CODEN: JASMAN 4966

THE JOURNAL of the Acoustical Society of America

Vol. 107, No. 1 January 2000

(Continued)

CONTENTS—*Continued from preceding page*

(Continued)

CONTENTS—*Continued from preceding page*

(Continued)

CONTENTS—*Continued from preceding page*

Scaling of turbulent wall pressure fluctuations downstream of a rearward facing step

Gerald C. Lauchle
Penn State University
Graduate Program in Acoustics and Applied Research Laboratory
State College, Pennsylvania 16804
gcl1@psu.edu

Walter A. Kargus IV
Johnson Electric Automotive
47660 Halyard Drive, Plymouth, Michigan 48170
wkargus@lear.com

Abstract: The turbulent boundary layer that forms downstream of a surface discontinuity is locally inhomogeneous. Here, we consider the boundary layer that occurs downstream of a rearward facing step discontinuity on a flat plate that is exposed to a zero incidence, uniform subsonic flow. The wall pressure "point" spectra are measured by small, flush-mounted pressure transducers located at various locations downstream of the step. A new form of the non-dimensional point wall pressure auto-frequency spectrum is proposed that includes the statistical variations of the reattachment location. This form is shown to collapse quite well all of the spectra measured slightly upstream, within, and downstream of the flow reattachment location.

PACS numbers: 43.50.Nm, 43.28.Ra, 43.50 Yw

1. Introduction

Flow over a rearward facing step is characterized as a discontinuous boundary-layer flow over a surface in which the elevation of the downstream surface is lower than that of the upstream surface. Lap-joints and cutouts on surfaces exposed to flow are examples. The assumed upstream turbulent boundary layer will separate at the step discontinuity forming a free shear layer and a local recirculation zone immediately downstream of the step. The shear layer eventually reattaches to the downstream surface, and a new highly energized turbulent boundary layer begins to form. This process produces wall pressure fluctuations that are significantly higher than those created by nonseparated, equilibrium turbulent boundary layers. In turn, this increases the direct flow-induced noise radiation and nonrigid surface vibrations that radiate as structural vibration-induced noise.

The scaling of the wall pressure point power spectrum under an equilibrium turbulent boundary layer (TBL) has been subdivided into major regions.[1] Each region conforms to different layers of the flow and has a particular pressure and time scale. The rms pressure fluctuations within the viscous sublayer, for example, scale on the wall shear stress and the viscous time scale. The convecting turbulence in the log-law region causes these pressures to scale on the wall shear stress and a larger time scale that is related to the TBL thickness and shear velocity. The region beyond the log-law region is termed the outer boundary layer. Here, the low-frequency pressure fluctuations scale on the dynamic pressure of the flow, $q = 1/2\rho_o U_o^2$, and on the time scale δ^*/U_o, where δ^* is the TBL displacement thickness, ρ_o is the fluid mean density, and U_o is the free stream velocity. The higher frequencies scale on viscous variables.

Each region of the TBL influences a different range of frequencies of the point wall

pressure spectrum. The regions beyond the log-law region influence the lower and mid frequencies, whereas the log-law region influences the ”overlapping" frequencies between the mid and high frequency range. The region of the viscous sublayer influences the high frequencies. These different scalings are still open to discussion[2] because of the complexity in modeling a TBL.

In this study, we consider the scaling of the point wall pressure spectrum downstream of a surface step discontinuity, which is more complex than that of a typical nonseparating TBL on a flat plate under zero pressure gradient conditions because of additional length scales, nonhomogeneous flow statistics, and reversed flow patterns. An experiment to characterize the statistics of the wall pressure fluctuations that occur downstream of a rearward facing, 2-D step on a flat plate has been conducted. Presented are scaling relationships that can be used to predict the auto-spectral characteristics of the wall pressure fluctuations for similar situations in which experimental data are unavailable. It is found that the spectra scale on the height of the step, the mean velocity upstream of the separation point, and on the *variance* of the estimated distance from the reattachment point-to-the point of measurement. By incorporating the variance between a fixed measurement location (or point of interest) and the reattachment point, which is known to be chaotic, a useful scaling law is established that has no singularity[3] when the measurement location happens to correspond to the reattachment location. This scaling relationship is different from earlier proposals[4,5] for a similar flow, and provides a better collapse of the experimentally measured spectra.

2. Experimental setup

A special facility was designed and used in a large anechoic chamber to measure the local wall pressure fluctuations and radiated sound from the flow over a rearward-facing step located on an otherwise flat, 2-D plate that supports a TBL on one side only. Figure 1 shows a schematic of the experiment, and the facility is described in complete detail elsewhere.[6]

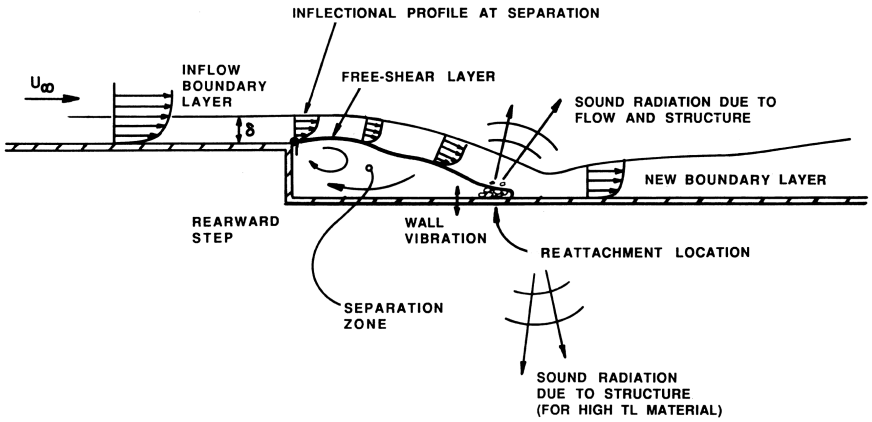

Fig. 1. Schematic of boundary-layer separation over a rearward-facing step. The inflow is from a convergent jet impinging on a 2-D flat plate that supports a TBL.

The flush-mounted pressure transducers are composed of B&K model 4165 (1.27 cm dia) microphones and supporting model 2639 preamplifiers powered by model 2087 power supplies. They are interfaced with the flow surface by a reduced area tube of 1.09 mm inside diameter and 5.7 mm in length. A cavity exists between the diaphragm of the microphone and

the inlet to the tube. It causes a microphone resonant response centered at 1 kHz. The peak response is 12 dB above the nominal free-field response of the microphone, and the half-power bandwidth of the resonance is ~200 Hz.

3. Flow reattachment

It is crucial to understand the fluid mechanics of the flow reattachment region to interpret the measured fluctuating wall pressure statistics. This can be accomplished conveniently by flow visualization. Figure 2 shows the flow pattern in the reattachment zone on the lower plate. This has been determined by photographing flourescent mini-tufts under black light conditions. The tufts are secured to the plate surface using cyanoacrylate adhesive. The flow direction and "steadiness" is indicated by the orientation and "blurriness," respectively of the individual tufts. One can see tufts aligned with the flow direction downstream of reattachment and regions of reversed flow upstream of the reattachment zone. Of particular interest is the overall width of this zone, identified by the band of tufts that have random orientations. Upon studying many different flow visualizations like this, under various velocity conditions, the reattachment location is clearly identified as a random variable with a mean value, $\bar{x}_r$, that is weakly dependent on flow speed being proportional to $U_o^{0.1}$. The variation of the reattachment location, $\sigma_{x_r}^2$, is also determined from these data and is found to be proportional to $U_o^{0.5}$.

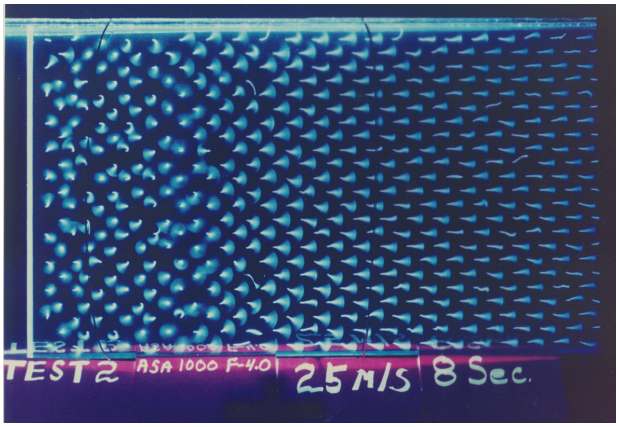

Fig. 2. An 8-s exposure of the mini-tufts exposed to 25 m/s mean flow velocity. The step is the vertical light line seen at the left.

4. Wall pressure fluctuations in reattachment region

The tube microphone was mounted at many streamwise locations along the centerline of the test plate. The signals were collected and analyzed using a Zonic System 7000 digital signal processor that was controlled by a Digital Equipment Corporation VAX Station 3100 m38. The spectral bandwidth is typically 3.125 Hz. Sufficient spectral averages were used to reduce random error to within ±1 dB. Figure 3 shows the variation of root-mean-square wall pressure through the reattachment region. The peak rms level is high; it is only 24 dB below the dynamic head of the flow. It is seen to occur from 7 to 8 step heights downstream of the step.

The mean position of the flow reattachment region occurs at approximately 6 step heights downstream. Figure 4 shows the details of these variations with flow speed. The location of peak rms wall pressure is a short distance downstream of the mean position of flow reattachment. This difference is possibly due to the short lag time required for the new TBL to form and generate pressure producing velocity fluctuations.

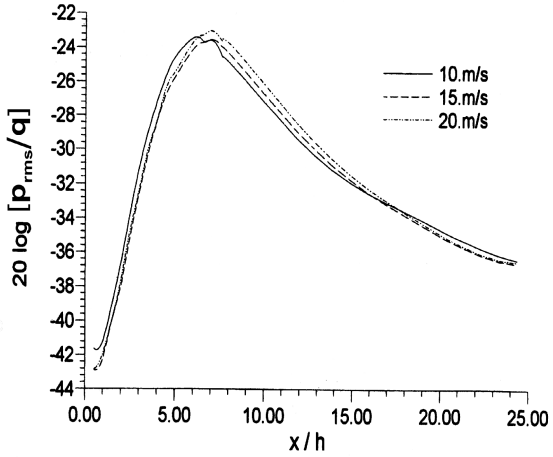

Fig. 3. Variation of rms wall pressure fluctuations with streamwise distance at different speeds.

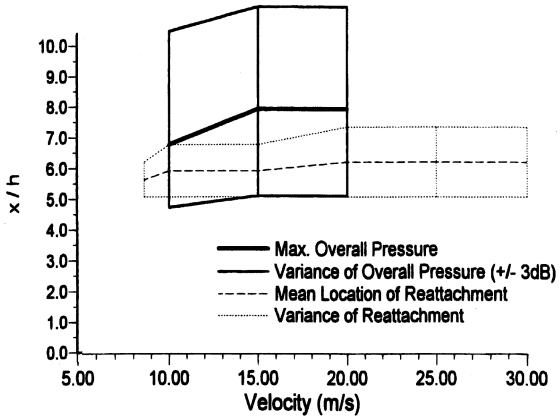

Fig. 4. Position of reattachment compared to the peak value of the rms wall pressure fluctuation.

The wall pressure spectral measurements were performed over extensive ranges of flow velocity ($7.82 \le U_o \le 25.1$ m/s) and streamwise location ($3.0 \le x/h \le 24.38$). The various types of TBL wall pressure spectrum scaling[1,4,5] were considered in an unsuccessful attempt to collapse the current spectral data into a single, reasonably well-bounded, universal function. Thus, traditional spectral normalization methods appear to be inappropriate for the pressure fluctuations occurring downstream of a step discontinuity. As noted previously,[3] and also from the data of Fig. 3, we recognize that on both sides of the mean reattachment location, the mean-square wall pressure decreases approximately as $|x-\bar{x}_r|^{-1}$. This means that the spectral amplitude should be weighted by such a factor to compare spectra measured at various locations. The dependence of the spectral magnitude on velocity is found to be satisfied by the outer (inertial) flow scaling typical of TBLs, i.e., spectrum level is proportional to q^2. The time scale h/U_o appears to be a more appropriate scale than δ^*/U_o. Physically, this means that the time scale of the wall pressure fluctuations is similar to that of the separation-induced vortex.

Now, Figs. 2 and 4 indicate that the reattachment location is chaotic; therefore, it must

be treated as a random variable. To use $|x-\bar{x}_r|^{-1}$ directly in a scaling formula without taking this fact into account will result in a singularity when the measurement point equals $\bar{x}_r$. To overcome this problem we define:

$$\Psi^2 = E[(x-x_r)^2] = (x-\bar{x}_r)^2 + \sigma_{x_r}^2 , \tag{1}$$

where E[ ] represents the expected value operation performed over N >> 1 individual records. The mean and variance terms of this expression are shown in Fig. 4. The new scaling formulation for the spectra, $G_{pp}(f)$, of the turbulent wall pressure fluctuations that occur at most locations downstream of a rearward facing step on a flat plate that supports a TBL and at any subsonic velocity is given by:

$$\frac{G_{pp}(f)\ \Psi\ U_o}{q^2\ h^2} \qquad vs. \qquad \frac{fh}{U_o} . \tag{2}$$

Using Eq. (2), point power spectral densities measured at locations slightly upstream, near, and downstream of $\bar{x}_r$ are nondimensionalized and presented for the considered range of velocities in Fig. 5. The collapse of these measured spectra into a single, well defined function is seen to be quite good. The variations for $1.5 < fh/U_o < 3$ are due to the microphone tube resonance. We note that the definition of Ψ assumes that the data shown in Fig. 3 are symmetric about the peak. This is strictly not the case, so the scaling is less valid for locations upstream of reattachment that are in the recirculation region. The spectra of Fig. 5 for x/h = 3.05 are measured as far upstream from $\bar{x}_r$ as the scaling appears to apply.[6] Equation (2) is actually most valid for locations that are within and farther downstream of the reattachment zone where the pressure fluctuations are created by energized boundary layer turbulence. In the recirculation zone, there is essentially no near-wall region of the boundary layer; thus, there would be less high-frequency pressure fluctuations created there. This statement is supported when comparing the spectra of Fig. 5 for x/h = 3.05 with those for x/h = 6.10 and 12.19. The spectral levels measured just upstream of $\bar{x}_r$ are some 11 to 15 dB lower than those measured within and downstream of $\bar{x}_r$ for $fh/U_o \gtrsim 1$.

5. Conclusions

The rms wall pressure fluctuations measured downstream of a rearward facing step discontinuity on a flat plate that supports a turbulent boundary layer are found to scale on the dynamic head of the flow, and to peak slightly downstream of the mean position of flow reattachment. The spectra of these fluctuations are found to be proportional to the inertial scales of the separated flow in addition to the statistical parameters describing the location of flow reattachment, which is a random variable. The scaling is most accurate within and downstream of the separation reattachment mean location. Upstream in the recirculation zone, the absence of any substantial near-wall turbulence results in pressure fluctuations that are quite low at high frequencies.

Acknowledgments

The work reported here was supported by Ford Motor Co., and ONR, Code 333.

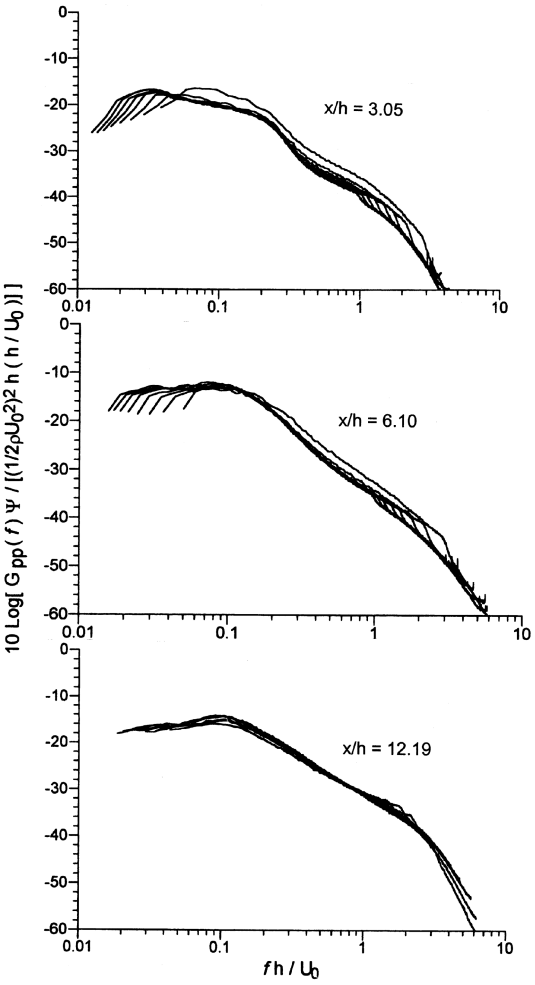

Fig.5. Dimensionless point power spectra of the local wall pressure fluctuations measured upstream (x/h = 3.05), near (x/h = 6.10), and downstream (x/h = 12.19) of the mean position of flow reattachment. The range of velocities for these measurements is from 7.82 to 25.1 m/s, and the step height, h = 2.5 cm.

References and links

[1] T. M. Farabee and M. J. Cassarella, "Spectral Features of Wall Pressure Fluctuations Beneath Turbulent Boundary Layers," Phys. Fluids A **3**, 2410-2420 (1991).
[2] W. L. Keith, D. A. Hurdis, and B. M. Abraham, "A Comparison of Turbulent Boundary Layer Wall-Pressure Spectra," Trans. ASME J. Fluids Eng. **114**, 338-347 (1992).
[3] T. A. Brungart, "Boundary Condition Effects on Turbulent Boundary Layer Wall Pressure Fluctuations," Ph.D. thesis, The Pennsylvania State University (1997).
[4] T. M. Farabee, "An experimental Investigation of Wall Pressure Fluctuations Beneath Non-Equilibrium Turbulent Flow," Ph.D. thesis, Catholic University of America (1986).
[5] T. M. Farabee and M. J. Casarella, "Effects of Surface Irregularity on Turbulent Boundary Layer Wall Pressure Fluctuations," Trans. ASME J. Vib., Acoust., Stress, and Relia. Des. **106**, 343-350 (1984).
[6] W. A. Kargus IV, "Flow-Induced Sound from Turbulent Boundary Layer Separation Over a Rearward Facing Step," Ph.D. thesis, The Pennsylvania State University (1997).

EDITORIAL

The article below, insofar as opinions are expressed, gives the views of the Editor-in-Chief at the time of submission, and they should not be construed as unchangeable. An ongoing discussion of the future of acoustics, the Society, and the Journal is desired, and readers and members are invited to submit their own views on any topic of general interest for publication in the Journal.

Things that are and things to come for the Society's publications: a myopic viewpoint

Allan D. Pierce
Acoustical Society of America, Office of the Editor-in-Chief, P.O. Box 323, East Sandwich, Massachusetts 02537

(Received 15 November 1999; accepted for publication 15 November 1999)

Several impending changes involving the *Journal* are discussed. These include proactive steps to facilitate publication of papers dealing with practical applications and of papers that may be helpful in the teaching of acoustics. Also discussed are virtual journals, the association of the *Journal* with *Acoustic Research Letters Online* (ARLO), possible changes in the handling of manuscripts, the desirability of encouraging good and concise writing, and the imposition of mandatory page charges for lengthy articles. © *2000 Acoustical Society of America.* [S0001-4966(00)07101-0]

PACS numbers: 43.10.Gi [ADP]

INTRODUCTION

The first issue in the year 2000 undoubtedly merits a nonstandard preamble; the dawn of a new century and of a new millennium tempts us to reflect on the past and to speculate on the future. The writer's plan is that such reflections and speculations be extended over a series of issues throughout this year with guest editorials from a number of prominent leaders in the acoustics community. The present article has rather modest objectives and deals with not entirely obvious matters that should be of current interest to the readers of the *Journal*. Although the changes that are currently taking place in the *Journal* and in the Society's publication portfolio will undoubtedly appear minor when viewed in the context of the overall history of the Society and of acoustics as a whole, they nevertheless require airing and discussing now, regardless of their coincidence with the start of a new century. The announcements here are similar in nature to editorial announcements that have appeared over the years (not just the recent past) in the *Journal*, but the author yields slightly to the temptation to discuss the status of the present and to speculate on the near future. The view is myopic and the scope is limited to matters within the purview of the Editor-in-Chief.

I. ACOUSTIC RESEARCH LETTERS ONLINE

Although initially envisioned as a stand-alone journal by its founding editor, Robert Apfel, *Acoustics Research Letters Online* (ARLO) has appeared over the past few months as an additional letters section in JASA. It has also been part of the on-line version of JASA (referred to as JASA-O). ARLO articles have appeared at the time of this writing in all of the 1999 issues (with the exception of the June issue) since May 1999. This, however, will change beginning with the second half of 2000, at which time ARLO will become a separate journal; the event will be a significant milestone in the history of electronic publishing. All members of the Society should take pride in that this milestone has been placed by the ASA.

ARLO has many unique features, with the dominant theme that almost all of the processing of manuscripts is done electronically. The feasibility of doing this with today's technology is enhanced with the requirement that the finished author-prepared manuscripts be limited to six single column pages. The actual implementation of the vision is not trivial, and it has required the development of a computer-based system with the joint efforts of the Acoustical Society and of the American Institute of Physics (AIP). The ARLO Manuscript Management System (MMS) has incited the interest of other societies affiliated with the AIP and will undoubtedly emerge as either the standard model or the genesis of a standard model for how a quality peer-reviewed on-line journal can be published making use of the full power of the Internet and of electronic publishing.

A full account of the details of the publication of ARLO can be found on the Internet at http://asa.aip.org/arlo. Notwithstanding the existence of ARLO as a stand-alone journal, an intimate connection between ARLO and JASA will continue indefinitely. Abstracts of ARLO articles will be published in JASA, and the administration of both journals, along with the Society's newsletter *Echoes*, will be overseen by the Editor-in-Chief; the editors of all three publications will be members of the Editorial Board. It so happens that the current Editor-in-Chief coincidentally serves as the Editor of JASA, but this could change in the distant future. The position of *Editor-in-Chief of the Acoustical Society of America* (in contradistinction to the position of Editor of the Journal of the Acoustical Society of America) was created in

June 1955 for the explicit purpose of insuring that there be a single administrative head if and whenever the Society might have more than one periodical.

II. QUICKER PROCESSING OF ARTICLES

A perpetual concern for peer reviewed journals has been the time required for an acceptable manuscript to pass through the process. One finds, for example, the statement

I am concerned that, on the average, we are not providing as prompt a publication service to our authors and our readers as they would like.

in an editorial titled ''Promoting prompt peer reviewing'' which Daniel Martin published in the October 1988 issue of the *Journal*. The present writer's view after many years of service on all three sides of the triangle is that very little of a speed-up can be achieved by imploring (or *riding*) reviewers and editors to act more quickly, given the present system with which JASA handles submitted manuscripts. The reviewers are in reality inducted volunteers; they usually have demanding full-time jobs. Some senior members of the acoustics community regularly receive papers for review from several JASA associate editors and, moreover, from editors of other journals. While persons who are regularly submitting papers themselves have sort of a moral obligation to also serve as reviewers, it is unfair to chastise a reviewer for tardiness when the number of papers that reviewer is being asked to review exceeds by a factor of, say, twenty the number the reviewer has submitted.

The envisioned remedy for the ''promptness problem'' is to adopt some prominent aspects of the ARLO Manuscript Management System. With this system, for example, each associate editor has access to information on the loads placed on individual reviewers by *all* of the associate editors. With a common electronic data file listing persons who have indicated willingness to review for the *Journal*, and with a knowledge of the responsibilities each such person has accepted, an associate editor will be better able to judiciously choose which reviewers to ask with the objective of achieving a quick review. Just how much of the MMS is presently feasible for JASA remains to be determined, and the transition, even if only in part, will undoubtedly take some time. Nevertheless, this is a direction in which we should go, and a committee is currently working on a plan that will make the shift palatable.

III. VIRTUAL JOURNALS

''Virtual journals'' is an idea that evidently originated within the American Institute of Physics and the American Physical Society; in retrospect, it appears to be an idea that the Acoustical Society should embrace and possibly advance. One conceives of a specialized subject whose leading papers appear in a number of different journals, each of which has an on-line version. The editors and organizations that publish those journals agree to enter into a cooperative endeavor whereby they allow selected papers of their journals to also be listed as ''papers'' in an on-line bibliographic list of such papers. However, this on-line list appears to the external world to be an on-line journal itself. One logs onto the Web-site for such a virtual journal, and finds for each ''issue'' a list of papers along with their abstracts. If a subscriber of the virtual journal seeks to read one of the articles in a given issue, then the subscriber is conveyed to the site of the actual (parent) on-line journal in which the paper is published. If that parent journal, for example, happens to be The Journal of the Acoustical Society of America–Online (JASA-O), then the virtual journal subscriber cannot access that paper unless either (1) the subscriber is already also a subscriber to JASA-O or (2) the virtual journal subscriber pays a pay-per-view fee to the Acoustical Society. Thus, in reality, all that the virtual journal provides is a pre-compiled bibliography and a speedy way of reaching the Internet sites where the individual papers reside.

Two such virtual journals have already been launched by the AIP and the APS, and it is envisioned that more will follow. At the recent Columbus meeting in November 1999, the Executive Council, on the recommendation of the Publication Policy Committee and with the full concurrence of the Editor-in-Chief, voted to participate in this endeavor. In retrospect, however, the basic idea transcends physics as such and transcends the organizations that are affiliated with the AIP. The idea of virtual journals is intrinsically attractive (although unanticipated pitfalls may be encountered) and should be given more consideration by various segments of the Society. Should, for example, the ASA team with the publishers of other of the world's leading acoustics journals to create virtual journals in each of several focused areas of acoustics?

IV. NOURISHMENT OF APPLIED ACOUSTICS

Perusal of the old back-issues of the *Journal* and especially of the various editorials and announcements that have appeared down through the years leads to the impression that there has been a sustained frustration concerning the *Journal*'s contribution to the second part of the ASA's stated mission—to increase and diffuse the knowledge of acoustics and to promote its practical applications. In the earliest issues of the *Journal*, a substantial fraction (if not the majority) of the papers were manifestly applied. Following the end of the Second World War, however, the *Journal* began to appear more unambiguously as an archival journal for original research. The Society apparently sensed a need for the publication of more papers that would be of immediate interest to readers concerned with practical applications and consequently, in January 1955, launched a second journal with the title *Noise Control*; this was replaced at the beginning of 1962 by a new journal with the title *Sound—its Uses and Control*, with R. Bruce Lindsay serving as editor for both JASA and *Sound*. (The archives are unclear as to whether *Sound* was intended as a simple continuation or as a replacement to *Noise Control*.) The publication of *Sound* was discontinued after two years. It is rumored that the vote in the Executive Council for the discontinuation was very close; the present writer's best guess is that the reason for the discontinuation was that the publication of *Sound* appeared to be an interminable financial drain on the Society's limited resources.

With perhaps the intention of partially restoring the loss of a tangible means for encouragement of the publication of applied papers caused by the demise of *Sound*, a new section of JASA titled ''Technical Notes and Research Briefs'' (TNRB) was created in 1966. The hope for this section, as stated by Lindsay in an editorial in February 1966 was that ''it will seek to provide brief accounts of new developments, particularly in various fields of applied acoustics.'' Although the section continued for over three decades, it failed dismally, in the present writer's opinion, to live up to Lindsay's stated hope. Perhaps for just this reason, Daniel Martin chose, in 1998, to discontinue TNRB.

One problem that frustrated the intended usage of TNRB was that many reviewers of submitted research articles came to regard it as a possible sop to authors whose papers did not meet the perceived standards for publication of regular articles. One would see, for example, statements in reviews such as ''this paper is not worthy for publication as a full-length article in JASA; I suggest the author condense it drastically and publish it as a technical note.'' Related problems were that the stated preamble to TNRB and the overall format of the section were not especially encouraging to potential authors who, for a different venue, might very well have submitted a high-quality applied paper that would have been well-received by a substantial minority of the *Journal*'s readership.

A new proactive solution to this seemingly interminable problem of disproportionately low attention to applied acoustics is now underway. A new associate editorship, that of Associate Editor for Applied Acoustics, has been created, with Stanley Ehrlich being appointed to that position. Relevant tasks are to actively encourage persons to submit applied acoustics papers, to give guidance to prospective authors on how to prepare such articles, and to insure that the accepted papers be of high standard. Peer reviewing will be continued, but the questions addressed to the reviewers will be somewhat different than those presented for research articles. Long term objectives are to nourish an attitude that writing such articles is a worthwhile thing to do and to establish JASA (or possibly some future ASA publication specifically emphasizing applied acoustics) as the best place to publish such articles.

V. EDUCATION IN ACOUSTICS

''Acoustics, like any other intellectual discipline, must be learned. It cannot merely be absorbed through one's pores.'' These two rousing sentences just cited are from a February 1965 editorial by R. Bruce Lindsay. At that time the ASA reacted to a perceived national need for professionals trained in acoustics with the creation of ''a special Committee on Education in Acoustics, headed by Alan Powell.'' In the intervening three and a half decades, that committee has flourished and has become one of the most lively groups in the Society. Nevertheless, a detached observer well versed in acoustics can still question whether the opportunity for learning acoustics has been sufficient for a substantial portion of the group of people who eventually earn their livelihood in acoustics. One can, for example, look over many of the papers (particularly in those areas with underpinnings in physics, engineering, and mathematics) that eventually became published in the *Journal* and speculate, even though they were deemed acceptable, just how much better they could have been if only the authors had had a little more thorough foundation in acoustics, not as a branch of physics or applied mathematics, but as a science in its own right. A richness in ''physical explanations'' of computed or experimental results, the earmark of a great paper, is often woefully lacking.

The ASA has done much to facilitate the education of acousticians, at all levels, including the post-graduate level, but it can and should do more. Much of what is currently being done, for example, could well be viewed by someone such as Lindsay as not much more than an encouragement to try to ''absorb acoustics through one's pores.'' Oral presentations at Education in Acoustics sessions, two-hour tutorials, and even short courses are not enough. A strong case can be made for printed materials of an archival nature which one can read over and over and which one can contemplate. Reprinting classic textbooks is an important service, but one must recognize that those who teach acoustics are continually discovering clearer ways of explaining acoustic concepts, continually inventing new demonstration experiments that illustrate those concepts, and continually seeking palatable explanations of the newer ideas so that students can be brought rapidly but honestly to the frontiers of the field. Note that there is no Association of Acoustics Teachers with its own journal. (The implied oblique reference is to the American Association of Physics Teachers, which publishes *The Physics Teacher* and *The American Journal of Physics*.) For acoustics, the ASA has to do it all; if articles are to be published that foster education in acoustics, then the only viable publication outlet is the Society's journal. *The American Journal of Physics* will not and cannot do a proper job in this regard because of its breadth, because of its page limitations, and because of the relatively negligible attention that acoustics characteristically receives in physics departments. It is sometimes argued, in regard to JASA publishing such papers, that it opens the door for publication of many second-rate papers. The counter-argument is that we can set high standards for the acceptance of such papers, as high or higher than those set by *The American Journal of Physics*, and we can stick to those standards.

With the arguments just stated in mind and, once again, with the guidance of the Society's mission statement, a new associate editorship has been created, that of Associate Editor for Education in Acoustics. The first holder of this important position is Thomas Rossing.

VI. ABANDONMENT OF PUNITIVE EXCESS PAGE CHARGES

Another long-term concern has been the perceived excessive length, and the actual increase in length over time, of articles published in the *Journal*. Lindsay published an editorial, for example, in October 1972 in which he laid down a strong case for conciseness and admonished authors to seek to write shorter and consequently better papers. The problem nevertheless did not go away and the length of papers continued to increase. Daniel Martin advocated that something

proactive needed to be done in this regard, and the Executive Council consequently voted at the Spring 1992 meeting to impose a mandatory excess page charge on all articles whose published length exceeded 12 pages. This was announced in an editorial published in October 1992. The plan was that the authors had to pay a mandatory page charge of double the ordinary page charge for each page beyond the first 12. Martin stated that this was to be a one-year experiment, but as far as the present writer knows the outcome of the experiment was never assessed, and the mandatory excess page charge has been continued until the present. The current fee for each such page is $160 per page. A safety valve was set in place with the Editor-in-Chief given the discretionary power to waive the excess page charges in unusual circumstances.

Examination of recent data supplied to the Editor-in-Chief by the AIP, which handles the billing and collection of page charges, indicates that the desired objectives of the ''experiment'' are not being achieved. Over a two year period beginning with April 1997, the percentage of published papers with more than 12 pages increased from 15% to 19%. The authors of these papers for the most part followed up on their agreed-upon commitment to pay the excess page charges, but a large majority declined to pay the customarily-asked ''voluntary'' page charges for the first 12 pages. Thus, for example, an author of a 13 page paper who had access to funds for publication page charges (or who had the power to sway the author's institution to pay such charges), but no real desire to help defray publication costs for the *Journal*, would pay only $160. A second author with a published paper of 12 pages who took the plea for ''honoring'' voluntary page charges seriously would pay $1080. In retrospect, a cynical author, and one who is not a meticulous writer, might easily yield to the temptation to pay the $160 rather than make the effort of following Strunk and White's admonition of omitting needless words (and needless equations, needless figures, needless reference citations, etc.).

Many possible solutions to the problem just described have been discussed by the Publication Policy Committee and by the Executive Council. Ideally, the pressure for conciseness should come from the associate editors and the reviewers, but human nature and the mechanics of the reviewing process makes this an ineffectual solution. Many authors evidently need a more tangible wake-up call, an alert to the fact that their writing and selection of included material may not be all that great. One can of course point to many great papers in the past, by giants such as Rayleigh, Helmholtz, Fletcher, and Sommerfeld, which did exceed the equivalent of 12 printed pages in JASA, and JASA wants to publish great papers, even when the authors, in spite of reasonable attempts to sway their institutions and research sponsors, are unable to pay any page charges. Nevertheless, the suspicion prevails that most long papers submitted to JASA are not in the truly great category; the great length is more often due to the authors' inexperience in writing or to the hastiness with which the manuscript was prepared.

The new policy that was eventually adopted, although not unanimously, was that there should be no excess page charges as such. The page charges for each and every page is to be the same. For papers with twelve pages or less, the policy remains the same, page charges are ''voluntary.'' However, if the published length exceeds 12 pages, then the author must insure that the page charges are paid. The mandatory page charges for a 12+n page article now becomes 12+n times $80. This policy will be enforced for all articles submitted after the first of January 2000.

SOUNDINGS

Section Editor: Richard Stern

This front section of the *Journal* includes acoustical news, views, reviews, and general tutorial or selected research articles chosen for wide acoustical interest and written for broad acoustical readership.

ACOUSTICAL NEWS—USA

Elaine Moran
Acoustical Society of America, Suite 1NO1, 2 Huntington Quadrangle, Melville, NY 11747-4502

Editor's Note: *Readers of this Journal are asked to submit news items on awards, appointments, and other activities about themselves or their colleagues. Deadline dates for news items and notices are 2 months prior to publication.*

Announcement of the 2000 Election

In accordance with the provisions of the bylaws, the following Nominating Committee was appointed to prepare a slate for the election to take place on 20 May 2000:

Lawrence A. Crum, *Chair* — Daniel L. Johnson
Sid P. Bacon — Sigfrid D. Soli
Dana S. Hougland — George S. K. Wong

The bylaws of the Society require that the Executive Director publish in the *Journal* at least 90 days prior to the election date an announcement of the election and the Nominating Committee's nominations for the offices to be filled. Additional candidates for these offices may be provided by any Member or Fellow in good standing by letter received by the Executive Director not less than 60 days prior to the election date and the name of any eligible candidate so proposed by 20 Members or Fellows shall be entered on the ballot.

Biographical information about the candidates and statements of objectives of the candidates for President-Elect and Vice President-Elect will be mailed with the ballots.

CHARLES E. SCHMID
Executive Director

The Nominating Committee has submitted the following slate:

FOR PRESIDENT-ELECT

William J. Cavanaugh

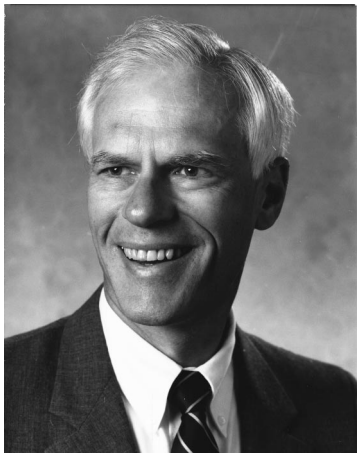

William M. Hartmann

 0001-4966/2000/107(1)/5/7/$17.00

FOR VICE PRESIDENT-ELECT

Sabih I. Hayek

Janet M. Weisenberger

FOR MEMBERS OF THE EXECUTIVE COUNCIL

Whitlow W. L. Au

Henry E. Bass

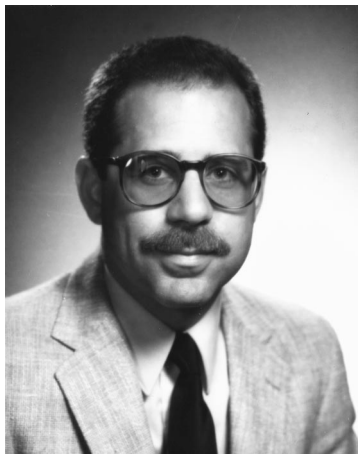

Elliott H. Berger

Donna L. Neff

Hideki Tachibana

Henrik Schmidt

President's Report on the Joint Meeting held in Berlin, Germany

The Joint Meeting: 137th Meeting of the Acoustical Society of America (ASA), the 2nd Convention of the European Acoustics Association (Forum Acusticum) integrating the 25th German Acoustics DAGA Conference was held 13–15 March 1999 at the Technical University of Berlin in Berlin, Germany. This was the first time that the Acoustical Society has met outside North America.

The meeting drew a total of 2263 registrants from 48 countries (see Table I). This was truly an international meeting. A total of 1955 papers organized into 198 sessions covered a wide variety of topics in acoustics.

The meeting began with an Opening Ceremony held in Berlin's famous Philharmonic Hall on Monday morning, 15 March. The ceremony included a special welcome to our international colleagues and addresses by the presidents of the Acoustical Society of America, the European Acoustics Association, and the German Acoustical Society. The meeting organizers were recognized for their meticulous planning of the meeting including Michael Möser and Jiri Tichy, Meeting Cochairs; David I. Havelock, Technical Program Chair; and Sigrid Bärndal, Conference Secretariat. Helmut A. Müller reviewed the history of the Berlin Philharmonic Hall including its acoustical particulars and Jürgen Meyer explained the influence of the special acoustical properties of the hall on orchestral sound. This was illustrated by an orchestra presenting short sound examples and the fourth movement of Brahms' second symphony.

TABLE I. Participants according to countries.

	Country	No. of participants
1	Algeria	1
2	Argentina	1
3	Australia	11
4	Austria	42
5	Belarus	1
6	Belgium	33
7	Brazil	6
8	Canada	38
9	China	10
10	Croatia	7
11	Czech Rep.	13
12	Denmark	53
13	Egypt	3
14	Estonia	4
15	Finland	15
16	France	165
17	Germany	644
18	Greece	12
19	Hungary	8
20	India	2
21	Iran	1
22	Ireland	1
23	Israel	2
24	Italy	33
25	Japan	75
26	Korea	11
27	Lebanon	2
28	Lithuania	7
29	Luxemborg	1
30	Mexico	4
31	Norway	31
32	Poland	44
33	Portugal	7
34	Romania	3
35	Russia	28
36	Singapore	4
37	Slovakian Rep.	2
38	Slovenia	4
39	South Korea	1
40	Spain	34
41	Sweden	53
42	Switzerland	39
43	Taiwan	5
44	The Netherlands	61
45	Turkey	2
46	Ukraine	6
47	UK	148
48	USA	585
	Total participants	2263

FIG. 1. President James E. West (l), President-Elect Patricia Kuhl (c), and Elaine Moran (r), recipient of the Distinguished Service Citation.

Technical sessions started on Monday afternoon and were scheduled through Friday evening. On Friday, 19 March, there were lectures held in German followed by the German Acoustical Society (DEGA) General Assembly. An international workshop on Active Noise and Vibration Control was an integral part of the meeting.

Other technical features of the meeting included joint meetings of ASA and DEGA technical committees, a student design competition sponsored by the ASA Technical Committee on Architectural Acoustics and the National Council of Acoustical Consultants, a Best Student Paper Award Program, and a Short Course on Thermoacoustics presented by Gregory Swift of the Los Alamos National Laboratory. A large and well-attended equipment exhibition was held from Monday afternoon to Thursday evening which included displays on state-of-the-art products and publications in acoustics. There were technical tours on the architectural acoustics of Preussischer Landtag (The Berlin Parliament House), the Konzerthaus (concert hall), and guided tours to various TU Berlin institutes and labs. A plenary session on Standards was held and all meeting participants were invited to attend. The ASA Committee on Women in Acoustics sponsored a luncheon which drew about 100 attendees. The press conference featured speakers from many countries and fields of acoustics.

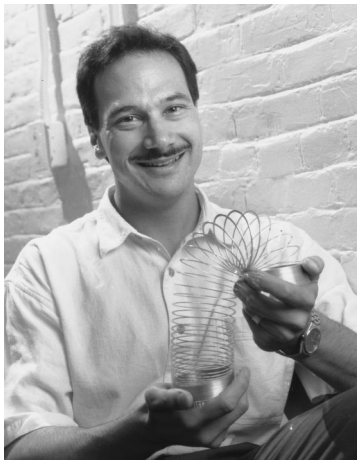

FIG. 2. Paul E. Barbone, recipient of the R. Bruce Lindsay Award.

FIG. 3. Jens Blauert (r), recipient of the Helmholtz-Rayleigh Silver Medal is introduced by Constantine Trahiotis (l).

A joint Medals and Awards plenary session included the presentation of awards by both the German Acoustical Society and the Acoustical Society of America, announcement of newly elected Fellows of the Acoustical Society, and recognition to the meeting organizers. Joachim Scheuren, the President of DEGA, presented two awards: The Helmholtz-Medal for the entire scientific life-work of an outstanding acoustician and the Lothar-Cremer-Preis for a single outstanding contribution of a junior scientist. James West, President of the ASA, presented five ASA awards (see Figs. 1–5). The Distinguished Service Citation was presented to Elaine Moran for ''*for sustained and dedicated service to the Acoustical Society, its officers and members, over many years*.'' The R. Bruce Lindsay Award was presented to Paul E. Barbone ''*for developing novel theoretical and computational acoustics techniques*.'' The Helmholtz-Rayleigh Interdisciplinary Silver Medal was presented to Jens P. Blauert ''*for contributions to sound localization, concert hall acoustics, signal processing, and acoustics standards*.'' Honorary Fellowship was conferred upon Leonid N. Brekhovskikh ''*for pioneering contributions to wave propagation and scattering*.'' The Gold Medal was presented to Henning E. von Gierke ''*for contributions to bioacoustics, psychoacoustics, vibrations, and for leadership in national and international acoustical standards*.'' Fellowships were announced and certificates were presented to Fellows elected at the Norfolk ASA meeting: Robert P. Carlyon, Alastair Cowley, Daniel E. Commins, Thomas R. Howarth, Rudolph Martinez, John C. Middlebrooks, Raymond Meddis, Stephen T. Neely, Philip Rubin, Narendra T. Sanghvi, Victor W. Sparrow, Gary Weismer, and Mei Q. Wu.

There were many opportunities for social interaction including a welcome reception on Monday evening, daily coffee breaks, a social reception on Tuesday held at the Orangerie of the castle (Schloss) Charlottenburg, a banquet on Wednesday in the fortress (Zitadelle) Spandau which included a medieval meal and medieval performers, and a farewell party on the last day of the meeting. Receptions were held for graduate students interested in the fields of Acoustical Oceanography and Underwater Acoustics and for graduate students interested in Speech Communication, Psychological and Physiological Acoustics, Animal Bioacoustics, and Musical Acoustics.

FIG. 4. President James E. West (l), Peter Mikhalevsky, and Leonid M. Brekhovskikh (r), new Honorary Fellow.

FIG. 5. President James E. West (r) presents the Gold Medal to Henning E. von Gierke.

The Society owes its gratitude to members of the Technical Program Organizing Committee for the outstanding organization of the technical sessions: *General Chairman*: David Havelock; *EAA Representatives*: Heinrich Kuttruff, Volker Mellert, Jürgen Meyer, Wolfgang Neise, Brigitte Schulte-Fortkamp; *ASA Representatives*: Whitlow Au, Angelo Campanella, Richard Campbell, James Candy, N. Ross Chapman, Nicholas Chotiros, Stanley Ehrlich, Carr Everbach, David Feit, Lawrence Feth, Christopher Fuller, Peter Gerstoft, William Hartmann, Sabih Hayek, Douglas Keefe, Armin Kohlrausch, Murray Korman, Christopher Lawrenson, James Lynch, Donna Neff, Richard Peppin, Mauro Pierucci, Joseph Pope, Subramanyan Rajan, Sally Revoile, Roger Richards, James Sabatier, Ralph Stephen, Emily Tobey, Dennis Walton, George Wong, and Allan Zuckerwar.

In addition, the Society is grateful to the large number of members from the three sponsoring organizations who participated in the conception, planning, and organization of the meeting which occurred over a two-year period. Their work produced a very successful joint meeting.

JAMES E. WEST
President 1998–1999

USA Meetings Calendar

Listed below is a summary of meetings related to acoustics to be held in the U.S. in the near future. The month/year notation refers to the issue in which a complete meeting announcement appeared.

2000

1–13 Jan.	38th AIAA Aerospace Sciences Meeting & Exhibit, Reno, NV [American Institute of Aeronautics and Astronautics, 1801 Alexander Bell Drive, Suite 500, Reston, VA 2019; Tel.: 703-264-7500 or 800-539-2422; E-mail: custserv@aiaa.org].
17–19 Feb.	National Hearing Conservation Association (NHCA) 25th Annual Conference, Denver, CO [NHCA, 9101 E. Kenyon Ave., Suite 3000, Denver, CO 80237; Tel.: 303-224-9022; Fax: 303-770-1812; E-mail: nhca@gwami.com; WWW: www.hearingconservation.org].
6–9 March	Society of Automotive Engineers Congress, Detroit, MI [SAE Headquarters, 400 Commonwealth Dr., Warrendale, PA 15096-0001; Fax: 724-776-1830; E-mail: congress2000@sae.org].
17–19 May	ASNE Day 2000, Arlington, VA [Andrea Zari, Meetings Department, American Society of Naval Engineers, 1452 Duke St., Alexandria, VA 22314-3458; Tel.: 703-836-6727; Fax: 703-836-7491; E-mail: azari@navalengineers.org].
30 May–3 June	139th Meeting of the Acoustical Society of America, Atlanta, GA [Acoustical Society of America, Suite 1NO1, 2 Huntington Quadrangle, Melville, NY 11747-4502; Tel.: 516-576-2360; Fax: 516-576-2377; E-mail: asa@aip.org; WWW: asa.aip.org].

13–16 July	ClarinetFest 2000, Norman, OK [Dr. Keith Koons, Music Dept., Univ. of Central Florida, P.O. Box 161354, Orlando, FL 32816-1354; Tel.: 407-823-5116; E-mail: kkoons@pegasus.cc.ucf.edu]. Abstract deadline: 15 January 2000.
4–8 Dec.	140th Meeting of the Acoustical Society of America, Newport Beach, CA [Acoustical Society of America, Suite 1NO1, 2 Huntington Quadrangle, Melville, NY 11747-4502; Tel.: 516-576-2360; Fax: 516-576-2377; E-mail: asa@aip.org; WWW:asa.aip.org].

2001

30 April–3 May	2001 SAE Noise & Vibration Conference & Exposition, Traverse City, MI [Patti Kreh, SAE Int'l., 755 W. Big Beaver Rd., Suite 1600, Troy, MI 48084; Tel.: 248-273-2474; Fax: 248-273-2494; E-mail: pkreh@sae.org]. Deadline for submitting abstracts: 14 July 2000.

Revision List

New Associates

Alhamdani, Ziad K., P.O. Box 38560, Bani Walid, Libya
Allyn, Stuart J., A.D.R. Studios, Inc., 250 Taxter Road, Irvington, NY 10533
Anderson, Samira B., 904 Greenvale Avenue, Northfield, MN 55057
Ang, Minni K., Music Department, Univ. of Putra Malaysia, Faculty of Human Ecology, Selangor 43400, Malaysia
Arvaniti, Amalia, Foreign Languages and Literatures, University of Cyprus, P.O. Box 20537, Nicosia 1678, Cyprus
Ball, Philip, Nature, Porters South, 4-6 Crunan Street, London N1 9XW, United Kingdom
Biaswi, Gianni, Communication Technology, Piazza Guidazzi 3, Cesena FO 47023, Italy
Brady, Steve D., 79 Grinsell Street, Newcastle, NSW 2289, Australia
Cassell, Christopher B., 1506 Bristol, Westchester, IL 60154
Cattafesta III, Louis N., AeMES, Univ. of Florida, P.O. Box 116250, Gainesville, FL 32611-6250
Craigie, Cameron J., LABTec, Inc., 1499 SE Tech Center Place, Suite 350, Vancouver, WA 98683
Denham, Susan L., School of Computing, Univ. of Plymouth, Drake Circus, Plymouth, Devon PL4 8AA, United Kingdom
Franck, Levassort, GIP Ultrasons/LUSSI-EIVL, Rue de la Chocolaterie, B.P. 3410, Blois, Cedex 41034, France
Frost, Karen L., 2KM Architects, Inc., 2275 Wrightsboro Road, Augusta, GA 30904
Goodman, Fred J., 9842 Dairyton Court, Gaithersburg, MD 20886
Guasca, Jose, 3202 Foothill Street, Woodbridge, VA 22192
Harada, Tatsuhiko, 1-1-806 Kaminoki-cho, Kanagawa-ku, Yokohama, Kanagawa 221-0015, Japan
Hentschel, Greg P., Marley Cooling Tower Company, 7401 West 129th Street, Overland Park, KS 66213
Hsueh, Wen-Jeng, Dept. of Naval Architecture and Ocean Eng., National Taiwan University, 73 Chow-shan Road, Taipei 106, Taiwan
Jahn, Andreas, R & D Center, Nokia Mobile Phones, Produktionsgesellschaft mbH, Meesmannstr. 103, Bochum D-44807, Germany
Klimanis, Gints, 105 Ballatore Court, San Jose, CA 95134
Kull, Jr., Robert C., Geo-Marine, Inc., 610 Thimble Shoals Boulevard, Suite 302B, Newport News, VA 23606
Lam, Yiu W., Dept. of Acoustics and Audio Eng., University of Salford, Salford M5 4WT, United Kingdom
Larsen, Erik, Kastelenplein 119, Eindhoven 5653LS, The Netherlands
Moss, Larry R., P.O. Box 9283, Alexandria, VA 22304
Navarro, Jaime, Univ. of Sevilla, Inst. Univ. de Ciencias de la construccion, School of Architecture, Avda Reina Mercedes S/N, Sevilla 41012, Spain
Paulson, Peter O., Pure Technologies, Ltd., #1050—340 12th Avenue, SW, Calgary, AB T2R 1L5, Canada
Pennington, Neil R., 36 Coal Point Road, Coal Point, NSW 2283, Australia
Riedel, Scott R., Scott R. Riedel and Associates, Ltd., 11040 West Bluemound Road, Wauwatosa, WI 53226
Riera-Gaxiola, Maritza, Center for Neurobiology UNAM, Psychophysiology, Campus UNAM Juriguilla, P.O. Box 1-1141, Queretaro, CP 76001, Mexico
Robert, Mark E., Auditory Implants & Perception, House Ear Institute, 2100 West Third Street, 5th Floor, Los Angeles, CA 90057-1922
Sendra, Juan J., Univ. of Sevilla, Inst. Univ. de Ciencias de la construccion, School of Architecture, Avda Reina Mercedes S/N, Sevilla 41012, Spain
Smith, Leslie S., Dept. of Computing Science, Stirling Hearing Systems, Univ. of Stirling, Stirling, Scotland FK9 4LA, United Kingdom
Tao, Fan-Chia, J. D'Addario & Company, Inc., 595 Smith Street, Farmingdale, NY 11735
Terra, Maria E., Center for Marine Science Research, UNC—Wilmington, 7205 Wrightsville Avenue, Wilmington, NC 28403
Tobis, Bruce J., 35510 River Pine Court, Farmington Hills, MI 48335
Wayland, Richard F., 20482 Chestnut Ridge Road, Leonardtown, MD 20650
Yiu, Edwin M., Dept. of Speech and Hearing Sciences, Univ. of Hong Kong, 5/F Prince Philip Dental Hospital, Hospital Road, Hong Kong

New Students

Bartlett, Christopher W., 308D Branch Brook Drive, Belleville, NJ 07109
Braasch, Jonas, Inst. fur Kommunikations Akustik, Ruhr-Univ. Bochum, Universitatstr. 150, Bochum D-44801, Germany
Cleary, Miranda, Evermann #675, Bloomington, IN 47408
Dusan, Sorin V., Electrical and Computer Engineering, University of Waterloo, 200 University Avenue, West, Waterloo, Ontario N2L 3G1, Canada
Fonseca, Luciano E. N., Geodesy and Geomatics Eng., Univ. of New Brunswick, Ocean Mapping Group, Fredericton, New Brunswick E3B 5A3, Canada
Frazier, Catherine H., Bioacoustics Research Lab., Dept. of Electrical and Computer Eng., Univ. of Illinois, 405 North Mathews Avenue, Urbana, IL 61801
Goldberg, Ari Z., 5323 Brody Drive, #104, Madison, WI 53705
Gunderson, Tom W., 225 East Rose Street, Glenwood, IL 60425
Hoffman, Justin P., Dept. of Applied Physics, Centre for Marine Science and Technology, Curtin University, G.P.O. Box U1987, Perth, WA 6845, Australia
Jerzak, Wayne, 18 25th Street, Troy, NY 12180
Kim, Kang, Applied Research Lab., Pennsylvania State Univ., Norther Atherton Street, State College, PA 16801
Kim, Mi-Ryoung, 1587 Beal Avenue, #12, Ann Arbor, MI 48105
Lewis, Clifford F., 3269 Altamont Avenue, Cleveland Heights, OH 44118-1807
Li, Zhiqiang, MIT, Linguistics Dept., 77 Massachusetts Avenue, E39-207, Cambridge, MA 02139
Lin, Hai, 458-3-1-611 Shibokuchi, Takatsuku, Kawasaki, Kanagawa 213-0023, Japan
Lineaweaver, Sean K., 9220 Sand Point Way, NE, Seattle, WA 98115
Panaso, Videe, 456 Wilson Street, Chippendale, NSW 2008, Australia
Raju, Balasundara I., Electrical Engineering & Computer Science, Massachusetts Inst. of Technology, 50 Vasser Street, Room 36-788, Cambridge, MA 02139
Scharine, Angelique A., Psychology Dept., Arizona State Univ., Mail Box 1104, Tempe, AZ 85287-1104
Taylor, Lawrence S., Electrical and Computer Eng., University of Rochester, P.O. Box 270126, Hopemann Engineering Building, Rochester, NY 14627
Uribe, Oscar X., 541 East Pacific Street, Carson, CA 90745
Urueta-Mazzilli, Dolly, 3227 Lutz Lake Fern Road, Lutz, FL 33549
Weil, Shawn A., 5633 Blue Lagoon Lane, Hilliard, OH 43026
West, Paula C., Phonetics Lab., Univ. of Oxford, 41 Wellington Square, Oxford, Oxfordshire OX1 2JF, United Kingdom
Yao, Jun, Electronic Engineering, The Chinese University of Hong Kong, Hong Kong, People's Republic of China
Yun, Ilsung, 277-1 Kaebong 3-dong, Kuro-gu, Seoul 152-093, Korea
Zhang, Zhaoyan, Ray W. Herrick Laboratories, 1077 Ray W. Herrick Laboratories, West Lafayette, IN 47907

Associates Elected Members

S. K. Alam, S. Ando, B. S. Aronov, J. M. Balash, P. W. Barnett, S. D. Beck, S. G. Benka, M. M. Boone, N. P. Cooper, T. Dau, D. Devries, M. A. Faltys, L. Feng, A. W. Gummer, K. Hartung, G. M. Hassell, N. I. Hill, K. Imano, L. J. Jacobs, P. Jiang, T. Kobayashi, T. Kundu, C. L. Kussmaul, T. Lawu, T. T. Luc, P. A. Manning, M. Matsukawa, R. Ming, J. W. Mooney, K. Mori, E. A. Skelton, C. L. Smith, J. Stepanek, H. Zhang

Students to Associates

J. A. Busenitz, J. A. Cook, D. A. Hock, D. U. Jeong, H-Y. Lai, R. D. G. Low

Resigned

H. Hoffmann, K. Yamamura—*Members*
J. Dunlop, L. W. Lee, J. Ohman, C. A. Papadimos, L. Saulnier, J. C. Scheinberg, J-H. Tarng—*Associates*

Deceased

F. S. Cooper—*Fellow*
R. J. E. Hemman—*Member*

Dropped

Catherine P. Browman, George Chertock, Donald G. Childers, Michael H. L. Hecker, C. S. Johnson, Ignacy Malecki, Roger G. Pridham, Nobuo Suga—*Fellows*

Leigh A. Abts, Hassam B. Ali, Hasan A. B. Alwi, Roger E. A. Arndt, James E. Atkinson, Robert M. Balonis, John C. Baumhauer, Jr., Edgar O. Bautista, Paul Bertaian, Mehmet Bilgen, Steven S. Black, Louis W. Boves, Marshall R. Bradley, Cary D. Bremigan, Joseph T. Brophy, Burlie A. Brunson, Stanley G. Chamberlain, Shoei-Sheng Chen, John E. Chlupsa, Arthur J. Collier, Robert K. Coulson, Richard G. De Jong, Edward J. DiPolvere, Philip V. Duckett, Jr., James E. Dukes, J. Salvador Echeverria-Villagomez, Gregory K. Essick, Neil L. Gerr, John J. Gilheany, Rena H. Glaser, John M. Green, Hans Groenig, Yueping Guo, Sandra L. Hamlet, Thomas E. Hayman, Howard Heemstra, Rolf S. Helgodt, Curtis A. Holsclaw, Jennifer M. Hood, John H. Huckans, David A. Hurdis, Dexter R. F. Irvine, Richard A. Jeans, Troy B. Jensen, Brian S. Johnson, James P. Kelly, Chamil Khalilullov, Chun-Duck Kim, Won-Ho Kim, Rena A. Krakow, Robert K. Kunze, Jr., Burney J. Le Boeuf, Wayne A. Lea, Chang-Hyo Lee, Gordon MacDonald, Lawrence J. Maga, Michael D. Max, Stanislav M. Mayevskyyi, Joe W. McClung, Michele D. McCollum, Sharon M. McFadden, Anthony F. Medeiros, Valery G. Mit'ko, Kevin G. Munhall, Anatoli G. Munin, Vernon L. Newhouse, Michael Nicholas, A. Michael Noll, James A. Nunley, William D. O'Neil, Aldo H. Ortiz Skarp, Viktor I. Passenchnik, Robert Perl, Larry D. Pope, Israel Raz, Sean M. Reilly, Ronald A. Roberts, Dale E. Schaeman, Dennis A. Seem, Jerome J. Sheehy, Michael D. Slurzberg, Howard G. Smith, James F. Smith, Giovanni Socino, Murray F. Speigel, Ronald L. Spross, William B. Swim, John R. Tanke, Jason A. Tomomeo, Rodrigo Varela, Thomas A. White, Charles R. Wilson, James H. Wilson, Lixue L. Wu, Edward J. Yoerger, Roger H. Yu, Seung S. Yun, Sergei T. Zavtrak, Jin Weng Zhang, Silvia Zorea—*Members*

Phillip B. Abraham, Kwin R. Abram, Murty A. Akundi, Javier Alpizar, Satoshi Amagai, Mohammed R. Amirinia, Michael J. Andruszkiewicz, John S. Antrobus, Chahe V. Apelian, Christian D. Audoly, B. Azpiroz, Jo-Anne Bachorowski, Christine Bartels, Gregory R. Bashford, Mahmood A. Bastaki, Michael L. Batzle, Robert L. Baum, William T. Baumann, William G. Beck, Todd B. Benjamin, Mark S. Bennett, Ronald D. Bennett, Frances S. Berge, Octavio L. Bentancourt, Kristian P. Biggs, Fernando Bitsie, Donald B. Bliss, Paul J. Book, P. Bowyer, James H. Boyden, Michael P. Brenner, Ronald I. Brent, Anthony D. Brescia, Bertrand Brevart, James R. Brewster, Carolyn J. Brown, Blair H. Brumley, Anthony B. Bruno, Ricardo A. Burdisso, Kirk G. Burlage, Ronald J. Burnosky, Phyllis H. Cahn, Peder U. Carlsson, Miguel Carrola, John W. Cartmill, Joseph E. Cates, David W. Chandler, Fang-Chu Chen, Kuo-Gen Chen, Ming-Te Cheng, Dmitry Chizhik, Myong-ki Cho, Woon Hyun Cho, Sunghoon Choi, Carl L. Chudy, Sang K. Chung, Alan B. Cobo-Lewis, John A. Colosi, Laurence N. Connor, Kathryn S. Copmann, David P. J. Coughtrie, James L. Curtis, David S. Cwalina, Ronald C. Dallman, William R. D'Angelo, Nolan R. Davis, Juan de Dios Esparza, Jerome F. DeJaco, Eugene F. Dell, Jr., Mauro De Ponti, Geert H. J. de Vries, Keith Denning, Laura Walsh Dickey, John F. Dorighi, John R. Dubberley, John I. Dunlop, Peirre E. Dupont, Bruce C. Edgar, Michael E. Edgerton, Rebecca E. Eilers, Mark C. Eldridge, John D. Elterich, Edward A. Estalote, Gail R. Feinman, Rainer J. Fink, Alison A. Flatau, Patrick J. Flynn, Antoine F. Folacci, Christopher S. Fortin, Paul A. France, Steven J. Franke, John R. Franks, Linda P. Franzoni, James H. Fu, Augusto Fuschini, Alaganandan Ganeshkumar, Brian Gardner, Eugene John Gehrig, Christian E. Gerard, Janice Giangrande, Robert V. Gillespie, Vin Gizzi, Michael P. Gokhale, David J. Goldfarb, Carlos T. Gomez-Fernandini, Grant A. Gordon, Frances K. Graham, Roy J. Greenfield, Doug M. Greenlee, Steven F. Griffin, Catherine Guigoy, Peter C. Guiod, Diane D. Gurdak, Peter-Peretz Halevi, Asa V. Hallgreen, Darren Hallman, Jeffrey F. Havens, Bruce P. Hayes, John G. Hayles, Roger D. Hayward, Shanjin He, Garry J. Heard, Cila Herman, Jose F. Hermano, Matthew L. Hettenhouse, Ingeborg J. Hochmair-Desoyer, Peter R. Holmes, Julie A. Hood, Klaas Hoogendoorn, Keith J. Howell, Ronald R. Hoy, Muh-Tsun Huang, Frank Wesley Ike, Paul W. Jameson, James A. Janko, Kirk E. Jenne, Bingli Jiau, Dilip N. Joharapurkar, Blane J. Johnson, Ramakrishna Kakarala, Jongmin Kang, Haruko Kawasaki-Fukumori, James A. Kearns, Michael H. Kelly, Khaldoun Khashanah, Hyun-Gwon Kil, Hiroo Kitagawa, Masakazu Konishi, Leslie G. Koshigoe, Geetha Krishnan, Harry A. Kunkel III, Young-Pil Kwon, Philip A. La Follette, Leo W. Lampone, Dong Hoon Lee, Minkyu Lee, Norman A. Lehtomaki, Sylvain S. Lerner, Alex J. S. Lin, Benjamin A. Lin, Hwei-Bing Lin, Weili Lin, D. L. Liu, Jingmei Liu, Russel K. Long, Christian Lorenzi, Molly A. Mack, Kenneth E. Malsky, Antonio Mancuso, Jason F. Manning, John D. Manning, Joseph J. Mariani, William H. Martin, Charles A. Marttila, Christophe Mattei, Anastasios Mauridis, Helen Ann McCaffrey, Mark McDonagh, Werner E. Mende, David S. Meyer, Scott K. Miller, Abdelfattah A. Moftah, Per Moren, Robert L. Morris, Douglas R. Munn, Nancy Tye Murray, N. Muthigyalu, Gary C. Muzzey, Kazuo Nakata, G. Patrick Nerbonne, Redwood W. Nero, Mark L. Neudorfer, Dan M. Nguyen, Stephen J. Norton, Robert J. Obara, Samuel G. Obeng, Robert N. Oerter, Thomas J. Owen, Andrea Paoloni, Theodore T. Papas, Claude Paradis, Serge Pare, Charles W. Parkins, Steen A. Parl, Michael Pavel, Xavier Pelorson, Diane C. Perrone, William R. Peterson, Alex Pidwerbetsky, James W. Pitton, Michael J. Pont, Anthony J. Popov, Miroslav Predny, William G. Proud, John D. Pyle, Gunnar G. Ramstrum, Curtis J. Randall, Najam A. Rauf, Satha T. Raveendra, Joelle Redner, Thomas J. Retka, Zane M. Rhea, Bernard P. Ricca, David M. Robinson, Harold C. Robinson, Ken L. Robinson, Ramiro Robledo, Christopher J. Rock, Andrew K. Rogers, Rick Rogers, Herbert L. Roitblat, Galina Rovner, Masahiko Sakai, Gerald M. Santos, Mohammed Sayeed, Stephen C. Schreppler, Timothy M. Scoggins, Jose A. Serpa, Kenneth W. Shearer, Angela G. Shoup, Todd W. Simmermacher, Kathleen A. Siren, Alice E. Smith, Dianna M. Smith, W. Gary Sokolich, Dimitrios A. Sotirpoulos, Nils Sponhein, Sheila V. Stager, Eckard Steiger, Joseph Steuwer, Paul N. Stevenson, Glen C. Steyer, John F. Straitz III, Ji Su, Ernest W. Swenson, Marialice O. Szpigel, Farokh Taghipour, Tapio I. Takala, Kushai K. Talukdar, Bazil Thomas, Suzzane Thwaites, Glynnis A. Tidball, Billy G. Tollison, J. Michael Trogolo, Ying-Chiao Tsao, Robert C. Turner, Michael A. Turturro, Sergion Vaiderrabano, David Van Tol, Nanette M. Veilleux, Theodore H. Venema, Judith R. Villemain, Brian E. Walden, J. Robin S. Waldstein, Jeff H. Waters, Christopher T. Welsh, Denise West, Gail M. Whitelaw, Leland Ray Whitney, Martin D. Wilde, Reiner F. Wilheims-Tricarico, Malcolm J. Williamson, James F. Willott, Betty Windham, Steven S. Wise, James M. Witting, Darrell Wong, Jae-Hak Woo, Stephen R. Wood, Xuefeng Yang, Shigong Ye, Miida Yoshiro, Chulsoo You, Xiaorong Zhang, Douglas C. Zhao, Yunxin Zhao, Stanley H. Zisk—*Associates*

Ron E. Ainsworth, Jr., Michele A. Aldridge, Inna V. Aleksandrovsky, Sherif F. Ali, Dennis L. Allen, Michael J. Anderson, Sevag H. Arzoumanian, Bradford L. Buckus, Bok-Dong Bang, Joy L. Barney-Tomalin, Todd R. Beiler, Jacklyn D. Bezemek, Tim G. Bofsford, Tamala S. Broadham, Ellen M. Bradley, David R. Brandt, Christine A. Brenner, Lynda B. Brooks, Christopher A. Brown, Holly A. Burch, Patricia A. Burton, Eric F. Bynum, Liang-Wu Cai, Greg H. Canfield, Terri E. Casey, Sabine Castagnet, Luca G. Cazzanti, Borka Josifovic Ceranic, Victor A. Chacon, Lin L. Chase, Chuan-Chiang Chen, Huxiong Chen, Jian-Feng Chen, Asim F. Choudhri, David S. Chow, Jean L. DeMerit, Brita J. Dean, Patricia C. Debergue, Max Deffenbaugh, Sumit Dhar, Carsten Draeger, Mike E. Duncan, Barry Joe Dunn, Bebashree Dutta, Chad L. Epinfanio, Michelle K. Estaphan, Daniel C. Fain, Tracie J. Ferguson, Christopher D. Field, Jamie M. Figueiredo, Liam Fitzpatrick, Dirk M. Fox Kruckenberg, Daniel J. France, Nathan C. M. Franzen, Cliff Frensley, Marcio de Avelar Gomes, Jeroen Groenenboom, Xinghui Shane Guan, Humberto Guarin, Mark A. Guisinger, Michiko Hashi, Clare L. Henderson, Paul D. Hernderson, Pablo A. Hernandez, Edson T. Hirohata, Cristian M. Hoffman, John F. Houde, John E. Huff, Jr., Willian D. Hula, Yi Bong Jung, Paulus Justianada, Christopher M. Karwoski, Paul A. Kienzle, Jyun Chul Kim, Michael D. Klein, Michael D. Knight, Beth A. Kopyar, Peter S. Kortenkamp, Paul H. Kraeutner, Hong-Kwang J. Kuo, Sylvia D. S. Kwakye, Hanif M. Ladak, David A. Laszlo, Bruce S. Lavoie, Michael J. Leamy, Hyo-Keun Lee, Jong-Hwa Lee, Sang-Kwong Lee, Zongbao Li, Car-

los R. Lopez, Xiaorong Lu, Margaret R. MacEachern, Michael J. Mack, Joyce Manzella, Yi Mao, Brett Martin, Linda V. Martin Traykovski, Earl T. McCullough, Donna L. McMorine, Michael M. Mielke, Jamaal Mitchell, Henmi Mitsuru, Abduljaleel K. Moidu, Joshua M. Montgomery, Bente H. Moxness, Christopher W. Myers, Richard C. Nadeau, David Nelson, Orlando Neto, Thomas Norris, Takatoshi Okuno, Felipe A. Otondo, Daniel J. Overholt, George J. Papadelis, Benoit Patry, Scott Paxton, Martin J. L. Pelser, Olegario Parales, Mauricio A. Pino, James E. Poplawski, Anahi M. Procel, Angie S. Reeder, Edward L. Riegelsberger, Philippe-E. M. Roche, Andrew R. Rollinger, Shiladitya Roy, Arthur R. Salindong, Ahmad Shamsoddini, Bernard J. Sklanka, Georgina R. Slavoff, Gordon P. Smith, Sandra A. Smith, Su W. Teoh, Eric J. Terrill, Mathew D. Turner, Ram Vakkayil, Edna E. Vasquez, Jeremie Voix, Shuh-Hau Wang, Ian Wann, Joseph F. Wayand, Martin L. Whitehead, Brian R. Wilson, Jane F. Wozniak, Xin Xiao, Ping Zhang—*Students*

Fellows	835
Members	2815
Associates	2795
Students	853
	7298

ACOUSTICAL STANDARDS NEWS

Avril Brenig, Standards Manager
Standards Secretariat, Acoustical Society of America, 120 Wall Street, 32nd Floor, New York, New York 10005-3993 [Tel.: (212) 248-0373; Fax: (212) 248-0146; e-mail: asastds@aip.org]

George S. K. Wong
Acoustical Standards, Institute for National Measurement Standards, National Research Council, Ottawa, Ontario K1A 0R6, Canada [Tel.: (613) 993-6159; Fax: (613) 990-8765; e-mail: george.wong@nrc.ca]

American National Standards (ANSI Standards) developed by Accredited Standards Committees S1, S2, S3, and S12 in the areas of acoustics, mechanical vibration and shock, bioacoustics, and noise, respectively, are published by the Acoustical Society of America (ASA) through the American Institute of Physics (AIP). In addition to these standards, ASA publishes Catalogs of Acoustical Standards, both National and International. To receive copies of the latest Standards Catalogs, please contact Avril Brenig.

Comments are welcomed on all material in Acoustical Standards News.

This Acoustical Standards News section in JASA, as well as the National and International Catalogs of Acoustical Standards, flyers on the draft international documents available, and other information on the Standards Program of the Acoustical Society of America, are available via the ASA home page: http://www.asa.aip.org.

Standards Meetings Calendar—National

The next meetings of the Accredited Standards Committees for national standards development, the review of International Standards, and planning of future meetings are scheduled to be held during the 139th ASA Meeting at the Western Peachtree Plaza Hotel, Atlanta, GA, 30 May–3 June 2000. Meetings of the Accredited Standards Committees are open to the public for participation. Organizations and individuals with expertise that may enhance the acoustical standards effort are encouraged to participate.

- ***Tuesday, 30 May 2000, 7:00 p.m. to 10:00 p.m.***
  ASA Committee on Standards (ASACOS) Steering
- ***Wednesday, 31 May 2000, 9:00 a.m. to 11:30 a.m.***
  ASA Committee on Standards (ASACOS). Meeting of the Committee that directs the Acoustical Standards Program of the Acoustical Society.

American National Standards Institute (ANSI) Calendar

1 January 2000
• Executive Standards Council (ExSC) Meeting & Appeals: 3 days, Finance Committee

10 January 2000
• Company Member Council Executive Committee (CMCEC) Meeting (Day 1 of 2)

11 January 2000
• Company Member Council Executive Committee (CMCEC) Meeting (Day 2 of 2)

12 January 2000
• ANSI International Committee (IC)

2 September 2000
• Organizational Member Council Meeting (OMC)

18 January 2000
• ANSI International Forum (AIF)

3 February 2000
• Board of Standards Review (BSR) Meeting

10 February 2000
• Board Executive Committee Meeting

29 February 2000
• ANSI National Issues Committee (NIC)

23 March 2000
• Board of Directors Meeting

2 May 2000
• Organizational Member Council Meeting

3 May 2000
• ANSI National Issues Committee (NIC)

4 May 2000
• Board of Standards Review (BSR) Meeting

11 May 2000
• ANSI Medical Device Standards Board

11 May 2000
• ISSB Meeting

24 May 2000
• ANSI International Committee (IC)

6 June 2000
• ANSI Executive Standards Council (ExSC) Meeting & Appeals: 3 days

20 June 2000
• Company Member Council Executive Committee (CMCEC) Meeting (Day 1 of 2)

21 June 2000
• Company Member Council Executive Committee (CMCEC) Meeting (Day 2 of 2)

19 July 2000
• Finance Committee Meeting of ANSI Board of Directors

20 July 2000
• ANSI Board Executive Committee Meeting

A listing of the Accredited Standards Committees, their Working Groups, their chairs (listed in parentheses) and published standards, Chair and Vice Chair of the ASA Committees on Standards (ASACOS), and the U. S. Technical Advisory Group (TAG) Chairs for the International Standards Committees, are given here for reference:

Accredited Standards Committee on Acoustics, S1

(G. S. K. Wong, Chair; T. Kuemmel, Vice Chair)

Scope: Standards, specifications, methods of measurement and test, and terminology in the field of physical acoustics including architectural acoustics, electroacoustics, sonics and ultrasonics, and underwater sound, but excluding those aspects which pertain to biological safety, tolerance and comfort.

S1 Working Groups

S1/Advisory—Advisory Planning Committee to S1 (T. Kuemmel);
S1/WG1—Standard Microphones and their Calibration (V. Nedzelnitsky);
S1/WG5—Band Filter Set (J. Pope);
S1/WG15—Noise Canceling Microphones (R. L. McKinley);
S1/WG16—FFT Acoustical Analyzers (R. J. Peppin, Chair; L. Wu, Vice Chair);
S1/WG17—Sound Level Meters and Integrating Sound Level Meters (T. J. Kuemmel);
S1/WG19—Insertion Loss of Windscreens (R. J. Peppin);
S1/WG20—Ground Impedance (Co-Chairs: K. Attenborough and J. Sabatier);
S1/WG21—Electromagnetic Susceptibility (EMS) of Acoustical Instruments (J. Seiler);
S1/WG22—Cavitation Detecting and Monitoring (W. L. Nyborg);
S1/WG23—Underwater Acoustics (F. Fisher);
S1/WG24—Design Response of Weighting Networks for Acoustical Measurements (G. S. K. Wong);
S1/WG25—Specification for Acoustical Calibrators (M. P. Valoski).

S1 STANDARDS ON ACOUSTICS

ANSI S1.1-1994 (R1999) American National Standard Acoustical Terminology.
ANSI S1.4-1983 (R1997) American National Standard Specification for Sound Level Meters.
ANSI S1.4A-1985 (R1997) Amendment to ANSI S1.4-1983.
ANSI S1.6-1984 (R1997) American National Standard Preferred Frequencies, Frequency Levels, and Band Numbers for Acoustical Measurements.
ANSI S1.8-1989 (R1997) American National Standard Reference Quantities for Acoustical Levels.
ANSI S1.9-1996 American National Standard Instruments for the measurement of Sound Intensity.
ANSI S1.10-1966 (R1997) American National Standard Method for the Calibration of Microphones.
ANSI S1.11-1986 (R1998) American National Standard Specification for Octave-Band and Fractional-Octave-Band Analog and Digital Filters.
ANSI S1.12-1967 (R1997) American National Standard Specifications for Laboratory Standard Microphones.
ANSI S1.13-1995 (R1999) American National Standard Measurement of Sound Pressure Levels in Air.
ANSI S1.14-1998 American National Standard Recommendations for Specifying and Testing the Susceptibility of Acoustical Instruments to Radiated Radio-Frequency Electromagnetic Fields, 25 MHz to 1 GHz.
ANSI S1.15-1997 Part 1 American National Standard Measurement Microphones—Part 1: Specifications for Laboratory Standard Microphones.
ANSI S1.18-1999 American National Standard Template Method for Ground Impedance.
ANSI S1.20-1988 (R1998) American National Standard Procedures for Calibration of Underwater Electroacoustic Transducers.
ANSI S1.22-1992 (R1997) American National Standard Scales and Sizes for Frequency Characteristics and Polar Diagrams in Acoustics.
ANSI S1.25-1991 (R1997) American National Standard Specification for Personal Noise Dosimeters.
ANSI S1.26-1995 (R1999) American National Standard Method for the Calculation of the Absorption of Sound by the Atmosphere.
ANSI S1.40-1984 (R1997) American National Standard Specification for Acoustical Calibrators.
ANSI S1.42-1986 (R1998) American National Standard Design Response of Weighting Networks for Acoustical Measurements.
ANSI S1.43-1997 American National Standard Specification for Integrating-Averaging Sound Level Meters.

Accredited Standards Committee on Mechanical Vibration and Shock, S2

(D. J. Evans, Chair; R. F. Taddeo, Vice Chair)

Scope: Standards, specifications, methods of measurement and test, and terminology in the field of mechanical vibration and shock, and condition monitoring and diagnostics of machines, but excluding those aspects which pertain to biological safety, tolerance, and comfort.

S2 Working Groups

S2/Advisory—Advisory Planning Committee to S2 (R. F. Taddeo);
S3/WG39(S2)—Human Exposure to Mechanical Vibration and Shock (D. D. Reynolds, Chair; H. E. von Gierke, Vice Chair);
S2/WG54—Atmospheric Blast Effects (J. W. Reed, Chair; J. H. Keefer, Vice Chair);
S2/WG65—Balancing Technology (R. Mehta, Chair; K. Won, Vice Chair);
S2/WG76—Measurement and Evaluation of Machinery Vibration (P. H. Maedel);
S2/WG77—Measurement and Evaluation of Ship Vibration (A. F. Kilcullen, Chair; P. C. Shang, Vice Chair);
S2/WG78—Measurement and Evaluation of Structural Vibration (C. G. Gordon);
S2/WG79—Characterization of the Dynamic Mechanical Properties of Viscoelastic Polymers (W. Madigosky, Chair; B. Hartmann, Vice Chair);
S2/WG80—Vibration and Shock Terminology (D. F. Muster);
S2/WG81—Use and Calibration of Vibration and Shock Measuring Instruments (D. J. Evans, B. E. Douglas);
S2/WG88—Measurement and Evaluation of Machine Tool Vibration (J. H. Pyne);
S2/WG89—Parallel to ISO/TC 108/SC5 Condition Monitor and Diagnostics of Machines (D. F. Muster);
S2/WG90—Parallel to ISO/TC 108/SC6 Vibration and Shock Generating Equipment (G. Booth);
S2/WG92—Training Accreditation in the Field of Condition Monitoring and Diagnostics of Machines (parallel to ISO/TC 108/SC5/WG7) (R. Eshleman);
S2/WG93—Condition Monitoring and Diagnostics of Power Transformers (parallel to ISO/TC 108/SC5/AGD) (T. H. Crum);
S2/WG94—Life Usage Monitoring (ISO/TC 108/SC5/WG9) (P. Gatlin);
S2/WG95—Survey of Techniques used for the Purpose of Condition Monitoring (parallel to ISO/TC 108/SC5/WG10) (Vacant);
S2/WG96—Condition Monitoring and Assessment of Structural Systems (parallel to ISO/TC 108/WG24 and ISO/TC 108/WG25) (B. E. Douglas);
S2/WG97—Signal Processing Methods (parallel to ISO/TC 108/WG27) (D. Groutage).

S2 STANDARDS ON MECHANICAL VIBRATION AND SHOCK

ANSI S2.2-1959 (R1997) American National Standard Methods for the Calibration of Shock and Vibration Pickups.
ANSI S2.3-1964 (R1997) American National Standard Specifications for High-Impact Shock Machine for Electronic Devices.
ANSI S2.4-1976 (R1997) American National Standard Method for Specifying Characteristics of Auxiliary Analog Equipment for Shock and Vibration Measurements.
ANSI S2.5-1962 (R1997) American National Standard Recommendations for Specifying the Performance of Vibration Machines.
ANSI S2.7-1982 (R1997) American National Standard Balancing Terminology.
ANSI S2.8-1972 (R1997) American National Standard Guide for Describing the Characteristics of Resilient Mountings.
ANSI S2.9-1976 (R1997) American National Standard Nomenclature for Specifying Damping Properties of Materials.
ANSI S2.10-1971 (R1997) American National Standard Methods for Analysis and Presentation of Shock and Vibration Data.
ANSI S2.11-1969 (R1997) American National Standard Selection of Calibrations and Tests for Electrical Transducers used for Measuring Shock and Vibration.
ANSI S2.13-1996 Part 1 American National Standard Mechanical Vibration of Nonreciprocating Machines—Measurements on Rotating Shafts and Evaluation—Part 1: General Guidelines.
ANSI S2.14-1973 (R1997) American National Standard Methods for Specifying the Performance of Shock Machines.
ANSI S2.15-1972 (R1997) American National Standard Specification for the Design, Construction, and Operation of Class HI (High-Impact) Shock-Testing Machine for Lightweight Equipment.
ANSI S2.16-1997 American National Standard Vibratory Noise Measurements and Acceptance Criteria of Shipboard Equipment.
ANSI S2.17-1980 (R1997) American National Standard Techniques of Machinery Vibration Measurement.

ANSI S2.19-1997 Part 1 American National Standard Mechanical Vibration—Balancing Quality Requirements of Rigid Rotors—Part 1: Determination of Permissible Residue Unbalance.
ANSI S2.20-1983 (R1997) American National Standard Estimating Air Blast Characteristics for Single Point Explosions in Air, with a Guide to Evaluation of Atmospheric Propagation and Effects.
ANSI S2.21-1998 American National Standard Method for Preparation of a Standard Material for Dynamic Mechanical Measurements.
ANSI S2.22-1998 American National Standard Resonance Method for Measuring the Dynamic Mechanical Properties of Viscoelastic Materials.
ANSI S2.23-1998 American National Standard Single Cantilever Beam Method for Measuring the Dynamic Mechanical Properties of Viscoelastic Materials.
ANSI S2.31-1979 Part 1 (R1997) American National Standard Method for the Experimental Determination of Mechanical Mobility—Part 1: Basic Definitions and Transducers.
ANSI S2.32-1982 Part 2 (R1997) American National Standard Methods for the Experimental Determination of Mechanical Mobility—Part 2: Measurements Using Single-Point Translation Excitation.
ANSI S2.34-1984 (R1997) American National Standard Guide to the Experimental Determination of Rotation Mobility Properties and the Complete Mobility Matrix.
ANSI S2.38-1982 (R1997) American National Standard Field Balancing Equipment—Description and Evaluation.
ANSI S2.40-1984 (R1997) American National Standard Mechanical Vibration of Rotating and Reciprocating Machinery—Requirements for Instruments for Measuring Vibration Severity.
ANSI S2.41-1985 (R1997) American National Standard Mechanical Vibration of Large Rotating Machines with Speed Range from 10 to 200 rev/s—Measurement and Evaluation of Vibration Severity *in situ.*
ANSI S2.42-1982 (R1997) American National Standard Procedures for Balancing Flexible Rotors.
ANSI S2.43-1984 (R1997) American National Standard Criteria for Evaluating Flexible Rotor Balance.
ANSI S2.45-1983 (R1997) American National Standard Electrodynamic Test Equipment for Generating Vibration—Methods of Describing Equipment Characteristics.
ANSI S2.46-1989 (R1997) American National Standard Characteristics to be Specified for Seismic Transducers.
ANSI S2.47-1990 (R1997) American National Standard Vibrations of Buildings—Guidelines for the Measurements of Vibrations and Evaluation of their Effects on Buildings.
ANSI S2.48-1993 (R1997) American National Standard Servo-Hydraulic Test Equipment for Generating Vibration, Method of Describing Characteristics.
ANSI S2.58-1983 (R1997) American National Standard Auxiliary Tables for Vibration Generators—Methods of Describing Equipment Characteristics.
ANSI S2.60-1987 Balancing Machines—Enclosures and Other Safety Measures.
ANSI S2.61-1989 (R1997) American National Standard Guide to the Mechanical Mounting of Accelerometers.

Accredited Standards Committee on Bioacoustics, S3

(R. F. Burkard, Chair; J. Franks, Vice Chair)

Scope: Standards, specifications, methods of measurement and test, and terminology in the fields of mechanical shock and physiological acoustics, including aspects of general acoustics, shock, and vibration which pertain to biological safety, tolerance, and comfort.

S3 Working Groups

S3/Advisory—Advisory Planning Committee to S3 (J. Franks);
S3/WG35—Audiometers (R. L. Grason);
S3/WG36—Speech Intelligibility (R. Schlauch);
S3/WG37—Coupler Calibration of Earphones (B. Kruger);
S3/WG39(S2)—Human Exposure to Mechanical Vibration and Shock—Parallel to ISO/TC 108/SC4 (D. D. Reynolds, H. E. von Gierke, Vice Chair);
S3/WG43—Method for Calibration of Bone Conduction Vibrator (J. Durrant);
S3/WG48—Hearing Aids (D. A. Preves);
S3/WG56—Criteria for Background Noise for Audiometric Testing (J. Frank);
S3/WG58—Hearing Conservation Criteria (D. L. Johnson);
S3/WG59—Measurement of Speech Levels (H. Levitt);
S3/WG60—Measurement of Acoustic Impedance and Admittance of the Ear (D. J. Lilly);
S3/WG62—Impulse Noise with Respect to Hearing Hazard (D. L. Johnson);
S3/WG67—Manikins (M. D. Burkhard);
S3/WG72—Measurement of Auditory Evoked Potentials (R. F. Burkhard);
S3/WG76—Computerized Audiometry (A. J. Miltich);
S3/WG78—Thresholds (W. A. Yost);
S3/WG79—Method for Calculation of the Speech Intelligibility Index (C. V. Pavlovic);
S3/WG81—Hearing Assistance Technologies (M. K. Wynne);
S3/WG82—Basic Vestibular Function Test Battery (C. Wall III);
S3/WG83—Sound Field Audiometry (T. R. Letowski);
S3/WG84—Otoacoustic Emission (G. R. Long);
S3/WG85—Hearing Loss and Exposure (R. A. Dobie);
S3/WG86—Audiometric Data Structures (G. J. Frye and B. Kruger, Co-Chairs);
S3/WG87—Human Response to Repetitive Mechanical Shock (N. Alem);
S3/WG88—Standard Audible Emergency Evacuation and other Signals (I. Mande);
S3/WG89—Spatial Audiometry in Real and Virtual Environments (J. Besing);
S3/WG90—Animal Bioacoustics (A. E. Bowles).

S3 Liaison Working Group:

S3/L-1 U.S. TAG Liaison to IEC/TC 87 Ultrasonics (W. L. Nyborg).

S3 STANDARDS ON BIOACOUSTICS

ANSI S3.1-1991 American National Standard Maximum Permissible Ambient Noise Levels for Audiometric Test Rooms.
ANSI S3.2-1989 (R1995) American National Standard Method for Measuring the Intelligibility of Speech over Communications Systems.
ANSI S3.4-1980 (R1997) American National Standard Procedure for the Computation of Loudness of Noise.
ANSI S3.5-1997 American National Standard Methods for the Calculation of the Speech Intelligibility Index.
ANSI S3.6-1996 American National Standard Specification for Audiometers.
ANSI S3.7-1995 (R1999) American National Standard Method for Coupler Calibration of Earphones.
ANSI S3.13-1987 (R1997) American National Standard Mechanical Coupler for Measurement of Bone Vibrators.
ANSI S3.14-1977 (R1997) American National Standard for Rating Noise with Respect to Speech Interference.
ANSI S3.18-1979 (R1993) American National Standard Guide for the Evaluation of Human Exposure to Whole-Body Vibration.
ANSI S3.20-1995 American National Standard Bioacoustical Terminology.
ANSI S3.21-1978 (R1997) American National Standard Method for Manual Pure-Tone Threshold Audiometry.
ANSI S3.22-1996 American National Standard Specification of Hearing Aid Characteristics.
ANSI S3.25-1989 (R1995) American National Standard for an Occluded Ear Simulator.
ANSI S3.29-1983 (R1996) American National Standard Guide to the Evaluation of Human Exposure to Vibration in Buildings.
ANSI S3.32-1982 (R1995) American National Standard Mechanical Vibration and Shock Affecting Man—Vocabulary.
ANSI S3.34-1986 (R1997) American National Standard Guide for the Measurement and Evaluation of Human Exposure to Vibration Transmitted to the Hand.
ANSI S3.35-1985 (R1997) American National Standard Method of Measurement of Performance Characteristics of Hearing Aids under Simulated *in situ* Working Conditions.
ANSI S3.36-1985 (R1996) American National Standard Specification for a Manikin for Simulated *in situ* Airborne Acoustic Measurements.
ANSI S3.37-1987 (R1997) American National Standard Preferred Earhook Nozzle Thread for Postauricular Hearing Aids.

ANSI S3.39-1987 (R1996) American National Standard Specifications for Instruments to Measure Aural Acoustic Impedance and Admittance (Aural Acoustic Immittance).
ANSI S3.40-1989 (R1995) American National Standard Guide for the Measurement and Evaluation of Gloves which are Used to Reduce Exposure to Vibration Transmitted to the Hand.
ANSI S3.41-1990 (R1996) American National Standard Audible Emergency Evacuation Signal.
ANSI S3.42-1992 (R1997) American National Standard Testing Hearing Aids with a Broadband Noise Signal.
ANSI S3.44-1996 American National Standard Determination of Occupational Noise Exposure and Estimation of Noise-Induced Hearing Impairment.
ANSI S3.45-1999 Procedure for Testing Basic Vestibular Function.
ANSI S3.46-1997 American National Standard Methods of Measurement of Real-Ear Performance Characteristics of Hearing Aids.

Accredited Standards Committee on Noise, S12

(P. D. Schomer, Chair; R. D. Hellweg, Vice Chair)

Scope: Standards, specifications, and terminology in the field of acoustical noise pertaining to methods of measurement, evaluation, and control, including biological safety, tolerance and comfort, and physical acoustics as related to environmental and occupational noise.

S12 Working Groups

S12/Advisory—Advisory Planning Committee to S12 (R. D. Hellweg);
S12/WG3—Measurement of Noise from Office and Data Processing Equipment (R. Lotz);
S12/WG11—Hearing Protector Attenuation and Performance (E. H. Berger);
S12/WG12—Evaluation of Hearing Conservation Programs (J. D. Royster, Chair; E. H. Berger, Vice Chair);
S12/WG15—Measurement and Evaluation of Outdoor Community Noise (P. D. Schomer);
S12/WG18—Criteria for Room Noise (R. J. Peppin);
S12/WG23—Determination of Sound Power (R. J. Peppin and B. Brooks, Co-Chairs);
S12/WG31—Predicting Sound Pressure Levels Outdoors (M. J. White);
S12/WG32—Revision of ANSI S12.7-1986 Methods for Measurement of Impulse Noise (A. H. Marsh);
S12/WG33—Revision of ANSI S5.1-1971 Test Code for the Measurement of Sound from Pneumatic Equipment (D. Bookshar);
S12/WG 34—Methodology for Hearing Conservation Program (R. Goodwin);
S12/WG35—Method for the Selection of Hearing Protectors that Optimize the Ability to Communicate (D. Byrne and K. L. Michael, Co-Chairs);
S12/WG36—Development of Methods for Using Sound Quality (G. L. Ebbit and P. Davies, Co-Chairs);
S12/WG37—Measuring Sleep Disturbance due to Noise (K. S. Pearsons);
12/WG38—Noise Labeling in Products (R. D. Hellweg and J. Pope, Co-Chairs);
12/WG39—Measurement of the Noise Attenuation of Active and/or Passive Level Dependent Hearing Protective Devices (D. Gauger);
12/WG40—Measurement of the Noise Aboard Ships (S. Fisher, Chair; A. F. Kilcullen, Vice Chair);
12/WG41—Model Community Noise Ordinances (C. Caccavari, Chair; M. Alexander, Vice Chair).
12/WG42—Classroom Acoustics (D. Lubman and L. Sutherland, Co-Chairs).

S12 Liaison Working Groups:

S12/L-1 IEEE 85 Committee for TAG Liaison—Noise Emitted by Rotating Electrical Machines (Parallel to ISO/TC 43/SC 1/WG 13) (R. G. Bartheld);
S12/L-2 Measurement of Noise from Pneumatic Compressors Tools and Machines (Parallel to ISO/TC 43/SC 1/WG 9) (Vacant);
S12/L-3 SAE Committee for TAG Liaison on Measurement and Evaluation of Motor Vehicle Noise (parallel to ISO/TC 43/SC 1/WG 8) (R. F. Schumacher);
S12/L-4 SAE Committee A-21 for TAG Liaison on Measurement and Evaluation of Aircraft Noise (J. Brooks);
S12/L-5 ASTM E-33 on Environmental Acoustics (to include activities of ASTM E33.06 on Building Acoustics, parallel to ISO/TC 43/SC 2 and ASTM E33.09 on Community Noise) (K. P. Roy);
S12/L-6 SAE Construction–Agricultural Sound Level Committee (W. H. Flint);
S12/L-7 SAE Specialized Vehicle and Equipment Sound Level (T. Disch);
S12/L-8 ASTM PTC No. 36 Measurement of Industrial Sound (R. A. Putnam, Chair; B. M. Brooks, Vice Chair).

S12 STANDARDS ON NOISE

ANSI S12.1-1983 (R1996) American National Standard Guidelines for the Preparation of Standard Procedures for the Determination of Noise Emission from Sources.
ANSI S12.2-1995 American National Standard Criteria for Evaluating Room Noise.
ANSI S12.3-1985 (R1996) American National Standard Statistical Methods for Determining and Verifying Stated Noise Emission Values of Machinery and Equipment.
ANSI S12.5-1990 (R1997) American National Standard Requirements for the Performance and Calibration of Reference Sound Sources.
ANSI S12.6-1997 American National Standard Methods for Measuring the Real-Ear Attenuation of Hearing Protectors.
ANSI S12.7-1986 (R1993) American National Standard Methods for Measurements of Impulse Noise.
ANSI S12.8-1998 American National Standard Methods for Determination of Insertion Loss of Outdoor Noise Barriers.
ANSI S12.9-1988 Part 1 (R1993) American National Standard Quantities and Procedures for Description and Measurement of Environmental Sound—Part 1.
ANSI S12.9-1992 Part 2 American National Standard Quantities and Procedures for Description and Measurement of Environmental Sound—Part 2: Measurement of Long-Term, Wide-Area Sound.
ANSI S12.9-1993 Part 3 American National Standard Quantities and Procedures for Description and Measurement of Environmental Sound—Part 3: Short-Term Measurements with an Observer Present.
ANSI S12.9-1996 Part 4 American National Standard Quantities and Procedures for Description and Measurement of Environmental Sound—Part 4: Noise Assessment and Prediction of Long-Term Community Response.
ANSI S12.9-1998 Part 5 American National Standard Quantities and Procedures for Description and Measurement of Environmental Sound—Part 5: Sound Level Descriptors for Determination of Compatible Land Use.
ANSI S12.10-1985 (R1997) American National Standard Methods for the Measurement and Designation of Noise Emitted by Computer and Business Equipment (Revision of ANSI S1.29-1979).
ANSI S12.11-1987 (R1997) American National Standard Methods for the Measurement of Noise Emitted by Small Air-Moving Devices.
ANSI S12.12-1992 (R1997) American National Standard Engineering Method for the Determination of Sound Power Levels of Noise Sources Using Sound Intensity.
DRAFT ANSI S12.13-1991 American National Standard Evaluating the Effectiveness of Hearing Conservation Programs.
ANSI S12.14-1992 (R1997) American National Standard Methods for the Field Measurement of the Sound Output of Audible Public Warning Devices Installed at Fixed Locations Outdoors.
ANSI S12.15-1992 (R1997) American National Standard For Acoustics—Portable Electric Power Tools, Stationary and Fixed Electric Power Tools, and Gardening Appliances—Measurement of Sound Emitted.
ANSI S12.16-1992 (R1997) American National Standard Guidelines for the Specification of Noise of New Machinery.
ANSI S12.17-1996 American National Standard Impulse Sound Propagation for Environmental Noise Assessment.
ANSI S12.18-1994 American National Standard Procedure for Outdoor Measurement of Sound Pressure Levels.
ANSI S12.19-1996 American National Standard Measurement of Occupational Noise Exposure.
ANSI S12.23-1989 (R1996) American National Standard Method for the Designation of Sound Power Emitted by Machinery and Equipment.
ANSI S12.30-1990 (R1997) American National Standard Guidelines for the Use of Sound Power Standards and for the Preparation of Noise Test Codes.

ANSI S12.31-1990 (R1996) American National Standard Precision Methods for the Determination of Sound Power Levels of Broadband Noise Sources in Reverberation Rooms.
ANSI S12.32-1990 (R1996) American National Standard Precision Methods for the Determination of Sound Power Levels of Discrete-Frequency and Narrow-Band Noise Sources in Special Reverberation Rooms.
ANSI S12.33-1990 (R1997) American National Standard Engineering Methods for the Determination of Sound Power Levels of Noise Sources in a Special Reverberation Test Room.
ANSI S12.34-1988 (R1997) American National Standard Engineering Methods for the Determination of Sound Power Levels of Noise Sources for Essentially Free-Field Conditions over a Reflecting Plane.
ANSI S12.35-1990 (R1996) American National Standard Precision Methods for the Determination of Sound Power Levels of Noise Sources in Anechoic and Hemi-Anechoic Rooms.
ANSI S12.36-1990 (R1997) American National Standard Survey Methods for the Determination of Sound Power Levels of Noise Sources.
ANSI S12.42-1995 American National Standard Microphone-In-Real-Ear and Acoustic Test Fixture Methods for the Measurement of Insertion Loss of Hearing Protection Devices.
ANSI S12.43-1997 American National Standard Methods for Measurement of Sound Emitted by Machinery and Equipment at Workstations and other Specified Positions.
ANSI S12.44-1997 American National Standard Methods for Calculation of Sound Emitted by Machinery and Equipment at Workstations and other Specified Positions from Sound Power Level.

ASA Committee on Standards (ASACOS)

ASACOS (D. L. Johnson, Chair and ASA Standards Director; P. D. Schomer, ASACOS Vice Chair).

U. S. Technical Advisory Groups (TAGS) for International Standards Committees:

ISO/TC 43 Acoustics, **ISO/TC 43 /SC1** Noise (P. D. Schomer, U.S. TAG Chair; H. E. von Gierke, U.S. TAG Vice Chair);
ISO/TC 108 Mechanical Vibration and Shock (D. J. Evans, U.S. TAG Chair);
ISO/TC 108/SC1 Balancing, including Balancing Machines (R. H. Mehta, U.S. TAG Chair; K. Won, U.S. TAG Vice Chair);
ISO/TC 108/SC2 Measurement and Evaluation of Mechanical Vibration and Shock as Applied to Machines, Vehicles and Structures (A. F. Kilcullen, U.S. Tag Chair);
ISO/TC 108/SC3 Use and Calibration of Vibration and Shock Measuring Instruments (D. J. Evans, U.S. Tag Chair);
ISO/TC 108/SC5 Condition Monitoring and Diagnostic Machines (D. J. Venditis, U.S. TAG Chair, R. F. Taddeo, U.S. Tag Vice Chair);
ISO/TC 108/SC6 Vibration and Shock Generating Systems (G. Booth, U.S. TAG Chair);
IEC/TC 29 Electroacoustics (V. Nedzelnitsky, U.S. Technical Advisor).

Standards News from the United States

(Partially derived from *ANSI Reporter*, and *ANSI Standards Action*, with appreciation)

Meetings of International Standards Committees

The following international standards committees are scheduled to meet in Newport Beach, CA, in conjunction with the 140th ASA Meeting:

- 28 November–1 December 2000 IEC/TC29: Electroacoustics.
- 12–16 December 2000 ISO/TC 43: Acoustics and ISO/TC 43/SC 1: Noise.

American National Standards Call for Comment on Proposals Listed

This section solicits comments on proposed new American National Standards and on proposals to revise, reaffirm, or withdraw approval of existing standards. The dates listed in parentheses are for information only.

ACOUSTICS

BSR S12.13, Evaluating the Effects of Hearing Conservation Programs through Audiometric Database Analysis (new standard) (23 November 1999)

Defines methods for evaluating the effectiveness of hearing conversation programs and for preventing occupational noise-induced hearing loss by using techniques for audiometric data base analysis. The rationale is given for using the variability of threshold measurements in annual monitoring audiograms as the basis for judging effectiveness.

Final actions on American National Standards

ANSI's Board of Standards Review has taken the final action indicated on the standards listed below.

ISO Standards

ACOUSTICS (TC 43)

ISO 1996-3:1987, Acoustics—Description and Measurement of Environmental Noise—Part 3: Application to noise limits.

ASTM Standards

ACOUSTICS

ANSI/ASTM E497-99, Practice for Installing Sound-Isolating Lightweight Partitions (revision of ANSI/ASTM E497-89 (R1994)): (10 August 1999)
ANSI/ASTM E976-99, Guide for Determining the Reproducibility of Acoustic Emission Sensor Response (revision of ANSI/ASTM E976-98): (10 September 1999)

Standards News from Abroad

(Partially derived from *ANSI Reporter* and *ANSI Standards Action*, with appreciation)

Newly published ISO and IEC Standards

Listed here are new and revised standards recently approved and promulgated by ISO—the International Organization for Standardization, and IEC—the International Electrotechnical Commission. They are all available from ANSI, the U.S. member of ISO and IEC and the sole source in the United States of ISO and IEC publications. Catalogs listing several thousand current ISO and IEC standards are also available from ANSI.

ISO Standards

ACOUSTICS (TC 43)

ISO 3741:1999, Acoustics—Determination of sound power levels of noise sources using sound pressure—Precision methods for reverberation rooms.
ISO 7779:1999, Acoustics—Measurement of airborne noise emitte by information technology and telecommunications equipment.

IEC Standards

AUDIO, VIDEO, AND MULTIMEDIA SYSTEMS AND EQUIPMENT (TC 100)

IEC 61595-3 Ed. 1.0 b: 1999, Multichannel digital audio tape recorder (DATR), reel-to-reel system, for professional use—Part 3: 24-bit operation for 16-bit media.

ISO Draft International Standards

This section lists proposed standards that the International Organization for Standardization (ISO) and the International Electrotechnical Commission (IEC) are considering for approval. The proposals have received substantial support within the technical committees or subcommittees that developed them and are now being circulated to ISO and IEC members for comment and vote. The final dates for offering comments, listed in parentheses, are for information only. Copies of these documents are available from ANSI.

ACOUSTICS (TC 43)

ISO/DIS 5129, Acoustics—Measurement of sound pressure levels in the interior of aircraft during flight (11 December)

ISO/DIS 13472-1, Acoustics—Procedure for measuring sound absorption properties of road surfaces *in situ*—Part 1: Extended surface method (20 November 1999)

MECHANICAL VIBRATION AND SHOCK (TC 108)

ISO/DIS 5349-1, Mechanical vibration—Measurement and evaluation of human exposure to hand-transmitted vibration—Part 1: General guidelines (20 November 1999)

ISO/DIS 5349-2, Mechanical vibration—Measurement and evaluation of human exposure to hand-transmitted vibration—Part 2: Practical guidance for measurement in the workplace (20 November 1999)

ISO/DIS 6954, Mechanical vibration—Guidelines for the measurement, reporting, and evaluation of vibration in merchant ships (4 December 1999)

ISO/DIS 13091-1, Mechanical vibration—Vibrotactile perception threshold for the assessment of nerve dysfunction—Part 1: Test methods for measurement at the fingertips (4 December 1999)

IEC Draft Standards

AUDIO, VIDEO, AND MULTIMEDIA SYSTEMS AND EQUIPMENT (TC 100)

100C/246/FDIS, IEC 60958-1: Digital audio interface—Part 1: General (30 September 1999)

100C/248/FDIS, IEC 60958-3: Digital audio interface—Part 3: Consumer applications (30 September 1999)

100C/249/FDIS, IEC 60958-4: Digital audio interface—Part 4: Professional applications (30 September 1999)

BOOK REVIEWS

P. L. Marston
Physics Department, Washington State University, Pullman, Washington 99164

These reviews of books and other forms of information express the opinions of the individual reviewers and are not necessarily endorsed by the Editorial Board of this Journal.

Editorial Policy: *If there is a negative review, the author of the book will be given a chance to respond to the review in this section of the Journal and the reviewer will be allowed to respond to the author's comments. [See ''Book Reviews Editor's Note,'' J. Acoust. Soc. Am.* ***81****, 1651 (May 1987).]*

Music, Cognition, and Computerized Sound: An Introduction to Psychoacoustics

Perry R. Cook (Editor)

The MIT Press, Cambridge, 1999.
xi+372 pp.+CD-ROM (formatted for Macintosh, for Windows 95, 98, and NT, and for Unix). Price: $60.000 hardcover.

Music, Cognition, and Computerized Sound derives from a course offered by the Stanford Center for Computer Research in Music and Acoustics and so is essentially a series of lectures focusing on the psychoacoustic roots of music perception. The lecturers are John Chowning, Perry R. Cook, Brent Gillespie, Daniel J. Levitin, Max Mathews, John Pierce, and Roger Shepard. The reader who accepts that music, not classical psychophysics, provides the foundation on which the book is built will find that it holds a few things to criticize but much to admire.

For clarity and coherence, I have lumped together all of the contributions of each author instead of taking the chapters in their order of appearance.

Mathews's chapter on ''The Ear and How It Works'' starts the book. It describes accurately and in remarkably few words the transmission of sound into and through the middle ear. It covers the basics of cochlear mechanics. His following chapter on ''The Auditory Brain'' explains how transduced acoustic signals find a pathway from the hair cells into the brain, again with surprising detail and with unrivaled simplicity. He even provides the book's first discussions of pitch perception and of binaural hearing. In two later chapters, Mathews deals with measuring percepts rather than measuring physical processes. ''What is Loudness?'' begins with the early Bell Labs work that defined equal loudness contours. The sections on the measurement of equal loudness in phons and of loudness in sones should be quite helpful to a beginner, but the section on phon arithmetic is disappointingly confusing. His ''Introduction to Timbre'' deals with an interesting, complex, and highly subjective set of musical phenomena.

Pierce's chapter on ''Sound Waves and Sine Waves'' introduces the reader to basic physical acoustics. Recognizing that pure tones ''are of crucial value in understanding the nature of musical sounds,'' he moves easily from the attributes of sine waves to the vibrations of strings to the deconstruction of a complex periodic signal into its constituent sinusoids. He shows how phase shifts can affect waveforms and how one may sample a complex waveform to determine its spectrum or to record a compact disc. He even manages to provide a short and easily understood discussion of wavelets. His ''Introduction to Pitch Perception'' includes a useful historical description of musical signals with missing fundamental frequencies and of the duplex theory of hearing (which is to say of pitch perception). In ''Hearing in Time and Space,'' he brilliantly covers audition's other major theoretical question: are two ears better than one? He analyzes the basic issues of binaural masking, of the precedence effect and listening to reverberant signals, and of making auditory judgments about the space around us. Pierce returns to the acoustics of music in ''Consonance and Scales'' where he discusses the relation between critical bandwidths and harshness or dissonance. Necessarily, he also brings up mistuning (especially the purposeful octave stretching of the piano) and the beats that may arise because of it. He examines the sounds produced by struck, plucked, or clashed musical instruments and their computer simulations in ''Passive Nonlinearities in Acoustics.'' In ''Storage and Reproduction of Music,'' Pierce reminds us that ''Music does not go on forever...'' and needs to be captured if we want to hear it later. His history of capturing-techniques ranges from memorizing tunes to writing scores to programming player pianos, music boxes, vocoders, and instruments that synthesize musical sounds. And of course he deals with various current means, mostly digital, for reproducing waveforms so we can listen to them whenever we want to.

Shepard's chapter on ''Cognitive Psychology and Music'' derives from his interest in illusions, mostly visual, and mostly different from the ones we all enjoyed when we were kids. By analyzing why the illusions work, one may abstract a number of organizing principles that apply to auditory perception. From those principles, Shepard infers bases for our abilities to judge room size, for example, or to recognize the nature of a sound source even in a reverberant space, or to select a single signal from a complex group of signals. In ''Stream Segregation and Ambiguity in Audition,'' he carries the idea of organizing principles further by considering circumstances in which they fail. The chapter on ''Pitch Perception and Measurement'' returns momentarily to classical psychophysics for a description of just noticeable differences and the development of the mel scale of pitch. But because the mel scale is nonmusical, because musical concepts such as fifths and especially octaves are so pervasive, and because some pitch-perception experiments result in musical scales instead of mel scales, Shepard spends most of his time not on conventional theories of pitch perception but on musical pitch, including its representation by helical models, and on examples of ambiguous melodies. He continues along the same line in ''Tonal Structure and Scales'' in which he says that experiments on musical tones in musical contexts are ''aimed at a measurement of musical sensibility rather than a traditional, purely objective, psychoacoustic measurement.'' Those who believe that nonobjective measurement leads to dubious data may have trouble accepting that these results are particularly valuable. Still, studies of dissimilar musical scales in diverse cultures seem to point to some innate constancies, and that possibility urges further experimentation.

Cook is particularly concerned with the acoustics of vocalization. His chapter ''Voice Physics and Neurology'' introduces vocal resonance and articulation structures, provides an understandable definition of *formant*, and sketches some of the brain's speech-analysis structures. In ''Formant Peaks and Spectral Valleys,'' he looks at vocal tract variations that modify vowels and that produce the kind of sound that permits trained singers to be heard over the playing of a 100-piece orchestra. Much of the chapter on ''Articulation in Speech and Sound'' derives from and expands on Harlan Lane's motor theory of speech. This theory proposes that in order to understand speech, listeners replicate (either in fact or in memory) the movements that created it. The concept is especially intriguing because it suggests that the speech signal alone may not provide the information required for accurate speech understanding. Cook then presents related ideas about the role of expectation in perception and of listeners choosing to hear easy-to-speak sounds even when the actual utterance is something more difficult. ''Pitch, Periodicity, and Noise in the Voice'' provides a segue from speech acoustics to singing acoustics. It opens with the marvelously clever question, ''Isn't Singing Just Strange Speech?'' which Cook approaches by spelling out some of the differences (such as pitch, vibrato, and spectral structure) between spoken and sung phrases. He also reminds us that aperiodicity and noise are normal elements of natural musical instruments including the voice, a fact that may help us distinguish them from synthesized instruments.

Chowning's ''Perceptual Fusion and Auditory Perspective'' provides a beautifully reasoned explanation of how performer/instrument imperfections provide the cues listeners need in order to judge what sort of instrument (including the voice) produced a sound, how many sources they are hearing, and how far away those sources are. The spectral components of perfect, nonvarying signals all blend together into featureless sounds whose charac-

 0001-4966/2000/107(1)/21/2/$17.00

ter is inherently impossible to guess. Only when a series of partials is wobbled (in pitch or loudness or both) as a group does the signal source become identifiable. Only when one series of partials is wobbled as a group while another series is wobbled differently but as a group does a signal split into two identifiable sources. And so on. A trained musician's superimposition of vibrato or tremolo enhances the effect. The question underlying Chowning's distance-perception discussion is intriguing: a loud singer stands at a distance; a quiet singer nearby produces a higher signal level at the ear; so how does a listener figure out that the distant one is singing more loudly? Experimental data confirm the intuitive answers: experience has taught us the nature of spectral changes with distance and the amount and nature of reverberation in near and distant signals. The next step is likely to be the application of these concepts to computer-generated musical sounds.

Gillespie's two interesting chapters on the senses of touch and kinesthesia, ''Haptics'' and ''Haptics in Manipulation,'' seem a bit out of place in a book on the acoustics and perception of music. However, he makes the case that a significant portion of a performer's feedback arises from palpating the instrument—from feeling its behavior with fingers or lips. His historical narrative runs from Aristotle through James Gibson and extends into current research and understanding. He details the uses of various aspects of touch in controlling mechanical and, by extension, mechano-acoustical devices. The chapters are well written and educational, but after readers finish them, they will still wonder why they are in a book on the acoustics and perception of music.

The first quarter of Levitin's ''Memory for Musical Attributes'' is a tutorial on the types and dimensions of memory. Like Gillespie's chapters on haptics, this section is interesting and easy to understand but not especially pertinent. The rest of the chapter, though, is quite pertinent. It covers every facet of memory for music. And its conclusions are based on careful experiments. People remember lyrics, melody, pitch, and tempo with surprising accuracy. Recalling the words to a song may seem easy until one realizes that some singers know thousands of lyrics. The data on pitch memory show that absolute pitch is not so rare as commonly believed but that it is often unrecognized even by the person who possesses it. Most people are very good at remembering tempos also without being aware that they are. Experiments on memory for timbre and loudness are already being done.

Levitin's ''Experimental Design in Psychoacoustic Research'' is amazing. It covers the subject completely yet with perfect simplicity and ought to be required reading for every beginner in any field of research.

Appendices include thought problems for students to consider and explore as well as suggestions for laboratory exercises.

A few minor complaints: Cook talks about ''perfect pitch'' where many prefer the term *absolute pitch* because of its contrast with *relative pitch.* Shepard confuses additive with subtractive color mixing. Pierce equates a hundredth of a semitone with a thousandth of an octave. Mathews talks about ''roughness'' not as the percept associated with frequency differences slightly greater than those that create beats but as a percept associated with some dissonances. Chowning's chapter opens with an unforeshadowed and unexplained homage to the one-named composer Ligeti; it only makes sense when the reader discovers in a footnote that the chapter was ''First authored...for Ligeti.'' Levitin's first chapter includes ''...environment of the the brain... .'' The lab-exercise appendix includes the definition $\log I = \log A2 = 2 \log A$ instead of $\log I = \log A^2 = 2 \log A$. The reference lists are quite variable: a couple are comprehensive and most are good, but some are sketchy and a few are very sketchy. A CD-ROM comes packaged with the book, but exploring it is confusing. The only files that my computer could see have either .c, .orc, or .sco extensions. These extensions are somewhere between difficult and impossible for a lot of people to use; that includes many students and me. And neither the CD-ROM nor the book contains any instructions. Only through frustration-driven experiment or lucky accident might one stumble onto the fact that activating the computer's music-CD player provides access to 80 sound samples that illustrate portions of the text. Except for the problem of figuring out how to use the CD-ROM, the complaints on this list are really trivial, but they all suggest careless editing.

The book's virtues are many, its authors include the people who created the ground floor over which computer music has been built, and the text is both interesting and informative.

JERRY V. TOBIAS
6 Huntington Way
Ledyard, Connecticut 06339

A time domain rough surface scattering model based on wedge diffraction: Application to low-frequency backscattering from two-dimensional sea surfaces

Richard S. Keiffer
Naval Research Laboratory, Code 7181, Stennis Space Center, Mississippi 39529-5004

Jorge C. Novarini
Planning Systems, Inc., 21294 Johnson Road, Long Beach, Mississippi 39560-9702

(Received 21 September 1998; revised 30 June 1999; accepted 16 September 1999)

A time domain method for calculating the acoustic impulse response of impenetrable, rough, two-dimensional (2D) surfaces is presented. The method is based on an extension of the wedge assemblage (WA) method to 2D surfaces and objects. Like the WA method for one-dimensional (1D) surfaces, the approach for 2D surfaces uses Biot's and Tolstoy's exact solution for the impulse response of an infinite impenetrable wedge [J. Acoust. Soc. Am. **29**, 381–391 (1957)] as its fundamental building block. The validity of the WA method for backscattering from 2D sea surfaces is assessed through comparisons with calculations based on Milder's operator expansion (OE) method [J. Acoust. Soc. Am. **89**, 529–541 (1991)]. Average intensities for backscattering from 2D fully developed seas (20 m/s wind speed) were computed by the WA and OE methods using 50 surface realizations and compared at 11 frequencies between 100 and 200 Hz. A single, moderately low grazing angle of incidence (20°) and several scattered grazing angles (90°, 45°, 20°, and 10°) were considered. Excellent overall agreement between the two models was obtained. The utility of the WA method as a tool to describe the physics of the scattering process is also discussed. [S0001-4966(00)04001-7]

PACS numbers: 43.20.Fn, 43.30.Hw [DLB]

INTRODUCTION

In the past and recent literature, one can find a large number of papers that have as their main topic the modeling of acoustic scattering from randomly rough surfaces. In nearly all of the published works on this subject, a time harmonic source is assumed and, usually after some approximation [still a computational necessity for large two-dimensional (2D) surfaces], the continuous wave (cw) solution for the scattered field is obtained. On the other hand, only a few papers address the solution of the transient acoustic scattering problem and even fewer proceed *directly* in the time domain.

The primary goal of this paper is to describe and test a model that helps to fill this particular gap in the literature. This model uses Biot's and Tolstoy's (BT) exact solution for the impulse response of an infinite impenetrable wedge[1] to construct an estimate for the impulse response of more complicated surfaces. Its application to scattering from 2D surfaces has been described previously in Ref. 2 and more recently in Ref. 3 where it was shown to be accurate for monostatic backscattering at moderate grazing angles (30°) from single realizations of 2D sea surfaces. In the current study, the ongoing assessment of the WA model is extended down to fairly low grazing angles (10°) and to rougher sea surfaces (20 m/s winds).

The idea of calculating the (finite) impulse response of a surface or an object by applying the BT solution to an assemblage of wedges that model the shape of the scatterer has been around for some time now. It is known as the wedge assemblage (WA) method. In its original form[4,5] for one-dimensional (1D) surfaces, the full BT solution was applied, essentially without modification, to an assemblage of long-crested (infinite apex) wedges that modeled the deterministic surface of interest. In the 17 years or so since the basic ideas for the WA method were formulated, several papers have been published[5–12] in which the WA model for 1D surfaces was compared with other model results, experimental data, or exact numerical solutions. In all cases, favorable results were reported which, considered in total, strongly supports the heuristic basis for this kind of modeling.

To extend the WA method to 2D surfaces, the application of the BT solution is modified in order to account for the fact that assemblage of wedges modeling the surface are truncated and no longer have infinite apexes. The accuracy of the WA method for 2D surfaces has been evaluated in studies involving scattering from 2D sea surfaces[3], hard and soft thin disks,[13] and spheres.[14] In these last two studies, through comparisons with a highly accurate numerical solution based on a *T*-matrix formulation,[15] it was found that the 2D WA method was stable and accurate even for extremely short wedge apexes. It was also clearly established in the disk study[13] that, as first proposed by Medwin,[7] multiple scattering effects could be accurately included in the WA method through successive time domain applications of Huygens' principle. In fact, the successive time domain application of Huygens' principle leads to a series of WA solutions approximating increasing orders of multiple scattering. This makes the WA method one of the few approaches that can, in principle, unambiguously address fundamental questions concerning the relative roles of multiply scattered contribu-

tions. In practice, computational constraints will probably limit this capability, even to ambitious programmers, to double scattering. Typically, as in this paper, the implementation of the WA approach is limited to single scattering.

The paper is organized as follows: in Sec. I a review of the wedge assemblage method is presented with particular attention paid to its application to rough 2D sea surfaces. Next follows a brief description of the recently developed (cw) method[16] that was used to generate the reference solutions for this study. It should be noted that for the very large scattering problems that are used in this study there are currently no true benchmark solutions available in the time or frequency domain. However, the second order solution obtained from Milder's operator expansion (OE) method has been shown for 1D sea surfaces to be quite accurate in predicting the average scattered intensity except very near grazing.[17] In Sec. III, results for the average backscattered intensity derived from the WA and OE models are compared and discussed. Finally, in Sec. IV, a couple of examples are given that demonstrate the utility of the WA model for describing the physics of the scattering process.

I. THE WEDGE ASSEMBLAGE MODEL

The concept of modeling the impulse response of a rough, complicated surface as the linear superposition of the responses from an assemblage of simpler shapes can be traced back to Trorey.[18] Basically Trorey's idea was to apply a Laplace transform to the Rubinowitz representation of the Kirchhoff diffraction integral[19] to obtain the impulse response of an infinite strip. The impulse response of a rough 1D surface could then be calculated from an assemblage of infinite strips ''fit'' to the surface. Clay[20] first applied this idea to ocean bottom scattering and later Novarini and Medwin[21] used it in a study of sea surface backscattering. Although this approach suffered from the limitations inherent to the Kirchhoff approximation, the idea of building up the impulse response directly in the time domain from basic scatterers survived. At the suggestion of Clay,[22] the building block of the calculation method was switched to the BT exact solution for the impulse response of an infinite, impenetrable wedge.

The Biot–Tolstoy solution assumes a point source and receiver, which may be arbitrarily located, and allows any wedge angle. The solution consists of two temporally distinct terms that have been interpreted as the impulsive reflection(s) from the wedge faces (these arrive first, if they exist) and the diffracted wave emitted from the wedge apex. The process of manipulating these two components to construct the impulse response of a more complicated surface defines the WA model. As we shall now discuss, the reflected and diffracted terms of the BT solution need not play equal roles. In fact, the very existence of the facet reflected component in WA method depends entirely on whether the surface being modeled (not the sampled version of it) actually has any finite-size flat facets from which to reflect. The following examples help to illustrate this point.

Consider first a surface like a sinusoid that is continuously curved everywhere on the surface. Clearly, the concept of an impulsive facet reflection does not apply to such a surface precisely because a continuously curved surface does not have any flat facets from which to reflect. If we include the phenomena of facet reflection in the WA modeling of the scattered response of such a surface then we will be including a phenomenon that does not actually occur. Consequently, the WA estimate for the impulse response of such a surface, regardless of the scattering geometry, is constructed from the apex-diffracted component alone. This modeling assumption was tested through demanding comparisons with exact numerical solutions for scattering from sinusoidal surfaces.[12] In those studies, the diffraction-only hypothesis was found to be completely valid, yielding excellent results over a broad range of scale kh (k is the acoustic wave number, h is the amplitude of the sinusoid). In particular, in the sinusoidal study it was shown that the diffraction-only WA model gave the correct results in the specular direction for $kh \ll 1$. In other words, it modeled correctly the reflectionlike response of a nearly flat surface. The reason for this result is simple: a reflection from a flat surface can be regarded as the limiting case of specular diffraction from a nearly flat wedge. In the case of the sinusoid, as the surface roughness becomes smaller, all the wedge angles approach π (i.e., flatter) and the diffractions from wedges on the surface become increasingly impulsive and directional, peaking strongly in the nominally specular direction of the mean ($\langle z \rangle = 0$) surface.

Now consider the problem of calculating the axial impulse response of a disk.[13] In this case, both the reflection from the flat interior and the diffraction from the edges of the disk are required to accurately model the impulse response. On the other hand, to calculate the axial impulse response of a sphere[14] only the diffracted component is used in the modeling. Again, this is because the scattering surface is continuously curved. For the simulated sea surfaces that are the subject of this paper, only the diffracted component is used to construct the impulse response. Although specified on a finite resolution grid, these sea surfaces should be regarded as having roughness at all scales. Like the continuously curved surfaces, they do not have any finite size flat facets from which to reflect. Thus the WA modeling of the scattering from surfaces presumed to have roughness at all scales only includes diffractions from the wedge apexes. As we shall see shortly, the results achieved by the WA model operating under this assumption clearly support this modeling approach.

Under the assumption that we need only consider the role of the diffracted component, the application of the Biot–Tolstoy solution to 1D rough surfaces becomes quite straightforward. A deterministic 1D surface specified on a uniform grid naturally decomposes into a collection of infinite strips or ''long'' rectangular facets. This collection of facets can be thought of as a collection of wedges; at every grid point two facets intersect and define an infinitely long wedge apex. The BT solution for the diffracted wave is then applied to each wedge and all of the individual responses are summed, with due respect to their time of arrival, to produce the impulse response of the entire surface.

In the development of a WA model for 2D deterministic surfaces, triangular shaped facets are used to model the shape of the surface. This results in an assemblage of wedges that

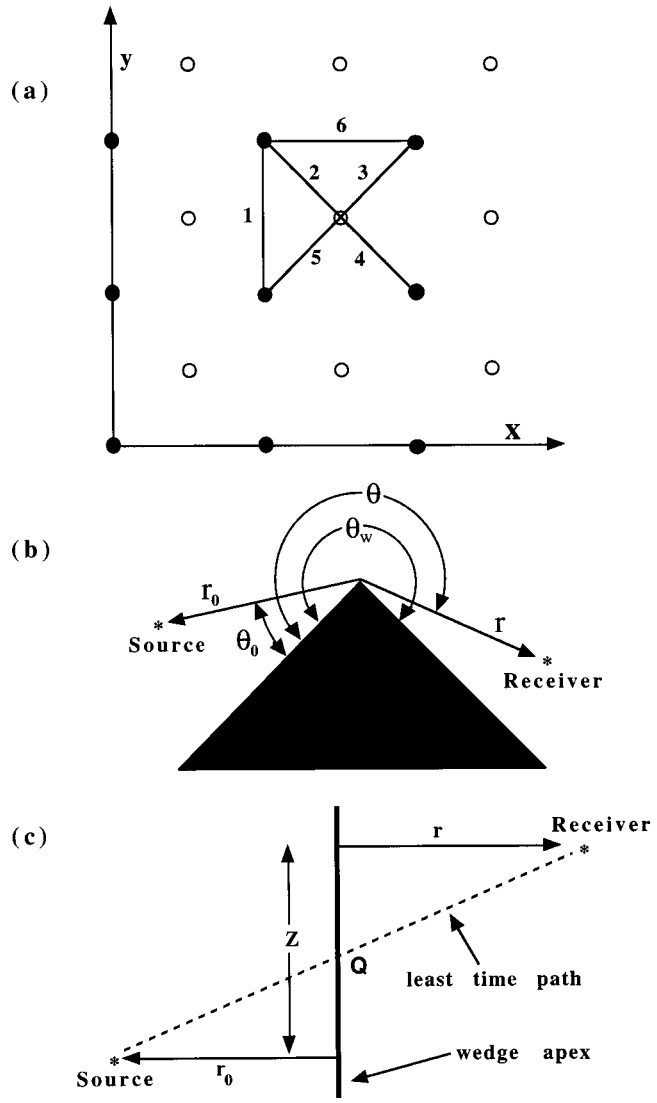

FIG. 1. (a) The unit cell and the six wedges that comprise it. Open circles represent the original grid on which the surface is defined. Closed circles represent grid points where interpolated values are defined. (b) and (c) Side and top views respectively of the geometry for the Biot–Tolstoy solution.

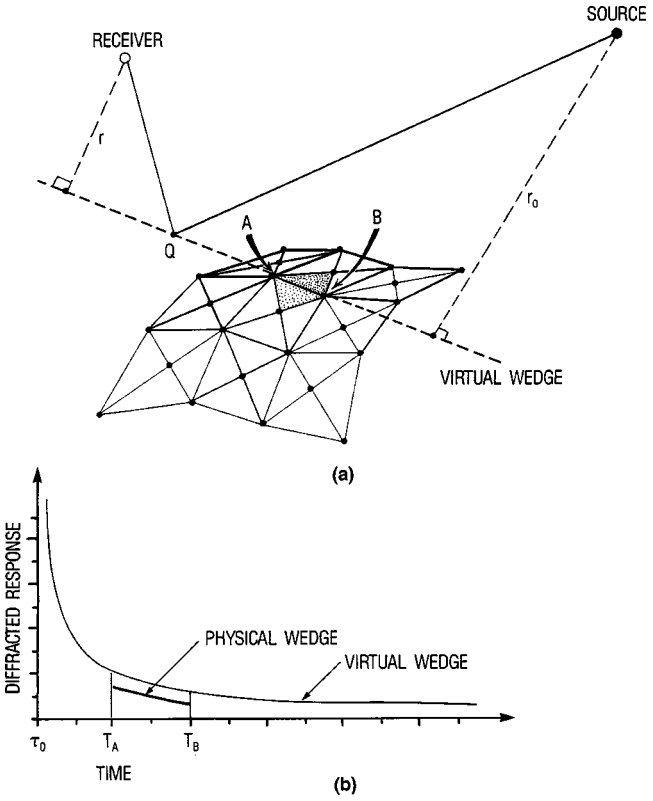

FIG. 2. The decomposition of a 2D surface into triangular facets. In part (a), the line segment **AB** represents a finite-length wedge apex (''the physical apex''), the dotted line containing **AB** represents the associated infinite wedge apex (''the virtual apex''). The least time point, *Q*, is the location on the wedge apex that yields the shortest source to apex to receiver travel time. In part (b), the diffracted response of the asymmetric segment **AB** is shown schematically to exist between times T_A and T_B and have half the amplitude of the associated infinite wedge.

have finite-length apexes. Consequently, a modification to the straightforward application of the BT solution for the diffracted wave is required. In the current implementation, under the assumption that the 2D rough surface is defined on a uniform grid ($\Delta x = \Delta y = \text{constant}$), the triangular facets that model the surface are specified as follows. First, as shown in part (a) of Fig. 1, a square unit cell can be defined from four grid points. The coordinates or indices of the upper left grid point can specify the location of the unit cell. At the center of each unit cell, a surface height is estimated (interpolated) from the average of the four surrounding grid values. With this interpolated point, the unit cell defines six wedges. The calculation of the impulse response of a surface reduces to calculating and accumulating the responses of all the unit cells that make up the surface.

Now consider Fig. 2 which shows a grided surface decomposed into triangular facets. Note that for each finite-length wedge apex one can imagine an infinitely long apex (having the same wedge angle) that passes through it. For convenience, we shall refer to the finite-length wedge apex as the *physical apex* and the imaginary, infinitely long apex that passes through it as a *virtual apex*. Whereas an infinite-length wedge apex has an infinitely long impulse response, a segment of it, i.e., the physical apex, can only respond (in the single-scatter approximation) for a finite length of time. In the example shown in Fig. 2, the time interval over which the physical apex has a response is $[T_A, T_B]$. The central assumption involved in the extension of the WA method to 2D surfaces is that, in the time interval that a physical apex can have a response, that response is proportional to the response of the associated virtual apex. This hypothesis for calculating the diffraction from a truncated wedge apex was first proposed by Medwin[5] who, by terminating the response of the BT solution, was able to fit and explain experimental scattering data from finite 2D objects. Medwin's hypothesis was put through demanding numerical tests in the WA studies of scattering from disks[12] and spheres[13] and found to hold in all cases.

Concerning the relationship of the diffracted response of the physical apex to that of its associated virtual apex, note the following: after the initial arrival of the diffracted wave, the diffraction is due to points on the wedge apex that are symmetric in time about the least time point [point *Q* Fig. 2 part (a)]. Therefore, if a physical apex is a segment of a virtual apex, and that segment is not symmetric about the

least time point, then the diffracted response of that physical apex is one-half of the time-gated response of the virtual apex. This is the case in the example shown in Fig. 2, where the physical apex defined between points **A** and **B**, does not contain the least time point *Q*. In this case the impulse response for this physical wedge is one-half of the full BT diffracted response [see part (b) of Fig. 2]. Of course it may happen that a physical apex has both symmetric and asymmetric parts. This will occur whenever the least time point (*Q*) is not at the center of the physical apex. In that case the computer code implementing the WA method can split the calculation of the wedge response into symmetric and asymmetric parts.

The impulse response of the entire scattering patch (which it may be assumed is defined on a grid having dimensions $m \times n$) as detected at a receiver located by $\mathbf{R}_R$ and due to a point source located by $\mathbf{R}_S$, is obtained by adding, with due respect to arrival times, the individual diffracted responses ($P_{\delta_{ijk}}$) of all the wedges:

$$P_{\text{scat}}(\mathbf{R}_R,t)=\sum_{i=1}^{m}\sum_{j=1}^{n}\sum_{k=1}^{6}\epsilon_{ijk}P_{\delta_{ijk}}(\mathbf{R}_S,\mathbf{R}_R,t). \tag{1}$$

Here i and j are the indices identifying the location of the upper left-hand corner of the unit cell and k labels the wedge number within the cell [see Fig. 1 part (a)]. The factor ϵ_{ijk} is either 1.0 or 0.5 depending on whether or not the physical wedge is symmetric about the least time point. Not indicated in Eq. (1) is the possibility that in some cases ϵ_{ijk} changes value from 1.0 to 0.5 along a single apex. This special case may arise because a single wedge apex can have both a symmetric and an asymmetric part. As previously mentioned, the computer code used for this paper does include the ability to split a wedge apex into symmetric and asymmetric parts as necessary. For a rigid wedge (Neumann boundary condition) the part of the BT solution that describes the apex diffracted wave, assuming a point source consisting of a Dirac delta function of volume flow ($\dot{V}$) at $t=0$, is given by

$$P_\delta(t)=\left(\frac{-\dot{V}\rho c}{8\pi\theta_w}\right)[rr_0\sinh(\eta)]^{-1}\times[D_{++}+D_{--}+D_{+-}+D_{-+}]. \tag{2}$$

In terms of measurable parameters for an impulse of pressure P_0, of duration Δt, at source range R_0, $\dot{V}$ is given by[3]

$$\dot{V}=\frac{4\pi P_0 R_0 \Delta t}{\rho}. \tag{3}$$

Along with the apex-diffracted component, the full BT solution includes all possible reflection(s) from the faces of the wedge. As we have already argued, the reflected component does not play a role in the WA modeling of the rough multiscale surfaces to be considered later.

Returning to Eq. (2) for pressure-release surfaces, the Biot–Tolstoy solution for the diffracted wave is the same except for a change of sign on the D_{++} and D_{--} terms. In both cases,

$$\eta=\cosh^{-1}\left[\frac{c^2t^2-(r^2+r_0^2+Z^2)}{2rr_0}\right], \tag{4}$$

and the terms D_{++}, D_{--}, D_{+-}, and D_{-+} are given by

$$D_{\pm\pm}=\frac{\sin\left[\frac{\pi}{\theta_w}(\pi\pm\theta_0\pm\theta)\right]}{\cosh\left[\frac{\pi\eta}{\theta_w}\right]-\cos\left[\frac{\pi}{\theta_w}(\pi\pm\theta_0\pm\theta)\right]}, \tag{5}$$

where the sign in the first subscript corresponds to the sign preceding θ_0 and the sign of the second subscript corresponds to the sign following θ_0. In Eq. (2), $\dot{V}$ is the source strength in units of $\text{m}^3\,\text{s}^{-1}$, c is the sound speed, and ρ is the density of the exterior medium. The variables r_0 and θ_0 locate the source and r and θ locate the receiver in the local wedge coordinate system [see Fig. 1(b) and (c)]. θ_w is the wedge angle measured in the exterior medium and Z is the offset distance along the wedge apex between perpendiculars drawn, respectively, from the source and receiver to the wedge apex. Note that, due to the term, $[\sinh(\eta)]^{-1}$, the diffracted response is singular when it first arrives at time t_0,

$$t_0=\frac{\sqrt{(r+r_0)^2+Z^2}}{c}. \tag{6}$$

To generate the sampled or finite impulse response at discrete time intervals given by $t_n=t_0+(2n+1)*\Delta t/2$; $n=0,1,2,3,...$, the mean value of the diffracted wave is calculated over a Δt time interval centered about the time of interest. For example, the first sampled value of the impulse response, which captures the initial arrival of the diffracted wave, is given by

$$\left\langle P_\delta\left(t_0+\frac{\Delta t}{2}\right)\right\rangle=\frac{1}{\Delta t}\int_{t_0}^{t_0+\Delta t}P_\delta(t)\,dt. \tag{7}$$

The singularity that occurs when the diffracted wave first arrives is integrable so Eq. (7) can be computed by a wide variety of existing numerical integration algorithms.

In the single-scatter approximation (which is adopted for this study), wedge apexes that are geometrically shadowed with respect to the source or receiver are not allowed to contribute to the received impulse response. Causality dictates that these shadowed apexes can contribute to the received signal only if multiple scattering is considered. In this view, geometric shadowing with respect to the source or receiver is inherent to the single-scatter term of the impulse response. Similarly, geometric shadowing by parts of the surface with respect to other parts of the surface is inherent to the higher order terms of a multiple scattering expansion of the impulse response. Therefore, in this context, geometric shadowing is not regarded as an additional approximation but may be part of every term of an expansion of the complete impulse response in terms of higher order scattering interactions. This treatment is self-consistent and distinct from the more familiar case (in the frequency domain) of geometric shadowing under the Kirchhoff approximation. There, geometric shadowing is regarded as a high frequency approximation, the theoretical validity of geometric shadowing is not at all clear,[23] and the main justification is based on

the fact that it approximately compensates for an energy excess in the Kirchhoff predictions at low grazing angles.

II. THE REFERENCE SOLUTION

As the reference solution we have adopted the operator expansion (OE) method developed by Milder.[16] Specifically, we have implemented the first and second even order terms of the inversion-symmetric form of the operator expansion hereafter labeled OE0 and OE2, respectively [for details see Eqs. (17) and (18) of Ref. 24]. Kaczkowski and Thorsos[17] have carried out a detailed analysis and testing of the OE2 solution against an integral equation technique for 1D surfaces assuming a Pierson–Moskowitz sea surface roughness spectrum. They considered the scattered field averaged over an ensemble of surfaces and found that (for wind speeds up to 20 m/s and for incident grazing angles down to 10°) the OE2 estimation for the scattering cross was accurate over all scattering angles except very near grazing. Among the conclusions of this study was that the rapid convergence of the OE series solution and its accuracy was expected to carry over to scattering from 2D randomly rough surfaces. Previously, for doubly periodic 2D eggcrate surfaces, it was shown through comparisons with exact solutions[24] that the accuracy of the OE solutions remained essentially unchanged by the added dimension of the problem. In the present work we have followed the Milder and Sharp prescription for implementing the second order formalism, replacing plane waves by spherical waves to handle finite source and receiver distances.

III. MODEL COMPARISONS

A. General remarks

In this section the accuracy of the wedge assemblage method for calculating the average total scattered intensity is examined for backscattering from modeled 2D sea surfaces driven by a 20 m/s wind speed (at 10 m height). Due to the huge computational burden of calculating ensemble averages for the full 3D scattering problem, the current study is limited to a single angle of incidence (20° grazing) and four backscattering directions (10°, 20°, 45°, and 90° grazing). For each geometry, the average scattered intensity is calculated from 50 surface realizations and compared at 11 evenly spaced frequencies between 100 and 200 Hz. For both models, the average scattered intensities were normalized by the image intensity which, holding $|\mathbf{R_R}|$ constant, is the intensity of the specular reflection from a flat surface of infinite extent. Grazing angles of incidence below 20° were not considered because this would require special computational precautions (padding with zero's and doing 2D FFTs that are 4 to 8 times larger) in order to maintain the accuracy of numerical estimates from the reference solution and this would increase the computational burden beyond the limits of this study. For similar reasons, scattered grazing angles below 10° are not considered.

Assuming a right-handed Cartesian coordinate system, the scattering geometry is defined by $\mathbf{R_S}$ and $\mathbf{R_R}$, the vectors drawn form the origin to the source and receiver locations, respectively. It is assumed that the center of the scattering surface is located at the origin of the coordinate system. The source radiation is incident from above and from the left ($x_S<0$, $y_S=0$, $z_S>0$) and the source and receiver distances are always equal, $|\mathbf{R_S}|=|\mathbf{R_R}|=50$ km unless otherwise noted, and large compared to the length of the scattering patch (1256 m). The fact that the scattering geometry is inverted with respect to an actual experiment conducted at sea is inconsequential because the modeled sea surfaces used ''look'' the same when viewed from above and from below. The direction of the insonification is into the windward direction of these 2D numerical sea surfaces and the azimuthal separation between source and receiver directions is zero. The sound speed in the half space above the rough surface is 1500.0 m/s.

In the usual manner, a taper function has been applied to the incident field in order to reduce the scattering from the truncation of the numerical sea surfaces. This insonification function is given by

$$A(x,y)=\exp\left[-36\left(\frac{x^2+y^2}{L^2}\right)\right], \quad x^2+y^2\leqslant L^2, \tag{8}$$

where L is the diameter of the largest circle that can fit on the surface. Outside of this circle the taper function is set to zero. With this insonification function, the intensity of the incident field at the edges of the surface is at least 78 dB down relative to the intensity at the center of the surface. For all scattering geometries considered, calculations (not shown) of the scattering from an identically insonified flat surface were used to verify that the diffractions from the surface truncation were much smaller than the scattering from the surface roughness. It should also be noted that the diameter of the circular area insonified with amplitude greater than half the peak value was approximately 2–3 surface correlation lengths. This ensures that the insonified surface is large enough to capture the effect of the longest waves on the statistics of the scattered field.

Although in principle a reference solution for the impulse response of a particular rough surface could be calculated from a series of accurate cw solutions, in practice there are several considerations that make this route toward validating the WA model an unattractive one. First, inevitably the frequency series calculated by the OE method or any other cw reference solution must be truncated. Truncation in the frequency domain gives rise to the well-known Gibbs phenomena[25] in the time domain. By performing the model comparisons in the frequency domain, the effects due solely to the truncation of the Fourier transform are not introduced into the *reference* solution. The effects of truncation of the time series, on the other hand, are not nearly so severe since the surfaces are finite and the insonification function applied to the incident field causes the beginning and end of the time series to ramp down to small values. Of course the WA method actually yields an estimate for the sampled or finite impulse response. Consequently it sufferers from aliasing effects which can be minimized in the frequency range of interest by sampling (i.e., calculating) the impulse response at a sufficiently short time interval. The second and perhaps more compelling reason to perform the comparisons in the

frequency domain is that the overall computational costs of the comparisons are significantly lower.

At this point, a few comments are in order concerning the modeled 2D sea surfaces that are used in this study. First, these numerical sea surfaces are the result of linear filtering random numbers having a Gaussian probability density function (PDF) of surface heights. Therefore, these modeled surfaces differ from real sea surfaces which result from nonlinear processes and do not have a truly Gaussian PDF. The details on how they are different are relatively unimportant since the comparisons we wish to make are not at all affected by the limitations of the sea surface modeling. Appendix A contains a complete description of the surface modeling process. The surfaces that were used in the current study have roughness power spectra compatible with fully developed seas as described by the (nondirectional) Pierson–Moskowitz[26] spectrum with a wave number independent cosine-squared azimuthal dependence (for details see the Appendix). Unless specified otherwise, the wind speed used was 20.0 m/s at 10 m above the sea surface and the surfaces generated employed 1024×1024 points with $\Delta x = \Delta y = 1.227$ m. Over the frequency band from 100 to 200 Hz the product of the acoustic wave number times the rms roughness ($k\sigma$) varied from 1.06 to 2.12.

Concerning requirements on the grid resolution, for backscattering perturbation theory[27] can be used to place an upper limit on the spectral information that needs to be included in the numerical surfaces. Assuming incident plane waves and a distant receiver, and given the highest acoustic wave number of interest ($k_{\max}$), the grid resolution of the surface must be such that surface components up to highest resonant (Bragg) wave number, $K_{\text{Bragg}} = 2.0k_{\max}\cos(\theta_g)$, are modeled. We have assumed a ''worst case'' scenario regardless of the grazing angle in the backscattering geometry and specified the surfaces with grid resolutions that exceed the criterion $K_{\max} = 2.0k_{\max}$.

B. Model comparisons

Comparisons between the WA and OE2 solutions for the average (image normalized) backscattered intensity are shown in Fig. 3. The 2D sea surfaces used were due to a 20 m/s wind, the angle of insonification was 20° grazing and the comparisons are shown for scattered angles of 90°, 45°, 20°, and 10° grazing. There is zero azimuthal separation between source and receiver directions, the incident and scattered wave vectors being in the same plane as the wind vector. Because of the relatively high frequency resolution of the transformed time series, the WA results are depicted as a continuous curve. For both models, the mean scattered intensities were derived from the same 50 surface realizations. This resulted in a calculated standard deviation of the mean that varied somewhat with frequency and grazing angle. In all cases, the mean plus one standard deviation and the mean minus one standard deviation resulted in scattering levels (in dB) that differed from the mean scattering levels by ±0.4 to ±0.8 dB.

With regard to the model comparisons, it can be seen from Fig. 3 that the WA model is in excellent agreement with the OE2 calculation at 90°, 45°, and 20° grazing. For

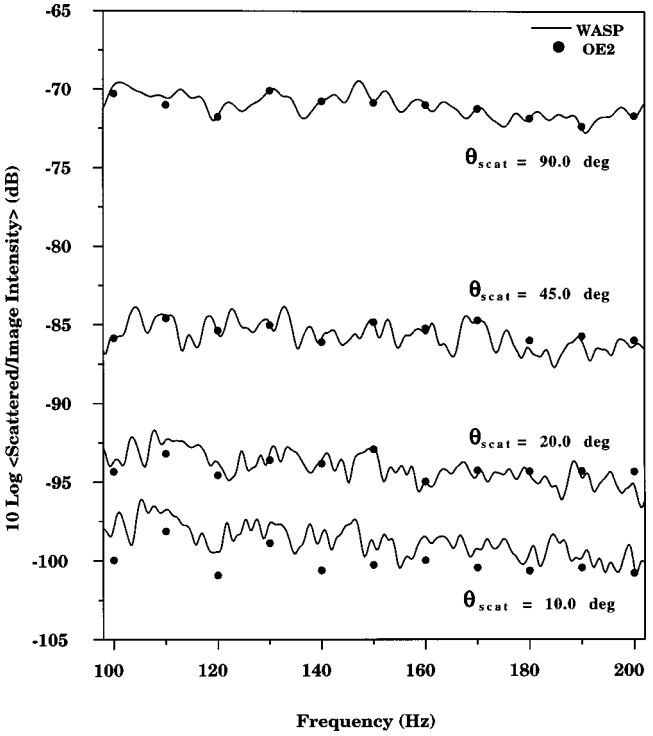

FIG. 3. Average scattered intensities predicted by the WA (solid line) and OE2 (dots) models for backward scattering from 2D fully developed seas due to a 20 m/s wind. The angle of insonification is 20° grazing and the scattered angles are (a) 90, (b) 45, (c) 20, and (d) 10° grazing. The incident and scattered wave vectors are in the same plane as the wind direction. Both the WA and OE2 calculations for the scattered field were normalized by the same image response.

these higher scattered angles, the differences between the WA and OE2 calculations were sometimes positive, sometimes negative, but always small (see Table I). The maximum differences in the estimated average intensities (⟨OE2⟩–⟨WA⟩) were −0.5, 0.5, and 0.9 dB respectively. For these three scattering angles, the difference between the WA and OE2 calculations, averaged over the 11 frequencies compared, was less 0.1 dB. This level of agreement is significant in light of the fact that similarly calculated differences between the mean scattering levels estimated by the OE2 and

TABLE I. Differences (dB) in the average backscattered intensities predicted by the WA and OE2 models. The 50 sea surfaces used in the study were 2D, fully developed, and due to a 20 m/s wind. The angle of insonification is 20° grazing.

Freq. (Hz)	$\theta_{\text{scat}} = 90°$ ⟨OE2⟩–⟨WA⟩	$\theta_{\text{scat}} = 45°$ ⟨OE2⟩–⟨WA⟩	$\theta_{\text{scat}} = 20°$ ⟨OE2⟩–⟨WA⟩	$\theta_{\text{scat}} = 10°$ ⟨OE2⟩–⟨WA⟩
100	−0.52	−0.15	−0.65	−2.07
110	−0.45	−0.17	−0.88	−1.39
120	−0.01	0.16	−0.80	−1.48
130	−0.05	−0.12	−0.44	−1.29
140	−0.02	−0.21	−0.22	−2.30
150	−0.12	−0.03	−0.04	−1.36
160	−0.05	0.35	0.12	−1.49
170	−0.05	0.02	0.27	−1.21
180	0.03	0.52	0.22	−1.15
190	0.11	0.33	0.43	−0.63
200	0.08	0.36	0.87	−0.32

TABLE II. Differences (dB) in the average backscattered intensities predicted by the OE2 and OE0 models. The 50 sea surfaces used in the study were 2D, fully developed, and due to a 20 m/s wind. The angle of insonification is 20° grazing.

Freq. (Hz)	$\theta_{scat}=90°$ $\langle OE2\rangle-\langle OE0\rangle$	$\theta_{scat}=45°$ $\langle OE2\rangle-\langle OE0\rangle$	$\theta_{scat}=20°$ $\langle OE2\rangle-\langle OE0\rangle$	$\theta_{scat}=10°$ $\langle OE2\rangle-\langle OE0\rangle$
100	0.81	1.00	1.36	1.65
110	0.76	0.82	1.88	1.33
120	0.74	1.04	0.92	1.22
130	0.99	0.90	1.40	1.48
140	0.79	0.80	1.03	1.48
150	0.70	0.79	1.31	1.48
160	0.78	0.91	1.53	1.69
170	0.81	1.01	1.54	1.19
180	0.77	0.89	1.64	1.80
190	0.72	0.99	1.62	1.84
200	0.89	0.79	1.53	1.90

OE0 solutions (averaged over the same 11 frequencies) are larger at all scattering angles and grow with decreasing grazing angle from 0.8 dB at 90° to 1.6 dB at 20°.

The comparison between the WA and OE2 models for the scattered angle of 10° is very interesting for two reasons: First, unlike the other angles, here the WA model consistently calculates a slightly higher scattering level than does the OE2 model. The difference between the WA and OE2 calculations, averaged over the 11 frequencies compared, increases from 0.1 dB (at 90°, 45°, and 20°) to 1.3 dB at 10°. Second, for this scattered angle, additional scattering phenomena come into play since 10–11 % of each surface realization is geometrically shadowed from the receiver. At the higher scattered angles there was no geometric shadowing. Unfortunately, a definitive analysis of the accuracy of the WA model at this low scattered angle is more complicated than the other cases due to the likelihood that small errors are showing up in the OE2 reference solution. From studies at 200 Hz involving 1D sea surfaces under similar insonification, wind speed, and other parameters, it is known[17] that in this angular range the OE2 solution for the mean scattered intensity tends to underestimate the exact (numerical) solution by few tenths of a dB. It seems reasonable, therefore, to expect that the OE2 calculation will similarly underestimate the scattering from rough 2D sea surfaces. If one accepts this speculation, then it appears that the departure of WA calculation from the OE2 calculation is in the direction of the true solution. Perhaps the WA model overestimates the correct scattering levels slightly, it is simply not possible to know based on these results. At the very least, indications are that both models are performing quite well in this low grazing angle geometry.

Evidence that the WA model stays in agreement with the OE2 prediction, even as the OE0 prediction begins to fail, can be found in Tables I and II and from Fig. 4 which shows (with an enlarged vertical scale) the monostatic case (20°) shown in Fig. 3 along with the OE0 calculation. Since the OE2 calculation is expected to be quite accurate down to 20° grazing, the agreement between the WA and OE2 results suggests that the essential scattering physics is well modeled by single scattering and wedge diffraction. Furthermore, the fact that the agreement between the WA and OE2 predictions

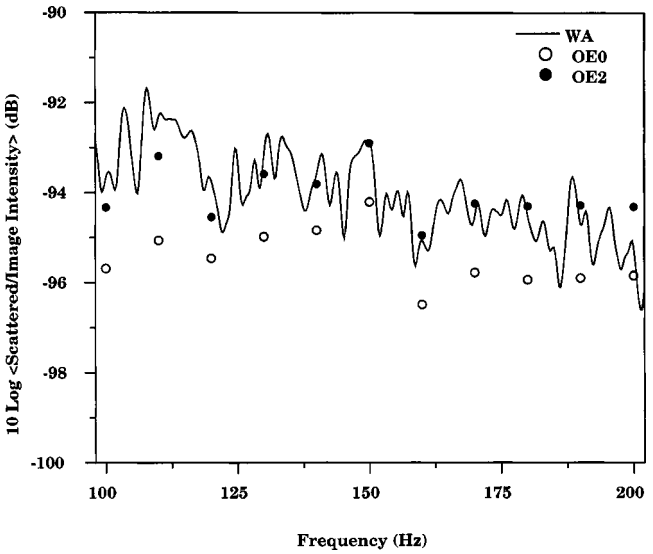

FIG. 4. Detailed comparison of OE2 (dots) and WA (solid line) model predictions for monostatic backscattering at 20° grazing (see Fig. 3) along with predictions by the zeroth order solution (OE0) of the operator expansion method (open circles).

persist down to moderately low grazing angles, where the scattering physics in the OE0 solution appears to become inadequate, suggests something about the nature of the additional physics included in the OE2 solution that is not in the OE0 solution. For example, it can be concluded that the differences between the OE2 and the OE0 predictions are not due to multiple scattering effects since, as just described, the single scattering in the WA model suffices to match the OE2 results. Rather, these results suggest that differences between the OE0 and OE2 results are due to a refining of the physics causing the scattering, not the addition of new scattering mechanisms.

In the previous comparisons, the scattered time series generated by the WA model were calculated using $\Delta t = 4.882\,82\times10^{-4}$ s. and varied in total length from about 1.61 seconds at 10° grazing to 0.79 seconds at 90°. Figure 5 shows (for a single surface realization) the time series generated by the WA model for the four scattered angles shown in Fig. 3. In each case, the WA scattered time series was normalized by the image response. Note the change in vertical scale for the different scattered angles. The WA averages shown in Fig. 3 were calculated by transforming time series like these to the frequency domain after padding with zeros out to 8192 points (4 s). This resulted in a nominal frequency resolution of 0.25 Hz. However, the true resolution, which is governed by the unpadded length of the time series and the details of the insonification function, varied from about 1.3 Hz to 0.6 Hz for scattering into 90° and 10° grazing, respectively.

Before leaving this section, we offer some idea of how the WA and OE models compare under near-field conditions where the incident and scattered wave front curvatures are important factors. Additionally, we make use of this opportunity to present WA–OE comparisons for a single deterministic sea surface. After all, it can be argued that by averaging the scattered intensities over an ensemble of sea surfaces the differences in the scattering physics included in the two

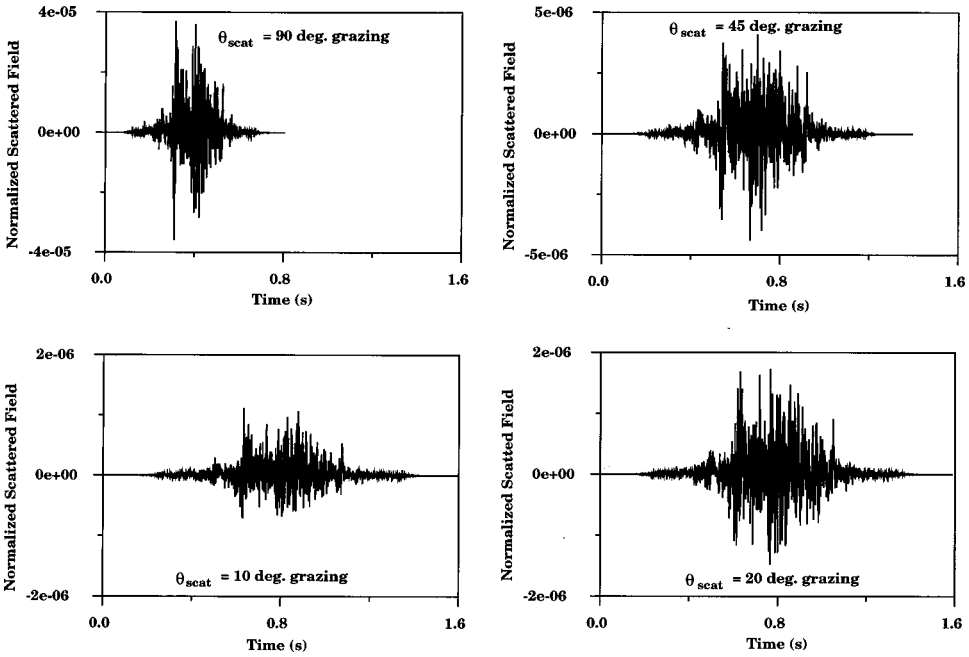

FIG. 5. Backscattered time series from a single realization of the 2D surfaces used to generate Fig. 3. Each time series is normalized by the same image response. The angle of insonification is 20° grazing and the scattered angles are 90°, 45°, 20°, and 10° grazing. The incident and scattered wave vectors are in the same plane as the wind direction.

models may be hidden. To this end, WA and OE calculations were made for backscattering from a single realization of a 20 m/s sea surface with source and receiver located 2000 m from the center of the surface. In the two cases considered, the source field was varied from 100 to 130 Hz at 0.125 Hz intervals and was incident at the nominal grazing angle of 20°. The grazing angles subtended by the 1256 m long surface ranged from 15.8° to 28.7°. Figure 6(a) and (b) show comparisons of the backscattered intensity for a receiver whose nominal scattered grazing angles were, respectively, 45° and 20°.

With regard to these additional comparisons, it can be seen that for both scattering geometries all three calculations (WA, OE0, and OE2) are in quite good agreement. There are ranges of frequencies where the agreement between the three calculations is nearly within a linewidth and there are bands where the differences are as much as 6 dB [excluding the narrow null at 122 Hz in Fig. 6(b)]. It can be noted that essentially all of the features (i.e., nulls or peaks) that appear in the OE calculations also appear in the WA calculations. This correlation of features indicates that the high level of agreement found for the ensemble averages was not achieved by some sort of fortuitous cancellation effect. As expected from the ensemble average results, the agreement between the three calculations is better for the case of scattering into 45° than it is for scattering into 20°. Lastly, there appears to be no noticeable degradation in the WA calculations as a result of the nearness of the scattering surface to the source and receiver.

IV. WA DISSECTION OF THE SCATTERING PROCESS

In this part of the paper, the modeling viewpoint imparted by the WA method is used to describe aspects of the scattering process. Our aim is a kind of ''dissection'' of the scattering process into components, which as it turns out, are generally inaccessible via other modeling approaches. In part, this unique capability is the result of working directly in the time domain and the particular manner in which the scattering problem is discretized. On the other hand, past experience has led to a familiarity with the behavior of the Biot–Tolstoy solution (and its components) in a wide variety of geometries. This past experience guides various aspects of the dissection.

To begin, let us examine the combined role that the scattering geometry and the surface curvature play in the scattering process. After all, in the WA method the diffracted response of each wedge is a function of (among other things) the wedge angle. The wedge angle is essentially a measure of the surface curvature in the direction perpendicular to the wedge apex. This idea that the scattering is controlled by the local surface curvature is in line with the recent findings by Wetzel[28] who has shown the importance of the role of local surface curvature as a ''scattering source.''

Recall that six distinct types (orientations) of wedges are defined by the particular manner in which the 2D rough surface has been discretized and interpolated (see Fig. 1). For a given unit cell, these six wedges describe the local wedge angles (and therefore the local curvature) along the **x** direction (wedge 1) and the **y** direction (wedge 6). Taken together, wedges 3 and 5 describe an average wedge angle along one of the diagonals of the unit cell and, taken together, wedges 2 and 4 describe an average wedge angle along the opposite diagonal. In other words, the total impulse response can be described as the superposition of these four contributions each of which senses the surface curvature in one of four directions. Thus for a given scattering geometry, the WA model can be used as tool to probe the sensitivity of the scattering process to the directional characteristics of the surface curvature.

The result of employing the WA model in the manner just described can be most directly understood by considering an example. A deterministic sea surface was generated having Pierson–Moskowitz spectrum due to a wind speed of 15 m/s. Two different monostatic scattering geometries were

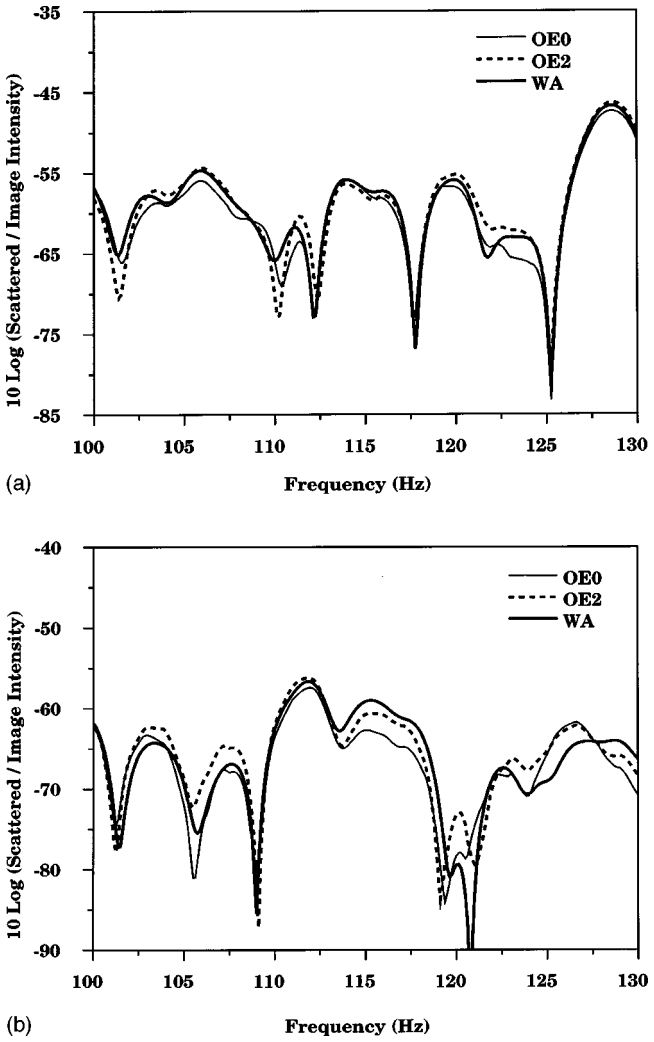

FIG. 6. Nearfield ($R_S = R_R = 2000$ m) frequency dependence of the scattered intensity from a single deterministic 20 m/s surface realization predicted by the OE0 (thin solid line), OE2 (thick dotted line), and WA (thick solid line) models. The angle of insonification is 20° grazing and the scattered angles are (a) 45° and (b) 20° grazing. The incident and scattered wave vectors are in the same plane as the wind direction. Both the WA and OE2 calculations for the scattered field were normalized by the same image response.

considered: normal incidence and 20° grazing. In both cases, $R_S = R_R = 15$ km and $\phi_S = \phi_R = 180°$. For these two grazing angles, the total impulse response was plotted along with the four components described above. These results are shown in Fig. 7. It can be seen that near normal incidence all four components contribute significantly to the total response; there is no preferential dependence of the scattering on the direction of the surface curvature. As the grazing angle decreases, the scattering associated with the surface curvature in the **x** direction (wedge 1) strongly dominates the other components.

In terms of the WA model, the explanation for this observed dependence on the direction of the surface curvature is quite straightforward and physically satisfying. Recall that for an infinite wedge the diffracted wave arrives with infinite amplitude and decays exponentially with time. Therefore, a segment of a wedge apex that is near the least time point (Q in Fig. 2) diffracts relatively strongly and a segment of an apex that is distant from the least time point diffracts weakly. Now, as the source/receiver grazing angle is reduced, the locations of the least time points change for every wedge in the assemblage. In other words, the time difference between the arrival of the diffraction from the physical wedge and the imaginary initial arrival of the diffraction from the virtual wedge apex changes. Referring again to Fig. 2, this time difference can be expressed as $(T_A - t_0)/t_0$ where generally speaking $(T_A - t_0)/t_0 < 1$ corresponds to early times and $(T_A - t_0)/t_0 > 1$ to late times. For the physical apexes perpendicular to the scattering plane (i.e., wedge 1 in this experiment) the change in this time difference as a result of lowering the grazing angle is much less than for the other (obliquely oriented) wedges. The net result is a weakening of the response of wedge types 2, 3, 4, 5, and 6 relative to the response due to wedge 1.

So far we have shown that for a low grazing angle monostatic geometry, the scattering from the surface curvature in the scattering plane dominates. We have explained why this occurs in terms of the BT wedge solution and WA modeling. Next we dissect the scattering process for this geometry further in order to begin to gain some insight as to why a particular feature on the scattering surface yields a negative or positive scattered pressure. In order to do this, we have developed a color map that shows the time integrated scattered pressure per unit time interval that each WA cell on the surface makes to received field:

$$\tilde{P}_{\delta_{ij}} = \frac{1}{\Delta t} \sum_{k=1}^{6} \int_{T_{A_{ijk}}}^{T_{B_{ijk}}} P_{\delta_{ijk}}\, dt. \tag{9}$$

For each unit cell, $T_{A_{ijk}}$ and $T_{B_{ijk}}$ are the lower and upper time limits of the kth wedge's diffracted response as indicated in the example shown in Fig. 2 and Δt is the time resolution for the calculation of the impulse response. To make this map, the calculation indicated in Eq. (9) was performed for each unit cell, normalized by the absolute magnitude of the time integrated response of the most energetic cell, assigned a color according to its amplitude, and mapped onto the surface grid. Because a unit cell can contribute either a positive or negative pressure to the received time series, the color scheme used to generate the map ranged from shades of blue to white to shades of red.

Figure 8 shows an example of such a map for monostatic backscattering from a small section of fully developed sea surface due to a 5 m/s wind ($\theta_g = 20°$, $\phi = 180°$, $R = 15$ km). Overlying the color map showing the scattered response is a contour plot of the surface heights. The grid spacing used to make this figure exceeded that used previously for the model comparisons ($\Delta x = \Delta y = 0.3$ m) and was selected to produce a smooth looking picture. Also the insonification function used in the validation section of this paper was not employed. Referring to the map, it can be seen that the scattering is due to a relatively weak background of scattering events punctuated by ''hot spots.'' Note that in most cases the sources of strong negative pressure (dark blue) and strong positive pressure (dark red) are spatial juxtaposed. Upon closer inspection it can be seen that there is almost always a thin patch of the surface having a near zero response (white) that separates the positive from the negative

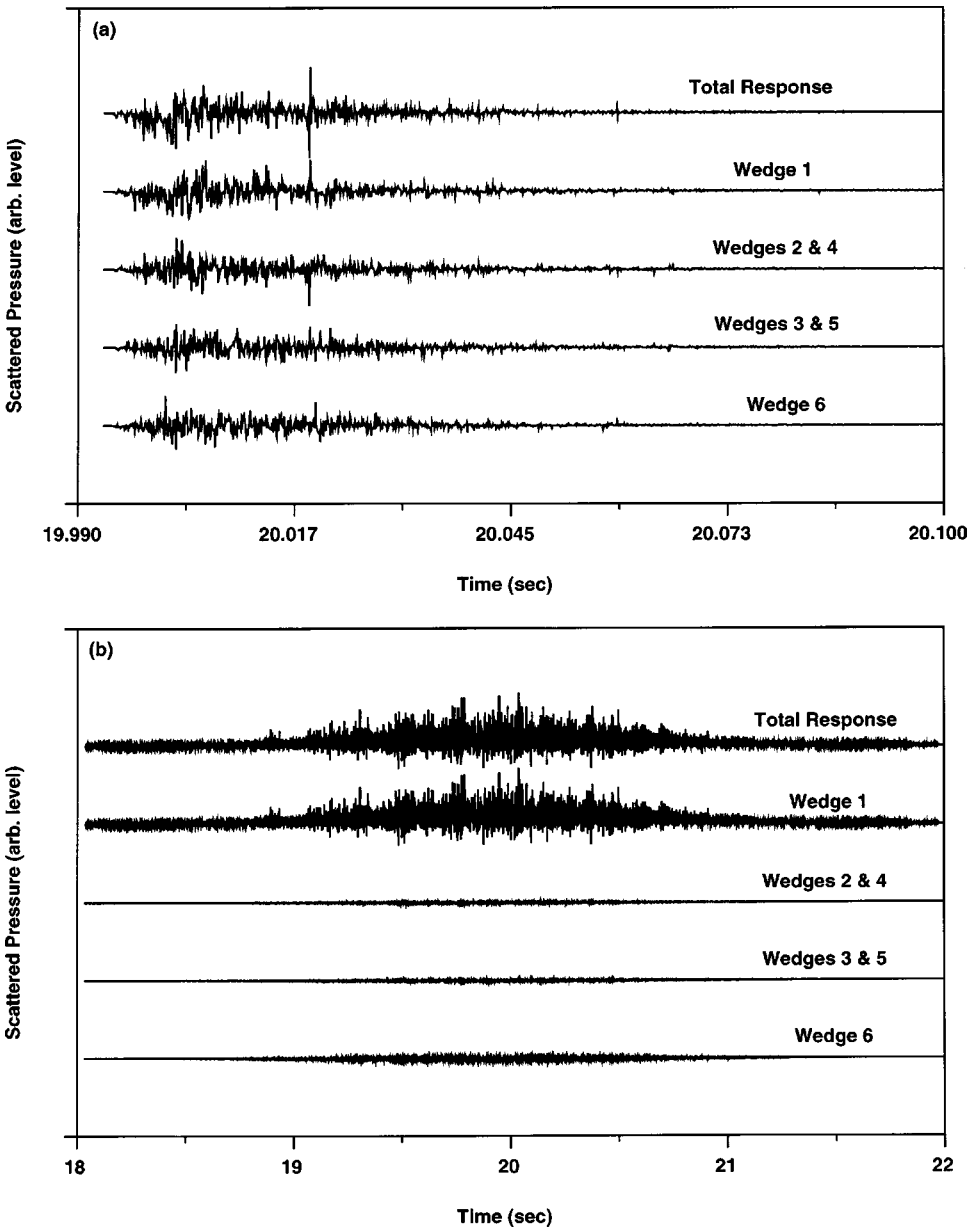

FIG. 7. The total impulse response and its decomposition into four parts each of which is associated with one of the four possible wedge orientations (see Fig. 1). The two cases shown correspond to monostatic backscattering from a 2D sea surface due to a 15 m/s wind at (a) normal incidence and (b) 20° grazing.

hot spots. It can be seen from the overlying contour map of the surface elevations that, as expected, the highlights of the scattering map are not fully explained by the surface features themselves. Obviously the source/receiver geometry influences the scattering and this information is not included in a contour plot of the surface heights. In particular, the surface elevations by themselves give no strong insight as to why a surface feature yields a strong compression or rarefaction. An examination of the BT solution, however, indicates that the features on the surface that yield negative diffracted pressures are all troughs (i.e., $\theta_w > 180°$) while the features of the surface that yield positive diffracted pressures are all crests (i.e., $\theta_w < 180°$). A more in depth study of this topic, which initial results indicate would be fruitful, is beyond the scope of the current effort. It may be the focus of a future study.

V. CONCLUDING REMARKS

A new time domain scattering model based on wedge diffractions that yields the impulse response of rough 2D surfaces has been shown to be suitable for large 3D scattering problems. Through comparisons with an accurate reference solution, the WA model has been shown to be very accurate for backscattering down to quite low grazing angles. It was shown that the single-scatter WA model gave quite good results even when significant shadowing was evident. Finally, although tested on sea surfaces, we see no reason why the accuracy of the WA method should not extend to arbitrarily rough surfaces without any limitation on slope. After all, the BT solution is valid for all wedge angles and source and receiver locations and, as shown in previous applications of the method, multiple scattering effects can be successfully modeled.

The WA approach is a very efficient method for computing the impulse response of a rough surface. Even an approach like OE method, which is efficient because it uses the FFT to calculate the scattered field, does not approach the performance of the WA method in this regard. As an example, consider the scattering geometry that led to Fig. 8.

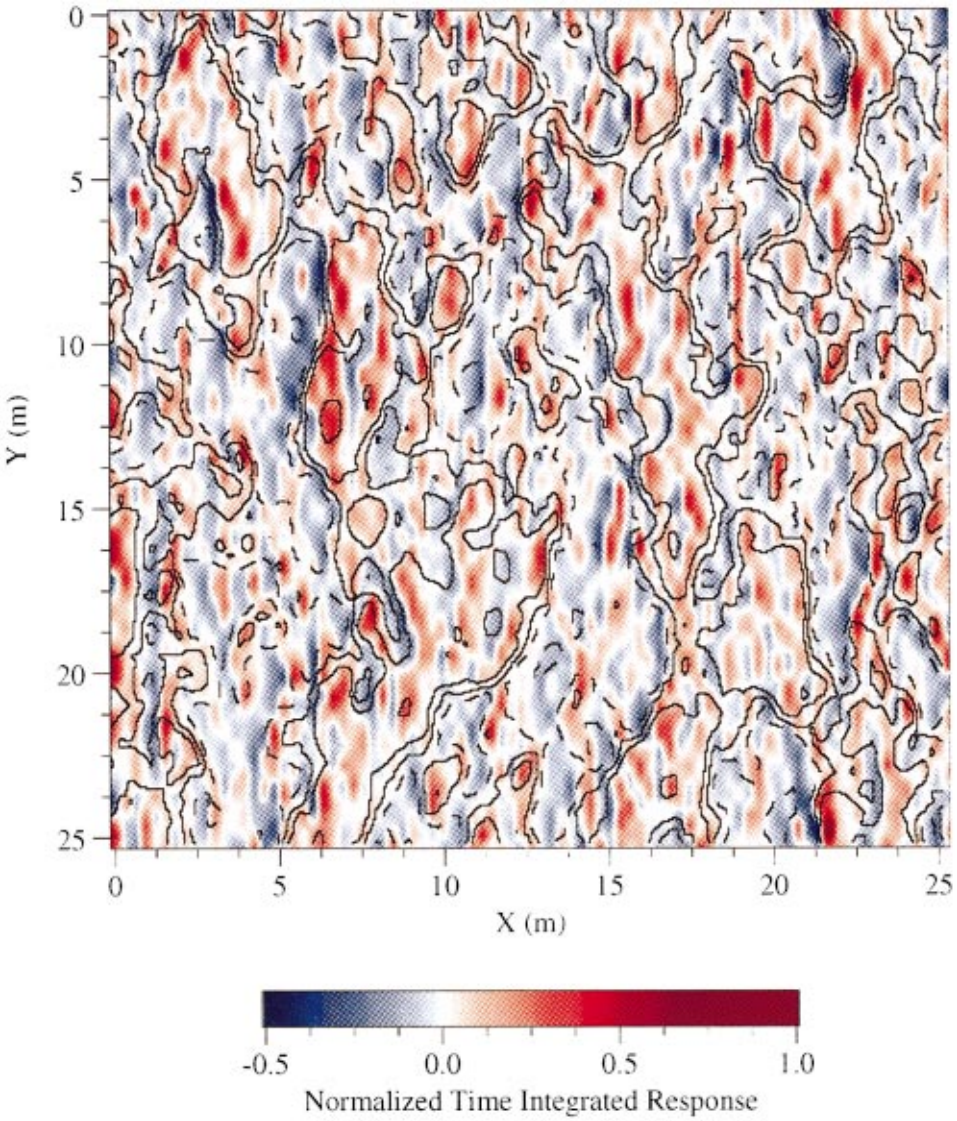

FIG. 8. Color map showing the amplitude of the time integrated response per unit time for each unit cell of the wedge assemblage. The overlying contours show the elevation of the sea surface at 5 values: −0.4, −0.1, 0.0, 0.1, and 0.4 meters. In this case, the scattering geometry is monostatic (20° grazing) and the sea surface was due to a 5 m/s wind.

The impulse response for that 20 m/s surface was approximately 1.44 seconds long. To synthesize this time series the OE method would have to generate a series of frequency domain solutions at 0.35 Hz intervals starting at 0 Hz and (as a result of the finite surface discretization) ending at around 600 Hz for a total of approximately 1715 cw calculations. Since each OE2 calculation takes approximately 60 seconds (single processor of a Cray C-90), the synthesis of the impulse response would take about 28.5 CPU hours (note that the OE2 code was not optimized for the Cray's vector architecture). The same calculation (also using a single processor of a Cray C-90) takes the vectorized WA code approximately 0.1 CPU hours. While comparisons of this nature can be misleading and will depend on the details of the benchmark, if the goal is to calculate the impulse response at a single receiver location there is no question that the time domain WA method is much faster than the more traditional harmonic synthesis approach.

ACKNOWLEDGMENTS

This work has been supported by the Office of Naval Research, Program Element No. 61153N-32 and by grants of computer time at two DoD High Performance Computing Shared Resource Centers (Stennis Space Center, MS and Vicksburg, MS). This document has been reviewed and is approved for public release.

APPENDIX: NUMERICAL GENERATION OF 2D SEA SURFACES

Realizations of 2D rough surfaces having a particular power spectrum (power spectral density function) can be generated in different ways. In this work, the process[29] is based on linear filter theory and is made efficient through the use of standard 2D fast Fourier transform algorithms. First, a 2D array of uncorrelated, normally distributed (unit standard deviation), real surface heights, $X(x,y)$, is generated through repeated calls to a random number generator. This array represents the surface heights obtained by sampling a white noise surface at even spatial intervals $(\Delta x, \Delta y)$. We used the intrinsic random number generator on a Cray C-90 to generate this array. To obtain a surface realization, $Z(x,y)$, having the desired power spectrum, $E_{\text{out}}(k_x k_y)$, we need only Fourier transform $X(x,y)$ to the wave number domain, apply the appropriate filter, $T(k_x, k_y)$, and transform back:

$$Z(x,y)=FT_{2D}^{-1}\{T(k_x,k_y)FT_{2D}\{X(x,y)\}\}. \quad \text{(A1)}$$

The output surface will have the desired power spectrum provided,

$$T(k_x,k_y)=\frac{\sqrt{E_{\text{out}}(k_x,k_y)}}{|FT\{X(x,y)\}|}. \quad \text{(A2)}$$

It can be noted that, due to the fact that the input surface was uncorrelated, the denominator in Eq. (A2) is nearly constant (i.e., white) and nonzero everywhere except at the origin. Special care is required at $k_x=k_y=0$, where, due to the zero mean requirement on the input surface the denominator is zero. For this special case we rely on the fact that the desired output surface must also have zero mean and simply set $T(0,0)=0.0$.

We have adopted a modified Pierson–Moskowitz (PM) spectrum[26] to describe the 2D fully developed sea surface used in this study. The PM spectrum was derived from observations of waves as a function of time at a fixed point and as a result is nondirectional. In its original form, it is given in terms of the angular frequency (ω) of the surface waves:

$$S_{\text{PM}}(\omega)=\alpha\left(\frac{g^2}{\omega^5}\right)e^{-\beta(\omega_0/\omega)^4}. \quad \text{(A3)}$$

Here, $\alpha=0.0081$, $\beta=0.74$, $g=9.81\,\text{ms}^{-2}$, and $\omega_0=g/U$, where U is the wind speed measured at 19.5 m above sea level. In the acoustics literature it is more common to find the wind speed reported at 10 m heights (u_{10}). In that case, the relationship $U=u_{10}/0.93$ can be used. Note that as originally defined the PM spectrum is a one-sided spectrum, that is, the total variance is obtained by integrating over all positive values of ω.

To make the original PM spectrum directional, we follow Kinsman[30] and impose a $\cos^2(\phi)$ azimuthal directionality pattern, use $\phi=0$ for the wind direction, and restrict ϕ to the interval $[-\pi/2,\pi/2]$. This new spectrum is given by

$$S_{\text{PM}}(\omega,\phi)=S_{\text{PM}}(\omega)A\cos^2(\phi). \quad \text{(A4)}$$

To ensure that the total variance remains unaffected we require that,

$$\int_{-\pi/2}^{\pi/2}A\cos^2(\phi)d\phi=1, \quad \text{(A5)}$$

which leads to $A=2/\pi$. The next step is to transform this spectrum to 2D wave number space. To accomplish this, we assume a deep-water environment and use the dispersion relation for gravity waves, $\omega=\sqrt{gk}$, along with $k=\sqrt{k_x^2+k_y^2}$, $\phi=a\tan(k_y/k_x)$, and the Jacobian of ω and ϕ with respect to k_x and k_y which is $g^{1/2}/2k^{3/2}$. The resulting directional power spectrum (units of m^4/rad^2) is only defined for k_x positive. To make a spectrum that is defined in all four quadrants of the 2D wave number space so that it can be used in the linear filter algorithm set forth in the previous section, we must split the energy in half and impose the correct symmetry:

$$E(-k_x,-k_y)=E(k_x,k_y). \quad \text{(A6)}$$

The resulting directional spectrum is

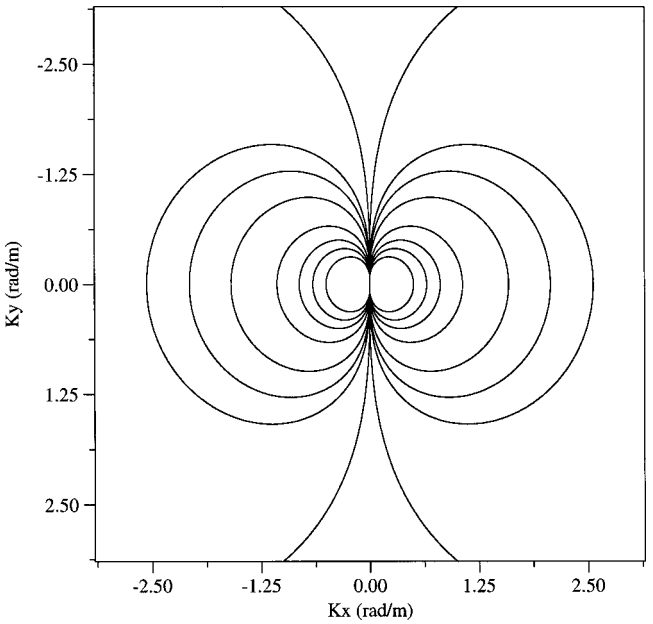

FIG. A1. Contour plot of the Pierson–Moskowitz sea surface roughness spectrum with a $\cos^2(\phi)$ azimuthal dependence for a 15 m/s wind speed (measured at 10 m above sea level). The eight contour levels shown have the values $2.0e$-2, $7.0e$-3, $3.0e$-3, $1.0e$-3, $2.0e$-4, $7.0e$-5, $3.0e$-5, and $1.0e$-6 in units of m^4/rad^2.

$$E_{\text{out}}(k_x,k_y)=\frac{\alpha}{2\pi k^4}\cos^2\left[a\tan\left(\frac{k_y}{k_x}\right)\right]\exp\left[\frac{-\beta g^2}{U^4k^2}\right]. \quad \text{(A7)}$$

Now the total variance is obtained by integrating this spectrum over all values of k_x and k_y. Figure A1 shows a contour plot of this spectrum in 2D wave number space for a wind speed of 15 m/s measured at 10 m above sea level.

[1] M. A. Biot and I. Tolstoy, ''Formulation of wave propagation in infinite media by normal coordinates with application to diffraction,'' J. Acoust. Soc. Am. **29**, 381–391 (1957).

[2] R. S. Keiffer and J. C. Novarini, ''The Wedge Assemblage method for 3D acoustic scattering from sea surfaces: comparison with a Helmholtz-Kirchhoff method,'' Proceedings of the Second International Symposium on Computational Acoustics IMACS (Princeton University, NJ, March, 1989).

[3] H. Medwin and C. S. Clay, *Fundamentals of Acoustical Oceanography* (Academic, New York, 1998), Chaps. 11–12.

[4] J. C. Novarini and H. Medwin, ''Backscattering Strength and the Range Dependence of Sound Scattered from the Ocean Surface,'' J. Acoust. Soc. Am. **69**, 108–111 (1981).

[5] W. A. Kinney, C. S. Clay, and G. A. Sanders, ''Scattering from a corrugated surface: Comparison between experiment, Helmholtz-Kirchhoff theory and the facet-ensemble method,'' J. Acoust. Soc. Am. **73**, 183–194 (1983).

[6] H. Medwin, ''Shadowing by a finite barrier,'' J. Acoust. Soc. Am. **69**, 1060–1064 (1981).

[7] H. Medwin, E. Childs, and G. Jebsen, ''Impulse studies of double diffraction: A discrete Huygens interpretation,'' J. Acoust. Soc. Am. **72**, 1005–1013 (1982).

[8] G. Jebsen and H. Medwin, ''On the failure of the Kirchhoff assumption in backscatter,'' J. Acoust. Soc. Am. **72**, 1607–1611 (1982).

[9] W. A. Kinney and C. S. Clay, ''The spatial coherence of sound scattered from a wind driven surface: Comparison between experiment, Eckart theory and the facet-ensemble method,'' J. Acoust. Soc. Am. **75**, 145–148 (1984).

[10] W. A. Kinney and J. G. Zornig, ''The azimuthal dependence of bistatic surface scattering: A comparison between theory and experiment,'' J. Acoust. Soc. Am. **77**, 1403–1408 (1985).

[11] J. C. Novarini and H. Medwin, ''Computer Modeling of Resonant Scat-

tering from a Periodic Assemblage of Wedges: Comparison with Electromagnetic Theories of Diffraction Gratings,'' J. Acoust. Soc. Am. **77**, 1754–1759 (1985).
[12] R. S. Keiffer, ''On the validity of the wedge assemblage method for pressure-release sinusoids,'' J. Acoust. Soc. Am. **93**, 3158–3168 (1993).
[13] R. S. Keiffer, J. C. Novarini, and G. V. Norton, ''The impulse response of an aperture: Numerical calculations within the framework of the wedge assemblage method,'' J. Acoust. Soc. Am. **95**, 3–12 (1993).
[14] R. S. Keiffer, J. C. Novarini, G. V. Norton, and J. R. Dubberley, ''Benchmarking the wedge assemblage method,'' Math. Modell. Sci. Comput. **4**, 414–419 (1994).
[15] G. Kristensson and P. C. Waterman, ''The *T* matrix for acoustic and electromagnetic scattering by circular disks,'' J. Acoust. Soc. Am. **72**, 1612–1625 (1982).
[16] D. M. Milder, ''An improved formalism for wave scattering from rough surfaces,'' J. Acoust. Soc. Am. **89**, 529–541 (1991).
[17] P. J. Kaczkowski and E. I. Thorsos, ''Application of the operator expansion method to scattering from one-dimensional moderately rough Dirichlet random surfaces,'' J. Acoust. Soc. Am. **96**, 957–972 (1994).
[18] A. W. Trorey, ''A simple theory for seismic diffractions,'' Geophysics **35**, 762–864 (1970).
[19] M. Born and E. Wolf, *Principles of Optics* (Pergamon, Oxford, 1980), pp. 375–382.
[20] C. S. Clay, ''Backscatter of an impulsive wave at a rough surface,'' J. Acoust. Soc. Am. **58** (S1), S67(A) (1975).
[21] J. C. Novarini and H. Medwin, ''Diffraction, reflection and interference during near grazing and near-normal ocean surface backscattering,'' J. Acoust. Soc. Am. **64**, 260–268 (1978).
[22] C. S. Clay (private communication).
[23] E. I. Thorsos, ''The validity of the Kirchhoff approximation for rough surface scattering using a Gaussian roughness spectrum,'' J. Acoust. Soc. Am. **83**, 78–92 (1988).
[24] D. M. Milder and H. T. Sharp, ''An improved formalism for wave scattering from rough surfaces. II: Numerical trials in three dimensions,'' J. Acoust. Soc. Am. **91**, 2620–2626 (1992).
[25] R. N. Bracewell, *The Fourier Transform and Its Applications* (McGraw-Hill, New York, 1978), pp. 209–211.
[26] W. J. Pierson and L. Moskowitz, ''A proposed spectral form for fully developed wind seas based on the similarity theory of S. A. Kitaigorodskii,'' J. Geophys. Res. **69**, 5181–5190 (1964).
[27] L. Brekhovskikh and Yu. Lysanov, *Fundamentals of Ocean Acoustics* (Springer-Verlag, New York, 1982), pp. 174–180.
[28] L. B. Wetzel, ''A time domain model for sea scatter,'' Radio Sci. **28**, 139–150 (1993).
[29] J. W. Caruthers and J. C. Novarini, ''Numerical modeling of randomly rough surfaces with applications to sea surfaces,'' Texas A&M University, Department of Oceanography, Technical Report Reference 71-13-T, 1971.
[30] B. Kinsman, *Wind Waves: Their Generation and Propagation in the Ocean Surface* (Prentice-Hall, Englewood Cliffs, NJ, 1965), Chap. 8.

Stop-pass behavior of acoustic waves in a 1D fractured system

Seiji Nakagawa, Kurt T. Nihei, and Larry R. Myer
Earth Sciences Division, E. O. Lawrence Berkeley National Laboratory, 1 Cyclotron Road, MS 90-1116, Berkeley, California 94720

(Received 10 February 1999; revised 21 September 1999; accepted 1 October 1999)

This study examines the dispersion and the stop-pass band behavior of acoustic waves propagating across periodically spaced and non periodically spaced parallel fractures. Laboratory ultrasonic wave measurements performed on a stack of synthetic fractures (identical steel plates with roughened interfaces) and numerical propagator matrix simulations show spectra with distinct stop-pass band structures that develop with decreasing fracture stiffness. To understand the physics behind these observations, an exact dispersion equation for wave propagation through an infinite series of equally spaced fractures is derived using displacement-discontinuity boundary conditions to model the constitutive behavior of the fractures and Floquet's (Bloch's) theory for the periodic boundary conditions. Both the measured and numerically simulated stop-pass band structures show good agreement with the theoretical predictions. Furthermore, the theory reveals that the left boundary of the stop-bands contains information about the fracture stiffness, suggesting the possibility of determining the stiffness of the parallel fractures from seismic waves. This paper also discusses the effects of fractured systems with random distributions of fracture spacings and stiffnesses on the stop-pass band structures of seismic waves in fractured rock. © *2000 Acoustical Society of America.* [S0001-4966(00)02801-0]

PACS numbers: 43.20.Bi, 43.20.Fn, 43.20.Hq, 43.20.Ks [ANN]

INTRODUCTION

The behavior of acoustic waves propagating through multiple parallel fractures (compliant interfaces) has been of considerable interest for geophysical study of fractured rock masses and nondestructive testing of structures and manufactured parts. Since a compliant fracture functions as a frequency-dependent filter on propagating waves, the characteristics of the fractures can be examined from the changes they impart to the waves.

The behavior of plane waves propagating through single fractures has been well studied and understood by many researchers. Schoenberg[1] showed that by modeling a fracture as a compliant interface with zero thickness between two elastic half spaces, frequency-dependent transmission and reflection coefficients of the wave result. The applicability of such an approach was proved by Angel and Achenbach[2] numerically for a fracture consisting of an array of open microcracks, and experimentally by Pyrak-Nolte *et al.*[3] for fractures in natural rock specimens. The effect of the fracture on transmitting plane waves can be represented by the complex transmission coefficient that reduces the amplitude and shifts the phase of the waves. The effect of the parallel multiple fractures on the wave may be evaluated by multiplying the transmission coefficients computed for individual fractures (e.g., Pyrak-Nolte *et al.*[4]). However, such an approach is shown in this paper to be valid only for the first-arriving part of the wave (ballistic pulse) and if the pulse is not strongly affected by the multiple reflections between fractures.

In this paper, an exact dispersion equation for wave propagation normal to an equally spaced infinite series of fractures with identical fracture stiffnesses is presented. It is shown that the spectra computed from the full waveform of the transmitted wave exhibit distinct frequency bands with large energy transmission (pass bands) and with near-zero energy transmission (stop bands). Such wave behavior is analogous to the behavior of the wave propagation through periodic systems composed of alternating units, and has been studied extensively.[5–7] Stop-pass bands in the stratified systems with welded interfaces are a function of the impedance contrast between layers and the layer thickness-to-wavelength. In contrast, in the fractured system, the stop-pass band structure is affected by both the frequency-dependent fracture acoustic impedance and the fracture spacing-to-wavelength. Due to this frequency-dependent nature, the width of the stop band increases monotonically with increasing wave frequency. The effect of a finite number of fractures and fractures with irregular fracture spacings and stiffnesses is also discussed using numerical simulations with the propagator matrix method. Finally, the stop-pass band behavior of the waves propagating through a multiply fractured medium is confirmed by laboratory ultrasonic wave measurements on a stack of roughened steel plates.

I. THEORY

A. Derivation of dispersion equation for a 1D fractured medium

In this section, the exact dispersion equation is derived for wave propagation across an equally spaced, infinite series of parallel fractures with identical fracture stiffnesses. The background medium is assumed to be elastic and isotropic. The wave is assumed to be normally incident on the fractures. The derivation of the dispersion equation for obliquely incident waves has been discussed elsewhere.[8] The specific fracture stiffness is defined in the context of the displacement-discontinuity boundary conditions,[1,3] i.e., it is the proportionality constant between the applied small incre-

ment of stress by the wave and the resulting closing (or opening) displacement of the fracture. The stresses on both sides of the fracture σ^+ and σ^- are related to the displacement jump across the fracture $[u]=u^+-u^-$ as

$$\sigma^-=\kappa[u], \tag{1}$$

$$\sigma^-=\sigma^+, \tag{2}$$

where superscripts ''+'' and ''−'' refer to the positive and the negative sides of the fracture and κ is the specific fracture stiffness.

The dispersion equation for the wave propagation in an infinite system with welded alternating layers has been studied by many researchers.[5,7,9] By taking advantage of the periodicity in the system and the resulting periodicity in the displacement and traction fields, the wave propagation in the infinite system can be analyzed using a unit cell that consists of a minimum unique sequence of alternating layers with different acoustic impedances (e.g., Bedford and Drumheller[10]). Boundary conditions at the ends of a single unit cell are related together using the Floquet (or Bloch) theory for steady-state wave fields.[11] This technique has also been applied to derive a dispersion relation for a medium containing a doubly periodic array of finite-length, identical open cracks.[12] A similar method is used in this paper to analyze wave propagation in a medium containing periodically spaced infinite fractures. For such a medium, the dispersion relation can be expressed in a compact form as a function of fracture stiffness and wave frequency.

The displacement of one-dimensional waves (waves propagating perpendicular to the fractures) in an intact layer is described by

$$u(z)=Ae^{i(kz-\omega t)}+Be^{-i(kz+\omega t)}, \tag{3}$$

where k is the wave number and ω is the angular frequency of the wave. The wave can be either a longitudinal (P-) wave or a transverse (S-) wave. A and B are coefficients to be determined by the boundary conditions. The stress is obtained by applying the spatial derivative to Eq. (3) as

$$\sigma(z)=i\omega Z(Ae^{i(kz-\omega t)}-Be^{-i(kz+\omega t)}), \tag{4}$$

where Z is the acoustic impedance of the intact medium (for P-waves, $Z=\sqrt{\rho(\lambda+2\mu)}$ and for S-waves, $Z=\sqrt{\rho\mu}$, where ρ, μ, λ are the material density and Lamé constants of the intact medium). Equations (3) and (4) do not describe the overall behavior of the wave that is reflected and transmitted by compliant fractures. Expressing a wave number for the overall (or effective) wave propagation in a single direction by $\hat{k}$ (Bloch wave number), the above expression can be rewritten as

$$u(z)=U(z)e^{i(\hat{k}z-\omega t)}, \tag{5}$$

$$\sigma(z)=\Sigma(z)e^{i(\hat{k}z-\omega t)}, \tag{6}$$

in which,

$$U(z)=Ae^{iK^-z}+Be^{-iK^+z}, \tag{7}$$

$$\Sigma(z)=i\omega Z(Ae^{iK^-z}-Be^{-iK^+z}), \tag{8}$$

where

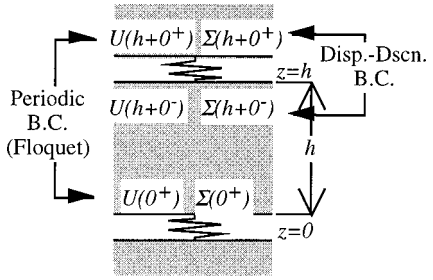

FIG. 1. Boundary conditions applied to the steady-state wave field. Periodic boundary conditions from Floquet theory are used in combination with the displacement-discontinuity boundary conditions to relate the variables in a single unit cell (thickness h) in a closed form.

$$K^+=k+\hat{k},\quad K^-=k-\hat{k}. \tag{9}$$

Equations (7) and (8) are independent of time. Floquet's (Bloch's) theory stipulates that a stationary wave field in a periodic system be also periodic. Therefore, $U(z)$ and $\Sigma(z)$ must be periodic functions of layer thickness h. Noting that the boundary conditions have to be applied to the same sides of the fractures (Fig. 1),

$$U(h+0^+)=U(0^+), \tag{10}$$

$$\Sigma(h+0^+)=\Sigma(0^+). \tag{11}$$

The displacement-discontinuity boundary conditions at $z=h$ are

$$\Sigma(h+0^+)=\kappa[U(h+0^+)-U(h+0^-)], \tag{12}$$

$$\Sigma(h+0^+)=\Sigma(h+0^-). \tag{13}$$

Equation (12) relates the stress and the displacement jump (opening displacement), and Eq. (13) states the continuity of the stress across the fracture, respectively. Using Eqs. (10) and (11), Eqs. (12) and (13) become

$$\Sigma(0^+)=\kappa[U(0^+)-U(h+0^-)], \tag{14}$$

$$\Sigma(0^+)=\Sigma(h+0^-), \tag{15}$$

respectively. By introducing Eqs. (7) and (8) into Eqs. (14) and (15), the following matrix equation is derived:

$$\begin{bmatrix} 1-e^{iK^-h} & -1+e^{-iK^+h} \\ \beta(1-e^{iK^-h})-2i & \beta(1-e^{-iK^+h})+2i \end{bmatrix}\begin{Bmatrix} A \\ B \end{Bmatrix}=0, \tag{16}$$

where $\beta=2\kappa/\omega Z$ is the impedance ratio of a single fracture. The condition for a nontrivial solution to exist is satisfied by equating the determinant of the matrix to zero, which yields

$$\cos(\hat{k}h)=\cos(kh)-\frac{1}{\beta}\sin(kh)$$

$$=\cos(kh)\left\{1-\frac{\tan(kh)}{\beta}\right\}. \tag{17}$$

This is the dispersion equation for the one-dimensional wave propagation in a medium containing an equally spaced infinite series of identical fractures. As shown in Appendix A, Eq. (17) can also be derived as a limiting case of the wave dispersion equation for a periodic binary material with a thin compliant layer constituent. By introducing dimensionless

frequencies (or wave numbers) $\alpha = kh = \omega h/c$, $\hat{\alpha} = \hat{k}h$ and a dimensionless fracture stiffness $b = \kappa h/M = \alpha\beta/2$, where $M = \rho c^2$ is the elastic modulus related to the wave velocity (*P*- or *S*-wave), the dimensionless frequency (wave number) can be computed explicitly by

$$\hat{\alpha} = \cos^{-1}\left[\cos(\alpha) - \frac{\alpha}{2b}\sin(\alpha)\right]. \tag{18}$$

B. Stop-pass band behavior

It is observed that the equation inside the bracket of Eq. (18) exhibits an oscillatory behavior that increases the amplitude with increasing frequency α. For the absolute magnitudes of the equation less than unity, the resulting effective wave number $\hat{k}$ from Eq. (18) is a real number ($\hat{\alpha} = \hat{k}h = \hat{k}_R h$). For the magnitudes larger than unity, $\hat{k}$ must be a complex number of the form $\hat{\alpha} = \hat{k}h = n\pi \pm i \cdot \hat{k}_I h$ ($n = 0,1,2,...$). Such wave numbers result in evanescent modes that are not propagating but decaying exponentially away from the source.

When real solutions of $\hat{k}$ are available, the wave does not attenuate as it propagates through the fractured system. As a consequence, if a transmission coefficient T is defined as a ratio between the complex amplitudes of the waves measured at two reference points, the magnitude of the transmission coefficient $|T|$ is always unity. In contrast, for the complex solutions of $\hat{k}$, the effective wave number has no term that contributes to the propagation of wave. Therefore, $|T|$ is an exponentially decreasing function of the propagation distance between the reference points. The frequency band where the transmission coefficient $|T| = 1$ is often called the *pass band* and the band between them the *stop band* (*forbidden band*). Such wave behavior has been studied extensively in elastic and electromagnetic wave propagation in periodic systems from atomic scale to geologic scale.[9,12–17]

Unlike the periodic binary media, the width of the pass band for the periodically fractured media decreases monotonically with increasing wave frequency. This is due to the frequency dependence of the transmission and reflection coefficients of individual fracture. Figure 2 is an example of the wave-number-frequency dispersion relation obtained from Eq. (18). Only real solutions are shown. The vertical axis is the normalized wave number and the horizontal axis is the normalized wave frequency. Multiple branches result due to the periodicity of the cosine function and waves propagating in the opposite directions. In the high stiffness limit, the branches shown in the thick curve connect one another and form a straight line that represents the nondispersive wave propagation in an intact medium.

C. Phase and group velocities

Phase and group velocities of the one-dimensional wave are computed by

$$c_{\text{phase}} = \frac{\omega}{k}, \tag{19}$$

and

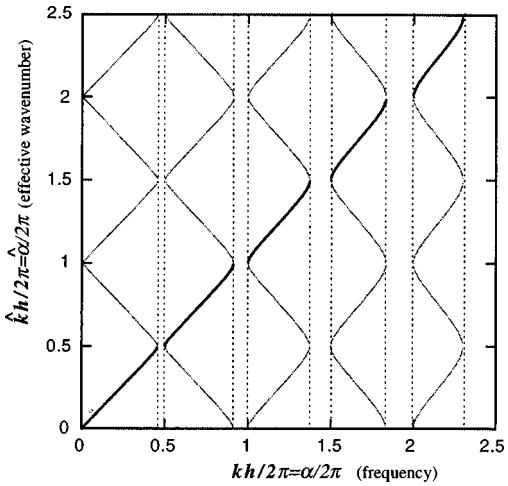

FIG. 2. Dispersion relation (wave number-frequency) of the fractured system with dimensionless fracture stiffness of $b = 10$. The horizontal axis is the dimensionless frequency and the vertical axis is the dimensionless wave number.

$$c_{\text{group}} = \frac{d\omega}{dk}, \tag{20}$$

respectively. For the effective wave propagation, from Eq. (15), the velocities can be computed explicitly by

$$\hat{c}_{\text{phase}} = \frac{\omega}{\hat{k}} = c \cdot P(\alpha, b), \tag{21}$$

$$\hat{c}_{\text{group}} = \frac{d\omega}{d\hat{k}} = c \cdot G(\alpha, b), \tag{22}$$

where

$$P(\alpha, b) = \alpha/\hat{\alpha}, \tag{23}$$

$$G(\alpha, b) = \sin\hat{\alpha}/[\sin\alpha + (\sin\alpha + \alpha\cos\alpha)/2b]. \tag{24}$$

Figure 3 shows an example of the phase and group velocity dispersion relations computed from Fig. 2. As can be seen from the plot, the maximum of the group velocity within each pass band shows negative dispersion. The group velocity approaches zero at both ends of the pass band, which indicates that the fractured system resonates at the boundaries between pass and stop bands.

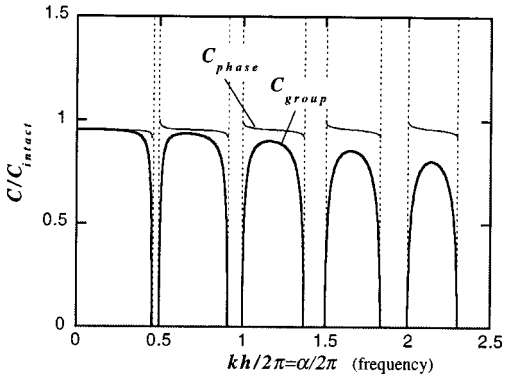

FIG. 3. Velocity dispersion of the fractured system with dimensionless fracture stiffness of $b = 10$.

When the stiffness of the fractures approaches infinity (high fracture stiffness limit), Eq. (17) becomes

$$\cos(\hat{\alpha}) = \cos(\alpha), \tag{25}$$

$$\therefore \hat{c}_{\text{phase}} = \hat{c}_{\text{group}} = c. \tag{26}$$

Therefore, the wave velocity becomes that of an intact medium.

When the frequency of wave approaches zero (static limit), a Taylor series expansion of Eq. (17) is performed as

$$1 - \frac{\hat{\alpha}^2}{2!} + \frac{\hat{\alpha}^4}{4!} - \cdots = 1 - \frac{\alpha^2}{2!} + \frac{\alpha^4}{4!} - \cdots - \frac{\alpha}{2b}\left\{\frac{\alpha}{1!} - \frac{\alpha^3}{3!} + \cdots\right\}. \tag{27}$$

Noting that the higher-order terms vanish as the frequency (α and $\hat{\alpha}$) approaches zero, the remaining first-order terms of the expression are

$$-\frac{\hat{\alpha}^2}{2} = -\frac{\alpha^2}{2} - \frac{\alpha^2}{2b}, \tag{28}$$

$$\therefore \hat{\alpha} = \alpha\sqrt{1 + \frac{1}{b}}. \tag{29}$$

Therefore, the phase velocity is

$$\hat{c}_{\text{phase}} = c \Big/ \sqrt{1 + \frac{1}{b}}. \tag{30}$$

The group velocity is obtained by taking the derivative of Eq. (27) with respect to ω and ignoring the higher-order terms as

$$\hat{c}_{\text{group}} = c \Big/ \sqrt{1 + \frac{1}{b}}, \tag{31}$$

which is identical to the phase velocity. Both velocities are related to the static stiffness of the fractured system as follows:

$$\frac{1}{\rho\hat{c}^2} = \frac{1 + 1/b}{\rho c^2} = \frac{1}{\rho c^2} + \frac{1}{\kappa h}, \tag{32}$$

$$\therefore \frac{1}{\hat{M}} = \frac{1}{M} + \frac{1}{\kappa h}, \tag{33}$$

where M is the elastic modulus of the intact layer ($M = \lambda + 2\mu$ for P-waves and $M = \mu$ for S-waves) and $\hat{M}$ is the effective (static) elastic modulus of the medium containing fractures. Equation (33) shows that the compliance of the system derived from a zero-frequency limit of velocities is equal to the static compliance that is given by a sum of the compliances in the intact medium and the fractures (i.e., the Backus average).

D. Localization of waves

When the frequency of the wave is within a stop band, the wave decays exponentially away from the source without propagating (evanescent wave). Therefore the wave can be best characterized by the decay rate $\hat{k}_I$ that also can be a measure of the wave localization near the source. The dimensionless decay rate $\hat{\alpha}_I$ is computed explicitly by

$$\hat{\alpha}_I = \hat{k}_I h = \cosh^{-1}\left|\cos(\alpha) - \frac{\alpha}{2b}\sin(\alpha)\right|. \tag{34}$$

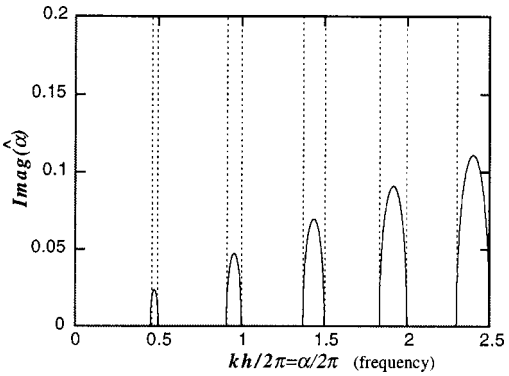

FIG. 4. Exponential decay factor within stop bands.

Figure 4 shows the magnitude of the dimensionless decay rate corresponding to the stop bands in Figs. 2 and 3. The decay rate becomes maximum near the center of each stop band and approaches zero at boundaries between the pass and stop bands.

If waves propagating in a homogeneous half-space impinge on a half-space containing periodically spaced fractures (Fig. 5), all waves are reflected without any energy loss. This is because no net transport of wave energy is allowed within the stop band. Schoenberg[18] examined the behavior of the reflection coefficient for such a system and showed that perfect reflection can result for certain frequency bands. It is noted that although perfect reflection occurs within the stop bands, standing waves exist within the fractured half-space with amplitude decaying away from the boundary between the two half spaces.

II. NUMERICAL SIMULATION

When the wave is transmitted through a finite system (fractured zone within a homogeneous infinite medium), the resulting transmission coefficients do not vanish to zero. Instead, waves can propagate through the fractured zone even within the stop band of the related infinite system. The amplitudes of the wave depend both on the decay rate and the width of the fractured zone. In this section, the characteristics of the waves transmitted through a finite fractured zone containing 11 fractures are examined using the propagator matrix method (Appendix B).

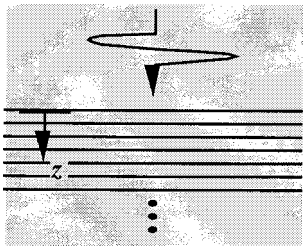

FIG. 5. Waves impinging on a regularly fractured half-space.

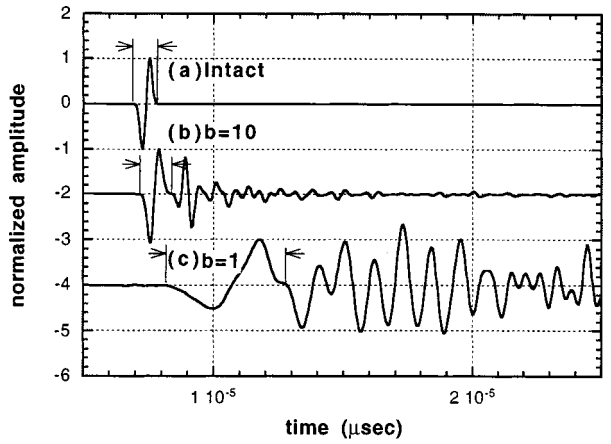

FIG. 6. Waves transmitted through (a) intact medium, and (b), (c) media containing equally spaced fractures. Amplitude of the waves are normalized.

A. First-arriving pulses

In geophysical applications, characteristics of the fractured zone are often evaluated from the first-arriving part of the transmitted wave (ballistic pulse). To see the frequency-dependent filtering effect of fractures on the ballistic pulse, absolute amplitudes of the transmission coefficient and delay time in energy propagation (group time delay) are examined for computed waveforms shown in Fig. 6. The dimensionless frequency corresponding to the central frequency of the source wavelet is $\alpha/2\pi=0.8$. Waves were transmitted through an equally spaced 11-fracture system with constant fracture stiffnesses [$b=\infty$ (intact), $b=10$ (high stiffness), and $b=1$ (low stiffness)]. Wave amplitudes are normalized by the maximum of the first-arriving pulses indicated in the figure.

Computed complex transmission coefficient T's of the ballistic pulses are computed from the ratios between spectra of the wave transmitted through the fractures and the wave transmitted through an intact medium for an identical distance. Normalized group-time delays are computed from T as

$$\hat{t}_g=\frac{1}{t_{g0}\cdot n}t_g, \tag{35}$$

where t_g is the group-time delay computed by

$$t_g=d\arg(T)/d\omega-t_{\text{intact}}. \tag{36}$$

$\arg(\cdot)$ designates phase angle and t_{intact} is the transmission time for the intact case. In Eq. (35), t_{g0} is a normalization factor given by $t_{g0}=Z/2\kappa$ and n is the number of fractures.

As a first-order approximation, the frequency-dependent filtering characteristics of the fractured zone are often evaluated by successively applying the transmission coefficient of each fracture as[4]

$$|T_{\text{all}}|=\prod_{i=1}^{n}|T_i|, \tag{37}$$

where $T_i\,(i=1,2,...,n)$ are the complex transmission coefficients of individual fractures given by

$$T_i=\frac{i\beta_i}{1+i\beta_i}. \tag{38}$$

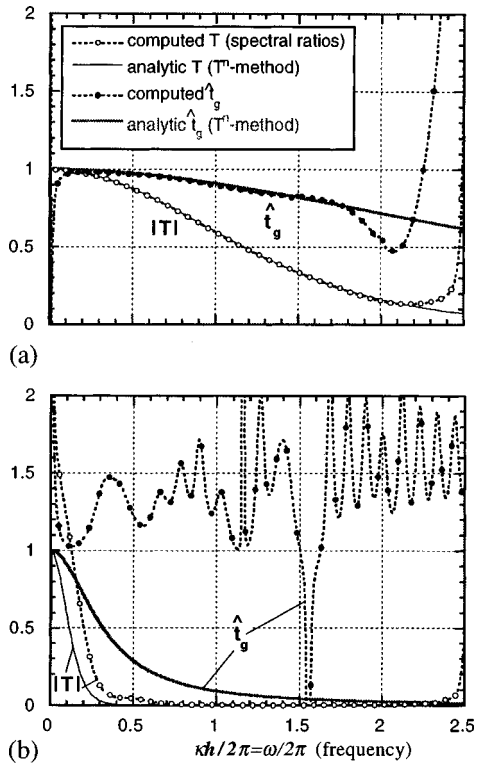

FIG. 7. Comparison between transmission coefficients and normalized group time delays from first-arriving pulses of computed waveforms and T^n-approximation. (a) High stiffness fractures ($b=10$); (b) low stiffness fractures ($b=1$).

β_i are the fracture-matrix impedance parameters.[1,3] For identical fracture stiffnesses with a transmission coefficient T_c, Eq. (37) is simply $|T_{\text{all}}|=|T_c|^n$ (T^n-method). Normalized group-time delays are computed as an average of group-time delays for n fractures as

$$\hat{t}_g=\frac{1}{t_{g0}\cdot n}\sum_{i=1}^{n}t_{gi}, \tag{39}$$

where t_{gi} is the group-time delay for each fracture computed by $t_{gi}=d\arg(T_i)/d\omega$.

To see the accuracy of this approximation, the amplitude of transmission coefficient and the normalized group-time delays given by the T^n-method are compared to the exact numerical solutions in Fig. 7(a) and (b). For a high fracture stiffness ($b=10$), both computed and analytic results are in good agreement except for very low and high frequencies where the source wave does not have significant energy. It is noted that the group-time delay decreases with increasing wave frequency, showing positive dispersion (group wave velocity increases with increasing frequency). In contrast, for low stiffness fractures ($b=1$), there are significant discrepancies. The plot indicates that the computed transmission coefficients (exact) show larger amplitudes than the T^n-prediction given by Eq. (37). Furthermore, the group velocity of the computed result exhibits an opposite behavior to the analytic prediction, showing increasing group-time delay with increasing frequency (negative group velocity dispersion). These differences for the low stiffness fractures are due to the multiple reflection of the waves that has a pre-

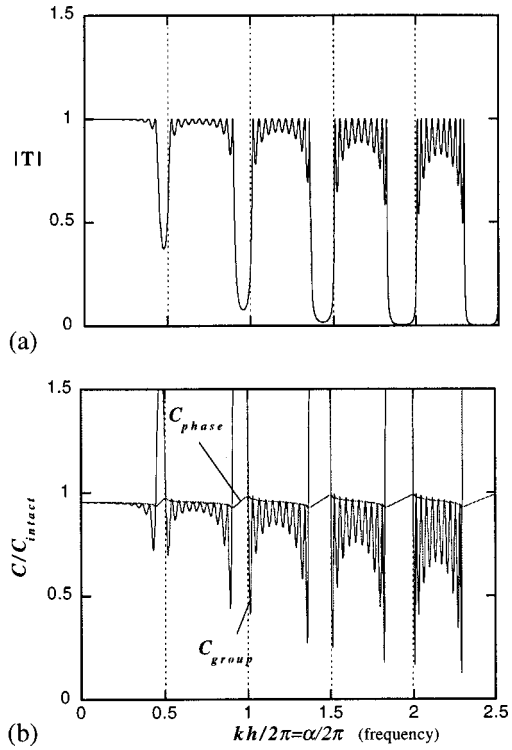

FIG. 8. Transmission coefficients and phase and group velocities for the 11-fracture system with constant fracture spacings and fracture stiffness $b=10$. (a) Transmission coefficient; (b) phase and group velocities.

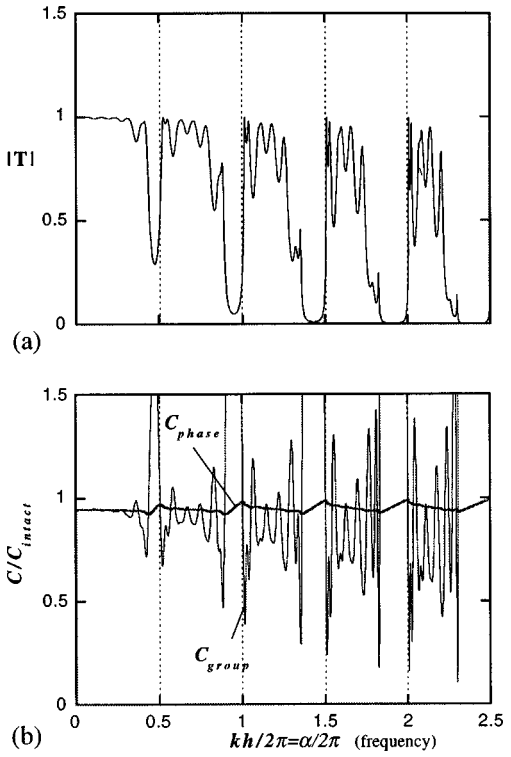

FIG. 9. Transmission coefficients and phase and group velocities for the 11-fracture system with random fracture stiffnesses. (a) Transmission coefficient; (b) phase and group velocities.

dominant effect on the shape of the first-arriving pulse. The results demonstrate that the T^n-method is valid only when the first-arriving pulse is not contaminated by the multiple reverberation of the waves. It is also noted that as seen in Fig. 6, it is difficult to determine from visual inspection whether the first-arriving pulse is affected by the reverberation.

B. Stop-pass band effect

The transmission coefficient of the fractured zone for monochromatic waves has quite different characteristics than the transmission coefficient of the first-arriving pulse. Such coefficients are computed using the propagator method described in Appendix B. Figure 8(a) and (b) show amplitudes of the transmission coefficients and phase and group velocities for the 11-fracture system with fracture stiffness $b=10$. These results are compared to those for the infinite fractures in Fig. 3. Phase velocities and the stop-pass band structure of the finite and infinite fractured system show good agreement. Transmission coefficients within low-frequency stop bands are finite due to the finite number of the fractures. Although the overall trend in the dispersion is the same, the group velocity of the finite system shows multiple peaks within each pass band. This is due to the resonance of the finite system seen as $10\,(=n-1)$ peaks of the transmission coefficient with perfect amplitude $|T|=1$.[8] Each trough of the group velocity corresponds to a single resonance peak. It is noted that each stop band of the transmission coefficient exactly corresponds to a single pass band in the reflection coefficient due to the conservation of energy ($|R|^2=1-|T|^2$). The reflection of the waves within the stop band of the transmission coefficient is known as Bragg reflection.[17]

C. Perturbed systems

Most natural fractured systems have irregularities in their geometry and mechanical properties. Therefore, the effects of the irregular fracture spacings and fracture stiffnesses are examined using the propagator method. Random, spatially uncorrelated fracture stiffnesses and spacings are generated from Gaussian distributions. The mean fracture stiffness is $b=10$ and the standard deviation is 40% of the mean. The standard deviation of the fracture spacings is 3.4% of its mean.

Figure 9(a) and (b) show transmission coefficients and phase and group velocities of the random stiffness system with equal fracture spacings. Despite the large perturbation in the stiffness, the stop-pass band structure is similar to the constant stiffness system in Fig. 8. However, unlike the constant stiffness system, the amplitudes of the transmission coefficient within each pass band do not become unity except for the first peak. This is due to the randomness in the system. The amplitude of the first peak is not affected by the perturbation of the stiffness since the displacements of the waves on both sides of individual fractures are in phase. This is also the reason for the lower-frequency limits of the pass bands that are identical to those for the constant stiffness system.

In contrast to the stiffness-perturbed system, small perturbations in the fracture spacing introduce significant changes in the transmission of the waves (Fig. 10). From the

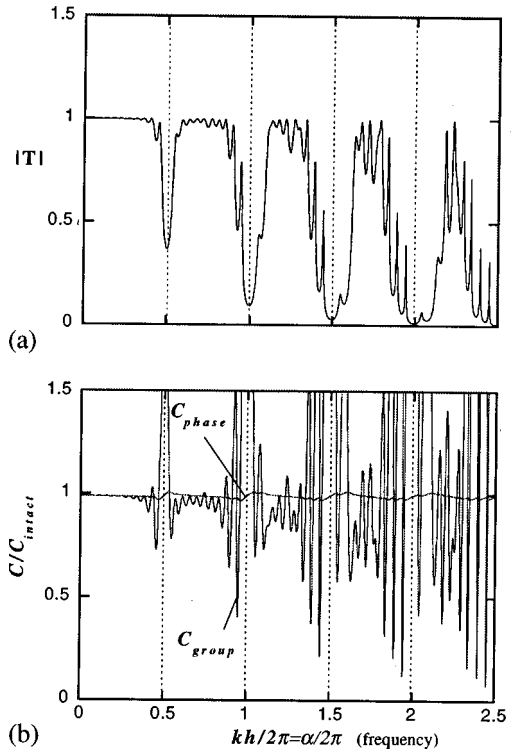

FIG. 10. Transmission coefficients and phase and group velocities for the 11-fracture system with random fracture spacings. (a) Transmission coefficient; (b) phase and group velocities.

plots, it can be seen that the spacing perturbation not only changes the shape of the pass bands, but also shifts the limits of the bands. Since the phases of the displacement on both sides of the fractures cannot be identical unless coincidental, there are no peaks that do not shift or attain unit amplitude.

III. EXPERIMENT

A. Experimental setup

To see the stop-pass band behavior of the regularly fractured media, laboratory ultrasonic transmission tests were conducted on a stack of ten steel plates with equal thicknesses. The diameter and the thickness of the plate are 50.8 and 2.90 mm, respectively. These plates were stacked between 6.25-mm-thick steel end pieces to form 11 interfaces. Each interface between the plates models a compliant fracture. The surfaces of the plates were sand-blasted so that the interface is sufficiently compliant to have an effect on the propagating waves. The steel has a *P*-wave velocity of 5751 m/sec, *S*-wave velocity of 3083 m/sec, and a density of 7940 kg/m^3.

The experimental setup for the transmission tests is shown in Fig. 11. Ultrasonic transducers that house piezoelectric crystals are attached to the top and the bottom of the specimen. On the interfaces between the transducers and the steel end pieces are placed thin lead foils to establish good acoustic coupling. The transducers generate *P*-waves with central frequency of 1 MHz excited by high-voltage pulses (500 V) from a pulse generator (IRCO M1k-20). The waves transmitted through the specimen are measured and recorded by a digital oscilloscope (LeCroy 9424E).

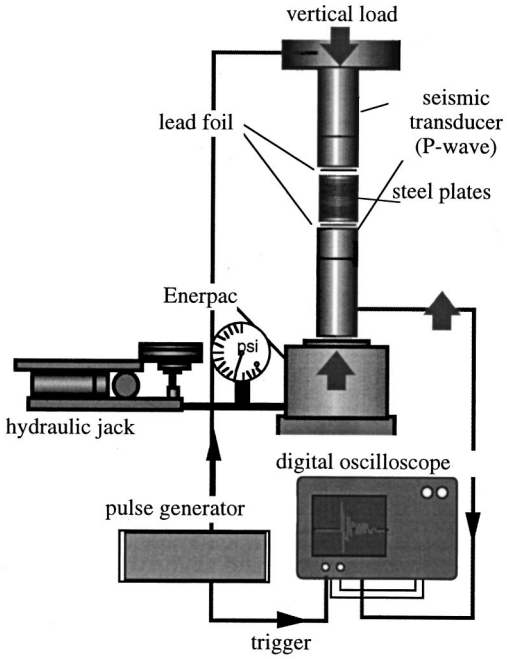

FIG. 11. Experimental setup for pulse transmission tests.

For comparison, an intact steel block of an identical size as the column of steel plates was first tested for the characteristics of the transmitted waves. Subsequently, the steel plate specimen with dry interfaces is tested under 3.3 MPa of axial stress. The test is repeated for the plate specimen with water-saturated interfaces.

To see the effect of a single fracture on the transmitting wave, the wave transmission tests are also conducted on a single interface between two steel plates. For the ''intact'' case, a piece of thin lead foil was placed on the interface and approximately 10 MPa of axial stress is applied to establish a good acoustic coupling between the plates.

B. Results and analysis

Waves transmitted through the intact specimen, plate specimens with dry and water-saturated interfaces are shown in Fig. 12. The large secondary pulses arriving approxi-

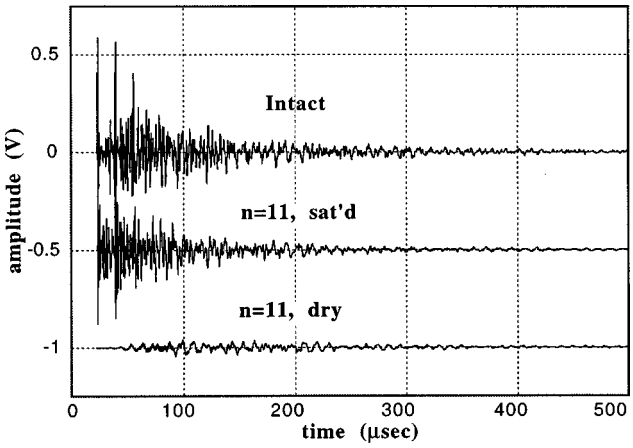

FIG. 12. Experimentally measured waveforms transmitted through a stack of ten steel plates (containing 11 interfaces). The waveform for an intact steel block with an identical size was also measured as a reference.

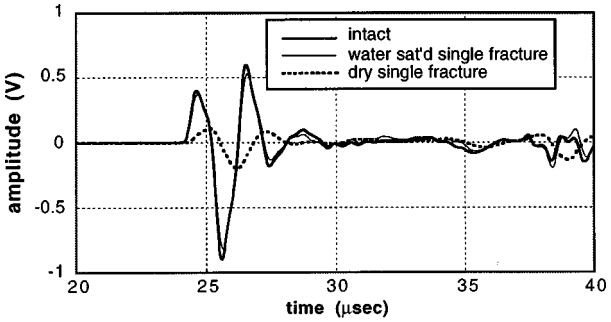

FIG. 13. Experimentally measured waveforms transmitted across a single fracture. The waveform for the intact specimen is measured by placing a lead foil in the fracture and applying an axial load of 10 MPa.

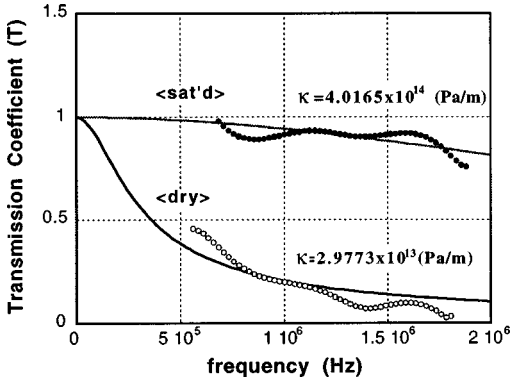

FIG. 14. Theoretical transmission coefficients fitted to the experimental transmission coefficients for both dry and water-saturated fractures. The coefficients were determined by taking the ratio between amplitude spectra for intact and fractured specimens.

mately 15 μsec after the first pulses for the intact and water-saturated specimens are the reflection from the transducer's backing material. The specimen with saturated fractures shows nearly identical waveform as the intact specimen, indicating a high dynamic fracture stiffness due to the intervening water. The specimen with dry fracture exhibits much smaller amplitude and decreased wave frequencies as well as a large delay in the first arrival of the wave. A close examination of the waveform also reveals the arrival of high-frequency components at later times (approximately 50 sec indicating the frequency dependence of the group velocity.

Waves transmitted through a single interface are shown in Fig. 13. Similar to the multiple-fracture case, a slight amplitude decrease and delay of the waveform is observed for the water-saturated fracture and significant changes are observed for the dry fracture. However, due to the lack of multiple scattering, a well-defined wavelet is observed for all three cases. From the ratio between the wave spectra computed for the fractured and intact specimens, experimental transmission coefficients of the single fracture were determined. Using the displacement-discontinuity boundary conditions, the transmission coefficient is given by

$$|T| = \frac{\beta}{\sqrt{1+\beta^2}}, \tag{40}$$

where $\beta = 2\kappa/\omega Z$ is the fracture-matrix acoustic impedance ratio for *P*-waves. Since the acoustic impedance of the matrix is known, the specific normal fracture stiffness κ can be determined by fitting the theoretical frequency-transmission coefficient relation to the experimental data (Fig. 14). It is noted that the behavior of the water-saturated fracture is also assumed to be elastic since the wave frequency is high.

Once the fracture stiffness is determined, theoretical dispersion relations and stop-pass bands for an infinite series of fractures can be computed from Eqs. (18), (21), and (22). Figure 15 shows the dispersion relations for the (a) water-saturated case and the (b) dry fracture case. It is noted that the overall trend in the dispersion of the group velocity is negative, particularly for the dry fracture case.

Finally, experimentally measured wave spectra for the multiple fracture (11-fracture) specimens are compared with the theoretically predicted stop-pass bands (Fig 16). These spectra are computed for the whole waveforms shown in Fig. 12. The stop bands can be recognized as decreases in the amplitude spectra from those for the intact block. It is noted that the horizontal axis is given by the normalized wave frequency, which is the ratio between fracture spacing and the wavelength (h/λ). As predicted, the lower-frequency limits of the pass band coincide with the half-multiples of the $h/\lambda(=0,0.5,1,....)$. In contrast, higher-frequency limits of the pass band shift with fracture stiffness, which, in turn, can be used to estimate the fracture stiffness. Since the width of the pass band becomes very narrow for higher-order pass bands, 3rd and 4th pass bands cannot be measured for the dry fracture.

The velocity dispersion of the wave was not measured quantitatively due to the noise in the experimental wave spectra. However, the results of time-frequency analysis shown in Fig. 17 were qualitatively consistent with the theoretical predictions. For this analysis, a moving-window fast fourier transform (FFT) analysis was employed to examine temporal changes in the spectral content of the waves. Measured waves were swept with a constant-duration window

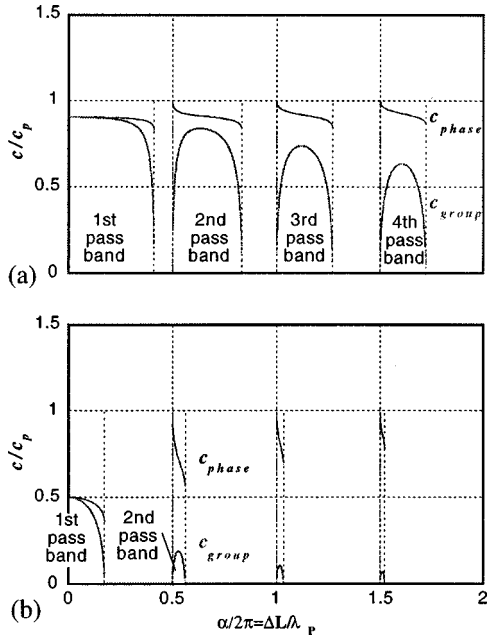

FIG. 15. Theoretical dispersion curves determined from the exact dispersion equation. (a) Water-saturated fractures; (b) dry fractures.

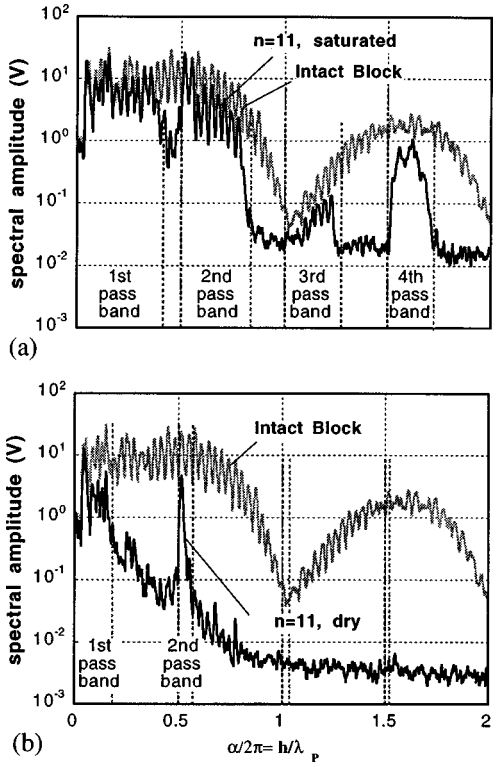

FIG. 16. Experimental amplitude spectra showing distinct pass and stop band structures. The location and the width of the pass bands from the analytic solutions are superposed on the plots showing a good agreement with the experimental results. (a) Water-saturated fractures; (b) dry fractures.

(5-μsec square window with 1 μ-sec half-cosine tapers) and amplitude spectra were computed for each location of the window. From the plots, development of distinct pass bands is seen with decreasing fracture stiffness (1st and 2nd bands are shown in dark gray). For the dry fracture case, arrivals of the waves are much delayed from the intact and water-saturated specimens. Furthermore, the arrival of the waves in the second pass band is clearly delayed from the waves in the first pass band, indicating a larger decrease in group velocity.

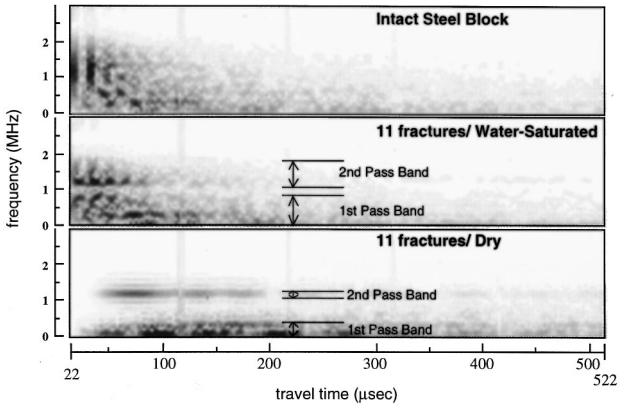

FIG. 17. Time-frequency analysis on the waveforms shown in Fig. 12. The plot shows the changes in temporal and spectral distribution of the measured waves. Each time section is the amplitude spectra computed for a single time window. Higher amplitudes are shown in darker gray and each plot is normalized to its maximum amplitude. Development of stop-pass band structures and a decrease in group velocity can be seen.

IV. CONCLUSIONS

In this paper, the effect of multiple parallel fractures on the normally incident acoustic waves was examined.

A dispersion equation was derived for waves propagating through equally spaced infinite series of fractures with identical fracture stiffnesses. It was revealed that waves transmitted through the fractures exhibit a distinct stop-pass band behavior that is analogous to the waves transmitted through a periodically layered medium with welded interfaces. The stop-pass band behavior for the multiple-fracture system, however, has some unique characteristics that distinguish it from those of the periodically layered system. For example, the width of the pass band is a function of fracture stiffness and decreases monotonically with increasing fracture stiffness. Such behaviors were confirmed experimentally using an idealized system of fractures made of steel blocks. To examine the effect of the randomness in the fractured system, propagator simulations were performed. The results showed that the behavior of the finite fractured systems is similar to the infinite system with the exception that the finite system exhibits distinct resonances in the pass band related to the width of the fracture zone. Perturbation to the fracture spacing resulted in more significant changes in the stop-pass behavior of the waves than the perturbation to the fracture stiffness.

The stop-pass behavior of the acoustic waves can be used to characterize materials containing fractures with periodic and near-periodic spacings and stiffnesses. Such a use of the waves is of great value for applications in geophysics and material testing to characterize fractured geomaterials and solid structures. It may also be applied to construct an acoustic filter whose properties can be altered by changing the stiffness of the fractures (compliant interfaces). The stop-pass behavior of electromagnetic waves in periodic materials has already been used widely in the field of materials science and optics. Therefore, the acoustic stop-pass behavior in fractured materials may also find a wide range of applications in geosciences and material evaluation.

ACKNOWLEDGMENTS

This research was supported by the Director, Office of Energy Research, Office of Basic Energy Sciences, under U.S. Department of Energy Contract No. DE-AC03-76SF00098.

APPENDIX A: DISPERSION EQUATIONS FOR PERIODICALLY FRACTURED MEDIA AS A LIMITING CASE OF PERIODIC BIMATERIAL WITH A THIN COMPLIANT LAYER COMPONENT

For alternating layers of thickness h_1 and h_2 (see Fig. A1), the dispersion equation of the wave propagating across the periodic system is given by[5,9]

$$\cos(\hat{k}h) = \cos(k_1h_1)\cdot\cos(k_2h_2) - \frac{1}{2}\left(\frac{Z_1}{Z_2}+\frac{Z_2}{Z_1}\right)\sin(k_1h_1)\cdot\sin(k_2h_2), \qquad \text{(A1)}$$

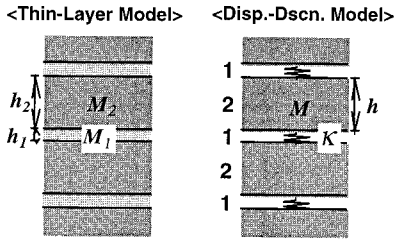

FIG. A1. Models for a fractured medium with equal fracture spacings. Fractures are modeled using thin compliant layers (thin-layer model) and displacement-discontinuity boundary conditions (displacement-discontinuity model).

where $h=h_1+h_2$. Z_1 and Z_2 are the acoustic impedances, k_1 and k_2 are the wave numbers for the layered media, respectively. From the derivation in the preceding section, the dispersion equation for a fractured medium is

$$\cos(\hat{k}h)=\cos(kh)-\frac{1}{\beta}\sin(kh). \tag{A2}$$

The objective here is to obtain Eq. (A2) from Eq. (A1) by approximating the static behavior of a fracture by that of a thin elastic layer.

Following the definition for the specific fracture stiffness κ, the static displacement across the fracture and the displacement within a compliant layer (layer 1) are made equal,

$$\Delta u=\frac{\sigma}{M_1(=\rho_1 c_1^2)}h_1=\frac{\sigma}{\kappa}. \tag{A3}$$

Therefore,

$$\kappa=\frac{\rho_1 c_1^2}{h_1}. \tag{A4}$$

From Eq. (A4), it can be seen that the elastic modulus M_1 $(=\rho_1 c_1^2)$ has to approach zero as the layer thickness h_1 approaches zero to produce a finite fracture stiffness (i.e., their magnitudes are of the same order). Since a fracture has to be ''massless'' in the limit $h_1\to 0$, a product $\rho_1 h_1\to 0$. Therefore, the limiting behavior of the phase term is

$$\varepsilon\equiv k_1h_1=\frac{\omega h_1}{c_1}=\omega\cdot\sqrt{\frac{\rho_1 h_1}{\kappa}}\to 0. \tag{A5}$$

The impedance ratios in Eq. (A1) can be expressed as

$$\frac{Z_2}{Z_1}=\frac{Z_2}{\rho_1 c_1}=\frac{Z_2}{\kappa h_1/c_1}=\frac{2c_1}{\omega h_1}\frac{\omega Z_2}{2\kappa}=\frac{2}{\varepsilon\beta}, \tag{A6}$$

$$\frac{Z_1}{Z_2}=\frac{\varepsilon\beta}{2}, \tag{A7}$$

and

$$\sin(k_1h_1)=\sin\varepsilon=\varepsilon+o(\varepsilon^3). \tag{A8}$$

By introducing the equations from Eq. (A4) to (A8) into Eq. (A1),

$$\cos(\hat{k}h)=\cos(\varepsilon)\cdot\cos(k_2h_2)-\frac{1}{2}\left(\frac{\varepsilon\beta}{2}+\frac{2}{\varepsilon\beta}\right)\times(\varepsilon+o(\varepsilon^3))\cdot\sin(k_2h_2). \tag{A9}$$

Taking the limit of ε and replacing k_2h_2 by kh results in

$$\cos(\hat{k}h)=\cos(kh)-\frac{1}{\beta}\sin(kh). \tag{A10}$$

The above expression is identical to the dispersion equation for a fractured medium [Eq. (A2)].

APPENDIX B: DISPLACEMENT PROPAGATOR MATRIX METHOD FOR FRACTURED 1D MEDIA

In a homogeneous medium with a density ρ and a wave velocity (P or S-wave) c (acoustic impedance of $Z=\rho c$), the displacement of a single Fourier component of the wave can be expressed as

$$\mathbf{u}(z+z_0)=E\mathbf{u}(z), \tag{B1}$$

where $\mathbf{u}=\{u_d,u_u\}^T$ is the displacement vector with down-going (propagates in the positive z-direction) and up-going (propagates in the negative z-direction) wave components. z_0 is an any reference coordinate. E is the phase-shifting matrix given by

$$E=\begin{bmatrix} e^{i\alpha} & 0\\ 0 & e^{-i\alpha}\end{bmatrix}, \tag{B2}$$

where $\alpha=\omega h/c$ is the phase shift over the layer thickness.

The relation between the components of displacement across a fracture is provided by the displacement-discontinuity boundary conditions

$$\sigma^-=\kappa(u^+-u^-)\equiv\kappa[u], \tag{B3}$$

$$\sigma^-=\sigma^+, \tag{B4}$$

where superscripts ''+'' and ''−'' represent the positive and negative sides of the fracture, $u=u_d+u_u$ is the displacement, κ is the specific fracture stiffness. Using the expressions for the displacement components

$$u_d(z)=u_d(z_0)\exp\left(\frac{i\omega}{c}(z-z_0)\right), \tag{B5}$$

$$u_u(z)=u_u(z_0)\exp\left(-\frac{i\omega}{c}(z-z_0)\right), \tag{B6}$$

and the constitutive relation

$$\sigma=M\varepsilon=M\frac{du}{dz}, \tag{B7}$$

where $M=\rho c^2$. Equations (A3) and (A4) are recast to a matrix-equation form

$$\mathbf{u}^+=P\mathbf{u}^-, \tag{B8}$$

with a transmission-reflection matrix

$$P=\begin{bmatrix} 1+(i/\beta) & -i/\beta\\ i/\beta & 1-(i/\beta)\end{bmatrix}, \tag{B9}$$

where $\beta=2\kappa/\omega Z$ is the fracture-matrix impedance ratio. Combining Eqs. (B1) and (B9), components of displacement on the negative side of the first fracture are related to the ones on the positive side of the last fracture as

$$\mathbf{u}(z_0+L)=P_{N+1}E_NP_NE_{N-1}\cdots E_1P_1\mathbf{u}(z_0)=F\mathbf{u}(z_0), \tag{B10}$$

where $L=\Sigma_{i=1}^{N}h_i$ is the total length of the fractured zone (h_i is the thickness of individual layer). The complex transmission and reflection coefficients are computed by setting $u_d(z_0)=1$ and $u_u(z_0+L)=0$ (radiation condition) and solving for $u_d(z_0+L)$ (transmission coefficient) and $u_u(z_0)$ (reflection coefficient). The transient response of the waves transmitted through the system can be obtained by multiplying the computed transmission coefficients with the Fourier spectra of the incident wave and then transforming back to the time domain.

[1] M. Schoenberg, ''Elastic wave behavior across linear slip interfaces,'' J. Acoust. Soc. Am. **68**(5), 1516–1521 (1980).

[2] Y. C. Angel and J. D. Achenbach, ''Reflection and transmission of elastic waves by a periodic array of cracks,'' J. Appl. Mech. **52**, 33–41 (1985).

[3] L. J. Pyrak-Nolte, L. R. Myer, and N. G. W. Cook, ''Transmission of seismic waves across single natural fractures,'' J. Geophys. Res. **95**, 8617–8638 (1990).

[4] L. J. Pyrak-Notle, L. R. Myer, and N. G. W. Cook, ''Anisotropy in seismic velocities and amplitudes from multiple parallel fractures,'' J. Geophys. Res. **95**, 11345–11358 (1990).

[5] S. M. Rytov, ''Acoustical properties of a thinly laminated medium,'' Sov. Phys. Acoust. **2**, 67–80 (1956).

[6] L. M. Brekhovskikh, *Waves in Layered Media* (Academic, New York, 1960).

[7] C. Sve, ''Time-harmonic waves traveling obliquely in a periodically laminated media,'' J. Appl. Mech. **38**, 477 (1971).

[8] S. Nakagawa, ''Acoustic resonance characteristics of rock and concrete containing fractures,'' Ph.D. thesis, University of California at Berkeley, 1998.

[9] K. Helbig, ''Anisotropy and dispersion in periodically layered media,'' Geophysics **49**(4), 364–373 (1984).

[10] A. Bedford and D. S. Drumheller, *Introduction to Elastic Wave Propagation* (Wiley, New York, 1994), pp. 141–151.

[11] G. Floquet, ''Sur les équations differentielles linéaires à coefficients periodiques,'' Annal. Ecole Normale (Ser. 2) **12**, 47–89 (1883).

[12] Y. C. Angel and J. D. Achenbach, ''Harmonic waves in elastic solid containing a doubly periodic array of cracks,'' Wave Motion **9**, 377–385 (1987).

[13] F. Abeles, ''Investigations on the propagation of sinusoidal electromagnetic waves in stratified media. Application to thin films,'' Ann. Phys. (Paris) **5**, 596 (1950).

[14] L. Brillouin, *Wave Propagation in Periodic Structures* (Dover, New York, 1953).

[15] P. W. Anderson, ''Absence of diffusion in certain random lattices,'' Phys. Rev. **109**, 1492–1505 (1958).

[16] P. Yeh, A. Yariv, and C. S. Hong, ''Electromagnetic propagation in periodic stratified media. I. General theory,'' J. Opt. Soc. Am. **67**, 423–437 (1977).

[17] A. Yariv and P. Yeh, *Optical Waves in Crystals* (Wiley, New York, 1984).

[18] M. Schoenberg, ''Reflection of elastic waves from periodically stratified media with interfacial slip,'' Geophysical Prospecting **31**, 265–292 (1983).

The reconstruction of a spatially incoherent two-dimensional source in an acoustically rigid rectangular cavity

J. C. Wendoloski[a)]
CSIRO, Telecommunications and Industrial Physics, P.O. Box 218, Lindfield NSW 2070, Australia

(Received 10 January 1998; accepted for publication 20 September 1999)

This paper applies Green's function modal expansion techniques to inverse source problems within an acoustically rigid rectangular cavity. In particular, solutions are developed for the reconstruction of a random spatially incoherent distributed source and a deterministic point source by using pressure-field measurements on adjacent walls. Such problems have seemingly not been addressed previously. Several example problems are studied in this paper. As is characteristic of inverse problems in general, numerical instabilities are encountered in the example problems addressed in this paper. These are linked to the notion of compactness in the forward operator, and dealt with using magnitude regularization and projections onto convex sets. The behavior of the example problems studied in this paper greatly deteriorates at frequencies near cavity resonances, particularly low frequency resonances (i.e., with $ka \lesssim 2\pi$, where a is the smallest cavity dimension). Other results concerning the example problems are also given. A proof of compactness of an infinite rank version of the type of operator used in this paper is given in the Appendix. This proof implies that the convergence of the Green's function modal expansion in the kernel of the forward problem is related to the instability of the inverse problem. This implies that, if it suffices to know an integral of the source profile rather than the actual profile, the problem becomes more stable. [S0001-4966(00)02101-9]

PACS numbers: 43.20.Bi, 43.20.Fn, 43.20.Rz [DEC]

LIST OF SYMBOLS

k	acoustic wave number
$\psi_k(\mathbf{x})$	velocity potential in the cavity (at wave number k)
$G_k(\mathbf{x}\|\mathbf{x}_0)$	Green's function for the cavity
ρ_k	source distribution function
K_{mn}	wave number of the (m,n)th cavity mode
ϵ_n	Neumann normalization factors
$z^\dagger$	complex conjugate of z
$\langle\ \rangle$	instruction to take ensemble averages
$A_k^{\psi}(x,0\|0,y')$	field autocorrelation function
$A_k^{\rho}(x_0,y_0\|x_0',y_0')$	source autocorrelation function
$\delta(x-x')$	Dirac delta function
$I_k(x_0,y_0)$	intensity profile of the source
$\delta(x-x',y-y')$	two-dimensional Dirac delta function
I_{pq}	Fourier cosine coefficients of $I_k(x_0,y_0)$
$A(x,y)$	shorthand for the autocorrelation function $A_k^{\psi}(x,0\|0,y)$
A_{mn}	Fourier cosine coefficients of $A(x,y)$
$\mathcal{Q}_{mnpq}$	component of the forward operator for the cavity problem
$D_{m,n,m',n'}$	basic form for terms in $\mathcal{Q}_{mnpq}$
Q	operator representation for the component form $\mathcal{Q}_{mnpq}$
$\mathbf{A}$	vector representation for the component form A_{mn}
$\mathbf{I}$	vector representation for the component form I_{mn}
A^*	conjugate transpose of matrix A
λ	regularizing parameter
e_f	error expression for source reconstructions
m_f	magnitude expression for source reconstructions
H	Hilbert space of square integrable functions L_2
$\mathcal{K}(x\|x_0)$	compact kernel of a first type Fredholm integral equation
$H_f(x)$	Heaviside step function

INTRODUCTION

This paper addresses a two-dimensional acoustic inverse source problem within the confines of an acoustically rigid rectangular cavity. The particular problem concerns the reconstruction of a random spatially incoherent source distribution in the interior of the cavity from field measurements on adjacent walls. Because of its mathematical similarity, the reconstruction of a deterministic point source in a rigid rectangular cavity is also demonstrated using the same techniques.

The problem of determining a two-dimensional source distribution from an implied one-dimensional set of measurements, made exterior to the source, appears in the most general case to be intractable.[1] This has been shown for free-field wave problems by Devaney,[2] and it will be shown that

a)Electronic mail: johncw@tip.csiro.au

it is also true for the cavity problem addressed in this paper. If, however, some *a priori* information is known about the source (deterministic or random), the problem may be rendered tractable (see Devaney[2]). For spatially incoherent sources, such information is present. This class of nondeterministic (or random) source distributions is characterized by a spatial autocorrelation function which reduces to the product of the source intensity profile and a Dirac delta function.

The ''spatial autocorrelation function'' mentioned above is related to the common temporal (time) cross-correlation function between distinct points in the source distribution (this will be qualified shortly). Hence, ''spatial incoherence'' occurs when different source points in the distribution vibrate in a manner which is statistically uncorrelated. This behavior would normally be found when the source is driven by a ''random'' process. If there were some degree of correlation between distinct points in the source distribution, one might expect a partially deterministic underlying process.

The reduction of the spatial autocorrelation function to the product of the source intensity profile and a Dirac delta function effectively reduces the dimensionality of the source. The inverse problem is thus rendered tractable (see Devaney[2]).

Norton and Linzer[3] comment that sources which may be well approximated as random and spatially incoherent are common in nature. They note the case in optics of blackbody sources, and acoustic emission from microcracking or material deformation in ultrasonics.

The term spatial autocorrelation function is here defined to be the statistical expectation of the product of Fourier amplitudes of acoustic sources or fields at different points (see Devaney[2]). At first glance this definition may appear unrelated to the temporal cross-correlation function discussed above (which was given for physical simplicity). If the condition of *ergodicity* is assumed (i.e., that the ensemble averaging in the expectation value is equivalent to time averaging), then the temporal cross-correlation function referred to above is essentially the inverse Fourier transform of the spatial autocorrelation function given in this paper. (Technically speaking, the autocorrelation function of Fourier amplitudes must include integration over an infinitesimal band of frequencies around the frequency of interest. A reference for this is given later.)

Although *ergodicity* is not strictly necessary for the development in this paper, it will be assumed that the fields and sources are at least statistically stationary. Background reading on these terms may be found in Harris and Ledwidge,[4] or probably any introductory text on noise or time-series analysis.

Solutions to the free-field version of the spatially incoherent inverse source problem using far-field data have been comprehensively reported on (see Devaney[2,5,6]). Solutions have also been developed using near-field data (see Norton and Linzer[3] and Ball *et al.*[7]).

The uniqueness of solution to the spatially incoherent inverse source problem still does, however, presuppose that enough measurements can be made to completely determine the intensity profile of the source. In the free-field problem, where the source is localized in a finite volume, it is clear that, in general, an infinite number of measurements is required to uniquely specify the intensity profile of the source.

The cavity problem appears to inherit most of the characteristics of the free-field problem. An important difference with the free-field problem arises due to the manifest localization of the source. The source will be localized even if it consists of a finite sum of cavity modes. (Note that the modes of the cavity form a complete set of functions and therefore are capable of describing any piece-wise continuous function.) In this case, the inverse source problem will possess a unique solution even if only a finite number of measurements is made.

A survey of the literature on inverse source problems was made by the author. No published literature was found on random inverse source reconstruction in two-dimensional acoustically rigid rectangular cavities. Random source reconstruction under the assumption of spatial incoherence and deterministic inverse scattering under the Born approximation can, however, produce equivalent integral equations. A recent paper by Novotný *et al.*[8] addresses a *one-dimensional* Born approximate inverse scattering problem under rigid boundary conditions. The authors, however, concur with the findings of this paper that the existing literature on inverse scattering deals almost exclusively with free-field problems.

In general, true inverse problems (as opposed to parameter optimization) are ill-conditioned. This property is intrinsic to inverse problems and is not a consequence of inadequate mathematical formulations (see Roger and Maystre,[9] who cite Hadamard[10]).

The behavior of an inverse diffraction problem can be shown to be related to properties of the corresponding forward diffraction problem (see Roger *et al.*[11]). In mathematical terms, the forward problem may be cast as a Fredholm integral equation of the first kind. The kernel of this equation acts under the integral sign as an operator from one vector space of functions to another (usually from a Hilbert space to itself). The forward operator in a diffraction problem will generally have infinite rank and be compact, which implies that the inverse operator will have arbitrarily small eigenvalues. It is the existence of these small eigenvalues which leads to the instability of the inverse problem.

A standard method of remedying this problem is ''regularization.'' What is meant by this term is basically a restriction of the solution space to remove solutions without certain (presumably *physical*) properties. Many varieties of this basic technique exist (see Ref. 12, Chap. 18).

Linear regularization techniques generally restrict the magnitude and derivatives of the solution. There are, of course, nonlinear techniques as well, which include the maximum entropy method and the Backus–Gilbert method. Still another technique is to solve the matrix equations iteratively and to impose deterministic constraints via projections onto convex sets (POCS). Linear regularization and POCS are employed in this paper in evaluating the present inverse source problem.

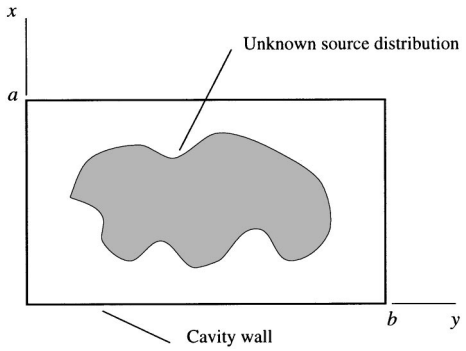

FIG. 1. An unknown source distribution within a rectangular cavity.

I. THE INVERSE SOURCE PROBLEM IN A RECTANGULAR CAVITY

The basic formulation for the spatially incoherent inverse source problem is as follows. A two-dimensional case of a source within a rectangular cavity with a rigid boundary is considered (see Fig. 1). Such a situation may be realized in a rigid air-filled cavity, with one dimension much smaller than the other two. This may be done by arranging the interior surface of one of the large walls to be composed in part of an array of flush-mounted vibrating pistons.

Unless stated otherwise, all the fields and source distributions described in this section are realizations of random processes. In the following, k is the wave number of an acoustic field.

Assume the velocity potential at some point in a rectangular cavity (with sides of lengths a and b) can be given as

$$\psi_k(\mathbf{x}) = \int_S \int d\mathbf{x}_0\, G_k(\mathbf{x}|\mathbf{x}_0)\rho_k(\mathbf{x}_0), \tag{1}$$

where ρ_k is the source distribution function, $S=[0,a]\times[0,b]$, and G_k is the Green's function incorporating the boundary conditions of the cavity. Expressions are now required for the field on the perimeter of the cavity. These are

$$\psi_k(x,0) = \int_S \int dx_0\, dy_0\, G_k(x,0|x_0,y_0)\rho_k(x_0,y_0), \tag{2}$$

and

$$\psi_k(0,y) = \int_S \int dx_0\, dy_0\, G_k(0,y|x_0,y_0)\rho_k(x_0,y_0), \tag{3}$$

for the field on a wall collinear to the x axis, and the field on a wall collinear to the y axis, respectively. The explicit form for the Green's function in the rectangular cavity is the well-known expansion

$$G_k(x,y|x_0,y_0) = \frac{1}{ab}\sum_{m,n=0}^{\infty} \epsilon_m\epsilon_n \times \frac{\cos(m\pi x/a)\cos(m\pi x_0/a)\cos(n\pi y/b)\cos(n\pi y_0/b)}{K_{mn}^2-k^2}, \tag{4}$$

for homogeneous Neumann boundary conditions on all walls. The symbol K_{mn} is defined by

$$K_{mn}^2 = \left(\frac{\pi m}{a}\right)^2 + \left(\frac{\pi n}{b}\right)^2, \tag{5}$$

and the ϵ_n symbols are the Neumann factors, which are defined by

$$\epsilon_n = \begin{cases} 1 & \text{if } n=0 \\ 2 & \text{if } n>0. \end{cases} \tag{6}$$

The quantity

$$\langle \psi_k(x,0)\psi_k^\dagger(0,y')\rangle = \int_{S_0}\int dx_0\, dy_0 \int_{S_0'}\int dx_0'\, dy_0' \times G_k(x,0|x_0,y_0)G_k(0,y'|x_0',y_0') \times \langle \rho_k(x_0,y_0)\rho_k^\dagger(x_0',y_0')\rangle, \tag{7}$$

may now be formed. The angle brackets $\langle\ \rangle$ represent ensemble averages. Equation (7) relates the autocorrelation function between the fields measured on adjacent walls (collinear with the x and y axes) to the autocorrelation function of the source. One may expect that for experimental work of the type required to verify results in this paper, time averaging may be more convenient than ensemble averaging. Ensemble averaging, on the other hand, is normally more convenient for theoretical developments such as that described in this paper, and correspondingly this type of averaging will be used. If, of course, we assume that the ensemble is *ergodic*, the two methods of averaging are equivalent. The field and source autocorrelation functions are, respectively, defined as

$$A_k^{\psi}(x,0|0,y') = \langle \psi_k(x,0)\psi_k^\dagger(0,y')\rangle, \tag{8}$$

and

$$A_k^{\rho}(x_0,y_0|x_0',y_0') = \langle \rho_k(x_0,y_0)\rho_k^\dagger(x_0',y_0')\rangle, \tag{9}$$

which is how they appear in Eq. (7).

Since we will be interpreting ψ_k and ρ_k as Fourier amplitudes of time-dependent stationary fields and sources, the autocorrelation functions as defined above must be modified to include an integration over an infinitesimal band of frequencies centered at k (see Marchand and Wolf[13]). In this case the resulting functions are the cross-spectral densities of the field and source at the primed and unprimed points. From here on, it may be assumed this integration has been performed without altering any of the argument.

It was stated in the Introduction that the discrete inverse cavity problems considered in this paper are in general intractable. Stated more precisely, these problems have nonu-

nique solutions. This statement may be proved directly for the deterministic case by expanding the source distribution function in Eqs. (2) and (3) in terms of orthonormal cavity modes and then substituting Eq. (4) in for the Green's function in these equations.

We shall assume that the source distribution function $\rho_k(x_0,y_0)$ is composed of an arbitrary but finite collection of modes; hence,

$$\rho_k(x_0,y_0) = \sum_{i,j=0}^{I-1,J-1} \sqrt{\frac{\epsilon_i \epsilon_j}{ab}} \cos(i\pi x_0/a)\cos(j\pi y_0/b) C_{i,j}. \quad (10)$$

The $C_{i,j}$ are arbitrary complex coefficients. Let X_i represent the ith Fourier cosine coefficient of the wave field $\psi_k(x,0)$ on the wall $(x,0)$

$$X_i = \sqrt{\frac{\epsilon_i}{a}} \int_0^a dx\, \psi_k(x,0)\cos(i\pi x/a). \quad (11)$$

Similarly, let Y_j represent the jth Fourier cosine coefficient of the wave field $\psi_k(0,y)$ on the wall $(0,y)$

$$Y_j = \sqrt{\frac{\epsilon_j}{b}} \int_0^b dy\, \psi_k(0,y)\cos(j\pi y/b). \quad (12)$$

Making the substitutions stated in the previous paragraph, the following equations result:

$$X_i = \frac{1}{\sqrt{b}} \sum_{j=0}^{J-1} \frac{\sqrt{\epsilon_j}}{K_{i,j}^2 - k^2} C_{i,j} \quad (0 \leqslant i < I), \quad (13)$$

and

$$Y_j = \frac{1}{\sqrt{a}} \sum_{i=0}^{I-1} \frac{\sqrt{\epsilon_i}}{K_{i,j}^2 - k^2} C_{i,j} \quad (0 \leqslant j < J). \quad (14)$$

By including field measurements on the walls ($x=a$ and $y=b$), another two sets of equations similar to (13) and (14) may be formed. This brings the total number of equations to $2(I+J)$. The number of unknowns is obviously equal to $I \times J$.

Consider now the nondeterministic case, where the symbols ψ_k, ρ_k, and C_{ij} now represent random processes. The structure of the source process will still be considered finite, being composed of $I \times J$ terms as in Eq. (10) (of course, the C_{ij} in this equation are now random processes).

Integral equations relating the field and source autocorrelation functions may be formed by multiplying the field equations [such as Eqs. (2) and (3)] on the walls together and then taking the ensemble average [as can be seen in Eq. (7)]. By generating all the possible non-redundant integral equations (using all the wall pairs) the field autocorrelation functions

$$\left\langle \psi_k\left(\begin{matrix} x,0 \\ x,a \\ 0,y \\ b,y \end{matrix}\right) \psi_k^{\dagger}\left(\begin{matrix} x',0 \\ x',a \\ 0,y' \\ b,y' \end{matrix}\right) \right\rangle \quad (15)$$

will be formed (where one ordered pair may be chosen from each large bracket) on the left-hand side of the integral equations. By following the discretization procedure (a discrete cosine transform) as before, it is seen that

$$4I^2 + 4(I \times J) + 4(J \times I) + 4J^2 = (2(I+J))^2 \quad (16)$$

equations are rendered.

The product of the complex conjugate of the source function over the primed coordinates, and the source function over the unprimed coordinates, appears in the source autocorrelation function in the kernel of all the integral equations. The discretization procedure will thus produce $(I \times J)^2$ unknowns. These unknowns correspond to all nonredundant autocorrelation values obtained at pairs of source points. (Remember the source structure is considered finite for this argument.)

Simply put, since the source distribution functions are multiplied in the integrands of the expressions for field autocorrelation functions, there will be $(I \times J)^2$ unknowns. Obviously, in both cases for I and J sufficiently large, the set of equations is under-conditioned.

Now, the assumption that the source is spatially incoherent is introduced. This implies

$$A_k^{\rho}(x_0,y_0|x_0',y_0') = I_k(x_0,y_0)\,\delta(x_0 - x_0')\,\delta(y_0 - y_0'), \quad (17)$$

where $I_k(x_0,y_0)$ is the intensity profile of the source, and is a real non-negative function. For the sake of brevity, the notation

$$\delta(x-x',y-y') \overset{\text{def}}{=} \delta(x-x')\,\delta(y-y'), \quad (18)$$

shall be used for the two-dimensional Dirac delta function in rectangular coordinates. Substituting Eq. (17) into Eq. (7) renders

$$A_k^{\psi}(x,0|0,y') = \int\int_{S_0} dx_0\, dy_0 G_k(x,0|x_0,y_0) G_k(0,y'|x_0,y_0) \times I_k(x_0,y_0). \quad (19)$$

The resolution of Eq. (19) will provide us with an expression for the unknown intensity profile. To achieve this, the intensity profile is expanded in a cosine series as

$$I_k(x_0,y_0) = \frac{1}{\sqrt{ab}} \sum_{pq=0}^{\infty} \sqrt{\epsilon_p \epsilon_q} I_{pq} \cos(p\pi x_0/a)\cos(q\pi y_0/b). \quad (20)$$

[The I_{pq} are the Fourier cosine coefficients of $I_k(x_0,y_0)$.] Now this expansion, along with the expression for the Green's function in Eq. (4), is substituted into Eq. (19).

The cosine terms containing the source arguments in the Green's functions are then reduced using standard trigonometric identities to yield the equation

$$A_k^{\psi}(x,0|0,y')$$
$$=\left(\frac{1}{ab}\right)^2 \sum_{mnm'n'=0}^{\infty} \epsilon_m\epsilon_n\epsilon_{m'}\epsilon_{n'} \times \frac{\cos(m\pi x/a)\cos(n'\pi y'/b)}{(K_{mn}^2-k^2)(K_{m'n'}^2-k^2)} \sum_{pq=0}^{\infty} \mathcal{P}_{mnm'n'pq} I_{pq}, \tag{21}$$

where

$$\mathcal{P}_{mnm'n'pq} = \frac{1}{4}\sqrt{\frac{\epsilon_p\epsilon_q}{ab}} \int_0^a \int_0^b dx_0\, dy_0 \times (\cos[(m+m')\pi x_0/a]\cos[(n+n')\pi y_0/b] + \cos[(m-m')\pi x_0/a]\cos[(n+n')\pi y_0/b] + \cos[(m+m')\pi x_0/a]\cos[(n-n')\pi y_0/b] + \cos[(m-m')\pi x_0/a]\cos[(n-n')\pi y_0/b]) \times \cos(p\pi x_0/a)\cos(q\pi y_0/b). \tag{22}$$

To make the following procedure clearer, n, n' and y' are relabeled as follows:

$$n \leftrightarrow n', \quad y' \rightarrow y. \tag{23}$$

For additional clarity, the function $A_k^{\psi}(x,0|0,y)$ will be identified by the symbol $A(x,y)$ Applying these relabelings to Eq. (21) results in

$$A(x,y) = \left(\frac{1}{ab}\right)^2 \sum_{mnm'n'=0}^{\infty} \epsilon_m\epsilon_n\epsilon_{m'}\epsilon_{n'} \times \frac{\cos(m\pi x/a)\cos(n\pi y/b)}{(K_{mn'}^2-k^2)(K_{m'n}^2-k^2)} \sum_{pq=0}^{\infty} \mathcal{P}_{mnm'n'pq} I_{pq}. \tag{24}$$

Notice that these relabelings do not alter $\mathcal{P}_{mnm'n'pq}$, which is symmetric in n and n' and independent of y'.

Both sides of Eq. (24) are now multiplied by

$$\sqrt{\frac{\epsilon_{n''}\epsilon_{m''}}{ab}}\cos(m''\pi x/a)\cos(n''\pi y/b), \tag{25}$$

and integrated from 0 to a and 0 to b for x and y, respectively, to obtain a doubly indexed set of equations

$$A_{mn} = \left(\frac{1}{ab}\right)^{3/2} \sum_{m'n'=0}^{\infty} \epsilon_{m'}\epsilon_{n'}\sqrt{\epsilon_m\epsilon_n} \times \frac{1}{(K_{mn'}^2-k^2)(K_{m'n}^2-k^2)} \sum_{pq=0}^{\infty} \mathcal{P}_{mnm'n'pq} I_{pq}, \tag{26}$$

where

$$A_{mn} \overset{\text{def}}{=} \int_0^a \int_0^b dx\, dy\, A(x,y) \sqrt{\frac{\epsilon_m\epsilon_n}{ab}}\cos(m\pi x/a)\cos(n\pi y/b). \tag{27}$$

[Of course the A_{mn} are just the Fourier cosine coefficients of the field autocorrelation function $A(x,y)$.] Note that the double primes on the indices m and n have been omitted for simplicity. The evaluation of the double integral within Eq. (22) greatly simplifies this result. The integrals will in fact be zero unless m' and n' are such that

$$m', n' \geqslant 0, \tag{28}$$

and

$$\begin{cases} |m-m'| = p \\ \text{or} \\ |m+m'| = p, \end{cases} \tag{29}$$

and

$$\begin{cases} |n-n'| = q \\ \text{or} \\ |n+n'| = q. \end{cases} \tag{30}$$

Taking these conditions together, it is necessary only to know whether p and q are equal to m and n in order to determine which of the integrals are nonzero. In this way, the sum over the primed variables (m' and n') is removed. The following doubly indexed set of linear equations results:

$$A_{mn} = \sum_{pq=0}^{\infty} \mathcal{Q}_{mnpq} I_{pq}, \tag{31}$$

where

$$\mathcal{Q}_{mnpq} = \frac{\sqrt{\epsilon_m\epsilon_n\epsilon_p\epsilon_q}}{4ab} \begin{cases} f_p f_q (D_{m,n,m+p,n+q} + D_{m,n,|m-p|,n+q} + D_{m,n,m+p,|n-q|} + D_{m,n,|m-p|,|n-q|}) & \text{if } p \neq m, q \neq n \\ g_m f_q (D_{m,n,2m,n+q} + 2D_{m,n,0,n+q} + D_{m,n,2m,|n-q|} + 2D_{m,n,0,|n-q|}) & \text{if } p = m, q \neq n \\ g_n f_p (D_{m,n,m+p,2n} + D_{m,n,|m-p|,2n} + 2D_{m,n,m+p,0} + 2D_{m,n,|m-p|,0}) & \text{if } p \neq m, q = n \\ g_m g_n (D_{m,n,2m,2n} + 2D_{m,n,0,2n} + 2D_{m,n,2m,0} + 4D_{m,n,0,0}) & \text{if } p = m, q = n, \end{cases} \tag{32}$$

and

$$D_{m,n,m',n'} = \frac{1}{(K_{mn'}^2-k^2)(K_{m'n}^2-k^2)}. \tag{33}$$

Also, the factors f_i and g_i are defined by

$$f_i = \begin{cases} \frac{1}{2} & \text{if } i = 0 \\ 1 & \text{if } i > 0, \end{cases} \tag{34}$$

and

$$g_i = \begin{cases} \frac{2}{3} & \text{if } i=0 \\ 1 & \text{if } i>0. \end{cases} \tag{35}$$

These factors occur since, in all but one of the sums, there is a reduction in the number of terms when one or two of the indices m, n, p, q are equal to zero. Equation (31) may be written symbolically as

$$\mathbf{A} = Q\mathbf{I}, \tag{36}$$

where Q is a linear operator between the vector spaces to which $\mathbf{A}$ and $\mathbf{I}$ belong. As Q derives from the linear integral Eq. (19) over the region $[0,a]\times[0,b]$ it may be interpreted as acting over a Hilbert space of square integrable functions defined over the said region, with the usual norm ($\mathbf{A}$ and $\mathbf{I}$ then belong to this space). In Eq. (31), Q has been projected onto a Fourier cosine basis and is represented as a four-dimensional array (see the Appendix).

If the expansion (20) converges uniformly over the region $[0,a]\times[0,b]$, then the expansion in Eq. (31) will converge absolutely for all m,n. This is the case, since the factors $D_{m,n,p\pm m,q\pm n}$ (for $p>m$ and $q>n$) all decrease with the square of p and q. Sometimes, even when the expansion (20) does not converge uniformly, as in the case of a point source (which is a delta function and therefore infinite at some point in $[0,a]\times[0,b]$), the expansion in Eq. (31) will still converge absolutely.

This, of course, is expected (in the case of a point source) since it is the same as saying that the Green's function series expansion (4) itself converges uniformly and absolutely (which it obviously does, providing k is not at a cavity resonance). However, a subtle point arises here. If one takes note of Eq. (21), it can be clearly seen that the integral sign and the summation sign have been interchanged. This is allowable when the summation is uniformly convergent and sometimes even when it is not. In general, a test described by Bromwich[14] must be used to determine the validity of this step. Since these results will be applied to a delta function later on, it is necessary to determine the validity of the interchange for this particular case. To do this, first note that a delta function in a rectangular enclosure may be expanded as follows:

$$\delta(x_0-x_s,y_0-y_s) = \frac{1}{ab}\sum_{pq=0}^{\infty} \epsilon_p\epsilon_q \cos(p\pi x_0/a)\cos(q\pi y_0/b) \times\cos(p\pi x_s/a)\cos(q\pi y_s/b). \tag{37}$$

This expansion is relatively standard and may be derived from the methods used by Morse and Feshbach[15] (p. 719). By substituting the left-hand side of Eq. (37) into Eq. (19) and the coefficients

$$I_{pq} = \sqrt{\frac{\epsilon_p\epsilon_q}{ab}}\cos(p\pi x_s/a)\cos(q\pi y_s/b), \tag{38}$$

on the right-hand side of Eq. (37) into Eq. (21), it can be seen that both Eqs. (19) and (21) yield the same expression upon evaluation of the associated integrals. (Both of these integrals are trivial: the first because it involves a delta function and the second because the eigenfunctions are orthogonal.)

Returning to Eq. (31), it can be seen that since the expansion on the right-hand side of this equation will be absolutely convergent for most practical cases (and certainly the ones examined here), the double summation may be reindexed in any fashion desired without affecting the limit. This is useful since the equation must be reduced to one of single indexation so that the usual matrix manipulations may be applied. Having said this, it must be admitted that a *square* mapping was used for converting the equation to one dimension. In other words, the mapping preserves the original indexing implied by the double summation signs (although no attempt was made to preserve the order of the summations), even though this is not necessary. This mapping was chosen essentially for convenience.

The absolute convergence of the series in (31) does, however, have another very important ramification. It can be noted that to obtain Eq. (31) from Eq. (26), it was necessary to interchange the orders of the double summations indexed by m', n' and p, q in Eq. (26). It is a well-known theorem that no divergent or conditionally convergent series may be rearranged to produce an absolutely convergent series. Hence, the interchange of the infinite summations is allowable given that the resultant summation [i.e., in Eq. (31)] is absolutely convergent.

Before turning to the resolution of Eq. (31), a discussion of the case of a point source is in order. Until now, it has been assumed that the source intensity profile we are reconstructing corresponds to a random (spatially incoherent) distributed source. Of course, this may also be a random point source; however, even a completely deterministic point source may be reconstructed by the same technique. This can be shown as follows. First, an equation similar to Eq. (7) is formed, but using delta functions for the deterministic point sources

$$\psi_k(x,0)\psi_k^{\dagger}(0,y') = \int_{S_0}\int dx_0\,dy_0 \int_{S_0'}\int dx_0'\,dy_0' \times G_k(x,0|x_0,y_0)G_k(0,y'|x_0',y_0')\rho_k \times \delta(x_s-x_0,y_s-y_0)\rho_k^{\dagger}\delta(x_s-x_0',y_s-y_0'), \tag{39}$$

where (x_s,y_s) is the point source position and ρ_k now represents the point source strength. We now recognize that

$$\delta(x_s-x_0,y_s-y_0)\,\delta(x_s-x_0',y_s-y_0') = \delta(x_0'-x_0,y_0'-y_0)\,\delta(x_0-x_s,y_0-y_s). \tag{40}$$

Substituting this expression into Eq. (39) results in

$$\psi_k(x,0)\psi_k^{\dagger}(0,y) = \int_{S_0}\int dx_0\,dy_0 G_k(x,0|x_0,y_0) \times G_k(0,y|x_0,y_0)I_k(x_0,y_0), \tag{41}$$

where $I_k(x_0,y_0)$ $(=\rho_k\rho_k^{\dagger}\delta(x_s-x_0,y_s-y_0))$ now represents the intensity of the point source. This equation is identical to Eq. (19) except for the ensemble averages (angled brackets) and hence may be resolved in the same manner.

It will be noted here that if the frequency of the point source is such that a highly restricted number of modes are strongly excited (for instance, near a resonance), then its position may be determined more simply. However, this is not the most general of cases and will not be discussed further here.

A. Fundamental instabilities

It was mentioned in the Introduction that a forward diffraction problem represented by a Fredholm equation of the first kind, with a kernel corresponding to a compact (infinite rank) operator, will imply that the associated inverse diffraction problem is fundamentally ill-posed. To briefly explain this, if the forward operator is of infinite rank and compact, it will have a series of eigenvalues which have zero as their limit. This property implies that an arbitrarily small variation in the image of the forward operator can produce an arbitrarily large variation in the image of the inverse operator. This fact has been well documented in the literature. (A proof of these statements may be found in Roger *et al.*[11]) This small variation in the image of the forward operator could in practice be due to experimental error, convergence errors (for infinite source expansions), or even the limitations of machine precision.

To see that the instabilities we have encountered are of this nature, it is necessary to show that the operator Q (which is represented by a four-dimensional array) defined by Eq. (32) is indeed compact. Such a proof is given in the Appendix. Of course, any operator we will be dealing with numerically will be finite. However, since the operator will be a truncated version of an infinite compact operator, it is possible for its eigenvalues to possess a dynamic range large enough to severely or completely corrupt reconstructions based on finite precision measurements. We will even see it is the case in some fairly modestly sized operators that the eigenvalues possess a dynamic range greater than that which is machine representable. The presence of these very small eigenvalues leads to numerical instability when the operator (or matrix, as the case will be) is inverted.

To overcome the instabilities that arise from inverting this compact operator, regularization techniques may be employed (again as mentioned in the Introduction). The general techniques used in this paper are well documented in Ref. 12 and Biemond.[16] Only the various adaptations of these techniques to our problem are mentioned.

Now, by writing the inverse problem as a matrix equation

$$A\mathbf{u}=\mathbf{b}, \tag{42}$$

the quantity may be formed

$$(A^*A+\lambda L)\mathbf{u}=A^*\mathbf{b}, \tag{43}$$

where $L=R^*R$ and R is the *regularizing operator*. The star above the operator (or matrix in this case) implies the adjoint of the operator (or transpose of the matrix) has been taken. The symbol λ represents a *regularizing parameter*. Linear regularization techniques usually seek to limit the magnitude and/or derivatives of the solution of the problem. One can think of linear regularization as a linear *filtering* procedure, whereby solutions of say an ''unphysical'' nature (too large, or too sharp, etc.) are weeded out. (Of course, filtering procedures usually corrupt the results by removing useful information as well as unwanted ''noise.'') The operator R used in this paper will limit only the magnitude of the two-dimensional solution. This was actually found to be the most successful choice of operator for the current problem. The regularizing operator is, therefore, simply the identity operator in this case, hence

$$L=R^*R=1, \tag{44}$$

or in matrix notation, L is simply the identity matrix.

The value of the regularizing parameter λ basically determines the degree to which one imposes the conditions, represented in L, on the solution. In our case, λ simply regulates the magnitude of the solution. There exist standard methods for determining L. A common one is this: if we know an upper bound for the error present in the solution, λ may be assigned a value such that

$$\|A\mathbf{u}-\mathbf{b}\|=\|\Delta\mathbf{b}\|, \tag{45}$$

where $\Delta\mathbf{b}$ represents an upper bound for the errors in $\mathbf{b}$. We have not found this method useful, however, and have used other techniques which will be discussed in Sec. I B.

Another common technique is an iterative solution of Eq. (43) coupled with projections onto convex sets (POCS). This technique has been used here only as a means of iteratively improving a solution obtained from a direct resolution of Eq. (43). The basic algorithm may be found in Ref. 12 (Chap. 18) and is of the form

$$\mathbf{u}^{i+1}=P_1P_2\cdots P_m(\mathcal{I}-\varsigma\lambda L)\mathbf{u}^i+\varsigma A^*(\mathbf{b}-A\mathbf{u}^i), \tag{46}$$

where ς is a real number which must satisfy the condition

$$0<\varsigma<\frac{2}{\max\ \text{eigenvalue}\ (A^*A+\lambda L)}, \tag{47}$$

to ensure convergence of the method. The symbol $\mathcal{I}$ represents the identity matrix. The symbol P_i refers to nonexpansive projection operators onto convex sets. The projection operators allow us to impose deterministic constraints. This technique will be applied to the first of the two examples that follow. Here, convex sets will be formed using approximate knowledge of the solution at the boundary.

It would also be possible, of course, to limit the magnitude and gradient of the solution with projection operators, as with the linear regularization techniques. However, this would be done explicitly rather than by use of a regularizing parameter. This avenue of research has not been explored, mainly because it was found that the iterative procedure converges very slowly. Hence, as stated above, the iterative technique has been used simply to improve a direct resolution of Eq. (43).

As our reconstructions will never be exact, it is necessary to define an error expression. This is given in terms of the Hilbert norm and is

$$e_f = \left(\frac{\int_0^a \int_0^b dx\, dy |f(x,y) - f_0(x,y)|^2}{\int_0^a \int_0^b dx\, dy |f_0(x,y)|^2} \right)^{1/2}, \tag{48}$$

where f_0 is the true solution and f is the approximate solution. Obviously, the magnitude of a solution, f, can be simply defined as precisely the Hilbert norm

$$m_f = \left(\int_0^a \int_0^b dx\, dy |f(x,y)|^2 \right)^{1/2}. \tag{49}$$

B. Examples

It was mentioned in the Introduction that the solution to the spatially incoherent inverse source problem dealt with in this paper can only be determined uniquely if either the source intensity profile has a finite modal structure, or an infinite number of field measurements is made. Two sets of examples of source reconstructions will now be given using the formalism above. In the first of these we will reconstruct a random spatially incoherent source whose intensity profile is a function composed of a finite number of cavity modes (i.e., a finite modal structure as mentioned above). This source is a *continuous distribution*, not a finite collection of discrete sources. The second set of examples will concern the reconstruction of a point source (which is obviously not representable by a finite modal expansion).

Both sets of examples will exhibit reconstruction errors, due to the fundamental instability outlined above. Obviously, finite operators, and finite matrices which represent them, are being dealt with here. Hence, the errors we shall be forced to consider are bounded. The instability referred to earlier will manifest itself in the matrices we are dealing with by causing them to be extremely ill-conditioned. All the sources dealt with in this paper are confined in a rectangular cavity of sides of $a=1$ and $b=2$. These lengths are dimensionless.

1. Band-limited spatially incoherent sources

In the first problem we address, the intensity profile of the source has been limited to include only the first 25 modes of the cavity. The inverse operator is also constructed using this number of modes. The reason for this size limitation is that we wish in this example to demonstrate explicitly the effect of adding random error of a known magnitude. It is obvious that this example is quite limited in scope. However, the limit of 25 modes still allows us, with double precision (on a Sparc 4 architecture), to reconstruct the source almost perfectly, when no random error is included. This is provided that the frequency at which the reconstruction is done is not too near a cavity resonance or higher than the highest eigenfrequency of the modes present in the source function. These conditions will be examined later. The problem is then extended to include the first 49 modes of the cavity, in the source profile and inverse operator, so as to examine the effect of increasing the rank of the inverse operator.

In general, the inverse problem has a matrix of order $N^2 \times N^2$, where A_{NN} [as defined in Eq. (27)] is the highest order coefficient of the measured field. So, a 25-mode problem would, for instance, contain a (5,5) mode, and the matrix would be a 25×25. So, the memory requirement goes up with the square of the number of modes involved (the number of operations in the matrix inversion is, therefore, of order N^6).

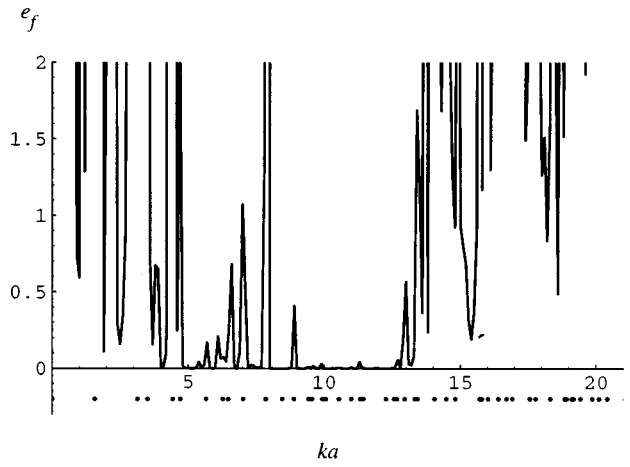

FIG. 2. The error e_f vs ka, for the 25-mode problem with $\lambda = 0$. The resonant wave numbers are shown as points in the negative region of the graph.

The forward problem was simulated simply by using Eq. (31) with a known set of coefficients in the expansion for $I_k(x,y)$. When it was required, a random number generator was used to add a random error of $\pm 1\%$ to the field coefficients A_{mn}. Equation (31) was then inverted, using the techniques described above, to recover the source profile.

As mentioned above, the frequency at which the reconstruction is attempted is critical to the accuracy of the procedure. As the reconstruction frequency approaches a resonant frequency of the cavity, the problem becomes increasingly unstable, which is to say that the error becomes very large near a resonant frequency. This is to be expected since, as the frequency approaches a cavity resonance, denominators of the form of those shown in Eq. (33) become large, increasing the dynamic range of the matrix eigenvalues. To see this, one can imagine that the row containing a ''large'' element could be made sufficiently large so that

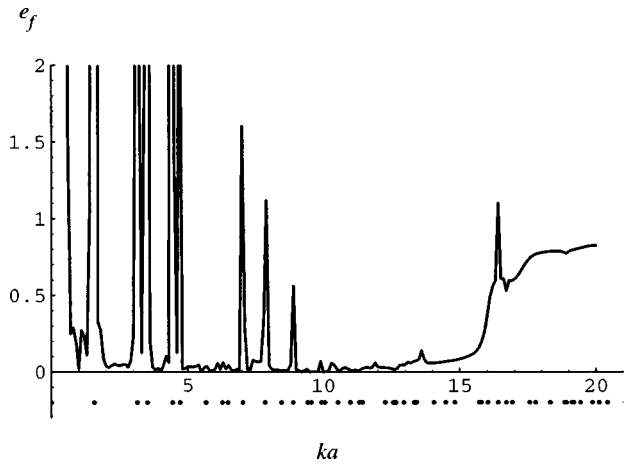

FIG. 3. The error e_f vs ka, for the 25-mode problem with $\lambda = 10^{-16}$. The resonant wave numbers are shown as points in the negative region of the graph.

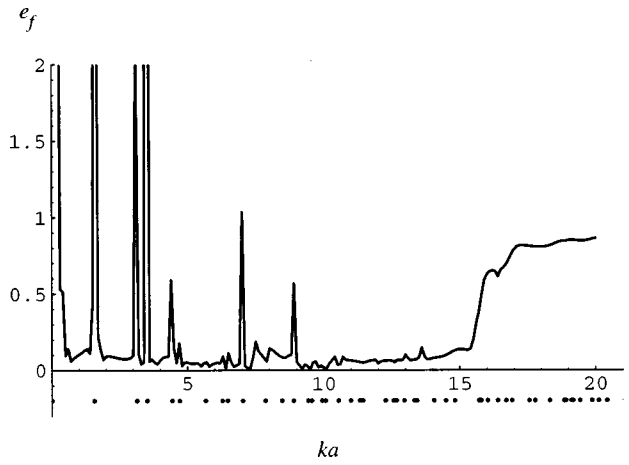

FIG. 4. The error e_f vs ka, for the 25-mode problem with $\lambda = 10^{-14}$. The resonant wave numbers are shown as points in the negative region of the graph.

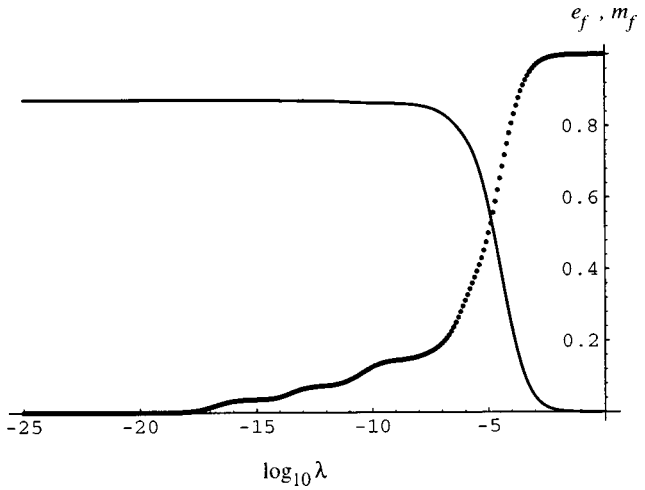

FIG. 5. The magnitude m_f and the error e_f vs λ, for the 25-mode problem, with no random error added ($ka = 12$). The magnitude is shown in solid line and must be multiplied by a factor of 10. The error is shown as points.

some other row not containing large elements becomes effectively a ''row'' of zeros, which is a singular state for a matrix. This effect can be countered to some extent by varying the regularizing parameter λ. Specifically, increasing λ appears to increase the stable region (or a region of relatively low error) around a resonant frequency, although obviously the regularization technique introduces an error of its own. Figures 2–4 illustrate this effect for the reconstruction of the test 25-mode source without added error. It can be seen that as the regularizing parameter is increased in magnitude, the stable regions in the error versus ka curves become larger. It is also apparent that the average minimum error becomes larger as the regularizing parameter is increased in magnitude.

It is interesting to note that the low-frequency resonances seem to affect a wider band of frequencies than the higher resonances, which in a large number of cases do not seem to excite instabilities at all. This is of course due to the fact that the curve was generated with a finite number of points (with equal ka spacing), none of which in fact lies exactly at any of the resonances (''exact'' in this case means to double-precision accuracy). In general, optimal values of the regularizing parameter must be worked out for each frequency. This has not been done for the error versus ka curves, since it would require a large amount of effort and the curves have been introduced mainly to illustrate the basic effect of the cavity's resonances.

It was also mentioned earlier that inaccurate reconstructions occur where the reconstruction frequency is higher than the highest eigenfrequency of the modes present in the source function. The highest eigenfrequency in the 25-mode source and autocorrelation functions corresponds to $ka = 14.05$. It can be seen from Figs. 3 and 4 that for ka slightly greater than this, there is a large rise in the error curves. (This same behavior is exhibited by the 49-mode source, as will be seen shortly.) In practice then, it is probably best to keep the reconstruction frequency as far away from a resonance as possible, especially for $ka \lesssim 2\pi$. It also appears necessary to avoid reconstruction frequencies higher than the highest eigenfrequency of the modes present in the autocorrelation function. (The highest eigenfrequency of the modes present in the autocorrelation function, by virtue of measurement, determines the highest eigenfrequency of the modes ''known'' to exist in the source function.) Perhaps this reconstruction error can be linked to the fact that some rows or columns [with denominators of the form of Eq. (33)] become very small with respect to others (i.e., those containing larger values of K_{nm}), when k becomes larger than the largest K_{nm} value present in the source function.

We now proceed to examine the effect of adding a random error of known magnitude to the ''measured field'' (which means the A_{mn} coefficients) before reconstructing the source. The magnitude of the added error will be $\pm 1\%$ of the field coefficients. It is noted here that in reality it would take quite a good experiment to achieve this low an error, but it will serve as an example for the present. It was mentioned earlier that the regularizing parameter, λ, needs to be optimized for the specific frequency one is using (due mainly to the presence of nearby resonances). The same is also true when random error is being added to the field.

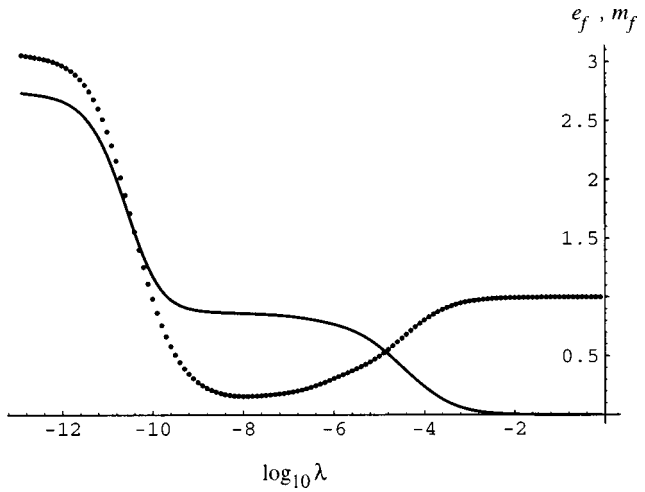

FIG. 6. The magnitude m_f and the error e_f vs λ, for the 25-mode problem, with $\pm 1\%$ random error added ($ka = 12$). The magnitude is shown in solid line and must be multiplied by a factor of 10. The error is shown as points.

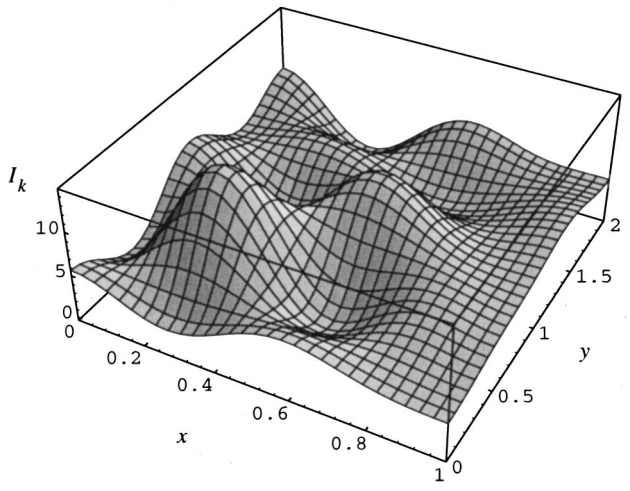

FIG. 7. The source reconstruction $I_k(x,y)$, for the 25-mode problem with $\pm 1\%$ random error added ($ka=12$). The error in this reconstruction is 17% with $\lambda = 10^{-8}$.

One method for achieving this optimization is to examine the magnitude of the solution as a function of λ. This technique has been used previously by Roger *et al.*[11] Figure 5 shows both the magnitude and error of the reconstructed source as a function of λ for the case of no added error when $ka=12$. Figure 6 is a graph of the same quantities at the same frequency, but for the case of an added random error of $\pm 1\%$. It can be seen from Fig. 5 that when $ka=12$, there is no need to regularize the problem when random error is not present. This provides a stark contrast to the case when a random error of $\pm 1\%$ exists in the field data, as can be seen in Fig. 6.

An examination of Fig. 6 reveals that there exists a relatively flat region (or ''plateau'') in the magnitude versus λ curve. This type of behavior was also observed by Roger *et al.*[11] These authors denoted the plateau region a *zone of insensitiveness,* as their reconstructions were apparently accurate anywhere in this region. In our case, it seems as if the error is minimized when the gradient of the magnitude versus λ curve is minimized in the plateau region. As an example, a reconstruction has been performed at $\lambda = 10^{-8}$,

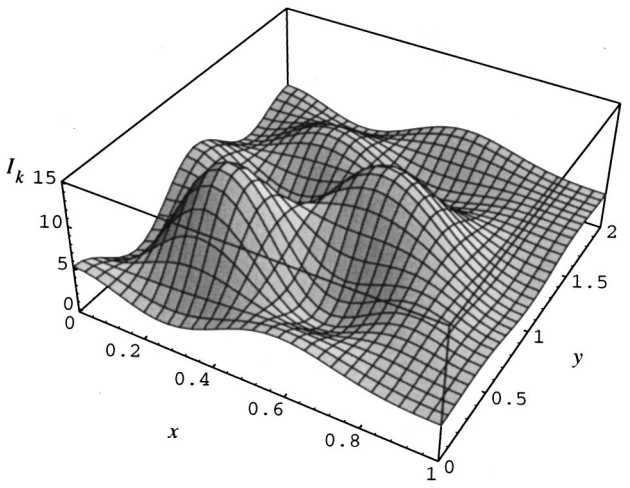

FIG. 8. The original source $I_k(x,y)$, for the 25-mode problem.

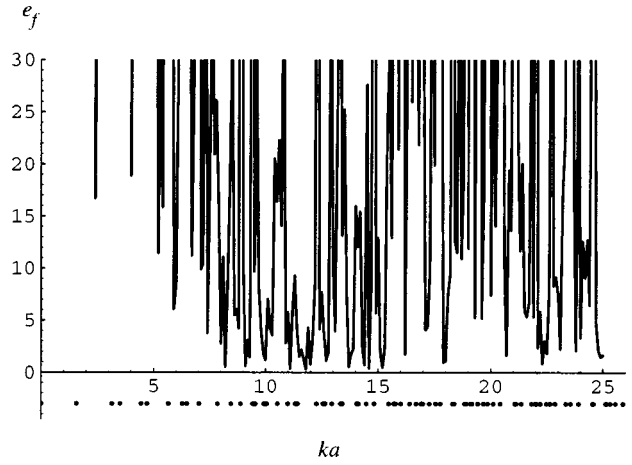

FIG. 9. The error e_f vs ka, for the 49-mode problem with $\lambda = 0$. The resonant wave numbers are shown as points in the negative region of the graph.

which is near the gradient minimum (in the plateau region) of the magnitude versus λ curve. This reconstruction is shown in Fig. 7, with the original profile shown in Fig. 8.

The 49-mode problem will now be considered. This problem demonstrates that the ill-conditioning we have observed can worsen with size. Error versus ka curves for this problem are shown in Figs. 9–11 for three different values of λ as before. A number of issues arise from these curves. To start with, it is apparent that the problem is more ill-conditioned, with the $\lambda = 0$ graph demonstrating errors much larger than 100% for almost all of the frequencies. The same punctuated nature appears to prevail in all of the curves, again due to the presence of the cavity's resonance frequencies. As λ is increased, it is again apparent that regions of relatively low error (or ''stable regions'') appear. It is also clear that the average minimum error, and in fact the absolute minimum error, is a good deal larger for the 49-mode problem for all values of λ, which tends to indicate again that the larger inverse operator is more poorly behaved. However, one advantage of having modes with higher eigenfrequencies in the source and autocorrelation functions is that the upper limit on the reconstructing frequency is higher.

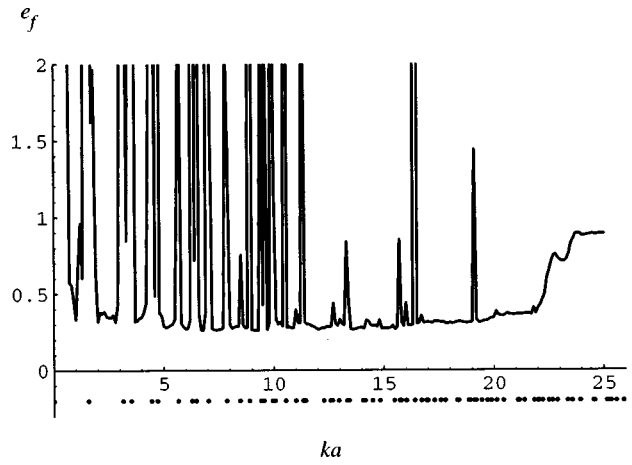

FIG. 10. The error e_f vs ka, for the 49-mode problem with $\lambda = 10^{-16}$. The resonant wave numbers are shown as points in the negative region of the graph.

One may verify this by examining Figs. 10 and 11, where it can be seen that the minimum error level does not start to rise sharply until $ka \approx 22$. This again corresponds to a frequency just slightly greater than the maximum eigenfrequency of the modes present in the source and autocorrelation functions (i.e., $ka = 21.07$).

Figures 12 and 13 are magnitude and error versus λ curves. These have again been made for the frequency corresponding to $ka = 12$. They demonstrate similar trends to the earlier 25-mode problem. However, it is evident from Fig. 12 that even when no error is added, the regularization procedure is advantageous. In this case, there appears to be a very sharp increase in the magnitude and error of the reconstructed profile at the end of the plateau region. This has been caused by the finite precision arithmetic of the computer. The reciprocal of the condition number of the regularized matrix with $\lambda = 10^{-20}$ was 1.3×10^{-17}. Obviously, if the condition number of the matrix is sufficiently high, then no precision can be obtained in the solution. It was found, however, that total loss of precision usually occurred for a condition number much higher than 10^{12}, which is the figure typically quoted. Total loss of precision generally occurred for condition numbers greater than about 1×10^{16}, for double precision in the Sparc 4 architecture used.

The case of no added error differs substantially from the case where errors have been added to the solution, as shown in Fig. 13. In this example, the magnitude of the solution rises much less sharply. The rise in magnitude here is associated simply with the ill-conditioning of the problem, not with a loss of precision.

It appears from the abrupt termination of the curves in Fig. 12 that, if the internal precision of the calculation had been increased, a curve similar to that in Fig. 5 or Fig. 13 may have been obtained. By stating this, we do not mean to imply that the actual (percentage) *accuracy* need be increased. The example in Fig. 13 makes it clear that even with inaccuracies of $\pm 1\%$, considerable precision is required in the internal calculation. The reciprocal of the condition numbers of the matrices in this case were of the order 10^{-7} to 10^{-11} for the section of the plateau region past the error minimum. If single precision were used in this case, there would have been a total loss of precision for at least some of the plateau region.

Again, it is not being suggested that the elements in the matrix need to be known with very high accuracy. Although this has not been simulated explicitly, it amounts to essentially the same thing as adding error to the field coefficients. The high level of precision required is necessary to keep track of the small values added to the matrix by the regularizing operator. These, in essence, seem to have the effect of keeping the diagonal elements in the matrix from becoming arbitrarily small.

If one compares the size of the plateau region in Fig. 12 with the case where random error has been added (Fig. 13), it can be seen that the random error has had the effect of reducing the size of the plateau region (especially since this region seems to have been truncated in Fig. 12). This latter phenomenon is expected and has been previously noticed by Roger *et al.*[11]

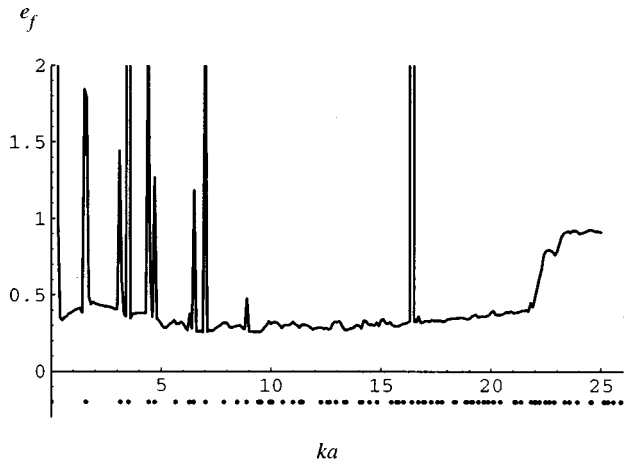

FIG. 11. The error e_f vs ka, for the 49-mode problem with $\lambda = 10^{-14}$. The resonant wave numbers are shown as points in the negative region of the graph.

Figures 14 and 15 show the original 49-mode source and its reconstruction after a random error of $\pm 1\%$ has been added. In this case, $\lambda = 10^{-10}$. It will now be demonstrated that improvement may be made by employing POCS, using some *a priori* information. For this purpose, it has been assumed that the original source profile was known at the boundaries to within $\pm 10\%$. Equation (46) has been used with a nonexpansive projection operator which projects onto the set of all functions over $[0,a] \times [0,b]$ with boundary values within $\pm 10\%$ of the actual value of the source profile. The parameter ς was crudely optimized by numerical experiment. (A value of 2000 was used.) The profile resulting from the procedure is shown in Fig. 16. As noted in the figure legend, the error in the profile has been reduced from 30% to 20%. This modest reduction is nevertheless visually noticeable and demonstrates the point that iterative improvement can be made if some *a priori* information is known about the solution. It should also be added that the method did converge slowly in the present case, as it does in general (see Biemond[16]). The number of iterations used was 20 000.

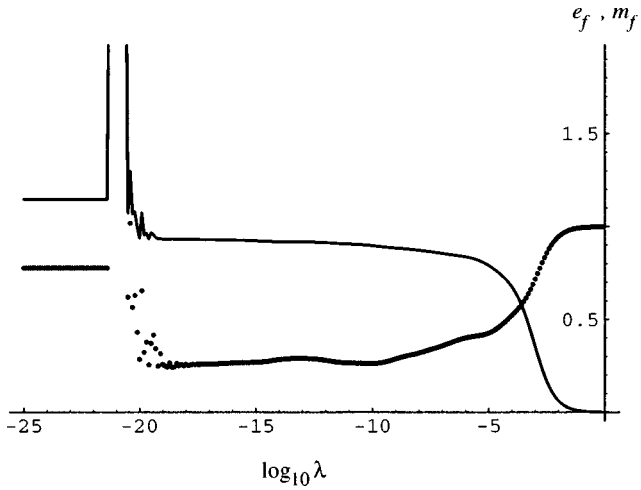

FIG. 12. The magnitude m_f and the error e_f vs λ, for the 49-mode problem, with no random error added ($ka = 12$). The magnitude is shown in solid line and must be multiplied by a factor of 10. The error is shown as points.

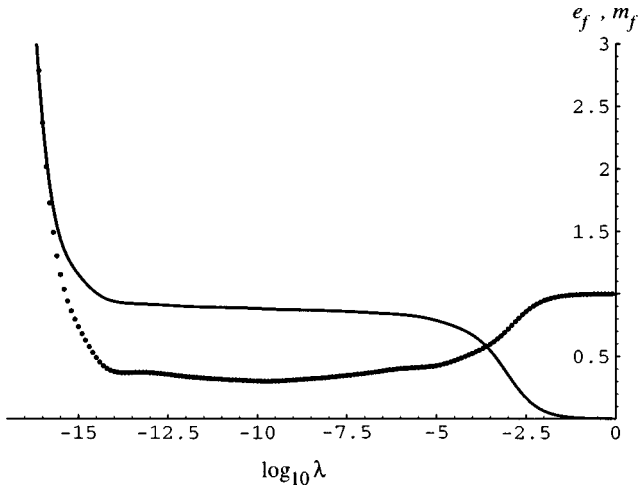

FIG. 13. The magnitude m_f and the error e_f vs λ, for the 49-mode problem, with $\pm 1\%$ random error added ($ka=12$). The magnitude is shown in solid line and must be multiplied by a factor of 10. The error is shown as points.

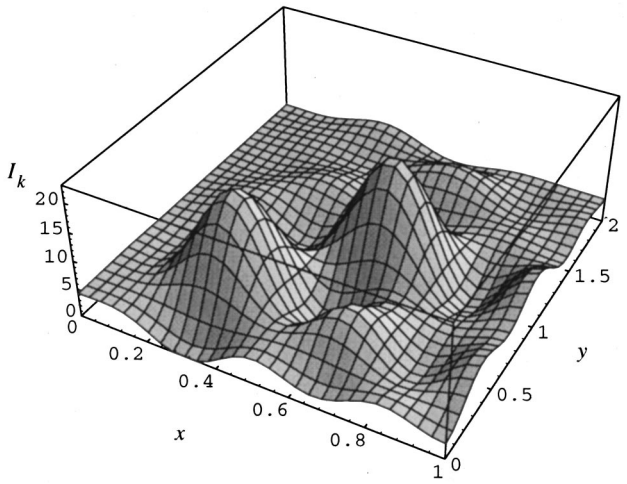

FIG. 15. The original source $I_k(x,y)$ for the 49-mode problem.

2. Point sources

The set of examples given in this section concerns the reconstruction of a point source in a rigid cavity. Given that a finite number of measurements is being made, and that a delta function is infinite and infinitely localized, we expect to recover only a ''low pass filtered'' version of the point source (see the discussion in the Introduction).

The forward problem has been generated in this case directly from the Green's function expansion (4), and has been truncated at the inclusion of 2000 modes in either direction. (This is to say 2000 modes were used in the expansion for the calculation of every coefficient of the ''measured'' field along the cavity wall in each coordinate direction.) Convergence errors will exist in the forward problem as only a finite number of modes is included; however, this number is still much larger than the number which would usually be included in the inverse problem. In practice, experimental limitations would generally dictate that only a relatively low number of measurements could be made for the reconstruction. As mentioned earlier, the inverse problem has a matrix of the order $N^2\times N^2$ [where A_{NN} as defined in Eq. (27) is the highest-order coefficient of the measured field]. This tends to imply it is desirable to use as few modes as possible, so that a direct, rather than iterative, approach may be taken to solving the matrix Eq. (31). Therefore, the convergence errors in the inverse problem will dominate those existing in the forward simulation. They will also imply that only fairly low frequencies are tractable. Convergence errors are exacerbated for large k, as one might expect from the form of the Green's function expansion.

The convergence errors in the forward and inverse problems excite the fundamental instability referred to earlier, and regularization is again necessary. (Of course, even if convergence errors were not present, machine precision would still be a limiting factor.) We will not add random error or use POCS for this example.

It is here that the problem appears to become better behaved as one increases the number of field coefficients used. This is expected, on the one hand, since the convergence errors will be reduced in the Green's function expansions in

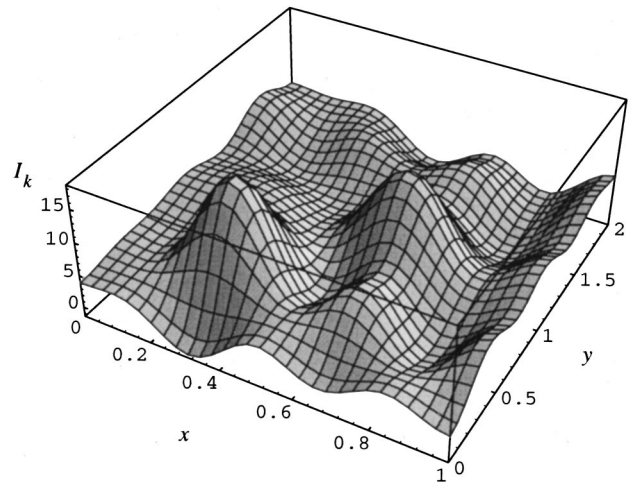

FIG. 14. The source reconstruction $I_k(x,y)$, for the 49-mode problem with $\pm 1\%$ random error added ($ka=12$). The error in this reconstruction is 30% with $\lambda=10^{-10}$.

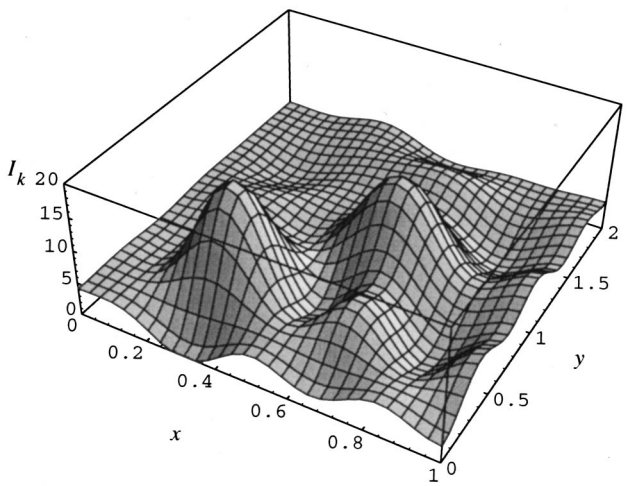

FIG. 16. The source reconstruction $I_k(x,y)$, for the 49-mode problem with $\pm 1\%$ random error added after application of POCS ($ka=12$). The error in this reconstruction is 20% and $\lambda=10^{-10}$.

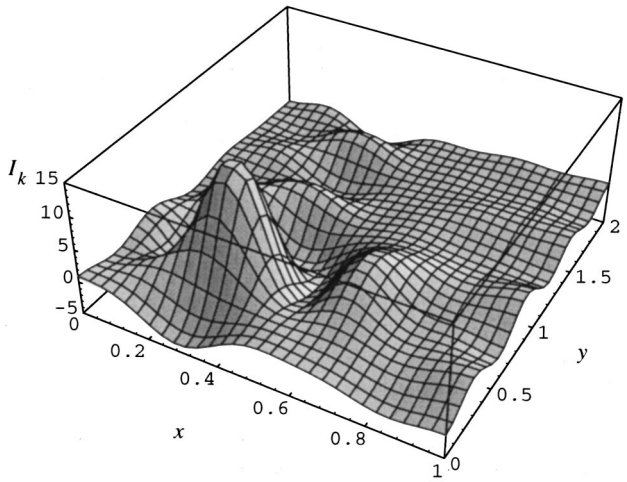

FIG. 17. The point source reconstruction $I_k(x,y)$, using 64 modes and 225 field coefficients, with original source coordinates: $(x,y)=(0.300,0.500)$. The reconstruction reaches a maximum at $(x,y)=(0.302,0.504)$. This should be compared with the coordinates of the maximum of the original truncated expansion, which are $(x,y)=(0.300,0.521)$. The magnitude estimate is in error by 33%. The reconstruction error is 53% and $\lambda=10^{-10}$ $(ka=6)$.

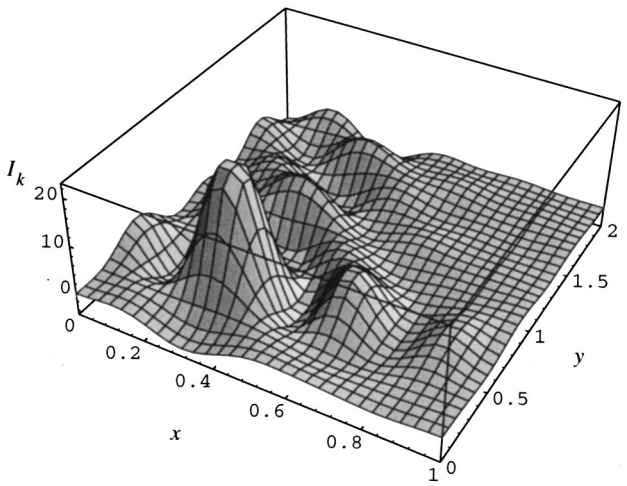

FIG. 18. The point source reconstruction $I_k(x,y)$, using 64 modes and 400 field coefficients, with original source coordinates: $(x,y)=(0.300,0.500)$. The reconstruction reaches a maximum at $(x,y)=(0.298,0.523)$. This should be compared with the coordinates of the maximum of the original truncated expansion, which are $(x,y)=(0.300,0.521)$. The magnitude estimate is in error by 0.1%. The reconstruction error is 31% and $\lambda=3\times10^{-16}$ $(ka=6)$.

the inverse operator. However, this should be counterbalanced by the fact that the larger operators are usually worse behaved (as was the case for the first problem), presumably due to the existence of more very-small singular values.

To demonstrate that the error does decrease when more field coefficients are used, two examples have been constructed. In each example, more field coefficients have been used than the required number of source coefficients, to facilitate convergence. This is to say our errors and plots will be based on a fixed number of source coefficients, this being a truncated set of the actual number calculated. In the first example, 225 field coefficients have been used in the inverse problem, and 64 of the resulting source coefficients have been used in the source reconstruction. In the second example, 400 coefficients have been used in the inverse problem and, again, 64 of the resulting coefficients have been used in the source reconstruction. These reconstructions are shown in Figs. 17 and 18 . The errors are listed in the figure legends and represent the normalized difference [in the sense of Eq. (48)] of the reconstructed point source and an equivalently truncated ideal modal expansion of the point source. Figure 19 is a plot of the original source.

The frequency of reconstruction corresponds to $ka=6$. It was found, using the methods described before, that the optimal value of λ for the 225-coefficient problem was approximately 1×10^{-10}, while the optimal value of λ for the 400-coefficient problem was approximately 3×10^{-16}. Using these values for λ, a graph of error versus ka was made for each problem, for the range $0<ka<6.5$. These graphs appear in Fig. 20. It can be seen from this figure that, although $ka=6$ indicates a relatively low wave number (i.e., $ka<2\pi$ as mentioned before), it isn't close enough to a resonance to put the solution in a high error region for the 400-coefficient plot (with $\lambda=3\times10^{-16}$). The 225-coefficient problem does not appear to be greatly affected by the presence of resonant frequencies, undoubtedly due to the fact that the regularizing parameter has a much larger value for this problem. This is important as we wish to compare errors of the point source reconstruction with respect to increasing the number of field coefficients. The comparison may be erroneous if we study the problem at a frequency for which the source reconstruction is in very large relative error.

These last two examples certainly show that increasing the number of field coefficients used can increase the accuracy of the reconstruction. The destabilizing effects which can accompany the use of a larger operator therefore seem to be less important here. It has been stated that the instability in the inverse problem is due to the compactness of the forward operator. A closer examination of the proof given in the Appendix for the compactness of the forward operator assumes we are operating on the Hilbert space L_2 defined over the region $[0,a]\times[0,b]$ (which will be denoted by the symbol H). It is evident, however, that the delta function is not a

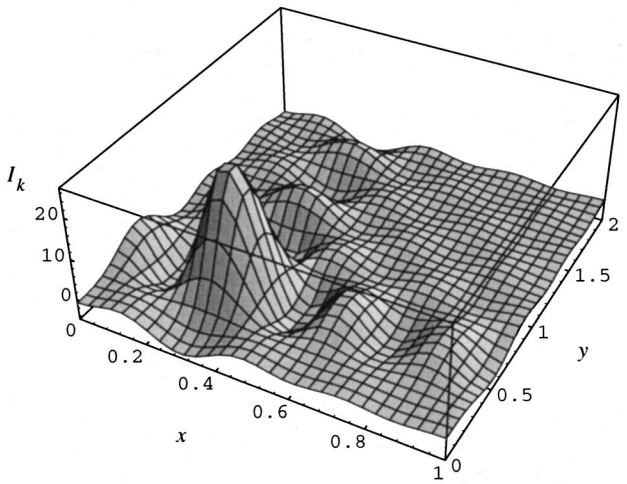

FIG. 19. The original point source expansion $I_k(x,y)$, truncated to 64 modes, with source coordinates: $(x,y)=(0.300,0.500)$.

square integrable function. In fact, it is not a function at all under the usual definition. (It is, however, an integrable generalized function.) This may be rigorously proved by squaring and integrating sequences equivalent to $e^{-nx^2}(n/\pi)^{1/2}$. The resulting sequence does not have a limit as $n\to\infty$ (see Lighthill,[17] p. 17).

It is still true that the forward operator maps the delta function onto H. In this sense, the forward operator may still be expressed as the limit of a sequence of finite rank operators. However, it is possible that the pathological nature of the delta function may in some way actually improve the behavior of the inverse problem. To justify this statement, note that the Fourier cosine expansion of a delta function does not converge in the usual sense; and it does seem to be the case, from the proof given in the Appendix, that the instability of the inverse problem is linked to the strength of the convergence of the forward problem (see Roger[18]). The proof of compactness in the Appendix, of course, is primarily a result for the operator rather than the source profile. It seems, however, that these two are related, since it is necessary to specify something about the source profile when defining compactness (i.e., that it is the member of a defined linear space).

This leads to an interesting aside. Consider a one-dimensional inverse problem represented by a Fredholm integral equation of the first type with a multipole function as the source profile

$$\psi(x)=\int_0^a \mathcal{K}(x|x_0)\,\delta^{(n-1)}(x_s-x_0)\,dx_0, \tag{50}$$

where ψ represents field measurements, $\mathcal{K}$ represents a compact kernel based on a wave operator of some description, δ is the Dirac delta function, and the integer superscripts enclosed in parentheses denote differentiation (with respect to x_0) a number of times equal to the value of the superscript.

Applying integration by parts to the integral equation results in

$$\psi(x)=\int_0^a \mathcal{K}(x|x_0)\,\delta^{(n-1)}(x_s-x_0)\,dx_0 \tag{51}$$

$$=\begin{cases} (-1)^i\displaystyle\int_0^a \mathcal{K}^{(i)}(x|x_0)\,\delta^{(n-i-1)}(x_s-x_0)\,dx_0 & n>1, \\ \mathcal{K}(x|x_0)H_f(x_0-x_s)\big|_0^a-\displaystyle\int_0^a \mathcal{K}^{(1)}(x|x_0) & \\ \quad\times H_f(x_s-x_0)\,dx_0 & n=1, \end{cases} \tag{52}$$

where H_f is the Heaviside step function and $0<x_s<a$.

It can be seen from Eq. (52), for $n>1$, that if we simply wish to localize a multipole source, and are not concerned about its structure (i.e., the order of the multipole), the derivatives may be transferred to the kernel of the equation so as to reduce the problem to resolving a point source with a multiply differentiated kernel. The kernel will in general be composed of Green's functions having modal expansions which weaken their convergence (and eventually diverge) under differentiation. The resulting inverse problem should therefore be more stable, the higher the order of the multipole. It would seem to follow that our original inverse source problem (before integration by parts) in Eq. (51) should increase in stability with increasing multipole order, provided our error metric is based in localization of the source rather than the source structure.

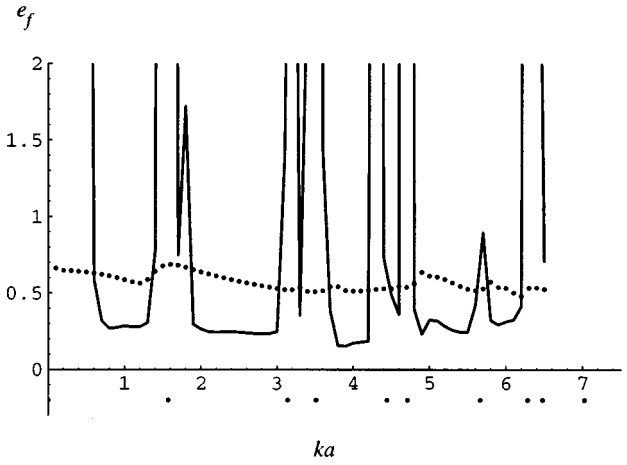

FIG. 20. The error e_f vs ka, for the 400-coefficient point source reconstruction (solid line), and the 225-coefficient point source reconstruction (points), with original source coordinates: $(x,y)=(0.300,0.500)$. The resonant wave numbers are shown as points in the negative region of the graph.

The case for a monopole source [Eq. (52) and $n=1$], which is similar to the problem at hand, is not quite as clear. Here, a point source has been converted through integration by parts to a Heaviside function, which is not manifestly localized like a delta function. Furthermore, another term appears in the integration by parts formula. This term, however, is a ''known'' in this problem, since it only involves evaluating the kernel at the boundary.

Even here, though, the same basic pattern seems to apply. The step change still gives an indication of the source position. Furthermore, it seems that the source position may be determined by magnitude measurements alone. That is, one may look for the point with coordinates nearest the half of the maximum value. This will only work if the profile is at least slightly imperfectly reconstructed, but this is almost by definition the case. The source position may, therefore, be inferred without differentiating the data. If differentiating the data were the only way of finding the source position, the latter argument about improved stability for this case would be circular. This completes the aside.

Given that a Fourier cosine expansion has been used for the delta function, what we expect to recover is a truncated set of Fourier cosine coefficients. These will produce a low-pass filtered version of the delta function when translated back into a Fourier cosine series (as mentioned at the beginning of this section). The maximum of the truncated series so formed should, however, give the approximate location of the point source. In addition, if the magnitude of the solution is compared with that of an equivalently truncated delta function expansion, it is possible to obtain information about the strength of the point source. Using this method, magnitude estimates have been included in the figure legends of the point source reconstructions.

What is of primary interest here, however, is the location

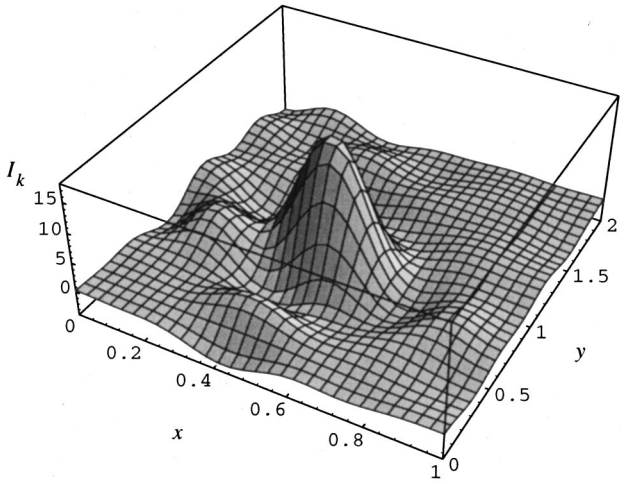

FIG. 21. The point source reconstruction $I_k(x,y)$, using 64 modes and 400 field coefficients, with original source coordinates: $(x,y)=(0.450,0.940)$. The reconstruction reaches a maximum at $(x,y)=(0.464,0.920)$. This should be compared with the coordinates of the maximum of the original truncated expansion, which are $(x,y)=(0.445,0.923)$. The magnitude estimate is in error by 22%. The reconstruction error is 56% and $\lambda=3\times10^{-17}$ $(ka=6)$.

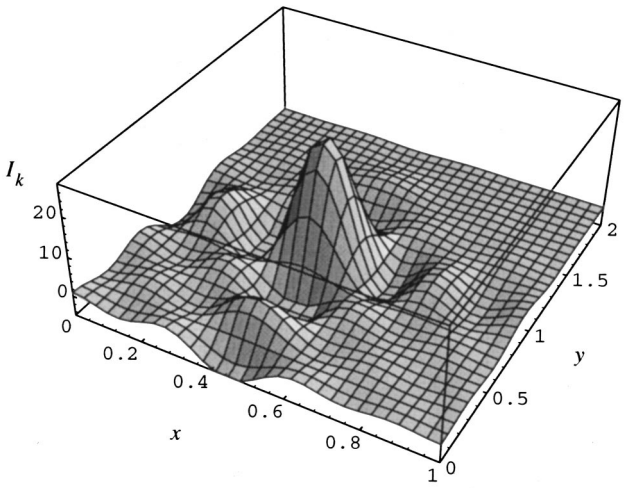

FIG. 22. The original point source expansion $I_k(x,y)$, truncated to 64 modes, with source coordinates $(x,y)=(0.450,0.940)$.

of the point source. To give some idea of the accuracy with which the source location may be found, the positions of the maxima of the reconstructed graphs have been compared with the actual locations of the original sources. We have also listed the coordinates of the maxima of equivalently truncated delta function expansions, in each case, to give an indication of the error present in this technique, even when a perfect reconstruction has been performed. These again are all shown in the figure legends of the point source reconstructions.

As a final example, we have reconstructed the source at a location farther away from the walls of the cavity where the field measurements were made. From Fig. 21, it can be seen that the reconstruction is in greater error (compared with Fig. 18), although its maximum still gives a very good indication of the position of the point source. This example has been generated with 400 field coefficients, and 64 modes have been plotted in the source expansion, as before. Again, $ka=6$. The original source expansion, truncated to 64 modes, is shown in Fig. 22. As it appears that reconstructions are less accurate the further the source is from the walls, it would in practice be best to measure the fields on all four walls and compare the four reconstructions obtained. In this way, the image could be built up in four sections, each of which would correspond to the measurements taken on the nearest pair of adjacent walls.

II. CONCLUSION

In this paper, Green's function modal expansion techniques have been applied to inverse source problems within a two-dimensional rigid rectangular cavity. In particular, solutions have been developed for the reconstruction of a spatially incoherent distributed source (with finite structure) and a deterministic point source by using field measurements on adjacent walls. To the author's knowledge, such problems have not previously been studied.

As is characteristic of inverse problems in general, numerical instabilities were encountered in the problems addressed in this paper. To counter these instabilities, magnitude regularization and projections onto convex sets have been employed. The use of the former technique was found necessary to achieve even a very approximate result. Projections onto convex sets, as applied in this paper, produced a slightly improved result. Concerning the magnitude regularization, it was noticed that there exists a relatively flat region in the graphs of reconstruction magnitude versus regularization parameter. Near the center of this region, reconstruction errors were at a minimum (roughly speaking). The reconstruction errors were also relatively insensitive to the regularization parameter in this region. This behavior has been noticed by other authors, such as Roger[11] in his work on electromagnetic inverse scattering.

We have found that the behavior of the inverse source problems studied greatly deteriorated at frequencies in the vicinity of cavity resonances, particularly low frequency resonances (i.e., with $ka \lesssim 2\pi$, where a is the smallest cavity dimension). The reconstruction frequencies should be chosen so to avoid these resonances when performing the source reconstruction. An interesting avenue of research would be to examine a similar problem but allow the walls to have finite acoustic impedance and to examine the effect on stability of varying this impedance. Concerning the finite structure spatially incoherent sources, it appears that when the frequency of reconstruction becomes greater than the highest eigenfrequency of modes in the source function, reconstruction errors (even with regularization) begin to increase sharply.

An interesting contrast in the change in stability with increasing size was evident between the finite structure spatially incoherent source and the point source. The finite structure spatially incoherent source displayed increasing instability in reconstruction as the number of modes in the source function was increased. This was expected as the eigenvalue dynamic range of truncated compact operators (matrices) at some point must increase with increasing size. The point source reconstruction example behaved in the opposite

fashion for the reconstruction frequency used. There are, however, competing effects in this case. The primary one is that convergence errors in the Green's function expansion are reduced when more field coefficients are used in the reconstruction. It is also suggested that the behavior of the point source reconstruction may be partly due to the pathological nature of the delta function (i.e., the fact that it is not square integrable and that cosine expansions of it cannot converge uniformly in the usual sense).

The proof of compactness given in the Appendix of this paper implies that the convergence of the Green's function modal expansion in the kernel of the forward problem is related to the instability of the inverse problem. We have indicated that, if it suffices to know an integral of the source profile rather than the actual profile (such as may be the case when localizing multipole sources or reconstructing collections of multipole sources), the problem becomes more stable. This was shown by using integration by parts to transfer the derivatives on the source to the Green's function-based kernel of the integral equation representing the inverse problem.

The problems given in this paper were two-dimensional. There is no *a priori* problem with tackling three dimensional problems. The matrices (as with all three-dimensional wave problems) would be $N^3 \times N^3$. Following through some of the arguments given above (on size versus instability), it might be expected that, for a given N, a general three-dimensional problem would be less well behaved than its two-dimensional counterpart.

APPENDIX: COMPACTNESS

First, we assume Q [defined in Eq. (32) as a four-dimensional array] is operating on a Hilbert space of square integrable functions, L_2, defined over the region $[0,a] \times [0,b]$ (with $0<a,b<\infty$), with the usual norm

$$\|\phi\| = \left(\int_0^a \int_0^b dx\, dy\, |\phi(x,y)|^2 \right)^{1/2}. \tag{A1}$$

We will refer to this Hilbert space as H. We also assume that k is fixed and that in addition it obeys

$$\begin{aligned} k &\neq [m^2/a^2 + (n \pm q)^2/b^2], \\ k &\neq [(m \pm p)^2/a^2 + n^2/b^2], \end{aligned} \tag{A2}$$

for all non-negative integers n, m, p, q, for our choice of a, b.

Now, for the present purpose, the functions and operators (of and on H) are projected onto a complete orthonormal basis with elements β^{pq} given by

$$\beta^{pq}(x,y) = \sqrt{\frac{\epsilon_p \epsilon_q}{ab}} \cos(p\pi x/a) \cos(q\pi y/b). \tag{A3}$$

Hence, the operators are matrices and the functions are vectors (actually two-dimensional sequences) of Fourier cosine coefficients. The functions will belong to H if, and only if, the sum of the modulus squares of Fourier cosine coefficients of the corresponding sequence form a convergent series (Riesz–Fischer theorem). Note that the index pq is superscripted. In this appendix, superscripts will be used to denote a particular function or sequence. A function will be denoted by using a plain or superscripted symbol (i.e., ϕ or ϕ^{pq}), whereas a component of the corresponding sequence (of cosine coefficients) will be denoted by using a subscript, i.e., by ϕ_{ij} or ϕ_{ij}^{pq}. The cosine sequence itself will be indicated by using curly brackets, i.e., by $\{\phi_{ij}\}$ or $\{\phi_{ij}\}^{pq}$ in this example. Furthermore, a sequence of functions ϕ^{pq} will be denoted by using curly brackets, i.e., $\{\phi^{pq}\}$.

A component of a projected operator will be referred to using Q_{nmpq} as before, while the operator itself will be symbolically referred to using the plain symbol (i.e., Q).

Furthermore, the norm becomes

$$\|\phi\| = \left(\sum_{pq=0}^{\infty} |(\phi, \beta^{pq})|^2 \right)^{1/2} = \left(\sum_{pq=0}^{\infty} |\phi_{pq}|^2 \right)^{1/2}. \tag{A4}$$

The symbol $(,)$ denotes an inner product, which in this case is defined by

$$(\phi, \psi) = \int_0^a \int_0^b dx\, dy\, \phi(x,y) \psi^{\dagger}(x,y) = \sum_{ij=0}^{\infty} \phi_{ij} \psi_{ij}^{\dagger}. \tag{A5}$$

1. Boundedness

It will first be shown that Q is a bounded operator on H, that is,

$$\|Qx\| \leqslant M\|x\|, \tag{A6}$$

for some real M and for any $x \in H$. Since x and Qx are vectors of Fourier cosine coefficients over the region $[0,a] \times [0,b]$, and $\|x\| < \infty$, the boundedness of Q implies that it maps from H to H.

To begin, let

$$S_{nm} = \sum_{pq} Q_{mnpq} x_{pq}, \tag{A7}$$

where x_{pq} are the elements of a doubly indexed vector of Fourier cosine coefficients for some $x \in H$, and Q_{mnpq} is the four-dimensional array representing the operator Q mentioned above. The notation Σ_{ij} is shorthand for $\Sigma_{ij=0}^{\infty}$. Now, assume first that the sum S_{nm} in Eq. (A7) is absolutely convergent. Then

$$|S_{nm}| \leqslant \sum_{pq} |Q_{mnpq}||x_{pq}|, \tag{A8}$$

$$\leqslant \|x\| \sum_{pq} |Q_{mnpq}|, \tag{A9}$$

$$\overset{\text{def}}{=} \|x\| T_{mn}, \tag{A10}$$

since $\|x\| = \sqrt{\Sigma_{pq}|x_{pq}|^2} \geqslant |x_{ij}|, \quad \forall\, i,j \in \mathbb{N} \cup \{0\}$. Then, from the definition of Q [in Eq. (32)], we have that:

$$T_{nm} \leqslant \frac{4}{ab} \sum_{pq} \sum_{\pm} \left| \frac{1}{\pi^2[m^2/a^2 + (n \pm q)^2/b^2] - k^2} \right| \times \left| \frac{1}{\pi^2[(m \pm p)^2/a^2 + n^2/b^2] - k^2} \right|. \tag{A11}$$

The notation $\Sigma_{\pm}$ means a summation over all forms of the summand while allowing each of the $\pm$ symbols to take either a positive or negative value (in this case, there will be four terms in the sum over $\pm$). By interchanging the summation over $\pm$ with the summation over pq, it is seen that the double summation over pq separates into the product of two single sums over p and q. Both of these sums are absolutely convergent, since the summands decrease as $1/p^2$ and $1/q^2$ for large p and q. Hence, when $x \in H$, the sum in Eq. (A7) is absolutely convergent, according to our first assumption. (This is because no series which is not absolutely convergent may be rearranged to produce an absolutely convergent series.) Further, we have shown that $|S_{nm}| \leqslant \|x\| T_{nm}$.

Following the manner of the preceding argument, we now assume that

$$S = \|Qx\| \tag{A12}$$

$$= \sqrt{\sum_{nm} |S_{nm}|^2} \tag{A13}$$

exists. In this case we have that

$$S \leqslant \|x\| \sqrt{\sum_{nm} |T_{nm}|^2} \tag{A14}$$

$$= \|x\| \times \left[\left(\sum_{\substack{0 \leqslant m \leqslant M \\ 0 \leqslant n \leqslant N}} + \sum_{\substack{m > M \\ 0 \leqslant n \leqslant N}} + \sum_{\substack{0 \leqslant m \leqslant M \\ n > N}} + \sum_{\substack{m > M \\ n > N}} \right) |T_{mn}|^2 \right]^{1/2}, \tag{A15}$$

where N is chosen such that $n/b > k/\pi$, $\forall n > N$, and M is chosen such that $m/a > k/\pi$, $\forall m > M$. In addition, the four double sums in Eq. (A15) will be referred to as $S^{(1)}$, $S^{(2)}$, $S^{(3)}$, and $S^{(4)}$, in respective order as they appear in the equation. Furthermore, the element T_{nm} in the summand of these sums will be indexed in the same fashion (i.e., $T_{nm}^{(i)}$) when the values taken by n,m are restricted to one of the four sums in question. The four sums are now dealt with separately, beginning with $S^{(4)}$.

Now for n and m appropriate to $S^{(4)}$ we have by Eqs. (32) and (33), and the triangle inequality, that

$$|Q_{mnpq}| \leqslant \frac{9}{ab} |D_{m,n,|m-p|,|n-q|}|. \tag{A16}$$

Hence,

$$T_{nm}^{(4)} \leqslant \frac{9}{\pi^4 ab} \sum_{pq} \left| \frac{b^2}{b^2 m^2/a^2 + (n-q)^2 - k^2 b^2/\pi^2} \right| \left| \frac{a^2}{(m-p)^2 + a^2 n^2/b^2 - k^2 a^2/\pi^2} \right|$$

$$= \frac{9}{\pi^4 ab} b^2 \left\{ \frac{1}{b^2 m^2/a^2 - k^2 b^2/\pi^2} + \left(\sum_{i=1}^{\infty} + \sum_{i=1}^{n} \right) \frac{1}{b^2 m^2/a^2 + i^2 - k^2 b^2/\pi^2} \right\}$$

$$\times a^2 \left\{ \frac{1}{a^2 n^2/b^2 - k^2 a^2/\pi^2} + \left(\sum_{j=1}^{\infty} + \sum_{j=1}^{m} \right) \frac{1}{a^2 n^2/b^2 + j^2 - k^2 a^2/\pi^2} \right\}, \tag{A17}$$

since all terms in the summands are positive. This fact also implies that the finite sums over i and j in the last expression are less than or equal to their infinite counterparts. Hence,

$$T_{nm}^{(4)} \leqslant \frac{36ab}{\pi^4} \left\{ \sum_{i=0}^{\infty} \frac{1}{b^2 m^2/a^2 + i^2 - k^2 b^2/\pi^2} \right\}$$

$$\times \left\{ \sum_{j=0}^{\infty} \frac{1}{a^2 n^2/b^2 + j^2 - k^2 a^2/\pi^2} \right\}$$

$$= \frac{36ab}{\pi^4} \left\{ \frac{\pi}{2X_m} \coth(\pi X_m) - \frac{1}{X_m^2} \right\}$$

$$\times \left\{ \frac{\pi}{2Y_n} \coth(\pi Y_n) - \frac{1}{Y_n^2} \right\}, \tag{A18}$$

where $X_m = \sqrt{b^2 m^2/a^2 - k^2 b^2/\pi^2}$ and $Y_n = \sqrt{a^2 n^2/b^2 - k^2 a^2/\pi^2}$. The reduction to closed form of the infinite summations follows from Eq. (124) in Jolley.[19] As n and m tend to infinity the expressions in the curly brackets decrease as $1/n$ and $1/m$ respectively, hence $|T_{nm}^{(4)}|^2$ is bounded from above by a term which tends to $C/(n^2 m^2)$, as n,m tend to ∞, for some real constant C. Thus $S^{(4)}$ is bounded by the product of two absolutely convergent sums and a real constant. Therefore,

$$S^{(4)} \leqslant M^{(4)}, \tag{A19}$$

for some real constant $M^{(4)}$.

For n and m appropriate to $S^{(2)}$, we have by Eqs. (32) and (33), and the triangle inequality, that

$$|Q_{mnpq}| \leqslant \frac{4}{\pi^4 ab} \sum_{\pm} \left| \frac{b^2}{b^2 m^2/a^2 + (n \pm q)^2 - k^2 b^2/\pi^2} \right|$$

$$\times \left| \frac{a^2}{(m \pm p)^2 + a^2 n^2/b^2 - k^2 a^2/\pi^2} \right|, \tag{A20}$$

where $\Sigma_{\pm}$ means the sum over all expressions which arise when the symbol $\pm$ is replaced by $+$ and $-$. This implies that

$$T_{mn}^{(2)} \leqslant \frac{4}{\pi^4 ab} \sum_{pq} \sum_{\pm} |\cdots||\cdots|$$

$$= \frac{4}{\pi^4 ab} \sum_{\pm} \sum_{q} |\cdots| \sum_{p} |\cdots|, \tag{A21}$$

where the symbol $|\cdots|$ is shorthand for the respective expression arising in Eq. (A20). Now,

$$\sum_{p=0}^{\infty} \left| \frac{1}{(m-p)^2 + a^2 n^2/b^2 - k^2 a^2/\pi^2} \right|$$

$$= \left(\sum_{i=0}^{m} + \sum_{i=1}^{\infty} \right) \left| \frac{1}{i^2 + a^2 n^2/b^2 - k^2 a^2/\pi^2} \right|. \tag{A22}$$

However, $\Sigma_{i=0}^{m} \leqslant \Sigma_{i=0}^{\infty}$ and $\Sigma_{i=1}^{\infty} < \Sigma_{i=0}^{\infty}$ of the summand on the right-hand side of Eq. (A22), since all terms are positive. Furthermore, the $\Sigma_{i=0}^{\infty}$ of this summand is convergent for fixed $n<N$ and k, since for large i the summand tends to $1/i^2$; hence,

$$\sum_{i=0}^{\infty} \left| \frac{1}{i^2 + a^2 n^2/b^2 - k^2 a^2/\pi^2} \right| = l_n, \tag{A23}$$

for some real l_n (where the dependence of the sum's limit on n has been included explicitly). Therefore,

$$\sum_{p=0}^{\infty} \left| \frac{1}{(m-p)^2 + a^2 n^2/b^2 - k^2 a^2/\pi^2} \right| \leqslant 2 l_n. \tag{A24}$$

From the above arguments, it is also clear that

$$\sum_{p=0}^{\infty} \left| \frac{1}{(m+p)^2 + a^2 n^2/b^2 - k^2 a^2/\pi^2} \right| \leqslant l_n. \tag{A25}$$

It is further evident from the arguments for $S^{(4)}$ that

$$\sum_{q=0}^{\infty} \left| \frac{1}{b^2 m^2/a^2 + (n \pm q)^2 - k^2 b^2/\pi^2} \right|$$

$$\leqslant 2 \left[\frac{\pi}{2X_m} \coth(\pi X_m) - \frac{1}{X_m^2} \right], \tag{A26}$$

since $m/a > k/\pi$. Hence,

$$T_{nm}^{(2)} \leqslant \frac{4ab}{\pi^4} 4 \left[\frac{\pi}{2X_m} \coth(\pi X_m) - \frac{1}{X_m^2} \right] 3 l_n. \tag{A27}$$

Therefore,

$$S^{(2)} \leqslant \left(\frac{48ab}{\pi^4} \right)^2 \sum_{m=M+1}^{\infty} \left[\frac{\pi}{2X_m} \coth(\pi X_m) - \frac{1}{X_m^2} \right]^2 \sum_{n=0}^{N} l_n^{21/2} \tag{A28}$$

$$\leqslant C(N+1) \max\{l_n^2 : 0 \leqslant n \leqslant N\}, \tag{A29}$$

where C is a real constant. Hence,

$$S^{(2)} \leqslant M^{(2)} \tag{A30}$$

for some real constant $M^{(2)}$.

Now, an identical argument to that for $S^{(2)}$ shows that

$$S^{(3)} \leqslant M^{(3)}. \tag{A31}$$

Furthermore, the argument for $S^{(2)}$ can be trivially extended to show that

$$S^{(1)} \leqslant M^{(1)}, \tag{A32}$$

since in this case the sums over p and q may both be treated using identical arguments to that for the sum over p in $S^{(2)}$. From the last statement, it follows that

$$S^{(1)} \leqslant C_1 \sum_{m=0}^{M} \lambda_m^2 \sum_{n=0}^{N} l_n^2 \tag{A33}$$

$$\leqslant C_2 (M+1) \max\{\lambda_m^2 : 0 \leqslant m \leqslant M\} \times (N+1) \max\{l_n^2 : 0 \leqslant n \leqslant N\}, \tag{A34}$$

where l_n is the limit for the sum over p, as in Eq. (A23), and λ_m is the limit for the corresponding sum over q in the present case. C_1 and C_2 are real constants.

Hence,

$$S \leqslant \|x\| \left(\sum_{nm} \left(\sum_{pq} |Q_{nmpq}| \right)^2 \right)^{1/2}$$

$$= \|x\| \left(\sum_{i=1}^{4} S^{(i)} \right)^{1/2} \leqslant \|x\| \left(\sum_{i=1}^{4} M^{(i)} \right)^{1/2}, \tag{A35}$$

therefore,

$$S = \|Qx\| \leqslant M \|x\|, \tag{A36}$$

for some real M, for any $x \in H$. So, Q is bounded.

2. Compactness

Now, given that Q is bounded, if $\{y^{kl}\}$ and $\{z^{ij}\}$ are two complete orthonormal sequences of functions belonging to H, then Q is compact if

$$\sum_{ijkl} |(Qy^{kl}, z^{ij})|^2 < \infty \tag{A37}$$

(see Jones,[20] pp. 184–185). Let y^{kl} be defined by

$$y_{pq}^{kl} = \begin{cases} 1 & \text{if } k=p \text{ and } l=q \\ 0 & \text{otherwise.} \end{cases} \tag{A38}$$

Let z^{ij} also be defined in the same fashion. Now, from Eq. (A35) we have

$$\sum_{ij} \left(\sum_{kl} |Q_{ijkl}| \right)^2 < \text{some real number.} \tag{A39}$$

But,

$$\sum_{ij} \left(\sum_{kl} |Q_{ijkl}| \right)^2 \geqslant \sum_{ij} \sum_{kl} |Q_{ijkl}|^2$$

$$= \sum_{ijkl} \left| \sum_{nmpq} Q_{nmpq} y_{pq}^{kl} z_{nm}^{ij} \right|^2$$

$$= \sum_{ijkl} |(Qy^{kl}, z^{ij})|^2. \tag{A40}$$

So, Q is compact.

Note that the proof depends on the convergence of infinite series of the form shown in Eq. (A11) which stems from the operator Q, which is based in turn upon the Green's function in Eq. (4). The convergence of the series in Eq. (4) is, therefore, related to the compactness of the forward operator and thus the instability of the inverse problem.

[1] It should be noted that for a free-field problem the far-field radiation pattern uniquely determines the field exterior to the source. It then follows that data obtained by field measurements external to a source have a lower dimensionality than the source.
[2] A. J. Devaney, ''The inverse problem for random sources,'' J. Math. Phys. **20**, 1687–1691 (1979).
[3] S. J. Norton and M. Linzer, ''Reconstructing spatially incoherent random sources in the nearfield: Exact inversion formulas for circular and spherical arrays,'' J. Acoust. Soc. Am. **76**, 1731–1737 (1984).
[4] R. W. Harris and T. J. Ledwidge, *An Introduction to Noise Analysis* (Pion Limited, London, 1974).
[5] A. J. Devaney, ''Inverse source and scattering problems in optics,'' in *Optics in Four Dimensions—1980* (American Institute of Physics, Woodbury, NY, 1980), pp. 613–626.
[6] A. J. Devaney, ''A new approach to emission and transmission CT,'' in *IEEE Ultrasonics Symposium Proceedings*, 1980, pp. 979–983.
[7] J. S. Ball, S. A. Johnson, and F. Stenger, ''Explicit inversion of the Helmholtz equation for ultra-sound insonification and spherical detection,'' in *Acoustical Imaging*, edited by K. Y. Wang (Plenum, New York, 1980), Vol. 9, pp. 451–461.
[8] T. Novotný, E. Matsumoto, and T. Shibata, ''Inversion scattering in finite space domain,'' J. Acoust. Soc. Am. **100**, 3600–3606 (1996).
[9] A. Roger and D. Maystre, ''The perfectly conducting grating from the point of view of inverse diffraction,'' Opt. Acta **26**, 447–460 (1979).
[10] J. Hadamard, *Le Problème de Cauchy* (Hermann, Paris, 1932).
[11] A. Roger, D. Maystre, and M. Cadilhac, ''On a problem of inverse scattering in optics: The dielectric inhomogeneous medium,'' J. Opt. (Paris) **9**, 83–90 (1978).
[12] W. H. Press, S. A. Teukolsky, W. T. Vetterling, and B. P. Flannery, *Numerical Recipes in Fortran*, 2nd ed. (Cambridge University Press, Cambridge, 1992).
[13] E. W. Marchand and E. Wolf, ''Angular correlation and the far-zone behavior of partially coherent fields,'' J. Opt. Soc. Am. **62**, 379–385 (1972).
[14] T. J. I. Bromwich, ''Note on double limits and on the inversion of a repeated infinite integral,'' Proc. Math. Soc. London Series 2 **1**, 176–201 (1903).
[15] P. M. Morse and H. Feshbach, *Methods of Theoretical Physics* (McGraw-Hill, New York, 1953).
[16] J. Biemond, R. L. Lagendijk, and R. M. Mersereau, ''Iterative methods for image deblurring,'' Proc. IEEE **78**, 856–883 (1990).
[17] M. J. Lighthill, *An Introduction to Fourier Analysis and Generalised Functions* (Cambridge University Press, Cambridge, 1958).
[18] A. Roger, *Problèmes inverses de diffraction en électromagnétisme. Théorie, traitement numérique, et applications a l'optique*, Ph.D. thesis, Université d'Aix-Marseille III, Centre de Saint-Jérôme, 1981, Appendice L.
[19] L. B. W. Jolley, *Summation of Series* (Dover, New York, 1961).
[20] D. S. Jones, *Methods in Electromagnetic Wave Propagation Vol. 1* (Clarendon Press, Oxford, 1987).

Acoustic X-wave reflection and transmission at a planar interface: Spectral analysis

Amr M. Shaarawi
Department of Engineering Physics and Mathematics, Faculty of Engineering, Cairo University, Giza 12211, Egypt

Ioannis M. Besieris
The Bradley Department of Electrical and Computer Engineering, Virginia Polytechnic Institute and State University, Blacksburg, Virginia 24061

Ahmed M. Attiya and Essam El-Diwany
Department of Microwave Engineering, Electronic Research Institute, Dokki, Giza, 12211, Egypt

(Received 5 March 1999; revised 31 August 1999; accepted 2 September 1999)

The spectral structure of a three-dimensional X-wave pulse incident on a planar surface of discontinuity is examined. Introducing a novel superposition of azimuthally dependent pulsed plane waves, it is shown for oblique incidence that the reflected pulse has a localized wave structure. On the other hand, the transmitted field maintains its localization up to a certain distance from the interface, beyond which it starts disintegrating. An estimate of the localization range of the transmitted pulse is established; also, the parameters affecting the localization range are identified. The reflected and transmitted fields are deduced for X-waves incident from either a slower medium or a faster one. For the former case the evanescent fields in the second medium are calculated and their explicit time dependence is deduced for a normally incident X-wave. Furthermore, at near-critical incidence the transmitted pulse exhibits significant pulse compression and focusing. © *2000 Acoustical Society of America.* [S0001-4966(99)05412-0]

PACS numbers: 43.20.Bi, 43.20.Px [ANN]

INTRODUCTION

Studies of the generation of acoustical and optical localized waves (LW)[1–7] and their use in high-resolution imaging and target identification[8–10] have advanced considerably in the past few years. Because of their large focusing depths and their wideband spectra, LWs have a potential in detecting objects buried at different depths and identifying wide ranges of the parameters characterizing a detected target.[8] A large number of different LW solutions have appeared in literature; they can be divided into two distinct categories. One category consists of solutions based on Brittingham's focus wave modes (FWM),[11–14] while the other is based on the X-waves deduced by Lu and Greenleaf.[15–18] A common attribute of these two categories of LWs is the spectral coupling between their spatial and temporal frequency components. This specific property characterizes LWs and differentiates them from other broadband pulses. In particular, such coupling causes the spectral depletion of radiated LWs to be different from that of other types of broadband fields.[19] It has been shown recently that the focus wave modes and the X-waves have the same spectral structure except that their spatio-temporal couplings are different.[20,21] Whereas the X-waves have a coupling for which the temporal frequency is proportional to the spatial frequency, the field of the FWMs is characterized by a temporal frequency that is proportional to the square of the spatial frequency.

In many applications, one expects acoustic localized waves to be transmitted from one medium to another. It is, therefore, important to study the details of a canonical problem involving the reflection and transmission of a localized wave obliquely incident on a planar interface separating two acoustically different materials. A similar problem has been investigated previously in two different papers.[22,23] In both cases, the authors used a two-dimensional variation of the Brittingham's FWM electromagnetic solution. In the first paper, Hillion has argued that FWMs are transmitted across a discontinuity surface only if they are normally incident on that surface, while for oblique incidence only reflection takes place.[22] Furthermore, he has demonstrated that for normal incidence the transmitted, reflected and incident fields have the same structure. Hillion's results have been criticized by Donnelly and Power.[23] They have used a geometrical approach to prove that the transmitted waveform of the two-dimensional FWM does not have a LW structure. In their approach, LW solutions are represented in the form of a space–time Fourier transform whose domain is constrained to a specific geometrical support. This is essentially a geometrical interpretation of the spectral coupling between the spatial and temporal frequency components.[7,19–21] Donnelly and Power have argued that for oblique incidence the reflected waveform has an LW structure, while the transmitted waveform does not. The aim of this paper is to clarify this point and to quantify the process of disintegration of the transmitted LW field.

In this work, we will investigate the case of reflection and transmission of the three-dimensional acoustic X-waves. There are several advantages associated with this choice, in contrast to working with vector fields or carrying out the analysis in two dimensions. In a three-dimensional framework, the pulses do not exhibit the extended tails appearing

in two-dimensional pulsed fields.[24,25] Trailing fields associated with 2-D pulses can obscure some of the wave phenomena associated with the reflection and transmission of transients.[25] In addition, the X-wave has a simpler spectral structure than the FWM solution and contains no backward traveling (acausal) components. Such acausal components can give rise to serious conceptual difficulties when dealing with an LW pulse incident on a planar interface. Furthermore, the study of transmission and reflection of a scalar LW pulse is free from the complexity associated with the polarization properties of an analogous vector field. This makes the mathematics more manageable and allows us to clearly identify the factors affecting the disintegration of the transmitted field. Finally, the peaks of a scalar X-wave lie on the axis of propagation, while those of the corresponding electromagnetic field components are located off-axis. Thus the decay of the peak of a scalar acoustic X-wave pulse is more tractable than that of an electromagnetic X-wave pulse.

In this paper, we elaborate on the spectral structure of LWs incident on an interface separating two different media. The analysis used in this paper follows basically that of Donnelly and Power; however, it is applied to the three-dimensional scalar X-wave solution instead of the two-dimensional vector FWM field. We show that for oblique incidence, the reflected X-wave has an LW structure. We also provide an explanation for the cause of disintegration of the transmitted field. This explanation is based on a spectral analysis that leads to a representation involving an integration of an angular distribution of azimuthally dependent elementary pulses. For the incident and reflected X-waves, all the azimuthally dependent pulses travel at the same speed and add up coherently at any observation point synthesizing a diffraction-free LW pulse. In contradistinction, the transmitted azimuthally dependent pulses travel at different speeds. The integration of such dispersed pulses results in a wave field having an axial width that increases with distance from the interface. This causes the central part of the transmitted pulse to become longer, and the amplitude of its peak to decrease with distance. The analysis used in this paper reveals that the transmitted field stays localized for a certain range, beyond which it starts to disintegrate. The disintegration of the transmitted wave field starts at a depth that depends on several parameters characterizing the incident pulse. The main goal of this work is to demonstrate how to estimate this localization depth and to identify the parameters that determine such a range.

The plan of this work is as follows: A Fourier spectral representation of the incident pulse is introduced in Sec. I. This is done for a 3-D X-wave incident normally on the planar interface separating two media. In the same section, we show that an obliquely incident X-wave can be derived by rotating the normally incident pulse. Expressions for the Fourier composition of both the reflected and transmitted pulses are deduced in Sec. II. The Fourier integrals associated with the incident, reflected and transmitted fields are transformed into azimuthal angular superpositions over elementary pulsed solutions of the scalar wave equation. These azimuthal angular representations are then used in Sec. III to explain the localization of the reflected LW field and the reason for the disintegration of the transmitted field. The dispersion of the transmitted pulse is quantified by deducing an expression for a dispersion-free distance in the second medium. In Sec. IV, we provide a detailed numerical study of the behavior of the reflected and transmitted fields, including situations involving total reflection and the generation of evanescent fields. This investigation shows that the dispersion-free distance deduced in Sec. III is fairly accurate.

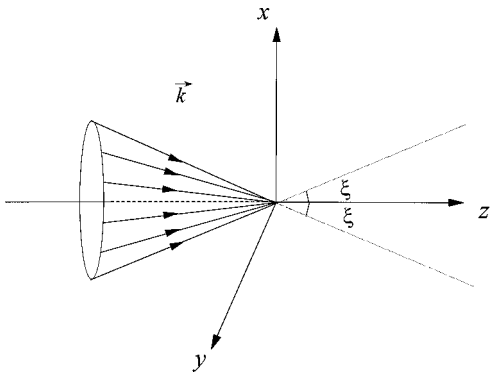

FIG. 1. Wave vectors of the normally incident X-wave lying on a conic surface having an apex angle ξ.

I. THE SPECTRAL COMPOSITION OF THE INCIDENT X-WAVE

In this section, we study the spectral composition of an acoustic X-wave pulse incident on an interface separating two different media. The spectral wave components will be used in later sections to study the behavior of the reflected and transmitted fields. The X-wave pressure field is a solution of the 3-D scalar wave equation

$$(\nabla^2 - c^{-2}\,\partial_t^2)p(\mathbf{r},t) = 0, \tag{1}$$

where $c = \sqrt{B/\rho_0}$ is the wave velocity in the medium, B being the bulk modulus of the medium and ρ_0 its density. We will restrict our analysis to compressive waves only; i.e., shear components will be neglected throughout the paper. This treatment models a large number of situations, e.g., an air–fluid or a gas–gas interface.

X-waves are wide-band pulses synthesized of plane waves components characterized by wave vectors lying on a conical surface defined by the apex angle $\theta_k = \xi$ in momentum space.[26,27] The superposition of such plane waves produces an interference pattern moving with the supersonic speed $\nu = c/\cos\xi$, although each individual plane wave propagates at the phase speed of the medium c along the cone surface.[26,27] An X-wave traveling in the positive z-direction has wave vectors forming the conical surface shown in Fig. 1. This represents the situation of normal incidence on an interface of discontinuity situated at $z = 0$. For oblique incidence, the cone shown in Fig. 1 must be rotated by an angle equal to the angle of incidence of the X-wave pulse. Sections of the tilted incident, reflected and transmitted cones taken at $x = 0$ are shown in Fig. 2. We will start with a normally incident X-wave propagating in the positive z-direction. Then, we will rotate this solution to obtain an obliquely incident X-wave.

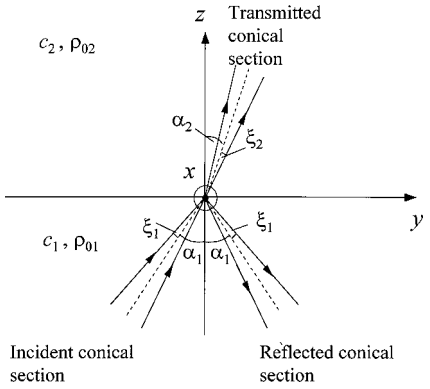

FIG. 2. Longitudinal sections of the spectral cones of the incident, reflected and transmitted fields. The surface of discontinuity between the two media is situated at the $z=0$ plane.

We commence our work by introducing the incident pressure field, which is represented by the fourfold Fourier transform of the zeroth order X-wave solution. Specifically,

$$p_{\mathrm{inc}}(\mathbf{r},t)=\int_{R^3} d^3\mathbf{k}\int_0^\infty d(\omega/c_1)e^{-i\mathbf{k}\cdot\mathbf{r}}e^{+i\omega t}A_{\mathrm{inc}}(\mathbf{k},\omega)\times\delta(k_z-(\omega/c_1)\cos\xi_1)\times\delta(k_x^2+k_y^2-(\omega/c_1)^2\sin^2\xi_1). \quad (2)$$

Here, $A_{\mathrm{inc}}(\mathbf{k},\omega)=A_0e^{-(\omega/c_1)a}$, a is a real positive parameter, A_0 is a constant spectral amplitude, the wave velocity in the first medium is c_1 and $\delta(\cdot)$ denotes the Dirac delta function. The integration over k_x and k_z yields

$$p_{\mathrm{inc}}(\mathbf{r},t)=\int_0^\infty d(\omega/c_1)\int_{-(\omega/c_1)\sin\xi_1}^{+(\omega/c_1)\sin\xi_1} dk_y\times\frac{A_0e^{-(\omega/c_1)a}}{\sqrt{(\omega/c_1)^2\sin^2\xi_1-k_y^2}}\times\cos\left(x\sqrt{(\omega/c_1)^2\sin^2\xi_1-k_y^2}\right)\times e^{-ik_yy}e^{-i(\omega/c_1)\cos\xi_1 z}e^{+i\omega t}. \quad (3)$$

The range of integration over k_y reflects the fact that X-waves have no evanescent fields. The integration over k_y in Eq. (3) yields (cf. 3.876.7 in Ref. 28)

$$p_{\mathrm{inc}}(\mathbf{r},t)=\pi\int_0^\infty d(\omega/c_1)J_0((\omega/c_1)\rho\sin\xi_1)\times A_0e^{-(\omega/c_1)a}e^{-i(\omega/c_1)(z\cos\xi_1-c_1t)}. \quad (4)$$

Finally, the integration over (ω/c_1) gives rise to the result

$$p_{\mathrm{inc}}(\mathbf{r},t)=\frac{\pi A_0}{[\rho^2\sin^2\xi_1+(a+i(z\cos\xi_1-c_1t))^2]^{1/2}}. \quad (5)$$

This is a localized pulse traveling in the positive z-direction with a peaked center propagating at the supersonic speed $c_1/\cos\xi_1$.

For obliquely incident X-waves, we need to rotate either the coordinates (x,y,z) or the wave vector components (k_x,k_y,k_z). A clockwise rotation by an angle α_1 around the x-axis is defined by the operation $\mathbf{r}'=M\mathbf{r}$, where

$$M=\begin{bmatrix}1 & 0 & 0\\ 0 & \cos\alpha_1 & -\sin\alpha_1\\ 0 & \sin\alpha_1 & \cos\alpha_1\end{bmatrix}. \quad (6)$$

This operation transforms a normally incident X-wave to the following obliquely incident one:

$$p_{\mathrm{inc}}(\mathbf{r},t)=\frac{\pi A_0}{[x^2\sin^2\xi_1+(y\cos\alpha_1-z\sin\alpha_1)^2\sin^2\xi_1+(a+i((y\sin\alpha_1+z\cos\alpha_1)\cos\xi_1-c_1t))^2]^{1/2}}. \quad (7)$$

Alternatively, we can rotate the components of the wave vector $\mathbf{k}$ using the procedure described by Donnelly and Power.[23] Specifically, the Fourier superposition of a rotated X-wave

$$p_{\mathrm{inc}}(M\mathbf{r},t)=\int_{R^3} d^3\mathbf{k}\int_R d\omega e^{-i\mathbf{k}\cdot M\mathbf{r}}e^{i\omega t}\tilde{p}_{\mathrm{inc}}(\mathbf{k},\omega)$$

is equivalent to having

$$p_{\mathrm{inc}}(M\mathbf{r},t)=\int_{R^3} d^3\mathbf{k}'\int_R d\omega e^{-i\mathbf{k}'\cdot\mathbf{r}}e^{i\omega t}\tilde{p}_{\mathrm{inc}}(\mathbf{k}',\omega), \quad (8)$$

where $\mathbf{k}'=M^T\mathbf{k}$ and $\mathbf{k}=M\mathbf{k}'$. Substituting these relations into the Fourier superposition Eq. (2) gives the following expression:

$$p_{\mathrm{inc}}(\mathbf{r},t)=\int_0^\infty d(\omega/c_1)\int_{R^3} d^3\mathbf{k}'e^{-i\mathbf{k}'\cdot\mathbf{r}}e^{i\omega t}\times A_0e^{-(\omega/c_1)a}\delta(k_y'\sin\alpha_1+k_z'\cos\alpha_1-(\omega/c_1)\cos\xi_1)\,\delta(k_x'^2+(k_y'\cos\alpha_1-k_z'\sin\alpha_1)^2-(\omega/c_1)^2\sin^2\xi_1).$$

Integrating over k_x' and k_z', the above expression reduces to

$$p_{\text{inc}}(\mathbf{r},t)=\int_0^{\infty} d(\omega/c_1)\int_{\Delta_-}^{\Delta_+} dk_y' \times\frac{A_0 e^{-(\omega/c_1)a}}{\cos\alpha_1\sqrt{(\omega/c_1)^2\sin^2\xi_1-\eta_1^2}} \times\cos(x\sqrt{(\omega/c_1)^2\sin^2\xi_1-\eta_1^2})e^{-ik_y' y} \times e^{iz(k_y'\sin\alpha_1/\cos\alpha_1-(\omega/c_1)\cos\xi_1/\cos\alpha_1)}e^{i\omega t}. \quad (9)$$

Here, we have used the simultaneous roots of the two Dirac delta functions; specifically,

$$k_z'=((\omega/c_1)\cos\xi_1-k_y'\sin\alpha_1)/\cos\alpha_1$$

and

$$k_x'^2=(\omega/c_1)^2\sin^2\xi_1-\eta_1^2,$$

where

$$\eta_1=k_y'\cos\alpha_1-k_z'\sin\alpha_1 =(k_y'/\cos\alpha_1)-(\omega/c_1)\sin\alpha_1\cos\xi_1/\cos\alpha_1.$$

The limits of the integration over k_y' can be determined by noting that $|k_y|<(\omega/c_1)\sin\xi_1$. Hence, $k_y'=k_y\cos\alpha_1+k_z\sin\alpha_1$ is limited so that $-(\omega/c_1)\sin\xi_1\cos\alpha_1+(\omega/c_1)\cos\xi_1\sin\alpha_1<k_y'<(\omega/c_1)\sin\xi_1\cos\alpha_1+(\omega/c_1)\cos\xi_1\times\sin\alpha_1$. Consequently, the two limits of the integration over k_y' in Eq. (9) are given by $\Delta_\pm=(\omega/c_1)\sin(\alpha_1\pm\xi_1)$.

Introducing the change of variables $k_y'\rightarrow\eta_1$ and rearranging terms, Eq. (9) can be rewritten as

$$p_{\text{inc}}(\mathbf{r},t)=\int_0^{\infty} d(\omega/c_1)\int_{-(\omega/c_1)\sin\xi_1}^{+(\omega/c_1)\sin\xi_1} d\eta_1 \times\frac{A_0 e^{-(\omega/c_1)a}}{\sqrt{(\omega/c_1)^2\sin^2\xi_1-\eta_1^2}} \times\cos(x\sqrt{(\omega/c_1)^2\sin^2\xi_1-\eta_1^2}) \times e^{i\omega t}e^{-i\eta_1(y\cos\alpha_1-z\sin\alpha_1)} \times e^{-i(\omega/c_1)\cos\xi_1(y\sin\alpha_1+z\cos\alpha_1)}. \quad (10)$$

Comparing Eqs. (10) and (3), we find that the above integration yields the same obliquely incident X-wave as that given in Eq. (7). We have, thus, demonstrated that we can change the direction of propagation of the X-wave by either rotating the position coordinates or by rotating the components of the wave vector $\mathbf{k}$. In later sections, the real part of $p_{\text{inc}}(\mathbf{r},t)$ will be used to represent the differential pressure of the incident acoustical field. The same criterion is applied in case of complex amplitudes representing reflected and transmitted pressure fields. The real parts of the pressure amplitudes have distinct peaks that are easy to trace. For such reason, we have preferred to use them in our study rather than the imaginary parts.

II. SPECTRAL REPRESENTATION OF THE REFLECTED AND TRANSMITTED X-WAVES

Consider the case of an acoustical X-wave obliquely incident on a surface of discontinuity separating two different media. Assume that the interface separating the two media is situated at $z=0$. Suppose that the first medium has a wave velocity c_1 and a density ρ_{01}, and that the second medium has a wave velocity c_2 and a density ρ_{02}. The axis of propagation of the X-wave incident from the negative z hemisphere makes an angle α_1 with the normal to the interface, as shown in Fig. 2. If the incident X-wave field has wave vector $\mathbf{k}$ components $k_{x\text{inc}}$, $k_{y\text{inc}}$ and $k_{z\text{inc}}$, then the components of the reflected and transmitted wave vectors become

$$k_{x\text{ref}}=k_{x\text{inc}},\quad k_{y\text{ref}}=k_{y\text{inc}}\ \text{ and }\ k_{z\text{ref}}=-k_{z\text{inc}}; \quad (11)$$

$$k_{x\text{tran}}=k_{x\text{inc}},\quad k_{y\text{tran}}=k_{y\text{inc}}\ \text{ and } k_{z\text{tran}}=\sqrt{(\omega/c_2)^2-k_{z\text{inc}}^2-k_{y\text{inc}}^2}. \quad (12)$$

Suppose that the pressure wave associated with a normally incident field is represented by the expression given in Eq. (2). The corresponding reflected and transmitted fields are given by

$$p_{\text{ref}}(\mathbf{r},t)=\int_{R^3} d^3\mathbf{k}\int_0^{\infty} d(\omega/c_1)e^{-i\mathbf{k}\cdot\mathbf{r}}e^{+i\omega t}A_{\text{ref}}(\mathbf{k},\omega) \times\delta(k_z+(\omega/c_1)\cos\xi_1) \times\delta(k_x^2+k_y^2-(\omega/c_1)^2\sin^2\xi_1) \quad (13)$$

and

$$p_{\text{tran}}(\mathbf{r},t)=\int_{R^3} d^3\mathbf{k}\int_0^{\infty} d(\omega/c_2)e^{-i\mathbf{k}\cdot\mathbf{r}}e^{+i\omega t} \times A_{\text{tran}}(\mathbf{k},\omega)\,\delta(k_z-(\omega/c_2)\cos\xi_2) \times\delta(k_x^2+k_y^2-(\omega/c_2)^2\sin^2\xi_2). \quad (14)$$

The apex angle of the spectral cones of the incident and transmitted X-waves are denoted by ξ_1 and ξ_2, respectively. In Eq. (14), the conditions $k_{x\text{tran}}=k_{x\text{inc}}$ and $k_{y\text{tran}}=k_{y\text{inc}}$ are satisfied because from Snell's law $(\omega/c_2)\sin\xi_2=(\omega/c_1)\sin\xi_1$. The condition $k_z=(\omega/c_2)\cos\xi_2$ imposed by the other Dirac delta function is another way of writing the relation $k_{z\text{tran}}=\sqrt{(\omega/c_2)^2-k_{z\text{inc}}^2-k_{y\text{inc}}^2}$. Notice that for normal incidence, the reflected and transmitted pressure fields have the same spectral structures as those of the incident field. Consequently, the reflected and transmitted fields due to a normally incident X-wave retain their LW structure.

The continuity conditions of the pressure and the normal displacement components at the boundary give the following relations between the spectral weighting functions[29,30]

$$A_{\text{ref}}=A_{\text{inc}}\frac{Z_2\sec\theta_{2k}-Z_1\sec\theta_{1k}}{Z_2\sec\theta_{2k}+Z_1\sec\theta_{1k}}, \quad (15)$$

$$A_{\text{tran}}=A_{\text{inc}}\frac{2Z_2\sec\theta_{2k}}{Z_2\sec\theta_{2k}+Z_1\sec\theta_{1k}}. \quad (16)$$

Here, the characteristic wave impedances for the two media are defined as $Z_1\equiv\rho_{01}c_1$ and $Z_2\equiv\rho_{02}c_2$. The angles between the z-axis and the wave vectors associated with the individual components contributing to the incident and transmitted fields are denoted by θ_{1k} and θ_{2k}, respectively. For normal incidence, these angles equal the apex angles ξ_1 and ξ_2. Before we substitute the reflection and transmission co-

efficients in the Fourier representations of the various fields, we need to express them in terms of the wave vectors, viz.,

$$A_{\text{ref}}=A_{\text{inc}}\frac{k_{z\text{inc}}-k_{z\text{tran}}(\rho_{01}/\rho_{02})}{k_{z\text{inc}}+k_{z\text{tran}}(\rho_{01}/\rho_{02})}, \tag{17}$$

$$A_{\text{tran}}=A_{\text{inc}}\frac{2k_{z\text{inc}}}{k_{z\text{inc}}+k_{z\text{tran}}(\rho_{01}/\rho_{02})}. \tag{18}$$

Therefore, for an obliquely incident X-wave, at an angle of inclination α_1, the reflected pressure field acquires the form

$$p_{\text{ref}}(\mathbf{r},t)=\int_0^\infty d(\omega/c_1)\int_{R^3} d^3\mathbf{k}' e^{-i\mathbf{k}'\cdot\mathbf{r}}e^{+i\omega t}A_0 e^{-(\omega/c_1)a}\,\frac{k_z'-\text{sgn}(k_z')\sqrt{(\omega/c_2)^2-k_x'^2-k_y'^2}(\rho_{01}/\rho_{02})}{k_z'+\text{sgn}(k_z')\sqrt{(\omega/c_2)^2-k_x'^2-k_y'^2}(\rho_{01}/\rho_{02})}$$
$$\times\,\delta(-k_z'\cos\alpha_1+k_y'\sin\alpha_1-(\omega/c_1)\cos\xi_1)\,\delta(k_x'^2+(k_y'\cos\alpha_1+k_z'\sin\alpha_1)^2-(\omega/c_1)^2\sin^2\xi_1), \tag{19}$$

where we have rotated the $\mathbf{k}$ vector and used the relation between $A_{\text{ref}}(\mathbf{k}',\omega)$ and $A_{\text{inc}}(\mathbf{k}',\omega)$ given in Eq. (17). Notice that the transformation $k_z'\rightarrow -k_z'$ in the arguments of the delta functions guarantees that the wave vectors are reflected in the correct direction. The delta functions in Eq. (19) imply that

$$k_z'=\eta_1\sin\alpha_1-(\omega/c_1)\cos\xi_1\cos\alpha_1,$$

and the argument of the square root contributing to the reflection coefficient becomes

$$(\omega/c_2)^2-k_x'^2-k_y'^2=(\omega/c_2)^2-(\omega/c_1)^2+\Lambda_1^2(\omega),$$

where $\Lambda_1(\omega)=\eta_1\sin\alpha_1-(\omega/c_1)\cos\alpha_1\cos\xi_1$. Notice that for α_1 and ξ_1 values obeying the condition $\alpha_1+\xi_1<\pi/2$, the quantity $\Lambda_1(\omega)$ is negative. This means that $\text{sgn}(k_z')$ is negative as expected for the reflected field. Carrying out the integration over k_x' and k_z' in Eq. (19) and changing the integration variable $k_y'\rightarrow\eta_1$, we obtain

$$p_{\text{ref}}(\mathbf{r},t)=\int_0^\infty d(\omega/c_1)\int_{-\omega/c\sin\xi}^{\omega/c_1\sin\xi} d\eta_1\,\frac{A_0e^{-(\omega/c_1)a}}{\sqrt{(\omega/c_1)^2\sin^2\xi_1-\eta_1^2}}\cos(x\sqrt{(\omega/c_1)^2\sin^2\xi_1-\eta_1^2})$$
$$\times\,e^{-i\eta_1(y\cos\alpha_1+z\sin\alpha_1)}e^{-i(\omega/c_1)\cos\xi_1(y\sin\alpha_1-z\cos\alpha_1)}e^{i\omega t}R(\eta_1,\omega), \tag{20a}$$

where the reflection coefficient may be rewritten as

$$R(\eta_1,\omega)=\frac{\Lambda_1(\omega)+\sqrt{(\omega/c_2)^2-(\omega/c_1)^2\sin^2\xi_1+\eta_1^2-\Xi_1^2(\omega)}(\rho_{01}/\rho_{02})}{\Lambda_1(\omega)-\sqrt{(\omega/c_2)^2-(\omega/c_1)^2\sin^2\xi_1+\eta_1^2-\Xi_1^2(\omega)}(\rho_{01}/\rho_{02})}, \tag{20b}$$

with $\Xi_1(\omega)=\eta_1\cos\alpha_1+(\omega/c_1)\sin\alpha_1\cos\xi_1$. The integration in Eq. (20a) cannot be evaluated explicitly in order to obtain a closed-form expression for the reflected pressure field and will be considered further in the next section.

The same procedure described above can be repeated in order to calculate the transmitted field. We have to be sure, however, that the continuity condition Eq. (12) is valid for the incident and transmitted plane wave components. Along this vein, consider Snell's law

$$(1/c_1)\sin\theta_{1k}=(1/c_2)\sin\theta_{2k}, \tag{21}$$

where θ_{1k} and θ_{2k} are the angles of the wave vectors associated with the incident and transmitted plane wave components, respectively. In particular,

$$\cos\theta_{1k}=(k_{z1}'/(\omega/c_1))=\cos\xi_1\cos\alpha_1-\eta_1\sin\alpha_1/(\omega/c_1). \tag{22}$$

Substituting Eq. (22) into Eq. (23), Snell's law may be rewritten as follows:

$$\cos^2\theta_{2k}=1-(c_2/c_1)^2(1-\cos^2\theta_{1k})=1-(c_2/c_1)^2(1-(\cos\xi_1\cos\alpha_1-\eta_1\sin\alpha_1/(\omega/c_1))^2). \tag{23}$$

Hence, the wave number k_{z2}' of the transmitted field is expressed explicitly as

$$k_{z2}'=(\omega/c_2)\cos\theta_{2k}=\sqrt{(\omega/c_2)^2-(\omega/c_1)^2+((\omega/c_1)\cos\xi_1\cos\alpha_1-\eta_1\sin\alpha_1)^2}. \tag{24}$$

The continuity of the tangential $\mathbf{k}$ components ($k_{x\text{tran}}=k_{x\text{inc}}$) yields

$$k_{x2}'^2=k_{x1}'^2=(\omega/c_1)^2\sin^2\xi_1-\eta_1^2. \tag{25}$$

The Fourier superposition of the transmitted field can thus be reduced to an expression analogous to Eq. (20); specifically,

$$p_{\text{trans}}(\mathbf{r},t)=\int_0^{\infty} d(\omega/c_1)\int_{-\omega/c_1\sin\xi}^{\omega/c_1\sin\xi} d\eta_1\,\frac{A_0 e^{-(\omega/c_1)a}}{\sqrt{(\omega/c_1)^2\sin^2\xi_1-\eta_1^2}}\cos(x\sqrt{(\omega/c_1)^2\sin^2\xi_1-\eta_1^2})e^{i\omega t}$$
$$\times e^{-iy(\eta_1\cos\alpha_1+(\omega/c_1)\cos\xi_1\sin\alpha_1)}e^{-iz\sqrt{(\omega/c_2)^2-(\omega/c_1)^2+((\omega/c_1)\cos\xi_1\cos\alpha_1-\eta_1\sin\alpha_1)^2}}T(\eta_1,\omega), \tag{26a}$$

where

$$T(\eta_1,\omega)=\frac{2\Lambda_1(\omega)}{\Lambda_1(\omega)+(\rho_{01}/\rho_{02})\sqrt{(\omega/c_2)^2-(\omega/c_1)^2+\Lambda_1^2(\omega)}}. \tag{26b}$$

One should point out that the coefficients of y and z in the arguments of the exponential functions cannot be mixed together to form a rotated coordinate. This should be compared to the reflected field where the coefficients of the y and z variables are combined into rotated coordinates that specify the trajectory of the reflected pulse. Similarly to the incident X-wave, wave vectors of the spectral plane wave components of the reflected pulse lie on a single conic surface. In contradistinction, the wave vectors defining the transmitted field components do not form a conic surface. This point has been emphasized in Ref. 31 and is elaborated further in the next section where a new pulsed wave representation is used to illustrate the process of the dispersion of the transmitted field. One should note, however, that for the special case of normal incidence $\alpha_1=0$, we have $k_{z1}=(\omega/c_1)\cos\xi_1$ and $k_{z2}=(\omega/c_2)\cos\xi_2$. Consequently, the transmission coefficient given in Eq. (26b) becomes independent of ω and the integration in Eq. (26a) can be evaluated explicitly to give a dispersion-free X-wave solution.

III. THE AZIMUTHALLY DEPENDENT PULSE REPRESENTATION

In this section, we introduce a representation of the incident, reflected and transmitted LW fields using an azimuthal angular superposition over elementary pulsed solutions of the scalar wave equation. This framework is then used to explain the localization of the reflected LW field and the reason for the disintegration of the transmitted field. In the preceding section, the quantity η_1 is essentially a rotated k_y component. Consequently, the integrations deduced for the incident, reflected and transmitted wave fields can be rewritten in a simpler form by introducing the azimuthal angular variable defined as $\cos\varphi=-\eta_1/\kappa_1\sin\xi_1$, where $\kappa_1=(\omega/c_1)$. Noting that $d(\omega/c_1)d\eta_1=\kappa_1\sin\varphi\sin\xi_1\,d\varphi\,d\kappa_1$, the incident pressure field given in Eq. (10) acquires the following form:

$$p_{\text{inc}}(\mathbf{r},t)=A_0\int_0^{\infty} d\kappa_1\int_0^{\pi} d\varphi e^{-\kappa_1 a}\cos(x\kappa_1\sin\xi_1\sin\varphi)$$
$$\times e^{i\kappa_1\cos\varphi\sin\xi_1 y'}e^{-i\kappa_1\cos\xi_1 z'}e^{i\kappa_1 c_1 t}. \tag{27}$$

The rotated coordinates associated with the obliquely incident X-wave are $z'=y\sin\alpha_1+z\cos\alpha_1$ and $y'=y\cos\alpha_1-z\sin\alpha_1$. The integration over κ_1 is a Laplace-type that can be easily evaluated to give an angular superposition over the azimuthally dependent pulse $\Psi_\varphi(\mathbf{r},t)$; specifically,

$$p_{\text{inc}}(\mathbf{r},t)=\int_0^{\pi} d\varphi\,\Psi_\varphi(\mathbf{r},t), \tag{28a}$$

where

$$\Psi_\varphi(\mathbf{r},t)=\frac{A_0}{2}\left\{\frac{1}{(a+i(z'\cos\xi_1-c_1t)-iy'\sin\xi_1\cos\varphi-ix\sin\xi_1\sin\varphi)}\right.$$
$$\left.+\frac{1}{(a+i(z'\cos\xi_1-c_1t)-iy'\sin\xi_1\cos\varphi+ix\sin\xi_1\sin\varphi)}\right\}. \tag{28b}$$

The angular superposition given in Eq. (28) is effectively a summation of pulses having shapes that depend on the azimuthal angular variable φ. The integration over φ in Eq. (28a) can be evaluated explicitly to yield the X-wave pressure field given in Eq. (7) and whose surface plot is displayed in Fig. 3; for $\alpha_1=25°$, $\xi_1=2°$ and $a=0.001$ m. The time dependence of the field is evaluated along the tilted axis of propagation, viz., the quantity $z'\cos\xi_1-c_1t$. The transverse dependence of the field is chosen as a function of $x'=x$ by setting the other transverse variable $y'=0$. One should note that for such a choice, $z'=z/\cos\alpha_1$. The field shown in Fig. 3 is calculated at the distance $z=-1$ m from the interface (for which $z'=-1/\cos\alpha_1$).

Similarly to Eq. (28), the reflected pressure field given in Eq. (20) can be transformed into the form

$$p_{\text{ref}}(\mathbf{r},t)=A_0\int_0^{\infty} d\kappa_1\int_0^{\pi} d\varphi e^{-\kappa_1 a}\cos(x\kappa_1\sin\xi_1\sin\varphi)$$
$$\times e^{-i\kappa_1\cos\varphi\sin\xi_1 y'}e^{-i\kappa_1\cos\xi_1 z'}e^{i\kappa_1 c_1 t}R(\varphi), \tag{29a}$$

where

$$R(\varphi)=\frac{\cos\xi_1\cos\alpha_1+\sin\xi_1\sin\alpha_1\cos\varphi-\sqrt{(c_1/c_2)^2-1+(\cos\xi_1\cos\alpha_1+\sin\xi_1\sin\alpha_1\cos\varphi)^2}(\rho_{01}/\rho_{02})}{\cos\xi_1\cos\alpha_1+\sin\xi_1\sin\alpha_1\cos\varphi+\sqrt{(c_1/c_2)^2-1+(\cos\xi_1\cos\alpha_1+\sin\xi_1\sin\alpha_1\cos\varphi)^2}(\rho_{01}/\rho_{02})} \tag{29b}$$

is independent of κ_1. The rotated coordinates associated with the reflected wave field are $z'=y\sin\alpha_1-z\cos\alpha_1$ and $y'=-y\cos\alpha_1-z\sin\alpha_1$. The integration over κ_1 leads to an angular superposition which is a generalization of the expression given in Eq. (28); specifically,

$$p_{\text{ref}}(\mathbf{r},t)=\int_0^{\pi}d\varphi R(\varphi)\hat{\Psi}_{\varphi}(\mathbf{r},t), \tag{30a}$$

where

$$\hat{\Psi}_{\varphi}(\mathbf{r},t)=\frac{A_0}{2}\left\{\frac{1}{(a+i(z'\cos\zeta_1-c_1t)+iy'\sin\xi_1\cos\varphi-ix\sin\xi_1\sin\varphi)}+\frac{1}{(a+i(z'\cos\zeta_1-c_1t)+iy'\sin\xi_1\cos\varphi+ix\sin\xi_1\sin\varphi)}\right\}. \tag{30b}$$

The expression given in Eq. (30b) indicates that all the reflected azimuthally dependent pulses $\hat{\Psi}_{\varphi}(\mathbf{r},t)$ travel at the same speed. At any observation point, the pulses $\hat{\Psi}_{\varphi}(\mathbf{r},t)$ will arrive at the same time to coherently synthesize the reflected field. As a consequence, the reflected field has an LW structure that does not disperse as the pulse travels away from the reflecting interface. This is consistent with having the wave vectors associated with the various plane wave components meet at the apex of a conical surface as explained in Ref. 31.

The azimuthal angular representation of the transmitted pressure wave can be deduced from Eq. (26) in a similar manner; it is given by

$$p_{\text{trans}}(\mathbf{r},t)=A_0\int_0^{\infty}d\kappa_1\int_0^{\pi}d\varphi e^{-\kappa_1 a}\cos(x\kappa_1\sin\xi_1\sin\varphi)e^{i\kappa_1 y(\sin\xi_1\cos\alpha_1\cos\varphi-\cos\xi\sin\alpha_1)}\times e^{-i\kappa_1 z\sqrt{(c_1/c_2)^2-1+(\cos\xi_1\cos\alpha_1+\sin\xi_1\sin\alpha_1\cos\varphi)^2}}e^{i\kappa_1 c_1 t}T(\varphi), \tag{31a}$$

where the transmission coefficient

$$T(\varphi)=\frac{2(\cos\xi_1\cos\alpha_1+\sin\xi_1\sin\alpha_1\cos\varphi)}{(\cos\xi_1\cos\alpha_1+\sin\xi_1\sin\alpha_1\cos\varphi)+\sqrt{(c_1/c_2)^2-1+(\cos\xi_1\cos\alpha_1+\sin\xi_1\sin\alpha_1\cos\varphi)^2}(\rho_{01}/\rho_{02})} \tag{31b}$$

is also independent of κ_1. The integration over κ_1 yields

$$p_{\text{trans}}(\mathbf{r},t)=\int_0^{\pi}d\varphi T(\varphi)\hat{\hat{\Psi}}_{\varphi}(\mathbf{r},t), \tag{32a}$$

where

$$\hat{\hat{\Psi}}_{\varphi}(\mathbf{r},t)=\frac{A_0}{2}\left\{\frac{1}{a+i(z\sqrt{(c_1/c_2)^2-1+(\cos\xi_1\cos\alpha_1+\sin\xi_1\sin\alpha_1\cos\varphi)^2}-c_1t)-iy(\sin\xi_1\cos\alpha_1\cos\varphi-\cos\xi_1\sin\alpha_1)-ix\sin\xi_1\sin\varphi}+\frac{1}{a+i(z\sqrt{(c_1/c_2)^2-1+(\cos\xi_1\cos\alpha_1+\sin\xi_1\sin\alpha_1\cos\varphi)^2}-c_1t)-iy(\sin\xi_1\cos\alpha_1\cos\varphi-\cos\xi_1\sin\alpha_1)+ix\sin\xi_1\sin\varphi}\right\}. \tag{32b}$$

In contrast to the incident and reflected cases, the transmitted azimuthally dependent pulses $\hat{\hat{\Psi}}_{\varphi}(\mathbf{r},t)$ have speeds that depend on φ. The square root coefficient of z depends on $\cos\varphi$ and this dependence cannot be eliminated by a simple rotation of the coordinates. As a result of this dependence on φ, the transmitted azimuthally dependent pulses arrive at a certain observation point with different speeds. Except for normal incidence ($\alpha_1=0$), these pulses do not arrive together at the same time to coherently construct an LW pulse. As a consequence, the transmitted pulse degenerates and its central peak decays as we move away from the surface of discontinuity.

The azimuthal angular representation of the transmitted field constitutes a framework that allows an accurate estimation of the localization depth of the transmitted field. Toward such a goal, we assume that the wave vectors of the trans-

mitted spectral components form an approximate conical surface. The inclination angle of the axis of such a surface is α_2 and its apex angle is ξ_2. Consider a section, taken at $x=0$, of the incident, reflected and transmitted cones, as illustrated in Fig. 2. Applying Snell's law to the rays shows that the following two equations are satisfied:

$$(1/c_1)\sin(\alpha_1 \pm \xi_1) = (1/c_2)\sin(\alpha_2 \pm \xi_2).$$

The combination of these two equations yields the relations

$$(1/c_1)\sin\xi_1 \cos\alpha_1 = (1/c_2)\sin\xi_2 \cos\alpha_2, \tag{33}$$

$$(1/c_1)\cos\xi_1 \sin\alpha_1 = (1/c_2)\cos\xi_2 \sin\alpha_2. \tag{34}$$

Eliminating the dependence on α_2 and after some algebraic manipulation, we obtain

$$\cos^4\xi_2 + ((c_2/c_1)^2\sin^2\xi_1\cos^2\alpha_1 - (c_2/c_1)^2\cos^2\xi_1\sin^2\alpha_1 - 1)\cos^2\xi_2 + (c_2/c_1)^2\cos^2\xi_1\sin^2\alpha_1 = 0. \tag{35}$$

The solution to this equation gives the apex angle of the transmitted field; specifically,

$$\cos\xi_2 = \sqrt{-(B/2) + \sqrt{(B/2)^2 - C}}, \tag{36}$$

where $B = ((c_2/c_1)^2\sin^2\xi_1\cos^2\alpha_1 - (c_2/c_1)^2\cos^2\xi_1\sin^2\alpha_1 - 1)$ and $C = (c_2/c_1)^2\cos^2\xi_1\sin^2\alpha_1$. After evaluating the apex angle ξ_2, the inclination angle α_2 can be calculated using either Eq. (33) or (34). This completes the analysis needed to calculate α_2 and ξ_2. These values can be used to estimate the deviation of the square root coefficient of z in Eq. (32b) from that of a rotated z variable appearing in an exact X-wave characterized by ξ_2 and tilted by an angle α_2. Toward such a goal, consider the denominators

$$D = a + i(z\sqrt{(c_1/c_2)^2 - 1 + (\cos\xi_1\cos\alpha_1 + \sin\xi_1\sin\alpha_1\cos\varphi)^2} - c_1 t) - iy(\sin\xi_1\cos\alpha_1\cos\varphi - \cos\xi_1\sin\alpha_1) \pm ix\sin\xi_1\sin\varphi \tag{37}$$

that appear in Eq. (32b). Using Eqs. (33) and (34), they can be rewritten in terms of the rotated coordinates of the transmitted field ($x' = x$, $y' = y\cos\alpha_2 - z\sin\alpha_2$, and $z' = y\sin\alpha_2 + z\cos\alpha_2$) as follows:

$$D = a + i(c_1/c_2)(z'\cos\xi_2 - c_2 t) + iz(c_1/c_2)\Delta(\varphi) - i(c_1/c_2)(y'\sin\xi_2\cos\varphi) \pm ix\sin\xi_1\sin\varphi. \tag{38}$$

Here $\Delta(\varphi)$ is the deviation from the assumed trajectory specified by α_2 and ξ_2 and is equal to

$$\Delta(\varphi) = \sqrt{1 - (c_2/c_1)^2 + (c_2/c_1)^2(\cos\xi_1\cos\alpha_1 + \sin\xi_1\sin\alpha_1\cos\varphi)^2} - \cos\xi_2\cos\alpha_2 - \sin\xi_2\sin\alpha_2\cos\varphi. \tag{39}$$

For short distances from the interface the condition $z(c_1/c_2)\Delta(\varphi) \ll a$ is satisfied for all values of $\Delta(\varphi)$. Hence, we introduce the hypothesis that the pulse stays localized with peak amplitude $\propto 1/a$ until it reaches the following distance along the direction of propagation of the pulse:

$$z'_d = \frac{z_d}{\cos\alpha_2} = \frac{(c_2/c_1)a}{|\overline{\Delta}(\varphi)|\cos\alpha_2}. \tag{40}$$

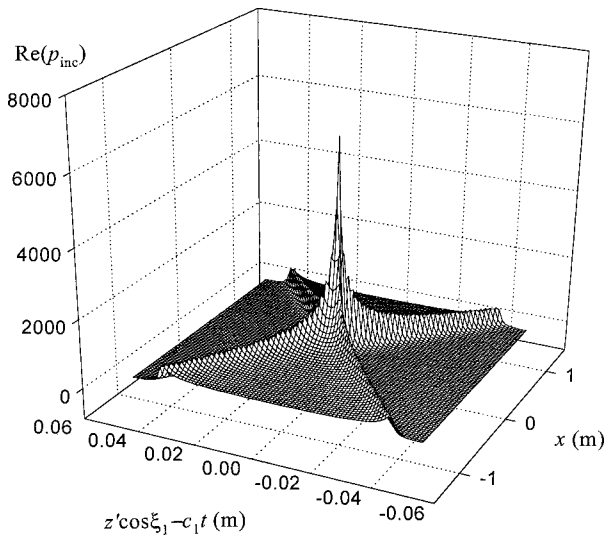

FIG. 3. Pressure field of the incident X-wave having $a=0.001$ m and $\xi_1 = 2°$ evaluated at $z=-1$ m.

Here, $\overline{\Delta}(\varphi)$ is the average deviation over the range $0 \leqslant \varphi < \pi$. From Eq. (40) it appears that z_d increases with (c_2/c_1); however, $|\overline{\Delta}(\varphi)| \propto (c_2/c_1)^n (n>1)$, resulting in z_d being inversely proportional to (c_2/c_1). The dispersion-free range given in Eq. (40) is a fairly accurate estimate as will be seen from the examples in the next section.

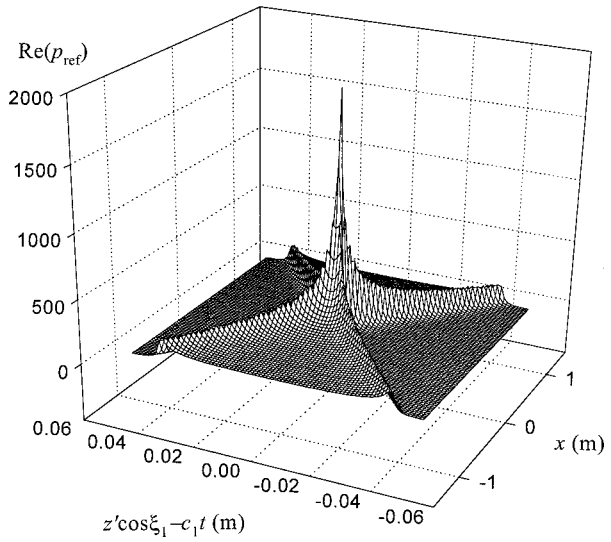

FIG. 4. Reflected pressure field evaluated for $(c_1/c_2)=2$ and $(\rho_{01}/\rho_{02}) = 0.25$. The incident X-wave has a propagation-axis tilted at $\alpha_1 = 25°$. The surface plot is calculated at $z=-1$ m.

IV. ILLUSTRATIONS AND EXAMPLES

In this section, we study the properties of the reflected and transmitted pressure fields resulting from an X-wave incident on a planar interface. The azimuthal angular representation introduced in the preceding section is used to numerically calculate surface plots of the reflected and transmitted pulses. The aim of the examples employed is to highlight certain properties of the reflected or transmitted fields and to illustrate that the disintegration of the transmitted field is caused by the spectral incoherence described in Sec. III. As such, the examples used will demonstrate the validity of the expression deduced for the dispersion-free length given in Eq. (40). Two main situations are considered; namely, the incident X-wave approaches the interface either from the side of the faster medium $[(c_1/c_2)>1]$ or the slower one $[(c_1/c_2)<1]$.

A. Reflected and transmitted fields for $(c_1/c_2)>1$

The X-wave is assumed to approach the surface of discontinuity from the side of the medium having the larger wave velocity; specifically, the values $(c_1/c_2)^2=4$ and $(\rho_{01}/\rho_{02})=0.25$ are chosen. In most numerical results presented in this section, the X-wave shown in Fig. 3 is assumed to be incident on the interface at an inclination angle $\alpha_1=25°$ and is characterized by the parameters $\xi_1=2°$ and $a=0.001$ m, except when explicitly stated otherwise. Furthermore, the calculated amplitudes of all incident, reflected and transmitted fields are displayed in terms of $(A_0/2)$. The time-variation of the reflected pressure field is plotted in Fig. 4 for $y'=0$, $z=-1$ m. The reflected X-wave retains the same LW structure characterizing the incident pressure field. At farther distances from the interface the reflected pulse preserves its shape and does not spread out.

As discussed in the preceding section, the refracted pulse should start disintegrating after traversing the estimated dispersion-free range given in Eq. (40). To illustrate this point the transmitted pressure field is plotted in Fig. 5 as a function of the transverse variable $x(y'=0)$ at distances $z=0.1$, 50, and 250 m from the interface. The time dependence of the field is evaluated along the tilted axis of propagation as a function of the quantity $z'\cos\xi_2-c_2t$. For an X-wave pulse having $\xi_1=2°$ and $a=0.001$ m incident at an angle $\alpha_1=25°$ on an interface separating two media characterized by $(c_1/c_2)^2=4$ and $(\rho_{01}/\rho_{02})=0.25$, the dispersion-free range given in Eq. (40) yields $z_d=45.77$ m. This result agrees nicely with the decay pattern illustrated in Fig. 5. The transmitted X-wave retains its shape for short distances, while the peak starts decaying at a distance of about 50 m. It appears, from the figures, that the disintegration of the transmitted field is accompanied by an increase in the axial width of the central portion of the pulse. This behavior is related to the dispersion in the velocities of the azimuthally dependent pulsed components. The disintegration of the pulse starts when the spread in the arrival time of the azimuthally dependent pulses is larger than a/c_2.

To achieve a better understanding of the decay properties of refracted X-wave, we consider the effect of changing the inclination angle α_1, the axicon angle ξ_1 and the param-

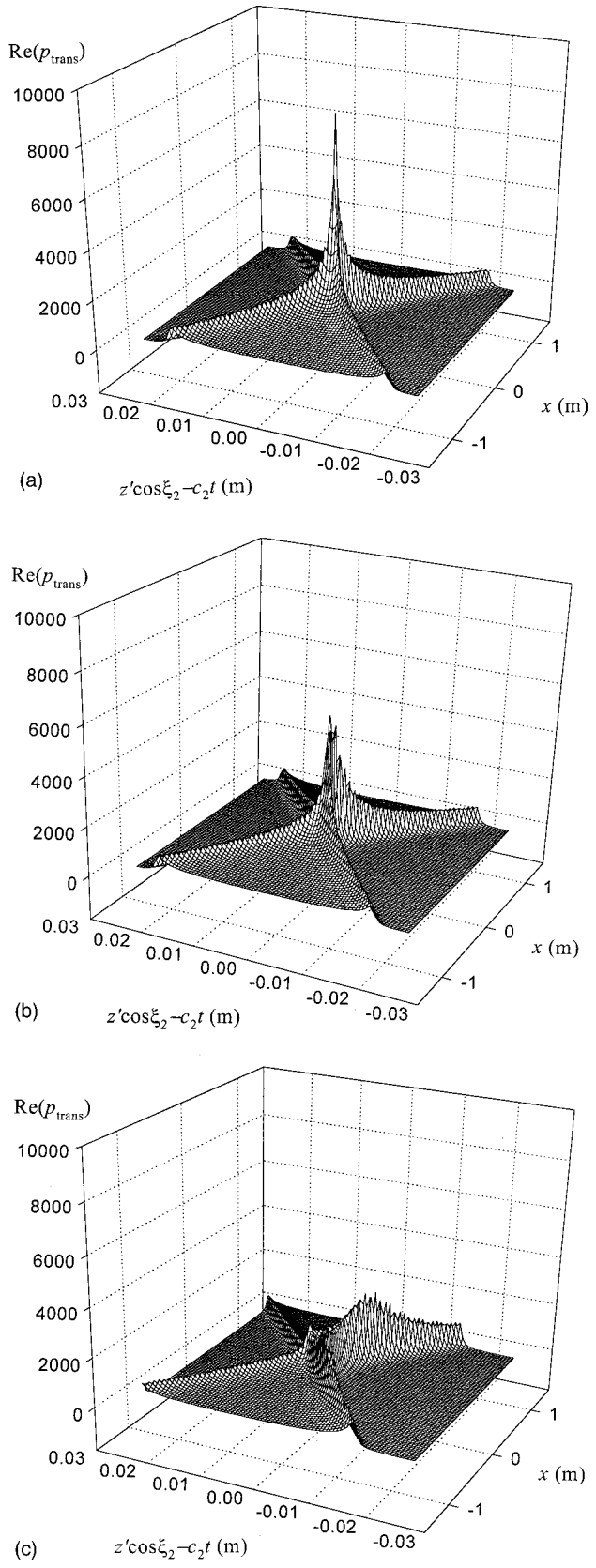

FIG. 5. Transmitted pressure field evaluated for $(c_1/c_2)=2$ and $(\rho_{01}/\rho_{02})=0.25$. The incident X-wave has a propagation-axis tilted at $\alpha_1=25°$. The surface plots are calculated at (a) $z=0.1$ m, (b) $z=50$ m and (c) $z=250$ m.

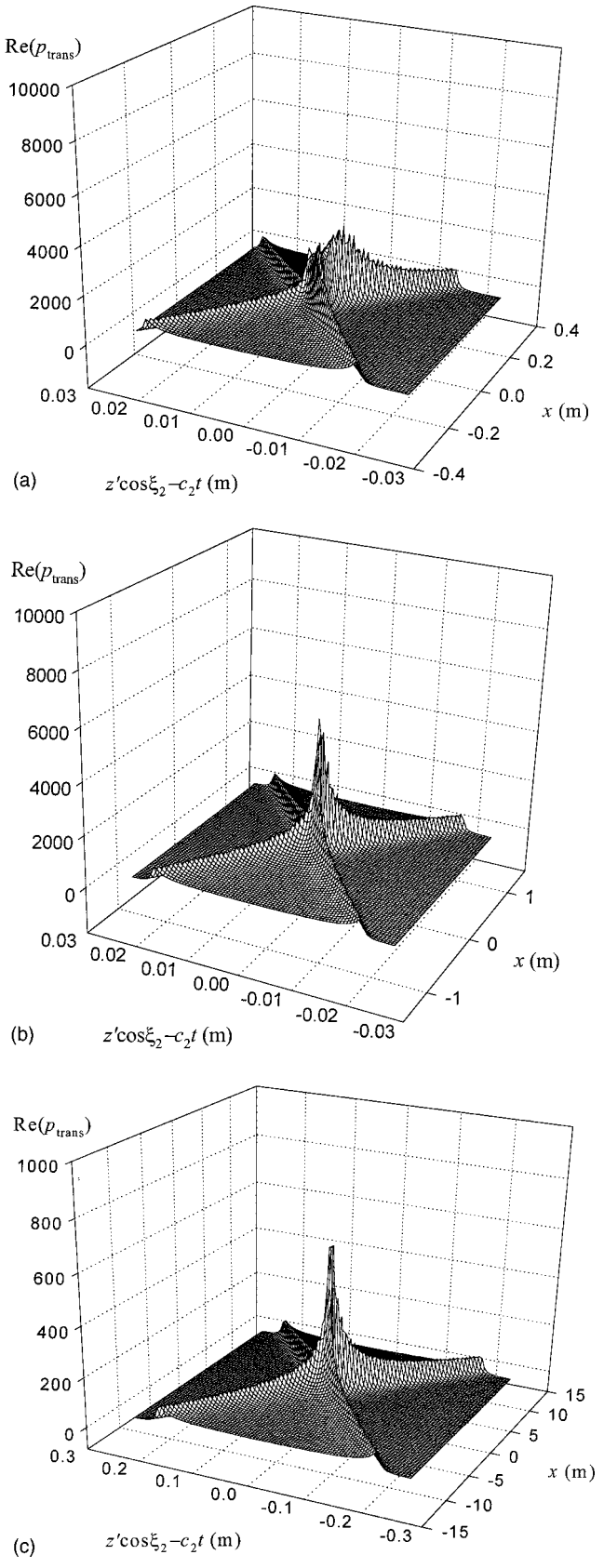

FIG. 6. Transmitted pressure field evaluated at $z=10$ m showing the change in the dispersion rate when (a) the apex angle ξ_1 is increased to 8° and (b) the inclination angle $\alpha_1=50°$. (c) The transmitted pressure field evaluated at $z=250$ m when the parameter a increases to 0.01 m. In each case the rest of the parameters are unchanged and are the same as in Fig. 5.

eter a on the dispersion-free range z_d. In Fig. 6(a), it is seen that increasing ξ_1 from 2° to 8° causes the transmitted pulse to decay at a much faster rate. The figure shows that for $\xi_1=8°$ the peak of the pulse has already decayed significantly at $z=10$ m. The resulting decay is a good demonstration of the fact that changing the apex angle to $\xi_1=8°$, while keeping the other parameters unchanged, reduces the dispersion-free depth to the value $z_d=2.86$ m. On the other hand, changing the inclination angle α_1 from 25° to 50°, while keeping $\xi_1=2°$, yields $z_d=11.76$ m. Figure 6(b) confirms this change in the dispersion-free length by demonstrating that increasing the inclination angle to $\alpha_1=50°$ causes the peak of the transmitted pulse to start decaying at $z=10$ m. Figure 6(c) shows the transmitted field at $z=250$ m for $a=0.01$ m. This agrees with the fact that increasing the parameter a to 0.01 m, while keeping α_1 and ξ_1 unchanged, extends the localization range to $z_d=457.73$ m. It is interesting to point out that parameter a controls the temporal frequency bandwidth.[20] As a increases, the bandwidth decreases. Thus X-waves with smaller frequency bandwidth undergo less dispersion, as they travel inside the second material.

B. Reflected and transmitted fields for $(c_1/c_2)<1$

In this subsection, the analysis introduced in Sec. III is applied to the case of an X-wave incident from the slower medium; specifically, we assume that $(c_1/c_2)^2=0.25$ and $(\rho_{01}/\rho_{02})=4$. The field components incident at spectral angles $\theta_k>\theta_c=\sin^{-1}(c_1/c_2)$ will be totally reflected and evanescent fields are generated inside the second medium. In this section, we investigate two cases involving the evanescent fields, associated with normally and obliquely incident X-waves, respectively. For the former case, the evanescent fields are generated when the axicon angle of the incident X-wave $\xi_1>\theta_c=\sin^{-1}(c_1/c_2)$. Consequently, the X-wave is totally reflected and all the spectral components produce evanescent fields in the second medium. For this particular case, the evanescent fields can be deduced in an exact closed-form. This allows for an interesting assessment of the time development of the evanescent field. For oblique incidence several possible situations are investigated, namely sub-critical, super-critical and near-critical incidence. For the first case, all the spectral components have $\theta_k<\sin^{-1}(c_1/c_2)$. This is completely analogous to the case discussed in Sec. III, except that the disintegration should be faster as seen from Eq. (40). The super-critical case corresponds to the situation when all the wave vectors lying on the tilted spectral cone are inclined at angles $\theta_k>\sin^{-1}(c_1/c_2)$. Near-critical incidence involves the situation when the tilted spectral cone has some wave vectors that are tilted at $\theta_k<\sin^{-1}(c_1/c_2)$, while the rest of the wave vectors have incidence angles greater than the critical angle. The field transmitted into the second medium is thus a mixture of propagating and evanescent fields. Near the interface, the lateral waves and the refracted ones become concentrated in a small region, thus producing a highly compressed and focused pulse.

Starting with normal incidence, we assume that the incident X-wave is characterized by an axicon angle $\xi_1=40°$

$>\sin^{-1}(1/2)=30°$. The transmitted field follows directly from Eqs. (26a) and (26b), where for normal incidence $\alpha_1=0$ and $\eta_1=k_y$, thus yielding

$$P_{\text{trans}}(\mathbf{r},t)=\int_0^{\infty} d(\omega/c_1)\int_{-\omega/c_1\sin\xi}^{\omega/c_1\sin\xi} dk_y \frac{A_0 e^{-(\omega/c_1)a}}{\sqrt{(\omega/c_1)^2\sin^2\xi_1-k_y^2}} \times\cos(x\sqrt{(\omega/c_1)^2\sin^2\xi_1-k_y^2}) \times e^{i\omega t}e^{-ik_y y}e^{-z(\omega/c_1)\sqrt{\sin^2\xi_1-(c_1/c_2)^2}}T(\xi_1), \tag{41a}$$

where

$$T(\xi_1)=\frac{2\cos\xi_1(c_1/c_2)^2}{\cos\xi_1(c_1/c_2)^2-i\sqrt{\sin^2\xi_1-(c_1/c_2)^2}}. \tag{41b}$$

In the above expression, we have used the negative imaginary branch for which $\sqrt{(\omega/c_2)^2-(\omega/c_1)^2\sin^2\xi_1}=-i(\omega/c_1)\sqrt{\sin^2\xi_1-(c_1/c_2)^2}$. This choice yields an exponentially decaying dependence on z in the integrand of Eq. (41a). In addition, we have assumed that $(\rho_{01}/\rho_{02})=(c_2/c_1)^2$ in order to simplify the resulting mathematical expressions. Since $T(\xi_1)$ is independent of (ω/c_1) and k_y, the double integration in Eq. (41a) can be evaluated exactly to give

$$p_{\text{trans}}(\mathbf{r},t)=\frac{(2A_0\cos\xi_1(c_1/c_2)^2)/(\cos\xi_1(c_1/c_2)^2-i\sqrt{\sin^2\xi_1-(c_1/c_2)^2})}{\sqrt{\rho^2\sin^2\xi_1+(a+z\sqrt{\sin^2\xi_1-(c_1/c_2)^2}-ict)^2}}. \tag{42}$$

This evanescent field exhibits a transverse wave motion along the interface through the terms $\rho^2\sin^2\xi_1-(c_1t)^2$ appearing in the square root in the denominator. This transverse motion is illustrated in Fig. 7 where surface plots of the real part of $p_{\text{trans}}(\mathbf{r},t)$ are shown for different times as a function of z, the normal distance from the interface. The two localized bumps that appear in Fig. 7(a) approach each other for negative time and coalesce into a single peak at $c_1t\approx 0$, as shown in Fig. 7(b). Henceforth, they split into two bumps and travel away from each other for $c_1t>0$ [cf. Fig. 7(c)]. The time evolution of the evanescent field is illustrated in Fig. 8(a). A surface plot of the real part of $p_{\text{trans}}(\mathbf{r},t)$ given in Eq. (42) is illustrated at distance $z=0.001$ m. At the farther distances, the evanescent field has the same shape but spreads out and its amplitude decreases. The time dependence of the evanescent field near the surface is an attenuated imprint of the reflected field [cf. Fig. 8(b)]. The reflected pulse could, thus, be perceived to exist for a certain period of time inside the second medium before being reflected back into the first one. This is analogous to the quantum mechanical picture that describes the state of a totally reflected wave packet from a finite-height potential barrier. In the latter situation, the wave packet dwells inside the reflecting barrier for a short time before being totally reflected. In both cases, the spectral components of the reflected fields undergo phase delays that distort the shape of the reflected pulses. Such phase delays are responsible for the distortion of the X-shape of the reflected field shown in Fig. 8(b). However, the reflected pulse preserves its shape from this time on and does not undergo any dispersion as it travels away from the interface.

To gain a better understanding of the time evolution of the evanescent field, we consider the case when $\rho=0$. As a consequence, the real part of the expression given in Eq. (42) acquires the following simple form:

$$\text{Re}\{p_{\text{trans}}(\mathbf{r},t)\}=\frac{A_0(2a\cos^2\xi_1(c_1/c_2)^2+2\cos\xi_1(c_1/c_2)^2\sqrt{\sin^2\xi_1-(c_1/c_2)^2}((c_1/c_2)^2\cos\xi_1 z-c_1t))}{((c_1t)^2+(a+z\sqrt{\sin^2\xi_1-(c_1/c_2)^2})^2)((c_1/c_2)^4\cos^2\xi_1+\sin^2\xi_1-(c_1/c_2)^2)}. \tag{43}$$

As shown in Fig. 8, this field has two peaks of opposite signs with a null in between. The null travels at the velocity $v_{\text{evan}}=c_2/(c_1/c_2)\cos\xi_1$ greater than the velocity c_2 of the medium. This explicit propagation in the z direction of the evanescent field is an interesting result in its own right. Thus in addition to the lateral wave motion of the evanescent field there is a longitudinal transfer of the field in a direction normal to the interface. This tunnelinglike effect may be used for ultra-fast signaling through a thin slab using evanescent fields.

For oblique incidence, we consider an incident X-wave characterized by an axicon angle $\xi_1=2°$. The axis of propagation of the X-wave is inclined at angles $\alpha_1=15°$, 30° and 45°, corresponding to sub-critical, near-critical and supercritical incidence, respectively. The angular superposition given in Eq. (32) is used to evaluate the transmitted fields in the above three cases, while Eq. (30) is employed to calculate the reflected fields. In these two equations, one should be careful when the argument of $\sqrt{(c_1/c_2)^2-1+(\cos\xi_1\cos\alpha_1+\sin\xi_1\sin\alpha_1\cos\varphi)^2}$ becomes negative. In such a case, the negative imaginary branch must be chosen to ensure the decay of the evanescent field along the positive z direction.

For sub-critical incidence, we assume that the X-wave

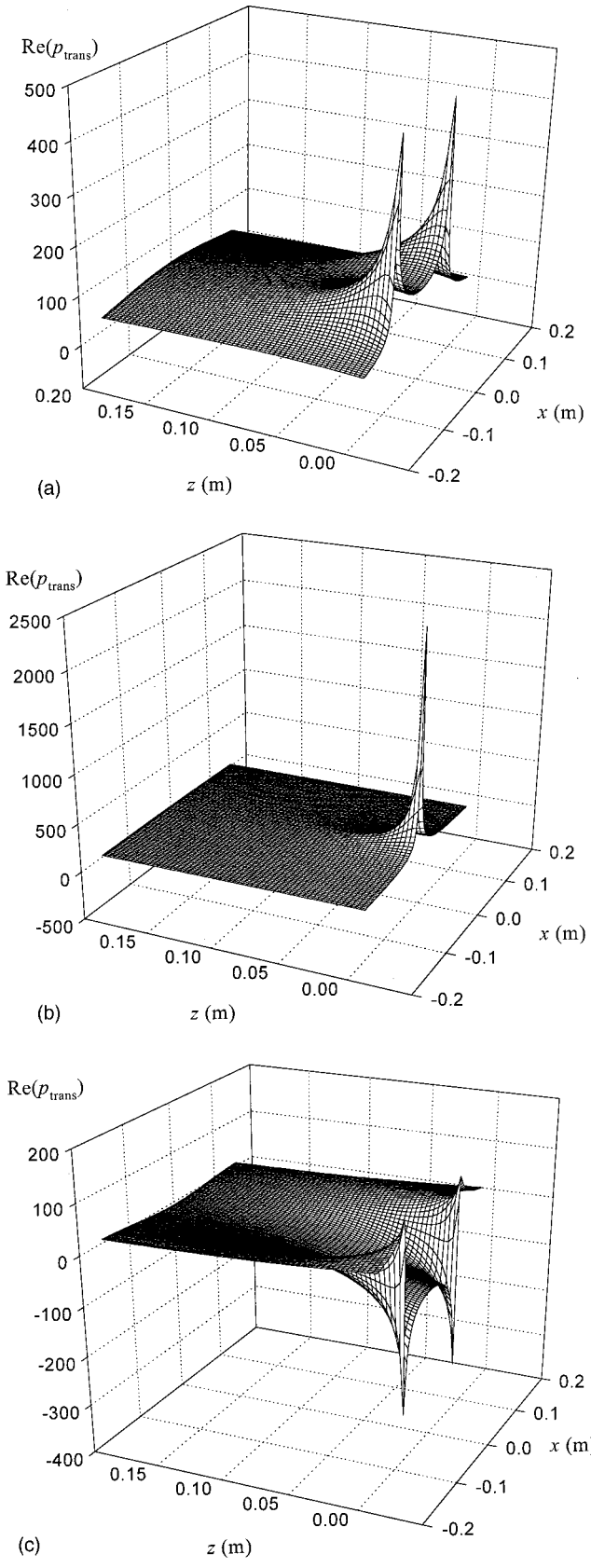

FIG. 7. Evanescent fields resulting from a normally incident X-wave having $a=0.001$ m and $\xi_1=40°$. The surface plots are evaluated for $(c_1/c_2)=0.5$ at (a) $c_1t=-0.05$ m, (b) $c_1t=0$ and (c) $c_1t=0.05$ m.

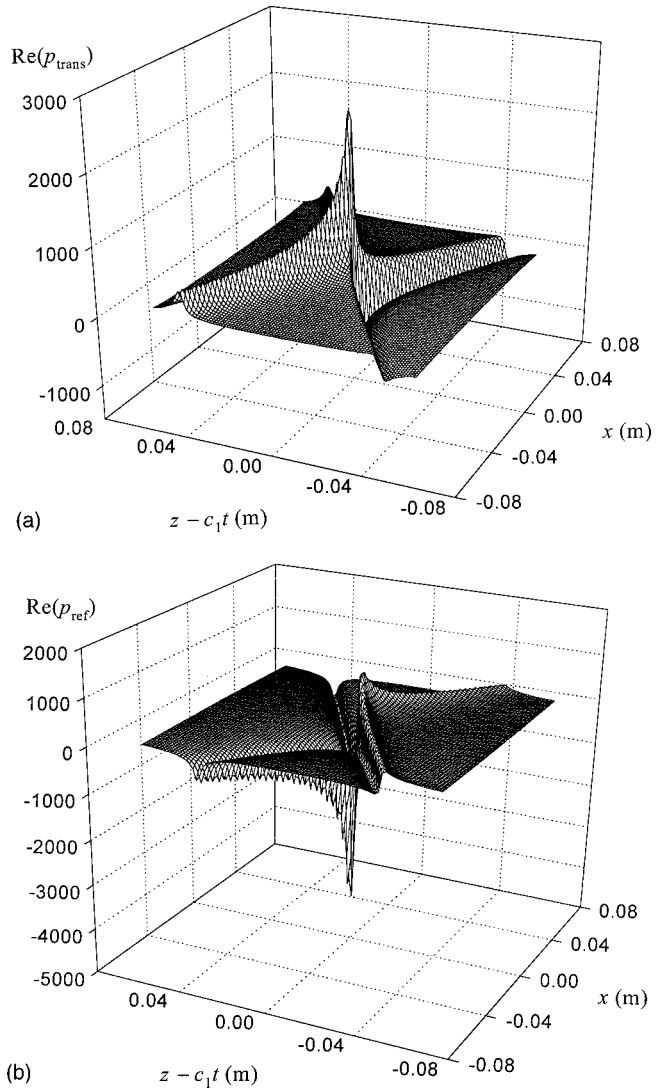

FIG. 8. (a) Time dependence of the evanescent fields resulting from a normally incident X-wave having $a=0.001$ m and $\xi_1=40°$. The surface plots are evaluated for $(c_1/c_2)=0.5$ at $z=0.001$ m. (b) The totally reflected pressure field evaluated at $z=-1$ m.

plotted in Fig. 3 is incident at an angle $\alpha_1=15°$ on the interface separating two media having $(c_1/c_2)=0.5$. The reflected pressure field calculated at $z=-1$ is shown in Fig. 9(a). The reflected pulse resembles the incident X-wave except for a change in the sign and magnitude of its amplitude. In Fig. 9(b)–(d), the transmitted field is plotted for distances $z=0.1$, 1 and 50 m normal to the interface. One should note that the decay of the peak of the transmitted field is much faster than in the case $(c_1/c_2)=2$. The pulse has already started to disperse at $z=1$ m and has decayed significantly at $z=50$ m. Another interesting difference between the two cases $(c_1/c_2)>1$ and $(c_1/c_2)<1$ is that in the former the pulse spreads backward along the lagging X-shaped arms, while in the latter the transmitted pulse spreads out along the forward X-shaped arms. This behavior is due to the fact that the wave vectors of the transmitted field lie on a convoluted conic surface.[31] Such a deformed cone is shaped by stretching the apex point of the cone associated with the incident X-wave into a line segment. For $(c_1/c_2)>1$, the apex point is drawn outward to form a line segment in a direction re-

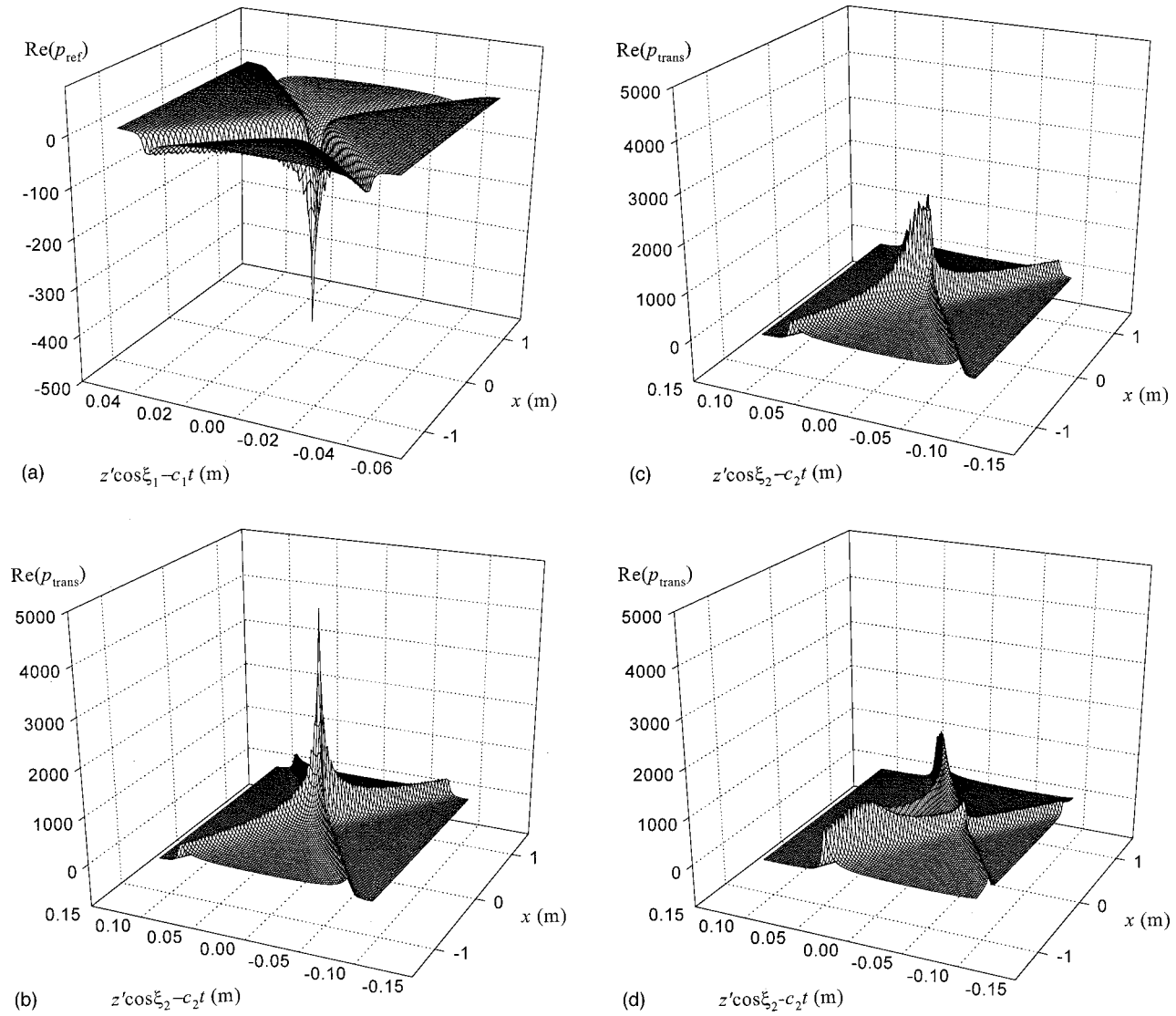

FIG. 9. Sub-critical incidence at $\alpha_1 = 15° < \theta_c = 30°$ $((c_1/c_2) = 0.5)$. (a) Reflected pressure field plotted at $z = -1$ m. Transmitted pressure field is evaluated at (b) $z = 0.1$ m, (c) $z = 1$ m and (d) $z = 50$ m.

moved away from the interface. Wave components arriving at different points on this line segment lag behind the peak. When $(c_1/c_2) < 1$, the apex is stretched inward toward the interface forming a folded surface. Wave components contributing to the transmitted field lead over the peak. Details of these ideas are presented in a separate work (cf. Ref. 31).

For the case of super-critical incidence, the pulse shown in Fig. 3 is incident on the surface of discontinuity at an angle $\alpha_1 = 45°$. All the plane wave components of the incident pressure field are inclined at angles θ_k larger than the critical angle $\theta_c = 30°$. Only evanescent fields exist in the second medium. The properties of the totally reflected field and the evanescent fields are similar to those discussed above for normal incidence with $\xi_1 > \theta_c$. To verify our claim, we provide in Fig. 10 a plot of the time variation of the totally reflected pressure field at $z = -1$ m. The reflected pulse has an LW structure and does not disperse as it travels away from the interface. The evanescent field dependence on z, the perpendicular distance to the interface, is similar to the case of normal incidence. In analogy to Fig. 7, the two lateral

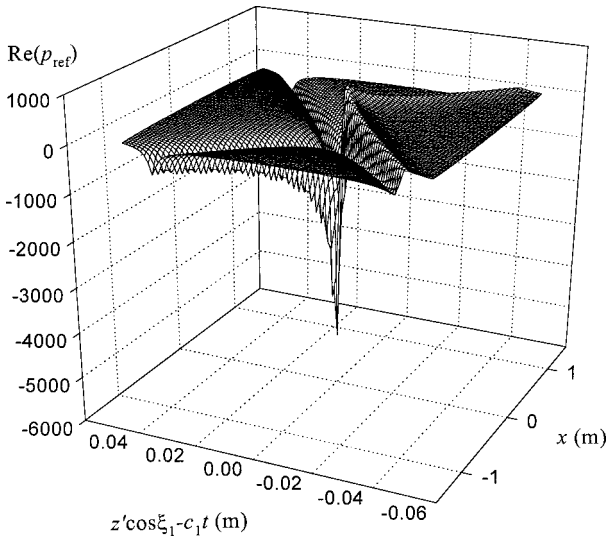

FIG. 10. Reflected pressure field plotted at $z = -1$ m for super-critical incidence at $\alpha_1 = 45° > \theta_c = 30°$ $[(c_1/c_2) = 0.5]$.

peaks of the evanescent field approach each other before coalescing at $c_1 t \approx 0$ and then start traveling away from each other.

Near-critical incidence corresponds to situations when the inclination angles of the wave vectors associated with the spectral components of the incident pressure field can have both values $\theta_k > \theta_c$ and $\theta_k < \theta_c$. The spectral components having $\theta_k < \theta_c$ generate propagating refracted fields in the second medium, while those having $\theta_k > \theta_c$ produce evanescent fields. The transmitted field, thus, consists of a combination of these two types of waves. Various transmitted field distributions are evaluated for different α_1 angles in the vicinity of $\theta_c = 30°$. This allows us to acquire a better understanding of the behavior of the transmitted mixture of refracted and evanescent fields. In Fig. 11 we plot the transmitted pressure fields resulting from an X-wave pulse (cf. the pulse shown in Fig. 3, having $\xi_1 = 2°$ and $a = 0.001$ m) incident at angles $\alpha_1 = 28°$, 29°, 30°, 31° and 32°. The transmitted fields, shown in Fig. 11(a) and (e), are similar to those occurring for sub-critical and super-critical incidence, respectively. This is the case because for $\xi_1 = 2°$, the pulse plotted in Fig. 11(a) is transmitted due to the incidence of an X-wave consisting of spectral components having $\theta_k < \theta_c$. The opposite is true for the pulse shown in Fig. 11(e). The transmitted field due to an X-wave inclined at $\alpha_1 = 31°$ is plotted in Fig. 11(d) and shows a close resemblance to that corresponding to $\alpha_1 = 32°$ shown in Fig. 11(e). The reason for this resemblance is that, for $\alpha_1 = 31°$, most of the spectral components have $\theta_k > \theta_c$. One should note, however, that the transmitted pulse shown in Fig. 11(d) is slightly compressed along the direction of propagation and has larger amplitude than the pulse plotted in Fig. 11(e). Far away from the interface, refracted components of the pulse shown in Fig. 11(d) will be stripped away from the decaying evanescent components, forming a propagating pulse that disperses with distance. The pulse shown in Fig. 11(e), however, consists solely of evanescent fields that will have negligibly small amplitudes at farther distances from the interface.

The pressure field displayed in Fig. 11(b) shows an extremely strong pulse-compression effect. It appears that the planar interface acts as a lens that focuses and compresses the field transmitted into the second medium. This effect can be used in applications requiring the delivery of high intensity ultra-short pulses near an interface. This pulse focusing effect may be understood by resorting to the ray-theoretic approach introduced in Ref. 31. For $(c_1/c_2) < 1$, the apex of the transmitted cone is stretched inwards into a line segment. This line segment is dragged up in the direction of the interface. For near-critical incidence, the line segment reaches the interface. Spectral components having $\theta_k < \theta_c$ will have refracted wave vectors ending up on different points of the line segment, while components with $\theta_k > \theta_c$ will produce lateral rays parallel to the interface. The concentration of such wave components in a small volume produces a highly focused pulse. At this point, we show that after traveling a short distance farther away from the interface, the amplitude of the transmitted field undergoes a sign inversion. In Fig. 12, we show that at $z = 0.001\,09$ m the transmitted pulse acquires very large negative amplitudes and is highly compressed. The extent of the compression of the pulse at $z = 0.001\,09$ m can be emphasized further by comparing Figs. 11(b) and 12. The scale of the transverse variable is reduced by 10-fold, while the longitudinal scale is shrunk by 20-fold. The peak amplitude of the transmitted pulse is 200 times larger than the incident X-wave. This compression effect is not restricted only to the angle $\alpha_1 = 29°$ but can occur for other angles at near-critical incidence. However, the position of the focus point varies with the various combinations of refracted and lateral rays. Consequently, incidence at different angles $\alpha_1 \sim \theta_c$ results in pulse compression at different distances from the interface. In fact, a surface plot of the transmitted pulse, displayed in Fig. 11(c) for $\alpha_1 = 30°$, shows that the inverted pulse is already focused at $z = 0.001$ m. This means that the strong focusing of the pulse occurs nearer to interface because the refracted rays are crowded together at a shorter distance from the surface of discontinuity. Furthermore, the field incident at $\alpha_1 = 30°$ contains spectral components having $\theta_k > \theta_c$ that are totally reflected. Since a number of the spectral components are totally reflected while the remaining ones give rise to both reflected and refracted fields, we expect the reflected pressure field to lose its X-shaped distribution. This effect is illustrated in Fig. 13 where the reflected field corresponding to $\alpha_1 = 30°$ is plotted at $z = -1$ m. One should note the deformation of the lagging X-shaped arms. However, this pulse still has an LW structure and it travels away from the interface without any dispersion.

V. CONCLUSION

In this work, the reflection and transmission of acoustic X-waves obliquely incident on a planar interface has been investigated. The analysis adopted is based on a spectral decomposition of the incident pulse into plane wave components specified by wave vectors forming a conical surface. The boundary conditions at the interface are satisfied by the individual plane waves and the reflected and transmitted fields are deduced as Fourier superpositions. Subsequently, it has been found profitable to transform each of these Fourier superpositions into an angular integration (synthesis) of azimuthally dependent pulsed plane waves. A study of the constituent pulsed solutions has been carried out for the problem under investigation in this paper. It has been shown that the incident and reflected pressure waves have azimuthally dependent pulses traveling at the same speed and, consequently, adding up coherently at any observation point to form an LW pulse. In contradistinction, the azimuthally dependent pulses associated with the transmitted field travel at different speeds, thus causing the dispersion of an LW pulse after traveling a certain distance from the interface. It has been shown that the localization range of the transmitted field depends on the temporal frequency bandwidth, the angle of inclination and the axicon angle of the incident X-wave pulse. The main factor affecting the disintegration of the transmitted pulse is the axial width of the incident X-wave along the direction of propagation (i.e., for $x' = y' = 0$). For larger axial widths of the incident X-wave, the transmitted pulse suffers less disintegration as it travels in-

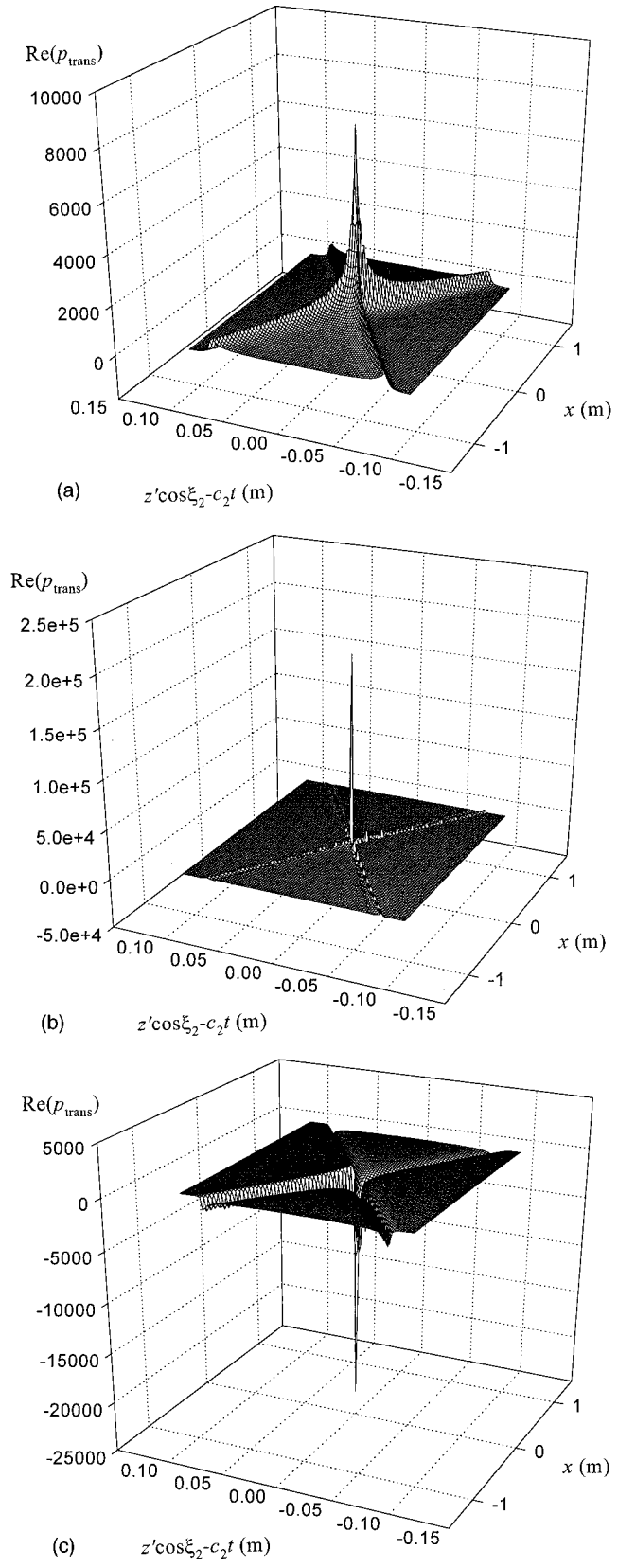

FIG. 11. Near-critical incidence for which $\alpha_1 \sim \theta_c = 30°$ $[(c_1/c_2) = 0.5]$. Transmitted pressure field evaluated at $z = 0.001$ m for (a) $\alpha_1 = 28°$, (b) $\alpha_1 = 29°$, (c) $\alpha_1 = 30°$, (d) $\alpha_1 = 31°$ and (e) $\alpha_1 = 32°$.

side the second medium. For zero angle of inclination (normal incidence), the transmitted fields retain their LW structure. These results are in agreement with the conclusions inferred from the ray-theoretic approach introduced in Ref. 31. The use of such angular superposition constitutes an efficient method for deducing the exact form of the transmitted field and for estimating its range of localization.

In previous investigations, the transmitted field was shown to lose the LW structure of the incident pulse. This may give the wrong impression that the transmitted field is not localized at all. An important contribution in the present work is the indication that the transmitted field stays localized up to a distance that depends on the characteristics of the incident field. A clear explanation is provided for the

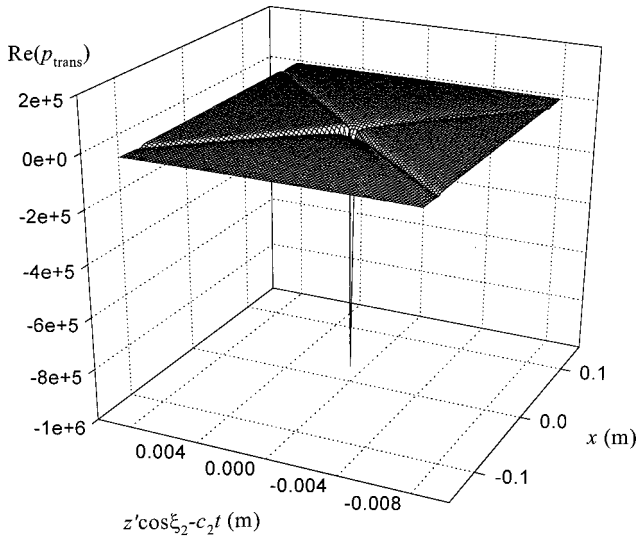

FIG. 12. Transmitted pressure field evaluated at $z=0.001\,09$ m for $\alpha_1=29°$; $(c_1/c_2)=0.5$.

dispersion of the transmitted pulse and the distance at which it starts. Such information is essential for practical applications that make use of the localized character of the transmitted field; e.g., in detection and identification of buried objects. The information should be used in conjunction with the fact that finite-energy LWs have a finite range of localization. Thus one should always be able to determine which effect will be the earliest to cause the decay of the transmitted field, the diffraction effect due to the initial finite energy source or the dispersion effect described in this paper. Such an assessment can be effected by comparing the estimate for the range of localization z_d' given in Eq. (40) to formulas specifying the diffraction lengths of LWs.[6,14,20,32,33]

Finally, one should note that we have basically studied the reflection and transmission of the infinite energy X-wave. As discussed earlier, the exact X-wave can be perceived as an interference of pulsed plane waves propagating along a conical surface and all having the same conical angle ξ with respect to the axis of propagation.[31] The resulting field has a slow radial decay and similarly to FWMs and to plane wave solution, X-waves have infinite energies. Finite energy X-shaped solutions can be obtained either by truncating the transverse support of the field of the X-wave[5,6,15,20] or by using superpositions of superluminally boosted elementary solutions.[21] Evidently, finite energy X-waves are fields of interest in physical situations. However, the mathematical analysis needed to study the reflection and transmission of such pulses can be quite tedious. This is the reason for considering the canonical problem analyzed in this work. The results of this paper are thus useful in situations when the distances traveled by the finite energy X-waves are smaller than their diffraction-free ranges. In addition, the extent of the planar interface should be much larger than the transverse width $(a/\sin\xi)$ of the highly focused central pulse of the X-wave. Since a is inversely proportional to the maximum frequency of the spectrum and $\sin\xi$ is a small quantity, the latter condition can be rephrased as having a planar interface of extent much larger than all wavelengths contributing to the spectrum of the X-wave. Furthermore, one should note that in earlier investigations the case of infinite energy FWMs has been considered instead of X-waves.[22,23] No attempt has been made at this stage to provide comparisons with recent work on the transmission and reflection of pulsed beams.[24,25] The latter are paraxial ultra-wide-band solutions to the scalar wave equation or Maxwell's equations, whereas X-waves are exact ones. We would like to point out that our investigation is not exhaustive. Further extensions are needed in the case of multi-layered media, for investigations concerned with curved interfaces and when accounts must be taken of medium loss and dispersion mechanisms.

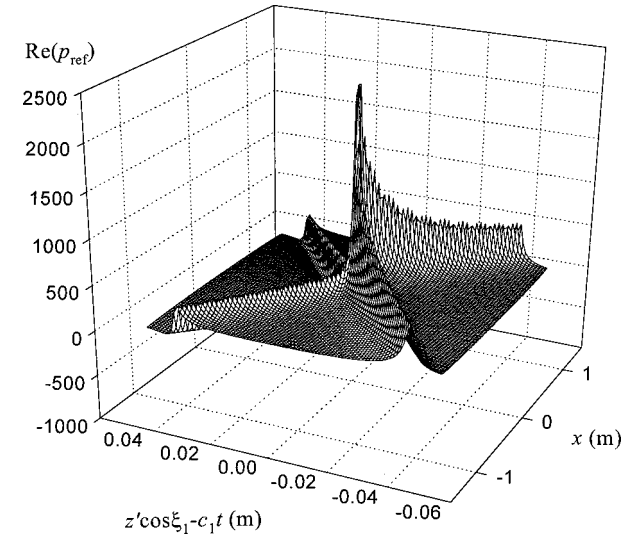

FIG. 13. Reflected pressure field evaluated at $z=-1$ m for $\alpha_1=30°$; $(c_1/c_2)=0.5$.

[1] P. Saari and K. Reivelt, ''Evidence of X-shaped propagation-invariant localized light waves,'' Phys. Rev. Lett. **21**, 4135–4138 (1997).

[2] J. Y. Lu and J. F. Greenleaf, ''Experimental verification of nondiffracting X waves,'' IEEE Trans. Ultrason. Ferroelectr. Freq. Control **39**, 441–446 (1992).

[3] R. W. Ziolkowski, D. K. Lewis, and B. D. Cook, ''Experimental verification of the localized wave transmission effect,'' Phys. Rev. Lett. **62**, 147–150 (1989).

[4] R. W. Ziolkowski, ''Localized wave physics and engineering,'' Phys. Rev. A **44**, 3960–3984 (1991).

[5] A. M. Shaarawi, I. M. Besieris, R. W. Ziolkowski, and S. M. Sedky, ''Generation of approximate focus wave mode pulses from wide-band dynamic Gaussian aperture,'' J. Opt. Soc. Am. A **12**, 1954–1964 (1995).

[6] P. R. Stepanishen, ''Acoustic bullets/transient Bessel beams: Near to far field transition via an impulse response approach,'' J. Acoust. Soc. Am. **103**, 1742–1751 (1998).

[7] A. A. Chatzipetros, A. M. Shaarawi, I. M. Besieris, and M. A. Abdel-Rahman, ''Aperture synthesis of time-limited X-waves and analysis of their propagation characteristics,'' J. Acoust. Soc. Am. **103**, 2287–2295 (1998).

[8] D. Power, R. Donnelly, and R. MacIsaac, ''Spherical scattering of superpositions of localized waves,'' Phys. Rev. E **48**, 1410–1417 (1993).

[9] J. Y. Lu, M. Fatemi, and J. F. Greenleaf, ''Pulsed-echo imaging with X wave,'' Acoust. Imaging **22**, 191–196 (1996).

[10] J. Y. Lu and J. F. Greenleaf, ''Diffraction-limited beams and their applications for ultrasonic imaging and tissue characterization,'' Proc. SPIE **1733**, 92–119 (1992).

[11] J. N. Brittingham, ''Focus wave modes in homogeneous Maxwell equations: Transverse electric mode,'' J. Appl. Phys. **54**, 1179–1189 (1983).

[12] R. W. Ziolkowski, ''Exact solutions of the wave equation with complex source locations,'' J. Math. Phys. **26**, 861–863 (1985).

[13] A. Sezigner, ''A general formulation of focus wave modes,'' J. Appl. Phys. **57**, 678 (1985).

[14] I. M. Besieris, A. M. Shaarawi, and R. W. Ziolkowski, ''A bidirectional traveling plane wave representation of exact solutions of the scalar wave equation,'' J. Math. Phys. **30**, 1254–1269 (1989).
[15] J. Y. Lu and J. F. Greenleaf, ''Nondiffracting X waves—Exact solutions to free space scalar wave equation and their finite aperture realization,'' IEEE Trans. Ultrason. Ferroelectr. Freq. Control **39**, 19–31 (1992).
[16] J. Y. Lu and J. F. Greenleaf, ''Sidelobe reduction for limited diffraction pulse-echo system,'' IEEE Trans. Ultrason. Ferroelectr. Freq. Control **40**, 735–746 (1993).
[17] J. Y. Lu and J. F. Greenleaf, ''Comparison of sidelobes of limited diffraction beams and localized waves,'' Acoust. Imaging **22**, 145–152 (1995).
[18] J. Y. Lu, ''Producing bowtie limited diffraction beams with synthetic array experiment,'' IEEE Trans. Ultrason. Ferroelectr. Freq. Control **42**, 893–900 (1996).
[19] A. M. Shaarawi, S. M. Sedky, F. M. Taiel, R. W. Ziolkowski, and I. M. Besieris, ''Spectral analysis of time-limited pulsed Gaussian wavefields,'' J. Opt. Soc. Am. A **13**, 1827–1836 (1996).
[20] A. M. Shaarawi, ''Comparison of two localized wavefields generated from dynamic apertures,'' J. Opt. Soc. Am. A **14**, 1804–1816 (1997).
[21] I. Besieris, M. Abdel-Rahman, A. Shaarawi, and A. Chatzipetros, ''Two fundamental representations of localized pulse solutions of the scalar wave equation,'' Progress in Electromagnetics Research (PIER) **19**, 1–48 (1998).
[22] P. Hillion, ''How do focus wave modes propagate across a discontinuity in a medium?'' Optik (Stuttgart) **93**, 67–72 (1993).
[23] R. Donnelly and D. Power, ''The behavior of electromagnetic localized waves at a planar interface,'' IEEE Trans. Antennas Propag. **45**, 580–591 (1997).
[24] E. Heyman and R. Ianconescu, ''Pulsed beam reflection and transmission at a dielectric interface: two-dimensional fields,'' IEEE Trans. Antennas Propag. **AP-38**, 1791–1800 (1990).
[25] E. Heyman, R. Strahilevitz, and D. Kosloff, ''Pulsed beam reflection and transmission at a planar interface: Exact solutions and local models,'' Wave Motion **18**, 315–343 (1993).
[26] J. Fagerholm, A. T. Friberg, J. Huttunen, D. P. Morgan, and M. M. Salomaa, ''Angular-spectrum representation of nondiffracting X waves,'' Phys. Rev. E **54**, 4347–4352 (1996).
[27] A. T. Friberg, J. Fagerholm, and M. M. Salomaa, ''Space-frequency analysis of nondiffracting pulses,'' Opt. Commun. **136**, 207–212 (1997).
[28] I. S. Gradshteyn and I. M. Ryzhik, *Tables of Integrals, Series and Products* (Academic, New York, 1965).
[29] W. C. Elmore and M. A. Heald, *Physics of Waves* (Dover, New York, 1985).
[30] A. D. Pierce, *Acoustics: An Introduction to its Physical Principles and Applications* (McGraw–Hill, New York, 1981).
[31] A. M. Attiya, E. A. El-Diwany, A. Shaarawi, and I. Besieris, ''Reflection and transmission of an electromagnetic X-wave in the presence of planarly layered media: The pulsed plane wave representation'' (unpublished).
[32] S. M. Sedky, A. M. Shaarawi, F. M. Taiel, and I. M. Besieris, ''On the diffraction length of localized waves generated by dynamic apertures,'' J. Opt. Soc. Am. A **13**, 1719–1727 (1996).
[33] B. Hafizi and P. Sprangle, ''Diffraction effects in directed radiation beams,'' J. Opt. Soc. Am. A **8**, 705–717 (1991).

Modeling of Lamb waves generated by integrated transducers in composite plates using a coupled finite element–normal modes expansion method

Emmanuel Moulin, Jamal Assaad, and Christophe Delebarre
IEMN, UMR CNRS 9929, OAE Department, Université de Valenciennes et du Hainaut Cambrésis, le Mont Houy, BP 311, 59304–Valenciennes Cedex, France

Daniel Osmont
ONERA, Solid Mechanics and Damage Department, BP 72, 92322–Chatillon Cedex, France

(Received 18 May 1999; revised 9 October 1999; accepted 14 October 1999)

Thin piezoelectric transducers attached to or embedded within composite structures could be used for *in situ* structural health monitoring. For plate-shaped structures, the useful ultrasonic vibration modes are Lamb waves. Preliminary testing has already demonstrated the suitability and practical feasibility of such integrated transducers, but better control of the generation of Lamb modes seems to be necessary. Therefore, an original modeling approach has been developed, which can be used to design and optimize these ''sensitive materials.'' This modeling technique allows the determination of the amplitude of each Lamb mode excited in a composite plate with surface-bonded or bulk-embedded piezoelectric elements. The method consists of a coupling of the finite element method (FEM) and the normal modes expansion method. The limited finite element mesh of the transducer and its vicinity enables the computation of the mechanical field created by the transducer, which is then introduced as a forcing function into the normal modes equations. The adequacy and accuracy of this modeling method have been numerically and experimentally verified.
 [S0001-4966(00)06401-8]

PACS numbers: 43.20.Ks, 43.20.Tb, 43.40.Le [ANN]

INTRODUCTION

Health monitoring of composite materials is a critical issue, particularly in aeronautic transportation. In order to increase safety and reduce maintenance costs, the concept of sensitive materials (or integrated health monitoring) has been under investigation in recent years. Since Lamb waves propagate over long distances and are affected by degradation of the propagation medium, they appear to be one promising method for sensing damage. This application of Lamb waves requires the investigation of a number of aspects, such as the study of their propagation in various structures, the understanding of their interaction with defects, and the optimization of their generation.

Intensive studies of the propagation of Lamb waves in various materials have been performed. The cases of isotropic,[1] then anisotropic,[2] and even multilayered and lossy[3,4] plates have been dealt with abundantly, and constitute an essential background for studies involving Lamb waves. As for the question of defect detection, several studies confirm the potentiality of Lamb waves. Their interaction with various types of defects, such as cracks,[5] notches,[6] and delaminations,[7] have been studied experimentally and theoretically. Even the evaluation of complex structures such as adhesive joints[8] or riveted plates[9] is possible. Datta *et al.*[10] have proposed a general method allowing the computation of the acoustic field scattered by any type of defect in a plate. This modeling technique is a hybrid method called the global local finite element method, which is of particular interest here because it is related in some aspects to the coupled method presented in this paper. In a recent publication,[11] the method has been applied to the case of a rivet hole, which required a three-dimensional treatment. This shows the promising potential of such hybrid techniques.

The important problem which constitutes the focal point of the work reported here is the generation of Lamb waves. A great deal of attention has already been given to the most classical generation methods, which consist of generating incident longitudinal waves at oblique incidence. In addition to the pioneer study of wedge transducers emitting in isotropic plates,[1] more recent works have been published on solid[12] and liquid[13] wedge transducers, as well as air-coupled transducers.[14] Other, more atypical excitation techniques have also been theoretically studied including comb transducers[15] and hertzian contact transducers.[16]

Whether intrinsically or with the help of the developed models, these techniques enable a relatively good control of the modes generated. However, the transducers used in these previous studies appear to be too bulky to be easily integrated into structures. For this reason, this paper reports the investigation of small piezoelectric elements bonded to, or embedded within, composite plates. Preliminary studies have shown the capability of the finite element method (FEM) for modeling such systems.[17] However, some aspects of the FEM (i.e., modeling of limited structures, lack of discrimination of modal components, necessity of a new complete computation for any parameter change, etc.) suggest that its use is likely to be insufficient or at least not well-suited. On the other hand, as already emphasized elsewhere,[13,16] the normal modes expansion method[18] appears to be particularly suitable for solving Lamb wave problems. However, for its

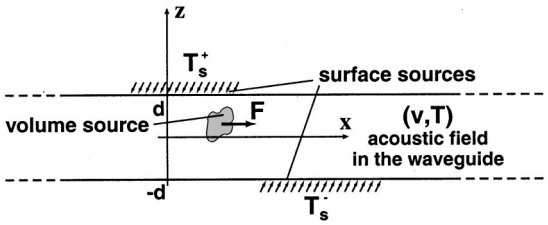

FIG. 1. Plate submitted to surface and volume excitations.

use, the mechanical excitation applied to the plate has to be known. This problem is not easy to solve by analytical methods and the FEM can naturally be used to compute it.

In the first section, a brief reminder of the normal modes expansion method is presented. Then in Sec. II, some considerations about the combination of the FEM (to compute the applied excitation) and the normal modes expansion (to determine the generated propagating modes), is given. Finally, the method will be applied to composite plates containing thin surface-mounted (Sec. III) and embedded (Sec. IV) piezoelectric elements.

I. NORMAL MODES EXPANSION

A. General review

Since Lamb waves are eigenmodes of a solid infinite and stress-free plate, the normal modes expansion method is suitable for this application. Indeed, this technique can be used to predict Lamb waves as a function of the plate excitation. Only the basic equations of this formalism are presented here.

The case which will be dealt with here is a solid plate considered as a two-dimensional acoustic waveguide. Mechanical excitation of this plate is provided by either an internal force field $\mathbf{F}$ or surface traction fields $\mathbf{T}_s^+$ and $\mathbf{T}_s^-$, respectively, acting on the upper and lower surfaces (Fig. 1). The notation of the corresponding created acoustic field in the plate is defined by the velocity vector $\mathbf{v}$ and the stress tensor $\mathbf{T}$, given by

$$\mathbf{v}(x,y,z,t)=\begin{pmatrix} v_x \\ v_y \\ v_z \end{pmatrix}=\frac{\partial \mathbf{u}}{\partial t}, \tag{1}$$

where $\mathbf{u}$ is the displacement vector, and

$$\mathbf{T}(x,y,z,t)=\begin{pmatrix} \sigma_{xx} & \sigma_{xy} & \sigma_{xz} \\ \sigma_{yx} & \sigma_{yy} & \sigma_{yz} \\ \sigma_{zx} & \sigma_{zy} & \sigma_{zz} \end{pmatrix}. \tag{2}$$

B. Basic equations

Let us consider two different volume and surface excitations $(\mathbf{F}_1,\mathbf{T}_{s1})$ and $(\mathbf{F}_2,\mathbf{T}_{s2})$ of a given nonpiezoelectric waveguide. In the case of harmonic excitation and assuming a lossless material, there exists a relation, called complex reciprocity relation, between both respective acoustic fields $(\mathbf{v}_1,\mathbf{T}_1)$ and $(\mathbf{v}_2,\mathbf{T}_2)$:[18]

$$\operatorname{div}(\mathbf{v}_2^*\cdot\mathbf{T}_1+\mathbf{v}_1\cdot\mathbf{T}_2^*)=-\mathbf{v}_2^*\cdot\mathbf{F}_1-\mathbf{v}_1\cdot\mathbf{F}_2^*, \tag{3}$$

where the asterisk * denotes complex conjugation.

This relation is the starting point of the normal modes theoretical development. By applying it to two distinct eigenmodes with wave numbers k_n and k_m and acoustic fields $(\mathbf{v}_n,\mathbf{T}_n)$ and $(\mathbf{v}_m,\mathbf{T}_m)$, respectively, the following orthogonality relation can be derived:[18]

$$P_{nm}=0 \quad \text{for } k_n\neq k_m^* \tag{4}$$

with

$$P_{nm}=\frac{1}{4}\int_{-d}^{d}(-\mathbf{v}_m^*\cdot\mathbf{T}_n-\mathbf{v}_n\cdot\mathbf{T}_m^*)\cdot\mathbf{x}\,dz. \tag{5}$$

Especially, in the case of propagating modes (k_n and k_m real), this relation is reduced to

$$P_{nm}=0 \quad \text{for } m\neq n. \tag{6}$$

Lamb waves are thus demonstrated to form a set of normal modes of a free plate. So the acoustic field $(\mathbf{v},\mathbf{T})$ created in a plate under arbitrary excitation fields $(\mathbf{F},\mathbf{T}_s^+,\mathbf{T}_s^-)$, can be expanded into a summation over the Lamb modes:

$$\begin{aligned}\mathbf{v}(x,z)&=\sum_m a_m(x)\mathbf{v}_m(z)\\ \mathbf{T}(x,z)&=\sum_m a_m(x)\mathbf{T}_m(z),\end{aligned} \tag{7}$$

where $(\mathbf{v}_m,\mathbf{T}_m)$ is the acoustic field related to the mth Lamb mode, and a_m is the corresponding modal amplitude.

The solution of the waveguide problem is then reduced to the determination of each modal amplitude a_m. To do that, both the complex reciprocity relation Eq. (3) and the orthogonality relation Eq. (6) are applied. Auld[18] has given details of this development, which will not be recalled here. The final point is the following modal amplitude equation:

$$4P_{mm}\left(\frac{\partial a_m}{\partial x}+jk_m a_m\right)=f_{Sm}+f_{Vm}, \tag{8a}$$

with

$$f_{Sm}(x)=\{\mathbf{v}_m^*(d)\cdot\mathbf{T}_s^+(x)-\mathbf{v}_m^*(-d)\cdot\mathbf{T}_s^-(x)\}\cdot\mathbf{z} \tag{8b}$$

and

$$f_{Vm}(x)=\int_{-d}^{d}\mathbf{v}_m^*(z)\cdot\mathbf{F}(x,z)dz, \tag{8c}$$

where f_{Sm} and f_{Vm} are the surface forcing function and the volume forcing function, respectively.

Assuming that there is no excitation source outside an interval $-L<x<L$ (Fig. 1), the solution of this differential equation for propagating modes travelling rightward (toward $+x$) is given by

$$a_m(x)=\frac{e^{-jk_m x}}{4P_{mm}}\int_{-L}^{L}[f_{Sm}(\eta)+f_{Vm}(\eta)]e^{jk_m\eta}\,d\eta \tag{9}$$

with

$$P_{mm}=-\frac{1}{2}\mathrm{Re}\left[\int_{-d}^{d}(v_{mx}^*\sigma_{mxx}+v_{mz}^*\sigma_{mxz})dz\right]. \tag{10}$$

Nonpropagating modes (complex wave numbers) will not be taken into account in this study. Since their ampli-

tudes decrease exponentially in the $+x$ direction, their effect is appreciable only near the source.

C. Comments on the mode amplitude equation

The use of the previously established Eq. (9) requires the preliminary knowledge of some terms. These terms, which are not *a priori* known, cannot be determined straightforwardly. So a few details have to be recalled here.

First of all, the wave number and acoustic field related to each eigenmode must be known. The method to determine them consists of using Christoffel's equations in the material and then applying the boundary conditions (stress-free surfaces). The wave number is then determined by setting the obtained 6*6 determinant (in the general case) to zero.[2] The related acoustic field (displacement and stress) in the plate is then derived from the corresponding singular system.

Second, the need to know the surface or volume forcing functions is evident. In the case of known, well-defined excitations (for example, piston traction), these terms are easily determined. However, if the waveguide is excited using an integrated transducer, then the applied stresses or forces are governed by complex interactions between the transducer and the host material and thus are not pre-defined. So a means to evaluate them is required. The next section will show how the finite element method can be used for this purpose.

II. COUPLING WITH THE FINITE ELEMENT METHOD

A. Determination of the forcing functions

Determining the forcing functions f_{Sm} and f_{Vm} requires the complete knowledge of the mechanical field (displacement and stress) in the immediate vicinity of the transducer. The finite element method provides a convenient method to compute the displacement values U_D^k at each mesh node, where D and k denote the displacement direction and the node number, respectively. From these values, the displacement and stress field can be determined using interpolation relations. These relations depend on the type of elements used in the mesh. Thus in the case of an element with n nodes, the displacement field is obtained as follows:[19]

$$\mathbf{u}=\begin{pmatrix} u_x \\ u_y \\ u_z \end{pmatrix} = \begin{pmatrix} N_1 & 0 & 0 & N_2 & 0 & 0 & \cdots & N_n & 0 & 0 \\ 0 & N_1 & 0 & 0 & N_2 & 0 & \cdots & 0 & N_n & 0 \\ 0 & 0 & N_1 & 0 & 0 & N_2 & \cdots & 0 & 0 & N_n \end{pmatrix} \cdot \begin{pmatrix} U_x^1 \\ U_y^1 \\ U_z^1 \\ \vdots \\ U_x^n \\ U_y^n \\ U_z^n \end{pmatrix}. \tag{11}$$

$N_1(x,y,z),\ldots,N_n(x,y,z)$ are called interpolation functions. They depend on the element geometry and the order and number of nodes.

The stress field is then simply given by

$$\sigma=\begin{pmatrix} \sigma_{xx} \\ \sigma_{yy} \\ \sigma_{zz} \\ \sigma_{yz} \\ \sigma_{xz} \\ \sigma_{xy} \end{pmatrix} = C\epsilon \tag{12}$$

with

$$\epsilon_{ij}=\frac{1}{2}\left(\frac{\partial u_i}{\partial x_j}+\frac{\partial u_j}{\partial x_i}\right). \tag{13}$$

It should be noted that the side of each element in the finite element mesh has to be smaller than $\lambda/4$,[20] where λ is the smallest wavelength to be considered.

B. Reflection at the plate boundary

The main problem in using the finite element method to determine the input mechanical field is that it requires the modeled structure to be spatially bounded. The aim of this work is to model the behavior of an infinite plate excited by integrated transducers. Thus unless a means to reduce wave reflection at the plate boundary is found, the obtained results would be corrupted by the presence of undesired stationary waves.

The proposed solution consists in attenuating the incident waves near the end of the modeled plate, by using a part of plate made of a lossy material (Fig. 2). Losses will be classically taken into account by introducing a nonzero imaginary part C_2'' of the elastic tensor C_2 (Fig. 2), with $C_2=C_2'+jC_2''$. In order to simplify the problem and by analogy with the isotropic case,[20] the existence of a loss angle δ_c, such as $C_2''=C_2'\tan\delta_c$, will be assumed.

The density ρ_2 and the elastic tensor C_2 of the material constituting the attenuating part, are simply chosen such as

$$\begin{aligned} &\rho_2=\rho_1, \\ &C_2=C_1(1+j\tan\delta_c), \end{aligned} \tag{14}$$

where (ρ_1,C_1) are the elastic properties of the lossless plate (C_1 real).

The proposed optimization criterion is the minimizing of the reflection coefficient R of x-polarized waves at the interface between the lossless plate and the attenuating part. Although taking into account the reflection of normally incident longitudinal waves only is a restrictive case, it will be

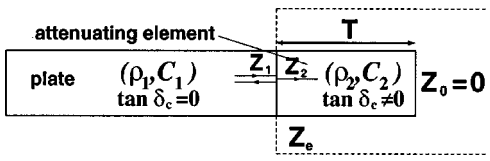

FIG. 2. Principle of the wave attenuation at the boundary of the plate.

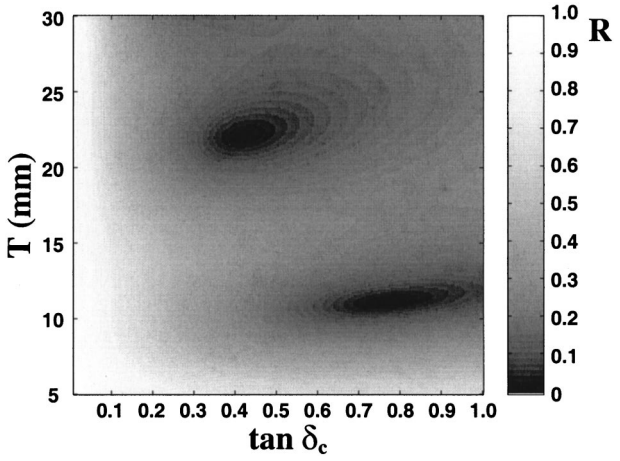

FIG. 3. Reflection coefficient as a function of the attenuating element parameters (T and $\tan \delta_c$).

shown that good enough results can be obtained by doing so. Using acoustic impedances, R is given by the following relation:

$$R = \frac{Z_e - Z_1}{Z_e + Z_1} \tag{15}$$

with Z_1, the acoustic impedance of the lossless plate and Z_e, the equivalent acoustic impedance seen at the interface (Fig. 2).

Since the acoustic impedance Z_0 of the vacuum is zero, this equivalent impedance is simply given by:[20]

$$Z_e = jZ_2 \tan(k_2 T), \tag{16}$$

where T is the length of the attenuating element, Z_2 its acoustic impedance, and k_2 is the wave number of longitudinal waves propagating in it.

By using Eqs. (14), (15), and (16), the reflection coefficient R can be expressed as a function of the two unknown parameters T and $\tan \delta_c$:

$$R = \frac{j \tan(k_2 T)\sqrt{1 + j \tan \delta_c} - 1}{j \tan(k_2 T)\sqrt{1 + j \tan \delta_c} + 1} \tag{17a}$$

with

$$k_2 = \omega \sqrt{\frac{\rho_1}{C_{11}(1 + j \tan \delta_c)}}. \tag{17b}$$

Designing the attenuating element is then enabled by finding proper values of T and $\tan \delta_c$, which minimize the reflection coefficient R.

The example presented here (Fig. 3) is the case of a T300/914 carbon/epoxy unidirectional $[0_{32}]$ composite plate, in the case of an excitation at 400 kHz. Two distinct suitable sets of parameters are evident from this figure. However, in order to restrict the size of the finite element mesh, it is better to consider as short an attenuating element as possible (smaller value of T). So the chosen features are the following:

$$\begin{aligned} &\tan \delta_c = 0.75, \\ &T = 11 \text{ mm}. \end{aligned} \tag{18}$$

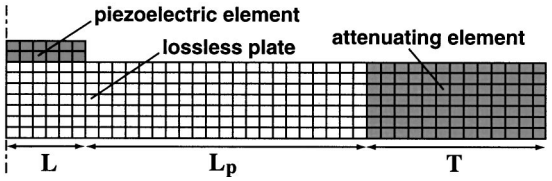

FIG. 4. Finite element mesh of the transducer, a part of lossless plate, and the attenuating element.

C. Considerations of mesh size

If the behavior of the attenuating element is assumed to be perfect, then the computed forcing functions are independent of the length L_p of the part of lossless plate between the transducer's end and the attenuating element's beginning (Fig. 4). Indeed, in that case, the modeled plate portion would then behave as an infinite plate, whatever the value of L_p.

In the case of finite element modeling, the computation time and the required memory space is a function of the mesh size. Consequently, it appears to be desirable to use as reduced a finite element mesh as possible. However, since the material properties have to be kept unchanged all around the piezoelectric element, in order to simulate the same interaction conditions, L_p has to be kept nonzero. Therefore, for the computation of the forcing functions, the value of L_p will be chosen to be a few percent of the length T of the attenuating element.

III. APPLICATION TO SURFACE-BONDED TRANSDUCERS

A. Formalism

The previously presented principles will be applied first to the case of harmonic surface excitation by a thin piezoelectric transducer bonded to the plate upper surface (Fig. 5).

This problem will be considered by assuming that the propagating normal modes in the plate are not altered too much by the presence of the surface-mounted transducer. Considering the size of this transducer in comparison to the plate dimensions, this assumption appears to be reasonable.

The volume forcing function f_{Vm} in Eqs. (8) and (9) is assumed here to be zero. The surface forcing function f_{Sm} depends on both the normal and lateral components of the applied surface traction. The mth mode amplitude [Eq. (9)] can then be expressed as

$$a_m(x) = \frac{e^{-jk_m x}}{4P_{mm}} [v^*_{mx}(d) I_{xz}(k_m) + v^*_{mz}(d) I_{zz}(k_m)] \tag{19a}$$

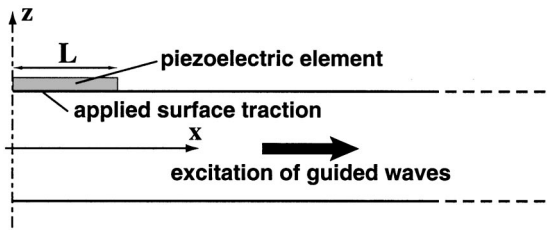

FIG. 5. Excitation of normal modes by a surface-bonded piezoelectric element.

with

$$I_{xz}(k)=\int_{-L}^{L}\sigma_{xz}(x,d)e^{jkx}\,dx,$$
$$I_{zz}(k)=\int_{-L}^{L}\sigma_{zz}(x,d)e^{jkx}\,dx, \tag{19b}$$

where $\sigma_{zz}(x,d)$ and $\sigma_{xz}(x,d)$ are the normal and lateral components, respectively, of the applied traction $\mathbf{T}_s^+$.

Since the acoustic fields related to the Lamb modes are assumed to be known, the only unknown terms are the components of the applied surface traction. As previously mentioned, these terms will be determined by using a limited finite element model consisting of the piezoelectric transducer, a small part of the composite plate, and the previously defined attenuating element. Perfect adherence conditions at the interface between the transducer and the plate will be assumed (displacement and stress continuity).

B. Example and numerical validation

The emitting transducer is a 4-mm wide ($L=2$ mm) and 0.5-mm thick parallelepiped made of PZT piezoelectric ceramic. Thus its corresponding width resonance (vibration along the x-axis, as defined in Fig. 5) is around 400 kHz. Its length is assumed to be much bigger than both other dimensions, so two-dimensional modeling is enabled.

The considered plate is a carbon reinforced epoxy $[0_{32}]$ composite plate. Since the thickness of a single ply is around 120–125 μm, the whole plate is about 4 mm thick. The x-axis is chosen to be the fiber direction.

The finite element mesh used to compute the traction applied by the piezoelectric transducer has a limited size. Indeed, L_p has been chosen to have a nonzero, but small value ($L_p/T\approx 0.07$). In addition, the model takes into account the attenuating element previously designed for an excitation at 400 kHz ($T=11$ mm; $\tan\delta_c=0.75$).

The computed surface traction is then introduced as an input to the mode amplitude Eq. (19). The different modal contributions are thus determined. In the present example, four Lamb modes are excited, with the following ratios (in terms of transported energy): $S_0(30\%)$, $A_0(44\%)$, $S_1(6\%)$, $A_1(20\%)$.

From the individual contribution of each Lamb mode, the whole displacement field in the plate can then be approximated. Actually, the exact displacement field would be obtained from an infinite summation of all eigenmodes. However, in our application, the nonpropagating (evanescent) modes are not considered, and only the propagating modes (which are in a finite number for a given frequency, according to the so-called dispersion curves) are summed. The error introduced is only significant in the vicinity of the source. Thus the displacements at both plate surfaces are presented (Fig. 6, solid lines) for a harmonic excitation of the transducer of 1-V amplitude and 400-kHz frequency. In fact, $e^{j\omega t}$ being implicit and the applied electrical potential being retained as reference, the real part [Fig. 6(a)] displays the picture of the displacement field at the initial time $t=0$, whereas the imaginary part [Fig. 6(b)] displays its picture at $t=\tau/4$, where $\tau=2\pi/\omega$ is the period. The real and imaginary parts together are sufficient to describe the displacement field at any time. In order to enable the displacements to be apparent in this graph, their values have been magnified by a factor of 3×10^6.

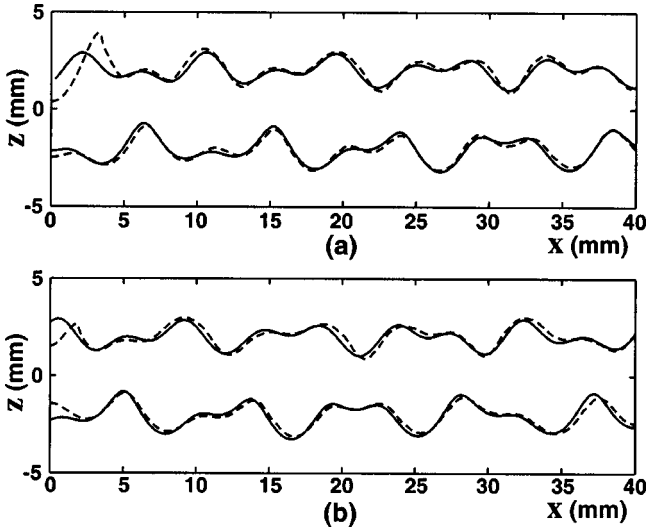

FIG. 6. Comparison between surface displacements at 400 kHz, magnified by a factor of 3×10^6, computed using respectively the coupled method (solid line) and the FEM only (dashed line). (a) Real part of the displacement. (b) Imaginary part.

A second, purely finite element modeling of the transducer, a portion of plate, and the attenuating element has been performed in order to validate the obtained results. But this time, the meshed plate length ($L_p/T\approx 3.5$) enabled to compute and visualize the whole displacement field caused by the generated Lamb waves, only using the finite element method. These results (Fig. 6, dashed lines) are then compared to the previous ones (solid lines).

The very good agreement observed suggests that the newly developed coupled method successfully solves this kind of problem. Additionally, the capability of the attenuating element technique to simulate infinite plates is demonstrated.

These two modeling techniques (coupled method and finite elements) provided equivalent results. However, several significant advantages of the coupled method over the purely FEM method are to be emphasized. First, significant time reduction is gained. Indeed, considering that the determination of the modal acoustic fields and phase velocities (calculated once and for all) do not contribute to the effective computation time, the calculation is approximately 75% to 95% faster when using the coupled method. In the case of the finite element modeling alone, the calculation time is typically of the order of a few minutes to more than half an hour, depending on the mesh definition and the type of computer used.

Second, as illustrated previously, the coupled method allows the direct isolation of the individual contribution of each Lamb mode, whereas the purely FEM model only gives the whole compound field in the plate. Even though it would be possible to post-determine the individual contributions from this global field, it would be more time consuming and

less accurate. Indeed, for health monitoring applications, it will be important to be able to control the excitation amplitude of a chosen mode versus the other modes, by optimizing the design of the transducer (work currently under progress). Therefore the knowledge of every mode contribution rather than the global acoustic field is desirable.

Finally, the next section will show that this coupled method can easily allow generalization.

C. Further developments

The coupled modeling method presented in this paper has proved to be suitable for the kind of application considered. However, some rigidity in applying the method is yet imposed by the finite element computation of the applied stress. Indeed it would be very interesting to be able to model easily the behavior of the system as a function of a variable parameter (such as the transducer width), in order to optimize it. Although theoretically feasible, this would require the modification of the finite element mesh and repeated computations for each variation of the considered parameter. Since this would be rather tedious and time consuming, an alternative method will be proposed here. Indeed, approximate scaling properties will be derived, in order to account for parametric changes. A similar approach had been recently dealt with, in the field of acoustic emission modeling.[21] This resulted in a possible generalization from a single computation. The same purpose is aimed at here.

From the linearity of the FEM it appears that the dynamic behavior at a frequency f of a structure whose dimensions are multiplied by a scaling factor a remains identical to the behavior of the initial structure at the frequency fa. But since only thin piezoelectric transducers (small thickness compared to the width) are considered here, and the frequency range corresponds to the transverse mode, then the vibration properties of the transducer (at a given frequency) essentially depend on its width. Thus if the material properties remain the same, then the dominant parameters are the excitation frequency f and the transducer half-width L.

The consequence of this would be that the stress profile under a piezoelectric element of width $2L$, computed for an excitation frequency f, is approximately the same as the one under a piezoelectric element of width $2La$ (providing that a is not too different from 1) at a frequency f/a, the thickness being kept constant.

In order to verify and to estimate the validity range of this interesting property, the normal (σ_{zz}) and transverse (σ_{xz}) stresses under the transducer have been computed and displayed (Fig. 7) for three different values of the half-width L and for the three corresponding values of f (fL remaining constant). In order to compare them, the curves have been normalized according to L.

The good agreement between the curves shows that this property is valid within a variation range of at least 10% around the initial frequency or half-width values. In fact, further testing has demonstrated a validity range of up to 20% around the initial value.

Consequently, from a single finite element computation, a whole parametric study, as a function of L, can be performed. Indeed, if the stress profile under a transducer of half-width L_0 at its transverse resonance frequency f_{r0} is known, then the stress profile under a transducer of any half-width L (within the validity range) at its corresponding resonance frequency f_r is also known, and can be simply introduced into the mode amplitude Eq. (19), f_r being given by

$$f_r = \frac{f_{r0} L_0}{L}. \tag{20}$$

Thus the method appears to be very easily adapted to various configurations.

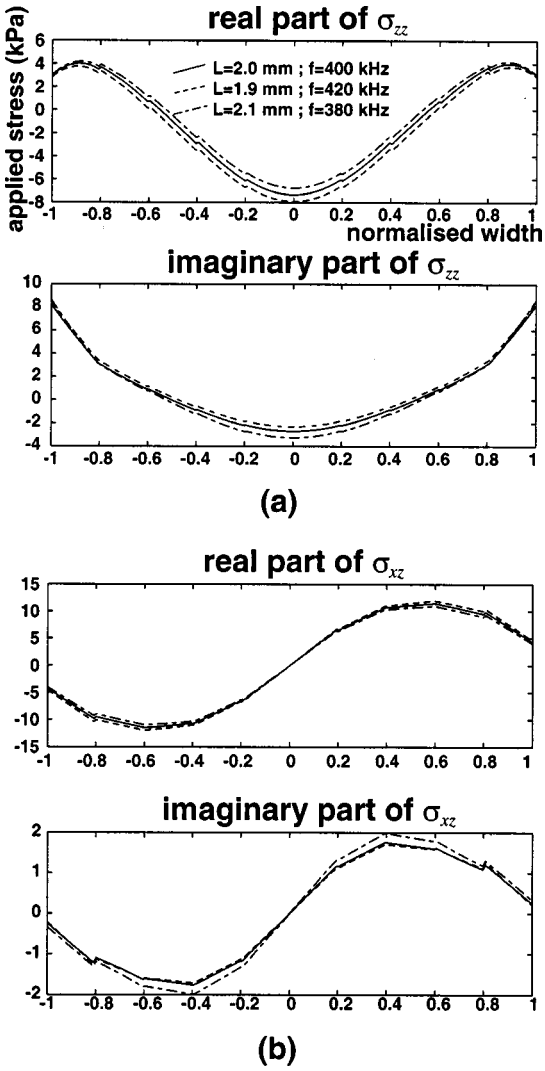

FIG. 7. Surface stresses applied to the plate by the bonded transducer. (a) Real and imaginary parts of σ_{zz}. (b) Real and imaginary parts of σ_{xz}.

IV. APPLICATION TO BULK-EMBEDDED TRANSDUCERS

A. Modeling principle

The case of a thin piezoelectric transducer embedded inside a plate will be considered. Here again, the normal mode expansion technique, coupled with the finite element method, will be used. Thus the surface forcing function is zero, and the determination of the volume forcing function

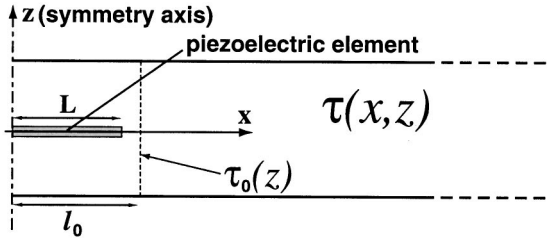

FIG. 8. Excitation by a bulk-embedded piezoelectric element.

could solve the problem in principle. However, an alternative resolution technique has appeared to be more suitable and easier to apply in this case.

For each eigenmode of the plate, the acoustic field vector is defined as:

$$\tau_m = \begin{pmatrix} v_{mx} \\ v_{mz} \\ \sigma_{mxx} \\ \sigma_{mxz} \end{pmatrix}. \tag{21}$$

Thus for any acoustic field τ excited in the plate, Eq. (7) gives

$$\tau(x,z) = \sum_m a_m(x)\,\tau_m(z). \tag{22}$$

Since Lamb waves propagate along the x-direction, the modes amplitudes can be written as $a_m(x) = A_m e^{-jk_m x}$.

If $\tau_0(z) = \tau(l_0, z)$ is defined to be the acoustic field in a section of the plate located at a short distance $(l_0 - L)$ from the transducer's edge (Fig. 8), then Eq. (22) implies

$$\tau_0(z) = \sum_n A_n \tau_n(z) e^{-jk_n l_0}. \tag{23}$$

The amplitude A_m of the mth mode can then be determined by considering an inner product (.,.) of the acoustic field vector space. Then we have

$$(\tau_0, \tau_m) = \sum_n A_n (\tau_n, \tau_m) e^{-jk_n l_0}. \tag{24}$$

By applying the orthogonality properties between each eigenmode, $(\tau_n, \tau_m) = 0$ if $n \neq m$, then the mth mode amplitude is directly given by

$$A_m = \frac{(\tau_0, \tau_m)}{(\tau_m, \tau_m)} e^{jk_m l_0}. \tag{25}$$

The orthogonality relation Eq. (6) suggests the choice of the following inner product:

$$(\tau_1, \tau_2) = -\frac{1}{4} \int_{-d}^{d} (v_{1x}\sigma^*_{2xx} + v_{1z}\sigma^*_{2xz} + v^*_{2x}\sigma_{1xx} + v^*_{2z}\sigma_{1xz})\,dz, \tag{26}$$

where

$$\tau_1 = \begin{pmatrix} v_{1x} \\ v_{1z} \\ \sigma_{1xx} \\ \sigma_{1xz} \end{pmatrix} \quad \text{and} \quad \tau_2 = \begin{pmatrix} v_{2x} \\ v_{2z} \\ \sigma_{2xx} \\ \sigma_{2xz} \end{pmatrix} \tag{27}$$

are two arbitrary acoustic field vectors.

Indeed, the inner product for two eigenmodes τ_m and τ_n is $(\tau_m, \tau_n) = P_{mn}$, and is thus zero if $m \neq n$.

Consequently, the mth mode amplitude is given by using Eqs. (25) and (26):

$$a_m(x) = -\frac{e^{jk_m(l_0 - x)}}{4P_{mm}} \int_{-d}^{d} (v_{0x}\sigma^*_{mxx} + v_{0z}\sigma^*_{mxz} + v^*_{mx}\sigma_{0xx} + v^*_{mz}\sigma_{0xz})\,dz. \tag{28}$$

It should be noted that this alternative resolution technique is perfectly applicable to the previous case of surface excitation as well. However, the first method, consisting in the determination of the forcing function (as presented in Sec. III), is more suited to the case of surface excitation, because it is versatile and allows generalization.

B. Example and experimental validation

This method has then been applied to a unidirectional $[0_{32}]$ carbon/epoxy composite plate of 4 mm thickness, containing a thin piezoelectric transducer embedded between its two central plies. The transducer is a 350-μm thick, 1-cm sided PZT ceramic. Two metallized, 25-μm thick polyamide films, in contact with the transducer's electrodes, enable the electric connection.

The source acoustic field $\tau_0(z)$ has been computed using the finite element method, with the same technique as presented in Sec. II A (attenuating element at the plate boundary), in order to reduce the mesh size. Then the determination of each mode amplitude a_m, using Eq. (28), enables recombing the global acoustic field in the plate.

An optical measurement technique, called shearography (or phase-shifting speckle interferometry), has been used to experimentally validate the theoretically obtained results. This technique enables us to visualize very small normal surface displacements. Its advantages over other optical techniques (e.g., heterodyne probe, Michelson interferometer...) are the relative insensitivity to experimental hazards such as thermal noise or surface rugosity of the sample, and also the capability of scanning an entire area rather than a single point. The principle of shearography[22,23] is based on interference between two spatially shifted images of a same object. In the case of static deformation, the derivatives of the surface displacement is measured. In the present case, however, (harmonic excitation of the plate), the technique has to be slightly adapted: synchronization of the laser beam to the acoustic frequency (acoustooptic modulation) along with phase-stepping technique, and spatial shift set to the half-wavelength of the acoustic wave. As a result of this adaptation, the actual surface displacement is measured and thus no integration is required. The surface reflectivity of the composite plate has been enhanced by using a reflective paint.

Thus the surface normal displacement along a line parallel to the fibers direction has been measured. The frequency of the transducer excitation has been set to 330 kHz, which gives the higher normal displacement values. The obtained curve has been compared to the normal surface displacement

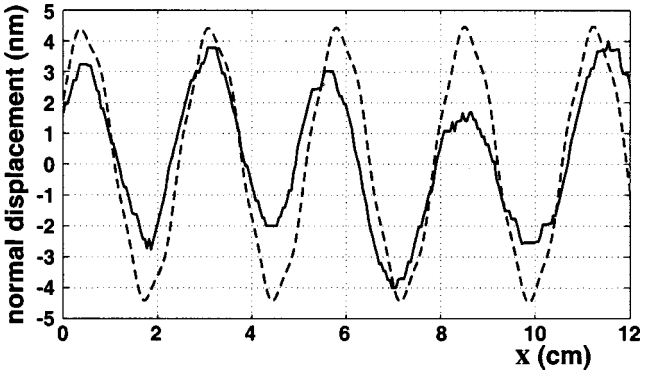

FIG. 9. Comparison between experimentally measured (solid line) and theoretically computed (dashed line) normal surface displacements at 330 kHz.

determined using the model (Fig. 9). Relatively good agreement is obtained between the experimental and theoretical curves. Although complementary studies would be necessary to determine precisely the involved parameters, it seems likely that the slight discrepancies could be explained either by model assumptions (unidirectional propagation and no losses taken into account, for instance) or by experimental uncertainties (such as the quality of the plate/transducer interface, or inaccuracy on so small displacement values).

The present case has been also successfully validated by using a pure FEM approach. As in the previous example (Fig. 6), the agreement between the two series of curves is very good, apart from the presence of evanescent modes in the very vicinity of the transducer. For convenience and conciseness, these results have not been displayed here.

V. CONCLUSION

In this paper, a modeling technique for Lamb waves transducers attached to or embedded within composite plates has been presented. It consists of a combination of the normal modes expansion method, which is suitable for waveguide excitation problems, and the finite element method, which enables the computation of the excitation actually applied by the piezoelectric transducer. In order to simulate infinite plates with a necessarily bounded finite element mesh, an attenuating element, located at the plate boundary, has been introduced. This solution gives satisfying results and the finite element mesh can thus be of very limited size. The cases of surface-mounted and embedded piezoelectric elements have been dealt with. In both cases the method has appeared to be practicable and valid. For surface transducers, it has even proved to be very flexible. Numerical simulation results and experimental results have been successfully compared to the results provided by the models.

For further investigation, additional testing of the method in various configurations is envisaged, such as arbitrary anisotropy of the plate and wave propagation along off-principal axes, and also cases of clearly multi-modal propagation (embedded transducer). Future possible extensions of this modeling approach concern Lamb wave generation into multilayered plates, and the case of multi-element sources.

ACKNOWLEDGMENTS

The authors wish to thank F. Taillade from ONERA-DMSE for having performed the shearography acquisitions, and the reviewers for helpful comments. This paper was presented in part at the 137th meeting of the Acoustical Society of America, Berlin, Germany, 15–19 March 1999. This work was supported by the EC, through a Brite EuRam Grant (project BE-97.4213 'DAMASCOS').

[1] I. A. Viktorov, *Rayleigh and Lamb Waves* (Plenum, New York, 1967).
[2] A. H. Nayfeh and D. E. Chimenti, ''Free wave propagation in plates of general anisotropic media,'' J. Appl. Mech. **56**, 881–886 (1989).
[3] A. H. Nayfeh, ''The general problem of elastic wave propagation in multilayered anisotropic media,'' J. Acoust. Soc. Am. **89**, 1521–1531 (1991).
[4] B. Hosten and M. Castaings, ''Transfer matrix of multilayered absorbing and anisotropic media. Measurements and simulations of ultrasonic wave propagation through composite materials,'' J. Acoust. Soc. Am. **94**, 1488–1495 (1993).
[5] S. I. Rokhlin, ''Diffraction of Lamb waves by a finite crack in an elastic layer,'' J. Acoust. Soc. Am. **67**, 1157–1165 (1980).
[6] D. N. Alleyne and P. Cawley, ''The interaction of Lamb waves with defects,'' IEEE Trans. Ultrason. Ferroelectr. Freq. Control **39**, 381–396 (1992).
[7] N. Guo and P. Cawley, ''The interaction of Lamb waves with delaminations in composite laminates,'' J. Acoust. Soc. Am. **94**, 2240–2246 (1993).
[8] S. I. Rokhlin, ''Lamb wave interaction with lap-shear adhesive joints: Theory and experiment,'' J. Acoust. Soc. Am. **89**, 2758–2765 (1991).
[9] S. Grondel, E. Moulin, and C. Delebarre, ''Lamb wave assessment of fatigue damage in aluminum plates,'' Proceedings of SPIE, Vol. 3668, Smart Structures and Integrated Systems (1999).
[10] S. K. Datta, Y. Al-Nassar, and A. H. Shah, ''Lamb wave scattering by a surface-breaking crack in a plate,'' in *Review of Progress in Quantitative NDE*, edited by D. O. Thompson and D. E. Chimenti (Plenum, New York, 1991), Vol. 10A, pp. 97–104.
[11] Z. Chang and A. Mal, ''Scattering of Lamb waves from a rivet hole with edge cracks,'' Mech. Mater. **31**, 197–204 (1999).
[12] J. J. Ditri and J. L. Rose, ''Excitation of guided waves in generally anisotropic layers using finite sources,'' J. Appl. Mech. **61**, 330–338 (1994).
[13] X. Jia, ''Modal analysis of Lamb waves generation in elastic plates by liquid wedge transducers,'' J. Acoust. Soc. Am. **101**, 834–842 (1997).
[14] M. Castaings and P. Cawley, ''The generation, propagation, and detection of Lamb waves in plates using air-coupled ultrasonic transducers,'' J. Acoust. Soc. Am. **100**, 3070–3077 (1996).
[15] J. L. Rose, S. P. Pelts, M. J. Quarry, ''A comb transducer model for guided wave NDE,'' Ultrasonics **36**, 163–169 (1998).
[16] F. L. Degertekin and B. T. Khuri-Yakub, ''Lamb wave excitation by hertzian contacts with applications in NDE,'' IEEE Trans. Ultrason. Ferroelectr. Freq. Control **44**, 769–778 (1997).
[17] E. Moulin, J. Assaad, C. Delebarre, H. Kaczmarek, and D. Balageas, ''Piezoelectric transducer embedded in composite plate: Application to Lamb wave generation,'' J. Appl. Phys. **82**, 2049–2055 (1997).
[18] B. A. Auld, *Acoustic Fields and Waves in Solids*, Vol. II, 2nd ed. (Krieger, Florida, 1990).
[19] O. C. Zienkiewicz, *The Finite Element Method*, 3rd ed. (McGraw-Hill, New York, 1977).
[20] J. Assaad, M. Ravez, and C. Bruneel, ''Application of the finite-element method for modeling backed transducers,'' J. Acoust. Soc. Am. **100**, 3098–3103 (1996).
[21] M. A. Hamstad, J. Gary, and A. O'Gallagher, ''Wide band acoustic emission displacement signals as a function of source rise-time and plate thickness,'' in *Progress in Acoustic Emission IX*, Proc. Intern. AE Conf., Hawaii, IV-48-57 (1998).
[22] K. Creath, ''Phase-shifting speckle interferometry,'' Appl. Opt. **24**, 3053–3058 (1985).
[23] T. Lamarque, ''Caractérisation de délaminages par interférométrie de speckle à cisaillement avec sollicitation thermique ou mécanique,'' Thèse de doctorat, Université Paris 6 (1998).

Sound scattering by bubble clouds near the sea surface

Guillermo C. Gaunaurd
Naval Surface Warfare Center, Carderock Division, Code 683, W. Bethesda, Maryland 20817-5700

Hanson Huang
13 200 Overbrook Lane, Bowie, Maryland 20715-1164

(Received 8 December 1998; revised 13 July 1999; accepted 22 September 1999)

The classical exact formulation required to evaluate the form function (or the scattering cross-section, SCS) of a single, ideal, air bubble in a boundless liquid is briefly recalled. It is then immediately generalized to the case of a round cloud of many possibly interacting such bubbles of known volume concentration, contained within the same boundless medium. This is further generalized to the case when the bubble cloud is near a free surface. The presence of the nearby pressure release surface, assumed flat, substantially alters the cloud's scattering cross-section relative to its value in the absence of boundaries. We then use an earlier technique of ours [i.e., see I.E.E.E. J. Ocean. Eng. **20**, 285–293 (1995)] based on the method of images that uses the addition theorem for the spherical wave functions, to relate all the scattered sound fields to a common origin and thus obtain the (modified) SCS of the cloud now near the boundary. This formulation accounts for all orders of multiple scattering and yields an infinite set of coupled algebraic equations for the coupling coefficients. This set is then solved for the coupling coefficients in terms of infinite sums of products of pairs of Wigner 3-j symbols, which are then used to construct and evaluate the form function. We display numerical results in four cases that correspond to geographical sites in which the bubble concentrations within the cloud have been measured along a couple of oblique upward directions, or have been assumed to have increasing (and in a few instances, purposely unrealistically high) values. In all cases considered here the bubble clouds are only a few meters beneath the sea surface and consist of ideal bubbles. The results are also compared to those found in the absence of a boundary in all the cases considered. [S0001-4966(00)05301-7]

PACS numbers: 43.20.Fn, 43.30.Gv [DLB]

BACKGROUND AND GENERALITIES

Consider a multitude of air bubbles contained within a spherical cloud of radius R in an infinite, external fluid medium. The density and sound speed in the pure outer fluid are ρ and c, respectively. The density and sound speed inside the bubbly cloud are ρ_c and c_c, respectively. A plane sound wave of time dependence $\exp(-i\omega t)$ is incident on the cloud from an arbitrary direction, α (see Fig. 1). For a properly chosen coordinate system so that the incident wave vector is along the polar (i.e., the z) direction on the spherical cloud, the scattered wave will have no azimuthal dependence, φ. The only angular dependence will be on the polar angle θ (i.e., the colatitude) and the (normalized) differential scattering cross-section (SCS) of the cloud is then given by

$$\frac{1}{R^2}\frac{d\sigma}{d\theta}=\left|\frac{1}{R}f_\infty(\theta,x)\right|^2, \tag{1}$$

where $x=kR$ and the form function $f_\infty(\cdot)$ is

$$f_\infty(\theta,x)=\frac{1}{ik}\sum_{n=0}^{\infty}(2n+1)T_n(x)P_n(\cos\theta). \tag{2}$$

Here, $k=\omega/c$, $P_n(\cdot)$ are the Legendre polynomials and the coefficients $T_n(x)$ are found by applying appropriate boundary conditions (B.C.) at the cloud's (conceptual) interface with the pure fluid. The B.C. are statements of continuity of pressure and particle velocity at the cloud's spherical surface $r=R$. The result for the coefficients $T_n(x)$ is

$$T_n(x)=-\frac{\rho_c x j_n'(x)j_n(\beta x)-\rho\beta x j_n'(\beta x)j_n(x)}{\rho_c x h_n^{(1)'}(x)j_n(\beta x)-\rho\beta x j_n'(\beta x)h_n^{(1)}(x)}, \tag{3}$$

where $\beta=c/c_c$. This result and many plots of partial waves and SCSs were given in Ref. 1 as particular cases of a more general situation, described in Ref. 2, in which the (''effective'') bubble cloud was contained inside a solid elastic medium. Note that in these early cases the cloud essentially consisted of a single ''effective'' ideal bubble of density ρ_c and sound speed c_c.

The external factor x cancels out in Eq. (3), and since the bubbly cloud usually has a small gas concentration, often a small fraction of 1%, the cloud density is essentially the same as that of the pure outer fluid, i.e., $\rho_c\cong\rho$. This result follows formally from the classical mixture law,

$$\rho_c=\rho(1-\phi)+\rho_g\phi, \tag{4}$$

where ρ_g is the gas (i.e., air) density and ϕ is the (small) volume fraction or concentration. It follows from Eq. (3) that

$$T_n(x)=-\frac{j_n'(x)j_n(\beta x)-\beta j_n'(\beta x)j_n(x)}{h_n^{(1)'}(x)j_n(\beta x)-\beta j_n'(\beta x)h_n^{(1)}(x)}, \tag{5}$$

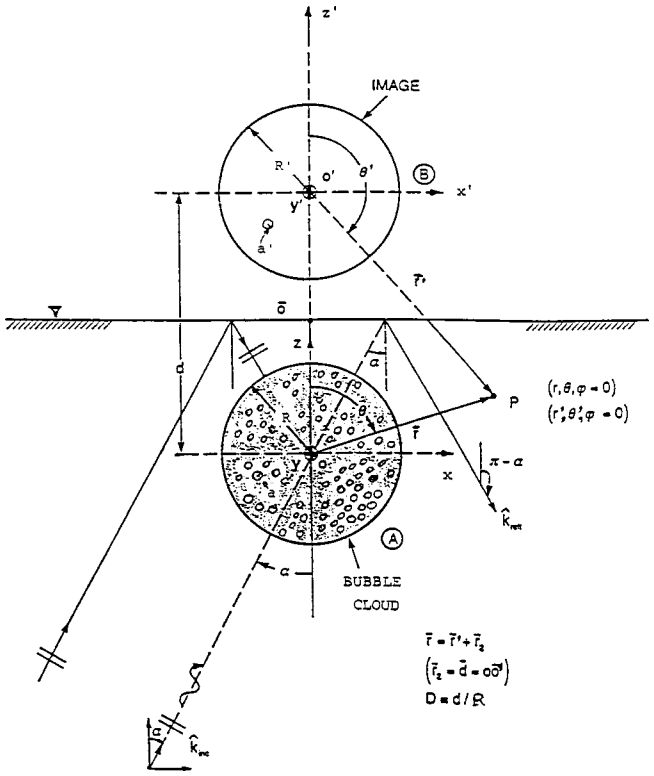

FIG. 1. The geometry of the scattering problem from the bubble cloud.

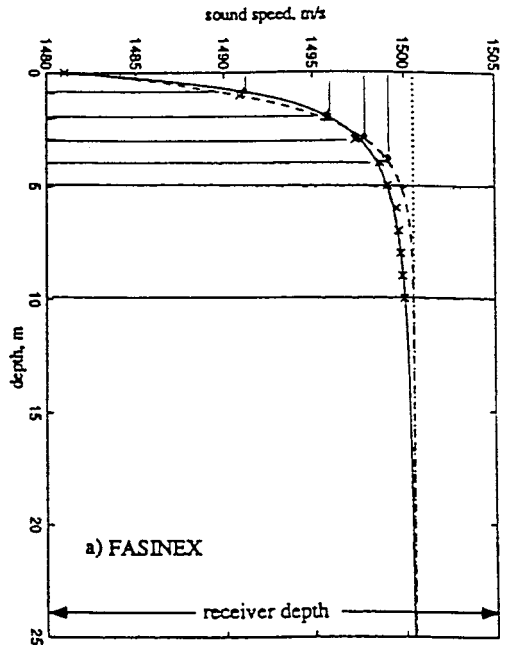

FIG. 2. Depth variation of the sound speed at the Fasinex site. [⋆⋆⋆ are the data of Ref. 5. Solid and dashed interpolating profiles are from Ref. 7.]

which is a set of coefficients no longer dependent on densities. To compute and display partial waves, form functions, or differential scattering cross sections, all that is now needed is the ''effective'' sound speed c_c in the cloud. In the backscattering direction $\theta=\pi$, one has $P(\cos\theta)=P_n(-1)=(-1)^n$. Then the pertinent form function is

$$f_\infty(\pi,x)=\frac{1}{ik}\sum_{n=0}^{\infty}(-1)^n(2n+1)T_n(x). \tag{6}$$

Below the resonance frequency of the bubbles contained in the cloud, one has $c_c \ll c$ (i.e., a relatively low sound speed inside the cloud, see Ref. 3). In this case, $\beta \gg 1$ and Eq. (5) yields the coefficients that should be used in the ''sound soft limit,'' viz.,

$$T_n(x)\to -\frac{j_n(x)}{h_n^{(1)}(x)}, \tag{7}$$

which is the familiar result for an impenetrable sphere with zero surface pressure. For small bubble concentrations within the cloud, the effective sound speed c_c cannot be expected to be *much* smaller than c, and then the more general coefficients given in Eq. (5) are to be retained.

For air bubbles in water, it is desirable to know the difference $c-c_c=\Delta c_c$ between the sound speed in the pure liquid and its value within the cloud. Using the familiar Wood's formula,[3] viz.,

$$c_c=c\left[\frac{\phi}{\rho_g}\left(\frac{c}{c_g}\right)^2+\frac{1}{\rho}(1-\phi)\right]^{-0.5}[(1-\phi)\rho+\rho_g\phi]^{-0.5}, \tag{8}$$

the difference $\Delta c_c=c-c_c$ can be expanded in powers of the parameter $(\rho c^2/\rho_g c_g^2)\phi$, where ρ/ρ_g and c^2/c_g^2 are large, but ϕ is small, so that the overall product is small, and then the result is

$$\Delta c_c \cong \frac{c}{2}\left(\frac{\rho}{\rho_g}\right)\left(\frac{c}{c_g}\right)^2\phi, \tag{9}$$

which is valid to first powers of $(\rho c^2/\rho_g c_g^2)$. For air bubbles in water all that is needed is the concentration ϕ in order to estimate the drop in sound speed inside the cloud. Substituting the familiar values of the air and water parameters one finds

$$\frac{c}{c_g}\cong\frac{1510.6}{340}=4.443 \quad \text{and} \quad \frac{\rho}{\rho_g}=\frac{1028.13}{1}=1028.13, \tag{9a}$$

and substitution into Eq. (9) yields

$$\Delta c_c=15.33\times 10^6\phi. \tag{10}$$

The concentration of air bubbles near the sea surface has been measured by several authors at several sites.[4,5] At the Fasinex site[5] it was found to be $\phi=1.4\times10^{-6}$. For this value, the decrease in sound speed in the bubbly mixture as found from Eq. (10) is $\Delta c_c\cong 21$ m/s. At depths below about 10 m, it decreases to zero, and then $c_c=c$. If the cloud is to exist more than a few seconds, the concentration values are quite small (see Fig. 2).

I. THE EFFECT OF PROXIMITY TO A FREE SURFACE

The analysis given above pertains to bubble clouds in boundless media. No boundary had yet been introduced. The SCS of a bubble cloud near the sea surface can no longer be accurately predicted by the formulation shown in the Introduction. The proximity to a free surface (or to any type of

surface) distorts the cross-section quite substantially, because of the complicated cloud interactions with the surface, which maintains a pressure release B.C. always acting on it. In previous work,[6] we analyzed the scattering problem of a bubble which is scattering plane sound waves near a free boundary. This work assumed a perfectly flat and smooth sea surface so that the method of images could be used to construct the solution. Furthermore, radiation damping was the only damping mechanism accounted for when modeling the bubble oscillations. In that work,[6] the bubble was a fluid sphere of density and sound speed different from those of the external fluid half-space. That same formulation, under the same assumptions, but with some modifications, can be adapted to the case of a spherical bubble *cloud* near the free surface. The sound speed within the cloud is the effective speed $c_{\mathbf{c}}$ given by Wood's formula [i.e., Eq. (8)]. The (effective) density within the cloud is governed by the simple mixture law in Eq. (4).

The bubble concentrations ϕ that have been measured in clouds observed near the sea surface are quite small. Clearly, these bubble clouds are fluid spheres, made mostly of liquid mixed with many minute air bubbles having a very small collective volume fraction. Hence, the cloud's effective density is essentially the same as that of the outer pure fluid. At the Fasinex site, the measured (and predicted) value of $c_{\mathbf{c}}$ is 1489 m/s, which is about 1.4% smaller than in bubble free water. Hence, at this site, it was found that $c_c = 0.986\,\mathrm{c}$ and $\rho_c \cong \rho = 1028.13\,\mathrm{Kg/m}$. The not uncommon concentration value of $\phi = 10^{-5}$ (see Ref. 7), produces an effective sound speed in the cloud of $c_c = 1377\,\mathrm{m/s}$ (according to Ref. 8), which represents about a 9% sound speed reduction from the value in bubble-free water. In this case, it follows that $c_c = 0.912\,\mathrm{c}$.

It has been postulated and observed[8–10] that bubble clouds exhibit a collective oscillatory behavior which makes them radiate sound at frequencies substantially lower than the resonance frequency of the individual constituent bubbles within the cloud. Such clouds vibrate like a system of coupled oscillators, which are known to have natural frequencies much lower than those of each individual oscillator.[10] The fundamental resonance frequency of the cloud is then given by [i.e., see Ref. 8, Eq. (39), in the present notation]

$$f_R^{(0)} = \left(\frac{\pi}{2\sqrt{3}}\right)\frac{1}{2\pi R}\sqrt{\frac{3\gamma P_0}{\phi\rho_c}} \to \approx \frac{1}{2\pi R}\sqrt{\frac{3\gamma P_0}{\phi\rho}}. \qquad (11)$$

Since $(\pi/2\sqrt{3})$ is close to unity and ρ_c is almost equal to ρ, this resonance can be expressed as a ''modified Minnaert formula,'' where the radius is now that of the cloud and the concentration is now present in the denominator.[9] For the present case of the cloud one should set $\gamma = 1$ for isothermal conditions, since the value of $\gamma = 1.4$ applies to the individual bubble oscillations. We recall[11] that the fundamental Minnaert resonance for a bubble of radius a is

$$f_R = \frac{1}{2\pi a}\sqrt{\frac{3\gamma P_0}{\rho}}. \qquad (12)$$

For standard atmospheric conditions near the surface (i.e., $P_0 = 10^5$ Pa) and for a cloud of radius $R = 1$ m in water (i.e., of density 1 g/cm^3), having a concentration value of $\phi = 10^{-5}$, then Eq. (11) predicts a resonance frequency of $f_R^{(0)} = 872\,\mathrm{Hz}$ for the cloud. In contrast, air bubbles of radius $a = 50\,\mu\mathrm{m}$ in water at atmospheric pressure, have a resonance frequency given by Eq. (12) of value $f_R = 65.3\,\mathrm{kHz}$. This value is 75 times higher than the one for the above cloud.

We remark that the original Minnaert formula, Eq. (12), applies to *ka* values that must remain small near resonance. For an air bubble in water near the surface, this small value is $ka \cong 0.0136$. In view of the global smoothing effect of the effective medium approach, the cloud's density is essentially that of water, and its (effective) sound speed is that given by Wood's Eq. (8). This will be true as long as Eq. (8) holds. In this case, the *modified* Minnaert formula Eq. (11) is the pertinent one. Now, *kR* takes on values a couple of orders of magnitude larger than those *ka* had for the single air bubble. Thus larger cloud radii and lower resonance frequencies result, in agreement with other published results for bubble clouds.[8–10]

Using a dimensionless scale of $0 \leqslant ka \leqslant 10$ with $a = 50\,\mu\mathrm{m}$, the corresponding frequency range is $0 \leqslant f \leqslant 50\,\mathrm{MHz}$. The resonance frequency of the individual minute bubbles (i.e., 65.3 kHz) and, of course, that of the cloud (i.e., 872 Hz) are at the extreme low end of the scale. It has been established[12] that for single bubbles, and frequencies above their resonance frequencies, the acoustic radiation damping effects (due to scattering) are dominant over the thermal or viscous ones. In the present situation of an idealized effective medium describing the cloud behavior, the cloud is essentially a water sphere with a minute air content that slightly decreases its (effective) sound speed. The cloud's behavior under this approach rests heavily on the validity of Eq. (8), and will not hold if it is invalid. We have assumed small void fractions to insure such validity. In Sec. II, below, only radiation damping will be included in the formulation applicable to the cloud, under the same validity assumption. In simpler models describing the bubble oscillation by means of one single degree-of-freedom harmonic oscillator with a single resonance frequency, there is a damping constant denoted by δ, which is the reciprocal of the oscillator's ''Q.'' Our general model includes all the n modes and resonance frequencies. The damping parameter now is found, by analogy, by reading from the vibratory response plot, the bandwidth at half-maximum of the scattering cross-section around the principal (i.e., $n = 0$, monopole) resonance, which is still dominant, and dividing it by that fundamental resonance frequency. We finally note that higher bubble concentrations within the cloud further reduce its collective resonance frequency, which follows from the presence of the void fraction ϕ in the denominator of Eq. (11).

II. ANALYTICAL FORMULATION VALID NEAR THE BOUNDARY

To generate numerical results we use the following modification of the formulation we gave earlier, Ref. 6. The form function (for $r \gg 1$) is

$$f_\infty(r,\theta,\varphi,k)=\frac{2}{ka}\left|\sum_{n=0}^{\infty}\sum_{m=0}^{n} i^{-(n+1)}b_{mn}\right.$$
$$\times\left[P_n^m(\cos\theta)-(-1)^{m+n}\ \frac{r}{r'}\right.$$
$$\left.\left.\times e^{ik(r'-r)}P_n^m(\cos\theta')\right]e^{im\varphi}\right|, \tag{13}$$

where the coefficients b_{mn} are the solutions of the following coupled, infinite system of algebraic equations with transcendental coefficients:

$$b_{mn}+T_n(x)\sum_{q=0}^{\infty}(-1)^{q+m}b_{mq}Q_{mqmn}(d)$$
$$=2T_n(x)i^n\left(\frac{2-\delta_{0m}}{N_{mn}}\right)P_n^m(\cos\alpha)$$
$$\times[1-(-1)^{n+m}e^{ikd\cos\alpha}], \tag{14}$$

where $T_n(x)$ was given in Eq. (5), the $P_n^m(\cdot)$ are the associated Legendre functions, α is the incidence angle of the plane wave with the normal to the boundary, $d/2$ is the distance from the cloud's center to the free surface, N_{mn} is the normalizing factor,

$$N_{mn}=\frac{2}{2n+1}\frac{(n+m)!}{(n-m)!}, \tag{15}$$

and the so-called ''translation coefficients'' are

$$Q_{mqmn}(d)=i^{n-q}\left(\frac{2}{N_{mn}}\right)\sum_{\sigma=|q-n|}^{q+n} i^{\sigma}(-1)^{\sigma}b_{\sigma}^{(qmnm)}$$
$$\times h_{\sigma}^{(1)}(kd), \tag{16}$$

where the weighing factors in Eq. (16) are

$$b_{\sigma}^{(qmnm)}=(-1)^{-m}(2\sigma+1)$$
$$\times\sqrt{\frac{(q+m)!(n+m)!}{(q-m)!(n-m)!}}\begin{pmatrix} q & n; & \sigma \\ 0 & 0; & 0 \end{pmatrix}$$
$$\times\begin{pmatrix} q & n; & \sigma \\ m & -m; & 0 \end{pmatrix} \tag{17}$$

and where the pairs of Wigner 3-j symbols appearing in Eq. (17) have been defined elsewhere.[6,13] The two indices m and n have the usual ranges, $0\leqslant n\leqslant\infty$ and $0\leqslant m\leqslant n$. If the r, θ coordinates of the field point are known, then the coordinates of its image r', θ' reflected on the free boundary are given by the relations,

$$r'=\sqrt{r^2+d^2-2rd\cos\theta} \tag{18a}$$

and if we define $B=\sin^{-1}[(r/r')\sin\theta]$, then θ' is given by

$$\begin{aligned}&\theta'=B \quad 0\leqslant\theta\leqslant\pi/2\\ &\theta'=\pi-B \quad \pi/2<\theta<3\pi/2\\ &\theta'=2\pi-B \quad 3\pi/2<\theta<2\pi\ .\end{aligned} \tag{18b}$$

We note that the solution Eqs. (13)–(18), valid for the cloud near the flat boundary, contain the coefficients $T_n(x)$ of the simpler solution in a boundless medium. These coefficients appear as factors in the infinite system of algebraic equations (14). The numerical procedure required to solve such an infinite system of coupled equations for the coupling coefficients b_{mn} is essentially the same we explained earlier in Ref. 6. A key difference between the present solution and the earlier one in Ref. 6 is that the present form function is evaluated with a different value of the parameter β, which appears in $T_n(x)$. In Ref. 6 we had $\beta=\rho c/\rho_g c_g$, while now β is equal to $\rho c/\rho_c c_c$. The value of c_c can be either measured or predicted by Eq. (8), and its introduction is what allows the treatment of the cloud as an effective medium. Also, the value of ρ_c is very close to that of ρ. For the site considered above, the new value to be used is $\beta=1.014$. As β approaches unity, a condition which occurs for depths about 10 m below the surface, the $T_n(x)=0$ for all n, and then the form function vanishes since there is no longer a cloud. In the more common case of $\phi=10^{-5}$, we find that $c_c=1377.3$ m/s, and thus $\beta=1.097$, a situation that we will analyze further, below, in Case B.

TABLE I. Typical concentration, cloud density, sound speed in cloud, and impedance ratio of pure to bubbly water, at four locations.

	ϕ	ρ_c (Kg/m)	c_c (m/s)	β^{-1}
Case A	1.4×10^{-6}	1028.1285	1489.0	0.9857
Case B	1.0×10^{-5}	1028.1197	1377.3	0.9118
Case C	3.0×10^{-5}	1028.0991	1190.97	0.7884
Case D	1.0×10^{-2}	1017.8587	106.31	0.0703

III. NUMERICAL RESULTS

The general formulation for the round bubble cloud near the sea surface in Sec. II will now be applied to the various cases in Table I, below. Case A corresponds to the Fasinex site. Cases A–D correspond to a variety of environments having different bubble concentrations. Only Cases A and B are realistic for bubble clouds near the sea surface. The others are hypothetical and have not been observed anywhere. In the computed cases the angle of incidence was assumed to be either 10 or 45 degrees. Thus the plane wave is assumed to be incident from below, as if it were projected at an upward but oblique inclination (of $\alpha=10°$, 45°) by an upward looking sonar.[4] In the backscattering direction one always has $\theta=\alpha+\pi$. It is convenient to first compute the form function for the bubble cloud for the cases in Table I, in the absence of any boundary. This can be done in two ways. One is using the simpler formulation in Eqs. (1)–(5) with the value of β given in Table I for each case. Another way is to use the more complex formulation in Eqs. (13)–(18), using the values of β in Table I, but setting the distance $d/2$ between the cloud's center and the free surface equal to infinity. (In the absence of boundaries, the angle of incidence is irrelevant.) Once the computer program is setup, the evaluation done in this seemingly harder way is not much more difficult to carry out than by the first (simpler) formulation. Figure 3 shows the form function f_∞ for a wide kR range for the cloud in free space, for Cases A, B, C, and D of Table I. In these cases, the bubble concentration is progressively increasing and the effective sound speed within the cloud is progressively decreasing. For the smallest concentration (i.e.,

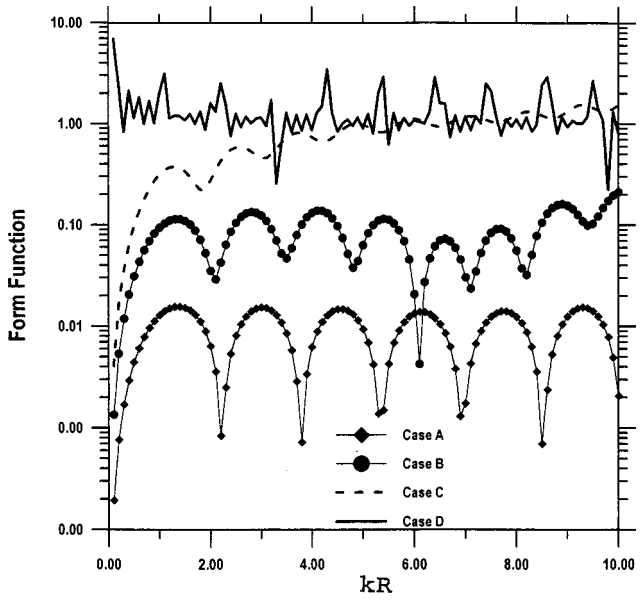

FIG. 3. The form function of a round bubble cloud in free-space in four cases (i.e., A, B, C, and D) in which the bubble concentration is progressively increasing. The parameter values are as given in Table I.

Case A) the peak amplitude of f_∞ is quite small (i.e., 0.01). As the concentration increases (i.e., in Cases B, C, and D), this peak amplitude grows to 0.1, 0.5, and ultimately 1.0, as it would be the case for an almost totally gaseous cloud (i.e., almost the situation for one large gas bubble in water). The target strength (TS) of these clouds is proportional to $(f_\infty)^2$ in all cases.

In the realistic cases actually observed (i.e., A and B), the TS of the clouds, even at its peaks, is quite small and never exceeds $(0.1)^2$. In all the cases in Fig. 3 the form functions exhibit oscillatory patterns that resemble a succession of ''inverted U's.'' These patterns have peaks/dips that reappear periodically as the ''creeping waves'' that revolve around the cloud interfere with the backscattered return after each circumnavigation. In the case of the ''almost liquid'' cloud (i.e., Case A, for very small ϕ), one observes asymptotic spacings of value $kR=\pi/2$, or which is the same, $2\pi R=(\pi/2)\lambda$. Here, $\pi/2$ wavelengths exactly fit the cloud's circumference. In the case of a more ''nearly gaseous'' cloud (i.e., Case D, of much higher concentration ϕ) one observes spacings between the dips of value $kR=1$, or equivalently, $2\pi R=\lambda$. In this case, only one wavelength exactly fits the cloud's circumference. The other two cases represent intermediate situations in which more than one but less than $\pi/2$ wavelengths—depending on the bubble concentration within the cloud—exactly fit the cloud's circumference.

We point out that the creeping waves revolving around the cloud are related, and in fact, are caused by the (low-order) resonances of the cloud, which can behave as a resonant cavity. These resonances are also related to circumferential waves internal to the cloud. The relation between these internal and external waves has been studied earlier.[14] In general, the internal resonance frequencies of a nearly **soft** object such as a bubble cloud, are obtained by solving the interior **Newmann** problem for the same object, contained in a rigid enclosure.[14] Only at the internal resonance frequencies, given by the roots of $j_n'(\beta x)=0$, where β is given after Eq. (3), will the incident field penetrate into the scatterer.

Figure 4(a), (b), (c) shows the effect of cloud proximity to the sea surface. These plots are here generated for an incidence angle of 45°, although other incidence directions could be equally computed. In the figures, $D=d/R$. For $D=2$, the cloud is just touching the sea surface, and for $D=2.5$, the cloud is at some depth beneath the surface. Actually, the cloud's apex is then a quarter of a cloud's radius R under the surface. For $D=\infty$, the cloud is in free space and the curves in these cases agree with the corresponding ones in Fig. 3. Observation of Fig. 4(a), (b), (c) shows that the boundary presence substantially enhances the amplitude of the form functions. All the peak values are increased by a factor of about 5 relative to the free-space curves (i.e., the $D=\infty$ curves). This is the main effect of proximity to a free surface. This large enhancement in all cases is easily explained and understood. Close to the boundary there is an additional reflection from the image cloud and also additional higher order interactions of various types, which constructively or destructively reinforce or weaken the return. The quasi-periodic dips/peaks observed in these patterns correspond to the interference phenomena caused by the phase difference between the cloud contribution to the scattered sound field, and that of its image. This behavior was observed earlier in Ref. 6 and has its origins in the analytical expression for the Lloyd's mirror effect of underwater acoustics. Figure 4(a) (Case A) shows that the peak amplitudes are not always largest when the cloud is closest to the surface. In fact, this figure shows that the peak amplitudes from a cloud slightly away from the sea surface can often be larger than when the cloud is right in contact with the surface. This statement seems to be true in the realistic cases of Fig. 4(a), (b). In Fig. 4(c) (Case C) the cloud touching the boundary exhibits form function peaks always larger than those of the slightly deeper cloud. In this case, the peak values of f_∞ for clouds near the surface are still 2–5 times larger in amplitude than in the absence of boundaries (i.e., for the $D=\infty$ curve).

Figure 5(a), (b), (c) is computed for the same parameter values used in Fig. 4, except that now the incidence angle is $\alpha=10°$. The curves for $D=\infty$, which pertain to the free-space condition, obviously agree with the results in Fig. 3 for the three cases shown. The main difference with the plots in Fig. 4 is the presence of the large broad peak seen in all cases. These relatively strong, broad, peaks are due to the contributions to the form function from the **forward** scattering produced by the reflected wave contribution that emerges from the **image** cloud. In each case shown, such peaks are pronounced within a relatively narrow sector around the forward direction from the image. This sector now encloses the nearly vertical direction of the incident plane wave. Such was not the case in Fig. 4, in which the more oblique incidence direction was outside the sector occupied by the forward scattered lobe from the image in that case. The interference patterns of ''inverted U's'' that were mentioned earlier, are still noticeable in Fig. 5, but now they are superimposed on the broad, forward scattering peak. In the large magnification needed in these plots to show the larger peak

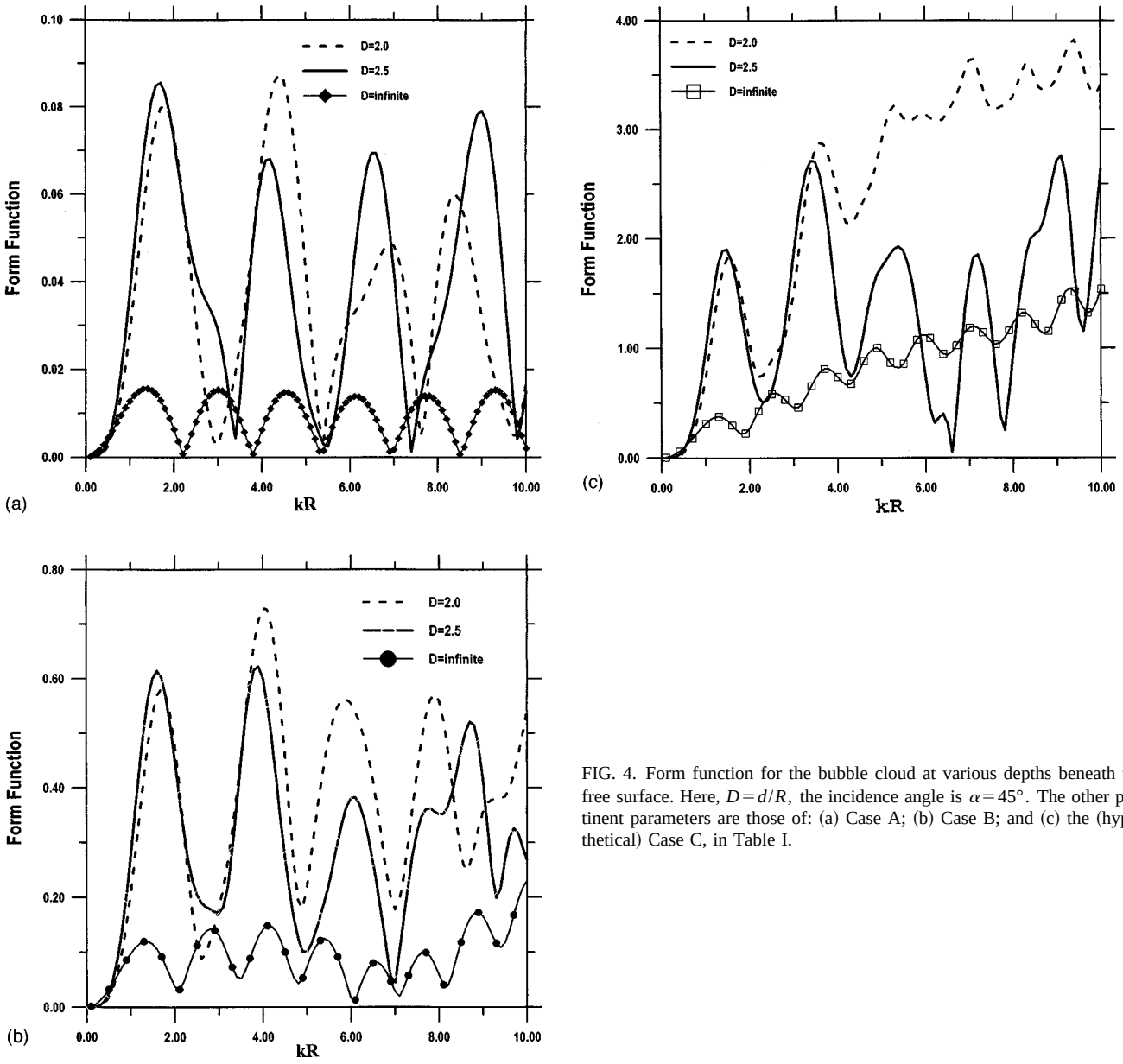

FIG. 4. Form function for the bubble cloud at various depths beneath the free surface. Here, $D=d/R$, the incidence angle is $\alpha=45°$. The other pertinent parameters are those of: (a) Case A; (b) Case B; and (c) the (hypothetical) Case C, in Table I.

amplitudes, they appear as small oscillatory perturbations added to the forward lobe. In view of this form function enhancement due to forward scattering from the image, the target strength of the cloud now takes on values about an order of magnitude higher than those in Fig. 4 for all the sites and depths shown. The closer the incidence direction comes to the vertical direction, the larger this enhancement becomes. This is a further consequence of the boundary proximity, in whose absence these enhancements would not be present.

We note in closing that the present formulation for clouds near boundaries replaces the multitude of minute bubbles near the sea surface by one effective spherical cloud of density very close to that of water, and of effective sound speed dominated by the small bubble concentration within the cloud. It is therefore not expected that the formulation will be very accurate at high frequencies. It is not unreasonable to expect it to hold for $\lambda/R>O(1)$. This translates into $kR<2\pi$, and thus, Figs. 3–5 are bound to contain some inaccuracies near their rightmost ends.

In general, it can be stated that the impedance contrast between the cloud and the outer pure liquid, and thus the target strength (TS) of the cloud, decreases with increasing depth, for the same concentration. It also decreases as the concentration decreases for the same depth. In fact, for increasing depth and consequent decrease in concentration, the TS of the cloud is reduced even more substantially. Eventually, as $\phi\rightarrow 0$, one has $c_c\rightarrow c$ and also $\rho_c\rightarrow\rho$. For very huge bubble concentrations in clouds—as one would never realistically find in the sea, such as when $\phi\rightarrow 1$—it would then follow that $\rho_c\rightarrow\rho_g$ and $c_c\rightarrow c_g$, and then the cloud would behave, in such hypothetical situation, as a single air bubble. Such normal and expected limiting behavior seems to contradict the possibility of effective sound speeds (i.e., phase velocities) in air bubble clouds having values *lower* than the value of c_g.

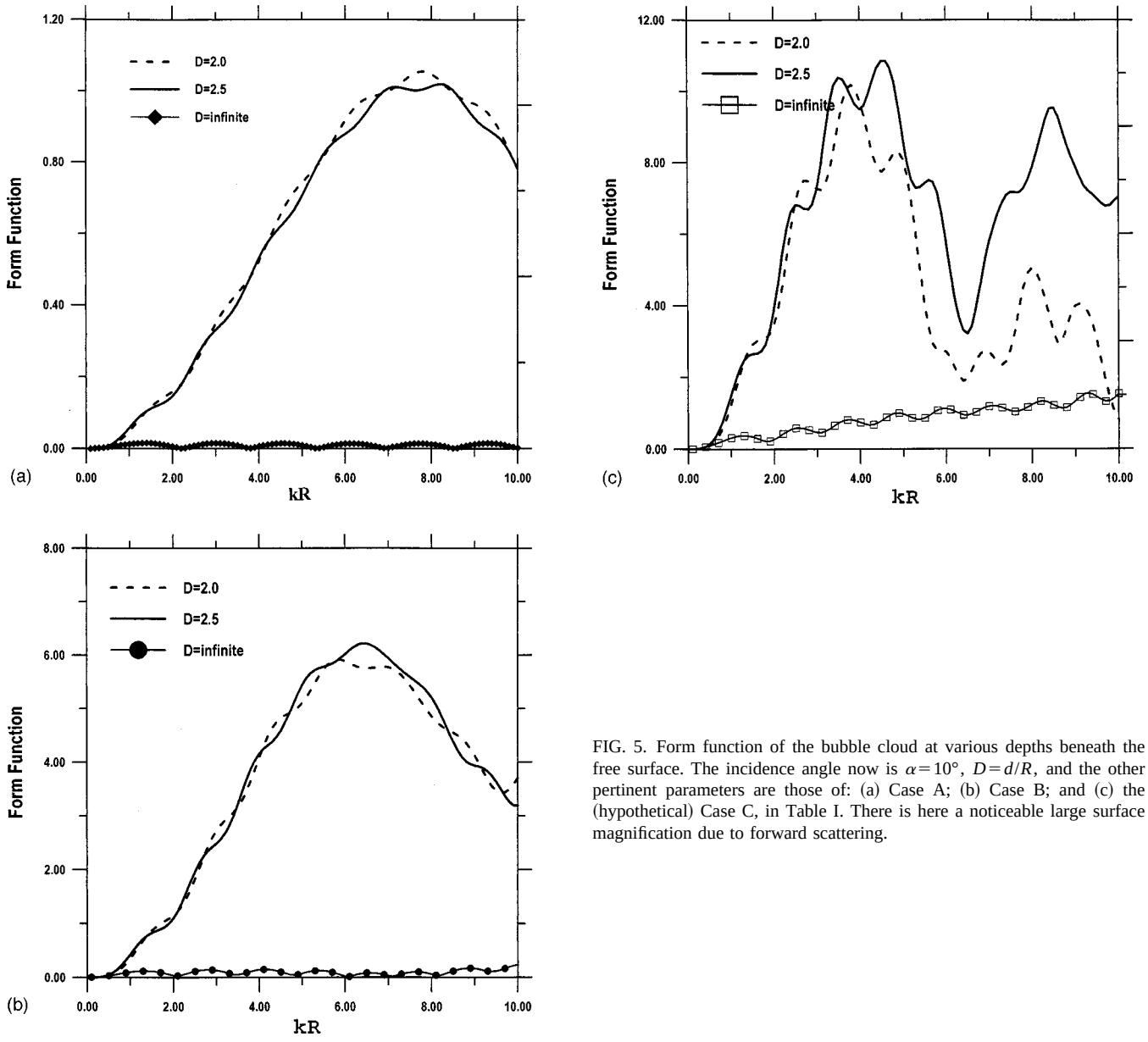

FIG. 5. Form function of the bubble cloud at various depths beneath the free surface. The incidence angle now is $\alpha = 10°$, $D = d/R$, and the other pertinent parameters are those of: (a) Case A; (b) Case B; and (c) the (hypothetical) Case C, in Table I. There is here a noticeable large surface magnification due to forward scattering.

IV. CONCLUSIONS

We have generalized an earlier formulation of ours[6] using an effective medium approach that permits the prediction of the form function (and/or the TS) of bubble clouds in the sea that may be present at various depths beneath the surface. We have evaluated the results and displayed them for several realistic and hypothetical cases in which the bubble concentration within the cloud varies over a reasonable range covered in Cases A to D of Table I. The results are compared to those obtained in the absence of a nearby boundary, and the main finding is the **quantitative** evaluation of the large enhancements (or amplitude peaks) that develop in the backscattering cross-section observed when the cloud is near the boundary. It is sometimes found that a deeper cloud exhibits larger peak enhancements than clouds just in contact with the surface. If the interrogating incidence direction is contained within the relatively narrow forward scattering lobe emerging from the reflected contribution from the **image** cloud, the enhancements are further enlarged. These enhancements can be explained on the basis of the same interference mechanism and the multiple scattering interactions between the cloud and the free surface that were pointed out in our earlier work[6] on single bubbles near boundaries.

ACKNOWLEDGMENT

Author G.C.G. acknowledges the partial support of the ILIR Program of the NSWC-CD.

[1] G. C. Gaunaurd, ''Multipole resonances in elastic wave-scattering from cavities, and in acoustic wave-scattering from bubbles and droplets,'' in *Mathematical Methods and Applications of Scattering Theory*, Lecture Notes in Physics, Vol. 130 (Springer, Berlin, 1979), pp. 114–121, Eq. (11).

[2] G. C. Gaunaurd and H. Uberall, ''Theory of resonance scattering from spherical cavities inside elastic and viscoelastic media,'' J. Acoust. Soc. Am. **63**, 1699–1712 (1978).

[3] A. B. Wood, *A Textbook of Sound* (Macmillan, New York, 1930), Fig. 100, p. 362.

[4] G. Crawford and D. Farmer, ''On the spatial distribution of ocean bubbles,'' J. Geophys. Res. **92**, 8231–8243 (1987).

[5] D. Farmer and S. Vagle, ''Waveguide propagation of ambient sound in the ocean surface bubble layer,'' J. Acoust. Soc. Am. **86**, 1897–1908 (1989).
[6] G. C. Gaunaurd and H. Huang, ''Acoustic scattering by an air bubble near the sea surface,'' IEEE J. Ocean Eng. **20**, 285–293 (1993).
[7] M. J. Buckingham, ''Sound speed and void fraction profiles in the sea surface bubble layer,'' Appl. Acoust. **51**, 225–250 (1997) (see p. 230).
[8] A. Prosperetti, N. Q. Lu, and H. S. Kim, ''Active and passive acoustic behavior of bubble clouds at the ocean's surface,'' J. Acoust. Soc. Am. **93**, 3117–3127 (1993).
[9] W. M. Carey, J. W. Fitzgerald, E. C. Monahan, and Q. Wang, ''Measurement of the sound produced by a tipping trough with fresh and salt water,'' J. Acoust. Soc. Am. **93**, 3178–3192 (1993).
[10] S. W. Yoon, L. A. Crum, A. Prosperetti, and N. Q. Lu, ''An investigation of the collective oscillations of a bubble cloud,'' J. Acoust. Soc. Am. **89**, 700–706 (1991) (see the references therein).
[11] M. Minnaert, ''On musical air-bubbles and the sounds of running water,'' Philos. Mag. **16**, 235–248 (1933).
[12] A. Prosperetti, ''Thermal effects and damping mechanisms in the forced radial oscillations of gas bubbles in liquids,'' J. Acoust. Soc. Am. **61**, 17–27 (1977) (see Figs. 8–12, Sec. III).
[13] A. Edmonds, *Angular Momentum in Quantum Mechanics* (Princeton University Press, Princeton, NJ, 1957).
[14] G. C. Gaunaurd *et al.*, ''Interior and exterior resonances in acoustic scattering, I. Spherical targets,'' Nuovo Cimento **76B**, 153–175 (1983).

Edge wave on axis behind an aperture or disk having a ragged edge

Penelope Menounou, Michael R. Bailey,[a] and David T. Blackstock[b]
Applied Research Laboratories, The University of Texas at Austin, Austin, Texas 78713-8029
and Department of Mechanical Engineering, The University of Texas at Austin, Austin, Texas 78712-1063

(Received 18 August 1998; revised 25 June 1999; accepted 18 July 1999)

Diffraction by a circular aperture or disk having a ragged edge is investigated. Theory and measurements are reported. The ragged edge is modeled as N arcs, of differing radii a_i, each of which contributes a scattered signal to the edge wave on axis behind the aperture or disk. The amplitude of each scattered signal is proportional to the angle of the arc, and the corresponding time delay is $\sqrt{a_i^2+s_0^2}/c_0$, where s_0 is the axial distance from the aperture plane and c_0 is the sound speed. Kirchhoff theory is used to make the calculation. A formula is derived for the rms pressure of the edge wave in terms of the rms pressure and autocorrelation function of the incident wave. The formula can be evaluated for incident waves that are sinusoidal, random (e.g., noise), or transient. Predictions agree reasonably well with underwater measurements made with a spark-generated pulse incident on various apertures. The main result is that making the edge ragged reduces the rms pressure of the edge wave. Indeed, an edge profile is presented that, for a given frequency and axial observation point, eliminates the edge wave completely.
[S0001-4966(99)02311-5]

PACS numbers: 43.20.Fn, 43.30.Es, 43.35.Bf [ANN]

INTRODUCTION

In most studies of diffraction by opaque objects, the edge of the object is assumed smooth or at least regular. Diffraction by a ragged, irregular edge has recently been investigated[1,2] and shown to have properties useful for certain practical applications, for example, in medical ultrasonics[3] and traffic noise barrier design.[4,5] The subject of the present work is diffraction by an aperture or disk that has a random (or ragged) edge. In particular we are concerned with the root-mean-square (rms) pressure of the scattered, or edge, wave on axis behind the aperture or disk.[6]

In certain practical applications, reduction of the effect of an edge wave is highly desirable. Consider, for example, panel tests to evaluate acoustical characteristics of materials. Measurements to determine the reflection coefficient of a sample of infinite surface area are made with a finite-size sample. However, diffracted signals from the edge of the sample contaminate the reflection measurement. To address this problem Piquette[7] developed a postprocessing technique to correct the experimental data by eliminating the edge wave component in the received signal. In other cases, however, postprocessing, which deals with data already contaminated by edge waves, is not enough. The edge wave itself must be decreased. Consider, for example, traffic noise barriers. Sound in the shadow zone is primarily due to edge waves diffracted from the top of the barrier. To protect the listener, the edge waves themselves must be reduced. This can be done by making the top edge of the barrier ragged.[4] A similar approach is reported in a biomedical experiment to measure damage to tissue by ultrasound.[3] Making the edge of a blocking plate ragged (technique described by Bailey and Blackstock[1]) suppressed an undesired edge wave.

A qualitative explanation of the effect of the ragged edge is as follows. Consider the axial field produced behind an aperture or disk by a normally incident plane wave or by a spherical wave generated by an on-axis source. If the edge is perfectly circular, every point on the rim is equidistant from an on-axis receiver. Because all scattered waves from the rim arrive simultaneously at the receiver, the edge wave is strong. For a receiver off axis, the scattered contributions lose their coherence, and the edge wave is weak. The axial position is therefore very special. When the aperture or disk is ragged, however, no receiver position is special. Even on axis, the contributions from the rim do not add coherently. Consequently, we expect the edge wave to be a diffuse signal of low amplitude. In this paper the rms value of the edge wave signal is used as the metric by which to measure the effect of raggedness of the rim.

For the theoretical study of diffraction by ragged edge apertures or disks the Kirchhoff theory of diffraction is used.[8] The solution for a perfectly circular aperture or disk is appropriately modified and generalized so that it can be applied to a ragged edge aperture or disk. The Kirchhoff theory, although it is approximate, is one of the most well-known theories of diffraction and has found extensive use in various diffraction problems, mainly because of the simplicity of its solution. A discussion of the approximations in Kirchhoff theory can be found in Ref. 9. Comparisons between the Kirchhoff solution and exact analytical solutions can be found in Ref. 10.

Because of Babinet's principle (complementary diffracting objects have complementary diffraction patterns),[8] it is not necessary to analyze apertures and disks separately. We

[a]Current address: Applied Physics Laboratory, College of Ocean and Fishery Science, University of Washington, 1013 NE 40th St., Seattle, WA 98105.
[b]Electronic mail: dtb@mail.utexas.edu

have chosen to concentrate on apertures and generally refer to disks only when a special point is to be made. It should be borne in mind, however, that changing the profile of the rim affects the edge wave for a disk the same as that for an aperture.

Section I below is devoted to theory. After diffraction by an aperture or disk having a circular edge is reviewed (Sec. I A), the theory for noncircular edges, in particular ones that are random, is developed (Sec. I B). The rms value of the diffracted pressure signal (on axis, behind the aperture or disk) is then used to compare various edges (Sec. I C). Section I D is devoted to the design of an aperture or disk for which the rms value of the edge wave vanishes. Such an aperture or disk constitutes a spatial notch filter. A generalization to cover diffraction by spherical waves from an on-axis source is given in Sec. I E. The remainder of the paper is devoted to experiments. Underwater measurements with a spark source and various apertures are described in Sec. II. The experimental results are discussed and compared with theoretical predictions in Sec. III.

I. THEORY

Our theoretical analysis is based on the Kirchhoff theory of diffraction. The starting point in Kirchhoff theory is the Helmholtz–Kirchhoff integral solution of the wave equation. The Helmholtz–Kirchhoff integral is evaluated under certain assumptions, sometimes called Kirchhoff boundary conditions. The solution for perfectly circular apertures or disks is reviewed, and it is then generalized to cover ragged-edge apertures and disks. We characterize the results by the rms value of the edge wave signal, which is calculated for a variety of edge profiles, including ragged. As a special application, a profile is designed that produces zero edge wave pressure (rms) for a given frequency at a given axial distance. The edge having this profile acts as a spatial notch filter. Finally, the analysis is extended to cover diffraction by spherical waves from an axially located source.

A. Background. Circular aperture

If the acoustic field on any closed surface S is known, the Helmholtz–Kirchhoff integral gives the acoustic pressure p at any interior point Q. Here the integral is used to predict the edge wave on axis behind a disk or an aperture. The time domain version of the Helmholtz–Kirchhoff integral is[8]

$$p(Q,t)=\frac{1}{4\pi}\int_S\left\{-\frac{1}{s}\left[\frac{\partial p}{\partial n}\right]+\frac{\partial}{\partial n}\left(\frac{1}{s}\right)[p]-\frac{1}{c_0 s}\frac{\partial s}{\partial n}\left[\frac{\partial p}{\partial t}\right]\right\}dS, \tag{1}$$

where c_0 is sound speed, t is time, s is the distance between Q and the surface element dS, $\partial()/\partial n$ is the normal derivative of $()$ on S (pointing inward), and brackets indicate that the quantity enclosed is to be evaluated at the retarded time $t-s/c_0$. Note that knowledge of the acoustic field on S means that p, $\partial p/\partial t$, and $\partial p/\partial n$ must be known there.

To use Eq. (1) to solve the aperture diffraction problem, begin with Fig. 1(a). The incident wave is a plane pressure disturbance of time waveform $f(t)$,

$$p_{\text{inc}}=f(t),$$

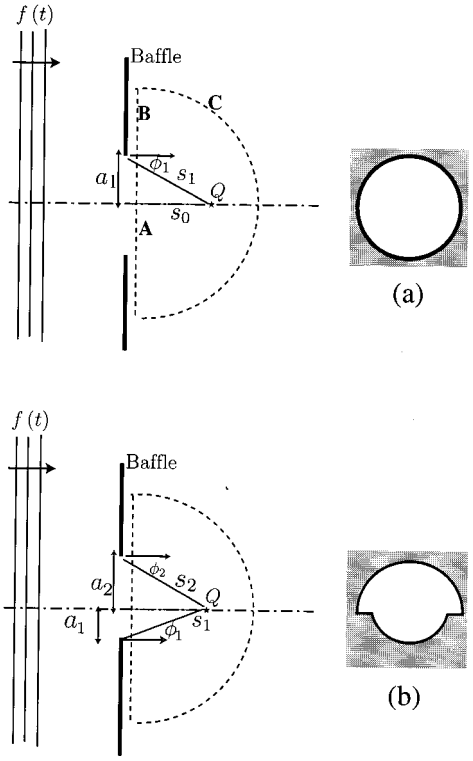

FIG. 1. Plane wave normally incident (a) on a circular aperture and (b) on a biradial aperture.

which is normally directed toward a circular aperture in an opaque baffle. In this section and the next, $t=0$ corresponds to the time the incident wave arrives at the aperture (in Sec. I C slightly different time origins are used). We wish to predict the pressure at point Q on axis behind the aperture and for this purpose use the Helmholtz–Kirchhoff integral. First take S to be the surface composed of elements A, B, and C as shown by the dashed lines in Fig. 1(a). If the radius of element C is made large enough that signals from it cannot reach Q in finite time, then the integral over C vanishes. Evaluation of the integrals over B and A requires the following assumptions (sometimes called Kirchhoff's boundary conditions[8]):

(1) On the back side of the baffle the pressure and its normal gradient are negligible. At least half of this assumption is justified if the baggle is either rigid or pressure release; the other half is justified for high frequencies, i.e., for wavelengths much smaller than the aperture radius.
(2) The pressure and its derivatives in the aperture itself have their free field values, that is, the scattered field in the aperture may be ignored.

Given assumption (1), the integral over B vanishes. Equation (1) thus reduces to an integral over surface A, which may be expressed as

$$p(Q,t)=\frac{1}{2}\int_{s_0}^{s_1}\left\{-\left[\frac{\partial p}{\partial n}\right]+\frac{s_0}{sc_0}\left[\frac{\partial p}{\partial t}\right]+\frac{s_0}{s^2}[p]\right\}ds, \tag{2}$$

where s_0 is the aperture-to-Q distance along the axis and s_1 is the rim-to-Q distance. Use of assumption (2) yields $[p]$

$=f$, $[\partial p/\partial t]=-c_0\partial f/\partial s$, and $[\partial p/\partial n]=\partial f/\partial s$, where the argument of f in each case is $t-s/c_0$. These substitutions render the integrand in Eq. (2) a perfect differential, and the final result, here called the total acoustic pressure p_T (notation explained below), is

$$p_T(Q,t)=f\left(t-\frac{s_0}{c_0}\right)-\Phi_1 f\left(t-\frac{s_1}{c_0}\right), \tag{3}$$

where $\Phi_1=\frac{1}{2}(1+\cos\phi_1)$ is called the obliquity factor,[11] and the diffraction angle ϕ_1 is defined in Fig. 1(a). As long as Q is more than a few aperture radii away from the aperture, the obliquity factor is approximately unity.

The physical interpretation of Eq. (3) is as follows. At Q the total received signal p_T is made up of the direct wave p_{direct} (the first term on the RHS), which has traveled a distance s_0 straight through the aperture. Arriving a little later and inverted (note the minus sign) is the edge wave (the second term), so-called because its travel distance s_1 is that from the edge to Q. Given this interpretation, Eq. (3) may be written

$$p_T(Q,t)=p_{\text{direct}}(Q,t)-p_{\text{edge}}(Q,t). \tag{4}$$

Notice that the edge wave is nearly as strong a signal as the direct wave. The strength is due to perfect coherence of all the arrivals from the rim when the aperture is circular.

If the aperture is replaced by an opaque disk, then by Babinet's principle the pressure at Q is given by

$$p_T(Q,t)=\Phi_1 f\left(t-\frac{s_1}{c_0}\right)=p_{\text{edge}}(Q,t), \tag{5}$$

which result may also be obtained directly by using the Helmholtz–Kirchhoff integral. The direct wave does not appear because it is blocked by the disk. The edge wave is the same as in Eq. (3), but without phase inversion.

In most of what follows, the edge wave is treated as a separate signal, resolved in time from the direct wave. The case in which the two waves are not resolved, i.e., when the duration of the incident wave exceeds $(s_1-s_0)/c_0$, is treated separately at the end of Sec. I C. Of course, for a disk the edge wave is the only signal.

B. Random-edge aperture

As explained in the Introduction, making the aperture ragged reduces the coherence of the edge wave and therefore decreases the axial pressure. To solve the ragged aperture problem, we begin by making small, deterministic changes in the circular perimeter. Biradial and triradial apertures are considered first. The random-edge aperture is then treated as a generalization of the multiradial aperture.

First some notation changes. Because for most of this section the edge wave is a completely separate signal (i.e., the edge and direct waves are assumed resolved), the subscript ''edge'' is now dropped. Instead, the simple symbol $p(Q,t)$ stands for the edge signal. Moreover, a circumflex ($\hat{}$) is used to denote pressure for a noncircular aperture. For example, $\hat{p}(Q,t)$ and $\hat{p}_{\text{rms}}$ are the pressure and its rms value for an edge wave produced by a noncircular aperture, whereas $p(Q,t)$ and p_{rms} are the corresponding values when the aperture is circular.

The biradial aperture shown in Fig. 1(b) has two semicircular edges, of radii a_1 and a_2. For this case the single integral in Eq. (2) is replaced by two integrals, which have upper limits s_1 (distance from the nearer edge to Q) and s_2 (distance from the farther edge), respectively, and the factor outside each integral is $\frac{1}{4}$ in place of $\frac{1}{2}$. The signal from the edge therefore has two components,

$$\hat{p}(Q,t)=\frac{1}{2}\Phi_1 f\left(t-\frac{s_1}{c_0}\right)+\frac{1}{2}\Phi_2 f\left(t-\frac{s_2}{c_0}\right), \tag{6}$$

where $\Phi_i=\frac{1}{2}(1+\cos\phi_i)$ is the obliquity factor for the ith edge (note that Φ_i depends on s_i). In terms of the edge signal p_i for a circular aperture, we have

$$\hat{p}(Q,t)=\tfrac{1}{2}p_1(Q,t)+\tfrac{1}{2}p_2(Q,t). \tag{7}$$

Because the two components have half the amplitude and arrive at different times, their sum is not as coherent as the edge wave for a single-radius aperture.

The triradial aperture produces a similar result. The rim is made up of three arcs of equal angle, $2\pi/3$ radians, but unequal radii a_1, a_2, a_3. The edge signal now has three $\frac{1}{3}$ amplitude components, which arrive at three different times. Coherence is thus further reduced.

The solution for biradial and triradial apertures may be extended to apertures or disks that have ragged edges. One may model a ragged edge as N arcs of equal angle (subtended from the center of the disk) but differing radii a_i. By extension of the previous results we obtain

$$\hat{p}(Q,t)=\frac{1}{N}\sum_{i=1}^{N}\Phi_i f\left(t-\frac{s_i}{c_0}\right)=\frac{1}{N}\sum_{i=1}^{N}p_i(Q,t). \tag{8}$$

Note that $p_i(Q,t)$ represents the edge wave for a circular aperture of radius a_i and thus includes the obliquity factor Φ_i. The various component signals p_i in the summation therefore have different amplitudes and different delay times.

Up to now all arc angles of the rim have been assumed equal. To generalize to unequal angles, let β_i be the angle of each arc. It may readily be seen that the solution is

$$\hat{p}(Q,t)=\frac{1}{N}\sum_{i=1}^{N}w_i\Phi_i f\left(t-\frac{s_i}{c_0}\right)=\frac{1}{N}\sum_{i=1}^{N}w_i p_i(Q,t), \tag{9}$$

where $w_i=\beta_i N/2\pi$ is a weighting factor to account for the contribution of each arc. For the special case of equal angles, β_i is $2\pi/N$, w_i is unity, and Eq. (8) is recovered.

Equation (8) [or (9)] is a complete description of the diffracted wave on axis behind a ragged-edge aperture or disk in the sense that all the information about the amplitude, waveform, and arrival time of each scattered component is given. The next step is to find means by which $\hat{p}$ and p may be compared for practical situations. The rms value of the pressure signals is proposed as a convenient and appropriate metric.

C. The rms pressure of the edge wave from a ragged-edge aperture

In this section a formula is derived to predict the rms value of the edge wave on axis behind a ragged-edge aperture or disk. The formula requires knowledge of the aperture geometry and the autocorrelation function of the incident signal (knowledge of the incident signal itself is not required). The formula reveals that the rms value of the edge wave behind a ragged-edge aperture is less than that behind a circular aperture. In the case of a disk, a ragged edge, by suppressing the strong on-axis signal, makes the disk a better shield.

The rms value p_{rms} and the autocorrelation $R_p(\tau)$ of a signal $p(t)$ are defined by

$$p_{\mathrm{rms}}^2=\frac{1}{t_{\mathrm{av}}}\int_0^{t_{\mathrm{av}}}p^2(t)dt, \tag{10}$$

$$R_p(\tau)=\frac{1}{t_{\mathrm{av}}}\int_0^{t_{\mathrm{av}}}p(t)p(t+\tau)dt, \tag{11}$$

where the integration time t_{av} depends on the type of waveform being considered. For periodic waves t_{av} is the period, for transient signals t_{av} is the duration of the transient, and for noise t_{av} must be ''a long time.'' The autocorrelation function is a measure of the similarity between the signal at times t and $t+\tau$, and it is an even function of the delay time variable τ:

$$R_p(-\tau)=R_p(\tau). \tag{12}$$

The rms value is associated with the intensity I of the wave (for progressive plane and spherical waves $I=p_{\mathrm{rms}}^2/\rho_0 c_0$). The rms value and the autocorrelation function are related by

$$R_p(0)=p_{\mathrm{rms}}^2, \tag{13}$$

where for all τ

$$R_p(0)\geqslant|R_p(\tau)|. \tag{14}$$

It should also be recalled that for periodic signals as well as for stationary noise the following is true:

$$p_{\mathrm{rms}}^2=\frac{1}{t_{\mathrm{av}}}\int_0^{t_{\mathrm{av}}}p^2(t)dt=\frac{1}{t_{\mathrm{av}}}\int_0^{t_{\mathrm{av}}}p^2(t+\tau)dt. \tag{15}$$

A formula is now derived to predict the rms value of the edge wave pressure behind a ragged-edge aperture $\hat{p}_{\mathrm{rms}}$ in terms of the rms pressure p_{rms} and the autocorrelation function R_p of the edge wave behind a circular aperture. The key is to express the solutions we have already found in a form convenient for calculating the rms value. After the formula for $\hat{p}_{\mathrm{rms}}$ is developed for a biradial aperture, the same procedure is used to obtain the prediction for a ragged-edge aperture. Finally, the formula is modified to include the case in which the edge wave is not resolved from the direct wave.

Up to this point no assumption has been made about the obliquity factors Φ_i. In order to simplify the calculation of $\hat{p}_{\mathrm{rms}}^2$, however, we now assume that the difference between the obliquity factors is small enough to be ignored. This assumption is satisfied if either (1) Q is several aperture radii away so that all the Φ_i are approximately unity or (2) the range of variation of the radii is small. Given this assumption, the signals p_i in Eq. (8) differ only by their delay times. To utilize the assumption about Φ and at the same time highlight the delay time differences, we introduce a new notation. The notation $p_i(Q,t)$ for the ith signal is replaced by $p(Q,t-\Delta s_i/c_0)$, where Δs_i is a difference in path length. Moreover, we redefine $t=0$ to correspond to the time of arrival of the first edge wave to reach Q. The first arrival is therefore represented by $p(Q,t)$, the second arrival by $p[Q,t-(s_2-s_1)/c_0]$, and so on.

Our first calculation of rms pressure is for the biradial aperture, for which the scattered pressure is given by Eq. (7), or, in terms of the new notation and time origin just introduced,

$$\hat{p}(Q,t)=\frac{p(Q,t)}{2}+\frac{p(Q,t-\tau)}{2}, \tag{16}$$

where $\tau=(s_2-s_1)/c_0$ is the time delay of the second edge wave, path s_2 in Fig. 1(b), relative to the first edge wave, path s_1. The rms value $\hat{p}_{\mathrm{rms}}$ may be found by substituting Eq. (16) into Eq. (10) and making use of Eqs (11), (12), and (15):

$$\hat{p}_{\mathrm{rms}}^2=\tfrac{1}{2}R_p(0)+\tfrac{1}{2}R_p(\tau). \tag{17}$$

To extend this approach to a ragged-edge aperture, we again start with the assumption that the ragged edge is made up of equal angle arcs. Equation (8) becomes

$$\hat{p}(Q,t)=\frac{1}{N}\sum_{i=1}^{N}p(Q,t-\tau_i), \tag{18}$$

where $\tau_i=(s_i-s_1)/c_0$ is the delay time for the ith arc. The same procedure used to produce Eq. (17) from Eq. (16) yields

$$\hat{p}_{\mathrm{rms}}^2=\frac{1}{N}R_p(0)+\frac{2}{N^2}\sum_{i=1}^{N}\sum_{j=i+1}^{N}R_p(\tau_j-\tau_i), \tag{19}$$

or, given Eq. (13),

$$\hat{p}_{\mathrm{rms}}^2=\frac{1}{N}p_{\mathrm{rms}}^2+\frac{2}{N^2}\sum_{i=1}^{N}\sum_{j=i+1}^{N}R_p(\tau_j-\tau_i). \tag{20}$$

The generalization to cover unequal arcs of the ragged rim is straightforward. The starting point is Eq. (9) and the result is

$$\hat{p}_{\mathrm{rms}}^2=\frac{p_{\mathrm{rms}}^2}{N^2}\sum_{i=1}^{N}w_i^2+\frac{2}{N^2}\sum_{i=1}^{N}\sum_{j=i+1}^{N}w_i w_j R_p(\tau_j-\tau_i). \tag{21}$$

The first term in Eq. (21) depends on the number and angle of the arcs that make up the rim. The second term depends on aperture geometry and the signal being diffracted. Again, the equation is in terms of the autocorrelation function of the incident signal, not the incident signal itself.

It is interesting to evaluate Eq. (21) when all time delays are zero:

$$\hat{p}_{\rm rms}^2=\frac{p_{\rm rms}^2}{N^2}\sum_{i=1}^{N} w_i^2+\frac{2}{N^2}\sum_{i=1}^{N}\sum_{j=i+1}^{N} w_i w_j p_{\rm rms}^2$$

$$=\frac{p_{\rm rms}^2}{N^2}\frac{N^2}{4\pi^2}\sum_{i=1}^{N}\beta_i^2+\frac{p_{\rm rms}^2}{N^2}\frac{N^2}{4\pi^2}\left(\sum_{i=1}^{N}\sum_{j=1}^{N}\beta_i\beta_j-\sum_{i=1}^{N}\beta_i^2\right)$$

$$=\frac{p_{\rm rms}^2}{4\pi^2}\sum_{i=1}^{N}\sum_{j=1}^{N}\beta_i\beta_j=p_{\rm rms}^2. \tag{22}$$

Two applications are the following. First, if Q is a finite distance from the aperture, all time delays zero means the aperture is circular; in this case Eq. (22) is just the expected result and simply constitutes a test of the consistency of Eq. (21). Second, all time delays approach zero when Q becomes very distant from the aperture. Equation (22) has a more substantive interpretation in this case: to an observer very far from the aperture, even a ragged aperture appears circular.

An important general conclusion: For any aperture geometry and any incident signal, Eqs. (14), (21), and (22) show that

$$\hat{p}_{\rm rms}^2\leqslant p_{\rm rms}^2. \tag{23}$$

Only for the special case in which $R_p(\tau_j-\tau_i)$ attains its maximum value for all τ_i and τ_j [Eq. (22)] does the second term in Eq. (21) take its maximum value to yield $\hat{p}_{\rm rms}^2=p_{\rm rms}^2$. If the aperture edge is irregular, the result is always $\hat{p}_{\rm rms}^2<p_{\rm rms}^2$. In the special case in which the incident wave is perfectly uncorrelated stationary noise, the second term in Eq. (21) is zero because the autocorrelation function vanishes ($\tau_j-\tau_i\neq 0$). Given the $1/N^2$ factor in front of the first term, $\hat{p}_{\rm rms}$ may be made increasingly small as the number N is made increasingly large.

Finally, we remove the restriction that the edge wave be resolved from the direct wave. The two waves overlap, for example, if the incident wave is a time harmonic, steady-state signal. Notation for the ensuing analysis is as follows: (1) $p_{T\rm rms}$ denotes the rms value of the complete signal p_T at Q, (2) $t=0$ corresponds to the time the direct wave arrives at Q, and (3) $\tau_i=(s_i-s_0)/c_0$ stands for the time delay (relative to the direct wave arrival) of the ith edge wave contribution. The calculation yields

$$p_{T\rm rms}^2=p_{\rm rms}^2+\frac{2}{N}\sum_{i=1}^{N} w_i R_p(\tau_i)+\frac{p_{\rm rms}^2}{N^2}\sum_{i=1}^{N} w_i^2$$

$$+\frac{2}{N^2}\sum_{i=1}^{N}\sum_{j=i+1}^{N} w_i w_j R_p(\tau_j-\tau_i), \tag{24}$$

where the two new terms (first two terms on the RHS) represent the direct wave and the edge wave-direct wave interaction, respectively. As an example, let the incident wave be time harmonic (angular frequency ω) and the aperture be circular. For this case we have $R_p(\tau)=p_{\rm rms}^2\cos\omega\tau$. Because all the delays are the same ($\tau_i=\tau$), the last two terms on the RHS reduce to $p_{\rm rms}^2$, as shown by Eq. (22). The final result is

$$p_{T\rm rms}^2=2p_{\rm rms}^2(1+\cos\omega\tau). \tag{25}$$

Thus $p_{T\rm rms}$ vanishes when the delay time is such that $\omega\tau=\pi$, which condition prevails when the edge wave arrives out of phase with the direct wave. At the other extreme, $\omega\tau=2\pi$ (the edge wave arrives in phase with the direct wave), Eq. (25) yields $p_{T\rm rms}=2p_{\rm rms}$. Although no such easy simplifications are available for ragged apertures, the general expression, Eq. (24), is still relatively easy to evaluate.

D. A spatial notch filter

Up to now the approach has been, given an edge profile, to find $\hat{p}_{\rm rms}$. However, the inverse problem is also of interest. An example is presented in this section, namely the design of an aperture or disk for which $\hat{p}_{\rm rms}$ vanishes at a specific axial position Q. Three assumptions are made: (1) the incident wave is a sinusoidal signal (frequency $f=\omega/2\pi$), (2) the edge of the aperture or disk is made up of N arcs of equal angle, and (3) Q is far enough from the aperture or disk that all obliquity factors Φ_i are unity.

The steps leading to the desired design are as follows. First, because the signal is a sinusoid, the autocorrelation function is

$$R_p(\tau)=p_{\rm rms}^2\cos\omega\tau, \tag{26}$$

and the rms pressure of the edge wave is given by Eq. (20). Next let the edge profile produce successive time delays that differ by a constant amount $\Delta\tau$, which is defined by $\tau_j-\tau_i=(j-i)\Delta\tau$. For this case the double summation in Eq. (20) reduces to the following single summation,

$$\hat{p}_{\rm rms}^2=\left(\frac{1}{N}+\frac{2}{N^2}\sum_{k=1}^{N-1}(N-k)\cos(k\omega\Delta\tau)\right)p_{\rm rms}^2. \tag{27}$$

It can be shown that the RHS vanishes if

$$\omega\Delta\tau=2\pi/N. \tag{28}$$

This relation may be used to specify an edge geometry that causes signals of frequency f to be nulled at the observation point Q. The aperture or disk then acts as a spatial notch filter.

Although the edge design to realize the notch filter is not unique, a simple approach is to use N radii that begin with the smallest value a_1 and increase monotonically to the largest value a_N. If a_1 is given, Eq. (28) may be satisfied by choosing all other radii a_i as follows:

$$a_{i+1}=\sqrt{\frac{2\lambda s_0}{N}+a_i^2}, \tag{29}$$

where s_0 is the axial distance from the disk or aperture to Q, and λ is the wavelength. The constant $2\lambda s_0/N$ determines the incremental change in edge radius and is termed the flare constant.

Observe that the effectiveness of the filter does not depend on N. As N increases, the difference between adjacent radii, a_i and a_{i+1}, decreases. Eventually, as N becomes very large, the profile of the disk converges to a smooth asymptotic profile. Figure 2 shows a filter designed by substituting the following values in Eq. (29): $f=500$ Hz, $c_0=1500$ m/s, $s_0=0.5$ m, $a_1=0.02$ m, and $N=500$.

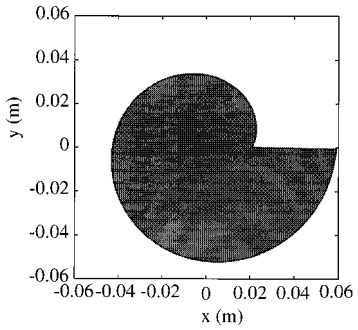

FIG. 2. A spatial notch filter.

E. Spherical wave incident on an aperture

Next consider the effect of changing the incident wave from plane to spherical. Axial symmetry is maintained by locating the spherical wave source at point S on axis in front of the aperture, while the observation point Q remains on axis behind the aperture; see Fig. 3. The Helmholtz–Kirchhoff integral may be evaluated to yield the following solution:[12,13]

$$p_T(Q,t)=\frac{r_1}{r_1+s_{01}}\left[f\left(t-\frac{s_{01}}{c_0}\right)-\Phi_1 f\left(t-\frac{s_1}{c_0}\right)\right]. \tag{30}$$

Here $f(t)$ is the incident wave at distance $r_1=SC$, where the spherical wavefront just touches the rim of the aperture, $s_{01}=CQ$ is the additional distance the incident wave travels to Q, and $\Phi_1=\frac{1}{2}(1+\cos\phi_1)$ is the obliquity factor.[14] A noticeable change from the plane wave solution, Eq. (3), is the appearance of the spherical spreading factor $r_1/(r_1+s_{01})$. However, observe that the factor is the *same* for both the direct wave and the edge wave. Also note the larger diffraction angle ϕ_1 when the incident wave is spherical (see Fig. 3) and consequently the smaller obliquity factor.

Because the spherical spreading factor for the edge wave is the same as that for the direct wave, it follows that only the change in obliquity factor Φ_1 affects the edge wave when the aperture is made larger or smaller. It is therefore very simple to convert the results for plane incident waves to equivalent ones for spherical incident waves.

For example, consider the biradial aperture. Recall that Eq. (6) gives the plane wave result for this case. Now let the incident wave be spherical. Imagine Fig. 3 to be modified so that the lower edge (edge 1) represents the smaller semicircle of the biradial aperture, while the upper edge (edge 2) represents the larger semicircle. The distances s_1 and s_2 are the same as in Fig. 1(b). Distance s_{02} is analogous to s_{01} in Fig. 3 but pertains to the upper edge. Let $f(t)$ describe the incident wave when it reaches edge 1. At this instant the incident wave is still a distance $s_{01}-s_{02}$ away from edge 2. If the delay (relative to the direct wave) for the edge 1 signal is s_1/c_0, then that for the edge 2 signal is $[s_2+(s_0-s_{02})]/c_0$. The predicted edge wave signal for the biradial aperture is therefore

$$\hat{p}(Q,t)=\frac{r_1}{r_1+s_{01}}\left[\frac{\Phi_1}{2}f\left(t-\frac{s_1}{c_0}\right)+\frac{\Phi_2}{2}f\left(t-\frac{s_2+s_{01}-s_{02}}{c_0}\right)\right]. \tag{31}$$

This result may also be obtained by direct evaluation of the Helmholtz–Kirchhoff integral. Next let the same changes described in the paragraph preceding Eq. (16) be made here, i.e., let differences in obliquity factors be assumed negligible, and $t=0$ be taken to be the time the first edge wave arrives at Q. Equations having the same form as Eqs. (16) and (17) follow except that now the function $p(Q,t)$ carries the appropriate spherical spreading factor, and $\tau=(s_2+s_{01}-s_{02})/c_0$.

The extension to a ragged aperture follows that for plane incident waves. In the experiment reported below, both source and receiver were far enough away from the aperture that for simplicity all the obliquity factors were approximated by unity. The plane wave formulas were therefore used to make theoretical predictions, for example, Eq. (21) in the case of a ragged aperture. However, delay times and spherical spreading appropriate for a spherical incident wave were used.

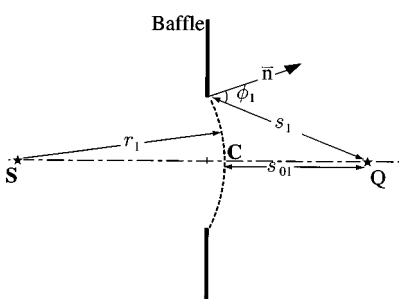

FIG. 3. Spherical wave normally incident on a circular aperture.

II. EXPERIMENT

Diffraction measurements were carried out in a water tank, length 57 cm, width 29 cm, depth 25 cm. A short, spherically diverging pulse was diffracted by an aperture in a plate and measured by a receiver on the other side of the plate. Source and receiver were both 8 cm from the plate on the axis of the aperture. Figure 4 shows a diagram of the experiment. Apertures with five different shapes were measured with this apparatus.[15]

The source was an underwater spark, produced at the open end of a coaxial cable (RG 58 A/U) when energy stored at 8 kV in a 0.1 μF capacitor was dumped across a triggered air gap onto the center lead of the cable. The left side of Fig. 4 shows the electronics used to charge the capacitor and trigger the airgap switch. More details about the source are given by Bailey.[2] The pressure disturbance generated by the spark was an apparently positive pulse. The inevitable negative tail was not measurable with the equipment available to us;[16] see also Campbell *et al.*[17]

Each aperture was an opening in an acoustically opaque plane barrier. The barrier was a sheet, $15\times23\,\mathrm{cm}^2$, of 1.59-mm-thick corprene, glued to a 2.29-mm-thick aluminum plate. The opacity of the plate was due to the corprene, which, because of its high cork content, acted as a pressure release surface. The aluminum sheet served mainly to provide mechanical support (by itself corprene tends to curl). Measurements showed that transmission through the plate itself was negligible. The control aperture was a 5-cm-diam

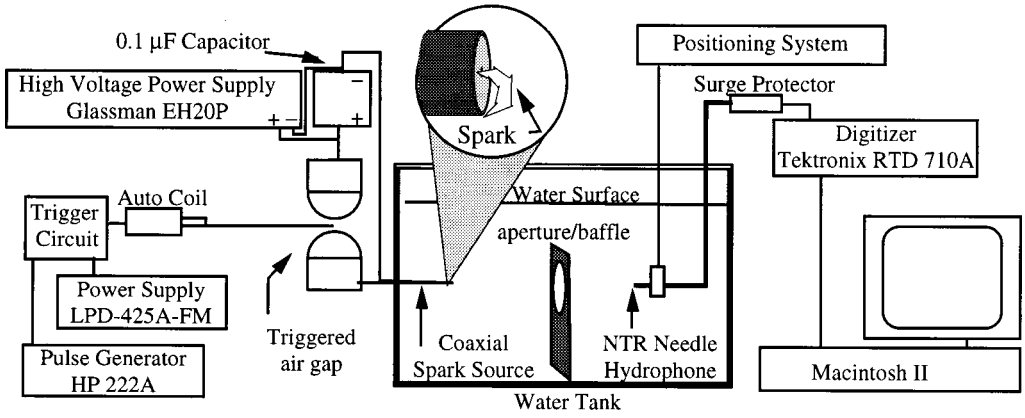

FIG. 4. Experimental apparatus.

circular hole cut in the plate [see the inset in Fig. 5(a)]. The obliquity factor for this aperture (see Fig. 3) was $\Phi_1 = 0.91$.

Noncircular apertures were cut from corprene sheet. Each was used as a mask, held in place by rubber bands, over the circular aperture. The insets in Fig. 5(b)–(e) show the different shapes that were used:

(i) Biradial—two semicircular arcs, radii 2.5 and 1.8 cm,
(ii) Triradial—three 120 degree arcs, radii 2.5, 2.0, and 1.5 cm,
(iii) Fringed or ''sunburst''—minimum radius 2.2 cm, maximum 2.35 cm,
(iv) Ragged—radius varies from 2.5 to 0.9 cm.

Tests with several ragged-edge apertures yielded similar results. The aperture shown in Fig. 5(e) is representative. The obliquity factor for the various apertures varies from 0.91 (radius 2.5 cm) to 0.99 (radius 0.9 cm).

The receiver, an NTR TNU 100A piezoceramic needle hydrophone having an active spot size (geometrical diameter) of 1.5 mm, was used to measure the sound field on axis. The time window was large enough to display both the direct wave and the edge wave. The frequency response of the hydrophone was peaked near 1 MHz, and 1 MHz ringing can be seen following the signals. Whenever the waveform had an abrupt initial rise (a shock), poor high-frequency response of the hydrophone caused the rise to be rounded.[18] Waveforms were recorded on an Sony Tektronix RTD 710A digitizer, saved to a computer via LabVIEW software (National Instruments, Austin, TX), and plotted by means of MatLab (The MathWorks, Natick, MA).

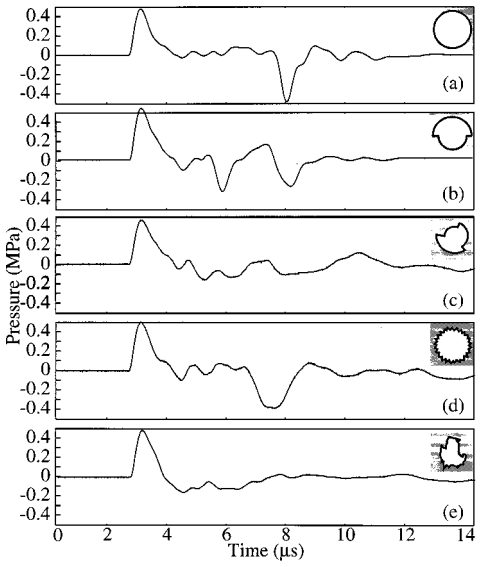

FIG. 5. Experimental time waveforms behind apertures of various shapes.

III. EXPERIMENTAL RESULTS. COMPARISON WITH THEORY

The measured pressure waveforms are displayed in Fig. 5. Measurements are shown for the five different aperture shapes described: circular, biradial, triradial, sunburst, and ragged. In each case the positive-pulse direct wave and the diffracted wave are resolved. Because of the geometry of the experiment, the approximation $\Phi = 1$ was used in comparing measured results with theoretical predictions. As explained at the end of Sec. II, formulas for plane incident waves, appropriately modified for spherical waves, were used for the predictions.

The waveform for the circular aperture (the control in the experiment) is presented in Fig. 5(a). In the main, the theoretical prediction, Eq. (3), is confirmed. The edge wave is a near replica, inverted, of the incident wave. Deviations from theory are minor. The slightly lower amplitude and longer duration of the direct wave may possibly be due to nonlinear propagation distortion, which would be expected to affect the direct wave more than the edge wave, since the latter is not a strong signal until it reaches the axis. The low level disturbance following both pulses is similar to that observed by Carstensen *et al.*[19] and may be due to the presence of residual bubbles at the source and/or the receiver.

The deterioration of the edge wave for noncircular apertures is easily seen in Fig. 5(b)–(e). The biradial aperture [Fig. 5(b)] generates two edge wave components, which have half the amplitude and are displaced from each other. Equation (7) is confirmed. Similarly, the triradial aperture [Fig. 5(c)] produces three one-third amplitude components. The trend toward a smearing out of the diffracted signal is clear. In the case of the sunburst aperture [Fig. 5(d)], how-

TABLE I. Measured rms values of direct and diffracted signals for five apertures.

Aperture	Direct rms (MPa)	Diffracted rms (MPa)	Difference (dB)
Circular	0.250	0.267	0.6
Bradial	0.296	0.140	−6.5
Triradial	0.264	0.088	−9.6
Sunburst	0.256	0.243	−0.5
Ragged	0.309	0.083	−11.4

ever, the variation in aperture radius is too small to have much effect. The edge pulse is still strong but somewhat broadened. Finally, Fig. 5(e) shows the result for the ragged-edge aperture. The high degree of incoherence of the scattered signals produces an edge wave so low in amplitude and long in duration that it can hardly be discerned from the background noise.

Table I provides a quantitative comparison of the direct and diffracted signals for each aperture. The entries are rms values computed from the measured waveforms. Variations in the rms value for the direct wave are due to jitter of the spark source, which causes a small variation in acoustic output from firing to firing. The data in the table confirm qualitative conclusions based on inspection of the waveforms in Fig. 5. The edge wave behind the circular aperture is strong. It is almost as strong for the sunburst aperture, for which the small fluctuation in radius produces an arrival time variation that is small compared to the pulse duration. The coherence of the diffracted wave decreases progressively, and the signal itself therefore weakens, as we progress from the biradial aperture to the triradial aperture to the ragged-edge aperture. For the latter the 11.4-dB drop of the edge wave is particularly striking.

Next measured and predicted rms values of the edge waves are compared for the four noncircular apertures. Predicted values are obtained from Eq. (21); values of τ_i and w_i were found by measuring the perimeter variation of the aperture used. In evaluating Eq. (21), we used the value of p^2_{rms} from the circular aperture measurement. Table II gives the results. The measured and predicted rms values appear to be in reasonably good agreement. Possible causes for disagreement are as follows. First, failure to include obliquity factor variation reduced the adequacy of Eq. (21) somewhat. Second, when the rms value of a measured signal was calculated, noise in the measured pressure signature made it difficult to select with precision the beginning and end of the signal. Third, to evaluate Eq. (21) for the noncircular apertures, we used the value of p^2_{rms} from the circular aperture measurement, which was from a different spark; some error was therefore introduced by spark jitter. Given these uncertainties, the results in Table II provide encouraging quantitative support to accompany the qualitative evidence shown in Fig. 5.

TABLE II. Comparison of predicted and measured rms values for edge waves from four apertures.

Aperture	Predicted rms (MPa)	Measured rms (MPa)	Difference (dB)
Biradial	0.140	0.118	−1.5
Triradial	0.088	0.078	−1
Sunburst	0.243	0.226	−1
Ragged	0.083	0.061	−2.7

IV. DISCUSSION AND SUMMARY

Diffraction by a ragged aperture is similar to diffraction by a circular aperture when the receiver Q is off axis. For both apertures, variation in the rim-to-Q distance decreases coherence of the scattered signals that arrive from the edge. Although the variation is random in one case but deterministic in the other, the net result is the same. How then do the two apertures differ in their scattering effect? The difference is that the circular aperture offers perfect coherence along its axis, whereas perfect coherence exists nowhere behind a ragged aperture. If the goal is a weak edge wave everywhere, therefore, the choice must be the ragged aperture.

This discussion brings up the question of what is meant by the axis for a ragged aperture.[6] We have used the axis for a circular aperture and maintained that location without regard to changes in the aperture profile. The choice was arbitrary (made for convenience), since no perpendicular line passing through a ragged aperture is more special than any other. Although it might be appealing to define axis as the perpendicular passing through the centroid of the aperture, it is difficult to imagine that such a definition would materially alter the results found in this paper. We therefore argue that the axis adopted in this paper is as good as any other.

Although apertures are stressed in this paper, a noncircular profile has the same effect on the edge wave from a disk. In applications where complete blocking of an incident wave is desired, a ragged disk would be particularly effective. An attractive aperturelike application would be to baffled piston radiators. A ragged mask used to make a circular piston into a ragged-edge piston should (1) greatly reduce sidelobes in the farfield and (2) make the nearfield much more uniform, since the axial peaks and nulls would be smoothed out.

The work presented in this paper may be summarized as follows. A formula based on the Helmholtz–Kirchhoff integral theorem has been derived for the rms value of the edge wave on axis behind an aperture (or a disk) having a ragged edge. Incident waves may be plane or spherical (source on axis), and the signal may be a sinusoid, a pulse, or noise. Knowledge of the aperture geometry is required, as well as the autocorrelation function of the incident wave. The prediction shows that the rms value of the edge wave behind a noncircular aperture is less than that behind a circular aperture. The difference increases as the aperture profile is made more ragged, provided the delay time variations are not small compared to the characteristic period of the incident wave. The design of a spatial notch filter—an aperture or disk for which the rms value of the edge signal vanishes (for a given frequency and receiver location)—has been demonstrated. Underwater experiments made with a spark source and various apertures show the effect of the ragged edge on the diffracted wave. The theoretical predictions agree reasonably well with the experimental measurements.

ACKNOWLEDGMENTS

This work was supported by the Texas Advanced Technology Program and by the U.S. Office of Naval Research. All computations were performed on Sparc 2000 SUN stations provided by the Applied Research Laboratories. The advice of Ilene Busch-Vishniac is appreciated as are the many helpful discussions the third author (DTB) had with E. L. Carstensen's group at the University of Rochester.

[1] M. R. Bailey and D. T. Blackstock, ''Isolation of a negative-pressure pulse by means of diffraction,'' in *Advances in Nonlinear Acoustics: 13th ISNA*, edited by H. Hobaek (World Scientific, Singapore, 1993), pp. 158–163.

[2] M. R. Bailey, ''Isolation of a Negative-Pressure Pulse and Studies of Irregular-Edge Diffraction,'' M.S. thesis, The University of Texas at Austin, 1994.

[3] M. R. Bailey, D. Dalecki, S. Z. Child, C. H. Raemon, D. P. Penney, D. T. Blackstock, and E. L. Carstensen, ''Bioeffects of positive and negative acoustic pressures *in vivo*,'' J. Acoust. Soc. Am. **100**, 3941–3946 (1996).

[4] S. S. T. Ho, I. J. Busch-Vishniac, and D. T. Blackstock, ''Noise reduction by a barrier with a random edge profile,'' J. Acoust. Soc. Am. **101**, 2669–2676 (1997).

[5] P. Menounou, ''Theoretical Study of Diffraction by Straight and Ragged Edge Noise Barriers,'' Ph.D. dissertation, The University of Texas at Austin, 1998.

[6] Although the terms ''center'' and ''axis'' are unambiguous for a circular aperture or disk, they have no clearcut meaning when the aperture or disk has no center of symmetry. In this paper the circular edge is used for reference. We therefore continue to use the original center and axis after the edge has been modified.

[7] J. C. Piquette, ''An analytical technique for reducing the influence of edge diffraction in reflection measurements made on thin acoustical panels,'' J. Acoust. Soc. Am. **80**, 19–27 (1986).

[8] M. Born and E. Wolf, *Principles of Optics*, 3rd ed. (Pergamon, New York, 1965), pp. 375–382.

[9] A. D. Pierce, *Acoustics: An Introduction to Its Physical Principles and Applications* (Acoustical Society of America, American Institute of Physics, New York, 1989).

[10] F. B. Sleator, ''The disc,'' in *Electromagnetic and Acoustic Scattering by Simple Shapes*, edited by J. J. Bowman, T. B. A. Senior, and P. L. E. Uslenghi (North-Holland, Amsterdam, 1969).

[11] B. Rossi, *Optics* (Addison-Wesley, Reading, MA, 1957), p. 21.

[12] C. L. Andrews, *Optics of the Electromagnetic Spectrum* (Prentice–Hall, Englewood Cliffs, NJ, 1960), pp. 258–264, 483–487.

[13] H. A. Wright, ''Time-domain analysis of broad-band refraction and diffraction,'' J. Acoust. Soc. Am. **46**, 661–666 (1969).

[14] For a derivation that includes absorption by the medium, see M. O. Anderson, ''The propagation of a spherical *N* wave in an absorbing medium and its diffraction by a circular aperture,'' Technical Report ARL-TR-74-25, Applied Research Laboratories, The University of Texas at Austin, 1974 (AD787878).

[15] The same apparatus was also used to measure diffraction by disks, both circular and ragged, and barriers, both straight and ragged. See Refs. 1 and 2.

[16] A property of a spherical pulse is that $\int_0^\infty p\,dt = 0$; see, for example, L. D. Landau and E. M. Lifshitz, *Fluid Mechanics* (Addison-Wesley, Reading, MA, 1959). This requirement is not violated if the negative tail is long but so weak that it is lost in the measurement noise.

[17] D. S. Campbell, H. G. Flynn, D. T. Blackstock, C. Linke, and E. L. Carstensen, ''The acoustic fields of the Wolf electrohydraulic lithotripter,'' J. Lithotripsy Stone Dis. **3**, 147–156 (1991).

[18] In other measurements the pulse from the source can be seen to begin as a true shock having a much faster rise time than shown here (Ref. 17).

[19] E. L. Carstensen, D. S. Campbell, D. Hollman, S. Z. Child, and E. J. Aymé-Bellegarda, ''Killing of *drosophilia* larvae by the fields of an electrohydraulic lithotripter,'' Ultrasound Med. Biol. **16**, 687–698 (1990).

Backscattering enhancements from Rayleigh waves on the flat face of a tilted solid cylinder in water

Karen Gipson[a] and Philip L. Marston[b]
Department of Physics, Washington State University, Pullman, Washington 99164-2814

(Received 7 August 1999; accepted for publication 1 October 1999)

When the face of a finite solid elastic cylinder is ensonified by an acoustic wave, a variety of backscattering contributions associated with acoustic wave coupling into elastic waves are observed. A significant backscattering enhancement is observed for tilts such that the acoustic wave is incident on the face of the cylinder in the vicinity of the coupling angle for launching Rayleigh waves across the face. The observed backscattering indicates that the Rayleigh waves are reflected at the edge of the face and subsequently radiate acoustic waves in the backscattering direction. The measured backscattering is compared to an approximate theoretical prediction. Approximating the focusing of the Rayleigh wave after reflection at the (circular) edge by a Gaussian beam pressure distribution on the cylinder's face yields simple expressions for the amplitude which are consistent with the measurements. In the vicinity of end-on incidence, other backscattering contributions due to the reflection of waves traveling down the length of the cylinder are observed. There is also evidence of a face-traversing longitudinal wave for slightly tilted cylinders. © *2000 Acoustical Society of America.* [S0001-4966(00)04601-4]

PACS numbers: 43.20.Fn, 43.30.Gv, 43.35.Pt [ANN]

INTRODUCTION

This investigation concerns high-frequency scattering processes which become important for backscattering by flat-ended solid cylinders at near end-on incidence. Previous investigations (e.g., Refs. 1 and 2) have emphasized waves which are transmitted down the length of the cylinder. At high frequencies there are several symmetric and antisymmetric modes supported by elastic cylinders, as reviewed in Refs. 3 and 4. While the present investigation includes evidence for various modes which have reflected from the far end of the cylinder, the emphasis is on a mechanism which becomes important for a range tilts sufficiently off of end-on incidence: a face-traversing Rayleigh wave. Our investigation of this Rayleigh wave contribution was stimulated by qualitative observations of the backscattering over a wide range of angles and frequencies shown in Fig. 1 for a solid steel rod in water. We previously investigated meridional ray contributions for this cylinder which occur for a different range of tilt angles than emphasized here.[5,6] In the figure $\gamma=0$ degrees corresponds to broadside and ka is the dimensionless frequency (wave number k multiplied by radius a). These data were obtained using an impulsive pressure PVDF sheet source in the same experimental configuration described in Ref. 7. The meridional ray contribution is evident near $\gamma=30$ degrees, and contributions from end-reflected helical Rayleigh waves[8,9] are evident for $\gamma<30$ degrees. Constructive interference associated with diffraction by the edges of the two ends of the cylinder produce the hyperbolic arcs[8] visible for $\gamma<20$ degrees and $ka<15$ while diffraction by the edges of the cylinder's closest face produce the lower arcs visible for $\gamma>45$ degrees.

A significant feature of Fig. 1 is the strong backscatter occurring in the angular vicinity of $\gamma=60$ degrees for a wide range of ka. This feature results from the reflection of Rayleigh waves launched on the cylinder's face. As illustrated in Fig. 2, a leaky Rayleigh wave will be launched on the cylinder's face when an acoustic wave is incident on the face of the cylinder such that its projection on the face satisfies the condition[10,11] $\theta_R=\sin^{-1}(c/c_R)=30.75$ degrees, where c is the speed of sound in water and c_R is the speed of the leaky Rayleigh wave at the water–steel interface. When the leaky wave reaches the edge of the cylinder's face, it will be partially reflected, and by reciprocity the resulting reversal of the wave vector will give rise to radiation leakage in the backscattering direction, also shown in Fig. 2. Since the face of the cylinder is flat, the wavefront of the Rayleigh wave is straight-crested prior to reflection for plane-wave incidence. However, as shown in Fig. 3(a), the circular curvature of the reflecting edge gives rise to a focusing of the reflected rays. The convolution method of Ref. 12 may be used to describe the launching of the leaky Rayleigh waves, but the effects of focusing must be accounted for in predicting the backscattered pressure amplitude. It will be seen in Sec. III that modeling the focusing as a Gaussian beam pressure distribution as shown in Fig. 3(b) yields a reasonable prediction of the far-field backscattered form function magnitude. With modification (to account for two-sided fluid loading[12]) the model should also apply to leaky wave backscattering enhancements from tilted circular discs.

In addition to coupling into Rayleigh waves, an acoustic wave incident on the cylinder's face at an arbitrary angle is expected to launch longitudinal waves within the cylinder's body up to the cutoff angle given by[11] $\theta_L=\sin^{-1}(c/c_L)$, where c_L is the speed of longitudinal waves. For most aspect angles, longitudinal waves undergo multiple reflections before radiating acoustic waves which are oriented in the back-

[a]Present address: Department of Physics, Grand Valley State University, 1 Campus Drive, Allendale, MI 49401.
[b]Electronic mail: marston@wsu.edu

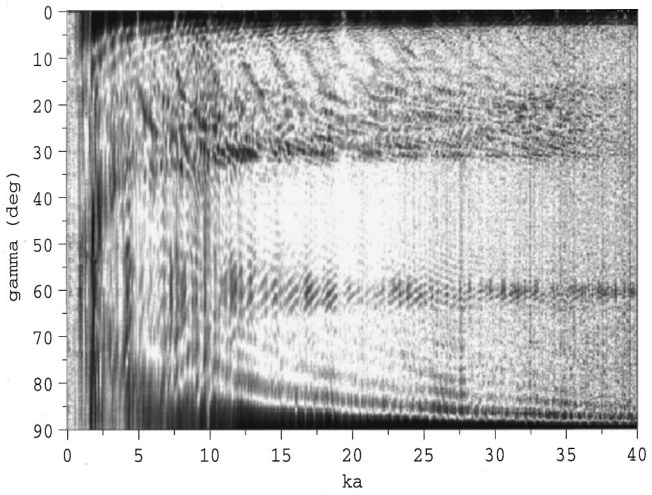

FIG. 1. Frequency scan of backscattering for a tilted solid steel cylinder, where broadside is defined as $\gamma=0$ degrees. Regions of strongest backscattering appear dark. Various elastic and geometric effects are visible, as noted in the Introduction.

scattering direction, so their amplitudes are significantly decreased due to mode conversion and wavefront spreading introduced by repeated reflections from curved surfaces. Therefore, backscattering contributions due to internally reflected longitudinal waves are usually expected to be weak. However, there are two conditions under which longitudinal waves will give rise to radiation in the backscattering direction after only one reflection: (i) for end-on incidence the acoustic wave launches a longitudinal wave down the length of the cylinder and its subsequent reflection at the opposite end of the cylinder gives rise to a backscattering contribution, and (ii) a longitudinal wave launched in the vicinity of the cutoff angle propagates across the face of the cylinder corresponding to a longitudinal lateral wave[11,13] and, after reflecting at the edge of the face, such a wave leaks radiation in the backscattering direction. The existence of waves which propagate down the bar at velocities close to c_L for high frequencies is reviewed, e.g., by Thurston.[4]

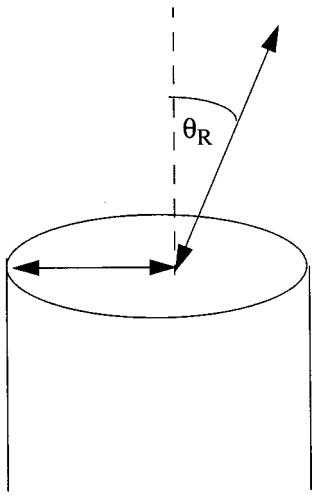

FIG. 2. Launching and reradiation of leaky Rayleigh waves on the face of a cylinder. Leaky Rayleigh waves are launched when the acoustic wave is incident in the vicinity of the coupling angle θ_R, and by reciprocity radiation leaks off at the same angle.

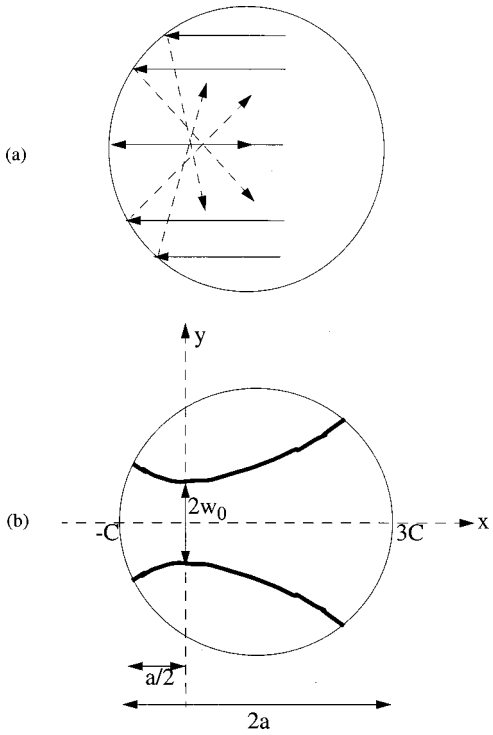

FIG. 3. Focusing of Rayleigh rays after reflection from the edge of the face. (a) Because parallel rays launched at different points on the face will be incident on the edge of the face at different angles, a focusing of the rays will occur. The aberration of the focus due to the circular nature of the edge of the face as shown in (a) is represented by the Gaussian beam pressure distribution shown in (b), where the beam waist is located at the focal plane $x=0$. If the radius of the cylinder is a, the focal plane is a distance $C=a/2$ from the central reflection point $x=-C$. The arcs represent equiamplitude contours in the limit of negligible attenuation. Subsequent reflections from the far edge are not included as explained in Sec. III.

In Sec. I we describe the relevant experiments, and the resulting data display the expected backscattering enhancements. In Sec. II we demonstrate that comparisons of the time returns of the various backscattering enhancements with predictions based on the dimensions of the cylinder and the known speeds for the various elastic waves support the interpretations discussed above, and in Sec. III we present a comparison of the measured backscattered pressure associated with the Rayleigh wave reflected diagonally across the face to an approximate theoretical prediction.

I. OBSERVED BACKSCATTERING CONTRIBUTIONS

Tone-burst scattering experiments were conducted using the same setup described in Ref. 6, and the target was the same stainless steel cylinder described there. The cylinder had a length of 254 mm and a radius of 19.0 mm and was composed of stainless steel 304. The elastic wave speeds for SS304 and those of the surrounding water are given in Table I and are needed to determine the coupling angles associated with the various mechanisms under investigation. A piston transducer (Parametrics model V302) was used as both source and receiver. The source-receiver and target were centered in the tank and separated by a distance of 168 cm in order to approximate plane wave incidence on the cylinder's face while ensuring that reflections from the tank walls were temporally distinct from the signals backscattered by the cyl-

TABLE I. Wave speeds (mm/μs). The elastic and acoustic wave speeds are needed to determine the coupling angles and predict the time delays associated with acoustic wave coupling into the elastic waves.

Cylinder (SS304)			
Tabulated		Derived	Water
Longitudinal wave	Shear wave	Rayleigh wave	Acoustic wave
5.675	3.141	2.904	1.485

inder. The envelope of the tone bursts was sufficiently rectangular that there was significant spectral content spread from the carrier frequency. The received signal was averaged over many pings by a digital oscilloscope.

The measurements were performed at experimentally determined optimum frequencies of the transducer: 620 kHz and 1.03 MHz, corresponding to *ka* of 50 and 83, respectively. The zero angle in these experiments was taken to be end-on incidence. Figure 4 shows an angular scan of backscattered pressure for 12 cycle tone bursts at 620 kHz; this 40-degree scan was recorded at 0.25-degrees steps. From the data in Table I, we obtain the longitudinal wave cutoff angle as 15.2 degrees and the Rayleigh wave coupling angle as 30.7 degrees. Thus we see that the expected features are evident in Fig. 4: (a) the first delayed echo in the angular region near 0 degrees supports the interpretation of a longitudinal wave down the length of the cylinder, (b) the weak signal observed coincident in time with the specular reflection from the far edge of the face for incidence in the angular region near 15 degrees supports the interpretation of a longitudinal wave across the face of the cylinder, and (c) the prominent signal observed coincident in time with the specular reflection from the far edge of the face for incidence in the angular region near 30 degrees supports the interpretation of a Rayleigh wave launched on the cylinder's face. In addition, the prominent signal occurring near the end of the time window for a wide range of tilt angles suggests the possibility of coupling into higher-order axisymmetric modes which propagate down the cylinder. The frequency is significantly higher than the threshold for the higher-order modes,[4] and some of the modes have group velocities in the appropriate range.[14,15] Phase velocities as a function of *ka* have been plotted for the lowest modes of this cylinder.[5]

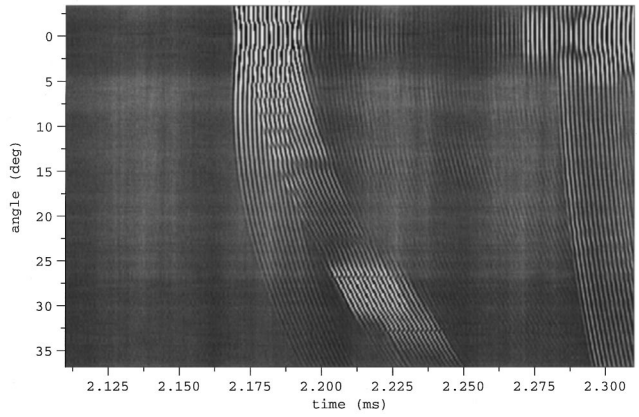

FIG. 4. Scan in tilt for 12 cycle tone bursts at 620 kHz. Zero backscattering is gray. Individual time records for a 40-degree scan at 0.25-degree steps have been cascaded in order to display the angular evolution of the backscattered pressure. End-on incidence corresponds to 0 degrees in these data, and the face-traversing longitudinal and Rayleigh reflections discussed in the text are evident near tilts of 15 and 30 degrees, respectively. The contributions which merge with the specular reflection at 0 degrees and 2.17 ms correspond to diffraction by the edges of the cylinder closest to the source. The longitudinal contribution near 15 degrees is associated with a variation in the signal contrast near 2.19 ms. It is also evident in a scan at 1.03 MHz (Ref. 8) but is always much weaker than the Rayleigh wave feature.

II. COMPARISONS OF OBSERVED TIME RETURNS TO THEORETICAL EXPECTATIONS

In order to identify scattering contributions, individual time traces in the angular vicinities of end-on incidence (0 degrees), the longitudinal wave cutoff angle (15 degrees), and the coupling angle for the Rayleigh waves (30 degrees) were carefully analyzed. Examples of individual time traces appear in Ref. 8, but the features of interest are all visible in Fig. 4.

The 0-degree region of Fig. 4 corresponds to end-on incidence, with the signal at 2.171 ms identified as the specular return from the face. The signal arriving 90 μs after the specular return is consistent with the predicted time of 89.5 μs for an end-reflected longitudinal wave down the length of the cylinder using the wave speeds in Table I. Also visible in Fig. 4 are stronger subsequent echos which are only slightly delayed from the longitudinal return. Figure 4 shows that one of these signals does not degrade when the cylinder is tilted. This signal is likely due to coupling into higher-order elastic modes of the cylinder.[4,14,15]

From Table I, the predicted cutoff angle for the longitudinal wave is $\theta_L = \sin^{-1}(c/c_L) = 15.2$ degrees. At this angle, a longitudinal wave is expected to propagate across the diagonal of the cylinder's face. This wave across the face is expected to arrive at the same time as an acoustic wave diffracted by the far edge of the face. Inspection of Fig. 4 in the vicinity of 15 degrees from end-on-incidence suggests that this expectation is confirmed; the figure shows an additional return interfering with diffracted returns from the edges of the cylinder's face for incidence near the longitudinal wave cutoff angle. The interference between the reflected longitudinal wave and the diffraction from the edges of the face renders a quantitative determination of the magnitude of the longitudinal reflection difficult, but the observed time delay of 12 μs after the leading diffracted return from the near edge of the face is close to the prediction of 13.4 μs.

Inspection of Fig. 4 in the vicinity of 30 degrees shows a large return approximately 27 μs after the diffracted return from the near edge of the face, which is consistent with the theoretical value of 26.2 μs for a reflected face-traversing Rayleigh wave, based on the diameter of the cylinder and the wave speeds given in Table I. The optimum coupling angle associated with this signal was determined by plotting the average peak pressure (measured near the center of the return) as a function of tilt angle. The results for frequencies of 620 KHz and 1.03 MHz, normalized as explained in Sec. III, are shown in Fig. 5. The observed optimum coupling angles are 28.5 degrees at 1.03 MHz and 29 degrees at 620 kHz. The observed optimum angles are expected to be shifted be-

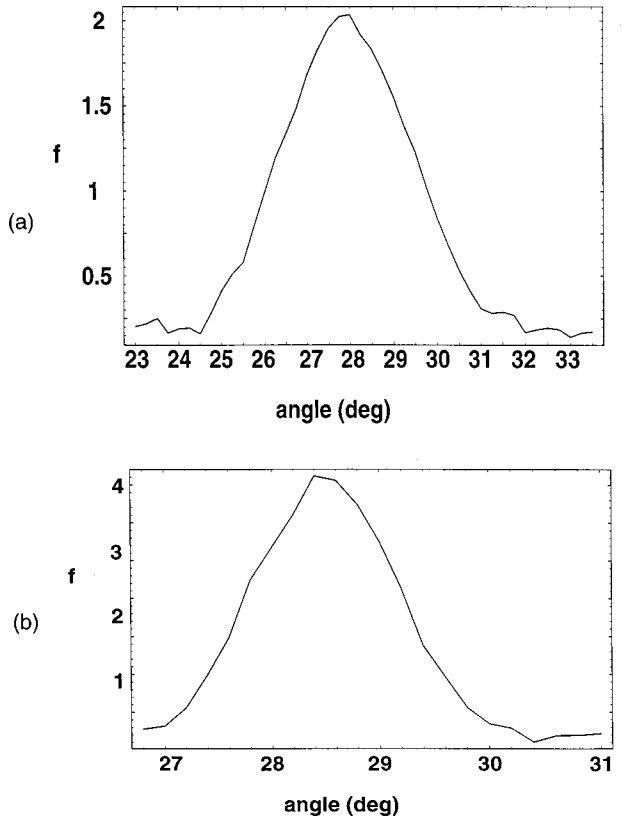

FIG. 5. Dephasing of measured form function moduli for the face-traversing reflected Rayleigh wave contribution at (a) 620 kHz and (b) 1.03 MHz. The peak magnitudes are greater than unity and indicate significant backscattering enhancements.

low the predicted value of 30.75 degrees as a consequence of a geometric shift due to the finite distance to the source.[6,16]

III. COMPARISON OF OBSERVED REFLECTED RAYLEIGH WAVE FORM FUNCTION TO THEORY

The convolution method of Ref. 12 can be used to analyze the launching of the Rayleigh wave on the face; Fig. 3(a) shows, however, that the curvature of the reflecting edge of the face will give rise to focusing of the reflected rays, which will affect the amplitude of the backscattered pressure. In the present application of the method of Ref. 12, the effects of focusing are approximated as giving rise to a Gaussian beam pressure distribution on the face of the cylinder, as shown in Fig. 3(b). This is a reasonable approximation of the imperfect focusing known to result from reflection from a circular (as opposed to parabolic) surface, where the Gaussian beam waist occurs at the geometric focus of the circular reflecting edge. The focal distance is[17] $C=a/2$, where a is the radius of curvature of the circular reflector (in this case the radius of the cylinder). Losses upon reflection are approximated using a reflection coefficient corresponding to normal incidence on a vacuum-backed elastic quarter-space.[18] The use of this coefficient is motivated by the large density of steel compared to water.[5,8,16] Neglecting the angular dependence of the reflection coefficient greatly simplifies the analysis.

Gaussian beams are solutions to the parabolic wave equation which results from simplifying the Helmholtz equation for cases where the magnitude varies slowly with propagation distance.[17] Taking the x coordinate to be the direction of the Rayleigh wave reflected along the diameter of the cylinder, the y coordinate to be transverse to the direction of propagation, and the z coordinate to be out of the plane of the cylinder's face [see Fig. 3(b)], the pressure distribution on the cylinder's face due to the leaky Rayleigh wave reflected by the edge may be written as a two-dimensional Gaussian beam:[19]

$$p_l(x,y,0)=\frac{p_f}{\sqrt{1+ix/b}}\exp[-\alpha x]\times\exp\left[ik_R x-ik_p\left(\frac{y^2}{2\rho}\right)-\frac{y^2}{2w^2}\right], \tag{1a}$$

where $\rho=\rho(x)=x+b^2/x$ is the local radius of curvature of the equiphase surface at x [measured with respect to the beam waist at $x=0$, as shown in Fig. 3(b)], $b=(k_R w_0^2)/2$ is a real valued parameter which from the form of Eq. (1a) affects the (complex) location of the source point,[17,19] $w=w(x)=w_0[1+(x/b)^2]^{1/2}$ gives the width of the beam at x relative to its minimum width w_0 in the focal plane $x=0$, and p_f indicates the pressure amplitude in the focal plane. The factor $\exp[-\alpha x]$ in Eq. (1) accounts for damping due to radiation leakage, with α defined from the complex wave number associated with the Rayleigh wave pole:[12] $k_p=k_R+i\alpha$. Note that the reference choice of $x=0$ at the beam waist means that the pressure amplitude will increase for $x<0$, in agreement with the physical situation that the pressure amplitude continually decreases after reflection point at $x=-C$. (We will subsequently use p_C to represent the leaky wave amplitude after reflection at the point $x=-C$ and incorporate a reflection coefficient B to account for energy losses upon reflection.) Fortunately, the final result for the contribution to the far-field scattering depends only weakly on b provided $b\ll a$, so that a detailed evaluation of w_0 is not required. Defining a new variable $X=x-ib$ as the distance from the complex source point location b, Eq. (1a) can be rewritten as

$$p_l(x,y)=p_f\sqrt{\frac{-ib}{X}}\exp[ik_R x]\exp[-\alpha x]\times\exp\left[\frac{ik_p y^2}{2X}\right]. \tag{1b}$$

The far-field pressure contribution due to the reflection of leaky Rayleigh waves is determined by applying the Rayleigh–Sommerfeld propagation integral to the reflected leaky wave pressure on the face as given by Eq. (1b). Taking the exit plane to be the face of the cylinder and using paraxial assumptions,[5,12] the Rayleigh–Sommerfeld integral[17] gives the far-field pressure as

$$p_{lsca}(z)\approx\frac{-ik\exp(ikR_C)}{2\pi R_C}\cos\overline{\gamma}\times\int\int_{-\infty}^{\infty}dx\,dy\,p_l(x,y)\exp(-ikx\sin\overline{\gamma}), \tag{2}$$

where R_C is the distance to the center of the reflecting edge, and $\overline{\gamma}=(90°-\gamma)$ is the angle between a normal to the exit plane and the propagation direction z. From Fig. 2, this angle is seen to be given by θ_R for the mechanism under investigation. Substituting Eq. (1b) into Eq. (2) yields the far-field pressure contribution due to reflected leaky Rayleigh waves as

$$p_{lsca}\approx\frac{-ikp_f\exp(ikR_C)}{2\pi R_C}\cos\theta_R\int_{-C}^{3C}dx\,\frac{\exp[-\alpha x]}{\sqrt{X}}\times\int_{-\infty}^{\infty}dy\exp\left[\frac{ik_p y^2}{2X}\right],\tag{3}$$

where the integration limits over x have been modified to account for the finite size of the face. Although the face of the cylinder is also finite in the y dimension, the infinite nature of the y integration introduces no significant error because the high frequencies used in this experiments indicate that the integrand will oscillate rapidly for large values of y and hence the primary contribution to the integral comes from the stationary phase points near the $y=0$ axis. A stationary phase approximation of the y integration yields $\sqrt{(2\pi X/k_p)}\exp(i\pi/4)$. The resulting cancellation of the $\sqrt{X}$ term renders the subsequent evaluation of the x integral trivial, and the resulting expression for the far-field pressure magnitude becomes

$$|p_{lsca}|\approx\frac{|p_C|}{2R_C}\cos\theta_R\,\frac{k}{\alpha}\sqrt{\frac{a}{\pi k_R}}[1-\exp(-2\alpha a)],\tag{4}$$

where we have used $|k_p|\approx k_R$ and from Eq. (1b) we see that $p_C=p_l(-C,0)$ is related to p_f by $p_f=p_C(1-i(C/b))^{1/2}\times\exp(-\alpha C+ik_lC)$. Taking into account the fact that the launching region along the diameter has a length $2a$ and simplifying the two-dimensional launching integral to a one-dimensional form [e.g., Eq. (10) of Ref. 12] gives $|p_C|=2|B||p_{\rm inc}|[1-\exp(-2\alpha a)]$, where $p_{\rm inc}$ is the incident acoustic amplitude and $|B|$ represents the amplitude of the reflection coefficient. Note that Eq. (4) in effect approximates the reflection coefficient as constant over the entire reflecting edge, so that the present result neglects B's dependence on incident angle for leaky waves incident at different y positions of the circular reflector and ignores the associated phase dependence of the reflected wave. Also note that Eq. (4) uses $C=a/2$ and the assumption that $b\ll a$.

In order to define a form function associated with this scattering mechanism, we assume that the far-field scattering from the end of the cylinder is expressible in the standard form of far-field scattering from a sphere:[6,17]

$$p_{\rm sph}=\frac{p_{\rm inc}f_{\rm sph}a_{\rm sph}}{2R_S}\exp(ikR_S),\tag{5}$$

where $a_{\rm sph}$ is the radius of the sphere, R_S is the distance from the sphere, and $f_{\rm sph}$ is a dimensionless form function describing the angular characteristics of the scattering pattern. Using Eq. (4) and assigning $a_{\rm sph}$ to be the cylinder radius a gives the form function magnitude for the reflected Rayleigh wave contribution as

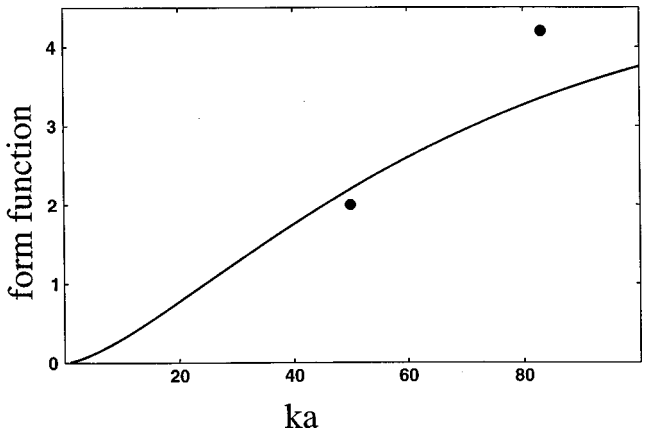

FIG. 6. Form function modulus for leaky Rayleigh wave reflection across the face of the cylinder. The solid curve is the theoretical approximation given by Eq. (6), and the points represent the experimental observations at *ka* values of 50 and 83.

$$|f_{\rm cyl}|\approx\frac{2|B|}{\tan\theta_R}\,\frac{k_R}{\alpha}\,\frac{1}{\sqrt{(ka)\pi\sin\theta_R}}[1-\exp(-2\alpha a)]^2,\tag{6}$$

where use has been made of $k_R=k\sin\theta_R$. The solid curve in Fig. 6 shows Eq. (6) plotted as a function of ka. The exponential factor is evaluated using $\alpha a=(c/c_R)(\alpha/k_R)ka$ with $c/c_R=0.511$, $\alpha/k_R=0.0116$, and $|B|=0.34$.[6,7]

To compare the approximate predictions to the observed backscattered pressure amplitudes, experimental measurements of p_{lsca} are normalized with respect to the measured specular reflection from a solid elastic sphere (thus eliminating the dependence on p_C). The resulting form function is then expressed in terms of measurable quantities of the cylinder and the sphere as discussed in Appendix B of Ref. 6:

$$|f_{\rm cyl}|=\left|\frac{p_{\rm cyl}}{p_{\rm sph}}\right|\left(\frac{a_{\rm sph}}{a_{\rm cyl}}\right)\left(\frac{t_C}{t_S}\right)^2|f_{\rm sph}|,\tag{7}$$

where the notation p_{lsca} has been changed to $p_{\rm cyl}$ and appropriate subscripts have been used to distinguish between parameters associated with the cylinder and the calibration sphere. This normalization was applied to the data displayed in Fig. 6, which show that the observed form function magnitudes are 2.0 and 4.2 for ka of 50 and 83, respectively. The data points are also plotted in Fig. 6, where it is obvious that the theory approximates the observed form function reasonably well. From Fig. 6 we see that the predicted form function magnitudes at these frequencies are approximately 2.1 and 3.3, which are within 5% and 25% of the respective observations. Thus we have approximated the backscattering enhancement for a case which is otherwise rather intractable. The simplification $b\ll a$ which was used in this approximation allows us to omit an $O(b/a)$ correction. This assumption was confirmed by estimating the b value required to match the decrease in the reflected amplitude with increasing $|y|$ resulting from the associated decrease in the length of the launching region.

IV. DISCUSSION

The analysis and experimental comparison shown are only for the earliest of the Rayleigh wave scattering contri-

butions. The reverberation of the Rayleigh wave along the cylinder's diameter is expected to give delayed and significantly weaker contributions. Neglecting the additional curvature of the wave crests resulting from each reflection at the curved edge, each subsequent reflection would be reduced in amplitude by a factor $|B|^2\exp(-4\alpha a)\approx 0.035$ and 0.016 for ka of 50 and 83, respectively. While Fig. 4 displays evidence of delayed contributions near θ_R, they are expected to be smaller than the single contribution we have investigated except at small ka where the $\exp(-4\alpha a)$ factor is closer to unity. The experimental comparison, Fig. 6, supports the approximations we have used at high frequencies and the identification of the band near 30 degrees in Fig. 1 as the result of leaky Rayleigh waves. Comparison of Fig. 5(b) with (a) shows that the angular width of the enhancement is greatest at low frequencies.

ACKNOWLEDGMENT

This work was supported by the Office of Naval Research.

[1] K. L. Williams, G. S. Sammelmann, D. H. Trivett, and R. H. Hackman, ''Transient response of an elastic spheroid: Surface waves and quasicylindrical modes,'' J. Acoust. Soc. Am. **85**, 2372–2377 (1989).
[2] R. H. Hackman and K. L. Williams, ''Axisymmetric monostatic and bistatic resonance excitation mechanisms of large aspect ratio targets: Impulse excitations and bipolar couplings,'' J. Acoust. Soc. Am. **91**, 1375–1382 (1992).
[3] J. Zemanek, Jr., ''An experimental and theoretical investigation of elastic wave propagation in a cylinder,'' J. Acoust. Soc. Am. **51**, 265–283 (1972).
[4] R. N. Thurston, ''Elastic waves in rods and clad rods,'' J. Acoust. Soc. Am. **64**, 1–37 (1978).
[5] P. L. Marston, ''Approximate meridional leaky ray amplitudes for tilted cylinders: End-back-scattering enhancements and comparisons with exact theory for infinite solid cylinders,'' J. Acoust. Soc. Am. **102**, 358–369 (1997); erratum **103**, 2236 (1998).
[6] K. Gipson and P. L. Marston, ''Backscattering enhancements due to reflection of meridional leaky Rayleigh waves at the blunt truncation of a tilted solid cylinder in water: Observations and theory,'' J. Acoust. Soc. Am. **106**, 1673–1680 (1999).
[7] S. F. Morse, P. L. Marston, and G. Kaduchak, ''High frequency backscattering enhancements by thick cylindrical shells in water at oblique incidence: Experiments, interpretations, and calculations,'' J. Acoust. Soc. Am. **103**, 785–794 (1998).
[8] K. Gipson, ''Leaky Rayleigh wave ultrasonic backscattering enhancements: Experimental tests of theory for tilted solid cylinders and cubes,'' Ph.D. thesis, Washington State University, 1998.
[9] X. L. Bao, ''Echos and helical surface waves on a finite elastic cylinder excited by sound pulses in water,'' J. Acoust. Soc. Am. **94**, 1461–1466 (1993).
[10] I. A. Viktorov, *Rayleigh and Lamb Waves: Physical Theory and Applications* (Plenum, New York, 1967).
[11] H. Uberall, ''Surface waves in acoustics,'' in *Physical Acoustics*, edited by W. P. Mason and R. N. Thurston (Academic, New York, 1973), Vol. 10, pp. 1–60.
[12] P. L. Marston, ''Spatial approximation of leaky wave surface amplitudes for three-dimensional high-frequency scattering: Fresnel patches and application to edge-excited and regular helical waves on cylinders,'' J. Acoust. Soc. Am. **102**, 1628–1638 (1997).
[13] G. V. Frisk, *Ocean and Seabed Acoustics* (Prentice–Hall, Englewood Cliffs, NJ, 1994), Chaps. 3 and 4.
[14] A. H. Meitzler, ''Mode coupling occurring in the propagation of elastic pulses in wires,'' J. Acoust. Soc. Am. **33**, 435–445 (1961).
[15] L. O. Wilson, ''The response of a semi-infinite fiber to a pulse applied asymmetrically to its end,'' J. Acoust. Soc. Am. **79**, 1798–1810 (1986).
[16] K. Gipson and P. L. Marston, ''Backscattering enhancements due to retroreflection of ultrasonic leaky Rayleigh waves at corners of solid elastic cubes in water,'' J. Acoust. Soc. Am. **105**, 700–710 (1999).
[17] P. L. Marston, ''Geometrical and catastrophe optics methods in scattering,'' in *Physical Acoustics*, edited by A. D. Pierce and R. N. Thurston (Academic, Boston, 1992), Vol. 21, pp. 1–234.
[18] A. K. Gautesen, ''Scattering of an obliquely incident Rayleigh wave in an elastic quarter-space,'' Wave Motion **8**, 27–41 (1986).
[19] L. B. Felsen, ''Evanescent waves,'' J. Opt. Soc. Am. **66**, 751–760 (1976).

Radiated noise characteristics of a modern cargo ship

Paul T. Arveson[a)]
Naval Surface Warfare Center, West Bethesda, Maryland 20817

David J. Vendittis
Florida Atlantic University, Boca Raton, Florida 33431

(Received 7 November 1996; revised 5 September 1998; accepted 15 September 1999)

Extensive measurements were made of the radiated noise of M/V OVERSEAS HARRIETTE, a bulk cargo ship (length 173 m, displacement 25 515 tons) powered by a direct-drive low-speed diesel engine—a design representative of many modern merchant ships. The radiated noise data show high-level tonal frequencies from the ship's service diesel generator, main engine firing rate, and blade rate harmonics due to propeller cavitation. Radiated noise directionality measurements indicate that the radiation is generally dipole in form at lower frequencies, as expected. There are some departures from this pattern that may indicate hull interactions. Blade rate source level (174 dB *re* 1 μPa/m at 9 Hz, 16 knots) agrees reasonably well with a model of fundamental blade rate radiation previously reported by Gray and Greeley, but agreement for blade rate harmonics is not as good. Noise from merchant ships elevates the natural ambient by 20–30 dB in many areas; the effects of this noise on the biological environment have not been widely investigated. © *2000 Acoustical Society of America.* [S0001-4966(99)07112-X]

PACS numbers: 43.20.Tb, 43.25.Yw, 43.30.Jx, 43.30.Nb [SAC-B]

INTRODUCTION

In spite of the fact that merchant shipping constitutes a major source of noise in the sea, few detailed studies of the radiated noise of modern cargo ships have been reported. *Physics of Sound in the Sea*, the World War II compendium,[1] described radiated noise of many ships of that period, as summarized in a textbook by Urick.[2] Strasberg[3] and Blake[4] contributed extensively to the literature on propeller cavitation noise of ships. In Europe, the sustained research program of The Netherlands has yielded several new measurement methods as well as insights into mechanisms of cargo ship noise.[5–7] Many researchers in Germany, Norway, Sweden, Finland, and other European countries have also contributed to ship noise and propeller research. Japan and China also have important and ongoing research programs. In recent years increasingly sophisticated numerical and experimental research on propeller cavitation has been conducted. For example, new attempts have been made to visualize and quantify propeller cavitation,[8] and advanced computational methods have been developed.[9,10] However, most of these studies have focused on improving propulsion efficiency and on habitability problems due to shipboard noise and vibration; they do not often report radiated noise levels.

Donald Ross studied the noise of commercial ships and trends in ship sizes and powering.[11] He also wrote a textbook that described the important general features of surface ship noise.[12]

Many of the published ship noise measurements were made with third-octave bandwidth analysis, which is too wide for separation of the individual spectral components of ship radiation. Also, the data were often acquired in shallow water, so the levels may not be representative of free-field values, especially at low frequencies. Due to the high cost of ship time as well as measurement facilities, it is perhaps not surprising that few detailed measurements of modern ships are available.

In 1975, the U.S. Navy initiated a new program for accurate narrow-band measurements of merchant ship noise. This research program, jointly sponsored by Naval Research Laboratory and Naval Ocean Research and Development Activity, was aimed at the development of a parametric model of surface ship noise based on two complementary phases of measurements: (1) accurate and comprehensive measurements on one representative ship to ''calibrate'' the parameters of the model; and (2) a large number (about 15) of limited measurements on a variety of merchant ships to permit extension of the parametric model to the world merchant fleet. The expectation of the NRL/NORDA program was that significant sources of radiated noise could be modeled in a general way by fitting the levels (via regression analysis) to readily available engineering parameters such as ship speed, draft, horsepower, length, and engine type.

In the 1970s, new theoretical research on ship noise prediction was undertaken by workers at Bolt, Beranek and Newman, Inc. Initial proposals for the parametric scaling laws were developed there by Gray, Greeley, and Heine. Special effort was focused on predicting propeller cavitation noise levels; this work will be reviewed in more detail below.

A pilot study was first conducted to determine whether relatively low-cost air-dropped sonobuoys would be adequate to make accurate measurements of cargo ship noise. The pilot study results for 12 ships-of-opportunity, including a supertanker, was conducted by Cybulski and Wright.[13] Results of these sonobuoy measurements were widely reported.[14–16] After careful analysis and comparison with

[a)]Electronic mail: arveson@balancedscorecard.org

TABLE I. Characteristics of M/V OVERSEAS HARRIETTE.

Deadweight tons	25 515
Length overall	567.2 ft. (172.9 m)
Beam	74.8 ft. (22.8 m)
Draft, full load	33.5 ft. (10.2 m)
Draft, ballasted, aft (condition during measurements)	26 ft. (7.9 m)
Speed, maximum (full load)	15.6 knots (145 rpm)
Turns/knot ratio	8.8
Propeller diameter	16 ft. (4.9 m)
Number of blades	4
Engine type	Direct-drive two-stroke diesel (Hitachi/Babcock & Wilcox 6K67GF, 6 cylinders)
Engine horsepower, maximum	11 200
Ship's service generator	Diesel, 5 cylinders (Hitachi/B&W)

other measurements, it was subsequently determined that these sonobuoy measurements were not sufficiently accurate for calibration of a surface ship noise model. There was evidence of contamination of the direct radiation with bottom reflections, and the electronics contributed a subtle form of distortion that elevated the low-frequency spectrum. Some of these measurements were compared (unsuccessfully) with theoretical calculations by Greeley. The disagreement between theory and experiment led some researchers to propose unlikely noise source mechanisms.[17] The exaggerated source levels—up to 232 dB *re*: 1 μPa/m—have been quoted in an ASA publication[18] and a National Research Council monograph.[19] The fact that these values were excessive was not realized until several years after the original measurements were reported, when new sonobuoy measurements were acquired concurrently with Atlantic Undersea Test and Evaluation Center (AUTEC) measurements. The discrepancy in levels and its cause were subsequently determined. The AUTEC results were initially reported at a meeting of the Acoustical Society;[20] this article is a long-overdue attempt to document the results in more detail.

Ross has observed that the trend in cargo ships is toward low-speed direct-drive diesel propulsion, because of its high energy efficiency.[11] Such a ship, M/V OVERSEAS HARRIETTE, was selected for the detailed phase of measurements. The ship is operated by the Military Sealift Command (MSC). Personnel from Naval Surface Warfare Center designed a comprehensive measurement plan and conducted acoustical measurements on this ship in 1980.

This article documents characteristics of the cargo ship's radiated noise data. The planned efforts in parametric analysis and extension to the world fleet were not completed. Nevertheless, the acquired data constitute an extensive measurement of a modern cargo ship. This ship is representative of many direct-drive diesel-powered vessels that make a significant contribution to noise in the world's oceans. It is hoped that these data can help to facilitate further efforts to develop models of shipping noise.

I. DESCRIPTION OF SHIP

M/V OVERSEAS HARRIETTE is a coal carrier owned by the Military Sealift Command and normally operated by a civilian U.S. crew. She was constructed in 1977 in Japan. Table I defines her characteristics.

At the time of the acoustical measurements in 1980, Overseas Harriette was nearly new, and her hull and propulsion machinery were observed to be in excellent condition. No fouling or damage was evident on the propeller.

II. MEASUREMENT CONDITIONS

Extensive planning was done to maximize the information to be obtained from the ship noise measurements, because of the high cost of diversion of the ship from its normal run and because of the large amount of radiated noise data required. A set of measurement criteria was developed to help ensure consistent data quality.

A cost-effectiveness analysis was conducted to determine the best facility and location in which to measure the ship noise. The Atlantic Undersea Test and Evaluation Center (AUTEC) system, located in Tongue of the Ocean, Bahamas, was selected for this experiment. It contains an accurate radiated noise measurement system consisting of a bottom-mounted hydrophone and tracking array and a radar surface ranging system. The bottom depth is 1830 m. Tongue of the Ocean (TOTO) is almost completely surrounded by shallow water of the Bahamas Bank. This means that TOTO is sheltered from open ocean shipping noise, and swells are usually absent in the sea state. Moreover, use of a bottom-mounted hydrophone array eliminated much of the extraneous low-frequency wave-induced noise that often influences measurements made from surface-suspended arrays and sonobuoys.

During the ship measurements, the mean wave height was less than 0.3 m, with wind speeds less than 3 m/s, so the ambient noise level was low. The sound speed profile at the time of the experiment was typical of the late summer: a smooth, gradually decreasing gradient without a mixed layer. At the relatively close ranges of the acoustic measurements (less than 600 m), the assumption of straight-line inverse-square propagation was valid within 1 dB at the frequencies and angles of interest. It is sometimes stated that at low frequencies (in the dipole region), propagation loss varies as 40 log range or 12 dB per double distance; but this is misleading. The distance in this case is the *horizontal* distance, whereas the actual source-to-receiver range, the *radial* distance, was used for these measurements. For the latter, 20 log range (spherical) spreading loss applies in the far field at all frequencies.

Five hydrophones at depths from 60 to 460 m were used to acquire the ship's radiated noise. The hydrophones were calibrated to frequencies as low as 3 Hz. An on-board vibration-monitoring system and two shakers were installed and operated during the experiment. Distance was measured both acoustically and by surface radar. The signal-to-noise ratio for the spectrum data was 25 dB or greater.

A total of 66 runs were tape recorded. The resulting spectra were used to provide an input to special directivity analysis programs used to generate the directivity plots. Simultaneous on-board vibration monitoring provided additional measurements of the bandwidth of tonals from the ship, diesel-engine cylinder pressure spectra, engine room hull and bottom response, ship hull ''beam mode'' response, and the transfer function between shaker force and radiation

TABLE II. Speeds measured on M/V OVERSEAS HARRIETTE, and wideband source levels at each speed.

Ship speed		Keel aspect wideband source level
RPM	knots	(dB *re*: 1 μPa at 1 m)
68	8	178
86	10	180
105	12	184
122	14	190
140	16	192

levels. Only limited on-board data were analyzed before project funding ended.

III. RESULTS—RADIATED NOISE LEVELS

A. Wideband noise levels

Table II indicates the speeds and shaft rpm values measured. Also included in this table are the overall (wideband) keel-aspect radiated noise source levels in dB *re*: 1 μPa at 1 m measured at each speed. (The keel aspect is in the direction downward below the ship.) Note that the wideband levels are seen to follow an S-shaped curve that increases rapidly above the propeller cavitation inception speed of 10 knots (5.1 m/s).

B. Third-octave bandwidth spectral analysis

A general quantitative description of the ship's radiated noise can be provided by power spectral analysis. This was accomplished for both third-octave bands and various narrow bandwidths. Figure 1 shows third-octave band keel-aspect spectra at all the speeds tested. The figure shows a prominent ''hump'' at 50 to 100 Hz, which is a typical feature in ship noise spectra. It is this source which also controls the high-frequency spectrum. Further descriptions of sources are given in Sec. III D.

C. Narrow-band spectral analysis

Figure 2 shows the dipole or keel aspect narrow-band power spectrum in 0.5 Hz bands at low (86 rpm) and maximum speed (140 rpm). These spectra were obtained from 8-s samples. The identification of various tonal harmonics is indicated. Figure 3 shows a higher-resolution power spectrum of low-frequency noise from a single keel-aspect run at 140 rpm. Here the bandwidth is 0.125 Hz, which was achieved by uniform sampling of an 8-s noise record at 8192 Hz.

The tonal levels of these short noise samples are somewhat variable, and should not be taken as representative. Better estimates of the mean source levels of several tonal frequencies are given in Table III and the directivity plots shown later. For the mean source levels in Table III, estimated uncertainty due to systematic errors is less than 2 dB. Long-term standard deviations of source levels (after removing directivity effects) were found to be about 2 to 5 dB, depending on the inherent source variability. The ship's service diesel generator (SSDG) tones showed more amplitude stability than the propulsion-related tonals. The discussion of these spectral data will be organized by the source of noise in the following section.

D. Description of major noise sources

1. Ship's service diesel generator

At low ship speeds, tonal components from the ship's service diesel generator (SSDG) contribute almost all of the radiated noise power of the ship. It radiates a series of 6-Hz harmonics that are independent of ship speed. Two of these harmonics, at 24 and 30 Hz, are strong enough to be contributors to the high-speed signature, as can be seen in Fig. 2. The keel-aspect source levels of these tones are 179 and 168 dB *re*: 1 μPa at 1 m, respectively (these frequencies and levels are independent of ship speed). The SSDG has five cylinders, as is typical on many large ships. Uneven vibration levels of individual cylinders may account for the higher levels of the harmonics that are multiples of 5. The SSDG

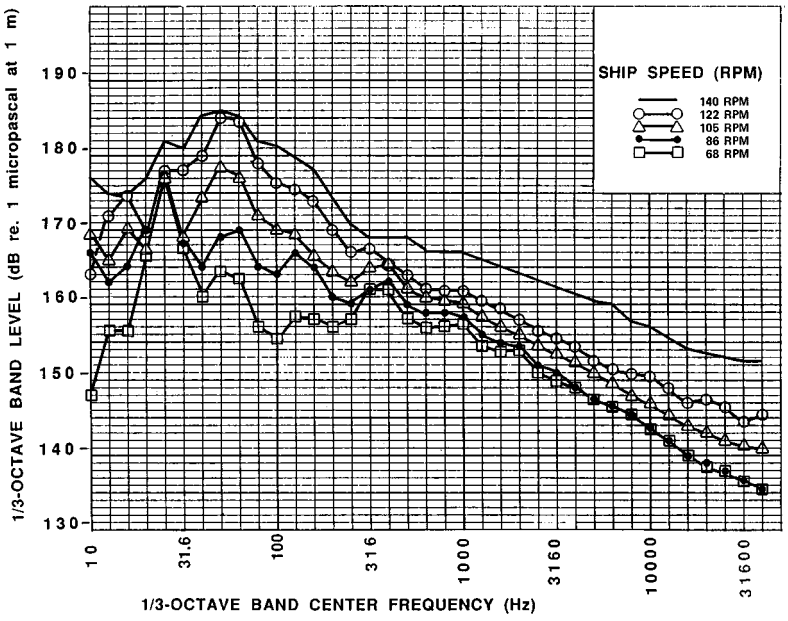

FIG. 1. Keel-aspect third-octave bandwidth spectra of M/V OVERSEAS HARRIETTE at all the speeds tested. Average of several runs at each speed.

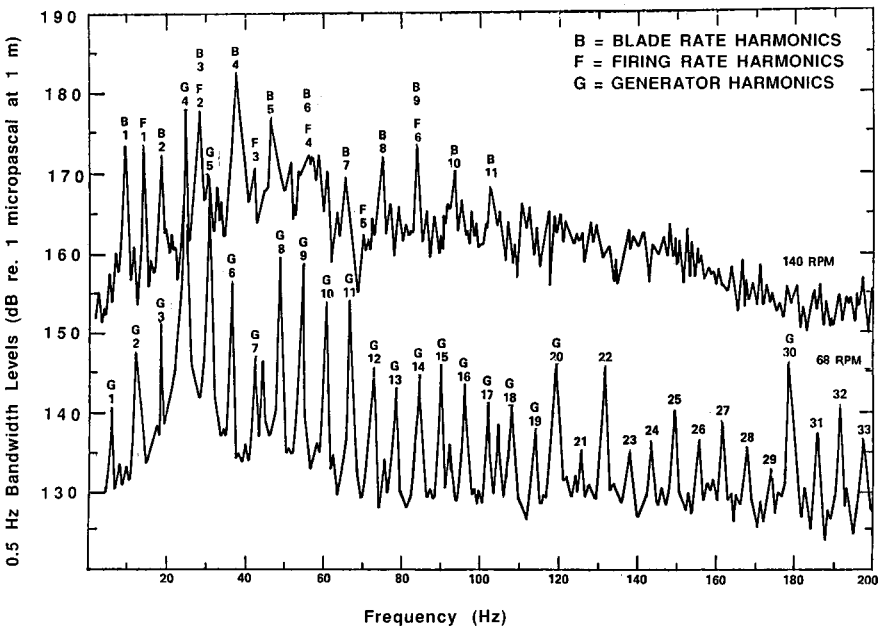

FIG. 2. Keel-aspect narrow-band spectra of M/V OVERSEAS HARRIETTE in 0.5 Hz bands at low speed (68 rpm) and maximum speed (140 rpm). The identification of various tonal harmonics is indicated; the symbols are G (ship's service diesel generator), B (blade rate), and F (diesel firing rate).

tonal levels were much more stable in amplitude and frequency than the tonals due to the propulsion system, probably because they are not subject to variations in loading as is the propeller. The ac power line frequencies (harmonics of 60 Hz) are distributed on machinery throughout the ship. In their initial cargo ship radiated noise model report, Gray and Heine proposed a scaling law for ac machinery noise on ships in which the wideband sum of ac machinery line energies is proportional to the square of generated power.[21]

2. Main propulsion diesel firing rate

At higher speeds, propulsion-related sources are dominant in the ship's radiated noise. OVERSEAS HARRIETTE is powered by a two-stroke six-cylinder diesel engine. Its shaft is directly coupled to the propeller. Hence in one revolution of the propeller there are six Diesel cylinder firing cycles. The Diesel firing rate is therefore defined as

$$\mathrm{FR}=\frac{6\times\mathrm{rpm}}{60}=\frac{\mathrm{rpm}}{10}\,\mathrm{Hz}. \tag{1}$$

Notice that every even harmonic of diesel firing rate coincides with every third harmonic of blade rate, because of the ratio of four blades to six cylinders per revolution. This causes an ambiguity in the interpretation of sources of the overlapping harmonics. In some of the measurements at 140 rpm, weak tones at the intermediate $\frac{1}{2}$-firing rate frequencies are also detected. These are evident at 7, 21, and 35 Hz in the high-resolution spectrum of Fig. 3.

In a calm sea, the frequency stability of the main engine during transit was found to be equivalent to a Q of about 100. In general, this value depends on sea state and the type of speed governor used on the ship.

Some studies have been undertaken to determine the mechanism of noise generation by diesel engines. Ross[12] and

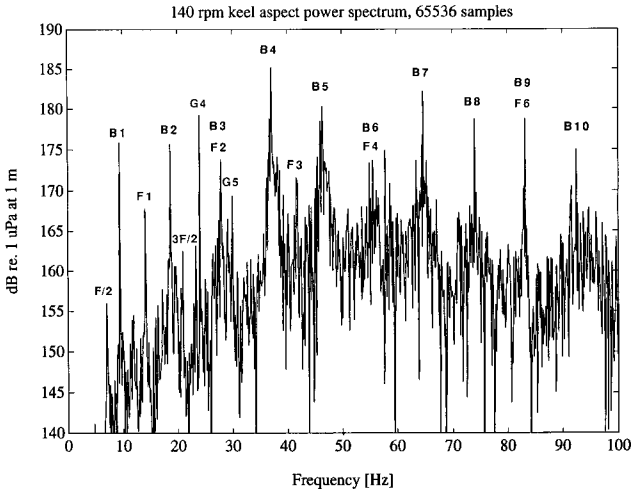

FIG. 3. High-resolution keel-aspect narrow-band power spectrum of low-frequency noise of OVERSEAS HARRIETTE at 140 rpm. The bandwidth is 0.125 Hz. Tonal harmonics are identified: G (ship's service diesel generator), B (blade rate), and F (diesel firing rate).

TABLE III. Measured source levels of significant tonal frequencies of M/V OVERSEAS HARRIETTE, keel aspect in dB *re*: 1 μPa at 1 m. These data represent the mean levels of several 8-s samples. They have standard deviations of 2 to 5 dB due to source variability (BR=blade rate, FR=engine firing rate).

Shaft rpm	68	86	105	122	140
Speed, knots	8	10	12	14	16
Source/Harmonic					
BR	<130	159	170	159	174
FR	···	175	170	174	174
2×BR	<130	161	165	167	175
3×BR=2×FR	···	···	160	<178	179
4×BR	···	···	···	173	185
3×FR	···	153	156	161	176
5×BR	···	···	···	177	175
6×BR=4×FR	···	···	168	177	175
7×BR	···	···	···	179	172
5×FR	···	···	···	177	163
8×BR	···	···	···	177	172
9×BR=6×FR	···	···	···	171	173
10×BR	···	···	···	171	170
340–360 band	156	156	159	162	163

others have concluded that the major source mechanism is ''piston slap,'' that is, the impact of the piston against the wall of the cylinder caused by reversals in the direction of the piston side force. Ross estimated that up to 0.1% of the engine power can be radiated as acoustic power by this mechanism. Heine[21] proposed a scaling law for merchant ship diesel engines in which the radiated power W at the fundamental firing rate frequency F is related to engine horsepower H as

$$W \sim (HF)^2. \tag{2}$$

Keel-aspect mean source levels of the more significant firing rate harmonics are shown as a function of ship speed in Table III. Note that the fundamental firing rate levels do not increase monotonically with ship speed. It is likely that the dynamics of the piston slap motions change with speed, which may cause significant differences in the spectrum of harmonics of diesel firing rate.

These measurements also suggest that structural resonances may play a role in determining the radiation efficiency of the ship's engine tones. The diesel engine is mounted on a thick bedplate that is nearly flush with the tank top, 2.7 m above the keel. Ohlrich[22] reported measurements of the mobility of bedplate structures; his data indicate that the fundamental bedplate resonance of a large diesel engine is as high as 400 Hz, below which the response is fairly smooth and mobile. This indicates that the engine bedplate itself is relatively stiff at low frequencies. Nilsson[23] measured vibration on a full-scale cargo ship and concluded that frequencies below 40 Hz are controlled by global vibration of the entire hull. Resonance modes of the hull at low frequencies therefore may be influencing the amplitude and directivity of engine tones. Additional evidence of such influence is offered by the directivity plots in Sec. IV.

3. Blade rate

An important source of radiated noise on surface ships is blade rate, that is, a signal at the blade passing frequency and its harmonics. This is usually the dominant source of low-frequency tonals at high speeds, when the propeller is heavily cavitating.

For OVERSEAS HARRIETTE, cavitation inception occurred at 10 knots or 86 rpm. (For an older ship, with some fouling or damage on the propeller, a lower inception speed could be expected.) The tip cavitation index was determined to be about 0.47, where the cavitation index is defined as

$$K_t = \frac{p_0 - p_v}{\frac{1}{2}\rho U_a^2}, \tag{3}$$

where p_0 is the ambient pressure at the tip depth, p_v is the water vapor pressure, r is water density, and U_a is the propeller tip velocity relative to the surrounding water. Due to the presence of the hull, the inflow velocity is reduced significantly near the top of the propeller (perhaps to as little as 10% of the ship's velocity). In this region the tip velocity is essentially given by the rotation rate times the propeller circumference.

The physical phenomena regarding the origin of blade rate noise and vibration have been widely reported;[24–27] they can be briefly outlined. A surface ship propeller operates behind a hull which creates a nonuniform wake inflow velocity; the pressure on a blade surface varies due to this wake and also due to the change in hydrostatic pressure as a function of its depth below the water surface. Both of these effects make the pressure lowest in the upper region of the propeller blade's motion. If the rotation speed is sufficiently high, a cavity will be formed; it rapidly collapses when pressure increases as the blade turns downward. Since this collapse occurs every time a blade passes through the region of low pressure, noise will be generated at blade rate and its harmonics. The distribution of blade rate harmonic amplitudes depends on the manner and rate at which the cavity changes in volume.

4. Propeller noise waveforms

The instantaneous free-field radiated acoustic pressure $P(t)$ from a pulsating monopole source can be derived by solving the acoustic wave equation for the case of a fluctuating mass source.[21] If its density change is assumed to be negligible, the solution can written in terms of time derivatives of volume changes using any of the following relationships:

$$P(t) = \frac{\pi f^2 \rho V(t)}{r} = \frac{f \rho V'(t)}{2r} = \frac{\rho V''(t)}{4\pi r}, \tag{4}$$

where V is the instantaneous cavity volume, V' is the volume velocity, V'' is the volume acceleration, f is frequency, ρ is the (constant) fluid density, and r is the distance from the source.

Equation (4) shows that the monopole pressure waveform $P(t)$ is directly proportional to the second derivative of the cavity volume changes. However, the proximity of the water surface alters the radiation field. The sea surface is a pressure-release boundary. For a source at depth d and depression angle q ($0 =$ horizontal), the received pressure is modified by a factor

$$D = 2 \sin(kd \sin \theta), \tag{5}$$

where k is $2\pi/\lambda = 2\pi f/c$, where c is the sound speed. For shallow sources at low frequencies, kd is small and the outer sine function can be removed, yielding

$$D_{\mathrm{LF}} \sim 2kd \sin \theta. \tag{6}$$

Physically D_{LF} is a dipole directivity pattern, which is universal for low-frequency sources under a pressure-release surface. The directivity factor modifies the monopole pressure to yield an expression for the dipole pressure $P_d(t)$. At $\theta = \pi/2$ (keel aspect), this dipole pressure becomes

$$P_d(t)_{\pi/2} = D_{LF} P(t) = 2kdP(t) = \frac{4\pi f d}{c} P(t), \tag{7}$$

but since $V'' = V'''/2\pi f$, we have from Eq. (4)

$$P_d(t) = \frac{d\rho V'''}{2\pi r c}, \tag{8}$$

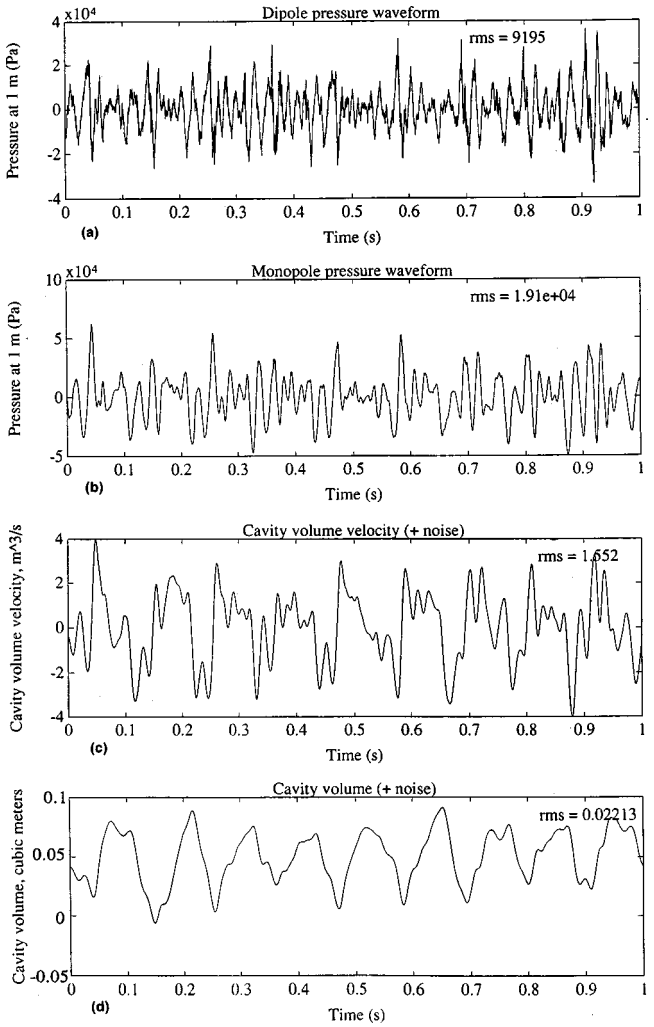

FIG. 4. (a) Waveform of radiated noise pressure from M/V OVERSEAS HARRIETTE at 140 rpm. This trace was recorded near the keel aspect. The upper frequency in the data is 3.2 kHz. Nine cycles of propeller blade rate are shown (1-s sample length). (b) One integration of the waveform in (a), which represents the monopole pressure waveform; (c) a second integration of the pressure waveform in (a), which approximately represents the waveform of cavity volume velocity; (d) a third integration of the waveform in (a), which approximately represents the changes in cavity volume. These waveforms include some contribution from the diesel engine and other sources.

and thus the proximity of the free surface produces a *third* differentiation of the volume waveform. Each differentiation is equivalent to a 6 dB/oct high-pass filter imposed on the cavity volume waveform. Hence, if the radiated dipole pressure waveform is known, in principle it is possible to infer the appearance of the cavity volume variations by means of three successive integrations in the time domain.

Dipole pressure waveforms were recorded from the AUTEC hydrophones. The waveform shown in Fig. 4(a) was measured at 140 rpm, near the keel aspect. The sample rate was 8192 Hz; the upper frequency in the data is 3200 Hz. At this ship speed the blade rate noise contributes most of the power, although there is some ''contamination'' with noise from the diesel engine and other sources. A sample 1-s long is shown, which contains nine blade rate pulses. (The polarity of this waveform is believed to be as shown based on other experimental observations of positive pressure peaks in collapsing cavities.[28]) Figure 4(a) clearly shows that the waveform is modulated at the blade rate frequency, and is asymmetrical. Examination of the duty cycle of high-frequency noise indicated that only one blade was cavitating at any given time.

Note the high values of the peak pressure, over 40 kPa at 1 m in some cases. This is equivalent to a *peak* sound pressure level of over 212 dB *re* 1 μPa at 1 m, which places this source (at least momentarily) in the nonlinear region in seawater.[29] At these levels, shock waves may be generated in the vicinity of the propeller.[30,31] Moreover, the presence of gas in the propeller wake reduces the local sound speed substantially, further suggesting the possible formation of shock waves in the wake. (However, measurements along the hydrophone string when it was under the ship show no evidence of significant deviations from spherical spreading among the hydrophones.)

By integrating the dipole pressure waveform once, the monopole waveform was obtained [Fig. 4(b)]. Successive integrations of the waveform yield approximations to the volume velocity [Fig. 4(c)] and cavity volume variations [Fig. 4(d)]. The rms levels at each stage are shown on the figures. Although it contains some contaminating ''noise'' from diesel tones, the waveform of Fig. 4(d) suggests the general appearance and duty cycle of the cavity volume variations. This waveform also resembles the expected shape of a typical cavity volume history as predicted by other studies.[32,33]

The amplitude of blade rate varies substantially, most likely due to changes in inflow caused by such effects as the pitch of the ship in the seaway. Even in a nearly calm sea, the rms level of fundamental blade rate sound (as seen on a level recorder with a time constant of 1 s) exhibited a long-term standard deviation of about 5 dB with most of the variations roughly correlating to the pitch period of the ship (about 6 s). At higher sea states the fluctuations in blade rate levels are likely to be higher than this.

Table III shows the mean keel-aspect source levels of blade rate harmonic source levels at each ship speed measured. The data for fundamental blade rate show a level-versus-speed trend of approximately 25 to 70 log rpm, which is not monotonic. Particularly surprising is the sharp decrease in level of fundamental blade rate at 122 rpm (about 15 dB below the trend). There may be a hydrodynamic cause for this drop in level. These are the kind of real-world effects that complicate the attempt to model the radiated noise of merchant ships.

Shaft rate is also sometimes seen in ship noise spectra; this may be caused when one blade is damaged or fouled much more than the others. Shaft rate was not a significant source of radiated sound on this ship, but vibration at this frequency and its harmonics was detected with on-board accelerometers.

5. Low-frequency continuum

Some of the previously reported sonobuoy measurements of cargo ship noise indicated a high level of continuum noise between the blade rate tonal peaks. This continuum increased down to the lowest frequencies measured

(about 2 Hz), showing spectrum levels over 200 dB *re*: 1 μPa at 1 m in some cases.[14–16] As we noted above, this high-level continuum has been found to be an artifact caused by distortion in the sonobuoy measurement equipment. There is no evidence for such high levels in the AUTEC measurements. For instance, the continuum in the 140 rpm keel-aspect spectrum near 10 Hz has a spectrum level of less than 155 dB *re* 1 μPa at 1 m. In any case, all shallow underwater sources will tend to decrease in level at low frequencies; the pressure-release boundary condition insures this.

6. High-frequency continuum

In addition to the blade rate harmonic series, cavitation generates a wideband spectrum due to the chaotic collapse of cavities. This spectrum has a broad, high-level ''hump'' centered at about 55 Hz, followed by a continuum that decreases by 6 dB per octave on a constant-bandwidth plot, or 3 dB per octave as seen on a $\frac{1}{3}$-oct plot (see Fig. 1). Its levels in the hump region are about 5 dB higher on the starboard side. A possible reason can be suggested for this asymmetry: most of the noise may originate from the collapse of the tip vortex cavity, which occurs downstream of the blades. Vortex shedding radiation is strongly forward directive, which projects a maximum level toward the starboard side, or slightly forward of this at the propeller pitch angle (the propeller is a right-hand screw).

At high speeds this continuum can contribute a significant fraction of the radiated noise power of the ship. Above the cavitation inception speed the shape and peak frequency of the wideband cavitation spectrum do not change appreciably with ship speed. Only the overall level changes; it increases smoothly with speed according to 104 log (rpm), or about 31 dB per double speed. Similar features are universally observed on surface ships; the only distinctions are in the overall noise level and the peak frequency and shape of the cavitation hump. Hence, scaling models of the cavitation noise have been developed.[3–5,12]

The wideband cavitation noise is strongly amplitude modulated at blade rate frequency and its harmonics. This modulation envelope is clearly evident in the waveform plot shown in Fig. 4(a). Such a signal has a very high ''crest factor'' (the ratio of peak to rms values). Examination of the duty cycle of the modulated noise indicates that propeller cavitation on one blade occurs for about 15 degrees of shaft revolution at 122 rpm, and 20 degrees at 140 rpm. Directivity of the cavitation noise in a typical spectral region (340–360 Hz) is discussed in Sec. IV.

7. On-board vibration measurements

In addition to the radiated noise measurements described above, vibration measurements were conducted aboard the ship during the test period by Gray and Heine. Hull bending modes were detected at 1.05 and 2.1 Hz. A shaker was installed on the fantail upper deck to provide stable signals for reciprocity measurements of the propeller noise. The far-field pressure/force transfer function showed a strong resonance near 14 Hz, but with an overall frequency dependence that is consistent with that observed on models and other ships.[6]

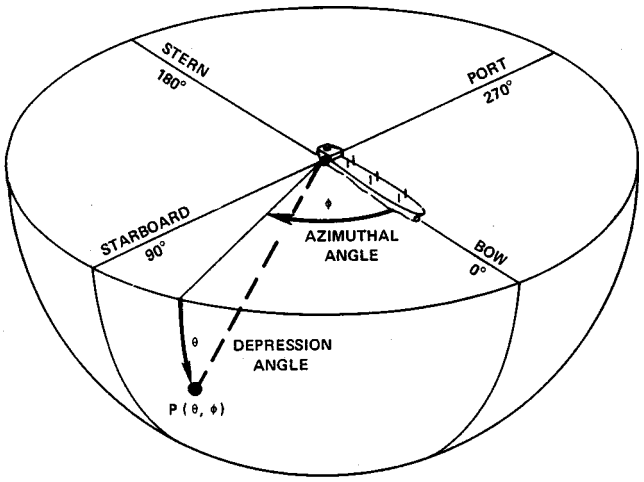

FIG. 5. Convention for defining aspect angles under the ship. The directionality is displayed as contours of source level plotted on a hemisphere of radius 1 m centered at the propeller. The hemisphere is projected onto a plan with uniform spacing of depression angles; this produces an *azimuthal equidistant projection* of the hemisphere.

IV. RESULTS—DIRECTIONALITY OF RADIATED NOISE

One of the major objectives of the measurement program was to determine the directivity of many components of the ship noise spectrum. Thousands of noise samples were processed, resulting in the directivity plots to be described below.

A. Directionality measurement considerations

For directionality measurements, the intent is to provide a more or less uniform distribution of valid measurements at all angles under the ship. This was done by developing an optimum set of measurement run geometries; the directionality data were required to have a resolution of 10×10 degrees.

Figure 5 shows the convention for defining angles under the ship. The directionality is displayed in terms of contours of constant far-field source level plotted as a function of azimuth and depression angles defining the field point direction centered at the propeller. The results are plotted (in the form of azimuthal equidistant projections) in Figs. 6–9. Contours are estimated in sectors where sample size is low; in these regions the contours are dashed. The unconventional contour level steps (154, 159, etc.) are the result of converting the original distance reference of 1 yard to 1 meter.

B. Analysis of directionality data

Some general observations can be made that apply generally to all the low-frequency radiation. For any underwater source near the free surface, the directivity pattern will contain a dipole component. The formulation of this dipole directivity pattern was given in Eq. (2). This dipole pattern will prevail when the frequency is less than about

$$f_L=\frac{rc}{4dh}, \tag{9}$$

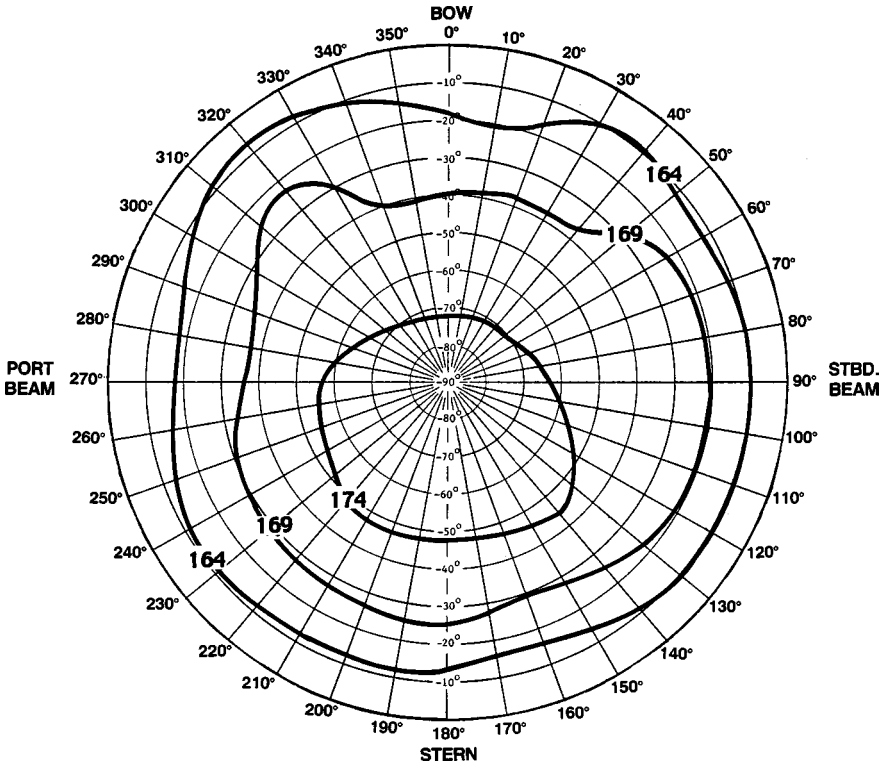

FIG. 6. Directionality of source levels of 9.3-Hz tone from blade rate at 140 rpm (16 knots), 777 samples. Format as described in the text and Fig. 5. (dB *re*: 1 μPa at 1 m.)

where h is hydrophone depth. This is the ''Lloyd frequency,'' below which the phase difference between direct and surface-reflected paths is less than π. At keel aspect, $r=h$, so the formula reduces to $f_L=c/4d$. For an assumed source depth of 1.8 m, this gives $f_L=200$ Hz. The fit to a dipole pattern tends to become better at lower frequencies and as the angle approaches the horizontal. Hence all of the directivity plots (except the figure for high-frequency noise above f_L) are dominated by a dipole pattern. Effects of multipoles, if any, will be perturbations on this basic dipole pattern.

The 9.3-Hz blade rate tone (Fig. 6) and the 24-Hz tone from the SSDG (Fig. 8) show nearly ideal dipole patterns; their contours in the azimuthal direction are approximately circular. However, the 14-Hz tone at diesel engine firing rate (Fig. 7) shows significant departures from azimuthal uniformity. On-board vibration measurements showed a strong resonance around 14 Hz that may indicate the presence of a

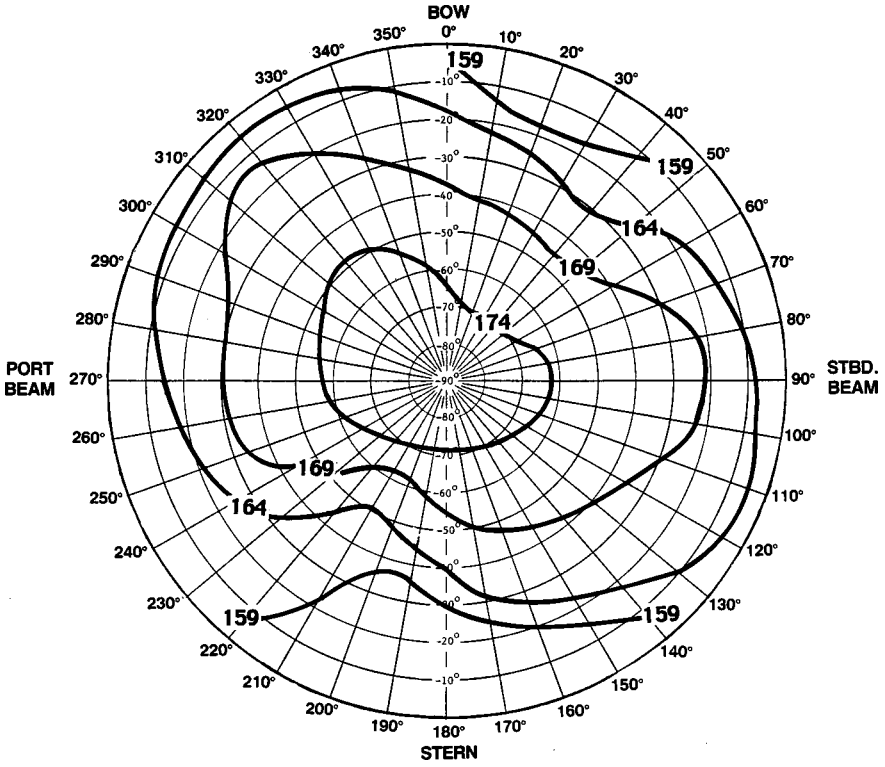

FIG. 7. Directionality of 14-Hz tone from main propulsion diesel firing rate at 140 rpm (16 knots), 719 samples. Format as described in the text and Fig. 5. (dB *re*: 1 μPa at 1 m.)

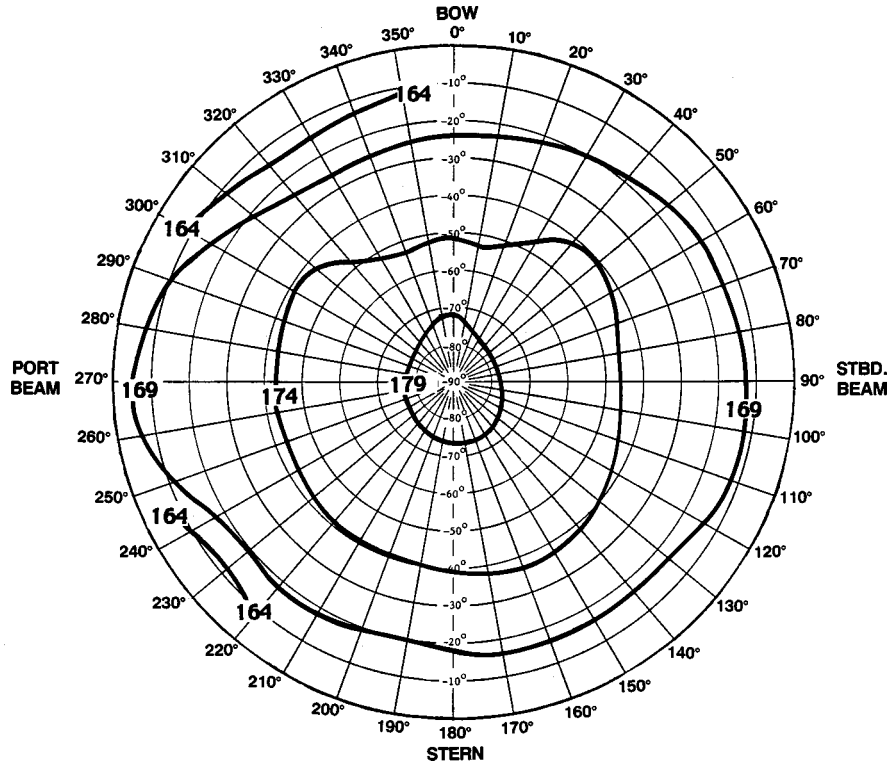

FIG. 8. Directionality of 24-Hz tone from 4× ship's service diesel generator (SSDG) rotation rate, 748 samples. Format as described in the text and Fig. 5. (dB *re*: 1 μPa at 1 m.)

hull mode that may influence the directivity in this region.

The directivity plot for a band of noise in the 340–360 Hz region (dominated by propeller cavitation) is shown in Fig. 9. At these higher frequencies, the directivity is slightly decreased in the fore and aft directions. This is a pattern that has been widely observed, in which the bow aspect radiation is partially blocked due the presence of the hull, and the stern aspect radiation is partially absorbed in the bubble wake of the ship. The levels are highest in directions somewhat forward of the beam aspects; this directivity could be the consequence of reflections of cavitation noise from the sides of the ship, or due to the geometry of the propeller.

V. PREDICTION OF PROPELLER BLADE RATE LEVELS

Since ship noise measurements are so expensive and scarce, it is important to determine whether theoretical esti-

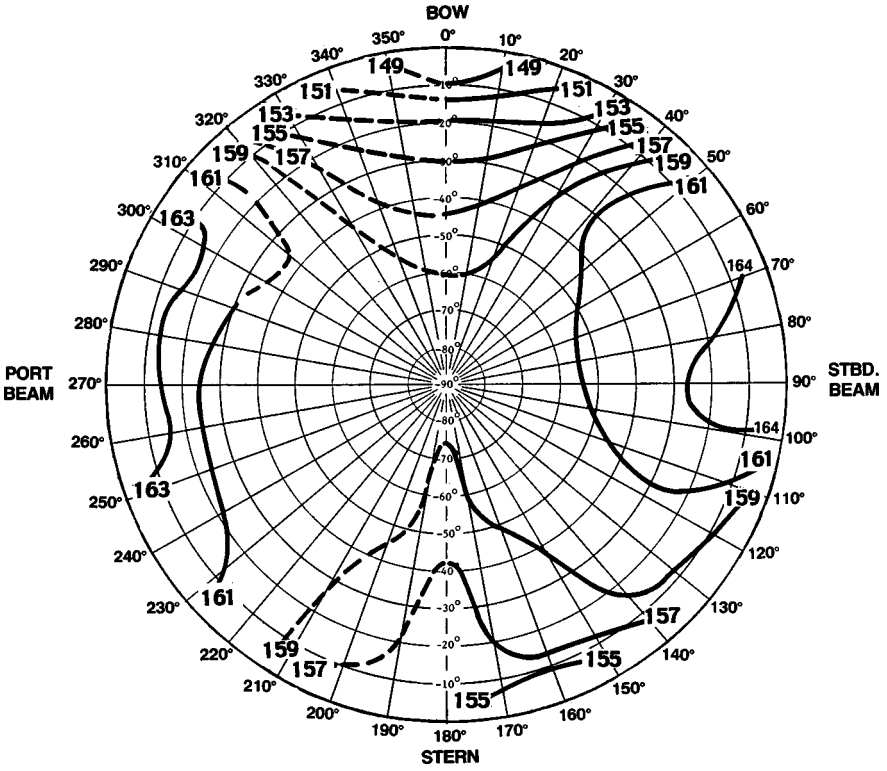

FIG. 9. Directionality of 340–360-Hz noise band from propeller cavitation at 122 rpm (14 knots), 950 samples. Format as described in the text and Fig. 5. (dB *re*: 1 μPa at 1 m.)

mates can be made with any validity. Prior to making the measurements, Gray and Greeley developed a theoretical approach to predicting blade rate noise and extended this model to the entire merchant fleet.[21,32–36] Interested readers should refer to the original reports for the details; the blade rate source level portion of their predictive model provides the following equation:

$$P_{d\mathrm{rms}} = \frac{\sqrt{2}\pi^2 \rho f^3 d V_{\max} \sin\theta}{rc}, \tag{10}$$

where $P_{d\mathrm{rms}}$ is the rms dipole pressure; r is the fluid density, f is frequency, d is the source depth, $V_{\max}$ is the maximum size of the cavity volume, θ is the radiation angle (0 = horizontal), r is distance to a field point, and c is the sound speed.

A. Complications

Notice that in Eq. (10) the acoustic pressure increases as f^3. This suggests that higher harmonics of blade rate are likely to radiate significant power. Hence the higher-order Fourier coefficients of the volume history are required for adequate modeling of blade rate radiation; but this is a very complex hydroacoustic problem. Cavity inception, growth and collapse behavior, and the consequent noise spectra are known to be affected by the following conditions:

(i) hull forms and propeller design;[34,37–39]
(ii) degree of fouling or damage of the propeller, which affects the radii of curvature of the surfaces and hence cavitation inception;
(iii) the density of cavitation nuclei in the seawater;[40] and
(iv) amount of entrained gas in the cavities,[41–43] which in turn is affected by wave height and pitch in the seaway.

These and other complexities could easily discourage any attempt to formulate a systematic prediction for propeller noise. However, it is still worthwhile to perform a comparison of the first-order prediction to these measurements to evaluate the adequacy of the simple theory.

B. Application of prediction to a specific ship

In order to deal with the effect of hull forms, Greeley devised elaborate algorithms that utilize the details of a particular ship's measured wake inflow profile and observations of the extent of cavitation on the blades in an attempt to calculate levels of the blade rate harmonic series.[33,34] Wake profiles and direct observations of cavitation were not obtained for Overseas Harriette, but use of relationships for a ship with similar hull shape and size allowed Gray and Greeley's theory to be applied to predict the dipole level of fundamental blade rate. Based on some empirical data on cavity sizes, the dipole source pressure level of blade rate is found to be given by

$$10\log_{10}(P_{d^2}) = 146 + 10\log_{10}(f^6 d^2 V_{\max^2}), \tag{11}$$

where the level is measured in dB *re* 1 μPa at 1 m. [This is Eq. (10) converted to decibels; it is a corrected version of Eq. (11) in Gray and Greeley's article.[36]] Using this approach, we obtain a predicted dipole source level of 171 dB *re* 1 μPa at 1 m at 140 rpm. The corresponding monopole level can be obtained by adding a value of $[-10\log(2kd)^2]$, which in this case adds 17 dB, yielding a monopole level of 188 dB *re* 1 MPa at 1 m.

C. Evaluation of the predictive model for blade rate levels

The measured blade rate dipole level at 140 rpm was 174 dB *re* 1 μPa at 1 m, with an uncertainty of about 2 dB. Its inferred monopole level, assuming a 1.8-m source depth, is 191 dB *re* 1 MPa at 1 m. Hence the prediction was 3 dB lower than the measured dipole source level for fundamental blade rate, but this difference is nearly within the uncertainty range of the measurements.

The AUTEC measurements (and their reasonable agreement with a simple volume-source model) indicate that, for fundamental blade rate at least, hull resonance is not an important modifier of the radiation, and continuous noise is a weak contributor to the ship noise spectrum in comparison to the pulsating cavity volume harmonics. Even entrained air in the cavity was not considered in this semi-empirical calculation. Nevertheless, Gray and Greeley's theoretical approach (which includes some estimated parameters) appears to be valid, at least for the case of fundamental blade rate of heavily-cavitating propellers at high ship speeds.

D. Determination of source depth

Most theoretical models of blade rate generation as well as models of sound propagation start by postulating an omnidirectional or monopole source under the sea surface. If acoustic data are ever to be compared on a monopole basis, or if they are to be interfaced to propagation models that require a monopole source, it is important to make an accurate determination of source depth. This point is also emphasized by Ross.[12]

Blade rate radiated levels are very sensitive to this source depth, because the dipole effect causes radiation to increase as +20 log depth, while the source level of blade rate sound decreases approximately as −50 log depth due to the decrease in cavity volume at deeper depths.[34] In the absence of direct imaging of cavitation, how can the source depth be defined accurately?

In this experiment it was determined that the ''source depth'' is also frequency dependent: the apparent monopole source depth for low-frequency blade rate harmonics is near 1.8 m, whereas the apparent depth for high-frequency wideband noise is 4.3 to 5.5 m, possibly because this is the region where tip cavities streaming off the blades collapse. Underwater images of cavitating propellers tend to support this conclusion.[45–47]

Because of the difficulties in defining actual source depths, it has been standard practice in the Navy to report surface ship noise measurements either at keel aspect or averaged over a 15–45 degree depression angle sector, ''as measured,'' with no monopole correction.[44] This method eliminates the need to make an assumption about source depth, although it does not provide sufficient information to

interface into long-range noise models. At any rate it is always important to report the propeller depth at time of testing, especially for cargo ships, in which the draft can vary widely with load conditions.

E. Determination of cavity volume

The predictive technique for blade rate outlined above is admittedly inexact; in particular more precise cavity volume estimates are desired. Imaging techniques have increasingly been applied to the direct observation and measurement of propeller cavitation. Several researchers have produced photographs of cavitating blades on full-scale ships,[45–47] and recently lasers have been used to map the shape and the volume of cavities in the laboratory.[48,49] The quantitative laboratory work, if applied to large ships, would be expected to improve the accuracy of blade rate source level models of the world fleet. However, the harmonics of blade rate sound are dependent on the time derivatives of the cavity volume. Such variations in cavity volume and shape are probably more difficult to determine even with direct imaging, because they are less repeatable than the cavity volume. At some level of detail, more precise measurements and theoretical analysis will become too expensive, and further progress in fleet noise predictions must revert to semi-empirical approaches based on statistical data from a large number of ships. This is the approach originally taken by Gray and Greeley, which still appears to be the only low-cost approach for predicting shipping noise levels.

F. Long-range propagation of surface ship noise

The directional radiation from surface ships is injected into the ocean environment, where refraction and boundaries affect acoustic propagation. At long ranges, low-frequency sound originates mainly from a fairly narrow sector of depression angles between about 4–10 degrees. The mean source levels in this sector are referred to as ''long-range effective source levels.'' At low frequencies (less than f_L) these values may be derived by subtracting $20\log[\sin q_e]$ from the dipole levels, where q_e is the long-range effective angle. Of course, for a specific environment the long-range effective angle can be more precisely calculated using a modern long-range propagation model such as that of Collins and Westwood.[50]

Data on ambient noise due to long-range shipping indicates that shipping noise constitutes a 20- to 30-dB elevation of ambient noise levels in the low frequencies relative to the natural ambient.[51] Furthermore, Ross noted that the level of noise due to shipping is increasing with time, due both to the increased number of ships and the increased engine power per ship.[11] The effect of this aspect of modern civilization on marine ecosystems is often ignored (unlike the furor generated by some underwater acoustics experiments), but it is beginning to be recognized as a problem worthy of further research.[19]

VI. SUMMARY

(1) At low speeds, the acoustic signature of the ship is dominated almost completely by tones from the ship's service Diesel generator, a series of 6-Hz harmonics. Above this speed, the ship's signature is dominated by three sources: main engine diesel firing rate harmonics, blade rate harmonics, and wideband cavitation noise. The diesel firing rate harmonics are a series of tones at six times the shaft rate. Propeller cavitation generated a series of harmonics at multiples of the blade rate frequency (four times the shaft rate). Cavitation inception speed is about 10 knots, or 86 rpm, this is the dominant source of noise at high speeds. The blade rate harmonic levels varied with speed in a complex manner. Researchers have attempted to predict the level of blade rate and its harmonics using basic engineering parameters (hull type, propeller dimensions, etc.) as inputs to predict the volume of the cavity.[34] These studies have been fairly successful in predicting levels of fundamental blade rate, but not its harmonics. This implies that the amount of cavity volume was accurately predicted. Agreement was less satisfactory for the higher harmonics of blade rate, indicating that the details of cavity volume change are not sufficiently understood to predict.

(2) It is recommended that all surface ship measurements should be accompanied by data on the propeller depth at the time of the measurements, and the angles of received radiation. This will permit data to be interfaced properly to propagation models. Also, measurements should be made in deep water and follow the other guidelines suggested in Sec. IV.

(3) Certain avenues for future research present themselves. Techniques recently developed for high-speed visualization of cavitation phenomena in the laboratory[48,49] could fruitfully be applied to full-scale ships at sea. Updated predictions of the shipping noise distribution in the world ocean, using the Gray and Greeley source modeling approach combined with advanced propagation codes,[50] could provide better estimates of the levels of ambient noise contributed by shipping for the benefit of marine mammal research programs.

ACKNOWLEDGMENTS

The efforts summarized here are derived from the work of many people from various Navy laboratories and private industry. John Cybulski of Naval Research Laboratory sponsored and coordinated the work of the program; unfortunately, he did not live to see all of its results. Orest Diachok continued to sponsor and maintain the project at the Naval Research Laboratory. Extensive theoretical studies and vibration analysis were conducted by Les Gray, David Greeley, John Heine, and others at Bolt, Beranek, and Newman, Inc. Supplementary data acquisition equipment at AUTEC was provided by Barry Douglass of Applied Measurement Systems, Inc. Data were processed by Hugh Charlton, using software developed by Michael Vandover and Johann Dretchen of Vector Research, Inc. Thanks also go to Maurice Sevik, Murray Strasberg, and Bill Blake of NSWC for encouragement and helpful discussions.

[1] *Physics of Sound in the Sea*, Summary Technical Report of Division 6, National Defense Research Committee, reprinted by Dept. of the Navy, Naval Material Command (1969).
[2] R. J. Urick, *Principles of Underwater Sound* (McGraw–Hill, New York, 1975), Chap. 10.
[3] M. Strasberg, ''Propeller Cavitation Noise After 35 Years of Study,'' in *Proceedings Symposium on Noise and Fluid Engineering* (ASME, New York, 1977), pp. 89–99.
[4] W. K. Blake, ''Aero-Hydroacoustics for Ships,'' David Taylor Naval Ship Research & Development Center Report 84/010 (June 1984), Chap. 4.
[5] T. ten Wolde and A. de Bruijn, ''A New Method for the Measurement of the Acoustical Source Strength of Cavitating Ship Propellers,'' Int. Shipbuilding Progress **22**, 385–396 (1975).
[6] T. ten Wolde, J. W. Verheij, and H. H. Steenhoek, ''Reciprocity method for the Measurement of Mechano-Acoustical Transfer Functions,'' J. Sound Vib. **42**(1), 49–55 (1975).
[7] A. de Bruijn, ''Acoustic Source Strength of Propeller Cavitation,'' in *Proceedings International Conference on Noise Control Engineering* (1979), pp. 659–664.
[8] S. Fish and J. N. Blanton, ''Analysis of Propeller Wake Flow Visualization Near a Free Surface,'' David Taylor Research Center Report DTRC/SHD-1268-03 (November 1988).
[9] P. Kaplan and S. J. Kim, ''Analysis and Extension of Theory for Predicting Propeller Field Pressures and Blade Forces Due to Cavitation,'' Virginia Polytechnic Inst. and State Univ. Report VPI-AERO-157 (December 1986).
[10] N. E. Fine, ''Nonlinear Analysis of Cavitating Propellers in Nonuniform Flow,'' Massachusetts Inst. of Technology Dept. of Ocean Engineering report, NTIS No. AD-A258215/3 (16 October 1992).
[11] D. Ross, ''Trends in Merchant Shipping (1969–1980),'' Tetra Tech, Inc. Report TT-SD-449-75-1 (April 1975).
[12] D. Ross, *Mechanics of Underwater Noise* (Pergamon, New York, 1976).
[13] ''A Pilot Study for Underwater Radiated Noise Measurements of Merchant Ships from Aircraft,'' Naval Oceanographic Office TN-6130-2-76 (1975).
[14] J. Cybulski and E. B. Wright, ''Contributions to VLF noise by merchant ships,'' J. Acoust. Soc. Am. (Suppl. 1) **67**, S96 (A) (1980).
[15] E. B. Wright and J. Cybulski, ''Low-Frequency Acoustic Source Levels of Large Merchant Ships,'' Naval Research Laboratory Report 8677 (March 1983).
[16] J. Cybulski, ''Probable Origin of Measured Supertanker Radiated Noise Spectra,'' in Oceans '77 Conference Record (1977), Vol. 1, 15C-1-8.
[17] S. H. Moritz, ''The Generation of Noise by Surface Ships: A Description of the Principal Sources,'' TRW Report for Naval Ocean Research and Development Activity (15 March 1980).
[18] A. Bowles, ''Noise rules for protecting marine mammals,'' in *Echoes* (newsletter of the Acoust. Soc. of Am.) **3**(2) (Summer 1993).
[19] ''Low-Frequency Sound and Marine Mammals: Current Knowledge and Research Needs,'' Committee on Low-Frequency Sound and Marine Mammals, Ocean Studies Board, National Research Council (National Academy, Washington, DC, 1994), Appendix C.
[20] P. T. Arveson, ''Radiated noise characteristics of M/V OVERSEAS HARRIETTE, a modern cargo ship,'' J. Acoust. Soc. Am. **89**, 1983(A) (1991).
[21] J. Heine and L. M. Gray, ''Merchant Ship Radiated Noise Model,'' Bolt Beranek and Newman, Inc. Report 3020 (August 1976).
[22] M. Ohlrich, ''Response of Bedplates and the Transmission of Structure-borne Sound in the Bottom Structure of Ships,'' in *Proceedings of the International Conference on Noise Control Engineering* (1979), pp. 635–639.
[23] A. Nilsson, ''Propeller Induced Hull Plate Vibrations,'' in *Proceedings of the International Conference on Noise Control Engineering* (1979), pp. 641–644.
[24] L. Noordzij, P. Van Oossanen, and A. M. Sturman, ''Radiated Noise of Cavitating Propellers,'' *Proc. Symposium on Noise and Fluid Engineering* (ASME, New York, 1977), pp. 101–108.
[25] P. Van Oossanen, ''Theoretical Prediction of Cavitation on Propellers,'' Marine Technol. Soc. J. **14**, 391–409 (1977).
[26] K.-Y. Chao, ''On the Practical Calculation of Pressure Distributions and Cavity Extents on Propeller Blades,'' in *2nd International Symposium on Practical Design in Shipbuilding* (1983), pp. 123–130.
[27] Y. Okamoto and Y. Kasahara, ''Experimental and Theoretical Investigations of Hull Pressure Fluctuations Caused by a Cavitating Propeller,'' in *Proceedings of the International Symposium on Propellers and Cavitation* (1986), pp. 79–86.
[28] Y. Yuanpei, Z. Youning, J. Zhiye, S. Minguan, and W. Tiankui, ''A Comparison of Suction and Pressure Side Cavitation Characteristics of Ducted Propeller Blades,'' in *Proceedings of the International Symposium on Propellers and Cavitation* (1986), pp. 250–260.
[29] R. T. Beyer, *Nonlinear Acoustics*, Naval Sea Systems Command (1974), Chap. 4.
[30] L. Noordzij and L. van Wijngaarden, ''Relaxation Effects, Caused by Relative Motion, on Shock Waves in Gas-bubble/Liquid Mixtures,'' J. Fluid Mech. **66**, 115–143 (1974).
[31] N. P. Tyvand and B. Persson, ''Prediction of Noise from a Cavitating Propeller,'' in *International Conference on Noise Control Engineering* (1979) pp. 649–652.
[32] L. M. Gray and D. S. Greeley, ''A Generalized Model for Predicting the Wake Field of Merchant Vessels,'' Bolt Beranek and Newman, Inc. Technical Memorandum 279 (February 1977).
[33] L. M. Gray, D. S. Greeley, and L. Sledjeski, ''Estimation of Propeller Cavitation Volume Velocity for Merchant Vessels,'' Bolt Beranek and Newman, Inc. Technical Memorandum 319 (February 1977).
[34] D. S. Greeley, ''Calculation of Low Frequency Cavitation Source Strength of Marine Propellers,'' Bolt Beranek and Newman, Inc. Technical Memorandum 459 (July 1978).
[35] L. M. Gray, ''Characteristics of low-frequency propeller noise generated by merchant vessels,'' J. Acoust. Soc. Am. Suppl. 1 **67**, S96 (1980).
[36] L. M. Gray and D. S. Greeley, ''Source level model for propeller blade rate radiation for the world's merchant fleet,'' J. Acoust. Soc. Am. **67**, 516–522 (1980).
[37] C. A. Johnsson, ''Simple Methods for First Estimate of Propeller Induced Pressure Fluctuations and Vibration,'' in *International Symposium on Practical Design in Shipbuilding* (1983), pp. 303–310.
[38] H. Yamaguchi, H. Kato, S. Tokano, and M. Maeda, ''Development of New Marine Propellers with Improved Cavitation Performance,'' in *International Symposium on Propeller and Cavitation* (1986), pp. 71–78.
[39] F. Lange and S. Zurnatzis, ''Shipboard Noise Caused by Cavitating Propellers and Design Methods to Reduce it,'' in *Proceedings of the European Conference on Underwater Acoustics* (1992), pp. 237–240.
[40] C. Brennen, ''Observations of Cavitating Flows,'' in *Twentieth Symposium on Naval Hydrodynamics* (National Academy, 1996), pp. 247–267.
[41] F. G. Hammitt, ''Effects of Gas Content Upon Cavitation Inception, Performance, and Damage,'' Michigan Univ. Report UMich-01357-19-T (June 1971).
[42] A. F. Lehman, ''The Influence of Free Air Bubbles on Cavity Volume and the Associated Noise Signature,'' Oceanics, Inc. Report 64-14 (August 1964).
[43] G. Reisman, E. McKenney, and C. Brennen, ''Cloud Cavitation on an Oscillating Hydrofoil,'' in *Twentieth Symposium on Naval Hydrodynamics* (National Academy, Santa Barbara, 1996), pp. 328–340.
[44] P. T. Arveson, ''Effects of Frequency, Temporal and Spatial Averaging on Image Interference,'' David Taylor Research Center Report SAD-90/35E/1975 (February 1990).
[45] K. O. Holden, A. Sorenson, S. Andersen, and D. Karlsen, ''Propeller Blade Cavitation as a Source of Vibrations—Full Scale Experiences,'' Norwegian Maritime Research **4**, 2–22 (1974).
[46] W. Dazheng, J. Dashan, and Z. Zhongye, ''Study on Cavity Characteristics and Fluctuating Pressure Induced by Cavitating Propeller,'' in *Proceedings International Symposium on Propeller and Cavitation* (1986), pp. 173–181.
[47] N. Bobanac, ''Full Scale Observation of Propeller Blade Cavitation on a Fast Small Ship,'' Brodogradnja [Quarterly J. of Naval Architecture and Shipbuilding Industry, Croatia] **40**, 117–120 (1992).
[48] H. D. Stinzing, ''Cavity Thickness on Rotating Propeller Blades—Measurements by Two Laser Beams,'' in *Eighteenth Symposium on Naval Hydrodynamics* (National Academy, Ann Arbor, 1991), pp. 319–330.
[49] Y. Ukon, T. Kudo, and Y. Kurobe, ''Measurement of Cavity Thickness Distribution on the Blade of Propeller Models by Laser-CCD Method,'' *ASME FED Symposium on Cavitation* (1991), pp. 99–104.
[50] M. D. Collins and E. K. Westwood, ''A higher-order energy-conserving parabolic equation for range-dependent ocean depth, sound speed, and density,'' J. Acoust. Soc. Am. **89**, 1068–1075 (1991).
[51] G. M. Wenz, ''Acoustic ambient noise in the ocean: spectra and sources,'' J. Acoust. Soc. Am. **34**, 1936–1956 (1962).

The Rayleigh-like collapse of a conical bubble

T. G. Leighton, B. T. Cox, and A. D. Phelps
Institute of Sound and Vibration Research, University of Southampton, Southampton SO17 1BJ, United Kingdom

(Received 1 June 1998; revised 24 February 1999; accepted 2 July 1999)

Key to the dynamics of the type of bubble collapse which is associated with such phenomena as sonoluminescence and the emission of strong rebound pressures into the liquid is the role of the liquid inertia. Following the initial formulation of the collapse of an empty spherical cavity, such collapses have been termed ''Rayleigh-like.'' Today this type of cavitation is termed ''inertial,'' reflecting the dominant role of the liquid inertia in the early stages of the collapse. While the inertia in models of spherical bubble collapses depends primarily on the liquid, experimental control of the liquid inertia has not readily been achievable without changing the liquid density and, consequently, changing other liquid properties. In this paper, novel experimental apparatus is described whereby the inertia at the early stages of the collapse of a conical bubble can easily be controlled. The collapse is capable of producing luminescence. The similarity between the collapses of spherical and conical bubbles is investigated analytically, and compared with experimental measurements of the gas pressures generated by the collapse, the bubble wall speeds, and the collapse times. © *2000 Acoustical Society of America.* [S0001-4966(90)00301-0]

PACS numbers: 43.25.Yw, 43.35.Ei [DLB]

INTRODUCTION

This paper compares experimental results with the predictions of an analysis for the collapse of a conical bubble, which adapts to a conical geometry the pioneering formulations of Rayleigh[1] and Noltingk and Neppiras.[2,3] Rayleigh considered the collapse of an empty cavity that remains spherical at all times, located in an incompressible liquid. The empty cavity is envisaged to be formed at rest ''as if a spherical portion of the fluid is suddenly annihilated'' [4] and, because of the hydrostatic pressure in the liquid, subsequently collapses. The wall speed becomes undefined as the radius approaches zero, a singularity that can be resolved by incorporating some permanent gas within the cavity.[1] Noltingk and Neppiras[2,3] incorporated this model of the collapse phase into a scheme in which the bubble first grows isothermally from an initial equilibrium size, subsequently undergoes adiabatic collapse, and then oscillates between maximum and minimum sizes (the addition of damping would cause the amplitude and period of these oscillations to decrease in time). Such so-called ''inertial'' collapses (reflecting the importance of the liquid inertia) were experimentally associated with the emission of liquid shocks at rebound, and the generation of sonoluminescence. Although theory has advanced considerably beyond the adiabatic models[5,6] (in line with developments in the observation of single-bubble sonoluminescence[7,8] and the issues it raises[9–14]), the transparency of the early models[1–3] has here been exploited to discuss the dynamics of conical bubbles, in a system where it is possible to modify the liquid inertia. The gas and liquid pressures can be measured, and the collapsing bubble wall photographed. The results are compared with a theory that adapts the analysis of Rayleigh, now more than 80 years old, for the inertial collapse of a conical bubble.

I. MATERIAL AND METHODS

A. Apparatus

Figure 1 shows the apparatus in which a gas pocket collapses into an otherwise liquid-filled conical hollow (of half-angle $\theta = 30$ degrees). Milled from polymethylmethacrylate (PMMA), the hollow has a circular horizontal cross section, 60-mm diameter at its base where it connects flush onto a steel U-tube. This is partially filled with degassed water at 15–17 °C, which can flow from the tube into the cone. At equilibrium, under ~0.1 MPa static pressure, a gas bubble of millimeter-order radius sits at the top of the cone. Then the top-plate is closed and the pumping train activated, reducing the static pressure in the tube so that the bubble undergoes relatively slow growth. After the bubble has expanded to the required size, the spring-loaded top-plate is opened. A pressure pulse of approximately 0.1 MPa propagates down the U-tube, causing the collapse of the bubble. The signal from an accelerometer on the top-plate provides the trigger for the various data acquisition systems (see below). The conical geometry not only allows the imaging of a ''cross section'' of the luminescing bubble (45% ± 5% of photons produced at the tip reaching the cone exterior). It also allows the positioning of pressure transducers within the gas, and within the surrounding liquid, since the center of the collapse is well defined. Define the variable ''bubble radius'' R_c as the vertical distance from the cone apex to the meniscus. Because the cross-sectional area in the cone increases with distance from the apex (r_c), the flow velocity of the liquid (of density ρ, assumed to be incompressible) decreases in proportion. Equating the flux at the position of the meniscus ($r_c = R_c$) to that across some cross section of the cone below it gives

$$\dot{R}_c dt \pi R_c^2 \tan^2\theta = \dot{r}_c dt \pi r_c^2 \tan^2\theta \Rightarrow \dot{R}_c/\dot{r}_c = (r_c/R_c)^2. \quad (1)$$

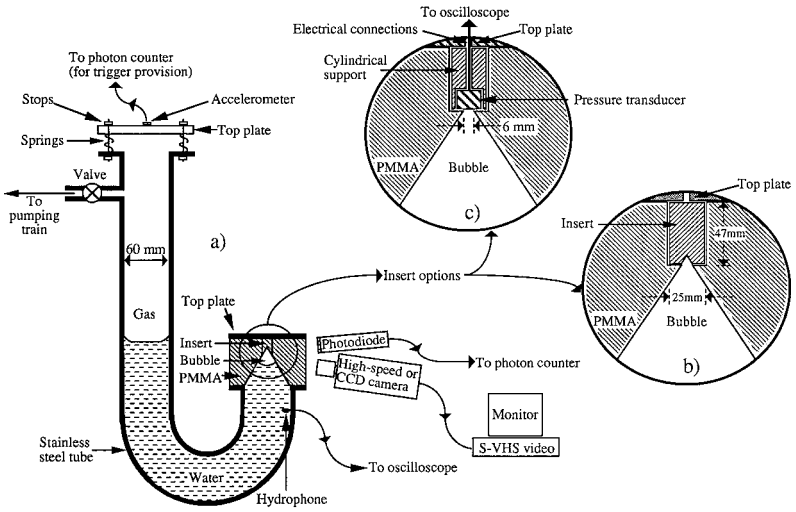

FIG. 1. (a) Diagram of the apparatus. (b) Insert showing the detail of the cone tip. (c) Insert showing detail of truncated cone, used for mounting pressure transducer.

Hence the liquid flow in the cone diverges and converges as in spherically symmetric conditions, within the limitations of the model (the actual nature of the flow is discussed in Sec. I B). In contrast, the flow in the U-tube has approximately one-dimensional geometry. This means that the inertia of the liquid is proportional to the length of fluid in the pipe.[15] Therefore, unlike the spherically symmetric case, the inertia does not converge to a finite value as one takes into account fluid at increasing distances from the bubble center. So by increasing the length of liquid in the U-tube, the inertia associated with the bubble collapse can be greatly increased.[16]

Optical instruments were deployed to study the collapse. A single frame was always taken with a stills camera immediately prior to the opening of the plate, in order to record the maximum bubble radius. Luminescence was monitored using a photon counting module (EG&G SPCM-200), which used a cooled avalanche silicon photodiode, and emitted a Transistor-Transistor Logic (TTL) pulse on detection of a photon. These were counted by a multi-channel scaler (EG&G T914P). The dark current was 25 counts/second. The counter was triggered by the accelerometer on the top-plate. Even when not required for photon counting, this system was always in use since, on receipt of the top-plate accelerometer signal, it provided the TTL signal which triggered the oscilloscope and provided a time marker for the high-speed film (see below).

During the photon counting, images of the luminescence were taken using a CCD camera (Photonic Science DS800). Operating at 25 f.p.s. (frames per second), it interlaced two fields, each of 40-ms duration but 20 ms out of phase (see Ref. 17 for details of exposure, persistence, video recording, etc.). High-speed images were taken of the bubble collapse using a Kodak Ektapro EM high-speed digital video camera. It could film at up to 1000 f.p.s. full-frame, or at 6000 f.p.s. with each frame occupying $\frac{1}{6}$ of the image screen. The top-plate accelerometer signal triggered a single flash signal, which allowed a common time basis between the film and the pressure signals, described below.

Because of their different ambient light requirements, the two camera systems could not be deployed simultaneously. However, instrumentation to measure the pressure of the liquid could be used simultaneously with each of them. These instruments were mounted in the 62-mm-tall PMMA extension to the shorter leg of the U-tube [Fig. 1(a)]. Within this extension, a pressure transducer (Bruel and Kjaer 8103 hydrophone), its center 10 cm below the apex of the cone, recorded the pressure fluctuations within the liquid. This system replaced the one used by Leighton *et al.*[17,18] which was prone to damage. Both systems could detect the rebound pressure pulses emitted by the bubble. (However, only the B&K 8103 system used here could be guaranteed to measure the amplitude of the rebound pressure pulses, since the amplitudes of these were beyond the range of the calibration available for the sensor used previously.[17]) Both systems could detect the reflections of these pressure pulses from the ends of the water column. However, unlike the sensor used by Leighton *et al.*,[17,18] the more robust Bruel and Kjaer device was not capable of measuring the pressure wave which propagates through the U-tube in response to the opening of the plate. According to the manufacturers, this hydrophone should behave linearly up to 4 MPa. Its calibration was checked regularly during the experiments and was stable to $\pm 0.5\%$. The spatial variation in the pressure pulses can be examined by the use of multiple sensors.[19]

The apex of the cone was itself designed to take two types of polycarbonate insert (described fully by Leighton *et al.*[17]), of 47-mm length and 25-mm outer diameter. The first [Fig. 1(b)] simply continues the conical hollow to the apex (and was used for all the results here except those of Fig. 8). If a collapse damaged the apex, it was easily replaced. The second type of insert [Fig. 1(c)] truncates the cone 5.25 mm before the apex by placing there a transducer (Keller PA-8, having 30-kHz resonance) which the manufacturers calibrate up to 100 MPa. However, here only the central circular area (6.05-mm diameter) of the full 13.0-mm-diam face of the transducer is exposed, and so an appropriate correction factor had to be employed in the measurement of gas pressure.[18] A third type of insert, not shown here, allows electrochemical sensors to be placed at the apex. These can monitor the regrowth of an oxide layer on an electrode there following its erosion by the collapse.[20] This allows measurement of the effects of erosion on a millisecond time scale.

The use of a U-tube with a conical termination was pioneered by Henwood and co-workers (Kosky and Henwood[19]

and Hawtin *et al.*[21]). It was used, however, to study a very different form of bubble activity: the condensation and oscillation of vapor bubbles. They had a particular interest in pressure transients, because of the implications for the generation and detection of accidental subcooled boiling in liquid-metal-cooled nuclear reactors. They photographed the vapor bubble, and recorded pressure transients along the length of the U-tube. Data from the system was compared with a model of the collapse of such vapor cavities by Hawtin *et al.*[21]

The theory and experiments reported in these earlier studies[19,21] are very different from the work reported here. In both cases it is the pressure difference exerted at the opposite ends of the water column that drives the motion. However, in the model used by Hawtin *et al.*[21] the pressure on the ''bubble wall'' is determined by the vapor pressure. In the current study the pressure is determined by the permanent gas, and the motion dominated by the inertia associated with the liquid.[18]

Hawtin *et al.*[21] concentrated on making measurements at higher temperatures, where the cavity dynamics are very different from the violent collapses studied here. For example, at temperatures in excess of 75 °C, they found that the pressure at the cone apex rose and fell relatively gently, over amplitudes of atmospheric order and time scales of around 50 ms, the rises coinciding with the contraction of the cavity and the falls with its expansion. The minimum bubble ''radius,'' achieved at the end of the compression phase, was in excess of 7 cm. This is the oscillation of a vapor cavity, and not an inertially dominated cavitation collapse of the type studied here. Inertia will in fact become a key factor at temperatures below ~55 °C, and Hawtin *et al.*[21] reported several difficulties in making observations in this lower temperature regime. These included the failure to find vapor cavities of an observable size at the first rebound below 69 °C (their theory had suggested this would be possible down to 50 °C), and to make measurements of the tip pressures below ~55 °C.

Summarizing their findings, Hawtin *et al.*[21] compare their theory against observations of tip pressures ($<$15 MPa), and collapse times ($>$30 ms), which are smaller and slower (respectively) than those found in the current study by around an order of magnitude. The minimum ''radius'' attained by their bubbles, at the end of the first collapse is, by comparison with the current study, very large ($>$5 cm). Measurements of these three parameters agree with their theory only for liquid temperatures in excess of ~60 °C.

The problems encountered by Hawtin *et al.*[21] when attempting to study and model their system at lower temperatures are not unexpected. Hawtin *et al.*[21] state that their theory cannot, for example, predict maximum pressures if the precollapse vapor pressure is below about 15 kPa. They give the reason as being the inapplicability of simple incompressible hydrodynamics when the collapse becomes more violent. It should be noted that 15 kPa corresponds to the vapor pressure of water at ~55 °C (the vapor pressure at the temperatures of the current study being roughly 1.7 kPa).[22] The theory outlined in the following section also assumes an incompressible liquid, but, by balancing the kinetic energy of the liquid with the work done by the liquid pressure and a permanent gas component, it can be compared with inertially dominated collapses at room temperature.

B. Analysis

Consider the following idealized bubble history. All the experiments begin with the injection of a small bubble into the cone, via a flexible pipe that is then removed, the top-plate remaining open to the atmosphere. Buoyancy causes the bubble to sit close to the cone apex, and prior to growth the bubble is sufficiently small to remain approximately spherical (with radius R_f). The ambient pressure (comprising atmospheric, hydrostatic, and Laplace components), and the gas pressure inside the bubble, are in equilibrium. The partial vacuum is applied, and the bubble grows to a maximum radius of R_i (defined as the vertical distance from the cone apex to the meniscus). At this time, the internal gas pressure is $p_{g,i}$. A still photograph is taken, recording R_i, and then the vacuum released. A pressure pulse travels down the U-tube. On reaching the bubble wall, it reflects back along the pipe, towards the flat meniscus at the top of the long leg of the U-tube. The bubble collapses into the cone, the increasing gas pressure eventually slowing the collapse. When the bubble reaches minimum radius $R_{\min}$ with maximum internal pressure $p_{g,\max}$, rebound occurs, and a pressure pulse is emitted down into the liquid. As with the initial pressure step, all the rebound pulses continually recross the tube, reflecting from either end, until dissipated.[17] The bubble expands to a maximum size, then collapses again. If there were no dissipation, this process would repeat endlessly, the bubble always achieving the same maximum and minimum sizes (with the same maximum gas pressures), and the time between the emission of rebound pressure pulses would be constant. Damping causes the amplitude of oscillation, and the time between rebounds, to decrease steadily, such that in the end a small spherical bubble is undergoing small-amplitude, linear pulsations near the cone apex. If there is no mass loss or gain from the bubble, and the ambient conditions are the same as those prior to the imposition of the vacuum, then that bubble will have radius R_f. In practice, the bubble fragments after its first rebound, although (because of subsequent coalescence and collective behavior of the fragments) continued growth/collapse cycles do occur which resemble the behavior that would be expected of a bubble which did not fragment.[17,18] The nature of these cycles will be explored in more detail in this paper.

The analysis[18] concentrates on the initial growth, and the first collapse up until the bubble reaches minimum size. Although the meniscus is assumed to be flat throughout, it is not difficult to adapt the calculation for a curved meniscus, though this is less relevant to the precollapse conditions. The analysis considers the energy balance before and after the start of the collapse. The increase of kinetic energy of the liquid in the tube and cone must be equal to the work done by the gas at the interface as the bubble collapses, and the radius reduces from its precollapse value, $R_c = R_i$. At the start of the collapse, when $R_c = R_i$ and $\dot{R}_c = 0$, the gas within the bubble has pressure $p_{g,i}$ and temperature T_i. If there is no heat flow across the bubble wall (which is valid if the

collapse speed is fast), the gas pressure p_g and bubble volume follow an adiabatic relationship. Balancing the energies during the collapse in the manner outlined above gives an expression for the speed of the bubble wall:

$$\dot{R}_c^2=\frac{\left(\frac{r_{\max}}{R_c}\right)^4\frac{\pi\tan^2\theta}{3}\left[p_L(R_i^3-R_c^3)-\frac{p_{g,i}R_i^3}{(\gamma-1)}\left(\left(\frac{R_i}{R_c}\right)^{3(\gamma-1)}-1\right)\right]}{\frac{1}{2}\rho A_0\left[\left(\frac{1}{R_c}-\frac{1}{r_{\max}}\right)r_{\max}^2+\left(h_i-\frac{1}{A_0}\frac{\pi}{3}\tan^2\theta(R_i^3-R_c^3)\right)\right]}, \tag{2}$$

where $r_{\max}=52$ mm is the vertical distance from the apex to the base of the cone (where the cross-sectional area is $A_0=2.8\times10^{-3}\,\mathrm{m}^2$, the same as that in the U-tube), γ is the ratio of the specific heat of the gas at constant pressure to that at constant volume, and p_L is the pressure in the liquid at the bubble wall.

The numerator in Eq. (2) represents the energy terms from the work done by the liquid and the gas. The $\dot{R}_c^2 \propto(r_{\max}/R_c)^4$ dependence arises naturally from the inverse square divergence with distance of the liquid particle velocity in the cone [Eq. (1)]. Since $p_{g,i}$ represents the initial pressure of the gas in the bubble, the terms in Eq. (2) with which it is multiplied account for the work done by the bubble gas on the liquid. The other term in the numerator of Eq. (2) represents the work done by the liquid pressure, p_L.

The denominator in Eq. (2) is the inertia multiplied by a factor of $\frac{1}{2}$. Multiplying it by $\dot{R}_c^2$ gives the kinetic energy term in the energy balance which Eq. (2) represents. The first term in the denominator represents the inertia of the liquid in the cone; and the second, that of the liquid in the tube. The symbol h_i represents the initial length of liquid in the U-tube. As the collapse proceeds, liquid flows from the tube into the cone (the length of liquid in the column at the end of the collapse is about 2 cm shorter than its initial value). This reduces the inertia of the liquid remaining in the U-tube, and the expression following h_i in Eq. (2) corrects for this.

Therefore if $p_{g,i}$ in Eq. (2) is set to zero, and the gas content of the bubble is effectively removed, this would give an expression for $\dot{R}_c^2$ which would be obtained were the conical bubble to collapse in the manner of a Besant cavity, as characterized by Rayleigh for the spherical bubble.[1] It is not possible to generate a formulation for the collapse time through integration of Eq. (2) in the way that Rayleigh did for the spherical cavity. However, the collapse times predicted from Eq. (2) can be calculated numerically for both empty and gas-filled cavities, and compared with experimental measurements (see Sec. II). The collapse time is given by

$$t_{\mathrm{coll}}=\int_{R_{\min}}^{R_i}\frac{dR_c}{\dot{R}_c}, \tag{3}$$

which was calculated numerically using a routine based on Simpson's midpoint rule.

As described earlier, the conical bubble starts the collapse with a zero wall velocity and a maximum radius R_i, the gas within the bubble having pressure $p_{g,i}$ and temperature T_i. The wall velocity will next be zero at the minimum radius $R_{\min}$, when the pressure and temperature of the gas within the bubble are at a maximum, $p_{g,\max}$ and $T_{\max}$, respectively. Assuming no break-up, the bubble will then rebound to a maximum size of $R_{\max}$ which, if there are no losses, will also equal R_i. The positions of maximum and minimum radius are found by setting $\dot{R}_c=0$ in Eq. (2), such that

$$\left[p_L(R_i^3-R_c^3)-\frac{p_{g,i}R_i^3}{(\gamma-1)}\left(\left(\frac{R_i}{R_c}\right)^{3(\gamma-1)}-1\right)\right]=0 \qquad (R_c=R_{\max},R_{\min}). \tag{4}$$

As expected, one solution to Eq. (4) gives the position of $R_{\max}=R_i$, the initial radius. The other solution occurs at $R_c=R_{\min}$. Simple estimates in the limit of $R_{\min}\ll R_i$ can be made by simplifying Eq. (4), to give

$$R_{\min}=R_i\left(\frac{p_{g,i}}{p_L(\gamma-1)}\right)^{1/3(\gamma-1)}. \tag{5}$$

The only value which is unknown in this expression is $p_{g,i}$, the initial gas bubble pressure. Provided mass transfer across the bubble wall is negligible, $p_{g,i}$ can be estimated from the final, postcollapse conditions, as follows. As described above, after the plate has been released and all the energy has been dissipated from the collapse, experimental observations have shown a spherical bubble lying at rest just below the tip of the cone. The differences in state between this bubble and the initial bubble (before plate opening) are governed by an isothermal relationship in volume and pressure, as both states will be at the initial temperature T_i. Hence,

$$p_{g,i}\frac{\pi}{3}R_i^3\tan^2\vartheta=p_L\frac{4}{3}\pi R_f^3\Rightarrow p_{g,i}=\frac{4}{\tan^2\vartheta}\left(\frac{R_f}{R_i}\right)^3p_L, \tag{6}$$

where R_f is the spherical radius of the final bubble in the cone tip. It is assumed that the static liquid pressure on the bubble prior to growth equals the pressure step p_L which collapses the bubble. Equation (6) ignores the contribution to the internal pressure of the bubble due to the difference in height of the liquid in the two legs of the U-tube, and also any contribution due to the Laplace pressure (which, for a 1-mm-radius bubble, will be ~0.1% of the static pressure contribution). A more complete form of the theory, which includes the height difference, predicts that there is a negligible change in the collapse conditions from the approximate version considered here.

However, although the estimate for $R_{\min}$ calculated from the assumption that $R_{\min}\ll R_i$ described in Eq. (5) is valid for large initial meniscal displacements, a more exact solution is available through calculation of $R_{\min}$ iteratively using Newton–Raphson's method. This is done by Leighton

et al.,[18] who showed that as the initial bubble size becomes smaller, Eq. (5) overestimates $R_{\min}$, compared to the predictions of the iterative calculation. This becomes important in calculating the maximum tip pressures, and the more complete form is used in the calculations presented in this paper. The maximum pressure achieved in the collapse, at a time when $R_c = R_{\min}$, can be found from assuming the collapse to be adiabatic, and using the expression for $p_{g,i}$ derived in Eq. (6):

$$p_{g,\max} = p_{g,i}\left(\frac{R_i}{R_{\min}}\right)^{3\gamma} = \left[\frac{4}{\tan^2\vartheta}\left(\frac{R_f}{R_i}\right)^3\right]^{1/(1-\gamma)}[(\gamma-1)]^{\gamma/(\gamma-1)}p_L. \quad (7)$$

Following the same reasoning and approximations, the maximum temperature reached in the bubble can be expressed as

$$T_{\max} = T_i\left(\frac{R_i}{R_{\min}}\right)^{3(\gamma-1)} = \left[\frac{4}{\tan^2\vartheta}\left(\frac{R_f}{R_i}\right)^3\right]^{-1}(\gamma-1)T_i. \quad (8)$$

This model, therefore, begins with an adaptation of the 1917 Rayleigh calculation, and then incorporates a permanent gas phase with an isothermal growth stage and an adiabatic collapse, which dates from the Noltingk–Neppiras model of the 1950s. The analysis will be compared with experimental observations in a system where direct visual observation is possible of both growth and collapse, where the precollapse bubble size can be controlled, and where pressure sensors can be placed within the bubble gas and within the liquid outside the bubble wall.

The emphasis is to show how far this historical analysis can be taken in predicting the bubble dynamics in this novel situation. There are clear approximations. The liquid is assumed to be incompressible. The vapor is ignored, and (as shown by Hawtin *et al.*[21]) this will have a role in certain circumstances. The tip pressure is assumed to be generated by gas compression and not, for example, by liquid impact. The Reynolds number for the flow in the pipe ($\mathrm{Re} = \rho d u/\eta$, where $d = 0.06$ m is the pipe diameter and u is the flow velocity there) takes a maximum value of $\sim 10^5$ (Fig. 5). This indicates turbulent conditions. Combining this with the wall roughness allows the pressure loss resulting from wall friction to be estimated[23] at around 250 Pa, which is small compared with both the 0.1-MPa pressure which initiates bubble collapse and the bubble gas pressures which retard it.

II. RESULTS

A. High-speed photography

Figures 2 and 3 show a selection of 16 frames from a consecutive sequence of 305, filmed at 1000 f.p.s. (each frame occupying full screen). In discussing the collapse shown here, attention will be paid to the highlights that appear in the cone as a result of reflection and refraction of the backlighting. This is because in Fig. 4, a sequence filmed at 6000 f.p.s., the use of similar highlights is necessary to locate the features in these more complicated images. Figure 2(b) is a frame-by-frame schematic illustration to assist in the identification of features in Fig. 2(a) [and Fig. 3(b) similarly relates to Fig. 3(a)]. The first highlight is indicated in frame 1, arrowed in Fig. 2(a) and labeled in Fig. 2(b). This frame corresponds to the precollapse phase, when the bubble fills the entire region of the cone shown in the figure. The highlight is a white line, aligned with the cone axis, extending from ~1 mm below the cone tip down to ~5 mm below the cone tip. The appearance of the apex highlight can be used to qualitatively distinguish between two states. If it is visible, the top 5 mm of the cone contains a coherent gas pocket that fills the apex to a sufficient degree (Fig. 2 frames 1–3, 15–16; Fig. 3, frame 25). If it is not visible, this region accommodates enough water to be described as containing either ''clear water'' (a loose description of water having a low void fraction), or ''bubbly water'' (water having a high void fraction), or a coherent gas pocket which is insufficient to generate the highlight (Fig. 3, frame 305). If the apex highlight is indeed absent, further evidence is required to distinguish between these three options.

Similarly, in the bottom half of frame 1, there is a broader axial vertical white line [arrowed in Fig. 2(a) labeled in Fig. 2(b)]. This ''bottom highlight'' also disappears when this region is liquid filled, to be replaced by a fainter, slightly curving and almost horizontal highlight [the ''curved highlight,'' arrowed in Fig. 3(a), frame 305]. These three lines are the clearest highlight indicators of whether gas or liquid fills the cone. The ''curved highlight'' in addition gives a qualitative assessment of the void fraction present. It is well defined when the void fraction is low (termed ''clear'' water, as seen in Fig. 2, frames 3, 16, 21–22; Fig. 3, frames 25–305). However, when it is high, the strong scatter from this region degrades the curved highlight (i.e., ''bubbly water'' is present at this location in Fig. 2, frames 8, 15, 17; Fig. 3, frame 23). Visual cross checks were regularly performed to ensure stability of the highlights by placing static menisci at varying heights.

Also arrowed in frame 1 is a dark horizontal line, which divides all the frames in half. Lying directly on top of this is a light horizontal line (which is more intense in later frames, e.g., frame 15). This pair forms the ''divisor highlight:'' it represents simply the physical boundary between the PMMA sections of the cone. The upper section is designed to take the cylindrical polycarbonate inserts. Where the aforementioned arrow meets the horizontal dark line in frame 1 corresponds to the left side of the base of the insert, and a vertical highlight above this point demarcates the extreme left edge of the insert [labeled ''edge highlight'' in Fig. 2(b), frame 1].

At this relatively low framing rate it is not possible to see the meniscus clearly during the first collapse. However, its approximate position can be inferred from the highlights. By frame 3 ''clear'' water is present in the lower part of the cone [the bottom highlight has been replaced by the curved highlight, arrowed and labeled in Fig. 2(a) and (b), respectively]. However, the apex highlight remains, implying that the top of the cone contains a coherent gas pocket.

By frame 4 water fills even more of the cone, the apex highlight having disappeared. In fact, frame 4 corresponds to a moment shortly after the first rebound (as can be confirmed

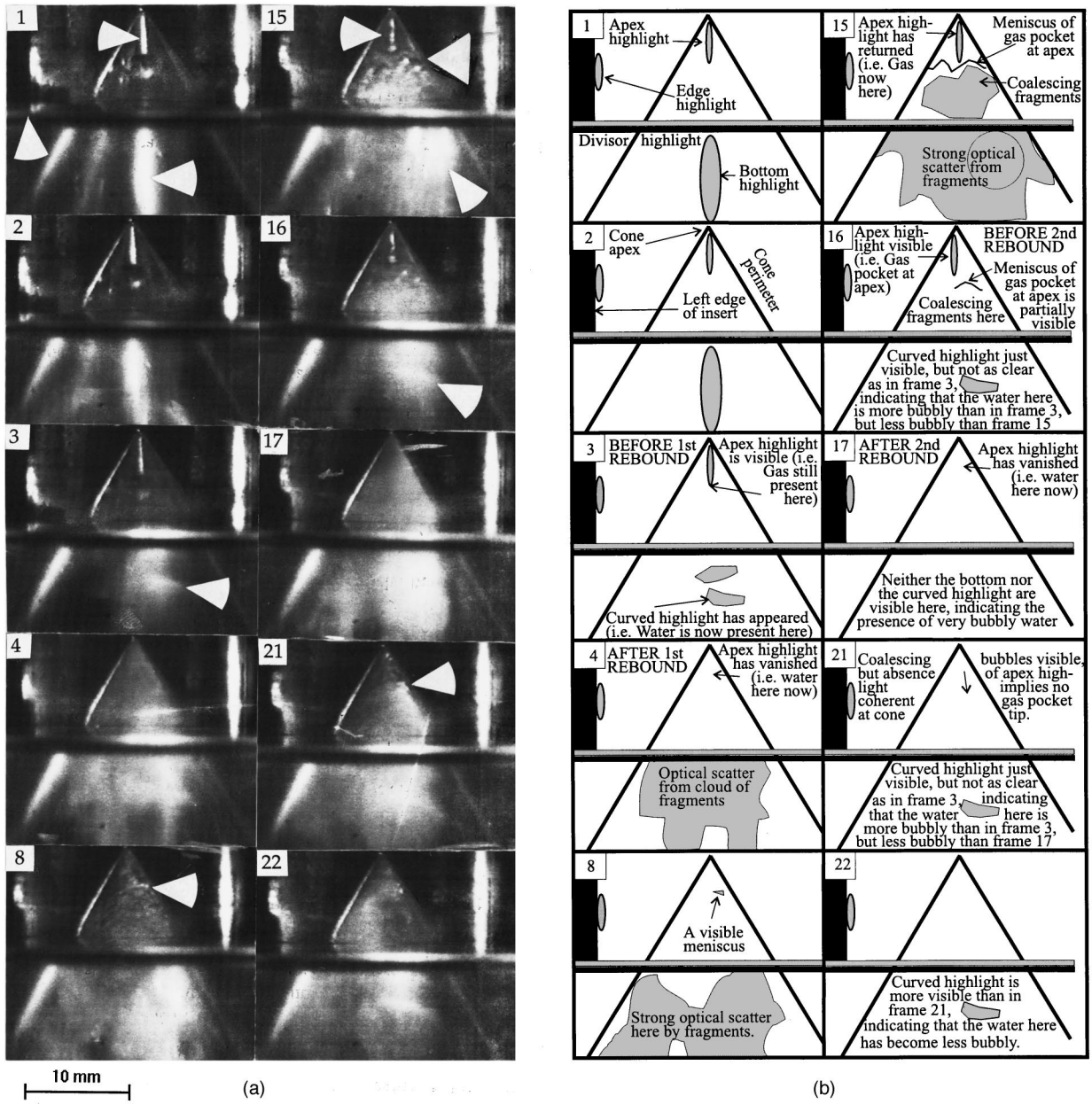

FIG. 2. (a) A selection of 10 frames from a consecutive sequence of 305, filmed at 1000 f.p.s. (each frame occupying full screen). Just prior to collapse the meniscus was $R_i = 60 \pm 5$ mm below the cone tip; after the collapse and subsequent bubble oscillation/fragmentation/coalescence features had ceased, there was a spherical bubble of diameter 2.7 ± 0.05 mm $(= 2R_f)$ remaining close to the cone tip. The device contained 1050 ml of degassed water ($h_i = 37.1$ cm). The arrowed features are described in the text. (b) A frame-by-frame schematic illustration to assist in the identification of features in (a).

through examination of pressure traces—see Sec. II B). A cloud of very small bubbles extends from the cone apex almost to the base of the frame. This interesting feature has been ejected away from the collapse center (the apex) during the rebound. These fragments are clear on the video sequence, but harder to see in still frames, and the cloud outline has been sketched in Fig. 2(b). By frame 8 these fragments have started to coalesce, and a meniscus is visible [arrowed and labeled in Fig. 2(a) and (b), respectively]. This meniscus is simply one feature in a complicated bubble cloud, which is large enough and slow enough to be captured on screen, and there is by no means a single air pocket above it and water below. However, by frame 15 there is clearly a coherent gas pocket at the tip, as opposed to a cloud of bubble fragments, as evidenced by the return of the ''apex highlight'' there [upper arrow, Fig. 2(a)]. The meniscus itself is not flat [middle arrow, Fig. 2(a)], but forming from the coalescence of bubble fragments, which fill much of the water below it [see, for example, the scatter around the lowest arrow of Fig. 2(a)]. These features are drawn schematically on frame 15 of Fig. 2(b). The cloud in the lower half of the cone is continually decreasing in void fraction. Compare, for example, the lower arrowed regions in frames 15 and 16: in the latter, the ''curved highlight'' is again visible, indicating the presence of water without a sufficient density of bubbles to degrade it. The relevant comment in Fig. 2(b) draws attention to the fact that the curved highlight has a clarity

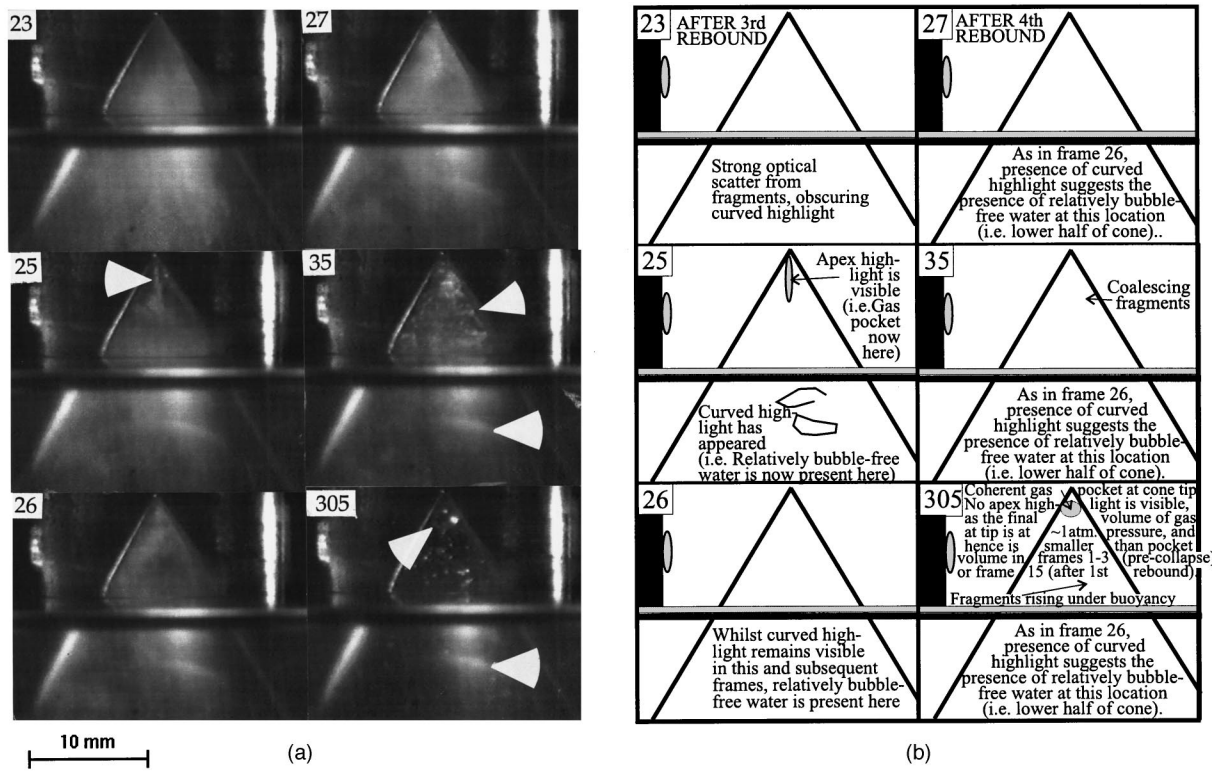

FIG. 3. (a) A selection of 6 further frames from the same consecutive sequence of 305 that is shown in Fig. 2. The arrowed features are described in the text. (b) A frame-by-frame schematic illustration to assist in the identification of features in (a).

intermediate between that found in frames 3 and 15, reflecting the void fractions present.

By frame 17 the second collapse/rebound has occurred (again, see the pressure traces—Sec. II B). The ''apex highlight'' has again disappeared, indicating the loss of a visible coherent gas pocket at the tip. Frames 17 and 21 correspond to similar periods after the second collapse, to those imaged after the first collapse in frames 4 and 8. There are similarities [for example, the menisci arrowed in frames 8 and 21 of Fig. 2(a)]. However, certain differences are clear from the comments in Fig. 2(b). Scatter from a higher void fraction in frame 8 degrades the curved highlight in frame 21.

The third rebound occurs between frames 22 and 23 (Fig. 3). By frame 25 the ''apex highlight'' has returned (arrowed), indicating the presence of a coherent gas pocket at the tip. The void fraction in the water in the lower half of the cone is decreasing, the curved highlight becoming visible in frame 25. It remains visible for the remainder of the film [see lower arrow in Fig. 3(a), frames 35 and 305]. There are two reasons why the void fraction here remains low. First, the progressively weakening rebounds are less able to fragment the tip gas pocket and project the fragments to depth (compare with the decreasing amplitude of the pressure trace in Fig. 6). Second, buoyancy provides a steady force for clearing bubbles from the lower part of the cone.

The fourth rebound occurs just before frame 27. After this one there are no more collapses that eject clouds of bubble fragments from the tip. In frame 35 of Fig. 3(a), the bubble cloud from the fourth collapse is coalescing, and will eventually form the final bubble, the meniscus of which is very faint but indicated by the upper arrow in frame 305.

Having identified the basic form of the collapse/rebound and fragmentation/coalescence cycles, the higher-speed sequences can now be interpreted. Figure 4(a) shows a selection of 60 frames from a consecutive sequence of 4020, filmed at 6000 f.p.s. Each frame occupies $\frac{1}{6}$ screen, the image corresponding to a vertical strip measuring 4 mm×34 mm high. It is presented rotated 90 degrees from true such that the left-hand edge of each image corresponds to a region close to the base of the cone, and the right-hand side of each image corresponds to a region close to the apex of the cone. Indeed, the cone apex is visible near the bottom right corner of each frame, so that the bottom edge of each frame is nearly aligned with the axis of the cone. Figure 4(b) shows a schematic illustration of this high-speed photographic sequence. For clarity, the gray scale in Fig. 4(b) has been inverted to form a negative image.

Arrowed in frame 2 of Fig. 4(a) are a pair of lines, dark and light, which form two of the three bands of the ''divisor highlight.'' This highlight physically corresponds to the boundary between the upper and lower sections of the cone (as arrowed in frame 1 of Fig. 2). These two bands [labeled B2 and B3, respectively, at the bottom left of Fig. 4(b)] are always present. However, the intensity of B3 varies (decreasing, for example, when clouds of bubble fragments scatter its emission, as in frames 23–30 and 55–60).

The third band of the divisor highlight (B1) appears as an intermittent white line in Fig. 4(a). The same is true of the highlight labeled ''*A*'' at the bottom left of Fig. 4(b) [and arrowed in frame 4020 of Fig. 4(a)]. Their appearance can be used to qualitatively distinguish between three states: whether at the location of each there is air, or water having

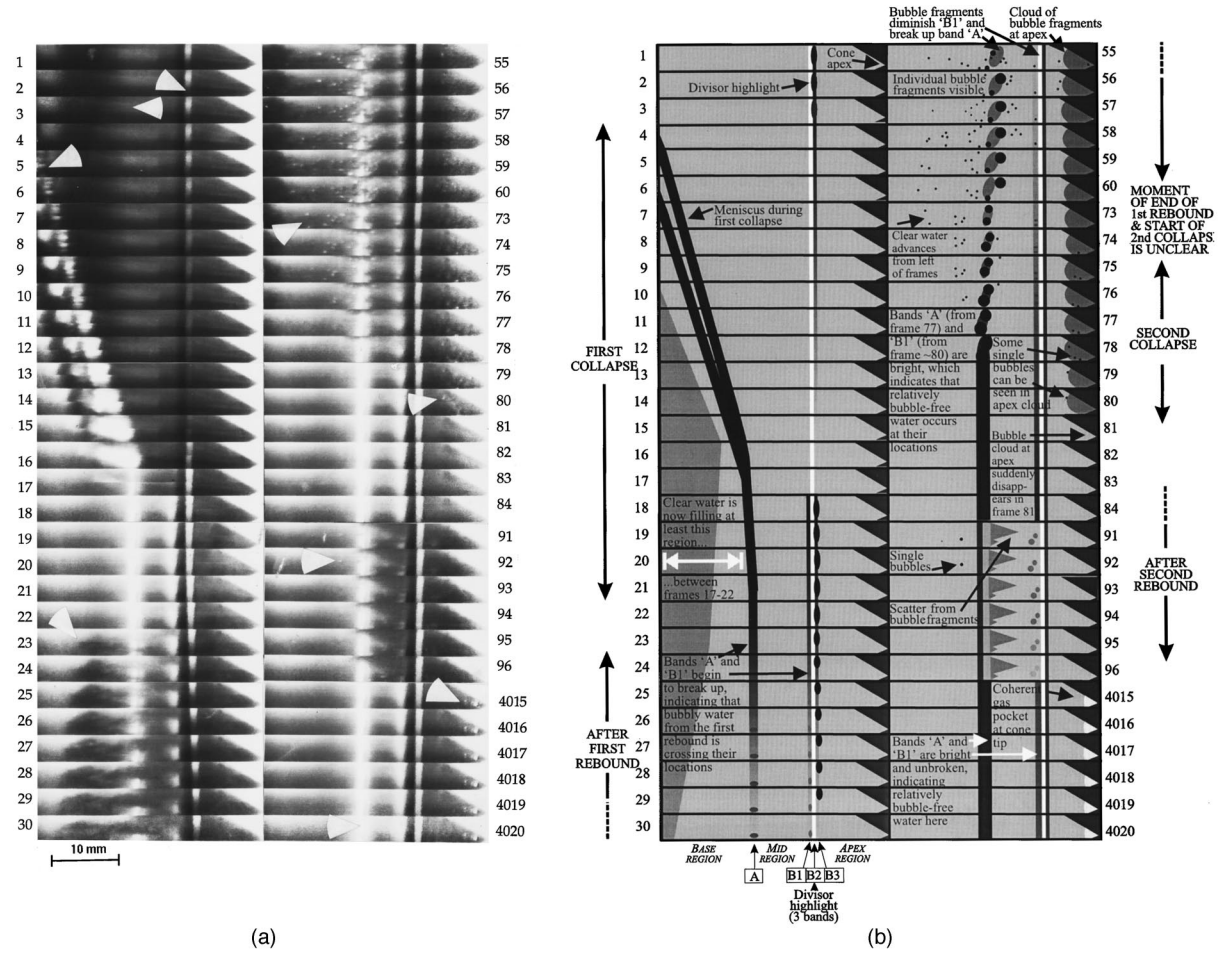

FIG. 4. (a) A selection of 60 frames from a consecutive sequence of 4020, filmed at 6000 f.p.s. Each frame occupies $\frac{1}{6}$ screen, the image corresponding to a vertical strip measuring 4 mm$\times$34 mm high. It is presented rotated 90 degrees from true such that the left-hand edge of each image corresponds to a region close to the base of the cone, and the right-hand side of each image corresponds to a region close to the apex of the cone. Indeed, the cone apex is visible near the bottom right corner of each frame, so that the bottom edge of each frame is nearly aligned with the axis of the cone. Unlike the other arrows in the figure, that in frame 3 does not point to any feature in the image; rather its tip precisely marks the location corresponding to the base of the image frames of Figs. 2 and 3. Just prior to collapse, the meniscus was $R_i = 50 \pm 5$ mm below the cone tip; after the collapse and subsequent bubble oscillation/fragmentation/coalescence features had ceased, there was a spherical bubble of diameter 1.5 ± 0.05 mm$(=2R_f)$ remaining close to the cone tip. The device contained 1050 ml of degassed water ($h_i = 37.1$ cm). The arrowed features are described in the text. (b) A frame-by-frame schematic illustration to assist in the identification of features in (a).

low void fraction (loosely termed ''clear water''), or water of high void fraction (''bubbly water''). When air is present, these bands are not visible (frames 1–17 for B1; frames 1–15 for A). They are intense when clear water is present (frames 18–22, 78–84, and 4015–4020 for both B1 and A). Their appearance is dimmer and broken when bubbly water at their locations scatters the light (frames 23–30, 55–76, and 91–96). Each frame can conveniently be divided into three regions [see labels at bottom left of Fig. 4(b)]. The ''apex region'' occurs between the divisor highlight and the cone tip; the ''mid region'' occurs between bands A and B1; and the base region occurs between band A and the left side of each frame (i.e., physically below band A, since the frames are shown rotated through 90 degrees).

Because of the higher framing rate, it is now possible to capture the image of the meniscus of the collapsing bubble. This appears around frame 5 [arrowed in Fig. 4(a)], and travels up the cone. It is not flat, but instead contains instabilities. The gradient mapped out by the meniscus in frames 5–16 of Fig. 4(a) gives the speed of the bubble wall, and it can readily be seen that this is accelerating (since the locus mapped out by any point on the meniscus follows a curve). From the image, the average speed between frames 6 and 8 is 6.9 ± 0.6 m/s, between frames 9 and 12 it is 8.5 ± 1.9 m/s, and between frames 13 and 15 it is 10.6 ± 2.0 m/s. These values are plotted in Fig. 5 against the solution of Eq. (2).

After frame 16 it is not simple to track the collapsing meniscus. This is because of both optical limitations and the fact that, as it accelerates to greater speeds, it becomes less distinct in the image. However, the intensity and integrity of band A in frames 17–22, and of band B1 in frames 18–21, indicate the presence of clear water. Hence the meniscus has passed these points at these times. The bubble collapses into the cone, the extent of this ''first collapse'' being indicated down the left side of Fig. 4(b). It then rebounds, ejecting a cloud of bubble fragments, which rapidly travels down the cone. This causes bands A and B1 to lose brightness and integrity (frame 23). Measurements of the image of the perimeter of this cloud [arrowed in Fig. 4(a), frame 23] show two features. First, the fragment cloud expands to well below

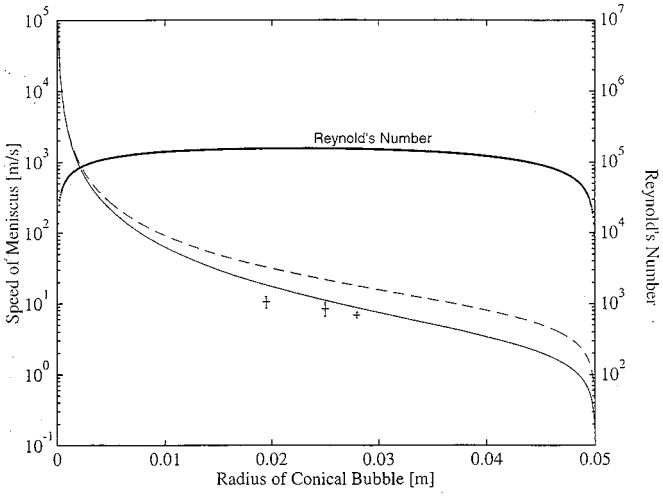

FIG. 5. Plot of meniscus velocity against (i) cone tip-to-meniscus distance for the collapse of a conical bubble containing gas (R_c) [solid, Eq. (2) for $p_{g,i}=12.9$ Pa], (ii) cone tip-to-meniscus distance for the collapse of an empty conical bubble (R_c) [dotted, Eq. (2) for $p_{g,i}=0$ Pa, and, in fact, indistinguishable from (i)], and (iii) bubble radius for the Rayleigh collapse of an empty spherical cavity (R) [dashed, calculated after Rayleigh (Ref. 1)]. The initial conditions are that $R=R_c=50$ mm, $\dot{R}_c=\dot{R}=0$, and $h_i=371$ mm. The fixed apparatus dimensions are given in the text. Also shown are the bubble wall speeds from the data of Fig. 4, and the estimated Reynolds number for the flow in the pipe (see text for the calculation of both).

the base of the images shown in Figs. 2 and 3 [as indicated by the arrow in Fig. 4(a), frame 3]. Second, the images in frames 25–28 suggest that the cloud perimeter is expanding away from the cone apex at 3.5 ± 0.8 m/s. However, details of the underlying optical scatter mean that this velocity should be treated with more caution than the other speeds measured from this film.

The bubble cloud continues to expand away from the cone apex, and during this some coalescence occurs. By frame 55 of Fig. 4, the cone still contains a significant amount of water, at least up to the level of band B1, as both it and band A are visible. However, their integrities are low, the light from both being strongly scattered. Individual bubble fragments are visible throughout the frame [dark points in Fig. 4(b), frame 55 onwards, are placed at the location of the clearest bubbles in Fig. 4(a)]. Note in particular the individual bubbles in the ''base region,'' and the presence of a cloud of bubbly water at the apex.

The indications from numerous video sequences such as this are that, immediately after the first rebound, there is no evidence of a sizeable ''main'' bubble remaining at the cone apex. [As marked in Fig. 4(b), the first rebound starts just before frame 24, and persists until some time after frame 60.] Instead, a cloud of tiny bubble fragments is ejected away from the apex. Coalescence occurs in the cloud, and the system contains ''bubbly water,'' a population of tiny bubbles with radii much smaller than R_f. This is the scenario shown in frames 55–60.

However, by frame 73 the second collapse has started, and the system changes dramatically. The second collapse appears, visually, as the convergence towards the cone apex of the region of ''bubbly water.'' The impression is that the bubble fragments are driven towards the apex. However, in addition to the translation of fragments, there will be a second contribution to this impression: as the local pressure increases, bubble fragments will be compressed, the void fraction will drop, and the water will appear to clear. The advance of a region of clear water from the left in frames 73–76, at 10 ± 6 m/s, can be seen by the progressive disappearance of fragments [Fig. 4(b)]. As a result, band A in frame 77 has become almost as bright as in frame 18, indicating that the water there has a low void fraction.

It is not so simple to see what happens close to the apex. Comparison of this region between frames 1–6 (when the apex is air filled) and frames 55–60 shows that, in the latter period, there appear to be bubble fragments near the apex. As the second collapse progresses, there is evidence of some structuring in the population, and it may be that coalescence occurs. Certainly the region contains a dense, compressing cloud of bubbles, with individual ones visible [one is arrowed in Fig. 4(a), frame 80; the approximate locations of others is indicated by dots in Fig. 4(b)]. The transition from frame 80 to 81 is critical: the apex region suddenly transforms from containing a bubbly cloud, to becoming ''clear'' water (the fragments presumably being compressed to give a low void fraction). The compression of the cloud is clearly rapid (as one would expect at the end of the collapse—see Fig. 5), since this region transforms from ''bubbly'' to ''clear'' in a single frame.

In Fig. 4(a), frames 81–84, bands A and B1 are bright and unbroken, and the cone apex is a clear, light gray: all three locations contain liquid of low void fraction. The same effects can be seen in frames 19–21 for the end of the first collapse. Between frames 84 and 91, the apex region darkens, and bands A and B1 dim and lose integrity. This is identical to the pattern seen at the end of the first collapse in frames 22 and 23 and the ejection/expansion of the bubble cloud from the apex after the second rebound. This ejection is not so energetic, and the cloud does not extend nearly so far from the apex (a very rough impression of the limit is given by the arrow in frame 92). The ''mid'' region contains visible bubble fragments. The cycle repeats, but as the rebounds become less energetic, the fragmentation at rebound is not complete, and eventually there is a coherent gas pocket undergoing small-amplitude oscillations close to the tip (arrowed in frame 4015).

It is interesting to note that, moments after the two rebounds, the images look very similar (frames 23–30 and 84–96) in all three regions (base, mid, and apex). This is because they contain water having similar void fractions. However, this is not the case when comparing the initial collapse (up to frame 21), and the second collapse (frames 71–81). The last four frames of each collapse appear to be very similar in the ''base'' and ''mid'' regions, but have obvious differences at the apex. Interestingly, the same applies for the period long after the collapse (frames 4015–4020). The ''base'' and ''mid'' regions here look very similar to those that occur towards the end of each collapse (frames 17–21 and 79–83), because these regions again contain water having a low void fraction, though for a very different reason: in frames 4015–4020 the fragments are

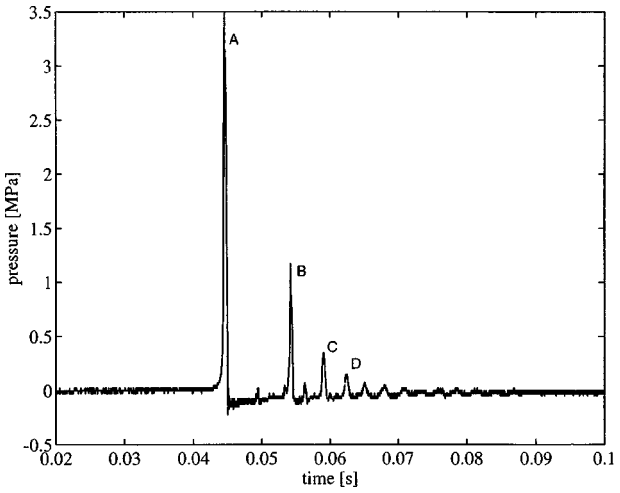

FIG. 6. Plot of a hydrophone signal (triggered at $t=0$) recorded 10 cm below the cone apex. Rebound pressure emissions are labeled: ''*A*'' corresponds to the signal emitted after the first collapse, ''*B*'' to that emitted after the second collapse, and so on. Transient signals between these correspond to reflections of these signals within the pipe (see Ref. 17).

smaller, being at equilibrium with atmospheric pressure.

B. Pressure records

Figure 6 shows the hydrophone record of the pressure in the liquid, measured 10 cm below the cone apex. Time $t=0$ corresponds to the common trigger signal produced by the photon-counting signal in response to the signal from the accelerometer mounted on the top-plate. This trigger signal also causes a single 12 μs flash, which Leighton *et al.*[20] record on high-speed sequences similar to Fig. 4. Comparison of these with simultaneous pressure traces allows the identification of the time at which, during each collapse, the bubble achieves minimum size, and the moment (a short time later) when the rebound pressure signal is detected by the sensor placed 10 cm below the bubble. The interval between the two can be used to give an estimate of the spatially averaged sound speed in the liquid between the bubble wall and the hydrophone. This is done in Table I for the first, second, and third rebounds, for a range of precollapse (R_i) and final (R_f) bubble sizes.

These figures can also be used to estimate the collapse times and compare these with theory, as obtained by integration of Eq. (2) described in Sec. I B. There are two ways of estimating the collapse time. First, the pressure sensor used by Leighton *et al.*[17] makes it possible to observe the passage over the pressure sensor of the pressure wave caused by the opening of the plate (see, as an example, their Fig. 4). From the interval between this and the measurement of the rebound pressure on the same sensor, it is possible to estimate the collapse time. However, quantifiable error arises both because, since the rebound pressure pulse saturated the pressure sensor, the signal was clipped and there was some uncertainty in the position of the pulse apex; and because, to correct for the travel time of the rebound pulse, a propagation speed must be assumed, which is by no means obvious (Table I). Second, high-speed images can be used. However, in the images presented in this paper, only the time between

TABLE I. The sound speed in the cone during the first, second, and third rebounds for various sizes of R_i and R_f. It was calculated from the time difference between the instant at which the bubble radius is a minimum (as measured from the high-speed video recording) and when the rebound pressure wave reaches the hydrophone.

Initial and final bubble sizes		(Sound speed/ m/s)$\pm$60 m/s		
$R_i\pm5$ mm	$R_f\pm0.05$ mm	First rebound	Second rebound	Third rebound
55	2.00	200	215	195
60	1.40	230	255	160
50	0.90	180	220	140
55	1.10	290	290	160
55	1.10	355	···	···
55	1.00	300	185	130
60	1.10	290	280	270

rebounds is directly observable. The initial collapse time can be extrapolated back from the inter-rebound times using the geometric series factor by which the inter-rebound collapse times decrease in duration as a result of damping.[24] This is clearly an approximation, given that from the images it is clear that fragmentation occurs. Using a different symbol for each, these two methods are used to estimate collapse times and compare with the predictions of Eq. (3) for a gas-filled conical bubble (Fig. 7). Also plotted, for comparison, is the collapse time of an empty spherical cavity, following Rayleigh.[1]

In the above data, and that of Sec. II C, the insert used retains the conical geometry right up to the cone apex. For the data of Fig. 8, that insert is replaced by the one that truncates the cone 5.25 mm below the apex, forming a horizontal window of 6.05-mm diameter over which the spatially averaged pressure can be monitored. The technique is detailed in Leighton *et al.*[18] who presented preliminary results. Figure 8 shows a larger set of results for the pressures generated by the first collapse, and compares the measurements

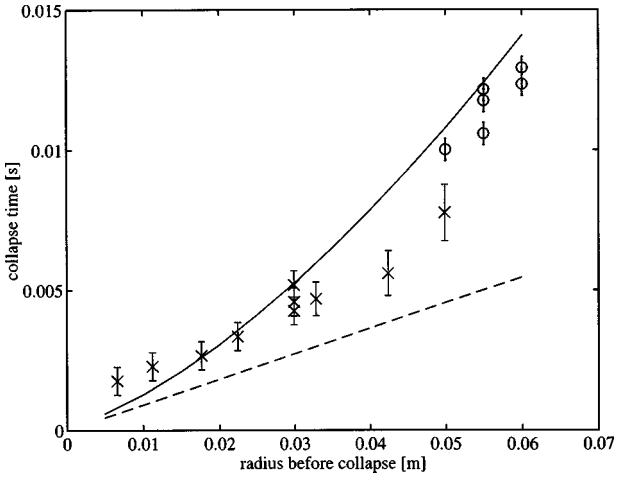

FIG. 7. Plots of the collapse time of (i) a gas-filled conical bubble [solid, found through integration of Eq. (2) using Eq. (3)] and (ii) an empty spherical Rayleigh cavity (dashed). The estimates of collapse times from data are shown, calculated from records of the pressure in the liquid ($\times$), and from extrapolation from the high-speed images of the rebounds ($\bigcirc$). In all the collapses from which these measurements were taken $R_f=0.95\pm0.05$ mm and the device contained 1050 ml of degassed water ($h_i=37.1$ cm).

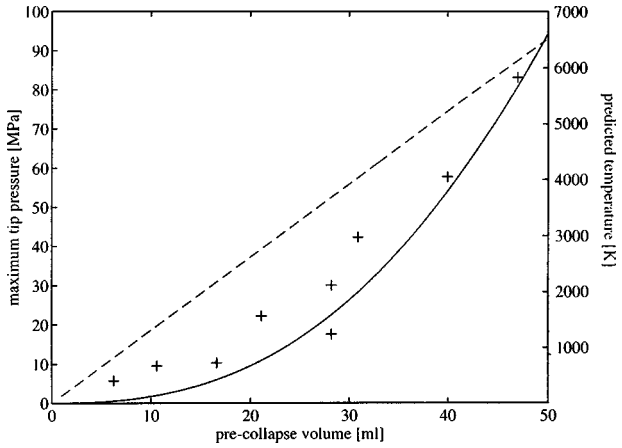

FIG. 8. Measurements of pressure taken at the top of a cone that has been truncated 5.25 mm below the normal position of the apex. The measurements are spatially averaged across the cross section at the position of the sensor. Predictions of theory for pressure are shown [Eq. (7), solid line]. Also shown are predicted temperatures that would occur under these conditions [Eq. (8), broken line]. The device contained 1050 ml of degassed water; the pregrowth bubble volume was 0.9 ml.

with those of theory [Eq. (7)]. The comparison is remarkably good, considering the assumptions of the theory. It is noted, however, that the latter assumes homogeneous conditions within the gas, and the measurement is spatially averaged over the sensor, which might artificially assist the fit. Although there are no measurements of the temperature in the device, given the degree of agreement in the pressure data, it was felt useful to show in Fig. 8 the gas temperatures predicted by theory [Eq. (8)]. Although in the absence of measurement this is by no means meant to indicate a belief that the thermal conditions within the bubble are homogeneous, the results are of interest given the role of such thermal criteria.[25–27]

C. Measurements of sonoluminescence[28]

Figure 9 shows a sequence of six frames from the CCD video. The vertical edges of the cone tip insert and the tip of the cone itself are marked with arrows in frame 4. Sonoluminescence is clearly visible in frames 3 and 4. The sonoluminescence does not appear to occur at the tip of the cone, but a few millimeters below the tip, and off center. A similar asymmetry was observed by Leighton *et al.*[16] Since the exposure per frame is around 40 ms (see Sec. I A), which is greater than the inter-rebound time, and there is finite persistence associated with the display, it requires better time resolution to determine the role of sonoluminescence in the time history of the collapse cycle. This is provided in Fig. 10 by the output of the photon counter, which is a histogram showing the number of photons per 0.1-ms interval. It records a single peak of 120 photons in the 0.1 ms associated with the end of the first collapse (as is evident from the simultaneous hydrophone trace, $t=0$ corresponding to the receipt of the trigger signal for both). The luminescence output at other times is within the noise. Given that the light detector has an active area of 1 mm^2 and a photon detection efficiency of $40\%\pm10\%$, that it is placed 50 mm from the cone tip, and

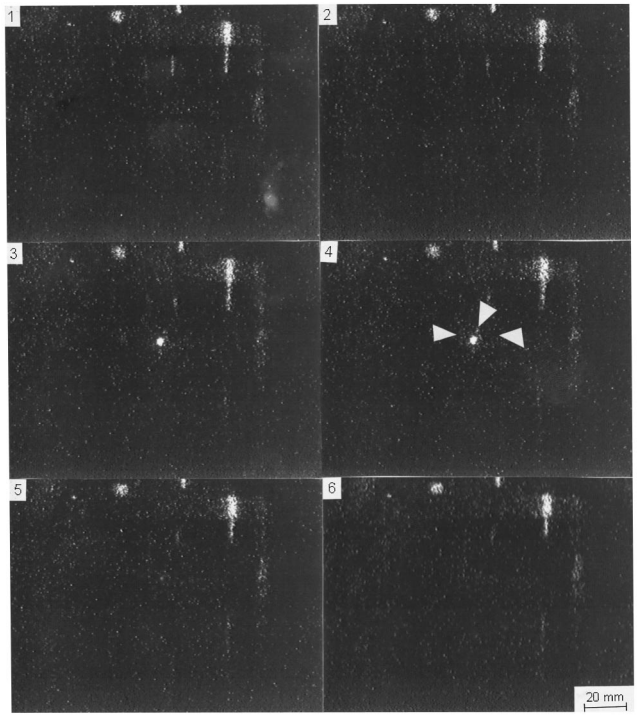

FIG. 9. A sequence of six frames from the CCD video. Exposure per frame is around 40 ms (see Ref. 18). Time-independent features are reflections of ambient low-level illumination from the insert. Just prior to collapse, the meniscus was $R_i=60\pm5$ mm below the cone tip; after the collapse and subsequent bubble oscillation/fragmentation/coalescence features had ceased, there was a spherical bubble of diameter 2 ± 0.05 mm ($=2R_f$) remaining close to the cone tip. The device contained 1050 ml of degassed water ($h_i=37.1$ cm). These frames correspond to the plots shown in Fig. 10.

that the PMMA absorbs $45\%\pm5\%$ of the photons which are generated at the apex, then the sonoluminescence flash contained $(2\pm0.5)\times10^7$ photons.

III. DISCUSSION AND CONCLUSIONS

Simple apparatus has been produced which generates the unstable collapse of a gas pocket. The bubble size prior to

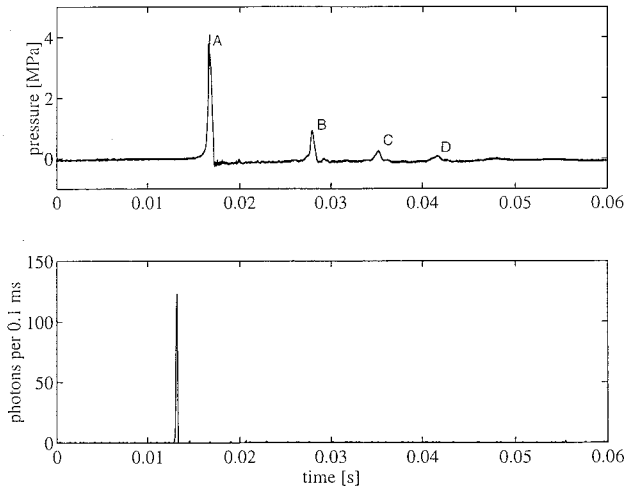

FIG. 10. Simultaneous records of (a) the hydrophone and (b) the photon counter, which is a histogram showing the number of photons per 0.1-ms interval. The datum $t=0$ corresponds to the receipt of the trigger signal for both traces. These plots correspond to the frames shown in Fig. 9.

growth, the size prior to the first collapse, and the inertia associated with the collapse can all be readily controlled. The pressure in the liquid (and, to a certain extent, the gas) can be monitored, and estimates made of the sound speed close to the bubble wall. The collapse can be photographed and the sonoluminescence imaged and quantified, and in all the records has only been produced by the first collapse. The bubble fragments after the first collapse, and the ''rebound'' appears to be in the form of an expanding cloud of bubble fragments. These coalesce during the subsequent collapse phase, and hence the bubble pressure trace resembles that which would be expected from the simple model of a single bubble, expanding and rebounding with decreasing amplitude until, at the end, one can observe a single bubble undergoing linear pulsations. A number of observations (wall speed, collapse time, and gas pressure) have been compared with a theory, adapted from Rayleigh, Noltingk, and Neppiras, based on initial isothermal bubble growth followed by adiabatic collapse.

ACKNOWLEDGMENTS

The conical bubble work described here and previously[17,18,20] has progressed unfunded through student projects. As such it would not have proceeded without the indulgence of the host laboratories in which I supervised the work (Cavendish Laboratory and the ISVR), and without the technical support of Ray Flaxman and Dave Johnson who constructed the apparatus on zero budget. I am also grateful to Dr. A. D. Fitt for suggestions on integration routines, and to the Engineering and Physical Sciences Research Council (GR/M24615) for the loan of the high speed camera. I am very grateful to Dr. P. R. Birkin for excellent discussions.

[1] Lord Rayleigh, ''On the pressure developed in a liquid during the collapse of a spherical cavity,'' Philos. Mag. **34**, 94–98 (1917).
[2] B. E. Noltingk and E. A. Neppiras, ''Cavitation produced by ultrasonics,'' Proc. Phys. Soc. London, Sect. B **63**, 674–685 (1950).
[3] E. A. Neppiras and B. E. Noltingk, ''Cavitation produced by ultrasonics: Theoretical conditions for the onset of cavitation,'' Proc. Phys. Soc. London, Sect. B **64**, 1032–1038 (1951).
[4] W. H. Besant, *A Treatise on Hydrostatics and Hydrodynamics* (Deighton, Bell, London, 1859), p. 158.
[5] C. C. Wu and P. H. Roberts, ''Shock-wave propagation in a sonoluminescing gas bubble,'' Phys. Rev. Lett. **70**(22), 3424–3427 (1993).
[6] W. C. Moss, D. B. Clarke, W. White, and D. A. Young, ''Hydrodynamic simulations of bubble collapse and picosecond sonoluminescence,'' Phys. Fluids **6**, 2979–2985 (1994).
[7] D. F. Gaitan and L. A. Crum, ''Observation of sonoluminescence from a single cavitation bubble in a water/glycerine mixture,'' in *Frontiers of Nonlinear Acoustics*, 12th ISNA, edited by M. F. Hamilton and D. T. Blackstock (Elsevier, New York, 1990), p. 459.
[8] B. P. Barber, R. Hiller, K. Arisaka, H. Fetterman, and S. Putterman, ''Resolving the picosecond characteristics of synchronous sonoluminescence,'' J. Acoust. Soc. Am. **91**, 3061–3063 (1992).
[9] L. A. Crum and S. Putterman, ''Sonoluminescence,'' J. Acoust. Soc. Am. **91**, 517 (1992).
[10] L. A. Crum and S. Cordry, ''Single-bubble sonoluminescence,'' in *Bubble Dynamics and Interface Phenomena*, Proc. IUTAM Symposium, Birmingham, UK, 6–9 September 1993, edited by J. R. Blake, J. M. Boulton-Stone, and N. H. Thomas (Kluwer Academic, Dordrecht, 1994), pp. 287–297.
[11] T. Lepoint, N. Voglet, L. Faille, and F. Mullie, ''Bubbles deformation and interface distortion as a source of sonochemical and sonoluminescent activity,'' in *Bubble Dynamics and Interface Phenomena*, Proc. IUTAM Symposium, Birmingham, UK, 6–9 September 1993, edited by J. R. Blake, J. M. Boulton-Stone, and N. H. Thomas (Kluwer Academic, Dordrecht, 1994), pp. 321–333.
[12] C. Eberlein, ''Sonoluminescence as quantum vacuum radiation,'' Phys. Rev. Lett. **76**, 3842 (1996).
[13] A. P. Prosperetti, ''A new mechanism for sonoluminescence,'' J. Acoust. Soc. Am. **101**, 2003–2007 (1997).
[14] T. J. Matula and R. A. Roy, ''Optical pulse width measurements of sonoluminescence in cavitation-bubble fields,'' J. Acoust. Soc. Am. **101**, 1994–2002 (1997).
[15] T. G. Leighton, P. R. White, and M. A. Marsden, ''Applications of one-dimensional bubbles to lithotripsy, and to diver response to low frequency sound,'' Acta Acust. **3**, 517–529 (1995).
[16] Simple theory predicts that increasing the inertia (by, for example, lengthening the tube) will not affect the minimum volume attained. However, it will reduce the bubble wall speed during collapse. Slower speeds will have important implications regarding the occurrence of meniscus fragmentation and shocks, and the thermodynamics of the collapse.
[17] T. G. Leighton, W.-L. Ho, and R. Flaxman, ''Sonoluminescence from the unstable collapse of a conical bubble,'' Ultrasonics **35**, 399–405 (1997).
[18] T. G. Leighton, A. D. Phelps, B. T. Cox, and W.-L. Ho, ''Theory and preliminary measurements of the Rayleigh-like collapse of a conical bubble,'' Acta Acust. **84**(6), 1014–1024 (1998).
[19] P. G. Kosky and G. A. Henwood, ''A new technique for investigating vapour bubble implosion experimentally,'' Br. J. Appl. Phys. **2**, 630–634 (1969).
[20] T. G. Leighton, B. T. Cox, P. R. Birkin, and T. Bayliss, ''The Rayleigh-like collapse of a conical bubble: Measurements of meniscus, liquid pressure, and electrochemistry,'' in *Proceedings of the 137th Regular Meeting of the Acoustical Society of America and the 2nd Convention of the European Acoustics Association (Forum Acusticum 99, integrating the 25th German Acoustics DAGA Conference)*, March 1999, Paper 3APAB_1.
[21] P. Hawtin, G. A. Henwood, and R. A. Huber, ''On the collapse of water vapour cavities in a bubble analogue apparatus,'' Chem. Eng. Sci. **25**, 1197–1209 (1970).
[22] T. G. Leighton, *The Acoustic Bubble* (Academic, London, 1994), Figure 2.8, §2.1.3b(iii).
[23] B. S. Massey, *Mechanics of Fluids* (Van Nostrand Reinhold, London, 1970), 2nd ed., Chap. 7.
[24] This assumes that the growth and collapse phases of the bubble are symmetrical in time profile. Although it is assumed that the first growth phase, performed here with the vacuum pump, is slow and hence isothermal, the subsequent growth phases can be assumed to be adiabatic, making the assumption of symmetric time profiles after the first rebound not unreasonable. See, for example, Fig. 16 in C. C. Church, ''A theoretical study of cavitation generated by an extracorporeal shock wave lithotripter,'' J. Acoust. Soc. Am. **86**, 215–227 (1989).
[25] C. K. Holland and R. E. Apfel, ''An improved theory for the prediction of microcavitation thresholds,'' IEEE Trans. Ultrason. Ferroelectr. Freq. Control **36**, 204–208 (1989).
[26] R. E. Apfel and C. K. Holland, ''Gauging the likelihood of cavitation from short-pulse, low-duty cycle diagnostic ultrasound,'' Ultrasound Med. Biol. **17**, 179–185 (1991).
[27] American Institute Of Ultrasound In Medicine/National Electrical Manufacturers Association (AIUM/NEMA), *Standard for real-time display of thermal and mechanical indices on diagnostic ultrasound equipment* (AIUM/NEMA, 1992).
[28] One reviewer made a very interesting point, which (with permission) I quote: ''I object very strongly to the use of the word sonoluminescence in section IIC, as the results here refer to nothing like what a normal reader would assume, given the excitement of the last few years about (true) sonoluminescence. There is no 'sono,' only luminescence here.'' To begin on a light note, first-time users of the device are unfailingly startled by the ''bang'' that accompanies the opening of the top plate (which generates the pressure pulse that causes the bubble to collapse). However, the absence of a conventional driving acoustic field, to which the reviewer refers, was also addressed in the review ''Sonoluminescence'' by A. J. Walton and G. T. Reynolds [Adv. Phys. **33**(6), 595–660 (1984)]. They state: ''Harvey (1939) introduced the name *sonoluminescence* (SL) for the luminescence caused by the sound field. A more apposite name might be 'cavitation luminescence,' since the light emission is associated with the presence of suitable size bubbles within the liquid...The appropriate cavitation conditions required for light emission can also be realized by flowing the liquid through a Venturi tube..., by impacting a water jet onto a stationary plate..., by focusing a pulsed laser beam into the liquid..., by

passing a spark discharge through the liquid...and even by smashing thin-walled glass spheres containing low pressure gas under water.'' As a final note, it would, in principle, be possible to generate even single-bubble sonoluminescence without the use of an acoustic field, using a noninertial frame to generate a stable oscillatory pressure field after the manner of T. G. Leighton, M. Wilkinson, A. J. Walton, and J. E. Field, ''The forced oscillations of bubbles in a simulated acoustic field,'' Eur. J. Phys. **11**, 352–358 (1990).

Mean force on a small sphere in a sound field in a viscous fluid

S. D. Danilov
Institute of Atmospheric Physics, Russian Academy of Sciences, 3 Pyzhevsky per., 109017 Moscow, Russia

M. A. Mironov
N. N. Andreev Acoustical Institute, Shvernika 4, 119036 Moscow, Russia

(Received 1 November 1997; revised 22 April 1998; accepted 1 September 1999)

A mean force exerted on a small rigid sphere by a sound wave in a viscous fluid is calculated. The force is expressed as a sum of drag force coming from the external steady flow existing in the absence of the sphere and contributions that are cross products of velocity and velocity derivatives of the incident field. Because of the drag force and an acoustic streaming generated near the sphere, the mean force does not coincide with the acoustic radiation pressure, i.e., the mean momentum flux carried by the sound field through any surface enclosing the sphere. If the sphere radius R is considerably smaller than the viscous wave penetration depth δ, the drag force can give the leading-order contribution (in powers of δ/R) to the mean force and the latter can then be directed against the radiation pressure. In another limit, $\delta \ll R$, the drag force and acoustic streaming play a minor role, and the mean force reduces to the radiation pressure, which can be expressed through source strengths of the scattered sound field. The effect of viscosity can then be significant only if the incident wave is locally plane traveling.
[S0001-4966(99)05512-5]

PACS numbers: 43.25.Yw [MAB]

INTRODUCTION

Acoustic radiation pressure exerted by a sound wave on compact obstacles is the subject of numerous studies (see, for example, Refs. 1–9). The interest in this problem was motivated by a variety of applications of acoustic radiation pressure in science and technology, such as calibration of high-frequency transducers,[3] acoustic levitation,[10] acoustic coagulation,[11] etc. Most of these works address the case of an ideal fluid, and typically the obstacle is a sphere.

Beginning with works by King[12] and Yosioka and Kawasima,[13] there was considerable progress in calculations of the radiation pressure on a sphere of various properties and arbitrary size in an ideal fluid. In acoustic coagulation, however, one deals with extremely small particles[11] of a size comparable with or even smaller than the penetration depths of viscous and thermal waves. For such particles, dissipative properties of the host fluid cannot be neglected. What modifications are introduced in the theory by the fluid viscosity and thermal conduction is a question still requiring further study.

In the last few years, the problem of mean force exerted by a sound wave on a sphere in a viscous and heat-conducting fluid has been examined thoroughly in a series of works.[4–9] The general result of these works can be applied to any axisymmetric sound field, and no restriction is imposed on the relation between the radius of the sphere, sound wavelength, and depths of penetration of viscous and thermal waves. While these works present some general background for the computation of the mean force in a real fluid in an axisymmetric sound field, they do not give a clear answer to the question when dissipative effects are important and when they are not, nor do they attempt to discuss the relevant physics introduced by dissipation.

It may, however, be anticipated from the very beginning that viscosity and thermal conduction are important only when the radius of the sphere is smaller than the sound wavelength. Indeed, in the opposite case the scattering cross section would be comparable to geometric cross section and very thin viscous and thermal layers near the sphere surface would not change the scattered sound field and hence the radiation pressure (one can hardly imagine a situation of practical significance when penetration depths of viscous and thermal wave exceed the sound wavelength).

One may go even further and assume, based on the same argument, that the radius of the sphere has to be smaller than or of the order of the penetration depths of viscous and thermal waves for the influence of viscosity and heat conduction to be discernible. This proves to be only partly true, because for a plane traveling wave, or any wave close to it, the viscosity and thermal conduction can influence the mean force even if the sphere radius exceeds the depth of penetration of viscous or thermal waves. The reason why a plane traveling wave makes this exception is very transparent and is explained in Ref. 14 (the reader may find examples of this influence in Refs. 4, 6, and 8). It is recapitulated briefly in Sec. I of this paper. The mean force is a quadratic quantity and depends not only on amplitudes of incident and scattered fields but also on phase differences between them. The phase differences are unfavorable for a plane traveling wave in an ideal fluid and even small phase shifts caused by dissipation can be important. But, even in this case the dissipative factors are noticeable only for a sphere that is small compared to the sound wavelength.

The assumption that the sphere is small compared to the scale of the sound field leads to substantial simplification of the computational part of the problem. For an axisymmetric

field and a rigid sphere, this problem was first treated in Ref. 15 for a viscous fluid and in Ref. 16 for a viscous and heat-conducting fluid. It turns out that the solutions obtained there yield to generalization to the case of arbitrary sound field (not necessarily axisymmetric, as in Refs. 15, 16, and 4–9), and can be represented more clearly and concisely. This generalization is the first goal of the present paper.

In order to make the exposition as simple as possible, we shall treat only the influence of viscosity, and assume that the sphere is rigid. The generalization for the case of thermal conduction, as well as accounting for the dependence of dynamic viscosity on temperature,[17] can be carried out in a similar way (these cases are examined in Ref. 16 for an axisymmetric field; see also Ref. 7). An account for the compressibility of the sphere does not raise any additional difficulties.

There is another goal as well. The problem of influence of viscosity and thermal conduction has a long history dating back to works by Westervelt.[17,18] Unfortunately, they are not mentioned in Refs. 4–9 and we should recall them here because they suggest terminology different from that used in Refs. 4–9 and point to some additional mechanisms that may lead to the formation of the mean force in a viscous and heat-conducting fluid. The point is that in the presence of viscosity one should distinguish between the two notions, that of the acoustic radiation pressure and that of the mean force exerted by a sound field on a particle. The acoustic radiation pressure is the rate at which the mean momentum transported by the sound field changes because of scattering on the particle. Only part of it contributes to the mean force applied to the particle, while another part is spent to generate acoustic streaming with dipole-type symmetry. This distinction is absent for an ideal fluid (no acoustic streaming). Additionally, the generation of incident sound field may be accompanied by production of mean ''acoustic wind'' whose magnitude depends on the boundary conditions on the source of the sound field and on the boundaries of volume where the sound field is created. In a viscous fluid, particles will experience a drag force from this mean streaming. This drag force is by no means associated with the ''pressure of radiation.''

Hence, the other goal of this paper is to explain the difference between the radiation force and the mean force in a viscous fluid and to show that they coincide if the sphere radius is much greater than the penetration depth of a viscous wave. In this case, effects of viscosity are significant only if the incident field is close to a plane traveling wave. The extraordinary strong influence of viscosity on the mean force in a plane traveling wave then receives the explanation in terms of phase relations between the incident and scattered sound fields.

The relation between the radiation force and the mean force in a viscous fluid and the role of phase relation are discussed in Sec. I. This section also contains a brief survey of the problem development. This, in our opinion, facilitates the understanding of subsequent results and eliminates some methodological drawbacks of the approach pursued in Refs. 4–9. Section II contains a derivation of the expressions for the mean force. Section III presents conclusions.

All calculations below are carried out in quadratic approximation, which is valid for sufficiently low amplitudes of incident sound wave. Lower indices ''*i*'' and ''*s*'' imply that the quantity in hand refers to incident or scattered waves, respectively. Combinations of indices designate respective quadratic quantities. Time dependence of the first-order fields is harmonic $\exp(-i\omega t)$, where ω is the frequency of incident sound wave, and will normally be omitted. The asterisk denotes complex conjugation. Linear (first-order) fields are denoted by prime, and quadratic (second order) fields by two primes.

I. ACOUSTIC RADIATION PRESSURE AND MEAN FORCE IN A VISCOUS FLUID

A. Radiation pressure on a small obstacle in an ideal fluid and the role of phase relations

In an ideal fluid, the radiation pressure exerted on an obstacle in a sound field is the *total mean force* applied to the obstacle

$$\langle F_j \rangle = -\left\langle \int_S \Pi_{jk}\, dS_k \right\rangle, \tag{1}$$

where S is any fixed surface enclosing the particle, $\Pi_{jk} = p\,\delta_{jk} + \rho v_j v_k$ is the momentum flux tensor which should be computed up to the second-order terms, p, ρ, $\mathbf{v}$ are the pressure, density, and velocity, respectively. Angular brackets denote averaging over sound wave period. The surface S can be arbitrary because the difference between mean values of the integral (1) over any surface S and the integral from $\Pi_{jk} - \rho v_j v_k$ over the surface of the particle S_0 equals zero in quadratic approximation. This can be easily verified by reducing the difference of surface integrals to a volume integral and making use of the Euler and continuity equations. As a result, the difference becomes

$$\int_S \Pi_{jk}\, dS_k - \int_{S_0} (\Pi_{jk} - \rho v_j v_k) dS_k = -\int_{\overline{V}} \partial(\rho v_k)/\partial t\, dV - \int_{V'(t)} \partial(\rho v_k)/\partial t\, dV + \int_{S_0} \rho v_j v_k\, dS_k .$$

Here, $\overline{V}$ is the volume between S and the surface of the particle in mean position $\overline{S}$; V' is the volume between $\overline{S}$ and S_0 (this volume is a first-order quantity). In quadratic approximation, the mean value of the first integral on the right-hand side is zero, since the integrand contains only terms oscillating at frequencies ω and 2ω, and two other terms on the right-hand side cancel each other out.

Physically, the picture is as follows. A sound wave carries the flux of momentum. As the wave scatters on the obstacle, some part of the momentum flux goes away with the scattered field. The rate of the momentum change within a volume containing the obstacle is given by the integral of the momentum flux over the boundary of the volume and repre-

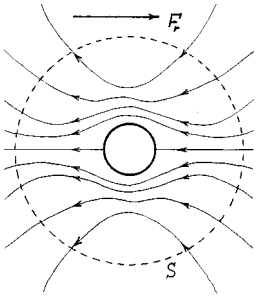

FIG. 1. Schematic pattern of dipole acoustic streaming that develops in the vicinity of the sphere. The arrow at the top shows the direction of the acoustic radiation pressure $\mathbf{F}_r$ that complies with the shown direction of the acoustic streaming.

sents the radiation force acting on the obstacle (note that the momentum flux is entirely due to the sound field).

An elegant derivation of expressions for the radiation pressure on a small obstacle in an arbitrary sound field in an ideal fluid belongs to Gor'kov.[19] In accordance with Ref. 19, the force (1) can be written as

$$\mathbf{F}=\mathbf{F}_{is}+\mathbf{F}_{ss}, \quad \mathbf{F}_{is}=-\frac{\rho_0}{4}\,Q^*\mathbf{v}_i-\left(\mathbf{P}^*\frac{1}{4i\omega}\,\nabla\right)\mathbf{v}_i+\text{c.c.},$$
$$\mathbf{F}_{ss}=-k^3\,\frac{1}{24\pi\omega}\,Q\mathbf{P}^*+\text{c.c.}, \tag{2}$$

where Q is the volume velocity of the monopole part of the scattered field, and $\mathbf{P}$ is the dipole force corresponding to the dipole part of the scattered field; ρ_0 is the unperturbed density of fluid, and k is the sound wave number. The expressions for $\mathbf{F}_{is}$ and $\mathbf{F}_{ss}$ presented here follow from the original expressions of Ref. 19 after simple manipulations. Usually the main contribution into the radiation pressure comes from the cross term $\mathbf{F}_{is}$, since it is potentially of lower power in k, and consequently, in kR, where R is the radius of the sphere. An exception is the case of plane traveling wave where the incident velocity field is approximately shifted by $\pi/2$ or $-\pi/2$ with respect to the monopole volume velocity, and the spatial derivative of incident velocity field is approximately in phase or antiphase with the dipole force.[14] As a result, the radiation pressure is proportional to $(kR)^4$ for a plane traveling wave (and waves close to it locally), and to kR in other cases. Correspondingly, even weak influence of viscosity can lead to shifts of the phase of $\mathbf{P}$ for the plane traveling wave and the radiation pressure can change noticeably (in fact, in an ideal fluid the nonzero contribution from the cross-term is entirely due to phase shifts caused by radiative losses).

B. Radiation pressure in a viscous fluid

Let us now turn to the case of a viscous fluid. In this case,[20] $\Pi_{kl}=p\,\delta_{kl}+\rho v_k v_l-\sigma_{kl}$, where $\sigma_{kl}=\nu[\partial v_k/\partial x_l+\partial v_l/\partial x_k-(2/3)\,\delta_{kl}\nabla\mathbf{v}]+\mu\,\delta_{kl}\nabla\mathbf{v}$ is the tensor of viscous stresses, while the scattered first-order field contains *viscous waves* in addition to sound waves.

The reasoning concerning the choice of the surface of integration in the case of ideal fluid also refers to the case of viscous fluid, and the mean force acting on an obstacle can be calculated over an arbitrary surface enclosing it. The proof is just the same, using the Navier–Stokes equation instead of the Euler equation. We choose the surface S to be distant from the obstacle, so that viscous waves can be neglected there. But, the presence of these waves in the volume near the obstacle is crucial because it leads to the excitation of second-order acoustic streaming in the vicinity of the obstacle. The main component of this streaming is of quadrupole symmetry. It is dealt with in most studies of acoustic streaming near a small sphere.[21] There is, however, a smaller component of dipole symmetry,[15,16,7–9] see Fig. 1. This dipole acoustic streaming carries the momentum flux and therefore the momentum flux carried by the sound field through the surface S enclosing the sphere is partly fluxed away. We shall refer to the momentum flux carried by sound waves (both incident and scattered) through the surface S as the acoustic radiation pressure in a viscous fluid. As a result, we shall distinguish between the radiation pressure and the mean force actually applied to an obstacle in a viscous fluid. The reason is that the momentum flux carried by the acoustic streaming is *not transported by sound waves*.

Another reason why we insist on making this distinction comes from the presence of an external acoustic streaming generated together with the incident sound field. We recall here the Eckart streaming which develops near piston sources of finite aperture (a sound wave is locally a plane traveling wave near the source) and the Rayleigh streaming in a standing wave between plane walls, to mention a few classical examples which the reader may find in textbooks on nonlinear acoustics (see, for example, Refs. 22 and 23). The external streaming will exert a drag force on the obstacle, which is apparently not connected with the transport of momentum flux by sound waves to the obstacle. In special cases, the external streaming can be computed by the local behavior of the incident first-order sound field.[7–9] In the general case, it depends on boundary conditions on the source and on the boundaries of the volume where the sound field is created. Thus, it is to be considered as an external, given field. Computation of the drift force based on the local behavior of incident first-order field, as is done in Refs. 7–9, may be misleading and should be avoided.

In adopting the above definition for the acoustic radiation pressure in a viscous fluid, we depart from the approach of Refs. 7–9, where the radiation pressure implies the total mean force, but follow the approach put forward by Westervelt more than 40 years ago.[18]

There is not only physical but also computational motivation behind this definition. As we show in Sec. II the mean force and acoustic radiation pressure are approximately equal if $\delta \ll R$ where $\delta=(2\nu/\omega)^{1/2}$ is the depth of penetration of viscous wave; computations of the radiation pressure force are elementary and require only the knowledge of monopole and dipole source strengths [and making use of (2)].

C. Mean force and radiation pressure in a viscous fluid: Previous development

Westervelt was the first who examined the problem of mean force acting on a small obstacle in a viscous fluid. In

particular, he found[18] that the radiation force exerted on a fixed sphere with a size smaller than the penetration depth of viscous wave in a traveling sound wave is

$$F=\frac{3}{2}\,\rho_0 v_0^2 \pi R^2 (kR)\,\frac{\delta^2}{R^2},$$

where v_0 is the amplitude of velocity in the sound wave. This result follows from the expression suggested by Westervelt,[18] which relates the radiation pressure in a plane traveling wave with scattering and absorption cross sections of a small sphere

$$F=E\left(\sigma_a+\sigma_s+\int \sigma_s(\theta,\phi)\sin\theta\, d\theta\, d\phi\right).$$

Here, E is the energy density, σ_a and σ_s are total cross sections of absorption and scattering, respectively, $\sigma_s(\theta,\phi)$ is the differential cross section of scattering, and θ, ϕ are angles of the spherical coordinate system. From this expression it is clear that viscosity or thermal conduction will lead to an abrupt increase in the radiation pressure force, since the absorption cross section of a small sphere in a plane traveling wave scales as kR and is much greater than the scattering cross section which scales as $(kR)^4$, a result well-known, for example, from the course of fluid mechanics by Landau and Lifshitz.[20] If kR increases, and reaches values of the order of unity, the scattering cross section is defined by the geometric cross section, and the absorption cross section becomes small in comparison to it.

Westervelt,[18] however, warned that the radiation force may not coincide with the total force on the obstacle because of the presence of acoustic streaming.

We mention here two other mechanisms predicted by Westervelt through which the mean force may form. The first is the dependence of dynamic viscosity on temperature.[17] Its contribution is of interest in that it has different signs for liquids and gases. In Ref. 17 this contribution, together with the drag force from the steady component of the incident field, is called the Stokes-type force. Also, Westervelt showed[17] that Oseen's formula for the force acting on a steady moving sphere predicts a strong mean force if the second harmonic of fundamental frequency is present in the incident sound field.

Thus, there was a question about the relation between the acoustic radiation pressure and the mean force on a small sphere. This question was solved in Ref. 15, where the case of plane traveling wave was considered; a sphere was assumed to be rigid and very heavy (fixed), and the external acoustic streaming was supposed to be absent (this can be achieved by an appropriate choice of boundary conditions at the source of traveling wave). In the case $\delta \gg R$, the mean force is

$$F=\frac{9}{5}\,\rho_0 v_0^2 \pi R^2 (kR)\left(\frac{\delta}{R}+\mathcal{O}(1)\right).$$

By comparing this result with Westervelt's, we see that in this limit, when one may expect the influence of viscosity to be strongest, the actual mean force is considerably smaller than the radiation pressure. From the physical viewpoint, this implies that the mean momentum flux the sound wave loses because of the presence of the sphere is largely redistributed, and is carried away by acoustic streaming excited near the sphere. Only a small fraction of the momentum flux ''reaches'' the sphere and contributes to the mean force. Certainly, the mean force remains large in comparison with that in the case of an ideal fluid, but not as large as one might expect.

In the opposite limit case, $\delta \ll R$, the role of acoustic streaming and the drag force proves to be small, and the mean force coincides with the acoustic radiation pressure up to terms of higher orders in δ/R. This is shown in Ref. 16 for an axisymmetric sound field and in the next section for a more general case. Therefore, all one needs if $\delta \ll R$ is the formula (2) which follows from the Gor'kov approach. The total mean force, i.e., the acoustic radiation pressure, can be computed immediately if one knows the dipole and monopole source strengths characterizing the scattered sound field. Because in this limit viscosity introduces only small corrections to the dipole force, the radiation pressure coincides with that in an ideal fluid in almost all cases, with exception, as is clear from the foregoing, of the case of a plane traveling wave, or any wave close to it locally. We reiterate that the phase relations between the incident field and the dipole force **P** [see (2)] are responsible for this behavior. Although dissipative correction is small by absolute value, it slightly shifts the phase of **P**, and thus leads to very strong effects. To illustrate how strong these effects may be, we again resort to the case of a fixed sphere.[14,15] In this case

$$F=\frac{3}{2}\,\rho_0 v_0^2 \pi R^2 (kR)\left(\frac{\delta}{R}+\mathcal{O}\left(\frac{\delta^2}{R^2}\right)\right).$$

Comparing this result to its counterpart for an ideal fluid, we find that on the order of value their ratio is $(kR)^{-3}(R/\delta)$ (in fact, it scales as the cross section of absorption in a viscous fluid divided by that of scattering in an ideal fluid). This ratio may be very large as far as (kR) is small. Taking $R=100\,\mu$m and a frequency of 10 kHz in air ($\delta \approx 23\,\mu$m) we find a value of 4×10^3. This obviously does not imply that the radiation pressure is extremely high: it is simply too weak in an ideal fluid. It seems clear that similar manifestations of extraordinary strong influence of viscosity should be expected in sound fields produced by point sources at distances where these fields become a plane traveling wave locally (see the discussion in Ref. 6, which does not point to this simple physics).

II. TOTAL MEAN FORCE ACTING ON A SMALL RIGID SPHERE IN A VISCOUS FLUID

We represent the velocity of an incident field in the form

$$\mathbf{v}_i=\mathbf{v}_i'+\mathbf{v}_i'', \tag{3}$$

where $\mathbf{v}_i'$ is the linear, i.e., oscillating part, and $\mathbf{v}_i''$ is the second-order correction to the linear field $\mathbf{v}_i'$. It is assumed that the incident field satisfies the Navier–Stokes equations and the equation of continuity in quadratic approximation. The spatial scale of the incident field, i.e., the minimum from the wavelength and the distance to a source l, is assumed to

be large compared to the sphere radius R. This is the only, yet essential, restriction we impose on the incident field. The consideration below hinges on the observation that the leading term in the expansion of the mean force in powers of kR or l/R depends only on the velocity and first derivatives of the velocity of the incident sound field (hence, for example, the first degree in kR for plane waves). Bearing this in mind, we expand the incident field (3) in a Taylor series about the mean position of the particle and retain only the first two terms in the expansion of $\mathbf{v}_i'$ and the first term in the expansion of $\mathbf{v}_i''$

$$(v_i)_m=(V_m+V_{mn}x_n)+(v_0'')m, \tag{4}$$

Here, $V_m=(v_i')_m|_{\mathbf{x}=0}$; $V_{mn}=\partial(v_i')_m/\partial x_n|_{\mathbf{x}=0}$, $v_0''=v_i''|_{\mathbf{x}=0}$, and $\mathbf{x}=\{x_m\}$ is the radius vector in the resting frame of reference (RFR) with $x=0$ at the mean position of the oscillating particle. The tensor of first derivatives is symmetric, that is, $V_{mn}=V_{nm}$, because the incident velocity field is potential. The great advantage of adopting this decomposition is the fact that fluid compressibility is important only in V_{mm} generally being nonzero. In all other respects the problem can be treated as incompressible, that is, the first-order scattering problem and calculations of locally induced acoustic streaming can be carried out for the incompressible case. Subsequent consideration can be conveniently carried out in the oscillating frame of reference (OFR) where the sphere is at rest (does not oscillate). It goes without saying that total mean forces in the OFR and RFR are equal. We shall denote the velocity in the OFR by $\mathbf{u}$ and the radius vector by $\mathbf{r}$ with $\mathbf{r}=0$ at the center of the sphere. Vectors $\mathbf{r}$ and $\mathbf{x}$ are connected by the relationship $\mathbf{x}=\mathbf{r}+\mathbf{d}$, $\mathbf{d}=\int dt\,\mathbf{U}_P$. Here, $\mathbf{U}_P$ is the velocity of sphere oscillations. Using an expression for the fluid reaction force in a viscous fluid[20]

$$\mathbf{N}=-[6\pi\eta R(1+R/\delta)-3i\pi\omega\rho_0\delta R^2(1+2R/9\delta)]\times(\mathbf{U}_P-\mathbf{v}_i'), \tag{5}$$

it is easy to show that the velocity of sphere oscillations can be written as

$$\mathbf{U}_P=\mathbf{V}GG_1, \tag{6}$$

where

$$G=[(1+\xi)^2+\xi^2(1+2\xi(1+2\zeta)/9)^2]^{-1},$$

$$\zeta=\rho_P/\rho_0,\quad \xi=R/\delta,$$

$$G_1=(1+\xi)^2+\xi^2(1+\tfrac{3}{2}\xi)(1+\tfrac{2}{9}\xi(1+2\zeta))+\tfrac{4}{9}i\xi^2(\zeta-1)(1+\xi).$$

Here, ρ_P is the density of the particle.

The incident velocity field in the OFR transforms to

$$(u_i)_m=V_m-(U_P)_m+V_{mn}x_n|_{\mathbf{x}=\mathbf{r}+\mathbf{d}}+(v_0'')_m=(U_m+V_{mn}r_n)+(u_0'')_m, \tag{7}$$

with $\mathbf{U}=\mathbf{V}-\mathbf{U}_P$ and $(u_0'')_m=(v_0'')_m+\int dt(U_P)_nV_{mn}$. Note that the OFR is not inertial and for that reason the force of inertia, $-\rho\partial\mathbf{U}_P/\partial t$, appears on the right-hand side of the Navier–Stokes equation

$$\rho\left(\frac{\partial\mathbf{u}}{\partial t}+(\mathbf{u}\nabla)\mathbf{u}\right)+\nabla p+\eta\nabla\times\nabla\times\mathbf{u}-\left(\frac{4}{3}\,\eta+\mu\right)\nabla\nabla\mathbf{u}=-\rho\frac{d\mathbf{U}_P}{dt}. \tag{8}$$

The continuity equation and the equation of state go without changes.

In the quadratic approximation, the total mean force acting on the sphere is expressed in the OFR as

$$F_m=-\int_S[\langle p''\rangle\delta_{mn}+\rho\langle u_m'u_n'\rangle-\eta\langle\partial u_m''/\partial r_n+\partial u_n''/\partial r_m-(2/3)\delta_{mn}\nabla\mathbf{u}''\rangle-\mu\delta\langle\nabla\mathbf{u}''\rangle]n_n\,dS-\langle M\partial(U_P)_m/\partial t\rangle, \tag{9}$$

where M stands for the total mass inside the surface S enclosing the sphere. As we have already pointed out, this force does not depend on S. We chose S to be concentric with the sphere. In a viscous fluid, the mean force that acts on a free particle would cause the drift of the particle and would be balanced with the drag from this drift. We shall assume that the particle is kept from drifting but is free to oscillate. The drift velocity of a free particle $\mathbf{v}_d$ is then calculated according to the Stokes formula $\mathbf{v}_d=\mathbf{F}/(6\pi\rho\nu R)$.

In accordance with (9), calculation of the mean force $\mathbf{F}$ requires determination of first-order scattered fields and then, the second-order mean velocity and pressure.

A. First-order scattered fields

The solution for the first-order scattered fields, valid in the vicinity of the particle, can be obtained under the assumption of incompressibility, as was stated above. This assumption is pertinent if r is small compared to the sound wavelength λ. In order to account for the case when $V_{mm}\neq 0$, a scattered field of monopole type should be taken into consideration. We express this part of the scattered field through the scalar potential $\Phi_s'=\phi(r)V_{mm}$. The remaining part is introduced through the vector potential Ψ_s' thus, $\mathbf{u}_s'=\nabla\phi_s'+\nabla\times\Psi_s'$. The scalar potential satisfies the Laplace equation (to which the Helmholtz equation reduces in the incompressible case). An equation to determine Ψ_s' is easily obtained after substitution of $\mathbf{u}_s'$ into the linearized Eq. (8) and taking curl from its both sides

$$-i\omega\nabla\times\nabla\times\Psi_s'+\nu\nabla\times\nabla\times\nabla\times\nabla\times\Psi_s'=0. \tag{10}$$

Ψ_s' is an axial vector. So, one can write for it

$$(\Psi_s')_j=\varepsilon_{jkl}U_kr_l\,f(r)+\varepsilon_{jkl}\tilde{V}_{km}r_lr_mf_1(r), \tag{11}$$

where ε_{jkl} is the fully antisymmetric tensor and $\tilde{V}_{km}=(1/2)[V_{km}+V_{mk}-(2/3)\delta_{km}V_{nn}]$. On substituting expressions for Φ_s' and Ψ_s' into the corresponding equations, we obtain separate equations for $\phi(r)$, $f(r)$, and $f_1(r)$. Taking solutions of these equations that satisfy the nonslip condition on the surface of the particle and vanish as $r\to\infty$, it is possible to express $\mathbf{u}'$ as

$$(u_s')_j = -\frac{R^3}{3} V_{kk}\frac{r_j}{r^3} + U_j A_1(r) + r_j r_k U_k A_2(r)$$

$$+ \tilde{V}_{jk} r_k A_3(r) + r_j r_k r_l \tilde{V}_{kl} A_4(r). \quad (12)$$

Expressions for $A_1(r)-A_4(r)$ are given in Appendix A.

B. Mean second-order velocity field

We consider next the mean second-order velocity field. It will be represented in a general form

$$\langle u'' \rangle = \nabla \times \langle \Psi'' \rangle + \nabla \langle \Phi'' \rangle + \langle \mathbf{u}_0'' \rangle. \quad (13)$$

To derive an equation on $\langle \Psi'' \rangle$, one should substitute $\langle \mathbf{u}'' \rangle$ given by (13) in time-averaged Eq. (8) and take curl from the result obtained. After making use of the identity

$$\frac{1}{\rho_0}\left\langle \frac{\rho' \partial(\mathbf{u}' + \mathbf{U}_p)}{\partial t} \right\rangle = -\frac{1}{\rho_0}\left\langle (\mathbf{u}' + \mathbf{U}_P)\frac{\partial \rho'}{\partial t} \right\rangle$$

$$= \langle (\mathbf{u}' + \mathbf{U}_P) \nabla \mathbf{u}' \rangle,$$

it transforms to

$$\nabla \times \nabla \times \nabla \times \nabla \times \langle \boldsymbol{\Psi}'' \rangle$$

$$= \frac{1}{\nu}\langle -(\mathbf{u}'\nabla)\nabla \times \mathbf{u}' + (\nabla \times \mathbf{u}'\nabla)\mathbf{u}' - 2\nabla \mathbf{u}' \nabla \times \mathbf{u}'$$

$$+ (\mathbf{U}_P + \mathbf{u}') \times \nabla \nabla \mathbf{u}' \rangle. \quad (14)$$

An equation to determine $\langle \Phi'' \rangle$ is a consequence of the time-averaged continuity equation $\nabla \langle \rho' \mathbf{u}' + \rho_0 \mathbf{u}'' \rangle = 0$, in which relationships between first-order fields are taken into account

$$\nabla^2 \langle \Psi'' \rangle = \left\langle \mathbf{u}' \nabla \nabla \int dt\, \mathbf{u}' \right\rangle. \quad (15)$$

Equations of this type are commonly used for considerations of averaged second-order fields.[24,23] Under assumptions that were made earlier in this section, $\nabla \nabla \mathbf{u}' = 0$ because $\nabla \mathbf{u}_s' = 0$ and $\nabla \mathbf{u}_i' = V_{jj} = \text{const}$, and the right-hand side of Eq. (15) is equal to zero while that of Eq. (14) is not. Hence, it is possible to accept $\langle \Phi'' \rangle = 0$. A velocity field that corresponds to solutions of homogeneous Eq. (15) with dipole or higher symmetry can be described by solutions of Eq. (14). Also note that the last term on the right-hand side of Eq. (14) is equal to zero for the same reason.

A careful reader can notice a trick here since our proof is essentially based on the specific form adopted for the incident field and the incompressibility of the scattered field. If effects of compressibility were taken into account, the right-hand side of Eq. (15) would be small, but nonzero. The problem with it is that it decays very slowly (algebraically if we neglect dissipation of sound waves) with the distance from the particle. Fortunately, it turns out that this contribution is insignificant. The proof is straightforward and is given in Appendix B.

The right-hand side of Eq. (14) is a source term that is responsible for the acoustic streaming generated in the vicinity of the sphere. According to Eq. (14), this streaming appears due only to viscous vortex waves ($\nabla \times \mathbf{u}' \neq 0$). Since the first-order velocity field is already known, the right-hand side of Eq. (14) can be easily calculated. It contains terms squared in U_j [or $(U_P)_j$] and $\tilde{V}_{jk}$, and respective cross terms. We leave only cross terms because the mean force is a vector and it is impossible to form a vector that is quadratic in U_j or V_{jk}. The expression for the right-hand side of Eq. (14) is given in Appendix C. However, even in this expression not all terms are of interest in the context of a mean force problem, and a straightforward solution of Eq. (14) would be unnecessarily involved.

The mean force $\mathbf{F}$ can be expressed only through products of U_j and V_{jk} or $(U_P)_j$ and V_{jk}. The second possibility exists because of the force of inertia in the Navier–Stokes equation (8). The mean value of inertia force is not zero when ρ' oscillates, that is when $V_{kk} \neq 0$. Therefore, possible combinations are $U_j V_{kk}$, $(U_P)_j V_{kk}$, and $U_j \tilde{V}_{jk}$, and the second of them appears only through the mean pressure field. Correspondingly, we are interested only in a part of $\langle \Psi'' \rangle$ that is associated with the vectors given by the first and the third combinations. $\langle \Psi'' \rangle$ is an axial vector and therefore we should leave only such terms on the right-hand side of Eq. (14) that give birth to $\langle \Psi'' \rangle$ in the form

$$\langle \Psi_j'' \rangle = \tfrac{1}{4} \varepsilon_{jkl} r_k [\psi_1(r) U_l V_{mm}^* + \psi_2(r) U_m \tilde{V}_{ml}^*] + \text{c.c.} \quad (16)$$

At this stage, it is convenient to consider terms that correspond to these two constituents of $\langle \Psi'' \rangle$ separately. Terms that are due to compressibility ($\propto V_{mm}$) appear on the right-hand side of Eq. (14) in just the form required (see Appendix C). Substituting the first constituent of $\langle \Psi'' \rangle$ (16) in Eq. (14) we obtain

$$\left(\frac{d^4}{dr^4} + \frac{8}{r}\frac{d^3}{dr^3} + \frac{8}{r^2}\frac{d^2}{dr^2} - \frac{8}{r^3}\frac{d}{dr} \right) \psi_1(r) = \frac{1}{\nu} s_1(r).$$

The expression for $s_1(r)$ is given in Appendix C.

The most simple way to find terms corresponding to the second constituent of $\langle \Psi'' \rangle$ is to compute the projection of the terms remaining on the right-hand side of Eq. (14) on the vector $\mathbf{r} \times \mathbf{D}$, where $D_l = U_m \tilde{V}_{lm}^*$. This projection in fact corresponds to the first term in the expansion of the right-hand side $\mathbf{S}$ (Appendix C) in associated Legendre polynomials $P_n^1(\cos\theta)$, where θ is the angle between $\mathbf{r}$ and $\mathbf{D}$. The projection is computed as

$$s_2(r) = \frac{3}{8\pi r^2} \int dS \frac{\mathbf{S}(\mathbf{r} \times \mathbf{D})}{r^2 |\mathbf{D}|^2},$$

and only terms containing $\tilde{V}_{lm}$ should be left in the expression for $\mathbf{S}$ and integration is implied over the surface of radius r enclosing the particle. The resulting equation for $\psi_2(r)$ follows from that for $\psi_1(r)$ after substitution of $s_2(r)$ instead of $s_1(r)$. The expression for $s_2(r)$ is given in Appendix C. Solving these equations, we can write $\langle \Psi'' \rangle$ in the following way:

$$\langle \Psi'' \rangle_j = \varepsilon_{jkl} r_k \left[r^2 \left(\frac{1}{30\nu} \int_R^r \sigma_l(a) a \, da + (C_1)_l \right) - \frac{1}{6\nu} \int_R^r \sigma_l(a) a^3 \, da + (C_2)_l + \frac{1}{r} \left(\frac{1}{6\nu} \int_R^r \sigma_l(a) a^4 \, da + (C_3)_l \right) + \frac{1}{r^3} \left(-\frac{1}{30\nu} \int_R^r \sigma_l(a) a^6 \, da + (C_4)_l \right) \right]. \quad (17)$$

In this expression, $\sigma_j = 1/4[U_j V_{kk}^* s_1(r) + U_k \tilde{V}_{kj}^* s_2(r) + \text{c.c.}]$. Constants of integration $\mathbf{C}_1$ and $\mathbf{C}_2$ are

$$\mathbf{C}_1 = -\frac{1}{30\nu} \int_R^r \sigma(a) a \, da, \quad \mathbf{C}_2 = \frac{1}{6\nu} \int_R^r \sigma(a) a^3 \, da, \quad (18)$$

since otherwise $\langle \Psi'' \rangle$ goes to infinity as $r \to \infty$. Two other constants can be determined from the nonslip condition on the surface of the sphere. Using the expression (13) for $\langle \mathbf{u}'' \rangle$, we have

$$\mathbf{C}_3 = -\tfrac{5}{2}\mathbf{C}_1 R^3 - \tfrac{3}{2}\mathbf{C}_2 R + \tfrac{3}{4} R \langle \mathbf{u}_0'' \rangle, \quad \mathbf{C}_4 = \tfrac{3}{2}\mathbf{C}_1 R^5 + \tfrac{1}{2}\mathbf{C}_2 R^3 - \tfrac{1}{4} R^3 \langle \mathbf{u}_0'' \rangle. \quad (19)$$

In accordance with Eqs. (13) and (17)–(19), the mean velocity field $\langle \mathbf{u}'' \rangle$ can be calculated. The next problem is to derive an expression for the mean pressure $\langle p'' \rangle$.

C. Mean second-order pressure

Again, we shall deal only with that part of $\langle p'' \rangle$ which is essential for calculations of mean force. The mean pressure is a scalar. So, its part which is essential for calculations of the mean force is expressed as

$$\langle p'' \rangle = \tfrac{1}{4}(p_1(r) \mathbf{r}\mathbf{u} V_{kk}^* + p_2(r) r_j U_k \tilde{V}_{kj}^* + p_3(r) \mathbf{r}\mathbf{U_P} V_{kk}^*) + \text{c.c.} \quad (20)$$

We make a substitution of this expression into the time-averaged Navier–Stokes equation

$$\nabla \langle p'' \rangle + \eta \nabla \times \nabla \times \langle \mathbf{u}'' \rangle = \langle \mathbf{P}_1 \rangle + \langle \mathbf{P}_2 \rangle, \quad (21)$$

where

$$\langle \mathbf{P}_1 \rangle = -\rho_0 \langle (\mathbf{u}' \nabla) \mathbf{u}' + \mathbf{u}' \nabla \mathbf{u}' \rangle, \quad \langle \mathbf{P}_2 \rangle = -\rho \langle \mathbf{u}_P \nabla \mathbf{u}' \rangle.$$

Derivatives of functions p_{1-3} enter this equation only in combinations $\mathbf{r} dp_{1-3}/dr$. They are eliminated by forming a vector product of $\mathbf{r}$ and Eq. (21). Following steps in determining $\langle p'' \rangle$ are elementary and the answer is

$$\langle p'' \rangle = \rho_0 \nu \mathbf{r} \left[-20 \left(\frac{1}{30\nu} \int_R^r \sigma(a) a \, da + \mathbf{C}_1 \right) - \frac{2}{r^3} \left(\frac{1}{6\nu} \int_R^r \sigma(a) a^4 \, da + \mathbf{C}_3 \right) \right] - \langle \mathbf{r}\mathbf{u}_P \nabla \mathbf{u}' \rangle + \tfrac{1}{4}(q_1(r) \mathbf{r}\mathbf{u} V_{kk}^* + q_2(r) r_j U_k \tilde{V}_{kj}^* + \text{c.c.}),$$

where $q_1(r)$ and $q_2(r)$ denote the functions that come from projecting $\langle \mathbf{r} \times \mathbf{P}_1 \rangle$ on vectors $\mathbf{r} \times \mathbf{U} V_{kk}^*$ and $\varepsilon_{jkl} r_k U_m \tilde{V}_{lm}^*$. Functions $q_1(r)$ and $q_2(r)$ are equal to zero at $r = R$ and their computation is not necessary if the surface of integration S coincides with the surface of the sphere.

D. The mean force

The last step is to substitute the expressions for $\langle \mathbf{u}'' \rangle$ and $\langle p'' \rangle$ derived above into (9) and implement integration. The result of integration is

$$\mathbf{F} = 8\pi\eta \left(\frac{1}{6\nu} \int_R^r \sigma(a) a^4 \, da + \mathbf{C}_3 \right) + \frac{4}{3} \pi r^3 \rho_0 \langle \mathbf{U}_P \nabla \mathbf{u}' \rangle + \mathbf{Q} - \rho_0 \int_S (\mathbf{U}_P + \mathbf{u}')(\mathbf{u}' \mathbf{n}) dS. \quad (22)$$

Here, $\mathbf{Q}$ denotes that part of the force which is connected with integration of $q_{1,2}(r)$ (if $r \neq R$). When the surface of integration S is taken at $r = R$, (22) reduces to

$$\mathbf{F} = 8\pi\eta \mathbf{C}_3 + \tfrac{4}{3} R^3 \langle \mathbf{U}_P \nabla \mathbf{u}' \rangle \rho_0 |_{r=R}. \quad (23)$$

In this form it will be used for calculations. It is noteworthy that another form which follows for $r \gg \delta$ may also be convenient

$$\mathbf{F} = 8\pi\eta \mathbf{C}_3 + (1/6\nu) \int_R^\infty \sigma(a) a^4 da + \mathbf{F}_r.$$

Here, $\mathbf{F}_r$ represents the sum of the last three terms in (22). In the case $r \gg \delta$, they include only products of sound fields and thus correspond to the radiation pressure. Since $\mathbf{F_r}$ is known (see Ref. 14), this second form of $\mathbf{F}$ may be used, in principle, for checking the results obtained.

Let us rewrite (23) using (19)

$$\mathbf{F} = 8\pi\eta[-\tfrac{5}{2}\mathbf{C}_1 R^3 - \tfrac{3}{2}\mathbf{C}_2 R] + 6\pi\eta R \langle \mathbf{u}_0'' \rangle + \tfrac{4}{3} R^3 \langle \mathbf{U}_P \nabla \mathbf{u}' \rangle \rho_0 |_{r=R}. \quad (24)$$

The second term in (24) corresponds to the Stokes drag force due to the steady component of velocity in the OFR. It is formed by the steady force $6\pi\eta R \langle \mathbf{v}_0'' \rangle$ in the RFR (the drag force due to the external acoustic streaming) and Dukhin's force[25] $6\pi\eta R \langle \int dt (U_P)_k V_{jk} \rangle$.

Integrals in constants $\mathbf{C}_1$ and $\mathbf{C}_2$ [see (18)] can be rearranged and expressed through linear combinations of elementary functions and integral exponents $E_1(a) = \int_1^\infty e^{-at} t^{-1} dt$ with $a \sim R/\delta$. In two-limit cases, $\delta \ll R$ and $\delta \gg R$, an asymptotic expansion and the Taylor expansion of $E_1(a)$, respectively, can be used to derive an analytical expression for the total mean force. Calculations are quite simple, yet rather cumbersome to be given here. Only resulting expressions for the mean force are presented below.

1. $\delta \ll R$

When $\delta \ll R$, up to leading terms

$$F_j = \pi R^3 \rho_0 \tfrac{1}{4}[U_j V_{kk}^* (2 + i\xi^{-1}) + U_k \tilde{V}_{jk}^* (2 + 3i\xi^{-1}) + \tfrac{4}{3}(U_P)_j V_{kk}^*] + \text{c.c.} \quad (25)$$

The term with the drag force drops out from (25) since it is $\mathcal{O}(\xi^{-2})$. It turns out that mean force given by (25) coincides with the radiation pressure in viscous fluid calculated with

the same accuracy. To show this, we recall that the dipole force due to a small sphere is the force which is necessary to apply to a fluid particle with the shape of the sphere to move it with the same amplitude as the real sphere moves under the action of sound field: $\mathbf{P}=-\mathbf{N}-(4/3)i\omega\rho_0\pi R^3(\mathbf{U}_P-\mathbf{v}_i')$. Here, $\mathbf{N}$ is the reaction force in a viscous fluid given by Eq. (5). We also recall that the volume velocity of monopole scattered field due to a rigid sphere $Q=-(4\pi/3)R^3V_{kk}$. Then, by applying (2), we immediately find that up to higher-order terms in small ratio $\delta/R=\xi^{-1}$

$$(F_r)_j=\pi\rho_0R^3\tfrac{1}{4}[U_kV_{jk}^*(2+3i\xi^{-1})+\tfrac{4}{3}V_jV_{kk}^*]+\text{c.c.},$$

which is exactly the result given by (25).

Small contribution $\propto\xi^{-1}$ in the last formula cannot be omitted because its phase differs by $\pi/2$ from that of the larger terms. For a plane traveling wave, namely, it determines the acoustic radiation pressure (because the product of U_k and V_{km} is imaginary). The viscosity of fluid is therefore crucial in this case even if $\delta\ll R$. Clearly, if this ratio is extremely small so that $\delta/R\leqslant(kR)^3$ (see Sec. I) the influence of viscosity can be neglected [the last formula cannot be applied in this limit since it does not account for term of higher order in (kR)]. This unequality, however, seldom holds for submillimeter particles in the frequency range used in the practice of acoustic coagulation. For standing waves, U_k and V_{km} are in phase and problems of this kind never occur.

2. $\delta\gg R$

In another limit, $\delta\gg R$, up to leading terms

$$F_j=\pi\rho_0R^3\tfrac{1}{4}[2(i+1)\xi^{-1}U_jV_{kk}^*+\tfrac{12}{5}(1+i)\xi^{-1}U_k\tilde{V}_{jk}^*+\tfrac{4}{3}(U_P)_jV_{kk}^*+3i\xi^{-2}(U_P)_kV*_{jk}]+\text{c.c.}+6\pi\eta R\langle v_0''\rangle_j. \quad (26)$$

It is necessary to note that in this case the integral which defines $\mathbf{C}_2$ (18) converges at distances comparable with δ. Consequently, the characteristic scale of incident sound field must significantly exceed $\max\{R,\delta\}$ if the expansion (4) is used. This fact should be kept in mind each time when formula (26) is applied.

The three first terms in square brackets in (26) represent that part of the radiation pressure (momentum flux associated with sound waves) which is transmitted to the sphere. Comparing it with the respective expression for the radiation pressure (see, for example, Westervelt's assessment given in Sec. I), one can conclude that this part is $\mathcal{O}(R/\delta)$ as we have already noted in Sec. I. The remaining terms in (26) are not connected with the radiation pressure and describe the drag force from the steady component of the incident field in the OFR. They include Dukhin's force (the fourth term in square brackets) and the drag from the external acoustic streaming. These terms are of higher order in ξ^{-1} and in fact dominate the mean force. Normally, only they are significant except for cases when phase relations are in favor of smaller terms.

Drag forces dominate in many practical situations with plane traveling waves. For example, given a piston radiation of a traveling wave $v_i'=v_0\exp(i\mathbf{kx})$ and a heavy sphere $(U_P=0)$, it is a simple exercise to show that the drag force is directed against the radiation pressure; the mean force is negative and practically equal to the drag force. To do this, we note only that for a piston source v_0'' is in fact governed by the constraint that the mean Lagrangian velocity is zero (otherwise there would be mass flux through the piston). In the quadratic approximation, $\mathbf{v}_L''=\mathbf{v}_i''+(\mathbf{d}_i\nabla)\mathbf{v}_i'=0$, where $\mathbf{d}_i=\int\mathbf{v}_i'\,dt$ is the displacement of a fluid particle. This immediately leads to $\mathbf{v}_0''=-\mathbf{k}v_0'^2/(2\omega)$ and

$$F\approx-\frac{3}{2}\,\rho_0v_0'^2\pi R^2(kR)\,\frac{\delta^2}{R^2}.$$

In other cases, when the incident wave is plane traveling only locally, computations of v_0'' are not so straightforward because mean Lagrangian velocity is not necessarily zero.

An important example of another kind constitutes a plane standing wave where the contribution coming from the last term in (26) can be made small if the particle is far from the walls of container or resonator (there is Rayleigh streaming otherwise).

We consider the case of plane standing wave in more detail. For $v_i'=v_0\sin(kx)$, the total mean force

$$F=G\pi\rho_0kR^3v_0^2\sin(2kx)[(\zeta-1)(\tfrac{8}{45}\zeta\xi^3-\tfrac{1}{3})+\tfrac{1}{3}]+6\pi\eta R\langle v_0''\rangle.$$

In this expression, we left only leading-order terms in ξ^{-1} and in density ratio ζ. For light particles these latter terms are unimportant.

Assume that the external acoustic streaming $\langle v_0''\rangle$ is equal to zero or suppressed. Then if the particle is rather dense, i.e., $\zeta\gg1$, the total mean force is directed against the radiation pressure when $\xi<\xi_{\text{cr}}\approx(15/8\zeta)^{1/3}$ (in this case, Dukhin's force prevails). For a water droplet in air, $\zeta\approx800$ and $\xi_{\text{cr}}\approx0.13\ll1(\delta/R\approx7.5)$. Particles with radii greater than $R=\xi_{\text{cr}}\delta$ must drift to pressure nodes and particles with smaller radii must drift to pressure crests. In this way, an aerosol can be divided into fine $(R<R_{\text{cr}})$ and coarse $(R>R_{\text{cr}})$ fractions with the critical radius R_{cr} determined by the sound frequency. In practice the value of ξ_{cr} may differ from that found here since the above expression for the mean force does not allow for all possible mechanisms contributing to the mean force. The main one is connected with the dependence of dynamic viscosity upon temperature variations caused by sound field. In air, it makes ξ_{cr} greater because the corresponding mean force is directed against Dukhin's force. In liquids, directions of both forces coincide but possible values of ζ are not as high as in gases. Drifting of small iron particles against the direction of the radiation force in a standing plane wave was observed experimentally[26] in water, ethyl alcohol, and glycerin for $R/\delta\leqslant3$.

III. CONCLUSIONS

In this paper, we addressed the problem of mean force exerted by a sound wave on a small rigid sphere in a viscous fluid and a number of closely related questions that clarify physical aspects of the influence of viscosity. Although the problem of mean force has recently received intense treat-

ment in Refs. 4–9, it required some additional analysis both to clarify the physical picture and to include more general fields into consideration.

We began by explaining the fact that viscosity and heat conduction may influence the mean force noticeably only when the sphere is small compared to the sound wavelength, and normally, to the depth of penetration of dissipative waves. The latter condition is not true for a plane traveling wave because of the phase relations between the quantities that characterize incident and scattered fields (Sec. I).

By resorting to the case of small sphere, we not only made the calculations simpler, but also were able to generalize them to the case of arbitrary sound field which varies slowly on the scale of the obstacle. The mean force was calculated within the accuracy of the leading term in the expansion in the parameter $\max\{kR, R/l\}$ and was expressed as a sum of drag force coming from the external steady flow existing in the absence of the sphere and contributions that are cross products of velocity and velocity derivatives of the incident field. We showed that calculations can be carried out under the assumption that scattered fields (sound and viscous waves) are incompressible. This implies that the compressibility of fluid is essential only as much as it is responsible for the gradients of incident velocity field. If a sphere were not rigid, its compressibility would be important only for calculating the volume velocity that characterizes the source of the monopole part of the scattered sound field.

We argue that in a viscous fluid a distinction should be made between the mean force on an obstacle and the radiation pressure. We define the latter as the mean momentum flux carried by sound waves through a surface enclosing the obstacle. In an ideal fluid, this quantity is the total mean force acting on the obstacle. The reason why these two forces are different in an viscous fluid is twofold. First, the generation of incident sound field is accompanied by production of acoustic streaming. This external streaming is dependent on the geometry of the domain as well as on on the boundary condition. The drag force coming from this streaming is not connected with the momentum flux carried by the sound wave to the obstacle. When the obstacle oscillates, there is an additional contribution to this drag, this time due to the fact that the obstacle ''sees'' the first-order incident field at points that oscillate with it. Second, even if this drag were absent, the radiation pressure is not the force exerted on the obstacle because another acoustic streaming is produced locally near the obstacle and carries away a part of the momentum flux brought by sound waves.

Computations of this streaming constitute the main difficulty in determining the mean force. It turns out that the streaming is really important if $\delta \geqslant R$. If $\delta \gg R$ it carries away the major part of the mean momentum flux brought by sound waves. The remaining part is usually next order in small parameter R/δ if compared to the drag force (nevertheless, it may be important depending on phase difference between the velocity and its derivative in the incident sound field).

If $\delta \ll R$ the streaming is unimportant and the mean force is approximately equal to the radiation pressure. This implies that one can use Gor'kov's approach (with properly determined source terms) to compute the mean force. Normally in this case the effects of viscosity are small and can be neglected. An exception is the case of a plane traveling wave (or any wave resembling it locally) where they may dominate. The radiation pressure in a plane traveling wave field is extraordinarily small if a host fluid is ideal because of phase relation, and small dissipative contribution is seen because it shifts the phase of the dipole component of the scattered sound field. To arrive at this conclusion one does not need to carry out all the very involved calculations of Refs. 4–9: it is a direct consequence of a much simpler approach.

Possible practical applications of the results obtained can be connected to the acoustic coagulation problem. Direct application of the expressions for the mean force derived above allows estimates of drift velocities to be made in sound fields of different type. These expressions can also be used to calculate forces of interaction between two spheres in a sound field. If the distance between spheres is large in comparison to their radii, one can treat the combination of the primary incident field and the scattered field from one of the obstacles as an incident field at the location of another obstacle. The mean force associated with this scattered field (treated as an incident one) is in fact the force of interaction (or repulsion) between obstacles (known as Bjerkness and König forces in the case of an ideal fluid[11]). Basic mechanisms that can lead to interparticle forces in a sound field have long been known,[11] but their relative importance is still debated, partly because of the lack of a rigorous theory which would account for effects of fluid viscosity that are expecially significant for very small particles. By virtue of assumptions made [the local representation (4)], our results can be applied only to estimate the interaction between well-separated particles (the distance between them must exceed δ). However, the temporal scale of interaction is most sensitive to passing the stage of maximum separation. Corresponding calculations will be given in a separate paper. The problem of interaction between particles in a sound field can also be analyzed from the viewpoint of collective interactions. In this case, a consistent theory needs an expression for the mean force too, as we showed in Ref. 27.

Discussing possible practical applications, we should analyze the region of applicability of underlying assumptions. Any theory developed in quadratic approximation is incomplete if a restriction on the amplitude of sound field is not imposed. For a small sphere, this restriction is

$$|\mathbf{v}_i' - \mathbf{U}_P|/\omega \ll \max(R, \delta), \tag{27}$$

implying that the displacement of fluid relative to the sphere must be small as compared with R when $R \gg \delta$ and with δ in another limit, $R \ll \delta$. If this constraint is violated, the linearization of hydrodynamical equations for deriving the first-order solution for scattered fields becomes impossible, as follows from the analysis of terms in the Navier–Stokes equation. In this case the perturbation theory should be based not on the linear solution, but on some other approach, and it is likely that in this case the Oseen-type mean force predicted by Westervelt[17] may appear. The restriction (27) can be fairly severe for heavy particles (not entrained by oscillating fluid) and, therefore, what occurs beyond the domain of ap-

plicability of quadratic approximation is really the question to be solved.

APPENDIX A

Expressions for functions $A_{1-4}(r)$ are as follows:

$$A_1(r)=a_1\frac{R^3}{r^3}-a_2\left(\frac{i}{y^3}+\frac{1}{y^2}-\frac{i}{y}\right)\exp(iy),$$

$$A_2(r)=-3a_1\frac{R^3}{r_5}+a_2\frac{1}{r^2}\left(\frac{3i}{y^3}+\frac{3}{y^2}-\frac{i}{y}\right)\exp(iy),$$

$$A_3(r)=-a_3\frac{2R^5}{5r^5}+a_4\left(\frac{6i}{y^5}+\frac{6}{y^4}-\frac{3i}{y^3}-\frac{1}{y}\right)\exp(iy),$$

$$A_4(r)=a_3\frac{R^5}{r^7}+a_4\frac{1}{r^2}\left(\frac{-15i}{y^5}-\frac{15}{y^4}+\frac{6i}{y^3}+\frac{1}{y^2}\right)\exp(iy).$$

In these expressions $y=\kappa r$, $\kappa=(1+i)/\delta$, and

$$a_1=\frac{1}{2}\left(-\frac{3}{y_0^2}+\frac{3i}{y_0}+1\right),\quad a_2=\frac{3y_0}{2i}\exp(-iy_0),$$

$$a_3=\frac{25}{3}\frac{3i+3y_0-iy_0^2}{iy_0^2+y_0^3}-\frac{5}{3},\quad a_4=\frac{5}{3}y_0^3(i+y_0)\exp(-iy_0),$$

$$y_0=\kappa R.$$

APPENDIX B

The right-hand side of Eq. (15) is not zero if fluid compressibility is taken into account. Although it is small (it contains k^2 due to the presence of $\nabla\nabla$ operator), it decays algebraically if sound absorption is neglected and therefore needs a separate treatment. The question with it can be solved by changing the representation for the second-order velocity field. By adding $\mathbf{U}_P\int dt\,\nabla\mathbf{u}_s'$ to the right-hand side of Eq. (13) and substituting the resultant expression into the averaged continuity equation, we arrive to a new expression for the right-hand side of Eq. (15) which contains terms squared in sound wave fields in the form

$$\left\langle \mathbf{v}_i'\int dt\,\nabla\nabla\mathbf{u}_s'+\mathbf{u}_s'\int dt\,\nabla\nabla\mathbf{v}_i'+\mathbf{u}_s'\int dt\,\nabla\nabla\mathbf{u}_s'\right\rangle.$$

Since the action of operator $\nabla\nabla$ is equivalent to multiplying by k^2, the above expression is equal to zero if k^2 is a real quantity, i.e., if dissipation of sound waves is neglected. However, even if the dissipation of sound waves is taken into account the contribution from the terms written above should be small as compared to a similar contribution from the terms squared in the incident sound field which is present in $\mathbf{v}_i''$. Indeed, the effect is accumulated over large volume where scattered field is much smaller than the incident one. Correspondingly, the only point which is still to be explained is that concerning the role of additional term $\mathbf{U}_P\int dt\,\nabla\mathbf{u}_s'$. Since it depends on the divergence of the scattered sound field, it does not contribute into the mean force in the first order in kR (in this respect it is different from the divergence of the incident field, which is proportional to k for plane waves).

APPENDIX C

$$S_j=\left\langle -(\mathbf{u}'\nabla)\varepsilon_{jkl}\frac{\partial u_l'}{\partial r_k}+(\nabla\times\mathbf{u}'\nabla)u_j'-2\nabla\mathbf{u}'\varepsilon_{jkl}\frac{\partial u_l'}{\partial r_k}\right\rangle$$

$$=\frac{1}{4}\left\{\varepsilon_{jkl}r_kU_lV_{mm}^*\left[-2L-\frac{r}{3}\left(1-\frac{R^3}{r^3}\right)\frac{dL}{dr}\right]\right.$$

$$+\varepsilon_{jkl}U_k\tilde{V}_{lm}^*r_m[-(A_1(r)+1)K^*+(A_3^*(r)+1)L]+\varepsilon_{jkl}r_k\tilde{V}_{lm}^*U_m[-(A_1(r)+1)K^*]+\varepsilon_{mkl}r_kU_l\tilde{V}_{jm}^*[L(A_3^*(r)+1)]$$

$$+\varepsilon_{jkl}r_k\tilde{V}_{lm}^*r_mU_nr_n\left[-\frac{dK^*}{dr}\left(\frac{A_1(r)}{r}+\frac{1}{r}+rA_2(r)\right)-K^*A_2(r)\right]$$

$$\left.+\varepsilon_{jkl}r_kU_lr_mr_n\tilde{V}_{mn}^*\left[-(A_3^*(r)+1)\frac{1}{r}\frac{dL}{dr}-A_4^*(r)\frac{rdL}{dr}\right]+\varepsilon_{mkl}r_kU_l\tilde{V}_{mn}^*r_nr_j[2LA_4^*(r)-K^*A_2(r)]+\text{c.c.}\right\}.$$

Here, functions $A_{1-4}(r)$ are those defined in Appendix A and

$$K=\frac{1}{r}\frac{dA_3(r)}{dr}-2A_4(r),\quad L=\frac{1}{r}\frac{dA_1(r)}{dr}-A_2(r).$$

Only a part of S_j can contribute to the mean force, as we have explained in Sec. II. The reduced form of S_j is as follows:

$$S_j=\varepsilon_{jkl}r_k\sigma_l(r),$$

$$\sigma_l(r)=\tfrac{1}{4}[U_lV_{mm}^*s_1(r)+\tilde{V}_{lm}^*U_ms_2(r)+\text{c.c.}],$$

where

$$s_1(r) = -2L - \frac{r}{3}\left(1 - \frac{R^3}{r^3}\right)\frac{dL}{dr},$$

$$s_2(r) = -\frac{3}{2}(A_1(r)+1)K^* - \frac{r^2}{5}\left[\frac{3}{2}\left(\frac{1}{r}(A_1(r)+1) + rA_2(r)\right)\frac{dK^*}{dr} + \frac{3}{2}A_2(r)K^* - \left(\frac{1}{r}(A_3^*(r)+1) + rA_4^*(r)\right)\frac{dL}{dr}\right].$$

[1] W. L. Nyborg, ''Radiation pressure on a small rigid sphere,'' J. Acoust. Soc. Am. **42**, 947–952 (1967).
[2] J. Wu and G. Du, ''Acoustic radiation force on a small compressible sphere in a focused beam,'' J. Acoust. Soc. Am. **87**, 997–1003 (1990).
[3] X. Chen and R. E. Apfel, ''Radiation force on a spherical object in an axisymmetric wave field and its application to the calibration of high-frequency transducers,'' J. Acoust. Soc. Am. **99**, 713–724 (1996).
[4] A. A. Doinikov, ''Acoustic radiation pressure on a compressible sphere in a viscous fluid,'' J. Fluid Mech. **267**, 1–21 (1994).
[5] A. A. Doinikov, ''Acoustic radiation pressure on a rigid sphere in a viscous fluid,'' Proc. R. Soc. London, Ser. A **447**, 447–466 (1994).
[6] A. A. Doinikov, ''Radiation force due to a spherical sound field on a rigid sphere in a viscous fluid,'' J. Acoust. Soc. Am. **96**, 3100–3105 (1994).
[7] A. A. Doinikov, ''Acoustic radiation force on a spherical particle in a viscous heat-conducting fluid. I. General formula,'' J. Acoust. Soc. Am. **101**, 713–721 (1997).
[8] A. A. Doinikov, ''Acoustic radiation force on a spherical particle in a viscous heat-conducting fluid. II. Force on a rigid sphere,'' J. Acoust. Soc. Am. **101**, 722–730 (1997).
[9] A. A. Doinikov, ''Acoustic radiation force on a spherical particle in a viscous heat-conducting fluid. III. Force on a liquid drop,'' J. Acoust. Soc. Am. **101**, 731–740 (1997).
[10] C. P. Lee, A. V. Anilkumar, and T. G. Wang, ''Static shape and instability of an acousticly levitated drop,'' Phys. Fluids A **3**, 2497–2515 (1991).
[11] N. L. Shirokova, ''Aerosol coagulation,'' in *Physical Principles of Ultrasonic Technology*, Vol. 2, edited by L. D. Rosenberg (Plenum, New York, 1973), pp. 477–539.
[12] L. V. King, ''On the acoustic radiation pressure on spheres,'' Proc. R. Soc. London, Ser. A **147**, 212–240 (1935).
[13] K. Yosioka and Y. Kawasima, ''Acoustic radiation pressure on a compressible sphere,'' Acustica **5**, 167–173 (1955).
[14] S. D. Danilov and M. A. Mironov, ''Radiation pressure force acting on a small particle in a sound field,'' Sov. Phys. Acoust. **30**, 276–279 (1984).
[15] S. D. Danilov, ''Average force acting on a small sphere in a travelling wave field in a viscous fluid,'' Sov. Phys. Acoust. **31**, 26–28 (1985).
[16] S. D. Danilov, ''The mean force acting on a small body in an axisymmetric sound field in a real medium,'' Fluid Dyn. (USSR) **21**, 812–820 (1986).
[17] P. J. Westervelt, ''The mean pressure and velocity in a plane acoustic wave in a gas,'' J. Acoust. Soc. Am. **22**, 319–327 (1950).
[18] P. J. Westervelt, ''The theory of steady forces caused by sound waves,'' J. Acoust. Soc. Am. **23**, 312–315 (1951); ''Acoustic radiation pressure,'' *ibid.* **29**, 26–29 (1957).
[19] L. P. Gor'kov, ''On the forces acting on a small particle in an acoustic field in an ideal fluid,'' Sov. Phys. Dokl. **6**, 773–775 (1962).
[20] L. D. Landau and E. M. Lifshitz, *Fluid Mechanics* (Pergamon, New York, 1959).
[21] C. A. Lane, ''Acoustical streaming in the vicinity of a sphere,'' J. Acoust. Soc. Am. **27**, 1082–1086 (1955).
[22] L. K. Zarembo and V. A. Krasil'nikov, *Introduction in Nonlinear Acoustics* (in Rusian) (Nauka, Moscow, 1966).
[23] W. L. Nyborg, ''Acoustical streaming,'' in *Physical Acoustics Principles and Methods*, edited by W. P. Mason, Vol. II, Part II, Properties of Polymers and Nonlinear Acoustics (Academic, New York/ London, 1965).
[24] P. J. Westervelt, ''The theory of steady rotational flow generated by sound field,'' J. Acoust. Soc. Am. **25**, 60–67 (1953).
[25] S. S. Dukhin, ''The theory of drift of aerosol particle in a standing sound wave,'' Kolloidn. Zh. (in Russian) **22**, 128–130 (1960).
[26] A. G. Avetisyan, V. S. Arakeylyan, O. V. Bagdasaryan, and A. K. Dudoyan, ''Behavior of a heavy particle in a viscous fluid in the field of a standing ultrasonic wave,'' Sov. Phys. Acoust. **31**, 227 (1985).
[27] S. D. Danilov and M. A. Mironov, ''Collective interaction of a suspension of particles in a sound field,'' Sov. Phys. Acoust. **38**, 250–253 (1992).

Study of horizontal multipaths and ray chaos due to ocean mesoscale structure

M. A. Wolfson
Earth Systems Science Center, Penn State University, University Park, Pennsylvania 16802

F. D. Tappert
Applied Marine Physics, University of Miami, RSMAS, 4600 Rickenbacker Cswy., Miami, Florida 33149

(Received 2 December 1997; revised 13 February 1998; accepted 6 October 1999)

Long-range ocean acoustic propagation in the presence of idealized mesoscale structure is studied by first deriving a two-dimensional horizontal-plane parabolic wave equation that follows from the adiabatic mode approximation. In the geometric limit, a nonautonomous Hamiltonian dynamical system having one degree of freedom is derived. A stochastic formalism is developed to analyze this nonintegrable dynamical system. The main result is that on average two rays that are initially separated by an infinitesimal amount diverge exponentially at a rate given by the Lyapunov exponent that has been calculated theoretically and compared to numerical experiments with agreement to two decimal places. The practical implication of this result is that tomographic inversions based on assumed pointwise accurate ray predictions might not be possible beyond the ''predictability horizon'' of many thousands of kilometers, due to horizontal-plane multipaths induced by naturally occurring mesoscale activity. © *2000 Acoustical Society of America.* [S0001-4966(00)05201-2]

PACS numbers: 43.30.Ft, 43.30.Cq, 43.30.Qd [DLB]

INTRODUCTION

When the geometric, or ray, approximation is made, the linear acoustic wave equation is replaced by a system of nonlinear ordinary differential equations that can be cast in the form of a Hamiltonian dynamical system. When, in addition, the ocean through which the sound waves propagate contains lateral inhomogeneities, then the ray equations are generically nonintegrable and ray trajectories exhibit chaotic behavior, i.e., extreme sensitivity to the initial conditions and to the environment. As a consequence, accurate predictions of individual ray trajectories might not be possible beyond a certain ''predictability horizon'' to be defined below. If individual ray trajectories are not accurately calculated, then predictions of intensities and phases (travel times) are also expected to not be pointwise accurate. This limitation of the ability to predict sound propagation is due ultimately to the finite precision of the measurement instruments that provide inputs to the propagation models.

The first published example of the above general observation concerning predictability of acoustic propagation was Palmer *et al.*[1] in the context of two-dimensional vertical plane (range, depth) propagation in the oceanic sound channel, perturbed by internal waves that were modeled as periodic in range. Analysis of chaotic behavior was based on Poincaré maps and numerically computed Lyapunov exponents that gave predictability horizons of a few hundred kilometers. A similar study that introduced area-preserving mappings was published by Brown *et al.*[2] Other studies of vertical plane propagation in shallow water with range-dependent bathymetric variations yielded predictability horizons of a few tens of kilometers.[3] A summary of this research was published by Brown *et al.*[4] More recently, general methods for analyzing chaos in vertical plane oceanic sound channel propagation were discussed by Smith *et al.*,[5] and effects of mesoscale perturbations were numerically computed by Smith *et al.*[6] to yield predictability horizons of a few thousand kilometers. Even more recently, some controversial aspects of ray chaos in ocean acoustics have been investigated.[7–10] In regard to internal wave induced chaos in the vertical plane, Simmen *et al.*[11] initiated numerical studies that revealed a sensitivity to the background sound speed profile as to which portion of a time front resulted from the propagation of chaotic rays.

The research reported in this article has two primary motivations: (1) to provide theoretical estimates of Lyapunov exponents and thereby predictability horizons, which heretofore had to be computed numerically; and (2) to estimate limitations of predictability for long-range low-frequency (LRLF) global ocean acoustic propagation. The basic acoustic model developed in this paper, adiabatic modes and horizontal ray tracing, follows the work of Weinberg and Burridge.[12] Using only climatology, and no mesoscale structure, horizontal multipaths in LRLF propagation were found in Refs. 13, 14. The same two-dimensional PE model developed in this paper including mesoscale structure, was also developed by Collins,[15] but without mesoscale structure. A preliminary version of this paper appeared in Ref. 16. We emphasize that our model of mesoscale structure is highly idealized in order to facilitate an analytical treatment.

In Sec. I, an idealized LRLF two-dimensional horizontal-plane acoustic propagation model is derived for each acoustic mode in depth. Mesoscale perturbations near the sound channel axis cause horizontal multipaths and ray chaos, which is rather different from the vertical plane chaos studied previously. In addition, the parabolic approximation and the geometric approximation are made, resulting in a nonautonomous Hamiltonian dynamical system having one

degree of freedom. In Sec. II, a stochastic formalism is developed based on the method of smoothing applied to the variational equations, and an analytical expression is derived for the expected value of the Lyapunov exponent. Relations between ray chaos and eigenrays are also discussed in Sec. II, and the predictability horizon is estimated. Section III describes numerical simulations that reveal the Hamiltonian chaos present in this problem and supports the theoretical analysis of Sec. II. Finally, Sec. IV summarizes the results of this research, describes the practical implications of the results, and states the conclusions.

I. DERIVATION OF DYNAMICAL SYSTEM EQUATIONS

The emphasis of this paper is on matters of principle, and not on a totally realistic ocean acoustic model. The starting point is the small-angle three-dimensional parabolic wave equation (PE) in Cartesian coordinates in which x is range, y is cross-range, and z is depth. Earth curvature effects are ignored because, although inclusion of such effects certainly alters acoustic predictions at long range, they do not influence the basic issue of predictability. Thus one obtains[17]

$$i\frac{\partial\Psi}{\partial x}+\frac{1}{2k_0}\left(\frac{\partial^2\Psi}{\partial y^2}+\frac{\partial^2\Psi}{\partial z^2}\right)-k_0U(x,y,z)\Psi=0. \tag{1}$$

Here $\Psi(x,y,z)$ is the reduced acoustic pressure, and k_0 is the reference wave number. The potential is expressed as

$$U(x,y,z)=U_0(z)+U_1(x,y,z), \tag{2}$$

where $U_0(z)$ represents the sound speed structure of the background ocean and $U_1(x,y,z)$ represents the ocean mesoscale structure.

The normal modes of the unperturbed, separable problem satisfy

$$-\frac{1}{2k_0^{i2}}\frac{d^2\phi_n}{dz^2}+U_0(z)\phi_n=\lambda_n\phi_n, \tag{3}$$

where the ϕ_n are the orthonormal acoustic modes. Expansion of the solution in terms of these normal modes,

$$\Psi(x,y,z)=\sum_n \psi_n(x,y)\phi_n(z)e^{-ik_0\lambda_n x}, \tag{4}$$

yields the coupled mode equations,

$$i\frac{\partial\psi_n}{\partial x}+\frac{1}{2k_0}\frac{\partial^2\psi_n}{\partial y^2}-k_0a_{nn}(x,y)\psi_n$$

$$=k_0\sum_{m\neq n} e^{ik_0(\lambda_n-\lambda_m)x}a_{mn}(x,y)\psi_n, \tag{5}$$

where the mode coupling coefficients are

$$a_{nm}(x,y)=\int \phi_n(z)U_1(x,y,z)\phi_m(z)dz. \tag{6}$$

Obviously the mode coupling matrix a_{nm} is real-valued and symmetric. Although it is believed that the mode coupling terms on the right-hand side of Eq. (5) are important in long-range acoustic propagation, these terms are neglected in the rest of this work. The results concerning chaos and predictability are not invalidated by the neglect of mode coupling; it is expected that mode coupling only adds to the chaos and decreases predictability. Thus the predictability horizon calculated in this paper is expected to be an upper bound to the true predictability horizon.

Defining $\epsilon_n=\langle a_{nn}^2(x,y)\rangle^{1/2}\ll 1$, where the brackets denote spatial averaging, and $\mu_n(x,y)=a_{nn}(x,y)/\epsilon_n$, Eq. (5) becomes

$$i\frac{\partial\psi_n}{\partial x}+\frac{1}{2k_0}\frac{\partial^2\psi_n}{\partial y^2}-k_0\epsilon_n\mu_n(x,y)\psi_n=0. \tag{7}$$

Thus a two-dimensional horizontal-plane parabolic wave equation is obtained for each acoustic mode. The potential, $\mu_n(x,y)$, is the integral over depth of the mesoscale structure weighted by the nth acoustic normal mode, and finally normalized by its rms value. The rms value, denoted by ϵ_n with $\epsilon_n\ll 1$, represents the strength of the sound speed fluctuations near the axis of the sound channel.

To model $\mu_n(x,y)$, the following simplifications are made: Given a choice of mode number n, it is assumed that the potential has unit-variance and zero-mean, is spatially stationary, isotropic, and has a single scale length, $L=O(100\,\text{km})$, and $10^{-3}\lesssim\epsilon\lesssim 10^{-2}$. The correlation function of the mesoscale structure is related to its power spectrum by

$$\langle\mu(x,y)\mu(x+\overline{x},y+\overline{y})\rangle=\int\int_{-\infty}^{\infty}S(k,l)\times\exp[i(k\overline{x}+l\overline{y})]dk\,dl. \tag{8}$$

In this paper, $\mu(x,y)$ is modeled with a bivariate Gaussian spectrum,

$$S(k,l)=(L^2/4\pi)\exp[-L^2(k^2+l^2)/4], \tag{9}$$

so that the spatial correlation function is also Gaussian:

$$\langle\mu(x,y)\mu(x+\overline{x},y+\overline{y})\rangle=\exp[-(\overline{x}^2+\overline{y}^2)/L^2]. \tag{10}$$

Real ocean mesoscale structure is believed to have a power law spectrum with at least two distinct scale lengths. Again, the simplified model adopted in this paper is intended to establish a methodology for investigating the basic issue of predictability. In future work, the mesoscale model will be made more realistic.

Dropping the mode number n, the basic equation becomes

$$ik_0^{-1}\frac{\partial\psi}{\partial x}=-\frac{k_0^{-2}}{2}\frac{\partial^2\psi}{\partial y^2}+\epsilon\mu(x,y)\psi. \tag{11}$$

The initial condition corresponds to a plane wave:

$$\psi_0(y)=\psi(0,y)=\exp(ik_0p_0y). \tag{12}$$

Here, p_0 represents the angle with respect to the x-axis of the direction of the plane wave. In the rest of this paper, it is assumed that $p_0=0$. More complicated and realistic initial conditions could be introduced, but again that would not influence the basic issue of predictability.

Since the medium is isotropic with a single scale length, the spatial variables in Eq. (7) are made nondimensional by scaling with L: $x\to x/L$, $y\to y/L$. Also define the small parameter

$$\delta=(k_0L)^{-1}. \tag{13}$$

To insure small-angle scattering, a necessary condition for the validity of the Eq. (1), we must have $\delta \ll 1$, and this is easily satisfied since $\delta = c_0/(2\pi f L) = O(10^{-5})$, using a reference sound speed of $c_0 = 1.5$ km/s, an acoustic frequency of $f = O(10^2)$ Hz, and $L = O(10^2)$ km. This transformation then yields

$$i\delta \frac{\partial \psi}{\partial x} = -\frac{\delta^2}{2}\frac{\partial^2 \psi}{\partial y^2} + \epsilon \mu(x,y)\psi, \tag{14}$$

with the plane wave initial condition, $\psi_0 = 1$. This equation is seen to be analogous to the time-dependent Schrödinger wave equation; the range variable x acts like time. The potential function is a member of an ensemble of scalar random fields which exhibit Gaussian correlations in both space and time (range).

The formal classical limit of Eq. (14), $\delta \to 0$, is readily obtained via the eikonal approximation. A more rigorous examination of this limit[18,19] that takes into account the smallness of ϵ shows that the small parameter is actually

$$\hbar = \delta \epsilon^{-2/3}. \tag{15}$$

Under this scaling, both the ray and wave process converge to a diffusion Markov process. This can be shown heuristically by explicitly introducing $\tilde{x} = \epsilon^{2/3} x$ into Eq. (14). Then Eq. (14) becomes

$$i\hbar \frac{\partial \psi}{\partial \tilde{x}} = -\frac{\hbar^2}{2}\frac{\partial^2 \psi}{\partial y^2} + \epsilon^{-1/3}\mu(\epsilon^{-2/3}\tilde{x}, y)\psi. \tag{16}$$

Considering a family of curves of constant $\hbar$, passing first to the limit $\epsilon \to 0$ is seen to reveal the potential to be delta function correlated in range. The classical limit is then the highly singular, inner expansion, $\hbar \to 0$. The $\epsilon^{-2/3}$ scaling seen here will be seen to play a primary role in the analysis of Sec. II A leading to the expected value for the Lyapunov exponent, i.e., Eq. (36). Taking the limit $\hbar \to 0$ of Eq. (16) [or the limit $\delta \to 0$ of Eq. (14)] yields the parabolic ray equations, equivalent to Newton's equations of motion in Hamiltonian form,

$$\dot{y} = p, \quad \dot{p} = -\epsilon\, \partial \mu(x,y)/\partial y, \tag{17}$$

where an overdot denotes the total derivative with respect to x. The variable p is interpreted as the angle of a ray with respect to the x-axis, and is small by assumption. This is the small-angle parabolic approximation. The plane wave initial condition is expressed as $y(0) = y_0$, $p(0) = p_0 = 0$.

Since this paper is concerned with the dynamics of rays that are initially separated by an infinitesimal amount, the variational equations, which correspond to the system just derived, are introduced. Label the phase space variables by their initial cross-range position y_0: $y = y(x, y_0)$, $p = p(x, y_0)$. The two variational quantities are defined as

$$\xi(x,y_0) = \frac{\partial y(x,y_0)}{\partial y_0}, \quad \eta(x,y_0) = \frac{\partial p(x,y_0)}{\partial y_0}. \tag{18}$$

The linear variational equations are found to be

$$\dot{\xi} = \eta, \quad \dot{\eta} = -\epsilon \mathcal{K}(x,y_0)\xi, \tag{19}$$

where

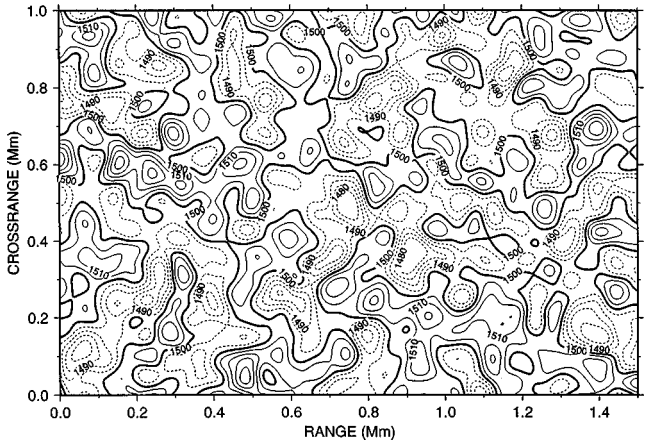

FIG. 1. A single realization of the mesoscale structure near the sound speed axis used for numerical simulations. Contours labels are of sound speed in m/s. This realization uses $\epsilon = 5.0 \times 10^{-3}$ and $L = 100$ km.

$$\mathcal{K}(x,y_0) = \partial^2 \mu(x, y(x,y_0))/\partial y^2. \tag{20}$$

The plane wave initial conditions are $\xi(0,y_0) = 1$, and $\eta(0,y_0) = 0$. These variational equations play a major role in looking for chaos in the Hamiltonian ray dynamical system just derived, as will be seen in the next section.

II. THEORETICAL ANALYSIS

In the following analysis, the physical picture concerns a single realization of horizontal-plane mesoscale structure that presumably is known through some sort of synoptic oceanographic measurements. Under these conditions, deterministic ray tracing is a reasonable procedure. As will be shown, however, ray trajectories are generically chaotic and are highly unstable. Since these ray trajectories are unpredictable in detail, the deterministic problem is analyzed as though it were a stochastic problem, and statistical methods of analysis are employed.

A numerically created realization of a field of mesoscale structure on the axis of the sound channel is shown in Fig. 1. A two-dimensional FFT is used to create this realization as is described in more detail in Sec. III below. The isotropic spectrum in Eq. (9) is used with $L = 100$ km, and $\epsilon = 5.0 \times 10^{-3}$. In Fig. 1, contours of constant sound speed are shown. This plot displays a complicated field of ''eddies'' that have a variety of sizes and shapes. Some have warm cores (higher sound speeds) and some have cold cores (lower sound speeds). Many earlier studies of ray chaos have used fluctuations that are periodic in range to simplify the analysis. In this work, the opposite tack is taken—a statistically homogeneous and isotropic field of sound speed fluctuations also simplifies the analysis. This model of mesoscale used is closer to oceanographic reality, although it is highly idealized.

A plot of numerically computed ray trajectories is shown in Fig. 2 for the same realization of mesoscale structure shown in Fig. 1. The numerical techniques are described in Sec. III below. The number of rays launched parallel to the x-axis is 250. Regions of lower sound speed tend to focus the rays, and regions of higher sound speed tend to defocus the rays. Cusped caustics begin to form at the range of about

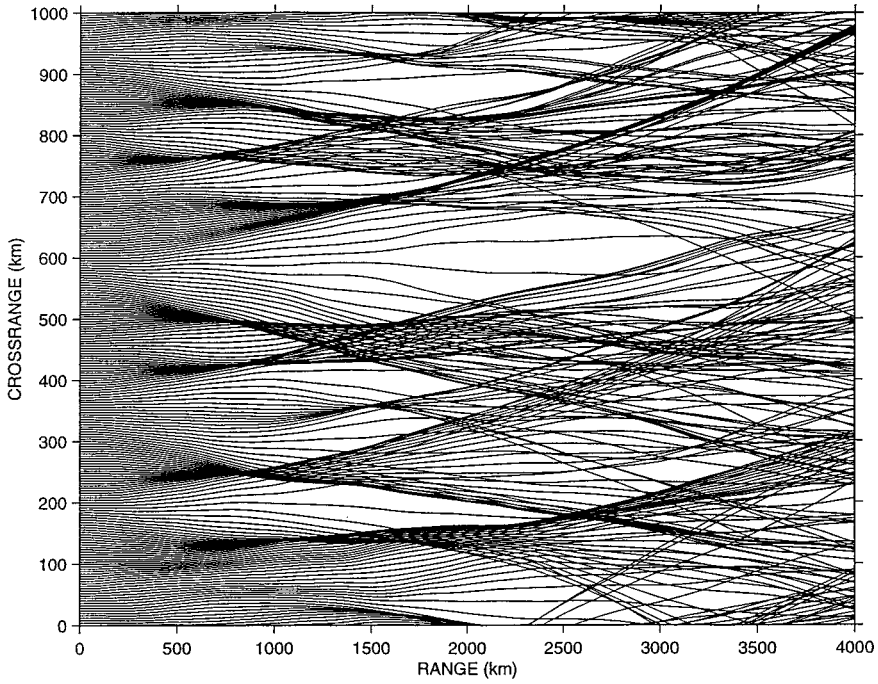

FIG. 2. Two hundred and fifty ray trajectories for the same realization of mesoscale structure shown in Fig. 1. Note the trajectories are plotted on an exaggerated scale in the crossrange coordinate. The trajectories initially have zero momentum and uniformly sample the crossrange with a spacing of 4 km.

1 Mm (1 Mm=1000 km), and generally strong focusing occurs at the range of about 2 Mm. At greater ranges, caustics form inside of caustics and the complexity of the field of rays increases without limit. Clearly a statistical method of analysis is required to describe this situation.

A. Variational equations

The ray equations are analyzed statistically by the method of smoothing (MOS). A good description of the method is given by Frisch[20] in Sec. IV C (pages 114–122) of the cited reference. This method has been applied to the same problem as here by Besieris and Tappert[21] in the context of wave-kinetic theory. It is common in the field of waves in random media to work with the so-called diffraction and strength parameters, Λ and Φ, which are defined in Ref. 22. For the problem considered here, one has

$$\Phi \sim \epsilon \delta^{-1} \sqrt{x}, \quad \Lambda \sim \delta x. \tag{21}$$

The saturation regime—where the normalized fluctuations in the wave field intensity become unity—is defined by $\Phi > 1$ and $\Lambda\Phi > 1$. This second condition implies that the saturation range for this problem requires the range to be beyond $O(\epsilon^{-2/3})$. This is the scale of the mean distance to the first focus, and turns out to be the shortest scale where exponential sensitivity is found. One of the conditions for the validity of Eq. (14) is that the rms multiple scattering angle is small, i.e., $\epsilon\sqrt{x} \ll 1$,[23] and Dashen[24] demonstrated that this is also the condition that must be satisfied for the validity of the strong Markov approximation for the problem addressed here, i.e., uniform background with homogeneous, isotropic index of refraction fluctuations that have a single characteristic scale size. The derivation is now presented.

For notational convenience, define

$$a(x,y_0)=\xi^2, \quad b(x,y_0)=\xi\eta, \quad c(x,y_0)=\eta^2. \tag{22}$$

For ranges much greater than L, it is valid to linearize the cross-range curvature of the potential, defined by Eq. (20), about the mean cross-range position, $\langle y\rangle = y_0$,

$$\mathcal{K}(x,y_0) \approx \mu_{yy}(x,\langle y\rangle) = \mu_{yy}(x,y_0), \tag{23}$$

where the subscript *yy* denotes the second partial derivative with respect to cross-range.

Taking the range derivative of Eq. (22), using Eq. (19), yields the system

$$\dot{a} = 2b, \tag{24a}$$

$$\dot{b} = c - \epsilon \mathcal{K}(x,y_0) a, \tag{24b}$$

$$\dot{c} = -2\epsilon \mathcal{K}(x,y_0) b. \tag{24c}$$

The method of smoothing is to be applied to this system. The quantities a, b, c are expressed as

$$a = \langle a\rangle + \delta a, \tag{25a}$$

$$b = \langle b\rangle + \delta b, \tag{25b}$$

$$c = \langle c\rangle + \delta c, \tag{25c}$$

where the angular brackets denote the ensemble average operation, and the random fluctuations about the mean are described by δ. Applying the ensemble averaging operation on the system of Eq. (24) yields

$$\langle \dot{a}\rangle = 2\langle b(x)\rangle, \tag{26a}$$

$$\langle \dot{b}\rangle = \langle c(x)\rangle - \epsilon\langle \mathcal{K}(x,y_0)\,\delta a(x,y_0)\rangle, \tag{26b}$$

$$\langle \dot{c}\rangle = -2\epsilon\langle \mathcal{K}(x,y_0)\,\delta b(x,y_0)\rangle, \tag{26c}$$

where in Eqs. (26b) and (26c), the fact that $\langle \mathcal{K}\rangle = 0$ has been used. The goal now is to express the fluctuating parts in Eq. (26) in terms of their means. This is accomplished by subtracting Eqs. (24) from Eqs. (25c), yielding

$$\delta\dot{a} = 2\,\delta b(x,y_0), \tag{27a}$$

$$\delta\dot{b} = \delta c(x,y_0) - \epsilon\mathcal{K}(x,y_0)\langle a(x)\rangle - \epsilon[\mathcal{K}(x,y_0)\,\delta a(x,y_0) - \langle\mathcal{K}(x,y_0)\,\delta a(x,y_0)\rangle], \tag{27b}$$

$$\delta\dot{c} = -2\epsilon\mathcal{K}(x,y_0)\langle b(x)\rangle - 2\epsilon[\mathcal{K}(x,y_0)\,\delta b(x,y_0) - \langle\mathcal{K}(x,y_0)\,\delta b(x,y_0)\rangle]. \tag{27c}$$

The last terms in Eqs. (27b) and (27c) are higher order in ϵ and are neglected in accordance with the method of smoothing. Reduction to quadrature then yields

$$\delta a = 2\int_0^x \delta b(x',y_0)\,dx', \tag{28a}$$

$$\delta b = -2\epsilon\int_0^x (x-x')\mathcal{K}(x',y_0)\langle b(x')\rangle dx' - \epsilon\int_0^x \mathcal{K}(x',y_0)\langle a(x')\rangle dx', \tag{28b}$$

$$\delta c = -2\epsilon\int_0^x \mathcal{K}(x',y_0)\langle b(x')\rangle dx'. \tag{28c}$$

Now it is simply a matter of substituting Eqs. (28b) and (28c) into Eqs. (26b) and (26c) to obtain a system of integro-differential equations for $\langle a\rangle$, $\langle b\rangle$, $\langle c\rangle$. One obtains

$$\langle\dot{a}\rangle = 2\langle b(x)\rangle, \tag{29a}$$

$$\langle\dot{b}\rangle = \langle c(x)\rangle + 2\epsilon^2\int_0^x (x-x')^2\langle\mathcal{K}(x,y_0)\mathcal{K}(x',y_0)\rangle \times\langle b(x')\rangle dx' + 2\epsilon^2\int_0^x (x-x') \times\langle\mathcal{K}(x,y_0)\mathcal{K}(x',y_0)\rangle\langle a(x')\rangle dx', \tag{29b}$$

$$\langle\dot{c}\rangle = 2\epsilon^2\int_0^x [2(x-x')\langle b(x')\rangle + \langle a(x')\rangle] \times\langle\mathcal{K}(x,y_0)\mathcal{K}(x',y_0)\rangle dx'. \tag{29c}$$

The long time Markovian approximation (LTMA) now is applied. The quantities $\langle a\rangle$, $\langle b\rangle$, $\langle c\rangle$ are linearized about $x' = x$, which is valid for potential functions which have a single scale Gaussian power spectrum in range, and $\epsilon \ll 1$. Since the correlation for $\mathcal{K}$ decays exponentially on the length scale L, and this work is concerned with propagation distances on the long-range scale $O(x \gg 1)$, the limit in the integral can be extended to infinity with exponentially small error. Thus Eqs. (29) becomes

$$\langle\dot{a}\rangle = 2\langle b(x)\rangle, \tag{30a}$$

$$\langle\dot{b}\rangle = \langle c(x)\rangle + 2\epsilon^2\alpha_2\langle b(x)\rangle + 2\epsilon^2\alpha_1\langle a(x)\rangle, \tag{30b}$$

$$\langle\dot{c}\rangle = 4\epsilon^2\alpha_1\langle b(x)\rangle + 2\epsilon^2\alpha_0\langle a(x)\rangle, \tag{30c}$$

where the constant coefficients are

$$\alpha_n = \int_0^\infty \zeta^n\langle\mathcal{K}(x-\zeta,y_0)\mathcal{K}(x,y_0)\rangle d\zeta, \quad n = 0,1,2. \tag{31}$$

The system represented by Eqs. (30a)–(30c) is closed, and it is straightforward to obtain the following linear, third order, differential equation for $\langle a\rangle$:

$$\frac{d^3\langle a\rangle}{dx^3} = 4\epsilon^2\alpha_0\langle a(x)\rangle + 8\epsilon^2\alpha_1\frac{d\langle a(x)\rangle}{dx} + 2\epsilon^2\alpha_2\frac{d^2\langle a(x)\rangle}{dx^2}. \tag{32}$$

The derivation of Eq. (32) is new, and is central to the theme of this paper. Assuming a solution of the form $\langle a\rangle \sim e^{2\nu x}$ yields the characteristic cubic equation

$$\nu^3 - \epsilon^2\alpha_0/2 - 2\epsilon^2\alpha_1\nu - \epsilon^2\alpha_2\nu^2 = 0. \tag{33}$$

Since the α_n of Eq. (31) are constants of $O(1)$, it is easy to establish that

$$\nu = \epsilon^{2/3}\tilde{\nu}_0 + O(\epsilon^{4/3}), \tag{34}$$

where $\tilde{\nu}_0$ are the three roots of $\tilde{\nu}_0^3 - \alpha_0/2 = 0$: $\tilde{\nu}_0 = (\alpha_0/2)^{1/3}$, $(\alpha_0/2)^{1/3}e^{i2\pi/3}$, $(\alpha_0/2)^{1/3}e^{i4\pi/3}$. Using the initial data for Eq. (32) corresponding to a plane wave, i.e., $\langle a(0)\rangle = 1$, $d\langle a(0)\rangle/dx = 0$, $d^2\langle a(0)\rangle/dx^2 = 0$, the leading order solution in ϵ for the cross-range variational quantity ξ is

$$\langle\xi^2(x) - 1\rangle = \tfrac{1}{3}[e^{2\nu_0 x} + 2e^{-\nu_0 x}\cos(\sqrt{3}\,\nu_0 x) - 3]. \tag{35}$$

The exponent ν_0 is given by

$$\nu_0 = \epsilon^{2/3}(\alpha_0/2)^{1/3}, \tag{36}$$

and is the desired Lyapunov exponent for this process. Third order differential equations and associated leading order solutions for the quantities $\langle\xi\eta\rangle$ and $\langle\eta^2\rangle$ are found by similar means.

An important fundamental result of this analysis is that the exponent is proportional to the strength of the mesoscale fluctuations to the 2/3 power. Looking back at Eq. (21), it is clear that this exponential sensitivity occurs at the saturation range, $x = O(\epsilon^{-2/3})$. Also, the subscript zero in ν_0 is intended as a reminder that this result follows from MOS, which is known to be exact in the Markov limit $\epsilon \to 0$ with $\epsilon^{2/3}x = O(1)$.

From Eq. (9) for a Gaussian spectrum, one obtains

$$\alpha_0 = 6\sqrt{\pi}, \quad \nu_0 = (3\sqrt{\pi})^{1/3}\epsilon^{2/3} \approx (1.7454...)\epsilon^{2/3}. \tag{37}$$

A positive Lyapunov exponent ν_0 characterizes classical chaos for the ray dynamical system expressed by Eq. (17). In Sec. III, numerical experiments are described that confirm this theoretical result. The cross-range variational quantity ξ describes the behavior of a pair of infinitesimally separated rays. Thus Eq. (35) states that, ''in the mean square sense,'' neighboring rays diverge exponentially at a rate given by ν_0, the Lyapunov exponent. This result is relevant to those using geometric acoustics in tomographic research, and will be further discussed in the following section.

Analysis of Eq. (35) for small $\nu_0 x$ yields the ''3/2 law'' of Chernov,[23] implying that the rms intensity fluctuations initially increase proportional to the 3/2 power of range. The large $\nu_0 x$ behavior shows the exponential growth characteristic of ray chaos. It is noted that the expression given in Eq.

(35) was previously obtained by other means.[25,26] The scaling of the Lyapunov exponent ν_0 as proportional to the strength of the perturbation to the 2/3 power, see Eq. (37), appears to be a new result in ocean acoustics, and is one of the main results of this work.

The quantity α_0 that appears in the Lyapunov exponent ν_0 may be interpreted, using Eq. (31) and Eq. (23), as follows: α_0 is proportional to the mean square curvature of the mesoscale structure in the cross-range direction, integrated in range along the unperturbed ray, $y=y_0=\text{const}$. In terms of the spectrum $S(k,l)$ of the mesoscale structure defined in Eq. (8), it is found that

$$\alpha_0=\pi\int_{-\infty}^{\infty} l^4 S(0,l)\,dl. \tag{38}$$

The factor l^4 corresponds to the mean square curvature in cross-range, and the fact that $S(k,l)$ is evaluated at $k=0$ corresponds to the resonance condition that is the fundamental physical mechanism responsible for ray chaos, as has been recently emphasized in Ref. 9. Since the unperturbed rays are straight lines in the x-direction in the two-dimensional model used in this study, the mesoscale structure that resonates with the unperturbed rays has arbitrarily long wavelength in the x-direction, or $k=0$ in the power spectrum. Whether real ocean mesoscale has significant power near $k=0$ is an interesting and important oceanographic question.

B. Predictability horizon

If $\nu_0 x \gg 1$, then Eq. (35) may be written as

$$|\Delta y(x)| \approx \Delta y_0 \exp(\nu_0 x), \tag{39}$$

where Δy_0 is the initial separation of the pair of rays, and $|\Delta y(x)|$ is their separation at range x. Thus an uncertainty, due to measurement errors, of the initial position of a ray is magnified by an exponentially large amount at greater ranges. Let the error in the initial position be $\Delta y_0 = rL$, where L is the scale length of the mesoscale structure. Then

$$|\Delta y(x)|L \approx r \exp(\nu_0 x). \tag{40}$$

The predictability horizon, x_p, is now estimated as the range where the error in ray position is $O(1)$, or $|\Delta y(x)|/L = O(1)$. This yields

$$x_p \approx \nu_0^{-1} \ln(r^{-1}). \tag{41}$$

For a 0.1% error in the measurement of the initial ray position, or $r=10^{-3}$, this yields

$$x_p \approx 7 \times \nu_0^{-1}. \tag{42}$$

In words, the predictability horizon may be estimated to be about seven e-folding distances. At this range, the measurement errors are magnified by a factor of about 1000, and the true ray position is unknown on the scale of the mesoscale perturbations. The value of $r=10^{-3}$ can also be interpreted as a minimum error of 0.1% for the precise location of mesoscale structure deduced from geophysical measurements.

From Eq. (37), the inverse Lyapunov exponent in dimensional units is

$$\nu_0^{-1} \approx 0.6 L \epsilon^{-2/3}. \tag{43}$$

Setting $L=100\,\text{km}$ and $\epsilon = 5\times 10^{-3}$, which are reasonable estimates, one obtains $\nu_0^{-1} \approx 2$ Mm, where 1 Mm=1000 km. Then the estimated predictability horizon is $x_p \approx 14$ Mm. Considering the uncertainties of the ocean model used in this work, it would be fair to say that the predictability horizon lies somewhere in the range between 10 Mm and 20 Mm. It is crucial to bear in mind that this is the limit of predictability due only to the effects of ocean mesoscale structure on propagation in the horizontal plane. Vertical plane effects due to mode coupling are expected to be about ten times stronger than horizontal-plane effects, leading to a predictability horizon about ten times smaller for the near-axial rays. Estimates of Lyapunov exponents due to vertical plance effects have been performed by Simmen *et al.*[11] due to internal waves and by Smith *et al.*[6] for mesoscale structure. Note that our predictability horizon estimate involved several approximations and assumptions in the acoustic model. In this regard, the parametric dependence of the predictability horizon, shown in Eq. (43), should be considered more relevant than the actual estimate. The order of magnitude of the estimate is also clearly relevant to basin scale, ray based acoustic tomography.

C. Multipaths and eigenrays

Suppose that a point receiver is located at range X and cross-range Y. Then rays labeled by y_0 that intercept the receiver satisfy the eigenray condition

$$y(y_0,X)=Y. \tag{44}$$

For given X and Y, this is a transcendental equation for y_0. Roots of this equation are denoted by y_{0j}; $j=1,2,...,J$. Here $J=J(X,Y)$ is the number of eigenrays at the receiver, and it depends sensitively on X and Y. This is also the number of multipaths at the given field point. It is not difficult to show that J is an odd number. The main connection between the eigenray concept and the ray chaos concept is that in a chaotic situation the number of eigenrays tends to grow exponentially with range X.[2,5,8,18] For the problem studied in this paper, it can be shown that

$$J \sim \exp(\nu_0 X), \quad \nu_0 X \gg 1, \tag{45}$$

where the Lyapunov exponent ν_0 has been calculated in Eq. (37). This phenomenon is known as the ''exponential proliferation of eigenrays.''

Caustics at the receiver must not only satisfy the eigenray condition of Eq. (44), but must also satisfy the condition

$$\xi(X,y_0)=\frac{\partial y(X,y_0)}{\partial y_0}=0. \tag{46}$$

Thus caustics correspond to extrema of the curves $y(X,y_0)$. This second condition selects certain values of Y, which are denoted as Y_m. The spacing between caustics at range X may be estimated by the same arguments that lead to Eq. (45), and it is found that

$$|Y_{m+1}-Y_m| \sim L \exp(-\nu_0 X), \quad \nu_0 X \gg 1. \tag{47}$$

The number of caustics per unit distance in cross-range Y increases exponentially with increasing range X, a phenomenon that may be called ''exponential proliferation of caustics.'' The spacing between caustics therefore decreases exponentially.

In the geometric acoustics limit, $\hbar \to 0$, the width of a caustic is vanishingly small and there is no limit to the spacing between caustics. At any finite frequency, however, the width of a caustic may be estimated to be

$$\Delta Y \sim \hbar L, \tag{48}$$

and interference effects with respect to computing the wave field become significant if

$$|Y_{m+1}-Y_m| \lesssim \Delta Y, \tag{49}$$

and the mean range where this occurs is found to be

$$X_b \sim \nu_0^{-1} \ln \hbar^{-1} \sim \nu_0^{-1} \ln(k_0 L \epsilon^{2/3}). \tag{50}$$

This is the well known ''log time'' (range) that was first introduced by Zaslavsky and Berman[27] and Berry and Balazs[28] in the context of quantum chaos. This is the range where fine structure in phase space develops on scales smaller than $O(\hbar)$. As an example, consider $L=100$ km, $\epsilon = 5\times 10^{-3}$, and the acoustic frequency 100 Hz. Then $\hbar \approx 10^{-3}$, and $X_b \approx 7\,\nu_0^{-1}$. This is the same as the predictability horizon that was estimated above. Thus for the horizontal-plane ocean acoustic propagation problem, interference effects in constructing the wave field based on ray-tracing techniques become significant at the same range (10–20 Mm) where prediction of individual trajectories becomes problematic. A more thorough analysis, which is beyond the scope of this paper, is demanded to formulate results presented here, which are indicative to a global breakdown of semi-classical mechanics applied to Eq. (14), as anything stronger than a conjecture. It is noted that this is an important fundamental problem in wave mechanics and is an active area of research.[29]

III. NUMERICAL EXPERIMENTS

In the above stochastic analysis, results were expressed for the statistics of a single ray trajectory. It is desirable to connect these results to deterministic propagation of a family of rays through a single realization of mesoscale sound speed fluctuations. Instead of stochasticity, one now speaks of complexity and deterministic chaos.

Since the mesoscale realization used is continuous to second order, the solution for the trajectories and variational quantities are continuous functions of the ray parameter y_0. This is an important criteria that is exploited in numerical simulations, where one must approximate the family of rays by a finite number of rays with some *a priori* sampling in y_0. If the sampling is appropriately dense, then it suffices to merely ''connect the dots'' to reconstruct the entire wavefront.

Numerical experiments help bridge the gap between the theoretical analysis performed in Sec. II A and what ocean acoustic experiments might yield in terms of observing deterministic ray chaos in ocean environments dominated by mesoscale eddies. The qualitative aspects of Hamiltonian chaos for this ray system are explored by numerically solving Eq. (17) using plane wave initial data for a single realization of mesoscale. The confirmation of the theoretical result regarding the Lyapunov exponent ν_0 involves solving Eq. (19) with $\xi(0,y_0)=1$, and $\eta(0,y_0)=0$; this will be discussed in more detail below. The numerical techniques employed are now briefly discussed.

The generation of an idealized, two-dimensional realization of sound speed fluctuations $\mu(x,y)$, due to ocean mesoscale eddies on the sound channel axis is accomplished by a discrete Fourier series representation, where each complex Fourier amplitude coefficient are taken to be independent Gaussian random numbers with mean zero and unit variance. The number of grid cells is 512×2048 for a realization that extends 1 Mm$\times$4 Mm in respective cross-range and range. Using $L=100$ km, there are 51.2 grid points per correlation length. Realizations constructed using these parameters revealed to be adequate in regards to their statistical properties. The mean and variance taken over an entire realization is found to agree within 3% of zero and unity, respectively. The discrete computation for the correlation function revealed a correlation length within 2% of the intended value of L. Upon multiplication by ϵ, this method produces a realization of the sound speed. A subsection of a single realization is shown in Fig. 1, where $c_0=1500$ m/s has been added to show actual values of sound speed contours. A fast Fourier transform technique enables the first and second derivatives with respect to cross-range of $\mu(x,y)$ to be computed on the same grid.

The first order differential equations, Eq. (17) and Eq. (19), are solved by a fixed step Runge-Kutta integrator. To evaluate $\mu_y(x,y)$ and $\mu_{yy}(x,y)$ between grid points, a biquadratic interpolation method is employed. The Fourier representation of the $\mu(x,y)$ and its corresponding derivatives allow us to periodically extend the medium in range, making it computationally trivial to propagate the ray quantities beyond the 4 Mm range extent of the medium.

There are two fundamental concerns that must be addressed concerning the numerical calculation of ν_0. The first deals with the fact that it is not feasible to use a single ray trajectory to determine ν_0, even if some type of range averaging is performed. This is clearly evident by examining Fig. 3, which is a portrait of the evolution of $\ln|\xi|$ for 50 different initial values of crossrange. The nulls represent zeros of ξ, which are the caustics described in Sec. II C. Even disregarding these nulls, the sample paths for ξ are seen to be wildly varying by orders of magnitude. Thus numerical simulations are employed to yield an ''expected value'' of the Lyapunov exponent, in agreement with the analysis performed in Sec. II A. The other fundamental concern to address is concerned with the Markov approximation. The value of ν_0 derived in Sec. II A is exact in the limit $\epsilon \to 0$, and numerical simulations must be performed using a positive, nonzero value for ϵ. Performing numerical simulations for different values of ϵ and extrapolating to $\epsilon=0$ suffices to allow us to obtain a numerical value of ν_0 that can be compared directly to Eq.

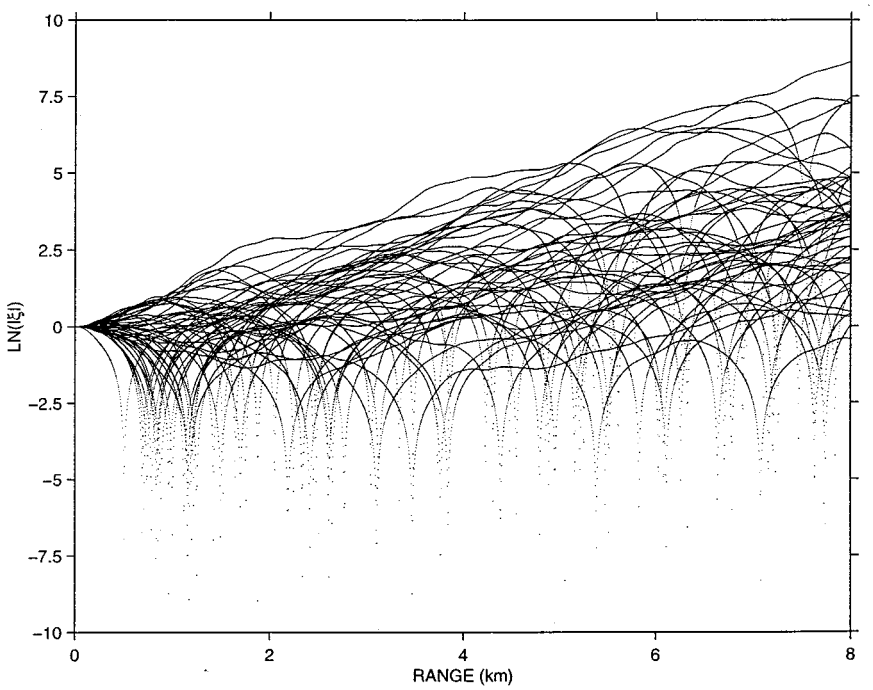

FIG. 3. Fifty sample paths of the magnitude of the cross-range variational quantity $\xi=\partial y/\partial y_0$, shown on a natural logarithm scale. The sample paths initially have $\xi(0,y_0)=1$, $\eta(0,y_0)=0$, and uniformly sample the cross-range with 20 km spacing.

(37). From Eq. (35), a natural definition for the Lyapunov exponent is

$$\nu=\lim_{x\to\infty} x^{-1}\ln\langle\xi(x,y_0)^2\rangle^{1/2}. \tag{51}$$

For the numerical simulations, the stationarity in cross-range of μ_{yy} is exploited, whereby ensemble averages are replaced by averages over y_0. Also, since it's not feasible to pass to the infinite range limit, linear regression is used to obtain the slope of

$$\ln\left(\frac{1}{M}\sum_{m=1}^{M}\left[\frac{\partial y_m(x)}{\partial y_0}\right]^2\right)$$

in the region of physical range corresponding to 2000 to 8000 km, where $M=25\,000$ is the total number of rays used to perform the average. Finally, since the Markov limit ($\lim \epsilon\to 0$) is used in deriving ν_0, the above slope is computed for successively smaller values of ϵ and the computational value of ν_0 is then extrapolated to $\epsilon=0$. This extrapolation procedure produces agreement to within 1% of the value of ν_0 given by Eq. (37).

IV. SUMMARY AND CONCLUSIONS

A horizontal mode propagation model has been introduced and examined in the geometric limit. The accumulated effects of horizontal refraction on the lowest vertical acoustic mode over long ranges of propagation [$O(10^4$ km)] has been investigated. This idealistic propagation model will be used in future work to investigate time statistics of the rays, which might help in understanding the late time mesoscale bias in impulse response data, which has been shown to be important if the data are to be used for tomographic inversion.[30] It is also being used to numerically investigate the breakdown of semi-classical mechanics. Using an idealized spatial correlation function to represent a realization of mesoscale-induced fluctuations of sound speed in an adiabatic sound channel allowed us to derive simple formulas for the statistics of the ray variational quantities. The shortest scale where the rms variational quantities exhibit exponential dependence with range was seen to be on the ''diffusion scale'' [$O(\epsilon^{-2/3}L)$], which was introduced first in the context of wave propagation in random media by Kulkarny and White.[26]

In order to understand the limits of predictability for deterministic acoustic propagation, methods from statistical analysis (MOS and LTMA) were employed. These methods inferred the chaotic nature of ray propagation through a single realization of mesoscale structure. This led to the analytical derivation of a Lyapunov exponent, which was used to define a predictability horizon, whereby, beyond this horizon, signal predictability might be highly degraded. For typical horizontal mesoscale [$L=O(100\,\text{km})$ and $\epsilon=5\times10^{-3}$], the predictability horizon, the distance at which the typical error in a cross-range ray position becomes $O(L)$, given that the initial error is $10^{-3}L$, is $O(14)$ Mm, which is on the scale of current long-range, ocean acoustic experiments. The fact that mode coupling was neglected indicates that the predictability horizon estimate reported here is an upper bound, i.e., mode coupling only complicates matters and will further decrease the estimate.

One way to interpret these results is to take for granted that the environment (realization of the ocean on the mean sound channel axis depth) is known exactly, but the transmitter location is in error. In this sense one is concerned with a deterministic dynamical system whose solution depends nonlinearly on the environment. This small error in the transmitter position ($10^{-3}L$) evolves to a large mean square cross-range separation distance to where the ray path should have gone. Another way to interpret these results is to surrender to the notion that the environment will never be

known accurately enough to predict individual ray trajectories at global scales of propagation.

All the above stated results depend on the strict classical limit, $\hbar \to 0$, or frequency becoming infinite. Global acoustic measurements are made at finite frequency (about 100 Hz), and then $\hbar \approx 10^{-3}$ which is very small but not zero. The study of finite frequency effects must be based on the linear wave equation, Eq. (14). Numerical and theoretical studies of Eq. (14) have not revealed any sign of exponential sensitivity to either initial or environmental perturbations, not even as a transient condition that saturates at long range. Inversion of acoustic signals to obtain mesoscale structure is therefore possible if full-wave methods are used, but might not be possible using ray-based methods, due to ray chaos.

ACKNOWLEDGMENTS

This work was supported by the Office of Naval Research, Code 321OA. Many helpful conversations with M. G. Brown are gratefully acknowledged.

[1] D. R. Palmer, M. G. Brown, F. D. Tappert, and H. F. Bezdek, ''Classical chaos in nonseparable wave propagation problems,'' Geophys. Res. Lett. **15**, 569–572 (1988).
[2] M. G. Brown, F. D. Tappert, and G. J. Goñi, ''An investigation of sound ray dynamics in a range dependent model of the ocean volume using an area-preserving mapping,'' Wave Motion **14**, 93–99 (1991).
[3] F. D. Tappert, M. G. Brown, and G. J. Goñi, ''Weak chaos in an area preserving mapping for sound ray propagation,'' Phys. Lett. A **153**, 181–185 (1991).
[4] M. G. Brown, F. D. Tappert, G. J. Goñi, and K. B. Smith, ''Chaos in underwater acoustics,'' in *Ocean Variability & Acoustic Propagation*, edited by J. Potter and A. Warn-Varnas (Kluwer Academic, The Netherlands, 1991), pp. 139–160.
[5] K. B. Smith, M. G. Brown, and F. D. Tappert, ''Ray chaos in underwater acoustics,'' J. Acoust. Soc. Am. **91**, 1939–1949 (1992).
[6] K. B. Smith, M. G. Brown, and F. D. Tappert, ''Acoustic ray chaos induced by mesoscale ocean structure,'' J. Acoust. Soc. Am. **91**, 1950–1959 (1992).
[7] M. D. Collins and W. A. Kuperman, ''Overcoming ray chaos,'' J. Acoust. Soc. Am. **95**, 3167–3170 (1994).
[8] F. D. Tappert and X. Tang, ''Ray chaos and eigenrays,'' J. Acoust. Soc. Am. **99**, 185–195 (1996).
[9] F. D. Tappert, ''Comment on 'Ray chaos in underwater acoustics in view of local instability,''' J. Acoust. Soc. Am. **99**, 2433–2434 (1996).
[10] M. G. Brown and F. D. Tappert, ''Comment on 'Overcoming ray chaos','' J. Acoust. Soc. Am. **100**, 1234–1239 (1996).
[11] J. Simmen, S. M. Flatté, and Guang-Yu Wang, ''Wavefront folding, chaos, and diffraction for sound propagation through ocean internal waves,'' J. Acoust. Soc. Am. **102**, 239–255 (1997).
[12] H. Weinberg and R. Burridge, ''Horizontal ray theory for ocean acoustics,'' J. Acoust. Soc. Am. **55**, 63–79 (1974).
[13] K. D. Heaney, W. A. Kuperman, and B. E. McDonald, ''Perth-Bermuda sound propagation (1960): Adiabatic mode interpretation,'' J. Acoust. Soc. Am. **90**, 2586–2594 (1991).
[14] B. E. McDonald, M. D. Collins, W. A. Kuperman, and K. D. Heaney, ''Comparison of data and model predictions for Heard Island acoustic transmissions,'' J. Acoust. Soc. Am. **96**, 2357–2370 (1994).
[15] M. D. Collins, ''The adiabatic mode parabolic equation,'' J. Acoust. Soc. Am. **94**, 2269–2278 (1993).
[16] M. A. Wolfson and F. D. Tappert, ''Chaos in an acoustic propagation model,'' in *The Chaos Paradigm: Developments and Applications in Engineering and Science*, edited by R. A. Katz, AIP Conf. Proc. **296** (AIP Press, New York, 1994), pp. 277–288.
[17] F. D. Tappert, ''The parabolic approximation method,'' in *Wave Propagation and Underwater Acoustics*, Lecture Notes in Physics, Vol. 70, edited by J. B. Keller and J. S. Papadakis (Springer-Verlag, New York, 1977), Chap. V, pp. 224–287.
[18] M. A. Wolfson, ''Kinetic Theory of Waves in Random Media and Amelioration of Classical Chaos,'' Ph.D. thesis, University of Arizona, Tucson, AZ (1994).
[19] B. Nair and B. S. White, ''High-frequency propagation in random media—A unified approach,'' SIAM (Soc. Ind. Appl. Math.) J. Appl. Math. **51**, 374–411 (1991).
[20] U. Frisch, ''Wave propagation in random media,'' in *Probabilistic Methods in Applied Mathematics*, Vol. 1, edited by A. T. Bharucha-Reid (Academic, New York, 1968).
[21] I. M. Besieris and F. D. Tappert, ''Stochastic wave-kinetic theory in the Liouville approximation,'' J. Math. Phys. **17**, 734–743 (1976).
[22] S. M. Flatté, R. Dashen, W. H. Munk, K. M. Watson, and F. Zachariasen, *Sound Transmission through a Fluctuating Ocean* (Cambridge University Press, New York, 1979).
[23] L. A. Chernov, *Wave Propagation in a Random Medium* (McGraw-Hill, New York, 1960).
[24] R. Dashen, ''Path integrals for waves in random media,'' J. Math. Phys. **20**, 894–920 (1979).
[25] A. N. Malakhov, S. N. Molodtsov, and A. I. Saichev, ''To the hypothesis of a logarithmically normal distribution law of amplitude fluctuations of a light wave propagating in a randomly-inhomogeneous medium,'' Radiophys. Quantum Electron. **20**, 169–176 (1977).
[26] V. A. Kulkarny and B. S. White, ''Focusing of waves in turbulent inhomogeneous media,'' Phys. Fluids **25**, 1770–1784 (1982).
[27] G. M. Zaslavsky and G. P. Berman, ''Condition of stochasticity in quantum nonlinear systems,'' Physica A **91**, 450–460 (1978).
[28] M. V. Berry and N. L. Balazs, ''Evolution of semiclassical quantum states in phase space,'' J. Phys. A **12**, 625–642 (1978).
[29] S. Tomsovic and E. J. Heller, ''Long-time semiclassical dynamics of chaos: The stadium billiard,'' Phys. Rev. E **47**, 282–299 (1993).
[30] M. A. Wolfson and J. L. Spiesberger, ''Full wave simulation of the forward scattering of sound in a structured ocean: A comparison with observations,'' J. Acoust. Soc. Am. **106**, 1293–1306 (1999).

An acoustic study of soils that model seabed sediments containing gas bubbles

T. N. Gardner
Department of Engineering Science, University of Oxford, Parks Road, Oxford OX3 7LD, United Kingdom

(Received 11 September 1999; revised 7 June 1999; accepted 28 September 1999)

The acoustic response of gassy seabed sediment is unique. It is a dispersive and extraordinarily attenuative natural material at frequencies which cause gas bubble resonance. It conceals the structure of the seabed from seismic profiling and it dampens acoustic signals that, for example, trigger acoustic mines. In the past, theoretical studies have formulated the probable cause of this response and crude experimental work has partially corroborated theory. This study measures compressional wave velocity and attenuation in a laboratory soil simulating natural gassy soil, and it investigates the structural properties that cause the unique acoustic response. It was confirmed that below the frequencies which cause resonance the soil behaves as a compressible material (containing gas), and above as a relatively incompressible material (containing no gas). Over the frequency range producing bubble resonance it is suggested that the soil should be modeled as a biphasic material of **gas** and a relatively incompressible **saturated soil matrix** (particles and fluid). Velocities for gassy soil were found to be as low as 220 m/s at frequencies below resonance and 1500 m/s above resonance; attenuations were found to be as high as 60 dB/cm for moderately gassy soil and as low as 1 dB/cm for soil with almost no gas. © *2000 Acoustical Society of America.* [S0001-4966(00)05101-8]

PACS numbers: 43.30.Pc, 43.30.Ma [DLB]

INTRODUCTION

An interest in gas bearing seabed sediments has been generated largely through the work of the oil industry in connection with foundation design for offshore structures and the exploration and appropriation of oil and gas. Gassy soils are very compressible and may suffer from reduced shear strengths due to certain combinations of seabed confining pressures.[1] Therefore, a knowledge of the content and the structure of gas pockets contained in a soil is essential for good foundation design. The presence of gas is also of importance in the field of exploration. Serious blowouts have occurred during drilling, when the penetration of layers of gas-charged sediments have caused sudden buoyancy. Therefore, research into gas detection in sediments may provide a measure of safety for those involved in locating submerged oil and gas. Acoustic devices may provide the most economic solution for detecting, surveying, and measuring gas-bearing sediments. They are already used for seabed surveys of submerged soils using seismic profiling techniques and remotely operated probes. Seismic surveys are generally successful in locating gas-bearing sediments because acoustic signals have been shown to be sensitive to the presence of gas. In addition, it can be seen from the work of Hamilton[2] and Hamilton and Bachman[3] on nongassy sediments that acoustic signals may be used more generally to classify the type and structure of submerged soils. It is anticipated that the same approach may be of use in determining the structure and content of gas-bearing soils.

Naturally occurring gassy soil is a product of either biogenic, thermogenic, or vulcanogenic processes in submerged sediments. The biogenic process is more common and consists of the anaerobic decomposition of organic matter by nitrate, sulphate, or carbonate reducing bacteria within oxygen-depleted soil. Gases produced are ammonia, hydrogen sulphide, and methane, respectively.[4] Although all three may be present in a given soil, methane tends to predominate in freshwater and also predominates in marine environments below the superficial layers of sediment that may contain sulphate. The gases are initially dissolved in the pore fluid where they may increase in concentration until one reaches supersaturation and forms free gas bubbles. Other dissolved gases may then diffuse across the bubble boundaries until diffusion equilibrium is reached. Gassy soil has been found in lakes, river deltas, harbors, and offshore locations throughout the world. It is perhaps more common in the first three areas since tributary streams carry a supply of organic matter with silt and clay particles that are settled out together in comparatively slow moving deep waters. Such areas include Chesapeake Bay,[5] the Mississippi Delta,[6,7] the Gulf of Mexico,[8] Suva Harbor, Fiji,[9] and Boston Harbor.[10] Offshore sites include the Irish Sea[11] and the North Sea.[12] Also reported are various gas induced erosion features such as ''mud volcanoes'' in the Caspian Sea,[13] ''gryphons and salses'' in several locations,[14] and ''pockmarks'' in the Scotian Shelf,[15] South China Sea,[16] and Aegean Sea.[14]

Bubbles observed in naturally occurring gassy soils appear to be between 0.5 and 5 mm diameter.[17,18] Maximum size seems to be controlled by consolidation[19] and may be influenced by particle size and shape due to their effect on the curvature of bubble menisci and on soil permeability. It is perhaps reasonable therefore to expect large bubbles to develop in surficial deposits that are loosely compacted. This material is less resistant to the local structural deformation arising from expanding pockets of gas during the initial diffusion process. Conversely, small bubbles may be expected to occur in well consolidated sediments at some depth below

the mudline or in shallow beds of overconsolidated material. Bubble shape is also influenced by consolidation. In surficial sediments they are largely spherical, but in well consolidated soils, that are anisotropic, bubbles are elongated in the weaker direction of the bedding plane. Further elongation may occur in a direction perpendicular to the stresses arising from overburden pressure.

Research into the acoustic response of gassy soils has been carried out by relatively few. Theoretical and experimental work is reported by Anderson and Hampton[17,18] who developed expressions for compressional wave sound speed and attenuation. Laboratory experiments were performed on plastic air-filled bubbles to examine the effects of bubble resonance. It was indicated that the bubbles pulsated radially at a frequency related to their diameter and that, over the frequency range during which resonance occurred, the medium behaved as a dispersive material with extremely high attenuation. Below this range it was predicted that gassy soil behaves as a single phase material that is very compressible, producing a relatively low velocity, and above the range it behaves as a biphasic material with the velocity of a saturated (nongassy) soil. To model the gassy soil over its resonance frequency, elastic properties derived from either a soil suspension (solids suspended loosely in fluid) or a saturated soil (solids combined with a compressible pore fluid) were used. Subsequently, it has been shown that the elastic behavior of gassy soil is not characteristic of such compressible fluids or saturated solids.[1] Further theoretical work by Bedford and Stern[20] used the principle of energy conservation to derive equations of motion for gassy soil. Resonance effects are manifested by an expression for the kinetic energy associated with the pulsating radial motion of bubbles. However, the model simulates a biphasic material; that of a saturated medium with a compressible fluid. Kepkay[21] provided both laboratory measurements and *in situ* testing results for velocities below resonance frequency. In the laboratory, methane gas was dissolved under pressure into water, which was then used to saturate a silty clay soil. Free gas then nucleated into bubbles as the pressure was released, providing a soil with a gas fraction of up to 0.2. Although a reduction in velocity of more than 66% is predicted by applying the theory of Anderson and Hampton[17,18] to a soil with this amount of gas, Kepkay's measured values indicated a fall of less than 11%. In conclusion, there is disagreement to date on the appropriate physical model which precisely simulates the acoustic behavior of gassy soil, and to date no controlled experiments have been performed on material which responds acoustically as gassy sediment.

Sediments that consist of the three phases of solid, liquid, and gas have been modeled as comprising two phases—(i) a saturated soil matrix containing gas-filled pockets greater in diameter than the soil particles, or (ii) a solid skeletal framework with free gas bubbles wholly contained within a pore fluid (a compressible fluid model). The later ''compressible fluid'' model of gas wholly surrounded by water may not be practical, since a silty clay sediment would be unlikely to contain interstitial pore sizes greater than 10 μm and Blanchard and Woodcock[22] state that a diameter of 10 μm is the theoretical minimum for bubbles in water at any degree of supersaturation. Therefore, the present study focused on the acoustic behavior of a soil characterized by the former model, a saturated soil containing gas pockets which was prepared in the laboratory under similar conditions as naturally occurring gassy soil. As Anderson and Hampton[17,18] predicted that bubble diameter determines the frequency at which resonance occurs, bubble size distributions (BSDs) of the soil specimens were measured and are discussed in relation to their influence upon the acoustic properties of the soil.

FIG. 1. Gassy soil produced in the laboratory to model commonly occurring seabed sediment containing gas bubbles. The figure (taken from Nageswaran, Ref. 23) shows 3 cm of dried silty clay soil (measured vertically) which has been consolidated to 35 kPa. Bubble sizes are between 0.2 and 1.0 mm diameter and gas fraction is 0.12.

I. METHOD

A. The laboratory gassy soil

Acoustic tests were performed on a silty clay soil prepared in the laboratory, containing a uniform distribution of methane gas bubbles of approximately 0.2 and 1.8 mm diameter. It can be shown that the structure of a laboratory gassy soil (Fig. 1) is similar to *in situ* gassy soils with occluded gas (Fig. 2) because the mechanical processes of formation are similar.[19] A brief description follows of the laboratory process used in this study; a more detailed description can be found in the Appendix, or in Nageswaran.[23] A soil slurry containing methane gas was deposited into two concurrently operated acoustic consolidation cells (Fig. 3) so that each soil specimen could be acoustically tested over two different frequency ranges. Each cell was used to form, consolidate, and acoustically test gassy soil specimens under a vertical stress of 25 kPa. During the first 36 h, free gas was formed in uniformly distributed bubbles within the saturated soil matrix, at a gas fraction controlled by the methane content. Subsequently, pressure was increased in the hydraulic reservoir below the piston to provide the required total stress during soil consolidation. Soil in cell 2 was drained through the piston from its bottom face in addition to the top face drainage also provided in cell 1. Since cell 1 had a consolidated soil depth of approximately 20 mm, and cell 2 of 65 mm, the periods of primary consolidation for both cells were made almost equal by draining cell 2 from both faces. This ensured that, as far as possible, all consolidated soil samples were of similar structure and bubble shape. Four soil slurries of different gas content produced eight soil samples of varying gas fraction. Following consolidation and final equilibra-

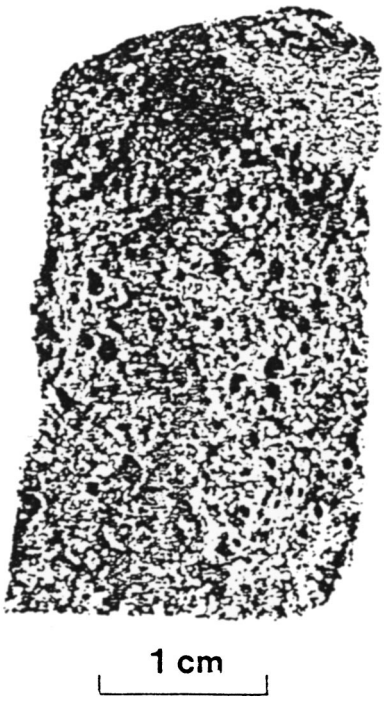

FIG. 2. Gassy soil occurring naturally in the seabed. The figure (taken from Fannin, Ref. 11) shows gassy soil cored from the North Sea.

tion of pore pressures, the soil was prepared for acoustic tests. It was raised in the cylinder to bear against a reaction plate assembly by releasing the top section securing bolts and applying a small increase in piston pressure. The pressure of consolidation was maintained on the soil during the lifting process by using a hydraulic ram between the top section and reaction plate. Figure 4 shows the reaction plate with the soil in the raised position and the top section 1 mm clear of the cell. The loss of contact between the cell and top section was found to decouple all signals of significant power that previously circumvented the direct route between the transducers by traveling around the soil via the cell wall. In addition, the 1 mm vertical face of the soil protruding from the cell was wiped free of grease and excess water to decouple surface waves. The reaction plates were fixed to a substantial steel section beam and the cell support frames were set in concrete at the base. Both the beam and the base were fitted with displacement gauges, the deflections being used to correct the measurements of signal path length described in the next section.

B. Acoustic methods

After consolidation equilibrium had been achieved, with the soil samples in the raised position, compressional wave velocity and attenuation were measured over the frequency range 10 kHz to 1 MHz. Compressional wave signals were propagated through the soil in plane waves between the transmitting transducer, in the cell top, and the receiver in the piston, with hydrophobic membranes placed between the faces of the transducers and the soil. The signal path length through the soil was measured to within ± 25 μm by fixing a linearly varying displacement transducer (LVDT) to a tube connected to the piston and passing through the base on

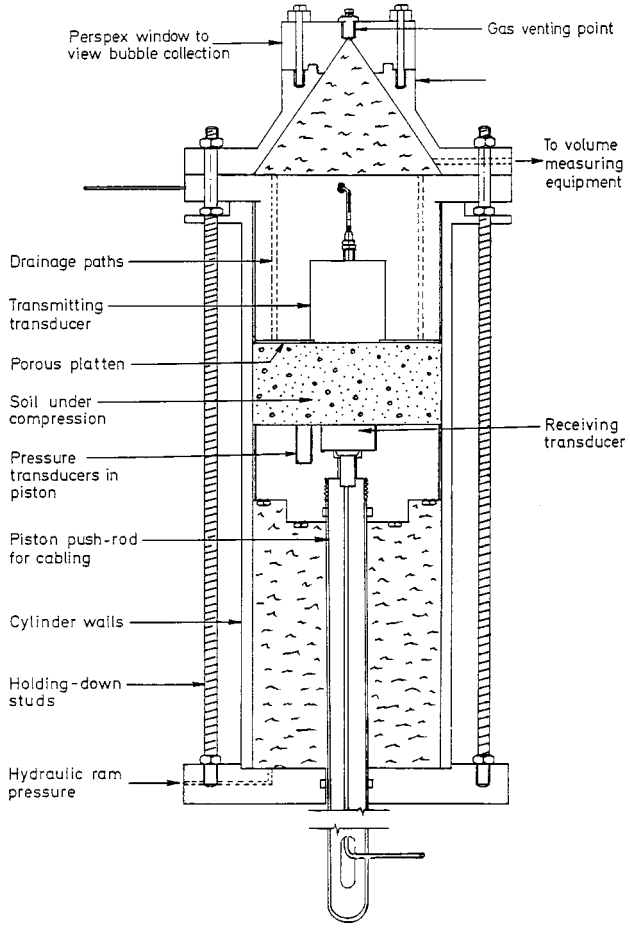

FIG. 3. Consolidation equipment was used to prepare the gassy soil specimens and to test them acoustically. Compressional wave velocity and attenuation was measured over frequencies between 1 kHz and 1000 kHz using transmitting and receiving transducers each end of the soil specimen; signals were pulsed sine waves or broadband spikes.

which the cylinder was mounted. The LVDT was supplied by a stabilized voltage and calibrated periodically to provide a mv/mm table to extrapolate position, since linearity proved unacceptable.

Path lengths were corrected for the error due to the elastic deformation of the equipment under consolidation pressure, but not for temperature since this was controlled to within $20+/0.25\,^{\circ}\mathrm{C}$. The piezoelectric transducers were made from pzt-4 elements recessed into air brick material to reduce sideways emission and faced with a thin layer of araldite. An aluminum and a steel disk were bonded to the faces of the transmitting element to increase bandwidth. The receiving transducers were similarly formed, using pzt-4 elements without the bonded disks.

Since the acoustic response of gassy soil was expected to cause severe constraints on the frequency range of testing, the design of apparatus and measurement technique was crucial to the success of the study. Since gassy soil is dispersive, the impedance mismatch at the soil/transducer interface varies with signal frequency. This makes it impossible to design the transducer face diameter to provide a maximum transmission of energy into the soil for a wide range of frequencies, while not exceeding the level of input that would cause damage to the araldite surfaces or nonlinear signal propaga-

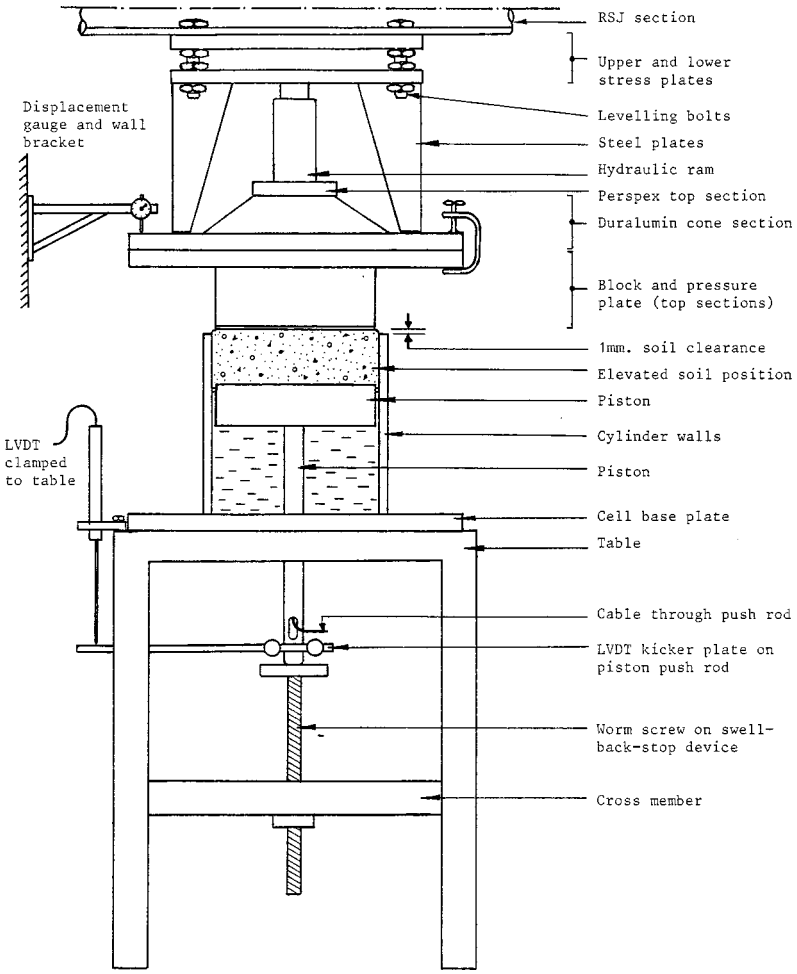

FIG. 4. Soil is shown in the raised position which decouples signals that are likely to circumvent the direct route through the soil between the transmitting and receiving transducers. The 1.0 mm gap between the bottom surface of the soil specimen and the cylinder wall was wiped clean of surface grease and fluid to decouple surface wave signals in the soil and compressional wave signals in the cylinder wall.

tion. As a compromise, two different face diameters were used to provide a limited range of output power over the required range of soil impedances and frequencies to be tested. Cell 1 contained the high frequency transmitting transducer with a 4 cm diameter face, designed to cover 40 to 95 kHz, and cell 2 the low frequency device of 5 cm diameter, for 20 to 40 kHz. Since bubble resonance effects in gassy soil may cause unusually large signal attenuation (45 dB/cm) soil depths were reduced to 20 mm in the high frequency cell and 65 mm in the low frequency chamber. This allowed a signal of sufficient strength and regularity to be received through a soil of large gas content, over the limited range of frequencies. In practice, the frequency operating ranges were extended well beyond this by varying the input excitation and using three different measurement techniques on each soil specimen. The three techniques were therefore used to provide complementary data to secure the best combination between the range and accuracy of results. Also, the range of soil impedances accommodated this way was extended to 0.3–2.56 ($\times 10$ kg/m^{2}s).

Two different transducer excitations were used for the three techniques. The first was a square wave 100 V pulse of up to 25 W rms, typically set at five cycles, adjustable over 10 to 412 kHz and providing a transducer output of the required dominant center frequency. This signal was used for the traditional method of obtaining velocity by measuring the time delay from transmission to the rise point of the received signal waveform (referred to here as the **leading edge method**), and using the corrected path length from the LVDT. Band pass filtering was not used, since off-center frequencies contained in the leading edge of the signal are phase-shifted and this affected transit time. With this method and the next, transit time was corrected by the delay caused within both transmitting and receiving transducers. This was found by measuring transit time for varying depths of water in both cells, and establishing the velocity and the delay error. Although this method proved most accurate for soils of low gas content, for greater gas fractions the dispersive nature of the soil caused the spectrum of frequencies generated by the transducer to be delayed by varying amounts. Therefore, the first arrival frequency marking the leading edge of the waveform was not generally the required center frequency; in this case, results were spurious. However, velocities were measured over the full range of frequencies possible, since reliable data were obtained for soils of low gas content and it was also useful to indicate the level of error found in more gassy soils when using the standard technique.

The second method, again using pulse transmission, was developed to overcome the acoustic problems caused by the soil and is referred to as the **transit time correction** method. Velocity was again found from the transit time and path length, although here the reference point for measuring transit time was a null amplitude position in the signal waveform rather than the leading edge. This position was selected in-

TABLE I. Accuracy of sound speed measurements. Note: accuracy was calculated by the following equation where C, S, and T are sound speed, soil depth, and transit time: $\Delta C = C(\Delta S/S + \Delta T/T)$.

	Leading edge method		TTC method		FT Method			
					Without TTC		With TTC	
	Cell 1	Cell 2	Cell 1	Cell 2	Cell 1	Cell 2	Cell 1	Cell 2
S (mm)	20	65	20	65	20	65	20	65
ΔS (mm)	±0.025	±0.025	±0.025	±0.025	±0.025	±0.025	±0.025	±0.025
$T=S/C$ (μs) ($C=1500$ m/s)	13.33	43.33	13.33	43.33	13.33	43.33	13.33	43.33
$T=S/C$ (μs) ($C=350$ m/s)	57.14	185.71	57.14	185.71	57.14	185.71	57.14	185.71
ΔT (μs) ($C=1500$ m/s)	±0.05	±0.05	±0.62	±0.62	±0.08	±0.16	±0.08	±0.13
ΔT (μs) ($C=350$ m/s)	±0.05	±0.05	±0.62	±0.62	±0.34	±0.56	±0.34	±0.56
ΔC (m/s) ($C=1500$ m/s)	±7.50	±2.31	±70.34	±22.04	±10.88	±5.08	±81.22	±27.12
ΔC (m/s) ($C=350$ m/s)	-	-	±4.24	±1.30	±2.52	±1.19	±6.76	±2.49

dividually for each signal frequency and test medium and marked the beginning of the section of waveform where the center frequency of transmission became established, following the initial rise period. The delay to the chosen null point was corrected for phase shifts not caused by passing through the soil, by using a calibration liquid of the same acoustic impedance. Six different fluids were installed in the consolidation cells under similar circumstances as the soils, and were tested at increments of 1 kHz to 10 kHz from low to high frequencies of transmission. The difference between the true transit time, measured by the leading edge method, and the value obtained using the null position, is the transit time correction (TTC). A table of TTC values was obtained from the liquids for each increment of frequency used in the soil tests and over the range of soil impedances. This corrected for displacements of the null point due to phase shifts at the transducer/medium interfaces, multiples and time delays within the transducers, and phase shifts caused by the electronic apparatus. Therefore, for soils of significant gas content, velocity was measured predominantly at the center frequency of transmission. This follows the initial rise period of the waveform, and precedes the decay. Here, unwanted frequencies may be suppressed using a tight bandpass filter on the center frequency without shifting its phase.

The third technique used spike excitation of up to 100 V, propagating through the soil a broadband signal of between 10 kHz and 1 Mhz and is referred to here as the **FT method**. Discreet Fourier transforms were used to provide phase angles from the received signals at frequency increments of approximately 2.4 kHz. By repeating the test with a calibration fluid of known velocity, a similar set of angles were provided that were correlated with the initial set to find compressional wave velocity for the soil specimen at each discrete frequency. Since the factors that influence phase were common to both tests, a comparison between the two provided the additional shift caused by transfer through the soil if the two sets of phase angles were referenced from the same datum. This common datum was provided by calculating the phase shifts at a frequency where the true transit time was known for both soil and fluid (from the TTC method). The predicted difference in phase between the soil and fluid was then compared with the actual difference found from the two tests and the error was equal to the phase shift required to bring about the common datum. The soil phase angles were therefore corrected by ''a/T'' [the proportion of a complete phase cycle, where a is the delay time correction constant and T is the period of each discrete frequency]. The soil transit times (t_s) were then calculated at each frequency using:

$$\frac{\Phi_s - \Phi_c}{360} = \frac{t_s - t_c}{T}, \tag{1}$$

where Φ_s and Φ_c are the total phase angles in the soil and fluid and t_c is the fluid transit time. (Total phase angles are the cumulative phase shifts from dc.)

A more detailed description of all three acoustic methods, together with a discussion of the theoretical error bounds, may be found in Gardner.[19] It can be seen from Table I that the leading edge method should be most accurate for soils of low gas content, and the TTC and FT methods are more appropriate for more gassy soils.

Although different power drive modules were used for the three acoustic methods, the signal recovery equipment was largely common to each. A two-stage post-amplifier was used to increase output in order to use the band pass filter (24 dB/octave attenuation over 10 Hz–1 MHz, Kron-hite Ltd.), before second stage amplification. Care was taken to center the high and low pass at the signal frequency under test, to avoid causing phase shifts. A 12-bit transient recorder (type 910, Data Laboratories Ltd.) was used to capture a digital received signal at up to 0.1 μs per sample point and signal analysis was performed by computer.

C. Measurement of gas fraction and bubble size distribution (BSD)

Since it has been shown in the literature that gas in soil fundamentally influences its elastic and acoustic properties, bubble size and gas fraction were measured to examine the structure of gas contained in soil and its effect on compressibility, and on velocity and attenuation.

The method of measuring the BSD in specimens of gassy soil is described in detail by Gardner[19] and Gardner and Goringe.[24] Twenty soil specimens of 25 mm $\times$10 mm (diameter$\times$depth) were sub-sampled using a cutting wire. Drying was achieved by initially replacing the soil pore fluid with acetone vapor, impregnating the pore spaces under high vacuum with a solution of polyester resin in acetone, and finally evaporating off the acetone and curing the resin. Surfaces of the specimens were prepared for image analysis by sectioning horizontally, leveling with 1200 grade silicon carbide, and coating with conductive carbon using a high vacuum carbon evaporator. A Joel JSM 35 scanning electron microscope (SEM) and computer were used to obtain multiple frame stored images of the surfaces with units of $512\times512\times8$ bit memory locations. Noise reduction was achieved by spatially resolved time averaging during acquisition from the SEM to the video. Computerized analysis of the stored images was facilitated by having selected a resin that increased the mismatch in atomic numbers at the soil/resin interface. Since the SEM was sensitive to atomic number, the images were bimodal in gray scale intensity, allowing the resin-filled void spaces to be discriminated from the soil solids. The void spaces were measured by area and then idealized as circles to be collated by diameter into groups of increasing size. The resulting planar sizes of voids were converted to spherical sizes by applying a probability distribution for each group of sphere diameters; similar to the method of Wicksell.[25] Each distribution indicated the probability of that sphere being observed in a smaller planar section for each of the size groups below it.

Examination of the laboratory soils by optical microscope indicated two types of void structure. ''Small'' voids were identified as interparticle spaces (of diameter less than a particle size), and ''large'' voids were identified as approximately spherical pockets (of much greater diameter than the particle size) formed from particle walls (Fig. 5). It was predicted that the small voids had been fluid-filled, consistent with interparticle spaces in fully saturated soils (containing no gas), and the large voids had been gas-filled bubbles. The rational for this was based upon two factors. First, interparticle spaces were identical to the interparticle spaces found in fully saturated laboratory soils prepared without methane gas, while the pockets were consistent in structure, size, and shape to those found to contain gas in river muds and marine sediments.[19] Second, when it is assumed that ''large'' voids are gas-filled and ''small'' voids are fluid-filled, it can be shown that calculated gas fractions of laboratory soil agree well with independent measurements of gas fractions from pycnometer tests.[19] Therefore, in the present study, threshold diameters above which voids ceased to be interparticle, fluid-filled spaces were identified from a microscope examination of each specimen. Voids measured by the BSD process that were greater than these threshold diameters were gas-filled bubbles, and gas fractions were calculated accordingly. Since all free gas in the laboratory soil was contained within gas pockets, and interparticle spaces were fluid-filled, the appropriate model was biphasic. This comprised a saturated soil (particle and fluid) matrix surrounding gas-filled pockets greater in diameter than the soil particles.

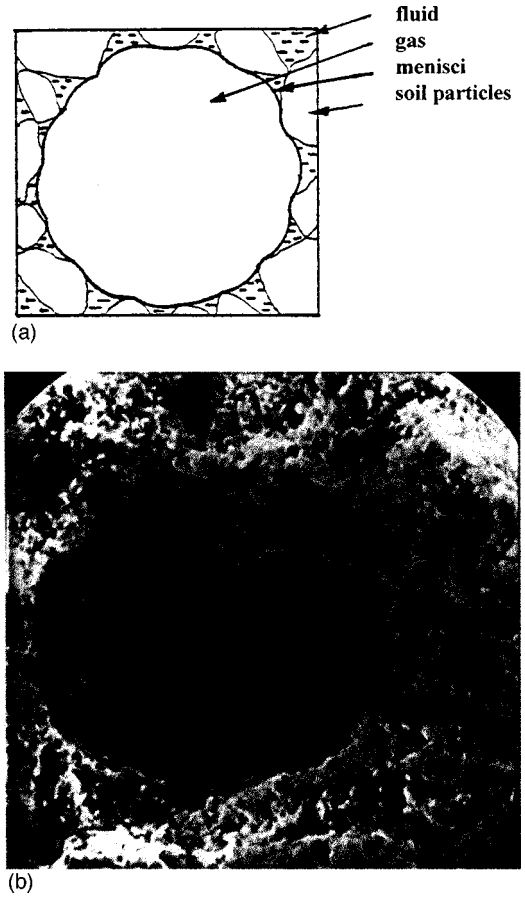

FIG. 5. The bi-phasic structure of gassy soil specimens (gas and a solid/fluid matrix). (a) Gas pockets are formed by the saturated soil matrix of fluid-filled, inter-particle voids. (b) Gassy soil specimen (scanning electron microscope image) showing the particulate formation around a spherical void assumed to have been gas-filled. The diameter of the void is approximately 6 μm.

II. RESULTS

A. Bubble size distributions and other physical properties

The properties of the four soil specimens (50, 51, 52, 53) each divided between cell 1 and 2 to provide eight samples, are shown in Table II. It can be seen from the gas fractions that the gas content was minimal for four of the samples (51-1, 2 and 53-1, 2), and was substantial for the other four (50-1, 2 and 52-1, 2). Despite sample 53 being prepared with a greater methane/zeolite proportion (17%), compared with sample 51 (2.5%), gas fractions were not very dissimilar. This was due to methane gas escaping within drainage fluid during consolidation of sample 53.

Threshold diameters ranged from 130 to 335 μm for the eight soils tested. Figure 6(a)–(h) illustrates the measured BSDs of the samples, which are presented as the total gas

TABLE II. Physical properties of the eight soil specimens.

Test	Methane/ zeolite Proportion (100%)	Gas fraction	Degree of saturation (%)	Bulk density (kg/m^3)	Void ratio	Total void fraction
E50-1	100	0.198	72	1322	2.311	0.698
E50-2	100	0.173	75	1363	2.215	0.689
E52-1	50	0.082	87	1513	1.899	0.655
E52-2	50	0.115	83	1459	2.003	0.667
E53-1	17	0.005 11	99.18	1639	1.674	0.626
E53-2	17	0.004 07	99.35	1640	1.674	0.626
E51-1	2.5	0.004 84	99.23	1640	1.674	0.626
E51-2	2.5	0.003 57	99.43	1643	1.667	0.625

fraction contained in each size of bubble. Each group covered a range of approximately 20 μm in diameter. The low gas content samples had bubble diameters of between approximately 140 μm and 500 μm, whereas the larger gas content samples had much larger bubbles predominantly between 220 and 900 μm but increasing to 1800 μm. Generally, gas was accumulated at the lower end of the bubble size range, with a more scattered presence at the upper end.

B. Compressional wave velocity

Compressional wave velocities for each of the three methods are presented as sound speed versus frequency [Fig. 7(a)–(d)]. The results for the four soil specimens (50, 52, 51, and 53) are shown individually in the four figures, with the exception of the FT method for sample E50-2 for which the transmitted spike signal was attenuated out. As expected, the Leading Edge Method indicates incorrectly that the soil was nondispersive over the range of frequencies tested. This was because components comprising the leading edge of the signal were at noncharacteristic frequencies outside the range influenced by resonance, giving rise to a constant time delay measurement at different frequencies. Nevertheless, the Leading Edge Method was accurate for velocity measurements at nonresonance frequencies, and it confirmed the degree of error arising from this common method of measurement for frequencies inducing resonance. With the TTC method, each data point was derived from individual mea-

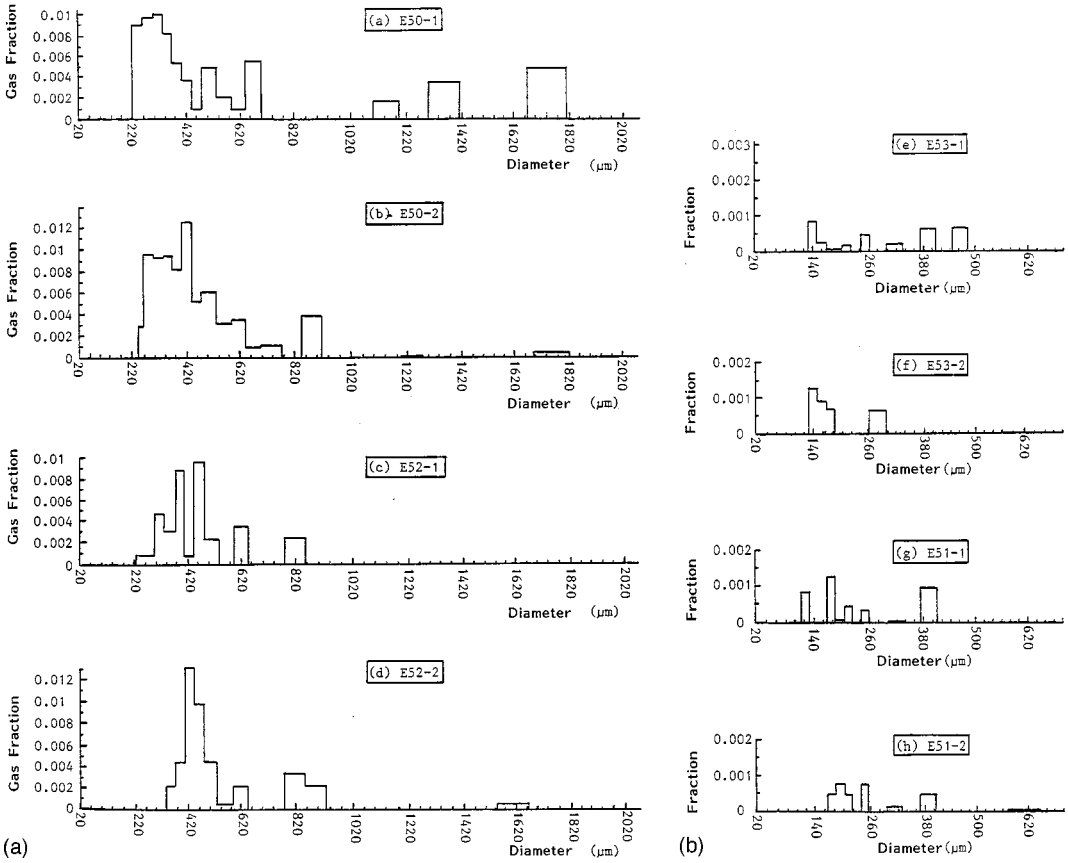

FIG. 6. Bubble size distributions (BSD) of the eight soil specimens. Gas fractions are those contained in each size of bubble. Sizes are in diameter increments of 20 μm.

surement and calibration. Therefore the smooth continuity of the curves indicated a consistent level of accuracy.

1. High gas content soils (50 and 52)

The single curve from the FT method for sample 50-1 agreed well with the TTC curves for both samples 50-1 and 50-2. Since it was apparent from Fig. 6 and Table II that the samples were of approximately the same BSD and gas fraction, the FT and TTC curves may be regarded as providing complementary results over a wide range of frequencies for approximately the same soil. Therefore, the velocity of soil ''50'' may be approximately constant (220 m/s) at frequencies below 20 kHz, consistent with the response of a dispersive material at frequencies below bubble resonance. At frequencies above 20 kHz velocity appears to be increasing, consistent with a dispersive material undergoing resonance. For soil ''52,'' velocities from 10 to 100 kHz appear to be constant, or reducing; since frequencies are likely to be below resonance, velocity would be expected to be constant rather than reducing. Both specimens (50 and 52) provide low velocities consistent with soils of high gas content (velocity being lower for the higher gas content of specimen 50 than for 52).

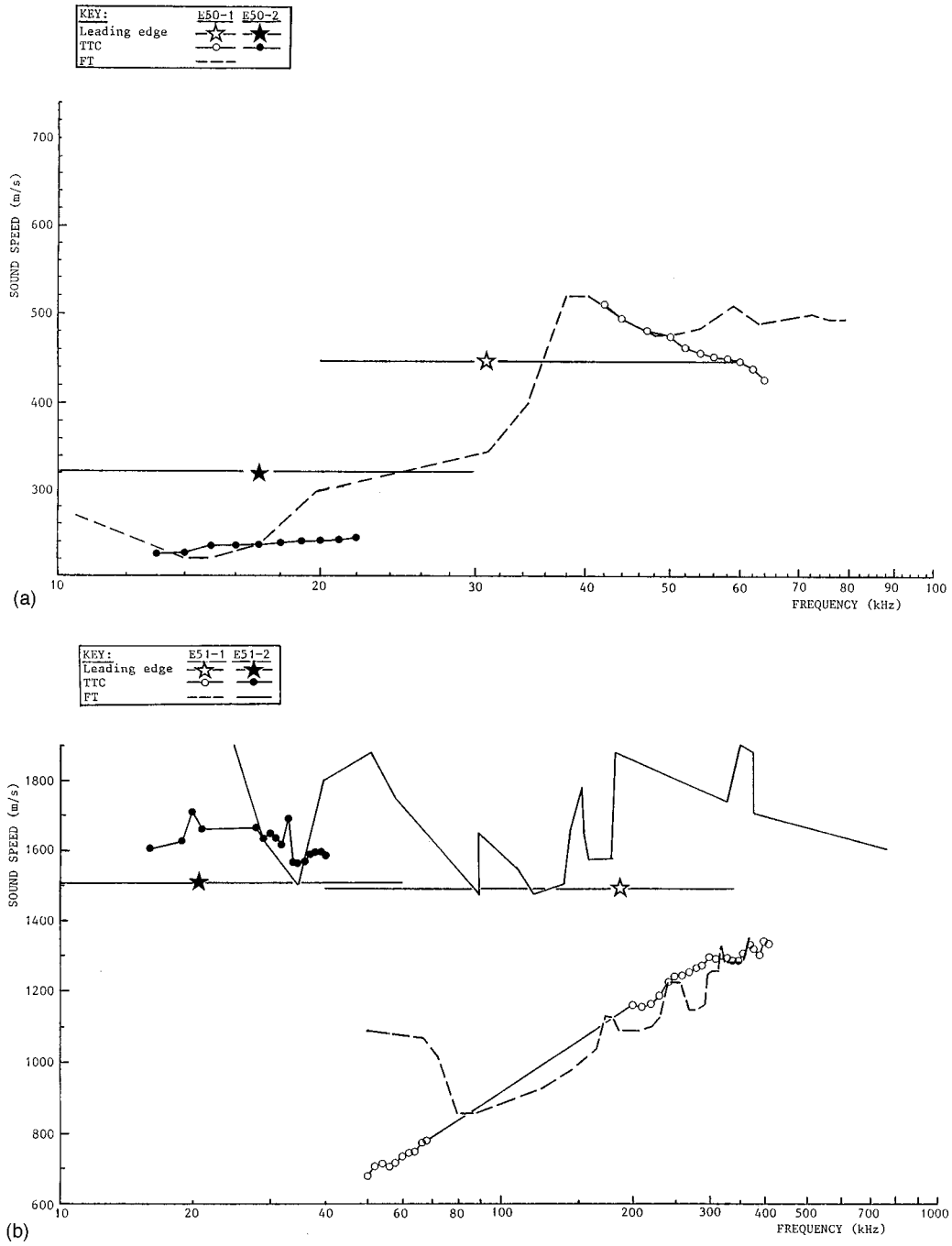

FIG. 7. Velocity versus signal frequency for the eight gassy soil specimens. Data are provided from each of the three test procedures to accumulate information.

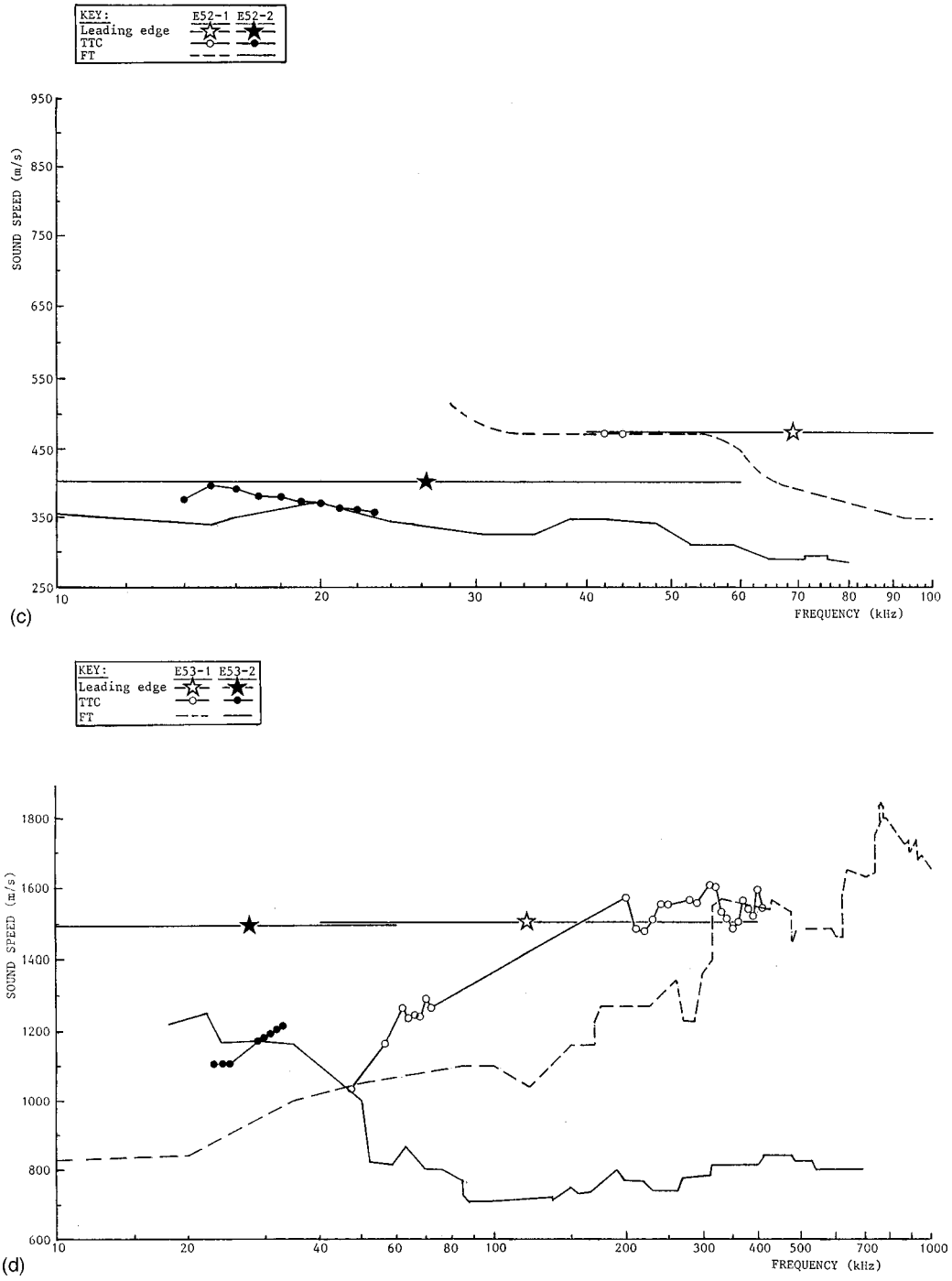

FIG. 7. (*Continued.*)

2. Low gas content soils (51 and 53)

For both pairs of low gas samples (''51'' and ''53'') similar to a fully saturated soil, the Leading Edge Method indicates a velocity of approximately 1500 m/s. This method is expected to produce more accurate velocities in the absence of a significant volume of gas, since it may be used successfully on nondispersive materials such as fully saturated soils. For soil 53, the continuity of data from the TTC Method was broken by a middle frequency region for which no data could be obtained, so the two sections in both samples have been joined by a straight line. Sample 53-1 behaves nondispersively at frequencies above 200 kHz, since it has the constant velocity of a saturated soil (1500 m/s) although the curve data become uncharacteristically unstable here. Below 200 kHz bubble resonance effects are apparent, since the soil is responding dispersively and the velocity decreases with reducing frequency. For soil 51, sample 51-1 behaves dispersively over the full range of frequencies tested, since velocity increases with increasing frequency. Again, there is instability in the measured velocity of sample 51-2 at around 1500 m/s, although the sample behaves nondispersively as a saturated soil exhibiting approximately a constant trend in velocity. Soil 53 (and to a lesser extent soil 51) does not indicate as satisfactory a correlation between

TTC and FT data as soils 50 and 52. This probably confirms that the Leading Edge Method is more reliable for nearly saturated soils, and the FT Method is better for more gassy soils. Sample 53-2 also shows unusually large inverse dispersion between 30 and 50 kHz.

C. Compressional wave attenuation

Figure 8(a)–(d) provides the attenuations of the four soils from the FT Method, with the exception of sample 50-2 where the signal was attenuated out by the soil.

1. High gas content soils (50 and 52)

Attenuations were high, from 6 to 60 dB/cm, and increased with both frequency and gas fraction. The rate of increase with frequency appeared to rise dramatically at 50 kHz with 50-1, and less abruptly with 52-1 and 52-2, indicating a nonlinear frequency response possibly due to bubble resonance.

2. Low gas content soils (51 and 53)

For these samples of relatively low gas content, attenuation is unexpectedly high; again, this is probably due to bubble resonance rather than the influence of a small gas content on the bulk elasticity of the material. The soil of lowest gas content, sample 51-2, appears neither to exhibit a response to gas nor to exhibit any bubble resonance effects. Attenuation remains below 1 dB/cm up to 700 kHz, similar to a fully saturated soil.[26] Also, the sample of next lowest gas content, 53-2, has a constant attenuation of 8–10 dB/cm at all frequencies.

III. DISCUSSION

A. Bubble size and shape

The structural examination implies that the laboratory gassy soil may be modeled as a composite material comprising a gas and a matrix, the matrix being a saturated soil of particles and fluid-filled interstitial voids. Since the mechanical process by which laboratory soil is formed is similar to

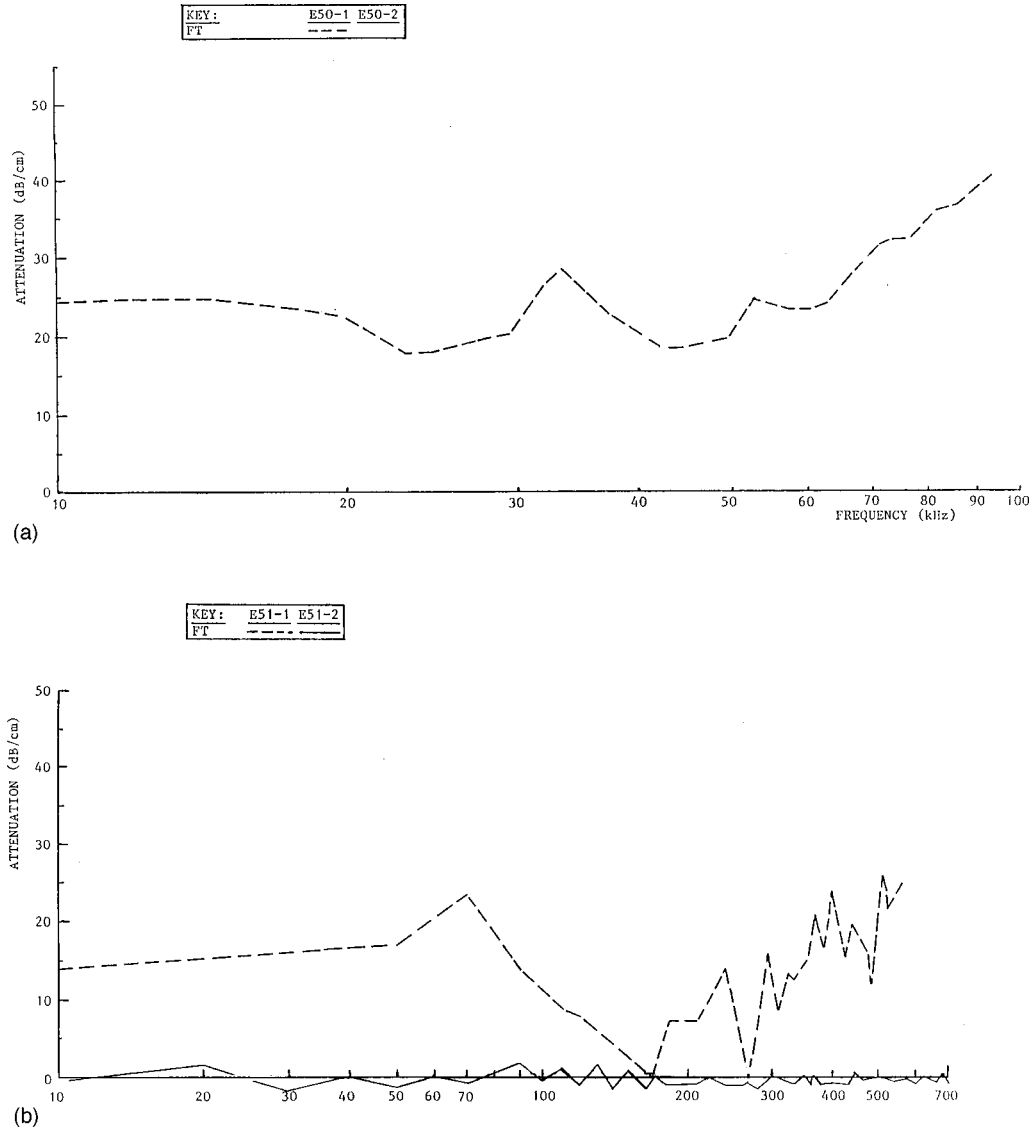

FIG. 8. Attenuation versus signal frequency for the eight gassy soil specimens from the Fourier Transform (FT) method.

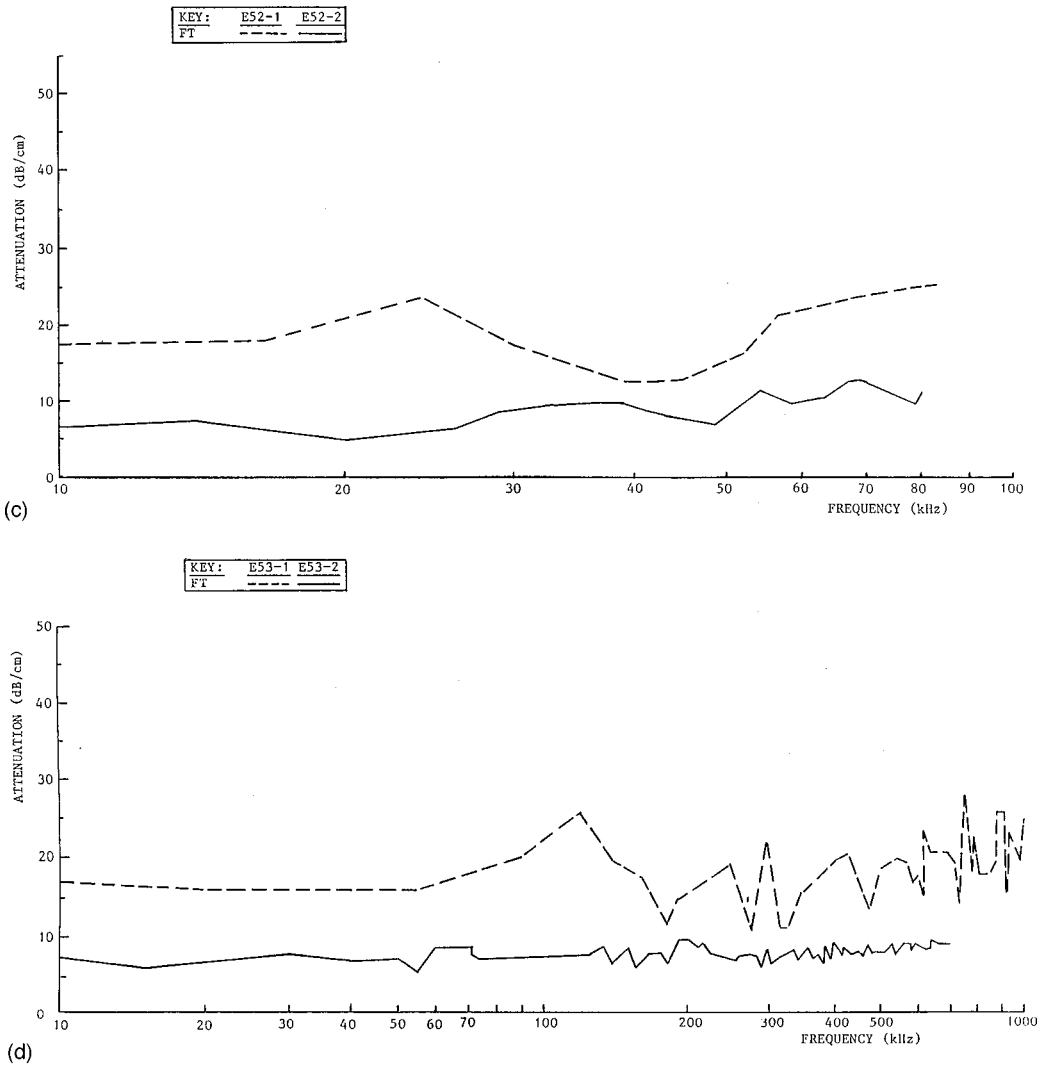

FIG. 8. (*Continued.*)

the formation of naturally occurring gassy soil, then it is appropriate to model natural soil similarly. The simulation of natural soil as a solid and a ''compressible fluid'' by Bedford and Stern[20] and by Anderson and Hampton[17,18] is likely to engender a totally different mechanical and acoustic behavior to typical gassy soils. Since laboratory soils of large gas content were found to have large bubbles, a prolific source of gas should produce natural soils with large bubbles as well as high gas contents.

B. Acoustic response

Anderson and Hampton[17,18] maintained that soils with a large gas content and large bubbles may be expected to substantially influence both velocity and attenuation at frequencies which cause bubble resonance. This has been confirmed by the present study that found low velocities and high attenuations in soils of high gas content using signals of relatively low frequency. Anderson and Hampton also predicted that low gas content soils with small bubbles would produce velocities and attenuations not very different to fully saturated (or nongassy) soils at frequencies which caused bubble resonance, and again this was confirmed in the present study. It was also confirmed that there is a frequency below which no bubble resonance occurs, and that gassy soil responds acoustically as a single phase material of great compressibility. At frequencies above this, resonance was said to occur over a range of frequencies related to the range of bubble sizes, and the influence of such resonance on velocity and attenuation is related to the gas contained in these bubbles. An examination of this relationship, using the structural parameters of the experimental soil to predict acoustic properties from Anderson and Hampton's theoretical model, will be reported separately. In this study it has been confirmed that velocity increases with frequency over a range determined by bubble resonance, and that resonance is influenced by the size of bubbles and the volume of gas within. Since the greater gas contents are held within the smaller bubble sizes (300 μm diameter for the large and 175 μm for the small), resonance is expected to be more dominant at 20 kHz for the large gas content soils and somewhat higher for the soils of lower gas content. Anderson and Hampton's prediction that gassy soil will behave as a single phase material for frequencies above resonance was confirmed. At such frequencies

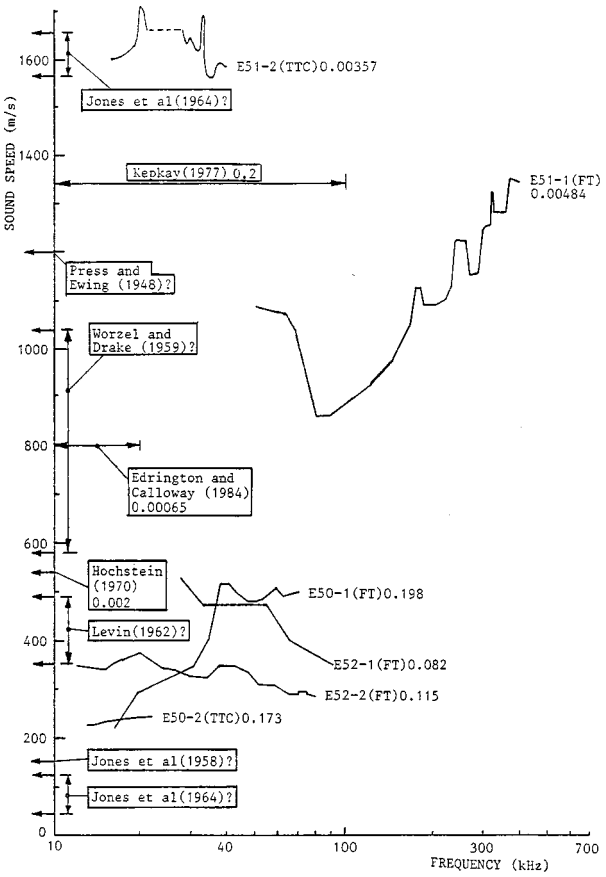

FIG. 9. Comparative acoustic data from other reports. Data are not comprehensive and are generally of low frequency. Gas fractions are given with the reference to each set of data; those of Kepkay and of the present study are measured values, whereas those of Edrington and Calloway and of Hochstein are estimates based on sound speed measurements. Question marks indicate that gas fractions are unknown.

gassy soil responds as a saturated soil in which the viscous and frictional response of the soil matrix dominate, and the gas phase has little influence.

C. Comparison with other studies

Comparative acoustic measurements on gassy soils are presented as sound speed versus frequency (Fig. 9). Largely FT data from the present study is included since frequency ranges are greater; soil 53 is omitted because the correlation with TTC data was not good. Data taken from the literature are not comprehensive, gas fractions are uncertain, and signal frequencies are generally low. Laboratory measurements by Kepkay[21] at between 3 and 100 kHz on soft silty clay of 0.2 gas fraction seem high in comparison with sample 50-1 which is of similar gas content, and also high in comparison with velocities predicted by Anderson and Hampton. Edrington and Calloway[27] experimenting on soft silty clay of low gas fraction (0.000 65) using a signal range of between 0.05 and 20 kHz found velocities vastly different to sample 51-2 with a gas fraction of 0.003 57. Since signal frequencies were higher in the present study, resonance effects in soil 51-2 may have influenced velocities at frequencies above 20 kHz. Hochstein[9] used a bandwidth of between 100 and 200 Hz, but although this is well below the signal frequencies used here velocities were commensurate with soils of gas fraction 0.08. Jones *et al.*[28] did not record the gas fraction of their soil, but their data for soft mud with signals of between 0.2 and 3.2 kHz imply that soil gas contents are above 0.2 for the 46 to 123 m/s results and around 0.0036 for the 1564 to 1656 m/s results. Press and Ewing,[29] Worzel and Drake,[30] Levin,[31] and Jones *et al.*[32] used low signal frequencies but no comparison is possible as gas contents were uncertain. However, the present study implies that their measured velocities were appropriate to soils with gas fractions between 0.004 and 0.2. In general, therefore, the diversity in soil properties and signal frequencies makes it impossible to obtain a good correlation with data reported in the literature.

In regard to attenuation, Nyborg *et al.*[33] found values of between 26 and 74 dB/cm over frequencies between 10 and 35 kHz for gassy soils formed by entraining air in loose Hagerstown silt of indeterminate gas fraction. Although the present study indicates that the gas fraction of their soil may have been 0.2 or higher, the unconsolidated loam silts were probably of lower elastic modulus than soils used in the present study and were therefore more likely to have high attenuations for a given gas fraction. This was also true of the laboratory soils measured by Wood and Weston[34] which were unconsolidated and achieved attenuations of 17 to 24 dB/cm for unreported gas fractions. Anderson and Hampton reported much lower attenuations of 0.13 dB/cm at 40 kHz in Lake Austin mud, probably similar in classification and consolidation to the laboratory soils of the present study. If this is so, gas fraction for the Lake Austin soils may be approximately 0.0036 to 0.0040.

IV. SUMMARY

In general, the acoustic response of gassy soil is broadly as predicted by Anderson and Hampton[17,18] below and above the frequencies that give rise to bubble resonance. However, a structural examination of soil containing gas revealed that the theoretical model used by Anderson and Hampton is probably inappropriate for the prediction of acoustic properties of gassy soil within the frequency range of bubble resonance.

APPENDIX: PREPARING THE SOIL

The laboratory soil was made by impregnating the pore spaces in a zeolite powder with methane gas under pressure. The zeolite was then added to a soil slurry of estuarine silty clay from the River Parrett, Combwich at a moisture content of 184% and a bulk density of 1280 kg/m^3. Water molecules replaced the methane molecules in the zeolite and the methane was liberated over a period of 36 h, during which the soil was consolidated to a vertical stress of 25 kPa. Free gas was formed in uniformly distributed bubbles within the saturated soil matrix, at a gas fraction that was controlled by adjusting the methane pressure or the zeolite/soil ratio.

The 170 mm steel cylinders forming the acoustic consolidation cells were provided with honed internal faces which, in conjunction with greased walls and low friction piston seals, reduced both wall/soil and wall/piston friction. Post-test sampling of soil moisture contents confirmed that there was no radial variation of consolidation due to loss of

vertical stress at the cell wall because of friction. Gassy soil slurry was poured into the cell cylinder above the hydraulic piston and the cylinder stopped-off from above by fixing the top section containing the water reservoir. Pressure was increased in the hydraulic reservoir below the piston to provide the required total stress during consolidation, which was measured by a pressure transducer in the piston. Drainage water and some gas, initially dissolved in the pore fluid, was discharged from the soil through the drainage passages in the top section where free gas collected in the top cone. Water was periodically forced back through the burette tubes used for volume change measurement to replace the volume of gas vented through the outlet point at the apex of the cone. The burettes were then used to measure the water volume discharged from the soil, the flow of which indicated when pressure equilibrium in the soil had been reached. Vyon filter material was used to bridge over the top and bottom drainage outlets and allow the water to drain over almost the entire area of the soil faces. Also, hydrophobic membranes of 2 μm pore size reduced the loss of fine material and avoided clogging of the filters.

A flow restricting device[35] was fitted to the inlet of the hydraulic reservoir through which pressure was applied below the piston for the consolidation process. This device was formed from assembling a group of hydrophobic filters of small pore size to inhibit flow to the reservoir. Vertical stress on the soil was therefore applied very slowly, allowing excess pore water pressures to remain lower and to be less divergent throughout the soil. This resulted in a more uniform consolidation stress from top to bottom of the sample with a correspondingly uniform structural development. The reduced pore water pressures contributed to the development of more spherical bubbles by reducing the consolidation period in relation to the period of bubble formation. It also produced increased bubble sizes, since, under lower pore pressures, less free gas was dissolved into the water and removed by drainage. Following consolidation and final equilibration of pore pressures, the soil was prepared for acoustic tests. It was raised in the cylinder to bear against a reaction plate assembly by releasing the top section securing bolts and applying a small increase in piston pressure. The pressure of consolidation was maintained on the soil during the lifting process by using a hydraulic ram between the top section and reaction plate.

Following completion of the test, the unloading process was performed over 12 h to allow pressures to equilibrate through the soil. This was completed by applying a vacuum to the flow restrictor side of the hydraulic reservoir inlet to release the small amount of consolidation pressure maintained by piston/wall friction after unloading. Full pressure release was important to avoid rupturing the soil by the sudden expansion of gas pockets arising from any drop in pore pressure, since the specimens were required for the measurement of gas fraction and bubble size in the acoustic analysis. It is worth noting that it is this expansion of gas which is thought to be the cause of structural damage to deep water gassy sediment core samples that have been removed to a condition of atmospheric pressure.

[1] S. J. Wheeler, ''The stress strain behavior of soils containing gas bubbles'' D. Phil. Thesis, University of Oxford (1986).
[2] E. L. Hamilton, ''Elastic properties of marine sediments,'' J. Geophys. Res. **76**, 579–604 (1971).
[3] E. L. Hamilton and R. T. Bachman, ''Sound velocity and related marine properties of marine sediments,'' J. Acoust. Soc. Am. **72**, (1982).
[4] R. R. Stainer, M. Doudoroff, and E. A. Adelberg, *The Microbial World* (Prentice-Hall, Englewood Cliffs, NJ, 1963).
[5] J. R. Schubel, *Gas Bubbles and the Acoustically Impenetrable or Turbid Character of Some Estuarine Sediments*, edited by I. R. Kaplan (Plenum, New York, 1974).
[6] T. Whelan III, J. M. Coleman, and J. N. Suhayda, ''The occurrence of methane in recent deltaic sediments and its effects on soil stability,'' Bull. Int. Assoc. Eng. Geol. **14**, 55–64 (1976).
[7] T. Whelan III, J. M. Coleman, J. N. Suhayda, and H. H. Roberts, ''Acoustical penetration and shear strength in gas-charged sediment,'' Marine Geotechnology **2**, 147–159 (1977).
[8] M. I. Esrig and R. C. Kirby, ''Implications of gas content for predicting the stability of submarine slopes,'' Marine Geotechnology **2**, 81–100 (1977).
[9] M. P. Hochstein, ''Seismic measurements in Suva Harbour (Fiji),'' N. Z. J. Geol. Geophys. **13**, 269–281 (1970).
[10] H. E. Edgerton, ''Sub-bottom penetration in Boston Harbour,'' J. Geophys. Res. **70**, 2931–2934 (1965).
[11] N. G. T. Fannin, ''I.G.S. pockmark investigations 1974–1978,'' IGS Report No. 98 (1979).
[12] R. McQuillin and N. G. T. Fannin, ''Explaining the North Sea's lunar floor,'' New Sci. **1163**, 90–92 (1979).
[13] A. A. Yakubov, A. A. Ali-Zade, and M. M. Zeinalov, ''Mud volcanos of the Azerbaijan,'' SSR; Atlas Academy of Science of Azerbaijan, SSR; Baku, U.S.S.R. **258**, (1971).
[14] R. S. Newton, R. C. Cunningham, and C. E. Schubert, ''Mud volcanoes and pockmarks: Sea floor engineering hazards or geological curiousities?,'' Offshore Techn. Conf. 12, **1**, 425–435 (1980).
[15] L. H. King and B. Maclean, ''Pockmarks of the Scotian shelf,'' Geol. Soc. Am. Bull. **81**, 3141–3148 (1970).
[16] J. Platt, ''Sigificance of pock marks for engineers,'' Offshore Engineer **45**, (1977).
[17] A. L. Anderson and L. D. Hampton, ''Acoustics of gas bearing sediments. I. Background,'' J. Acoust. Soc. Am. **67**, 1865–1889 (1980).
[18] A. L. Anderson and L. D. Hampton, ''Acoustics of gas bearing sediments. II. Measurements and models,'' J. Acoust. Soc. Am. **67**, 1890–1903 (1980).
[19] T. N. Gardner, ''The acoustic properties of gassy soil,'' D. Phil. Engineering Thesis, University of Oxford (1988).
[20] A. Bedford and M. Stern, ''A model for wave propagation in gassy sediments,'' J. Acoust. Soc. Am. **73**, 409–417 (1983).
[21] P. E. Kepkay, ''Preliminary investigation of free gas as the control of a sub-bottom acoustic reflector in the fine-grained sediments of Halifax Harbour and St. Margaret's Bay, Nova Scotia,'' M. Sc. Thesis, Dalhousie University (1977).
[22] D. C. Blanchard and A. H. Woodcock, ''Bubble formation and modification in the sea and its meteorological significance,'' Tellus **9**, 145–158 (1957).
[23] S. Nageswaran, ''Effect of gas bubbles on the sea bed behaviour,'' D. Phil. Engineering Thesis, University of Oxford (1983).
[24] T. N. Gardner and M. Goringe, ''The measurement of gas bubble size distribution in a three phase gassy soil,'' ASTM Geotech. Test. J. **11**, 49–55 (1988).
[25] S. D. Wicksell, ''The corpuscle problem. A mathematical study of a biometric problem,'' Biometrika **17**, 127–136 (1925).
[26] E. L. Hamilton, ''Compressional-wave attenuation in marine sediments,'' Geophysics **37**, 620–646 (1972).
[27] T. S. Edrington and T. M. Calloway, ''Sound speed and attenuation measurements in gassy sediments in the Gulf of Mexico,'' Geophysics **49**, 297–299 (1984).
[28] J. L. Jones, C. B. Leslie, and L. E. Barton, ''Acoustic characteristics of underwater bottoms,'' J. Acoust. Soc. Am. **36**, 154–157 (1964).
[29] F. Press and M. Ewing, ''Low-speed layer in water-covered areas,'' Geophysics **13**, 127–132 (1948).
[30] J. L. Worzel and C. L. Drake, ''Structure section across the Hudson River at Nyack, N.Y. from seismic observations,'' Ann. (N.Y.) Acad. Sci. **80**, (1959).

[31] F. K. Levin, ''The seismic properties of Lake Maracaibo,'' Geophysics **27**, 35–47 (1962).
[32] J. L. Jones, C. B. Leslie, and L. E. Barton, ''Acoustic characteristics of a lake bottom,'' J. Acoust. Soc. Am. **30**, 142–145 (1958).
[33] W. L. Nyborg, I. Rudnick, and H. K. Schilling, ''Experiments on acoustic absorption in sand and soil,'' J. Acoust. Soc. Am. **22**, 422–425 (1950).
[34] A. B. Wood and D. E. Weston, ''The propagation of sound in mud,'' Acustica **14**, 156–162 (1964).
[35] K. Lee, ''The analytical and experimental study of large strain soil consolidation,'' D. Phil. Engineering Thesis, University of Oxford (1979).

A model for the horizontal directionality of breaking wave noise in the surf zone

Grant B. Deane
Marine Physical Laboratory, Scripps Institution of Oceanography, UCSD, La Jolla, California 92093-0238

(Received 27 May 1998; revised 2 April 1999; accepted 13 September 1999)

A model is presented for the horizontal directionality of the noise generated by individual breaking waves in the surf zone. The model is based on the interaction between sound radiated by ringing bubbles created in a breaking wave crest and the population of acoustically quiescent bubbles left on the seaward side of the wave in the shallow water waveguide. The effect of the quiescent bubbles is to absorb sound from all but the very ends of the breaking crest, resulting in the formation of ''acoustic hot-spots.'' The model calculations are in good agreement with observations of the horizontal directionality of noise from individual breaking waves in the surf zone. © *2000 Acoustical Society of America.* [S0001-4966(00)00501-4]

PACS numbers: 43.30.Nb [DLB]

INTRODUCTION

During November of 1996, a series of recordings of the underwater sound from single breaking waves were made in the surf zone off Red Beach, Southern California as part of the Adaptive Beach Monitoring Experiment.[1] The measurements were made in 2 m of water, some 25 m on the seaward side of breaking surf. An analysis of the wave noise showed that the noise from individual breaking waves appears to radiate from compact regions, or ''acoustic hot-spots,'' which follow the wave break-points through the surf zone (see Fig. 1 for a definition of the term ''wave break-point''). As a wave shoals, the wave break-points move through the surf zone causing systematic temporal variations in the noise field directionality. Details of the experiment off Red Beach, and analysis of the wave noise measurements showing the formation of acoustic hot-spots, are the subject of an earlier paper.[2] Two mechanisms that could be responsible for the formation of hot-spots, a source effect and a propagation effect, were discussed in the earlier work. The source effect is based on the idea that the ends of the breaking wave crest might be more acoustically energetic than the central regions, resulting in the formation of diverging pairs of hot-spots. The second mechanism is based on the strongly absorbing bubbly residue left behind (i.e., on the seaward side of) the breaking wave absorbing the seaward propagating sound radiated by all of the breaking crest except for the end regions, which radiate into relatively bubble-free water. The observed behavior of hot-spots tends to favor the latter explanation, providing the motivation for the present work. Here we present a model for the coherence and directionality of the noise radiated by individual breaking waves which includes the interaction between the sound generated by the breaking wave crest and the population of acoustically quiescent bubbles behind the breaking wave.

The coherence of oceanic ambient noise in shallow water has been the subject of a number of studies; some important contributions have been made by Kuperman and Ingenito,[3] Buckingham,[4–6] Harrison,[7–9] and Hamson.[10,11] In the early 1980's Karnovskii[12–14] published a trio of papers considering the properties of noise in a wedge and Harrison[9] has published a study of noise directionality in the surf zone. The present work differs from these earlier efforts in that the primary concern is with the noise radiated by individual breaking waves in the surf zone, and investigating how the wave noise interacts with the residue of bubbles left behind the breaking wave. Although the model presented does have a statistical component, one of the main results is the calculation of deterministic and systematic variations in wave noise directionality associated with movement of the breaking wave crest through the surf zone. The focus on time-varying patterns of noise directionality associated with the noise radiated by individual breakers makes it difficult to compare the results of this work with those presented by Karnovskii,[12] Buckingham,[6] and Harrison.[9] Harrison,[9] for example, has calculated the noise directionality in a wedge as a function of elevation and azimuth for a random spatial distribution of noise sources, which is appropriate for a calculation of surf noise directionality at a large enough range from the surf line that no single breaking event dominates the noise field.

The paper is arranged as follows. A summary of the observations of breaking wave noise and the formation of acoustic hot-spots reported in Ref. 2 is given in Sec. I. A model for the wave noise directionality is developed in Sec. II. This section opens with a discussion of the issues relating to wave noise generation and propagation through surf zone, which leads into a theoretical model for the breaking noise coherence and directionality of isolated breakers. A comparison of the model calculations with observations of wave noise is given in Sec. III. Finally, the concluding remarks are made in Sec. IV.

I. OBSERVATIONS OF SURF NOISE DIRECTIONALITY

The observations of surf noise that motivated the present study are the subject of an earlier work,[2] which contains a full account of the experiment and wave noise analysis. This section reproduces only those details necessary to provide a context for the model of wave noise directionality developed in Sec. II. Figure 1 illustrates the regions of a breaking wave that will be referred to throughout the paper. The breaking

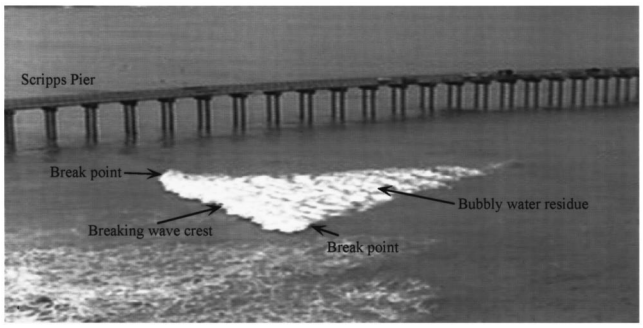

FIG. 1. Image of a shoaling wave in the surf zone north of Scripps Pier. The spacing between the pier pilings is 9 m. The white water at the leading edge of the wave is the breaking wave crest, and the regions of overturning wave at the ends of the breaking crest are the wave break-points. The population of bubbles left in the water column by the passage of the wave causes the triangular region of surface foam labeled bubbly water residue.

wave crest is the region of foamy water at the leading edge of the breaking wave. The wave break-points are the regions of overturning crest at the edges of the breaking region, and occur at the transition between breaking and unbroken wave crest. The bubbly residue is the region of bubble-filled water trailing the breaking crest. The bubbly residue is evident at the water surface by the foam created by bubbles rising to the water's surface, and which remains visible to the naked eye for a few seconds after the passage of the wave.

A. The experiment

An experiment to measure the sound radiated by isolated breaking waves in the surf zone was conducted as part of the Adaptive Beach Monitoring Experiment off Red Beach, Camp Pendleton during November, 1996. A two-element hydrophone array was deployed on a frame jetted into the sea floor in approximately 0.3 m of water at low tide. The axis of the hydrophone array was aligned parallel with the still ocean surface, perpendicular to the shore line and positioned 0.9 m above the sea floor. At high tide, the water depth at the frame was approximately 2 m, and surf tended to break between the hydrophone array and the shore line, roughly 25 m to 50 m shoreward of the frame. Sound pressure time-series data were cabled to shore and recorded on a digital tape deck with a 20 Hz–22.5 kHz bandwidth. Wave conditions in the region of the surf frame were recorded synchronously with the hydrophone data using a video camera mounted on a bluff overlooking the deployment site.

B. Wave noise coherence, directionality, and the formation of acoustic hot-spots

During a breaking event, the wave noise rose above background levels for typically 3 to 5 s after the wave initially overturned. Figure 2 shows a summary analysis of a single breaking event. The four video frames at the bottom of the figure show the evolution of the breaking wave crest at 0.5, 1, 1.5, and 2 s after the beginning of the data record. The camera recording the images was mounted on a bluff above and to the southwest of the array. The wave break-point is on the far left of the field of view at 0.5 s, and travels from left to right across the image as time progresses.

The color contour plot immediately above the video images shows the ambient noise directionality, computed from the coherence measured across the entire frequency band of wave noise frequencies that were measured. The time of the video images relative to the directionality plot is indicated by the arrows connecting the figures. Each vertical slice in the plot represents an estimate of the ambient noise directionality as a function of angle, integrated around the array axis and color coded according to the scale to the right. The result is a color contour plot of the angle and time dependence of the ambient noise directionality. Negative and positive angles, respectively, correspond to sound arriving from sources on the shoreward and seaward sides of the array. An isotropic noise field has a constant noise directionality with unity magnitude. A noise field consisting of a single plane wave is represented by a noise directionality with a delta function at the angle of the plane wave. In practice, the maximum response of the broadband beam former depends on the highest frequency component of the coherence measurement and the hydrophone separation (see Appendix A of Deane[2]). For the measurements presented here, the theoretical maximum array response is 21.

During the acoustically active part of the wave breaking event, the ambient noise showed a strong directionality, with energy from sources on the shoreward side of the frame predominating. The pronounced, red band between 0.5 and 2.5 s in the lower half of the plot indicates the presence of a localized source, or acoustic hot-spot, moving systematically through the surf zone. The video recordings show that the hot-spot movement roughly corresponds to the movement of the northernmost wave break-point along the shore line. The noise directionality estimates show that energy from sources on the seaward side of the frame predominates before and after the breaking event. The band of energy at the top of the plot between 2 s and 4 s is due to spatial aliasing of the array.

The plate directly above the directional density contour plot shows a spectrogram of the ambient noise at the shoreward hydrophone of the two-element array and illustrates that the onset of the wave noise is coincident with the change in the noise field directionality. The two plots at the top of the figure show time averages of the noise power spectral density and directionality through the period labeled ''Averaging Interval'' at the top of the spectrogram. The noise field directionality is strongly peaked, showing a 9° beam at −55°. The angular resolution of the array is determined by the highest frequency component of the coherence measurement and the separation of the hydrophone elements, which, respectively, were 22.5 kHz and 0.327 m for the experiment. These values imply an angular resolution of approximately 9°, so that the length of the acoustically dominant region of the breaking wave crest may have been shorter than implied by the measured beamwidth of the peak in the noise field directionality.

The measurements of wave noise directionality 25 m or so behind the breaking surf show that, while the ambient noise field is dominated by breaking wave noise, only a small fraction of the total length of a breaking wave crest is audible. The two explanations for this are that either we are observing an effect inherent to the noise source (i.e., the

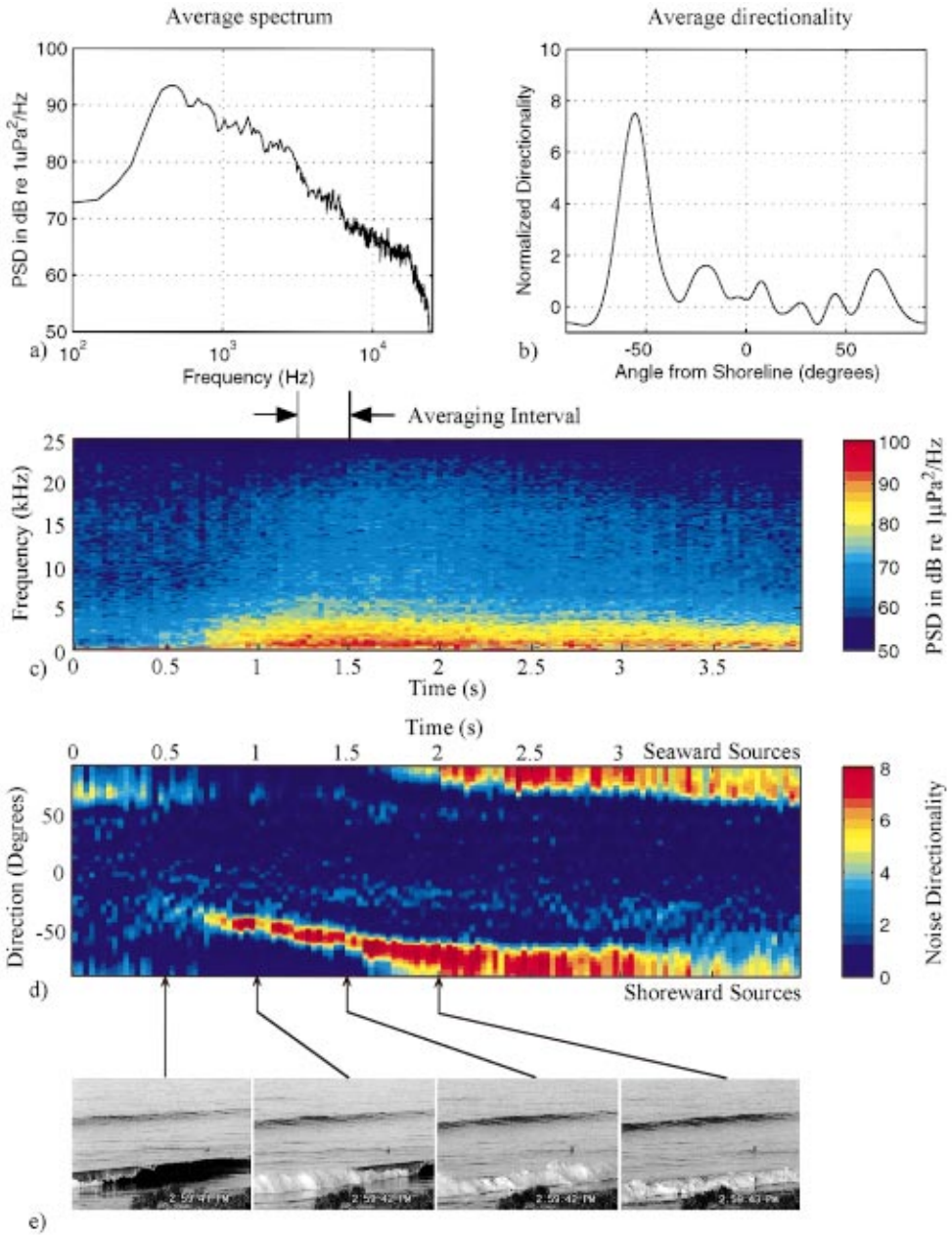

FIG. 2. Analysis of the noise directionality from a single breaking event at Red Beach. (a) The wave noise power spectral density, averaged over the interval indicated on the spectrogram beneath. The rapid roll-of above 22.5 kHz is caused by the recording system anti-aliasing filter. (b) The ambient noise directionality, measured behind the breaking wave and averaged over the same interval as the power spectral density plot. The peak in the directionality at $-55°$ is caused by the wave noise. (c) A spectrogram of the ambient noise. The onset of the wave noise can be seen roughly 0.5 s into the plot. (d) The ambient noise directionality plotted as color contours versus angle and time. Positive angles correspond to sources on the seaward side of the array and negative angles correspond to sources on the shoreward side. The red shows that the breaking wave noise originates from a well-defined spatial region that moves through the surf zone. (e) Video images of the breaking wave taken from a bluff overlooking the experiment site. The images were taken at 0.5 s intervals, and correspond to the times on the directionality plot as indicated by the arrows.

wave noise is generated preferentially in a limited region of breaking crest), or the hot-spots are caused by a propagation effect. As the hot-spots tend to track the wave break-point trajectories, a plausible model is that the wave break-points are more acoustically energetic than the rest of the breaking wave crest. If this were the case then hot-spots, like wave break-points, would always be observed in diverging pairs. In practice, however, hot-spots usually appear as isolated peaks in the noise directionality. When pairs are observed, they most frequently appear as not diverging, but converging pairs.

An alternative hypothesis is that the hot-spots are caused by a screening effect. The residue of bubbles left in the water column is a strong absorber of sound, and may be screening the seaward-propagating sound radiated by all of the breaking wave crest except for the wave break-points which radiate into relatively bubble-free water. Assuming such a screening effect, hot-spots are formed in pairs, but not *observed* in pairs, at least not at a single observation point. In general, the noise from one wave break-point will have a clear transmission path to the array while the other is blocked. The occasional observation of converging hot-spot pairs can be explained by noting that a single shoaling wave can have more than one region of breaking crest. An array positioned behind the unbroken wave crest separating two regions of the breaking crest will receive energy from two converging break-points; the sound from the outer, diverging wave break-points will be screened by the bubbly residue. Without the screening effect of the bubbles, four hot-spots would be observed from the two breaking regions, two of which would be converging and two diverging. This combination of hot-spots was not observed in the directionality patterns of the 100 or so waves analyzed.

The screening versus source effect hypotheses are discussed further in Deane.[2] The weight of the data tends to favor the screening hypothesis, and expressions for the wave

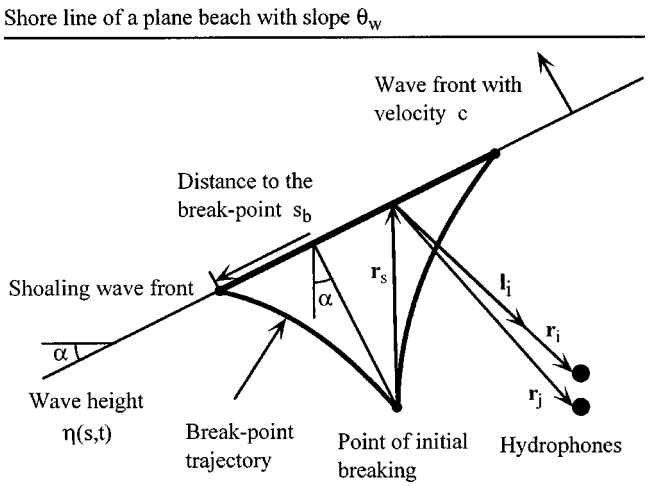

FIG. 3. The geometry for the wave noise coherence model. A plane wave is shoaling with constant velocity c and at an angle α to a plane beach with slope θ_w. Coordinates are measured relative to the point of initial wave breaking. The variable s_b measures distance along the breaking wave crest to the wave break-points. Sources of wave noise are distributed along the entire region of breaking wave crest, and the position vector from the coordinate system origin to a chosen point on the breaking crest is denoted by $\mathbf{r}_s$. The straight-line propagation paths from $\mathbf{r}_s$ to the hydrophone array are denoted by $\mathbf{r}_i$ and $\mathbf{r}_j$. The vector $\mathbf{l}_i = \mathbf{r}_s + \mathbf{r}_i l / r_i$ defines the straight-line propagation path from the sources at $\mathbf{r}_s$ to $\mathbf{r}_i$.

noise directionality based on this model are developed in the following sections.

II. A MODEL FOR WAVE NOISE DIRECTIONALITY

It has been established by Cox[15] that the directionality of oceanic ambient noise is related to its coherence. If the noise field is a superposition of plane waves, and therefore homogeneous in space, the coherence and directionality are related via a spatial Fourier transform. We will use this relationship to calculate the wave noise directionality for individual breaking waves from a model for the wave noise coherence. This method of analysis follows the measurement methodology used in the experiment, and will allow a meaningful comparison between the model predictions and measurements of surf noise. The transformation between noise directionality and coherence relies on Fourier series expansion of the broadband coherence between two fixed points. The details of the calculation and performance of a two-element hydrophone used in this way have been presented in Deane,[2] and are not reproduced here.

A. A note on coordinate systems

The geometry and coordinate systems used in the wave noise model are shown in Fig. 3, which illustrates a shoaling wave incident on a plane beach. The wave is assumed to show some height variation along its wavefront, so that the wave does not initially break simultaneously along the entire front. The spatial coherence is calculated at two nearby points on the seaward side of the breaking wave. The origin of the coordinate is the point at which the wave first overturns. Sources of wave noise are distributed along the entire region of breaking wave crest, and the position vector from the coordinate system origin to a chosen point on the breaking crest is denoted by $\mathbf{r}_s$. The straight-line propagation paths from $\mathbf{r}_s$ to the field evaluation points are denoted by $\mathbf{r}_i$ and $\mathbf{r}_j$. The magnitude of a vector is indicated by the plain type counterpart of the bold type symbol.

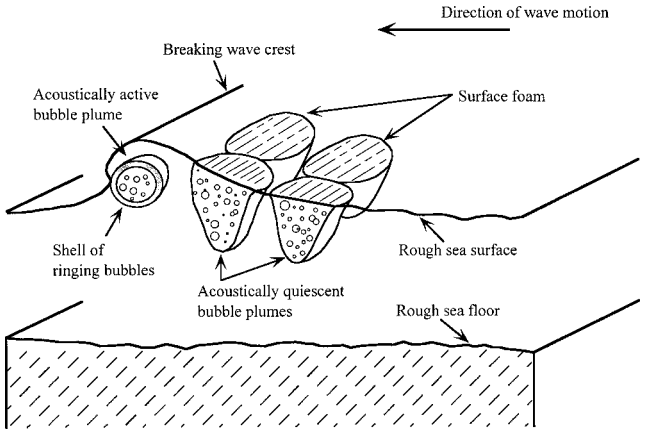

FIG. 4. A schematic of the distribution of acoustically active and quiescent bubbles entrained by the breaking wave. The acoustically active bubbles are created in forming bubble plumes within and beneath the breaking wave crest, shown propagating from right to left across the figure. Fully formed, acoustically quiescent plumes are left in the water column behind the breaking crest.

B. The source model

Breaking surf radiates underwater sound over a broadband of frequencies, from a few hundred Hertz or lower up to at least 20 kHz.[16,17] A discussion of sound source mechanisms associated with surf is given in Deane.[16] As with breaking waves in the open ocean, the source of the underwater noise above 500 Hz or so from surf is thought to be the pulses of sound emitted by bubbles when they are formed within the breaking wave crest.[18–23] Thus the sound at frequencies above 500 Hz is expected to be radiated from regions within the crest where bubbles are being formed, which is the entire length of breaking wavefront. There are various mechanisms that could contribute to the breaking wave noise below 500 Hz, including bubble-amplified turbulence[24] and collective oscillations.[23,25] The noise model developed below assumes that the noise sources are newly formed bubbles, and is thus restricted to frequencies above 500 Hz or so.

As a wave shoals into increasingly shallow water, the region of breaking crest, and therefore active bubble creation and noise generation, lengthens and moves shoreward, resulting in a space–time distribution of the wave noise sources. Thus there are two questions that need to be considered in establishing a source model for breaking surf noise: what is the small-scale distribution of the acoustically active bubbles within the breaking wave crest, and what is the motion of the breaking wave crest through the surf zone?

1. A source model for wave noise

Figure 4 shows a schematic representation of the distribution of bubbles entrained by a breaking wave in the surf zone. The wave is shoaling from right to left across the figure. Photographs of the assemblages of surf-generated bubbles from above and below the water surface show that

they are initially packed into dense plumes[16] whose void fraction of air can exceed 50%.[26] The acoustically quiescent plumes shown in Fig. 4 are fully formed plumes that have been left behind the breaking wave crest. These plumes evolve through the processes of bubble advection, diffusion, and dissolution, and persist in the water column for hundreds of seconds after the passage to the breaking wave. Fully developed plumes are acoustically quiescent in the sense that bubble creation has ceased, and therefore they do not radiate the noise that accompanies bubble formation. Quiescent plumes do, however, strongly absorb and scatter sound incident from the water column. This point is discussed in greater detail in Sec. II C.

Bubbles are created, and radiate pulses of sound, within and beneath a breaking wave crest during the formation of a bubble plume. The plume labeled ''acoustically active'' in Fig. 4 is meant to represent a plume forming at the leading edge of the breaking wave. There is acoustical evidence that time-scale for bubble formation and sound generation within a forming plume is around 0.1 s.[16] Two large-scale flow features have been identified as important in the entrapment of air by plunging breakers, which are air entrainment under the falling water jet caused by the overturning wave crest, and air entrainment at the point where the falling water jet meets the vortex formed at the rear of the splash-up.[27,28] A detailed description of the physical processes resulting in bubble formation by these large-scale flow features does not exist at the present time, although there is some photographic evidence which suggests that bubble splitting and the unstable break-up of small filaments of air both play a role in the generation of bubbles.[29]

In the absence of detailed physical measurements, it is necessary to make some assumptions about the spatial distribution and creation rate of bubbles during the acoustically active phase of plume formation. The details of a simple model have been given in Ref. 16 (also see Loewen and Melville,[22] Hollett and Heitmeyer,[30] and Finette and Heitmeyer[31]). The essential assumptions are that the bubbly mixture of the forming plume can be modeled as a linear, time-invariant system for the time interval over which the plume is radiating sound, so that superposition holds, and that bubbles are created at random times throughout the plume volume.

Consider an element of volume dv on the outer edge of a forming plume at a position $\mathbf{r}_s$ along a breaking wave crest. Within dv, bubbles are assumed to be created randomly at a mean rate of $\lambda(a)$ bubbles per unit radius, per second, where a is the bubble radius and the creation rate is assumed to be independent of position within the plume. At the instant of its creation, each bubble radiates a pulse of sound with a pressure spectrum $Q(\omega,a)$, which is a function of angular frequency ω and radius a. The element of volume is assumed to be on the outer edge of the forming plume because the dense mixture of bubbles inside the forming plume strongly absorbs the sound radiated by bubbles interior to the plume,[16,32] leading to the conclusion that only bubbles on the outer edges of the plume contribute to the wave noise. Given that the audible bubbles are all formed in a similar environment, on the plumes' outer edges, it is reasonable to assume that the pressure spectrum of the audible bubbles of the same radius are also similar. If different bubble creation mechanisms are operating within the plume, each with its own characteristic emission spectrum, then the source spectrum Q represents a rate-weighted mean of all the source spectra.

Following the analysis of earlier authors (see Cron and Scherman,[33] Kuperman and Ingenito,[3] Buckingham,[5] and Harrison[7]), the contribution to the noise field cross-spectrum at two chosen points $\mathbf{r}_i$ and $\mathbf{r}_j$ from the bubbles created in dv with radii between a and $a+da$ is given by

$$dS_{ij}=\lambda(a)|Q(\omega,a)|^2 G(\omega,\mathbf{r}_s,\mathbf{r}_i)G^*(\omega,\mathbf{r}_s,\mathbf{r}_j)da\,dv, \qquad (1)$$

where $G(\omega,\mathbf{r}_s,\mathbf{r})$ is the Green's function for sound propagation between $\mathbf{r}_s$ and $\mathbf{r}_i$ or $\mathbf{r}_j$, $\|$ denotes taking the absolute value, and* denotes complex conjugation. Equation (1) holds on time-scales sufficiently long that many bubbles have been created in the element of volume dv, but sufficiently short that the propagation environment can be considered time-invariant. A time-scale that satisfies these constraints is the acoustically active period of a forming bubble plume, which is about 0.1 s.[16]

A more sophisticated treatment of surf noise generation would model the formation of individual plumes statistically (see Finette and Heitmeyers' open-ocean noise model,[31] for example), and would account for the varying sound speed and rough boundary at a plume's edge. The current state of knowledge of surf-induced bubble plumes does not permit such a treatment, and some simplifying assumptions need to be made. The model adopted here is that the sound from the breaking wave crest is radiated by ringing bubbles distributed along a tube below the breaking wave crest. By assuming a uniform source strength along the breaking crest, the possibility of hot-spots being formed by acoustically energetic wave break points is explicitly excluded from the model. The justification for this is that acoustically energetic wave break-points cannot, on their own, explain the observed numbers and behavior of hot-spots, and so is already discounted as a sole mechanism on other grounds. The intention here is to study the screening effect of the bubbly residue on wave noise directionality without assuming preferred regions of radiation along the length of breaking crest.

The total contribution to the cross-spectrum due to the breaking wave is found by integrating Eq. (1) between the smallest and largest bubbles created in the plume, respectively, a_0 and a_1, and the total volume of the tube within which ringing bubbles are assumed to be audible. Performing this integration yields

$$S_{ij}=\int_{a_0}^{a_1}\lambda(a)|Q(\omega,a)|^2 da \times \int\int_V\int G(\omega,\mathbf{r}_s,\mathbf{r}_i)G^*(\omega,\mathbf{r}_s,\mathbf{r}_j)dv. \qquad (2)$$

The wave noise coherence between $\mathbf{r}_i$ and $\mathbf{r}_j$ is now defined as

$$\Gamma=\frac{S_{ij}}{(S_{ii}S_{jj})^{1/2}}. \qquad (3)$$

Equation (3) can be evaluated from Eq. (2) once a suitable form for the Green's function has been determined, which is the topic of Sec. II C.

2. The movement of a breaking wave crest through the surf zone

A model of the movement of wave break points through the surf zone has been presented in the paper describing the experimental observations of individual breaking waves in the surf zone.[2] The break-point model yields the length of a breaking wave crest, the spatial extent of the bubbly region created behind the breaking crest and the variation of both of these parameters with time, all of which are required for a calculation of the wave noise coherence. The model is based on the McCowan breaking criterion, which relates the still water depth to the height of the wave crest at which initial breaking occurs. The result of applying this criterion to an individual wave shoaling on a plane beach is an expression relating the beach slope, θ_w, and time after the wave initially overturned, t_b, to the distance of the wave break-point along the wave crest, s_b, and waveheight at the break-point, η_b. In this simple model, the waveheight profile along the wave crest is parameterized by a two-parameter set of exponential profiles:

$$\eta_b = K_m h_0 \exp(-|s_b/s_0|^{\gamma}), \tag{4}$$

where K_m is a constant in the range 0.7 to 1.5 depending on beach slope and wave period, h_0 is the still water depth at which the wave initially overturns, s_0 is a length scale characterizing the change of waveheight along the wave crest, and γ is a dimensionless parameter of order unity that will be called the profile index. For waves normally incident on a plane beach, the model yields

$$s_b = \pm s_0 \left\{ \ln\left(\frac{h_0}{h_0 - c t_b \tan\theta_w} \right) \right\}^{1/\gamma}, \tag{5}$$

where c is the wave speed. The $\pm$ sign in Eq. (5) arises because there are two break-points on either side of the point at which s_b equals 0. Equation (5) provides a means of calculating the length of the breaking wave crest as a function of time after initial breaking, and can also be used to calculate the spatial distribution in a horizontal plane of quiescent bubbles behind the wave.

C. A model for wave noise propagation through the surf zone

There are three main environmental factors that characterize acoustic propagation through the surf zone. These are the proximity of the sea surface, the proximity of the sea floor, and the distributions of bubbles created by the passage of breaking waves. The proximity of the sea surface and sea floor results in waveguide propagation, and scattering from the rough surface and bottom boundaries. The presence of bubbles in the water column results in strong sound absorption and scattering, and in addition lowers the speed of sound. All of these effects need to be considered in the development of a Green's function for the wave noise cross-spectrum.

The effects of sea surface and bottom roughness on propagation through shallow water have been well studied. Various propagation models are available, including parabolic equation codes and normal mode solutions.[34–37] Considered in terms of modal propagation, surface and bottom scattering cause modal coupling, mode attenuation, and add a random factor to the mode phases.

There are also theories of sound propagation through oceanic bubble plumes.[38–40] A treatment which is particularly relevant to the present problem has been presented by Sarkar and Prosperetti[38] (although we are more concerned here with forward scatter by bubble plumes than back scatter). The main effects of bubble plumes are to reduce the sound speed and increase absorption in the water column, and to scatter the acoustic field. Measurements of the acoustical properties of acoustically quiescent bubble plumes in the surf zone were made as part of the experiment that motivated the modeling work presented here.[2] Acoustical absorptions up to 10 Nepers per meter and sound speeds as low as 500 m/s were observed at mid-water depth in 1.7 m of water in the bubbly residue left by the passage of a wave overhead.

The difficulty in applying existing theories of wave scattering and absorption to propagation in the surf zone is a lack of detailed environmental information to use as inputs to the models. As commented by Rouseff and Ewart,[37] ''The difficulty in simulating shallow-water propagation lies not in the quality of acoustic modeling, but rather in the lack of knowledge about the environment.'' Our resolution to this difficulty is to establish a model which contains only the gross features of the environment, such as beach slope and spatial extent of the bubbly water behind the breaking wave crest, about which some information is available. The effects of scattering from the sea surface, sea floor, and bubbly residue behind the breaking wave crest are modeled by randomizing the phase of the acoustic modes propagating through the water column. This feature of the acoustic model is justified later by an analysis of actual measurements of wave noise propagation through the surf zone. Although this may seem tautological, the feature of the wave noise field used to justify randomizing the mode phases, which is the absence of a modal interference structure in the wave noise spectrum, is quite distinct from the computation of wave noise directionality, which is the ultimate model output.

1. The propagation model

The geometry for the propagation calculations is shown in Fig. 5. As discussed earlier, coherence calculations are done on time-scales that are long compared with bubble creation rates, but short compared with changes in the environment, such as movement of the breaking wave crest. Thus for a given coherence estimate, the breaking wave crest is assumed to be frozen in the water column. The problem is to calculate the propagation of sound radiated from bubble sources positioned at $\mathbf{r}_s$ to the hydrophones located at $\mathbf{r}_i$ and $\mathbf{r}_j$. The starting point for the propagation model is an adiabatic mode expansion of the Green's function solution of the

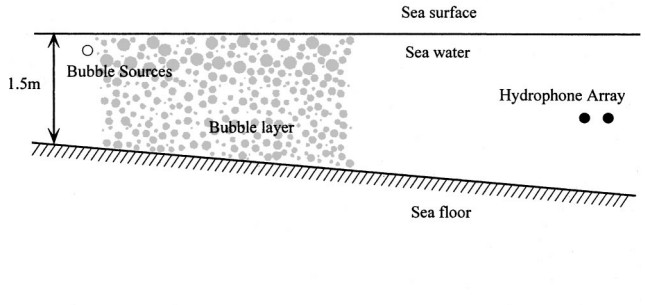

Acoustical Properties

Material	Sound Speed (m/s)	Density (Kg/m^3)	Absorption (dB/wavelength)
Sea floor	1700	1500	0.5
Seawater	1500	1000	0
Bubbly water	1000	1000	0.5

FIG. 5. A vertical slice through the propagation geometry assumed for the coherence model. The bubble layer left behind the bubble sources is assumed to extend through the entire vertical extent of the water column. Range dependence in the waveguide is included in the model, as indicated by the sloping sea floor. The acoustical properties used in the coherence calculations are tabulated below the figure.

Helmholtz equation at angular frequency ω. The expansion can be expressed as a sum of normal modes (see, for example, Zhang and Tindle[41]):

$$G(\omega,\mathbf{r}_s,\mathbf{r}_j)=i\sqrt{2\pi}\sum_{n=1}^{n_{\max}}\left(\frac{\phi_n(\omega,\mathbf{r}_s)\phi_n(\omega,\mathbf{r}_i)}{\sqrt{k_n(\omega,\mathbf{r}_i)r_i}}\times\exp\left(i\int_0^{r_i}k_n(\omega,\mathbf{l}_i)dl\right)\right), \tag{6}$$

where $i=\sqrt{-1}$ (except when used as a subscript), ϕ_n and k_n, respectively, are the amplitude and horizontal wave number of mode n, and the integral appearing in the mode sum is taken along the path that connects the sources at $\mathbf{r}_s$ to the hydrophone at $\mathbf{r}_i$. The maximum number of modes that needs to be included in the sum, $n_{\max}$, is determined by the critical angle of the sea floor α_c, the speed of sound in the water column c_w, and angular frequency ω:[42]

$$n_{\max}=\frac{\omega h}{\pi c_w}\sin\alpha_c. \tag{7}$$

Even at 20 kHz, in the shallow waters of interest here no more than 25 modes need be included in the mode sum. The vector $\mathbf{l}_i(l)=\mathbf{r}_s+\mathbf{r}_i l/r_i$ follows the straight-line propagation path between the source position $\mathbf{r}_s$ and the field evaluation point $\mathbf{r}_i$. The mode amplitude ϕ_n and horizontal wave number k_n depend on water depth, and so are functions of position in the wedge geometry. Expressions for ϕ_n and k_n and a computationally efficient method for their evaluation can be found in Zhang and Tindle.[41] Equation (6) does not account for three-dimensional propagation effects through the surf zone, so the effect of bathymetric refraction, for example, is not included in the model. Although three-dimensional propagation effects might be important for contributions to the noise field from distant breaking waves,[8] they are unlikely to be important or the short propagation paths of interest here (less than 50 m).

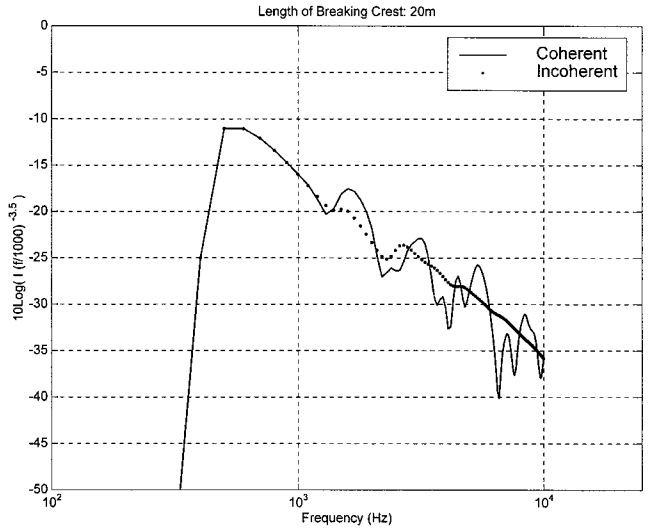

FIG. 6. Plots of the coherent and incoherent calculations of the Green's function integral that arises in Eq. (8) for the wave noise power spectrum. The breaking wave crest was given a length of 20 m, and placed 25 m on the shoreward side of a receiver. The calculated values of I have been scaled by $(f/1000)^{-3.5}$ and plotted as a function of frequency on a log–log scale to allow a comparison with the measured wave noise power spectrum plotted in Fig. 2. The coherent form of I shows a pronounced modal interference structure in the form of preferred frequency bands of propagation. The incoherent form of I does not show a strong modal interference structure.

2. Mode scattering

Equation (6) is a fully coherent expression for the sound field, and does not account for the scattering of sound at the sea surface, at the sea floor, or from bubbles in the water column. In the absence of detailed environmental measurements, the simplest way to estimate the effect of scattering on wave noise is to study noise that has actually traveled through the surf zone. We have available estimates of the power spectral density of breaking wave noise from the same experiment that provided the wave noise directionality. A theoretical expression for the power spectral density is given by Eq. (2) calculated with $\mathbf{r}_j=\mathbf{r}_i$. Making this substitution yields

$$S_{ii}=A\int_{a_0}^{a_1}\lambda(a)|Q(\omega,a)|^2da\int_L G(\omega,\mathbf{r}_s,\mathbf{r}_i)G^*(\omega,\mathbf{r}_s,\mathbf{r}_i)ds, \tag{8}$$

where s parameterizes length along the region of wave crest which is breaking, the integral on the right hand side of Eq. (7) is over the entire length of breaking crest, L, and the factor A represents the cross-sectional area of the hypothetical tube of ringing bubbles beneath the breaking wave crest discussed toward the end of Sec. II B. The integral over L in Eq. (7), which will subsequently be referred to as I, has been evaluated numerically assuming both coherent and incoherent propagation from a radiating breaking wave crest to a receiver placed 25 m behind the wave. The geometry for the calculations is described in the caption of Fig. 6, which also shows the numerical evaluation of I. Note that in the figure, the integral has been scaled by the factor $(f/1000)^{-3.5}$, where $f=\omega/(2\pi)$, to give roughly the same spectral roll-off as the wave noise measurements. This scaling is introduced for purposes of comparison only. The figure shows both co-

herent and incoherent calculations, which are described below.

The coherent form of I was established by substituting Eq. (6) for the Green's function directly into the integral in Eq. (8), which was then evaluated numerically. The product of the Green's function and its complex conjugate contains product terms of the form:

$$\int_L \frac{\phi_n(\omega,\mathbf{r}_s)\phi_n(\omega,\mathbf{r}_j)}{\sqrt{k_n(\omega,\mathbf{r}_i)r_i}} \frac{\phi_m^*(\omega,\mathbf{r}_i)\phi_m^*(\omega,\mathbf{r}_i)}{\sqrt{k_m^*(\omega,\mathbf{r}_i)r_i}} \times \exp\left(i\int_0^{r_i} k_n(\omega,\mathbf{l}_i)k_m^*(\omega,\mathbf{l}_i)dl \right) ds,$$

which add coherently to the sound field. Cross-terms for which $n \neq m$ have a phase associated with them, and they give rise to a modal interference pattern which, at a fixed range, appear as oscillations in I as a function of frequency. This interference structure can be clearly seen in the coherent calculation of I in Fig. 6 in the form of preferred frequency bands for propagation to the chosen range, at center frequencies of roughly 1.5 kHz, 3.1 kHz, 5.5 kHz, and 8.4 kHz. The length of the breaking wave crest for this calculation was 20 m. In general, the number and center frequencies of the bands will be a function of the composition and bathymetry of the sea floor, and the range between the source and receiver. The rapid roll-off of the integral below 400 Hz corresponds to the low frequency cutoff of the shallow water channel, which was about 1.5 m deep at the bubble sources.

The incoherent form of I was calculated by assuming that scattering adds a random factor to the mode phases which, when integrated along the breaking wave crest and propagation path, eliminates the cross-terms from the product of Green's functions in I. Thus the incoherent calculation retains only the $n=m$ form of the product terms. The incoherent form of I for a 20 m length of breaking wave crest is shown in Fig. 6, and does not show a modal interference structure. There are no clearly preferred frequency bands for propagation. The slight rise in level in the curve at 1.5 kHz, 2.7 kHz, and 4.5 kHz correspond to the water column successively supporting two, three, and four propagating modes.

Figure 7 shows coherent and incoherent calculations of I for a receiver placed 25 m behind 100 m of breaking wave crest. Over this longer length of breaking wave crest, the variations in phase of the mode cross-terms are sufficient for them to be averaged out of the integral over L, and the coherent calculation of I does not show significant levels of modal interference structure.

The conclusion is that sufficiently short (roughly less than 20 m) lengths of breaking crest should show preferred frequency bands of propagation to a given range, if modes are propagating coherently through the surf zone. The peak-to-trough level of the computed bands is in the neighborhood of 5 dB to 10 dB, and structure of this sort should be evident in measured wave noise spectra, particularly during the initial segments of the wave noise spectrograms when the length of breaking wave crest is short. However, the measured wave noise power spectrum plotted in Fig. 2 compares most favorably with the incoherent propagation model.

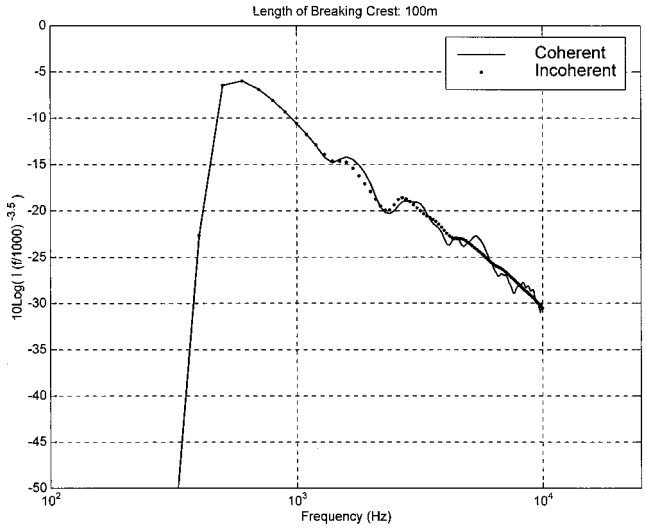

FIG. 7. Plots of the coherent and incoherent calculations of the Green's function integral as calculated in Fig. 6, but with a longer, 100 m length of breaking wave crest. The extended length of breaking crest has caused the mode cross-terms in the coherent calculation of I to average out, and the coherent and incoherent calculations yield similar values for the integral.

There is little evidence of the preferred frequency bands of propagation predicted from the coherent calculations in most of the wave noise spectrograms collected during the experiment, although some structure is occasionally apparent (not shown). Given the weight of evidence favoring the assumption of incoherent propagation, the incoherent propagation model is used for the wave noise coherence calculations below.

3. Bubble absorption

In this section we will consider the transmission of sound through the region of bubbly water that trails the breaking wave crest. Although detailed measurements of the horizontal and vertical distribution of bubbles in the water column and their evolution in time during the acoustically active phase of the wave breaking event do not exist, some information about the plumes is available. The horizontal extent of the bubbly mixture is apparent at the sea surface from the white foam left by bubbles rising to the surface through buoyancy (see the surface foam patterns in Fig. 1, for example). A simple model for these patterns has been presented in Deane,[2] and a discussion of them can be found in Sec. II B 2. Measurements of the plumes' acoustical properties shows that they can extend at least 0.8 m into the water column and are strongly absorbing. Figure 8 shows bubble plume absorption between 1 kHz and 20 kHz averaged over a 3 s interval and 32 cm path length immediately after the passage of a breaking wave 0.8 m above the measurement system in 1.7 m deep water. The values of absorption are so high that if the plumes fill the entire vertical extent of the water column, all seaward propagating energy from a few kHz up to at least 20 kHz would be absorbed. However, underwater photographs taken a few seconds after the passage of a breaking wave show the existence of a rough, but fairly well-defined boundary underneath the plumes (see, for example, Fig. 4 of Ref. 16). Thus there exists the possibility

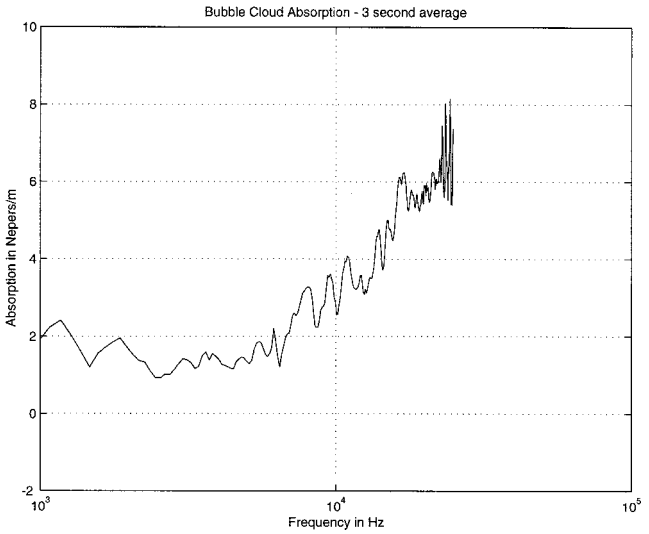

FIG. 8. Values of acoustic absorption in quiescent bubble plumes, measured 0.8 m below the water surface directly after the passage of a breaking wave overhead. The absorption values were inferred from a 3 s average of broadband acoustic transmissions over a 0.32 m path length. Above about 6 kHz, the absorption scales as f^8. The high values of absorption shown here are representative of bubble plume properties a few seconds after plume creation.

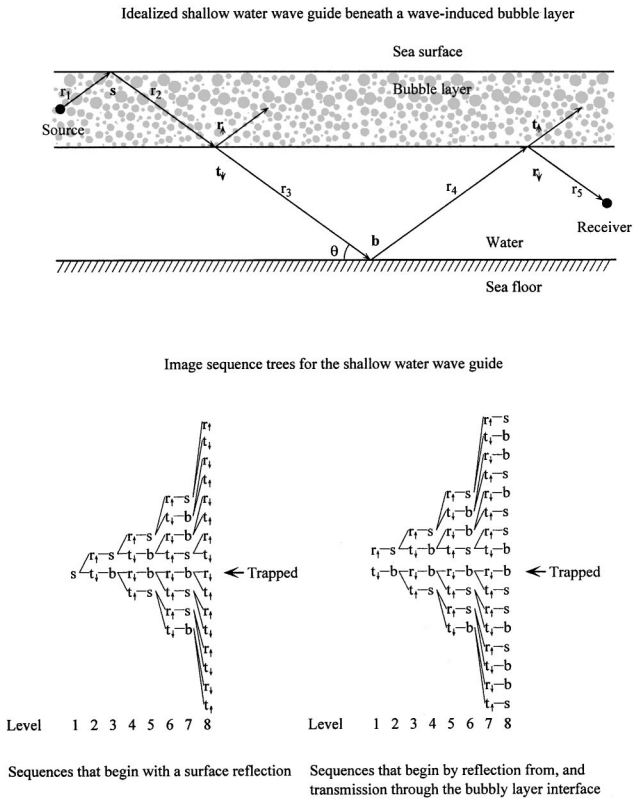

FIG. 9. The idealized, three-layer waveguide used to calculate propagation below the bubble cloud layer. Sound sources are placed 0.25 m below the sea surface in a 0.5 m thick bubble layer in a 1.7 m deep channel. The field evaluation point is 0.5 m beneath the bubble layer. The sound speeds and densities for the water column and sea floor, respectively, were 1500 m/s and 1000 kg/m^3, and 1700 m/s and 1600 kg/m^3. The sound speed and density of the bubble layer was assumed to be 1100 m/s and 1000 kg/m^3. The absorptions were 1.6 Nepers/m at 1 kHz and 3 Nepers/m at 10 kHz in the bubble layer. The sea floor absorption was assumed to be proportional to frequency and 0.057 56 Nepers/m at 1700 Hz (i.e., an absorption of 0.5 dB per wavelength).

of a waveguide between the bottom of the bubble plumes and the sea floor. The focus of this section is a study of the coupling of wave noise into, and transmission through, such a waveguide.

The waveguide, shown in Fig. 9, has been represented by a bubble-free layer of water resting between the sea floor and a homogeneous layer of bubbly water above. The propagation path of interest is between the source located near the surface on the left of the waveguide and the receiver in the bubble-free layer on the right. The source has been placed in the bubble layer to simplify the initial discussion. In reality, the bubble sources lie on the shoreward side of the bubble layer, and the effect of the source placement relative to the bubble layer on the coupling of sound into the waveguide is discussed toward the end of this section.

The waveguide geometry shown in Fig. 9 can be analyzed using the method of images, which will also allow us to draw conclusions about propagation through a more physically realistic representation of the waveguide. The method of images is based on the geometrical construction of ''image'' sources (see, for example, Brekhovskikh[42]). Each interaction of propagating wavefronts with a boundary leads to an image, and the field at the receiver point is found by summing the contributions from all image sources. The images arising from a specified configuration of boundaries can be exhaustively enumerated by systematically constructing all possible boundary interactions. The six types of boundary interaction arising from the waveguide geometry are illustrated in Fig. 9. Each boundary interaction is represented by one of the following symbols: s (surface reflection), b (bottom reflection), $t_{\downarrow}$ (transmission through the bottom boundary of the bubble layer into the water), $r_{\uparrow}$ (upward reflection from the bubble layer/water boundary), $t_{\uparrow}$ (transmission from the water into the bubble layer), and $r_{\downarrow}$ (downward reflection from the bubble layer/water boundary). In addition to specifying a type of boundary interaction, the interaction symbols will also be used to denote the angle-dependent ratio of the complex amplitudes of the energy leaving the boundary (reflected or transmitted according to the interaction) to the energy incident on the boundary. To simplify the calculations, refraction caused by differences in the sound speed in the bubbly and bubble-free layers has been neglected. This approximation is justified on the grounds that including the effects of absorption alone will provide a first-order estimate of transmission through the water waveguide and considerably simplifies the geometrical construction of the image sources. Image sources arising from a specified series of interactions can be represented by a corresponding sequence of interaction symbols, forming an ''image sequence.'' For example, the energy traveling along the path indicated by r_1 through r_5 in Fig. 9 corresponds to the image sequence $st_{\downarrow}br_{\downarrow}$.

The general expression for the magnitude the arrival from a unity magnitude image source at a receiver point is

$$P=\frac{\Pi K_j}{\Sigma(r_b+r_w)}\exp\left(ip_b\sum r_b\right)\exp\left(ip_w\sum r_w\right), \qquad (9)$$

where ΠK_j is the product of boundary interaction terms in

the image sequence, p_b and p_w, respectively, are the complex wave numbers for propagation in the bubble and water layers, and r_b and r_w, respectively, are the ray path segment lengths in the bubble and water layers. The product of interaction symbols accounts for change in amplitude and phase at each boundary interaction, the sum of ray path segments in the denominator accounts for geometrical spreading, and the exponential factors account for absorption and changes in wavefront phase due to propagation through the bubble and water layers. This expression is an approximation because it neglects wavefront curvature at the boundary interactions, but is sufficiently accurate for a first-order estimate of transmission through the water waveguide. For example, the amplitude of the arrival for the sequence $st_{\downarrow}br_{\downarrow}$ is approximated by

$$P=\frac{s(\theta)t_{\downarrow}(\theta)b(\theta)r_{\downarrow}(\theta)}{r_1+r_2+r_3+r_4+r_5}\exp(ip_b(r_1+r_2))\times\exp(ip_w(r_3+r_4+r_5)), \quad (10)$$

where θ is the grazing angle of the ray path (assumed to be constant in the two layers), and r_1 through r_5 are the lengths of the path segments indicated in Fig. 9.

Images can be classified according to the number of interactions in their sequence, which will be called their length. The image sequence trees in Fig. 9 can be used to generate all image sequences with length less than or equal to 8. There are two sequence frees in the diagram, corresponding to images that begin with a surface reflection and images that begin with an interaction with the bubble layer/water boundary. The image sequences of a given length are generated by traversing the sequence trees from left to right along all possible paths, accumulating interactions and stopping when a sequence of the desired length is obtained. Because the number of boundary interactions increases with increasing sequence length, long image sequences have long ray paths with steep grazing angles.

Any sequence containing either the $r_{\uparrow}$ or $t_{\uparrow}$ interactions implies a wavefront passing into the bubble layer and therefore a ray path that must traverse the full width of the bubble layer twice before re-emerging into the waveguide. The bubble layer is highly absorbing and propagating waves have a wave number with a large imaginary component. Thus the exponential factor $\exp(ip_b\Sigma r_b)$ in the expression for the amplitude of such images is small and they can be neglected from a sum of image contributions. Prohibiting traverses along the sequence tree that contain the $r_{\uparrow}$ and $t_{\uparrow}$ interactions leaves only two paths with the potential to transmit significant levels of sound energy, both of which correspond to energy trapped between the sea floor and the bottom boundary of the bubble layer. The sequences for these images are labeled ''Trapped'' in Fig. 9.

The amplitude of the trapped sequences can be factored into coupling, reverberation, and geometrical losses. The coupling term accounts for the losses associated with propagation from the source into the water layer, and is the product of transmission loss through the bubble layer boundary with absorption by the layer: $K\exp(ip_br_b)$ where K is either one of the image sequences $st_{\downarrow}$ or $t_{\downarrow}$. The length of the propagation path through the bubble layer, r_b, is shortest for large grazing angles, and thus high-angle wavefronts couple most effectively into the water layer. The reverberation losses are the product of reflection terms from the sea floor and the lower boundary of the bubble layer, and has the form $b^n r_{\downarrow}^m$, where n is the number of bottom reflections and m is the number of reflections from the bubble layer. The geometrical losses are just the reciprocal of the ray path length between the image source and the receiver, and account for geometrical spreading of the wavefronts.

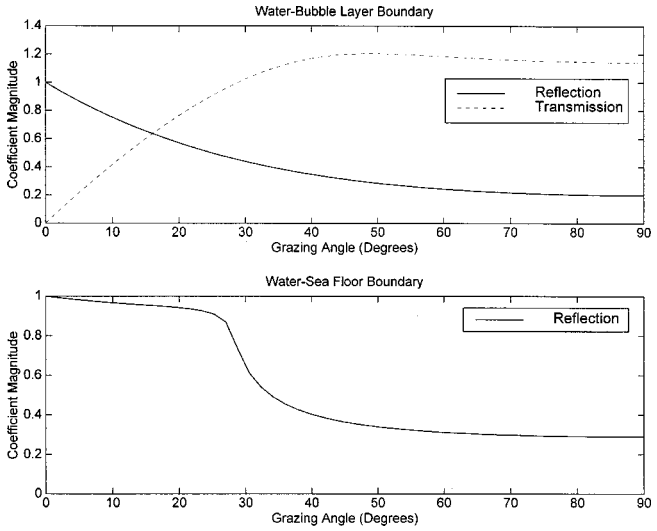

FIG. 10. The top plot shows the plane wave reflection coefficients plotted as a function of incident grazing angle for transmission through the lower bubble layer boundary into the water layer ($\mathbf{t}_{\downarrow}$), and reflection from the lower bubble layer boundary of energy incident from the water column ($\mathbf{r}_{\downarrow}$). The bottom plot shows the plane wave reflection coefficient for the sea floor ($\mathbf{b}$). The critical grazing angle for the sea floor is 28°.

Figure 10 shows estimates of $r_{\downarrow}$ and $t_{\downarrow}$, respectively, labeled ''Reflection'' and ''Transmission'' in the top plot and the reflection coefficient for the sea floor in the bottom plot. Expressions for the plane wave reflection and transmission coefficients for layered media can be found in Brekhovskikh.[42] The acoustical properties chosen as being typical of the layers are listed in the caption of Fig. 9. The reflection and transmission coefficients have been calculated assuming plane wave energy incident on a planar boundary. This is a reasonable approximation for the sea floor, which was composed of a relatively smooth layer of sand. Photographs of the water/bubble layer interface show that it is not planar. Significant scattering can be expected from this boundary, and the curves plotted in Fig. 10 provide an upper estimate for the reflection and transmission coefficients. That is, losses from interaction with this boundary will be greater than indicated in the plots. Energy propagating at grazing angles greater than 28°, which is the critical grazing angle for the sea floor, is rapidly attenuated by bottom interactions. The water–bubble layer boundary does not have a critical angle for energy incident from the water side and reflection losses are significant for grazing angles less than the critical angle of the sea floor.

Table I shows estimates of the arrival amplitudes for a source placed 0.25 m below the sea surface in a 0.5 m thick bubble layer over a 1 m thick layer of water, calculated using

TABLE I. Calculated image amplitude logarithms for a source in a 0.5 m thick surface bubble layer and receiver in a 1.2 m deep bubble-free layer of sea water beneath. The source and receiver depths, respectively, were 0.25 m and 1 m, and were spaced 1 cm apart. The source frequency was set to 1000 Hz, and the bubble cloud absorption was taken to be 1.6 Nepers per m. ''Bottom reflections'' and ''Bubble layer reflections,'' respectively, correspond to the number of sea floor and bubble layer reflections for the source image. ''Source image angle'' is the grazing angle of the ray path between the source image and receiver, in degrees. ''Reverberation,'' ''Coupling,'' and ''Spreading,'' respectively, correspond to the logarithm of the energy loss due to boundary interactions, propagation through the bubble layer and geometrical spreading. The ''Total'' column is the sum of the three loss mechanisms.

Bottom reflections	Bubble layer reflections	Source image angle	Reverberation loss	Coupling loss	Spreading loss	Total loss
0	0	2.9	0.0	−4.5	−1.2	−5.7
1	0	8.2	0.0	−1.0	−1.2	−2.2
1	1	11.9	−0.1	−0.6	−1.2	−1.9
2	1	16.9	−0.2	−0.4	−1.2	−1.8
2	2	20.3	−0.4	−0.3	−1.2	−1.9
3	2	24.9	−0.5	−0.2	−1.2	−1.9
3	3	27.9	−1.0	−0.2	−1.2	−2.4
4	3	31.9	−1.8	−0.2	−1.2	−3.2
4	4	34.6	−2.4	−0.2	−1.3	−3.9

Eq. (9). Note that values in all the ''loss'' columns are the logarithms of the computed losses. Only arrivals that start with a $t_{\downarrow}$ are shown; the arrivals beginning with a surface reflection are very similar, and not required for the present argument. The receiver point for the arrivals was 0.5 m below the bubble layer. The sound speed and density of the sea floor were, respectively, set to 1700 m/s and 1600 kg/m^3, which are typical values for a medium-grained sand. The sound speed in the bubble layer was set to 1100 m/s, which was the average value observed during the same averaging interval used for the bubble plume absorption plot shown in Fig. 8. The absorption in the bubble layer was set to the lower limit of absorption observed during transmission measurements through bubble plumes, which was 1.6 Nepers/m. The frequency, source depth, bubble layer thickness, and receiver range were all chosen to minimize the effects of transmission and boundary interaction losses for energy coupled into and trapped in the water layer and thus provide a conservative estimate of losses, while maintaining values that are representative of the known factors in the environment.

There are two competing factors which determine the amplitude of arrivals from the trapped sequences. The first is the coupling of the wavefronts from the image source into the water waveguide, as described above and tabulated in the ''Coupling loss'' column of Table I. Because the exponential decay associated with propagation through the bubble layer decreases with increasing grazing angle, and transmission through the lower boundary of the bubble layer increases with increasing grazing angle, the coupling loss decreases as the number of boundary interactions (and therefore grazing angle) increases. The reverberation losses, however, increase as the number of boundary interactions, and therefore grazing angle, increases. The net effect is an optimal angle of transmission into the waveguide, which occurs at a grazing angle of about 17° in Table I. Table II shows the results of a similar computation, but at a frequency of 10 kHz and with the absorption in the bubble layer set to 3 Nepers/m. Both increased coupling and reverberation losses combine to give weaker arrivals than the 1 kHz calculations. For comparison, arrival amplitudes in a waveguide without a bubble layer are shown in Table III. The source image angles differ from the previous two cases because energy reverberates between the sea floor and the sea surface rather than the bottom of the bubble layer, resulting in longer ray path lengths for a given sequence of boundary interactions. Coupling losses are zero in this case, and reverberation losses are small until the ray path grazing angle exceeds the critical angle for the sea floor. The result is a total loss that is very similar to the geometri-

TABLE II. Calculated image amplitude logarithms for a source and receiver in the same waveguide geometry described in the caption of Table I. In this case, the source frequency has been increased to 10 kHz, and the absorption in the bubble layer set to 3 Nepers per m.

Bottom reflections	Bubble layer reflections	Source image angle	Reverberation loss	Coupling loss	Spreading loss	Total loss
0	0	2.9	0.0	−4.0	−1.2	−5.2
1	0	8.2	−0.0	−1.1	−1.2	−2.3
1	1	11.9	−0.5	−0.8	−1.2	−2.5
2	1	16.9	−0.7	−0.6	−1.2	−2.5
2	2	20.3	−1.7	−0.5	−1.2	−3.4
3	2	24.9	−2.1	−0.4	−1.2	−3.7
3	3	27.9	−3.5	−0.4	−1.2	−5.1
4	3	31.9	−4.5	−0.3	−1.2	−6.0
4	4	34.6	−6.2	−0.3	−1.3	−7.8

TABLE III. Calculated image amplitude logarithms for a source and receiver in the same waveguide geometry described in the caption of Table I, but with the upper bubble layer removed. There is no coupling loss in this case.

Bottom reflections	Bubble layer reflections	Source image angle	Reverberation loss	Coupling loss	Spreading loss	Total loss
0	0	2.9	0	0	−1.2	−1.2
1	0	8.2	−0.0	0	−1.2	−1.2
1	1	15.5	−0.0	0	−1.2	−1.2
2	1	20.3	−0.1	0	−1.2	−1.3
2	2	26.7	−0.1	0	−1.2	−1.3
3	2	30.8	−0.7	0	−1.2	−1.9
3	3	36.1	−1.0	0	−1.3	−2.3

cal spreading loss over the short propagation path considered. The incoherent sum of the tabulated arrivals for the 1 kHz and 10 kHz bubble layer cases, respectively, are a factor of 4.6 and 24 less than the sum of arrivals without a layer (including the surface reflected images would approximately double the sums in all three cases, yielding the same ratios). These factors increase with increasing range from the sources.

The conclusion is that a conservative calculation of transmission losses from sources near the sea surface in the presence of a surface bubbly layer shows moderate (at 1 kHz) to significant (at 10 kHz) attenuation compared with the layer-free case. These calculations are only indicative of the expected absorption. The coupling loss calculation, for example, depends on the details of the spatial distribution of bubbles around the breaking wave crest, which are not known. If the quiescent bubbles do not extend to the assumed depth of 0.5 m near the wave crest, and they may not as the acoustically active bubbles are formed on the shoreward side of the quiescent bubble plumes, then the high grazing angle coupling loss will be less than the calculated values. On the other hand, the actual reflection losses from the lower boundary of the bubble layer are almost certainly significantly higher than the estimated values because of rough boundary scattering and the presence of sound speed and absorption gradients at the outer edges of the layer which would improve propagation into the layer.

Rather than build the complexities of a three layer model into a calculation of wave noise coherence, we have made the simplifying assumption that the bubble layer fills the water column, which eliminates the possibility of sound transmission through a bubble-free water layer near the sea floor. This step is justified to some extent by the calculations described above, which show that sound radiated by sources at the leading edge of the bubble layer and near the sea surface does not couple effectively into, or propagate well through, such a layer. In addition, the absorption assumed for the bubble layer is set to 0.5 dB per wavelength, corresponding to 0.038 Nepers/m at 1 kHz and 0.38 Nepers/m at 10 kHz. These values are more than a factor of 10 less than the absorption observed at 0.8 m depth after the passage of a breaking wave, but may well be representative of absorption close to the sea floor at the seaward end of the bubble layer after turbulence and bubble advection has distributed the bubbles throughout the water column.

D. A model for wave noise coherence

The collected results from Secs. II B and II C form the basis of a model for cross-spectrum of the noise from a single shoaling wave in the surf zone. Substituting Eq. (6) for the waveguide Green's function into Eq. (2) for the cross-spectrum yields

$$S_{ij} = \int_{a_0}^{a_1} \lambda(a)|Q(a)|^2 da A \times \int_L \sum_{n=1}^{n_{\max}} \frac{\phi_n(\mathbf{r}_s)\phi_n(\mathbf{r}_i)\phi_n^*(\mathbf{r}_s)\phi_n^*(\mathbf{r}_i)}{\sqrt{k_n(\mathbf{r}_i)k_n^*(\mathbf{r}_j)r_i r_j}} \times \exp\left(i\int_0^{r_i} k_n(\mathbf{l}_i)dl - i\int_0^{r_j} k_n^*(\mathbf{l}_j)dl \right) ds, \quad (11)$$

where the explicit dependence of variables on angular frequency ω has been dropped. For reasons explained in Sec. II C 2, cross-mode terms have been eliminated from the Green's function product. The absorption due to the bubbly layer behind the breaking wave crest and the effects of variable bottom bathymetry enter Eq. (11) through calculation of the mode horizontal wave numbers k_n. The line integrals of horizontal wave number are evaluated by dividing the propagation paths into regions inside and outside the bubbly region and computing separate integrals along each path. Values for the mode amplitude and horizontal wave number are calculated using the iterative technique described in Zhang and Tindle[41] using values of sound speed and absorption appropriate for the bubbly mixture or seawater, depending on whether the calculation is for wave numbers inside or outside the bubbly region.

Equation (11) can be further simplified by considering the special geometry of interest here. We are concerned with the wave noise coherence between nearby points, sufficiently close that the propagation paths from a source to the points are almost parallel, and the water depth at the points is almost constant. In this case, a far-field approximation can be made to eliminate one of the line integrals in Eq. (11):

$$\int_0^{r_j} k_n(\mathbf{l}_j)dl \approx \int_0^{r_j} k_n(\mathbf{l}_i)dl + (r_j - r_i)k_n(\mathbf{r}_i). \quad (12)$$

Also, since the water depth is almost the same at the two points, $\phi_n(\mathbf{r}_j) \approx \phi_n(\mathbf{r}_i)$ and $k_n(\mathbf{r}_j) \approx k_n(\mathbf{r}_i)$. With these approximations, Eq. (11) can be rewritten as

$$S_{ij}=\int_{a_0}^{a_1}\lambda|Q(a)|^2 da A\sum_{n=1}^{n_{\max}}\int_L \frac{|\phi_n(\mathbf{r}_i)\phi_n(\mathbf{r}_j)|^2}{|k_n(\mathbf{r}_i)|\sqrt{r_i r_j}} \times\exp\left(-2\int_0^{r_i}\Im(k_n(\mathbf{l}_i))dl - i(r_j-r_i)k_n^*(\mathbf{r}_i)\right)ds, \tag{13}$$

where $\Im$ denotes taking the imaginary part of a complex variable. Equation (13) is the final expression for the cross-spectral density. This is not a new result, and can be compared directly with Eq. (30) of Kuperman and Ingenito,[3] and also with Eq. (A5) from Harrison.[7] Substitution of Eq. (13) into Eq. (3) yields an expression for the wave noise coherence:

$$\Gamma(\omega,\mathbf{r}_i,\mathbf{r}_i)=\frac{\sum_{n=1}^{n_{\max}}\int_L \frac{|\phi_n(\omega,\mathbf{r}_s)\phi_n(\omega,\mathbf{r}_j)|^2}{|k_n(\omega,\mathbf{r}_i)|\sqrt{r_i r_j}}\exp(-2\int_0^{r_i}\Im(k_n(\omega,\mathbf{l}_i))dl - i(r_j-r_i)k_n^*(\omega,\mathbf{r}_i))ds}{\sum_{n=1}^{n_{\max}}\int_L \frac{|\phi_n(\omega,\mathbf{r}_s)\phi_b(\omega,\mathbf{r}_i)|^2}{|k_n(\omega,\mathbf{r}_i)\sqrt{r_i r_j}}ds}. \tag{14}$$

III. COMPARISON WITH EXPERIMENT

Equation (14) can be compared with measurements of the wave noise coherence in the following way. The trajectory of an acoustic hot-spot through the surf zone for a given breaking event is determined from measurements of the wave noise directionality versus time, allowing estimates of the waveheight profile parameters to be made. The length of breaking wave crest and spatial distribution of bubbles behind the wave are then modeled from the time of initial overturning until the end of the acoustically active phase of the breaking event. This provides sufficient information to evaluate Eq. (14) for the wave noise coherence as a function of frequency and time. For purposes of comparison with the data set, the calculated noise coherence is transformed into a normalized horizontal directional density function using the Fourier series expression in Deane.[2] In addition to providing an easy comparison with the measured noise directionality, this procedure includes a model of the two-element hydrophone array performance.

A. Estimation of the waveheight profile parameters

The trajectory of a hot-spot through the surf zone can be determined as follows. During the few seconds between the passage of a breaking wave over the measurement system and the end of its acoustically active phase, the wave moved less than 40 m or so shoreward, and to first order the wave speed can be assumed constant and given by the shallow water approximation $c=\sqrt{gh_0}$, where g is the acceleration due to gravity and h_0 is a representative water depth. Taking $h_0\approx 2$ m yields a wave speed of $c\approx 4.5$ m/s. The point of initial overturning relative to the array is estimated from

$$x_0=-c\Delta t, \tag{15}$$

$$y_0=\pm x_0\cot\theta_0, \tag{16}$$

where Δt is the time between the passage of the wave over the array and its initial overturning, estimated from the onset of breaking wave noise, and θ_0 is the initial angle formed between the array and the hot-spot, estimated from the plot of wave noise directionality versus time. The ambiguity in sign associated with the calculation of y_0 arises from an along-shore ambiguity in the arrival angle estimated from the two-element hydrophone array. The subsequent trajectory of the hot-spot is determined by propagating the wave forward at a constant speed and estimating the along-shore position from the noise directionality.

Figure 11 summarizes the result of this analysis applied to the event shown in Fig. 2. The broken line on the left hand side of the plot represents the measured trajectory of the hot-spot. The right hand side of the plot is simply a reflection of the measured trajectory in the vertical axis. The trajectory of the wave break-point computed from the Eq. (5) and the profile parameters $\gamma=2.5$, $h_0=1.7$ m, and $s_0=94$ m is plotted as a broken line in Fig. 11.

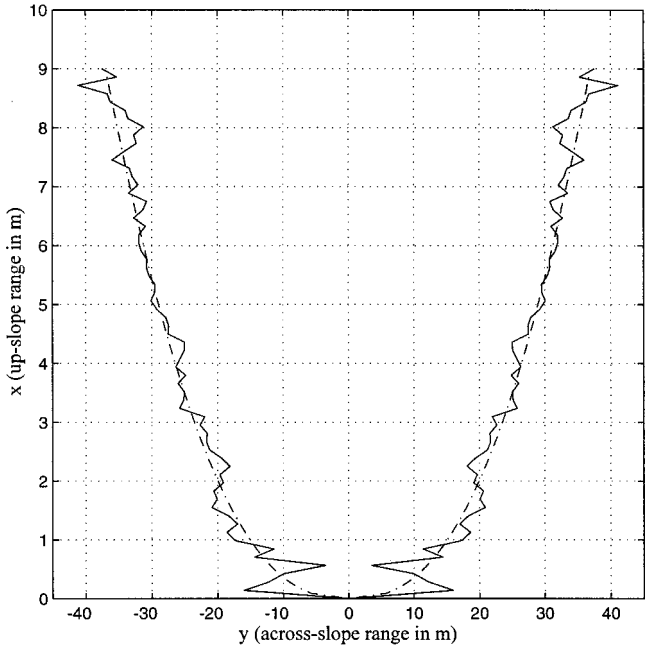

FIG. 11. The hot-spot trajectory for the breaking event shown in Fig. 2. The solid line is the measured trajectory, estimated from the variation with time of the peak in the wave noise directionality. The broken line was calculated with the break-point model described in Sec. II B 2 using the profile parameters $\gamma=2.5$, $h_0=1.7$ m, and $s_0=94$ m. The curves for positive values of across-slope range are a mirror image of the left hand curves, and do not represent actual data.

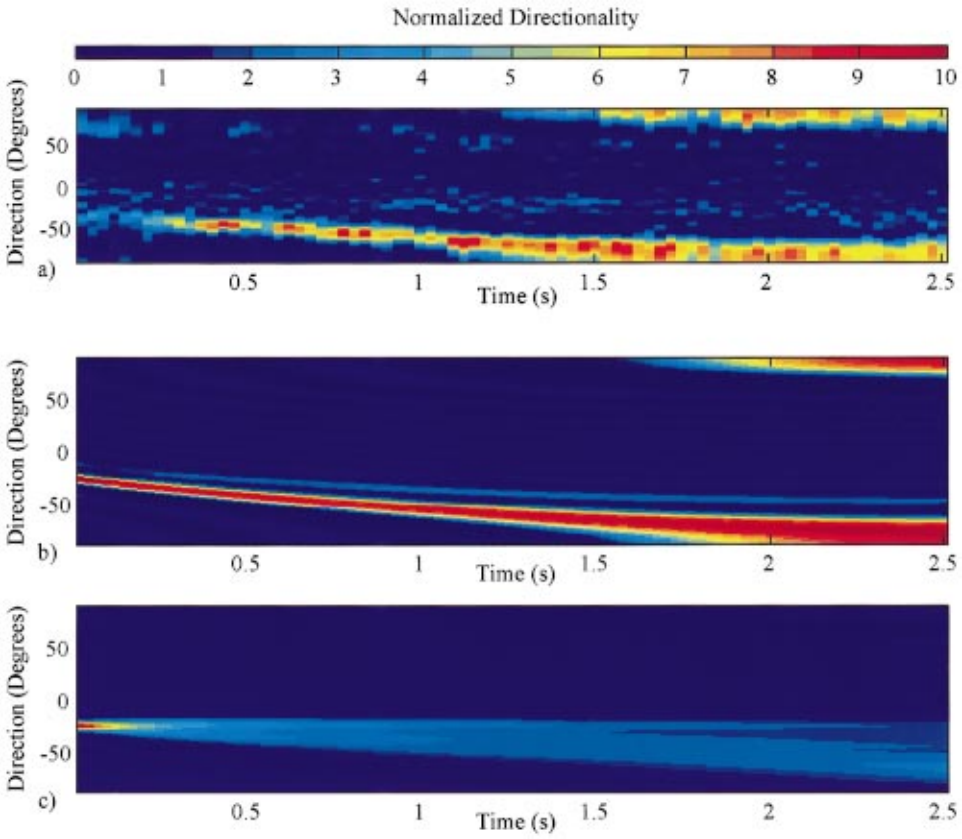

FIG. 12. Color contour plots of (a) the wave noise directionality from the event shown in Fig. 2; (b) the modeled wave noise directionality, including the effects of the absorbing residue of bubbles behind the wave; and (c) the wave noise directionality calculated without a bubbly residue.

B. Calculation of the wave noise directionality

The waveheight profile parameters determined in the previous section are sufficient to allow a calculation of Eq. (14) for the wave noise coherence as a function of time, and hence the wave noise directionality. The waveheight profile parameters were chosen as described in the section above, and the mean depth of the tube of ringing bubbles and receiver depths were, respectively, taken to be $z_s = 0.1$ m and $z_r = 0.8$ m. Figure 12 shows the results of such a calculation. Figure 12(a) is the measured noise directionality, determined from the wave noise coherence measurements. Figure 12(b) shows the model result calculated using the waveheight profile parameters chosen to fit the observed hot-spot trajectory. Figure 12(c) shows the noise directionality calculated by setting the acoustical properties of the bubbly region to those of the surrounding water, thus eliminating the bubbly residue.

The effect of the bubbles on the wave noise directionality is demonstrated by the differences between the calculations with and without a screening bubbly residue. The calculation with the bubble screen shows that only a localized region of braking wave crest is audible at the receiver array. The bubble-free noise directionality calculation does not show the formation of an acoustic hot-spot, and is quite different from the observed directionality. In the bubble-free case, the directionality shows a much broader spread of arrival angles. Since the energy is spread over a wider band of angles, the directional density function also has a lower value than the bubble layer calculation.

Note that the simulation accounts for the limited angular resolution of the two-element hydrophone array. The differences in simulated directionality between Fig. 12(b) and (c) demonstrate that the angular resolution is sufficient to distinguish between radiation from a localized region of breaking crest and radiation from the entire length of breaking crest. The simulation also includes the effects of changing bathymetry and range between different source locations along the wave crest and the hydrophone array. Because of the poor agreement between the simulation without bubbles (which includes these effects) and the measured directionality, we can conclude that propagation effects through bubble-free water do not account for the formation of hot-spots.

The detailed agreement between the measured and modeled hot-spot trajectories was built into the simulations by a judicious choice of the waveheight profile parameters. These parameters were chosen to fit the measured trajectory, and the agreement between the trajectories is not substantiating evidence for the wave break-point or wave noise coherence models. The substantiating evidence comes from the fact that hot-spots are only formed when bubbles are included in the simulations, ruling out effects arising from range-dependent propagation and the limited angular resolution of the array.

IV. CONCLUDING REMARKS

The main result of this study is the calculation of the time-varying directionality of noise radiated by individual breaking waves in the surf zone. Motivated by the observation of acoustic hot-spots in the surf zone, the model is able to account the interaction between sound radiated by the breaking wave crest and the residue of bubbly water left behind the breaking wave. The underlying premise of the wave noise coherence model is that the quiescent bubbles left in the water column behind the wave act to screen the

sound radiated by the breaking wave crest, with the exception of the wave break-points at the ends of the breaking crest. The relatively bubble-free water surrounding the break-points allows the sound they radiate to propagate to deeper water behind the wave. The net result is the formation of acoustic hot-spots, which move through the surf zone on trajectories determined by the along-shore waveheight profile and bottom bathymetry. The comparison between the modeled and measured directionality discussed in Sec. III provides some supporting evidence for the model.

The model developed here assumes that the noise radiated by the breaking wave crest is constant along the entire length of the crest, which may be an oversimplification. It is possible that wave break-points, which are undergoing initial overturning, are more acoustically energetic than the inner region of crest which has already broken. Without the bubble screen, however, hot-spots caused by preferential radiation from the wave break-points would always be observed in pairs, one for each break-point. The bubble-free simulation in Fig. 12(c) shows that the wave noise directional density measurements had sufficient spatial resolution to distinguish between break-points at the along-shore ends of the breaking wave crest had they both been audible at the sensor frame. However, only a single hot-spot is apparent in the measured wave noise directionality, suggesting that noise from the screened break-point, more acoustically energetic or not, is absorbed before reaching the array.

ACKNOWLEDGMENTS

I am indebted to three anonymous reviewers who suggested significant improvements to the original manuscript. This work would not have been possible without the support of the other scientists who participated in the Adaptive Beach Monitoring Program, and the assistance of the military and civilian personnel at the Camp Pendleton Marine Base. I am also pleased to acknowledge the support of the U.S. Office of Naval Research, who supported this work through Grants Nos. N00014-96-1-0120 and N00014-96-1-0852.

[1] G. L. D'Spain *et al.*, ''Environmental observations during the 1995 Adaptive Beach Monitoring Experiment,'' Marine Physical Laboratory, Scripps Institution of Oceanography, UCSD, TM-446, 1996.
[2] G. B. Deane, ''Acoustic hot-spots and breaking wave noise in the surf zone,'' J. Acoust. Soc. Am. **105**, 3151–3167 (1999).
[3] W. A. Kuperman and F. Ingenito, ''Spatial correlation of surface generated noise in a stratified ocean,'' J. Acoust. Soc. Am. **67**, 1988–1996 (1980).
[4] M. J. Buckingham, ''A theoretical model of ambient noise in a low-loss, shallow water channel,'' J. Acoust. Soc. Am. **67**, 1186–1192 (1980).
[5] M. J. Buckingham, ''Spatial coherence of wind-generated noise in a shallow ocean channel,'' J. Acoust. Soc. Am. **70**, 1412–1420 (1981).
[6] M. J. Buckingham, ''A theoretical model of surface-generated noise in a wedge-shaped ocean with pressure-release boundaries,'' J. Acoust. Soc. Am. **78**, 143–148 (1985).
[7] C. H. Harrison, ''Formulas for ambient noise level and coherence,'' J. Acoust. Soc. Am. **99**, 2055–2066 (1996).
[8] C. H. Harrison, ''Noise directionality for surface sources in range-dependent environments,'' J. Acoust. Soc. Am. **102**, 2655–2661 (1997).
[9] C. H. Harrison, ''Noise directionality in the surf zone: A model,'' in *Natural Physical Processes Associated with Sea Surface Sound* (CBC Print and Media resources, Fordingbridge, Hampshire, U.K., Southampton, 1997), pp. 101–110.
[10] R. M. Hamson, ''Vertical array response to shipping noise: Model/measurement comparisons for range-dependent Mediterranean sites,'' J. Acoust. Soc. Am. **94**, 386–395 (1993).
[11] R. M. Hamson, ''The theoretical responses of vertical and horizontal line arrays to wind-induced noise,'' J. Acoust. Soc. Am. **78**, 1702–1712 (1985).
[12] A. M. Karnovskii, ''Spatial correlation function of the noise field of sources near the edge of a wedge,'' Sov. Phys. Acoust. **27**, 132–135 (1981).
[13] A. M. Karnovskii, ''Noise field of sources localized near the bounding surfaces of a wedge,'' Sov. Phys. Acoust. **28**, 465–468 (1982).
[14] A. M. Karnovskii, ''Structure of the noise field in a wedge,'' Sov. Phys. Acoust. **29**, 337–338 (1983).
[15] H. Cox, ''Spatial correlation in arbitrary noise fields with application to ambient sea noise,'' J. Acoust. Soc. Am. **54**, 1289–1301 (1973).
[16] G. B. Deane, ''Sound generation and air entrainment by breaking waves in the surf zone,'' J. Acoust. Soc. Am. **102**, 2671–2689 (1997).
[17] S. J. Bass and A. E. Hay, ''Ambient noise in the natural surf zone: Wave-breaking frequencies,'' IEEE J. Ocean Eng. **22**, 411–424 (1997).
[18] H. Medwin and M. M. Beaky, ''Bubble sources of the Knudsen sea noise spectra,'' J. Acoust. Soc. Am. **86**, 1124–1130 (1989).
[19] H. Medwin and A. C. Daniel, Jr., ''Acoustical measurements of bubble production by spilling breakers,'' J. Acoust. Soc. Am. **88**, 408–412 (1990).
[20] M. L. Banner and D. H. Cato, ''Physical Mechanisms of Noise Generation by Breaking Waves—A Laboratory Study,'' in *Sea Surface Sound*, Series C: Mathematical and Physical Sciences (Kluwer Academic, Dordrecht, 1988), pp. 429–436.
[21] W. K. Melville, M. R. Loewen, and E. Lamarre, ''Bubbles, noise and breaking waves: A review of laboratory experiments,'' in *Sea Surface Sound* (Kluwer Academic, Dordrecht, 1993), pp. 483–501.
[22] M. R. Loewen and W. K. Melville, ''A model of the sound generated by breaking waves,'' J. Acoust. Soc. Am. **90**, 2075–2080 (1991).
[23] A. Prosperetti, ''Bubble-related ambient noise in the ocean,'' J. Acoust. Soc. Am. **84**, 1042–1054 (1988).
[24] A. P. Dowling and J. E. Ffowcs Williams, *Sound and Sources of Sound* (Ellis Horwood, Chichester, 1983), p. 321.
[25] W. M. Carey and D. Browning, ''Low frequency ocean ambient noise: measurement and theory,'' in *Natural Mechanisms of Surface Generated Noise in the Ocean* (Kluwer Academic, Dordrecht, 1988), pp. 361–376.
[26] E. Lamarre and W. K. Melville, ''Void fraction measurements and sound-speed fields in bubble plumes generated by breaking waves,'' J. Acoust. Soc. Am. **95**, 1317–1328 (1994).
[27] D. H. Peregrine, ''Breaking waves on beaches,'' Annu. Rev. Fluid Mech. **15**, 149–178 (1983).
[28] P. Bonmarin, ''Geometric properties of deep-water breaking waves,'' J. Fluid Mech. **209**, 405–433 (1989).
[29] G. B. Deane and M. D. Stokes, ''Air entrainment processes and bubble size distributions in the surf zone,'' J. Phys. Oceanogr. **29**, 1393–1403.
[30] R. D. Hollett and R. M. Heitmeyer, ''Noise generation by bubbles formed in breaking waves,'' in *Sea Surface Sound*, Series C: Mathematical and Physical Sciences (Kluwer Academic, Dordrecht, 1988), pp. 449–462.
[31] S. Finette and R. M. Heitmeyer, ''Angle-time-frequency resolution of the noise field generated by wind-induced breaking waves,'' J. Acoust. Soc. Am. **99**, 209–221 (1996).
[32] L. d'Agostino and C. E. Brennen, ''Acoustical absorption and scattering cross sections of spherical bubble clouds,'' J. Acoust. Soc. Am. **84**, 2126–2134 (1988).
[33] B. F. Cron and C. H. Sherman, ''Spatial correlation functions for various noise models,'' J. Acoust. Soc. Am. **38**, 885 (1965).
[34] G. V. Norton and J. C. Novarini, ''The effect of sea-surface roughness on shallow water waveguide propagation: A coherent approach,'' J. Acoust. Soc. Am. **99**, 2013–2021 (1996).
[35] M. J. Beran and S. Frankenthal, ''Combined volume and surface scattering in a channel using a modal formulation,'' J. Acoust. Soc. Am. **100**, 1463–1472 (1996).
[36] D. D. Ellis, ''A shallow-water normal-mode reverberation model,'' J. Acoust. Soc. Am. **97**, 2804–2814 (1995).
[37] D. R. Rouseff and T. E. Ewart, ''Effect of random sea surface and bottom roughness on propagation in shallow water,'' J. Acoust. Soc. Am. **98**, 3397–3404 (1995).
[38] K. Sarkar and A. Properetti, ''Coherent and incoherent scattering by oceanic bubbles,'' J. Acoust. Soc. Am. **96**, 332–341 (1994).
[39] K. Sarkar and A. Prosperetti, ''Backscattering of underwater noise by

bubble clouds,'' J. Acoust. Soc. Am. **93**, 3128–3138 (1993).
[40] A. Prosperetti, N. Q. Lu, and H. S. Kim, ''Active and passive acoustic behavior of bubble clouds at the ocean's surface,'' J. Acoust. Soc. Am. **93**, 3117–3127 (1993).
[41] Z. Y. Zhang and C. T. Tindle, ''Complex effective depth of the ocean bottom,'' J. Acoust. Soc. Am. **93**, 205–213 (1993).
[42] L. M. Brekhovskikh and Y. Lysanov, *Fundamentals of Ocean Acoustics* (Springer-Verlag, Berlin, 1982).

Multifrequency acoustical volume backscattering patterns in the Arabian Sea—265 kHz to 3 MHz

Duncan E. McGehee, Charles F. Greenlaw, and D. V. Holliday
Tracor Aerospace, 4669 Murphy Canyon Road, San Diego, California 92123

Richard. E. Pieper
University of Southern California/Southern California Marine Institute, 820 South Seaside Avenue, Terminal Island, California 90731

(Received 5 October 1998; revised 6 May; accepted 21 September 1999)

High-frequency acoustical volume backscattering was examined during three periods of the annual cycle of winds in the Arabian Sea—the Winter Northeast (NE) Monsoon, the Summer Southwest (SW) Monsoon, and the Fall Intermonsoon—using a multifrequency acoustic profiling system deployed on an undulating towed body. This system measured acoustical volume backscattering strengths at six frequencies ranging from 265 kHz to 3.0 MHz. Measurements were made from near the surface to 250 m depth along a ship track that paralleled the coast of Oman, then proceeded away from the coast towards the middle of the Arabian Sea. At all frequencies, volume backscattering strength was highest near the surface, decreasing with increasing depth. Contrary to expectation, backscattering was generally lower during the Summer SW Monsoon than during the Winter NE Monsoon. Also contrary to expectation, backscattering was not appreciably higher near the coast than it was offshore during the Summer SW Monsoon, although it was higher near the coast during the Winter NE Monsoon. Generally speaking, regional and seasonal differences were smaller than expected, and much smaller than the fine-scale spatial and temporal variability, particularly at frequencies below 1 MHz. There was a daily pattern of increased nighttime backscattering in the upper 100 m at 265 and 420 kHz. This pattern was less evident at 1.1 MHz and above. [S0001-4966(00)01901-9]

PACS numbers: 43.30.Pc, 43.30.Sf [DLB]

INTRODUCTION

The monsoon winds that bring warm summer rains from the south and cold dry winter air from the north to southern Asia also affect the circulation and the biology of the Arabian Sea. In the summer a high-pressure zone builds over the Indian Ocean, while a low-pressure zone builds over Asia. The resulting flow of air over the Arabian Sea—the Southwest (SW) Monsoon—is characterized by an intense jet, first described by Findlater (1969). This wind leads to coastal upwelling along the coast of Yemen and Oman (Currie *et al.*, 1973; Currie, 1992), and also general upwelling out to 400 km from the coast (Smith and Bottero, 1977; Swallow, 1984) associated with the wind-stress maximum within the Findlater jet (Bauer *et al.*, 1991). These upwelling regions contain higher-than-usual concentrations of chlorophyll-*a* (Banse, 1987; Bauer *et al.*, 1991). In December and January, continental cooling generates a high-pressure zone over Asia, and the Northeast (NE) Monsoon winds blow across the Arabian Sea, generally with less force and concentration than during the Summer SW Monsoon (Banse, 1987; Bauer *et al.*, 1991). Bauer *et al.* (1991) have shown that Eckman pumping can occur in the central Arabian Sea during this time, but generally chlorophyll-*a* levels are lower during the Winter NE Monsoon (Banse, 1987; Bauer *et al.*, 1991). Zooplankton biomass responds to food supply and therefore should be higher during and after the Summer SW Monsoon event than at other times of year (Smith, 1995). Zooplankton are major contributors to high frequency (>100 kHz) acoustic volume backscattering. Therefore, monsoonal forcing would be expected to lead indirectly to significant changes in high-frequency acoustic volume backscattering levels and patterns.

Between 1994 and 1996, a multiprogram study was made of the interaction between atmosphere and ocean in the Arabian Sea. Among the various programs involved were the U.S. component of the Joint Global Ocean Flux Study (U.S. JGOFS); the World Ocean Circulation Experiment (WOCE); the U.S. component of the Global Ocean Ecosystems Dynamics Program (U.S. GLOBEC); and an accelerated research initiative (ARI) on forced upper ocean dynamics of the Arabian Sea, sponsored by the Office of Naval Research (ONR). The particular goal of the ONR ARI was to study the physical and biological response of the upper ocean to atmospheric forcing. One part of the program was a set of survey cruises whose purpose was to map the upper ocean physics and biology from near the surface to approximately 300 m depth. These cruises used a towed body called SeaSoar (Brink and Bahr, 1996; Fucile *et al.*, 1998). SeaSoar had hydrodynamic control surfaces that permitted it to undulate from near the surface to approximately 300-m depth and back [Fig. 1(a)]. It was towed at 8 knots along a path that varied little from cruise to cruise (Fig. 2). The SeaSoar contained a suite of instruments including a conductivity, temperature, and depth (CTD) sensor; a fluorometer; a transmissometer; a solar irradiance sensor; and a Tracor acoustic profiling system (TAPS™). TAPS measures acoustic volume

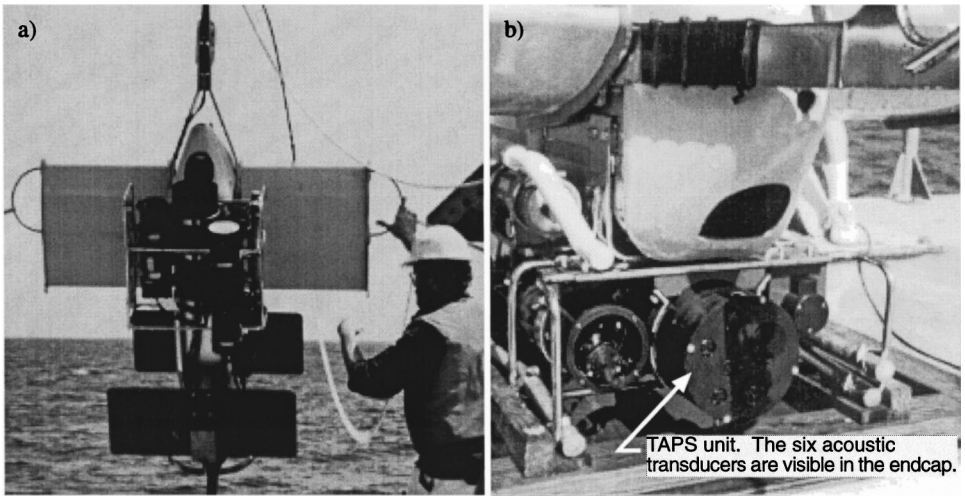

FIG. 1. (a) The SeaSoar towed body had hydrodynamic control surfaces that permitted it to ''fly'' from near the surface to approximately 300-m depth and back again in an undulating pattern while being towed at 8 knots. (b) SeaSoar carried a suite of instruments, including a conductivity, temperature, and depth (CTD) sensor; a fluorometer; a transmissometer; a solar irradiance sensor; and a Tracor acoustic profiling system (TAPS), an instrument which measures acoustic volume backscattering at six frequencies ranging from 265 kHz to 3.0 MHz. Photos are courtesy of Frank Bahr, Woods Hole Oceanographic Institution.

backscattering strength at six frequencies ranging from 265 kHz to 3.0 MHz [Fig. 1(b)].

Volume reverberation is often more important than either electronic or ambient noise in limiting the performance of underwater acoustic systems. In this context, volume backscattering strength becomes an important environmental parameter in its own right, and has been mapped in many of the world's oceans at frequencies ranging from 2 to 88 kHz (NDRC, 1946; Anderson, 1967; Farquhar, 1970; Hall, 1971, 1973; Scrimger and Turner, 1973; Batzler, 1975; Greenblatt, 1982). The purpose of this article is to report measurements of high-frequency (265 kHz to 3.0 MHz) volume backscattering at a variety of locations in the Arabian Sea for different stages of the monsoonal cycle. These measurements should be of interest to oceanographers intending to use high-frequency acoustics in the region. A few observations are made in this article regarding the zooplankton distributions that underlie the acoustic measurements. However, these are addressed in much more detail in a related paper (Pieper *et al.*, submitted).

I. DATA COLLECTION AND ANALYSIS

A. Data collection

SeaSoar was towed from the R/V THOMAS G. THOMPSON on four cruises at different stages of the monsoon cycle. The TAPS unit was included on three of these cruises. The first was during the height of the Winter NE Monsoon, from 28 November 1994 to 17 December 1994. The second was during the height of the Summer SW Monsoon, from 21 June 1995 to 13 July 1995. The third was at the onset of the Fall Intermonsoon period, from 18 September 1995 to 11 October 1995. The cruises all sailed from Muscat, Oman, went south along the coast of Oman (Fig. 2), did an inshore grid survey (Radiator 1, or Rad1), made a transect out to a long-term mooring array located at 15 °30′N, 61 °30′E, made a survey

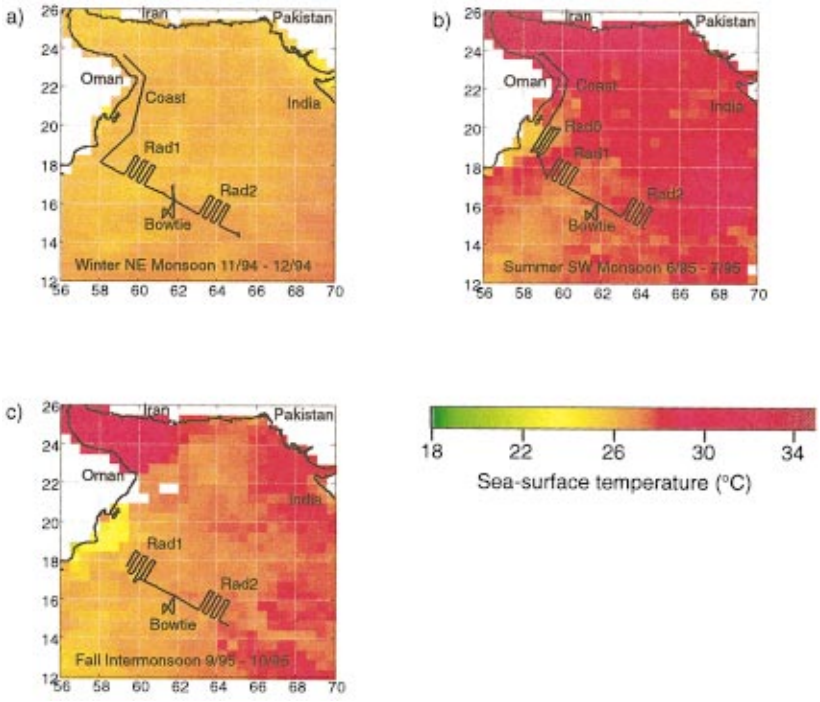

FIG. 2. Ship tracks during the three SeaSoar cruises in the Arabian Sea when a TAPS was used: (a) the Winter NE Monsoon cruise, (b) the Summer SW Monsoon cruise, and (c) the Fall Intermonsoon cruise. The ship tracks are shown only for portions of the cruises when SeaSoar was deployed. Each of the labeled cruise segments was carried out for a particular reason. The Coast transect was designed to sample a coastal upwelling environment, Radiator 1 (Rad1) sampled a ''nearshore'' environment (still presumably within the upwelling zone), and Radiator 2 (Rad2) sampled an open-ocean environment. The Bowtie was centered on a long-term mooring array. During the Summer SW Monsoon cruise an additional study was made, Radiator 0 (Rad0), when the ship encountered an offshore filament with lower-than-usual temperature, high nutrients, and high chlorophyll.

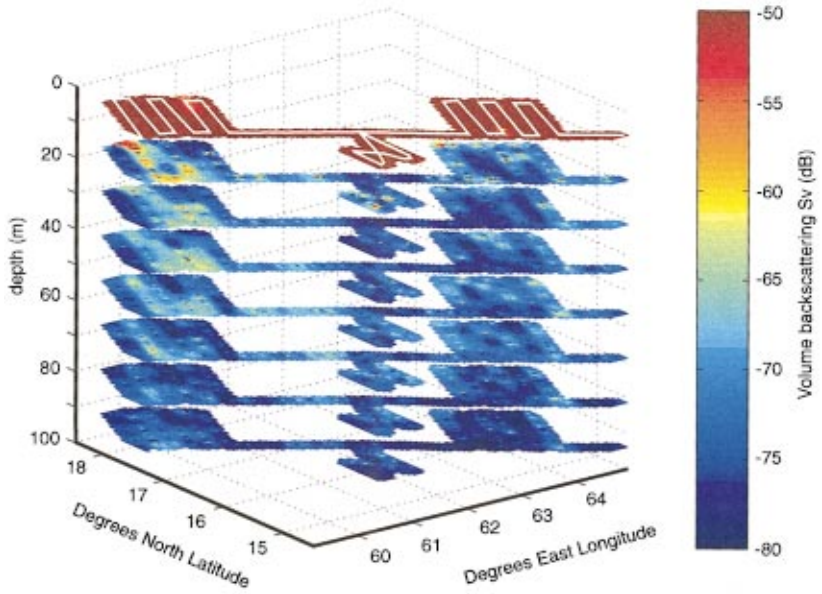

FIG. 3. Acoustical volume backscattering at 420 kHz in the upper 100 m of the water column during the Summer SW Monsoon. Transect is from Rad1 to Rad2. The ship track is shown as a white line. Each horizontal slab represents a 12.5-m depth bin. Values away from the cruise track were interpolated using a modified form of the Kriging algorithm. Values were limited to those within 10 nautical miles of the cruise track. The general pattern here and on all the cruises was of substantially higher acoustic backscattering near the surface, generally decreasing with depth. Backscattering varied at all depths, indicating patchiness, some of which was due to daily vertical migration of zooplankton (see Fig. 10).

centered on the array (the Bowtie), then moved further offshore to do another grid survey (Rad2). During the Summer SW Monsoon cruise, the scientific party observed a cool water filament extending offshore from the coast. The feature was distinguished by cool surface temperatures, high nutrients, and high chlorophyll (Brink, 1995). An *ad hoc* grid survey was made of the filament [Rad0 in Fig. 2(b)]. Normally SeaSoar was deployed soon after leaving port, although during the Fall Intermonsoon cruise it was not deployed until the beginning of Rad1. SeaSoar was ''undulated'' from near the surface to approximately 300-m depth and back, with a round-trip time of approximately 11 min. Consequently it averaged just under 1 m/s vertical speed, moving vertically faster near the center of the cycle and slower at the top and bottom.

The TAPS unit was mounted on SeaSoar facing forward [Fig. 1(b)]. It measured acoustic volume backscattering from a fixed sample volume (approximately 5 liters at 1.5 m range) at six frequencies: 265 kHz, 420 kHz, 700 kHz, 1.1 MHz, 1.85 MHz, and 3.0 MHz. Echo envelopes were sampled eight times on each ping and mean-square averaged over 24 pings sequentially on each channel. Date, time, depth, and temperature were measured in the middle of the echo ensemble. After all measurements were made, the echo

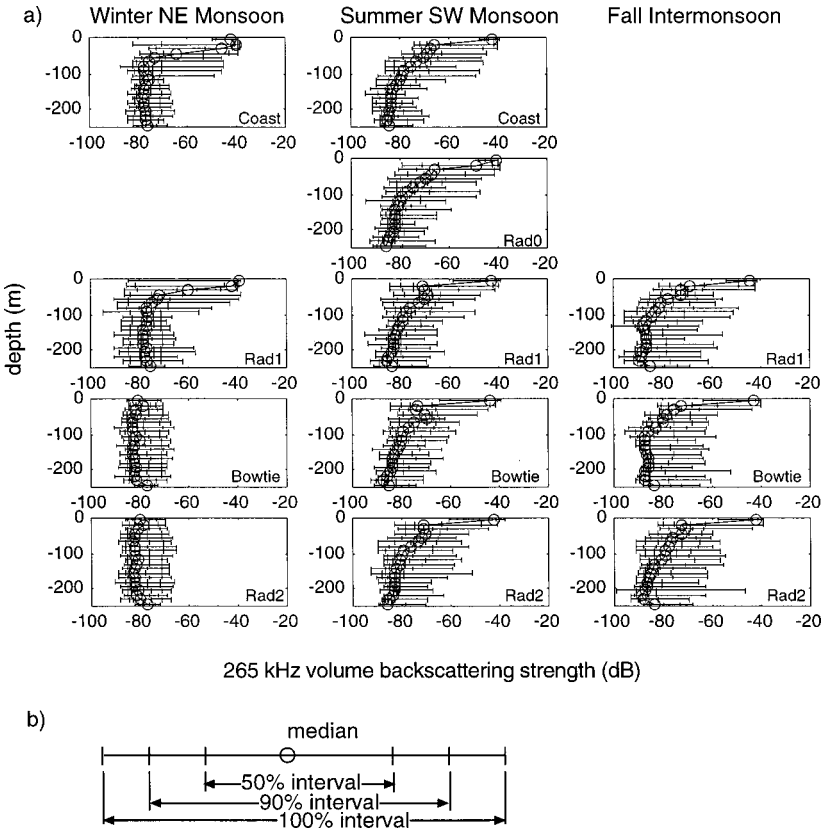

FIG. 4. (a) Profiles showing distribution of 265-kHz volume backscattering strength measurements as functions of depth for the different components of each cruise. (b) The distribution at each depth is shown with a circle to mark the median value, and 50%, 90%, and 100% intervals to show how the data were distributed.

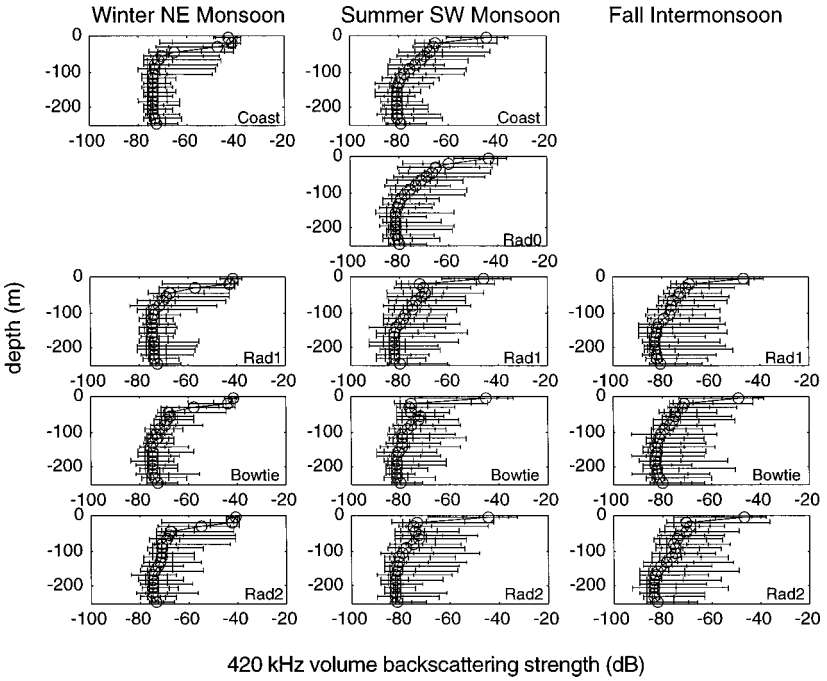

FIG. 5. Profiles showing distribution of 420-kHz volume backscattering strength measurements as functions of depth for the different components of each cruise. The same nomenclature is used as in Fig. 4.

intensities were converted to volume backscattering strengths and transmitted by serial link to a datalogger on the ship. Approximately 6 s were needed to collect, process, and transmit a full six-frequency data set. Geographic locations and data from the other instruments on SeaSoar were recorded on a separate datalogger. At 5 liters, the TAPS sampling volume was small enough to exclude significant contributions from large and relatively rare organisms such as fish and large zooplankton. The volume backscattering strengths reported here therefore represent scattering primarily from the smaller, more numerous zooplankton (e.g., copepods and smaller). TAPS was calibrated before the winter cruise, before the summer cruise, and after the fall cruise.

B. Data analysis

TAPS data were collected during both ascent and descent of the SeaSoar towed body. However, only data from the descents were analyzed because echoes from the tow cable appeared in the ascent data. Data were binned vertically into 20 uniformly sized 12.5-m-depth bins over the upper 250 m of the water column. The large vertical bin size was chosen to maximize the likelihood that there would be data in every bin, a concern due to SeaSoar's rapid vertical speed. Data from each downcast were treated as having been collected in a single geographic location, chosen as the ship's location at the middle of the downcast. Distance be-

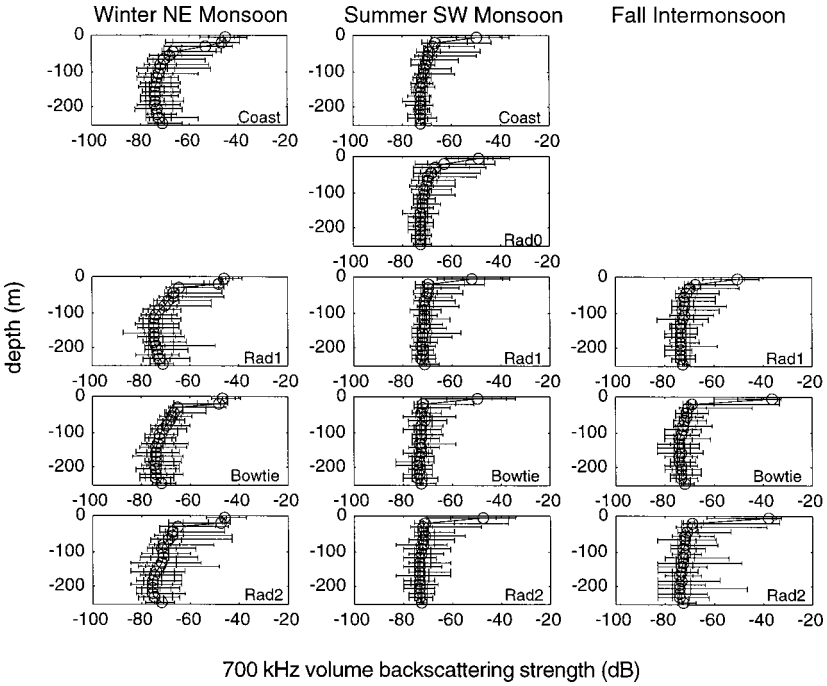

FIG. 6. Profiles showing distribution of 700-kHz volume backscattering strength measurements as functions of depth for the different components of each cruise. The same nomenclature is used as in Fig. 4.

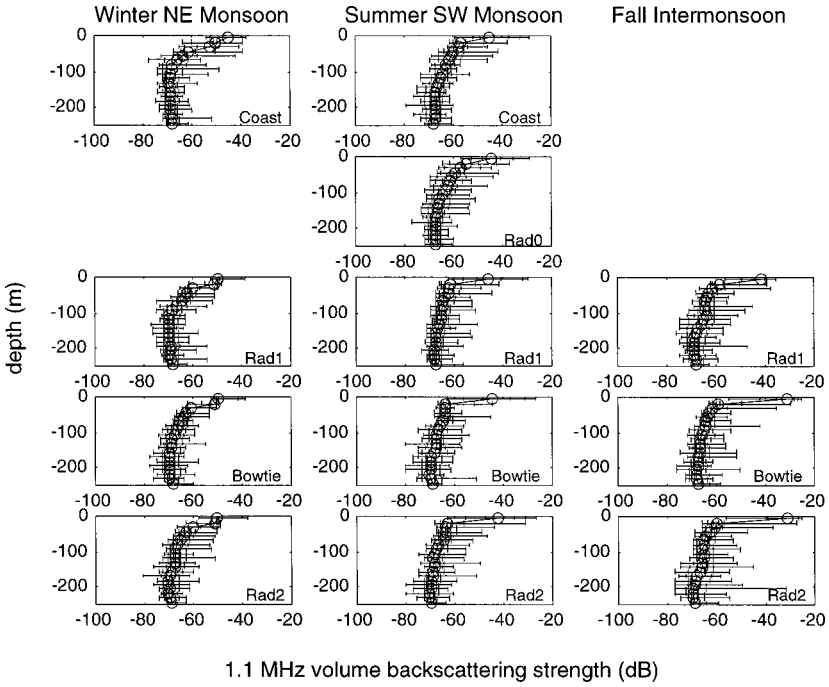

FIG. 7. Profiles showing distribution of 1.1-MHz volume backscattering strength measurements as functions of depth for the different components of each cruise. The same nomenclature is used as in Fig. 4.

tween downcasts varied around a mean of 2.8 km. By treating each downcast as having been made in a single location, it was possible to treat the volume backscattering data at the six frequencies as functions of three dimensions: depth, latitude, and longitude (Fig. 3), keeping in mind that the data were also functions of time of day. A total of 1254 downcasts was made during the Winter NE Monsoon cruise, 1284 during the Summer SW Monsoon cruise, and 1031 during the Fall Intermonsoon cruise.

The volume backscattering measurements were examined statistically by combining all data from each cruise segment (Coast, Rad0, Rad1, Bowtie, and Rad2) by depth and acoustic frequency (Figs. 4–9). An effort was also made to compare acoustic backscattering at each frequency by season and by location. The integrated column backscattering strength (Scrimger and Turner, 1973; Batzler, 1975) from 0- to 250-m depth was calculated for each downcast in the Coast, Rad1, and Rad2 segments of each cruise. Column backscattering was then compared between cruise segments for each season (Table I), and between seasons for each cruise segment (Table II) using the median test (Mood, 1950 as cited in Zar, 1984) (H_0: medians were the same; H_A: medians were different, $\alpha = 0.05$). Column backscattering strength was dominated in most cases by the high scattering levels found in the depth bins nearest the surface. However, we found that the conclusions from the regional and seasonal comparisons in Tables I and II did not change drastically when the analysis was repeated with column backscattering

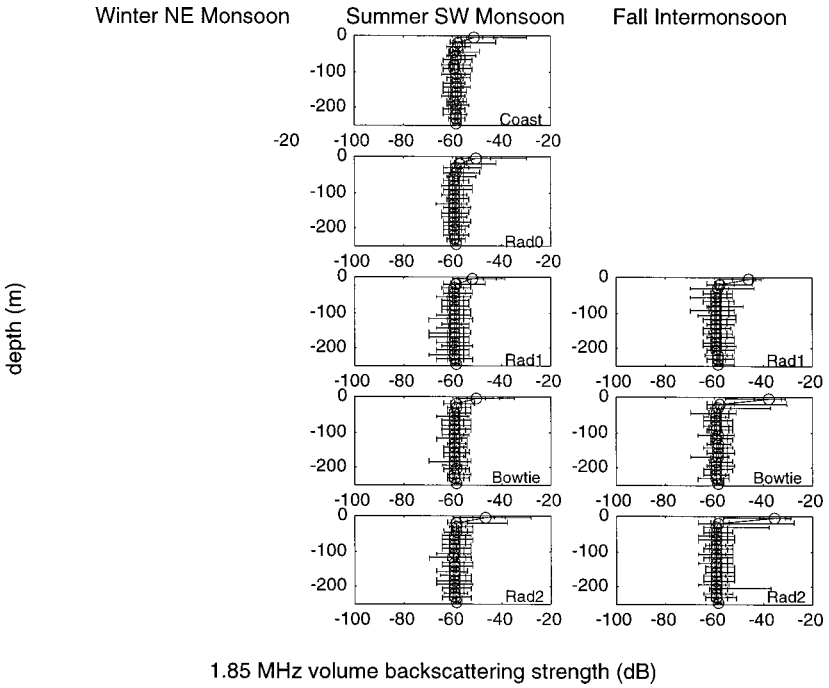

FIG. 8. Profiles showing distribution of 1.85-MHz volume backscattering strength measurements as functions of depth for the different components of each cruise. The same nomenclature is used as in Fig. 4. Data from the Winter NE Monsoon cruise are not shown because high noise levels on that channel made the results suspect.

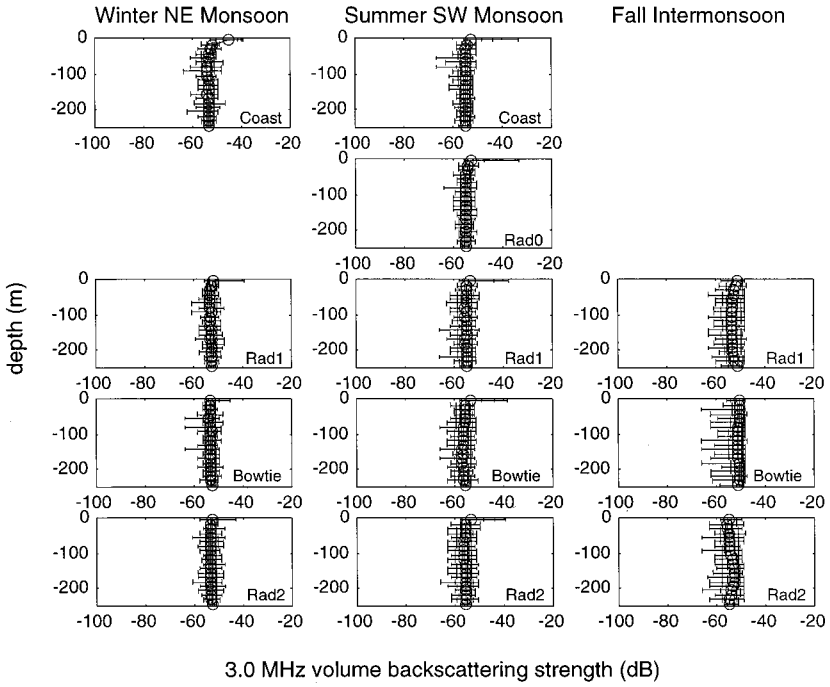

FIG. 9. Profiles showing distribution of 3.0-MHz volume backscattering strength measurements as functions of depth for the different components of each cruise. The same nomenclature is used as in Fig. 4.

limited to the deeper part of the water column (the 37–250-m-depth range).

II. RESULTS

A. Effect of depth and geographic region on volume backscattering

Volume backscattering generally decreased with depth at all frequencies and in all cruise segments (Figs. 4–9), although this effect was less pronounced for the higher frequencies (1.85 and 3.0 MHz) than for the lower ones. The high volume backscattering in the surface depth bin was undoubtedly due in part to scattering from bubbles, as well as to scattering from zooplankton. We had expected acoustic backscattering to be higher near the coast than further offshore (Rad1 and Rad2) due to upwelling, particularly during the Summer SW Monsoon period. We found to our surprise that while this was mostly true for the Winter NE Monsoon (Table I), coastal backscattering was generally not greater than offshore backscattering during the Summer SW Monsoon (Table I). Also, the differences in median column backscattering were typically less than 6 dB, whereas the volume backscattering at any given depth often varied locally by 30 dB (Figs. 3–9).

TABLE I. Regional comparison of volume backscattering as a function of season and acoustical frequency. Integrated column backscattering from 0 to 250-m depth is compared using the median test (see the text) at a 5%-significance level. Comparisons involving the Fall Intermonsoon's Coast segment are marked N/A because SeaSoar was not deployed for that part of the cruise. Comparisons involving the 1.85-MHz data from the Winter NE Monsoon are marked N/A because high noise levels on that channel made the results suspect.

		Winter NE Monsoon	Summer SW Monsoon	Fall Intermonsoon
265 kHz	Coast vs Rad1	Coast>Rad1	Coast>Rad1	N/A
	Coast vs Rad2	Coast>Rad2	Coast=Rad2	N/A
	Rad1 vs Rad2	Rad1>Rad2	Rad2>Rad1	Rad2>Rad1
420 kHz	Coast vs Rad1	Coast>Rad1	Coast=Rad1	N/A
	Coast vs Rad2	Coast>Rad2	Coast=Rad2	N/A
	Rad1 vs Rad2	Rad2>Rad1	Rad2>Rad1	Rad1=Rad2
700 kHz	Coast vs Rad1	Coast>Rad1	Coast=Rad1	N/A
	Coast vs Rad2	Coast>Rad2	Coast=Rad2	N/A
	Rad1 vs Rad2	Rad2>Rad1	Rad2>Rad1	Rad2>Rad1
1.1 MHz	Coast vs Rad1	Coast>Rad1	Coast=Rad1	N/A
	Coast vs Rad2	Coast>Rad2	Coast=Rad2	N/A
	Rad1 vs Rad2	Rad1>Rad2	Rad2>Rad1	Rad2>Rad1
1.85 MHz	Coast vs Rad1	N/A	Coast>Rad1	N/A
	Coast vs Rad2	N/A	Rad2>Coast	N/A
	Rad1 vs Rad2	N/A	Rad2>Rad1	Rad2>Rad1
3.0 MHz	Coast vs Rad1	Rad1>Coast	Coast=Rad1	N/A
	Coast vs Rad2	Rad2>Coast	Coast>Rad2	N/A
	Rad1 vs Rad2	Rad1>Rad2	Rad1>Rad2	Rad1>Rad2

B. Effect of monsoon season on volume backscattering

Acoustic backscattering during and after the Summer SW Monsoon had been predicted to be higher than during the Winter NE Monsoon due to the direct and indirect effects of wind-driven upwelling, particularly near the coast. In fact the opposite was found to be true: Acoustic backscattering was generally higher at all three locations (Coast, Rad1, and Rad2) during the winter than during the summer (Table II), with Fall Intermonsoon backscattering levels falling between. As with the regional differences, however, these differences were much smaller than the fine-scale (O [10 km]) horizontal variability.

C. Fine-scale spatial and temporal patterns of volume backscattering

Regions of high volume backscattering were patchy in distribution, both horizontally at scales of 10 km and up and vertically at scales of 12 m and up (Fig. 3), with much greater variability at 265 kHz through 1.1 MHz than at 1.85 and 3.0 MHz (Figs. 4–9). Part of the variability at the lower

TABLE II. Seasonal comparison of volume backscattering as a function of location and acoustical frequency. Integrated column backscattering from 0 to 250-m depth is compared using the median test (see the text) at a 5%-significance level. Comparisons involving the Fall Intermonsoon's Coast segment are marked N/A because SeaSoar was not deployed for that part of the cruise. Comparisons involving the 1.85-MHz data from the Winter NE Monsoon are marked N/A because high noise levels on that channel made the results suspect.

		Coast	Rad1	Rad2
265 kHz	Winter NE Monsoon vs Summer SW Monsoon	Winter>Summer	Winter>Summer	Summer>Winter
	Winter NE Monsoon vs Fall Intermonsoon	N/A	Winter>Fall	Fall>Winter
	Summer SW Monsoon vs Fall Intermonsoon	N/A	Summer>Fall	Summer=Fall
420 kHz	Winter NE Monsoon vs Summer SW Monsoon	Winter>Summer	Winter>Summer	Winter>Summer
	Winter NE Monsoon vs Fall Intermonsoon	N/A	Winter>Fall	Winter>Fall
	Summer SW Monsoon vs Fall Intermonsoon	N/A	Summer=Fall	Summer>Fall
700 kHz	Winter NE Monsoon vs Summer SW Monsoon	Winter>Summer	Winter>Summer	Winter>Summer
	Winter NE Monsoon vs Fall Intermonsoon	N/A	Winter>Fall	Fall>Winter
	Summer SW Monsoon vs Fall Intermonsoon	N/A	Fall>Summer	Fall>Summer
1.1 MHz	Winter NE Monsoon vs Summer SW Monsoon	Summer>Winter	Summer>Winter	Summer>Winter
	Winter NE Monsoon vs Fall Intermonsoon	N/A	Fall>Winter	Fall>Winter
	Summer SW Monsoon vs Fall Intermonsoon	N/A	Fall>Summer	Fall>Summer
1.85 MHz	Winter NE Monsoon vs Summer SW Monsoon	N/A	N/A	N/A
	Winter NE Monsoon vs Fall Intermonsoon	N/A	N/A	N/A
	Summer SW Monsoon vs Fall Intermonsoon	N/A	Fall>Summer	Fall>Summer
3.0 MHz	Winter NE Monsoon vs Summer SW Monsoon	Winter>Summer	Winter>Summer	Winter>Summer
	Winter NE Monsoon vs Fall Intermonsoon	N/A	Fall>Winter	Winter>Fall
	Summer SW Monsoon vs Fall Intermonsoon	N/A	Fall>Summer	Fall>Summer

frequencies was due to the daily vertical migration, probably of larger crustacean zooplankton. At 420 kHz for example, daily vertical migration contributed to a daily fluctuation in volume backscattering on the order of 10 dB at 44-m depth (Fig. 10). The effect of daily vertical migration was much less pronounced at the higher frequencies (1.1 MHz and up).

III. CONCLUSION

The most unexpected discovery from this study of high-frequency acoustic backscattering in the Arabian Sea was that backscattering was generally lower during the Summer SW Monsoon than it was during the Winter NE Monsoon. We can offer no certain explanation of this, although it is possible that the winds and currents were anomalous during the study period. Geographic variation was less significant than predicted, with greater onshore–offshore differences during the Winter NE Monsoon period than during the Summer SW Monsoon period. Neither seasonal nor geographic differences were as important as fine-scale patchiness in affecting the observed variations in volume backscattering. In

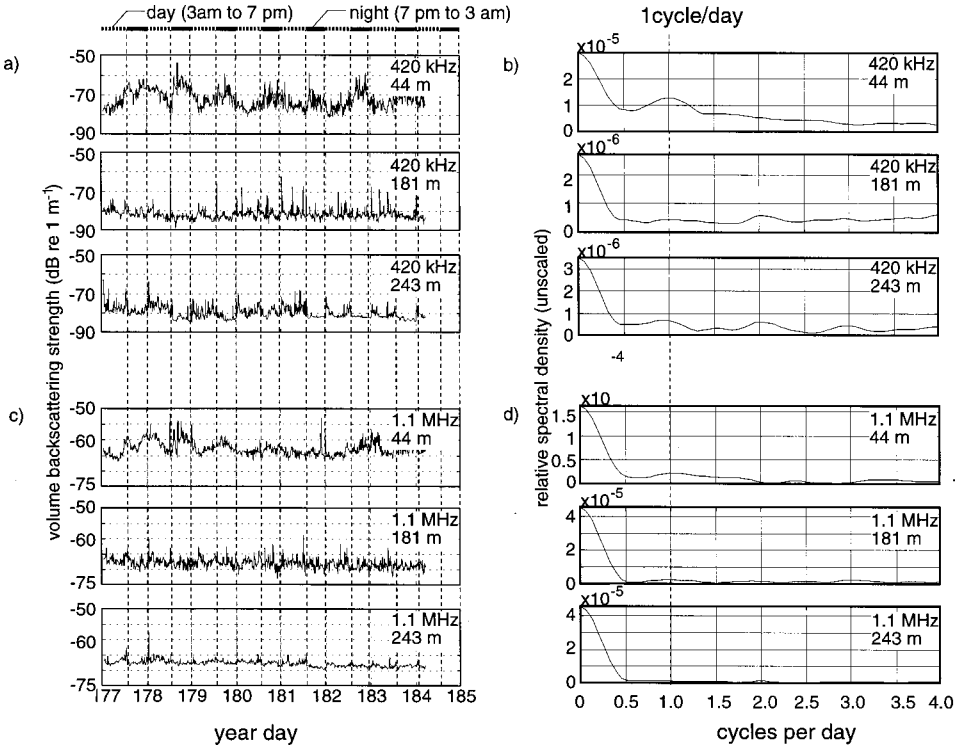

FIG. 10. Acoustic volume backscattering varied on a daily cycle at low frequency, but not at high frequency. (a) 420-kHz acoustic volume backscattering strength at three depths, 44, 181, and 243 m. Volume backscattering was higher during the night at 44-m depth than during the day. Conversely, volume backscattering was lower during the night at 243 m than during the day. The message at 181 m was more confused. (b) Unscaled spectra of the three time signals in (a) showed a local peak at 1 cycle per day at 44 m and at 243 m, and a local peak at 2 cycles/day at 181-m depth. An obvious interpretation is that large zooplankton stayed in the deeper water by day, rose to the photic zone at night, and returned at dawn to the inky depths, passing through the intermediate depths twice per day. (c), (d) 1.1-MHz volume backscattering strength at the same three depths showed a much weaker daily signal. These data are from the Summer SW Monsoon period.

particular, the daily vertical migration of zooplankton had a strong influence on the observed variability of volume backscattering, mostly at the lower frequencies.

ACKNOWLEDGMENTS

We would like to thank the WHOI SeaSoar Group, in particular Ken Brink and Frank Bahr, for deploying TAPS with SeaSoar, and for multiple discussions since then. We also would like to thank Sharon Smith for numerous discussions. AVHRR sea-surface temperature data were obtained from the NASA Physical Oceanography Distributed Active Archive Center at the Jet Propulsion Laboratory, California Institute of Technology. This work was supported by ONR Code 322BC under Contract No. N00014-C-91-0069.

Anderson, V. C. (**1967**). ''Spatial and spectral dependence of acoustic reverberation,'' J. Acoust. Soc. Am. **42**, 1080–1088.

Banse, K. (**1987**). ''Seasonality of phytoplankton chlorophyll in the central and northern Arabian Sea,'' Deep-Sea Res. **34**, 713–723.

Batzler, W. E. (**1975**). ''Deep-scattering-layer observations off New Zealand and comparison with other volume scattering measurements,'' J. Acoust. Soc. Am. **58**, 51–71.

Bauer, S., Hitchcock, G. L., and Olson, D. B. (**1991**). ''Influence of monsoonally-forced Ekman dynamics upon surface layer depth and plankton biomass distribution in the Arabian Sea,'' Deep-Sea Res. **38**, 531–553.

Brink, K. H. (**1995**). Personal communication.

Brink, K. H., and Bahr, F. (**1996**). ''Changing winds and ocean mixing—Studies of the Arabian Sea monsoon,'' Oceanus **39**, 24.

Currie, R. I. (**1992**). ''Circulation and upwelling off the coast of south-east Arabia,'' Oceanol. Acta **15**, 43–60.

Currie, R. I., Fisher, A. E., and Hargreaves, P. M. (**1973**). ''Arabian Sea Upwelling,'' in *The Biology of the Indian Ocean*, edited by B. Zeitzschel (Springer, New York), pp. 57–63.

Farquhar, G. B., Ed. (**1970**). *Proceedings of an International Symposium on Biological Sound Scattering in the Ocean* (U.S. Government Printing Office, Washington, D.C.).

Findlater, J. (**1969**). ''A major low-level air current near the Indian Ocean during the northern summer,'' Q. J. R. Meteorol. Soc. **95**, 362–380.

Fucile, P., Gordon, A., Bahr, F., and Dean, J. (**1998**). ''Optic control of undulating platform,'' Sea Technol. **39**(5), 63–66.

Greenblatt, P. (**1982**). ''Distributions of volume scattering observed with an 87.5 kHz sonar,'' J. Acoust. Soc. Am. **71**, 879–885.

Hall, M. (**1971**). ''Volume backscattering in the South China Sea and the Indian Ocean,'' J. Acoust. Soc. Am. **50**, 940–945.

Hall, M. (**1973**). ''Volume backscattering in the Tasman Sea, the Coral Sea, and the Indian Ocean,'' J. Acoust. Soc. Am. **54**, 473–477.

NDRC (**1946**). *Physics of Sound in the Sea, Part II, Reverberation—Summary Technical Report of Division 6*, Vol. 8 (National Defense Research Committee, Washington, D.C.).

Pieper, R. E., McGehee, D. E., Greenlaw, C. F., and Holliday, D. V. (**1998**). ''Acoustically Measured Seasonal Patterns of Zooplankton in the Arabian Sea,'' Deep-Sea Res. II (submitted).

Scrimger, J. A., and Turner, R. G. (**1973**). ''Backscattering of sound from the ocean volume between Vancouver Island and Hawaii,'' J. Acoust. Soc. Am. **54**, 483–493.

Smith, S. L. (**1995**). ''The Arabian Sea: mesozooplankton response to seasonal climate in a tropical ocean,'' ICES J. Mar. Sci. **52**, 427–438.

Smith, R. L., and Bottero, J. S. (**1977**). ''On upwelling in the Arabian Sea,'' in *A Voyage of Discovery*, edited by M. Angel (Pergamon, New York), pp. 291–304.

Swallow, J. C. (**1984**). ''Some aspects of the physical oceanography of the Indian Ocean,'' Deep-Sea Res. **31**, 639–650.

Zar, J. H. (**1984**). *Biostatistical Analysis* (Prentice-Hall, Englewood Cliffs, NJ).

Acoustic normal mode fluctuation statistics in the 1995 SWARM internal wave scattering experiment

Robert H. Headrick,[a] James F. Lynch, John N. Kemp, Arthur E. Newhall, and Keith von der Heydt
Woods Hole Oceanographic Institution, Woods Hole, Massachusetts 02543

John Apel
Global Ocean Associates, PO Box 12131, Silver Spring, Maryland 20908

Mohsen Badiey
Ocean Acoustic Laboratory, Graduate College of Marine Studies, U. Delaware, Newark, Delaware 19716

Ching-sang Chiu
Naval Post Graduate School, Monterey, California 93943

Steve Finette, Marshall Orr, Bruce Pasewark, Alton Turgot, and Steve Wolf
Naval Research Laboratory, Washington DC 20375-5350

Dirk Tielbuerger
Forschnungsanstalt der Bundeswehr für Wasserschall und Geophysik, Klausdorfer Weg 2-24, 24148 Kiel, Germany

(Received 21 July 1997; revised 21 July 1998; accepted 13 September 1999)

In order to understand the fluctuations imposed upon low frequency (50 to 500 Hz) acoustic signals due to coastal internal waves, a large multilaboratory, multidisciplinary experiment was performed in the Mid-Atlantic Bight in the summer of 1995. This experiment featured the most complete set of environmental measurements (especially physical oceanography and geology) made to date in support of a coastal acoustics study. This support enabled the correlation of acoustic fluctuations to clearly observed ocean processes, especially those associated with the internal wave field. More specifically, a 16 element WHOI vertical line array (WVLA) was moored in 70 m of water off the New Jersey coast. Tomography sources of 224 Hz and 400 Hz were moored 32 km directly shoreward of this array, such that an acoustic path was constructed that was anti-parallel to the primary, onshore propagation direction for shelf generated internal wave solitons. These nonlinear internal waves, produced in packets as the tide shifts from ebb to flood, produce strong semidiurnal effects on the acoustic signals at our measurement location. Specifically, the internal waves in the acoustic waveguide cause significant coupling of energy between the propagating acoustic modes, resulting in broadband fluctuations in modal intensity, travel-time, and temporal coherence. The strong correlations between the environmental parameters and the internal wave field include an interesting sensitivity of the spread of an acoustic pulse to solitons near the receiver. [S0001-4966(00)00601-9]

PACS numbers: 43.30.Re, 43.30.Bp [DLB]

BACKGROUND

One of the hallmarks of the shallow water acoustic environment is its variability. Due to the importance of bottom interaction in shallow water, much attention has been paid to the variability of the bottom geology and the geoacoustic parameters of the bottom. However, in recent years, it has been recognized that the water column and its fluctuations also have a large impact on modulating acoustic signals in shallow water. Of particular interest has been the internal wave field, which can impress large fluctuations on shallow water signals, both in amplitude and phase/travel time. These fluctuations have important implications for array signal processing for both source localization and medium (inverse problem) studies.

One of the first indications of strong internal wave induced fluctuations came from the Yellow Sea work of Zhou and his co-workers, where anomalously large, frequency and azimuth dependent propagation losses were noted in tandem with high internal wave activity.[1,2] Zhou and other investigators postulated a ''Bragg resonant internal wave scattering plus bottom loss'' mechanism to explain this important observation.[1–4] However, the Yellow Sea data were not detailed enough, particularly the physical oceanography, to firmly prove or disprove this propagation loss hypothesis (or any other such reasonable hypothesis). The need for further higher resolution data was soon recognized. In order to understand both the acoustic scattering and losses produced by coastal internal waves, and their physical oceanography

[a]Robert H. Headrick was associated with the MIT/WHOI Joint Program in Oceanography and Oceanographic Engineering during the performance of this work. He is currently on active duty in the U.S. Navy.

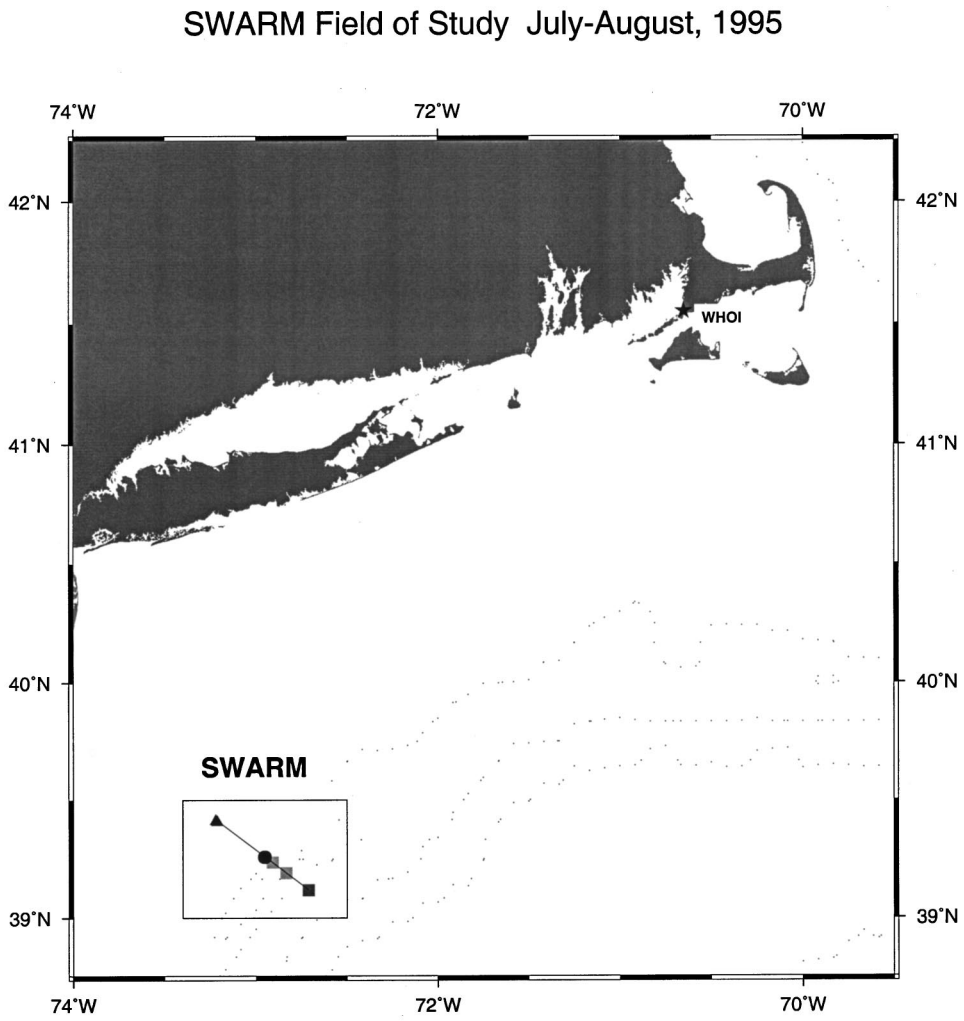

FIG. 1. Locations of acoustic moorings. The tomography sources, moored in close proximity, are a pair, 224 Hz and 400 Hz. The receiver is the 16 element WHOI vertical line array (WVLA). Coastal shelfbreak (at 200-m isobath) is main producer of the shoreward-propagating internal wave field affecting the acoustics transmissions.

(which is not perfectly known, especially for nonlinear coastal internal waves), a number of focused experiments were performed in the ensuing years. A semi-inclusive list of such experiments would include: (1) the 1995 SWARM experiment, which concentrated on acoustic pulse amplitude and travel-time variations as well as the physical oceanography of the nonlinear internal wave field;[5] (2) the 1995 STANDARD EIGER experiment, which looked at the issue of azimuthal variations in the acoustic field due to cnoidal, nonlinear waves;[6] (3) the Intimate '96 experiment, which examined the effects of the M2 internal tide (internal waves at M2 semidiurnal tidal frequency);[7] (4) the 1996–97 PRIMER experiments, which simultaneously examined both internal wave and coastal front effects on acoustic propagation;[8,9] (5) the 1995–96 SESAME I and II experiments, which had goals similar to those of the PRIMER experiments;[10] (6) the Strait of Gibraltar tomography experiment, which looked at scattering of acoustic energy for paths along the crests of nonlinear soliton trains;[11] and (7) the Yellow Sea follow-on experiment, in which Zhou and his colleagues (both from the U.S. and China) reconfirmed and extended their initial Yellow Sea measurements.[12] In addition, there have recently been a number of strictly physical oceanographic studies looking at the nature of the coastal internal wave field, which is quite different from the deep ocean field; however, discussion of these is beyond the scope of the present paper.

Our discussions in this paper will focus on the first experiment in our above list, the SWARM (Shallow Water Acoustic Random Medium) experiment. This experiment featured the highest resolution physical oceanography and acoustics combination achieved to date, which was necessary to understand acoustic fluctuations. In particular, we will focus on the travel-time fluctuations impressed upon acoustic pulses by the shallow water internal wave field. These include both the ''wander'' of the pulse (a change of pulse travel-time without change of pulse shape, an adiabatic mode effect) and the pulse ''spread'' (a change in pulse shape, due to mode coupling). The problem of the amplitude fluctuation of the fields, which was also measured in the SWARM experiment, is briefly treated here. In the main, however, this latter topic is outside the scope of this paper. We refer the reader mainly interested in internal wave induced amplitude fluctuations to the recent papers by Creamer, Tielbuerger *et al.*, Tang and Tappert, and Preisig and Duda.[13–16]

Our paper is organized as follows. In Sec. I, we present the description of the SWARM experiment, focusing on the mooring positions and their relation to the internal wave oceanographic field. In Sec. II, we discuss the characteristics of the acoustic data collected, including key elements of the

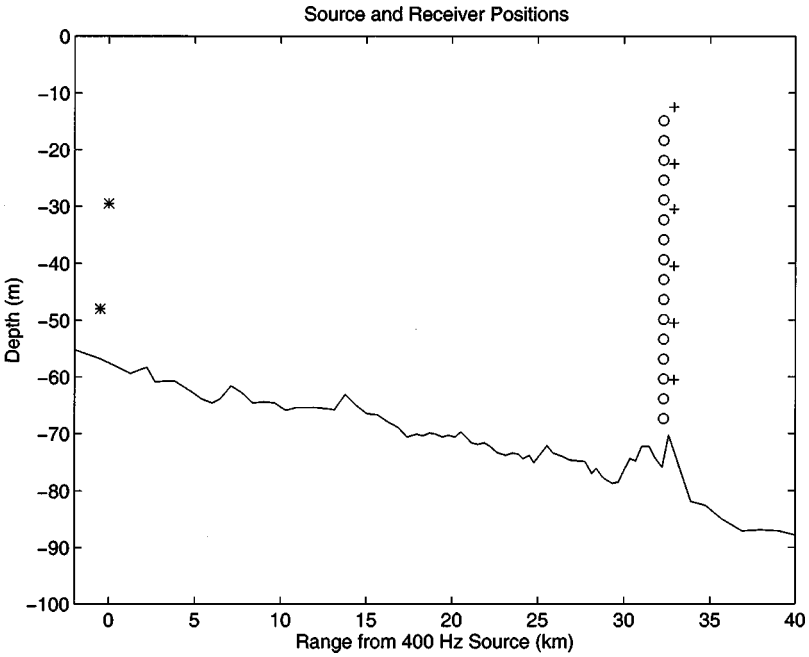

FIG. 2. Source positions are noted by ''*.'' The 400-Hz source is the shallower of the two. WVLA hydrophone positions are noted by ''○'' and the thermistors on the array are marked as ''+.''

subsequent data processing. Attention is paid to the mode filtration issue, as we later analyze data on a mode-by-mode basis. Section III of the paper treats the temporal variability observed in the mode filtered pulse arrivals, particularly their spread, wander, and bias. The strong correlation of these fluctuation statistics to the details of the internal wave field is one of the main results of the paper. This section also contains some analysis of the temporal coherence time of the acoustic modes, as well as a brief look at their amplitude fluctuations. Our final section, Sec. IV, contains a brief synopsis of the paper's results, our conclusions to date, and some thoughts on future directions for such work. The Appendix contains a short derivation showing how solitons near the acoustic receiver have the largest effect on time spreading, an effect noted in the data and dubbed ''near receiver dominance.''

I. EXPERIMENT DESCRIPTION

The SWARM experiment[5] was conducted off the coast of New Jersey near the continental shelfbreak in July and August of 1995. The experiment was primarily dedicated to understanding acoustic normal mode scattering effect due to both linear internal waves and nonlinear solitary internal waves (solitons) in shallow water, and so was performed in late summer in order to see the strongest possible internal wave effects. In order to quantify the physical oceanography as well as the acoustics, the experiment included a myriad of acoustic and ocean environmental sensors; these sensors, their sampling schemes, and a complete overview of the data they produced in SWARM are given in Apel *et al.*[5] The present paper is chiefly concerned with the analysis of acoustic mode travel time data taken from the 16 element WHOI vertical line array (WVLA). Its mooring location, in about 70 m of water, is shown in Fig. 1. A pair of tomography sources, with center frequencies 224 Hz and 400 Hz, were moored for nearly three weeks 32 km shoreward of the WVLA receiver, such that the acoustic path was anti-parallel to the primary propagation direction for shelf generated internal wave solitons. Figure 2 shows a side view of the experiment, emphasizing the array extent in the water column. The temperature profile at the WVLA was monitored by six thermistors attached to the array at various depths. These temperature sensors, measuring twice per minute, gave good temporal resolution of the internal wave fluctuations and adequate spatial resolution in the vertical direction.

The SWARM region was well suited for an internal wave experiment. The internal solitary wave packets that we desired to study are so plentiful in summer that a nearly continuous stream of solitons would pass over a fixed instrument in the course of several hours. This is illustrated in Fig. 3, in which the array of thermistors attached to the WVLA records the passage of *many* waves over a 6-h period.

The mixture of time and space in this figure creates a distorted view of the soliton shapes. In terms of physical dimensions, typical soliton phase speeds of between 0.6 and 0.8 m/s would require on the order of a tenfold increase in the horizontal dimension of the lowest panel in Fig. 3 to achieve a properly scaled representation of a soliton. The resulting horizontal gradients in sound speed are still quite strong, however, and the level of soliton activity was more than sufficient to ensure some highly coupled mode arrivals at the WVLA. The magnitude of the horizontal gradient at mid-depth can be seen in Fig. 4, which shows the sound speed in the middle of a typical soliton and just outside it.

II. SWARM ACOUSTIC DATA CHARACTERISTICS

The 400-Hz (100-Hz bandwidth) tomography source produced a 511 digit, phase-modulated signal sequence with a digit length of 4 cycles, giving a total of 5.11 s per sequence. The sequence was repeated 23 times during each transmission, for a total transmission time of 117.53 s. (We only used 22 of the transmissions in practice.) The 400-Hz transmissions started on the hour and were repeated every 6 min. They were received at the WVLA about 22 s later.

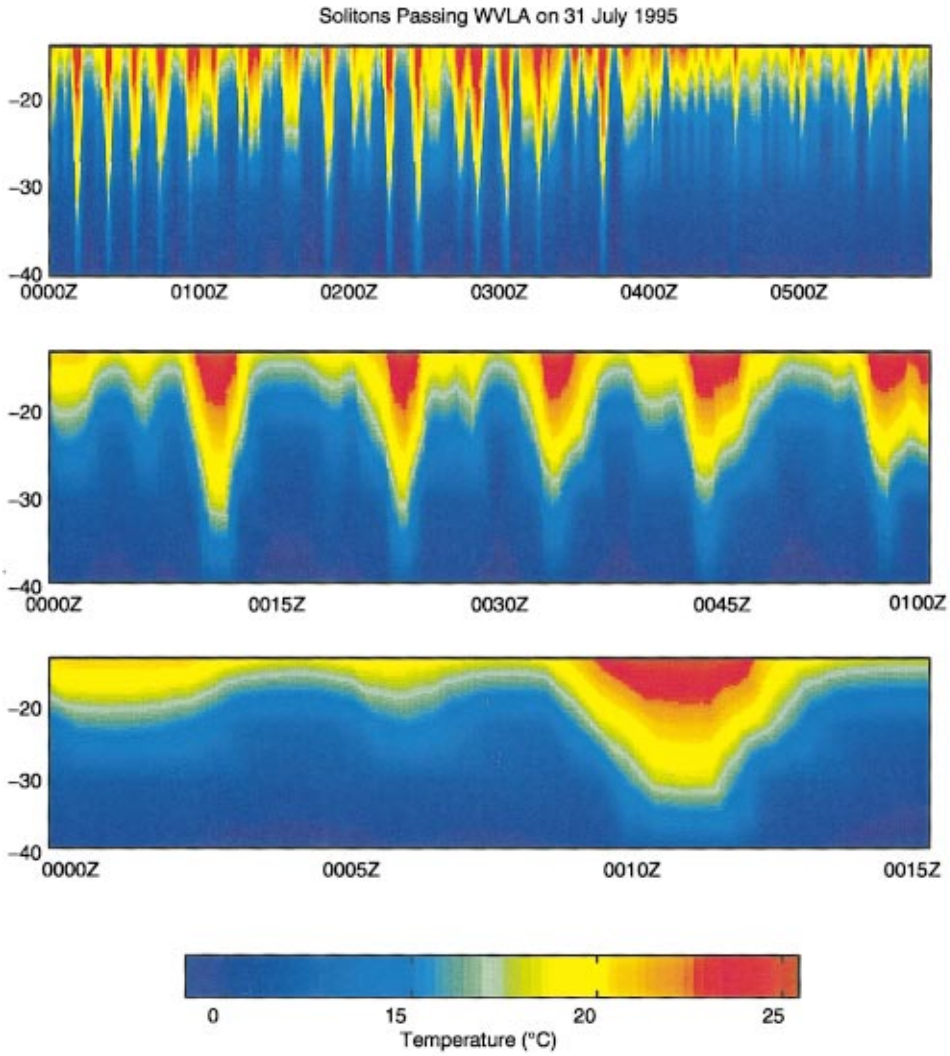

FIG. 3. Time and space interpolation of four thermistor records. The thermistors were attached to the WVLA at water depths of 12.5, 20.5, 30.5, and 40.5 m and sampled at 30-s intervals.

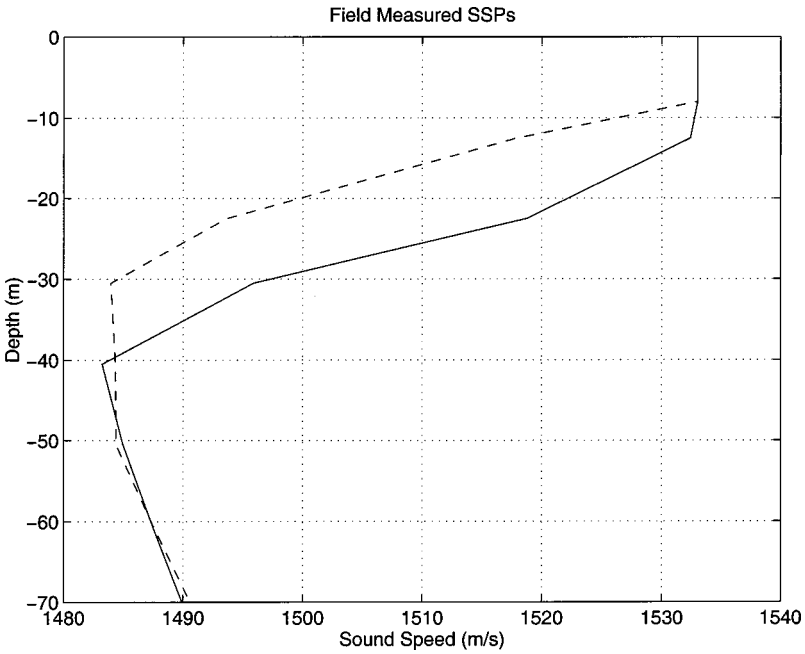

FIG. 4. Sound speed profiles in the center of a typical soliton (solid) and just outside it (dashed). Horizontal sound speed gradients of up to 25 m/s over 100 m can be inferred from such profiles.

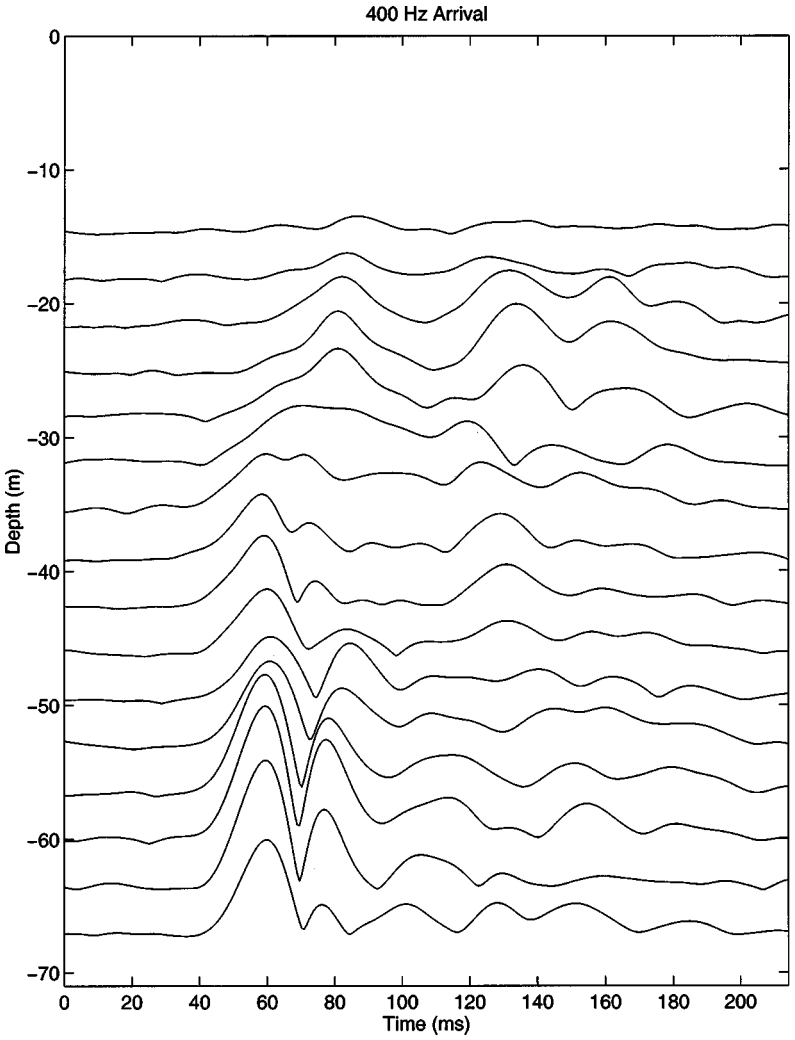

FIG. 5. Typical 400-Hz arrivals observed at the WVLA hydrophones during SWARM. Plot shows pressure field amplitude in linear units.

Figure 5 shows a typical set of 400-Hz pulse-compressed arrivals for the 16 hydrophones at the WVLA. The term ''typical'' is used rather loosely here, as the scattering from internal waves in the waveguide causes significant temporal variability in the individual hydrophone arrivals. What *is* typical here is that a set of arrivals generally consists of an early packet of energy with a mode one amplitude and phase depth dependence followed by a signal of about about 100-ms duration having ''mixed mode'' characteristics.

The 224-Hz arrivals are similar, but the narrower bandwidth (16 Hz) yields a broader pulse width ($\cong$60 ms). The 224-Hz source produced a 63 digit, phase-modulated signal with a digit length of 14 cycles, with period 3.9375 s per sequence. The sequence was repeated 30 times during each transmission, for a total transmission time of 118.125 s. The transmissions were repeated every 5 min, starting on the hour. They were received at the WVLA about 22.5 s later.

We should note in closing this section that this sampling schedule, while reasonable for looking at internal waves, was still somewhat sub-optimal. Although the 5- and 6-min repetition rates were perfectly adequate for M2 tidal period (12.42 h) studies, they somewhat aliased the interval between individual solitons, which are typically on the order of 4 to 10 min. A 100% duty cycle transmission would have been preferred, but battery limitations in the source and (circa 1995) disk storage limitations in the receiver precluded that option.

A. Mode filtering of received signals

The modal analysis of 400-Hz acoustic arrivals at the WVLA begins by treating the acoustic signal at each hydrophone as a sum of vertical modes

$$p_h(t)=\sum_{n=1}^{N} A_n(t)\phi_n(z_h), \tag{1}$$

where $\phi_n(z)$ is the modal pressure depth function, $A_n(t)$ is the mode coefficient, and z_h is the depth of the hth hydrophone. The number of propagating normal modes, N, as well as the mode shapes themselves are frequency dependent.

The six thermistors on the WVLA, which are sampled every 30 s, adequately provided the water column sound speed profiles needed for computing a time-dependent set of 400-Hz mode shapes using the KRAKEN[17] normal-mode code. (Bottom parameters are taken from Apel *et al.*[5]) The basis for this code, a numerical normal-mode solution of the Helmholtz equation at angular frequency ω,

$$[\nabla^2+k^2(r,\omega)]p(r,\omega)=0, \tag{2}$$

TABLE I. Auto and cross-mode rejection levels for best case, worst case, and average mode arrival/filter scenarios.

Input mode	Auto and cross-mode rejection levels (dB)											
	Best filter				Worst filter				Average filter			
	1	2	3	4	1	2	3	4	1	2	3	4
1	0	47	46	40	0	13	24	32	0	31	35	36
2	49	0	34	31	13	1	11	20	31	1	22	26
3	46	34	0	26	24	11	1	11	34	22	1	18
4	40	31	26	1	32	21	11	2	36	26	18	1

where $p(r,\omega)$ is the Fourier component of the pressure field, can be found in Jensen *et al.*[18]

The KRAKEN mode shapes are orthonormal in the sense that,

$$\int \frac{\phi_m(z)\phi_n(z)}{\rho(z)}dz = \delta_{mn}, \tag{3}$$

so given $p(z,t)$,$A_n(t)$ can be readily computed by applying the operator

$$\int (\cdot)\frac{\phi_n(z)}{\rho(z)}dz. \tag{4}$$

Since the pressure field, $p(z,t)$, is only sampled at the 16 hydrophone locations, the integral computation of the mode coefficients, $A_n(t)$, must be approximated by

$$A_n(t) \simeq \sum_{h=1}^{16} \frac{p(z_h,t)\phi_n(z_h)\Delta z}{\rho(z_h)}, \tag{5}$$

where Δz is the spacing between hydrophones. This discrete sum is easily implemented through matrix multiplication of mode shape vectors with 16 channel hydrophone data vectors (i.e., narrow-band direct-projection mode-filtering). A more accurate filter would take into account the frequency dependence of the modal depth functions over the bandwidth of the acoustic arrivals, but the effects were shown by our calculations to be minimal and thus the increased computation time was not warranted.[19]

The direct projection method works well for the low modes that are adequately sampled by the WVLA. A typical SWARM mode 1 shape will yield,

$$\sum_{h=1}^{16} \frac{\phi_1(z_h)\phi_1(z_h)\Delta z}{\rho(z_h)} = 0.9989, \tag{6}$$

very close to the ideal output of 1.0. Higher order modes have more energy outside the depths sampled by the WVLA, so the above projection-filtration scheme degrades, yielding outputs of 0.9949, 0.9881, 0.9803, 0.9681, 0.9269, and 0.8243 for modes 2 through 7, respectively. The higher order modes suffer more from partial vertical coverage than they do from undersampling, so that a simple output gain factor (such as one obtained by dividing the filter output by its projection-filtration level) may be useful if level comparisons between mode arrivals are to be made. However, an output gain factor will not provide relief from modal crosstalk, which is inherent with undersampling and partial coverage.

Two other factors to consider in mode-filter performance are array tilt and deviations between the calculated and actual modal depth functions at the receiver. Tilt for the WVLA seldom exceeds 1°, except during the passage of a particularly large soliton where it may approach 2°.[19] Time offsets between the actual modal depth functions at the WVLA and the mode-filter being used can range from 0 to 42 s.[19] These factors, and thus the levels of cross-mode rejection, are time dependent, i.e., we see fluctuations in the cross-mode rejection performance of the mode-filters. Worst case assumptions can drop the nearest neighbor (adjacent mode order) rejection levels down to the 10-dB level, but on average the performance is in the 20-dB range.

Table I gives best case, worst case, and average cross-mode rejection estimates for the mode-filters. The best case scenario assumes zero tilt and no time offset, and the worst case assumes a constant tilt of one degree and a 30-s offset between the arrivals and the mode-filters. As stated before, tilts may exceed 1 m from time to time and time offsets of up to 42 s are possible, so the ''true worst case'' is a fairly elusive concept; mode shapes can only be tabulated at 30-s intervals, and the tail of the tilt distribution function is difficult to quantify. Given all this, the term ''nearly worst case'' might be better for the tabulation presented above.

B. Acoustic impact of solitons

Internal wave induced coupling between acoustic normal modes, combined with differences in the acoustic modal group velocities, causes the time spreading of pulses as energy is transferred between different acoustic modes. In the SWARM waveguide, mode one usually has the highest group speed (see Table II), so that energy which transits in other modes for a portion of the source-to-receiver trip and then couples to mode one is of necessity delayed with respect to energy that traveled exclusively in mode one. This

TABLE II. Calculated modal group speeds at 400 Hz for sound speed profiles inside and outside the soliton shown in Figs. 3 and 4. The calculation of group speeds was performed using a range independent model.

Mode	Group speeds	
	Outside soliton	Inside soliton
1	1484.1	1484.2
2	1483.2	1482.8
3	1481.1	1480.0
4	1478.2	1477.7
5	1475.6	1475.2
6	1472.9	1479.7
7	1472.2	1488.6
8	1471.4	1488.4

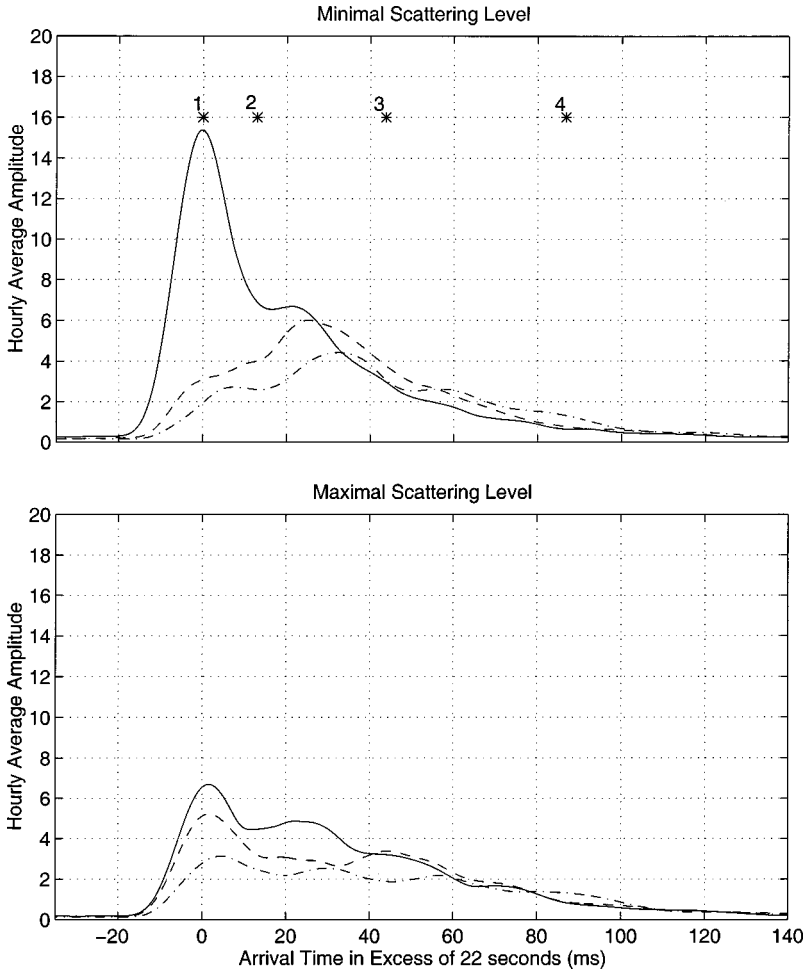

FIG. 6. Two different 1-h incoherent averages of mode one (solid), mode two (dashed), and mode three (dot-dash) filtered outputs. The top figure represents a period of minimal scattering of energy between modes and the lower figure a period of maximal scattering. The periods are separated by about 12.5 h. The numbered asterisks in the top figure represent predicted adiabatic mode arrival times for modes 1–4.

causes the spread of mode one energy to be all in one direction (i.e., there is a positive bias in the mean and median travel time of mode one energy relative to an unscattered mode one arrival). Higher order modes may have some energy arriving earlier (from traveling part of the path in lower order modes) and some arriving later (from traveling part of the path in higher order modes); thus there may be negative, positive, or even zero bias in the travel-time of the spread high order mode arrivals.

The effect of the spreading/smearing of energy on the intensity of mode one arrivals is two-fold. First, the spreading itself reduces the intensity of the mode one peak and, second, the attenuation level for higher order acoustic modes is greater, so energy that transits even a portion of the waveguide in some mode higher than mode one will suffer increased attenuation. This second effect was first proposed to explain intensity fluctuations observed in previous shallow water CW experiments.[1,20]

The amount of mode spreading and attenuation is quite variable. To illustrate this variability, Fig. 6 shows two different 1-h incoherent averages of mode 1–3 filtered outputs. The pulse distortion increases very dramatically over the 12.5 h separating these two averages.

III. TEMPORAL FLUCTUATIONS IN MODE ARRIVAL STATISTICS

Figure 6 provides a good illustration of the variability inherent in the mode filtered outputs of the acoustic data. Some of the important observables in the acoustic data are spread, bias, wander, intensity, and temporal coherence. All of these statistics are interrelated to varying degrees, and with the exception of wander, they are all sensitive to the numbers and location of solitons in the waveguide. We now examine them in some detail.

A. Spread, bias, and wander

1. 400-Hz mode 1 arrivals

We first look at the wander in travel-time of acoustic mode one. The nature of the SWARM waveguide is such that this mode generally has the highest group speed, making the energy that travels nearly exclusively in mode one the earliest possible arrival for most transmissions. This energy is referred to as the pseudo-adiabatic mode one arrival (PAM1).[19] It is not always the strongest peak in the envelope of a mode one arrival, but energy arrives at or near the PAM1 arrival time strongly enough so that distributions of mode one peak arrival times have observable leading edges. There are exceptions. During the early hours of day 212, at the WVLA, mode two has a higher group velocity than mode one; if and when this is the case for the majority of the waveguide, the PAM2 arrival will precede the PAM1 arrival, allowing for some positively biased mode one energy. The leading edge of mode one, when observable, is quite useful

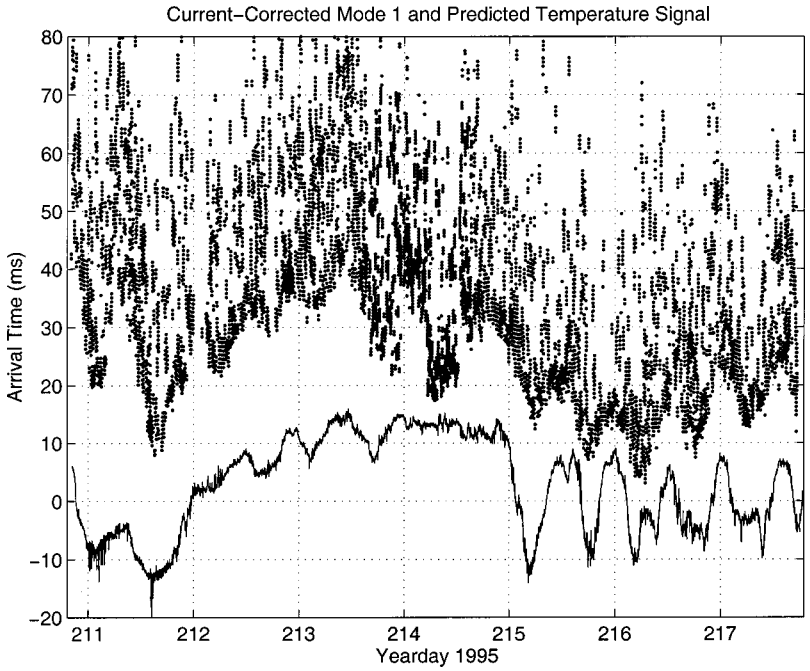

FIG. 7. Predicted temperature fluctuation effects on PAM1 arrival time (solid curve) plotted along with the distribution of ''current-corrected'' acoustic peak arrival times (dots). The peaks are picked from over 32 000 mode one arrival envelopes that are similar to those shown in Fig. 6. Only the highest peak from each envelope is plotted. The solid curve prediction is zero mean (by definition) and is offset from the acoustic data for convenience. Generally good agreement between the prediction and the leading edge of the acoustic pulses in noted.

in that its travel-time wander is a sensitive measure of the oceanic heat content variation along the path connecting the source and receiver.

The ''current-corrected'' distribution of SWARM mode one peak arrival times, which is our cleanest data set for the modes, is shown in Fig. 7. The arrivals have a fairly sharp leading edge; there is little or no indication of negatively biased peaks. [The current-correction to travel-time is derived from a bottom moored current meter near the WVLA. Specifically, the predicted travel-time fluctuations (order ± 3 ms) obtained from applying the measured barotropic (depth independent) currents (predominantly M2 tidal, i.e., the strong 12.42-h period semidiurnal tidal component) to the entire acoustic path were subtracted from raw peak arrival times.] The mode one wander, as seen in Fig. 7, is substantial, and a good portion of it can be correlated with temperature fluctuations in the vicinity of the WVLA. These fluctuations were logged in thermistor records from the WVLA and three dedicated thermistor strings moored in a cluster 4.5 km shoreward of the WVLA. The solid curve in Fig. 7 is obtained by using the average change in sound speed seen at seven of these thermistors to calculate travel-time variations. The seven thermistor records used (three from the WVLA, four from the dedicated strings) were in the depth band of interest for acoustic mode one (40–60 m) and judged to be reliable records. The foot of the shelfbreak front, which has been observed in CTD profiles to extend across the position of the WVLA, seems a very likely source of the temperature fluctuations.[5] The actual range between the thermistors used is only 4.5 km, but the effects may be reasonably extrapolated farther along the acoustic path, since the foot of the front extends somewhat farther inshore. The choice we made of 8 km provides a level of predicted variance close to that observed in the acoustic data. However, the PAM1 wander occurring on yearday 214 is a clear indicator that large temperature fluctuations are not entirely restricted to the frontal area around the WVLA, and it is likely that changes in temperature along the entire 32-km path contribute at various times and in varying degrees to the acoustic mode one wander.

We next look at the spread of the mode one arrival at 400 Hz. The range and variability of positive bias seen in the Fig. 7 peak arrival distribution is indicative of significant time spreading in the mode one arrival patterns. Spread is perhaps the simplest quantitative measure of signal distortion and also is a clear indicator of coupled mode scattering being produced by the waveguide.

Spread is conceptually simple, yet the choice of which mathematical definition of spread is ''best'' to use is somewhat subjective. Four typical measures that could be considered are: (1) the interquartile range (IQR) of the arrival envelope; (2) the standard deviation of the arrival envelope; (3) the absolute value of the peak minus the mean arrival time; and (4) the standard deviation of the peak times in a 22 sequence transmission. This list is obviously not exhaustive but is a good selection of the possibilities. We will eventually concentrate on IQR in our work, where the IQR time spread is defined here as the difference in time between where 25% of the total pulse integrated amplitude (always positive, i.e., absolute value of amplitude) has arrived and where 75% of the total pulse integrated amplitude has arrived. One can use energy definitions of IQR as well; we chose amplitude simply for ease of processing.

Using method one, the IQR, analysis results for the WVLA mode one arrival spread are shown in Fig. 8. The upper frame of Fig. 8 is a plot of the spread averaged over each 22-sequence transmission, while the lower frame includes five different bin averages ranging from 1.4 to 4.1 h for comparison. The upper frame of Fig. 8 reveals significant spread variability over time scales ranging from several minutes up to semidiurnal tidal oscillations. The M2 tidal oscillations, along with other low frequency signals, are readily evident in the longer bin averages shown in the lower frame.

The second method of estimating spread, standard de-

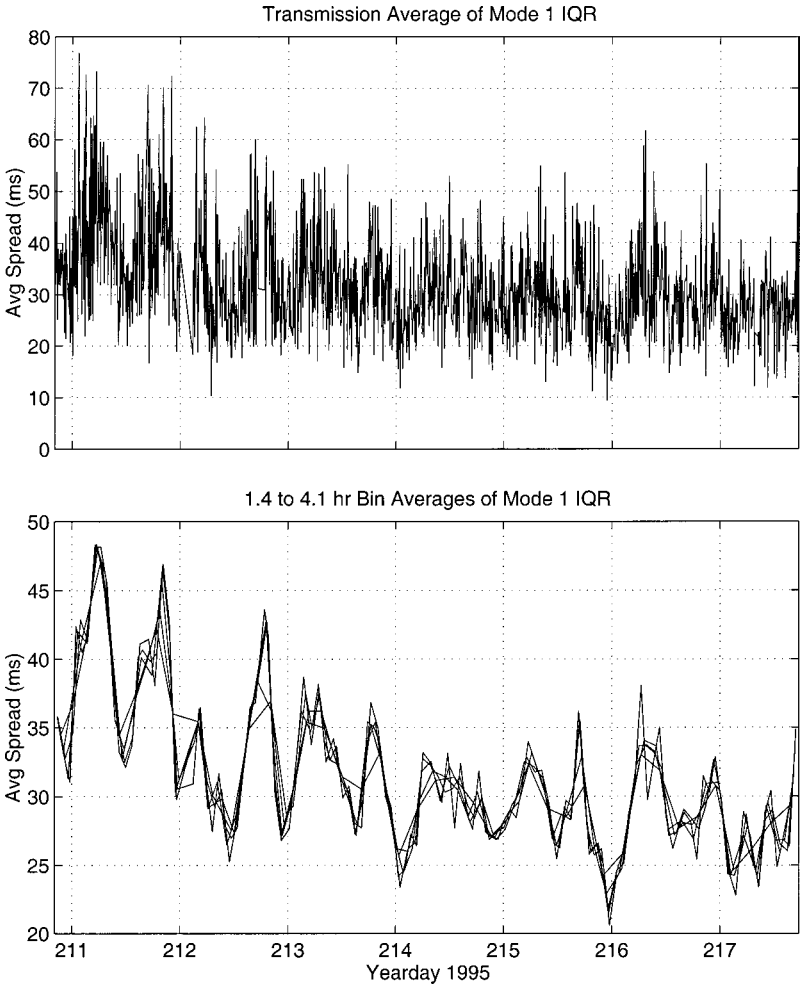

FIG. 8. Mode one arrival spread, as measured by the IQR of the arrival envelope (unscattered IQR is about 7.2 ms). The upper frame of Fig. 8 is a plot of the spread when averaged over each transmission (22 sequences per transmission). The lower frame shows bin averaged spreads for five bin widths ranging from 1.4 to 4.1 h.

viation, is very similar to the first; the main difference is in its sensitivity to outlying energy. The third method, absolute value of peak minus mean, strictly speaking, is more a measure of ''non-Gaussianess'' than a measure of spread, but these usually go hand-in-hand. Whereas the first three methods require evaluation of the arrival envelope, the fourth method, standard deviation of peak times, only requires the peak arrival times to be recorded. The tradeoff for this is that only one measurement can be obtained per transmission, as opposed to 22 per transmission for the other three.

Applying each of these methods to the mode one arrival records from SWARM produces varying degrees of similarity between methods. Using 1.4-h bin averages (see Fig. 8) as benchmarks, the following matrix of zero-lag cross-correlation values between the time series generated by the different methods can be constructed:

$$\begin{bmatrix} 1.00 & 0.97 & 0.85 & 0.57 \\ & 1.00 & 0.82 & 0.60 \\ & & 1.00 & 0.29 \\ & & & 1.00 \end{bmatrix}.$$

As expected, the correlation is the strongest between methods one and two, and the other combinations show limited similarity. The IQR will from here on be the primary method by which spread is measured.

We also looked at our Fig. 8 time series in the frequency domain. The spectra (not shown) reconfirm the existence of significant variability near the M2 semidiurnal tidal frequency. This tidal variability is consistent with our understanding of the most probable source of the spread in the arrivals: internal wave solitons associated with nonlinear M2 internal tides called ''solibores.'' [21]

The relationship between tides and soliton formation appears to be strong, but it is not simple, and it is certainly not linear; the numbers and sizes of solitons, as well as the extent of the internal tidal bores (long wavelength, nonlinear internal tide isotherm depressions) they are often associated with, can change dramatically from one tidal cycle to the next. This, coupled with multiple soliton-generation sites and the complicated relationship between acoustic spread and soliton density, produces a rather broad M2 line in the pulse spread spectrum. Figure 9 graphically illustrates this variability in the soliton packets from cycle to cycle. Figure 9 also displays another very important effect—the mean spread levels are seemingly controlled by the density of solitons in the near-receiver portion of the waveguide. The sensitive dependence of the pulse spreading to solitons near the receiver is an important point in this paper, as well as in the sequel paper to this one.[22] A brief explanation of the physics of why the spreading depends most crucially on near-receiver solitons is to be found in the Appendix of this paper; a more

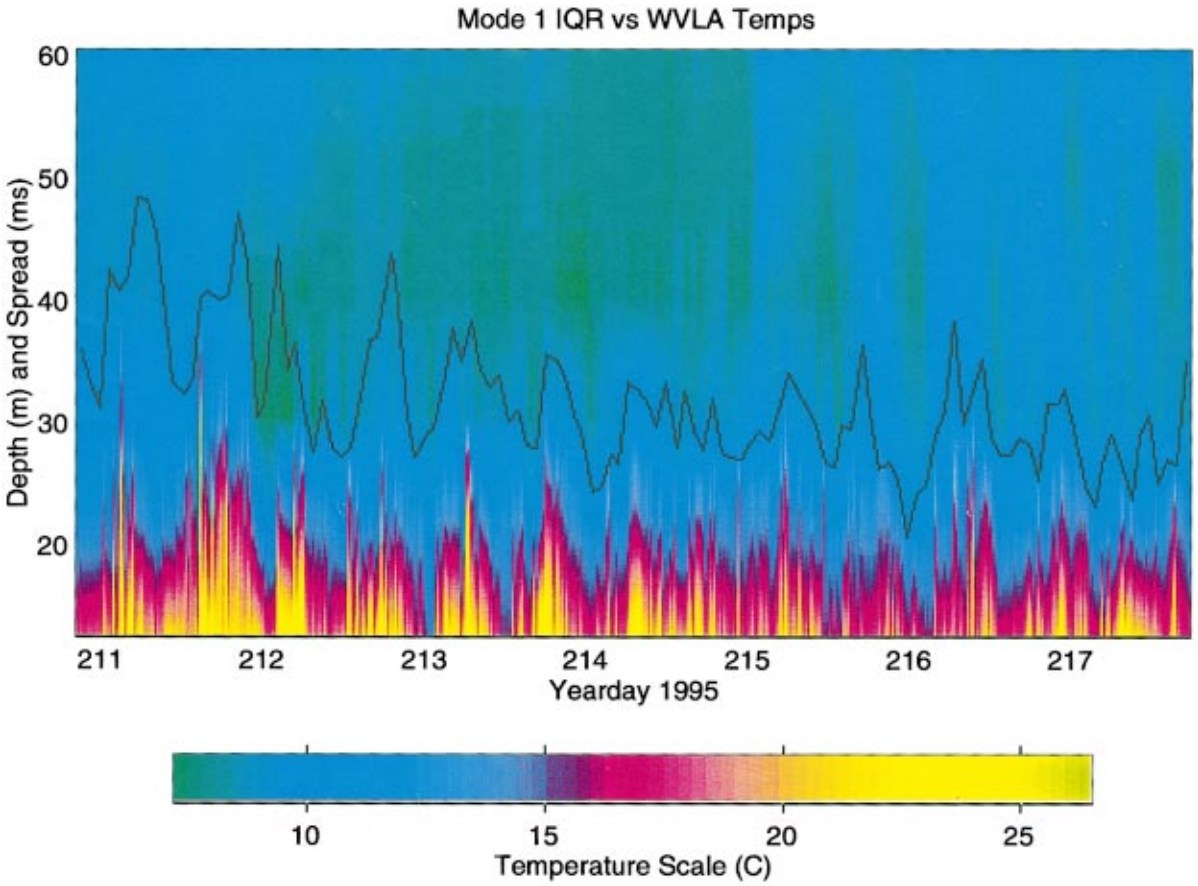

FIG. 9. WVLA temperature as function of time and depth overlaid by the 1.4-h bin averaged IQR estimate of mode one arrival spread at the WVLA. Both the variability in the fields and the correlation of the spread to the near-receiver temperature fluctuations are of note here.

detailed explanation can be found in the sequel paper.

To further understand the relationship between the oceanography and the acoustic spread and bias seen, we will look at the propagation of the solibores along our acoustic track. This oceanography and its relation to the sound speed field is most easily seen in the isotherm displacement records made by the thermistor strings placed along the acoustic path. (We have already looked at these records somewhat in examining the acoustic wander.) Since the majority of solitons in the SWARM region propagate anti-parallel to the acoustic path, one can assume, to first order, that most of the temperature disturbances seen at the WVLA will propagate in some fashion across the shelf toward the acoustic source region at speeds from 0.6 to 0.8 m/s.[19] To show this, Fig. 10 illustrates an analysis of three thermistor records from various locations along the acoustic path. The first is record is from a thermistor on the WVLA at a depth of 12.5 m. The second record, at a range of 5 km, is from a thermistor from Temperature String 598 at a depth of 17.5 m. The final record, at a range of 32 km, is from a thermistor on the Naval Research Laboratory (NRL) source mooring at a depth of 18 m. (The NRL source was moored about 0.6 km downslope from the 400-Hz tomography source. It did not function, but the thermistor pod on it did.) The diagonal lines on Fig. 10 correspond to a nominal solibore propagation speed of 0.8 m/s; this speed reasonably connects many of the tidal period disturbances evident in the three records, especially the low frequency M2 ''solibore envelope.'' Later portions of all three records (past yearday 214, e.g., see Fig. 9 for the WVLA record) have weaker M2 internal tidal signals that are hard to correlate between moorings. Assuming this fixed propagation velocity of 0.8 m/s anti-parallel to the acoustic path, the disturbances at the WVLA would reach the acoustic sources some 670 min later. Thus using Fig. 9, an inference can be made that the temperature profiles in the graph up to 670 min earlier than a given spread reading at time t_0, when converted to distance using 0.8 m/s, are a rough approximation to what the waveguide looked like at the time of the transmission. This inference is basically a ''frozen field,'' constant velocity advection approximation that follows Rubenstein and Brill.[20] Such an approximation ignores the the spatial and temporal evolution of the solibores,[23] but given that we did not have the extensive data needed to quantify the evolution of individual solibores, it is a reasonable, ''data based'' first approximation.

As mentioned, a visual analysis of Fig. 9 reveals a reasonable degree of correlation between mode one spread levels and soliton induced thermal activity near the receiver. The estimated WVLA-receiver-to-source transit time of 11.2 h is sufficiently short to place the bulk of the previous tidal cycle's solitons outside the acoustic path when a solibore packet of interest is in the region of the waveguide near the receiver. However, the situation reverses if slightly lower, but still reasonable, soliton propagation speeds are assumed; a speed of 0.6 m/s yields a receiver–source transit time of 14.9 h, placing two sets of solitons in the acoustic path at the

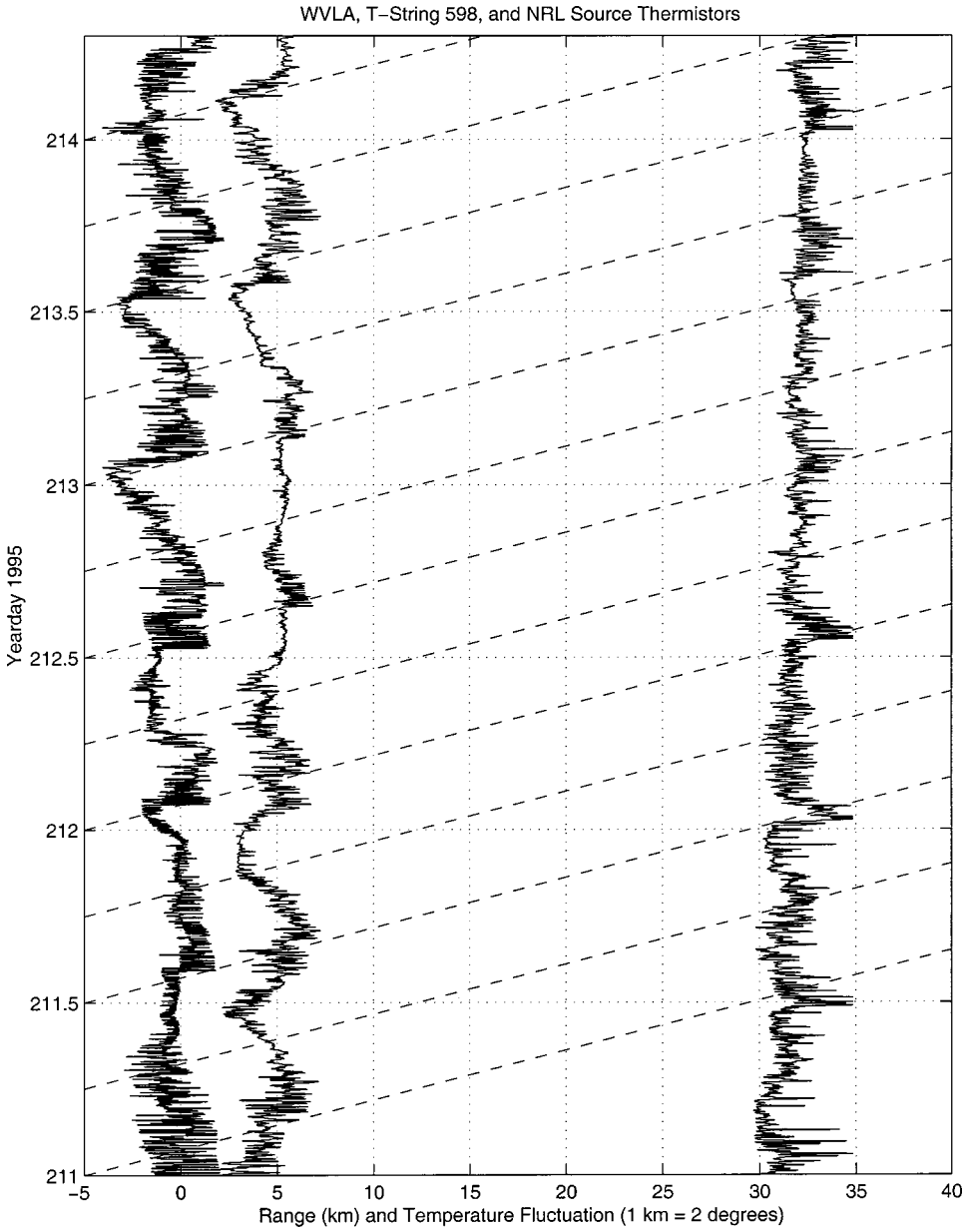

FIG. 10. The temperature fluctuations at three shallow thermistors plotted as a function of time, offset by their respective shoreward distances from the WVLA. The first is a thermistor on the WVLA at a depth of 12.5 m, the second at range of 5 km is a thermistor from Temperature String 598 at a depth of 17.5 m, and finally at a range of 32 km is a thermistor from the NRL source mooring at a depth of 18 m. The diagonal lines correspond to a propagation speed of 0.8 m/s.

times when large numbers of solitons are near the receiver. Also, it is observed that ''M2 arrival times'' of trains of solitons at a fixed point a few tens of kilometers shoreward from the shelfbreak fluctuate by $\pm 10-20$ percent, due to changes in oceanographic conditions. Thus 11.2 h is really just a mean of a distribution of solibore transit times between the WVLA and the source location. This is reflected in the Fig. 10 data, and implies that our present data thus cannot unambiguously differentiate between effects due to solitons near the acoustic sources and near the acoustic receivers. (The third array deployed, which failed due to flooding, would have been able to make such an unambiguous separation due to its shorter source-to-receiver path.) We thus must still appeal somewhat to physics arguments that the time spreading observed is due to near-receiver solitons, as opposed to solitons near the source. Again, we refer the reader to the Appendix and to our sequel paper.[22]

Even with an assumed 11.2-h transit time, it is difficult from Fig. 9 to exactly quantify correlations between soliton activity and spread levels visually. However, if the standard deviation of the temperature at 22.5-m depth over the previous 4.3 h (a reasonable binning time and ''much less'' than either the 11.2-h transit time or the 12.42-h M2 period) is used as a measure of soliton activity near the receiver, then we can see a clearer picture of the time series correlation, as shown in the upper panel of Fig. 11. A correlation level of 0.65 is obtained (see Fig. 11, lower panel). This level is rather good, given the inherent variability in the oceanographic field and the acoustic pulse shapes.

2. Higher modes

Peak arrival scattergrams for the higher order modes look similar to the mode one scattergram shown in Fig. 7. The scattergram data for the first four modes are summarized, using their leading edges and bin averaged mean arrival times, in the plots shown in Fig. 12. These figures show two more statistics with a strong M2 tidal influence. The

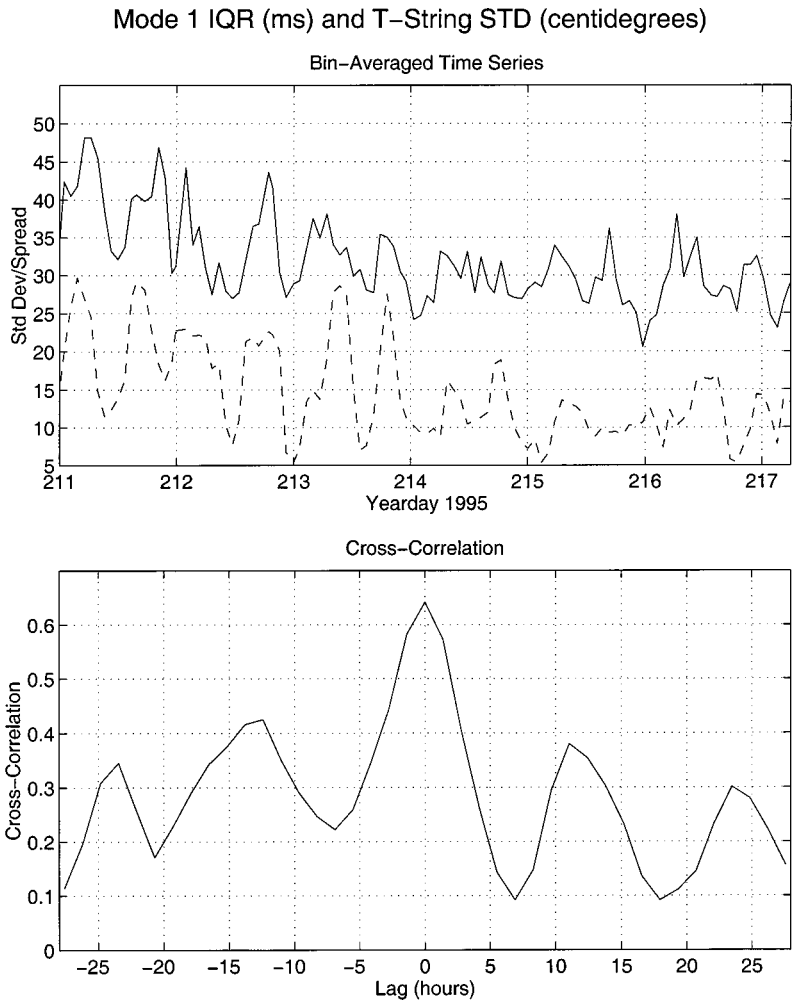

FIG. 11. The upper frame shows a comparison of 1.4-h bin averaged IQR levels for the SWARM data (solid line) and the standard deviation of the temperature at 22.5-m depth over the previous 4.3 h (dashed line). The standard deviation of the temperature is in tenths of a degree C to facilitate comparison with the IQR levels in milliseconds. The lower frame shows the cross-correlation of the two time series.

mean mode four arrival time has an M2 tidal variability that is greater than the tidal modulation of the PAM1 arrival (i.e., the peaks in the upper panel dotted line have larger amplitudes than the peaks in the lower panel solid line). These mean mode four arrivals are also negatively biased relative to the predicted PAM4 arrival, and are generally within 80 ms or less of the mode one leading edge (80 ms is the average difference between computer simulated PAM1 and PAM4 arrivals). In physical terms, this implies that the mode four arrival structure is more sensitive to mode coupling than is the mode one arrival structure, which is sensible, since mode four would be extremely weak (due to bottom attenuation) were it not for mode coupling.

Following Fig. 11 for mode one, Fig. 13 compares 1.4-h bin-averaged spread statistics for modes 2–4 to the standard deviation of the temperature at 22.5-m depth over the previous 4.3 h. The behavior of the mode two spread is very similar to the mode one behavior, and the correlation with the temperature statistic is equally strong. As the mode number increases past mode two, the tidal signal appears to decorrelate from our measure of ''near-receiver'' soliton activity. Physically, we believe that this is due to a larger fraction of the high mode energy being due to mode coupling whenever it is seen, so that it will have a more constant amount of spread versus clock time.

3. 224-Hz arrivals

The 224-Hz tomography source, moored about 1000 m farther up the shelf, provides a second source of acoustic arrivals at the WVLA. The narrower bandwidth of the 224-Hz source yields a pulse width of about 60 ms versus the 10-ms pulse width of the 400-Hz signal.

The wider pulse width of the 224-Hz source no doubt contributes to the somewhat fuzzy distribution of 224-Hz mode one peak arrival times shown in Fig. 14. It is difficult to estimate just what portion of the variability in the 224-Hz peak arrival time wander should be attributed to measurement uncertainty associated with the broader pulse, but using the shape of the 400-Hz pulse leading edge as a guide, an uncertainty of around ± 5 ms appears to be appropriate. A similar qualitative analysis of Fig. 7 leads us to believe the uncertaintity for the 400-Hz peak arrival times is less than about ± 2 ms. An interesting feature of the Fig. 14 plot is the apparent divergence between the leading edges of the 224-Hz and 400-Hz distributions of peak arrival time. Frequency dependence in the mode one group velocity is not large enough to explain all of this divergence. One possibility is that the leading edge in the mode one 224-Hz arrivals may not be as strongly tethered to the PAM1 arrival time as is the case for the 400-Hz mode one arrivals.[19]

The time histories of the 224-Hz and 400-Hz bin aver-

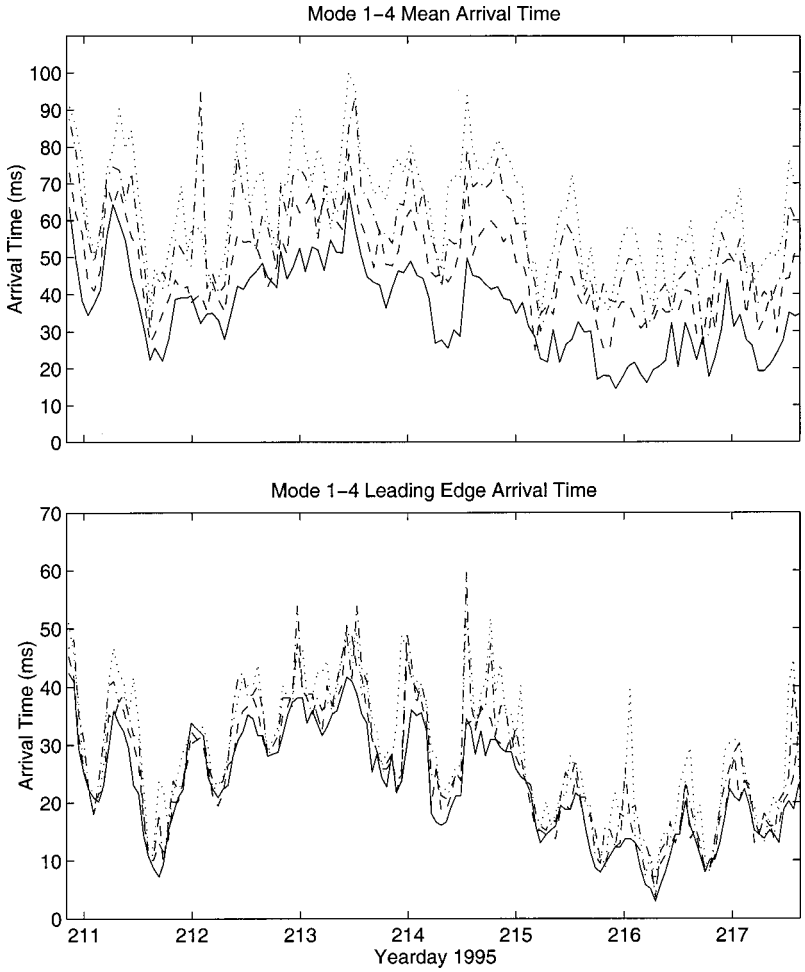

FIG. 12. The lower panel shows plots of the mode one (solid), mode two (dashed), mode three (dot-dashed), and mode four (dotted) peak arrival time distribution leading edges (the plots connect the earliest peak arrivals in 1.1-h bins). The upper frame shows the corresponding 1.4-h bin average mean peak arrival times.

aged mode one spread (IQR) statistics are compared in Fig. 15. Both records exhibit fairly strong M2 tidal modulation of the spread during the first part of the recorded period. The latter portions of both records have more limited tidal signatures, but the modulation that does exist is somewhat similar, and the mean levels of spread exhibited are both about 23 ms above their respective unscattered levels of 7 and 37 ms. (We note that we have included the natural width of the pulse in the spread both in Fig. 15 and our other work, i.e., reported ''total pulse width'' as spread.) The zero-lag cross-correlation between the two entire records is 0.72. The closeness of the spread numbers (23 ms) is easily understood from our receiver dominance argument in the Appendix. The strength of the two-frequency cross-correlation (0.72) needs a more complex picture of the coupled scattering to explain it, and we refer the reader to the papers by Duda and Preisig.[16,24]

B. Temporal coherence and intensity fluctuations

Given the significant spread observed in the mode-filtered outputs, which implies significant scattering, one would expect to observe fairly short average decorrelation times. To illustrate this, Fig. 16 shows mode 1–4 filtered outputs for five sequences separated by 20 s and five sequences separated by 6 min, over a 30-min period. This figure shows fairly strong correlation between sequences separated by up to 1 min and 22 s; however, the temporal variability over a 6-min period is quite dramatic. The mode pressure amplitude patterns at 6-min lag are basically uncorrelated.

A more quantitative measure of the individual mode temporal coherences can be reached using our data by computing the correlation coefficient between the first sequence (arrival structure) of a transmission and the 20 subsequent sequences in that transmission. Figure 17 displays the results of such computations when averaged over ten transmissions. For the analyzed time period, the average 3-dB down points for the correlation functions fall between 70 and 90 s.

Analysis of this limited number of records tends to confirm suspicions that decorrelation times for the mode arrivals are fairly short, but further analysis shows the decorrelation times themselves to be highly variable. Figure 18 shows the variations of 1.4-h bin averaged 3-dB down decorrelation times for modes 1–4 over a one week period. The broken nature of the data (approximately 2 min of data followed 4 min of silence) is such that quadratic extrapolation is needed to estimate decorrelation times beyond the 107-s point. This extrapolation leads to some large correlation time estimates that are obviously unrealistic; this is an unavoidable error, given our data sampling.

A semidiurnal tidal signature is evident in each of the four plots in Fig. 18. This modulation is a direct consequence of the semidiurnal fluctuations in the distribution of solitons in the waveguide. They cause most of the coupled scattering,

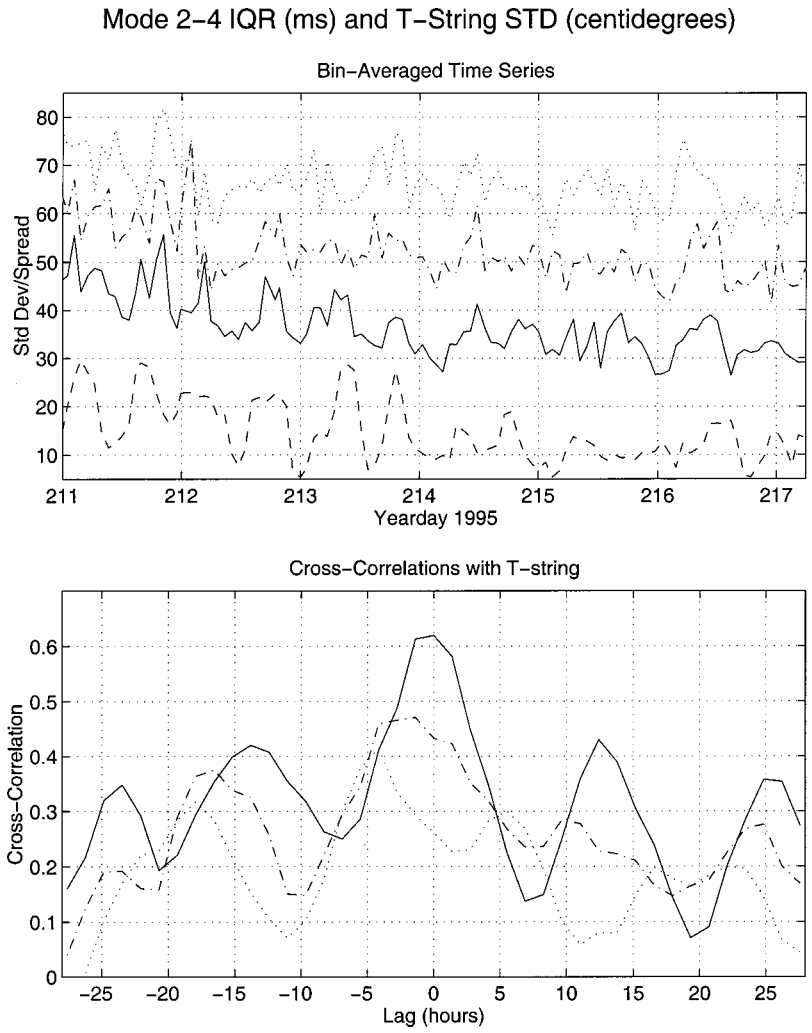

FIG. 13. The upper frame shows a comparison of 1.4-h bin averaged IQR levels for mode two (solid line), mode three (dot-dash line, offset by an additional 10 ms), and mode four (dotted line, offset by an additional 20 ms), and the standard deviation of the temperature at 22.5-m depth over the previous 4.3 h (dashed line). The standard deviation of the temperature is in tenths of a degree C to facilitate comparison with the IQR levels in milliseconds. The lower frame shows the cross-correlation of the temperature statistic with the three bin-averaged spread statistics.

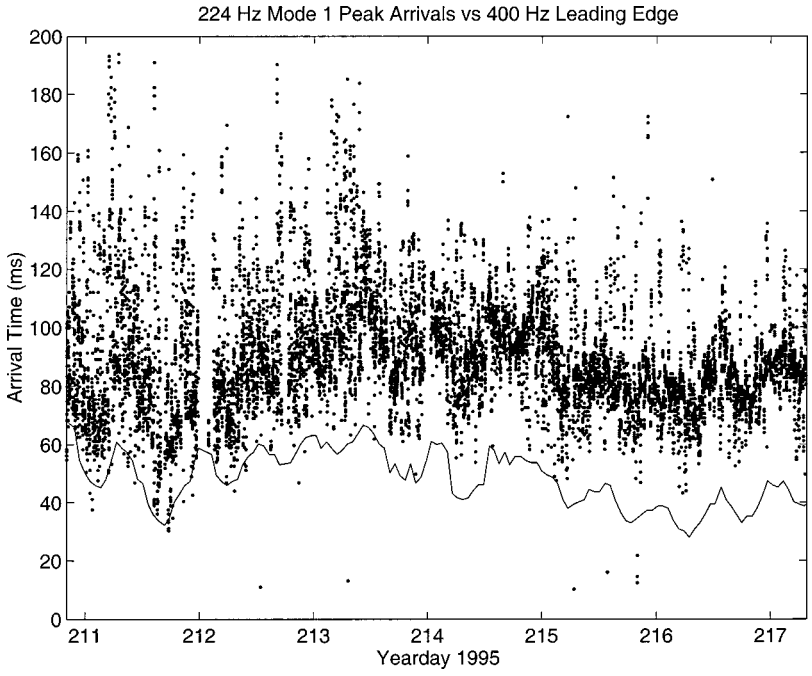

FIG. 14. Distribution of SWARM 224-Hz mode one peak arrival times. The zero reference is at an arrival time of 22.453 s. The plotted transmissions occurred every 5 min. Only 8 sequences (every 4th from 1 to 29) are shown of the 29 available. An upshifted leading edge of the 400-Hz peak arrival distribution is also shown for comparison. The later zero reference time, relative to Fig. 7, stems from the difference in source mooring locations.

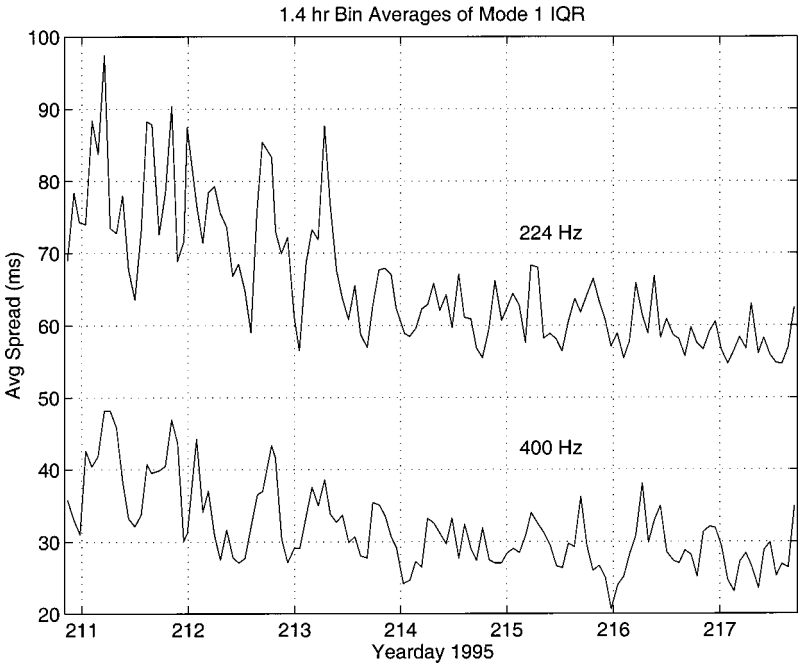

FIG. 15. Comparison of 224-Hz and 400-Hz 1.4-h bin averaged IQR (spread). The IQR pulse width of an unscattered 224-Hz pulse would be about 37 ms (7 ms for a 400-Hz pulse).

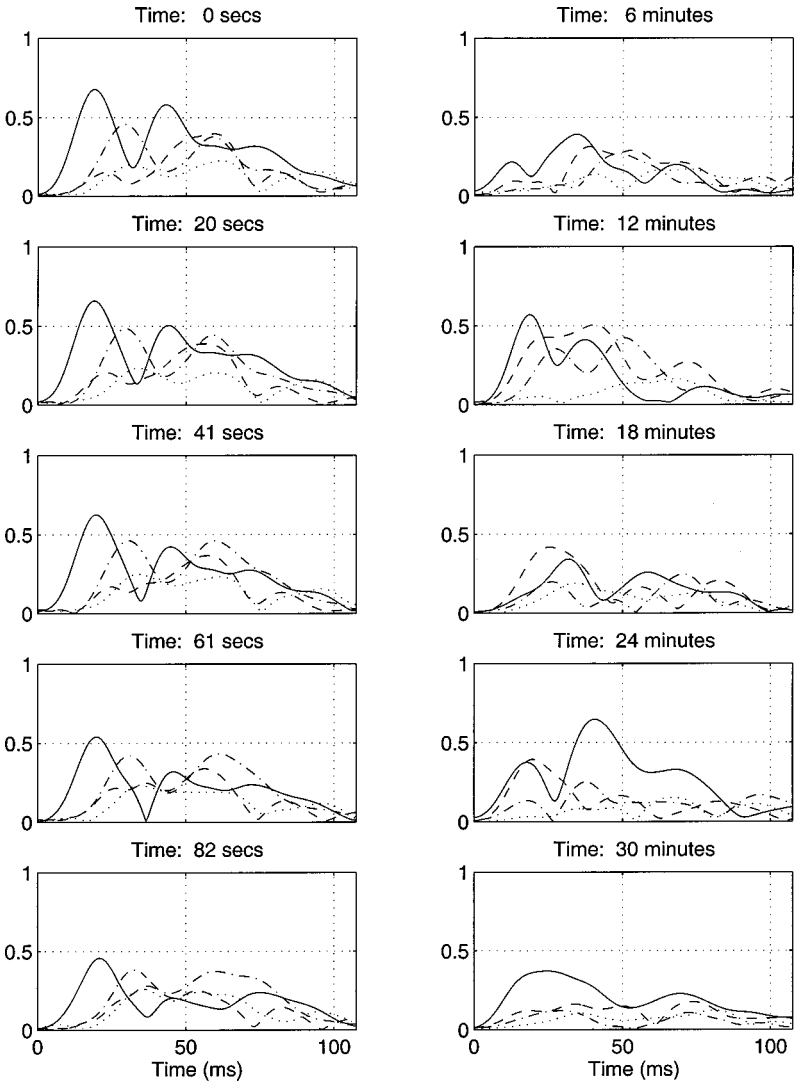

FIG. 16. Mode coefficient outputs, A_1 (solid), A_2 (dashed), A_3 (dot-dash), and A_4 (dotted), as a function of time. The five plots in the left column depict the evolution of the mode arrivals over a period of 82 s. The plots in the right hand column depict the evolution of the mode arrivals over a period of 30 min.

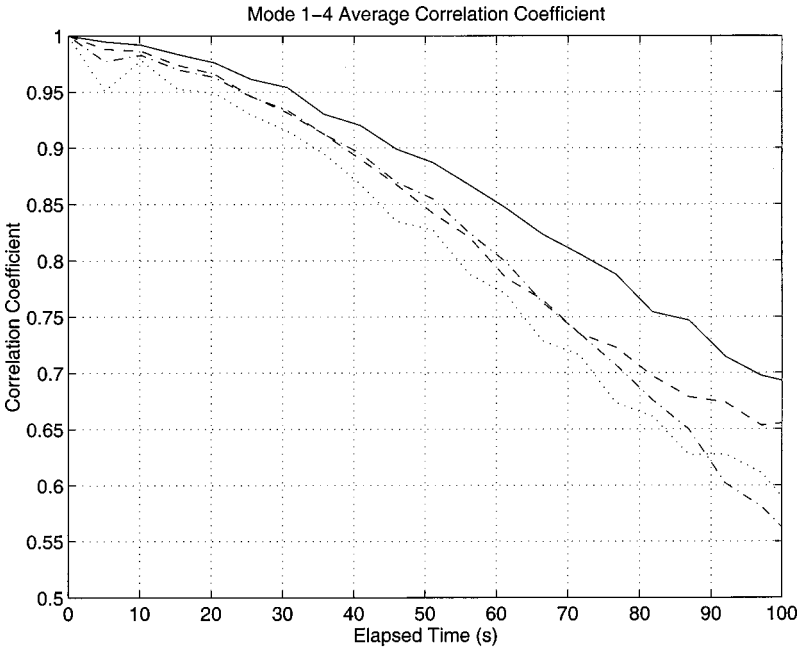

FIG. 17. Average correlation coefficients for outputs, A_1 (solid), A_2 (dashed), A_3 (dot-dash), and A_4 (dotted), as a function of elapsed time. The average is taken over the ten transmissions of Fig. 6.

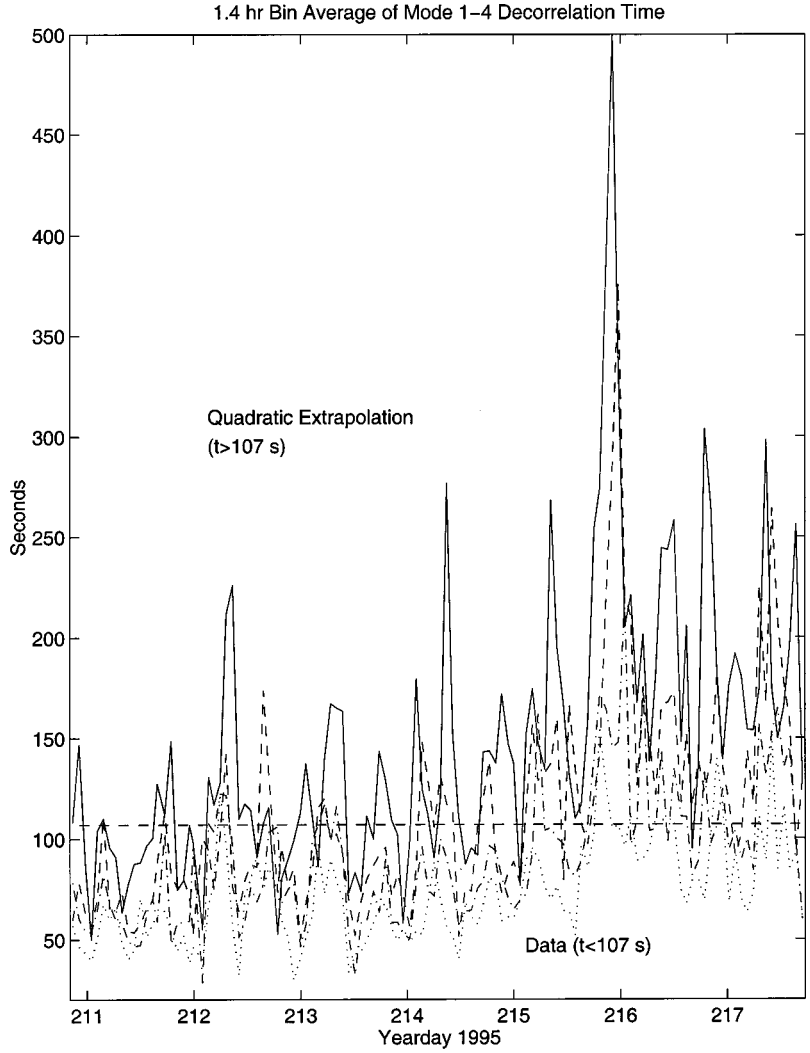

FIG. 18. Decorrelation times for 400-Hz modes 1–4. Mode one is solid, mode two is dashed, mode three is dot-dashed, and mode four is dotted.

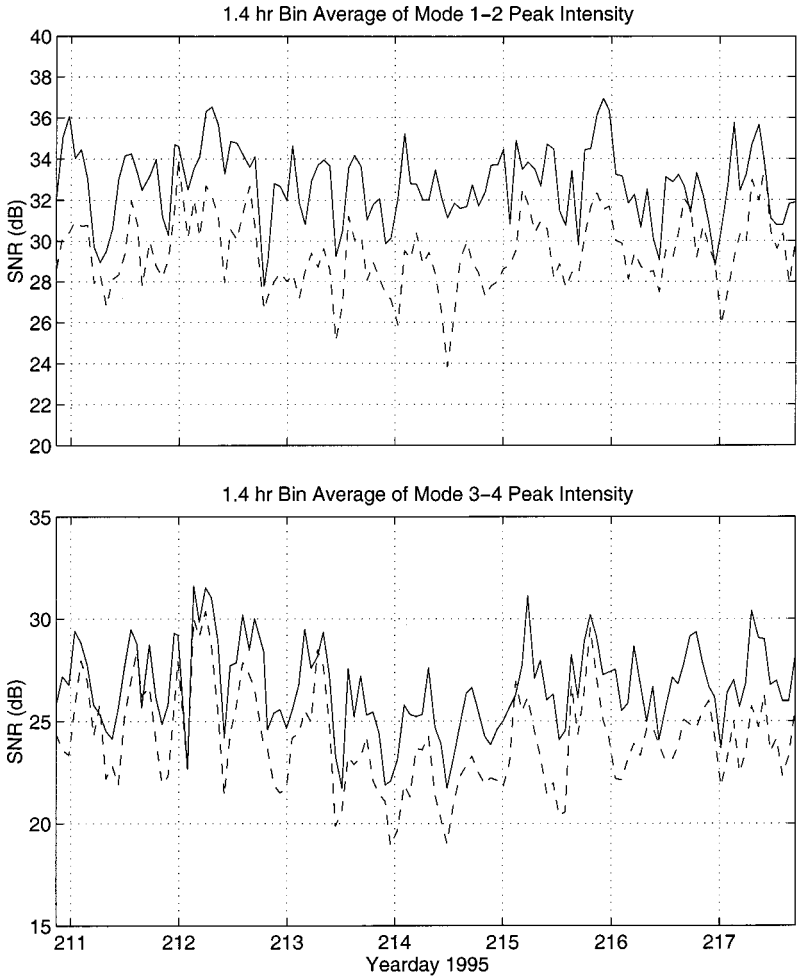

FIG. 19. A comparison of 1.4-h averaged peak-SNR fluctuations for the first four modes of the SWARM data. In the upper frame, mode one is solid and mode two is is dashed. In the lower frame, mode three is solid and mode four is is dashed.

and as the overall amount of mode coupling increases, the level of temporal coherence decreases. The individual mode temporal coherence decrease again correlates well with soliton activity near the receiver.

Increased coupling between modes also affects the peak intensities of the mode arrivals, as evidenced by the strong tidal modulation seen in the Fig. 19 plots of 1.4-h bin averaged peak SNR levels for modes 1–4. Intensities of these lower order modes are reduced as scattering levels increase, so their peak intensity tends to oscillate in phase with temporal coherence and decorrelation time.

The strength of the correlation between the modal intensity and mode decorrelation time appear to increase with mode number, as evidenced by the cross-correlations shown in the upper frame of Fig. 20. The cross-correlation between mode 1–4 peak intensity and our general measure of ''near-receiver'' soliton activity is shown in the middle frame of Fig. 20. Whereas mode one and two *spread* levels were shown to be ''in-phase'' with soliton activity near the receiver (see Figs. 10 and 12), the peak negative correlations with intensity fluctuations occur when the intensities lead (by 2 or 3 h) our soliton activity measurement. One possible explanation for this result is that, given our experimental configuration, solitons from the previous tidal cycle that are near the source are scattering energy from the low modes into the high modes, which are more quickly attenuated. This sensitivity of amplitude effects to soliton activity near the source would also be in agreement with recent numerical studies by Duda and Preisig.[24]

Finally, the plots in the lower frame of Fig. 20 show the cross-correlations between intensity and spread levels for modes 1–4; no phase lags are evident, but only mode one shows a significant negative peak. The mode one result is not too surprising, as its phase lag in the middle panel is only 1.4 h (one unit of resolution).

IV. SYNOPSIS OF MAIN RESULTS, CONCLUSIONS, AND FUTURE DIRECTIONS

The following conclusions and thoughts on future directions can be drawn from our data analyses.

To begin with, acoustic normal mode arrival time spread and bias, and the modal intensities and decorrelations times measured in the 1995 SWARM experiment show distinct M2 tidal period fluctuations. These are highly correlated to the passage of trains of solitons between the source and receiver. A particular interesting correlation was that of the maximum modal pulse spread with solitons near the acoustic receiver. Although we have not shown it here, there are no other oceanic or bottom acoustic phenomena which can create this same M2 type of signal in our data, so we can reasonably state that these effects *are* due to internal tide solibores. (The interested reader is referred to the thesis by Headrick.[19])

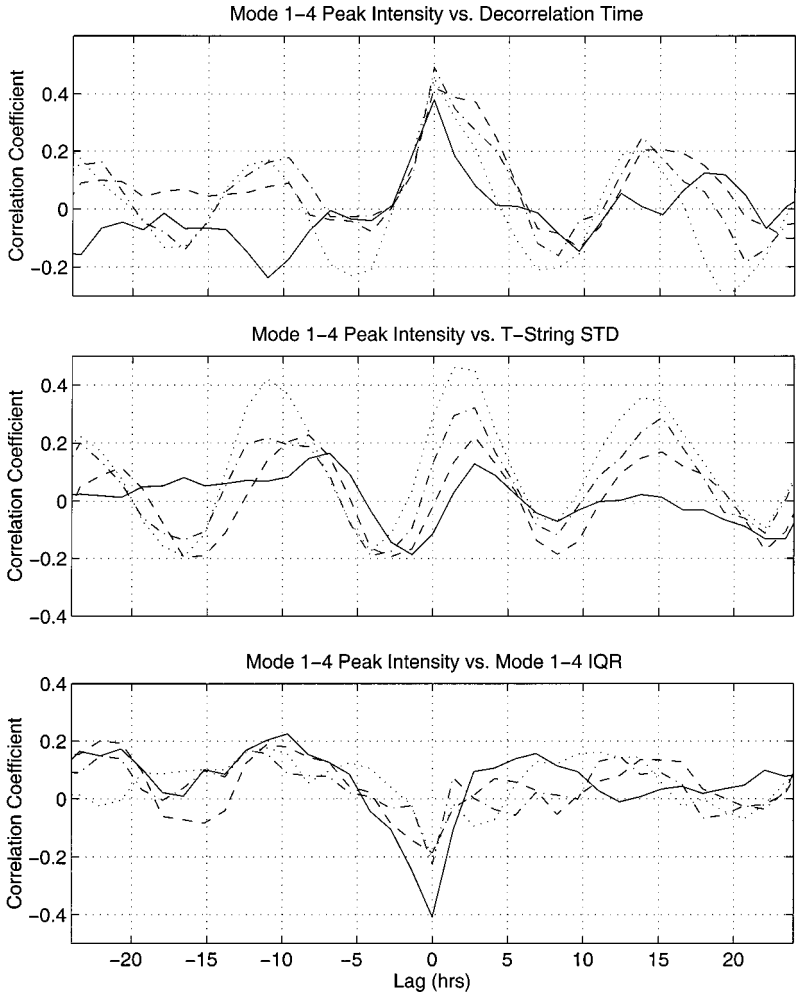

FIG. 20. The upper frame shows cross-correlations between peak intensities and decorrelation times for 400-Hz modes 1–4. The middle frame shows the cross-correlations between mode 1–4 peak intensities and the standard deviation of the temperature at 22.5-m depth over the previous 4.3 h. The lower frame shows the cross-correlations between mode 1–4 peak intensities and the mode 1–4 spread levels (IQR). Mode one is solid, mode two is dashed, mode three is dot-dashed, and mode four is dotted.

Next, under a common shallow water circumstance, i.e., when mode one has the highest group speed, a pseudo-adiabatic mode one (PAM1) arrival time can be estimated from a distribution of peak mode one arrival times by finding the leading edge envelope of the distribution. We saw that mode one had the highest path-averaged group speed for most, if not all, of the duration of the SWARM experiment. This leading edge peak can be very useful for ocean thermometry (or tomography) studies. As an example of this, we observed that large fluctuations in the path-averaged mode one group speed occurred over tidal and subtidal periods during the course of the experiment. A significant percentage of the mode one group speed fluctuations could be attributed to warm water advection in the seaward 5 to 10 km of the SWARM waveguide. This advection, which is probably associated with movement of the foot of the warm, salty shelf-break front, was clearly seen in deep thermistor records near the receiver.

Additionally, although the M2 signal was stressed in this paper, our time series also showed that soliton-filled waveguides produce significant mode arrival structure distortions with fluctuation time scales ranging from minutes to days. We need both better high frequency data and low frequency data to study the 0–10 min and 3 days– 3 months variability signals due to internal waves.

Finally, our data had at least one ''feature'' we wish we could have avoided. The tomography sources and the WVLA receiver were spaced at a distance which corresponds to ~11.2 h for the time of propagation of a soliton train between the two. This is very close to the 12.42-h M2 tidal period at which solitons are generated. Since: (1) the soliton trains have ''time spreads'' of ~3 h to transit a given point, and (2) the times of propagation can also very 10–20 percent due to oceanographic conditions, we often have solitons close to both the source and the WVLA receiver. Thus our data cannot resolve perfectly well whether the acoustic scattering due to solitons was due to solitons near the source or near the receiver. It can, however, distinguish between scattering at the endpoints and scattering in the middle of the path. Working with model predictions has allowed us to resolve this experimental ambiguity to some extent.

As to the future, there are still many gaps that need to be filled in our studies of modal acoustic scattering by soliton-filled ocean waveguides. These include: (1) examining a broader range of acoustic frequencies; (2) obtaining data along a shorter path where the source/receiver scattering ambiguity we encountered does not exist ($R \leqslant 20$ km) (we actually had such a path in our SWARM experiment, but the receiver flooded); (3) examining longer continuous time series of acoustic transmissions (as our 2-min transmissions obviously did not give us quite enough time to fully estimate modal acoustic temporal decorrelation and our one week time series could not see longer term effects such as spring neap cycles); (4) looking at along-shelf propagation paths;

and (5) examining arrivals across a horizontal array. This list is obviously an incomplete one, but represents some of the first order issues the SWARM group sees as important. Our study here also obviously does not encompass full wave acoustic studies, array coherences, or modeling issues—these topics are being pursued, but are beyond the scope of the one pursued in this paper.

ACKNOWLEDGMENTS

We would first like to heartily acknowledge all of our SWARM collaborators; without their superb efforts, the success of the SWARM experiment would not have been possible. Our principal Office of Naval Research sponsor, Dr. Jeff Simmen, is also warmly acknowledged for his strong support of the project. The support of Dr. Lou Goodman of ONR for some of the oceanographic analyses is gratefully acknowledged as well. The funds for the data analyses by R. Headrick were provided by the Office of Naval Research through an ONR Fellowship (Massachusetts Institute of Technology award 002734-001); the general funds for SWARM were provided by the Office of Naval Research through ONR Grant No. N00014-95-0051. This is Woods Hole Oceanographic Institution contribution number 10076.

APPENDIX: A SIMPLE MODEL OF PULSE BROADENING DUE TO NEAR RECEIVER MODE COUPLING

One of the major results that our SWARM experimental work indicates is ''near-receiver dominance'' of the time spreading of acoustic pulses by soliton scattering. This sensitivity of the time spreading to near-receiver mode coupling is also seen clearly in the rather elaborate numerical modeling efforts by Headrick *et al.*[19,22] However, there is an even simpler way to see how this effects works physically in the context of an simple, two-coupled-mode ''toy'' model. Such a model allows one to show *analytical* forms for the modal time spreading versus the distance along the acoustic path of the acoustic mode coupler (in this case a train of solitons).

To begin with, let us consider a two mode system, with trapped modes one and two present only. Mode one is the faster mode, with group speed $v_1^G > v_2^G$. Also, let us assume that mode one has a very small modal attenuation coefficient, $\beta_1 \simeq 0$, whereas β_2 is somewhat larger ($\beta_2 \neq 0$). For the coupling matrix, no assumption is really necessary, as it is an amplitude effect. One can assume equal coupling into and out of the two modes for simplicity, if desired.

We now look at the propagation from the source at $x=0$ to the receiver at $x=L$. For mode one, the time of flight is $L/v_1^G = t_1$; for mode two we get $L/v_2^G = t_2$. Now let's consider looking at time spread arrivals in mode one where we can have both an unscattered arrival (travel is purely in mode one) and a single scattered arrival (one coupling by the soliton from mode two to mode one occurs at some distance x along the path from source-to-receiver) comprising the spread arrival. The time spread between the initial mode one arrival at $t_1 = L/v_1^G$ and the later scattered arrival is

$$\Delta t_1 = |L/v_1^G - (x/v_2^G + (L-x)/v_1^G)|. \tag{A1}$$

The amplitude (ignoring the coupling strength and spreading, and just including modal attenuation for simplicity) of the single coupled mode arrival is

$$A_1 = A_1^0 e^{-\beta_2 x}. \tag{A2}$$

Clearly Eq. (A1) gives the greatest time spread of the pulse when $x=L$, i.e., when the scattering is near the receiver. However, there is a decrease in amplitude of the single scattered arrival, which produces a *minimum* amplitude when $x=L$ in this case. Thus there is some trade-off between time spread maximization (best at $x=L$) and scattered arrival amplitude maximization (best at $x=0$). In the case of the mode two arrivals, things are in fact a bit more favorable to ''near-receiver dominance.'' The time spread between the unscattered mode two arrival and the (faster) coupled mode arrival is simply expressed as

$$\Delta t_2 = |L/v_2^G - (x/v_1^G + (L-x)/v_2^G)|, \tag{A3}$$

which again is a maximum when $x=L$. The amplitude of the single scattered coupled mode arrival is

$$A_2 = A_2^0 e^{-\beta_2 (L-x)}. \tag{A4}$$

The amplitude in Eq. (A4) is clearly a *maximum* when $x=L$, thus giving the maximum amplitude for the scattered arrival when the scatterer is near the receiver.

The above argument gives the simple physical rationale for why near-receiver scattering produces the most time spread, but does not pretend to handle the details of the scattering, propagation, or coupling in any exact sense. For these details, we refer the reader to the thesis and modeling paper by Headrick *et al.*[19,22]

[1] J. X. Zhou, X. Z. Zhang, and P. H. Rogers, ''Resonant interaction of sound wave with internal solitons in the coastal ocean,'' J. Acoust. Soc. Am. **90**, 2042–2054 (1991).
[2] J. X. Zhou, X. Z. Zhang, P. H. Rogers, D. Wang, and E. Luo, ''Anomalous sound propagation in shallow water due to internal wave solitons,'' Proc. IEEE Oceans '93 **1**, 87–92 (1993).
[3] D. B. King, S. A. Chin-bing, and R. W. McGirr, ''Ocean variability and acoustic propagation,'' in *Theoretical and Computational Ocean Acoustics*, Vol. 2, edited by D. Lee and M. Schultz (World Scientific, Singapore, 1994), pp. 793–807.
[4] M. K. Broadhead and H. B. Ali, ''Dissipative shallow water internal waves and their acoustical properties,'' Proc. MTS/IEEE Oceans '95 (IEEE, 1995).
[5] The SWARM Group (J. R. Apel *et al.*), ''An overview of the 1995 SWARM shallow water internal wave acoustic scattering experiment,'' IEEE J. Ocean Eng. **22**, 465–500 (1997).
[6] D. Rubenstein, ''Observations of cnoidal internal waves and their effect on acoustic propagation in shallow water,'' J. Acoust. Soc. Am. **101**, 3016 (1997).
[7] X. Demoulin, Y. Stephan, E. Coelho, S. Jesus, and M. B. Porter, ''Intimate96: A shallow water tomography experiment devoted to the study of internal tides,'' in *Shallow-Water Acoustics*, edited by R. Zhang and J. Zhou (China Ocean Press, Beijing, April 21–25, 1997), pp. 485–490.
[8] G. G. Gawarkiewicz, R. Pickart, J. F. Lynch, C. S. Chiu, K. B. Smith, and J. H. Miller, ''The shelfbreak front PRIMER experiment,'' J. Acoust. Soc. Am. **101**, 3016 (1997).
[9] J. F. Lynch, G. G. Gawarkiewicz, C. S. Chiu, R. Pickart, J. H. Miller, K. B. Smith, A. Robinson, K. Brink, R. Beardsley, B. Sperry, and G. Potty, ''Shelfbreak PRIMER—An integrated acoustic and oceanographic field study in the Mid-Atlantic Bight,'' in *Shallow-Water Acoustics*, edited by R. Zhang and J. Zhou (China Ocean Press, Beijing, April 21–25, 1997), pp. 205–212.
[10] R. L. Field, C. Mire, Z. Hallock, J. George, and M. Broadhead, ''The SESAME experiments—the effects of internal solitons on acoustic propa-

gation at the Malin Shelf,'' in *Shallow-Water Acoustics*, edited by R. Zhang and J. Zhou (China Ocean Press, Beijing, April 21–25, 1997), pp. 227–232.
[11] P. F. Worcester, U. Send, B. D. Cornuelle, and C. Tiemann, ''Acoustic monitoring of flow through the Strait of Gibraltar,'' in *Shallow-Water Acoustics*, edited by R. Zhang and J. Zhou (China Ocean Press, Beijing, April 21–25, 1997), pp. 471–478.
[12] J. X. Zhou, P. H. Rogers, G. W. Caille, R. Zhang, G. Jin, L. Lei, P. H. Dahl, R. C. Spindel, and Z. Gan, ''Overview of the joint China-U.S. ''Yellow Sea '96'' experiment,'' in *Shallow-Water Acoustics*, edited by R. Zhang and J. Zhou (China Ocean Press, Beijing, April 21–25, 1997), pp. 17–22.
[13] D. B. Creamer, ''Scintillating shallow water waveguides,'' J. Acoust. Soc. Am. **99**, 2825–2838 (1996).
[14] D. Tielbuerger, S. Finette, and S. Wolf, ''Acoustic propagation through an internal wave field in a shallow water waveguide,'' J. Acoust. Soc. Am. **101**, 789–808 (1997).
[15] X. Tang and F. D. Tappert, ''Effects of internal waves on sound pulse propagation in the Straits of Florida,'' IEEE J. Ocean Eng. **22**, 245–255 (1997).
[16] J. Preisig and T. F. Duda, ''Coupled acoustic mode propagation through continental shelf internal solitary waves,'' IEEE J. Ocean Eng. **22**, 256–269 (1997).
[17] M. B. Porter, ''The KRAKEN normal mode program,'' Technical report, SACLANT Undersea Research Center, November 1992.
[18] F. B. Jensen, W. A. Kuperman, M. B. Porter, and H. Schmidt, *Computational Ocean Acoustics* (American Institute of Physics, New York, 1994).
[19] R. H. Headrick, ''Analysis of internal wave induced mode coupling effects on the 1995 SWARM acoustic transmissions,'' Ph.D. thesis, MIT/WHOI Joint Program in Oceanography and Oceanographic Engineering, June 1997.
[20] D. Rubenstein and M. H. Brill, ''Acoustic variability due to internal waves and surface waves in shallow water,'' in *Ocean Variability and Acoustic Propagation*, edited by J. Potter and V. Warn-Varnas (Kluwer Academic, Boston, 1991), pp. 215–228.
[21] F. S. Henyey and A. Hoering, ''Energetics of borelike internal waves,'' J. Geophys. Res. **102**, 3323–3330 (1997).
[22] R. H. Headrick, J. F. Lynch, and the SWARM group, ''Modeling mode arrivals in the 1995 SWARM experiment acoustic transmissions,'' J. Acoust. Soc. Am. (submitted).
[23] J. R. Apel, S. I. Finette, M. H. Orr, and J. F. Lynch, ''The ''dnoidal'' model for internal solitons and tides on the continental shelf,'' J. Geophys. Res. (submitted).
[24] T. F. Duda and J. Preisig, ''Acoustic effects of moving coastal solitary wave packets,'' IEEE J. Ocean Eng. **24**, 16–32 (1999).

Modeling mode arrivals in the 1995 SWARM experiment acoustic transmissions

Robert H. Headrick,[a] James F. Lynch, John N. Kemp, Arthur E. Newhall, and Keith von der Heydt
Woods Hole Oceanographic Institution, Woods Hole, Massachusetts 02543

John Apel
Global Ocean Associates, PO Box 12131, Silver Spring, Maryland 20908

Mohsen Badiey
Ocean Acoustics Laboratory, Graduate College of Marine Studies, U. Delaware, Newark, Delaware 19716

Ching-sang Chiu
Naval Post Graduate School, Monterey, California 93943

Steve Finette, Marshall Orr, Bruce Pasewark, Alton Turgot, and Steve Wolf
Naval Research Laboratory, Washington DC 20375-5350

Dirk Tielbuerger
Forschnungsanstalt der Bundeswehr für Wasserschall und Geophysik, Klausdorfer Weg 2-24, 24148 Kiel, Germany

(Received 21 July 1997; revised 6 February 1998; accepted 13 September 1999)

As part of the Shallow Water Acoustics in a Random Medium (SWARM) experiment, a 16 element WHOI vertical line array (WVLA) was moored in 70 m of water off the New Jersey coast. A 400-Hz acoustic tomography source was moored some 32-km shoreward of this array, such that an acoustic path was created that was anti-parallel to the primary propagation direction for shelf-generated internal wave solitons. The presence of these soliton internal waves in the acoustic waveguide causes significant coupling of energy between propagating acoustic modes, creating fluctuations in modal intensities and modal peak arrival times, as well as time spreading of the pulses. Two methods by which acoustic propagation and scattering in soliton-filled waveguides can be modeled are presented here in order to understand and explain the scattering observed in the SWARM field data. The first method utilizes the Preisig and Duda [IEEE J. Ocean. Eng. **22**, 256–269 (1997)] Sudden Interface Approximation (SIA) to represent the solitons. The second method, which is computationally slower, uses a finely meshed, ''propagated'' thermistor record to simulate the solitons in the SWARM experiment waveguide. Both numerical methods are found to generate scattering characteristics that are similar to the SWARM field data. © *2000 Acoustical Society of America.* [S0001-4966(00)00701-3]

PACS numbers: 43.30.Re, 43.30.Bp [DLB]

INTRODUCTION

The Shallow Water Acoustics in a Random Medium (SWARM) experiment,[1] conducted off the coast of New Jersey near the continental shelfbreak in July and August of 1995, was dedicated to furthering our understanding of acoustic scattering effects of internal waves, especially nonlinear solitary internal waves (solitons), in shallow water. The experiment employed a large number of acoustic and environmental sensors which are discussed in detail by Apel *et al.*[1] One of the primary purposes of the experiment was to understand the temporal distortion of acoustic pulses caused by internal wave scattering. The experimental expression of this effect was seen clearly in the source-to-receiver data from a 16 element WHOI vertical line array (WVLA) and a 400-Hz tomography source moored about 32-km shoreward. These data are discussed in detail in a paper by Headrick *et al.*,[2] to which we refer the reader for details. The issue of modeling the mechanisms by which the acoustic energy is time spread was only treated cursorily in the previous Headrick *et al.* paper, and it is that issue we wish to address here. As in the previous paper, our emphasis will be on the modal picture of propagation and scattering, as the vertical line arrays employed gave us the capability to make modal decompositions of the data which provide useful physical insight.

Two approaches to modeling the nonlinear internal wave field are examined in this paper: (1) the Sudden Interface Approximation (SIA), in which individual solitons in a train are treated as square wells, each with two sharp edges that induce mode coupling; and (2) a conversion of a thermistor time series record of solitons at a certain spatial point into a 2-D spatial picture, using the assumption of a constant, nondispersive propagation speed for the solitons. Both of these techniques have their advantages and drawbacks, as will be discussed. There are also other possibilities for modeling the

[a]Robert H. Headrick was associated with the MIT/WHOI Joint Program in Oceanography and Oceanographic Engineering during the performance of this work. He is currently on active duty in the U.S. Navy.

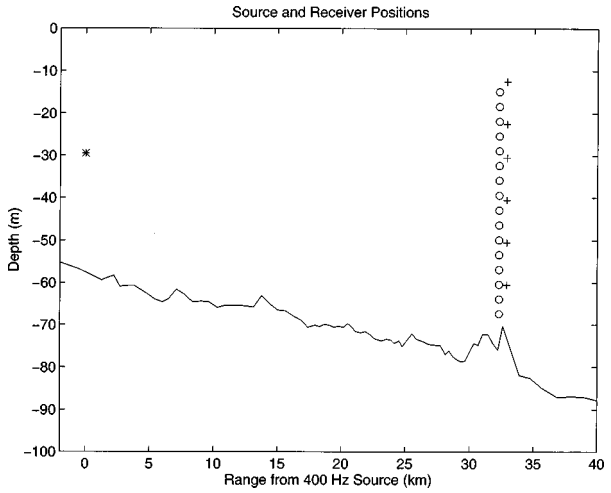

FIG. 1. The 400-Hz source position is noted by ''*.'' WVLA hydrophone positions are noted by ''○'' and the thermistors on the array are marked as ''+.''

internal wave field for input into acoustic calculations; detailed hydrodynamic modeling of the soliton trains is one strong candidate that is currently being explored, e.g., by Colosi and Sperry[3] and Apel *et al.*[4] We will limit ourselves here to the two approaches mentioned above, while realizing that there are other possibilities.

One of the major loose ends from the previous Headrick *et al.* paper was proving the hypothesis of ''receiver dominance.'' Specifically, the data strongly suggested that the time spread of an individual acoustic normal mode arrival by soliton induced mode coupling was most pronounced when the soliton(s) were near the receiver. However, due to the experimental geometry, there was a source/receiver ambiguity in our data. We endeavor to show in this paper that there is indeed receiver dominance in the time spreading of individual modes by solitons. Models, which can easily vary their geometries, allow us in this case to go beyond the limitations that were imposed on our real-world experiment.

Our paper is broken into six basic sections: Introduction, Experiment Description, A Basic Description of Two Soliton Models and Their Inclusion into Acoustics Models, The SIA Model, the ''Propagated Temperature Field Model,'' and our Conclusions. In the Introduction, we explain the rationale and directions of our work. In Sec. I, the Experiment Description, we briefly describe the SWARM acoustic data and some of the processing that was done to render it into useful form (particularly mode filtering). In Sec. II, we discuss the two soliton models that are used in our acoustic calculations. The strengths and weaknesses of each model are examined. Emphasis is given to the details of acoustic pulse propagation through these two models. In Sec. III, we show the results of acoustic calculations using the first soliton model, the SIA model. The effects of the number of solitons and their placement are shown, and the ''near-receiver dominance effect'' (most time spread observed for scatterers near the receiver) is numerically demonstrated. In Sec. IV, we look at the results of sending acoustic pulses through the ''propagated thermistor string'' model of the ocean soliton field. Pulse spreads and biases are predicted using the model, and reasonably good qualitative agreement with the SWARM experiment is seen. In Sec. V, we present our conclusions and suggest directions for future work.

I. A BRIEF DESCRIPTION OF RELEVANT SWARM EXPERIMENT RESULTS

This paper is chiefly concerned with numerically modeling the SWARM data obtained from the acoustic source/receiver combination illustrated in Fig. 1, i.e., data from a 400-Hz Webb tomography source transmitting through a strong soliton field to a 16 element WHOI vertical line array (WVLA). The recorded data, which result from 2-min duration strings of phase encoded sequences sent every 6-min over the course of nearly 2 weeks, clearly show internal wave induced scattering effects, which make them of interest. The data and their acquisition are discussed in detail in Headrick *et al.*[2] and we refer the reader to that paper for more detailed experimental information. Environmental data along the acoustic propagation path were provided by both thermistor strings and ship ''tow-yo's,'' as related by Apel *et al.*[1] Of critical importance were the six thermistors located on the WVLA. These temperature sensing pods, which were sampled every 30 s, provided the sound speed profiles needed for computing the time-dependent 400-Hz mode shapes (using the KRAKEN[5] normal-mode code), a key step in mode filtering. In that mode filtering of the acoustic data follows directly from this environmental measurement, we discuss it next.

The modal analysis of 400-Hz acoustic arrivals at the WVLA begins by treating the acoustic signal at each hydrophone as a sum of vertical modes

$$ph(t)=\sum_{n=1}^{N} A_n(t)\phi_n(z_h), \tag{1}$$

where $\phi_n(z)$ is the mode (pressure) depth function, $A_n(t)$ is the mode pressure coefficient time series, and z_h is the depth of the hydrophone in question. The number of propagating normal modes, N, as well as the mode depth functions themselves are frequency dependent. The KRAKEN mode functions are orthonormal in the sense that

$$\int \frac{\phi_m(z)\phi_n(z)}{\rho(z)}dz=\delta_{mn}, \tag{2}$$

so given $p(z,t)$, $A_n(t)$ can be readily computed by applying the operator

$$\int (\cdot)\frac{\phi_n(z)}{\rho(z)}dz \tag{3}$$

to Eq. (1). Since the pressure field, $p(z,t)$, is sampled only at the 16 hydrophone locations, the integral computation of the mode coefficients, $A_n(t)$, must be approximated by

$$A_n(t)\simeq\sum_{h=1}^{16}\frac{p(z_h,t)\phi_n(z_h)\Delta z}{\rho(z_h)}, \tag{4}$$

where Δz_z is the spacing between hydrophones. This discrete sum is easily implemented through matrix multiplication of mode depth function vectors with 16 channel hydrophone

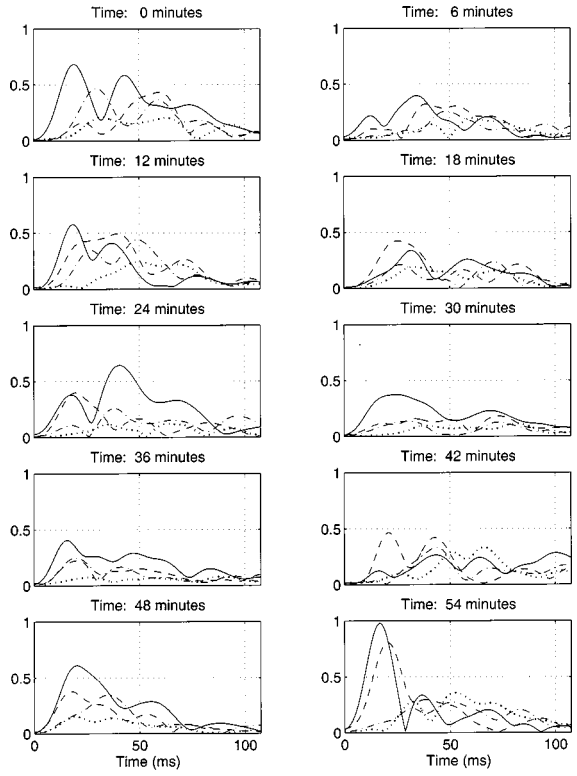

FIG. 2. Mode coefficient outputs, A_1(solid), A_2(dashed), A_3(dot-dash), and A_4(dotted), as a function of time. The 10 plots depict the arrival structure for the first portions of 10 sequential transmissions. Significant variability is seen in the position of the maximum (the ''mode peak'') for each mode, in the shape of the arrival and in the maximum amplitude for each mode.

data vectors (i.e., narrow-band direct-projection mode-filtering).

As mentioned above, one of the important goals of the SWARM experiment was to understand the arrival time structure of acoustic pulses sent through the waveguide, particularly their time spreading. Internal wave induced coupling between acoustic normal modes combined with differences in the acoustic modal group speeds cause time spreading of pulses (in addition to normal dispersion) as energy is transferred between different acoustic modes. In the SWARM waveguide, mode 1 has the highest group speed, so that the energy that transits in higher order modes for a portion of the path is delayed with respect to energy that has traveled exclusively in mode 1. This delay causes the time spreading of mode 1 energy to be all in one direction (i.e., there is a positive bias in the mean and median travel-time of mode 1 energy relative to an unscattered mode 1 arrival time). Higher order mode arrivals may have some energy coming in earlier (as a result of traveling part of the track in lower order modes) and some energy coming in later (due to traveling part of the path in higher order modes), so there may be negative, positive, or even zero bias in the travel-time of these ''smeared'' arrivals.

The effect of this coupling induced time spreading of energy on the intensity of mode 1 arrivals is two-fold. First, the spreading itself generally reduces the intensity of the mode 1 peak. Second, the modal attenuation coefficients of higher order modes are usually greater than those of lower order modes, so that energy that transits even a portion of the waveguide in modes higher than mode 1 will exhibit increased attenuation. The degree to which this spreading and attenuation occurs is quite variable. Figure 2 illustrates this by showing examples of the variability in mode filtered outputs of the SWARM acoustic data. A central task of this paper will be to generate similar mode-coupling induced distortions in modeled transmissions.

II. MODELING OF SOLITONS AND ACOUSTIC PROPAGATION THROUGH THEM

In this section of the paper, we examine the basic modeling of both the internal wave solitons and acoustic pulse propagation through them. A number of specific issues are addressed which are important both to the modeling and to the interpretation of the SWARM data by using such models. Later sections of the paper describe the results obtained with these models.

A. Modeling efforts to date

The two models of solitons we will pursue in this paper are in many ways extensions of work by previous investigators. We briefly describe here the work which has anticipated ours. In 1991 an internal soliton modeling effort by Rubenstein and Brill[6] introduced the ''propagated thermistor string environmental model,'' in which a measured temperature time series is advected at a constant phase speed in an appropriate direction to simulate a dispersionless train of internal waves. This approach was a reasonable way to convert an easy-to-obtain time series into a harder-to-obtain space series, and had been commonly used by physical oceanographers in other contexts. Another approach to creating ocean input for acoustic propagation models is to make models of ocean processes which contain their essential physical features. One of the seemingly robust features of solitons was their regularly spaced wavetrains. Based on this cue, Zhou *et al.*[7] presented a three-layer gated sine wave model for internal soliton packets; this model was later modified to employ a more realistic sech^2 waveform in the soliton packets.[8] The top and bottom layers are isovelocity; the middle layer undulates in accordance with the soliton model and provides a linear gradient sound speed connection between the top and bottom layers. However, other observations of solitons showed far less evenly spaced wavetrains than those that Zhou observed, and taking this as a cue, Preisig and Duda[9] decided to look at single soliton scattering events, which could later be extended to look at scattering by trains of solitons, either regularly or irregularly spaced. Physically, they took the three-layer model in the opposite direction and simplified the model of a single internal solitary wave down to an inverted square wave, via a sudden interface approximation (SIA). Though our work here concentrates on the nonlinear internal wave field (solitons), which seem to be the dominant oceanographic scattering mechanism encountered at the SWARM site, the effects of the linear field in shallow water also need to be eventually quantified. Tielbuerger *et al.*[10] have analyzed simulated waveguides that included both linear and nonlinear internal waves, indicating that the linear waves can play an important role in scattering. Recent

calculations by Duda (private communication), based on experimentally measured wave strengths, indicate that the linear field is perhaps less important. It would probably be fair to say that the importance of the linear internal wave field in shallow water is still a research issue. In that our propagated thermistor string model propagates both the linear and nonlinear waves on an equal footing, we have tacitly included the linear field somewhat in our work. We do not attempt to separate it from the nonlinear field in this case, in that such a separation is far from trivial.

We should also mention the acoustic propagation code aspects of the modeling effort. The previous modeling efforts we have mentioned employed CW Parabolic Equation (PE) algorithms, so the describable acoustic effects of the solitons were limited to intensity fluctuations and modal decompositions. The two soliton models presented in this paper are inputs for a broadband coupled mode approach that can be used to analyze travel-time fluctuations, as well as intensity fluctuations.

B. Normal-mode pulse propagation

We will briefly discuss here how we treat broadband pulse propagation numerically. We start with a full solution of the Helmholtz equation for a point source in range-independent cylindrical geometry:[11]

$$p(r,z) \simeq \frac{i}{\rho(z_s)\sqrt{8\pi r}} e^{-i\pi/4} \sum_{m=1}^{\infty} \phi_m(z_s)\phi_m(z) \frac{e^{ik_{rm}r}}{\sqrt{k_{rm}}}, \tag{5}$$

where the k_rm are the mode eigenvalues (horizontal wave numbers). We now truncate the sum to the M trapped modes and rearrange:

$$p(r,z) = \sum_{m=1}^{M} S_m \phi_m(z) \frac{e^{ik_{rm}r}}{\sqrt{r}}, \tag{6}$$

where

$$S_m = \frac{i}{\rho(z_s)\sqrt{8\pi k_{rm}}} e^{-i\pi/4} \phi_m(z_s). \tag{7}$$

Adding time and frequency dependence and removing cylindrical spreading yields

$$p(r,z,\omega,t) = \sum_{m=1}^{M} A_m P(\omega) e^{-i\omega t} \phi_m(\omega,z) e^{ik_{rm}(\omega)r}, \tag{8}$$

where

$$A_m P(\omega) = S_m(\omega). \tag{9}$$

Attenuation is modeled through the addition of an imaginary term, $i\alpha_{rm}(\omega)$, to the horizontal wave number. Now, integrating over the pulse bandwidth for a single mode,

$$\tilde{p}_m(r,t) = \frac{1}{2\pi} \int P(\omega) e^{-i\omega t} e^{ik_{rm}(\omega)r} \, d\omega, \tag{10}$$

yields the mode pulse arrival shapes that can be summed over the modes to get the signal at an individual receiver:

$$p(r,z,t) = \sum_m A_m \phi_m(z) \tilde{p}_m(r,t). \tag{11}$$

These range-independent propagation concepts can be carried over rather simply to a coupled mode model that is step-wise range independent. The modeled acoustic signal is treated as a sum of modes,

$$p_s(z,t) = \sum_n A_n \phi_n(z) \tilde{p}(t), \tag{12}$$

where $\phi_n(z)$ is the mode depth function, A_n is the mode coefficient, and $\tilde{p}(t)$ is the pulse-shape of the transmitted sequence after baseband replica correlation. Each of the modes transmitted is then allowed to couple into other modes at discrete locations between the source and receiver.

To estimate the coupling of modes across the steps, an *approximate single-scatter* one-way coupled mode approach from Jensen *et al.*[11] is employed that uses an arithmetic mean of pressure and velocity matching conditions across the interface to produce the elements of the coupling matrix,

$$C_{lm}^{j+1}(z,t) = \frac{1}{2} \int \frac{\phi_l^{j+1}(z)\phi_m^j(z)}{\rho^{j+1}(z)} dz + \frac{k_{rm}^j}{2k_{rl}^{j+1}} \int \frac{\phi_l^{j+1}(z)\phi_m^j(z)}{\rho^j(z)} dz, \tag{13}$$

where k_{rm}^j is the horizontal wave number of mode m in region j, and the coupling among mode coefficients is given by

$$A_l^{j+1} = C_{lm}^{j+1} A_m^j, \tag{14}$$

or in matrix notation,

$$A^{j+1} = C^{j+1} A^j. \tag{15}$$

C. SIA waveguide propagation basics—The SIA soliton, bottom properties, and pulse dispersion effects

We now examine the first technique by which we include the soliton internal wave field into our acoustics calculations, the ''SIA Soliton.'' Preisig and Duda's[9] PE simulations indicate that, at frequencies of a few hundred hertz, the mode coupling caused by a single soliton (whose width is less than about 400 m, a good assumption for coastal solitons) can be reasonably modeled by a sharp transition into and out of the soliton's sound speed profile (SSP). This sharp interface approximation (SIA), illustrated in Fig. 3, provides an avenue for studying simulated soliton-filled waveguides with only two mode-coupling calculations per soliton in the waveguide.

Creation of the SIA solitons was guided by the thermistor data, particularly those taken at the WHOI VLA. These data were principally used to create the time-dependent mode filters used to analyze the acoustic arrivals at the array, but they were also a convenient source of realistic SSPs for use in the pulse propagation model. The SSPs chosen for the SIA soliton waveguides are shown in the lower frame of Fig. 3.

To complete the waveguide model, we need to make some mention of the bottom. A bottom model was created

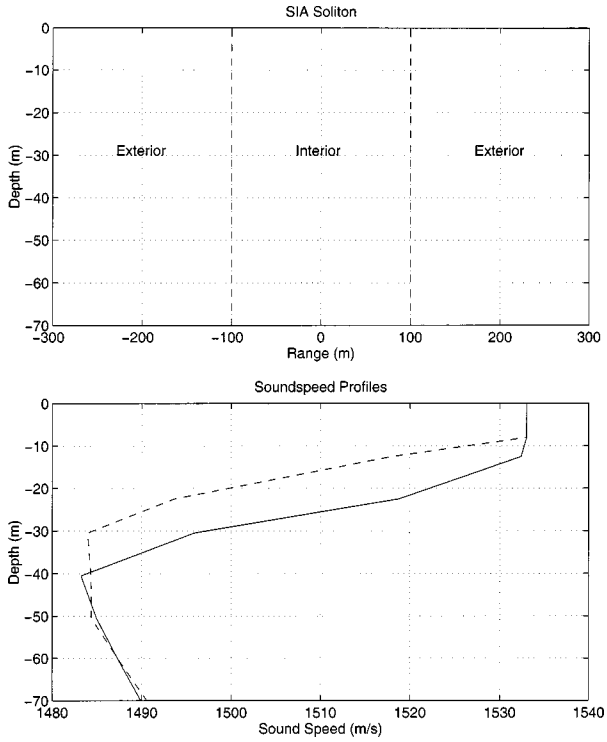

FIG. 3. An illustration of the SIA approximation for solitons (above), and the field measured SSPs (below) used to model the interior and exterior regions of the SIA soliton. The dashed SSP curve represents the exterior or background region, and the solid curve represents the interior or ''soliton'' SSP.

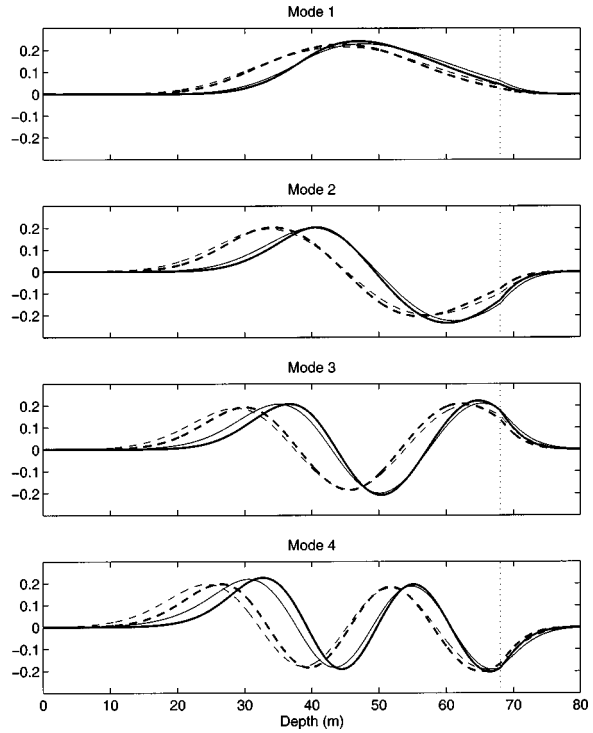

FIG. 4. Mode shapes for field measured (SWARM) SSPs. The dashed lines are the 355-Hz (thin lines) and 445-Hz (thick lines) mode shapes corresponding to the standard SSP with no soliton. The solid lines are the same modes for the SSP with a soliton included. The dotted line at 68 m indicates the water–sediment interface.

based on acoustic inverses and sedimentary analyses in the vicinity of the WVLA.[1] Numerous trials, gauged by comparisons with actual data, indicate that the average 400-Hz compressional wave attenuation in the bottom, along the SWARM acoustic path, is in the neighborhood of 0.02 to 0.03 dB/m. A sedimentary compressional wave attenuation coefficient of 0.092 dB/m can be inferred from chirp sonar inversions for sound speed (which shows an increase from 1500 to 1800 m/s at around 30-m depth in the sediment, due to a reflector underlying the surface sediment) and density (1.8 g/cm^3) in sediment near the WVLA. Extending these bottom parameters in a range-independent fashion toward the source produces almost complete attenuation of energy above mode 2 in simulated transmissions, but the actual data show significant energy transmission up through and including mode 4. An attenuation level of around 0.0115 dB/m proved to be appropriate for our modeled 30-m subbottom; slightly higher levels (0.02 to 0.03 dB/m) would be more appropriate if observed along track reductions in the actual SWARM subbottom thickness were considered.[12]

We now examine the characteristics of acoustic propagation in a waveguide containing SIA solitons, emphsizing dispersion effects. Figure 4 compares *soliton present* and *soliton absent* mode depth functions at the extremes of the pulse frequency domain (355–445 Hz). The mode depth functions for these SWARM SSPs have a frequency dependence that appears minimal in modes 1 and 2, but it becomes somewhat more visible in modes 3 and 4. Mode depth function frequency dependence also implies frequency dependence in horizontal wave number and group speed. The model propagates individual Fourier components $P(\omega)$, prior to synthesis at the receiver, so the resulting transmitted pulse shape,

$$\tilde{p}_n(r,t)=\frac{1}{2\pi}\int P(\omega)e^{i\omega t}e^{-ik_{rn}(\omega)r}\,d\omega, \tag{16}$$

shows the spreading and intensity loss that is due to frequency dispersion. The synthesis results for different modes will reflect the differences in group speed between modes through the frequency dependence of the horizontal wave

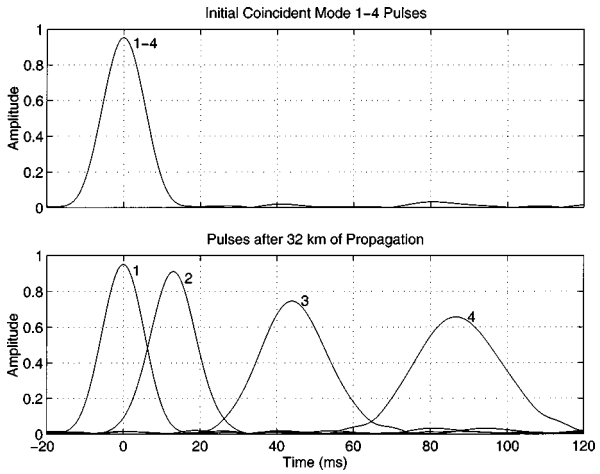

FIG. 5. Effects of mode and frequency dispersion on single mode transmission over 32 km. The transmissions include no soliton scattering or intrinsic mode attenuation. The attenuation in the higher modes is due solely to frequency dispersion.

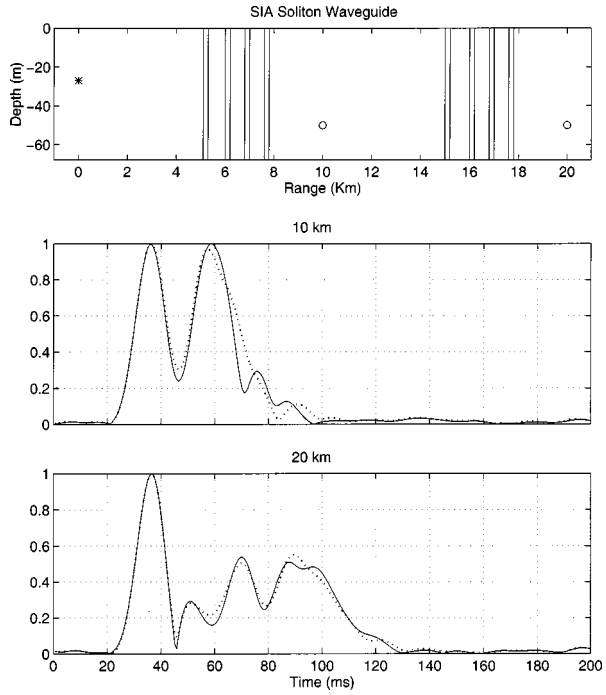

FIG. 6. An eight soliton waveguide (upper panel) and two corresponding arrivals computed from the PPM (solid) and KFS (dotted) methods. The modeled waveguide uses the SWARM SSPs shown in Fig. 3 to simulate the solitons. The source (*) depth is 27 m and the receiver (○) depth at both ranges is 50 m.

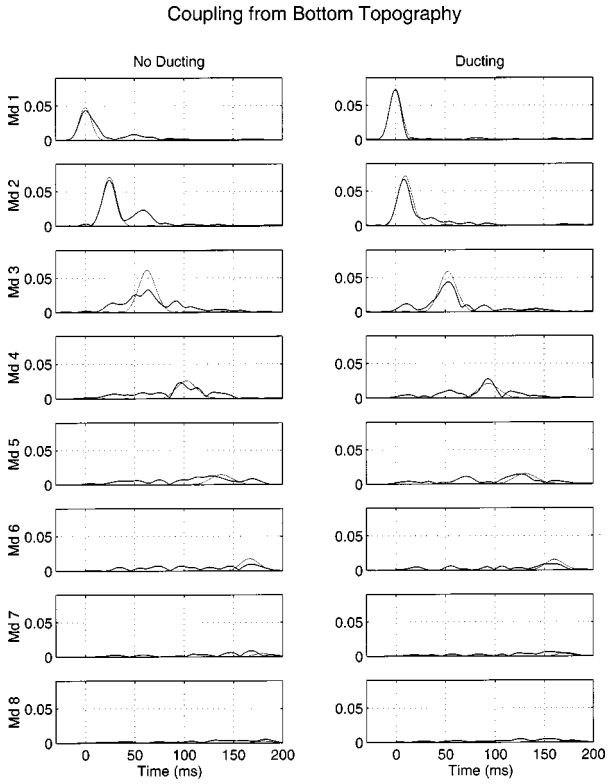

FIG. 7. Mode coupling effects of the bottom topography shown in Fig. 1 when the SSP is a modified version of the ''nonsoliton'' SSP of Fig. 3. The ''No Ducting'' modification consists of imposing the 50.5-m temperature from 50.5 m to the bottom depth, and the ''Ducting'' modification consists of imposing the 60.5-m temperature from 50.5 m to the bottom depth. The thinner lines in this figure represent predicted arrival shapes for modes that propagate adiabatically.

numbers, $k_{rn}(\omega)$. Figure 5 illustrates both the separating effects of mode dispersion and the pulse distortion effects of frequency dispersion that might be expected for individual mode pulses that travel the entire 32-km waveguide without any soliton scattering.

An ideal frequency domain propagation model would also include frequency dependence in the coupling matrices, and in fairly simple waveguides, this is a possibility. For instance, the acoustic model we are using computes the complex pressure field, $C(r,z,\omega)=a(r,z,\omega)+ib(r,z,\omega)$, at a number of selected ranges and depths for a given source depth, source frequency, and acoustic environment. If the transfer function is evaluated at a number of frequencies (covering the bandwidth of the transmitted signal), we can calculate the received signal pulse shape by using Fourier synthesis, i.e.,

$$p(r,z,t)=\frac{1}{2\pi}\int C(r,z,\omega)P(\omega)e^{i\omega t}\,d\omega. \tag{17}$$

Since complex pressure fields are not smooth functions of frequency, an accurate solution using the SWARM 400-Hz source requires 1201 CW runs for each different SSP in a range-dependent problem. This procedure, which we will refer to as KRAKEN Field Synthesis (KFS), computes the arrival at a single hydrophone; it can be extended to predict mode arrivals by mode-filtering the predicted arrivals at vertical array of hydrophones.

Conversely, the mode arrival predictions of our method, termed the pulse propagation model (PPM), can be synthesized to yield the arrival at a given single hydrophone. This computation,

$$p(r,z,t)=\sum_n \tilde{p}_n(r,t)\phi_n(z_s)\phi_n(z), \tag{18}$$

is very simple and provides an output for direct comparison with the KFS method. Since the modal wave number spectra it uses for propagation are fairly smooth functions of frequency, the PPM method requires only five computer model runs for each SSP. The wave numbers and attenuation levels for each mode's 1201 nonzero frequency bins are then computed through cubic spline interpolation. The five model runs with interpolation used in the PPM are orders of magnitude more efficient than the 1201 model runs needed in KFS.

Figure 6 shows a comparison between the two computational methods for a fairly complicated SIA soliton scenario. The results are not exactly matched but they are close, even at 20-km range. The narrow-band approximation used in the PPM coupling matrices is the major contributor to the deviations, as range-independent comparisons show negligible deviation between the two methods.[12]

D. The effects of bottom topography

Waveguides with little horizontal variation in water column properties may still produce mode-coupling, if there is significant variability in bottom topography. (We ignore coupling by water wave surface scattering in this study, in part because the SWARM field data shown here were gathered during fairly calm conditions.) For soliton-filled waveguides,

the coupling caused by bottom topography produces a baseline level of scattering to which is added the time-varying volume (soliton) scattering. Given the sloping bottom topography of the SWARM waveguide (see Fig. 1), some nonzero level of bottom scattering is expected.

The simulations shown in Fig. 7, which used a range-dependent waveguide based on the bottom topography of Fig. 1, can provide a good estimate of this baseline. The range-independent SSP used in what we call the ''No Ducting'' case is a modified version of the ''nonsoliton'' SSP of Fig. 3. The modification consists of imposing the 50.5-m temperature from 50.5 m down to the bottom, producing a ''worst case'' scenario for mode 1 bottom scattering. The ''Ducting'' SSP is the same, except the 60.5-m temperature is imposed from 50.5 m to the bottom depth, noticeably reducing the topographic coupling effects for the lower modes. The thinner lines in this figure represent predicted arrival shapes for modes that propagate adiabatically (i.e., no scattering of energy between modes). The difference between the two is, obviously, a measure of the effects of bottom coupling. It is quickly seen that the coupling effects are largest for the higher modes and the ''No Ducting'' case. In that the ''Ducting present'' case is more realistic for the SWARM site (due to warm bottom water being present due to the foot of the shelfbreak front), the Fig. 7 result allows us to claim that the bottom scattering effects can be ignored to first order for low order modes in the SWARM data.

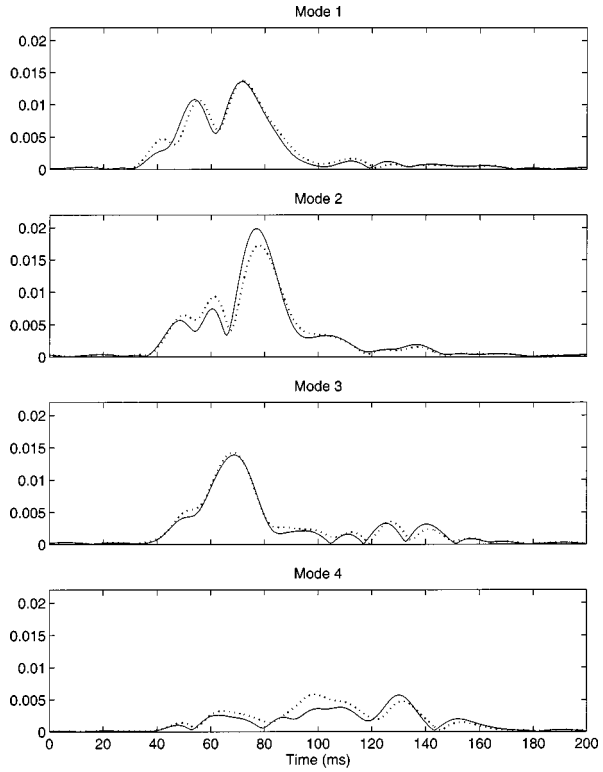

FIG. 8. Comparison of fine scale coupled mode arrivals using 24-m (solid) and 48-m (dotted) step-sizes. The 32-km waveguide under evaluation was generated from range-propagated WVLA thermistor records.

E. Propagated thermistor string coupled mode computations

A second, fine-scale, range-dependent, frequency-domain, coupled-mode model can be developed by using the equation (13) narrow-band coupling matrix. The environmental range dependence of the model is determined by following the procedure of Rubenstein and Brill[6] and ''propagating,'' without dispersion, the SSPs measured at the WVLA shoreward toward the source at 0.8 m/s. (This is roughly the speed of the leading soliton seen in the trains of solitons in SWARM. This is *not* the speed of the following solitons, so this procedure has some inherent error.) Sampling the WVLA SSPs every minute yields a 48-m step-size for the ''propagated thermistor string'' waveguide; a series of coupling matrices can then be calculated for the transitions between the SSPs. Equation (13), as it stands, works well enough for the limited numbers of coupling events required with SIA solitons, but it requires some modification if this finer scale (48-m) range dependence is to be employed. Ideally, a numerical computation of Eq. (13) using the same SSP on both sides would yield

$$C=\frac{1}{2}\int\frac{\phi(z)\phi(z)}{\rho(z)}dz+\frac{k}{2k}\int\frac{\phi(z)\phi(z)}{\rho(z)}dz=I, \quad (19)$$

an identity matrix. However, the six decimal place, 1001 point, ASCII mode depth functions provided by the KRAKEN[5] plotting routine ''plotmodeM'' yield

$$\int\frac{\phi_n(z)\phi_n(z)}{\rho(z)}\neq 1. \quad (20)$$

The integrals are very close to one, typically around 0.9996 for the higher order modes, but the cumulative effect over hundreds of coupling events is noticeable. The numerical implementation of Eq. (13) also produces small (fourth decimal place) errors in the off-diagonal terms.

All these small error sources can be readily eliminated for the trivial case of coupling into an identical environment by multiplying Eq. (13) coupling matrix by its inverse, creating,

$$C'=C^{-1}C=I, \quad (21)$$

the desired identity matrix. In a fine scale implementation, the coupling matrices are nontrivial, but the differences between SSPs in adjacent regions are small. This suggests a corrected coupling matrix,

$$C'_{12}=C_{22}^{-1}C_{12}. \quad (22)$$

Kuperman *et al.*[13] deal with a truncated coupling coefficient integral in a similar fashion. The correction matrix, C_{22}^{-1}, is always close to an identity matrix, insignificant over a small number coupling calculations, but it can be important when small range steps are used over large distances. Consider a 32-km waveguide with a 48-m step-size. The 670 coupling matrices it requires will generate significant cumulative errors from small individual errors in coupling coefficients (e.g., $0.9996^{670}=0.765$). (We should also note here that the correction matrix C_{11}^{-1} works as well.)

The effectiveness of this correction factor can be seen in the close fit of the mode arrival patterns in Fig. 8. Both sets of patterns were generated using the same 32-km waveguide, but one used a 48-m step-size (dotted), and the other em-

ployed a 24-m step-size (solid), requiring twice as many coupling calculations. The 32-km waveguide is derived directly from range propagated WVLA thermistor records. Had the coupling matrices not been corrected properly, the smaller step-size model, with 1340 coupling events, would have diverged noticeably from the 48-m step-size model. The closeness of fit also indicates that the 48-m step-size produces a convergent solution.

F. Model summary

In summary, we have introduced two ''approximate soliton'' models. The first model, emphasizing computational simplicity and speed, is implemented via the following steps:

(1) Create range varying waveguides by alternating between two different SSPs, representing solitons via the Preisig and Duda[9] SIA. The SSPs, shown in Fig. 3, are from the WVLA at periods with and without a soliton present.
(2) Conduct mode propagation in the frequency domain, using interpolated modal wave number and attenuation spectra over the (100-Hz) bandwidth of the SWARM (400-Hz center frequency) signal.
(3) Use the narrow-band approximation in creating the coupling matrices.

This model will be used in sections to follow primarily for the purpose of analyzing the effects of solitons on mode 1 arrivals. The addition of bottom topography in this model is feasible, but complicated, and, as shown in Fig. 7, it would have a very limited impact on mode 1 scattering for our SWARM case.

We have also proposed a second simple model of how to compute acoustic propagation through solitons. It is implemented as follows:

(1) Create range-dependent waveguides (32 km long in SWARM) directly via propagated (WVLA) thermistor records. The transformation from time dependence to range dependence is made by assuming all the temperature disturbances are propagating without dispersion at some speed (0.8 m/s in SWARM) along the same line as the acoustic transmission path. (We used a 48-m step-size that corresponds conveniently to the 1-min sampling of the slowest thermistor records in SWARM.)
(2) Conduct mode propagation in the frequency domain, using interpolated modal wave number and attenuation spectra over the bandwidth of the signal.
(3) Use the narrow-band approximation to generate the coupling matrices.

As mentioned, this method implicitly includes the sound speed perturbations from both linear and nonlinear internal waves. The addition of bottom topography in this model is not presently feasible, as the ability to ''march'' the coupling matrices forward in range as the solitons propagate is critical to the computational efficiency of the model. Even with the fast, cheap computational power currently available, describing the fully range-dependent, broadband scattering of sound by solitons remains at the edges of our computational ability, at least with coupled mode approaches.

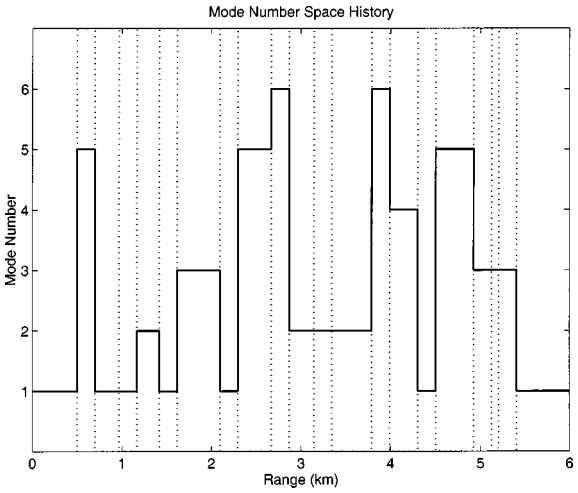

FIG. 9. The solid line shows the mode number space history of one of the 6^{20} subarrivals that would make up the mode 1 arrival from a six mode transmission through the ten SIA soliton waveguide that is indicated by the dotted lines.

III. MONTE CARLO ANALYSES OF MODAL ARRIVALS USING THE SIA MODEL

The main purpose of the simulation runs to be shown in this section is to study the effects of varying the numbers and locations of solitons on the mode 1 arrival spread and bias. With the computer, we can manipulate the ocean in ways that were unavailable to the SWARM experiment, and perhaps resolve some of the ambiguities left by the real world data. In particular, we will look at the issue of the ''near-receiver dominance'' in the time spread of individual modal arrivals, which the SWARM data indicated, but could not fully resolve.

A. Relevant statistics and modal path histories

The mode arrival structures of actual data (see Fig. 2) are very complicated, and this complexity is echoed in the models. As mentioned, two measures of this complexity are pulse spread and bias. The spread is a measure of the width of an arrival pulse and the bias is a measure of the difference between the average arrival time of mode 1 energy and the ''PAM1 arrival time,'' which we now define. The nature of both the actual and modeled SWARM waveguides is such that mode 1 generally has the highest group speed, making the energy that travels nearly exclusively in mode 1 the earliest possible arrival for most transmissions. This energy packet is referred to as the ''pseudo-adiabatic mode 1 arrival (PAM1)'';[12] it is not always the strongest peak in the envelope of a mode 1 arrival, but the highest peak arrives at or near the PAM1 arrival time often enough so that distributions of mode 1 peak arrival times have observable leading edges. In actual transmissions, the PAM1 arrival time is estimated from this leading edge, but in simulated transmissions, the PAM1 arrival time can be actually calculated for each transmission.

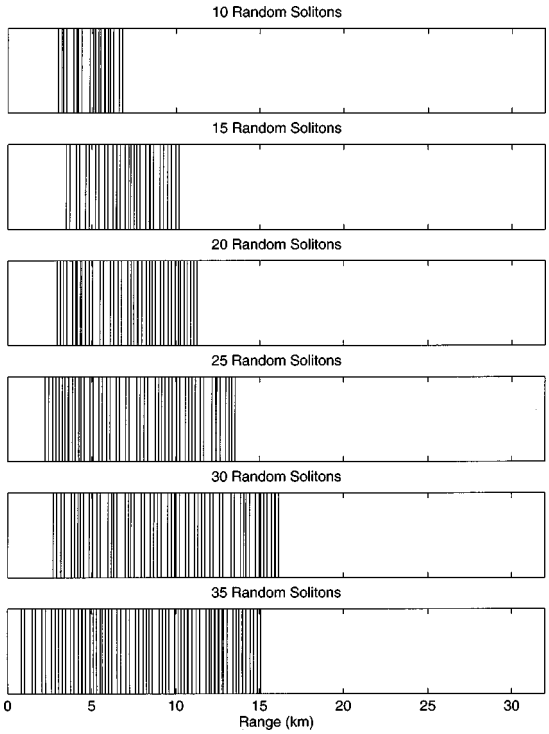

FIG. 10. Random realizations of test waveguides with from 10 to 35, 200 m width, SIA solitons over 32 km. The first soliton is placed randomly about 2.5 km from the source, and the remainder are added randomly from there, with an average of 450 m between leading edges. Adding more solitons progressively ''fills'' the waveguide from left to right in this scheme.

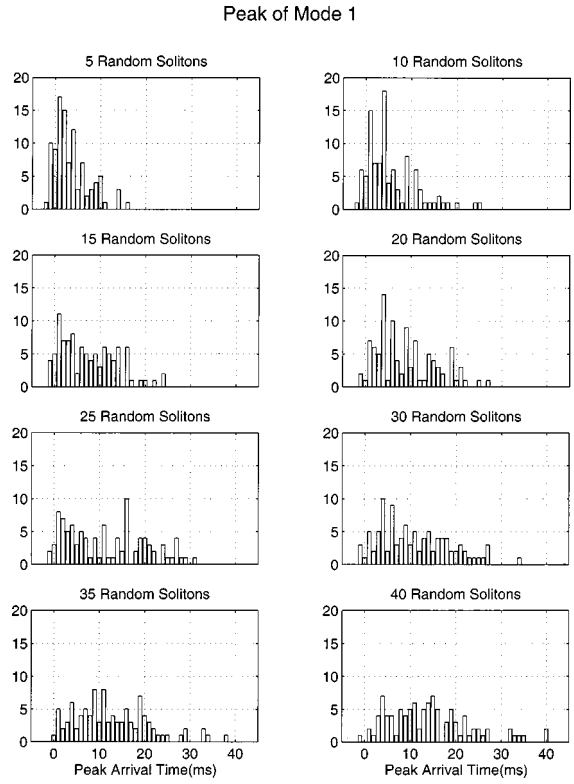

FIG. 11. Histograms for peak position of mode 1 arrivals for 5 through 40 random solitons. The solitons start about 2.5 km from the source with an average separation of 450 m between soliton leading edges. Time zero corresponds to the PAM1 arrival.

Let us now consider the single-mode arrivals at the receiver to be made up of the coherent sum of numerous ''mode multipaths,'' each having a phase and amplitude determined by its mode number–space history. In this picture, the spread and bias of a mode 1 arrival depends on the histories of the dominant subarrivals that make up a given arrival. The solid line in Fig. 9 shows the mode number space history of one of the 6^{20} subarrivals that would make up a mode 1 arrival in the 10 SIA soliton waveguide that is indicated by the dotted lines in the same figure. The phase relationships between the subarrivals are very important, but, on average, higher percentages of time spent by a single subarrival in higher order modes in the histories cause greater bias, and greater diversity in mode number histories of the dominating subarrivals causes greater spread. In other words, on average, the bias in an arrival is determined by the mean mode number history of the subarrivals and the spread of the arrival is determined by the variance of the mode number histories of the subarrivals, where the mean and variance are of course range averaged and weighted by the group slowness.

Quantitative measurement of spread and bias in an arrival is somewhat subjective; there are many similar mathematical measures that give slightly different results; the subjectivity comes from choosing which is ''best.'' Some reasonable bias measurement candidates are the displacements of the peak, mean, and median arrival times of the mode 1 arrival envelopes relative to the PAM1 arrival time. There are several candidates for gauging the spread: the standard deviation of the arrival envelope; the interquartile range (the difference between the the 75th and 25th percentile of the arrival envelope); and the difference between the mean and peak arrival time.

B. Simulation parameters

Eight modes were propagated and scattered through the simulated waveguides, six random realizations of which are shown in Fig. 10. The modeled waveguides support upwards of 40 propagating modes for the 400-Hz source, but the modes above 8 are of little consequence after about 5 km. The most serious drawback of this truncated sum approach is exposed when one considers the problem of adequately modeling coupling events that occur within the first few kilometers of the source. The ''near-source'' coupling of energy from modes above 8 might reasonably affect the mode 1–8 arrivals at the receiver. However, trials using 6, 8, and 10 modes in the model show convergence for the mode 1–4 arrivals at the receiver when 8 modes are used in ''near-source'' coupling scenarios.

C. Soliton number and placement effects—Near receiver dominance

Ten computer runs of 100 realizations each were conducted to evaluate the effects of adding a number of solitons between the source and receiver. The 200-m width solitons are randomly placed with an average separation of 250 m between solitons, starting at an average distance of 2.5 km from the source. Figure 11 shows that the addition of solitons is clearly accompanied by an increase in the probability that

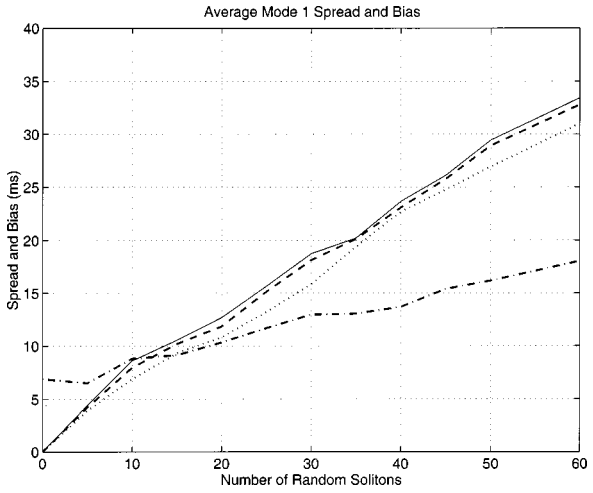

FIG. 12. The average mean (-), median (- -), and peak (···) lag with respect to the pseudo-adiabatic arrival, and standard deviation (-·) of scattered mode 1 arrivals plotted as a function of the number of solitons placed between the source and the receiver, where the solitons are added starting from the source end. The upper three lines are all bias measures, and the lower line is a measure of spread.

dispersed mode 1 energy will dominate the arrival pattern. The averages of spread and bias statistics taken over the 100 trials are displayed as function of the number of solitons in Fig. 12. Note the close agreement between all three measures of signal bias; the small differences among the three are indicative of a fairly regular mean pulse shape with a longer tail on the trailing edge. Figure 13 shows the situation to be entirely different if the solitons are added starting from the receiver end. The data in Fig. 12 are plotted with additional curves for averages of spread and bias statistics when the solitons are added starting near the receiver.

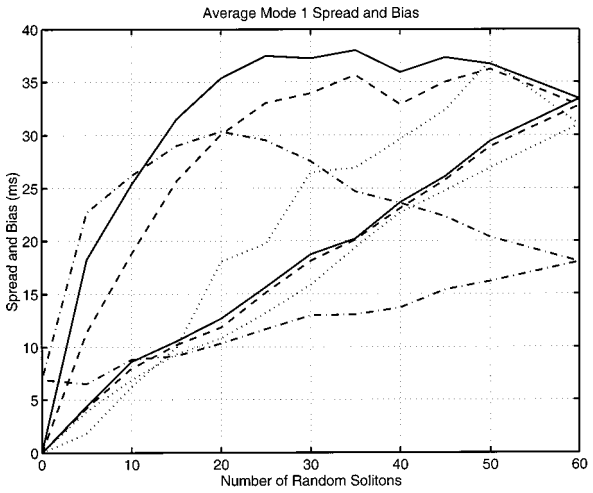

FIG. 13. The average mean (-), median (- -), and peak (···) lag with respect to the pseudo-adiabatic arrival, and standard deviation (-·) of scattered mode 1 arrivals plotted as a function of the number of solitons placed between the source and the receiver. The upper curves, averages over 50 realizations, represent the case where the solitons are added starting at the receiver end. The lower set of curves is replotted from Fig. 12, i.e., the waveguide is filled starting at the source end. 60 solitons is essentially saturation, and the same points are used in both sets of curves. Looking at the 20 soliton point, one notices nearly three times the spread and bias for near receiver solitons as opposed to near source. This is a graphical demonstration of ''near-receiver dominance'' in mode spreading by soliton scattering.

Adding a few solitons near the receiver dramatically affects the spread of mode 1 arrivals, building quickly to a peak spread for about 20 solitons. The effect on bias is also dramatic when measured by the mean arrival, but it is less so when the median is used. Both of these measures of bias seem to be approaching asymptotic levels as the number of solitons increases beyond 25. When peak position for fewer than 15 solitons is considered, no real difference can be seen between the ''adding near the source'' and the ''adding near the receiver'' results. The large differences between mean, median, and peak position for moderate numbers of near receiver solitons are indicative of a mean pulse shape with a substantial tail on the trailing edge.

All these effects can be understood when one considers the amount of modal dispersion produced by this waveguide over a distance of 32 km (see Fig. 5). If scattering interactions are constrained to occur only near the receiver, the peak of the mode 1 arrival is difficult to affect, but the tail of that arrival will be dramatically altered. The mean arrival time and the standard deviation of the arrival envelope are very sensitive to changes in the tail. The median and IQR of the arrival envelope are less sensitive, and the peak is by definition insensitive to the tail, unless, of course, the tail becomes the peak.

The asymptotic level of bias reached in the ''adding near the receiver'' case is to be expected. With no scattering, the history of the mode 1 arrival (single subarrival) is mode 1 only. As the number of scattering events is increased, the mean mode number history is weighted more and more by higher order modes, but there is a limiting value for the average percentage of mode *n* history in a mode 1 arrival, particularly when attenuation strips out the energy in the higher order modes.

Dozier and Tappert[14] have shown in a simplified model of scattering with no modal attenuation that the equilibrium energy state is an equipartition of energy between the modes. The asymptotic limit for mode 1 mode number history will, therefore, approach equal percentages of all modes, with some additional weighting (which depends on the average distance required to randomly redistribute the energy in mode 1, relative to the total distance traveled) given to mode 1. Similar arguments hold for the other modes. In more realistic scenarios, the asymptotic mode 1 mode number history percentages will still approach the equilibrium energy partitions, but, as shown by Creamer,[15] with attenuation there will not be equal percentages of each mode. The energy partitions and mode number histories will be weighted toward the modes with the least attenuation.

The soliton effects on spread, though with **no** attenuation, can be easily visualized by considering the simplistic case of two modes that sequentially scatter with all four coupling coefficients equal to 0.5. For equal mode 1 and mode 2 intensities and equally spaced scattering events, with the last occurring just before the receiver, this scenario will yield an average mode 1 subarrival mode number history of 50 percent travel in mode 1 and 50 percent travel in mode 2. There will of course be some variance between the individual subarrival histories with some subarrivals spending more time in mode 1 and others more time in mode 2. For narrow pulses

TABLE I. Subarrival statistics for the simple two mode 50/50 scattering scenario where there are four equally spaced increments and the difference between the PAM1 and PAM2 arrival times is $\Delta T=1$.

Simple two mode scattering scenario with four evenly spaced increments	Subarrival *k*-group					
	0	1	2	3	4	Total
Number in Group	1	4	6	4	1	16
Group Bias	0	.25	.50	.75	1.00	.50
Group Spread	0	0	0	0	0	.25

with adiabatic mode 1 and mode 2 travel-times separated by ΔT, the spread of a mode 1 arrival, as measured by the N normalized arrival standard deviation is

$$\sigma=\frac{\Delta T}{2\sqrt{n}}, \tag{23}$$

where n is the number of scattering events and $N=2^n$ is the number of subarrivals. Of the N mode 1 subarrivals, one is the PAM1 arrival, a second is coincident with PAM2 arrival (scattered into mode 1 right before the receiver), and the remaining 2^n-2 arrive in k groups, where k is number of increments traveled in mode 2. The number of subarrivals in a given k-group is given by the binomial coefficient,

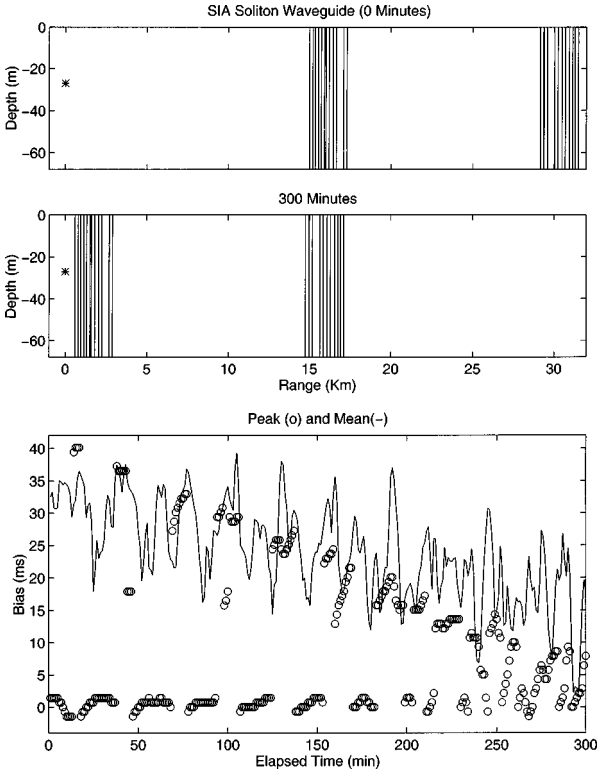

FIG. 14. Time-dependent waveguide with two sets of six SIA solitons. The upper frame shows the starting positions, the middle frame shows the positions five hours later, and the lower frame is plot of peak position bias (*re*: PAM1) as a function of time. The solitons propagate in lock-step, traversing 48 m per min, the time between each peak position data point (*o*). The mean arrival data is also in 1-min increments, but the points are connected by a solid line.

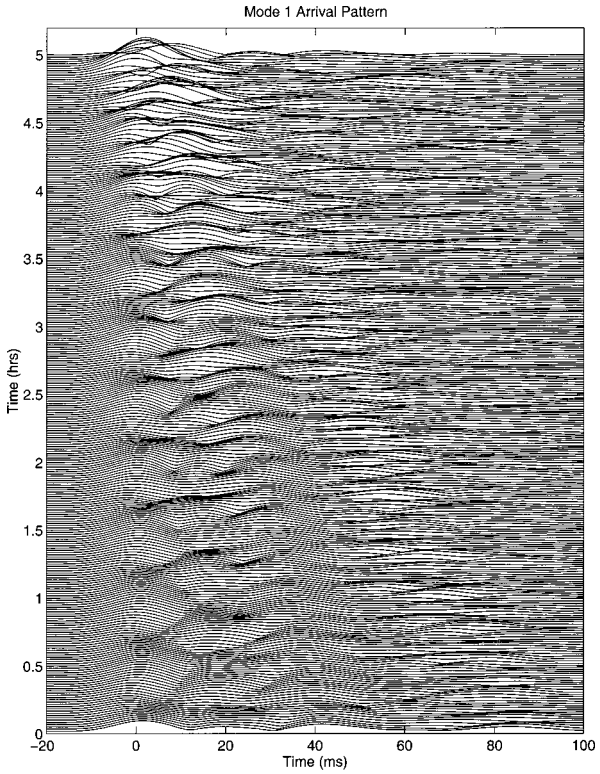

FIG. 15. Waterfall of mode 1 arrival patterns from the time dependent waveguide with two sets of six SIA solitons. The 300 peak positions in the lower frame of Fig. 14 were picked from these arrival patterns.

$$\frac{n!}{k!(n-k)!}, \tag{24}$$

for finding the number of ways of putting n distinguishable items into two groups, one containing k items.[16] The PAM1 and ''coincident with PAM2'' arrivals can also be considered as k-groups, with k equal to 0 and n, respectively.

Table I summarizes the subarrival statistics for the case where $n=4$ and $\Delta T=1$. Clearly, the same scenario with only one increment (i.e., one scattering at the very end) will still yield an average bias value of 0.50, but the spread will be maximized (also equal to 0.50). Any additional scattering prior to this late event decreases the spread, with no change in bias. Conversely, the two-mode case with only a single scatter occurring early in the path will produce a small amount of spread and bias; additional scattering events occurring later will cause an increases in both. Figure 13 simulation runs are more complicated than the above two-mode example, but the same effects can be seen. The eight-mode cross-modal coupling coefficients are much less than 0.5, so the ''adding near the receiver'' peak spread is not reached until around 20 solitons. We can also see the bias stabilize at about the same number of solitons, indicating saturation in the mean mode number history of subarrivals. The two-mode ''adding near the receiver'' example was saturated from the outset.

D. Soliton location effects

The above section has illustrated, via Fig. 13 in particular, that the location of solitons in a waveguide has more

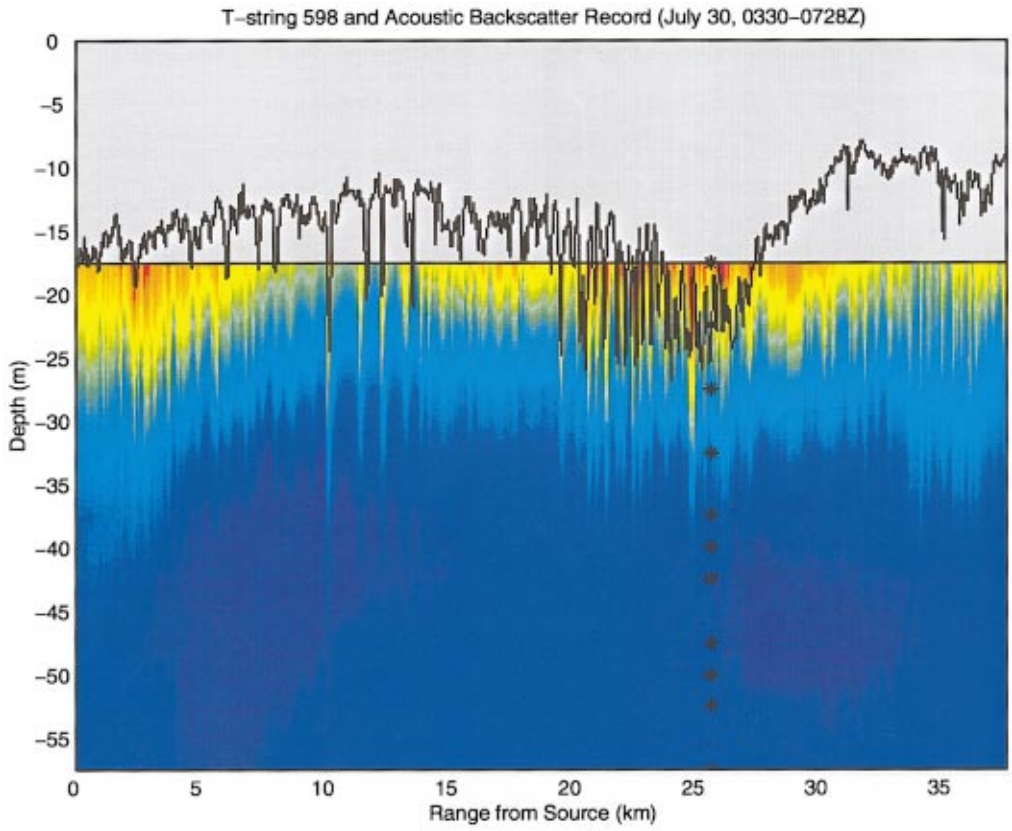

FIG. 16. Pycnocline (large density gradient region) displacements (white line) from an acoustic backscatter record compared to a thermistor string record using a propagation speed of 0.62 m/s over the distance between the back scatter instrument and the thermistor string at each backscatter reading. Asterisks show thermistor depths.

impact on spread and bias values of the received mode 1 field time series than does the number of solitons. In this section we show that, in addition to the general ''large scale'' location, the specific location of the solitons along the acoustic path contributes significantly to the nature of the mode 1 arrival patterns. This dependence on soliton location shows up as a higher frequency modulation of the lower (tidal) frequency trend. Figure 14 demonstrates this with two trains of six SIA solitons propagating in the waveguide without dispersion at the same speed of 0.8 m/s. As the soliton trains progress toward the source, the location of the last scattering event moves toward the source, reducing the potential for mode 1 arrival bias. As expected, this general decreasing trend in mean and peak arrival bias is evident in Fig. 14. Equally interesting is the fact that the mean and peak arrival time bias is sensitive to small shifts in the exact soliton train position.

Figure 15, a companion to Fig. 14, provides a good qualitative sense of the mode 1 arrival pattern's dependence on the exact position of the soliton trains. The outline of the first arrival at the bottom of the figure shows four distinct humps that roughly correspond in location to the mode 1–4 arrivals shown in Fig. 5. For the majority of the arrivals (see Fig. 14), the peak arrival resides on the mode 1 hump, but it often, almost periodically, shifts to the mode 3 hump, and it occasionally resides on the mode 2 hump. The mean arrival fluctuations are equally dramatic. The sensitivity of the arrival shapes and bias measurements to small changes in the location of solitons is chiefly due to the constructive and destructive interference patterns of scattered subarrivals. The undulations evident in the ''mode 1'' hump in Fig. 15 contribute significantly to the peak position jumps in Fig. 14. The source of these undulations is alternating constructive and destructive interference between mode 1 and 2 in the first soliton train. The mode cycle distance between mode 1 and 2 is about 1420 m; this, combined with a soliton train speed of 48 m per min, yields the half-hour cycles evident in both figures. This type of fluctuation has been discussed in some detail in the recent paper by Duda and Preisig.[17]

IV. ANALYSES USING THE ''PROPAGATED THERMISTOR STRING MODEL''

In this section, we again generate acoustic variability statistics via a computer model, but with a somewhat different soliton model. At the present time, the exact soliton model that one should use and the sensitivity of the results to which model is used are open research questions. Thus we feel justified to look at this second model and its output. We invest some effort into discussions of how sensible the model is, in that the input to acoustic calculations is a critical item. Again, we will compare our outputs as best we can to the SWARM data, with the realization that exact comparisons of our simplified model output and the complex acoustic data are not strictly possible.

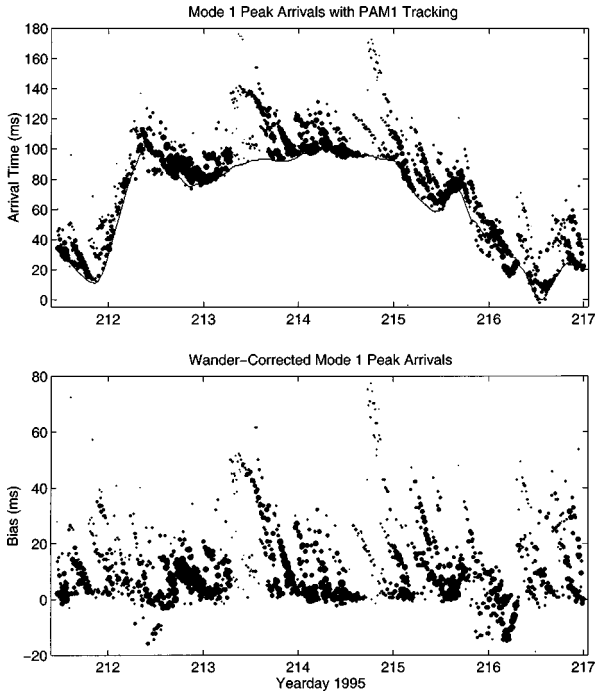

FIG. 17. Distribution of peaks for the mode 1 arrivals of simulated transmission using sequential WVLA thermistor string generated waveguides. The sequential 32 160 by 68 m waveguides are separated by 6 min. The size of each arrival dot is scaled by the amplitude of the peak arrival. The upper frame includes a plot of the PAM1 arrival time in conjunction with the individual peak arrival times; the zero reference on the arrival time axis corresponds to 21.6 s. The lower frame plots the bias or offset of the peak arrivals relative to the PAM1 arrival time for each realization.

A. An example waveguide

The fine-scale ''propagated thermistor string'' model described earlier is computationally much slower than the SIA model, but the use of thermistor string data brings in more realistic size and spacing characteristics for solitons, as well as added scattering from other sources (e.g., the linear internal waves). An example of this type of data-generated model waveguide is shown in Fig. 16. The temperature plot is overlaid with isopycnal (constant density) surface displacements taken from a high frequency backscatter record in order to show consistency between the propagated thermistor string method and an independent ''standard'' method of experimentally measuring internal waves. Specifically, constant temperature surfaces are considered good, passive tracers of the vertical displacement of the water due to internal waves, and so are backscatter records. In the latter measurement, the assumption made is that the backscatter seen is mainly due to marine micro-organisms which ''ride'' on constant density surfaces, which are displaced in exactly the same way as the constant temperature surfaces. The waveguide in this case is produced from records from a dedicated thermistor string (not the WVLA thermistors) used during SWARM. These ''T-string 598'' data were used strictly to make this comparison with the backscatter record, because the WVLA was not deployed early enough. Comparisons between the two different instruments point to nonlinear internal wave propagation speeds in the range of 0.6–0.8 m/s. The propagation speed of 0.62 m/s used in Fig. 16 was chosen for best overall agreement between the two records. The agreement is, in fact, quite good—better than one might have expected using the ''constant velocity'' assumption for soliton and internal tide propagation. We regard this agreement as a rough justification for using the propagated thermistor string model with the range of wave propagation speeds mentioned (0.6–0.8 m/s). However, one must still be careful in using this model—the soliton field does evolve in range, and as one goes to larger and larger distances, this simple assumption breaks down to some degree.

B. Model results

The WVLA, with its thermistors spanning 12.5 m to 60.5 m in depth, generally provides good data-generated waveguides for simulating our tomographic transmissions. Thus we will use the WVLA thermistor data for the modeling calculations that follow. Due to coverage gaps, the sound speeds are extrapolated for depths above 12.5 m and below 60.5 m. By assuming a WVLA temperature signal propagation speed of 0.8 m/s along the acoustic path, each 670 min of thermistor string data is transformed into a 32 160 by 68 m waveguide. The profile at the source determines the ''eight mode'' starting field for the acoustic model, and an ''eight mode'' transmission is then propagated through the waveguide and relevant statistics are obtained from the mode arrivals.

1. PAM1 peak arrival characteristics

Figure 17 shows several days of simulated 400-Hz mode 1 peak arrival times (both absolute and wander-corrected). There are 6 min between each acoustic transmission, and, in order to provide some qualitative sense of the variability in the strength of the arriving signals, the size of each arrival dot is scaled by the amplitude of the peak arrival. The peak arrivals consistently display a tendency toward positive travel-time bias relative to the PAM1 arrival, but there are exceptions, e.g., the periods around day 212.5 and 216. During these periods, the PAM2 arrival is actually slightly earlier than the PAM1 arrival, allowing for some negative bias in mode 1 arrival times.

For periods where the PAM1 arrival is the earliest arrival, the distributions of mode 1 peak arrivals tend to exhibit a fairly clean leading edge that coincides with the PAM1 arrival time. The arrivals with the largest peak amplitudes tend to fall within 10 to 20 ms of this leading edge. Arrivals with peak bias levels in the 40 to 60 ms range are partially the result of interference among the mode 1, nonadiabatic subarrivals, and as a result, the peak heights are noticeably smaller.

2. Spread statistics

The interquartile range (IQR) of a mode arrival envelope provides a robust estimate for that mode's time spreading. Figure 18 plots these spread statistics for mode 1 in 1.4-h bin averages, as an overlay with the WVLA temperature profiles for the simulation test period. For a given spread reading, the coincident temperature profile was used in modeling the SSP at the receiver. The profile at a time 0.46 days to the left of the receiver profile was used at the source, and the profiles between these were used in the interior of the modeled

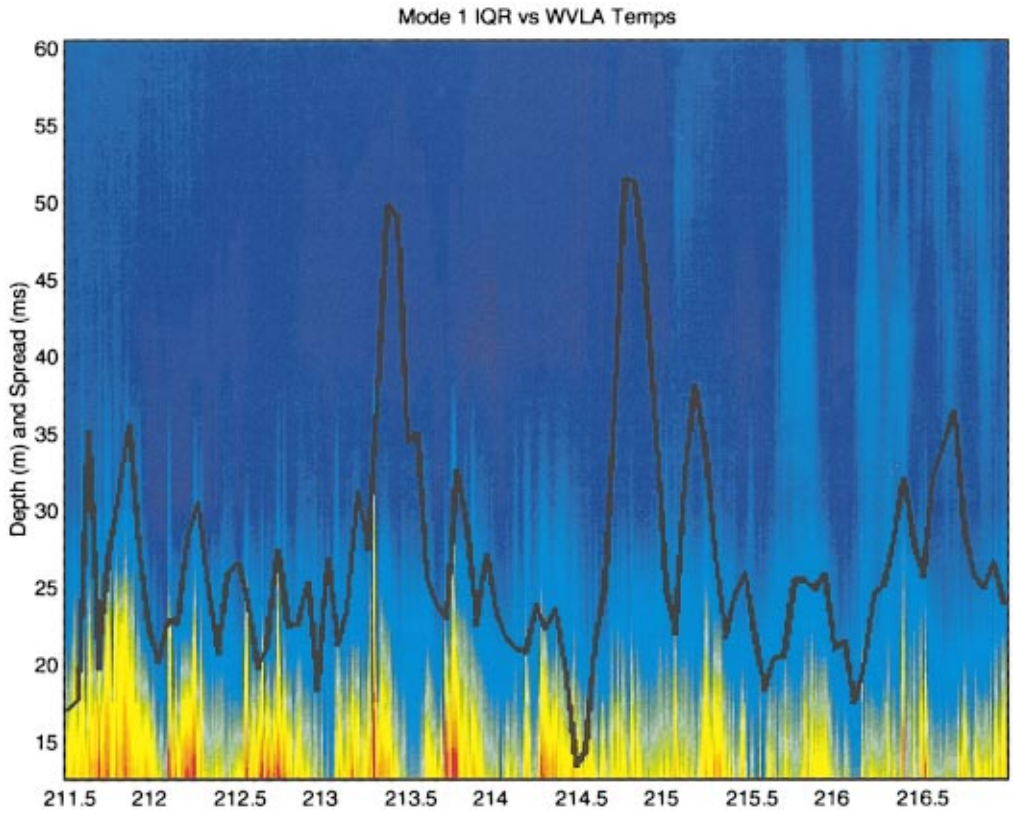

FIG. 18. Thirty-minute bin averaged IQR measurements versus the WVLA temperature profile for the simulation test period. The profiled temperatures range from 7.2 to 25.9 °C.

32-km waveguide. On average, larger amounts of spread tend to be accompanied by a significant amount of soliton activity in the latter half of the waveguide (i.e., in the near-receiver region from the time in question to about 0.25 days to the left in Fig. 18), but this is not always the case. The large peaks in the the mode 1 spread history around yeardays 213.4 and 214.8, for example, are inexplicable in terms of the accompanying soliton activity in the waveguide or the excitation levels at the source. These are further examples of the sensitivity of the instantaneous spread and bias statistics to the finer details of the modeled waveguide.

The correlation between ''instantaneous'' spread levels and soliton activity is difficult to quantify on a realization by realization basis, but if the standard deviation of the temperature at 22.5-m depth taken over the previous 4.3 h is used as a measure of soliton activity near the receiver, then a reasonable attempt at measuring a correlation can be made. A long (~12 km) reach is necessary to encompass the most critical region for soliton scattering. Figure 19 shows 1.4-h bin averaged spread statistics for both the acoustic model output and the actual SWARM data[2] plotted against this averaged temperature statistic.

The lower panel of this figure shows the cross-correlations between the statistics, indicating a weak correlation between the mean spread levels from the simulations and the mean spread levels found in the data. Obviously the similarities could be coincidental, as the correlation is not strong and consistent, but given the nonlinear spread response to soliton density and the unavoidable differences between the modeled and actual waveguides, one cannot ex-

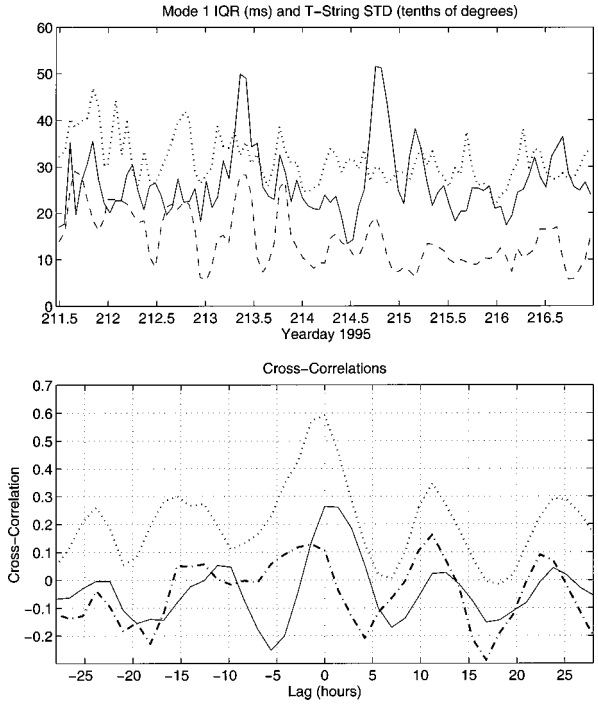

FIG. 19. The upper frame shows a comparison of 1.4-h bin averaged IQR levels for the simulated data (solid line), the actual data (dotted line) and the standard deviation of the temperature at 22.5-m depth over the previous 4.3 h (dashed lines). The standard deviation of the temperature is in tenths of a degree centigrade to facilitate comparison with the IQR levels in milliseconds. The lower frame shows the cross-correlations: the model/T-string (solid line); SWARM data/T-string (dotted line); and the model/SWARM data (dot-dash line).

TABLE II. Zero-lag cross-correlations between 1.4-h bin averaged mode 1–4 peak heights and mode 1–4 mean spread levels.

	Zero-lag cross-correlations Peak height mode			
Spread mode	1	2	3	4
1	−0.67	−0.36	−0.07	0.06
2	−0.27	−0.72	−0.35	−0.17
3	0.10	−0.46	−0.62	−0.21
4	0.30	0.04	0.23	−0.26

pect extremely close agreement. (The periods and phases of the correlations do seem to agree, however, which is encouraging.) The strongest correlation seen is between the data and the ''near-receiver'' soliton activity statistic from the T-string.

C. Bias statistics

As observed in the modeling results of Fig. 17, increased bias in mode 1 peak position is generally accompanied by a reduction in the mode 1 peak height. Table II shows the same type of relation holds between the mode 1 spread and mode 1 peak height; peak height fluctuations for mode 2 and 3 also have strong negative a zero-lag correlations with their spread statistics. Not unexpectedly, the amounts of cross-mode correlation vary considerably, reflecting the complicated relationship between the degree of modal coupling and the amount of spread and peak intensity in higher mode number arrivals.

The bias in peak arrival time for the mode 1 arrivals is quite variable in both the actual SWARM data[2] and the model results shown in Fig. 17. Mode 1 peak arrival time bias histograms for both data and model arrivals are shown in Fig. 20. The histograms are quite similar, even though the ''Data'' histogram is based on over 32 000 arrivals and the ''Model'' histogram uses only 1329. Not surprisingly, the ''Model'' histogram is not quite as smooth; it also shows a

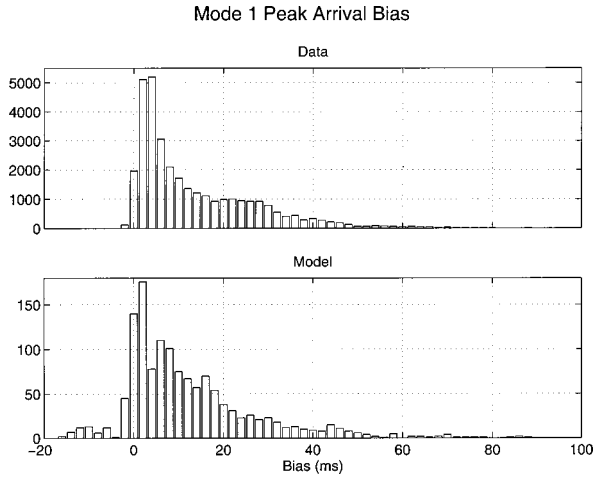

FIG. 20. Mode 1 peak arrival time bias histograms for the actual SWARM data and the model distribution shown in Fig. 17. The bias measurements are relative to estimated PAM1 arrival times (i.e., the leading edge) for the data and calculated PAM1 arrival times for the model.

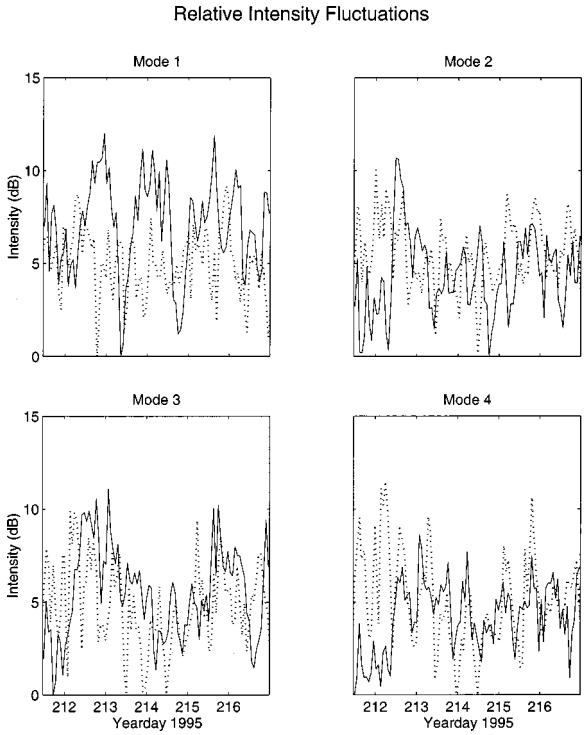

FIG. 21. Relative intensity fluctuations (1.4-h bin averages) in the mode 1–4 peak arrivals for both the modeled data from Fig. 17 (solid lines) and the actual SWARM data (dotted lines).

negatively biased pocket that stems from the periods when the modeled path averaged group speed for mode 2 was higher than mode 1 (see Fig. 17).

1. Modal intensity fluctuations

The intensity fluctuations observed in the modeled mode 1–4 arrivals were in the 10-dB range. The levels are quite close to those observed in the actual SWARM data;[2] a comparison is provided in Fig. 21. The M2 tidal influence is not strong in the mode 1 arrivals, for either the data or model, but it increases noticeably in the higher mode numbers. For example, the M2 tidal influences in the mode 4 intensity fluctuations are quite strong in both the data and the model. This is to be expected if the higher modes seen near the receiver are primarily due to mode coupling by near-receiver solitons, which arrive at the M2 period.

V. CONCLUSIONS

There are a number of conclusions that can be drawn from these modeling efforts. We will try to summarize some of the more important ones here.

We begin with our hypothesis of ''near-receiver dominance.'' Individual mode arrival spread and bias statistics can be very sensitive to the specific locations of soliton scattering events, but, in general, the more soliton activity there is in the portion of the waveguide closest to the receiver, the greater the spread and bias will be in the mode arrivals. The SIA model results show this very clearly, with the ''propagated thermistor string'' and actual SWARM[2] data providing good support. One should note that this obviously assumes that the pulse has not already been spread appreciably by

competing processes (e.g., rough surface scattering). If the pulse has already been spread in time by other processes to the (rough) limit defined by the source/receiver distance divided by the difference in group velocities of the fastest and slowest trapped modes, then soliton scattering will have little or no additional effect on time spreading.

Another interesting observation is that, under a common shallow water circumstance (i.e., when mode 1 has the highest group speed), a ''PAM1'' (pseudo-adiabatic mode one) arrival time can be estimated from a distribution of peak mode 1 arrival times by finding the leading edge envelope of the distribution. This noncoupled arrival is very useful for both tomographic analyses (e.g., water temperature estimation using time-of-flight) and for using as a baseline to understand coupled mode arrival structures.

A rather obvious conclusion, but one that bears repeating is that soliton-filled waveguides will produce arrival structure distortions with fluctuation time scales ranging from minutes to days. The two most interesting time scales seem to be the ''minutes'' time scale (i.e., the time it takes individual solitons to transit over a source or receiver) and the tidal time scale (i.e., the M2 tidal cycle over which packets of solitons will transit over sources and receivers). Our emphasis in this paper and its predecessor have been these two time scales, with perhaps a heavier weight on the M2 tidal cycle.

Another major issue, which this paper has just scratched the surface of, is modeling of the coastal internal wave field, both linear and nonlinear. The generation, propagation, and dissipation of the coastal internal wave field is incompletely known at present. There remains much oceanographic work to be done before we can confidently input the internal wave environment into acoustic propagation and scattering codes. In our SWARM experiment, we took a great deal of environmental data, especially for the internal wave field, and were able to constrain the problem ''adequately'' at best. This allowed us to understand certain aspects of the acoustic scattering processes. But even in SWARM, more sampling would have been valuable (perhaps thermistor strings every 5 km to monitor the soliton packet's evolution). The eventual hope is that, by doing more oceanographic research to understand the physics of the internal wave field, numerical ocean models can be generated so that one may make minimal measurements at a site like the SWARM site, and allow the models to fill in most of the details. There is certainly more work that needs to be done as regards shallow water scattering of sound by internal waves!

ACKNOWLEDGMENTS

We would first like to thank all our fellow SWARM collaborators. Without them, this research would not have been possible. We would also like to thank the reviewers, whose comments have greatly improved our manuscript. The funds for the model development were provided by the Office of Naval Research through an ONR Fellowship (Massachusetts Institute of Technology award 002734-001); the general funds for SWARM were also provided by the Office of Naval Research through ONR Grant No. N00014-95-0051. This is Woods Hole Oceanographic Institution contribution number 10077.

[1] The SWARM Group (J. R. Apel *et al.*), ''An overview of the 1995 SWARM shallow water internal wave acoustic scattering experiment,'' IEEE J. Ocean Eng. **22**, 465–500 (1997).
[2] R. H. Headrick, J. F. Lynch, and The SWARM Group, ''Acoustic normal mode fluctuation statistics in the 1995 swarm internal wave scattering experiment,'' J. Acoust. Soc. Am. **107**, 201–220 (2000).
[3] B. Sperry, ''Analysis of acoustic propagation in the region of the New England continental shelfbreak,'' Ph.D. thesis, MIT/WHOI Joint Program, April 1999.
[4] J. R. Apel, S. I. Finette, M. H. Orr, and J. F. Lynch, ''The ''dnoidal'' model for internal solitons and tides on the continental shelf,'' J. Geophys. Res. (submitted).
[5] M. B. Porter, ''The kraken normal mode program,'' Technical report, SACLANT Undersea Research Center, November 1992.
[6] D. Rubenstein and M. H. Brill, ''Acoustic variability due to internal waves and surface wave in shallow water,'' in *Ocean Variability and Acoustic Propagation*, edited by J. Potter and V. Warn-Varnas (Kluwer Academic, Boston, 1991), pp. 215–228.
[7] J. X. Zhou, X. Z. Zhang, and P. H. Rogers, ''Resonant interaction of sound wave with internal solitons in the coastal ocean,'' J. Acoust. Soc. Am. **90**, 2042–2054 (1991).
[8] J. X. Zhou, X. Z. Zhang, P. H. Rogers, D. Wang, and E. Luo, ''Anomalous sound propagation in shallow water due to internal wave solitons,'' IEEE J. Ocean Sc. **90**, 2042–2054 (1993).
[9] J. Preisig and T. F. Duda, ''Coupled acoustic mode propagation through continental shelf internal solitary waves,'' IEEE J. Ocean Eng. **22**, 256–269 (1997).
[10] D. Tielbuerger, S. Finette, and S. Wolf, ''Acoustic propagation through an internal wave field in a shallow water waveguide,'' J. Acoust. Soc. Am. **101**, 789–808 (1997).
[11] F. B. Jensen, W. A. Kuperman, M. B. Porter, and H. Schmidt, *Computational Ocean Acoustics* (American Institute of Physics, New York, 1994).
[12] R. H. Headrick, ''Analysis of Internal Wave Induced Mode Coupling Effects on The 1995 SWARM Acoustic Transmissions,'' Ph.D. thesis, MIT/WHOI Joint Program, June 1997.
[13] W. A. Kuperman, M. B. Porter, J. S. Perkins, and R. B. Evans, ''Rapid computation of acoustic fields in three dimensional ocean environments,'' J. Acoust. Soc. Am. **89**, 125–133 (1991).
[14] L. B. Dozier and F. D. Tappert, ''Statistics of normal mode amplitudes in a random ocean. ii. Computations,'' J. Acoust. Soc. Am. **64**, 533–547 (1978).
[15] D. B. Creamer, ''Scintillating shallow-water waveguides,'' J. Acoust. Soc. Am. **99**, 2825–2838 (1996).
[16] A. W. Drake, *Fundamentals of Applied Probability Theory* (McGraw-Hill, New York, 1967).
[17] T. F. Duda and J. Preisig, ''Acoustic effects of moving coastal solitary wave packets,'' IEEE J. Ocean Eng. **24**, 16–32 (1999).

Reverberation at the Mid-Atlantic Ridge during the 1993 ARSRP experiment seen by R/V ALLIANCE from 200–1400 Hz and some modeling inferences

John R. Preston
ARL, The Pennsylvania State University, P.O. Box 30, State College, Pennsylvania 16804

(Received 1 July 1997; revised 22 February 1999; accepted 16 September 1999)

In July 1993 SACLANTCEN participated in an experiment for the Acoustic Reverberation Special Research Program (ARSRP). The primary objective was to take high resolution measurements to shed light on the detailed physical processes dominating the low frequency scattering from rough topographic features and from deep sediment pond areas. A very detailed set of monostatic and bistatic scattering experiments were conducted just west of the Mid-Atlantic Ridge near 26° N, 47° W. Results from SACLANTCEN's R/V ALLIANCE are presented which show monostatic and bistatic scattering from selected bathymetric features using pulsed sources from 200–1400 Hz and SUS charges. Area water depths ranged from 3300 to greater than 5200 m. The receivers were a horizontal array of 128 elements spaced at 0.5, 1, and 2 m. Source depths varied from 120 to 1200 m and receiver depths ranged from 400 to 500 m. Received reverberation levels are presented as functions of the estimated scatterer position on area bathymetry maps. Results show the same high scattering areas from one seamount were observed in three distinct frequency bands centered at 227, 350, and 700 Hz. Even at 1350 Hz the correlation of scattering highlights with nearby bathymetric features is quite good. Comparisons of measured reverberation and modeled reverberation are presented which suggest that the dominant longer range scattering from the large features is driven by the steep slopes present above the critical depth but that small scale roughness is also essential for strong backscatter. [S0001-4966(00)04201-6]

PACS numbers: 43.30.Gr, 43.30.Vh, 43.30.Hw [DLB]

INTRODUCTION AND BACKGROUND

This experiment was a joint effort between the Office of Naval Research (ONR) and SACLANTCEN under the ONR research program entitled the Acoustic Reverberation Special Research Program (ARSRP) to study low frequency long range reverberation and scattering from the sea floor.[1,2] The primary objective of the experiment was to take high resolution measurements to shed light on the detailed physical mechanisms dominating the low frequency reverberation and scattering processes from rough topographic features and from deep sediment pond areas. To this end a very detailed set of monostatic and bistatic scattering experiments were conducted during July 1993 in the frequency range from 200 to 1400 Hz near the Mid-Atlantic Ridge (MAR). The results are being compared with existing and developing models for scattering from bottom, sub-bottom, and volume inhomogeneities and for basin feature reverberation. Major participants in the United States included NRL Washington and NRL SSC, Hawaii Institute of Geophysics, MIT, Scripps, and WHOI. There are numerous examples of selected analysis on this data set.[3–17] This paper summarizes the observations on reverberation made on the R/V ALLIANCE platform using a wider band of frequencies than previously reported. Some inferences for important reverberation mechanisms are made using available two-way scattering models.

The operations area was a 270 km by 470 km area called the Atlantic Natural Laboratory. It is just west of the Mid-Atlantic Ridge roughly bounded by 27.5° N, 49° W and 25.5° N, 45° W. Four principal measurement sites: A, B′, C′, and D were selected (Figs. 1, 2, and Table I).

Figure 1 shows the bathymetry in an area called the B′–C′ corridor. Previous cruises collected detailed supporting geological and high-resolution bathymetric data and will be alluded to as needed here. In the experiment, many beam time series were collected from direct path insonification of distinct features including scattering at various aspect angles. These data are being used to study the scattering zone near these features while limiting much of the complicated forward-scattered field that characterizes shallow water feature scattering. The primary objectives of this work are to

(1) Summarize salient features of the backscatter data seen by the R/V ALLIANCE during the fine scale ARSRP experiment.

(2) Infer from the data and models the circumstances giving rise to strong coherent backscatter from rough steep basin features.

(3) Distill results for input to simpler models using scattering kernels and interface statistics, etc. (A longer range goal.)

Section I provides a brief overview of the ARSRP experiment. Section II contains a description of the data processing and data handling. Section III contains a presentation of the monostatic and bistatic reverberation data. Section IV briefly presents a summary of some sediment thickness measurements made shortly after the ARSRP experiment. Sec-

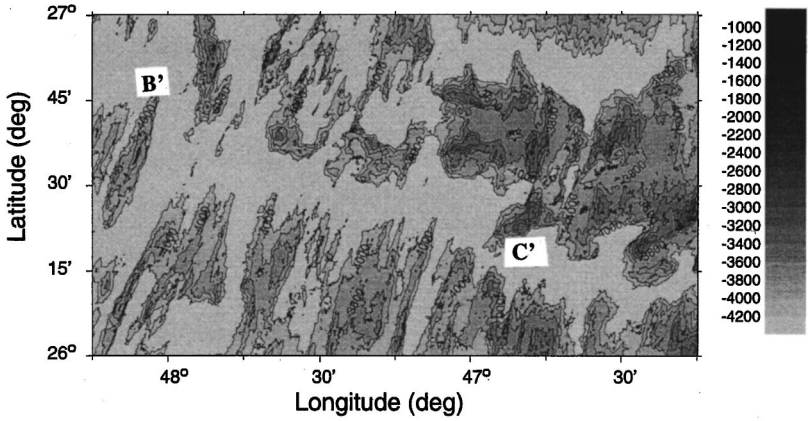

FIG. 1. Area of study near the Mid-Atlantic Ridge showing the seamounts B′ and C′ and the sedimented corridor between them. Bathymetry is truncated at 4200 m to simplify salient details.

tion V contains modeling inferences using a finite element parabolic equation (FEPE) two-way model. Finally, Sec. VI presents the summary and conclusions to date. Appendix A contains sound speed data and descriptions of the key experimental assets onboard ALLIANCE.

I. EXPERIMENT OVERVIEW

The ARSRP acoustics experiment called for a series of monostatic and bistatic reverberation runs using towed arrays and pulsed sources on R/V CORY CHOUEST and R/V ALLIANCE. R/V CORY CHOUEST was the lead ship in the experiment. In addition, the R/V KNORR was to deploy deep moored vertical arrays at three sites, conduct near bottom scattering measurements using DTAGS in the 250–650 Hz band and conduct coring and dredging operations in the area. From July 12 to July 22, 1993 all operations were conducted with the three ships present. On July 22 the R/V CORY CHOUEST departed the area and the R/V ALLIANCE and R/V KNORR operated independently for an additional 5 days.

During this cruise R/V ALLIANCE conducted nine bistatic reverberation runs with R/V CORY CHOUEST, three monostatic reverberation runs (without the CORY), and three airgun/Uniboom passes in the operations area (also without the CORY). In addition, R/V ALLIANCE took five CTDs to depths of 3500 m or more and numerous XBTs were taken. Appendix A contains a composite plot of the 5 deep CTDs taken by ALLIANCE during the period from July 10 to July 22, 1993. Deep moored vertical line arrays deployed by R/V KNORR recorded the bistatic data during Runs 1 and 6 (sites A and B′). A vertical line array deployed near the sea surface by R/V ALLIANCE also recorded ~7 h of data during Run 6 and ~7 h of data for the reverberation pentagon at site D. The nominal tracks for acoustic work with the CORY can be found in the ARSRP Cruise Report for the R/V CORY CHOUEST[1] (actual tracks were somewhat different). A short cruise report also exists for R/V ALLIANCE, which contains more tracks and additional information about data formats and other environmental information.[18]

The R/V ALLIANCE collected monostatic data using a horizontal line array and a towed source (described in Appendix A). The R/V CORY CHOUEST was used as the primary source for the bistatic experiments. The general experimental area will be shown in subsequent sections on each of the plots presenting reverberation data vs location. The water depth in the sediment ponds was ~4000–4800 m over much of the scattering area but these ponds are small and are surrounded by steep very rough outcrops of basalt and gabbro.[6] (Appendix A, Fig. A1 contains a typical sound speed profile taken from the ALLIANCE CTD casts made during the trial.) The sea state was estimated to be 2 or less over much of the trial (wind speed approximately 8–12 knots). The critical depth for ALLIANCE was ~4150±250 m so blockages shallower than ~3900 m and which were located near 1/2 CZ range cut off most of the long range propagating paths from ALLIANCE. Before starting the bistatic runs, clocks onboard CORY and ALLIANCE were synchronized to 1 ms. However, the GPS unit on ALLIANCE was accurate only to ±100 m, while the CORY GPS was much more accurate.

In all there were nine joint acoustic subexperiments (Runs 1 through 9), containing many array orientations each

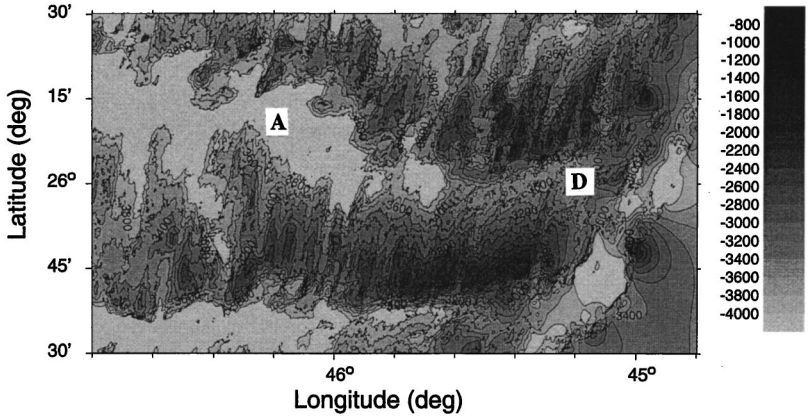

FIG. 2. Area of study near the Mid-Atlantic Ridge showing site D through the west to site A. Bathymetry is truncated at 4200 m to simplify salient details.

TABLE I. Main ARSRP sites.

Site No.	Actual location	
A	26° 11.0′ N	46° 16.0′ W
B′	26° 34.9′ N	48° 06.2′ W
C′	26° 23.28′ N	46° 50.4′ W
D	26° 0.0′ N	45° 15.0′ W

plus three additional monostatic experiments done by R/V ALLIANCE (Runs A, D and a pentagon at site D). This work will discuss examples from Runs 5, 6, 9 and Runs A and D.

II. DATA PROCESSING AND DISPLAY CONVENTIONS

All beam levels presented here are power levels in dB *re* 1 μPa over the signal band, source power levels are in dB *re* 1 μPa at 1 m, and scattering strengths are in dB (unit-less) for scattered intensity from a 1 m^2 area patch.

A. Matched filter processing

Matched filtering (or replica correlation) is an optional step in the signal processing chain to compare the transmitted signal with received data. This cross correlation provides improved range resolution. This procedure is fully equivalent to a standard quadrature correlation operation. This algorithm[19] normalizes the data such that the value of the correlation peak at the output is equal to the rms amplitude at the input for a signal that is perfectly correlated with the signal replica. The theoretical processing gain through this replica correlator for a signal in uncorrelated Gaussian random noise is 10 Log(BT), where B is the signal bandwidth of the pulse in Hz and T is the pulse length in seconds.

B. Data display algorithm

The raw beam time series samples exhibit variances typical of complex Gaussian random variables with unity time-bandwidth product. To reduce this variability, an average over 0.126 s (~19 samples) is performed on each beam time series for data from the 350 Hz band and an average of 0.125 s (~25 samples) for higher frequency bands. In this study, each block of 0.126 s (over which the average is taken) is referred to as a time bin. As the final step to suppress noiselike spikes, the correlator output also uses a clutter reduction method consisting of a peak detector when returns are signal-like and an averager when they are not.[19] Beam power data are linearly interpolated (in dB) across all beam directions where beam data have been taken.

A reference time t_0 is selected as the time when the leading edge of the pulse leaves the source. Display of the reverberation data presents all beam power received monostatically at time t as though it has propagated out horizontally a distance of $c(t-t_0-t_b)/2$, where c is the average sound speed in the water column and t_b is one-half the data block acquisition length (~0.063 s). A consequence of this display technique is that the fathometer returns, when visible, appear in the broadside beam as equally spaced in range.

For a bistatic geometry, the source and receiver positions determine the baseline for an annular ellipse that locates all scatterers at time $t-t_0-t_b$. For a given received backscatter on beam θ possessing a power level $\mathrm{RL}(t,\theta)$, the relative look directions corresponding to that beam are used to compute the two possible locations on the ellipse corresponding to time $t-t_0-t_b$. By doing this calculation over all angles and times, a matrix of received levels is produced. The results (either received level or scattering strength) are interpolated over a Mercator map grid area and then displayed.

It is important to note that at any given time the received energy in a horizontal line array beam can be an average of several multipath arrivals, each path scattered from possibly a different grazing angle. Incidence angle spreads of 10–20 degrees are not unusual at ranges away from convergence zones.[20] However, not all eigenrays will contribute equally, especially on a horizontal line array—there is a tendency for the first waterborne arrivals to be the strongest. This will be illustrated later in the section on low frequency results.

Also it is assumed that received levels on a beam are caused by energy that is incident directly on the main beam axis, so no attempt has been made to correct for loss due to the array receiver response pattern.

C. Display conventions

All plots of received level versus location that are discussed below contain two marker ellipses (or circles). The outermost marker ellipse shows scatterer positions associated with arrival times that are 60 s after the start of reception at the receiver (t_r) of the direct blast. For the monostatic cases, the marker ellipses are nearly circular (as mentioned, the source and receiver on the ALLIANCE were typically ~1450 m apart). Consequently, for monostatic plots that marker (circle) translates to approximately 45 km in range. The innermost marker ellipse is drawn at T s after the start of signal reception, where T is the pulse length. Inside the inner marker ellipse, the direct blast signal is being received. In the monostatic cases, the proximity of the source to the array causes the acquisition system to be overloaded while the signal is being transmitted. For this reason, the inner monostatic marker ellipse becomes a series of ellipses spaced 1 s apart out to the end of signal transmission. Each plot shows an arrow along the horizontal line array heading. If the run is bistatic, a line is also drawn connecting source and receiver.

III. MATCHED FILTER RESULTS

Two types of displays will be presented in the following section.

(1) Monostatic matched filtered received beam level versus location on an area map.

(2) Bistatic matched filtered received beam level versus location on an area map.

All of the plots shown are for a single horizontal line array heading and consequently will show backscatter that includes the same data on the mirror image bearing (the bearing ambiguity). Hence, monostatic plots are symmetric about

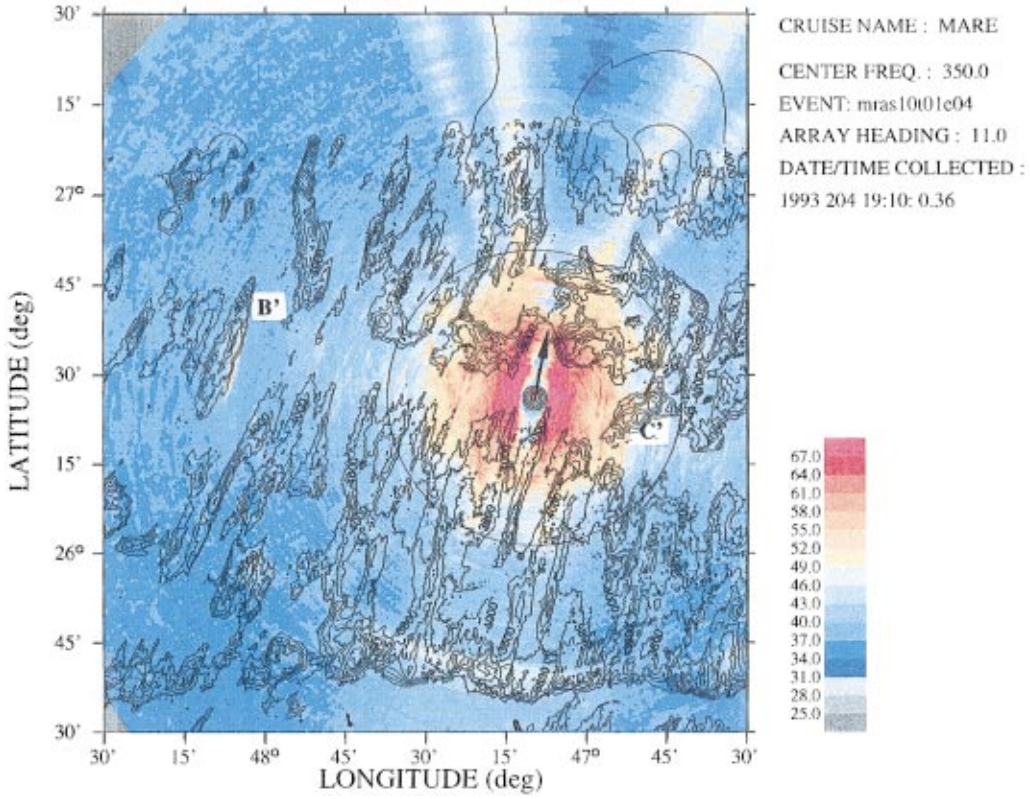

FIG. 3. Received beam power in dB versus location for the horizontal line array near site C′ with 4 s LFM pulse: in the 325–375 Hz band. Bathymetry is truncated at 4200 m to simplify salient details.

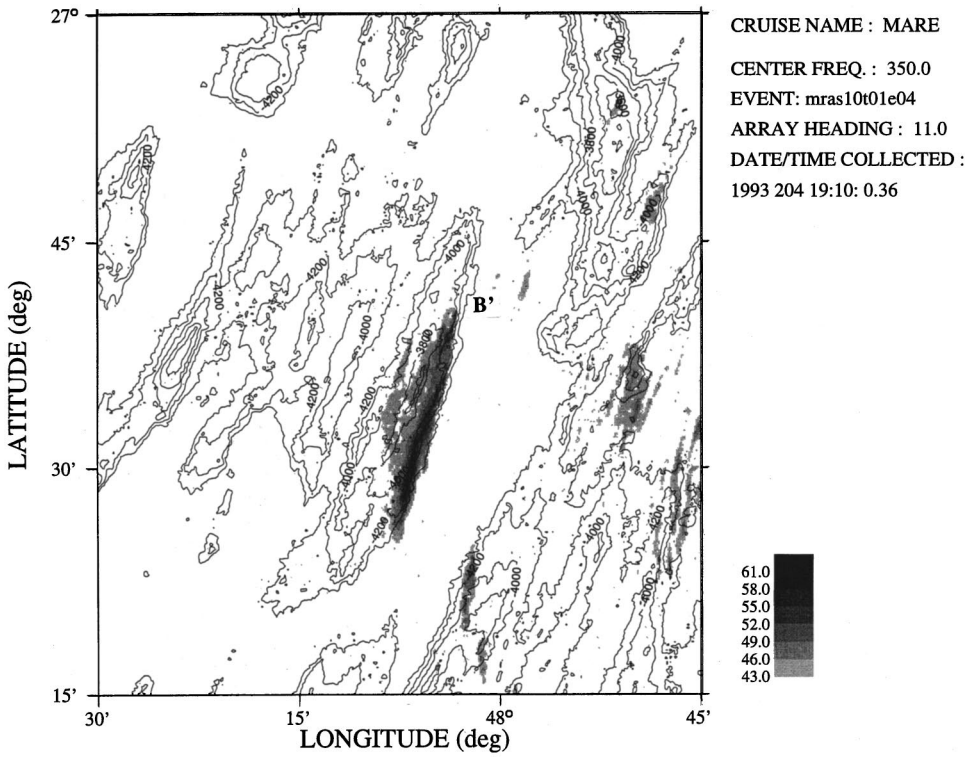

FIG. 4. Same as Fig. 3 but expanded plot around the B′ seamount showing the return from the lower scarp. Bathymetry is truncated at 4600 m for this plot only.

the array heading line. In order to simplify the plots, the bathymetric overlays are generally truncated to 4200 m (or in some cases 4400 m) which is approximately equal to the deepest depth reached by the low loss eigenrays for ALLIANCE during this experiment. After inspection of the eigenrays using the Generic Sonar Model (GSM), it was decided to use an average speed of propagation on the plots to be shown of 1503.6 m/s. This slightly over-propagated energy for the CORY source for the two bistatic examples discussed here, since the depth excursions of the ray paths from the CORY were not quite as deep as those from the ALLIANCE.

Typical standard deviations on the correlator output data for Run 5 and Run 6 were measured for both the noise regions and the reverberation regions on selected broadside beams. For the noise only region of the plots to be presented, typical standard deviations ranged from $\sigma \sim 0.9$–1.8 dB with 1.0–1.2 dB being typical. After removing the slope, standard deviations for the incoherent regions of reverberation ranged from as small as 1.3 dB to 2.6 dB with 2.0–2.5 dB being typical. These values are consistent with Makris' predictions for signal or noise variability versus time bandwidth product.[21]

A. Lower frequency (200–400 Hz) results

In this frequency region both the R/V ALLIANCE and R/V CORY CHOUEST were able to transmit and receive bistatically. The first example of backscatter data is from R/V ALLIANCE, Run A at a range of 1-1/2 convergence zones (CZs) from the B′ seamount. Figure 3 shows the monostatic matched filtered results from one LFM ping (4 s long, 325–375 Hz). The B′ and C′ seamounts are indicated in the plot. The bathymetric overlay includes depths only down to 4200 m. The lower depth limit changes from plot to plot. Inside the 60 s marker circle (~0.7 of a convergence zone range), there are high levels of incoherent backscattered energy across most beams. There are also patterns of high backscatter levels that follow some of the steeper bathymetry, especially around the C′ seamount and its northern neighbors. The radial lines to the north of the 60 s marker circle represent directional ambient noise. But most striking is the elongated return from the B′ seamount (Fig. 4 is the expanded view of the return from B′ in Fig. 3). The lower scarps of B′ at ~3900–4200 m are illuminated sharply by the LFM pulse. Figure 4 shows that the peak illumination has an extent of ~2 km in the down range direction from ALLIANCE. This LFM pulse has a nominal range resolution of ~15 m at high signal to noise levels but because of the 0.126 s averaging the actual resolution shown is ~95 m.

The backscatter result can be understood using the range-dependent acoustic model (RAM) to look at just the propagation loss.[22] RAM is a split step, high angle parabolic equation model, which uses Padé approximations to march solutions out in range. Figure 5(a) and (b) show RAM propagation loss predictions (in dB) for the two element source on ALLIANCE from the ping location out along the two ambiguous broadside beam bearings from the array (101° and 281° T). Note that the energy to the east is bathymetrically blocked by the C′ seamount at ~30 km (1/2 CZ) while to the west it is able to insonify the lower scarp of B′ at 1-1/2 CZs.

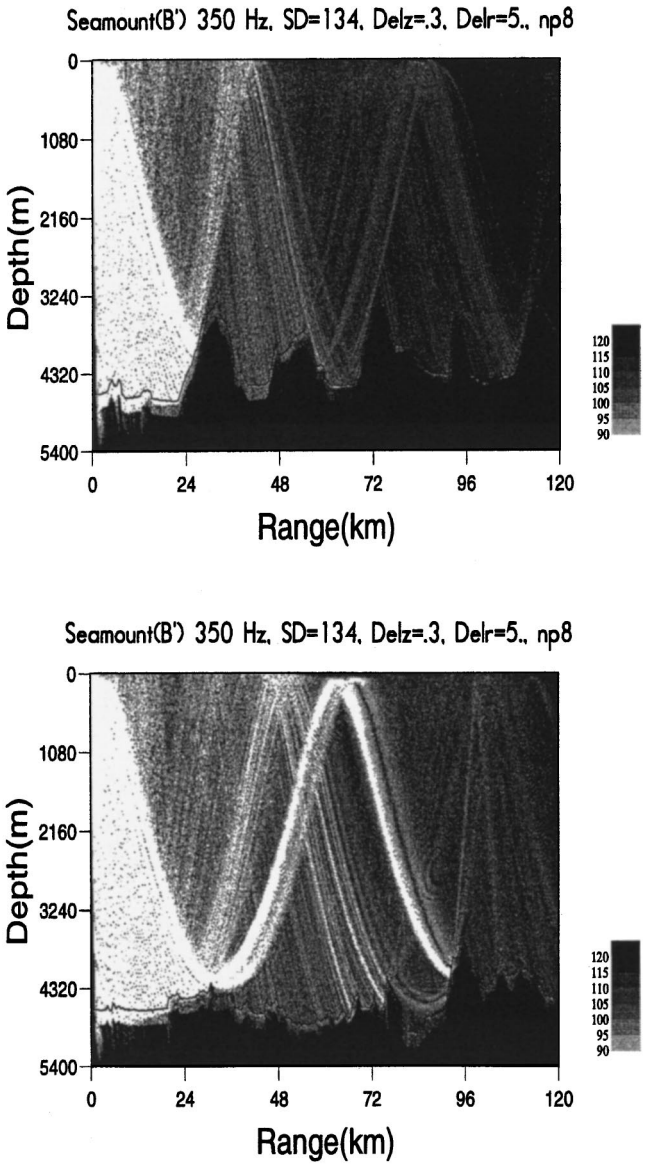

FIG. 5. (a) RAM one way propagation field showing bathymetric shielding of the broadside beam energy by the C′ seamount to the East of the ALLIANCE position shown. (b) RAM one way propagation field showing the 1-1/CZ energy hitting the lower scarp of the B′ seamount to the west of R/V ALLIANCE position shown.

This means that the return shown in Fig. 4 is unambiguously a return from the B′ seamount. [This geometry was designed by Makris for the CORY CHOUEST for Run 8 and was repeated by ALLIANCE at the higher frequency (325–375 Hz) band during Run A.]

Figure 6 looks at the very different character of the matched filter time series from B′ for 11 adjacent beams around broadside. These returns are from the lower scarp shown in Fig. 4. The significant energy for these 11 returns is spread over ~2.5 s corresponding to an equivalent range spread of ~1900 m.

Figure 7 shows a spectrogram of the broadside beam in Fig. 6 (fifth trace from the top) for this 50 Hz wide LFM. Zero time is the direct arrival (monostatic), after a gap of ~5 s the bottom returns plus reverberation are seen on the array. Between 50 and 90 s there are a series of 5 weak but visible arrivals. The last of these could correspond to a return from

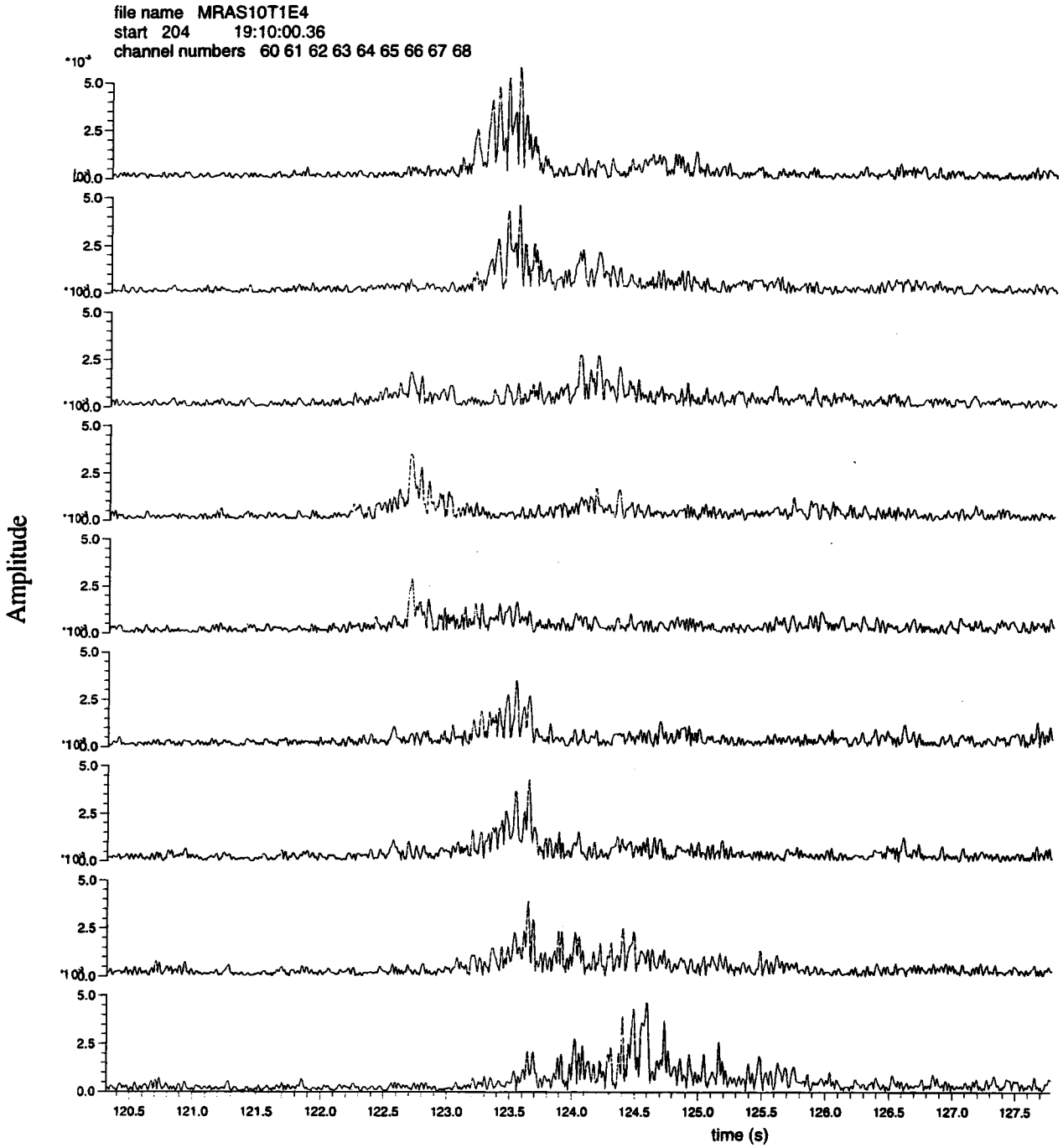

FIG. 6. Sample beam time series after matched filtering of the 1-1/2 CZ reverberant return from B′ for the eleven adjacent beams around broadside from the data in Fig. 4.

a 1 CZ range, i.e., the sea surface (since the ALLIANCE source was not very directional). Note the strong and sharp first arrival from the B′ seamount at ~122 s sweeping from −25 to 25 Hz.

Now a series of selected monostatic pings from R/V ALLIANCE are shown. The endfire beams (dead ahead or dead aft on the array), contain unambiguous bearing data. A forward endfire return from the top of B′ and from two successive features behind it to the west is shown in Fig. 8 from Run 6. Note that a sharp return is visible near the 4000 m contour of B′ in this direction and another is visible from the top of B′ at ~3500 m depth. There appears to be a return from the backside of B′ as well (next to the back of the arrow head) but this might also be a multipath return from closer in since the time difference is ~5 s. As corroboration, Fig. 5(b) shows a faint forward scatter path from the lower scarp of B′ to the surface and down to the back side of B′. The extra surface bounce takes ~5 s. If the returned energy followed that same path back to the source the display program would erroneously map that energy to a point 5 s beyond the back side of B′. Smith, Hodgekiss, and Tappert[7] discuss this point and show broadband predictions for an LFM pulse (200–255 Hz) from the CORY source. They predict one way pulse spreads of ~4–6 s at 30 km range from B′ which is similar to the Fig. 8 case. However, most of the time in deep water, the strongest reverberant arrivals seem to

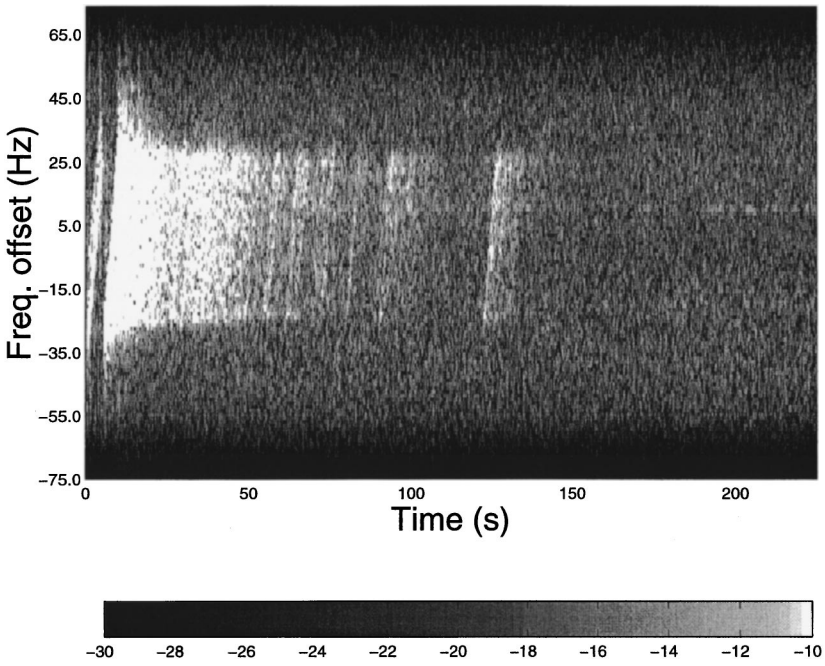

FIG. 7. Sample spectrogram of the 4 s LFM (325–375 Hz) reverberant time series including the return from the B′ seamount at 1-1/2 CZ range and at ~120 s (see Fig. 6). The frequencies shown (−25–+25 Hz) were down shifted by 350 Hz before the computation was made.

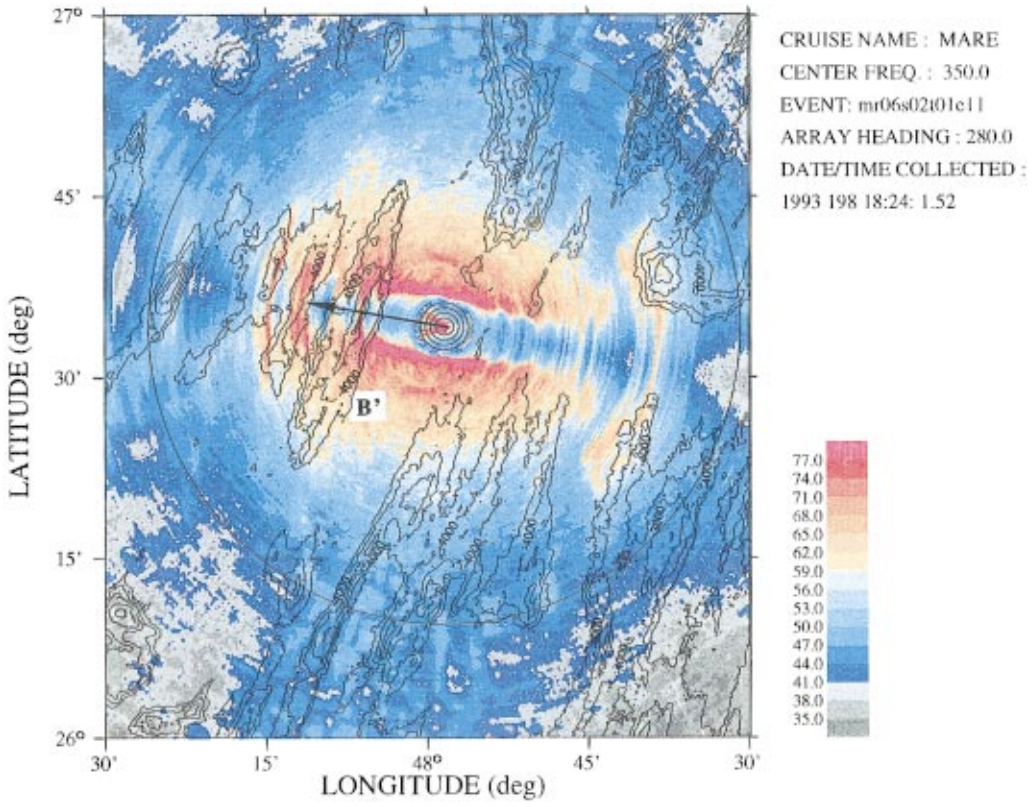

FIG. 8. Received beam power in dB vs location for the horizontal line array about to cross over the top of B′ with 4 s LFM pulse in the 325–375 Hz band. Note the unambiguous forward endfire return from B′.

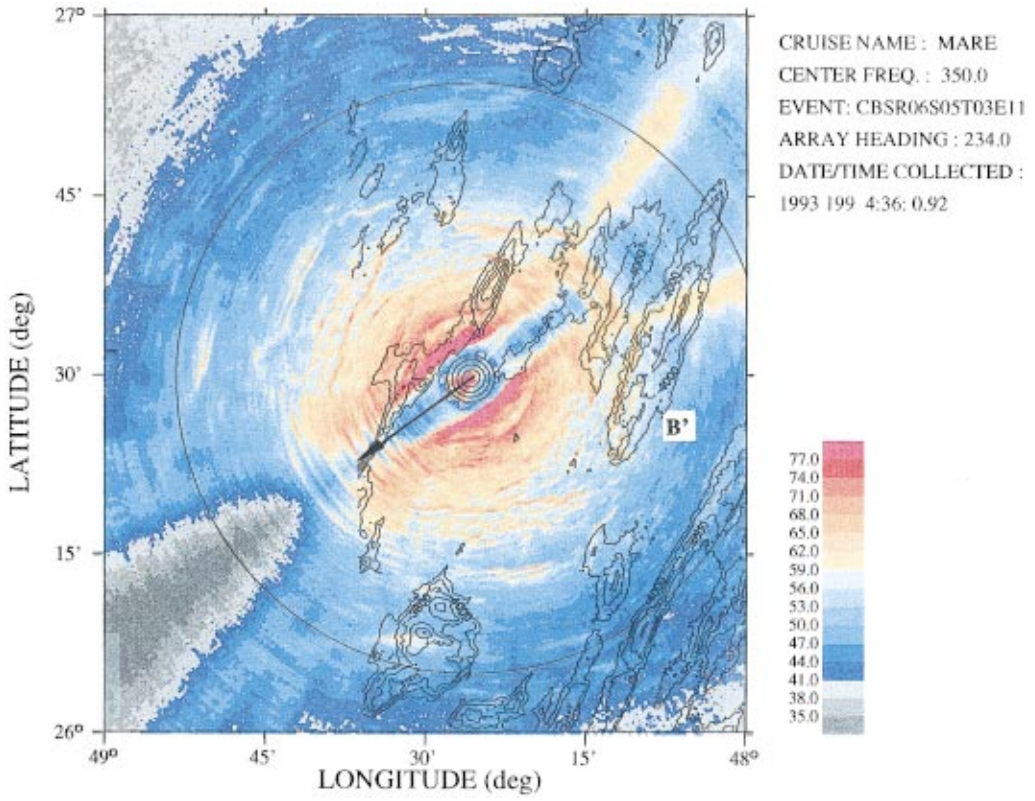

FIG. 9. Received beam power in dB versus location for the horizontal line array near the west side of B′ with 4 s LFM pulse in the 325–375 Hz band.

correlate well with bathymetry since the leading edge of the pulse contains the least amount of surface and bottom interactions and so it usually carries more energy than the pulse tail.

Figure 9 shows scattering from the west side of B′ during Run 6—in particular from the lower scarp of B′ at ~4000 m depth coming from the aft ~140° bearing relative to the array heading arrow on the plot at approximately 30 s after the pulse emission. Note the ambiguous bearing does not correlate with the bathymetry and is therefore unlikely to be a contributor. The bathymetric data set (collected by the WHOI using the R/V EWING in a 1992 ARSRP cruise[23]) ends at ~48° 37′ W. A feature at ~26° 40′ N and 48° 35′ W also shows high correlation with the scattered energy on the beams just forward of array broadside, while the mirror image energy running horizontally near 26° 20′ N does not.

Starting with the ping shown in Fig. 9, Fig. 10(a) shows what the three consecutive pings from this run from those lower scarps on the back of B′ look like after matched filtering. They were spaced 180 s apart and the ALLIANCE speed of advance was ~4 kts leading to a spatial offset of ~360 m. Levels above 0.003 are signal like. One can see that the signals like portions are quite different in appearance.

For the intervals shown in Fig. 10(a), Fig. 10(b) shows an incoherent cross covariance of the matched filtered output between these 3 pings. This suggests a moderately high (incoherent) ping to ping correlation for these sharp returns from the west side of B′ despite the ping to ping difference in appearance shown in Fig. 10(a). This is probably expected since strong backscattering from large basin features is often observed.

A probable insonification of the C′ seamount from 2-1/2 CZs during Run 6 while ALLIANCE was on the western side of the B′ seamount is shown in Fig. 11. There is just barely enough clearance for the convergence zone ray paths to clear the B′ seamount and get out into the sound channel of the sedimented B′–C′ corridor. The eastern side of B′ is 3800 m deep at ~21 400 m range and ray tracing showed that only the strong limiting ray bundle which vertexes at the shallowest depth at ~4200 m and at 1/2 CZ in range can clear the seamount. A check on ambiguous bearing bathymetry inferred using gravitational anomalies from GEOSAT data at the same range as C′ showed no features of significance meaning that the return shown most probably comes from the C′ seamount.

The insonification of B′ from the South during Run 5b is shown in Fig. 12. One can see 7–8 separate lineated returns from B′ progressing up the southern slope. The bathymetry includes the 4400 m contour which becomes more important when ranges are less than 1/2 CZ (~35 km). The mirror image returns (not shown here) do not correlate well with the bathymetry and so we again argue that the lineations are due almost entirely to the steeper scarps on B′.

Figure 13 shows a closely related bistatic example from Run 5b using the stronger and more directional source from the CORY CHOUEST. This ping was an HFM pulse from 200–255 Hz with about 20 dB more source level than the 350 Hz pings from ALLIANCE. For this case the source receiver separation was ~23.65±0.1 km. We define horizontal incident

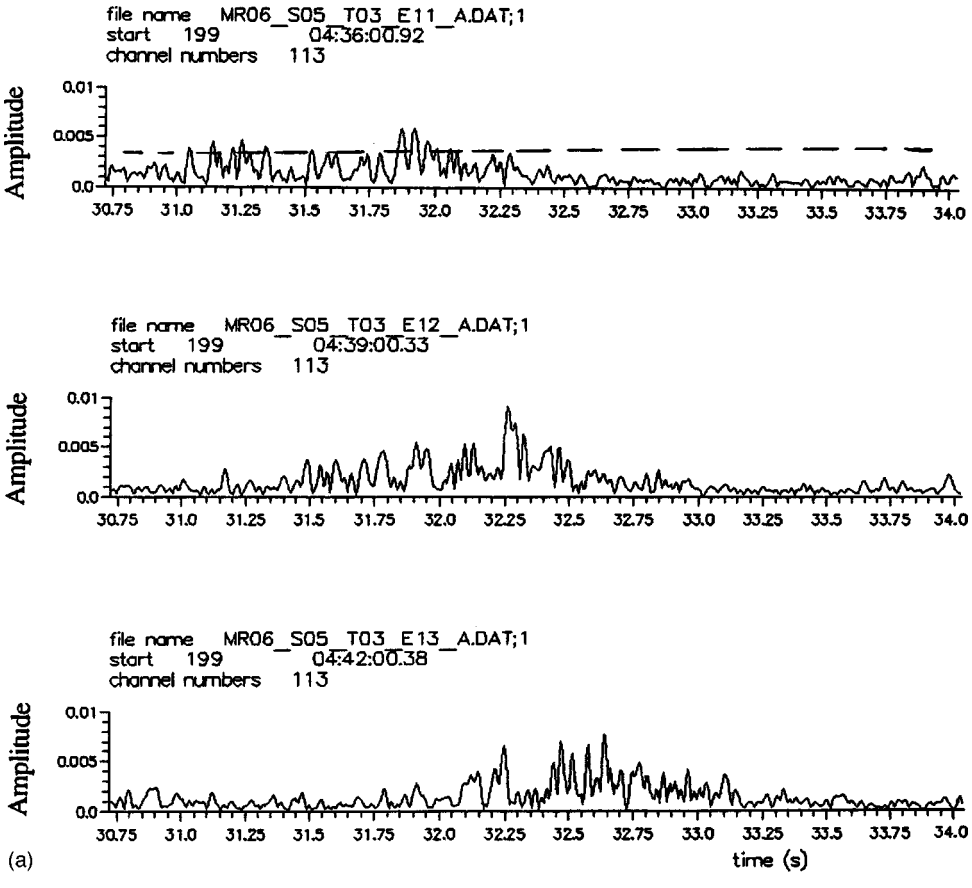

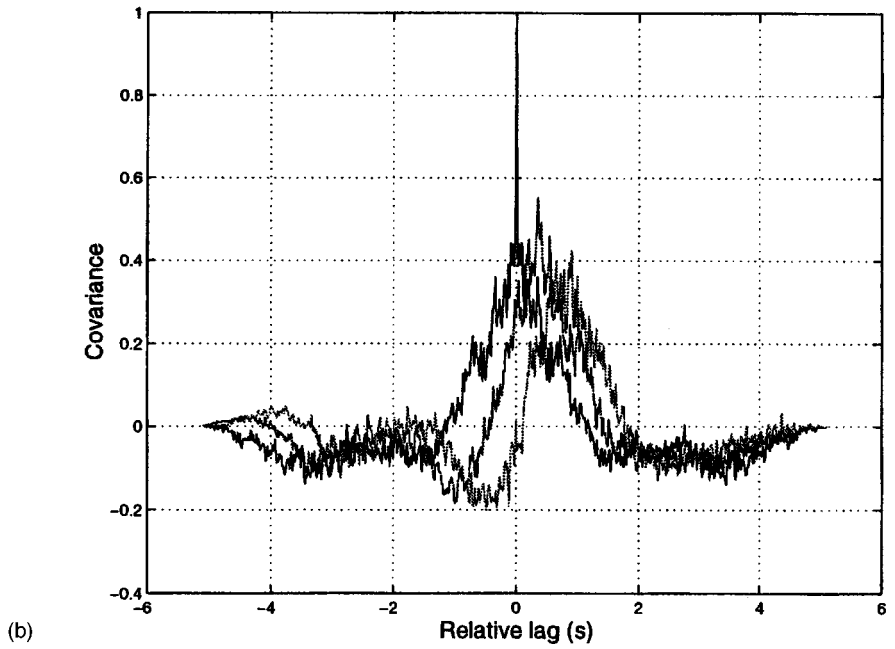

FIG. 10. (a) Sample of three sets of beam time series after matched filtering from three consecutive pings spaced 180 s apart of return from the West side of B′ at around 31–33 s. (b) Cross covariance of the matched filtered time series of ping 1 with pings 1, 2, and 3, respectively. The solid line is the auto covariance of the first ping, then the next peak at ~0.55 is the covariance of the first with the second ping and the last peak at ~0.4 is the covariance of the first ping with the third.

angles to be the angles [looking down on Figs. 12 or 13(a)] that a line from the source to the center of scattered returns makes with the long axis of a bathymetric feature. Then the monostatic horizontal incidence angle from source to B′ in Fig. 12 is about 90°. The horizontal bistatic angle (the mean of the transmit incident angle and receive incident angle) on the southern part of B′ is nearly the same as the 90° horizontal incident angle in Fig. 12 for the monostatic case. We see about 6 sets of lineated returns from the southern part of B′ even though this is a bistatic return. The advantage of the CORY's higher source level is manifested here since the bistatic imaging of the B′ scarps with the strong source of the CORY appears to show more detail than the monostatic image using the ALLIANCE source.

In all the polar plots presented so far one can see that many of the strongest and sharpest returns are associated with large changes in the bathymetry (where the spacing of the contour lines is the smallest) and which are most nearly perpendicular to the horizontal incidence angle. In other words, when a feature can be insonified, the stronger coher-

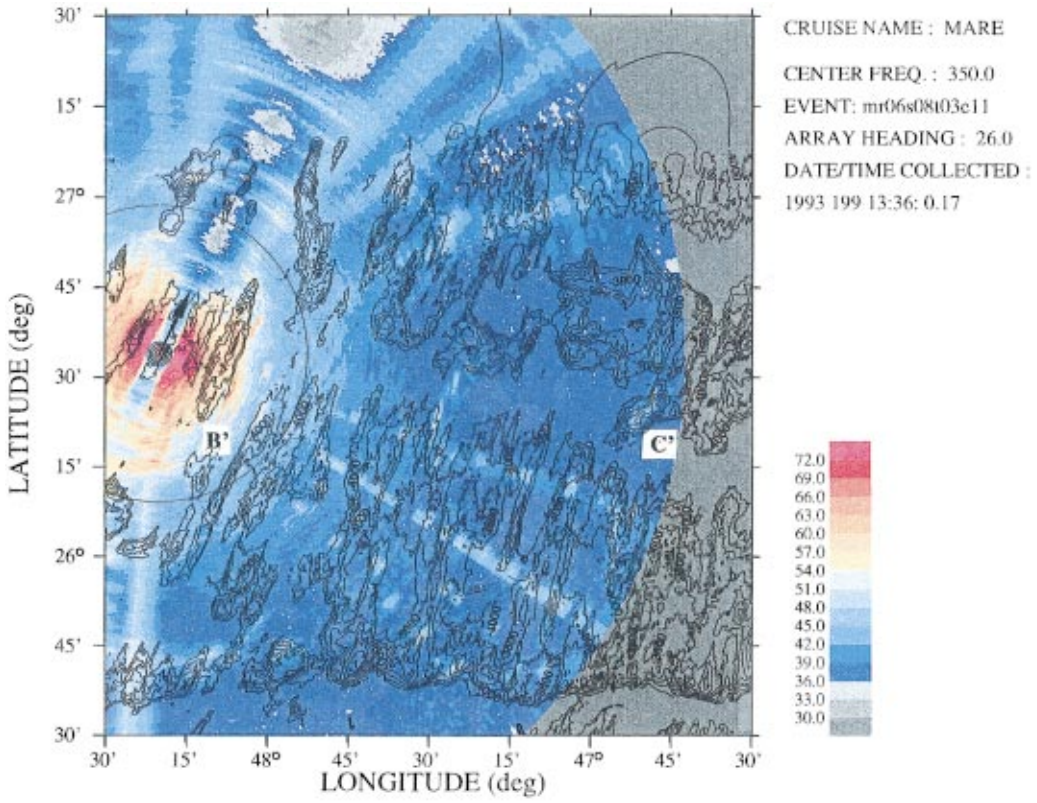

FIG. 11. Received beam power in dB versus location for the horizontal line array near the west side of B′ with 4 s LFM pulse in the 325–375 Hz band. This shows a probable insonification of the C′ seamount from 2-1/2 CZs by R/V ALLIANCE.

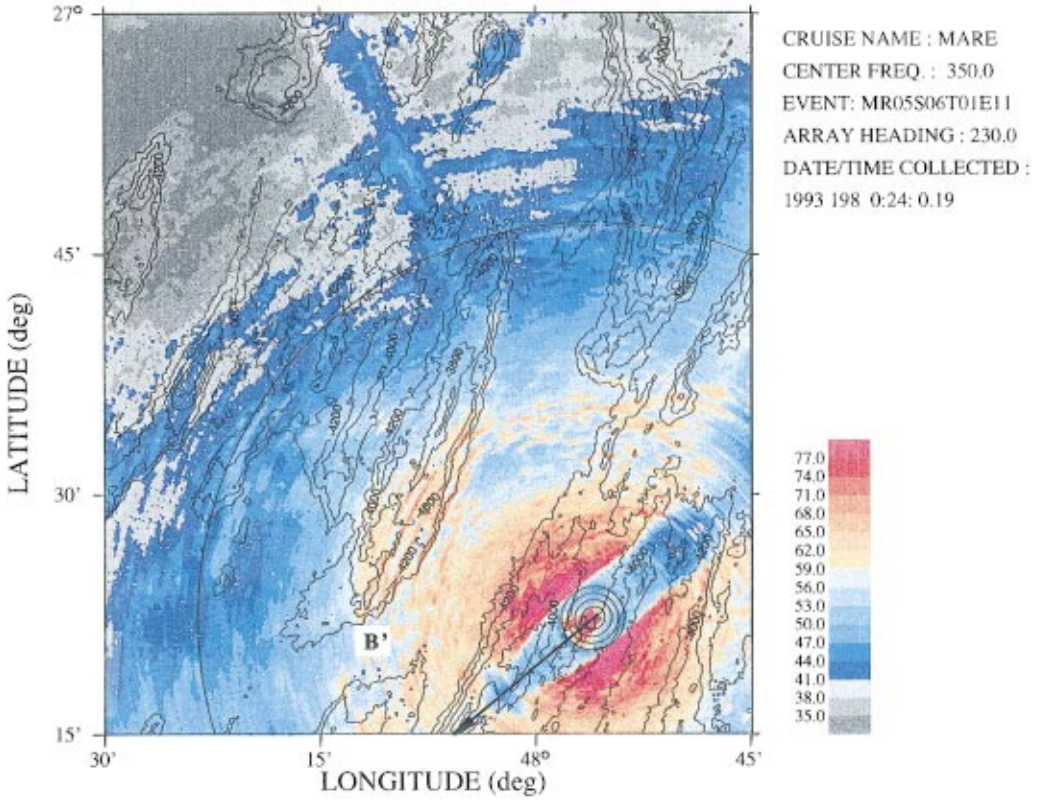

FIG. 12. Monostatic received beam power in dB versus location for the horizontal line array, southwest side of B′ with 4 s LFM pulse in the 325–375 Hz band. This shows 8 lineated arrivals from the southern slope of B′.

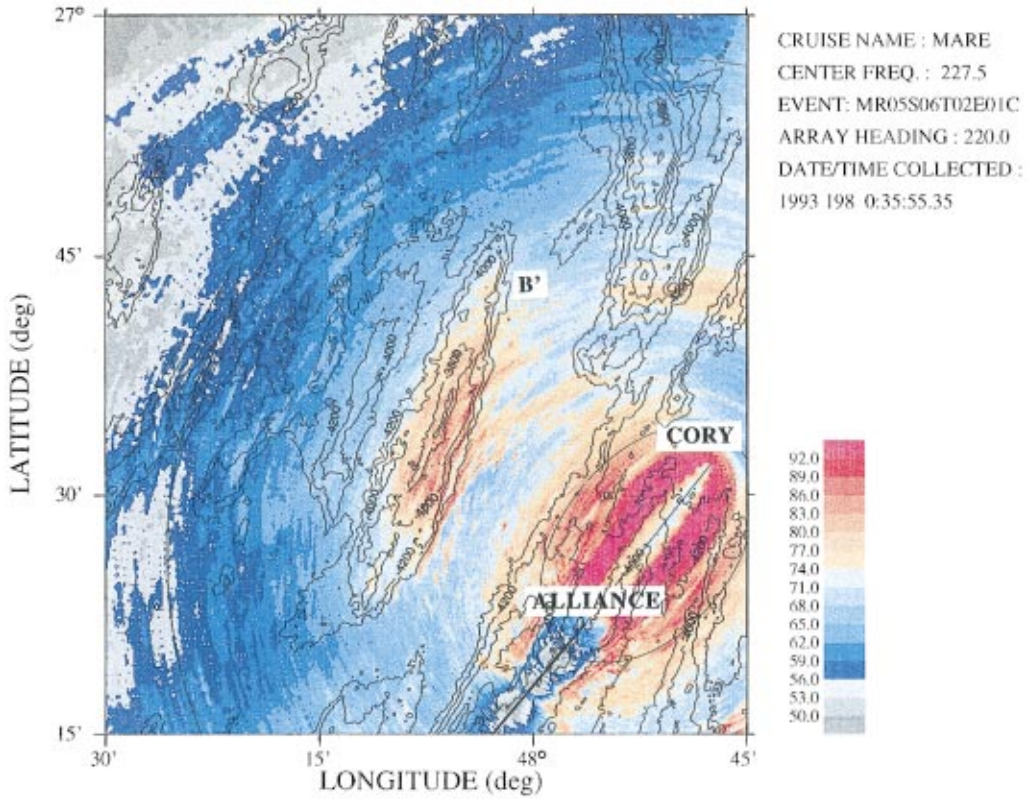

FIG. 13. Bistatic received beam power in dB versus location for the horizontal line array; southwest side of B′ with 5 s LFM pulse in the 200–255 Hz band. This shows 5–6 lineated arrivals from the southern slope of B′. R/V CORY CHOUEST position is indicated on the plot.

ent backscatter is most likely from slopes where incidence angles are large and the orientation of the slope is perpendicular to the horizontal incidence angle (in a top view sense).[24] Makris[4,5] used bathymetric directional derivatives overlaid with backscatter to show similar results for the CORY in the 200–280 Hz band.

The seismic and waterborne direct arrival structure from the bistatic event shown in Fig. 13 is fairly complex and includes forward-scattered energy. A rectangular plot of received beam power versus time and relative azimuth is shown in Fig. 14(a). Indicated on the plot are four major arrival groups for this particular ping from the CORY CHOUEST. The times in Fig. 14(a) all have an offset so 4.60 s must be subtracted from these values to get actual travel times. The source depth was 181 m and the receiver depth was 437 m. The water depth was taken to be 4000 m at the mean of the bistatic source and receiver positions for this ping. The bathymetry indicates the source receiver mid-point is somewhat elevated relative to the nearby sedimented corridors and is therefore more likely to be basalt or gabbro that is thinly sedimented.[6]

Some simplified explanations for each of these four arrivals are summarized in Table II. Column 2 shows the four distinct arrival times. In order to identify the arrivals, columns 3, 4, and 5 make different assumptions about the type of path the arrivals may have taken. Where the computations lead to nonphysical answers an NP is inserted next to the speed estimate. Column 3 computes mean water speed assuming a straight-line path from source to receiver. Column 4 computes mean water speed assuming a straight-line bottom bounce path (off the 4000 m sea floor). Column 5 computes mean water speed assuming a straight-line trapezoidal path like that from a head wave. Since a head wave loss goes roughly as $1/r^2$ at longer ranges, this is approximately 87 dB so there would be ample detectable energy at these source levels.

If a direct waterborne path is assumed, arrival 3 in column 3 is the only arrival in that column that is physically possible. Figure 14(b) is a range dependent ray trace (using Bellhop[25]) for this case showing that according to ray theory there is no direct path from source to receiver due to the shadow zone so only bottom bounce paths are possible. One possibility is that arrival 3 is a diffracted or scattered path across the shadow zone and the 1507 m/s speed is closest to the water sound speed of 1525 m/s near the source depth.

For the bottom bounce path, the Generic Sonar Model (GSM) was used to compute the waterborne eigenrays for approximate comparison to the observed data[26] GSM is a range independent model but it accounts for all the array source and receiver geometry for towed arrays, making it useful for model comparisons with real data. Arrival 4 in column 4, is the only arrival predicted by the GSM MULTIP submodel and the only one in that column that is physically possible.

For the last column in Table II it was assumed that the entrance, exit and bottom critical angles were equal. Angles and bottom speeds were computed using simple straight lines of a trapezoidal path (the sound speed at the source and the speed at 4000 m only differed by 2.2 m/s. The angles in the last column correspond to a match in the calculation of the total travel time vs critical angle). Arrivals 1, 2, and 3, with

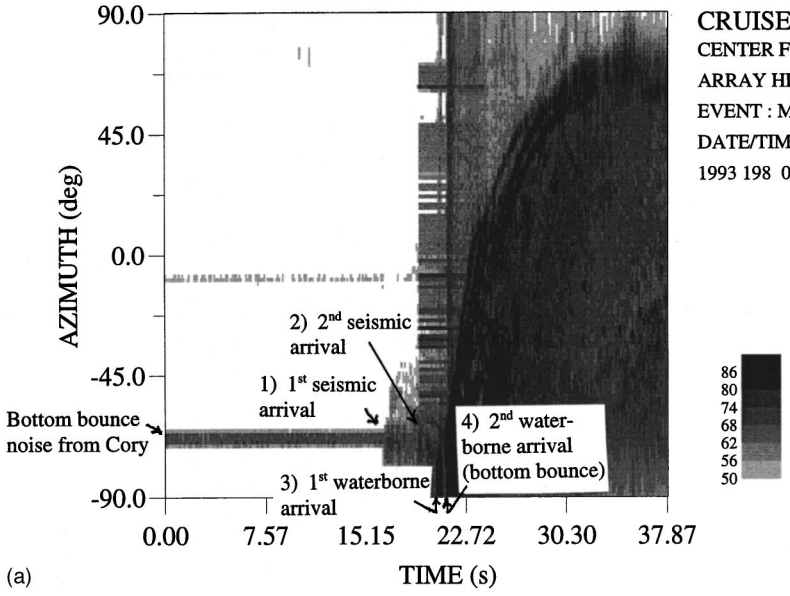

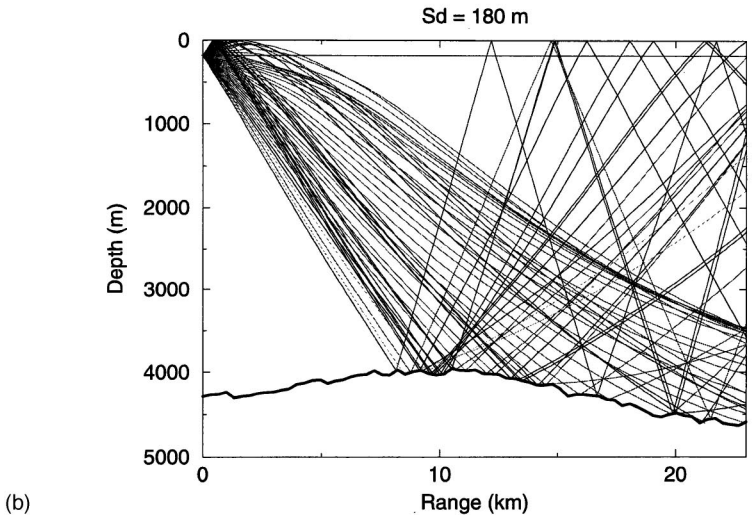

FIG. 14. (a) Detailed plot of direct arrival structure of the CORY ping in Fig. 13. Plot of received level versus azimuth and time showing seismic arrivals preceding the water borne arrivals. (b) Ray trace from the R/V CORY CHOUEST source for the ping of Fig. 13. ALLIANCE HLA depth is indicated by the dotted line and ALLIANCE range of 23 650 m by the arrows.

critical angles of 63°, 46°, and 32°, respectively, are consistent with head-wave like paths. The sound speeds of 2200 and 3360 m/s are not inconsistent with the compressional speeds of basalt and gabbro.

The interpretation of the above analysis is that arrival 1 is probably a deeper bottom refracted path, but could be a head wave, while arrivals 2 and 3 are probably head waves. However, arrival 3 could less likely be a diffracted or scattered water borne path across the shadow zone between the source and receiver. Arrival 4 is the normal water borne bottom bounce path (really a group of 4 paths).

TABLE II. Summary of major arrivals for ping shown in Fig. 14(a) NP means not physically possible.

Arrival No.	Corrected time [Fig. 14(a) —4.6 s]	Effective mean c_w if dir. path (m/s)	Effective mean c_w if bot. bounce path (m/s)	Effective mean c_b if bot. head wave path
1	11.8	2021.5—NP	2177—NP	3363/63°
2	14.4	1654—NP	1732—NP	2198/46°
3	15.8	1506.5?	1578—NP	1800/32°
4	16.5	1442.2—NP	1510	NP

Figure 15 presents a final example of a bistatic return from Run 6 showing the insonification of most of the northern half of B′ (the triangular reddish patch). In this case the source receiver separation was ~15.08 km. Note the ambiguous bearing patch south of the array line of bearing on the plot that is uncorrelated with any bathymetry. The entire top of B′ above the 3800 m contour and north of the heading arrow scattered energy back to ALLIANCE. Features on the near aft endfire (probably the feature east–northeast of ALLIANCE were also strong scatterers. Although not shown here, an arrival structure qualitatively very similar to Fig. 14(a) and Table II was observed for this ping as well.

B. Beam statistics

Standard detection and estimation theory requires that a statistical characterization is needed for any signal processing schemes seeking to minimize the effects of reverberation. Therefore, an illustration of beam time series statistical fluctuations is presented which were observed near the B′ seamount (the analysis routines were provided courtesy of Sheckler and McCammon[27]). We select a sample broadside beam time series (not shown), with reverberation from a 4 s

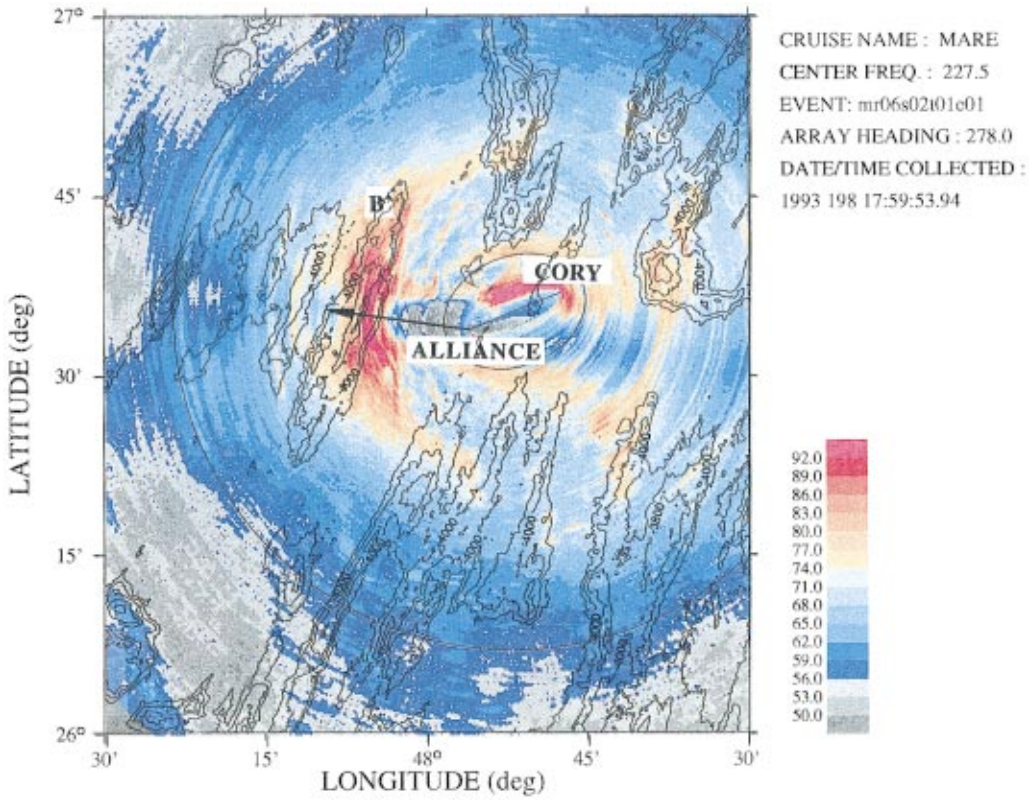

FIG. 15. Bistatic received beam power in dB versus location for the horizontal line array east of B′ with 4 s LFM pulse in the 200–255 Hz band. This shows the northern half of B′ being imaged by the reverberation returns (above the array heading vector) while the mirror image below that vector does not correlate with the bathymetry at all. R/V CORY CHOUEST position is indicated on the plot.

LFM ping centered at 350 Hz (before match filtering). These data were taken from the broadside beam for the polar plot shown as Fig. 9. Two 30 s time intervals were selected for reverberation only and noise-only processing. The data are subsampled in time and beam space until the samples are independent. When the noise only portion is averaged over 13 separate independent beams about broadside and the data are normalized by the mean, Fig. 16(a) is the result. As expected when the noise is a Gaussian random variable, the amplitudes obey a Rayleigh distribution (plotted as the dashed line). When the reverberation segment is processed in a similar manner, however, the spiky reverberation results in a PFA curve that is higher than a Rayleigh distribution [Fig. 16(b)]. This observation is consistent with a multimodal amplitude distribution for the reverberation.

Similar results were generated for a bistatically received LFM ping recorded at about the same time in the 227 Hz band (see Fig. 9 for the monostatic geometry) and quite different results were observed. The source on the CORY for this event was about 45 km east of ALLIANCE and the broadside-beams were about 60° off the line of bearing from ALLIANCE to the CORY CHOUEST. Figure 17(a) shows a PFA curve for the noise using averages of 13 beams as before. One can see the noise data falls somewhat below the Rayleigh distribution curve but Fig. 17(b) shows that the reverberation data fall on the Rayleigh curve. Inspection of the original time series showed the reverberation portion was less spiky than the monostatic result and looks more like a decaying Gaussian pressure field than was the case at the first site. When normalized by the time varying mean the reverberation distribution is primarily Rayleigh-like. Note that in both these cases the tails of the reverberation data exceed the tails of the noise data. There is one important difference in the second data set and that is that the system gain into the A/D converter was set low to minimize clipping of the direct arrival signal from the CORY. As a result the 12 bit A/D sees a biased version of the actual amplitude distribution for ambient noise since the A/D never properly samples lower level ambient noise. This means the upper tail region of the noise is never filled in resulting in a lower than Rayleigh CDF.

C. Higher frequency (650–1400 Hz) results

In this section the broad bandwidth of ALLIANCE data is used to extend the observations on ARSRP reverberation to higher frequency regions. Figures 18 and 19 show higher frequency examples of reverberation data from LFM pulses centered at 700, 950, and 1350 Hz, respectively. In all three cases shown the bathymetric contours extend down to 4400 m. Figure 18 is a high frequency version of Fig. 12 but on a scale that shows the ambiguous bearing bathymetry. The 700 Hz plot correlates well with the bathymetry of the southern part of B′. Again ~6 lineated returns are visible from the south side of B′ and the ambiguous bearing bathymetry is either uncorrelated with these returns or is correlated with negative gradient (down slope) bathymetry.

Figure 19 is from a site in the B′–C′ corridor near C′. These data are from Run 9. While these frequencies are at-

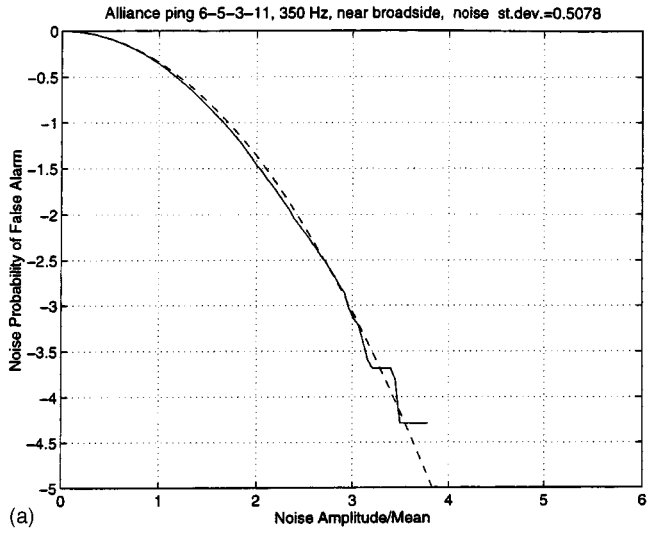

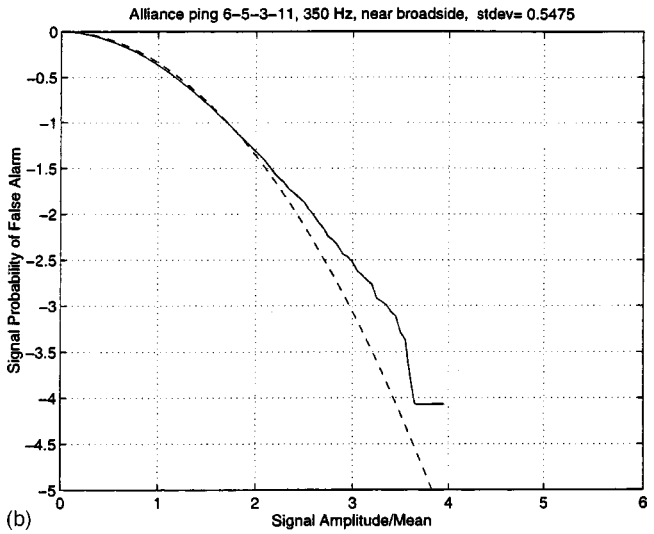

FIG. 16. Statistics from 13 beams near broadside of the 350 Hz LFM windowed in the (a) noise and (b) signal portions. Plots are log [1 minus the cumulative probability density function (CDF)] labeled probability of false alarm (PFA) versus the normalized amplitude. The dashed lines are Rayleigh.

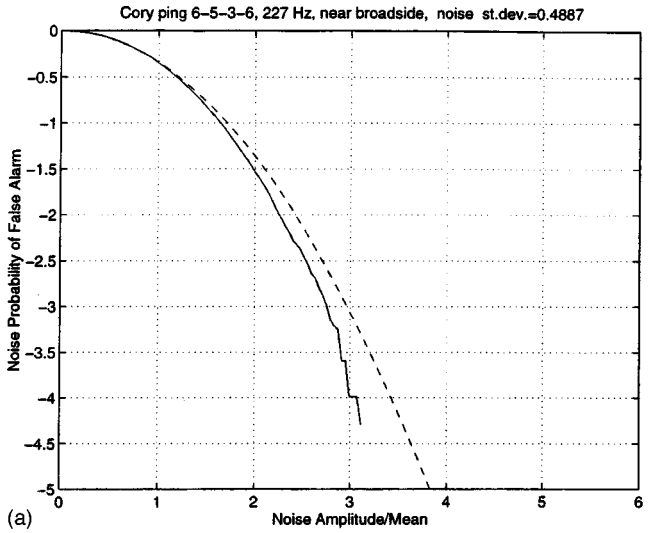

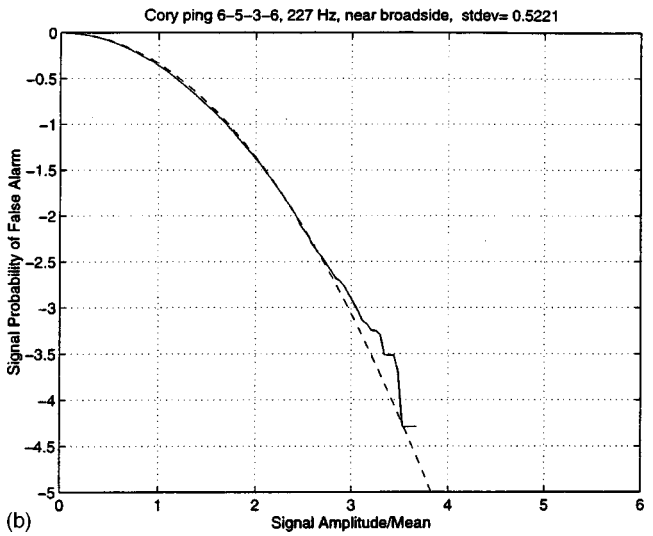

FIG. 17. Statistics from 13 beams near broadside of the 227 Hz LFM windowed in the (a) noise and (b) signal portions. Plots are log [1 minus the cumulative probability density function (CDF)] labeled probability of false alarm (PFA) versus the normalized amplitude. The dashed lines are Rayleigh.

tenuated faster than the 200–350 Hz frequency bands, for these higher frequency pulses analyzed there is still a reasonable degree of correlation with the bathymetry inside the 1/2 CZ range (~35 km or about 1-1/2 arrow lengths). At 1350 Hz, Fig. 19 shows there are some bathymetric features north of ALLIANCE which correlate well with smaller but very visible returns at about 15 km (~3/4 arrow length). Similar results were noted for 950 Hz data (not shown). As might be expected generally the 950 and 1350 Hz data become more patchy than the 350 Hz band data but also are very finely detailed, i.e., smaller in range and cross range extent. A key observation here is that even at higher frequencies the large bathymetric features have a strong deterministic component to the backscatter.

D. High and low frequency comparisons of reverberation data and model results

In this section scattering strength estimates are presented for two sites. Three broadside beam time series have been selected to compare with estimated reverberation using the Generic Sonar Model. Sample broadside beam data were selected at 3 frequencies; 700, 1350, and 350 Hz. Data segments were taken which showed fathometer returns because these provide an immediate way to calibrate the 90° bottom loss estimates. Array geometry can be simulated with GSM and the techniques recommended by Ellis are used to properly account for reverberation on a line array.[28] To estimate scattering strength, a forward model and match approach was used. The starting point was to use a 10 layer hybrid of the geo-acoustic models from Wilkens *et al.*[29] and Bowles.[30] Due to the many layers postulated in these geo-acoustic models, the reflection loss vs grazing angle becomes fairly complicated. Averaging over the frequency band of the ping gives smoother results which are more representative of that band. Figure 20 shows an example computation for the 650–750 Hz band using the OASES model[31] with shear. That curve was put into GSM, however the GSM predicted reverberation was found to be fairly insensitive to the roughly

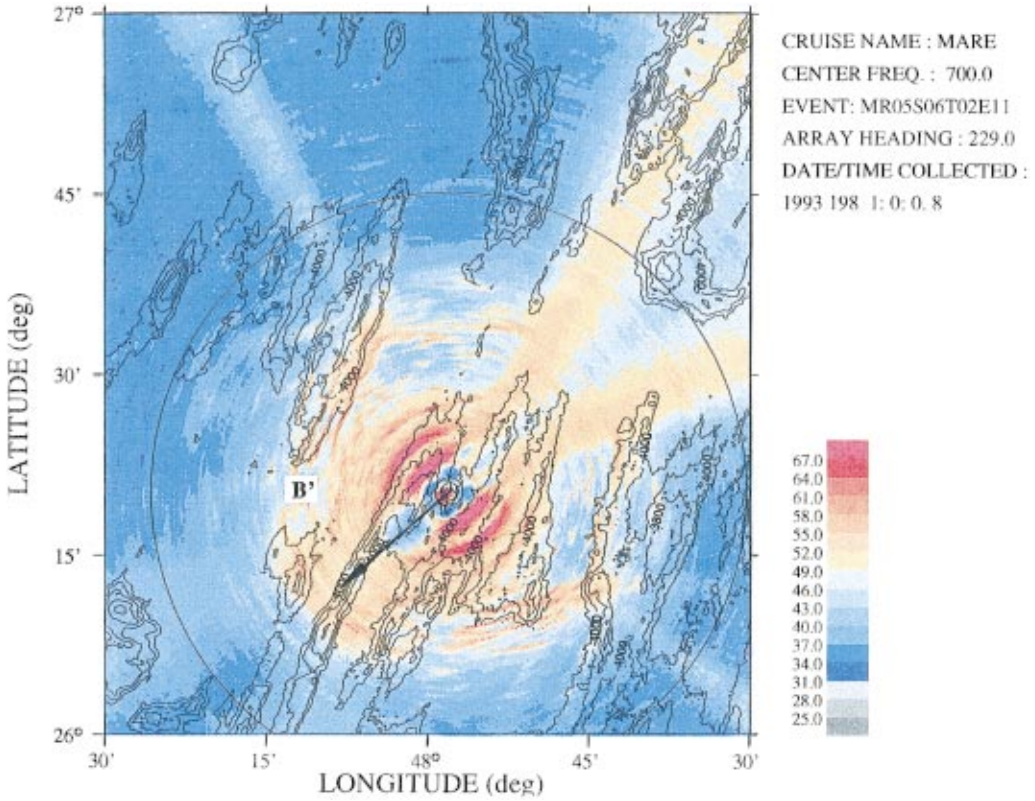

FIG. 18. Received beam power in dB versus location for the horizontal line array near the southeast side of B′ with 2 s LFM pulse in the 650–750 Hz band at 1/2 CZ range.

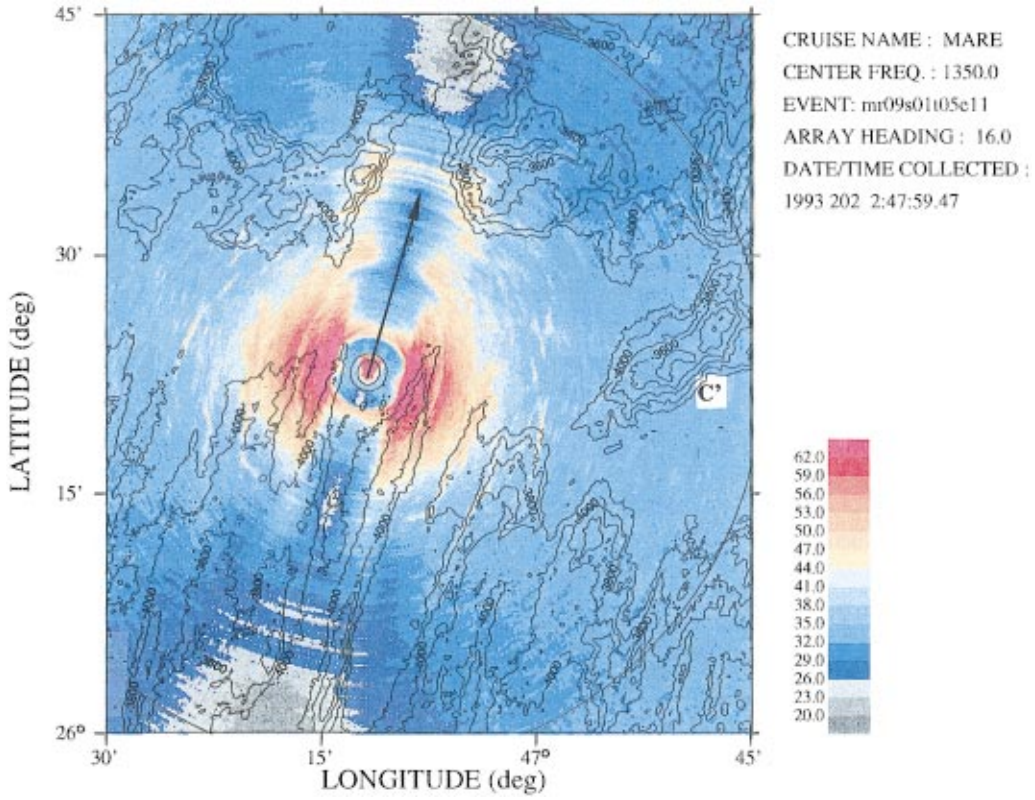

FIG. 19. Received beam power in dB versus location for the horizontal line array near the west side of C′ with 2 s LFM pulse in the 1300–1400 Hz band.

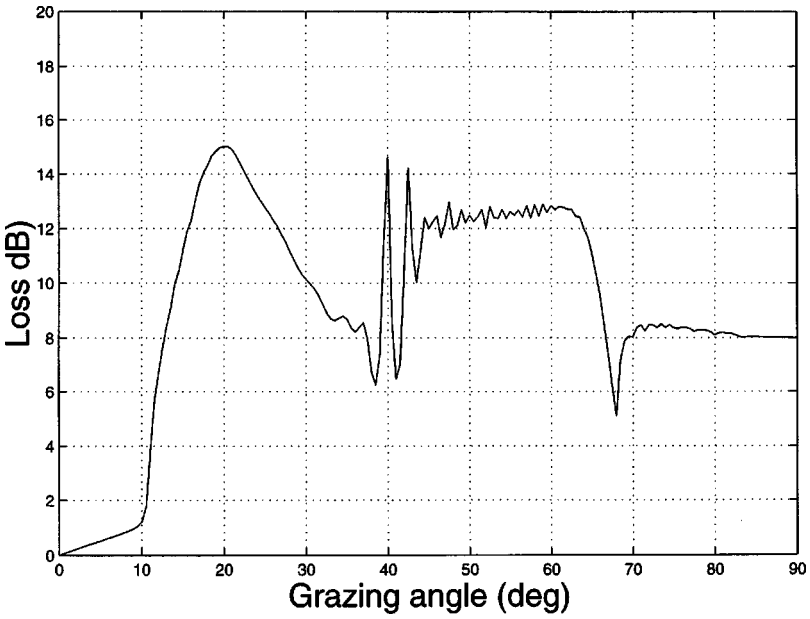

FIG. 20. Reflection loss versus grazing angle for the actual geo-acoustic model near the B′ seamount at 700 Hz.

20°–80° angular region shown in Fig. 20. This suggests that, except for the fathometer returns, only the low angle region of the reflection loss curve is important for these reverberation predictions in the ARSRP environment.

GSM modeling proceeds by making as few changes as possible to achieve an acceptable match to the data. After a few perturbations of the 90 degree reflection losses and the parameter in Lambert's rule for scattering strength, one can arrive at the smoothed bottom loss versus grazing angle curve shown in Fig. 20. (Physically the adjustment to bottom loss at 90° was equivalent to changing the depth from the seafloor to the start of the basement layer.) This estimate was put into GSM and Fig. 21 shows the resulting model data comparison for a 700 Hz LFM pulse from a beam looking on array broadside. The first fathometer return shown in these plots was usually clipped and so the 2nd, 3rd, and 4th fathometer returns are used to estimate the 90° bottom loss. The data was taken near the B′ seamount from Run 5 with approximately 4700 m depth. (The monostatic prediction was made at the average of the source and receiver depths=280 m.) The final geo-acoustic model that gave the best match to the reverberation at 700 Hz was the bottom loss versus reflection curve of Fig. 20, a near surface compressional attenuation α_p of 0.027 dB/m-kHz and a 90° bottom reflection loss of 8 dB. A Lambert's rule coefficient of $\mu=-22$ dB (above average backscattering), for this ping was used in the final model/data comparison. The 90° transmit pattern loss for the ALLIANCE source in this frequency band was only ~0.75 dB. (The low frequency source pair has a grating lobe near 90°.)

A similar model data comparison was done for a 1350 Hz LFM pulse from a beam looking on array broadside. The data was also taken near the B′ seamount from Run 5 with water depth approximately 4600 m. The final geo-acoustic model that gave the best match to the reverberation at 1350 Hz (not shown here) was also a similar 10 layer model with near surface compressional attenuation α_p, of 0.027 dB/m-kHz and a 90° bottom reflection loss of 10 dB. A Lambert's rule coefficient of $\mu=-22$ dB (high backscattering), fit this data well. The 90° transmit pattern loss for the ALLIANCE source in this frequency band was ~8.5 dB.

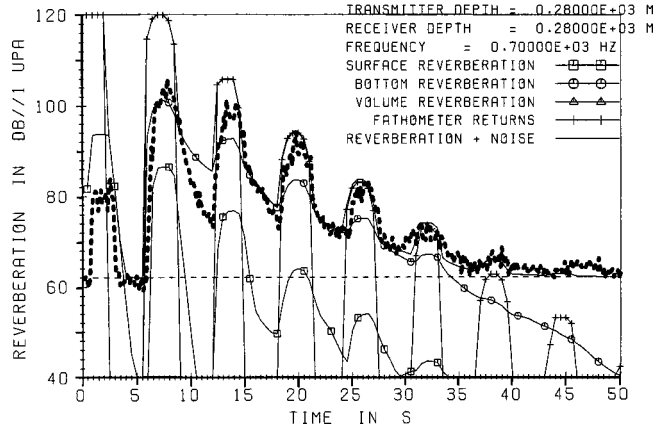

FIG. 21. Comparison of the broadside beam data at 700 Hz (heavy dashed line) with GSM modeled reverberation+noise versus time for the ping of Run 5, Seq. 3, Table 2, Ev. 12 using the 2 s LFM pulse (before matched filtering).

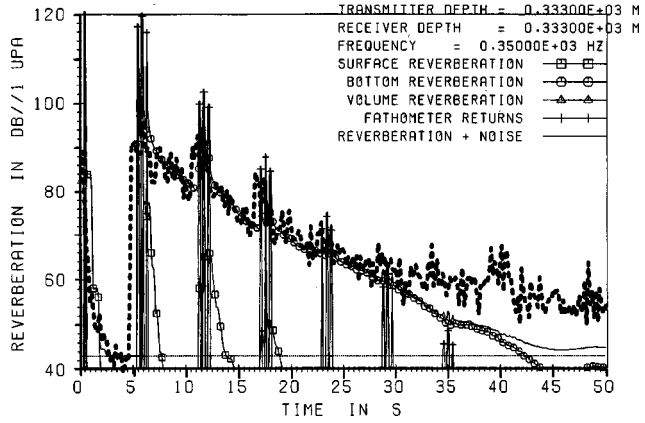

FIG. 22. Comparison of the broadside beam data at 350 Hz (heavy dashed line) with GSM modeled reverberation+noise versus time for the 240 m SUS charge of Run D, Leg 1.

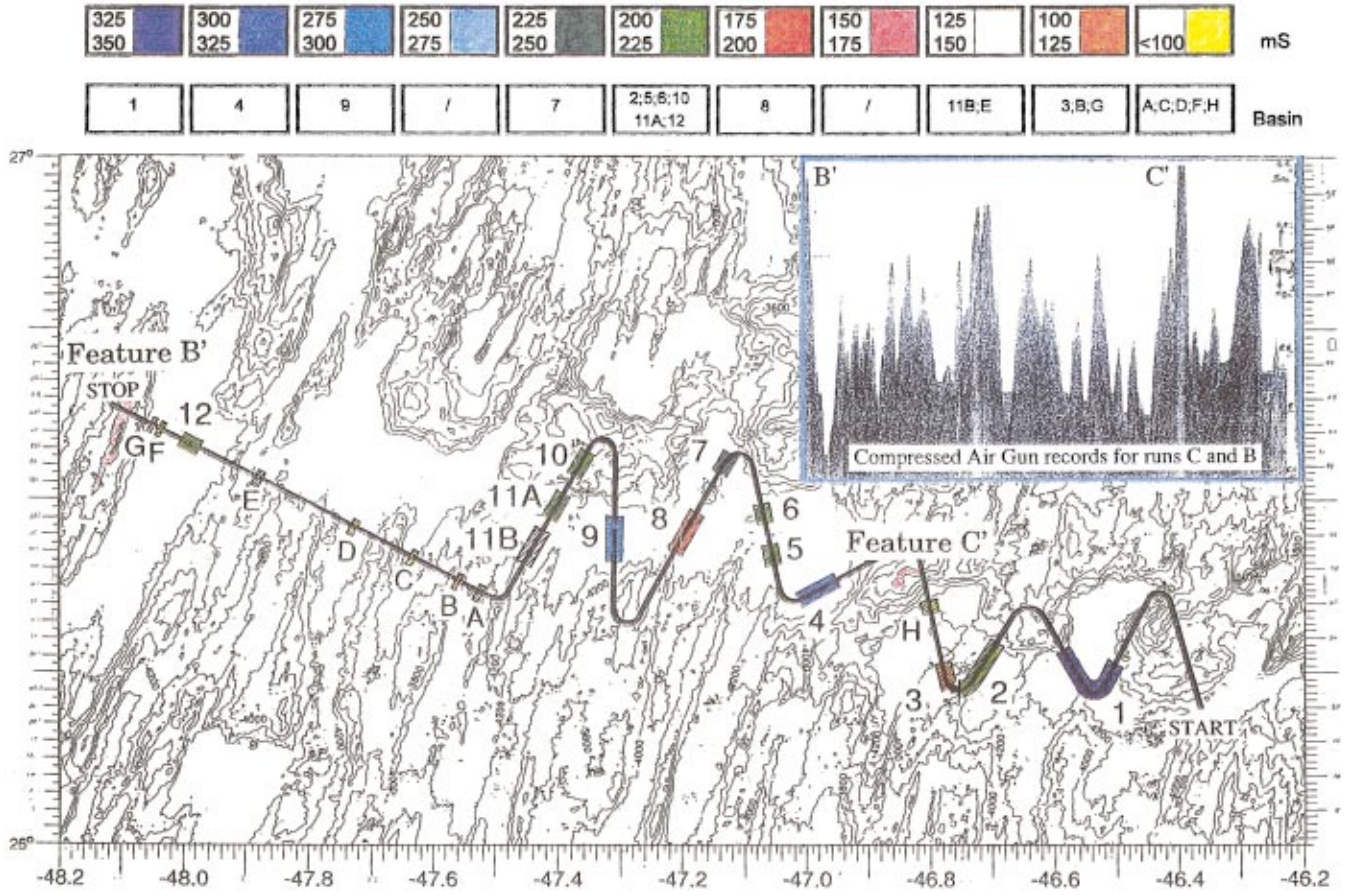

FIG. 23. Track plot for Runs B and D—across the B′–C′ corridor starting just west of site A. This shows estimated sediment thickness as two way travel time for 21 segments along the track.

The 350 Hz data presented some special challenges using this approach. The 90° pattern loss for the ALLIANCE source was theoretically at least 13 dB down in this frequency band and no discernible fathometer returns could be found in all the 350 Hz pings examined. Therefore it was necessary to use some SUS data to augment the reverberation broadside beam samples across frequency. Figure 22 shows a model data comparison at 350 Hz for a 240 m SUS charge taken during Run D (the monostatic prediction was made at the average of the source and receiver depths, 333 m). This run was conducted about midway between sites C′ and A (see Fig. 2). The water depth was approximately 4400 m. The plot is also for a beam from array broadside. The final geo-acoustic model that gave the best match to reverberation data at 350 Hz was a similar 11 layer model with near surface compressional attenuation α_p of 0.027 dB/m-kHz, and a 90° bottom reflection loss of 11 dB. A Lambert's rule coefficient of $\mu=-17$ dB (very high backscattering), was needed to fit this data but this is probably more indicative of general scattering from nearby rocky outcrops than in the first two cases.

The above geo-acoustic parameters are probably not unique. If layers with velocity gradients were used rather than iso-velocity layers, similar matches might be obtainable with different geo-acoustic characterizations. However, if one uses the model and parameters described here, data–model comparisons for similar experiments in this area should be favorable. The best that can be said for this type of bottom estimation technique is that it starts with as much *a priori* information as possible, attempts to make very small deviations from that information, and end up with a model that is as close as possible to the original a priori information. The simple adjustment of μ to provide the best fit to the reverberation levels is the last step in this model–data comparison.

IV. SEISMIC DATA COLLECTION

To help verify bottom properties, ALLIANCE also collected ancillary bottom sedimentation data using airguns and sparkers. Figures 23 and 24 show a summary of results presented previously by Michelozzi and Preston.[32] Figure 23 is the seismic data collection track plot for Runs B and D. The purpose of these runs was to estimate sediment thickness and record reflection data on the SACLANTCEN towed array along the B′ to C′ to site A corridors. Figure 23 also shows the measured thickness for 21 sites along the track. The measurement track started near site A.

Figure 24 shows the low-resolution airgun data for the 12 main sediment ponds along the track in Fig. 23. The counterintuitive result that the sediment thickness decreases from near site A and C′ to B′ is clearly shown (data between the numbered ponds is not included). This has phenomenon has already been reported by Jaroslow[33] as being due to a

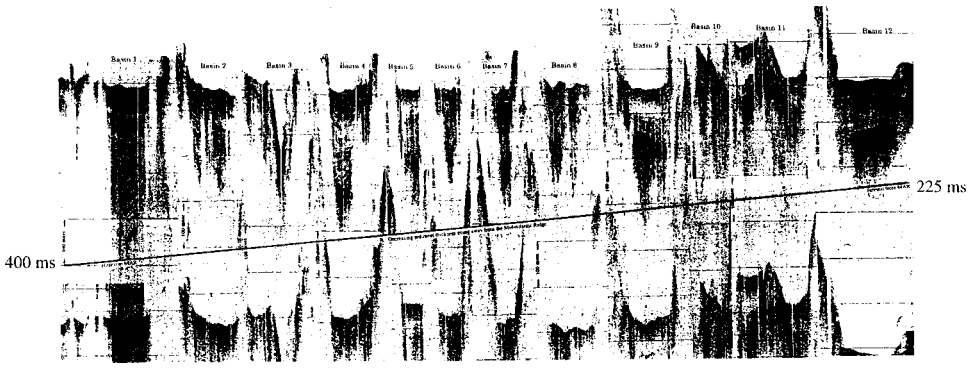

FIG. 24. Estimated sediment thickness as two way travel time for the 12 major basins of Fig. 23 vs distance from the Mid-Atlantic Ridge.

change in the calcium carbonate deposition rate near the Mid-Atlantic Ridge during the particular epoch when that part of the seafloor was being created. Site A is estimated to be ~10 million years old (ma) versus site B′ which is estimated at ~24 ma. The slope of the line in Fig. 24 assumes that there is no bias due to variations in sediment sound speed. There is additional deviation from the trend line due to failure of the track to pass through the pond centers (e.g., basins 2, 3, and 10).

V. FEPE TWO-WAY BACKSCATTER MODELING INFERENCES FOR ARSRP

Knowledge of wavelength scale roughness is critical to understanding the reverberant energy seen in the ARSRP experiment. WHOI (Tucholke) has provided the 1992 Hydrosweep bathymetry[23] for the ARSRP area and the 1993 DSL 120 data[34] at site B′ to the ARSRP researchers. These data have been used together with a best estimate of parameters for the Goff–Jordan and Webb–Jordan models to reconstruct/extrapolate the morphology near B′ down to scales as small as 0.1λ.[35,36] Using estimates based on the ARSRP Hydrosweep, DSL 120, and the Mesotech data, spectral analysis of the B′ surface has been done to estimate the degree of non-stationarity and improve the surface roughness estimates near B′.

Two-way backscatter model estimates of scattering near B′ have been made using the fine scale bathymetry near B′ and have also been made with some low resolution approximations to the bathymetry in order to assess the effects of fine scale roughness. However, for the modeling work below we assume nothing more than the measured data and linear slopes in between measured points.

Figure 25 shows the high-resolution bathymetry near B′ collected in 1993 in the fine scale geophysics part of the ARSRP effort. Referring back to Figs. 3 and 4, a cut in bathymetry was taken from the ALLIANCE position along the broadside beam direction up the slope of the B′ seamount. The data are interpolated from the gridded data base along the line of bearing from the ALLIANCE position in Fig. 3 out to and up the slopes of B. The plot starts at the base of the B′ seamount at about 91.5 km range.

Model inferences can be made about reverberation from the B′ seamount as seen by the CORY and ALLIANCE at center frequencies from 227–350 Hz. Backscatter is modeled using the FEPE2WAY model of Collins[37] (but modified for improved stability[38]), and using the high resolution bathymetry from the B′ seamount.

The FEPE2WAY model was used to model backscatter from a sample bathymetry slice at a 1.5 CZ standoff range from B′. Strong backscatter was observed on R/V ALLIANCE and R/V CORY CHOUEST for this geometry. It is important to note that we are using FEPE2WAY to model qualitatively, the results for the near broadside beams. These beams have ~1° beamwidths in azimuth but essentially no vertical discrimination. Due to run time considerations the modeling was done at 100 Hz and bathymetry was greatly simplified up to the start of the B′ feature. A grid size of 0.75 m in depth and 2 m in range was used. The FEPE2WAY run assumed a geo-acoustic model based on Bowles estimates, similar to that previously described in Sec. III D, but with six simpler layers including the basement instead of 10. Backscatter is plotted as two-way transmission loss in dB. Two-dimensional geometry (rather than the cylindrical spreading option) is used in the plots.

Figure 26(a) shows the predicted backscattered field at 100 Hz from a model seamount similar to B′ using the idealized low resolution bathymetry described above and

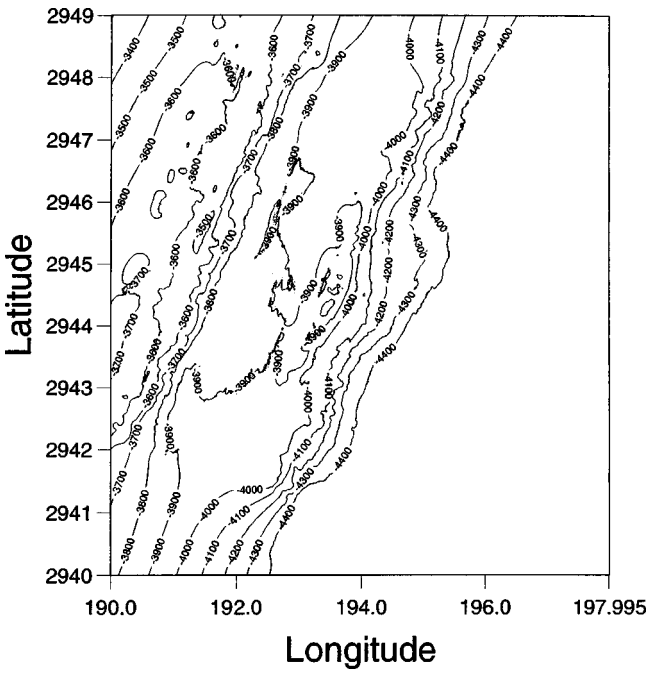

FIG. 25. Fine scale (5 m) bathymetry near B′ from the DSL 120 data taken in 1993.

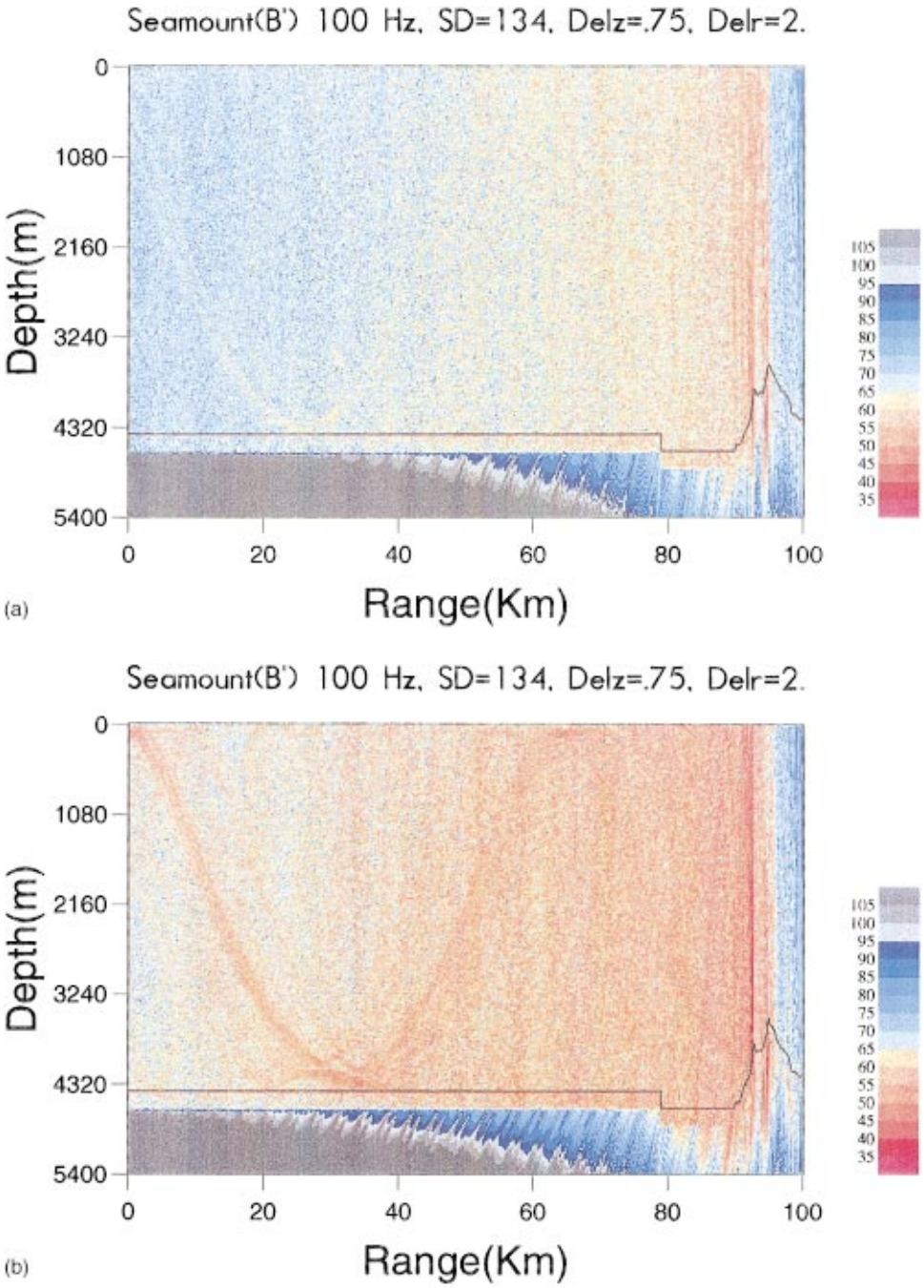

FIG. 26. (a) Predicted backscatter from the B′ seamount using the low resolution (200 m) bathymetry across B′. (b) Predicted backscatter from the B′ seamount using the high resolution (5 m) bathymetry across B′ (2 way loss in dB-plane geometry assumed) bathymetry from −282° bearing from Run A event S10T1E4.

sampled every 200 m. Qualitatively this predicted backscatter is much weaker and more diffuse than experimentally observed results. Using the same bottom parameters, Fig. 26(b) shows the greatly increased backscatter at 100 Hz predicted when the high resolution bathymetry from the 1993 R/V KNORR data, sampled every 5 m, is used in the FEPE2WAY model run. The backscatter levels near the 1-1/2 CZ point are ~10–15 dB greater using the high resolution bathymetry than when using the low resolution data.

Figure 27 shows an estimated power spectrum for the slice through the eastern face of B′ starting at 91.5 km from ALLIANCE and going up. Estimates are given for both the low and high resolution rough surfaces respectively. These data were first linearly interpolated onto a 0.75 m grid spacing that was also used for the FEPE model runs. The estimate was computed using Welch's method of averaging windowed sub-sequences and using 256 point FFTs. The FFT windows were Hann weighted and demeaned to remove edge effects in the estimate. The 95% confidence limits were approximately +2.6 and −7.5 dB. Assuming a k^{-n} functional form for the high resolution data, a least squares fit to this curve gives a $k^{-2.8}$ dependence on wave number for this slice.

Consistent with Fig. 26(a) and (b), Fig. 27 shows 10 to 20 dB more power in the high resolution data than in the low resolution data for the 0.2 to 0.628 m^{-1} wave number band.

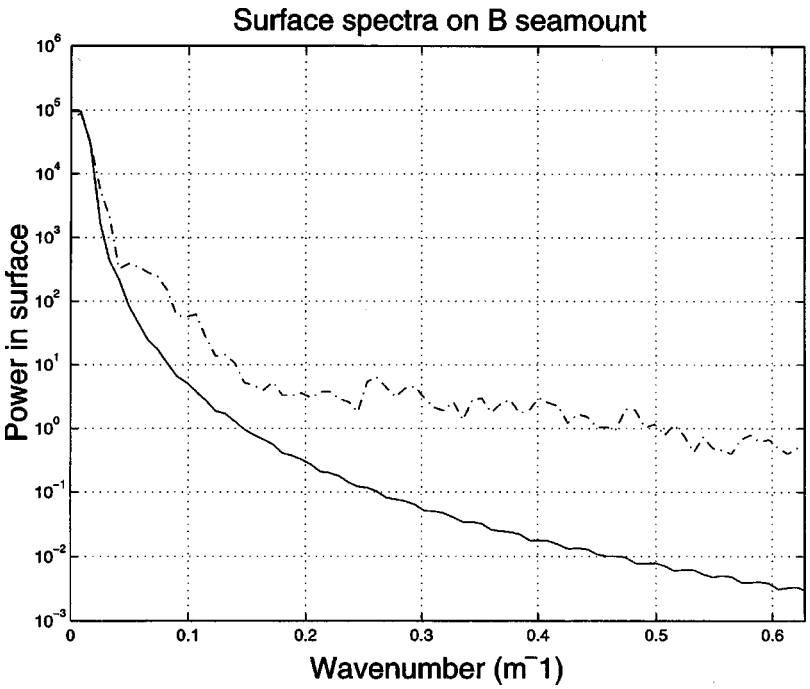

FIG. 27. Comparison of bottom interface roughness spectrum for low resolution bathymetry (solid line) and high resolution bathymetry (dashed line) across the B′ seamount.

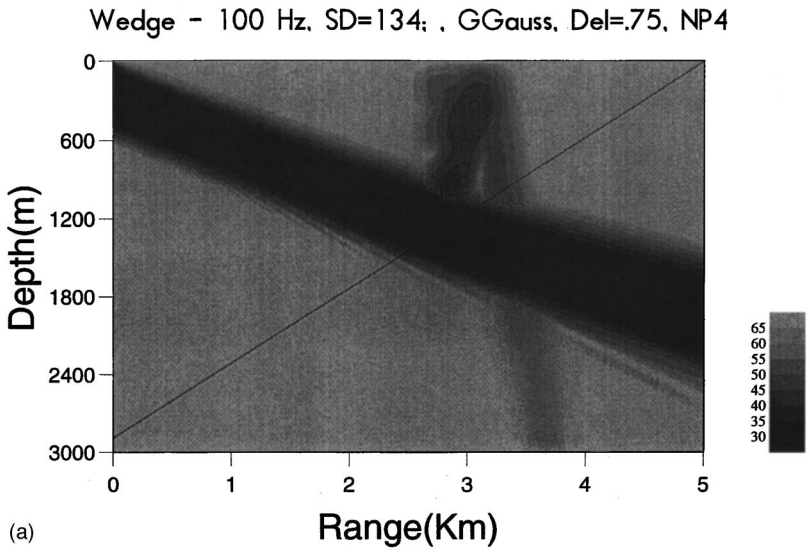

(a)

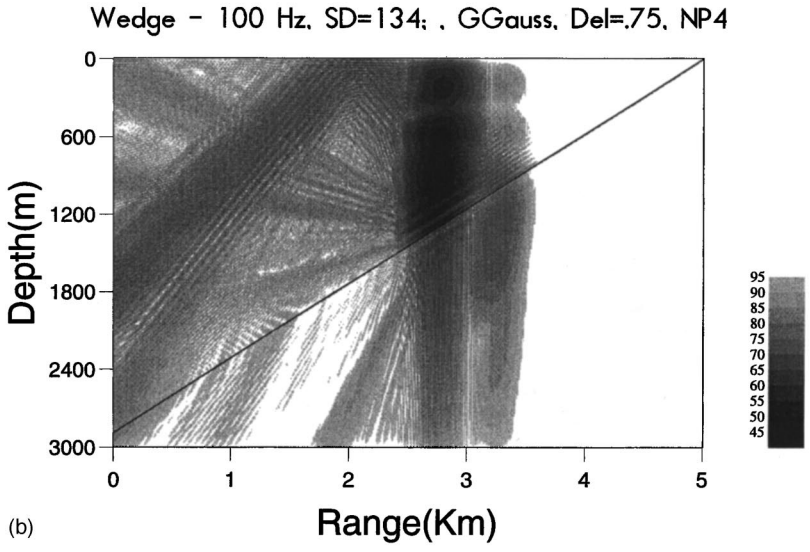

(b)

FIG. 28. (a) FEPE model run showing incident Gaussian beam steered 20° down at a 30° smooth wedge. Note the forward specular beam is incident on the wedge at 80° from the horizontal after one bottom reflection. (b) FEPE two way model run showing energy returned by the second specular bounce from the wedge at an angle of 50° from the horizontal (with a surface bounce at ~2 km).

This strongly suggests that roughness at the Bragg wave numbers is crucial for even these large coherent backscatter returns to occur. Others have pointed this out before,[7,39,40] for example. Large-scale facets on seamounts that reach into the sound channel are also essential. The combination is required if backscatter is to be strong relative to the reverberation from primarily horizontal (but rough) water-bottom interfaces. This finding is in general agreement with composite roughness theories.

One final example using the FEPE2WAY model will be discussed to illustrate that multiple forward scattering is a viable mechanism for returning energy incident on a feature in some circumstances.[41] Figure 28(a) shows a 20° Gaussian beam incident on a 30° wedge with no roughness (a 1/20th of a wavelength sample grid was used). The FEPE2WAY run assumed a nonelastic half-space below the wedge surface with sound speed c_b, of 1600 m/s density ρ, of 1.1 g/cm^3, and absorption α, of 1.0 dB/wavelength.

FEPE2WAY predicts returned energy via this mechanism after 2 specular bottom bounces which turns a ray bundle back toward the source at 50° from the horizontal, strikes the surface at ~2 km and continues back toward the source range at a downward angle of 50° [Fig. 28(b)]. This indicates that ray bundle turnaround on large slopes is also a viable mechanism for returning energy from a source. As a further example, range dependent ray tracing on the same bathymetry as used in Fig. 26(a) and (b), showed four rays out of 30 turning around before they reached the B′ seamount using only simple geometric reflection as the return mechanism.

VI. CONCLUSIONS

Results have been presented that show the range of reverberation data observed on R/V ALLIANCE during the fine scale acoustics experiment. Estimated received levels from 200–1400 Hz have been presented as a function of scatterer location. Conclusions regarding this work to date are.

(1) Large facets ($\geqslant 1\lambda$) from features which protrude into the sound channel dominate the coherent backscatter but small scale roughness must be included even on steep slopes.
(2) The stronger coherent backscatter is most likely from slopes where incidence angles are large and the orientation of the slope is nearly perpendicular to the horizontal incidence angle (in a top view sense).
(3) Ray bundle turn around from a high impedance wedge (equivalent to multiple forward scattering) could also be a competitive mechanism to backscattering when the feature geometry supports it.
(4) For the pings analyzed, noise histograms were close to theoretical Rayleigh curves but for the bistatic and monostatic reverberation data the tails of the PDFs were higher than the noise PDFs. This is consistent with the model that reverberation is often a mixture of Gaussian processes and has important consequences for signal processors.
(5) For one strong feature the ping to ping correlation from 3 sample pings, each 180 s apart, remained relatively high suggesting that scattering from large features has a strong deterministic component.
(6) GSM modeling of 3 sample pings in the 350 to 1350 Hz region containing fathometers showed normal incidence bottom losses from 8–11 dB and Lambert's rule coefficients from −17 to −22 dB.

ACKNOWLEDGMENTS

The author thanks ONR Code 321OA for their support of this work and to Dr. M. Collins at NRL for the use of his FEPE based models and for his help in using them. The author would also like to thank Dr. N. Makris of MIT and Dr. K. Gilbert and Dr. D. McCammon at ARL Penn State for their constructive comments and very helpful discussions on this work and to K. Gerstof for help in the initial data processing. The author wishes to thank the anonymous reviewers for many good comments and suggestions. Finally, special thanks is extended to the excellent technicians and engineering coordinators of the SACLANT Undersea Research Center (including Dr. R. Hollett, E. Michelozzi, and L. Troiano) onboard R/V ALLIANCE for their dedication and outstanding support during the ARSRP experiment.

APPENDIX A: SUMMARY OF SOUND SPEED CONDITIONS AND DESCRIPTION OF R/V ALLIANCE EXPERIMENT ASSETS

Figure A1 provides a composite of all five CTD casts by R/V ALLIANCE over the course of the ARSRP fine scale

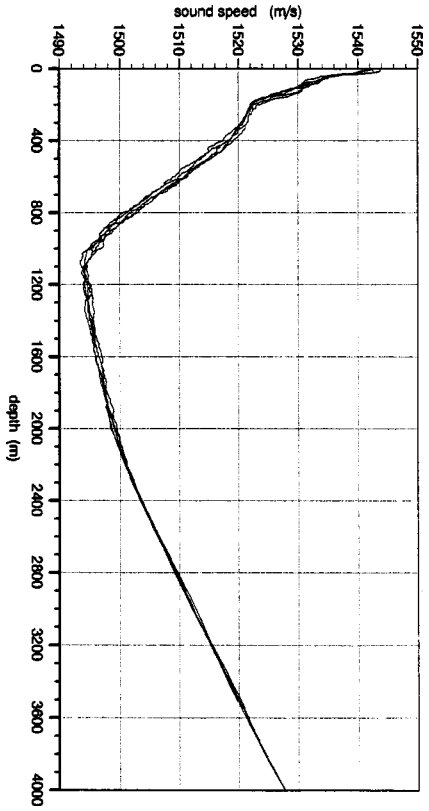

FIG. A1. Composite of all five CTD casts by R/V ALLIANCE over the course of the ARSRP fine scale acoustics experiment.

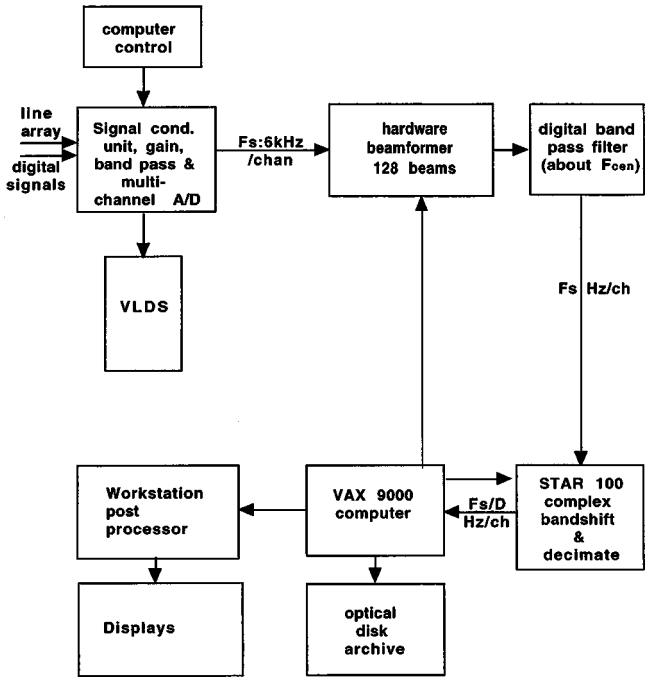

FIG. A2. Block diagram of data processing chain on R/V ALLIANCE.

acoustics experiment. The following sub-sections describe some key assets on R/V ALLIANCE in more detail.

1. Horizontal line array system

The line array receiver used on R/V ALLIANCE is approximately 254 m in length. It consists of three nested apertures of 128 hydrophones at 0.5, 1.0, and 2.0 m spacing. For this experiment the acoustic center of the array was located 1692 m behind the center of the ship. The towed array data are digitized after the preamplifiers and multiplexed before being sent up the cable to the dry-end processing center onboard. The element data digitization used 12 bits and a sample rate of 6000 Hz for each hydrophone. The array elements are individually preamplified in the array and data is carried via twisted pairs into an onboard signal conditioning unit (SCU) that contains a variable high-pass filter. These raw data (all 256 phones) were stored on the Center's VLDS tapes. Simultaneously, the data from one selected array aperture were beamformed using a Hann weighted time domain beamformer with 128 output beams (including exact forward and aft endfire directions but not exact broadside). Figure A2 shows a block diagram of the data flow. 128 beams were formed equally spaced in cosine space from forward to aft endfire. The signals out of the beamformer were passed through a bank of programmable bandpass filters. Following these filters, the data were frequency shifted and decimated to a low output sample rate, which resulted in a complex time series. The processed time series were then recorded on optical disks and passed to the VAX computers for further processing (including matched filtering).

2. Towed source system description

The pulsed source used by R/V ALLIANCE was a towed body with two pairs of flextensional transducers. One pair has a peak response at 400 Hz and a vertical separation of 1.9 m while the other pair has a double peak response at 900 and 1240 Hz and vertical separation of 0.7 m. Only one pair transmitted for any given wave train and the transmission is in phase so the main response axis (MRA) should be 0°, i.e., along the horizontal direction.

The source levels used by R/V ALLIANCE were 210 dB/μPa/Hz at 350 Hz; 202 dB at 700 Hz; 208 dB at 950 Hz and 204 dB at 1350 Hz. The given levels assume a standard dry voltage was applied but the actual voltage applied may vary and has to be cross checked in the ping logs. These levels are on axis but effectively apply to all but the very nearly vertical paths since only two elements are forming the beam pattern.

[1] ARSRP Office of Naval Research Initial Report Acoustics Experiment R/V CORY CHOUEST, 5–26 July 1993.
[2] A. B. Baggeroer and J. A. Orcutt, in *Ocean Reverberation*, edited by D. D. Ellis, J. R. Preston, and H. G Urban (Kluwer, Dordrecht, Holland, 1993), pp. 183–188.
[3] N. C. Makris, ''Imaging ocean basin reverberation via inversion,'' J. Acoust. Soc. Am. **94**, 983–999 (1993).
[4] N. C. Makris and J. M. Berkson, ''Long range backscatter from the Mid-Atlantic Ridge,'' J. Acoust. Soc. Am. **95**, 1865–1881 (1994).
[5] N. C. Makris, ''Deterministic reverberation from ocean ridges,'' J. Acoust. Soc. Am. **97**, 3547–3574 (1995).
[6] B. E. Tucholke and J. Lin, ''A geological model for the structure of ridge segments in slow spreading ocean crust,'' J. Geophys. Res. **99**, 11937–11958 (1994).
[7] K. B. Smith, W. S. Hodgkiss, and F. D. Tappert, ''Propagation and analysis issues in the prediction of long range reverberation,'' J. Acoust. Soc. Am. **99**, 1387–1404 (1996).
[8] K. B. Smith, F. D. Tappert, and W. S. Hodgekiss, ''Comparison of UMPE/PEREV bistatic predictions with observations in the ARSRP Natural Lab,'' J. Acoust. Soc. Am. **94**, 1766(A) (1993).
[9] E. I. Thorsos and S. L. Broschat, ''An investigation of the small slope approximation for scattering from rough surfaces: Part I—Theory,'' J. Acoust. Soc. Am. **97**, 2082–2093 (1995).
[10] J. M. Berkson, N. C. Makris, R. Menis, T. L. Krout, and G. L. Gibian, in *Ocean Reverberation*, edited by D. D. Ellis, J. R. Preston, and H. G. Urban (Kluwer, Dordrecht, Holland, 1993), pp. 189–194.
[11] J. W. Caruthers and J. C. Novarini, ''Modeling bistatic bottom scattering strength including a forward scattering lobe,'' IEEE J. Ocean Eng. **18**, 100–106 (1993).
[12] J. A. Goff, ''The relationship between local and global scattering functions for fractal surfaces under a separation of scales hypothesis,'' J. Acoust. Soc. Am. **97**, 1586–1595 (1995).
[13] A. K. Kalra and J. K. Fulford, in *Ocean Reverberation*, edited by D. D. Ellis, J. R. Preston, and H. G. Urban (Kluwer, Dordrecht, Holland, 1993), pp. 209–214.
[14] R. A. Stephen, in *Ocean Reverberation*, edited by D. D. Ellis, J. R. Preston, and H. G. Urban (Kluwer, Dordrecht, Holland, 1993), pp. 227–232.
[15] R. J. Greaves and R. A. Stephen, ''Seafloor acoustic backscattering from different geological provinces in the Atlantic Natural Laboratory,'' J. Acoust. Soc. Am. **101**, 193–208 (1997).
[16] H. F. Webb and T. H. Jordan, ''Quantifying the distribution and transport of pelagic ocean sediments on young abyssal hills,'' Geophys. Res. Lett. **20**, 2203–2206 (1993).
[17] J. E. Bondaryk, I. Dyer, and E. Dorfman, ''Estimation of bottom scattering characteristics from Acoustic Reverberation Special Research Program bistatic data,'' J. Acoust. Soc. Am. **98**, 2988(A) (1995).
[18] J. R. Preston, E. Michelozzi, L. Troiano, and R. Hollett, Cruise report on R/V ALLIANCE cruise MARE July 5–August 1, 1993: SACLANTCEN's joint experiment with ONR's ARSRP group, SACLANTCEN Report # M 112, Sept. 1993.
[19] J. R. Preston and W. Kinney, ''Monostatic and bistatic reverberation using low-frequency linear FM pulses,'' J. Acoust. Soc. Am. **93**, 2549–2565 (1993).
[20] J. R. Preston, T. Akal, and J. Berkson, ''Analysis of Backscattering Data

in the Tyrrhenian Sea,'' J. Acoust. Soc. Am. **87**, 119–134 (1991).
[21] N. C. Makris, ''Effect of saturated transmission scintillation on ocean acoustic intensity measurements'', J. Acoust. Soc. Am. **100**, 769–783 (1996).
[22] M. D. Collins, ''A split-step Pade solution for parabolic equation method,'' J. Acoust. Soc. Am. **93**, 1736–1742 (1993).
[23] B. E. Tucholke, J. Lin, M. A. Tivey, M. C. Kleinrock, T. B. Reed, J. A. Goff, and G. E. Jaroslow, ''Segmentation and crustal structure of the western Mid-Atlantic Ridge flank, 25 25′ −27 10′ N and 0-29 m.y.,'' J. Geophys. Res. **102**, 10203–10223 (1997).
[24] J. R. Preston, Bistatic and monostatic scattering in basins of the IBERLANT area, SACLANTCEN Report, SR-198, Sept. 1992.
[25] M. Porter, The KRAKEN normal mode program, SACLANTCEN Report, SRM-245, Sept. 1991.
[26] H. Weinberg, Generic Sonar Model, Naval Underwater Systems Center, New London, CT, TD # 5971D, Jun. 1985.
[27] L. Deliman and D. F. McCammon (private communication).
[28] D. Ellis, ''Effective Vertical Beam Patterns for Ocean Acoustic Reverberation Calculations,'' IEEE J. Ocean Eng. **16**, 208–211 (1991).
[29] S. S. Fu, R. H. Wilkens, and L. N. Frazer, ''Acoustic LANCE: New *in situ* seafloor velocity profiles,'' J. Acoust. Soc. Am. **99**, 234–242 (1996).
[30] F. A. Bowles, ''A Geoacoustic model for fine grained unconsolidated sediments (ARSRP Natural Laboratory),'' NRL-SSC Report. NRL/MR/7432-93-7082, March 9, 1994.
[31] H. Schmidt, OASES ver. 1.7 Application and Upgrade Notes, MIT, April 1995.
[32] E. Michelozzi and J. R. Preston, ''High resolution sediment profiler for deep water,'' Simposio Internazionale—The Ocean Floor: Observations, Theory and Imagination, Acedemie Nazionale Dei Lincei, Rome, Italy, Oct. 13–14 (1994).
[33] G. E. Jaroslow, ''The geologic record of ocean crystal accretion and tectonism at slow spreading ridges,'' Ph.D. thesis, M.I.T.—Woods Hole Oceanographic Institute Joint Program in Oceanography, 1997.
[34] B. E. Tucholke, W. K. Stewart, and M. C. Kleinrock, ''Long term denudation of ocean crust in the central North Atlantic Ocean,'' Geology **25**, 171–174 (1997).
[35] J. A. Goff and T. H. Jordan, ''Stochastic modeling of seafloor morphology: inversion of Sea Beam data for second order statistics,'' J. Geophys. Res. **93**, 13589–13608 (1988).
[36] J. A. Goff, H. F. Webb, and T. H. Jordan, ''Stochastic interpolation of a wide beam bathymetric profile within the ONR-ARSRP acoustic reverberation corridor,'' Woods Hole Technical Report ARSRP #2, April 1992.
[37] M. D. Collins and R. B. Evans, ''A two way parabolic equation for acoustic backscattering in the ocean,'' J. Acoust. Soc. Am. **91**, 1357–1368 (1992).
[38] M. D. Collins and P. Nielsen (private communication).
[39] I. Dyer, A. B. Baggeroer, H. Schmidt, J. R. Fricke, N. Ozleur, and D. Giannoni, in *Ocean Reverberation*, edited by D. D. Ellis, J. R. Preston, and H. G. Urban (Kluwer, Dordrecht, Holland, 1993), pp. 51–57.
[40] K. E. Gilbert, ''A stochastic model for scattering from the near surface oceanic bubble layer,'' J. Acoust. Soc. Am. **94**, 3325–3334 (1993).
[41] I. Blatstein and J. Goertner, Naval Surface Weapons Center (private communication).

Wave scattering on a fractal surface

Z. W. Qian[a)]
National Laboratory of Acoustics, Institute of Acoustics, Chinese Academy of Sciences, Beijing 100080, People's Republic of China

(Received 30 April 1998; revised 10 June 1999; accepted 21 September 1999)

A generalized Von Koch surface was constructed. On the basis of Freedman's formulation for wave scattering and by applications of the Lipchitz transform under Hölder conditions in fractals, a demonstration was given that the Hausdorff dimension of the solid-angle discontinuity on the scattering surface is the same as the one of the surface itself, and an expression of the scattering strength of the fractal surface has been given. A comparison with the Schulkin–Shaffer empirical formula for the sound scattering from sea surface proposes that, in this situation, the generalized (continuous) Koch surface seems to degenerate into the (discrete) four-two Cantor sets, only the latter make a contribution to the backscattering. © *2000 Acoustical Society of America.* [S0001-4966(00)01101-2]

PACS numbers: 43.30.Hw, 43.25.Rq [DLB]

The scattering from rough surfaces is an interesting topic in the areas of both acoustics and electromagnetics. Many papers presenting experiments in underwater acoustics (for example, as collected in Ref. 1) were published. Schulkin and Shaffer summarized the data published by many authors up to that time and proposed an empirical expression as follows:[2]

$$S_s = 10\log(fh\sin\vartheta)^{0.99} - 45, \tag{1}$$

where S_s is the scattering strength, f is the acoustical frequency, ϑ the grazing angle to the sea plane, and h is the crest-to-trough height of the ocean waves. It was found that the data could be fitted by this expression with a standard deviation of 5 dB over a range of $fh\sin\vartheta$ between 4 and 200 except when the incidence is near vertical or grazing. A lot of theoretical work which deals with the scattering from the regular and random (differentiable everywhere) surfaces[3–5] cannot explain such frequency and angle relationship as given in Eq. (1).[1]

As pointed out in Ref. 6, ''there is no acceptable rationale for a general solution of the problem on the fractal-surface scattering. The very first work, Ref. 7, used the phase screen approximation; in other words, it examined diffraction of a wave that passed through a thin phase screen with the optical width distribution $kh(x)$ rather than undertake to solve the problem of wave scattering on a rough surface $h(x)$.[7] In Ref. 8, the single-fold statistics of rays emanating from an infinite, corrugated, Gaussian surface with fractal slope were investigated. Following Twersky's interaction theory, Ref. 9 presented the scattering by scatterers, the distribution of which is fractal. Taking multiple-scattering interaction and the fractal shape of the grains into account, Ref. 10 investigated the sound attenuation and the fractal dimension of the grains in marine sediments. However, the theories both of Refs. 9 and 10 are inconvenient for the scattering by fractal surfaces.

In this paper, the scattering from a generalization of a Von Koch surface will be investigated by use of Freedman's scattering formulation.[11]

By means of Mandelbrot's fractals,[12] a generalized Von Koch surface can be generated by following procedure:

$$n=0,\quad a^{(0)}=1,\ n=1,\quad a_1^{(1)}=\frac{1}{2\sqrt{2}},$$
$$a_2^{(1)}=\frac{1}{\sqrt{2}},\quad a_3^{(1)}=\frac{1}{2\sqrt{2}},\quad \text{etc.,} \tag{2}$$

the geometrical outline of which is illustrated in Fig. 1. According to the heuristic method, its Hausdorff measure satisfies

$$2\left(\frac{1}{2\sqrt{2}}\right)^D+\left(\frac{1}{\sqrt{2}}\right)^D=1, \tag{3}$$

where D is the fractal dimension. It can easily be obtained from Eq. (3) that D is equal to 1.524.

The fractal surface mentioned above is only a special situation that the vertex angles made by the line segments neighbored are rectangular to each other (Fig. 1). Now we attempt to generate a type of fractal surface that can describe the ocean waves approximately as follows;

$$n=0,\quad a^{(0)}=\Lambda_0,\quad n=1,$$
$$a_1^{(1)}=\frac{\Lambda_0}{4}\sqrt{1+\left(\frac{4A_0}{\Lambda_0}\right)^2}=\frac{\Lambda_0}{2\sqrt{2}\sqrt{(1-\cos\Theta)}}=a_3^{(1)}, \tag{4}$$
$$a_2^{(1)}=2a_1^{(1)},\ldots,$$

where Θ is the angle made by two neighbor line elements of the fractal set. Obviously, the Hausdorff measure of the set satisfies

$$(2^{1-D}+1)(a_2^{(1)})^D=1. \tag{5}$$

Let

a)Electronic mail: qzwnoe@ihw.com.cn

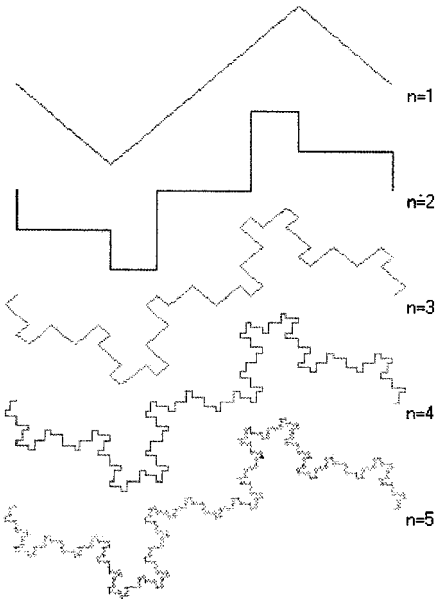

FIG. 1. Generalized Von Koch fractal surface.

$$\alpha = \frac{4A_0}{\Lambda_0} = \cot\frac{\Theta}{z}. \tag{6}$$

Then the solution of Eq. (5) can be obtained by a numerical computation as listed in Table I.

By the Kirchhoff approximation, a formulation for sound scattering has been given by Freedman[11] that scattered radiation is generated whenever there is a discontinuity with respect to range, r, in $d^n W(r)/dr^n$, where $W(r)$ is the directivity-weighted solid angle subtended at the observer by those parts of the scattering surface within range r.

In the two-dimensional situation, an ideal sea surface can be referred to as a sinusoidal one. If we use a scale such as the sound wavelength λ ($\lambda < \Lambda_0, A_0$) to observe a real surface, however, it appears that a rough one can be described by a fractal surface (curve) approximately. As noted, its derivative exists nowhere, i.e., there is discontinuity of the solid angle subtended at the observer by each element of the fractal surface (curve) everywhere. Thus, the scattered radiation in the far field will be generated by it. Following Ref. 11, it can be denoted as

$$I = \int_S \frac{dW(r)}{dr} \exp(-2jkr)\, dr, \tag{7}$$

where S is the fractal surface (curve). In the following, it can be seen that the Freedman formulation facilitates treatment of the problem.

In order to integrate Eq. (7), we define

$$I_n = \int_{S_n} \frac{dW(r)}{dr} \exp(2jkr)\, dr, \tag{8}$$

TABLE I. Fractal dimension of a generalized Von Koch surface vs α.

α	0.2	0.4	0.6	0.8	1.0	1.2	1.3	1.4
D	1.08	1.13	1.15	1.3	1.5	1.74	2.0	2.13

where S_n is a subset of the set S in which n is a definite number. Obviously, W has discontinuity at each convex angle point (see Fig. 1), so that $W(r)$ can be denoted by

$$W(r) = W(r_m)\mathrm{H}(r - r_m).$$

where $\mathrm{H}(x)$ represents a Heaviside step function, the derivative of which is the Dirac function. Substituting it into Eq. (8) yields

$$I_n = \int_{S_n} W(r_m)\,\delta(r - r_m)\exp(2jkr)\,dr = \sum_m W(r_m) e^{2jkr_m},$$

and

$$|I_n|^2 = \sum_m |W(r_m)|^2 + \sum_m \sum_{l \neq m} W(r_m) W(r_l) \times \exp 2jk(r_m - r_l),$$

where r_m and r_l are two different discontinuous points. Averaging this expression, the cross terms can be neglected because of the interference of each other, and

$$|I_n|^2 = \sum_m |W(r_m)|^2. \tag{9}$$

When $n \to \infty$, $I_n = I$, and the set becomes a fractal curve s, the dimension of which is D, one can use an integral in place of the sum in Eq. (9), i.e.,

$$|I|^2 = \int_s d|W(s)|^2. \tag{10}$$

Obviously, the number of the discontinuities in the fractal curve is proportional to its length ds. According to the Lipchitz transform under Hölder's condition,[13] the dimension of $|W(s)|$ will equal that of the curve itself, so that

$$|I|^2 \sim |W|^{2D}. \tag{11}$$

In the Appendix A, W was given as follows:

$$W \sim 2\, fA \tan\left(\frac{\Theta}{2}\right) \sin\vartheta,$$

where ϑ is the grazing angle of the incidental wave with respect to the sea plane, f is the frequency of the sound wave, and A_0 is the wave height. It is worth reminding that the solid angle should be weighted by the directivity of both the

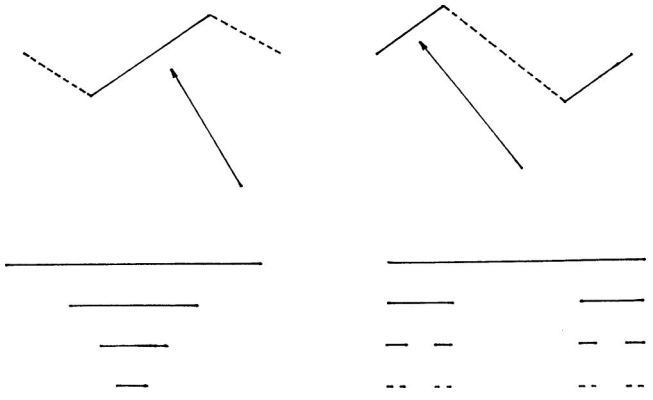

FIG. 2. Geometry to calculate the discontinuous change of a solid angle.

transmitter and the receiver. Substituting W into Eq. (11) yields

$$|I|^2 \sim \left[2\, fA_0 \tan\left(\frac{\Theta}{2}\right) \sin\vartheta \right]^{2D}. \tag{12}$$

From Eq. (12), the scattering strength S_s of the fractal surface can be denoted by

$$S_s = 10\log|I|^2 = S_s^{(0)} + 10\log\left[fh\tan\left(\frac{\Theta}{2}\right)\sin\vartheta \right]^{2D}. \tag{13}$$

By comparison of Eqs. (13) and (1), it can be seen that their appearances are the same when $\Theta \approx \pi/2$, which means that in those data of the scattering strength measured by underwater-reverberation technique, the backscattering only results from the fractal set of which the fractal dimension D is equal to 0.5 approximately. As is well known, however, the dimension of a continuous fractal curve is not less than 1 (see Table I). A possible explanation is that during the scattering process, the continuous curve may degenerate into a discrete set, for example, the generalized Von Koch curve ($D>1$) degenerates into four-two Cantor sets ($D=0.5$) (see Fig. 2).

In the underwater-reverberation measurements, the incident wave onto the sea surface can be regarded as a plane wave. If a line element in the fractal curve is almost parallel to the incidental wave vector, the next one will be vertical to it because $\Theta \approx \pi/2$. The contribution of latter one to the backscattering can be neglected since the receiver has its directivity. Thus, only those alternately separated line elements that constitute two kinds of (discrete) four-two Cantor sets (see Fig. 2) can contribute to the backscattering.

ACKNOWLEDGMENTS

This is a project supported by NSFC. The author is grateful to Professor Y. Cai, Professor G. Dai, and X. Li for helpful drawing by computer.

APPENDIX: A CALCULATION FOR *W*

In order to integrate Eq. (9), let $n=1$ in Fig. 1, in which the fractal subset consists of broken lines and two neighbor broken lines construct a vertex angle. Suppose that the sound wave can insonify a part of the surface including N vertex angles. Now, we attempt to calculate the discontinuous change of the solid angle as a vertex angle Θ is rounded. Figure A1 shows the geometry, where AB is the horizontal plane of the surface, $ACEDB$, θ is the grazing angle, θ_1 is the angle made by the surface element CD and the wave front

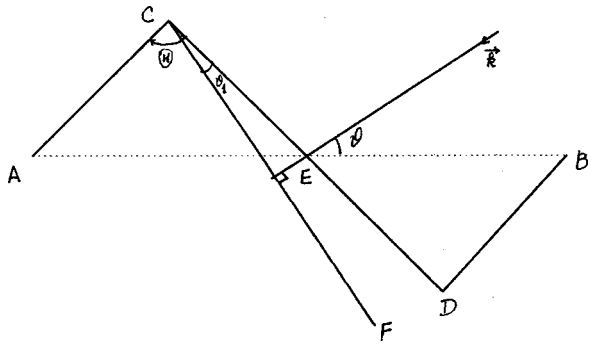

FIG. A1. Generalized Von Koch surface degenerated into four-two Cantor sets.

CF, and A_0 is the wave height. Obviously, $\theta_1 = \Theta/2 - \theta$, and the projection of both CE and DB to the wave front are

$$CE\cos\vartheta_1 = \frac{A_0}{\cos(\Theta/2)}\cos\left(\frac{\Theta}{2} - \vartheta\right)$$

and

$$DB\cos(\vartheta_1 - \Theta) = \frac{A_0}{\cos(\Theta/2)}\cos\left(\frac{\Theta}{2} + \vartheta\right),$$

respectively. Thus, when the vertex angle D is rounded the discontinuous change of the solid angle is proportional to

$$CE\cos\vartheta_1 - DB\cos(\vartheta_1 - \Theta) = 2A_0\tan\left(\frac{\Theta}{2}\right)\sin\vartheta,$$

and the change of the solid angle will be

$$W \sim 2\, fA_0\tan\left(\frac{\Theta}{2}\right)\sin\vartheta,$$

when we use a scale such as sound wavelength λ to observe it.

[1] R. J. Urick, *Principle of Underwater Sound*, 3rd ed. (McGraw-Hill, New York, 1983), Chap. 8.
[2] M. Schulkin and R. Shaffer, J. Acoust. Soc. Am. **36**, 1699 (1964).
[3] P. Beckman and A. Spizzichino, *The Scattering of Electromagnetic Waves from Rough Surface* (Macmillan, New York, 1963).
[4] C. Eckart, J. Acoust. Soc. Am. **25**, 566 (1953).
[5] H. W. Marsh, J. Acoust. Soc. Am. **33**, 330 (1961).
[6] V. V. Zosimov and L. M. Lyamshev, Phys. Usp. **38**, 347 (1995).
[7] M. V. Berry, J. Phys. A **12**, 781 (1979).
[8] E. Jakeman, J. Phys. A **15**, L55 (1982).
[9] Z.-S. Wang and B.-W. Lu, Waves Random Media **4**, 97 (1994).
[10] Z. W. Qian, Phys. Rev. E **53**, 2304 (1996).
[11] A. Freedman, Acustica **12**, 10 (1962).
[12] B. B. Mandelbrot, *Fractal Geometry of Nature* (Freeman, New York, 1982).
[13] K. J. Falconer, *Fractal Geometry* (Wiley, New York, 1990).

Modeling of subcritical penetration into sediments due to interface roughness

Eric I. Thorsos, Darrell R. Jackson, and Kevin L. Williams
Applied Physics Laboratory, University of Washington, 1013 NE 40th Street, Seattle, Washington 98105

(Received 5 October 1998; revised 15 July 1999; accepted 19 July 1999)

Recent experimental results reveal acoustic penetration into sandy sediments at grazing angles below the critical angle. A mechanism for this subcritical penetration is described based on scattering at a rough water–sediment interface. Using perturbation theory, a numerically tractable three-dimensional model is used for simulating experiments. The rough interface scattering has been treated using formally averaged methods as well as with single rough surface realizations. Data-model comparisons show that scattering by interface roughness is a viable hypothesis for the observed subcritical penetration. © *2000 Acoustical Society of America.*
[S0001-4966(00)02301-8]

PACS numbers: 43.30.Gv, 43.30.Hw, 43.30.Vh [DLB]

INTRODUCTION

High frequency acoustic penetration into seafloor sediment at low grazing angles is of interest for buried object detection, e.g., pipelines, mines. For sandy sediments the critical angle can be in the 25°–30° range, which suggests that penetration at lower grazing angles might be quite limited. However, recent experimental results reported by Chotiros[1] reveal acoustic penetration into sandy sediments at grazing angles below the critical angle over a broad frequency range (5–80 kHz). In addition, the propagation speed in the sediment was inferred to be near 1200 m/s, significantly lower than the compressional sound speed of about 1700 m/s in unconsolidated sands. Chotiros interprets these results to indicate the excitation of a Biot slow wave in the sediment. However, our previous modeling studies[2,3] have indicated that the results presented by Chotiros could also be explained by the mechanism of scattering by roughness at the water–sediment interface.

Subcritical acoustical penetration into sediments has also been reported by Lopes,[4] Simpson and Houston,[5] and Maguer *et al.*[6] Simpson and Houston have reported laboratory measurements in which the penetrating field was observed to increase markedly when the interface was deliberately roughened; they also indicate that their measurements showed no evidence of a slow wave. Maguer *et al.* report on measurements in the 2–15 kHz range, and argue based on modeling studies that the subcritical penetration they observed below 5–7 kHz is due to the evanescent wave, while above 5–7 kHz it is due to rough interface scattering.

In this article, the acoustic penetration mechanism based on rough interface scattering will be examined in detail using simulations. Data-model comparisons will be given showing that scattering by interface roughness is a viable hypothesis for the observed subcritical penetration. For this mechanism the propagation speed for the sound penetrating the sediment is the standard compressional wave speed, but the apparent speed found through processing techniques similar to those used in the experiments by Chotiros can be significantly less and ranges from about 1200 m/s to about 1500 m/s depending on the roughness conditions assumed. A simple explanation for this lower apparent speed will be given.

Before considering simulations of experiments, results are presented in Sec. I for the penetrating field in two dimensions obtained with an exact integral equation method. These results show the potential for a rough interface to couple sound into the sediment at subcritical grazing angles. In Sec. II exact results are used to demonstrate that perturbation theory is valid in a 2-D geometry for roughness conditions of interest and thus should be valid for the 3-D geometry as well. Formally averaged perturbation theory is used in Sec. III to simulate a high frequency penetration experiment[1] in 3-D. An alternative approach is used in Sec. IV, where perturbation theory is used in 3-D Monte Carlo simulations to examine the variability due to the use of different rough interface realizations that are consistent with an assumed roughness spectrum. A comparison is also given between the formal-average and Monte Carlo approaches. Section V gives a simple explanation of the tendency of interface scattering to yield processing artifacts which mimic slow wave behavior. With the Monte Carlo simulation approach, coherent processing of the acoustic data can also be simulated. In Sec. VI simulations are used to examine the results of a mid-frequency penetration experiment[7] for which coherent processing was utilized. The results of applying coherent processing to the high frequency experiment are also simulated, and concluding remarks are given in Sec. VII.

I. EXACT 2-D SIMULATIONS OF ACOUSTIC PENETRATION INTO SEDIMENT

The sediment is modeled as a homogeneous fluid supporting only compressional waves, since for sand sediments it can be shown that coupling into shear waves is negligible.[8,9] The problem of scattering from and transmission through a rough two-fluid interface can be solved exactly in the CW case for individual rough interface realizations using an integral equation method. Because of high computational requirements, this method is essentially limited to a 2-D geometry with a 1-D rough interface. Nevertheless, such results illustrate that surface roughness can couple acoustic energy into sediments when the incident

 1063-7834/2000/107(1)/15/$17.00

grazing angle is below the critical angle. A detailed exposition of the integral equation method for electromagnetic scattering at a rough surface separating two media (closely analogous to the two-fluid case) is given in Ref. 10 (see Appendix A), and the simpler case of a single fluid with rough surface subject to a Dirichlet boundary condition is treated in Ref. 11.

With a specified incident pressure field on the rough surface, solution of the integral equation (actually two coupled integral equations) gives the field and the normal derivative of the field on the surface. With these quantities known, it is possible to compute, via the Helmholtz–Kirchhoff integral formula, the field at any point on either side of the interface and thus construct maps of the field structure. Absorption in the sediment is incorporated by using a complex wave number in the fluid below the interface.

To illustrate the effects of roughness on acoustic penetration into sediment, parameters similar to those for the Acoustic Testbed Experiment (ATBE) near Panama City[1] are used. Denoting the sound speed and density by c_1 and ρ_1 in the water and by c_2 and ρ_2 in the sediment, respectively, we use $c_2/c_1=1.13$ (which gives a critical angle of 27.8°), $\rho_2/\rho_1=2.0$, and a sediment absorption of 0.5 dB/m/kHz. The 2-D spectrum of sediment roughness was not measured during ATBE. For numerical simulations in two dimensions we require a 1-D roughness spectrum, $W(K_x)$, which we model with the following modified power law form:

$$W(K_x)=\frac{w_1}{K_x^2+K_L^2}. \tag{1}$$

The spectrum in Eq. (1) is the appropriate 1-D analogue of one form of 2-D roughness spectrum discussed later in Sec. III. In our notation, w_1 gives the spectral level for a 1-D spectrum, while w_2 is the corresponding quantity for a 2-D spectrum. The spectrum is defined such that $W(-K_x)=W(K_x)$, where $K=|K_x|$ is the spatial wave number, and the mean square surface height, h^2, is given by

$$h^2=\int_{-\infty}^{\infty} dK_x W(K_x). \tag{2}$$

In Eq. (1) a ''lower cutoff'' K_L has been introduced to yield a finite mean square surface height. A similar cutoff will be used in Sec. III with the 2-D roughness spectrum and discussed further there. For the example in this section, $w_1=0.02\,\mathrm{cm}$ and $K_L=0.1\,\mathrm{cm}^{-1}$, which yield a roughness parameter $k_1h=0.66$ (where k_1 is the wave number in the water for $c_1=1500$ m/s and a frequency of 20 kHz). The results shown are essentially unaffected if K_L is made smaller.

Examples of CW pressure fields obtained with the integral equation method for both a flat and rough surface are shown in Fig. 1. In these figures the mean water-sediment interface is at 0.0 cm on the vertical scale, and the color display represents the ratio of the pressure to the magnitude of the incident field and is linear in pressure. A 20-kHz plane wave is incident from the left at a grazing angle of 20°, which is below the critical angle of 27.8°; this incident wave has been omitted to simplify the field structure in the water. In Fig. 1(a) the surface is flat, and the phase fronts of the reflected wave can be seen moving up and to the right above the interface. For this flat surface case the field in the sediment is evanescent; it decreases exponentially with depth and has significant magnitude for only about a wavelength into the sediment.

It has been noted[12] that a critical angle does not exist in the usual sense when acoustic absorption in the sediment is taken into account. The most important consequence of this change is that the reflection coefficient is no longer unity when the incident grazing angle is below the nominal critical angle due to absorption of the evanescent wave within the sediment. Another consequence of this absorption, barely visible in Fig. 1(a), is that the lower tips of the phase fronts in the sediment slightly lag the phase fronts at the interface, an indication that the wave in the sediment is not strictly evanescent. With absorption, the vertical component of the wave vector in the sediment has a small real part, which leads to a rapidly attenuating wave that propagates slightly downward from horizontal. While in a strict sense this means a critical angle does not exist, the field structure in the sediment is so little affected by absorption that this distinction has little consequence, as shown by Fig. 1(a). Thus we will refer to the field in the sediment in Fig. 1(a) as the evanescent wave and consider the incident grazing angle to be below the critical angle, defined in terms of the phase velocity obtained from the real part of the wave number in the sediment. It is important to note that absorption in no way increases field penetration into the sediment for subcritical grazing angles.

In Fig. 1(b) the rough surface realization is consistent with the spectrum given by Eq. (1). Energy can be seen to radiate down into the sediment at relatively steep angles, in part because absorption will tend to remove energy propagating closer to horizontal. One might expect acoustic penetration into the sediment to occur at regions along the surface where the local grazing angle (accounting for the local surface slope) exceeds the critical angle. However, acoustic penetration due to roughness occurs even if this condition is not met anywhere on the surface. It is evident from Fig. 1 that the field scattered down into the sediment is spatially incoherent, while for the Biot slow wave hypothesis, the penetrating field would be a spatially coherent wave (assuming that interface and volume scattering effects are negligible). We use the term ''spatially incoherent'' when any spatial coherence is confined to spatial separations of less than about a wavelength. In the example of Fig. 1(b), for separations large compared to a wavelength, the field is not even partially coherent.

In order to see if the rough surface scattering mechanism can explain the acoustic penetration results reported by Chotiros, it is necessary to model the full 3-D experiment geometry, which is not practical using the integral equation approach. Thus we have employed perturbation theory to account for the effects of scattering. In doing this we sometimes consider levels of surface roughness, as indicated by the parameter k_1h, which are uncomfortably large for the normal application of lowest-order perturbation theory. Therefore, we first turn to the question of the applicability of perturbation theory for our regime of interest. This is done in

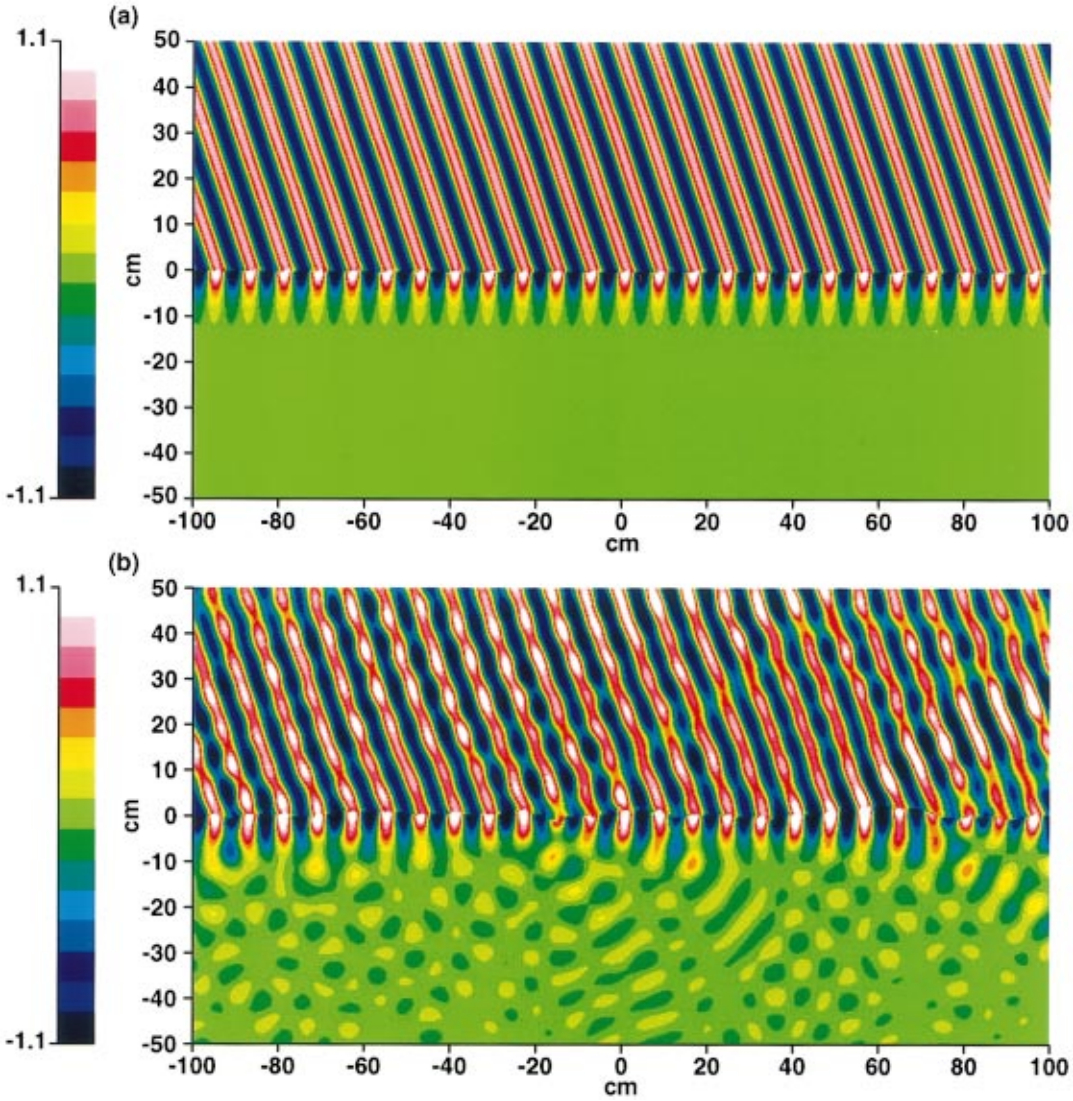

FIG. 1. Pressure fields above (in water) and below (in sediment) a flat surface (a) and a rough surface (b) obtained for a 2-D geometry using the exact integral equation method. The in-water incident field (not shown) propagates from the left at a grazing angle of 20°, which is below the critical angle of 27.8°. The pressure is expressed in units of the incident field magnitude.

two dimensions, where integral equation results can serve as ground truth.

II. VALIDITY OF PERTURBATION THEORY FOR ACOUSTIC SCATTERING INTO SEDIMENT

It would normally be expected that $k_1 h \ll 1$ is necessary for lowest-order perturbation theory to be accurate in predicting bistatic scattering from rough surfaces.[13] For bistatic scattering back into the water from a rough bottom that is modeled as a homogeneous fluid, results from numerical studies using the integral equation method are in agreement with this expectation. The numerical results show that, as $k_1 h$ increases, the inaccuracy of perturbation theory first becomes noticeable at a $k_1 h$ of about 0.3–0.4. For scattering into the sediment, however, numerical results show that perturbation theory accuracy extends to much higher roughness levels. It is possible to show that the phase perturbation caused by the rough surface is much less for the field transmitted into the sediment compared to that for the field scattered back into the water. Essentially, the smallness of the sound speed contrast between the water and sediment reduces the effective roughness (i.e., phase perturbation) of the interface for the transmission scattering problem. As a result, perturbation theory remains accurate for much larger $k_1 h$ than might be expected.

Here we simply illustrate this improved accuracy with an example without pursuing a fundamental explanation. Figure 2 shows a comparison between perturbation theory[14,15] and exact integral equation bistatic scattering results for an example with $k_1 h = 1.0$. The sound speed and density ratios are the same as in Fig. 1, and the roughness spectrum is again given by Eq. (1) with $w_1 = 0.02$ cm, but K_L has been reduced to 0.044 cm^{-1} to obtain $k_1 h = 1.0$ (for $c_1 = 1500$ m/s and a frequency of 20 kHz). Again, as in Fig. 1, the incident grazing angle of 20° is below the critical angle of 27.8°. For simplicity, absorption in the sediment has been suppressed in this example. For this two-dimensional scattering problem, the scattering strength is $10 \log_{10} \sigma$, where σ is the bistatic scattering cross section given by $\langle I_s \rangle r/(I_i L)$. Here I_i is the incident intensity on the surface of length L,

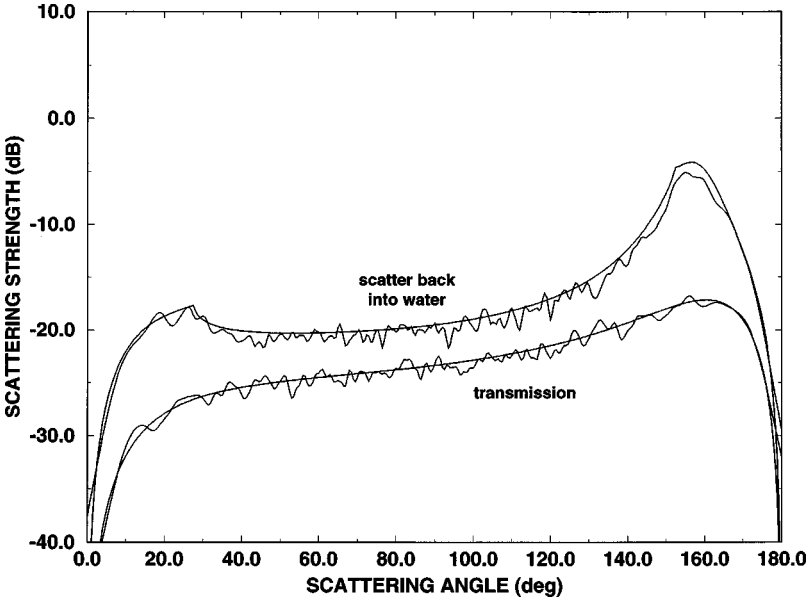

FIG. 2. Bistatic scattering strengths for scattering from a rough sediment surface for a 2-D geometry. The smooth curves are obtained using lowest-order perturbation theory, and the fluctuating curves (averages using 50 surface realizations) are found with the integral equation method. The incident grazing angle is 20°, the critical angle is 27.8°, and $k_1h=1.0$.

and $\langle I_s \rangle$ is the average intensity at far-field range r. With the integral equation method, the average scattered intensity was obtained using 50 surface realizations, and a tapered plane wave incident field was employed as described in Ref. 11. Finally, for scatter back into the water, the coherent intensity (over the ensemble of surface realizations) was removed, leaving only the incoherent intensity, which is the appropriate quantity to compare with perturbation theory. The coherent intensity is removed by subtracting the result of a coherent average as described in Ref. 16. For scatter into the sediment, there is no coherent field in the far zone since the incident angle is below the critical angle.

Figure 2 shows that for scattering back into the water lowest-order perturbation theory over predicts the scattering level by about 1 dB near the specular direction (a scattering angle of 160°), which is not surprising since $k_1h=1.0$. Nevertheless, accuracy for scattering into the sediment is excellent, and this agreement extends to even higher values of k_1h, well beyond what is needed for experiment simulations. [For the simulations to be discussed later, $k_1h=0.28$ for Figs. 4(b), 6, 7, and 11, and $k_1h=1.54$ for the highest frequency case (8 kHz) in Fig. 10.] As noted earlier, absorption in the sediment has been neglected. When absorption is included, the comparison is again excellent, except within about 10° of grazing where the situation becomes much more complicated. Low grazing angle paths will be unimportant in our experiment modeling, however, since these paths will be highly attenuated. Thus we believe perturbation theory is highly accurate for simulating the effects of sediment roughness on acoustic penetration into sediment.

III. SIMULATIONS USING FORMALLY AVERAGED PERTURBATION THEORY

In this section we use full 3-D simulations to examine whether the rough surface scattering mechanism for penetration into sediment can explain results reported by Chotiros[1] for the ATBE. In the ATBE an acoustic projector on a movable tower transmitted short sound pulses to an array of buried hydrophones (Fig. 3). Because the projector was movable, the incident grazing angle could be varied, and (after processing) the temporal resolution was about 0.1 ms. The received signals from the buried array were used to deduce the propagation speed and direction in the sediment. Because the hydrophone locations were not known to the precision of a fraction of a wavelength (the frequency range covered in these measurements was 5–80 kHz), these deductions were made with an incoherent processing technique as described in Ref. 1 and outlined in Appendix B.

We consider the ATBE data obtained at 20 kHz.[1] The measured sediment sound speed at this site was reported to be 1729 m/s and the critical angle was about 27°. For incident grazing angles well above the critical angle, the propagation speed deduced from incoherent processing is consistent with the measured sediment sound speed, and the direction is consistent with Snell's law. For angles below the critical angle, the situation changes markedly. Figure 4(a)

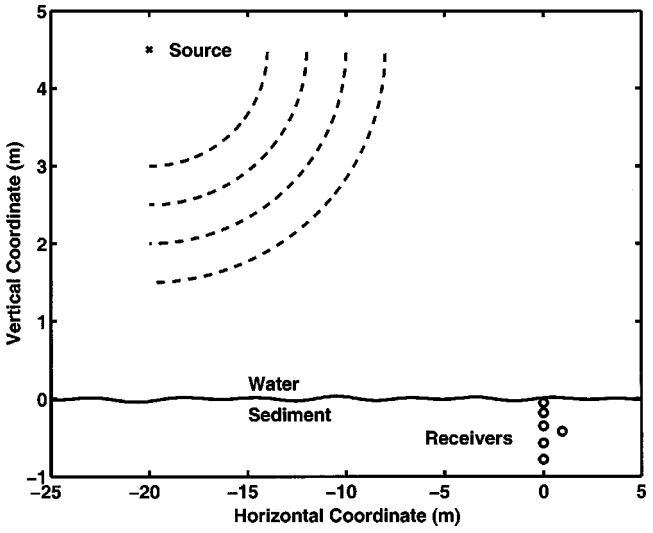

FIG. 3. A schematic, 2-D rendition of the simulation geometry for acoustic penetration measurements reported by Chotiros (Ref. 1). Note exaggeration of vertical scale. Receiver coordinates are given in the top half of Table II.

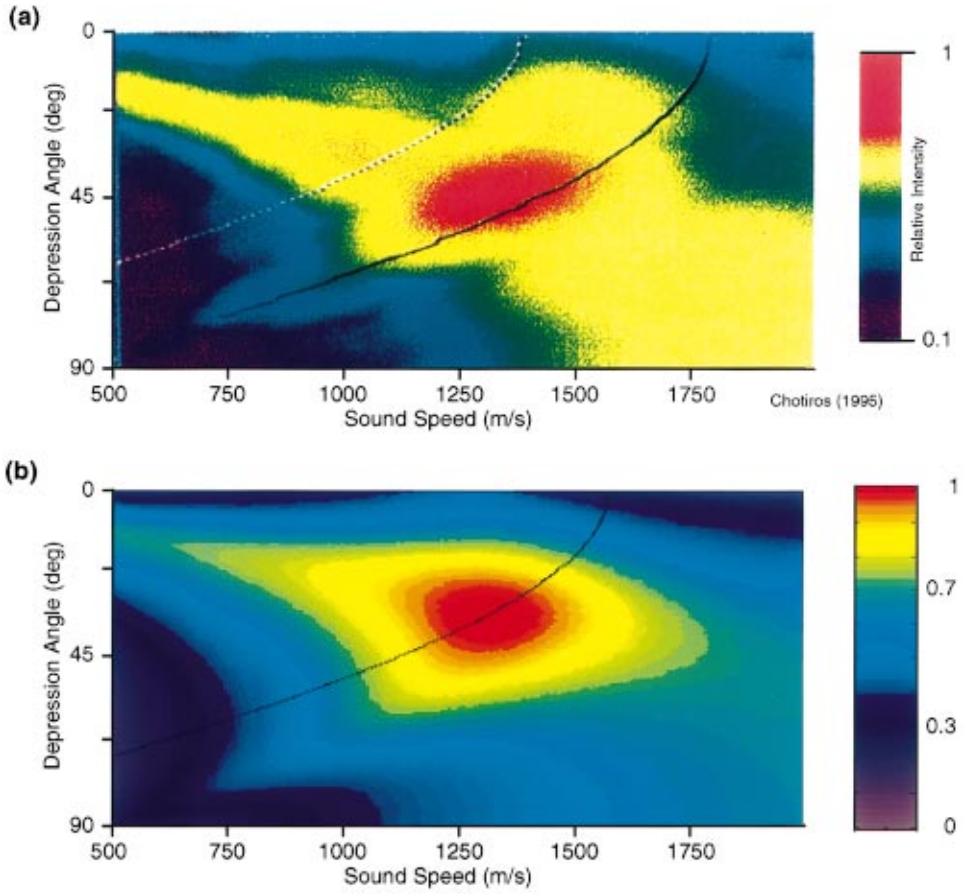

FIG. 4. Ambiguity plot for apparent sound speed and depression angle in sediment: (a) Experimental results reported by Chotiros (Ref. 1), and (b) simulation results based on scattering from a rough sediment interface. The frequency is 20 kHz and the incident grazing angle is 12.7°. In (a) the region between the lines is considered consistent with Snell's law, given the experimental uncertainties (Ref. 1); in (b) points on the line are consistent with Snell's law. The ambiguity plot was normalized so that the maximum possible value is unity (see Appendix B).

(adapted from Ref. 1) shows an ambiguity plot in sound speed and depression angle obtained using field data with an incident grazing angle of 12.7°, well below the critical angle. The ambiguity plot indicates a propagation speed for this case of about 1300 m/s. For the region between the solid and dotted lines, the propagation direction and speed were considered consistent with Snell's law, given the experimental uncertainties.[1]

A detailed description of the experiment simulation is given by Moe[14] and the derivation of relevant equations is summarized in Ref. 15. The sediment acoustic parameters[1,17] are summarized in Table I. The absorption/frequency ratio (α/f) was chosen to yield a reasonable value $\delta \approx 0.016$ for the absorption parameter defined by Eq. (C11) in Appendix C. The source and buried hydrophone coordinates[17] are given in Table II. The intensity time series at each hydrophone is obtained as a sum of incoherent and coherent intensities, the latter only being important in the evanescent region near the interface. A Gaussian pulse with envelope $\exp(-t^2/t_s^2)$ with $t_s = 0.1$ ms is used to approximate the filtered pulse shape appropriate to the ATBE data. The incoherent part is found by dividing the surface area into a large number of subareas and summing the time delayed contributions from each using the bistatic scattering cross section (lowest-order perturbation theory[14,15]) appropriate for each subarea. The signal level is reduced by spherical spreading from the source to each area element and by spherical spreading and attenuation due to absorption from each area element to each hydrophone. The coherent intensity is found ignoring interface roughness and is computed by wave number integration.[18]

A 2-D spectrum of surface roughness is needed to evaluate the perturbation theory cross section, and, as mentioned previously, the roughness spectrum was not measured during ATBE. Some guidance is provided by spectra obtained in the same region with similar water depths and sediment properties in 1984,[19] about two years before ATBE. These data

TABLE I. Physical parameters used in simulations.

Fig. No.	Freq. (kHz)	c_1 (m/s)	c_2 (m/s)	ρ_2/ρ_1	α/f (dB/m/kHz)	Spectral strength, w_2	Spectral exponent, γ	Cutoff parameter
4(b),6 7,11	20	1536	1729	2.0	0.565	6.2×10^{-3} (cm)	3.0	a =4 cm
10	2,4, 6,8	1489	1530	1.83	0.583	5.0×10^{-3} ($\text{cm}^{0.5}$)	3.5	K_L =0.01 cm^{-1}

TABLE II. Source and hydrophone coordinates used in simulations. For high frequency simulations [Figs. 4(b), 6, 7, 11], receiver 1 was used as a reference. For mid-frequency simulations (Fig. 10), receiver 4 was used as a reference.

Fig. No.	Coord. (m)	Source	Rec. 1	Rec. 2	Rec. 3	Rec. 4	Rec. 5	Rec. 6	Rec. 7	Rec. 8
4(b),6	x	−20.0	0.0	0.0	0.0	0.0	0.0	0.95		
7,11	y	0.0	0.0	0.0	0.0	0.0	0.0	0.0		
	z	4.5	−0.05	−0.18	−0.35	−0.57	−0.78	−0.42		
10	x	62.4	0.0	0.0	0.0	0.0	1.9	1.9	1.9	1.9
	y	14.5	0.0	0.0	0.0	0.0	2.0	2.0	2.0	−2.0
	z	4.5	−2.6	−1.8	−1.0	−0.01	−1.6	−0.8	−0.01	−0.01

cover a length scale range from about 50 cm down to 0.8 cm (for $2\pi/K$) and can be approximated by the isotropic form (see parameters in Fig. 9 of Ref. 20)

$$W(\mathbf{K}) = \frac{w_2}{K^3}, \tag{3}$$

where $w_2 = 6.2\times 10^{-3}$ cm, and $K = |\mathbf{K}|$. Unfortunately, owing to the spatial separation and the time lapse between the spectrum and the penetration measurements, we cannot have confidence that Eq. (3) applies to the sediment surface near ATBE. In addition it is likely that the sediment was disturbed in the process of burying hydrophones. For simulations we have modified and generalized Eq. (3) with two different forms of low wave number cutoff: a ''Gaussian'' cutoff form

$$W(\mathbf{K}) = \frac{w_2}{K^\gamma}\{1-\exp[-(Ka)^2/2]\}^2, \tag{4}$$

and an ''algebraic'' cutoff form analogous to Eq. (1),

$$W(\mathbf{K}) = \frac{w_2}{(K^2+K_L^2)^{\gamma/2}}. \tag{5}$$

For the high frequency simulations of this section, the spectral strength parameter, w_2, and the spectral exponent, γ, were assigned the values 0.0062 cm and 3.0, respectively. Different values were used in the mid-frequency simulations to be described in Sec. VI. Differing values were assigned to the cutoff parameters (a or K_L) in order to vary the low wave number content of the spectrum as shown in Fig. 5 for the case $\gamma=3$. As the cutoff is changed, the mean-square roughness, h^2, changes. The mean-square roughness is the integral of $W(\mathbf{K})$ over all $\mathbf{K}$ including both positive and negative wave vector components.

Using Eq. (4) with $a=4$ cm yields a spectrum deficient in low wave number structure and relatively rich in high wave number structure with normalized roughness $k_1 h = 0.28$. Doing the simulation with these parameters and using an incoherent processing technique (Appendix B) similar to that used for the experimental data yields the ambiguity plot shown in Fig. 4(b), which agrees closely with Fig. 4(a). It must be emphasized that in this simulation the actual propagation speed in the sediment is 1729 m/s, but the apparent speed as measured by this processing method is close to 1300 m/s in this example. Snell's law is satisfied for points on the black line in Fig. 4(b), which passes through the maximum in the simulation ambiguity plot. Section V gives a simple explanation for the low apparent wave speeds seen in the simulations and the tendency of the (incorrect) speed and angle to satisfy Snell's law.

By using different choices for the form of the spectrum and for the cutoff parameter, we obtain apparent propagation speeds in roughly the 1200–1500 m/s range. As the cutoff parameter is changed to increase the low wave number content of the roughness spectrum, the apparent speed increases and finally stabilizes at about 1500 m/s becoming insensitive to further change. For example, using Eq. (5) with $K_L < 0.2\,\mathrm{cm}^{-1}$ gives about 1500 m/s. Thus if the spectrum were of the form of Eq. (3) down to length scales of about 30 cm or beyond, we would predict an apparent speed of about 1500 m/s. (The example in Fig. 1 corresponds to this case.) With roughness spectra relatively richer in high wave number components, apparent speeds in the 1100–1300 m/s range can be obtained. It should be expected that these results would be insensitive to very low wave number components of the roughness spectrum. In particular, because of attenuation in the sediment, the region on the water–sediment interface that contributes significantly to the scattered fields received by the buried hydrophones is an area only a few meters on a side. Interface roughness with length

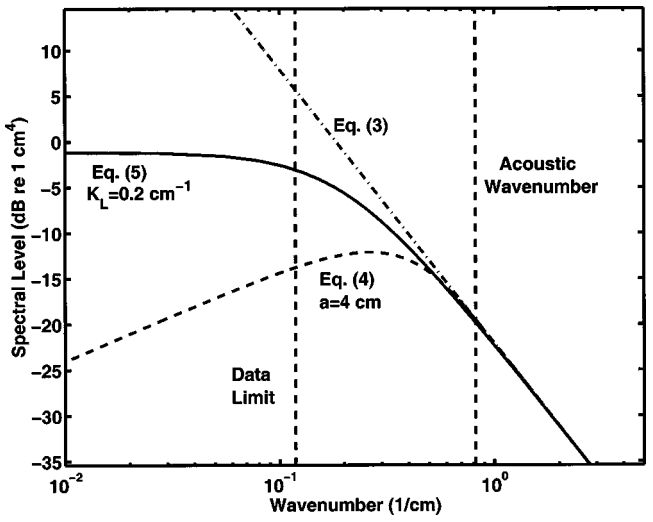

FIG. 5. Comparison of roughness spectrum models used in simulations with the power law model given by Eq. (3). The spectrum shown using the algebraic cutoff model of Eq. (5) is equivalent to Eq. (3) for simulation purposes. The spectrum shown using the Gaussian cutoff model of Eq. (4) yields apparent speeds in agreement with Ref. 1.

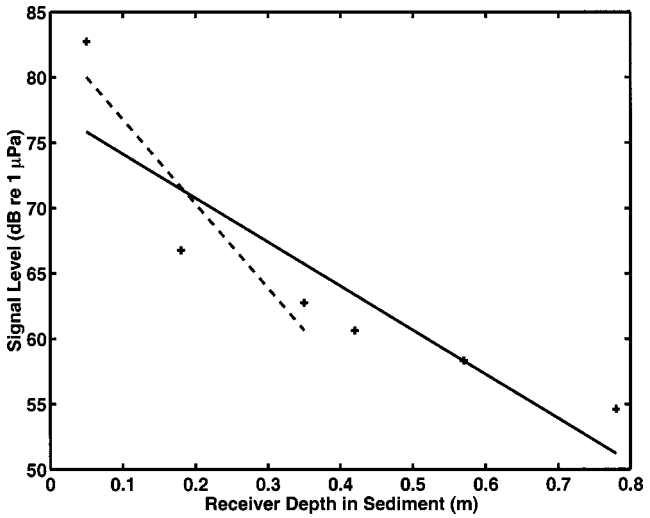

FIG. 6. Simulation results for peak signal level versus receiver depths for a source level of 120 dB *re*: 1 μPa at 1 m. Simulation parameters were the same as for Fig. 4(b). The dashed line (fit using three shallowest receiver depths) corresponds to an attenuation of 36.0 dB/m. The solid line (fit for all receiver depths) corresponds to an attenuation of 18.9 dB/m.

scales exceeding or even approaching this range will not contribute to the scattered fields.

In addition to propagation speed and direction in the sediment, attenuation in the sediment is also of interest. For ATBE Chotiros reports slow-wave attenuations of 30–40 dB/m at 20 kHz.[1] To compare with these values, we assume the simulated signal levels are due to a propagating slow wave. For the simulation used to obtain Fig. 4(b), $\theta_i = 12.7°$ and $c_1 = 1536$ m/s (Table I). From Fig. 4(b), the apparent slow wave speed $c_2' \approx 1300$ m/s, and by Snell's law the slow wave would propagate at angle $\theta_2' = 34.3°$ down from the horizontal. (See Sec. V for related discussion.) Thus when attenuation occurs over a path length Δr, the same reduction in signal level would be observed over a depth change $|\Delta z| = \sin\theta_2' \Delta r$. It follows that the attenuation is the negative of the slope of the appropriate line in Fig. 6 multiplied by $\sin\theta_2'$. As shown in Fig. 6, a fit to the signal levels for all six hydrophones used in our simulation yields an attenuation of 19 dB/m. However, if only the top three hydrophones are used in the fit, an attenuation of 36 dB/m is obtained. This difference occurs because the top hydrophone is strongly affected by the evanescent wave, whereas the signal at the deeper hydrophones is made up primarily of scattered waves propagating steeply.

IV. MONTE CARLO SIMULATIONS USING PERTURBATION THEORY

In the previous section formally averaged perturbation theory was used in simulations of experimental results obtained by Chotiros using an incoherent processing technique. The agreement between the simulation and experimental results in Fig. 4 is good, but to obtain this agreement a particular form of the interface roughness spectrum, a form relatively rich in high wave numbers, was used. If a more typical spectrum for undisturbed sediment is used, the maximum in the simulated ambiguity plot occurs at an apparent speed of about 1500 m/s versus the measured value of about 1300 m/s. We consider in this section how simulation results for these more typical roughness spectra may in fact also be consistent with the experimental results. The simulation method used in Sec. III is based on average scattering levels, the average taken over an ensemble of rough water–sediment interfaces. The experimental results, on the other hand, are for a single realization of the rough interface, and we should expect the results to fluctuate from realization to realization. To study the magnitude and significance of such fluctuations we have generalized the simulation method to accommodate single realizations of rough interfaces, i.e., developed a Monte Carlo simulation method.

To model this experiment with Monte Carlo simulations we use unaveraged first-order perturbation theory with specific realizations of the rough interface. This approach allows study of fluctuations in the outputs of incoherent processors and also allows simulations using coherent processors, discussed in Sec. VI. Realizations of rough 2-D interfaces were generated from isotropic 2-D roughness spectra given by Eq. (4) or (5) using a generalization of the method described for 1-D rough surfaces in Ref. 11. Moe[14] and Moe and Jackson[15] give an expression for the plane wave T-matrix for scattering into a rough, homogeneous, sediment. This expression applies to scattering of CW plane waves and, to adapt this result to the present time-domain problem, a stationary phase approximation is employed to increase computation speed (Appendix C).

The Monte Carlo simulation method provides a means of studying properties of the incoherent processor that cannot be examined using the formal-average approach. In particular, when scattering is the dominant penetration mechanism, the hydrophone output envelopes are random with irregular shapes, while the formal average approach assumes that these envelopes can be approximated by the smooth curves generated using the theoretical scattering cross section and the sonar equation. Thus one expects the processor output to be less smooth than predicted by the formal-average method and to fluctuate from realization to realization. Also, one may question the use of the scattering cross section (defined in the far field) in these near-field calculations. Moe[14] and Jackson *et al.*[21] have given arguments to justify this approach and, as the Monte Carlo simulations do not employ the scattering cross section, they provide a means of checking the conclusions of Refs. 14 and 21.

In the simulations of this section, all parameters are the same as those used to obtain Fig. 4(b), including the parameters defining the roughness spectrum. Figure 7 shows the output of the incoherent speed-angle processor for four independent realizations. While each realization produces an output that bears some resemblance to the formal-average simulation of Fig. 4(b), which has a peak at an apparent propagation speed of about 1300 m/s, fluctuations in both the peak output and the position of the peak are pronounced. Note that the peak generally lies near the Snell's law line but need not fall on the line as in the formal-average simulation. Note also that the peak for realization No. 4 occurs at an apparent speed of about 1500 m/s, similar to what is found using formally averaged perturbation theory with the algebraic cutoff form of the spectrum given by Eq. (5) with K_L

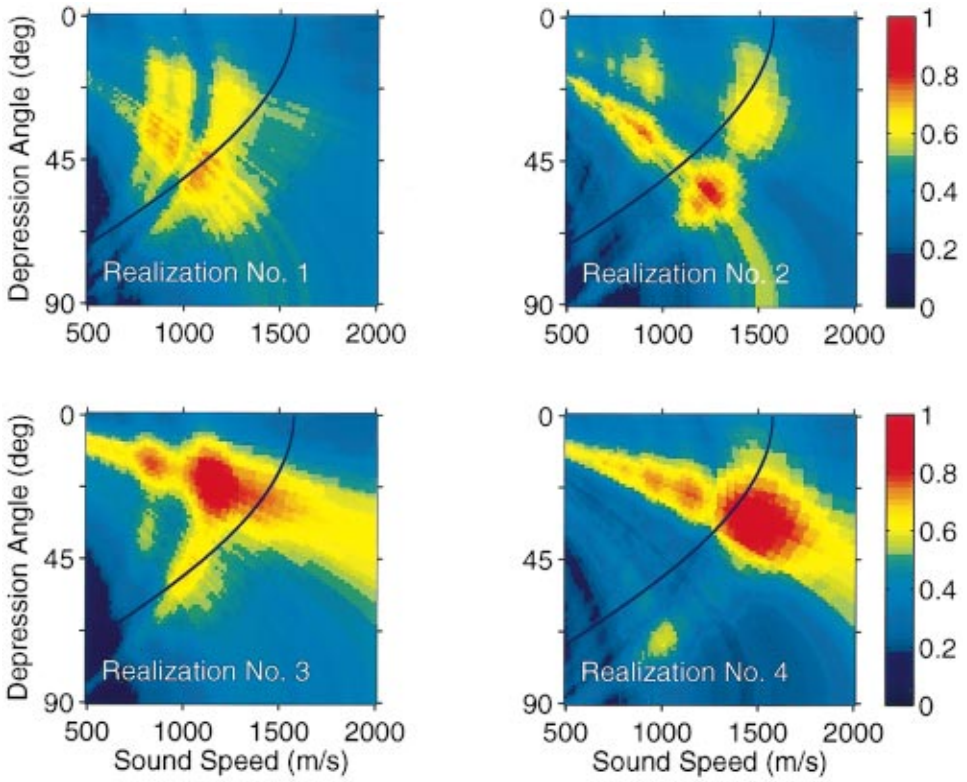

FIG. 7. Monte Carlo simulation results for ambiguity plots for apparent sound speed and depression angle in sediment. Simulation parameters were the same as in Fig. 4(b), and incoherent processing was used. Results for four independent rough interface realizations are shown. The ambiguity plots were normalized so that the maximum possible value is unity (see Appendix B).

$<0.2\,\mathrm{cm}^{-1}$. [This form of the spectrum is equivalent to the canonical power law form Eq. (3) for the present purpose, since there is no dependence on K_L for $K_L<0.2\,\mathrm{cm}^{-1}$.] Conversely, other simulations show that use of the algebraic cutoff form with $K_L<0.2\,\mathrm{cm}^{-1}$ produces some realizations that yield apparent speeds as low or lower than 1300 m/s. Therefore, if the slow apparent speeds reported in Ref. 1 were the result of penetration due to interface scattering, then fluctuations associated with the particular realization existing in the experiments reported there could be responsible for the difference (or part of the difference) between experimental and simulation results using canonical power law forms of the roughness spectrum.

We have also averaged the outputs for several realizations to see if this average approaches that of the formal-average method. Returning to the parameters used in Fig. 4(b), an average over 10 realizations yielded a peak whose width and position compared favorably with Fig. 4(b), but the average peak output was about 0.65 compared to a value near 1.0 for the formal average approach. It may seem surprising that the Monte Carlo average differs from the formal average result, but there is no reason the two should be the same. This is because the Monte Carlo average is taken after the nonlinear speed-angle processor has acted on the data, while the formal average is taken before the data are input to the processor. On the other hand, when the mean-square pressure at each receiver is averaged over all Monte Carlo realizations, the result is found to agree within expected statistical error with the result obtained using the scattering cross section of formally averaged perturbation theory. This validates theoretical arguments[14,21] that the far-field cross section can be used in these near-field situations.

The fluctuations seen in Fig. 7 can be taken to be one of the signatures of interface scattering, and would be expected in any penetration experiment dominated by scattering. In order to observe such fluctuations, more than one realization of the rough interface must be available. This could be accomplished by deliberate alteration of roughness. It may also be possible to achieve nearly independent realizations by altering the source location or changing acoustic frequency. While it is unclear whether the data of Ref. 1 show diminution and displacement of the processor output peak from the Snell's law curve, other cases from the ATBE measurements[17] show effects similar to those seen in Fig. 7, in particular, strong fluctuation as frequency is changed.

The Monte Carlo method is more accurate and better simulates stochastic behavior than the formal average method. However, the formal-average method requires considerably less calculation and provides a useful approximate simulation tool.

V. SPEED-ANGLE ARTIFACTS DUE TO INTERFACE SCATTERING

The way in which scattered waves traveling at the normal sediment compressional speed, c_2, can appear to be traveling at a much slower speed is illustrated in Fig. 8. Consider a short-pulse plane wave whose leading edge at some time is aligned with the arrows on the water side of the interface. Assume the pulse scatters at the surface and for simplicity propagates straight down. The leading edge will propagate down at speed c_2 and at some later time be aligned with the arrows shown in the sediment. If one assumes the propagation direction is normal to this leading edge (as done for these experiments and in our simulations), the apparent speed will be $c_2'<c_2$. In the more general case in which the

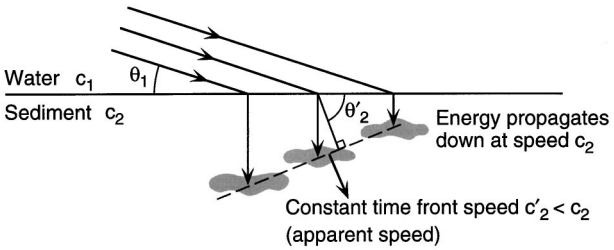

FIG. 8. Schematic showing how scattering at the sediment interface can mimic a slow wave in the sediment. For simplicity energy is assumed to scatter straight down.

scattered energy travels at an angle, θ_2, in the sediment the apparent wave speed, c_2', and apparent angle, θ_2', are given by[14]

$$\theta_2' = \theta_2 - \tan^{-1}[(c_2 \cos\theta_1 / c_1 - \cos\theta_2)/\sin\theta_2], \tag{6}$$

$$c_2'/\cos\theta_2' = c_1/\cos\theta_1 . \tag{7}$$

Figure 9 displays the corresponding dependence of apparent speed on incident grazing angle assuming vertical scattering, $\theta_2 = 90°$. For c_2 about 1700 m/s with $c_2/c_1 = 1.13$, for low incident grazing angles, and for vertical propagation in the sediment, it follows from Fig. 9 that c_2' is about 1100–1200 m/s. As the mean propagation direction moves forward (backward) from vertical, c_2' increases (decreases) so that a range of apparent speeds can be obtained depending on the mean propagation direction, which in turn depends on the properties of the sediment roughness spectrum. The apparent wave speed and angle will always be consistent with Snell's law, Eq. (7), in this simple model of a single propagation direction in the sediment, whether vertical or not. In general, scattering will not occur at a well-defined angle but, as noted in Sec. I, absorption will tend to remove energy that is propagating at angles significantly away from the vertical. This was the case in the simulations of Secs. III and IV at 20 kHz, but may not apply at lower frequencies since absorption will be reduced.

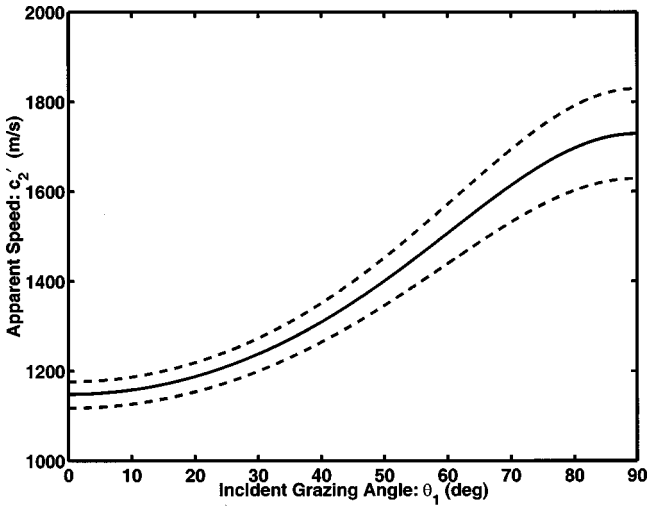

FIG. 9. Dependence of the apparent slow wave speed on incident grazing angle assuming the scattered field propagates in the vertical direction. For the solid line the speed in the sediment (water) is 1729 m/s (1536 m/s). The dashed lines show the dependence for sediment speeds that are 100 m/s above and below the 1729-m/s value; the higher speed gives the top curve.

VI. SIMULATIONS OF COHERENT PROCESSING

Because the scattering cross section contains no phase information, the formal-average simulation method cannot be used to study the result of coherent processing. However, the Monte Carlo method described in Sec. IV can be used for simulations of coherent processing. In this section two simulation examples will be given. The first example is a simulation of mid-frequency experimental results reported by Chotiros *et al.*,[7] and the second is a simulation of the high frequency experiment (also by Chotiros[1]) discussed in Secs. III and IV. At lower frequencies, the longer wavelengths reduce the importance of uncertainties in buried hydrophone positions, and coherent processing can be effected without making special provisions for the determination of hydrophone locations. While coherent processing was not used for the high frequency experimental results, simulations allow us to examine the potential benefits of this type of processing in removing ambiguity in the inferred sediment sound speed.

A. Mid-frequency simulations

The Mediterranean experiment of Chotiros *et al.*[7] employed lower frequencies (2–8 kHz) than used in ATBE, and the authors used a coherent processing scheme (see Ref. 7 or Appendix B of the present article). Our interest in simulating this experiment derives from the results shown in Fig. 12 of Ref. 7 coupled with the supporting analysis given. The authors discuss features shown in the elevation angle-sound speed ambiguity plots of their Fig. 12 that lie below or to the left of the white curved lines labeled c_m. The authors give an analysis that they contend shows that such features cannot be due to scattering from roughness at the water–sediment interface. Therefore, the authors ascribe such features (e.g., the four features circled in their Fig. 12) to the existence of slow propagating waves, and suggest these may be Biot slow waves. We show in our simulations that such features can result from scattering from roughness and point out the limitations of their interpretation.

In simulating roughness scattering effects for the mid-frequency experiment of Chotiros *et al.*,[7] we use the sediment sound speed and density of their ''baseline'' model. The absorption/frequency ratio (α/f) was chosen to yield a reasonable value $\delta \approx 0.016$ (Ref. 20) for the absorption parameter defined by Eq. (C11). The roughness spectrum approximates one measured at a site having a similar sandy silt sediment (the ''Puget Sound'' site of Ref. 20). The simulation acoustic parameters are given in Table I, and the source and receiver coordinates[7,22] are given in Table II. These coordinates correspond to those of the actual experiment except that the ''reference'' receiver (No. 4) was taken to be 1 cm below the interface in the simulations whereas it was actually 40 cm above the interface.[7] Receivers 7 and 8 were also taken to be 1 cm below the interface rather than *on* the interface as in Ref. 7. A Gaussian pulse envelope, $\exp(-t^2/t_s^2)$, with $t_s = 0.2$ ms was used in the simulations to approximate the bandwidths employed in processing the ex-

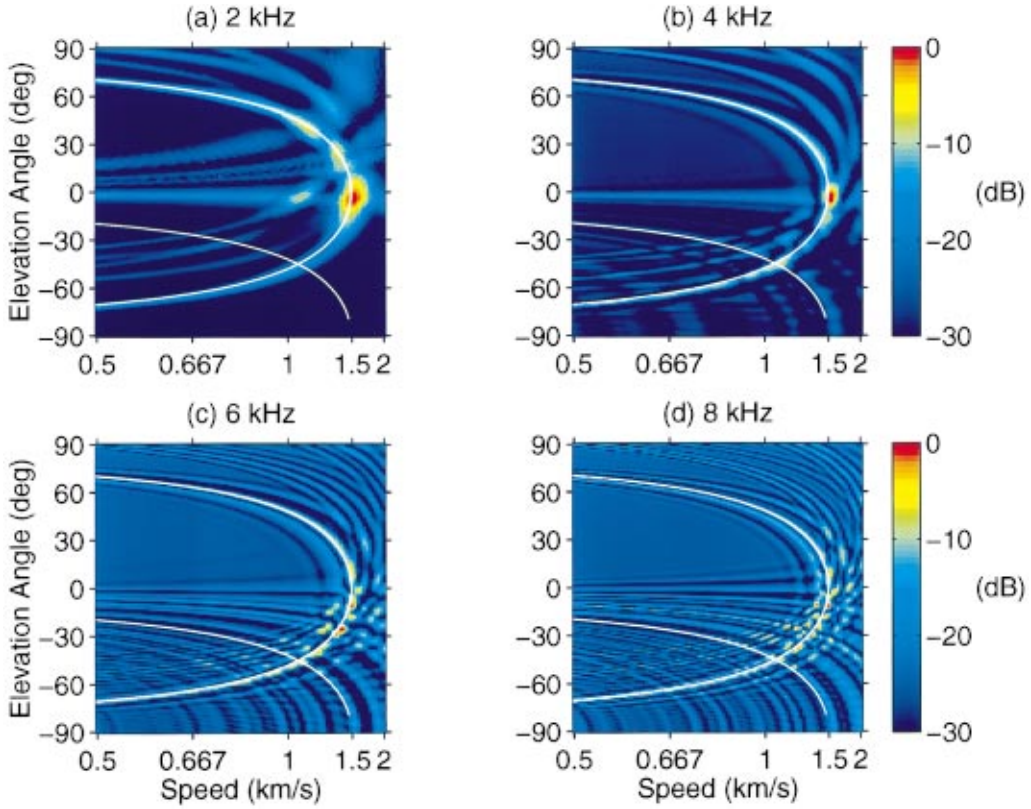

FIG. 10. Monte Carlo simulations of speed-angle ambiguity plots for the mid-frequency experiment of Chotiros *et al.* (Ref. 7). Simulation parameters are given in Tables I and II, and coherent processing was used. See text for description of superimposed white lines. The ambiguity plots were normalized so that in each case the peak value is unity.

perimental data.[7] The spectrum equation (5) was used to generate independent rough-interface realizations, $f(\mathbf{R})$, for insertion into Eq. (C15).

Figure 10 shows the results of a simulation for the elevation angle-sound speed ambiguity plot using a single realization with center frequencies of 2, 4, 6, and 8 kHz. The format of this figure was chosen for similarity with Ref. 7 and differs from that of Figs. 4 and 7. Equivalent results were obtained using a second, independent rough-interface realization. Two white lines are superimposed on each figure. The first, which doubles back to intersect the left vertical boundary twice and is the more difficult to see, is the locus of points consistent with Snell's law for transmission from the water into the sediment. Note that only negative elevation angles correspond to downward propagation within the sediment; this is the region of primary interest. The second line, which curves down and to the right, is a bound for scattering artifacts proposed by the authors; they contend that all features due to scattering should lie above and to the right of this curve.

Chotiros *et al.*[7] state that artifacts due to scattering will necessarily lie above a bound determined by the following equations:

$$c \geqslant \frac{c_f c_h}{\sqrt{c_f^2 + c_h^2}}, \tag{8}$$

$$\theta = \tan^{-1}(c_h / c_f). \tag{9}$$

In Eqs. (8) and (9), c_f is the compressional wave speed and c_h is a horizontal phase speed treated as an unknown. In Fig. 12 of Ref. 7 and Fig. 10 of the present article, the region defined by Eqs. (8) and (9) lies above the line defined by using equality in Eq. (8) and allowing c_h to range over all positive values. As is evident in Fig. 10, scattering produces features that fall below this line, contrary to the assertion made in Ref. 7 (see also Fig. 11). This is because, while Eqs. (8) and (9) represent a limit for the artifact discussed in Ref. 7, they do not represent a limit for all possible scattering artifacts. The particular artifact discussed in Ref. 7 arises when the coherent processor interprets the signals from two separate waves as arising from one coherent wave: one wave being an evanescent wave, the other being a scattered wave taken as propagating vertically to obtain the bound. It turns out that important artifacts are also produced when two or more scattered waves are interpreted as one coherent wave, and there is no limit in speed-angle space for the resulting artifacts as explained in Sec. V. Thus the argument in Ref. 7 that there is a bound on speed for artifacts due to interface scattering is incorrect.

B. High frequency simulations

Finally, we give a simulation example of coherent speed-angle processing at high frequency. This allows us to examine the expectation that coherent processing will prove superior to incoherent processing owing to the incorporation of phase information, provided hydrophone positions are

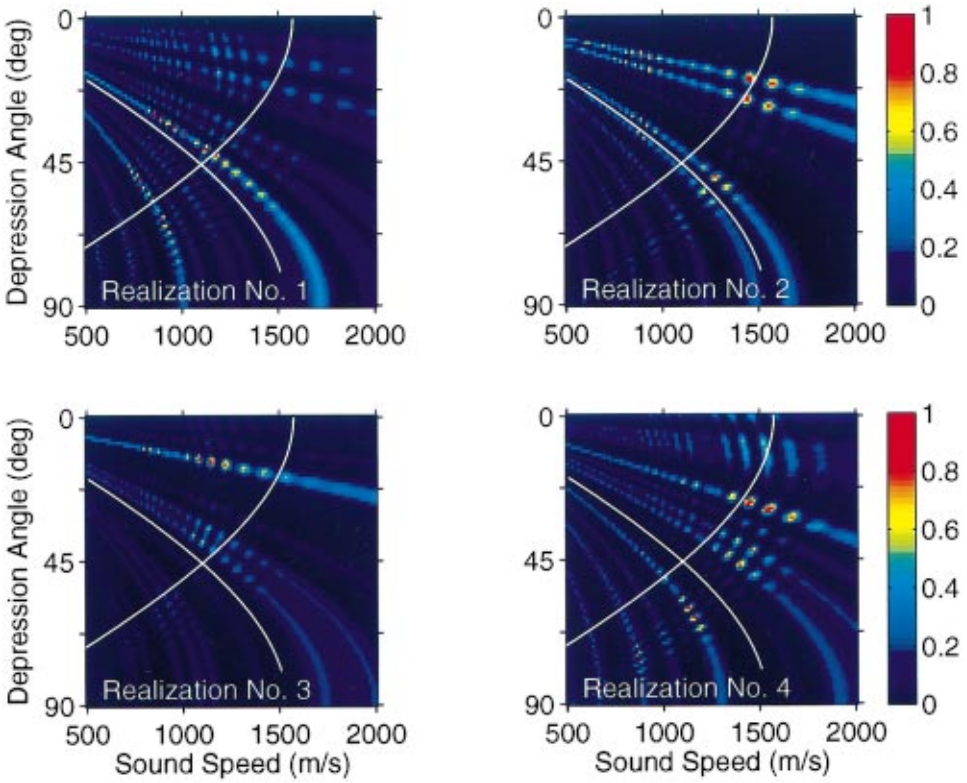

FIG. 11. Monte Carlo simulations of speed-angle ambiguity plots employing coherent processing for the same simulation parameters and rough interface realizations used for Fig. 7. The ambiguity plots were normalized so that in each case the peak value is unity.

known to within a fraction of a wavelength. We return to the 20-kHz example of Figs. 4 and 7. The slow propagation speed implied by the simulation outputs is an artifact of the processing method, since the actual sediment propagation speed was 1729 m/s in the simulation. For the coherent processing simulations, all parameters, including hydrophone locations, were kept the same as for the incoherent simulations described in Secs. III and IV. Figure 11 shows the speed-angle plots obtained by coherent processing using the same four realizations employed in Fig. 7. The two white lines superimposed on the figure are the same as described in Sec. VI A in reference to Fig. 10.

Note that in Fig. 11 strong peaks (red) occur at a speeds between 1200 and 1500 m/s near the Snell's law curve, and a few strong peaks lie at even lower speeds. In realizations 1 and 4, strong features appear well below the bound on scattering effects proposed in Ref. 7 and given by the white line which curves down and to the right. While some signal is evident at speeds near 1700 m/s (at angles near $-90°$), this output has the appearance of side-lobe structure to stronger features at lower speeds. Unfortunately, merely switching to coherent processing does not remove the speed ambiguity in the processor output.

In other simulations we have found that the poor performance of the coherent processor is related to the sparseness of the buried array in this example. Using denser arrays (subwavelength spacing) the expected result can be recovered, that is, a strong dominant feature is obtained at speeds near 1700 m/s. The trade-off between processor performance and array configuration is the subject of ongoing simulation studies.

VII. CONCLUSIONS

In summary, we have shown that scattering from a rough water–sediment interface is a viable hypothesis for subcritical penetration into sediments. With a suitable choice of roughness spectrum, this mechanism can explain the observation of apparent slow wave speeds in sediments. Simulated attenuations are less than reported experimentally, but if the analysis is restricted to a subset of hydrophones closest to the surface, simulation results are consistent with the reported values. Acoustic penetration experiments with the roughness spectrum measured in the precise experimental area should be able to determine if scattering from sediment roughness is the actual mechanism. While coherent processing should be superior to incoherent processing in penetration measurements, additional study is needed to determine acceptable array configurations and processing methods.

ACKNOWLEDGMENTS

This work was supported by the U.S. Office of Naval Research, Code 321OA. Dr. John Moe, in his thesis work at APL-UW, contributed significantly to the initial phase of this work. The authors benefited from numerous technical discussions with Dr. Dajun Tang, who provided the computer code used to generate rough-interface realizations and who assisted in checking the accuracy of the stationary phase approximations used here. We also wish to thank anonymous reviewers for their helpful comments.

APPENDIX A: COUPLED INTEGRAL EQUATIONS FOR THE TWO-FLUID INTERFACE

In Ref. 10, coupled integral equations for a *p*-polarized electromagnetic field incident on a dielectric rough surface are given by Eqs. (3.32) and (3.33) or by Eqs. (3.49a) and (3.49b). The coupled integral equations for an acoustic pressure field incident on a rough two-fluid interface can be obtained from the equations in Ref. 10 using the following associations: The total pressure field, $p(\mathbf{r})$, on the rough surface is analogous to the magnetic field, $H(x_1|\omega)$, in Ref. 10. The quantity

$$\left(-\frac{df(x)}{dx}\frac{\partial}{\partial x}+\frac{\partial}{\partial z}\right)p(\mathbf{r})$$

on the rough surface, which is proportional to the normal derivative of the total pressure field on the rough surface, with $f(x)$ the rough surface profile, is analogous to $L(x_1|\omega)$, in Ref. 10. Finally, the density ratio of the two fluids, ρ_2/ρ_1, where the field is incident on the side with density ρ_1, is analogous to the dielectric constant $\epsilon(\omega)$ in Ref. 10.

APPENDIX B: SPEED-ANGLE PROCESSING METHODS

Both the incoherent[1,17] and coherent[7] processing methods of Chotiros and collaborators employ signal normalization to compensate for signal loss in the deeper hydrophones due to absorption. In each method, one hydrophone is designated as a reference, and the time instant at which the signal envelope for this hydrophone reaches its peak value is used to provide a time reference, t_0, while the location of this hydrophone provides a spatial reference, $\mathbf{r}_0$. Considering the *n*th hydrophone located at position $\mathbf{r}_n$, the arrival time, t_n, of a pulse moving at speed c and in direction given by the unit vector $\mathbf{e}$ is

$$t_n=t_0+\mathbf{e}\cdot(\mathbf{r}_n-\mathbf{r}_0)/c. \tag{B1}$$

To form speed-angle ambiguity plots, such as those in Figs. 4, 7, 10, and 11, the speed-angle domain is represented by a discrete grid, with each grid point representing a hypothetical speed-angle pair, (c,θ), where $\mathbf{e}$ is directed at angle θ relative to the horizontal. Equation (B1) is used to obtain the arrival times for this hypothetical case, the signals at each hydrophone are sampled at these times, and the samples are summed and normalized to provide the processor output for (c,θ).

In order to replicate as closely as possible the processing methods used by Chotiros and collaborators, the signal normalization was chosen differently for the incoherent and coherent methods. In the incoherent method, the signals of interest are the squared envelopes, and these signals are normalized to have unit peak values. The sum of delayed samples (including the value unity for the reference hydrophone) is normalized by dividing by the number of hydrophones so that the maximum possible processor output is unity.

In the coherent method, the signals of interest are the complex baseband time series, $s_n(t)$, representing the output of each hydrophone. These are normalized to have the same energy (same area under squared envelope), and the processor output is

$$p(c,\theta)=A\left|\sum_n s_n(t+t_n)\exp(-i\omega_0 t_n)\right|^2. \tag{B2}$$

Note that the factor $\exp(-i\omega_0 t_n)$ accounts for the carrier phase shift corresponding to the hypothetical time shift, t_n, and that the sign of this phase shift must be consistent with the baseband carrier reference chosen in generating the synthetic time series. As noted in Appendix C, the carrier phase is defined as $\exp(-i\omega_0 t)$. In the results presented here, the normalizing constant, A, was chosen so the peak of the processor output in (c,θ) space was always unity.

APPENDIX C: STATIONARY PHASE APPROXIMATION FOR PENETRATING FIELD

The Monte Carlo simulations employ stationary phase approximations for the zeroth-order coherent pressure and the first-order incoherent scattered pressure. The incoherent scattered pressure is computed using an expression for the plane wave T-matrix for scattering into a rough, homogeneous sediment.[14,15] This expression applies to scattering of plane waves and, to adapt this result to the present problem, a plane wave decomposition of the field of a point source is used.

For a CW point source at $\mathbf{r}_i=(x_i,y_i,z_i)$ in the water, the incident field above the sediment is

$$\psi_i(\mathbf{r})=\frac{e^{ik_1|\mathbf{r}-\mathbf{r}_i|}}{4\pi|\mathbf{r}-\mathbf{r}_i|}, \tag{C1}$$

where k_1 is the wave number in medium 1 (water) with sound speed c_1. A plane wave decomposition of $\psi_i(\mathbf{r})$ for a field point, $\mathbf{r}$, below the source, but above the sediment yields

$$\psi_i(\mathbf{r})=\int d^2K' e^{i\mathbf{K}'\cdot\mathbf{R}-ik_1\beta_1(K')z}\Psi_i(\mathbf{K}'), \tag{C2}$$

with

$$\Psi_i(\mathbf{K}')=\frac{i}{2(2\pi)^2 k_1\beta_1(K')}e^{-i\mathbf{K}'\cdot\mathbf{R}_i+ik_1\beta_1(K')z_i}. \tag{C3}$$

In these equations, capital bold symbols denote horizontal vectors. Thus $\mathbf{r}=\mathbf{R}+z\mathbf{z}$ and $\mathbf{k}'=\mathbf{K}'+k_z\mathbf{z}=\mathbf{K}'-ik_1\beta_1(K')\mathbf{z}$, where $\beta_1(K')=(1-K'^2/k_1^2)^{1/2}$, and where $\mathbf{z}$ denotes a unit vector in the positive z-direction. The field at $\mathbf{r}_s=(x_s,y_s,z_s)$ in the sediment (medium 2) can be represented by

$$\psi_s(\mathbf{r}_s)=\int d^2K'' e^{i\mathbf{K}''\cdot\mathbf{R}_s-ik_2\beta_2(K'')z_s}\Psi_s(\mathbf{K}''), \tag{C4}$$

where the plane wave coefficients of the scattered field, $\Psi_s(\mathbf{K}'')$, are given in general by

$$\Psi_s(\mathbf{K}'')=\int d^2K' T_{12}(\mathbf{K}'',\mathbf{K}')\Psi_i(\mathbf{K}'), \tag{C5}$$

where $T_{12}(\mathbf{K}'',\mathbf{K}')$ is the transmission T-matrix for refraction and scattering from medium 1 to medium 2.

The transmission T-matrix is obtained to first order in $k_1 h$ using perturbation theory in Refs. 14,15. We write

$$T_{12}(\mathbf{K}_s,\mathbf{K}_i)=T_{12}^{(0)}(\mathbf{K}_s,\mathbf{K}_i)+T_{12}^{(1)}(\mathbf{K}_s,\mathbf{K}_i), \tag{C6}$$

where $T_{12}^{(0)}(\mathbf{K}_s,\mathbf{K}_i)$ is the unperturbed (or flat surface) T-matrix, and $T_{12}^{(1)}(\mathbf{K}_s,\mathbf{K}_i)$ accounts for scattering to first order in $k_1 h$. Expressions for $T_{12}^{(0)}$ and $T_{12}^{(1)}$ are given in Refs. 14,15. In particular,

$$T_{12}^{(0)}(\mathbf{K}_s,\mathbf{K}_i)=T_{12}(\mathbf{K}_i)\,\delta(\mathbf{K}_s-\mathbf{K}_i)=\Gamma_{12}(\theta_1)\,\delta(\mathbf{K}_s-\mathbf{K}_i), \tag{C7}$$

where θ_1 is the incident grazing angle given by $\sin\theta_1=\beta_1(K_i)$. The transmission coefficient, $\Gamma_{12}(\theta_1)$, is given by

$$\Gamma_{12}(\theta_1)=2z_{12}/(z_{12}+1), \tag{C8}$$

where the normalized impedance, z_{12}, is given by

$$z_{12}=\frac{\rho\beta_1(K_i)}{\kappa\beta_2(K_i)}=\frac{\rho\sin\theta_1}{\kappa\sin\theta_2^{(s)}}. \tag{C9}$$

In Eq. (C9), $\rho=\rho_2/\rho_1$ and $\kappa=k_2/k_1$, where the complex wave number ratio depends upon the loss parameter, δ, as follows:

$$\kappa=(1+i\delta)c_1/c_2. \tag{C10}$$

The loss parameter can be related to the ratio of absorption coefficient to frequency (α/f) appearing in Table I:

$$\delta=\alpha c_2\log_e 10/(40\pi f). \tag{C11}$$

The angle, $\theta_2^{(s)}$, is the complex angle in the sediment obtained using Snell's law

$$\cos\theta_2^{(s)}\kappa=\cos\theta_1. \tag{C12}$$

The first-order transmission T-matrix, $T_{12}^{(1)}(\mathbf{K}_s,\mathbf{K}_i)$, is given in Refs. 14,15 and will not be repeated here. For the point source given by Eq. (C1), the field in the sediment, $\psi_s(\mathbf{r}_s)$, given by Eq. (C4) is also the transmission Green's function, $G_{12}(\mathbf{r}_s,\mathbf{r}_i)$. From Eqs. (C2)–(C5) with $T_{12}^{(0)}(\mathbf{K}'',\mathbf{K}')$ from Eq. (C7) used for $T_{12}(\mathbf{K}'',\mathbf{K}')$ in Eq. (C5), the zero-order (or unperturbed) Green's function can be written

$$G_{12}^{(0)}(\mathbf{r}_s,\mathbf{r}_i)=\int d^2K'\,e^{i\mathbf{K}'\cdot\mathbf{R}_s-ik_2\beta_2(K')z_s}\Psi_i(\mathbf{K}')T_{12}(\mathbf{K}'). \tag{C13}$$

Similarly, the first-order Green's function is obtained using $T_{12}^{(1)}(\mathbf{K}'',\mathbf{K}')$ for $T_{12}(\mathbf{K}'',\mathbf{K}')$ in Eq. (C5). The wave vector integrals that result can be evaluated formally to obtain the following expression:

$$\begin{aligned}G_{12}^{(1)}(\mathbf{r}_s,\mathbf{r}_i)=-\int_{z=0}d^2R f(\mathbf{R})[&(k_1^2-k_2^2/\rho)\\&\times G_{12}^{(0)}(\mathbf{r}_s,\mathbf{r})G_{12}^{(0)}(\mathbf{r},\mathbf{r}_i)-(1-1/\rho)\\&\times\nabla G_{12}^{(0)}(\mathbf{r}_s,\mathbf{r})\cdot\nabla G_{12}^{(0)}(\mathbf{r},\mathbf{r}_i)].\end{aligned} \tag{C14}$$

In this expression, $\mathbf{r}=(\mathbf{R},0)$, where $\mathbf{R}=(x,y)$ is the two-dimensional integration coordinate vector and $z=0$ is the mean plane of the rough interface. The rough surface elevation relative to $z=0$ is $f(\mathbf{R})$, and $G_0(\mathbf{r}_a,\mathbf{r}_b)$ is the Green's function for the unperturbed (flat interface) problem with either coordinate $\mathbf{r}_a$ or $\mathbf{r}_b$ allowed to be in the water or sediment. In Eq. (C14), the coordinate $\mathbf{r}$ in $G_0(\mathbf{r}_s,\mathbf{r})$ is evaluated immediately above the (flat) interface while $\mathbf{r}$ in $G_0(\mathbf{r},\mathbf{r}_i)$ is evaluated immediately below the interface. As the pressure is continuous across the interface, this distinction is immaterial in the first term in the integral, but it is important in the second term, where noncontinuous gradients appear.

At this stage, a time-domain result can be obtained by Fourier synthesis, that is, the desired time series for the hydrophone output is computed as the inverse Fourier transform of the product of Eq. (C14) and the Fourier transform of the transmitted waveform. Because signals of appreciable bandwidth were used in the experiments to be simulated, the frequency dependence of absorption over the signal band should be considered. As an approximation, we assume absorption increases linearly with frequency, and that sound speed is independent of frequency, realizing that this entails a slight, but negligible, violation of causality.[23] In the present notation, this is equivalent to assuming that both c_2 and δ are frequency independent.

The Fourier synthesis approach requires considerable numerical effort, as the double integral of Eq. (C14) must be evaluated at a number of frequencies (of order 100) before the inverse transform can be performed. Instead, we evaluate the unperturbed Green's functions in the stationary phase approximation, which assumes the path lengths are large compared to the wavelength. Since, in some cases, the path length in the sediment was of the order of the wavelength, the accuracy of the stationary phase approximation was verified for the geometries of interest using exact wave number integration for the Green's functions. In the stationary phase approximation, the only frequency dependence of the Green's functions appears in an exponential time shift factor. Because of this, time-domain results can be obtained by the simple expedient of scaling and delaying the transmitted waveform. The resulting time series for the complex baseband scattered pressure at the point $\mathbf{r}_s$ in the sediment is

$$\begin{aligned}p_s(\mathbf{r}_s,t)=-[k_{10}^2\rho/(4\pi)^2]&\\\times\int d^2R\Gamma_{12}(\theta_1)\Gamma_{21}(\theta_2)f(\mathbf{R})B(\mathbf{R})&\\\times s(t-t_1-t_2)\exp[i\omega_0(t_1+t_2)]/(r_1r_2),&\end{aligned} \tag{C15}$$

where

$$\begin{aligned}B(\mathbf{R})=1-\kappa^2/\rho-\kappa(1-1/\rho)[&(\mathbf{R}_s-\mathbf{R})\cdot(\mathbf{R}-\mathbf{R}_i)/(r_1r_2)\\&+\sin\theta_1^{(s)}\sin\theta_2^{(s)}].\end{aligned} \tag{C16}$$

The parameter, $k_{10}=\omega_0/c_1$, is the acoustic wave number at the center frequency, ω_0, and $s(t)$ is the baseband representation of the transmitted pulse. The carrier phase convention has been chosen as $\exp(-i\omega_0 t)$ so that positive time delays correspond to positive phase shifts. The vector $\mathbf{r}_1=\mathbf{r}-\mathbf{r}_i$ connects the source, located at $\mathbf{r}_i=(\mathbf{R}_i,z_i)$, to the scattering patch located at $\mathbf{r}=(\mathbf{R},0)$, and $\mathbf{r}_2=\mathbf{r}_s-\mathbf{r}$ is the vector connecting the scattering patch to the hydrophone situated at $\mathbf{r}_s$. Similarly, $t_1=r_1/c_1$, and $t_2=r_2(1+i\delta)/c_2$ are the corresponding acoustic travel times, with t_2 being complex. This complex time delay, when inserted in Eq. (C15), accounts

for attenuation and pulse dispersion due to losses.[14,15] Pulse dispersion effects are found to be small for the bandwidths of interest, and, in fact, another mechanism causing slight pulse distortion has been ignored. The double time derivative implied by the factor k_1^2 in Eq. (C14) acting on $s(t)\times\exp(-i\omega_0 t)$ produces three terms, and only the largest (containing a factor ω_0^2) is retained. The next largest term, containing a factor ω_0 and a single derivative of $s(t)$ is smaller by an approximate factor $1/\omega_0 t_s$. If this term and the remaining term were retained, there would be a slight change in the waveforms at the buried receivers, equivalent to a slight change in the transmitted waveform. As the Gaussian transmitted waveform is chosen for convenience, there is no reason in the present application to refine this aspect of the simulations. Equation (C15) includes a factor $\Gamma_{12}(\theta_1)$ giving the water–sediment transmission coefficient for a plane wave having real grazing angle $\theta_1=\tan^{-1}(z_i/|\mathbf{R}_i-\mathbf{R}|)$ in the water and a factor $\Gamma_{21}(\theta_2)$ giving the sediment–water transmission coefficient for a plane wave having real grazing angle $\theta_2=\tan^{-1}(|z_s|/|\mathbf{R}-\mathbf{R}_s|)$ in the sediment. The pressure transmission coefficient, $\Gamma_{12}(\theta_1)$, is given by Eq. (C8) and

$$\Gamma_{21}(\theta_2)=2z_{21}/(z_{21}+1), \tag{C17}$$

with

$$z_{21}=\kappa\sin\theta_2/(\rho\sin\theta_1^{(s)}), \tag{C18}$$

where $\theta_1^{(s)}$ is complex and is found using Snell's law for the real grazing angle in the sediment, θ_2, corresponding to $\mathbf{r}_2$:

$$\cos\theta_1^{(s)}=\kappa\cos\theta_2. \tag{C19}$$

In this approach, a double integral over the scattering region must be performed once for each time sample, but, apart from the factor $s(t-t_1-t_2)\exp[i\omega_0(t_1+t_2)]$, the integrand is independent of time and need only be evaluated once for each hydrophone. Additional efficiency is obtained by computing and storing the factor $[k_{10}^2\rho/(4\pi)^2]\Gamma_{12}(\theta_1)\times\Gamma_{21}(\theta_2)B(\mathbf{R})$ for each hydrophone and each grid point, as this factor is the same for each realization and for all times. This approach results in much faster computation than the Fourier synthesis approach.

The double integration in Eq. (C15) was performed by simple summation over a square grid with equal *x*- and *y*-intervals. The size of this grid was chosen so that the integrand reached negligible values at the edges, and the grid interval was conservatively chosen so that an increase by a factor of 2 (that is, the grid is made more sparse) produced negligible change in results. An interval of 1 cm (about 1/7.5 wavelength) was used in the 20-kHz simulations with a 512 ×512 grid. In the 4-kHz simulations, a 512×512 grid with 5-cm interval was used, again giving 1/7.5 wavelength sampling. This grid was also used in the other mid-frequency simulations and, though it was rather sparse at 8 kHz, it should yield acceptable results given the conservative nature of the grid interval criterion. Note that the Bragg condition for downward scattering is met by interface roughness Fourier components having wavelength comparable to the acoustic wavelength (about 20 cm at 8 kHz). The grid interval provides about four samples/wavelength for these components, which should be adequate.

The coherent pressure will be broken into two parts due to the refracted and evanescent waves:

$$p_c(\mathbf{r}_s,t)=p_r(\mathbf{r}_s,t)+p_e(\mathbf{r}_s,t). \tag{C20}$$

The refracted pressure is computed using the stationary phase approximation with loss neglected. Loss is then introduced by allowing the delay time due to propagation in the sediment to be complex and by including the effect of loss on the magnitude of the transmission coefficient. This is equivalent to the usual ray tracing practice in slightly lossy media.

$$\begin{aligned}p_r(\mathbf{r}_s,t)=&\frac{1}{4\pi}s(t-t_1^{(r)}-t_2^{(r)})\exp[i\omega_0(t_1^{(r)}+t_2^{(r)})]\\&\times\sqrt{\rho}\Gamma_{12E}(\theta_1^{(r)})\{|\mathbf{R}_s-\mathbf{R}_i|\tan\theta_2^{(r)}\\&\times[|z_i|/\sin^2\theta_1^{(r)}\\&+|z_s|c_2\sin\theta_1^{(r)}/(c_1\sin^3\theta_2^{(r)})]\}^{-1/2}.\end{aligned} \tag{C21}$$

The function

$$\Gamma_{12E}(\theta_1^{(r)})=\sqrt{1-|1-\Gamma_{12}(\theta_1^{(r)})|^2} \tag{C22}$$

is a real transmission coefficient that neglects the phase shift due to losses. The square of $\Gamma_{12E}(\theta_1)$ is the energy transmission coefficient.

In Eqs. (C21) and (C22), $\theta_1^{(r)}$ is the angle in water for the refracted path connecting the source at $\mathbf{r}_i$, to the receiver at $\mathbf{r}_s$ obtained by solving

$$|\mathbf{R}_s-\mathbf{R}_i|=\cot\theta_1^{(r)}|z_i|+\cot\theta_2^{(r)}|z_s|. \tag{C23}$$

The angles $\theta_1^{(r)}$ and $\theta_2^{(r)}$ are connected by Snell's law with loss neglected

$$\cos\theta_1^{(r)}/c_1=\cos\theta_2^{(r)}/c_2. \tag{C24}$$

This necessitates the solution of a quartic equation in $\cot\theta_1^{(r)}$; only the real, positive root that satisfies Eq. (C23) is retained. The times, $t_1^{(r)}$ and $t_2^{(r)}$, are the real and complex time delays corresponding to the distances, $r_1^{(r)}$ and $r_2^{(r)}$, for the refracted path connecting the source and receiver in the water and sediment, respectively.

The evanescent pressure is

$$\begin{aligned}p_e(\mathbf{r}_s,t)=&s(t-t_1^{(e)}-t_2^{(e)})\exp[i\omega_0(t_1^{(e)}+t_2^{(e)})]\\&\times\Gamma_{12}(\theta_1^{(e)})/(4\pi r_1^{(e)}),\end{aligned} \tag{C25}$$

where

$$r_1^{(e)}=\sqrt{|\mathbf{R}_s-\mathbf{R}_i|^2+z_i^2} \tag{C26}$$

is the distance from the source to a point on the mean (flat) interface immediately above the receiver at $\mathbf{r}_s$, and

$$t_1^{(e)}=r_1^{(e)}/c_1, \tag{C27}$$

$$t_2^{(e)}=\kappa\sin\theta_2^{(e)}|z_s|/c_1, \tag{C28}$$

$$\sin\theta_1^{(e)}=|z_i|/r_1^{(e)}, \tag{C29}$$

with the complex angle $\theta_2^{(e)}$ obtained from Snell's law,

$$\cos\theta_1^{(e)}/c_1=\cos\theta_2^{(e)}/c_2. \tag{C30}$$

The evanescent contribution is set to zero if the incident angle, $\theta_1^{(e)}$, is greater than the critical angle, $\cos^{-1}(c_1/c_2)$. Note that when the incident angle is less than the critical angle, $\sin\theta_2^{(e)}$ is purely imaginary and $t_2^{(e)}$ is almost purely imaginary. This imaginary time, when inserted in Eq. (C25), gives the exponential decay with depth associated with the evanescent wave.

[1] N. P. Chotiros, ''Biot model of sound propagation in water-saturated sand,'' J. Acoust. Soc. Am. **97**, 199–214 (1995).

[2] E. I. Thorsos, D. R. Jackson, J. E. Moe, and K. L. Williams, ''Modeling of subcritical penetration into sediments due to interface roughness,'' in *High Frequency Acoustics in Shallow Water*, edited by N. G. Pace *et al.* (NATO SACLANT Undersea Research Centre, La Spezia, Italy, 1997), pp. 563–569.

[3] J. E. Moe, E. I. Thorsos, D. R. Jackson, and K. L. Williams, ''The effect of roughness on acoustic penetration of the seafloor as given by a fluid-fluid perturbation model and comparison with recent sediment penetration experiments,'' J. Acoust. Soc. Am. **97**, 3315(A) (1995).

[4] J. L. Lopes, ''Observations of anomalous acoustic penetration into sediments at shallow grazing angles,'' J. Acoust. Soc. Am. **99**, 2473(A) (1996).

[5] H. J. Simpson and B. H. Houston, ''A synthetic array measurement of a fast compressional and a slower wave in an unconsolidated water-saturated porous medium,'' J. Acoust. Soc. Am. **102**, 3210(A) (1997).

[6] A. Maguer, E. Bovio, W. L. J. Fox, E. Pouliquen, and H. Schmidt, ''Mechanisms for subcritical penetration into a sandy bottom: Experimental and modeling results,'' J. Acoust. Soc. Am. (to be published).

[7] N. P. Chotiros, A. M. Mautner, A. Lovik, A. Kristensen, and O. Bergem, ''Acoustic penetration of a silty sand sediment in the 1–10-kHz band,'' IEEE J. Ocean Eng. **22**, 604–615 (1997).

[8] D. R. Jackson and A. N. Ivakin, ''Scattering from elastic sea beds: First-order theory,'' J. Acoust. Soc. Am. **103**, 336–345 (1998).

[9] A. N. Ivakin and D. R. Jackson, ''Effects of shear elasticity on sea bed scattering: Numerical examples,'' J. Acoust. Soc. Am. **103**, 346–354 (1998).

[10] A. A. Maradudin, T. Michel, A. R. McGurn, and E. R. Mendez, ''Enhanced backscattering of light from a random grating,'' Ann. Phys. **203**, 255–307 (1990).

[11] E. I. Thorsos, ''The validity of the Kirchhoff approximation for rough surface scattering using a Gaussian roughness spectrum,'' J. Acoust. Soc. Am. **83**, 78–92 (1988).

[12] R. D. Stoll, *Sediment Acoustics*, Vol. 26 in Lecture Notes in Earth Sciences, edited by S. Bhattacharji *et al.* (Springer-Verlag, Berlin, 1989), p. 32.

[13] E. I. Thorsos and D. R. Jackson, ''The validity of the perturbation approximation for rough surface scattering using a Gaussian roughness spectrum,'' J. Acoust. Soc. Am. **86**, 261–277 (1989).

[14] J. E. Moe, ''Near and far-field acoustic scattering through and from two dimensional fluid-fluid rough interfaces,'' Technical Report No. APL-UW TR 9606, Applied Physics Laboratory, University of Washington, October 1996.

[15] J. E. Moe and D. R. Jackson, ''Near field scattering through and from a two-dimensional fluid-fluid rough interface,'' J. Acoust. Soc. Am. **103**, 275–287 (1998).

[16] E. I. Thorsos, ''Acoustic scattering from a 'Pierson–Moskowitz' sea surface,'' J. Acoust. Soc. Am. **88**, 335–349 (1990).

[17] N. P. Chotiros, ''High frequency bottom penetration: Panama City experiment analysis III,'' Technical Report No. ARL-TR-91-18, Applied Research Laboratories, University of Texas at Austin, July, 1991.

[18] L. M. Brekhovskikh, *Waves in Layered Media* (Academic, San Diego, 1980), Chap. 4.

[19] S. Stanic, K. B. Briggs, P. Fleischer, R. I. Ray, and W. B. Sawyer, ''Shallow-water high-frequency bottom scattering off Panama City, Florida,'' J. Acoust. Soc. Am. **83**, 2134–2144 (1988).

[20] P. D. Mourad and D. R. Jackson, ''High frequency sonar equation models for bottom backscatter and forward loss,'' in Proceedings of OCEANS '89 (IEEE Press, New York, 1989), Vol. 4, pp. 1168–1175. Spectral parameters for Table I in the current article were based on measured values given in Figs. 7 and 9 in Ref. 20. Two values are listed in these figures for each parameter: the first was obtained using model equations, and the second is a fit to site measurements.

[21] D. R. Jackson, E. I. Thorsos, and J. E. Moe, ''Far field considerations in boundary scattering,'' in *Shallow-Water Acoustics*, edited by R. Zhang and J. Zhou (China Ocean, Beijing, 1997), pp. 297–302.

[22] N. P. Chotiros, personal communication.

[23] D. J. Wingham, ''The dispersion of sound in sediments,'' J. Acoust. Soc. Am. **78**, 1757–1760 (1985).

Localization using Bartlett matched-field processor sidelobes

Aaron M. Thode, W. A. Kuperman, G. L. D'Spain, and W. S. Hodgkiss
Marine Physical Laboratory, Scripps Institution of Oceanography, San Diego, California 92093-0205

(Received 8 May 1998; revised 28 April 1999; accepted 20 September 1999)

Ambiguity surface sidelobes generated by the Bartlett matched-field processor (MFP) shift location with frequency. This sidelobe shift can be viewed as a continuous trajectory in a range-frequency plane at a fixed depth, where the trajectories converge to the correct source range for a perfectly matched surface. In isovelocity or bottom-interacting environments the sidelobe trajectories are straight lines that converge to the true range at zero frequency, while environments with upward-refracting sound-speed profiles have trajectories that asymptotically converge as the frequency approaches infinity. This behavior can be explained by the theory of waveguide invariants, which predict the local behavior of interference maxima/minima of acoustic intensity in the frequency-range plane. As the ambiguity surface of the Bartlett matched-field processor has a physical interpretation in terms of a time-reversed acoustic field, with the sidelobes analogous to local interference maxima, these invariant concepts can be reformulated for application to MFP. These interference trajectories are demonstrated to exist in simulations, broadband source tows, and a type A blue whale vocalization. Sidelobe trajectories also exist in the range-depth plane, but they contain no information about the correct source depth. An appendix demonstrates how these sidelobe properties can be exploited when combining ambiguity surfaces through use of gradient and Radon transform information. The resulting range estimators demonstrate better peak-to-sidelobe ratios than a simple incoherent average. [S0001-4966(00)01001-8]

PACS numbers: 43.30.Pc, 43.30.Sf [DLB]

INTRODUCTION

This paper shows that sidelobes of the Bartlett matched-field processor (MFP) contain information about both the source location and the waveguide environment. The derivation of these properties is a straightforward extension of the acoustic invariant concept as first developed by Chuprov[1] and extended in subsequent papers.[2,3] These sidelobe properties are demonstrated to exist in both simulations and data.

Bartlett ambiguity surfaces typically are incoherently averaged across frequency when performing matched-field processing on a broadband source.[4] This method assumes that the true source location at each frequency remains fixed, while the sidelobes will appear at different locations at different frequencies, and thus will be suppressed by the averaging. This shift of sidelobe location with frequency can be viewed as a continuous trajectory in a range-frequency plane, where the depth is fixed and the Bartlett surfaces are generated at small increments of frequency. These trajectories form patterns that converge to the true source range and their shape is dependent on the type of waveguide being modeled.

Section I presents the derivation of these trajectories in the range-frequency plane for perfectly matched, range-independent environments. Section II provides examples of these patterns in simulation and data. In Appendix A we address the behavior of sidelobe trajectories with ambiguity surface depth. Finally, in Appendix B we discuss two simple postprocessing methods for improving the peak-to-sidelobe performance of frequency-averaged Bartlett surfaces, using these sidelobe properties. This appendix will also demonstrate that the correct range of a source can be recovered from sidelobe information alone.

I. DERIVATION OF SIDELOBE TRAJECTORIES IN THE RANGE-FREQUENCY PLANE

In this section the Bartlett surfaces will be assumed to be generated from range-independent, perfectly matched environments. The case of mismatched MFP surfaces is the subject of later work.

At ranges greater than a few water depths, a source at depth z_s and range R will produce a pressure field at a depth z_n that can be expressed as a sum of normal modes.[5]

$$p(z_n,z_s,R,\omega)=p(z_n)=\frac{ie^{-i\pi/4}}{\rho(z_s)\sqrt{8\pi R}}\sum_l U_l(\omega,z_s)U_l(\omega,z_n)\frac{e^{i\xi_l(\omega)R}}{\sqrt{\xi(\omega)_l}}, \tag{1}$$

where ξ is the horizontal wave number of the lth mode, and n is the index of the receiving hydrophone along a vertical array. Similarly, a normalized MFP replica generated by a hypothetical source at range, depth (r,z) will have the form

$$\hat{p}(z_n,z,r,\omega)=\hat{p}(z_n)=N\sum_l \hat{U}_l(\omega,z)\hat{U}_l(\omega,z_n)\frac{e^{i\hat{\xi}_l(\omega)r}}{\sqrt{\hat{\xi}_l(\omega)r}}, \tag{2}$$

where N is a normalization constant. The complex pressure field received across a vertical array of hydrophones can be expressed as a vector, each element representing the field detected by a single receiving hydrophone. The Bartlett surface can be expressed as the power of the inner product between the vectors formed from (1) and (2):[4]

$$B(r,\omega,z)=\frac{|\Sigma_n p(z_n)\hat{p}^*(z_n)|^2}{\Sigma_n|p(z_n)|^2\Sigma_n|\hat{p}(z_n)|^2}. \tag{3}$$

For the case of a perfectly matched Bartlett processor, the expression can be simplified by assuming that the aperture of the array is sufficient to exploit the orthogonality of the modes:

$$\sum_n (\Delta z)U_l(\omega,z_n)\hat{U}_m(\omega,z_n)/\rho(z_n)=\delta_{lm}. \tag{4}$$

This approximation yields the following formula for the Bartlett ambiguity surface:

$$\begin{aligned} &B(z_s,z,r,R,\omega)=N\sum_{l,m} P_l P_m \cos(\hat{\chi}_{lm}r-\chi_{lm}R),\\ &\hat{\chi}_{lm}=\hat{\xi}_l-\hat{\xi}_m, \quad \chi_{lm}=\xi_l-\xi_m,\\ &P_i=U_i(\omega,z_s)U_i(\omega,z)/\sqrt{\xi_i}. \end{aligned} \tag{5}$$

The hatted variables represent the modeled environment, and the $r^{(-1/2)}$ terms have been merged with the normalization constant. Written this way, it is obvious that with the depth z fixed, the Bartlett function will show a series of interference maxima and minima, with the maxima corresponding to sidelobe locations. In order to locate the contours of constant correlation in the range-frequency plane, the total differential of the Bartlett surface is taken, following Brekhovskikh:[3]

$$dB=\frac{\partial B}{\partial r}dr+\frac{\partial B}{\partial \omega}d\omega=0, \tag{6}$$

where ω is the frequency of the source. Thus an expression for the slope of the contour is obtained:

$$\begin{aligned} &\frac{\partial \omega}{\partial r}=-\frac{\partial B/\partial r}{\partial B/\partial \omega},\\ &\frac{\partial B}{\partial r}\cong\sum_{l,m} P_l P_m \hat{\chi}_{lm}\sin(\hat{\chi}_{lm}r-\chi_{lm}R),\\ &\frac{\partial B}{\partial \omega}\cong\sum_{l,m} P_l P_m\left[r\frac{\partial \hat{\chi}_{lm}}{\partial \omega}-R\frac{\partial \chi_{lm}}{\partial \omega}\right]\sin(\hat{\chi}_{lm}r-\chi_{lm}R). \end{aligned} \tag{7}$$

To first order the mode shapes have been assumed independent of frequency, and the cylindrical spreading terms have been neglected. The expressions χ and $\delta\chi/\delta\omega$ can be redefined in terms of modal phase and group velocities c_p and c_g:

$$\chi_{lm}=\omega\left[\frac{1}{c_p^l}-\frac{1}{c_p^m}\right]\equiv\omega\Delta(1/c_p), \tag{8a}$$

$$\frac{\partial\chi_{lm}}{\partial\omega}=\left[\frac{1}{c_g^l}-\frac{1}{c_g^m}\right]\equiv\Delta(1/c_g). \tag{8b}$$

Following Brekhovskikh,[3] the phase slowness can be expressed as a Taylor expansion of the group slowness:[1]

$$\frac{1}{c_p^l}=\frac{1}{c_p^m}+\left(\frac{\Delta(1/c_p)}{\Delta(1/c_g)}\right)_{\omega,l,m}\left[\frac{1}{c_g^l}-\frac{1}{c_g^m}\right]. \tag{9}$$

Now assume that the number of modes in the system is large enough that mode order can be considered a continuous variable. Then, in the continuous limit, one can define the following quantity:

$$\beta\equiv-\frac{d(1/c_p)}{d(1/c_g)}. \tag{10}$$

This term, labeled the acoustic invariant by Chuprov,[1] is argued to be independent of mode order and frequency, provided that the frequency band in question is far from most modal cutoff frequencies. Equivalently stated, β is constant if the group velocities of a waveguide environment can be expressed as an explicit function of modal phase velocity only. Two standard examples of β that can be derived analytically are an isovelocity waveguide, and a so-called n^2 profile. These two cases will appear in the specific examples in Sec. II.

For an isovelocity waveguide with a perfectly reflecting bottom, the following relation holds:

$$c_p c_g=c^2, \tag{11}$$

where c is the speed of sound of the medium. Thus the phase velocity does not explicitly depend on mode order or frequency. Using Eqs. (10) and (11), β is

$$\beta=\cos^2\theta\approx 1, \tag{12}$$

where θ, the effective ray angle of the mode with respect to the horizontal, is small. This relationship applies to many shallow-water environments, even if the sound-speed profile is not strictly isovelocity.

Another example is a waveguide with a linear variation in the square index of refraction, i.e.,

$$n^2(z)=c_0^2/c_1^2=1-az, \tag{13}$$

where c_0 represents the surface sound speed. Note that a linear sound-speed profile is a special case of this form wherein $az\ll 1$. The group and phase velocities[1] are related by

$$c_g=\frac{3c_p}{2+(c_p/c_0)^2}. \tag{14}$$

The β for this environment can be written as

$$\beta=\frac{-3}{2-(c_p/c_0)^2}\approx -3, \tag{15}$$

where c_p has been assumed approximately equivalent to c_0.

These expressions for β are only approximate. In reality, different combinations of modes at different frequencies will show slightly different values of β. Also, a single environment can contain mode groups that have properties of both Eqs. (12) and (15). For example, a shallow-water environment with an upward-refracting profile may have low-frequency mode groups that obey Eq. (12), but once the frequency becomes large enough that a group of modes becomes trapped in the waveguide, Eq. (15) will become relevant. However, for the rest of this paper, β will be assumed constant for a particular environment.

Combining Eqs. (7)–(10) allows several terms that are independent of mode number to be factored outside the summations. Terms with an explicit dependence on mode num-

ber then cancel and an expression for the slope of a constant-correlation contour in the Bartlett range-frequency plane can be derived:

$$\frac{\partial \omega}{\partial r} = \beta \frac{\omega}{r - R}. \tag{16}$$

This differential equation can be solved for the curves of constant Bartlett intensity:

$$\omega = C(r - R)^{\beta}, \tag{17}$$

where C is a constant of the integration, independent of r. Because $\beta \approx 1$ is a good approximation for shallow-water waveguides, the trajectories in these environments are straight lines that converge to $r = R$, which is the true range.

To determine the value of the constant in (17) for shallow-water environments, the following approximation can be made for low-order modes in an ideal waveguide:[2]

$$\chi_{lm} \cong \frac{(l^2 - m^2) c \pi^2}{\omega D^2}, \tag{18}$$

where D is the depth of the waveguide. Since the distance between interference maxima generated between modes l and m is $2\pi/\chi_{lm}$, interference maxima will occur at ranges r where the following relationship holds:

$$r - R = \frac{2\pi k}{\chi_{lm}}, \quad k = 0, \pm 1, \pm 2, \ldots . \tag{19a}$$

The resulting expression for the Bartlett sidelobe trajectories in an ideal waveguide becomes

$$\omega = \frac{(l^2 - m^2) c \pi}{2kD^2}(r - R),$$

$$l, m = 1, 2, 3 \ldots, \quad k = 0, \pm 1, \pm 2, \ldots . \tag{19b}$$

The behavior of sidelobes with respect to ambiguity surface depth is discussed in Appendix A.

II. EXAMPLES

This section provides four examples of MFP sidelobe trajectories. Subsection A describes a simulation of an acoustic source in a shallow water environment. Subsection B uses data recorded in a similar environment from a broadband source tow off San Diego in 1994. Subsection C contains a simulation of a source in 2-km-deep water with a idealized Arctic profile (linear sound-speed profile). Lastly, subsection D demonstrates the patterns generated by a blue whale call recorded off the Southern California Channel Islands in 1996.

A. Shallow-water environmental simulation

This example uses an optimized geoacoustic model of the shallow water environment off Point Loma, San Diego, and is shown in Fig. 1. The model was constructed in conjunction with the SWellEx series of experiments performed in the area,[6,7] and consists of a basement of mudstone topped by a 26-m layer of slit. Using the normal-mode model Kraken,[8] a broadband acoustic source was modeled at 30-m depth and a range of 6 km from a 64-element vertical array placed in the lower half of the water column. No noise was added to the model. A series of Bartlett MFP ambiguity surfaces was generated using the same environment from 10 to 100 Hz. The results are stacked and viewed along the fixed depth of 30-m, and the resulting plot is shown in Fig. 2. The sidelobe trajectories clearly indicate the correct source range. The fact that the trajectories are straight indicates that a nearly isovelocity model has been used to generate the replica vectors.

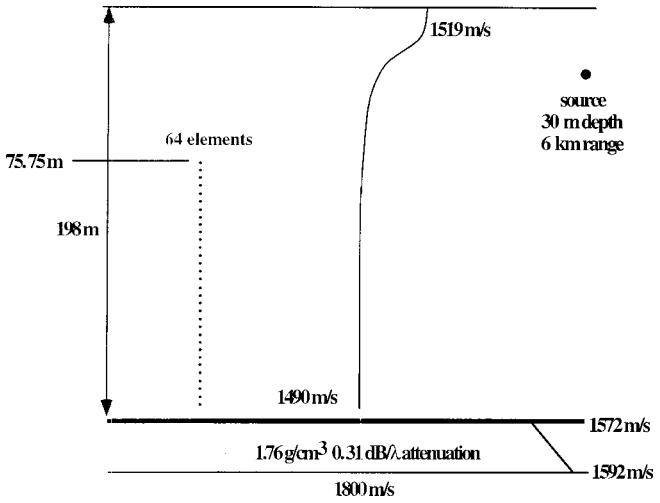

FIG. 1. Schematic of the shallow-water waveguide environment used in the simulations. The environment represents summer conditions off Point Loma, San Diego, CA. An acoustic source is simulated at 30-m depth and 6-km range, and its signal is received across a 120-m aperture vertical array with 64 elements spaced 1.875 m apart. The top element is at 75.75-m depth. The bottom is a 26-m layer of silt overlying a half-space of mudstone.

Figure 3 demonstrates that these interference patterns converge to the correct range when viewed along a fixed depth different from the true source depth. In this figure, the range-frequency plane was made along a fixed depth of 158 m, or 128 m deeper than the correct source depth.

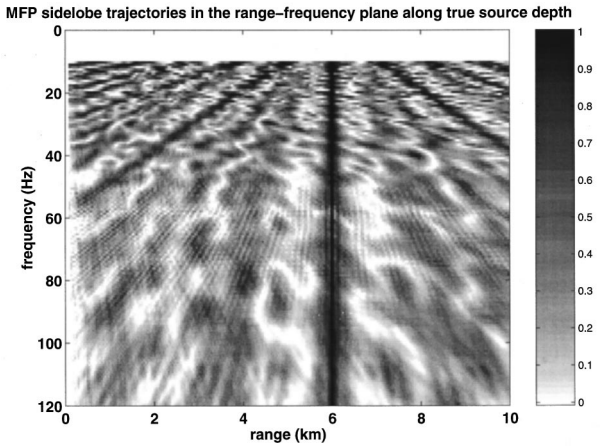

FIG. 2. The MFP sidelobe trajectories generated using the environment in Fig. 1, where $\beta \sim 1$. The intensity scale is a linear measure of the normalized Bartlett power. The replicas were generated using Kraken, using all 64 array elements. Low-order mode interferences are visible across the entire frequency band; higher-order mode interferences generate partial trajectories, because the sidelobes change depth with frequency. The vertical line indicates the presence of the mainlobe. All trajectories converge to the correct source range.

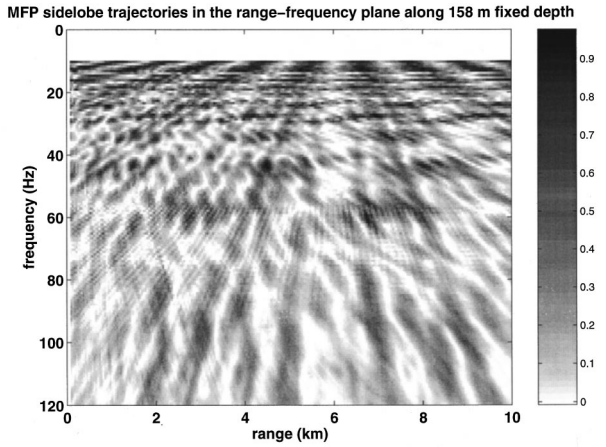

FIG. 3. Same as Fig. 2 but the range-frequency plane is viewed along an ambiguity surface depth of 158 m or 128 m deeper than the true source. While the mainlobe is absent, the sidelobe trajectories still converge to the true source range.

B. Data from shallow-water environment

This example uses data from a source tow performed during the SWellEx-3 experiment conducted off the coast of San Diego[6] beginning on 27 July 1994 at 18:00 GMT. The J13 source projected pseudo-random noise at a 30-m depth over a 85–150-Hz bandwidth with a frequency-integrated source level of 170 dB *re* 1 μPa @ 1 m. The source was fixed in place during this time, and the bathymetry profile between the source ship and the vertical array was mostly range independent. The environmental model of Fig. 1 was used to produce the replicas for the MFP and a slice of the range-frequency plane at the correct source depth is shown in Fig. 4. As theory predicts, the sidelobes converge to the correct range of 6 km.

C. Arctic profile simulation

This example was constructed to demonstrate sidelobe trajectories in an environment where $\beta=-3$. Figure 5 outlines the model, which consists of a 2-km-deep ocean with an upward-refracting sound-speed profile and a bottom half-space of 1700 m/s. A 120-m aperture vertical array covering less than 10% of the water column is placed in the water, recording a signal produced by a source at 30-m depth and 6-km range. The poor coverage of the water column violates the orthogonality condition in Eq. (4), yet the result presented in Fig. 6 demonstrates that at low frequencies the sidelobe trajectories behave as predicted by Eq. (17). At higher frequencies the orthogonality condition fails and the trajectories blur and merge. For environments where β is negative, the trajectories asymptotically converge to the correct range at infinite frequency. This is a consequence of the fact that modal group velocity increases with phase velocity for this environment [Eq. (14)]. It is intriguing that a successful localization can be achieved with little vertical water column coverage.

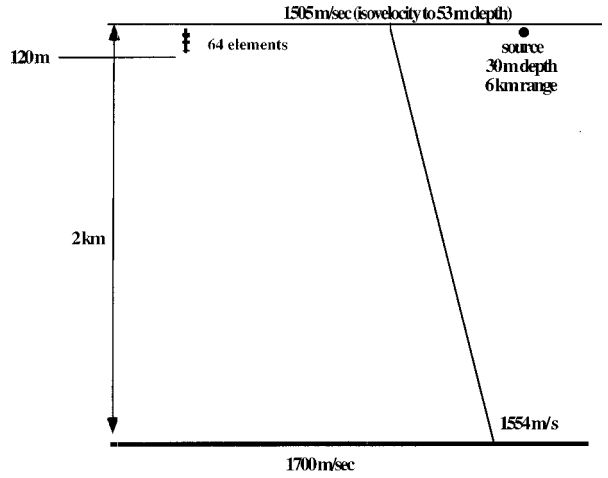

FIG. 5. Schematic of upward-refracting environment used for $\beta=-3$ simulation. The sound-speed profile is isovelocity at 1505 m/s to 53 m, then increases linearly to 1554 m/s at 2-km depth. The simulated source and receivers are at the same location as in Fig. 1. Note that the vertical array covers less than 10% of the water depth. The bottom consists of a 1700-m/s half-space.

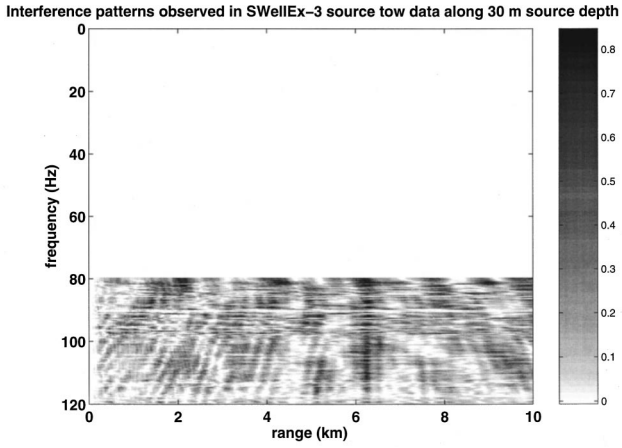

FIG. 4. Sidelobe trajectories generated from ocean acoustic data along a fixed depth of 30 m. The replicas from Fig. 1 were correlated with spectral estimates derived from 2.73 s of data recorded during the SWellEx-3 experiment. The true source location is 30-m depth and 6-km range. The signal consisted of pseudo-random noise with a bandwidth of 85–120 Hz.

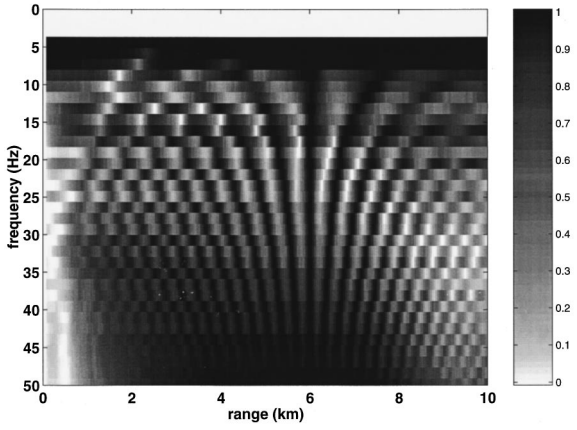

FIG. 6. The MFP sidelobe trajectories for the environment outlined in Fig. 5. The ambiguity function is sliced along the modeled source depth. In this type of environment the sidelobe trajectories converge asymptotically to the correct range as $f\rightarrow\infty$. The blurring of the individual trajectories above 40 Hz is likely due to insufficient water column coverage by the vertical array.

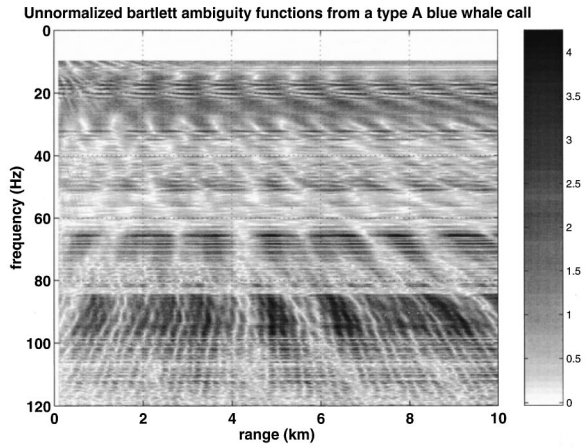

FIG. 7. Unnormalized backpropagated PE ambiguity range-frequency surface from a type A blue whale vocalization, recorded on Julian Day 203 at 20:52 GMT. Ten seconds of data have been used to form an averaged cross-spectral density matrix from which the eigenvector with the greatest eigenvalue was selected for backpropagation. The call contains energy bands at 17, 32, 48, 65, 95, and 110 Hz. The water depth was 128 m and the bottom speed was estimated to be ~1650 m/s.

D. Blue whale vocalization

This final example was obtained from processing a blue whale sound recorded off San Miguel Island in Southern California in 1996.[9] This vocalization is the ''type A'' call typically made by Northeastern Pacific populations[10] and generally lasts 15–20 s. It is a pulsed call with pulse period 0.7 s, containing energy in the 15–120-Hz frequency range. Resonances near 17, 34, 51, 65, 95, and 110 Hz result in a considerable variation in signal-to-noise ratio (SNR) with frequency. Typically the strongest frequency bands are between 17–20 Hz and 85–95 Hz.

The geoacoustic environment and sound-speed profile in this area were estimated using standard geoacoustic inversion methods,[11–13] on several high SNR calls. A very fast back-propagated PE algorithm[14] then was used to perform localization on other type A calls, including the one shown here. Holding the source depth constant at 15 m (a typical calling depth for the animal), the resulting range-frequency MFP plane for this call is shown in Fig. 7.

Two features from this figure merit further discussion. The first is the well-defined sidelobe patterns that lie between 85 and 120 Hz and which seem to converge to ~5-km range. The signal quality is worse at lower frequencies, but the convergence pattern is still visible in the frequency band between 65 and 75 Hz. Below 60 Hz a second feature appears: interference maxima and minima that converge to the range-frequency origin. This type of convergence often appears when processing signals with significant noise, or surfaces with severe environmental mismatch, particularly mismatch in vertical array tilt. A full explanation of this feature is involved and will be the subject of future work.

Ever when the relatively high SNR region between 85–120 Hz is incoherently averaged, the output reveals only a weak mainlobe with numerous high-amplitude sidelobes. In Appendix B we demonstrate how the sidelobe interference structure apparent in Fig. 7 can be exploited to improve the performance of the final averaged range estimate.

III. CONCLUSION

Broadband Bartlett matched-field processing sidelobes contain source location and environmental information, which is readily apparent when viewed in the range-frequency plane along a fixed ambiguity surface depth. The existence and shapes of the sidelobe trajectories can be derived using waveguide invariant theory. Several examples of these patterns using both simulation and ocean acoustic data have been presented. One intuitive explanation for this sidelobe behavior is that the Bartlett ambiguity surface has a physical interpretation in terms of a time-reversed acoustic field.[15] From this viewpoint, MFP sidelobes are analogous to zones of constructive interference in the ocean and should therefore contain useful information about the source location.

Two interesting research avenues follow from this fundamental observation. The first is that this sidelobe behavior can be exploited to improve the mainlobe-to-sidelobe performance of a broadband Bartlett processor. The exact details of how this can be achieved are complex and thus have been relegated to Appendix B. The second avenue concerns the effect of environmental mismatch and ocean noise on the structure of these patterns. As hinted in Sec. II D, the results are intriguing and are intimately intertwined with the concept of MFP ''mirages.'' [16] A description of these properties will have to described separately.

ACKNOWLEDGMENTS

The authors would like to thank MPL technical staff and the crew of the R/P FLIP for making the collection of the data used in this paper possible. The contributions of Hee Chun Song and James Murray are particularly appreciated. This research was funded by the Office of Naval Research Grant No. N00014-97-0593 and N00014-96-0603.

APPENDIX A: DEPTH DEPENDENCIES OF SIDELOBE SHIFTS

In addition to the range shift discussed earlier. MFP sidelobes display spatial shifts along the depth axis with changes in frequency. According to the Wantzel–Kramers–Brillouin (WKB) approximation, a mode can be represented as a sum of $\exp(\pm i\gamma Z)$ terms where γ is the depth-dependent modal vertical wave number associated with a depth-dependent ray arrival angle $\theta = a\tan(\gamma/\xi)$. If the acoustic energy intercepting a vertical array is associated with a particular arrival angle, one of the exponential terms dominates and the Bartlett surface can be written as

$$B(r,z) \approx \sum_{l,m} \cos[\alpha_{lm}(z-z_s) + \chi_{lm}(r-R)],$$

$$\alpha_{lm} \equiv \gamma_l \gamma_m, \tag{A1}$$

from which can be derived

$$\frac{\partial \omega}{\partial z} = -\frac{\partial B/\partial z}{\partial B/\partial \omega}, \quad \frac{\partial B}{\partial z} = \sum_{l,m} \alpha_{lm} P_l P_m \sin(\chi_{lm}[r-R]),$$
$$\frac{\partial B}{\partial \omega} = \sum_{l,m} \frac{\partial \chi_{lm}}{\partial \omega}(r-R) P_l P_m \sin(\chi_{lm}[r-R]). \tag{A2}$$

Note that $\delta\gamma d\omega = 0$ reflecting the fact that mode shape is independent of frequency at this order (e.g., $\gamma_m = m\pi/D$ in an ideal waveguide). In order to factor the double sums, a relation is needed between α and $\delta\gamma/\delta\omega$. A Taylor series expansion can be constructed between the wave numbers:[1]

$$\gamma_l = \gamma_m + (\xi_l - \xi_m)\frac{d\gamma}{d\xi}. \tag{A3}$$

Simplifying

$$\frac{\alpha_{lm}}{\chi_{lm}} = \frac{d\gamma}{d\xi} = \frac{d\sqrt{k^2-\xi^2}}{d\xi} = -\frac{\xi}{\gamma} = -\cot\theta, \tag{A4}$$

one obtains, using (8),

$$\alpha_{lm} = \frac{d\gamma}{d\xi} = \beta\omega\cot\theta\frac{\partial\chi_{lm}}{\partial\omega}, \tag{A5}$$

which, when combined with (A2), yields

$$\frac{\partial\omega}{\partial z} = -\beta\frac{\omega}{r-R}\cot\theta. \tag{A6}$$

One sees that sidelobes trajectories generated by high-order modes experience greater shifts in the vertical than those from low-order modes. These shifts are not large. The low-order sidelobes generated by a 50 Hz source in a 200-m-deep ideal waveguide will shift around 3-m depth per kilometer range. Note also that the true source depth does not appear anywhere in Eq. (A6), a consequence of the fact that $\delta\gamma/\delta\omega \approx 0$. Therefore, the sidelobe trajectories in the z-ω plane should contain no source depth information.

The trajectories generated by the lower-order modes shift vertically only a small amount with a change in frequency. Thus, in Fig. 2 the low-order trajectories remain visible over a large frequency range at 30-m depth. By contrast, the finer-scale intensity trajectories shift considerably in the z direction across this frequency range so only partial trajectories for the high-order modes are visible.

APPENDIX B: TWO ALGORITHMS FOR IMPROVING RANGE ESTIMATION USING SIDELOBES

One potential application investigated here is the possibility of ''enhancing'' incoherent broadband Bartlett averaging by exploiting knowledge of sidelobe behavior. The first method uses a simple trick to effectively cancel all sidelobes during averaging, and the second method uses the Radon transform to estimate the range at which all sidelobe trajectories converge. Using this latter approach it is possible to obtain a correct range estimate without using the mainlobe, which suggests that the mainlobe does not even have to lie on the plot.

To illustrate both methods, a simple, abstracted model of a MFP range-frequency plane is shown in Fig. B1(a). The model represents a shallow-water environment wherein the

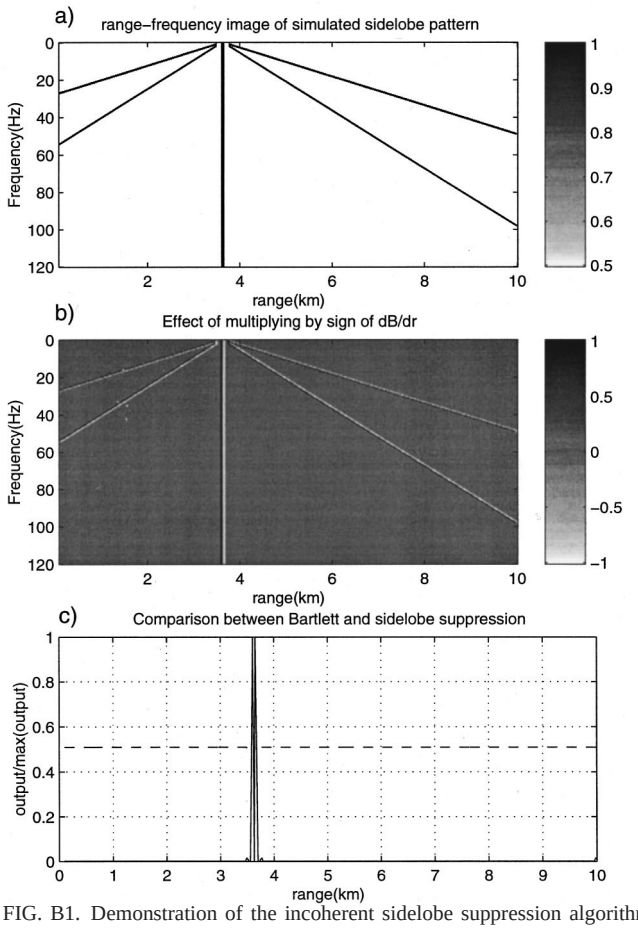

FIG. B1. Demonstration of the incoherent sidelobe suppression algorithm. (a) Simple abstracted model of sidelobe trajectories in a MFP range-frequency plane. Each trajectory is three range bins wide and is assigned a value of one. Other range-frequency bins are assigned a value of 0.5. (b) Effect of multiplying a by $(\partial B(r,\omega)/\partial r)B(r,\omega)$. (c) Result of averaging along the frequency axis in (b).

mainlobe lies at 3.75 km and four sidelobes converge to the correct range at 0 Hz from angles of ± 45 and ± 62 degrees from the vertical. At every frequency the sidelobes and mainlobe are three range bins wide and each of these bins is assigned a value of one. During standard broadband MFP processing, the ambiguity surfaces are averaged [i.e., an integration is performed along a vertical line for each range bin in Fig. B1(a)]

$$\overline{B}_0(r) = \frac{\Delta\omega}{\omega 2 - \omega 1}\int_{\omega 1}^{\omega 2} B(r,\omega)\, d\omega, \tag{B1}$$

where B represents the Bartlett ambiguity function and $\Delta\omega$ is the width of a frequency bin in rad/s. Examination of this example suggests that if positive values could be assigned to the left edge of each trajectory and negative values to the right edge, then the sidelobe at frequency $\omega + \delta\omega$ will tend to cancel out the sidelobe at frequency ω. An easy way to achieve this is to multiply each ambiguity surface by the sign of its derivative with respect to r:

$$\overline{B}_1(r) = \frac{\Delta\omega}{\omega 2 - \omega 1}\left\| \int_{\omega 1}^{\omega 2} \operatorname{sgn}\left(\frac{\partial B(r,\omega)}{\partial r}\right) B(r,\omega)\, d\omega \right\|. \tag{B2}$$

The effect of performing this operation on our sample surface is shown in Fig. B1(b). As desired, every trajectory now

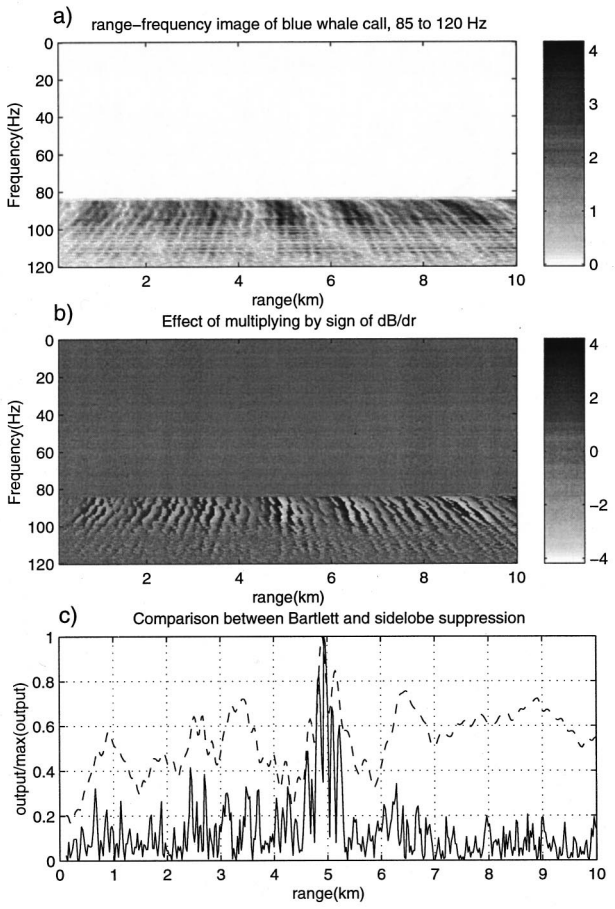

FIG. B2. Demonstration of the incoherent sidelobe suppression algorithm on the data shown in Fig. 7. (a) Reproduction of Fig. 7, retaining only the frequencies above 85 Hz. (b) Effect of multiplying by $(\partial B(r,\omega)/\partial r)B(r,\omega)$. (c) Comparison of Eq. (B2) (solid line) with the standard Bartlett average given in B1 (dashed line). Both curves are normalized relative to their maximum values.

has a value of $+1$ on the left edge and -1 on the right. When integrated vertically, every positive value on the sidelobe is canceled by a negative at an adjacent frequency, except for the vertical trajectory (mainlobe). In that case, all the positive and negative values add constructively and the sharp spike displayed in Fig. B1(c) is obtained.

Figure B2 illustrates the effectiveness of this simple postprocessing on the blue whale ambiguity function shown in Fig. 7. Figure B2(a) shows the 85–120-Hz: band region of this function. Applying Eq. (B2) produces the surface in Fig. B2(b), and averaging across frequency then yields the solid-line output in Fig. B2(b). For comparison the regular Bartlett average from Eq. (B1) is plotted as a dashed line. Both plots are normalized with respect to their maximum values. It is clear that Eq. (B2) generates a result with lower peak-to-sidelobe ratios (2.5) than regular averaging (1.25), while requiring little additional computational effort.

A more exotic approach than sidelobe suppression involves estimating the range at which the sidelobe trajectories converge—a ''sidelobe beamformer.'' If a shallow water environment is being modeled so that $\beta \approx 1$, then the sidelobe trajectories are straight lines. Thus, the integral from Eq. (B2) can be modified to allow the integration path to transect

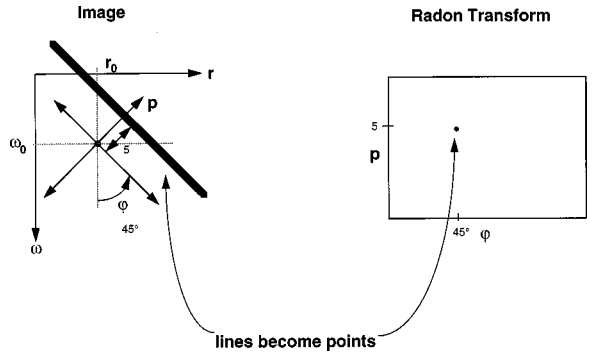

FIG. B3. Illustration of the Radon transform. Given a reference point (r_0,ω_0), the transform outputs line integrals as a function of rotation angle φ from the vertical and unitless distance p along the p axis. Thus straight lines in the image are transformed into points in the (p,φ) plane.

the image along any angle φ with respect to the frequency (vertical) axis beginning from the point $(r,0)$:

$$\overline{B}_2(r,\varphi) \equiv \frac{1}{N(r,\varphi)} \left\| \int_0^T B_e(r(t),\omega(t))\, dt \right\|,$$

$$B_e(r,\omega) \equiv \mathrm{sign}\left(\frac{\partial B(r,\omega)}{\partial r} \right) B(r,\omega), \tag{B3}$$

$$r(t) = r + (\Delta r)t \sin\varphi, \quad \omega(t) = (\Delta r)t \cos\varphi.$$

Here, t is a unitless parameter of integration, Δr is a scaling factor that converts t into range units, and $\Delta\omega$ is an equivalent scaling factor for frequency. When $\varphi = 0$, this formula reduces to Eq. (B2) and represents an integration along a possible mainlobe at range r. This incoherent output is now a function of two parameters, source range and integration angle with respect to that range. Theoretically, the normalization factor N will also be a function of range and φ, but experience has shown that N can be treated as constant.

Equation (B3) is a special case of the Radon transform[17,18] which often is found in image processing:

$$\begin{aligned} &\Re(p,\varphi,B_e(r,\omega)) \\ &\quad \cong \Re(p,\varphi)|_{r0,\omega 0} \\ &\quad = \int_{-\infty}^{\infty} B_e\left(\frac{p\cos\varphi + t\sin\varphi}{\Delta r}, \frac{p\sin\varphi + t\cos\varphi}{\Delta\omega} \right) dt \Bigg|_{r0,\omega 0}. \end{aligned} \tag{B4}$$

Here p represents a unitless distance from a reference point $(r0,\omega 0)$ in an image, which is typically the center pixel. Figure B3 provides an illustration of the Radon transform. Given the reference point, the transform outputs image line integrals as a function of both a rotation angle φ around the reference and a displacement p along the rotated axis. Put another way, the line integral is performed along a line perpendicular to this rotated axis and crosses the axis a distance p away from the reference. Therefore, a line lying at an angle φ with respect to the ω axis and passing a minimum distance of p units away from the reference point will be transformed into a point at the coordinates (p,φ).

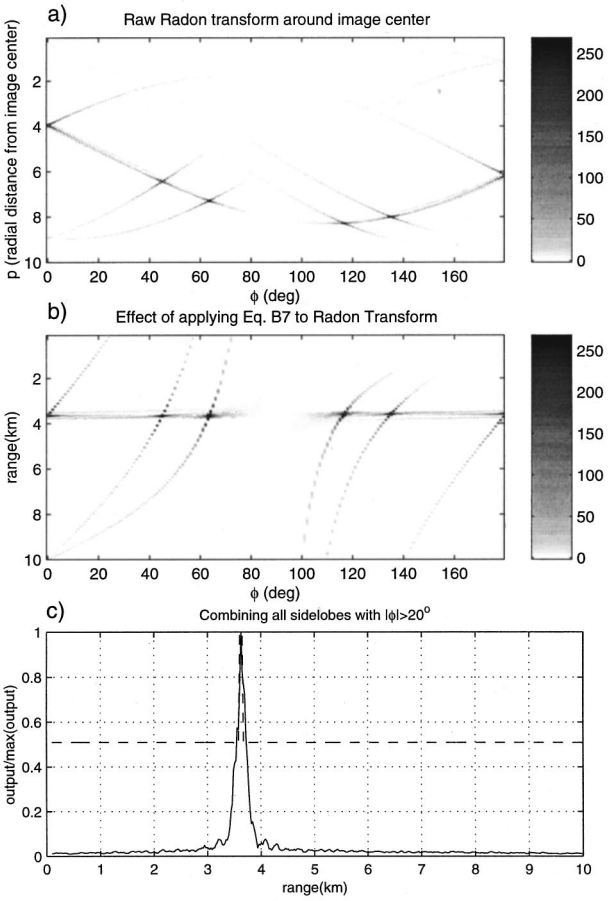

FIG. B4. Demonstration of sidelobe beamforming on the simulated surface shown in Fig. B1(a). (a) Radon transform of the surface performed around the center of the image (5 km, 0). Note that the five lines are now points in the (p,ω) plane. (b) Effect of applying Eq. (B7) to the radon surface. Each point (r,φ) now represents a line integral that intersects the range axis at r, along an angle φ relative to the frequency axis. (c) Effect of averaging the beamformed sidelobes [summing along the φ axis in (b)]. The mainlobe has not been included in the average and the output is normalized by its maximum.

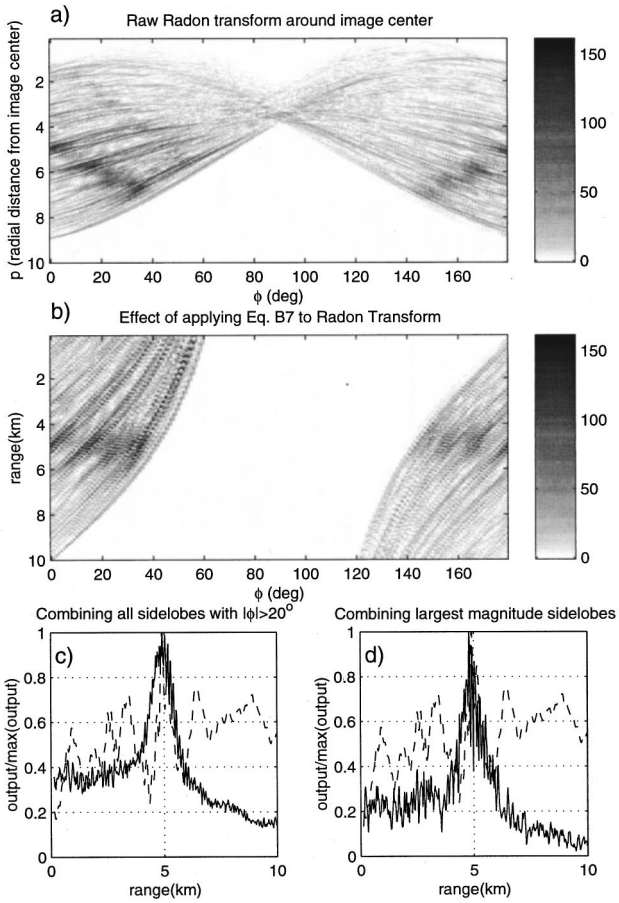

FIG. B5. Demonstration of sidelobe beamforming on backpropagated MFP data. (a) Radon transform of Fig. B2(a). (b) Output of Eq. (37), using transform on (a). (c) Effect of averaging all sidelobe beams with $|\varphi|>20$ degrees (solid line). The incoherent Bartlett result is overlain for comparison (dashed line). Both curves are normalized by their maximum values. (d) Same as (c) but using only sidelobes whose maximum amplitude exceeds a cutoff value. This is an attempt to eliminate angles along which there is no sidelobe energy.

Comparison of Eqs. (B4) and (B3) shows that the sidelobe beamformer can be expressed as a radon transform around the point $(r,0)$:

$$\overline{B}_2(r,\omega)=\|\Re(0,\omega)|_{r,0}\|. \tag{B5}$$

It might appear that if the MFP function has N range bins, then N Radon transforms would have to be conducted, which would be a time consuming process. In practice, only a single transform of the range-frequency plane is required, because a Radon transform produced around one reference point (r,ω) can be related to a transform around another reference point (r',ω') via a ''translation theorem:'' [17]

$$\Re(p,\varphi)|_{(r',\omega')}=\Re(p-\mathbf{d}\cdot\mathbf{a},\varphi)|_{(r_0,\omega_0)},$$
$$\mathbf{d}=\left(\frac{r'-r_0}{\Delta r},\frac{\omega'-\omega_0}{\Delta\omega}\right),\quad \mathbf{a}=(\cos\varphi,\sin\varphi). \tag{B6}$$

Thus the final expression for the sidelobe beamformer becomes

$$\overline{B}_2(r,\varphi)=\|\Re(p(r,\varphi),\varphi)|_{r_0,\omega_0}\|,$$
$$p(r,\varphi)=\left(\frac{r-r_0}{\Delta r}\right)\cos\varphi+\left(\frac{\omega_0}{\Delta\omega}\right)\sin\varphi. \tag{B7}$$

Figure B4 illustrates this process on the idealized image displayed in Fig. B1(a): The raw Radon transform is shown in Fig. B1(c) where the five lines in the (r,ω) plane have been transformed into the five points in the (p,φ) plane. The reference point for this transform was the center of the image at approximately 5 km and 60 Hz. Applying Eq. (B7) yields the output shown in Fig. B4(b); which shows the convergence ranges of all the sidelobe trajectories. The mainlobe integration is revealed by the bright spot shown near $\varphi=0°$, and the sidelobes by the remaining four points. It is clear that all trajectories converge to 3.75 km. This can be displayed by averaging along the phi axis and plotting the final result in Fig. B4(c). In this case, Fig. B4(c) does not include the mainlobe, which is accomplished by only averaging beams with $|\varphi|>20$ degrees. The mainlobe has been excluded to illustrate that the sidelobes alone contain enough information to obtain the true range.

Figure B5 applies the sidelobe beamformer to Fig. B2(a), using only frequency components greater than 85 Hz. The Radon transform is shown in Fig. B5(a): and the application of Eq. (B7) produces Fig. B5(b). The effects of averaging all beams for $|\varphi|>20$ degrees is shown in Fig. B5(c), and the result of using a more selective average (using only the largest-amplitude beams) is shown in Fig. B5(d). As before, the standard Bartlett average is plotted alongside the new beamformer's output. Clearly the sidelobe beamformer also displays a superior mainlobe sidelobe ratio, at the cost of a broadened peak around the correct range. This broadening seems to occur for two reasons: first, β for shallow-water environments is not exactly one so the sidelobe trajectories will not be exactly straight lines. Second, the peak width produced by a beamformed sidelobe will be on the order of a sidelobe width; which tends to be wider than a mainlobe. The reason for this difference is that the sidelobe is generated by constructive interference between a few modes, while the mainlobe is generated by constructive interference between all modes, including the high-order modes that permit finer resolution.

In summary, the structures contained in the sidelobe trajectories can be incorporated into incoherent sidelobe suppression or sidelobe beamforming algorithms that improve the peak/sidelobe ratio of the final averaged estimator. However, the latter approach only works for modeling shallow-water environments where $\beta-1$, is more computationally intensive, and has a broader peak in range.

[1] S. D. Chuprov, ''Interference Structure of a Sound Field in a Layered Ocean,'' in *Akustika Okeana Sovremennoe Sostoyanie (Ocean Acoustics, Current State)*, edited by L. M. Brekhovskikh and I. B. Andreevoi (Nauka, Moscow, 1982), pp. 71–91.

[2] G. A. Grachev, ''Theory of acoustic field invariants in layered waveguide,'' Acoust. Phys. **39**, 33–35 (1994).

[3] L. M. Brekhovskikh and Y. Lysanov, *Fundamentals of Ocean Acoustics*, 2nd ed. (Springer-Verlag, Berlin, 1991).

[4] A. B. Baggeroer, W. A. Kuperman, and H. Schmidt, ''Matched field processing: Source localization in correlated noise as an optimum parameter estimation problem,'' J. Acoust. Soc. Am. **83**, 571–587 (1988).

[5] F. B. Jensen, W. A. Kuperman, M. B. Porter, and H. Schmidt, *Computational Ocean Acoustics* (American Institute of Physics, New York, 1994).

[6] N. O. Booth, P. A. Baxley, J. A. Rice, P. W. Schey, W. S. Hodgkiss, G. L. D'Spain, and J. J. Murray, ''Source localization with broad-band matched-field processing in shallow water,'' IEEE J. Ocean Eng. **21**, 402–412 (1996).

[7] R. T. Bachman, P. W. Schey, N. O. Booth, and F. J. Ryan, ''Geoacoustic databases for matched-field processing: Preliminary results in shallow water off San Diego, California,'' J. Acoust. Soc. Am. **99**, 2077–2085 (1996).

[8] M. B. Porter, ''The KRAKEN normal mode program,'' SACLANTCEN, Memorandum SM-245, 1991.

[9] A. M. Thode, G. L. D'Spain, and W. A. Kuperman, ''Matched-field processing and geoacoustic inversion of blue whale vocalizations,'' J. Acoust. Soc. Am. (accepted).

[10] W. C. Cummings and P. O. Thompson, ''Underwater sounds from the blue whale, *Balaenoptera musculus*,'' J. Acoust. Soc. Am. **50**, 1193–1198 (1971).

[11] P. Gerstoft, ''Inversion of seismoacoustic data using genetic algorithms and a posteriori probability distributions,'' J. Acoust. Soc. Am. **95**, 770–782 (1994).

[12] P. Gerstoft, ''Inversion of acoustic data using a combination of genetic algorithms and the Gauss–Newton approach,'' J. Acoust. Soc. Am. **97**, 2181–2190 (1995).

[13] P. Gerstoft, ''SAGA Users Guide 2.0, an inversion software package,'' SACLANT Undersea Research Centre SM-333, 1997.

[14] F. D. Tappert, L. Nghiem-Phu, and S. C. Daubin, ''Source Localization using PE method,'' J. Acoust. Soc. Am. Suppl. 1 **78**, 530 (1985).

[15] W. A. Kuperman, W. S. Hodgkiss, H. C. Song, and T. Akal, ''Phase conjugation in the ocean: Experimental demonstration of an acoustic time-reversal mirror,'' J. Acoust. Soc. Am. **103**, 25–40 (1998).

[16] G. L. D'Spain, J. J. Murray, W. S. Hodgkiss, N. O. Booth, and P. W. Schey, ''Mirages in shallow water matched field processing,'' J. Acoust. Soc. Am. **105**, 3245–3265 (1999).

[17] S. R. Deans, *The Radon Transform and Some of its Applications* (Wiley, New York, 1983).

[18] J. R. Fricke and A. B. Baggeroer, ''Modal-slowness analysis of plate vibrations,'' J. Acoust. Soc. Am. **92**, 3228–3238 (1992).

On analytic design of loudspeaker arrays with uniform radiation characteristics

Ronald M. Aarts and A. J. E. M. Janssen
Philips Research Laboratories, 5656 AA Eindhoven, The Netherlands

(Received 5 May 1999; accepted for publication 18 September 1999)

Some notes on analytical derived loudspeaker arrays with uniform radiation characteristics are presented. The array coefficients are derived via analytical means and compared with so-called maximal flat sequences known from telecommunications and information theory. It appears that the newly derived array, i.e., the quadratic phase array, has a higher efficiency than the Bessel array and a flatter response than the Barker array. The method discussed admits generalization to the design of arrays with desired nonuniform radiating characteristics. © *2000 Acoustical Society of America.* [S0001-4966(00)00901-2]

PACS numbers: 43.38.Ar, 43.38.Hz [SLE]

INTRODUCTION

There is a vast amount of literature on loudspeaker arrays radiating sound in a particular direction; see, e.g., Ref. 1 and the classical paper, Ref. 2. The directional characteristics of such an array—when depicted graphically—assume the form of a major or principal lobe and several minor or secondary lobes. Instead of making the array directive, one may desire an array having a directional response proportional to that of a single loudspeaker with a gain factor as high as possible. The application of such an array could be to address an audience, where a single loudspeaker does not radiate sufficient power while it is desired that the perception of the listeners is independent of their position to the array. The calculation of the array coefficients is the topic of the present paper. In Ref. 3 another approach is followed where the problem is treated as an approximation to a continuous distributed sensor.

The directional response of a linear loudspeaker array depends on the coefficients assigned to the individual loudspeakers. The sound pressure of a loudspeaker array with N identical equally spaced loudspeakers is given by

$$p(\Omega,\theta,r)=A(\omega,\theta)R(\omega,r)\sum_{l=-M}^{M} x_l e^{il\Omega}, \tag{1}$$

where θ is the angle of observation, $A(\omega,\theta)$ the directional response of a single loudspeaker, d is the distance between the loudspeakers, $\Omega=\omega d\sin(\theta)/c$, ω is the radial frequency of the sound, r is the common distance to the array, c is the velocity of sound, $R(\omega,r)=r^{-1}e^{-i\omega r/c}$, x_l is the coefficient for the lth loudspeaker, and $N=2M+1$ is the number of loudspeakers. We assume here that the observation point is in the far field so that $r\gg c/\omega$ and $r\gg 2Md$.

In general terms the paper discusses various loudspeaker array coefficients: one based on Bessel functions, a newly derived array called ''the Quadratic Phase array,'' and coefficients with optimal autocorrelation properties known from telecommunications and information theory [such as Barker, Huffman, and binary maximally flat (MF) sequences].[4] The paper is organized as follows: In Sec. I we consider arrays in which we take as the array coefficients $x_l=J_l(z)/\sigma$, with appropriately chosen z and σ which we call ''Bessel array.'' Using the asymptotics of the Bessel functions we indicate values for z (depending on their length N) such that the resulting array has a good trade-off between spectral flatness and efficiency [see Eq. (15) for the definition of efficiency]. In Sec. II we present some considerations that lead to new arrays which we call the ''Quadratic Phase arrays.'' These arrays turn out to have efficiencies much better than the Bessel arrays, and a better spectral flatness than the Barker and other binary arrays ($|x_l|=1$). Contrary to Barker arrays (which have at most 13 elements), there are no length limitations for Quadratic Phase arrays. Moreover, the coefficients of the Quadratic Phase arrays are easy to compute since they are given in analytical form. Such a thing does not hold for Barker, binary (MF) sequences, and (nonbinary) Huffman arrays, for which an exhaustive search must be done to find the coefficients.

I. BESSEL ARRAY

It was suggested by N. V. Franssen and elaborated by W. Kitzen[5] to use $x_l=J_l(z)/\sigma$. Here J_l is the Bessel function of the first kind of order l, the argument z is to be chosen appropriately, and σ is a normalization constant such that $\max|x_l|=1$. Using the generating function of $J_l(z)$ [Ref. 6, Eq. 9.1.41]:

$$e^{z(t-1/t)/2}=\sum_{l=-\infty}^{\infty} t^l J_l(z), \tag{2}$$

with $t=e^{i\Omega}$, Eq. (1) can for $M\to\infty$ be written as

$$p(\Omega,\theta,r)_{M\to\infty}=A(\omega,\theta)Re^{iz\sin\Omega}. \tag{3}$$

Equation (3) shows that, apart from a phase factor, the array exhibits a directional response proportional to that of a single loudspeaker, i.e.,

$$|p(\Omega,\theta,r)_{M\to\infty}|_{\text{Bessel}}=|A(\omega,\theta)R|. \tag{4}$$

It appears from Eq. (4) that the amplitude of the sound pressure does not depend on z. However, for practical Bessel arrays, where M is finite, a judicious choice of z is necessary. Since the right-hand side of Eq. (3) has an absolute value

independent of Ω, the array exhibits as an acoustical all-pass filter. It is known from psycho-acoustic theory that the human ear is not very sensitive to phase distortion, whence ignoring the phase factor does not cause serious problems.

To obtain a finite sum as in Eq. (1), the infinite series of Eq. (2) must be truncated at both sides to a finite length M, the coefficients x_l must be normalized by a suitable factor σ, and an appropriate fixed value of z must be chosen, depending on M and such that the modulus of the sound pressure is, to a good approximation, independent of Ω. These topics, including the influence of the truncation, are discussed below.

A. Calculation of appropriate fixed value of z

The error introduced due to the truncation of the infinite sum in Eq. (2) is equal to

$$\Delta = e^{iz\sin\Omega} - \sum_{l=-M}^{M} J_l(z) e^{il\Omega}. \tag{5}$$

This error will influence the array behavior when we use the truncated version of Eq. (2) to implement Eq. (1). Clearly Δ depends on Ω, and we are interested in particular in the maximal error $\hat{\Delta}$. For fixed $z = z_F \approx M$, and Ω such that the error is maximal, it can be shown from the asymptotics of the Bessel functions [Ref. 6, Sec. 9.3] that

$$|\hat{\Delta}| \approx \int_{\gamma}^{\infty} \mathrm{Ai}(s)\, ds, \tag{6}$$

where

$$\gamma = \left(\frac{2}{M+1}\right)^{1/3} (M+1-z_F), \tag{7}$$

and $\mathrm{Ai}(s)$ is an Airy function [Ref. 6, Sec. 10.4]. As to the choice of γ there is a trade-off between taking large $\gamma \geqslant 0$ so that $|\hat{\Delta}|$ is small and taking small $\gamma \geqslant 0$ so that the efficiency of the array is large.

A value suggested by N. V. Franssen was $z_F = M - 1$, which yields $0.5 \leqslant \gamma \leqslant 1.4$ for $100 \geqslant M \geqslant 5$. Using the asymptotic expansion [Ref. 6, Eq. 10.4.82]

$$\int_0^x \mathrm{Ai}(s)\, ds \sim \frac{1}{3} - \frac{1}{2}\pi^{-1/2} x^{-3/4} e^{-(2/3)x^{3/2}}, \tag{8}$$

we obtain

$$|\hat{\Delta}| \approx \tfrac{1}{2}\pi^{-1/2}\gamma^{-3/4} e^{-(2/3)\gamma^{3/2}}; \tag{9}$$

the right-hand side of Eq. (9) is plotted in Fig. 1.

Using $\gamma = 2^{1/3}$ gives $\hat{\Delta} \approx 0.1$ and $z_F = M + 1 - (M+1)^{1/3}$. The advantage of this ''rule of thumb'' value of z_F over Franssen's rule is that it yields an error $\hat{\Delta}$ independent of M.

B. Calculation of the scaling factor

To compare the performance of the array with that of a single loudspeaker, we normalize the coefficients by a scalar σ such that the largest coefficient in the summation of Eq. (2) is equal to unity. Therefore the value of ν where the maximum value of $J_\nu(z_F)$ occurs, must be calculated.

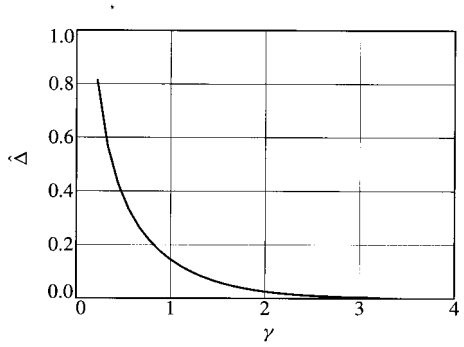

FIG. 1. The approximate truncation error $\hat{\Delta}$ vs γ; see Eq. (9).

To that end we use the asymptotic expansion [Ref. 6, Eq. 9.3.23] of J_ν in the transition region where J_ν takes its largest value (see Fig. 2). Thus

$$J_\nu(\nu + a\nu^{1/3}) \approx (2/\nu)^{1/3}\,\mathrm{Ai}(-2^{1/3}a). \tag{10}$$

It appears that $\mathrm{Ai}(-2^{1/3}a)$ has maximum value ≈ 0.5357 at $a \approx 0.8086$. Solving $z_F = \nu + a\nu^{1/3}$ for ν, keeping in mind that $\nu \approx z_F$, gives

$$\nu \approx z_F - a(z_F)^{1/3}. \tag{11}$$

Using Eq. (10), with ν as in Eq. (11) and $z_F \approx M = (N-1)/2$, yields

$$J_\nu(z_F) \approx 0.85 N^{-1/3}. \tag{12}$$

When we truncate the infinite sum in Eq. (2) to $\pm M$ and use

$$\sigma_M = J_\nu(z_F) \tag{13}$$

as a normalization factor, the maximum coefficient is equal to one. Finally, the summation of Eq. (1) becomes

$$|p(\Omega,\theta,r)|/\sigma_M \approx |A(\omega,\theta)R| \sum_{l=-M}^{M} J_l(z_F)/\sigma_M. \tag{14}$$

C. The efficiency of Bessel arrays

The efficiency of an array is defined as

$$\eta = E/(N \max|x_i|^2), \tag{15}$$

with normalization factor $E = \Sigma_{l=-M}^{M}|x_l|^2$. Using the addition theorem for the Bessel functions [Ref. 6, Eq. 9.1.76], the efficiency for a Bessel array is

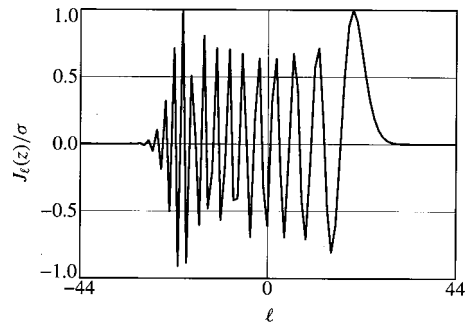

FIG. 2. $J_l(z)/\sigma$ vs l, with $\sigma = 0.243$ and $z = 70/\pi$.

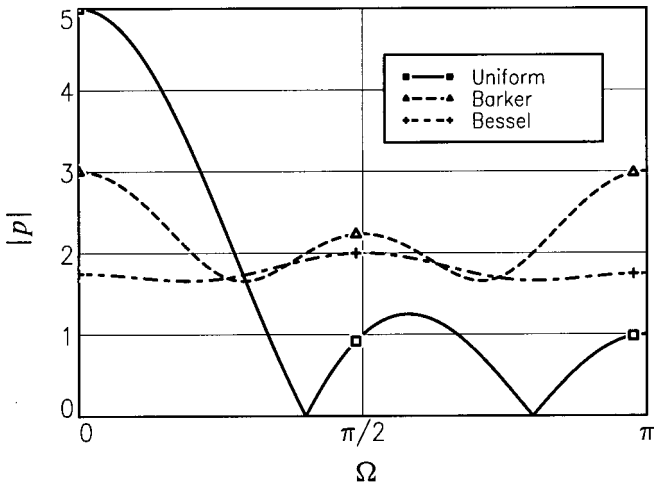

FIG. 3. Comparison of the directional dependency ($|p/R|$ vs Ω) of a uniform, a Barker and a Bessel array, with $N=5$ loudspeakers ($M=2$).

$$\eta_{\text{Bessel}} \approx 1/(N\sigma_M^2), \tag{16}$$

so that for large N [using Eqs. (12)–(13)]

$$\eta_{\text{Bessel}} \approx 1.4N^{-1/3}. \tag{17}$$

Clearly, for large Bessel arrays the efficiency decreases.

D. Comparison with Barker arrays

A different approach for array beam forming was given in Refs. 7 and 8 where, instead of Bessel coefficients, Barker sequences were used, where $x_l = \pm 1$. The largest Barker sequence known is for $N=13$. A comparison between a uniform, a Barker, and a Bessel array, using $z=z_F$ as presented at the end of Sec. I A, with five loudspeakers, is shown in Fig. 3.

One can state in general that for loudspeaker array applications, sequences with good autocorrelation properties (that is, having a high efficiency and a maximally flat amplitude spectrum) are superior to Bessel arrays with respect to efficiency. This can be shown easily as follows.

The spectrum X_j of such sequences x_l is approximately flat, or $\forall j |X_j| \approx C$. Using Parseval's theorem we have

$$E = \sum_l |x_l|^2 \approx C^2, \tag{18}$$

and with Eq. (15) we can write

$$C \approx \sqrt{N\eta}. \tag{19}$$

For a flat binary sequence ($\eta=1$) we get

$$C_F = \sqrt{N}, \tag{20}$$

and for a Bessel sequence [using Eq. (17)]

$$C_B \approx 1.18N^{1/3}. \tag{21}$$

Using the above and considering C as the gain factor of using N loudspeakers instead of one, we can write for an array with coefficients equal to a flat binary sequence

$$|p(\Omega,\theta,r)|_{\text{binary}} = \sqrt{N}|A(\omega,\theta)R|, \tag{22}$$

while for Bessel coefficients we get

$$|p(\Omega,\theta,r)|_{\text{Bessel}} = 1.18N^{1/3}|A(\omega,\theta)R|. \tag{23}$$

Here we see that to obtain an array with a directional response proportional to that of one single loudspeaker, the increase in sound pressure level is, at best, proportional to $\sqrt{N}$. To obtain a level of 10 times a single loudspeaker we need approximately 600 loudspeakers in a Bessel configuration.

II. QUADRATIC PHASE ARRAY

In the previous section it was shown that the gain of Bessel arrays is of the order of $N^{1/3}$ [Eq. (23)]. This power of 1/3 is due to the relatively large values of the Bessel coefficients (for fixed z) in the transition region. In order to improve the efficiency, the following idea was developed. The reason for using the Bessel array was that the generating function of $J_l(z)$ [see Eq. (2)] is the Fourier transform of the sequence $(J_l(z))_l$. Substitution of $t=e^{i\theta}$ in Eq. (2) gives

$$e^{iz\sin\theta} = \sum_{l=-\infty}^{\infty} e^{i\theta l} J_l(z). \tag{24}$$

Applying the inverse Fourier transform to both sides of Eq. (24) gives the integral representation of the Bessel function [Ref. 6, Eq. 9.1.21]:

$$J_l(z) = 1/(2\pi)\int_{-\pi}^{\pi} e^{i(z\sin\theta - l\theta)}\, d\theta. \tag{25}$$

From Eq. (25) one can derive the behavior of $J_l(z)$ for $|l| \leqslant z$ by employing the stationary phase method.[9] It can thus be seen that for values of l with $|l| \approx z$ one must expect $|J_l(z)|$ to be relatively large since $z\sin\theta - l\theta$ has a nearly vanishing second derivative with respect to θ at $\theta=0$ or π for these values of l. Such a thing can be avoided by replacing the $\sin\theta$ in the exponential at the left-hand side of Eq. (24) by a phase function $\phi(\theta)$ for which the second derivative of $z\phi(\theta)$ always stays away from 0. We thus propose to choose $C_l(z)$ such that

$$c(\theta;z) := e^{iz\phi(\theta)} = \sum_{l=-\infty}^{\infty} e^{il\theta} C_l(z), \tag{26}$$

whence

$$C_l(z) = 1/(2\pi)\int_{-\pi}^{\pi} e^{i(z\phi(\theta) - l\theta)}\, d\theta, \tag{27}$$

where

$$\phi(\theta) = (1 - |\theta|/\pi)\,\theta/\pi, \tag{28}$$

with $|\theta| \leqslant \pi$. Thus $c(\theta;z)$ and $C_l(z)$ are a Fourier pair, and since $|c(\theta;z)| = 1$ it is guaranteed that the sequence C_l has a flat spectrum.

We call the sequence C_l the ''Quadratic Phase array.'' It is not easy to calculate the values of C_l directly, but by evaluating Eq. (26), and applying a discrete Fourier transform to this result, the C_l can be computed and are plotted in Fig. 4 (dashed curve). Instead of using a discrete Fourier transform, C_l can be approximated directly, as discussed in the Appendix.

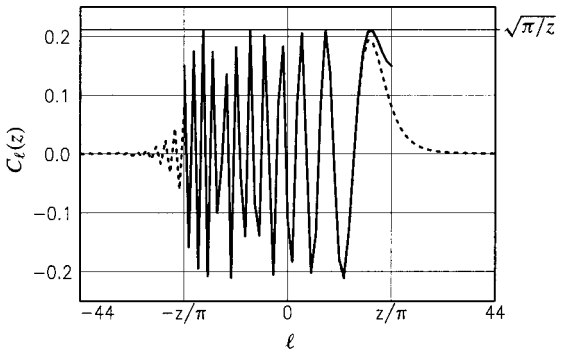

FIG. 4. Exact and approximated sequence C_l for $z=70$. Dashed curve: C_l (exact via a 1024 point FFT). Solid curve: [with Eq. (33)] approximated C_l for $|l|\leqslant z/\pi$.

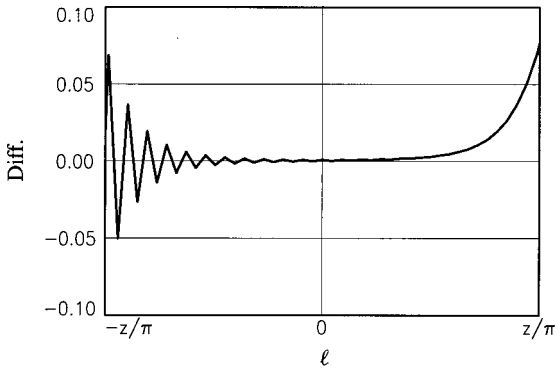

FIG. 5. The difference between the exact and approximated version of C_l (for $z=70$).

As the figure shows, there is no peaking of the sequence C_l in the transition region, as occurred in the Bessel coefficients case. The sequence C_l has a nice compact burstlike behavior. This is an attractive feature because the efficiency will be higher than for the Bessel coefficients.

Using the method of stationary phase,[9] the integral in Eq. (27) when $|l|\leqslant z/\pi$ can be approximated. The stationary points follow from

$$z\phi'(\theta)=l, \tag{29}$$

and using Eq. (28) we obtain

$$\theta_l=\pi^2(1/\pi-l/z)/2. \tag{30}$$

Now we get from the stationary phase method

$$C_l(z)\approx 2\Re\left\{1/(2\pi)e^{i[z\phi(\theta_l)-l\theta_l]}\int_{-\infty}^{\infty}e^{iz\phi''(\theta_l)(\theta-\theta_l)^2/2}\,d\theta\right\}. \tag{31}$$

Then for $0\leqslant l\leqslant z/\pi$ we have $\phi''(\theta)=-2/\pi^2$, and using

$$\int_{-\infty}^{\infty}e^{-\gamma(\theta-\theta_l)^2}\,d\theta=\sqrt{\pi/\gamma}, \tag{32}$$

with $\gamma=-iz\phi''/2$ we finally obtain

$$C_l(z)\approx\sqrt{\pi/z}\cos(z(1-l\pi/z)^2/4-\pi/4). \tag{33}$$

For $-z/\pi\leqslant l\leqslant 0$ we use that $C_{-l}=(-1)^l C_l$.

The approximated sequence C_l [with Eq. (33)] is plotted in Fig. 4 (dotted curve). The difference between the exact and approximated version of C_l is plotted in Fig. 5. The Fourier transform of the approximated C_l [using Eq. (33) without the leading term $\sqrt{\pi/z}$] is plotted in Fig. 6 for $z=70$, together with two Fourier transforms of sequences known from telecommunications and information theory as maximal-efficient Huffman sequence and a maximal-flat binary sequence (MF) [Ref. 4, Table III], respectively, and finally a Bessel array ($z=20.2$). Since the maximal length of a Barker sequence corresponds to $M=6$, the Barker array is not included in the comparison, where we have 45 loudspeakers ($M=22$).

Figure 6 shows that—due to the approximation and truncation of C_l—there appears a ripple in the response. However, it has a good efficiency. If one desires a flatter response, C_l can be obtained by using Eqs. (26) and (28) an FFT, and a smaller value for z_F, however, this is at the expense of a smaller efficiency. The Huffman array has a good performance, but there are neither analytical methods available to calculate the coefficients nor their efficiency, and the efficiency behaves somewhat as an erratic function of array length.

The aim of the proposed quadratic phase array was, as in the case of the Bessel array, to radiate uniformly over the entire Ω range. To meet this end with an efficiency that compares favorably with that of a Bessel array, we have chosen $\phi(\theta)$ such that the envelope of the $C_l(z)$ is approximately constant in the range $|l|\leqslant z$ of interest [see Eq. (33)]. When one prefers a different envelope, this can be achieved by choosing $\phi(\theta)$ in such a way that the desired envelope results in terms of ϕ'' in the same manner as this occurred in Eqs. (31)–(33) for the case of a uniform envelope. This makes the method very flexible and can be implemented even as an adaptive array. We finally observe that our method generalizes in a straightforward way when the desired radiation characteristic is a slowly varying function of Ω, rather than a constant. We intend further investigation on this point.

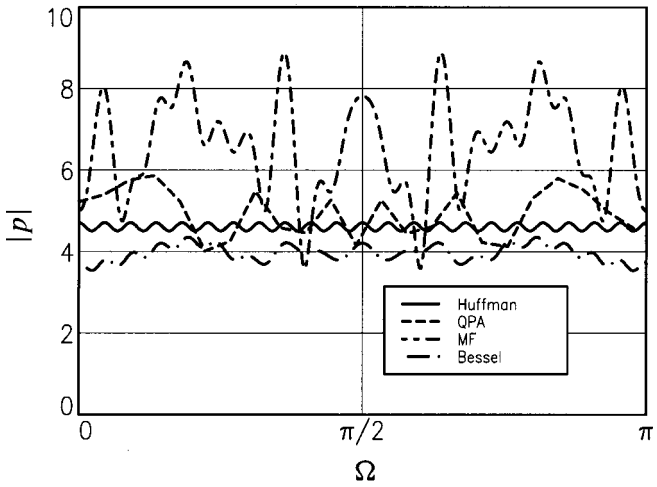

FIG. 6. Comparison of the direction dependency ($|p|$ vs Ω) of a maximal-efficient Huffman sequence, a Quadratic Phase array (QPA, $z=70$) a maximal-flat binary sequence (MF, Ref. 4, Table III), and a Bessel array ($\gamma=2^{1/3}$, $z=20.2$), each with 45 loudspeakers ($M=22$).

TABLE I. Design example of various array types of length $N=13$, with their efficiency η. The first coefficients are given, the others are found by using the skew-symmetry property $C_{-l}=(-1)^l C_l$. MF is the best possible Maximally Flat sequence, the so-called Barker sequence. For the Bessel array $z=5.0$, for the QPA [using Eq. (33)] $z=18.0$.

l	MF	Bessel	QPA
0	−1	−0.454	−0.864
1	1	−0.837	−0.670
2	1	0.119	0.447
3	−1	0.933	1.000
4	1	1.000	0.957
5	−1	0.667	0.778
6	1	0.335	0.735
η	1	0.499	0.628

III. DESIGN EXAMPLE

To gain some insight into the coefficients of the various arrays, a design example is given in Table I for an array with 13 loudspeakers. The table shows that the Quadratic Phase array has a higher efficiency than the Bessel array. The maximally flat sequence (MF) has—because it is a binary array—the maximally attainable efficiency, but does not allow us to trade flatness against efficiency as opposed to Quadratic Phase arrays by varying the value of the parameter z. Using the coefficients of Table I the array responses are calculated and are shown in Figs. 7–9, together with an uniform array Fig. 10 (all coefficients equal to one). The frequency axis in the plots are normalized as

$$\omega_n=\omega d/c. \tag{34}$$

It appears that the newly derived array, the Quadratic Phase array, has a higher efficiency than the Bessel array and a flatter response than the Barker array. The ripple in the MF array (Fig. 7) looks similar as that of the Quadratic Phase array (Fig. 9). However, for the MF array there is a rather strong increase in output for values of Ω in the neighborhood of integer multiples of π (e.g., small values of ω_n or θ). This can be seen more clearly in the plot for the smaller array of Fig. 3. For the larger array ($N=45$) there is for the MF array not such a ridge (see Fig. 6), but the response is a somewhat erratic function of Ω.

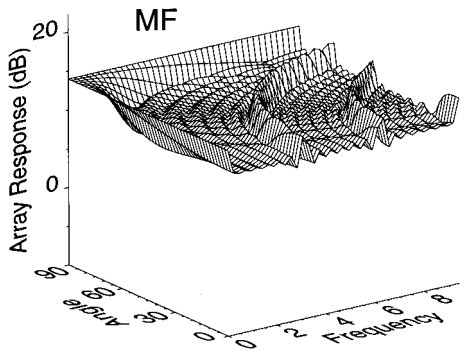

FIG. 7. Design example of an MF array ($N=13$), the best possible Maximally Flat sequence (Barker sequence). Frequencies have been normalized and are expressed in terms of ω_n.

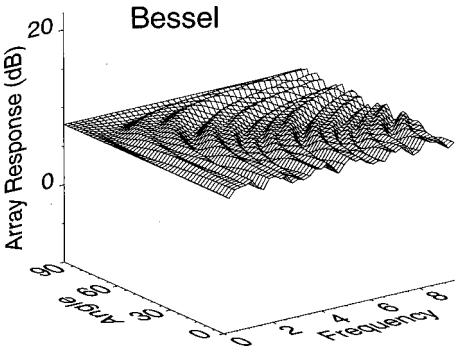

FIG. 8. Design example of a Bessel array ($N=13$, $z=5.0$). Frequencies have been normalized and are expressed in terms of ω_n.

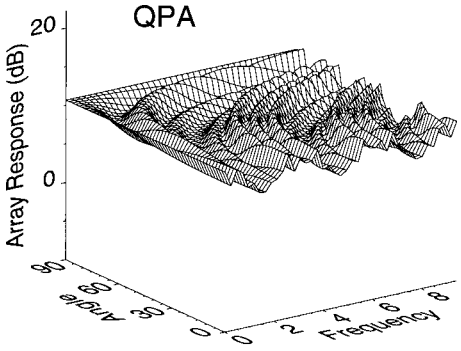

FIG. 9. Design example of a QPA array [using Eq. (33), $N=13$, $z=18.0$]. Frequencies have been normalized and are expressed in terms of ω_n.

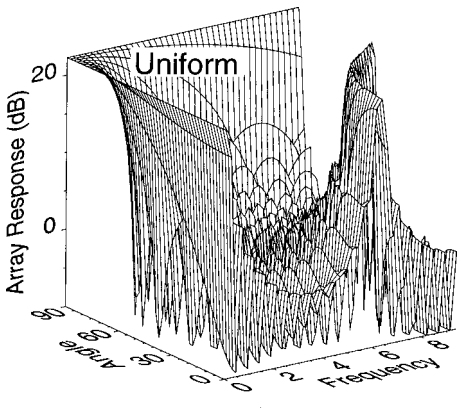

FIG. 10. Design example of a uniform array (all coefficients equal to one, $N=13$). Frequencies have been normalized and are expressed in terms of ω_n.

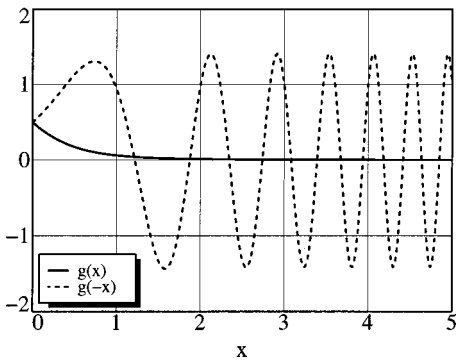

FIG. 11. Auxiliary function $g(x)$ (solid) and $g(-x)$ (dotted).

IV. CONCLUSIONS

It appears that the newly derived array, the Quadratic Phase array, has a higher efficiency than the Bessel array and a flatter response than the Barker array. The Quadratic Phase array and the Bessel array allow for trading flatness against efficiency by varying the value of the parameter z. The proposed method allows generalization of the design of arrays with desired nonuniform radiating characteristics.

APPENDIX: EXPRESSION OF $C_l(z)$ IN TERMS OF THE FRESNEL AUXILIARY FUNCTION

The integral in Eq. (27) can be expressed in terms of the Fresnel integrals and, using the auxiliary function $g(x)$ [see Ref. 6, Eq. 7.3.6], we have

$$C_l(z)=\sqrt{\pi/(2z)}(g(-\omega_l)-(-1)^l g(\omega_{-l})), \tag{A1}$$

where $\omega_l=\sqrt{z/\pi}(1-l\pi/z)$. Accurate asymptotic approximations of $g(x)$ are given in Ref. 6, Eq. 7.3.28. A rational approximation of $g(x)$ for $x\geqslant 0$ is given in Ref. 6, Eq. 7.3.33; for $x<0$ we can write (using Ref. 6, Eqs. 7.3.6, 7.3.17)

$$g(-x)=\cos(\pi x^2/2)+\sin(\pi x^2/2)-g(x). \tag{A2}$$

The function $g(x)$ is plotted in Fig. 11.

[1] R. L. Pritchard, ''Optimum directivity patterns for linear point arrays,'' J. Acoust. Soc. Am. **25**, 879–891 (1953).
[2] S. A. Schelkunoff, ''A mathematical theory of linear arrays,'' Bell Syst. Tech. J. **22**, 80–107 (1943).
[3] D. B. Ward, R. A. Kennedy, and R. C. Williamson, ''Theory and design of broadband sensor arrays with frequency invariant far-field beam patterns,'' J. Acoust. Soc. Am. **97**, 1023–1034 (1995).
[4] T. A. C. M. Claasen, G. F. M. Beenker, and P. W. C. Hermens, ''Binary sequences with a maximally flat amplitude spectrum,'' Philips J. Res. **40**, 289–304 (1985).
[5] W. J. W. Kitzen, ''Multiple loudspeaker arrays using Bessel coefficients,'' Philips Electronic Components & Applications **5**, 200–205 (1983).
[6] M. Abramowitz and I. A. Stegun, *Handbook of Mathematical Functions* (Dover, New York, 1972).
[7] H. Kuttruff and H.-P. Quadt, ''Elektroakustische Schallquellen mit ungebündelter Schallabstrahlung,'' Acustica **41**, 1–10 (1978).
[8] H. Kuttruff and H.-P. Quadt, ''Ebene Schallabstrahlergruppen mit ungebündelter Abstrahlung,'' Acustica **50**, 273–279 (1982).
[9] R. Wong, *Asymptotic Approximations of Integrals* (Academic, New York, 1989).

Plane harmonic waves in orthorhombic thermoelastic materials

J. N. Sharma
Department of Mathematics, Regional Engineering College, Hamirpur (H.P.) 177 005, India

Vinod Kumar
Department of Physics, MLSM College, Sunder Nagar (HP) 174401, India

S. P. Sud
Department of Physics, HP University, Shimla (HP) 171 005, India

(Received 6 October 1998; accepted for publication 14 September 1999)

Keeping in view the increased usage of orthorhombic materials in the development of advanced engineering materials such as fibers and composites and other multilayered media, the aim of the present paper is to give a detailed account of the plane harmonic generalized thermoelastic waves in orthorhombic materials. According to the frequency equation, the four waves, a quasi-longitudinal, two quasi-transverse, and a quasi-thermal wave, can propagate in an orthorhombic crystal. When plane waves propagate along the axis of an orthorhombic solid, then only the longitudinal and thermal waves are coupled, whereas the transverse waves get decoupled from the rest of the motion. For plane waves propagating in one plane of the solid, only the SH wave in that plane remains purely transverse and gets decoupled from the rest of the motion and vice versa. The other three waves are coupled and get modified due to thermal variations and relaxation time. The particle paths and stability of the waves have been discussed and the results verified numerically. These have been represented graphically for single crystals of solid helium and cobalt material. © *2000 Acoustical Society of America.* [S0001-4966(99)06912-X]

PACS numbers: 43.40.At [PJR]

INTRODUCTION

The theory of elastic wave propagation in anisotropic solids is well known.[1] Chadwick and Seet[2] and Chadwick[3] discussed propagation of plane harmonic waves in transversely isotropic and homogeneous anisotropic heat conducting solids, respectively, in the coupled theory of thermoelasticity. Banerjee and Pao[4] and Pao and Banerjee[5] investigated the propagation of plane harmonic waves in homogeneous anisotropic solids and dielectric crystals with thermal relaxation times, respectively. The generalized theory of thermoelasticity developed by Lord and Shulman[6] has been extended to homogeneous anisotropic media by Dhaliwal and Sherief.[7] Sharma,[8] and Sharma and Singh[9] discussed the propagation of thermoelastic waves in transversely isotropic materials and cubic crystals, respectively. Sharma and Sidhu,[10] and Sharma and Singh[11,12] studied the wave propagation in anisotropic solids in generalized theory of thermoelasticity.[7]

Keeping in view the increased usage of orthorhombic materials in the development of advanced engineering materials such as fibers and composites and other multilayered media, the aim of the present paper is to give a detailed account of the plane harmonic generalized thermoelastic waves in orthorhombic materials in the context of a theory developed in Ref. 7. According to the frequency equation, four waves, a quasi-thermal wave, a quasi-longitudinal, and two quasi-transverse waves, can, in general, propagate in an orthorhombic media. When plane waves are propagating along the axis of orthorhombic solid, then only longitudinal and thermal waves are coupled, whereas the transverse wave gets decoupled from the rest of the motion. For plane waves propagating in one of the planes of the solid, only the SH wave in that plane remains purely transverse and gets decoupled from the rest of the motion and vice versa. The other waves are coupled and get modified due to thermal variations and relaxation time. The particle paths have also been discussed and found to be elliptic. The stability of waves is also discussed. The results have been verified numerically and are represented graphically for single crystals of solid helium (He) and cobalt.[2,4]

I. THE PROBLEM AND THE SECULAR EQUATION

We consider an unbounded, homogeneous orthorhombic thermoelastic body at a uniform temperature T_0 in the undisturbed state. The medium is assumed to be subjected to a sudden rise in temperature. Let $\vec{u}(x_1,x_2,x_3,t)=(u_1,u_2,u_3)$ and $T(x_1,x_2,x_3,t)$, be the displacement vector and temperature change, respectively, of the medium at time t. The equations of motion and heat conduction equation in the absence of body forces and heat sources for such materials are[7]

$$c_{11}u_{1,11}+c_{66}u_{1,22}+c_{55}u_{1,33}+(c_{12}+c_{66})u_{2,21}+(c_{13}+c_{55})u_{3,31}-\beta_1 T_{,1}=\rho\ddot{u}_1, \tag{1}$$

$$c_{66}u_{2,11}+c_{22}u_{2,22}+c_{44}u_{2,33}+(c_{23}+c_{44})u_{3,32}+(c_{12}+c_{66})u_{1,21}-\beta_2 T_{,2}=\rho\ddot{u}_2, \tag{2}$$

$$c_{55}u_{3,11}+c_{44}u_{3,22}+c_{33}u_{3,33}+(c_{13}+c_{55})u_{1,13}+(c_{23}+c_{44})u_{2,23}-\beta_3 T_{,3}=\rho\ddot{u}_3, \tag{3}$$

 1063-7834/2000/107(1)/13/$17.00

$$K_1T,_{11}+K_2T,_{22}+K_3T,_{33}-\rho C_e(\dot{T}+\tau_0\ddot{T})$$
$$=T_0\left(\frac{\partial}{\partial t}+\tau_0\frac{\partial^2}{\partial t^2}\right)(\beta_1u_1,_1+\beta_2u_2,_2+\beta_3u_3,_3), \tag{4}$$

where

$$\beta_1=c_{11}\alpha_1+c_{12}\alpha_2+c_{13}\alpha_3, \quad \beta_2=c_{12}\alpha_1+c_{22}\alpha_2+c_{23}\alpha_3,$$

$$\beta_3=\alpha_{13}\alpha_1+c_{23}\alpha_2+c_{33}\alpha_3,$$

c_{ij} are the isothermal elasticities, ρ, C_e, and τ_0 are the density, specific heat at constant strain, and thermal relaxation time, respectively, and K_i and α_i $(i=1,2,3)$ are, respectively, the thermal conductivities and coefficients of linear thermal expansion of the material. Comma notation is used for spatial derivatives and a superposed dot represents differentiation with respect to time.

We may take plane harmonic wave solutions as

$$u_k=U_k\exp\{i\omega(v^{-1}x_pn_p-t)\}, \quad k=1,2,3 \tag{5}$$

$$T=\Theta\exp\{i\omega(v^{-1}x_pn_p-t)\}, \tag{6}$$

where ω is the angular frequency (assumed to be real), v is the phase velocity (in general complex) of the waves, and the unit vector $\vec{n}=(n_1,n_2,n_3)$ is the wave normal specifying the direction of wave propagation.

Substituting from Eqs. (5) and (6) in Eqs. (1) to (4) and simplifying, we obtain the frequency equation

$$zD(\xi^3-a_1\xi^2+a_2\xi-a_3)+(1+\epsilon_1)^4$$
$$\times\tau^*\zeta(\zeta^3-A_1\zeta^2+A_2\zeta-A_3)=0, \tag{7}$$

where

$$\zeta=\frac{\xi}{1+\epsilon_1}, \quad \xi=\frac{\rho v^2}{c_{11}}, \quad \tau=\tau_0\omega_1^*, \quad z=i\chi,$$

$$\chi=\frac{\omega}{\omega_1^*}, \quad \omega_1^*=\frac{C_ec_{11}}{K_1}, \quad \epsilon_1=\frac{\beta_1^2T_0}{\rho C_ec_{11}}, \tag{8}$$

$$\tau^*=1-\tau z.$$

Here a_i, A_i $(i=1,2,3)$, and D are given in the Appendix.

Equation (7) is the secular equation for plane harmonic waves and contains all information regarding the phase velocities of the waves. This equation, being a fourth degree in ξ, has four roots and hence, in general, there are four waves, namely, a quasi-longitudinal (QL), two quasi-transverse (QT), and a quasi-thermal wave (T-mode), which can propagate in such types of media. All the waves are coupled with each other.

II. WAVES OF ASSIGNED FREQUENCY

In this case, the frequency ω is real and the wave number η is complex so that the phase velocity $v=\omega/\mathrm{Re}(\eta)$. Taking $\eta=p+iq$ (p,q are real), the right-hand side of Eqs. (5) and (6) are of the form $\exp(-qx_pn_p)\exp[i(px_pn_p-\omega t)]$. For $x_pn_p>0$, if $q<0$, the waves amplitudes are amplified (which relates to the ideal case), while for $q>0$ the waves attenuate in space (happens practically). The secular equation (7) in terms of η is

$$i\chi c_{11}^4a_3\eta^8-(i\chi a_2-\tau^*A_3)c_{11}^3\rho\omega^2\eta^6$$
$$+(i\chi a_1+\tau^*A_2)c_{11}^2\rho^2\omega^4\eta^4$$
$$-(i\chi-\tau^*A_1)\rho^3\omega^6c_{11}\eta^2-\tau^*\rho^4\omega^8=0. \tag{9}$$

Equation (9) is a quartic in η^2 so, in general, it has eight roots of the form $\pm(p^r\pm iq^r)$, $r=1,2,3,4$. Corresponding to each pair of roots there are two waves traveling in opposite directions with distinct speeds equal to $\omega/R_e(\eta)$. Thus there are four distinct waves, namely, a quasi-longitudinal, two quasi-transverse, and a thermal wave in such types of media.

A. Low- and high-frequency behavior

In low- and high-frequency regimes, characterized by $\chi\ll1$ and $\chi\gg1$, the wave like modes are determined by isentropic (constant entropy) and isothermal acoustical tensors, respectively. A motivating argument runs as follows:

Consider the transport of energy over a distance ''d'' in the direction defined by $\vec{n}=(1,0,0)$. Representative times for this process are $t_M=d(c_{11}/\rho)^{-1/2}$, when the energy is mechanical and the means of transfer is a displacement wave and $t_T=d^2(K_1/\rho C_e\tau^*)^{-1}$, when the energy is thermal and the operative mechanism is heat conduction. The frequency of the wave is $\omega=t_M^{-1}$, hence from the definition of Eq. (8), $|t_M/t_T|=\chi[1-\tau^2\chi^2/2+o(\tau^4)]$. We deduce that $t_M\ll t_T$ when, $\chi\ll1$, indicating that at low frequencies mechanical energy transfer is much more effective than thermal conduction and that conditions locally are therefore nearly isentropic. Whereas, at the opposite extreme, $\chi\gg1$, thermal energy transfer is a more predominant process, and the prevailing conditions are nearly isothermal. Thus at the low-frequency limit, the wavelike modes are identifiable with the small amplitude waves in an elastic material that does not conduct heat and may be regarded as inherent in the classical elastodynamics derived strictly from mechanical principles.

1. Waves at low frequency

In the case of low frequency, $\omega\ll\omega^*$, letting $\chi\to0$, i.e., $|z|\to0$. The frequency equation (7) reduces to

$$\zeta(\zeta^3-A_1\zeta^2+A_2\zeta-A_3)=0. \tag{10}$$

Equation (10) has one root $\zeta=0$, which corresponds to the thermal mode (T-mode) and predicts that the thermal wave does not exist at all in this limiting case of low frequency at which the conditions are isentropic. The other roots of Eq. (10) are given by

$$\zeta^3-A_1\zeta^2+A_2\zeta-A_3=0. \tag{11}$$

This equation is the same as that obtained in the case of non-heat-conducting elastic materials and gives the same type of wave propagation.

2. Waves at high frequency

In case of high frequency, $\omega\gg\omega^*$, letting $\chi\to\infty$, i.e., $|z|\to\infty$. The secular equation (7) takes the form

$$\tau\xi^4-[D+\tau(1+\epsilon_1)A_1]\xi+[Da_1+\tau(1+\epsilon_1)^2A_1]\xi^2$$
$$-[Da_2+\tau(1+\epsilon_1)^3A_3]\xi+Da_3=0. \tag{12}$$

This equation being a biquadratic in ξ gives four isothermal wave speeds which are influenced by the thermal relaxation time τ_0. In the absence of thermal relaxation time τ_0, Eq. (12) has one root, $\xi^{-1}=0$, that corresponds to the thermal mode and predicts infinite speed of heat propagation. The other roots of Eq. (12) are given by

$$\xi^3-a_1\xi^2+a_2\xi-a_3=0. \tag{13}$$

Equations (13) and (11) are of the same form. Thus we conclude that low-frequency waves under isentropic conditions and high-frequency waves under isothermal conditions, in the absence of thermal relaxations, are of the same type. Also, it is observed that the thermal relaxation time has no effect on low-frequency waves in the limiting case which supports the conclusion that the ''second sound'' effects are short lived.

B. Case I: Wave propagation in a principal plane

We consider plane waves propagating in a principal plane perpendicular to the principal direction (0,1,0) i.e., the wave normal $\vec{n}=(\sin\theta,0,\cos\theta)$, where θ is the inclination of wave normal to the x_3 axis. The frequency equation (7) reduces to

$$c_5\sin^2\theta+c_3\cos^2\theta-\xi=0 \tag{14}$$

and

$$(1-\tau z)\xi(\xi-\lambda_1^*)(\xi-\lambda_2^*)+zD'(\xi-\lambda_1)(\xi-\lambda_2)=0, \tag{15}$$

where

$$\begin{aligned}
&\lambda_1,\lambda_2=[b_1\pm(b_1^2-4b_2)^{1/2}]/2,\\
&\lambda_1^*,\lambda_2^*=(1+\epsilon_1)[B_1\pm(B_1^2-4B_2)^{1/2}]/2,
\end{aligned} \tag{16}$$

$$\begin{aligned}
b_1&=(1+c_4)\sin^2\theta+(c_2+c_4)\cos^2\theta,\\
b_2&=c_4\sin^4\theta+(c_2+c_4^2-c_6^2)\sin^2\theta\cos^2\theta+c_2c_4\cos^4\theta,\\
B_1&=(1+C_4)\sin^2\theta+(C_2+C_4)\cos^2\theta,\\
B_2&=C_4\sin^4\theta+(C_2+C_4^2-C_6^2)\sin^2\theta\cos^2\theta\\
&\quad+C_2C_4\cos^4\theta,\\
D'&=\sin^2\theta+\overline{K}_3\cos^2\theta,
\end{aligned} \tag{17}$$

and c_2, c_4, c_6 and C_2, C_4, C_6 are given in the Appendix.

Equation (14) corresponds to the purely transverse (SH) wave, which is not affected by thermal variations and vice versa. This wave propagates without dispersion or damping with speed

$$V=\left[\frac{1}{\rho}(c_{66}\sin^2\theta+c_{44}\cos^2\theta)\right]^{1/2} \tag{18}$$

and decouples from rest of the motion. Equation (15) being a cubic in ξ gives three roots and hence yields three dispersive waves which are affected by thermal variations and relaxation time. In case of $\omega\to 0$, i.e., $|z|\to 0$, Eq. (15) reduces to

$$\xi(\xi-\lambda_1^*)(\xi-\lambda_2^*)=0, \tag{19}$$

whose roots are $\xi_1=\lambda_1^*$, $\xi_2=\lambda_2^*$, $\xi_3=0$. The first two roots correspond to the usual elastic waves at isentropic conditions and the third one to the thermal mode. Thus, at low frequency, the elastic waves propagate with real isentropic speeds $(c_{11}\lambda_1^*/\rho)^{1/2}$, $i=1,2$, without dispersion, and the thermal wave does not exist at all. Again, when $\omega\to\infty$, i.e., $|z|\to\infty$, Eq. (15) becomes

$$\xi^{-1}(\xi-\lambda_1)(\xi-\lambda_2)-\tau(\xi-\lambda_1^*)(\xi-\lambda_2^*)=0. \tag{20}$$

Its roots may be obtained as a special case from the high-frequency approximations given in the following analysis. However, if $\tau_0\to 0$, then (20) reduces to

$$\xi^{-1}(\xi-\lambda_1)(\xi-\lambda_2)=0, \tag{21}$$

whose roots are $\xi_1=\lambda_1$, $\xi_2=\lambda_2$, $\xi_3=\infty$. Velocities of the first two modes associated with elastic waves have real values. The third mode (T-mode) has infinite velocity of propagation and is thus diffusive in nature. The approximation to the roots of Eq. (15) combined with (9) and (10) can be obtained by following the approach presented by Sharma and Sidhu[10] and Sharma[8] at low and high frequencies, respectively.

1. Low-frequency approximation ($\chi\ll 1$)

Here

$$\begin{aligned}
&\xi_i(z)=\lambda_i^*\left[1+\sum_1^\infty c_n^{(i)}(-z)^n\right],\quad i=1,2,\\
&\xi_3(z)=\sum_1^\infty d_n(-z)^n,
\end{aligned} \tag{22}$$

where the first two coefficients in these series are given by

$$\begin{aligned}
c_1^{(i)}&=g(\lambda_i^*)/\lambda_i^*f'(\lambda_i^*),\\
c_2^{(i)}&=c_1^{(i)}[g'(\lambda_i^*)-\tau^{f'}(\lambda_i^*)-c_1^{(i)}\lambda_i^{*f''}(\lambda_i)^*/2]/f(\lambda_i^*),\\
d_1&=g(0)/f'(0),\\
d_2&=d_1[g'(0)-\tau_0\omega_1^{*f'}(0)-d_1{}^{f''}(0)/2]/{}^{f'}(0),\\
f(\xi)&=\xi(\xi-\lambda_1^*)(\xi-\lambda_2^*),\quad g(\xi)=D'(\xi-\lambda_1)(\xi-\lambda_2),
\end{aligned} \tag{23}$$

and primes denote derivatives with respect to the argument. The values of wave speed (V) and attenuation coefficient (q) for different modes in this case are obtained as

$$V_i=V_i^*\sqrt{R_i}/\cos(\phi_i/2),\quad q_i=\omega\sin(\phi_i/2)V_i^*\sqrt{R_i}, \tag{24}$$

where

$$\begin{aligned}
&R_i=(L_i^2+M_i^2)^{1/2},\quad \phi_i=\tan^{-1}\left(\pm\left|\frac{M_i}{L_i}\right|\right),\quad i=1,2,3,\\
&L_i=1-c_2^{(i)}\chi^2,\quad M_i=c_1^{(i)}\chi,\\
&V_i^*=(c_{11}\lambda_i^*/\rho)^{1/2},\quad \text{for elastic waves},\\
&L_3=-\chi^2d_2,\quad M_3=d_1\chi,\quad V_3^*=(c_{11}/\rho)^{1/2},\\
&\qquad\text{for thermal wave (T-mode).}
\end{aligned} \tag{25}$$

The + or − sign in ϕ_i is taken according to whether $x_p n_p > 0$ or <0, and here we have taken $v^{-1} = V^{-1} + i\omega^{-1} q$, V and q being real.

2. High-frequency approximations ($\chi \gg 1$)

Here

$$\xi_i(\hat{z}) = \lambda_i \left[1 + \sum_1^\infty c_n^{(i)} (-\hat{z})^n \right],$$
$$\xi_3(\hat{z}) = \eta(\hat{Z})/\hat{Z}, \quad \eta(\hat{Z}) = \sum_0^\infty d_n (-\hat{Z})^n, \tag{26}$$

where $\hat{Z} = \hat{z} - \tau$, $\hat{z} = z^{-1}$ and the first two coefficients in these series are given by

$$c_1^{(i)} = f(\lambda_i)/\lambda_i g'(\lambda_i),$$
$$c_2^{(i)} = c_1^{(i)} [f(\lambda_i) - \lambda_i c_1^{(i)} g''(\lambda_i)]/g'(\lambda_i),$$
$$d_0 = -1, \quad d_1 = \lambda_1^* + \lambda_2^* - \lambda_1 - \lambda_2),$$
$$d_2 = 2[\lambda_1^* \lambda_2^* - \lambda_1 \lambda_2 + d_1 \{2(\lambda_1^* + \lambda_2^*) - \lambda_1 - \lambda_2 + 2d_1\}],$$

and $f(\xi)$, $g(\xi)$ are given by (23).

In this case, the wave speeds and attenuation coefficients are obtained as

$$V_i = \hat{v}_i \sqrt{r_i}/\cos(\psi_i/2), \quad q_i = \omega \sin(\psi_i/2)/\hat{v}_i \sqrt{r_i}, \tag{27}$$

where

$$r_i = (l_i^2 + m_i^2)^{1/2}, \quad \psi_i = \tan^{-1}\left(\pm \left| \frac{m_i}{l_i} \right| \right)$$
$$l_i = 1 - r\cos\psi c_1^{(i)} + r^2 \cos 2\psi c_2^{(i)},$$
$$m_i = -r \sin\psi c_1^{(i)} + r^2 \sin 2\psi c_2^{(i)}, \tag{28}$$
$$\hat{v}_i = (c_{11}\lambda_i/p)^{1/2}, \quad \text{for elastic waves}$$

and

$$l_3 = -\cos(\psi)/r + r d_1 \cos\psi + r^2 d_2 \cos 2\psi,$$
$$m_3 = \sin(\psi)/r + r d_1 \sin\psi + r^2 d_2 \sin 2\psi, \tag{29}$$
$$\hat{v}_3 = (c_{11}/p)^{1/2} \quad \text{for thermal waves},$$
$$r = (\chi^{-2} + \tau^2)^{1/2}, \quad \psi = \tan^{-1}(1/\tau). \tag{30}$$

The + or − sign in the determination of ψ_i is to be taken according to whether $x_p n_p > 0$ or <0. The approximate values of the roots of Eq. (20) can be obtained from Eq. (26) on letting $\chi \to 0$. We obtain

$$\xi_i = \lambda_i [1 - \tau c_1^{(i)} + (\tau)^2 c_2^{(i)} + \cdots], \quad i = 1,2,$$
$$\xi_3 = (\tau)^{-1} + d_1 - d_2 \tau + \cdots. \tag{31}$$

The real value of propagation speed follows from the above expansions directly. We get

$$V_i = \hat{v}_i (1 + \tau c_1^{(i)} + (\tau)^2 c_2^{(i)} + \cdots) \quad \text{for elastic waves},$$
$$V_3 = \hat{v}_3 \{(\tau)^{-1} + d_1 - \tau d_2 + \cdots\} \quad \text{for thermal waves}. \tag{32}$$

This last result shows that the T-mode now has a finite velocity of propagation, whereas in the coupled thermoelasticity ($\tau_0 \to 0$) this mode is evidently diffusive.

C. Case II: Wave propagation in other planes

We consider plane wave propagation in principal planes perpendicular to the principal direction (1,0,0) or (0,0,1), i.e., the wave normal $\vec{n} = (0, \sin\theta, \cos\theta)$ or $\vec{n} = (\sin\theta, \cos\theta, 0)$, where θ is now the inclination of wave normal to the x_3 and x_2 axes, respectively. The SH wave (purely transverse) again gets decoupled from the rest of the motion and is not affected by thermal variations in these directions. This wave now propagates without dispersion or damping with velocity

$$V = \left[\frac{1}{\rho} (c_{66} \sin^2\theta + c_{55} \cos^2\theta) \right]^{1/2}$$

and (33)

$$V = \left[\frac{1}{\rho} (c_{55} \sin^2\theta + c_{44} \cos^2\theta) \right]^{1/2}$$

in the principal planes perpendicular to (1,0,0) and (0,0,1), respectively.

The rest of the motion is coupled and governed by the secular equation of the type similar to Eq. (15) with minor adjustments of elastic and thermal parameters in these directions, and the corresponding velocities as well as the attenuation coefficients of the constituent wave modes can be obtained in a similar fashion as was done in case I. In all these cases the waves are found to be dispersive in character and attenuated in space.

D. Case III: Wave propagation along and perpendicular to axis of symmetry

For waves travelling in a direction perpendicular to the axis of symmetry we have $\theta = 90$ degrees and hence the wave normal $\vec{n} = (1,0,0)$. The secular equation (7) reduces to

$$c_5 - \xi = 0, \tag{34}$$

$$c_4 - \xi = 0, \tag{35}$$

and

$$\tau^* \xi^2 - a\xi - z = 0, \quad a = (1 + \epsilon)\tau^* - z. \tag{36}$$

Equations (34) and (35) give us two purely transverse waves, which get decoupled from rest of the motion and vice versa. These waves are not affected by thermal relaxation and propagate without dispersion or damping with velocities $(c_{66}/\rho)^{1/2}$ and $(c_{55}/\rho)^{1/2}$, respectively, independent of the thermodynamic conditions. The roots of Eq. (36) are given by

$$\xi_i, \xi_2 = \frac{1}{2\tau^*} \{[a \pm \sqrt{[a^2 + 4z\tau^*]}]\}. \tag{37}$$

When $\omega \to \infty$, i.e., $|z| \to \infty$, the root $\xi_1 \to 1 + \epsilon$ and $\xi_2 \to 0$. Thus the longitudinal wave in this limiting case travels with isentropic velocity $(c_{11}(1 + \epsilon_1)/\rho)^{1/2}$, and the thermal wave

does not exist at all. Again, when $\omega \to 0$, i.e., $|z| \to 0$, the roots ξ_1 and ξ_2 reduce to

$$\xi_1^*, \xi_2^* = \frac{1}{2\tau}\{1+\tau+\epsilon_1\tau \pm [(1+\tau+\epsilon_1\tau)^2 - 4\tau]^{1/2}\} \quad (18)$$

because

$$(1+\tau+\epsilon_1\tau)^2 - 4\tau = (1-\tau+\epsilon_1\tau)^2 + 4\epsilon_1\tau > 0,$$

and therefore ξ_1^*, ξ_2^* are real. Thus, there are two waves called longitudinal and thermal, corresponding to ξ_1^* and ξ_2^* in this limiting case, which can travel with real velocities given by $(c_{11}\xi_i^*/\rho)^{1/2}$, $i=1,2$, and depend upon the thermal relaxation time. The approximations (22) and (26) to roots ξ_1 and ξ_2 in this case reduce to the following.

1. Low-frequency approximation ($\chi \ll 1$)

Here

$$\xi_1 = 1 + \epsilon_1 \frac{\epsilon_1 z}{1+\epsilon_1} + \frac{\epsilon_1\{1-\tau(1+\epsilon_1)^2\}^2}{(1+\epsilon_1)^3} + \cdots,$$
$$\xi_2 = \frac{z}{1+\epsilon_1} - \frac{\epsilon_1 + \tau(1+\epsilon_1)^2 z^2}{(1+\epsilon_1)^3} + \cdots. \quad (38)$$

2. High-frequency approximations ($\chi \gg 1$)

We have

$$\zeta_1 = 1 + \epsilon_1\hat{Z} - \epsilon_1(1+\epsilon_1)\hat{Z}^2 + \cdots,$$
$$\zeta_2 = -\hat{Z}^{-1} + \epsilon_1\hat{Z} + \cdots, \quad (39)$$

where $\hat{Z} = \hat{z} - \tau$ and $\hat{z} = z^{-1}$.

The corresponding wave speeds and attenuation coefficients can also be obtained in a similar way as was done in case I. A similar type of discussion can be made for the waves propagating along the axis of symmetry, i.e., for $\theta = 0$.

III. PATHS OF THE PARTICLES

In order to discuss the paths of the particles of the modified QL and QT waves during the motion, we omit purely transverse waves. It is also observed that when thermomechanical coupling is operative, the amplitude and slowness of the waves are no longer real. This means that the wave is damped and that phase differences exist between each pair of the functions u_1, u_3, and T. We take $\vec{n} = (\sin\theta, 0, \cos\theta)$. Therefore, from Eqs. (5) and (6) we may have

$$u_1 = Ae^{-i\alpha}\exp\{i\omega(v^{-1}x_p n_p - t)\},$$
$$u_3 = Be^{-i\beta}\exp\{i\omega(v^{-1}x_p n_p - t)\}, \quad (40)$$
$$T = \Theta\exp\{i\omega(v^{-1}x_p n_p - t)\},$$

Here $U_1 = A\exp(-i\alpha)$ and $U_2 = B\exp(-i\beta)$, A, B being real.

Upon simplifying and eliminating $p = \omega\{v^{-1}(x_1\sin\theta + x_3\cos\theta) - t\}$ after retaining only the real parts in Eqs. (40) for real frequency, we obtain

$$\frac{u_1^2}{U^2\sin^2\theta} + \frac{u_3^2}{U^2N^2\cos^2\theta} - \frac{2\cos(\alpha-\beta)u_1u_3}{NU^2\sin\theta\cos\theta} = \sin^2(\alpha-\beta), \quad (41)$$

where

$$U = A\exp(-qx_p n_p) = A\exp[-q(x_1\sin\theta + x_3\cos\theta)], \quad (42a)$$

$$N = |B/A| = \frac{[(\overline{\beta}_3 - c_6)\sin^2\theta + \overline{\beta}_3 c_4\cos^2\theta] - \overline{\beta}_3\xi}{[c_4\sin^2\theta + (c_2 - c_6\overline{\beta}_3)\cos^2\theta] - \xi}. \quad (42b)$$

The ratio B/A, i.e., N has two values corresponding to two roots ξ_1, ξ_2 of the frequency equation (15) representing QL and QT waves, respectively. Thus Eq. (41) represents the path of a typical particle of the medium corresponding to the roots ξ_1 and ξ_2, which is an ellipse in the u_1u_3, plane. The major axes M_1, M_2, minor axes m_1, m_2, and eccentricities e_1, e_2 of the particle paths for the modified QL and QT waves are respectively given by

$$M_i^2 = \frac{2\{\tan^2\theta + N_i^2 + [(\tan^2\theta - N_i^2)^2 + 4N_i^2\tan^2\theta\cos^2(\alpha-\beta)]^{1/2}\}\cos^2\theta}{U_i^2N_i^2\sin^2(2\theta)\sin^2(\alpha-\beta)}, \quad (43)$$

$$m_i^2 = \frac{2\{\tan^2\theta + N_i^2 - [(\tan^2\theta - N_i^2)^2 + 4N_i^2\tan^2\theta\cos^2(\alpha-\beta)]^{1/2}\}\cos^2\theta}{U_i^2N_i^2\sin^2(2\theta)\sin^2(\alpha-\beta)}, \quad (44)$$

$$e_i^2 = \frac{2[(\tan^2\theta - N_i^2)^2 + 4N_i^2\tan^2\theta\cos^2(\alpha-\beta)]^{1/2}}{\tan^2\theta + N_i^2 + [(\tan^2\theta - N_i^2)^2 + 4N_i^2\tan^2\theta\cos^2(\alpha-\beta)]^{1/2}}. \quad (45)$$

If δ_i is the inclination of the major axes to the wave normal, then

$$\tan(2\delta_i)=\frac{2[\tan^2\theta+N_i^2+4N_i^2\cos^2(\alpha-\beta)(1-\tan^2\theta)]\tan\theta}{\tan^4\theta-[4N_i\cos(\alpha-\beta)+N_i^2]\tan^2\theta+N_i^2}. \tag{46}$$

As $N_i\cos(\alpha-\beta)=\mathrm{Re}(U_3/U_1)$, δ_i and e_i can be determined from Eq. (42). During the propagation of waves in a given direction the orientation and eccentricity of the particle paths remain fixed but, due to the presence of exponential factor of U in (42a), the lengths of the axes decrease steadily. From Eq. (45) it is clear that the elliptical paths degenerate into straight lines when $\theta=0$, $\pi/2$, and θ_d where

$$\theta_d=\tan^{-1}\left[\frac{c_2-c_4-\overline{\beta}_3c_4}{1-c_4-c_6/\overline{\beta}_3}\right]=\tan^{-1}\left[\frac{C_2-C_4-\overline{\beta}_3C_6}{1-C_4-C_6/\overline{\beta}_3}\right], \tag{47}$$

and when the phase difference $\alpha-\beta=0$, that is, when U_3/U_1 is real. We find that for both waves, $I_m(u_3/u_1)=0$ when $\theta=\theta_d$. It follows that for each wave the sense of describing the elliptical path changes as the wave normal crosses the plane $x_3=0$. Further, if $\theta=\theta_d$ given by Eq. (47) is real, then the sense also changes when the wave normal crosses the cone with semi-vertical angle $\theta=\theta_d$ with the x_3 axis as the axis of the cone.

We note that when $\theta=\pi/2$, i.e., for the direction of propagation along the x_1 axis, the behavior of the modified QL wave is identical to that of the modified dilatational wave in an isotropic heat conducting elastic material with thermoelastic coupling constant ϵ_1 and characteristic thermoelastic frequency ω_1^*, while the modified QT wave has constant phase velocity and is undamped. A similar remark applies when $\theta=0$ (i.e., for propagation along the x_3 axis), the operative values of the coupling constant and the characteristic frequency then are

$$\epsilon_3=\beta_3^2T_0/\rho C_e c_{33}=(\overline{\beta^2}/c_1)\epsilon_1,$$

$$\omega_3^*=C_ec_{33}/K_3=(c_2/\overline{K_3})\omega_1^*.$$

IV. STABILITY OF WAVES

A plane wave is said to be stable if its amplitude remains bounded at all distances in the direction of travel. For $\omega>0$ this requires $\mathrm{Im}(\xi)\leqslant 0$. Thus in order to prove the stability of all plane waves with positive frequency in generalized thermoelasticity, we must show that $\xi_i(\chi)$ remains entiretly within the lower half of the complex ξ plane for $\omega\geqslant 0$, though a branch may touch the positive real ξ axis. In the low-frequency limit the four branches may be approximated by their Taylor expansions in Eqs. (22) as

$$\xi_i(z)=\lambda_i^*-zg(\lambda_i^*)/f'(\lambda_i^*)+o(z^2),\quad i=1,2, \tag{48}$$

$$\xi_3(z)=-zg(0)/f'(0)+o(z^2), \tag{49}$$

while in the high-frequency limit we have

$$\xi_i(\hat{z})=\lambda_i+\hat{z}f(\lambda_i)/g'(\lambda_i)+o(\hat{z}^2),\quad i=1,2, \tag{50}$$

$$\xi_3(\hat{z})=-\frac{1}{\hat{Z}}+\lambda_1+\lambda_2-\lambda_1^*-\lambda_2^*+o(\hat{z}^2), \tag{51}$$

where $\hat{z}=z^{-1}$ and $\hat{Z}=\hat{z}-\tau$.

Thus even for nonzero τ_0, since τ_0 does not appear until the $o(\omega^2)$ terms in (48) and (49), therefore each wave is certainly stable for small enough frequencies.[14] However, with $\tau_0>0$, the high-frequency limit differs from that in the case of the coupled theory of thermoelasticity ($\tau_0=0$). As $\omega\to\infty$ we see that the three limiting values of ξ are given by the three roots of the real cubic equation,

$$F(\xi)=-\tau f(\xi)+g(\xi)=0, \tag{52}$$

where $f(\xi)$, $g(\xi)$, and D' are defined in Eqs. (23) and (17), respectively.

Theorem: For each $\tau>0$, Eq. (52) has four real roots $\xi=\overline{\lambda}_i$ (say), $i=1,2,3$, which interlace according to

$$\overline{\lambda}_1<\lambda_1<\lambda_1^*<\overline{\lambda}_2<\lambda_2<\lambda_2^*<\overline{\lambda}_3 \tag{53}$$

with $\overline{\lambda}_1>0$, provided that the four acoustic values are distinct.

Proof: From Eq. (52), we have

$$\begin{aligned}
&F(0)=D'\lambda_1\lambda_2>0,\\
&F(\lambda_1)=-\tau\lambda_1(\lambda_1-\lambda_1^*)(\lambda_1-\lambda_2^*)<0,\\
&F(\lambda_1^*)=D'(\lambda_1^*-\lambda_1)(\lambda_1^*-\lambda_2)<0,\\
&(\lambda_2)=-\tau\lambda_2(\lambda_2-\lambda_1^*)(\lambda_2-\lambda_2^*)>0,\\
&F(\lambda_2^*)=D'(\lambda_2^*-\lambda_1)(\lambda_2^*-\lambda_2)>0,\\
&F(+\infty)=-\infty<0.
\end{aligned} \tag{54}$$

Since $F(\xi)$ is a cubic polynomial continuous in ξ, it is an immediate consequence of these inequalities (54) that Eq. (52) has three real roots that satisfy the inequalities (53).

If the four eigenvalues are not distinct, then factors may be removed from (15), $f(\xi)$ and $g(\xi)$, as was done by Scott.[14] Such factors also occur in (52) showing that if there is a coincidence between one of the values λ_i and one of the value λ_i^*, then one of the $\overline{\lambda}_i$ is also equal to this common value. When all such coincident eigenvalues have been removed it is found that the remaining (distinct) eigenvalues satisfy strict inequalities of the form (53) and, defining the real cubic polynomial

$$h(\xi)=(\xi-\overline{\lambda}_1)(\xi-\overline{\lambda}_2)(\xi-\overline{\lambda}_3), \tag{55}$$

we find that for high frequencies the three branches $\xi(\hat{z})$ given by (50) and (51) for $\tau>0$ become

$$\xi_i(\hat{z})=\overline{\lambda}_i-\tau\hat{z}f(\overline{\lambda}_i)/h'(\overline{\lambda}_i)+o(\hat{z}^2),\quad i=1,2,3. \tag{56}$$

The high-frequency branch in the case $\tau_0=0$ which terminates at $-i\infty$ has been replaced for $\tau_0>0$ by the branch (56) that terminates at the finite point $\overline{\lambda}_3$. This is the chief distinguishing feature between the cases $\tau_0=0$ and $\tau_0>0$. Of course, there is no claim that the low- and high-frequency branches of $\xi(\omega)$ are connected together in the order in which they have been numbered and, in general, they are not.[15]

The inequalities (53) may be used to verify that each of the branches (56) satisfies $I_m(\xi(\omega))<0$ for ω large enough and is therefore stable. Thus we see that each of the three generalized thermoelastic waves is stable for low and high frequencies. This may be extended to the following.

Theorem: For all $\tau_0>0$ and for all positive frequencies, each of the three branches $\xi(\omega)$ of

$$(1-\tau z)f(\xi)+zg(\xi)=0, \tag{57}$$

satisfies $I_m(\xi(\omega))<0$ and so gives a stable wave.

Proof: We have seen that branches of $\xi(\omega)$ touch the real ξ, axis at the points 0, λ_1^*, λ_2^* (corresponding to $\omega=0$) or $\overline{\lambda_1}$, $\overline{\lambda_2}$, $\overline{\lambda_3}$ (corresponding to $\omega=\infty$) and lie in $I_m(\xi(\omega))<0$ close to these points. However, no branch may cut the real axis in any other point as (57) may be written as

$$f(\xi)/g(\xi)=-z/(1-\tau z), \quad z=i\chi=i\omega/\omega_1^*,$$

indicating that for finite, nonzero χ the ratio $f(\xi)/g(\xi)$ is complex so that ξ may not be real. Thus each branch must remain within the region $I_m(\xi(\omega))<0$, proving the stability.

For most materials that exhibit nonzero τ we find that[15] τ lies between 10^{-3} and 1 which implies that $\tau\ll 1$ and then the roots $\overline{\lambda_i}$ of (52) are approximately

$$\overline{\lambda_i}=\lambda_i+\tau f(\lambda_i)/g'(\lambda_i)+o(\tau^2), \quad i=1,2,$$

$$\overline{\lambda_3}=1/\tau+\lambda_1^*+\lambda_2^*-\lambda_1^*-\lambda_2^*+o(\tau).$$

Thus the first two roots $\overline{\lambda_i}$ differ little from λ_i while the third is radically different from its counterpart in classical thermoelasticity.

V. PARTICULAR CASES

A. Transversely isotropic materials

This type of medium has only one axis of thermal and elastic symmetry. We take the x_3 axis along the axis of symmetry. Then the nonvanishing elastic and thermal parameters are

$$c_{11}=c_{22},\ c_{33},\ c_{12},\quad c_{13}=c_{23},\quad c_{44}=c_{55},$$

$$c_{66}=(c_{11}-c_{12})/2,\quad K_1=K_2,K_3,\quad \alpha_1=\alpha_2,\alpha_3,$$

$$\beta_1=\beta_2=(c_{11}+c_{12})\alpha_1+c_{13}\alpha_3,\quad \beta_3=2c_{13}\alpha_1+c_{33}\alpha_3.$$

Using these values in the above analysis most of the results are reduced to those obtained by Sharma and Singh[11] in the case of transversely isotropic materials.

B. Cubic crystals

For cubic crystals, the nonvanishing elastic and thermal parameters are

$$c_{11}=c_{22}=c_{33},\quad c_{12}=c_{23}=c_{13},\quad c_{44}=c_{55}=c_{66},$$

$$K_1=K_2=K_3=k,\quad \beta_1=\beta_2=\beta_3=\beta,$$

$$\alpha_1=\alpha_2=\alpha_3=\alpha_t,\quad \beta=(c_{11}+c_{12})\alpha_t.$$

Using these values of parameters in the above analysis we recover the results obtained by Sharma and Singh.[9]

TABLE I. Physical data for a single crystal of cobalt and solid helium.

Quantity	Units	Cobalt	Helium
T_0	°K	298	0.8500
ρ	kg m^{-3}	8.836×10^3	0.1910
C_{11}	Nm^{-2}	3.071×10^{11}	0.4040×10^{10}
C_{12}	Nm^{-2}	1.650×10^{11}	0.2120×10^{10}
C_{13}	Nm^{-2}	1.027×10^{11}	0.01050×10^{10}
C_{33}	Nm^{-2}	3.581×10^{11}	0.5530×10^{10}
C_{44}	Nm^{-2}	0.7550×10^{11}	0.1245×10^{10}
β_1	$Nm^{-2}deg^{-1}$	7.040×10^6	2.3620×10^6
β_2	$Nm^{-2}deg^{-1}$	6.900×10^6	2.641×10^6
C_e	$Jkg^{-1}deg^{-1}$	4.270×10^2	1.4770×10^5
K_1	$Wm^{-1}deg^{-1}$	0.6900×10^2	0.3000×10^2
K_3	$Wm^{-1}deg^{-1}$	0.6900×10^2	0.2000×10^1
ϵ_1	⋯	0.129	0.04162
ω_1^*	s^{-1}	1.880×10^{12}	1.9890×10^{13}
τ_0	⋯	0.02	0.02

C. Isotropic media

For isotropic material every direction is a direction of elastic as well as thermal symmetry and the nonvanishing elastic and thermal parameters are

$$c_{11}=c_{22}=c_{33}=\lambda+2\mu,\quad c_{12}=c_{23}=c_{13}=\lambda,$$

$$c_{44}=c_{55}=c_{66}=\mu,\quad K_1=K_2=K_3=K,$$

$$\alpha_1=\alpha_2=\alpha_3=\alpha_t,\quad \beta_1=\beta_2=\beta_3=\beta=(3\lambda+2\mu)\alpha_t.$$

Using these values of parameters in the foregoing analysis we obtain the well-established results[13] of plane harmonic wave propagation in homogeneous isotropic materials.

VI. NUMERICAL RESULTS AND DISCUSSION

The material chosen for the purpose of numerical evaluation was cobalt and solid helium which fall in the category of transversely isotropic materials. The physical data for a single crystal of cobalt and solid helium materials is given in Table I.[2,4]

The velocities and attenuations of modified waves have been computed by using Eqs. (24)–(27) for different values of the angle of incidence $0\leqslant\theta\leqslant\pi/2$ and $\chi=0.01,0.03,0.1,0.3,1.0,3.0,10.0,30.0$. The variations with nondimensional frequency of the phase velocities v_j and the attenuation coefficients q_j, $j=1,2,3$, are represented graphically in Figs. 1 and 9 for various directions of propagation. The values of isothermal and isentropic wave speeds V, V_1, V_2 and V_1^*, V_2^* in a cobalt (Co) and solid helium (He) crystals are given in Table II for several angles of incidence in the range $0\leqslant\theta\leqslant\pi/2$, respectively.

The curves in Fig. 1 show that for each value of θ in the interval $(0,\pi/2)$ the phase velocity of the modified QL wave in solid helium first increases monotonically from the isentropic value V_1^* at $\chi=0.0$ up to $\chi=0.3$, and decreases up to the critical value $\chi=1.0$ and then ultimately becomes closer to the isothermal value V_1 as $\chi\to\infty$. It is also observed that variations in the phase velocity of the QL-wave lie between the lowest value for $\theta=30$ degrees and highest for $\theta=90$ degrees. The variation of v_1 is confined to a band of frequencies about two decades in width, the center point of which (transition frequency) lies approximately at

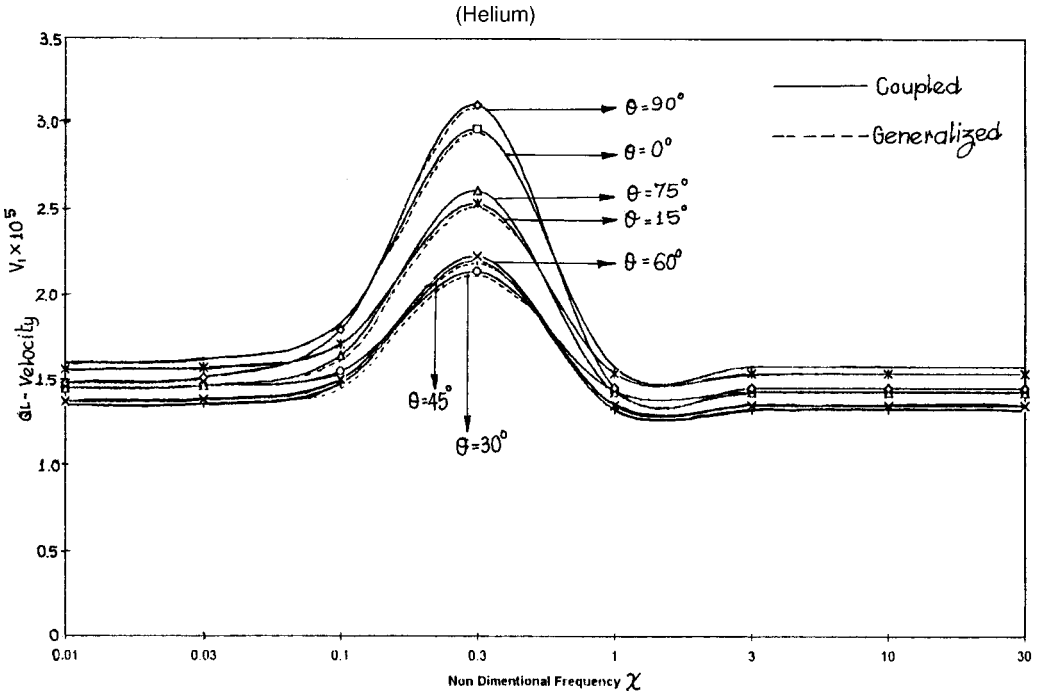

FIG. 1. Variation of QL wave velocity with nondimensional frequency in various directions of propagation.

$\chi=\omega_3^*/\omega_1^*=0.3$. The effect of thermal relaxation time is visible on the velocity of these waves in solid helium crystal.

From Fig. 2 the variations with frequency of the phase velocity of the modified QT wave in solid helium are seen to have the same trend of variations as the curves for v_1 but the variations are less dependent in each direction as compared to those of the QL wave, and for the QT wave the transition frequency is weakly dependent on the directions of propagation, which justifies the fact that shear motion is less affected due to the thermal effects. The variations in the phase velocity of the QT wave are observed to lie between the lowest value at $\theta=0$ degrees and the highest value at $\theta=45$ degrees. The waves along the axis of symmetry at 45 degrees are less affected due to thermal effects.

Figures 3 and 4 show that the phase velocity and attenuation coefficient of the thermal wave (T-mode) in solid helium vary logistically and are dependent on the anisotropy of the medium. While the variations in phase velocity increase as θ increases from 0 to 90 degrees, the variations in attenuation coefficient increases for $\theta=0$ degrees to $\theta=90$ degrees. It is observed from Fig. 5 that the attenuation coefficient of the modified QL wave is negative and decreases for $0\leqslant\chi\leqslant0.3$, increases for $0.3\leqslant\chi\leqslant1.0$, and ultimately become closer to zero as $\chi\rightarrow\infty$. The attenuation coefficient of the QT wave remains positive and observed to increase for $0\leqslant\chi\leqslant0.3$, decrease for $0.3\leqslant\chi\leqslant1.0$ and remain constant for $\chi\rightarrow\infty$ for various directions of propagation as represented in Fig. 6 for solid helium.

The curves in Fig. 7 show that the variations of phase velocity of QL wave with frequency in a cobalt crystal increases from the isotropic value V_1^* at $\chi=0.0$ up to $\chi=0.3$ and decreases up to the critical value $\chi=1.0$ and ultimately becomes closer to the isothormal value $\hat{v}_1$ as $\chi\rightarrow\infty$. The phase velocity of the QL wave lies between its lowest value at $\theta=30$ degrees and highest value at $\theta=90$ degrees and confined to the band of frequencies about two decades in width, the center point of which (transition frequency) lies approximately at $\chi=\omega_3^*/\omega_1^*=0.3$. The thermal relaxation effects are observed to be negligibly small in cobalt material.

From the curves in Fig. 8 it is observed that the trend of variation of phase velocity of QT waves in cobalt crystal is same that of QL waves, but the variations are independent in each direction and are quiet small in magnitude as com-

TABLE II. Isentropic and isothermal wave speeds (ms^{-1}) of QL and QT-waves in various directions of propagation in a single crystal of solid helium and cobalt.

θ	00		15		30		45		60		75		90	
(degrees)	He	Co	He	Co	He	Co	He	Co	He	Co	He	Co	He	Co
V	80 736	2993	82 189	3008	86 034	3229	91 024	3509	95 754	3768	99 074	3947	100 057	4010
V_1	167 022	6333	162 540	6178	150 003	5765	134 248	5348	132 161	5436	139 382	5733	142 502	5888
V_2	57 089	2067	65 186	2412	82 567	3113	96 761	3588	89 565	3238	68 314	2470	57 089	2067
V_1^*	170 156	6360	165 651	6220	153 116	5800	137 655	5388	135 423	5475	142 361	5771	145 437	5895
V_2^*	57 089	2667	65 022	2414	82 203	3117	96 664	3589	89 425	3239	68 168	2471	57 089	2067

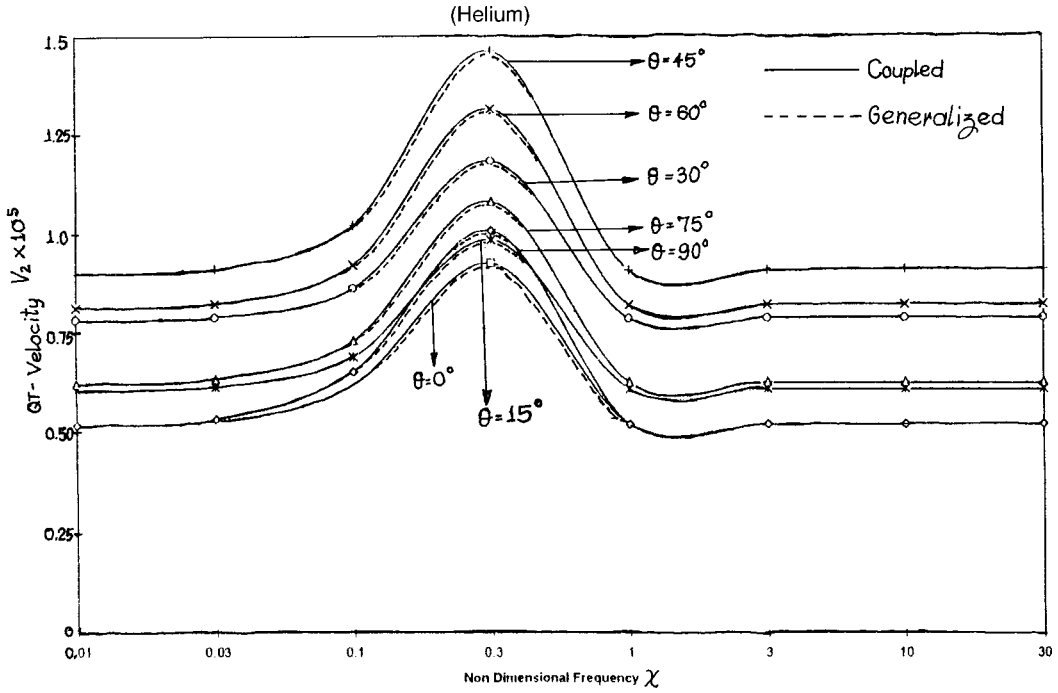

FIG. 2. Variation of QT wave velocity with nondimensional frequency in various directions of propagation.

pared to those in Fig. 7, which justifies the fact that shear motion is less affected due to thermal effects. No modification is noticed due to thermal relaxation time on these waves.

The curves in Fig. 9 suggests that approximately there is no effect of anisotropy of the medium on the thermal wave (T-mode) although the phase velocity varies logistically with frequency in cobalt material.

The comparison of Figs. 1 and 7 with Figs. 2 and 8 supports the conclusion, not unexpected, that the modified QL wave is more strongly affected by the thermomechanical interactions than the QT wave. It is also observed that the modified QL waves propagating in directions perpendicular to the axis of symmetry of cobalt and solid helium crystals are subjected to greater thermoelastic modification than those traveling in the proximity of the basal plane. The QT waves propagating in the directions inclined at $\pi/4$ to the axis of symmetry are subjected to greater modifications. The variations in QL and QT-wave velocities along and perpendicular to the axis of symmetry are quite close, and behavior of these quantities in these direction seems to be similar to the elastic

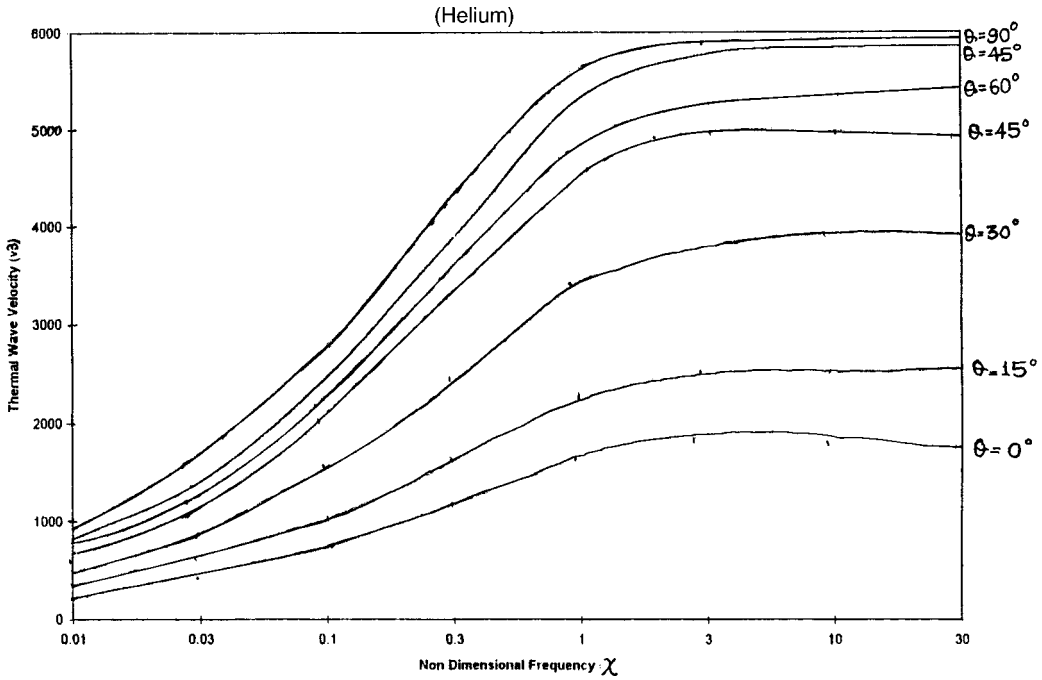

FIG. 3. Variation of thermal wave velocity with nondimensional frequency in various directions of propagation.

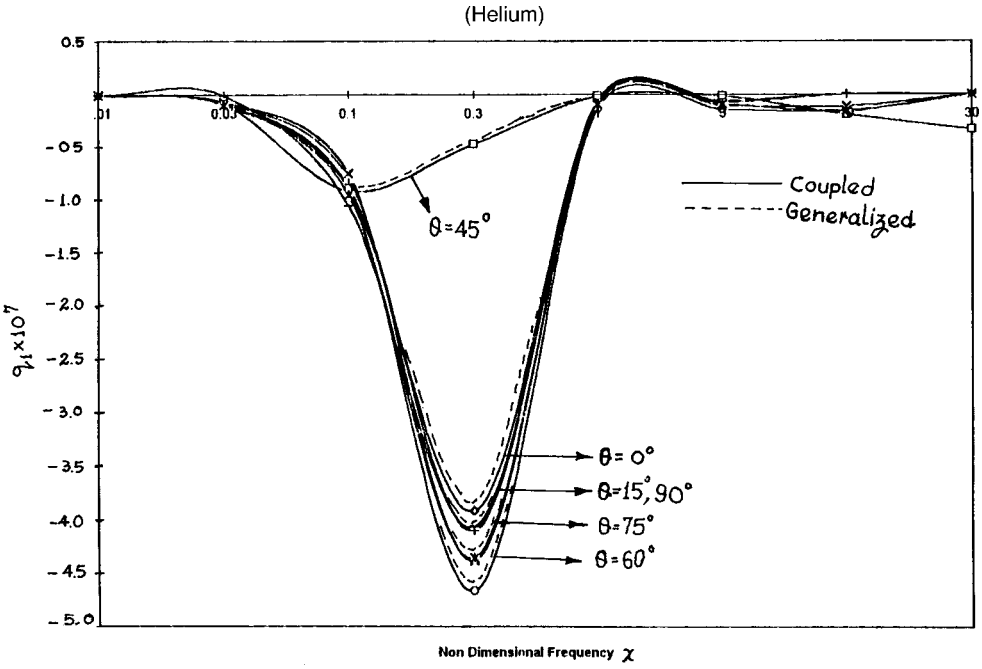

FIG. 4. Variation of attenuation coefficient of the thermal wave with nondimensional frequency in various directions of propagation.

case and independent, as the effect of thermoelastic coupling is lost at these angles. The maximum variations in the velocities and attentuations occur in the low-frequency range ($\chi \leqslant 1$), whereas these quantities for QL and QT waves almost remain constant in the high-frequency range ($\chi \leqslant 1$). Thus the low-frequency limits are of greater physical interest. The eccentricities of the particle paths are found to be very close to unity for all frequencies and directions of propagation. Thus the modified QL and QT waves are very nearly polarized. The calculations have been done on an Intel-586, 133-MHz computer.

VII. CONCLUSIONS

In a general case, the secular equation of plane harmonic waves in orthorhombic materials permits four waves to propagate, namely, a quasi-longitudinal (QL), two quasi-transverse (QT), and a thermal wave (T-mode) which are coupled to each other. At low and high frequencies the wave-like modes are determined by isentropic (constant entropy) and isothermal acoustical tensors, respectively. In the limiting case thermal relaxation time has no effect on low-frequency waves which supports the conclusion that ''second

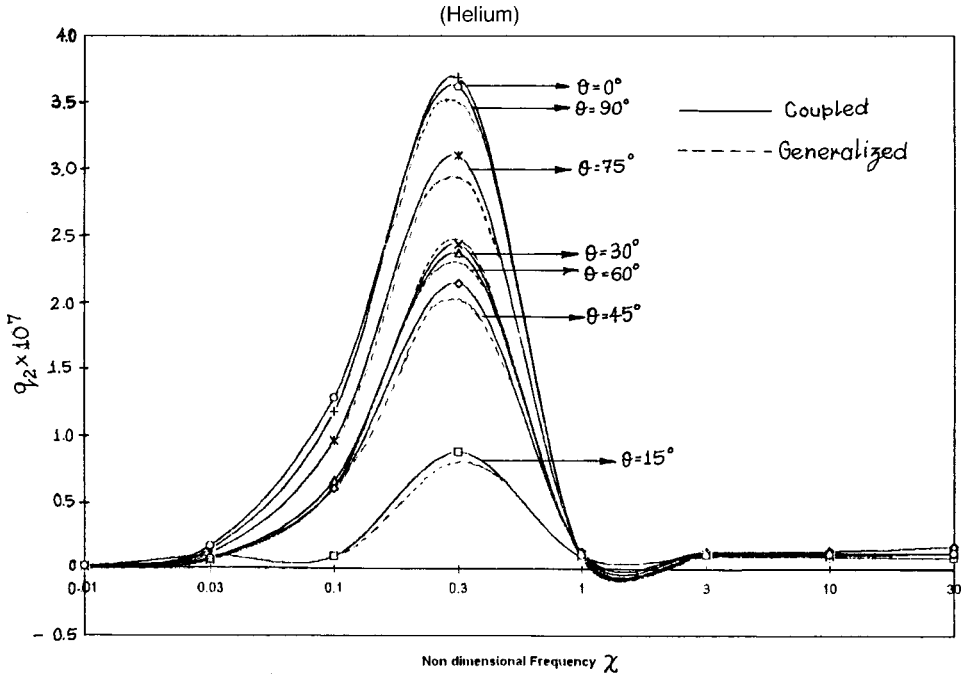

FIG. 5. Variation of attenuation coefficient of the QL wave with nondimensional frequency in various directions of propagation.

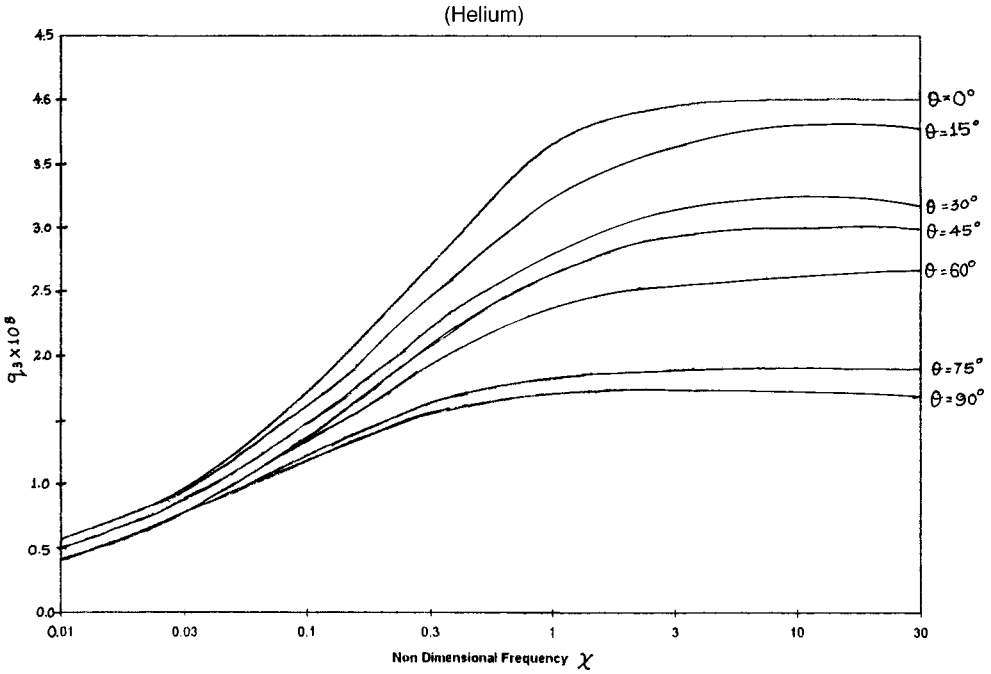

FIG. 6. Variation attenuation coefficient of the QT wave with nondimensional frequency in various directions of propagation.

sound'' effects are short lived. For the wave propagation along one of the principal axis of the solid, only longitudinal and thermal waves remain coupled and the transverse motion which gets decoupled from rest of the motion propagates without dispersion or damping and is not affected by thermal relaxation time and thermaodynamical conditions.

In case of wave propagation in a principal plane the purely transverse (SH) wave gets decoupled from the rest of the motion and propagates without dispersion or damping and remains unaffected by thermal variations. Neglecting the shear horizontal (SH) motion, the frequency equation, in general, permits three waves identified as QL, QT, and T-mode. The low-frequency regimes are found to be of more physical interest than the high-frequency regimes. The modified QT waves are observed to be less affected due to thermomechanical effects than the modified QL waves. This is not unexpected but supports the corresponding conclusion in the case of isotropic materials.

The waves propagating in the proximity of the basal plane are much affected due to thermal effects as compared

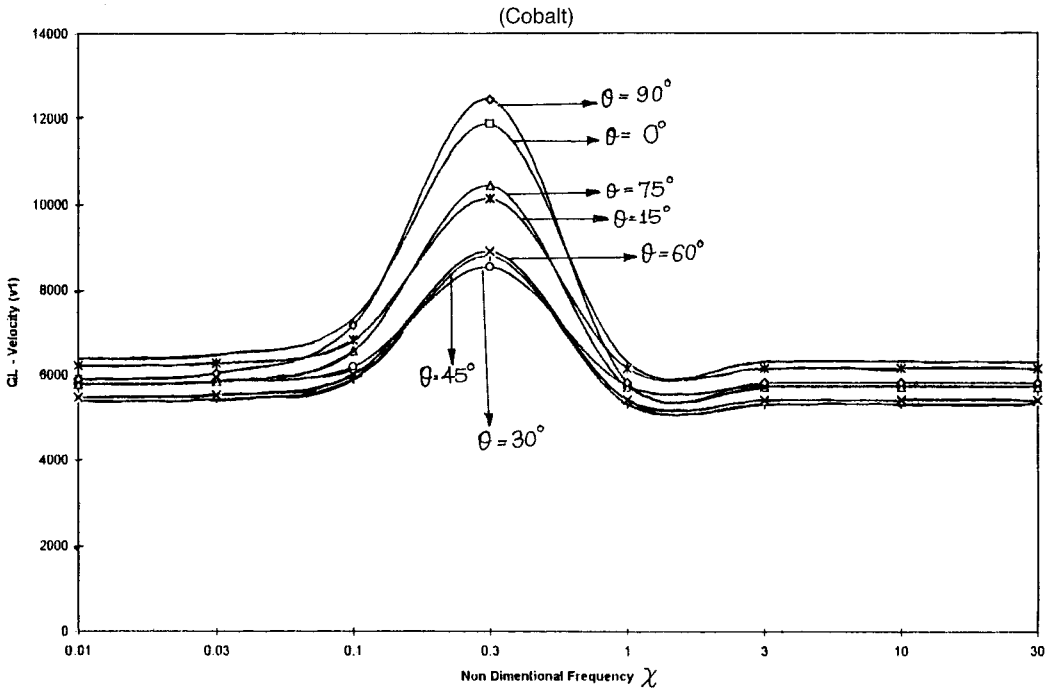

FIG. 7. Variation of QL wave velocity with nondimensional frequency in various directions of propagation.

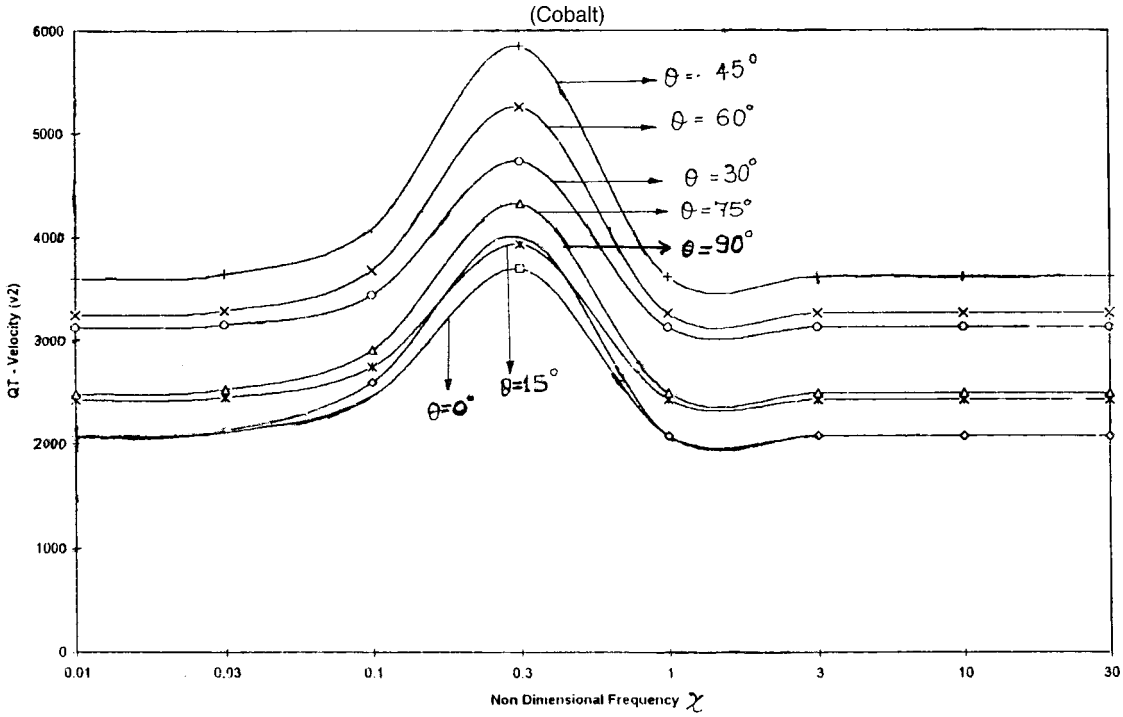

FIG. 8. Variation of QT wave velocity with nondimensional frequency in various directions of propagation.

to those traveling along or close to the directions perpendicular to it in single crystals of solid helium and cobalt.

The paths of the particles during the motion are found to be elliptical, whose major axes are inclined at angles δ_i $(i=1,2)$. The paths of particles degenerate into straight line segments when the wave is propagating

(i) along the x_3 axis,

(ii) perpendicular to the x_3 axis and possibly

(iii) along the surface of the cone with axis of symmetry as the axis of cone and semivertical angle θ_d given by Eq. (47). This also happened when there is no phase difference in QL and QT waves, i.e., when $\alpha=\beta$. The modified QL and QT waves are also found to be very nearly polarized. The generalized thermoelastic waves

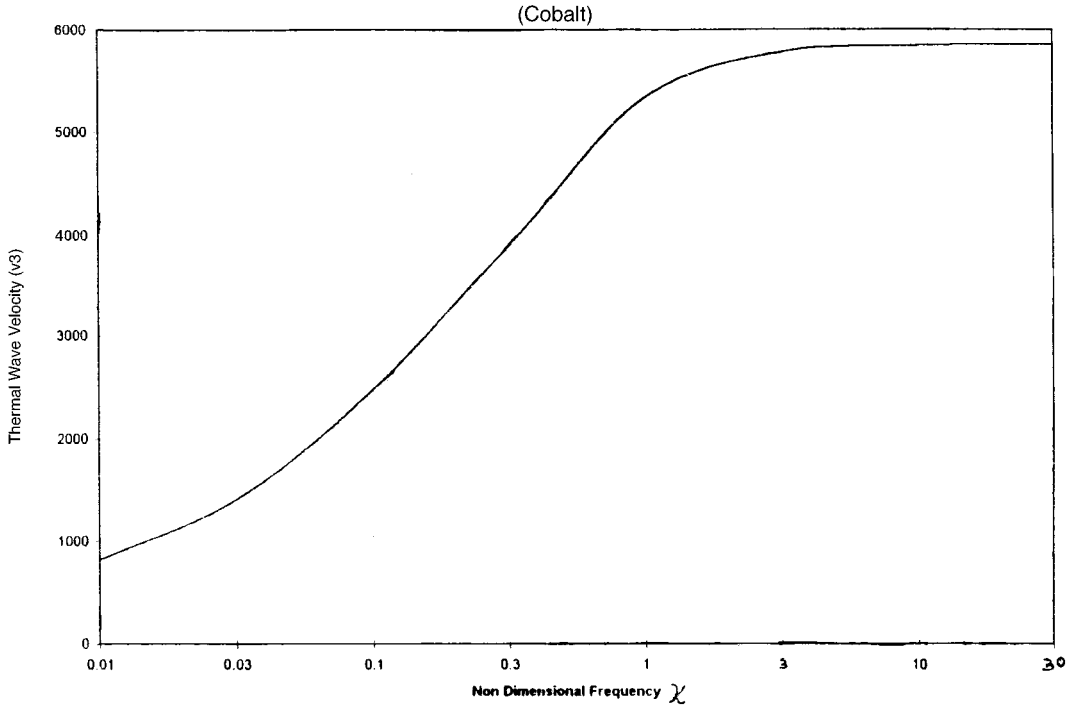

FIG. 9. Variation of thermal wave velocity with nondimensional frequency in various directions of propagation.

discussed herein are found to be stable. The T-mode which was diffusive in nature in the case of coupled thermoelasticity now becomes wavelike in generalized thermoelasticity, which propagates with finite, though quite large, speed.

ACKNOWLEDGMENTS

The authors are thankful to the refrees for their useful suggestions. The first author (JNS) is also thankful to Regional Engineering College authorities and MHRD, Government of India, for providing financial assistance through FIP under Center of Excellence (CoE) scheme to complete this work.

APPENDIX

The various coefficients in Eq. (7) are obtained as follows:

$$D=n_1^2+\overline{K}_2n_2^2+\overline{K}_3n_3^2,$$

$$a_1=(1+c_4+c_5)n_1^2+(c_1+c_3+c_5)n_2^2+(c_2+c_3+c_4)n_3^2,$$

$$a_2=(n_1^2+c_5n_2^2+c_4n_3^2)(c_5n_1^2+c_1n_2^2+c_3n_3^2)+(n_1^2+c_5n_2^2+c_4n_3^2)(c_4n_1^2+c_3n_2^2+c_2n_3^2)+(c_5n_1^2+c_1n_2^2+c_3n_3^2)(c_4n_1^2+c_3n_2^2+c_2n_3^2)-c_6^2n_1^2n_3^2-c_7^2n_1^2n_2^2-c_8^2n_2^2n_3^2,$$

$$a_3=(n_2^1+c_5n_2^2+c_4n_3^2)(c_5n_1^2+c_1n_2^2+c_3n_3^2)\times(c_4n_1^2+c_3n_2^2+n_3^2)(c_4n_1^2+c_3n_2^2+c_2n_3^2)-c_8^2n_2^2n_3^2(n_1^2+c_5n_2^2+c_4n_3^2)+2c_6c_7c_8n_1^2n_2^2n_3^2-c_6^2n_1^2n_3^2(c_5n_1^2+c_1n_2^2+c_3n_3^2),$$

$$A_1=(1+C_4+C_5)n_1^2+(C_1+C_3+C_5)n_2^2+(C_2+C_3+C_4)n_3^2,$$

$$A_2=(n_1^2+C_5n_2^2+C_4n_3^2)(C_5n_1^2+C_1n_2^2+C_3n_3^2)+(n_1^2+C_5n_2^2+(C_4n_3^2)(C_4n_1^2+C_3n_2^2+C_2n_3^2)+(C_5n_1^2+C_1n_2^2+C_3n_3^2)(C_4n_1^2+C_3n_2^2+C_2n_3^2)-C_6^2n_1^2n_3^2-C_7^2n_1^2n_2^2-C_8^2n_2^2n_3^2,$$

$$A_3=(n_1^2+C_5n_2^2+C_4n_3^2)(C_5n_1^2+C_1n_2^2+C_3n_3^2)(C_4n_1^2+C_3n_2^2+n_3^2)+2C_6C_7C_8n_1^2n_2^2n_3^2-C_6^2n_1^2n_3^2(C_5n_1^2+C_1n_2^2+C_3n_3^2)-C_7^2n_1^2n_2^2(C_4n_1^2+C_3n_2^2+C_2n_3^2)-C_8^2n_3^2n_2^2(n_1^2+C_5n_2^2+C_4n_3^2),$$

$$C_1=\frac{c_1+\epsilon_1\overline{\beta}_2^2}{1+\epsilon_1},\quad C_2=\frac{c_2+\epsilon_1\overline{\beta}_3^2}{1+\epsilon_1},\quad C_3=\frac{c_3}{1+\epsilon_1},$$

$$C_4=\frac{c_4}{1+\epsilon_1},\quad C_5=\frac{c_5}{1+\epsilon_1},\quad C_6=\frac{c_6+\epsilon_1\overline{\beta}_3}{1+\epsilon_1},$$

$$C_7=\frac{c_7+\epsilon_1\overline{\beta}_2}{1+\epsilon_1},\quad C_8=\frac{C_8+\epsilon_1\overline{\beta}_2}{1+\epsilon_1},$$

$$c_1=\frac{c_{22}}{c_{11}},\quad c_2=\frac{c_{33}}{c_{11}},\quad c_3=\frac{c_{44}}{c_{11}},\quad c_4=\frac{c_{55}}{c_{11}},\quad c_5=\frac{c_{66}}{c_{11}},$$

$$c_6=\frac{c_{13}+c_{55}}{c_{11}},\quad c_7=\frac{c_{12}+c_{66}}{c_{11}},\quad c_8=\frac{c_{23}+c_{44}}{c_{11}},$$

$$\overline{K}_2=\frac{K_2}{K_1},\quad \overline{K}_3=\frac{K_3}{K_1},\quad \overline{\beta}_2=\frac{\beta_2}{\beta_1},\quad \overline{\beta}_3=\frac{\beta_3}{\beta_1}.$$

[1] M. J. P. Musgrave, *Crystal Acoustics* (Holden-Day, San Francisco, CA, 1970).
[2] P. Chadwick and L. T. C. Seet, ''Wave propagation in transversely isotropic heat conducting elastic materials,'' Mathematika **17**, 255–272 (1970).
[3] P. Chadwick, ''Basic properties of plane harmonic waves in a prestressed heat-conducting elastic material,'' J. Thermal Stresses **2**, 193–214 (1979).
[4] D. K. Banergee and Y. H. Pao, ''Thermoelastic waves in anisotropic solids,'' J. Acoust. Soc. Am. **56**, 1444–1454 (1974).
[5] Y. H. Pao and D. K. Banergee, ''Thermal pulses in dielectric crystals,'' Lett. Appl. Eng. Sci. **1**, 33–41 (1973).
[6] H. W. Lord and Y. Shulman, ''The generalized dynamical theory of thermoelasticity,'' J. Mech. Phys. Solids **15**, 299–309 (1967).
[7] R. S. Dhaliwal and H. H. Sherief, ''Generalized thermoelasticity for anisotropic media,'' Q. Appl. Math. **38**, 665–673 (1986).
[8] J. N. Sharma, ''On the low and high-frequency behavior of generalized thermoelastic waves,'' Arch. Mech. **38**, 665–673 (1986).
[9] J. N. Sharma and H. Singh, ''Propagation of generalized thermoelastic waves in cubic crystals,'' Arch. Mech. **42**, 19–30 (1990).
[10] J. N. Sharma and R. S. Sidhu, ''On the propagation of plane harmonic waves in anisotropic generalized thermoelasticity,'' Int. J. Eng. Sci. **24**, 1511–1516 (1986).
[11] H. Singh and J. N. Sharma, ''Generalized thermoelastic waves in transversely isotropic media,'' J. Acoust. Soc. Am. **77**, 1046–1053 (1985).
[12] J. N. Sharma and H. Singh, ''Generalized thermoelastic waves in anisotropic media,'' J. Acoust. Soc. Am. **85**, 1407–1413 (1985).
[13] I. N. Sneddon and R. Hill, *Progress in Solid Mechanics* (North-Holland, Amsterdam, 1964), Vol. 1, p. 265.
[14] N. H. Scott, ''A theorem in thermoelasticity and its application to linear stability,'' Proc. R. Soc. London, Ser. A **424**, 143–153 (1989).
[15] N. H. Scott, ''The stability of plane waves in generalized thermoelasticity,'' *Elastic Wave Propagation*, edited by M. F. McCarthy and M. A. Hayes (North-Holland, Amsterdam, 1989), pp. 623–628.

The influence of backward wave transmission on quantitative ultrasonic evaluation using Lamb wave propagation

T. Liu
Department of Civil Engineering, The University of Queensland, Brisbane, Qld 4072, Australia

W. Karunasena
Department of Civil and Environmental Engineering, School of Engineering, James Cook University, Townsville, Qld 4811, Australia

S. Kitipornchai[a)]
Department of Civil Engineering, The University of Queensland, Brisbane, Qld 4072, Australia

M. Veidt
Department of Mechanical Engineering, The University of Queensland, Brisbane, Qld 4072, Australia

(Received 8 December 1998; revised 30 August 1999; accepted 31 August 1999)

In view of the various novel quantitative ultrasonic evaluation techniques developed using Lamb wave propagation, the influence of an important related phenomenon, backward transmission, is investigated in this paper. Using the discrete layer theory and a multiple integral transform method, the surface displacement and velocity responses of isotropic plates and cross-ply laminated composite plates due to the Lamb waves excited by parabolic- and piston-type transmitting transducers are evaluated. Analytical expressions for the surface displacement and velocity frequency response functions are developed. Based on this a large volume of calculations is carried out. Through examining the characteristics of the surface displacement and velocity frequency response functions and, especially, the different propagation modes' contributions to them, the influence of the backward wave transmission related to quantitative ultrasonic nondestructive evaluation applications is discussed and some important conclusions are drawn. © *2000 Acoustical Society of America.* [S0001-4966(99)04212-5]

PACS numbers: 43.40.Dx, 43.35.Cg [CBB]

INTRODUCTION

In recent years, the use of Lamb wave propagation to develop modern quantitative ultrasonic evaluation techniques has attracted rapidly growing interest for various purposes, for example, quick inspection of long gas or petroleum pipe lines, evaluation of complex damage state of composite structures and even real-time monitoring of composite manufacturing processes. Consequently, a clear understanding of the characteristics of the wave propagation involved is very important for the interpretation of measurement results as well as for the further optimization of the corresponding measurement techniques.

There has been a considerable amount of investigation on general characteristics of Lamb wave propagation, for example, Refs. 1–8. However, investigation of an important phenomenon related to the Lamb wave propagation, namely, backward wave transmission, is still limited. Based on the frequency equation for isotropic plates or cylinders, some researchers such as Tolstoy *et al.*[9] first predicted the presence of backward wave motion in which phase and group velocities have opposite signs. This means that energy is carried in a direction opposite to the motion of the waves. Several years later Meitzler[10] reported his experimental observations to give evidence of this interesting prediction and also gave an interpretation by comparing the displacement components, stress components, and the average energy-flux density for the forward and backward motions. After that, Torvik[11] reconfirmed the presence of backward wave motion for a limited range of frequency during his investigation of the reflection of an infinite train of waves from the free edge of an isotropic plate. He also found that there exists a critical frequency in the second mode (nonpropagating mode) well below the first cutoff frequency near which the wave reflection coefficient experiences a sharp resonance in amplitude.

Considering the abnormal properties discovered for backward wave transmission in isotropic plates, the influence of backward waves involved in some quantitative ultrasonic evaluation techniques such as acousto-ultrasonics or stress wave factor technique for composite laminates is considered in this paper. Using discrete layer theory and a multiple integral transform method, the surface displacement and velocity responses of isotropic plates and cross-ply composite laminated plates due to Lamb waves excited by contact-type transducers such as adhesively bonded piezoceramic transducers are evaluated. Analytical expressions for the surface displacement and velocity frequency response functions are developed. Based on this, numerical calculations are carried out to examine the influence of backward wave transmission related to ultrasonic nondestructive evaluation applications.

I. FORMULATION OF THE PROBLEM

Consider a transmitting transducer attached to the upper surface of a composite laminated plate of thickness h as

a)Electronic mail: e2kitip@brolga.uq.edu.au

FIG. 1. The problem considered in this paper.

shown in Fig. 1. It is assumed that the surface displacement or velocity is to be measured at another position. A Cartesian coordinate system (x,y,z) with origin on the upper surface of the laminate is introduced. Each lamina is modeled as a transversely isotropic material. For simplicity, we confine our attention to cross-ply laminates with the three axes coinciding with the axes of orthotropy and a plane strain condition with the y axis being perpendicular to the plane. Then, in the absence of body forces, the basic governing equations for the ith lamina bounded by $z=z_i$ and $z=z_{i+1}$ are

$$\begin{Bmatrix} \sigma_{xx} \\ \sigma_{zz} \\ \sigma_{xz} \end{Bmatrix} = \begin{bmatrix} c_{11} & c_{13} & 0 \\ c_{13} & c_{33} & 0 \\ 0 & 0 & c_{55} \end{bmatrix} \begin{Bmatrix} \epsilon_{xx} \\ \epsilon_{zz} \\ \gamma_{xz} \end{Bmatrix}, \tag{1}$$

$$\epsilon_{xx}=\frac{\partial u}{\partial x}, \quad \epsilon_{zz}=\frac{\partial w}{\partial z}, \quad \gamma_{xz}=\frac{\partial u}{\partial z}+\frac{\partial w}{\partial x}, \tag{2}$$

$$\frac{\partial \sigma_{xx}}{\partial x}+\frac{\partial \sigma_{xz}}{\partial z}=\rho\frac{\partial^2 u}{\partial t^2}, \tag{3a}$$

$$\frac{\partial \sigma_{xz}}{\partial x}+\frac{\partial \sigma_{zz}}{\partial z}=\rho\frac{\partial^2 w}{\partial t^2}, \tag{3b}$$

$$\sigma_{zz}|_{z=0}=-p_1(x,t), \tag{4a}$$

$$\sigma_{xz}|_{z=0}=-p_2(x,t), \tag{4b}$$

where σ_{ij} and ϵ_{ij} are stress and strain components, respectively; u and w denote displacement components in x and z axis directions, respectively; c_{ij} and ρ are elements of the constitutive matrix and density of the ith lamina, respectively; t denotes the time variable; and $p_1(x,t)$ and $p_2(x,t)$ represent the distributed traction excited by the transmitting transducer.

An approximate approach called the stiffness method[12–14] or discrete layer method[15] is used to solve the above equations. The essence of the method is to divide the plate into a number of mathematical layers in the thickness direction so that the variation of the displacements through the thickness of each layer can be approximated by various polynomials using interpolation for some unknown displacements. Using the principle of virtual work, the differential equations of the wave motion in the plate can then be expressed in a form in which there is no differentiation with respect to the variable in the thickness direction.

Following the procedure described in Refs. 12–15, it is assumed that the plate, as shown in Fig. 1, is divided into N mathematical layers. For the ith layer, the vector of displacements at an arbitrary point denoted by $\mathbf{U}_i(x,z)=[u_i(x,z),w_i(x,z)]^T$ is expressed by a quadratic polynomial interpolation as

$$\mathbf{U}_i=(x,z)=\mathbf{N}\mathbf{q}_i, \tag{5}$$

where the matrix $\mathbf{q}$, a displacement vector composed of the displacement vectors for the upper surface, the middle plane and the lower surface of the ith layer, and the matrix $\mathbf{N}$, the corresponding shape function, can be expressed as

$$\mathbf{q}_i^T=[\mathbf{U}_i^T|_{\eta=0},\mathbf{U}_i^T|_{\eta=1/2},\mathbf{U}_i^T|_{\eta=1}], \tag{6}$$

$$\mathbf{N}=[2\eta^2-3\eta+1)\mathbf{I},(-4\eta^2+4\eta)\mathbf{I},(2\eta^2-\eta)\mathbf{I}], \tag{7}$$

in which $\mathbf{I}$ is a 2×2 identity matrix and η is the normalized measure for the ith layer defined by

$$\eta=(z-z_{iu})/h_i, \tag{8}$$

where z_{iu} and h_i are the z coordinate of the upper surface and the thickness of the ith layer, respectively.

Applying the principle of virtual work to the ith layer, we have

$$\delta\mathbf{q}_i^T\mathbf{T}_i=\delta\mathbf{q}_i^T\mathbf{S}_i+\int_{z_{iu}}^{z_{iu}+h_i}\delta\mathbf{U}_i^T(\rho_i\ddot{\mathbf{U}}_i-\mathbf{L}^T\sigma_i-\mathbf{f}_i)dz, \tag{9}$$

with

$$\sigma_i^T=[\sigma_{xx},\sigma_{zz},\sigma_{xz}], \tag{10a}$$

$$\mathbf{f}_i^T=[f_x,f_z], \tag{10b}$$

$$\mathbf{S}_i^T=[-\sigma_{xz}|_{\eta=0},-\sigma_{zz}|_{\eta=0},0,0,\sigma_{xz}|_{\eta=1},\sigma_{zz}|_{\eta=1}], \tag{10c}$$

$$\mathbf{T}_i^T=[p_{xz}|_{\eta=0},p_{zz}|_{\eta=0},p_{xz}|_{\eta=1/2},p_{zz}|_{\eta=1/2},\ p_{xz}|_{\eta=1},p_{zz}|_{\eta=1}], \tag{10d}$$

$$\mathbf{L}^T=\begin{bmatrix} \frac{\partial}{\partial x} & 0 & \frac{\partial}{\partial z} \\ 0 & \frac{\partial}{\partial z} & \frac{\partial}{\partial x} \end{bmatrix}, \tag{10e}$$

where σ_i, $\mathbf{f}_i$, $\mathbf{S}_i$ and $\mathbf{T}_i$ represent the stress vector, the body force vector, the upper and lower interface traction vector, and the probable external load vector for the ith layer, respectively. Here p_{xz} and p_{zz} are the shear and normal external traction. ρ_i is its mass density. The symbol ''$\cdot$'' indicates differentiation with respect to time.

Substituting Eqs. (5)–(7) into Eq. (9) and using the general relations among stresses, strains and displacements, the governing equation for the ith layer can be expressed as

$$\mathbf{M}^{(i)}\frac{\partial^2}{\partial t^2}\mathbf{q}_i+\left[-\mathbf{K}_1^{(i)}\frac{\partial^2}{\partial x^2}-\mathbf{K}_4^{(i)}\frac{\partial}{\partial x}+\mathbf{K}_6^{(i)}\right]\mathbf{q}_i=\mathbf{T}_i, \tag{11}$$

where $\mathbf{M}^{(i)}$, $\mathbf{K}_1^{(i)}$, $\mathbf{K}_4^{(i)}$ and $\mathbf{K}_6^{(i)}$ and 6×6 matrices which are given in the Appendix (item 1). In the derivation of Eq. (11), it is assumed that no body forces exist.

In the same way, obtaining all the governing equations for the N layers, and then assembling them from the top layer to the bottom layer, the governing equation for the laminated plate can be finally expressed as

$$\mathbf{M}\frac{\partial^2}{\partial t^2}\mathbf{q}+\left[-\mathbf{K}_1\frac{\partial^2}{\partial x^2}-\mathbf{K}_4\frac{\partial}{\partial x}+\mathbf{K}_6\right]\mathbf{q}=\mathbf{T}, \tag{12}$$

where $\mathbf{q}$, $\mathbf{T}$, $\mathbf{M}$, $\mathbf{K}_1$, $\mathbf{K}_4$, and $\mathbf{K}_6$ are the global matrices produced by assembling $\mathbf{q}_i$, $\mathbf{T}_i$, $\mathbf{M}^{(i)}$, $\mathbf{K}_1^{(i)}$, $\mathbf{K}_4^{(i)}$ and $\mathbf{K}_6^{(i)}$ $(i=1,2,3,...,N)$, respectively.

In order to simplify the problem, as presented in Refs. 16 and 17 it is assumed that the pressure distribution between the transducer and the plate can be approximated by a piston distribution or a parabolic distribution. The contact pressure $p_i(x,t)$ exerted on the surface of the plate by the transducer can therefore be expressed as

$$p_i(x,t)=[\mathrm{H}(x+a)-\mathrm{H}(x-a)]D(x,a)p_i(t), \quad i=1,2, \tag{13}$$

in which a is the aperture of the transmitting transducer, $\mathrm{H}(x)$ stands for the Heaviside function, $p_i(t)(i=1,2)$ are the normal and tangential forces exerted on the plate by the transmitting transducer, and $D(x,a)$ is the contact pressure distribution function which for a piston distribution is defined as

$$D(x,a)=\begin{cases}1, & |x|\leqslant a,\\ 0, & |x|>a,\end{cases} \tag{14}$$

and for a parabolic distribution as

$$D(x,a)=\begin{cases}\frac{3}{2}[1-(x/a)^2], & |x|\leqslant a,\\ 0, & |x|>a.\end{cases} \tag{15}$$

The resultant force is the same in both cases.

Expressing the above contact pressure in the form of the external load vector given in (12) yields to

$$\mathbf{T}=p_1(x,t)\mathbf{C}_1+p_2(x,t)\mathbf{C}_2 \tag{16}$$

where $\mathbf{C}_1$ and $\mathbf{C}_2$ are constant vectors of length $2(2N+1)$, which are given by

$$\mathbf{C}_1^T=[0,1,0,0,...,0], \tag{17a}$$

$$\mathbf{C}_2^T=[1,0,0,0,...,0]. \tag{17b}$$

II. FREQUENCY DOMAIN SOLUTION AND INVERSION

Applying the Fourier time transform and spatial transform defined as

$$\overline{g}(x,\omega)=\int_0^{\infty} g(x,t)e^{-i\omega t}dt, \tag{18}$$

$$\tilde{g}(\kappa,t)=\int_{-\infty}^{+\infty} g(x,t)e^{-i\kappa x}dx, \tag{19}$$

to Eqs. (12) on t and x, respectively, we have

$$(\kappa^2\mathbf{K}_1-i\kappa\mathbf{K}_4+\mathbf{K}_6-\omega^2\mathbf{M})\tilde{\overline{\mathbf{q}}}=\tilde{\overline{\mathbf{T}}}. \tag{20}$$

Solving the above equation yields to[18]

$$\tilde{\overline{\mathbf{q}}}=i\sum_{m=1}^{2M}\frac{\boldsymbol{\psi}_{ml}^T\tilde{\overline{\mathbf{T}}}}{(\kappa-\kappa_m)\boldsymbol{\psi}_m^T\mathbf{R}\boldsymbol{\varphi}_m}\boldsymbol{\varphi}_{mu}, \tag{21}$$

where $M=2(2N+1)$ and $\kappa_m=i\lambda_m$. φ_m, ψ_m and λ_m $(m=1$ to $2M)$ are the eigenvectors and eigenvalues of the following two characteristic equations:

$$(\mathbf{Q}-\lambda\mathbf{R})\varphi=\mathbf{0}, \tag{22a}$$

$$(\mathbf{Q}^T-\lambda\mathbf{R}^T)\psi=\mathbf{0} \tag{22b}$$

in which

$$\mathbf{Q}=\begin{bmatrix}\mathbf{0} & \mathbf{I}\\ \omega^2\mathbf{M}-\mathbf{K}_6 & -\mathbf{K}_4\end{bmatrix}, \tag{23a}$$

$$\mathbf{R}=\begin{bmatrix}\mathbf{I} & \mathbf{0}\\ \mathbf{0} & -\mathbf{K}_1\end{bmatrix}, \tag{23b}$$

where $\mathbf{I}$ is an identity matrix of the same dimension as $\mathbf{M}$, $\mathbf{K}_1$, $\mathbf{K}_4$, and $\mathbf{K}_6$. φ_{mu} and ψ_{ml} are the upper and lower halves of the eigenvectors φ_m and ψ_m, respectively.

Substituting Eqs. (13)–(15) to Eq. (16) and then applying the Fourier transformations (18) and (19) to resulting equation on variable t and x, respectively, yields

$$\tilde{\overline{\mathbf{T}}}=\overline{p_1}(\omega)I(\kappa)\mathbf{C}_1+\overline{p_2}(\omega)I(\kappa)\mathbf{C}_2, \tag{24}$$

in which $I(\kappa)$ is given as for piston-type force distribution,

$$I(\kappa)=i[e^{i\kappa(x-a)}-e^{i\kappa(x+a)}]/\kappa, \quad x>a, \tag{25a}$$

and for parabolic-type force distribution,

$$I(\kappa)=3[(i-\kappa a)e^{i\kappa(x-a)}-(i+\kappa a)e^{i\kappa(x+a)}]/(\kappa^3a^2)], \quad x>a. \tag{25b}$$

Applying the inverse Fourier spatial transform of Eq. (19) to Eqs. (21) and (24), we have

$$\overline{\mathbf{q}}(x)=\overline{\mathbf{q}}_1+\overline{\mathbf{q}}_2 \tag{26}$$

with

$$\overline{\mathbf{q}}_j=\frac{i}{2\pi}\overline{p}_j(\omega)\int_{-\infty}^{\infty}\sum_{m=1}^{2M}\frac{I(\kappa)\boldsymbol{\psi}_{ml}^T\mathbf{C}_j}{(\kappa-\kappa_m)\boldsymbol{\psi}_m^T\mathbf{R}\boldsymbol{\varphi}_m}\boldsymbol{\varphi}_{mu}d\kappa, \quad j=1,2. \tag{27}$$

Considering the real measurements, from the general displacement expression (26), the frequency domain solution of the top surface displacement $w(x,0,t)$ and velocity $V(x,0,t)$ of the plate are expressed as

$$\overline{w}(x,0,\omega)=G_1(\omega)\overline{p}_1(\omega)+G_2(\omega)\overline{p}_2(\omega), \tag{28}$$

$$\overline{V}(x,0,\omega)=-i\omega G_1(\omega)\overline{p}_1(\omega)-i\omega G_2(\omega)\overline{p}_2(\omega), \tag{29}$$

in which

$$G_j(\omega)=\frac{i}{2\pi}\int_{-\infty}^{\infty}\sum_{m=1}^{2M}\frac{(\boldsymbol{\psi}_{ml}^T\mathbf{C}_j)(\boldsymbol{\varphi}_{mu}^T\mathbf{C}_1)}{(\kappa-\kappa_m)\boldsymbol{\psi}_m^T\mathbf{R}\boldsymbol{\varphi}_m}I(\kappa)d\kappa, \quad j=1,2, \tag{30a}$$

$$H_j(\omega)=-i\omega G_j(\omega), \quad j=1,2. \tag{30b}$$

Applying the contour integration technique[19] to Eq. (30a), $G_j(\omega)$ can be simplified as

TABLE I. Engineering constants of two types of plates used in the calculation.

Material	E_1 (Gpa)	E_2 (Gpa)	G_{12} (Gpa)	G_{13} (Gpa)	G_{23} (Gpa)	ν_{12}	ρ (Kg/m^3)
Aluminum	73	73	28.077	28.077	28.077	0.3	2770
Glass/epoxy	38.612	8.274	4.137	4.137	3.448	0.26	1800

$$G_j(\omega)=-\sum_{m=1}^{M_i}\frac{(\boldsymbol{\psi}_{ml}^T\mathbf{C}_j)(\boldsymbol{\varphi}_{mu}^T\mathbf{C}_1)}{\boldsymbol{\psi}_m^T\mathbf{R}\boldsymbol{\varphi}_m}I(\kappa_m)-\sum_{m=1}^{M_c}\frac{(\boldsymbol{\psi}_{ml}^T\mathbf{C}_j)(\boldsymbol{\varphi}_{mu}^T\mathbf{C}_1)}{\boldsymbol{\psi}_m^T\mathbf{R}\boldsymbol{\varphi}_m}I(\kappa_m),\quad j=1,2, \tag{31}$$

where M_r is the number of the real wave modes with positive group velocities, i.e., carrying energy towards the positive x-axis direction, and M_c is the number of complex wave modes corresponding to the κ_m with $\mathrm{Im}(\kappa_m)>0$.

In view of Eqs. (28) and (29) $G_1(\omega)$, $G_2(\omega)$ and $H_1(\omega)$, $H_2(\omega)$ can be called the displacement and velocity frequency response functions corresponding to the normal traction and shear traction excited by the transmitting transducer.

Applying the inverse Fourier time transformation to the frequency domain solution Eqs. (28) and (29), the time domain solution of the surface displacement and velocities can be expressed as

$$w(x,0,t)=\int_{-\infty}^{\infty}[G_1(\omega)\overline{p_1}(\omega)+G_2(\omega)\overline{p_2}(\omega)]e^{i\omega t}d\omega, \tag{32a}$$

$$V(x,0,t)=\int_{-\infty}^{\infty}[H_1(\omega)\overline{p_1}(\omega)+H_2(\omega)\overline{p_2}(\omega)]e^{i\omega t}d\omega. \tag{32b}$$

The computation of Eqs. (32a) and (32b) can be carried out using the fast Fourier transform (FFT) technique.

III. THE SOLUTION BASED ON SIMPLIFED THEORIES

Although simplified plate theories such as the classical plate theory and the Mindlin plate theory cannot be used to examine backward wave transmission, they are still useful for result comparison or program check in low-frequency regions. In this section, the corresponding solution based on the Mindlin plate theory is presented.

Using the same coordinate system as above, the equations of the motion for the plate in a state of plane strain parallel to the x-z plane are

$$kA_{55}\left(\frac{\partial\varphi_x}{\partial x}+\frac{\partial^2 w}{\partial w^2}\right)+p_1=\rho h\frac{\partial^2 w}{\partial t^2}, \tag{33a}$$

$$D_{11}\frac{\partial^2\varphi_x}{\partial x^2}-kA_{55}\left(\varphi_x+\frac{\partial w}{\partial x}\right)=\frac{\rho h^3}{12}\frac{\partial^2\varphi_x}{\partial t^2}, \tag{33b}$$

where w is the transverse displacement; φ_x is the rotation of the plane section perpendicular to the x axis; p_1 is seen in Eq. (13); $k(=\pi^2/12)$ is a shear correction factor; and A_{55} and D_{11} are the plate transverse-shear and plate bending rigidities, respectively. A_{55} and D_{11} are given by

$$A_{55}=\sum_{k=1}^{N}\overline{Q}_{55}^{(k)}(\overline{z}_{k+1}-\overline{z}_k), \tag{34a}$$

$$D_{11}=\frac{1}{3}\sum_{k=1}^{N}\overline{Q}_{11}^{(k)}(\overline{z}_{k+1}^3-\overline{z}_k^3), \tag{34b}$$

$$\overline{Q}_{55}^{(k)}=Q_{55}^{(k)}\cos^2\theta_k+Q_{44}^{(k)}\sin^2\theta_k, \tag{34c}$$

$$\overline{Q}_{11}^{(k)}=Q_{11}^{(k)}\cos^4\theta_k+Q_{22}^{(k)}\sin^4\theta_k, \tag{34d}$$

$$Q_{11}^{(k)}=E_1^{(k)}/(1-\nu_{12}^{(k)}\nu_{21}^{(k)}), \tag{34e}$$

$$Q_{22}^{(k)}=\nu_{12}^{(k)}E_2^{(k)}/(1-\nu_{12}^{(k)}\nu_{21}^{(k)}), \tag{34f}$$

$$Q_{44}^{(k)}=G_{23}^{(k)}, \tag{34g}$$

$$Q_{55}^{(k)}=G_{13}^{(k)}, \tag{34h}$$

$$\nu_{21}^{(k)}=\nu_{12}^{(k)}E_2^{(k)}/E_1^{(k)}, \tag{34i}$$

where $\overline{z}_k=z_k-h/2$, $Q_{ii}^{(k)}$ $(i=1,2,4,5)$ is the material stiffness constant of kth layer, θ_k is the angle between the fiber direction of kth layer and the x axis (0 or 90 degrees), and $E_1^{(k)}$, $E_2^{(k)}$, $G_{13}^{(k)}$, $G_{23}^{(k)}$, and $\nu_{12}^{(k)}$ are the engineering constants for the kth layer.

Based on Eqs. (33a), (33b) and (13)–(15), using a similar Fourier transformation procedure, the solution corresponding to Eq. (28) can be obtained as follows:

For parabolic source,

$$\overline{w}(x,0,\omega)=\overline{p_1}(\omega)[\mu_{11}e^{-i\kappa_1(x-a)}+\mu_{12}e^{i\kappa_1(x+a)}+\mu_{21}e^{-\gamma(x-a)}+\mu_{22}e^{-\gamma(x+a)}],\quad |\omega|<\omega_c, \tag{35a}$$

$$\overline{w}(x,0,\omega)=\overline{p_1}(\omega)[\mu_{11}e^{-i\kappa_1(x-a)}+\mu_{12}e^{-i\kappa_1(x+a)}+\mu_{21}e^{-i\kappa_2(x-a)}+\mu_{22}e^{-i\kappa_2(x+a)}],\quad |\omega|\geqslant\omega_c. \tag{35b}$$

For piston source,

$$\overline{w}(x,0,\omega)=\overline{p_1}(\omega)\{\nu_1[e^{-i\kappa_1(x-a)}-e^{-i\kappa_1(x+a)}]+\nu_2[e^{-\gamma(x-a)}-e^{-\gamma(x+a)}]\},\quad |\omega|<\omega_c, \tag{36a}$$

$$\overline{w}(x,0,\omega)=\overline{p_1}(\omega)\{\nu_1[e^{-i\kappa_1(x-a)}-e^{-i\kappa_1(x+a)}]+\nu_2[e^{-i\kappa_2(x-a)}-e^{i\kappa_2(x+a)}]\},\quad |\omega|\geqslant\omega_c, \tag{36b}$$

where the coefficients μ_{ij}, ν_i $(ij=1,2)$ are given in the Appendix (item 2), and the cutoff frequency ω_c and wave number κ_1 and κ_2 are given by

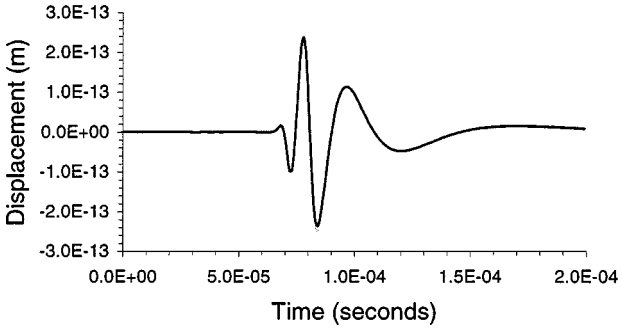

FIG. 2. Time history of the surface displacement evaluated by the discrete layer theory (thin line) and Mindlin plate theory (thick line) (composite plate 0/90/0, $h=2$ nm, $x=100$ mm; parabolic source $a=5$ mm, $f_0=0.125$ MHz, $n_0=2$; $f_c=0.368$ MHz).

$$\kappa_1=\left[\frac{1}{2}\left(\frac{1}{c_0^2}+\frac{1}{c_s^2}\right)\omega^2+\sqrt{\frac{1}{4}\left(\frac{1}{c_0^2}-\frac{1}{c_s^2}\right)^2\omega^4+\frac{1}{c_0^2\alpha^2}\omega^2}\right]^{1/2},\quad |\omega|<\infty, \tag{37}$$

$$\kappa_2=i\gamma \quad \text{for } |\omega|\leqslant\omega_c, \tag{38a}$$

$$\kappa_2=\left[\frac{1}{2}\left(\frac{1}{c_0^2}+\frac{1}{c_s^2}\right)\omega^2-\sqrt{\frac{1}{4}\left(\frac{1}{c_0^2}-\frac{1}{c_s^2}\right)^2\omega^4+\frac{1}{c_0^2\alpha^2}\omega^2}\right]^{1/2}\quad \text{for } |\omega|>\omega_c, \tag{38b}$$

in which

$$\gamma=\left[\sqrt{\frac{1}{4}\left(\frac{1}{c_0^2}-\frac{1}{c_s^2}\right)^2\omega^4+\frac{1}{c_0^2\alpha^2}\omega^2}-\frac{1}{2}\left(\frac{1}{c_0^2}+\frac{1}{c_s^2}\right)\omega^2\right]^{1/2}, \tag{39a}$$

$$c_0=\sqrt{\frac{12D_{11}}{\rho h^3}}, \tag{39b}$$

$$c_s=\sqrt{\frac{A_{55}k}{\rho h}}, \tag{39c}$$

$$\alpha=\frac{h}{\sqrt{12}}, \tag{39d}$$

$$\omega_c=\sqrt{\frac{12A_{55}k}{\rho h^3}}. \tag{39e}$$

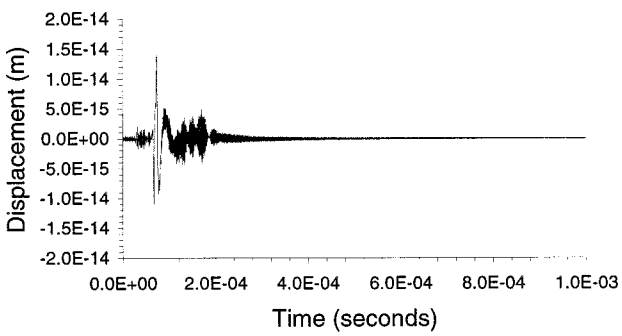

FIG. 3. Time history of the surface displacement evaluated by the discrete layer theory (composite plate 0/90/0, $h=2$ mm, $x=100$ mm; parabolic source $a=5$ mm, $f_0=0.4$ MHz, $n_0=2$; $f_c=0.368$ MHz).

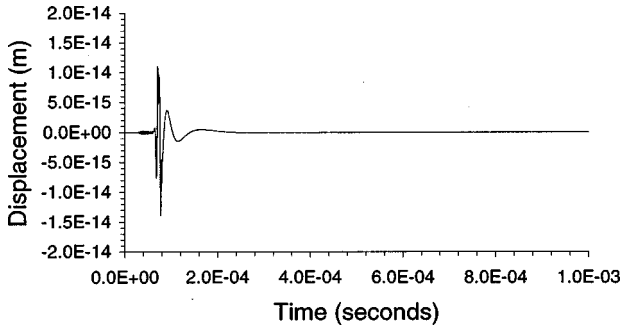

FIG. 4. Time history of the surface displacement evaluated by the Mindlin plate theory (composite plate 0/90/0, $h=2$ mm, $x=100$ mm; parabolic source $a=5$ mm, $f_0=0.4$ MHz, $n_0=2$; $f_c=0.368$ MHz).

Similarly, applying the inverse Fourier time transformation to Eqs. (35a), (35b), (36a), and (36b), the time domain solutions of the surface displacement can be obtained.

IV. NUMERICAL RESULTS AND DISCUSSION

In this section, based on the above analytical formulations, some numerical calculations are carried out to examine the characteristics of backward wave motion and its influence on the surface displacement and velocity responses of the plate interrogated by the transmitting transducer.

Two types of materials were used in the calculations. One is an isotropic aluminum, and the other is a glass/epoxy composite. Their engineering material constants are given in Table I.

Also, in the calculation the input pulse used is the delayed sine pulse with Haning window, i.e.,

$$p_i(t)=\begin{cases}0.5[1-\cos(2\pi f_0 t/n_0)]\cos(2\pi f_0 t), & t\leqslant n_0/f_0,\\ 0, & t>n_0/f_0,\end{cases} \tag{40}$$

where f_0 is the central frequency and n_0 is the number of periods.

As a program check, the surface displacement response of a composite laminate (0°/90°/0°) of thickness $h=2$ mm due to parabolic source pulse is evaluated by both the discrete layer theory and the Mindlin plate theory. Figure 2 shows both results for low-frequency input (the dominant frequency is 0.125 MHz). It is seen that they are very close to each other. Using the same program the results for relatively high-frequency input (the dominant frequency is 0.4 MHz) are evaluated by the two theories in Figs. 3 and 4, respectively. For this frequency range the results of the two analysis models show some differences. It is evident that the above results are reasonable, considering the approximation involved in the Mindlin plate theory. This demonstrates, to some extent, the validity of the analysis and the computer program. Based on this, the backward wave motion characteristics and its influence are examined in the following paragraphs.

The dispersion curves for the aluminum plate which can be obtained by solving characteristic equation (22a) or (22b),

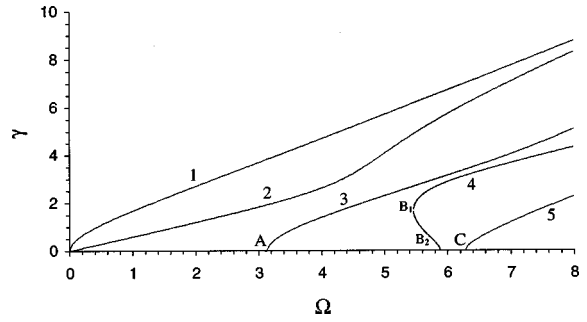

FIG. 5. The dispersion curves of normalized frequency $\Omega=\omega h/c_s$ and normalized wave number $\gamma=\kappa h$ for an isotropic plate with Poisson's ratio $\nu=0.3$.

are shown in Fig. 5. Since the wave number κ and the frequency ω have been normalized by $\Omega=\omega h/c_s$ and $\gamma=\kappa h$, respectively, where $c_s=\sqrt{G/\rho}$ with G and ρ being the shear modulus and the mass density, the dispersion curves obtained are valid for a wide range of isotropic plate cases as long as the Possion's ratio $\nu=0.3$. In this figure, the backward wave branch is marked by B_1B_2, in which the phase and group velocities are of opposite sign. It is necessary to point out that branch B_1B_2 here should be understood as its image with respect to the Ω axis, which has a positive group velocity. Additionally, for simplicity B_1 and B_2 are called the beginning and end points of the backward wave region in this paper, although B_2 is usually called the cutoff frequency of the second symmetric real branch.

Referring to Eq. (28), Fig. 6 shows the variation in amplitude of the normalized displacement frequency response function $G_1(\omega)$ at two different surface points due to a normal pressure pulse transmitted by a parabolic source. There are two singularities at the beginning and end points of the backward wave region, while at their two neighboring points A and C which are the first and second cutoff frequencies of antisymmetric modes there exist no singularities. This phenomenon is useful for understanding the peaks in the corresponding amplitude spectrum of a response signal when the input frequency covers this region. Additionally, it can also be seen that in relatively high-frequency cases, the displacement frequency response function has larger amplitude within and near the backward wave region. This means in such regions Lamb waves can carry more energy. However,

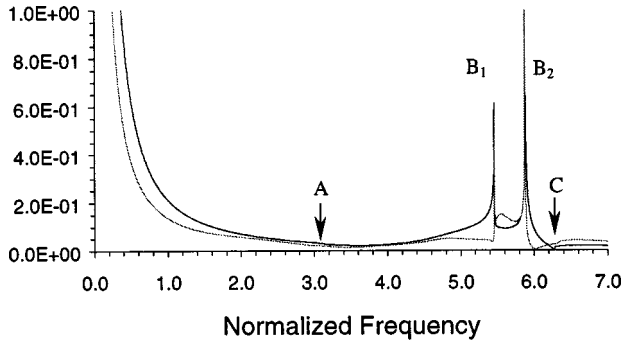

FIG. 6. Surface displacement frequency response $(GG_1/h\sim\omega h/c_s)$ at two different points $x/h=0.833$ (solid line) and 8.33 (dashed line) on an isotropic plate ($\nu=0.3$) due to a normal pressure pulse transmitted by a parabolic source ($a/h=0.5$).

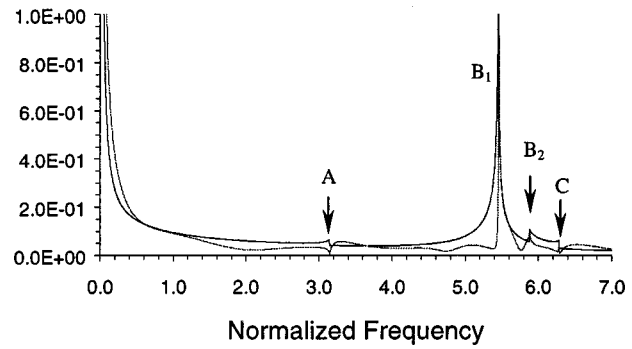

FIG. 7. Surface displacement frequency response function $(GG_2/h\sim\omega h/c_s)$ at two different points $x/h=0.833$ (solid line) and 8.33 (dashed line) on an isotropic plate ($\nu=0.3$) due to a shear force pulse transmitted by a parabolic source ($a/h=0.5$).

since there are several wave branches which have different group velocities, such regions will therefore cause more dispersion or distortion of time domain signals if many wave modes are involved in measurements.

Under the same condition as in Fig. 6, the displacement frequency response function $G_2(\omega)$ due to a shear force source is examined in Fig. 7. It is found that, (1) at the beginning point of the backward wave region there still exists a singularity, and near this singularity point $G_2(\omega)$ still has higher amplitude, while at the end point there is only a little discontinuity. (2) At the points A and C which correspond to the cutoff frequencies of the second and third antisymmetric real branches, there occur small discontinuities. (3) Compared with $G_1(\omega)$, $G_2(\omega)$ is of smaller amplitude in the low-frequency region.

In order to further understand the influence of backward wave transmission at the observation point farther away from the transmitting transducer, the contributions of different real branches (i.e., the propagation modes) to the displacement frequency response function due to a normal pressure pulse transmitted by a parabolic source are shown in Fig. 8. The figure clearly shows that the backward wave branch causes two singularities at its beginning and end points and, compared with other branches in this frequency region it has apparently higher amplitude. This implies that the backward wave branch makes the major contribution to the peak area of the overall frequency spectrum when multiple wave modes are excited as shown in Fig. 6. In other words, the

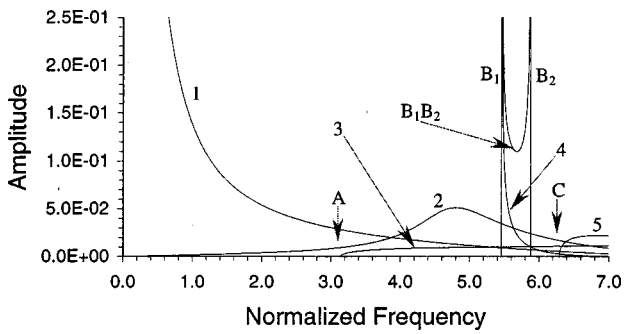

FIG. 8. Contributions of different real branches to the surface displacement frequency response function $(GG_1/h\sim\omega h/c_s)$ at $x/h=8.33$ on an isotropic plate ($\nu=0.3$) due to a normal pressure pulse transmitted by a parabolic source ($a/h=0.5$) (referring to Fig. 5).

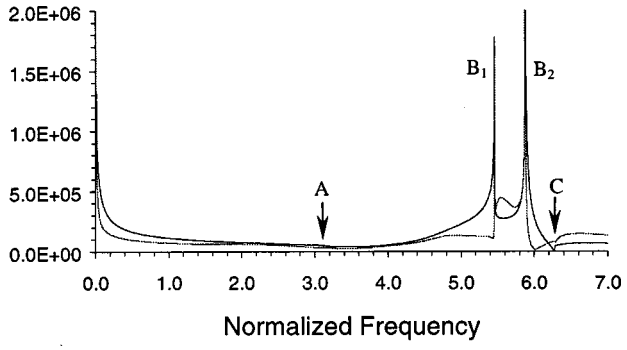

FIG. 9. Surface velocity frequency response function ($GH_1/h \sim \omega h/c_s$) at two different points $x/h=0.833$ (solid line) and 8.33 (dashed line) on an isotropic plate ($\nu=0.3$) due to a normal pressure pulse transmitted by a parabolic source ($a/h=0.5$).

peak area of the overall spectrum is dominated by the backward wave mode. But, unfortunately, since the backward wave mode has much smaller wave number, i.e., much longer wave length (see Fig. 5) than other branches in this region, the backward wave propagation will decrease the overall sensitivity for damage detection in this frequency region. On the other hand, however, if the damage size concerned can be compared with the wave length of the backward wave or long distance wave interrogation is required, then the use of the single backward wave mode which can be achieved by interdigital transducers could probably have some advantages because it appears that the backward wave can be excited more efficiently.

The contributions of different real branches to the displacement frequency response function $G_1(\omega)$ due to a normal pressure pulse transmitted by a piston-type source have also been examined. Compared with Fig. 8, it is found that there is no apparent difference in the backward wave contribution between the parabolic and piston source cases.

In consideration of the common use of the noncontact Doppler laser vibrometer system to measure surface velocity,[20] in Fig. 9 the frequency response function of surface velocities $H_1(\omega)$ [see Eq. (29)] due to a normal pressure pulse transmitted by a parabolic source is shown, and in Fig. 10 different real branches' contributions to $H_1(\omega)$ for the point farther away from the source are illustrated. The same behavior induced by the backward wave transmission in the

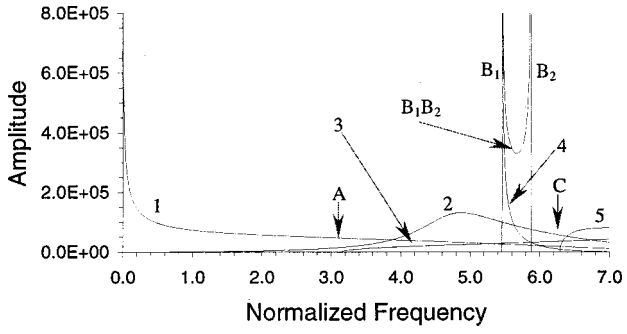

FIG. 10. Contributions of different real branches to the surface velocity frequency response function ($GH_1/h \sim \omega h/c_s$) at $x/h=0.833$ on an isotropic plate ($\nu=0.3$) due to a normal pressure pulse transmitted by a parabolic source ($a/h=0.5$) (referring to Fig. 5).

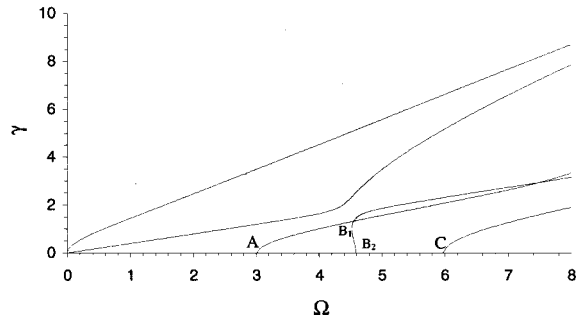

FIG. 11. The dispersion curves of normalized frequency $\Omega=\omega h/\sqrt{G_{12}/\rho}$ and normalized wave number $\gamma=\kappa h$ for a glass/epoxy composite laminated plate [(0/90/0/90/0)s].

case of surface displacement measurement can be found in velocity measurement. So the above discussions about the backward transmission measured by surface displacement also applies to the cases for velocity measurement. However, it is of interest to note that $H_1(\omega)$ has relatively lower amplitude than $G_1(\omega)$ in the low frequency region.

Figure 11 shows the normalized dispersion curves of a glass/epoxy composite plate laminated as (0°/90°/0°/90°/0°)s. In Fig. 12 its surface velocity frequency response function due to normal pressure pulses transmitted by a parabolic-type transducer is presented. It can be seen that no matter whether the plate is isotropic or orthotropic, the behavior caused by the backward wave transmission is similar. This is because the characteristics of the dispersion curves in both cases are similar.

V. CONCLUSION

In this paper, in recognition of the various quantitative ultrasonic evaluation techniques using Lamb waves propagation, the influence of backward wave transmission in isotropic plates and cross-ply laminated composite plates has been investigated. Using the discrete layer theory, the surface displacement and velocity responses due to the Lamb waves excited by transmitting transducers have been evaluated. Expressions of the surface displacement and velocity frequency response functions have been presented. For comparison, analytical results using the Mindlin plate theory have also been developed. Based on the analytical results numerical

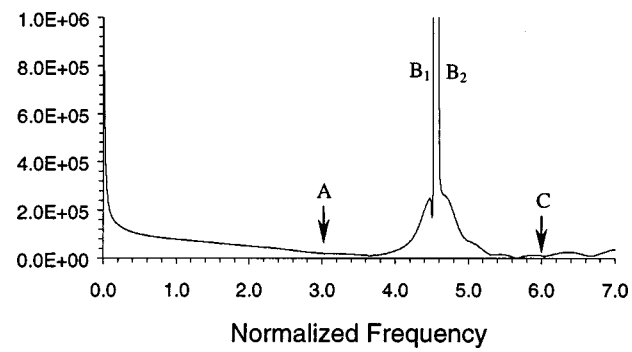

FIG. 12. Surface velocity frequency response function ($GH_1/h \sim \omega h/\sqrt{G_{12}/\rho}$) at point $x/h=10$ on a glass/epoxy composite laminated plate [(0/90/0/90/0)s] due to a normal pressure pulse transmitted by a parabolic source ($a/h=1$).

calculations were carried out to check the validity of the analysis and then to examine the behavior of the backward wave transmission. The following conclusions have been drawn:

(1) For a moderately thick plate or relatively high-frequency input pulses, there exists apparent backward wave transmission. It is essential to consider its influence in this frequency regime for the development of guided wave quantitative nondestructive evaluation techniques.
(2) At the beginning point of the backward wave region, the normal surface displacement and velocity frequency response functions have a singularity no matter whether the transducer transmits normal forces or shear forces, while at the end point a singularity occurs only for the case of a normal pressure source. This is important for the interpretation of peak points in the output frequency spectra.
(3) The backward wave branch carries much more energy than other branches in the backward wave frequency regime. This implies that the backward transmission, on one hand, will decrease the resolution of damage detection if the ultrasonic techniques involve multiple wave modes and their input frequency cover this region since the corresponding wave lengths are large. On the other hand, however, it could be an advantage for some single-wave-mode related ultrasonic evaluation techniques.
(4) The surface displacement and velocity frequency response functions have the same behavior in the backward wave frequency region, e.g., relatively higher amplitude, but in the low-frequency region, the former has relatively higher amplitude than the latter.
(5) The presented figures for the different real branches' contributions to the surface displacement and velocity frequency response functions are of significance for selecting optimized input frequency regimes and the interpretation of the corresponding measurement results.
(6) It should be noted that in the analysis presented in this paper no damping was introduced, so the conclusions obtained above are only valid for structures with no or only small damping. For highly damped structural systems, it is necessary to take into account the damping influence when similar investigations are carried out.

APPENDIX

(1) The matrices in Eq. (11) for the ith layer are

$$\mathbf{M}^{(i)}=\frac{1}{30}h_i\rho_i\begin{bmatrix} 4\mathbf{I} & 2\mathbf{I} & -\mathbf{I} \\ & 16\mathbf{I} & 2\mathbf{I} \\ \textbf{Sym.} & & 4\mathbf{I} \end{bmatrix},$$

$$\mathbf{K}_1^{(i)}=\frac{1}{30}h_i\begin{bmatrix} 4\mathbf{A}_1 & 2\mathbf{A}_1 & -\mathbf{A}_1 \\ & 16\mathbf{A}_1 & 2\mathbf{A}_1 \\ \textbf{Sym.} & & 4\mathbf{A}_1 \end{bmatrix},$$

$$\mathbf{K}_4^{(i)}=\frac{1}{6}\begin{bmatrix} -6\mathbf{B}_4+3\mathbf{A}_4 & -4\mathbf{A}_4 & \mathbf{A}_4 \\ & 0 & -4\mathbf{A}_4 \\ \textbf{Antisym.} & & 6\mathbf{B}_4-3\mathbf{A}_4 \end{bmatrix},$$

$$\mathbf{K}_6^{(i)}=\frac{1}{3h_i}\begin{bmatrix} 7\mathbf{B}_6 & -8\mathbf{B}_6 & \mathbf{B}_6 \\ & 16\mathbf{B}_6 & -8\mathbf{B}_6 \\ \textbf{Sym.} & & 7\mathbf{B}_6 \end{bmatrix},$$

in which $\mathbf{I}$ is a 2×2 identity matrix, and $\mathbf{A}_1$, $\mathbf{A}_4$, $\mathbf{B}_4$, and $\mathbf{B}_6$ are given by

$$\mathbf{A}_1=\begin{bmatrix} c_{11} & 0 \\ 0 & c_{55} \end{bmatrix},\quad \mathbf{A}_4=\begin{bmatrix} 0 & c_{13}+c_{55} \\ c_{13}+c_{55} & 0 \end{bmatrix},$$

$$\mathbf{B}_4=\begin{bmatrix} 0 & c_{55} \\ c_{13} & 0 \end{bmatrix},\quad \mathbf{B}_6=\begin{bmatrix} c_{55} & 0 \\ 0 & c_{33} \end{bmatrix},$$

where c_{ij} $(ij=1,3,5)$ are the stiffness matrix elements in (1) for the ith layer, and h_i and ρ_i are its thickness and mass density, respectively.

(2) The coefficients μ_{ij}, ν_i $(ij=1,2)$ in Eqs. (35a), (35b), (36a) and (36b) are given by

$$[\mu]=\frac{1}{D_{11}a^2\omega^2}\begin{bmatrix} \lambda_1(i\kappa_1 a_1-1)/\kappa_1^2 & \lambda_1(i\kappa_1 a_1+1)/\kappa_1^2 \\ \lambda_2(i\hat{\kappa}a_1-1)/\hat{\kappa}^2 & \lambda_2(i\hat{\kappa}a_1+1)/\hat{\kappa}^2 \end{bmatrix},$$

$$[\nu]=\frac{1}{D_{11}a^2\omega^2}[-\lambda_1 a_1^2/3 \quad -\lambda_2 a_1^2/3],$$

in which

$$\lambda_1=\frac{2}{\eta\delta},\quad \lambda_2=\frac{c_0^2\alpha^2\eta}{2\delta},$$

$$\eta=\delta+(1/c_0^2-1/c_s^2)\omega,\quad \delta=\left[\left(\frac{1}{c_0^2}-\frac{1}{c_s^2}\right)^2+\frac{4}{c_0^2\alpha^2}\right]^{1/2},$$

where $\hat{\kappa}=-i\gamma$ for $|\omega|\leqslant\omega_c$ and $\hat{\kappa}=\kappa_2$ for $|\omega|>\omega_c$.

[1] K. F. Graff, *Wave Motion in Elastic Solids* (Clarendon, Oxford, England, 1975).
[2] J. Miklowitz, *Elastic Waves and Waveguides* (North-Holland, Amsterdam, 1978).
[3] S. K. Datta, J. D. Achenbach, and Y. S. Rajapakse, *Elastic Waves and Ultrasonic Nondestructive Evaluation* (North-Holland, Amsterdam, 1990).
[4] A. N. Ceranoglu and Y. H. Pao, ''Propagation of elastic pulses and acoustic emission in a plate, part 1: theory,'' J. Appl. Mech. **48**, 125–132 (1981).
[5] A. N. Ceranoglu and Y. H. Pao, ''Propagation of elastic pulses and acoustic emission in a plate, part 2: epicentral responses,'' J. Appl. Mech. **48**, 133–138 (1981).
[6] A. N. Ceranoglu and Y. H. Pao, ''Propagation of elastic pulses and acoustic emission in a plate, part 3: general responses,'' J. Appl. Mech. **48**, 139–147 (1981).
[7] A. K. Mal and S. S. Lih, ''Elastodynamic response of a unidirectional composite laminate to concentrated surface loads: part I,'' J. Appl. Mech. **59**, 878–886 (1992).
[8] S. S. Lih and A. K. Mal, ''Elastodynamic response of a unidirectional composite laminate to concentrated surface loads: part II,'' J. Appl. Mech. **59**, 887–892 (1992).
[9] I. Tolstoy and E. Usdin, ''Wave propagation in elastic plates: low and high mode dispersion,'' J. Acoust. Soc. Am. **29**, 37–42 (1957).
[10] A. H. Meitzler, ''Backward-wave transmission of stress pulses in elastic cylinders and plates,'' J. Acoust. Soc. Am. **38**, 835–842 (1965).
[11] P. J. Torvik, ''Reflection of wave trains in semi-infinite plates,'' J. Acoust. Soc. Am. **41**, 346–353 (1967).
[12] S. B. Dong and R. B. Nelson, ''On natural vibrations and waves in laminated orthotropic plates,'' J. Appl. Mech. **39**, 739–745 (1972).
[13] S. B. Dong and K. H. Huang, ''Edge vibrations in laminated composite plates,'' J. Appl. Mech. **52**, 433–438 (1985).
[14] W. Karunasena, A. H. Shah, and S. K. Datta, ''Wave propagation in a

multilayered laminated cross-ply composite plate,'' J. Appl. Mech. **58**, 1028–1032 (1991).
[15] K. Kausel, ''Wave propagation in anisotropic layered media,'' Int. J. Numer. Methods Eng. **23**, 1567–1578 (1986).
[16] J. L. Rose, J. J. Ditri, and A. Pilarski, ''Wave mechanics in acousto-ultrasonic nondestructive evaluation,'' J. Acoust. Emiss. **12**, 23–26 (1994).
[17] S. Pelts and J. L. Rose, ''Source influences on elastic guided waves in an orthotropic plate,'' J. Acoust. Soc. Am. **99**, 2124–2129 (1994).
[18] G. R. Liu, J. Tani, T. Ohyoshi, and K. Watanabe, ''Transient waves in anisotropic laminated plates, part I: theory,'' Trans. ASME, J. Vib. Acoust. **113**, 230–234 (1991).
[19] R. V. Churchill and J. W. Brown, *Complex Variables and Applications* (McGraw–Hill, New York, 1990).
[20] M. Veidt and W. Sachse, ''Ultrasonic evaluation of thin, fiber-reinforced laminates,'' J. Compos. Mater. **28**, 329–342 (1993).

Development of an on-line diagnosis system for rotor vibration via model-based intelligent inference

Mingsian R. Bai,[a] Ilong Hsiao, Hsuming Tsai, and Chinteng Lin
Department of Mechanical Engineering, Chiao-Tung University, 1001 Ta-Hsueh Road, Hsin-Chu 30050, Taiwan, Republic of China

(Received 22 July 1998; revised 30 September 1999; accepted 2 October 1999)

An on-line fault detection and isolation technique is proposed for the diagnosis of rotating machinery. The architecture of the system consists of a feature generation module and a fault inference module. Lateral vibration data are used for calculating the system features. Both continuous-time and discrete-time parameter estimation algorithms are employed for generating the features. A neural fuzzy network is exploited for intelligent inference of faults based on the extracted features. The proposed method is implemented on a digital signal processor. Experiments carried out for a rotor kit and a centrifugal fan indicate the potential of the proposed techniques in predictive maintenance. © *2000 Acoustical Society of America.* [S0001-4966(00)03201-X]

PACS numbers: 43.40.Le, 43.40.At [CBB]

INTRODUCTION

Process automation has been a trend in mass-production industries worldwide. In process automation, direct contact with the human operators is reduced and automatic means are generally employed to monitor the health of process elements. Early detection and isolation of machine faults has been a key issue of productivity and safety.

Traditionally, fault detection and isolation (FDI) is carried out on a periodic basis to check either the overall level or the band level of vibrations with regard to a certain threshold and alarms are triggered if the limits are exceeded. This class of methods is known as limit checking.[1–3] As a more advanced approach, computer-based expert systems can also be used.[4,5] However, faults are usually detected by these methods at a rather late stage near failure. Motivated by the need for early FDI, this paper proposes an on-line model-based diagnosis technique for rotator vibration. The required model must be identified on the basis of the input–output relationship of the system of interest. These techniques make use of more information than the pure signal-based methods that are based on only the outputs to the system. The advantage of including a model lies in the early detection and isolation of faults and reduced number of sensors. Model-based methods have been utilized for vibration monitoring of cracked beams and rotors from the structure point of view.[6–9] This paper has a slightly different perspective that is aimed primarily at the common rotor faults in the discrete components and the system as a whole.

The general architecture of these methods can be divided into two major steps: (1) generation of features from the monitored signals and (2) inference and isolation of the faults. The dynamic model of the physical system of interest is identified via either a recursive continuous-time algorithm or a discrete-time parameter estimation algorithm.[10] On the basis of extracted features, fault types are determined by using the neural fuzzy intelligent inference algorithms.[11] The architecture of the model-based method is depicted in Fig. 1.

Rotating machines are chosen as the target application to validate the proposed FDI techniques because they represent a large class of industrial machinery. In particular, we use a rotor kit that is capable of producing several kinds of common faults of rotating machinery. Then, we use a centrifugal fan to justify the practicality of the integrated FDI system.

I. RECURSIVE PARAMETER ESTIMATION FOR ROTORS

A. Continuous-time parameter estimation

Model-based diagnosis algorithms generally fall into two categories: the state estimation methods[1,12] and the parameter estimation methods.[10,13–16] State estimation methods can further be classified into three kinds of schemes: the fault detection filter,[17] the parity space method,[18,19] and the dedicated observer method.[20] In this paper, we choose the parameter estimation method because it reflects more directly the change of system characteristics and is also robust against disturbances and uncertainties.

For processes with lumped parameters that can be linearized about the operating point, the dynamic models usually take the forms of ordinary differential equations

$$y(t)+a_1y^{(1)}(t)+\cdots+a_ny^{(n)}(t) = b_0u(t)+b_1u^{(1)}(t)+\cdots+b_mu^{(m)}(t), \quad (1)$$

with

$$y(t)=Y(t)-Y_0 \text{ and } u(t)=U(t)-U_0, \quad (2)$$

where U_0, Y_0 are the steady-state (or direct current) values of the input signal $U(t)$ and the output signal (t) around the operating point, and $y^{(n)}(t)=d^ny(t)/dt^n$. The process model in Eq. (1) can be written more compactly in a linear regression form

$$y(k)=\psi^T(k)\,\theta(k), \quad (3)$$

with the parameter vector

[a]Electronic mail: msbai@cc.nctu.edu.tw

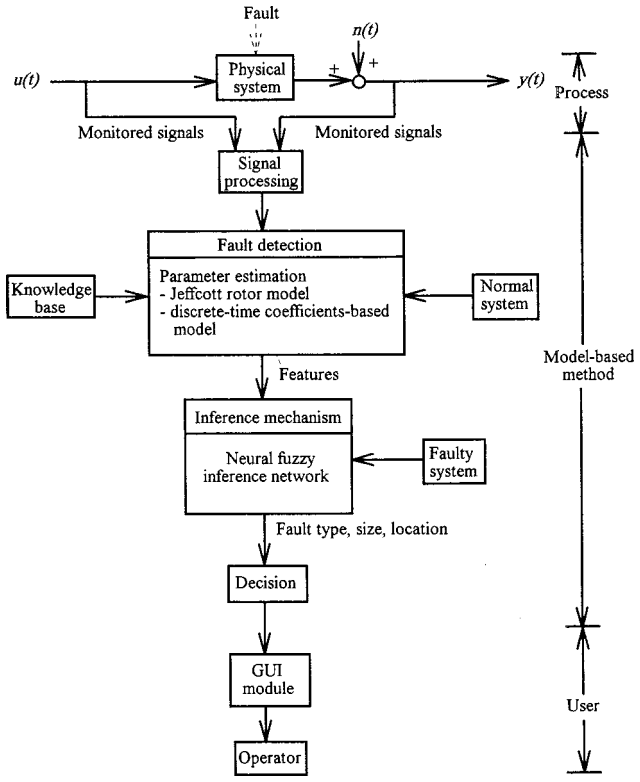

FIG. 1. Architecture of the model-based method for the fault diagnosis system.

$$\theta^T(k)=[a_1\cdots a_n b_0\cdots b_m] \tag{4}$$

and the data vector

$$\psi^T(k)=[-y^{(1)}(t)\cdots-y^{(n)}(t)u(t)\cdots u^{(m)}(t)], \tag{5}$$

where k is the iteration index on the discrete-time base. The task of feature extraction here consists of estimating θ based on the measured ψ. In this paper, the recursive least-square (RLS)[21] algorithm with forgetting factor is utilized to estimate the parameters. Defining the data matrix

$$\psi_k^T=[\psi(1)\psi(2)\psi(3)\cdots\psi(k)], \tag{6}$$

and the covariance matrix

$$\mathbf{P}(k)=[\psi_k^T\psi_k]^{-1}, \tag{7}$$

the procedures are summarized as follows:

(1) Initialize the parameter vector $\hat{\theta}(k=0)$ and the covariance matrix $\mathbf{P}(k=0)=p\mathbf{I}$, with p being a very large constant and $\mathbf{I}$ being the identity matrix.
(2) Obtain the input and output data to form the new data matrix $\psi(k)$ and $y(k)$.
(3) Form the a priori prediction error $\varepsilon(k)$ using

$$\varepsilon(k)=y(k)-\psi^T(k)\hat{\theta}(k-1). \tag{8}$$

(4) Update the parameter estimates $\hat{\theta}(k)$ using

$$\hat{\theta}(k)=\hat{\theta}(k-1)+\mathbf{F}(k)\varepsilon(k), \tag{9}$$

where

$$\mathbf{F}(k)=\frac{\mathbf{P}(k-1)}{\lambda+\psi^T(k)\mathbf{P}(k-1)\psi(k)}\psi(k), \tag{10}$$

and λ is called the forgetting factor that introduces increasing weaker weighting on the old data in the quadratic cost function of $\varepsilon(k)$.[22]

Update the covariance matrix $\mathbf{P}(k)$ using

$$\mathbf{P}(k)=\frac{1}{\lambda}[I-\mathbf{F}(k)\psi^T(k)]\mathbf{P}(k-1). \tag{11}$$

(5) Set $k=k+1$ and go to step (2).

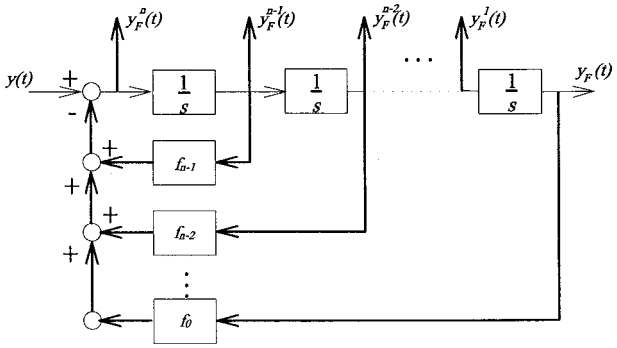

FIG. 2. Block diagram of the state variable filter (SVF).

Some remarks should be made on the practical implementation of the RLS algorithm. In principle, large initial $\mathbf{P}(0)$ (corresponding to large uncertainty and rapid fluctuations) and large forgetting factors λ (close to unity) should be selected if the input signals are not sufficiently persistently exciting or spectrally rich,[22] which is usually the case in the constant-speed operations of rotating machines. Also, proper scaling may be necessary to improve the convergence when some of the model coefficients are out of proportion to the others.

There remains one problem to resolve before the application of the continuous-time parameter estimation. The time derivatives in the data vector ψ are usually unavailable if only the signals $u(t)$ and $y(t)$ are measured. One way to overcome the difficulty is to use the state variable filter (SVF).[23] It is a state representation of an nth-order low-pass transfer function $F(s)$,

$$F(s)=\frac{y_F(s)}{y(s)}=\frac{1}{f_0+f_1 s+\cdots+f_n s^n}, \tag{12}$$

where $y_F(s)$ and $y(s)$ represent the Laplace transform of the filtered output $y_F(t)$ and the original output $y(t)$, respectively. It provides simultaneously the time derivatives (without direct differentiation) and filtering of the noise (Fig. 2). In the paper, we choose a fourth-order Butterworth filter with a cutoff frequency of 200 Hz.

After all the derivatives are obtained from the SVF, the RLS algorithm is employed to calculate the model parameters θ. Assume that the relationship between the model parameters θ and the process coefficients ρ is

$$\theta=f(\rho), \tag{13}$$

or, in matrix form,

$$\theta=\mathbf{C}\mathbf{z}, \tag{14}$$

where $\mathbf{z}$ is a function of ρ, i.e.,

$$\mathbf{z}=g(\rho). \tag{15}$$

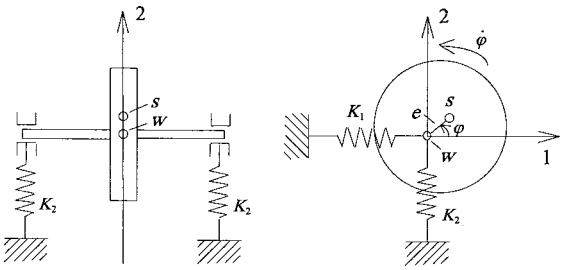

FIG. 3. The Jeffcott rotor model with flexible bearings.

Thus the process coefficients ρ can be obtained from the inverse relationship

$$\rho = f^{-1}(\theta). \tag{16}$$

A useful alternative to the forgoing continuous-time parameter algorithm is the discrete-time parameter estimation algorithm. The discrete-time algorithm follows basically the same line as the continuous-time version, except that the data vector ψ contains the present and past data samples instead of time derivatives. There is no need for the SVF processing in constructing the data. The advantage of the discrete-time algorithm lies in the fact that it accommodates better than the continuous-time version the high-order dynamics of more complicated systems that cannot be modeled as simple rotors.

B. Modeling of rotor dynamics

In the paper, we model the rotor systems in terms of lateral vibrations that reflect the rotor faults commonly encountered in practical applications. A classical rotor model suited for this purpose is the Jeffcott model.[24,25]

The Jeffcott model illustrated in Fig. 3, consists of a massless circular shaft with a fixed rigid circular disc supported by flexible bearings at the center of the shaft. The disc is mounted with its plane perpendicular to the shaft axis. Its mass center S has a radial offset e with the shaft center W. The disc is assumed to move only in the 1-2 plane. The movement of the shaft center W relative to the unloaded position is given by coordinates (y_1, y_2) and the angle of the disc position is given by φ. The position of the point S can be expressed as

$$z_1 = y_1 + e\cos\varphi, \tag{17}$$

$$z_2 = y_2 + e\sin\varphi. \tag{18}$$

Assume that the damping coefficients in directions 1 and 2 are d_1 and d_2, respectively, the stiffness of shaft is K, and two bearings have equal pairs of stiffness K_1 and K_2 in the directions 1 and 2, respectively. The total stiffness of the shaft and bearings is

$$K_1' = \frac{K}{1 + K/2K_1}, \tag{19}$$

$$K_2' = \frac{K}{1 + K/2K_2}. \tag{20}$$

The equations of motion (as functions of y_1, y_2, and φ) can be obtained from applying Newton's second law in translation and rotation.

$$M\ddot{y}_1 + d_1\dot{y}_1 + K_1' y_1 = \mathrm{Me}(\ddot{\varphi}\sin\varphi t + \dot{\varphi}^2\cos\varphi t), \tag{21}$$

$$M\ddot{y}_2 + d_2\dot{y}_2 + K_2' y_2 = \mathrm{Me}(-\ddot{\varphi}\cos\varphi t + \dot{\varphi}^2\sin\varphi t) - G, \tag{22}$$

$$I_p\ddot{\varphi} + e(d_1\dot{y}_1 + K_1' y_1)\sin\varphi t - e(d_2\dot{y}_2 + K_2' y_2)\cos\varphi t = T(t), \tag{23}$$

where M is the mass of the disc, G is the weight of the disc, I_p is the polar moment of inertia of disc, and $T(t)$ is the mechanical torque input. Assuming that y_1 and y_2 are measured with reference to the equilibrium position, we can rewrite Eqs. (21) and (22), adjusted with an angle offset φ_0 that is the angle between the reference point and the center of mass,

$$\ddot{y} + 2\xi_1\omega_{01}\dot{y}_1 + \omega_{01}^2 y_1 = e[\ddot{\varphi}\sin(\varphi + \varphi_0) + \dot{\varphi}^2\cos(\varphi + \varphi_0)], \tag{24}$$

$$\ddot{y}_2 + 2\xi_2\omega_{02}\dot{y}_2 + \omega_{02}^2 y_2 = e[-\ddot{\varphi}\cos(\varphi + \varphi_0) + \dot{\varphi}^2\sin(\varphi + \varphi_0)]. \tag{25}$$

Or,

$$\ddot{y}_1 + 2\xi_1\omega_{01}\dot{y}_1 + \omega_{01}^2 y_1 = e\cos\varphi_0(\ddot{\varphi}\sin\varphi + \dot{\varphi}^2\cos\varphi) + e\sin\varphi_0(\ddot{\varphi}\cos\varphi - \dot{\varphi}^2\sin\varphi), \tag{26}$$

$$\ddot{y}_2 + 2\xi_2\omega_{02}y_2 + \omega_{02}^2 y_2 = e\cos\varphi_0(-\ddot{\varphi}\cos\varphi + \dot{\varphi}^2\sin\varphi) + e\sin\varphi_0(\ddot{\varphi}\sin\varphi + \dot{\varphi}^2\cos\varphi), \tag{27}$$

where

$$\omega_{0i} = \sqrt{\frac{K_i'}{M}}, \tag{28}$$

$$\xi_i = \frac{\sqrt{K_i' M}}{2d_i}. \tag{29}$$

Equations (26) and (27) form the basis of the continuous-time parameter estimation which can be recast into the linear regression forms

$$y_i(k) = \psi_i^T(k)\,\theta_i(k), \quad i = 1,2, \tag{30}$$

where

$$\psi_1^T(k-1) = [\ddot{y}_1\dot{y}_1\ddot{\varphi}\sin\varphi + \dot{\varphi}^2\cos\varphi\ddot{\varphi}\cos\varphi - \dot{\varphi}^2\sin\varphi], \tag{31}$$

$$\psi_2^T(k-1) = [\ddot{y}_2\dot{y}_2\dot{\varphi}^2\sin\varphi - \ddot{\varphi}\cos\varphi\ddot{\varphi}\sin\varphi + \dot{\varphi}^2\cos\varphi], \tag{32}$$

$$\theta_1^T(k) = [-a_{11} - a_{21}b_{11}b_{21}], \tag{33}$$

$$\theta_2^T(k) = [-a_{12} - a_{22}b_{12}b_{22}], \tag{34}$$

and

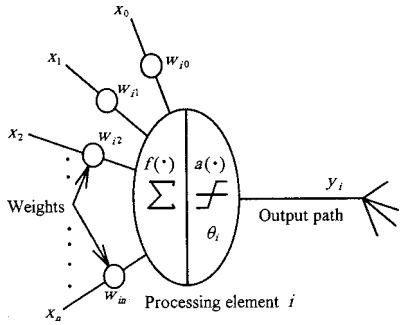

FIG. 4. A schematic diagram of a McCulloch–Pitts neuron (Ref. 26).

$$a_{1i}=1/\omega_{0i}^2, \quad a_{2i}=2\xi_i/\omega_{0i}, \quad b_{11}=b_{12}=e\cos\varphi_0, \quad b_{21}=b_{22}=e\sin\varphi_0. \tag{35}$$

From the model parameters, the process coefficients can be recovered as

$$\omega_{0i}=\frac{1}{\sqrt{a_{1i}}}, \quad i=1,2, \tag{36}$$

$$\xi_i=\frac{a_{2i}}{2\sqrt{a_{1i}}}, \quad i=1,2, \tag{37}$$

$$e=\sqrt{b_{11}^2+b_{21}^2}=\sqrt{b_{12}^2+b_{22}^2}. \tag{38}$$

II. INTELLIGENT INFERENCE ALGORITHMS FOR FDI

In the paper, artificial neural network and fuzzy theory are utilized for inference of rotor faults. Figure 4 shows a mathematical model of the biological neuron, usually called an M-P neuron,[26,27] where the ith processing element computes a weighted sum of its inputs $x_0, x_1, x_2, \ldots, x_n$ and outputs $y_i=1$ (firing) or 0 (not firing) according to whether this weighted input sum is above or below a certain threshold θ_i,

$$y_i(k+1)=a(f)\sum_{j=0}^{n} w_{ij}x_i(k)-\theta_i, \tag{39}$$

where k is the iteration index of input and output and the activation function $a(f)$ is a unit step function,

$$a(f)=\begin{cases}1, & \text{if } f\geqslant 0\\ 0, & \text{otherwise}\end{cases}. \tag{40}$$

In the paper, the supervised learning network with back-propagation is employed. The algorithm generally includes two phases: the learning (training) process and the recall process. In the supervised learning, the objective is to reduce the error between the desired output and the calculated output. To quantify the quality of learning, an error function is utilized,

$$E=\frac{1}{2}\sum_i (T_i-A_i)^2, \tag{41}$$

where T_i is the desired output vector and A_i is the calculated output vector. Methods such as the gradient search algorithm can be used for finding the minimum of E. In the training phase, the network weightings are updated according to the sensitivity of the error function with respect to the weightings

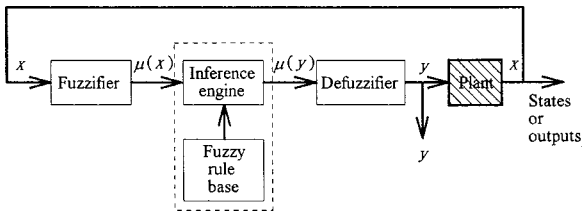

FIG. 5. Block diagram of a fuzzy logic controller (FLC) (Ref. 26).

$$\Delta w_{ij}^n=-\eta\frac{\partial E}{\partial w_{ij}^n}, \tag{42}$$

where Δw_{ij}^n is the increment of the weighting between the ith processing element of the $(n-1)$th layer and the jth processing element of the nth layer, and η is the step size for the gradient search algorithm.

Since Zadeh introduced in 1965 the fuzzy sets to represent vagueness of linguistics, a rapid growth in the use of fuzzy theories is witnessed in many scientific applications.[26] In contrast to classical sets that are crisp sets based on the binary logic (''Truth'' or ''False''), the fuzzy sets are not only to classify one element belonging to a set or not, but to fuzzify in ''Truth'' with some degree of membership. Let $\tilde{A}$ be a fuzzy set and U be its universe of discourse

$$\tilde{A}=\{(x,\mu_{\tilde{A}}(x))|x\in U\}, \tag{43}$$

where $\mu_{\tilde{A}}(x)$ is the membership function of x in the fuzzy set $\tilde{A}$ that represents the degree of x belonging to the fuzzy set $\tilde{A}$, and its value is usually in the interval [0, 1]. A general architecture of a fuzzy logic control (FLC) system including a fuzzifier, a fuzzy rule base, an inference engine, and a defuzzifier, is shown in Fig. 5. If the output from the defuzzifier is not a control action (as in our case) for a plant, the system becomes a fuzzy logic decision system.

In this study, a Self-cOnstructing Neural Fuzzy Inference Network (SONFIN), which is inherently a fuzzy rule-based model possessing neural network,[26] is employed for intelligent inference and isolation of faults. This technique integrates the advantages of both artificial neural network and the fuzzy theory, and is well suited for automatic inference required in the FDI application. The structure of the SONFIN is shown in Fig. 6, whereby the network consists of six layers: the input layer, the membership layer, the fuzzy rule layer, the normalization layer, the consequent layer, and the output layer. The network realizes the following fuzzy model:

$$\text{Rule } i\text{: IF } (x_1 \text{ is } A_{i1} \text{ and}\cdots\text{and } x_n \text{ is } A_{in})$$
$$\text{THEN } (y \text{ is } m_{0i}+a_{ji}x_j+\cdots), \tag{44}$$

where A_{ij} is a fuzzy set, m_{0i} is the center of a symmetric membership function on y, and a_{ji} is a consequent parameter. There are no rules initially, but they are created and adapted as on-line learning proceeds via simultaneous structure and parameter identification. The learning process involves four steps: input/output space partitioning, construc-

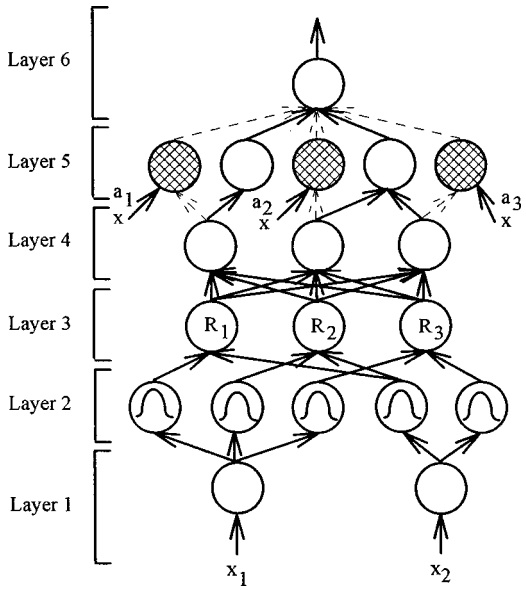

FIG. 6. Structure of the Self cOnstructing Neural Fuzzy Inference Network (SONFIN). In the figure, *x*'s are input variables; *R*'s are fuzzy rules; *a*'s are weightings in back-propagation.

tion of fuzzy rules, optimal consequent structure identification, and parameter identification. The first three steps are for structure learning and the last step for parameter learning. In the structure identification of the precondition part, the input space is partitioned by using an aligned clustering-based algorithm, while in the structure identification of the consequent part only a single value selected by a clustering method is assigned to each rule initially. Afterwards, some additional significant input variables selected via the Gram–Schmidt orthogonalization for each rule will be added to the consequent part incrementally. Furthermore, to enhance the knowledge representation, a linear transformation for each input variable is incorporated into the network so that fewer rules are needed. Finally, in parameter identification, the RLS algorithm is used to tune the parameters in layer 5 and the back-propagation algorithm is used to update the parameters of the membership functions in layer 2. The trained neural fuzzy network is used for the subsequent inference for faults. The unique features of SONFIN are twofold. First, the structure and the weights of the network are automatically adjusted. Second, a high-dimensional fuzzy system is implemented with a small number of rules and fuzzy terms. Due to the physical meaning of the fuzzy if–then rule, each input node in the SONFIN is only connected to its related rule nodes through its term nodes, instead of being connected to all the rule nodes in layer 3. This results in a small number of weights to be tuned. In some cases, however, it is time consuming to train the network provided the number of inputs is large. To alleviate the difficulty, a Discriminatory Information (DI) method[4] can be

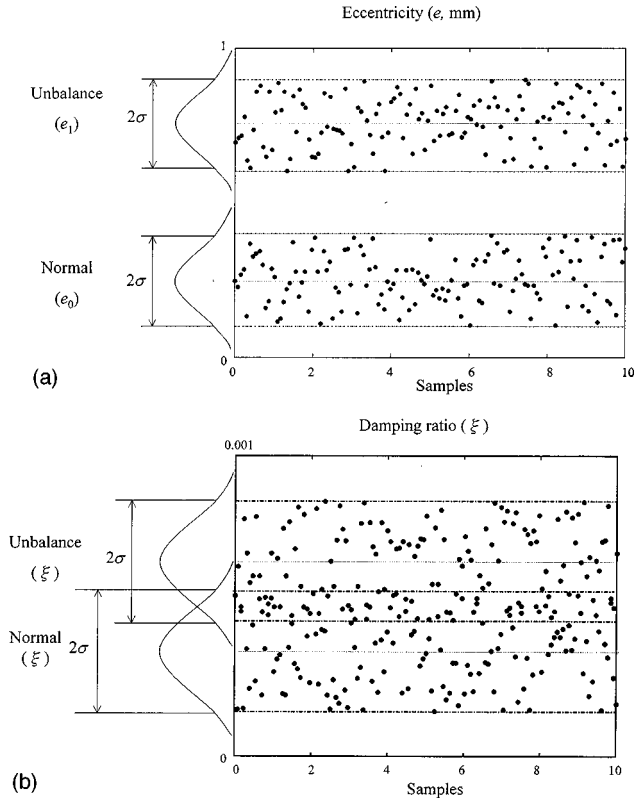

FIG. 7. Schematic of the discriminatory information (DI) method. (a) A more discriminatory feature; (b) a less discriminatory feature.

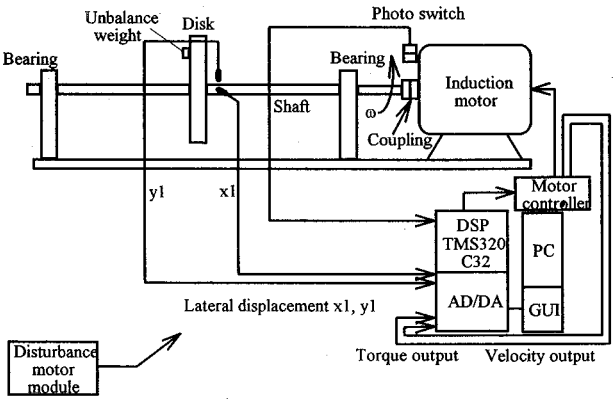

FIG. 8. Experimental arrangement of the rotor kit.

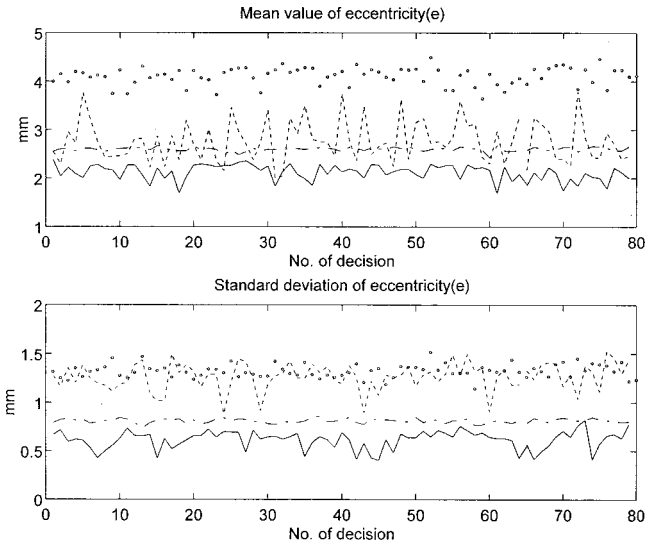

FIG. 9. The time variation of *e* in the normal, imbalanced, looseness, and faulty bearing conditions of the rotor kit. Normal: ——, imbalanced: · · , looseness: –·–, and faulty bearing: --.

TABLE I. Effects of different faults on the estimated continuous-time process coefficients for the rotor kit. ($\overline{x}$: average; σ: standard deviation; +: increase; −: decrease; *: insignificant).

Condition	Parameters									
	$\overline{x}$ of ω_{01}	$\overline{x}$ of ω_{02}	$\overline{x}$ of ξ_1	$\overline{x}$ of ξ_2	$\overline{x}$ of e	σ of ω_{01}	σ of ω_{02}	σ of ξ_1	σ of ξ_2	σ of e
Disturbance	−	−	*	+	*	+	+	+	+	+
Imbalance	+	*	−	*	+	+	*	−	*	+
Misalignment	+	+	+	+	+	+	+	+	+	+
Looseness	*	−	−	−	−	*	*	−	−	−
Faulty bearing	−	*	+	*	*	+	*	+	*	+

used to calculate the statistics of the data and retain only the inputs that account for the distinct features associated with the different conditions. The basic idea of the DI method is to choose the features that have distributions of distinct means and small spreads with respect to different conditions. The procedure is summarized as follows:

(a) A test is performed to collect 128 samples of system parameters, e.g., eccentricity, damping ratio, natural frequency, etc.
(b) Probability density functions (pdf) are calculated for the extracted parameters in an off-line manner.
(c) If the mean value deviates from the normal case by 20% and the ''2-σ'' regions do not overlap, then the parameter is considered a good discriminator for the fault type of interest and thus serves as an input variable to the network. Otherwise, the parameter is discarded.

An example of the use of the DI method is shown in Fig. 7. The feature of Fig. 7(a) shows more isolated mean values and smaller variances than that of Fig. 7(b). Thus the former feature is preferably used as the principal input to the network.

III. EXPERIMENTAL INVESTIGATIONS

Experiments were carried out to validate the proposed FDI technique. In particular, we verified the feature generation and fault inference algorithm by using a rotor kit that is capable of producing common rotor faults. Then, a centrifugal fan was also used to justify the practicality of the FDI system.

A. Rotor kit

A rotor kit is used in the first part of the experiments (Fig. 8). The rotor kit consists of a constant-speed (1500 rpm) induction motor, a coupling, a steel shaft, two ball-bearing supports, an aluminum disk, and a disturbance motor module. Five common rotor faults, imbalance, misalignment, disturbance, mechanical looseness, and faulty bearings can be conveniently produced by the rotor kit. Imbalance is created by adding an imbalanced weight on the disk. Misalignment is created by dislocating the coupling with a radial offset. Disturbance is created by a frictional disk driven by another induction motor running at a different angular frequency. The mechanical looseness is created by loosening one of the four bolts at the two bearing supports. The bearing fault is created by using a damaged outer ring. On the other hand, the FDI system consists of two eddy-current probes, a photo switch (for angular frequency measurement), and a personal computer equipped with a DSP card (TMS320C32) and 32 analog I/O channels.

In case 1, the FDI method based on continuous-time parameter estimation is investigated. Lateral displacements in both horizontal and vertical directions near the center of the disc are measured by two eddy-current probes. The angular velocity Ω is measured by a photo switch. The measured signals are fed to the DSP via the analog I/O module with a sampling rate 200 Hz. Using the SVF method, the time derivatives of displacements are calculated. Based on the data, the continuous-time RLS algorithm is employed to generate the features including five process coefficients. The DI procedure is used to preprocess the features and remove the insignificant inputs. These data features then become the input vector to the neural fuzzy network. In the first (training) stage of 12-sec measurement, five types of fault and the normal condition are produced by the rotor kit, and the data features are calculated to train the neural fuzzy network. In the second (recall) stage, the rotor is restarted for five times and for each time the faults are regenerated to verify the trained network. Each time record is further divided into ten sets to represent ten experiments. There are altogether $6\times5\times10=300$ experiments. Figure 9 shows the variations of e in the normal, imbalanced, mechanical looseness, and faulty bearing conditions, respectively, of the rotor kit. The variations of the other process coefficients in the other conditions during an ongoing experiment are similarly calculated. The effects of five types of fault on the estimated process coefficients for the rotor kit are summarized in Table I. Appar-

TABLE II. Performance of the continuous-time model-based FDI technique for the rotor kit.

Result	Condition					
	Normal	Disturbance	Imbalance	Misalignment	Looseness	Faulty bearing
Normal	100%	0%	0%	0%	0%	0%
Disturbance	0%	92%	0%	0%	0%	0%
Imbalance	0%	8%	100%	0%	0%	0%
Misalignment	0%	0%	0%	100%	2%	0%
Looseness	0%	0%	0%	0%	98%	8%
Faulty bearing	0%	0%	0%	0%	0%	92%
Average rate of correct inference: 97.0%						

TABLE III. Performance of the discrete-time model-based FDI technique model for the rotor kit.

Result	Condition					
	Normal	Disturbance	Imbalance	Misalignment	Looseness	Faulty bearing
Normal	100%	0%	0%	0%	0%	0%
Disturbance	0%	100%	0%	0%	0%	0%
Imbalance	0%	0%	98%	0%	0%	0%
Misalignment	0%	0%	0%	96%	0%	0%
Looseness	0%	0%	2%	4%	100%	0%
Faulty bearing	0%	0%	0%	0%	0%	100%
Average rate of correct inference: 99.0%						

ently, it is very difficult for an experienced operator to detect and isolate the fault by merely looking at the trends in the table. This calls for the capability of automatic machine-learning of the neural fuzzy network. Table II summarizes the performance of the continuous-time FDI technique with neural fuzzy inference for the rotor kit. The result appears acceptable (average rate of correct inference $=97\%$).

In case 2, the FDI technique based on discrete-time parameter estimation is examined. The foregoing assumption that the angular frequency is constant is relaxed. It is assumed that the discrete-time model of the rotor system is of the form

$$\begin{aligned} y_1(k) = & -a_{1i}y_1(k-1) - a_{2i}y_1(k-2) \\ & + b_{1i}\dot{\omega}\cos(\omega k) + b_{2i}\dot{\omega}\cos(\omega(k-1)) \\ & + b_{3i}\dot{\omega}\sin(\omega k) + b_{4i}\dot{\omega}\sin(\omega(k-1)), \\ & i = 1,2, \end{aligned} \tag{45}$$

where a's and b's are model parameters to be determined and $\dot{\omega}$ is the time derivative of ω that is calculated by the SVF. The above equations can be cast into the linear regression form $y(k) = \psi^T(k)\theta(k)$ with the data vectors

$$\begin{aligned} \mathbf{\Psi}_i^T(k-1) = & [y_i(k-1)y_i(k-2)\dot{\omega}\cos(\omega k)\dot{\omega} \\ & \times \cos(\omega(k-1))\dot{\omega}\sin(\omega k) \\ & \times \dot{\omega}\sin(\omega(k-1))], \quad i = 1,2, \end{aligned} \tag{46}$$

and the parameter vectors

$$\theta_i^T(k) = [-a_{1i} - a_{2i} b_{1i} b_{2i} b_{3i} b_{4i}]. \tag{47}$$

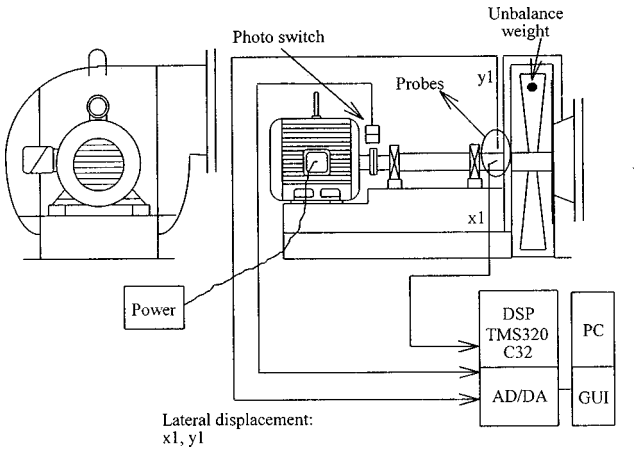

FIG. 10. Experimental arrangement of the centrifugal fan.

Other than the parameter estimation model, the experimental setup remains the same as in the continuous-time case. The discrete-time parameter estimation algorithm is employed to generate the features that in turn become the input vectors to the neural fuzzy inference network. Following a procedure similar to the continuous-time algorithm, the neural fuzzy network is necessary to infer the fault types, based on the features (model parameters in this case) extracted earlier by the discrete-time RLS algorithm. Table III summarizes the performance of the discrete-time FDI technique with neural fuzzy inference for the rotor kit. In comparison with the continuous-time method, the result appears to be slightly improved (average rate of correct inference $=99.0\%$).

B. Centrifugal fan

A more practical system, a two-horsepower centrifugal fan, is chosen for validating the proposed FDI technique. The experimental setup including the fan and the FDI system is shown in Fig. 10. The fan system consists of a constant-speed (1750 rpm) AC induction motor, a steel shaft, a coupling, two bearing supports, and 12 impellers. Four common faults of centrifugal fans, including imbalance, misalignment, mechanical looseness, and faulty bearing are investi-

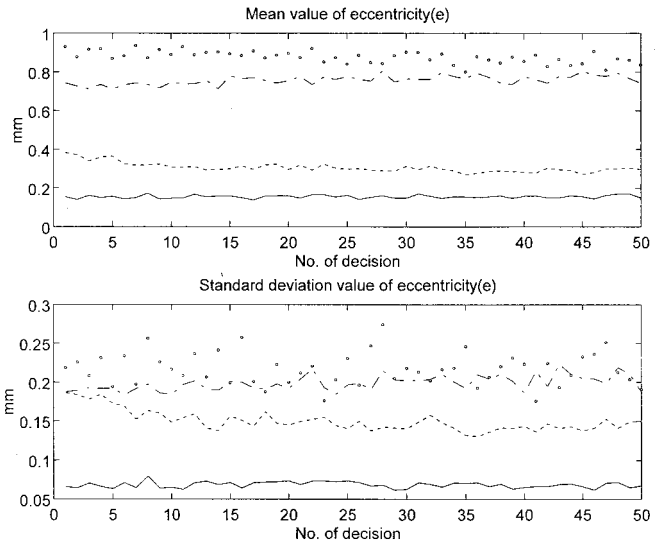

FIG. 11. The time variation of e in the normal, imbalanced, looseness, and faulty bearing conditions of the centrifugal fan. Normal: ——, imbalanced: · ·, looseness: –·–, and faulty bearing: --.

TABLE IV. Performance of the continuous-time model-based FDI technique for the centrifugal fan.

Result	Condition				
	Normal	Imbalance	Misalignment	Looseness	Faulty bearing
Normal	92%	0%	0%	0%	0%
Imbalance	0%	100%	0%	0%	0%
Misalignment	0%	0%	100%	0%	0%
Looseness	8%	0%	0%	100%	0%
Faulty bearing	0%	0%	0%	0%	100%
Average rate of correct inference: 98.4%					

gated in the experiment. The faults are created the same way as the earlier procedures in rotor kit, except that the faulty bearing was replaced with a lubricated bearing.

In case 1, the FDI technique based on continuous-time parameter estimation is examined. Lateral displacements in both horizontal and vertical directions near the impellers are measured by two eddy-current probes. The angular velocity Ω is measured by the photo switch. The other conditions are the same as in case 1 of the rotor kit. Following a procedure similar to the continuous-time algorithm, the neural fuzzy network is necessary to infer the fault types, based on the features extracted earlier by the RLS algorithm. Figure 11 shows the variations of e in the normal, imbalanced, mechanical looseness, and faulty bearing conditions, respectively. The neural fuzzy network is used to infer the fault types, based on the features (process coefficients in this case) extracted earlier by the continuous-time RLS algorithm. Table IV summarizes the performance of the continuous-time FDI technique with neural fuzzy inference for the centrifugal fan. The result appears acceptable (average rate of correct inference$=$98.4%).

In case 2, the FDI method based on the discrete-time parameter estimation technique is examined. The foregoing assumption that the angular frequency is constant is relaxed. The other conditions remain unchanged from case 2 of the rotor kit. Following a procedure similar to the continuous-time algorithm, the neural fuzzy network is necessary to infer the fault types, based on the features extracted earlier by the RLS algorithm. Table V summarizes the performance of the discrete-time FDI technique with neural fuzzy inference for the centrifugal fan. Compared to the continuous-time method, the result appears excellent (average rate of correct inference$=$100.0%). It is noted from Tables II–V that the ''false alarm'' rates and ''failure-to-alarm'' rates are all zero except the case of the centrifugal fan, where 8% of the data under ''normal'' conditions are misinterpreted as looseness faults. In these experiments, 97% detection rate is considered sufficient.

TABLE V. Performance of the discrete-time model-based FDI technique for the centrifugal fan.

Result	Condition				
	Normal	Imbalance	Misalignment	Looseness	Faulty bearing
Normal	100%	0%	0%	0%	0%
Imbalance	0%	100%	0%	0%	0%
Misalignment	0%	0%	100%	0%	0%
Looseness	0%	0%	0%	100%	0%
Faulty bearing	0%	0%	0%	0%	100%
Average rate of correct inference: 100.0%					

IV. CONCLUDING REMARKS

An on-line FDI system for rotator vibration is presented. The development of the proposed methods is divided into two stages. First, data features are generated based on two model-based methods. Second, fault types are determined based on the extracted features via neural fuzzy inference algorithms. The proposed FDI system is implemented on a DSP. The usefulness of the proposed technique in identifying common rotor faults has been justified by experiments conducted for a rotor kit and a centrifugal fan. From the experimental results, the discrete-time parameter estimation approach that does not require analytical modeling of the system yields better performance than the continuous-time approach. However, the success of the methods hinges on the proper choices of the model structures.

The proposed FDI technique can readily be extended to other systems such as centrifugal pumps, centrifugal compressors, and machine tools. The system will be extended for handling multiple faults. In practical applications, information is generally incomplete. The machine condition is generally unknown so that the field data are insufficient for reliable training of the network. Thus enhancing the present neural fuzzy inference network, in light of machine learning and human knowledge, for an expert system suited for robust FDI will be the focus of future research.

ACKNOWLEDGMENTS

Special thanks go to Dr. G. H. Chen for the helpful discussions on the FDI subject. The work was supported by the Institute of Occupational Safety and Health (IOSH), Council of Labor Affairs, Executive Yuan in Taiwan, Republic of China, under the project ''Development of Hazard-Preventive Techniques of Major Hydraulic Machinery.''

[1] P. M. Frank, ''Fault diagnosis in dynamic systems using analytical and knowledge-based redundancy—A survey and some new results,'' Automatica **26**, No. 3, 459–474 (1990).
[2] S. J. Mitchell, *Machinery Analysis and Monitoring* (Penn Well, Oklahoma, 1981).
[3] J. E. Berry, ''Proven method for specifying both spectral alarm bands as well as narrowband alarm envelopes using today's predictive maintenance software system,'' BandAid Technical Literature, Technical Associates of Charlotte, Inc., Charlotte, NC, 1993.
[4] S. Braun, *Mechanical Signature Analysis—Theory and Applications* (Academic, Orlando, Florida, 1986).
[5] H. Kumamoto, ''Application of expert system techniques to fault diagnosis,'' Chem. Eng. J. **29**, 1–9 (1984).
[6] R. L. Actis and A. D. Dimarogonas, ''Non-linear effects due to closing cracks in vibrating beams,'' ASME Des. Eng. Div. Publ. DE Struct. Vib. Acoust. **18**, 99–104 (1989).
[7] J. Wauer, ''On the dynamics of cracked rotors: A literature survey,'' Appl. Mech. Rev. **43**, 13–17 (1990).
[8] X. T. C. Man, L. M. McClure, Z. Wang, and R. D. Finch, ''Slot depth resolution in vibration signature monitoring of beams using frequency shift,'' J. Acoust. Soc. Am. **95**, 2029–2037 (1994).
[9] X. T. C. Man and R. D. Finch, ''Vibration monitoring of slotted beams using an analytical model,'' J. Acoust. Soc. Am. **102**, 382–390 (1997).

[10] R. Isermann, ''Fault diagnosis of machines via parameter estimation and knowledge processing—tutorial paper,'' Automatica **29**, No. 4, 815–835 (1993).
[11] C. F. Juang and C. T. Lin, ''An on-line self-constructing neural fuzzy inference network and its applications,'' IEEE Trans. Fuzzy Systems **6**, No. 1,12–13 (1998).
[12] P. M. Frank, ''Analytical and qualitative model-based fault diagnosis—A survey and some new results,'' European J. Control **2**, 6–28 (1996).
[13] R. Isermann, ''Process fault detection based on modeling and estimation methods—A survey,'' Automatica **20**, No. 4, 387–404 (1984).
[14] R. Isermann, ''Process fault diagnosis based on process model knowledge—Part I. Principles for fault diagnosis with parameter estimation,'' J. Dyn. Syst., Meas., Control **113**, No. DEC, 620–626 (1991).
[15] R. Isermann, ''Process fault diagnosis based on process model knowledge—Part II: Principles for fault diagnosis with parameter estimation,'' J. Dyn. Syst., Meas., Control **113**, No. DEC, 627–633 (1991).
[16] R. Isermann, ''Estimation of physical parameters for dynamic processes with application to an industrial robot,'' Int. J. Control **55**, No. 6, 1287–1298 (1992).
[17] K. L. Jones, ''Failure detection in linear systems,'' The Charles Stark Draper Laboratory, Cambridge, MA, Rep. T-608.
[18] E. Y. Chow and A. S. Willsky, ''Analytical redundancy and the design of robust failure detection systems,'' IEEE Trans. Autom. Control. **AC-29**, No. 7, 603–614 (1984).
[19] J. Gertler, ''Residual generation in model-based fault diagnosis,'' Control Theory Advanced Technology **9**, No. 1, 259–285 (1993).
[20] R. J. Patton and J. Chen, ''Robust fault detection of jet engine sensor systems using eigenstructure assignment,'' J. Guid. Control. Dyn. **15**, No. 6, 1491–1497 (1992).
[21] L. Ljung, *System Identification: Theory for the User* (Prentice-Hall, Englewood Cliffs, NJ, 1987).
[22] G. C. Goodwin and K. S. Sin, *Adaptive Filtering Prediction and Control* (Prentice-Hall, Englewood Cliffs, NJ, 1984).
[23] P. C. Young, ''Parameter estimation for continuous-time models—A survey,'' Automatica **17**, 23–39 (1981).
[24] *Handbook of Rotordynamics*, edited by E. F. Ehrich (McGraw-Hill, New Delhi, India, 1992).
[25] K. Erwin, *Dynamics of Rotors and Foundations* (Springer-Verlag, Berlin, 1993).
[26] C. T. Lin and Lee C. S. George, *Neural Fuzzy Systems* (Prentice-Hall, Englewood Cliffs, NJ, 1996).
[27] T. Kohonen, ''An introduction to neural computing,'' Neural Networks **1**, 3–16 (1988).

Active control of the plate energy transmission in a semi-infinite ribbed plate

Nicole J. Kessissoglou
Mechanical Engineering, James Cook University, Townsville QLD 4811, Australia

(Received 29 March 1999; accepted for publication 10 September 1999)

Active control of the plate flexural wave transmission through the beam in a semi-infinite beam-reinforced plate is analytically investigated. The ribbed plate is modeled as a continuous system, using equations of motion to describe the plate in flexure and the beam in both flexure and torsion. The maximum transmission of the plate flexural waves through the reinforcing beam is found to occur at resonance frequencies corresponding to the optimal coupling between the plate flexural waves and the flexural and torsional waves in the beam. A single control force is applied to the beam, and a cost function is developed to attenuate the far-field flexural energy transmission. It can be observed that the transmission peaks corresponding to the flexural resonances in the beam are reduced. Similarly, the transmission peaks corresponding to the torsional resonance conditions in the beam can be attenuated using a single control moment applied to the beam. Significant attenuation of all the resonance peaks in the flexural wave transmission can also be achieved with the application of a single force and a single moment collocated on the beam. In this paper, the feasibility of attenuating the flexural wave transmission due to both the flexural and torsional resonance conditions by using a single point force and point moment collocated on the beam is demonstrated. © *2000 Acoustical Society of America.* [S0001-4966(99)06612-6]

PACS numbers: 43.40.Vn [PJR]

INTRODUCTION

The effect of a reinforcing rib attached to a plate on the structural response is fundamental in the study of noise and vibration problems in aerospace and marine industries. The scattered structural wave field at the beam discontinuity can produce vibrations problems, as well as the efficient radiation of structure-borne sound. Previous works conducted on plates reinforced by a single rib have examined in great detail the interaction between the beam and the plate, by concentrating on the dynamic stresses and couplings at the beam-plate boundaries.[1] However, most work on periodically stiffened structures tends to approximate the rib stiffeners in a variety of ways such as exerting line forces and/or line moments at the rib location,[2,3] adding mass and stiffness discontinuities in the plate at the beam location,[4] or even replacing the beam as a line impedance operator.[5] Heckl[6] examined a semi-infinite simply supported plate with a reinforcing beam. Expressions for the transmitted and reflected plate flexural waves are given in terms of traveling waves along the infinite direction, and summation of the modes in the finite direction. Heckl found that the heavier the beam is, the more the transmitted energy is concentrated in the vicinity of the resonance frequency of the beam, where there exist many more bending wave resonances of the beam than torsional wave resonances. Only a handful of researchers have investigated active control of the response of ribbed plates.[7,8] In this paper, the dynamic nature of the flexural wave transmission in a semi-infinite simply supported beam-reinforced plate is examined in detail. Maximum transmission is shown to occur at resonance frequencies corresponding to the optimal coupling between the plate flexural and the beam flexural or torsional waves. Active control systems are then optimally designed in order to attenuate the plate energy transmission. A single point control force and a single control moment are applied to the beam to attenuate the transmission peaks corresponding to the flexural and torsional resonances, respectively. Attenuation of all the resonance peaks in the flexural wave transmission can also be achieved with the application of a single force and a single moment collocated on the beam. In this paper, the feasibility of using a single control force and moment collocated on the beam to globally attenuate the plate wave transmission through a reinforcing beam is demonstrated. It is shown that the mechanisms involved with the attenuation of the plate vibration correspond to the reduction of the beam vibration.

I. PRIMARY FLEXURAL WAVE MOTION IN THE PLATES

A. Plate flexural plane wave incident on the beam discontinuity

The beam-plate system consists of a semi-infinite thin elastic plate symmetrically reinforced by two identical finite uniform beams of rectangular cross section. The beams and plate are simply supported along the same edges at $y=0$ and $y=L_y$, as shown in Fig. 1, and the plate is infinite in the x direction. An incident flexural plane wave, W_{in}, propagates in the positive x direction in plate 1 at an angle φ to the x axis. The scattering of the structural wave field due to the incident wave impinging on the beam discontinuity generates both reflective and transmitted waves in plates 1 and 2, respectively.

Due to the simply supported boundary conditions, the incident wave can be expressed as the summation of all the individual modes that contribute to the flexural wave motion at the frequency of excitation, and is described by

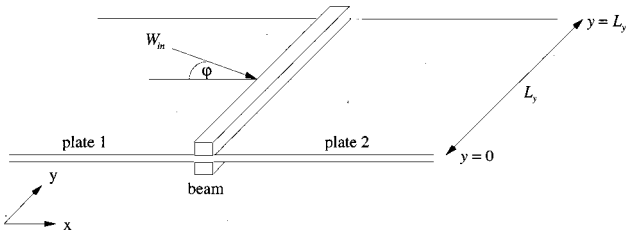

FIG. 1. Semi-infinite simply supported ribbed plate showing the flexural wave incident at the beam boundary.

$$W_{\text{in}}(x,y)=\sum_{m=1}^{\infty} A_{p_m} e^{-jk_p \cos\varphi_m x} \sin(k_{y_m} y), \tag{1}$$

where A_{p_m} is the modal amplitude of the incident wave, $k_p = \sqrt{\omega}(\rho_p h/D)^{1/4}$ is the plate flexural wave number, where $D=E_p h^3/12(1-\nu^2)$ is the plate flexural rigidity, and ρ_p, h, E_p, and ν are, respectively, the density, thickness, Young's modulus, and Poisson's ratio of the plate. Here $k_{y_m} = m\pi/L_y$ is the modal wave number of the incident wave in the y direction, where m is the mode number, and $k_p \cos\varphi_m$ is the wave number of the incident wave in the x direction. The wave number in the x direction can also be described by $k_{y_m}=k_p\cos\varphi_m=\sqrt{k_p^2-k_{y_m}^2}$, where $k_p \geqslant k_{y_m}$ is necessary for a nondecaying propagating wave. From the expression $k_p = k_{y_m}$, it can be shown that each mode has a corresponding ''cut-on'' frequency, which is determined by

$$f_{\text{co}}=\frac{1}{2\pi}\left(\frac{m\pi}{L_y}\right)^2\sqrt{\frac{D}{\rho_p h}}. \tag{2}$$

When the excitation frequency of the incident wave is greater than the cut-on frequency for a certain mode, then the component of the incident wave traveling in the x direction will exist for that mode. Due to the cut-on frequency for each mode, there is also a limiting range for the angle of propagation for each mode, corresponding to

$$\cos^{-1}\left(\frac{\sqrt{k_p^2-k_{y_m}^2}}{k_p}\right)<\varphi_m<\frac{\pi}{2}. \tag{3}$$

Hence, a given mode can only propagate at incident angles for excitation frequencies greater than or equal to the cut-on frequency for that mode.

Using the simply supported and infinite boundary conditions, the primary displacements in plates 1 and 2 can be expressed in terms of modal coefficients $(R_{p_m}, R_{n_m}, T_{p_m}, T_{n_m})$ and modal wave numbers $(k_{x_m}, k_{n_m}, k_{y_m})$. The flexural displacement in plate 1 is described by a modal solution for the standing wave in the y direction, and a traveling wave solution along the x direction:

$$W_1^p(x,y)=\sum_{m=1}^{\infty}\left(A_{p_m}e^{-jk_p\cos\varphi_m x}+R_{p_m}e^{jk_{x_m}x} + R_{n_m}e^{k_{n_m}x}\right)\sin(k_{y_m}y), \tag{4}$$

where R_{p_m} and R_{n_m} are the amplitudes of the reflected propagating and near-field decay waves, respectively. Here $k_{x_m}=\sqrt{k_p^2-k_{y_m}^2}$ and $k_{n_m}=\sqrt{k_p^2+k_{y_m}^2}$ respectively represent the wave numbers of the propagating and decay waves along the x direction. Similarly, the primary flexural displacement in plate 2 can be described by

$$W_2^p(x,y)=\sum_{m=1}^{\infty}\left(T_{p_m}e^{-jk_{x_m}x}+T_{n_m}e^{-k_{n_m}x}\right)\sin(k_{y_m}y), \tag{5}$$

where T_{p_m} and T_{n_m} are the amplitudes of the propagating and near-field transmitted waves, respectively. It is important to note that the incident plate wave of the mth mode excites transmitted and reflected waves in the plate of the mth mode only.

The beam-reinforced plate is modeled as a continuous system, using the equations of motion to describe the plate in flexure and the beams in flexure and torsion. Due to their simply supported ends, the induced beam primary flexural and torsional displacements are also described by a modal solution. Continuity equations are used to describe the coupling at the beam-plate boundaries.[9]

Solutions for the plate modal coefficients T_{p_m}, T_{n_m}, R_{p_m}, and R_{n_m} can be obtained by making use of the coupling conditions between the beam and plate, the equations of motion, and the general solutions for the beam and plate displacements, resulting in

$$T_{p_m}=\frac{X_1+X_2}{2}, \tag{6}$$

$$T_{n_m}=\frac{Y_1+Y_2}{2}, \tag{7}$$

$$R_{p_m}=\frac{X_1-X_2}{2}, \tag{8}$$

$$R_{n_m}=\frac{Y_1-Y_2}{2}, \tag{9}$$

where

$$X_1=1+\frac{k_{n_m}}{jk_{x_m}-k_{n_m}+2jk_{x_m}k_{n_m}k_p^2\Phi_m}, \tag{10}$$

$$X_2=\frac{k_{n_m}+k_{x_m}+2k_p^2\Psi_m}{k_{n_m}-jk_{x_m}+2k_p^2\Psi_m}, \tag{11}$$

$$Y_1=1+\frac{2k_{x_m}}{k_{x_m}+jk_{n_m}+2k_{x_m}k_{n_m}k_p^2\Phi_m}, \tag{12}$$

$$Y_2=\frac{-2jk_{x_m}}{k_{n_m}-jk_{x_m}+2k_p^2\Psi_m}, \tag{13}$$

$$\Phi_m=\frac{2D}{E_b I(k_B^4-k_{y_m}^4)}, \tag{14}$$

and

$$\Psi_m=-\frac{2D}{GJ(k_T^2-k_{y_m}^2)}, \tag{15}$$

where E_bI and GJ are the beam flexural and torsional rigidities, respectively, and k_B and k_T are the beam flexural and torsional wave numbers.

B. Resonance conditions

For heavy reinforcing beams (where the beam stiffness is significantly greater than the plate stiffness), the values for D/E_bI and D/GJ are very small, and the transmitted energy is in the vicinity of the resonance frequencies for the bending and torsional waves in the beam.[6] The resonances occur when the modal wave number component of the incident wave in the y direction matches the natural flexural or torsional wave numbers in the beam, that is, when $k_{y_m}=k_B$ (flexural resonance) or $k_{y_m}=k_T$ (torsional resonance). Under these trace wave matching conditions, there is optimal coupling between the plate and beam motions, resulting in the greatest transmission of the plate flexural waves through the reinforcing beam. Closer examination of the resonance conditions reveals that for each individual mode of the incident wave, there is a frequency corresponding to the beam flexural resonance condition, which can be described by

$$f_{B_m}=\frac{1}{2\pi}\left(\frac{m\pi}{L_y}\right)^2\sqrt{\frac{E_bI}{\rho_bA}}, \tag{16}$$

where ρ_b and A are the density and cross-sectional area of the beam, respectively. Similarly, the corresponding frequency for the beam torsional resonance condition is described by

$$f_{T_m}=\frac{1}{2\pi}\left(\frac{m\pi}{L_y}\right)\sqrt{\frac{GJ}{\rho_bI_p}}, \tag{17}$$

where I_p is the polar moment of inertia of the beam.

To investigate the flexural wave transmission in the far field of plate 2, it is sufficient to only consider the transmitted propagating coefficient T_{p_m}. For an incident wave with unit magnitude ($A_{p_m}=1$), the transmitted flexural energy can be measured by the mean squared plate displacement in the far field by

$$\Pi_p=\frac{1}{L_y}\int_0^{L_y}W_2^p(W_2^p)^*\,dy=\frac{1}{2}\sum_{m=1}^{\infty}T_{p_m}T_{p_m}^*. \tag{18}$$

Hence, the far-field flexural energy transmission can be described solely in terms of the modal transmitted propagating coefficient T_{p_m}, and the expression $\frac{1}{2}\Sigma_{m=1}^{\infty}T_{p_m}T_{p_m}^*$ simply describes the ratio of the transmitted energy (per unit length in the x direction) to the incident wave energy.

II. ACTIVE CONTROL OF THE PLATE FLEXURAL ENERGY TRANSMISSION

For this semi-infinite beam-plate system, attenuation of the flexural energy transmission in the far field of plate 2 may be realized with the application of just a single, properly located point control force and a single point control moment collocated on the beam, as shown in Fig. 2. The point control force is arranged to excite only flexural wave motion in the beam and the control moment excites only torsional motion in the beam. For each control system application, a cost function is set up to minimize the far-field flexural energy transmission corresponding to each individual mode of the incident wave. In order to optimally design the active control system, attenuation of the far-field flexural energy transmission under point force control and point moment control are initially examined separately.

A. Point force control

A point control force of amplitude F_s at a location of y_f on the beam generates secondary flexural motion in the beam. The total force acting on the beam consists of two parts: the point force excitation, and a force F_{BR} which is a result of the backward reaction from the plates acting on either side of the beam.[10] The equation of motion for the secondary flexural waves of the beam excited by a point force has been previously described.[9] Due to the simply supported ends, the secondary beam flexural displacement is described by the following modal solution:

$$u_s(y)=\sum_{m'=1}^{\infty}u_{s_{m'}}\sin(k_{y_{m'}}y), \tag{19}$$

where $u_{s_{m'}}$ is the modal amplitude of the beam secondary flexural displacement, m' is the mode number of the secondary vibrations, and $k_{y_{m'}}=m'\pi/L_y$ is the modal wave number in the y direction of the secondary waves. Using the equation of motion for the beam secondary flexural motion,[9] the backward reaction force F_{BR} can be described in terms of the modal wave number components and the secondary flexural displacement in the beam by

$$F_{\mathrm{BR}}=-2jD(k_p^4-k_{y_{m'}}^4)((k_p^2-k_{y_{m'}}^2)^{-1/2}+j(k_p^2+k_{y_{m'}}^2)^{-1/2})u_s(y). \tag{20}$$

Taking the following steps: substituting Eq. (20) into the equation of motion for the beam in flexure, multiplying the resultant equation by an orthogonal mode, integrating over the length of the beam, and making use of modal orthogonality relationships, results in the following expression to describe the modal amplitude of the beam secondary flexural displacement by

$$u_{s_{m'}}=\frac{2F_s}{E_bIL_y}H_{f_{m'}}\sin(k_{y_{m'}}y_f), \tag{21}$$

where

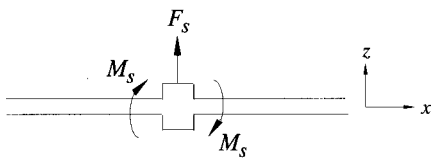

FIG. 2. Application of a single point control force and control moment to the reinforcing beam.

$$H_{f_{m'}} = \frac{1}{k_{y_{m'}}^4 - k_B^4 + (2jD/E_bI)\,(k_p^4 - k_{y_{m'}}^4)((k_p^2 - k_{y_{m'}}^2)^{-1/2} + j(k_p^2 + k_{y_{m'}}^2)^{-1/2})}. \tag{22}$$

Initial examination of the beam secondary flexural amplitude as a function of frequency shows that the maximum amplitude occurs in the vicinity of the resonance frequencies, corresponding to the modal wave number in the y direction being equal to the beam flexural wave number ($k_{y_{m'}} = k_B$). This coincides with the results from the primary wave transmission, where the maximum plate flexural wave transmission occurs at the flexural resonance condition corresponding to when the modal wave number component of the incident wave in the y direction is equal to the natural flexural wave number in the beam.

The general solution for the secondary flexural displacement in plates 1 and 2 can be described in terms of a modal and a traveling wave solution by

$$W_1^s(x,y) = \sum_{m'=1}^{\infty} (R_{p_{m'}} e^{j\sqrt{k_p^2 - k_{y_{m'}}^2}\,x} + R_{n_{m'}} e^{\sqrt{k_p^2 + k_{y_{m'}}^2}\,x}) \sin(k_{y_m} y), \tag{23}$$

$$W_2^s(x,y) = \sum_{m'=1}^{\infty} (T_{p_{m'}} e^{-j\sqrt{k_2^p - k_{y_{m'}}^2}\,x} + T_{n_{m'}} e^{-\sqrt{k_p^2 + k_{y_{m'}}^2}\,x}) \sin(k_{y_m} y). \tag{24}$$

For wave motion continuity, the coupling conditions between the plates and the beam require that the beam flexural displacement is equal to the flexural displacement in plates 1 and 2, and the torsional displacement of the beam is equal to the rotation of the plates about the y axis.[10] Also, from the symmetry of the control force application, the secondary displacements in plates 1 and 2 are the same ($T_{p_{m'}} = R_{p_{m'}}$ and $T_{n_{m'}} = R_{n_{m'}}$).[11] As the point force control is arranged to only excite flexural motion in the beam, the secondary torsional displacement in the beam is equal to zero. Using the coupling conditions, an expression for the secondary flexural displacement in plate 2 can be obtained as

$$W_2^s(x,y) = \frac{2F_s}{E_bIL_y} \sum_{m'=1}^{\infty} (A_{1_{m'}} e^{-j\sqrt{k_p^2 - k_{y_{m'}}^2}\,x} + A_{2_{m'}} e^{-\sqrt{k_p^2 + k_{y_{m'}}^2}\,x}) H_{f_{m'}} \sin(k_{y_{m'}} y_f) \sin(k_{y_{m'}} y), \tag{25}$$

where

$$A_{1_{m'}} = \frac{\sqrt{k_p^2 + k_{y_{m'}}^2}}{\sqrt{k_p^2 + k_{y_{m'}}^2} - j\sqrt{k_p^2 - k_{y_{m'}}^2}}$$

and

$$A_{2_{m'}} = \frac{-j\sqrt{k_p^2 - k_{y_{m'}}^2}}{\sqrt{k_p^2 + k_{y_{m'}}^2} - j\sqrt{k_p^2 - k_{y_{m'}}^2}}$$

represent the coefficients of the secondary propagating and near-field decay waves, respectively.

The plate vibrations are to be minimized at error sensors which are located in the far field of plate 2 at $x_e = 10\lambda_p$ (where $\lambda_p = 2\pi/k_p$). The total flexural displacement in plate 2 is the superposition of the primary transmitted flexural waves and the secondary flexural waves generated by the point control force, that is,

$$W_2^{\text{tot}}(x,y) = W_2^p(x,y) + W_2^s(x,y). \tag{26}$$

The primary transmitted flexural waves in the far field of plate 2 can be approximated using Eq. (5) as

$$W_2^p(x,y) = \sum_{m=1}^{\infty} T_{p_m} e^{-j\sqrt{k_p^2 - k_{y_m}^2}\,x} \sin(k_{y_m} y). \tag{27}$$

Similarly, by considering only the propagating secondary waves in the far field of plate 2, Eq. (25) can be simplified as

$$W_2^s(x,y) = F_s \sum_{m'=1}^{\infty} G_{f_{m'}} e^{-j\sqrt{k_p^2 - k_{y_{m'}}^2}\,x} \sin(k_{y_m} y), \tag{28}$$

where

$$G_{f_{m'}} = \frac{2}{E_bIL_y} A_{1_{m'}} H_{f_{m'}} \sin(k_{y_{m'}} y_f). \tag{29}$$

A cost function is developed to minimize the far-field flexural energy transmission by means of minimizing the total averaged squared plate displacement at the error sensors. The total power flow at the error sensor location becomes

$$\Pi_f = \frac{1}{L_y} \int_0^{L_y} W_2^{\text{tot}}(x_e, y)(W_2^{\text{tot}}(x_e, y))^* \, dy. \tag{30}$$

By standard methods, the cost function can be expressed as a quadratic function of the control force F_s:[11]

$$\Pi_f = F_s A_f F_s^* + B_f F_s^* + F_s B_f^* + C_f, \tag{31}$$

where

$$A_f = \frac{1}{L_y} \int_0^{L_y} \sum_{m'=1}^{\infty} G_{f_m} G_{f_{m'}}^* \sin^2(k_{y_{m'}} y) \, dy = \frac{1}{2} \sum_{m'=1}^{\infty} G_{f_{m'}} G_{f_{m'}}^*, \tag{32}$$

$$B_f = \frac{1}{L_y} \int_0^{L_y} \sum_{m=1}^{\infty} T_{p_m} e^{-j\sqrt{k_p^2 - k_{y_m}^2}\,x} \sin(k_{y_m} y) \times \sum_{m'=1}^{\infty} G_{f_{m'}}^* (e^{-j\sqrt{k_p^2 - k_{y_{m'}}^2}\,x})^* \sin(k_{y_{m'}} y) \, dy, \tag{33}$$

and

$$C_f=\frac{1}{L_y}\int_0^{L_y}\sum_{m=1}^{\infty} T_{p_m}T_{p_m}^{*}\sin^2(k_{y_m}y)\,dy$$

$$=\frac{1}{2}\sum_{m=1}^{\infty} T_{p_m}T_{p_m}^{*}. \tag{34}$$

Using the orthogonality relationship of the vibrational modes shows that the only nontrivial solution for Eq. (33) occurs when $m'=m$, resulting in

$$B_f=\frac{1}{2}\sum_{m=1}^{\infty} T_{p_m}G_{f_m}^{*}. \tag{35}$$

Using standard methods, the optimal control force is obtained by differentiating the cost function with respect to the real and imaginary components of the control force, where the optimal force corresponds to when both derivatives are zero.[11] The optimal control force resulting in the minimum averaged squared plate displacement is obtained as

$$F_s|_{\text{opt}}=-\frac{B_f}{A_f}, \tag{36}$$

and the corresponding minimum flexural energy transmission at the error sensor location is

$$\Pi_f|_{\min}=C_f-\frac{B_f^{*}B_f}{A_f}. \tag{37}$$

B. Point moment control

Similar arrangements can be made for point moment control, where a single, properly located point moment is applied to the beam to excite only torsional wave motion in the beam. The total moment acting on the beam can also be described by two parts: the control moment of amplitude M_s acting at a location of y_m on the beam, and a backward reaction from the plates. Under point moment control, the rotation in the plates about the y axis is equal to the secondary torsional displacement in the beam at the beam-plate coupling interfaces, and the secondary flexural displacements in the plates and beam are equal to zero. A general solution for the beam secondary torsional displacement is

$$\theta_s(y)=\sum_{m'=1}^{\infty}\theta_{s_{m'}}\sin(k_{y_{m'}}y), \tag{38}$$

where $\theta_{s_{m'}}$ is the modal amplitude of the beam secondary torsional displacement. Using the equations of motion of the beam torsional displacement, the backward reaction moment becomes

$$M_{\text{BR}}=2D\left(\sqrt{k_p^2+k_{y_{m'}}^2}+j\sqrt{k_p^2-k_{y_{m'}}^2}\right)\theta_s(y). \tag{39}$$

Using the same steps to obtain Eq. (21), the beam torsional amplitude can be obtained as

$$\theta_{s_{m'}}=\frac{M_s}{GJ}H_{m_{m'}}\sin(k_{y_{m'}}y_m), \tag{40}$$

where

$$H_{m_{m'}}=\frac{1}{k_{y_{m'}}^2-k_T^2+\frac{2D}{GJ}\left(\sqrt{k_p^2+k_{y_{m'}}^2}+j\sqrt{k_p^2-k_{y_{m'}}^2}\right)}. \tag{41}$$

Initial examination of Eqs. (40) and (41) reveals that the maximum amplitude of the beam secondary torsional displacement occurs when $k_{y_{m'}}=k_T$, which corresponds to the torsional resonance condition of the primary wave transmission. Hence, the secondary responses of the beam and plate are also dominated by the torsional resonance frequencies described by Eq. (17). Making use of the general solutions for the plate secondary flexural displacements and the beam-plate coupling conditions results in the following expression for the secondary flexural displacement in the far field of plate 2 under point moment control:

$$W_2^s(x,y)=\frac{2M_s}{GJL_y}\sum_{m'=1}^{\infty}B_{1_{m'}}e^{-j\sqrt{k_p^2-k_{y_{m'}}^2}x}H_{m_{m'}}$$

$$\times\sin(k_{y_{m'}}y_m)\sin(k_{y_{m'}}y), \tag{42}$$

where

$$B_{l_{m'}}=\frac{1}{j\sqrt{k_p^2-k_{y_{m'}}^2}-\sqrt{k_p^2+k_{y_{m'}}^2}},$$

is the amplitude of the secondary propagating flexural waves in the plate under the point moment application.

A cost function is set up as a quadratic function of the control moment amplitude in order to minimize the far-field flexural energy transmission. By considering each individual mode of the incident wave and using orthogonality relationships between the modes, the cost function can be described by

$$\Pi_m=M_sA_mM_s^{*}+B_mM_s^{*}+M_sB_m^{*}+C_m, \tag{43}$$

where

$$A_m=\frac{1}{2}\sum_{m'=1}^{\infty}G_{m_{m'}}G_{m_{m'}}^{*}, \tag{44}$$

$$B_m=\frac{1}{2}\sum_{m=1}^{\infty}T_{p_m}G_{m_m}^{*}, \tag{45}$$

$$C_m=\frac{1}{2}\sum_{m=1}^{\infty}T_{p_m}T_{p_m}^{*}, \tag{46}$$

and

$$G_{m_{m'}}=\frac{2}{GJL_y}B_{1_{m'}}H_{m_{m'}}\sin(k_{y_{m'}}y_m). \tag{47}$$

The optimal control moment resulting in the minimum power flow at the error sensor location x_e is obtained as

$$M_s|_{\text{opt}}=-\frac{B_m}{A_m}, \tag{48}$$

and the corresponding minimum far-field flexural energy transmission is

$$\Pi_m|_{\min} = C_m - \frac{B_m^* B_m}{A_m}. \tag{49}$$

C. Collocated force and moment control

Finally, the control performance is investigated using a combination of both force and moment control. The control actuators are applied to the beam and consist of a single point force and a single point moment collocated on the beam. The total flexural displacement in the far field of plate 2 now becomes the superposition due to three wave components: the primary transmitted waves, the secondary waves under point force control, and the secondary waves under point moment control, described by

$$W_2^{\text{tot}}(x,y) = W_2^p(x,y) + W_2^{F_s}(x,y) + W_2^{M_s}(x,y), \tag{50}$$

where $W_2^p(x,y)$, $W_2^{F_s}(x,y)$ and $W_2^{M_s}(x,y)$ are described by Eqs. (27), (28), and (42), respectively. The total power flow at the error sensors located in the far field of plate 2 is described by the total averaged squared plate flexural displacement:

$$\begin{aligned}\Pi_{fm} &= \frac{1}{L_y}\int_0^{L_y} W_2^{\text{tot}}(x_e,y)(W_2^{\text{tot}}(x_e,y))^* \, dy \\ &= [F]^H[A_{fm}][F] + [F]^H[B1_{fm}] + [B2_{fm}][F] + [C_{fm}],\end{aligned} \tag{51}$$

where $[F] = [\begin{smallmatrix} F_s \\ M_s \end{smallmatrix}]$ is the matrix form of the control force and moment, and $[\ ]^H = [\ ]^{*T}$ denotes the complex conjugate and transpose of a matrix;

$$[A_{fm}] = \frac{1}{L_y}\int_0^{L_y} [G]^H[G]\sin^2(k_{y_{m'}}y)dy = \frac{1}{2}[G]^H[G], \tag{52}$$

where $[G] = [G_{f_{m'}} \quad G_{m_{m'}}]$ and $G_{f_{m'}}$ and $G_{m_{m'}}$ are described by Eqs. (29) and (47), respectively; and

$$\begin{aligned}[B1_{fm}] = \frac{1}{L_y}\int_0^{L_y} \sum_{m'=1}^{\infty} [G]^H \sin(k_{y_{m'}}y) \\ \times \sum_{m=1}^{\infty} T_{p_m} \sin(k_{y_m}y)\, dy,\end{aligned} \tag{53}$$

$$\begin{aligned}[B2_{fm}] = \frac{1}{L_y}\int_0^{L_y} \sum_{m=1}^{\infty} T_{p_m}^* \sin(k_{y_m}y) \\ \times \sum_{m'=1}^{\infty} [G]\sin(k_{y_{m'}}y)\, dy,\end{aligned} \tag{54}$$

and

$$\begin{aligned}[C] &= \frac{1}{L_y}\int_0^{L_y} \sum_{m=1}^{\infty} T_{p_m} T_{p_m}^* \sin^2(k_{y_m}y)\, dy \\ &= \frac{1}{2}\sum_{m=1}^{\infty} T_{p_m} T_{p_m}^*.\end{aligned} \tag{55}$$

Using the orthogonality relationship of modes, it is found that the only nontrivial solutions for Eqs. (53) and (54) exist when $m' = m$, resulting in

$$[B1_{fm}] = \frac{1}{2}\sum_{m=1}^{\infty} T_{p_m}[G]^H \tag{56}$$

and

$$[B2_{fm}] = \frac{1}{2}\sum_{m=1}^{\infty} T_{p_m}^*[G], \tag{57}$$

where $[G]$ is a function of m only. It can be observed in Eqs. (56) and (57) that $[B1_{fm}]$ is the complex conjugate and transpose of $[B2_{fm}]$. By separating the complex power flow Π_{fm} into real and imaginary parts, and differentiating the real part with respect to the real and imaginary components of the control force, a solution for the optimal control force is obtained corresponding to the control force when both derivatives are zero. The optimal control force can be described by[11]

$$[F]_{\text{opt}} = -\frac{1}{2\,\text{Re}([A_{fm}])}([B1_{fm}] + [B2_{fm}]^H), \tag{58}$$

and the corresponding power flow at the error sensors is a minimum.

III. RESULTS AND DISCUSSION

A. Results of the primary flexural wave transmission

The theoretical model is based on the requirement that the beam-plate system is constructed of the same material throughout, and that the plate is symmetrically reinforced by two identical rectangular beams. For this analysis, the properties of aluminum were chosen for the material parameters, where $\rho = 2700\,\text{kg/m}^3$, $E = 6.9\times10^{10}\,\text{N/m}^2$, and $\nu = 0.33$. The internal distributed damping in the structure is included in the complex Young's modulus by $E_p^* = E_p(1 + j\eta)$, where $\eta = 0.001$ is the structural loss factor. For a plate thickness of 1.6 mm and reinforcing beams of both width and height 20 mm, the plate and beam flexural and torsional rigidity ratios are very small, where $D/E_bI = 3.2\times10^{-3}\,\text{m}^{-1}$ and $D/GJ = 6.9\times10^{-3}\,\text{m}^{-1}$. This results in the transmission peaks be-

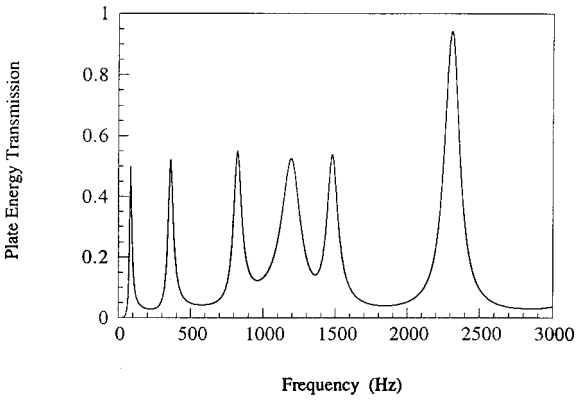

FIG. 3. Flexural energy transmission through a finite reinforcing beam.

TABLE I. Flexural and torsional resonance frequencies (Hz) for the first six modes of the incident wave.

$f_{B_1}=95.4$	$f_{T_1}=1121.9$
$f_{B_2}=381.4$	$f_{T_2}=2243.9$
$f_{B_3}=858.2$	$f_{T_3}=3365.8$
$f_{B_4}=1525.8$	$f_{T_4}=4487.8$
$f_{B_5}=2384.0$	$f_{T_5}=5609.7$
$f_{B_6}=3433.0$	$f_{T_6}=6731.7$

ing in the vicinity of the resonance frequencies for the heavily stiffened plate. The finite length of the plate and length of the beams is $L_y=1$ m.

Figure 3 corresponds to the flexural energy transmission in the far field of plate 2 as described by Eq. (18), as a function of frequency and for a specific incident wave field. For this case, the incident waves have the same amplitude in all directions ($A_{p_m}=1$), and all possible angles of incidence are simultaneously considered corresponding to their mode number and cut-on frequency. A frequency range of up to 3000 Hz was chosen in order to show an adequate number of the resonance peaks. For this frequency range, 27 modes were found present in the incident wave, where there are a greater number of flexural wave modes in the beam than torsional modes. Table I shows the flexural and torsional resonance frequencies described by Eqs. (16) and (17), respectively, for the first six modes of the incident wave. Figure 3 shows that the transmission peaks are dominated by the resonance frequencies, corresponding to the first five flexural resonance frequencies in the beam and the first two torsional resonance frequencies. At 2300 Hz, a very large transmission peak can be observed. This is due to the simultaneously excited flexural and torsional wave resonances in the beam contributed by the fifth flexural mode and the second torsional mode of the incident wave. Away from the resonance frequencies, there is very little transmission of the plate flexural energy as the beam is acting as a passive attenuation device.

B. Control results

The control force was located at a position of $y_f=0.618L_y$ on the reinforcing beam. This corresponds to a structural location which results in excitation of all the structural modes. Figure 4 shows that the application of a single, properly located point control force attenuates those peaks in the far-field flexural plate wave transmission corresponding to the flexural wave resonances only. The control forces generate flexural wave motion only in the beam resulting in significant reduction of the beam flexural vibration, as shown in the proceeding section. Similarly, Fig. 5 shows that a single, properly located point control moment on the beam will attenuate the transmission peaks corresponding to the torsional resonance conditions only. Attenuation of the plate flexural energy transmission due to the torsional resonances is achieved due to significant reduction of the beam torsional vibration under moment control. However, to achieve global attenuation of the far-field flexural energy transmission, it is necessary to apply both a control force and a control moment. This results in the attenuation of the transmission peaks at all resonance conditions, as shown in Fig. 6.

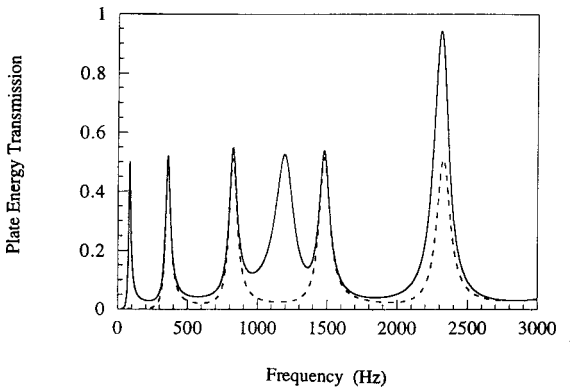

FIG. 5. Primary (———) and attenuated (---) responses of the flexural energy transmission under point moment control.

IV. EFFECT OF THE ACTIVE CONTROL ON THE BEAM VIBRATION

In order to obtain more physical insight into the mechanisms involved with the reduction of the plate vibration, the beam vibration was examined. Under the single control force application, the primary, secondary, and total beam flexural energy distributions were obtained as a function of frequency, as shown in Fig. 7. The beam flexural energies were averaged over the length of the beam. The beam secondary

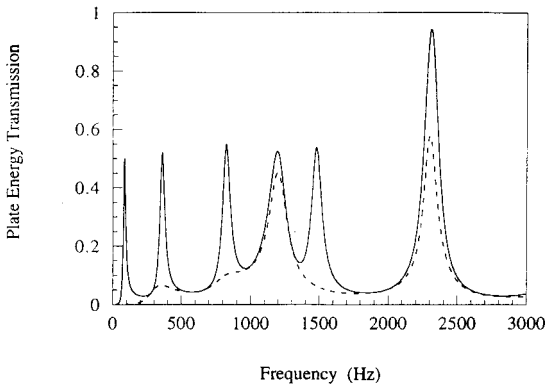

FIG. 4. Primary (———) and attenuated (---) responses of the flexural energy transmission under point force control.

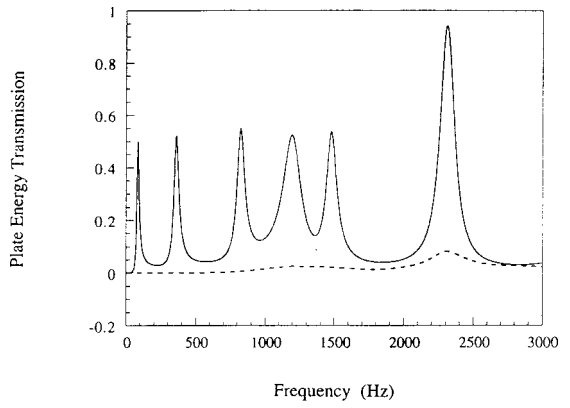

FIG. 6. Primary (———) and attenuated (---) responses of the flexural energy transmission using collocated force and moment control.

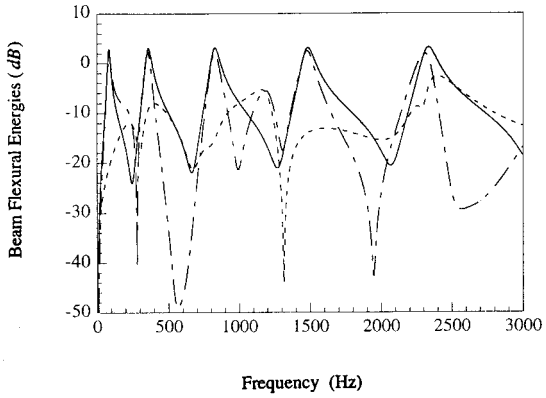

FIG. 7. Total beam flexural energy (---) showing the contributions by the primary (———) and secondary (- — -) beam flexural displacements.

flexural displacement was evaluated using the optimal control force obtained from the minimization of the far-field plate flexural energy transmission at the error sensor location. In Fig. 7, the primary beam flexural energy displays the peaks corresponding to the flexural resonance frequencies. A small peak corresponding to the first torsional resonance of the beam secondary vibration can also be observed. The beam secondary response matches the primary response at the resonance frequencies but 180 degrees out of phase, resulting in a reduction in the total beam flexural energy. However, at the frequency corresponding to the first torsional resonance, there is an increase in the total beam flexural energy. Similarly, at the frequency corresponding to the second torsional resonance, only a small reduction in the total beam flexural energy is observed. Similar results are found when examining the total beam torsional energy under point moment control, where only the peaks of the primary beam torsional energy are attenuated. Using collocated force and moment control, significant global attenuation of the beam flexural and torsional energy distribution is achieved.

V. CONCLUSIONS

Active attenuation of the plate flexural wave transmission through a reinforcing beam on a semi-infinite simply-supported ribbed plate has been analytically investigated. It has been shown that the maximum plate flexural wave transmission occurs at the optimal coupling between the plate flexural waves and the flexural and torsional waves in the beam. These optimal coupling conditions occur at resonance frequencies, where for each mode of the incident wave, there is a corresponding flexural and torsional resonance frequency. The far-field plate flexural energy transmission of the primary wave motion exhibits peaks which are dominated by the resonance frequencies. Active attenuation of the transmission peaks corresponding to the flexural resonance frequencies was achieved using a single point force applied to the beam. Similarly, attenuation of the transmission peaks due to torsional resonance was achieved under moment control. Using collocated force and moment control, global attenuation of the plate wave transmission through a reinforcing beam was achieved. Mechanisms involved with the attenuation of the plate vibration correspond to reduction of the beam vibration.

[1] E. E. Ungar, ''Transmission of plate flexural waves through reinforcing beams,'' J. Acoust. Soc. Am. **33**, 633–639 (1961).
[2] M. L. Rumerman, ''Vibration and wave propagation in ribbed plates,'' J. Acoust. Soc. Am. **57**, 370–373 (1975).
[3] R. F. Keltie, ''Structural acoustic response of finite rib-reinforced plates,'' J. Acoust. Soc. Am. **94**, 880–887 (1993).
[4] G. P. Eatwell and D. Butler, ''The response of a fluid-loaded, beam-stiffened plate,'' J. Sound Vib. **84**(3), 371–388 (1982).
[5] G. Maidanik, A. J. Tucker, and W. H. Vogel, ''Transmission of free waves across a rib on a panel,'' J. Sound Vib. **49**(4), 445–452 (1976).
[6] M. A. Heckl, ''Wave propagation on beam-plate systems,'' J. Acoust. Soc. Am. **33**, 640–651 (1961).
[7] A. J. Young and C. H. Hansen, ''Control of flexural vibration in a stiffened plate using piezoceramic actuators and an angle stiffener,'' Int. J. Active Control **1**, 277–301 (1995).
[8] J. Dickey and G. Maidanik, ''Active control of response of ribbed panels,'' in *Proceedings of the Conference on Recent Advances in Active Control of Sound and Vibration*, Virginia Polytechnic Institute and State University, Blacksburg, VA (1991), pp. 525–533.
[9] N. J. Kessissoglou and J. Pan, ''An analytical investigation of the active attenuation of the plate flexural wave transmission through a reinforcing beam,'' J. Acoust. Soc. Am. **102**, 3530–3541 (1997).
[10] M. A. Heckl, *Compendium of Impedance Formulas* (Bolt Beranek and Newman, Cambridge, MA, 1961), Report No. 774.
[11] J. Pan and C. H. Hansen, ''Active control of total vibratory power flow in a beam: I. Physical system analysis,'' J. Acoust. Soc. Am. **89**, 200–209 (1991).

Radiation modal expansion: Application to active structural acoustic control

Gary P. Gibbs
NASA Langley Research Center, Hampton, Virginia 23681-0001

Robert L. Clark
Duke University, Durham, North Carolina 27708-0302

David E. Cox
NASA Langley Research Center, Hampton, Virginia 23681-0001

Jeffrey S. Vipperman
University of Maine, Orono, Maine 04469

(Received 11 May 1998; accepted for publication 14 September 1999)

This paper demonstrates active structural acoustic control using multiple input/output adaptive sensoriactuators combined with radiation filters and a feedback control paradigm. A new method of reduced order modeling/design of radiation filters termed radiation modal expansion (RME) is presented. For the experiments detailed in this paper, the RME technique reduced the modeling of the radiation matrix from 400 transfer functions to 6 transfer functions (multiplied by a constant transformation matrix). Experimental results demonstrate reductions of radiated sound power on the order of 5 dB over the bandwidth of 0–800 Hz. © *2000 Acoustical Society of America.* [S0001-4966(00)00401-X]

PACS numbers: 43.40.Vn [PJR]

INTRODUCTION

In this paper, we examine the experimental implementation of a controller designed to minimize structure-borne sound radiation from a panel with clamped boundary conditions and subjected to acoustic excitation. The successful implementation of the control scheme detailed in this paper relies on the combination of several recent technological advances. The control system uses adaptive piezoelectric sensoriactuators (Vipperman and Clark, 1996) in a multiple input/output topology for simultaneous control actuation and output sensing. The plant was modeled using experimental measurements of input/output transfer functions (frequency domain) where the sensor outputs were augmented with plate velocity measurements made using a scanning laser vibrometer. The radiated acoustic energy was estimated with discrete radiation filters, and used as the cost function in the controller design (Elliott and Johnson, 1993). A new method termed radiation modal expansion was developed to facilitate the implementation of radiation filters with currently available digital signal processing hardware. A brief summary of related previous research will be detailed in the following paragraphs.

Active control of sound radiation from structures using structural based control inputs has seen much development in the recent past. A paper reviewing the concepts in controller design for active structural acoustic control was presented by Silcox *et al.* (1995). Work by Clark *et al.* (1993) investigated the use of shaped piezoelectric sensors for active structural acoustic control. Johnson and Elliott (1997) analytically investigated the use of arrays of discrete actuator tiles to locally reduce the volume velocity of a vibrating surface. Maillard and Fuller (1994) developed new structural acoustic sensing techniques and untilized these methods to control acoustic radiation from baffled beams. Also, Baumann *et al.* (1992) and Elliott and Johnson (1993) considered the control of radiated sound power using structural based measurements and radiation filters. The work presented in this paper extends the work of Elliott and Johnson (1993) by providing an approximation to the radiation filters which is experimentally implementable using current digital signal processing (DSP) technology.

Considerable research has concentrated on the modeling of acoustic radiation from vibrating structures such as beams and plates. Cunefare (1991) examined the minimum multimodal radiation efficiency of finite beams, and Currey and Cunefare (1995) and Elliott and Johnson (1993) addressed the characteristics of radiation modes and their convergence and accuracy. Borgiotti and Jones (1994) examined the frequency-independent properties of the radiation filters.

I. PROBLEM OVERVIEW

The primary difficulty in designing adaptive structures with complex geometry and/or complex boundary conditions is that the modes must usually be developed from a series expansion. This can be tedious for certain boundary conditions or high bandwidth applications. In this paper, we explore an alternative approach using the discretization of Rayleigh's integral (Elliott and Johnson, 1993; Maillard and Fuller, 1994) to predict the radiated power. The approach presented follows that proposed by Elliott and Johnson (1993).

A picture of the test structure (flat, aluminum panel) mounted in the Transmission Loss Test Facility at the Structural Acoustics Branch of the NASA–Langley Research Center is illustrated in Fig. 1. The plate is configured with

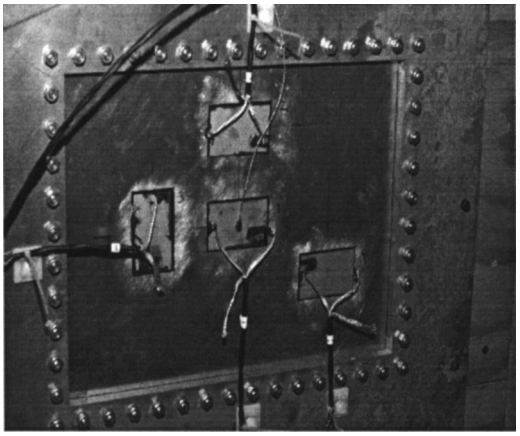

FIG. 1. Picture of the Transmission Loss Test Facility at the Structural Acoustics Branch of the NASA Langley Research Center.

four piezoelectric transducers. Again, each transducer is configured to operate as an adaptive sensoriactuator as detailed by Vipperman and Clark (1996). The control system is implemented on a TMS320C40 digital signal processor, and the identified test-based model and frequency-shaped cost functional required for structural acoustic control are detailed in the following discussion.

The primary purpose of this paper is to identify the level of complexity introduced to the frequency-shaped cost function in an attempt to accurately model the essential physics of the structural acoustic radiation. Radiation filters are designed based upon a spatial discretization of the structure into elemental radiators. Singular value decomposition of this frequency-dependent radiation matrix is used to identify the dominant radiation modes and the dominant singular values. Model reduction/truncation is then applied to minimize the number of states required in the radiation filters. Finally, effects of the model truncation on closed-loop performance are studied.

II. DESCRIPTION OF THE PLANT

The test structure illustrated in Fig. 1 measures 355.6 $\times 254 \times 1$ mm^3, and the positions of the sensoriactuators are identified in the schematic diagram presented in Fig. 2. The locations were selected such that the actuators could couple into the first five modes of the panel (clamped–clamped

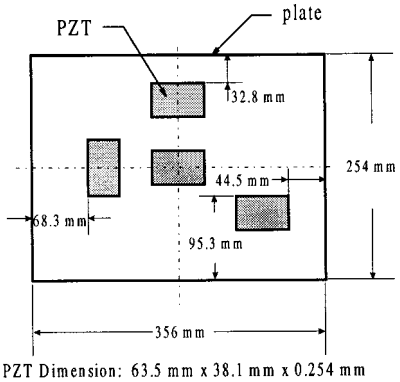

FIG. 2. Schematic diagram of the test panel used in structural acoustic control experiments.

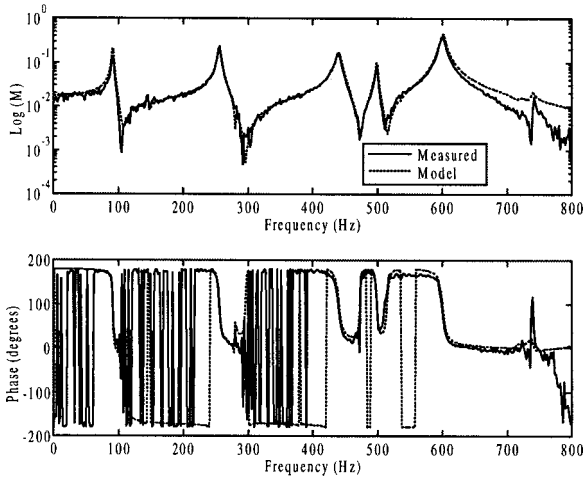

FIG. 3. Exemplary frequency response of sensoriactuator and curve-fit of the dynamic response.

modes) with the following exceptions. The actuators mounted on the horizontal centerline cannot observe/control modes with even indecies in the *y* direction (vertical). The actuators mounted on the vertical centerline cannot observe/control modes with even indecies in the *x* direction (horizontal). Thus the center-mounted actuator can only observe/control the odd–odd modes.

In addition to the strain measurements obtained from the sensoriactuators, velocity measurements are obtained at 20 locations on the plate using an Ometron VPI sensor (scanning laser Doppler velocimeter). The laser provides a noninvasive means of measuring the open- and closed-loop velocity of the structure at the discrete points indicated. Additionally, as will be outlined in a subsequent section, discrete velocity measurements are required to generate the performance objective since the structural acoustic radiation is estimated from a discretized version of the Rayleigh integral (Elliott and Johnson, 1993; Maillard and Fuller, 1994).

The frequency responses of the 4-input, 24-output system are determined using a Bruel & Kjaer 2032 spectrum analyzer over a bandwidth extending from DC to 1600 Hz. The SMARTID (1996) software package is used to identify the state-variable model of the system from the measured frequency response functions (FRFs). The FRF of adaptive piezoelectric sensoriactuator (APSA) 1 is presented in Fig. 3. As illustrated, the measured response and predicted response with the identified system are approximately the same up to a frequency of 700 Hz. The desired control bandwidth is between 20 and 500 Hz, so the structural model is truncated at 800 Hz. As will be discussed in the section devoted to control synthesis, this rolloff due to the unmodeled dynamics can be used to assist in the loop shaping since increasing the level of sensor noise in proportion to the plant response provides a means of indicating the bandwidth over which noise dominates the measured response.

The frequency responses between all four transducers and the 20 velocity measurements are all used in the identification of the model. These FRFs define the performance path which serves to ''shape'' the dynamic compensator; however, the measurements are not required during control

implementation. The model of the structure with the four-input, four-output array of sensoriactuators is required to implement the controller, and the model of the structure from the four piezoelectric inputs to the 20 velocity outputs is required to generate the performance metric. An acoustic loudspeaker is used to generate the acoustic disturbance on one side of the panel in the transmission loss facility, and a model of the disturbance source is also included to create the performance path associated with the typical two-port model (disturbance-to-error). The radiation filter design, required to implement a cost functional emphasizing reduction of radiated sound power, will be presented in the section devoted to the augmented plant model.

III. TRANSDUCER SELECTION AND PLACEMENT

Piezoceramic elements are selected to meet the need for compact transducers which might ultimately be integrated into the host structure for the ASAC application. Additionally, the piezoceramic elements are readily surface mounted, and thus require no reaction force from an additional support structure or mass. The piezoelectric devices create a strain when subjected to an applied voltage. When mounted off the neutral axis of the plate the actuators apply moments (torques) in the panel. The transducers can also act as distributed sensors measuring the integral of the strain (response) under the actuator. For this experiment, the transducers are operated as adaptive, piezoelectric sensoriactuators providing simultaneous sensing and actuation (Vipperman and Clark, 1996).

IV. AUGMENTED PLANT MODEL DEVELOPMENT: APPROXIMATION OF RADIATION FILTERS USING RME

Before assembling the augmented plant model, a model which incorporates the physics associated with the structural acoustic coupling must be developed. This dynamic model is used to ''filter'' the discrete velocity measurements such that the rms sound power radiated from the structure can be estimated. The radiated sound power and the control energy generate the performance metric for the structural acoustic control problem. Thus, once the frequency-dependent filter modeling the structural acoustic coupling is developed, the augmented plant can be assembled.

In this example, the modes of the test structure will not be explicitly identified; therefore, a different method is required to implement the radiation filters. Following the work of Elliott and Johnson (1993), the sound power radiating from a vibrating planar surface mounted in an infinite rigid baffle can be estimated using a discretization of Rayleigh's integral. The formulation will be omitted from this paper for brevity, but can be found in the reference by Elliott and Johnson (1993). If a planar surface extends over an infinite half-space, then one can demonstrate that the acoustic pressure at any field point can be described by the Rayleigh integral as follows (Fahy, 1985):

$$p(\mathbf{r})e^{j\omega t}=\frac{j\omega\rho_0}{4\pi}e^{j\omega t}\int_S\left\{2v_n(\mathbf{r}_s)\left(\frac{e^{-jkR}}{R}\right)\right\}dS, \tag{1}$$

where $p(\mathbf{r})$ is the acoustic pressure at the vector position $\mathbf{r}$, R is the magnitude of the difference between the vector to the vibrating surface $\mathbf{r}_s$ and the vector to the field point, $\mathbf{r}$: $|\mathbf{r}-\mathbf{r}_s|$, $v_n(\mathbf{r}_s)$ is the normal velocity of the vibrating surface at vector position $\mathbf{r}_s$, ρ_0 is the density of the fluid, and ω is the circular frequency.

The Rayleigh integral presented in Eq. (1) describes the radiation from a continuous vibrating surface in an infinite baffle in terms of continuous functions. For the test panel of this example, analytic functions describing the spatial vibration characteristics are unknown. Using a laser Doppler velocimeter (laser vibrometer), the out-of-plane velocities at a finite number of discrete locations are determined. This discretized measurement approach allows the surface to be considered as differential elements vibrating with known velocity. The pressure at some location off the surface can then be found through numerical integration of Eq. (1).

The radiated power from a vibrating surface described by a discrete number of velocity measurements can be found by the following relation:

$$\overline{P}=\mathbf{v}(j\omega)^H\mathbf{R}(j\omega)\mathbf{v}(j\omega), \tag{2}$$

where $\mathbf{v}(j\omega)$ is an $m\times 1$ vector of panel velocity measurements, and $\mathbf{R}(j\omega)$ is an $m\times m$ radiation matrix. $\mathbf{R}(j\omega)$ is real, symmetric, and positive definite. Thus the total radiated power of a vibrating surface (estimated by a discrete number of points) can be determined with only local panel vibration measurements. $\mathbf{R}(j\omega)$ can be calculated for a distribution of velocity points as follows [dropping the $(j\omega)$ terminology for convenience] (Elliott and Johnson, 1993):

$$\mathbf{R}=\frac{\omega^2\rho S^2}{4\pi c}\times\begin{bmatrix}1 & \frac{\sin(kr_{12})}{kr_{12}} & \cdots & \frac{\sin(kr_{1m})}{kr_{1m}}\\ \frac{\sin(kr_{21})}{kr_{21}} & 1 & \frac{\sin(kr_{23})}{kr_{23}} & \vdots\\ \vdots & \vdots & \ddots & \\ \frac{\sin(kr_{m1})}{kr_{m1}} & \cdots & \frac{\sin(kr_{mm-1})}{kr_{mm-1}} & 1\end{bmatrix}, \tag{3}$$

where ω is the circular frequency in rad/s, ρ is the density of air, S is the area associated with the discretized radiator, c is the speed of sound in air, k is the wave number (ω/c), and r_{ij} is the distance between the center of the ith and jth velocity locations. Since $r_{ij}=r_{ji}$, the radiation matrix is symmetric. Since the radiation matrix is also a function of frequency, a singular value decomposition can be performed to determine the dominant radiation modes of the system at each frequency. Singular value decomposition is performed at frequency ω_i as follows:

$$\mathbf{R}(\omega_i)=\mathbf{u}\mathbf{\Sigma}\mathbf{u}^{\mathbf{H}}, \tag{4}$$

where $\mathbf{u}$ is an $m\times m$ matrix whose columns are the normalized radiation modes of the matrix at frequency ω_i, and $\mathbf{\Sigma}$ is an $m\times m$ diagonal matrix whose elements are the singular

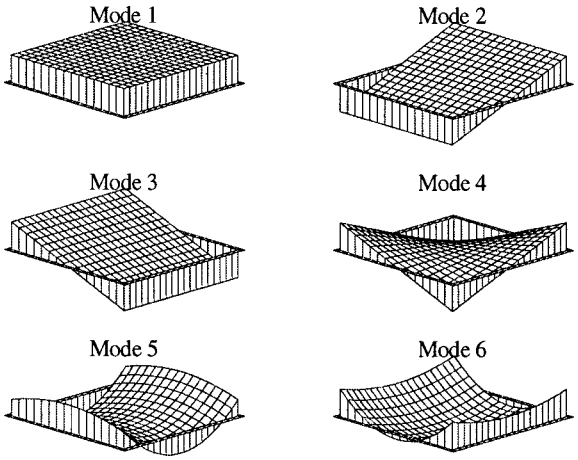

FIG. 4. Radiation modes 1–6 at 5 Hz.

values, decreasing monotonically along the diagonal. The magnitude of the *j*th diagonal element, σ_j, of $\mathbf{\Sigma}$ determines the relative importance of the *j*th radiation mode compared to other radiation modes.

For the aluminum panel used in this experiment (355.6 $\times 254 \times 1$ mm^3), a plot of the first six radiation modes at 5 and 500 Hz are shown in Figs. 4 and 5. Note how the shape of the first radiation mode transitions from a uniform ''piston'' mode to one with rounded edges (''dome'' shaped). A plot of the first six singular values, σ_1 through σ_6, as a function of frequency is presented in Fig. 6. Note that the radiation in the low-frequency range is dominated by the first mode, and for frequencies between 300 and 500 Hz the radiation is dominated by at most six modes.

In order to predict the total power radiated over some bandwidth, the characteristics of the **R** matrix must be modeled over that bandwidth. Thus, for an $m \times m$ matrix, a total of m^2 transfer functions must be modeled (curve fit). For this experiment a 5×4 grid of velocity points was used which corresponds to 400 transfer functions or approximately 1000 states. This level of complexity is impractical for control system design and synthesis, not to mention real-time implementation, since the order of the dynamic compensator is typically the same order as the augmented plant. ''Optimal'' controllers cannot be improved by going to higher orders. In this paper, a special curve fitting technique termed radiation modal expansion (RME) is presented which provides a reasonable approximation to the dynamics of the **R** matrix using a small fraction of the original number of states.

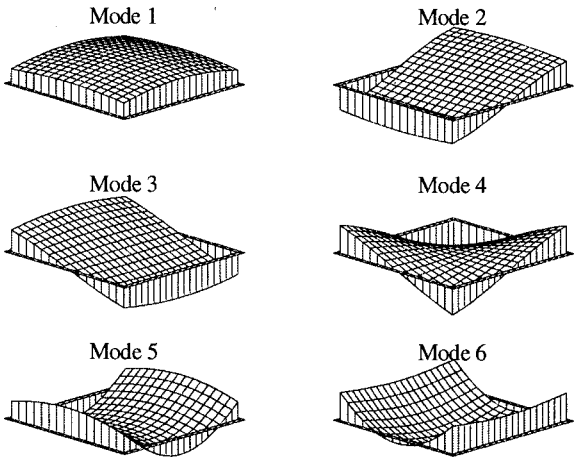

FIG. 5. Radiation modes 1–6 at 500 Hz.

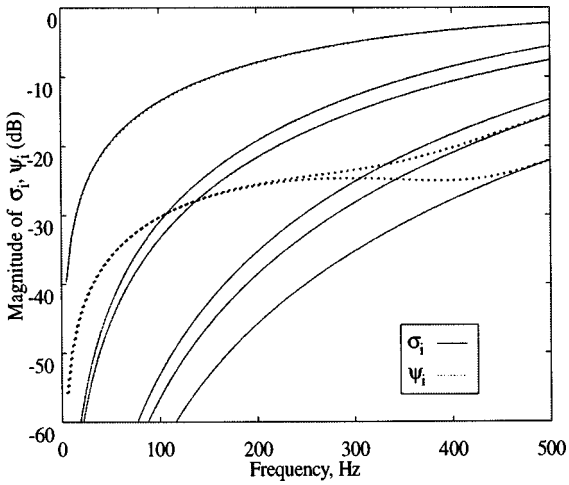

FIG. 6. Comparison of six dominant singular values (σ_i) of the radiation matrix **R** to the radiation modal expansion coefficients (ψ_i) for the first six radiation modes.

Work by Borgiotti and Jones (1994) described the ''nesting'' property of the radiation modes. In their work, they assert that the space spanned by the *significant* radiating modes at frequencies below some arbitrary maximum frequency of the bandwidth $\omega_{\max}$ is a subspace of the space spanned by the radiating modes at the frequency $\omega_{\max}$. Thus, the set of singular vectors at $\omega_{\max}$ corresponding to the significant radiating modes can be used as a basis to describe the radiation at any frequency below $\omega_{\max}$.

The key to incorporating the essential physics of structural acoustic coupling rests in curve fitting the dominant radiating modes over the bandwidth, which is performed using the RME technique outlined in this section. In this technique, the significant radiation modes at the upper frequency of the bandwidth of interest are used as a basis to curve fit the properties of the **R** matrix over the entire bandwidth. The amplitude-weighting coefficients are determined by the radiated power of each respective normalized radiation mode shape at each frequency ω over the bandwidth as follows:

$$\psi_i^2(\omega) = \mathbf{u}_{i,\max}^H \mathbf{R}(j\omega)\mathbf{u}_{i,\max}, \tag{5}$$

where $\psi_i^2(\omega)$ is the radiated power of the *i*th radiating mode (shape determined at $\omega_{\max}$), and $u_{i,\max}$ is the *i*th radiating mode shape determined at $\omega_{\max}$. A plot of the amplitude-weighting coefficients $\psi_i(\omega)$ for the first six radiation modes is shown in Fig. 6. Note that the magnitude of the RME coefficients, ψ_1 through ψ_4 (dashed), agree reasonably well with the actual singular values, σ_1 through σ_4 (solid), over the entire frequency range. The RME coefficients, ψ_5 and ψ_6, agree well with the actual singular values, σ_5 and σ_6, above about 400 Hz. Below 400 Hz, the two curves diverge due to the differences in shape between the actual singular vectors, μ_i, and shapes used for the curve fit, $u_{i,\max}$. In this frequency range, the basis functions or shapes, $u_{i,\max}$, are not completely orthogonal. Thus, for example, a normalized dis-

placement of $u_{5,\max}$ applied to the plate at some arbitrary low frequency is comprised of contributions from the actual radiation mode 5 as well as small contributions of other modes. The main goal of this paper is to create an efficient estimate of the radiation filter that can be implemented using currently available DSP hardware. Orthogonality over the entire bandwidth would be nice but is not required. As indicated in Fig. 6, the control system must yield levels of reduction on the order of 20 dB over the bandwidth of interest before the nonorthogonal characteristics of the radiation filter are of relative importance. As will be demonstrated in the results, this level of attenuation cannot be achieved in most practical realizations of feedback control for structures displaying high modal density and with limited model fidelity. The degree of orthogonality and the implications of this on the control problem are the subjects of future work.

In order to create a model of the RME system it is only necessary to curve fit the dynamics described by the RME coefficients, ψ_i, shown in Fig. 6. Thus the model transforms the velocity measurements into radiation mode coordinates with a set of constant transformation matrices (20×6 in this example), and then each mode passes through a model of the RME coefficients. The complexity is reduced from modeling 400 transfer functions to that of modeling 6 transfer functions (for the ψ_i's) and a simple (constant with ω) transformation matrix of vectors $u_{i,\max}$.

V. AUGMENTED PLANT MODEL ASSEMBLY

From the system identification process, we obtained a model of the structural plant, including 1 disturbance input, 4 piezoelectric inputs, 4 piezoelectric outputs, and 20 velocity outputs. To incorporate the appropriate performance metric, radiation filters are designed using RME to develop a frequency-weighted cost functional which incorporates a physical model of the structural acoustic coupling. For this example, three different performance metrics are explored, and closed-loop performance resulting from each design metric is evaluated. In developing the augmented plant, a state-variable model is generated which includes all three performance metrics, and the **sel** function of the μ-analysis and synthesis toolbox of Matlab is used to choose appropriate outputs for the error incorporated in the different cost functionals.

Consider the block diagram of the augmented plant presented in Fig. 7. The numbers presented in brackets, [*:*], indicate the vector entries for the respective inputs/outputs for the model. For example, outputs 1–6 are the outputs of the six radiation filters. As illustrated, there is a state-variable model of the structural plant (Ap, Bp, Cp, Dp), a state variable model of the radiation filters including six radiation modes ($A6$, $B6$, $C6$, $D6$), a state variable model of the radiation filter including one radiation mode ($A1$, $B1$, $C1$, $D1$), and a state-variable model which weights the structural velocities (Av, Bv, Cv, Dv) to provide a rms average of the sum. The rms average of the sum as opposed to the sum of the rms average of the velocity measurements was used to provide a better estimate of volumetric radiation. The inputs to each of the performance filters are obtained from the velocity outputs over the 5×4 grid of the structural model. Thus, for the radiation filters, the volumetric velocity of each elemental radiator of the panel is assumed to be that of the velocity measured at the center point of the elemental radiator. The remaining outputs of the augmented plant are constructed from the vector sum of the piezoelectric sensoriactuators and the assumed sensor noise, which is filtered with the state-variable model (Aw, Bw, Cw, Dw) as illustrated in Fig. 7 . The inputs to the system include the model of the disturbance path, the four piezoelectric sensoriactuators, and the sensor noise. Notice that the control effort penalty is weighted by a filter (Af, Bf, Cf, Df) also. Filters for control effort penalty and sensor noise are included for future flexibility as both of these vector inputs can be frequency weighted; however, for the purpose of this example, a uniform weighting over the bandwidth is assumed.

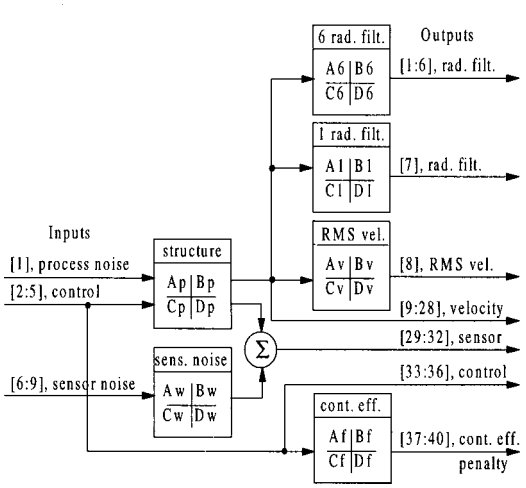

FIG. 7. Block diagram of the structural acoustic system used in the design process.

Once the augmented plant model is developed, there are a total of 9 inputs and 40 outputs. Now, at this point, one might question why the system architecture includes three different performance paths. As outlined earlier, the objective is to try each of the three different error paths, but not all three concurrently. Using Matlab and the μ-analysis and synthesis toolbox, it turns out that it is easiest to simply include all dynamics desired in a single model, and then select the desired inputs and outputs when you are ready to design the control system. The **sel** function can be used for this purpose and was incorporated into the script file which was used to design the control system. The vector array of inputs and outputs are grouped, and when ''selecting'' the design system, the appropriate inputs and outputs are identified for the desired plant.

VI. CONTROL STRATEGY

Thus far, a model of the structural plant has been identified, and a model which incorporates the physics of structural acoustic coupling has been constructed. The complete system is coupled as illustrated in Fig. 7. The compensator was designed with the objective to compare the performance (with respect to control of sound radiation) of each control system design based upon the three different cost function-

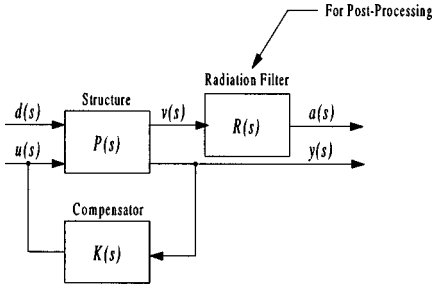

FIG. 8. Block diagram of the compensated plant.

als: six radiation filters, one radiation filter, and no radiation filters (rms average of summed point velocities). As illustrated in Fig. 8 the closed-loop plant includes the compensator, $K(s)$, and the structural plant, $P(s)$. The measured outputs of the adaptive sensoriactuators, $y(s)$, are provided as inputs to the compensator, and the compensator generates the control inputs, $u(s)$, to the structural plant. To evaluate the radiated sound power, the point-velocity measurements, $v(s)$, are postprocessed with radiation filters, $R(s)$. Thus, the closed-loop performance is represented by the transfer matrix, $T_{ad}(s)$, of the system between the applied disturbance, $d(s)$, and the measured radiation, $a(s)$.

The design parameters which are utilized in this experiment are the control effort penalty weighting and the sensor noise weighting. Due to the chosen weighting functions, the frequency weighted $\mathcal{H}_2$ synthesis is structured analogous to the standard Linear Quadratic Gaussian (LQG) problem. By increasing the control effort penalty, the closed-loop performance can be limited. Additionally, due to the rolloff in the modeled system (only a finite number of modes are included in the system identification), increasing the sensor noise tends to decrease the performance and the effective bandwidth of operation for the closed-loop system. Conceptually, one recognizes that the frequency at which the sensor noise is of the same order of magnitude as the plant output corresponds to the limit of the bandwidth over which the control system should perform. Thus, considering the rolloff in the plant model, as the level of sensor noise is increased, the frequency at which the sensed variables and the sensor noise are of the same order of magnitude decreases. By considering the maximum and minimum singular values of the loop transfer function, including the dynamic compensator, one can assess the gain cross-over frequency. For a fixed control effort penalty, increasing the sensor noise relative to the plant response tends to decrease the gain cross-over frequency.

Two figures were used extensively in the design process: a comparison of the open- and closed-loop radiated sound power and a plot of the singular values corresponding to the loop transfer matrix. As detailed in Chap. 8 of Clark *et al.* (1997), the maximum and minimum singular values of the multiple input multiple output (MIMO) loop transfer matrix have an analogous interpretation to the Bode plot of a single input single output (SISO) system. For this example, the objective is to maximize performance over the bandwidth of operation while minimizing the control effort expended at higher frequencies where the dynamics of the structure are

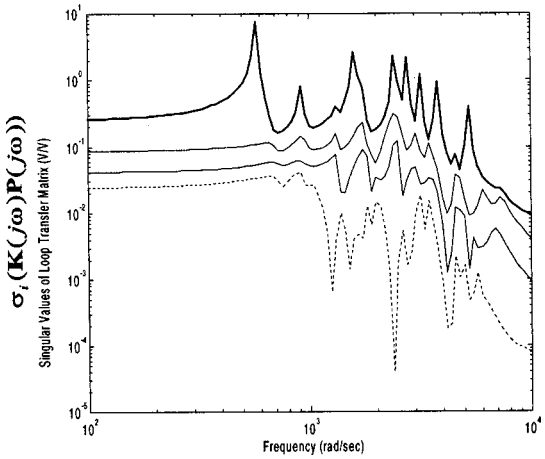

FIG. 9. Magnitude of the singular values of the loop transfer matrix.

not modeled. To accomplish this ''rolloff,'' the sensor noise is adjusted to effectively lower the corner frequency of the dynamic compensator. The singular values of the loop transfer matrix, $P(j\omega)K(j\omega)$, as a function of frequency are illustrated in Fig. 9. The maximum singular values never exceed unity above a frequency of approximately 600 Hz (3770 rad/s). This is below the bandwidth of the modeled dynamics but exceeds the bandwidth targeted for performance (20–500 Hz). Weighting for sensor noise and process noise were set at 10^{-3} and 2×10^{-2}, respectively.

VII. ANALYTICAL RESULTS

The $\mathcal{H}_2$ norm at each frequency of the closed-loop transfer matrix is computed between the disturbance input and the radiation filter output. For the given compensator design, the result is presented in Fig. 10. Note that the inputs and outputs are not converted to engineering units; however, this does not affect the relative performance of the system as the results presented in Fig. 10 are representative of the relative power for the open and closed-loop system. As illustrated, the predicted closed-loop performance is greatest at low frequency, in the bandwidth of the resonant frequency corresponding to the fundamental mode with approximately 20 dB of attenuation. The closed-loop performance extends to

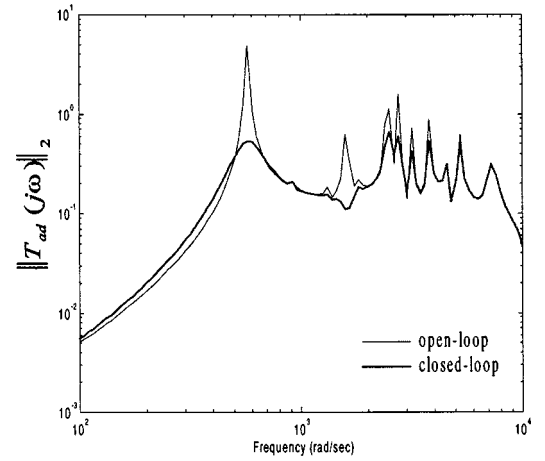

FIG. 10. Predicted open and closed-loop performance of test panel based upon dynamics obtained through modeling and system identification.

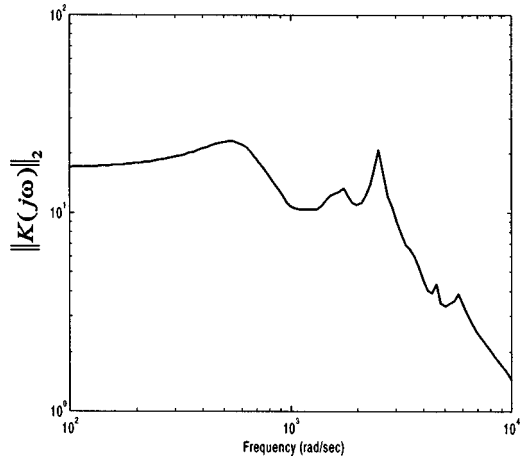

FIG. 11. Root mean square of squared singular values of the dynamic compensator plotted as a function of frequency.

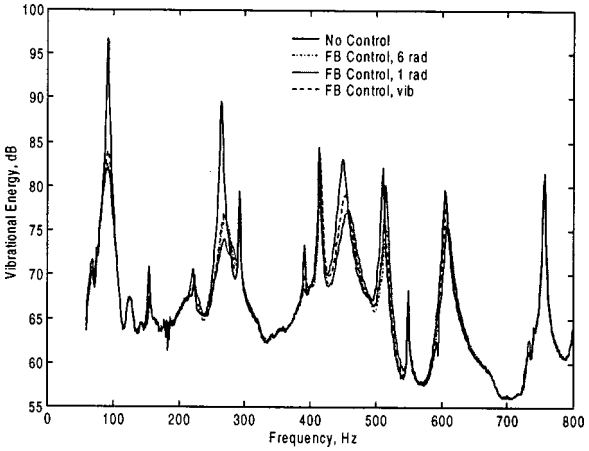

FIG. 13. Measured open- and closed-loop structural power.

approximately 600 Hz, which is the frequency at which the maximum singular values of the loop transfer matrix fell below unity.

In Fig. 11, the $\mathcal{H}_2$ norm at each frequency of the dynamic compensator is presented. As illustrated, the bandwidth of the compensator is limited to approximately 500 Hz. Beyond this bandwidth, the dynamic response decreases with increasing frequency, which is also reflected in the singular values of the loop transfer matrix presented in Fig. 9. This rolloff is necessary to minimize the control energy expended at higher frequencies where model uncertainty is greatest. The measured performance of the closed loop system with the given compensator is presented in the following section.

VIII. EXPERIMENTAL RESULTS

As detailed at the beginning of this paper, the objective was to design a compensator for three different cost functions. In this section, the closed-loop performance for compensators designed from each alternative cost function is presented.

As illustrated in Fig. 12, the open- and closed-loop sound power radiated from the structure is presented. In the legend, there are four cases identified: no control (No control), feedback control based upon a six radiation filter design (FB Control, 6 rad), feedback control based upon a single radiation filter design (FB Control, 1 rad), and feedback control based upon minimizing the sum of the velocity over an array of points on the structure (FB Control, vib). As indicated, approximately 15 dB of reduction in sound power is observed at the resonance corresponding to the fundamental panel mode for both the six radiation filter design and the single radiation filter design. As was detailed in the section devoted to the design of the radiation filters, the first radiation mode is the dominate mechanism for sound radiation at low frequency. As such, the curve-fit and model fidelity associated with the higher-order radiation modes is less important. The vibration control system design results in approximately 12 dB of attenuation at the resonance of the fundamental structural mode. Also notice that the acoustic response at some of the resonant frequencies (between 100 and 200 Hz) is insignificant compared to that corresponding to the resonance of the fundamental mode. This results from the radiation efficiency of the modes which characterize the structural acoustic control problem since structural modes with even indices are inefficient radiators at low frequency (i.e., when the structural wavelength is shorter than the acoustic wavelength). To see this effect, consider the plot of the structural power illustrated in Fig. 13 and obtained from a rms average of the velocity measurements. As indicated in the results, the resonant response of structural modes which were not significant radiators now appears in the plot of the vibrational energy. However, the modes corresponding to these resonances do not play a significant role in the frequency-shaped cost functional since their relative contribution to the radiated sound power is insignificant when the acoustic wavelength is much greater than the structural wavelength. Thus, the frequency-shaped cost functional, made possible by the implementation of the radiation filters, provides a means of incorporating this physical mechanism into the control system design. The overall performance of the two control system designs based upon radiation filters as opposed to vibration control resulted in an additional 0.5 dB of sound power attenuation over the bandwidth. Considering that the total reduction for the vibration controller was 3.5 dB, the increase in performance was on the order of 15%.

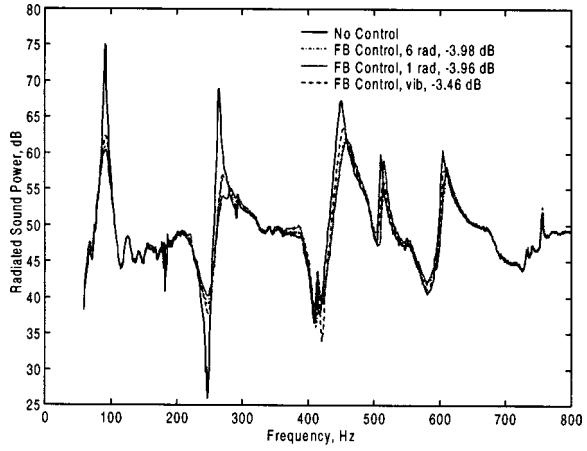

FIG. 12. Measured open- and closed-loop acoustic power radiated.

However, since the vibration controller chosen for this experiment was based upon the rms of the sum as opposed to the sum of the rms measure of velocity over the panel, it also targeted volumetric radiation on the panel. While effective, it was not as effective as the simple model of a single radiation mode.

IX. CONCLUSIONS

A method of developing a frequency-shaped cost functional incorporating the structural acoustic coupling for an experimental test structure was presented. The order of the state-variable model of the structural acoustic coupling was significantly reduced through a new technique termed radiation modal expansion, and models incorporating six radiation filters and a single radiation filter were used to design dynamic compensators for control of a structure clamped at all boundaries and configured with four piezoelectric sensoriactuators. The relative performance of the compensator designs from the two different choices of radiation filters was indistinguishable; however, a marginal improvement was observed when compared to the implementation of a controller based solely on a rms measure of the summed point velocities over the structure, which was also chosen to target volumetric radiation. The importance of the frequency-shaped cost was demonstrated as was the need to provide a practical method of rendering such model-based control system designs. As indicated by the results presented herein, a model of the first radiation mode is likely sufficient to provide acceptable levels of performance for low-frequency, structural acoustic control applications.

ACKNOWLEDGMENTS

The authors would like to gratefully acknowledge the support of the Structural Acoustics Branch of the NASA Langley Research Center under NCC-1-250, Dr. Richard Silcox, Contract Monitor. The authors would also like to acknowledge Dr. Ran Cabel of the Structural Acoustics Branch for his assistance in developing the DSP code.

Baumann, W. T., Ho, F.-S., and Robertshaw, H. H. (**1992**). ''Active structural acoustic control of broadband disturbances,'' J. Acoust. Soc. Am. **92**, 1998–2005.

Borgiotti, G. V., and Jones, K. E. (**1994**). ''Frequency independence property of radiation spatial filters,'' J. Acoust. Soc. Am. **96**, 3516–3524.

Clark, R. L., Burdisso, R. A., and Fuller, C. R. (**1993**). ''Design approaches for shaping polyvinylidene fluoride sensors in active structural acoustic control (ASAC),'' J. Intell. Mater. Syst. Struct. **4**, 354–365.

Clark, R. L., Saunders, W. R., and Gibbs, G. P. (**1997**). *Adaptive Structures: Dynamics and Control* (Wiley, New York).

Cunefare, K. A. (**1991**). ''The minimum multimodal radiation efficiency of baffled finite beams,'' J. Acoust. Soc. Am. **90**, 2521–2529.

Currey, M. N., and Cunefare, K. A. (**1995**). ''The radiation modes of baffled finite plates,'' J. Acoust. Soc. Am. **98**, 1570–1580.

Elliott, S. J., and Johnson, M. E. (**1993**). ''Radiation modes and the active control of sound power,'' J. Acoust. Soc. Am. **94**, 2194–2204.

Fahy, F. (**1985**). *Sound and Structural Vibration* (Academic, New York).

Johnson, M. E., and Elliott, S. J. (**1997**). ''Active control of sound radiation from vibrating surfaces using arrays of discrete actuators,'' J. Sound Vib. **207**(5), 743–759.

Maillard, J., and Fuller, C. R. (**1994**). ''Advanced time domain wavenumber sensing for structural acoustic systems. I. Theory and design,'' J. Acoust. Soc. Am. **95**(6), 3252–3261.

Silcox, R. J., Fuller, C. R., and Burdisso, R. A. (**1995**). ''Concepts on an integrated design approach to the active control of structurally radiated noise (ASAC),'' *Transactions of the ASME Special 50th Anniversary Design Issue* **117**, 261–270.

SMARTID (**1996**). Active Control eXperts, 215 First Street, Cambridge, MA 02142-1227.

Vipperman, J. S., and Clark, R. L. (**1996**). ''Implementation of an adaptive piezoelectric sensoriactuator,'' AIAA J. **34**(10), 2102–2109.

Acoustical design of the Tokyo Opera City (TOC) concert hall, Japan[a)]

Takayuki Hidaka
Takenaka R&D Institute, 1-5-1, Otsuka, Chiba 270-1395, Japan

Leo L. Beranek[b)]
975 Memorial Drive, #804, Cambridge, Massachusetts 02138

Sadahiro Masuda, Noriko Nishihara, and Toshiyuki Okano
Takenaka R&D Institute, 1-5-1, Otsuka, Chiba 270-1395, Japan

(Received 25 August 1998; revised 5 July 1999; accepted 30 August 1999)

The Tokyo Opera City concert hall seats 1632, volume 15 300 m^3, and reverberation time, with audience and orchestra, 1.95 s. As part of the design process, measurements on CAD computer and 1:10 wooden models of the hall and full-sized materials samples were conducted over a 5-yr. period. The hall in plan is rectangular. The ceiling is a distorted pyramid, with its peak 28 m above the main floor and nearer the stage than the rear of the hall. This unique shape was analyzed on the models so that all interior surfaces combine to distribute sources on the stage uniformly over the seating areas and to yield optimum values for reverberation time (RT), early decay time (EDT), interaural cross-correlation coefficient ($IACC_{E3}$), bass ratio (BR), initial-time-delay gap (ITDG), strength (G), and sound diffusion index (SDI) [for definitions see L. Beranek, *Concert and Opera Halls: How They Sound* (Acoustical Society of America, Woodbury, NY, 1996)]. On the long ceiling facing the stage, Schroeder QRD diffusers provide diffusion, eliminate a possible echo, and strengthen lateral reflections. Performers and critics judge the acoustics excellent. © *2000 Acoustical Society of America.* [S0001-4966(00)00101-6]

PACS numbers: 43.55.Br, 43.55.Fw, 43.55.Ka, 43.55.Mc [JDQ]

INTRODUCTION

The Tokyo Opera City complex (TOC) is contiguous with the New National Theatre complex (NNT). The NNT is on a 6-acre site and consists of an opera house, drama theater, experimental theater, and many other spaces. The TOC involves 5 acres on which are located the concert hall, rehearsal and education spaces, a 54-story sky-scraper, an art museum, and an arcade with shops and restaurants. A multilevel garage underlies the entire 11-acre site.

Nine Japanese companies own the property on which TOC is built. They formed the ''Owners Council of Tokyo Opera City Project,'' and named an Executive Committee to oversee the design, construction, and operation. Because of the size and diversity of buildings, a joint-venture design team was assembled by the Executive Committee, and Takahiko Yanagisawa of TAK Associated Architects was commissioned as the lead architect for the concert hall. [See the *Architects Preface* in the companion paper on the NNT opera house (Beranek *et al.*, 2000).]

Composer Toru Takemitsu was first commissioned as musical consultant and later as artistic director of the concert hall. Sadly, he died before completion and the concert hall is now designated the *Takemitsu Memorial*.

The requirements presented to the Acoustical Consultants by the Executive Committee and the Architect were (1) the hall should seat approximately 1630; (2) it must be planned primarily for concerts and recital performances; and (3) its reverberation time should lie in the range of 1.8–2.0 s with full occupancy. Several designs were produced by the architect before 1991, all of which had wooden side walls and ceiling.

Beranek was commissioned as the Acoustical Design Consultant for the TOC concert hall in April 1991. The acoustical staff of the Takenaka R&D Institute of Chiba, Japan, headed by Hidaka, was retained to make models and perform all necessary acoustical measurements. The first move was to review throughly the technical literature on concert hall design. Notable work in the past 30 years has come from Goettingen and Berlin in Germany, New Zealand, England, Canada, Denmark, Japan, and USA. [A summary and references are given in Beranek (1992).] Eight acoustical parameters, six of which are orthogonal, were identified as contributing to acoustical quality.

Hidaka and staff made modern acoustical measurements on 23 halls in Europe, Japan, and the Americas. Simultaneously, a systematic effort was accelerated to complete the assembly of drawings, photographs, details on materials, and acoustical data for 66 concert halls in regular use in 22 countries. Beranek (1996) determined, from interviews of qualified listeners, rank orderings of 34 concert halls for which binaural acoustical data were available (see Table I of Hidaka *et al.*, 1995), and by correlation determined an optimum range for each of the six orthogonal parameters and produced charts for combining the measurements on them into a physical rating scheme adapted from a procedure proposed by Ando (1985).

[a)]Presented at the ASA/ICA meeting in Seattle, Washington, 25 June 1998.
[b)]Electronic mail: beranekleo@mediaone.net

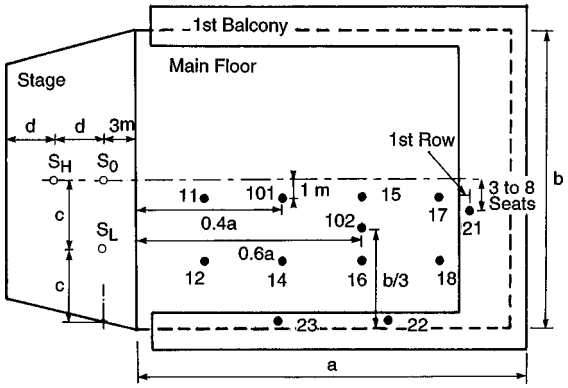

FIG. 1. Measuring positions used by the Takenaka R&D Institute group. For symmetrical halls, the measurements are generally made at least at the eight positions shown, and at more positions if there are more balconies or if there are a number of terraces. The letters a–d relate to the dimensions of the hall and determine the locations of sources and receivers. For three source positions and nine receiver positions, this gives 27 observations on the main floor. Each balcony or ring chosen has three or more positions.

I. ACOUSTICAL MEASUREMENTS

In all of the acoustical measurements made in 23 halls, a dodecahedral sound source was placed on the stage at one to four positions shown as examples in Fig. 1, of which S_0 was used in every hall. Each sector of the dodecahedral sound source, with a loudspeaker, is 21.5 cm on a side. For the binaural measurements in the halls, standard ''dummy'' heads fitted with microphones in the ear canals, or persons with two tiny microphones taped to the entrance of the ear canals (Fig. 2) were employed. The wearer of the microphones recorded their output on a DAT recorder. Accuracies of this kind of measurement were covered in Hidaka *et al.* (1995).

A modified stretched impulse signal was used (Aoshima, 1981) as shown in Fig. 3. The interaural cross-correlation functions corresponding to the measured impulse responses were calculated in the laboratory using the Wiener–Khinchin theorem (IEEE, 1979). Using a synchronous summation technique, a sequence of ten stretched pulses was recorded to improve the S/N ratio. The recorded signal is also the timing signal for starting the A/D conversion, which is possible by starting the stretched impulse with a lower frequency component than that specified by Aoshima. With a high-

FIG. 2. Subject wearing miniature microphones at outer ear canals and DAT recorder in his lap for binaural measurements at audience positions.

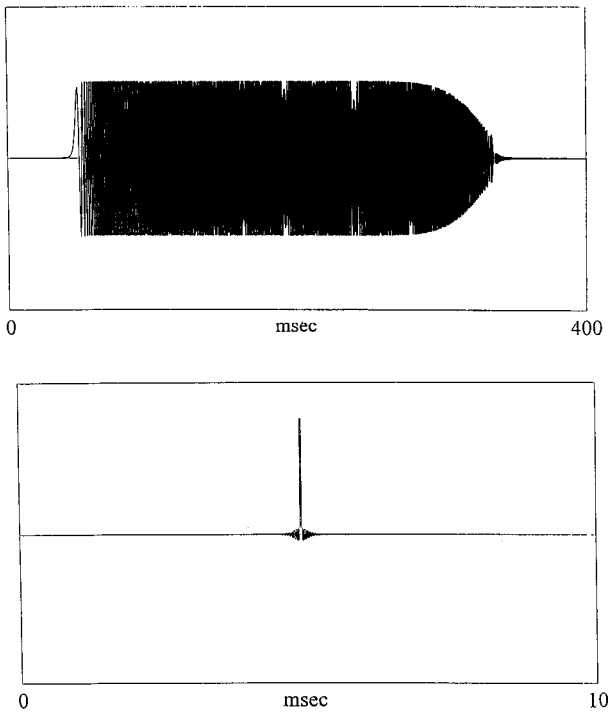

FIG. 3. (Upper) Waveform of the stretched impulse signal, $s(t)$. (Lower) Waveform of the exact impulse, $FT^{-1}[\exp[-B]\cdot FT[s(t)]$, compressed by the phase shift filter.

frequency component such a timing signal is not possible because of the waveform distortion at the impulse's beginning, which is apparently caused by phase fluctuations that modulate the refraction index of air.

Seven acoustical parameters were measured in eight frequency bands by these techniques: RT, EDT, $[1\text{-IACC}_E]$, C_{80}, BR, ITDG, and G (definitions are given in the Appendix). An eighth important acoustical parameter has not yet received an approved physical measurement, and must be estimated from visual inspection, namely, the sound diffusion index SDI. Diffusion of the sound field is produced by the architectural irregularities on both the ceiling and side walls of a hall, both large and small in scale. The correlations among the objective acoustical factors measured in the concert halls are listed in Table I. It is seen that RT_M and EDT_M are highly correlated and that $C_{80}(3)$ is also highly correlated (negatively) to these two parameters. The other acoustical parameters have low correlations among themselves and with RT_M, EDT_M, and $C_{80}(3)$. Obviously, SDI has low correlation with the other factors.

II. DESIGN PROCEDURE

In May 1991, the architect presented preliminary drawings which showed a hall whose lower part was rectangular in shape. The upper part was a distorted pyramid whose base started at the lighting trough which is located above the second balcony. The acoustical design process involved three stages from that time to the opening of the hall. First, a computer simulation of the hall was programmed. With it, ray traces through the second reflection, including air attenuation and diffraction from reflecting surfaces, was used to determine the feasibility of a rectangular/pyramidal shape

TABLE I. Correlation coefficients among objective acoustical factors calculated from the results of measurements in 39 concert halls. The subscripts ''*M*'' and ''3'' mean, respectively, that the octave band average was for 500 and 1000 Hz, and 500, 1000, and 2000 Hz. The significant correlations are in **bold** type.

	RT_M	EDT_M	$C_{80}(3)$	G_M	1-$IACC_{E3}$	BR	ITDG	V	N
RT_M	1.00								
EDT_M	**0.99**	1.00							
$C_{80}(3)$	**−0.84**	**−0.87**	1.00			**Bold**:>0.6			
G_M	0.31	0.31	−0.34	1.00					
1-$IACC_{E3}$	0.17	0.20	−0.37	0.46	1.00				
BR	0.08	0.04	0.04	0.04	−0.16	1.00			
ITDG	−0.48	−0.50	0.57	−0.43	−0.13	−0.04	1.00		
V	0.27	0.23	−0.03	−0.55	−0.51	0.21	0.25	1.00	
N	0.11	0.09	0.05	−0.53	−0.55	0.29	0.18	**0.84**	1.00

and the approximate values of the acoustical parameters. Second, a 10:1 wooden scale model of the hall was constructed as soon as the broad design was set, in which the shaping of reflecting surfaces, the height necessary to achieve the desired reverberation times, and the values for acoustical attributes were set. Third, after construction of the hall and several months before the opening, a test concert, with invited orchestra and audience, was arranged to determine the balance among the sections of the orchestra, whether the musicians heard each other well, and whether there were any peculiarities in the sound in the audience areas or on stage that had not been detected in the 10:1 model.

III. NUMERICAL CRITERIA AND INITIAL DECISIONS ADOPTED IN 1991

Reverberation time, **RT_M**, **and early decay time**, **EDT_M**: RT_M is the average of the RTs at 500 and 1000 Hz, with full audience and orchestra. For the nine halls rated highest in the survey of conductors and music critics (Beranek, 1996, Table 5.2; Hidaka *et al.*, 1995, Table I) the average reverberation time is 1.9 s, with a range from 1.8 to 2.0 s. It was agreed that the goal for RT_M would be 1.9 ± 0.1 s. In very good to excellent halls, the EDT_M (measured when unoccupied) is on average about 0.5 s longer than RT_M (measured when occupied). Previous experience has been that EDT is more critical in setting the acoustical quality of a hall for music than RT, but that if either the energy or the decay time in the RT portion of the sound decay is too low, the hall will lack the highly desirable ''singing tone'' of halls like those in Amsterdam, Boston, and Vienna. EDT is highly correlated with RT in all halls except for those of unusual shape or with addable volumes.

Shape: Because 6 of the highest rated halls in the 34 hall list in the two references above are shoebox shaped, a rectangular shape for the lower part of the TOC hall, which includes the main floor and balconies, was immediately judged acceptable. The unique pyramidal shape for the upper part of the hall, proposed by the architect, did not appear to present an insurmountable problem if proper diffusion and echo control were incorporated. This, of course, needed confirmation in the models.

Intimacy: The attribute that causes listeners to feel, acoustically, that they are in close contact with the performing group, is measured by the initial-time-delay gap, ITDG. Because the seating capacity is 1632, and the width of the hall is about 20 m, the resulting ITDG, at mid-main floor, is about 15 ms, well below the maximum acceptable value of 25 ms.

Spaciousness is defined as the combination of (a) subjective acoustical width of the performing body (called ASW, the apparent source width), and (b) the listener's feeling of being surrounded by the reverberant sound field (called LEV, listener envelopment). The rectangular shape is perfect for achieving the desired ASW provided all sound reflecting surfaces are properly oriented to yield a high measured value of $[1-IACC_{E3}]$. For the best halls this parameter exceeds 0.6. In regard to LEV, listeners feel surrounded by the reverberant sound if there is an unobstructed volume above the balconies, the RT is large enough, and there is adequate large-scale diffusion in the room [see Hidaka *et al.* (1995) and Okano *et al.* (1998)]. There is no agreed-on physical means for measuring LEV.

Clarity, **$C_{80}(3)$**, is highly (inversely) correlated with the early decay time EDT_M when the initial-time-delay gap is short and there are a number of reflections between it and 80 ms. In the best concert halls, the measured $C_{80}(3)$ (unoccupied) is between −1.0 and −4.0 dB (Beranek, 1996, Tables 5.2 and 12.1). The goal is a value within this range.

Diffusion, sound index, SDI is defined as the homogenizing of the sound field produced by irregularities on all reflecting surfaces. The halls most highly rated subjectively have highly irregular side walls and ceiling. One of the basic acoustical problems in the ill-fated Philharmonic Hall in New York was the lack of irregularities on any of the sound reflecting surfaces (eliminated for budgetary reasons). Diffusion must be of two types, fine scale and large scale. In the TOC it was decided to recommend fine-scale diffusion on the side walls beneath the balconies and large scale diffusion on the balcony fronts and the ceiling. Haan and Fricke (1993) have shown SDI to be a primary acoustical parameter for concert halls. No objective measurement has been standardized, so SDI is presently judged visually.

Strength G has been shown generally to be related to the ratio of (a) the early decay time EDT to (b) the cubic volume of the room (see Beranek, 1996, p. 445). In this hall with a seating capacity of 1632, this ratio will be similar to that in Vienna and Zurich if the desired EDT is achieved. The design problem is to make the SPL as uniform throughout the hall as possible.

Bass ratio, BR, is the ratio of the average RT at 125 and 250 Hz to RT_M. From measurements in the best halls, it was found that BR should exceed 1.0 (Beranek, 1996, Table 8.5).

Over-stage reflector: The sound radiated upward by an orchestra must be captured and reflected in part to the front portion of the audience area on the main floor and in part to the musicians on stage. In the TOC hall, because of the pyramidal ceiling, an overhead reflector is absolutely necessary to achieve these purposes.

Stage floor: A satisfactory stage floor must be wooden and not too thick or overly braced if it is to augment the vibrations of the pins on the cellos and basses.

Stage enclosure: Experience has shown that there should be sloping reflecting surfaces around the three sides of the stage, not far above the heads of the players, so that the players at the extreme sides of the orchestra can hear the music of the others. Further, the side (end) walls of the stage enclosure should be splayed, so as to send sound energy toward the audience and not to confine it to the stage alone. This is especially important for small orchestral groups and recitals. It was also decided that the area of the stage should not be too large, because if it is as wide as in many contemporary halls, the players cannot maintain good ensemble. For chamber groups and recitals, a large stage is a definite disadvantage. It was decided to make the stage area 10% larger than that in Boston Symphony Hall, which has been adequate there for nearly a century. Of course, if the stage area is thus limited, it needs to be extended for large choral works.

Seats and carpets: Because the interior surfaces of the TOC hall are of wood, which, even though 25 mm thick with a mass of 40 kg/m^2, absorb more bass than plaster walls, the audience seats must be chosen to absorb less bass. No added absorbing materials, including carpets, can be permitted.

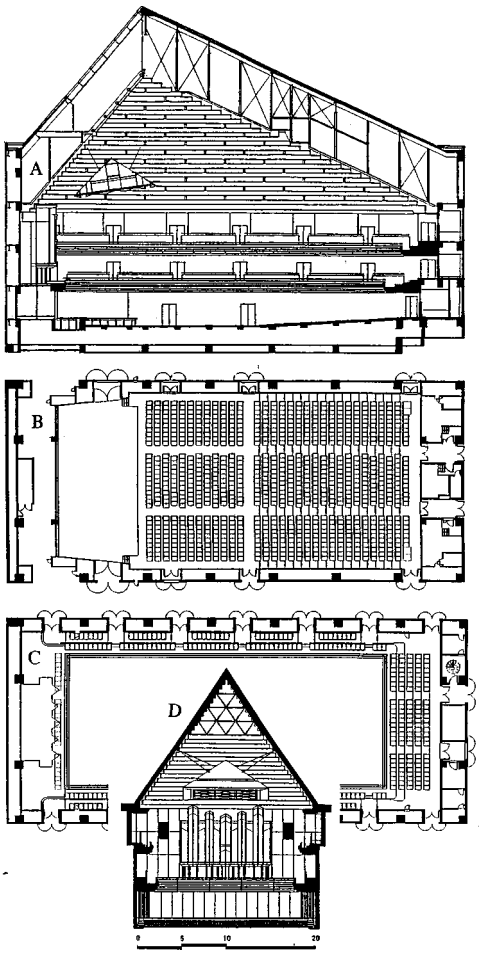

FIG. 4. The TOC concert hall as built: (a) Longitudinal cross section. (b) Main floor. (c) First balcony. (d) Lateral cross section at highest ceiling point. The second balcony is similar to the first, except it has three rows of seats at the rear. Many variations were presented originally by the architect for acoustical evaluation. Architect: Takahiko Yanagisawa, TAK Associated Architects, Tokyo.

IV. COMPUTER AND 10:1 WOODEN SCALE MODEL TESTS

By February 1992, the Takenaka Laboratories had completed both the computer model and the 10:1 wooden model of the TOC concert hall. With the 10:1 model, not only could the acoustical attributes listed above be measured, but the sounds of the hall could actually be heard, which is especially valuable for detecting echoes. The principal limitation with a 10:1 model is that there is no way to simulate 100 players performing simultaneously on stage, nor to determine their reactions to the hall's sound.

Drawings of the TOC hall, as built, are shown in Fig. 4. The main floor is 32.2 m long and 20 m wide. The sections show the distorted pyramidal shape of the ceiling. In the 10:1 tests, five ceiling configurations were evaluated: case 1 was with smooth ceiling surfaces; case 2 with uniform steps, and case 3 with uniform steps and a stage house like that in Boston Symphony Hall. Case 4 was with non-uniform steps, and case 5 with nonuniform steps and a canopy over the stage. Case 2 with uniform steps and diffusing blocks and a canopy over the stage was selected for architectural and acoustical reasons.

Throughout the acoustical tests four positions of the sound source on the stage were used, designated S_0, S_L, S_R, and S_H, shown in Fig. 5. Because the hall is symmetrical, eight receiving positions were selected on the main floor and four or five positions in the balconies. Position 102 on the main floor is of particular interest because it is both off center and is an important audience position.

In Fig. 6, photographs of the interior of a late version of the 10:1 wooden model and of the dodecahedral sound source are shown. Movable throughout the ''audience'' areas were (1) $\frac{1}{8}$-in. electret microphones for monaural measurements and (2) ''dummy'' heads, each about 2 cm in diameter fitted with two tiny microphones at the ear positions, for binaural measurements. The numbering of the audience positions is also shown in Fig. 5. In Fig. 7, reflectograms from the computer model and the 10:1 model are shown for comparison. The sound source was at S_0. In the upper half of Fig. 7, the ''listener'' was at main-floor position 102 and in the lower half at first balcony position 23. Early reflections are very important, both as to time of arrival, amplitude, and direction. It is apparent that position 102 was superior to position 23 at that stage of the development, because there are 13 reflections in the first 80 ms, while at position 23 there are only 6, and the levels of the first 5 reflections at position

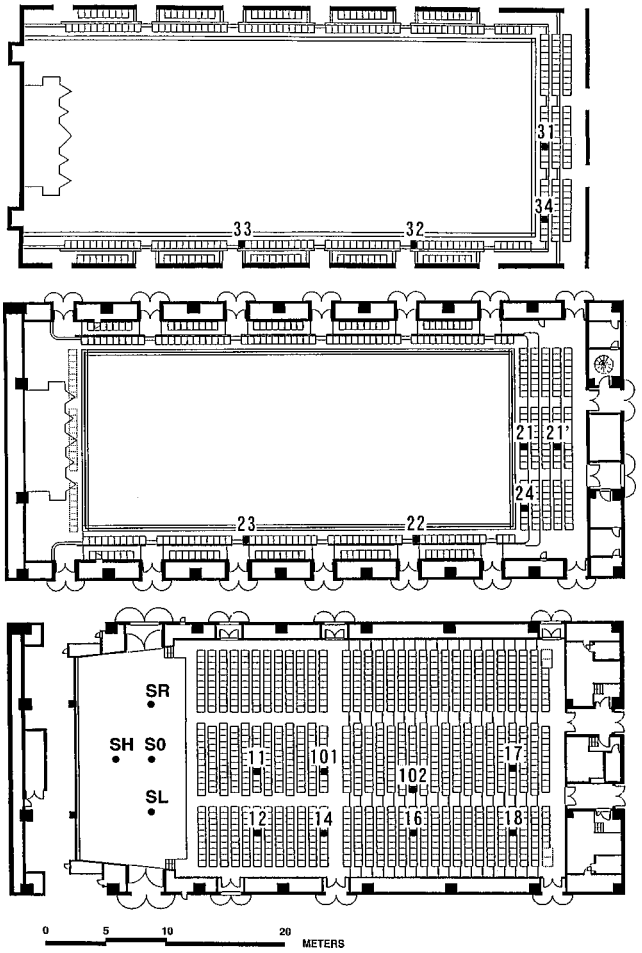

FIG. 5. Stage and audience measuring positions used by Takenaka Research and Development Institute for symmetrical models and halls. (Lower) Four positions of omnidirectional sound source on stage, with S_0 being referred to most often in this paper, and eight audience measuring positions on main floor, with Nos. 101 and 102 being referred to most often. (Middle) Five audience positions in first balcony with Nos. 21 and 23 being referred to most often. (Upper) Four audience measuring positions in second balcony, with No. 32 being referred to most often.

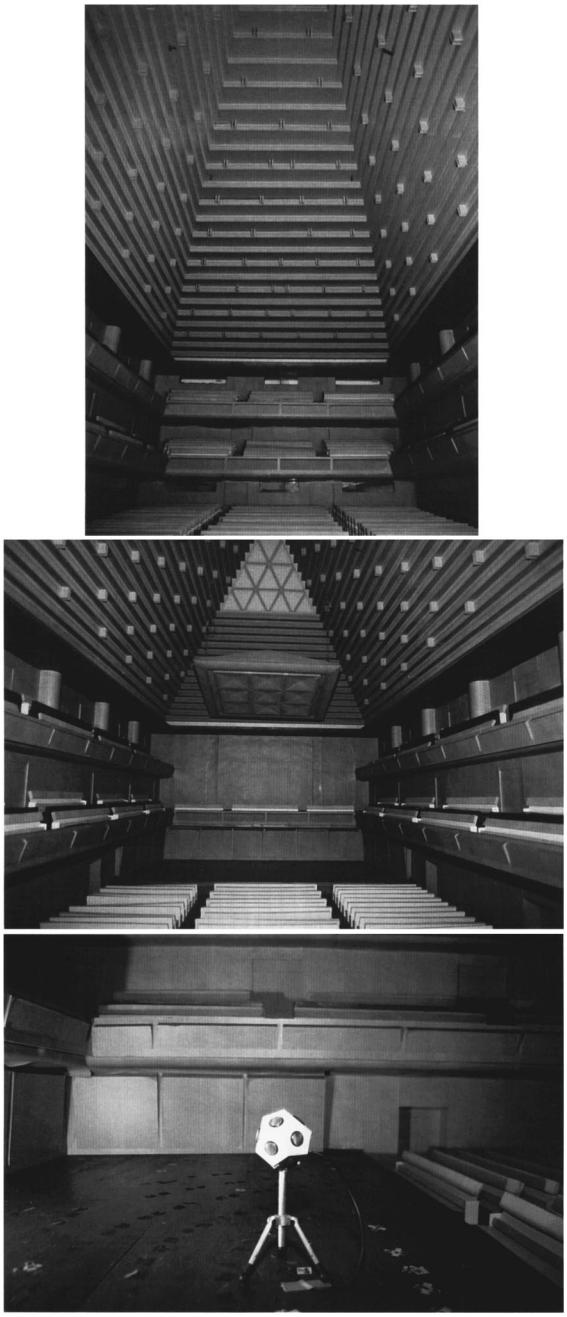

FIG. 6. Photographs of 10:1 wooden model, taken at late stage of the TOC design project.

23 are well below those at 102. By adjusting the slopes of the balcony faces, adding large scale diffusion to them, and adjusting the angle of the lighting trough at the upper edge of the rectangular portion, the sound at position 23 was later improved. The discrete reflections shown in the lower halves were spread out when diffusion was added, as will be shown later in the reflectograms for the finished hall. The tests in the models assured that the rectangular/pyramidal shape of the hall desired by the architect would yield values of intimacy, loudness, spaciousness, and clarity that would be near ideal. Attention was then focused on reverberation time, bass ratio, hanging reflector, and sound diffusion on ceiling and side wall surfaces.

Determination of reverberation times in the 10:1 model was more difficult than expected because no satisfactory method was then available for simulating the audience. This difficulty was improved on after we learned the effectiveness of the cloth covering that is described in Sec. VI below. In Fig. 8, the sound pressure distributions at mid-frequencies on the main floor and the balconies, using pink noise in eight octave bands, are shown in comparison with the level at position 101 in the center of the hall. No long-path echoes were discovered on-stage or in the audience either by listening or by measurement.

By the Fall of 1992, the results of acoustical tests of the various architectural features that had been installed in the models were reported to the architect. Because the ceiling of TOC is shaped like a pyramid, the architect wanted the over-stage reflector to be pyramidal with its dimensions as small as possible consistent with accomplishing the necessary acoustical results. He also requested that the space at the front of the hall, above the first balcony, must be tall enough to accommodate the organ pipes, which appeared to be in conflict with the lower height needed to achieve the desired reverberation time.

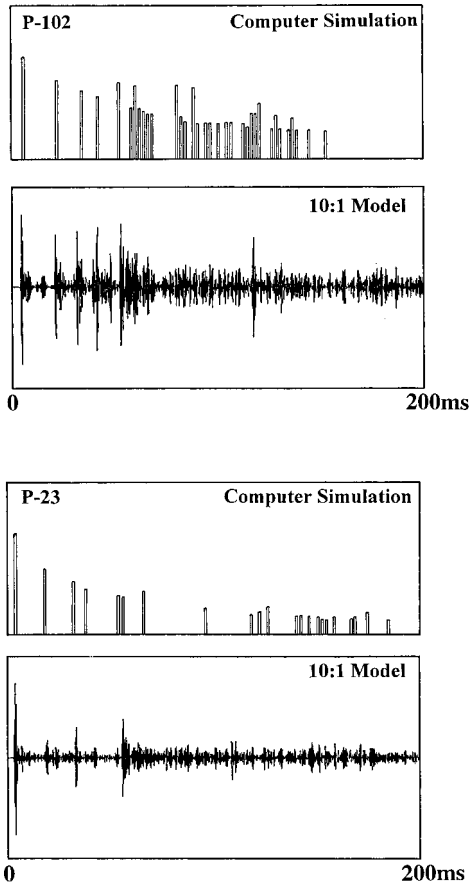

FIG. 7. Comparison of computer CAD model and 10:1 model reflectograms for 2000 Hz at positions 102 and 23, with omnidirectional source at S_0 on stage. These charts are from an early stage of the design project.

The consultants concluded that the interior surfaces could be comprised of two layers of heavy wood with an overall thickness of 25 mm.

At this point, attention was turned to the detailed designs of the over-stage reflector and the pyramidal ceiling which must produce the desired sound diffusion. A specific design for the chairs also followed so that samples could be fabricated and tested acoustically in a reverberation chamber. Other items that needed laboratory consideration were (1) the fine-scale sound-diffusing irregularities on the side walls beneath the first balcony; (2) the large-scale sound-diffusing irregularities for the balcony fronts, and (3) the final orientation of all reflecting surfaces.

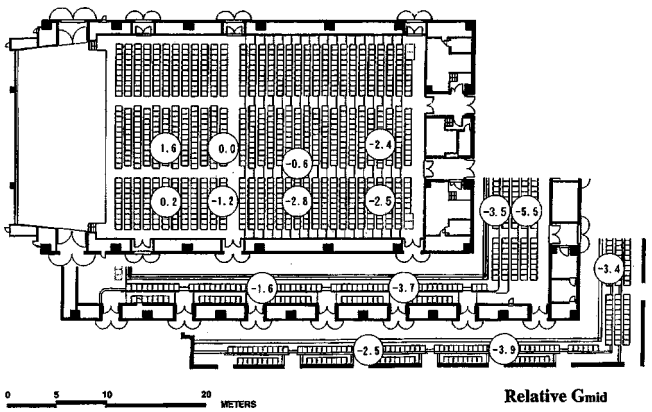

FIG. 8. Relative values of the strength factor G_M (average of 500- and 1000-Hz values) measured at 15 audience positions with an unidirectional source on stage at S_0. The reference position is No. 101.

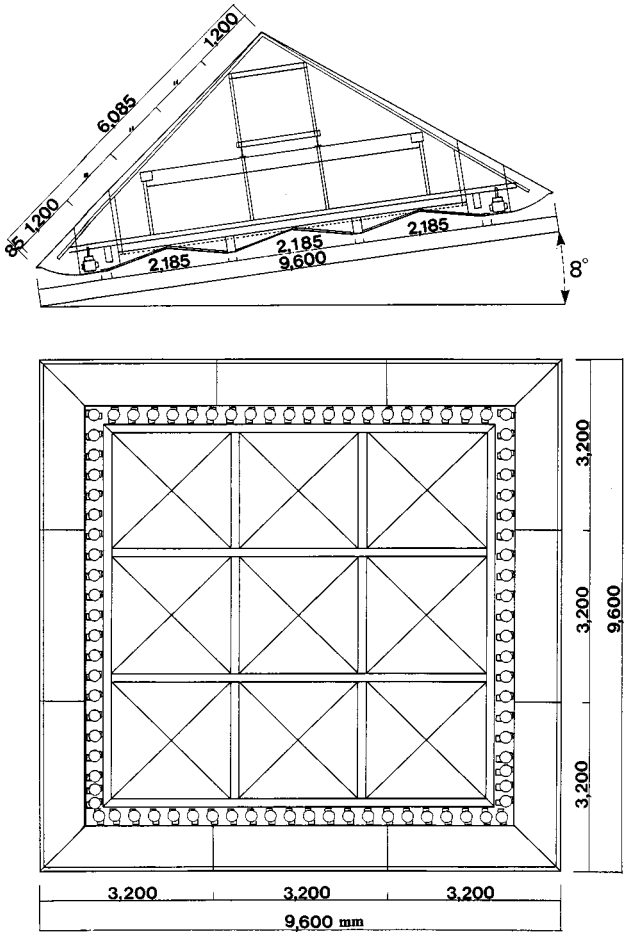

FIG. 9. Outline drawing of the pyramidal sound reflector hung above stage in TOC concert hall. The nine sections act to diffuse the sound so that performers on the stage can hear themselves and other players. The reflector also strengthens the early sound in the front rows of the audience. The dimensions are in millimeters.

V. LABORATORY DESIGNS, TESTS, AND RECOMMENDATIONS

In response to the above lists of needs, the following designs, tests, and recommendations were made by the acoustical consultants:

Reflecting canopy: Using the 10:1 model it was determined that (1) the lateral dimensions of the lower surface of the canopy should be no smaller than about 10 m on a side, (2) its slope, that is to say, its angle relative to horizontal, should be about 8 degrees; (3) the detailed shaping of the lower surface must be irregular, preferably with both large- and small-scale irregularities so as to diffuse the reflected sound, thus making the balance better among the sections of the orchestra as heard on stage and in the audience; and (4) the outer 0.5 m around the reflecting surface should preferably be curved up to increase the canopy's reach. The final design of the reflecting surface is shown in Fig. 9.

Organ pipe space: The consultants insisted that the height of the ceiling must be chosen to produce the desired

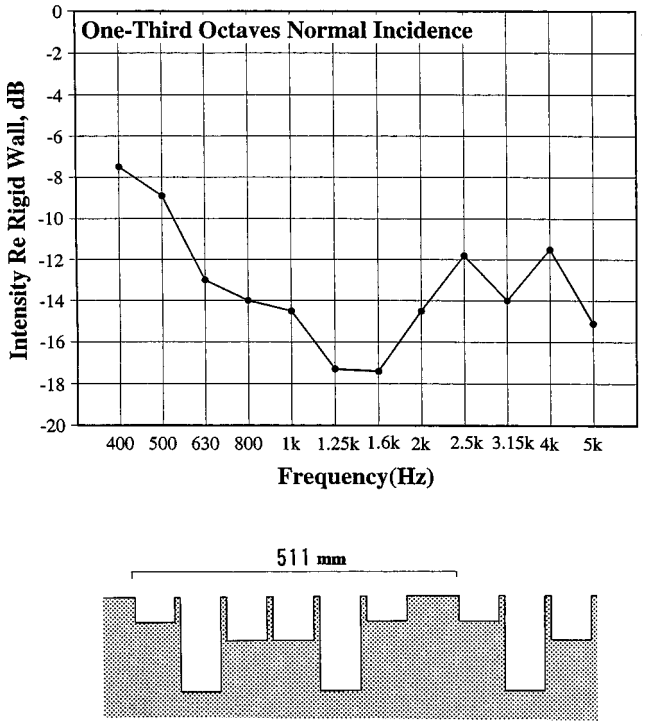

FIG. 10. (Lower) Design of Schroeder QRD sound diffusers installed horizontally on the rear wall of the pyramid facing the stage. (Upper) Reflected intensity measured in one-third-octave bands at normal incidence. The sound reflected back to the stage is reduced by more than 12 dB in the frequency bands from 630 to 5000 Hz. The QRD directs a considerable part of the diffused sound energy to the side walls of the pyramid which, on reflection, strengthens early lateral reflections.

reverberation time. Because only the lowest-frequency pipes need be long, it was urged that the organ builder bend them to fit the necessary space.

Pyramidal ceiling details: To preserve the aesthetic feel of the room, the architect demanded that the steps in the ceiling be uniform. To permit this, it was recommended that the long pyramidal surface be covered with Schroeder quadratic residue diffusers (QRD) and that sound-reflecting blocks be placed at intervals of 4.5 m on alternate steps along the lengths of the other three surfaces. As designed, the QRDs (Fig. 10, lower) scatter the sound laterally, thus the scattered sound strikes the side surfaces of the ceiling where they are further diffused laterally by the steps and the reflecting blocks. Laboratory tests showed that there would be no coloration owing to the steps. Sound directly striking the sides of the ceiling is also diffused by this combination. A further advantage of the QRDs is that they reduce the level of sound that is reflected directly back to the stage, thus eliminating what might have been a weak, but disturbing, on-stage echo (Fig. 10, upper).

Selection of chairs: The basis for the selection of the chairs turned out to be a sizable research project. The results are given in Beranek and Hidaka (1998). The design selected is similar to the chairs in the Grosser Musikvereinssaal of Vienna and is shown in Fig. 11. The seat cushion is about 5 cm thick, and 60% of the front of the seat back is a 2-cm-thick cushion.

Fine-scale diffusion on lower side and rear walls: It had been learned from listening tests in New York's Philharmonic Hall that sound reflected from smooth surfaces gave a peculiar ''acoustical glare'' to the music which could be eliminated by reducing the amount of sound reflected at the high frequencies (above 1000 Hz). The laboratory program developed several fine-scale irregularities for the lower side walls that scattered the high-frequency sound on reflection, thus giving the sound an ''acoustical patina.'' The detailed design acceptable to the architect is shown in Fig. 12.

Large-scale diffusion on balcony fronts: The model tests showed that for producing the best reflectograms at all parts of the audience, the balcony fronts would need to be sloped forward as shown in Fig. 13. Large-scale diffusion was created by the steps and the bottom edges were rounded to reflect the high frequencies more uniformly over the audience areas. In addition, vertical interruptions (protruding wooden blocks) are placed along the lengths of the balcony fronts on alternate steps, about 1.8 m apart (see Fig. 4).

All of the above changes were incorporated into the 10:1 scale model and RTs, reflectograms and C_{80}'s at 15 audience positions, as well as ST1 and reflectograms for various source positions on stage were determined. The improvement in the sound for 2000 Hz at seat 23 can be seen from Fig. 14 by comparison with the reflectogram for the 10:1

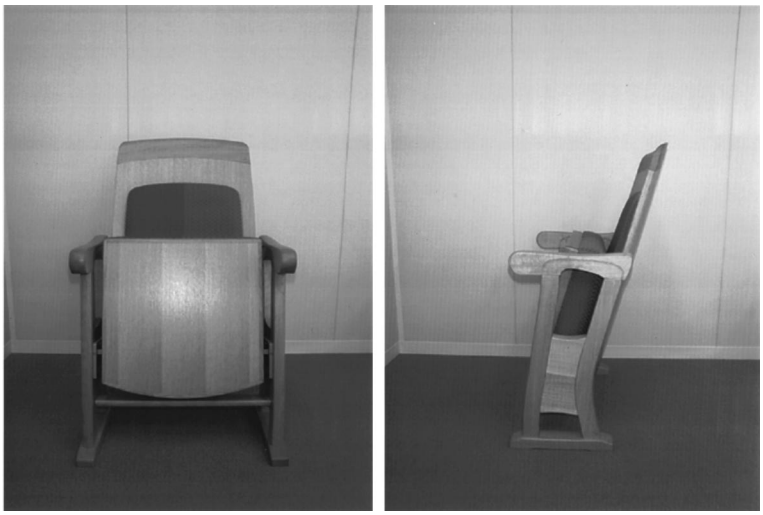

FIG. 11. Photographs of the audience seats. These are similar to those in the Vienna, Grosser Musikvereinssaal.

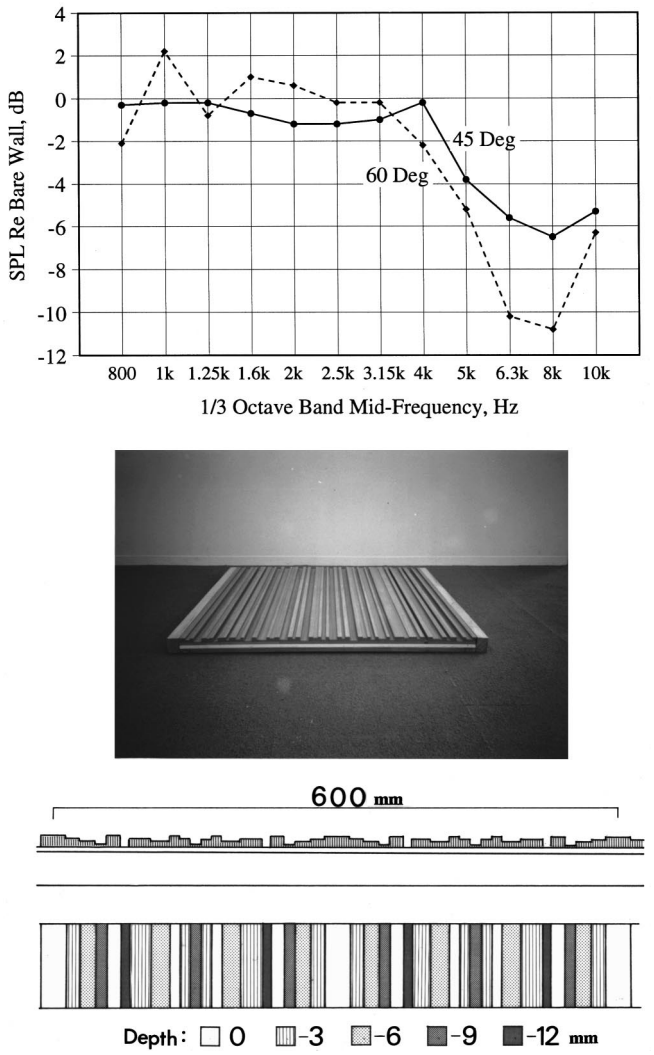

FIG. 12. Fine-scale diffusing surfaces on the side and rear walls of the rectangular portion of the TOC concert hall. (Lowest) Depth in millimeters of the grooves. (Next up) Section view of the pattern of the grooving. (Middle) Photograph of the diffusing panel as tested in the laboratory. When installed on the sidewalls the grooves are vertical. (Upper) The sound pressure level relative to that from a hard flat surface, with the sound wave incident at 45 and 60 degrees. The microphone was located at the optical reflection angle.

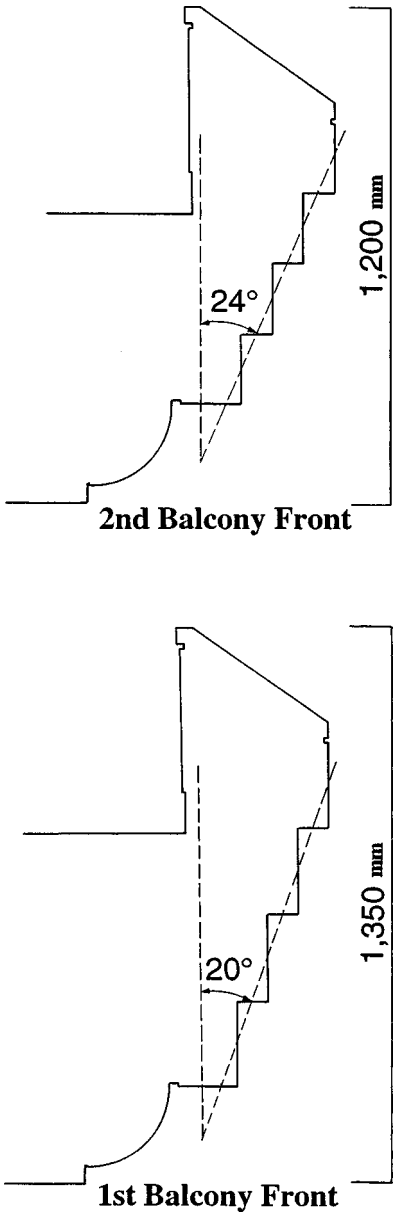

FIG. 13. Design of the balcony fronts. The angles of the facia were set to produce the most uniform sound reflectograms among the audience seats. The curved lower edge is to spread the early sound at high frequencies more uniformly over the main floor seating areas.

model of Fig. 7. Although there was some variation in the reflectograms in different parts of the TOC hall, the uniformity achieved seemed excellent and the architect proceeded with the final drawings in early 1993.

VI. THE HALL AS BUILT

The hall as finally constructed is shown by the photographs in Fig. 15. Construction was completed in late fall of 1996, nearly a year ahead of its opening! Reverberation times were measured before installation of the seats on June 8, 1996 and the RTs and residual absorption coefficients are given in Table II. After installation of the seats, the RTs were again measured and the absorption of the seats determined. The results are shown in Table III along with absorption coefficients measured in the reverberation chamber using the ISO procedures. The large difference between the two measurements of the two absorption coefficients are due in part to the difference in the sound fields, but more because the upholstery of the chairs as installed differed from that of the sample chairs tested in the reverberation chamber. Apparently, the cloth covering was back-sprayed, thus reducing its

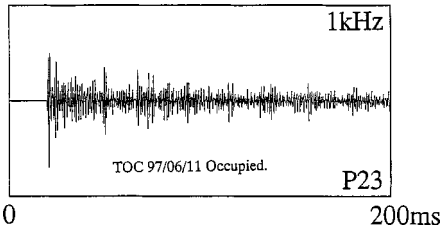

FIG. 14. Measured reflectogram in the completed hall for 2000 Hz at position 23.

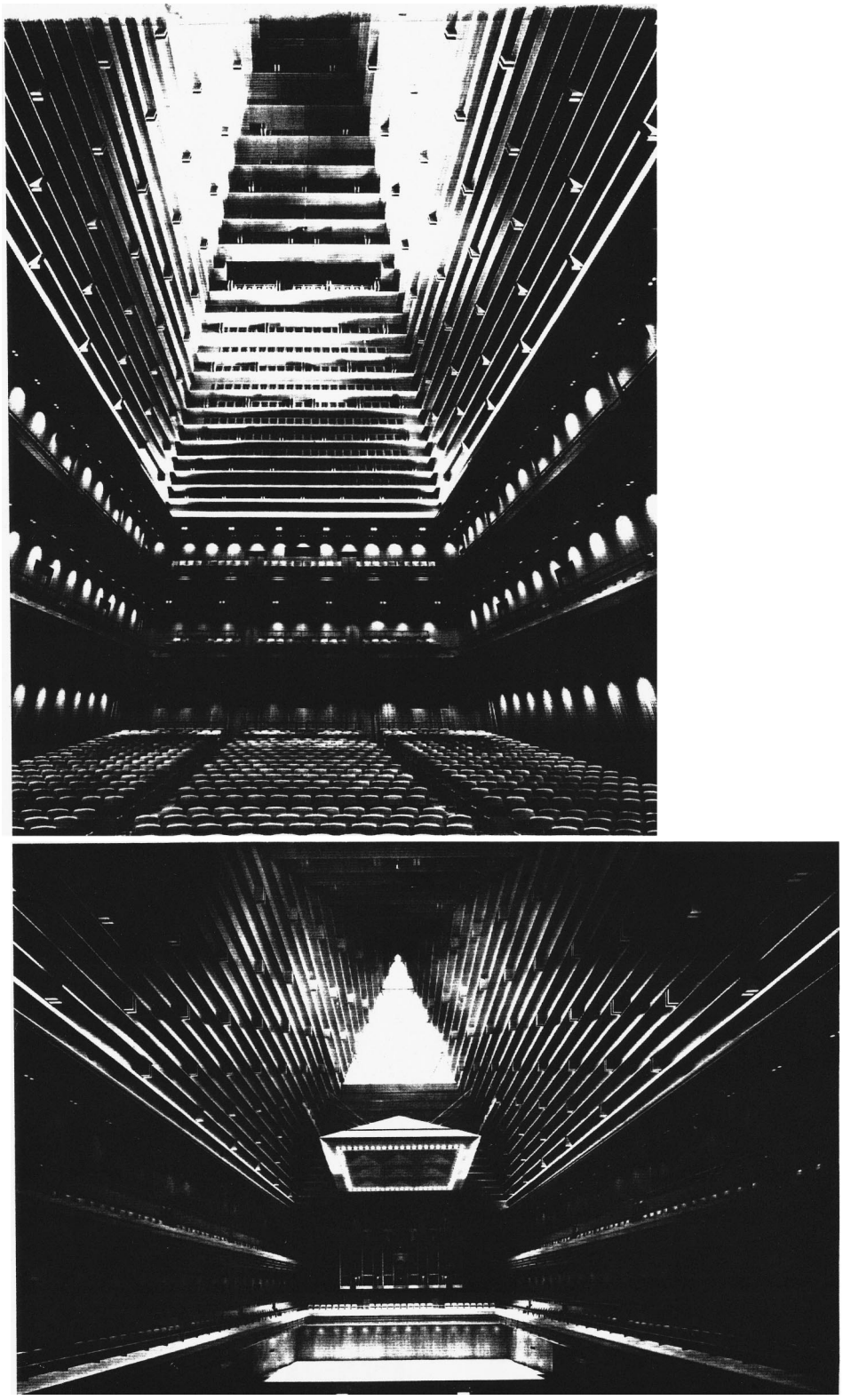

FIG. 15. The TOC concert hall. (Upper) View of hall from stage. Irregular balcony fronts and sides of pyramidal ceiling create diffusion of the sound field. The long rear side of the pyramid is fully covered with Schroeder quadratic residue diffusers QRD to diffuse a large portion of the sound laterally and to reduce the intensity of the sound returned to the stage. (Lower) View of the hall from the first balcony center. The 9.6-m square pyramidal canopy hangs over the stage. With its irregular undersurface and hanging at an angle of 8 degrees, sound from all instruments is reflected uniformly to the front half of the audience on the main floor and the sound of every musician is reflected to every other musician. The wooden interior and the pipe organ add to the beauty of the hall. **Architect**: Takahiko Yanagisawa. **Photos**: Studio Murai, Tokyo.

porosity. A rehearsal curtain, hung from the ceiling about a $\frac{1}{3}$ of the way back in the main floor seating, is available.

In a separate paper it is shown that a simple means can be used to simulate the occupied condition of a concert hall so that the objective acoustical parameters can be measured at will without involving real people (Hidaka *et al.*, 1998). The means consists of laying a sheet of cloth (flow resistance between 630 and 870 Pa*s/m, and thickness about 0.5 mm) over the seats. Measurements of RT in the NNT opera house for (people) occupied and simulated (cloth cover) occupied conditions are shown in Table IV. This discovery meant that many days of tests could be scheduled in the hall with equivalent ''full occupancy.''

Reverberation measurements were made in the TOC concert hall after laying the cloth covering over all seats, but before installation of the pipe organ. The measured RT was

FIG. 15. (*Continued.*)

greater than expected, making it seem desirable to add a sound-absorbing blanket above the lighting cove at the top of the rectangular section [see Fig. 4(d)]. This was done. In the next few months, the pipe organ was installed. The RTs measured preceding the tuning concert, with cloth covering, are shown by the uppermost curve in Fig. 16.

VII. TUNING CONCERT

The tuning concert was held 11 June 1997. Seiji Ozawa conducted the New Japan Philharmonic Orchestra. Three compositions were performed: Brahms, *Symphony #3*; Tchaikovsky, *Piano Concerto, #1 B-Flat-Minor*; and Brahms, *Alto Rhapsody, Op. 53*. At the rehearsal in the afternoon, with the cloth covering over the seats to simulate the audience, the sound was excellent. At the tuning concert that evening with a real audience, the sound was unexpectedly different, at least to some observers at some seats and to some orchestra members. The reverberation time with real audience is shown as the lowest curve in Fig. 16, a greater difference from the uppermost curve than shown in (A) and

TABLE II. (A) Reverberation times and (B) residual sound absorption coefficients for the TOC hall measured before installation of seats. *Residual* means average absorption coefficients for all surfaces, except those that would be covered by audience and orchestra seating, but including absorption by chandeliers, ventilation grilles, doors, etc.

	Frequency (Hz)					
	125	250	500	1000	2000	4000
(A)	3.18	3.86	4.54	4.61	4.22	3.50
(B)	0.14	0.11	0.09	0.08	0.08	0.065

TABLE III. (A) Reverberation times and (B) sound absorption coefficients for the unoccupied seats in TOC hall measured after installation of seats. (C) Sound absorption coefficients for 20 TOC seats (5 seats×4 rows) measured in the reverberation chamber using ISO procedures.

	Frequency (Hz)					
	125	250	500	1000	2000	4000
(A)	2.23	2.62	2.86	2.98	3.12	2.92
(B)	0.41	0.37	0.37	0.33	0.25	0.19
(C)	0.27	0.40	0.52	0.47	0.40	0.34

TABLE IV. (A) Reverberation times measured in NNT opera house with actual audience. (B) Same, but with cloth covering over seats to simulate the audience.

	Frequency (Hz)					
	125	250	500	1000	2000	4000
(A)	1.62	1.59	1.49	1.49	1.42	1.32
(B)	1.59	1.56	1.46	1.48	1.40	1.22

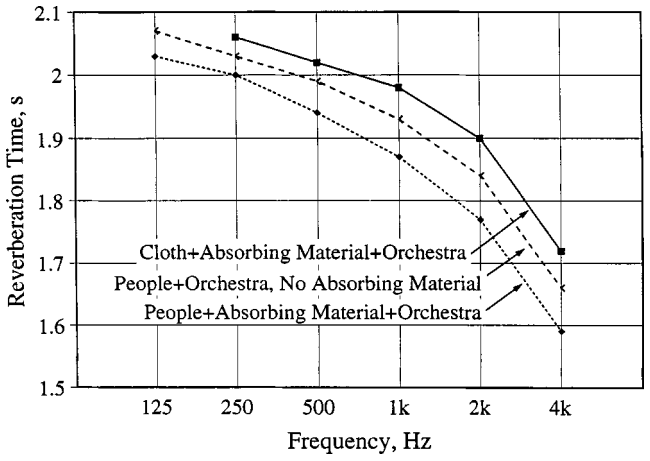

FIG. 16. Measured reverberation times after installation of the pipe organ: (Upper) Occupied hall simulated by cloth covering, with orchestra on-stage and with sound absorbing material in the lighting cove. (Middle) Occupied hall as finally configured, with real audience and orchestra on stage and without sound absorbing material. (Lower) Occupied hall, with real audience and orchestra and with sound absorbing material in the lighting cove.

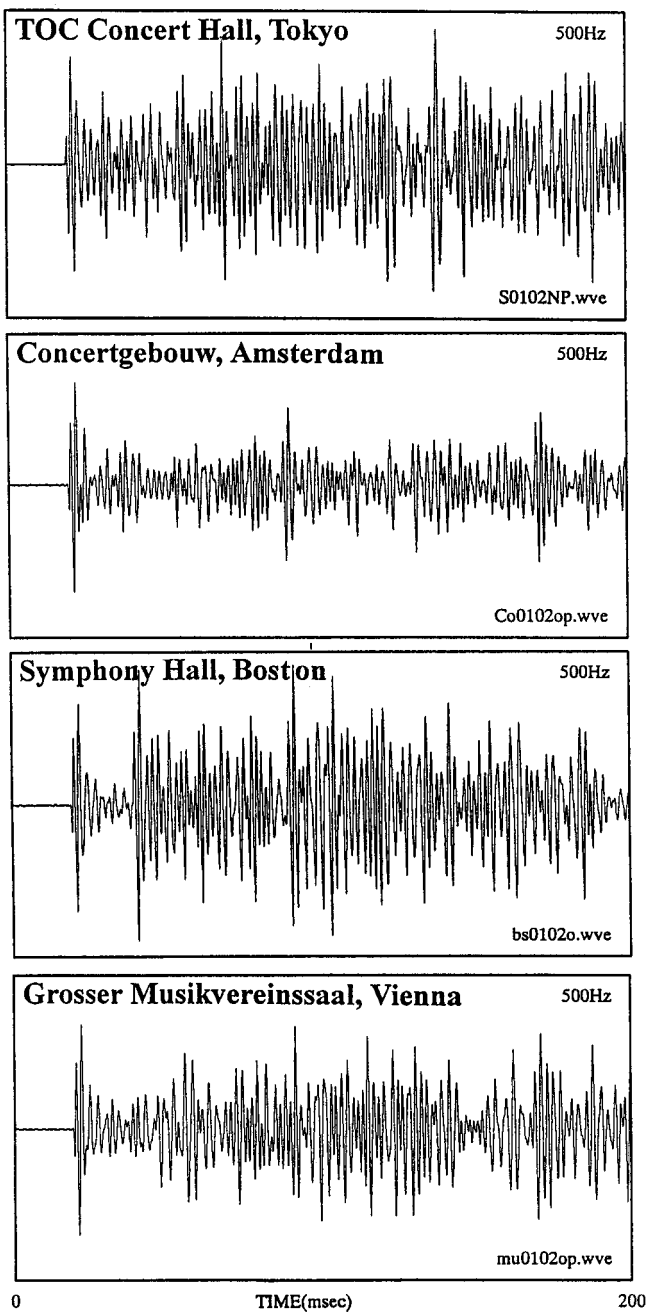

FIG. 17. Reflectograms for 500 Hz measured at seat 102 on main floor of four concert halls. The Amsterdam, Boston, and Vienna halls are rated subjectively by conductors and music critics as ''superior halls'' (Beranek, 1996, p. 58). The TOC reflectograms here and in the next two figures resemble those of Boston most closely.

(B) of Table IV. Because the sound at the same seats with the cloth covering was judged to be better, it was decided to remove the added absorbing material in the lighting cove. The RTs with (people) audience and no absorbing material are shown by the middle curve of Fig. 16, measured opening night.

Reflectograms at position 102 (see Fig. 5, lower) at 500, 1000, and 2000 Hz are shown in Figs. 17–19 for TOC, Amsterdam, Boston, and Vienna concert halls, all measured with the same equipment and by the same personnel. All halls were unoccupied. The reflectograms for the TOC hall appear to be closest to those for Boston Symphony Hall.

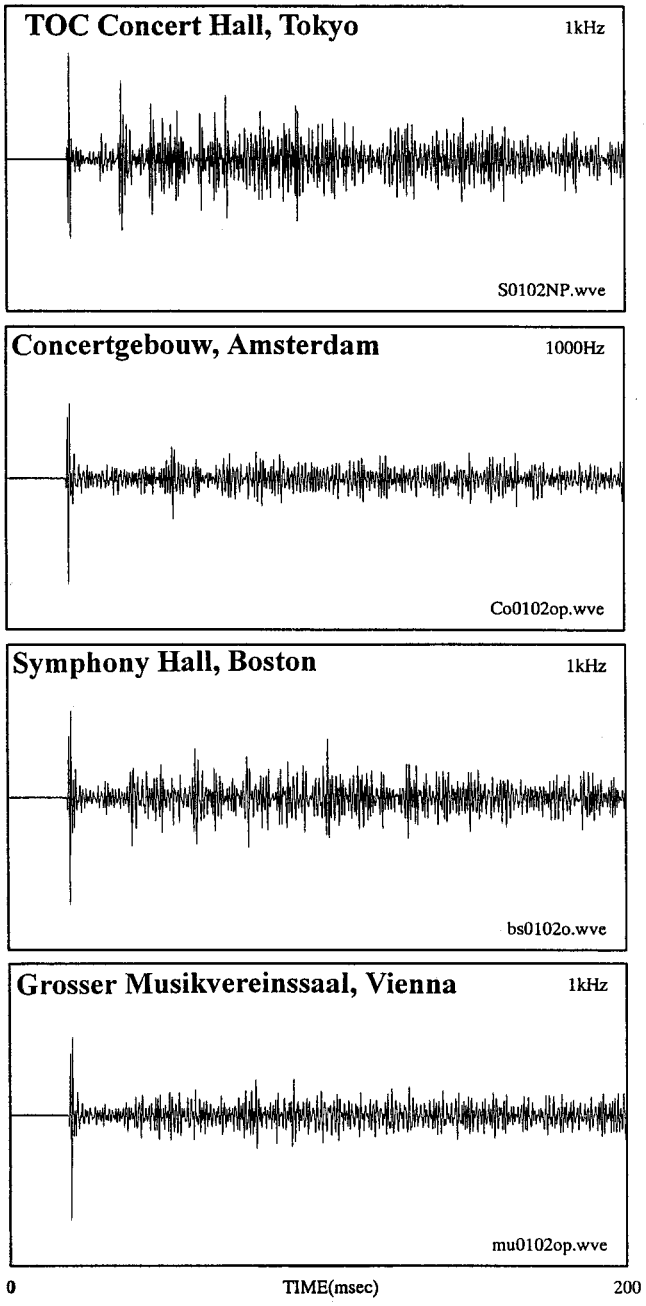

FIG. 18. Same as Fig. 17, except for 1000 Hz.

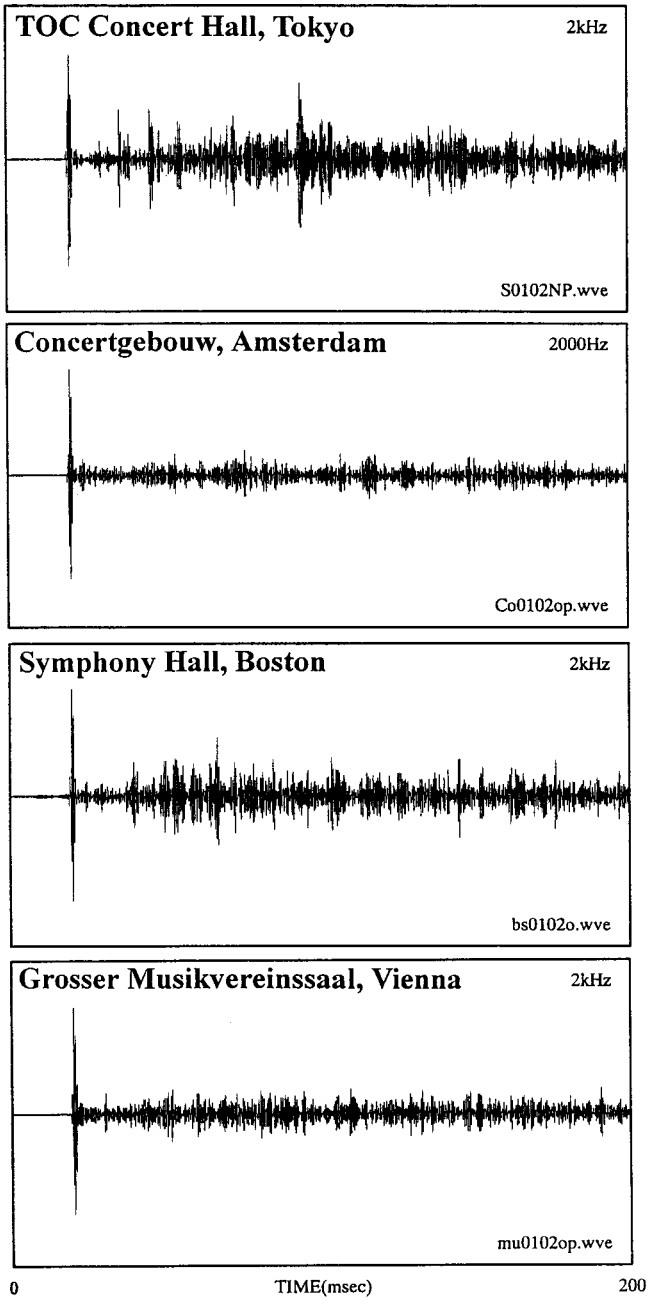

FIG. 19. Same as Fig. 17, except for 2000 Hz.

VIII. OPENING NIGHT, 10 SEPTEMBER 1997, AND PROFESSIONAL EVALUATION

The TOC Concert Hall opened 10 September 1997, with the Emperor and Empress of Japan in attendance. Seiji Ozawa conducted J. S. Bach's *B-Minor Mass* with the Saito Kinen Orchestra. The concert was excellent in every respect. The acoustics were successful. Concerts by visiting symphony orchestras, string ensembles, concertos for piano, violin and cello soon followed. The reviews by music critics were excellent. Letters were received from some of the performers and interviews were held with others. All praised the acoustics and there were no negatives. Excerpts from three letters are:

Yo Yo Ma, cello concerts, 30 September and 1 October: ''This hall simply has some of the best acoustics in which I have ever had the privilege to play...the pyramid-like structure and the unusual lighting gives...[the TOC Hall] a spiritual feel that I never experienced in any other hall... What has been accomplished is a miracle!''

Kent Nagano, Music Director, Opera National de Lyon, two ONL orchestral concerts, 27 and 28 September: ''From the perspective of having visited many concert halls throughout the world together, we found in this concert hall that rare combination of esthetic, emotion, spirit and acoustical balance that conspire to make a concert hall great...the architectural vision and the marvelously excellent acoustics seem to at once provoke imagination, generate a warmth of intimacy, while providing a sense of quiet timelessness, mystery and awe.''

TABLE V. Measured acoustical parameters for Tokyo Opera City concert hall, opened 10 September 1997 (1632 seats).

	Frequency (Hz)					
	125	250	500	1000	2000	4000
RT, unoccupied	2.16	2.51	2.72	2.88	2.98	2.72
RT, occupied	2.07	2.03	1.99	1.93	1.84	1.66
EDT, unoccupied	2.03	2.24	2.65	2.73	2.84	2.54
EDT, occupied	1.76	1.77	1.84	1.81	1.73	1.51
$IACC_A$, unoccupied	0.89	0.68	0.18	0.12	0.11	0.12
$IACC_A$, occupied	0.86	0.66	0.26	0.19	0.17	0.21
$IACC_E$, unoccupied	0.92	0.75	0.36	0.25	0.22	0.25
$IACC_E$, occupied	0.88	0.66	0.33	0.29	0.26	0.31
$IACC_L$, unoccupied	0.88	0.66	0.15	0.09	0.07	0.05
$IACC_L$, occupied	0.85	0.69	0.23	0.13	0.08	0.06
$C_{80}(3)$, dB, unoccupied	−2.0	−3.5	−2.9	−2.7	−2.6	−2.2
$C_{80}(3)$, dB, occupied	−2.5	−1.6	−0.8	0.2	0.7	1.8
G, dB, unoccupied	4.0	5.4	6.0	6.3	6.9	6.3
G, dB, occupied	3.5	4.2	4.7	4.5	4.6	3.9

András Schiff, Schubert Piano Sonatas, 24 and 27 November: ''This is a wonderful auditorium, an architectural masterpiece...The sound is warm, round, and reverberant, when the audience is present this is just ideal. It's like a beautiful cathedral without the echo...the feeling of intimacy—so important in music—is achieved.''

An interesting thread throughout these three letters (and letters and interviews of others) relates to the overall impression that the hall makes on listeners and performers. Many of the letters and interviews used words like, ''mystery and awe,'' ''spiritual feel,'' ''intimacy,'' and ''like an Aztec pyramid.'' These words signify, at least to the authors, that a successful collaboration between the architect and the acoustical consultants took place.

IX. MEASURED ACOUSTICAL PARAMETERS

The measured acoustical parameters for the TOC Concert Hall are given in Table V. The occupied conditions for IACC were measured at the test concert with eight dummy heads on the main floor and nine in the balconies, each head fitted with binaural microphones. The other occupied parameters were measured at the same positions with omnidirectional microphones. The values are the averages of the numbers at the 17 positions. All unoccupied data were taken at all positions shown in Fig. 5 and averaged. Comparisons between these data (given first) and the ranges of the data measured in the Vienna Musikvereinssaal, Amsterdam Concertgebouw, and Boston Symphony Hall (given in parentheses) are as follows. (The values for RT and BR are for full occupancy and the other parameters are for the halls unoccupied, because those are the only data available): $RT_{MID}=1.96$ s (three-hall range 1.9–2.0 s); $EDT_{MID}=2.69$ s (range 2.4–3.0 s); ITDG=15 ms (range 12–21 ms); $C_{80}(3)=-2.7$ dB (range −3.7 to −2.7 dB); $[1-IACC_{E3}]=0.72$ (range 0.62–0.71); BR=1.05 (range 1.03–1.11); $G_{mid}=6.2$ dB (range 5.4–7.8 dB); and ST1=−12.1 dB (range −17.8 to −13.7 dB). All data are for equivalent positions and were taken by the same measuring crews. By comparison with the three acknowledged world's best halls, the numbers indicate that TOC has optimum reverberation, clarity, intimacy, spaciousness, warmth, and strength of sound. The noise levels measured in the unoccupied hall with the HVAC in operation are shown in Fig. 20 which yield a rating of NCB-14.

X. CONCLUSION

As documented above, the subjective judgments and the measured data place the TOC concert hall in the category ''Excellent.'' This success with an entirely new architectural solution, the pyramidal ceiling, indicates that it is not necessary to duplicate previously successful halls precisely to achieve excellent results, provided the principal acoustical parameters for the audience areas listed in the previous para-

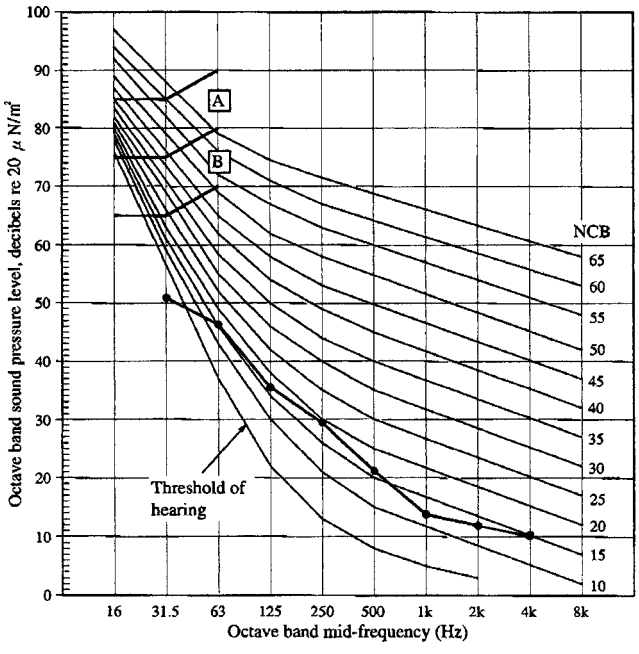

FIG. 20. Measured noise levels in unoccupied TOC Hall with HVAC systems in operation.

graph have values consistent with those for the best halls, and the stage acoustics are acceptable to the musicians.

ACKNOWLEDGMENTS

We wish to express our deep appreciation for the excellent cooperation and relationship with architect Takahiko Yanagisawa and his project managers, Paul Baxter and Hiroshi Wada. Thanks are owed the administrations of the concert halls in which acoustical measurements were made.

APPENDIX: EQUATIONS FOR ACOUSTICAL PARAMETERS

Interaural cross-correlation coefficient, $\mathbf{IACC_{E3}}$: This quantity is a measure of the difference in the sound pressures $p(t)$ at the two ears,

$$\mathrm{IACC}_{E3}=\left|\frac{\int_0^{0.08} p_L(t)p_R(t+\tau)\,dt}{(\int_0^{0.08} p_L^2(t)\,dt \int_0^{0.08} p_R^2(t)\,dt)^{1/2}}\right|_{\substack{\text{MAX \&}\\ \text{3-BAND}}}$$

$$\text{for } -1<\tau<+1,$$

where L and R designate the entrances to the left and right ears, respectively, and the measurement is usually made with a standard dummy head or with tiny microphones at the ears of a person with head dimensions approximating that of the standard. Time ''0'' is the time of arrival of the direct sound from the impulse radiated by the source on the stage or in the pit. The function is determined for values of τ between -1 and $+1$ and the magnitude of the maximum value so obtained is used. Because of the short range for τ, the function is meaningful in room acoustics for measurements in octave bands of 500 Hz and above. The letter ''*E*'' stands for ''early sound,'' i.e., the sound that arrives within the first 80 ms after the direct sound and ''3'' stands for averaging the measured quantity in the three octave bands, 500, 1000, and 2000 Hz.

As a measure of spaciousness IACC_{E3} eliminates sound waves arriving from the direction of the source and measures the difference in the waves arriving at the two ears, making it a binaural measurement, and at frequencies critical to the fast moving tones of string instruments. It takes into account both phase and amplitude in this difference and has been shown by Beranek (1996), Hidaka *et al.* (1995), and Okano *et al.* (1998) to be superior to lateral fraction LF_{E4}. Lateral fraction is a monaural measurement which only measures the magnitude of sound pressure arriving at directions other than directly ahead weighted by $\cos^2\theta$, where $\theta=90$ degrees is in the direction of the source. It considers the sound pressures mainly at low frequencies, and it does not correlate as well as IACC_{E3} with subjective judgments of acoustical quality of concert halls as rated by conductors, music critics, and qualified symphonic listeners.

Strength factor, G: This quantity, expressed in decibels, is a measure of the sound pressure level at a point in a hall, $p(t)$, with an omni-directional source on stage, minus the SPL that would be measured at a distance of 10 m from the same sound source operating at the same power level and located in an anechoic chamber $p_A(t)$,

$$\mathrm{G}=10\ \log\frac{\int_0^3 p^2(t)\,dt}{\int_0^3 p_A^2(t)\,dt}\ \text{dB},$$

where $p_A(t)$ is the free-field sound pressure level at a distance of 10 m. $\mathrm{G_{mid}}$ means average of the measured values for the 500- and 1000-Hz octave bands.

Bass ratio, BR: This quantity is the ratio of the low- to mid-frequency reverberation times for halls fully occupied,

$$\mathrm{BR}=\frac{\mathrm{RT}_{125}+\mathrm{RT}_{250}}{\mathrm{RT}_{500}+\mathrm{RT}_{1000}},$$

where the RTs are the reverberation times at the frequencies shown in the subscripts measured in halls fully occupied.

Clarity factor, $\mathbf{C_{80}}$: This quantity, expressed in decibels, is the ratio of the early sound energy (0 to 80 ms) to the late (reverberant) sound energy (80 to 3000 ms),

$$\mathrm{C}_{80}=10\ \log\frac{\int_0^{0.08} p^2(t)\,dt}{\int_{0.08}^3 p^2(t)\,dt}\ \text{dB}.$$

$\mathrm{C}_{80}(3)$ means the average of the clarity factor over the three octave bands, 500, 1000, and 2000 Hz.

RT and EDT: RT is the reverberation time in seconds measured starting after the decay has progressed -5 dB and until it reaches -35 dB, the result multiplied by 2. When measurements are made from stop chords recorded during performances, Schroeder's integration method must be used to detect unusable decay curves. EDT is the reverberation time obtained during the first 10 dB of sound decay. It generally is not measured from stop chords because uniform decay curves are generally not obtained in the first few decibels of sound decay.

Support factor, ST1: The support factor ST1 is the difference in decibels between two measurements of sound pressure level on a stage where the orchestra members play. The nondirectional sound source emits an impulse and the microphone receives it at a point 1 m removed from the center of the source. The first measurement is of the energy in the time interval from 0 to 10 ms and the second measurement is from 20 to 100 ms. Nearby music stands and chairs are moved to prevent their influencing the measurement.

Ando, Y. (**1985**). *Concert Hall Acoustics* (Springer-Verlag, Berlin).

Aoshima, N. (**1981**). ''Computer-generated pulse signal applied for sound measurement,'' J. Acoust. Soc. Am. **69**, 1484–1488.

Beranek, L. (**1992**). ''Concert hall acoustics–1992,'' J. Acoust. Soc. Am. **92**, 1–39.

Beranek, L. (**1996**). *Concert and Opera Halls: How They Sound* (Acoustical Society of America, Woodbury, NY).

Beranek, L., and Hidaka, T. (**1998**). ''Sound absorption in concert halls by seats, occupied and unoccupied, and by the hall's interior surfaces,'' J. Acoust. Soc. Am. **104**, 3169–3177.

Beranek, L., Hidaka, T., and Masuda, S. (**2000**). ''Acoustical design of the Opera House of the New National Theater, Tokyo, Japan,'' J. Acoust. Soc. Am. **107**, 355–367.

Haan, C. H., and Fricke, F. R. (**1993**). ''Surface diffusivity as the measure of

acoustic quality of concert halls,'' in *Proceedings of Conference of the Australia and New Zealand Architectural Science Association*, Sydney, pp. 81–90.

Hidaka, T., Beranek, L., and Okano, T. (**1995**). ''Interaural cross-correlation, lateral fraction, and low- and high-frequency sound levels as measures of acoustical quality in concert halls,'' J. Acoust. Soc. Am. **98**, 988–1007.

Hidaka, T., Nishihara, N., and Beranek, L. (**1998**). ''Relation of acoustical parameters with and without audiences in concert halls and a simple method for simulating the occupied state,'' presented at the ASA/ICA meeting in Seattle, WA, 25 June 1998, J. Acoust. Soc. Am. **104**, 2955(A).

IEEE (**1979**). *Programs for Digital Signal Processing* (IEEE, New York), Chap. 1.

Okano, T., Beranek, L., and Hidaka, T. (**1998**). ''Relations among interaural cross-correlation coefficient ($IACC_E$), lateral fraction (LF_E), and apparent source width (ASW) in concert halls,'' J. Acoust. Soc. Am. **104**, 255–265.

Acoustical design of the opera house of the New National Theatre, Tokyo, Japan[a)]

Leo L. Beranek[b)]
975 Memorial Drive, Suite 804, Cambridge, Massachusetts 02138

Takayuki Hidaka and Sadahiro Masuda
TAK Associated Architects, 1-7 Kanda-Nishiki-cho, Chiyoda-ku, Tokyo 101, Japan

(Received 25 August 1998; revised 5 July 1999; accepted 30 August 1999)

Architect Takahiko Yanagisawa's preface explains his approach to the design. The NNT opera house seats 1810, its volume is 14 500 m^3, and its reverberation time, with audience, is 1.5 s (proscenium curtain open). Measurements on CAD computer and 1:10 wooden models and full-sized materials samples were conducted over a 7-yr. period. The main floor is almost rectangular, the three balconies have modest fan shape in plan, although the balcony facia at each level create a rectangular shape. The unique design has a large curved reflector in front of and above the proscenium and six curved reflecting surfaces at the front ends of the three side balconies to form, in combination, an ''acoustic trumpet.'' These surfaces, along with the balcony faces and the shaped ceiling, distribute the singers' voices uniformly over the seating areas from a large portion of the large stage at sound levels that easily override the orchestra in the pit. © *2000 Acoustical Society of America.* [S0001-4966(00)00201-0]

PACS numbers: 43.55.Br, 43.55.Fw, 43.55.Ka, 43.55.Mc [JDQ]

ARCHITECT'S PREFACE: TAKAHIKO YANAGISAWA, TAK ARCHITECTS, TOKYO

The theater or hall is a place where one is able to experience directly the power of humanity. The live sensory information that is physically transmitted by the people on stage is also perceived physically by the members of the audience. The theater is therefore a place where there is direct, ''heart to heart'' communication among people.

The theater space facilitates the exchange of energy through a multi-faceted network. It goes without saying that this network includes the exchange between those on the stage and the audience. There is also, however, an extremely powerful force which results in the unconscious bonding between the members of the audience as they coexist in space and time. The excitement of the theater is to be found in those moments in which the performers on stage and the audience become a single, unified entity. This mutual exchange of energy and innervation of the five senses creates a place of great intensity. It is therefore necessary, when designing theaters and halls, to create spaces that heighten the whole range of human senses. Of course, in this respect sound is second to none in its importance.

The design of the hall itself must be based upon principles that intensify the exchange of energies described above. We felt that the best way to achieve this was to have the people in the audience positioned so that they surround the stage as much as possible. In particular it was felt that the role of the balconies, both in reflecting the sound and encouraging empathy amongst the members of the audience as they face each other across the hall, was very important.

In the opera house of the New National Theater, multiple balconies are wrapped around the hall on the three sides, while in plan the overlaying of a fan-shaped main floor by a rectangular balcony geometry has resulted in a new kind of opera house. With a quite different approach, the concert hall of the Tokyo Opera City, adjacent to this hall, combines a rectangular plan form for the seating spaces with a dramatic pyramidal ceiling section, which represents a new departure for its genre of performance space.

The architectural team visited many of the world's great halls with the acoustical design team to listen and take measurements, overlaying the latest scientific data with the sensual evaluation made possible by actually listening to the halls' acoustics. I believe that the design of these two halls shows that in order to create original theater spaces it is absolutely vital that the organization of the design team should allow a more organic relationship among the specialist fields.

INTRODUCTION

An international architectural competition was announced in 1985 by the (National) Agency for Cultural Affairs and the Japan Arts Council for the design of the overall New National Theater (NNT) Project which embodies an opera house, a medium-sized (drama) theater, a small (experimental) theater, a sunken garden, and associated spaces for rehearsals, dressing rooms, workshops, training rooms, reading and documents rooms, offices, and a large multilevel garage underneath.

TAK Architects of Tokyo with Takahiko Yanagisawa, president, and architect in charge, won the competition. The characteristics specified before the competition that would bear on the acoustics of the opera house were (1) approximately 1800 seats; (2) adequate visibility of performers' movements and expressions from all seats; (3) to be used

[a)]Presented at the ASA/ICA meeting in Seattle, WA, 25 June 1998.
[b)]Electronic mail: beranekleo@mediaone.net

TABLE I. Acoustical characteristics judged to be important for the design of an opera house in the Italian style (Hidaka *et al.*, 2000a).

(A) Reverberation time RT: Room reverberation gives fullness and singing tone to the music, but must not be so great as to destroy voice intelligibility. In the best opera houses the RT's at mid-frequencies range from 1.3 to 1.6 s. A reverberation time of 1.5 s was the design goal for the NNT opera house. This requires the proper cubic volume in relation to the areas covered by the audience, the top of the pit and the proscenium opening.

(B) Early Decay Time EDT: EDT affects principally the hall's support to the voice and adds definition to the higher tones of the music. If EDT is too high, it reduces the intelligibility of the voice. The magnitude of EDT measured in unoccupied opera houses is usually about 0.1 to 0.2 s higher than RT measured occupied, with the proscenium open. To achieve this result, a satisfactory combination of RT and of surfaces for reflecting early sound to all seats is necessary. A goal of 1.7 s was chosen.

(C) Bass Strength BR: BR, the bass ratio, is a measure of the support the reverberation in the hall gives to the low notes of the music. Many factors, including surface materials and chair design, contribute to BR. Its value should be greater than 1.0.

(D) Intimacy: The music should sound as if heard in a small hall—the listener should feel in intimate contact with the performers. The arrival time of the first reflections after the direct sound must be short, i.e., should be less than 25 ms in an opera house.

(E) Spaciousness: The sound at listeners' seats should include a sizable number of early reflections that arrive from near lateral directions. This is saying that the source of the music should sound broadened. In good concert halls, its measure, $[1-\mathrm{IACC}_{E3}]$, should exceed 0.6. The same criterion was assumed for an opera house.

(F) Diffusion: Every successful hall for music has irregularities, both large and small, on the walls, balcony facia, and ceiling to give the sound a rich patina. The usual measure of adequate diffusion is by observation of the irregularities.

(G) Strength: The strength of the sound, which is related to loudness, is a quantity that must be as uniform as possible throughout the house. It is related to the ratio of the volume of the hall in m^3 divided by the early decay time EDT in s. Early decay time depends on whether the proscenium is open or closed.

(H) Reflecting surfaces: Special reflecting surfaces above the proscenium and at the six fronts of the side balconies were to be specially designed to enhance the strength of the singers' voices in the audience seating areas.

(I) ST1, a measure of the strength of orchestral sound returned by nearby reflecting surfaces to the ears of each player in the orchestra pit: This measure is technical and is described in the companion paper (Hidaka *et al.*, 2000a).

(J) Quiet: The hall must be quiet, both in regard to external and to internal noise and vibration sources. A goal of NCB less than 18 dB was chosen.

(K) Echoes: The room and stage must be free from echoes.

primarily for presentation of opera and ballet in the manner of an Italian opera house; (4) reverberation time in the range of 1.4 to 1.6 s with full occupancy; and (5) orchestra pit to accommodate up to about 120 musicians. In the competition the architect chose a moderate fan-shaped plan for the main floor and three balconies, each rectangular in plan. The architect's desire was to minimize the distance between the front of the stage and the most remote listener while maintaining adequate visibility from all seats. Also, he wished to line the interior of the hall with richly colored wood. Masuda was acoustical consultant during the competition stage.

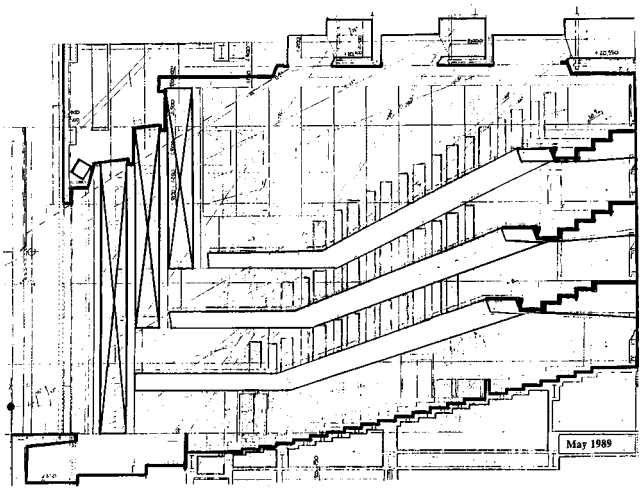

FIG. 1. Architect's suggested design that was presented to the acoustical design consultant in May 1989.

FIG. 2. Photographs of a late version of the 10:1 scale model of the NNT opera house.

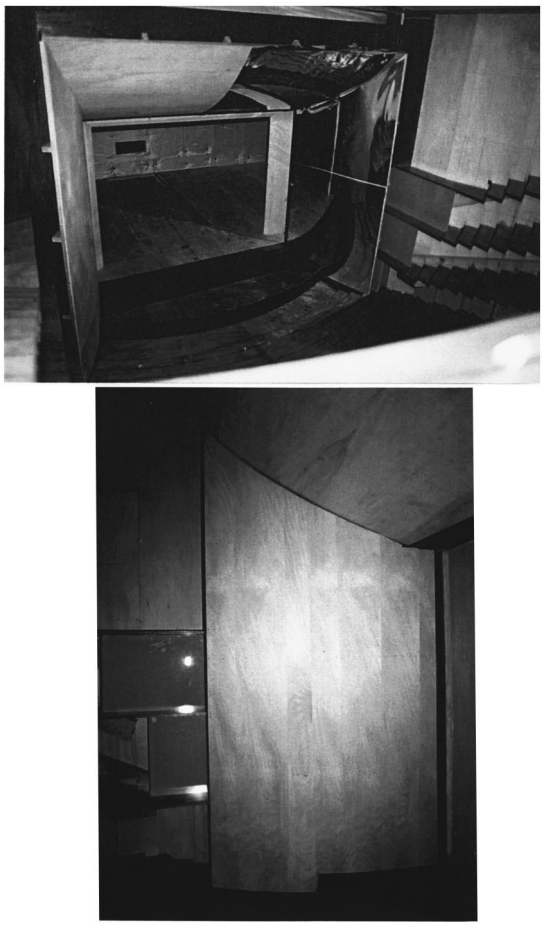

FIG. 3. Early study of the efficacy of an ''acoustical trumpet'' on the three sides of the proscenium.

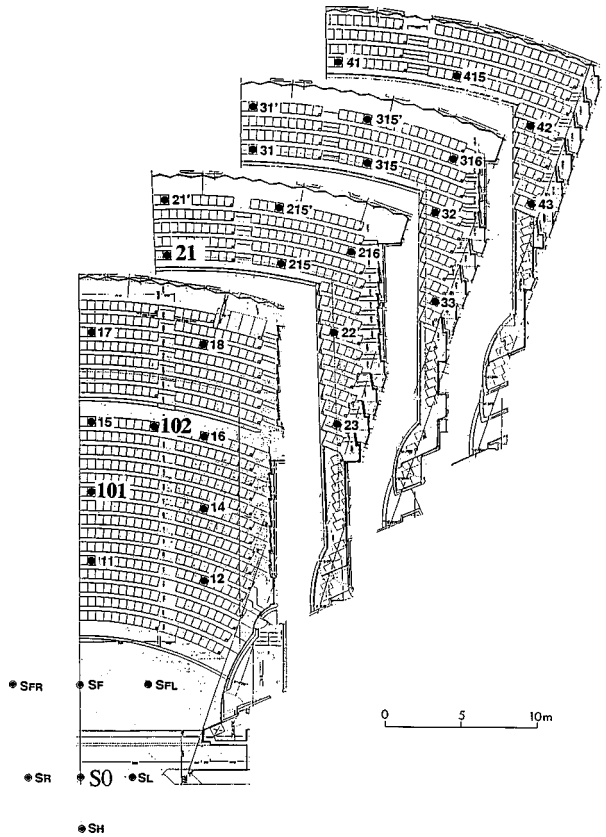

FIG. 4. Source and receiver positions used by Takenaka R & D Institute for the acoustical measurements in the models and the completed opera house.

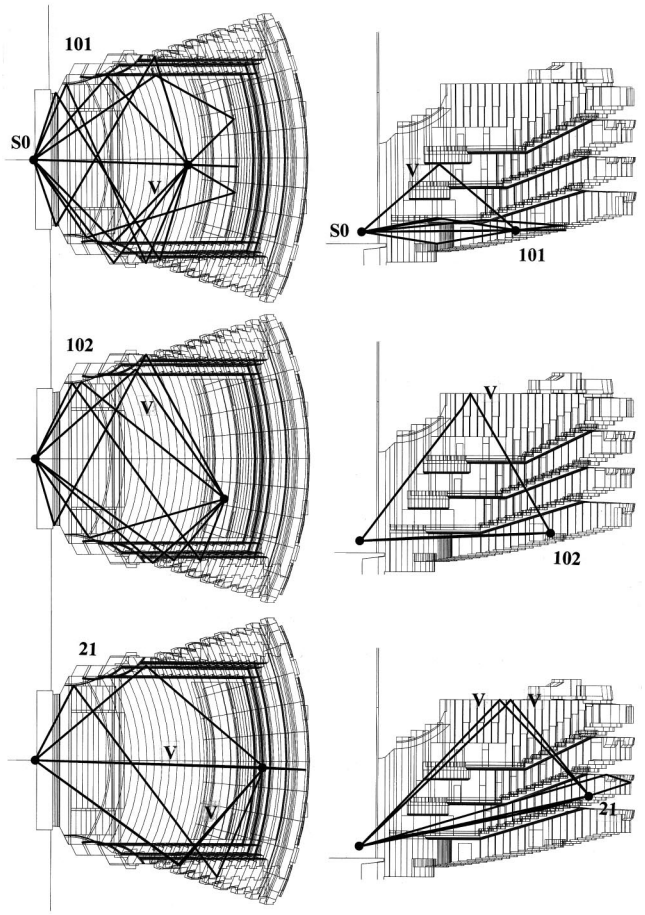

FIG. 5. Drawings showing early reflections obtained in an early computer CAD model of the NNT opera house. The source is at S_0 and the rays to audience seats 101, 102, and 21 are shown. All reflections are lateral except those marked ''V'' for vertical, directly in front and directly from rear.

On receiving the commission of Acoustical Design Consultant for the NNT in April 1989, Beranek reviewed in depth the researches carried out on the acoustics of halls for music by groups in Germany, England, Denmark, New Zealand, Canada, Japan, and USA (Beranek, 1992). Simultaneously, a systematic endeavor was made to bring to a close the assembling of drawings, photographs, and details on materials obtained from architects and the acoustical data measured by acoustical engineers worldwide for 12 opera houses in Salzburg, Vienna, Milan, Paris, New York, Philadelphia, San Francisco, Washington, DC, Buenos Aires, London, Bayreuth, and Tokyo. The architect's technical staff under the direction of Hidaka made new acoustical measurements in 14 European opera houses and theaters for music: Vienna, Milan, Paris, Dresden, Hamburg, Berlin, Amsterdam, Budapest, Prague, and Essen. The results of those efforts were published in Beranek (1996) and in a companion paper in this issue (Hidaka *et al.*, 2000a).

I. BASIC ACOUSTICAL PARAMETERS AND MEASUREMENTS

A list of the acoustical parameters that came from the concert hall studies and that were assumed also to be important in combination for aiding in the successful design of the acoustical environment for Italian opera is compiled in Table

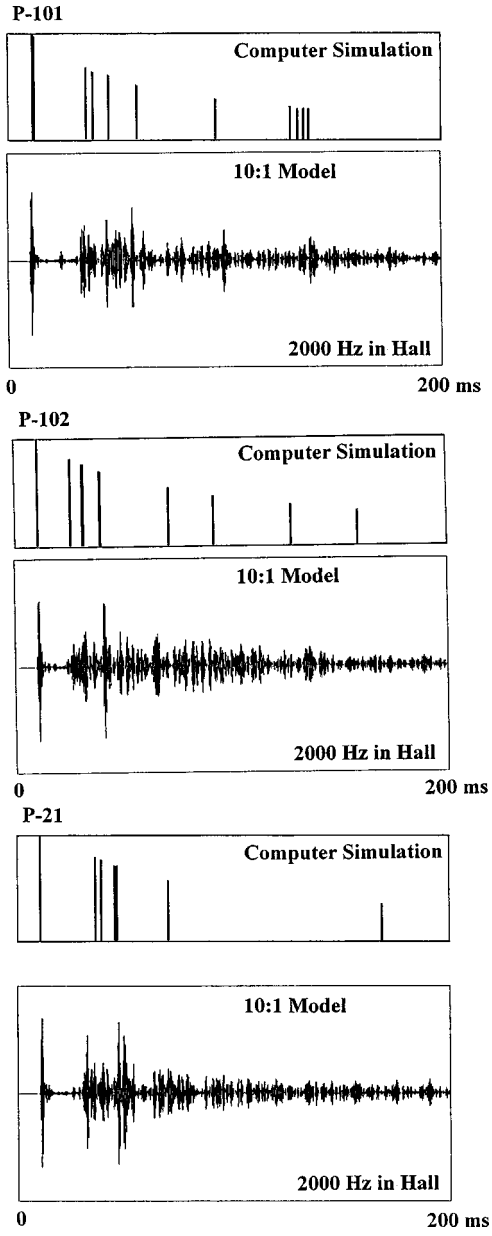

FIG. 6. Comparison of reflectograms at three seat positions obtained in computer CAD model with those obtained in 10:1 wooden model of the NNT opera house. Data from 1993.

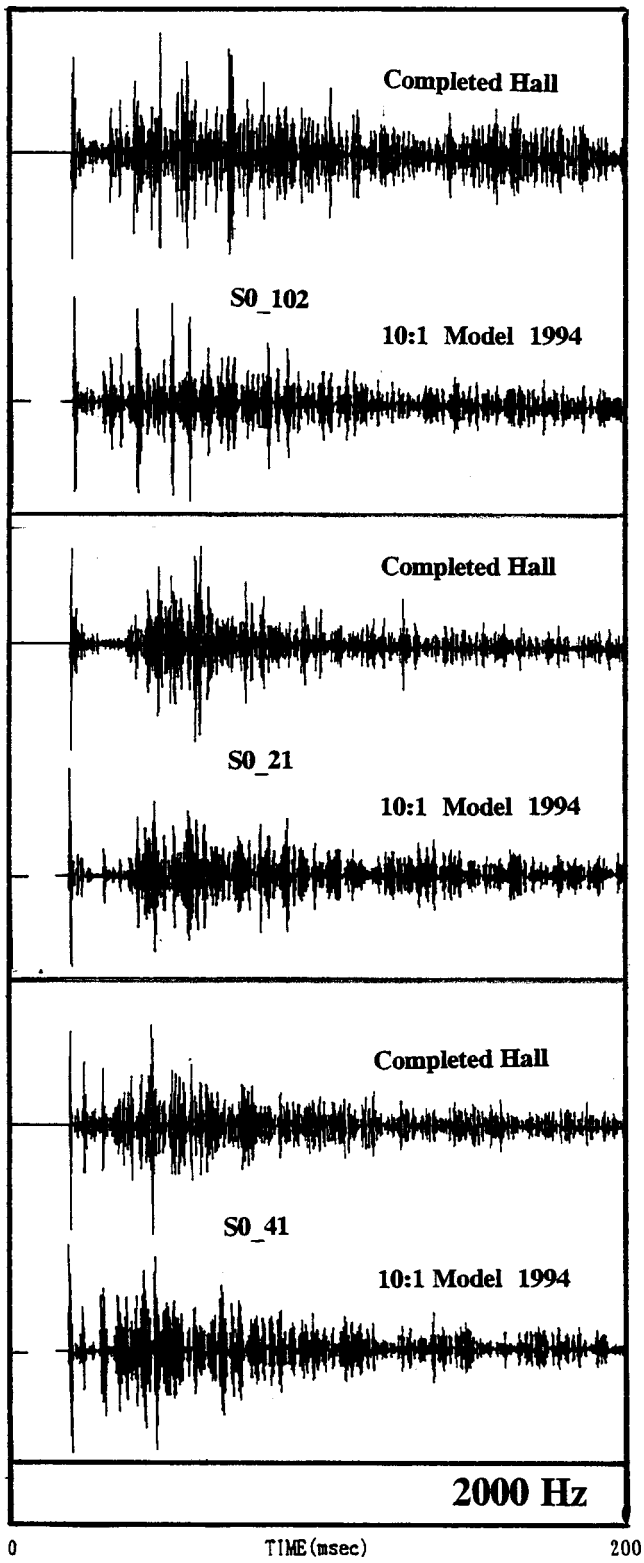

FIG. 7. Comparison of reflectograms measured in 10:1 model (1994) and those measured in the completed (NNT) opera house (1997), both for occupied condition.

I. The definitions of these quantities are given in the companion paper (2000a) in this issue of JASA on the design of the TOC Concert hall, which is located on a contiguous site in Tokyo (Hidaka *et al.*, 2000b). The second companion paper presents recent research on the subjective ratings and objective measurements for 23 opera houses and their correlations and shows that items A–G in Table I are orthogonal to each other except for EDT which is highly correlated with RT. Procedures and precautions for the measurement of these quantities are given in Hidaka *et al.* (1995), Okano *et al.* (1998), and Hidaka *et al.* (1998).

From the outset, the acoustical design consultant emphasized that the most critical problem in almost all opera houses is the difficulty the singers have in attempting to override the music of a 60-piece, or larger, orchestra. The solution to this problem became a major part of the architect/consultant cooperation.

Shown in Fig. 1 is the drawing of the NNT opera house that was presented to the acoustical design consultant at the outset. This design concept greatly resembles the NNT as constructed—in gross shape and dimensions, including three balconies that have front arms that slope downward. But, satisfactory acoustical reinforcement of the singer's voices

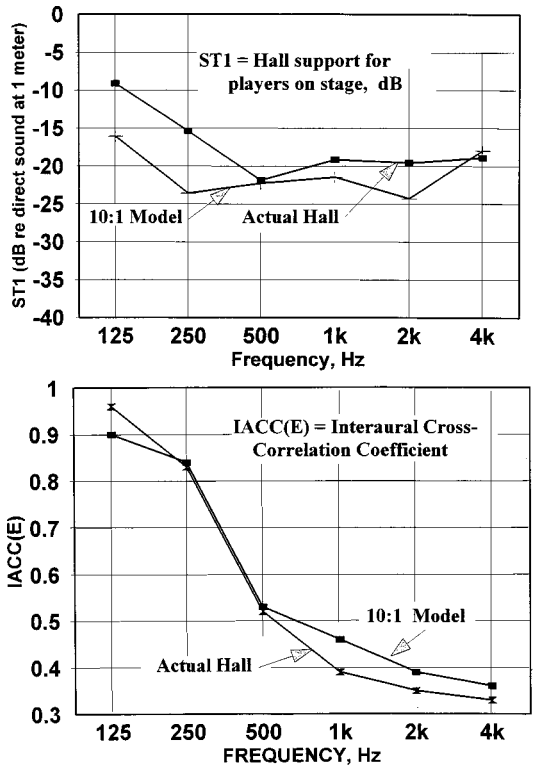

FIG. 8. Comparison of ST1 (average on stage) and $IACC_E$ (average in audience areas) as measured in 10:1 model and the completed NNT opera house.

was inhibited by three lighting bridges in the ceiling and three large lighting coves on either side of the front of the hall and by a loudspeaker bridge above the proscenium. The reverberation time of 1.2 s for this design was too low. Also, sound diffusion was only shown on the balcony faces.

The first acoustical recommendation was a new architectural concept in opera house design, namely, that the six ends of the sidewall balconies nearest the proscenium and the space immediately above the proscenium should, together, resemble the bell of a brass wind instrument, for example a trumpet or French horn. These constructions, if properly shaped, will amplify the voices of the singers without amplifying the orchestral music. The result will be less strain on the voices and will reduce the feeling by the pit orchestra that its music must continually be restrained.

II. THE RESEARCH AND DEVELOPMENT PHASE

A. CAD and 10:1 models

The architect's technical staff, under the direction of Hidaka, constructed a computer CAD model and a 10:1 wooden model. The first tasks were to confirm and to correct the acoustical deficiencies of the original design and to investigate and refine the proposed concept of an acoustic horn structure around the proscenium. The 10:1 model, actually photographed at a later stage, is shown in Fig. 2. An early construction of the horn concept is shown in Fig. 3. Although the arrangement of Fig. 3 tested well acoustically, it was obviously not an acceptable architectural solution.

Figure 4 delineates the source and audience positions that were used for measurements in both models. Very little difference among the results measured at the audience positions were found for the four source positions on stage or the three in the pit. Twenty-seven audience positions were selected in this symmetrical hall.

As Fig. 5 shows, the CAD computer model was used to trace the number and directions of the early reflections and to determine the length of the initial-time-delay gap. On this figure are shown the positions that are primarily used as illustrations in this paper, namely, S_0, the source location, and 101, 102, and 21 (first balcony), audience positions. All reflections shown occur within 150 ms and arrive at the listener's position from lateral directions, except for those marked ''V,'' meaning, arriving from the overhead, directly forward, or directly backward direction.

Typical comparisons of the results from the computer and 10:1 models are illustrated in Fig. 6. The computer data of that era gave both the time of arrival and the angle of each reflected wave, but not much detail. The levels of the components were often greatly different from those of the 10:1 model. The wooden model gives detail, out to 200 ms and beyond, including all reflections generated as a result of dispersion from irregular surfaces.

With the 10:1 model, the measurements could determine the acoustical coverage pattern from the various reflecting surfaces, the spaciousness measure $[1-\mathrm{IACC}_{E3}]$; the strength of the sound throughout the hall G; the initial-time-delay gap ITDG; and any echoes.

To show how the data from the 10:1 model relate to

TABLE II. Calculated reverberation times with proscenium curtain open, highly absorbent scenery tower, and no stage set. Volume: $V=14\,500\ \mathrm{m}^3$; pit area: $S_0=102\ \mathrm{m}^2$; audience area with edge correction: $S_A=1153\ \mathrm{m}^2$; proscenium area: $S_p=205\ \mathrm{m}^2$; and residual wall and ceiling areas, with unoccupied pit area: $S_R=4308\ \mathrm{m}^2$. The residual absorption was measured before the seats were installed. The audience absorption was measured at the tuning concert and the proscenium opening was measured with and without a heavy metal fire curtain with the house unoccupied.

	125	250	500	1000	2000	4000
α_R=residual absorption	0.17	0.16	0.13	0.11	0.11	0.10
$A_R=4308\times\alpha_R$, includes pit	732	689	560	474	474	431
α_A for S_A, occupied,	0.39	0.44	0.60	0.62	0.65	0.54
$A_T=1153\times\alpha_A$, occupied w/o pit	450	507	692	715	738	623
$A_R+A_T\ \mathrm{m}^2$	1182	1197	1252	1189	1212	1053
Proscenium absorption (approximate)	220	302	302	302	302	378
A_{total}=total absorption	1402	1499	1554	1491	1514	1391
4 mV	0	16	41	76	138	349
RT=0.161*14 500/(A_{total}+4 mV)	1.67	1.54	1.46	1.49	1.41	1.34
Measured RT, occupied, 2/15/97	1.62	1.59	1.49	1.49	1.42	1.32

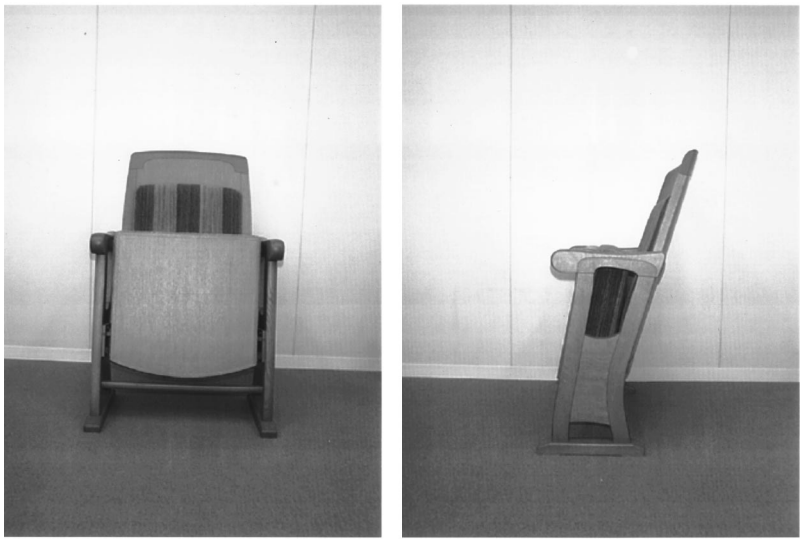

FIG. 9. Photograph of audience seat in the NNT opera house.

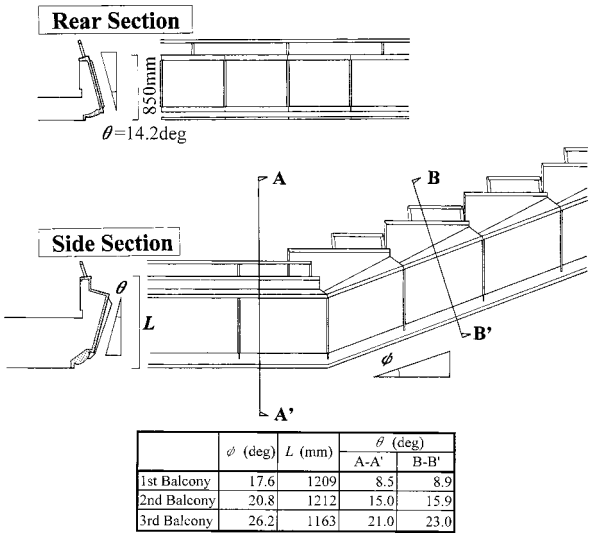

	φ (deg)	L (mm)	θ (deg)	
			A-A'	B-B'
1st Balcony	17.6	1209	8.5	8.9
2nd Balcony	20.8	1212	15.0	15.9
3rd Balcony	26.2	1163	21.0	23.0

FIG. 10. Details of the three balcony faces, shaped to provide early reflections at all parts of the house and to eliminate possibility of echo from the rear section.

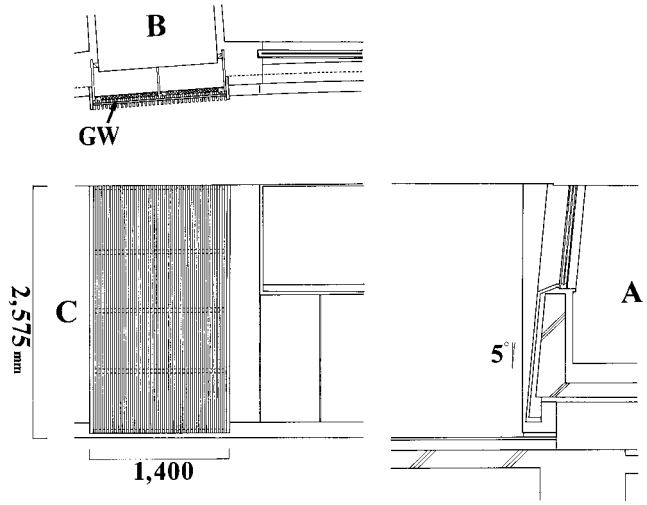

FIG. 11. Design of the curved (in plan) rear walls. The slope is indicated by A. The sound absorbing portion of the rear wall is shown by B and C. The same treatment as C was used under the soffit of the first balcony and at the rear of the ceiling.

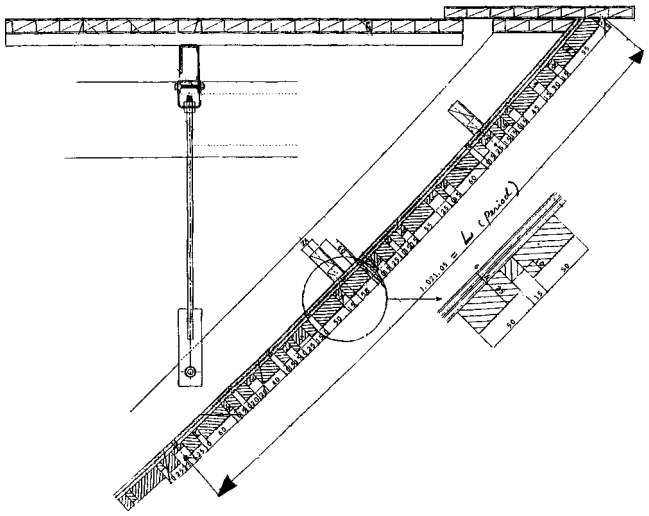

FIG. 12. Detail drawing of the fine-scale diffusion on the sound reflector above the proscenium and the front ends of side-wall balconies.

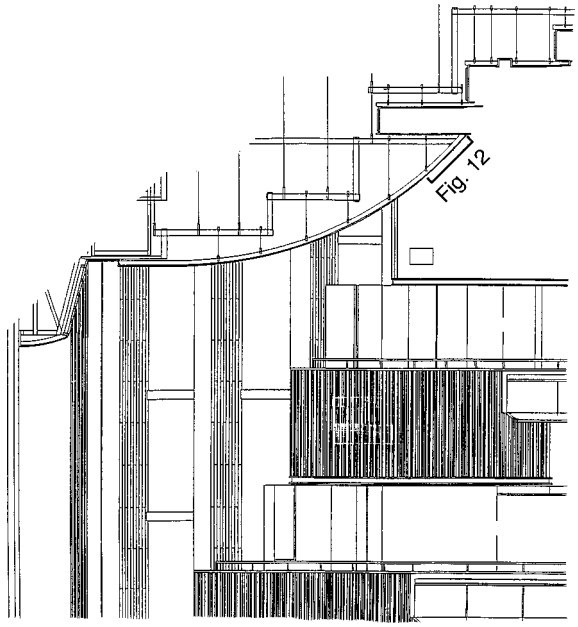

FIG. 13. Drawing showing the shape of the over-proscenium sound reflector. The location of the fine-scale diffusion on the proscenium reflector and the balcony fronts is also indicated.

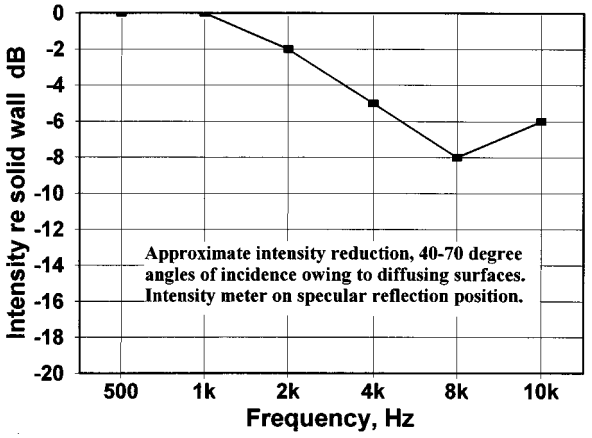

FIG. 14. Approximate intensity reduction in a range of 40- to 70-degree angles of incidence of a sound wave on a sound-diffusing surface like that shown in Fig. 12. The surface was flat during the measurement and the intensity meter was at the optical angle of reflection of the incident wave.

those measured in the actual hall, Fig. 7 presents comparisons of reflectograms measured at 2000 Hz, the approximate center of the spectrum of the singing voice, in the completed hall and in the 10:1 model. The source position was S_0 and the audience positions were seats 102, 21, and 41, i.e., main floor and first and third balconies. Although the reflectograms are not exactly alike, the general nature of the patterns are the same. Desired are a uniformly spaced set of reflections along the time axis, with considerable energy in the first 50 to 80 ms.

In Fig. 8, two of the most important measures of acoustical quality ST1 (on stage) and $IACC_E$ (in audience) are seen to be well predicted from the 10:1 model. We had our least success in determining the reverberation time from the 10:1 model measurements, mostly because of that date, we did not know how to simulate the audience seats that would eventually be used in the hall. Consequently, we relied on calculations like those described in Beranek (1996) and Beranek and Hidaka (1998).

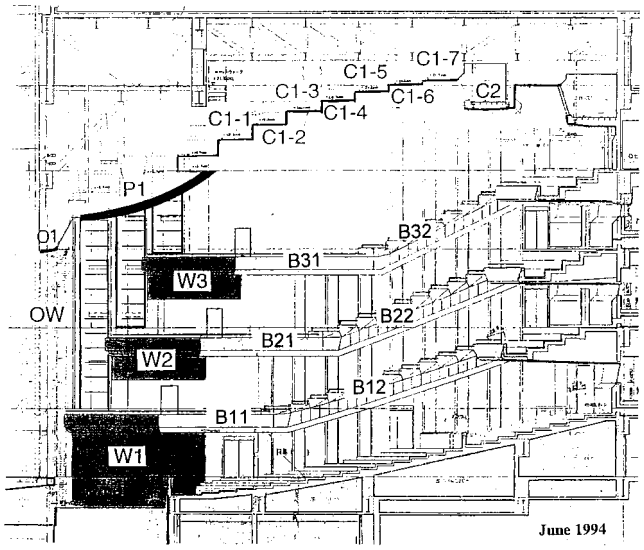

FIG. 15. Reflecting surfaces O1, OW, P1, W1, W2, W3, B11, B12, B21, B22, B31, B32, C1 group, and C2, all designed and adjusted to distribute the sound of orchestra and on-stage singers uniformly to the audience areas.

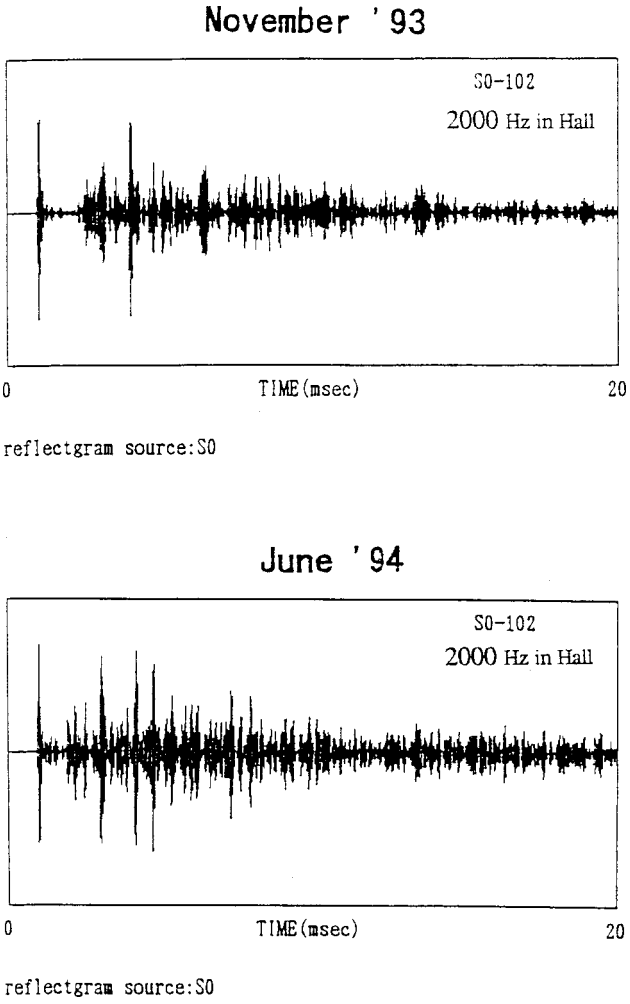

FIG. 16. Reflectograms showing the improvement achieved in the 10:1 model between November 1993 and June 1994 as a result of adjustments in the reflecting surfaces shown in Fig. 15. The source was at S_0 and the receiver at audience seat 102.

B. Seats

The acoustical characteristics of the seats as a function of frequency must be planned along with those of the sidewall and ceiling surfaces. The house has a wooden interior, which absorbs low-frequency sound more than it does the high-frequency sound (see Table II, first line). In order to avoid a deficiency in the strength of the bass and a short reverberation time at low frequencies, the choice of seats becomes very important. When the audience enters the house it adds absorption to that of the empty seats mainly at high frequencies. The absorption at low frequencies is heavily dependent on the thickness of the cushions over which the audience sits. An extensive series of tests of the sound absorption of different chairs, occupied and unoccupied, was made in the reverberation chamber and was preliminarily reported in Hidaka *et al.* (1996). The chair selected, similar to those in Vienna's Grosser Musikvereinssaal, is shown in Fig. 9. The thickness of the seat cushion is 6 cm and 65% of the front of the back rest is covered with a cushion 2 cm in thickness. Thus the sound absorption coefficient by the seated audience in this house at 125 Hz is only about 40% (see third line of Table II) compared to about 70% for an

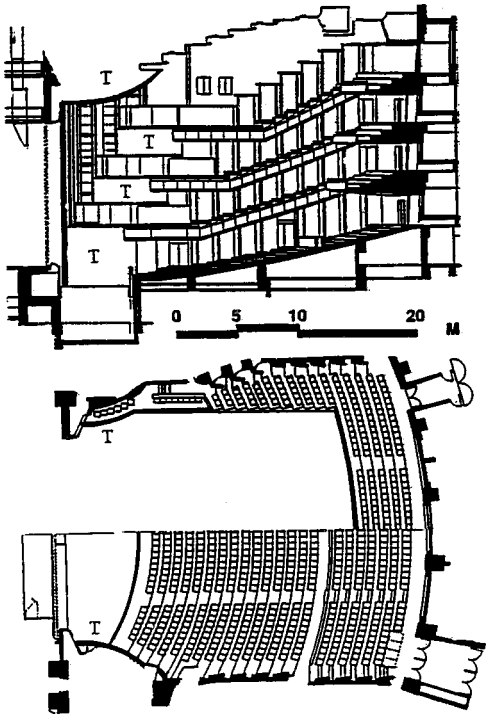

FIG. 17. The NNT opera house as built. (Upper) Longitudinal section drawing. (Lower) Plan drawings of main floor and first balcony. The ''T''s show the trumpet reflecting surfaces.

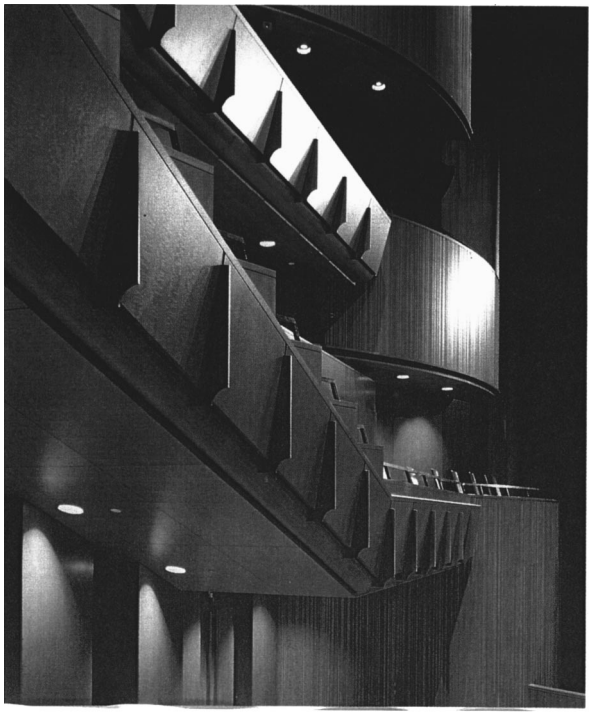

FIG. 18. Photograph showing the three reflecting surfaces W1, W2, and W3 in the completed NNT opera house. The large scale diffusing elements on the fronts of the balconies are also seen.

occupied seat with thick upholstering. The absorption at higher frequencies is less than that of samples tested in the reverberation chamber because the upholstery cloth of those installed was apparently back-sprayed (Beranek and Hidaka, 1998).

C. Sound-reflecting and -absorbing surfaces

To achieve adequate lateral sound-reflected energy over the entire seating area, the balcony fronts had to be individually shaped. In Fig. 10 the details for the three different parts of the three balconies are shown, the rear part being the same at all levels and shaped to eliminate the possibility of echo.

Also to prevent echo, all of the back walls of the house were tilted backwards 5 degrees [see Fig. 11(A)], except for six vertical structural columns at each level, so as to throw the sound incident from the stage to the underside of the

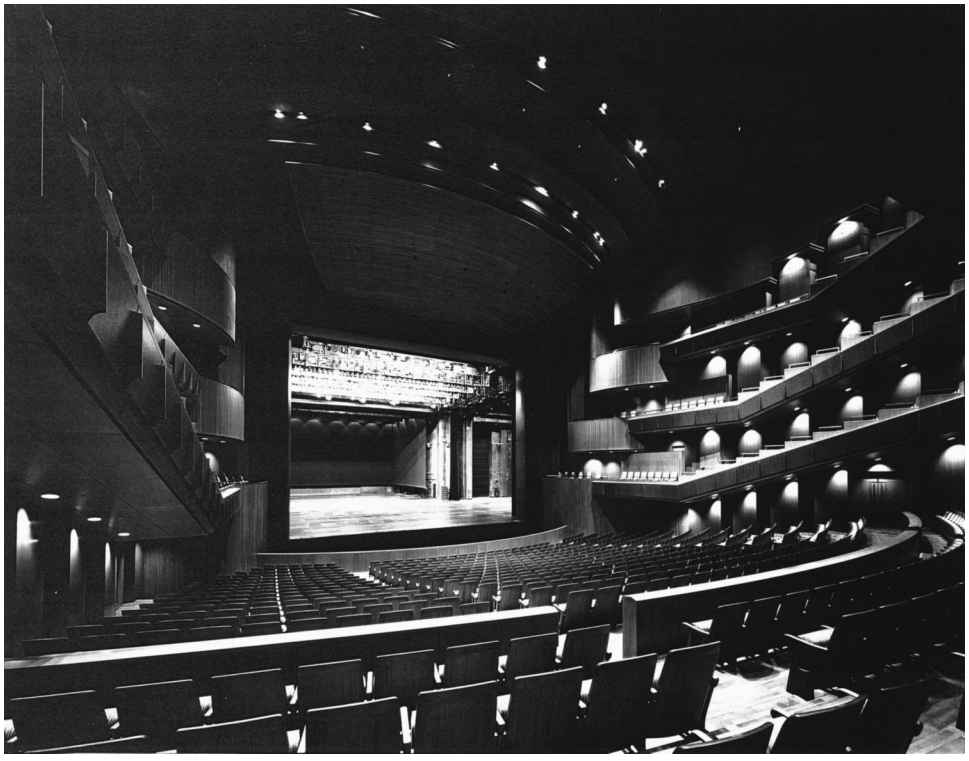

FIG. 19. Photograph of the NNT opera house taken from the rear of the hall looking toward the proscenium. (Photo by Murai, Tokyo.)

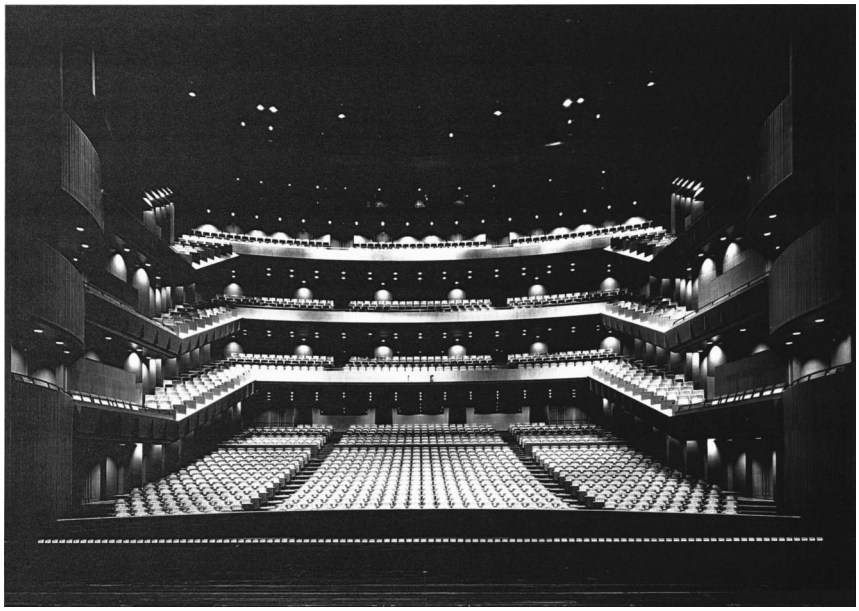

FIG. 20. Photograph of the NNT opera house taken from the stage looking toward the rear of the hall. (Photo by Murai, Tokyo.)

balconies and the rear part of the ceiling and not directly back to the stage. The total area of the back wall on the main floor (most critical acoustically) is 84 m^2. Of this 65% is reflecting, that is, the windows for the booths and the wooden panels beneath, and 35% is sound absorbent. The sound-absorbing portion includes the doors, which have perforated wooden faces, and the columns which are covered with a series of small vertical slats backed by a layer of glass wool (GW) over an airspace as seen in sketches (B) and (C). To absorb the reflections from the lowest and the highest tilted back walls, which were most capable of creating echoes, this same construction was incorporated as follows: (1) the rear 70% of the soffit on the underside of the first balcony with the strips running parallel to the front/rear axis of the hall and made removable so that the amount of sound-absorbing material could be varied to send more or less reflected sound back to the stage, and (2) a sound-absorbing area 1.2 m wide running the full spread of the rear of the ceiling.

Parenthetically, by trial and error after construction, with baritone and soprano singers at various positions on stage, adjustment in the amount of sound absorption by these surfaces was made until the singers expressed approval of the hall support to their voices.

Experience in halls with smooth reflecting surfaces has shown the value of small-scale irregularities, which serve to scatter the reflected sound and give it a warm ''patina.'' This type of irregularity had both to be effective acoustically and to satisfy the architect's desire to avoid visual ''disturbance.'' Extensive research was undertaken to find a solution to satisfy both needs. The result is shown in Fig. 12. This fine-scale sound diffusion (small irregularities) was added to the sound reflector over the proscenium and to the curved surfaces at the fronts of the side balconies (Fig. 13). The width of the dips are 10, 15, 20, 23.6, 25, 30, 40, 45, 50, 55, and 60 mm, and are distributed randomly. Each wooden slat is firmly glued to wooden boards, 25 mm thick. The whole period L is 1021.05 mm, which number was selected as non-integer. The pattern was repeated alternately, making the acoustical period $2L$. The laboratory program that designed these irregularities yielded the approximate reduction in specular reflection shown in Fig. 14.

D. Orchestra pit

The orchestra pit is conventional in shape, except it is normally set up for 60 to 80 musicians. The back wall is removable so that, under the stage, the size is expandable to accommodate 120 musicians. The dividing back wall, when in place, is made of individual reversible panels, one side of which is hard, the other sound absorbent.

III. THE COMPLETED OPERA HOUSE

By June 1994, the acoustical design was near complete (see Fig. 15). The ceiling design, C1s, was stepped to make it acoustically more effective, and W1 was extended down into the pit. The curvatures of W1, W2, W3, and P1 (see also Fig. 13) were finalized. The surface O1 at the top edge of the proscenium was shaped to reflect more sound to the players in the pit.

The improvements in the reflectograms, typically like those at seat 102 for 2000 Hz, are shown in Fig. 16. The coverage pattern, as determined in the 10:1 model, showed that the levels within the front two-thirds of the main floor and the centers of the balconies were within ± 1.3 dB. Only in the corners beneath the second and third balconies did the levels drop to -5 to -6 dB below that near the front of the main floor, position 11. Elsewhere the levels were within -2.2 and -4 dB of position 11.

The longitudinal section and plan drawings of the NNT opera house as built are shown in Fig. 17. The ''trumpet'' reflectors are indicated by ''T'''s, —the main reflector overhead and the three reflectors on each side at the fronts of the side balconies. A photograph of the balcony reflectors is shown in Fig. 18, and photographs of the finished house are shown in Figs. 19 and 20.

To illustrate that the primary goal of increasing the strength of the singers' voices as heard in the audience was

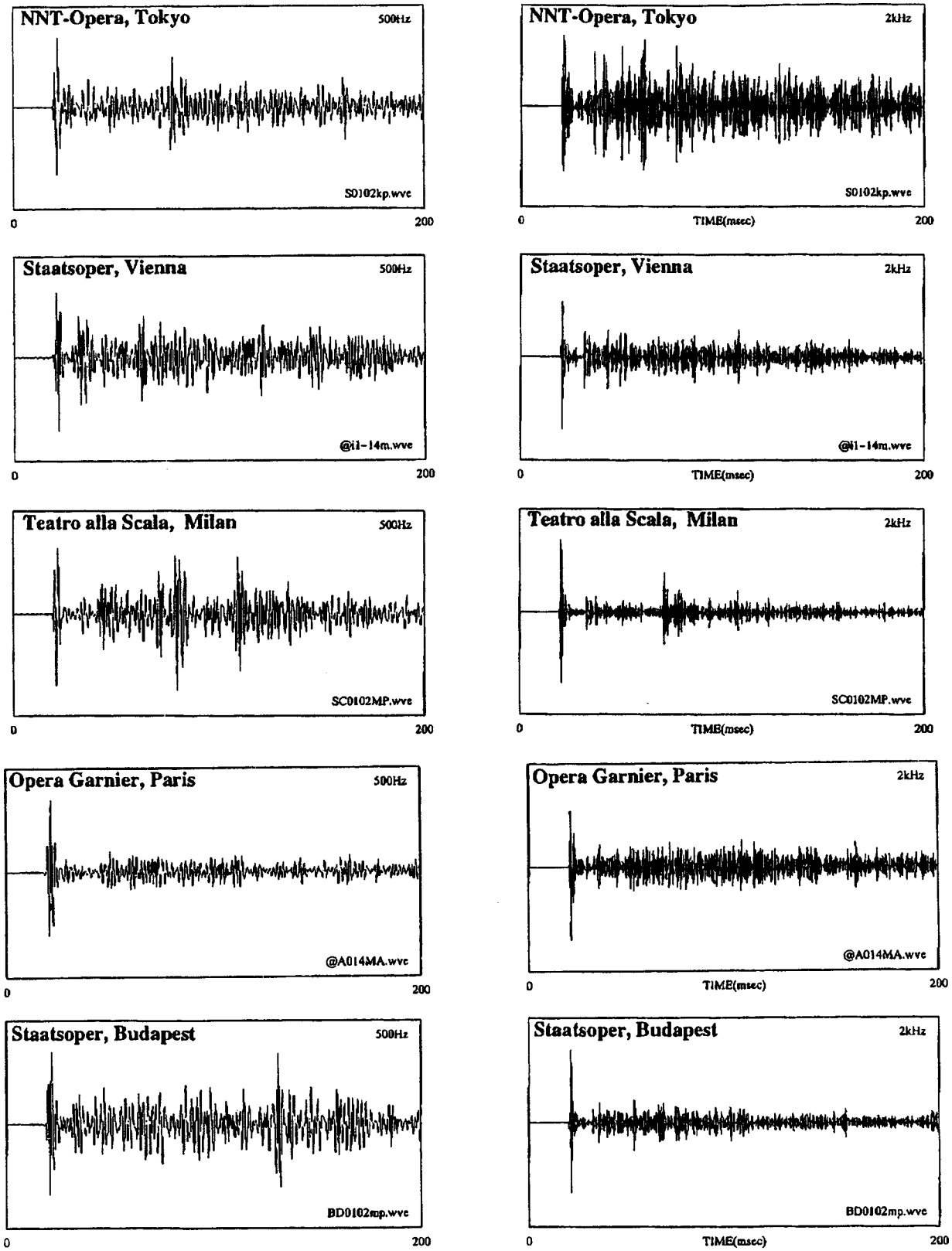

FIG. 21. Comparisons of reflectograms, using the same omnidirectional source on stage at position S_0 and the receiver at audience position 102, for NNT, Vienna, Milan, Paris, and Budapest opera houses. The reflectograms have approximately equal SPLs at 500 Hz, but the SPLs are much greater at 2000 Hz in the NNT opera house than in the others. Note that the center of the intelligibility range of voice frequencies is about 1600 Hz for men and near 2000 Hz for women.

accomplished, comparisons of reflectograms in the audience at seat positions 102 *with the same omnidirectional source at* S_0 *used in all the halls* are shown in Figs. 21 and 22 where eight well-known opera houses of Europe are represented. The distances of position 102 from the source S_0 are NNT (23 m); Vienna (21 m); Milan (20 m); Garnier (20 m); Budapest (*S*) (16 m); Berlin (22 m); Dresden (19 m); Amsterdam (22 m); and Budapest (E) (21 m).

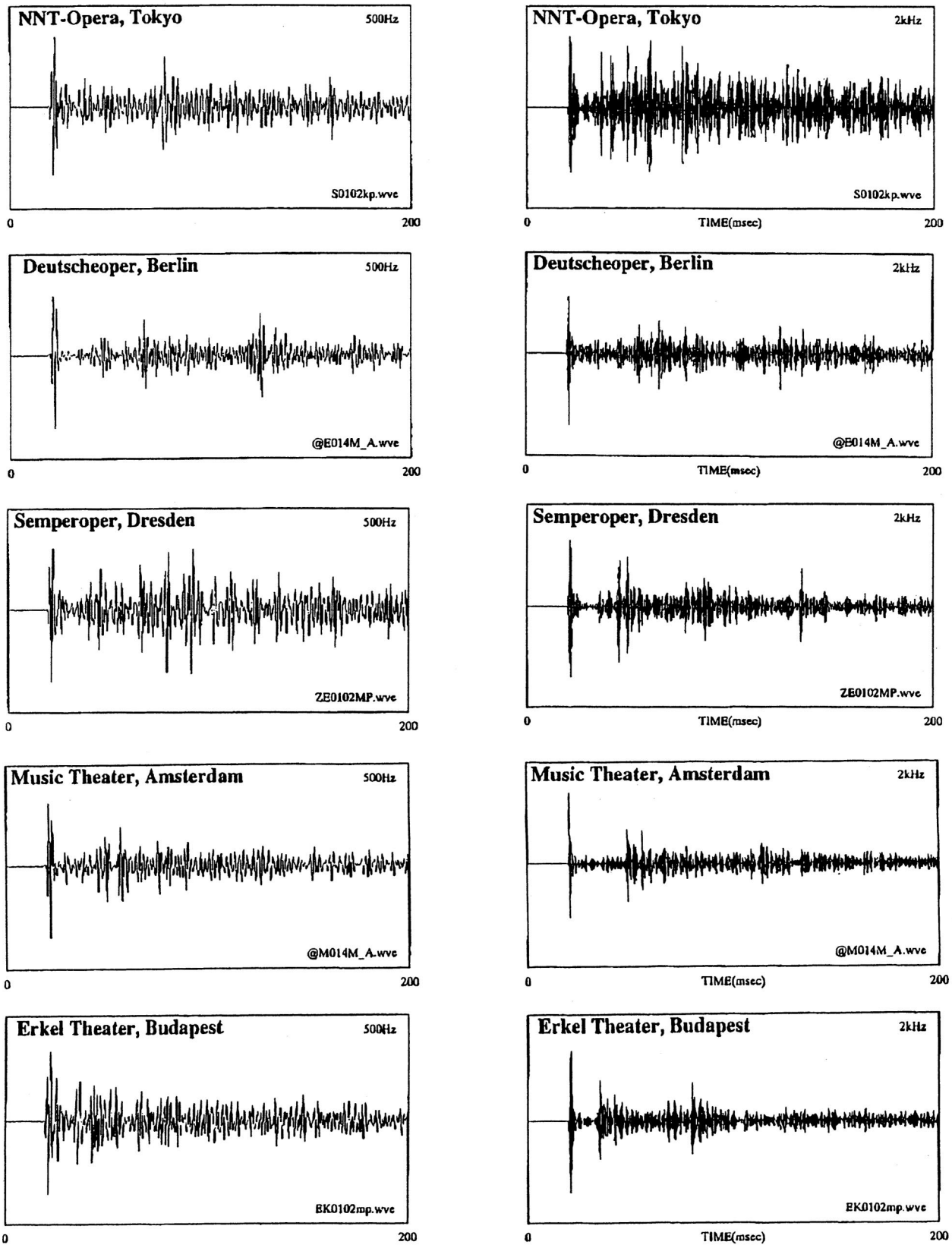

FIG. 22. Same as Fig. 21, except comparison is with NNT, Berlin (Deutscheoper), Dresden, Amsterdam (Music Theater), and Budapest (Erkel).

Reflectograms for the octave band centered on 2000 Hz were chosen as best for this comparison, because it is nearest the center of the frequency range important to the singing voice. It is obvious that the singers voices are substantially augmented in the NNT house.

The reverberation times measured and calculated with audience and open proscenium are shown in Fig. 23 and Table II. Finally, there is no echo and the background noise (NCB-16) with no audience and HVAC in operation is plotted in Fig. 24.

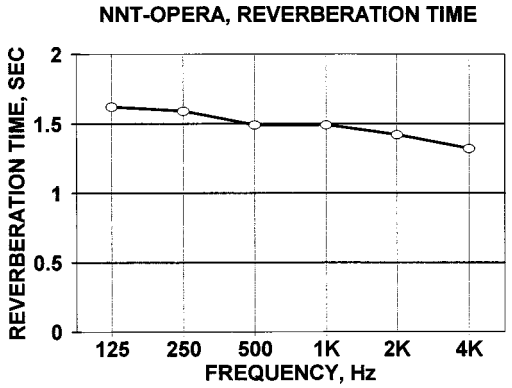

FIG. 23. Reverberation times as a function of frequency for the fully occupied NNT opera house, with orchestra in pit and stage curtain raised and performing set in place on stage.

IV. MEASURED ACOUSTICAL PARAMETERS

The major objective parameters as measured in the finished NNT opera house are listed in Table III. A comparison of these data (which are given first) and those measured in the Buenos Aires Opera Colón, Dresden Semperoper, and Vienna Staatsoper, all world standards (given in parentheses), are $RT_{MID}=1.5$ s (1.4 to 1.6 s); $EDT_{MID}=1.7$ s (1.4 to 1.8 s); ITDG=17 ms (17 to 20 ms); $C_{80}(3)=1.6$ dB (0.8 to 2.7 dB); $[1-IACC_{E3}]=0.65$ (0.60 to 0.72); BR=1.1 (1.2); and $(V/EDT_{MID})\times 10^{-2}=85$ (74 to 119) (see Beranek, 1996, p. 445). Note that RT_{MID} and BR are for the houses when occupied, while all other numbers are for the houses unoccupied. These numbers indicate that the NNT opera house has rich reverberation, clarity, spaciousness, warmth, and strength of sound equal to those in three of the world's highly rated opera houses (see Hidaka and Beranek, 2000a).

V. TUNING CONCERT

The hall was fully completed by January 1997, eight months ahead of its grand opening date, and the tuning concert was held on February 15. The measured reverberation time at mid-frequencies was 1.5 s occupied with orchestra, open stage curtain, and a performance set on stage. Unoccupied it measured 1.8 s. No acoustical problems were detected and no changes were made.

VI. GRAND OPENING AND PROFESSIONAL CRITICISM

The grand opening took place 10 and 11 October 1997. The Emperor and Empress of Japan attended and Prime Minister Ryutaro Hashimoto spoke from the stage, saying that the New National Theater and the adjoining TOC concert hall now make Tokyo a world center for music and ballet. The performance was a success.

Excerpts from reviews and comments for this opera and Bizet's *Carmen* and Wagner's *Lohengrin* that followed were as follows.

Yasutoshi Nakagawa, *Asahi Shimbun* (newspaper), 15 October 1997: ''This house is as grand as any first-rate opera house in the world...Evidence of the excellent acoustics is that one does not feel as if in a strange place even at one's first experience.''

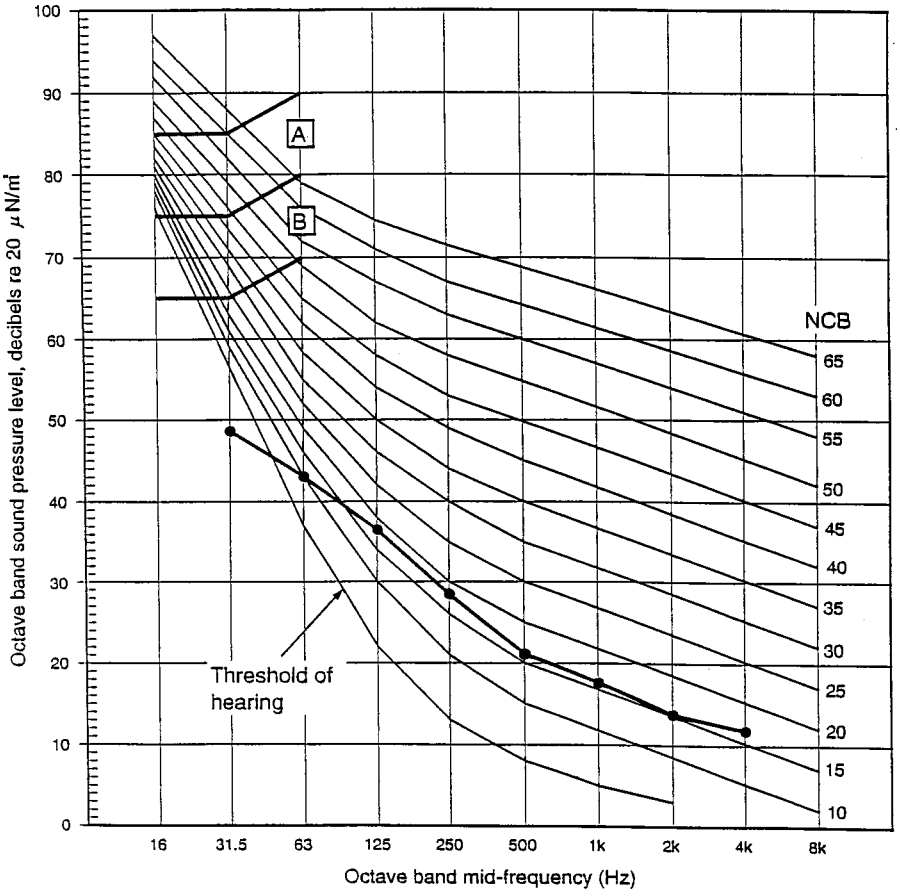

FIG. 24. Average noise level in audience areas of the unoccupied NNT opera house (NCB-16). The HVAC system was in operation.

TABLE III. Measured acoustical parameters for the New National Theater (NNT) opera house (opened 10 October 1997, 1810 seats). The occupied conditions for the IACC's were measured at the tuning concert with full audience, using seven dummy heads fitted with binaural microphones. Four were on the main floor and three in the balconies. The other occupied parameters were measured at the same positions as for the unoccupied measurements with omni-directional microphones. The unoccupied data were taken at 27 audience positions. The data at the various locations were averaged. The source was at position S_0.

	Frequency (Hz)					
	125	250	500	1000	2000	4000
RT, unoccupied	1.65	1.66	1.73	1.85	1.83	1.60
RT, occupied	1.60	1.58	1.48	1.49	1.40	1.31
EDT, unoccupied	1.55	1.59	1.65	1.75	1.73	1.48
EDT, occupied	1.56	1.51	1.38	1.26	1.23	1.09
$IACC_A$, unoccupied	0.93	0.78	0.29	0.20	0.21	0.24
$IACC_A$, occupied	0.87	0.78	0.41	0.31	0.27	0.27
$IACC_E$, unoccupied	0.94	0.82	0.42	0.31	0.31	0.34
$IACC_E$, occupied	0.90	0.83	0.52	0.39	0.35	0.33
$IACC_L$, unoccupied	0.92	0.74	0.19	0.13	0.11	0.08
$IACC_L$, occupied	0.85	0.72	0.22	0.15	0.13	0.10
C_{80} (dB), unoccupied	−0.1	0.9	1.7	1.6	1.4	2.2
C_{80} (dB), occupied	0.90	1.3	2.9	3.7	3.3	3.8
G (dB), unoccupied	−0.4	0.2	1.2	2.2	2.4	−0.3
G (dB), occupied	−0.3	−0.1	−0.1	0.9	0.2	−1.5

Tokihiko Umezu, *Nami* (art magazine), November 1997: ''What surprised me first was the wonderful acoustics of the opera theater...The acoustics are sure to guarantee remarkable joy to listeners.''

Toshiya Inagaki (lead tenor, sang the part of *Takeru*): ''It is very easy to sing in this opera house. The reverberation...is just right. The sound of the large orchestra does not burden the singing at any time even in the loudest passages. I heard that the audience hears the singers easily above the orchestra.''

Ikuma Dan, libretto and composer of the opera, *Takeru*: ''The quality of sound—high tones and low tones—was beautifully balanced. The conductor played full strength. There was no holding back of the orchestra. Yet, every voice and every instrument were clear; everything went together as if one...I have heard operas in many theaters in the world, but this house is my most favorite one...This hall is like a great musical instrument.''

Maestro Gustav Kuhn of Austria wrote, after conducting four performances of *Carmen* in January 1999: ''The National Theatre Opera House is absolutely 'One of the Best' [in the world]. Congratulations on your wonderful work.'' (The only other opera house with this high a rating among the fourteen that Maestro Kuhn ranked was the Teatro di San Carlo in Naples, Italy.)

Other reviews and performers' comments: ''The sound in the pit is excellent. The singing was clearly heard in the pit, even when the orchestra played full strength.'' Another said: ''The acoustics are wonderful. The conductor let the orchestra go full force and the orchestra blended with the singers, not covering their voices.'' Another: ''Perfectly balanced acoustics.'' Another: ''I can say the hall is a success-...The theater gives the voice full reach, while eliminating any masking of the voice by the orchestra. With the Wagner work, the acoustics of this theater reached a high level of perfection.''

VII. CONCLUSION

To summarize, the goal set at the beginning to strengthen the projection of the singers' voices, while preserving the beauty of the music from both the stage and the pit, has been accomplished. The sound is of equal quality and near-equal strength throughout the house. The critical evaluations show that the architectural design of the opera house fully meets the esthetic and sight line requirements desired by the architect. And, highly significant, the acoustical characteristics as measured and appraised equal those of the world's best opera houses, all without resort to the ''horse-shoe'' shape of the conventional Italian opera house.

ACKNOWLEDGMENTS

We wish to express our deep appreciation for the excellent cooperation and relationship with Architect Takahiko Yanagisawa and his project managers, Paul Baxter and Hiroshi Wada. We deeply appreciate the professional help of Noriko Nishihara, who assisted with the measurements and reduction of data. Thanks are owed to the administrations of the opera houses in which acoustical measurements were made and to Toshiyuki Okano, who spent three years, full time, supervising the acoustical and vibrational aspects of the construction of this theater as well as the drama and experimental theaters at the NNT site, for which we also were consultants.

Beranek, L. (**1992**). ''Concert Halls—1992,'' J. Acoust. Soc. Am. **92**, 1–39.
Beranek, L. (**1996**). *Concert and Opera Halls: How They Sound* (Acoustical Society of America, Woodbury, NY).
Beranek, L., and Hidaka, T. (**1998**). ''Sound absorption in concert halls by seats, occupied and unoccupied, and by the hall's interior surfaces,'' J. Acoust. Soc. Am. **104**, 3169–3177.
Hidaka, T., and Beranek, L. (**2000a**). ''Objective and subjective evaluations of 23 opera houses in Europe, Japan, and Americas,'' J. Acoust. Soc. Am. **107**, 368–383.
Hidaka, T., Beranek, L., and Okano, T. (**1995**). ''Interaural cross-correlation, lateral fraction, and low- and high-frequency sound levels as measures of acoustical quality in concert halls,'' J. Acoust. Soc. Am. **98**, 988–1007.
Hidaka, T., Nishihara, N., and Beranek, L. (**1996**). ''Mechanism of sound absorption by seated audiences in concert halls,'' J. Acoust. Soc. Am. **100**, 2705.
Hidaka, T., Nishihara, N., and Beranek, L. (**1998**). ''Relation of acoustical parameters with and without audiences in concert halls and a simple method for simulating the occupied state,'' J. Acoust. Soc. Am. **103**, 2955 (A).
Hidaka, T., Beranek, L., Masuda, S., Nishihara, N., and Okano, T. (**2000b**). ''Acoustical design of the Tokyo Opera City (TOC) Concert hall, Japan,'' J. Acoust. Soc. Am. **107**, 340–354.
Okano, T., Beranek, L., and Hidaka, T. (**1998**). ''Relations among interaural cross-correlation coefficient ($IACC_E$), lateral fraction (LF_4), and apparent source width (ASW) in concert halls,'' J. Acoust. Soc. Am. **104**, 255–265.

Objective and subjective evaluations of twenty-three opera houses in Europe, Japan, and the Americas

Takayuki Hidaka
Takenaka R&D Institute, 1-5-1, Otsuka, Inzai, Chiba 270-1395, Japan

Leo L. Beranek
975 Memorial Drive, #804, Cambridge, Massachusetts 02138

(Received 5 July 1999; revised 20 October 1999; accepted 21 October 1999)

The room acoustical parameters, reverberation time RT, early decay time EDT, clarity factor C_{80}, bass ratio BR, strength G, interaural cross-correlation coefficient IACC, and initial-time-delay gap ITDG [definitions in Hidaka *et al.*, J. Acoust. Soc. Am. **107**, 340–354 (2000) and Beranek, *Concert and Opera Halls: How They Sound* (Acoustical Society of America, New York, 1996)], were measured in 23 major opera houses under unoccupied conditions in 11 countries: Argentina, Austria, Czech, France, England, Germany, Hungary, Italy, Japan, The Netherlands, and the USA. Questionnaires containing rating scales on the acoustical quality of 24 opera houses were mailed to 67 conductors, 22 of whom responded. The objective measurements were analyzed for reliability and orthogonality, and were related to the subjective responses. Presented are (a) the rankings of 21 opera houses each rated by at least 6 conductors for acoustical quality as heard by them both in the audience areas and in the pit; (b) relations between objective room acoustical parameters and subjective ratings; (c) findings of the most important of the parameters for determining acoustical quality: RT (or EDT), G_M, ITDG, $[1-\mathrm{IACC}_{E3}]$, texture (appearance of reflectograms in the first 80–100 ms after arrival of the direct sound), a lower limiting value for BR, and major concern for diffusion and avoidance of destructive characteristics (noise, vibration, echoes, focusing, etc.); (d) the differences between average audience levels with and without enclosed stage sets; and (e) the differences between average levels in audience areas for sounds from the stage and from the pit.
 [S0001-4966(00)06801-6]

PACS numbers: 43.55.Fw, 43.55.Hy, 43.55.Gx, 43.55.Mc [JDQ]

INTRODUCTION

For concert halls, measurements of current room acoustics parameters and their correlation with subjective ratings have been reported in Beranek (1996). There are only a few reported cases of similar studies for opera houses (Barron, 1993). It seems important to learn whether the acoustical parameters that correlate well with subjective ratings of concert halls are useful in evaluating opera houses, therefore a survey of a number of important opera houses is an obvious need. The purpose of this paper is (1) to assemble contemporary acoustical data for 23 houses used for opera; (2) to report on a survey of important opera conductors to learn their acoustical ratings on 24 well-known opera houses of the world; (3) to examine the ranges of various room acoustical parameters determined from the measurements; (4) to compare the subjective judgments by the conductors with the objective parameters; (5) to establish a framework for evaluating opera houses; and (6) to suggest guidelines for use in the acoustical design of new opera houses.

I. OBJECTIVE MEASUREMENTS

A. The halls surveyed

The opera houses to be investigated were selected from the standpoints: (1) they should be widely known as venues for classical opera; (2) their architectural characteristics should either be available in the literature or be determinable; and (3) they should supplement and extend the range of size and shape beyond information now existing in the acoustical literature.

We must emphasize that regular subscribers to performances in *all* of these houses spoke favorably of their acoustics.

Combining these guidelines with practical possibilities, measurements of the 22 opera houses listed in Table I were conducted by the staff of the Takenaka R. & D. Institute, and the data for an additional one were taken from Beranek (1996). Further information about the geometrical properties of the halls are available in that reference and other references (e.g., Beranek, 1962 and 1997; Cremer *et al.*, 1982; Veneklasen and Christoff, 1964; Schmidt, 1985; Moatti *et al.*, 1989; Beauvert, 1996). The seating numbers in these 23 opera houses vary from 1125 to 3816, while the volume and reverberation times (occupied) range from 7000 to 24 724 m^3 and 1.1 to 2.0 s, respectively.

B. Measurement procedures

The measurements were executed under the following conditions: (1) without audiences; (2) with fire and performing curtains open; (3) with major musical instruments and chairs in the orchestral pit (except for the Essen, the Tokyo New National Theater, and Seattle Opera House); and (4) with an orchestral enclosure at Rochester. (An example of the measuring positions is shown in Appendix A, Fig. A1.)

TABLE I. Opera houses for which objective measurements are available. Source at S_0. Listing is alphabetical. All except LO were measured by the Takenaka R. & D. Institute. LO was taken from Beranek (1996).

	Hall name	V m^3	N	V/S_T m	$RT_{occ,M}$ s	$EDT_{unocc,M}$ s	$BR_{occ.}$ -	$C_{80,3}$ dB	G_M dB	$1-IACC_{E3}$ -	ITDG ms	Stage set
AM	Amsterdam, Music Theater	10 000	1689	-	1.30	1.30	1.30	1.9	1.7	0.55	32	n
BD	Berlin, Deutscheoper	10 800	1900	7.5	1.36	1.60	1.30	0.7	1.2	0.39	33	n
BK	Berlin, Komischeoper	7000	1222	7.1	1.25	1.23	1.30	3.1	6.0	0.62	20	y
BE	Budapest, Erkel Theater	17 000	2340	-	1.30	1.40	1.14	3.8	3.3	0.45	17	y
BS	Budapest, Staatsoper	8900	1450	-	1.34	1.37	1.14	1.9	4.4	0.65	15	y
BA	Buenos Aires, Teatro Colón	20 570	2487	9.6	1.56	1.72	1.23	1.1	2.4	0.65	18	y
CC	Chicago, Civic Opera House	23 000	3563	9.1	1.51	1.49	1.32	2.1	0.3	0.53	41	n
DS	Dresden, Semperoper	12 480	1300	10.3	1.60	1.83	1.23	0.8	2.7	0.72	20	n
EO	Essen, Opera House	8800	1125	-	1.61	1.90	1.31	1.3	−0.4	0.54	16	n
HS	Hamburg, Staatsoper	11 000	1679	7.4	1.23	1.35	1.12	2.2	1.3	0.46	34	y
LO	London, Royal Opera House[a]	12 250	2120	7.7	1.10	1.04	1.07	4.5	0.7	0.53	18	n
MS	Milan, Teatro alla Scala	11 252	2289	6.9	1.24	1.14	1.26	3.6	−0.3	0.48	16	y
NM	N.Y., Metropolitan Opera	24 724	3816	9.1	1.47	1.62	1.07	1.7	0.5	0.62	18	n
PG	Paris, Opéra Garnier	10 000	2131	6.9	1.18	1.16	1.31	4.6	0.7	0.50	15	y[a]
PS	Prague, Staatsoper	8000	1554	-	1.23	1.17	1.29	3.1	2.2	0.64	16	y
RE	Rochester, Eastman Theater	23 970	3347	10.2	1.63	1.90	1.32	0.8	3.6	0.54	22	y
SF	Salzburg, Festspielhaus	14 020	2158	8.9	1.50	1.80	1.11	1.5	1.2	0.40	27	n
SO	Seattle, Opera House	22 000	3099	11.2	2.02	2.50	1.26	−0.4	2.7	0.48	25	n
TB	Tokyo, Bunka Kaikan	16 250	2303	9.8	1.51	1.75	1.18	1.1	0.3	0.56	14	n
TN	Tokyo, New National Theater	14 500	1810	9.9	1.49	1.70	1.07	1.6	1.7	0.65	20	n
NT	Tokyo, Nissei Theater	7500	1340	7.4	1.11	1.06	1.24	4.4	5.3	0.58	17	y
VS	Vienna, Staatsoper	10 665	1709	7.3	1.36	1.43	1.19	2.7	2.8	0.60	17	y
WJ	Washington, JFK Center, Opera House	13 027	2142	8.2	1.28	1.27	1.21	4.3	3.1	0.53	15	y

[a]Steel shutter behind main stage closed.

In some houses additional measurements were made with full occupancy and in others the occupied values were estimated using the procedures of Hidaka *et al.* (1998).

C. Measuring system

The block diagram of the measurement setup is shown in Fig. 1. The general outline for the measurements is in accordance with the ISO 3382 (1997), and has been described in more detail in Hidaka *et al.* (1998). A revised stretched impulse was radiated from a calibrated dodecahedral loudspeaker five to ten times, and recorded on DAT in the field. Subsequently, in the laboratory, the S/N ratio was improved from the multiple measurements using the synchronous summation method and later processing.

It is to be noted in the block diagram that a definite pre-triggering signal for the impulses is not used at the time of the field recordings. Such signals are usually employed to permit accurate sync summation subsequently. To eliminate the usual pre-triggering signal, one of the recorded signals, whose waveform was trimmed by a low-pass filter, is also used as the trigger signal for the sync summation. After passing through a digital delay unit, the recorded signals are digitally sampled. If the stretched impulse were to begin from a high frequency component, as is commonly specified (Aoshima, 1981), this sync summation method could not be utilized because of the waveform distortion at the pulse's beginning, which apparently is due to phase fluctuations that modulate the refraction index of the air. To accomplish this method, the revised signal using a lower frequency component [shown in Fig. B1(A) in Appendix B] was employed.

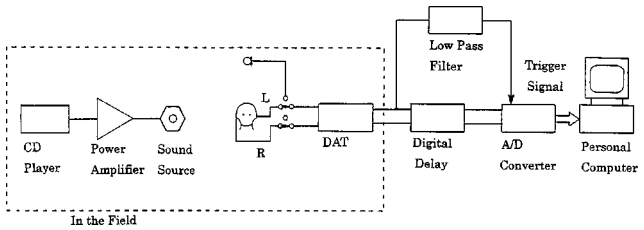

FIG. 1. Block diagram of the measuring system used by the Takenaka R. & D. Institute.

D. Source and receiver positions

Up to four on-stage source positions using the omnidirectional loudspeaker (height = 1.5 m) were selected depending on the time available for measurement, where S_0 (3 m from the stage edge on the center line) was used in every hall. The source position, S_{pit}, near the conductor's position in the orchestra pit was used whenever possible. The number of receiving points (height = 1.1–1.2 m) were distributed uniformly at 10–27 seats corresponding to the seating capacity of each (Fig. A1). The receivers were carefully placed at the position of a seated listener's ear position. The binaural measurements were made with tiny microphones taped to the outer ear canals of seated persons with DAT recorders held in their laps. The numbers of monaural and binaural measurements were almost the same.

The variations of objective parameters in the opera houses were of the same orders as for concert halls, the standard deviations (houses unoccupied) of RT_{low}, RT_{mid}, EDT_{mid}, $C_{80,3}$, G_{mid}, and $IACC_{E3}$, from source position S_0 (for NM which is the greatest in size) were 0.07 s, 0.04 s, 0.28 s, 1.3 dB, 1.4 dB, and 0.11, respectively. With the source in the pit at S_{pit}, these were 0.09 s, 0.05 s, 0.17 s, 2.9 dB, 1.8 dB, and 0.12, respectively.

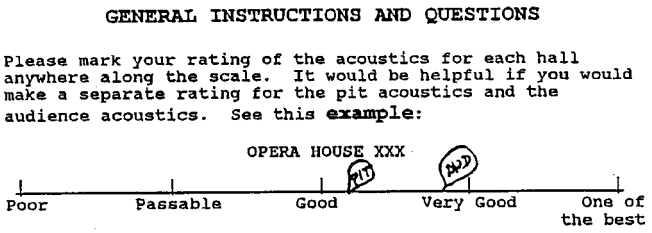

FIG. 2. The rating scale employed in the questionnaire for each of the opera houses, including general instructions for the conductors. The ''questions'' referred to are listed in the text.

II. SUBJECTIVE DETERMINATIONS

A. Questionnaires mailed to conductors

Questionnaires were mailed to 67 important opera conductors and 22 responded, with one response not usable. They were asked for ratings of the acoustics of the opera halls that they knew well on scales that had five steps: *Poor*, *Passable*, *Good*, *Very Good*, and *One of the Best*, which were assigned the numbers 1 to 5 (Fig. 2). Because 13 of the respondents preferred to remain anonymous, all names have been withheld in this paper.

The 24 halls that were included in the questionnaire are those in Table I plus some additions and eliminations. Inclusions were Munich Bayerische Staatsoper, Naples Teatro di San Carlo, Rome Opera da Roma, San Francisco War Memorial, Paris Opera Bastille, Amsterdam Stadtsschouwburg, and Tokyo NHK Hall, for which we have no acoustical data. Not included on the questionnaire were Budapest Erkel Theater, Rochester Eastman Theater, Washington JFK Opera House, Tokyo Bunka Kaikan, Tokyo NNT, and the Seattle Opera House, for which there are data.

The conductors' responses for 21 halls are given in Fig. 3. Four of the 24 halls were rated by fewer than 6 conductors and were not included in Fig. 3; added, as explained later, is Tokyo NNT. Nine halls received ten or more ratings. Note that higher ratings for the acoustics of the pits were made for three halls, NS, PS, and NM.

The standard deviations for the ratings for the audience areas ranged from 0.4 to 1.3 with the median at 0.8. The largest s.d.'s (0.9 to 1.0) were for New York NM, Naples NS, Paris Bastille PB, Chicago CC, and San Francisco SO; and Tokyo NHK Hall TK at 1.3. The smallest s.d.'s (0.4 to 0.6) were Berlin Komische BK, Rome RO, and Vienna VS.

Comments

New York NM (13 conductors) and Naples NS (10 conductors) are two of the three halls in which the pit ratings were significantly higher than the audience ratings. The houses TK, NM, SO, CC, and PB have large seating capacities. Houses BK, RO, and VS have low seating capacities. Thus the most obvious correlations with the magnitudes of the s.d.'s are (1) the seating capacities of the houses and (2) the magnitude of the differences between the pit and audience ratings.

Another factor of the rating system was that some conductors (3) used the full range of 1–5 for their ratings, while some others (3) used a range as little as 2–4. The main group used 2–5. If there was some way to justify expanding or

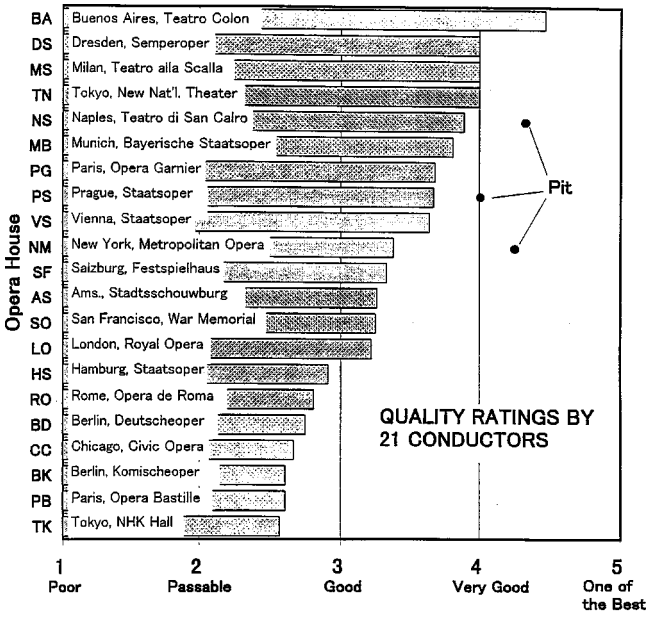

FIG. 3. Acoustical quality ratings in the audience areas of 21 opera houses by 21 opera conductors. The rating sheets contained scales for 24 houses. Only houses that received six or more ratings are included in this figure. All conductors rated the acoustics of the pits as well, but for only three houses were their ratings significantly different (higher) than the ratings for the audience areas, as shown by the large dots. A nonparametric rank ordering, without reference to the rating numbers yields nearly the same sequence—the differences are only among those with almost the same numerical ratings. The rating for TN, which opened in October 1997, was obtained from two opera conductors, two opera singers, two opera directors, two visiting listeners, and four music critics, all with world opera experience. The standard deviations are discussed in the text.

contracting the breadth of the scales of the ratings so that they all covered the same range, the s.d.'s might be reduced, but this manipulation of the data seemed precarious because all conductors did not make the same choice of halls.

Finally, a nonparametric rank-order comparison of the houses, disregarding the numerical ratings given them by the conductors, was made. The halls fell into the following order: BA, DS, MS, MB, NS, PG, PS, VS, SF, NM, AS, LO, SO, HS, RO, BD, CC, PB, TK, BK. Although there are some reversals from the numerical ordering of Fig. 3, they do not affect the conclusions that are given in this paper because they are for houses with almost the same numerical ratings.

B. Comments by respondents to questionnaires

The two questions below were included in the letter in an attempt to find the keys to which objective parameters might be dominant. A summary of their responses is:

Question 1: ''What mostly makes you judge the sound in some opera houses better than in others?''

This question was answered by 10 of 12 respondents. Typical responses are the following (edited for uniformity of language):

- Can singers project without forcing? Are there dead spots on stage? Does the pit have warmth, but also clarity? Is the pit large enough to place horns and brass together?
- The singers must be clearly heard.
- There must be clarity of texture and richness in the sound.

- There must be presence and beauty of the sound.
- There must be early reflection['s?] and no echo and fast transport of tone.
- It is important that there be adequate resonance and warmth of blend between orchestra and singer while allowing absolute clarity to the sung text.
- One conductor wrote, Kangverhaltniss Buhne-Orch. Mischungsverhaltniss des OrchesterKlangs. Klarheit und Raumlichkeit. [Translation: Acoustical balance stage-orchestra. Ensemble balance among orchestra sounds. Clarity and spaciousness.]
- Depends on what piece was performed. Vienna is excellent in the balance between orchestra and singers. Of course, particular performance of the singers and the orchestra create different impressions of sound quality—that is, eternal issue.

From these comments, we can conclude that good opera houses should satisfy four fundamental demands, assuming no harmful factors: (1) hall support for singers; (2) uniformity of singer projection from a wide area on the stage; (3) good balance between orchestra and singer; and (4) clarity and richness of the orchestral and singing tones.

Question 2: ''Which halls on the list do you enjoy the most and why?''

This question was answered by 10 of 21 respondents. The halls which were nominated by more than two respondents were; Milan (4), Dresden (3), Naples (3), NY (3), Tokyo NNT (3), and Garnier (3). One stated strongly, ''Buenos Aires is extraordinary, as is Dresden. In Paris, I like the Garnier very much and the Bastille not. A basic problem, as ever, is clarity versus liveness. Houses like London (Royal Opera House before 1999 reconstruction) and Amsterdam are simply too dry.'' Another world famous conductor said that the New York Metropolitan Opera House should be ranked equal to the Dresden Semperoper in spite of the fact that only the most experienced and powerful voices can successfully perform in the Met because of its huge size (3816 seats vs 1300). A famous Austrian conductor wrote, ''The National Theater Opera House [TN, Tokyo] is absolutely 'One of the Best.' ''

One world famous conductor, who was not counted in the respondents above, wrote ''There is only one opera house existing which is excellent on all counts and which has never been able to be imitated by anyone, and that is Bayreuth.'' In part, this reflects the difficulty in choosing the best opera acoustics because the reputation of a house is influenced by the performing styles commonly presented and by the backgrounds and personal preferences of its principal conductors. Opera has a longer history than most orchestral music and the beauty of an operatic performance depends on a number of factors in addition to acoustics—the voice and personality (including acting styles) of the singers, the beauty of the orchestral music, the costume and scenery design, and the view of the stage. Opera is truly a composite art.

Parenthetically, it is common consensus that the Bayreuth Festspielhaus is especially suited to the performance of Wagner's compositions—particularly his *Parsifal*.

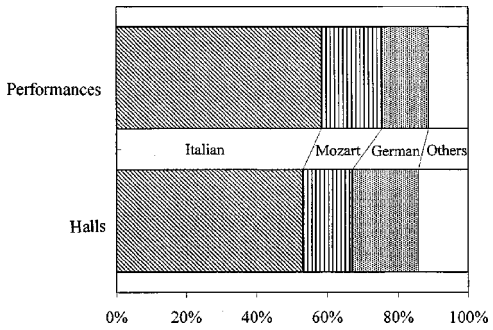

FIG. 4. Statistics of opera performances at 32 opera houses in the 1997–98 seasons taken from *Music and Opera*.

It is generally not believed suitable for Italian opera. The authors analyzed the statistics of opera performances in the 1997–98 seasons at 32 major opera houses around the world (*Music & Opera*, 1997–1998), where opera types, each of which was performed at more than ten halls, were classified into Italian, German, Mozart, and others. The result in Fig. 4 shows that Italian and Mozart type operas are dominant. For them intimacy and clarity are vital because the orchestras are usually not large, and the singers/orchestra together often include delicate ensembles and there are recitatives requiring understandable speech. This information seems to be one reason why horse-shoe halls of compact size have predominated throughout much of operatic history.

III. FINDINGS FROM THE OBJECTIVE MEASUREMENTS AND RELATIONS TO QUESTIONNAIRES

A. Introduction

A complete set of measurements of RT, EDT, C_{80}, G, IACC, and ITDG [definitions in Hidaka *et al.* (2000) and Beranek (1996)] was made in each of the 23 opera houses and is listed in Table I. The IACC_{E3}'s were measured for the 500 to 2000 Hz bands, since they have little meaning at lower frequencies. Only the IACC_{E3} data for the London Royal Opera House LO were converted from LF_{E4} values (Okano *et al.*, 1998). All the acoustical parameters were derived from measurements made with the omnidirectional source located at position S_0, except where indicated otherwise. The correlation matrix for these objective measures are given in Table II, where the suffix ''*L*,'' ''*M*,'' and ''3'' mean the average over 125 and 250 Hz, 500 and 1000 Hz, and 500, 1000, and 2000 Hz, respectively. The correlation matrix was calculated for unoccupied values except for BR which was taken from RTs for occupied halls. The correlation, not shown here, between RT for unoccupied and occupied halls is in the high 90's. It is seen that relatively low correlations exist among RT_M, G_L, G_M, IACC_{E3}, BR, and ITDG, while the correlations are high among RT_M, EDT_M and $C_{80,3}$. The correlation matrix for six octave bands is attached in Table AI of Appendix A.

B. Effect of source position on-stage and in pit

In the Tokyo New National Theater TN, on stage, each acoustical parameter was measured for three source posi-

TABLE II. Correlation coefficients among objective acoustical factors calculated from the results of measurements in 23 opera houses listed in Table I. The subscript ''*L*,'' ''*M*,'' and ''3'' mean, respectively, that the octave band average is for 125 and 250 Hz, 500 and 1000 Hz, and 500, 1000, and 2000 Hz. The significant correlations are in **bold** type.

	RT_M	EDT_M	$C_{80,3}$	G_L	G_M	$IACC_{E3}$	BR	ITDG	*V*	*N*
RT_M	-									
EDT_M	**0.98**	-								
$C_{80,3}$	**−0.86**	**−0.88**	-							
G_L	−0.02	−0.06	0.02	-			**Bold**: > 0.6			
G_M	−0.11	−0.12	0.14	**0.89**	-					
$IACC_{E3}$	−0.05	0.04	0.06	−0.37	−0.34	-				
BR	0.13	0.05	−0.09	0.30	0.08	0.07	-			
ITDG	0.18	0.17	−0.35	−0.17	−0.20	0.42	0.19	-		
V	**0.63**	0.58	−0.46	−0.19	−0.21	0.05	−0.12	0.23	-	
N	0.42	0.35	−0.24	−0.29	−0.30	0.22	−0.06	0.25	**0.92**	-

tions. In the orchestra pit, measurements were made for four distributed positions (see Fig. A1). Both cases were with and without audience. As shown in Table III, the differences in the values of the parameters measured on average in the audience for the different source positions is within a tolerably small range. Similar measurements for various source positions on stage were executed at Berlin Komischeoper BK, Dresden DS, and Milan MS, with the same results for the latter two. We can say that in most houses, e.g., TN, DS, and MS, the different source positions on stage have little influence on the measurements in the audience as long as they are not extremely far from the singer's main position, S_0. The effect of stage position on the sound distribution in Berlin BK will be discussed later. The same conclusion holds for different source positions in the pit. Therefore two source positions, S_0 and S_{pit}, which are often selected in this paper, appear sufficiently reliable for our purposes.

The sound from the orchestra pit is of primary importance, so each acoustical parameter for it was measured in the audience areas of 13 opera houses as shown in Table IV. $RT_{M,\text{occ}}$ and BR_{occ} had nearly the same values as listed in Table I whether the source was on stage or in the pit. With the source in the pit, $C_{80,3}$, G_M, and $[1-IACC_{E3}]$ change their values from those for the sound source on stage because of weakened direct sound and the different paths for early reflections. An interesting finding is that the values of $C_{80,3}$ and G_M are similar from hall to hall, except for Vienna VS where G_M is 4 dB for the pit source, which also means that $C_{80,3}$ is small.

The question is, ''Why is G_{pit} for VS so large?'' Beranek has sat in the Vienna pit (second violin position at the rail) during an opera performance and saw and heard nothing unusual. The answer is that the ceiling, particularly above the pit, is shaped to reflect pit sounds to the main floor. The singers' voices are reflected to the rear of the main floor and to the higher boxes and balconies. There is recent indication that the opera producers in Vienna are aware of this unusual difference, because for two operas, *I Puritani* and *Les Contes D'Hoffman*, produced in late March 1999, stage sets were employed that were nearly closed, both ceiling and side walls, even for outdoor scenes. Also, any important singer's passage was performed very near stage center at the plane of the proscenium. With these arrangements, the singers had no apparent difficulty in making themselves heard above the orchestra. The acoustical consequences of closed sets are discussed shortly.

C. Applicability of the simplified Sabine equation for calculations

The volumes and areas of the different surfaces for the halls that are tabulated in the various tables are for the audience chamber only, as though the stage house was bounded at the proscenium by a wall with an appropriate absorption coefficient. In *Concert and Opera Halls: How They Sound* (C&OH) by Beranek, p. 437, it was shown that for concert halls, in which the sound absorption at mid frequencies of the audience is about 0.85 and the average absorption of all other surfaces in the room is about 0.1, the Sabine equation becomes, approximately, $RT_M = 0.14(V/S_T)$, where V is the volume in m^3 and S_T is the acoustical area of the audience and the proscenium, if open (plus that of the pit if the players

TABLE III. Range of objective parameters measured for three source positions on the stage and four in the orchestra pit under unoccupied and occupied conditions at Tokyo New National Theater Opera House TN.

	RT_L s	RT_M s	EDT_L s	EDT_M s	$C_{80,3}$ dB	G_L dB	G_M dB	$IACC_{E3}$ -
Unoccupied								
Stage	1.6–1.7	1.8	1.5–1.6	1.6	1.7–2.7	−1.7–−0.2	0.3–1.7	0.37–0.43
Pit	1.6–1.7	1.8	1.6–1.8	1.7–1.8	−2.6–0.3	−2.0–1.0	1.7–2.9	0.31–0.44
Occupied								
Stage	1.6	1.5	1.5–1.6	1.3–1.4	3.3–3.9	−1.1–−0.2	−0.4–0.4	0.42–0.51
Pit	1.5–1.6	1.4–1.5	1.5–1.6	1.3–1.4	0.1–1.6	−2.6–−0.5	−1.9–0.0	0.39–0.40

TABLE IV. Measurements made in audience areas of 13 opera houses with sound source in orchestra pit. There were no musical instruments or chairs in the pits at Essen and Tokyo TN. The sequence of the first nine houses is by conductors' ratings. The remaining four (''b'') were not rated. Note that for the source in the pit the clarity in the audience is often negative, good for orchestral music.

	Hall name	$RT_{M,occ}$ s	BR_{occ} -	$C_{80,3}$ dB	G_M dB	$1-IACC_{E3}$ -
BA	Buenos Aires, Teatro Colón	1.53	1.19	−2.6	1.9	0.66
TN	Tokyo, New National Theater[a]	1.49	1.03	−2.3	1.8	0.68
PG	Paris, Opéra Garnier	1.15	1.19	0.3	0.1	0.65
PS	Prague, Staatsoper	1.21	1.28	−0.4	2.5	0.67
VS	Vienna, Staatsoper	1.35	1.12	−0.5	4.0	0.65
NM	NY, Metropolitan Opera	1.48	1.07	−2.3	0.2	0.63
HS	Hamburg, Staatsoper	1.23	1.09	−0.7	1.4	0.57
BD	Berlin, Deutscheoper	1.32	1.28	−1.4	1.0	0.54
CC	Chicago, Civic Opera House	1.52	1.26	−0.2	−2.1	0.66
AM	Amsterdam, Music Theater[b]	1.29	1.20	−1.4	0.3	0.61
EO	Essen, Opera House[a,b]	1.46	1.25	−0.6	−0.1	0.71
TB	Tokyo, Bunka Kaikan[b]	1.49	1.15	−0.5	-	0.58
WJ	Washington, JFK Center, Opera House[b]	1.25	1.13	2.1	1.3	0.58

[a]No musical instruments or chairs in pit.
[b]Not rated by conductors.

are present during the measurements) in m^2. Note that in concert halls the reverberation times (occupied) range from 1.6 to 2.2 s.

We have only one opera house, the Tokyo New National Theater (TN), where we have measured *separately* the acoustic absorption of (1) the audience area, both occupied and unoccupied, (2) the remaining areas of the hall (residual absorption), and (3) the proscenium, with the results shown in Table V (Beranek and Hidaka, 1998). The walls of the stage house (fly-tower) of TN are highly absorbent.

The absorption of sound by a proscenium is a matter of how it is measured and of what conditions exist in the stage house. In the Tokyo NNT Opera House, the omnidirectional loudspeaker was placed either at position S_0 with the proscenium open, or moved forward so that a heavy fire curtain could be dropped behind it. The RTs were then measured for the two cases at seats throughout the opera house and averaged. From those data we could calculate the absorption of the open proscenium, as given in Table V, which, in the middle four bands, is about 1.5 times its area, i.e., 302 vs 205 m^2. This increase in absorption is possibly explained by coupled room theory, but the authors have not attempted verification. The same experimental result was obtained in the 10:1 wooden model. In a contiguous drama theater with 55% of the cubic volume and a highly absorbent stage house, the same measurement was made and the absorption was about 1.23 times the area of the proscenium. We would suppose that in a small theater where the stage house has hard walls, and only a limited amount of hung scenery, the absorption coefficient for the proscenium in those four bands might be near 1.0. We used 1.0 in another case with such a

TABLE V. Calculation of the reverberation times for the Tokyo, New National Theater Opera House TN with proscenium curtain open, a highly absorbent fly (scenery) tower and no stage set. The Sabine equation, $RT = 0.161V/(A_{total} + 4\ mV)$, was used for the calculations. The absorption coefficients for the residual surfaces and the occupied chairs were determined from the reverberation times measured before and after installation of the chairs. The mid-frequency audience absorption (0.61) in this opera house is lower than that in most houses (0.80), because of the characteristics of the audience chairs which are similar to those in the TOC Concert Hall (see Beranek and Hidaka, Fig. 6, 1998). A photograph of the chair is in Beranek *et al.*, Fig. 9 (2000). Volume, $V = 14\,500\ m^3$; Pit area, $S_0 = 102\ m^2$; Audience area with edge correction, $S_A = 1153\ m^2$; Proscenium opening, $S_p = 205\ m^2$; Residual wall and ceiling areas, $S_R = 4206\ m^2$. Total residual area without orchestra, $S'_R = S_R + S_0 = 4308\ m^2$.

	Frequency, Hz					
Calculations:	125	250	500	1000	2000	4000
Alpha (R), residual absorption	0.17	0.16	0.13	0.11	0.11	0.10
$A_R = 4308 \times$ Alpha (R)	732	689	560	474	474	431
Alpha's, S_A, occupied,	0.39	0.44	0.60	0.62	0.65	0.54
$A_T = 1153 \times$ Alpha (S_A)	445	503	692	711	747	623
$A_R + A_T$, m^2	1177	1192	1252	1185	1221	1053
Proscenium absorption (Approx)	220	302	302	302	302	378
A_{total} = total absorption	1397	1494	1554	1487	1523	1391
4 mV, Air absorption	0	16	41	76	138	349
$RT = 0.161 \times 14\,500/(A_{total} + 4\ mV)$	1.67	1.55	1.46	1.49	1.41	1.34
Measured RT, Occup., 2/15/97	1.62	1.59	1.49	1.49	1.42	1.32

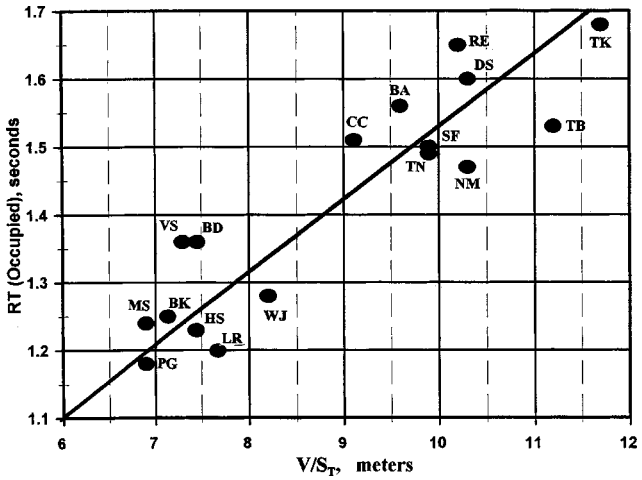

FIG. 5. Plot of the reverberation times for occupied opera houses versus the volume divided by the acoustical area of the audience. The text discusses how the RTs (occupied) were derived from the RTs (unoccupied) where they were not directly measured. The simplified Sabine equation is $RT = KV/S_T$. The mid-value of K for opera houses is 0.16, for the lower group 0.17 and for the upper group 0.15. For concert halls with larger RTs, $K = 0.14$.

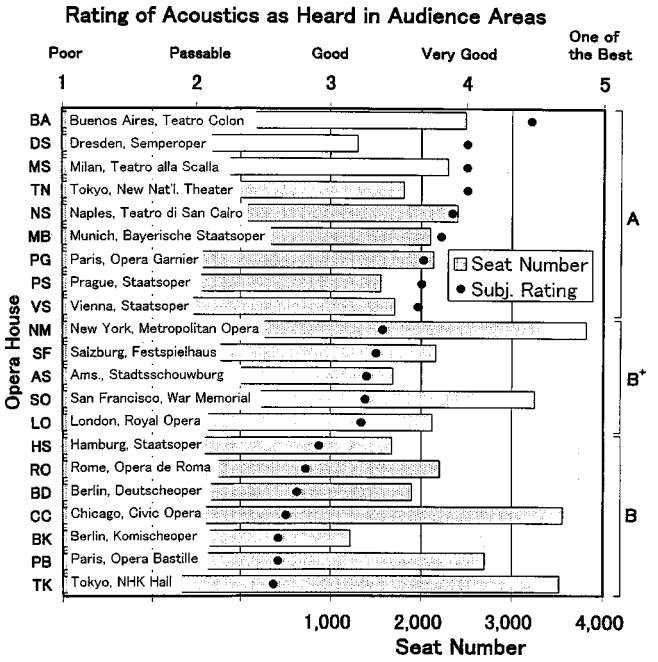

FIG. 6. Conductors' ratings of the acoustics in the audience areas compared to seating capacity. The opera houses are sequenced along the Y axis according to Fig. 3, with the rating shown by the solid points according to the scale on the upper X axis. The seating capacities are shown by the horizontal bars according to the scale on the lower X axis.

stage house and obtained reverberation times equal to those measured.

The RT_M's for 17 houses for which full-occupancy data are available are plotted as a function of V/S_T in Fig. 5. Because S_T is the acoustical audience area (''acoustical area'' means the area over which the audience sits plus edge corrections and plus the area of the proscenium when it is open), the abscissa is approximately equivalent to determining RT as a function of the volume assigned to the acoustical area over which each person sits, i.e., $(V/N)/(S_T/N)$. For estimating reverberation times during early design, the simplified Sabine equation with a suitably selected value of K would seem to provide sufficient accuracy. As discussed above, the RT of an opera house is a function of what is behind the proscenium. If the stage house is heavily sound absorbent (very low RT, say, 0.5 s) and the audience area with the proscenium closed off has a much higher RT (say, 1.7 s), opening the proscenium wall reduces RT in the audience area much more than if the two RTs are nearly alike. This says that the ''sound absorption coefficient'' for the proscenium opening is a variable depending on the stage-house condition.

There is another problem in calculation created by the boxes in a vertical, horseshoe-shaped ''wall'' whose surface is less than 50% perforated for the box openings, e.g., Milan La Scala 43%. Thus the RT in the main-floor audience chamber of such a house will be higher than in a house like the Philadelphia Academy of Music where there is no wall in front of the boxes, only balcony fronts, and no separating walls between the boxes. Depending on which architecture is being evaluated, the volume in the Sabine formula for La Scala should probably only be that of the main floor audience room, while the volume for Philadelphia should include the volume of the open boxes. In the former case, the absorption of the ''wall'' is that of the box openings, while in Philadelphia, the absorption is that of the audience area inside the ''boxes.''

Despite the fact that all types of architecture and stage acoustics are involved, the mean line of Fig. 5 is usually within 0.1 s of the measured values. One should note that the reverberation times for occupied houses that are reported in the literature generally were measured with a few stop chords at only one or two seats, and thus are expected to be off by ± 0.1 s, and if the decay curves are not properly evaluated (Hidaka *et al.*, 1998), even more.

D. Room volume *V*, shape, and number of seats *N*

The volumes of the halls of Table I range from 7000 to 24 724 m^3 and S_T from 980 to 2718. Newly built opera houses have not merely a variety of shapes, but also the acoustical area per seat S_T/N is generally larger than in the traditional horseshoe ones. From Fig. 6 it is seen that none of the houses with large seating capacities (above 2500 as shown on the lower scale), rank subjectively above the value of 3.6 on the five-point rating scale of the upper abscissa. With a large volume, assuming evenly distributed sound, there is less soloist energy per square meter of audience space. For the architect, a large house with modern seats occupying larger area per person, necessitates special construction around the proscenium to fully project voices to the audience areas.

Of the top nine houses, only one, TN, is not horseshoe shaped (see Fig. A1). The measured acoustical data also indicate that the horseshoe shape is not necessary to obtain a good opera house acoustically. Visual factors certainly have entered into the decisions to build horseshoe-shaped houses. In those houses, the distance of most of the listeners is

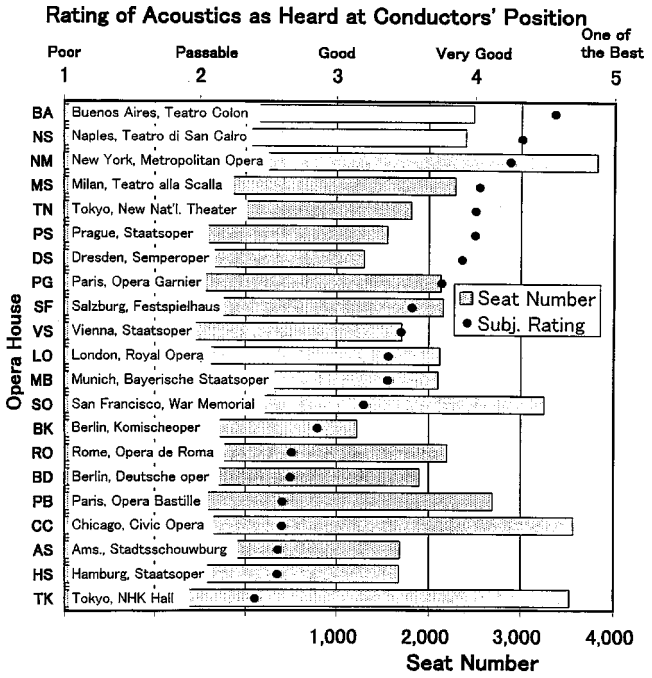

FIG. 7. Same as Fig. 6, except the conductor's ratings are for the acoustics of the pits.

shorter than in conventional auditoriums. Further, in the old houses, the percentage of seats on the main floor is less than in modern houses and the halls are narrower, which makes them more intimate, a fact confirmed shortly by the ITDG data. From Fig. 7 we see that the acoustical conditions around the proscenium and in the pit can increase the conductor's rating of the sound heard in the pit for a large hall, particularly in the case of the New York Metropolitan Opera House NM.

E. Occupied RT obtained from unoccupied RT

An empirical method (Hidaka *et al.*, 1998) for calculating occupied RTs at all six frequencies from unoccupied RTs produced many of the values of RT_{occ} in Table I. The others were determined from analysis of chords recorded during concerts. The accuracy of the empirical method can be illustrated by comparing calculations and measured RT_{occ}'s at the New National Theater, Tokyo. They were, respectively, 1.49 and 1.51 s. The correlation matrix of Table II is the same for the occupied condition because the empirical equation is a linear transformation.

EDT_M has high correlations with both RT_M ($r=0.98$) and $C_{80,3}$ ($r=-0.88$). Hence, the subjective meaning of reverberance in opera houses may be explained by any one of RT, EDT, or $C_{80,3}$. When selecting reverberation times during design, acoustical clarity $C_{80,3}$ may be more meaningful to laymen than RT, because, in fact, the selection of RT is based on rendering singers' voices adequately articulate.

F. Bass ratio BR

The bass ratio for occupied houses (Table I) is distributed from 1.07 to 1.32, which is a narrower range than that of the concert halls, 0.92 to 1.45.

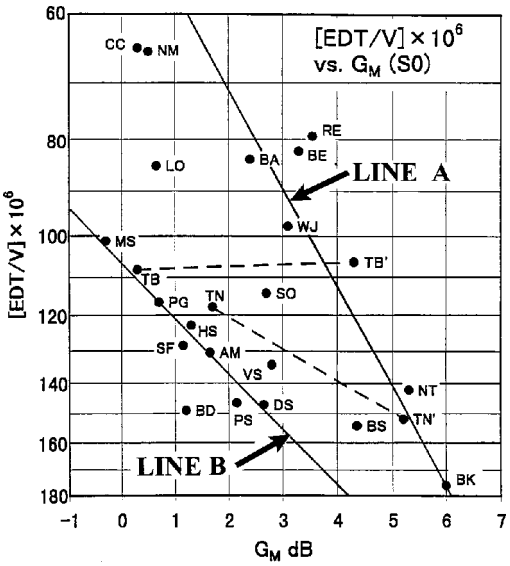

FIG. 8. The early decay time EDT_M divided by the volume V is plotted against the strength factor G_M, both quantities for unoccupied houses with the source at S_0. The measurements were the average of the positions throughout the audience areas. The houses divide into two groups, with four houses falling between. Line A is taken from Beranek (1996, p. 445) and is for opera houses that, during the measurements, had an orchestra enclosure in place, or a stage set that represented a closed room (with ceiling), or a stage house (fly-tower) that was highly reverberant. Line B is for houses with highly absorbent stage houses and either no stage set or a stage set that allowed free acoustical communication between the stage house and the audience auditorium. The letters TB' and TN' are for measurements made in houses TB and TN with silicated-calcium-board fire curtains down.

G. Strength factor *G*

The strength factor G_M (average sound pressure level in dB for 500 and 1000 Hz bands) is important because it is a means for estimating the strength of the singing voice located at the position S_0 on the stage. It has been found that when the Sabine equation is valid, G_M is proportional to RT and inversely proportional to V (C & OH, p. 444). Because the ratio of EDT_{unocc} to RT_{occ} is approximately 1.1 for the halls in this study, and assuming as before that the acoustic audience absorption is not less than 75% of the total room absorption with the proscenium closed off, we find that we should have the logarithmic relation shown by Line A in Fig. 8, where the omnidirectional source is at S_0 and the values of EDT_M and G_M are averaged over the audience areas.

Line A in Fig. 8 is the same as that for concert halls (C & OH, p. 445). It is valid for those houses that had, at the time of measurement, either (a) substantial stage sets (i.e., returning most of the energy from the back side of the omnidirectional source to the hall), or (b) either highly reverberant stage houses (fly-towers) or orchestra enclosures on stage. Line B was determined by those halls for which the absorption in the stage house was high and, for that condition, either there was no orchestra enclosure on stage or the stage set was sparse. The separation between the two lines illustrates clearly the approximate increase in the singer's voice that occurs when a roomlike stage set is used instead of a sparse set that opens into a dead stage house. The difference between A and B is 2–4 dB.

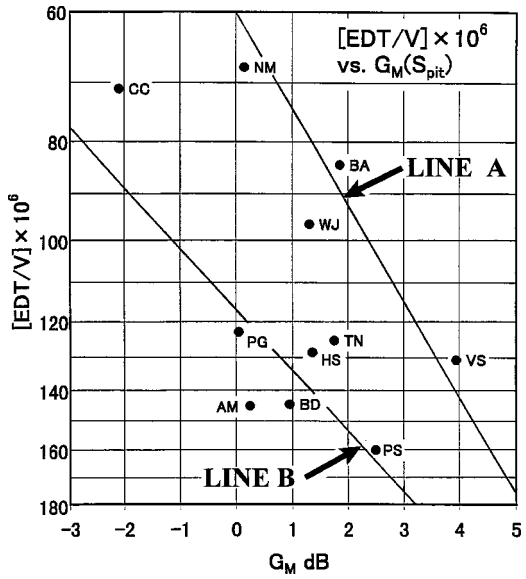

FIG. 9. Same as preceding figure, except the EDT_M and G_M figures are for the source at the position S_{pit}.

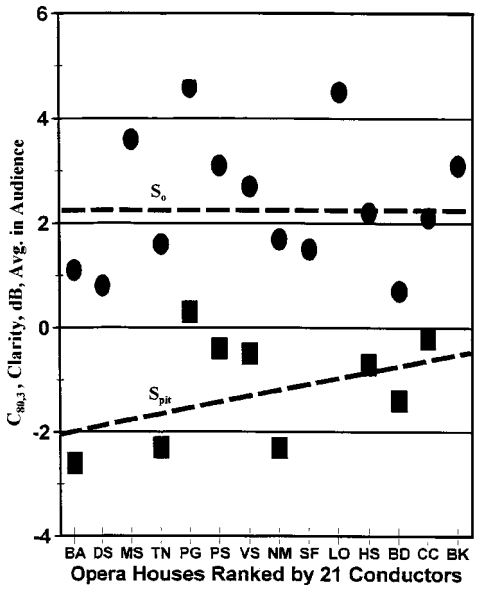

FIG. 10. The clarity factor $C_{80,3}$ plotted against the rank-orderings of the opera houses by the conductors. The upper half is for the source at S_0 and the lower at S_{pit}.

Comment

During the time of the measurements in the Teatro Colón in Buenos Aires BA, a room-tight stage set was in place. Hence, the BA plot lies on the A line. Two halls have relatively small stage houses, Washington WJ and Budapest Erkel BE, so their plots are near line A. The ratios between the stage houses' volumes and the audience chambers were smaller in Chicago CC and Seattle SO than those along line B, so they lie between A and B. At the time of the New York NM measurements, a steel shutter was closed at the rear of the front stage and both sides were largely closed off by reflective stage sets. So its plot lies near Chicago. Obviously, the acoustics behind the proscenium opening is an important factor in determining *G*, and indicates to opera producers the value of fairly complete and heavy (preferably wooden) stage sets.

Figure 9 is the same as Fig. 8, except that the omnidirectional source was in the center of the pit. Lines A and B are shifted from their values in Fig. 8 by about 1.0 dB to the left, i.e., the pit location reduces the energy radiated by the source by that amount, except for the Vienna Staatsoper VS for which G_M *increases* by 1.2 dB. (The probable reason is discussed in Sec. III B above.) The output of the source in the pit (Fig. 9) is affected by the acoustics behind the proscenium opening, also showing a difference between the lines of about 3 dB.

Although a decrease of 1.0 dB in the radiated strength of an orchestra is significant, the total power from a large orchestra is much larger than that from a singer, so that the orchestra generally has to be restrained in important singing passages. Assistance to the strength of the singers' voices can be obtained architecturally by incorporating special sound reflecting surfaces above and to the sides of the proscenium as are found in Tokyo's New National Theater TN (Beranek *et al.*, 2000).

H. Clarity factor $C_{80,3}$

The clarity factor $C_{80,3}$ (average over the 500, 1000, and 2000 Hz bands) is a measure, in dB, of the strength of the early sound to the reverberant sound, and, hence, a greater positive value indicates that the room reverberation does not decrease the intelligibility of the singing voice as much. Shown by the circles in Fig. 10, values of $C_{80,3}$, with the source at S_0 and averaged over the house, are plotted against the ratings of the acoustics in the audience areas by the conductors (highest rating at the left of the bottom axis). These data with the source in the pit are shown by the squares. For the source at S_0 the mean value is $+2.3$ dB and the standard deviation is 1.2. With the source in the pit, the mean value is -1.2 dB and the standard deviation is 1.0. The dashed lines show that for singers, all values of clarity between $+1$ and $+5$ seem acceptable, while for the orchestral music, less clarity, i.e., 0 to -3 dB, is favored. C_{80} is a function of both the architectural and the stage set design. In general, C_{80} has little or no effect on the overall rating of the acoustics by these 21 conductors.

I. Spaciousness $[1-\mathrm{IACC}_{E3}]$

Of the objective parameters that we tested against the subjective judgments of acoustical quality by conductors, the ''spaciousness'' factor $[1-\mathrm{IACC}_{E3}]$, for the source at S_0, had the highest correlation. Its value is increased by stronger early lateral reflections from side walls, balcony fronts, and reflecting panels that arrive at the listeners' ears within 80 ms after the direct sound. This measure is most effective for judging acoustical quality when its value is determined from the average of its values in the three octave bands, 500, 1000, and 2000 Hz (Hidaka *et al.*, 1995; Okano *et al.*, 1998).

The measured values of $[1-\mathrm{IACC}_{E3}]$, for all halls for which both ratings and these measured data exist, are plotted against the conductor's ratings in Fig. 11. From house to

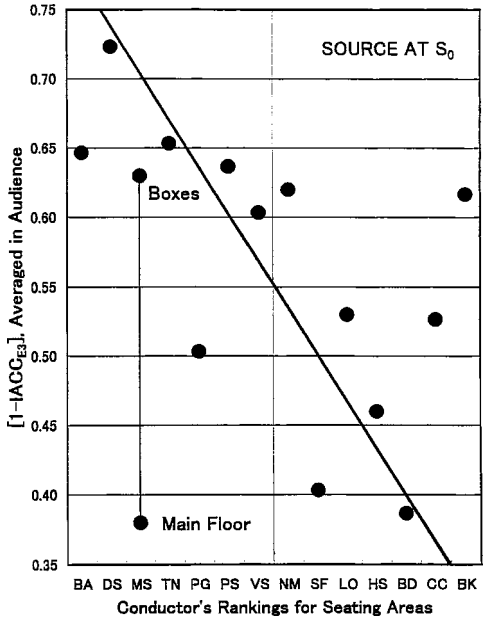

FIG. 11. The spaciousness factor $[1-\mathrm{IACC}_{E3}]$ with the source at S_0 is plotted against the names of the halls rank-ordered according to the conductors' ratings of the acoustical quantities for the audience areas. The higher ratings are toward the left end of the abscissa.

house the variation in spaciousness is the same as for concert halls (Beranek, 1996), i.e., 0.72–0.39 vs 0.71–0.41.

Comment

One sees that there are several discrepancies between measured $[1-\mathrm{IACC}_{E3}]$ and the conductors' ratings, which can mostly be explained by deficiencies in the other important factors. The high measured spaciousness value of 0.62 for the New York Metropolitan NM is accompanied by a lower rating mainly because of its very large size (Table I), which demands that only singers with strong voices be engaged. Milan La Scala MS is a mixed-bag case. In the boxes its values for measured spaciousness average 0.63 (four measurements at two levels) compared to an average of 0.38 on the main floor (six measurements) and its rating is ''one of the best.'' Unquestionably, conductors enjoy MS's pit acoustics, and, in addition, one might speculate that when they listen to an opera they sit in the management's box. One European conductor who rated La Scala one category below the top rating wrote, ''It [the acoustic] was quite disappointing....But ''La Scala'' gives a lot of atmosphere and...this ...distracts the objective acoustic sensitivity. If you feel, that Serafin, De Sabata, Toscanini and others did not complain about the acoustic, why should you....something like this.'' The Paris Garnier House PG is rated higher than its spaciousness measure, probably because of its high intimacy factor (Table VIII) and its great beauty. The measured high spaciousness value for the Berlin Komischeoper BK is counterbalanced by its poor Texture (Fig. 14), which is certainly apparent to trained ears. The excellent sound in the pit of the Prague Staatsoper PS may influence the magnitude of the conductors' subjective rating for the audience areas. Interestingly, when the omnidirectional source is in the pit the spa-

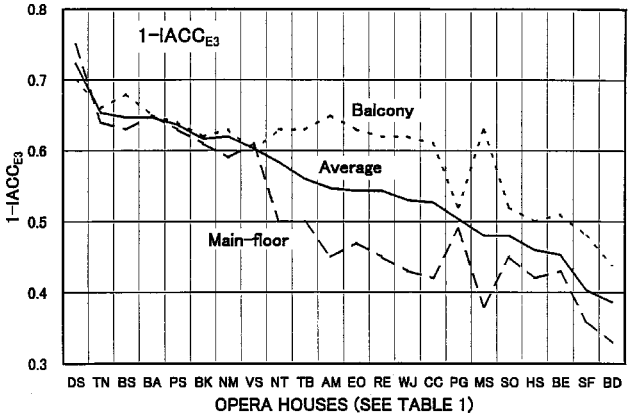

FIG. 12. Plot of $[1-\mathrm{IACC}_{E3}]$ against the names of the halls rank-ordered according to the values of measured spaciousness, which were averaged for the seating areas indicated. The solid line is the average at all receiver positions; the two broken lines are the averages for the balconies and the main floor, respectively. Source at position S_0.

ciousness values (averaged throughout the audience area) are almost equal in all but the lowest rated halls (Table IV)!

Because the correlation between $[1-\mathrm{IACC}_{E3}]$ and the subjective judgments is sufficiently high overall (see Appendix D), it is an important objective parameter to be used *along with the others* in the design and evaluation of opera houses.

Figure 12 illustrates that in over half of the opera houses measured spaciousness is lower on the main floors than in the balconies (boxes). The main reason is that an insufficient number of early lateral reflections are directed to the main floor in many classical horseshoe-shaped opera houses. That is to say, the balcony fascia do not direct early reflections into those areas and the side wall surfaces have a large number of openings. Also, there may be improperly oriented surfaces next to the proscenium or (open) boxes almost at the proscenium, both cases near stage level. We have learned from discussions with local opera-goers that for these types of houses the sound is superior in the upper tiers.

Another reason for believing that $[1-\mathrm{IACC}_{E3}]$ is a good parameter to use in opera house design is that it seems to be less affected by conditions on stage than others. In Table VI, where in one case a highly reflective fire curtain was closed and in two cases the proscenium curtains were open, its values varied over a relatively small range, 0.58 to 0.65, although RT_M varied greatly: 1.49–2.26 s. In only two halls, Tokyo Bunka Kaikan TB and Osaka Festival Hall OF, measurements were made (unoccupied) with and without an orchestra enclosure (Beranek, 1972, Japanese language). In the former, the values were 0.6 with and 0.56 without, and in the latter 0.52 and 0.49, respectively. Thus even in a multi-

TABLE VI. Measurements of $[1-\mathrm{IACC}_{E3}]$ and reverberation time in the Tokyo NNT Opera House TN, under the three different conditions indicated.

Stage condition	Audience area	$1-\mathrm{IACC}_{E3}$	RT_M (s)
Fire curtain closed	Unoccupied	0.61	2.26
Nothing	Unoccupied	0.65	1.79
Reflecting stage set	Occupied	0.58	1.49

TABLE VII. Comparison of $[1-\mathrm{IACC}_{E3}]$ for several source positions in three opera houses. The data for the different source positions are averaged at the same seats in the different houses. The source position S_H is on the center line at the distance behind S_0 given in the parentheses. S_L of Milan is moved 4 m from S_0 to state right, and S_L of Paris is moved 3 m to stage left and 1.5 m behind S_0. Number in parentheses refers to the distance behind S_0.

Source position	BK, Berlin, Komischeoper	MS, Milan, Teatro alla Scala	PG, Paris, Opera Garnier
S_0	0.65	0.48	0.57
S_H	0.49 (5 m)	0.48 (7 m)	-
S_L	-	0.49	0.64

purpose hall, $[1-\mathrm{IACC}_{E3}]$ seems to be a useful parameter for assistance in rating acoustical quality.

One other factor, which needs more investigation, may explain in part why conductors rate Milan MS high and Berlin Komischeoper BK low. Table VII shows that $[1-\mathrm{IACC}_{E3}]$ in MS varies hardly at all for three positions of the sound source on stage, while in BK it is 0.49 and 0.65 for two stage positions. Further discussion is given in Appendix C.

IV. THE REFLECTOGRAMS

A. Introduction

Reflectograms were faithfully taken at every seat position and for every source and stage condition in every hall that was measured by the Takenaka Institute for each of six frequency bands. Do reflectograms aid in evaluating the acoustical quality of opera houses? Three aspects were studied in an attempt to answer this question: (a) initial-time-delay gap; (b) number of significant reflection peaks in the first 80 ms after arrival of the direct sound (in C&OH, p. 485, this is called ''TEXTURE''); and (c) visual rating of the ''quality'' of the reflection stream in the first 200 ms, i.e., the absolute amplitude and the evenness of the reflections both in amplitude and time distribution. The results were: (a) ITDGs are of significance; (b) there are a greater number of reflection peaks in the best houses, but the range is not large enough to be reliable for estimating acoustical quality; and (c) visual ratings of the reflectograms are purely subjective and not reliably quantifiable.

B. Intimacy ITDG

The initial-time-delay gap measured near the center of the main floor (a position or positions near there are usually chosen as the lone number to be used for indicating the ''intimacy'' of a hall for music) is generally determined by the first sound reflection from a side wall or a balcony front after arrival of the direct sound. In practice, this generally means that ITDG is shorter in smaller halls and can be made shorter in larger halls if the walls, balcony fronts, and reflecting panels are shaped to return early reflections to the seats on the main floor. By proper design, which is easier if the house is not horseshoe-shaped, ITDG can be made less than 20 ms. Table VIII lists the ITDGs as determined from the average of the values found at audience positions 101 and 102 on the main floor of 19 opera houses with the source at S_0. All halls rated high in quality have ITDGs in the region of 20 ms or less. This is consistent with the findings for concert halls (C&OH, p. 483). Four of the lowest ranked houses have ITDGs greater than 30 ms.

TABLE VIII. Values of the initial-time-delay gap ITDG determined from the reflectograms. The numbers are the average of the ITDGs at audience positions 101 and 102, near the center of the main floor.

	Opera house	ITDG ms
WJ	Washington, JFK Center, Opera House	15
BS	Budapest, Staatsoper	15
PG	Paris, Opéra Garnier	15
MS	Milan, Teatro alla Scala	16
PS	Prague, Staatsoper	16
VS	Vienna, Staatsoper	17
BE	Budapest, Erkel Theater	17
NM	NY, Metropolitan Opera	18
BA	Buenos Aires, Teatro Colón	18
BK	Berlin, Komischeoper	20
TN	Tokyo, New National Theater	20
DS	Dresden, Semperoper	20
SO	Seattle, Opera House	25
RE	Rochester, Eastman Theater	26
TB	Tokyo, Bunka Kaikan	26
AM	Amsterdam, Music Theater	32
BD	Berlin, Deutscheoper	33
HS	Hamburg, Staatsoper	34
CC	Chicago, Civic Opera House	41

C. Texture

Texture is defined in Beranek (p. 25, 1996): ''Texture is the subjective impression the listeners derive from the patterns in which the sequence of early sound reflections arrive at their ears. In an excellent hall those reflections that arrive soon after the direct sound follow in a more-or-less uniform sequence. In other halls there may be a considerable interval between the first and the following reflections. Good texture requires a large number of early reflections, uniformly but not precisely spaced apart, and with no single reflection dominating the others.''

Counting the number of significant reflection peaks from a reflectogram is not easy. A single reflection will often appear to be divided in two. Using best judgment, a count of the number of reflections in the first 80 ms for 22 houses was made at 2 frequencies and averaged. The most were found for Milan, Buenos Aires, Tokyo TN, Budapest Staatsoper, and Berlin Deutsche. The least were found for Hamburg, Seattle, Prague, and Rochester. But the most was 15 and least was 11, so that use of the reflectograms to rank-order acoustical quality does not seem very helpful.

The visual rankings of the reflectograms of the same 22 houses were made by comparisons like those shown in Figs. 13 and 14. Because the length of these reflectograms is 200 ms, they relate to the definition above plus the beginnings of the reverberant sound field discussed next. The three chosen as best are Tokyo NT, Buenos Aires, and Vienna. The three chosen as of lower quality are Hamburg, Chicago, and Berlin Deutsche. The others are inbetween. This exercise seems

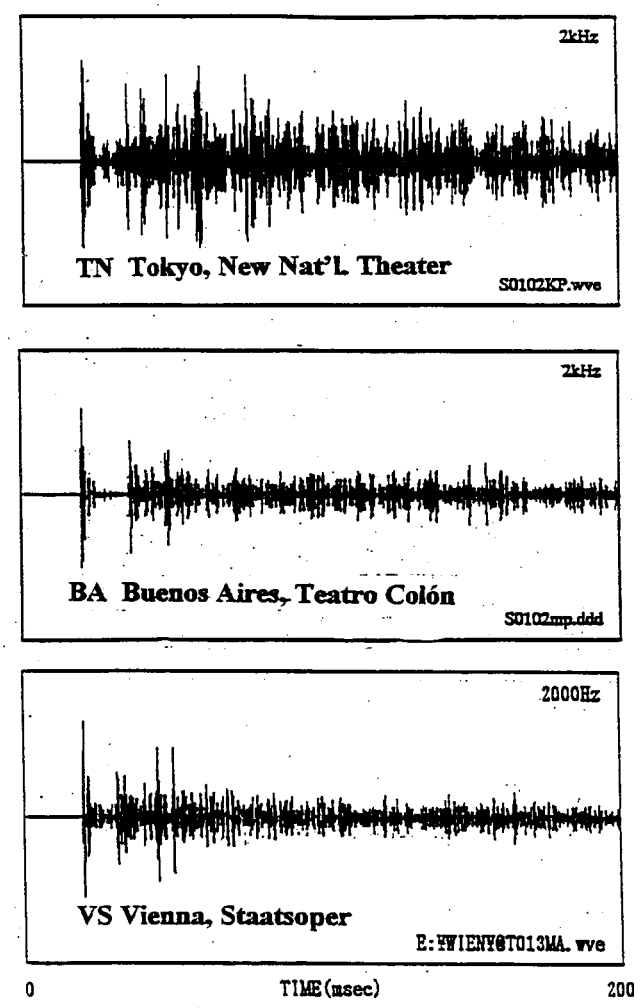

FIG. 13. Reflectograms at receiver position 102 on main floor and source at S_0. These three reflectograms were chosen by visual judgments of ''texture,'' and represent those of the 22 houses that were judged best.

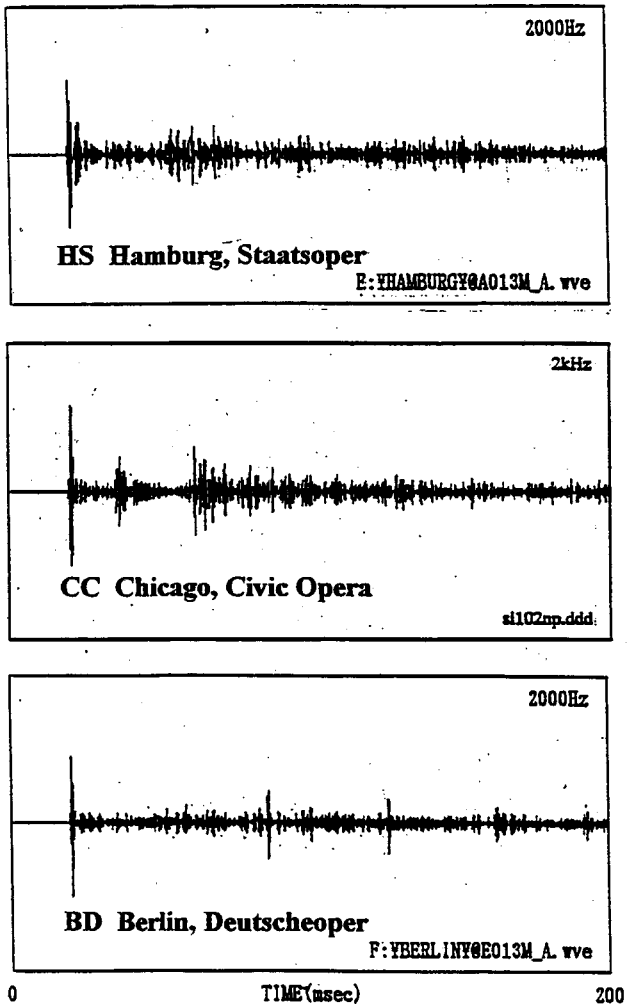

FIG. 14. Same as Fig. 13 except it includes the three halls for which the visual judgments indicated the ''texture'' to be least good among the 22 houses.

helpful in separating the very best from the ones of lesser quality, but it is not a quantitative measure and is of limited help in establishing relative ratings.

D. Diffusion

Every opera house and concert hall with ratings above the level of ''passable'' has architectural means for bringing about diffusion of the reverberant sound field [Haan and Fricke have shown that sound-diffusion in concert halls is a major acoustical parameter (1993)]. A few of the best venues have small-scale irregularities on balcony fronts, lower side walls, and reflecting panels. Such irregular surfaces diffuse the high frequency portions of the early reflected sound waves, thus adding ''patina'' to the overall sound.

Diffusion of the reverberant sound field is usually accomplished by means of coffers, niches, projecting curved, or triangular surfaces and the like on walls and ceiling, particularly in the upper parts of the hall. Unfortunately there is no standardized way to measure the amount or effectiveness of diffusion on the quality of sound and there are no data available on opera houses. But anyone who has ever heard sound in a venue for music with flat smooth walls and ceiling can understand the importance of sound diffusing surfaces. Lacking measurements for evaluating the quality of diffusion in the 23 halls of Table I, we are unable to use it as an objective parameter to add to the five important parameters, reverberance (clarity), spaciousness, initial-time-delay gap, strength, and bass response. It remains, along with texture, of great importance, but with no means for quantifying it except visually.

V. CONCLUSIONS

Five independent (orthogonal) objective acoustical parameters in opera houses were measured and studied: reverberation time at mid-frequencies, RT_M (occupied house); spaciousness $[1-IACC_{E3}]$ (unoccupied); intimacy ITDG (determined from reflectograms); strength of sound throughout the house at mid-frequencies G_M (unoccupied); and bass ratio BR (occupied), which is the ratio of summed reverberation times in the 125/250 Hz bands to those in the 500/1000 Hz bands.

(1) The reverberation times with full occupancy in the four most highly rated houses (aside from Munich and Naples which are highly rated but for which we have no data) (Fig. 3) are 1.6, 1.6, 1.2, 1.5, respectively. Conductors

and music critics have stated that houses with RTs of 1.1–1.3 s are too dry and that 1.4–1.6 s is the optimum range. Although highly correlated with RT and EDT, the (unoccupied) house-averaged clarity factor, $C_{80,3}$, should lie between 1 and 3 dB throughout the audience areas with the source at S_0. Negative values are desired for orchestral music (source at S_{pit}).

(2) The optimum range for (either unoccupied or occupied) hall-averaged spaciousness factor $[1-\text{IACC}_{E3}]$ should exceed 0.6 (Fig. 11). To achieve such values, the side walls and balcony fronts must be shaped to provide an adequate number of early, lateral sound reflections to the main floor, a deficiency of which was found to exist in half of the houses. Sound reflecting surfaces adjacent to the audience side of the proscenium can profitably be added to strengthen the levels of the singers' voices to the main floor and lower balconies. The favorable results accruing from using such surfaces is shown by the TN reflectogram in upper Fig. 13. These surfaces should also be designed to provide uniform sound radiation from singers located over a large area of positions on the stage.

(3) The initial-time-delay gap ITDG measured at locations near the center of the main floor, which is an acceptable measure of intimacy, should be 20 ms or less (Table VIII).

(4) The optimum range for (unoccupied) hall-averaged sound strength G_M with the omnidirectional source on stage at position S_0 is 1–4 dB (Fig. 8). With this same source condition on stage, the use of an acoustically closed stage set (simulating a room with a closed ceiling) results in an increase in G_M of about 3 dB over that measured in a highly absorbent stage house without a set. Although the increase in strength of a soprano's voice will not be this great at high frequencies because of the directionally of her voice, a large part of this increase will be effective for the lower voices. An increase of 2–3 dB is a significant difference.

(5) The bass ratio, determined from the reverberation times in the four octave bands from 125 to 1000 Hz, should, in opera houses, be larger than 1.05 (Table I).

(6) The texture factor, as observed from reflectograms, should be favorable. That is to say, there should be at all seats a substantial number of early reflections, many of them lateral, in the first 80 ms after the direct sound arrives, and they should be uniformly spaced, adequate in level and as nearly uniformly strong as possible. In the best houses, the number of such reflections near the center of the main floor is about 15 (Figs. 13 and 14).

(7) Finally, a hall aspiring to be in the top ranks, must have diffusion and ''patina'' producing surfaces—large irregularities on the walls and ceiling where the reverberant sound is formed, and small irregularities on lower side walls and balcony fronts from where early sound is reflected. Haan and Fricke (1993) have found diffusion in concert halls to be of major importance.

The authors have attempted to incorporate all of these factors into the design of the Opera House in the New National Theater of Japan, located in Tokyo (Beranek *et al.*, 2000). Although only time will reveal the true success of that venue for opera, two years of service without complaints and a high rating to date from conductors and music critics, give us confidence in offering the above conclusions. Above all, this result shows that an opera house which is not in the tradition of a horseshoe-shape, can share the praise given the best of houses of that shape and yields the same measured data.

ACKNOWLEDGMENTS

The authors wish to express their gratitude to N. Nishihara of Takenaka R&D Institute for her assistance in the data analysis. Thanks are due A. Kotschy of Budapest, Dr. D. Stanzial of Ferrara, and Dr. J. Novak of Prague for their efforts in arranging for the measurements in part of the halls and in helping invite conductors to respond to questionnaires, and to Dr. John A. Swets for helpful suggestions. We are especially grateful to the 22 opera conductors who responded to the questionnaire. We wish also to acknowledge that during our measurements the staffs of all the houses were very cooperative.

APPENDIX A: CORRELATION MATRIX AMONG OBJECTIVE PARAMETERS IN OCTAVE BANDS

Listed in Table AI are correlation coefficients among objective parameters calculated from the results of measure-

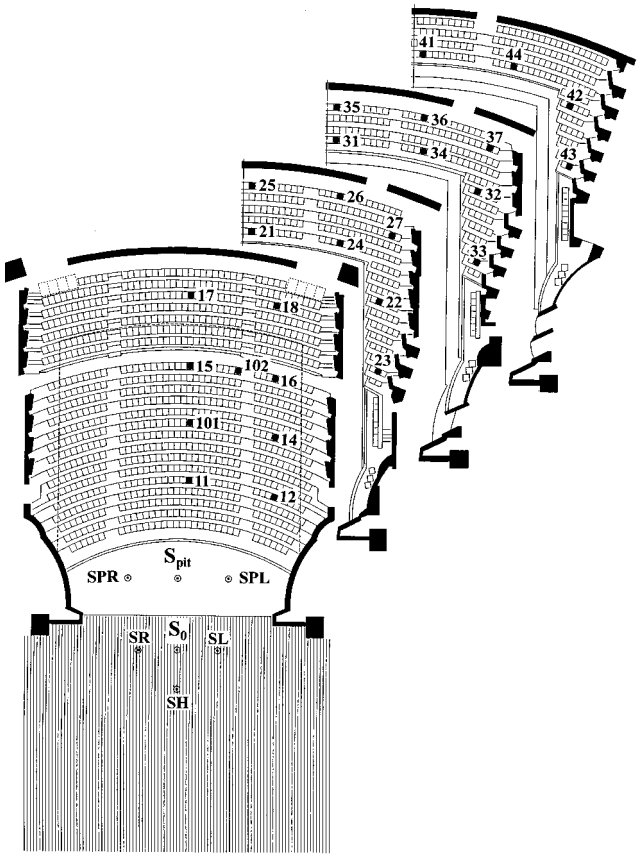

FIG. A1. Source positions and receiver locations in the New National Theatre Opera House, Tokyo. These positions and locations were used typically in all of the opera houses studied, although the time available for the measurements may have reduced the number of audience locations to as few as 10 to 15. Positions S_0 and S_{pit} represent the source positions most often quoted in this paper and Position 102 represents the main-floor position most quoted because it is off center and is usually a choice seat.

TABLE AI. Correlation coefficients among objective acoustical factors calculated from the results of measurements in 23 opera houses listed in Table I in each of the six octave bands with mid-frequencies from 125 to 4000 Hz.

		RT	EDT	C_{80}	G
125 Hz	RT	-			
	EDT	0.93	-		
	C_{80}	−0.68	−0.83	-	
	G	−0.05	−0.01	−0.02	-
250 Hz	RT	-			
	EDT	0.95	-		
	C_{80}	−0.85	−0.84	-	
	G	0.22	0.20	−0.43	-
500 Hz	RT	-			
	EDT	0.96	-		
	C_{80}	−0.79	−0.83	-	
	G	−0.04	−0.02	−0.03	-
	$IACC_E$	0.12	0.20	−0.18	−0.26
1000 Hz	RT	-			
	EDT	0.98	-		
	C_{80}	−0.86	−0.87	-	
	G	−0.13	−0.16	0.11	-
	$IACC_E$	−0.08	0.03	0.12	−0.47
2000 Hz	RT	-			
	EDT	0.94	-		
	C_{80}	−0.87	−0.90	-	
	G	0.07	−0.05	0.06	-
	$IACC_E$	−0.12	0.05	0.20	−0.28
4000 Hz	RT	-			
	EDT	0.91	-		
	C_{80}	−0.80	−0.86	-	
	G	−0.14	−0.25	0.16	-
	$IACC_E$	−0.14	0.08	0.10	−0.19

ment in 23 opera houses listed in Table I. The values are determined for each of the six octave bands with mid-frequencies from 125 to 4000 Hz. Typical measurement positions are shown in Fig. A1.

APPENDIX B: MEASUREMENT METHOD OF IMPULSE RESPONSE BY STRETCHED PULSE

The stretched impulse is a modification from the delta function, whose phase term in each frequency is shifted in the frequency domain from the original function (Aoshima, 1981; Hidaka *et al.*, 1998). Since this impulsive signal has a stretched waveform on the time axis as shown in Fig. B1(A), the sound power for each frequency of this signal can be much larger than that of the original delta function, provided the sound generating system has sufficient power. Accordingly, the impulse response measurement of the room under noisy circumstances can be achieved with superior S/N ratio, when the stretched impulse is utilized instead of the delta function. In this case, the impulse response is numerically obtained later by inverse filtering of the phase shift filter above mentioned. Figure B1(B) shows the ideal impulse with limited frequency range up to 20 000 Hz that is obtained by the convolution of the inverse filter.

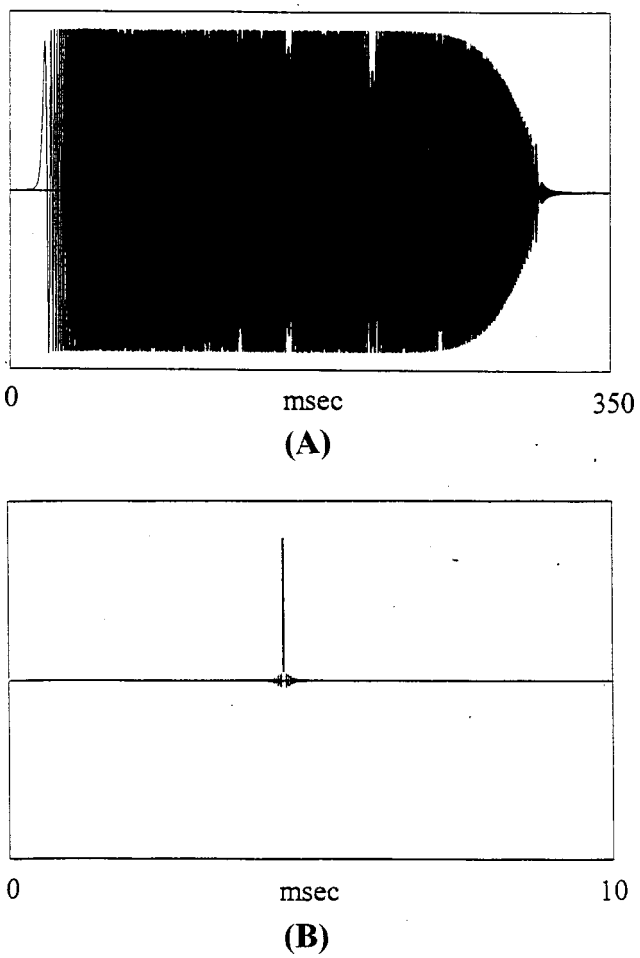

FIG. B1. Waveform of (A) the stretched impulse signal, and (B) the exact impulse wave compressed by the phase shift filter.

APPENDIX C: DISTRIBUTION OF LATERAL REFLECTIONS IN A HORSESHOE HALL

As a supplemental study to the result discussed in Section IV.B the distribution of the first-order reflections from the side walls to the main floor was determined by ray tracing for the cases of the on-stage source position at S_0 and at a position on the centerline backward for the houses BK, PG, and MS. Table CI shows the ratio of the audience area at which first-order lateral reflection arrives versus the whole audience area of the main floor. In the Berlin Komischeoper, the ratio of the covered area to the total floor audience area

TABLE CI. The ratio of audience area covered by reflections from the side walls versus the whole audience area of the main floor, calculated for the three opera houses: Berlin Komischeoper BK, Paris Garnier PG, and Milan La Scala MS. The source position S_0 is on the centerline, 3 m from the edge of the stage. The lower two rows show the source at 8 and 10 m, respectively, from the stage edge.

	BK	PG	MS
S_0	81	98	100
S_0+5 m	61	97	97
S_0+7 m	50	90	86

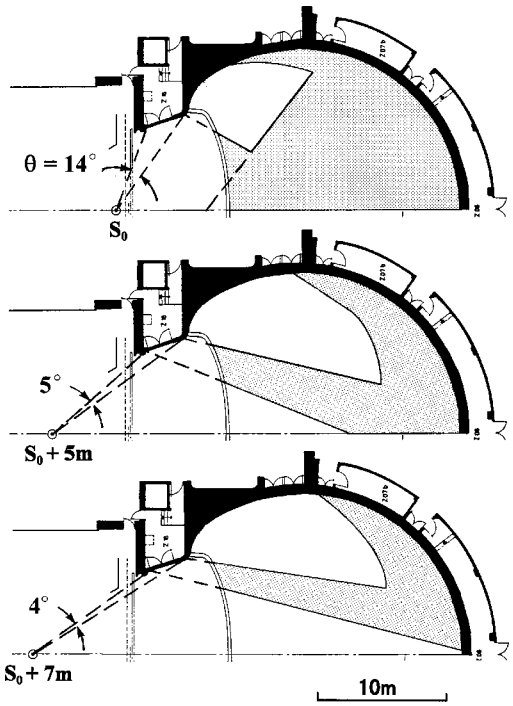

FIG. C1. Area covered by lateral reflections from lower side walls on main floor in Berlin Komischeoper for three source positions: S_0 (upper) and S_0 plus five and seven meters backward (middle and lower). At S_0, a larger portion of a singer's voice energy ($\theta = 14°$) reaches the main floor audience than reaches there when the singer moves up-stage 5 or 7 m ($\theta = 5°$ or 4°). Also, the area covered by the reflected sound decreases.

by the lateral reflections is fairly low. But for the Paris, Garnier and the Milan, La Scala the ratio is high, even though the source is moved backward by up to 7 m, which is approximately the maximum acting zone. Most of the first-order reflections come from the side walls around the proscenium opening and at the level of the main audience area.

Figure C1 shows the covered area for the Berlin Komischeoper BK, where not only the lateral reflections do not cover enough of the center audience area, which is most important, but also the covered area shifts when the sound source moves. This result comes from the circular shape of BK, the only one with this shape among the researched 23 halls. The comparison indicates that the sound changes greatly when the sound source is moved. In opera houses, acoustical uniformity over a great range of a singer's position is vital. Accordingly, the lower subjective judgements for BK might be caused by this effect, although the acoustical coverage for the S_0 position is not unfavorable. Practically, there can exist strong (first-order) reflections from the part of the ceiling near the proscenium opening and, often, from the stage set in addition to the lateral reflections discussed here. However, reflections like those shown in Fig. C1 are very important since they arrive first at the receiving point on the main floor.

APPENDIX D: MULTIPLE REGRESSION ANALYSIS BETWEEN SUBJECTIVE JUDGEMENT AND OBJECTIVE PARAMETERS

By executing a multiple regression analysis between the subjective judgments of acoustical quality in the audience area (Fig. 3) and the seemingly two most important measurable room acoustics parameters in Table I, the best regression equation, which minimizes Akaike's Information Criterion, defined as -2 (maximum log-likelihood of statistical model) $+2$ (number of parameters in the model) was determined (Akaike, 1973). The model that produced the least AIC is,

$$\mathrm{SR} = 1.2[1 - \mathrm{IACC}_{E3}] - 0.039\mathrm{ITDG} + 3.67. \qquad \text{(A1)}$$

SR means the subjective rating from 1 to 5 as in Fig. 2. The relations between the conductors' SRs (measured) and those calculated from Eq. (A1) are shown in Fig. D1. The multiple coefficients of correlation of Eq. (A1) is 0.69, which judges this prediction as ''rather good,'' and the partial regression coefficients of $[1 - \mathrm{IACC}_{E3}]$ and ITDG are 0.49 and -0.67, respectively. Hence, using only 2 of the 7 identified acoustical parameters for this calculation, 12 opera houses out of the 14 fall between ± 0.5 of the measured values, and the remaining 2 are within ± 1. (Note that the conductors' ratings of the acoustics in the audience areas show that values of ITDG between 15 and 20 ms are equally good as are values of $[1 - \mathrm{IACC}_{E3}]$ greater than 0.6.) But, even this two-parameter result can be considered acceptable for practical purposes because we must also consider that the judgements by the opera conductors based on criteria like ''Poor'' to ''One of the Best'' are heuristic. When BK is excluded from the data base, because it appears to be heavily influenced by other factors, as discussed in Appendix C, R increases to 0.83. We could expect to obtain a more reliable equation if the other five parameters could be taken into account. This exercise demonstrates, however, that $[1 - \mathrm{IACC}_{E3}]$ and ITDG are important objective parameters for approximating the acoustical quality of opera houses, provided the RT_M is 1.3 s or greater, the house is not overly large (or reflective sets are used so that G_M is reasonable), there are adequate sound diffusing surfaces in the house and the bass ratio BR is above 1.0. This also assumes that there are no negative effects, such as noise, echoes or focusing.

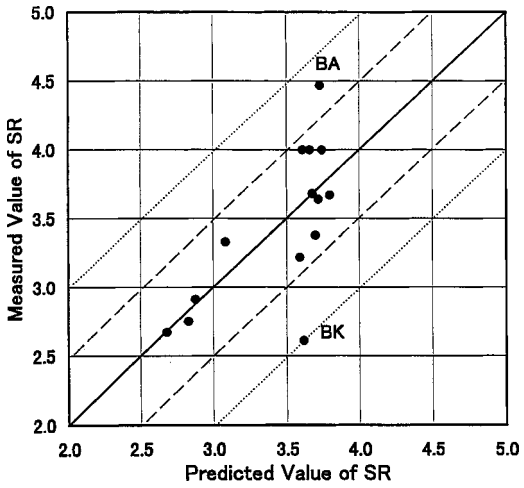

FIG. D1. Plot of the predicted subjective ratings (SR) of the acoustics in the audience areas of 14 opera houses. The solid line means that the predicted values equal the measured values. The broken lines and dotted lines mean ± 0.5 and ± 1 relative to the solid line.

Akaike, H. (**1973**). *Information Theory and an Extension of the Maximum Likelihood Principle* (Akademiai Kiado, Budapest).
Aoshima, N. (**1981**). ''Computer-generated pulse signal applied for sound measurement,'' J. Acoust. Soc. Am. **69**, 1484–1488.
Barron, M. (**1993**). *Auditorium Acoustics and Architectural Design* (E and FN Spon and Chapman & Hall, London).
Beauvert, T. (**1996**). *Opera Houses of the World* (The Vendomes Press, New York).
Beranek, L. L. (**1962**). *Music, Acoustics, and Architecture* (Wiley, New York; in Japanese, Kajima Institute, Tokyo, 1972).
Beranek, L. L. (**1972**). [Same as Beranek (1962), except translated with additions into Japanese] Kajima Institute, Tokyo.
Beranek, L. L. (**1992**). ''Concert hall acoustics—1992,'' J. Acoust. Soc. Am. **92**, 1–39.
Beranek, Leo (**1996**). *Concert and Opera Halls: How They Sound* (Acoustical Society of America, Woodbury, NY).
Beranek, L. L., and Hidaka, T. (**1998**). ''Sound absorption in concert halls by seats, occupied and unoccupied, and by the hall's interior surfaces,'' J. Acoust. Soc. Am. **104**, 3169–3177.
Beranek, L. L., Hidaka, T., and Masuda, S. (**2000**). ''Acoustical design of the Opera House of the New National Theatre, Tokyo, Japan,'' J. Acoust. Soc. Am. **107**, 355–367.
Cremer, L., Mueller, H., and Schultz T. J. (**1982**). *Principles and Applications of Room Acoustics, Vol. 1* (Applied Science Publishers, Essex, England and Elsevier, New York). [Originally published in German without later additions: Cremer L., and Mueller, H., *Die Wissenschaftlichen Grundlagen der Raumakustik*, Vol. 1, Hirzel Verlag (1978)].
Haan, C. H., and Fricke, F. R. (**1993**). ''Surface diffusivity as a measure of the acoustic quality of concert halls,'' Proceedings of the Conference of the Australian and New Zealand Architectural Science Association, Sidney, pp. 81–90.
Hidaka, T., Beranek, L. L., and Okano, T. (**1995**). ''Interaural cross-correlation, lateral fraction, and low- and high-frequency sound levels as measures of acoustical quality in concert halls,'' J. Acoust. Soc. Am. **98**, 988–1007.
Hidaka, T., Beranek, L. L., Masuda, S., Nishihara, N., and Okano, T. (**2000**). ''Acoustical design of the Tokyo Opera City (TOC) Concert Hall, Japan,'' J. Acoust. Soc. Am. **107**, 340–354.
Hidaka, T., Beranek, L., and Nishihara, N. (**1998**). ''Relation of acoustical parameters with and without audiences in concert halls and a simple method for simulating the occupied state,'' J. Acoust. Soc. Am. **103**, 2955(A).
ISO 3382 (**1997**). ''Acoustics—Measurement of the reverberation time of rooms with reference to other acoustical parameters.''
Moatti, J., Kleinefern, F., Vermeil, J., and Laulhére-Vigneau, C. (**1989**). *Operas d'Europe* (Plume, Paris).
Okano, T., Beranek, L. L., and Hidaka, T. (**1998**). ''Relations among interaural cross-correlation coefficient ($IACC_E$), lateral fraction (LE_E), and apparent source width (ASW) in concert halls,'' J. Acoust. Soc. Am. **104**, 255–265.
Schmidt, W. (**1985**). ''Die Raumakustik in Zuschauerraum, Die neue Semperoper in Dresden,'' Institute für Kulturbauten, Berlin, **2**, 20–24.
Veneklasen, P., and Christoff, J. P. (**1964**). ''Seattle Opera House—Acoustical design,'' J. Acoust. Soc. Am. **36**, 903–910.

Adaptive eigenvalue decomposition algorithm for passive acoustic source localization

Jacob Benesty
Bell Laboratories, Lucent Technologies, 700 Mountain Avenue, Murray Hill, New Jersey 07974-0636

(Received 6 May 1998; accepted for publication 29 September 1999)

To find the position of an acoustic source in a room, the relative delay between two (or more) microphone signals for the direct sound must be determined. The generalized cross-correlation method is the most popular technique to do so and is well explained in a landmark paper by Knapp and Carter. In this paper, a new approach is proposed that is based on eigenvalue decomposition. Indeed, the eigenvector corresponding to the minimum eigenvalue of the covariance matrix of the microphone signals contains the impulse responses between the source and the microphone signals (and therefore all the information we need for time delay estimation). In experiments, the proposed algorithm performs well and is very accurate. © *2000 Acoustical Society of America.* [S0001-4966(00)03801-7]

PACS numbers: 43.60.Bf, 43.60.Gk, 43.60.Lq [JCB]

INTRODUCTION

Time delay estimation (TDE) between two (or more) microphone signals can be used as a means for the passive localization of the dominant talker in applications such as camera pointing for teleconferencing and microphone array beam steering for suppressing reverberation in all types of communication and voice processing systems. This problem is difficult because of the nonstationarity of speech and of room acoustic reverberation. Isotropic noise in the room can also be a problem if the signal-to-noise ratio becomes smaller than 20 dB, but that rarely occurs in teleconferencing rooms.

Generalized cross-correlation (GCC)[1] is the most commonly used method for TDE. In this technique, the delay estimate is obtained as the time-lag that maximizes the cross-correlation between filtered versions of the received signals. Several authors[2–4] have proposed techniques to improve the GCC in the presence of noise. However, it is believed that the main problem in practical TDE is reverberation as is clearly shown in Refs. 5 and 6. Accordingly, the same authors proposed an interesting method that is based on cepstral prefiltering. The basic idea is to first estimate the reverberation in the cepstral domain, subtract it from the microphone signals, and then use the GCC to determine the delay.[7,8]

Another interesting idea was proposed in Ref. 9 and was tested in a real time implementation in Ref. 10. The principle of this approach is to identify the onset of pitch periods and to cross-correlate these within a certain acceptance window. The problem of this algorithm is that it might take a very long time before it gives an accurate estimation of the time delay.

Most of the existing methods are based on an ideal signal model (single propagation path from the source to the sensors). In this paper, a new approach is proposed based on a real signal model (with reverberation) using eigenvalue decomposition. Indeed, the eigenvector corresponding to the minimum eigenvalue of the covariance matrix of the microphone signals contains the impulse responses between the source and the microphone signals (and therefore all the information we need for time delay estimation).

All of the above methods can be improved by using several pairs of microphones, e.g., by hyperbolic curve fitting of multiple delay estimates[11] or by linear 3-D intersection of multiple bearing lines.[12–14]

Section I discusses two models used for the TDE problem. In Sec. II, the GCC method is described and it is demonstrated how this method can fail. In Sec. III, the new proposed approach is developed which can also be seen as a generalization of the algorithm proposed in Ref. 15 where a single multipath is assumed. Section IV gives some experimental results and comparison of different algorithms.

I. MODELS FOR THE TDE PROBLEM

In this section, two models that are often used for the TDE problem are discussed. First, the ''ideal model'' is described and then the ''real model'' that more accurately describes a real acoustic environment.

A. Ideal model

A simple and widely used signal model for the classical TDE problem is the following. Let $x_i(n)$, $i=1,2$, denote the i-th microphone signal, then:

$$x_i(n)=\alpha_i s(n-\tau_i)+b_i(n), \tag{1}$$

where α_i is an attenuation factor due to propagation effects, τ_i is the propagation time from the unknown source $s(n)$ to microphone i, and $b_i(n)$ is an additive noise signal at the ith microphone. It is further assumed that $s(n)$, $b_1(n)$, and $b_2(n)$ are zero-mean, uncorrelated, stationary Gaussian random processes. The relative delay between the two microphone signals 1 and 2 is defined as

$$\tau_{12}=\tau_1-\tau_2. \tag{2}$$

This model is ideal in the sense that the solution for determining τ_{12} is clear. Indeed, let's first write Eq. (1) in the frequency domain

$$X_i(f)=\alpha_i S(f)e^{-j2\pi f\tau_i}+B_i(f), \tag{3}$$

and then take the (complex) sign of the cross-spectrum $S_{x_1x_2}(f)$ between $X_1(f)$ and $X_2(f)$,

$$\mathrm{sgn}[S_{x_1x_2}(f)]=\mathrm{sgn}[E\{X_1(f)X_2^{\star}(f)\}]=e^{-j2\pi f\tau_{12}}, \tag{4}$$

where $\mathrm{sgn}(z)=z/|z|$, $E\{\cdot\}$ denotes mathematical expectation, and * denotes complex conjugate. We can easily see that the inverse Fourier transform of Eq. (4) will result in a sharp peak in the time domain corresponding to the delay τ_{12}.

B. Real model

Unfortunately, in a real acoustic environment we must take into account the reverberation of the room and the ideal model no longer holds. Then, a more complicated but more complete model for the microphone signals $x_i(n), i=1,2$, can be expressed as follows:

$$x_i(n)=g_i*s(n)+b_i(n), \tag{5}$$

where $*$ denotes convolution and g_i is the acoustic impulse response between the source $s(n)$ and the ith microphone. Moreover, $b_1(n)$ and $b_2(n)$ might be correlated which is the case when the noise is directional, e.g., from a ceiling fan or an overhead projector.

In this case, we do not have an ''ideal'' solution to the problem, as is the case for the previous model, unless we can very accurately determine the two impulse responses between the source and the two microphones, which is a very challenging problem.

II. THE GCC METHOD

This method is based on the ideal model but is the most commonly used even in very reverberant environments.[14,16–18]

In the GCC technique,[1] the time-delay estimate is obtained as the value of τ that maximizes the generalized cross-correlation function given by

$$\psi_{x_1x_2}(\tau)=\int_{-\infty}^{+\infty}\Phi(f)S_{x_1x_2}(f)e^{j2\pi f\tau}df$$

$$=\int_{-\infty}^{+\infty}\Psi_{x_1x_2}(f)e^{j2\pi f\tau}df, \tag{6}$$

where $\Phi(f)$ is a weighting function and

$$\Psi_{x_1x_2}(f)=\Phi(f)S_{x_1x_2}(f) \tag{7}$$

is the generalized cross-spectrum. Then, the GCC TDE may be expressed as:

$$\hat{\tau}_{\phi}=\arg\max_{\tau}\psi_{x_1x_2}(\tau). \tag{8}$$

The choice of $\Phi(f)$ is important in practice. For example, the maximum likelihood (ML) weighting function, which is roughly equivalent to a frequency-dependent SNR, seems to be optimal for a high level of uncorrelated noise. However in practice, this algorithm performs best (within this class of algorithms) only for low SNR ($\leqslant$10 dB), as is shown in Ref. 2. Given that our problem is reverberation, the ML estimator will not help with reasonable SNR ($\geqslant$20 dB) and can even perform poorly.[2]

If we take $\Phi(f)=1$, we obtain the classical cross-correlation (CC) method. In the noiseless case, knowing that $X_i(f)=S(f)G_i(f)$, $i=1,2$, we have

$$\Psi_{x_1x_2}(f)=\Psi_{cc}(f)=G_1(f)E\{|S(f)|^2\}G_2^{\star}(f). \tag{9}$$

The classical phase transform (PHAT) technique is obtained by taking $\Phi(f)=1/|S_{x_1x_2}(f)|$. In the noiseless case, we show easily that

$$\Psi_{x_1x_2}(f)=\Psi_{pt}(f)=G_1(f)G_2^{\star}(f)/|G_1(f)G_2^{\star}(f)| \tag{10}$$

does depend only on the impulse responses and can perform well in a moderately reverberant room.

Another interesting weighting function is $\Phi(f)=1/\sqrt{S_{x_1x_1}(f)S_{x_2x_2}(f)}$. In this case, the corresponding normalized cross-spectrum $\Psi_{cf}(f)$ is simply the complex coherence function. We note that in the noiseless case, $\Psi_{cf}(f)=\Psi_{pt}(f)$, which is not true, in general, in the presence of noise.

The GCC methods can give good results when the reverberation of the room is not very high, but when the reverberation becomes important all of these techniques will fail because they are based on a simple signal model that does not represent reality.

III. THE PROPOSED METHOD

In this section a completely different approach than GCC is proposed. This new method focuses directly on the impulse responses between the source and the microphones in order to estimate the time-delay. First, the principle of this approach is explained and then an algorithm is presented.

A. Principle

We assume that the system (room) is linear and time invariant; therefore, we have the following relation:[19]

$$\mathbf{x}_1^T(n)\mathbf{g}_2=\mathbf{x}_2^T(n)\mathbf{g}_1, \tag{11}$$

where

$$\mathbf{x}_i(n)=[x_i(n)\quad x_i(n-1)\quad\cdots\quad x_i(n-M+1)]^T,\quad i=1,2$$

are vectors of signal samples at the microphone outputs, ''T'' denotes the transpose of a vector or a matrix, and the impulse response vectors of length M are defined as

$$\mathbf{g}_i=[g_{i,0}\quad g_{i,1}\quad\cdots\quad g_{i,M-1}]^T,\quad i=1,2.$$

This linear relation follows from the fact that $x_i=s*g_i$, $i=1,2$, thus $x_1*g_2=s*g_1*g_2=x_2*g_1$.

The covariance matrix of the two microphone signals is:

$$\mathbf{R}=\begin{bmatrix}\mathbf{R}_{x_1x_1} & \mathbf{R}_{x_1x_2}\\ \mathbf{R}_{x_2x_1} & \mathbf{R}_{x_2x_2}\end{bmatrix}, \tag{12}$$

where

$$\mathbf{R}_{x_ix_j}=E\{\mathbf{x}_i(n)\mathbf{x}_j^T(n)\},\quad i,j=1,2. \tag{13}$$

Consider the $2M\times 1$ vector

$$\mathbf{u}=\begin{bmatrix}\mathbf{g}_2\\ -\mathbf{g}_1\end{bmatrix}.$$

From Eqs. (11) and (12), it can be seen that $\mathbf{Ru}=\mathbf{0}$, which means that the vector $\mathbf{u}$ (containing the two impulse responses) is the eigenvector of the covariance matrix $\mathbf{R}$ corresponding to the eigenvalue 0. Moreover, if the two impulse responses $\mathbf{g}_1$ and $\mathbf{g}_2$ have no common zeros and the autocorrelation matrix of the source signal $s(n)$ is full rank, which is assumed in the rest of this paper, the covariance matrix $\mathbf{R}$ has one and only one eigenvalue equal to 0.[20]

In practice, accurate estimation of the vector $\mathbf{u}$ is not trivial, because of the nature of speech, the length of the impulse responses, the background noise, etc. However, for this application we only need to find an efficient way to detect the direct paths of the two impulse responses. In the following, it is explained how this can be done.

B. Adaptive algorithm

In practice, it is simple to estimate iteratively the eigenvector (here $\mathbf{u}$) corresponding to the minimum (or maximum) eigenvalue of $\mathbf{R}$, by using an algorithm similar to the Frost algorithm which is a simple constrained Least-Mean-Square (LMS),[21] or by using the algorithms proposed in Ref. 22. In the following, we show how to apply these techniques to our problem. Minimizing the quantity $\mathbf{u}^T\mathbf{Ru}$ with respect to $\mathbf{u}$ and subject to $\|\mathbf{u}\|^2=\mathbf{u}^T\mathbf{u}=1$ will give us the optimum filter weights $\mathbf{u}_{\text{opt}}$.

Let us define the error signal:

$$e(n)=\frac{\mathbf{u}^T(n)\mathbf{x}(n)}{\|\mathbf{u}(n)\|}, \tag{14}$$

where $\mathbf{x}(n)=[\mathbf{x}_1^T(n)\quad \mathbf{x}_2^T(n)]^T$. Note that minimizing the mean square value of $e(n)$ is equivalent to solving the above eigenvalue problem. Taking the gradient of $e(n)$ with respect to $\mathbf{u}(n)$ gives

$$\nabla e(n)=\frac{1}{\|\mathbf{u}(n)\|}\left[\mathbf{x}(n)-e(n)\frac{\mathbf{u}(n)}{\|\mathbf{u}(n)\|}\right], \tag{15}$$

and we obtain the gradient-descent constrained LMS algorithm:

$$\mathbf{u}(n+1)=\mathbf{u}(n)-\mu e(n)\nabla e(n), \tag{16}$$

where μ, the adaptation step, is a positive constant.

Substituting Eqs. (14) and (15) into Eq. (16) gives

$$\mathbf{u}(n+1)=\mathbf{u}(n)-\frac{\mu}{\|\mathbf{u}(n)\|}\left[\mathbf{x}(n)\mathbf{x}^T(n)\frac{\mathbf{u}(n)}{\|\mathbf{u}(n)\|}-e^2(n)\frac{\mathbf{u}(n)}{\|\mathbf{u}(n)\|}\right] \tag{17}$$

and taking mathematical expectation after convergence, we get

$$\mathbf{R}\frac{\mathbf{u}(\infty)}{\|\mathbf{u}(\infty)\|}=E\{e^2(n)\}\frac{\mathbf{u}(\infty)}{\|\mathbf{u}(\infty)\|}, \tag{18}$$

which is what is desired: the eigenvector $\mathbf{u}(\infty)$ corresponding to the smallest eigenvalue $E\{e^2(n)\}$ of the covariance matrix $\mathbf{R}$.

In practice, it is advantageous to use the following adaptation scheme to avoid roundoff error propagation:[23]

$$\mathbf{u}(n+1)=\frac{\mathbf{u}(n)-\mu e(n)\nabla e(n)}{\|\mathbf{u}(n)-\mu e(n)\nabla e(n)\|}. \tag{19}$$

Note that if this trick is used, then $\|\mathbf{u}(n)\|$ [which appears in $e(n)$ and $\nabla e(n)$] can be removed, since we will always have $\|\mathbf{u}(n)\|=1$.

C. A simplified algorithm

The algorithm Eq. (19) presented above is a little bit complicated and is very general to find the eigenvector corresponding to the smallest eigenvalue of any matrix $\mathbf{R}$. If the smallest eigenvalue is equal to zero, which is the case here, the algorithm can be simplified as follows:

$$e(n)=\mathbf{u}^T(n)\mathbf{x}(n) \tag{20}$$

and

$$\mathbf{u}(n+1)=\frac{\mathbf{u}(n)-\mu e(n)\mathbf{x}(n)}{\|\mathbf{u}(n)-\mu e(n)\mathbf{x}(n)\|}. \tag{21}$$

Note that this algorithm can be seen as an approximation of the previous one by neglecting the terms in $e^2(n)$ [in Eq. (19)], which is reasonable (since the smallest eigenvalue is equal to zero). In this application, the two algorithms Eqs. (19) and (21) should have the same performance after convergence even with low SNRs. Moreover, in all experiments the unconstrained frequency-domain adaptive filter (UFLMS)[24] is used to implement the impulse response estimation algorithm. Note that this algorithm is still efficient from a complexity point of view but it requires seven FFT operations per block (because we need to go back to the time-domain to apply the norm constraint), while the PHAT requires only three FFT operations per block.

D. Discussion

The goal here is not to accurately estimate the two impulse responses g_1 and g_2 but rather the time-delay. For that, we need to detect the two direct paths. Thus initialization of the proposed algorithm is a key issue. During adaptation, the first half of vector $\mathbf{u}$ will contain an estimate of the impulse response g_2; initializing by 1 (at time $n=0$) a tap of $\mathbf{u}$ somewhere in the middle of the first half part (in order to take into account negative and positive relative delays), say $u_{M/2}(0)=1$, and adjusting the parameters of the adaptive algorithm (which is easy to do) in such a way that this (positive) peak will always be dominant (during adaptation) in comparison with the $M-1$ other taps of the first half of $\mathbf{u}$, $u_{M/2}(n)$ will be considered an estimate of the direct path of g_2. A ''mirror'' effect will appear in the second half of $\mathbf{u}$ (containing an estimation of the impulse response $-g_1$): a negative peak will dominate and that will be an estimation of the direct path of $-g_1$. Thus the relative delay will simply be the difference between the indices corresponding to these two

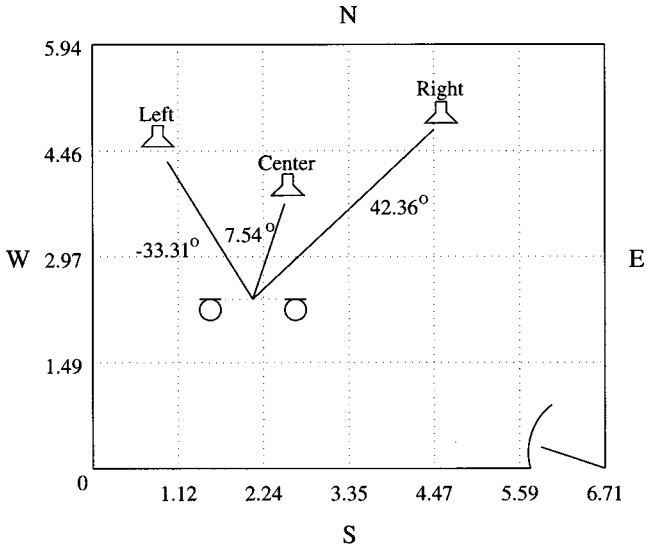

FIG. 1. Varechoic chamber floor plan (coordinate values measured in meters) with the position of the two microphones and the sources.

peaks. If reality corresponds to the ideal model, it is clear that the vector **u** will converge to the two peaks and the other taps will be close to zero.

The proposed algorithm can be seen as a generalization of the LMS TDE proposed in Refs. 25 and 26, where the minimization criterion of the direct paths as well as echoes are accounted for, whereas the LMS TDE considers only the two direct paths. Mathematically speaking, the LMS TDE is based on a criterion using the following error signal:

$$e(n)=x_1(n-D)-\mathbf{w}_2^T(n)\mathbf{x}_2(n), \tag{22}$$

whereas the proposed method is based on a criterion using the error signal

$$e(n)=\mathbf{w}_1^T(n)\mathbf{x}_1(n)-\mathbf{w}_2^T(n)\mathbf{x}_2(n). \tag{23}$$

The two algorithms will have exactly the same performance in an environment that corresponds to the ideal model. In practice, the LMS TDE performs like the CC method.

IV. EXPERIMENTAL RESULTS

Now, the performance of the proposed method is compared to PHAT, CC, and the Fischell–Coker (FC) algorithm. All the measurements were made in the Varechoic chamber at Bell Labs, which is a room with computer-controlled absorbing panels which vary the acoustic absorption of the walls, floor, and ceiling.[27] Each panel consists of two perforated sheets whose holes, if aligned, expose sound absorbing material behind, but if shifted to misalign, form a highly reflective surface. The panels are individually controlled so that the holes are either fully open (absorbing state) or fully closed (reflective state). Three different panel configurations were selected: panels all open, half of the panels open (ran-

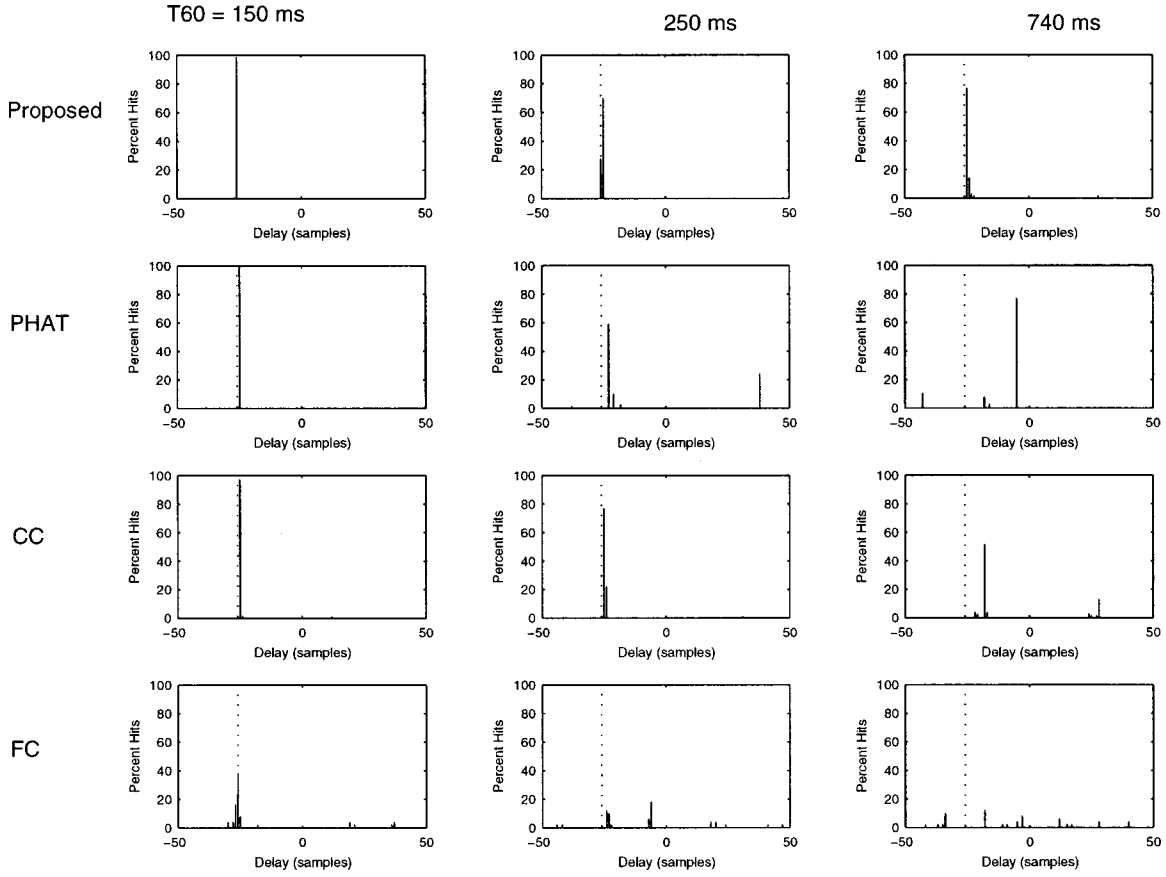

FIG. 2. Histograms of TDE with a pair of cardioid microphones. The source is a speech signal and its position is on the right in Fig. 1. The first, second, and third columns correspond, respectively, to a reverberation time of 150 ms, 250 ms, and 740 ms. The first, second, third, and fourth lines correspond, respectively, to the TDE by the proposed algorithm, PHAT, CC, and FC. The true delay is plotted with a dotted line.

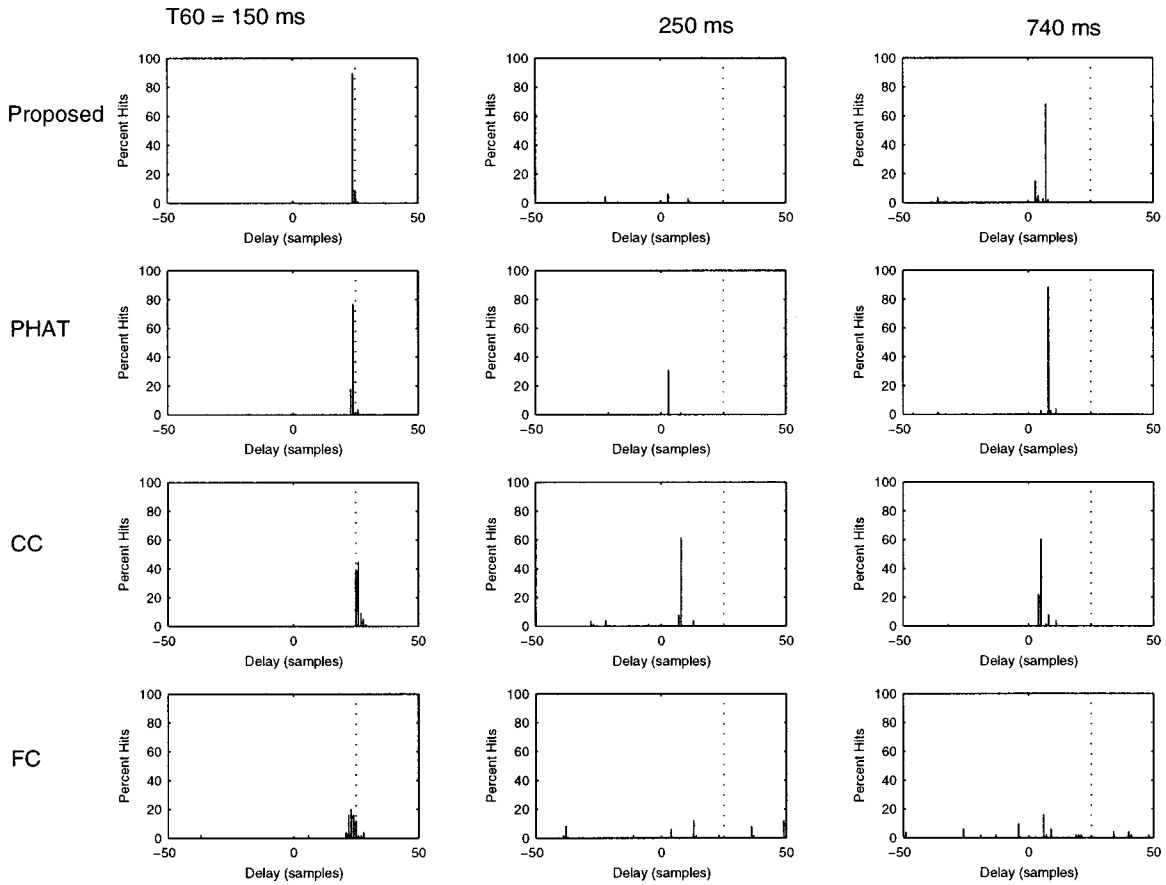

FIG. 3. Histograms of TDE with a pair of omni microphones. The source is a speech signal and its position is on the left. Presentation the same as in Fig. 2.

dom selection), and panels all closed; and the corresponding 60 dB reverberation time in the 400–1600 Hz band is, respectively, 150 ms, 250 ms, and 740 ms. Two different pairs of microphones were used: cardioid and omni. The distance between the two microphones was about 95 cm (37.25 in.). The source was simulated by placing a loudspeaker in four different positions (left, center, right, and far-right). Figure 1 shows a diagram of the floor plan layout with the position of the sources and the two microphones. A total of 14 different pairs of microphone signals were recorded, 12 with a speech source signal, and 2 with a white noise source signal. The original sampling rate was 48 kHz, but all the files were subsequently converted to a 16 kHz sampling rate. Each recording was about 5 s long.

For PHAT and CC, a 64 ms Kaiser window was used for the analysis frame. These two algorithms were well optimized in order to get the best results in terms of accuracy of TDE. For FC, a 100 ms window was used.[10] For the new method, we have used the UFLMS[24] with $\mu=0.003$. The length of the adaptive vector u is taken as $L=2M=512$. The power of the two microphone signals $X_i(f,n), i=1,2$, was estimated in the frequency-domain as follows:

$$P_i(f,n)=\gamma P_i(f,n-1)+(1-\gamma)|X_i(f,n)|^2, \tag{24}$$

with $\gamma=0.999$. We initialized the algorithm with $P_i(f,0)=2L\sigma_{x_i}^2$ ($\sigma_{x_i}^2$ is the average power of x_i).

It is not always easy to compare fairly different algorithms and the proposed choice of parameters of the previous algorithms may be argued, since in practice another set may be used for a better tracking. But this choice was done deliberately. We tried to find these parameters in order to have the best accuracy possible for all the algorithms. Note that this choice does not favor our algorithm. All of these simulations were made in a ''blind'' way, without using any information about the true delay. Moreover, we have used the same parameters for all the examples.

Figure 2 shows histograms of TDE with a pair of cardioid microphones. The source is a speech signal and its position is on the right. The first, second, and third columns correspond, respectively, to a reverberation time of 150 ms, 250 ms, and 740 ms. The first, second, third, and fourth lines correspond, respectively, to the TDE by the proposed algorithm, PHAT, CC, and FC. The true delay is plotted with a dotted line. It can be seen from this example that the new method performs better and is the most accurate. Notably with a 740 ms reverberation time, all methods fail except for the proposed algorithm.

Figures 3, 4, and 5 show histograms of TDE with a pair of omni directional microphones, which presents a more difficult problem. The source is again a speech signal and the presentation is the same as in Fig. 2. For Fig. 3, the source is on the left. All the methods fail for reverberation time of 250 ms and 740 ms. In Fig. 4, the source is in the center and here again the proposed algorithm seems to give better results. For Fig. 5, the source is on the right. It can be noticed that the new method fails completely only for a 250 ms reverberation time, whereas the other methods fail for 250 ms and 740 ms reverberation time.

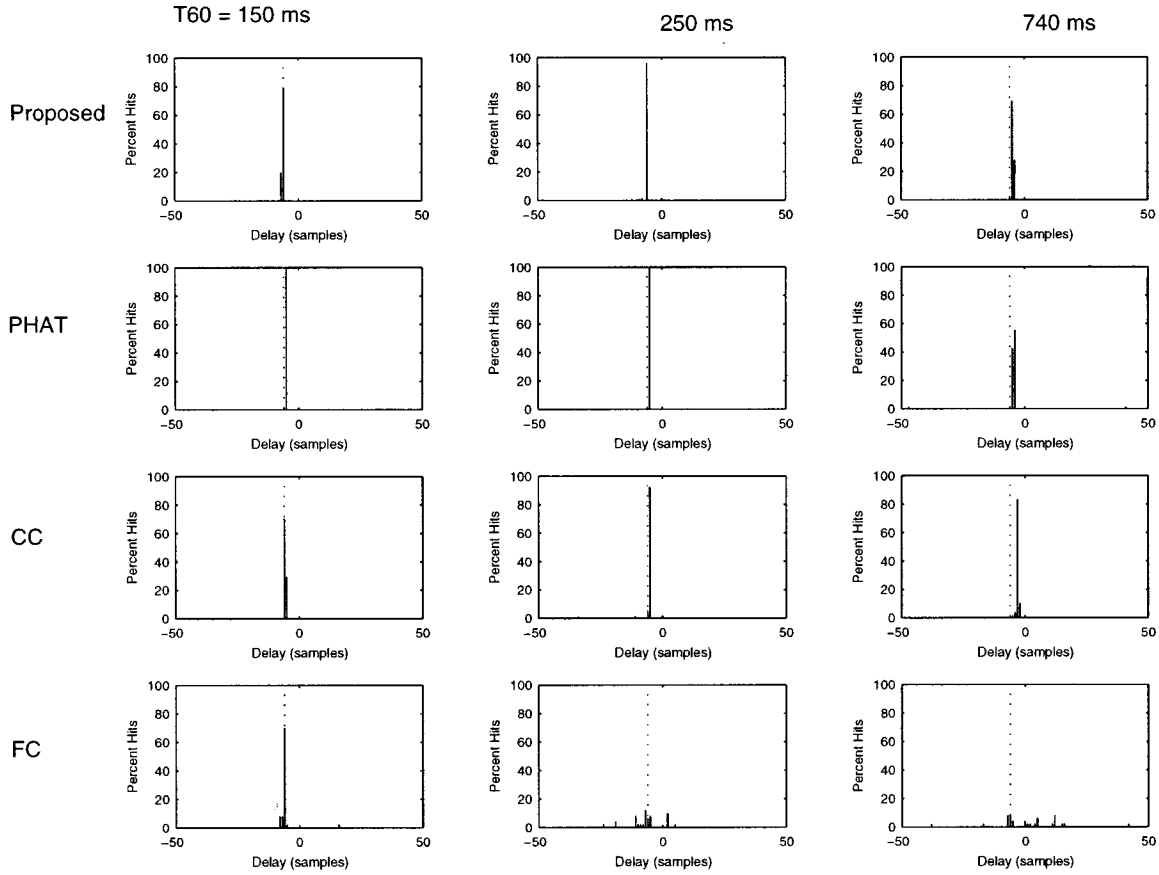

FIG. 4. Histograms of TDE with a pair of omni microphones. The source is a speech signal and its position is on the center. Presentation the same as in Fig. 2.

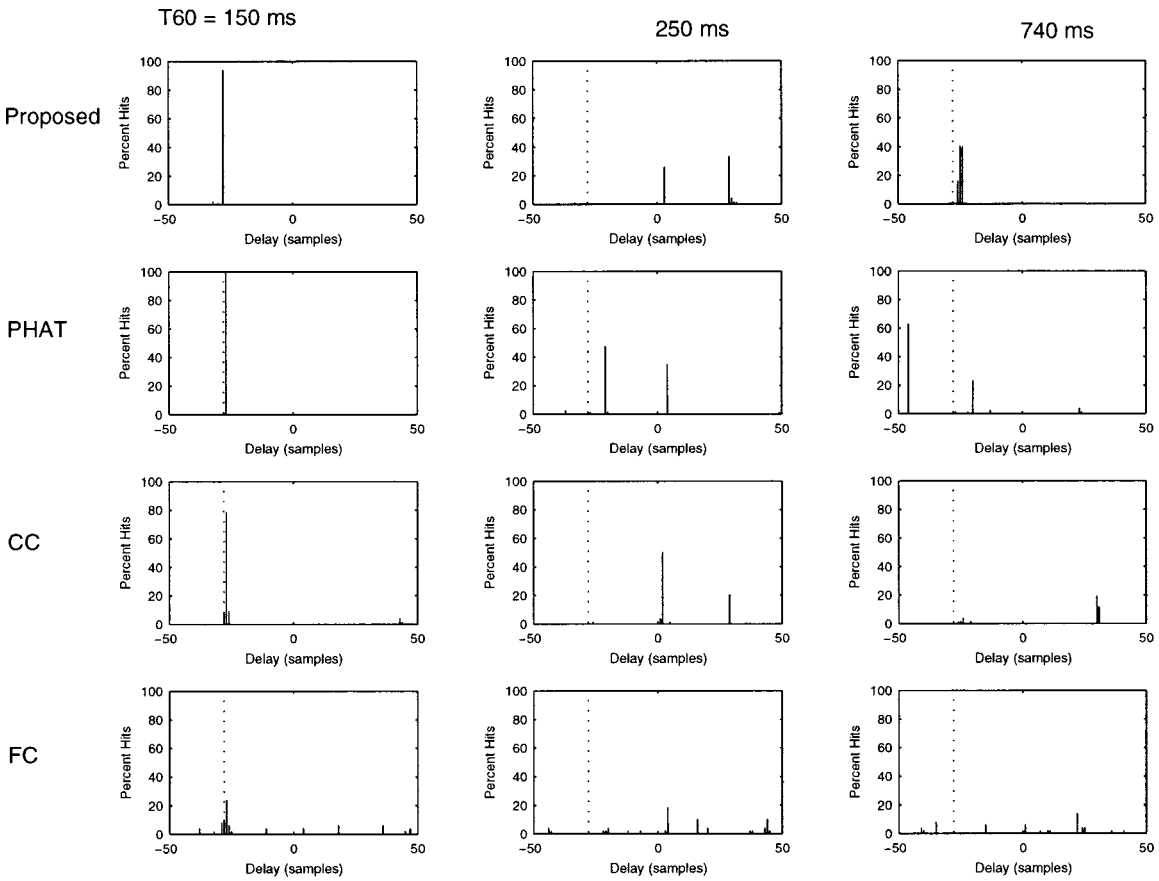

FIG. 5. Histograms of TDE with a pair of omni microphones. The source is a speech signal and its position is on the right. Presentation the same as in Fig. 2.

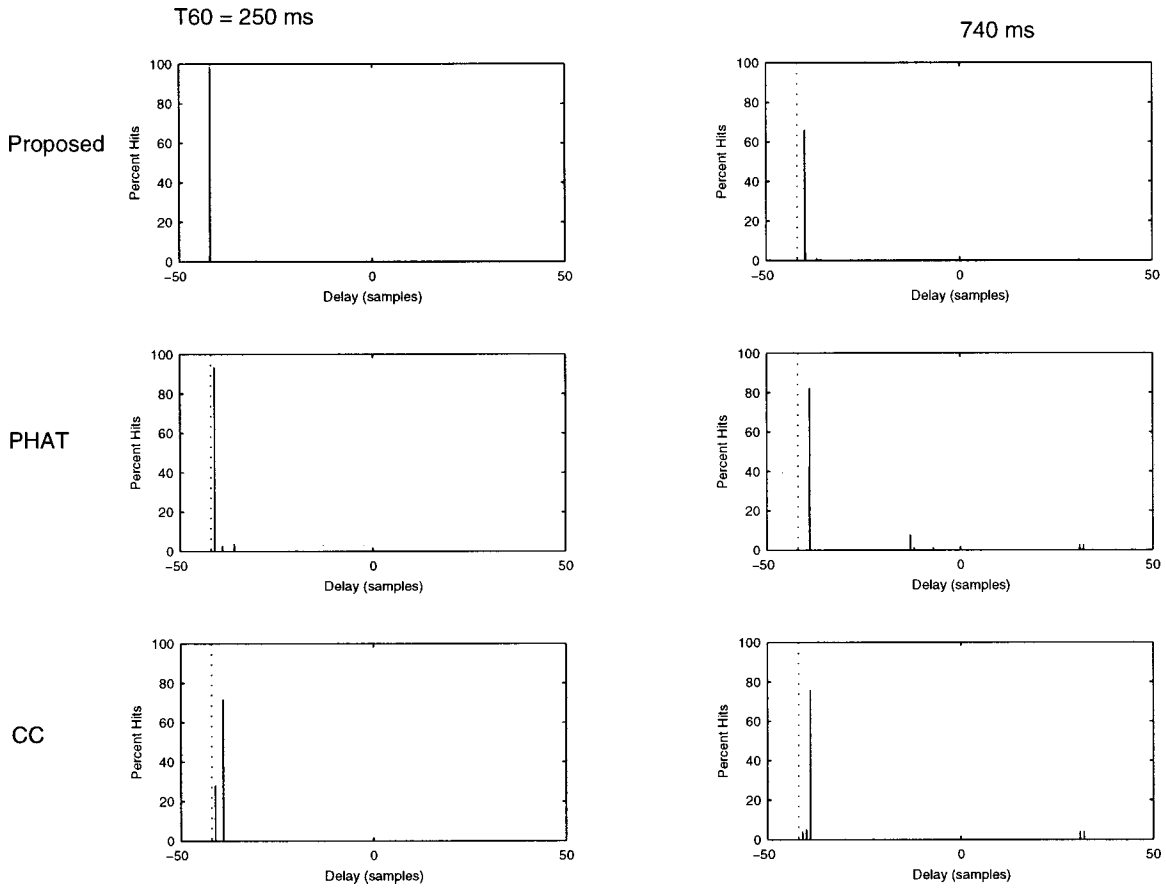

FIG. 6. Histograms of TDE with a pair of omni microphones. The source is a white noise signal and its position is on the far-right. The first and second columns correspond, respectively, to a reverberation time of 250 ms and 740 ms. The first, second, and third lines correspond, respectively, to the TDE by the proposed algorithm, PHAT, and CC. The true delay is plotted with a dotted line.

Figure 6 shows histograms of TDE with a pair of omni microphones, and a white noise source positioned on the far-right (not shown in Fig. 1). The first and second columns correspond, respectively, to a reverberation time of 250 ms and 740 ms. The first, second, and third lines correspond, respectively, to the TDE by the proposed algorithm, PHAT, and CC. Results for FC are not shown, since it is a pitch-based algorithm. Again, the true delay is plotted with a dotted line. All the algorithms are close to the solution but the new one is by far the most accurate.

The proposed algorithm converges very fast to a good time-delay estimate, it converges in less than 250 ms. Moreover, it is very robust to noise even with an SNR as low as 10 dB. Figure 7 compares the proposed algorithm to the PHAT, with a speech source on the right, a pair of cardiod microphones, a 250 ms reverberation time, and a white noise source in the center with an SNR equal to 10 dB.

V. CONCLUSION

In this paper, a new and simple approach to time-delay estimation has been proposed. The method consists of detecting the direct paths of the two impulse responses between the source signal and the microphones that are estimated in the eigenvector corresponding to the smallest eigenvalue of the covariance matrix of the microphone signals. In comparison with other methods, the proposed one seems to be more efficient in a reverberant environment and much more accurate.

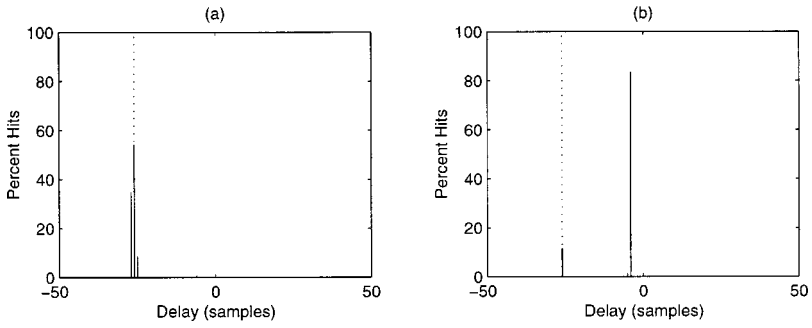

FIG. 7. Comparison of (a) the proposed algorithm to (b) the PHAT, with a speech source on the right, a pair of cardiod microphones, a 250 ms reverberation time, and a white noise source in the center with an SNR equal to 10 dB.

ACKNOWLEDGMENTS

I would like to thank Gary W. Elko and Jens Meyer for recording the data in the Varechoic chamber, and Dennis R. Morgan and again G. W. Elko for a careful reading of a preliminary draft and providing many useful comments for improvement. Also thanked are the anonymous reviewers for helpful suggestions.

[1] C. H. Knapp and G. C. Carter, ''The generalized correlation method for estimation of time delay,'' IEEE Trans. Acoust., Speech, Signal Process. **ASSP-24**, 320–327 (1976).
[2] M. S. Brandstein, ''A pitch-based approach to time-delay estimation of reverberant speech,'' in Proceedings of the IEEE ASSP Workshop Applications on Signal Processing Audio Acoustics, New Paltz, NY, 1997.
[3] P. G. Georgiou, C. Kyriakakis, and P. Tsakalides, ''Robust time delay estimation for sound source localization in noisy environments,'' in Proceedings of the IEEE ASSP Workshop Applications on Signal Processing Audio Acoustics, New Paltz, NY, 1997.
[4] H. Wang and P. Chu, ''Voice source localization for automatic camera pointing system in video-conferencing,'' in Proceedings of the IEEE ASSP Workshop Applications on Signal Processing Audio Acoustics, New Paltz, NY, 1997.
[5] S. Bédard, B. Champagne, and A. Stéphenne, ''Effects of room reverberation on time-delay estimation performance,'' in Proceedings of the IEEE ICASSP, Adelaide, Australia, 1994, pp. II-261–II-264.
[6] B. Champagne, S. Bédard, and A. Stéphenne, ''Performance of time-delay estimation in the presence of room reverberation,'' IEEE Trans. Speech Audio Process. **4**, 148–152 (1996).
[7] A. Stéphenne and B. Champagne, ''Cepstral prefiltering for time delay estimation in reverberant environments,'' in Proceedings of IEEE ICASSP, Detroit, MI, 1995, pp. 3055–3058.
[8] A. Stéphenne and B. Champagne, ''A new cepstral prefiltering technique for time delay estimation under reverberant conditions,'' Signal Process. **59**, 253–266 (1997).
[9] D. R. Fischell and C. H. Coker, ''A speech direction finder,'' in Proceedings of IEEE ICASSP, 1984, pp. 19.8.1–19.8.4.
[10] D. R. Morgan, V. N. Parikh, and C. H. Coker, ''Automated evaluation of acoustic talker direction finder algorithms in the varechoic chamber,'' J. Acoust. Soc. Am. **102**, 2786–2792 (1997).
[11] H. F. Silverman and S. E. Kirtman, ''A two-stage algorithm for determining talker location from linear microphone array data,'' Comput. Speech Lang. **6**, 129–152 (1992).
[12] M. S. Brandstein, J. E. Adcock, and H. F. Silverman, ''A closed-form method for finding source locations from microphone-array time-delay estimates,'' in Proceedings of IEEE ICASSP, Detroit, MI, 1995, pp. 3019–3022.
[13] M. S. Brandstein, J. E. Adcock, and H. F. Silverman, ''A closed-form location estimator for use with room environment microphone arrays,'' IEEE Trans. Speech Audio Process. **5**, 45–50 (1997).
[14] D. V. Rabinkin, R. J. Renomeron, A. Dahl, J. C. French, and J. L. Flanagan, ''A DSP implementation of source location using microphone arrays,'' Proc. SPIE **2846**, 88–99 (1996).
[15] P. C. Ching, Y. T. Chan, and K. C. Ho, ''Constrained adaptation for time delay estimation with multipath propagation,'' IEE Proc. F, Radar Signal Process. **138**, 453–458 (1991).
[16] M. Omologo and P. Svaizer, ''Acoustic event localization using a crosspower-spectrum phase based technique,'' in Proceedings of IEEE ICASSP, Adelaide, Australia, 1994, pp. II-273–II-276.
[17] M. Omologo and P. Svaizer, ''Acoustic source location in noisy and reverberant environment using CSP analysis,'' in Proceedings of IEEE ICASSP, Atlanta, GA, 1996, pp. 921–924.
[18] D. V. Rabinkin, R. J. Renomeron, J. C. French, and J. L. Flanagan, ''Estimation of wavefront arrival delay using the cross-power spectrum phase technique,'' J. Acoust. Soc. Am. **104**, 2697(A).
[19] J. Benesty, F. Amand, A. Gilloire, and Y. Grenier, ''Adaptive filtering algorithms for stereophonic acoustic echo cancellation,'' in Proceedings of IEEE ICASSP, Detroit, MI, 1995, pp. 3099–3102.
[20] L. Tong, G. Xu, and T. Kailath, ''Fast blind equalization via antenna arrays,'' in Proceedings of IEEE ICASSP, Minneapolis, MN, 1993, Vol. IV, pp. 272–275.
[21] O. L. Frost III, ''An algorithm for linearly constrained adaptive array processing,'' Proc. IEEE **60**, 926–935 (1972).
[22] N. L. Owsley, ''Adaptive data orthogonalization,'' in Proceedings of IEEE ICASSP, 1978, pp. 109–112.
[23] M. Bellanger, *Analyse des signaux et filtrage numérique adaptatif* (Masson et CNET-ENST, Paris, 1989).
[24] D. Mansour and A. H. Gray, Jr., ''Unconstrained frequency-domain adaptive filter,'' IEEE Trans. Acoust., Speech, Signal Process. **ASSP-30**, 726–734 (1982).
[25] F. A. Reed, P. L. Feintuch, and N. J. Bershad, ''Time delay estimation using the LMS adaptive filter-static behavior,'' IEEE Trans. Acoust., Speech, Signal Process. **ASSP-29**, 561–571 (1981).
[26] D. H. Youn, N. Ahmed, and G. C. Carter, ''On using the LMS algorithm for time delay estimation,'' IEEE Trans. Acoust., Speech, Signal Process. **ASSP-30**, 798–801 (1982).
[27] W. C. Ward, G. W. Elko, R. A. Kubli, and W. C. McDougald, ''The new Varechoic chamber at AT&T Bell Labs,'' in Proceedings of the Wallace Clement Sabine Centennial Symposium, Acoustical Society of America, Woodbury, NY, 1994, pp. 343–346.

Nearfield broadband array design using a radially invariant modal expansion

Thushara D. Abhayapala and Rodney A. Kennedy
Telecommunications Engineering Group, Research School of Information Sciences and Engineering, Australian National University, Canberra ACT 0200, Australia

Robert C. Williamson
Department of Engineering, Faculty of Engineering and Information Technology, Australian National University, Canberra ACT 0200, Australia

(Received 22 December 1997; revised 5 February 1999; accepted 29 September 1999)

This paper introduces an efficient parameterization for the nearfield broadband beamforming problem with a single parameter to focus the beamformer to a desired operating radius and another set of parameters to control the actual broadband beampattern shape. The parameterization is based on an orthogonal basis set of elementary beampatterns by which an arbitrary beampattern can be constructed. A set of elementary beamformers are then designed for each elementary beampattern and the desired beamformer is constructed by summing the elementary beamformers with frequency and source-array distance dependent weights. An important consequence of our result is that the beamformer can be factored into three levels of filtering: (i) beampattern independent elementary beamformers; (ii) beampattern shape dependent filters; and (iii) radial focusing filters where a single parameter can be adjusted to focus the array to a desired radial distance from the array origin. As an illustration the method is applied to the problem of producing a practical array design that achieves a frequency invariant beampattern over the frequency range of 1:10 (which is suitable for speech acquisition using a microphone array), and with the array focused either to farfield or nearfield where at the lowest frequency the radial distance to the source is only three wavelengths. [S0001-4966(00)03901-1]

PACS numbers: 43.60.Gk, 43.38.Si, 43.30.Wi [JCB]

INTRODUCTION

Consider the problem of designing a microphone array for speech acquisition. Not only does the array require a narrow main beam, but it should operate uniformly over a large bandwidth and be able to cope with nearfield sources. While there has been a deal of progress in designing broadband arrays, having them operate well in the nearfield still requires rather *ad hoc* solutions. In this paper, we will present a systematic way of designing nearfield broadband sensor arrays. In particular, we will explicitly show how to parameterize the beamformer in order to focus the array to practically any operating radius from the array origin using a single parameter while maintaining a predetermined broadband angular beampattern using another set of parameters.

Most of the array processing literature assumes a farfield source having only plane waves impinging on the sensor array. However, in many practical situations, such as microphone arrays in car environments,[1] the source is well within the nearfield. The use of farfield assumptions to design the beamformer in these situations may severely degrade the beampattern. In many cases the approximate distance at which the farfield assumption begins to be valid is $r = 2L^2/\lambda$, where r is the distance from an arbitrary array origin, L is the largest array dimension, and λ is the operating wavelength.[2] However, we will show in Sec. I C that this common rule-of-thumb for farfield approximation is not a necessary condition.

There appears to be little work in the literature on nearfield beamforming. One method uses time delays to compensate for differing propagation delays due to spherical propagation.[3] However, this ignores the variation of the magnitude with distance and angle and assumes a point source. In another method,[4] there was consideration initially for nearfield theoretical development but this was ignored in the actual array design. The few other related works we are aware of dealing with design of nearfield arrays can be found in the references.[5–10]

A novel methodology to obtain precise nearfield array designs has been recently developed.[11] It is based on writing the solution to the wave equation in terms of spherical harmonics and allowing a nearfield beampattern specification to be transformed to the farfield, and the subsequent use of well understood farfield theory, to design the nearfield beamformer. These nearfield–farfield transformations have been used for many years in the radio antenna community for reconstructing farfield antenna patterns from nearfield measurements,[12] though these transformations are computationally involved. The theory of nearfield–farfield transformation was used to establish a computationally simple design procedure that numerically implements the nearfield–farfield transformation.[13] Farfield broadband beamforming has been considered[14–16] and reviewed in Ref. 14.

In this paper, a new method of beamforming is proposed in which an arbitrary desired beampattern in both frequency and angle may be produced either in nearfield or farfield. We have used the wave equation based representation of beampatterns[11] to identify the class of elementary beampat-

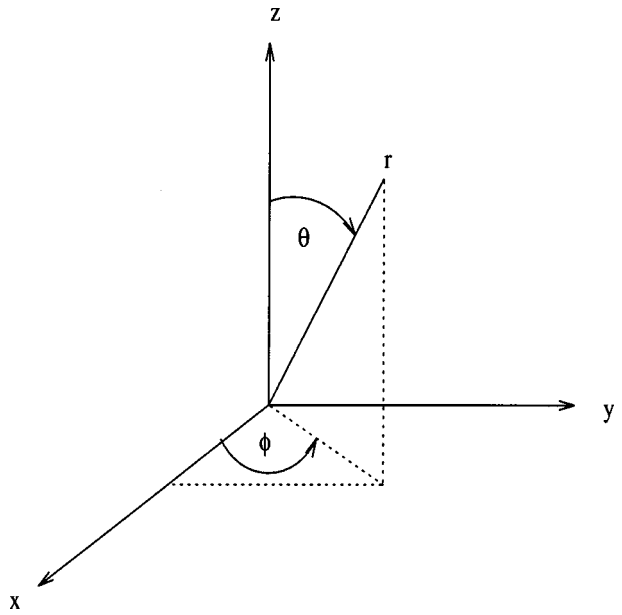

FIG. 1. Spherical coordinate system.

terns by which any arbitrary beampattern can be constructed. These elementary beampatterns form an orthogonal basis set. We use the concept of a theoretical continuous sensor to design elementary beamformers for each elementary beampattern. Then the desired beamformer is constructed by summing the elementary beamformers with frequency and radial distance dependent weights. The proposed beamformer structure has three major processing blocks: (i) a beampattern independent filtering block consisting of elementary beamformers; (ii) a beampattern shape dependent filtering block; and (iii) a radial focusing filter block, where a single parameter can be adjusted to focus the array to different radial distances from the array origin. Hence this design provides an efficient parametrization for adaptive beamformers, where only the beampattern shape dependent filters and a radial distance dependent parameter need to be adapted.

The paper is organized as follows: Section I introduces the notion of elementary shape invariant beampatterns as building blocks of beampatterns. The design of a general broadband theoretical continuous sensor as a sum of elementary continuous sensors is discussed in Sec. II. Section III shows how to approximate the theoretical continuous sensor by a practical discrete array of sensors. Guidelines for choosing the nonuniformly spaced sensor locations and the consequence of spatial sampling are addressed in Sec. IV. We conclude with an example broadband beamformer, which can be focused to either nearfield or farfield, in Sec. V.

I. THEORY OF ELEMENTARY SHAPE INVARIANT BEAMPATTERNS

A. Beampattern formulation

The nearfield–farfield transformation is obtained by solving the physical problem governed by the classical wave equation in the spherical coordinate system.[11] Let r denote radial distance, and ϕ and θ be the azimuth and elevation angles as shown in Fig. 1. Then a general valid beampattern is constructed by combination of all possible modes of the form[11]

$$r^{1/2}H^{(1)}_{n+1/2}(kr)P^{|m|}_n(\cos\theta)e^{jm\phi}, \tag{1}$$

where integers $n\geqslant 0$ and m (such that $|m|\leqslant n$) index the modes, $k=2\pi fc^{-1}$ is the wave number, f is the frequency of the wave, and c is the speed of wave propagation. The functions $P^m_n(\cdot)$ are associated Legendre functions and $H^{(1)}_{n+1/2}(\cdot)$ is the half-odd integer order Hankel function of the first kind which is defined by $H^{(1)}_{n+1/2}(\cdot)=J_{n+1/2}(\cdot)+jY_{n+1/2}(\cdot)$, where $J_{n+1/2}(\cdot)$ and $Y_{n+1/2}(\cdot)$ are the half-integer order Bessel functions of first and second kind, respectively. A property we will rely on is that there is no nonnegative integer n and no real number $r>0$ such that $H^{(1)}_{n+1/2}(r)=0$. This result follows from the fact that there are no common zeros for the functions $J_{n+1/2}(r)$ and $Y_{n+1/2}(r)$ (Ref. 17, p. 30).

The modes Eq. (1) are associated with waves propagating toward the origin (the half-odd integer order Hankel functions of the *second* kind give the waves propagating away from the origin). We assume that the propagation speed c is independent of frequency, implying k is a constant multiple of frequency f. Consequently, throughout this paper we will often refer to k as ''frequency.'' By combining modes for all possible n and m an arbitrary beampattern can be written as

$$b_r(\theta,\phi;k)=\sum_{n=0}^{\infty}\sum_{m=-n}^{n}\alpha^m_n(k)r^{1/2}H^{(1)}_{n+1/2}(kr)P^{|m|}_n(\cos\theta)e^{jm\phi}, \tag{2}$$

where $\{\alpha^m_n(k)\}$ is a set of frequency dependent coefficients. By introducing frequency dependence to the coefficients, we can use Eq. (2) to represent an arbitrary beampattern specification in both space (angle) and frequency. To complete the beampattern transformation model, it can be shown[11] that the $\alpha^m_n(k)$ coefficients can be obtained from the *analysis* equation:

$$\alpha^m_n(k)=\frac{(n+\frac{1}{2})}{2\pi r^{1/2}H^{(1)}_{n+1/2}(kr)}\frac{(n-m)!}{(n+m)!}\times\int_0^{2\pi}\int_0^{\pi}b_r(\theta,\phi;k)P^{|m|}_n(\cos\theta)e^{-jm\phi}\sin\theta\,d\theta\,d\phi. \tag{3}$$

Since we can invert the representation Eq. (2) via Eq. (3) we conclude that the $\alpha^m_n(k)$ uniquely represent an arbitrary beampattern. Equations (2) and (3) form an orthogonal transform pair. This implies the following linearity property which will be used later: if we have more than one beampattern at one fixed radius, then linearly adding them and transforming their sum to another radius is equivalent to the transformation of each beampattern separately to the second radius and then adding them together.

B. Elementary beampatterns

As we have seen in Eq. (2), any physically realizable beampattern can be constructed by combining modes of Eq.

(1). Inversely, an arbitrary beampattern can be decomposed into modes by Eq. (3). These modes in Eq. (1) are also valid beampatterns. Let us denote these beampatterns by

$$E_n^m(r,\theta,\phi;k) \triangleq R_n(r,k)\epsilon_n^m(\theta,\phi), \tag{4}$$

where

$$R_n(r,k) \triangleq r^{1/2}H_{n+1/2}^{(1)}(kr) \tag{5}$$

and

$$\epsilon_n^m(\theta,\phi) \triangleq P_n^{|m|}(\cos\theta)e^{jm\phi}. \tag{6}$$

The quantity $\epsilon_n^m(\theta,\phi)$ can be considered as an elementary beam shape and the quantity $R_n(r,k)$ is a complex function parameterized by distance r and frequency k. Therefore, the shape of the beampattern Eq. (4) is invariant with frequency as well as with distance. Hence we denote these beampatterns as *Elementary Shape Invariant Beampatterns* (ESIB). These are elementary because any physically realizable beampattern can be decomposed into a weighted sum of ESIBs:

$$b_r(\theta,\phi;k) = \sum_{n=0}^{\infty}\sum_{m=-n}^{n} \alpha_n^m(k)E_n^m(r,\theta,\phi;k), \tag{7}$$

where $\alpha_n^m(k)$ are the decomposition coefficients. From this point onward, we refer to Eq. (7) as the *modal representation* of beampatterns. Some examples of the lower order elementary beam shapes $\epsilon_n^m(\theta,\phi)$ for $m=0$ (which implies the shape is invariant with ϕ) are illustrated in Fig. 2 where the magnitude of $\epsilon_n^0(\theta,\phi)$ is plotted against θ. The shapes in Fig. 2 are the standard omni-directional, dipole, etc., patterns. It is evident that the number of *lobes* present is proportional to the mode n.

C. Radially invariant beampatterns

As a simple illustration of the modal representation Eq. (7), we now introduce a novel class of beampatterns related to ESIBs which are radially invariant with respect to their shape. A radially shape invariant beampattern $b_r(\theta,\phi;k)$ has the following property: For r_A, $r_B>0$, $\theta\in[0,\pi]$ and $\phi\in[0,2\pi)$ there exists a complex constant $C\equiv C(r_A,r_B)$ such that

$$b_{r_A}(\theta,\phi;k) = Cb_{r_B}(\theta,\phi;k). \tag{8}$$

One such class of beampatterns can be found excluding all but a single index n in Eq. (7) as

$$b_r(\theta,\phi;k)_{\text{invariant}} = R_n(r,k)\sum_{m=-n}^{n}\alpha_n^m(k)\epsilon_n^m(\theta,\phi), \tag{9}$$

where, in Eq. (8), the complex scaling factor $C = R_n(r_A,k)/R_n(r_B,k)$. Here, the shape of the beampattern is fixed with respect to radius r but its amplitude and phase are scaled with the distance from the array origin. However, this variation of phase and amplitude is same for all angles. The beampattern class Eq. (9) covers only a subset of all possible arbitrary beampatterns Eq. (7). An example of a beampattern of the form Eq. (9) is illustrated in Fig. 3. All radially invariant beam shapes of the form Eq. (9) need two-dimensional arrays [where $\alpha_n^m(k)=0$ for $m\neq 0$ in Eq. (9)] except trivial beam shapes such as omni-directional, dipole, etc.

The standard farfield design techniques can be applied to beampatterns such as Eq. (9) with the resulting beamformer automatically inheriting the radial invariance property if the farfield pattern is accurately realized. Note that the rule-of-thumb for farfield approximation[2] is not applicable for radial invariant beampatterns. For an arbitrary beampattern, the accuracy of this rule depends on the relative combination of ESIBs in Eq. (7).

A possible application of radially invariant beampatterns is in the microphone array design with a mixed nearfield/farfield problem,[10] where the array needs to focus to a nearfield source (the talker) but to attenuate farfield interference (reverberation). Keeping the same shape in both nearfield and farfield could be a useful solution to such a problem.

Radially invariant beampatterns are only one of the possible applications of ESIBs. In the remainder of this paper we will illustrate how ESIBs can be used to develop theory for more general broadband beamforming.

II. BROADBAND CONTINUOUS SENSOR DESIGN

A. Elementary continuous sensors

In previous sections we developed a new method for decomposing a given beampattern into elementary shape invariant beampatterns (ESIBs). We will now address the engineering problem of physically realizing these ESIBs using an array of sensors. We begin with the concept of *continuous sensor*, in order that an exact relationship between ESIBs and aperture illumination can be developed. The illumination function of the continuous sensor will then be approximated by a discrete sensor array to permit practical implementation.

In order to be able to completely describe results for different array configurations we introduce the notation $\rho(x,y,z;k)$ for the broadband aperture illumination or the response of the aperture at a point (x,y,z) and for a frequency k. The response of a continuous sensor to planar waves (i.e., those generated by a farfield point source) impinging from an angle (θ,ϕ) is then

$$b_\infty(u,v,w;k) = \int_{-\infty}^{\infty}\int_{-\infty}^{\infty}\int_{-\infty}^{\infty}\rho(x,y,z;k)e^{jk(ux+vy+wz)}\,dx\,dy\,dz, \tag{10}$$

where $(u,v,w)=(\sin\theta\cos\phi,\sin\theta\sin\phi,\cos\theta)$, $\theta\in[0,\pi]$ and $\phi\in[0,2\pi]$. Equation (10) is the standard three-dimensional Fourier transform relating the farfield beampattern to aperture illumination for a frequency k. The three-dimensional inverse Fourier transform corresponding to Eq. (10) is given by

$$\rho(x,y,z;k) = \left(\frac{k}{2\pi}\right)^3\int\int\int b_\infty(u,v,w;k) \times e^{-jk(ux+vy+wz)}\,du\,dv\,dw, \tag{11}$$

where the three-dimensional integration is over the unit sphere.

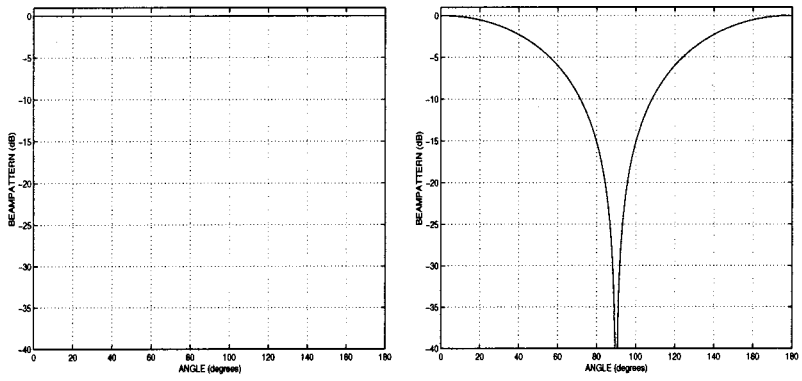

(a) mode: $m=0, n=0$ (b) mode: $m=0, n=1$

(c) mode: $m=0, n=2$ (d) mode: $m=0, n=3$

(e) mode: $m=0, n=4$ (f) mode: $m=0, n=5$

FIG. 2. Magnitude of few lower order elementary beam shapes $\epsilon_n^m(\theta,\phi)$ [given by Eq. (6)] for $m=0$ plotted against the angle θ. Note that these shapes are the standard omni directional, dipole, etc. patterns.

In order to establish an exact relationship between the ESIBs Eq. (4) and the aperture illumination function $\rho(x,y,z;k)$, we write an arbitrary farfield beampattern in the modal representation Eq. (7) as

$$b_\infty(u,v,w;k)=\sum_{n=0}^{\infty}\sum_{m=-n}^{n}\alpha_n^m(k)E_n^m(\infty,u,v,w;k), \quad (12)$$

where $\{\alpha_n^m(k):n\in\mathbb{Z}^+,\ m\in\mathbb{Z},\ |m|\leqslant n \text{ and } k\in\mathbb{R}^+\}$ are the decomposition coefficients and $E_n^m(\infty,u,v,w;k) \triangleq \lim_{r\to\infty} E_n^m(r,u,v,w;k)$ is the farfield beampattern given in Eq. (4) but expressed in the (u,v,w) coordinates. Substituting Eq. (12) into Eq. (11) and rearranging, we obtain the desired relationship as

$$\rho(x,y,z;k)=\sum_{n=0}^{\infty}\sum_{m=-n}^{n}\alpha_n^m(k)R_n(\infty,k)\varrho_n^m(x,y,z;k), \quad (13)$$

where

$$\varrho(x,y,z;k)\triangleq\left(\frac{k}{2\pi}\right)^3\int\int\int \epsilon_n^m(u,v,w) \times e^{-jk(ux+vy+wz)}\,du\,dv\,dw, \quad (14)$$

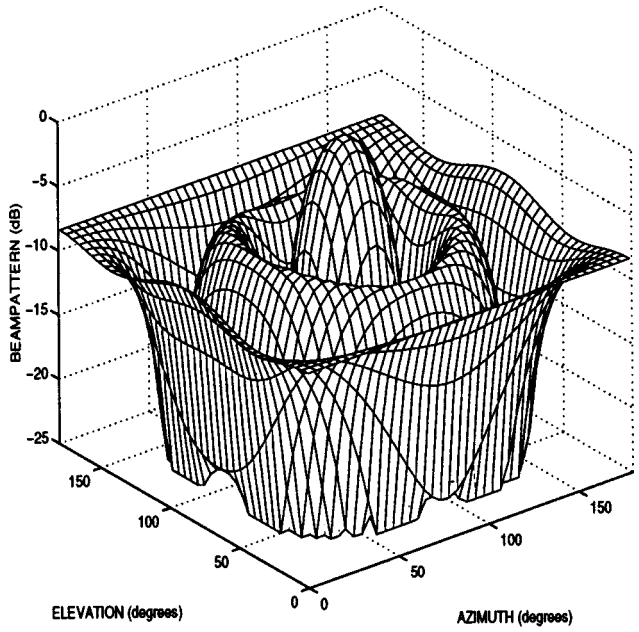

FIG. 3. An example of a shape invariant beampattern given by Eq. (9): $N=4$, $\alpha_4^4=0.05$, $\alpha_4^3=0$, $\alpha_4^0=0.35$, $\alpha_4^1=0$, $\alpha_4^0=7.0$, and $\alpha_4^{-m}=\alpha_4^m$.

and $R_n(\infty,k)\triangleq\lim_{r\to\infty}R_n(r,k)$. Using the results of Ref. 17 (p. 198) and Eq. (5) we have

$$R_n(\infty,k)=\lim_{r\to\infty} r^{1/2}H_{n+1/2}^{(1)}(kr)=(-j)^{n+1}\sqrt{\frac{2}{\pi k}}e^{j(k-k_0)}, \tag{15}$$

where k_0 is an arbitrary chosen nominal frequency. We can consider $\varrho_n^m(x,y,z;k)$ as the elementary aperture illumination functions. We can make following comments:

(1) An arbitrary farfield beampattern can be represented by Eq. (12). That means it can be decomposed in to ESIBs using Eq. (3) by calculating the coefficients $\alpha_n^m(k)$.
(2) Equation (14) could be used to find the elementary aperture illumination $\varrho_n^m(x,y,z;k)$ for each $\epsilon_n^m(\theta,\phi)$. Note that these elementary aperture functions are independent of the specific beampattern and they can be calculated beforehand in a practical situation.
(3) The coefficients $\alpha_n^m(k)$ have two interpretations: (i) they decompose the beampatterns Eq. (12) into a weighted sum of ESIBs, and (ii) they construct the aperture illumination Eq. (13) as a weighted sum of elementary aperture illumination functions.

B. Nearfield equivalence

In Sec. II A we introduced a technique to obtain a continuous aperture illumination function $\rho(x,y,z;k)$ for a broadband farfield beampattern using ESIBs. In this section, we generalize this result for broadband beampatterns at any radial distance from the array origin using the nearfield–farfield transformation technique.[11]

Theorem 1. *Let $b(\theta,\phi;k)$ be an arbitrary broadband beampattern specification. Then the aperture illumination, $\rho^{(r)}(x,y,z;k)$ of a continuous sensor which realizes this beampattern at a radius r from the sensor origin is given by*

$$\rho^{(r)}(x,y,z;k)=\sum_{n=0}^{\infty}\sum_{m=-n}^{n}\alpha_n^m(k)\frac{[R_n(\infty,k)]^2}{R_n(r,k)}\varrho_n^m(x,y,z;k), \tag{16}$$

where the elementary aperture illumination functions Eq. (14) $\varrho_n^m(x,y,z;k)$ and the complex functions $R_n(\cdot,k)$ [see Eq. (5)] are independent of the given beampattern and $\alpha_n^m(k)$ are the modal coefficients which give rise to the beampattern $b(\theta,\phi;k)$ in the farfield.

The proof is given in the Appendix. The theorem provides a method to achieve a desired beampattern response at any radius r from the array origin by a single parameter r adjustment of the continuous sensor $\rho^{(r)}(x,y,z;k)$.

C. One-dimensional sensor

The broadband array theory developed in the previous section is sufficiently general to capture quite arbitrary three-dimensional sensor geometries. In an attempt to bring the result into focus and provide a more concrete presentation of the ideas we examine a linear sensor aligned with the z axis. Specifically, we derive a closed form expression for the elementary aperture functions in the one-dimensional case. In this case, the beampattern is rotationally symmetric with respect to ϕ, and a farfield beampattern can be expressed as $b_\infty(\theta;k)=b_\infty(\theta,\phi;k)$.

By symmetry, the only nonzero components of the representation Eq. (12) are those for which $m=0$. Thus we obtain

$$b_\infty(\theta;k)=\sum_{n=0}^{\infty}\alpha_n(k)R_n(\infty,k)P_n^0(\cos\theta), \tag{17}$$

and

$$\rho^{(r)}(z,k)=\sum_{n=0}^{\infty}\alpha_n(k)\frac{[R_n(\infty,k)]^2}{R_n(r,k)}\varrho_n^0(z;k), \tag{18}$$

where $\alpha_n(k)\triangleq\alpha_n^0(k)$ and $\varrho_n^0(z;k)$ are the elementary aperture functions and $\rho^{(r)}(z,k)$ is the aperture illumination which will realize the desired response at a radius r from the array origin. By evaluating the integral in Eq. (14) for this case, we obtain a closed form expression for the elementary aperture functions for a linear sensor aligned with the z axis as:

$$\varrho_n^0(z;k)=\frac{k}{2\pi}\int_{-1}^{1}P_n(w)e^{-jkwz}\,dw \tag{19}$$

$$=\frac{k}{\sqrt{2\pi}}(-j)^n\frac{J_{n+1/2}(kz)}{\sqrt{kz}}, \tag{20}$$

where $P_n(\cdot)$ is the Legendre function of order n. Thus we have an exact expression for elementary aperture functions, although they are infinite in length. In the following section, we show how to discretize and truncate the continuous aperture functions derived.

III. BROADBAND DISCRETE ARRAY DESIGN

A. Background

We will now show how to exploit the above ideas for broadband array design. An array is a finite set of identical, discrete, omni-directional broadband sensors arranged in a regular geometry. We will only consider one-dimensional sensor arrays, although the results can be generalized to two and three dimensions. We consider a double sided array aligned to the z axis. There are few techniques discussed in the literature[18,19] for discretization of a continuous sensor; we closely follow the procedure given in Ref. 14.

B. Approximation

An array of sensors can only approximate the continuous aperture distribution described by Eq. (18). In our formulation this reduces to a numerical approximation of the following integral representation, which gives the output frequency response of the ideal continuous sensor for an arbitrary signal, having the frequency response $S(z,k)$, impinging on the array at position z:

$$Y(k)=\int_{-\infty}^{\infty}\rho^{(r)}(z,k)S(z,k)dz. \tag{21}$$

We use the well-known Trapezoidal integration method as used in Ref. 14 to approximate Eq. (21) by

$$\tilde{Y}(k)=\sum_{i=-L}^{L} g_i\rho^{(r)}(z_i,k)S(z_i,k), \tag{22}$$

where $\{z_i\}_{i=-L}^{L}$ is a set of $2L+1$ discrete sensor locations and g_i is a spatial weighting term which is used to account for the (possibly) nonuniformly spaced sensor locations. The role of g_i is better understood at the end of Sec. IV, where g_i is expressed in terms of sensor locations. The above approximation introduces two kind of errors: (i) the physical array is finite in extent and thus an infinite length integral has been replaced by a finite length summation; (ii) two spatially continuous functions $\rho^{(r)}(z,k)$ and $S(z,k)$ are replaced by their corresponding spatially discrete counterparts and hence there is a possibility of spatial aliasing and quantization errors.

C. Beamformer structure

We can consider $\rho^{(r)}(z_i,k)$ in Eq. (22) as the frequency response of a filter attached to the sensor at point z_i. By combining Eqs. (18) and (22) we write,

$$\tilde{Y}(k)=\sum_{i=-L}^{L} g_i S(z_i,k)\sum_{n=0}^{\infty}\alpha_n(k)G_n(r,k)F_n^0(z_i,k), \tag{23}$$

where

$$F_n^m(z_i,k)\triangleq\frac{\sqrt{2\pi}}{k}\varrho_n^m(z_i;k), \tag{24}$$

$$G_n(r,k)\triangleq\frac{k}{\sqrt{2\pi}}\frac{[R_n(\infty,k)]^2}{R_n(r,k)}. \tag{25}$$

The filters $F_n^0(z_i,k)$ depend on the elementary beam shapes and the position of the sensors. Using Eqs. (20) and (24), we get

$$F_n^0(z_i,k)=(-j)^n\frac{J_{n+1/2}(kz_i)}{\sqrt{kz_i}}, \tag{26}$$

where $J_{n+1/2}(\cdot)$ is the half-odd integer order Bessel function. We will call $F_n^m(z_i,k)$ the *elementary filters* (consistent with same terminology of ESIBs and elementary aperture functions). As in the case of ESIBs, these elementary filters are same for all beamformers, thus they may be useful in developing an effective parameterization for adaptation of beampatterns. Figure 4 illustrates the magnitude of the frequency response of the elementary filters of the first six modes versus the product of wave number k and the distance z to the associated sensor. We now demonstrate an important result regarding the elementary filters as a consequence of Eq. (26). Note that in Eq. (26), $F_n^0(z_i,k)$ is a symmetric function of spatial variable z_i and of the frequency variable k. Thus, these elementary filters have a *dilation property*:

Theorem 2. *All elementary filter responses $F_n^0(z_i,k)$ of the same mode n at different sensor locations z_i are identical up to a frequency dilation. That is*

$$F_n^0(z_i,k)=F_n^0\left(z_0,\frac{z_i}{z_0}k\right), \tag{27}$$

where z_0 is a reference sensor location.

The proof is given in the Appendix. With the output of the double-sided one-dimensional broadband array as defined in Eq. (23) and the dilation property of the elementary filters Eq. (41), we are led to a block diagram as shown in Fig. 5.

Regarding the beamformer structure we can make following comments:

(1) The proposed general beamformer has three levels of filtering associated with it. The first level consists of elementary beamformers, which are shown inside the dashed-line boxes in Fig. 5. Each of the elementary beamformers consists of elementary filters of the same mode which are connected to different sensors but are related by the dilation property. As a consequence, we have a set of unique beamformers for each and every mode n. In other words, the elementary beamformer of mode n produces the ESIB of the mode n. Further, the elementary beamformers are independent of the required beampattern specifications.

(2) The characteristic coefficients $\alpha_n(k)$ form the second level of filtering. Since the $\alpha_n(k)$ determine the shape of the beampattern, we call them *Beam Shape Filters*.

(3) The final set of filters $G_n(r,k)$ are independent of sensor locations but dependent on the operating radius r and the mode, and can be simplified using Eqs. (5), and (15), and (25),

$$G_n(r,k)=\frac{(-1)^{n+1}}{\pi^{3/2}}\sqrt{\frac{2}{r}}\frac{e^{j2(k-k_0)}}{H_{n+1/2}^{(1)}(kr)}, \tag{28}$$

where k_0 is an arbitrary chosen nominal frequency. By adjusting the parameter r in $G_n(r,k)$, the beamformer

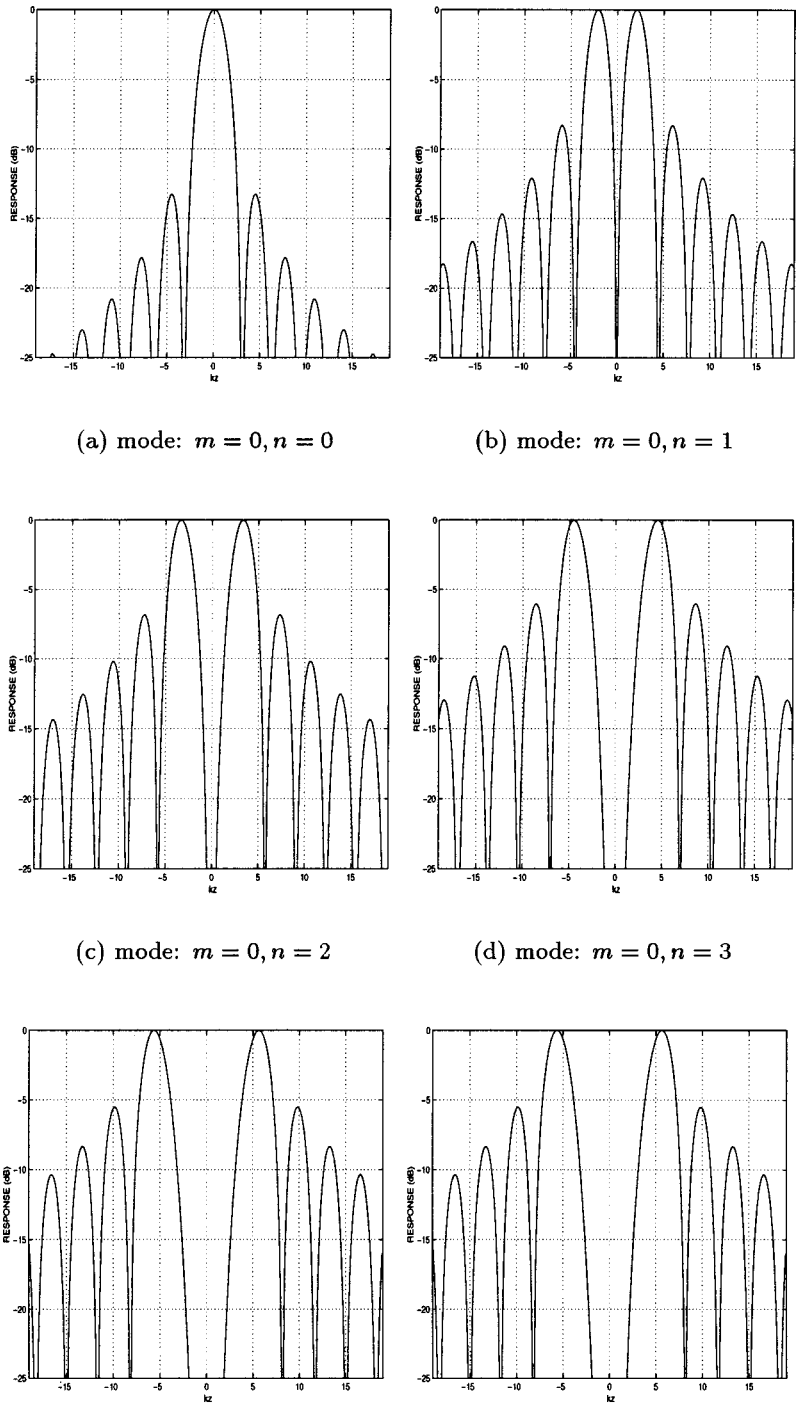

(a) mode: $m = 0, n = 0$ (b) mode: $m = 0, n = 1$

(c) mode: $m = 0, n = 2$ (d) mode: $m = 0, n = 3$

(e) mode: $m = 0, n = 4$ (f) mode: $m = 0, n = 5$

FIG. 4. Magnitude response of elementary filters $F_n^m(z,k)$ for $m=0$, plotted against the product of wave number k and the distance z to the associated sensor.

can be focused to a particular operating radius r either in nearfield or farfield. To highlight this important property we call the filters $G_n(r,k)$ *Radial Focusing Filters*.

(4) In Sec. I B we showed that an arbitrary beampattern can be decomposed into a weighted sum of ESIBs, where the weights are the characteristic coefficients $\alpha_n(k)$. Since each elementary beamformer produces an ESIB, an arbitrary beamformer can be implemented by adding them together with the decomposition coefficients $\alpha_n(k)$ of the required beampattern and the focusing filters $G_n(r,k)$. Because of these properties, our design is readily convertible to adaptive implementations, where only the beam shape filters and radial focusing filters need to be adapted.

(5) Finally, we will give some remarks about the general beamforming structure for two- and three-dimensional arrays. We can generalize the one-dimensional beamforming structure Eq. (23) for higher dimensions:

$$\tilde{Y}(k)=\sum_i g_i S(\mathbf{x}_i,k)\sum_{n=0}^{\infty} G_n(r,k)\sum_{m=-n}^{n}\alpha_n^m(k)F_n^m(\mathbf{x}_i,k), \tag{29}$$

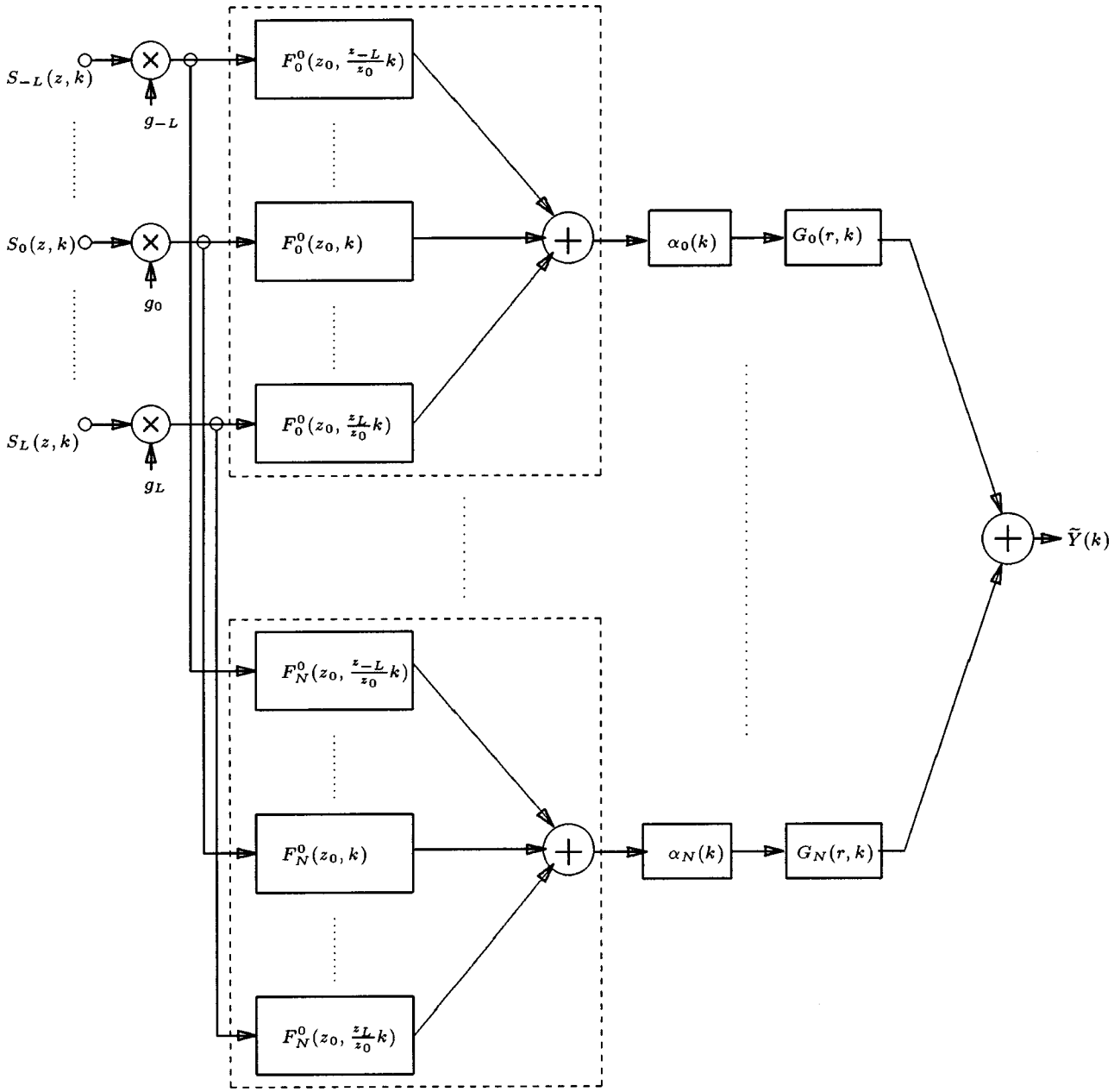

FIG. 5. Block diagram of a general one-dimensional broadband beamformer described by Eq. (23) where $F_n^0(z,k)$ is the elementary filters, $G_n(r,k)$ is the radial focusing filters, and $\alpha_n(k)$ are the beam shape filters.

where i is an integer and the sensors are placed at points $\{\mathbf{x}_i\}$ in the three-dimensional space. Let us assume that $\alpha_n^m(k)=0$ for $n>N$, where N is a positive integer. Then, there will be $N(N+2)$ elementary beamformers whose outputs are connected to the shape filters $\alpha_n^m(k)$. Compared with the one-dimensional beamformer (Fig. 5), there are additional summing points before the radial focusing filters $G_n(r,k)$ which add the outputs from the $(2n+1)$ shape filters $\alpha_n^m(k)$ of the same mode n but different m values.

D. Frequency invariant beamforming

We now consider the design of frequency invariant beamformers as a special case of the general beamforming theory developed above. This method generalizes the previous work.[14] The response of a frequency invariant beamformer is constant over an arbitrary design bandwidth. This type of beamformer is particularly useful for speech acquisition with microphone arrays.

An arbitrary beampattern over an arbitrary bandwidth can be expressed (in the farfield) by Eq. (17). It can be easily seen from Eq. (17) that if there is a sequence $\{\beta_n\}$ of mode dependent constants such that

$$\alpha_n(k)=\frac{\beta_n}{R_n(\infty,k)}, \tag{30}$$

for a range of frequencies $k\in[k_l,k_u]\subset(0,\infty)$, then the beampattern is frequency invariant over $k\in[k_l,k_u]$. This simplifies the general beamformer structure in Fig. 5, and in particular the product $G_n(r,k)\alpha_n(k)$ appearing in Eq. (23) can be simplified using Eqs. (25), (30), and (15):

$$G_n(r,k)\alpha_n(k)=\begin{cases}\beta_n\dfrac{k}{\sqrt{2\pi}} & \text{for farfield as } r\to\infty\\ \beta_n\dfrac{(-j)^{n+1}}{\pi}\sqrt{\dfrac{k}{r}}\dfrac{e^{j(k-k_0)}}{H^{(1)}_{n+1/2}(kr)} & \\ & \text{for nearfield at radius } r.\end{cases}\tag{31}$$

Here, to determine β_n, we need only to calculate $\alpha_n(k)$ for some nominal frequency $k_0\in[k_l,k_u]$ and then use Eq. (30).

IV. CHOICE OF SENSOR LOCATIONS

As an engineering problem, it is desirable to minimize the number of sensors required while maintaining acceptable performance. The major factor determining the minimum number of sensors possible is *spatial aliasing*. It is well known from the array literature[20] that a sensor spacing of $\lambda/2=\pi/k$ is needed to avoid spatial aliasing for a narrowband array operating at frequency k. For a broadband array, the upper limit of the design band frequency k_u must be used to avoid spatial aliasing in all frequencies, which suggests that a uniformly spaced array with π/k_u spacings is needed. However, such an array will give a smaller effective aperture for lower frequencies and larger aperture for a high frequencies which is undesirable. We will now show how to overcome this problem.

It has been shown,[13] by using the Parseval relation that the lower order modes (ESIBs) are the significant ones that give the broad beampattern features, whereas the higher order modes give the finer detail. We assert that sensible beampattern specifications should involve only the lower order modes. Hence, for most practical beampatterns, the characteristic coefficients $\alpha_n(k)$ are zero for larger n (typically $n>15$ or so). Let us assume $\alpha_n(k)=0$ for $n>N$, and thus we need to consider only ESIBs up to the mode N and the corresponding elementary filters.

We observe from Fig. 4 that the all elementary filters tend to have the characteristics of a bandpass filter except $n=0$ mode filter which has low-pass characteristics. Due to the dilation property of the elementary filters (see Theorem 2), the bandwidth and the cutoff frequencies of elementary filters are scaled with the location of the sensor to which they are connected. Therefore, as we move away from the origin, sensors become relatively inactive at higher frequencies. This means that the sensor spacings can be increased according to the highest frequency for which that sensor is effectively active. Consequently we can minimize the number of sensors as well as avoid the spatial aliasing.

For a given sensor location, the effective cutoff frequency of these filters increases as mode n increases. Let a_n be the product of the upper cutoff frequency $k_{c,n}$ of the mode n filter and the distance z to the associated sensor from the origin (i.e., $a_n=k_{c,n}z$), where $k_{c,n}$ is defined as the first zero crossing point above the pass band. (Note that these elementary filters are not ideal band pass filters and other definitions for cutoff frequencies such as half-power point can be used.) Table I lists the a_n of the first 16 elementary filters. Clearly the upper cutoff frequencies of elementary filters are related by $k_{c,1}<k_{c,2}<\cdots<k_{c,N}$. Therefore to make a sensor inactive for a given frequency k, it is sufficient to have $k_{c,N}<k$.

TABLE I. Upper cutoff frequencies of the first 16 elementary filters as a product of sensor location z and cutoff frequency $k_{c,n}$.

Mode (n)	$a_n=k_{c,n}z$
0	3.142
1	4.493
2	5.763
3	6.988
4	8.183
5	9.356
6	10.51
7	11.05
8	12.79
9	13.91
10	15.03
11	16.14
12	17.25
13	18.35
14	19.44
15	20.54

We can now give complete guidelines for choosing discrete sensor locations. Here we consider a double-sided array and begin with a sensor located at the array origin. Initially, to avoid spatial aliasing we need a sampling distance of $d_{k_u}=\lambda_u/2=\pi/k_u$. As long as the cutoff frequency k_i of the sensor located at z_i (which is equal to the cutoff frequency $k_{c,N}$ of the highest mode elementary filter attached to that sensor) is greater than the upper design frequency k_u, we need to maintain the above sampling distance. In this central portion of the array, the cutoff frequency of the ith sensor from either side of the origin is given by

$$k_i=\frac{a_N}{|i|\pi}k_u \quad \text{for } 0<|i|\leq Q,$$

where Q is the number of uniformly spaced sensors in one side of the array. As we move further away from the origin, i.e., as i grows, k_i decreases and will become less than k_u. The number of uniformly spaced sensors Q required to satisfy this constraint is given by

$$Q=\left\lceil\frac{a_N}{\pi}\right\rceil,\tag{32}$$

where $\lceil\cdot\rceil$ is the ceiling function. At this point, we can increase the sampling distance, just to avoid spatial aliasing at k_Q. Since the cutoff frequency k_{Q+1} of the $(Q+1)$th sensor is less than that of Qth sensor, the sampling distance can be further reduced for the next location. This process can be continued until the cutoff frequency of the last sensor becomes less than the lower design frequency k_l. The result of this is that the location of the ith sensor relative to the origin is given by

$$z_i=\begin{cases}\dfrac{i\pi}{k_u} & \text{for } |i|\leq Q\\ \dfrac{Q\pi}{k_u}\left(1+\dfrac{\pi}{\alpha_N}\right)^{|i|-Q} & \text{for } Q<|i|\leq L,\end{cases}\tag{33}$$

where L is the total number of sensors in one side of the array. Using the fact that the cutoff frequency of the last sensor has to be less than or equal to the lower design frequency k_l, the number of minimum sensors per one side required to implement a broadband array over the design band is

$$L = Q + \left\lfloor \frac{\log\left(\frac{a_N k_u}{Q\pi k_l}\right)}{\log\left(1+\frac{\pi}{a_N}\right)} \right\rfloor, \tag{34}$$

where $\lfloor\cdot\rfloor$ is the floor function. Note that we need a total of $2L+1$ sensors altogether to have double-sided array.

In order to complete the guidelines for a practical realization of the beamformer given by Eq. (22), we now consider the spatial weighting term g_i introduced in Eq. (22). Recall that the Trapezoidal rule has been used to approximate the integral in Eq. (21) by the summation in Eq. (22), hence the spatial weighting term g_i is given by (possibly) nonuniform sensor locations Eq. (33) as

$$g_i = \begin{cases} \frac{1}{2}(z_{i+1} - z_{i-1}) & \text{if } |i| < L \\ \frac{1}{2}(z_L - z_{L-1}) & \text{if } |i| = L \end{cases}. \tag{35}$$

Note that any other integral approximation method can be used instead of Trapezoidal rule and the spatial weighting term g_i needs to be derived appropriately.

V. DESIGN EXAMPLE

We will now consider an example of broadband beamforming design using the techniques introduced above.

Suppose we wish to design a one-dimensional microphone array for operations in the air at sea level so $c = 345\,\mathrm{ms}^{-1}$. Suppose the desired design frequency range is 300–3000 Hz, which is suitable for speech applications. Let us limit the maximum modes index N to be 15 as suggested in Sec. IV; thus we assume all beampatterns of our interest can be approximately decomposed to 16 ESIBs. Now we can determine the sensor locations and 16 elementary filters, which are independent of the desired response once the design band and the number of modes are decided. From Table I, the product of cutoff frequency $k_{c,n}$ and the sensor location z of the highest (15th) mode elementary filter is $a_N = 20.54$. Next the sensors are placed according to Eq. (33) and it is found from Eq. (34) that the total number of sensors required is 41 and the length of the double-sided array is 4.9 m. The sensor locations are given in Table II and the frequency response of the elementary filters are given by Eq. (26).

Now we consider an example beampattern which is for a beamformer having a constant Chebyshev 25-dB beampattern (shown in Fig. 6) over the frequency range 300–3000 Hz. The example chosen is a frequency invariant beampattern, although we stress that our design method is not restricted to frequency invariant beamformers. The frequency responses of the combined filters $G_N(r,k)\alpha_n(k)$ are given by Eq. (31). For this case, the beampattern is characterized by the coefficients β_n and we have calculated them for $n = 0,1,\ldots,15$ using Eqs. (38) and (3).

TABLE II. Locations z_i of the ith sensor of the example double-sided symmetric array in Sec. V (given in terms of the upper design wavelength λ_u).

i	z_i/λ_u
0	0.0
1	0.5
2	1.0
3	1.5
4	2.0
5	2.5
6	3.0
7	3.5
8	4.0
9	4.6
10	5.4
11	6.2
12	7.1
13	8.2
14	9.5
15	10.9
16	12.6
17	14.5
18	16.7
19	19.3
20	22.3

For the sake of efficient implementation, all the filters are collapsed into one filter per each sensor. This is possible, since the proposed beamformer structure (Fig. 5) consists of linear combinations of various filters.

The resulting beamformer is focused at the farfield by setting the parameter $r = 100\lambda_l$ in the focusing filter $G_n(r,k)$. The response of the beamformer to a farfield source is given in Fig. 7(b), which is close to the desired response. The response of the same farfield focused beamformer to a nearfield source at a radius $3\lambda_l$ is given Fig. 7(a).

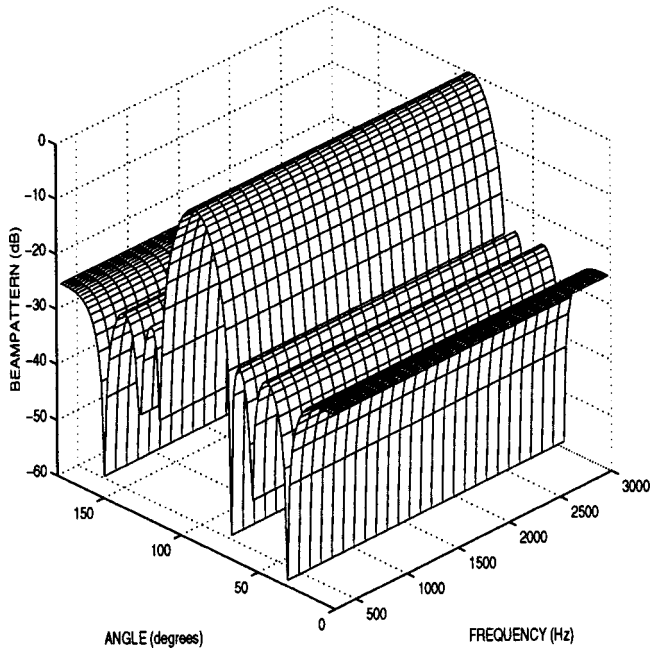

FIG. 6. Desired beamformer response used in the example in Sec. V: 25-dB Chebyshev beampattern over 300–3000 Hz.

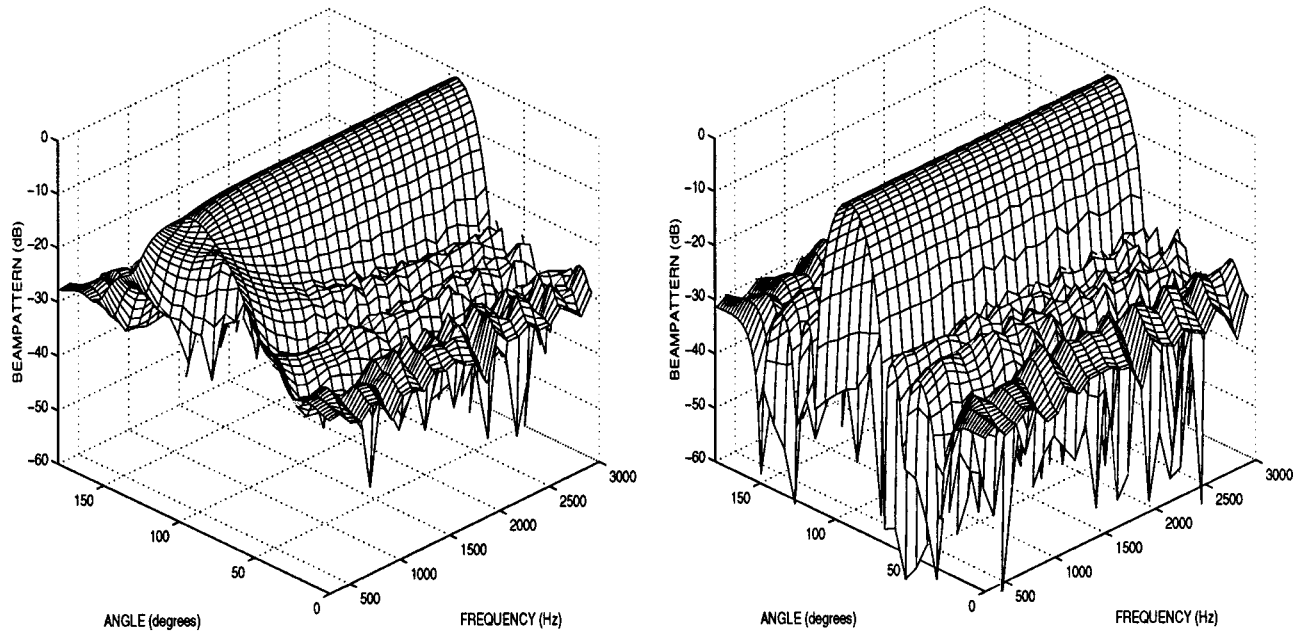

(a) (b)

FIG. 7. Response of the farfield focused [by setting $r=100\lambda_l$ in the focusing filter $G_n(r,k)$] beamformer (see Fig. 5) with 25-dB Chebyshev beampattern to (a) a nearfield source at a radius $3\lambda_l$, (b) a farfield source at $100\lambda_l$. This figure demonstrates that the farfield design is inadequate for the desired nearfield performance.

It is evident from this figure that the farfield design is inadequate for the desired nearfield performance. Next we focus the same beamformer to the nearfield by simply adjusting the variable r in the focusing filter $G_n(r,k)$ to $3\lambda_l$. The resulting beamformer is simulated in the nearfield and we observe an improved response in Fig. 8(a). The focused array response is close to the desired response with neglible variation in the main beam and slight ripples in the side lobes. We conclude that the approximation involved in discretizing and truncating the continuous sensor was sufficiently accurate. For completeness, we find the response of nearfield focused beamformer to a farfield source and show this in Fig. 8(b).

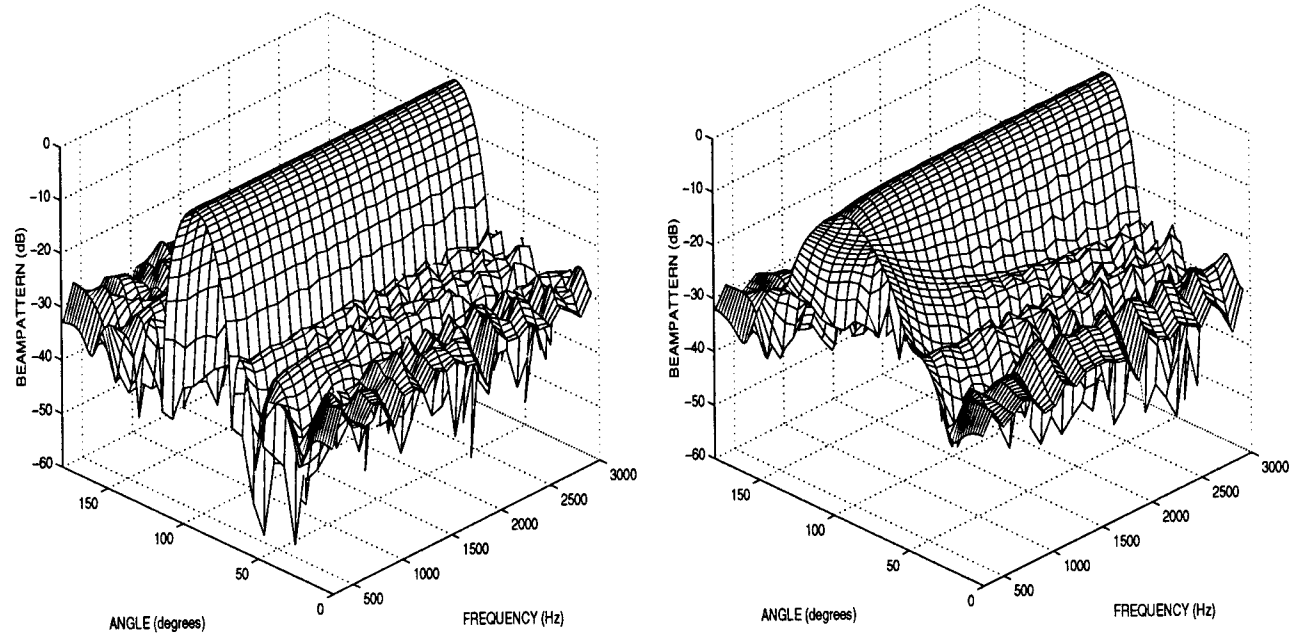

(a) (b)

FIG. 8. Response of the nearfield focused [by setting $r=3\lambda_l$ in the focusing filter $G_n(r,k)$] beamformer (see Fig. 5) with 25-dB Chebyshev beampattern to (a) a nearfield source at a radius $3\lambda_l$, (b) a farfield source at $100\lambda_l$.

The similar appearance of Figs. 7(a) and 8(b) can be explained by our previous work[13] on radial reciprocity, which established the asymptotic equivalence of two transformation problems: (i) determining the nearfield performance of a farfield beampattern specification, and (ii) determining the equivalent farfield beampattern corresponding to a nearfield beampattern specification. We can view Figs. 8(b) and 7(a) as the result of problems (i) and (ii), respectively, with beampattern specification given in Fig. 6 for both cases.

VI. CONCLUSIONS

A new method of general broadband beamforming covering farfield and nearfield operations has been proposed in this paper. The efficient parameterization afforded by this technique enables the beamformer to be focused to a desired radial distance using a single parameter and the shape of the beampattern can be controlled by another set of parameters. These properties make it potentially useful for adaptive beamformer design.

APPENDIX

Proof of Theorem 1: Let $b_\infty(\theta,\phi;k)=b(\theta,\phi;k)$ be the beampattern specification in the farfield and let $a_{r_A}(\theta,\phi;k)=b(\theta,\phi;k)$ be a separate design with the same beampattern shape but at radius r_A (nearfield) from the sensor origin. Then we use Eqs. (2) and (4) to write,

$$b_\infty(\theta,\phi;k)=\sum_{n=0}^{\infty}\sum_{m=-n}^{n}\alpha_n^m(k)R_n(\infty,k)\epsilon_n^m(\theta,\phi), \quad \text{(A1)}$$

$$a_{r_A}(\theta,\phi;k)=\sum_{n=0}^{\infty}\sum_{m=-n}^{n}\beta_n^m(k)R_n(r_A,k)\epsilon_n^m(\theta,\phi). \quad \text{(A2)}$$

Note that the two sets of coefficients $\alpha_n^m(k)$ and $\beta_n^m(k)$ uniquely represent two different beampatterns, $a_r(\theta,\phi;k)$ and $b_r(\theta,\phi;k)$ in $(r,\theta,\phi;k)$ space. We will equate Eqs. (A1) and (A2) and observe that Eq. (A1) is the beampattern b_r evaluated at $r=\infty$ and Eq. (A2) is the beampattern a_r evaluated at $r=r_A$. Hence $\alpha_n^m(k)$ and $\beta_n^m(k)$ are related by $\alpha_n^m(k)R_n(\infty,k)=\beta_n^m(k)R_n(r_A,k)$ and thus

$$\beta_n^m(k)=\frac{R_n(\infty,k)}{R_n(r_A,k)}\alpha_n^m(k), \quad \text{(A3)}$$

since $R_n(r_A,k)=r_A^{1/2}H_{n+1/2}(kr_A)\neq 0$. Using the nearfield–farfield transformation, the farfield equivalent to a_{r_A} is given by

$$a_\infty(\theta,\phi;k)=\sum_{n=0}^{\infty}\sum_{m=-n}^{n}\beta_n^m(k)R_n(\infty,k)\epsilon_n^m(\theta,\phi). \quad \text{(A4)}$$

From Eq. (13) the aperture illumination function corresponding to this farfield pattern is

$$\rho(x,y,z;k)=\sum_{n=0}^{\infty}\sum_{m=-n}^{n}\beta_n^m(k)R_n(\infty,k)\varrho_n^m(x,y,z;k). \quad \text{(A5)}$$

Finally, by substituting Eq. (A3) into Eq. (A5) completes the proof.

Proof of Theorem 2: Let $F_n^0(z_0,k)$ and $F_n^0(z_i,k)$ be the frequency response of two elementary filters of the same mode n and associated with sensors at $z_0\neq 0$ and z_i, respectively. Then from Eq. (26),

$$\begin{aligned}F_n^0(z_i,k)&=(-j)^n\frac{J_{n+1/2}(kz_i)}{\sqrt{kz_i}}\\&=(-j)^n\frac{J_{n+1/2}\left(k\dfrac{z_i}{z_0}z_0\right)}{\sqrt{k\dfrac{z_i}{z_0}z_0}}\\&=F_n^0\left(z_0,\frac{z_i}{z_0}k\right),\end{aligned} \quad \text{(A6)}$$

which is a dilation in the frequency domain.

[1] Y. Grenier, ''A microphone array for car environments,'' Speech Commun. **12**, 25–39 (1993).
[2] R. J. Mailloux, *Phased Array Antenna Handbook* (Artech House, Boston, 1994).
[3] F. Khalil, J. P. Jullien, and A. Gilloire, ''Microphone array for sound pickup in teleconference systems,'' J. Aud. Eng. Soc. **42**, 691–700 (1994).
[4] J. L. Flanagan, D. J. Johnston, R. Zahn, and G. W. Elko, ''Computer-steered microphone arrays for sound transduction in large rooms,'' J. Acoust. Soc. Am. **78**, 1508–1518 (1985).
[5] F. Pirz, ''Design of wideband, constant beamwidth, array microphone for use in the near field,'' Bell Syst. Tech. J. **58**, 1839–1850 (1979).
[6] S. Nordebo, I. Claesson, and S. Nordholm, ''Weighted Chebyshev approximation for the design of broadband beamformers using quadratic programming,'' IEEE Signal Process. Lett. **1**, 103–105 (1994).
[7] M. F. Berger and H. F. Silverman, ''Microphone array optimization by stochastic region contraction,'' IEEE Trans. Signal Process. **39**, 2377–2386 (1991).
[8] J. G. Ryan and R. A. Goubran, ''Nearfield beamforming for microphone arrays,'' Proceedings of the IEEE International Conferences on Acoustic Speech Signal Processing, pp. 363–366 (Munich, 1997).
[9] J. G. Ryan and R. A. Goubran, ''Optimum nearfield response for microphone arrays,'' in *Workshop on Applications of Signal Processing to Audio and Acoustics*, Oct. 1997.
[10] D. B. Ward and G. W. Elko, ''Mixed nearfield/farfield beamforming: A new technique for speech acquisition in a reverberant environment,'' in *Workshop on Applications of Signal Processing to Audio and Acoustics*, Oct. 1997.
[11] R. A. Kennedy, T. D. Abhayapala, and D. B. Ward, ''Broadband nearfield beamforming using a radial beampattern transformation,'' IEEE Trans. Signal Process. **46**, 2147–2156 (1998).
[12] A. C. Ludwig, ''Calculation of scattered patterns from asymmetrical reflectors,'' Tech. Rep. 32–140, Jet Propulsion Laboratory, California Institute of Technology, Pasadena, California, Feb. 1970.
[13] R. A. Kennedy, D. B. Ward, and T. D. Abhayapala, ''Nearfield beamforming using radial reciprocity,'' IEEE Trans. Signal Process. **47**, 33–40 (1999).
[14] D. B. Ward, R. A. Kennedy, and R. C. Williamson, ''Theory and design of broadband sensor arrays with frequency invariant farfield beampatterns,'' J. Acoust. Soc. Am. **97**, 1023–1034 (1995).
[15] J. H. Doles III and F. D. Benedict, ''Broadband array design using the asymptotic theory of unequally spaced arrays,'' IEEE Trans. Antennas Propag. **36**, 27–33 (1988).
[16] M. M. Goodwin and G. W. Elko, ''Constant beamwidth beamforming,'' Proc. IEEE Int. Conf. Acoust. Speech Sig. Process. (ICASSP93), Vol. 1, pp. 169–172 (1993).
[17] N. W. McLachlan, *Bessel Functions for Engineers* (Oxford University Press, London, 1961).
[18] R. S. Elliott, ''On discretizing continuous aperture distributions,'' IEEE Trans. Antennas Propag. **AP-25**, 617–621 (1977).
[19] C. F. Winter, ''Using continuous aperture illumination discretely,'' IEEE Trans. Antennas Propag. **AP-25**, 695–700 (1977).
[20] J. L. Flanagan, ''Beamwidth and useable bandwidth of delay-steered microphone arrays,'' AT&T Tech. J. **64**, 983–995 (1985).

Inverse problem of the wave equation and the Schwinger approximation

M. A. Hooshyar and Tuan H. Lam
University of Texas at Dallas, Programs in Mathematical Sciences, P.O. Box 830688, Richardson, Texas 75083-0688

M. Razavy
Theoretical Physics Institute, Department of Physics, University of Alberta, Edmonton, Alberta T6G 2J1, Canada

(Received 5 January 1998; accepted for publication 29 September 1999)

A new method of profile inversion for acoustic waves propagating in a medium with spherical inhomogeneity based on the Schwinger variational method is presented. The wave equation of interest is transformed into a Schrödinger equation, so that the Born approximation and the new method could also be applied at high frequencies. It is shown that the new method is stable and is more accurate than the Born approximation. To illustrate the method, an exactly solvable analytical example is presented. Also numerical examples using synthetic data, with and without additive noise, are given and the corresponding inversion results and the stability of the method are studied. © *2000 Acoustical Society of America.* [S0001-4966(00)03701-2]

PACS numbers: 43.60.Pt, 03.65.Nk [JCB]

INTRODUCTION

Efficient and stable methods for nonobtrusive estimation of radially dependent acoustical wave speed of a spherical flaw is of great interest in many diverse areas such as nondestructive testing and remote sensing. Exact methods for solving such a problem are known.[1–3] However, these methods appear to be computationally intensive and sensitive to the range of the available data. There exists a rich literature on profile inversion based on the Born approximation.[4,5] Such methods based on Born approximation are stable and are not computationally too intensive, however, their range of applicability are usually limited to weak scatterers. This limitation is due to the fact that the Born approximation is based on the assumption that the field inside the scattering region is the same as the incident field. For the Schrödinger equation, this assumption is not valid for low incident energies. On the other hand, for the wave equation, the Born approximation is more accurate at lower frequencies. However, in the inverse problem the input data entail the complete spectrum of the scattering amplitude from the very low to the high frequencies, therefore an approximate form of the amplitude which is valid for all frequencies is desirable. To this end we apply the Liouville transform to the wave equation and change it to a Schrödinger equation, where the Born approximation works well at high frequencies. To arrive at the desired approximation, we take the next step and appeal to the Schwinger formalism with plane wave trial wave functions and find an approximation that works at low as well as high frequencies.[6–8] A method of inversion using Schwinger's approach has already been applied to construct the potential in the Schrödinger equation from the knowledge of the *s*-wave scattering amplitude.[7] Here we want to show that the same method can be extended to the case of the Helmholtz equation and compare the results of this inversion to those obtained from the Born approximation for radially inhomogeneous media. In Sec. I we develop the needed relations, based on Schwinger approximation, for the scattering problem of a plane pressure wave incident on a spherical flaw. Section II deals with the inversion problem and develops a new procedure for recovery of the wave speed of the medium from the scattering data. Results and conclusions based on a detailed study of an exactly solvable realistic acoustic medium are presented in Sec. III. In addition, numerical performance of the proposed inversion method using synthetic data with and without added noise is also investigated.

I. THE DIRECT PROBLEM

In this section the propagation of an acoustic plane pressure wave, traveling in a medium with constant density, in a direction denoted by the unit vector $\hat{\mathbf{k}}$ is studied. The wave speed of the medium, $c(r)$, is assumed to depend on the radial coordinate, with the radial distance being measured from the origin of the coordinate system. We also assume that the wave speed $c(r)$ will approach a constant value c_0 as r tends to infinity. It is known that the wave field $P(k,\mathbf{r})$ associated with such a problem obeys the Helmholtz equation:[9]

$$\Delta P(\mathbf{k},\mathbf{r}) + \frac{\omega^2}{c^2(r)} P(\mathbf{k},\mathbf{r}) = 0. \tag{1}$$

A time dependence of the form $\exp(-i\omega t)$ with fixed frequency ω is assumed for the above wave field. The constant $k \equiv \omega/c_0$ is the wave number for the region sufficiently away from the center of the coordinate system, $\mathbf{k} = k\hat{\mathbf{k}}$, and $\mathbf{r}$ is the position vector where the field is being considered. Expansion of the wave field is spherical harmonics, Y_l^m, leads to

$$P(\mathbf{k},\mathbf{r}) = (kr)^{-1} \sum_{lm} Y_l^m(\hat{\mathbf{r}}) Y_l^{m*}(\hat{\mathbf{k}}) \psi_l(k,r), \tag{2}$$

where $\hat{\mathbf{r}}=\mathbf{r}/r$ and ψ_l is the radial dependent part of the wave field, which satisfies the following differential equation:

$$\psi_l''(k,r)+k^2U(r)\psi_l(k,r)=\frac{l(l+1)}{r^2}\psi_l(k,r), \tag{3}$$

with prime denoting differentiation with respect to r, the index of refraction is denoted by $n(r)=c_0/c(r)$, and $U(r)=n^2(r)$. The regular solution of the above equation is of special interest. Such a solution satisfies the boundary condition[1]

$$\lim_{r\to 0}(2l+1)!!r^{-l-1}\psi_l(k,r)=1. \tag{4}$$

It should be noted that information on $U(r)$ for large values of r can be directly measured. Hence, only the recovery of the function $U(r)$ for small values of r from the asymptotic information on $\psi_l(k,r)$ is of interest in this study. However, from Eq. (3) it can be noted that for small values of r the term $l(l+1)/r^2$ for $l\neq 0$ will dominate over $U(r)$, making the scattering data not very sensitive to the form of $U(r)$ for small values of r. From these observations it follows that behavior of $U(r)$ for small values of r can be best studied from the asymptotic behavior of the radial wave field for $l=0$. In other words the wave function of interest in this study is the regular solution to the differential equation

$$\psi_0''(k,r)+k^2U(r)\psi_0(k,r)=0. \tag{5}$$

In order to make use of existing results[10] for the above equation, let us make use of the Liouville transformation and consider the modified wave field $\phi(k,x)=E(x)\psi_0(k,r)$ which satisfies the equation

$$\frac{d^2}{dx^2}\phi(k,x)+[k^2-u(x)]\phi(k,x)=0, \tag{6}$$

with

$$x=\int_0^r n(s)ds, \quad E(x)=n^{1/2}(r),$$

and

$$u(x)=E^{-1}(x)\frac{d^2}{dx^2}E(x)=-n^{-3/2}(r)\frac{d^2}{dr^2}n^{-1/2}(r). \tag{7}$$

The choice of x value at $r=0$ is motivated by the desire to make Eq. (6) to be the exact analog of the Schrödinger equation for $l=0$ waves. For the physical index of refraction $n(r)>0$ and $n(r)\to 1$ as $r\to\infty$, therefore the defined variable x will have the desired form, $x\in[0,\infty)$. In other words, just like the Schrödinger equation for central potentials, the differential equation (6) is defined on the half-line $x\geqslant 0$. Based on existing results for the Schrödinger equation,[1] sufficient conditions for the existence of a physically acceptable solution to Eq. (6) are

$$\int_0^\infty |u(x)|dx<\infty \quad \text{and} \quad \int_0^\infty x|u(x)|dx<\infty. \tag{8}$$

In order to express these sufficient conditions in terms of the wave speed $c(r)$ and also to be able to relate the asymptotic behavior of $\phi(k,x)$ to the asymptotic behavior of $\psi_0(k,r)$, let us make use of Eq. (7) and derive the relation

$$x(r)=\alpha+r, \text{ as } r\to\infty, \quad \text{with } \alpha=\int_0^\infty [n(s)-1]ds. \tag{9}$$

Substituting Eq. (9) in Eq. (8) we note that $dx=n(r)dr$ leads to following inequalities:

$$\begin{aligned}\int_0^\infty |u(x)|dx&=\int_0^\infty \left|n^{-1/2}(r)\frac{d^2}{dr^2}n^{-1/2}(r)\right|dr\\&=\frac{1}{c_0}\int_0^\infty c^{1/2}(r)\left|\frac{d^2}{dr^2}c^{1/2}(r)\right|dr,\end{aligned} \tag{10}$$

$$\begin{aligned}\int_0^\infty x|u(x)|dx&=\int_0^\infty x(r)\left|n^{-1/2}(r)\frac{d^2}{dr^2}n^{-1/2}(r)\right|dr\\&=\frac{1}{c_0}\int_0^\infty x(r)c^{1/2}(r)\left|\frac{d^2}{dr^2}c^{1/2}(r)\right|dr,\\&\leqslant\frac{|\alpha|}{c_0}\int_0^\infty c^{1/2}(r)\left|\frac{d^2}{dr^2}c^{1/2}(r)\right|dr\\&\quad+\frac{1}{c_0}\int_0^\infty rc^{1/2}(r)\left|\frac{d^2}{dr^2}c^{1/2}(r)\right|dr.\end{aligned} \tag{11}$$

From the above inequalities and Eq. (8), it follows that sufficient conditions for the existence of a solution to Eq. (6) can be stated as:

$$\begin{aligned}&|\alpha|<\infty, \quad c(r)<\infty, \quad \frac{d^2}{dr^2}c^{1/2}(r) \text{ exists for } r\in[0,\infty),\\&\int_0^\infty\left|\frac{d^2}{dr^2}c^{1/2}(r)\right|dr<\infty \quad \text{and} \quad \int_0^\infty r\left|\frac{d^2}{dr^2}c^{1/2}(r)\right|dr<\infty.\end{aligned} \tag{12}$$

With the above conditions satisfied, it can be shown that the regular solution to Eq. (6) is also the solution of the following Fredholm integral equation:

$$\phi(k,x)=\phi_0(k,x)+\int_0^\infty G(k,x,s)u(s)\phi(k,s)ds, \tag{13}$$

with $\phi_0(k,x)=\sin(kx)$ and $G(k,x,s)$ being the free Green's function for Eq. (6):

$$G(k,x,s)=-\frac{1}{k}\begin{cases}\sin(kx)\cos(ks) & \text{if } x\leqslant s\\ \cos(kx)\sin(ks) & \text{if } x\geqslant s\end{cases}. \tag{14}$$

From Eqs. (13) and (14), it follows that

$$\lim_{x\to 0}\phi(k,x)=0, \tag{15}$$

which is consistent with the boundary condition for regular solutions as given by Eq. (4). We also note that as x tends to infinity, Eqs. (13) and (14) can be used to find the asymptotic form of $\phi(k,x)$:

$$\phi(k,x)\sim\sin(kx)-\frac{D(k)}{k}\cos(kx) \quad \text{for } x\to\infty, \tag{16}$$

with $D(k)$ being directly related to the wave speed by the relation

$$D(k)=\langle\phi_0|u|\phi\rangle\equiv\int_0^\infty \phi_0(k,x)u(x)\phi(k,x)dx. \tag{17}$$

Since $D(k)$ is related to the asymptotic behavior of the wave function, Eq. (16), hence information on $D(k)$ can be obtained and used as the input to the inversion problem at hand. However, we need to develop the connection between $D(k)$ and the wave speed further before we proceed with the inversion problem. In order to deduce the needed relations, following Ref. 7, let us consider the Born series expansion of the solution to Eq. (13). Using the operator notation, we can write the Born series as:

$$\phi=\phi_0+Gu\phi_0+(Gu)^2\phi_0+(Gu)^3\phi_0+\cdots. \tag{18}$$

Substitution of above equation in Eq. (17) leads to the relation

$$D(k)=\sum_{n=0}^{\infty} M_n(k) \quad \text{with} \quad M_n(k)=\langle\phi_0|u(Gu)^n|\phi_0\rangle. \tag{19}$$

In the direct problem, where $u(x)$ is known and if it is such that Eq. (18) is convergent, then the advantage of using Eq. (19) over Eq. (17) for computing $D(k)$ resides on the fact that unlike Eq. (17) we can compute $D(k)$ from Eq. (19) without having to first find the wave function ϕ. Furthermore, Eq. (19) is more amenable to approximation. For example,

$$D_B(k)\equiv M_0(k)=\langle\phi_0|u|\phi_0\rangle \tag{20}$$

is the first Born approximation to $D(k)$ and, as can be seen from Eq. (20), it is equivalent to approximating ϕ by ϕ_0 in Eq. (17). Of course, if the Born series as given by Eq. (18) is convergent, then a finite sum of $M_n(k)$ would approximate $D(k)$ very well.[11] However, in the direct problem, higher order Born approximations are cumbersome to calculate, and inversions based on these approximations are computationally sensitive to the input data. In order to overcome this difficulty and work with a better and simpler estimate of $D(k)$, we consider the Schwinger approximation. To this end we start with a quadratic functional $S[\phi]$:

$$S[\phi]=2\langle\phi_0|u|\phi\rangle-\langle\phi|u-uGu|\phi\rangle. \tag{21}$$

The extremum of $S[\phi]$ which is obtained by variation of ϕ and satisfies the integral equation (13); however, other trial functions for ϕ can also be used in Eq. (21) to find approximate solutions. In particular if we replace ϕ by $d_0\phi_0$, then the Schwinger functional $S[\phi]$ becomes a quadratic form in d_0 and the extremum of $S[d_0\phi_0]$ obtained by setting $(d/dd_0)S[d_0\phi_0]$ equal to zero yields the following expression for d_0:

$$d_0=\frac{M_0(k)}{M_0(k)-M_1(k)}. \tag{22}$$

This trial plane wave used in the Schwinger's functional yields accurate results even at low k values[8] for the Schrödinger equation.

Making use of such an approximation of ϕ in Eq. (17), we find the Schwinger approximation to $D(k)$:

$$D_S(k)=\frac{M_0^2(k)}{M_0(k)-M_1(k)}. \tag{23}$$

Because of the appearance of $M_1(k)$ in Schwinger approximation, one may wonder about the relative accuracy of Schwinger approximation as compared to the second Born approximation, as given by Eq. (19):

$$D_{2B}(k)\equiv M_0(k)+M_1(k). \tag{24}$$

Denoting the difference between the exact $D(k)$ and its Schwinger and second Born approximations as $e_S=D(k)-D_S(k)$ and $e_{2B}=D(k)-D_{2B}$, respectively, one can show from Eqs. (23) and (24) that

$$e_S(k)=e_{2B}-\frac{M_1^2(k)}{M_0(k)-M_1(k)}. \tag{25}$$

In other words, when the Born series is rapidly convergent so that $M_1(k)$ is small, then the Schwinger approximation and the second order Born approximation have about same degree of accuracy. In fact, further information about these approximations can be found if we consider the regular solution to Eq. (6) with the following boundary conditions:

$$\lim_{x\to 0}\tilde{\phi}(k,x)=0 \quad \text{and} \quad \lim_{x\to 0}\frac{d}{dx}\tilde{\phi}(k,x)=1. \tag{26}$$

In this case the solution to Eq. (6), $\tilde{\phi}(k,x)$, satisfies the Voltera integral equation:[1]

$$\tilde{\phi}(k,x)=\frac{\sin(kx)}{k}+\int_0^\infty \frac{\sin k(x-s)}{k}u(s)\tilde{\phi}(k,s)ds. \tag{27}$$

Also, it can be shown[1] that for large real values of k

$$\tilde{\phi}(k,x)=\frac{\sin(kx)}{k}+O\left(\frac{1}{k^2}\right). \tag{28}$$

The connection between the regular solution $\tilde{\phi}(k,x)$ and the physical solution $\phi(k,x)$ is found by determining the asymptotic behavior of $\tilde{\phi}(k,x)$ from Eq. (27);

$$\tilde{\phi}(k,x)=\tilde{A}(k)\sin(kx)+\tilde{B}(k)\cos(kx) \quad \text{for } x\to\infty, \tag{29}$$

where

$$\tilde{A}(k)=\frac{1}{k}+\int_0^\infty \frac{\cos(ks)}{k}u(s)\tilde{\phi}(k,s)ds, \tag{30}$$

and

$$\tilde{B}(k)=-\int_0^\infty \frac{\sin(ks)}{k}u(s)\tilde{\phi}(k,s)ds. \tag{31}$$

Comparison between Eqs. (29) and (16) leads to the desired connection:

$$\phi(k,x)=\frac{\tilde{\phi}(k,x)}{\tilde{A}(k)} \quad \text{and} \quad D(k)=-k\frac{\tilde{B}(k)}{\tilde{A}(k)}. \tag{32}$$

Making use of above relations and Eq. (28) one can find the behavior of the quantities under consideration for large real values of k:

$$\phi(k,x)=\sin(kx)+O\left(\frac{1}{k}\right),\quad M_1(k)=O\left(\frac{1}{k}\right), \tag{33}$$

$$D(k)=M_0(k)+O\left(\frac{1}{k}\right),\quad D_S(k)=M_0(k)+O\left(\frac{1}{k}\right), \tag{34}$$

$$e_S=e_B+O\left(\frac{1}{k}\right),\quad \text{and}\quad e_S=e_{2B}+O\left(\frac{1}{k^2}\right), \tag{35}$$

where $e_B=D(k)-D_B(k)=D(k)-M_0(k)$. As expected, the above relations indicate that for large values of k the Schwinger approximation and second Born approximation rapidly approach each other and as k tends to infinity all the above approximations tend to the first Born approximation, M_0 defined by Eq. (20), which can be rewritten as

$$M_0(k)=\tfrac{1}{2}[\tilde{u}_0-\tilde{u}(2k)], \tag{36}$$

with

$$\tilde{u}_0=\int_0^\infty u(x)dx\quad\text{and}\quad \tilde{u}(2k)=\int_0^\infty u(x)\cos(2kx)dx. \tag{37}$$

Appealing to the Riemann–Lebesque theorem,[12] we note that for $u(x)\in L^1$, the function $\hat{u}(2k)$ will tend to zero as k tends to infinity. Combining the above asymptotic information, we find

$$\lim_{k\to\infty} D(k)=\lim_{k\to\infty} D_S(k)=\lim_{k\to\infty} M_0(k)=\tfrac{1}{2}\tilde{u}_0. \tag{38}$$

From Eq. (37) it is evident that if one can find $M_0(k)$ from information on $D(k)$, then $u(x)$ can be recovered by making use of the inverse cosine transform. With this aim in mind, let us then conclude this section by connecting $D(k)$ to the actual acoustic wave function $\psi_0(k,r)$, by noting that $\psi_0(k,r)=n^{-1/2}\phi(k,x)$ and $x=\alpha+r$ as r tends to infinity. Thus as r tends to infinity, x will also tend to infinity, $n\to 1$, and since the asymptotic form of the acoustic wave function will be a linear combination of $\sin(kr)$ and $\cos(kr)$, we come to the conclusion that:

$$\begin{aligned}\psi_0(k,r)&=\phi(k,\alpha+r)\\&=A(k)\sin(kr)+B(k)\cos(kr)\quad\text{for } r\to\infty.\end{aligned} \tag{39}$$

Substituting the asymptotic form of $\phi(k,x)$ as r tends to infinity in the above equation and making use of Eq. (16), we find the desired connection:

$$D(k)=-k\frac{D_0(k)-\tan(k\alpha)}{1+D_0(k)\tan(k\alpha)}, \tag{40}$$

where $D_0(k)=[B(k)]/[A(k)]$, which is directly related to the physical acoustic wave function and therefore measurable. From Eq. (40), it follows that the data of interest, $D(k)$, can be determined from the empirical data $D_0(k)$ if α is known. Of course, in the direct problem where $c(r)$ is known, α can be found from Eq. (9). However, in the inverse problem, where $c(r)$ is not known, we need to deduce the constant α from the empirical data $D_0(k)$. To accomplish this aim, let us relate $A(k)$ and $B(k)$ to $\tilde{A}(k)$ and $\tilde{B}(k)$:

$$A(k)=\tilde{A}(k)\cos(k\alpha)-\tilde{B}(k)\sin(k\alpha), \tag{41}$$

$$B(k)=\tilde{A}(k)\sin(k\alpha)+\tilde{B}(k)\cos(k\alpha). \tag{42}$$

Next we make use of Eqs. (28), (30), and (31) in the above equations, and we find

$$\tilde{A}(k)=\frac{1}{k}+O\left(\frac{1}{k^2}\right)\quad\text{and}\quad\tilde{B}(k)=O\left(\frac{1}{k^2}\right)\ \text{ as }\ k\to\infty. \tag{43}$$

Substitution of Eq. (43) in Eqs. (41) and (42) leads to following estimates:

$$A(k)=\frac{\cos(k\alpha)}{k}+O\left(\frac{1}{k^2}\right)$$

and (44)

$$B(k)=\frac{\sin(k\alpha)}{k}+O\left(\frac{1}{k^2}\right)\ \text{ as }\ k\to\infty.$$

From Eq. (44) it follows that

$$D_0(k)=\frac{B(k)}{A(k)}=\tan(k\alpha)+O\left(\frac{1}{k}\right)\ \text{ as }\ k\to\infty. \tag{45}$$

In order to estimate α, let us consider the relation

$$\begin{aligned}&\cos^2(k\alpha)\frac{d}{dk}[D_0(k)-\tan(k\alpha)]\\&=\frac{2\alpha\tilde{A}(k)\tilde{B}\sin(k\alpha)\cos(k\alpha)}{A^2}\\&\quad+\frac{[\tilde{B}'(k)\tilde{A}(k)-\tilde{B}(k)\tilde{A}'(k)+\alpha\tilde{B}^2(k)]\cos^2(k\alpha)}{A^2},\end{aligned} \tag{46}$$

where prime indicates differentiation with respect to k. Next, following the same procedure that led to Eq. (28), one finds

$$\tilde{A}'(k)=O\left(\frac{1}{k^2}\right)\quad\text{and}\quad\tilde{B}'(k)=O\left(\frac{1}{k^2}\right)\ \text{ as }\ k\to\infty. \tag{47}$$

Taking the limit of Eq. (46) as k tends to infinity leads to the desired estimate of α:

$$\alpha=\lim_{k\to\infty}\cos^2[\tan^{-1}(D_0(k))]\frac{d}{dk}[D_0(k)]. \tag{48}$$

Having found all the needed relations and the connection between $D(k)$ and the empirical data $D_0(k)$, we are now in a position to present the new inversion procedure based on the Schwinger approximation.

II. THE INVERSE PROBLEM

A direct method of inversion of the problem of acoustic waves using successive Born approximation has been advocated previously (e.g., in Ref. 13), which avoids Liouville transformation and thus can be applied to cases where there are discontinuities in the medium, such as layers. However, in this direct method of inversion, multiple Fourier transforms are needed to obtain accurate results. But it is well-known that the numerical computation of these transforms is very sensitive to initial data and cutoff frequencies. Thus in

this section the problem of finding the wave speed $c(r)$ from the information on $D(k)$ as a function of k using the formulation of the previous section will be studied. The main relation which allows such a connection to be possible is Eq. (36). Let us rewrite Eq. (36) in the form of cosine Fourier transform of the unknown function $u(x)$:

$$\tilde{u}(2k)=\int_0^\infty u(x)\cos(2kx)dx=\tilde{u}_0-2M_0(k). \tag{49}$$

Taking the inverse Fourier cosine of above equation, we find

$$u(x)=\frac{4}{\pi}\int_0^\infty [\tilde{u}_0-2M_0(k)]\cos(2kx)dk. \tag{50}$$

It should be stated that the above relation is an exact relation and knowing $M_0(k)$ enables us to find $u(x)$ exactly. However, the available inversion data are not $M_0(k)$, but it is $D(k)$ which can be found from $D_0(k)$ via Eq. (40). From Eq. (35), it follows that zeroth approximation to $M_0(k)$ can be achieved if we replace $M_0(k)$ in Eq. (50) by $D(k)$. In other words, the data $D(k)$ are assumed to be well approximated by the first term of the Born series:

$$M_0(k)=D_B(k)\approx M_0^0(k)=D(k). \tag{51}$$

With such an assumption the potential $u(x)$ is then estimated to be

$$u_B(x)=\frac{4}{\pi}\int_0^\infty [\tilde{u}_0-2M_0^0(k)]\cos(2kx)dk. \tag{52}$$

However, based on the analysis presented in Sec. I, we would expect a better approximation to $u(x)$ could be obtained if we assume that the data are well approximated by the Schwinger function $D_S(k)$:

$$D_S(k)\approx D(k), \tag{53}$$

and use Eq. (23) to find a better approximation to $M_0(k)$ as compared to the Born approximation, $M_0^0(k)$. Since knowing $D_S(k)$ does not directly lead to evaluation of $M_0(k)$, we develop an iterative procedure to find $M_0(k)$. The starting value for $M_0(k)$ in this iterative procedure will be its Born approximation, $M_0^0(k)$. However, since $M_1(k)$ is not known, we also need to develop a method to find $M_1(k)$ from the information on $M_0(k)$. A simple procedure can be developed, if we make use of another representation for the Green's function defined in Eq. (14):

$$G(k,x,s)=\frac{2}{\pi}\mathbf{P}\int_0^\infty \frac{\sin(qx)\sin(qs)}{k^2-q^2}dq. \tag{54}$$

Substitution of the above form of the Green's function in Eq. (19) leads to direct relation between $M_1(k)$ and $M_0(k)$:

$$M_1(k)=\frac{2}{\pi}\mathbf{P}\int_0^\infty \frac{\left[M_0\left(\frac{k+q}{2}\right)-M_0\left(\frac{k-q}{2}\right)\right]^2}{k^2-q^2}dq. \tag{55}$$

Here we note that for *s*-wave scattering by local potentials, the off-shell matrix elements of the scattering matrix in the Born approximation can be found from the knowledge of the on-shell elements only.[14] Having found the relation between $M_1(k)$ and $M_0(k)$, the desired iterative procedure for finding $M_0(k)$ is obtained if we view the solution to Eq. (23) as equivalent to the problem of finding the zero of the function $\tilde{F}(M_0(k))=D_S(k)[M_0(k)-M_1(k)]-M_0^2(k)=0$. Rewriting this problem as a fixed point problem, an iterative solution to it takes the form

$$M_0^{(n+1)}(k)=M_0^{(n)}(k)+\text{sign}[D(k)]\times[D(k)(M_0^{(n)}(k)-M_1^{(n)}(k))-(M_0^{(n)}(k))^2]. \tag{56}$$

In arriving at the above equation, we have made use of Eq. (53) and have also introduced the quantity sign$[D(k)]$, so that the fixed point iteration could converge. Following a similar procedure as presented by Prosser,[11] one can show that for suitably restricted data $\hat{F}(M_0(k))\equiv M_0(k)+\text{sign}[D(k)][D(k)[M_0(k)-M_1(k)]-M_0^2(k)]$ is a contraction mapping. Thus the solution to the fixed point problem $M_0(k)=\hat{F}(M_0(k))$ exists and can be found by iteration. The formal analysis of needed conditions on data for $\hat{F}(M_0(k))$ to be a contraction mapping is beyond the scope of this article. In this preliminary study we limit our investigation to numerically testing the performance of the present inversion method for some realistic profiles.

To carry out the proposed iteration procedure for suitably restricted input data, once $M_0^{(n+1)}(k)$ is found from Eq. (55), the associated $M_1^{(n+1)}(k)$ is calculated using Eq. (55). In other words,

$$M_1^{(n+1)}(k)=\frac{2}{\pi}\mathbf{P}\int_0^\infty \frac{\left[M_0^{(n+1)}\left(\frac{k+q}{2}\right)-M_0^{(n+1)}\left(\frac{k-q}{2}\right)\right]^2}{k^2-q^2}dq. \tag{57}$$

That is, to find a better approximation of $M_0(k)$, we first start with $M_0^0(k)$, as given by Eq. (51). Then we use Eq. (57) to find $M_1^0(k)$ which will enable us to find the next approximation to $M_0(k)$, that is, $M_0^{(1)}(k)$, from Eq. (56). Such an iterative approximation to $M_0(k)$ can be continued until the found $M_0^{(n)}(k)$ does not vary appreciably from its previous value. That is,

$$\int_0^\infty |M_0^{(n+1)}(k)-M_0^{(n)}(k)|dk<\epsilon, \tag{58}$$

where $\epsilon>0$ is a sufficiently small number and is related to the desired accuracy of our numerical computations.

Having found $M_0^{(n)}(k)$ in the framework of the Schwinger approximation, the potential $u(x)$ can then be found by substituting $M_0^{(n)}(k)$ in Eq. (50):

$$u_S(x)=\frac{4}{\pi}\int_0^\infty [\tilde{u}_0-2M_0^{(n)}(k)]\cos(2kx)dk. \tag{59}$$

Since the potential $u(x)$ is given as a function of the auxiliary variable x and not the actual variable r, one needs to find a relation between these two variables both representing distance, by making use of Eq. (7):

$$\frac{d^2}{dx^2}E(x)=u(x)E(x)$$

$$\text{with } \lim_{x\to\infty}E(x)=1 \quad \text{and } \lim_{x\to\infty}\frac{d}{dx}E(x)=0. \tag{60}$$

Having found $E(x)$ from Eq. (60), we are then in a position to relate the variable x to the radial variable of interest r, using Eq. (7) and the fact that $dx=n(r)dr$:

$$r=\int_0^x \frac{1}{E^2(x')}dx'. \tag{61}$$

Since $n(r)=E^2(x)>0$, it follows from above relation that $r(x)$ is a one-to-one function of the auxiliary variable x. By calculating this one-to-one relation using Eq. (61), the relation between the auxiliary variable x and the actual variable r can be deduced. From this found relation, $x(r)$, we are then in a position to determine the wave speed as a function of the radial distance r:

$$c(r)=\frac{c_0}{E^2(x(r))}. \tag{62}$$

III. RESULTS AND DISCUSSION

To illustrate the proposed method further, we first study an analytically solvable example which will enable us to see some of the important details of the inversion procedure. Having studied this particular example, we then study other examples numerically so that we can evaluate the numerical performance of the new inversion procedure and compare it with the Born method.

For the analytical example, let us consider a medium with following index of refraction:

$$n(r)=\begin{cases}(\lambda r+\beta)^{-2} & \text{if } 0\leqslant r\leqslant b\beta\\ 1 & \text{if } b\beta\leqslant r\end{cases}, \tag{63}$$

where $\beta=(\lambda b+1)^{-1}$, with λ and b being two arbitrary but positive constants. It can be shown by direct substitution that for such an index of refraction, the following function is the solution to Eq. (5):

$$\psi_0(k,r)=F(r)\left[\sin(kf(r))+\frac{\lambda\sin(kb)}{1+(\lambda/2k)\sin(2kb)}G(k,f(r),b)\right], \tag{64}$$

where the Green's function, G, is defined by Eq. (14),

$$F(r)=\begin{cases}\lambda r+\beta & \text{if } 0\leqslant r\leqslant b\beta\\ 1 & \text{if } b\beta\leqslant r\end{cases},$$

and (65)

$$f(r)=\begin{cases}\dfrac{r}{\lambda\beta r+\beta^2} & \text{if } 0\leqslant r\leqslant b\beta\\ \alpha+r & \text{if } b\beta\leqslant r\end{cases},$$

and $\alpha=\lambda\beta b^2$. As can be seen from Eq. (63), the proposed profile does not belong to the class of profiles considered by our method, Eq. (12), however, as we will see, for this special example the proposed procedure can be carried out analytically, the technical difficulties can be overcome, and our inversion method can be applied to recover the profile.

In order to find the scattering data associated with the proposed profile, we look at the asymptotic form of Eq. (64) and compare it with Eq. (39) to find that

$$D_0(k)=\frac{\sin(k\alpha)-\dfrac{\overline{D}(k)}{k}\cos(k\alpha)}{\cos(k\alpha)+\dfrac{\overline{D}(k)}{k}\sin(k\alpha)}$$

$$\text{with } \overline{D}(k)=\frac{\lambda\sin^2(kb)}{1+\dfrac{\lambda}{2k}\sin(2kb)}. \tag{66}$$

Having computed the synthetic data $D_0(k)$, for the inverse problem we can use these data as input and find the associated profile. An interesting observation can be made here regarding the data. If the functional dependence of the data is given like in Eq. (66), then the value of α and the function $\overline{D}(k)$ are known and no further processing is necessary. However, in actual applications where the synthetic data $D_0(k)$ are only known for different values of k, then such information by itself is not enough to give us both α and the function $D(k)$. However, by using Eq. (45), and taking the asymptotic form of the data, $D_0(k)$, one is able to find α. Having found α, then $\overline{D}(k)$ for different k values are found from $D_0(k)$. Knowing α and $\overline{D}(k)$, we obtain $D(k)$ from Eq. (40):

$$D(k)=\overline{D}(k)=\frac{\lambda\sin^2(kb)}{1+\dfrac{\lambda}{2k}\sin(2kb)}. \tag{67}$$

Having computed the needed input data $D(k)$, following the proposed procedure, we assume $D_S(k)=D(k)$ and make use of Eq. (23) to find $M_0(k)$ which satisfies the following equation:

$$D_S(k)=\frac{\lambda\sin^2(kb)}{1+\dfrac{\lambda}{2k}\sin(2kb)}=\frac{M_0^2(k)}{M_0(k)-M_1(k)}. \tag{68}$$

An iterative procedure for finding $M_0(k)$, solution to Eq. (68), is given in Sec. II. However, for this example, we can find the solution by inspection:

$$M_0(k)=\lambda\sin^2(kb). \tag{69}$$

To prove that the above $M_0(k)$ is the solution to Eq. (68), we find $M_1(k)$ from Eq. (55):

$$M_1(k)=\frac{2}{\pi}\mathbf{P}\int_0^\infty \frac{\left[\lambda\sin^2\left(\frac{k+q}{2}b\right)-\lambda\sin^2\left(\frac{k-q}{2}b\right)\right]^2}{k^2-q^2}dq$$

$$=-M_0(k)\frac{\lambda}{2k}\sin(2kb). \tag{70}$$

Substitution of Eqs. (69) and (70) in the right-hand side of Eq. (68) verifies that $M_0(k)$ defined by Eq. (69) is the solution of interest.

Once $M_0(k)$ is determined, we are in the position to find the potential $u(x)$ from Eq. (50), if we first find the constant $\tilde{u}_0$ from Eq. (38). However, since the example under consideration does not satisfy the sufficiency conditions stated in Eq. (12), the limit of $M_0(k)$ in the usual sense does not exist. But if we interpret the limit appearing in Eq. (38) in the distributional sense, and appeal to the Riemann–Lebesque theorem and similar arguments as given for deriving Eq. (38), we find

$$\tilde{u}_0=\lambda. \tag{71}$$

Substitution of Eqs. (69) and (71) in Eq. (50) and performing the necessary integrals lead to the following relation:

$$u(x)=\lambda\,\delta(x-b), \tag{72}$$

where at this stage, $x\epsilon[0,\infty)$ is just an auxiliary variable. Next we make use of Eq. (72) in the differential equation (60) and solve the resulting equation:

$$E(x)=\begin{cases}[\lambda(b-x)+1] & \text{if } 0\leqslant x\leqslant b\\ 1 & \text{if } b\leqslant x\end{cases}. \tag{73}$$

Substitution of Eq. (73) in Eq. (7) will result in finding the index of refraction as a function of the auxiliary variable x:

$$n=E^2(x) \tag{74}$$

Of course the inversion procedure is complete only when we have recovered the index of refraction as a function of the actual variable r. To do so, we substitute Eq. (73) in Eq. (61) and integrate the resulting equation:

$$r=\begin{cases}\lambda^{-1}[(\lambda(b-x)+1)^{-1}-\beta] & \text{if } 0\leqslant x\leqslant b\\ x-\alpha & \text{if } b\leqslant x\end{cases}. \tag{75}$$

Solving Eq. (75) for x as a function of r, we find

$$x=\begin{cases}\dfrac{r}{\lambda\beta r+\beta^2} & \text{if } 0\leqslant r\leqslant b\beta\\ \alpha+r & \text{if } b\beta\leqslant r\end{cases}. \tag{76}$$

Substituting of Eq. (76) in Eq. (74), we find the recovered index of refraction $n(r)$ is identical to the index of refraction which we started with i.e., Eq. (63). In view of the fact that the proposed inversion method is based on the Schwinger approximation, such an exact recovery of the index of refraction is unexpected. However, similar results have been found by Razavy[13] and Devaney and Weglein[15] for approximate inversion of the delta function potentials. What we find especially remarkable about our finding is that in previous known examples, e.g., Refs. 13, 15, one is dealing with a nonrealistic medium where the index of refraction is directly related to the delta function; however, in the exactly solvable example presented in this work, we are dealing with a very physical and reasonable medium whose index of refraction is given by Eq. (63). This observation raises a tantalizing question regarding the class of potentials which can be exactly recovered by approximate inversion methods, and also the possibility of extending the proposed method to media with index of refractions which do not satisfy all of the sufficiency conditions specified by Eq. (12).

Having presented an analytically solvable example illustrating the details of the proposed inversion procedure, we now test the new inversion method numerically by first computing $D_0(k)$ for some specified realistic inhomogeneous media, and then use this numerically computed synthetic data, $D_0(k)$, to find the associated profile. In all of our numerical experimentations, we assume that the wave speed $c(r)$ becomes a constant c_0 after a sufficient distance away from the origin, $r\geqslant R$. With such an assumption, it then follows that the synthetic data $D_0(k)$ can be found from the relations

$$D_0(k)=\frac{k\cos(kR)-\tilde{D}(k,R)\sin(k,R)}{k\sin(kR)+\tilde{D}(k,R)\cos(kR)}$$

$$\text{with } \tilde{D}(k,R)=\frac{\psi_0'(k,R)}{\psi_0(k,R)}. \tag{77}$$

The logarithmic derivative of the wave function $\psi_0(k,R)$, that is, $\tilde{D}(k,R)$, is found by solving Eq. (5) numerically, for different values of k. Once $D_0(k)$ is calculated, we use it for large values of k to find α from Eq. (48). Knowing α, the modified data $D(k)$ for different values of k are found from Eq. (40). Next, from the information on $D(k)$ for large values of k and Eq. (38) we estimate the constant $\tilde{u}_0$ which is defined by Eq. (37). Having obtained all the needed quantities for the inversion procedure, we are then in a position to find $u(x)$ from Eq. (50). In this preliminary study we have used the trapezoidal rule for integration. Also the integration appearing in Eq. (50) over the infinite interval $[0,\infty)$ was only carried out over the finite interval $[0,k_{\max}]$, where $k_{\max}$ is sufficiently large enough so that Eq. (59) can be well approximated by

$$u_S(x)=\frac{4}{\pi}\int_0^{k_{\max}}[\tilde{u}_0-2M_0^{(n)}(k)]\cos(2kx)dk. \tag{78}$$

Making use of Eqs. (35)–(38), we note that Eq. (57) can be well approximated by the following equation where the integration is only over a finite interval:

$$M_1^{(n)}(k)=\frac{2}{\pi}\mathbf{P}\int_0^{3k_{\max}}\frac{\left[M_0^{(n)}\left(\frac{k+q}{2}\right)-M_0^{(n)}\left(\frac{k-q}{2}\right)\right]^2}{k^2-q^2}dq. \tag{79}$$

Based on the asymptotic behavior of $M_0(k)$ studied in Sec. I, we have made use of Eq. (38) and approximated $M_0^n(k)$ for $k_{\max}\leqslant k\leqslant 2k_{\max}$ appearing in Eq. (79) by the asymptotic value $\frac{1}{2}\tilde{u}_0$. Also in evaluating the integral appearing in Eq. (79), we have used the fact that $M_0^{(n)}(k)$ is an even function of k.

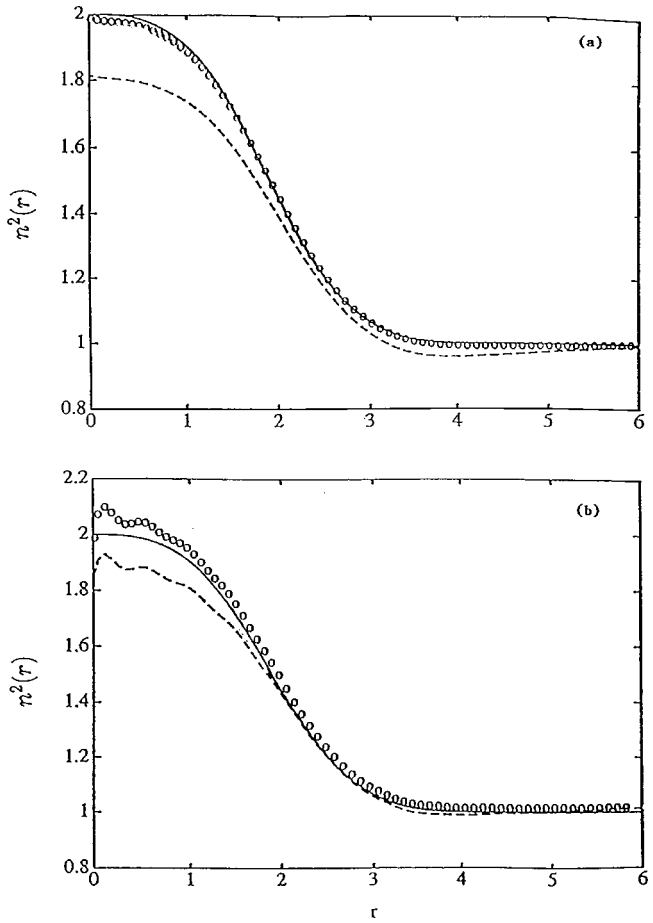

FIG. 1. The solid line represents the profile $n^2(r)=1+e^{-r^3/10}$ used as input. The dashed line is the result of inversion obtained from Born approximation. The points shown as *o* are the results of using the proposed inversion method. (a) presents inversion results using exact synthetic data and (b) recovers the potential from data with 5% random error added to the exact synthetic data.

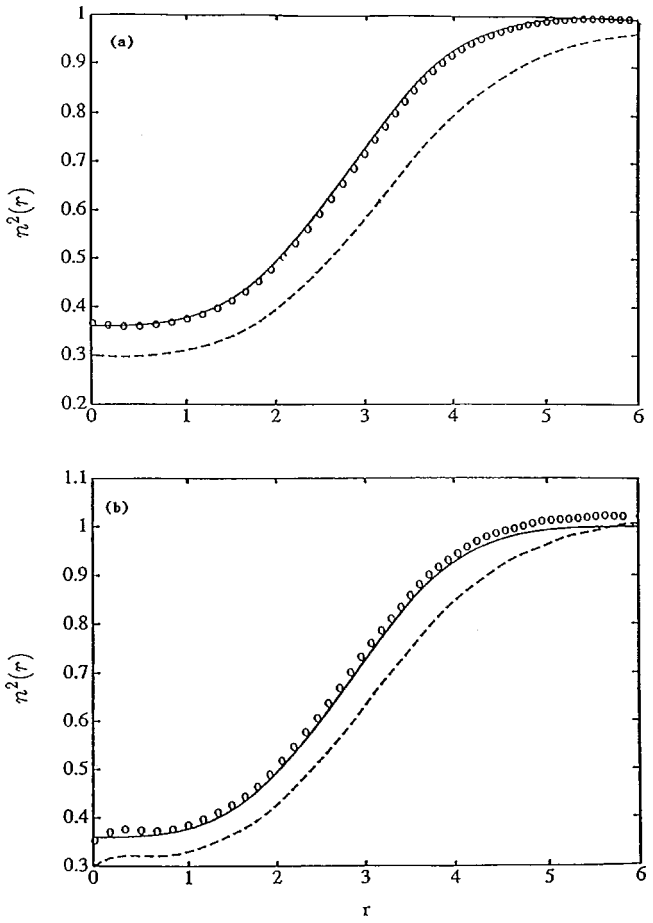

FIG. 2. Same as Fig. 1, except that the wave speed inside the flaw is higher than outside. $n^2(r)=(1-0.4e^{-r^3/27})^2$.

After finding $u_S(x)$ from Eq. (78), we are now in a position to use Eq. (60) and obtain the connection between the auxiliary variable x and the radial variable r. This task is considerably simplified if we note from Eqs. (7) and (9) that if the wave speed $c(r)=c_0$ for $r\geqslant R$, then $u(x)=0$, for $x \geqslant x_R\equiv\alpha+R$. Therefore, we need not solve the differential equation (60) for all values of $x\geqslant 0$, but just for values of $x\epsilon[0,x_R]$. In other words, we only need to solve the following modified version of Eq. (7):

$$\frac{d^2}{dx^2}E(x)=u(x)E(x)$$

$$\text{with } E(x_R)=1 \quad \text{and} \quad \frac{d}{dx}E(x)\Big|_{x_R}=0. \quad (80)$$

This differential equation is solved for $E(x)$ by using the finite difference method. With the help of Eq. (61) the connection between the auxiliary variable x and the actual variable r is established. Knowing the relation between x and r, we then use Eq. (62) to find the wave speed of the medium. Numerical results for some representative profiles are presented in Figs. 1–4. In order to make the examples scale independent, we have divided the distance r and the wave number k by their respective units. $R=10$ and $k_{\max}=5$ were used for all the numerical examples presented in this study. Two thousand partitions were used for all the integrations. It was found that 50 iterations were enough to make ϵ appearing in Eq. (58) to become less than 10^{-4} for all the examples considered. Stability of the Born and the Schwinger methods was tested numerically by adding random error of not more than 5% to the exact synthetic data. The inversion results for the synthetic data with added noise are also shown in Figs. 1–4. As expected, inversion results using Schwinger approximation reproduce the profiles more accurately than the Born approximation. The procedure also does well both in low and high velocity zones. The two methods show significant stability in the presence of additive random error in the synthetic data. However, it seems that in some of the examples the Born inversion does show a little more stability as compared with the Schwinger inversion. However, this does not appear to be the case for all examples considered. For example, in Fig. 4, the Schwinger inversion method seems to show better stability as compared to Born inversion. Of course, in general since the proposed inversion method requires more computation, it may show more sensitivity to the random error as compared to the Born approach. However, the numerical results presented in Figs. 1–4 indicate that this inversion method is sufficiently stable.

We conclude this section by noting that the present inversion method based on the Schwinger wave function can

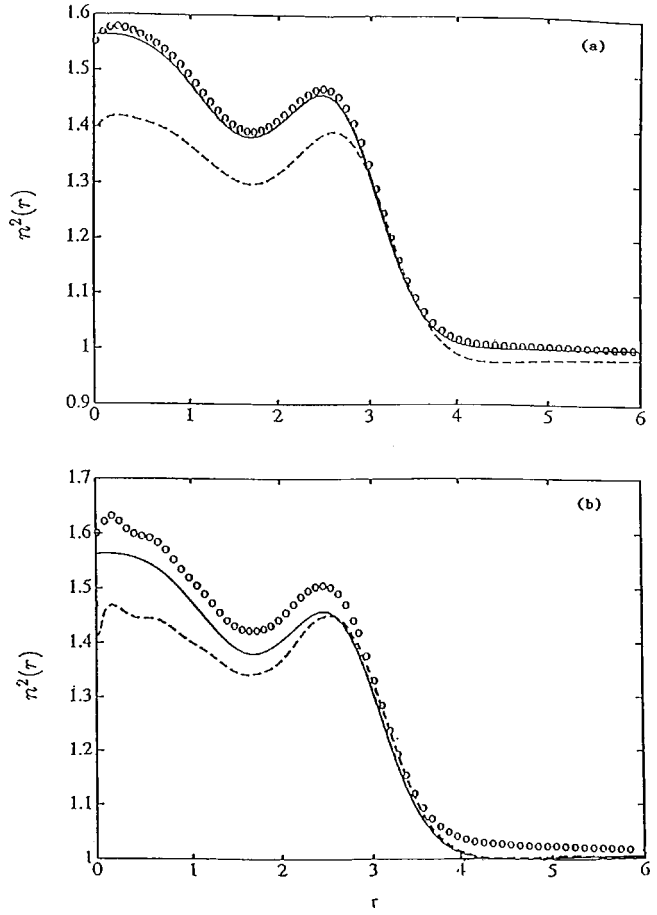

FIG. 3. Result of inversion for the profile $n^2(r)=[1+(e^{-(r/2)^2}+0.4r^{-(r-2.7)^2})^2]^2$. Other details are as in Fig. 1.

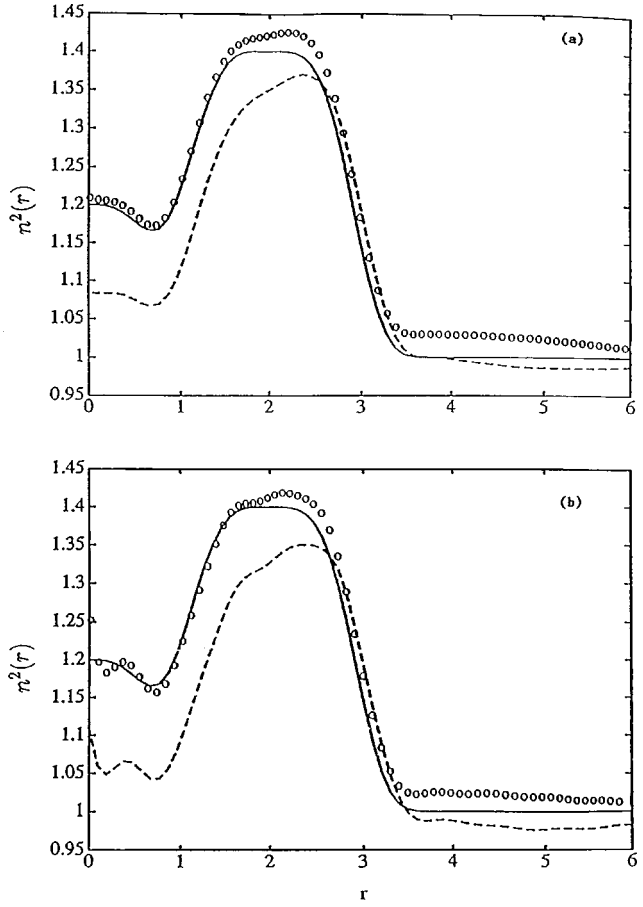

FIG. 4. Same as Fig. 3, expect for different flaw structure. $n^2(r)=1+0.2e^{-r^3}+0.4e^{-(r-2)^4}$.

be extended and better approximation to the wave function inside the scattering region can be found by using the nth order variational wave function:

$$\phi_{n\text{th}}=[d_0+d_1(Gu)+d_2(Gu)^2+\ldots,d_n(Gu)^n]\phi_0, \tag{81}$$

where d_j's are the variational constants. Similar to the procedure presented in Sec. I, Eq. (21), these constants can be found by making the associated functional extremum. Also, following similar procedure as presented in Sec. I, the scattering data, $D(k)$, can be represented in a form which is analogous to Eq. (23):

$$D_{n\text{th}}(k)=M_0+M_1+M_2+\cdots+\frac{M_{n-1}^2(k)}{M_{n-1}(k)-M_n(k)}, \tag{82}$$

with M_j having a similar form as given by Eq. (55):

$$M_j(k)=\left(\frac{2}{\pi}\right)^j \mathbf{P}\int_0^\infty\cdots\int_0^\infty \frac{W(k,q_1)W(q_1,q_2)\cdots W(q_{j-1},q_j)W(q_j,k)}{(k^2-q_1^2)(k^2-q_2^2)\cdots(k^2-q_j^2)}\,dq_1\,dq_2\cdots dq_j, \tag{83}$$

where $j=1,2,\ldots,n$ and

$$W(k,q)=M_0\left(\frac{k+q}{2}\right)-M_0\left(\frac{k-q}{2}\right). \tag{84}$$

It can be noticed that for the case when $n=1$, Eqs. (81) and (83) reduce to their analogs, which are Eqs. (23) and (55), respectively. We find the form of Eq. (83) to be remarkable, since it follows from Eq. (84) that if $M_0(k)$ is known, then all the other needed $M_j(k)$'s can be found from Eq. (83). In other words, the procedure presented for the Schwinger approximation can be directly extended to higher order approximations. That is, we again start with the Born approximation of the data, $M_0^0(k)=D(k)$ as the input and find the associated $M_1^0(k),M_2^0(k),\ldots,M_n^0(k)$ from Eq. (83). Next an updated version of $M_0(k)$, which is denoted by $M_0^1(k)$, is found from Eq. (82) in a similar manner as described for the case of the Schwinger approximation, Eq. (56). Therefore, in principle, the proposed method can be extended and more accurate inversion results could be found at the expense of more intensive computations.

Finally one may inquire whether this method can be

applied to two- or three-dimensional cases where the wave speed is a function of both radial and angular coordinates. The problem, apart from a very special and unrealistic case where $\omega^2/c^2(\mathbf{r})$ in Eq. (1), is of the form

$$\frac{\omega^2}{c^2(\mathbf{r})} = k^2\left[U(r) + \frac{f(\theta)}{r^2} + \frac{g(\phi)}{r^2 \sin^2\theta}\right], \tag{85}$$

is not separable and for nonseparable problems there is no simple Liouville transformation. Thus a straightforward extension of the present method does not seem feasible. However, it should be pointed out that for the two-dimensional Helmholtz equation, a Liouville transformation has been found by Bellman.[16] It is applicable to wave speeds whose logarithms are harmonic functions. It is very tantalizing to see if Bellman's Liouville transformation can be used to extend the present inversion method to two-dimensional problems.

[1] K. Chadan and P. C. Sabatier, *Inverse Problems in Quantum Scattering Theory*, 2nd ed. (Springer-Verlag, New York, 1989).

[2] G. A. Baker, Jr., ''Solution of an inverse, elastic-wave scattering problem,'' J. Acoust. Soc. Am. **71**, 785–789 (1982).

[3] M. A. Hooshyar, ''An inverse scattering problem of elastic-waves,'' J. Acoust. Soc. Am. **77**, 844–849 (1985).

[4] R. Clayton and R. Stolt, ''A Born–WKBJ inversion method for an acoustic reflection data,'' Geophysics **46**, 1559–1567 (1981).

[5] R. G. Keys and A. B. Weglein, ''Generalized linear inversion and the first Born theory for acoustic stratified media,'' J. Math. Phys. **24**, 1444–1449 (1983).

[6] C. Duneczky and R. E. Wyatt, ''Lanczos recursion, continued fractions, Padé approximants, and variational principles in quantum scattering theory,'' J. Chem. Phys. **89**, 1448 (1988).

[7] M. A. Hooshyar, T. H. Lam, and M. Razavy, ''Inverse scattering problem and the Schwinger approximation,'' Can. J. Phys. **70**, 282–288 (1992).

[8] H. H. Chan and M. Razavy, ''Plane wave approximation for the scattering amplitude,'' Can. J. Phys. **42**, 1017–1029 (1964).

[9] P. M. Morse and K. V. Ingard, *Theoretical Acoustics* (McGraw-Hill, New York, 1968).

[10] R. G. Newton, *Scattering Theory of Waves and Particles*, 2nd ed. (Springer-Verlag, New York, 1982).

[11] R. T. Prosser, ''Formal solution of inverse scattering problem IV,'' J. Math. Phys. **23**, 2127–2130 (1982).

[12] E. Hewitt and K. Stromberg, *Real and Abstract Analysis* (Springer-Verlag, New York, 1965).

[13] M. Razavy, ''Determination of the wave velocity in an inhomogeneous medium from reflection coefficient,'' J. Acoust. Soc. Am. **58**, 956 (1975).

[14] M. Razavy and R. J. W. Hodgson, ''Dispersion relation approach to the nuclear structure calculation,'' Nucl. Phys. A **149**, 65–85 (1970).

[15] A. J. Devaney and A. B. Weglein, ''Inverse scattering using the Heitler equation,'' Inverse Probl. **5**, L49 (1989).

[16] R. Bellman, ''On a Liouville transformation of $u_{xx}+u_{yy}+a^2(x,y)u=0$,'' Bollettino della Unione Mathematica Italiano **13**, 535 (1958).

Correlated cortical populations can enhance sound localization performance

Rick L. Jenison[a)]
Department of Psychology, University of Wisconsin, Madison, Wisconsin 53706

(Received 8 March 1999; revised 16 July 1999; accepted 20 September 1999)

Neurons within cortical populations often evidence some degree of response correlation. Correlation has generally been regarded as detrimental to the decoding performance of a theoretical vector-averaging observer making inferences about the physical world—for example, an observer estimating the location of a sound source. However, if an alternative decoder is considered, in this case a Maximum Likelihood estimator, performance can improve when responses in the population are correlated. Improvement in sound localization performance is demonstrated analytically using Fisher information, and is also shown using Monte Carlo simulations based on recordings from single neurons in cat primary auditory cortex. © *2000 Acoustical Society of America.* [S0001-4966(00)01501-0]

PACS numbers: 43.64.Bt, 43.64.Qh [RDF]

INTRODUCTION

Statistical independence of cortical responses is often assumed for the theoretical study of neural coding. Under the assumption of independence, simple population averaging of even weakly correlated sensory neurons can result in diminished performance compared to a neural population composed of independent neurons (Zohary *et al.*, 1994; Shadlen *et al.*, 1996; Shadlen and Newsome, 1998). However, it can be shown that a Maximum Likelihood (ML) estimator with knowledge of the population response covariance matrix can demonstrate improvement in estimation performance when the responses within a population are correlated. This perhaps surprising result can be demonstrated both analytically using Fisher information, and confirmed using Monte Carlo simulation. Much has been written on the topic of estimation theory, the roots of which extend back to Ronald Fisher (1925). Estimation theory is concerned with the problem of finding a best value for an unknown parameter from a measured sample. We, as well as others, have previously investigated the consequences of broad receptive fields on population coding using Fisher information and the Cramer–Rao lower bound (CRLB) under the assumption of independence (Paradiso, 1988; Seung and Sompolinsky, 1993; Jenison, 1998). More recently Abbott and Dayan (1999) have shown that, in theory, correlation can have a positive impact on the acuity of a population code using the analytic tools of Fisher information and the CRLB. However, their analysis was restricted to the coding of a single parameter, hence they did not consider the impact of correlation on cross-information between parameters such as sound source localization in two dimensions, i.e., azimuth and elevation.

The CRLB is a lower bound on the variance of any unbiased estimator, and is derived from Fisher information with respect to a family of parametric probability distributions. The CRLB is inversely related to Fisher information mathematically, and intuitively. As the magnitude of Fisher information increases, we expect estimation error variance to diminish. In addition, it can be shown that ML estimation performance asymptotically approaches the CRLB as the number of measurements becomes large (Blahut, 1987). If the CRLB can be derived analytically, it can be used to compute the minimum possible variance about any value estimated by a theoretical ideal observer. The power of this analysis is the following: whatever form of biological information processing ensues on the population of cortical responses, the very best performance, defined in terms of estimation variability, is given by the CRLB. This lower bound applies to the brain, as well as any other decoding mechanism. Under the assumption of independence, even very broad and nonuniform spatial receptive fields in primary auditory AI cortex can demonstrate psychophysical localization acuity with as few as ten cells in the population (Jenison, 1998). Although it is quite unlikely that this optimal form of estimation is literally performed by cortical circuitry, some recent modeling work has shown that simple recurrent neural networks can be used to approximate the mechanics of ML estimation (Pouget *et al.*, 1998). ML estimation provides an upper bound on performance given empirically measured responses and affords one way of assessing the relative magnitude of information available at different levels along a sensory pathway.

I. MODELS

We have recently described a methodology by which cortical receptive fields that depend on the location (azimuth θ and elevation ϕ) of a virtual sound source in space can be functionally modeled (Jenison *et al.*, 1998). The methods used to collect the single neuron responses that constrain the receptive field models are described in Brugge *et al.* (1996), which are briefly summarized here. Barbiturate-anesthetized cats were fitted with hollow ear pieces sealed into the external ear canals through which virtual acoustic space stimuli (Musicant *et al.*, 1990) were presented. Single neurons were recorded extracellularly in the high-frequency region of the left AI field of auditory cortex. The latency of the first-spike

[a)]Electronic mail: jenison@wavelet.psych.wisc.edu

in response to transient virtual acoustic space stimuli was used as the primary response variable for von Mises basis function approximation[1] (Jenison *et al.*, 1998). Although we have found these basis functions to yield accurate models of spatial receptive fields, the analysis described here does not depend on any specific receptive field model. Hence the ith modeled spatial receptive field in a cortical population will be denoted *symbolically* as $\widehat{\mathbf{SRF}}_i(\theta,\phi)$. The derivative operators applied to the receptive fields, i.e., $(\partial/\partial\theta)\widehat{\mathbf{SRF}}_i(\theta,\phi)$ and $(\partial/\partial\phi)\widehat{\mathbf{SRF}}_i(\theta,\phi)$, denote the receptive field gradient or slope relative to a change in azimuth or elevation. The ''hat'' ($\hat{}$) implies a mathematical model that approximates the behavior of a set of actual measurements.[2]

In this study, performance is measured in terms of estimation variability of a chosen target direction resulting from a sample of population responses. The structure of the noise covariance between neurons, under a simplifying assumption of homogeneous correlation[3] within the population, can be formally characterized as

$$\mathbf{G}_{\text{resp}}=\begin{bmatrix} \sigma_1^2 & \rho_{\text{resp}}\sigma_1\sigma_2 & \cdots & \rho_{\text{resp}}\sigma_1\sigma_N \\ \rho_{\text{resp}}\sigma_2\sigma_1 & \sigma_2^2 & \vdots & \rho_{\text{resp}}\sigma_2\sigma_N \\ \vdots & \cdots & \ddots & \vdots \\ \rho_{\text{resp}}\sigma_N\sigma_1 & \rho_{\text{resp}}\sigma_N\sigma_2 & \cdots & \sigma_N^2 \end{bmatrix}, \quad (1)$$

where σ_i^2 is the variance of the noise about the ith modeled receptive field and ρ_{resp} is the response correlation coefficient. The off-diagonal cells correspond to covariance between the ith and jth neurons. Given this covariance structure, the probability density function of the population response array, denoted $\overrightarrow{\text{resp}}$, given a particular location in space (θ, ϕ) under a Gaussian assumption is

$$p(\overrightarrow{\text{resp}}\,|\,\theta,\phi)=\frac{1}{\sqrt{(2\pi)^N|\mathbf{G}_{\text{resp}}|}} \times\exp\left(-\tfrac{1}{2}(\overrightarrow{\text{resp}}-\widehat{\mathbf{SRF}}(\theta,\phi))^T \times\mathbf{G}_{\text{resp}}^{-1}(\overrightarrow{\text{resp}}-\widehat{\mathbf{SRF}}(\theta,\phi))\right), \quad (2)$$

where $\mathbf{G}_{\text{resp}}^{-1}$ denotes the covariance matrix inverse, $|\mathbf{G}_{\text{resp}}|$ is the determinant of $\mathbf{G}_{\text{resp}}$, and $\widehat{\mathbf{SRF}}(\theta,\phi)$ is the array of modeled receptive fields. The multivariate Gaussian is a well-known probability distribution (Freund, 1992), and we have previously shown that the Gaussian assumption is reasonable for first-spike latency auditory spatial receptive fields (Jenison *et al.*, 1998).

A population of 65 modeled spatial receptive fields from the left AI field in the cat was used to examine ML localization performance for a target direction (AZ 0° EL 0°) under different levels of correlated noise. The method of ML estimation entails choosing estimates of θ and ϕ that maximize the conditional probability or likelihood function described by Eq. (2). In this study ML estimates were obtained from the population of modeled receptive fields under a range of positive correlations between 0 and 1. Monte Carlo response simulations were performed by selecting multivariate random deviates generated by the probability model of Eq. (2), and computing the ML estimate of direction. Each experiment (simulation) entailed 300 random selections from the theoretical probability distribution. Spatial receptive fields $\widehat{\mathbf{SRF}}(\theta,\phi)$ were modeled using a spherical approximation technique described in Jenison *et al.* (1998), and an example receptive field is shown in Fig. 1(A). All neurons in the population were equally ''tuned'' using a linear combination of two radially symmetric von Mises basis functions. The width of the spatial receptive field was constructed to be approximately 60° halfway between the maximum and minimum response latencies, which is typical of contralateral virtual space receptive fields (Jenison *et al.*, 1998). The degree to which receptive fields overlap is illustrated in Fig. 1(B). The standard deviation σ_i of the noise about the ith modeled receptive field was chosen to be a value of 4 ms for purposes of this paper. This is a very conservative value and represents the upper tail region of the distribution of latency standard deviations (Jenison *et al.*, 1998). The assumption of homogeneity of correlated noise is certainly not a necessary condition for computing CRLBs, however, this assumption does afford a more tractable algebraic expansion, and it may be a reasonable assumption across isofrequency bands in AI auditory cortex (Eggermont, 1992).

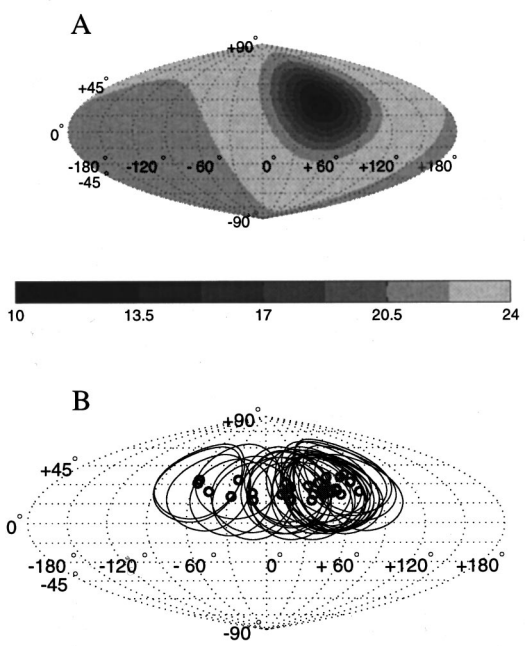

FIG. 1. (A) Example of a modeled AI cortical $\widehat{\mathbf{SRF}}$ (first-spike latency) with best direction (shortest latency at AZ 57° EL 25°). The $\widehat{\mathbf{SRF}}$ is modeled using a linear combination of spherical von Mises basis functions (Jenison *et al.*, 1998) and shown projected onto an equal-area map of auditory space. (B) A representative distribution of best directions for 65 AI $\widehat{\mathbf{SRF}}$s (circles) (from Brugge *et al.*, 1996) surrounded by iso-latency contours 50% up from the minimum latency.

II. RESULTS

A. Monte Carlo confirmation of theoretical lower bounds

The scatter of 300 estimates for each of the three conditions of neural response correlation is shown in Fig. 2. It is evident that the variability of the estimates generally decreases as the correlation of the response noise ρ_{resp} in-

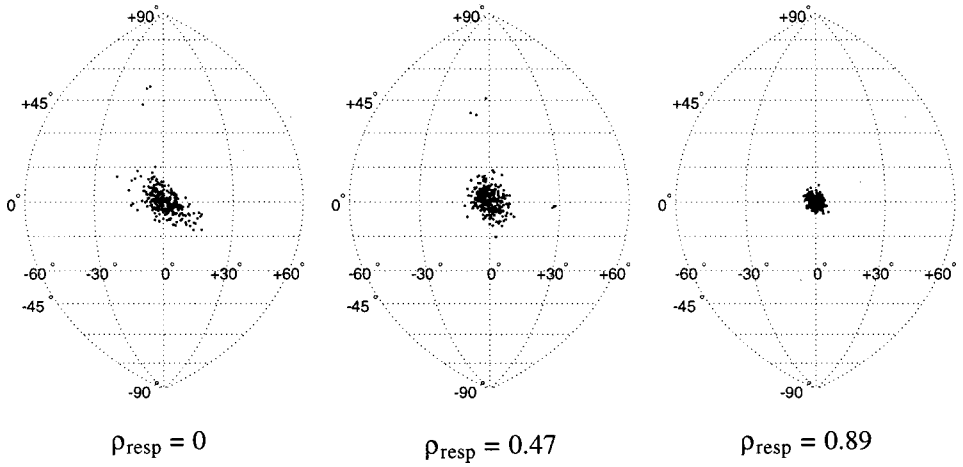

FIG. 2. Monte Carlo simulations of maximum-likelihood estimates for three levels of response correlation, ρ_{resp}. Each dot represents a localization estimate of a target sound source located at AZ 0° EL 0°.

creases. To reveal this trend in greater detail, 20 Monte Carlo experiments (300 estimates each) were statistically summarized as a function of ρ_{resp} and are shown in Fig. 3 as circles. Plotted on top of the Monte Carlo statistics are the theoretical CRLBs. The CRLB represents a theoretical lower bound for the covariance matrix of parameter estimates, where the variance of the estimates is defined as

$$\sigma_{\hat{\theta}}^2 = E[(\hat{\theta} - E[\hat{\theta}])^2] \tag{3}$$

and

$$\sigma_{\hat{\phi}}^2 = E[(\hat{\phi} - E[\hat{\phi}])^2]. \tag{4}$$

The covariance of the estimates, $\hat{\theta}$ and $\hat{\phi}$, are defined as the product $(\rho_{\hat{\theta},\hat{\phi}})(\sigma_{\hat{\theta}})(\sigma_{\hat{\phi}})$, where $\rho_{\hat{\theta},\hat{\phi}}$ is the correlation coefficient of the estimates. The difference in definition of ρ_{resp} and $\rho_{\hat{\theta},\hat{\phi}}$ may introduce some confusion at this point. ρ_{resp} is the degree to which the neural noise is correlated between neurons, whereas $\rho_{\hat{\theta},\hat{\phi}}$ is the correlation between azimuth and elevation parameter estimates of sound direction generated by the theoretical ideal observer/estimator. Although $\rho_{\hat{\theta},\hat{\phi}}$ is theoretical, it is revealed empirically as the degree of tilt observed in the scatter of Monte Carlo ML estimates as evident in Fig. 2. The CRLB and elements of the Fisher information matrix provide analytic insights into how correlation impacts the ML estimates. The CRLB of the estimation covariance matrix is formally defined as the matrix inverse of the Fisher information matrix (Blahut, 1987; Cover and Thomas, 1991),

$$\begin{bmatrix} \sigma_{\hat{\theta}}^2 & \rho_{\hat{\theta},\hat{\phi}}\sigma_{\hat{\theta}}\sigma_{\hat{\phi}} \\ \rho_{\hat{\theta},\hat{\phi}}\sigma_{\hat{\theta}}\sigma_{\hat{\phi}} & \sigma_{\hat{\phi}}^2 \end{bmatrix} \geqslant \mathbf{J}_{\theta,\phi}^{-1}, \tag{5}$$

where the Fisher information matrix is defined as

$$\mathbf{J}_{\theta,\phi} = \begin{bmatrix} E\left\{\frac{\partial}{\partial\theta}\log p(\overrightarrow{\text{resp}}\,|\,\theta,\phi)\right\}^2 & E\left\{\frac{\partial}{\partial\theta}\log p(\overrightarrow{\text{resp}}\,|\,\theta,\phi)\,\frac{\partial}{\partial\phi}\log p(\overrightarrow{\text{resp}}\,|\,\theta,\phi)\right\} \\ E\left\{\frac{\partial}{\partial\phi}\log p(\overrightarrow{\text{resp}}\,|\,\theta,\phi)\,\frac{\partial}{\partial\theta}\log p(\overrightarrow{\text{resp}}\,|\,\theta,\phi)\right\} & E\left\{\frac{\partial}{\partial\theta}\log p(\overrightarrow{\text{resp}}\,|\,\theta,\phi)\right\}^2 \end{bmatrix}. \tag{6}$$

Equation (5) in words states that regardless of the form of the estimator, estimation variance can never be any *smaller* than the CRLB (denoted by the inequality). The diagonal of the Fisher information matrix [Eq. (6)] corresponds to information with respect to each parameter, and the off-diagonals correspond to coupled information between parameters. Note that elements of the matrix have very subtle differences that depend on the differential operator with respect to each of the parameters, θ and ϕ. Evaluating the expected value in the formula for Fisher information (see the Appendix) yields a computational formula for each cell in the Fisher information matrix

$$\mathbf{J}_{\theta,\phi} = \begin{bmatrix} \left\{\left[\frac{\partial}{\partial\theta}\widehat{\mathbf{SRF}}(\theta,\phi)\right]^T \mathbf{G}_{\text{resp}}^{-1}\,\frac{\partial}{\partial\theta}\widehat{\mathbf{SRF}}(\theta,\phi)\right\} & \left\{\left[\frac{\partial}{\partial\theta}\widehat{\mathbf{SRF}}(\theta,\phi)\right]^T \mathbf{G}_{\text{resp}}^{-1}\,\frac{\partial}{\partial\phi}\widehat{\mathbf{SRF}}(\theta,\phi)\right\} \\ \left\{\left[\frac{\partial}{\partial\phi}\widehat{\mathbf{SRF}}(\theta,\phi)\right]^T \mathbf{G}_{\text{resp}}^{-1}\,\frac{\partial}{\partial\theta}\widehat{\mathbf{SRF}}(\theta,\phi)\right\} & \left\{\left[\frac{\partial}{\partial\phi}\widehat{\mathbf{SRF}}(\theta,\phi)\right]^T \mathbf{G}_{\text{resp}}^{-1}\,\frac{\partial}{\partial\phi}\widehat{\mathbf{SRF}}(\theta,\phi)\right\} \end{bmatrix}. \tag{7}$$

Equation (7) illustrates the general dependence of Fisher information on the gradients of the modeled receptive fields, $(\partial/\partial\theta)\widehat{\mathbf{SRF}}(\theta,\phi)$ and $(\partial/\partial\phi)\widehat{\mathbf{SRF}}(\theta,\phi)$, and the variability of responses about the modeled receptive fields represented by the matrix $\mathbf{G}_{\mathbf{resp}}$. Recall that ρ_{resp} appears in the off-diagonal cells of $\mathbf{G}_{\mathbf{resp}}$ [see Eq. (1)].

Figure 3 confirms that the variance of the ML estimates approaches the CRLB over many trials, as stated previously

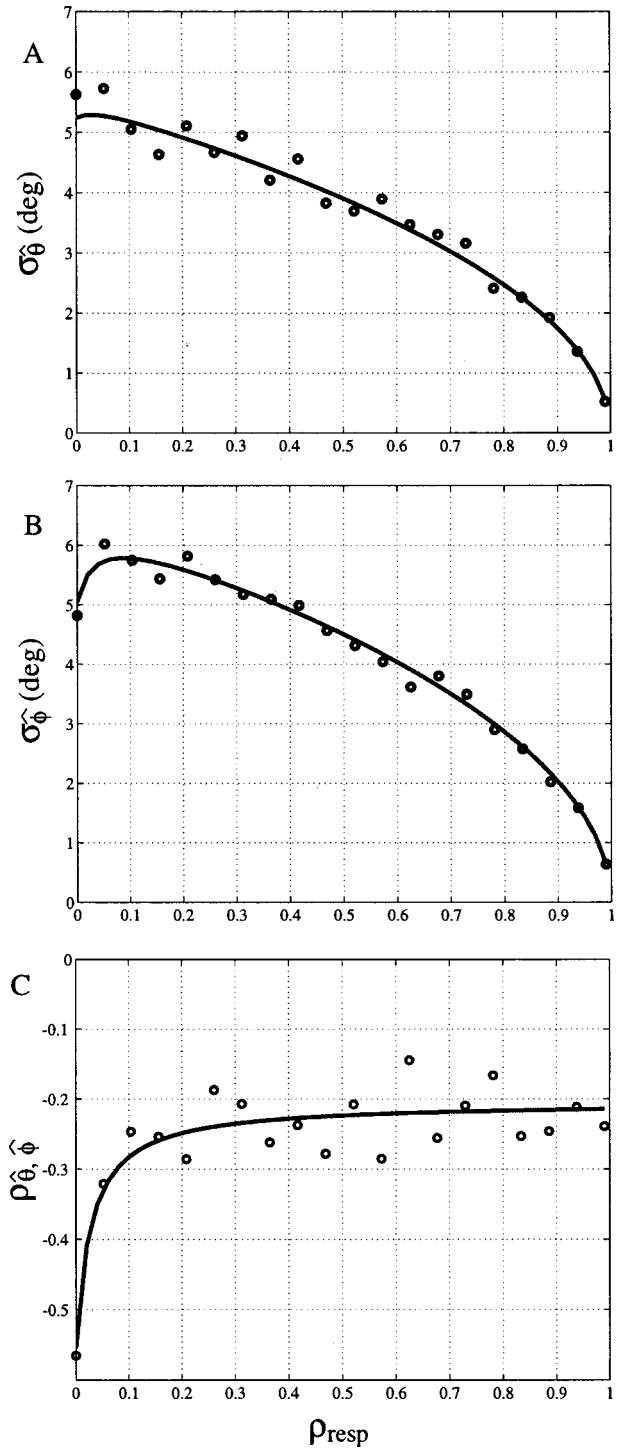

FIG. 3. Cramer–Rao Lower Bound covariance matrix [converted to (A) azimuth and (B) elevation standard deviation of the estimates, $\sigma_{\hat{\theta}}$ and $\sigma_{\hat{\phi}}$, and (C) correlation coefficients between the estimates, $\rho_{\hat{\theta},\hat{\phi}}$] (lines) for the target (true) location (AZ 0° EL 0°) as a function of response correlation, ρ_{resp}. Corresponding Monte Carlo statistics (circles) computed on empirical estimates as a function of response correlation, ρ_{resp}.

in the Introduction. It should be emphasized that each CRLB function is computed directly from the characteristics of the modeled population, and is not simply a ''fitted function'' of the Monte Carlo ML estimates. Both the Monte Carlo ML estimates and the CRLB demonstrate the trend of reduced variability of the estimates as ρ_{resp} increases. Another trend that is revealed by these analyses is an asymptotic approach to a constant value of $\rho_{\hat{\theta},\hat{\phi}}$.

The shape of the CRLB functions is dependent on the position of the target (true) sound direction relative to the best directions of the population of simulated neurons. It is difficult to make general statements regarding the behavior of specific CRLB functions because they are dependent on many factors such as the slope of the receptive fields and degree of receptive field overlap. Several example sound targets are shown in Fig. 4. Since the theoretical CRLB reliably predicts the behavior of the ML estimates in the limit, only the CRLB functions of ρ_{resp} are shown. Again two general trends—a reduction in variability of the estimates and the asymptotic approach to a constant value of $\rho_{\hat{\theta},\hat{\phi}}$—are evident for different target directions. The specific characteristics of the CRLB are different depending on where the target is located relative to the best directions of the cortical population. Variability of the estimates generally increases as the target moves lateral to the cluster of best directions. The magnitude and sign of the asymptotic values of $\rho_{\hat{\theta},\hat{\phi}}$ also depend on where the target is located relative to the cluster of best directions. To lend further explanation to these differences, elements of the Fisher information matrix were examined under an algebraic expansion.

B. Analytical examination

Taylor series expansion of each cell in the Fisher information matrix helps to reveal the impact of correlation on estimation performance (acuity). The diagonal cells of the Fisher information matrix [Eq. (7)] were Taylor series expanded with respect to ρ_{resp} for a population of N neurons.[4] Below is shown the second-order expansion for azimuth (θ) information, located in cell [1, 1] of Eq. (7):

$$J_{\theta,\phi}[1,1] \approx \sum_{i=1}^{N} \left\{ \frac{\frac{\partial}{\partial\theta}\widehat{SRF}_i(\theta,\phi)}{\sigma_i} \right\}^2 + (\mathbf{N}-1)\rho_{\text{resp}}^2 \sum_{i=1}^{N} \left\{ \frac{\frac{\partial}{\partial\theta}\widehat{SRF}_i(\theta,\phi)}{\sigma_i} \right\}^2 + ((\mathbf{N}-2)\rho_{\text{resp}}^2 - \rho_{\text{resp}}) \times \sum_{i\neq j}^{N} \left\{ \frac{\frac{\partial}{\partial\theta}\widehat{SRF}_i(\theta,\phi)\frac{\partial}{\partial\theta}\widehat{SRF}_j(\theta,\phi)}{\sigma_i\sigma_j} \right\}. \tag{8}$$

The impact of ρ_{resp} can now be examined more easily because the higher-order terms of the resulting series polynomial, which have progressively less influence on the infinite series, have been removed. The removal of the higher-order terms is appropriate because higher powers of ρ_{resp} must necessarily diminish because $|\rho_{\text{resp}}|<1$, which is also a necessary condition for the convergence of the series.[5] Abbott and Dayan (1999) employed a similar approach to understanding the impact of correlation, however, they focused on whether a ceiling on acuity exists as the population size approaches infinity. Here, the Taylor expansion is not restricted to large

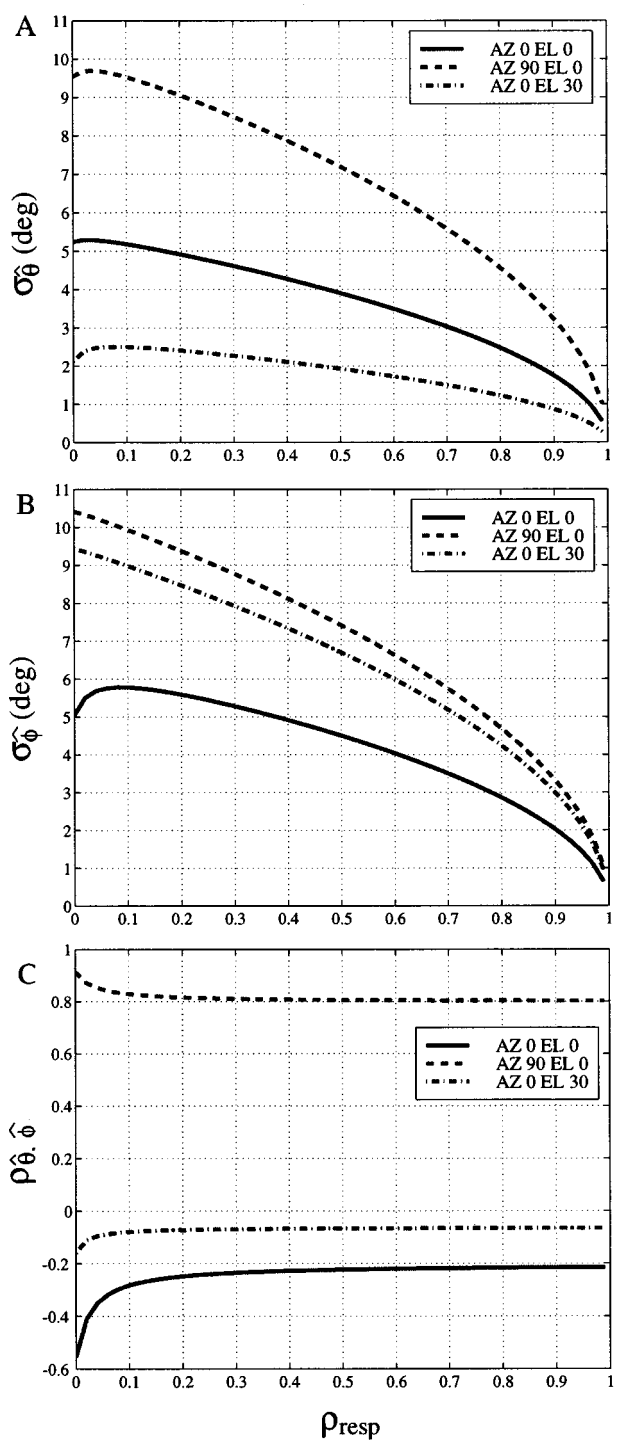

FIG. 4. Cramer–Rao Lower Bound covariance matrix [converted to (A) azimuth and (B) elevation standard deviations, $\sigma_{\hat{\theta}}$ and $\sigma_{\hat{\phi}}$, respectively, and (C) correlation coefficients between the estimates, $\rho_{\hat{\theta},\hat{\phi}}$] for three target (true) locations as a function of response correlation, ρ_{resp}.

N but considers the case of small populations. Several important influences on the magnitude of Fisher information can be observed. The first term does not depend on ρ_{resp}, and corresponds to the sum-of-squared $\widehat{\mathbf{SRF}}$ gradients that elevate Fisher information as *N* grows and gradients steepen, thus decreasing the lower bound on the variability of estimates. However, increasing levels of noise (σ) deflate Fisher information. Both of these observations were noted earlier by Paradiso (1988) under conditions of independence ($\rho_{resp}=0$). The second term, which *is* ρ_{resp} dependent, will elevate the first term by an additional gain of $(\mathbf{N}-1)\rho_{resp}^2$. However, the story becomes more complex upon examination of the third term, where the consequence of positive correlation also depends on the direction of the receptive field gradients at a particular sound direction (θ, ϕ). Under the condition where the sum-of-products of gradients is negative, positive correlation will further elevate Fisher information with respect to the first two terms only when the corresponding gain $((\mathbf{N}-2)\rho_{resp}^2-\rho_{resp})$ has a negative sign. A negative gain necessarily occurs when ρ_{resp} approaches zero and the population is small. Conversely, when the gradients possess the same sign, the third term will tend to lower Fisher information until ρ_{resp} increases to a sufficiently large value. Hence, the third term in Eq. (8) provides analytical insight into the nonmonotonic behavior of the theoretical CRLBs at low values of ρ_{resp} observed in Figs. 3 and 4. To survey the gain surfaces, iso-gain contours for the second and third terms are shown in Fig. 5(A) and (B), respectively. The negative region of the surface, shown in gray in Fig. 5(B), is actually concave upward with the edges corresponding to zero. It should be noted that the gain represents multiplicative factors applied to sums-of-squares and -products of gradients, and as such are isolated from the population specific characteristics (gradients and noise levels) of the receptive fields. This separation also serves to highlight the difference between systematic changes in $\widehat{\mathbf{SRF}}(\theta,\phi)$ and unsystematic covariation of the noise, which is characterized by ρ_{resp}. Hypothetically, two neurons with similar, but slightly different best-directions would have similar noise covariation, ρ_{resp}. However, depending on the direction of a sound source, the sum-of-products of gradients could be negative (when the target is between the two best-directions) or positive (when the target is lateral to the two best-directions).

C. Violation of independence assumption

The previous analysis was based on the use of an ideal observer/estimator that has knowledge of the response covariance structure. When the response variability is correlated, the derived estimator is assumed to take advantage of this knowledge. However, the case most similar to that described by Shadlen and colleagues is when the observer is not ideal, and fails to exploit correlated variability. To contrast the nonideal case with the ideal ML estimator, Monte Carlo estimates were again obtained for the condition where the observer incorrectly assumes response independence, while response correlation is titrated into the population of responses. These results are shown in Fig. 6 under the conditions when the target was at AZ 0° EL 0° and AZ 90° EL 0°. Depending on the target direction, performance either degrades or remains relatively constant as ρ_{resp} increases, for both azimuth and elevation estimates. This is in contrast to the performance of the ideal ML estimator shown in Figs. 3 and 4. Finally, correlation of the estimates $\rho_{\hat{\theta},\hat{\phi}}$ fails to approach a constant level when the assumption of response independence is violated [Fig. 6(B)]. Since the observer is suboptimal, there is not a formalism, such as a misinformed CRLB

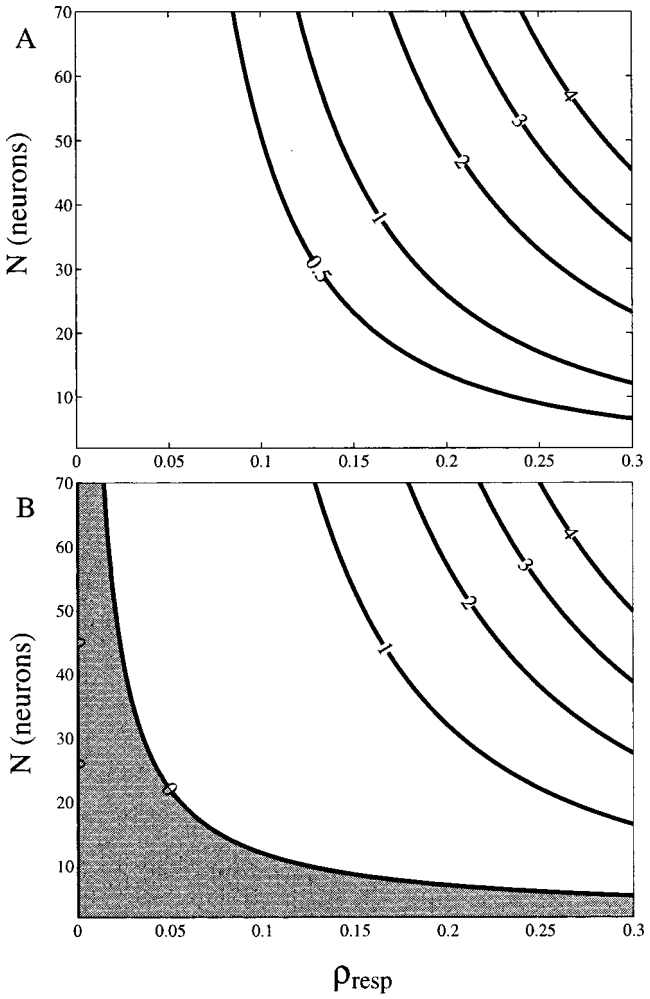

FIG. 5. Iso-gain contours for the gain functions (A) $(\mathbf{N}-1)\rho_{\text{resp}}^2$ and (B) $((\mathbf{N}-2)\rho_{\text{resp}}^2-\rho_{\text{resp}})$ of the Taylor series expanded Fisher information [Eq. (8)]. Only the lower interval of ρ_{resp} is appropriate for the series expansion about the origin. Assuming ρ_{resp} is nonnegative, the function in (A) is always nonnegative, and the case where the gain is negative in (B) is shown in gray.

to examine analytically. Consequently, it is difficult to interpret why estimate variability grows in certain cases, while others remain relatively constant with increasing ρ_{resp}. Regardless, performance does not improve with increasing ρ_{resp} *under the assumption of independence*, which is a result generally consistent with earlier reports.

III. DISCUSSION

These findings challenge the common interpretation that correlated noise between information channels always compromises ideal performance. Under the assumption of a maximum likelihood ideal observer with knowledge of the response covariance structure, the theoretical lower bounds on estimation variance generally decrease as correlation is titrated into a population of cortical neurons; we will assume that the covariance structure can be learned by the observer. Recently, this finding, while surprising, has been noted independently by several laboratories that study visual cortex (Dan *et al.*, 1998; Oram *et al.*, 1998; Abbott and Dayan, 1999). Prior to these studies, Snippe and Koenderink (1992) examined the effects of correlated noise in channel-coded

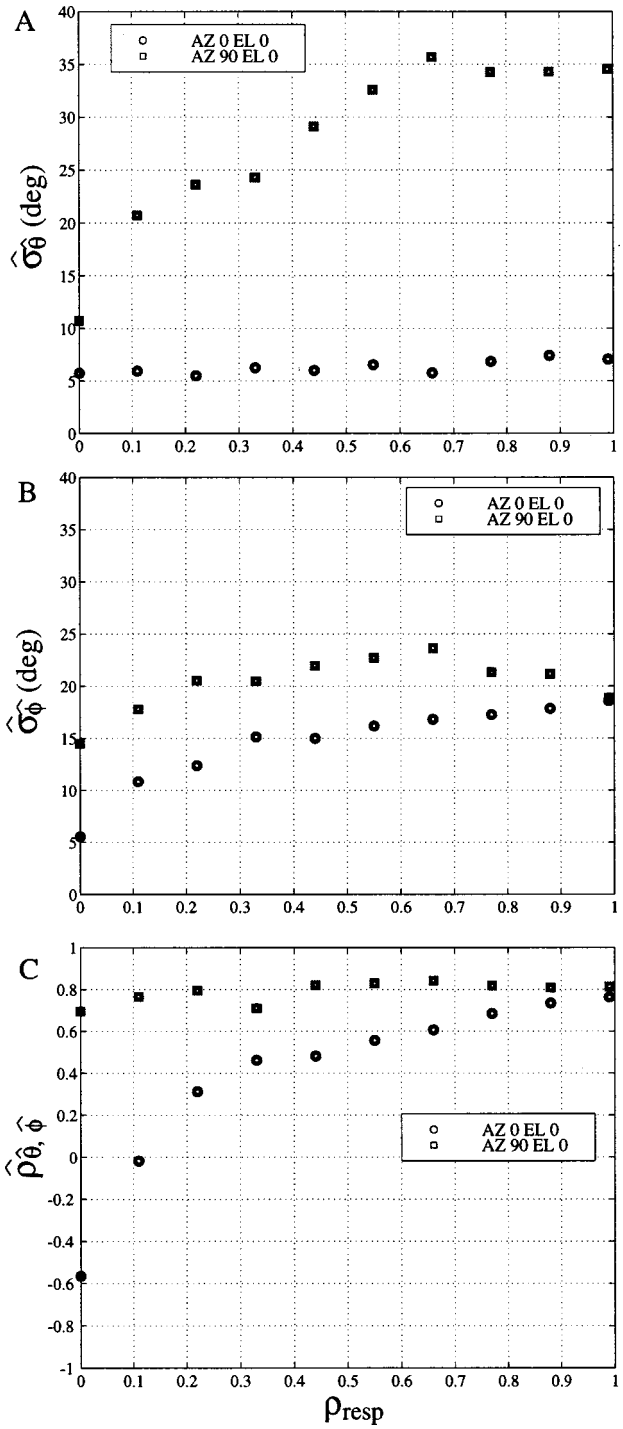

FIG. 6. Monte Carlo statistics for (A) azimuth and (B) elevation standard deviations. $\hat{\sigma}_{\hat{\theta}}$ and $\hat{\sigma}_{\hat{\phi}}$, and (C) correlation coefficients between the estimates, $\hat{\rho}_{\hat{\theta},\hat{\phi}}$ for two target (true) locations as a function of response correlation, ρ_{resp}, when the ML estimator incorrectly assumes independence.

systems on discrimination thresholds, coming to roughly similar conclusions, however, without the analytic tool of Fisher information. Although Abbott and Dayan (1999) have recently employed Fisher information, they did not consider the impact of correlation on cross-information between parameters. Estimation correlation, or the tilt of the estimates, approaches a constant value as more correlation is titrated into the population; that is, patterns of ML *estimates* of direction (θ, ϕ) are remarkably robust to different levels of

response correlation. Tilt in behavioral estimates of sound direction relative to the median and horizontal planes have occasionally been observed in the cat (May and Huang, 1996; Huang and May, 1996). The analyses here predict that direction estimates lateral to the acoustic axis will tend to evidence stronger correlation between the azimuth and elevation estimates than those near the acoustic axis. At the midline, the tilt in the scatter of estimates ultimately may be cancelled when the convergence of the two contributing hemispheres is considered. Perhaps the greatest contribution of the CRLB to the analysis of the neural code is that it shares a common currency with psychophysical performance measures—that of estimation variance and d'. Therefore, the CRLB affords a bridge between physiology and psychophysics. Patterns of estimation error decoded from neural responses can be compared directly to patterns of estimation error generated by behavioral studies, which will help constrain the possible decoding mechanisms.

ACKNOWLEDGMENTS

I would like to thank Dr. Rick Reale and Dr. John Brugge for their invaluable suggestions on a draft of the manuscript. I would also like to thank the two anonymous reviewers for their helpful comments. This research was supported, in part, by NIH Grant Nos. DC02804 and DC00116.

APPENDIX

Derive cell [1, 1] in Eq. (6) from cell [1, 1] in Eq. (7):

$$\left[\frac{\partial}{\partial\theta}\widehat{\mathbf{SRF}}(\theta,\phi)\right]^T\mathbf{G}_{\mathbf{resp}}^{-1}\frac{\partial}{\partial\theta}\widehat{\mathbf{SRF}}(\theta,\phi) = E\left\{\frac{\partial}{\partial\theta}\log p(\overrightarrow{\text{resp}}\,|\,\theta,\phi)\right\}^2. \tag{A1}$$

The conditional probability density of the response is assumed to be a multivariate Gaussian PDF:

$$p(\overrightarrow{\text{resp}}\,|\,\theta,\phi) = \frac{1}{\sqrt{(2\pi)^N|\mathbf{G}_{\text{resp}}|}} \times\exp\left(-\tfrac{1}{2}(\overrightarrow{\text{resp}}-\widehat{\mathbf{SRF}}(\theta,\phi))^T \times\mathbf{G}_{\text{resp}}^{-1}(\overrightarrow{\text{resp}}-\widehat{\mathbf{SRF}}(\theta,\phi))\right), \tag{A2}$$

and taking the natural logarithm of $p(\overrightarrow{\text{resp}}\,|\,\theta,\phi)$ of Eq. (A1) yields

$$\log\left(p(\overrightarrow{\text{resp}}\,|\,\theta,\phi)\right) = \log\left(\frac{1}{\sqrt{(2\pi)^N|\mathbf{G}_{\text{resp}}|}}\right) - \tfrac{1}{2}(\overrightarrow{\text{resp}}-\widehat{\mathbf{SRF}}(\theta,\phi))^T\mathbf{G}_{\text{resp}}^{-1}(\overrightarrow{\text{resp}}-\widehat{\mathbf{SRF}}(\theta,\phi)). \tag{A3}$$

Taking the derivative of the log probability w.r.t. θ yields the bilinear form

$$\frac{\partial}{\partial\theta}\log(p(\overrightarrow{\text{resp}}\,|\,\theta,\phi) = \left[\frac{\partial}{\partial\theta}\widehat{\mathbf{SRF}}(\theta,\phi)\right]^T\mathbf{G}_{\text{resp}}^{-1} \times(\overrightarrow{\text{resp}}-\widehat{\mathbf{SRF}}(\theta,\phi)). \tag{A4}$$

We now square Eq. (A4) and take the expected value, letting

$$\mathbf{x} = (\overrightarrow{\text{resp}}-\widehat{\mathbf{SRF}}(\theta,\phi))$$

and

$$\mathbf{y} = \frac{\partial}{\partial\theta}\widehat{\mathbf{SRF}}(\theta,\phi),$$

$$E\left\{\frac{\partial}{\partial\theta}\log p(\overrightarrow{\text{resp}}\,|\,\theta,\phi)\right\}^2 = E\{\mathbf{y}^T\mathbf{G}_{\text{resp}}^{-1}\mathbf{x}\mathbf{x}^T\mathbf{G}_{\text{resp}}^{-1}\mathbf{y}\}. \tag{A5}$$

Rearrange the expected value operator

$$E\left\{\frac{\partial}{\partial\theta}\log p(\overrightarrow{\text{resp}}\,|\,\theta,\phi)\right\}^2 = \mathbf{y}^T\mathbf{G}_{\text{resp}}^{-1}E\{\mathbf{x}\mathbf{x}^T\}\mathbf{G}_{\text{resp}}^{-1}\mathbf{y}. \tag{A6}$$

$E\{\mathbf{x}\mathbf{x}^T\}$ is the covariance matrix $\mathbf{G}_{\text{resp}}$, so

$$E\left\{\frac{\partial}{\partial\theta}\log p(\overrightarrow{\text{resp}}\,|\,\theta,\phi)\right\}^2 = \mathbf{y}^T\mathbf{G}_{\text{resp}}^{-1}\mathbf{G}_{\text{resp}}\mathbf{G}_{\text{resp}}^{-1}\mathbf{y}, \tag{A7}$$

and $\mathbf{G}_{\text{resp}}^{-1}\mathbf{G}_{\text{resp}}$ is the identity matrix $\mathbf{I}$:

$$E\left\{\frac{\partial}{\partial\theta}\log p(\overrightarrow{\text{resp}}\,|\,\theta,\phi)\right\}^2 = \mathbf{y}^T\mathbf{I}\mathbf{G}_{\text{resp}}^{-1}\mathbf{y}. \tag{A8}$$

Substituting back for $\mathbf{x}$ and $\mathbf{y}$ yields the result

$$E\left\{\frac{\partial}{\partial\theta}\log p(\overrightarrow{\text{resp}}\,|\,\theta,\phi)\right\}^2 = \left[\frac{\partial}{\partial\theta}\widehat{\mathbf{SRF}}(\theta,\phi)\right]^T \times\mathbf{G}_{\text{resp}}^{-1}\frac{\partial}{\partial\theta}\widehat{\mathbf{SRF}}(\theta,\phi). \tag{A9}$$

The same steps can be applied to derive the remaining cells of the Fisher information matrix, under the assumption of multivariate Gaussian noise.

[1]The details of spherical functional approximation can be found in Jenison *et al.* (1998). The spatial receptive field model is expressed as:

$$\widehat{\mathbf{SRF}}(\theta,\phi) = \sum_{m=1}^{M} W_m\exp\{k_m[\sin\phi\sin\beta_m\cos(\theta-\alpha_m)+\cos\phi\cos\beta_m]\},$$

where M is the number of basis functions, α_m and β_m are the coordinates of the basis function centroids, κ_m is the concentration parameter, and w_m is a weight.

[2]Sometimes a source of confusion, the ''hat'' ($\hat{}$) is also used to denote a physical parameter estimate, such as $\hat{\theta}$. It is also used in connection with Monte Carlo simulations where a population parameter is being estimated from a random sample; for example, $\hat{\sigma}_{\hat{\theta}}^2$ is the Monte Carlo estimate of the theoretical $\sigma_{\hat{\theta}}^2$.

[3]The assumption of homogeneity refers only to correlation, not the covariance matrix. The standard deviations are not assumed to be homogeneous, hence the covariance matrix is not homogeneous.

[4]The Taylor series expansions differ only by the gradients $(\partial/\partial\theta)\widehat{\mathbf{SRF}}_i(\theta,\phi)$ and $(\partial/\partial\phi)\widehat{\mathbf{SRF}}_i(\theta,\phi)$. The series expansion is performed about $\rho_{\text{resp}}=0$.

[5]Sufficient conditions have also been met such that the Taylor series expansion of Eq. (7) is guaranteed to converge.

Abbott, L. F., and Dayan, P. (**1999**). ''The effect of correlated variability of a population code,'' Neural Comput. **11**, 91–94.
Blahut, R. E. (**1987**). *Principles and Practice of Information Theory* (Addison-Wesley, Reading, MA).
Brugge, J. F., Reale, R. A., and Hind, J. E. (**1996**). ''The structure of spatial receptive fields of neurons in primary auditory cortex of the cat,'' J. Neurosci. **16**, 4420–4437.
Cover, T. M., and Thomas, J. A. (**1991**). *Elements of Information Theory* (Wiley, New York).
Dan, Y., Alonso, J. M., Usrey, W. M., and Reid, R. C. (**1998**). ''Coding of visual information by precisely correlated spikes in the lateral geniculate nucleus,'' Nat. Neurosci. **1**, 501–507.
Eggermont, J. J. (**1992**). ''Neural interaction in cat primary auditory cortex. Dependence on recording depth, electrode separation, and age,'' J. Neurophysiol. **68**, 1216–1228.
Fisher, R. A. (**1925**). ''Theory of statistical estimation,'' Proc. Cambridge Philos. Soc. **22**, 700–725.
Freund, J. F. (**1992**). *Mathematical Statistics* (Prentice-Hall, Englewood Cliffs, NJ).
Huang, A. Y., and May, B. J. (**1996**). ''Sound orientation behavior in cats. II. Mid-frequency spectral cues for sound localization,'' J. Acoust. Soc. Am. **100**, 1070–1080.
Jenison, R. L. (**1998**). ''Models of sound location acuity with broad cortical spatial receptive fields,'' in *Central Auditory Processing and Neural Modeling*, edited by P. Poon and J. F. Brugge (Plenum, New York), pp. 161–174.
Jenison, R. L., Reale, R. A., Hind, J., and Brugge, J. F. (**1998**). ''Modeling auditory spatial receptive fields with spherical approximation functions,'' J. Neurophysiol. **80**, 2645–2656.
May, B. J., and Huang, A. Y. (**1996**). ''Sound orientation behavior in cats. I. Localization of broadband noise,'' J. Acoust. Soc. Am. **100**, 1059–1069.
Musicant, A. D., Chan, J. C. K., and Hind, J. E. (**1990**). ''Direction-dependent spectral properties of cat external ear: New data and cross-species comparisons,'' J. Acoust. Soc. Am. **87**, 757–781.
Oram, M. W., Foldiak, P., Perrett, D. I., and Sengpiel, F. (**1998**). ''The 'Ideal Homunculus': Decoding neural population signals,'' Trends Neurosci. **21**, 259–265.
Paradiso, M. A. (**1988**). ''A theory for the use of visual orientation information which exploits the columnar structure of striate cortex,'' Biol. Cybern. **58**, 35–49.
Pouget, A., Zhang, K., Deneve, S., and Latham, P. E. (**1998**). ''Statistically efficient estimation using population codes,'' Neural Comput. **10**, 373–401.
Seung, H. S., and Sompolinsky, H. (**1993**). ''Simple models for reading neuronal population codes,'' Proc. Natl. Acad. Sci. USA **90**, 10749–10753.
Shadlen, M. N., Britten, K. H., Newsome, W. T., and Movshon, J. A. (**1996**). ''A computational analysis of the relationship between neuronal and behavioral responses to visual motion,'' J. Neurosci. **16**, 1486–1510.
Shadlen, M. N., and Newsome, W. T. (**1998**). ''The variable discharge of cortical neurons: Implications for connectivity, computation, and information coding,'' J. Neurosci. **18**, 3870–3896.
Snippe, H. P., and Koenderink, J. J. (**1992**). ''Information in channel-coded systems: Correlated receivers,'' Biol. Cybern. **67**, 183–190.
Zohary, E., Shadlen, M. N., and Newsome, W. T. (**1994**). ''Correlated neuronal discharge rate and its implications for psychophysical performance,'' Nature (London) **370**, 140–143.

Vibration characteristics of bone conducted sound *in vitro*

Stefan Stenfelt and Bo Håkansson
Department of Signals and Systems, Division of Medical Electronics, Chalmers University of Technology, Göteborg, Sweden

Anders Tjellström
Department of Otolaryngology, Head and Neck Surgery, Sahlgrenska University Hospital, Göteborg, Sweden

(Received 1 February 1999; revised 22 July 1999; accepted 20 September 1999)

A dry skull added with damping material was used to investigate the vibratory pattern of bone conducted sound. Three orthogonal vibration responses of the cochleae were measured, by means of miniature accelerometers, in the frequency range 0.1–10 kHz. The exciter was attached to the temporal, parietal, and frontal bones, one at the time. In the transmission response to the ipsilateral cochlea, a profound low frequency antiresonance (attenuation) was found, verified psycho-acoustically, and shown to yield a distinct lateralization effect. It was also shown that, for the ipsilateral side, the direction of excitation coincides with that of maximum response. At the contralateral cochlea, no such dominating response direction was found for frequencies above the first skull resonance. An overall higher response level was achieved, for the total energy transmission in general and specifically for the direction of excitation, at the ipsilateral cochlea when the transducer was attached to the excitation point closest to the cochlea. The transranial attenuation was found to be frequency dependent, with values from −5 to 10 dB for the energy transmission and −30 to 40 dB for measurements in a single direction, with a tendency toward higher attenuation at the higher frequencies. [S0001-4966(00)01601-5]

PACS numbers: 43.64.Bt, 43.66.Ba, 43.66.Ts [RDF]

INTRODUCTION

Bone conduction audiometry and bone conduction hearing aids are two fields for which the response of a skull to bone conducted stimulation is of fundamental importance. Although there have been thorough investigations during the twentieth century (e.g., Bárány, 1938; Kirikae, 1959; von Békésy, 1960; Tonndorf, 1966), the complete picture of hearing by bone conduction has not yet been achieved. There are several reasons for this. Bone conduction is a very complex phenomenon, which makes it difficult to describe as a comprehensive whole. The geometrical structure of the skull, together with the fact that the human head comprises soft tissue, layered bone, and brain tissue, has made it impossible to date to achieve an analytical solution to the problem. Furthermore, it is not possible, for ethical reasons, to perform direct measurements of the motion of the basilar membrane in a living human cochlea. Hence, either a subjective measurement of the human skull or objective measurements of a cadaver, dry skull, or an animal have been used to link the response of an applied vibration of the skull to that of the cochlea.

Briefly, vibrations applied to the skull are transmitted through the skull bones until they reach the cochlea, where they are transformed to a wave motion of the basilar membrane. This motion is coded by the neurones and interpreted in the primary and secondary auditory cortices as sounds. The response in the cochlea seems to be equal for both air and bone conducted sound (von Békésy, 1960). Hence, at the basilar membrane level, it is impossible to distinguish a bone conducted tone from that of an air conducted one. According to Tonndorf (1966), the applied vibration, depending on the position of application and frequency, is transmitted to the cochlea in three basic modes: (a) the reception of sound energy radiated into the external ear canal; (b) the inertial response of the middle-ear ossicles and the inner-ear fluids; and (c) the compressional response of the inner ear spaces. These three modes can be subdivided to account for the specific physical phenomena that yield a wave motion of the basilar membrane. To describe each mode quantitatively, when feasible, specially designed measurements have to be performed.

The bone anchored hearing aid (BAHA) (Tjellström and Håkansson, 1995) is, according to the surgical manual, positioned approximately 55 mm behind the opening of the ear canal (in the parietal bone). This placement, which was chosen only for practical reasons (although important), has no audiological rationale whatsoever. However, it is widely assumed that the closer the attachment point to the cochlea, the better the sound transmissions. One of the limiting factors of a BAHA, or of any bone conduction hearing aid, is that the electrical energy requirement manifests itself as the limited output power of the transducer. A position of higher sensitivity might extend the use of these aids and minimize the amount of distortion and battery consumption. Furthermore, where to place a totally implantable bone conduction device and how to excite the bone in order to achieve maximal sensitivity are not yet known.

A well-known phenomenon of bone conduction is the lateralization effect. This effect arises when the stimulation of one cochlea is either temporally ahead of or at a higher

level than the other cochlea (Tonndorf, 1966). Even if the stimulation point is essentially closer to one of the cochleae, e.g., applied to the mastoid portion of the temporal bone, the contralateral cochlea can at some frequencies be stimulated at a higher level than the ipsilateral cochlea. This is most probably due to anti-resonances in the transfer function from the excitation point to the closest cochlea. In an audiometric bone conduction test, this phenomenon could be present for one or several of the test tones, and hence, if masking is used, interpreted as a neural hearing loss at the ipsilateral cochlea. Investigators who have pointed out the presence of these anti-resonances in the bone conduction path have usually measured the response in one direction only (e.g., Kirikae, 1959; Brandt, 1989; Håkansson *et al.*, 1994), while it could be so that the responses in the other directions are large. This could explain the difference between these objective measurements and subjective measurements (e.g., Nolan and Lyon, 1981) regarding transcranial attenuation.

Although there have been a large number of studies on the subject of skull response to bone conducted stimuli, none has measured the response for all three rectilinear directions at both cochleae when exciting the skull at different positions.

This investigation is designed to answer the following questions:

(1) How do the three rectilinear response directions of the acceleration at the cochlea vary with frequency and excitation point?
(2) What is the difference in acceleration response between the three rectilinear directions?
(3) What is the difference in acceleration response between the ipsilateral and contralateral cochlea (transcranial attenuation)?
(4) Would the response acceleration gain if the exciter were implanted closer to the cochlea, e.g., in the proximity of the semi circular canals?

I. MATERIAL AND METHOD

A. The skull measured

All measurements were performed on a dry skull of a male adult; no other information of the skull is available. The sutures between the plates of a dry skull are not firmly attached; thus nonlinearities in the transfer function could be introduced. Therefore, the main sutures were glued together with a low viscosity glue (Loctite IS 420) so that they could be considered rigid. Furthermore, the resonances of the living skull are highly damped, as shown by Håkansson *et al.* (1994). Since the resonances and anti-resonances of the dry skull were highly undamped, the data obtained were hard to interpret. To better simulate a real human head, an approximately 5-mm-thick layer of viscous damping material (Polyurethane, Swedac DG-Ul, ratio 7:1, Swedish Acoustic Products Innovations AB, Göteborg, Sweden) was attached to the cranial vault. This increased the relative damping of the resonances. In total, the mass of the skull was 810 g of which 340 g was the damping material added to it.

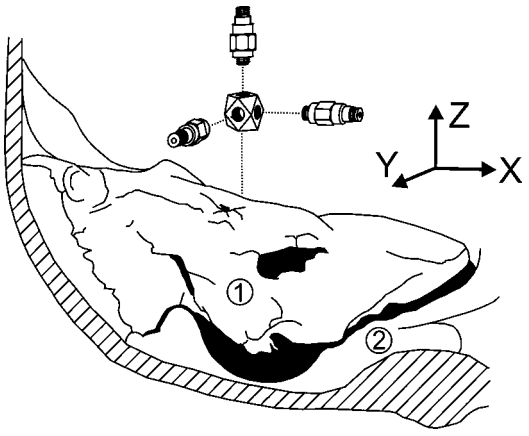

FIG. 1. A view of (1) the petrous part of the left temporal bone and (2) the occiptial bone at the base of the skull. The attachment point for the adapter holding the three accelerometers, at the arcuate eminence (top portion of the petrous part of the temporal bone), is also indicated in the illustration.

B. The measurement setup

With a specially built adapter (Fig. 1), it was possible to measure the acceleration of the cochlea in the three rectilinear directions. Three accelerometers (PCB 353B66), with a mass of 1.5 g each, were attached to the adapter which had a mass of 0.8 g. The adapter was cemented with X-60 (Schnellklebstoff X-60, CLC Systems AB, Stockholm, Sweden) at the arcuate eminence (top portion of the petrous part of the temporal bone); see Fig. 1. This position was judged to be the point closest to the cochlea that the gauges could be attached to without deforming or drilling the temporal bone. Three orthogonal directions, *x*, *y*, and *z*, were chosen so that the *x* direction pointed medially (toward the midplane), the *y* direction pointed posteriorly (backward), and the *z* direction pointed cranially (upward), as illustrated in Figs. 1 and 2. At the two cochleae, the *x* directions for the accelerometers were aligned toward each other (180° out of phase), whereas the *y* and *z* directions were the same at both cochleae. The distance between the two adapters was 49 mm. The accelerometers, which were of ICP® type (PCB Piezotronics, Inc.), were connected by way of a power supply to a two-channel FFT analyzer, Hewlett–Packard 3562A, as shown in Fig. 2. As an excitation source, a BAHA transducer was used (Tjellström and Håkansson, 1995). The transducer was fed by a random noise signal generated by the internal source of the FFT analyzer and amplified by a Brüel and Kjær type 2706

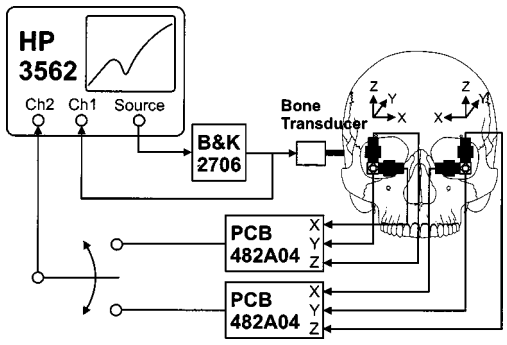

FIG. 2. Arrangement for measuring accelerance.

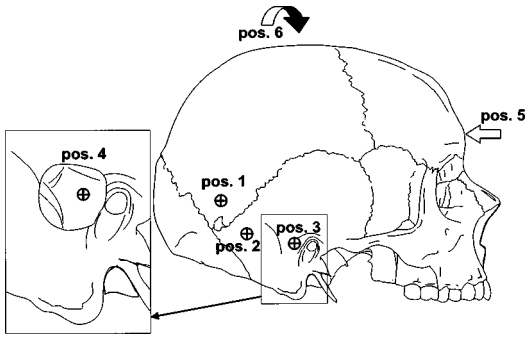

FIG. 3. The six transducer attachment positions: (pos. 1) At the parietal bone 55 mm behind the opening of the ear canal, (pos. 2) at the posterior part of the temporal bone 35 mm behind the opening of the ear canal, (pos. 3) 5 mm behind the opening of the car canal, (pos. 4) at the semi-circular canals, (pos. 5) at the frontal bone, and (pos. 6) same as pos. 2 but on the contralateral side.

power amplifier. The output from the power amplifier was also applied to one of the input channels of the FFT analyzer.

The transducer was rigidly connected to the bone with a threaded screw to a threaded hole in the skull. The transfer functions from the transducer to the cochleae were measured for six attachment points, as shown in Fig. 3: (pos. 1) the anterior caudal corner of the parietal bone just below the temporal line, where an ordinary BAHA is attached; (pos. 2) the posterior caudal part of the temporal bone, where a bone transducer for conventional bone conduction audiometry is attached; (pos. 3) the outer ear canal opening, 3-mm posterior to Henly's spine (approx. 5 mm behind the ear canal); (pos. 4) the otic capsule close to the ampulla of the posterior semi-circular canal, level with the lateral genu of the facial nerve (approx. 22 mm under pos. 3 where an implantable BAHA can be attached); (pos. 5) the center of the frontal bone, 10-mm cranial to (above) the suture of the nasal bone; and (pos. 6) the same as (pos. 2) but on the opposite side. As one of the intentions of the study was to investigate whether bone conduction would be improved by attaching the vibrator closer to the cochlea, a portion of the mastoid bone was opened down to the semi-circular canals (the bone around pos. 3 was removed), and a threaded bone screw was attached in the bottom of this hole (pos. 4); see Figs. 3 and 4. Making this hole in the skull means that the skull anatomy is slightly deformed and, hence, might affect the frequency response functions from the other stimulation points. However,

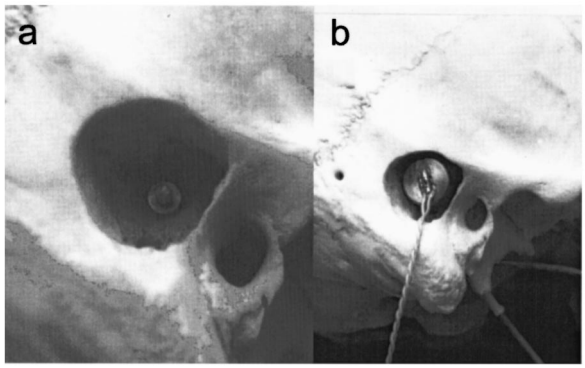

FIG. 4. (a) Position 4 with the bone screw *in situ*, and (b) with the transducer attached to the bone screw.

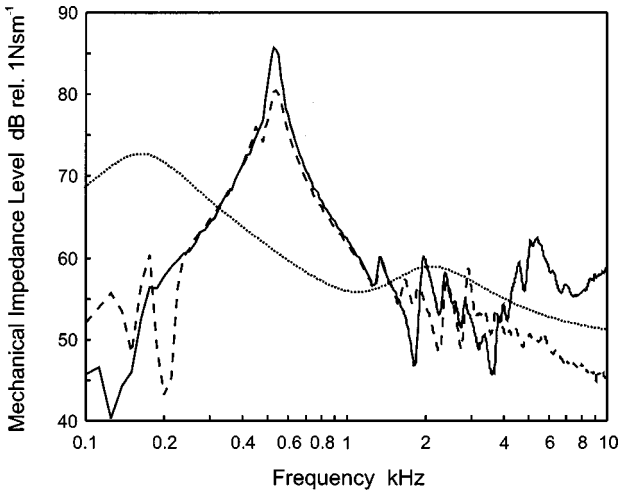

FIG. 5. The mechanical impedance level measured on the dry skull. The solid line shows the measurement at pos. 4, and the dashed line, the measurement at pos. 2. The frequency resolution for the measurements is 12.5 Hz. The dotted line is the skull impedance of a model of the human head, taken from Håkansson *et al.* (1986).

the frequency response functions were measured for all stimulation positions (except for the third, which disappeared when the hole was drilled), before and after the drilling of the hole. No effect whatsoever on the response functions due to the hole could be found.

The transducer was calibrated both before and after each measurement on a Skull Simulator TU-1000 (Håkansson and Carlsson, 1989). The difference between the two calibration runs was always less than 0.5 dB. These measurements were used in a subsequent calculation to achieve the transfer function

$$H(jf)=\frac{A(jf)}{F(jf)}, \tag{1}$$

where $H(jf)$, $A(jf)$, and $F(jf)$ are the complex accelerance, acceleration, and force frequency functions, respectively. Each measured accelerance function was calculated as an average of 30 measurements using random noise excitation, where the frequency range was 0.1–10 kHz and the frequency resolution was 12.5 Hz.

C. The mechanical impedance

To compare the results of the damped dry skull with that of a living human head, the mechanical impedance of the skull was measured for each position shown in Fig. 3 for the frequency range 0.1–10 kHz. The mechanical impedance data were measured by means of an impedance head (Brüel and Kjær type 8001) connected to a threaded adapter for rigid attachment between the impedance head and the bone screw. The apparent mass (force/acceleration) of a known mass, approximately 30 times the mass above the force gauge, was measured in order to calibrate the impedance head. The apparent mass of the impedance head with the adapter unloaded was then measured; this was used for the compensation of the mass above the force gauge in the post-processing of the impedance data.

Figure 5 gives the mechanical impedance of pos. 4

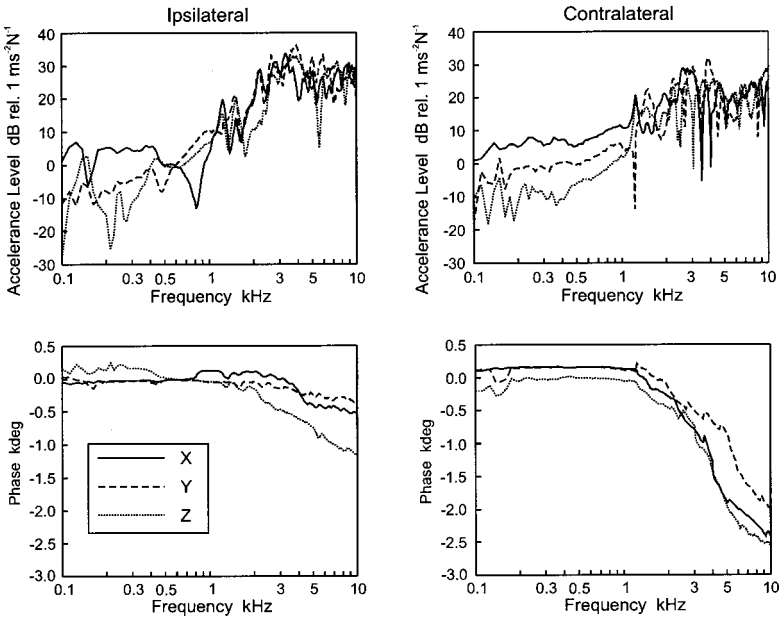

FIG. 6. The ipsi- and contralateral responses with the transducer attached at pos. 1, in the parietal bone. The solid line is the *x* direction, the dashed line is the *y* direction, and the dotted line represents the *z* direction. The frequency resolution is 12.5 Hz.

(solid line) and pos. 2 (dashed line). The mechanical impedance of the other measurement points lay close to the result of pos. 2. Further, the mechanical impedance data of a model of the living skull are included in Fig. 5 (dotted line). This model is taken from Håkansson *et al.* (1986) who measured the mechanical point impedance on seven patients equipped with osseointegrated titanium fixtures implanted for BAHAs. The original data comprise a coupling compliance (C_0 in the model in the article by Håkansson *et al.*) which has been removed here, as the transducer is rigidly attached to the bone screw. As can be seen, the anti-resonance of the damped dry skull is of a higher frequency and less damped than that of a real human head; this is due to the lower mass and less damping of the dry skull. For frequencies above 1 kHz, the impedance levels correspond fairly well.

D. The transverse sensitivity

To ensure further the validity of the measurements, the transverse vibration sensitivity of the accelerometers (including the adapter attached to a specimen of bone) was tested. According to the manufacturer, the accelerometer's transverse sensitivity is less than -26 dB. A square piece of mastoid bone was cut out, with sides of 20 mm and a thickness of approximately 8 mm. The measurement adapter was glued to the middle of this specimen with X-60 and the three accelerometers were attached to the adapter in the three orthogonal directions. Measurements were then conducted with the transducer attached in each of the three directions (the same as the gauges). The attachment of the transducer was aligned with the mass center of the bone specimen for all directions. The measurements showed a transverse sensitivity of lower than -10 dB for all directions throughout the frequency range 0.1–10 kHz. This means that, if the difference in response between the directions is 10 dB or more, the lowest response could be an artifact that originates in the transverse response of other directions.

E. The coherence function

The coherence function, $\gamma^2(f)$, can be used to evaluate the quality of a measurement using random noise excitation (Bendat and Piersol, 1980). For each measurement, $\gamma^2(f)$ was examined to determine whether that measurement should be accepted or rejected. The acceptance criteria, $\gamma^2(f)>0.95$, was used for all excitation positions over the frequency range 0.2–10 kHz in the *x* direction and 0.3–10 kHz in the *y* and *z* directions, with a few exceptions. The lower limiting frequency for pos. 5 (frontal bone) was 200 Hz in the *y* direction and 300 Hz in the *x* and *z* directions. Exceptions from the acceptance criteria, $\gamma^2(f)>0.95$, were also made at frequencies close to either a resonance or an anti-resonance in the accelerance function.

II. RESULTS

The results of the accelerance measurements are presented for both the ipsilateral and the contralateral cochlea, for the three response directions, as level and phase responses (in all, four graphs). Results of measurements when the transducer was attached at pos. 1 are shown in Fig. 6, at pos. 2 in Fig. 7, at pos. 4 in Fig. 8, and at pos. 5 in Fig. 9. All of the measurements are presented in more detail below.

A. Position 1: BAHA attachment

The results from the measurement obtained when the transducer was attached to the parietal bone (pos. 1) are presented in Fig. 6. From the phase response it is clear that the skull moves as a rigid body for the low frequencies. At the ipsilateral cochlea, a drop in the level of the frequency response function for the *x* direction occurs at 800 Hz, a phenomenon not present in the response at the contralateral cochlea. This is a forced anti-resonance due to local compliance in the area around the point of excitation. This anti-resonance also shows clearly in the phase response for the *x* direction where a phase shift of 180° occurs around 800 Hz. The excitation direction at this position deviates approxi-

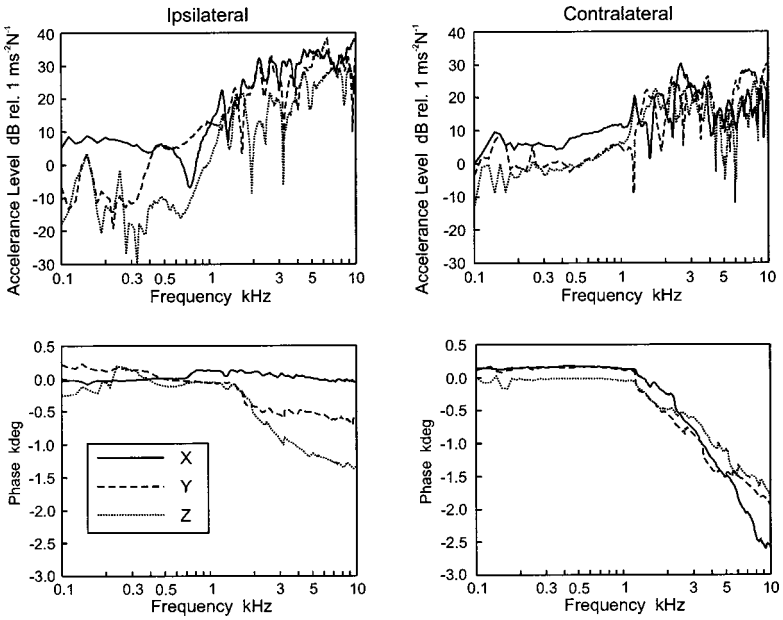

FIG. 7. The ipsi- and contralateral responses with the transducer attached at pos. 2, at the posterior part of the temporal bone. The solid line is the *x* direction, the dashed line is the *y* direction, and the dotted line represents the *z* direction. The frequency resolution is 12.5 Hz.

mately 20° from the *x* direction and is almost orthogonal to the *z* direction. As a result, the low frequency responses at both cochleae are considerably higher in the *x* direction than in the other two. The first free skull resonance appears at 1.2 kHz, while above this frequency several resonances and anti-resonances occur. Here, the distinct difference in the response for the different directions disappears, specifically the contralateral responses for which the response curves become quite similar.

Except for the low frequency anti-resonance, no major total level differences between the ipsilateral and contralateral responses were found below 2 kHz. For frequencies above 2 kHz, the level response at the ipsilateral cochlea becomes an overall 5–10 dB higher than at the contralateral cochlea. Above the first skull resonance the phase response at both cochleae starts sloping, indicating a nonrigid body behavior. This phase slope is most pronounced at the contralateral side, due to the longer time delay between excitation and response points than at the ipsilateral side. The phase response for the ipsilateral side is rather flat, indicating only a minor time delay between the excitation and response points.

B. Position 2: Audiometric bone conductor attachment

Figure 7 presents the results from the measurements with the transducer attached at the posterior part of the temporal bone (pos. 2). The direction of excitation is almost exactly the same as for pos. 1, and the results have an overall resemblance to those in Fig. 6 except for a slightly higher response level at the ipsilateral cochlea for the higher frequencies. The low frequency anti-resonance in the *x* direction is at a slightly lower frequency (720 Hz) and the first skull resonance appears again at 1.2 kHz, indicating a true structural resonance independent of the excitation position.

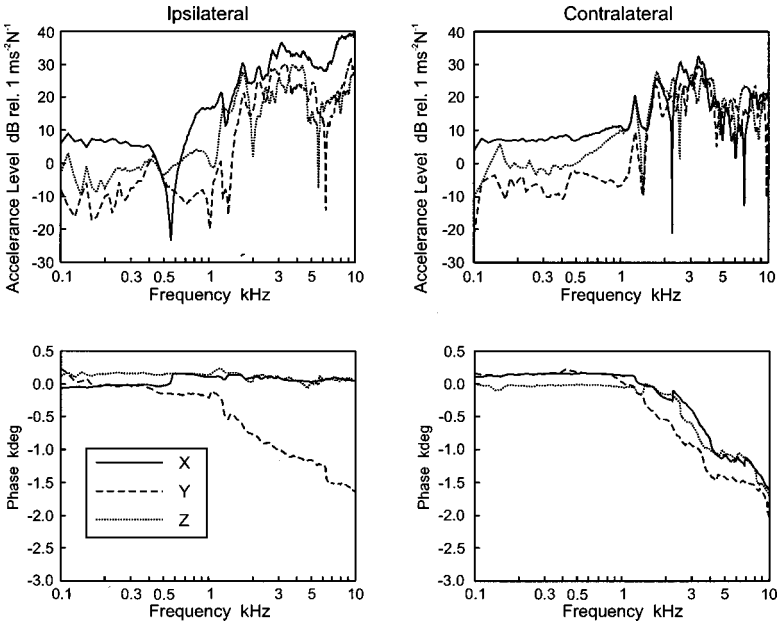

FIG. 8. The ipsi- and contralateral responses with the transducer attached at pos. 4, in the proximity of the semi-circular canals. The solid line is the *x* direction, the dashed line is the *y* direction, and the dotted line represents the *z* direction. The frequency resolution is 12.5 Hz.

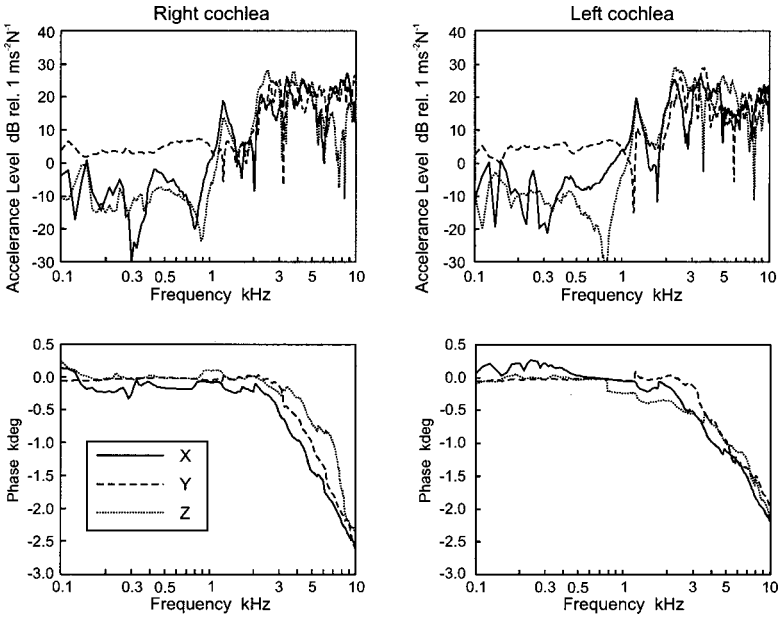

FIG. 9. The responses at the right and left cochlea with the transducer attached at pos. 5, in the frontal bone. The solid line is the *x* direction, the dashed line is the *y* direction, and the dotted line represents the *z* direction. The frequency resolution is 12.5 Hz.

For the *x* direction at the ipsilateral cochlea, the response shows a flat phase, indicating almost no time delay between excitation and response points, whereas for the other two directions the result shows the same behavior as when the stimulus was applied at pos. 1.

C. Position 3: Directly behind the ear canal

Excitation positions 2 and 3 were separated by only 25 mm and were both placed in the temporal bone. The responses for both cochleae were nearly the same as those for the stimulation at pos. 2, shown in Fig. 7.

D. Position 4: Implantable BAHA

The results from the measurements when the transducer was attached at pos. 4 are shown in Fig. 8. The low frequency anti-resonace for the ipsilateral response is around 580 Hz, which is lower than for the other stimulation points. In the *x* direction, the ipsilateral response level is approximately 10 dB or more higher than in the other two directions for almost the whole frequency range. The overall response levels at the ipsilateral and contralateral sides are the highest and lowest, respectively, among the different stimulation positions in this investigation; hence, the difference in response levels between the two cochleae is largest at this stimulation position. In the phase response at the ipsilateral side, no time delay for the *x* and *z* directions seems to be present; this indicates rigid body motion up to 10 kHz. On the contralateral side, the phase response flattens out between 4 and 8 kHz and shifts from a sloping phase, indicating a time delay, to a more or less constant phase, indicating an infinity phase velocity. This result suggests different vibratory pathways or different types of wave motion or, most truly, a combination of both.

E. Position 5: Frontal bone

Figure 9 shows the results from the accelerance measurement with excitation applied at pos. 5, the frontal bone. At this position, the excitation point is symmetrically placed with respect to the two cochleae, indicated as right and left cochlea in Fig. 9. As the excitation is in the *y* direction, the response level in that direction dominates for frequencies below 1 kHz. The responses at both sides are quite similar: no major differences between them can be seen. The phase starts sloping at approximately 2 kHz which is slightly higher than that obtained when stimulating at the other positions. The difference of 0.5 kdeg at 10 kHz between the two is most probably due to a minor time delay difference in the two sound paths.

F. Position 6: Bone conductor attachment opposite to position 2

Stimulation position 6 is, on the opposite side of the skull, in exactly the same position as pos. 2. The measurements at this position were merely for validation of the symmetry of the skull; no significant differences were found between these two positions.

III. DISCUSSION

A. Response of a dry skull

In this study the vibrations were measured by accelerometers. There are several drawbacks with such measurement technique compared with the noncontact methodologies such as interferometry, e.g., Ogura *et al.* (1979), Hoyer and Dorheide (1983), and Dorheide and Hoyer (1984). Those studies, however, reported vibration modes of the skull for a rather limited frequency range; not the same as here where the transfer function between the surface of the skull and the cochlea was measured. The results obtained in this study indicate that the petrous pyramid moves almost as a rigid body. Consequently, only minor loss of information is made by measuring at one specific point solely. Moreover, the weight of the accelerometers is approximately one-eighth of the temporal bone. In a verification of the mass-loading effect on the measurements (mass was added to the accelerom-

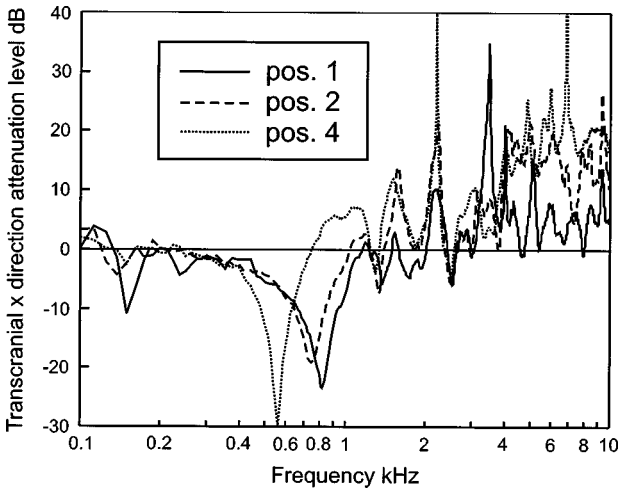

FIG. 10. Comparison of *x* direction ipsilateral and contralateral level responses (transcranial attenuation) when excitation is applied at the positions 1, 2, and 4. Solid line: stimulation at pos. 1. Dashed line: stimulation at pos. 2. Dotted line: stimulation at pos. 4. The frequency resolution is 12.5 Hz.

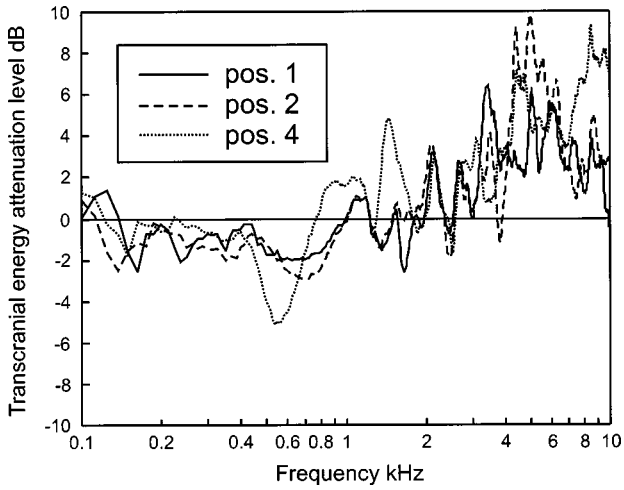

FIG. 11. Comparison of the energy levels transmitted to the ipsilateral cochlea and the contralateral cochlea (transcranial energy attenuation) when excitation is applied at positions 1, 2, and 4. Solid line: stimulation at pos. 1. Dashed line: stimulation at pos. 2. Dotted line: stimulation at pos. 4. The frequency resolution is 12.5 Hz.

eters), it was shown that the bias due to this is less than 1 dB. Further, by using accelerometers it was possible to make measurements in all three directions at both cochleae, with a high sensitivity and frequency resolution, in one single session.

To draw general conclusions from measurements of a dry skull, data should be linked to measurements of a normal living human head. It should also be remembered that only the acceleration of the petrous part of the temporal bone, assumed to rigidly encapsulate the cochlea, is measured here. This is not the same as the subjectively perceived bone conducted sound. To make a more complete interpretation of these results, knowledge of the frequency function transforming acceleration of the cochlea to a perceived sound level for all three directions must be obtained. Also, due to changing nature of skull and elasticity, it is not possible to extrapolate these results with regard to varying age groups. Franke (1956) showed that the first fundamental resonance frequency was shifted down 39% when the dry skull was filled with gelatine. Khalil *et al.* (1979) filled the cranial cavity with liquid and took into account bone stiffness and skin damping; then they calculated the free resonance frequency shift to be 53%. Furthermore, damping of the skull resonances due to wet bone, the brain, and skin should be included in the calculated response functions. Even if such transformations were made, it can be assumed that the results would still have to be adjusted by some additional correction factors. However, as a first assumption, one can assume that the cochlea is sensitive to one direction alone (the *x* direction). A second assumption would be to assume that the mechanical vibration energy (quadratic summation of all three directions) transmitted to the cochlea represents a realistic measure of the total cochlear response.

B. Single direction response

Figure 10 shows the difference in response levels for the *x* direction between the ipsilateral and contralateral cochleae for excitation at positions 1, 2, and 4. These results are a measure of the single-direction transcranial attenuation. Between 0.5 and 1 kHz, the contralateral response level is higher than the ipsilateral one, an effect of the anti-resonance in the ipsilateral sound transmission path, as explained below. Above 1 kHz, the response levels at the ipsilateral cochlea become higher than those at the contralateral one. When the excitation is applied at pos. 4, it can also be seen that the transcranial attenuation is higher overall than when it is applied at pos. 2 or 1. This indicates that stimulating close to the cochlea gives a greater directivity, an important issue for hearing aids. It can also be concluded that the vibrations are transmitted mostly by the shell of the skull rather than by the junctions between the petrous part of the temporal bones and the occipital bone at the base of the skull; see Fig. 1. The medial part of the apex of the petrous bone is attached to the occipital bone by means of syncondros (cartilage and fibrous tissues) in a human head; this is simulated by the damping material added in the dry skull used here. Both yield a significant attenuation of the vibration transmitted. A finding at the ipsilateral cochlea is an improvement for the sensitivity in the *x* direction when the stimulation position is closer to the cochlea, especially for frequencies above 1 kHz. Stimulating at pos. 2 yields 5–10 dB higher sensitivity than stimulating at pos. 1, and stimulating at pos. 4 gives 10–15 dB higher sensitivity.

C. Mechanical energy transmission

The next approximation was to assume that the cochlea was sensitive to the transmitted energy, i.e., the sum of the three orthogonal components individually multiplied by their complex conjugates; see Eq. (2):

$$E = xx^* + yy^* + zz^*. \tag{2}$$

Figure 11 presents the transcranial energy attenuation, similar to the single *x* direction attenuation presented in Fig. 10. As can be seen, the relative peak levels of the energy measurements are much lower, a result caused by the lesser influence of the anti-resonances on the energy transmission.

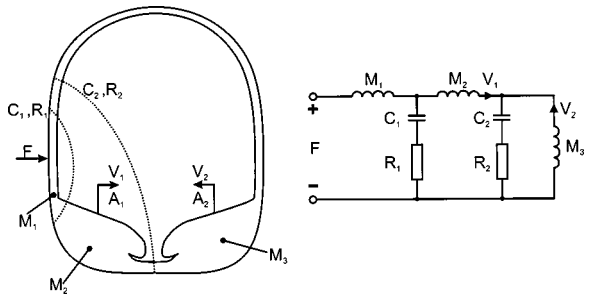

FIG. 12. A cross-section of the skull (left), indicating the dynamic behavior of the skull at low frequencies (<1 kHz), and a corresponding lumped network model (right). V_1 and A_1 stand for the velocity and acceleration, respectively, at the ipsilateral cochlea; the same holds for V_2 and A_2 at the contralateral cochlea. F is the force at the stimulation point; M, C, and R are the model masses, compliances, and dissipative elements, respectively.

Consequently, a smoother transcranial attenuation curve is obtained. A trend similar to but weaker than that shown in Fig. 10 is apparent in Fig. 11: at the low frequencies only some negative attenuation (amplification) of a couple of dB, due to the low frequency anti-resonance, is present; while at the higher frequencies the attenuation is between 0 and 10 dB, with an increase of attenuation at the highest frequencies. Furthermore, there is some indication of higher transcranial attenuation when the stimulation is closer to the ipsilateral cochlea.

When comparing the differences in energy transmitted from the three positions, 1, 2, and 4, to the ipsilateral cochlea with the one obtained for the x direction, the energy transmission differences are smaller. The sensitivity for stimulation at pos. 2 compared with pos. 1 does not reveal any sign of an overall better transmission to the ipsilateral cochlea at either of the two positions, whereas the sensitivity at pos. 4 versus pos. 1 shows a slightly better overall energy transmission of approximately 5 dB in favor of pos. 4.

D. Low frequency anti-resonance and sound lateralization

The low frequency anti-resonance appearing in the ipsilateral x direction response when stimulation is at or near the temporal bone is a forced phenomenon. Accordingly, its frequency varies for different stimulation points. The temporal and the nearby parietal bone form a rather flat surface and can be seen more or less as a plate attached at the border. Such a plate has mass and stiffness distributed throughout. As a result, the further the stimulation point is from the receiver position, the more of this plate is in the sound transfer path, which means there is higher compliance and more mass of the transfer path. This is illustrated in Fig. 12, where a cross-section of the skull is shown together with a lumped parameter network model. This network model illustrates the single-direction dynamic behavior for frequencies below 1 kHz. Above this frequency, this model is no longer sufficient to describe the dynamics of the skull. The acceleration can be calculated from the velocity obtained in the model according to the relation

$$A(j\omega) = j\omega V(j\omega). \tag{3}$$

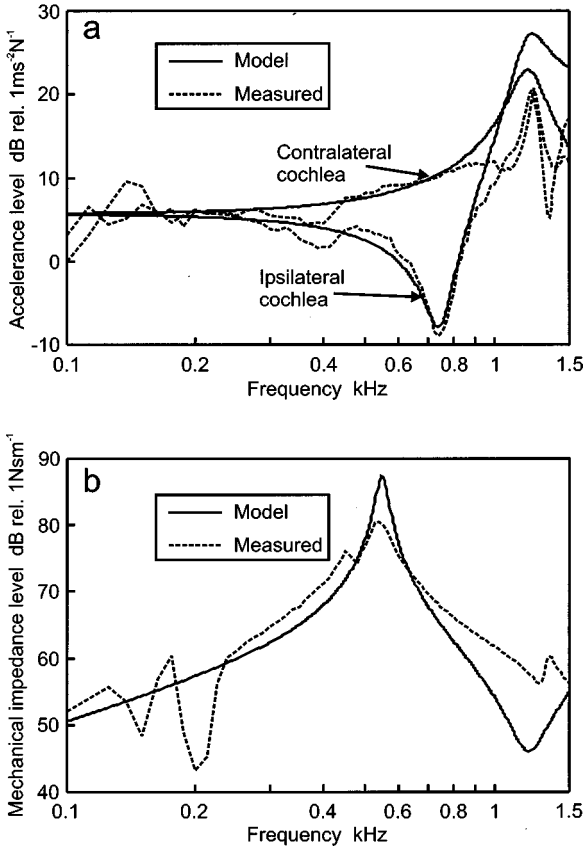

FIG. 13. (a) Comparison of the x direction model accelerance (solid line) and measured accelerance (dashed line) stimulating at pos. 2 for both ipsi- and contralateral cochlea (b) the model (straight line) and measured (dashed line) mechanical point impedance at pos. 2.

As seen in Fig. 12, all components can be given a physical interpretation; M_1 is the mass of the bone surrounding the stimulation point, M_2 is the mass of the bone part next to M_1 on the ipsilateral side of the skull including the ipsilateral cochlea, and M_3 is the mass of the rest of the skull including the contralateral cochlea. The compliance between M_1 and M_2 is modeled with C_1, and between M_2 and M_3 with C_2. Further, R_1 and R_2 are the dissipative elements at C_1 and C_2, respectively. For the model, values of the components were determined to fit the x direction ipsilateral and contralateral responses when stimulating at pos. 2 (x direction responses in Fig. 7). The values of the components obtained are: $M_1 = 0.07$ kg, $M_2 = 0.1$ kg, $M_3 = 0.35$ kg, $C_1 = 100$ nm/N, $C_2 = 130$ nm/N, $R_1 = 100$ Ns/m, and $R_2 = 200$ Ns/m. The results for the frequency range 0.1–1.5 kHz are given in Fig. 13(a). As a validation, the mechanical impedance of the model is compared with the measured mechanical impedance at pos. 2 (from Fig. 5).

It can be seen from the model that the total effective mass ($M_1 + M_2 + M_3$) is only 0.52 kg, which is less than the 0.81 kg stated earlier for the skull used here. This discrepancy originates in the fact that the excitation direction does not pass through the mass center, hence, there is also a rotational motion. As both the translational and the rotational motion of the skull add in phase at the response point, the effective mass of the accelerance is less than the total mass of the skull.

It can be anticipated that the low frequency anti-resonance found here will affect the bone conduction when the transducer is applied in the mastoid area. An example of this would be in bone conduction audiometry, and manifest itself as a sound lateralization to the contralateral cochlea around that frequency. To show that this lateralization is also present in a living human head, the subjective lateralization was measured on three living subjects with normal head structure and hearing for the frequencies from 100 to 1000 Hz. The bone conduction receiver (Radioear B-71) was attached to the mastoid portion of the temporal bone (approximately pos. 2 in this study). All three showed a marked lateralization effect to the contralateral side in the frequency range 290–500 Hz, with a bandwidth of approximately 150 Hz.

E. Response of the human head *in vivo*

A comparison can be made between the mechanical impedance obtained here (Fig. 5), where the first anti-resonance occurs at 550 Hz, and the results by Håkansson *et al.* (1986) where they found the first anti-resonance frequency between 100 and 350 Hz among the seven patients investigated. Such a comparison indicates that the results here should be frequency shifted downward by a factor of 2, which is in agreement with the findings by Khalil *et al.* (1979). Furthermore, the internal free skull resonances, from around 800 Hz and upward, were reported in the same study by Håkansson *et al.* (1986), to have no effect on the mechanical point impedance. That finding shows that the layer of damping material used in this study did not attenuate the resonances of the dry skull enough. A comparison can be made with another study by Håkansson *et al.* (1994), where the objective was to investigate the resonance frequencies of the human skull. A single-direction (normal to the skull) transcranial accelerance function was measured between two bilateral osseointegrated fixtures (the same as pos. 1 in this study but on both sides of the skull in their study). Even though the response location differs between the two studies and no absolute comparisons can be made, some indications can be noted. The overall accelerance levels are somewhat higher in this investigation, specifically below the first free resonance frequency where the skull moves as a rigid body. This can partially be explained by the mass difference between the dry skull and a real human head. Above the first skull resonance, 828–1164 Hz in the study by Håkansson *et al.* and 1200 Hz here, the responses agree fairly well, except that the resonances are less damped in this study. We believe, therefore, that the overall results obtained here can be linked to the response of a human skull *in vivo*.

F. Compression of the cochlea and ossicular inertia

For frequencies below the first skull resonance, the skull moves as a rigid body and no wave motion appears; except for stimulation at positions 1 and 5, this is actually so for the response in the *x* direction at the ipsilateral side throughout the whole frequency range investigated. The responses exhibit a damped mass-spring system behavior, hence the only cochlear response obtained in this direction would be that caused by relative movement: relative jaw movement (von Békésy, 1960), ossicular inertia (Bárány, 1938), and inner ear fluid inertia (Bárány, 1938). If this finding can be applied to the living human head, the contribution to bone conduction due to compression at the ipsilateral cochlea would be of minor importance. However, it is possible that some compression of the ipsilateral cochlea due to the wave motions in the other directions is present, and also at the contralateral side. Several investigators (e.g., von Békésy, 1960; Tonndorf, 1962, 1966) have tried to measure the contribution to bone conduction from compression of the cochlea, with respect to both the frequency range and the level. It is difficult, however, to isolate one specific contributing phenomenon without affecting others. Therefore, the results obtained in those investigations might suffer from uncertainty about the actual origin of the response.

An indication of a dominating *x* direction sensitivity of the cochlea (first assumption here) is the findings of Studebaker (1962), where he investigated the bone conduction acuity on patients with defective middle ears. It was shown in that study that the bone conduction loss was about 5 dB less when stimulating at the frontal bone than when stimulating at the mastoid, for frequencies between 0.5 and 4 kHz. In addition, Goodhill *et al.* (1970) found that for frequencies up to 4 kHz, bone conduction is more sensitive to the condition of the middle ear when stimulating at the mastoid than at the frontal bone. It can be seen in Fig. 7 that the *x* axis is the dominating response direction for stimulation of the mastoid bone, whereas Fig. 9 shows no dominating response direction above 1 kHz for stimulation at the frontal bone. Accordingly, ossicular inertia has a major influence on bone conducted sound, even at frequencies as high as 4 kHz, when excitation is applied in the mastoid area.

IV. CONCLUSIONS

A damped dry skull was used to investigate the vibratory pattern of bone conducted sound. Due to differences in mass-loading and damping properties between the skull used in this study and a normal human head, absolute findings here cannot be applied directly to the living human head. Nevertheless, findings such as differences in response directions at the cochleas, structural phenomena, transcranial attenuation, and level differences due to variation of excitation positions can give indications of the response of bone conducted sound in a living human head.

For stimulation at or close to the temporal bone, the following results were obtained: (1) A profound low frequency forced anti-resonance in the ipsilateral transmission path was found, which was also psychoacoustically proven to yield a distinct lateralization effect toward the contralateral side: (2) For the ipsilateral side, a general dominant response direction was found to coincide with the excitation direction, whereas the same dominating vibration direction was found only for frequencies below the first free skull resonance in the contralateral response. Above the first skull resonance, no overall dominating response direction whatsoever could be seen in the contralateral response. (3) The transcranial attenuation between the cochleae is frequency dependent, with values between −30 and 40 dB for the mea-

surements in a single direction and from −5 to 10 dB for the total energy transmission, with higher attenuation at the highest frequencies. (4) The time delay for the ipsilateral response in the excitation direction was almost zero (constant phase), indicating only a minor contribution of the transversal wave motion to the total response in that direction. If this is also true for the living human head, the major response to bone conducted sound would be of inertia origin for the ipsilateral side.

ACKNOWLEDGMENT

The authors wish to thank the Department of Applied Signal Processing at the University of Karlskrona/Ronneby for their support in selecting and supplying equipment for this investigation.

Bárány, E. (**1938**). ''A contribution to the physiology of bone conduction,'' Acta Oto-Laryngol. Suppl. **26**, 129.

Békésy, G. von (**1960**). *Experiments in Hearing*, edited by E. G. Wever (McGraw-Hill, New York), p. 745.

Bendat, J. S., and Piersol, A. G. (**1980**). *Engineering Applications of Correlation and Spectral Analysis* (McGraw-Hill, New York), p. 302.

Brandt, A. (**1989**). ''On sound transmission characteristics of the human skull *in vivo*,'' Licentiate thesis No. 61L, Chalmers University of Technology, Göteborg.

Dorheide, J., and Hoyer, H.-E. (**1984**). ''Holographic investigation of the impact response of human heads,'' J. Neurosurg. **60**, 718–723.

Franke, E. (**1956**). ''Response of the human skull to mechanical vibrations,'' J. Acoust. Soc. Am. **28**, 1277–1284.

Goodhill, V., Dirks, D., and Malmquist, C. (**1970**). ''Bone-conduction thresholds. Relationships of frontal and mastoid measurement in conductive hypacusis,'' Arch. Otolaryngol. **91**, 250–256.

Hoyer, H.-E., and Dorheide, J. (**1983**). ''A study of human head vibrations using time-averaged holography,'' J. Neurosurg. **58**, 729–733.

Håkansson, B., Brandt, A., Carlsson, P., and Tjellström, A. (**1994**). ''Resonance frequency of the human skull *in vivo*,'' J. Acoust. Soc. Am. **95**, 1474–1481.

Håkansson, B., and Carlsson, P. (**1989**). ''Skull simulator for direct bone conduction hearing devices,'' Scand. Audiol. **18**, 91–98.

Håkansson, B., Carlsson, P., and Tjellström, A. (**1986**). ''The mechanical point impedance of the human head, with and without skin penetration,'' J. Acoust. Soc. Am. **80**, 1065–1075.

Khalil, T. B., Viano, D. C., and Smith, D. L. (**1979**). ''Experimental analysis of the vibrational characteristics of the human skull,'' J. Sound Vib. **63**, 351–376.

Kirikae, I. (**1959**). ''An experimental study on the fundamental mechanism of bone conduction,'' Acta Oto-Laryngol. Suppl. **145**, 110.

Nolan, M., and Lyon, D. J. (**1981**). ''Transcranial attenuation in bone conduction audiometry,'' J. Laryngol. Otol. **95**, 597–608.

Ogura, Y., Masuda, Y., Miki, M., Takeda, T., Watanabe, S., and Ogawara, T. (**1979**). ''Vibration analysis of the human skull and auditory ossicles by holographic interferometry,'' in *Holography in Medicine and Biology*, edited by G. von Bally (Springer-Verlag, Berlin), pp. 218–222.

Studebaker, G. (**1962**). ''Placement of vibrator in bone-conduction testing,'' J. Speech Hear. Res. **5**, 321–331.

Tjellström, A., and Håkansson, B. (**1995**). ''The bone-anchored hearing aid. Design principles, indications, and long-term clinical results,'' Otolaryngologic Clinics of North America **28**, 53–72.

Tonndorf, J. (**1962**). ''Compressional bone conduction in cochlear models,'' J. Acoust. Soc. Am. **34**, 1127–1131.

Tonndorf, J. (**1966**). ''Bone conduction. Studies in experimental animals,'' Acta Oto-Laryngol. Suppl. **213**, 132.

A performance adequate computational model for auditory localization

Wing Chung
Systems Engineering and Design Automation Laboratory, Department of Electrical and Information Engineering, University of Sydney, Sydney 2006, Australia

Simon Carlile[a)]
Auditory Neuroscience Laboratory, Department of Physiology, University of Sydney, Sydney 2006, Australia

Philip Leong
Department of Computer Science and Engineering, The Chinese University of Hong Kong, Shatin NT, Hong Kong

(Received 13 February 1998; revised 26 April 1999; accepted 23 July 1999)

A computational model of auditory localization resulting in performance similar to humans is reported. The model incorporates both the monaural and binaural cues available to a human for sound localization. Essential elements used in the simulation of the processes of auditory cue generation and encoding by the nervous system include measured head-related transfer functions (HRTFs), minimum audible field (MAF), and the Patterson–Holdsworth cochlear model. A two-layer feed-forward back-propagation artificial neural network (ANN) was trained to transform the localization cues to a two-dimensional map that gives the direction of the sound source. The model results were compared with (i) the localization performance of the human listener who provided the HRTFs for the model and (ii) the localization performance of a group of 19 other human listeners. The localization accuracy and front–back confusion error rates exhibited by the model were similar to both the single listener and the group results. This suggests that the simulation of the cue generation and extraction processes as well as the model parameters were reasonable approximations to the overall biological processes. The amplitude resolution of the monaural spectral cues was varied and the influence on the model's performance was determined. The model with 128 cochlear channels required an amplitude resolution of approximately 20 discrete levels for encoding the spectral cue to deliver similar localization performance to the group of human listeners. [S0001-4966(99)04411-2]

PACS numbers: 43.64.Bt, 43.64.Ha, 43.66.Qp [RDF]

INTRODUCTION

Humans can locate the source of a sound with remarkable accuracy using a variety of acoustic cues (Carlile, 1996). The location-dependent information contained in the sounds at each ear results from the interaction between the auditory periphery and the incident sound. The binaural localization cues include the interaural time difference cue (ITD) and the interaural level difference cue (ILD) (Middlebrooks and Green, 1991). The ITD operates principally at low frequencies and, conversely, the ILD is a reliable localization cue for the middle to high frequencies. Because of the relative symmetry of the ears on the head, a set of points in space can have the same binaural time or level values. That is, a binaural cue defines a ''cone of confusion'' centered on the interaural axis which leads to ambiguities in the vertical position of the sound source and front–back confusions (Oldfield and Parker, 1986). The auditory system most probably uses the spectral cues provided by the location-dependent filtering of the outer ear to resolve the cone of confusion (Middlebrooks, 1992; Carlile, 1996).

The head-related transfer function (HRTF) is defined as the acoustic transformation function from a point in space to the outer ear and describes the location-dependent filtering of a sound by the auditory periphery. The HRTF captures both the frequency domain and time domain aspects of the cues to a sound's location. Various models of the peripheral processing by the auditory system suggest that the fidelity of the acoustical information encoded by the nervous system is considerably degraded in the frequency domain when compared to the fidelity with which the HRTF is routinely measured (see Carlile and Pralong, 1994).

In the work reported here, we were interested in developing a model of localization that combined biologically plausible processing of the acoustical input with the input–output mapping provided by an artificial neural network (ANN). There were several key motivators for this approach.

First, preprocessing the input to the ANN in a biologically plausible manner would ensure that the mapping provided by the ANN would be a more reasonable model, in performance terms, of human localization performance. Thus, our first objective was to develop a model with a number of biologically plausible constraints that would provide a similar performance level as that found in humans. This necessitated the degradation of the model over the best that could be achieved without these constraints.

Second, a model with human-like performance could

a)Electronic mail: simon@physiol.usyd.edu.au

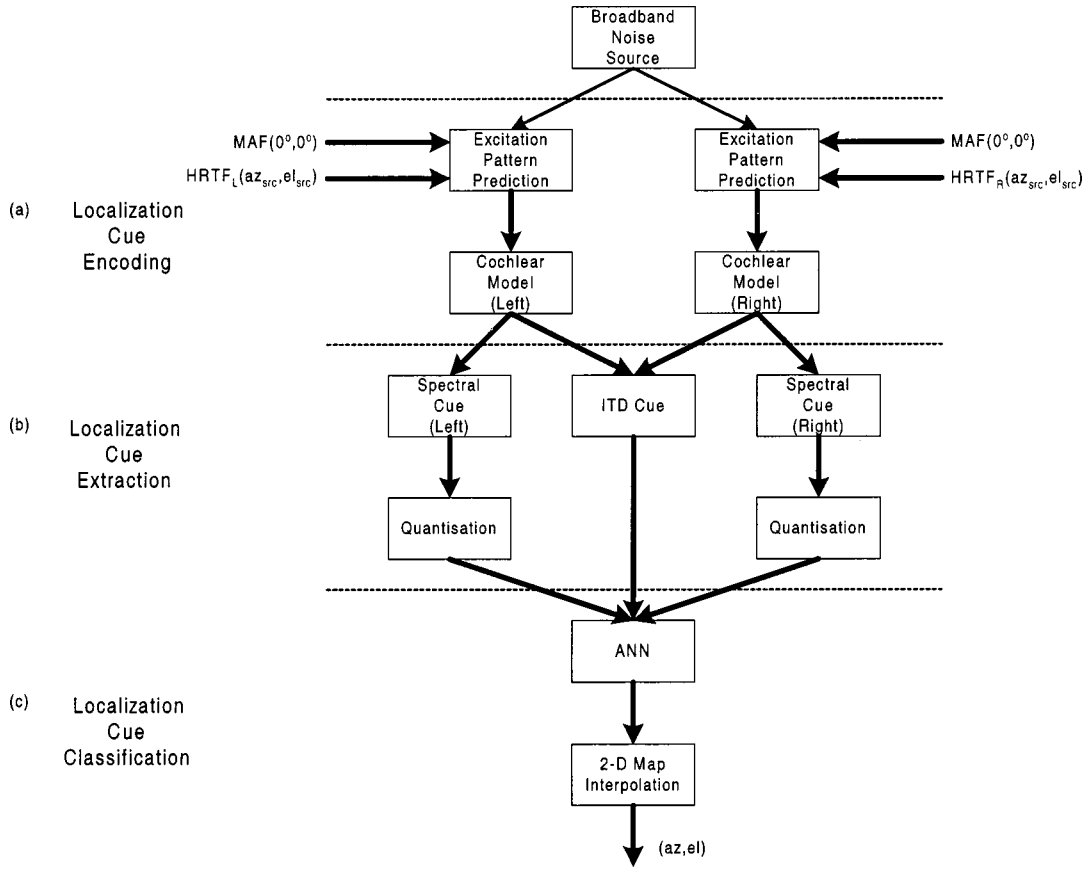

FIG. 1. Localization model architecture.

then provide the basis for exploring aspects of preprocessing to the ANN by varying biologically constrained parameters and observing the impact on the subsequent localization performance. In this way we could explore the limits of the ''biological resolution'' of inputs to the model that are necessary to sustain human levels of localization performance. In addition, benchmarking the model's performance against human localization performance would provide some insights into the likely biological relevance of various encoding and output parameters of the model.

Third, the output of the ANN was postprocessed using a spatial interpolator that attempted to model the behavior of a neuronal population of spatial location detectors. Previous neurophysiological studies of auditory space maps in the deep layers of the Superior Colliculus of mammals and the MLD of Owls have demonstrated significant difference in the size of the auditory spatial receptive fields of neurones in these nuclei [see King (1994) for review]. It has been proposed that some aspects of localization behavior may well be mediated by the output of the population of these neurones [for example, see Middlebrooks (1984)], in which case, the neuronal point image, or extent of the nucleus which was activated by a single point stimulus in space, would vary significantly between these species. We were interested in varying the ''point image'' of the output layer in our model to see what effect this may have on the subsequent localisation accuracy of the model.

The preprocessing components of the model described in this report attempts to account for (i) the spectral smoothing of cochlear encoding, (ii) the frequency-dependent variation in auditory sensitivity, (iii) the encoding of acoustical information as spike trains, and (iv) the parallel streaming of interaural timing information and spectral amplitude information. Once a combination of parameters had been determined that produced human-like localization performance, two main experiments were conducted using the model. First, we explored the fidelity of the spectrum amplitude quantization of the input required to sustain human localization performance. Second, the impact of the size of the ''point image'' of the ANN output was explored by varying the extent of the ANN output layer over which the spatial interpolator took its input. A third control experiment was also carried out to ensure that the behavior of the ANN was not limited by the information encoding capacity of the network architecture. In this case the effects of varying the number of hidden layer neurones on localization performance was examined.

I. STRUCTURE OF THE LOCALIZATION MODEL

A. Model overview

The model consists of three parts. First, a broadband sound in free field space was simulated using white noise [Fig. 1(a)]. The noise was filtered by the filter function of the outer ear, or head-related transfer function (HRTF), adjusted using the frequency sensitivity function of the auditory system and then used as input to the Patterson–Holdsworth cochlear model (Slaney, 1994). The monaural and binaural lo-

calization cues (left and right monaural spectral cue and ITD cue) were extracted from the cochlear output [Fig. 1(b)]. An artificial neural network (ANN) was trained to classify these localization cues [Fig. 1(c)]. The model was developed using the Matlab scripting language (version 4) and the C programming language. In this model, the direction of a sound source with respect to the listener is given using the vertical, single-pole coordinate system with azimuth 0 degrees and elevation 0 degrees indicating the position directly ahead of the subject. Locations above the audio-visual horizon and to the right of the anterior of the midline are indicated by positive degrees elevation and azimuth, respectively (Carlile, 1996).

B. Stimulus generation and localization cue encoding

Due to the various level-dependent nonlinearities in auditory encoding, the capacity of the system to encode spectral shape is dependent upon the overall input level (Sachs and Young, 1979). This will also be modified by the frequency dependency of auditory sensitivity that reflects, in part, the acoustical transmission properties of the auditory periphery (the pinna, concha, ear canal, and middle ear). The minimum audible field (MAF) describes the minimum detectable pressure level determined at the position of the subject's head for a free-field, pure tone stimulus located on the median plane (ISO R.226; see also Glasberg and Moore, 1990). This variation of sensitivity should affect the audibility of different frequency components of a complex sound. In this context, the MAF will weight the spectral cues according to the human audiometric sensitivity so that some of the features of the HRTF will be more salient than the others.

Carlile and Pralong (1994) argued that the neural excitation pattern for a spectrally flat broadband noise directly in front of a subject (azimuth 0 degrees, elevation 0 degrees) could be estimated by passing the inverted MAF through a cochlear model. This study extended this method to estimate the neural excitation pattern for a sound at any location for which the HRTF had been determined. The MAF used in this model was taken from Glasberg and Moore (1990) and was assumed to correspond to the human sensitivity for a sound located at (0 degrees, 0 degrees) in our system. The MAF curve was extrapolated with a low-order spline to estimate the low- and high-frequency tails of the sensitivity function not covered by the original measurements. The neural excitation pattern for a location (az, el) was then estimated by passing a weighted spectrum $Ws_{(\mathrm{az,el})}$ for a broadband sound source at (az, el) to the cochlear model where $Ws_{(\mathrm{az,el})}$ was an approximation of the MAF at (az, el). The magnitude response of $Ws_{(\mathrm{az,el})}$ was estimated using the HRTFs measured at (az, el) and (0 degrees, 0 degrees) using Eq. (1):

$$|Ws_{(\mathrm{az,el})}(f)| = \left| \frac{k^{*}\mathrm{HRTE}_{(\mathrm{az,el})}(f)}{\mathrm{HRTF}_{(0^{\circ},0^{\circ})}(f)^{*}\mathrm{MAF}_{(0^{\circ},0^{\circ})}(f)} \right|. \quad (1)$$

Equation (1) computes the magnitude response of $Ws_{(\mathrm{az,el})}$ by adjusting the MAF at location (0 degrees, 0 degrees) by the difference between the HRTF at (az, el) and (0 degrees, 0 degrees). The constant k adjusts the weighted spectrum to a reasonable level corresponding to a spectrum amplitude of 30 dB (i.e., $k=31.6$) (see also Carlile and Pralong, 1994). Since no phase information was included with the published MAF, it was assumed that the phase of $\mathrm{HRTF}_{(\mathrm{az,el})}$ and $Ws_{(\mathrm{az,el})}$ are identical [Eq. (2)]:

$$\arg(Ws_{(\mathrm{az,el})}(f)) = \arg(\mathrm{HRTF}_{(\mathrm{az,el})}(f)). \quad (2)$$

A randomly generated white noise was filtered with $Ws_{(\mathrm{az,el})}$ and produced the input to the cochlear model needed to predict the neural excitation pattern for location (az, el). The duration of the noise stimulus was 100 ms.

The Patterson–Holdsworth cochlear model provided the simulation of the auditory transduction model using a gamma-tone filter bank and the Meddis hair cell model (Slaney, 1994). The output of the gamma-tone filter bank was connected to an array of Meddis hair cells. The compressive nonlinearity of the Meddis hair cell model limited the output of the cochlear model. The output of the hair cell gives the firing probability at each sampling interval. Each cochlear model contained 128 Meddis hair cells. The number of hair cells in the model is a trade-off between spectral resolution and computational efficiency and our choice was influenced by the model of Neti *et al.* (1992) who used the same number of channels to represent a spectral cue.

C. Extraction of ITD cues

Figure 1(b) shows the circuit for the extraction of the ITD and the left and right monaural spectral cues encoded in the output of the cochlear model. Figure 2 shows the circuit that extracts the ITD cue from the left and right cochlear outputs. This design was based on the silicon model of the time-coding pathway of the owl described in Lazzaro and Mead (1989) which operates on binary pulse/trains. The modified ITD circuit calculates the cross-correlation coefficients from the profile of the left and right inputs to the circuit.

The output of the hair cells in the left and the right cochlear outputs with the same center frequency were passed through a pair of time delay lines. Assuming that the ears are two points on a spherical head, the path difference d between the two ears is approximated by $d=r(\theta+\sin\theta)$ where r is the radius of the head and θ is the direction of the sound source measured from the median plane in radians (Woodworth, 1938). The maximum path length-occurs at $\theta=\pi/2$. From this equation the maximum path difference d is 0.26 m for $r=0.1$ m and corresponds to a time delay of 780 μs. This defines the maximum time delay to be modelled for a signal to propagate from the start to the end of the delay line. The time delay elements updated their output by copying the output of the preceding time delay element to its own output at a rate of 40 kHz (i.e., $\Delta t=25\,\mu$s). Each time delay line contained a chain of 32 determined by the relationship between the maximum output rate of the cochlear model (40 kHz) and the need for the number of time delay elements to span the maximum ITD (i.e., $N=40\,000\times 780\,\mu\mathrm{s}\approx 32$). In addition, 32 delay elements would quantize the ITD to approximately 25 μs which is similar to the human just noticeable difference (JND) for an ITD of 10 μs (Yost, 1974). The output of all hair cells propagated through the time delay elements at the same rate. The cross correlation was calcu-

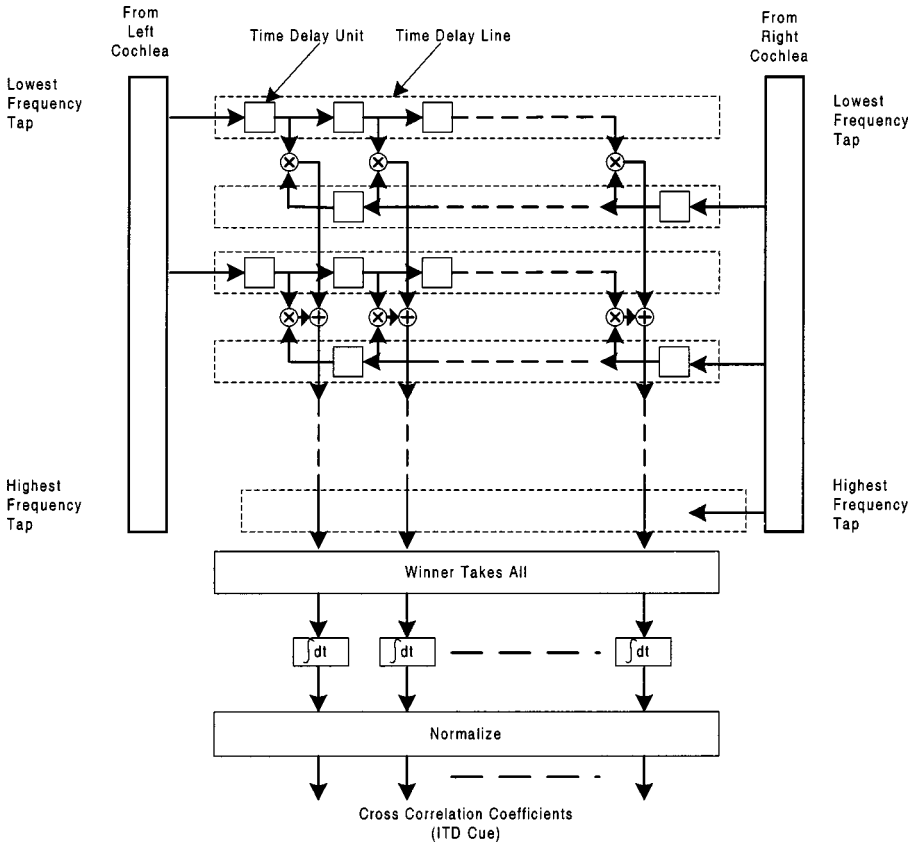

FIG. 2. The ITD cue extractor.

lated by multiplying the output of cochlear models passing through the two time delay lines [Eq. (3)], where cgm_l and cgm_r are the left and right cochlear outputs and N is the number of delay elements in a delay line:

$$xcorr_k(t)=\sum_{f=100\ \text{Hz}}^{1.4\ \text{kHz}} cgm_l(f,t-k\Delta t) \times cgm_r(f,t-(N-k-1)\Delta t) \quad \text{for } 0\leqslant k<N. \tag{3}$$

The ITD cue extractor summed the cross-correlation coefficients for all hair cells with center frequency below 1.4 kHz as described in Eq. (3). A ''winner takes all'' function converted the cross-correlation coefficients into a binary vector $\mathrm{ITD}(t)$, where the ith component of this vector, $\mathrm{ITD}_i(t)$, was computed using Eq. (4):

$$\mathrm{ITD}_i(t) = \begin{cases} 1 & \text{if } xcorr_i(t)\geqslant xcorr_j(t) \quad \text{for all } 0\leqslant j<N, \\ 0 & \text{otherwise.} \end{cases} \tag{4}$$

Bit i in the binary vector $\mathrm{ITD}(t)$ was set to one if it corresponded to the maximum cross-correlation coefficient, otherwise it was set to zero. The binary versions of the instantaneous ITD cues were accumulated [Eq. (5)] to estimate the normalized ITD cue [Eq. (6)]. In most cases when the model was stimulated by a broadband stimulus, only one component in $\mathrm{ITD}_{\mathrm{norm}}$ was set to one while the other components were close to zero:

$$\mathrm{ITD}_i=\sum_{t=25\ \text{ms}}^{100\ \text{ms}} \mathrm{ITD}_i(t) \quad \text{for } 0\leqslant i<N, \tag{5}$$

$$\mathrm{ITD}_{\mathrm{norm}}=\left(\frac{\mathrm{ITD}_0}{\mathrm{ITD}_{\max}},\frac{\mathrm{ITD}_1}{\mathrm{ITD}_{\max}},\ldots,\frac{\mathrm{ITD}_{N-1}}{\mathrm{ITD}_{\max}}\right) \quad \text{where } \mathrm{ITD}_{\max}=(\max \mathrm{ITD}_0,\ldots,\mathrm{ITD}_{N-1}). \tag{6}$$

Within a particular frequency channel, the ITD information corresponded to the phase relationships between the signals received from the left and right ears. As a result, only frequencies with a wavelength greater than the distance between the ears offer an unambiguous ITD.

D. Extraction of spectral cues

The monaural spectral cue for the model was the time average of the cochlear output from 25 to 100 ms. The first 25 ms of output was discarded to allow the cochlear output to reach a steady state. Note that the left and right monaural spectral cues were extracted simultaneously and presented to the ANN together. This arrangement allowed the ANN to derive binaural cues such as the interaural spectral difference cue or the interaural level difference cue using the two monaural spectral cues.

E. Artificial neural network classifier and feature vector coding

A two-layer artificial neural network (Rumelhart and McCelland, 1986; Lippmann, 1987) was trained to transform the localization cues to a two-dimensional output matrix that indicated the direction of the sound source. A feed-forward

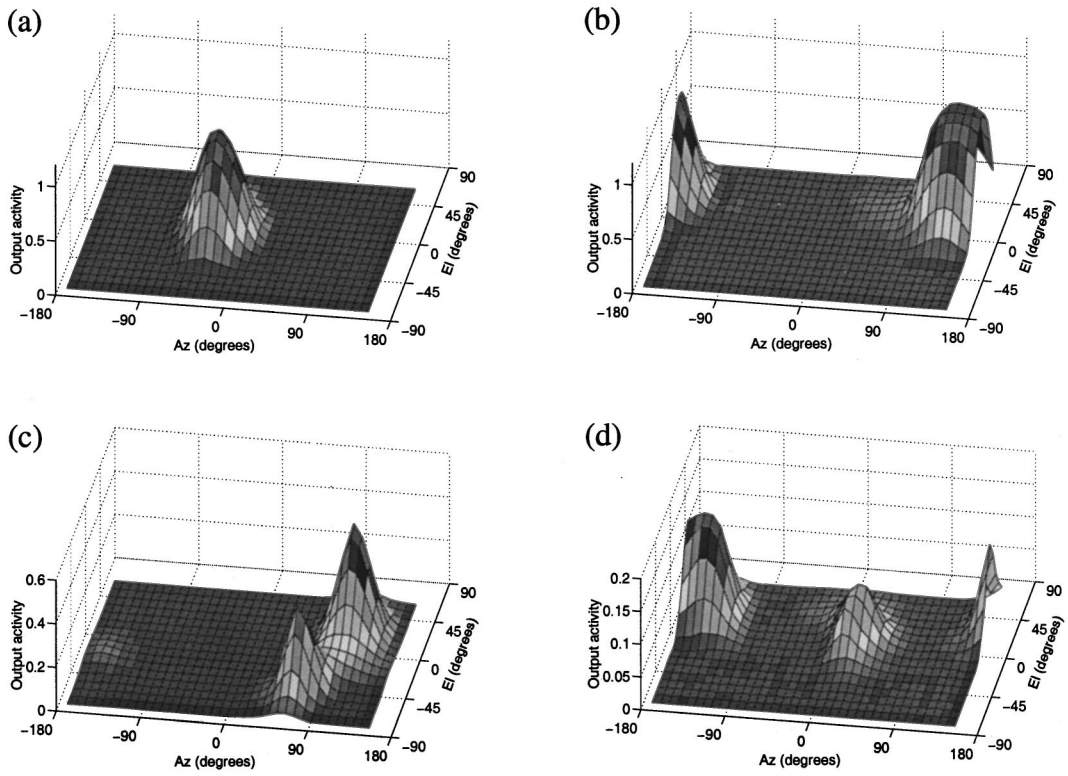

FIG. 3. Examples of ANN outputs. (a) A single clear peak for an estimated source located at (−40 degrees, 0 degrees). (b) A single clear peak for a source estimated to be at (140 degrees, 40 degrees). (c) Output of ANN which led to elevation confusion with source located at (80 degrees, −40 degrees). (d) Output of ANN which led to front–back confusion with source located at (40 degrees, 20 degrees). Data points were interpolated at 10 degrees rather than 1 degree as described in Sec. I E for clarity of this illustration.

back-propagation algorithm was used to train the network. A neural network simulator, NevProp (Goodman *et al.*, 1993), was used to implement the neural network.

The ANN contained 288 input neurones: 128 neurones to receive the left spectral cue, another 128 neurones to receive the right spectral cue, and 32 neurones to receive the normalized ITD cue. The model used in the experiment that was described in Sec. III A contained eight hidden layer neurones. The output layer contained 162 neurones which formed a 9×18 neurone matrix. Each neurone in the matrix was associated with a point (az,el), where $-180\leqslant \text{az} <180$ degrees and $-80\leqslant \text{el}\leqslant 80$ degrees, with a 20-degrees step size. The neurones in the input and the hidden layer were fully interconnected, and likewise for the neurones in the hidden layer and the output layer. There were no assumptions about how the network would use the localization cues. Although the two poles (north and south) were not represented directly by any neurones, the localization model could still specify these directions by passing the ANN outputs to a space-map interpolator (described below).

Each training vector presented to the ANN consisted of two parts: the ANN input vector and the target output vector. The input vector consisted of the left and right spectral cues and the ITD cue for direction (az,el). The left and right spectral cues in each input vector were scaled by the normalization factor $1/m$, where m was the maximum value in each pair of left and right spectral cues. The target output vector specified the output activity of the output layer neurones during training. When the neurone output activity is plotted over its associated coordinates, the profile of the plot resembles a double Gaussian distribution. The coordinates with the highest output activity was taken as the source direction. Equation (7) was used to calculate the output activity for an output neurone d_{ij} located at position ($20i$ degrees, $20j$ degrees) where $-9<i\leqslant 9$ and $-4<j\leqslant 4$ for a sound source located at (az, el). The variable σ is the standard deviation of the double Gaussian distribution. A large value of σ causes more output neurones to respond to an input stimulus. The value of σ was set to 30 degrees in all model experiments unless otherwise stated:

$$d_{ij}=e^{-[(20i^\circ-\text{az})/(\sigma/\cos(20j^\circ))^2+((20j^\circ-el)/\sigma)^2]}. \tag{7}$$

The single pole representation of space used in the study has the disadvantage that as elevation diverges from the greater circle indicating the equator, there is a decrease in the area of space corresponding to one degree azimuth. A scaling factor, $1/\cos(20j)$ (where $20j$ is the elevation associated with the output neurone) has been included in Eq. (7) to adjust the spread of the activity to compensate for the change in density of neurones under a fixed area at different elevations.

The ANN output was interpolated using the Matlab function griddata to give the final location estimate. The algorithm interpolates the ANN outputs from a 20-degree grid to a 1-degree grid. The most active output neurone was identified and the interpolation operation was applied to the local 3×3 output neurone matrix centered on the most active output neurone. Figure 3 illustrates four examples of the

ANN outputs. The plots show the pattern of activity of the output layer which reflects stimulation at four different points in space. Note that the maximum output activity shown in Fig. 3(a) and (b) is close to 1, whereas in Fig. 3(c) and (d) the maximum output activity is lower. In the latter two cases, the ANN had difficulty in estimating the source location, and generated output activities for two regions which indicates an increase of elevation [Fig. 3(c)] or front–back confusion [Fig. 3(d)] errors.

II. EXPERIMENT

A. Psychophysical test setup

Since the model was designed to deliver human level performance, it was necessary to assess the model performance against the free-field localization performance of the human listener who provided the HRTFs to the model. The free-field localization tests have been described in detail elsewhere (Carlile *et al.*, 1997) but are briefly outlined below. All localization tests that involved human listeners were carried out in the same anechoic chamber that was used for the HRTF recording (Carlile *et al.*, 1997). A 150-ms broadband stimulus was played through a loudspeaker mounted on a computer-controlled, semi-circular hoop (1-m radius) centered on the listener's head. The listener was asked to point his/her nose toward the perceived location of the sound source. An electromagnetic tracking device was mounted on the listener's head which measured the position of the head. This procedure was repeated for all 76 locations with four trials per location. The localization estimates were analyzed using the same procedures applied for the model's results for comparison.

B. Data analysis

The azimuth and elevation systematic errors, the spherical angular error of localization estimates, and the overall spherical correlation coefficient (SCC) were calculated for the model results to assess the performance of the model. The randomness in the stimuli supplied as input to the model would certainly cause some variations in the estimated source location, and therefore multiple estimates for each source location were collected. The difference between the source position and the mean direction of the distribution gives the systematic error in azimuth and elevation directions (referred to as E_{az} and E_{el}, respectively) (Leong and Carlile, 1997). For the set of estimates made for the same source location, the spherical angular error is defined as the average of the angle between the line joining the center of the head of listener to the mean direction and the line joining the head of the listener to each of the estimates.

The spherical correlation coefficient is a measure of the correspondence between the actual location of the target and the location indicated by either the human subjects (Carlile *et al.*, 1997) or the model. Consistent with other studies we have used this coefficient as a global metric of localization accuracy (for methods of calculation see Wightman and Kistler, 1989; Fisher *et al.*, 1993; Carlile *et al.*, 1997). Front–back confusion errors were processed separately during data analysis. An estimate was considered front–back confused if the source and the estimate were on different sides of the interaural axis and greater than 5 degree from the vertical plane through the interaural axis. In addition, an estimate was considered front–back confused only if it lay within ± 20 degrees azimuth of the mirrored source location. This operation was employed to separate the large azimuth errors from front–back confusion errors. All data analysis was performed using the Matlab toolbox, SPAK (Leong and Carlile, 1997).

C. Vector generation

The HRTFs were used to simulate sound sources located at different positions in space. The HRTF library of a human subject was recorded using the procedures described in Pralong and Carlile (1996). A total of 724 pairs of HRTFs were recorded for equally spaced stimulus positions.

Localization cue vectors were generated by passing filtered noise stimuli through the cue coding and extraction components of the model as described in Sec. I. A range of input levels were prepared: 40, 50, 60, 65, 70, 80, and 90 dB. In addition, at each input level, ten samples were generated for each pair of HRTFs contained in the 724-point HRTF library. This provided a vector pool that contained a total of 50 680 localization cue vectors. Training and testing vector sets were formed by selecting localization cue vectors from this large pool that corresponded to the particular stimulus characteristics of interest. Humans are most likely trained to localize on a wide range of stimulus levels. This was simulated in the training of the model by using training cue vectors generated at different input levels. The training vector set was composed of one sample per point in the HRTF library for each input level. This gives a total of 5068 cue vectors in the training set. The testing vector set was composed of a subset of 76 positions that were used in the training, with ten samples of localization cue vectors generated at 65-dB input level. The performance of the model on this test set was compared with the localization results of human listeners using the same set of 76 stimulus locations. The human psychophysical experiments were performed at a fixed 65-dB sound pressure level (SPL) and used the same set of stimulus locations as that used in the generation of the testing vector set.

III. RESULTS

A number of parameters were available to control the performance of the model which was then compared to the performance of the single subject who provided the HRTFs used in the model as well as the performance data pooled from a population of 19 other subjects. Localization performance was measured in terms of the spherical correlation coefficient of the localization estimates against the actual target locations and the percentage of front–back confusion errors. We have included comparisons of both the single subject and the population response as it is likely that the performance of the single human subject also contains idiosyncrasies that reflect factors other than the sensory inputs. Therefore, a more robust comparison of the model performance might be against the population response where individual effects should have been cancelled out to some extent.

TABLE I. Localization performance of individual listener (Human), a group of 19 human listeners (Group), and the reported model with different configuration (E1 to E14). The test stimuli were generated at 65 dB SPL.

Result	Trial no.	Quantization levels	Cochlear channels	Hidden neurone	σ (degrees)	SCC (no MAF)	% fb (no. MAF)	SCC (MAF)	% fb (MAF)
Human	304	n/a	n/a	n/a	n/a	n/a	n/a	0.957	1.0%
Group	6909	n/a	n/a	n/a	n/a	n/a	n/a	0.983	3.2%
E1	780	10	128	8	30	0.958	8.1%	0.884	7.5%
E2	780	20	128	8	30	0.966	3.7%	0.944	3.3%
E3	780	40	128	8	30	0.962	5.9%	0.972	0.8%
E4	780	100	128	8	30	0.970	5.4%	0.975	1.5%
E5	780	20	64	8	30	0.934	7.6%	0.950	4.1%
E6	780	20	256	8	30	0.969	3.3%	0.974	2.7%
E7	780	20	128	6	30	0.883	7.2%	0.823	6.7%
E8	780	20	128	10	30	0.964	4.7%	0.956	3.7%
E9	780	20	128	8	5	0.274	33.7%	0.477	12.1%
E10	780	20	128	8	10	0.925	9.9%	0.886	4.6%
E11	780	20	128	8	20	0.957	4.1%	0.984	0.4%
E12	780	20	128	8	40	0.969	6.5%	0.968	1.6%
E13	780	20	128	8	60	0.955	3.1%	0.941	2.1%
E14	780	20	128	8	90	0.939	3.1%	0.948	0.0%

In Table I the summary results for all 28 experiments with the model are presented. Experiments E1–E4 examined the variation of the spectral cue amplitude resolution; E2, E5, and E6 examined the effects of varying the frequency resolution of the input to the ANN; E2, E7, and E8 examined variation in the number of neurones contained in the ANN hidden layer; and E2 and E9–E14 examined the variation in the size of the neural ''point image'' of the output. All experiments were conducted both with and without the MAF correction.

A. Broadband localization

The objective of the first series of experiments was to develop a model with the most human-like localization performance. In this series, we systematically varied the frequency resolution [64 (E5), 128 (E2), and 256 (E6) cochlear channels] and the size of the neural point image (5, 10, 20, 40, 60, and 90 degrees: E9–14). The SCC provides only a rough guide for comparisons of localization accuracy between the subject group and the model as this measure is sensitive to the number of samples. Therefore, as an initial screening of performance, we sought a combination of parameters that provide a SCC that was close to that of the individual listener and a front–back confusion rate that was closer to the group. This was provided by a model with 128 channels and a neural point-image of 30 degrees. For each model we also examined the azimuth and elevation systematic errors and the spherical angular error and these also demonstrated the best fit to the human data for our standard model. These measures have more explicit and detailed measures of localization performance, offering more information than the SCC.

The ''standard'' model result and the individual and group human results were analyzed and plotted as a function of the azimuth of the sound source. The plots include the azimuthal and elevational systematic errors (Figs. 4 and 5), the spherical angular error (Fig. 6) of the localization estimate distributions at ±40-, ±20-, and 0-degrees elevation, as well as the distribution of the front–back confusions (Fig. 7). On average the error magnitudes were very similar among the three sets of results.

The azimuthal systematic errors for the individual listener showed more abrupt changes than the data obtained from the group. For instance, Fig. 4 shows that at elevation 40 degrees, the azimuthal systematic error for the individual listener (circles) changed from 10 degrees at azimuth −150

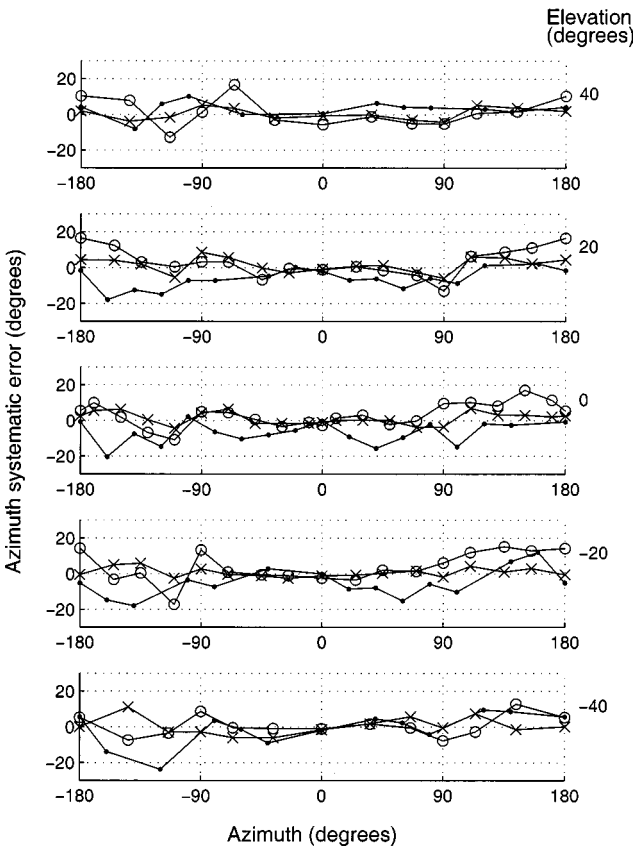

FIG. 4. E_{az} of the estimate distribution of the model (dot), the human listener whose HRTFs are used by the model (circle), and the group of 19 listeners (cross).

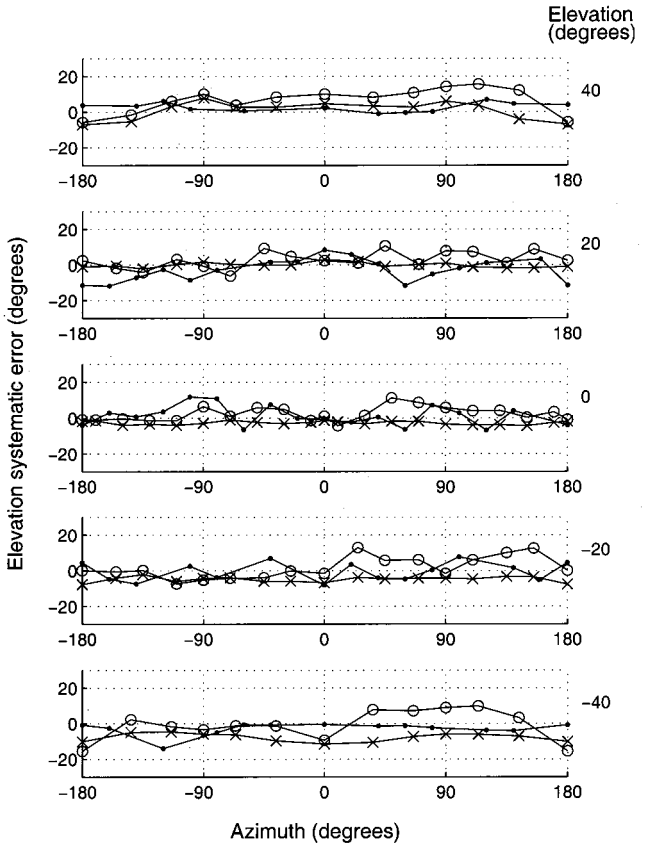

FIG. 5. E_{el} of the estimate distribution of the model (dot), the human listener whose HRTFs are used by the model (circle), and the group of 19 listeners (cross).

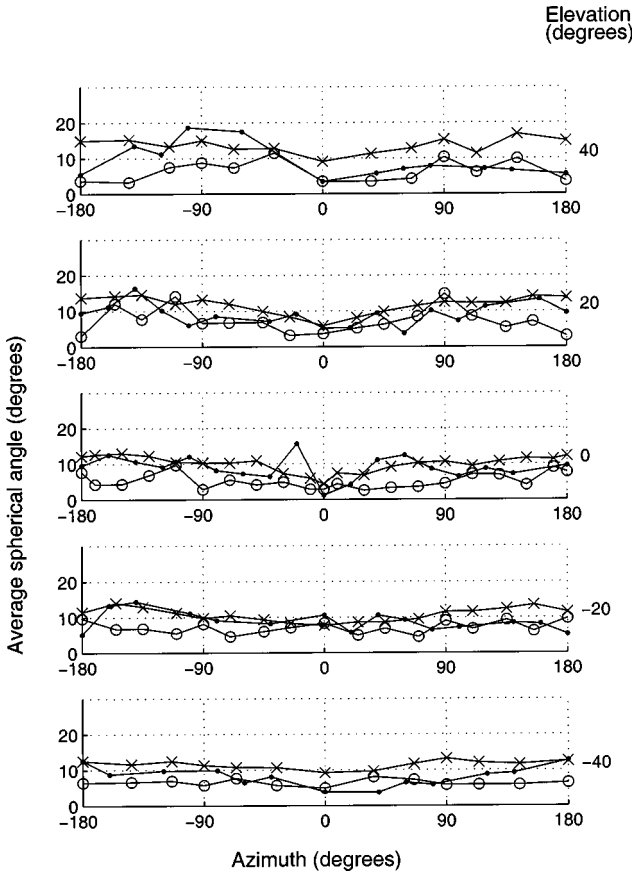

FIG. 6. Spherical angular error of estimate distribution of the model (dot), the human listener whose HRTFs are used by the model (circle), and the group of 19 listeners (cross).

degrees to −15 degrees at azimuth −110 degrees, then back to 20 degrees at −70 degrees.

The elevational systematic error is shown in Fig. 5 and indicates that the magnitudes for the elevational systematic error were similar for the three sets of data. At higher elevations, for example at 40 degrees, the magnitude of the elevational systematic error of the model (dots) was generally lower than those of the listener (circles) and the group results (crosses). The individual listener gave greater elevational systematic error at ±40 degrees elevations than at ±20 degrees and 0 degrees elevations, and often had positive elevational systematic errors when the source was on the right hemisphere. This feature was not found on the left hemisphere, and also not obvious in the model or the group result. This may represent a bias related to the response measure rather than the perception of the location.

Figure 6 shows the magnitude of the average spherical angular error of the estimates for the model, single subject, and group. The spherical angular error between the model (dots) and the individual listener results (circles) are similar at 20, −20, and −40 degrees elevation. The spherical angular error of the group (crosses) is generally greater than that of the model and the individual listener at all elevations. The average spherical angular error of the model remained within the limits defined by the individual listener and group results at most test locations.

The magnitude of systematic errors shown in Figs. 4 and 5 indicate that the individual listener exhibited performance that was close to the group results, and that the distribution of estimates were usually within the range of the group results. The model gave similar systematic errors for most locations to that shown for the single and group results.

The distribution of front–back confusion errors in the three sets of results with data collapsed across elevation are illustrated in Fig. 7. In the model result [Fig. 7(a)], the front–back confusion errors occurred more often with source locations on the left hemisphere. However, for the results of the group [Fig. 7(c)], the front–back confusion errors were more equally distributed for the right and left hemispheres.

B. Effects of frequency resolution

Increasing the number of cochlear channels from 64 (E5) to 128 (E2) resulted in only minor differences in the performance of the model, but that an increase to 256 (E6) channels resulted in a substantial increase in accuracy. In any event, the model with 128 cochlear channel provided the best match to the human performance.

C. Effects of amplitude resolution

To explore the role played by the fine structure of the spectral cues in localization performance, the spectral amplitude components of the monaural spectral cues were subjected to a linear quantization operation. The magnitude of the quantization step applied to the monaural spectral cues was varied and four models were trained using spectral cues

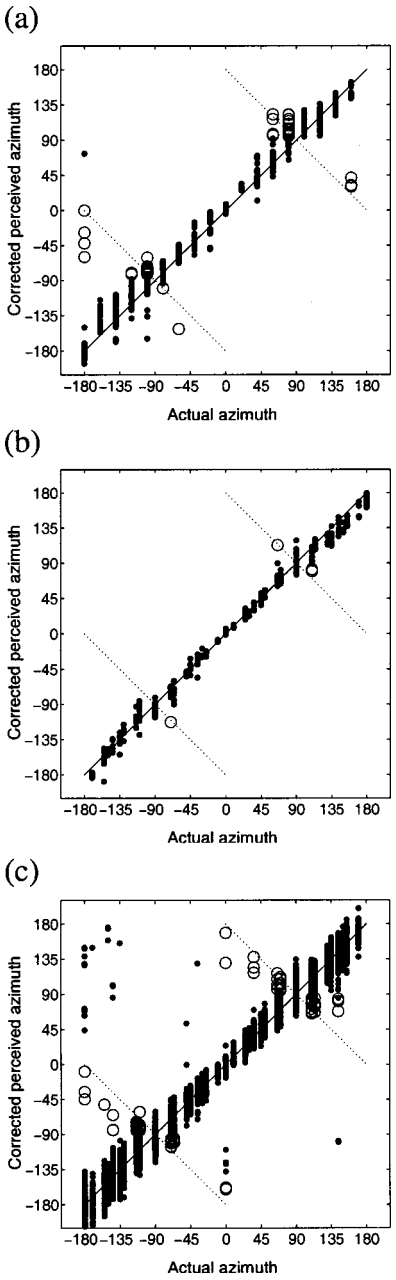

FIG. 7. Front–back confusions of the (a) model, (b) human listener, and (c) the group of 19 listeners. Front–back confused data are plotted using empty circles and non-front–back confused data are plotted using dots.

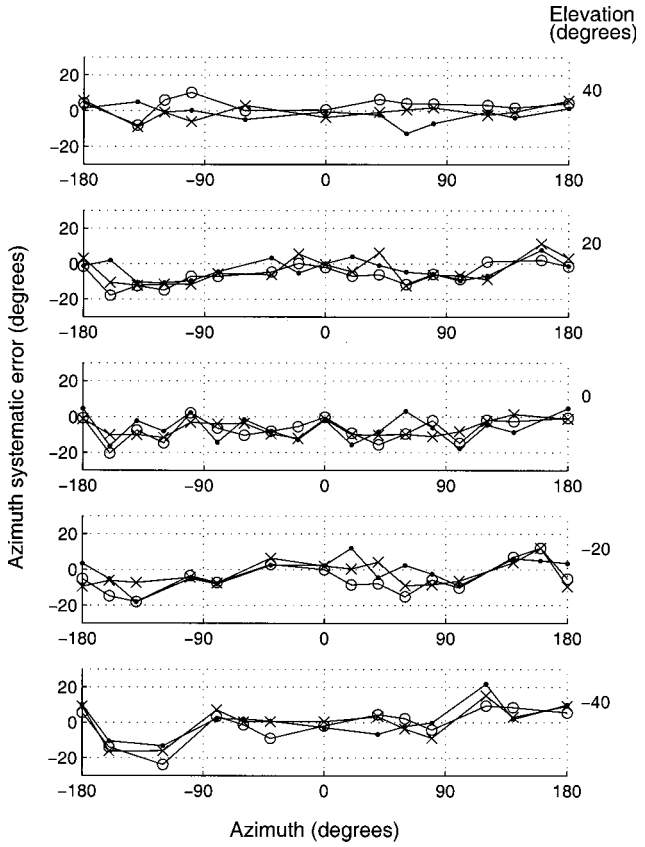

FIG. 8. E_{az} for models trained with spectral cues quantized to 10 (dot), 20 (circle), and 40 (cross) levels.

that were quantized to 10, 20, 40, and 100 levels over the total dynamic range of the normalized spectral cues. For instance, when the quantization parameter was set to 40 levels, a normalized monaural spectral cue was approximated by 40 equally spaced discrete values between 0 to 1 (inclusive). Each analog value of spectrum amplitude was rounded to the closest quantization level. The azimuth and elevation systematic errors (Figs. 8 and 9), spherical angular error (Fig. 10), and the front–back confusion errors (Fig. 11) have been plotted for 10, 20, and 40 quantization levels. E1–E4 in Table I correspond to the models trained with spectral cues quantized to 10, 20, 40, and 100 quantization levels, respectively.

The pattern and magnitude of the systematic errors demonstrated by the different models showed only marginal changes with variation in the number of quantization levels (azimuth: Fig. 8 and elevation: Fig. 9). The random errors of localization indicated by the extent of the distribution of the estimates showed clear changes when the number of quantization levels were changed (Fig. 10). At all elevations, the model that used spectral cues with higher amplitude resolution (greater number of quantization levels) gave smaller average spherical angles for the distributions. For the directions close to (0 degrees, 0 degrees), however, all three models had similar spherical angular error. In addition, the extent of the front–back (FB) confusions were also negatively correlated to the number of quantization levels (10 to 40 levels). From Fig. 11, the model with 10 quantization levels produced the most front–back confusion errors among the three models; the model with 40 quantization levels gave almost no front–back confused estimates.

The levels of performance with 20 quantized levels was closest to that exhibited by the human subjects (Figs. 4, 5, and 6). Increasing the number of quantized levels beyond 40 produced only a slightly higher SCC and more front–back confused estimates.

D. Effects of number of hidden layer neurone

The number of hidden layer neurones will affect the information storage capacity of the ANN (Baum and Haussler, 1989). As a control experiment, it was important in this study to demonstrate that the ANN architecture we were employing was not a limiting factor in the performance of the model. In experiments E7, E2, and E8, the number of hidden

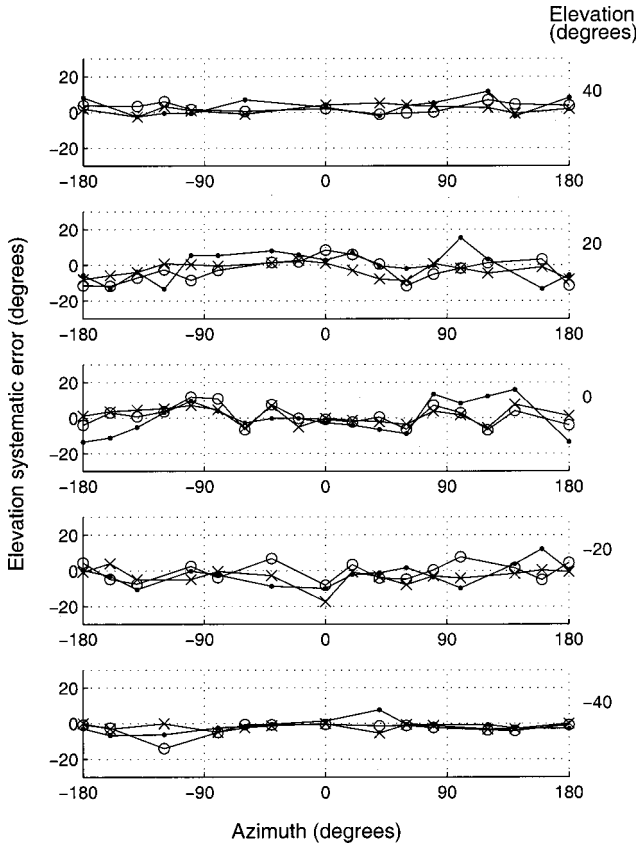

FIG. 9. E_{el} for models trained with spectral cues quantized to 10 (dot), 20 (circle), and 40 (cross) levels.

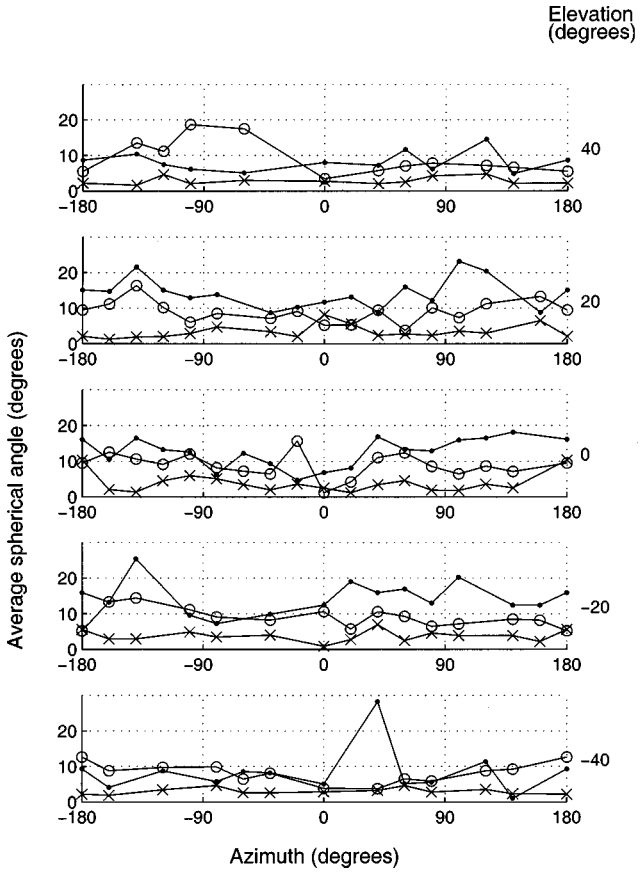

FIG. 10. Spherical angular error for models trained with spectral cues quantized to 10 (dot), 20 (circle), and 40 (cross) levels.

layer neurones was six, eight, and ten, respectively. With six hidden layer neurones, there was a substantial decrease in the SCC and a twofold increase in the number of FB confusions when compared to the model with eight hidden layer neurones. In contrast, an increase to ten neurones had only a marginal effect on the SCC and a similar number of FB confusions. We concluded from this experiment that the performance of our standard model was not bound by capacity of our ANN with eight hidden layer neurones required to carry out an effective input–output mapping.

IV. DISCUSSION

A. Broadband localization

The localization performance of the model was compared with the individual listener from whom the HRTFs were obtained and with a group of 19 human listeners (Carlile *et al.*, 1997). Although there is a good match between the three sets of data, there are some characteristic differences. Some of these differences can probably be attributed to the differences in the sample sizes for each group. This is particularly evident with the sharp variations in the azimuthal systematic errors (Fig. 4) for the individual human data compared to the group data and to a lesser extent the model.

A second source of difference is likely to originate from the response measures. In testing human localization performance, the listener was asked to point his or her nose in the direction of the source (Carlile *et al.*, 1997). Although turning to face towards a sound source is a highly ecological process, there are at least two types of errors that may be present in the estimates. First, for sound locations that require very small or large movements of the head to the mechanical limits of motion, there is a tendency for the listener to point towards the source using a combined movement of the head and the eyes, rather than only the movement of the head. As the method of detecting the perceived location of the sound source involves tracking the position of the head (rather than the eyes), the ''eye capture'' of the perceived target location may produce systematic errors in estimating the perceived location. This type of systematic error is classified as a motor error (for a full discussion see Carlile *et al.*, 1997). In addition to motor error, there are also spatially dependent variations in the localization performance found in experiments that have minimized the presence of motor errors (Gilkey *et al.*, 1995; Carlile *et al.*, 1997) which can be attributed to sensory error. Since the model used the HRTFs of the individual listener, one would expect similar features to be found in their results if the behavior of the model was constrained similarly to that of the human even though the magnitudes of the model systematic errors were close to the individual listener and the group results. The systematic errors (Figs. 4 and 5) made by the model were more symmetrical about the median plane than that of the individual listener. The asymmetry in the single listener's errors might have resulted from motor errors or other response biases. We have not attempted to include any of these latter kinds of errors in our model.

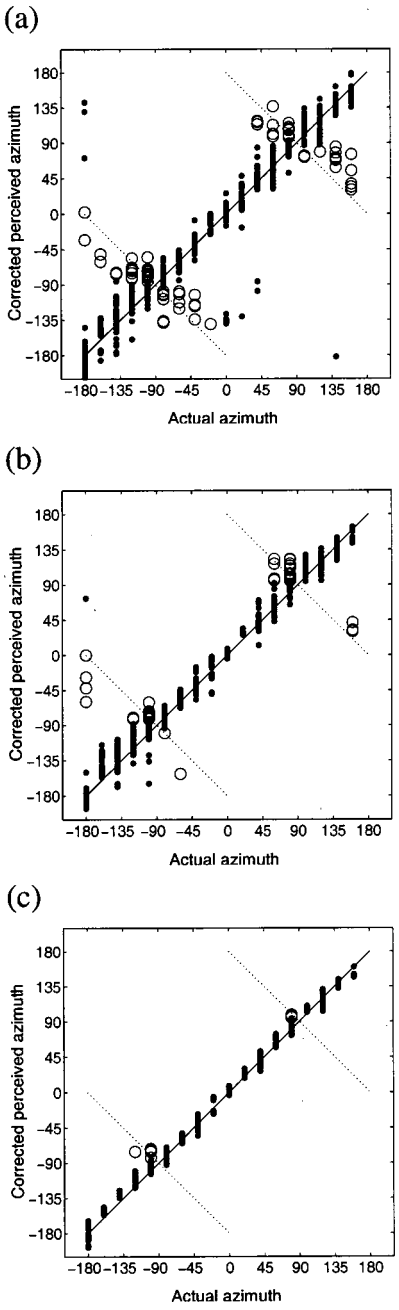

FIG. 11. Front–back confusions for models trained with spectral cues quantized to (a) 10, (b) 20, and (c) 40 levels.

For instance, both the systematic error and the size of the error distributions were observed to increase with the azimuth of the sound source. In localization experiments that involved a human listener, when the sound source was behind the listener, the listener was unable to swivel his/her head towards the back without body movement to point their nose at the perceived sound location. The judgment of the azimuthal angle traveled may well be less accurate than relatively smaller azimuth movements accomplished by the head alone. This is consistent with observations that for the human listeners, the azimuthal localization error was smallest when the source was on the median plane and close to the audio-visual horizon. The slightly greater accuracy demonstrated by the model for more lateral and posterior location may be due to the absence of motor error in the model's result.

The close similarities between the average spherical angular error and systematic error close to the median plane in the results collected from the model and the human listeners also suggests that localization cue features used by the model were similar to those used by human listeners. This in turn provides support for the notion that the model parameters were set to psychophysically plausible values.

B. Effect of amplitude quantization on localization performance

There was no significant change in the pattern of the systematic errors with the variations in the number of quantization levels applied to the monaural spectral cues. Rather, the more significant changes were in the magnitude of the distribution of the estimates. In general, the spherical angular error of the distribution of estimates increased as the number of quantization levels was decreased. This indicates that the detail in the monaural localization cues can provide information important for accurate localization performance. It was interesting that even with a quantization level of only ten steps, the extent of the systematic errors was similar to the other models, and the distribution of estimates was only slightly greater than models with higher quantization. However, with ten-step quantization, there was a significant increase in front–back confusions.

This strongly suggests that the detail in the spectral cues could contribute to the processes involved in resolving front–back confusions. Of interest, the model with 100 quantization levels showed slightly more front–back confusions than the model with 40 quantization levels although the SCCs at 40 and 100 were the same. This may indicate that the fine detail in the spectral cues caused by the randomness of the white noise had an undue influence on the development of the network during training. As a result the model became more sensitive to such random detail which resulted in increased front–back confusions.

This result suggests that the auditory system may not need to exploit the full detail of the spectral cues available to perform accurate localization. Alternatively, the auditory system may be unable to encode or resolve high resolution changes in amplitude that are characterized by the measured acoustical HRTF. From the experiments, the model that used spectral cues with 20 discrete levels produced a performance most similar to that of the human, which implies that the auditory system might only require about 4 bits of resolution on the spectral amplitude cues to perform reliable localization.

C. Effect of MAF correction on model performance

An initial design decision in the model front end was to include the frequency sensitivity function of the auditory system in the form of the minimum audible field (MAF) function in line with earlier excitation pattern estimates of Carlile and Pralong (1994). The underlying rationale was that the MAF weighting should affect the saliency of various spectral components of the broadband sound. The cochlear model itself does not have a frequency dependence in threshold sensitivity; however, the use of the MAF, determined

TABLE II. Model architecture summary.

	Neti *et al.* (1992)	Janko *et al.* (1995)	Chau and Duda (1995)	This work
Spectral analysis	n/a	FFT	FFT and gammatone filter bank	Patterson–Holdsworth cochlear model
Spectral cues	Yes	Yes	Yes	Yes
Interaural time difference cue	No	Yes	Yes	Yes
Interaural level difference cue	No	Yes	Yes	No
ANN	128 input 8 hidden 187 output	1 to 23 input 50 hidden 30 output	No	288 input 8 hidden 162 output
Azimuth and elevation range	$-75 \leqslant az \leqslant 75$ degrees $-30 \leqslant el \leqslant 90$ degrees	$-180 < az \leqslant 180$ degrees $-54 \leqslant el \leqslant 54$ degrees	Not stated	$-180 < az \leqslant 180$ degrees $-80 \leqslant el \leqslant 80$ degrees
Distortion on localization cues	No	Amplitude and time jitter	No	Quantization and MAF

psychophysically, lumps together all of the threshold sensitivity components of the auditory system. To test whether this weighting was relevant at the simulated stimulus levels used in this model we repeated the experiment using our standard model in the absence of MAF filtering. In the absence of MAF weighting, the SCC in experiment E2 increased from 0.944 (with MAF) to 0.966 (without MAF) but the front–back confusion weights were largely unchanged (3.3% with MAF to 3.7% without MAF). This suggests that, at the simulated stimulus levels used in training and testing the current model, the MAF has only a minor effect on the quality of the information available to the ANN. It is a matter for future investigation to explore the impact of the MAF at higher and lower input levels where the nonlinearity of cochlear encoding would more likely result in distortions of the encoded spectra.

D. Comparison with previously reported models

Several previously reported models have been reviewed (Searle *et al.*, 1976; Lazzaro and Mead, 1989; Middlebrooks, 1992; Neti *et al.*, 1992; Horiuchi, 1994; Chau and Duda, 1995; Lim and Duda, 1995; Janko *et al.*, 1995). Neti *et al.* (1992), Chau and Duda (1995), and Janko *et al.* (1995) employ models with a similar architecture to the model reported in this paper. Table II summarizes the architecture of these model and the model reported in this paper. Apart from the models by Lazarro *et al.* and Horiuchi which extracted only the ITD cue, the other models reviewed together with this work used separate processing streams to extract the localization cues (e.g., spectral cues and ITD cue).

All the models also used the HRTF to filter the acoustic cues into neural excitation patterns. Neti *et al.* (1992) used the HRTF measured in anaesthetized cats, and assumed that the HRTF and the neural excitation pattern had the same profile. Chau and Duda (1995) estimated the neural excitation pattern by filtering a broadband noise with the HRTF and passing the result through a cochlear model. However, neither model used the MAF to adjust the amplitude of the inputs to the model. All of the previously reported models used the full precision of the estimated neural excitation pattern, although Lim and Duda (1995) noted that the spectral fine structures were not necessary for accurate localization in their model. In contrast, we have explicitly examined the role of amplitude features using a quantization parameter which determines the number of equally spaced quantized levels available to code the monaural spectral cues.

The model reported by Neti *et al.* (1992) used an ANN for the transformation of auditory cues into a two-dimensional output map to indicate the position of the sound source. An important point of departure with this study was that Neti *et al.* employed HRTFs measured from cats. The ear of the cat is a quite different in acoustical structure to that of the human and is well modelled as a truncated conical horn (Calford *et al.*, 1984) whereas the human outer ear demonstrates more complex acoustic behavior (Shaw, 1974; Carlile, 1996, Chap. 2). As a consequence, the nature of the spectral cues to localization are likely to be quite different between these species. For instance, the HRTF of the cat displays a number of middle frequency notches whose center frequencies vary systematically with location (Rice *et al.*, 1992) where similar systematic changes in notches are not evident in the human HRTF (Carlile and Pralong, 1994). Not withstanding these differences in what is being modelled, the model itself provides important insights in the approach and we have adopted much of the architecture for the model reported here. For instance, all neurones in successive layers were fully connected, and the ANNs were trained to generate output activities which resemble a double Gaussian distribution when mapped to the two-dimensional output map. Sixty-four spectral channels were used as monaural inputs in Neti's model although we settled on 128 cochlear channels after exploring this parameter experimentally. Additionally we have included an ITD analysis stream which was not included by Neti *et al.* Their model with ten hidden layer neurones which was trained using both left and right monaural spectral cues gave the best results. This is consistent with the findings reported here.

The model reported by Janko *et al.* (1995) provided an amplitude and time jitter operator which is not found in other models. After filtering a sound with the HRTF, each point of the left and right channels were multiplied by a normally distributed amplitude jitter factor and subjected to a normally distributed time delay. The standard deviation of the amplitude jitter was 0.25 and the standard deviation of the time

jitter was 20 μs. Application of quantization is similar to the addition of noise to the signal. When a neural excitation pattern is rounded to one of the closest ten equally spaced discrete amplitudes, the equivalent ''amplitude jitter'' is 5% of the maximum value, compared with 25% (0.25 standard deviation) used in Janko's model. The model by Janko *et al.* also used an ANN to classify the localization cues and provide location estimates. In contrast, the ANN used in Janko's model contained 50 hidden layer neurones although no output interpolator was used. The estimated azimuth was indicated by 1 of 24 output neurones and the estimated elevation by 1 of 6 output neurones.

E. General discussion of the model

This model has attempted to simulate the processes of localization cue encoding and extraction using a physiologically and psychophysically plausible preprocessor and a two-layer neural network. This model exhibited very similar localization performance to human listeners when the model parameters were set to a particular range of values.

When constrained using physiologically realistic parameters, the model described here achieved localization performance close to that of human listeners. Increasing the amplitude resolution of the monaural spectral cues beyond 20 quantized steps resulted in only small improvements in the model's performance. It was also found that the model's performance was positively correlated with the number of cochlear channels for a given number of quantization levels. The model with 256 cochlear channels and using a MAF correction showed a greater SCC than that found for the human listener. Together, these results indicate that the model's localization performance is at human levels using monaural spectral cues with relatively low amplitude and frequency resolution when compared to the level of resolution that is commonly employed in recording the HRTFs. The results indicate that the model can operate on monaural spectral cues with lower amplitude resolution and still deliver similar performance if the cues have sufficient frequency resolution. The important implication here is that, even with considerable ''degradation'' of the input by the preprocessor, the fidelity or quality of the localization cue information is still very high.

In the reported model, there was no assumption on how the monaural cues (left and right spectral cues) and binaural cues were combined to estimate the source direction. The model was free to select a combination that minimized an error measure. The model was free to determine the limit of localization performance accuracy when there were no restrictions on the usage of localisation cues. Although we expect strong evolutionary pressures to maximize the use of the available localization cues, it is likely that other biological constraints ensure that the central nervous system is not as free in its processing. An ANN that uses a topology which reflects the structure of the central nervous system and incorporates other ''realism constraints'' (Zipser, 1992) into the design may give further insights into the usage and effect of the auditory cues.

ACKNOWLEDGMENTS

This research project was supported by the University of Sydney Research Grants Scheme, the Australian Research Council, and the National Health and Medical Research Council (Australia).

Baum, E. B., and Haussler, D. (**1989**). ''What net size gives valid generalization?'' Neural Comput. **1**, 151–160.

Calford, M. B., and Pettigrew, J. D. (**1984**). ''Frequency dependence of directional amplification at the cat's pinna,'' Hear. Res. **14**, 13–19.

Carlile, S., ed. (**1996**). *Virtual Auditory Space: Generation and Applications* (Landes, Austin).

Carlile, S., and Pralong, D. (**1994**). ''The location-dependent nature of perceptually salient features of the human head-related transfer function,'' J. Acoust. Soc. Am. **95**, 3445–3459.

Carlile, S., Leong, P., and Hyams, S. (**1997**). ''The nature and distribution of errors in the localization of sounds by humans,'' Hear. Res. **114**, 179–196.

Chau, W., and Duda, R. O. (**1995**). ''Combined monaural and binaural localization of sound sources,'' in *29th Asilomar Conference on Signals, Systems, and Computers* (Asilomar, CA).

Fisher, N. I., Lewis, T., and Embleton, B. J. J. (**1993**). *Statistical Analysis of Spherical Data* (Cambridge UP, Cambridge).

Gilkey, R. H., Good, M. D., Ericson, M. A., Brinkman, J., and Stewart, J. M. (**1995**). ''A pointing technique for rapidly collecting localisation responses in auditory research,'' Behav. Res. Methods Instrum. Comput. **27**(1), 1–11.

Glasberg, B. R., and Moore, B. C. (**1990**). ''Derivation of auditory filter shapes from notched-noise data,'' Hear. Res. **47**(1–2), 103–138.

Goodman, P., Rosen, D., and Plummer, A. (**1993**). University of Nevada Center of Biomedical Modelling Research, Washoe Medical Center, H-166, 77 Pringle Way, Reno, NV 89520. Goodman@unr.edu

Horiuchi, T. (**1994**). ''An auditory localization and co-ordinate transform chip,'' Neural Information Processing 7, Abstract of Papers, p. 43. http://www.klab.caltech.edu/~timmer/respapers/respaper.html.

Janko, J., Anderson, T., and Gilkey, R. (**1995**). ''Using Neural Networks to Evaluate the Viability of Monaural and Interaural Cues for Sound Localization,'' in *Binaural and Spatial Hearing in Real and Virtual Environments*, edited by R. Gilkey and T. Anderson (Erlbaum, Mahwah, NJ), Chap. 26, pp. 557–570.

King, A. J., and Carlile, S. (**1994**). ''Neural coding for auditory space,'' in *The Cognitive Neurosciences* (MIT, Boston).

Lazzaro, J., and Mead, C. A. (**1989**). ''A silicon model of auditory localization,'' Neural Comput. **1**, 47–57.

Leong, P., and Carlile, S. (**1997**). ''Methods for spherical data analysis and visualization,'' J. Neurosci. Methods **80**, 191–200.

Lim, C., and Duda, R. O. (**1994**). ''Estimating the azimuth and elevation of a sound source from the output of a cochlear model,'' in *Proceedings of the 28th Asilomar Conference on Signals, Systems and Computers* (Asilomar, CA). Available at http://www-engr.sjsu.edu/~duda/Duda.Research.Refs.html

Lippmann, R. P. (**1987**). ''An introduction to computing with neural nets,'' IEEE Trans. Accoust. Speech Signal Process. ASSP **2**, 4–22.

Middlebrooks, J. C., and Carlile, S. (**1984**), ''A neural code for auditory space in the cat's superior colliculus,'' J. Neurosci. **4**, 2621–2634.

Middlebrooks, J. C. (**1992**). ''Narrow-band sound localization related to external ear acoustics,'' J. Acoust. Soc. Am. **92**, 2607–2624.

Middlebrooks, J. C., and Green, D. M. (**1991**). ''Sound localization by human listeners,'' Annu. Rev. Phys. Chem. **42**, 135–159.

Neti, C., Young, E. D., and Schneider, M. H. (**1992**). ''Neural network models of sound localization based on directional filtering by the pinna,'' J. Acoust. Soc. Am. **92**, 3140–3156.

Oldfield, S. R., and Parker, S. P. A. (**1986**). ''Acuity of sound localization: a topography of auditory space. III Monaural hearing conditions,'' Perception **15**, 67–81.

Pralong, D., and Carlile, S. (**1996**). ''The role of individualized headphone calibration for the generation of high fidelity virtual auditory space,'' J. Acoust. Soc. Am. **100**, 3785–3793.

Rice, J. J., May, B., Spiron, G. A., and Young, E. D. (**1992**), ''Pinna-based spectral cues for sound localization in cat,'' Hearing Res. **58**, 132–152.

Rumelhart, D. E., and McCelland, J. L. (**1986**). *Parallel Distributed Processing: Exploration in the Microstructure of Cognition I* (MIT, Boston).
Sachs, M. B., and Young, E. D. (**1979**). ''Encoding of steady-state vowels in the auditory nerve: representation in terms of discharge rate,'' J. Acoust. Soc. Am. **66**, 470–479.
Searle, C. L., Braida, L. D., Davis, M. F., and Colburn, H. S. (**1976**). ''Model for auditory localization,'' J. Acoust. Soc. Am. **60**, 1164–1175.
Shaw, E. A. G (**1974**), ''The External Ear,'' in *Handbook of Sensory Physiology*, edited by W. D. Keidel and W. D. Neffs, Vol. VIII, Auditory System (Springer-Verlag, New York), pp. 455–490.
Shaney, M. (**1994**). *Auditory Toolbox: A MATLAB Toolbox for Auditory Modelling Work*, Apple Technical Report #45, Apple Computer, Inc., Advanced Technology Group.
Wightman, F. L., and Kistler, D. J. (**1989**). ''Headphone simulation of free-field listening. II: Psychophysical validation,'' J. Acoust. Soc. Am. **85**, 868–878.
Woodworth, R. S. (**1938**). *Experimental Psychology* (Holt, New York).
Yost, W. A. (**1974**). ''Discrimination of interaural phase differences,'' J. Acoust. Soc. Am. **55**, 1299–1303.
Zipser, D. (**1992**). ''Identification models of the nervous system,'' Neuroscience (NY) **47**, 853–862.

Distortion product otoacoustic emission ($2f1$-$f2$) amplitude growth in human adults and neonates

Carolina Abdala[a)]
House Ear Institute, Children's Auditory Research and Evaluation Center, 2100 West Third Street, Los Angeles, California 90057

(Received 8 June 1999; revised 21 September 1999; accepted 22 September 1999)

Distortion product otoacoustic emissions (DPOAEs) are thought to be by-products of an active amplification process in the cochlea and thus serve as a metric for evaluating the integrity of this process. Because the cochlear amplifier functions in a level-dependent fashion, DPOAEs recorded as a function of stimulus level (i.e., a *DPOAE growth function*) may provide important information about the range and operational characteristics of the cochlear amplifier. The DPOAE growth functions recorded in human adults and neonates may provide information about the maturation of these active cochlear processes. Two experiments were conducted. Experiment I included normal-hearing adults and term-born neonates. The $2f1$-$f2$ DPOAE growth functions were recorded for both age groups at three $f2$ frequencies. Experiment II was an extension of the first experiment but added a subject group of premature neonates. The results of these studies indicate that DPOAE growth functions most often show amplitude saturation and nonmonotonic growth for all age groups. However, premature neonates show monotonic growth and the absence of amplitude saturation more often than adults. Those premature neonates who do show saturation also show an elevated threshold for amplitude saturation relative to adults. In contrast, term neonates are adultlike for most measures except that they show a larger percentage of nonsaturating growth functions than adults. These results may indicate immaturity in cochlear amplifier function prior to term birth in humans. Outer hair cell function and/or efferent regulation of outer hair cell function are hypothesized sources of this immaturity, although some contribution from the immature middle ear cannot be ruled out. [S0001-4966(00)01201-7]

PACS numbers: 43.64.Jb, 43.64.Kc [BLM]

INTRODUCTION

In the last 20 years, it has become apparent that the motion created within the cochlea by external input is altered by intrinsic, active processes, i.e., the *cochlear amplifier*. Auditory sensitivity and frequency resolution are enhanced because the cochlear amplifier works to augment basilar membrane vibration only near the characteristic frequency or peak of the traveling wave evoked on the basilar membrane (Neely and Kim, 1986). The motile properties of the outer hair cells appear to be responsible for cochlear amplification of sound.

Distortion product otoacoustic emissions (DPOAEs) are by-products of cochlear amplifier function and, thus, serve as a metric for evaluating the integrity of this active process. DPOAEs are tones created by the cochlea when the ear is presented with two simultaneous pure tones. When a DPOAE of given frequency is generated over a wide range of stimulus levels, a DPOAE input/output function or *amplitude growth function* is generated. Because the cochlear amplifier is level dependent and functions efficiently at low-to-moderate levels only, DPOAE amplitude recorded across the stimulus level provides information about the range and boundaries of cochlear amplifier function and can help to characterize active processes.

In small mammals, it has been shown that DPOAEs generated by low-level primary tones are based in cochlear amplifier activity and are susceptible to noise and toxins that damage the outer hair cells. A marked amplitude plateau or ''notch'' at moderate primary tone levels represents saturation of cochlear amplifier function; DPOAEs generated by high-level tones are unaffected by outer hair cell (OHC) toxins and are thought to reflect primarily passive motion of the basilar membrane (Whitehead *et al.*, 1992; Mills and Rubel, 1996). It is unclear whether DPOAE amplitude growth reflects cochlear amplifier function in the same manner for humans. Human DPOAE growth functions show a tremendous amount of variability in shape and often do not have three distinct segments (Lasky, 1998; Lonsbury-Martin and Martin, 1990; Stover and Norton, 1993; Popelka *et al.*, 1993).

Development of cochlear amplifier function has been minimally studied in humans, primarily due to inaccessibility since the inner ear develops almost completely *in utero* (Lavigne-Rebillard and Pujol, 1987, 1988) and because a noninvasive assay for detailed cochlear amplifier function in humans has not been available. However, maturation of the cochlear amplifier has been well defined in gerbils by use of loop diuretics (Mills and Rubel, 1996). Loop diuretics such as furosemide reduce the endocochlear potential drastically. Since the endocochlear potential provides the battery for OHC motility and subsequent DPOAE generation, DPOAEs are eliminated if the endocochlear potential is significantly reduced. Mills and colleagues have recorded pre- and post-

a)Electronic mail: Cabdala@hei.org

furosemide DPOAE growth functions in gerbils of various ages. On a DPOAE growth function, the horizontal difference (in dB) between a prefurosemide growth function and a postfurosemide function can be used to calculate the gain of the cochlear amplifier. The gain of the cochlear amplifier in this species develops from birth through approximately 42 days after birth when it looks adultlike and provides relatively flat gain across frequency (Mills and Rubel, 1996).

In human neonates, it is not possible to use loop diuretics for obvious reasons. However, changes in the pattern of DPOAE amplitude growth, saturation characteristics, and slope or rate of DPOAE amplitude growth in neonates at different stages of prematurity may provide a similarly dynamic condition for investigating human cochlear amplifier function. Few investigators have examined DPOAE amplitude growth in human neonates (Popelka *et al.*, 1995; Lasky, 1998), and these have produced inconclusive results with respect to maturation of the cochlear amplifier. The objective of this study was to examine the effect of age, $f2$ frequency, and $f2/f1$ ratio on $2\,f1\text{-}f2$ DPOAE growth function in human adults and neonates, and, in doing so, provide insight into the maturation of human cochlear amplifier function. Two experiments were conducted to address these issues.

I. METHODS—EXPERIMENT I

A. Subjects

Ten normal-hearing adults and 12 term-born neonates were used as subjects in experiment I. The average age of the adults was 29 years (range=24–35); six adult subjects were male and four female. All adults had audiometric thresholds $<$15 dB HL between 500 and 8000 Hz and negative history of otologic pathology.

The 12 term neonates were born at Women and Children's Hospital, Los Angeles County—University of Southern California Medical Center between 37 and 41 weeks of gestation. They were tested within 72 h of birth after informed parental consent was obtained. Their average birthweight was 3227 g and average 5- and 10-min APGARs were 8.4 and 8.9, respectively.

B. Instrumentation and signal analysis

An Ariel DSP16+ signal processing and acquisition board housed within a Compaq Prolinea 590 personal computer with Pentium processor was used to generate stimuli and acquire data. The Ariel board was connected to an Etymotic Research ER-10C probe-mic system. The ER-10C probe contains two output transducers and a low-noise microphone. The two primary tones were generated by the DSP processor.

Energy at the probe microphone was high-pass filtered (12 dB/oct: 710 Hz high-pass cutoff) and sampled at a rate of 50 kHz with a sweep length of 4096 samples, giving a frequency resolution of 12.2 Hz. Twenty-five sweeps of the microphone signal were added and comprised one block for $f2=3000$ and 6000 Hz. Due to elevated noise in the low frequencies, 50 sweeps were added to make up one block at 1500 Hz. The sum of each block was stored as 32-bit integer values. Two acceptable blocks of data were summed (see Sec. I C), averaged, and the power spectrum was obtained by applying a 4096-point fast Fourier transform (FFT). The level of the DPOAE was computed using the summed 32-bit data directly and 8-byte IEEE-format floating-point computations in the discrete Fourier transform.

Intermodulation distortion produced by the recording system at $2\,f1\text{-}f2$ was measured with the probe in a Zwislocki coupler for all test conditions. The mean level of system distortion was -21 dB SPL. In no case did the level exceed -17 dB SPL. The recording system noise floor was determined using a similar method with no tones present. The level of system noise floor ranged between -22 and -27 dB SPL depending on frequency.

C. Data acceptance criteria

The DPOAE measurements were accepted and recorded as valid data if they met the following criteria: (1) Noise measurements for three frequency bins on either side of the $2\,f1\text{-}f2$ frequency had to be $<$0 dB SPL to ensure appropriate subject state. Preliminary work has shown that subjects with noise of 0 dB SPL or lower are more likely to generate DPOAE data with low amplitude variability. (2) The measured DPOAE level had to be at least 5 dB above the average noise measured in the same six bins around the DPOAE frequency to be accepted into the grand average.

The program attempted up to six blocks of either 25 or 50 sweeps to obtain two acceptable blocks. If two blocks of data were not collected after six attempts, no data were collected and the next condition was initiated. In addition, sweeps were accepted into a block of data only when the estimated rms level in that sweep did not exceed a user-controlled artifact rejection threshold. This level was set for each subject based on observations of baseline activity level determined early in the test session and modified if necessary during the experiment.

D. Procedure

Adult subjects were tested in a sound-treated booth at the House Ear Institute while reading, sleeping, or sitting quietly. Neonates were tested within the hospital in an acoustically treated infant isolette (Eckels ABC-100 acoustic isolette) that provided 25 dB of attenuation from 500 to 2000 Hz and up to 45 dB of attenuation between 2000 and 8000 Hz. The neonates were fed if necessary prior to the test, swaddled, and placed in the isolette to sleep.

An initial *in situ* calibration procedure was conducted on both output transducers before each subject was tested. Tones of fixed voltage were presented to the transducers at 250 Hz intervals from 500 to 10 000 Hz and the resulting SPL of these tones was recorded in the ear canal. Based on this information, an equalization of output levels was performed for each subject to achieve target stimulus levels across all test frequencies.

In experiment I DPOAE growth functions were generated at primary tones ranging from 30 to 80 dB SPL (L1) in 5 dB steps. The level separation between primary tones was always 10 dB (L1$>$L2). The growth functions were generated at 1500-, 3000-, and 6000-Hz $f2$ frequencies with $f2/f1$

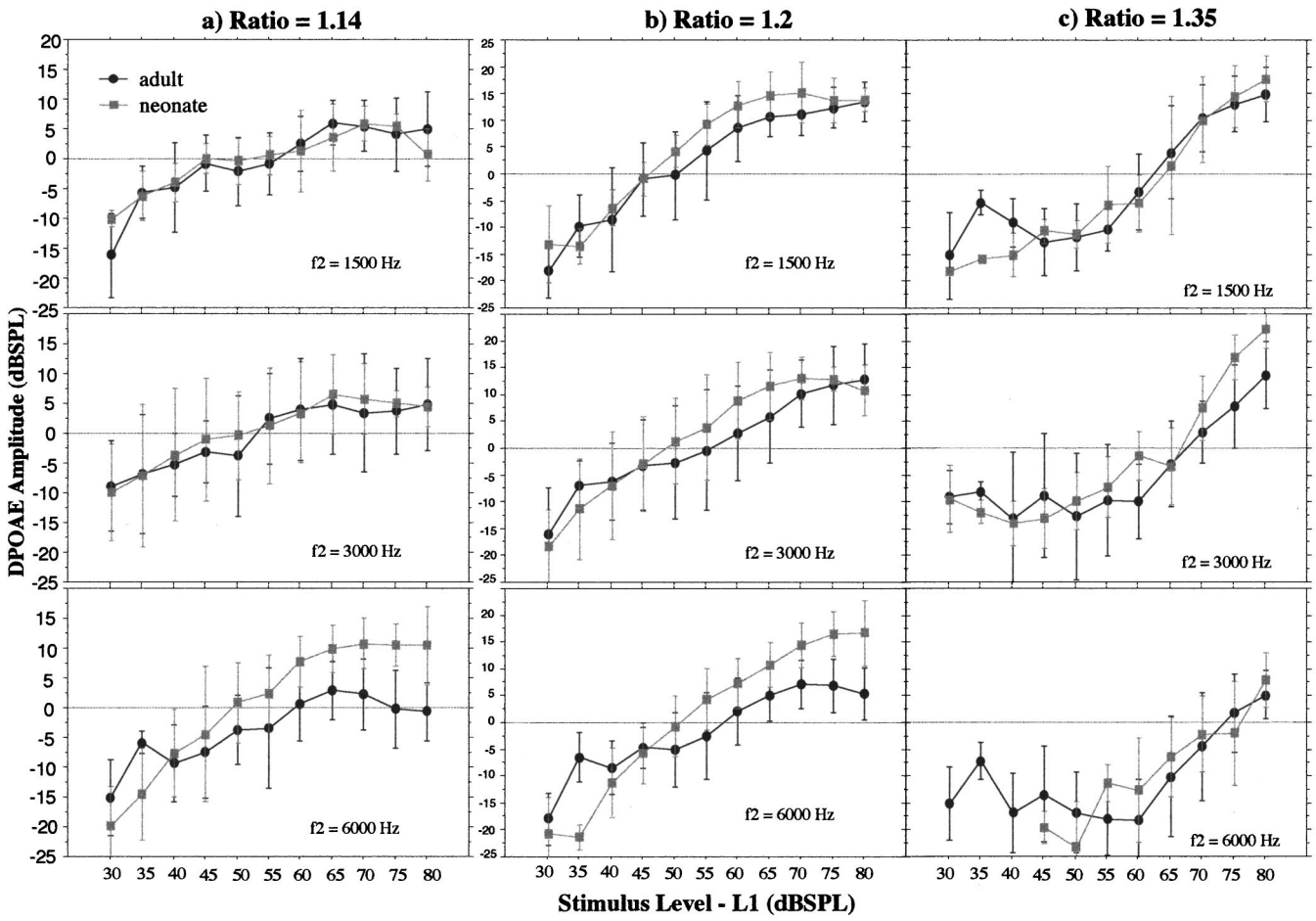

FIG. 1. Mean DPOAE growth functions for three $f2/f1$ ratios: 1.14, 1.2, and 1.35, and three $f2$ frequencies: 1500, 3000, and 6000 Hz. Age is the parameter. Vertical bars represent ∓ 1 s.d.

frequency ratios of 1.14, 1.2, or 1.35. Three growth functions were collected per ear. Only the mean of these three growth functions was entered into data analysis for each ear. This initial averaging of DPOAE amplitude data from any one ear was conducted to reduce the influence of intrasubject, run to run variability.

E. Analysis

(1) A plateau in DPOAE amplitude at mid-levels has been attributed to saturation of the cochlear amplifier and appears to provide an important landmark in the growth function. Therefore, *configuration* or pattern of DPOAE amplitude growth was quantified by making a categorical decision about the absence or presence of amplitude saturation in each individual growth function. If amplitude did not saturate, the growth function was considered to be monotonic; if there was an amplitude plateau, the function was considered to be saturating and nonmonotonic. An average percentage of growth functions with and without saturation for each age group, $f2$ frequency, and $f2/f1$ ratio was determined.

(2) *Saturation threshold* was measured as the second point along a marked plateau in DPOAE amplitude. The criteria used for establishing a saturation threshold are provided in Appendix A. A sharp notch or drop in amplitude at only one primary tone level with recovery at the

TABLE I. The number and percentages of growth functions that were nonsaturating and monotonic for adults and neonates at three $f2/f1$ ratios and three $f2$ frequencies.

	$f2$ frequency 1500			3000			6000		
	$f2/f1$ ratio 1.14	1.2	1.35	1.14	1.2	1.35	1.14	1.2	1.35
Adult	1/7 (14%)	2/7 (28%)	3/7 (43%)	1/8 (12%)	1/8 (11%)	5/8 (62%)	1/9 (11%)	1/9 (11%)	5/9 (55%)
Neonate	0/4 (0%)	2/6 (33%)	2/4 (50%)	0/7 (0%)	1/7 (14%)	7/7 (100%)	0/6 (0%)	3/7 (43%)	3/5 (60%)

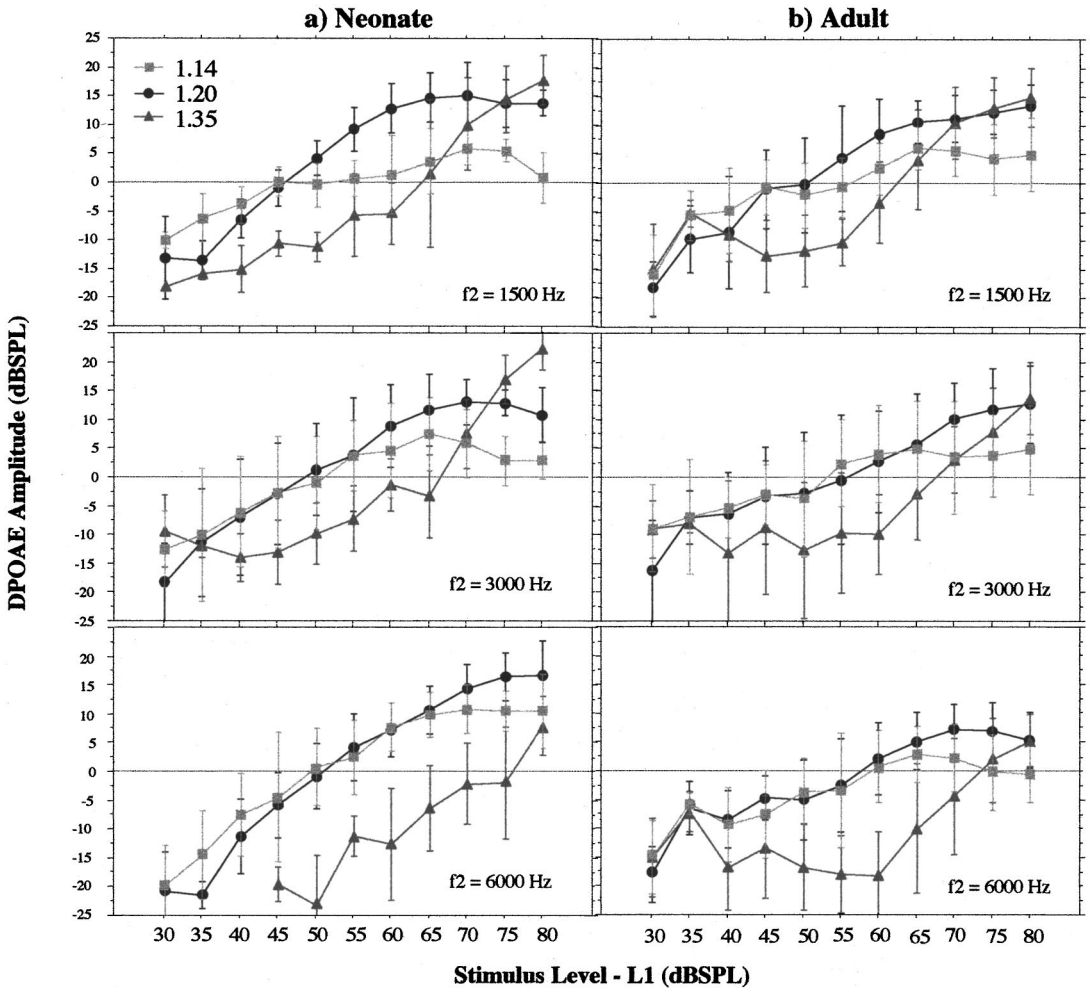

FIG. 2. The same data displayed in Fig. 1 are replotted to show differences among growth functions generated with three $f2/f1$ ratios. Mean DPOAE growth functions for two ages and three $f2$ frequencies. $F2/f1$ ratio is the parameter. Vertical bars represent ∓ 1 s.d.

subsequent level was not sufficient to be considered saturation. This study sought to detect consistent, highly reliable trends in DPOAE amplitude growth in designated age groups, rather than identify the many idiosyncratic patterns of amplitude growth that exist in humans. In addition, transient, sharp changes in DPOAE amplitude can sometimes be attributed to the presence of spontaneous emissions or spurious noise, thus sharp notches were not measured in this study, even though they are thought to reflect some aspects of cochlear amplifier function as well.

(3) The DPOAE *growth function slope* (i.e., amplitude growth rate) was measured by fitting a regression equation to the monotonically growing portion of the growth function only. Any region of saturation was excluded from the slope calculation.

Age and $f2$ frequency effects on saturation threshold and slope were measured with analyses of variance (ANOVA) conducted separately at each of the three $f2/f1$ ratios.

II. RESULTS—EXPERIMENT I

A. Configuration of DPOAE amplitude growth

The majority of growth functions from either adults or term neonates showed non-monotonic growth patterns that included saturation of DPOAE amplitude. Generally, amplitude of the DPOAE grew consistently up to moderate or moderate-high levels then plateaued and often decreased (Fig. 1).

There was no systematic difference in the overall average percentage of nonsaturating, monotonically growing functions observed between adults and term neonates; 25% of the adult growth functions did not show DPOAE amplitude saturation while an average of 31% neonatal growth functions did not saturate. Table I includes the breakdown of the growth functions in both age groups that did not show saturation and were monotonic in their amplitude growth. The number of observations varies because not all neonates provided growth functions at each of the three $f2$ frequencies. There are no consistent age-related trends in the data, although at 3000 Hz ($f2/f1 = 1.35$) and 6000 Hz ($f2/f1 = 1.2$) term neonates have higher percentage of monotonic growth functions than adults do.

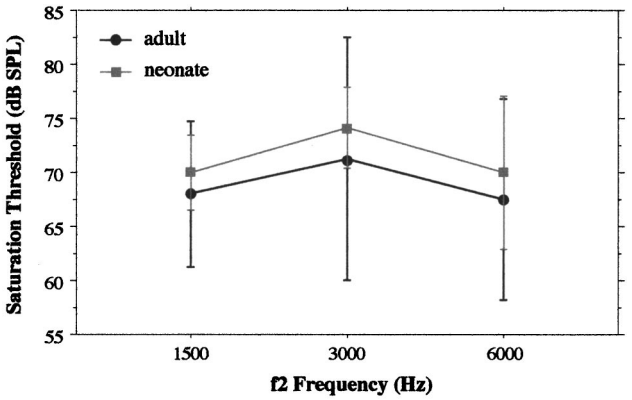

FIG. 3. Mean saturation threshold as a function of $f2$ frequency for adults and neonates. Vertical bars represent ∓ 1 s.d.

A non-monotonic, saturating growth function was observed most frequently when an $f2/f1$ ratio of 1.14 was used, followed by 1.21, and least often when a ratio of 1.35 was used. In adults, 50% of the growth functions generated with $f2/f1=1.35$ never showed an amplitude plateau. In neonates, 75% of their growth functions recorded with a 1.35 $f2/f1$ ratio did not saturate [Fig. 1(c)]. Thus, prevalence of saturation was clearly related to $f2/f1$ ratio. Growth functions generated with a ratio of 1.35 were also the most steeply growing functions.

Growth functions generated with ratios of 1.2 and 1.14 appeared similar in morphology at low primary tone levels but then diverged at moderate-high levels between 50 and 70 dB SPL (Fig. 2). Beyond this divergence point, the 1.14 amplitude typically dropped or plateaued and the DPOAE amplitude generated with a 1.2 ratio continued to grow. The primary tone level at the divergence point between 1.14 and 1.2 did not appear to differ in any systematic fashion between age groups, but divergence did occur at progressively higher primary tone levels as $f2$ frequency increased [see Fig. 2(a)].

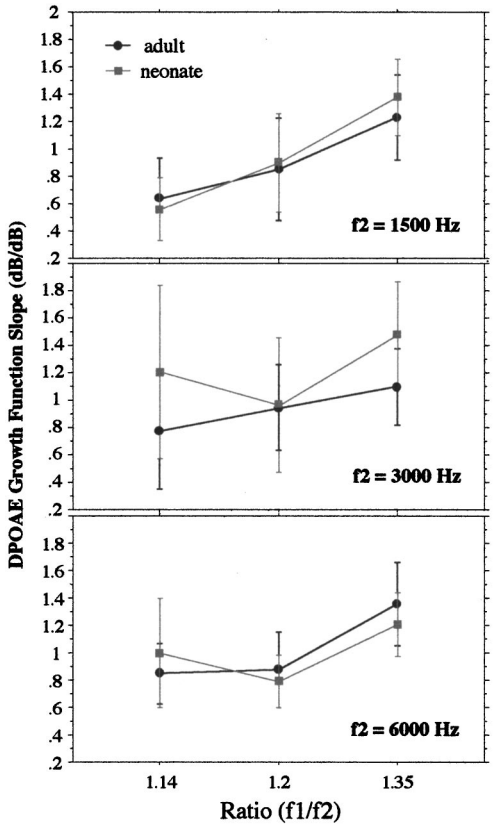

FIG. 4. Mean DPOAE growth function slope as a function of $f2/f1$ ratio for three $f2$ frequencies. Age is the parameter. Vertical bars represent ∓ 1 s.d.

B. Saturation threshold

Neonates showed a trend toward slightly elevated saturation thresholds as illustrated in Fig. 3 for $f2/f1$ ratio $=1.2$. The DPOAE amplitude saturated on average at 69.7 dB SPL for neonates and 67.9 dB SPL for adults; however, there are no statistically significant differences in saturation threshold between age groups for any of the three $f2/f1$ ratios. There are also no significant differences in saturation threshold among the three $f2$ frequencies.

C. Growth function slope

There was no significant age difference for slope at any of the three $f2/f1$ ratios (infants$=1.06$ dB/dB; adults $=0.95$ dB/dB), therefore, data were summed over age and an ANOVA of ratio$\times f2$ frequency was conducted. This was not conducted as a repeated measures ANOVA because not all subjects had data present at the three ratios. Mean overall growth function slope was 0.84 dB/dB at $f2/f1=1.14$; 0.89 dB/dB at 1.2, and 1.29 dB/dB at 1.35. The DPOAE amplitude slope increased significantly for all frequencies as $f2/f1$ ratio went from 1.14 to 1.35 ($df=2;F=19.8;p=0.0001$) (see Fig. 4). Additionally, slope increased significantly with increased $f2$ frequency only when a ratio of 1.14 was used ($df=2;F=3.29;p=0.04$).

D. Summary of results

These results indicate that human DPOAE growth functions are most often non-monotonic, saturating functions. Growth functions from term-born neonates are adultlike in general configuration, amplitude saturation characteristics, and in the slope of amplitude growth. The DPOAE growth slope increased with increasing $f2$ frequency and as $f2/f1$ ratio got larger. The DPOAE growth functions generated with large ratios (1.35) cause reduced DPOAE amplitude and a very steep, nonsaturating growth of the DPOAE.

III. METHODS—EXPERIMENT II

A. Subjects

Twenty-four ears (12 left and 12 right) from 15 normal-hearing adults were tested with the experimental protocol. The adults had a mean age of 28 years and had audiometric thresholds <15 dB between 500 and 8000 Hz. Seven of the adult subjects were male and eight were female. None of the adult subjects had a history of noise exposure or otologic disease.

Because experiment I established that term neonates were basically adultlike in DPOAE amplitude growth, premature neonates were included in experiment II to define the

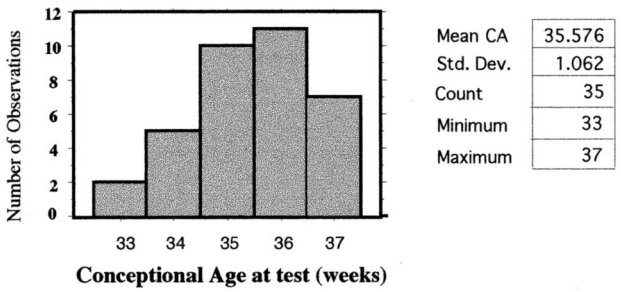

FIG. 5. Conceptional age (weeks) at the time of test for all premature neonatal subjects.

time course for maturation. Fifty-two term-born and 35 premature neonates were included as subjects in this study. Data from these same neonates had been analyzed previously in a study of efferent system maturation (Abdala *et al.*, 1999). The term-born neonates were born between 37 and 41 weeks gestation, averaged 3393 g at birth and had average 5- and 10-min APGAR scores of 8.3 and 8.8, respectively. Just over 50% of the term neonates were tested within 72 h of birth. The other half were tested no more than 7 days after birth. Availability for test depended on many factors including the health status of the mother and procurement of an informed consent.

The 35 premature subjects were born between 27 and 36 weeks of gestation and their mean conceptional age at test was 35 weeks (Fig. 5); 80% of premature subjects were tested prior to 37 weeks conceptional age. Thus, the premature subjects were not only prematurely born but most were preterm at the time of our evaluation. Average birthweight for premature subjects was 2095 g and average 5- and 10-min APGAR scores were 7.1 and 8.7, respectively. All premature neonates had passed hearing screenings with the auditory brainstem response prior to inclusion in this study.

B. Instrumentation and signal analysis

See details described under experiment I.

C. Procedure

In the second experiment, DPOAE growth functions were generated at primary tone stimuli ranging from 30 to 85 dB in 5-dB steps. An additional 5 dB was added to the high end of the stimulus level range (*re*: experiment I) in an attempt to better identify amplitude saturation when it occurred. The level separation was 10 dB (L1>L2) and $f2/f1$ ratio was fixed at 1.2. This ratio was selected because it optimizes DPOAE amplitude across level as results of experiment I indicated. Three $f2$ frequencies were used: 1500, 3000, and 6000 Hz.

D. Analysis

(1) *Configuration* of DPOAE amplitude growth was quantified in two ways:

(a) As in Experiment I, a categorical decision of absence/presence of saturation was made for each individual growth functions. A mean percentage of nonsaturating functions for each age group and $f2$ frequency was generated.

(b) A regression line was fit to each complete growth function. A high squared correlation coefficient was interpreted as an indication that amplitude growth was monotonic and could be appropriately fit by a single line. A low $r2$ indicated that a simple linear growth pattern was not adequate to characterize DPOAE amplitude growth. Thus, the squared correlation coefficient value was used as a metric to judge whether growth was simple and monotonic or more complex and included saturation.

(2) *Saturation threshold*: The same DPOAE amplitude saturation criteria were applied for experiments I and II (see Appendix A).

(3) *Slope of amplitude growth*: Slope was determined by measuring only the monotonically growing portion of the growth function. Any region of saturation was excluded from the slope calculation.

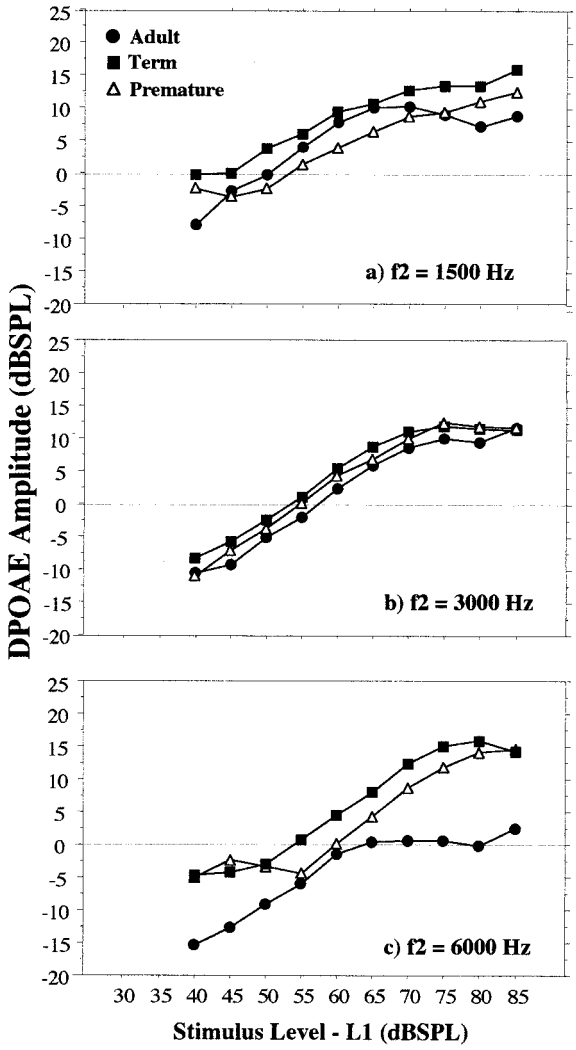

FIG. 6. Mean DPOAE growth functions for three $f2$ frequencies and three age groups: adults, term, and premature neonates. The individual amplitude growth data from which these average functions were derived, are included in Appendix B.

TABLE II. Percentages of growth functions that were nonsaturating and monotonic for adults, term, and premature neonates at three $f2$ frequencies. The data were collected with an $f2/f1$ ratio of 1.2.

	$f2$ frequency		
	1500	3000	6000
Adult	0%	13%	0%
Term	26%	9%	37%
Premature	31%	6%	20%

ANOVAs were conducted to test for age and $f2$ frequency effects on saturation threshold and growth function slope. When required, additional *post hoc* evaluations were performed using a Bonferoni correction factor for multiple tests on the same data set.

IV. RESULTS—EXPERIMENT II

A. Configuration

Mean growth functions for the three age groups are shown superimposed in Fig. 6(a)–(c). These mean data suggest that saturation is more evident in adult than neonatal data. This age-related trend is particularly evident at $f2 = 1500$ Hz where mean adult saturation clearly occurs at approximately 65 dB SPL whereas the premature growth function continues to grow monotonically to the highest primary tone levels presented and saturation is not observed.

Table II shows the distribution of growth functions that did not show saturation. These data indicate that adults rarely have monotonic growth and nearly all of their growth functions saturate. This is consistent with the $f2/f1 = 1.2$ adult data from experiment I. Experiment II shows that both term and premature neonates have an average of between 20% to 37% of growth functions for 1500 and 6000 Hz growing monotonically and not saturating. Overall, neonates have a higher percentage of nonsaturating, monotonically growing amplitude growth functions.

Both adult and neonatal growth functions were fit with a linear regression to assess whether amplitude growth could be well predicted or characterized by a straight line. A good linear fit for amplitude data (i.e., high $r2$) was interpreted to indicate that DPOAE amplitude growth was monotonic. The $r2$ values are shown in Table III. These data indicate that neonatal amplitude growth was often adequately characterized by a straight line whereas adult growth was not. (An example is shown in Fig. 7.) At 1500 Hz, mean $r2$ for premature neonates was 0.81 and mean $r2$ for adult growth was 0.59. At 6000 Hz, a straight line characterized DPOAE amplitude growth in premature neonates with a mean fit of 0.89 and for adults, a mean fit of 0.56. At 3000 Hz, DPOAE growth from adults and neonates was equally well characterized by a linear fit. The exemplar data presented in Fig. 7 reflect the fact that most of the adult data require a more sophisticated polynomial fit to approximate the curvilinear pattern of amplitude growth. This is due to the consistent presence of saturation at moderate to high levels in adult data. The high mean squared correlation coefficients observed in premature neonatal data, in contrast, indicate that a linear fit is adequate much of the time for characterizing the pattern of DPOAE amplitude growth in this age group.

TABLE III. The $r2$ for linear regression line fit to DPOAE amplitude growth in adults, term neonates, and premature neonates at three $f2$ frequencies.

	$f2$ frequency		
	1500	3000	6000
Adult	0.59	0.83	0.56
Term	0.78	0.71	0.80
Premature	0.81	0.76	0.89

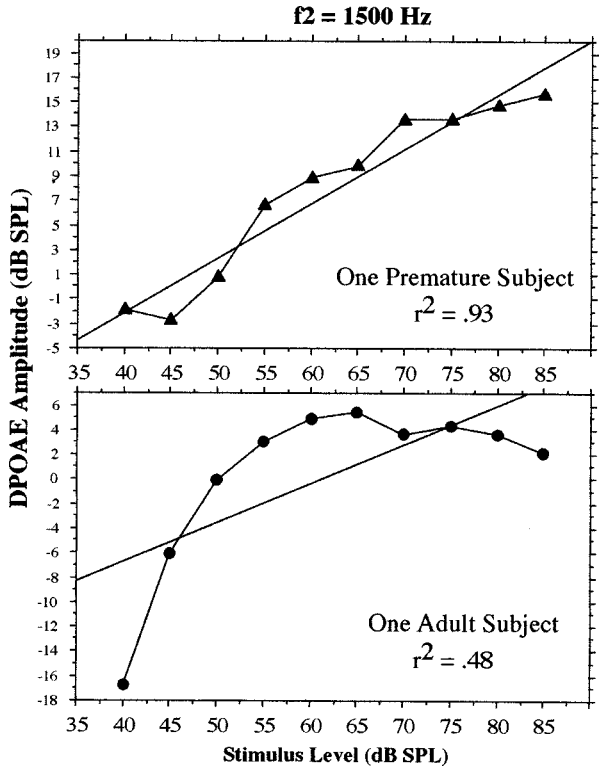

FIG. 7. The DPOAE growth functions at $f2 = 1500$ Hz from one representative premature neonate and one adult. Each growth function has been fit with a linear regression equation and the resulting squared correlation coefficient is shown. The neonatal growth function is adequately characterized by a linear equation whereas the adult function is not.

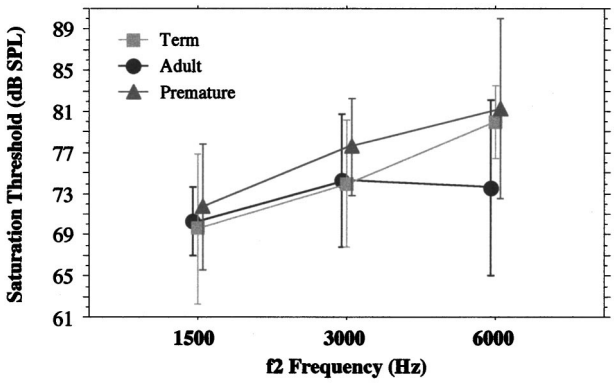

FIG. 8. Mean saturation threshold as a function of $f2$ frequency for adults, term, and premature neonates. Vertical bars represent ∓ 1 s.d.

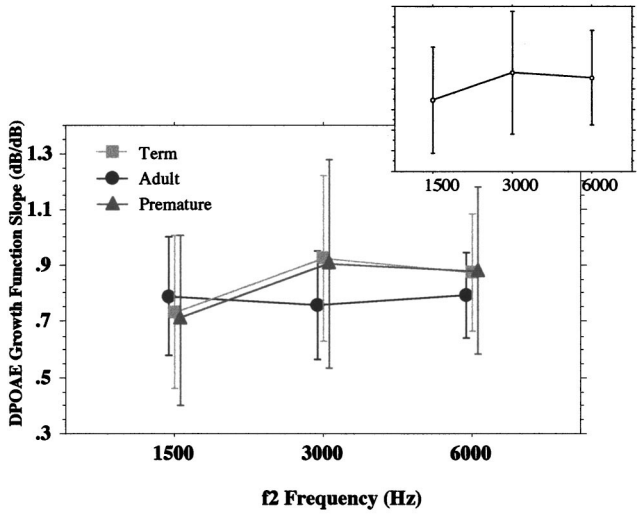

FIG. 9. Mean DPOAE growth function slope as a function of $f2$ frequency for adults, term, and premature neonates. The inset graph displays mean slope summed over age. Vertical bars represent ∓ 1 s.d.

B. Saturation threshold

Figure 8 shows mean saturation thresholds for the three age groups and $f2$ frequencies. An ANOVA of frequency×age effects on saturation showed both age and $f2$ frequency to be significant factors ($df=2$; $F=3.47$; $p=0.03$, and $df=2$; $F=11.35$; $p=0.0001$, respectively). Upon *post hoc* analyses, only the adult versus premature neonate age contrasts were significant, indicating that saturation threshold from premature neonates was elevated relative to adult thresholds ($p=0.003$). Premature versus term contrasts were borderline significant ($p=0.02$). Consistent with experiment I results, adult saturation threshold was no different from saturation threshold observed in term neonates.

C. Growth function slope

There were no significant differences in slope among age groups, thus an ANOVA was conducted for frequency effects summed over age. This analysis showed that slope became steeper as $f2$ frequency increased ($df=2; F=3.22; p=0.04$). This result can be best observed in the inset of Fig. 9, where slope is summed over age.

D. Summary of results

Configuration of DPOAE amplitude growth is primarily saturating for both adults and neonates. However, neonates have a greater percentage of nonsaturating, monotonic growth functions and, on average, their data are well characterized by a simple linear equation. When saturation is present in premature neonates, saturation threshold is higher than in adults. Slopes of the DPOAE growth functions are comparable among adult, term, and premature subjects. Both saturation threshold and slope increase with increasing $f2$ frequency.

V. DISCUSSION

Consistent with previous work, results show that DPOAE amplitude growth in humans grows at a rate approaching 1 dB/dB (Lasky, 1998; Lonsbury-Martin and Martin, 1990; Popelka *et al.*, 1993, 1995; Stover and Norton, 1993). Human DPOAE amplitude growth functions are complex and 80%–100% show non-monotonic patterns of amplitude growth when using optimum $f2/f1$ ratios. It is thought that the non-monotonic pattern of amplitude growth for the $2\,f1\text{-}f2$ DPOAE reflects level-dependent functioning of the cochlear amplifier. The DPOAE saturation at moderate-high levels may represent the level at which active processes of the cochlea cease to function effectively. In small mammals, it has been shown that at least two sources of distortion exist; a low-level source which is based in cochlear amplifier activity and a high-level source which appears to be primarily passive in nature (Whitehead *et al.*, 1992). The transition point between these two modalities of function is defined by a plateau in amplitude and sometimes a sharp notch in amplitude growth. It is believed that this plateau is caused by nearly equal contribution from active and passive sources of distortion generation that are 180 degrees out of phase.

In humans, it has been much more difficult to identify dual active–passive components of the DPOAE growth function. There is much more variability in DPOAE amplitude configuration, and transitions from active- to passive-dominated distortion are not clearly evident. Additionally, often sound cannot be presented at levels high enough to observe passive distortion, if present. Despite these limitations, this study, along with previous work, confirms that saturation is present in most DPOAE growth functions from human adults and present to a lesser extent in human neonates (Lasky, 1998; Popelka *et al.*, 1995). If this saturation point in DPOAE amplitude reflects the limits of cochlear amplifier function, data suggest that the human cochlear amplifier saturates between 65 and 75 dB SPL. Cochlear amplifier function appears to have a relatively flat frequency response although the functional range might be slightly larger at high $f2$ frequencies, as evidenced by the higher saturation thresholds at 6000 Hz.

A. *f2/f1* ratio

Experiment I examined the effect of $f2/f1$ ratio on DPOAE amplitude growth. Clearly, a large ratio (1.35) that minimizes the overlap between traveling wave patterns generated by these two tones produces a steep, monotonically growing growth function that drops into the noise floor rapidly. The only level at which a ratio of 1.35 shows DPOAE amplitude greater than or equal to amplitude generated with either 1.14 or 1.2 is at the very highest primary tone levels. This is consistent with previous work showing that a large $f2/f1$ ratio optimizes DPOAE amplitude at high stimulus levels (Harris *et al.*, 1989; Abdala, 1996). However, in general, it appears that a growth function generated with an $f2/f1$ ratio of 1.35 is limited in its ability to characterize the cochlear amplifier because the DPOAE is observed at only a few high levels and it is a minimally featured function. Thus, the landmarks that appear to be associated with cochlear amplifier function cannot be distinguished and quantified when using an $f2/f1$ ratio of 1.35 to generate distortion.

The $f2/f1$ ratios of 1.14 and 1.2 produced relatively

similar patterns of amplitude growth in adults and term neonates but diverged in some predictable ways. At low frequencies, a larger $f2/f1$ ratio is optimal (i.e., generates a more robust DPOAE) (Harris *et al.*, 1989). Consistent with this, DPOAEs generated at 1500 Hz remain robust across level with ratios of 1.21, while the smaller ratio (1.14) produces a drop in amplitude once moderate-high stimulus levels are reached [Fig. 2(a) and (b)]. Likewise, at 6000 Hz, where a smaller $f2/f1$ ratio optimizes amplitude, ratios of 1.2 and 1.14 produce comparable DPOAE amplitude. Either 1.14 or 1.2 can be used for probing cochlear function; however, 1.2 is the $f2/f1$ ratio that optimizes DPOAE amplitude across level.

B. Maturation of the cochlear amplifier

1. Term neonates

Results of experiments I and II indicate that, in most ways, adult and term neonatal growth functions are comparable. The primary tone level at which saturation occurred and the slope or rate at which amplitude grew with increased primary tone level was comparable between these two age groups. Others have reported similar findings in neonates (Lasky, 1998; Popelka *et al.*, 1995). This suggests that by term birth the cochlear amplifier and its range of function is mature as measured by DPOAE amplitude growth. This observation is consistent with previously reported developmental data on related aspects of cochlear function. For example, human neonates show DPOAE suppression tuning that is adultlike by term birth (Abdala *et al.*, 1999; Abdala, 1998), bandpass functions produced by plotting DPOAE amplitude as a function of $f2/f1$ ratio are adultlike in term neonates (Abdala, 1996; Brown *et al.*, 1994), and estimates of cochlear travel time produced by measuring DPOAE phase delays also suggest a normal periphery by term birth (Eggermont *et al.*, 1996).

The only way in which adults and term neonates differed was in the percentage of monotonic growth functions. Both adults and term neonates showed the majority of their functions to be saturating; however, term neonates had a higher percentage of nonsaturating, monotonically growing functions than adults, particularly in experiment II. In experiment I, if only the 1.2 $f2/f1$ ratio condition is considered, term neonates also show a larger proportion of nonsaturating growth functions than adults, particularly at 6000 Hz (see Table I). Lasky (1998) also observed a larger proportion of nonlinear growth functions in a small group of term neonates relative to adults. He attributes this to transducer limitations that did not allow him to present adult subjects with high-level stimuli. The reason for the apparent immaturity in the saturation characteristics of term neonates in the present study is unclear.

2. Premature neonates

Premature neonates also had a higher percentage of nonsaturating DPOAE growth functions than adults. They showed monotonic DPOAE amplitude growth and excellent fit with a linear regression equation for all frequencies, indicating that amplitude growth in premature neonates can often be characterized appropriately with a single line. These nonadultlike patterns of DPOAE amplitude growth in preterm neonates may reflect cochlear immaturity. When the cochlear amplifier of small mammals is ''turned off'' by loop diuretics, the DPOAE growth function loses its amplitude plateau and becomes monotonic, although the slope of amplitude growth does not change. Like small mammals with a dysfunctional cochlear amplifier, premature neonates have more monotonic amplitude growth.

Interestingly, although they are nonadultlike in configuration of DPOAE growth function and in their saturation threshold, the slope of amplitude growth is adultlike in premature neonates. Adultlike slope has also been reported in premature neonatal growth functions by Popelka and colleagues as well (1995). These investigators found that DPOAE amplitude grew at a rate approximating 1 dB/dB for premature neonates and adults. These findings are consistent with the finding that slope of DPOAE amplitude growth is NOT altered in small mammals that have been given loop diuretics, even after the cochlear amplifier has been disabled and the configuration of the function has become monotonic.

It is difficult to pinpoint the developmental period during which the cochlea becomes adultlike based on this small group of premature neonates with a limited age range (average=35 weeks CA at test). Given what is known about the time course of anatomical development of cochlea, it is unlikely that some of the older premature neonates were nonadultlike in cochlear function. It is likely that the youngest neonates, at 33–34 weeks conceptional age, account for the age-related findings in DPOAE amplitude growth. A study with a larger subject group, including a larger range of conceptional ages, might help solve this issue and focus in on the age at which the cochlear amplifier becomes mature.

The mechanism of cochlear amplifier immaturity is not clear. In small mammals, monotonic growth of the DPOAE suggests the absence of cochlear amplifier function. This cannot be the case with the premature human neonates tested in experiment II. Anatomical studies of human cochlea indicate that these neonates (35 weeks CA on average) probably had morphologically normal outer hair cells and stria vascularis, both critical to cochlear amplifier function (Lavigne-Rebillard and Bagger-Sjoback, 1992; Lavigne-Rebillard and Pujol, 1988). Thus, these subjects cannot be equated with animals whose cochlear amplifier has been completely disabled. If cochlear immaturity exists in these neonatal subjects, its is likely to be subtle and reflect the final stages of reaching adultlike status.

The decreased presence of saturation and the elevated saturation threshold in premature neonates may suggest that the range for cochlear amplifier function is larger in this group than in adults. Many models of cochlear function have considered the OHC as critical for compressing the dynamic range of the cochlea into a useable range for inner hair cell transduction. The DPOAE saturation appears to provide evidence of this compression. If the extent and range of OHC compression is not mature in the most immature neonates tested, it could explain the nonadultlike pattern of amplitude growth observed in experiment II.

Outer hair cells are largely innervated by the medial

olivo-cochlear bundle at the mid-brainstem (Fex, 1962); Thus, immaturity in efferent regulation of OHC function could cause an alteration in cochlear amplifier compression and result in nonadultlike DPOAE amplitude growth. The efferent system should also be considered as a potential site of immaturity in premature neonates showing nonadultlike patterns of DPOAE amplitude growth. From these results it is not possible to differentiate between these two potential sources of the immaturity.

Differences in the growth functions of adults and premature neonates were only present at 1500 and 6000 Hz and the shape of neonatal growth functions was fairly adultlike at 3000 Hz. This has been noted consistently in studies from our laboratory comparing adult and neonatal DPOAE responses. For example, the only differences in DPOAE suppression tuning between adults and premature neonates is also observed at 1500 and 6000 Hz. It appears that cochlear function in neonates is mature earliest in the mid-frequency range. As discussed in a previous report (Abdala, 1998), this may reflect the fact that outer hair cells achieve mature morphology first in the mid-basal region of the cochlea and then proceed to mature basally and apically (Pujol and Marty, 1970; Bredberg, 1968).

C. Middle ear immaturity

An immature middle ear may have contributed to these age-related findings. Anatomically, there are various immaturities in the conductive pathway of human neonates (Anson and Donaldson, 1981; Himelfarb *et al.,* 1979; Margolis and Shanks, 1985). Keefe and colleagues have shown that there is reduced efficiency of transmission through the neonatal middle ear (Keefe *et al.,* 1993, 1994). The DPOAE saturation threshold used in this study is completely dependent upon primary tone level; thus, if primary tone level is attenuated as it passes through an immature neonatal middle ear, it is expected that saturation characteristics could be altered in a predictable fashion. That is, the point on the growth function representing a stimulus of 85 dB SPL, for example, may actually represent responses recorded from the premature cochlea at 70 dB SPL (i.e., with 15-dB attenuation due to conductive factors). If this attenuation occurs, it is possible that the stimulus in this experiment could not be presented at sufficiently high levels to reach DPOAE saturation threshold in neonates.

However, if high-level primary tones are attenuated by 15 dB as in the above-mentioned example, the low-level primary tones are likewise attenuated by 15 dB. Thus, the lowest level primary tones would have reached the neonatal cochlea at stimulus levels of 15 dB (L1) and 5 dB SPL (L2) rather than the target values of 30 and 20 dB SPL. It is difficult to argue that the DPOAEs in this study were recorded above the noise floor when using primary tone levels of 15–5 dB SPL. The DPOAEs from humans are typically recorded from 50 to 60 dB below primary tone levels, depending on the stimulus parameters used (Probst, 1991). Thus, it is unlikely that attenuation of sound through the immature neonatal middle ear caused attenuation as large as 15 dB.

If slight attenuation occurred, it cannot account for the absence of DPOAE amplitude saturation in many premature DPOAE growth functions. Average adult saturation threshold was between 67 and 72 dB SPL. Given that the highest stimulus levels presented were 85 dB SPL, middle ear attenuation of <15 dB should not have eliminated saturation in most premature neonatal growth functions. In conclusion, an immature middle ear cannot easily explain the high percentage of premature growth functions that were nonsaturating, although it might explain the slightly elevated saturation threshold in this age group. It is likely that immaturities in the middle ear contribute to the nonadultlike patterns of DPOAE amplitude growth observed in premature subjects in this study. However, it is difficult to attribute these age differences solely to this factor.

D. Summary

Differences in the pattern of DPOAE amplitude growth between adults and premature neonates suggest a peripheral immaturity in the auditory system is present prior to term birth. Premature neonates show a more monotonic pattern of DPOAE amplitude growth and an elevated saturation threshold, possibly indicating a larger range or instability in the range for cochlear amplifier function. Maturation of OHC morphology and innervation occur late in human development; thus, it is hypothesized that the site of this immaturity is the OHC and/or its efferent innervation. It is not possible to entirely rule out influence of the immature middle ear on these findings. It is most likely that the findings result from a combination of middle ear and cochlear immaturities.

ACKNOWLEDGMENTS

This work was partially supported by Research Grant No. 1 R29 DC03552 from the National Institutes of Deafness and Other Communication Disorders, National Institutes of Health. The author would like to thank Sandy Oba for assistance in data collection and management and in the preparation of graphics for this manuscript.

APPENDIX A: CRITERIA FOR ESTABLISHING AMPLITUDE SATURATION THRESHOLD

(1) $\leqslant$1-dB amplitude change among at least three consecutive points, unless they are the two highest levels (80 and 85 dB SPL), then only two consecutive points with $\leqslant$1 dB are required. The second point (going from low to high levels) along a two- or three-sequence plateau is saturation threshold.
(2) $\leqslant$2-dB amplitude change among at least four consecutive points. Second point in this sequence is saturation threshold.
(3) At least two consecutive points with decreased amplitude. Second point in this sequence is saturation threshold.
(4) If the last point on the growth function (i.e., at the highest level presented) shows decreasing amplitude, the point just adjacent to it is considered saturation threshold.

APPENDIX B: INDIVIDUAL GROWTH FUNCTIONS USED TO GENERATE THE MEAN DATA PRESENTED IN FIGS. 6(a)–6(c)

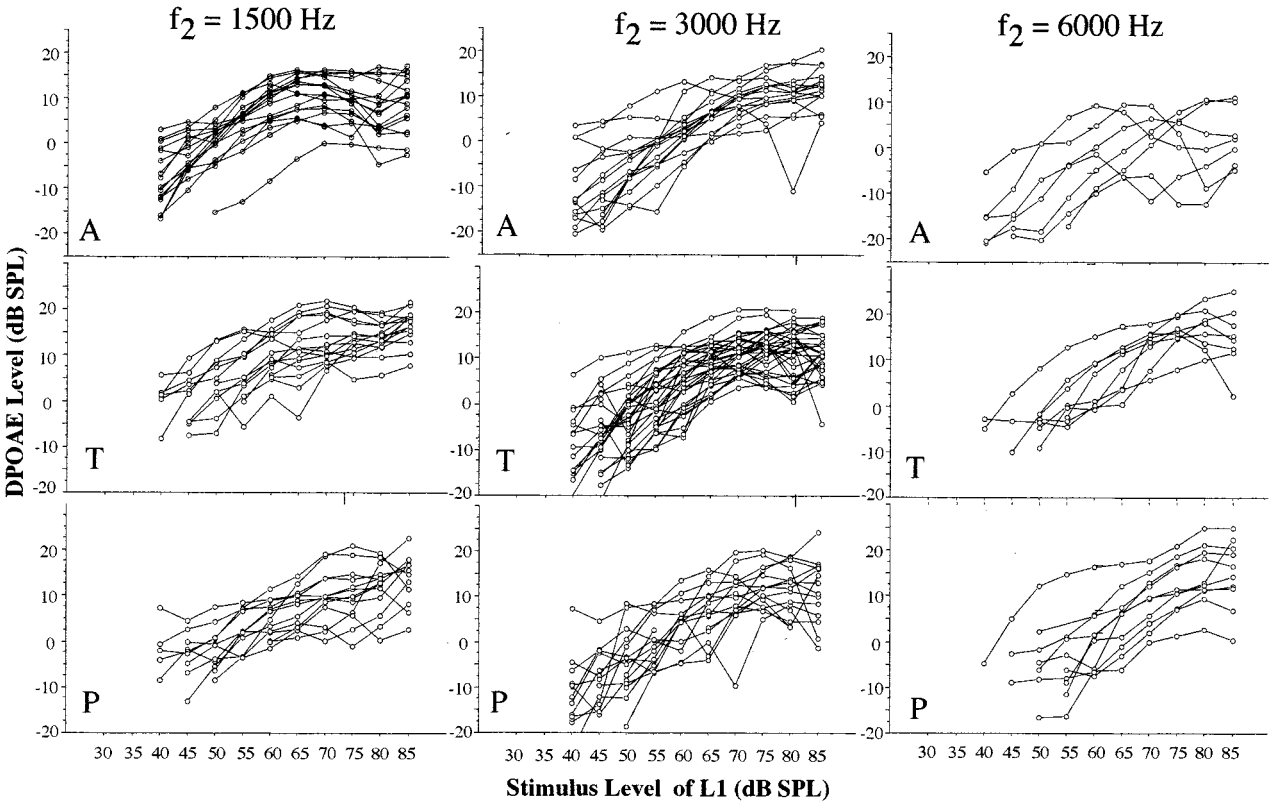

FIG. B1.

Abdala, C. (**1996**). ''DPOAE Amplitude ($2f1$-$f2$) as a function of $f2/f1$ frequency ratio and primary tone level separation in human adults and neonates,'' J. Acoust. Soc. Am. **100**, 3726–3740.

Abdala, C., Sininger, Y., Ekelid, M., and Zeng, F.-G. (**1996**). ''Distortion product otoacoustic emission suppression tuning curves in human adults and neonates,'' Hear. Res. **98**, 38–53.

Abdala, C. (**1998**). ''A developmental study of DPOAE ($2f1$-$f2$) suppression in humans,'' Hear. Res. **121**, 125–138.

Abdala, C., Ma, E., and Sininger, Y. S. (**1999**). ''Maturation of medial efferent system function in humans,'' J. Acoust. Soc. Am. **105**, 2392–2402.

Anson B., and Donaldson J. (**1981**). *Surgical Anatomy of the Human Temporal Bone* (Saunders, Philadelphia).

Bredberg, G. (**1968**). ''Cellular pattern and nerve supply of the human organ of Corti,'' Acta Oto-Laryngol. Suppl. **236**, 1–135.

Brown, A., Sheppard, S., and Russell, P. (**1994**). ''Acoustic distortion products (ADP) from the ears of term infants and young adults using low stimulus levels,'' Br. J. Audiol. **28**, 273–280.

Eggermont, J., Brown, D., Ponton, C., and Kimberley, B. (**1996**). ''Comparison of DPE and ABR traveling wave delay measurements suggests frequency specific synapse maturation,'' Ear Hear. **17**, 386–394.

Fex, J. (**1962**). ''Auditory activity in centrifugal and centripetal cochlear fibers in cat. A study of a feedback system,'' Acta Physiol. Scand. **55**, 1–68.

Harris, F., Lonsbury-Martin, B., Stagner, B., Coats, A., and Martin, G. (**1989**). ''Acoustic distortion-products in humans: Systematic changes in amplitude as a function of $f2/f1$ ratio,'' J. Acoust. Soc. Am. **85**, 220–229.

Himelfarb, M., Popelka, G., and Shanon, E. (**1979**). ''Tympanometry in normal neonates,'' J. Speech Hear. Res. **22**, 179–191.

Keefe, D., Bulen, J., Arehart, K., and Burns, E. (**1993**). ''Ear-canal impedance and reflection coefficient in human infants and adults,'' J. Acoust. Soc. Am. **94**, 2617–2638.

Keefe, D., Bulen, J., Arehart, K., and Burns, E. (**1994**). ''Pressure transfer function and absorption cross section from the diffuse field to the human infant ear canal,'' J. Acoust. Soc. Am. **95**, 355–371.

Lasky, R. (**1998**). ''Distortion product otoacoustic emissions in human newborns and adults: II. Level effects,'' J. Acoust. Soc. Am. **103**, 992–1000.

Lavigne-Rebillard, M., and Bagger-Sjoback, D. (**1992**). ''Development of the human stria vascularis,'' Hear. Res. **64**, 39–51.

Lavigne-Rebillard, M., and Pujol, R. (**1987**). ''Surface aspects of the developing organ of Corti,'' Acta Oto-Laryngol, Suppl. **436**, 43–50.

Lavigne-Rebillard, M., and Pujol, R. (**1988**). ''Hair cell innervation in the fetal human cochlea,'' Acta Oto-Laryngol. **105**, 398–402.

Lonsbury-Martin, B., and Martin, G. (**1990**). ''The clinical utility of distortion product OAEs,'' Ear Hear. **11**, 144–154.

Margolia, R., and Shanks, J. (**1985**). ''Tympanometry,'' in *Handbook of Clinical Audiology*, 3rd ed., edited by J. Katz (Williams and Wilkins, Baltimore).

Mills, D., and Rubel, E. (**1996**). ''Development of the cochlear amplifier,'' J. Acoust. Soc. Am. **100**, 428–441.

Neely, S., and Kim, D. (**1986**). ''A model for active elements in cochlear biomechanics,'' J. Acoust. Soc. Am. **79**, 1472–1480.

Popelka, G., Osterhammel, P., Nielsen, L., and Rasmussen, A. (**1993**). ''Growth of distortion product otoacoustic emissions with primary-tone level in humans,'' Hear. Res. **71**, 12–22.

Popelka, G., Karzon, R., and Arjmand, E. (**1995**). ''Growth of the $2f1$-$f2$ distortion product otoacoustic emission for low-level stimuli in human neonates,'' Ear Hear. **16**, 159–165.

Probst, R., Lonsbury-Martin, B., and Martin, G. (**1991**). ''A review of otoacoustic emissions,'' J. Acoust. Soc. Am. **89**, 2027–2065.

Pujol, R., and Marty, R. (**1970**). ''Postnatal maturation in the cochlea of the cat,'' J. Comp. Neurol. **139**, 115–126.

Stover, L., and Norton, S. (**1993**). ''The effects of aging on otoacoustic emissions,'' J. Acoust. Soc. Am. **94**, 2670–2681.

Whitehead, M., Lonsbury-Martin, B., and Martin, G. (**1992**). ''Evidence for two discrete sources of $2f1$-$f2$ distortion-product otoacoustic emission in rabbit: I. Differential dependence on stimulus parameters,'' J. Acoust. Soc. Am. **91**, 1587–1607.

Indications of different distortion product otoacoustic emission mechanisms from a detailed f_1, f_2 area study

Richard D. Knight and David T. Kemp
Auditory Biophysics Group, Institute of Laryngology and Otology, University College London, 330/332 Gray's Inn Road, London WC1X 8EE, United Kingdom

(Received 2 March 1999; revised 26 August 1999; accepted 1 September 1999)

The primary site of generation on the basilar membrane for the $2f_1-f_2$ distortion product (DP) is generally considered to be near where the higher-frequency stimulus tone peaks. This site has also been shown to be a source of DP otoacoustic emission (DPOAE) in the ear canal, but a second source of emission is known to exist in the region of the DP frequency place. The DPOAE phase versus frequency gradient provides a means of investigating the emission mechanisms. ''Wave-fixed'' and ''place-fixed'' mechanisms have been proposed to account for the very different phase gradients found depending on whether the $2f_1-f_2$ DPOAE is evoked by a small or large stimulus-frequency ratio. DPOAE phase versus frequency gradients can be investigated either by sweeping f_1, f_2 or by sweeping both frequencies maintaining a constant frequency ratio. Each manipulation gives only a partial description of DP behavior. In this study, the place-fixed/wave-fixed dichotomy is analyzed using extensive $2f_1-f_2$ and $2f_2-f_1$ DP stimulus-frequency sweep data presented on matrices of f_1 vs f_2 and f_2/f_1 ratio versus DP frequency. These show how the DPs are related and provide a more complete picture of $2f_1-f_2$ and $2f_2-f_1$ DPOAE phase and amplitude versus frequency behavior. The phase data contain evidence for a systematic variation in the proportions of wave- and place-fixed emission. The results suggest that $2f_1-f_2$ DPOAEs with a wide stimulus frequency ratio are wave fixed, while all other DPOAEs are place fixed. A transition occurs within the $2f_1-f_2$ DP data region at a frequency ratio of about $f_2/f_1=1.1$. The $2f_1-f_2$ DP and $2f_2-f_1$ DP phase behavior is continuous across the $f_2/f_1=1$ boundary. As the $2f_2-f_1$ DP generation region must be strongly influenced by the DP frequency place, the results imply that the place-fixed component of the $2f_1-f_2$ DP is also linked to its frequency place. A similar pattern was obtained with the $3f_1-2f_2$ and $3f_2-2f_1$ DPs. The results support the following model: For the limited set of stimulus conditions that gives rise to $2f_1-f_2$ wave-fixed emissions, DP energy is largely generated in the f_2 region and is emitted directly. All other DPOAEs are place-fixed emissions, and while nonlinearity within the f_2 stimulus envelope remains the generator, the DP is not directly emitted but travels apically until it is re-emitted basally via a separate reflection mechanism in the region of the DP place.
[S0001-4966(99)05212-1]

PACS numbers: 43.64.Jb, 43.64.Kc, 43.64.Ri [BLM]

INTRODUCTION

All evoked otoacoustic emissions (OAEs) exhibit delay relative to the stimulus; therefore, OAE phase is dependent on frequency. Phase versus stimulus frequency gradients have been shown, for example, with transient-evoked otoacoustic emissions (TEOAE) (e.g., Kemp and Chum, 1980a; Wilson, 1980), distortion product otoacoustic emissions (DPOAE) (Kemp and Brown, 1983), and stimulus frequency otoacoustic emissions (SFOAE) (Kemp and Chum, 1980b). The group delay implied by these phase gradients (often referred to as ''OAE latency'') is believed to contain information about the mechanism underlying otoacoustic emissions.

The possibility of two cochlear sources of lower sideband DPOAE was suggested by Kim (1980). Two modes of distortion product emission mechanism were first put forward by Kemp and Brown (1983), and Kemp (1986) introduced the terms wave- and place-fixed to describe these two modes. These have recently been discussed by Shera and Guinan (1998, 1999), who referred to the wave-fixed and place-fixed modes of emission as ''distortion'' or ''reflection'' emissions and emphasized fundamental differences between them.

In the case of the wave-fixed mode, the emission site is supposed to be an integral part of and to move smoothly with the stimulus traveling wave envelope as stimulus frequency is swept. Since the cochlear frequency scaling is approximately geometric, with the result that frequency shifts cause little change to the traveling wave shape, when a stimulus pattern is swept in frequency the phase at any point moving with the traveling wave envelope changes little. Therefore, any OAE contribution from that point would have a very shallow phase gradient. With the place-fixed model, a series of reflecting or scattering sites is supposed to exist at fixed locations along the basilar membrane. As a stimulus is swept in frequency and its excitation pattern moved along the basilar membrane, the stimulus phase at each reflector will change, thus changing the OAE phase and creating a steep phase gradient.

Shera and Guinan (1999) showed that the wave-fixed

mechanism was consistent with the shallow DPOAE phase gradient obtained with the most commonly used stimulus parameters in a constant frequency ratio sweep, but was incapable of generating the steep phase gradients obtained with stimulus frequency (SF) OAE and transiently evoked (TE) OAE. Therefore, they argued, OAEs fell into two entirely separate categories—a distortion-emission class and a reflection-emission class.

However, the steep and shallow phase-gradient characteristics can both be observed in $2f1-f2$ distortion product OAEs obtained with constant stimulus frequency ratio sweeps. Kemp (1986) and Knight and Kemp (1999) have shown that the $2f_1-f_2$ DPOAE has a shallow phase gradient consistent with the wave-fixed model when stimulated using typical clinical stimulus parameters (f_2/f_1 is usually between 1.2 and 1.25 for clinical use), but has a steep phase gradient when stimulated using a small stimulus frequency ratio, e.g., $f_2/f_1=1.05$. Therefore, the $2f_1-f_2$ DP appears to change emission mode depending on whether a wide or small stimulus frequency ratio is used.

DPOAE phase gradients are not entirely smooth and monotonic. In addition to an overall gradual change in phase gradient from low to high frequency, there are also small scale irregularities. These irregularities are not only due to the effects of noise, as they occur when the DPs are well above the noise floor. The irregularities are permanent and repeatable and are often associated with the fine structure of DPOAE amplitude (Moulin and Kemp, 1996). The irregularities could arise from interference caused by multiple reflections between the DP frequency place in the cochlea and the middle ear (Stover *et al.*, 1996), or by interference between either two DP sources (e.g., Brown *et al.*, 1996; Talmadge *et al.*, 1999), or between different parts of a distributed source region (e.g., Zweig and Shera, 1995; Sun *et al.*, 1994). It may be that more than one of these effects can occur, either simultaneously or under different stimulus conditions.

Usually, test strategies are adopted for obtaining DP phase gradients with either f_1 (e.g., Kimberley *et al.*, 1993) or f_2 (e.g., O Mahoney and Kemp, 1995) being swept in frequency while the other is held constant. In the case of the ''f_1 sweep,'' the $2f_1-f_2$ DP generation region [which is related to the f_2 frequency place (e.g., Brown and Kemp, 1984)] remains stationary, whereas with an ''f_2 sweep,'' the $2f_1-f_2$ DP generation region moves. It has been shown that in the case of the $2f_1-f_2$ DP, f_2 sweeps result in a higher value for group delay than f_1 sweeps (Kimberley *et al.*, 1993; O Mahoney and Kemp, 1995). The $2f_2-f_1$ DP behaves differently. No significant difference between f_1 and f_2 sweep latencies is reported (Moulin and Kemp, 1996).

DPOAE latency does not directly indicate the site of generation. Using an f_2 sweep paradigm, the group delay of the $2f_2-f_1$ DP has been reported by Wable *et al.* (1996) to be shorter than that of the $2f_1-f_2$ DP; this finding was used to support the generally accepted view that the generation region of the $2f_2-f_1$ DP is more basal than the $2f_1-f_2$ DP (Martin *et al.*, 1998). However, this result is in fact dependent on the test paradigm—the opposite result could have been found using a sweep with a constant frequency ratio (Knight and Kemp, 1999). The ''latency'' derived from DPOAE phase versus frequency gradients requires careful interpretation as an indicator of true time delay because of the dispersive nature of the cochlea and because the path length varies with frequency. The phase gradient also does not directly indicate the relative source locations of the DPs along the basilar membrane, as the DPs have different frequencies and would therefore travel at different speeds at the same location in the cochlea and also because different mechanisms may be involved in generating the reverse traveling waves. The onset delays measured by Whitehead *et al.* (1996) are an alternative method of evaluating DP delay and the result is a more physically meaningful time delay, although the onset can be gradual, resulting in uncertainty regarding the exact onset time. Despite the difficulties in interpretation, phase gradient-derived delays are useful as comparative probes of the mechanisms involved in cochlear function.

Logically, the $2f_1-f_2$ DP must be generated in a region where both stimulus tones are present, which in practice means within the f_2 envelope, probably near the f_2 traveling wave peak. Once the DP is generated it may travel in either direction—either straight back out or onwards to the DP place. From the DP place it may be re-emitted back to the base as a ''stimulus-frequency'' emission. Group delays consistent with both wave- and place-fixed emission modes have been found in $2f_1-f_2$ DPOAE measurements. The place-fixed part would be consistent with a stimulus-frequency OAE from the DP place, and the wave-fixed part would be consistent with a direct emission from the region of the f_2 frequency place as suggested by Whitehead *et al.* (1996), Fahey and Allen (1997), and Brown *et al.* (1996).

The emitted $2f_2-f_1$ DP, meanwhile, must originate in the region of the f_2 envelope which embraces the DP characteristic frequency place on the basilar membrane, since frequencies propagate very poorly from positions apical to their characteristic place. These conclusions are supported by suppression studies (e.g., Martin *et al.*, 1987, 1998; Kemp, 1998). The DP could be produced at the sites of the reflectors and immediately travel basally, or it may be generated at a site removed from the reflectors and initially travel apically until a reflector is encountered.

Inverse Fourier transform techniques have been used to view complex DPOAE data obtained with f_1 stimulus frequency sweeps in the time domain. This has revealed coexisting DP components with different latencies whose relative strength varies depending on stimulus level (Fahey and Allen, 1997; Stover *et al.*, 1996). Stover *et al.* also found that with low stimulus amplitudes a series of DPOAE amplitude peaks is sometimes seen in the time domain, which could be an indication of multiple reflections between the DP place and the stapes.

Generally, the literature has centered on the wide-frequency ratio case with the $2f_1-f_2$ DP, and tended to avoid small and intermediate frequency ratios and phase data with the $2f_2-f_1$ DP.

As discussed above, the use of f_1 and f_2 sweeps to investigate latency, while useful, provides an incomplete picture of DP phase behavior and the true significance of the

''partial'' latencies obtained via these methods remains unclear. The aim of this study was to reach a better understanding of which stimulus conditions result in DPOAE of the wave-fixed and the place-fixed type and determine how the production of $2f_2-f_1$ DPOAE is similar to or different from the $2f_1-f_2$ DP in this respect. Previous reports on DPOAE phase behavior have been fragmentary and invariably presented as isolated sweeps of either f_1, f_2 or occasionally constant f_2/f_1 sweeps. In the present study, we adopt a new representation in which multiple sweeps are combined within two-dimensional stimulus domains, providing a more complete picture of DPOAE phase versus frequency behavior.

Phase gradients over the stimulus-frequency surfaces rather than over isolated linear sweeps allow the delineation all of the conditions in which the DPOAE behavior is consistent with the wave-fixed mechanism and when it matches the place-fixed emission mechanism. Also, the transition region between the two domains can be visualized, previously only known from single-sweep data. Direct comparison of the $2f_1-f_2$ and $2f_2-f_1$ DPs allows exploration of the links between them and identification of any common characteristics.

A. Two-dimensional DP data representation

1. Phase behavior expected from wave- and place-fixed emissions

Because of the near-geometric frequency scaling of the cochlea, the phase of a wave-fixed DPOAE would be expected to be roughly constant through a frequency sweep maintaining a constant stimulus-frequency ratio.

If the frequency ratio changes, the relative phases of f_1 and f_2 must change over the whole excitation region and the DP phase must also change. In the case of an f_1 change, even if the DP generator itself were fixed to the f_2 wave envelope the DP generator would still ''read'' the changing phase of f_1 at the generator site. Similarly, for an f_2 frequency change the generator site would be moved to a new location where the phase of f_1 would be different. Therefore, for either an f_1 or f_2 sweep the DPOAE phase would change smoothly with a changing frequency ratio.

In the case of a place-fixed lower-sideband DPOAE, DP energy is released from a region inside the f_2 excitation envelope basal to the DP frequency place and propagates apically towards the DP frequency place, from where it is then re-emitted. (Upper-sideband DPOAE may also travel apically before being reflected basally in this way, or may be generated at fixed points already traveling in a basal direction.) Much of the latency would be associated with the traveling wave behavior near the DP place. In this case, it is helpful to consider a constant DP frequency sweep as the phase of a place-fixed DPOAE may remain relatively constant during such a sweep.

For the $2f_2-f_1$ DP at wide frequency ratios, the inward travel time of the stimulus tones to the DP place would be very short and almost constant with f_1 and f_2 frequency changes because the f_1 and f_2 peaks would be far removed apically from the DP place. The DPOAE phase would therefore depend only on the DP frequency, and so the phase contours for the $2f_2-f_1$ DP would be expected to closely follow lines of equal DP frequency. In the case of a constant-DP-frequency sweep (for which, in the case of the $2f_2-f_1$ DP, f_1 changes at twice the rate of f_2) a flat phase characteristic would in this case be observed. With a smaller frequency ratio, some inward f_1 and f_2 delay could accumulate and so the DPOAE phase may then develop a steeper gradient in a constant-DP-frequency sweep. However, the DP may be generated basal to the DP place and propagated apically before being reflected at the DP place. The amount of inward delay would depend on how close the DP generator is to the DP frequency place on the basilar membrane: the closer to the DP place, the more the inward travel time would increase.

For the $2f_1-f_2$ DP, in the case of a place-fixed emission, substantial phase delays for the primaries would be expected to accumulate by the DP generation site which would add to the phase delay contributed by the re-emission from the DP place. $2f_1-f_2$ DPOAE phase contours would not necessarily, therefore, be expected to lie along lines of constant DP frequency.

2. f_1, f_2 area

Figure 1(a) defines the first way in which we will present DPOAE data in this study. In this representation we can show what phase-contour pattern can be expected for different DPOAE emission mechanisms. Constant ratio frequency sweeps are straight lines in this representation radiating from the 0, 0-Hz point. Phase contours would be expected to follow this pattern in the case of a wave-fixed emission mechanism.

Lines of constant DP frequency are a family of parallel lines and cross the chart with a gradient of 2 (because the stimulus frequency which is more distant to the DP frequency must change at twice the amount of the closer stimulus frequency in order to maintain a constant DP frequency). Phase contours would be expected to follow this pattern in the case of a place-fixed emission mechanism.

3. f_2/f_1 ratio, DP frequency area

Figure 1(b) defines the second way in which we will present DPOAE data in this study. Amplitude data have been shown using a related presentation method by Moulin *et al.* (1999) (but with $f2/f1$ vs f_2 instead of DP frequency). In this case, by definition, lines of constant frequency ratio are horizontal and lines of constant DP frequency are vertical. Therefore, phase contours which are horizontal on this chart are consistent with a wave-fixed emission mechanism and phase contours which are vertical are consistent with a place-fixed emission mechanism.

I. METHOD

A. Subjects

Data presented in this paper are drawn from an exhaustive study of DPOAE conducted using the left ears of two subjects: a male (RDK), aged 29 and a female (RN), aged 24. Prior to commencing the DPOAE study, the ears were confirmed as having normal auditory thresholds and middle-ear function. In addition, standard DP grams ($f_1/f_2=1.22$, L_1

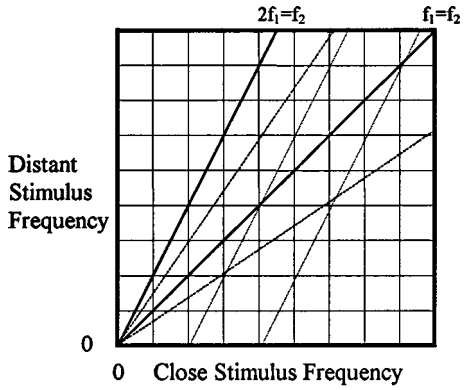

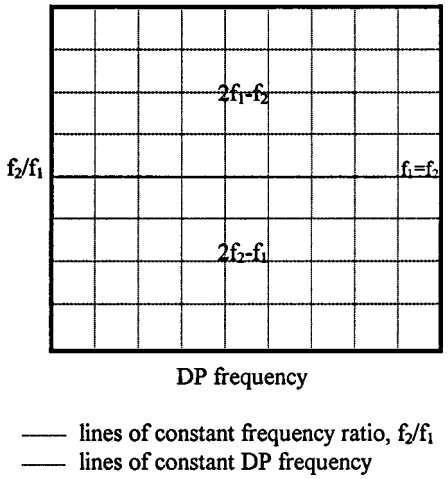

FIG. 1. (a) The f_1, f_2 scheme for presenting DPOAE data. The frequency scales are linear and the *x* and *y* axes are the ''close'' and ''distant'' stimulus frequencies, respectively. These terms refer to the stimulus frequencies which are closer to or further away from the DP frequency, i.e., the close stimulus frequency to the $2f_1-f_2$ DP is f_1 and the close stimulus frequency to the $2f_2-f_1$ DP is f_2. The reason for employing this definition for the axes rather than simply using f_1 and f_2 is that it allows both upper-sideband and lower-sideband DP data to be combined on one chart. The leading diagonal line on the chart is $f_1=f_2$, a condition at which DP measurements are not possible. Above this line is the $2f_1-f_2$ DP area; below the line is the $2f_2-f_1$ DP area. The line running from the origin with a gradient of 2 is $f_2=2f_1$. At this line, the $2f_1-f_2$ DP frequency falls to 0 Hz and therefore becomes mathematically impossible. In practice, the DP becomes unmeasurable well before this. No similar limitation exists with the $2f_2-f_1$ DP, although the DP also becomes unmeasurable if f_1 and f_2 are very widely separated. Dotted lines show the orientation of constant f_2/f_1 and constant DP frequency sweeps. (b) The f_2/f_1 versus DP frequency scheme for presenting DPOAE data. $f_1=f_2$ is a horizontal line at the center of the chart (i.e., $f_2/f_1=1$). Above this is the $2f_1-f_2$ DP; below it is the $2f_2-f_1$ DP.

$=65$, $L_2=55$ dB SPL) were obtained which were within normal limits (Gorga *et al.*, 1997). RDK was one of a small normal-hearing group investigated for TEOAE and DPOAE phase characteristics and was typical of that group (Knight and Kemp, 1999).

B. Experimental method

An ILO88 DPi instrument was used with a standard adult two port probe (RDK) and a standard child probe (RN), which deliver the two stimulus tones via separate amplification and loudspeakers. Custom stimulus ''sweeps'' could be preprogramed with either f_1, f_2 or f_1 and f_2 in increments with time. Each measured DP sweep data point was obtained from averaging of 64 (RDK) or 32 (RN) signal samples, each of 80-ms duration. The equipment has a noise rejection facility in which individual 80-ms samples were excluded if the noise exceeded a preset noise threshold. This was set to between 2 or 4 mPa depending on the ear fitting and on the frequency range to be tested. The equipment was situated in a quiet room with a typical background noise level of 40 dBA SPL.

Level differences between L_1 and L_2 were not explored as these are usually devised to optimize $2f_1-f_2$ DPOAE amplitude for a specific frequency ratio. For measurements with RDK with $L_1=L_2=60$ or 75 dB SPL, sequential measurements were mostly in the form of f_2 sweeps with 12-Hz steps, supplemented by some f_1 sweeps and constant frequency ratio sweeps. Successive f_2 sweeps were separated by f_1 intervals of approximately 50 Hz. Subsequently, where required to clarify detail, additional f_2 sweeps were added which halved the frequency spacing between adjacent sweeps to approximately 25 Hz. For RDK and RN with $L_1=L_2=70$ dB SPL, the data were obtained in constant f_2/f_1 sweeps, with the ratio in increments of 0.25 for adjacent sweeps. The overall stimulus-frequency range studied extended from 1300 Hz to approximately 3 kHz for the f_1, f_2 area representation, which was extended to a DP frequency range of 1–4.1 kHz for the f_2/f_1 versus DP frequency area representation.

In order to be accepted, each DP sweep data measurement was required to exceed the mean measured noise level in the adjacent ten harmonic frequencies of the 80-ms data sample by at least 1 s.d. In order to be visible above the floor in the amplitude chart, the DP amplitude also needed to exceed -15 dB SPL. Constant frequency ratio sequences swept from low frequency towards higher frequencies.

The stimulus levels used were $L_1=L_2=75$, 70, and 60 dB SPL. The 75-dB SPL level was chosen because of the large amplitude and therefore better signal-to-noise (S/N) ratio of the DPs. The stimulus levels also facilitated successful measurements at wider frequency ratios than could have been obtained using smaller-amplitude stimuli. This level is higher than that typically employed for clinical assessment but did not lead to a significant risk of artifactual DP contamination and did not generate measurable DPs in a 1-cc test cavity. Similar sets of measurements were obtained using lower stimulus levels for comparison. At each frequency point, the data for the first pair of DPs were obtained simultaneously, i.e., the $2f_1-f_2$ and $2f_2-f_1$ DP data were obtained simultaneously for frequency points on the chart with the stimulus frequencies transposed.

C. Testing procedure

The probe was sealed in the external auditory meatus with a disposable foam tip. Each DP sweep was preceded by a ''checkfit'' procedure in which the frequency response of the ear canal was measured using wideband clicks. In the event of the response not being substantially flat in the fre-

quency region to be tested, the probe was removed and reinserted. The f_1 or f_2 sweep sequences began with a small frequency ratio, with either f_2 in successive increments or f_1 in decrements until several successive $2f_1-f_2$ and $2f_2-f_1$ DPOAEs were unobtainable or until the limits of the frequency range under investigation were reached. Constant frequency ratio sweeps began at low frequency and swept towards higher frequencies.

D. Data analysis

DP amplitude and phase data from every DP sweep were entered into the two-dimensional frequency plane in EXCEL spreadsheets. To complete a single area chart, up to approximately 3500 data points were obtained per DP from up to approximately 70 f_1 and f_2 sweeps. On occasion, single points were repeated at intersections of f_1 and f_2 sweeps and in these cases an average was taken. Typically, repeated points agreed to within 2 dB or 20°. Linear interpolation was employed between unmeasured data points. However, no interpolation was allowed across data points which failed to meet the S/N criteria or at data points where adjacent measured data implied that a DPOAE would not have met the S/N criteria if attempted. This restriction was to prevent excessive ''filling in'' of amplitude notches or smoothing of irregularities in the phase data.

The phase was unwrapped by adding or subtracting multiples of 360° so as to minimize adjacent phase steps. The absolute number of whole 360° cycles is unknown for each DP. With the $2f_1-f_2$ DP, a choice was necessary whether to optimize the smoothing of the phase at small or large stimulus-frequency ratios. This was because optimizing the smoothing of the phase with small f_2/f_1 led to some large phase steps with large f_2/f_1, and vice versa. This curious feature of the phase data is described in more detail in Results, Sec. II C.

E. Data analysis in the time domain

In order to observe the relative contributions of the various components of the DPOAEs, long sweeps of DPOAE data were obtained and subsequently analyzed in the time domain via an inverse Fourier transform. This resulted in the different DPOAE components being separated by their latencies. This is similar to the method of Stover *et al.* (1996) except that they used f_2 sweeps. Two hundred-and-fifty-six-point constant frequency ratio sweeps of the $2f_1-f_2$ DP were obtained with $L_1=L_2=70$ dB SPL using 12-Hz steps through an f_1 frequency range from 1 to 4 kHz. Before the data were inverse-Fourier transformed to enter the time domain, the frequency intervals within the DP sweeps were converted to a log scale. This was in order to linearize the underlying phase gradient, which would otherwise gradually change from low to high frequency as a result of the logarithmic frequency scaling of the cochlea and give rise to a broad peak in the time domain with different parts of the peak representing different parts of the frequency sweep. Use of a logarithmic frequency scale counteracts the effect of cochlear frequency scaling and results in a linearized underlying phase gradient and therefore well-defined peaks in the time domain. The time scales in the time domain were derived from the average DP frequency step size in each of the logarithmic frequency scales.

II. RESULTS

A. f_1, f_2 area representation

1. Subject RDK

a. $L_1=L_2=75$ dB SPL

i. Amplitude features. The amplitude data for the $2f_1-f_2$ and $2f_2-f_1$ DPs are shown in Fig. 2(a). In general, the maximum amplitude tended to occur with the $2f_1-f_2$ DP using a frequency ratio of 1.3–1.35, consistent with the results of Harris *et al.*, 1989. In addition, for this ear the DP amplitude was generally raised in two broad areas, one in the $2f_1-f_2$ DP below $f_1=1.8$ kHz and one in both DPs above approximately $f_1=2.2$ kHz.

Also in this ear, two well-defined valleys with a depth of 10–15 dB can be seen in the $2f_2-f_1$ DP data. The notches occur at constant DP frequencies and possibly continue into the $2f_1-f_2$ DP data. The $2f_2-f_1$ DP was measurable at very wide frequency ratios away from the center line, extending up to $f_2/f_1=1.9$. This contrasts with the $2f_1-f_2$ DP, which was not measurable at frequency ratios greater than $f_2/f_1=1.5$. Notches are typically seen in DP gram data and the 2D representation shows how these notches would shift position for DP grams constructed with different primary ratios. The amplitude data of the $2f_1-f_2$ DP contain a smooth plateau along the maximum amplitude region of $f_2/f_1=1.3$–1.4, whereas at smaller frequency ratios a series of valleys occurred which followed lines of approximately constant DP frequency. There are missing data in both DPs at $f_2/f_1=1.5$, which was caused in the $2f_1-f_2$ DP by the fact that the difference tone was coincident, and in the $2f_2-f_1$ DP by harmonic distortion at $2f_1$ (most likely from the transducers) appearing in the noise spectrum.

ii. Phase. Overall, the 2D representation shows lines of equal phase running from lower left to upper right bending to become less steep as they do so.

It is highly significant that the $2f_2-f_1$ DP phase contours (lower-right region) all lie along constant DP frequencies [Fig. 2(b)] in contrast to the $2f_1-f_2$ DP region (upper left).

The $2f_2-f_1$ DP data also contained phase steps which occurred at constant DP frequencies and coincided with the amplitude notches described in Sec. *i.* above.

With a small frequency ratio (close to the diagonal $f_1=f_2$ line), the $2f_1-f_2$ DP phase contours tend to be a continuation of the $2f_2-f_1$ DP phase contours with isophase lines crossing directly between the two DP regions. At larger frequency ratios the $2f_1-f_2$ DP phase contours turn to follow constant frequency ratios. The transition occurs at a frequency ratio of around $f_2/f_1=1.1$–1.15.

b. Reduced stimulus levels, $L_1=L_2=60$ dB SPL

The overall pattern of results obtained at $L_1=L_2=75$ dB SPL was not specific to that stimulus level, although signifi-

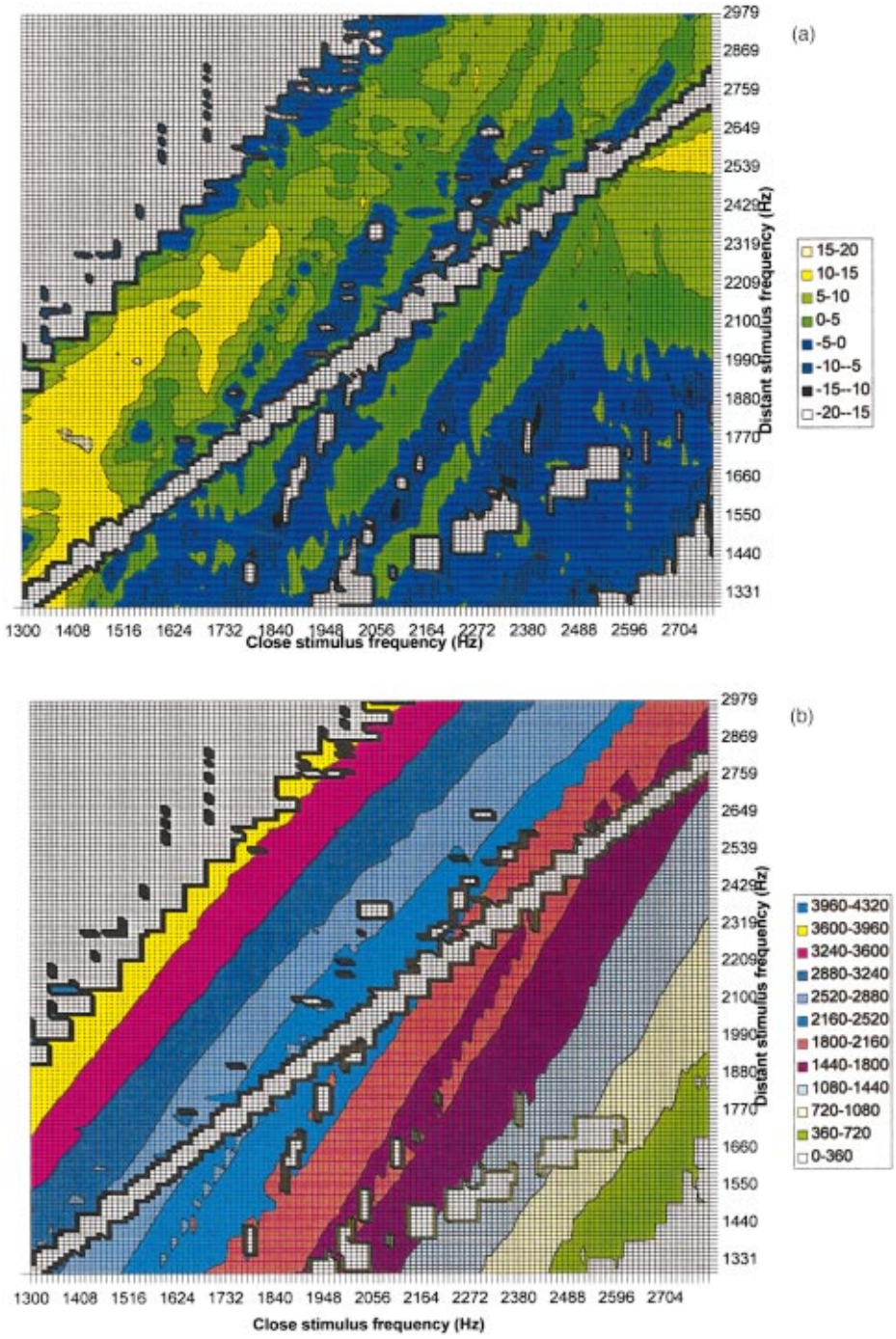

FIG. 2. f_1, f_2 area representations of (a) level, dB SPL (upper chart), and (b) phase, deg (lower chart) of $2f_1-f_2$ and $2f_2-f_1$ DPOAE with $L_1=L_2=75$ dB SPL with subject RDK. In each chart, $2f_1-f_2$ DP data are above the leading diagonal line; $2f_2-f_1$ DP data are below the line. Major amplitude features include two valleys in the $2f_2-f_1$ DP data which follow approximately constant DP frequencies, and in the $2f_1-f_2$ DP data there are complex amplitude patterns when f_2/f_1 is small, but a smooth amplitude function when f_2/f_1 is between 1.2 and 1.4. Phase contours typically follow lines of constant DP frequency, but there is a transition within the $2f_1-f_2$ DP data at approximately $f_2/f_1=1.1-1.15$, above which the phase contours follow lines of constant stimulus-frequency ratio.

cant differences were found with stimulus level, mainly in the amplitude data.

i. Amplitude differences. The measurements were repeated with the stimulus reduced to $L_1=L_2=60$ dB SPL. The amplitude data obtained using a lower stimulus amplitude [Fig. 3(a)] are much more complex. The two pronounced valleys in the $2f_2-f_1$ DP data are no longer present, but have been replaced by another at approximately 3 kHz. The $2f_2-f_1$ DP amplitude is still strong at small frequency ratios, but at frequency ratios above $f_2/f_1=1.2$ there has been a larger reduction in amplitude, resulting in difficulty obtaining measurements. The $2f_1-f_2$ DP data also appear more complex, with valleys which are not always straight following approximately constant DP frequencies. The valleys in some cases appear to divide into two, for example when the close stimulus frequency (f_1) is 1700 and 1900 Hz. The amplitude features are not just noise, as the data are well above the noise floor (except the very lowest amplitude points), are repeatable, and related patterns occur across adjacent data sweeps. No smooth plateau occurs in the $2f_1-f_2$ DP data and the maximum amplitude occurs at a smaller frequency ratio than was the case with the stimulus levels at 75 dB SPL (approximately $f_2/f_1=1.2$ instead of 1.3).

ii. Phase. The phase data [Fig. 3(b)] essentially follow the same patterns as with the higher stimulus levels, where the data met the S/N criteria. In the case of the $2f_1-f_2$ DP, the transition at which the phase contours turn from follow-

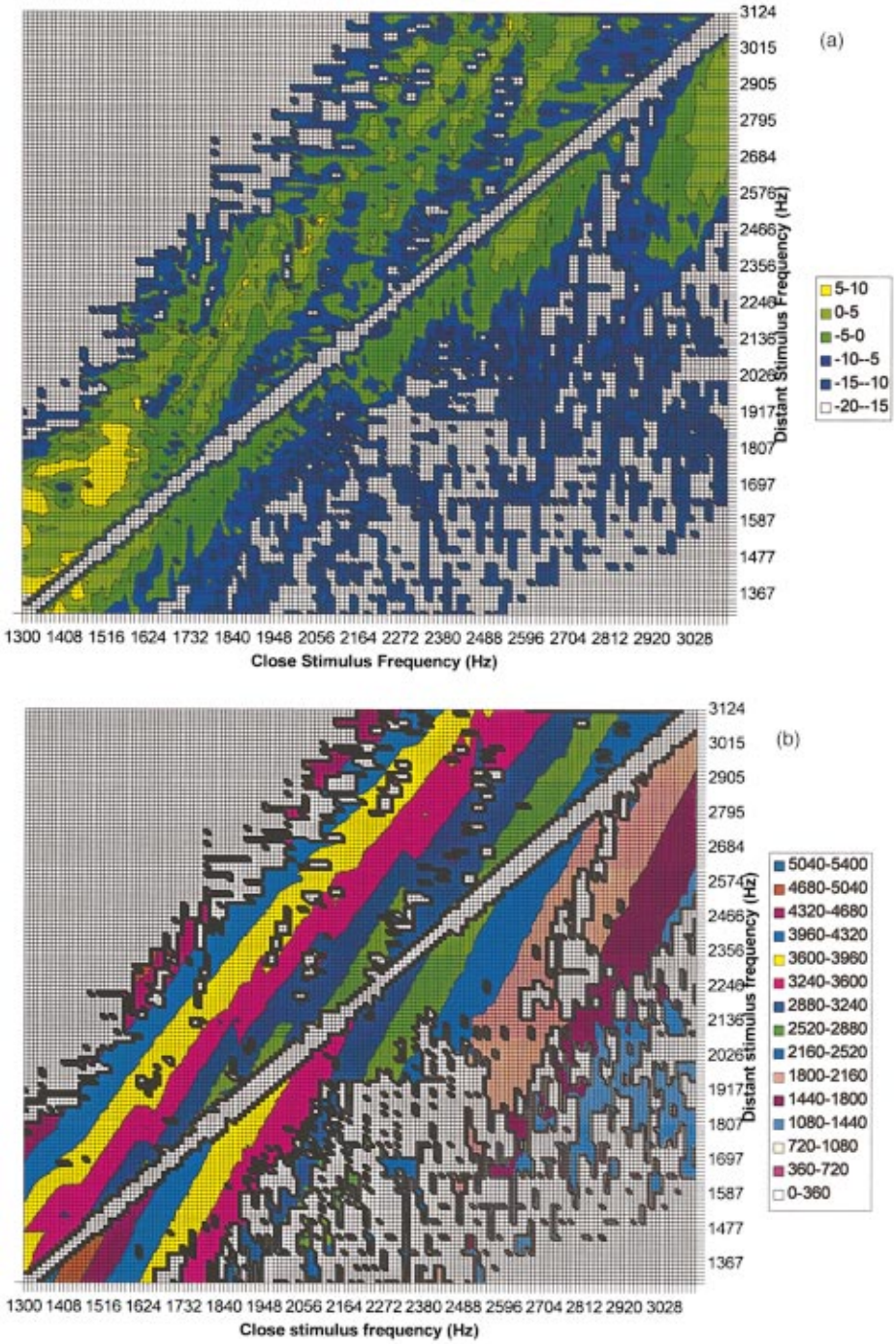

FIG. 3. f_1, f_2 area representations of (a) level, dB SPL (upper chart), and (b) phase, deg (lower chart) of $2f_1-f_2$ and $2f_2-f_1$ DPOAE with $L_1=L_2=60$ dB SPL with subject RDK. In each chart, $2f_1-f_2$ DP data are above the leading diagonal line; $2f_2-f_1$ DP data are below the line. Compared to Fig. 2, the $2f_1-f_2$ DP amplitude is much more complicated with no smooth plateau at any ratio of f_2/f_1. The $2f_2-f_1$ DP is difficult to measure at wide stimulus-frequency ratios, and the two amplitude valleys which were found when $L_1=L_2=75$ dB SPL are no longer present, but another valley has appeared at a higher frequency. The phase behavior is similar to that seen in Fig. 2, except that the transition region within the $2f_1-f_2$ DP data occurs at a slightly larger stimulus-frequency ratio.

ing a constant DP frequency to following a constant frequency ratio occurs at a slightly larger frequency ratio of approximately $f_2/f_1=1.15$.

c. Higher-order DPOAEs $3f_1-2f_2$ and $3f_2-2f_1$

The data obtained using stimulus levels $L_1=L_2=75$ dB SPL are shown in Fig. 4(a) and (b). As with the $2f_2-f_1$ DP, the $3f_2-2f_1$ DP phase contours always tend to follow constant DP frequencies; however, in this case the lines of constant DP frequency have an aspect ratio of 3:2 because of the different order of the DP components. The ''transition'' region at which the phase contours turn from following DP frequencies to following frequency ratios occurs at a smaller frequency ratio with the $3f_1-2f_2$ DP ($f_2/f_1=1.05$) than was the case with the $2f_1-f_2$ DP ($f_2/f_1=1.1-1.15$), and the DPs are not measurable with ratios greater than $f_2/f_1=1.1-1.15$. However, as the emission frequency of the $3f_1-2f_2$ DP is twice as far from f_2 as that of the $2f_1-f_2$ DP for the same stimulus frequencies, the transition is occurring at comparable frequency spacings from f_2 for both DPs.

2. $L_1=L_2=70$ dB SPL, subject RN

a. Amplitude

The amplitude data, shown in Fig. 5(a), contain many of the features which were seen with subject RDK. Amplitude ''valleys'' are seen in the $2f_2-f_1$ DP data, which follow

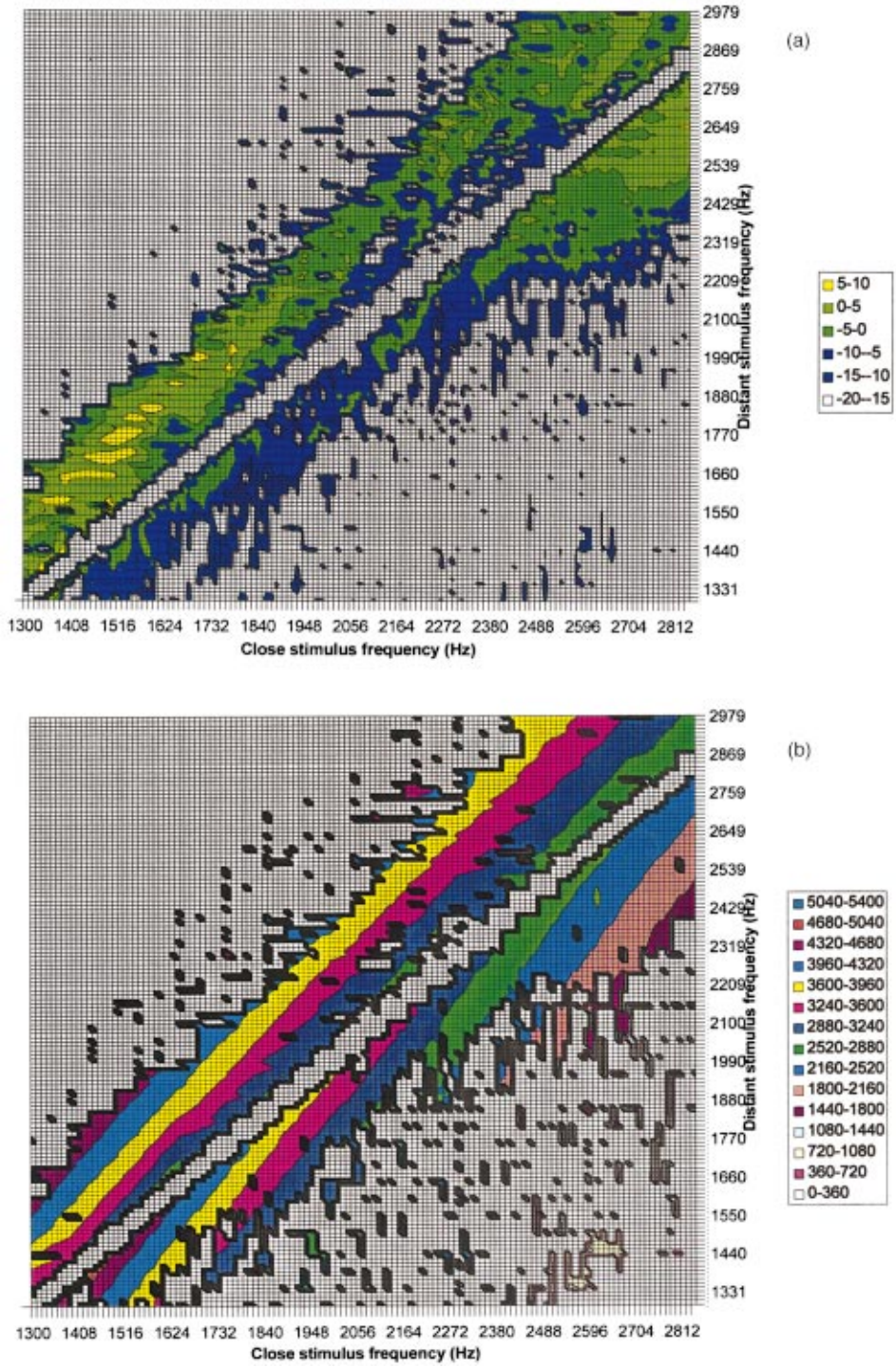

FIG. 4. Area representations of (a) level, dB SPL (top), and (b) phase, deg (lower) of $3f_1-2f_2$ and $3f_2-2f_1$ DPOAE with $L_1=L_2=75$ dB SPL with subject RDK. In each chart, $3f_1-2f_2$ DP data are above the leading diagonal line; $3f_2-2f_1$ DP data are below the line. These DPs are only measurable with small stimulus-frequency ratios. The phase is comparable to Fig. 2, except that where the phase contours follow constant DP frequencies, the direction has an aspect of 3:2 instead of 2:1 because of the different DP. The transition between phase contours following constant DP frequency or following constant f_2/f_1 occurs at a smaller stimulus-frequency ratio.

constant DP frequencies and continue into the $2f_1-f_2$ DP. The $2f_1-f_2$ data become smoother at wider frequency ratios, rising to a peak at a ratio of approximately $f_2/f_1=1.25$ before falling into the noise floor at approximately $f_2/f_1=1.4-1.45$. The $2f_2-f_1$ DP, meanwhile, reduces in amplitude gradually towards wider frequency ratios, but remains above the noise floor up to frequency ratios of 1.7–1.8.

There are differences in the detail of the results from the two subjects. The results from RN are of higher amplitude and contain more valleys in the $2f_2-f_1$ DP data. The amplitude ridge and valley features do not occur at the same frequencies in the two subjects.

b. Phase

The phase data from RN [Fig. 5(b)] follow the same pattern as RDK, with $2f_2-f_1$ DP phase contours following constant DP frequencies and crossing to the $2f_1-f_2$ DP. The $2f_1-f_2$ DP phase contours also follow constant DP frequencies when f_2/f_1 is small, but switch to following constant frequency ratios when $f2/f1$ exceeds approximately 1.1–1.15.

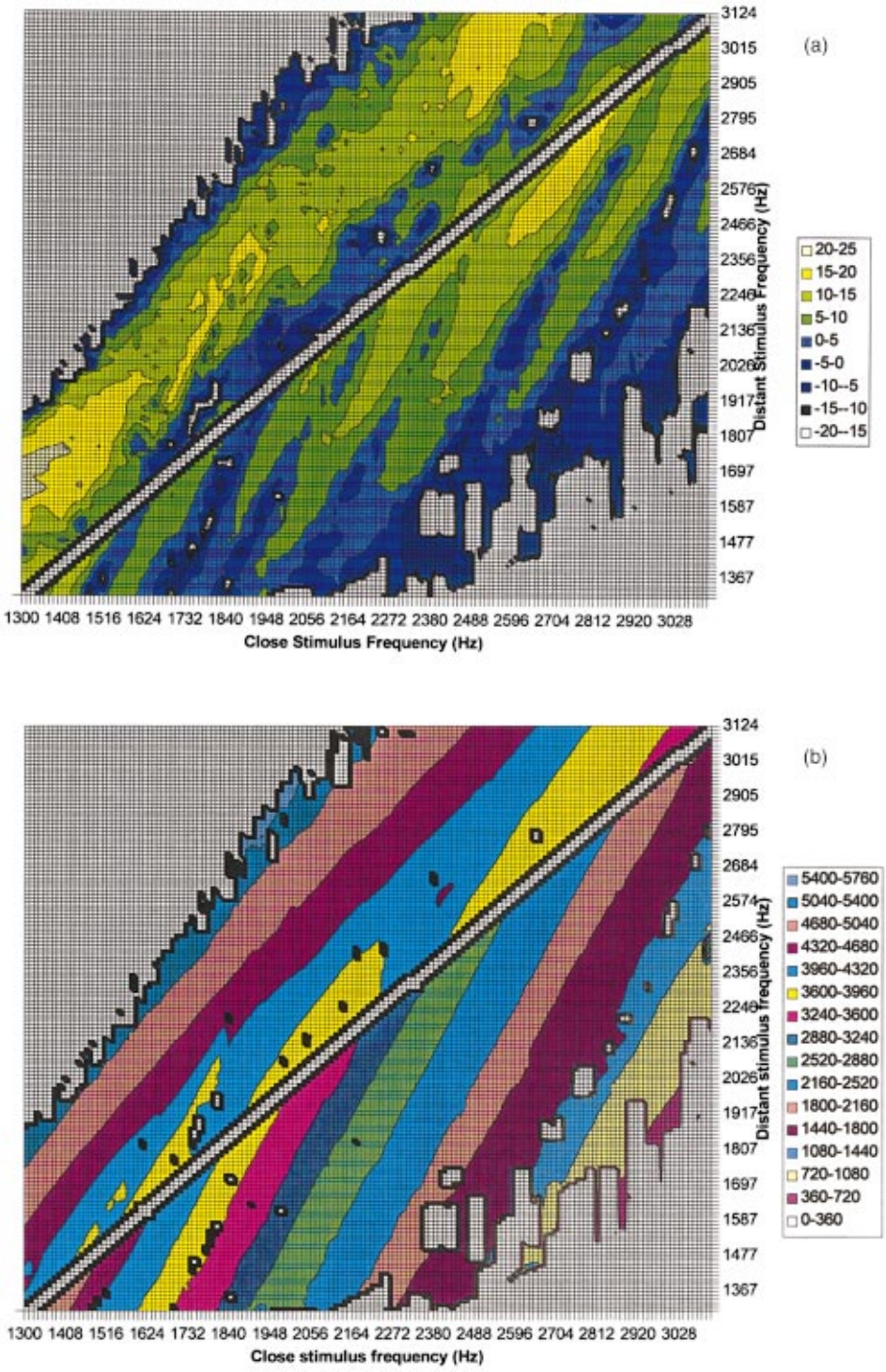

FIG. 5. f_1, f_2 area representations of (a) level, dB SPL (upper chart), and (b) phase, deg (lower chart) of $2f_1-f_2$ and $2f_2-f_1$ DPOAE with $L_1=L_2=70$ dB SPL with subject RN. In each chart, $2f_1-f_2$ DP data are above the leading diagonal line; $2f_2-f_1$ DP data are below the line. Data were obtained in constant f_2/f_1 sweeps. Compared to RDK, there is a greater amount of fine structure in the $2f_2-f_1$ DP with valleys and ridges occurring across the whole frequency range; the level of the DPs is also a little higher generally, but otherwise the overall pattern of the results is very similar.

B. f_2/f_1 versus DP frequency representation

1. $L_1=L_2=70$ dB SPL, RDK and RN

Figures 6 and 7 show data for each subject with $L_1=L_2=70$ dB SPL using the alternative presentation format, plotting stimulus-frequency ratio f_2/f_1 against DP frequency.

a. Amplitude

With this format [Figs. 6(a) and 7(a)] the amplitude valleys in the $2f_2-f_1$ DP are approximately vertical, indicating that they are defined by the DP frequency. The valleys cross to the $2f_1-f_2$ DP. The amplitude fine structure in the $2f_1-f_2$ DP at frequency ratios above 1.1 is not fixed to emission frequency, but instead drifts towards lower frequencies at larger frequency ratios. With subject RDK, the amplitude data become more smooth when the DP frequency is above 3 kHz, whereas with RN the fine structure continues across the whole frequency range investigated.

b. Phase

The $2f_2-f_1$ phase contours [Figs. 6(b) and 7(b)] are almost vertical, with a slight drift towards lower DP fre-

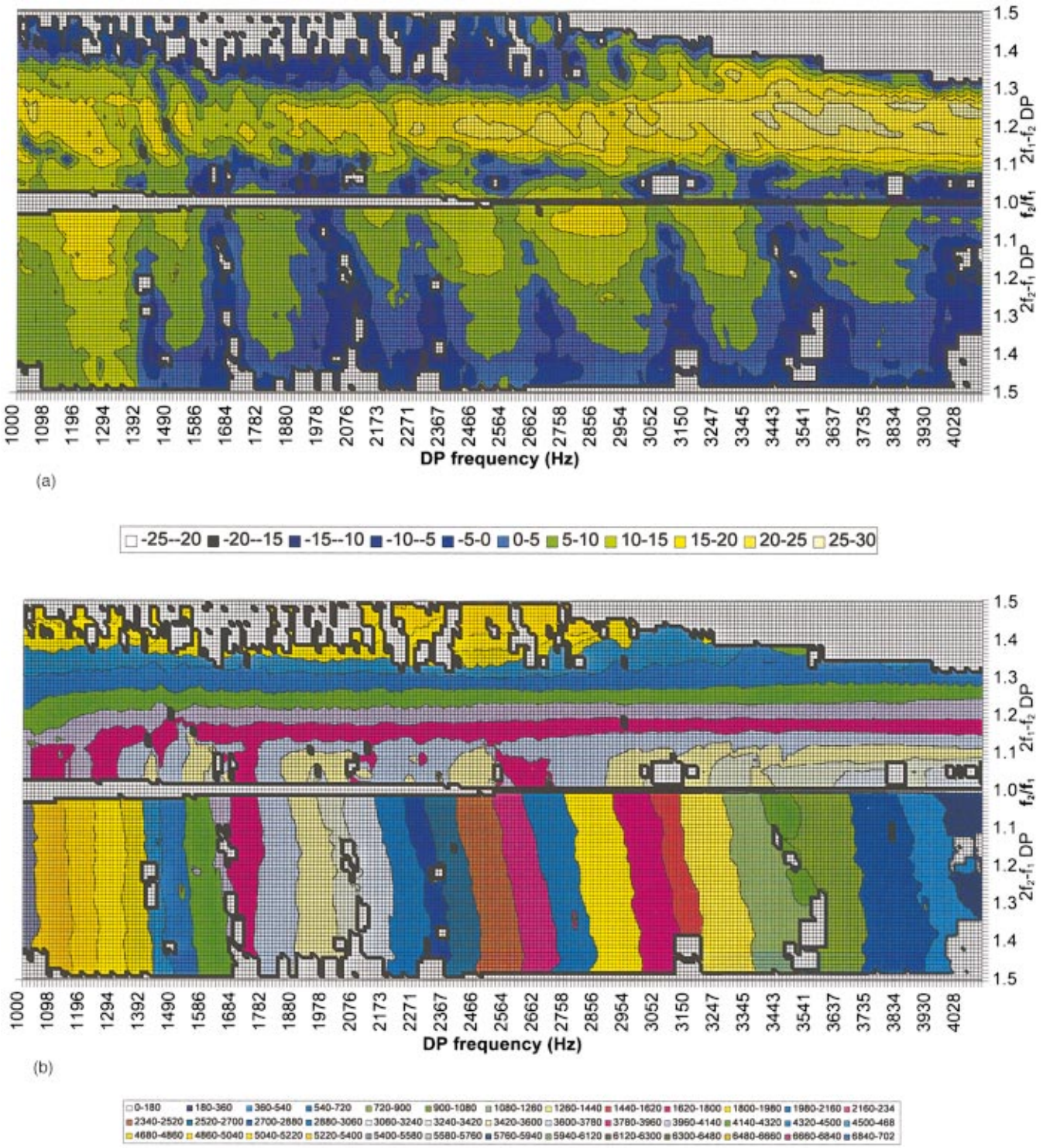

FIG. 6. f_2/f_1 versus DP frequency area representations of (a) level, dB SPL (upper chart), and (b) phase, deg (lower chart) of 2 f_1-f_2 and 2 f_2-f_1 DPOAE with $L_1=L_2=70$ dB SPL with subject RN. The data in Fig. 5 are drawn from these charts. Using this presentation, the transition within the 2 f_1-f_2 data between the wave-fixed and place-fixed behavior can clearly be seen.

quency at small f_2/f_1 which is more marked above approximately 2 kHz. This is to be expected from Figs. 2, 3, and 5 and is consistent with a place-fixed emission mechanism. The slight deviation from vertical indicates a very small influence of the stimulating frequencies on the resulting phase of the DPOAE. It is unclear whether this results from greater inward delay in the cochlea to the DP place because of the smaller frequency ratio (and hence the DP place is closer to $f2$), a small movement of the DP generating region, or whether it merely reflects greater inward phase change of the stimuli as they travel along the ear canal because of the higher frequency and therefore shorter wavelength of the primaries.

The phase contours clearly cross directly between the 2 f_2-f_1 and 2 f_1-f_2 DPs in both subjects, suggesting a continuity of emission mechanism, but with the 2 f_1-f_2 DP the

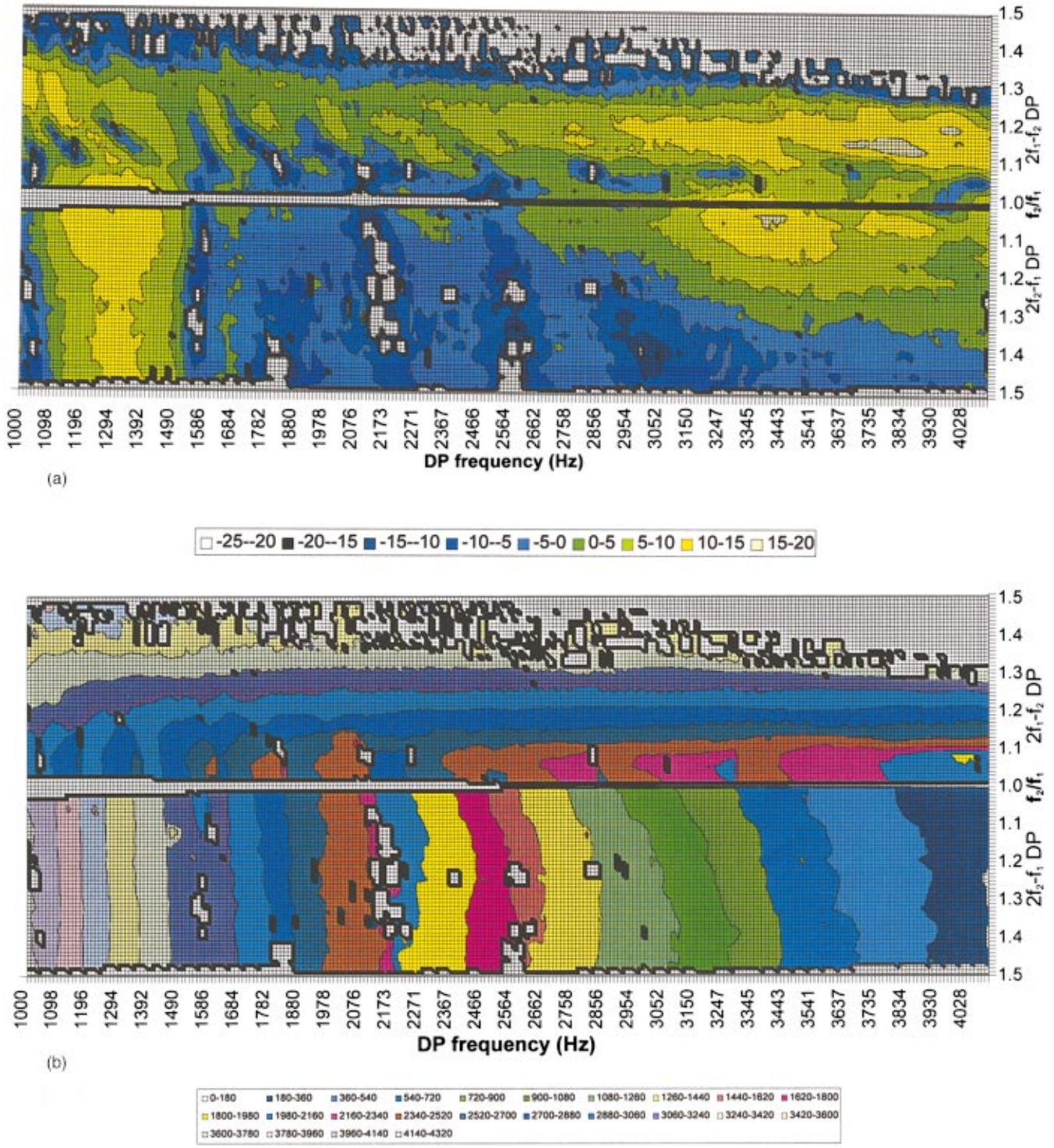

FIG. 7. f_2/f_1 versus DP frequency area representations of (a) level, dB SPL (upper chart), and (b) phase, deg (lower chart) of 2 f_1-f_2 and 2 f_2-f_1 DPOAE with $L_1=L_2=70$ dB SPL with subject RDK. The same general pattern is seen as in Fig. 6, except that no notches in level are seen above 2.5 kHz in the 2 f_2-f_1 DP.

phase contours switch from vertical (phase determined by DP frequency) to horizontal (phase determined by f_2/f_1) at larger ratios. This is consistent with a change from the place-fixed to the wave-fixed emission mechanism.

C. The 2 f_1-f_2 DP transition

In order to investigate the 2 f_1-f_2 DP transition between the wave- and place-fixed mechanisms, successive short constant frequency ratio sweeps were obtained with the frequency ratio in increments for each sweep. Each sweep covered the 2 f_1-f_2 DP frequency range 1490–1678 Hz. The stimulus level was $L_1=L_2=70$ dB SPL, and the frequency ratio was varied from $f_2/f_1=1.08$ up to 1.2 (Fig. 8).

When the frequency ratio was large, the DP sweeps had shallow phase gradients. As the frequency ratio reduced, the phase gradient became steeper with an upward step. When

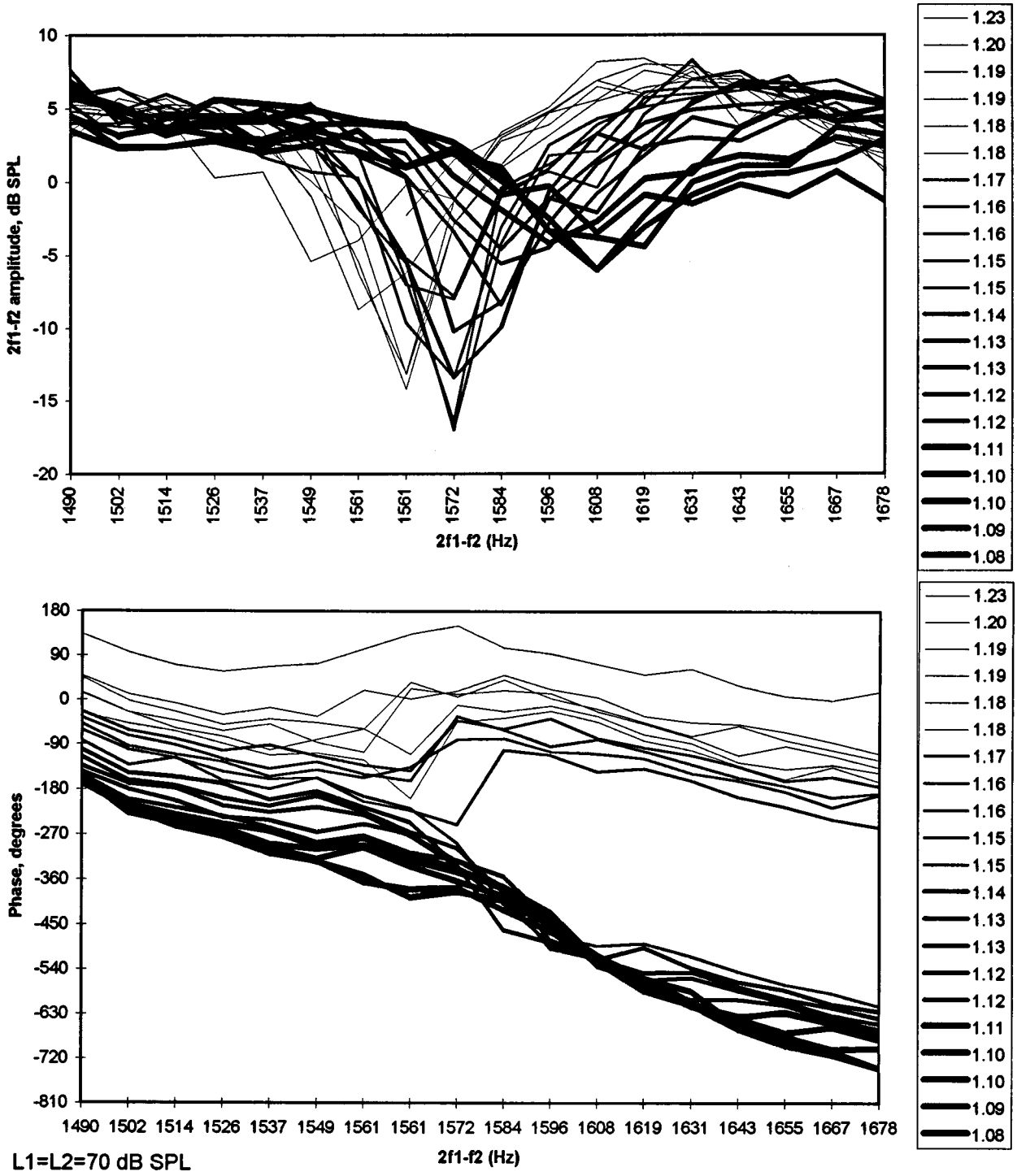

FIG. 8. Detail of a 2 f_1-f_2 DPOAE phase discontinuity which occurred in the transition between wave- and place-fixed behavior (subject RDK). Sweeps are constant f_2/f_1 and successive sweeps are in increments of f_2/f_1. Phase is seen to switch between a steep or a shallow gradient by gaining or losing a 360°-step. A corresponding level notch comes and goes during this transition, moving slightly towards lower frequencies at larger f_2/f_1.

the frequency ratio reached 1.15, the upward step exceeded 180° and so was logically stepped downwards. Ultimately, at the narrowest ratios ($f_2/f_1 \approx 1.1$) the step approached 360° and the phase resolved to a new steep gradient. The frequency at which the step occurred increased slightly with smaller stimulus-frequency ratios. There was a corresponding amplitude notch which came and went during this transition.

This process by which 360° is ''lost'' as the stimulating-frequency ratio is increased explains the necessity in the area DP data for either downward 360° steps at low-frequency ratios or upward 360° steps at high ratio when attempting to join the phase data in a 2D frequency array.

D. Time-domain analysis

In order to observe the relative contributions of the various components of the DPOAEs, we transformed the data into the time domain.

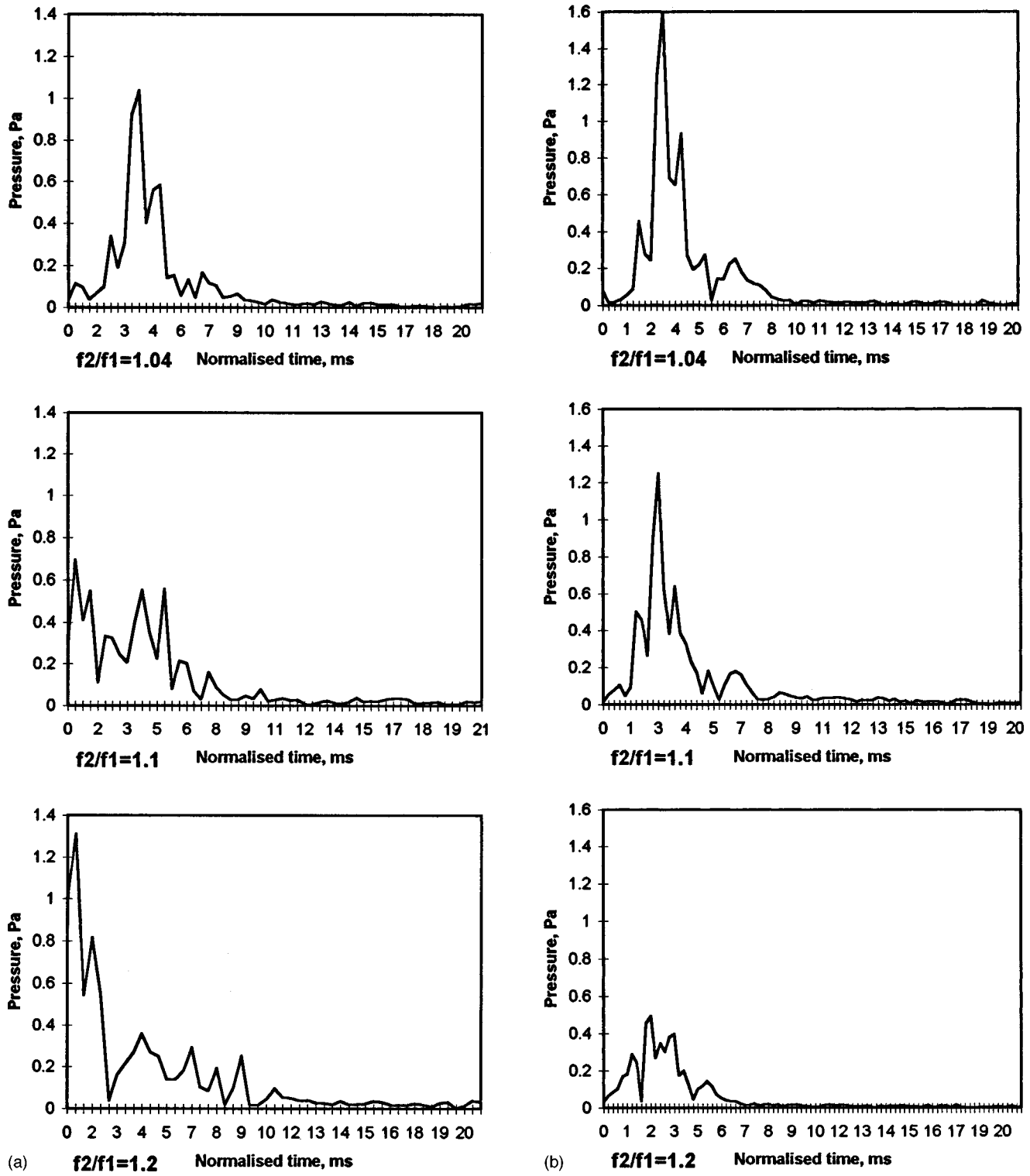

FIG. 9. Magnitudes of Fourier transforms of 256-point constant frequency ratio DP sweeps with $L_1=L_2=70$ dB SPL (subject RDK). f_1 was in increments of 12-Hz steps, starting at 1 kHz. The frequency intervals were converted to a log scale prior to the Fourier transform to remove an underlying gradual change in phase gradient. (a) $2f_1-f_2$ DP—A low-latency and a high-latency component can be identified. When $f_2/f_1=1.04$, there is almost no trace of the low-latency component; when $f_2/f_1=1.1$, both components are present and approximately equal in amplitude, and when $f_2/f_1=1.2$, the low-latency component dominates although higher-latency elements are also present. (b) $2f_2-f_1$ DP—The level is lower with wider frequency ratios, but the latency remains about the same.

The magnitudes of the inverse Fourier transforms derived from three DPOAE sweeps are shown in Fig. 9(a), using stimulus-frequency ratios of $f_2/f_1=1.04$, 1.1, and 1.2. Each peak has an implied group delay, derived from the rate of change of phase in the DP sweep. The group delay associated with the frequency ratio of $f_2/f_1=1.04$ is 3–4 ms, compared to 0.5–1 ms with a frequency ratio of 1.2. When the frequency ratio is 1.1, components with both group delays are seen, rather than a single peak with an intermediate time delay. Therefore, two components of DPs are identified,

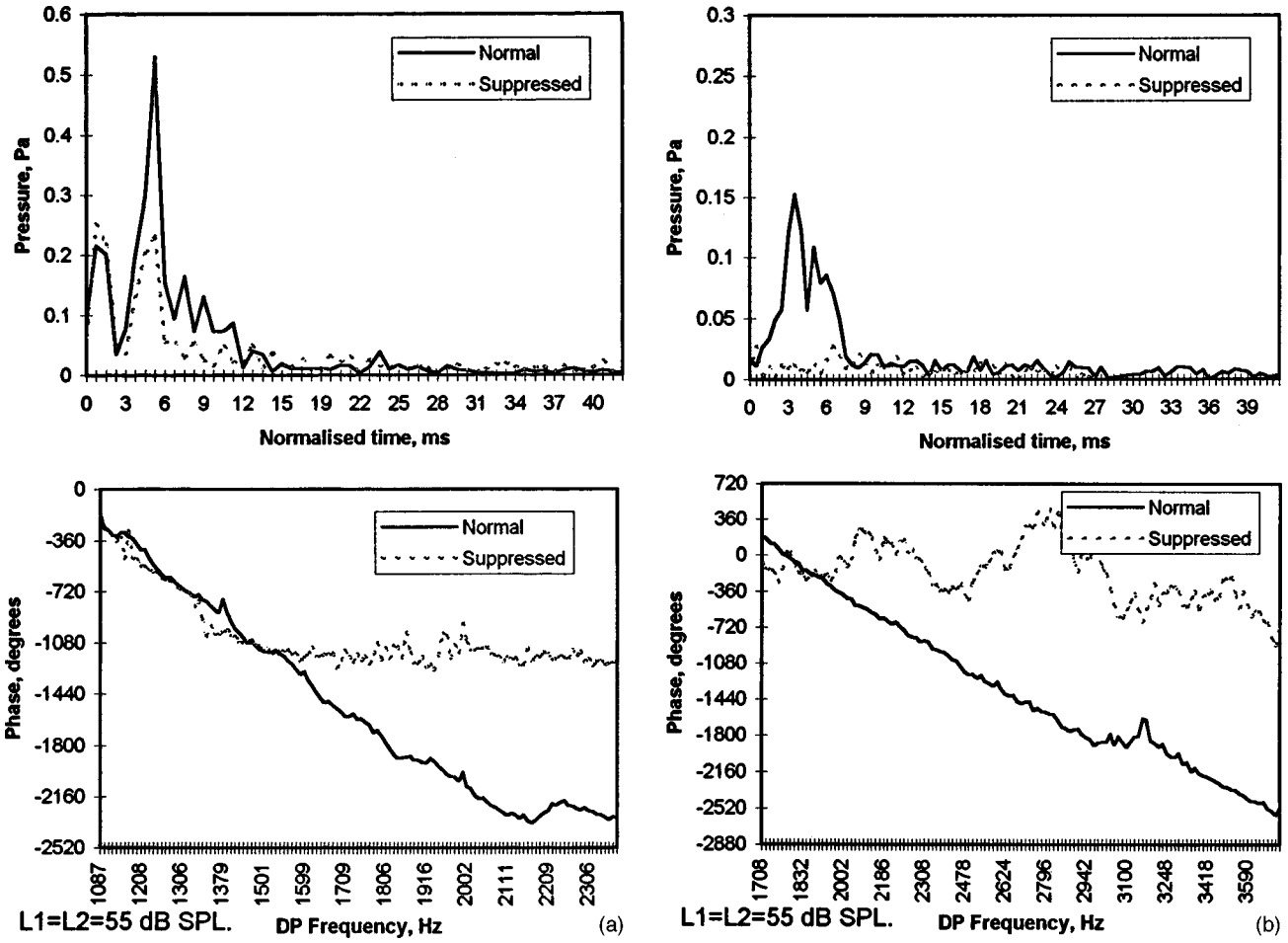

FIG. 10. Phase and amplitude of Fourier transform data from constant frequency ratio DP sweeps with $L_1=L_2=55$ dB SPL and with f_2/f_1 fixed at 1.15 (subject RDK). (a) $2f_1-f_2$ DP: Insertion of a third stimulus tone of 55 dB SPL at 50 Hz above the DP frequency selectively suppresses the high-latency emission and results in a predominantly flat phase characteristic. (b) $2f_2-f_1$ DP: The suppressor tone suppresses the entire DP, leaving only noise.

with two distinct group delays. As the sweeps had constant stimulus-frequency ratios, the peak with a small group delay is consistent with the wave-fixed emission mechanism, whereas the later peak is consistent with the place-fixed emission mechanism. Which one dominates the measured DPOAE depends on the ratio f_2/f_1.

Similar data have been obtained for the $2f_2-f_1$ DP [Fig. 9(b)]. In this case, there is no sign of the low-latency peak that was seen with the $2f_1-f_2$ DP.

Further DP sweeps were obtained using 128 points in the $2f_1-f_2$ DP frequency range of 1087–2381 Hz with a frequency ratio of 1.15 and a stimulus level of $L_1=L_2=55$ dB SPL. The measurement was then repeated with a third tone of 55 dB SPL introduced at 50 Hz above the DP frequency. Figure 10(a) contains both a time-domain response and the unwrapped phase data. It can be seen that the third tone selectively ''suppresses'' the more delayed component of the DP and the overall phase gradient changes from a steep gradient to a shallow gradient. No such gradient change could be induced by introducing a third stimulus tone at frequencies close to the frequencies of f_1 and f_2. Figure 10(b) shows the corresponding data for the $2f_2-f_1$ DPOAE. In this case, the suppressor close to the DP frequency obliterates the entire DP, leaving just noise.

III. DISCUSSION

A. Comparison with literature

We can compare the results of this study with that available in the literature by using our f_1 and f_2 sweep-phase data obtained with $L_1=L_2=60$ dB SPL (Fig. 3) to calculate ''partial'' latencies from the phase gradients as follows:

$$\text{Latency} = -\delta(\phi/2\pi)/\delta(f),$$

where ϕ is the DP phase in radians and f is the DP frequency in Hz. The frequency ranges of the examples were selected to avoid discontinuous data or data containing large irregularities.

In the case of the $2f_2-f_1$ DP the latencies calculated via the f_2 sweep method were only marginally greater than the f_1 sweep latencies (ratio of f_1 sweep/f_2 sweep latency $=0.92-1.00$). In this respect the results are consistent with those of Moulin and Kemp (1996), who used stimulus parameters of $L_1=65$, $L_2=60$ dB SPL $f_2/f_1=1.2-1.22$, and reported no significant difference between f_1 and f_2 sweep latencies for the $2f_2-f_1$ DPOAE. Each individual latency found here is also consistent with those found by Moulin and Kemp [which in the frequency range 1–3 kHz ranged from 9.5 to 6 ms ($2f_1-f_2$, f_2 sweep), 7.7 to 4 ms ($2f_1-f_2$, f_1

sweep), 9 to 4.5 ms ($2f_2-f_1$, f_2 sweep), and 7 to 4.5 ms ($2f_2-f_1$, f_1 sweep)]. For our $2f_1-f_2$ data, the f_2 sweep-derived latencies exceed the f_1 sweep latencies when measured using large frequency ratios (ratio of f_1 sweep/f_2 sweep latency$=0.75-0.86$). This was consistent with studies by Kimberley *et al.* (1993) and O Mahoney and Kemp (1995), who found that f_1 sweeps were 20% lower than f_2 sweeps. However, when f_2/f_1 was small, the latencies calculated via the f_2 sweep method were only marginally greater than the f_1 sweep latencies (ratio of f_1 sweep/f_2 sweep latency$=0.89-1.02$), as was the case with the $2f_2-f_1$ DP.

B. Emission modes

In describing the DP frequency versus f_2/f_1 ratio representation of DP data, we indicated that wave-fixed emission mechanisms would result in horizontal phase contours. It can be seen from the results in Figs. 6 and 7 that the $2f_1-f_2$ DP does follow this trend when $f_2/f_1>1.1-1.15$. Meanwhile, place-fixed DPs would tend to result in vertical phase contours, following lines of constant DP frequency. The $2f_2-f_1$ DP and the $2f_1-f_2$ DP with $f_2/f_1<1.1-1.15$ tend to be of this form. The division is not simply between the upper- and lower-sideband distortion products (where $f_2/f_1=1$ on the charts), but instead the transition occurs within the $2f_1-f_2$ DP data at a frequency ratio of approximately 1.1, with a transition region in which both mechanisms coexist and give rise to interference effects.

To summarize, at large frequency ratios the $2f_1-f_2$ DP phase behavior implies a wave-fixed emission mode, whereas the $2f_1-f_2$ DP with a small frequency ratio and the $2f_2-f_1$ DP are consistent with a place-fixed emission mode.

As TEOAE and SFOAE phase behavior is also consistent with the place-fixed model (Kemp and Chum, 1980a; Wilson, 1980; Kemp and Chum, 1980b), the clinical $2f_1-f_2$ DPOAE, for which the frequency ratio is normally approximately 1.2, is part of a subset of wave-fixed OAEs which includes only lower-sideband DPOAEs stimulated with a wide frequency ratio. All other stimulated OAEs appear to be place-fixed.

C. The origins of DPOAE fine structure

The issue of whether the fine structure associated with the $2f_1-f_2$ DP is caused by interference between two distinct regions of DP emission or a local effect of interactions within one source region remains controversial. Clearly, two sources of differing latency would give rise to fine structure by interference, but repeated reflections between the base and a single DP place-fixed reflector could also produce a fine structure (as in SFOAE). Mechanisms have been proposed by which interference could also arise from within a single distributed source region. Initially, the place-fixed reflectors were thought of as single scattering points (Kemp, 1978). Subsequently, to explain the extended segmented nature of the reflector-phase behavior, models requiring regularly spaced impedance changes along the basilar membrane (e.g., Strube, 1989) were introduced, although no physiological anatomical correlate was known. More recently, Zweig and Shera (1995) have shown that OAE fine structure could be generated with a random spacing of impedance irregularities which could, for example, be linked to the irregularities in primate outer hair-cell (OHC) arrangements. Evidence that part of the $2f_1-f_2$ DPOAE may be from the DP place under some conditions has been provided by suppression tuning curves (Kummer *et al.*, 1995) and suppression of the fine structure (Heitmann *et al.*, 1998). The mechanism underlying such a ''re-emission'' or reflection is expected to be place-fixed by logical argument, because the situation with a forward-going DP from the region of the stimulus frequencies proceeding to its frequency place and then returning as an OAE is essentially the same as a stimulus-frequency otoacoustic emission, which has a phase characteristic consistent with a place-fixed mechanism.

D. Wave- and place-fixed emissions

The results presented in the present study provide further evidence that the high-latency place-fixed part of the $2f_1-f_2$ DP arises from the region of the DP frequency place. At small ratios, the continuation of the phase contours between the $2f_1-f_2$ and $2f_2-f_1$ DPs across the $f_1=f_2$ or $f_2/f_1=1$ line suggests a continuation of the same emission mechanism between the upper and lower sidebands. As the $2f_2-f_1$ DP must be primarily emitted from the region of or basal to the DP frequency place, this result strongly suggests that the place-fixed $2f_1-f_2$ DP is also emitted largely from the region of its DP frequency place via a reflection mechanism. In the case of the $2f_1-f_2$ DP, this is a re-emission of a DP which was originally generated in the frequency region of the primary tones on the basilar membrane.

Further support for the theory of the DP frequency place region being the site of reflection for the place-fixed emission is provided by the inverse Fourier transform and suppression data (Figs. 9 and 10).

With a small primary frequency ratio, the inverse Fourier-transformed DP data contain almost no trace of the wave-fixed (low latency) emission in the $2f_1-f_2$ DP, which suggests that the distortion source may not be simply bidirectional. If DP energy was always sent equally towards the base and the apex of the cochlea, a wave-fixed component to the $2f_1-f_2$ DP would always be present. In addition, the high-latency emission reduces in amplitude as the ratio f_2/f_1 increases. While the intensity of DP generation might be expected to decrease with increasing frequency separation of equal-level primaries, an increase in place-fixed emission amplitude relative to wave-fixed emission could be expected because of a reduction in suppression of the DP frequency ''amplifier'' region by the primaries. This result implies that less DP energy is directed towards the apex from the f_2 region when stimulated with larger ratios of f_2/f_1. A mechanism by which the distortion source may be directional and dependent on the ratio f_2/f_1 is presented by Kemp and Knight (1999).

E. Characteristics of DPOAE fine structure

The $2f_1-f_2$ DP showed a quite smooth amplitude function with wide frequency ratios when stimulated by $L_1=L_2$

=75 dB SPL (Fig. 2), but when the stimulus tones were reduced to 60 dB SPL the amplitude function remained complex at all frequency ratios, up until the DP sank into the noise floor at approximately $f_2/f_1=1.4$ (Fig. 3). The uneven amplitude of the $2f_1-f_2$ DPOAE at wide ratios with lower stimulus levels could be a result of the wave-fixed emission failing to completely dominate the place-fixed emission, or an increase in interference between out-of-phase elements within a single DP-generating region, or multiple reflections between the base of the cochlea and the DP place becoming more significant.

The most striking feature of the $2f_2-f_1$ DP (upper sideband) amplitude data from RDK in Fig. 2 is the two valleys which approximately follow constant DP frequencies (2150 and 2550 Hz). Similar features were also seen with RN across the whole frequency range under investigation. The possible causes would seem to be an interference effect or localized cochlear anatomical features; however, the notches disappear at lower stimulus levels (RDK) and so localized anatomical irregularities are unlikely. As there is one obvious region on the basilar membrane from which this DP is emitted (unlike lower-sideband DPs), i.e., the DP frequency place, the remaining possible sources of interference are from different parts of a large region of generation or reflection, or from cancellation between multiple reflections between the DP place and the stapes. The latter is less likely as the reflections would be unlikely to become relatively more significant with higher stimulus levels. Recently, Martin *et al.* (1999) have suggested that a source of the $2f_2-f_1$ DP exists basal to the DP frequency place due to the interference of the harmonic $2f_2$ with f_1 to produce another source of the $2f_2-f_1$ DP, reintroducing the possibility of interference between two DP-generating sites. The situation is therefore potentially quite complex.

F. Location of the $2f_2-f_1$ DP generator in this data

It is interesting that the $2f_2-f_1$ DP phase contours in our data do not deviate much from following lines of equal DP frequency even with a very low frequency ratio, despite the expectation that under these conditions the DPOAE would gain delay from the increased traveling time of the stimuli to the DP place. The two possible reasons for this are (1) The outward traveling time reduces at the same rate as the inward traveling time increases, or (2) The inward traveling time doesn't increase.

Option 1 would require that the region from which a DP reflection occurs should move depending on the frequency ratio by which the DP was generated, being further towards the base with smaller frequency ratios. Option 2 would require that the $2f_2-f_1$ DP generation region is significantly basal to the DP frequency place (Martin *et al.*, 1998, 1999), therefore remaining far enough from the region of the stimulus frequencies so as not to accumulate much inward traveling time even when the DP frequency is close to f_2. The region of place-fixed reflections could occur anywhere between the DP generation region and the DP frequency place, maintaining a fixed relationship with the DP frequency place.

G. Are the results typical?

The results presented in this study contain some features that have been previously shown, and others that are new. Both subjects had a change in phase behavior in the $2f_1-f_2$ DP in constant f_2/f_1 frequency sweeps, with steep phase gradients recorded with f_2/f_1 below approximately 1.1 and shallow phase gradients at wider frequency ratios. This has been shown previously (Kemp, 1986; Knight and Kemp, 1999) and is undoubtably a normal feature. The exact ratio at which the changeover occurs is known to be variable across subjects and also to be slightly frequency- and stimulus-level dependent. Both subjects also produced maximum levels of $2f_1-f_2$ DPOAE with frequency ratios of approximately 1.2–1.25 [Figs. 6(a), 7(a)] and this is also known to be typical (Harris *et al.*, 1989). The exact ratio at which the maximum level occurs is also known to vary between subjects and is also frequency- and stimulus-level dependent.

Where data are dominated by place-fixed behavior, the phase is almost entirely dependent on the DP frequency. As this occurs in both subjects, this interesting result is likely to be typical of normal ears. The continuity of the amplitude and phase contours between the lower- and upper-sideband DPOAEs also occurs in both subjects and appears to indicate a continuity of emission mechanism which would be true of all normal ears.

The presence of amplitude ridges and valleys in the $2f_2-f_1$ DP data appears to be less certain in other subjects, as in subject RDK they didn't occur across the whole frequency range or at all stimulus levels. This is therefore likely to be a common but not necessarily universal feature. Data from both subjects with the $2f_1-f_2$ DP wave-fixed emission show evidence of amplitude valleys which drift towards lower emission frequencies at wider frequency ratios. However, the exact location of specific amplitude features are not correlated between the two subjects.

IV. SUMMARY

For lower-sideband DPOAEs, whether the wave- or place-fixed mechanism dominates depends on the stimulus-frequency ratio, the DP, order and the stimulus amplitude. Therefore, the wave-fixed emission mode cannot be explained as the uncomplicated leakage of DP energy and may depend on a source region which has variable directivity. Upper-sideband DPOAEs are always dominated by the place-fixed emission mode.

The phase of corresponding place-fixed upper- and lower-sideband DPs appeared to be continuous between the DPs at small frequency ratios, suggesting continuity of mechanism. Whilst the presence of two separate emission regions for the $2f_1-f_2$ DP is presumably the cause of much of the amplitude fine structure seen in this DP, the presence of amplitude notches in the $2f_2-f_1$ DP indicates that fine structure may also arise from either multiple reflections within the cochlea or from interference within a distributed DP generating or reflecting region.

The emission model which is suggested by these results can be summarized as follows. For the wave-fixed emission, distortion in the basilar-membrane motion is the generator

and the DP is emitted directly. For the place-fixed emission, distortion occurring within the f_2 envelope is still the generator of the DP, but DP energy is projected apically and is emitted via a separate reflection process in the region of the DP frequency place.

The two-dimensional and time-domain analysis methods have been shown to be valuable. Further work is required to investigate variability among other ears and the effect of using other stimulus levels.

ACKNOWLEDGMENTS

The authors would like to thank Ruchi Narang for her considerable patience as a subject for this study and the Auditory Biophysics Laboratory at the Institute of Laryngology and Otology, London for financially supporting this project.

Brown, A. M., Harris, F. P., and Beveridge, H. A. (**1996**). ''Two sources of acoustic distortion products from the human cochlea,'' J. Acoust. Soc. Am. **100**, 3260–3267.

Brown, A. M., and Kemp, D. T. (**1984**). ''Suppressibility of the 2 $f1-f2$ stimulated acoustic emissions in gerbil and man,'' Hearing Res. **13**, 29–37.

Fahey, P. F., and Allen, J. B. (**1997**). ''Measurement of distortion product phase in the ear canal of the cat,'' J. Acoust. Soc. Am. **102**, 2880–2891.

Gorga, M. P., Neely, S. T., Ohlrich, B., Hoover, B., Redner, J., and Peters, J. (**1997**). ''From laboratory to clinic: a large scale study of distortion product otoacoustic emissions in ears with normal hearing and ears with hearing loss,'' Ear Hear. **18**(6), 440–455.

Harris, F. P., Lonsbury-Martin, B. L., Stagner, B. B., Coats, A. C., and Martin, G. K. (**1989**). ''Acoustic distortion products in humans: systemic changes in amplitude as a function of f_2/f_1 ratio,'' J. Acoust. Soc. Am. **85**, 220–229.

Heitmann, J., Waldmann, B., Schnitzler, H., Plinkert, P. K., and Zenner, H. (**1998**). ''Suppression of distortion product otoacoustic emissions (DPOAE) near 2 $f1-f2$ removes DP-gram fine structure—Evidence for a secondary generator,'' J. Acoust. Soc. Am. **103**, 1527–1531.

Kemp, D. T. (**1978**). ''Stimulated acoustic emissions from within the human auditory system,'' J. Acoust. Soc. Am. **64**, 1386–1391.

Kemp, D. T. (**1986**). ''Otoacoustic emissions, travelling waves and cochlear mechanisms,'' Hearing Res. **22**, 95–104.

Kemp, D. T. (**1998**). ''Otoacoustic emissions: distorted echoes of the cochlea's travelling wave,'' *in Otoacoustic Emissions Basic Science and Clinical Applications*, edited by C. I. Berlin (Singular, San Diego), Chap. 1, pp. 1–59, Figs. 1–12.

Kemp, D. T., and Brown, A. M. (**1983**). ''An integrated view of cochlear mechanical nonlinearities observable from the ear canal,'' *in Cochlear Mechanics*, edited by E. DeBoer and M. A. Viergever (Delft University Press, Holland).

Kemp, D. T., and Chum, R. A. (**1980a**). ''Properties of the generator of stimulated acoustic emissions,'' Hearing Res. **2**, 213–232.

Kemp, D. T., and Chum, R. A. (**1980b**). ''Observations on the generator mechanism of stimulus frequency acoustic emissions—two tone suppression,'' in *Psychophysical, Physiological and Behavioural Studies in Hearing*, edited by van den Brink and Bilsen (Delft University Press, Holland), pp. 34–42.

Kemp, D. T., and Knight, R. D. (**1999**). ''Virtual DP reflector explains DPOAE wave and place fixed dichotomy,'' in *Association for Research in Otolaryngology Abstracts* 396.

Kim, D. O. (**1980**). ''Cochlea mechanics: Implications of electrophysiological and acoustical observations,'' Hearing Res. **2**, 297–317.

Kimberley, B. P., Brown, D. K., and Eggermont, J. J. (**1993**). ''Measuring human cochlear travelling wave delay using distortion product emission phase responses,'' J. Acoust. Soc. Am. **94**, 1343–1350.

Knight, R. D., and Kemp, D. T. (**1999**). ''Relationships between DPOAE and TEOAE characteristics,'' J. Acoust. Soc. Am. **106**, 1420–1435.

Kummer, P., Janssen, T., and Arnold, W. (**1995**). ''Suppression tuning characteristics of the 2 $f1-f2$ distortion-product otoacoustic emission in humans,'' J. Acoust. Soc. Am. **98**, 197–210.

Martin, G. K., Lonsbury-Martin, B. L., Probst, R., Scheinin, S. A., and Coats, A. C. (**1987**). ''Acoustic distortion products in rabbit ear canal. II. Sites of origin revealed by suppression contours and pure tone exposures,'' Hearing Res. **28**, 191–208.

Martin, G. K., Jassir, D., Stagner, B. B., Whitehead, M. L., and Lonsbury-Martin, B. L. (**1998**). ''Locus of generation for the 2 f_1-f_2 vs 2 f_2-f_1 distortion-product otoacoustic emissions in normal-hearing humans revealed by suppression tuning, onset latencies, and amplitude correlations,'' J. Acoust. Soc. Am. **103**(4), 1957–1971.

Martin, G. K., Stagner, B. B., Fahey, P. F., and Lonsbury-Martin, B. L. (**1999**). ''Influence of even-order nonlinearities on the suppression and enhancement of DPOAEs above $f2$ in rabbits,'' in *Association for Research in Otolaryngology Abstracts* 22, p. 382.

Moulin, A., and Kemp, D. T. (**1996**). ''Multicomponent acoustic distortion product otoacoustic emission phase in humans. I. General characteristics,'' J. Acoust. Soc. Am. **100**, 1617–1639.

Moulin, A., Jourdain, F., and Collet, L. (**1999**). ''Using acoustic distortion product otoacoustic emissions in clinical applications: Influence of $f2/f1$ on DPOAE gram,'' Br. J. Audiol. **33**, 89.

O Mahoney, C. F., and Kemp, D. T. (**1995**). ''Distortion product otoacoustic emission delay measurement in human ears,'' J. Acoust. Soc. Am. **97**(6), 3721–3735.

Shera, C. A., and Guinan, J. J. (**1998**). ''Reflection emissions and distortion products arise by fundamentally different mechanisms,'' in *Association for Research in Otolaryngology Abstracts* 21, p. 344.

Shera, C. A., and Guinan, J. J. (**1999**). ''Evoked otoacoustic emissions arise by two fundamentally different mechanisms: A taxonomy for mammalian OAEs,'' J. Acoust. Soc. Am. **105**, 782–798.

Stover, L. J., Neely, S. T., and Gorga, M. P. (**1996**). ''Latency and multiple sources of distortion product otoacoustic emissions,'' J. Acoust. Soc. Am. **99**, 1016–1024.

Strube, H. W. (**1989**). ''Evoked otoacoustic emissions as cochlear Bragg reflections,'' Hearing Res. **38**, 35–46.

Sun, X., Schmiedt, R. A., He, N., and Lam, C. F. (**1994**). ''Modelling the fine structure of the 2 $f1-f2$ acoustic distortion product. I. Model development,'' J. Acoust. Soc. Am. **96**, 2166–2174.

Talmadge, C. L., Long, G. R., Tubis, A., and Dhar, S. (**1999**). ''Experimental confirmation of the two-source interference model for the fine structure of distortion product otoacoustic emissions,'' J. Acoust. Soc. Am. **105**, 275–292.

Wable, J., Collet, L., and Chéry-Croze, S. (**1996**). ''Phase delay measurements of distortion product otoacoustic emissions at 2 $f1-f2$ and 2 $f2-f1$ in human ears,'' J. Acoust. Soc. Am. **100**, 2228–2235.

Whitehead, M. L., Stagner, B. B., Martin, G. K., and Lonsbury-Martin, B. L. (**1996**). ''Visualization of the onset of distortion-product emissions and measurement of their latency,'' J. Acoust. Soc. Am. **100**, 1663–1679.

Wilson, J. P. (**1980**). ''Evidence for a cochlear origin for acoustic re-emissions, threshold fine-structure and tonal tinnitus.'' Hearing Res. **2**, 233–252.

Zweig, G., and Shera, C. A. (**1995**). ''The origin of periodicity in the spectrum of evoked otoacoustic emissions,'' J. Acoust. Soc. Am. **98**, 2018–2047.

Three-dimensional numerical modeling for global cochlear dynamics[a)]

Anand A. Parthasarathi
Department of Biomedical Engineering, 3304 G. G. Brown, University of Michigan, Ann Arbor, Michigan 48109

Karl Grosh
Department of Mechanical Engineering and Applied Mechanics, 2350, Hayward Avenue, University of Michigan, Ann Arbor, Michigan 48109

Alfred L. Nuttall
Oregon Health Sciences University, 3181 SW Sam Jackson Park Road, Portland, Oregon 97201 and Kresge Hearing Research Institute, 1301 East Ann Street, Ann Arbor, Michigan 48109

(Received 16 November 1998; revised 1 July 1999; accepted 17 September 1999)

A hybrid analytical-numerical model using Galerkin approximation to variational equations has been developed for predicting global cochlear responses. The formulation provides a flexible framework capable of incorporating morphologically based mechanical models of the cochlear partition and realistic geometry. The framework is applied for a simplified model with an emphasis on application of hybrid methods for three-dimensional modeling. The resulting formulation is modular, where matrices representing fluid and cochlear partition are constructed independently. Computational cost is reduced using two methods, a modal–finite-element method and a boundary element–finite-element method. The first uses a cross-mode expansion of fluid pressure (2.5D model) and the second uses a waveguide Green's-function-based boundary element method (BEM). A novel wave number approach to the boundary element formulation for interior problem results in efficient computation of the finite-element matrix. For the two methods a convergence study is undertaken using a simplified passive structural model of cochlear partition. It is shown that basilar membrane velocity close to best place is influenced by fluid and structural discretization. Cochlear duct pressure fields are also shown demonstrating the 3D nature of pressure near best place. [S0001-4966(99)08012-1]

PACS numbers: 43.64.Kc, 43.64.Bt [RDF]

INTRODUCTION

Cochlear models are formulated as a fluid structure interaction problem where the various components of the cochlear partition interact with one another and with the fluid governed by physical balance laws. Many current models of the cochlea are based on a phenomenological approach designed to explain the mechanisms underlying certain measured cochlear responses. The basic approach in these models is to assume a simplified geometry and represent the cochlear partition by one-dimensional impedance. While these models have provided much insight into the working of the cochlea and also facilitated hypothesis propositions, the mechanisms relating to the interaction of fluid and the various structural components are often omitted. Given the complex nature of the cochlear partition and the geometry of the cochlea, there are two essential requirements in a model. First, a structural model of the cochlear partition which includes the structural details of the various components, such as their spatial orientation and connectivity is needed. A structural model requires details of the constitutive equations governing the different components. However, given the current uncertainty of information, it would be convenient if one could include these data in the model as they become available. Of course, the model variation should be achieved in a modular fashion without significant changes in the problem formulation and the solution techniques. The second requirement of the model is a three-dimensional representation of the fluid. The fluid effects are dependent on the geometry of the cochlea and could introduce significant computational costs. Hence effective solution strategies are required in a three-dimensional formulation. It should be noted that the level of structural and geometric complexity introduced into the model should be influenced by the purpose of the modeling effort. At the same time, the model should be flexible to accommodate more features and hence serve as an open framework.

The purpose of this paper is to present a computational framework using finite-element methodology (FEM). The generalized framework is flexible, and capable of incorporating realistic geometry and structural model of the cochlear partition.

In this paper a simplified model consisting of an unwrapped rectangular idealization of the cochlea and a passive linear model of the cochlear partition is studied using the general finite-element framework. The simplified model was primarily used to study discretization and convergence issues with an emphasis on the application of the hybrid methods to

[a)]Part of this material has been presented at the 135th meeting of ASA and the 21st meeting of ARO.

simplify the numerical computations involved for three-dimensional modeling. The converged results, it turns out, also yield interesting information for the response slightly apical to the best place, showing differences for 2D and 3D models. In the finite-element formulation, the matrices representing the fluid and the cochlear partition are independently constructed, thereby achieving the desired modularity. Hence, once the fluid matrices are formed, for example, one could use them for other representations of the structure and vice versa. The influence of micromechanical structures of the OoC are not included here. However, the fact that this model may be extended to directly include the complex structures of the OoC, including transient behavior, nonlinearities, and longitudinal coupling, is a great attraction of this framework. The computational cost, resulting from a three-dimensional representation of the fluid, is reduced through development of two hybrid techniques to represent the fluid effects. In one method, the fluid pressure is expanded in terms of the acoustic cross modes. The formulation in terms of modes makes the problem two dimensional and simplifies computations. The 3D pressure is obtained as the sum of the modal pressures. In the other method, a Green's function is used to eliminate the pressure equations based on a boundary element method. Only the structural element displacements are solved for, and this reduces the size of the matrices.

In the past, Kolston and Ashmore (Kolston and Ashmore, 1996) and Kagawa *et al.* (Kagawa *et al.*, 1987) have reported numerical cochlear models. Kagawa *et al.* develop a variational formulation similar to that in this paper. They do not, however, apply hybrid methods for the problem solution nor discuss convergence aspects, but rather focus on the geometric effects of coiling and changes in the cross section of the cochlea (our general framework also has the flexibility for handling such geometric studies). Kolston and Ashmore's study includes the different components of OoC in their true anatomical position relative to the rectangular geometric idealization. Also, their formulation includes the fluid velocity which is eliminated in our model (since there is no fluid viscosity), reducing the size of the formulation relative to theirs. However, their approximation of the differential equations is closer to a finite difference scheme than a finite-element technique. The finite-element method is more accurate when boundaries are more curved and the meshing irregular (Strang and Fix, 1973).

The organization of the paper is as follows. The general finite-element framework is first described. Next, a hybrid modal–finite-element solution and a hybrid boundary element–finite-element formulation for the fluid are developed for a rectangular idealization of the geometry of the cochlea. Finally, discretization and convergence issues are addressed, followed by discussion and future work.

I. FINITE-ELEMENT FRAMEWORK

In this section, the general finite-element framework is described. The formulation results in matrices representing the structural and fluid contributions along with their coupling. The development of the matrices makes a few assumptions on the geometry and the structural model of the cochlear partition. The cochlea is taken to be a dual-chambered, fluid-filled duct. The cochlear partition is loaded by the fluid, which is modeled as an incompressible liquid. [Fluid compressibility increases the time of travel of the traveling wave but does not have a significant influence on the characteristic frequency location of the wave (Lighthill, 1981).] Fluid viscosity is accounted for approximately through damping in the structural equations (Viergever and Kalker, 1974); other approaches are also possible (Chadwick *et al.*, 1996; Holmes and Cole, 1984; Steele, 1979). In the inviscid fluid approximation, at the fluid–structure interface (denoted by Γ), the structure's acceleration is related to fluid pressure gradient through Euler's relation and continuity conditions [Eq. (3)]. The coupled fluid–structure governing equations may be written symbolically as

$$\mathcal{L}_s\mathbf{u} = -\hat{\mathbf{n}}p|_\Gamma, \tag{1}$$

$$\nabla^2 p = 0, \tag{2}$$

$$\frac{\partial p}{\partial \mathbf{n}} = -\rho_f \hat{\mathbf{n}}\cdot\ddot{\mathbf{u}} \quad \text{on} \quad \Gamma. \tag{3}$$

Equation (1) is the structural equation and Eq. (2) is the Laplace's equation governing the fluid. Here $\mathbf{u}$ represents the displacement of the stapes or the components of the cochlear partition, p is the fluid pressure, and $\hat{\mathbf{n}}p|_\Gamma$ represents the fluid forcing of the structures. As just mentioned, Γ is the surface where fluid and structural components (e.g., the BM) are in contact, $\hat{\mathbf{n}}$ is the unit normal to fluid loaded surfaces, and ρ_f is the fluid density. The operator $\mathcal{L}_s$ acts on the displacement vector and symbolically represents the differential operator governing the response of the structural components.

A (Bubnov–)Galerkin finite-element formulation is obtained from the variational form of the governing equations (Hughes, 1987). The variational equations for a given structural model may be obtained via integration of the product of displacement and pressure weighting functions ($\overline{\mathbf{u}}$ and $\overline{p}$, respectively) with Eqs. (1) and (2), respectively (Hughes, 1987; Morse and Feshbach, 1953) over the fluid–structure domain. The variational equations are written symbolically as

$$a^s(\overline{\mathbf{u}},\mathbf{u}) = -(\overline{\mathbf{u}},\hat{\mathbf{n}}p)_\Gamma, \tag{4}$$

$$a^f(\overline{p},p) + (\hat{\mathbf{n}}\overline{p},-\rho_f\ddot{\mathbf{u}})_\Gamma = 0. \tag{5}$$

The fluid operator $a^f(\overline{p},p)$ is equal to $\int_\Omega \nabla\overline{p}\cdot\nabla p\, d\Omega$, where Ω is the entire fluid domain. The structural operator $a^s(\overline{\mathbf{u}},\mathbf{u})$ is equal to $\int_\Gamma \overline{\mathbf{u}}\mathcal{L}_s\mathbf{u}\, d\Gamma$. [The form of $a^s(\overline{\mathbf{u}},\mathbf{u})$ will depend on the structural model used]. The notation, $(\cdot,\cdot)_\Gamma$, denotes the inner product over Γ.

Obtaining the finite-element discretization using a Galerkin scheme involves the introduction of approximate solutions via the interpolation functions $N_A(\mathbf{x})$ (Fig. 1). The approximate displacement, u^h, and its weighting function, $\overline{u}^h$, are given by

$$u^h(\mathbf{x}) = \sum_{A=1}^{N} d_A N_A(\mathbf{x}), \quad \overline{u}^h(\mathbf{x}) = \sum_{B=1}^{N} c_B N_B(\mathbf{x}),$$

where A and B are the finite-element node numbers, d_A represents the approximate solution at a node of the finite-

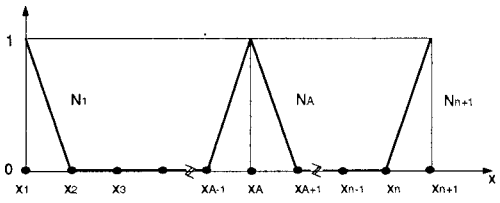

FIG. 1. One-dimensional interpolation function $N_A(x)$.

element interpolation, and c_B are the weighting function amplitudes.

The same interpolation functions are used for the solution and weighting functions, see, e.g., Hughes, 1987. The displacement d_A will depend on time or frequency (depending on whether we are studying time-dependent or time-harmonic solutions) as well as node number. Finite-element interpolation of the fluid pressure leads to a set of linear equations. Hence, the pressure may be eliminated from the discrete equations by: (1) analytic extraction before discretization by using either modal or Green's function methods (hybrid finite-element method); (2) substructuring of the finite-element equations resulting in the added mass effect of the fluid pressure. This will be influenced by Ω and the assumed boundary conditions.

The next step is to formulate the matrix equations. Obtaining the matrix elements would, however, require knowledge of the differential operator $\mathcal{L}_s$. A more detailed derivation of the matrix formulation is described for a simplified model in the next section. In general, if the structural model depends on acceleration, velocity, and displacement then the matrix equations, when fluid pressure is condensed out, will take the form,

$$\underbrace{\mathbf{K}^s\mathbf{d}(t)+\mathbf{C}^s\dot{\mathbf{d}}(t)+\mathbf{M}^s\ddot{\mathbf{d}}(t)}_{\text{structure}}+\underbrace{\mathbf{M}^{\text{fl}}\ddot{\mathbf{d}}(t)}_{\text{coupling}}=\mathbf{f}_T(t), \tag{6}$$

where the matrices above arise from the integration, $a^s(\bar{\mathbf{u}},\mathbf{u})$, over the element domains only (Hughes, 1987). The terms $\mathbf{K}^s$, $\mathbf{C}^s$, and $\mathbf{M}^s$ are the stiffness, damping, and mass matrices, respectively, representing the structure. $\mathbf{M}^{\text{fl}}$ represents the fluid pressure acting on the structure and $\mathbf{f}_T(t)$ is the forcing term that includes the effects of the stapes motion driving the system.

Computing the elements of $\mathbf{M}^{\text{fl}}$, as will be clear in the following section, will depend on the method used to eliminate the fluid pressure equations. In a simple substructuring of the finite-element equations, it consists of two components, a fluid stiffness matrix and a coupling matrix. The fluid stiffness matrix arises from the fluid operator, $a^f(\bar{p},p)$, and is determined by the shape of the fluid domain Ω. The coupling matrix elements are determined by the fluid–structure interaction surface Γ. (This is true even in the hybrid method using modes to expand fluid pressure prior to discretization.) Evaluation of the coupling elements, and in turn the modularity of the formulation, is hence influenced by the ''complexity'' of Γ. For example, the basilar membrane could be the only structure in contact with the fluid while the other components of the OoC influence the BM motion but do not interact with the fluid. In such a model, one can achieve significant modularity. In reality, however, the structures do interact with the fluid. Also, viscous effects could exist between the microstructures. The finite-element formulation can include these effects, although the modularity of the formulation and the associated computational simplifications may not be achievable. A second hybrid approach, that also results in the matrix equation, Eq. (6), uses a Green's function to represent the fluid pressure. The Green's function approach is especially useful when Γ is simple.

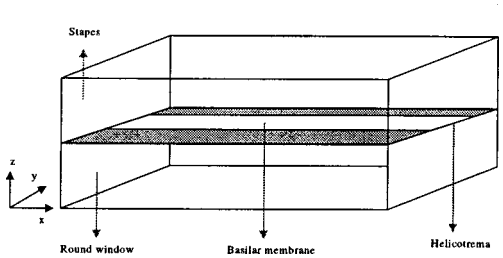

FIG. 2. Unwrapped, rectangular idealization of the cochlea.

II. SIMPLIFIED MODEL

A. Assumptions

As mentioned earlier, the fluid pressure equations are represented either by substructuring the finite-element matrix or by using modal/Green's function. This depends on the geometry of the cochlea. A rectangular geometry (Fig. 2), which has been extensively studied in the past by several authors (see, e.g., de Boer, 1981), is used here. Also fluid-structure interaction takes place only at the BM and stapes. Hence Γ has only two components, Γ_{BM} and Γ_{stapes}. Their motion is normal to the walls of the duct. Hence the pressure gradient normal to the wall is used to relate to the velocity of the structures. The walls of the ducts are modeled as rigid except at the basilar membrane surface and at the stapes. Only antisymmetric pressure is studied in this paper, therefore only one chamber is considered. (The formulation can be extended to study the total pressure by having two chambers, one each above and below the cochlear partition.)

In the simplified structural model, the microstructures are omitted and the cochlear partition is represented only by the BM. The BM is assumed to be a strongly orthotropic structure governed by

$$\mathcal{L}_s u(x,y)=EI(x)\frac{\partial^4 u(x,y)}{\partial y^4}+\rho A(x)\frac{\partial^2 u(x,y)}{\partial t^2}$$
$$=-2p(x,y,z=0), \tag{7}$$

where $u(x,y)$ is the BM displacement (x is the axial dimension and y is the cross cochlear direction), $EI(x)$ and $\rho A(x)$ are the spatially varying material properties of the BM, and $p(x,y,z=0)$ is the unsymmetric fluid pressure on the surface of the BM (see, e.g., Allen, 1977); symmetric pressure distributions do not excite the basilar membrane. The negative sign on the right side of Eq. (7) is because the positive direction for the displacement is toward the *scala vestibuli*, while a positive pressure forces the membrane away from the

scala vestibuli. The factor of 2 is for the upper and lower duct pressure contributions. A modal solution to the beam equations is introduced in the y direction and a piecewise linear finite-element interpolation is used in the x direction. Hence the BM deflection, u, is approximated by the function u^h,

$$u^h(x,y)=\sum_{j=1}^{n_{\text{modes}}}\sum_{A=1}^{n_{\text{nodes}}} d_{jA}\psi_j(y)N_A(x), \tag{8}$$

where n_{modes} is the number of cross modes used and n_{modes} is the number of finite-element nodes used down the length of the cochlea. $\psi_j(y)$ satisfies the boundary conditions for the beam. Simply supported mode shapes are used in this paper, hence $\psi_j(y)=\sin(j\pi y/\epsilon(x)b)$, where b is the width of the duct, and $\epsilon(x)$ is the fraction of the duct width occupied by the BM. Therefore, $u(x,y)=0$ for $|y|>\epsilon b/2$. The amplitude of the solution is d_{jA}. Given this approximation, the relation between the fluid pressure and the structural displacement is found by substituting Eq. (8) into Eq. (7), multiplying the equations by the structural mode shape, and integrating across the width

$$\sum_{j=1}^{n_{\text{modes}}}\sum_{A=1}^{n_{\text{nodes}}}\frac{1}{A(x)}(\omega_j^2(1-i\eta)-\rho A(x)\omega^2)\frac{1}{2}d_{jA}\alpha_j N_A(x) = -\int_{-\epsilon b/2}^{\epsilon b/2}\psi_j(y)p(x,y)dy, \tag{9}$$

where ω_j is the x-dependent resonance frequency of the basilar membrane for a particular mode, η is the damping factor, and $\alpha_j=\int_{-\epsilon b/2}^{\epsilon b/2}\psi_j^2(y)dy$.

The introduction of a single cross-mode model, $n_{\text{modes}}=1$, simplifies Eq. (9) and renders this formulation equivalent to an x-dependent impedance model for the basilar membrane and its attached structures. The impedance, $Z(x)$, has the expression (de Boer, 1981),

$$Z(x)=i\omega m_0+\frac{c_0}{i\omega}e^{-\alpha x}+\delta(m_0c_0)^{1/2}e^{-0.5\alpha x}, \tag{10}$$

where m_0 is the mass constant, c_0 the stiffness constant, α the rate constant, and δ the damping factor. The values of the parameters used are: $m_0=0.05$, $c_0=10^9$, $\alpha=3.0$, $\delta=0.05$ (all in cgs units). Other parameters of the cochlea are: $L=5.0$, $h=0.1$, $b=0.1$ (cgs units) and $\epsilon=0.1$, a constant. The use of piecewise linear shape functions, $N_A(x)$ (Fig. 1), results in banded $\mathbf{K}^s$, $\mathbf{C}^s$, and $\mathbf{M}^s$ matrices and hence save storage and computational cost. The (A,B)th element of the stiffness matrix, K^s, is given by

$$[K^s]_{AB}=\int_{\Gamma_{\text{BM}}}c_0e^{-\alpha x}N_AN_Bd\Gamma_{\text{BM}}. \tag{11}$$

Similar expressions can be obtained for the damping and mass matrix. For this simplified structural model we develop a modal–finite-element solution and a boundary element–finite-element formulation of the fluid. The two techniques and their advantages are discussed below.

B. 2.5D model

For the rectangular geometry, the cross modes of the duct satisfying rigid wall conditions are cosine functions and these mode shapes may be used in the variational equations (before approximate discretization) to reduce the dimensionality of the discretization by decomposing the solution in terms of the duct cross mode number, m. Therefore, only a 2D mesh is needed for a three-dimensional solution, and hence the name ''2.5D model.'' The fluid pressure is expanded in a modal sum,

$$p(x,y,z)=\sum_{m=0}^{M}p_m(x,z)\phi_m(y), \tag{12}$$

where the modes $\phi_m(y)=\cos(2m\pi y/b)$ satisfy the rigid boundary conditions at the walls.

The strong form of the reduced model in terms of the modal pressure amplitudes, p_m, is given by

$$\left(\frac{\partial^2}{\partial x^2}+\frac{\partial^2}{\partial z^2}\right)p_m-\beta_m^2p_m=0, \tag{13}$$

$$\frac{\partial p_m}{\partial \mathbf{n}}=-\rho_f\chi_m \quad \text{on} \quad \Gamma, \tag{14}$$

where $\beta_m^2=(2m\pi/b)^2$ is the modal wave number in the y direction. χ_m depends on fluid-structure coupling, and is given by

$$\chi_m=\frac{\int_{-b/2}^{b/2}\phi_m(y)\hat{\mathbf{n}}_{0,1,1}\cdot\ddot{\mathbf{u}}_{\text{stapes}}(0,y,z)dy}{\int_{-b/2}^{b/2}\phi_m^2(y)dy} \quad \text{at stapes,} \tag{15}$$

$$\chi_m=\frac{\int_{-b/2}^{b/2}\phi_m(y)\hat{\mathbf{n}}_{1,1,0}\cdot\ddot{\mathbf{u}}_{\text{BM}}(x,y,0)dy}{\int_{-b/2}^{b/2}\phi_m^2(y)dy} \quad \text{at BM.} \tag{16}$$

The fluid domain, Ω_{2d}, is now two dimensional. $\mathbf{n}_{0,1,1}$ and $\mathbf{n}_{1,1,0}$ are normals in the corresponding directions. The modal pressure variational equation is given by

$$a^f(\overline{p}_m,p_m)+(\overline{p}_m\hat{\mathbf{n}},-\rho_f\ddot{\mathbf{u}})_\Gamma=0. \tag{17}$$

Galerkin formulation results in discrete equations,

$$\sum_D[K_m^f]_{CD}p_{mD}+\rho_f\sum_A[Q_m]_{AC}d_A=f_C \quad \forall \text{C}, \tag{18}$$

where,

$$[K_m^f]_{CD}=\int_{\Omega_{2d}}(\nabla N_C.\nabla N_D+\beta_m^2N_CN_D)d\Omega_{2d}. \tag{19}$$

$N_C(x,z)$ is the bilinear shape function used to interpolate the pressure. The fluid-structure coupling matrix, $\mathbf{Q}_m$, couples the acoustic cross y modes to the BM displacement $\mathbf{u}$ and arises from the coupling terms in the variational equation, Eq. (17).

$$[Q_m]_{AC}=\int_{\Gamma_{\text{BM}}}\chi_mN_A(x)N_C(x,0)d\Gamma_{\text{BM}}. \tag{20}$$

For steady-state dynamics, the matrix equations of the 2.5D model will then have the form

$$\begin{bmatrix} \mathbf{K}_0^f/\rho_f\omega^2 & 0 & \cdots & 0 & \mathbf{Q}_0^T \\ 0 & \mathbf{K}_1^f/\rho_f\omega^2 & \cdots & 0 & \mathbf{Q}_1^T \\ 0 & 0 & \ddots & 0 & \vdots \\ 0 & 0 & \cdots & \mathbf{K}_M^f/\rho_f\omega^2 & \mathbf{Q}_M^T \\ \mathbf{Q}_0 & \mathbf{Q}_1 & \ddots & \mathbf{Q}_M & \mathbf{K}^s+i\omega\mathbf{C}^s-\omega^2\mathbf{M}^s \end{bmatrix} \begin{pmatrix} \mathbf{p}_0 \\ \mathbf{p}_1 \\ \vdots \\ \mathbf{p}_M \\ \mathbf{d} \end{pmatrix} = \begin{pmatrix} \mathbf{f}_0 \\ \mathbf{f}_1 \\ \vdots \\ \mathbf{f}_M \\ 0 \end{pmatrix}. \tag{21}$$

The modal forcing terms $\mathbf{f}_i$ are determined by the stapes displacement y distribution. In the simplified model, the stapes is assumed to occupy a uniform fraction of the duct height, with uniform displacement. Hence, only the zeroth mode is excited and only $\mathbf{f}_0$ is nonzero. The inclusion of the complex microstructures of the OoC in this model will lead to a change in $\mathbf{K}^s+i\omega\mathbf{C}^s-\omega^2\mathbf{M}^s$ and $\mathbf{Q}_m$ only, while the rest of the matrix elements remain unchanged. In the above formulation, if fluid pressure distributions are not desired, then it is possible to condense out the fluid pressure. The basilar membrane displacement response is then obtained from the following equations:

$$[\underbrace{\mathbf{K}^s+i\omega\mathbf{C}^s-\omega^2\mathbf{M}^s}_{\text{structure}}\underbrace{-\omega^2\mathbf{M}^{\text{fl}}}_{\text{coupling}}]\mathbf{d}=\mathbf{f}_T, \tag{22}$$

where $\mathbf{M}^{\text{fl}}$ is the fluid pressure acting on the surface of the basilar membrane (''added mass'') given by

$$\mathbf{M}^{\text{fl}}=\frac{1}{\rho_f}\sum_{m=1}^{M}\mathbf{Q}_m^T[\mathbf{K}_m^f]^{-1}\mathbf{Q}_m \tag{23}$$

and

$$\mathbf{f}_T=\frac{1}{\rho_f}\sum_{m=1}^{M}\mathbf{Q}_m^T[\mathbf{K}_m^f]^{-1}\mathbf{f}_m. \tag{24}$$

The piecewise linear shape functions, $N_C(\mathbf{x})$, result in a banded $\mathbf{K}_m^f$ matrix. Bandwidth is determined by the node numbers of adjacent elements (Hughes, 1987). The node numbering in the fluid and structural mesh is done is such a way that the bandwidth of $\mathbf{K}_m^f$ matrices are minimal. For a $\mathbf{N}\times\mathbf{M}$ $x-z$ discretization, node numbering along x results in half-bandwidth of $(N+1)m+1$ and numbering along z results in half-bandwidth of $(M+1)m+1$. Here m is the number of fluid modes. Since $N\gg M$, node numbering was usually done along the z direction.

C. Hybrid boundary element/finite-element solution

For a rectangular cross section (i.e., no variation in width and height), the following boundary conditions are specified:

$$\left.\frac{\partial p}{\partial \mathbf{n}}\right|_{y=\pm b/2,z=h}=0, \tag{25}$$

$$\frac{\partial p}{\partial \mathbf{n}}=-\rho_f\hat{\mathbf{n}}\cdot\ddot{\mathbf{u}} \quad \text{on} \quad \Gamma, \tag{26}$$

$$p(x=L)=0. \tag{27}$$

Note that Eq. (27) is valid for the antisymmetric pressure field studied here because the antisymmetric pressure field should be zero at the helicotrema. A special Green's function, $G(x,\xi)$, is sought, satisfying the following boundary value problem,

$$\nabla^2 G(\mathbf{x},\boldsymbol{\xi})=-4\pi\delta(x-\xi)\delta(y-\eta)\delta(z-\zeta), \tag{28}$$

$$\left.\frac{\partial G}{\partial n}\right|_{x=0,y=\pm b/2,z=0,h}=0, \tag{29}$$

$$G(x=L)=0, \tag{30}$$

where δ is the Dirac delta function. Here, $\mathbf{x}=(x,y,z)$ and $\xi=(\xi,\eta,\zeta)$ refer to the observer and source locations, respectively, in Cartesian coordinates. The boundary integral equation relating surface pressure to surface normal displacement is obtained by multiplying Eq. (28) by pressure and Eq. (2) by the Green's function, subtracting the result and integrating over the fluid domain. After applying the divergence theorem, the selection of the boundary conditions for the Green's function, Eqs. (29) and (30), and for the pressure solution, Eqs. (25) and (27), results in a cancellation of many of the terms usually present in the boundary integral formulation (Junger and Feit, 1986). The integral relation between the pressure p at $\mathbf{x}$ and the normal surface displacement, u, arising from these manipulations is

$$p(\mathbf{x})=-\rho_f\omega^2\int_\Gamma G(\mathbf{x},\boldsymbol{\xi})u(\boldsymbol{\xi})d\Gamma(\boldsymbol{\xi}) \quad \text{for} \quad \mathbf{x}\in\Gamma. \tag{31}$$

The Green's function is written as a sum of the duct cross modes. The rigid boundary conditions in the cross section result in modes $\phi_{mn}(y,z)=\cos(2m\pi y/b)\cos(n\pi z/h)$, where h is the height of the duct, and m and n are the mode numbers in the y and z directions, respectively. Hence the Green's function is given by

$$G(\mathbf{x},\xi)=\sum_{m,n}\phi_{mn}(y,z)g_{mn}(x,\boldsymbol{\xi}), \tag{32}$$

where $g_{mn}(x,\xi)$ satisfies the boundary value problem,

$$\frac{\partial^2 g_{mn}(x,\boldsymbol{\xi})}{\partial x^2}-\gamma_{mn}^2 g_{mn}(x,\boldsymbol{\xi})=\frac{-4\pi\phi_{mn}(\eta,\zeta)}{\alpha_{mn}}\delta(x-\xi), \tag{33}$$

$$\left.\frac{\partial g_{mn}}{\partial n}\right|_{x=0}=0, \tag{34}$$

$$g_{mn}(x=L)=0. \tag{35}$$

Here, $\gamma_{mn}^2=(2m\pi/b)^2+(n\pi/h)^2$ and $\alpha_{mn}=\int_{-b/2}^{b/2}\int_0^h \phi_{mn}^2(y,z)dydz$. For the $m=n=0$ case, g_{00} is easily found to be

$$g_{00}(x,\boldsymbol{\xi})=\frac{4\pi\phi_{00}(\eta,\zeta)}{\alpha_{00}}\left[L-\frac{|x-\xi|+|x+\xi|}{2}\right]. \tag{36}$$

One could also solve for the higher-order contributions in closed form. Instead, using the method of images, a novel wave number formulation of the boundary element formulation is developed. This results in an efficient method for computation of the fluid ''added mass'' matrix elements as shown below.

The governing equation for $g_{mn}(x,\boldsymbol{\xi})$ with image sources is

$$\frac{\partial^2 g_{mn}(x,\boldsymbol{\xi})}{\partial x^2}-\gamma_{mn}^2 g_{mn}(x,\boldsymbol{\xi}) = \frac{-4\pi\phi_{mn}(\eta,\zeta)}{\alpha_{mn}}\sum_p (-1)^p[\delta(x-(2pL+\xi)) + \delta(x-(2pL-\xi))], \tag{37}$$

where p is the number of image sources chosen to match the boundary conditions. For a source at $\boldsymbol{\xi}=(\xi,\eta,\zeta)$, a positive image source exists at $\boldsymbol{\xi}=(-\xi,\eta,\zeta)$, and this source pair repeats periodically at intervals of $4L$. These positive images are required to satisfy the rigid boundary condition imposed at the base. Negative images source pairs occur at $\boldsymbol{\xi}=(2L\pm\xi,\eta,\zeta)$ and also repeat periodically at intervals of $4L$. These negative images are needed to satisfy the pressure release boundary condition at the apex. Solving Eq. (37) using Fourier transform, $\mathcal{F}(x,k_x)$, results in

$$g_{mn}(x,\boldsymbol{\xi})=\frac{\phi_{mn}(\eta,\zeta)}{\alpha_{mn}}\sum_p (-1)^p \times\int_{-\infty}^{\infty}\frac{e^{ik_x(2pL+\xi-x)}+e^{ik_x(2pL+\xi-x)}}{k_x^2+\gamma_{mn}^2}dk_x. \tag{38}$$

The x dependence of the Green's function is left in wave number space, k_x, in anticipation of substitution into the variational equations.

In the variational formulation [Eq. (4)], the coupling of the fluid pressure to the structural response is embodied by the integral of the pressure times the displacement weighting function,

$$(\overline{\mathbf{u}},\hat{\mathbf{n}}p)_{\Gamma_{\mathrm{BM}}}=\int_{\Gamma_{\mathrm{BM}_{\mathbf{x}}}}\overline{u}(\mathbf{x})\int_{\Gamma_{\mathrm{BM}_{\boldsymbol{\xi}}}}G(\mathbf{x},\boldsymbol{\xi})u(\boldsymbol{\xi})d\Gamma_{\mathrm{BM}_{\mathbf{x}}}d\Gamma_{\mathrm{BM}_{\boldsymbol{\xi}}}. \tag{39}$$

The stapes force is propagated through

$$(\overline{\mathbf{u}},\hat{\mathbf{n}}p)_{\Gamma_{\mathrm{STP}}}=\int_{\Gamma_{\mathrm{STP}_{\mathbf{x}}}}\overline{u}(\mathbf{x})\int_{\Gamma_{\mathrm{STP}_{\boldsymbol{\xi}}}}G(\mathbf{x},\boldsymbol{\xi}) \times u(\boldsymbol{\xi})d\Gamma_{\mathrm{STP}_{\mathbf{x}}}d\Gamma_{\mathrm{STP}_{\boldsymbol{\xi}}}. \tag{40}$$

Substituting the finite-element interpolation of the nodal displacement, u^h, and the weighting function, $\overline{u}^h$, into the boundary integral equations [Eqs. (39) and (40)] eliminates the pressure from the structural equations [Eq. (4)]. The elements of the fluid ''added mass'' matrix, $\mathbf{M}^{\mathrm{fl}}$, are now given by, $\Sigma_{m,n}(4\rho\omega^2/2\pi\alpha_{mn})\Sigma_p(-1)^p M^{\mathrm{fl}}_{m,n,p}$, where

$$M^{\mathrm{fl}}_{m,n,p}=\int_{-\infty}^{\infty}\int_x\int_{\xi}\frac{e^{ik_x(2pL+\xi-x)}+e^{-ik_x(2pL-\xi-x)}}{k_x^2+\gamma_{mn}^2} \times N_B(\xi)N_A(x)d\xi dx dk_x. \tag{41}$$

In this equation, A is the measurement location and B is the source location. For a uniform discretization and using piecewise linear interpolation functions, the above expression simplifies to a convolution,

$$M^{\mathrm{fl}}_{m,n,p}=\underbrace{[\Theta(x)\oplus\Lambda_{mn}(x)]_{x=((A-B)\Delta-2pL)}}_{M^{\mathrm{fl1}}_{m,n,p}} +\underbrace{[\Theta(x)\oplus\Lambda_{mn}(x)]_{x=((A+B)\Delta-2pL)}}_{M^{\mathrm{fl2}}_{m,n,p}}, \tag{42}$$

where $\oplus$ refers to convolution, Δ is the internodal distance, and

$$\Theta(x)=\mathcal{F}^{-1}\left[\frac{\sin\frac{k_x}{2}}{\frac{k_x}{2}}\right]^4, \tag{43}$$

$$\Lambda_{mn}(x)=\mathcal{F}^{-1}\left[\frac{1}{k_x^2+\gamma_m^2}\right]. \tag{44}$$

$\Theta(x)$ is hence the convolution of two triangles (the interpolation functions $N_A(x)$ and $N_B(\xi)$ used in our formulation refer to Fig. 1) and has compact support. $\Lambda_{mn}(x)$ is a symmetric function and represents the x dependence of the modal Green's function $g_{mn}(x)$ (up to a constant factor). $(A-B)\Delta-2pL$ and $(A+B)\Delta-2pL$ refer to the points where the convolution is evaluated without further computation. Hence, once the convolution integral is evaluated for a given m,n, and p and for an arbitrary shift of $\Lambda_{mn}(x)$, then the elements $M^{\mathrm{fl1}}_{m,n,p}$ and $M^{\mathrm{fl2}}_{m,n,p}$ can be evaluated directly. Special consideration of end nodes is needed for which $\Theta(x)$ changes, since either one or both of $N_A(x)$ and $N_B(\xi)$ could be half triangles (Fig. 1).

In the BEM formulation, although the fluid mesh is removed, matrix sparseness cannot be achieved. But $\mathbf{M}^{\mathrm{fl1}}$ and $\mathbf{M}^{\mathrm{fl2}}$ exhibit ''neat'' properties. $\mathbf{M}^{\mathrm{fl1}}$ is a Toeplitz symmetric matrix, and hence only the first-row elements are determined. $\mathbf{M}^{\mathrm{fl2}}$ is a Hankel matrix and hence the first row and the last column are evaluated. The end elements, however, do not follow this relation and are treated separately. A look-up table consisting of convolution integrals for different $\Theta(x)$ was generated for rapid evaluation of the matrix elements.

Formulation of the Green's function in the wave number space [Eq. (38)] leads to the convolution integral in Eq. (42). Closed form solutions for g_{mn}, instead, would require performing the double integral,

$$\int_x \int_\xi g_{mn}(x,\xi) N_B(\xi) N_A(x) d\xi dx,$$

for each measurement location, A, for a given source at B. This matrix does not have the Toeplitz or Hankel matrix properties. Hence for an N point discretization (excluding the end points), this would require calculating $N(N+1)/2$ elements. Using the method of images, on the other hand, requires estimating only $3N$ elements (N for the Toeplitz matrix and $2N$ for the Hankel matrix). As mentioned above, the convolution integral can be performed once, and the matrix elements determined by evaluating the integral at different points as given in Eq. (42). This also obviates the need to keep track of the shape function support (i.e., the domain where the shape functions are nonzero).

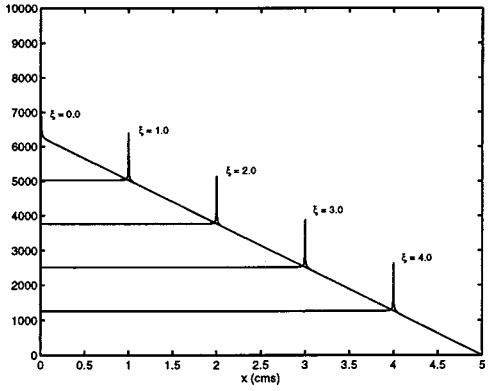

FIG. 3. Green's function for the rectangular model, measured at $\mathbf{x}=[x,0,0]$ for sources located at $\xi=[\xi,0,0]$. In this figure, 6 y modes, 60 z modes, and 20 images were used.

III. DISCRETIZATION AND CONVERGENCE

A. Fluid–structure coupling

The fluid discretization, apart from depending on the geometry, is directly influenced by the structural model. The number of y modes is determined by the structural vibration pattern along y. Similarly, the x and z discretization is determined by the properties of the traveling wave, which is again dependent on the structural model.

B. Fluid discretization

The number of nodes and modes required for determining the numerical results were determined based on a convergence study increasing the nodes and the cross modes. Preliminary results obtained using a uniform discretization of the 2.5D formulation predicted rapid changes in response only close to the BM resonance location (as predicted by previous modelers, e.g., de Boer (de Boer, 1981)). Hence an equispaced $x-z$ discretization is not required. A nonuniform discretization was used in such a way that close to the BM resonance location, where the wave number of the traveling wave is very high, the x discretization was very dense. Also, in the z direction the discretization close to the BM was very fine, as the wave decays away from BM requiring such refinement. For the assumed structural model, the internodal distance along the x direction was changed from 0.001 cm close to the resonance location to 0.1 cm near the stapes and apex. Along the z direction, mesh density was changed from 1000 nodes per cm near the BM to 40 nodes per cm close to the wall. The resulting $x-z$ discretization had a size of 269×21. Nonuniform meshing significantly reduces the computational cost by reducing the number of unknowns. However, a disadvantage is the need for a priori information about the wave number and the resonance location, and the mesh has to be tailor-made for each frequency of excitation. Another disadvantage is the high aspect ratio for some of the elements, although comparison of results from uniform mesh indicate mismatch only close to the best place. In general, a nonuniform mesh could be used to obtain preliminary results. For a given $x-z$ discretization, the number of y modes required was determined by the shape of BM deflection. For a single structural mode expansion of the BM deflection, 20 acoustic cross modes were found to be sufficient for convergence.

In the BEM formulation, the Green's function is influenced by the number of y and z modes used. Figure 3 shows the Green's function for different source locations along the duct. Except for very near the source, the function exhibits a linear behavior. The function is singular at the location of the source. The peak at the singularity depends on the number of y and z modes and the number of image sources used. In Fig. 4 the dependence on number of z modes is shown. It can be seen that for a given number of y modes, increasing the z modes gives a better approximation of the singularity. Similarly, an increase in y modes leads to a better approximation.

For results using BEM, a sufficiently large number of z modes were required. This was essential since the z modes were cosine functions, while the fluid pressure exhibits an exponential decay in the z direction, requiring many such modes to perform the expansion. BEM computations in this paper were done using 300 z modes and 20 y modes. Increasing the number of Green's function modes increases only the setup cost of computing the added mass matrix and not of the solution of the resulting matrix equations (which have only BM displacement as the unknown). For a uniform x discreti-

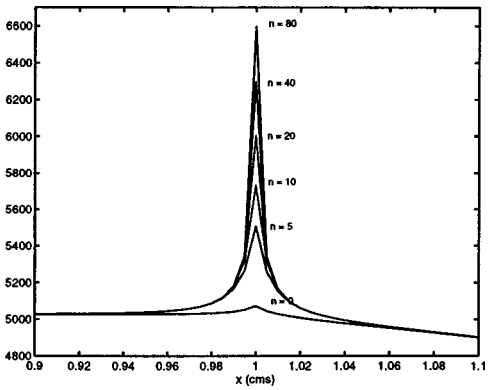

FIG. 4. Influence of z modes on the Green's function. Increasing the number of z modes (denoted by n) leads to a better approximation of the singularity. Increasing the number of y modes also has the same effect. Six y modes were used in this figure.

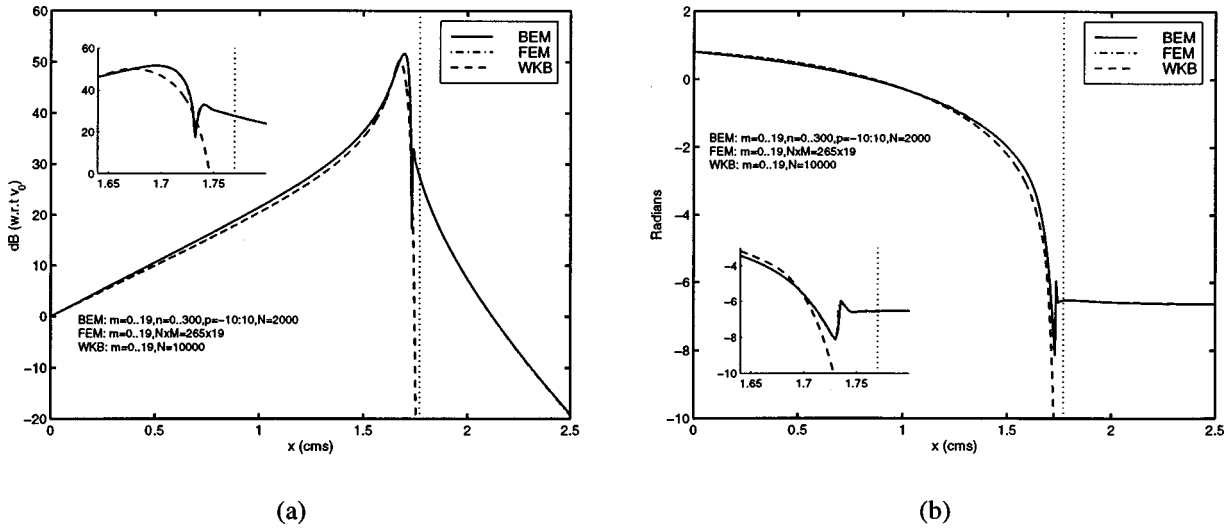

FIG. 5. (a) BM velocity amplitude versus distance. A comparison of finite-element and WKB solutions (Grosh *et al.*, 1998). (b) Phase versus distance. The geometry is the ''box'' model of the cochlea using de Boer's parameters (de Boer, 1981). Excitation frequency $f=1.6$ kHz. The dotted line is the location of the BM resonance location. The inset boxes in (a) and (b) are an enlargement of the corresponding responses near the resonance location. FEM and BEM solutions are indistinguishable.

zation, 2000 nodes were used in the x direction to accurately resolve the response near the resonance location.

C. Velocity and pressure convergence

BM velocity response obtained using the 2.5D and BEM formulations were compared to an asymptotic solution obtained using Wentzel–Kramers–Brillouin (WKB) theory (Steele and Taber, 1979; de Boer and Viergever, 1982). These are shown in Fig. 5. In the figure (and in the subsequent figures), FEM refers to the 2.5D simulation and BEM to the boundary element simulation.

In Fig. 6, the influence of meshing on the BM velocity response is shown in a close-up region around the best place.

It can be seen that, for a given number of y modes, the response close to the peak is sensitive to both the x discretization and the z discretization or modes. The response peak shifts basally with finer z discretization in the 2.5D model and with increasing z modes in the BEM. The basal shift also occurs with increasing y modes. This corroborates the fact that BM velocity response in a 3D model of the cochlea has a more basal peak than the corresponding one- and two-dimensional models (de Boer, 1981). In the figure it is also seen that increasing the z discretization or modes, keeping the x discretization fixed, deepens the post-peak notch. However, if the x discretization is also increased then the depth of the notch is less.

In Fig. 5 it is seen that the WKB solution provides a

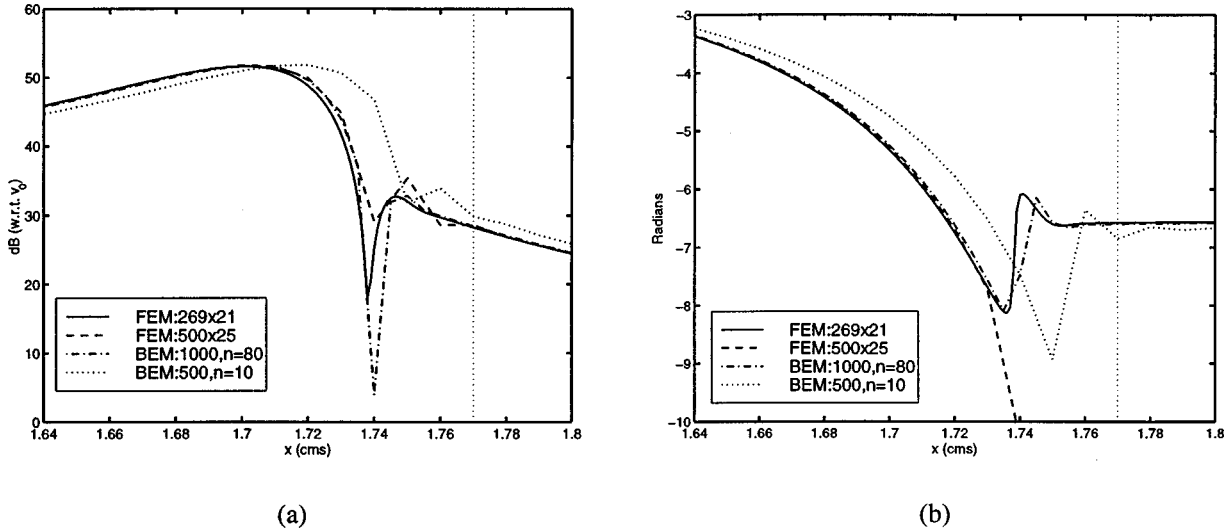

FIG. 6. ''Zoom in'' of (a) BM velocity and (b) phase response around the BM resonance location (dotted line) to study the influence of meshing in the 2.5D model. Two results are shown for the 2.5D simulation, one using the 269×21 adaptive mesh and the other using a much coarser 500×25 mesh. For the BEM, a fine 1000 x nodes and 80 z nodes discretization and a coarse 500 x nodes and 10 z nodes discretization, are shown. 20 y modes were used in all these simulations. Excitation frequency $f=1.6$ kHz.

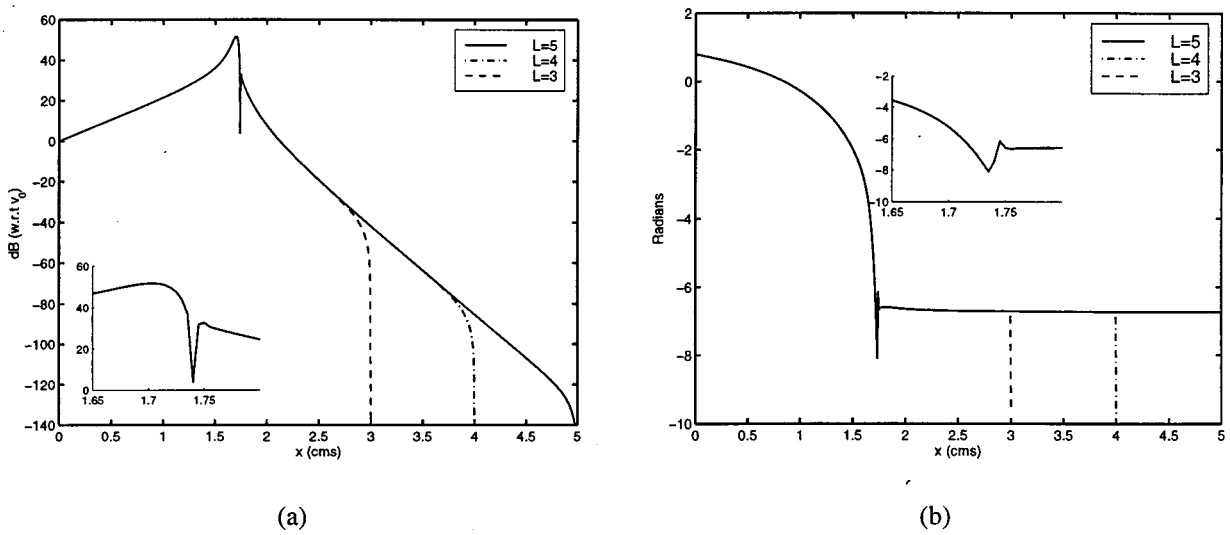

FIG. 7. Influence of apex position on finite-element solution (a) BM velocity amplitude and (b) phase. The intermodal width for all three cases is 0.005. The inset boxes in (a) and (b) are an enlargement of the corresponding responses near the resonance location and are unaffected by the length change. Excitation frequency $f = 1.6$ kHz.

good approximation to the response, except that it peaks earlier and predicts a faster post-peak response decay. In Fig. 7 the length of the cochlea is artificially reduced to determine if any artificial numerical end effects (due to numerical contamination resulting from approximating the boundary condition at the apex) were influencing the response decay predicted by the numerical method. Dramatic changes in the length do not alter the important features around the response peak. A possible explanation for the discrepancy between the WKB and numerical results is discussed by Parthasarathi *et al.* (Parthasarathi *et al.*, 1998) and Watts (Watts, 1993).

The post-peak notch has been reported in 2D cochlear simulations also (Neely, 1981). In Fig. 8, the influence of meshing on the notch in 2D model is shown. The response was obtained using only the first acoustical cross *y* mode (hence 2D) and using Neely's parameters. If 250 points were used along the *x* direction (Neely assumed a cochlear length of 3.5 cm and used 70 points per cm), a notch is seen in the response close to the BM resonance location. However, the post-peak notch disappears with a finer mesh in the 2D model. As will be seen in the pressure plots, the notch in the 3D model is increasingly predominant in higher-order fluid pressure modes. Higher-order modes decay rapidly in the *z* direction and exist only close to the BM. Also, they have a much smaller wavelength (along the *x* direction). As such, they require a finer mesh. Hence, the notch seen in the 3D model is a function of how effectively these modes are discretized using fine meshing in the *x* and the *z* direction.

The antisymmetric pressure field is shown in Fig. 9. Close to the stapes the pressure varies very slowly with *z* (confirming a long wave behavior). While the stapes occupies only a fraction of the height (assumed between $z = 0.01$ to $z = 0.04$), the incompressibility of the fluid rapidly flattens the pressure distribution along *z*. Close to the re-

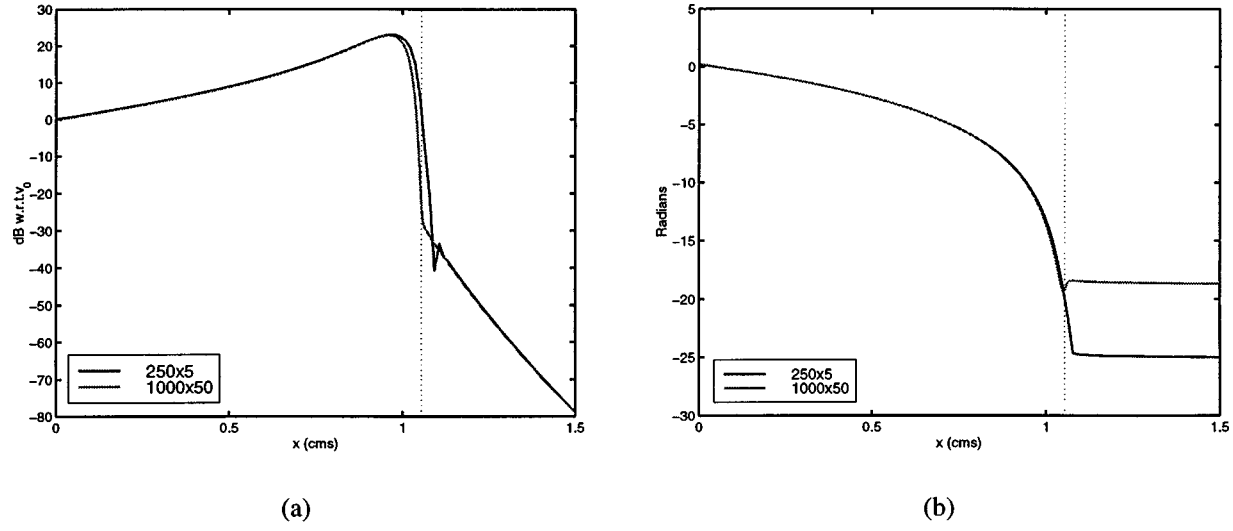

FIG. 8. Influence of meshing in the 2D model using Neely's parameters (Neely, 1981). The dotted line is the location of the BM resonance location. Excitation frequency $f = 4.53$ kHz.

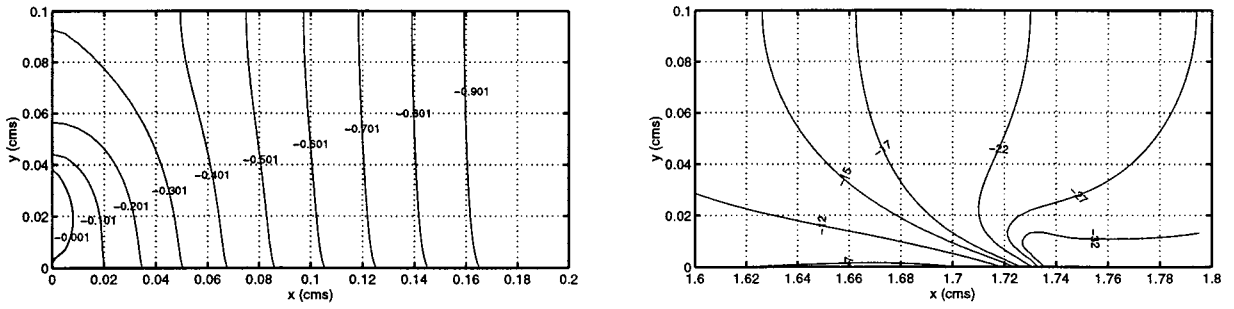

(a) (b)

FIG. 9. Midline pressure (a) close to stapes and (b) close to response peak. The contours are plotted at the indicated dB levels, calculated using the pressure at $x=y=z=0$ as reference. Excitation frequency $f=1.6$ kHz.

sponse peak, the pressure sharply decays away from the BM (confirming a short wave behavior). This is due to the low impedance of the BM and the conversion of the propagating structural acoustic wave to a evanescent wave.

In Fig. 10 the contribution of each cross mode to the total midline pressure is plotted, normalized by the total pressure amplitude at the stapes. A striking feature of the amplitude plot is that, as the wave moves away from the stapes, the higher-order modes become increasingly dominant. Also, as mentioned earlier, the post-peak notch is more prominent in the higher-order modes. Close to the upper wall of the duct, modal decomposition reveals that the zeroth mode is dominant throughout.

Across the duct, the pressure distribution in the y direction does not remain constant (Fig. 11). For small values of z, the pressure distribution is influenced by the structural mode shapes, while farther away the distribution becomes uniform. In Fig. 11, it is seen that a large number of cross modes are required to capture the pressure variation across the duct close to the resonance location. Close to the stapes, however, the pressure varies only minimally across the duct. The pressure variation predicted in the $y-z$ direction validates the need for a 3D formulation, especially close to the response peak, rather than the more traditional 2D formulation which assumes constant pressure distribution across the duct.

D. Computing time

2.5D simulations were performed using FORTRAN77. For 6 y modes and a 1000×50 uniform $x-z$ discretization, matrix setup for calculating the BM displacement and the fluid pressure distribution using Sun ultra-10 (300 MHz, 128-MB RAM, and 2-GB virtual memory) took 15 hours. Solving the matrix for one excitation frequency took an additional 7 hours. Using a 269×21 adaptive mesh (and using 20 y modes) the above timings were 3 and 2 hours, respectively.

BEM simulations were performed in MATLAB. For calculating the BM displacement only, setting up the matrices for a 2000 x node, 20 y mode, 300 z mode, and 20-image formulation took 7 hours on the same machine. Solving the

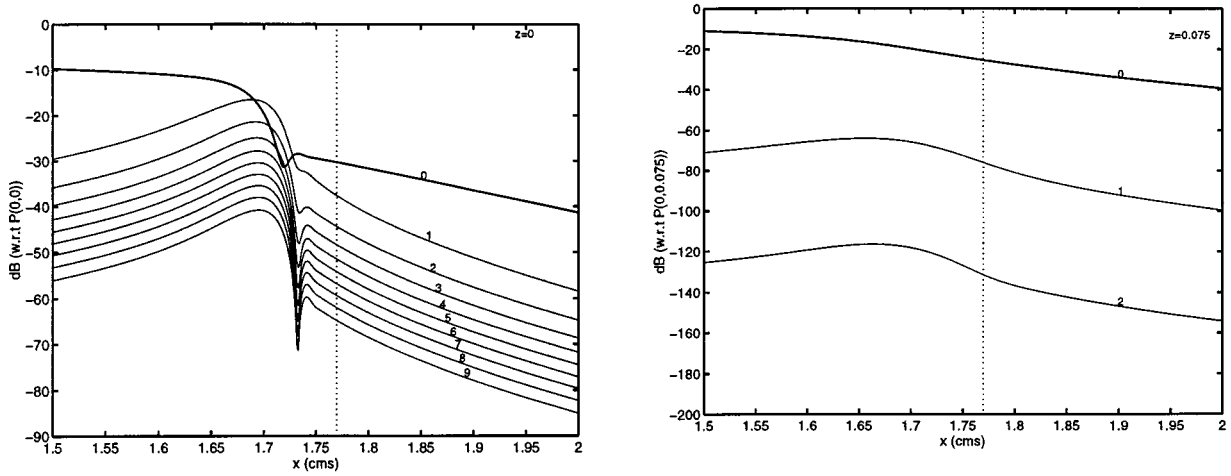

(a) (b)

FIG. 10. Modal decomposition of pressure versus x (a) on the BM surface at $z=0$ cm and (b) slightly off the BM surface at $z=0.075$ cm. The corresponding total pressure at the base is used to normalize the response.

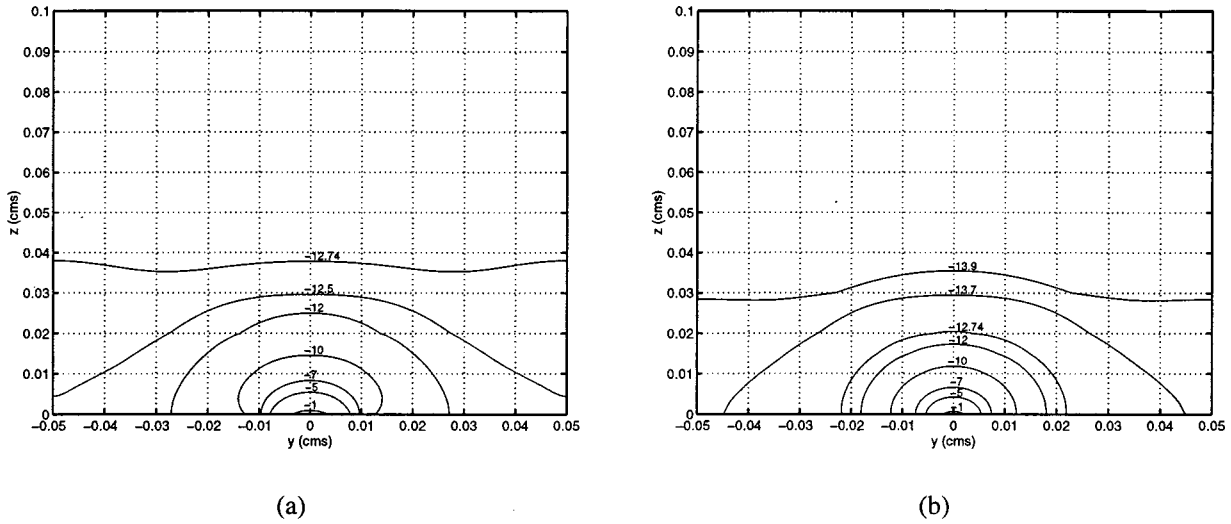

FIG. 11. Pressure in cross section at $x=1.69$ cm using (a) six cross y modes and (b) 20 y modes. The BM resonance location is $x=1.77$ cm. The contours are plotted at the indicated dB levels, obtained using pressure at $x=1.69$ cm and $y=z=0$ as reference. Excitation frequency $f=1.6$ kHz.

matrix problem took an additional 30 min for each excitation frequency.

IV. DISCUSSION AND FUTURE WORK

In this paper, a general variational framework for cochlear mechanics is developed and then specialized to a simplified cochlear model. Hybrid modal–finite-element (2.5D model) and boundary element methods are developed with specific advantages and flexibilities. For example, the 2.5D model allows for easy variations of the duct height and boundary conditions. The BEM does not have such ''easy'' variation, but does analytically extract the fluid pressure from direct computation, thereby reducing the degrees of freedom computed. Definitive convergence studies are performed on an impedance representation of the BM for a uniform duct. These results show the three dimensionality of the pressure field and the differences between 2D and 3D models.

Several models of the cochlea have been proposed in the past. Neely and Kim (Neely and Kim, 1986; Neely, 1993) and Geisler (Geisler, 1991) have proposed models using limited fluid models, representing the fluid in one dimension only. A model using Green's function to represent two-dimensional fluid effects was proposed by Allen (Allen and Sondhi, 1979; Allen and Neely, 1992), while Mammano and Nobili (Mammano and Nobili, 1993; Nobili and Mammano, 1996) use a Green's function formulation for a three-dimensional model. In de Boer's (de Boer, 1984; de Boer, 1991) model the three-dimensional effects are captured using a kernel of an integral equation. These models are all based on a phenomenological approach to explain the properties of the cochlear filter and assume a simplification of the cochlear partition in the form of a mechanical impedance (such as is used in this paper). This limitation was partly due to the absence of detailed information about the various microstructures of the cochlear partition. Recently, however, more complete in vivo information has become available (e.g., Tolomeo and Steele, 1998; Spector *et al.*, 1998; Ren and Nuttall, 1997; Zetes and Steele, 1997; Laffon and Angelini, 1996). These developments, in part, motivate the need for a modeling framework capable of incorporating the various microstructures and make global response predictions to various stimuli under different operating conditions.

The hybrid numerical–analytical formulation developed in this paper provides a framework to introduce complex micromechanical structures. A variational formulation for the OoC requires information about the governing equations of the associated structures. Nevertheless, it is possible to use a simplified multidegree of freedom system to enable hypothesis proposition and test models for activity and nonlinearity (Parthasarathi *et al.*, 1999). Also, the analytical solutions of the above-mentioned models do not have the flexibility to introduce the complex geometry of the cochlea and to study the total fluid pressure (symmetric and antisymmetric) effects in the various cochlear ducts. Introduction of complex geometry is possible in our general finite-element framework. The boundary integral method also admits arbitrary geometries. For a more realistic geometry of the cochlea, Mammano and Nobili (Mammano and Nobili, 1993) have developed a simplified Green's function to save computations. Our Green's function based method involves no approximation in the kernel functions and the accuracy of the results will depend only on discretization used. However, for complex geometries, the computational simplifications such as obtained in the BEM formulation in this paper may not be achieved. Information on the symmetric and antisymmetric pressure could be obtained from the 2.5D model by discretizing two chambers, one above and one below the cochlear partition. Preliminary results indicate this is particularly useful to study pressure distribution arising from the direct electrical stimulation of OHC motility.

While most features of the BM velocity response were captured using a relatively coarse discretization, the response close to the peak was heavily influenced by the discretization used (Fig. 6). Convergence in the BEM formulation depends on the x discretization and the number of y and z modes. Since image sources were used only for higher-order contributions to the Green's function, they did not play a signifi-

cant role in convergence. For the 2.5D formulation, convergence depends on the $x-z$ discretization and the number of cross modes used.

The convergence studies provide details of the response close to the BM resonance location. The post-peak notch has been critically analyzed by various modelers. In a 2D model it has been interpreted as origination from microscale reflections (deBoer and Viergever, 1982) or destructive interference of traveling wave and cutoff modes (Watts, 1993). Our 2D simulations show it to be the result of insufficient discretization. However, in the 3D model the notch does not disappear even at the highest mesh density that could be used. Fluid pressure modal analysis close to the BM reveals that the higher-order modes become more important than the plane-wave mode close to the BM resonance location. These results in part indicate the need for a three-dimensional formulation of the cochlea.

ACKNOWLEDGMENTS

This research was supported in part by NIH Grant Nos. RO1 DC00141 and PO1 DC00078. The authors would like to thank Dr. Egbert de Boer for his many valuable comments in the preparation of this manuscript and Dr. Jont Allen for discussions on the influence of the apex boundary conditions on result convergence.

Allen, J. (**1977**). ''Two-dimensional cochlear fluid model: New results,'' J. Acoust. Soc. Am. **61**, 110–116.

Allen, J., and Neely, S. (**1992**). ''Micromechanical models of the cochlea,'' Phys. Today **45**(7), 40–47.

Allen, J., and Sondhi, M. (**1979**). ''Cochlear macromechanics: Time domain solutions,'' J. Acoust. Soc. Am. **68**, 123–132.

Chadwick, R., Dimitriadis, E., and Iwasa, K. (**1996**). ''Active control of waves in a cochlear model with subpartitions,'' Proc. Natl. Acad. Sci. USA **93**, 2564–2569.

de Boer, E. (**1981**). ''Short waves in three-dimensional cochlea models: Solution for a 'block' model,'' Hear. Res. **4**, 53–77.

de Boer, E. (**1984**). ''Auditory physics. Physical principles in hearing theory. II,'' Phys. Rep. **105**, 141–226.

de Boer, E. (**1991**). ''Auditory physics. Physical principles in hearing theory. III,'' Phys. Rep. **203**, 125–231.

de Boer, E., and Viergever, M. (**1982**). ''Validity of the Liouville-Green (or WKB) method for cochlear mechanics,'' Hear. Res. **8**, 131–155.

Geisler, C. (**1991**). ''A cochlear model using feedback from motile outer hair cells,'' Hear. Res. **54**, 105–117.

Grosh, K., Parthasarathi, A. A., and Nuttall, A. L. (**1998**). ''Three-dimensional numerical modeling for global cochlear dynamics,'' in *Abstracts of the 21st Midwinter Research Meeting*, Association for Research in Otolaryngology.

Holmes, M., and Cole, J. (**1984**). ''Cochlear mechanics: Analysis for a pure tone,'' J. Acoust. Soc. Am. **76**, 767–778.

Hughes, T. J. R. (**1987**). *The Finite Element Method: Linear Static and Dynamic Finite Element Analysis* (Prentice-Hall, Englewood Cliffs, NJ).

Junger, M., and Feit, D. (**1986**). *Sound and Structures* (MIT Press, Cambridge, MA).

Kagawa, Y., Yamabuchi, T., Watanabe, N., and Mizoguchi, T. (**1987**). ''Finite element cochlear models and their steady state response,'' J. Sound Vib. **119**, 291–315.

Kolston, P. J., and Ashmore, J. F. (**1996**). ''Finite element micromechanical modeling of the cochlea in three dimensions,'' J. Acoust. Soc. Am. **99**, 455–467.

Laffon, E., and Angelini, E. (**1996**). ''On the Deiters cell contribution to the micromechanics of the organ of Corti,'' Hear. Res. **99**, 106–109.

Lighthill, J. (**1981**). ''Energy flow in the cochlea,'' J. Fluid Mech. **106**, 149–213.

Mammano, F., and Nobili, R. (**1993**). ''Biophysics of the cochlea: Linear approximation,'' J. Acoust. Soc. Am. **93**, 3320–3332.

Morse, P. M., and Feshbach, H. (**1953**). *Methods of Theoretical Physics* (McGraw-Hill, New York).

Neely, S. (**1981**). ''Finite difference solution of a two-dimensional mathematical model of the cochlea,'' J. Acoust. Soc. Am. **69**, 1386–1393.

Neely, S. (**1993**). ''A model of cochlear mechanics with outer hair cells motility,'' J. Acoust. Soc. Am. **94**, 137–146.

Neely, S., and Kim, D. (**1986**). ''A model for active elements in cochlear biomechanics,'' J. Acoust. Soc. Am. **79**, 1472–1480.

Nobili, R., and Mammano, F. (**1996**). ''Biophysics of the cochlea II: Stationary nonlinear phenomenology,'' J. Acoust. Soc. Am. **99**, 2244–2255.

Parthasarathi, A. A., Bladh, R., Grosh, K., and Nuttall, A. L. (**1999**). ''Numerical formulation for a micromechanical model of the cochlea,'' in *Abstracts of the 22nd Midwinter Research Meeting*, Association for Research in Otolaryngology.

Parthasarathi, A. A., Grosh, K., and Nuttall, A. L. (**1998**). ''Determination of roots of the Eikonal equation for WKB solution in cochlear models,'' J. Acoust. Soc. Am. **103**, 2811(A).

Ren, T., and Nuttall, A. L. (**1997**). ''Frequency dependence of acoustic modulation of electrically evoked otoacoustic emission in intact gerbil cochlea,'' in *Abstracts of the 20th Midwinter Research Meeting*, Association for Research in Otolaryngology.

Spector, A., Brownell, W., and Popel, A. (**1998**). ''Estimation of elastic moduli and bending stiffness of the anisotropic outer hair cell wall,'' J. Acoust. Soc. Am. **98**, 1007–1011.

Steele, C. (**1979**). ''Comparison of WKB calculations and experimental results for three-dimensional cochlear models,'' J. Acoust. Soc. Am. **65**, 1007–1018.

Steele, C., and Taber, L. (**1979**). ''Comparison of WKB calculations and experimental results for three-dimensional cochlear models,'' J. Acoust. Soc. Am. **65**, 1007–1018.

Strang, G., and Fix, G. (**1973**). *An Analysis of the Finite Element Method* (Prentice-Hall, Englewood Cliffs, NJ).

Tolomeo, J., and Steele, C. (**1998**). ''A dynamic model of outer hair cell motility including intracellular and extracellular fluid viscosity,'' J. Acoust. Soc. Am. **103**, 524–534.

Viergever, M., and Kalker, K. (**1974**). ''On the adequacy of the Peterson-Bogert model and the effects of viscosity in cochlear dynamics,'' J. Eng. Math. **8**, 149–156.

Watts, L. (**1993**). ''Cochlear mechanics: Analysis and analog VLSI,'' Ph.D. thesis, California Institute of Technology.

Zetes, D., and Steele, C. (**1997**). ''Fluid-structure interaction of the stereocilia bundle in relation to mechanotransduction,'' J. Acoust. Soc. Am. **101**, 3593–3601.

Neural responses to the onset of voicing are unrelated to other measures of temporal resolution

Donal G. Sinex
Arizona State University, Department of Speech and Hearing Science, Box 871908, Tempe, Arizona 85287-1908

Guang-Di Chen
University of Oklahoma Health Sciences Center, School of Pharmacy, 1110 N. Stonewall Street, PO Box 26901, Oklahoma City, Oklahoma 73190

(Received 16 February 1999; revised 13 September 1999; accepted 20 September 1999)

Voice onset time (VOT) is a temporal cue that can distinguish consonants such as /d/ from /t/. It has previously been shown that neurons' responses to the onset of voicing are strongly dependent on their static spectral sensitivity. This study examined the relation between temporal resolution, determined from responses to sinusoidally amplitude-modulated (SAM) tones, and responses to syllables with different VOTs. Responses to syllables and SAM tones were obtained from low-frequency neurons in the inferior colliculus (IC) of the chinchilla. VOT and modulation period varied from 10 to 70 ms in 10-ms steps, and discharge rates elicited by stimuli whose amplitude envelopes were modulated over the same temporal interval were compared. Neurons that respond preferentially to syllables with particular VOTs might be expected to respond best to the SAM tones with comparable modulation periods. However, no consistent agreement between responses to VOT syllables and to SAM tones was obtained. These results confirm the previous suggestion that IC neurons' selectivity for VOT is determined by spectral rather than temporal sensitivity. © *2000 Acoustical Society of America.* [S0001-4966(00)01701-X]

PACS numbers: 43.64.Qh, 43.64.Sj, 43.64.Bt [RDF]

INTRODUCTION

Speech sounds may differ from one another in either spectral or temporal properties. For example, vowels are usually distinguished by the shape of the spectrum, in particular the placement of spectral peaks associated with resonances of the vocal tract. Consonants, on the other hand, may be distinguished by spectral differences, temporal differences, or both. The voiced–voiceless distinction in initial stop consonants is an example of a contrast based primarily on temporal differences (Lisker and Abramson, 1964). Syllables such as /da/ and /ta/ differ in the time after the onset of the syllable at which the vocal folds begin to vibrate. This property of articulation is referred to as voice onset time (VOT). Consonant–vowel syllables that differ in VOT may exhibit similar movement of the formants, but the intensity and periodicity of the energy associated with the formants will vary, depending on whether voicing has or has not started.

We have previously studied the responses of neurons in the auditory system of the chinchilla to syllables that differ in VOT. Sinex and McDonald (1988, 1989) described the representation of VOT in the responses of auditory nerve fibers. Most individual auditory nerve fibers exhibited a discharge rate increase at the onset of the syllable, followed by a discharge rate decrease and a second rate increase some time later. For neurons with characteristic frequencies (CF) below about 1 kHz and for VOTs greater than about 10 ms, the latency of the discharge rate increase associated with the onset of voicing closely matched the nominal VOT of the syllable. For neurons with higher CFs and for VOTs of 0 and 10 ms, the latencies did not change in proportion to VOT. To determine the stimulus properties that accounted for the response, the VOT syllables were passed through narrow-band filters whose center frequencies matched the CFs of the neurons under study. For most neurons, the latency of the second discharge-rate increase matched the latency of an amplitude increase in the filtered stimulus (Sinex and McDonald, 1988; Sinex *et al.*, 1991; Sinex, 1993). This was also true for neurons with higher CFs and for the shortest VOTs, whether or not the latency of the amplitude change or the discharge-rate increase matched the stimulus VOT. That is, after frequency selectivity was taken into account, the temporal pattern of the responses of auditory nerve fibers reflected in a fairly simple way the temporal pattern of spectral change in the syllables used to elicit the responses.

Chen *et al.* (1996) measured the responses of neurons in the inferior colliculus (IC) of the chinchilla to the same syllables. The responses of IC neurons were similar in some ways to those of auditory nerve fibers, and different in other ways. The discharge pattern often included a transient burst of spikes at the onset of voicing; Chen *et al.* referred to this burst as the ''VOT response.'' In general, the temporal pattern of the VOT response was consistent with the shape of the peristimulus time (PST) histogram elicited by CF tones (Nuding *et al.*, 1999). Neurons that exhibited transient responses to tones responded transiently at voicing onset, and neurons that exhibited sustained responses to tones responded at voicing onset and to the following vowel, much like auditory nerve fibers do. As was done for auditory nerve fiber responses, the latencies of the VOT responses were measured with respect to syllable onset. For IC neurons with low CFs, VOT-response latencies increased with increases in

 1063-7834/2000/107(1)/10/$17.00

VOT, similar to the pattern of latency change observed in the periphery. The absolute latencies of IC neurons were several ms longer than those of auditory nerve fibers, of course.

In the previous study, the discharge rates of some IC neurons varied nonmonotonically with VOT; they exhibited selectivity for VOT. For example, some neurons exhibited large VOT responses for syllables with intermediate VOTs, and smaller responses for short and long VOTs. As was done in the previous studies of the responses of auditory nerve fibers, Chen *et al.* attempted to determine what properties of the neurons and the stimuli account for the selectivity (or lack of selectivity). Since many IC neurons responded transiently to the syllables, the discharge patterns did not correspond to the pattern of spectral change in the same sustained way that auditory nerve fibers did. Even so, it was argued that to a first approximation, the responses of IC neurons to the onset of voicing could be attributed to static spectral properties of the syllables. The spectral cue was estimated by calculating the ''effective level'' of the syllable at the onset of voicing; the ''effective level'' was a measure of the stimulus energy that fell within the neuron's excitatory tuning curve. The amplitude of the discharge rate peak that followed the onset of voicing was correlated with the effective level of the syllable, also measured at the onset of voicing. That is, the short-term response of an IC neuron to the onset of voicing could be predicted from knowledge of a static property of the neuron, its tuning curve, and the short-term spectrum of the syllable, also measured in a brief time window without reference to the stimulus before or after the analysis window. It was concluded that the VOT response was not influenced directly by the length of the preceding aspirated interval.

Most descriptions of VOT emphasize the length of the interval that separates the onset of the syllable and the onset of voicing, since that is the property that best distinguishes a voiced consonant like /d/ from a voiceless consonant like /t/ (Lisker and Abramson, 1964). During the interval from syllable onset to the onset of voicing, the envelope of a VOT syllable may be thought of as undergoing a cycle of amplitude modulation, analogous to but more complicated than a cycle of a sinusoidally amplitude-modulated (SAM) tone. Thus it is tempting to think that the responses of an IC neuron to syllables in which the VOT interval varies would be affected by a more general ability of the neuron to follow envelope fluctuations. We will refer to this ability as ''temporal resolution.'' As the term is used here, it obviously excludes certain kinds of specialized temporal processing, such as binaural processing of interaural time differences. Temporal resolution is usually assessed with SAM tones and quantified by a modulation transfer function (MTF), a plot of discharge rate versus modulation frequency. Responses of auditory neurons, including IC neurons, to SAM tones have been reported by others (Rees and Møller, 1983; Langner and Schreiner, 1988; Schreiner and Langner, 1988; Rees and Palmer, 1989). One rationale for measuring the MTF is that it may lead to a better understanding of the representation of other sounds with nonsinusoidal envelopes. For example, Delgutte *et al.* (1998) have developed a model based in part on neural MTFs obtained with SAM tones that was reasonably successful in predicting responses to the envelope of speech. Predictions for IC neurons were less accurate than predictions for auditory nerve fibers and cochlear nucleus neurons, however.

In many cases, the overall discharge rate of IC neurons varies in a way that is referred to as ''bandpass selectivity'' for modulation frequency (Langner and Schreiner, 1988). Consequently, one might hypothesize that selectivity for VOTs within a certain range would be correlated with bandpass selectivity for tones modulated at the same rates. Similarly, IC neurons that lack selectivity for VOT might also fail to show bandpass selectivity for SAM tones.

Chen *et al.* (1996) specifically argued that their results were inconsistent with this hypothesis, for the reasons stated above. However, they did not explicitly compare responses to VOT syllables to responses to SAM tones. In the present study, those comparisons were made. It was found that responses of IC neurons to the onset of voicing were unrelated to the responses of the same neurons to sinusoidally amplitude-modulated CF tones. The results confirm the suggestion of Chen *et al.* (1996) that an IC neuron's sensitivity to sinusoidal amplitude modulation does not account for the responses that occur following intervals of similar length in VOT syllables.

I. METHODS

A. Stimuli

The stimuli were consonant–vowel syllables differing in VOT or SAM tones. The syllables were a subset of a continuum of synthesized VOT syllables that has been used previously and for which detailed descriptions have been provided (Sinex and McDonald, 1988, 1989; Sinex *et al.*, 1991; Chen *et al.*, 1996; Chen and Sinex, 1999). Briefly, the syllables had an overall duration of 205 ms, and VOT varied from 10 to 70 ms, in 10-ms steps. Each syllable consisted of a burst of frication noise at onset, followed by aspiration noise that lasted until the onset of voicing. The particular pattern of amplitude change during the interval from syllable onset to voicing onset varied, depending upon the frequency band being measured and, to a lesser extent, the length of the VOT interval. An example is shown in Fig. 1, and additional examples obtained with slightly different techniques have been shown previously (Figs. 2–8 in Sinex and McDonald, 1988; Fig. 5 in Sinex *et al.*, 1991). Figure 1(A) shows the first 100 ms of the waveform of the syllable with VOT=50 ms. The amplitude was low during the first 50 ms, at which time the onset of voicing produced a large amplitude increase. From 50 ms until the end of the syllable, the waveform envelope was modulated with a period, 8.77 ms, that reflects the fundamental frequency of voicing, 114 Hz. In Fig. 1(B), the heavy line shows a smoothed representation of the waveform envelope. The rms amplitude was calculated in 10-ms windows and expressed in dB. Shown in this way, the envelope was modulated before the onset of voicing, the overall amplitude increased by about 22 dB from the envelope minimum to the onset of voicing, and the envelope was relatively flat after the onset of voicing.

The envelopes were similar for the other syllables, ex-

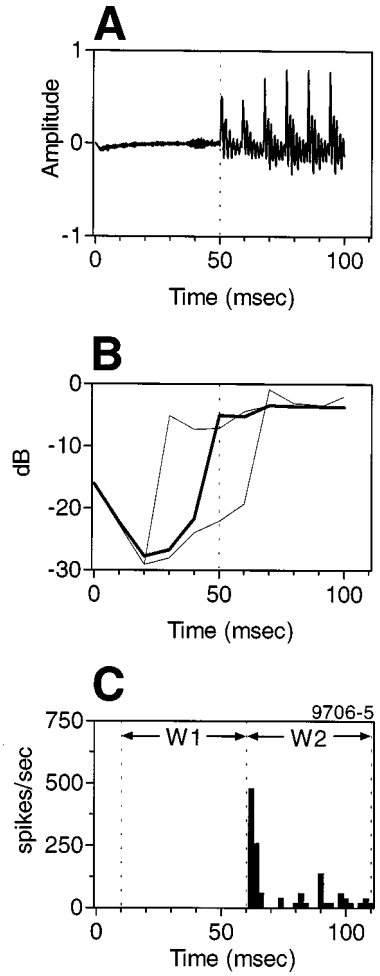

FIG. 1. (A) Waveform of the syllable with VOT=50 ms. Only the first 100 ms of the 204-ms syllable are shown. (B) Representations of syllable envelopes. rms amplitude was calculated for 10-ms rectangular windows, then expressed in dB. Heavy line: Envelope for the waveform shown in (A), VOT=50 ms. The envelope varied by 22 dB during the aspirated interval from 0 to the onset of voicing at 50 ms, but was relatively flat after voicing onset. Thin lines: envelopes calculated in the same way for syllables with VOTs of 30 and 70 ms. (C) Response of one neuron to the syllable shown in (A), presented at 60 dB SPL to the contralateral ear. ''W1'' and ''W2'' represent the windows over which discharge rate was calculated. The window length was always equal to VOT (in this example, 50 ms), and the windows were always delayed to compensate for the neuron's response latency measured with CF tones. Neuron 9706-5, CF=0.91 kHz, threshold=20 dB SPL, PST type=Pauser.

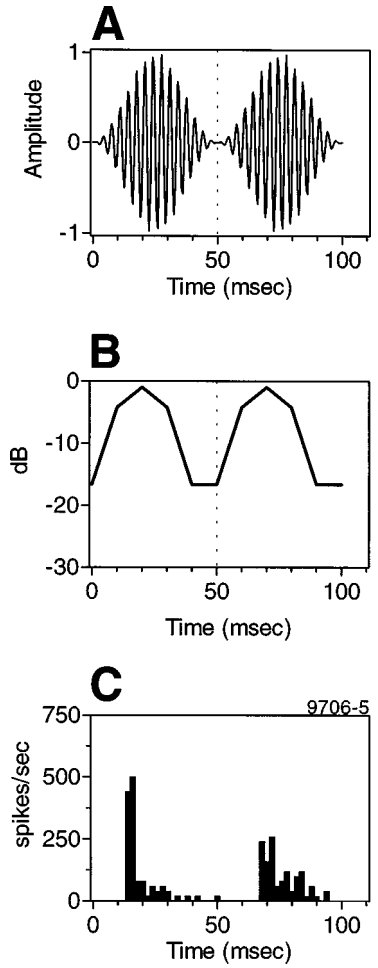

FIG. 2. (A) Waveform of a SAM tone. For this illustration, the carrier frequency was 300 Hz, modulated with a period of 50 ms (modulation frequency=20 Hz). Only the first 100 ms of the 200-ms tone are shown. (B) A representation of the SAM tone envelope. Calculations were as described for Fig. 1(B). (C) Response of the same neuron shown in Fig. 1(C) to a SAM tone presented at 60 dB SPL to the contralateral ear. The modulation interval was 50 ms (modulation frequency=20 Hz), as shown in (A) and (B), and the carrier frequency was 0.8 Hz. Neuron 9706-5, CF=0.91 kHz, threshold=20 dB SPL. PST type=Pauser.

cept that the length of the modulated interval, before the onset of voicing, changed with VOT. In Fig. 1(B), the thin lines represent the envelopes for the syllables with VOTs of 30 and 70 ms, for comparison. The interval over which the envelope was modulated varied as expected with VOT. In contrast, the envelope after the onset of voicing did not change significantly with VOT; the waveform was modulated at 114 Hz (and the smoothed envelope was relatively flat) in every case. The short-term spectrum did vary with VOT during this segment, as described previously (Sinex *et al.*, 1991).

SAM tones were synthesized online by multiplying a sine wave carrier by a second sine wave, the modulator. The depth of modulation was always 100%, chosen to produce the largest possible amplitude change and for consistency with many previous neurophysiological studies. The carrier frequency for SAM tones was chosen to match the neuron's CF, rounded to the nearest 100 Hz. The modulation period varied from 10 to 70 ms in 10-ms steps, to match the VOT intervals in the syllables; thus the modulation frequencies varied from a maximum of 100 Hz down to approximately 14 Hz. IC neurons normally respond to modulation frequencies throughout this range (Langner and Schreiner, 1988), and a broader range would have been presented if the goal of the experiment had been to fully characterize the neurons' MTFs. The duration of SAM tones was nominally 200 ms, constrained to be an integer multiple of the modulation period. For example, when the modulation period was 70 ms, the duration was increased to 210 ms. Figure 2(A) shows the first 100 ms of the waveform of a SAM tone whose modulation period, 50 ms, is the same as the VOT of the waveform shown in Fig. 1(A). Two cycles of modulation are shown, so that the time axis matches that of Fig. 1. Fig. 2(B) shows the pattern of amplitude change in dB for the SAM tone, calculated in the same way as in Fig. 1(B). Over the

50-ms interval from the first peak to the second, the SAM tone envelope changed in a way that was similar but obviously not identical to the pattern of change from 0 to 50 ms in Fig. 1(B). The shape of the modulation was different, and the depth of modulation was shallower, 16 dB from valley to peak in the smoothed envelope, compared to 24 dB for the syllable. The phase of modulation also did not match that in the syllable, but since no phase-dependent response measures were obtained, this phase shift did not influence the outcome of the experiment.

In the figures that follow, results are shown as a function of the time interval over which the stimulus was modulated: VOT for syllables, and modulator period for SAM tones. The convention normally followed in neurophysiological (Langner and Schreiner, 1988) and also psychophysical (Viemeister, 1979) studies of temporal resolution is to display data as a function of modulator frequency. VOT, however, is normally stated as a time interval (Lisker and Abramson, 1964). To simplify comparisons to the syllables, the temporal characteristics of all stimuli including SAM tones will always be specified as the length of the modulated interval in ms.

B. Animal preparation

Responses were obtained from single neurons in the IC of the chinchilla. The procedures were similar but not identical to those described by Chen *et al.* (1996; Chen and Sinex, 1999). Animals were anesthetized by an intraperitoneal (i.p.) injection of sodium pentobarbital (65 mg/kg). Supplemental i.p. injections of sodium pentobarbitol were given as required to maintain a surgical level of anesthesia. The skull was opened, and a portion of the cerebral cortex was aspirated to expose the dorsal surface of the IC. Tungsten electrodes insulated with Parylene-C (Microprobe) with impedances greater than 1 megOhm were placed above the IC under visual control, then advanced with a hydraulic microdrive (Trent-Wells). The electrode trajectory passed through the central nucleus of the IC, in a parasagittal plane. The neurons exhibited secure responses to tone bursts, and sharp tuning with CFs that increased with increasing depth. These properties are consistent with those of neurons in the central nucleus of the IC (Langner and Schreiner, 1988; Nuding *et al.*, 1999), and it is assumed that all of the neurons studied were from the central nucleus.

C. Data collection and analysis

Stimulus presentation and data collection were controlled by a PC-compatible computer. When a neuron was isolated, estimates of CF and binaural sensitivity were obtained manually. Following the initial characterization of the neuron, a detailed response map was obtained with an automated procedure (Nuding *et al.*, 1999). These data were used to make a more precise estimate of CF and threshold at CF. Responses to steady-state CF tones were also obtained and used to classify each neuron according to the shape of its PST histogram (Nuding *et al.*, 1999).

In most cases, SAM tones and VOT syllables were presented monaurally to the contralateral ear, but binaural presentation was also used, if a neuron exhibited weak responses to contralateral stimulation or if the recording time allowed both monaural and binaural data to be collected. When binaural presentations were used, the stimuli were presented at the interaural time delay (ITD) that elicited the largest response to CF tones. In the small number of cases for which both monaural and binaural stimuli were presented, the results were not strongly dependent on the ear or ears of presentation.

Each stimulus waveform was repeated 25 times, with a nominal silent interval of 205 ms between presentations. The actual silent interval was always a few msec longer than 205 ms because of computer processing carried out between presentations. The length of the silent interval did not vary systematically across stimulus types. Each stimulus type was presented at a series of levels, usually from 30 to 70 dB SPL. For each stimulus type, the nominal level is the rms pressure of the entire syllable. For syllables, this is the same convention used in previous studies (Sinex and McDonald, 1988; Chen *et al.*, 1996). For SAM tones, the rms level is independent of modulation frequency; however, the peak sound pressure of the SAM tones is always 4.3 dB greater than the peak sound pressure of an unmodulated tone at the same frequency. The order of presentation of modulation frequencies was varied quasi-randomly. For each modulation frequency, SAM tones were alternated with syllables. The stimulus type presented first was also varied.

For syllables, spikes were counted in windows whose lengths matched the VOT of the syllable. Counts were obtained for two successive windows, called Window 1 and Window 2, delayed with respect to the stimulus onset to compensate for the neuron's response latency. Window 1 included spikes elicited during the aspirated segment prior to the onset of voicing, that is, during the segment for which the amplitude envelope varied with VOT. Window 2 included spikes elicited during the voiced segment, that is, during the segment for which the amplitude envelope did not vary with VOT but the short-term spectrum did. Figure 1(C) shows the discharge pattern elicited from a representative neuron by the syllable shown in the top panel. In this example, there was little or no response during the modulated interval, prior to the onset of voicing, and a robust VOT response, after the onset of voicing. This pattern is common for IC neurons responding to VOT syllables.

The response to SAM tones was calculated over the entire duration of the tone, as has been done in previous studies (Langner and Schreiner, 1988). Figure 2(C) illustrates the responses of the same neuron shown in Fig. 1(C) to the first 100 ms of a SAM tone with a modulation period of 50 ms (a modulation frequency of 20 Hz). For this stimulus, there was a similar response during both modulation cycles, although the response to the first modulation cycle was slightly larger. Calculating discharge rate over the duration of the tone minimizes the effects of cycle-by-cycle fluctuations in discharge rate, eliminates any effects of stimulus or response phase, and as noted above is consistent with previous studies of responses to SAM tones. It should be noted that this response measure tends to underestimate the response to tones modulated at low frequencies, which necessarily have fewer modulation cycles to elicit spikes. As a consequence, neu-

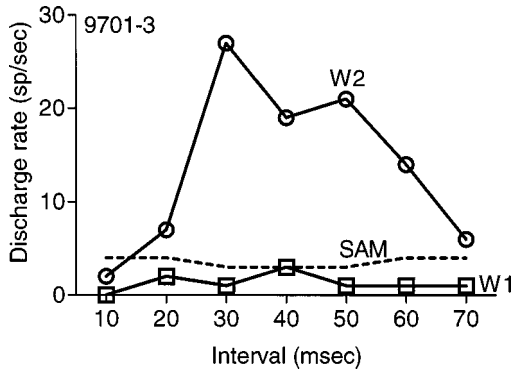

FIG. 3. Discharge rate elicited by VOT syllables and by SAM tones. The curve marked ''W2'' (circles) represents discharge rate after the onset of voicing. The curve marked ''W1'' (squares) represents discharge rate before the onset of voicing. The curve marked ''SAM'' (dashed line without symbols) represents discharge rates to SAM tones. The abscissa represents the interval over which the stimulus envelope was modulated: equal to VOT for syllables, and equal to modulation period for SAM tones. All stimuli were presented at 60 dB SPL to the contralateral ear. Carrier frequency for SAM tones=0.5 kHz. Neuron 9701-3, CF=0.52 kHz, threshold=20 dB SPL, PST type=Transient.

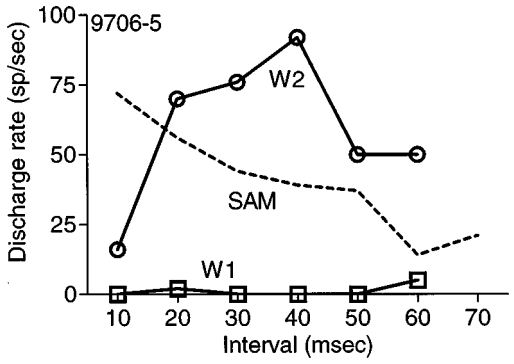

FIG. 4. Similar to Fig. 3 for a different neuron. All stimuli were presented at 60 dB SPL to the contralateral ear. Carrier frequency for SAM tones=0.8 kHz. Neuron 9706-5, CF=0.91 kHz, threshold=20 dB SPL, PST type =Pauser.

rons that respond strongly to individual modulation cycles when the modulation frequency is low may still be categorized as having ''bandpass'' MTFs. Since it was not a goal of this study to determine the proportion of neurons having particular types of MTFs, the conclusions were not affected by the choice of response measure.

The two estimates of discharge rate to syllables, in Window 1 and in Window 2, were compared to the overall discharge rate elicited by SAM tones. The relation between discharge rate elicited by the two types of stimuli was quantified by calculating the ''Normalized Rate,'' the ratio of discharge rate elicited by a segment of a syllable to the overall discharge rate elicited by a SAM tone modulated with the same period.

II. RESULTS

The data presented below were obtained from 19 neurons from 8 chinchillas. Although the sample size is small, the neurons were consistent in that they showed no systematic relation between the magnitude of response to VOT syllables and the magnitude of response to SAM tones modulated over the same interval. Examples of discharge rates for three individual neurons, illustrating the range of patterns, are shown first. The responses of all the neurons are summarized in plots of normalized rate. Finally, the effect of stimulus level on responses to syllables, and the relative lack of an effect of level on responses to SAM tones is illustrated.

A. Selectivity for VOT and for modulation period

Three sets of discharge rates obtained from one IC neuron are shown as a function of temporal interval in Fig. 3. The line marked ''W2'' in the figure represents the rates obtained in response to VOT syllables, after the onset of voicing. The highest rates were elicited by VOTs from 30 to 50 ms. This pattern of nonmonotonicity was described by Chen *et al.* (1996); patterns such as this one raise the question of whether the nonmonotonicity or selectivity for VOT is a consequence of a more general temporal resolution. The responses of the same neuron to SAM tones are shown by the dashed line. In this case, the neuron exhibited low and relatively constant discharge rates at each of the tested modulation periods; tones modulated over 30- to 50-ms periods did not elicit higher discharge rates than tones modulated over longer or shorter periods. The neuron exhibited little or no selectivity for SAM tones, and thus the selectivity for VOTs of intermediate length was not predicted by its responses to SAM tones.

As noted above, all of the VOT syllables had the same amplitude envelope during analysis Window 2. The line marked ''W1'' in Fig. 3 represents discharge rates obtained during analysis Window 1, that is, the aspirated interval during which the pattern of change in the amplitude envelope did vary with VOT. For this neuron, however, discharge rates during Window 1 were consistently low, and even though there was a small peak at 40 ms, no selectivity for VOT should be inferred because the spike counts were so low. Again, there was no suggestion that the response to the aspirated segment of the syllable was correlated with the response to SAM tones.

A second example of the lack of correlation between rates is shown in Fig. 4. This neuron exhibited selectivity for intermediate VOTs that was similar to that shown in the previous figure. Responses during Window 2 varied nonmonotonically with VOT, while responses during Window 1 were nearly absent. For this neuron, the pattern of responses to SAM tones differed from the pattern in the previous example: the discharge rate was highest for the tone modulated at 10 ms (100 Hz) and decreased as modulation period increased (or modulation frequency decreased). The highest discharge rate elicited by a SAM tone occurred for the interval for which the response to the onset of voicing was smallest. Again, there was no suggestion that the discharge rate elicited by one type of stimulus could be predicted from the rate elicited by the other stimulus.

The third example is from a neuron that exhibited the opposite pattern: strong responses to SAM tones, but weak responses to both segments of the syllables. For the neuron shown in Fig. 5, the response to the onset of voicing was lowest for the intermediate VOTs for which the neurons in the previous figures exhibited their highest discharge rates.

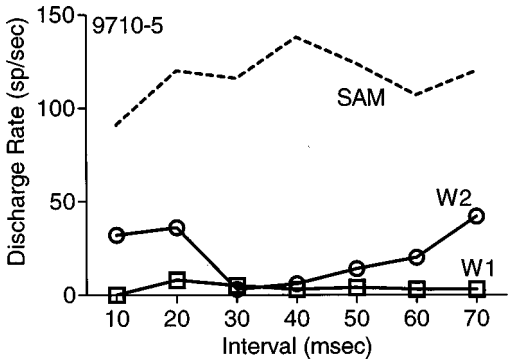

FIG. 5. Similar to Fig. 3 for a different neuron. All stimuli were presented at 60 dB SPL with an interaural time difference of 0.4 ms (contralateral ear leading). Carrier frequency for SAM tones=0.2 kHz. Neuron 9710-5, CF =0.2 kHz, threshold=10 dB SPL, PST type=Sustained.

Although no strong selectivity for SAM tones was observed, the highest rate was observed at 40 ms, an interval for which the response to the syllables was close to its minimum.

B. Normalized rates

Figure 6 summarizes the patterns shown in the three examples. The response measure, Normalized Rate, would have a value of one if both types of stimuli elicited exactly the same discharge rate. The Normalized Rate during Window 2 [Fig. 6(A)] rarely approached one for any single point. In addition, over the range of intervals, it took on values greater than or less than one, varied by an order of magnitude for each of the individual neurons, and varied by about two and a half orders of magnitude across all three neurons. Of course, it would not be necessary for the Normalized Rate to be equal to one to indicate a relation, as long as the ratio was constant across modulation intervals; points falling along any horizontal line would indicate a simple scale relation between discharge rates. However, even when plotted on a log scale, the normalized rates did not appear to be independent of the modulation interval.

The Normalized Rate during Window 1 [Fig. 6(B)] also varied across modulation intervals. In this case, the measure was consistently much less than one, indicating that the aspirated segment of the syllables elicited a weaker response (or no response at all) than a SAM tone modulated over the same interval. During this analysis window, the syllables exhibited modulation that varied with VOT; however, there was no suggestion of a relation between the responses elicited by those modulated intervals and the responses elicited by SAM tones.

Figure 7 illustrates the Normalized Rates for 15 neurons for which at least 5 modulation intervals were studied. As in the previous figure, Normalized Rate varied over several orders of magnitude, and there was no suggestion for either window of a systematic relation between Normalized Rate and modulation interval. There were many individual points for which the Normalized Rate was zero, indicating no response to that particular segment of the syllable. There were also a few examples (plotted as ''infinite'') for which the Normalized Rate could not be calculated because responses were elicited by the syllable but not by the SAM tone.

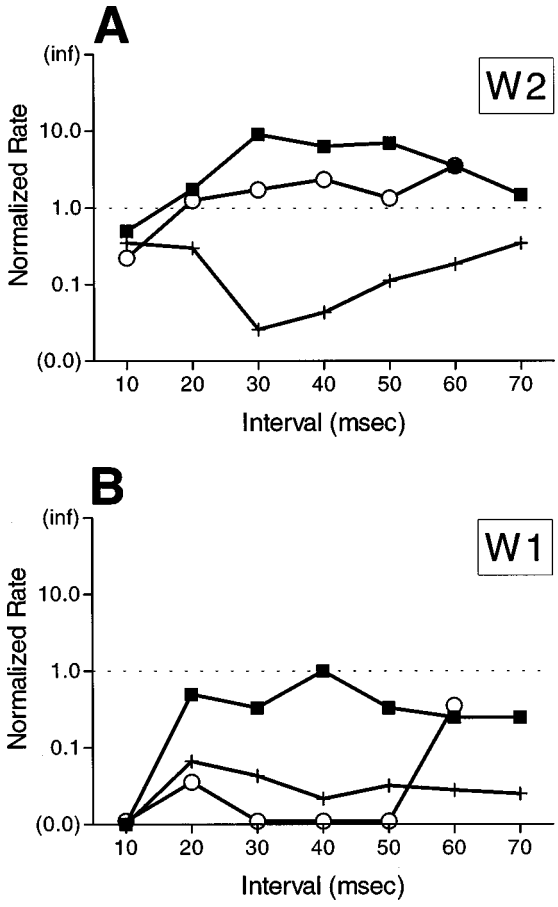

FIG. 6. ''Normalized Rate'' to VOT syllables for the neurons shown in Figs. 3–5. See text for explanation of the response measure. The label ''(0.0)'' on the ordinate indicates the coordinate for Normalized Rates for which the numerator was zero. The label ''(inf)'' on the ordinate indicates the coordinate for Normalized Rates for which the denominator was zero. Panel A: Normalized Rates for responses occurring in analysis Window 2, after voicing onset. Filled squares: data from Neuron 9701-3, shown in Fig. 3. Open circles: data from Neuron 9706-5, shown in Fig. 4. Plusses: data from Neuron 9710-5, shown in Fig. 5. Panel B: Normalized Rates for responses occurring in analysis Window 1, before voicing onset. Symbols are the same as in A.

At first glance, it may appear that some of the lines in this figure are nearly horizontal. However, no line remained horizontal across the full range of intervals, as would be necessary for the response to SAM tones to be a useful predictor of the response to voicing for any individual neuron. Also, for the lines for which Normalized Rate appeared to have a relatively constant value, that value could be as low as 0.5 or as high as 8 or 10. If there were a simple relation between responses to SAM tones and responses to the syllables, one might expect that the Normalized Rate would take on similar values for different neurons, but Fig. 7 indicates that was not the case.

The logarithmic ordinate and the large range of Normalized Rates represented in Fig. 7 made small but real deviations from zero slope difficult to see. This is illustrated in Fig. 8, which replots a data set for which the Normalized Rate in analysis Window 2 appeared to be nearly constant. For this neuron, shown in Fig. 7 as the thick line with filled circles, Normalized Rates varied between 1 and 2 over the

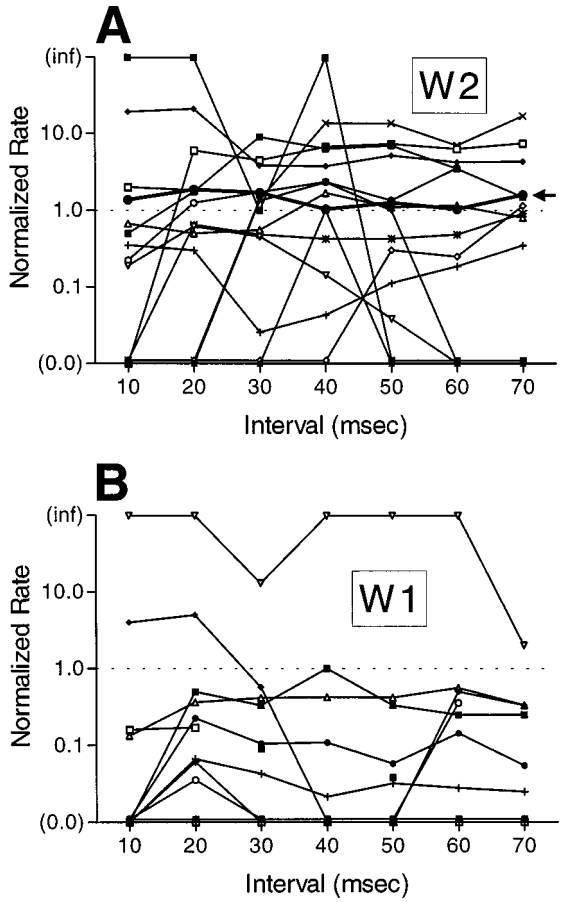

FIG. 7. Similar to Fig. 6 for 15 neurons. Panel A: Responses occurring in Window 2. The thicker line marked by the arrow is replotted with different scaling in Fig. 8. Panel B: responses occurring in Window 1.

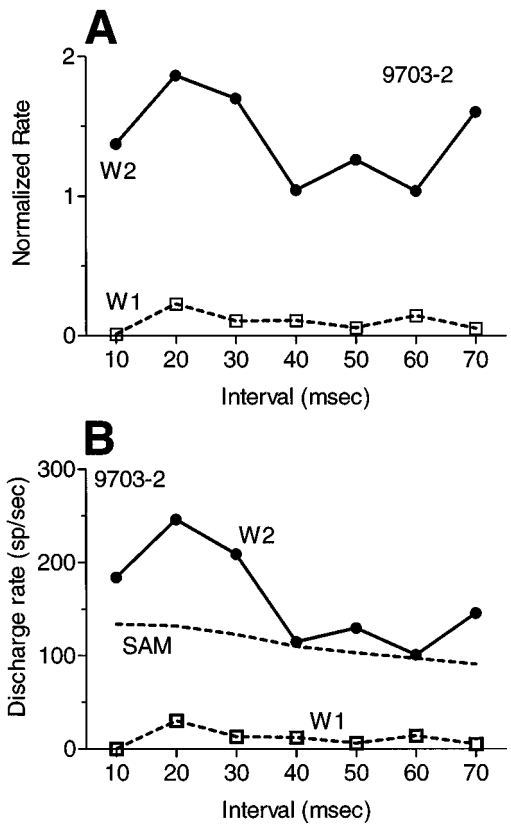

FIG. 8. Panel A: Normalized Rates for responses occurring in analysis Window 2, for a neuron exhibiting high discharge rates. Panel B: Discharge rates, shown as in Fig. 3. Carrier frequency for SAM tones=0.3 kHz. Neuron 9703-2, CF=0.32 kHz, threshold=30 dB SPL, PST type=Sustained.

range of intervals tested, an amount of change that was difficult to appreciate in Fig. 7 but is more apparent when a restricted linear ordinate is used [Fig. 8(A)]. The discharge rates generated by this sustained neuron were high, so that these differences in Normalized Rate represented large, reliable differences in the number of spikes elicited [Fig. 8(B)]. The plot of discharge rates in Fig. 8(B) indicates that the neuron exhibited a selectivity for VOTs less than 40 ms for which there was no corresponding selectivity for SAM tones.

C. Effects of stimulus level

For these VOT syllables, both the number of response components and the latencies of individual response components can vary with level (Chen *et al.*, 1996). However, the temporal pattern of the response to SAM tones was more stable with changes in level than the temporal pattern in response to syllables. The finding that changes in presentation level affect the responses to syllables and SAM tones differently provides further evidence that temporal resolution does not account for the responses to VOT syllables. The effects of level on the responses of one neuron are shown in Fig. 9, for the syllable with VOT=20 ms. The histograms on the right side of Fig. 9 show the discharge patterns in response to the syllables. As level increased, the overall discharge patterns changed, both in the number and latency of response components; the differences were especially apparent when responses at 30, 60, and 80 dB SPL are compared. At the lowest level shown, 30 dB SPL (top panel), the syllable elicited only a few spikes with a latency of about 70 ms. At higher levels, the latency of that response decreased and stabilized at about 35 ms; the number of spikes reached a maximum at 60 dB SPL. The VOT response at 60 dB SPL is indicated in Fig. 9 by a small arrow. At still higher levels, however, the size of this response component decreased. A second response component elicited by the steady-state vowel appeared at 40 dB SPL, increased over the next few level steps, and then decreased at the highest levels.

The responses of the same neuron to SAM tones are shown on the left side of Fig. 9. Although the number of spikes increased, most noticeably between 30 and 40 dB SPL, the latency of the first spike elicited within a particular modulation cycle was stable to within 2–4 ms across the range of levels from 40 to 80 dB SPL. There were no changes in the temporal discharge pattern in response to SAM tones that were comparable to those observed in response to the syllable.

III. DISCUSSION

The goal of this experiment was to determine whether the representation of VOT might be understood in terms of a general ability of neurons to represent temporal intervals. In auditory neurophysiology, that general ability has often been characterized by the pattern of responses elicited by SAM tones. So one would like to know whether selectivity for

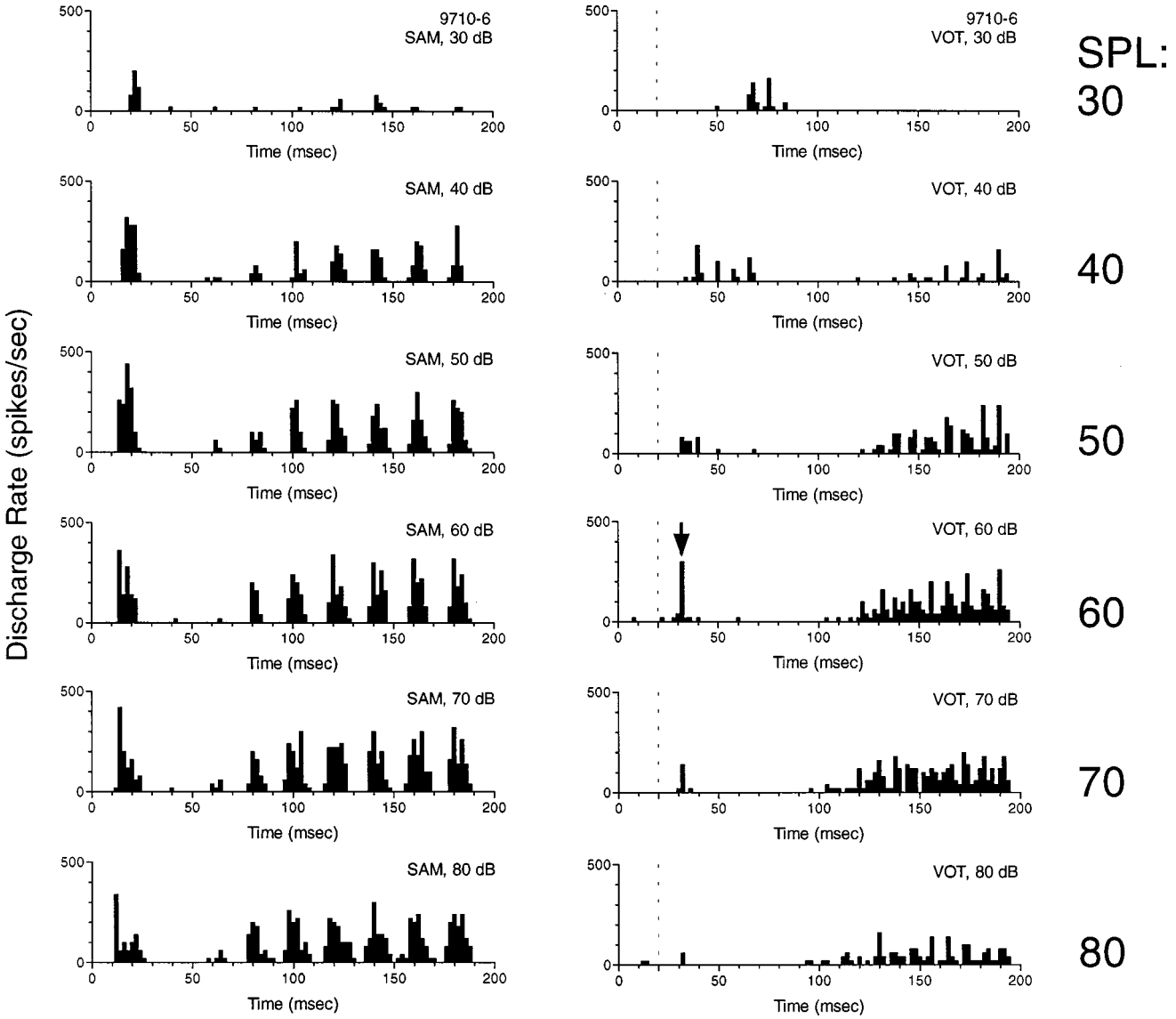

FIG. 9. Effects of stimulus level. Level increases from top to bottom, as indicated by the labels on the right side of the figure. Right column: responses to the syllable with VOT=20 ms (the vertical dashed line marks the syllable VOT). The arrow in the PST histogram obtained at 60 dB SPL marks the VOT response component. Left column: responses to SAM tones with carrier frequency=0.75 kHz and modulation period=20 ms (modulation frequency=50 Hz). Neuron 9710-6, CF=0.78 kHz, threshold=20 dB, PST type=Pauser.

SAM tones predicts or accounts for selectivity for VOT. Although the results of previous experiments suggested that this was not the case (Sinex *et al.*, 1991; Chen *et al.*, 1996), a direct empirical test had not been made. Overall, a neuron's responses elicited by the onset of voicing were unrelated to its responses to SAM tones. Some neurons exhibited moderate selectivity for VOT, but that selectivity was unrelated to selectivity for tones modulated over the same intervals. Many neurons exhibited strong responses to the onset of voicing but only weak responses to SAM tones. The opposite pattern was also observed; some neurons exhibited robust responses to modulated tones but only weak responses to the onset of voicing. Selectivity for VOT was observed only for responses elicited after the onset of voicing, when the waveform envelope did not distinguish between syllables. Responses obtained before the onset of voicing, when the envelope did vary with VOT, were weak or absent. Finally, it was shown that stimulus level affected the temporal pattern of responses to syllables in more complex ways than it affected responses to SAM tones.

In a previous study of the representation of VOT syllables in the auditory cortex of the cat (Eggermont, 1995), two measures of temporal resolution, the ''limiting click interval'' and the ''limiting SAM period,'' were compared to responses to syllables. The limiting intervals were the shortest intervals for which successive clicks or modulation periods elicited a response; for shorter intervals, the trailing stimulus was ineffective. It was noted that neurons often responded to the beginning and end of VOT intervals that were shorter than the limiting intervals estimated with other stimuli. Although responses obtained over the full range of interclick and modulation intervals were not shown, the conclusions of the study with respect to temporal resolution were consistent with those drawn here.

Why aren't responses to SAM tones good predictors of responses to VOT? It is because in the component of the VOT syllable that is effective in eliciting spikes, the rate of modulation was independent of VOT. At the onset of voicing, the stimulus available to neurons with low CFs changed from low to high amplitude abruptly; overall amplitude could increase by 20 dB or more [Fig. 1(B)] and the amplitude in a narrow frequency band could change by an even larger amount (Sinex *et al.*, 1991). This pattern of amplitude change more closely resembled the onset of a tone than a complete cycle of a SAM tone. Because of the large amplitude increase, the neurons' responses to the onset of voicing were most influenced by acoustic events that occurred in the few ms after the onset of voicing, not by events that occurred over the entire unvoiced segment of the syllables.

After the onset of voicing, the amplitude envelope was relatively constant across syllables; it was modulated at the fundamental frequency of voicing, 114 Hz, in every case. Selectivity for syllables based on spikes elicited during this segment must be based on the static, short-term spectrum, since that is the acoustic property that distinguished one syllable from another. This was first reported for IC neurons by Chen *et al.* (1996), who noted that the magnitude of the response to the onset of voicing varied with the amplitude of the syllable within a frequency band that matched the neuron's tuning curve. They referred to the acoustic measure as the ''effective level'' of the syllable. Chen *et al.* (1996) also described the changes in response latency that accompany changes in presentation level, as shown here in Fig. 9. Those latency changes were larger than those that occurred when the level of a pure tone or a SAM tone was changed. They occurred because increases in the overall level of the syllable could raise previously sub-threshold spectral components to a level high enough to drive the neuron. Those newly effective components could occur tens of msec earlier than the components that were effective at lower overall levels, accounting for the large latency changes. The most important point for the present study is that these changes, which reflect only the static, short-term spectrum of the syllable and the frequency selectivity of the neuron, combine to produce large changes in the temporal pattern of the response. As indicated by Fig. 9, they are not indicative of a change in the neuron's underlying temporal sensitivity as indicated by responses to SAM tones; that sensitivity did not change with level.

The pattern of responses of IC neurons to SAM tones modulated at different frequencies is often assumed to serve as an adequate measure of the temporal resolution of IC neurons (Langner and Schreiner, 1988; Schreiner and Langner, 1988; Delgutte *et al.*, 1998). It is intuitively appealing to assume that temporal resolution is a general property of auditory neurons that contributes to, among other things, the representation of speech sounds. Although it is certainly true that there must be a limit to temporal resolution, the present results and those from a companion study (Sinex and Chen, 1998) indicate that the pattern of responses to SAM tones does not completely specify what that limit is. Also, while there must be a relation between temporal resolution of auditory neurons and their ability to represent speech, the present results and those of Delgutte *et al.* (1998) and Eggermont (1995) indicate that the relation is not always the simplest or most obvious one.

The sinusoidal modulation frequencies to which auditory neurons respond best overlap with the envelope frequencies of speech sounds; that was true for the stop consonants used in the present study but it is true for other sounds as well. However, apparent similarity between temporal resolution, as indicated by responses to SAM tones, and selectivity for more complex modulated sounds such as consonant–vowel syllables, does not prove that one form of selectivity is responsible for the other. If it did, responses elicited by the onset of voicing following an aspirated segment would not differ as greatly from the responses elicited by SAM tones as they do.

The present results should not be interpreted to mean that the timing or latency of spikes is unimportant for the neural representation of VOT, or that auditory temporal resolution plays no role in the perception or discrimination of VOT syllables. The correct interpretation is that the *encoding* of VOT syllables is not constrained by neurons' temporal resolution, at least at the level of the IC. These results do not address the role of auditory temporal resolution in *decoding* the neural representation. That process is not understood, even to the point of attributing it to auditory or nonauditory mechanisms. In either case, it seems likely that any constraints on the processing of VOT syllables provided by temporal resolution would have to be imposed at the decoding stage.

VOT is a relatively simple temporal property of speech and the one that has been studied more often than any other. The absence of a simple relation between neural temporal resolution (as revealed by responses to SAM tones) and the neural representation of VOT syllables suggests that hypotheses that such a relation may hold for other speech sounds should be made with caution. This is important to remember, in light of the recent increase in interest in the role of auditory temporal processing in both normal and abnormal perception of speech (Merzenich *et al.*, 1996; Kraus *et al.*, 1996; Phillips and Farmer, 1990).

IV. CONCLUSIONS

Neurons in the IC of the chinchilla could exhibit moderate selectivity for VOTs near the middle of the range from 10 to 70 ms. This selectivity was unrelated to the neurons' selectivity for SAM tones modulated over the same intervals. This result confirms our previous suggestion that responses of IC neurons to the onset of voicing are largely explained by the short-term spectra of the syllables and the frequency selectivity of the neurons. Thus temporal resolution does not account for nonmonotonicity in the representation of VOT syllables that may be observed in the responses of IC neurons.

ACKNOWLEDGMENTS

A preliminary report of these results has been presented (Sinex and Chen, 1997). Supported was provided by Grant No. DC341 from NIDCD to D.G.S.

Chen, G. D., and Sinex, D. G. (**1999**). ''Effects of interaural time differences on the responses of chinchilla inferior colliculus neurons to consonant–vowel syllables,'' Hear. Res. (in press).
Chen, G. D., Nuding, S. C., Narayan, S. S., and Sinex, D. G. (**1996**). ''Responses of single neurons in the chinchilla inferior colliculus to consonant–vowel syllables differing in voice-onset time,'' Aud. Neurosci. **3**, 179–198.
Delgutte, B., Hammond, B. M., and Cariani, P. A. (**1998**). ''Neural coding of the temporal envelope of speech: Relation to modulation transfer functions,'' in *Psychophysical and Physiological Advances in Hearing*, edited by A. R. Palmer, A. Rees, A. Q. Summerfield, and R. Meddis (Whurr Publishers, London), pp. 595–603.
Eggermont, J. J. (**1995**). ''Representation of a voice onset time continuum in primary auditory cortex of the cat,'' J. Acoust. Soc. Am. **98**, 911–920.
Kraus, N., McGee, T. J., Carrell, T. D., Zecker, S. G., Nicol, T., and Koch, D. B. (**1996**). ''Auditory neurophysiologic responses and discrimination deficits in children with learning problems,'' Science **273**, 971–973.
Lisker, L., and Abramson, A. (**1964**). ''A cross-language study of voicing in initial stops: Acoustical measurements,'' Word **20**, 384–422.
Langner, G., and Schreiner, C. E. (**1988**). ''Periodicity coding in the inferior colliculus of the cat. I. Neuronal mechanisms,'' J. Neurophysiol. **60**, 1799–1822.
Merzenich, M. M., Jenkins, W. M., Johnston, P., Schreiner, C. E., Miller, S. L., and Tallal, P. (**1996**). ''Temporal processing deficits of language-learning impaired children ameliorated by training,'' Science **271**, 77–84.
Nuding, S. C., Chen, G. D., and Sinex, D. G. (**1999**). ''Monaural response properties of single neurons in the chinchilla inferior colliculus,'' Hear. Res. **131**, 89–106.
Phillips, D. P., and Farmer, M. E. (**1990**). ''Acquired word deafness, and the temporal grain of sound representation in the primary auditory cortex,'' Behav. Brain Res. **40**, 85–94.
Rees, A., and Møller, A. R. (**1983**). ''Responses of neurons in the inferior colliculus of the rat to AM and FM tones,'' Hear. Res. **10**, 301–330.
Rees, A., and Palmer, A. R. (**1989**). ''Neuronal responses to amplitude-modulated and pure-tone stimuli in the guinea pig inferior colliculus, and their modification by broadband noise,'' J. Acoust. Soc. Am. **85**, 1978–1994.
Schreiner, C. E., and Langner, G. (**1988**). ''Periodicity coding in the inferior colliculus of the cat. II. Topographical organization,'' J. Neurophysiol. **60**, 1823–1840.
Sinex, D. G. (**1993**). ''Simulation of neural responses that underlie speech discrimination,'' in *Neural Systems: Analysis and Modeling*, edited by Frank H. Eeckman (Kluwer Academic, Norwell, MA), pp. 307–313.
Sinex, D. G., and Chen, G. D. (**1997**). ''Neural responses to the onset of voicing are unrelated to other measures of temporal sensitivity,'' J. Acoust. Soc. Am. **102**, 3162(A).
Sinex, D. G., and Chen, G. D. (**1998**). ''Responses of chinchilla inferior colliculus neurons to different types of amplitude-modulated tones,'' Abstracts of the Assoc. for Res. in Otolaryngol.
Sinex, D. G., and McDonald, L. P. (**1988**). ''Average discharge rate representation of voice-onset time in the chinchilla auditory nerve,'' J. Acoust. Soc. Am. **83**, 1817–1827.
Sinex, D. G., and McDonald, L. P. (**1989**). ''Synchronized discharge rate representation of voice-onset time in the chinchilla auditory nerve,'' J. Acoust. Soc. Am. **85**, 1995–2004.
Sinex, D. G., McDonald, L. P., and Mott, J. B (**1991**). ''Neural correlates of nonmonotonic temporal acuity for voice onset time,'' J. Acoust. Soc. Am. **90**, 2441–2449.
Viemeister, N. (**1979**). ''Temporal modulation transfer functions based upon modulation threshold,'' J. Acoust. Soc. Am. **66**, 1364–1380.

Vestibular responses to loud dance music: A physiological basis of the "rock and roll threshold"?

Neil P. McAngus Todd[a)]
Department of Psychology, University of Manchester, Manchester M13 9PL, United Kingdom

Frederick W. Cody
Department of Biological Sciences, University of Manchester, Manchester M13 9PL, United Kingdom

(Received 14 May 1999; revised 27 August 1999; accepted 30 September 1999)

In this paper new evidence is provided to indicate that vestibular responses may be obtained from loud dance music for intensities above 90 dB(A) SPL (Impulse-weighted). In a sample of ten subjects acoustically evoked EMG were obtained from the sternocleidomastoid muscle in response to a sample of techno music typical of that which may be experienced in a dance club. Previous research has shown that this response is vestibularly mediated since it can be obtained in subjects with loss of cochlear function, but is absent in subjects with loss of vestibular function (Colebatch *et al.* [J. Neurol. Neurosurg. Psychiatr. **57**, 190–197 (1994)]. Given that pleasurable sensations of self-motion are widely sought after by more normal means of vestibular stimulation, it is suggested that acoustically evoked sensations of self-motion may account for the compulsion to exposure to loud music. Given further the similarity between the thresholds found, and the intensities and frequency distributions that are typical in rock concerts and dance clubs, it is also suggested that this response may be a physiological basis for the minimum loudness necessary for rock and dance music to work—the ''rock and roll threshold'' [Dibble, J. Audio Eng. Soc. **43**(4), 251–266 (1995)].
 [S0001-4966(00)04801-3]

PACS numbers: 43.64.Ri, 43.66.Lj [RDF]

INTRODUCTION

An issue of increasing concern is the damage that may be caused to the cochlea by loud music (Dibble, 1995; Florentine *et al.*, 1999) in public places such as restaurants, bars, and dance clubs where sounds may reach levels well in excess of 120 dB SPL. However, given that loud music is also considered to be pleasurable, where the loudness of itself is a source of pleasure, to a certain extent independent of other aspects such as rhythm and tempo, then the following question arises. What are the attributes of the sound that contribute respectively to damage and pleasure? According to Dibble (1995) loud music, unlike industrial noise which is known to be harmful, may not be stressful even up to 105 dBL_{Aeq}, and, in his view, ''rock and roll just does not work below a certain threshold level, ...somewhere around 96 dBL_{Aeq}, provided there is sufficient low frequency energy present.'' He suggests further that ''live performance spectra requires at least a 10 dB differential between the mean midband energy level and that of the 50–100 Hz bands, that discotheque systems require 20 dB, and that for 'rave' music, anything up to 30 dB is common place.'' This stands in contrast with industrial noise which tends to have a more flat broadband character. Thus, the source of pleasure appears to be the low frequencies above a certain threshold.

Given this predominance of high-intensity low frequencies in loud music then, it is of immense interest whether it may be the case that acoustically evoked sensations other than normal hearing are being sought after in these environments. One obvious such sensation is vibrotactile (Verillo, 1993). Another less obvious sensation is vestibular (Todd, 1993). While labyrinthine sensitivity to loud sound and vibration is well documented (e.g., von Bekesy, 1935; Lackner and Graybiel, 1974; Young *et al.*, 1977; McCue and Guinan, 1995) for clicks and tone pips, it is not known whether more natural stimuli, as may be found in the sound environment at a rock concert or dance club, may evoke a vestibular response. The goal of this paper then, is to determine the thresholds and growth functions for acoustically evoked vestibular responses to loud dance music. We first briefly review the physiological evidence for acoustic sensitivity of the vestibular system.

It is well established (Popper *et al.*, 1982) that there is a division, in the fish inner ear, between the organs of balance (the three canals and the utricle) and organs which are auditory in function (the sacculus and the lagena). While, during the course of evolution, the cochlea has come to replace the saccule as the primary organ of hearing, evidence suggests that the saccule may have retained some acoustic function in higher vertebrates. For example, auditory sensitivity of the saccule has been demonstrated in amphibians (Moffat and Capranica, 1976), birds (Wit *et al.*, 1984), and, among mammals, in guinea pigs (Cazals *et al.*, 1983), cats (McCue and Guinan, 1995), and squirrel monkeys (Young *et al.*, 1977). Evidence suggests strongly that it is the saccule, rather than the utricle or canals, which is maximally sensitive to sound. The acoustically responsive saccular fibers have irregular spontaneous discharge rates, a range of best stimulus frequencies lying between about 200 and 1000 Hz in the cat, and a rate threshold at about 90 dB SPL, while the synchronization threshold is about 20 dB lower (McCue and Guinan, 1995; Young *et al.*, 1977).

The primary target for saccular afferent fibers is the lateral vestibular nucleus (LVN or Deiter's nucleus) (Didier

a)Electronic mail: todd@fs4.psy.man.ac.uk

et al., 1987; Cazals *et al.*, 1987). In turn, the LVN exerts a major descending influence on spinal motoneurones, particularly muscles innervating the cervical spinal cord, by way of the lateral vestibulo-spinal-tract (LVST) (Wilson and Peterson, 1981). Given that the sacculus has an acoustic sensitivity, the LVST is thought to mediate evoked myogenic responses to acoustic stimuli which may be obtained in humans. In early work, Bickford *et al.* (1964) demonstrated an evoked electromyographic (EMG) response, in a variety of muscles, to clicks. These authors went on to rule out the possibility that the evoked myogenic responses simply constituted a component of the auditory startle reflex (which, unlike the observed responses, adapts very quickly) and came to the conclusion that the myogenic response was vestibular rather than cochlear in origin, since the response was present in patients with neurosensory deafness, but was abolished in those with loss of labyrinthine function. Later work on the myogenic inion response (Townsend and Cody, 1971), using 10-ms tone pips rather than clicks, showed that the response was frequency dependent, with a maximum response between 250 and 500 Hz.

More recently, Colebatch *et al.* (1994) have provided further evidence for an otolithic component of the acoustically evoked, myogenic response by measuring EMG responses of the sternocleidomastoid muscle evoked by loud clicks. They found four main components in the averaged response: n13, p23, p34, and n44. It was established in normal subjects that n13–p23 represented an ipsilateral response to unilateral stimulation (see Fig. 1), whereas p34–n44 reflected a bilateral response to unilateral stimulation. Further recordings from patients with unilateral and bilateral inner-ear deficits showed that the n13–p23 peaks were present in patients with bilateral sensorineural deafness, while p34–n44 peaks were absent. On the other hand, n13–p23 peaks were not present in recordings from patients with loss of vestibular function ipsilateral to the stimulation.

In the work reported here, we set out to investigate whether such EMG responses could be evoked in natural, everyday sound environments, such as may be experienced in a dance club. In order to go some way to answering this we determined the threshold and response growth as a function of stimulus intensity for a natural sound obtained from a sample of dance music.

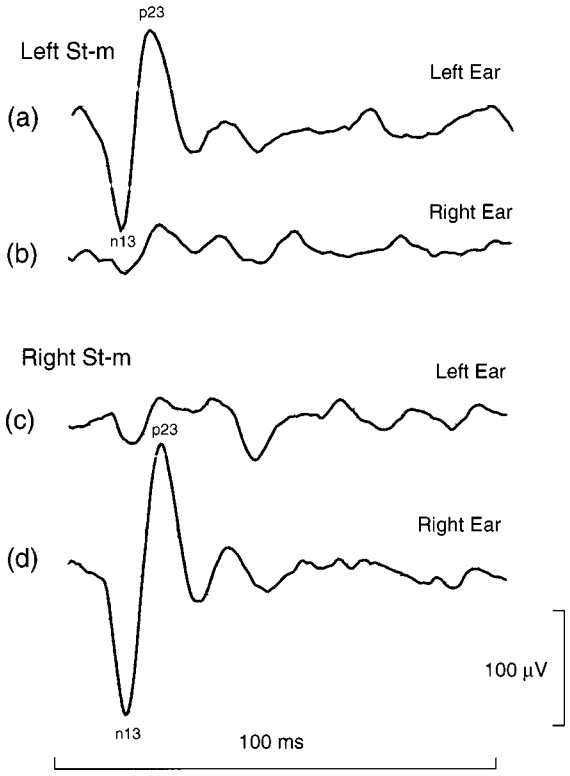

FIG. 1. Averaged, unrectified EMG response recorded from the left and right sternocleidomastoid muscles of one subject in response to a monaurally presented 1-ms click at 110 dB SPL: (a) left sternocleidomastoid, left ear; (b) left sternocleidomastoid, right ear; (c) right sternocleidomastoid, left ear; (d) right sternocleidomastoid, right ear. All labels on the right of the figure refer to the stimulus ear, labels on the left refer to the response muscle. Note the presence of a diphasic negative–positive wave at approximately 13 and 23 ms, consistent with earlier data using click stimuli. A diphasic negative–positive wave corresponds to the passage of depolarizing compound muscle action potentials from positive to negative electrodes.

I. METHOD

A. Subjects

Ten Manchester University undergraduate and postgraduate students were used, five males and five females. Subjects were screened for any neurological impairments, vestibular impairments, and chronic medication. All subjects had pure tone thresholds in the normal range, apart from one subject who had a mild hearing impairment. All subjects were right handed.

B. Apparatus

Stimuli were generated by CED Signal software and delivered via a pair of Sennheiser HD420 headphones. Stimulus intensity was calibrated by means of a B&K 2260 in conjunction with a B&K 4163 artificial ear and 4134 pressure microphone. Differential recordings of EMG were made using two small, surface electrodes. A CED 1902 was used for EMG amplification and analogue filtering. The EMG was sampled by means of a CED 1401 plus. Visual feedback for maintenance of steady background activity was provided by means of an oscilloscope. A standard screening audiometer was used to obtain pure tone thresholds.

C. Stimuli

The stimulus selected was a sample of a single cycle of techno music which consisted of a repetitive percussive sound (Fig. 2). This sample, which sounds like a thud, is quite typical of that which might be experienced in a dance club. The stimulus power spectrum showed that it had peaks at around 100 Hz and 240 Hz, but with a broad distribution. The natural repetition rate was about 2.5 Hz, making it suitable for an EMG averaging run. The stimulus intensity levels to be used were from 90–120 dB SPL in 5-dB steps (A-frequency-weighted and Impulse-time-weighted). These levels were chosen so as to provide a useful range, but to remain below the limits set by the *Noise at Work Regulations (1989)* issued by the *Health and Safety Executive* in order to avoid the possibility of permanent damage. These limits are

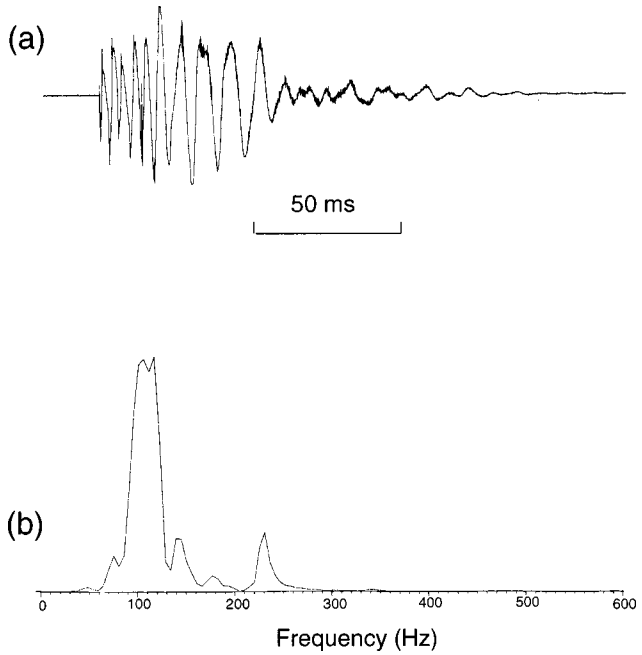

FIG. 2. (a) The stimulus waveform—a sample selected from a single cycle of techno music which consisted of a repetitive percussive sound. (b) The stimulus power spectrum shows that it has peaks at around 100 and 240 Hz but with a broad distribution.

a daily personal noise exposure of 90 dB(A) and a peak sound level (PSL) of 140 dB re 20 μPa. For this purpose two other measures were monitored, in addition to SPL, the equivalent continuous level L_{Aeq} and the PSL.

D. Procedure

Before starting the experiment pure tone audiograms were obtained and a handedness questionnaire was also administered for each subject.

Subjects were informed the purpose of the experiment, that it would involve EMG recording from muscles of the neck, that they would be required to maintain the neck muscles in a state of tension during a recording which may involve some discomfort, and that they would be stimulated by repetitive loud sounds up to 120 dB SPL. Subjects were then asked to read and sign a consent form in order to conform with local ethical committee guidelines.

After subjects had understood and signed the consent form two small, surface electrodes were placed over the upper part of the left sternocleidomastoid muscle. The positive electrode was placed rostral the negative electrode, while the reference electrode was placed on the sternum. After amplification and low-pass filtering at 1 kHz by means of the CED 1902, the EMG was sampled at 2.5 kHz by means of the CED 1401plus. Rectified EMG was used to provide feedback to enable the subject to maintain a suitable level of background muscular contraction, fixed at 80 μV, by voluntarily turning the head to one side. Before the averaging run subjects were given an opportunity to find a sitting position which would minimize discomfort.

Once the subject has found a suitable position the evoked EMG recording was started. The sampled, unrectified EMG was averaged over a run of 512 multiple repetitions of the stimuli. The repetition rate was 2.5 Hz, the natural beat rate of the music. All stimuli were presented monaurally and EMG recorded ipsilateral to the stimulated ear. The averaging procedure was repeated at the seven intensity levels from 90 to 120 dB SPL in 5-dB steps. Between each recording run subjects were allowed to relax. When the procedure was completed for the left side, subjects were given a short break and the whole procedure repeated for the right sternocleidomastoid.

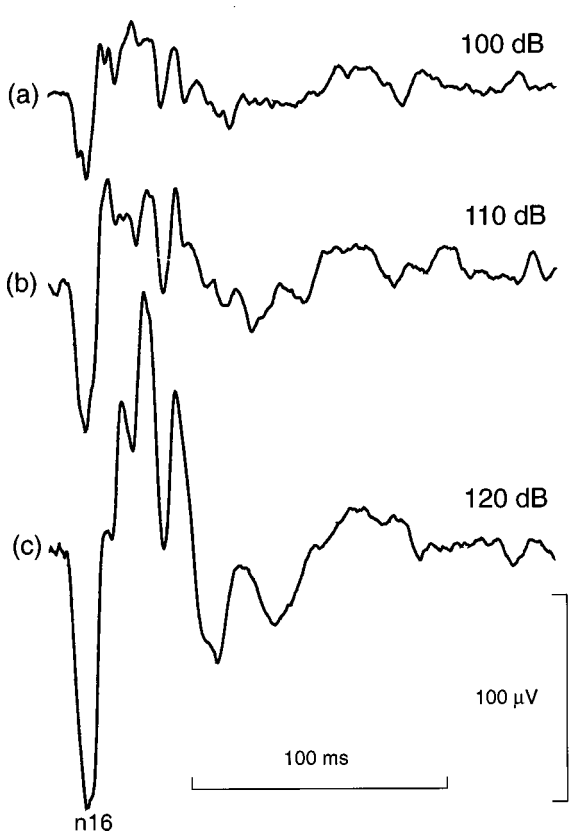

FIG. 3. Average unrectified EMG responses recorded from the left sternocleidomastoid muscle of one subject in response to the techno music sample at (a) 100 dB, (b) 110 dB and (c) 120 dB SPL presented monaurally to the left ear. Note that although the response is more complex than the response to click stimuli there is a clear negative wave at the same latency of about 13 ms, although it arrives about 3 ms later than in response to clicks.

In order to be sure that no permanent damage was being done by this procedure, one subject was monitored extensively before and after measurements. There was no evidence of any significant change in pure tone thresholds for this subject.

II. RESULTS

Although the average response to our particular stimulus is more complex than that to the simple stimuli (see Fig. 3), it still retains a well-defined ipsilateral n13 wave. In order to avoid any contamination the analysis was carried out only on the amplitude of the n13 component measured as the negative deviation from zero.

Figure 4(a) and (b) shows the amplitude of the n13 wave in the ten subjects as a function of intensity in respectively the left and right sternocleidomastoid muscle. The average response is shown in Fig. 4(c). It is clear that there is con-

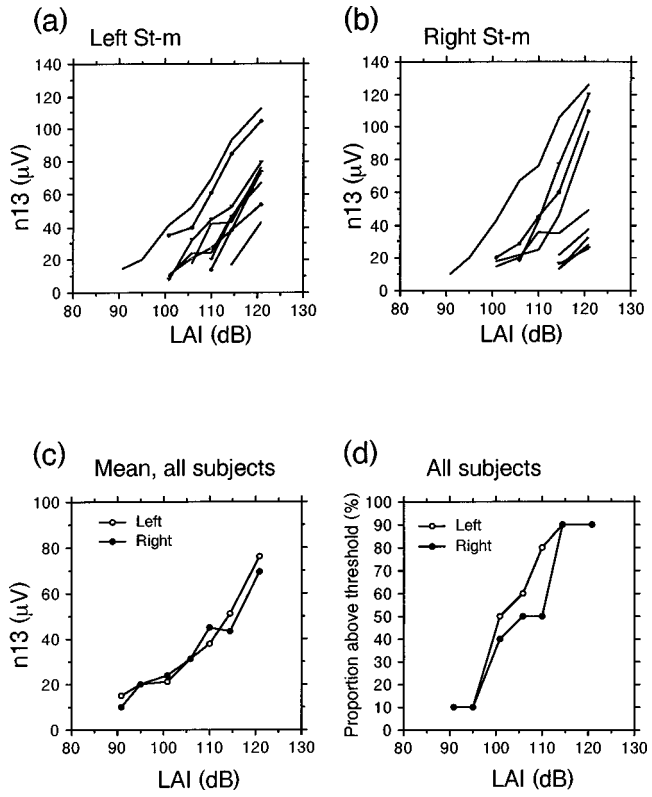

FIG. 4. Effect of stimulus intensity on amplitude of the N13 wave for ten right-handed subjects: (a) left sternocleidomastoid and (b) right sternocleidomastoid. (c) The mean response averaged over those subjects above threshold. (d) The proportion of the subjects above threshold as a function of intensity. All intensities are in dB SPL, A-frequency-weighted and Impulse-time-weighted (notated as LAI).

siderable variation in responsiveness between subjects. However, at 120 dB SPL, 90% of the subjects showed a response [Fig. 4(d)] and the most sensitive subjects had a threshold at about 90 dB. In some subjects an exponential function gave a better fit to the data than a linear function. The population average also shows an exponential growth function. In the interests of health and safety we did not measure the response at intensities higher than 120 dB SPL and so it is not clear whether the exponential growth curve would continue.

In order to check that this response was not related to the function of the cochlea, a product moment correlation was computed with pure tone thresholds (range 0 to 35 dB). A coefficient of 0.135 ($p=0.5748$, $N=20$) indicates no relationship between the strength of the response and thresholds.

III. DISCUSSION

To summarize our results then, in a sample of ten subjects, acoustically evoked vestibularly mediated responses may be obtained above 90 dB(A) SPL (Impulse-weighted) for a natural sound, with frequencies between 100 and 300 Hz, as may be typically experienced in a bar or dance club. Fifty percent of subjects show a response at 105 dB SPL, 90% show a response at 120 dB SPL. In order to determine whether these data are relevant to natural sound environments we need to consider two factors, i.e., the intensity and frequency distributions typically found in dance clubs and rock band concerts.

For intensity distribution, Davis *et al.* (1985) cite a range of 89–119 dB(A) mean intensities for rock groups measured between 1968–1980. The same report cite ranges from 83 to 107 dB(A) for discotheques between 1970–1979. Both these surveys show a trend of increasing loudness with time. Dibble (1988) gives a range of 99–107 dB(A) for discotheques. Griffiths and Staunton (1991) cite values ranging from 94 to 113 L_{Aeq} for a variety of live concerts. In our own survey of dance clubs in Manchester we have obtained measurements somewhat higher than Davis *et al.* or Dibble (1988), depending on where the measurements were taken. In the proximity of the speakers typically the average intensities (*I*-weighted) are nearer 120 dB(A) and often exceed 130 dB(A) SPL.

For frequency distributions, Dibble's summary of data, taken from Cabot *et al.*'s (1979) survey of rock bands and Bickerdike and Gregory's (1979) survey of 49 discotheques, indicates that the peak in the frequency distribution lies between 125 Hz and 500 Hz. Dibble's own measurements give a peak at 50–100 Hz for discotheques and 125–350 Hz for rock bands. Mawhinny and McCullagh's (1993) analysis of sound profiles for different instruments give peaks between 125 and 500 Hz. Our own measurements of Manchester dance clubs are broadly consistent with these results with frequencies between 50–500 Hz being dominant, depending on the location, the style of music, and the venue.

Given these data concerning dance club and rock band sound environments, we may infer that a large proportion of dance club and rock concert attendees will experience acoustically evoked vestibular responses. The distribution of frequencies in the stimuli used here and which are typically dominant in dance club and rock concert sound environments are somewhat lower than the distribution of best frequencies for acoustically responsive saccular fibres in the cat (McCue and Guinan, 1995). However, the data that is available for humans (Townsend and Cody, 1971) and our own data (Todd *et al.*, submitted) indicate that acoustically evoked vestibularly mediated EMG has a minimum threshold at frequencies between 200 and 400 Hz. This is consistent with it being saccularly mediated, since the greater otolith mass of the human sacculus would give it a lower resonant frequency than that of the cat. Thus, the frequency distributions of club sound environments are well matched to the maximal sensitivity of the sacculus.

It is tempting therefore to suggest that Dibble's ''rock and roll threshold'' corresponds to the threshold for acoustic activation of the sacculus. The 96 dBL_{Aeq} corresponds to a value of about 106 dB(A) for the stimuli used here at which 50% of subjects show a response. Although Dibble's value for this threshold is arrived at from his experience as an audio engineer, it is consistent with the above extensive measurements of intensities at rock concerts and discotheques that have been made since the 1960s.

Why should acoustic saccular stimulation be sought after? Anecdotally, it seems clear that sensations of self-motion are widely sought after by more normal means of vestibular stimulation, such as may be obtained from swings, rocking chairs, and fun parks, for example. In a recent study (Todd and Gascoyn, in preparation) we found in a sample of

48 undergraduate students that on a five-point scale the distributions for enjoying the sensations of loud music and enjoying the sensations of swings were extremely close. Approximately 60% responded independently that they enjoyed the sensation of loud music and swings ''quite a lot,'' 20%–30% responded that they enjoyed the sensation of loud music and swings ''a great deal.'' Only about 10% responded that they enjoyed the sensation of loud music and swings ''not much'' or ''not at all.'' A paired means comparison showed no significant difference in these distributions. This implies at least that the sensation of loud music and the sensation of self-motion induced by swings are equally pleasurable.

On their own, the above data do not prove that acoustically evoked saccular responses are a source of pleasure in loud music. The thresholds for vibrotactile sensations also have a minimum for frequencies of about 200 Hz and there is a tendency for people who enjoy loud music to also enjoy vibrations ($r=0.55$, $p<0.0001$) (Todd and Gascoyn, in preparation). Hence, it is also quite plausible to suggest vibrotactile sensations as being a source of pleasure. However, the distribution on the pleasure scale is quite different. Only 25% responded that they enjoyed the sensation of vibrations ''quite a lot.'' We suggest therefore that both vibrotactile and acoustically evoked vestibular sensations may be sources of pleasure in loud music.

IV. SUMMARY AND CONCLUSION

In this paper we have provided further evidence that activation of the vestibular system may be evoked by ''natural'' acoustic stimuli above about 90 dB SPL with frequencies between 100 and 300 Hz. The coincidence of these intensity and frequency values with those typically encountered in dance clubs and rock concerts suggests that the threshold for acoustic activation of the sacculus could be a physiological basis of the ''rock and roll threshold.'' In our sample this corresponds to a level of about 105 dB(A) (Impulse-weighted), where 50% of subjects showed an acoustically evoked response. However, further experiments are required to show a direct relationship between our physiological measure and any possible associated sensation or pleasure. One way this could be done is by means of a parallel psychophysical procedure carried out on each subject in order to estimate the onset of any pleasurable sensation, or any change in the quality of sensation as a function of intensity. Further research is also needed to establish the relative importance of vibrotactile and vestibular sensations as the source of pleasure derived from loud music and the subjective nature of such sensations.

ACKNOWLEDGMENTS

We are grateful to Jon Banks in Biological Sciences at Manchester for his technical assistance with the EMG recording and to Ian Mackenzie in the Department of Audiology for his help with audiometry. We are grateful also to anonymous reviewers for suggestions for improvement of the original manuscript. This work was supported by an equipment grant from the Royal Society.

Bickerdike, J., and Gregory, A. (**1979**). ''An evaluation of hearing damage risk to attenders of discotheques,'' DoE Contract No. DGR481/99, Noise Advisory Council/DoE Project Report, Leeds Polytechnic School of Constructional Studies, UK.

Bickford, R., Jacobson, J., and Cody, D. (**1964**). ''Nature of averaged evoked potentials to sound and other stimuli in man,'' Ann. (N.Y.) Acad. Sci. **112**, 204–223.

Cabot, R. C., Gentner, C. R., and Lucke, T. (**1979**). ''Sound levels and spectra of rock music,'' J. Aud. Eng. Soc. **27**, 267–284.

Cazals, Y., Erre, J., and Aurousseau, C. (**1987**). ''Eighth nerve evoked responses recorded at the base of the vestibular nucleus in the guinea pig,'' Hear. Res. **31**, 93–98.

Cazals, Y., Aran, J., Erre, J., Guihaume, A., and Aurousseau, C. (**1983**). ''Vestibular acoustic reception in the guinea pig: A saccular function?'' Acta Oto-Laryngol. **95**, 211–217.

Colebatch, J., Halmagyi, G., and Skuse, N. (**1994**). ''Myogenic potentials genereated by a click-evoked vestibulocollic reflex,'' J. Neurol. Neurosurg. Psychiatr. **57**, 190–197.

Davis, A., Fortnum, R., Coles, A., and Lutman, M. (**1985**). ''Damage to hearing arising from leisure noise—A review of the literature,'' Report by the Medical Research Council Hearing Research Unit, University of Nottingham, UK.

Dibble, K. (**1988**). ''The 1988 BEDA Discotheque Survey Project,'' in *Proceedings of the Institute of Acoustics*, Vol. 10(7), pp. 275–285.

Dibble, K. (**1995**). ''Hearing loss and music,'' J. Aud. Eng. Soc. **43**(4), 251–266.

Didier, A., Cazals, T., and Aurousseau, C. (**1987**). ''Brainstem connections of the anterior and posterior parts of the saccule in the guinea pig,'' Acta Otolaryngol. (Stockholm) **104**, 385–391.

Florentine, M., Hunter, W., Robinson, M., Ballou, M., and Buus, S. (**1999**). ''On the behavioural characteristics of loud music listening,'' Ear Hear. **19**(6), 420–428.

Griffiths, J. E., and Staunton, J. S. (**1991**). ''Audience exposure to sound at pop concerts and the impact of proposed guidelines,'' in *Proceedings of the Institute of Acoustics*, Vol. 13(7).

Lackner, J., and Graybiel, A. (**1974**). ''Elicitation of vestibular side effects by regional vibration of the head,'' Aerosp. Med. **45**(11), 1267–1272.

Mawhinney, C., and McCullagh, G. (**1993**). ''Music induced hearing loss in musicians playing different musical instruments,'' in *Proceedings of the Institute of Acoustics*, Vol. 14(5), pp. 95–105.

McCue, M., and Guinan, J. (**1995**). ''Spontaneous activity and frequency selectivity of acoustically responsive vestibular afferents in the cat,'' J. Neurophysiol. **74**(4), 1563–1572.

Moffat, A., and Capranica, R. (**1976**). ''Auditory sensitivity of the saccule in the American toad (*Bufo americanus*),'' J. Comp. Physiol. **105**, 1.

Popper, A., Platt, C., and Saidal, W. (**1982**). ''Acoustic functions in the fish ear,'' Trends Neurosci. **5**, 276–280.

Todd, N. P. M. (**1993**). ''Vestibular feedback in music performance,'' Music Perception **10**(3), 379–382.

Todd, N. P. M., and Gascoyn, E. (**in preparation**). ''Effects of music exposure and drug consumption on hearing loss.''

Todd, N. P. M., Cody, F., and Banks, J. (**submitted**). ''A saccular origin of frequency tuning in myogenic vestibular evoked potentials?: Inplications for human responses to loud sounds,'' Hearing Res.

Townsend, G., and Cody, D. (**1971**). ''The average inion response evoked by acoustic stimulation: its relation to the saccule,'' Ann. Otol. Rhinol. Laryngol. **80**, 121–131.

Verrillo, R. (**1992**). ''Vibration sensation in humans,'' Music Perception **9**(3), 281–302.

von Bekesy, G. (**1935**). ''Uber akustische Reizung des Vestibularapparates,'' Arch. Ges. Physiol. **236**, 59.

Wilson, V., and Peterson, B. (**1981**). in *Handbook of Physiology, Section 1: The Nervous System, Vol. II. Motor Control, Part 1*, edited by V. B. Brooks (American Physiological Society, Bethesda, MD), pp. 667–702.

Wit, H., Bleeker, J., and Mulder, H. (**1984**). ''Response of pigeon vestibular nerve fibres to sound and vibration with audio frequencies,'' J. Acoust. Soc. Am. **75**, 202–208.

Young, E., Fernandez, C., and Goldberg, J. (**1977**). ''Responses of squirrel monkey vestibular neurons to audio-frequency sound and head vibration,'' Acta Oto-Laryngol. **84**, 352–360.

Basilar-membrane nonlinearity estimated by pulsation threshold

Christopher J. Plack[a)]
Department of Psychology, University of Essex, Wivenhoe Park, Colchester CO4 3SQ, England

Andrew J. Oxenham
Research Laboratory of Electronics, Massachusetts Institute of Technology, Cambridge, Massachusetts 02139

(Received 22 July 1999; revised 16 September 1999; accepted 21 September 1999)

The pulsation threshold technique was used to estimate the basilar-membrane (BM) response to a tone at characteristic frequency (CF). A pure-tone signal was alternated with a pure-tone masker. The frequency of the masker was 0.6 times that of the signal. For signal levels from around 20 dB above absolute threshold to 85 dB SPL, the masker level was varied to find the level at which a transition occurred between the signal being perceived as ''pulsed'' or ''continuous'' (the pulsation threshold). The transition is assumed to occur when the masker excitation is somewhat greater than the signal excitation at the place on the BM tuned to the signal. If it is assumed further that the response at this place to the lower-frequency masker is linear, then the shape of the masking function provides an estimate of the BM response to the signal. Signal frequencies of 0.25, 0.5, 1, 2, 4, and 8 kHz were tested. The mean slopes of the masking functions for signal levels between 50 and 80 dB SPL were 0.76, 0.50, 0.34, 0.32, 0.35, and 0.41, respectively. The results suggest that compression on the BM increases between CFs of 0.25 and 1 kHz and is roughly constant for frequencies of 1 kHz and above. Despite requiring a subjective criterion, the pulsation threshold measurements had a reasonably low variability. However, the estimated compression was less than in an earlier study using forward masking. The smaller amount of compression observed here may be due to the effects of off-frequency listening. [S0001-4966(00)02201-3]

PACS numbers: 43.66.Dc, 43.66.Ba, 43.66.Mk [SPB]

INTRODUCTION

The basilar membrane (BM) in the cochlea has a response function that is highly nonlinear and compressive (Rhode and Robles, 1974; Robles *et al.*, 1986; Murugasu and Russell, 1995; Ruggero *et al.*, 1997; Russell and Nilsen, 1997). Recent results suggest that the BM is the primary source of the nonlinearities observed in psychophysical masking experiments (Oxenham and Moore, 1995; Moore and Oxenham, 1998; Oxenham and Plack, 1998; Plack and Oxenham, 1998). Furthermore, cochlear nonlinearities have a significant influence on a wide range of basic auditory processes, such as frequency selectivity (Hicks and Bacon, 1999; Moore *et al.*, 1999), temporal integration (Oxenham *et al.*, 1997), and loudness growth (Yates, 1990; Moore and Glasberg, 1997; Moore and Oxenham, 1998). It is clear that future models of hearing will need to incorporate a simulation of the characteristics of the BM if they are to provide an accurate account of our perceptions.

While direct physiological measurements of BM vibration have provided a great deal of information about the nature of the nonlinearity, these measurements have been restricted to very high (Ruggero *et al.*, 1997; Russell and Nilsen, 1997) and low (Rhode and Cooper, 1996) characteristic frequencies (CFs): Only the basal and apical turns of the cochlea are readily accessible. In addition, of course, it is not practical to make such measurements in live human beings.

Oxenham and Plack (1997) attempted to estimate the BM response in humans using a psychophysical forward-masking technique. A brief pure-tone signal was presented shortly after a pure-tone masker with a frequency an octave below the signal. A forward-masking design was used so that there could be no interaction between the masker and the signal on the BM (Arthur *et al.*, 1971; Ruggero *et al.*, 1992; Nelson and Schroder, 1997). In this respect the design differed from those that used simultaneous masking to estimate BM compression (Stelmachowicz *et al.*, 1987; Bacon *et al.*, 1999). For a range of signal levels, the masker level was varied to find threshold. The technique relies on the finding that the BM response to a tone well below CF is roughly linear (Murugasu and Russell, 1995; Ruggero *et al.*, 1997; Russell and Nilsen, 1997). In other words, a 10-dB increase in masker level will produce a 10-dB increase in BM vibration (excitation) at the place tuned to the signal frequency. If it is assumed that the signal is detected using the information at this place, and if it is assumed further that the ratio of signal excitation to masker excitation is constant at threshold, then any BM compression applied to the signal will be reflected in the slope of the masking function. For example, if the compression ratio is 5:1, then a 10-dB increase in signal level will produce only a 2-dB increase in BM excitation. Hence, the masker level will only need to be increased by 2 dB for the signal to remain at threshold. In other words, a shallow masking function (masker level plotted against signal level) with a slope less than 1 indicates compression.

a)Electronic mail: cplack@essex.ac.uk

Using the forward-masking technique, Oxenham and Plack (1997) estimated the CF response at 2 and at 6 kHz. They found approximately 5:1 compression for signal levels between about 45 and 80 dB SPL, with a more linear response at low and high levels. The results were consistent with the physiological data (Yates *et al.*, 1990; Ruggero, 1992; Murugasu and Russell, 1995), suggesting that the assumptions of the technique are valid. Furthermore, measurements on hearing-impaired listeners revealed much less compression, consistent with the physiological consequences of cochlear damage (Ruggero and Rich, 1991; Ruggero *et al.*, 1993). Indeed, the experiments of Moore *et al.* (1999), comparing several behavioral measures of BM nonlinearity in normal and impaired listeners, suggest that the forward-masking design may provide a reliable indication of the state of the active mechanism.

Although the results of Oxenham and Plack (1997) are encouraging, there is a serious limitation to their technique. In order to obtain a substantial amount of masking for such a large frequency separation between the masker and the signal, the signal needed to be very brief (4 ms) and presented very shortly after masker offset. The silent interval between the masker and the signal was only 2 ms. At low frequencies it is not advisable to use the same parameters. First, the width of the auditory filter becomes narrow compared to the spectral extent of the signal, so that the effects of ''spectral splatter'' become a serious concern. Second, the longer temporal response of the auditory filters at low frequencies (Kiang *et al.*, 1970) means that the masker and the signal may overlap on the BM, producing nonlinear effects such as suppression that could confound the results (Ruggero *et al.*, 1992; Nelson and Schroder, 1997).

The present article explores an alternative design based on the pulsation threshold technique devised by Houtgast (1972). This technique relies on an auditory illusion whereby an interrupted sound is perceived as being continuous if there is sufficient energy from another sound during the interruption. Consider the situation in which a signal is alternated with a low-frequency masker. If the masker excitation at the place tuned to the signal is greater than the signal excitation, then the signal may be perceived as continuous. As described earlier, for a masker much lower in frequency than the signal, the masker excitation at the signal place is related linearly to the masker level. If threshold is defined as the masker level at which the perception of the signal changes from ''pulsed'' to ''continuous,'' then a plot of masker level at threshold against signal level should provide an estimate of the BM response to the signal, in the same way as in the Oxenham and Plack (1997) forward-masking design.

The advantage of the pulsation threshold technique is that long signals and long maskers can be used, avoiding the frequency limitations inherent in the forward-masking design. Any short-term interactions on the BM at masker and signal transitions are likely to be insignificant with regard to the overall perception of the signal as pulsed or continuous.

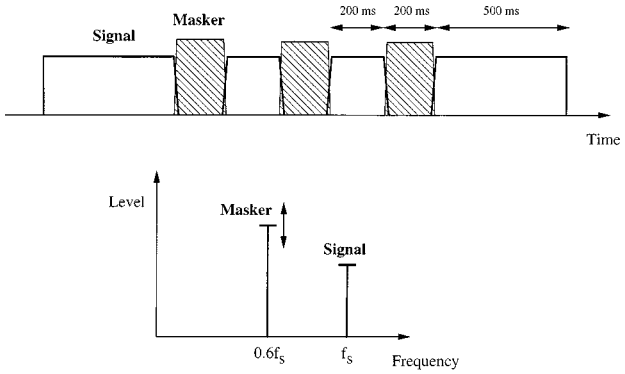

FIG. 1. A schematic illustration of the temporal and spectral characteristics of the stimuli.

I. METHOD

A. Stimuli

The maskers and signals were sinusoids, gated with 20-ms raised-cosine ramps. The masker was presented diotically, and the signal was presented monaurally. This had the effect of spatially separating the two stimuli, such that the masker and signal were lateralized to the center and side, respectively. This made it easier for the listeners to concentrate on the signal, while attempting to ignore the masker. Also, it had the benefit of ruling out the detection of signal pulsation in the contralateral ear, due to acoustic or electric crosstalk. Each interval began with a 540-ms (total duration) signal, followed by an alternating sequence of three maskers and two signals, each with a total duration of 240 ms, and finishing with another 540-ms signal (see Fig. 1). All stimuli began 30 ms before the end of the previous stimulus, so that the ramps of the maskers and signals overlapped and crossed at a point where the envelopes were approximately 1.4 dB below their peak values. This was done to prevent an audible gap between the maskers and the signals being used as a cue for whether the signal was pulsed or continuous.

Signal frequencies of 250, 500, 1000, 2000, 4000, and 8000 Hz were tested. The masker frequency was set at 0.6 times the signal frequency. At each frequency, signal levels from about 20 dB above absolute threshold (as measured in each listener individually) to 85 dB SPL were tested.

The maskers and signals were generated digitally and played out separately via a D/A converter (TDT DD1) at a sampling rate of 50 kHz. The stimuli were then low-pass filtered at 20 kHz (TDT FT5) and attenuated (TDT PA4) before being combined (TDT SM3), passed through a headphone buffer (TDT HB6), and presented via a Sony MDR-V6 headset.

B. Procedure

Pulsation thresholds were measured using a one-interval interleaved adaptive procedure, similar to that described by Jesteadt (1980). In a given run, the masker level was varied and the signal level was held constant. Listeners were asked after each trial to decide whether the signal sounded ''pulsed'' or ''continuous'' by pressing the appropriate button. To help them get accustomed to the task, a demonstration program was used before the experiment started, and

occasionally before the start of a new session. In this program, the signal level was set at either 55 or 65 dB and the masker level was set 10 dB lower, making any gating of the signal clearly audible. Listeners could then elect to hear either a pulsed or a continuous signal by pushing one of two buttons. In the pulsed case, a stimulus was presented where the gating of the stimuli was identical to that used within the experiment itself. In the continuous case, the signal actually was continuous (and was heard as such), while the masker was gated in the same way as in the experiment. There was no difference in level between the two conditions. This demonstration was found to be very useful in helping naive listeners focus on the temporal characteristics of the signal, while trying to ignore the masker, which was always gated.

Each run consisted of two interleaved tracks, one tracking the point on the psychometric function corresponding to 70.7% of continuous responses (track 1), and the other tracking the point corresponding to 29.3% of continuous responses (or 70.7% of pulsed responses; track 2). The initial levels of tracks 1 and 2 were 95 and 60 dB SPL, respectively. These levels were chosen as they were found in pilot tests to almost always result in continuous and pulsed responses, respectively, in all conditions. For track 1, two consecutive continuous responses resulted in a decrease in masker level, while every pulsed response resulted in an increase in level. For track 2, two consecutive pulsed responses were required to increase the masker level, while one continuous response resulted in a decrease in masker level.

The initial step size of the masker level was 5 dB. For each track independently, the step size decreased to 2 dB after three reversals. Each track was terminated after seven reversals and the mean of the last four reversals was defined as the threshold. The means from both tracks were averaged to estimate the 50% point, at which a pulsed response was as likely as a continuous response. Some difference between the two tracks is expected, given that they were tracking different points on the psychometric function. However, if the difference between the two tracks was 10 dB or more, the run was discarded and rerun at a later time. If more than two of the four runs had to be discarded, that data point was abandoned. This occurred for some listeners at the lowest signal levels tested. The highest allowable masker level was 107 dB SPL at signal frequencies of 250 and 500 Hz, and 100 dB SPL for all other frequencies. If the adaptive procedure called for a level higher than this, the level was set to the maximum allowable level. If the maximum level was used more than five consecutive times in a track, the run was terminated.

Each threshold reported is the mean of at least four threshold estimates (except for listener AO who only completed three repetitions for each condition).

C. Listeners

A total of six listeners participated in the experiment. Their ages ranged from 20 to 45 years (median age 24). All except author AO were college students who were paid for their participation. Absolute thresholds for a 500-ms pure-tone signal, at octave frequencies between 250 and 8000 Hz, were measured using a two interval, forced-choice (2IFC), three-down one-up adaptive procedure. These values are presented in Table I. All listeners had thresholds of 15 dB HL or less over this frequency range.

TABLE I. The absolute thresholds for the six listeners (in dB SPL) at the six frequencies tested in the experiment. The signal was a 500-ms pure tone.

Subject	250 Hz	500 Hz	1 kHz	2 kHz	4 kHz	8 kHz
EF	28	12	8	4	12	18
BT	20	4	−2	2	6	23
KS	28	22	11	19	16	31
EL	18	9	10	13	10	34
YO	25	13	12	10	8	18
AO	26	12	7	10	12	11

All listeners except AO were naive. Between 2 and 4 h practice was needed for performance to stabilize on the pulsation-threshold task.

II. RESULTS

The individual and mean results are shown in Fig. 2. The average standard deviation across listeners and conditions was 3.2 dB. The missing data points are for conditions in which the signal was too close to absolute threshold for a reliable masked threshold to be found, or where the masker exceeded the highest allowable level. While listener YO shows lower thresholds than the others (note that lower thresholds suggest *less* frequency selectivity), overall the form of the data is consistent between the six listeners. The thick lines show the mean results for conditions where thresholds were available from all six listeners. As explained in the Introduction, the masking function is an estimate of the BM response function for the place with CF equal to the signal frequency. The dotted lines in Fig. 2 show a slope of 1 (linear growth) for comparison. Slopes shallower than unity indicate compression. It is clear that the masking functions for the two lower frequencies (250 and 500 Hz) are steeper than those for the higher frequencies. Indeed, the slopes at 250 Hz do not differ greatly from unity.

Table II shows the slopes of the masking functions for the six listeners together with the mean slopes. These values were obtained by straight-line fits to the data for signal levels from 50 to 80 dB SPL inclusive. (The earlier data of Oxenham and Plack, 1997, suggest that compression is maximal between 50 and 80 dB SPL.) A within-subjects analysis of variance (ANOVA) conducted on these values found a highly significant main effect of frequency $[F(5,25)=18.095,\ p<0.000\,05]$. Pairwise comparisons (Tukey) revealed that the slopes at 250 Hz differed from the slopes for all the other frequencies, and that in addition the slopes at 500 Hz differed from the slopes at 2 kHz. No other comparisons were significant. Table II also shows the compression ratios for each frequency. These values are simply the inverse of the mean slopes.

III. DISCUSSION

A. Comparison with previous results

The masking function slopes for high signal frequencies from the present study are about twice those reported by

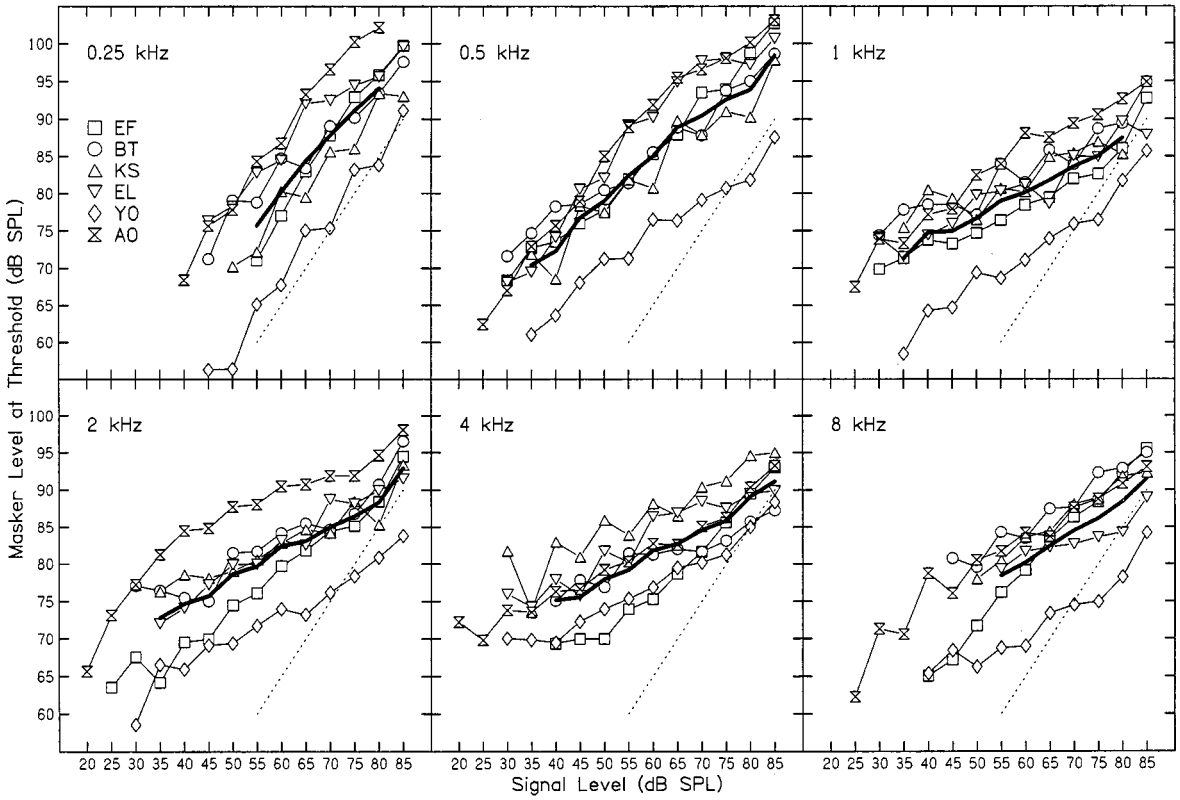

FIG. 2. The results from the main experiment, showing the masker level at pulsation threshold as a function of signal level. The thick lines show the mean results. The dashed lines show a slope of 1 (linear response) for comparison.

Oxenham and Plack (1997). Consequently, the estimated compression (around 2.8:1) is half as great as that derived from the earlier study. Part of the discrepancy may be attributed to a difference in the stimuli. Oxenham and Plack used a high-pass noise to restrict off-frequency listening on the high-frequency side of the excitation pattern. No such noise was used in the present study.

Off-frequency listening may have a strong influence on thresholds in the presence of a low-frequency masker (Johnson-Davies and Patterson, 1979; O'Loughlin and Moore, 1981). As signal level is increased, excitation spreads to the higher CFs. The resulting ''expansive'' improvement in detectability as more channels become available may counteract the on-frequency compression to some extent, reducing the effect of BM nonlinearity on the slope of the masking function. Furthermore, if listeners use auditory filters with CFs greater than the signal frequency, the amount of compression will be less (compression decreases as the input frequency is moved away from CF, see for example Ruggero *et al.*, 1997). When Oxenham and Plack (1997) ran a control condition without the high-pass noise, the slope they found was much less than for the noise conditions, and was in fact very similar to the slopes reported in Table II. Moore *et al.* (1999) found slopes similar to those reported here for their normal listeners using forward masking in the absence of a high-pass noise.

B. BM nonlinearity as a function of frequency

The results suggest that the amount of compression on the BM increases from 250 Hz to 1 kHz and is roughly constant for frequencies of 1 kHz and above. In this respect,

TABLE II. The slopes of the masking functions (for signal levels from 50 to 80 dB SPL) for the six listeners in the experiment. Also shown are the compression ratios (the inverse of the mean slopes).

Subject	250 Hz	500 Hz	1 kHz	2 kHz	4 kHz	8 kHz
EF	1.007	0.681	0.357	0.461	0.629	0.668
BT	0.501	0.507	0.349	0.275	0.216	0.430
KS	0.732	0.457	0.317	0.258	0.306	0.450
EL	0.596	0.503	0.306	0.371	0.285	0.177
YO	0.900	0.379	0.410	0.357	0.343	0.385
AO	0.819	0.489	0.324	0.213	0.339	0.347
Mean slope:	0.759	0.502	0.344	0.323	0.353	0.410
Compression ratio (dB/dB):	1.318	1.992	2.908	3.101	2.833	2.442

the results are consistent with those of Oxenham and Plack (1997), who found no difference between the slopes of the masking functions at 2 and 6 kHz. Hicks and Bacon (1999) examined the effect of frequency on three different psychophysical measures of auditory nonlinearity: frequency selectivity as a function of level; two-tone suppression; and growth of forward masking with masker frequency lower than the signal frequency. All the measures showed a progressive increase in nonlinearity from 750 Hz to 3 kHz with no evidence of nonlinear processing at 375 Hz. The results of Hicks and Bacon, particularly those for the growth-of-masking experiment, are broadly consistent with the results reported here. Similarly, Bacon *et al.* (1999), using the upward spread of simultaneous masking to estimate BM nonlinearity, found evidence for less compression at 400 to 750 Hz than at 1944 to 5000 Hz.

The conclusions based on psychophysical data do depend on an important assumption, however. In the design of Oxenham and Plack (1997), and in the present design, the masking-function slopes will only differ from unity if there is *differential* compression between the signal and the masker. If both the masker and the signal are compressed equally, then the two effects should cancel out and the slope of the masking function will be unity. In other words, the present results are consistent with the possibility that the BM response function is just as compressive at low frequencies as at high frequencies. If this is the case, however, the region of compression at low frequencies must extend over a wider range of frequencies relative to CF.

The two additional techniques used by Hicks and Bacon (1999) may also depend on this assumption. Frequency selectivity will change as a function of level only if the growth of excitation differs between frequency regions relative to CF. In other words, the compression must be frequency selective. Psychophysical two-tone suppression, the other frequency-dependent measure of compression reported by Hicks and Bacon, is more complex. However, it is possible to imagine situations in which there is a great deal of compression without any suppression. For example, if compression is applied after filtering, then the (nominal) suppressor can only add to the overall output of the channel, not reduce it. Incidentally, this is also a situation in which the compression would not be frequency selective.

The apical BM displacement measurements of Rhode and Cooper (1996) suggest that the compression may indeed be less frequency selective at low frequencies than at high, with a broad band of frequencies affected relative to CF. Although the overall compression they measured was less than that found basally, consistent with the psychophysical results, it could be argued that the techniques used to investigate the apex of the cochlea are more disruptive to the physiology than those used in the basal region. Specifically, Reissner's membrane is opened in the apical procedure, which may disrupt the ionic balance of the scala media, thereby damaging the active mechanism.

Another concern with the present data is that the masker frequency was always a constant fraction of the signal frequency. Estimates of the equivalent rectangular bandwidth (ERB) of the auditory filter show that, when expressed as a proportion of CF, the ERB increases with decreasing frequency (Moore and Glasberg, 1983; Glasberg and Moore, 1990). Considered together with the findings of Rhode and Cooper, it could be argued that for low signal frequencies the masker frequency was too close to CF to be within the linear response region. To test this idea, additional masking functions were measured for a 250-Hz signal with a masker frequency of only 100 Hz. Three listeners were tested; the results are shown in Fig. 3. The slopes of the masking functions (for signal levels from 50 to 80 dB SPL) were 0.583, 0.803, and 1.107 for listeners EL, YO, and AO, respectively. These values are similar to those for the equivalent conditions from the main experiment, and there is certainly no evidence that the slope of the masking function decreases as the masker is moved away from the signal frequency. This conclusion is similar to that drawn by Bacon *et al.* (1999) using simultaneous masking. They found little difference between using a masker that was a fixed fraction of the signal frequency (about 0.69), or a masker that was a fixed number of ERBs (3) below the signal frequency. The data lend support to the hypothesis that BM compression decreases at low CFs in humans, although it is still conceivable that the compressive range reported by Rhode and Cooper would encompass both masker and signal, even for the wide frequency separation in the final experiment. At least it can be argued that there is strong psychophysical and physiological evidence for a larger frequency-selective component of nonlinearity at high CFs than at low.

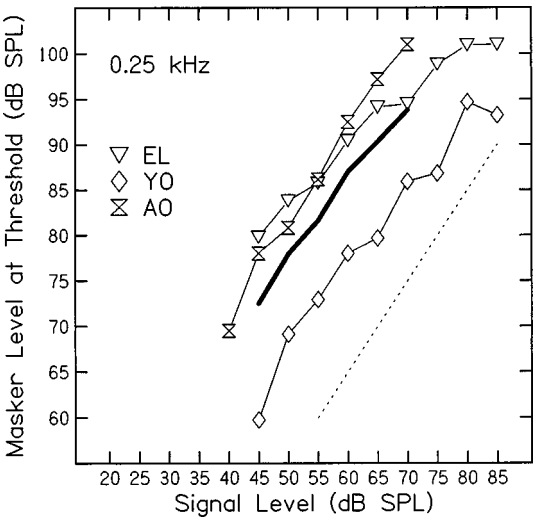

FIG. 3. The results from the experiment described in Sec. III B, showing the masker level at pulsation threshold as a function of signal level, for a 100-Hz masker and a 250-Hz signal. The thick line shows the mean results.

C. An evaluation of the pulsation-threshold technique

As described in Sec. III A, the estimates of compression at high frequencies from the present experiment are less than those reported by Oxenham and Plack (1997), and less than those predicted by the physiology (Murugasu and Russell, 1995; Ruggero *et al.*, 1997; Russell and Nilsen, 1997). It was suggested that the difference could be explained by off-frequency listening. Oxenham and Plack (1997) argued that the effects of off-frequency listening could be minimized by

using the ratio of slopes for an off-frequency masker and an on-frequency masker as the estimate of compression. The reasoning is that the expansive effects of off-frequency listening on the two masking functions should cancel out to some extent. The pilot data of Oxenham and Plack (1997) using one listener supported this argument. Moore *et al.* (1999) also used the ratio-of-slopes technique to estimate compression in their study. The argument is correct if one assumes that off-frequency listening increases detectability by increasing the number of channels that can contribute to detection, as this would be the same for both on- and off-frequency maskers. However, the argument may not be sound for situations in which the signal is detected through a channel with a much higher CF than the signal frequency. In this case, the excitation due to both the signal and the masker will grow roughly linearly (the BM response to a tone well below CF is linear). When the masker and the signal have the same frequency and a similar level, the form of the BM response function has little effect on threshold (since the masker and signal are either both compressed or both passed linearly). In other words, the slope of the masking function for the on-frequency condition should not be affected greatly by listening at a higher CF. However, for the case where the masker frequency is less than the signal frequency (the crucial condition), the use of a channel with a CF higher than the signal frequency may produce a more *linear* masking function. Thus, the ratio of slopes for the on- and off-frequency maskers may not provide an accurate estimate of BM compression, if off-frequency listening is not accounted for. With respect to the present design, Houtgast (1972) and Duifhuis (1980) used on-frequency pulsation maskers and found that signal thresholds were about 3 dB lower than the masker level and generally increased linearly with masker level. In other words, with respect to the present data it is unlikely that the ratio-of-slopes estimate would predict any more compression than that reported in Table II.

It may be necessary instead to modify the pulsation threshold stimuli to include a high-pass noise to mask the spread of excitation. Some pilot experiments were run with a background noise, but listeners found the task much harder under these conditions and produced much more variable results, leading to the attempt being abandoned. It remains to be seen whether additional manipulations will prove more successful.

With respect to the reliability of the design, the results are quite encouraging. Despite the fact that threshold depends on a subjective criterion (whether or not the signal sounds pulsed), the standard deviation between replications was quite low, with an average of 3.2 dB. The average standard deviation between replications for the Oxenham and Plack (1997) forward-masking study was 2.1 dB, so the ''subjective'' tracking procedure is by no means disgraced by the conventional 2AFC adaptive technique. The finding of reasonably consistent results supports a similar conclusion drawn by Duifhuis (1980). Using on-frequency maskers in conjunction with a suppressor, he found that the within- and across-session standard deviations were very similar for forward masking and pulsation threshold.

The amount of time taken to reach stable performance on the present task varied between listeners. Some were stable right away while others took a few hours' practice to stabilize. Again, the pulsation-threshold technique did not differ from the forward-masking technique in this regard.

IV. CONCLUSIONS

(i) Masking functions generated by the pulsation-threshold technique showed a strong dependence on signal frequency. The slopes were roughly constant for frequencies of 1 kHz and above but became more linear as the signal frequency decreased from 1 kHz to 250 Hz. The estimated BM compression varied from 1.3:1 at 250 Hz to around 2.8:1 at the higher frequencies.

(ii) The pulsation-threshold technique for estimating BM compression yields thresholds with a reasonably low variability, and allows a wide range of frequency regions to be explored. However, the technique may underestimate the amount of compression, possibly because listeners use information on the high-frequency side of the excitation pattern which was not masked in the present study.

ACKNOWLEDGMENTS

The first author was supported by a Royal Society University Research Fellowship and the second author by NIH/NIDCD Grant No. R03DC03628. The collaboration was made possible by a grant from the Wellcome Trust. The data were collected while the second author was at the Institute for Hearing, Speech, and Language, Northeastern University, Boston. The authors thank Sid Bacon and two anonymous reviewers for constructive comments on an earlier version of the article.

Arthur, R. M., Pfeiffer, R. R., and Suga, N. (**1971**). ''Properties of 'two tone inhibition' in primary auditory neurones,'' J. Physiol. (London) **212**, 593–609.

Bacon, S. P., Boden, L. N., Lee, J., and Repovsch, J. L. (**1999**). ''Growth of simultaneous masking for $fm<fs$: Effects of overall frequency and level,'' J. Acoust. Soc. Am. **106**, 341–350.

Duifhuis, H. (**1980**). ''Level effects in psychophysical two-tone suppression,'' J. Acoust. Soc. Am. **67**, 914–927.

Glasberg, B. R., and Moore, B. C. J. (**1990**). ''Derivation of auditory filter shapes from notched-noise data,'' Hear. Res. **47**, 103–138.

Hicks, M. L., and Bacon, S. P. (**1999**). ''Psychophysical measures of auditory nonlinearities as a function of frequency in individuals with normal hearing,'' J. Acoust. Soc. Am. **105**, 326–338.

Houtgast, T. (**1972**). ''Psychophysical evidence for lateral inhibition in hearing,'' J. Acoust. Soc. Am. **51**, 1885–1894.

Jesteadt, W. (**1980**). ''An adaptive procedure for subjective judgements,'' Percept. Psychophys. **28**, 85–88.

Johnson-Davies, D. B., and Patterson, R. D. (**1979**). ''Psychophysical tuning curves: Restricting the listening band to the signal region,'' J. Acoust. Soc. Am. **65**, 765–770.

Kiang, N. Y.-S., Moxon, E. C., and Levine, R. A. (**1970**). ''Auditory-nerve activity in cats with normal and abnormal cochleas,'' in *Sensorineural Hearing Loss*, edited by G. E. W. Wolstenholme and J. Knight (Churchill, London), pp. 241–268.

Moore, B. C. J., and Glasberg, B. R. (**1983**). ''Suggested formulae for calculating auditory-filter bandwidths and excitation patterns,'' J. Acoust. Soc. Am. **74**, 750–753.

Moore, B. C. J., and Glasberg, B. R. (**1997**). ''A model of loudness perception applied to cochlear hearing loss,'' Aud. Neurosci. **3**, 289–311.

Moore, B. C. J., and Oxenham, A. J. (**1998**). ''Psychoacoustic consequences of compression in the peripheral auditory system,'' Psychol. Rev. **105**, 108–124.

Moore, B. C. J., Vickers, D. A., Plack, C. J., and Oxenham, A. J. (**1999**). ''Inter-relationship between different psychoacoustic measures assumed to be related to the cochlear active mechanism,'' J. Acoust. Soc. Am. (in press).

Murugasu, E., and Russell, I. J. (**1995**). ''Salicylate ototoxicity: The effects on basilar membrane displacement, cochlear microphonics, and neural responses in the basal turn of the guinea pig cochlea,'' Aud. Neurosci. **1**, 139–150.

Nelson, D. A., and Schroder, A. C. (**1997**). ''Linearized response growth inferred from growth-of-masking slopes in ears with cochlear hearing loss,'' J. Acoust. Soc. Am. **101**, 2186–2201.

O'Loughlin, B. J., and Moore, B. C. J. (**1981**). ''Improving psychoacoustical tuning curves,'' Hear. Res. **5**, 343–346.

Oxenham, A. J., and Moore, B. C. J. (**1995**). ''Additivity of masking in normally hearing and hearing-impaired subjects,'' J. Acoust. Soc. Am. **98**, 1921–1934.

Oxenham, A. J., Moore, B. C. J., and Vickers, D. A. (**1997**). ''Short-term temporal integration: Evidence for the influence of peripheral compression,'' J. Acoust. Soc. Am. **101**, 3678–3687.

Oxenham, A. J., and Plack, C. J. (**1997**). ''A behavioral measure of basilar-membrane nonlinearity in listeners with normal and impaired hearing,'' J. Acoust. Soc. Am. **101**, 3666–3675.

Oxenham, A. J., and Plack, C. J. (**1998**). ''Suppression and the upward spread of masking,'' J. Acoust. Soc. Am. **104**, 3500–3510.

Plack, C. J., and Oxenham, A. J. (**1998**). ''Basilar membrane nonlinearity and the growth of forward masking,'' J. Acoust. Soc. Am. **103**, 1598–1608.

Rhode, W. S., and Cooper, N. P. (**1996**). ''Nonlinear mechanics in the apical turn of the chinchilla cochlea in vivo,'' Aud. Neurosci. **3**, 101–121.

Rhode, W. S., and Robles, L. (**1974**). ''Evidence from Mossbauer experiments for nonlinear vibration in the cochlea,'' J. Acoust. Soc. Am. **55**, 588–596.

Robles, L., Ruggero, M. A., and Rich, N. C. (**1986**). ''Basilar membrane mechanics at the base of the chinchilla cochlea. I. Input–output functions, tuning curves, and response phases,'' J. Acoust. Soc. Am. **80**, 1364–1374.

Ruggero, M. A. (**1992**). ''Responses to sound of the basilar membrane of the mammalian cochlea,'' Curr. Opin. Neurobiol. **2**, 449–456.

Ruggero, M. A., and Rich, N. C. (**1991**). ''Furosemide alters organ of Corti mechanics: Evidence for feedback of outer hair cells upon the basilar membrane,'' J. Neurosci. **11**, 1057–1067.

Ruggero, M. A., Rich, N. C., and Recio, A. (**1993**). ''Alteration of basilar membrane responses to sound by acoustic overstimulation,'' in *Biophysics of Hair Cell Sensory Systems*, edited by H. Duifhuis, J. W. Horst, P. v. Dijk, and S. M. v. Netten (World Scientific, Singapore), pp. 258–264.

Ruggero, M. A., Rich, N. C., Recio, A., Narayan, S. S., and Robles, L. (**1997**). ''Basilar-membrane responses to tones at the base of the chinchilla cochlea,'' J. Acoust. Soc. Am. **101**, 2151–2163.

Ruggero, M. A., Robles, L., Rich, N. C., and Recio, A. (**1992**). ''Basilar membrane response to two-tone and broadband stimuli,'' Philos. Trans. R. Soc. London, Ser. B **336**, 307–315.

Russell, I. J., and Nilsen, K. E. (**1997**). ''The location of the cochlear amplifier: Spatial representation of a single tone on the guinea pig basilar membrane,'' Proc. Natl. Acad. Sci. USA **94**, 2660–2664.

Stelmachowicz, P. G., Lewis, D. E., Larson, L. L., and Jesteadt, W. (**1987**). ''Growth of masking as a measure of response growth in hearing-impaired listeners,'' J. Acoust. Soc. Am. **81**, 1881–1887.

Yates, G. K. (**1990**). ''Basilar membrane nonlinearity and its influence on auditory nerve rate-intensity functions,'' Hear. Res. **50**, 145–162.

Yates, G. K., Winter, I. M., and Robertson, D. (**1990**). ''Basilar membrane nonlinearity determines auditory nerve rate-intensity functions and cochlear dynamic range,'' Hear. Res. **45**, 203–220.

Perceptual salience of individually distinctive features in the calls of adult king penguins

Thierry Lengagne and Thierry Aubin
NAMC-UMR 8620 bat 446, Université Paris Sud. F-91400 Orsay, France

Pierre Jouventin
CEFE-CNRS UPR 9056, 1919 Route de Mende 34293, Montpellier, France

Jacques Lauga
UMR 5552 Laboratoire d'Ecologie Terrestre, Université Paul Sabatier, 118 route de Narbonne 31062, Toulouse Cedex, France

(Received 5 February 1999; revised 28 June 1999; accepted 6 October 1999)

In the king penguin, *Aptenodytes patagonicus*, incubation and brooding duties are undertaken alternately by both partners of a pair. Birds returning from foraging at sea find their mate in the crowded colony using acoustic signals. Acoustic recognition of the mate maintains and strengthens the mate's fidelity and favors synchronization in the different stages of reproduction. In this study it was found that the king penguin vocalizes in response to the mate's playback calls, but not to those of neighbors or unfamiliar conspecific individuals. To study individual features used by the birds for individual recognition of mates, various experimental signals consisting of synthesized modifications of the mate's call were played back to the incubating bird. Results indicated that birds attend to the FM profile of the call, in particular its initial inflexion. The frequency modulation shape of the syllable can be assimilated to a vocal signature repeated though the different syllables of the call. King penguins pay little attention to the call's AM envelope or its absolute frequency. © *2000 Acoustical Society of America.* [S0001-4966(00)05001-3]

PACS numbers: 43.66.Gf, 43.80.Lb [DWG]

INTRODUCTION

Many birds show an ability to respond selectively to particular individuals in their social environment. They may respond only to the call of their own species (see review on species recognition in Becker, 1982) or to the call of one individual (see review on individual recognition in Falls, 1982). For species breeding in colonies, birds are continuously exposed to the calls of conspecific birds, but most respond only to the call of one individual: the mate or the chick (Evans, 1970; White, 1971; Jouventin, 1982). The best evidence of voice-based individual recognition (IR) in birds comes from colonial species for which the omnidirectional properties of sound make acoustic signals more reliable than visual signals in a crowded colony (Beer, 1970). In breeding colonies where nest sites are closely spaced, the close proximity of neighbors makes reliable individual recognition (IR) especially important. IR provides a basis for the development of exclusive and stable social bonds between partners of a breeding pair and allows them to coordinate their efforts, especially in seabirds when both sexes brood and rear the chicks.

According to Beer (1970), investigators have used three approaches in the study of IR: field observation, acoustic analysis of signals, and playback experiments. Field observations show that birds can respond to songs of their own mates, even when they cannot see them (Nelson, 1965; Tinbergen, 1959). Acoustic analysis of the variation in calls has been the most widely employed tool to predict which features could be used in the discrimination process. Most studies have shown that significant variation exists among the calls of different individuals beyond that found in repeated calls of the same individual. This prerequisite for individual recognition has been demonstrated by numerous authors (White *et al.*, 1970; Bretagnolle and Lequette, 1990; Mathevon, 1996). However, absolute measures of variation are hard to interpret in the absence of information concerning which features of a signal are detected and used by a bird. The most direct way to demonstrate IR by sound is to compare responses of birds to recordings of different individuals. White (1971), Brooke (1978), and Moseley (1979) have, respectively, demonstrated IR in the gannet (*Sula Bassana*), the manx shearwater (*Puffinus puffinus*) and the least stern (*Sterna albifrons*) by playback experiments in the field, where birds may be expected to perform normally in a complex natural environment. Contrary to the species recognition process, individual recognition requires very precise information and it can be supposed that individual identity is conveyed by detailed structure. However, few studies have been conducted using playback experiments to determine which properties of calls are important in eliciting IR.

The king penguin, *Aptenodytes patagonicus*, is a highly colonial seabird. It breeds in large and dense colonies on the seashore of subantarctic islands and, as in other colonial breeders, its social behavior can be expected to have features that reflect adaptations to its colonial way of life. Furthermore, the king penguin breeds without a nest, incubating its single egg on its feet where it is covered by a brood patch. Birds move with the egg but stay in an area of the colony that has been named the ''attachment zone'' by Barrat (1976). Incubation and brooding duties are undertaken alter-

nately by both partners of a pair (Weimerskirch *et al.*, 1992). Field observations of the breeding behavior have shown that IR of mates by each other is achieved though a display call (Stonehouse, 1960). The mate returning from the sea makes its way to the attachment zone and calls. The incubating bird, recognizing its mate's call, becomes agitated and calls back without moving. After a few calls, the incoming bird finds the incubating one and the two birds exchange the egg or the young chick. Previous studies tried to evaluate the potential of different features of the signal for coding individual information. Jouventin (1982), Robisson (1992b) and Lengagne *et al.* (1997) showed that individual information can be conveyed by either temporal or frequency parameters. Playback experiments conducted by Derenne *et al.* (1979) demonstrated that the king penguin discriminates the display calls of its mate from the calls of other birds in the colony. But it is not known whether recognition is achieved by a complex discrimination between calls of numerous birds (discrimination between different neighbors' calls and stranger's call) or by a binary discrimination (discrimination between familiar and unfamiliar calls). Derenne *et al.* (1979) and Robisson (1992a) used playback experiments to assess how information concerning individual identity is decoded. Many features, such as spectral composition, time-varying amplitude or time-varying frequency might be involved in IR. The organization of this coding–decoding process has probably evolved under the influence of several factors such as physical constraints imposed by the environment (Wiley and Richard, 1978; Morton, 1975) and masking properties of vocalizations from conspecific birds (Aubin and Jouventin, 1998). The coding decoding process is probably based on sound features that are best able to survive transmission across the colony (Brémond and Aubin, 1990).

The aim of this study was first to investigate the features of the signal that convey identity by means of playback of modified synthetic versions of the mate's display call. This coding–decoding system of individual recognition between mates is discussed in regard to the parent–chick recognition system previously studied (Jouventin *et al.*, 1999) and to the physical constraints imposed by the environment. In a second step, we investigate the kind of individual discrimination that the king penguin can do and the biological function of individual recognition between adults.

I. MATERIAL AND METHODS

A. Study areas

The recordings and experiments were performed at La Baie du Marin, Possession Island, Crozet Archipelago (46°25 S, 51°45 E) during the beginning of the breeding season 1994–1995 (from December to February). The king penguin colony consisted of about 40 000 pairs of birds (Guinet, C., unpublished data).

B. Recording and analysis procedure

During the incubation and brooding stage, members of a pair alternate care duties on land and foraging trips at sea. The ability to communicate using acoustic signals is an advantage in a crowded colony of morphologically similar birds and we have shown that acoustic signals appears to be more effective than visual signals in locating birds within a colony (Lengagne *et al.*, in press). Moreover, experiments proved that birds cannot find each other without acoustic signal (Jouventin, 1982). The display call of king penguins was recorded at the changeover using an omnidirectional Beyer Dynamic M69 microphone mounted on a perch and connected to a Nagra III tape recorder (19.05 cm/s). The microphone was placed at 1 m in front of the beak of the recorded bird. Display calls of the two birds of 50 pairs were recorded and all birds were flipper-banded for their identification in the colony.

Signals were digitized through a 16-bit acquisition card equipped with an antialiasing filter (low pass filter, $fc = 6.4$ kHz; -120 dB/octave) at a sampling rate of 16 kHz. Signals were then examined and modified with the SYNTANA analytic package (Aubin, 1994).

C. Playback procedure

The experimental technique used enabled us to test the effects of the sound itself in isolation from other factors that might sometimes be associated with it, such as specific visual and olfactory stimuli and specific location.

The experiments were performed under clear and dry weather conditions. To avoid problems of masking due to wind (Eve, 1991; Lengagne *et al.*, 1999b), experiments were conducted when the wind speed was less than 4 m/s. To prevent habituation, each bird was tested only once a day. The broadcast chain consisted of an Uher 4000C connected to a Nagra Kudelski amplifier (7 W) and a loudspeaker. To prevent differences in the intensity of the response of the bird, all the signals were broadcast with the same intensity and at a same distance from the tested bird (Evans, 1970). Signals were played back at 95 dB (SPL), measured at 1 m from the loudspeaker, with a Bruel & Kjaer Sound Level Meter type 2235 (linear scale, slow setting). This level was equivalent to that produced in natural conditions (Robisson, 1993). The loudspeaker was placed 7 m from the tested bird, a distance that allows penguins to discriminate without difficulty the call of the mate in the background noise of the colony (Lengagne *et al.*, in press).

Two experimental signals separated by a 15-s silence were broadcast. The response obtained was compared with that induced by a reference signal, i.e., two natural calls from the mate broadcast 20 min later and separated by a 15-s silence. The order of presentation of both experimental and reference signals was randomized. The presentation of 24 experimental signals was also randomized during the whole experimental period.

D. Classification of reactions and statistical analysis

To evaluate the intensity of response of tested bird to playback signals, a four-point scale was used, ranked as follows:

class 0: no reaction
class 1: agitation
class 2: agitation then calls in response to the second broadcast
class 3: agitation then calls in response to the first broadcast

TABLE I. Main characteristics of the 24 signals used in acoustic experiments: RS (Reference Signals), 3 Natural Signals (NS) and 21 Experimental Signals (ES). The number of tests conducted for each signal was indicated. (AM: Amplitude Modulation; FM: Frequency Modulation.)

Signals compared to the reference signal	Characteristics	Number of tested birds
Natural Signals (NS)		
	NS 1 signal of an alien conspecific	16
	NS 2 signal of neighbor 1	13
	NS 3 signal of neighbor 2	13
Experimental Signals (ES)		
modified temporal patterns		
	ES 1 signal with AM of RS, without FM	16
	ES 2 signal without AM, with FM of RS	25
	ES 3 signal with AM of RS, with FM of NS	15
	ES 4 signal with AM of NS 1, with FM of RS	16
	ES 5 first syllable (524 ms)	15
	ES 6 first part of the first syllable (152 ms)	15
	ES 7 second part of the first syllable (372 ms)	15
	ES 8 first half of ES 6 (76 ms)	15
modified frequency patterns		
	ES 9 low frequencies	16
	ES 10 high frequencies	16
	ES 11 fundamental frequency	18
	ES 12 shift+100 Hz	11
	ES 13 shift+85 Hz	11
	ES 14 shift+70 Hz	11
	ES 15 shift+50 Hz	11
	ES 16 shift+25 Hz	11
	ES 17 shift−100 Hz	11
	ES 18 shift−85 Hz	11
	ES 19 shift−70 Hz	11
	ES 20 shift−50 Hz	11
	ES 21 shift−25 Hz	11

This behavioral scale is similar to those used in previous studies dealing with the king penguin (Derenne *et al.*, 1979; Robisson, 1990). Responses falling in classes 2 and 3 were considered positive since they allowed the birds to carry out the changeover, while responses falling in classes 0 and 1, not followed by a changeover, were considered negative.

Responses obtained after the broadcast of 24 signals were compared with the responses obtained by the reference signal. The sign test on related samples was used to assess the significance of the differences observed on scores following the broadcast of experimental and reference signals. The null hypothesis is that $p(Xa>Xb)=p(Xa<Xb)$ where Xa is the score observed under reference signal and Xb the score under experimental signal. Computations were carried out using statistical analysis software SPSS statistic package.

E. Reference and experimental signals

We broadcast 25 signals: 1 was the reference signal (call of the mate), 3 were natural display calls of other conspecific birds (natural signals), and the last 21 were experimental signals obtained by acoustic modifications of the reference signal. All responses obtained were compared with the response obtained by the reference signal. Several studies have shown the low intra-individual variation of the call emitted by each birds (Derenne *et al.*, 1979; Robisson, 1992b; Lengagne *et al.*, 1997). This high stereotypy can be considered from an ethological point of view. We have shown that all the calls produced by a bird elicit a strong response by its mate. This explains why we used only one call of the mate as the reference signal for each tested bird. Main characteristics of the 24 signals used are summarized in Table I.

1. The reference signal

The Reference Signal (RS) is the natural display call of the mate of the bird under test (Fig. 1). It consists of a fundamental frequency (between 400 and 500 Hz) and numerous harmonics. The majority of energy is concentrated between 400 and 3000 Hz. The waveform of the call revealed large amplitude modulations (AM) which separated sound elements named syllables. The spectrogram revealed frequency modulations (FM) in each syllable. The duration of the ascending part of the FM is on average 152 ± 3 ms (mean $\pm$SE) with a modulation rate of 1887 ± 36 Hz/s (mean$\pm$SE). Concerning the second part of the syllable, its duration is 372 ± 11 ms with a modulation rate of 568 ± 24 Hz/s. The small variation of the call has been demonstrated previously. By using the coefficient of variation (CV), Derenne *et al.* (1979) first demonstrated a weak variation of the call of each bird in either the frequency domain (average of CV: 2.8%) or the temporal domain (average of CV: 5.1%). This intra-individual variation is weaker than the inter-individual variation (respectively, 19.9% and 37.4%). In addition, by statistic methods (Analysis of variance, *t* test or independent time and frequency decomposition) other studies have shown that all

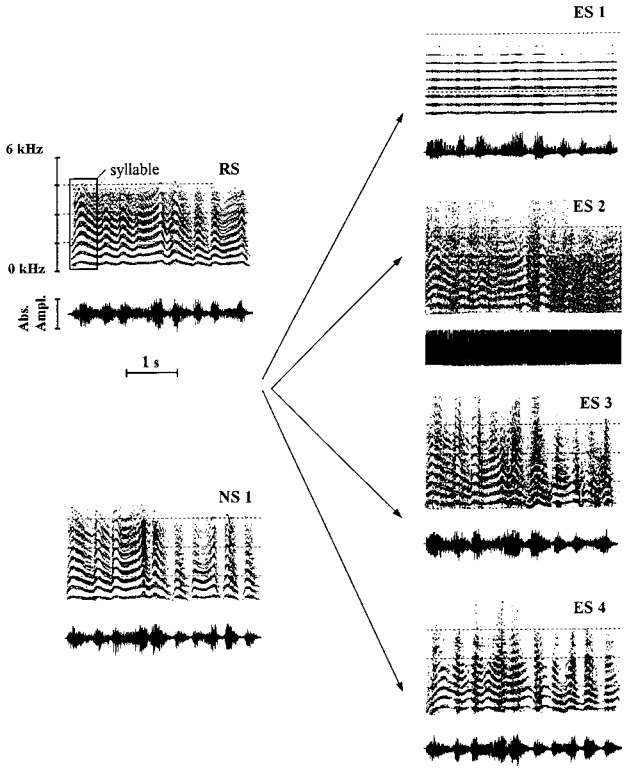

FIG. 1. Spectrograms and waveforms of six signals used in our experiments. Signals on the left, RS (reference signal) and NS 1 (natural signal of an alien conspecific) were used to synthesize the four experimental signals on the right: ES 1 (signal with amplitude modulation of RS and without frequency modulation), ES 2 (signal without amplitude modulation and with frequency modulation of RS), ES 3 (signal with amplitude modulation of RS and frequency modulation of NS 1) and ES 4 (signal with amplitude modulation of NS 1 and frequency modulation of RS).

the calls produced by a bird kept the same temporal and spectral characteristics (Robisson, 1992a, b; Lengagne *et al.*, 1997).

2. Natural signals of other conspecific birds

Three Natural Signals (NS) corresponding to the display calls of different conspecific birds were used:

- NS 1, natural display call of a conspecifics (a different call for each bird tested) located in a distant area of the colony, 200 m away (Fig. 1). We believe that it was a signal that the tested bird had not heard previously.
- NS 2 and NS 3, natural display calls of two conspecific neighbors located less than 3 m from the tested bird. The tested bird received these signals numerous times at each exchange of the neighbor pairs. Thirteen birds were tested with NS 2 and NS 3, these calls being different for each experiment.

3. Experimental signals

The reference signal of the bird under study was modified either in the temporal or the frequency domain. During our experiments, 21 Experimental Signals (ES) were broadcast. Since the different calls emitted by one bird are highly stereotyped, only one call for each bird serves as RS. This call was then modified to obtain the different experimental signals. There were only two exceptions in building these signals: experimental signals 3 and 4 had hybrid characteristics between the Reference Signal and an alien call (see below).

a. Signals with modified AM and FM. Four types of modifications of AM and FM were used.

(1) Experimental Signal 1 (ES 1). A natural envelope was applied to a carrier frequency without FM. A carrier frequency was composed by the fundamental frequency and by the harmonic series of the mate's call. The fundamental frequency corresponds to the mean value between the maximum and the minimum of the frequency modulation calculated on each entire RS. The amplitude envelope applied was extracted from the call of the mate, using the analytic signal calculation (Mbu-Nyamsi *et al.*, 1994). As a result, we obtained a signal with the same temporal succession of syllables and spectral content as the mate's call, but without any modulation in the frequency domain (Fig. 1). This signal was termed ''with mate AM, without FM.''

(2) Experimental Signal 2 (ES 2). The amplitude modulation of the mate's call was removed by application of analytic signal calculation (Mbu-Nyamsi *et al.*, 1994). We obtained a signal with the same spectral content and the same FM as those of the mate's call but without any AM. This signal was termed ''without AM, with mate FM.''

(3) Experimental Signal 3 (ES 3). Using methods described above for ES 1 and ES 2, we synthesized an hybrid signal made of mate AM and alien FM and spectral content. We applied the amplitude envelope previously extracted from the call of the mate (see ES 1) to the spectral content of the alien call without AM (removed as ES 1). As a result, we obtained a signal with the same temporal succession of syllables (AM) of the mate's call but with the spectral content and the FM of the alien call (Fig. 1). Calls of 30 birds were used to synthesize this experimental signal (15 alien calls emitted by different birds and the RS corresponding to each of the 15 tested birds). This signal was termed ''with mate AM, with alien FM.''

(4) Experimental Signal 4 (ES 4). We synthesized a hybrid signal made of alien AM and mate FM and spectral content. We applied the amplitude envelope extracted from an alien call to the spectral content of the mate's call without AM (see ES 2). We obtained a signal with the spectral content and FM of the mate's call but with the temporal succession of syllables (AM) of an alien call (Fig. 1). Calls of 32 birds were used to synthesize this experimental signal (16 alien calls emitted by different birds and the RS corresponding to each of the 16 tested birds). This signal was termed ''with alien AM, with mate FM.''

b. Signals with modified call duration. Experimental Signals 5 to 8 (ES 5 and 8, Fig. 2). Four signals were synthesized with different modifications of the call duration. In a previous study, Derenne *et al.* (1979) showed that the first half of the mate's song is sufficient to elicit the response from the tested bird. We applied accurate modifications of signal duration so as to test the importance of tempo (number of elements by unit of time), rhythm (ratio sound/silence) or syntax (order of the elements) in IR. At the same time, we emphasized an important redundancy of the individual infor-

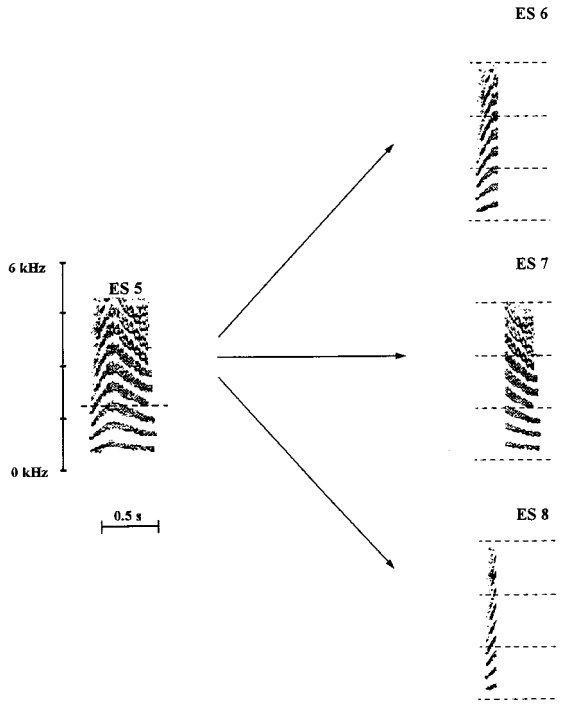

FIG. 2. Spectrograms of four signals used in our experiments. The signal on the left, ES 5 (first syllable of the call) was used to synthesize the three experimental signals on the right: ES 6 (first part of the first syllable), ES 7 (second part of the first syllable) and ES 8 (first half of ES 6).

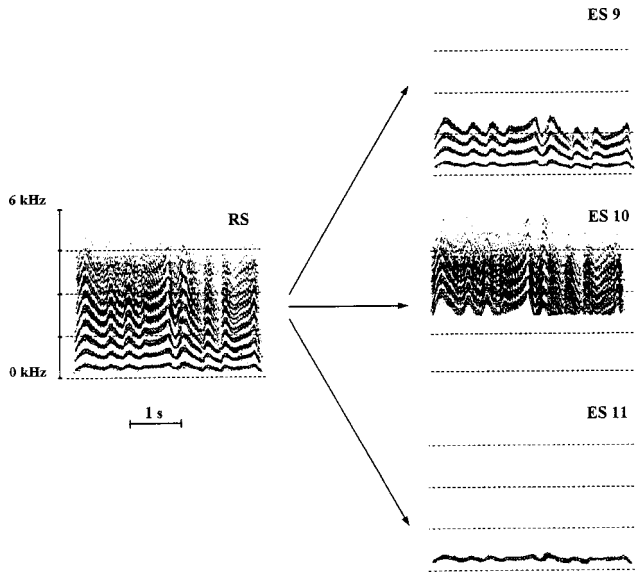

FIG. 3. Spectrograms of four signals used in our experiments. The signal on the left, RS (reference signal) was used to synthesize the three experimental signals on the right: ES 9 (signal with low frequencies), ES 10 (signal with high frequencies) and ES 11 (signal with the fundamental frequency and without any harmonics).

mation content if a small part of the signal allowed IR between mates. ES 5 was composed of the first syllable of the mate's call (mean duration ± SE: 524 ms ± 13 ms). ES 6 was composed of the first part of the first syllable containing the inflexion point of the frequency modulation, i.e., the point situated at the inversion of the slope between the increasing frequency part and the decreasing (mean duration ± SE: 152 ms ± 5 ms). ES 7 was composed of the second part of ES 5 (mean duration ± SE: 372 ± 12 ms) and ES 8 corresponded to the first half of ES 6 (mean duration ± SE: 76 ms ± 3 ms).

c. Signals with modified frequency patterns. Two methods were used for the modification of the frequency patterns of the reference signals.

(1) Experimental Signals 9 to 11 (ES 9 to 11, Fig. 3). We synthesized three signals with different modifications of the spectral content by digital filtering. We applied optimal filtering with the FFT (Press *et al.*, 1988). The window size of the FFT was 4096 points (precision in frequency: $\Delta F = 4$ Hz). ES 9 corresponded to the lower part of the spectrum (the fundamental frequency and the first three harmonics). ES 10 corresponded to the complementary part of the spectrum of ES 9. Finally, ES 11 corresponded to the fundamental frequency of the mate's call. Thus, the three signals had the same duration and temporal succession of syllables, the same FM as the reference call, but a modified spectral content.

(2) Experimental Signals 12 to 21 (ES 12 to 21). We shifted the frequency of each reference signal. We applied short-termed overlapping (50%) FFT followed by a linear shift (+ or −) of each spectrum and by a short-term inverse FFT (Randall and Tech, 1987). We used a 4096-point window size ($\Delta F = 4$ Hz). Signals 12–16 and 17–21 were shifted positively and negatively, respectively, by 100, 85, 70, 50 and 25. All of these signals kept the normal (natural) frequency range of the species while moving the whole call either up or down in frequency.

II. RESULTS

Scores obtained after broadcast of ES were compared to scores of RS.

A. Natural Signals of other conspecific birds (NS)

For signals NS 1, NS 2, and NS 3, strong differences from the reference signal were found ($P < 0.001$). Responses obtained after broadcast of the three signals were not statistically different: These calls were not recognized as a mate's display call (class 0 for all responses obtained). Birds responded only to the call of their mate (between 85 and 100% of positive responses).

B. Experimental signals

1. Signals with modified AM and FM

When the experimental signals had the FM of the mate's call but not its AM (no AM or AM of an alien bird: ES 2 and ES 4), no significant differences were found from the reference signal (Fig. 4). When the experimental signals had the AM of the mate's call but not its FM (no FM or FM of an alien bird: ES 1 and ES 3), birds discriminated these signals from the mate's display call ($P < 0.001$). Thus, the FM of the signal seems to give the bird a distinctive cue in identifying the emitter.

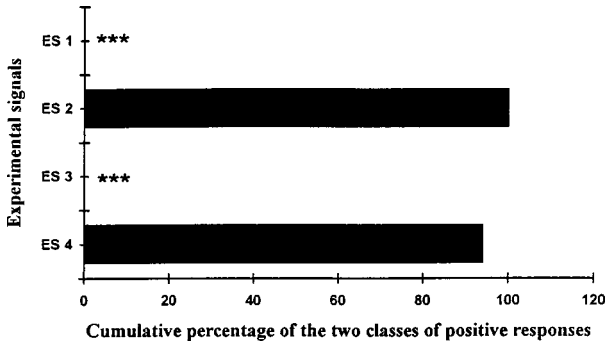

FIG. 4. Cumulative percentage of the two classes of positive responses (classes 2 and 3) obtained for four Experimental Signals with amplitude modulation (AM) or frequency modulation (FM) modifications (ES 1: signal with AM of RS, without FM; ES 2: signal without AM, with FM of RS; ES 3: signal with AM of RS, with FM of NS 1; ES 4: signal with AM of NS 1, with FM of RS). The response of the tested bird on a four-point behavioral scale was compared with the response obtained for the RS by a sign test. (***$p<0.001$.)

2. Signals with modified call duration

Concerning the modifications of syllable duration, it appears that the broadcast of only the first syllable was sufficient to elicit recognition (no significant difference was found between ES 5 and RS; see Fig. 5). Indeed, individual recognition still occurred when only the first part of the first syllable was broadcast (no significant difference was found between ES 6 and RS). This signal presented only a small part of the call (on average 4.1% of the whole call duration). However, significant differences ($P<0.001$) were found for the broadcast of either the second part of the first syllable (ES 7) or the first 74 ms of the first syllable (ES 8). Tested birds did not recognize the mate's call. Thus, the whole call seems not to be necessary to elicit discrimination of the mate's call, and the beginning of the syllable seems more important than its end.

3. Signals with modified frequency patterns

There were no significant differences between the responses to RS and the responses to experimental signals containing only the lower frequency band (ES 9) or containing only the fundamental frequency (ES 11). On the other hand,

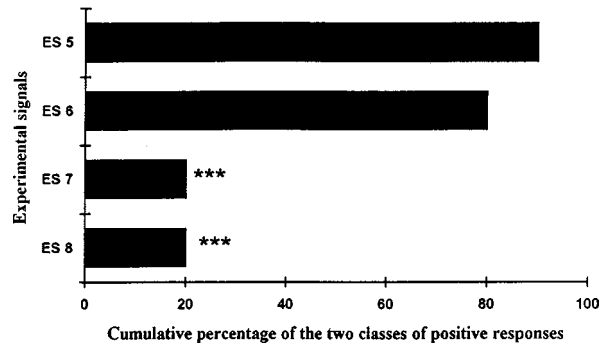

FIG. 5. Cumulative percentage of the two classes of positive responses (classes 2 and 3) obtained for four Experimental Signals with modified call duration (ES 5: first syllable; ES 6: first part of the first syllable; ES 7: second part of the first syllable; ES 8: first half of ES 6). The response of the tested bird on a four-point behavioral scale was compared with the response obtained for the RS by a sign test. (***$p<0.001$.)

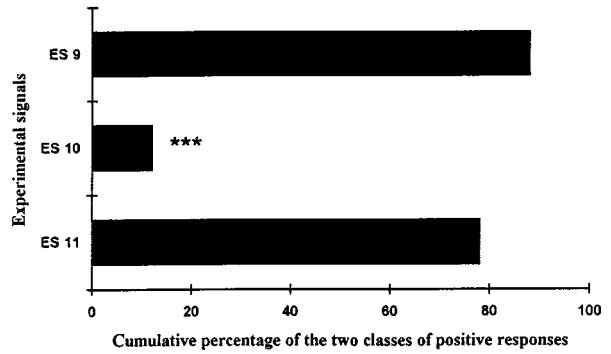

FIG. 6. Cumulative percentage of the two classes of positive responses (classes 2 and 3) obtained for three Experimental Signals with modified spectral content (ES 9: low frequencies; ES 10: high frequencies; ES 11: fundamental frequency). The response of the tested bird on a four-point behavioral scale was compared with the response obtained for the RS by a sign test. (***$p<0.001$.)

a significant difference was found between ES 10 (high frequency band) and the reference signal ($P<0.001$). Thus, as for call duration, the whole frequency content of the call does not seem to be necessary to elicit discrimination of the mate's call (Fig. 6).

Concerning the frequency shift series (ES 12 to ES 21), significant differences appeared for a positive frequency shift of 75 Hz or more and for a negative frequency shift of 85 Hz or more. Results with statistical differences between ES and RS are shown in Fig. 7. It seems that birds did not utilize frequencies precisely.

III. DISCUSSION

A. Coding–decoding processes of individual information between mates

The sounds of birds are characterized by a large number of combinations of acoustic characteristics. Only some of

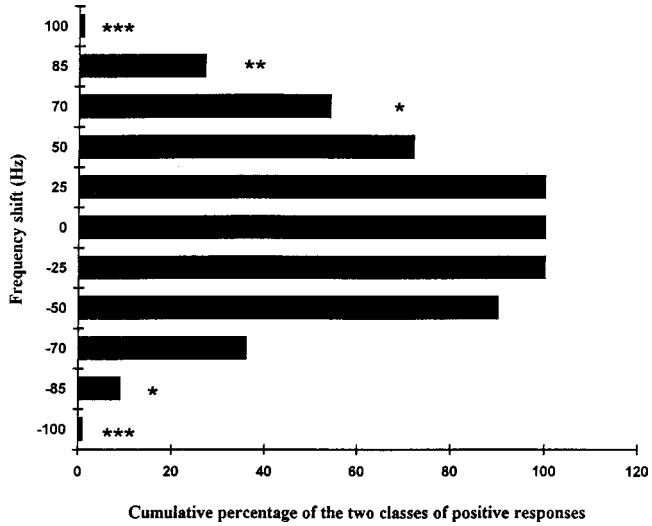

FIG. 7. Cumulative percentage of the two classes of positive responses (classes 2 and 3) obtained for eight experimental signals (frequency shift from −100 Hz to +100 Hz). The shift 0 Hz corresponds to the Reference Signal (RS). The response of the tested bird on a four-point behavioral scale was compared with the response obtained for the RS by a sign test. (*$p<0.05$; **$p<0.01$; ***$p<0.001$.)

them act as releasers for IR. Hopkins (1983) and Okanoya and Dooling (1991) suggested that vocal recognition (for individuals or species) may involve some common perceptual mechanisms across a wide variety of avian species. The parameters of an input signal can be utilized by the receiver either in the frequency domain (using a power spectral profile) or in the temporal domain (using combinations of elements in the signal or using the structure of single elements) or both.

Different studies showed that biologically relevant information can be encoded in the frequency pitch: Birds can pay attention to the timber of signals (Bertram, 1970; Robisson, 1987; Aubin and Brémond, 1992). Our frequency shift series (ES 12 to ES 21) demonstrated that recognition still occurred until the reference call was shifted 75 Hz up or 85 Hz down (corresponding to a total variation of 160 Hz). The experimental calls shifted up or down, remaining in the natural range of king penguin calls. A frequency decrease of a certain amount (in Hz) seems to be perceived as less of a change than an equivalent increase. Our filtering experiments (ES 9 to ES 11) showed that a small part of the spectra of the call seems sufficient to elicit IR. The reference signal (with numerous harmonics), filtered so as to obtain a pure tone (corresponding to the fundamental frequency), allowed tested birds to recognize their mate's call. According to these experiments, it seems that king penguins do not utilize with precision the spectrum of the signal in regard to IR of mates.

Each species has its own strategy for the use of temporal parameters as species or individual markers. Previous studies of Falls (1963), Abs (1963), and Aubin and Brémond (1983), showed that in several species, birds use a combination of elements to code species or individual information. The releasing function can be supported by tempo, rhythm or syntax. In king penguins, the playback of the first half of the first syllable alone (mean duration: 152 ms) allows IR. This experiment proved that a combination of successive elements (i.e., syllables) is not necessary to elicit IR. Heavy perceptual weighting of the initial part of a vocal signal has been shown in other studies (Horning *et al.*, 1993; Johnrude *et al.*, 1994).

Another possibility is that king penguins utilize the structure of each syllable for the IR coding–decoding process. Birds have the possibility to use in each syllable either amplitude modulation or frequency modulation (Heidemann and Oring, 1976; Ficken and Ficken, 1973; Becker, 1982). Our experiments emphasized the releasing value of the FM and the absence of role of the AM for coding individual information in the king penguin. Indeed, the reference signal without AM (ES 2) was still recognized as the mate's call whereas a reference signal without FM (ES 1) was not recognized at all. Moreover, we tested birds with two complex signals: we played back two hybrid calls composed of characteristics of the mate's call and an alien bird's call. Only the signal with an FM of the mate's call (ES 4) was recognized, whereas the signal with the FM of an alien bird (ES 3) was not. Consequently, the frequency modulation of calls seems to act as a main releaser for IR of mate.

B. Comparisons with parent–chick recognition system

Stonehouse (1960) showed that to be fed, a king penguin chick must recognize its parents calls in the colony. Parents arriving from the sea call regularly in the area of the colony where the chick is usually located (the rendezvous site). The chick in the flock holds up its head, calls in reply and moves toward the parent. The signal emitted by the adult is the same for a parent–chick recognition purpose or a mate recognition one. Previous statistical analysis dealing with IR in king penguin calls (Robisson, 1992a; Lengagne *et al.*, 1997) has shown that individual information could be conveyed by either temporal or frequency parameters. Our playback experiments (Jouventin *et al.*, 1999) have shown that chicks do not precisely utilize the power spectral profile of the parent's call. As we described here for adults, chicks do not use a combination of elements to code their information. For mate recognition, we have shown the releasing value of frequency modulation for the IR coding–decoding process. In the king penguin, as in other colonial birds, the individual recognition process is established in the first weeks of the chick's life, by which time the young chicks are capable of moving out of the nesting area (Beecher *et al.*, 1981; Burtt, 1977; Davies and Carrick, 1962; Loesche *et al.*, 1991; Davis and McCaffrey, 1989). The fact that colonial constraints on acoustic communication are the same for both adults and chicks may explain why the same coding–decoding process is used by both.

C. Adaptation to the colonial environment

Acoustic communication in a colonial environment appears to be very difficult. Two main problems have to be solved: the degradation of sound features of the signal during propagation and the masking effect of the continuous background noise generated by other birds in the colony.

Physical constraints imposed by the environment seem to have selective influences on the structure of bird sounds (Chappuls, 1971; Morton, 1975). In numerous cases, it has been demonstrated that the coding–decoding process of a signal is based on sound features that are relatively resistant to degradation (Robisson, 1987; Brémond and Aubin, 1990). In penguin colonies, propagating acoustic signals are degraded to some extent by blurring of amplitude and frequency parameters and also by attenuation. Moreover, the screening effect of the birds bodies that the signal must cross increases the degradation (Aubin and Jouventin, 1998). The lack of recognition obtained with the playback of the high-pass signal (ES 10) was not surprising if we consider the characteristics of the transmission channel: Sound intensity attenuates as a function of frequency, and higher frequencies are rapidly lost with distance (Lengagne *et al.*, 1999a). Moreover, during propagation through the penguin's bodies, frequencies around 1000 Hz are more severely attenuated (Aubin and Jouventin, 1998). These strong degradations of the signal frequencies could explain why the spectral profile was not used by birds for the precise coding–decoding process of individual information. In the same way, amplitude patterns were also subject to various distortions in the chan-

nel of transmission (Lengagne *et al.*, 1999a), and therefore are not suitable as releasers for IR. On the contrary, the FM of the carrier, well preserved during propagation, seems to be a more reliable strategy to ensure accurate transmission under constraining conditions (Wiley and Richards, 1982). A sequential redundancy may be important to counteract modifications of the signal during propagation. The redundancy in the king penguin's call is considerable since our experiments indicated that 4.1% of the whole duration of the call, i.e., 152 ms, was sufficient to achieve recognition.

In a dense colony, the most pervasive problem for mates is the difficulty of recognizing the mate's vocalizations in the continuous background sounds of other pairs. This process, termed the ''cocktail party effect,'' was first studied by Cherry (1966). In king penguins, recognition still occurs even if the level of the signal is well below the level of the background noise (Aubin and Jouventin, 1998). One way to enhance the discrimination of the signal in the noise is to increase the localizability of the emitter. Birds can localize a wide-spectrum signal better than any pure tone (Konishi, 1973). In addition, sounds with sharp changes in amplitude result in maximal localizability (Konishi, 1977). Wide spectra and strong gaps of amplitude are found in the king penguin call, and these particular features of the call besides FM could be important for IR by virtue of enhancing detection of the call in the background noise. Such acoustic characteristics are also found in the call of many colonial birds (White and White, 1970; Wiley, 1976).

D. Biological functions of individual recognition

Playback experiments in the field demonstrate that several territorial passerines discriminate among their different neighbors and not only between familiar and unfamiliar calls (Wiley and Wiley, 1977; Stoddard *et al.*, 1991). This complex process of recognition assumes that birds store representations of all neighbors' signals and that a stimulus is compared to each prototype before a decision is made about the identity of the emitter. In the colonial species in which parent–young and mate recognition by calls occurs, this complex process of recognition does not appear to have been found, even when it has been looked for (Beer, 1970; White, 1971; Wooler, 1978; Jouventin, 1982). In the king penguin we observed a strong response when we broadcast the display call of the mate but no responses were obtained after broadcast of either neighbor's call or an alien bird's call. No difference was found with our behavioral scale between these responses (responses class 0 for NS 1, NS 2 and NS 3). During the playback of these signals, any behavioral change (agonistic behavior, fights, calling...) was observed. The lack of behavioral responses with NS 1, NS 2, and NS 3 (birds on its egg does not move at all) may be explained by the lack of biological function. Contrary to territorial passerine birds, in the crowded conditions of a colony, neighbors and stranger birds represent the same threat or irrelevance to the task of egg and chick exchange for a breeding pair. A given bird may not spend energy to communicate with other birds, except if it is the mate (or the chick). The lack of behavioral change in response to playback of NS 1, NS 2, and NS 3 does not meant that birds are unable to distinguish a neighbor call from an alien one. It can be only stated that such a complex discrimination, if it exists, cannot be appreciated by a bahavioral scale.

In seabirds, the two mates of a pair can ensure offspring survival only by subtle cooperative behavior. It appears obvious that such behavior depends on coordination and synchronization of reproductive effort of mates (Falls, 1982). The adaptative value of the acoustic IR appears clearly in terms of time and energy saved during the nest relief in the incubation or brooding period (Brooke, 1978; Guillotin and Jouventin, 1980). This process can be interpreted as an adaptation to monogamy in breeding species when both sexes coordinate their efforts in brooding and rearing the chicks. During changeover, the acoustic communication allowing birds to identify mates without ambiguity in a few seconds is a particularly efficient strategy.

ACKNOWLEDGMENTS

The study was supported by the Institut Français pour la Recherche et al Technologie Polaires (I.F.R.T.P.) and the Center National de la Recherche Scientifique (C.N.R.S.). We thank the 1995 winter team in Crozet for help on the field. Many thanks are due to Lance Barrett-Lennard for improving the English and valuable criticism. We are grareful to three anonymous reviewers for their constructive critical readings of the text.

Abs, M. (**1963**). ''Field tests on the essential components of the European nightjar's song,'' Proc. Int. Ornithol. Congr. **13**, 202–205.

Aubin, T. (**1994**). ''Syntana: A software for the synthesis analysis of animal sounds,'' Bioacoustics **6**, 80–81.

Aubin, T., and Brémond, J. C. (**1983**). ''The process of species-specific song recognition in the skylark *Alauda arvensis*. An experimental study by means of synthesis,'' Z. Tierpsychol. **61**, 141–152.

Aubin, T., and Brémond, J. C. (**1992**). ''Perception of distress call harmonic structure by the starling (*Sturnus vulgaris*),'' Behaviour **120**, 151–163.

Aubin, T., and Jouventin, P. (**1998**). ''Cocktail-party effect in king penguin colonies,'' Proc. R. Soc. London, Ser. B **265**, 1665–1673.

Barrat, A. (**1976**). ''Quelques aspects de la biologie et de l'écologie du manchot royal *Aptenodytes patagonicus* des îles Crozet,'' Com. Nat. Fr. Rech. Ant. **40**, 9–51.

Becker, P. H. (**1982**). ''The coding of species-specific characteristics in birds,'' in *Acoustic Communication in Birds, Vol. 1*, edited by D. E. Kroodsma and E. H. Miller (Academic, New York), pp. 213–252.

Beecher, M. D., Beecher, I. M., and Hahn, S. (**1981**). ''Parent–offspring recognition in bank swallows (*Riparia riparia*): Development and acoustic basis,'' Anim. Behav. **29**, 95–101.

Beer, C. G. (**1970**). ''Individual recognition of voice in the social behaviour of birds,'' Adv. Study Behav. **3**, 27–74.

Bertram, B. (**1970**). ''The vocal behavior of the Indian Hill Myna *Gracula religiosa*,'' Anim. Behav. Monogr. **3,** Part 2, 81–189.

Brémond, J. C., and Aubin, T. (**1990**). ''Responses to distress calls by black-headed gulls, *Larus ridibundus*: The rôle of nondegraded features,'' Anim. Behav. **39**, 503–511.

Bretagnolle, V., and Lequette, B. (**1990**). ''Structural variation in the call of the Cory's Shearwater (*Calonectris diomedea, aves, Procellariidae*),'' Ethology **85**, 313–323.

Brooke, M. L. (**1978**). ''Sexual differences in the voice and individual vocal recognition in the manx shearwater (*Puffinus puffinus*),'' Anim. Behav. **26**, 622–629.

Burtt, E. H. (**1977**). ''Some factors in the timing of parent–chick recognition in swallows,'' Anim. Behav. **25**, 231–239.

Chappuis, C. (**1971**). ''Un exemple de l'influence du milieu sur les émissions vocales des oiseaux: l'évolution des chants en forêt équatoriales,'' Terre et Vie **25**, 183–202.

Cherry, C. (**1966**). *On Human Communication*, 2nd ed. (MIT Press, Cambridge, MA).

Davies, S. J. J. F., and Carrick, R. (**1962**). ''On the ability of crested terns (*Sterna bergii*) to recognize their own chicks,'' Aust. J. Zool. **10**, 171–177.
Davis, L. S., and McCaffrey, F. T. (**1989**). ''Recognition and Parental Investment in Adélie penguins,'' Emu **89**, 155–158.
Derenne, M., Jouventin, P., and Mougin, P. (**1979**). ''Le chant du Manchot royal (*Aptenodytes patagonica*) et sa signification adaptative,'' Le Gerfaut **69**, 211–224.
Evans, M. R. (**1970**). ''Parental recognition of the mew call in black-billed gulls (*Larus bulleri*),'' The Auk **87**, 503–513.
Eve, R. (**1991**). ''L'environnement acoustique d'un peuplement d'oiseaux en forêt tropicale; organisation ou chao?,'' Terre et Vie **46**, 191–229.
Falls, J. B. (**1963**). ''Properties of bird song eliciting responses from territorial males,'' Proc. Int. Ornithol. Congr. **13**, 259–271.
Falls, J. B. (**1982**). ''Individual recognition by sounds in birds?'' in *Acoustic Communication in Birds, Vol. 2*, edited by D. E. Kroodsma and E. H. Miller (Academic, New York), pp. 237–278.
Ficken, M. S., and Ficken, R. W. (**1973**). ''Effects of number, kind and order of song elements on playback responses of the Golden-winged Warbler,'' Behaviour **46**, 114–128.
Guillotin, M., and Jouventin, P. (**1980**). ''Le pétrel des neiges à Pointe Géologie,'' Gerfaut **70**, 51–72.
Heidemann, M. K., and Oring, L. W. (**1976**). ''Functional analysis of spotted sandpiper (*Actitis macularia*) song,'' Behaviour **56**, 181–193.
Hopkins, C. P. (**1983**). ''Sensory mechanisms in animal communication,'' in *Animal Behaviour Communication*, edited by T. R. Halliday and P. J. B. Slater (Blackwell Scientific, Oxford).
Horning, C. L., Beecher, M. D., Stoddard, P. K., and Campbell, S. E. (**1993**). ''Song perception in the song sparrow: Importance of different parts of the song in song type classification,'' Ethology **94**, 46–58.
Johnsrude, I. S., Weary, D. M., Ratcliffe, L. M., and Weisman, R. G. (**1994**). ''Effect of motivational context on conspecific song discrimination by brown-headed cowbirds (*Molothrus ater*),'' J. Comp. Psych. **108**, 172–178.
Jouventin, P. (**1982**). *Visual and Vocal Signals in Penguins, Their Evolution and Adaptative Characters* (Verlag Paul Parey, Berlin), pp. 42–61.
Jouventin, P., Aubin, T., and Lengagne, T. (**1999**). ''Finding a parent in a king penguin colony: The acoustic system of individual recognition,'' Anim. Behav. **57**, 1175–1183.
Konishi, M. (**1973**). ''Locatable and non locatable acoustic signals for Barn Owls,'' Am. Nat. **107**, 775–785.
Konishi, M. (**1977**). ''Spatial localization of sound,'' in *Dahlem workshop on recognition of complex acoustic signals*, edited by T. Bullock (Dahlem Konf., Berlin), pp. 127–143.
Lengagne, T., Lauga, J., and Jouventin, P. (**1997**). ''A method of independent time and frequency decomposition of bioacoustic signal: Inter-individual recognition in four species of penguins,'' C. R. Acad. Sci. Paris, Life Sciences **320**, 885–891.
Lengagne, T., Aubin, T., Jouventin, P., and Lauga, J. (**1999a**). ''Acoustic communication in a king penguin's colony: Importance of bird location within the colony and of the body position of the listener,'' Polar Biol. **21**, 262–268.
Lengagne, T., Aubin, T., Lauga, J., and Jouventin, P. (**1999b**). ''How do king penguins (*Aptenodytes patagonicus*) apply the Mathematical Theory of Information to communicate in windy conditions?'' Proc. R. Soc. London, Ser. B **266**, 1623–1628.
Lengagne, T., Jouventin, P., and Aubin, T. (in press). ''Finding one's mate in a king penguin colony: efficiency of acoustic communication,'' Behaviour.
Loesche, P., Stoddard, P. K., Higgins, B. J., and Beecher, M. D. (**1991**). ''Signature versus perceptual adaptations for individual vocal recognition in swallows,'' Behaviour **118**, 15–25.
Mathevon, N. (**1996**). ''What parameters can be used for individual acoustic recognition by the greater flamingo?,'' C. R. Acad. Sci Paris, Science de la vie **319**, 29–32.
Mbu-Nyamsi, R. G., Aubin, T., and Brémond, J. C. (**1994**). ''On the extraction of some time dependant parameters of an acoustic signal by means of the analytic signal concept. Its application to animal sound study,'' Bioacoustics **5**, 187–203.
Morton, E. S. (**1975**). ''Ecological sources of selection on avian sounds,'' Am. Nat. **108**, 17–34.
Moseley, L. J. (**1979**). ''Individual recognition in the least tern (*Sterna albifrons*),'' The Auk **96**, 31–39.
Nelson, J. B. (**1965**). ''The behaviour of the Gannet,'' Brit. Birds **58**, 233–288.
Okanoya, K., and Dooling, R. J. (**1991**). ''Detection of species-specific calls in noise by zebra finches *Poephila guttata* and budgerigars *Melopsittacus undulatus*: Time or frequency domain?,'' Bioacoustics **3**, 163–172.
Press, W. H., Flannery, B. P., Teukolsky, S. A., and Vetterling, W. T. (**1988**). ''Numerical recipes in C,'' in *The Art of Scientific Computing* (Cambridge University Press, New York).
Randall, R. B., and Tech, B. (**1987**). *Frequency Analysis* (Naerum, Bruel & Kjaer).
Robisson, P. (**1987**). ''L'adaptation des règles de décodage des signaux acoustiques des oiseaux au canal de transmission. Etude appliquée aux cris de détresse du vanneau huppé (*Vanellus vanellus*),'' C. R. Acad. Sc. Paris **304**, 275–278.
Robisson, P. (**1990**). ''The importance of the temporal pattern and the syllable structure of display calls for individual recognition in the genus *Aptenodytes*,'' Behav. Processes **22**, 157–163.
Robisson, P. (**1992a**). ''Roles of pitch and duration in the discrimination of the mate's call in the King Penguin *Aptenodytes patagonicus*,'' Bioacoustics **4**, 25–36.
Robisson, P. (**1992b**). ''Vocalizations in *Aptenodytes* penguins: Application of the two voice theory,'' The Auk **109**, 654–658.
Robisson, P. (**1993**). ''Adaptation du transfert de l'information individuelle au milieu colonial chez les manchots,'' Terre et Vie **48**, 133–141.
Stoddard, P. K., Beecher, M. D., Horning, C. L., and Campbell, S. E. (**1991**). ''Recognition of individual neighbors by song in the song sparrow, a species with song repertoires,'' Behav. Ecol. Sociobiol. **29**, 211–215.
Stonehouse, B. (**1960**). ''The king penguin, *Aptenodytes patagonicus* of South georgia. 1 Breeding behaviour and development,'' Falk. Is. Dep. Surv. Sci. Rep. **23**, 1–81.
Tinbergen, N. (**1959**). ''Comparative studies of the behaviour of gulls (*Laridae*): A progress report,'' Behaviour **15**, 1–70.
Weimerskirch, H., Stahl, J. C., and Jouventin, P. (**1992**). ''The breeding biology and population dynamics of king Penguins *Aptenodytes patagonica* on the Crozet Islands,'' Ibis **134**, 107–117.
Wiley, R. H. (**1976**). ''Communication and spatial relationships in a colony of Common Grackles,'' Anim. Behav. **24**, 570–584.
Wiley, R. H., and Wiley, M. S. (**1977**). ''Recognition of neighbors' duet by stripe backed wrens *Campylorhynchus nuchalis*,'' Behaviour **62**, 10–34.
Wiley, R. H., and Richards, D. G. (**1978**). ''Physical constraints on acoustic communication in the atmosphere: Implications for the evolution of animal vocalizations,'' Behav. Ecol. Sociobiol. **3**, 69–94.
Wiley, R. H., and Richards, D. B. (**1982**). ''Adaptations for acoustic communication in birds: sound transmission and signal detection,'' in *Acoustic Communication in Birds, Vol. 1*, edited by D. E. Kroodsma and E. H. Miller (Academic, New York), pp. 131–181.
White, S. J. (**1971**). ''Selective responsiveness by the Gannet (*Sula Bassana*) to played-back calls,'' Anim. Behav. **19**, 125–131.
White, S. J., and White, R. E. C. (**1970**). ''Individual voice production in gannets,'' Behaviour **37**, 41–54.
White, S. J., White, R. E. C., and Thorpe, W. H. (**1970**). ''Acoustic basis for individual recognition by voice in the Gannet,'' Nature (London) **225**, 1156–1158.
Wooler, R. D. (**1978**). ''Individual vocal recognition in the kittiwake gull, *Rissa tridactyla*,'' Z. Tierpsychol. **48**, 68–86.

Binaural sluggishness in the perception of tone sequences and speech in noise

John F. Culling[a] and H. Steven Colburn
Department of Biomedical Engineering, Boston University, 44 Cummington Street, Boston, Massachusetts 02215

(Received 2 November 1998; revised 19 July 1999; accepted 28 September 1999)

The binaural system is well-known for its sluggish response to changes in the interaural parameters to which it is sensitive. Theories of binaural unmasking have suggested that detection of signals in noise is mediated by detection of differences in interaural correlation. If these theories are correct, improvements in the intelligibility of speech in favorable binaural conditions is most likely mediated by spectro-temporal variations in interaural correlation of the stimulus which mirror the spectro-temporal amplitude modulations of the speech. However, binaural sluggishness should limit the temporal resolution of the representation of speech recovered by this means. The present study tested this prediction in two ways. First, listeners' masked discrimination thresholds for ascending vs descending pure-tone arpeggios were measured as a function of rate of frequency change in the NoSo and NoSπ binaural configurations. Three-tone arpeggios were presented repeatedly and continuously for 1.6 s, masked by a 1.6-s burst of noise. In a two-interval task, listeners determined the interval in which the arpeggios were ascending. The results showed a binaural advantage of 12–14 dB for NoSπ at 3.3 arpeggios per s (arp/s), which reduced to 3–5 dB at 10.4 arp/s. This outcome confirmed that the discrimination of spectro-temporal patterns in noise is susceptible to the effects of binaural sluggishness. Second, listeners' masked speech-reception thresholds were measured in speech-shaped noise using speech which was 1, 1.5, and 2 times the original articulation rate. The articulation rate was increased using a phase-vocoder technique which increased all the modulation frequencies in the speech without altering its pitch. Speech-reception thresholds were, on average, 5.2 dB lower for the NoSπ than for the NoSo configuration, at the original articulation rate. This binaural masking release was reduced to 2.8 dB when the articulation rate was doubled, but the most notable effect was a 6–8 dB increase in thresholds with articulation rate for both configurations. These results suggest that higher modulation frequencies in masked signals cannot be temporally resolved by the binaural system, but that the useful modulation frequencies in speech are sufficiently low (<5 Hz) that they are invulnerable to the effects of binaural sluggishness, even at elevated articulation rates. [S0001-4966(00)02601-1]

PACS numbers: 43.66.Pn, 43.66.Ba, 43.66.Dc, 43.66.Hg [DWG]

INTRODUCTION

This investigation combines two recent concepts in binaural research and applies them to the practical issue of how the binaural system assists the understanding of speech in noise. The first concept is the theory that when signals are added to noise at a differing interaural phase or delay, they are detected by virtue of the changes in interaural correlation, which target signals induce in noise (Durlach *et al.*, 1986); the second is the sluggishness of the binaural system, which seems unable to follow rapid changes in the temporal relationships between the sound reaching the two ears, as though this information is temporally smeared within the auditory system (Grantham and Wightman, 1978, 1979). Taken together, these ideas imply first, that the modulations of a speech signal within different frequency bands are detected by the binaural system as modulations in the interaural correlation of those frequency bands, and second, that these modulations in correlation are perceived only at low modulation rates. For the situations encountered within this study, addition of the signal always causes a reduction in interaural correlation.

It will be demonstrated below that, according to this logic, the binaural system should lose the spectrotemporal information which codes formant movements, while preserving information associated with the enunciation of syllables. One might expect the loss of formant-movement information to reduce the usefulness of the binaural system in speech understanding. The effectiveness of the binaural system for speech recognition can be measured by comparing the masked speech-reception thresholds (SRTs) in the NoSo and NoSπ configurations. The difference in threshold is called the binaural intelligibility level difference (BILD). However, although the BILD is only 5–6 dB, whereas masked pure-tone thresholds can show differences of 15 dB, this difference in the size of the masking release can be fully accounted for without reference to binaural sluggishness.

Levitt and Rabiner (1967a,b) showed that the smaller size of the BILD compared to binaural masking level differ-

[a]Current address: School of Psychology, Cardiff University, P.O. Box 901, Cardiff CF10 3YG, U.K. Electronic mail: cullingj@cardiff.ac.uk

ences (BMLDs) can be fully explained by the limited range of frequencies over which the binaural system is effective. They predicted a BILD of 5-6 dB from pure-tone data by using Fletcher's articulation index (Fletcher and Galt, 1950; Kryter, 1962a,b). The articulation index, originally developed for the telecommunications industry, predicts the intelligibility of speech through a given transmission channel using information about that channel's frequency response and noise; Levitt and Rabiner's calculations assumed that the effective noise level at each frequency was reduced in favorable binaural configurations in accordance with the corresponding pure-tone BMLD at that frequency. In terms of the structural features of speech, the BILD is only 5–6 dB, because only the first formant region is strongly assisted by the binaural system. The articulation index does not, however, take into account the channel's modulation transfer function (MTF), a measure of the fidelity with which a channel transmits different modulation frequencies. The MTF was developed for the purpose of predicting speech intelligibility in reverberant auditoria which produce temporal smearing of the signal (Houtgast and Steeneken, 1985). Since the binaural system seems likely to lose the higher-modulation frequencies, one should expect predictions of the BILD based on the MTF to be smaller than those based on the articulation index, and, therefore, smaller than those observed. Unfortunately, there are, at present, insufficient empirical data on the importance of different modulation frequencies in speech perception to make quantitative predictions of the BILD on this basis.

The fact that binaural sluggishness seems to be irrelevant to accurate predictions of the BILD consequently poses a problem for the idea that speech is heard via a temporally smeared representation of spectro-temporal modulations in interaural correlation. It is possible that this idea is flawed, since Yost (1985) has suggested an alternative hypothesis; binaural sluggishness might be related to the time it takes the binaural system to adapt to a changing masker. He pointed out that within the context of Durlach's equalization-cancellation model (Durlach, 1972), such sluggishness could be represented as the time required for the system to calculate a new equalization operation. If binaural sluggishness took that form, it would be important for changing noises, but not for changing signals, like speech, because the equalization operation depends on the interaural configuration of the noise and that remains the same throughout the stimulus. In that case, the binaural spectrogram idea proposed here would be quite inappropriate. It should be noted that attempts to measure binaural temporal resolution using signal-detection tasks have all used temporally changing masking noises, rather than changing signals (Bell, 1972; Grantham and Wightman, 1979; Shackleton and Bowsher, 1989; Kollmeier and Gilkey, 1990; Culling and Summerfield, 1998). Thus, Yost's account of binaural sluggishness does not affect the prediction of the BILD and is consistent both with Levitt and Rabiner's findings, as well as with the binaural-temporal-resolution literature. However, Kohlrausch (1990) has found some evidence against Yost's account. He showed that when the interaural phase of a masker is different in different frequency regions, listeners have no difficulty detecting antiphasically presented tones in either region, when there is trial-by-trial uncertainty as to the tone frequency. He also noted that in a condition where So and Sπ thresholds were measured at the same frequency, with trial-by-trial uncertainty as to the signal phase, the results could only be accounted for if the system was employing different equalization delays in parallel within the same frequency channel.

The present investigation compares two hypotheses: (1) binaural sluggishness does not extend to the discrimination of signals according to their spectro-temporal patterns; (2) the modulation frequencies in speech that make the most important contribution to intelligibility are too low to be affected by binaural sluggishness. Sections A–C of this introduction briefly outline the evidence that the binaural system is sluggish, the evidence that interaural decorrelation is interpreted by the binaural system as the presence of a masked signal, and the implications of combining these concepts into a representation of speech as recovered from masking noise by the binaural system—a ''binaural spectrogram.'' Section D outlines the experiments which follow.

A. Binaural sluggishness

The binaural system is unable to follow rapid changes in the interaural parameters of the stimulus. This sluggishness can be illustrated by asking listeners to discriminate between a stimulus whose binaural parameters are sinusoidally modulated in some way and a comparison stimulus which has the same average binaural characteristics, but unmodulated. If a binaural parameter is modulated at 10 Hz or more, the stimulus is much more difficult to discriminate from the unmodulated standard than at low modulation rates (Grantham and Wightman, 1978; Grantham, 1982).[1] Recently, there have been several attempts to characterize binaural sluggishness as a moving-average filter, termed a binaural temporal window, which integrates information over time according to a weighting function that defines the window. These studies have sought to measure both the shape and equivalent rectangular duration (ERD) of the window (Kollmeier and Gilkey, 1990; Culling and Summerfield, 1998) or only its ERD (Akeroyd and Summerfield, 1999). The ERDs measured in these studies range from 40–200 ms. For the purposes of the present investigation, the measurements of Culling and Summerfield will be employed, since these authors measured both the shape and the ERD of the window, and since their method afforded greater protection against the effects of off-time listening (Moore *et al.*, 1988; Plack and Moore, 1990) than that of Kollmeier and Gilkey. The window measured by Culling and Summerfield had an ERD of about 110 ms, and a Gaussian shape. The modulation transfer function for such a window, which is shown in Fig. 1, has a slope of about −18 dB/oct. It is worth noting for future reference that by 10 Hz (roughly the frequency at which the binaural beat is no longer heard as a moving stimulus) the attenuation is 28 dB.

B. Interaural decorrelation, the BMLD, and dichotic pitches

A number of studies have converged on the idea that signals in noise can be detected by the binaural system via

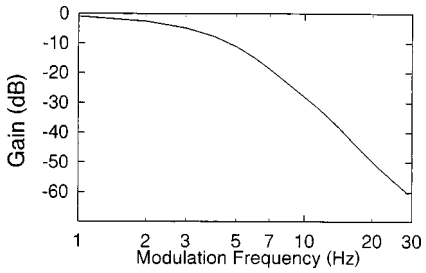

FIG. 1. Modulation transfer function of the binaural temporal window, measured by Culling and Summerfield (1998) at a frequency of 500 Hz and spectrum level of 40 dB(SPL)/Hz.

the differences in interaural correlation that they induce (Osman, 1971; Gabriel and Colburn, 1981; Durlach *et al.*, 1986; Koehnke *et al.*, 1986; Jain *et al.*, 1991; Bernstein and Trahiotis, 1992, 1996a,b; Culling and Summerfield, 1995; Culling *et al.*, 1998a,b,c). In particular, Jain *et al.* showed a correspondence between the amount of decorrelation that was induced by a pure-tone signal at masked threshold in a 1/10th-octave band of noise and the amount of decorrelation which could be detected in a just-noticeable-difference task, where correlation was controlled directly by mixing noises. Culling *et al.* (1998a,b) showed that this quantitative correspondence in the data is complemented by qualitative similarities in the perceptual experience. They showed that a group of phenomena known as dichotic pitches could be explained as illusions produced by the mechanism of binaural unmasking, since each of these phenomena involved stimuli which varied in correlation across frequency; although no ''signal'' is added to the noise, an additional sound is heard whose pitch corresponds to the interaurally decorrelated frequencies. Finally, Culling *et al.* (1998c) have found that the perceived loudness of decorrelated bands of noise fringed by correlated noise is consistent with the idea that decorrelation acted as a perceptual surrogate for signal intensity. Specifically, cumulative d' for binary discriminations based on loudness was an approximately linear function of the ''equivalent signal-to-noise ratio'' in dB, where equivalent signal-to-noise ratio (SNR) was the SNR at which a signal in the NoSπ configuration would produce the interaural decorrelation used in the experiment.

In the past, models of binaural unmasking have generally featured a process of applying internal delays to compensate for the interaural delays or phase shifts that have been applied to the noise, followed by some assessment of the correlation. If the noise is coherent, but a signal is present, the correlation will deviate from unity. For instance, in Durlach's equalization–cancellation (E-C) model, delays (or phase shifts) are used to ''equalize'' the stimulus at the two ears and then the degree of correlation is assayed by a ''cancellation'' process that subtracts the stimulus at one ear from that at the other. In most cases, the greater the residue from cancellation, the greater the decorrelation. Osman (1971) developed a similar scheme in which the correlation after equalization was used directly as the decision variable. In order to account for BMLDs when the frequency and phase of a 20-ms signal were uncertain, and could not be predicted from the noise (which had different phases at each frequency), Kohlrausch (1990) suggested a modification to Durlach's E-C scheme, in which all equalization operations are processed in parallel at all frequencies and equalization delays. Coming from a quite different perspective, Culling and Summerfield (1995) suggested that independently selected delays are employed in each frequency channel in order to account for listeners' inability to perceptually segregate ''whispered'' vowels. Colburn (1973, 1977) employed a similar delay-only scheme, except that the within-channel cross product was calculated at a range of delays, and deviations of these cross products from reference values (supplied by the nonsignal interval, or by other frequency channels) indicated the presence of a signal. Such models may be most simply described as systems that are sensitive to within-channel incoherence in the stimulus. That is to say that the output at each frequency reflects the deviation from unity of the maximum in the cross-correlation function as a function of internal delay. When we refer to ''decorrelation'' we refer to such incoherence, and conversely when we refer to ''correlation'' we refer to coherence (i.e., the maximum value in the interaural cross-correlation function); the application of an optimum internal delay is assumed. For NoSπ, the optimum delay is always zero. Given that reductions in correlation (from a coherent background) are widely thought to be the relevant cue for binaural detection, it seems sensible to calculate decorrelation directly, rather than use the various surrogate measures which have been used in previous models.

C. Binaural spectrograms

The idea of a binaural spectrogram is that the binaural system derives a spectro-temporal representation of interaural correlation as a function of time and frequency and that this representation provides a parallel input to the speech recognition system. In order to produce a perceptually valid binaural spectrogram, one must complete four stages of processing: (a) simulate realistic frequency selectivity; (b) derive the within-channel interaural decorrelation as a function of time; (c) smooth that function in accordance with the binaural temporal window; (d) transform the resulting function according to the sensitivity of the binaural system to decorrelation. Data have already been published which enable the first three stages to be implemented. The fourth stage has recently been addressed by Culling *et al.* (1998c). However, only the first three stages will be implemented here (Fig. 2).

The width of binaural critical bands appears to be similar to that of monaural critical bands (Kohlrausch, 1988; Kollmeier and Holube, 1992), so a conventional auditory filterbank such as that developed by Patterson *et al.* (1987, 1988) may be used as a front end [stage (a)]. The temporally smoothed within-channel correlation [stages (b) and (c)] may be implemented as follows. The interaural correlation is calculated directly from the stimulus (signal and noise) within a series of overlapping binaural temporal windows. The Gaussian window, derived by Culling and Summerfield (1998) at 500 Hz and at a noise spectrum level of 40 dB/SPL(Hz) is employed throughout this paper. As published, the window represents the weighting of interaural correlation as a function of time and not the weighting of raw waveforms whose correlation is to be determined. In the process

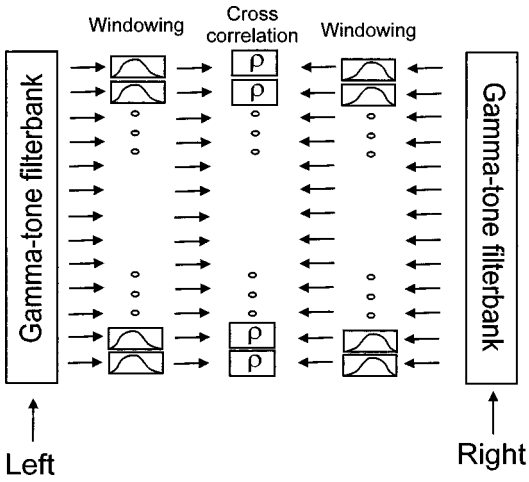

FIG. 2. The stages of making a binaural spectrogram. The left- and right-hand channels are filtered by a gamma-tone filterbank (Patterson *et al.*, 1987, 1988) and overlapping temporal windows are extracted. The windows of corresponding frequency and timing from the two ears are cross-correlated. The differences between the maximum interaural cross correlations and 1.0 as a function of delay for each frequency and time form the binaural spectrogram.

of calculating correlation, the waveforms are multiplied together, multiplying, at the same time, any weighting that has been applied to them. For this reason, the weights of the window were square-rooted before being applied to both input waveforms, and the correlations between the corresponding windowed segments calculated. Finally, in order to gain a representation that reflects listeners' sensitivity to interaural correlation, the temporally smoothed interaural correlation function derived from a series of overlapping windows may be scaled according to the relationship between decorrelation and sensitivity [stage (d)].

Figures 3 and 4 illustrate the effects of the monaural and binaural temporal windows [stages (a)–(c)] on the representation of speech. The speech segment contains the words ''pirates' gold.'' For Fig. 3 the speech segment is processed with no noise. A psychoacoustic spectrogram was generated using the Patterson *et al.* (1987, 1988) gamma-tone filterbank. The squared Hilbert envelopes of each output frequency channel were extracted. These waveforms were then convolved with the *monaural* temporal window measured by Plack and Moore (1990), which has a frequency-dependent ERD of 8–13 ms, and plotted for each channel as functions of time. For Fig. 4, the speech segment was first added to speech-shaped noise in the NoSπ configuration at an overall signal-to-noise ratio of −15 dB. A *binaural* psychoacoustic spectrogram was generated using the method described above and illustrated in Fig. 2. Figure 4 differs dramatically in appearance from Fig. 3 because the binaural temporal window is an order of magnitude longer than the monaural temporal window and so greatly attenuates the representation of higher-modulation frequencies. Notice, in particular, that the formant movements which are clear in Fig. 3 at the onset of and during enunciation of the diphthong /əʊ/ of the word ''gold'' are almost entirely smoothed out in Fig. 4. Thus, it appears that a prediction which comes from this representation is that the binaural system can recover information chiefly about the frequency and amplitude of the first formant in each syllable, but not about any formant movements.

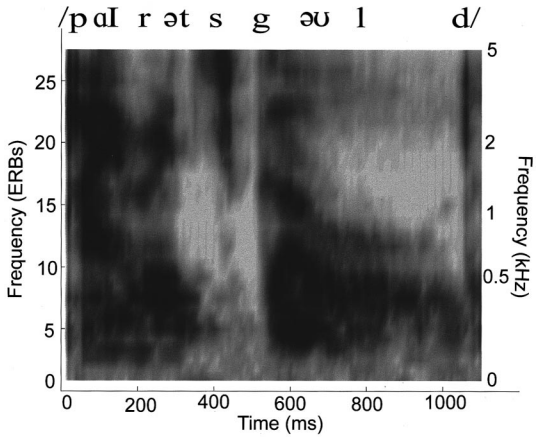

FIG. 3. Psychoacoustic spectrogram of the words ''pirate's gold'' spoken by a male voice, generated by filtering with a gamma-tone filterbank, extracting the Hilbert envelope of each frequency channel, and convolving with Plack and Moore's (1990) monaural temporal window. It is traditional to represent spectrograms with a grayscale image. Since other representations would be unfamiliar and are difficult to read, grayscales have been used here, but an ambiguity is thereby introduced to the scaling of the *z* dimension. The grayscale in the figure was generated using the MATLAB™ *surf* function, viewed from directly above. The darker tones represent increased intensity in dB.

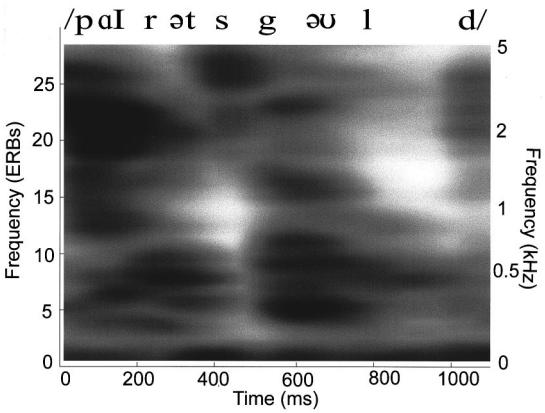

FIG. 4. As Fig. 3, except that the words have been mixed with speech-shaped noise and a binaural psychoacoustic spectrogram generated using the method illustrated in Fig. 2. The grayscale represents decreased correlation and, in order (crudely) to reflect the greater sensitivity of the binaural system to deviations from perfect correlation than to deviations from other reference values (Pollack and Trittipoe, 1959a,b; Culling *et al.*, 1998c), the correlation values, ρ, were subjected to the transform $\log(1-\rho)$ before plotting.

It should be noted that the representation in Fig. 4 lacks any consideration of the relative effectiveness of the binaural system at different frequencies. Information above 1 kHz ($\approx$15 ERBs) should be greatly attenuated. It is thought that the underlying reason for this lack of sensitivity is that the binaural system is relying upon the normalized interaural correlation (rather than the normalized interaural covariance) of the signal envelope at high frequencies (van de Par and Kohlrausch, 1995; Bernstein and Trahiotis, 1996a,b).

Formant movements are widely regarded as very important in speech perception. They provide information about both consonants and vowels. For instance, Strange *et al.* (1983) have shown that the formant movements entering and

leaving a steady-state vowel (from a ''briskly'' spoken CVC syllable) are more useful to listeners in identifying the vowel than the steady-state portion. The binaural spectrogram suggests that such information would not be recovered from noise by the binaural system.

D. The present investigation

The first experiment verifies the binaural spectrogram concept by testing whether binaural sluggishness can be observed in the discrimination of signals according to their spectro-temporal patterns. The threshold levels for discriminating different repeated signal patterns (ascending vs descending arpeggios) were measured in the NoSo and NoSπ configurations. Where a lower discrimination threshold is observed in NoSπ than in NoSo, the binaural system may be presumed to be responsible. By varying the rate at which the spectro-temporal pattern of the signal is repeated, the modulation frequencies in the signal and, therefore, the rate of modulations in interaural correlation for the NoSπ stimuli can be controlled. It will be shown that the difference between NoSo and NoSπ discrimination thresholds diminishes with increasing repetition rate consistent with a loss of information about the modulations in interaural correlation furnished by the binaural system. At high repetition rates the binaural system is too sluggish to substantially assist the listener, resulting in similar discrimination thresholds for NoSo and NoSπ.

Having established that changing signals *do* display effects of binaural sluggishness, the second experiment explores the possibility that, for speech, the *most important* modulation frequencies are sufficiently low that they are not affected by binaural sluggishness. This experiment tests whether speech perception in noise will begin to show the detrimental effects of binaural sluggishness if the modulation frequencies in speech are artificially increased.

I. EXPERIMENT 1

A. Stimuli

Experiment 1 tests the hypothesis that binaural sluggishness will be observed when listeners try to distinguish two masked signals which have different spectro-temporal patterns. For this purpose, two simple spectro-temporal patterns were used. These signals were three-tone arpeggios, made up from pure-tone bursts of variable duration (32–100 ms) which included 5-ms, raised-cosine onset/offset ramps. Each tone began at the offset of the previous tone, so that a shorter tone duration would result in a more rapid arpeggio. The arpeggios began on a randomly selected tone and were repeated throughout a 1.6-s, white noise burst (0–10 kHz). The three pure tones had frequencies of 400, 500, and 625 Hz. The onsets and offsets of the resulting 1.6-s sequence of arpeggios was ramped on and off using a 50-ms, raised-cosine function, while the noise was ramped on and off more rapidly, using a 10-ms raised cosine function. The random starting tone and the slower ramping of the signal were intended to remove listeners' opportunity to exploit the initial or final tone in the sequence as a cue to the direction of frequency change. The durations of the constituent tones (held constant during a given threshold run) were 32, 40, 50, 64, 80, or 100 ms, resulting in arpeggios of three times these durations. The corresponding rates of repetition were, therefore, 10.41, 8.33, 6.67, 5.21, 4.17, and 3.33 arp/s. The signals were presented in either the NoSo or NoSπ binaural configurations. The noise was presented at a spectrum level of 38 dB(SPL)/Hz.

As well as measuring the masked thresholds for 70.7% discrimination performance for different tone durations, the masked *detection* thresholds were also measured. This test was run in exactly the same way, except that the downward arpeggios were removed, so that listeners discriminated masked upward arpeggios from noise alone. Measurements of the detection thresholds facilitated the calculation of discrimination thresholds expressed in sensation level.[2]

All stimuli were generated on-line using a TDT AP2 array-processor card and presented to listeners in a sound-treated chamber via a TDT System-2 psychoacoustic rig (DD1, PA4, FT5-9, HB6) and Sennheiser HD414 headphones.

B. Procedure

Listeners attended a number of 1-h practice sessions followed by eight experimental sessions. The first four experimental sessions measured discrimination thresholds and the second four measured detection thresholds. In each session, they completed 12 runs which covered all combinations of the six rates of arpeggios and the two binaural configurations. Each run was a 2-down/1-up adaptive threshold measurement (Levitt, 1971), with 14 reversals. The average signal level at the last ten reversals was taken as the threshold. The stepsize was 4 dB until two reversals had been completed, and 2 dB thereafter. Each trial was a two interval, forced-choice (2I-FC) task, in which the listener was required to indicate the interval which contained ascending arpeggios. Trial-by-trial feedback was given. The listeners were trained on a predictable sequence of runs that had progressively faster arpeggios throughout the session, but were tested using a random sequence of runs. After collecting four thresholds for each condition in the discrimination task, four detection thresholds were measured for the same conditions. For this purpose the downward arpeggios were removed from each trial, so that listeners simply indicated the noise burst which contained an upward arpeggio. Four discrimination thresholds in dB sensation level (SL) were derived by subtracting the discrimination thresholds from the corresponding detection thresholds.[3]

The discrimination task was found to be very difficult by most listeners. Often the adaptive staircase returned to the initial (and maximum) signal level of 84 dB SPL during a run at one of the fastest presentation rates. Three listeners could not discriminate the direction of movement accurately at the lowest presentation rate and at high signal-to-noise ratios, and were immediately rejected. Another four were trained for many hours without achieving stable thresholds at the highest rates. Five listeners eventually achieved stable thresholds across all presentation rates. Of these, only two (AM and MT) were able to do this without at least 5–10 h of

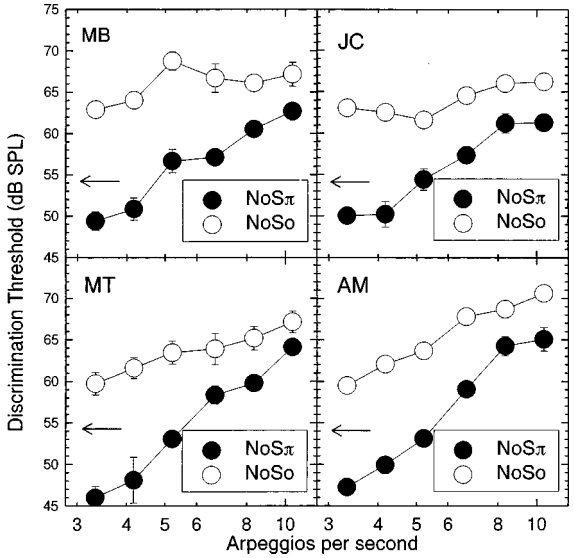

FIG. 5. Masked-discrimination thresholds in dB SPL for the discrimination of ascending versus descending pure-tone arpeggios as a function of their repetition rate. Each panel shows the results for a different listener. The error bars are one standard error of the mean. The arrow at a signal level of 54 dB indicates the signal-to-noise ratio at which Figs. 7, 8, and 9 were generated. The decrease in signal level resulting from the greater number of onset and offset ramps in the more rapid tone sequences (a difference of 0.66 dB between 32- and 100-ms tones) has been compensated for.

training. Four listeners produced a complete data set with stable thresholds throughout. Their data are presented below.

C. Results

Mean thresholds, averaged across four runs, for the four listeners are plotted in separate panels of Figs. 5, 6, and 7. Figure 5 shows the masked discrimination thresholds in dB. For each listener, the discrimination thresholds for NoSo and NoSπ differ by 12–14 dB at a rate of 3.33 arp/s, but this binaural advantage reduces to 3–5 dB at 10.4 arp/s. The

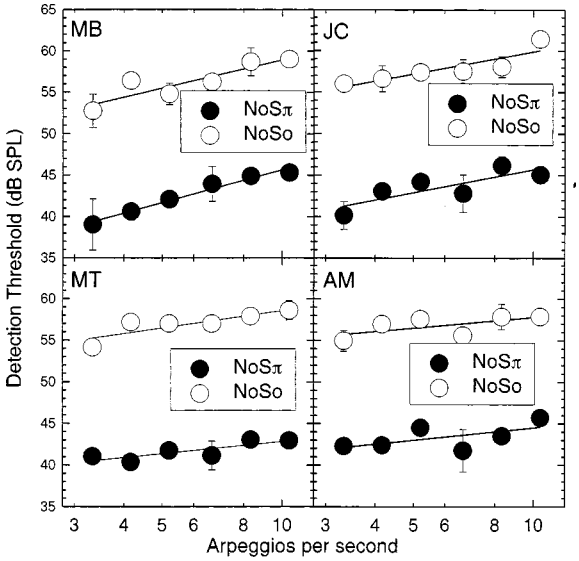

FIG. 6. As Fig. 5, but showing masked-detection thresholds in dB SPL for the detection of ascending pure-tone arpeggios as a function of their repetition rate. The lines are linear regression functions fitted to the data for each binaural configuration.

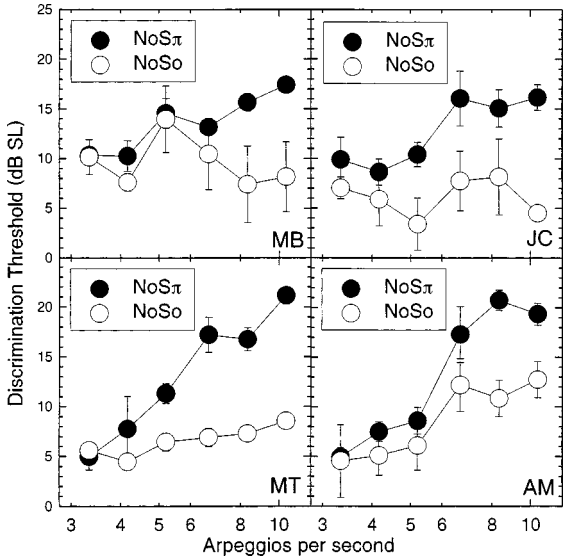

FIG. 7. As Fig. 5, but plotted in sensation level.

difference in discrimination level at 3.33 arp/s is therefore similar to the BMLD for detection of static tones in noise, but much smaller when the repetition rate is higher. Although both NoSo and NoSπ thresholds increase with presentation rate, NoSπ thresholds increase more. An analysis of variance (ANOVA) covering the four runs, six presentation rates, and two binaural conditions showed significant main effects of rate of presentation [$F(5,15)=42.2$, $p<0.0001$] and of binaural condition [$F(1,3)=466$, $p<0.0005$], and a significant interaction between those two [$F(5,15)=117$, $p<0.0001$]. There were no effects associated with the 'run' factor. Tukey HSD pair-wise comparisons showed that the difference between NoSo and NoSπ was significant at the 5% level or less at all presentation rates.

Figure 6 shows the *detection* thresholds for ascending arpeggios using the same scale. The detection thresholds also increased as a function of presentation rate; the most rapid sequences gave detection thresholds which were up to 7 dB higher than the slowest for both NoSo and NoSπ. The slope of this increase in threshold with presentation rate varies across the listeners, but is similar for each listener in NoSo and NoSπ

Figure 7 shows the discrimination thresholds in dB SL (i.e., the thresholds from Fig. 6 have been subtracted from those from Fig. 5). Before the detection thresholds were subtracted, the discrimination thresholds in the NoSo condition showed a substantial increase with presentation rate. Since detection thresholds increase with presentation rate, discrimination thresholds in NoSo increase less when measured in sensation level than when measured in absolute level. The thresholds in sensation level are similar for NoSo and NoSπ at low presentation rates and separate as the presentation rate increases for all listeners. Listeners can make the discrimination at a sensation level of 5–10 dB in the NoSo condition across all presentation rates. In the NoSπ condition, however, the threshold is similar to NoSo at the lowest presentation rate but is substantially higher at higher presentation rates; the listeners can discriminate the direction of the fast-

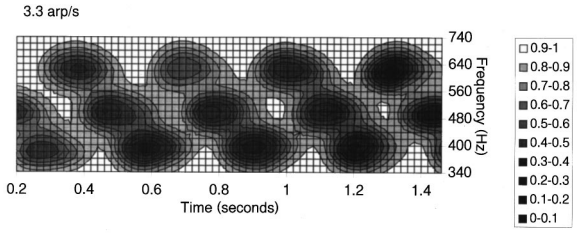

FIG. 8. Binaural spectrogram of masked-arpeggio stimuli from experiment 1 at presentation rates of 3.3 arp/s at the signal level indicated with arrows in Fig. 5.

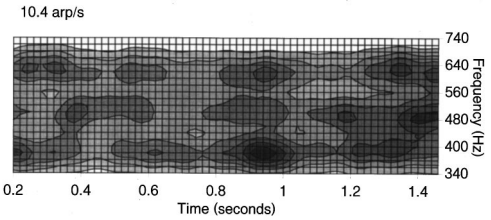

FIG. 10. As Fig. 4, but for 10.4 arp/s.

est arpeggios in NoSπ only when they are as much as 15–20 dB above detection threshold.

D. Discussion

The results show that the binaural advantage for discriminating two simple spectro-temporal patterns in noise can be greatly reduced if the patterns change rapidly. This reduction is consistent with a lack of temporal resolution for binaural processing. Binaural sluggishness has therefore been observed in the discrimination of spectro-temporal patterns among masked signals. This result is inconsistent with Yost's (1985) suggestion that binaural sluggishness might reflect the time taken for the binaural system adapt to a changing *masker*, since the masker was constant in this experiment. The data therefore corroborate Kohlrausch's (1990) conclusions on this matter, using a quite different approach. However, while the reduction in binaural advantage was progressive, the binaural advantage was not completely abolished at the highest rate. This aspect of the results appears inconsistent in some respects with the Gaussian window shape of 110-ms ERD measured by Culling and Summerfield (1998). Such a window should result in a high degree of attenuation (about 28 dB) for modulations of correlation at 10.4 Hz (cf. Fig. 1). The point may perhaps be better illustrated using the binaural spectrogram itself. Figures 8, 9, and 10 show binaural spectrograms of descending arpeggios with presentation rates of 3.3, 5.2, and 10.4 arp/s, respectively. These spectrograms have been plotted as grey-scale plots with discrete contours so that the exact correlations are shown explicitly at the boundaries. The signal-to-noise ratio used is indicated by arrows in Fig. 5. At this signal-to-noise ratio, the presence of the signal causes substantial decorrelation of the masker for all rates, consistent with detection performance well above threshold. However, the representation of the spectro-temporal pattern of decorrelation depends upon the arpeggio rate; the binaural spectrogram contains clear regular modulations for downward sweeps at 3.3 arp/s, rather less distinct modulation for downward sweeps at 5.2 arp/s, and no discernible detail at 10.4 arp/s. Figure 10 shows some random fluctuations in correlation. These are caused by fluctuations in the level of the noise; whenever the noise fluctuates downward in level, the decorrelation caused by the presence of the signal increases. According to a visual inspection of Fig. 10, the binaural spectrogram model predicts that listeners should be unable to use binaural cues at 10.4 arp/s and so should have similar thresholds for NoSo and NoSπ conditions at that presentation rate. These thresholds in fact differ by 3–5 dB, suggesting that the model overpredicts the increase in thresholds with increasing presentation rate.

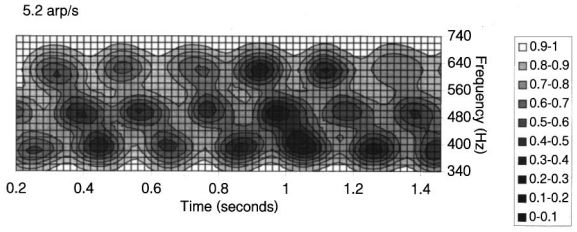

FIG. 9. As Fig. 4, but for 5.2 arp/s.

The fact that the model overpredicts this increase was confirmed by some more formal modeling. Stimuli were created with signals at the listeners' average discrimination threshold from the experiment for presentation rates of 3.3 and 10.4 arp/s. The interaural correlation at the output of a pair of 500-Hz gamma-tone filters was measured during the 500-Hz tone bursts. This average correlation value was then used to create a boxcar correlation modulation function with a 2/3 duty cycle (i.e., with a correlation of 1.0 for 2/3 of a cycle). This function represented the idealized modulation in interaural correlation at the output of a matched pair of auditory filters with 500-Hz center frequencies when listening to the arpeggios. The function was convolved with the binaural temporal window and the modulation of the correlation at the output of the window assessed. At 3.3 arp/s the correlation varied between 0.998 and 0.941, a difference of 0.057. This value is comparable with just-noticeable differences (jnd's) reported in the literature for a reference correlation close to 1.0 (Pollack and Trittipoe, 1959a; Gabriel and Colburn, 1981; Koehnke *et al.*, 1986; Culling *et al.*, 1998c), which vary between 0.03 and 0.005. At 10.4 arp/s the correlation varied between 0.628 and 0.572, a difference of 0.055. The range of correlations at the outputs of the temporal window is, therefore, very similar at each presentation rate. However, it is well established that listeners are progressively less sensitive to changes in interaural correlation as the reference correlation is reduced from 1.0 (Pollack and Trittipoe, 1959a; Culling *et al.*, 1998c). So, at threshold, there should be a larger range of correlation change at the output of the temporal window for the faster arpeggios than for the slower ones due to their lower average interaural correlation ($\approx$0.6). Since this is not observed, the listeners are coping better with the increase in presentation rate than the model would predict. This said, the model did predict a reduction in discrimination level difference over the approxi-

mate range of presentation rates over which this reduction took place.

The increase in detection thresholds with rate of presentation (Fig. 6) was an unexpected result. The effect remains when the reductions in signal level produced by the onset and offset ramps is accounted for. Some informal follow-up experiments (using listener JC, the first author) suggest that the effect is produced by the use of multifrequency spectro-temporal sound patterns. When two of the tones were switched off, there was no increase in threshold for the remaining tone as its repetition rate was increased. It seems likely that the effect arises from listeners attempting to attend to the tone pattern one tone at a time; if listeners can succeed in attending to the appropriate frequency channel throughout part of the stimulus, then they may hear it better. Of course, the listener must have heard the preceding tones in order to know what frequency will come next, but since the stimulus is extended in time, listeners may have the opportunity to confirm or refute a hypothesis about how the frequency is changing during the course of the stimulus, by attempting to follow the frequency changes. When the sequence is too rapid for listeners to switch their attention between frequency channels, the strategy is confounded and thresholds increase. The effect may be worthy of further study.

The failure of some listeners to perform the task at all also deserves some comment. Two listeners could not discriminate the upward from downward arpeggios not only at the slowest rates presented in the experiment, but even at 2.08, 1.67, and 1.04 arp/s specially prepared by the experimenter for initial training. Lower rates than this were impractical without increasing the stimulus duration, as fewer than two arpeggios were already being presented at 1.04 arp/s. In this situation, it is very difficult to know whether listeners have simply not grasped the instructions, although one would expect the trial-by-trial feedback to resolve any confusions provided that the stimuli were discriminable. It seems that some listeners with apparently normal hearing and speech can find abstract spectro-temporal sound patterns very difficult to discriminate.

II. EXPERIMENT 2

Experiment 2 investigated the effect of speech rate on speech-reception thresholds (SRTs) in NoSo and NoSπ binaural configurations. If the binaural system responds sluggishly to the changes in interaural correlation induced by the fluctuating presence of speech energy in the NoSπ configuration, and if detection of those correlation changes is the basis of the binaural intelligibility level difference (BILD), then high articulation rates should reduce the BILD.

A. Stimuli

The speech consisted of recorded sentences from the Harvard sentence list (Rothauser *et al.*, 1969). The speech was processed digitally in order to increase the articulation rate without altering the pitch, using a method similar to the phase vocoder. This acceleration of the articulation rate was implemented using the Hilbert transform. The procedure was as follows. (1) The digital waveforms were filtered by the Patterson *et al.* (1987, 1988) gamma-tone filterbank. (2) Each filtered channel was converted to an instantaneous amplitude and an instantaneous phase function. (3) The instantaneous phase function was unwrapped to produce a monotonically increasing function. (4) the phase function was scaled down (by the reciprocal of the acceleration factor), in order to prevent an increase in carrier frequency. (5) The phase and amplitude functions were resampled at a reduced sampling rate in order to compress the same changes in frequency and amplitude over time into a smaller number of samples. (6) An inverse Hilbert transform recovered the accelerated waveforms. (7) All channels were summed back together to get the accelerated speech signal.[4]

The masking noise was speech-shaped according to the long-term spectra of the speech materials used in the experiment. Fifty samples of such noise were prepared. Speech and noise were prepared off-line using |WAVE software (Culling, 1996) and mixed adaptively during the experiment using a TDT AP2 array processor.

B. Procedure

The noise was mixed with the speech and presented to the listener at a signal-to-noise ratio determined by a procedure adapted from one developed by Zurek (1996). SRTs were measured in a series of 1-up/1-down adaptive runs to determine the 50%-intelligibility level (Levitt, 1971). Each run began with a sentence at a poor SNR. For this sentence, the listener was instructed to increase the signal level progressively and rehear the sentence until it was perceived as partially intelligible, and then to attempt a transcription. By this means, the adaptive staircase was started at approximately the 50%-intelligibility level without wasting any speech material. The listener entered the transcript on a computer terminal. When the transcript was complete, the listener pressed ''return'' and the computer gave the listener the actual transcript of the speech with the keywords in upper case. The listener self-marked the number of correct keywords out of the five in each sentence and the computer adjusted the signal level by 2 dB for the next trial. For subsequent trials, the listener heard each sentence only once and immediately offered a transcript. The SNR was increased for two or fewer keywords correct and decreased for three or more correct. The listeners were not informed of this criterion, but were aware that the computer was using their self-reported performance to control the speech level and also that the entire transaction was both visible on the experimenter's monitor and being logged. A complete adaptive run consisted of a total of ten sentences. The new signal level selected after each trial was averaged over the last eight trials to give the measured speech-reception threshold for that run.

The listeners attended either six or ten 1-h sessions. All listeners began with two sessions of practice with the experimental procedure for unprocessed sentences in the NoSo and NoSπ configurations. This practice familiarized listeners with the procedure, ensuring that their judgments of partial intelligibility at the start of each run were acceptably accurate, and also gave an initial estimate of the binaural intelligibility level difference (BILD). At this stage, one listener showed no BILD and was rejected from the study. The other listeners averaged a BILD of 5.4 dB. Six listeners went

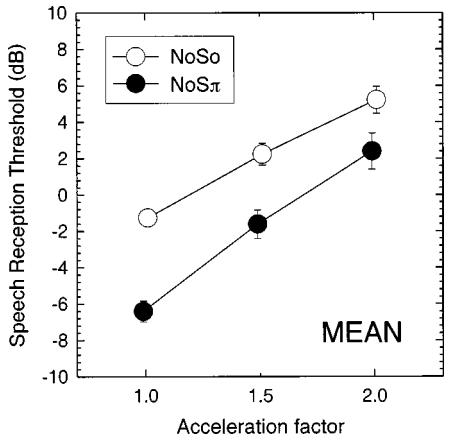

FIG. 11. Mean speech reception thresholds for 12 listeners in each binaural configuration and for each speech acceleration factor. The error bars are 95% confidence intervals for the mean of 84 SRTs (12 listeners × 7 repeated measurements).

straight on to the experimental sessions, and six listeners were given further training designed to acclimatize them to accelerated speech. This training consisted of listening to a series of story tapes for a recently published thriller, using a variable-speed tape player (Radio Shack VSC-2002). This machine was also equipped with a pitch control[5] (Variable Speech Control Co.), which could be used to offset the pitch changes produced by changing the tape speed. These listeners were instructed to attend to the story, which none of them had heard before, and to increase the tape speed progressively until they were following the story at double the original speed. All six of these listeners increased the speed to double by the end of the first acclimatization session and listened comfortably at double speed throughout the following three sessions.

In the four experimental sessions, listeners completed a total of 44 runs. The first two runs in the first session were further practice, but using accelerated speech material. The remaining 42 runs were seven repeated measures for the six conditions (3 acceleration factors × 2 binaural conditions). The speech materials used were new to the listeners, and were counterbalanced across the six conditions, so that each sentence was presented in each of the six conditions; for a given set of six listeners, each sentence was presented once in each of the six conditions, each time to a different listener.

C. Results

Figure 11 shows the results of experiment 2 for the two groups of listeners combined. The results are averaged across all 12 listeners because they would otherwise be distorted by differences in the intrinsic intelligibility of the different sentence lists (only across a group of six listeners are all lists used for all six conditions) and because an analysis of variance, covering the seven repeated-threshold measurements, the three speech rates (1, 1.5, and 2 times original speed), the two binaural conditions (NoSo/NoSπ), and the two training regimes (with/without accelerated-speech acclimatization) showed no effect of acclimatization to accelerated speech.

Listeners produced SRTs that were 3–5 dB lower for NoSπ (filled symbols) than for NoSo (open symbols) [$F(1,10)=27$, $p<0.0005$]. An analysis of simple main effects shows that the difference was significant at each speech rate [at original speed, $F(1)=16.8$, $p<0.002$; at 1.5 times original speed, $F(1)=9.4$, $p<0.02$; at twice original speed, $F(1)=5.0$, $p<0.05$]. Meanwhile, their thresholds in both conditions rose with increasing articulation rate by around 8 dB [$F(2,20)=172$, $p<0.0001$]. The increase in SRT was around 2 dB greater for NoSπ than for NoSo, as reflected by an interaction between acceleration factor and binaural condition in the ANOVA [$F(6,60)=2.6$, $p<0.05$].

D. Discussion

In both experiments 1 and 2, the principal effect of interest was the interaction between rate of change in the signal and binaural condition. In experiment 1, increasing the repetition rate of the arpeggios substantially reduced the effect of the binaural configuration, broadly in agreement with the predictions of a binaural spectrogram model. However, in experiment 2, the most striking effect of accelerated speech was a 6–8-dB increase in SRTs. In addition to this effect there was a reduction in the binaural advantage for accelerated speech. However, the 6–8-dB increase in sensation level makes it difficult to interpret the reduction in binaural advantage with certainty. Thus, it would appear that while accelerated speech is difficult to understand in noise, this effect has relatively little to do with binaural sluggishness. This result was somewhat unexpected, and requires explanation.

Given that experiment 1 is persuasive in its demonstration of an effect of binaural sluggishness on spectrotemporal pattern discrimination, the most likely explanation for the relative indifference of the binaural system to increased speech rate is that the binaural system is still able to recover useful information which is within the temporal window's MTF. In order to assess the likelihood of this explanation, one needs to know what modulation frequencies are present in speech and how important they are to intelligibility. Plomp (1983) measured the average modulation spectrum for ten male voices. He found that the modulation spectrum was similar in all measured frequency bands; in each 1/3rd-octave band the modulation spectrum peaked at about 4 Hz (approximately the syllable rate), but featured extensive shallow slopes towards higher and lower modulation frequencies. A similar demonstration appears in Houtgast and Steeneken (1985). The dominant modulation frequencies of speech are therefore quite low compared to the passband of the temporal window, and doubling the articulation rate would not remove them. However, these frequencies might not be the most important.

Drullman *et al.* (1994a,b) have investigated the role of different modulation frequencies in speech intelligibility. In their first paper (1994a), they temporally smeared speech using each of a wide range of low-pass cutoff frequencies (4, 8, 16, 32, and 64 Hz) before adding noise. They found that the 16-, 32-, and 64-Hz cutoffs produced very similar SRTs. The 8-Hz cutoff increased the SRT by about 1 dB and the 4-Hz cutoff increased it by a further 4 dB. Their experiment suggested, therefore, that frequencies between 4 and 8 Hz are

quite important to the intelligibility of speech in noise, although it was not clear whether they are more or less important than still lower frequencies. Their subsequent paper (1994b) used high-pass filtering of the modulation spectrum in order to address this question. By combining the results of the two studies, they demonstrated that the most important modulation frequency was, in fact, about 8 Hz.

Their first experiment was similar, in a sense, to experiment 2 of the current study: Drullman *et al.* directly smeared the speech, while experiment 2 assumed that such smearing would be a side effect of binaural processing; Drullman *et al.* varied the low-pass cutoff of the modulation spectrum, while Experiment 2 varied the speech rate. In either case, speech was heard in noise with a low-pass-filtered modulation spectrum. If we say that the binaural system recovers no information about the modulation spectrum above about 10 Hz (28-dB attenuation according to Fig. 1), the information in the original modulation spectrum is effectively low-pass filtered at 10, 6.7, and 5 Hz for acceleration factors of 1, 1.5, and 2×, respectively. Experiment 2 found only partial abolition of the BILD for an equivalent 5-Hz low-pass cutoff. Assuming that the original speech rate of our materials was similar to Drullman's, it is surprising that no more substantial effect was observed in experiment 2. It may be that most of the modulation frequencies above 4 Hz that are important to intelligibility are in higher spectral regions than those recovered by the binaural system. In any case, the present results indicate that binaural sluggishness does not limit the ability of the binaural system to facilitate speech understanding in noise at normal speech rates.

It is possible that across-frequency processing may help explain the discrepancy between the results obtained with tone patterns and with speech. Gordon (1997a,b) has shown that above-threshold information from remote spectral regions can ''protect'' temporally coherent signals from masking. He observed a modest reduction in threshold (≈2 dB) for a brief signal in low-pass noise when a cosignal was simultaneously presented at higher frequencies. The cosignal was presented in both the signal and nonsignal intervals and apparently served only as a temporal marker for the signal, since discrepancies between the onset and offset times of the signal and cosignal destroyed the effect. Conceivably, a similar effect may occur when listening to speech in noise. The low-frequency, low-modulation rate information recovered by the binaural system may act as a cosignal which assists detection of temporally coherent parts of the speech signal in higher spectral regions. Akeroyd *et al.* (1998) have recently demonstrated that the auditory system can integrate speech information furnished simultaneously by monaural and binaural cues and the requirement for temporal coherence should be fulfilled by speech signals because all frequencies tend to modulate coherently at 4 Hz or so due to the enunciation of syllables.

The experiments and modeling described here demonstrate that binaural sluggishness can affect the auditory system's ability to extract fine temporal detail from signals in noise. However, the indications are that this effect is of marginal importance to the BILD. It is not yet clear why the effect of binaural sluggishness does not have a more detrimental effect on speech understanding. A better understanding of how binaural information is employed in the unmasking of speech will be required to resolve this issue.

III. CONCLUSIONS

(1) Binaural sluggishness reduces the binaural advantage for discriminating spectro-temporal patterns in noise when those patterns change rapidly.

(2) Accelerated speech is more difficult to understand in noise than the same speech at the original rate regardless of binaural configuration.

(3) The speech signal may contain information that is sufficient to facilitate understanding at low-modulation frequencies in the 200–1500-Hz spectral region where the binaural system is effective.

ACKNOWLEDGMENTS

We would like to thank Gerald Kidd and Christine Mason for many helpful suggestions about the design of the experiments, Katrin Krumbholz for advice on the Hilbert transform, and Armin Kohlrausch and an anonymous reviewer for their thorough and thought-provoking reviews. Work supported by an M.R.C. Career Development Award (J.F.C.) and by NIDCD (H.S.C.).

[1]In each of these studies stimulus artifacts enabled listeners to make discriminations at modulation rates much higher than 10 Hz. Generally performance reached a trough in the 10–50 Hz region.

[2]Thresholds in sensation level were calculated because Yost (1997) has pointed out that binaural advantages can become smaller as sensation level is increased. Since there was a general trend for thresholds to increase for faster presentation rates, it was thought possible that the increase in sensation level might itself reduce the binaural advantage, rather than binaural sluggishness *per se.* In fact, we found that the detection thresholds *also* increased with presentation rates, so the increase in sensation level was small.

[3]Listener MB was only available for two sessions of detection threshold measurements, so the two resulting thresholds for each condition were subtracted from two different discrimination thresholds.

[4]The resulting accelerated speech was of very high quality. Occasionally, the excitation had a slightly gurgling quality, which, upon investigation, could be attributed to the broad high-frequency channels of the gammatone filterbank. Because these channels admitted a number of frequency components, the instantaneous amplitude function displayed modulation at the original fundamental frequency. After resampling, this modulation was increased in frequency. Thus, in the finished stimuli the fundamental frequency information at low frequencies was fully controlled by scaling the phase of the isolated components in these channels, and was identical to the original, while the high frequencies were giving amplitude modulation cues to a higher fundamental. The perceptual salience of this conflicting information was very low due to the dominance of low frequencies in pitch perception.

[5]The real-time pitch control of this device appeared to be based on the pitch period deletion principle rather than a phase vocoder. Although the pitch was controlled by a slider, the pitch changes were discrete.

Akeroyd, M. A., and Summerfield, Q. (**1999**). ''A binaural analog of gap detection,'' J. Acoust. Soc. Am. **105**, 2807–2820.

Akeroyd, M. A., Summerfield, Q., and Foster, J. R. (**1998**). ''Integrating monaural and binaural spectral information,'' J. Acoust. Soc. Am. **103**, 2976(A).

Bell, D. (**1972**). ''Effect of fringe on masking-level difference when gating from uncorrelated to correlated noise,'' J. Acoust. Soc. Am. **52**, 525–529.

Bernstein, L. R., and Trahiotis, C. (**1992**). ''Discrimination of interaural envelope correlation and its relation to binaural unmasking at high frequencies,'' J. Acoust. Soc. Am. **91**, 306–316.

Bernstein, L. R., and Trahiotis, C. (**1996a**). ''On the use of normalized correlation as an index of interaural envelope correlation,'' J. Acoust. Soc. Am. **100**, 1754–1763.
Bernstein, L. R., and Trahiotis, C. (**1996b**). ''The normalized correlation: Accounting for binaural detection across center frequency,'' J. Acoust. Soc. Am. **100**, 3774–3784.
Colburn, H. S. (**1973**). ''Theory of binaural interaction based on auditory nerve data. I. General strategy and preliminary results on interaural discrimination,'' J. Acoust. Soc. Am. **54**, 1458–1470.
Colburn, H. S. (**1977**). ''Theory of binaural interaction based on auditory nerve data. II. Detection of tones in noise,'' J. Acoust. Soc. Am. **61**, 525–533.
Culling, J. F., and Summerfield, Q. (**1995**). ''Perceptual segregation of concurrent speech sounds: absence of across-frequency grouping by common interaural delay,'' J. Acoust. Soc. Am. **98**, 785–797.
Culling, J. F. (**1996**). ''Signal processing software for teaching and research in psychoacoustics under UNIX and X-windows,'' Behav. Res. Methods Instrum. Comput. **28**, 376–382.
Culling, J. F., and Summerfield, Q. (**1998**). ''Measurements of the binaural temporal window using a detection task,'' J. Acoust. Soc. Am. **103**, 3540–3553.
Culling, J. F., Summerfield, Q., and Marshall, D. H. (**1998a**). ''Dichotic pitches as illusions of binaural unmasking. I. Huggins' pitch and the 'binaural edge pitch','' J. Acoust. Soc. Am. **103**, 3509–3526.
Culling, J. F., Marshall, D. H., and Summerfield, Q. (**1998b**). ''Dichotic pitches as illusions of binaural unmasking. II. the Fourcin pitch and the dichotic repetition pitch,'' J. Acoust. Soc. Am. **103**, 3527–3539.
Culling, J. F., Spurchise, M., and Colburn, H. S. (**1998c**). ''Interaural correlation sensitivity,'' J. Acoust. Soc. Am. **103**, 3081–3082(A).
Drullman, R., Festen, J. M., and Plomp, R. (**1994a**). ''Effect of temporal envelope smearing on speech reception,'' J. Acoust. Soc. Am. **95**, 1053–1064.
Drullman, R., Festen, J. M., and Plomp, R. (**1994b**). ''Effect of reducing temporal modulations on speech reception,'' J. Acoust. Soc. Am. **95**, 2570–2680.
Durlach, N. I. (**1972**). ''Binaural signal detection: Equalization and cancellation theory,'' in *Foundations of Modern Auditory Theory, Vol. II*, edited by J. V. Tobias (Academic, New York).
Durlach, N. I., Gabriel, K. J., Colburn, H. S., and Trahiotis, C. (**1986**). ''Interaural correlation discrimination. II. Relation to binaural unmasking,'' J. Acoust. Soc. Am. **79**, 1548–1557.
Fletcher, H., and Galt, R. H. (**1950**). ''The perception of speech and its relation to telephony,'' J. Acoust. Soc. Am. **22**, 89–151.
Gabriel, K. J., and Colburn, H. S. (**1981**). ''Interaural correlation discrimination. I. Bandwidth and level dependence,'' J. Acoust. Soc. Am. **69**, 1394–1401.
Gordon, P. C. (**1997a**). ''Coherence masking protection in speech sounds: The role of formant synchrony,'' Percept. Psychophys. **59**, 232–242.
Gordon, P. C. (**1997b**). ''Coherence masking protection in brief noise complexes: Effects of temporal patterns,'' J. Acoust. Soc. Am. **102**, 2276–2283.
Grantham, D. W. (**1982**). ''Detection of time-varying interaural correlation in narrow band noise stimuli,'' J. Acoust. Soc. Am. **72**, 1178–1184.
Grantham, D. W., and Wightman, F. L. (**1978**). ''Detectability of varying interaural temporal differences,'' J. Acoust. Soc. Am. **63**, 511–523.
Grantham, D. W., and Wightman, F. L. (**1979**). ''Detectability of a pulsed tone in the presence of a masker with time-varying interaural correlation,'' J. Acoust. Soc. Am. **65**, 1509–1517.
Houtgast, T., and Steeneken, H. J. M. (**1985**). ''A review of the MTF concept in room acoustics and its use for estimating speech intelligibility in auditoria,'' J. Acoust. Soc. Am. **77**, 1069–1077.
Jain, M., Gallagher, D. T., Koehnke, J., and Colburn, H. S. (**1991**). ''Fringed correlation discrimination and binaural detection,'' J. Acoust. Soc. Am. **90**, 1918–1926.
Koehnke, J., Colburn, H. S., and Durlach, N. I. (**1986**). ''Performance in several binaural-interaction experiments,'' J. Acoust. Soc. Am. **79**, 1558–1562.
Kohlrausch, A. (**1988**). ''Auditory filter shape derived from binaural masking experiments,'' J. Acoust. Soc. Am. **84**, 573–583.
Kohlrausch, A. (**1990**). ''Binaural masking experiments using noise maskers with frequency-dependent interaural phase differences. I. Influence of signal and masker duration,'' J. Acoust. Soc. Am. **88**, 1737–1756.
Kollmeier, B., and Gilkey, R. H. (**1990**). ''Binaural forward and backward masking: Evidence for sluggishness in binaural detection,'' J. Acoust. Soc. Am. **87**, 1709–1719.
Kollmeier, B., and Holube, I. (**1992**). ''Auditory filter bandwidths in binaural and monaural listening conditions,'' J. Acoust. Soc. Am. **92**, 1889–1901.
Kruyter, K. D. (**1962a**). ''Methods for calculation and use of the articulation index,'' J. Acoust. Soc. Am. **34**, 1689–1697.
Kruyter, K. D. (**1962b**). ''Validation of the articulation index,'' J. Acoust. Soc. Am. **34**, 1698–1702.
Levitt, H. (**1971**). ''Transformed up–down methods in psychoacoustics,'' J. Acoust. Soc. Am. **49**, 467–477.
Levitt, H., and Rabiner, L. R. (**1967a**). ''Binaural release from masking for speech and gain in intelligibility,'' J. Acoust. Soc. Am. **42**, 601–608.
Levitt, H., and Rabiner, L. R. (**1967b**). ''Predicting binaural gain in intelligibility and release from masking for speech,'' J. Acoust. Soc. Am. **42**, 620–629.
Moore, B. C. J., Glasberg, B. R., Plack, C. J., and Biswas, A. K. (**1988**). ''The shape of the ear's temporal window,'' J. Acoust. Soc. Am. **83**, 1103–1116.
Osman, E. (**1971**). ''A correlation model of binaural masking level difference,'' J. Acoust. Soc. Am. **50**, 1494–1511.
Patterson, R. D., Nimmo-Smith, I., Holdsworth, J., and Rice, P. (**1987**). ''An efficient auditory filterbank based on the gammatone function,'' paper presented to the IOC speech group on auditory modeling at RSRE, 14–15 Dec.
Patterson, R. D., Nimmo-Smith, I., Holdsworth, J., and Rice, P. (**1988**). ''Spiral VOS final report, Part A: The auditory filter bank,'' Cambridge Electronic Design, Contract Report (APU 2341).
Plack, C. J., and Moore, B. C. J. (**1990**). ''Temporal window shape as a function of frequency and level,'' J. Acoust. Soc. Am. **87**, 2178–2187.
Plomp, R. (**1983**). ''The role of modulation in hearing,'' in *Hearing: Physiological Bases and Psychophysics*, edited by R. Klinke and R. Hartmann (Springer, Berlin), pp. 270–276.
Pollack, I., and Trittipoe, W. J. (**1959a**). ''Binaural listening and interaural noise cross correlation,'' J. Acoust. Soc. Am. **31**, 1250–1252.
Pollack, I., and Trittipoe, W. J. (**1959b**). ''Interaural noise correlation: Examination of variables,'' J. Acoust. Soc. Am. **31**, 1616–1618.
Rothauser, E. H., Chapman, W. D., Guttman, N., Hecker, M. H. L., Nordby, K. S., Silbiger, H. R., Uranek, G. E., and Weinstock, M. (**1969**). ''IEEE recommended practice for speech quality measurements,'' IEEE Trans. Audio Electroacoust. **17**, 226–246.
Shackleton, T. M., and Bowsher, J. M. (**1989**). ''Binaural effects of the temporal variation of a masking noise upon the detection thresholds of tone pulses,'' Acustica **69**, 218–225.
Strange, W., Jenkins, J. J., and Johnson, T. L. (**1983**). ''Dynamic specification of coarticulated vowels,'' J. Acoust. Soc. Am. **74**, 695–705.
van de Par, S., and Kohlrausch, A. (**1995**). ''Analytical expressions for the envelope correlation of certain narrow-band stimuli,'' J. Acoust. Soc. Am. **98**, 3157–3169.
Yost, W. A. (**1985**). ''Prior stimulation and the masking level difference,'' J. Acoust. Soc. Am. **78**, 901–907.
Yost, W. A. (**1997**). ''The cocktail party problem: forty years later,'' in *Binaural and Spatial Hearing in Real and Virtual Environments*, edited by R. H. Gilkey and T. A. Anderson (Elbaum, Mahwah, NJ), pp. 239–248.
Zurek, P. M. (**1996**). Personal communication.

Fidelity of three-dimensional-sound reproduction using a virtual auditory display

Erno H. A. Langendijk[a] and Adelbert W. Bronkhorst
TNO Human Factors Research Institute, P.O. Box 23, 3769 ZG Soesterberg, The Netherlands

(Received 3 February 1999; revised 24 May 1999; accepted 22 September 1999)

The fidelity of reproducing free-field sounds using a virtual auditory display was investigated in two experiments. In the first experiment, listeners directly compared stimuli from an actual loudspeaker in the free field with those from small headphones placed in front of the ears. Headphone stimuli were filtered using head-related transfer functions (HRTFs), recorded while listeners were wearing the headphones, in order to reproduce the pressure signatures of the free-field sounds at the eardrum. Discriminability was investigated for six sound-source positions using broadband noise as a stimulus. The results show that the acoustic percepts of real and virtual sounds were identical. In the second experiment, discrimination between virtual sounds generated with measured and interpolated HRTFs was investigated. Interpolation was performed using HRTFs measured for loudspeaker positions with different spatial resolutions. Broadband noise bursts with flat and scrambled spectra were used as stimuli. The results indicate that, for a spatial resolution of about 6°, the interpolation does not introduce audible cues. For resolutions of 20° or more, the interpolation introduces audible cues related to timbre and position. For intermediate resolutions (10°–15°) the data suggest that only timbre cues were used. © *2000 Acoustical Society of America.* [S0001-4966(00)02001-4]

PACS numbers: 43.66.Qp, 43.66.Pn [DWG]

INTRODUCTION

In recent years, techniques for generation of spatialized sounds using headphone presentation have received increasing scientific attention (Wenzel *et al.*, 1988; Wightman and Kistler, 1989a,b; Bronkhorst, 1995). These techniques, sometimes referred to as ''virtual acoustics,'' have applications in various fields such as avionics (Sorkin *et al.*, 1989; McKinley *et al.*, 1994; Bronkhorst *et al.*, 1996) and music reproduction (Blauert, 1997). Virtual acoustics has also been used as a tool in the study of spatial hearing (Asano *et al.*, 1990; Kistler and Wightman, 1992; Wenzel *et al.*, 1993; Bronkhorst and Houtgast, 1999).

The techniques for creating virtual sound sources are based on the use of head-related transfer functions (HRTFs). These functions represent the acoustic transfer from a sound source in the free field to a listener's eardrums. They contain the acoustic effects of body, head, and ears, and reflect time and intensity differences between the ears and spectral level changes at the ears. These acoustic effects code the angle of incidence of a sound wave (Gardner and Gardner, 1973; Blauert, 1997). When a headphone signal is filtered with the HRTFs and inversely filtered with the headphone transfer function (HPTF), the signals of a free-field sound source at the eardrums can be reproduced (Wightman and Kistler, 1989a). Given that the signals at the eardrums determine the auditory percept, it is, in principle, possible to create a virtual sound source that is indistinguishable from an actual loudspeaker in the free field.

An important question with respect to actual applications of virtual acoustics is whether the simulation is sufficiently accurate. In previous studies (Wightman and Kistler, 1989b; Bronkhorst, 1995) the quality of the simulation was verified by comparing absolute localization performance for real sources with that for virtual sources. This method has, however, two drawbacks. First, the comparison is hampered by the rather large variability normally found in absolute localization experiments. Second, it only answers the question whether real and virtual sources are perceived in the same direction, not whether they generate identical percepts. This means that considerable differences might occur between original and simulated sounds, even when a perfect match is found in the comparison. It is interesting that, in the studies cited above, some differences were found between localization performance for real and virtual sources; increased confusion rates (mainly front–back) were observed for virtual sources. Thus, these studies have not answered the question whether accurate simulation of sound sources can be achieved.

From a theoretical point of view, there is only one way to investigate whether a virtual source is indistinguishable from a real source: by performing a direct A/B-comparison. For obvious reasons, it is, however, rather difficult to implement such a test. The headphone that is required for generation of the virtual source should, in principle, be absent when the real source is presented. One solution might be to ask the listener to remove and replace the headset during trials, but this has severe methodological drawbacks: the HRTF and HPTF will be affected by head movements and headphone replacements (Pralong and Carlile, 1996), respectively, and performance will suffer from the long intervals between presentations. In addition, no blind comparison can be made, because listeners know when real and virtual sound sources are presented. Alternatively, an acoustically open transducer can be used for the virtual sound that is left in place during presentation of the real source. This approach has, in fact,

[a]Electronic mail: erno@tm.tno.nl

been used in two earlier studies (Zahorik *et al.*, 1995; see also Zahorik *et al.*, 1996; Hartmann and Wittenberg, 1996).

In the study by Zahorik *et al.* (1995), a two-interval, two-alternative forced choice (2AFC) task was used in which the listener had to detect the interval with the virtual sound. Scores were measured as a function of filter length, used for generating virtual sounds. Although real and virtual sources were judged to be identical in some of the conditions, certain aspects of the methodology might be improved. For example, the relatively large headphones distorted the position percept of the free-field sound source in some of their listeners. Another aspect is the order of presentation of the conditions. Because conditions with different filter lengths were mixed randomly within a block of trials, the cue to detect the virtual source could have been different from trial to trial, which made the discrimination of real and virtual sounds more difficult. A somewhat different approach was taken by Hartmann and Wittenberg (1996). Their listeners performed a yes–no task to discriminate real from virtual loudspeaker. However, the scope of the results presented by Hartmann and Wittenberg can be questioned, because they not only employed a rather large headphone, but also used stimuli with a limited bandwidth, in spite of the fact that spectral cues for spatial hearing occur especially in the high frequencies (Bronkhorst, 1995; Blauert, 1997).

The first experiment presented in this paper is, in essence, a replication of the study by Zahorik, using an improved methodology and a wider range of sound-source positions. One of the improvements was the use of a smaller transducer used for the generation of the virtual sound sources. With this transducer in front of the ear, only small effects on the open-ear HRTF are to be expected. Other improvements were that the stimulus was compensated for the loudspeaker response and that it was broadband (flat up to 16 kHz). Sound-source positions ranged from $-60°$ to $+60°$ in elevation and included front and rear positions, as well as positions at both sides of the listener, i.e., a wide range of loudspeaker positions covering the entire sphere around the listener. Discrimination of real and virtual sources was tested for three paradigms. The first paradigm was a yes–no task as used by Hartmann and Wittenberg (1996). The second paradigm was a 2AFC task as used by Zahorik *et al.* (1995). In pilot experiments listeners had some difficulties with both tasks, because discrimination cues, if present, had to be learned from trial to trial, putting a substantial demand on a listener's memory. Therefore, a third paradigm, using an oddball design, was added that does not suffer from these drawbacks (Gescheider, 1997). In this paradigm, stimuli were presented in four intervals. One stimulus, the oddball, was presented in the second or third interval, the other stimulus in the remaining intervals. Listeners had to indicate the interval with the oddball.

A second aspect of the present study concerns the generation of virtual sound sources at positions for which no actual HRTFs are measured. Because HRTFs are always measured for a limited number of source positions, specific algorithms are normally implemented in virtual auditory displays that allow continuous interpolation between these positions. The question of how well the intermediate positions are simulated has, however, received very little scientific attention. Wenzel and Foster (1993) investigated the interpolation effect on localization performance, but their results were obscured by the effect of using nonindividual HRTFs. Given that an adequate algorithm is used (that treats amplitude and phase differences separately), the only relevant factor is the spatial resolution of the measured positions. In the second experiment presented here, the ability to discriminate between virtual sound sources created with measured and interpolated HRTFs was investigated for three spatial resolutions using the same oddball paradigm as in the first experiment. The interpolated HRTFs were calculated, using linear interpolation, on either two measured HRTFs that differed in azimuth or in elevation, or on four measured HRTFs differing in both dimensions. The interpolation effect was studied for eight spatial regions and two signal conditions. In one condition, listeners could discriminate on minute spectral differences, whereas in the other condition directional cues were the major discrimination cue.

I. EXPERIMENT I

A. METHOD

1. Virtual sound-source generation

The mathematics used for simulating a free-field loudspeaker over headphones can be derived as follows. Suppose that the signal at a listener's eardrum is $y_{FF}(t)$ for a signal $x(t)$ delivered to a loudspeaker in the free field and $y_{HP}(t)$ for the same signal delivered to a pair of headphones. In the frequency domain, this can be written as

$$Y_{FF}(w) = T_{FF}(w)X(w), \tag{1}$$

and

$$Y_{HP}(w) = T_{HP}(w)X(w), \tag{2}$$

where the transfer function $T_{FF}(w)$ includes the loudspeaker transfer function and the free field to eardrum transfer function (HRTF) and where $T_{HP}(w)$ is the headphone to eardrum transfer function (HPTF). When a signal $z(t)$ delivered to the headphones should give the same signal as in the free-field situation

$$Y_{FF}(w) = T_{HP}(w)Z(w), \tag{3}$$

the required transfer functions can be solved from Eqs. (1) and (3)

$$Z(w) = \frac{T_{FF}(w)}{T_{HP}(w)}X(w). \tag{4}$$

The ratio of $T_{FF}(w)$ and $T_{HP}(w)$ will be referred to as the ''virtual headphone filter.'' The above equations apply to one ear and to one single loudspeaker position in the free field. In order to simulate different loudspeaker positions, different filters have to be designed for each ear separately.

The transfer functions $T_{FF}(w)$ and $T_{HP}(w)$ are normally measured with two probe microphones (one for each ear) positioned close to a listener's eardrums. The microphones, which have a certain frequency response, influence both free-field and headphone transfer functions. However, when the microphones remain in position between both measurements,

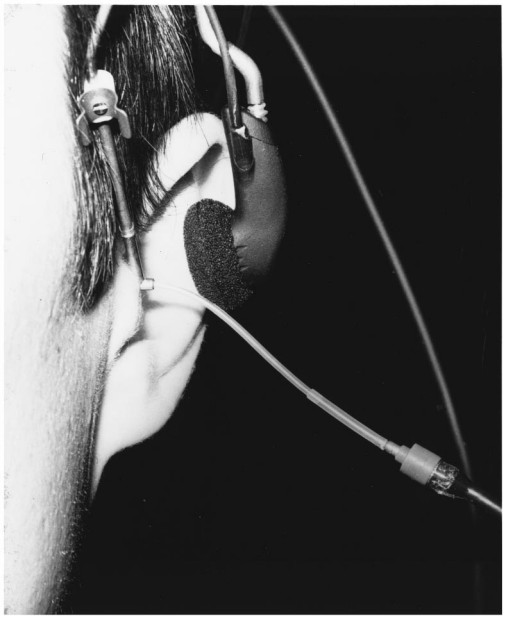

FIG. 1. Picture of a listener's ear with probe microphone and headphone.

the effect on both transfer functions will be equal and thus will be canceled in the virtual headphone filter.

In the present experiment, the filters were implemented with finite impulse responses of 20.48 ms. The filter length was taken such that it included the acoustical effects of body, head, and ears and any spurious reflections from the measurement setup.

2. Listeners

Six listeners, with normal hearing (hearing levels $\leqslant 20$ dB, at octave frequencies between 250 and 8000 Hz), participated in the experiment. All listeners had previous experience in sound localization and other listening experiments.

3. Acoustical measurements

The experiments were done in a soundproof anechoic chamber. The free-field sound source was a Philips AD 2110/SQ8 midrange dome tweeter mounted on a trolley that could move along a semicircular arc, such that the distance from the loudspeaker to the center of the arc was always 1.14 m. The arc was supported at the ends by aluminum struts and could rotate about a horizontal axis. Both arc, struts, and trolley were covered with sound-absorbing foam. A PC controlled the rotation of the arc and the movement of the trolley. With this setup, the loudspeaker could be placed at any azimuth and any elevation above $-60°$, with an angular resolution of less than 1°.

The listeners wore a headband with the sensor of a Polhemus Isotrak head tracker mounted on top. Attached to either side of the headband was a small brass rod that held a Sennheiser KE 4-211 microphone. A Sony MDR E-575 earphone was attached to a second rod (see Fig. 1). The earphone had a diameter of 1.7 cm. The distance from earphone to concha was approximately 1 cm. The microphones were put into a plastic casing to which a 5-mm brass tube was connected at the side of the microphone opening. The tube (inner diameter of 1.2 mm) was extended by a stiff 75-mm-long polyethylene tube with inner and outer diameters of 0.8 and 1.2 mm, respectively. At the tip of this probe was a flexible 8-mm-long silicon tube with inner and outer diameters of 0.8 and 1.4 mm, respectively. Each microphone output was amplified by a custom-built amplifier.

The acoustic transfer functions were measured using a PC board with a DSP32C processor and two 16-bit AD/DA channels (sampling rate at 50 kHz per channel). The signal for the acoustical measurements was a 3.4-ms time-stretched pulse (Aoshima, 1981), calculated on 170 points at a sampling rate of 50 kHz. The DSP generated the measurement signal and recorded it on 1024 points after a short delay. The delay was different for loudspeaker and headphone presentations and taken such that the main peak of the signal was at about one quarter of the measurement window. In order to improve the signal-to-noise ratio, 25 measurements were averaged. The signal for the HRTF measurements was filtered so as to compensate for the loudspeaker response. This resulted in a loudspeaker output that was flat within 1 dB between 250 Hz and 16 kHz. The signal for the HPTF measurements was not compensated for the headphone response.

For the generation of the virtual sounds, a second DSP board was used to perform real-time filtering (1024 points at 50 kHz) using the overlap–add algorithm. The first and the last 128 points of the filter were multiplied with the skirts of a Hanning window.

At the beginning of the experiment the listener was seated with his/her head in the center of the loudspeaker arc. The headband was put on and the probe tubes were aligned by the experiment leader. The listener then inserted the probes into the ear canals till the tip of the probe touched the eardrum, then pulled the probe out 1–2 mm. In order to check if the tip of the probe was close enough to the eardrum, HRTF measurements were done for several loudspeaker positions. If the spectral notch, caused by the quarter wave resonance in the ear canal (Chan and Geisler, 1990), was at less than 16 kHz, the probe tube was moved closer to the eardrum and the test was repeated.

Then, HRTF measurements were carried out for all speaker positions. Subsequently, the Sony headphones were positioned in front of the ears and the HRTF measurements were repeated. The two sets of measurements were used to investigate the influence of the headphones. During the rest of the experiment, probe microphones and headphones remained in position.

In order to verify how accurately the acoustical waveforms were reproduced by the headphones, ''acoustical verification'' measurements were carried out. First, the HRTF and HPTF measurements for the current loudspeaker position were done. From these measurements the virtual headphone filter was calculated and loaded into a DSP. Next, the measurement signal was fed to the DSP, presented over the headphones, and recorded with the probe tube microphones. After correction of the microphone response, the result was compared with the HRTF measurement.

For the psychophysical experiments, 200-ms Gaussian white-noise bursts with 20-ms cosine-square on- and offset ramps were used as stimuli. The noise bursts were bandpass

filtered between 500 Hz and 16 kHz and stored in files on a hard disk of a PC. For each presentation a noise file was chosen at random out of a set of 25, played over a D/A converter (Tucker Davis Technologies, DD1) and fed into one of the DSPs. In the DSP the signal could either be filtered by the inverse amplitude spectrum of the loudspeaker or by the virtual headphone filter.

When the measurement signal was played through the loudspeaker, the A-weighted level in the center of the arc was about 65 dB. For the acoustical verification measurements and in the psychophysical validation the signal was attenuated 10 dB. This was done to prevent distortion in the headphones, which had to play at a loud level because they were placed at a relatively large distance from the ear.

4. Design

Real and virtual sources were compared for six loudspeaker positions using three paradigms. The loudspeaker positions, expressed in degrees azimuth and elevation, were at: $(-90,-60)$, $(180,-30)$, $(-90,0)$, (30,0), (90,30), and (0,60). For each loudspeaker position the three paradigms were presented successively. The first paradigm was, in essence, a yes–no paradigm. Listeners had to indicate, by pressing one of two buttons, if they heard the real or the virtual sound source. The second paradigm was a two-interval, two-alternative forced choice (2AFC) paradigm with *AB* and *BA* as possible presentation orders, where *A* is the real and *B* is the virtual sound source. In the third paradigm, an oddball design with four intervals was used. The oddball could be presented in either the second or the third interval, giving four possible orders of presentation (*ABAA*, *BABB*, *AABA*, and *BBAB*). For all paradigms, listeners got auditory feedback after each trial indicating whether or not their response was correct. In the paradigms with multiple intervals, stimuli were separated by 200-ms pauses. For each paradigm 50 trials were presented in a row. The order of presentation of loudspeaker positions and paradigms was balanced across listeners.

The acoustical and psychophysical measurements for each loudspeaker position were carried out in the following order. First, the HRTF and HPTF were measured. From these two measurements the virtual headphone filter was calculated and loaded into the DSP. Next, the acoustical verification measurement was carried out. The acoustical measurements took less than 15 s. After that, the psychophysical validation was performed (i.e., three series of 50 trials). This took about 8 min. Listeners were instructed not to move their heads and bodies during the measurements. A headrest helped them in retaining a fixed head position. This was important, because head movements would cause the virtual sound source to move also (whereas the free-field loudspeaker would remain at its position) and movement of the limbs and torso could change the acoustic transfer function. After the measurements for a specific source position, listeners were allowed to relax, while being careful not to move the probe microphones or the headphones. By pressing a button, the listener moved the loudspeaker to the next position.

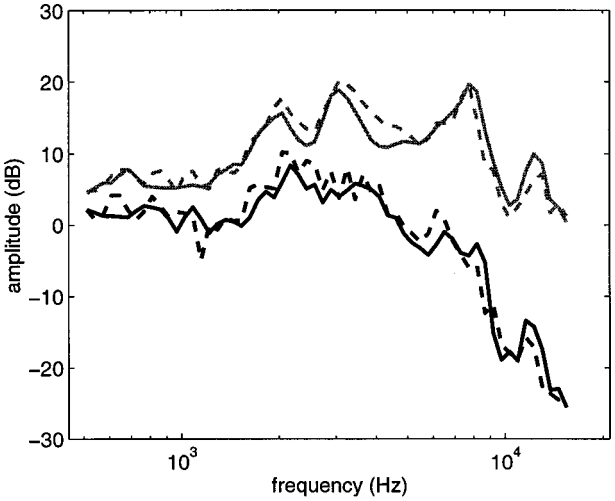

FIG. 2. Illustration of the effect of the headphones on the HRTFs for left (black lines) and right (gray lines) ears of one listener for loudspeaker position (90,30). HRTFs measured with and without the headphones placed in front of the ears are displayed with broken and solid lines, respectively. HRTFs were averaged in 1/12-octave bands.

B. Results

1. Headphone effect on HRTFs

Figure 2 illustrates the influence of the headphones on the HRTFs for one loudspeaker position. Amplitude differences between HRTFs measured with and without headphones placed in front of the ears are within 5 dB for most frequencies. In general, for frequencies above 1 kHz, the major peaks and valleys of the HRTFs measured with and without the presence of the headphones occurred at about the same frequencies. Amplitude differences introduced by the presence of the headphones were on the order of amplitude differences between HRTFs that occur for loudspeaker positions differing about 10° in azimuth/elevation. The effect of the headphones on the interaural phase difference was smaller than 10° for frequencies up to 3 kHz. The headphones had no effect on the interaural difference in arrival time of the signal.

2. Acoustical differences

Typical free-field and virtual free-field HRTFs, obtained from one of the listeners, are displayed in Fig. 3. Large variations in the amplitude spectra occur as a function of frequency and for different loudspeaker positions. The dynamic range of the amplitude spectra is approximately 50 dB. Across listeners, spectral differences of more than 20 dB were quite normal for frequencies above 4 kHz.

Figure 3 also shows that the differences between real and virtual free-field HRTFs were, in general, quite small. Across all listeners, amplitude differences were typically within 1 dB at the ipsilateral ear and up to 5 dB at the contralateral ear. Phase differences were in all cases less than 1° for frequencies up to 10 kHz and less than 6° for higher frequencies. For one listener and at one single loudspeaker position (90,30), amplitude differences of 6 dB were found in the ipsilateral ear for high frequencies. Because this was probably caused by a saturation of the headphones, the corresponding psychophysical data were removed.

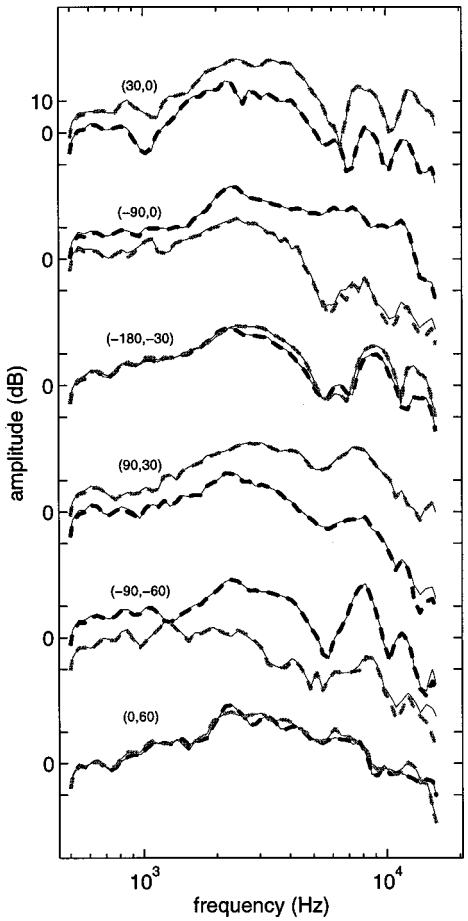

FIG. 3. Illustration of the acoustical verification. HRTFs for left (black lines) and right (gray lines) ears of one listener, averaged in 1/12-octave bands, for a real (thick broken lines) and a virtual (thin solid lines) sound source at different positions. HRTFs for different loudspeaker positions are shifted over 40 dB.

3. Psychophysical validation

Figure 4 shows the mean percentages correct and the 95%-confidence intervals for each of the three paradigms collapsed across loudspeaker positions and listeners. It shows that the scores for the yes–no and 2AFC paradigms were not significantly different ($p<0.05$) from chance, whereas it was for the oddball paradigm. However, the average score in the oddball paradigm (53%) is only slightly above chance.

An analysis of variance (ANOVA) showed a significant effect ($p<0.05$) of loudspeaker position, but not of paradigm. The former effect was due to a single outlier (score larger than three standard deviations from the mean) that occurred for one of the listeners for one loudspeaker position and which could not be related to acoustical differences. Because the outlier occurred in the paradigm that was tested last, while no high scores were obtained for the other two paradigms, it is likely that the listener had moved his head and thus introduced discrimination cues.

II. EXPERIMENT II

A. Method

1. Interpolation

Using linear interpolation, the HRTF for an arbitrary loudspeaker position **y** can be calculated as follows. Suppose

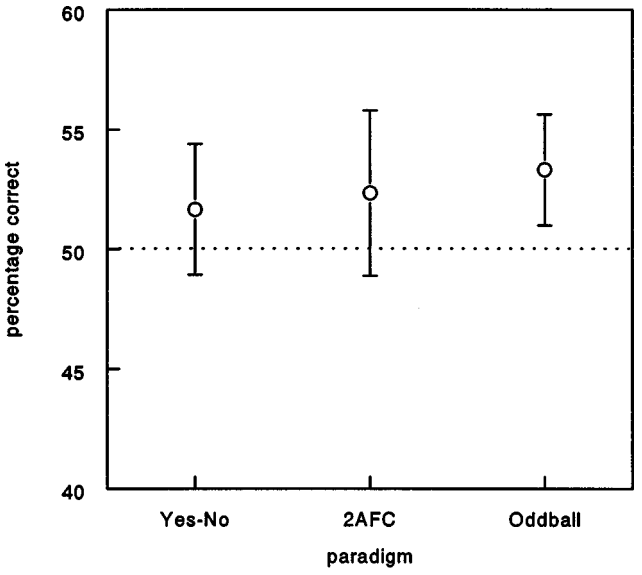

FIG. 4. Mean percentages correct and the 95%-confidence intervals of the mean for each of the paradigms, collapsed across loudspeaker positions and listeners.

a set of HRTFs with level L_k (in dB) and phase Φ_k is measured for loudspeaker positions $\mathbf{x}_k$, with a spatial resolution Δ, such that the angle between the vectors pointing at two loudspeaker positions, given by

$$\alpha = \arccos(\mathbf{x}_m \cdot \mathbf{x}_n), \tag{5}$$

is greater than or equal to Δ. Then, the level (L) and the phase (Φ) of the interpolated HRTF can be written as

$$L = \frac{1}{W} \sum_{k=1}^{N} w_k L_k, \tag{6a}$$

$$\Phi = \arg\left(\sum_{k=1}^{N} w_k e^{i\Phi_k} \right) \tag{6b}$$

where

$$w_k = \begin{cases} 1 - \dfrac{\theta}{\Delta}, & \theta < \Delta \\ 0, & \theta \geqslant \Delta \end{cases},$$

and

$$W = \sum_{k=1}^{N} w_k,$$

where θ is the angle between vectors **y** and $\mathbf{x}_k$, and N is the number of HRTFs contributing to the interpolation. In what follows, the loudspeaker positions $\mathbf{x}_k$ will be referred to as the grid positions and the corresponding HRTFs will be called the grid HRTFs. Likewise, the resolution of the grid positions Δ will be called the grid resolution.

In general, HRTFs are measured on a regular grid of positions. Sometimes these positions are based on making equal steps in azimuth and elevation. In the azimuth direction, however, two loudspeaker positions that are 10° apart are closer to one another near the poles ($\pm 90°$ elevation) than near the equator (0° elevation). In order to calculate the

azimuths of two loudspeaker positions at elevation ϵ, with a constant angular separation Δ, the following formula can be used:

$$\Delta_{Az} = 2 \arcsin\left(\frac{\sin(\frac{1}{2}\Delta)}{\cos(\epsilon)} \right). \quad (7)$$

Thus at, for example, 45° elevation Δ_{Az} is about 1.4 times as large as Δ.

2. Listeners

Six listeners, with normal hearing (hearing levels $\leqslant$20 dB, at octave frequencies between 250 and 8000 Hz), participated in the experiment. Half of the listeners had previous experience in psychoacoustical experiments.

3. Design

Prior to the interpolation experiment, HRTF measurements were carried out for 104 loudspeaker positions. The HRTF measurements were performed in a similar way as in the first experiment (but no headphones were worn). Headphone measurements were made after the free-field measurements using Sennheiser HD 520 headphones. These were placed carefully over the listeners ears in order not to disturb the positions of the probe tubes. The acoustical measurements took about 15 min.

During the HRTF measurements listeners wore a headband with a sensor of a Polhemus head tracker. The sensor registered position and orientation of the head. When the listener's head was more than 1 cm from the center of the arc, the listener got auditory feedback (a sampled voice) indicating how the head should be moved back into position. The orientation of the head was calibrated just before the experiment. The loudspeaker position was compensated for small rotations (within 5°) of the head. When larger deviations occurred the listener also got auditory feedback.

For the listening experiment, the sound stimulus was a 200-ms Gaussian white-noise burst, bandpass filtered between 200 Hz and 16 kHz, with 20-ms cosine-square on- and offset ramps. A total of 25 different noise bursts was stored on disk. For each presentation one of the noise files was chosen at random and played over a D/A converter. The output was filtered with either measured or interpolated HRTFs and inverse filtered with the HPTF. The filters were implemented with 10.24-ms finite impulse response (FIR) filters. The filters were long enough to include the acoustical effects of the body, head, and ears of a listener, yet short enough to exclude any spurious reflections from the arc that was used to measure the HRTFs. The A-weighted level of the headphone signal corresponded to 65 dB, measured at 1.14 m from a free-field sound source.

There were three independent variables that determined the experimental conditions. The first was the grid resolution Δ, which could be 5.6°, 11.3°, or 22.5°. The second was the direction of interpolation: horizontal, vertical, or diagonal. In the horizontal and vertical conditions, two HRTFs contributed to the interpolation. The loudspeaker positions for these HRTFs differed Δ only in azimuth or elevation. In the diagonal condition there were four contributing HRTFs for which the loudspeaker positions differed in azimuth, in elevation, or in both directions. The third independent variable was the amount of scrambling of the stimulus, which could be either 0 or $\pm$3 dB per 1/3-octave. The scrambling was accomplished by filtering the stimulus with a filter that had a random amplitude (uniform distribution, $\pm$3 dB-range) assigned to each 1/3-octave band.

TABLE I. Formulas to calculate target and grid positions for three different directions of interpolation, given the base direction (Az,El) of the spatial region of interest and the grid resolution. See the text for details.

Interpolation direction	Target position	Grid positions
Horizontal	$(Az+\frac{1}{2}\Delta_{Az}, El)$	$(Az, El), (Az+\Delta_{Az}, El)$
Vertical	$(Az, El+\frac{1}{2}\Delta_{El})$	$(Az, El), (Az, El+\Delta_{El})$
Diagonal	$(Az+\frac{1}{2}\Delta_{Az}, El+\frac{1}{2}\Delta_{El})$	$(Az, El), (Az+\Delta_{Az}, El), (Az, El+\Delta_{El}), (Az+\Delta_{Az}, El+\Delta_{El})$

The target positions were taken from eight different spatial regions, defined by the following base directions: (0,90), (45,45), (135,45), (0,0), (90,0), (180,0), (45,−45), and (135,−45). The exact target positions, as well as the grid positions, depended on the experimental conditions. Table I shows how target and grid positions were calculated for the three different interpolation directions, given the grid resolution and the base direction (Az,El). Note that Eq. (7) is used to calculate the azimuth difference Δ_{Az} in order to get the correct angular difference Δ between the positions. The elevation difference Δ_{El} is equal to Δ.

The conditions and target positions were pooled in six blocks. One block contained all trials for one interpolation direction, four target positions, two scrambling conditions, and three grid resolutions. Within blocks, the presentation order of target positions and scrambling conditions was varied across listeners. The resolution conditions were always presented in the same order, going from low to high resolution. For each condition, 12 trials were presented in a row. The order of the six blocks was balanced across listeners using a Latin square design.

Listeners were presented with stimuli that were generated with measured HRTFs (*A*) or with interpolated HRTFs (*B*). The task for the listener was the four-interval oddball paradigm also used in experiment I. In this paradigm the stimulus order could be *ABAA*, *BABB*, *AABA*, or *BBAB* and the listener had to detect the interval with the oddball.

The experiment was carried out in a soundproof room. Listeners were seated on a chair and were instructed to look straight forward during stimulus presentation. They started with a training session that contained a subset of the conditions (22.5°-grid resolution, vertical and diagonal interpolation directions, and both scrambling conditions) presented for four loudspeaker positions. The training took about 10 min. The experiment took about 2.5 h, including 10-min breaks every half hour. During the experiment, listeners could take additional short breaks on request.

B. Results

1. Acoustical differences

Figure 5 illustrates the errors that occurred when HRTFs were interpolated. In this example, the measured HRTF

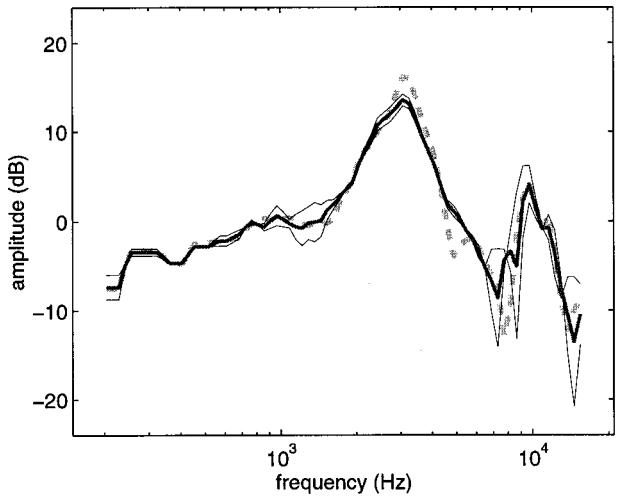

FIG. 5. Typical example of measured and interpolated HRTFs. The measured HRTF for target position (180,11.25) and the corresponding interpolated HRTF in the vertical interpolation direction condition are plotted as a thick dotted line and a thick solid line, respectively. The two thin black lines represent the grid HRTFs for loudspeaker positions (180,0) and (180,22.5), which contributed to the interpolation.

(thick dotted line) has a sharp notch between 6 and 9 kHz, with a center frequency that changes with elevation. The interpolated HRTF (thick solid line) has a notch at a different frequency that is less deep and broader than the notch of the measured HRTF. At other frequencies, interpolation errors of a few dB occur. These errors are due to the nonlinear behavior of the HRTFs as a function of azimuth and elevation.

On average, interpolation errors were within 1 dB per 1/12-octave band for the highest (5.6°) grid resolution and within 2 dB for the lowest grid resolution. The maximum error, however, could be as high as 12 (20) dB for the highest (lowest) grid resolution. The errors were larger for high frequencies than for low frequencies.

In order to estimate the perceptual effect of the interpolation, HRTFs were averaged in critical bands (1/3-octave) between 200 and 16 kHz and the maximum of the absolute difference of each pair of measured and interpolated HRTFs was taken as an error measure. Figure 6 shows a histogram of the maximum interpolation errors for each of the three grid resolutions (pooled across listeners, loudspeaker positions, and interpolation directions). The figure shows that errors for the ipsilateral ear are smaller than for the contralateral ear. The errors increase when the grid resolution is decreased. For the highest resolution for the ipsi(contra)lateral ear, over 95% (85%) of the errors are smaller than 2 dB, whereas it is about 45% (40%) for the lowest resolution.

2. Psychophysical validation

In the analysis of the psychophysical data, an arc–sine transformation was used in order to normalize the distribution of the scores. In the final presentation of the data, arc–sine scores were transformed back to percentages.

Figure 7 shows the percentage correct as a function of grid size for the three interpolation directions and the two scrambling conditions. Data were averaged across loudspeaker positions. It appears that, without scrambling, only scores for the highest grid resolution are near chance. When

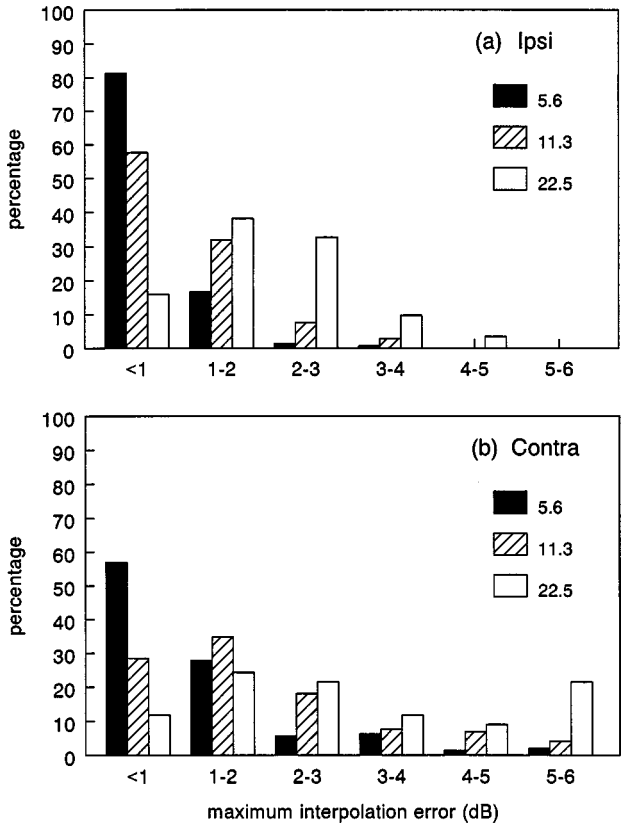

FIG. 6. Histograms of the maximum interpolation error for ipsi- and contralateral ears (upper and lower panel, respectively) and for three different resolution conditions (coded by the pattern of the bar). Results were pooled for six listeners, eight loudspeaker positions, and three interpolation directions.

scrambling is introduced, scores between 50% and 60% are also obtained for the 11.3° grid. Interpolation appears to be worst for the diagonal direction. With the 22.5° grid, the percentage correct increased to 88% (no scrambling) and 76% (±3-dB scrambling).

Results were submitted to a four-way repeated-measures ANOVA, separating effects of grid resolution, interpolation

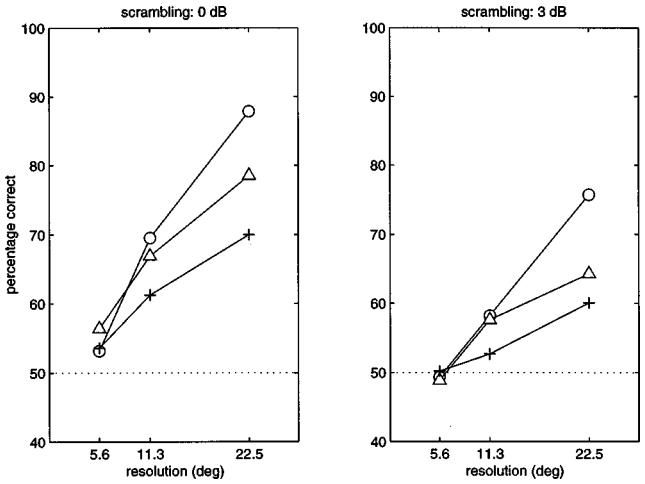

FIG. 7. Percentage correct as a function of grid resolution. Left and right panels show the results for the 0-dB and ±3-dB scrambling conditions, respectively. The results for the horizontal, vertical and diagonal interpolation directions are indicated by +, △, and ○, respectively.

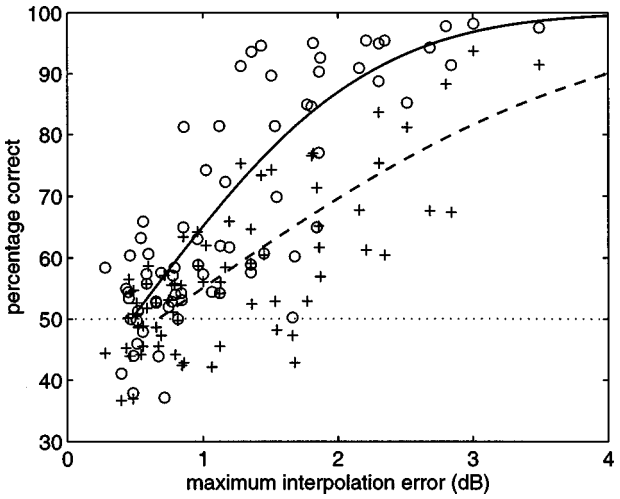

FIG. 8. Correlation between the maximum interpolation error for the ipsilateral ear and the percentage correct detection. Data points were averaged across listeners. The ○ and + represent the results for the 0-dB and ±3-dB scrambling conditions, respectively. The lines represent linear least-squares fits through the data points when expressed as *z*-scores (solid for 0-dB and dashed for ±3-dB scrambling).

direction, amount of scrambling, and loudspeaker position. The outcome of the ANOVA showed that all effects were significant ($p<0.01$), as well as the two-way interactions between loudspeaker position and interpolation direction and between interpolation direction and grid resolution ($p<0.05$). The main effects were subjected to a Tukey HSD *post hoc* analysis. It appeared that results for all three grid resolutions were significantly different ($p<0.05$). The mean score for the highest resolution was near chance (52%). For the 11.3° and 22.5° resolutions, the mean score increased to 61% and 73%, respectively. The significant effect of interpolation direction was due to the difference between the horizontal and diagonal interpolation directions ($p<0.01$). On average, the ±3-dB scrambling condition decreased the scores by 9%.

An analysis of the effect of loudspeaker position showed that scores were significantly higher for one position (45, −45). In general, scores for loudspeaker positions at high elevations (45° and 90°) were lower than those for loudspeaker positions with lower elevations (0° and −45°). Likewise, scores for frontal positions were higher than those for rear positions. This pattern is in good agreement with the acoustical differences (not shown).

In order to investigate whether the audible differences between measured and interpolated HRTFs could be explained by the maximum interpolation error (cf. Fig. 6), a correlation analysis was performed. Correlations for the two scrambling conditions were investigated separately for ipsi- and contralateral ears. In the analysis, percentages were first transformed to *z*-scores and then averaged across listeners. For the ipsilateral ear, correlation coefficients of 0.84 and 0.77 were found for the 0-, and ±3-dB scrambling conditions, respectively. For the contralateral ear, there appeared to be a trend that correlation coefficients were lower (0.72, $p=0.07$ and 0.64, $p=0.126$, respectively).

Figure 8 shows the percentage correct as a function of the maximum interpolation error for the ipsilateral ear and for the two scrambling conditions. The lines in the figure represent linear least-squares fits through the data points, when these are expressed as *z*-scores. The slope of the line for the 0-dB scrambling condition is significantly higher ($p<0.01$) than for the ±3-dB scrambling condition. The intercepts were not significantly different. In the no-scrambling condition, listeners scored above 75% correct when the maximum interpolation error was more than 1.4 dB. For the ±3-dB scrambling condition, the 75%-correct detection threshold was found to be 2.5 dB.

III. DISCUSSION

A. Experiment 1

The results of the first experiment demonstrate that it is possible to accurately reproduce the free-field acoustic waveforms at the eardrum, such that the percept of the virtual sound source that it generates is practically indistinguishable from an actual loudspeaker in the free field, even in very sensitive *A*/*B* comparison tasks. Listeners did not score significantly different from chance in the yes–no and 2AFC tasks and only slightly above chance in the oddball task. This indicates that there were no perceptual differences in position (as these would have been detected in the yes–no and 2AFC tasks) and only very small spectral differences that could serve as a cue (which are difficult to detect in the yes–no and 2AFC tasks, because they are hard to memorize/label; Gescheider, 1997). These small spectral differences could have been those encountered in the acoustical verification measurements, but might as well be due to small head movements in the course of the experiment.

The purpose of the first experiment was to prove the null hypothesis (i.e., showing there is no difference). This is, of course, difficult and it should be noted that listeners could have lost concentration after a number of trials when they were unable to detect a difference. This could be prevented by mixing in trials with a just noticeable difference, a procedure used by Zahorik *et al.* (1995), who randomly mixed trials with different filter lengths for the virtual source. However, listeners might as well be put on the wrong track in this way, because they get trained on detecting the cue that filter length provides (for example, direction or distance), whereas the actual cue might have been a timbre cue. For this reason, no dummy conditions with detectable cues were mixed in.

Our findings are in agreement with the results of previous studies. Zahorik *et al.* (1995) demonstrated that listeners could not discriminate between broadband noise bursts generated by real and virtual sound sources when sufficiently long filter lengths were used. Hartmann and Wittenberg (1996) found that listeners could not discriminate real from virtual sounds in a task using a synthesized vowel /a/ as a stimulus and a filter length of 1 s. In spite of the general agreement between our results and those of Zahorik *et al.* (1995) and Hartmann and Wittenberg (1996), several methodological differences between the studies should be considered, because these determine the scope of the conclusions that were drawn.

The first aspect that deserves attention is the size of the headphones. Zahorik *et al.* (1996) found that in their experi-

ment the headphones, with a diameter of about 4 cm, decreased sound localization performance in some of their listeners. Hartmann and Wittenberg (1996) reported that sound sources directly in front of or behind the listener were poorly externalized when listeners were wearing headphones (6-cm diameter). In the present study, however, the headphones were much smaller (1.7-cm diameter) and they had a relatively small effect on the HRTFs for the high frequencies that contain the major spectral localization cues. The effect for those frequencies is comparable to an HRTF difference for loudspeaker positions that are about 10° apart. Thus, although we did not measure localization performance itself, it is unlikely that the presence of the headphones had a significant effect. This was confirmed by the listeners themselves, who reported that the sounds always seemed to originate from the real loudspeaker (when visible).

Another aspect is the position of the probe microphone in the ear canal. Hartmann and Wittenberg (1996) measured HRTFs with the tip of the probe at the ear-canal entrance, whereas in the present study and in the study by Zahorik *et al.* (1995) HRTFs were measured at the eardrum. The problem with measuring away from the eardrum is that a notch occurs in the audible range of the spectrum due to standing waves in the ear canal (Chan and Geisler, 1990). Near the notch frequency there is a low signal-to-noise ratio, which could affect a precise reproduction of the signal. It is interesting that in spite of this, listeners could not detect a difference between real and virtual sounds in the experiment of Hartman and Wittenberg. One has to take into consideration, however, that the frequency spectrum of the stimulus used in their experiment dropped off rapidly above 7 kHz, obscuring a possible effect of the notch. Another aspect involving their stimulus is that the spectral localization cues, which are especially important in the high-frequency range (4–16 kHz), were not well represented. In the present study, on the other hand, a broadband (500–16 000 Hz) stimulus was used that had a flat spectrum in the entire frequency range.

The last aspect to be considered is the range of loudspeaker positions. Zahorik *et al.* (1995) tested for 15 positions on the left side of the listener at elevations of $-30°$, 0°, and $+30°$. Hartmann and Wittenberg (1996) did their experiments for only four positions on the horizontal plane. In the present study, investigations were performed for six loudspeaker positions that ranged from $-60°$ to $+60°$ in elevation and that included positions in the front, the rear, and at both sides of the listener. Since a representative selection of loudspeaker positions for the entire sphere around the listener was tested, it is expected that realistic virtual sound sources can be created for intermediate loudspeaker positions as well.

The above findings validate the assumption made in virtual acoustics that if the pressure signatures of signals at the eardrum for loudspeaker and headphones are (virtually) the same, the percepts are also the same. The fact that a sufficiently long filter should be used (as demonstrated by Zahorik *et al.*, 1995) is of specific interest here, because it appeared that the minute reflections caused by the equipment in the vicinity of the listener produced a clear distance percept yielding scores close to 100%. Only by including the first-order reflections in the HRTFs could this cue be removed.

A final issue that deserves attention is that, according to signal-detection theory (e.g., Gescheider, 1997) a comparison between different paradigms should not be made on a percentage-correct basis, but on an unbiased and criterion-free measure of discriminability, such as d'. In case of an ideal observer, d' scores for all three paradigms would be the same (by definition). However, converting to d' increased the relative difference between the oddball score ($d'=0.5$) on the one hand and the yes–no and 2AFC scores ($d'=0.08$) on the other. This indicates that the listeners in the present experiment do not act like ideal observers as is the case, for example, in a simple task like tone-in-noise detection. As already indicated, this can be accredited to the difficulty in labeling the real and virtual sounds. The results suggest that in discrimination experiments with spectral cues, as in both experiments in the present study, an oddball paradigm is more suitable than a yes–no or 2AFC paradigm.

B. Experiment 2

When HRTFs are measured for loudspeaker positions with a certain spatial resolution, the HRTFs for intermediate positions can be calculated using linear interpolation. The results of the second experiment demonstrate that when the spatial resolution is approximately 6°, virtual sound sources generated with interpolated HRTFs give exactly the same auditory percept as those generated with measured HRTFs. When scrambled noise is used as a stimulus the spatial resolution can be decreased to 10°–15°, without introducing significant perceptual differences.

The latter result probably applies to realistic situations, because when listeners perform an A/B comparison for flat-spectrum noise, they can use even minute (timbre) cues, which are not relevant for sound localization. On the other hand, for the scrambled-spectrum noise, it is very unlikely that listeners used timbre cues, because they were different for each condition and the scrambling itself introduced differences in timbre, which varied from one presentation to another. It is more likely that listeners used localization cues, which were not, or only slightly, affected by the scrambling (acoustical differences between the HRTFs for neighboring loudspeaker positions in the 5.6°-resolution condition were on the order of the differences introduced by the scrambling). These arguments were confirmed by the listeners who reported that in the scrambling condition the only reliable cue was the loudspeaker position.

The same arguments explain the difference in the relationship between the maximum acoustical differences and the percentage-correct detection in the 0- and ± 3-dB scrambling conditions (cf. Fig. 8). The results indicate that if acoustical differences between interpolated and measured HRTFs are between 1.5 and 2.5 dB per 1/3-octave, this will introduce timbre differences, whereas acoustical differences that exceed 2.5 dB can also affect the position of the sound source. This finding can be used to analyze more sophisticated ways of interpolation (e.g., cubic splines) without doing a time-consuming psychophysical validation.

In analyzing the relationship between the maximum acoustical differences and the percentage-correct detection, it is somewhat surprising to find lower correlations for the contralateral ear, for which larger interpolation errors occurred than for the ipsilateral ear. This could be explained by the fact that the amplitudes of the HRTFs for the contralateral ear are, in general, more than 15 dB below the amplitudes of the ipsilateral HRTFs for frequencies above 3 kHz.

The above findings are in clear contrast to the results obtained by Wenzel and Foster (1993), who found that sound localization was not affected by the interpolation, even for a spatial resolution of 60° in azimuth and 36° in elevation. The difference is most probably due to the fact that they used a localization task, which is less sensitive than an A/B comparison. In addition, they used nonindividual HRTFs, which appeared to have such a large impact on the localization accuracy that it probably obscured the interpolation effect.

C. General

The experimental setup of the first experiment allowed the presentation of both real and virtual sound sources. In most applications of virtual acoustics, however, all sources are virtual and HRTF measurements can be made without the presence of the headphones, as in the second experiment. The advantage is that bigger headphones with better dynamics in the low frequencies can be used. Care has to be taken with the measurement of the headphone-to-eardrum transfer function (HPTF). because the headphone placement could disturb the position of the probe in the ear canal. As a result, the quarter wave resonance notch could occur at a different frequency than for the HRTF measurements. Hence, the two notches will not cancel in the division of the calculation of the virtual headphone filter. Thus, when open-ear HPTF measurements are performed, the best procedure is with the tip of the probe within a few millimeters from the eardrum, because then the notches will occur outside the audible frequency range. However, recent studies have shown that blocked ear-canal measurements also provide reliable ways of measuring HPTFs in the case of acoustically open headphones (Møller *et al.*, 1995). Apart from disturbing the position of the probe, the headphone placement itself also introduces variability in the HPTF of a few dB per 1/3 octave band (Pralong and Carlile, 1996).

In the present study, the fidelity of sound reproduction using a virtual auditory display was tested for an actual loudspeaker in the free field. In order to simulate a loudspeaker in other environments, like a reverberant room, the acoustics of such a room has to be incorporated in the simulation as well. This could be done by measuring the HRTF in such a room with a filter long enough to include all acoustic reflections from the environment. However, the disadvantage of measuring the HRTF directly is twofold. First, the impulse response will be different for every other room and for every different position of loudspeaker and listener in the room, whereas in an anechoic chamber only the direction of the vector from listener to loudspeaker is of importance. Second, rooms for which the impulse response is not (yet) measured or rooms that still have to be built cannot be simulated. A more sophisticated way to simulate a loudspeaker in a reverberant room is to calculate the reflections from the environment and incorporate these with the appropriate (interpolated) free-field HRTFs in order to create a realistic simulation. That with this technique a realistic simulation of the distance percept can be generated using only few reflections has in fact been shown in a recent study by Bronkhorst and Houtgast (1999). Future research, using A/B comparison techniques as described in the first experiment, could reveal if identical percepts of real and virtual loudspeakers can also be created in reverberant rooms.

Aoshima, N. (**1981**). ''Computer-generated pulse signal applied for sound measurement,'' J. Acoust. Soc. Am. **69**, 1484–1488.

Asano, F., Suzuki, Y., and Sone, T. (**1990**). ''Role of spectral cues in median plane localization,'' J. Acoust. Soc. Am. **88**, 159–168.

Blauert, J. (**1997**). *Spatial Hearing* (MIT Press, Cambridge, MA).

Bronkhorst, A. W. (**1995**). ''Localization of real and virtual sound sources,'' J. Acoust. Soc. Am. **98**, 2542–2553.

Bronkhorst, A. W., Veltman, J. A., and Breda, L. (**1996**). ''Application of a three-dimensional auditory display in a flight task,'' Hum. Factors **38**, 23–33.

Bronkhorst, A. W., and Houtgast, T. (**1999**). ''Auditory distance perception in rooms,'' Nature (London) **397**, 517–520.

Chan, J. C., and Geisler, C. D. (**1990**). ''Estimation of eardrum acoustic pressure and of ear canal length from remote points in the canal,'' J. Acoust. Soc. Am. **87**, 1237–1247.

Gardner, M. B., and Gardner, R. S. (**1973**). ''Problem of localizing in the median plane: Effect of pinnae cavity occlusion,'' J. Acoust. Soc. Am. **53**, 400–408.

Gescheider, G. A. (**1997**). *Psychophysics: The Fundamentals* (Erlbaum, Mahwah, NJ), pp. 142–165.

Hartmann, W. M., and Wittenberg, A. (**1996**). ''On the externalization of sound images,'' J. Acoust. Soc. Am. **99**, 3678–3688.

Kistler, D. J., and Wightman, F. L. (**1992**). ''A model of head-related transfer functions based on principal components analysis and minimum-phase reconstruction,'' J. Acoust. Soc. Am. **91**, 1637–1647.

McKinley, R. L., Erickson, M. A., and D'Angelo, W. R. (**1994**). ''3-dimensional auditory displays: Development, applications, and performance,'' Aviat. Space Environ. Med. 31–38.

Møller, H., Hammershoi, D., Jensen, C. B., and Sorensen, M. F. (**1995**). ''Transfer characteristics of headphones measured on human ears,'' J. Audio Eng. Soc. **43**, 203–217.

Pralong, D., and Carlile, S. (**1996**). ''The role of individualized headphone calibration for the generation of high fidelity virtual auditory space,'' J. Acoust. Soc. Am. **100**, 3785–3793.

Sorkin, R. D., Wightman, F. L., Kistler, D. J., and Elvers, G. C. (**1989**). ''An exploratory study of the use of movement-correlated cues in an auditory head-up display,'' Hum. Factors **31**, 161–166.

Wenzel, E. M., Wightman, F. L., and Foster, S. H. (**1988**). ''A virtual display system for conveying three-dimensional acoustic information,'' Proc. Hum. Factors Soc. **32**, 86–90.

Wenzel, E. M., Arruda, M., Kistler, D. J., and Wightmann, F. L. (**1993**). ''Localization using nonindividualized head-related transfer functions,'' J. Acoust. Soc. Am. **94**, 111–123.

Wenzel, E. M., and Foster, S. H. (**1993**). ''Perceptual consequences of interpolating head-related transfer functions during spatial synthesis,'' in *Proceedings of the ASSP (IEEE) Workshop on Applications of Signal Processing to Audio and Acoustics* (IEEE, New York).

Wightmann, F. L., and Kistler, D. J. (**1989a**). ''Headphone simulation of free-field listening. I. Stimulus synthesis,'' J. Acoust. Soc. Am. **85**, 858–867.

Wightmann, F. L., and Kistler, D. J. (**1989b**). ''Headphone simulation of free-field listening. I. Psychophysical validation,'' J. Acoust. Soc. Am. **85**, 858–867.

Zahorik, P., Wightman, F. L., and Kistler, D. J. (**1995**). ''On the discriminability of virtual and real sound sources,'' in *Proceedings of the ASSP (IEEE) Workshop on Applications of Signal Processing to Audio and Acoustics* (IEEE, New York).

Zahorik, P., Wightman, F. L., and Kistler, D. J. (**1996**). ''The fidelity of virtual auditory displays,'' J. Acoust. Soc. Am. **99**, 2596(A).

Use of context by young and aged adults with normal hearing

Judy R. Dubno,[a] Jayne B. Ahlstrom, and Amy R. Horwitz
Department of Otolaryngology and Communicative Sciences, Medical University of South Carolina, 39 Sabin Street, P.O. Box 250150, Charleston, South Carolina 29425

(Received 12 May 1999; accepted for publication 30 September 1999)

Word recognition in sentences with and without context was measured in young and aged subjects with normal but not identical audiograms. Benefit derived from context by older adults has been obscured, in part, by the confounding effect of even mildly elevated thresholds, especially as listening conditions vary in difficulty. This problem was addressed here by precisely controlling signal-to-noise ratio across conditions and by accounting for individual differences in signal-to-noise ratio. Pure-tone thresholds and word recognition were measured in quiet and threshold-shaped maskers that shifted quiet thresholds by 20 and 40 dB. Word recognition was measured at several speech levels in each condition. Threshold was defined as the speech level (or signal-to-noise ratio) corresponding to the 50 rau point on the psychometric function. As expected, thresholds and slopes of psychometric functions were different for sentences with context compared to those for sentences without context. These differences were equivalent for young and aged subjects. Individual differences in word recognition among all subjects, young and aged, were accounted for by individual differences in signal-to-noise ratio. With signal-to-noise ratio held constant, word recognition for all subjects remained constant or decreased only slightly as speech and noise levels increased. These results suggest that, given equivalent speech audibility, older and younger listeners derive equivalent benefit from context. © *2000 Acoustical Society of America.* [S0001-4966(00)03501-3]

PACS numbers: 43.66.Sr, 43.66.Dc, 43.71.Lz, 43.66.Ba [SPB]

INTRODUCTION

An important aspect of speech recognition is the benefit derived from contextual information. When acoustic-phonetic information in speech is degraded, either from increased noise level or threshold elevation, listeners are forced to rely more on redundancy or contextual information. However, to provide benefit from context, words must be heard and recalled in a certain order and should be resistant to a breakdown of selective attention. Given that these functions may be diminished in older listeners, it is reasonable to assume that their use of context in speech would also be reduced. However, the results of several studies are equivocal and suggest that the ability of older listeners to benefit from context is unclear.

Kalikow *et al.* (1977), in their development of the Speech Perception in Noise (SPIN) test, found that differences in recognition of final words in high- and low-context sentences were equivalent for older and younger listeners, a result consistent with Divenyi and Haupt (1997) and with van Rooij and Plomp (1991) who used a variation of context known as ''linguistic entropy.'' Results of Pichora-Fuller *et al.* (1995) suggest that older subjects with and without hearing loss benefit from context *more* than young subjects. However, Schum and Matthews (1992) found that for some elderly hearing-impaired subjects, the use of context was poorer than expected, given these listeners' speech understanding abilities without context. In that study, individuals with ''depressed'' scores for high-context sentences tended to have higher pure-tone thresholds and poorer word recognition (for monosyllabic words and for low-context sentences).

A primary reason for these conflicting conclusions is the interactive effects of elevated absolute thresholds and use of context, especially as listening condition varies in difficulty. In an attempt to control these factors, Pichora-Fuller *et al.* (1995) assessed benefit from context under conditions in which scores for low-context sentences were equated for all subjects. Greater improvement in scores for high-context sentences achieved by older subjects was interpreted as better use of context. However, equating performance for low-context sentences among subjects with varying degrees of hearing loss is not straightforward. For normal-hearing subjects, scores for low-context sentences are determined by the level and spectrum of the masker. Therefore, scores will change in a predictable manner as a function of signal-to-noise ratio, as reflected in the slope of the psychometric function. For subjects with hearing loss (even relatively mild loss), scores for low-context sentences may be determined partially by subjects' absolute thresholds and partially by the masker. As signal-to-noise ratio is adjusted, the relative contributions of these two factors to word recognition may vary, resulting in changes in relative audibility in different frequency regions. Such changes in the slope of the psychometric function for low-context sentences may yield differences between it and the psychometric function for high-context sentences that are inappropriately attributed to the use of context. In the current experiment, this problem is avoided by using a continuous, broadband noise masker which provides a fixed threshold shift relative to quiet threshold at each frequency for each subject in both high- and low-

[a]E-mail: dubnojr@musc.edu

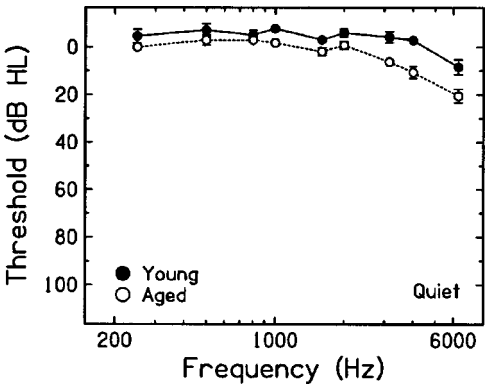

FIG. 1. Mean (±1 standard error) thresholds (in dB HL) measured in quiet for eight young subjects (filled) and eight aged subjects (open).

context sentences. Thus, any observed differences between psychometric functions for low- and high-context sentences may be attributed to benefit from context, and any differences observed between young and aged subjects may be attributed to differences in their use of context.

In the current study, measurements of word recognition in high- and low-context sentences were obtained over a wide range of speech and noise levels. This design allowed further exploration of the additional question of whether speech recognition deteriorates at high signal levels. This topic has been under investigation for many years (e.g., French and Steinberg, 1947; Hawkins and Stevens, 1950) as have the negative effects of high noise levels on speech recognition (e.g., Pollack and Pickett, 1958). These issues have been raised again recently in studies of the benefit of high-frequency amplification for listeners with high-frequency hearing loss (Ching *et al.*, 1998; Hogan and Turner, 1998). When speech was amplified to high levels to make speech audible for hearing-impaired subjects, recognition for some subjects in these studies was poorer than predicted using a simple audibility model. These results provided further evidence of possibly adverse effects of high speech and noise levels on speech recognition of hearing-impaired individuals. Indeed, results of Studebaker *et al.* (1999) suggested that speech recognition in noise by normal-hearing and hearing-impaired listeners decreased at signal levels just exceeding conversational levels when signal-to-noise ratio was held constant. The design of the current study, in which signal-to-noise ratio for each subject was held constant across a range of speech levels, provided a unique opportunity to assess these effects.

I. METHOD

A. Subjects

Eight young subjects (mean age: 25; range: 22–28) and eight aged subjects (mean age: 68; range: 63–74) with normal hearing participated. The criteria for normal hearing were pure-tone thresholds ≤20 dB HL (ANSI, 1989) at octave frequencies from 250 to 4000 Hz and immittance measures within normal limits. One ear of each subject was selected for testing. For the aged subjects, the test ear was typically the ear with better thresholds; for young subjects, test ear was selected randomly. Mean audiometric thresholds (in dB HL) for young and aged subjects are shown in Fig. 1. Although thresholds for all subjects were within ''normal'' limits, thresholds for aged subjects were higher than those of young subjects.

B. Apparatus and stimuli

Tonal signals were digitally generated (TDT PD1), 350-ms pure tones with 10-ms raised-cosine rise/fall ramps. Speech items were 200 high-context sentences and 200 low-context sentences from the revised Speech Perception in Noise (SPIN) test (Kalikow *et al.*, 1977; Bilger *et al.*, 1984). Original SPIN recordings obtained from Bilger were modified to separate high- and low-context sentences and were recorded onto digital audio tape (DAT) for playback. The subject's task was to repeat the last word of each sentence. In high-context sentences, the last word was predictable from context (''I've got a cold and a sore *throat*''); in low-context sentences, the last word was not predictable from context (''He is considering the *throat*''). Low-context sentences were similar to conventional tests of monosyllabic word recognition and were assumed to reflect the use of acoustic-phonetic speech information. A focus of this investigation was on older listeners' ability to benefit from contextual information in speech. This was assessed by examining differences in psychometric functions relating word recognition for high- and low-context sentences to speech level.

Pure-tone thresholds and word recognition in high- and low-context sentences were measured in quiet and in two levels of broadband noise whose spectrum was adjusted at one-third-octave intervals to achieve specific masked thresholds for each subject (see below). To generate the spectrally shaped noise, broadband noise (TDT WG1) was routed through two cascaded, digitally programmable, one-third-octave equalizers (Applied Research and Technology, IEQ). Pure-tone signals (or speech) and spectrally shaped broadband noise were individually attenuated (TDT PA4), mixed (TDT SM3), and delivered through one of a pair of TDH-49 earphones. Spectral characteristics of all signals were verified on a signal analyzer.

C. Procedures

1. Pure-tone thresholds

Pure-tone thresholds at one-third-octave center frequencies ranging from 200 to 6300 Hz were measured in quiet using a single-interval (yes–no) maximum-likelihood psychophysical procedure. Then, for each subject, a broadband noise was introduced whose one-third-octave band levels were initially set using critical ratio predictions with the goal of producing thresholds at all signal frequencies that were 20 dB higher than the subject's thresholds in quiet. Prior to data collection, masked thresholds were then measured and minor adjustments (1–3 dB) made in the one-third-octave band levels of the noise until the subject's thresholds were within ±3 dB of the predicted values (20 dB above quiet thresholds). This final noise was called the ''+20-dB masker.'' Next, 20 dB was added to each band level to produce thresholds that were 40 dB higher than the subject's thresholds in quiet. Thresholds were measured again to confirm that in this

''+40-dB masker,'' thresholds were within ±3 dB of the predicted values (40 dB above quiet thresholds). Using these individually assigned maskers, pure-tone thresholds were shifted by equal amounts at each frequency for each subject.

2. Word-recognition scores

Word recognition was measured in quiet, in the +20-dB masker, and in the +40-dB masker. In each condition, word-recognition scores were obtained at a minimum of four speech levels to generate psychometric functions. In quiet, scores were obtained at speech levels of 20, 23, 26, and 29 dB SPL for high-context sentences and at 24, 30, 36, and 42 dB SPL for low-context sentences. Scores at higher speech levels were obtained if scores at 29 dB (high context) or 42 dB (low context) were <80%. In the +20- and +40-dB maskers, speech levels were increased by 20 and 40 dB, respectively. Thus, for high-context sentences, scores were obtained at 40, 43, 46, and 49 dB SPL in the +20-dB masker, and at 60, 63, 66, and 69 dB SPL in the +40-dB masker; for low-context sentences, scores were obtained at 44, 50, 56, and 62 dB in the +20-dB masker, and at 64, 70, 76, and 82 dB SPL in the +40-dB masker. Speech levels were presented in a randomized order; noise levels and context were counterbalanced.

Subjects were instructed to respond by repeating aloud the last word of each sentence and were encouraged to guess. Word-recognition scores were the correct responses to 25 high-context or 25 low-context sentences. Scores in percent correct were transformed to rationalized arcsine units (rau) before statistical analyses so that the variance was homogeneous over the range of the obtained scores (Studebaker, 1985). Two outcome measures were included: (1) slopes of psychometric functions relating word recognition to speech level (in rau/dB), and (2) word-recognition thresholds, defined as speech levels (or signal-to-noise ratios) corresponding to 50 rau (50.0%) and 69.04 rau (70.7%) correct recognition. Differences due to age, masker level, and context were assessed by repeated-measures analyses of variance (ANOVA) on rau-transformed scores, with age (young, aged) as a grouping factor, and masker level (0 [quiet], +20, +40) and context (high context, low context) as repeated measures. Note that the relatively small sample size may increase the possibility of missing some small- or medium-size effects.

II. RESULTS AND DISCUSSION

A. Pure-tone thresholds

Mean thresholds in the +20-dB masker and in the +40-dB masker are shown in Fig. 2 for young and aged subjects. To facilitate comparisons across conditions and subject groups, in the upper panel 20 dB was added to each quiet threshold for comparison to thresholds measured in the +20-dB masker; in the lower panel 40 dB was added to each quiet threshold for comparison to thresholds measured in the +40-dB masker. The overlap within these pairs of curves demonstrates that in the presence of the threshold-shaped maskers, thresholds were shifted by appropriate amounts at each one-third-octave center frequency for both subject groups. The average difference between quiet thresholds and

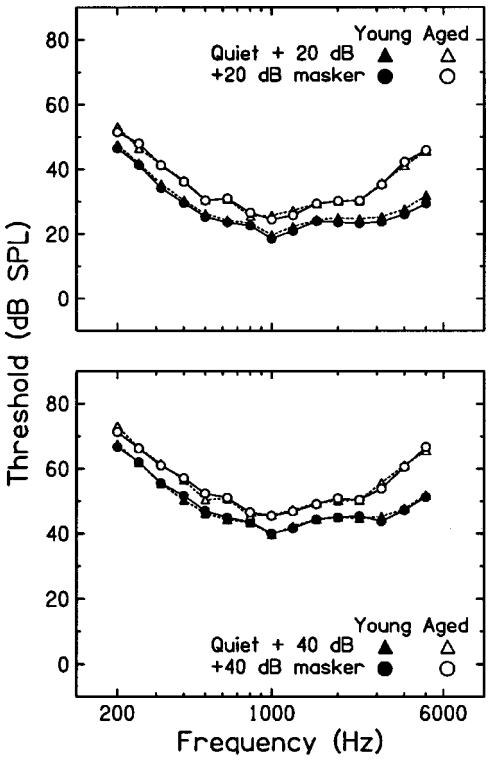

FIG. 2. Mean thresholds for pure tones at one-third-octave center frequencies in the +20-dB masker and in the +40-dB masker for young and aged subjects. In the upper panel, 20 dB was added to quiet thresholds (triangles) for comparison to the thresholds measured in the +20-dB masker (circles). In the lower panel, 40 dB was added to quiet thresholds (triangles) for comparison to the thresholds measured in the +40-dB masker (circles).

thresholds in the +20-dB masker was 19.0 dB for young subjects and 19.9 dB for aged subjects. The average difference between quiet thresholds and thresholds in the +40-dB masker was 40.1 dB for young subjects and 40.0 dB for aged subjects.

Quiet thresholds of aged subjects were higher than those of young subjects by an average of 7.0 dB (see Fig. 1). As a result, overall levels of the +20-dB and +40-dB maskers were higher for aged subjects than for young subjects. Overall levels of the +20-dB masker averaged 56.9 dB SPL (range: 48–65 dB SPL) for young subjects and 64.7 dB SPL (range: 59–72 dB SPL) for aged subjects, a difference of 7.8 dB. Of course, overall levels of the +40-dB masker were 20 dB higher than these levels for all subjects.

Recall that for measurements of word recognition, speech levels in the +20-dB masker and in the +40-dB masker were also increased by 20 and 40 dB, respectively, relative to the levels used in quiet. By increasing pure-tone thresholds and speech levels by precisely the same amount, signal-to-noise ratio for each subject was maintained across the three conditions, as illustrated for high-context sentences in Fig. 3. The contents of the left panels will be discussed first. The upper left panel shows mean pure-tone thresholds (circles) for young subjects in quiet, in the +20-dB masker, and in the +40-dB masker and speech spectra (dotted lines) for the respective levels of 20, 40, and 60 dB SPL, which were the lowest of the speech levels used in each condition. The lower left panel shows the same thresholds (quiet, +20,

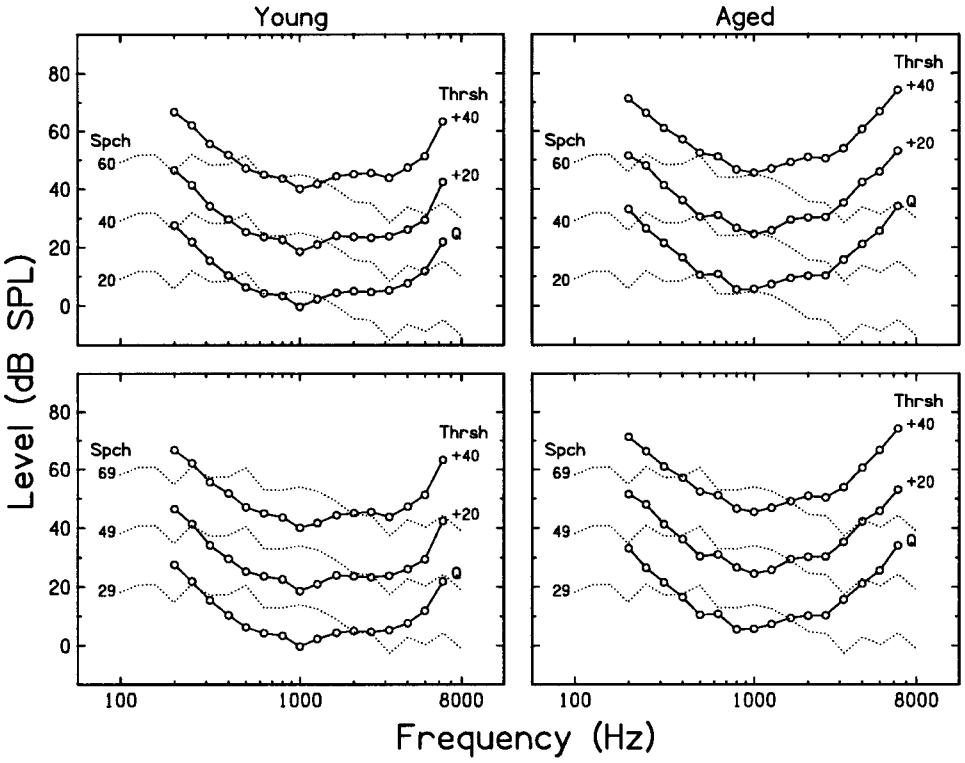

FIG. 3. Illustration of speech spectra and thresholds in quiet, in a +20-dB masker, and in a +40-dB masker for young subjects (left panels) and aged subjects (right panels). Spectra for the lowest speech levels are in the top panels and spectra for the highest speech levels are in the bottom panels. See text for discussion.

+40) and spectra for the respective speech levels of 29, 49, and 69 dB SPL, which were the highest speech levels used (except if the subject's score was <80%). Note that, within each panel, the relative position of the thresholds and the speech spectra (i.e., the solid line with circles and the dotted line) was identical for the three pairs of lines, demonstrating that the signal-to-noise ratio remained constant for the three conditions. For each pair of lines, the area where the dotted line is above the solid line indicates the audible speech area. The lower panel, where speech levels were higher, shows a constant, but higher, signal-to-noise ratio and more audible speech. The same pattern of constant signal-to-noise ratios may be seen in the right panels which contain the same speech levels, but thresholds for aged subjects, which were slightly higher than those of young subjects. Thus, signal-to-noise ratios were lower (less advantageous) for aged subjects than for young subjects. Moreover, because each subject's signal-to-noise ratio was determined by the individual's quiet thresholds, individual differences in signal-to-noise ratio were observed, even within the young and aged subject groups.

B. Word-recognition scores

Because speech levels and pure-tone thresholds at each center frequency were increased by precisely equal amounts, psychometric functions measured in quiet, in the +20-dB masker, and in the +40-dB masker should be parallel. That is, relative to functions in quiet, functions in noise should be shifted to the right by 20 and 40 dB, respectively (Studebaker *et al.*, 1993; Dubno and Ahlstrom, 1997).

Figure 4 plots psychometric functions relating word recognition (in rau) to speech level for young subjects (filled) and aged subjects (open). Scores for high-context sentences are in the upper panel and scores for low-context sentences are in the lower panel. Scores obtained in quiet (squares), in the +20-dB masker (circles), and in the +40-dB masker (triangles) are plotted at their respective speech levels. As expected, functions obtained in quiet, in the +20-dB masker, and in the +40-dB masker were generally parallel within each subject group; relative to the function in quiet, functions in noise were shifted to the right by approximately 20 and 40 dB. Within each condition (quiet, +20, +40), there was an additional rightward shift of the functions for aged subjects relative to those for young subjects. That is, poorer scores were obtained for aged subjects than for young subjects for speech presented at equal levels. These age-related differences in word recognition may be attributed to aged subjects' higher quiet and masked thresholds (Figs. 1 and 2). As suggested by results of Dubno and Ahlstrom (1997), even relatively small threshold differences between young and aged subjects can produce substantial divergence in word recognition under certain conditions. This topic will be discussed in more detail in later sections.

C. Slopes of psychometric functions

To quantify age-related and condition-related differences in recognition of words in high-context and low-context sentences, slopes of psychometric functions relating word recognition to speech level were computed for each subject and condition. The slope was determined from a linear regression fit by the least-squares method to scores for high- or low-context sentences obtained for an individual. Logistic functions were also fit to the data using a nonlinear optimization method (Microsoft® Excel Solver). Slope and threshold parameters of best-fit logistic functions were found to be nearly identical to those obtained from linear regres-

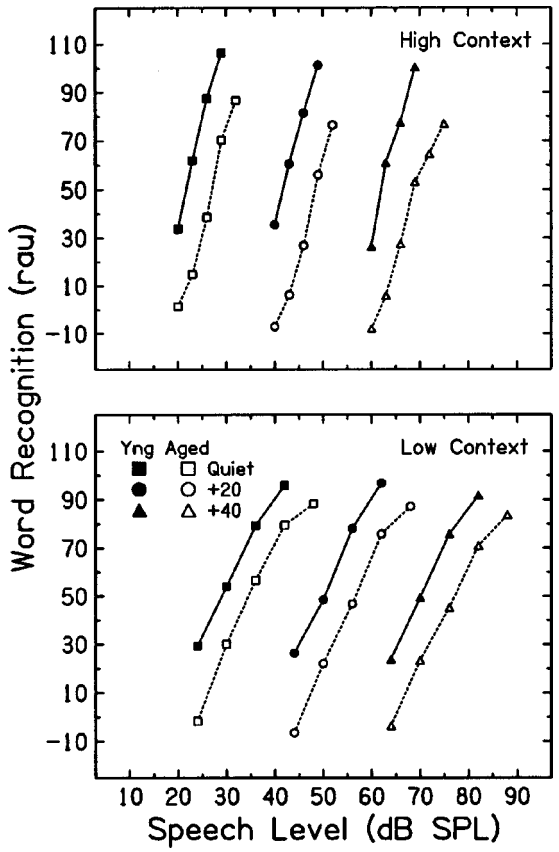

FIG. 4. Mean word-recognition scores (in rau) as a function of speech level for high-context and low-context sentences presented in quiet (squares), +20-dB masker (circles), and +40-dB masker (triangles) for young subjects (filled symbols) and aged subjects (open symbols).

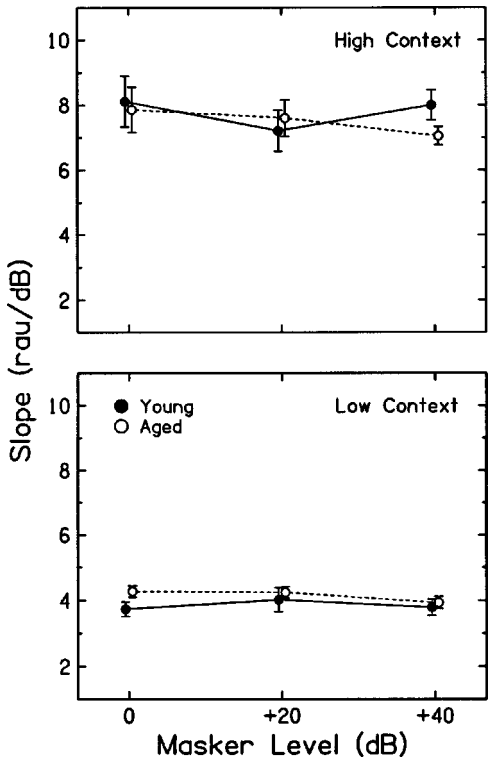

FIG. 5. Mean (±1 standard error) slopes (in rau/dB) calculated from psychometric functions relating word-recognition score to speech level for young and aged subjects plotted as a function of masker level (0 [quiet], +20, +40). Slopes of functions for high-context sentences are in the upper panel and slopes of functions for low-context sentences are in the lower panel.

sion. Given the similarity of the results of the two fitting methods, the decision was made to use parameters from the more straightforward and well-known linear regression procedure.

Figure 5 includes mean slopes of psychometric functions (in rau/dB) for high- and low-context sentences plotted as a function of masker level (0 [quiet], +20, +40) for young and aged subjects. Results of repeated measures ANOVA revealed that, as expected, slopes of psychometric functions were significantly steeper ($F[1,14]=203.07$; $p<0.000\,01$) for high-context sentences than for low-context sentences (e.g., Kalikow *et al.*, 1977; Dirks *et al.*, 1986). However, slopes were equivalent for young and aged subjects ($F[1,14]=0.0025$; $p=0.96$) and for functions obtained in quiet, in the +20-dB masker, and in the +40-dB masker ($F[2,28]=0.88$; $p=0.426$). There were no statistically significant interactions among age, masker level, or context. That is, differences in slopes of psychometric functions for sentences with and without context were maintained in the three masker conditions, confirming that the psychometric functions shown in Fig. 4 were parallel. Importantly, differences in slopes for high- and low-context sentences were equivalent for young and aged subjects, which suggested that aged subjects derived benefit from context that was equal to that of young subjects.

D. Word-recognition thresholds

Recall that Fig. 4 revealed an additional rightward shift of the functions for aged subjects relative to those for young subjects, indicating that word recognition was poorer for aged subjects at equal speech levels. To examine these differences with more precision, the speech level corresponding to the 50 rau (50.0%) point on the psychometric function was determined and used as an estimate of the word-recognition threshold (in dB SPL). The word-recognition threshold in quiet, in the +20-dB masker, and in the +40-dB masker was determined from the linear regression fit to each subject's psychometric function relating word-recognition score (in rau) to speech level. Figure 6 shows mean word-recognition thresholds for high- and low-context sentences plotted as a function of masker level (0 [quiet], +20, +40) for young and aged subjects.

As pure-tone thresholds were increased by 20 and 40 dB, average word-recognition thresholds increased by 20.8 and 41.5 dB, relative to quiet (see Fig. 6). This statistically significant main effect of masker level was expected ($F[2,28]=3760.0$; $p<0.000\,01$); no statistically significant interactions with context or age were observed. Word-recognition thresholds were significantly lower for words in high-context sentences than in low-context sentences ($F[1,14]=372.77$; $p<0.000\,01$), consistent with previous results of Dubno *et al.* (1984). Threshold differences due to context were equivalent for both age groups and for the three masker levels. Finally, word-recognition thresholds were

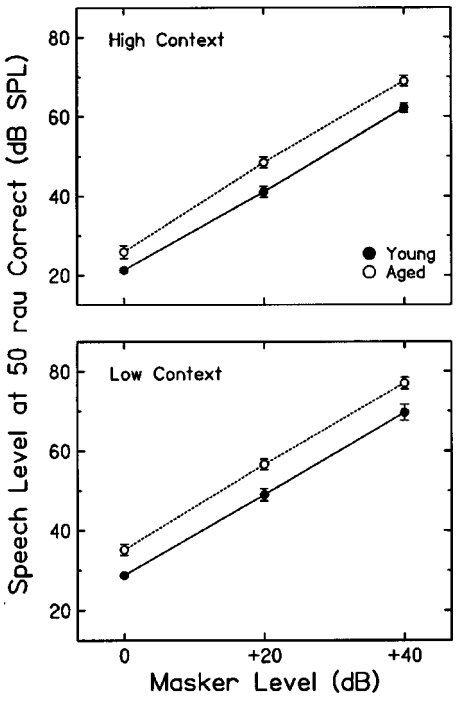

FIG. 6. Mean (±1 standard error) word-recognition thresholds (in dB SPL) for high- and low-context sentences plotted as a function of masker level (0 [quiet], +20, +40) for young and aged subjects. Threshold was defined as the speech level corresponding to 50 rau (50.0%) correct recognition on the psychometric function.

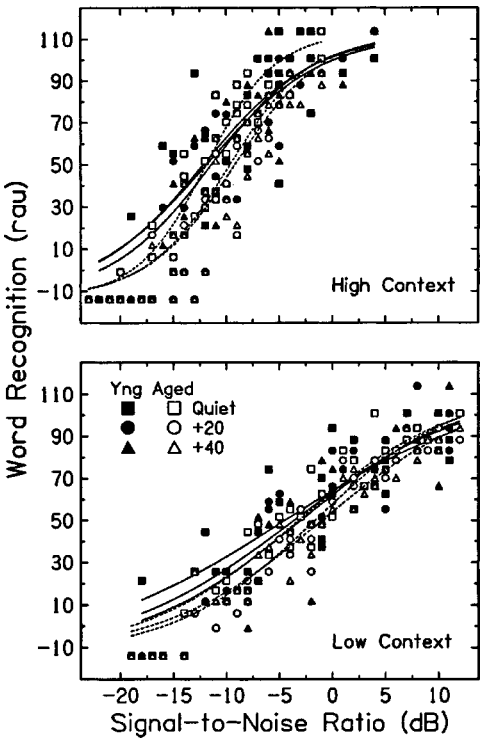

FIG. 7. Word-recognition scores (in rau) as a function of signal-to-noise ratio for high- and low-context sentences for young subjects (filled symbols) and aged subjects (open symbols). The solid and dashed lines are logistic functions fit to scores of young and aged subjects, respectively, for each of the three masker conditions.

higher for aged subjects than for young subjects by an average of 6.7 dB[1] ($F[1,14]=13.87$; $p=0.0023$), but no statistically significant interactions with context or masker level were observed. Similar patterns of thresholds and ANOVA results were obtained for word-recognition thresholds measured at speech levels corresponding to 69.04 rau, or 70.7% correct (not shown).

Recall that pure-tone thresholds of aged subjects were higher than those of young subjects by an average of 7.0 dB. Given this average 7-dB difference between groups, word-recognition thresholds should also differ by 7 dB (if threshold curves for young and aged subjects were precisely parallel). Thus, the correspondence between the average differences in pure-tone and word-recognition thresholds suggested that aged subjects' higher word-recognition thresholds may be attributed to their higher quiet and masked thresholds. Moreover, the agreement in word-recognition threshold differences for high- and low-context sentences between young and aged subjects did not support the assumption of an age-related difference in the benefit derived from contextual information in speech.

E. Effects of signal-to-noise ratio

The correspondence between average age-related differences in pure-tone and word-recognition thresholds was consistent with the assumption that word recognition was strongly associated with pure-tone thresholds. To provide additional evidence of this association, signal-to-noise ratios for individual young and aged subjects were computed for high- and low-context sentences. Individual differences in signal-to-noise ratio occurred, particularly between young and aged subjects, because the same speech levels were used for all subjects whereas pure-tone thresholds varied within and between subject groups. The following analysis was conducted to determine if individual differences in word recognition could be explained by individual differences in signal-to-noise ratio.

Signal-to-noise ratio for each subject was estimated as the difference between average one-third-octave band levels for the SPIN sentences and average one-third-octave band levels for each subject's threshold-shaped noise. Each one-third-octave band from 200 to 6300 Hz was included and contributed equally to the average. For ease of measurement, the +40-dB masker was used to determine the band levels; signal-to-noise ratios for the +20-dB and quiet conditions were determined by subtracting 20 and 40 dB, respectively, from those measurements. Recall that signal-to-noise ratios for individual subjects were identical in the +20-dB masker and in the +40-dB masker because both thresholds and speech levels were increased by 20 or 40 dB (e.g., see Fig. 3). Figure 7 displays word-recognition scores (in rau) plotted as a function of signal-to-noise ratio. Each data point is a score for an individual young subject (filled symbols) or aged subject (open symbols). The solid and dashed lines are logistic functions fit to scores of young and aged subjects, respectively, for each of the three masker conditions.

When scores were plotted as a function of signal-to-noise ratio rather than as a function of speech level, psychometric function slopes remained the same as shown previously in Figs. 4 and 5. That is, slopes of functions for high-context sentences were steeper than those for low-context

sentences (note that in Fig. 7, the abscissa plots a 30-dB range of levels whereas the abscissa in Fig. 4 includes an 80-dB range of levels). However, in contrast to the functions shown in Fig. 4, the positions of the functions along the abscissa in Fig. 7 were generally similar for the three masker conditions and for young and aged subjects. That is, when word recognition was plotted as a function of signal-to-noise ratio, the functions for quiet, +20-dB masker, and +40-dB masker were no longer shifted along the abscissa by 20 and 40 dB and there was no longer an additional rightward shift of the functions for aged subjects relative to those for young subjects.

To determine if significant age-related or condition-related differences in word recognition remained when word recognition was assessed as a function of signal-to-noise ratio, word-recognition thresholds (in dB signal-to-noise ratio) were computed for each subject. Here, word-recognition threshold was defined as the 50-rau (50.0%) point on the psychometric function relating word recognition to signal-to-noise ratio for each subject. Word-recognition thresholds for young subjects averaged only 1.3 dB lower than those for aged subjects, a value that was not statistically significant ($F[1,14]=1.29$; $p=0.275$). There were no significant interactions with context or masker level. Thus, word-recognition thresholds measured in terms of signal-to-noise ratio (rather than speech level) were equivalent for young and aged subjects. Thresholds for all subjects remained significantly higher for words in low-context sentences than for words in high-context sentences ($F[1,14]=379.04$; $p<0.000\,01$). Finally, there were significant differences in word-recognition thresholds among the three masker levels ($F[2,28]=6.02$; $p=0.0067$). The average signal-to-noise ratio at threshold was −7.64 dB in quiet, −6.62 dB in the +20-dB masker, and −5.95 dB in the +40-dB masker. *Post hoc* testing revealed that word-recognition thresholds measured in the +40-dB masker were significantly higher than those measured in quiet ($F[1,14]=8.09$; $p=0.013$) and in the +20-dB masker ($F[1,14]=4.70$; $p=0.0478$). These differences were not expected, given that each subject's signal-to-noise ratio remained the same for the three conditions as speech and masker levels increased. These results suggested that word recognition may decrease at higher overall speech and noise levels when signal-to-noise ratio was held constant. This finding was explored further and is discussed in the following section.

F. Effects of speech and noise levels

In Fig. 8, mean word-recognition scores (in rau) are plotted as a function of speech level for high-context sentences (filled) and low-context sentences (open). The three data points in each function are average scores obtained in quiet, in the +20-dB masker, and in the +40-dB masker at the same signal-to-noise ratio. The data in Fig. 8 have been replotted from the data previously shown in Fig. 4. For example, scores for young subjects in the upper-most function for high-context sentences in Fig. 8 are identical to the highest score on each of the three functions for young subjects in the upper panel of Fig. 4.

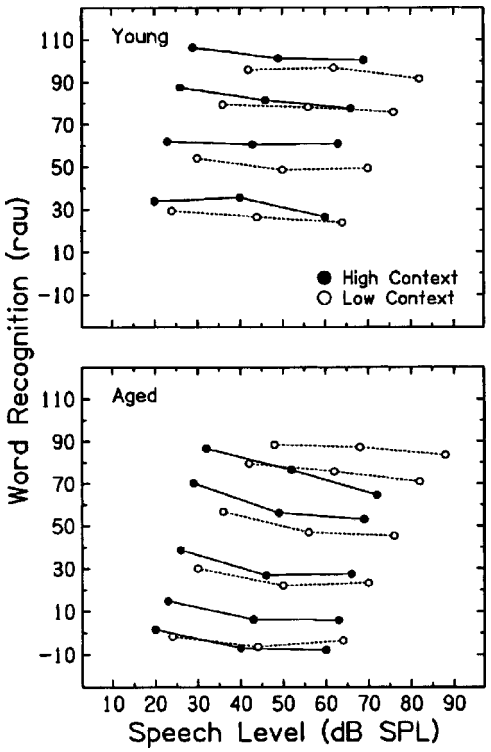

FIG. 8. Mean word-recognition scores (in rau) as a function of speech level for high-context sentences (filled) and low-context sentences (open). Scores for young subjects are in the upper panel and scores for aged subjects are in the lower panel. Scores obtained at the same average signal-to-noise ratio are connected by lines. The parameter is signal-to-noise ratio (signal-to-noise ratio improves as the lines move from the bottom to the top of each panel).

The functions in Fig. 8 differ from typical psychometric functions relating word recognition to speech level. Each of the functions in Fig. 4 was plotted with masker level as the parameter; scores increased with speech level as signal-to-noise ratio improved. The functions in Fig. 8 were plotted with signal-to-noise ratio as the parameter; scores remained relatively constant with speech level because, as speech level increased, noise level also increased, maintaining a constant signal-to-noise ratio and constant speech audibility. Thus, if word recognition was determined entirely by audibility and was independent of overall speech and noise level, scores should remain constant and the slopes of the functions in Fig. 8 should be zero. The degree to which the slopes of these functions deviated from zero provided evidence of the adverse effects of high speech and noise levels. The slope of each function (in rau/dB) was determined by linear regression on the individual data. The general trend was for the slopes to be slightly negative. The mean slope was −0.2 rau/dB but only one slope (−0.554 rau/dB, for high-context sentences at the highest signal-to-noise ratio for aged subjects) was statistically significantly different from zero ($F[1,18]=7.067$, $p=0.016$). Thus, over the range of speech and noise levels used in this study, word recognition generally remained constant or decreased slightly.

Another method of assessing effects of signal levels is to determine the change in signal-to-noise ratio required to maintain a constant word-recognition score. As reported in the previous section, the signal-to-noise ratio required to

achieve 50 rau correct recognition was determined for each subject and condition. The average signal-to-noise ratio at this word-recognition threshold was −7.64 dB in quiet, −6.62 dB in the +20-dB masker, and −5.95 dB in the +40-dB masker; this pattern was consistent for young and aged subjects and for high and low-context sentences. Thus, with a 40-dB increase in pure-tone thresholds and masker spectrum level, the signal-to-noise ratio needed to maintain constant performance increased by 1.69 dB, equivalent to a slope of 0.042 dB/dB. This value is less than has been observed in several previous studies, as reported in Table VII of Studebaker *et al.* (1999).[2] As noted earlier, the results suggest that at a constant signal-to-noise ratio, word-recognition thresholds decreased only slightly as speech and noise levels increased. Discrepancies among studies may be due to differences in speech materials and masker spectra. Studebaker *et al.* (1999, p. 2440) noted that effects were largest for nonsense syllables and monosyllabic words and for maskers that matched the speech spectrum. The current study used sentences and a masker whose spectrum approximated the shape of the audiogram.

Further evidence of the limited effect of speech and noise levels may be inferred from results of young and aged subjects. As noted previously, although the same speech levels were used for all subjects, the overall levels of the +20- and +40-dB maskers were necessarily higher for aged subjects due to their higher quiet thresholds. For example, overall levels of the +40-dB masker averaged 76.9 dB SPL for young subjects and 84.7 dB SPL for aged subjects. Notwithstanding these higher noise levels, average word recognition for aged subjects did not decrease with signal level more than that of young subjects.

III. SUMMARY AND CONCLUSIONS

The benefit derived from contextual information by older adults has been difficult to determine, in part due to the confounding effect of even mildly elevated thresholds on the use of context, especially as listening conditions vary in difficulty. This problem was addressed here by precisely controlling signal-to-noise ratio across conditions and by accounting for individual differences in signal-to-noise ratio among subjects. Subjects were eight young and eight aged individuals with normal but not identical audiograms. Pure-tone thresholds and recognition of final words in high- and low-context sentences were measured in quiet, and in maskers whose spectrum was adjusted for each subject to produce thresholds at one-third-octave center frequencies that were 20 and 40 dB higher than the subject's thresholds in quiet. Scores were obtained at several speech levels in each condition; threshold was defined as the speech level (or signal-to-noise ratio) corresponding to the 50-rau point on the psychometric function. Results may be summarized as follows.

(1) Psychometric functions relating word recognition to speech level measured in broadband maskers that increased pure-tone thresholds by 20 and 40 dB were parallel to functions measured in quiet. In these maskers, word-recognition thresholds increased by 20 and 40 dB.
(2) Thresholds for words in high-context sentences were lower than for words in low-context sentences. Slopes of psychometric functions for high-context sentences were steeper than those for low-context sentences. These context-related differences were equivalent for young and aged subjects.
(3) Individual differences in word recognition for all subjects, young and aged, were accounted for by individual differences in signal-to-noise ratio. Thus, given equivalent speech audibility, the understanding of words in sentences with or without context did not differ between young and aged subjects with normal hearing.
(4) With signal-to-noise ratio held constant, recognition of words in high- and low-context sentences remained constant or decreased only slightly as speech and noise levels increased.
(5) Relatively small differences in absolute thresholds among subjects can result in substantial differences in speech audibility under certain conditions. Thus, studies comparing speech recognition by young and aged subjects should be designed to minimize differences in effective signal-to-noise ratio among subjects or to otherwise account for these individual differences.

ACKNOWLEDGMENTS

This work was supported (in part) by Grant Nos. P50 DC00422 and R01 DC00184 from NIH/NIDCD. The authors would like to thank Elizabeth A. Poth for assistance with data collection, Fu-Shing Lee for advice on data analysis, and Johanna J. Larsen for help with figures.

[1]The word-recognition threshold for high-context sentences in quiet for one aged subject was exceptionally low, that is, more than two standard deviations better than the mean for young subjects. With this single data point omitted, the average difference in word-recognition thresholds between young and aged subjects was 6.95 dB.

[2]To be directly comparable to the values in Table VII of Studebaker *et al.* (1999), a value of 1.0 should be added to the slope value obtained in the present study (i.e., 1.042 dB/dB).

ANSI (**1989**). ANSI S3.6-1989, *Specifications for Audiometers* (American National Standards Institute, New York).

Bilger, R. C., Nuetzel, J. M., Rabinowitz, W. M., and Rzeczkowski, C. (**1984**). ''Standardization of a test of speech perception in noise,'' J. Speech Hear. Res. **27**, 32–48.

Ching, T. Y. C., Dillon, H., and Byrne, D. (**1998**). ''Speech recognition of hearing-impaired listeners: Predictions from audibility and the limited role of high-frequency amplification,'' J. Acoust. Soc. Am. **103**, 1128–1140.

Dirks, D. D., Bell, T. S., Rossman, R., and Kincaid, G. (**1986**). ''Articulation index predictions of contextually-dependent words,'' J. Acoust. Soc. Am. **80**, 82–92.

Divenyi, P. L., and Haupt, K. M. (**1997**). ''Audiological correlates of speech understanding deficits in elderly listeners with mild-to-moderate hearing loss. I. Age and lateral asymmetry effects,'' Ear Hear. **18**, 42–61.

Dubno, J. R., and Ahlstrom, J. B. (**1997**). ''Additivity of multiple maskers of speech,'' in *Modeling Sensorineural Hearing Loss*, edited by W. Jesteadt (Erlbaum, Mahwah, NJ), pp. 253–272.

Dubno, J. R., Dirks, D. D., and Morgan, D. E. (**1984**). ''Effects of age and mild hearing loss on speech recognition in noise,'' J. Acoust. Soc. Am. **76**, 87–96.

French, H., and Steinberg, J. C. (**1947**). ''Factors governing the intelligibility of speech sounds,'' J. Acoust. Soc. Am. **19**, 90–119.

Hawkins, J. E., and Stevens, S. S. (**1950**). ''The masking of pure tones and of speech by white noise,'' J. Acoust. Soc. Am. **22**, 6–13.

Hogan, C. A., and Turner, C. W. (**1998**). ''High-frequency audibility: Benefits for hearing-impaired listeners,'' J. Acoust. Soc. Am. **104**, 432–441.
Kalikow, D., Stevens, K., and Elliott, L. (**1977**). ''Development of a test of speech intelligibility in noise using test material with controlled word predictability,'' J. Acoust. Soc. Am. **61**, 1337–1351.
Pichora-Fuller, M. K., Schneider, B. A., and Daneman, M. (**1995**). ''How young and old listen to and remember speech in noise,'' J. Acoust. Soc. Am. **97**, 593–608.
Pollock, I., and Pickett, J. M. (**1958**). ''Masking of speech by noise at high sound levels,'' J. Acoust. Soc. Am. **30**, 127–130.
Schum, D. J., and Matthews, L. J. (**1992**). ''SPIN test performance of elderly hearing-impaired listeners,'' J. Am. Acad. Audiol **3**, 303–307.
Studebaker, G. A. (**1985**). ''A rationalized arcsine transform,'' J. Speech Hear. Res. **28**, 455–462.
Studebaker, G., Gilmore, C., and Sherbecoe, R. L. (**1993**). ''Performance-intensity functions at absolute and masked thresholds,'' J. Acoust. Soc. Am. **93**, 3418–3421.
Studebaker, G. A., Sherbecoe, R. L., McDaniel, D. M., and Gwaltney, C. A. (**1999**). ''Monosyllabic word recognition at higher-than-normal speech and noise levels,'' J. Acoust. Soc. Am. **105**, 2431–2444.
van Rooij, J. C., and Plomp, R. (**1991**). ''The effect of linguistic entropy on speech perception in noise in young and elderly listeners,'' J. Acoust. Soc. Am. **90**, 2985–2991.

Pitch estimation by early-deafened subjects using a multiple-electrode cochlear implant

P. A. Busby[a] and G. M. Clark
Department of Otolaryngology, University of Melbourne, Parkville, 3052, Victoria, Australia

(Received 18 November 1998; revised 4 May 1999; accepted 27 August 1999)

Numerical estimates of pitch for stimulation of electrodes along the 22-electrode array of the Cochlear Limited cochlear implant were obtained from 18 subjects who became deaf very early in life. Examined were the relationships between subject differences in pitch estimation, subject variables related to auditory deprivation and experience, and speech-perception scores for closed-set monosyllabic words and open-set Bamford–Kowal–Bench (BKB) sentences. Reliability in the estimation procedure was examined by comparing subject performance in pitch estimation with that for loudness estimation for current levels between hearing threshold and comfortable listening level. For 56% of subjects, a tonotopic order of pitch percepts for electrodes on the array was found. A deviant but reliable order of pitch percepts was found for 22% of subjects, and essentially no pitch order was found for the remaining 22% of subjects. Subject differences in pitch estimation were significantly related to the duration of auditory deprivation prior to implantation, with the poorest performance for subjects who had a longer duration of deafness and a later age at implantation. Subjects with no tonotopic order of pitch percepts had the lowest scores for the BKB sentence test, but there were no differences across subjects for monosyllabic words. Performance in pitch estimation for electrodes did not appear to be related to performance in the estimation procedure, as all subjects were successful in loudness estimation for current level. © *2000 Acoustical Society of America.* [S0001-4966(99)04312-X]

PACS numbers: 43.66.Ts, 43.64.Me, 43.66.Hg, 43.71.Ky [JWH]

INTRODUCTION

In multiple-electrode cochlear implants, electrode position is one of the most important parameters for coding acoustic information. Stimulation of electrodes along a multiple-electrode array typically evokes pitch percepts that are generally consistent with the tonotopic organization of the cochlea (Busby *et al.*, 1994; Collins *et al.*, 1997; Cohen *et al.*, 1996a,1996b; Dorman *et al.*, 1990; Eddington *et al.*, 1978; Nelson *et al.*, 1995; Shannon, 1983; Tong and Clark, 1985; Tong *et al.*, 1982; Zwolan *et al.*, 1997). The term ''pitch'' is used in this context and throughout this paper to denote what is frequently described as ''place-pitch'' in the normally hearing ear (Nelson *et al.*, 1995). In the speech-processing strategies of multiple-electrode prostheses, the outputs of a series of bandpass filters are typically mapped or assigned to the different electrodes in a tonotopic order (Eddington, 1980; McDermott *et al.*, 1992; Skinner *et al.*, 1994; Tong *et al.*, 1982; Wilson *et al.*, 1991). It should be noted that different methods for measuring the distinctiveness of pitch percepts elicited by stimulating electrodes along the array, such as pitch estimation, electrode discrimination, electrode identification, and pitch ranking, have produced fairly consistent results with respect to the tonotopic order of percepts. In some cases, however, there were differences in the number of perceptually distinct electrodes calculated from the results of the different methods (Collins *et al.*, 1997).

There are a number of variables that would influence the tonotopic order of pitch percepts when stimulating electrodes on a multiple-electrode array. These include the distribution of surviving auditory-nerve fibers in the cochlea, the current distributions produced by the stimulating electrodes, and the integrity of the auditory pathway and cortex. It has been shown that electrode discrimination in the nonhuman primate (Pfingst *et al.*, 1985) and pitch ranking in the human subject (Clark *et al.*, 1988) were poorer at locations in the cochlea with very poor auditory-nerve survival, with better performance at locations with better nerve survival. Current distributions in the cochlea can be influenced by the impedance characteristics of the surrounding medium and the method of stimulation. For instance new bone formation changes the electric resistance between the active and return electrodes, and between electrodes and the stimulated auditory-nerve fibers (Kawano *et al.*, 1998), which may result in abnormal current flow to more distant fibers and/or produce a greater current spread (Clark *et al.*, 1988). It has been shown that pitch estimates and neural excitation profiles, estimated using forward masking, can vary for different electrode configurations using the 22-electrode prosthesis manufactured by Cochlear Limited (Busby *et al.*, 1994; Cohen *et al.*, 1996a,b). Marked departures from a tonotopic order in pitch estimates and neural excitation profiles were recorded in some subjects for common ground stimulation, but not for bipolar stimulation. In common ground, a single electrode is activated and the other electrodes on the array are connected together to serve as the return. In bipolar stimulation, the electric current is passed between two electrodes in close proximity on the array. One factor which may have influenced our findings for common-ground stimulation would be abnormal current distributions produced by variations in the

[a]Electronic mail: p.busby@medoto.unimelb.edu.au

impedances of the return electrodes (Black *et al.*, 1983).

It is not surprising, therefore, that between- and within-subject variability in measures of pitch perception for stimulating electrodes on a multiple-electrode array have been frequently found (Busby *et al.*, 1994; Collins *et al.*, 1997; Nelson *et al.*, 1995; Zwolan *et al.*, 1997). For instance, Nelson *et al.* (1995) reported considerable between-subject variation in the pitch ranking scores of 12 postlinguistically deaf adults using the Cochlear Limited prosthesis. Within-subject variability, such as localized regions of indistinguishable electrodes or departures in the tonotopic order of pitch percepts, have been found for electrode discrimination (Collins *et al.*, 1997; Zwolan *et al.*, 1997), pitch ranking (Nelson *et al.*, 1995), and pitch estimation (Busby *et al.*, 1994; Collins *et al.*, 1997).

The studies described above were conducted with postlinguistically deafened adults, where it is assumed that there would have been a relatively normal tonotopic order of pitch percepts prior to the onset of deafness. A second group of subjects is those whose onset of profound deafness was at birth or a very early age. These early-deafened subjects have been profoundly deaf for most of their lives and almost all of their auditory experience has been via electric stimulation. They are, therefore, an important subject group for investigation as performance may indicate the effects of auditory deprivation at or near birth and electric stimulation as the primary means of auditory experience. However, there have been very few investigations with this group of subjects. Eddington *et al.* (1978) reported that pitch percepts were not consistent with the tonotopic organization of the cochlea in the one early-deafened adult tested using a six-electrode prosthesis. Nelson *et al.* (1995) found that the pitch-ranking scores for one early-deafened adult with a progressive loss were similar to scores for postlinguistically deaf adults, using the Cochlear Limited prosthesis. For the second early-deafened adult tested whose etiology was meningitis, however, pitch-ranking scores were extremely poor.

We have conducted studies with small groups of early-deafened subjects using the Cochlear Limited prosthesis that measured the discrimination of electrode trajectories and time-invariant electrodes (Busby and Clark, 1996; Busby *et al.*, 1993). There was some evidence suggesting that differences in performance across subjects was negatively related to the duration of auditory deprivation prior to implantation. In one study of electrode trajectory discrimination (Busby *et al.*, 1993), three of four early-deafened subjects were less successful than four postlinguistically deaf adults in the discrimination of trajectories that spanned a small number of electrodes. The early-deafened subject with the best performance became deaf at a later age and was deaf for a shorter period of time than the other three early-deafened subjects. In a second study with six early-deafened subjects (Busby and Clark, 1996), the discrimination of electrode trajectories and time-invariant electrodes was measured at the apical, mid, and basal positions on the array. Difference limens for electrode trajectories and time-invariant electrodes were very similar, and were less than 2–3 electrodes for most subjects. For one subject, difference limens were larger, 4–8 electrodes, and this subject was implanted at a later age and was deaf for a longer period of time than the other subjects. We also found within-subject differences in limens across three positions on the array for several subjects.

It is possible that differences between the postlinguistically deaf and early-deafened subject groups, and also differences between early-deafened subjects, could be related to morphological and physiological differences in the neural structure of the auditory pathway caused by the early onset of profound deafness and limited auditory experience. Experimental animal studies have shown that auditory deprivation can result in incomplete maturation and/or degeneration within the auditory system (Hardie *et al.*, 1998; Harrison *et al.*, 1991; Moore, 1990; Saada *et al.*, 1996). The extent of degeneration appears to be considerably greater when auditory deprivation is during development in the very young animal than in the more mature animal (Hashisaki and Rubel, 1989; Moore, 1990; Tierney *et al.*, 1997). However, it appears that auditory deprivation from birth may not result in the complete loss of tonotopic projections in the auditory pathway, as studies in the congenitally deaf white cat have shown some tonotopic organization at the auditory cortex (Hartmann *et al.*, 1997), with evidence of intact afferent projections at least to the level of the inferior colliculus (Heid *et al.*, 1997). Similar findings have also been recorded in neonatally deafened cats with both short and long durations of auditory deprivation prior to the mapping of the tonotopic projections in the inferior colliculus (Shepherd *et al.*, 1999).

Additional changes in the auditory pathway may also arise as a consequence of postoperative experience with electric stimulation. Chronic electric stimulation in the neonatally deafened cat may lead to an increase in spiral ganglion cell survival at the site of stimulation (Leake *et al.*, 1991), although this has not been the case in all investigations (Shepherd *et al.*, 1994). An expansion in the representation of the site of stimulation at the inferior colliculus with chronic electric stimulation in the neonatally deafened cat has also been recorded (Snyder *et al.*, 1990). The auditory system is responsive to variations in sensory input well into maturity, as changes in the spatial representation of the tonotopic order at the primary auditory cortex have been produced by unilateral partial lesions in the normally hearing adult cat (Rajan *et al.*, 1993). Thus, it is possible that electric stimulation using a multiple-electrode prosthesis may lead to further changes in the auditory pathway for both child and adult cochlear-implant users.

The main objective of this study was to determine whether pitch estimates for stimulated electrodes on a multiple-electrode array were tonotopically ordered in early-deafened cochlear-implant subjects. The prosthesis manufactured by Cochlear Limited, consisting of a scala tympani array of 22 electrodes spaced 0.75 mm apart, was used. It was hypothesized that there could be an absent or severely degraded tonotopic order of pitch percepts because of severe degradation of the residual peripheral auditory fibers, the tonotopic projections in the auditory pathway, or representations at the primary auditory cortex. Thus, the performance of early-deafened subjects could differ from that of postlinguistically deafened adults.

TABLE I. Summary of subject histories.

Subject	Age at confirmation of profound-total hearing loss (months)	Cause of deafness	Age at implantation (years)	Age at testing (years)	Duration of implant use (years)
S1	39	meningitis	4.8	10.2	5.4
S2	47	meningitis	5.2	10.8	5.6
S3	11	congenital, unknown	6.6	11.3	4.7
S4	24	Klippel–Feil and Mondini syndromes	8.6	11.7	3.1
S5	16	cytomegalovirus	4.6	11.7	7.1
S6	12	congenital, unknown	10.4	11.7	1.3
S7	9	congenital, unknown	8.2	11.7	3.5
S8	10	cytomegalovirus	7.8	12.2	4.4
S9	24	meningitis	3.5	12.9	9.4
S10	15	rubella	5.2	13.3	8.1
S11	6	congenital, unknown	8.0	13.5	5.5
S12	24	meningitis	8.1	13.7	5.6
S13	15	congenital, unknown	11.6	13.7	2.1
S14	16	rubella	12.0	13.7	1.7
S15	12	congenital, unknown	13.5	14.5	1.0
S16	6	Usher's syndrome	14.8	20.6	5.8
S17	18	Usher's syndrome	20.0	20.8	0.8
S18	12	congenital, unknown	17.5	21.0	3.5

The second objective was to determine the relationships between subject variables related to auditory deprivation and experience, and pitch estimation performance. It is possible that departures in the tonotopic order of pitch percepts may be more marked in subjects with a long duration of auditory deprivation. Experience with electric stimulation may lead to the development or enhancement of a tonotopic order of pitch percepts because of adjustments in the tonotopic projections and neural connections in response to electric stimulation.

The third objective was to determine the relationships between speech-perception performance and pitch estimation in these early-deafened subjects. It may be the case that a tonotopic order of pitch percepts is an important factor influencing speech perception in early-deafened subjects, as has been the case in postlinguistically deaf adults. It has been shown that consonant-recognition scores positively correlated with pitch-ranking scores in postlinguistically deaf adults using the Cochlear prosthesis (Nelson *et al.*, 1995). In addition, speech scores were markedly reduced when the tonotopic order of speech-envelope information was distorted in normally hearing listeners using bandpass-filtered speech (Shannon *et al.*, 1998).

In this study with early-deafened subjects, it was also considered important to determine subject reliability in numerical estimation procedures. Subject performance was compared over two estimation tasks: pitch estimation for stimulating electrodes on the array, and loudness estimation for variations in electric current levels. It was hypothesized that poor performance in both loudness and pitch estimation would indicate an inability to adequately perform the numerical estimation task.

I. METHOD

A. Subjects and electric stimulation hardware

The histories of the 18 early-deafened subjects are summarized in Table I, ordered according to age at the time of testing. Four subjects were deafened as a result of meningitis; at 39, 47, 24, and 24 months of age for S1, S2, S9, and S12, respectively. The other 14 subjects were congenitally deaf from a variety of etiologies. All subjects had a profound-total bilateral sensorineural hearing loss and were fitted with high-gain hearing aids at the time of diagnosis, at an average age of 17.6 months (s.d.=10.9 months) with a range of 6 to 47 months. Preoperative speech-perception testing indicated that the subjects received minimal benefit from amplification, which was a clinical prerequisite for implantation. The subjects were implanted with the Cochlear Limited prosthesis of 22 electrodes, spaced 0.75 mm apart (Clark *et al.*, 1987), and the average age of the subjects at the time of implantation was 9.5 years (s.d.=4.7 years), with a range of 3.5 to 20 years. The electrode array was fully inserted into the cochlea for most subjects. However, some electrodes were not available for stimulation in several cases because they were external to the cochlea, there was a short or open circuit, or stimulation produced unpleasant sensations. Details of the number of electrodes used in the pitch-estimation study are given in Sec. I B 2 and Table II. The average age of the subjects at the time of testing was 13.8 years (s.d.=3.4 years), with a range of 10.2 to 21.5 years, and the average duration of implant use at the time of testing was 4.4 years (s.d.=2.5 years), with a range of 0.8 to 9.4 years. Subjects were typically seen once per week at their school for about 45 min per session.

The residual auditory-nerve fibers were stimulated using biphasic current pulses with a pulse duration of 200 μs phase. The Cochlear Limited prosthesis delivers electric current using a scale of 239 levels, with approximately a 2.5% increase in current for each level (Skinner *et al.*, 1991). These current levels are reported in dB (*re* 1 μA) using values from calibration tables supplied by Cochlear Limited for each subject's implant. The stimulus duration was 500 ms and the pulse rate was 250 pulses/s. Bipolar stimulation was used for all subjects. For most subjects, except S4 and S8,

TABLE II. Electrodes used in the pitch-estimation study.

Subject	Number of electrodes	Electrodes (apical to basal)
S1	10	20, 18, 16, 14, 12, 10, 8, 6, 4, 2
S2	10	20, 18, 16, 14, 12, 10, 8, 6, 4, 2
S3	10	20, 18, 16, 14, 12, 10, 8, 6, 4, 2
S4	19	19, 18, 17, 16, 15, 14, 13, 12, 11, 10, 9, 8, 7, 6, 5, 4, 3, 2, 1
S5	10	20, 18, 16, 14, 12, 10, 8, 6, 3, 1
S6	10	20, 18, 16, 14, 12, 10, 8, 6, 4, 2
S7	10	19, 18, 16, 14, 12, 10, 8, 6, 4, 2
S8	15	19, 18, 17, 16, 15, 14, 13, 12, 11, 10, 9, 8, 7, 6, 5
S9	10	20, 18, 16, 14, 12, 10, 8, 6, 4, 2
S10	10	20, 18, 16, 14, 12, 10, 8, 6, 4, 2
S11	20	20, 19, 18, 17, 16, 15, 14, 13, 12, 11, 10, 9, 8, 7, 6, 5, 4, 3, 2, 1
S12	14	20, 19, 18, 17, 16, 15, 14, 13, 12, 11, 10, 9, 8, 7
S13	19	20, 19, 18, 17, 16, 15, 14, 13, 12, 11, 10, 9, 8, 7, 6, 5, 4, 3, 2
S14	16	20, 19, 18, 17, 16, 15, 14, 13, 12, 11, 10, 9, 8, 7, 6, 5
S15	20	20, 19, 18, 17, 16, 15, 14, 13, 12, 11, 10, 9, 8, 7, 6, 5, 4, 3, 2, 1
S16	15	20, 19, 18, 17, 16, 15, 14, 13, 12, 11, 7, 6, 4, 2, 1
S17	20	20, 19, 18, 17, 16, 15, 14, 13, 12, 11, 10, 9, 8, 7, 6, 5, 4, 3, 2, 1
S18	20	20, 19, 18, 17, 16, 15, 14, 13, 12, 11, 10, 9, 8, 7, 6, 5, 4, 3, 2, 1

the two electrodes of the bipolar pair were separated by one electrode which corresponds to BP+1 in the Cochlear Limited clinical procedures. For S4 and S8, the two electrodes were separated by two electrodes corresponding to BP+2 in the clinical procedures. The term ''electrode'' describes the basal member of the bipolar pair. Electrodes are numbered 22–1 in an apical–basal direction in this paper, consistent with the clinical numbering system.

B. Procedure

1. Threshold and comfortable-listening levels

For each subject, hearing threshold (*T*) and comfortable-listening (*C*) levels were obtained for all electrodes available for stimulation using the procedures in our previous study with postlinguistically deaf adults (Busby *et al.*, 1994). The *T* and *C* levels were measured using single presentations of the stimuli and the step-size was two current levels. The *T* levels were measured using the Hughson–Westlake ascending technique (Carhart and Jerger, 1959). The *C* levels were measured using an ascending–descending technique, where current was increased until stimulation became too loud or uncomfortable and it was then decreased to a level corresponding to the comfortable listening level. The *C* levels were further adjusted to ensure that the electrodes across the array were approximately of equal loudness. First, a group of four adjacent electrodes was stimulated in succession, with a 500-ms interval between successive electrodes, and the subject indicated whether any electrodes required adjustment for equal loudness. This was repeated for consecutive groups of four electrodes, with an overlap of one electrode with the previous group, until all electrodes had been assessed. Second, all electrodes in the set were sequentially presented in an apical–basal direction and the subject indicated whether any electrode needed further adjustment to the *C* level.

2. Pitch estimation

A single-interval numerical-estimation procedure (Busby *et al.*, 1994; Collins *et al.*, 1997) was used to measure pitch percepts for stimulation of electrodes at the *C* level. The electrodes selected as stimuli for each subject are shown in Table II. Typically for the older subjects, all of the available electrodes were selected as stimuli. Usually for the younger subjects, every second electrode was selected in order to keep the number of stimuli in the set within reasonable limits so that interest in the task was maintained. Two sets of stimuli were used for testing, with each electrode randomly selected five times in each set, and the number of stimuli in each set was from 50 to 100 across subjects. Thus, ten estimates for each electrode were obtained, and means and standard deviations were then calculated from these data for each subject.

The subjects were instructed to assign a number in the range 1–100 to the pitch of a single presentation. A low pitch was assigned a low number and a high pitch a high number. The subjects were also advised that the numerical scale could be expanded in either direction, if required. The scale with written descriptions was displayed on a sheet of paper for reference. Prior to presenting each set of stimuli, subjects listened to the electrodes in the stimulus set in an apical–basal order. During testing, the subjects either entered their responses on a computer keyboard or responded verbally, and the tester then entered the responses.

Training was provided prior to data collection. For those subjects with good pitch-estimation skills, there were one to two sessions of training as these subjects clearly showed that they were able to complete the task without difficulty. For those subjects who found pitch estimation more difficult, four to six sessions of training were provided. All subjects demonstrated that they were able to perform the numerical-estimation task, as shown by the results for loudness estimation.

3. Loudness estimation

Loudness-estimation data for a set of current levels between the *T* and *C* levels were obtained from all subjects. Stimulation was on electrode 14 in all cases. The number of current levels selected as stimuli ranged from seven to ten across subjects because of differences in the size of the dynamic range between *T* and *C* levels. Within each set of stimuli for each subject, a uniform incremental step-size in current level was used. Each current level in the stimulus set for each subject was presented ten times, typically using one block of randomized stimuli. In some cases two blocks of stimuli were used, with five randomized presentations of each stimulus in each block, to maintain interest in the task. This was the case for some of the younger subjects or where there was a large number of stimuli in the set. Calculated

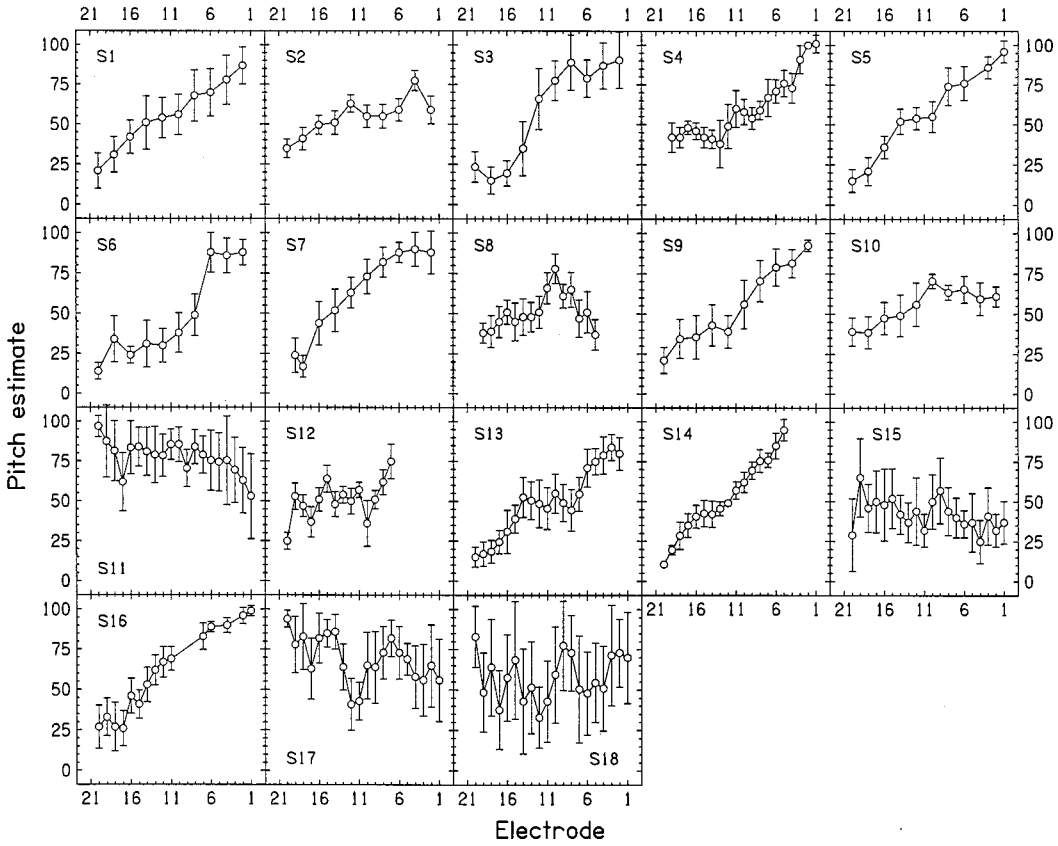

FIG. 1. Pitch estimates from the 18 subjects for stimulation of electrodes on the array. Electrodes are numbered 21–1 in an apical–basal direction. The error bars indicate ±1 standard deviation around the mean.

from these data were the means and standard deviations of the loudness estimates for each current level.

The loudness-estimation procedure was similar to that used for pitch estimation. A single-interval numerical-estimation task was used, where the subject was instructed to assign a number in the range 1–100 to the loudness of a single presentation. A soft sound was assigned a low number and a loud sound a high number. The numerical scale and written descriptions were displayed on a sheet of paper for reference. Subject responses were obtained by direct computer entry by the subject or by verbal response. The subjects received one to two sessions of training and all subjects were able to complete the task without difficulty.

II. RESULTS

A. Pitch estimation for electrodes

For a considerable proportion of subjects, pitch estimates across electrodes were generally consistent with the tonotopic organization of the cochlea in that the estimates increased as the stimulating electrode became more basal (Fig. 1). Subjects were divided into three groups using two criteria: the size of the standard deviations of pitch estimates, and the slope of the estimate by standardized electrode function. The electrodes for each subject were standardized to the numerical range 1–100 in an apical-basal direction (Fig. 2). Standardization was useful as it allowed for a more direct comparison of the functions across subjects. This is because the pitch estimates were relative to the set of electrodes used as stimuli and not all electrodes were available for stimulation for all subjects, as was the case for S8 and S12 at the basal end of the array, for example. Standardization of the electrodes therefore enabled the calculation of the slope of uniform functions across subjects, using linear regression.

For the 10 Group1 subjects (S1, S3, S4, S5, S6, S7, S9, S13, S14, and S16), the standard deviations of the estimates were small (an average of 9.9 units and a range of 5.9 to 13.6 units on the estimation scale) and the slopes of the estimate functions, in degrees, were considerably steeper than those for the other subjects (an average of 36.1° and a range of 30.5° to 40.9° for standardized electrodes). For the four Group2 subjects (S2, S8, S10, and S12), the standard deviations of the estimates were also small (an average of 8.3 units and a range of 6.8 to 9.8 units on the estimation scale), but the slopes of the estimate functions were shallow (an average of 12.8° and a range of 7.4° to 16.1° for standardized electrodes). For the four Group3 subjects (S11, S15, S17, and S18), there was essentially no pitch order of estimates as the standard deviations of the estimates were considerably larger than those of the other subjects (an average of 19.0 units and a range of 16.3 to 26.9 units on the estimation scale) and the slopes of the estimate function were flat or negative (an average of −7.0° and a range of −12.7° to 4.5° for standardized electrodes). While a negative slope could be interpreted as an inverse pitch order, the very large standard deviations for the Group3 subjects indicated that the pitch order was

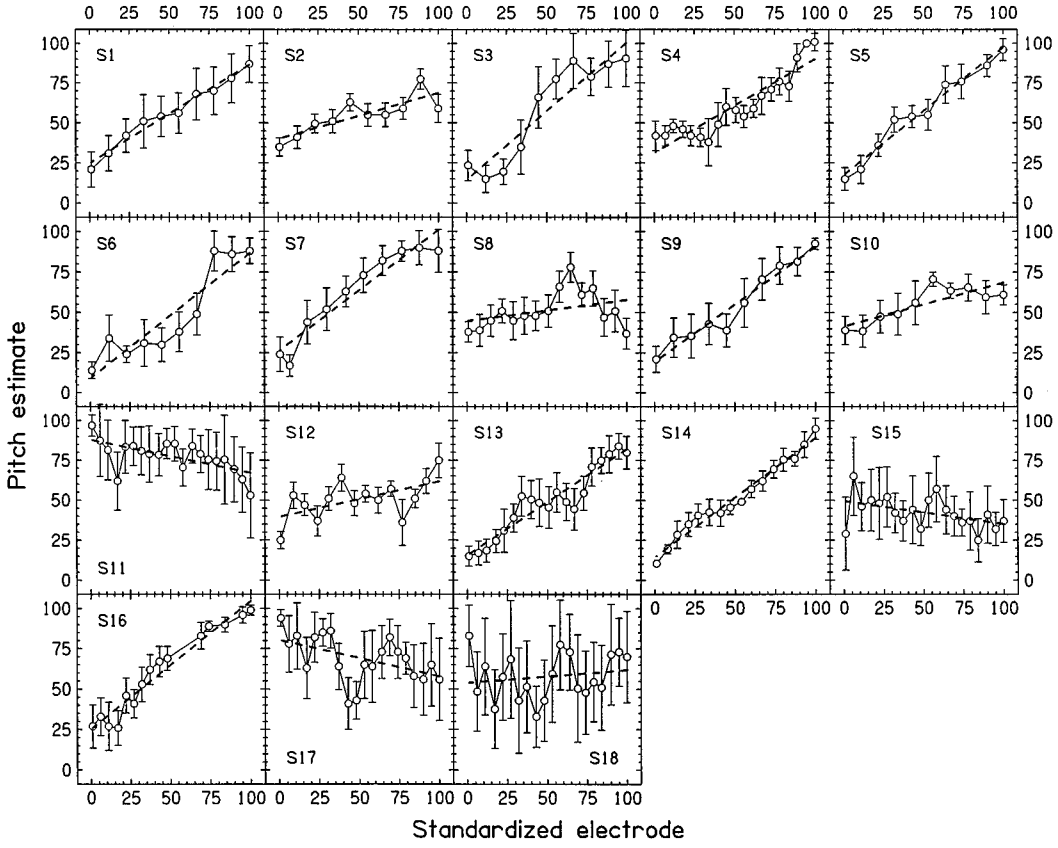

FIG. 2. Pitch estimates from the 18 subjects using standardized electrodes in the numerical range of 1–100 (apical to basal). A linear regression line has been fitted to the estimate data, shown by the dashed line in each graph. The error bars indicate ±1 standard deviation around the mean.

very poorly defined. Thus, these data were interpreted as indicating that there was essentially no tonotopic order in the pitch estimates.

The size of the standard deviations and the slopes of the estimate function using standardized electrodes were separately analyzed using a one-way analysis of variance to determine whether values differed across the three subject groups. *Post hoc* Tukey tests were used to identify which subject group contributed to the significant effect at a $p < 0.05$ significance level. A significant difference was found for the size of the standard deviations [$F(2,17) = 15.66$, $p < 0.001$], which was due to larger standard deviations for the Group3 subjects. A significant difference was found for the slopes of the estimate function [$F(2,17) = 15.66$, $p < 0.001$], and the three subject groups were different from each other and ordered Group1, Group2, and Group3, from largest to smallest slopes, respectively. Note that the standard deviations for the Group1 and Group2 subjects were in the same range as those found for postlinguistically deaf adults using the same procedure, typically less than 12 units on the estimation scale (Busby *et al.*, 1994).

On visual inspection of the data (Figs. 1 and 2), it was clear that there were deviations in the tonotopic order of pitch estimates across the electrode array for a number of Group1 and Group2 subjects. For the Group1 subjects, there were instances where the estimates did not vary across small sections of the array: at the apical end for S4 and S16, at the middle of the array for S13, and at the basal end for S3, S6, and S7. For Group2 subjects, there were more marked departures from a tonotopic order of estimates. For S8 and S10, the highest estimates were found at the middle of the array and estimates remained relatively unchanged (S10) or decreased as the electrode became more basal (S8). The range of estimates along the array was also small: from 35 to 59 units for S2 and from 39 to 61 units for S10, using the average values for each electrode. Similar findings to these two subjects have also been found for some postlinguistically deaf adults (Busby *et al.*, 1994; Collins *et al.*, 1997), which may suggest some difficulty with the pitch-estimation procedure. For S12, there was a broad region of variation in estimates at the apical and mid electrodes, and estimates increased for the basal electrodes. Unfortunately, the six most basal electrodes were not available as stimulation produced very high-pitched and unpleasant sensations. Thus, it is possible that the increase in estimates for electrodes 10–7 may not represent a consistent trend, given the small number of electrodes involved.

To determine whether there were any differences between these three subject groups with respect to variables related to auditory deprivation and experience with (acoustic and electric) hearing, the data were analyzed using a series of one-way analysis of variance. *Post hoc* Tukey tests were used to identify which subject groups contributed to the significant effect at a $p < 0.05$ significance level. The variables related to auditory deprivation were age at onset of profound deafness, duration of deafness prior to implantation, and age

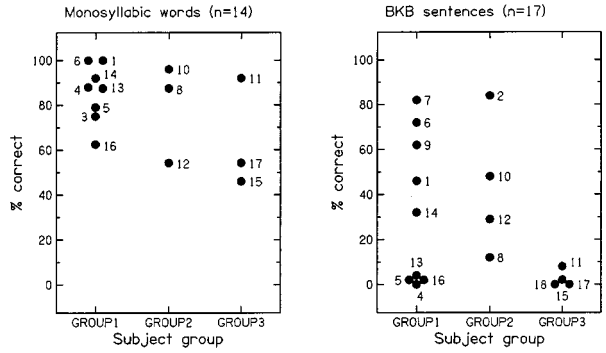

FIG. 3. Speech perception scores for a monosyllabic word test and word scores for the BKB sentence test. Subjects are numbered and grouped according to their performance in pitch estimation.

at implantation. For the congenitally deaf subjects, the duration of deafness values was the same as those for age at implantation. The variables related to auditory experience were duration of implant use and the total time period of auditory experience (age at onset of deafness plus duration of implant use). In addition, age at the time of testing was included as a variable to determine whether differences between the three groups were influenced by any cognitive or task-dependent factors related to chronological age.

Significant differences were recorded between the three subject groups for three variables. The results suggested that the absence of a tonotopic order of pitch estimates for electrodes in Group3 subjects was related to a long duration of auditory deprivation prior to implantation for this subject group. A significant difference $[F(2,15)=5.36,\ p=0.018]$ was recorded for duration of deafness, which was due to a longer duration of deafness for Group3 subjects than for Group1 and Group2 subjects. A significant difference $[F(2,15)=5.45,\ p=0.017]$ was recorded for age at implantation, which was due to a later age of implantation for Group3 subjects than for Group1 and Group2 subjects. A significant difference $[F(2,15)=3.93,\ p=0.042]$ was recorded for age at testing, which was due to a later age of testing for Group3 subjects than for Group1 subjects. However, this significant effect for age at testing was because subjects tested at a later age had a longer duration of deafness and were implanted at a later age. The Pearson product moment coefficient was used to examine the correlations between these three variables, and is expressed using the coefficient of determination (R^2) to indicate the proportion of variance. Significant positive correlations were found between all three variables ($R^2>73.4\%,\ p<0.001$).

The relationship between a tonotopic order of pitch percepts for electrodes on the array and speech perception was examined using scores from two speech tests presented in the audition-alone condition: a 12-alternative forced-choice monosyllabic word test (Plant, 1984) and word scores for BKB sentences (Bench and Bamford, 1979). Data were obtained from the clinic files using scores collected on average within 0.35 years (s.d.=0.30 years) of the pitch-estimation data. Data were not available from four subjects for the monosyllabic word test (S2, S7, S9, and S18) and from one subject for the BKB sentence test (S3). Figure 3 shows the speech scores for the three subject groups. To determine whether there were any differences in scores between subject groups, the scores for each test were separately analyzed using a one-way analysis of variance.

For the monosyllabic word test, most subjects scored above 60% and there was no significant difference in scores across the three subject groups $[F(2,11)=1.68,\ p=0.230]$. For BKB sentences, the lowest scores were recorded for Group3 subjects, where all scores were below 10%, but there was no significant difference in scores across subject groups $[F(2,14)=2.28,\ p=0.139]$. The lack of significant difference between subject groups for BKB scores could have been influenced by the unequal variance in scores for the three groups, as shown by significant results for both the Bartlett's ($p=0.014$) and Levene's ($p=0.022$) tests for homogeneity of variance (Minitab, Inc., 1998). The wide range of BKB scores for the Group1 and Group2 subjects, from 0% to 84%, suggested that a tonotopic order of pitch estimates was not always related to high sentence scores. For example, low scores were found for S5 and S16 (Fig. 3) who had large slopes of the estimate function (Fig. 2). In addition, high BKB scores were found for subjects with small slopes of the estimate function. For example, a small slope was recorded for S2 (Fig. 2) and the BKB sentence score was high, 84% (Fig. 3). These findings were consistent with the results of correlation analysis which showed no significant correlation between scores for both tests and the slopes of the estimate function ($R^2<17.3\%,\ p>0.137$).

To determine whether speech scores for those subjects with small standard deviations of estimates (Group1 and Group2 subjects) were different from scores for subjects with large standard deviations (Group3 subjects), *t*-tests assuming unequal variances were used to analyze the data. This would indicate whether consistent performance in pitch estimation resulted in higher speech-perception scores. Scores for the Group3 subjects were significantly lower than those for the combined Group1 and Group2 subjects for BKB sentences $[t(13)=3.81,\ p=0.002]$, but not for monosyllabic words $[t(2)=1.34,\ p=0.310]$. This finding suggested that the absence of a consistent pitch order for electrodes along the array may result in poor speech-perception performance.

B. Threshold and comfortable-listening levels

The current levels which elicited the threshold (T) and comfortable listening (C) levels for each subject are shown in Fig. 4. The size of the average dynamic range across electrodes, the difference between T and C levels, did not correlate with subject variables of auditory deprivation and experience ($R^2<21.6,\ p>0.052$). Also, the correlations between the average dynamic range and speech scores for the monosyllabic word and BKB sentence tests were not significant ($R^2<9.4,\ p>0.286$).

It is possible that variations in pitch estimates and corresponding variations in T or C levels could be related to variations in the status of peripheral auditory fibers. It has been shown that pitch ranking (Clark *et al.*, 1988) and electrode discrimination (Pfingst *et al.*, 1985) were poorer at locations with very poor nerve survival. It is also possible that these variations may be related to the status of the auditory pathway or cortex. For instance, it has been shown that el-

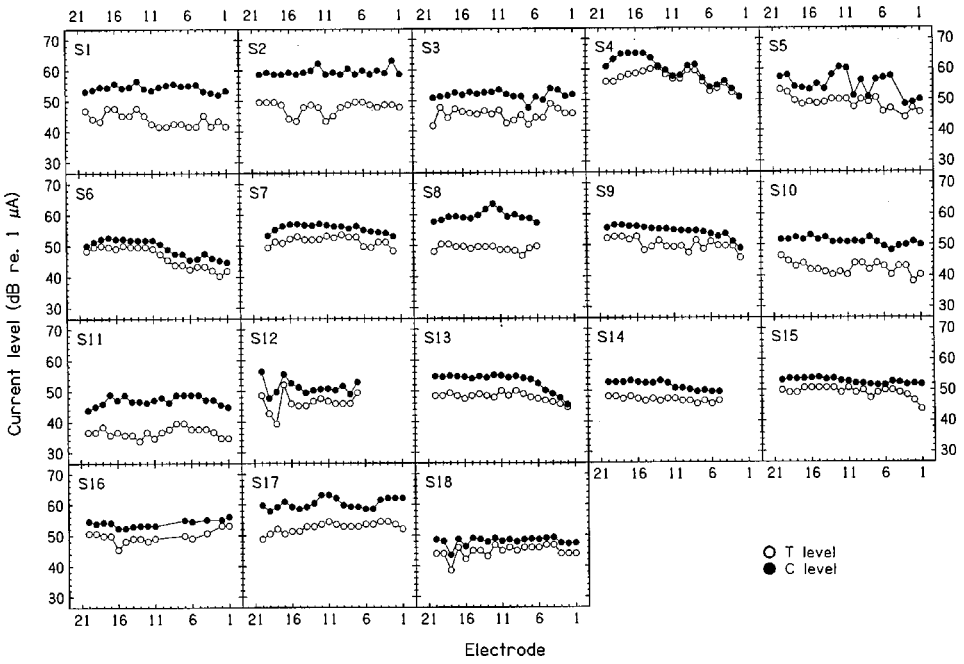

FIG. 4. Threshold (*T*) and comfortable-listening (*C*) levels for the 18 subjects.

evated thresholds can be induced by localized lesions in the auditory cortex (Heffner and Heffner, 1986). Visual examination of the *T* and *C* levels (Fig. 4) and the pitch-estimation data (Fig. 1) suggested that for three subjects (S4, S8, and S17), the location of variations in pitch estimates corresponded to the location of variations in the *C* level. Figure 5 shows the data for these three subjects. The surgical reports and postoperative x rays indicated that there were no marked deviations in the location of the electrode array in the cochlea for these subjects.

For S4, there was essentially no variation in pitch estimates for apical electrodes and there was a marked increase in the current levels used to elicit the *C* level for these electrodes (Fig. 5). It is possible that the same group of auditory fibers was stimulated by these apical electrodes because of the similarity in pitch estimates. The increase in *C* levels for the apical electrodes could indicate that there was a reduced number of residual fibers at this location and that relatively more current was required to recruit sufficient fibers to obtain the comfortable-listening level. For S8 and S17, the re-

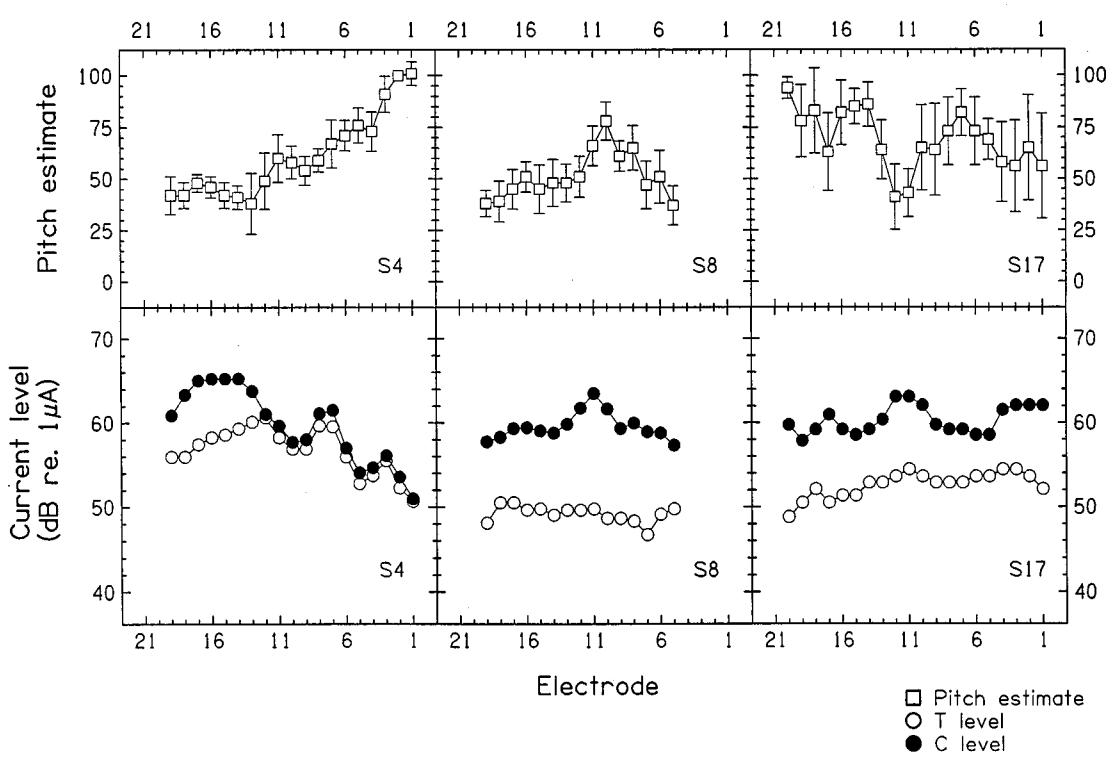

FIG. 5. Pitch estimates, and threshold and comfortable-listening levels for three subjects: S4, S8, and S17.

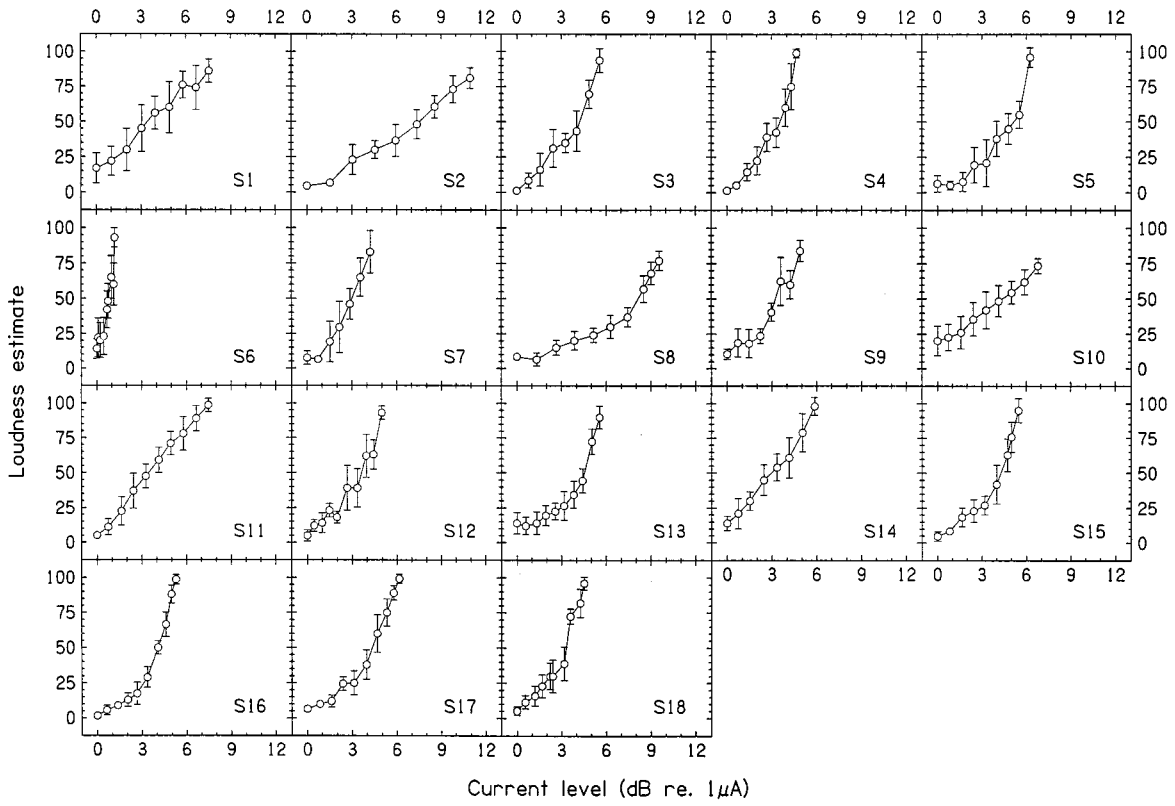

FIG. 6. Loudness estimates from the 18 subjects for variations in current level. The current levels for each subject are expressed in dB and have been adjusted so that the lowest level is at 0 dB. The error bars indicate ±1 standard deviation around the mean.

lationship was less clear because the tonotopic order of pitch estimates was not uniform for S8 and essentially absent for S17. However, it appears that stimulation of electrodes in the vicinity of electrode 11 for S8 and electrode 12 for S17 resulted in a change of percept which was regarded as a higher pitch for S8 and as a lower pitch for S17. This may suggest that electrodes in the vicinity of electrode 11 stimulated a basal group of auditory fibers for S8, while electrodes in the vicinity of electrode 12 stimulated an apical group of auditory fibers for S17. Alternatively for S8, stimulation of basal electrodes may have resulted in the stimulation of more remote auditory fibers emanating from the apical portion of the cochlea. These variations could also be indicative of more central processes, such as reorganization of tonotopic projections or the result of localized neural degeneration in the auditory pathway and/or cortex. However, given the lack of consistent tonotopic order for these two subjects, these interpretations are speculative.

There were several instances where there was a departure from a tonotopic order of pitch estimates but no corresponding variation in *T* or *C* levels. For example, estimates were relatively unchanged at the basal electrodes for S3 and S6 (Fig. 1), but there was no corresponding variation in *T* or *C* levels (Fig. 4). This may suggest that the lack of variation in pitch percepts was not related to any variation in auditory-nerve-fiber density at these locations, but could be related to more central mechanisms in the auditory pathway and/or cortex. Note that this interpretation does not assume that there were no variations in the distribution of surviving auditory fibers in the cochlea, which may be reflected by variations in *T* and *C* levels, but that variations in residual fiber density were not related to variations in pitch estimates. The data for S5 would be an example, where there were marked variations in *C* levels at two locations on the array (Fig. 4) but a consistent tonotopic order of pitch estimates (Fig. 1).

C. Loudness estimation

All subjects were able to successfully estimate loudness for variations in current level (Fig. 6). In all cases, loudness increased with increases in current level. There were considerable differences in the size of the dynamic range across subjects, from 1.21 dB for S6 to 10.96 dB for S2. The average of the standard deviations of the loudness estimates across subjects was 8.7 units on the estimation scale, with a range of 5.1 (S16) to 12.9 (S1) units. These standard deviation values were similar to those found in pitch estimation for electrodes for the Group1 and Group2 subjects, where the average standard deviation was 9.3 units on the estimation scale. There were no significant differences in the average size of the standard deviations of the loudness estimates between Group1, Group2, and Group3 subjects [$F(2,15) = 1.64$, $p = 0.228$]. These findings indicated that all subjects were able to perform the numerical-estimation task with a similar degree of consistency.

III. DISCUSSION

The main finding of this study was that a tonotopic order of pitch percepts for stimulation of electrodes on the Cochlear Limited array was recorded for 56% of the 18 early-deafened subjects, as shown by the small standard deviations of the pitch estimates and the large slopes of the estimate function for the Group1 subjects. A consistent but deviant tonotopic order of pitch percepts was found for 22% of subjects, as shown by the small standard deviations of the pitch estimates and small slopes of the estimate function for the Group2 subjects. There was essentially no pitch order for the remaining 22% of subjects, as shown by the very large standard deviations for the Group3 subjects. Some of the between-subject differences in pitch estimation were related to the duration of auditory deprivation prior to implantation, with the poorest performance for the Group3 subjects, who had a longer duration of deafness and were implanted at a later age than the other subjects. The Group3 subjects also had the lowest scores for the BKB sentence test.

With the exception of the four Group3 subjects, the pitch-estimation results for these early-deafened subjects did not appear to be markedly different from those previously reported for postlinguistically deaf adults. This is because the extent of the between- and within-subject variability in pitch estimates for the Group1 and Group2 subjects was similar to that found for postlinguistically deaf adults in pitch estimation (Busby *et al.*, 1994; Collins *et al.*, 1997) and pitch ranking (Collins *et al.*, 1997; Nelson *et al.*, 1995). In the case of the Group1 subjects, the slopes of the estimates by standardized electrodes were similar to those found for postlinguistically deaf adults. We calculated the slopes of the functions using data for bipolar stimulation collected in our previous study (Busby *et al.*, 1994). With the exception of one subject, the average slope was 32.6°, with a range of 22.1° to 41.3°. The slope for the excluded subject was very small, 4.5°. The small slopes of the estimate functions from the Group2 subjects were similar to the small slopes of the estimate functions and low pitch-ranking scores recorded from several postlinguistically deaf adults in previous studies (Busby *et al.*, 1994; Collins *et al.*, 1997). With respect to within-subject variability in the tonotopic order of pitch percepts, there were a number of instances where estimates did not vary, or the tonotopic order was reversed, across small sections of the array. Similar findings have been found frequently for postlinguistically deaf adults. Thus, it appears that both the postlinguistically deaf and early-deafened subject groups show considerable variability in measures of pitch perception for stimulation of electrodes on a multiple-electrode array, and that there is no clear difference between the two subject groups, except for the Group3 subjects where there was essentially no tonotopic order of estimates.

It has been hypothesized that some of the between- and within-subject variability in the tonotopic order of pitch percepts could be related to variations in the distribution of surviving peripheral auditory fibers, as demonstrated in a small number of studies which have shown a correlation between auditory-nerve survival and electrode discrimination (Pfingst *et al.*, 1985) and pitch ranking (Clark *et al.*, 1988). It could be expected that variation in auditory-nerve survival would be related to variations in the electric stimulation levels used to obtain hearing threshold and comfortable-listening levels. For instance, Kawano *et al.* (1998) have shown correlations between comfortable-listening levels and spiral ganglion-cell density in adults who used the Cochlear Limited prosthesis. However, there was no clear pattern of correspondence between the electric stimulation levels for threshold and comfortable-listening levels and pitch estimates in our study. In only one instance, S4, a clear correspondence between pitch estimates and comfortable-listening levels was found (Fig. 5), which would be consistent with this hypothesis. There could be other important factors influencing pitch percepts and electric stimulation levels, such as auditory pathway and cortex integrity (Heffner and Heffner, 1986; Moore, 1990, 1994; Trune, 1982). In further studies, it would be useful to determine the relative contributions of peripheral or central mechanisms to variations in pitch percepts and the electric stimulation levels for threshold and comfortable-listening levels.

The tonotopic order of pitch percepts for stimulating electrodes along the array in early-deafened subjects is consistent with recent animal studies which have reported a tonotopic organization at the inferior colliculus and auditory cortex in the congenitally deaf and neonatally deafened cat (Hartmann *et al.*, 1997; Heid *et al.*, 1997; Shepherd *et al.*, 1999). In these animal studies, the onset of profound deafness was prior to the onset of measurable hearing responses, suggesting that the tonotopic ordering of neural projections develops at a very early stage of development. However, Shepherd *et al.* (1999) noted that there was a smaller distance between the best locations of the spatial tuning curves for stimulation of apical and basal electrodes in the neonatally deafened cat when compared to the normally hearing animal, suggesting that sensory stimulation in the normal animal leads to further development and enhancement of these projections. This would be consistent with several studies which have demonstrated that sensory input is essential for normal auditory development (Moore, 1990, 1994; Trune, 1982).

There were significant differences between early-deafened subjects in pitch estimation which were related to the duration of auditory deprivation prior to implantation. The Group3 subjects, where there was essentially no tonotopic pitch order, had the longest period of auditory deprivation. This suggests that auditory stimulation may be important for both maintaining tonotopic projections and further maturation of the auditory pathway, consistent with the animal studies showing that sensory input contributes to auditory development (Moore, 1990, 1994; Saada *et al.*, 1996; Trune, 1982). However, several subjects were implanted as teenagers in our study and a tonotopic order of pitch estimates was recorded: S13, S14, and S16, for example (Fig. 1). Thus, it appears that despite the lack of auditory stimulation over a long time period, the tonotopic projections were maintained and/or were responsive to electric stimulation. It is possible that postoperative experience could also result in changes to the mechanisms underlying a tonotopic order of pitch percepts. Experimental studies in juvenile and adult animals have shown that the auditory system is responsive to

stimulation-induced changes. It has been shown that chronic electric stimulation in the neonatally deafened cat at a single location in the cochlea resulted in an expansion of the site of stimulation at the inferior colliculus (Snyder *et al.*, 1990). In adult animals, rapid changes in the spatial representation of the tonotopic order at the auditory cortex have been produced by partial cochlear lesions (Irvine *et al.*, 1997; Rajan *et al.*, 1993).

There did not appear to be any within-group similarities with respect to etiology of deafness. In the case of the four subjects with meningitic deafness, it is likely that there would have been a normal tonotopic order of pitch percepts prior to the onset of deafness. However, for only two of the four meningitically deaf subjects, S1 and S9, a clear tonotopic order of pitch estimates was recorded. This suggests that the long duration of auditory deprivation prior to implantation for these two subjects did not result in any degenerative processes influencing the maintenance of the tonotopic ordering of neural connections in the auditory pathway and cortex. For S2, the small slope of the estimate function could be related to poor pitch-estimation skills. For S12, it is possible that the deviant pitch estimates may be due to idiopathic postmeningitic damage to the cochlea and peripheral neural structures, such as new bone formation and a reduction in the number of spiral ganglion cells (Nadol, 1997). The inability to stimulate electrodes at the basal end of the array for this subject because of unpleasant sensations would be consistent with considerable damage in the cochlea, as it suggests abnormal current flow in the cochlea. For the other three meningitic subjects, virtually all electrodes were available for stimulation, suggesting that any postmeningitic damage to the cochlea did not appear to be a factor influencing their performance.

Subjects with essentially no tonotopic order of pitch estimates for electrodes (Group3 subjects) also had lower speech-perception scores for BKB sentences, but not for monosyllabic words (Fig. 2). However, not all Group1 subjects obtained good scores for BKB sentences and it is likely that there are other important factors influencing performance, such as language competence and vocabulary knowledge (Sarant *et al.*, 1997). Our findings with this small group of subjects may suggest that a tonotopic order in pitch percepts for stimulation of electrodes on the array is an important prerequisite for successful speech perception using the implant. This would be consistent with previous studies which have shown significant relationships between electrode discrimination or electrode pitch ranking with speech perception in implanted children (Busby *et al.*, 1993) and postlinguistically deaf adults (Nelson *et al.*, 1995; Zwolan *et al.*, 1997). In addition, it has been shown that speech scores are markedly reduced in normally hearing listeners using bandpass-filtered speech when the tonotopic order of the speech-envelope information is distorted (Shannon *et al.*, 1998). For monosyllabic words, scores were similar for the three subject groups, suggesting that the tonotopic pitch order was not a factor influencing performance and that there may have been sufficient temporal and amplitude cues to obtain reasonable scores for this test. Nelson *et al.* (1995) have shown that postlinguistically deaf adults with poor electrode pitch ranking were able to obtain reasonable scores for consonant recognition on the basis of speech-envelope information.

ACKNOWLEDGMENTS

This work was supported by the National Health and Medical Research Council of Australia, the Human Communication Research Center at the Department of Otolaryngology, University of Melbourne, Lions Clubs International, and the Cooperative Research Center for Cochlear Implant, Speech and Hearing Research. The authors wish to thank the reviewers for their constructive suggestions, Mark Harrison for assistance in software development, the subjects for their participation, and the Cochlear Implant Clinic of the Royal Victorian Eye Ear Hospital, Melbourne, for access to clinic data.

Bench, R. J., and Bamford, J. (Eds.) (**1979**). *Speech-Hearing Tests and the Spoken Language of Hearing-Impaired Children* (Academic, London).

Black, R. C., Clark, G. M., Tong, Y. C., and Patrick, J. F. (**1983**). ''Current distributions in cochlear stimulation,'' Ann. (N.Y.) Acad. Sci. **405**, 137–145.

Busby, P. A., and Clark, G. M. (**1996**). ''Electrode discrimination by early-deafened cochlear implant patients,'' Audiology **35**, 8–22.

Busby, P. A., Tong, Y. C., and Clark, G. M. (**1993**). ''Electrode position, repetition rate, and speech perception by early- and late-deafened cochlear implant patients,'' J. Acoust. Soc. Am. **93**, 1058–1067.

Busby, P. A., Whitford, L. A., Blamey, P. J., Richardson, L. M., and Clark, G. M. (**1994**). ''Pitch perception for different modes of stimulation using the Cochlear multiple-electrode prosthesis,'' J. Acoust. Soc. Am. **95**, 2658–2669.

Carhart, R., and Jerger, J. (**1959**). ''Preferred method for clinical determination of pure tone thresholds,'' J. Speech Hear. Disord. **24**, 330–245.

Clark, G. M., Blamey, P. J., Busby, P. A., Dowell, R. C., Franz, B. K., Musgrave, G. N., Nienhuys, T. G., Pyman, B. C., Roberts, S. A., Tong, Y. C., Webb, R. L., Kuzma, J. A., Money, D. K., Patrick, J. F., and Seligman, P. M. (**1987**). ''A multiple-electrode intracochlear implant for children,'' Arch. Otolaryngol. **113**, 825–828.

Clark, G. M., Shepherd, R. K., Franz, B. K-H., Dowell, R. C., Tong, Y. C., Blamey, P. J., Webb, R. L., Pyman, B. C., McNaughtan, J., Bloom, D. M., Kakulas, B. A., and Siejka, S. (**1988**). ''The histopathology of the human temporal bone and auditory nervous system following cochlear implantation in a patient,'' Acta. Oto-Laryngol. Suppl. **488**, 1–65.

Cohen, L. T., Busby, P. A., Whitford, L. A., and Clark, G. M. (**1996a**). ''Cochlear implant place psychophysics. I. Pitch estimation with deeply inserted electrodes,'' Audiol. Neuro-Otol. **1**, 265–277.

Cohen, L. T., Busby, P. A., and Clark, G. M. (**1996b**). ''Cochlear implant place psychophysics. II. Comparison of forward masking and pitch estimation data,'' Audiol. Neuro-Otol. **1**, 278–292.

Collins, L. M., Zwolan, T. A., and Wakefield, G. H. (**1997**). ''Comparison of electrode discrimination, pitch ranking, and pitch scaling data in postlingually deafened adult cochlear implant subjects,'' J. Acoust. Soc. Am. **101**, 440–455.

Dorman, M. F., Smith, L., McCandless, G. A., Dunnavant, G., Parkin, J., and Dankowski, K. (**1990**). ''Pitch scaling and speech understanding by patients who use the Ineraid cochlear implant,'' Ear Hear. **11**, 310–315.

Eddington, D. K., Dobelle, W. H., Brackman, D. E., Mladejovsky, M. G., and Parkin, J. L. (**1978**). ''Auditory prostheses research with multiple channel intracochlear stimulation in man,'' Ann. Otol. Rhinol. Laryngol. Suppl. **53**, 5–39.

Eddington, D. K. (**1980**). ''Speech discrimination in deaf subjects with cochlear implants,'' J. Acoust. Soc. Am. **68**, 885–891.

Hardie, N. A., Martsi-McClintock, A., Aitkin, L. M., and Shepherd, R. K. (**1998**). ''Neonatal sensorineural hearing loss affects synaptic density in the auditory midbrain,'' NeuroReport **9**, 2019–2022.

Harrison, R. V., Nagasawa, A., Smith, D. W., Stanton, S., and Mount, R. J. (**1991**). ''Reorganization of auditory cortex after neonatal high frequency cochlear hearing loss,'' Hear. Res. **54**, 11–19.

Hartmann, R., Shepherd, R. K., Heid, S., and Klinke, R. (**1997**). ''Response of the primary auditory cortex to electrical stimulation of the auditory nerve in the congenitally deaf white cat,'' Hear. Res. **112**, 115–133.

Hashisaki, G. T., and Rubel, E. W. (**1989**). ''Effects of unilateral cochlea removal on anteroventral cochlear nucleus neurons in developing gerbils,'' J. Comp. Neurol. **303**, 2–15.

Heffner, H. E., and Heffner, R. S. (**1986**). ''Hearing loss in Japanese macaques following bilateral auditory cortex lesions,'' J. Neurophysiol. **55**, 256–271.

Heid, S., Jahn-Siebert, T. K., Klinke, R., Hartmann, R., and Langner, G. (**1997**). ''Afferent projection patterns in the auditory brainstem in normal and congenitally deaf white cats,'' Hear. Res. **110**, 191–199.

Irvine, D. R. F., and Rajan, R. (**1997**). ''Injury-induced reorganization of frequency maps in adult auditory cortex: the role of unmasking of normally-inhibited inputs,'' Acta Oto-Laryngol. Suppl. **532**, 39–45.

Kawano, A., Seldon, H. L., Clark, G. M., Ramsden, R. T., and Raine, C. H. (**1998**). ''Intracochlear factors contributing to psychophysical percepts following cochlear implantation,'' Acta Oto-Laryngol. **118**, 313–326.

Leake, P. A., Hradek, G. T., Rebscher, S. J., and Snyder, R. L. (**1991**). ''Chronic intracochlear electrical stimulation induces selective survival of spiral ganglion cells in neonatally deafened cats,'' Hear. Res. **54**, 251–271.

McDermott, H. J., McKay, C. M., and Vandali, A. E. (**1992**). ''A new portable sound processor for the University of Melbourne/Nucleus Limited multielectrode cochlear implant,'' J. Acoust. Soc. Am. **91**, 3367–3371.

Minitab, Inc. (**1998**). MINITAB STATISTICAL PACKAGE, Version 12.22 for Windows (State College, PA).

Moore, D. R. (**1990**). ''Auditory brainstem of the ferret: bilateral cochlear lesions in infancy do not effect the number of neurones projecting from the cochlear nucleus to the inferior colliculus,'' Dev. Brain Res. **54**, 125–130.

Moore, D. R. (**1994**). ''Auditory brainstem of the ferret: long term survival following cochlea removal progressively changes projections from the cochlear nucleus to the inferior colliculus,'' J. Comp. Neurol. **339**, 301–310.

Nadol, J. B. (**1997**). ''Patterns of neural degeneration in the human cochlea and auditory nerve: implications for cochlear implantation,'' Otolaryngol.-Head Neck Surg. **117**, 220–228.

Nelson, D. A., Van Tasell, D. J., Schroder, A. C., Soli, S., and Levine, S. (**1995**). ''Electrode ranking of 'place pitch' and speech recognition in electrical hearing,'' J. Acoust. Soc. Am. **98**, 1987–1999.

Pfingst, B. E., Glass, I., Spelman, F. A., and Sutton, D. (**1985**). ''Psychophysical studies of cochlear implants in monkeys: clinical implications,'' in *Cochlear Implants*, edited by R. A. Schindler and M. M. Merzenich (Raven, New York), pp. 305–321.

Plant, G. (**1984**). ''A diagnostic speech test for severely and profoundly hearing-impaired children,'' Aust. J. Audiol. **6**, 1–9.

Rajan, R., Irvine, D. R. F., Wise, L. Z., and Heil, P. (**1993**). ''Effect of unilateral partial cochlear lesions in adult cats on the representation of lesioned and unlesioned cochleas in primary auditory cortex,'' J. Comp. Neurol. **338**, 17–49.

Saada, A. A., Niparko, J. K., and Ryugo, D. K. (**1966**). ''Morphological changes in the cochlear nucleus of congenitally deaf white cats,'' Brain Res. **736**, 315–328.

Sarant, J. Z., Blamey, P. J., Cowan, R. S., and Clark, G. M. (**1997**). ''The effect of language knowledge on speech perception—what are we really assessing,'' Am. J. Otology **18**, S135–S137.

Shannon, R. V. (**1983**). ''Multichannel electrical stimulation of the auditory nerve in man. I. Basic psychophysics,'' Hear. Res. **11**, 157–189.

Shannon, R. V., Zeng, F.-G., and Wygonski, J. (**1998**). ''Speech recognition with altered spectral distribution of envelope cues,'' J. Acoust. Soc. Am. **104**, 2467–2476.

Shepherd, R. K., Baxi, J. H., and Hardie, N. A. (**1999**). ''Response of inferior colliculus neurons to electrical stimulation of the auditory nerve in neonatally deafened cats,'' J. Neurophysiol. **82**, 1363–1380.

Shepherd, R. K., Matsushima, J., Martin, R. L., and Clark, G. M. (**1994**). ''Cochlear pathology following chronic electrical stimulation of the auditory nerve. II. Deafened kittens,'' Hear. Res. **81**, 150–166.

Skinner, M. W., Clark, G. M., Whitford, L. A., Seligman, P. M., Staller, S. J., Shipp, D. B., Shallop, J. K., Everingham, C., Menapace, C. M., Arndt, P. L., Antogenelli, T., Brimacombe, J. A., Pijl, S., Daniels, P., George, C. R., McDermott, H. J., and Beiter, A. L. (**1994**). ''Evaluation of a new spectral peak coding strategy for the Nucleus 22 channel cochlear implant system,'' Am. J. Otology **15**, 15–27.

Skinner, M. W., Holden, L. K., Holden, T. A., Dowell, R. C., Seligman, P. M., Brimacombe, J. A., and Beiter, A. L. (**1991**). ''Performance of postlinguistically deaf adults with the wearable speech processor (WSP III) and mini speech processor (MSP) of the Nucleus multi-electrode cochlear implant,'' Ear Hear. **12**, 3–22.

Snyder, R. L., Rebscher, S. J., Cao, K., Leake, P. A., and Kelly, K. (**1990**). ''Chronic intracochlear electrical stimulation in the neonatally deafened cat. I. Expansion of central representation,'' Hear. Res. **50**, 7–34.

Tierney, T. S., Russell, F. A., and Moore, D. R. (**1997**). ''Susceptibility of developing cochlear nucleus neurons to deafferentation-induced death abruptly ends just before the onset of hearing,'' J. Comp. Neurol. **378**, 295–306.

Tong, Y. C., Clark, G. M., Blamey, P. J., Busby, P. A., and Dowell, R. C. (**1982**). ''Psychophysical studies for two multiple-channel cochlear implant patients,'' J. Acoust. Soc. Am. **71**, 153–160.

Tong, Y. C., and Clark, G. M. (**1985**). ''Absolute identification of electric pulse rates and electrode positions by cochlear implant patients,'' J. Acoust. Soc. Am. **77**, 1881–1888.

Trune, D. R. (**1982**). ''Influence of neonatal cochlea removal on the development of mouse cochlear nucleus. I. Number, size, and density of its neurons,'' J. Comp. Neurol. **209**, 409–424.

Wilson, B. S., Finley, C. C., Lawson, D. T., Wolford, R. D., Eddington, D. K., and Rabinowitz, W. M. (**1991**). ''New levels of speech recognition with cochlear implants,'' Nature (London) **352**, 236–238.

Zwolan, T. A., Collins, L. M., and Wakefield, G. H. (**1997**). ''Electrode discrimination and speech recognition in postlingually deafened adult cochlear implant subjects,'' J. Acoust. Soc. Am. **102**, 3673–3685.

Effects of pitch-shift velocity on voice F_0 responses

Charles R. Larson,[a] Theresa A. Burnett, and Swathi Kiran
Department of Communication Sciences and Disorders, Northwestern University, Evanston, Illinois 60208

Timothy C. Hain
Departments of Otolaryngology—Head and Neck Surgery, and Neurology, Northwestern University Medical School, Chicago, Illinois 60611

(Received 12 May 1999; revised 17 September 1999; accepted 11 October 1999)

Previous studies have shown that voice fundamental frequency (F_0) is modified by changes in the pitch of vocal feedback and have demonstrated that the audio–vocal control system has both open- and closed-loop control properties. However, the extent to which this system operates in closed-loop fashion may have been underestimated in previous work. Because the step-type stimuli used were very rapid, and people are physically unable to change their voice F_0 as rapidly as the stimuli, feedback responses might have been reduced or suppressed. In the present study, pitch-shift stimuli, consisting of a disparity between voice F_0 and feedback pitch of varying ramp onset velocities, were presented to subjects vocalizing a steady /ah/ sound to examine the effect of stimulus onset on voice F_0 responses. Results showed that response velocity covaried with stimulus velocity. Response latency and time of the peak response decreased with increases in stimulus velocity, while response magnitude decreased. A simple feedback model reproduced most features of these responses. These results strongly support previous suggestions that the audio-vocal system monitors auditory feedback and, through closed-loop negative feedback, adjusts voice F_0 so as to cancel low-level fluctuations in F_0. © *2000 Acoustical Society of America.*
[S0001-4966(00)05601-0]

PACS numbers: 43.70.Aj [AL]

INTRODUCTION

The study of the role of pitch feedback in the control of voice fundamental frequency (F_0) has been advanced through the use of the feedback pitch-shift technique (Burnett *et al.*, 1996; Burnett *et al.*, 1994; Elliott and Niemoeller, 1970; Kawahara, 1994; Kawahara, 1995; Kawahara and Aikawa, 1996; Kawahara *et al.*, 1993; Larson *et al.*, 1994; Larson *et al.*, 1995). There are several convincing lines of evidence for a closed-loop control component, perhaps used as a ''trim'' or fine-tuning mechanism for small magnitude F_0 fluctuations (Burnett *et al.*, 1998).

There are also several lines of evidence for open-loop control. Previously, it was reported that neither feedback loudness values between 65 and 85 dB SPL nor feedback loudness combined with pink masking noise alter subjects' responses to pitch-shift stimuli (PSS) (Burnett *et al.*, 1998). Also, the magnitude of the F_0 response was limited to about 50 cents despite variations in the PSS magnitude from 25 to 300 cents (1200 cents=1 octave). For this reason, it was suggested that the control of voice F_0 by pitch feedback operates primarily in an open-loop mode.

Nevertheless, because of the nature of our previous experimental paradigms, it is possible that we underestimated the amount of closed-loop control. In particular, because the onset of step-type stimuli used previously was very rapid, closed-loop-type responses might have been reduced or suppressed. In previous studies, the onset velocity of the PSS was on the order of 10 000 cents/sec. Such a rapid onset would be unlikely to occur naturally. If vocal tracking is organized similarly to ocular motor tracking, there might be two tracking modes—a ballistic mode and a continuous tracking mode, with ballistic changes (saccades) being used to null large target disparities and smooth, continuous tracking (so-called ''smooth pursuit'') used to null gradual or small target disparities. If this is true, the rapid onset of the PSS might have favored the use of a ballistic tracking mode. There is, in fact, good evidence for a second, longer latency response to audio-vocal responses from other studies of our group and others (Burnett *et al.*, 1998; Kawahara, 1995). Thus following this conjecture, small and/or slowly changing PSS might be more effective in eliciting early closed-loop-type responses than larger and/or rapidly changing PSS.

A second reason why the speed of onset might have influenced the response also derives from analogy to other biological tracking systems. It is common for tracking systems to respond to a weighted sum of an input signal and its derivatives (position, velocity, acceleration, etc.), that is, to have both tonic and phasic responses, as this behavior allows more rapid or accurate tracking than would otherwise be the case (Franklin *et al.*, 1994). In industrial control applications, a popular and effective controller style is called the ''PID'' (proportional-integral-derivative) controller (Callender *et al.*, 1936), which uses a weighted sum of a sensor signal, its derivative, and its integral to control a wide variety of processes. For vocal control then, the feedback-related response might be driven by a combination of the difference between

[a]Author to whom correspondence should be addressed; electronic mail: clarson@casbah.acns.nwu.edu

pitch of acoustic feedback and the intended pitch, as well as the velocity or integral of the difference signal. In the present study, ramps of disparity between vocalization and feedback, of varying ramp velocities, were presented to subjects vocalizing a steady /ah/ sound. Results were reproduced by a mathematical model and were consistent with a mixture of open-loop control and closed-loop control driven by a partially integrated difference signal, similar to that found in previous experiments using steps.

METHODS

Subjects: 35 normal young adults (30 females and 5 males, ages 18–22) served as subjects. All subjects passed a hearing screening at 20 dB (500–8 kHz), reported no neurological deficits, had no speech or voice disorder, and were not trained singers.

Apparatus and procedures: Subjects were seated in a sound-treated room, their voices recorded with an AKG boom-set microphone, amplified with a Mackie mixer (model 1202), processed for auditory feedback pitch shifting through an Eventide (SE 3000) Ultraharmonizer, mixed with 70 dB (SPL) pink masking noise, and presented to the subject over AKG earphones (Model K 270 H/C). Subjects maintained their vocal loudness at 70 dB SPL, aided by a Dorrough loudness monitor placed in front of them, resulting in voice feedback loudness of about 80 dB SPL. Although slight masking noise was presented, it was established previously that the presence or absence of masking noise has no effect on the responses. Moreover, if the feedback signal itself is presented at a lower level than 80 dB, subjects still respond to it despite the fact that they might be able to hear their own nonshifted, bone-conducted signal. For additional methodological details see Burnett *et al.*, 1998.

Subjects were instructed to vocalize for 5 sec, pause for a breath, then repeat. During each vocalization, one pitch-shift stimulus was presented at a random time from 500 to 2500 ms after vocalization onset. The pitch-shift stimulus, which we call a ''ramp-hold,'' was a continuously increasing difference (disparity) between the feedback pitch and the subject's F_0, starting at 0, and peaking at a magnitude of 100 cents. Then the 100-cent disparity between the subject's vocal output and the auditory feedback was held constant throughout the remainder of the subject's vocalization, despite any changes the subject might make to the voice F_0. After vocalization offset, the feedback disparity was reset to 0 prior to the next vocalization.

Figure 1 displays examples of voice F_0 responses, feedback pitch, and the disparity between F_0 and feedback for two stimulus velocity conditions. Following the ramp onset of the stimulus, the harmonizer system performed reasonably well in maintaining a 100-cent disparity between feedback and output. At the offset of the ramp-shaped stimulus, there is some overshoot and ringing, which is due to the harmonizer itself. Such overshoot was observed most frequently with faster stimulus velocities. Although regrettable, such overshoot probably did not affect the data significantly since its magnitude was small compared to the primary stimulus.

Thirty vocalizations (trials) of one ramp speed constituted one block. Five blocks were recorded: one for each of

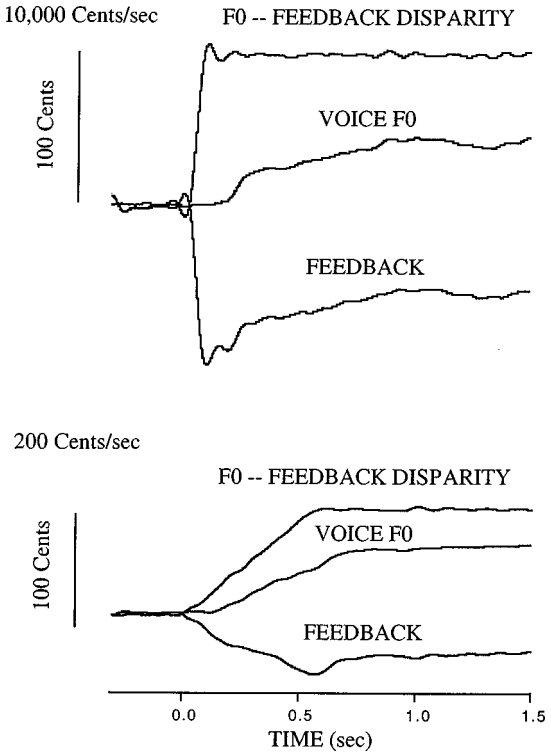

FIG. 1. Examples of feedback stimulus, voice F_0, and disparity between feedback and voice for two velocity conditions. See text for details.

the following ramp velocities: 10 000, 1000, 500, 200, and 100 cents/sec. The sequence of blocks was varied randomly. All five blocks of 30 trials contained both 15 increasing and 15 decreasing PSS (randomly presented), resulting in a total of ten experimental conditions.

During the experiment, the subject's voice, the feedback signal to the subject, and a control pulse triggering the harmonizer were digitized at a sampling frequency of 2 kHz. The subject's voice and the feedback signal were low-pass filtered at 200 Hz (females) or 100 Hz (males) prior to digitization.

The F_0 of the digitized acoustical signals was extracted using a software algorithm resulting in direct current (dc) signal whose voltage corresponded to F_0. This algorithm detected zero crossings, interpolated the time fraction between the two sample points that constituted each positive-going zero crossing, and calculated the reciprocal of the period defined by the center points to signify the voice F_0.[1] The resulting analog F_0 trace was then smoothed slightly with a five-point, binomial, sliding window. Signals were then time-aligned with the PSS onset and averaged with like trials of the same stimulus conditions. Response latency, peak time, and maximum response magnitude were automatically measured, while response onset velocities were measured by manually placing cursors at the points of onset and offset of maximum changes in slope of the averaged response traces (see Fig. 2). Voice and feedback signal magnitudes were converted to cents. The absolute value of the averaged response onset velocity was calculated by taking the ratio of the magnitude of the F_0 change to the duration of the change in voice F_0. These measures, as well as the latency measures, were charted and submitted to significance

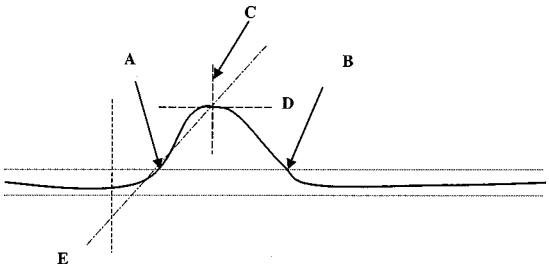

FIG. 2. Schematic illustration of measurements. Dotted horizontal lines=2 standard deviations of prestimulus mean F_0. Vertical dashed line=stimulus onset. A=latency, B=end point, C=time of peak response, D=response magnitude, E, double-dashed line intersecting latency point and time of peak response indicates method of response velocity calculation.

testing using a MANOVA and ANOVA in Data Desk (Data Description, Inc., Ithaca, NY).

RESULTS

A total of 324 valid responses out of a possible 350 were measured and analyzed. From this total, five responses changed in the same direction (1.5%) as the stimulus (''following'' response) and the remainder (98.5%) changed in the opposite direction (compensating response).

Figure 3 shows data from one subject, illustrating characteristic response patterns in each condition. The major findings are that, as the feedback pitch increased, voice F_0 decreased, and as feedback pitch decreased, voice F_0 increased (excepting the 15 instances of ''following'' responses). Moreover, the response velocity tended to vary with that of the stimulus, and response latency decreased with increasing stimulus velocity.

The box plots in Fig. 4 present quantitative measures of response velocity, magnitude, latency, and peak time as a function of stimulus velocity. Overall, the four dependent variables were significantly affected by stimulus velocity ($F=38$, $df=20,1042$, $p<0.005$). Significant differences between conditions are indicated by shared symbols below the boxes in Fig. 4. In general, response velocity increased with stimulus velocity, response latency and peak time decreased

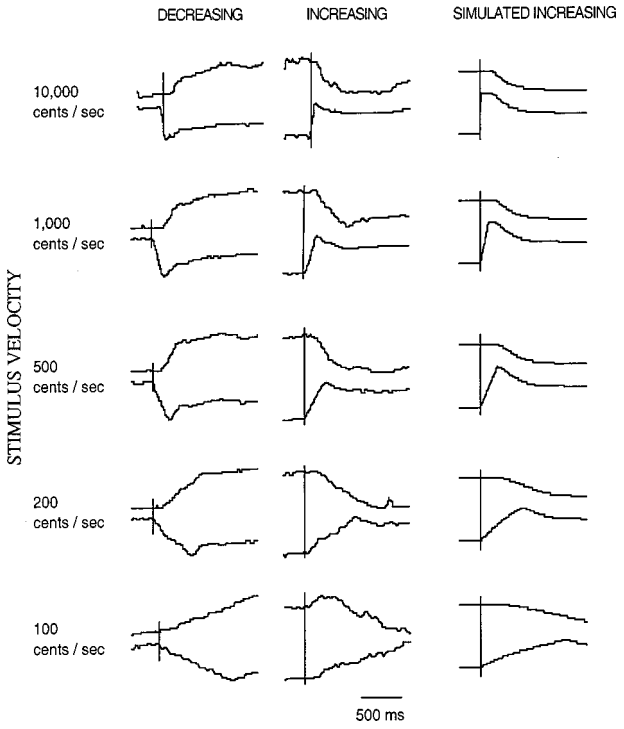

FIG. 3. Data from one subject, illustrating characteristic response patterns in each condition. Left column represents five conditions of decreasing pitch feedback (lower traces), with F_0 responses (upper traces). Middle column shows similar results for increasing pitch feedback. Right column shows simulation of increasing data using model of Fig. 5. Vertical scales are in relative units. See Fig. 4 for a more accurate depiction of response magnitudes.

with stimulus velocity, and response magnitude was significantly greater in the 200 cent/sec condition compared with the 10 000 cents/sec stimulus condition.

As with previous studies, responses were analyzed to determine if compensating responses differed from ''following'' responses. The relatively few numbers of ''following'' responses precluded statistical analysis. Nevertheless, ''following'' responses had a much smaller magnitude (18 vs 49 cents), slower velocity (51 vs 143), and longer latency (364 vs 243 ms) than compensating responses. It was also found that the latency of upward responses (217 ms) was less than

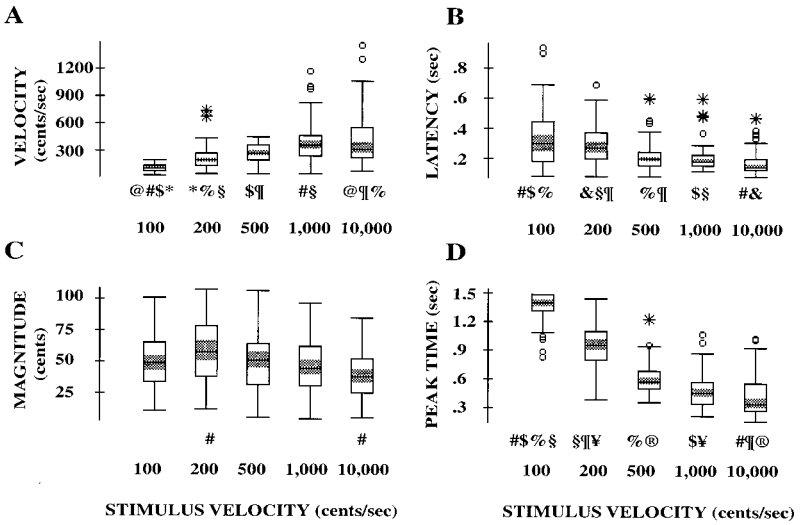

FIG. 4. Quantitative measures of response velocity, latency, magnitude, and peak time as a function of stimulus velocity (compensating responses only). Significant differences between conditions are indicated by shared symbols below the boxes ($p<0.005$). Box plot definitions: upper and lower limits of boxes (hinges) represent the 75th and 25th percentiles, respectively. Horizontal line through box is the median. Gray boxes =95% confidence limits. Whiskers extend to upper and lower limits of main body of data, defined as: high hinge+1.5 (high hinge–low hinge) and low hinge–1.5 (high hinge–low hinge). Points depicted as ''○'' extend beyond the above limits, unless they exceed high hinge +3.0 (high hinge–low hinge) or low hinge −3.0 (high hinge–low hinge), in which case they are shown as ''*'' (Data Desk, Data Description, Inc.).

the downward responses (273 ms), regardless of whether they were compensating or ''following'' types ($F=5.48$, $p<0.005$).

DISCUSSION

In the present study, we describe voice F_0 responses to ramp-hold-type pitch-shift stimuli with varying ramp velocities. Response timing, velocity, and magnitude were all affected by the changes in stimulus velocity. In general, with higher stimulus velocities, response velocity increased and responses occurred with shorter latencies. The changes in latency measures may have been an artifact of our measurement technique, see below. Response magnitude tended to remain relatively constant, although there was a difference between the 10 000 and 200 cent/sec stimulus conditions.

These results support the hypothesis that the audio-vocal system attempts to maintain stability of voice F_0 output by modulating F_0 to eliminate differences between an internal reference and the feedback pitch (compensating responses only) (Burnett *et al.*, 1998). During normal vocal events, e.g., singing, the system monitors auditory feedback and adjusts voice F_0 output so as to reduce the error between feedback and either an internal or external reference pitch, depending on the behavioral context. Thus the audio-vocal system is sensitive to direction of pitch feedback and is able to adjust the speed of F_0 changes according to the velocity of the feedback change.

Negative feedback tracking systems can have complex and nonintuitive results. In the Introduction, we proposed two different conjectures as to why stimulus velocity might modify response characteristics, involving mode switching and proportional-integral-derivative control, respectively. Accordingly, in an attempt to organize our observations, we propose a schematic for an F_0 tracking system in Fig. 5. Figure 5(a) shows a qualitative schematic for orientation purposes (Hain *et al.*, in press), and Fig. 5(b) shows a more explicit mathematical model representing the ''compensatory response'' part of Fig. 5(a), driven with the same input waveforms as used in this experiment.

In the model of Fig. 5(b), the input is the F_0 drive signal, derived from vocal motor cortex, and the output is vocalization (F_0). Two delays are postulated to represent latencies. ''Loop delay'' represents the sum of all delays between F_0 drive, F_0 generation, and auditory cortex. ''Copy delay'' represents a compensatory delay used to process desired F_0 signals so that they are temporally aligned with auditory input. The net result is for feedback responses to show a 130-msec delay.

After F_0 error is computed, the result is partially integrated using a low-pass filter (element ''filter''). The integration allows a corrected F_0 to continue even should auditory input be temporarily unavailable, and the low-pass aspects of the integrator, which make it function as an imperfect or ''leaky'' integrator, are helpful to explain velocity sensitivity aspects of the data, as discussed later. In a more complete model, the filter also incorporates a limiting nonlinearity to prevent response magnitude from exceeding 50 cents. While the nonlinearity is necessary to simulate other data sets related to F_0 feedback, it is not relevant to the simulation of this particular experiment and for this reason, details are not shown.

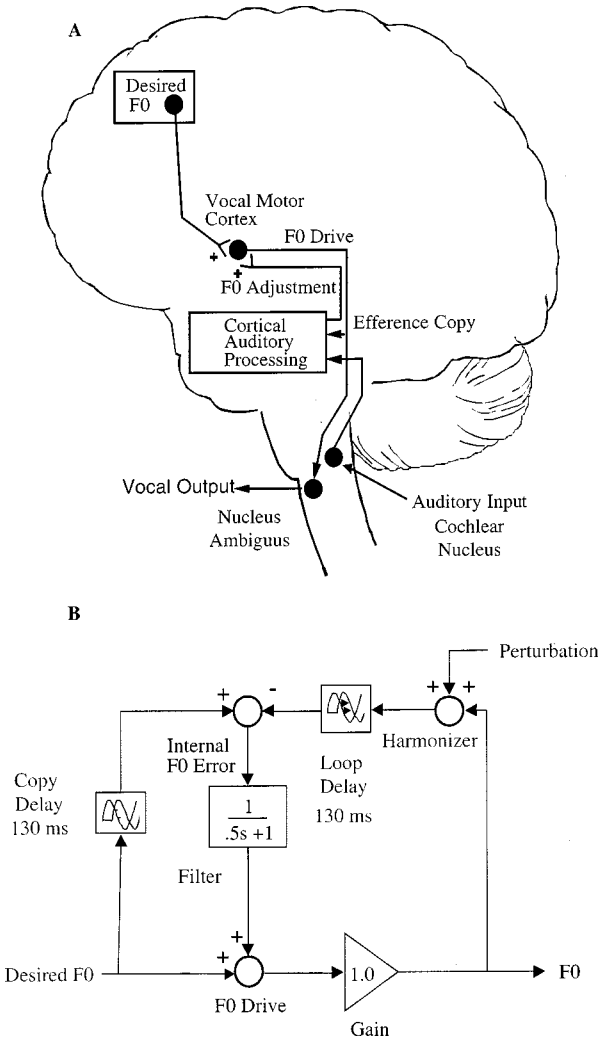

FIG. 5. (a) The auditory input and vocal motor output signal flow superimposed upon a sagittal drawing of the human cerebral cortex and brainstem. (b) Mathematical model of compensatory responses composed of an open-loop pathway (desired $F_0 \rightarrow$ Gain $\rightarrow F_0$), and a feedback pathway (upper portion of diagram). Dynamics are implemented with two delays, and a low-pass filter (Laplace notation), having a time constant of 0.5 sec. See text for details.

As shown in Fig. 3, this negative feedback model performs well in reproducing the main features of experimental data. While this mathematical model is doubtless oversimplified, it does demonstrate its feasibility and provides a quantitative hypothesis that can be tested in future experiments.

Returning to the discussion of features of the data, there was covariation in the timing between stimulus and response. The three measures of timing: latency, time of peak response, and velocity were all affected by the stimulus velocity. As stimulus velocity increased, the latency and peak response times decreased and the response onset velocity increased.

The finding that response velocity is correlated with stimulus velocity [Fig. 4(a)] is important for revealing other details about the system. Although there was not a perfect correlation between the timing of the feedback and output

signals, the fact that there was a relationship, indicates the system is sensitive to changes in feedback regardless of the rate of change. The system is not solely responding to sudden acoustical stimuli, such as the auditory–laryngeal reflex (Sapir *et al.*, 1983a,b), but rather may respond to very slow variations in feedback as well. During normal vocalization, the system could track variations in F_0 output regardless of the rate of change and adjust the output so as to reduce the error between the feedback and a referent signal.

Although response velocity was correlated with stimulus velocity, it was not directly proportional and rather appeared limited to an average value of approximately 150 cents/sec. In the context of the schematic of Fig. 5, this behavior can be directly attributed to the action of the low-pass filter. With a filter time constant of 0.5 sec, simulated response velocity was limited to a slope of 200 cents/sec, and the simulated velocity scaled quite similarly to the experimental data.

A decrease in response latency with increase in stimulus velocity, possibly artifactual, was noted [Fig. 4(b)]. This behavior may have been an artifact of our measurement methodology, because as stimulus velocity increased, the voice F_0 response velocity increased and hence exited the 2 SD criterion range (indicating response onset) at an earlier time for each progressively increasing stimulus velocity condition. Had it been possible to measure response onset more accurately, there may not have been any latency change as a function of stimulus velocity. Alternatively, in the context of the model of Fig. 5, this effect could be obtained by postulating nonlinear adjustments of the delay parameters as a function of a derivative of F_0 error.

The decreases in response magnitude with increases in stimulus velocity [Fig. 4(c)], although rather modest, support the hypothesis that lower velocity stimuli may be more effective in eliciting a corrective type of response than more rapid onsets. As the model of Fig. 5 did not reproduce this behavior, either the model is inaccurate, or the behavior is mediated by circuitry outside the model. Additionally, as response velocities did track the stimulus input, the findings suggest that while for small signal inputs there is a proportionality between input and output, the total response is limited to about 50 cents. The model of Fig. 5 also exhibited this behavior. This pattern is consistent with previous work (Burnett *et al.*, 1998), where it was established that the response magnitude did not increase beyond 25 to 50 cents even though stimulus magnitude increased from 25 to 300 cents.

In this study, 98.5% of the responses were compensating, regardless of whether the pitch-shift feedback signal increased or decreased in frequency. Moreover, the compensating responses were larger in magnitude and had faster onset velocities than the ''following'' responses. Thus the audio–vocal system is capable of generating different types of responses (compensating or ''following''), and the two types of responses differ in their magnitude and onset speed.

CONCLUSION

It was demonstrated in this study that when subjects hear their voice feedback pitch increase or decrease at different velocities, their voice F_0 compensates with a reciprocal change. Moreover the response onset velocity is proportional to that of the stimulus. These results support the hypothesis that the audio–vocal system monitors auditory feedback and controls voice F_0 through a closed-loop negative feedback system. This behavior was reproduced by a mathematical model incorporating a leaky integrator with a limiting nonlinearity that prevents response magnitude from exceeding 50 cents. These findings indicate the audio–vocal system is sensitive to changes in pitch of auditory feedback and is capable of adjusting the response output in accordance with the velocity of the input.

ACKNOWLEDGMENTS

This research was supported by NIH Grant No. DC02764-01. We gratefully acknowledge the assistance of Dr. Mary Kay Kenney and Ms. Danielle Lodewyck in the data analysis. Portions of this study have been reported in abstract form (Burnett *et al.*, 1997). We also acknowledge the significant contributions made by two anonymous reviewers of a previous draft of this manuscript.

[1]This method of F_0 extraction represents a change from previous studies (Burnett *et al.*, 1998). In the present study, a software algorithm was used to extract a dc F_0 signal from the original alternating current (ac) audio signal. Previously, a Kay Visi-Pitch was used for this purpose. By comparing the two different F_0 extraction methods, it became clear that the software algorithm was much more sensitive than the Visi-Pitch, and hence this allowed us to detect a greater proportion of valid responses than in our previous studies.

Burnett, T. A., Freedland, M. B., Larson, C. R., and Hain, T. C. (**1998**). ''Voice F_0 responses to manipulations in pitch feedback,'' J. Acoust. Soc. Am. **103**, 3153–3161.

Burnett, T. A., Larson, C. R., Freedland, M. B., and White, J. P. (**1996**). ''Differential effects of pitch shift duration on voice F_0 control,'' Speech Motor Control Conference, Amelia Island, Florida.

Burnett, T. A., Senner, J. E., Carrell T. D., and Larson, C. R. (**1994**). ''Changes in F_0 following auditory feedback pitch shifting,'' American Speech-Language and Hearing Association Conference, New Orleans.

Burnett, T. A., Senner, J. E., and Larson C. R. (**1997**). ''Voice F_0 responses to pitch-shifted auditory feedback; A preliminary study,'' J. Voice **11**, 202–211.

Callender, A., Hartree, D. R., and Porter, A. (**1936**). ''Time lag in a control system,'' Philos. Trans. R. Soc. London, Ser. A.

Elliott, L., and Niemoeller, A. (**1970**). ''The role of hearing in controlling voice fundamental frequency,'' Int. Audiology **IX**, 47–52.

Franklin, G. F., Powell, J. D., and Emami-Naeini, A. (**1994**). *Feedback Control of Dynamic Systems*, 3rd ed. (Addison-Wesley, Reading, MA).

Hain, T. C., Larson, C. R., Burnett, T. A., Kiran, S., and Singh, S. (in press). ''Instructing participants to make a voluntary response reveals the presence of two vocal responses to pitch-shift stimuli,'' Exp. Brain Res.

Kawahara, H. (**1994**). ''Interactions between speech production and perception under auditory feedback perturbations on fundamental frequencies,'' J. Acoust. Soc. Jpn. **15**, 201.

Kawahara, H. (**1995**). ''Hearing voice: Transformed auditory feedback effects on voice pitch control,'' *Computational Auditory Scene Analysis and International Joint Conference on Artificial Intelligence*, Montreal.

Kawahara, H., and Aikawa, K. (**1996**). ''Contributions of auditory feedback frequency components on F_0 fluctuations,'' J. Acoust. Soc. Am. **100**, 2825(A).

Kawahara, H., Hirai, T., and Honda, K. (**1993**). *Laryngeal Muscular Control under Transformed Auditory Feedback with Pitch Perturbation* (SP93-39) (The Institute of Electronics, Information and Communication Engineers).

Larson, C. R., Carrell T. D., Senner, J. E., and Burnett, T. A. (**1994**). ''Pitch shifting for the study of voice F_0 control,'' American Speech-Language and Hearing Association, New Orleans.

Larson, C. R., Carrell, T. D., Senner, J. E., Burnett, T. A., and Nichols, L. L.

(**1995**). ''A proposal for the study of voice F_0 control using the pitch shifting technique,'' in *Vocal Fold Physiology: Voice Quality Control*, edited by O. Fujimura and M. Hirano (Singular, San Diego), pp. 321–331.
Sapir, S., McClean, M., and Luschei, E. S. (**1983a**). ''Effects of frequency-modulated auditory tones on the voice fundamental frequency in humans,'' J. Acoust. Soc. Am. **73**, 1070–1073.
Sapir, S., McClean, M. D., and Larson, C. R. (**1983b**). ''Human laryngeal responses to auditory stimulation,'' J. Acoust. Soc. Am. **73**, 315–321.

Viscoelastic shear properties of human vocal fold mucosa: Theoretical characterization based on constitutive modeling

Roger W. Chan and Ingo R. Titze
National Center for Voice and Speech, Department of Speech Pathology and Audiology, The University of Iowa, Iowa City, Iowa 52242

(Received 8 March 1999; revised 24 August 1999; accepted 10 September 1999)

The viscoelastic shear properties of human vocal fold mucosa (cover) were previously measured as a function of frequency [Chan and Titze, J. Acoust. Soc. Am. **106**, 2008–2021 (1999)], but data were obtained only in a frequency range of 0.01–15 Hz, an order of magnitude below typical frequencies of vocal fold oscillation (on the order of 100 Hz). This study represents an attempt to extrapolate the data to higher frequencies based on two viscoelastic theories, (1) a quasilinear viscoelastic theory widely used for the constitutive modeling of the viscoelastic properties of biological tissues [Fung, *Biomechanics* (Springer-Verlag, New York, 1993), pp. 277–292], and (2) a molecular (statistical network) theory commonly used for the rheological modeling of polymeric materials [Zhu *et al.*, J. Biomech. **24**, 1007–1018 (1991)]. Analytical expressions of elastic and viscous shear moduli, dynamic viscosity, and damping ratio based on the two theories with specific model parameters were applied to curve-fit the empirical data. Results showed that the theoretical predictions matched the empirical data reasonably well, allowing for parametric descriptions of the data and their extrapolations to frequencies of phonation. [S0001-4966(99)06512-1]

PACS numbers: 43.70.Bk, 43.35.Mr, 43.75.Rs [AL]

INTRODUCTION

Previous studies have shown that the viscoelastic shear properties of the vocal fold mucosa (the cover, i.e., the epithelium plus the superficial layer of lamina propria) are not only important for the theoretical study of voice production, but also for the surgical management of vocal fold disorders (Chan, 1998; Chan and Titze, 1998, 1999a, 1999b; Gray *et al.*, 1999). Specifically, data on the elastic properties (elastic shear moduli) and viscous properties (viscous shear modulus and dynamic viscosity) of the vocal fold mucosa and other tissue layers are needed for the computer simulation of vocal fold vibration (Alipour and Titze, 1983, 1988; Berry and Titze, 1996; Titze and Story, 1999). Viscous properties of the mucosa are also important for determining phonation threshold pressure, an objective measure of vocal function and the ease of phonation (Titze, 1988, 1992). Clinically, a lowered phonation threshold pressure following a surgical procedure may be an indication of surgical success because it suggests that a smaller amount of energy is expended to sustain vocal fold oscillation (Chan and Titze, 1998, 1999a).

In our previous study, a parallel-plate rotational rheometer was employed to deform tissue samples of human vocal fold mucosa in small-amplitude sinusoidal oscillatory shear (Chan and Titze, 1999b). Data on elastic shear modulus, viscous shear modulus, dynamic viscosity, and damping ratio were quantified as a function of oscillation frequency. However, dynamic shear data were only obtained at relatively low frequencies (0.01–15 Hz) because of mechanical limitations of the rheometer (inertia of the rotating plate and sample inertia) (Chan and Titze, 1999b). As this was approximately an order of magnitude below typical frequencies of vocal fold oscillation (usually >100 Hz), extrapolations of the data to frequencies of phonation are needed so that the data become relevant for voice production.

In addition to data extrapolation, parametric descriptions of tissue shear properties are possible with constitutive modeling of the linear viscoelastic data. If dynamic shear data of the vocal fold mucosa agree with theoretical predictions based on a model with a specific set of parameters, viscoelastic behaviors of the vocal fold mucosa may be efficiently represented by the model's constitutive equations and the particular set of model parameters. Dynamic shear data can be conveniently reproduced, while other viscoelastic data (e.g., stress relaxation and strain creep data) may also be predicted from the constitutive equations and the model parameters.

This paper attempts to characterize the viscoelastic shear properties of human vocal fold mucosa with two commonly used constitutive models, namely a quasilinear viscoelastic model and a molecular model (statistical network model). The quasilinear viscoelastic theory proposed by Fung (1972, 1981, 1993) has been successfully applied to characterize the viscoelastic properties of many biological tissues, including the shear properties of soft tissues. The statistical network theory (the revised version of Zhu *et al.*, 1988, 1991) has been extensively applied to characterize the rheological properties of polymeric materials, as well as the extracellular matrices of connective tissues. Prior to a discussion of these theories, however, it is helpful to first review the traditional approach to viscoelastic modeling.

I. TRADITIONAL LINEAR VISCOELASTIC MODELS

Traditional models for viscoelasticity are one-dimensional lumped-element models made of basic elastic and viscous elements, namely linear springs and dashpots (or

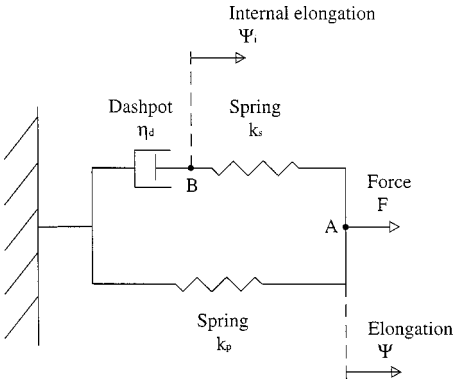

FIG. 1. The standard linear model (Kelvin model) of viscoelasticity.

dampers), respectively. Different combinations of springs and dashpots have been used to model different time-dependent and strain history-dependent viscoelastic behaviors, e.g., hysteresis, stress relaxation, and strain creep. The simplest combinations are the Maxwell model (a spring and a dashpot connected in series), the Voigt model (or Kelvin–Voigt model; a spring in parallel with a dashpot), and the standard linear model (or Kelvin model; a Maxwell model in parallel with a spring; see Fig. 1) (Barnes *et al.*, 1989; Ferry, 1980; Fung, 1993). Many other variations have also been developed by adding more springs and dashpots in series and in parallel. However, all of these models of discrete springs and dashpots are associated with a *discrete* spectrum of the relaxation function, as we shall illustrate below. The *relaxation function* of a model describes the gradual reduction of stress as a function of time, during the process of stress relaxation when a material sample is subject to a constant strain. For example, consider the standard linear model (Kelvin model) shown in Fig. 1. The series spring (k_s) and the parallel spring (k_p) are the elastic elements, while the dashpot (η_d) is the viscous element. The constitutive equation for the model is

$$\tau_s \dot{\sigma}_k + \sigma_k = E(\tau_p \dot{\varepsilon}_k + \varepsilon_k), \tag{1}$$

where σ_k is stress, ε_k is strain, both functions of time t (the subscript ''k'' stands for the Kelvin model). The ''dot over'' notation represents time differentiation. τ_s is a series time constant, τ_p is a parallel time constant, and E is an elastic modulus defined in terms of the spring constants (k_s and k_p) and the dashpot viscosity (η_d),

$$\tau_s = \frac{\eta_d}{k_s}, \quad \tau_p = \eta_d\left(\frac{k_p + k_s}{k_p k_s}\right), \quad E = \frac{k_p L_0}{A}, \tag{2}$$

where L_0 is the reference length and A is the cross-sectional area of the material sample described by the model. Consider the case when the model is subject to a step strain input $\varepsilon_k(t)$,

$$\varepsilon_k(t) = 0 \quad \text{when } t < 0,$$
$$= \varepsilon_0 \quad \text{when } t \geq 0, \tag{3}$$

where ε_0 is a constant. In response to this step strain, the model will undergo stress relaxation following a relaxation function $k(t)$ (Ferry, 1980; Fung, 1993),

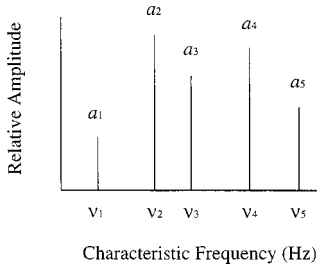

FIG. 2. A discrete spectrum of the relaxation function (after Fung, 1993).

$$k(t) = \frac{\sigma_k(t)}{\varepsilon_0} = E\left[1 + \left(\frac{\tau_p}{\tau_s} - 1\right)e^{-t/\tau_s}\right]. \tag{4}$$

It is clear that the relaxation function of the Kelvin model is an exponential function with a relaxation time constant τ_s. In fact, the relaxation functions of linear viscoelastic models are always composed of exponential terms, each with a time constant τ_i. By adding more springs and dashpots to a model, more derivative terms are introduced into its constitutive equation, yielding more exponential terms in the relaxation function. In general, the relaxation function can be expressed as a sum of N exponential terms with N characteristic time constants, each associated with a characteristic coefficient (Fung, 1993),

$$k(t) = \sum_{i=1}^{N} a_i e^{-t/\tau_i}, \tag{5}$$

where τ_i are the characteristic time constants and a_i are the characteristic coefficients associated with τ_i. A series of characteristic frequencies ν_i can be defined as the inverse of the characteristic time constants τ_i. The discrete function $a_i(\nu_i)$ is called the spectrum of the relaxation function, or *relaxation spectrum*, which is a density or weighting function of τ_i. This spectrum is *discrete* for models with a finite number of exponential terms, or a finite number of mechanical elements (see Fig. 2 for an example).

A discrete relaxation spectrum is not adequate for the description of viscoelastic properties of many biological soft tissues (Fung, 1993). In particular, traditional linear models with discrete relaxation spectra are associated with a finite number of peaks (at the characteristic frequencies) in their frequency-dependent damping characteristics. However, relatively flat or frequency-insensitive damping characteristics have been commonly observed for biological soft tissues, which can only be accurately described with a *continuous* relaxation spectrum (Fung, 1993). Continuous relaxation spectra have been implemented in the contexts of the quasilinear viscoelastic theory and the statistical network theory, which are summarized next.

II. THE QUASILINEAR VISCOELASTIC THEORY

Fung (1972, 1981, 1993) proposed a quasilinear viscoelastic theory (QLV) to describe commonly observed nonlinear viscoelastic properties of biological tissues, including nonlinear stress–strain characteristics, differences in stress response between loading and unloading (hysteresis phenomena), and the general dependence of stress on time and

strain history. Many biomechanics researchers have successfully applied the theory to model the time-dependent and strain history-dependent viscoelastic properties of various animal and human soft tissues in the passive state (i.e., relaxed state for contractile tissues), including tendons (Chun and Hubbard, 1986; Woo *et al.*, 1982, 1993), ligaments (Woo *et al.*, 1981, 1982, 1993), mesentery (Fung, 1972), aorta (Tanaka and Fung, 1974), cardiac muscles (Pinto and Fung, 1973; Pinto and Patitucci, 1980), smooth muscles (Price *et al.*, 1979), spinal cords (Bilston and Thibault, 1996), and articular cartilages (Simon *et al.*, 1984; Spirt *et al.*, 1989; Woo *et al.*, 1980; Zhu *et al.*, 1986). Fung first developed the theory in the context of stress relaxation, but formulations of the theory can be generalized for other modes of deformation, including oscillatory shear deformation. For instance, the theory has been used for the modeling of viscoelastic shear properties of articular cartilage (e.g., Mak, 1986; Spirt *et al.*, 1989; Zhu *et al.*, 1986). Let us first review Fung's basic formulations of the theory in the context of stress relaxation, with the use of a continuous relaxation spectrum. Applications of the theory to oscillatory shear deformation are then discussed.

A. Formulation of the theory

Consider a viscoelastic tissue sample subject to an ideal step increase of strain, with an infinite strain rate at time $t=0$,

$$\begin{aligned} \varepsilon(t) &= 0 \quad \text{when } t<0, \\ &= \varepsilon_0 \quad \text{when } t\geqslant 0, \end{aligned} \tag{6}$$

where $\varepsilon(t)$ is strain and ε_0 is a constant. The fundamental assumption of the QLV is that the stress relaxation function K is both time-dependent and strain history-dependent and can be expressed as the product of a function of time and a function of strain,

$$K \equiv K[\varepsilon(t),t] = G(t)\sigma^e[\varepsilon(t)], \tag{7}$$

where $K[\varepsilon(t),t]$ is the relaxation function, $G(t)$ is the *reduced relaxation function*, which is a function of time only, and $\sigma^e[\varepsilon(t)]$ is the *elastic response* (the superscript ''*e*'' stands for ''elastic''), which is defined as the instantaneous stress developed in the sample in response to the ideal step increase of strain. The reduced relaxation function $G(t)$ is defined as the time-dependent relaxation function normalized by the relaxation function at $t=0^+$,

$$G(t) = \frac{K(t)}{K(0^+)}, \quad G(0^+)=1. \tag{8}$$

This function is dimensionless and by definition dependent on time only. With this definition, the relaxation function K is equal to the elastic response $\sigma^e[\varepsilon]$ at $t=0^+$, which is an instantaneous stress response due to the sample's elastic component [cf. Eq. (7)].

Consider the strain history as a series of infinitesimal step increases in strain. According to the Boltzmann superposition principle of linearity, which states that the effects of sequential (step) changes in strain are additive, the stress contributions from all individual step strains at past times can be summed up to yield the stress at time t (Bird *et al.*, 1977a; Ferry, 1980; Fung, 1993). Therefore the stress σ at time t can be expressed in the form of a hereditary or convolution integral between the reduced relaxation function $G(t)$ and the rate of change of the elastic response $\sigma^e[\varepsilon]$,

$$\sigma(t) = \int_0^t G(t-\tau)\frac{\partial \sigma^e[\varepsilon]}{\partial \varepsilon}\frac{\partial \varepsilon}{\partial \tau}d\tau, \tag{9}$$

where $\sigma(t)$ is the overall stress response (Lagrangian stress) at time t due to a history of strain $\varepsilon(t)$ (Green's strain), for a time history beginning at $t=0$. It is clear that this constitutive equation is mathematically similar to that of the generalized linear viscoelastic model, i.e., $G(t)$ and $\sigma^e[\varepsilon]$ are playing the roles of relaxation function and strain in linear viscoelasticity, respectively (Bird *et al.*, 1977a; Ferry, 1980),

$$\sigma(t) = \int_0^t k(t-\tau)\frac{d\varepsilon}{d\tau}d\tau. \tag{10}$$

These analogies explain why the theory is ''quasilinear,'' which allows the simple yet powerful mathematical tools of analysis for linear systems to be applicable, e.g., in the context of oscillatory shear deformation. Prior to such linear analysis, however, a continuous relaxation spectrum has to be implemented so that biological tissues may be adequately described.

B. Continuous relaxation spectrum

The damping characteristics of many biological soft tissues have been found to remain relatively insensitive to the rate of deformation (frequency or strain rate), often across several decades of variation (Fung, 1993). As discussed in Sec. I, this frequency insensitivity cannot readily be accounted for by the finite number of exponential terms in the relaxation functions of traditional linear viscoelastic models. Rather, a generalized model with an infinite number of springs and dashpots must be considered. Equivalently speaking, a *continuous* relaxation spectrum corresponding to an infinite number of exponential terms in the relaxation function should be used. In order to accommodate such a continuous relaxation spectrum in the context of the QLV, Fung (1972, 1981) derived the following *generalized* reduced relaxation function:

$$G(t) = \left(1+\int_0^\infty S(\tau)e^{-t/\tau}d\tau\right) \Big/ \left(1+\int_0^\infty S(\tau)d\tau\right), \tag{11}$$

where $S(\tau)$ is the continuous relaxation spectrum, τ is a continuous variable playing the role of ''time constants'' in the exponential terms, while in fact there are no time constants in the continuous integrals. Note that $G(0^+)=1$, fulfilling the definition of the reduced relaxation function in Eq. (8). A specific continuous relaxation spectrum $S(\tau)$ was proposed by Fung (1972, 1981) to account for frequency-insensitive damping,

$$\begin{aligned} S(\tau) &= \frac{c}{\tau} \quad \text{for } \tau_1 \leqslant \tau \leqslant \tau_2, \\ &= 0 \quad \text{elsewhere}, \end{aligned} \tag{12}$$

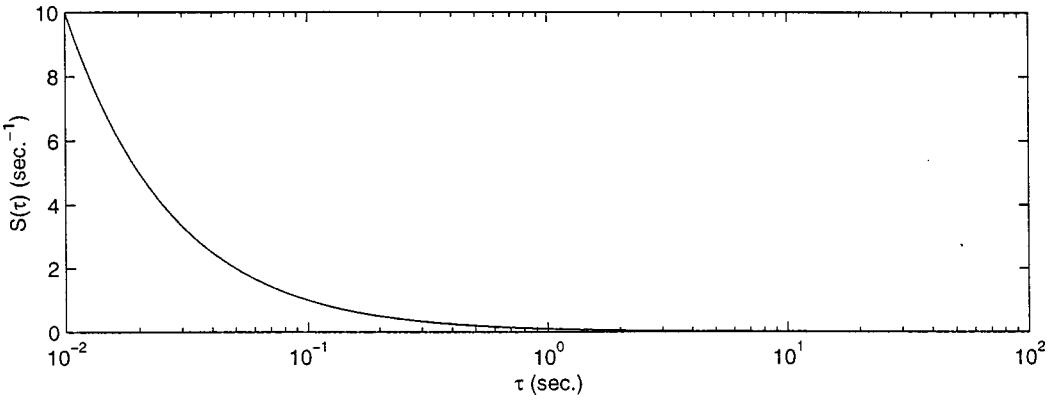

FIG. 3. A continuous spectrum of the relaxation function [cf. Eq. (12)].

where c is a dimensionless constant. The constants c, τ_1, and τ_2 are the model parameters of the QLV, to be adjusted for the theory to match the empirical data. Figure 3 shows a generic example of the continuous spectrum with $c=0.1$, $\tau_1=0.01$ s, and $\tau_2=100$ s, which results in a rather flat damping for $\tau_1 \leqslant 1/\omega \leqslant \tau_2$ (Fung, 1993). It has been shown repeatedly that the viscoelastic properties of many biological soft tissues are closely described by the QLV using this spectrum (for references, see the paragraph at the beginning of this section). A similar spectrum had also been used for the descriptions of hysteresis and damping in other fields of scientific studies, e.g., in the descriptions of dielectricity (Wagner, 1913), metal electromagnetism (Becker and Doring, 1939; Neubert, 1963), and airplane flutter (Theodorsen and Garrick, 1940).

Based on this specific continuous relaxation spectrum, the QLV can be applied to the experimental condition of oscillatory shear deformation, which is illustrated below.

C. Application to oscillatory shear deformation

Consider the condition of oscillatory shear deformation, where the overall stress response $\sigma(t)$ and the elastic response $\sigma^e(t)$ can be expressed as complex harmonic functions of time,

$$\sigma^*(t)=\sigma_0 e^{i(\omega t+\delta)}, \tag{13}$$

$$\sigma^{e*}(t)=\sigma_0^e e^{i\omega t}, \tag{14}$$

where σ_0 and σ_0^e are amplitudes, i is the imaginary number $\sqrt{-1}$, ω is angular frequency of oscillation, and δ is the phase shift between the two complex quantities. Since the elastic response is playing the role of strain [Eqs. (9) and (10)], $\sigma^{e*}(t)$ can be regarded as the sinusoidal input to a linear viscoelastic system, yielding a sinusoidal stress output $\sigma^*(t)$ at the same oscillation frequency but shifted by a phase of δ. Therefore, the definition of the complex shear modulus as the ratio of complex shear stress to complex shear strain in the context of linear viscoelasticity can be applied here (Chan and Titze, 1999b; Ferry, 1980; Fung, 1993),

$$\mu_q^*(\omega)=\frac{\sigma^*}{\sigma^{e*}}, \tag{15}$$

where $\mu_q^*(\omega)$ is the complex shear modulus of elasticity (the subscript ''q'' stands for the QLV). On substituting the complex overall stress and complex elastic response [Eqs. (13) and (14)] into the constitutive equation [Eq. (9)], $\mu_q^*(\omega)$ can be expressed in terms of the reduced relaxation function $G(t)$,

$$\mu_q^*(\omega)=\frac{\sigma_0}{\sigma_0^e}e^{i\delta}=i\omega\int_0^t G(t)e^{i\omega t}dt. \tag{16}$$

Substituting the continuous relaxation spectrum $S(\tau)$ [Eq. (12)] into the generalized reduced relaxation function $G(t)$ [Eq. (11)], and integrating from τ_1 to τ_2 with respect to τ, the reduced relaxation function becomes

$$G(t)=\frac{1+c[E_1(t/\tau_2)-E_1(t/\tau_1)]}{1+c\,\ln(\tau_2/\tau_1)}, \tag{17}$$

where $E_1(z)$ is the exponential integral function defined by

$$E_1(z)=\int_z^\infty \frac{e^{-t}}{t}dt \quad (|\arg z|<\pi). \tag{18}$$

With Eqs. (17) and (18), the integral in Eq. (16) can be evaluated by using Laplace transform. Using the Laplace transform for the exponential integral function $E_1(z)$ (Abramowitz and Stegun, 1964),

$$\mathcal{L}\{E_1(t/\tau)\}=\frac{1}{s}\ln(1+\tau s), \quad \tau>0, \tag{19}$$

the final expression for the complex shear modulus can be obtained (Fung, 1981, 1993),

$$\mu_q^*(\omega)=\frac{1+(c/2)[\ln(1+\omega^2\tau_2^2)-\ln(1+\omega^2\tau_1^2)]+ic[\tan^{-1}(\omega\tau_2)-\tan^{-1}(\omega\tau_1)]}{1+c\,\ln(\tau_2/\tau_1)}. \tag{20}$$

By definition, the real part of $\mu_q^*(\omega)$ is the elastic shear modulus μ_q, while the imaginary part is the viscous shear modulus $\omega\eta_q$,

$$\mu_q = \frac{1+\frac{c}{2}[\ln(1+\omega^2\tau_2^2)-\ln(1+\omega^2\tau_1^2)]}{1+c\ln(\tau_2/\tau_1)}, \tag{21}$$

$$\omega\eta_q = \frac{c[\tan^{-1}(\omega\tau_2)-\tan^{-1}(\omega\tau_1)]}{1+c\ln(\tau_2/\tau_1)}. \tag{22}$$

Once μ_q and $\omega\eta_q$ are computed, the dynamic viscosity η_q and the damping ratio ζ_q can be readily derived ($\eta_q = \omega\eta_q/\omega$ and $\zeta_q = \omega\eta_q/\mu_q$). These analytical expressions represent theoretical predictions of the viscoelastic shear properties of biological soft tissues based on the QLV. The three model parameters c, τ_1, and τ_2 can be adjusted to curve-fit these predictions to the empirical data of different tissues, including those of the vocal fold mucosa.

According to a sensitivity analysis of the QLV, changes of the model parameters c, τ_1, and τ_2 are critically related to the stress relaxation function and the frequency-dependent damping ratio predicted by the theory (Sauren and Rousseau, 1983). Their results showed that the parameter c indicates the amount of viscous effects present with respect to elastic effects, such that larger values of c correspond to a higher damping ratio across a wide range of frequency ($10^{-3}-10^{3}$ Hz), a more ''sharply tuned'' damping ratio curve (i.e., more frequency-sensitive), and an increase in stress relaxation magnitude and rate. The other model parameters τ_1 and τ_2 are ''time constants'' which define the range of the continuous relaxation spectrum and hence the frequency-insensitive range of the damping curve. The smaller τ_1 governs the ''fast viscous phenomenon,'' i.e., the high-frequency limit of the relatively flat range of the damping curve, analogous to the upper cutoff frequency of the frequency response of a bandpass filter. The larger τ_2 governs the ''slow viscous phenomenon,'' i.e., the low-frequency limit of the relatively flat range of damping, analogous to a lower cutoff frequency (Sauren and Rousseau, 1983). A decrease in τ_1 or an increase in τ_2 tends to expand the ''bandwidth'' of the damping curve, making it more ''broadly tuned'' or frequency-insensitive.

III. MOLECULAR THEORIES

The molecular structure of the vocal fold lamina propria has been studied considerably (see summary in Chan and Titze, 1998, 1999a, 1999b). As most of the molecular constituents found in the lamina propria extracellular matrix are biomacromolecules (or biopolymers), it seems logical to apply rheological molecular theories to describe the viscoelasticity of the vocal fold mucosa.

Molecular theories attempt to model the rheological properties of macromolecular or polymeric materials based on their molecular dynamics and kinetics. The viscoelastic properties of polymeric materials and polymers in solutions arise from both intramolecular and intermolecular interactions among the macromolecules, as well as intermolecular interactions between the macromolecules and the solvent (usually water) molecules (Bird *et al.*, 1977b; Ferry, 1980). Intramolecularly, there is a resting equilibrium state associated with each macromolecule in which the orientations of chemical bond vectors are distributed randomly, resulting in a state of minimum internal energy (Barnes *et al.*, 1989; Bird *et al.*, 1977b). When the macromolecule is deformed by an external force (or stress), the orientations of chemical bond vectors are changed and elastic energy is stored in the new orientations. Elastic recovery represents reorientation of the bond vectors back to the equilibrium state. On the other hand, resistance to flow and dissipation of internal energy (viscous behaviors) are caused by a molecule's interactions with other molecules and solvent molecules, which introduce frictional drag on the molecules and delay the process of bond vector reorientation (Barnes *et al.*, 1989; Bird *et al.*, 1977b). There are many types of molecular models, one of which is the transient network model or *statistical network model.*

A. Statistical network theory

The statistical network theory for the rheological modeling of polymeric fluids and materials has been developed extensively by Lodge (1968), Bird *et al.* (1977a, 1977b), De Kee and Carreau (1979), and Zhu and his co-workers (Zhu and Mow, 1990; Zhu *et al.*, 1988, 1991). Based on earlier analytical work by Lodge (1968) and De Kee and Carreau (1979), Zhu *et al.* (1988, 1991) described a network theory capable of relating the rheological properties of macromolecular materials to structural parameters defining a molecular network model of the material. In order to describe the transient non-Newtonian flow properties of concentrated macromolecular solutions not predicted by previous network theories (e.g., stress-overshoot and thixotropic responses[1] of concentrated proteoglycan solutions), Zhu *et al.* (1988, 1991) developed a nonlinear second-order constitutive equation for the network theory. This updated and extended version of the statistical network theory has been shown to closely describe the viscoelastic properties of some biopolymeric materials, including proteoglycan solutions (Zhu and Mow, 1990; Zhu *et al.*, 1988, 1991) and collagen-proteoglycan mixtures (Zhu *et al.*, 1996).

The theory assumes that polymeric materials form a macromolecular network through intermolecular interactions of chains of macromolecules, particularly physical entanglement. The network is composed of *chain segments* (or network segments) and *junction sites* (or interaction sites). A chain segment is defined as the molecular chain between two adjacent junction sites. A junction site is defined as a common point where molecular chains are constrained to coincide and where forces can be transferred between molecules. It is assumed that these junction sites are confined to local interactions only and that they are constrained to move as part of the continuum of macromolecules. They are *transient* junctions but not permanent bonds. During deformation, both chain segments and junction sites are created and lost continuously. At any given time, the network consists of a distribution of chain segments created at different past times. This distribution is a function of the history of strain, or *memory* of the network. A memory function is incorporated

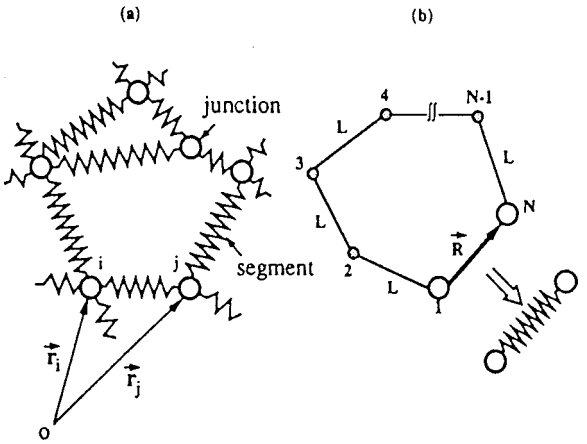

FIG. 4. Schematic of the statistical network model. (Reprinted from Zhu *et al.* (1991), with permission from Elsevier Science).

into the model's constitutive equation and is defined in such a way that it depends on the rate of creation and the rate of loss of junction sites (or chain segments), as illustrated in the next section.

B. Constitutive equation and complex shear modulus

Figure 4 shows the schematic of the molecular network model. Part (a) illustrates the connections between several chain segments and junction sites, while part (b) shows the details of one chain segment. The chain segment is modeled as a molecular chain which consists of N beads connected together with $(N-1)$ rigid rods of length L. Each chain segment can be described by a configuration vector $\mathbf{R}$, defined in terms of the junction position vectors $\mathbf{r}_i$ and $\mathbf{r}_j$, at the ith and jth junctions, respectively (Fig. 4). According to statistical mechanics, a time-average force is developed in the chain segment because of random molecular (Brownian) motions and the constrains of the chain at the junction sites. The time-average force makes the chain segment behave like a Hookean spring with a spring constant H (Bird *et al.*, 1977b),

$$H=\frac{3kT}{(N-1)L^2}, \tag{23}$$

where k is the Boltzmann constant ($=1.3807\times10^{-23}\,\mathrm{JK}^{-1}$) and T is the absolute temperature (in Kelvin). Elastic energy can be stored in these network springs during deformation. At any given point in time, the network consists of a continuous distribution of chain segments with various configuration vectors $\mathbf{R}$, which depends on the creation and loss of individual chain segments at different past times, i.e., the strain history, which is described by a *memory function*. The overall stress developed in the network is assumed to be the sum of individual stress contributions from all chain segments existing at the present time t and created at all past times t'. Using tensor notations, the second-order constitutive equation for the network developed by Zhu *et al.* (1988, 1991) is

$$\boldsymbol{\tau}=\int_{-\infty}^{t} m(t,t')\boldsymbol{\Gamma}(t,t')dt', \tag{24}$$

where $\boldsymbol{\tau}$ is the extra stress tensor, $m(t,t')$ is the memory function, and $\boldsymbol{\Gamma}(t,t')$ is the Finger strain tensor. Note that $\boldsymbol{\tau}$ includes the stress contributions from all chain segments but not the stress contributions from the interstitial fluid. In fact, the total stress tensor is given by $-p\mathbf{I}+\boldsymbol{\tau}$, where p is the interstitial fluid pressure associated with the fluid's incompressibility, and $\mathbf{I}$ is the identity tensor. The Finger strain tensor $\boldsymbol{\Gamma}$ is defined by

$$\boldsymbol{\Gamma}=\mathbf{F}^{-1}(\mathbf{F}^{-1})^T-\mathbf{I}, \tag{25}$$

where $\mathbf{F}$ is the deformation gradient relating a past junction position $\mathbf{r}_i'$ to the current junction position $\mathbf{r}_i(\mathbf{r}_i=\mathbf{F}^{-1}\mathbf{r}_i')$. Note that under this formulation it is assumed that elasticity only comes from the deformation of individual chain segments from past times t' to the present time t, as each chain segment behaves like an equivalent spring and the junction sites are confined to local interactions only (i.e., they are being considered as isolated points of entanglements). The memory function $m(t,t')$ in the constitutive equation is expressed as a function of the creation rate and the loss rate of the chain segments, which are assumed to be continuous functions of the second invariant[2] of the first Rivlin–Ericksen tensor[3] ($\boldsymbol{\Pi}_1$) as well as the second invariant of the second Rivlin–Ericksen tensor[3] ($\boldsymbol{\Pi}_2$),

$$m(t,t')=\int_0^{\infty} C(\boldsymbol{\Pi}_1,\boldsymbol{\Pi}_2,s)e^{-\int_{t'}^{t}[dt''/L(\boldsymbol{\Pi}_1,\boldsymbol{\Pi}_2,s)]}ds, \tag{26}$$

where C is the rate of creation and L is the rate of loss of chain segments (and junction sites), both continuous functions of $\boldsymbol{\Pi}_1$ and $\boldsymbol{\Pi}_2$. The second invariant of a tensor is an indication of the magnitude of the tensor, thus $\boldsymbol{\Pi}_1$ quantifies the rate of deformation of the network, while $\boldsymbol{\Pi}_2$ quantifies the accelaration of deformation. It becomes clear that the constitutive equation is indeed second order, because of the dependence of $m(t,t')$ on both $\boldsymbol{\Pi}_1$ and $\boldsymbol{\Pi}_2$ (see Appendix for the specific forms of the functions C and L). s is called the ''segment complexity,'' a spectral variable showing the diversity of chain segment types on a continuous scale, i.e., the distribution of the chain segment configuration vectors $\mathbf{R}$. With the above constitutive equation and memory function, Zhu *et al.* (1988, 1991) obtained the following expressions for the real part and the imaginary part of the complex shear modulus μ^* under small-amplitude oscillatory shear conditions,

$$\mu(\omega)=\int_0^{\infty}\frac{\eta(s)\lambda(s)\omega^2}{1+[\lambda(s)\omega]^2}ds, \tag{27}$$

$$\omega\eta(\omega)=\int_0^{\infty}\frac{\eta(s)\omega}{1+[\lambda(s)\omega]^2}ds, \tag{28}$$

where μ is the elastic shear modulus, $\omega\eta$ is the viscous shear modulus, $\lambda(s)$ is the network relaxation spectrum (with the dimension of time), and $\eta(s)$ is a function of $\lambda(s)$ (with the dimension of viscosity). They are given by

$$\lambda(s)=\frac{\lambda_0}{(1+s)^{\alpha}}, \tag{29}$$

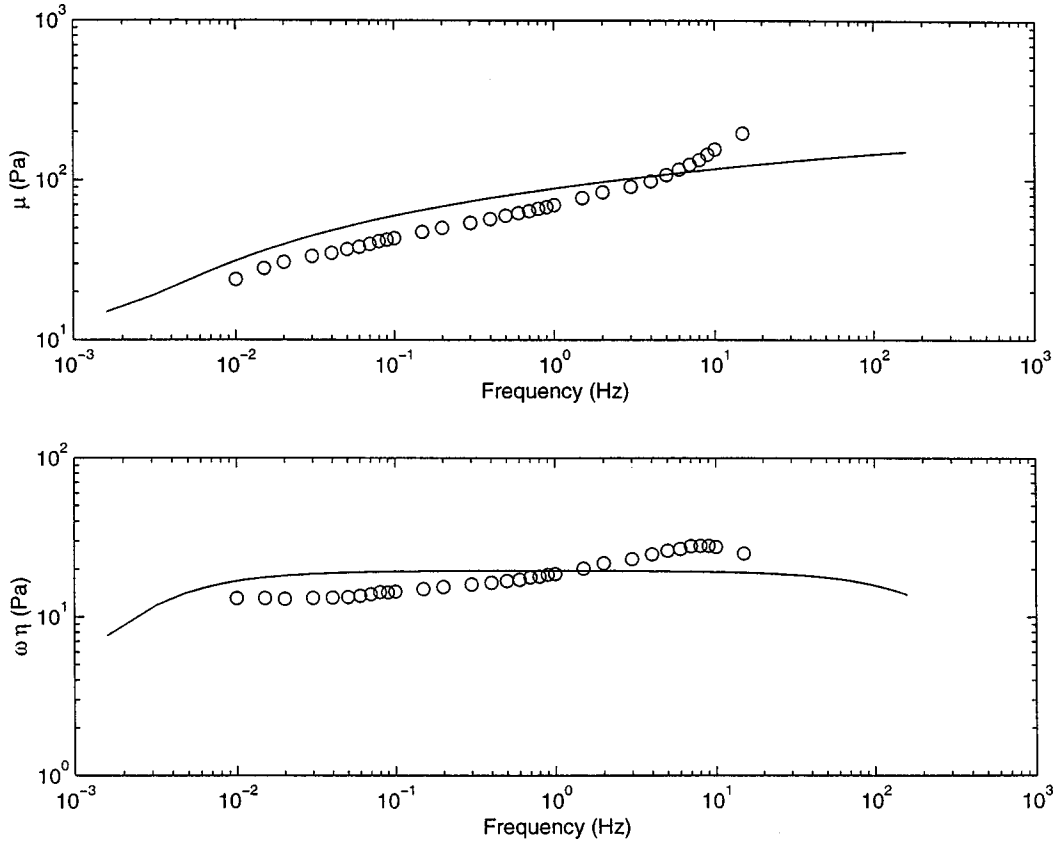

FIG. 5. Curve-fitting of elastic shear modulus μ (upper graph) and viscous shear modulus $\omega\eta$ (lower graph) of human male vocal fold mucosa by the QLV.

$$\eta(s)=\frac{\eta_0\lambda(s)}{\int_0^\infty \lambda(s)ds}, \tag{30}$$

where λ_0 is maximum relaxation time of the network, α is a spectral parameter greater than 1.0 (see below), and η_0 is zero shear-rate viscosity. Note that the network relaxation spectrum $\lambda(s)$ is *continuous*, as s is a continuous variable. This implementation of a continuous relaxation spectrum is similar to that in Fung's quasilinear viscoelastic theory, as discussed in Sec. II. This similarity suggests that the statistical network theory is capable of the description of a frequency-insensitive damping in biological soft tissues, like the QLV. The spectral parameter α can be expressed as

$$\alpha=1+\frac{\ln(\eta_0/\eta_\infty)}{\ln(1+s_0)}, \tag{31}$$

where η_∞ is infinite shear-rate viscosity and s_0 is the maximum number of ''segment complexity'' which defines the range of chain segments under shear deformation, such that $0\leqslant s\leqslant s_0$.

In summary, four independent parameters (η_0, η_∞, λ_0, s_0) and one dependent parameter (α) are needed for the description of linear viscoelastic shear properties using the present version of the statistical network theory. Among the shear properties, the elastic shear modulus μ and the viscous shear modulus $\omega\eta$ are computed from Eqs. (27) and (28), while the dynamic viscosity η and the damping ratio ζ can be derived from μ and $\omega\eta$. The model parameters can be adjusted to curve-fit these theoretical predictions to the empirical data of specific polymeric materials and tissues, including vocal fold mucosal tissues. Knowledge of the parameters provides insights on how the network model of molecules might interact and contribute to deformation and shear properties. Specifically, the total number of chain segments per unit volume (number density of chain segments) in the network, $N(t)$, may be expressed as a function of time and strain history. When the molecular network is at rest (momentarily), the chain segments are randomly oriented and a maximum of $N(t)$ is maintained. The maximum number density of chain segments (N_0) corresponds to this peak of $N(t)$ and is related to the model parameters by

$$N_0=\frac{\eta_0 s_0(\alpha-1)}{kT\lambda_0}. \tag{32}$$

This number denotes an estimation of the effective amount (or extent) of molecular interactions in a polymeric material (Zhu and Mow, 1990; Zhu *et al.*, 1991). In the next section, the viscoelastic data of human vocal fold mucosa reported previously (Chan and Titze, 1999b) are interpreted in terms of this index of molecular interactions, as well as the statistical network theory and the quasilinear viscoelastic theory in general.

IV. RESULTS AND DISCUSSION

A. Quasilinear viscoelastic theory

Figures 5 and 6 show the viscoelastic shear properties of human male vocal fold mucosa as a function of oscillation frequency, including the elastic shear modulus μ, the viscous shear modulus $\omega\eta$, the dynamic viscosity η, and the damping

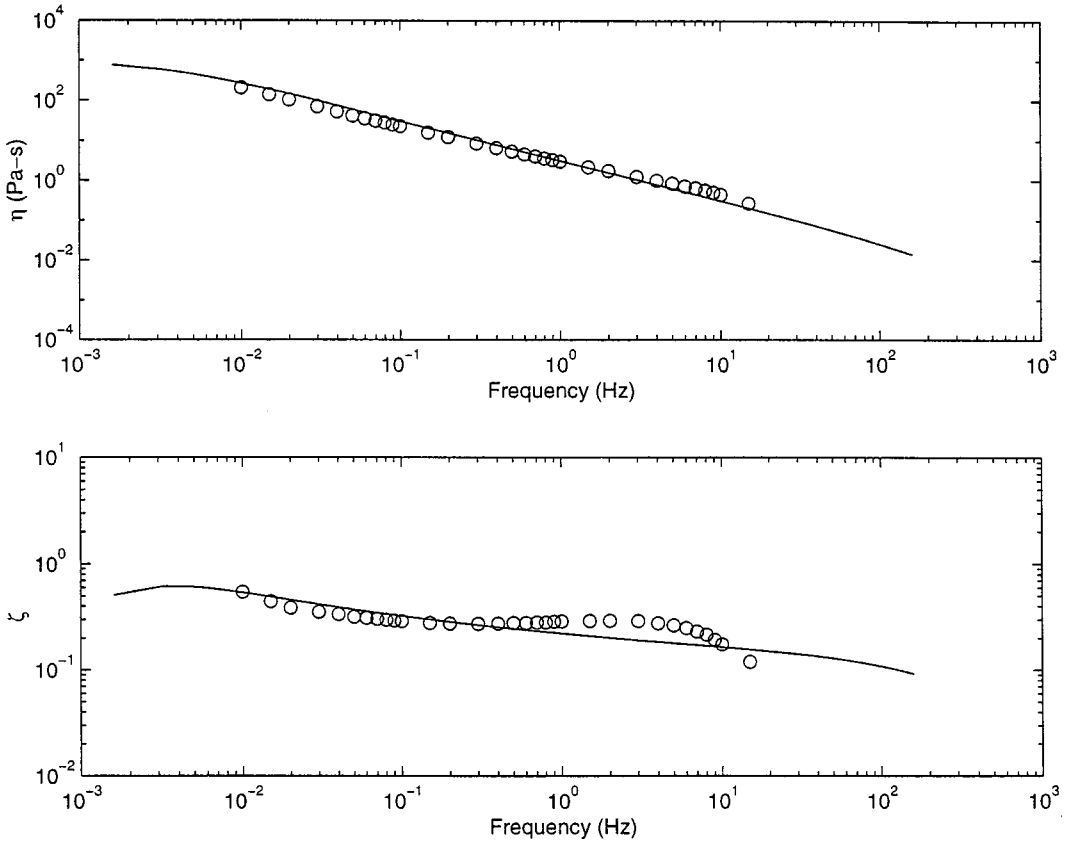

FIG. 6. Curve-fitting of dynamic viscosity η (upper graph) and damping ratio ζ (lower graph) of human male vocal fold mucosa by the QLV.

ratio ζ. The data points (in circles) represent the average empirical data of ten male subjects, while the solid lines are the ''best-fit'' theoretical curves based on the QLV. Agreement between the empirical data and the theoretical predictions for *each* of the shear properties was assessed by computing a correlation coefficient r as the goodness-of-fit statistic,

$$r=\sqrt{1-\frac{\Sigma_i(x_i-y_i)^2}{\Sigma_i(x_i-\overline{x})^2}}, \tag{33}$$

where x_i are the empirical data of one of the shear properties, y_i are the corresponding model predictions, and $\overline{x}$ is the average of x_i. Two steps were involved in the curve-fitting procedure: (1) Beginning with an initial set of parameters that correspond to the generic continuous relaxation spectrum shown in Fig. 3 ($c=0.1$, $\tau_1=0.01$ s, $\tau_2=100$ s), an approximate graphical fit was found empirically by varying the model parameters (c, τ_1, and τ_2) individually; (2) Next, the ''best fit'' was found by fine-tuning the model parameters until the sum of the correlation coefficients (for different shear properties) was maximized. For the average data of ten human male subjects, the best fit was achieved with $c=1.0$, $\tau_1=0.0005$ s, and $\tau_2=70$ s. Table I summarizes the correlations between theory and data using this set of model parameters.

Figures 5 and 6 show that in general the theoretical curves of the QLV fit the empirical data quite well, with reasonably high correlation coefficients in three of the four shear properties, except the viscous shear modulus $\omega\eta$ (Table I). There were certain discrepancies between theory and data, however, especially at higher frequencies (around 10–15 Hz). For instance, the empirical elastic shear modulus data (μ) appeared to be increasing with frequency at a slightly larger slope when higher frequencies were approached, yet the QLV predicted a smooth curve increasing only slowly with frequency, without any significant change of slopes (Fig. 5). The result was an underprediction of the data at high frequency. Predictions of the QLV did not match very well for $\omega\eta$ and ζ, again particularly at higher frequencies (Figs. 5 and 6), yielding correlation coefficients of only 0.2453 and 0.6596, respectively. The viscous shear modulus $\omega\eta$ was actually slightly increasing with frequency across the whole frequency range, as opposed to the very flat (frequency-independent) curve predicted by the QLV. This discrepancy was clearly shown by the low correlation coefficient (0.2453). Meanwhile, there was an excellent match between theory and data for η (Fig. 6), whose correlation coefficient was higher than 0.9.

TABLE I. Correlation coefficients of curve-fitting with QLV modeling of human male vocal fold mucosa (cf. Figs. 5 and 6).

Shear properties	r
μ	0.8584
$\omega\eta$	0.2453
η	0.9069
ζ	0.6596

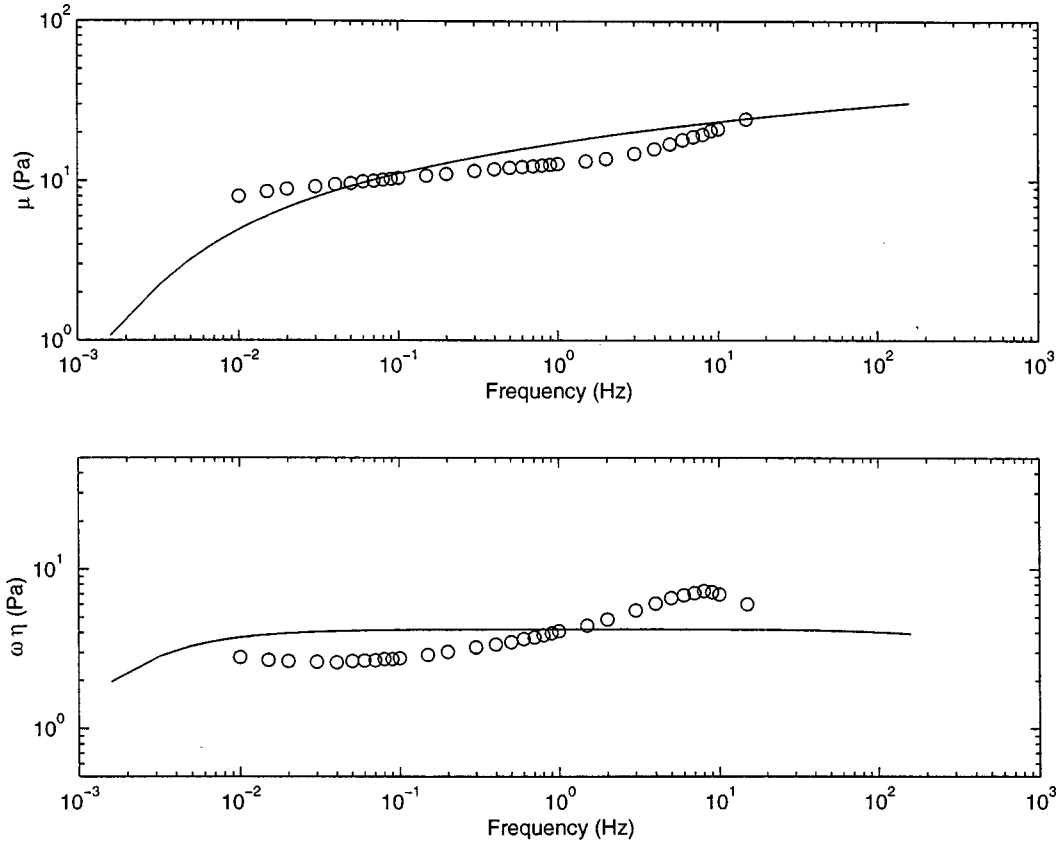

FIG. 7. Curve-fitting of elastic shear modulus μ (upper graph) and viscous shear modulus $\omega\eta$ (lower graph) of human female vocal fold mucosa by the QLV.

Figures 7 and 8 show the average empirical data for ten female subjects (in circles) and the best-fit theoretical predictions of μ, $\omega\eta$, η, and ζ based on the QLV. A similar curve-fitting procedure as described above was performed. The best fit was achieved with $c=10$, $\tau_1=0.0001$ s, and $\tau_2=90$ s. Table II shows the correlations between theory and data associated with this set of model parameters.

Comparing with the results for the male data, the theoretical curves of the QLV generally fit the female data less well, with lower correlation coefficients across all shear properties (Table II). Discrepancies between theory and data were quite significant for $\omega\eta$ and ζ, where only a general trend with an approximate slope was predicted in each case. The theory failed to closely predict the course of slope changes across the frequency range, yielding rather low correlation coefficients (0.2223 and 0.5951). Both $\omega\eta$ and ζ actually showed a ''peak'' at around 10 Hz, which was more prominent than the ''peak'' observed in the male data and hence a larger deviation from the flat curves predicted by the QLV. On the other hand, there was a much better match between theory and data for η (Fig. 8), where the correlation coefficient was again the highest.

Differences in the model parameters for achieving best fits for the male and the female data may be interpreted in terms of the findings of the sensitivity analysis of the QLV (Sauren and Rousseau, 1983). Recall that the parameter c indicates the relative amount of viscous effects, where a larger c corresponds to a higher damping ratio and a more sharply tuned damping curve (i.e., more frequency-sensitive). Also, recall that the other parameters τ_1 and τ_2 define the range of the continuous relaxation spectrum and the relatively frequency-insensitive range of the damping curve. A decrease in τ_1 or an increase in τ_2 is associated with a broader or more flat damping curve. Our findings showed that a larger value of c was obtained for modeling the female data ($c=10$) than for the male data ($c=1.0$), suggesting a higher and a more frequency-sensitive damping ratio for female than for male. On the other hand, the female data were modeled with a smaller τ_1 and a larger τ_2 ($\tau_1=0.0001$, $\tau_2=90$ s), than the male ($\tau_1=0.0005$, $\tau_2=70$ s), suggesting a less frequency-sensitive damping ratio curve. Thus it seemed that the model parameters of the QLV were apparently capable of offsetting the effects of one another on the frequency sensitivity of the damping ratio, yielding a damping ratio with similar frequency dependence for both male and female. It also seemed that the QLV was capable of predicting a larger damping ratio for female based on the magnitude of the continuous relaxation spectrum, i.e., a larger parameter c. These theoretical predictions on the damping ratio of male and female vocal fold mucosal tissues indeed agreed with their empirical data, where (1) ζ was found to be larger for female at higher frequencies, and (2) there was a comparably flat range of ζ for both male and female data (cf. Chan and Titze, 1999b).

B. Statistical network theory

Figures 9 and 10 show the average empirical data for ten male subjects (in circles) and the theoretical predictions of viscoelastic shear properties (μ, $\omega\eta$, η, and ζ) based on the

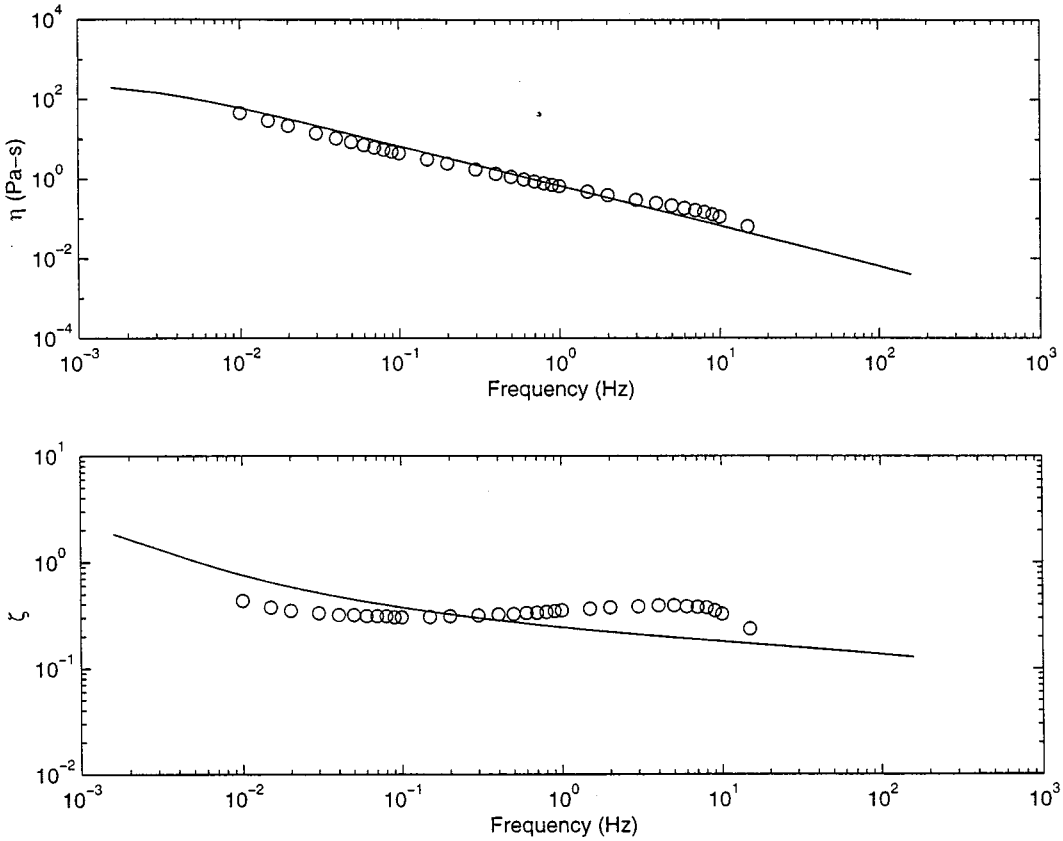

FIG. 8. Curve-fitting of dynamic viscosity η (upper graph) and damping ratio ζ (lower graph) of human female vocal fold mucosa by the QLV.

statistical network theory. The ''best fit'' between the theoretical curves and the empirical data was again determined empirically in a way similar to that described for the QLV, i.e., by adjusting the model parameters individually until the correlation coefficients were maximized. For the average data of ten human male subjects, the best fit was achieved with the four independent model parameters $\eta_0 = 3.2 \times 10^7$ Pa-s, $\eta_\infty = 0.32$ Pa-s, $\lambda_0 = 10^8$ s, $s_0 = 100$, and with $\alpha = 4.991\,38$. Table III summarizes the correlations between theory and data with a list of correlation coefficients for the shear properties.

It is observed that theoretical curves of the statistical network theory generally fit the empirical data quite well, with all correlation coefficients higher than 0.7 (Table III). Similar to the case of the QLV, there were some discrepancies between theory and data at higher frequencies (around 10–15 Hz), especially for μ and $\omega\eta$. The empirical μ data appeared to be increasing with frequency at a slightly larger slope at high frequency than that at lower frequencies, yet a smooth curve was predicted with a slightly smaller slope at high frequency than that at lower frequencies (Fig. 9). The result was an underprediction of the empirical data above 10 Hz. This relative disagreement between theory and data at higher frequencies was similar to the deviation observed for the QLV. Also similar to what was observed for the QLV, predictions of the statistical network theory did not match too well with the empirical $\omega\eta$ and ζ data, again particularly at higher frequencies (Figs. 9 and 10). However, curve-fitting based on the statistical network theory seemed to be better than the fit based on the QLV (cf. Figs. 5 and 6). In fact, correlation coefficients associated with the best fit of the statistical network theory were 0.7547 for $\omega\eta$ and 0.7265 for ζ, compared to only 0.2453 and 0.6596, respectively, for the QLV.

TABLE II. Correlation coefficients of curve-fitting with QLV modeling of human female vocal fold mucosa (cf. Figs. 7 and 8).

Shear property	r
μ	0.6328
$\omega\eta$	0.2223
η	0.8587
ζ	0.5951

Figure 9 also shows that the statistical network theory was more capable of predicting the slightly increasing trend of $\omega\eta$ with frequency, compared to the QLV, which predicted a very flat or frequency-independent $\omega\eta$ curve. Predictions of ζ based on the statistical network theory (Fig. 10) also showed the decreasing trend of the data at high frequency (>5 Hz) better than those of the QLV. Meanwhile, the theory matched the empirical dynamic viscosity data (η) as well as the QLV, with an almost excellent match and a correlation coefficient higher than 0.97.

Figures 11 and 12 show the average empirical data for ten female subjects (in circles) and the best-fit theoretical curves of μ, $\omega\eta$, η, and ζ based on the statistical network theory. The best fit was achieved with the model parameters $\eta_0 = 2.0 \times 10^6$ Pa-s, $\eta_\infty = 0.02$ Pa-s, $\lambda_0 = 2.5 \times 10^7$ s, s_0

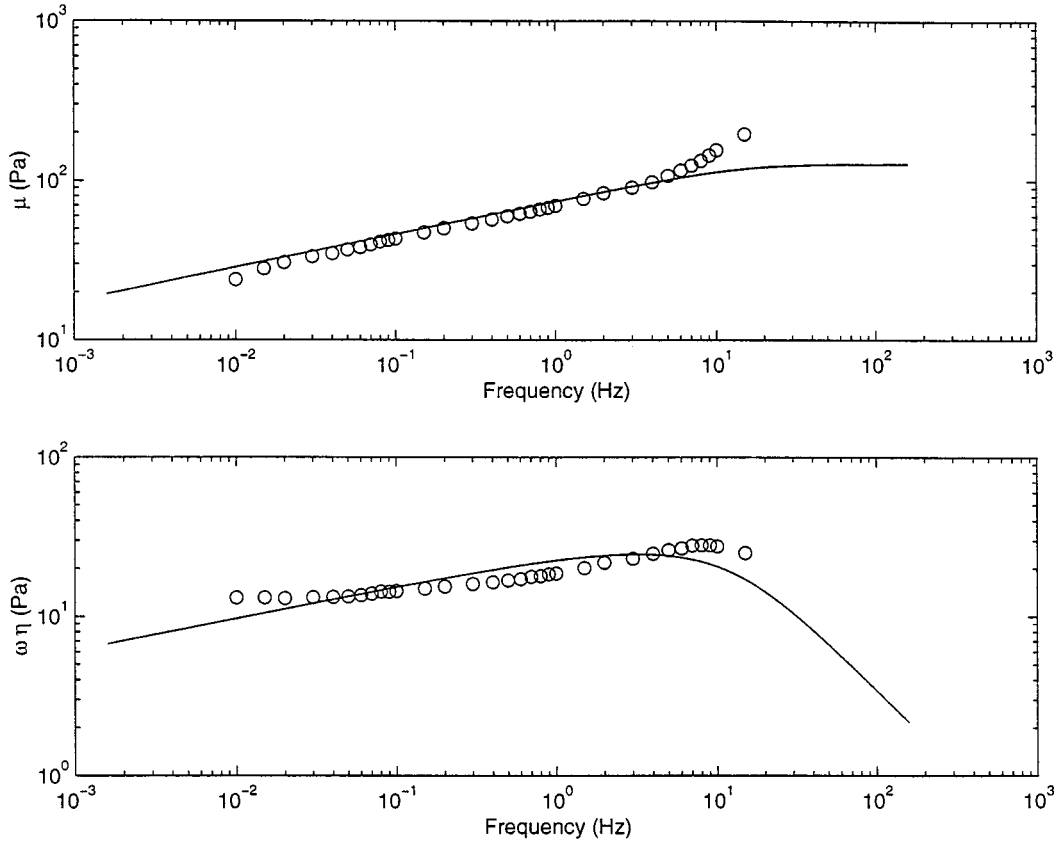

FIG. 9. Curve-fitting of elastic shear modulus μ (upper graph) and viscous shear modulus $\omega\eta$ (lower graph) of male vocal fold mucosa by the statistical network model.

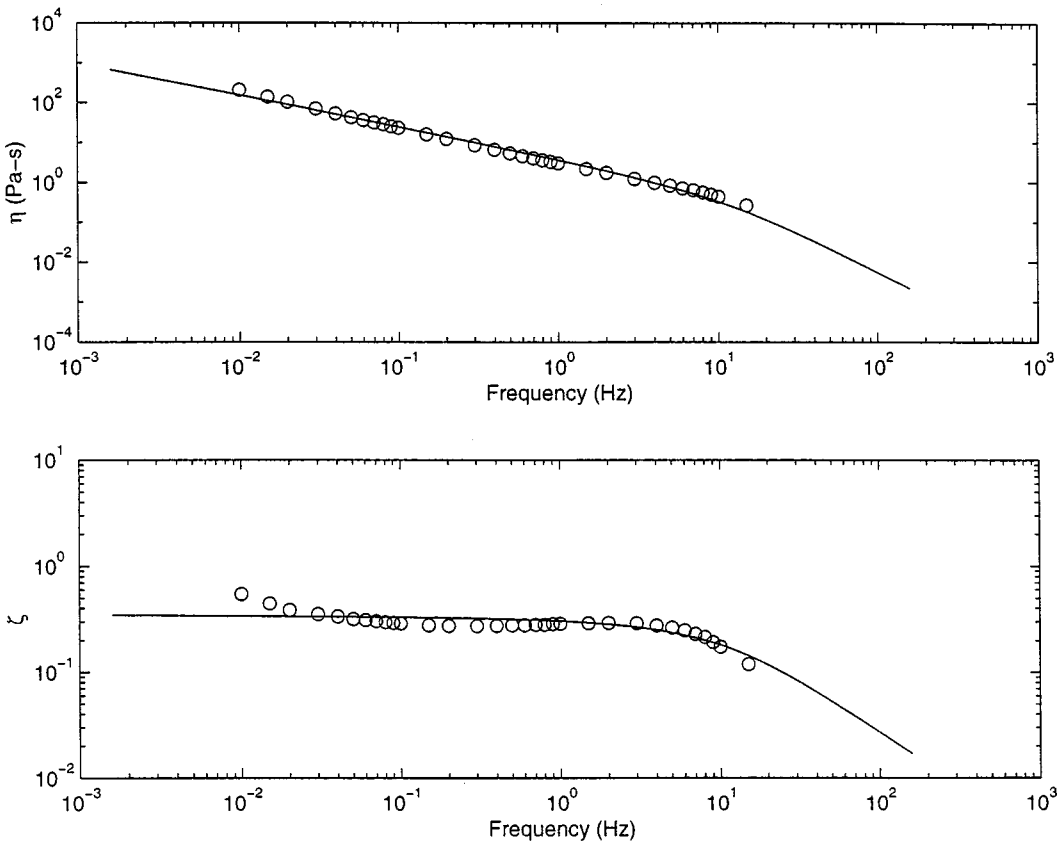

FIG. 10. Curve-fitting of dynamic viscosity η (upper graph) and damping ratio ζ (lower graph) of male vocal fold mucosa by the statistical network model.

TABLE III. Correlation coefficients of curve-fitting with statistical network modeling of human male vocal fold mucosa (cf. Figs. 9 and 10).

Shear property	r
μ	0.9042
$\omega\eta$	0.7547
η	0.9757
ζ	0.7265

$=100$, and with $\alpha=4.991\,38$. Table IV lists the correlation coefficients for the female data using this set of model parameters.

Comparing with the results of curve-fitting for the male data, Figs. 11 and 12 show that predictions of the statistical network theory fit the female data even better than the male data, with all correlation coefficients higher than 0.8 (Table IV). In particular, the theoretical curves matched the female μ and $\omega\eta$ data rather closely at high frequency, compared to the male data (cf. Figs. 9 and 11). This finding was in direct contrast with that of the QLV, where the agreement between theory and data was better for the male data than for the female data. Also contrary to what was observed for the QLV, predictions of the statistical network theory matched quite well with the female $\omega\eta$ and ζ data (Figs. 11 and 12). Compared to the QLV, the theory was again more capable of predicting the slightly increasing trend of $\omega\eta$ with frequency and the decreasing trend of ζ at high frequency, similar to what was observed for the male data. Indeed, there seemed to be actually a better match between theory and data for $\omega\eta$ and ζ for the female than the male data, both in terms of visual comparisons and correlation coefficients. Meanwhile, the statistical network theory matched the female η data as well as the male data, with a good agreement and a correlation coefficient higher than 0.95.

With the two sets of model parameters known for the average male and the average female vocal fold mucosa, the maximum number density of chain segments (N_0) in the molecular network model can be computed according to Eq. (32). N_0 is an indication of the extent of molecular interactions of the network. Zhu and his colleagues (1991, 1996) found that N_0 increases with the concentration of proteoglycan solutions, as well as the relative content of collagen in collagen-proteoglycan mixtures. They also found that N_0 is positively correlated with the shear elasticity and viscosity of the proteoglycan solutions and the collagen-proteoglycan mixtures, supporting the hypothesis that the viscoelastic shear properties of polymeric materials increase with the extent of molecular interactions.

For the male vocal fold mucosa, $N_0=2.9841\times10^{22}\,\mathrm{m}^{-3}$, while for the female vocal fold mucosa, $N_0=7.4602\times10^{21}\,\mathrm{m}^{-3}$, which was approximately four times smaller than that of the male. These findings suggested that the male vocal fold mucosa has effectively four times more molecular interactions sites than the female mucosa, in the language of the statistical network theory. This may be related to the molecular finding that the male vocal fold lamina propria has higher contents (concentrations) of certain molecular constituents than the female, particularly *hyaluronic*

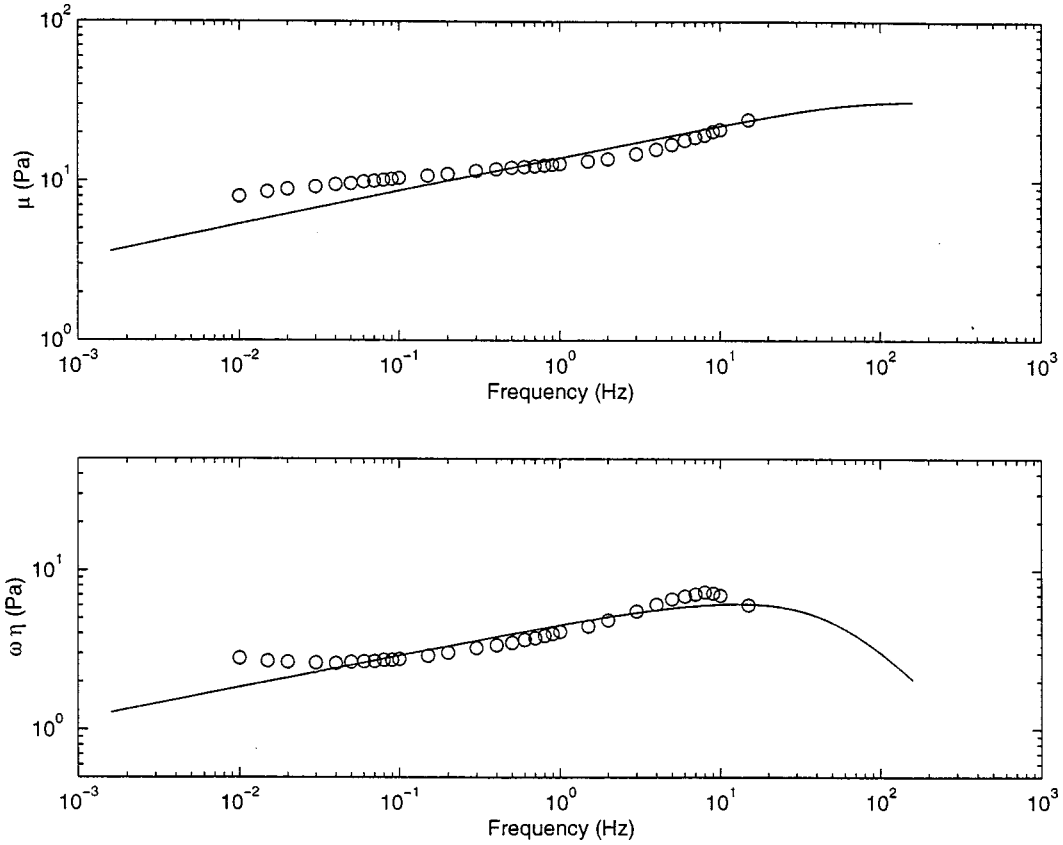

FIG. 11. Curve-fitting of elastic shear modulus μ (upper graph) and viscous shear modulus $\omega\eta$ (lower graph) of female vocal fold mucosa by the statistical network model.

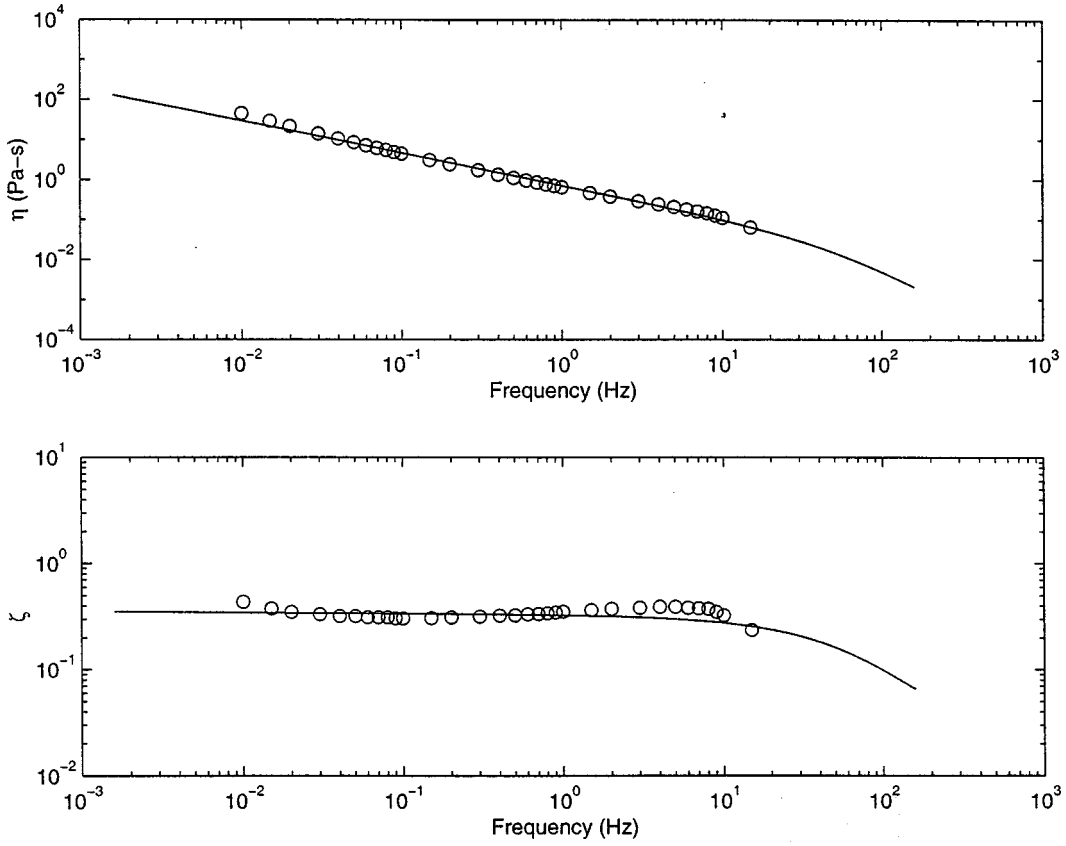

FIG. 12. Curve-fitting of dynamic viscosity η (upper graph) and damping ratio ζ (lower graph) of female vocal fold mucosa by the statistical network model.

acid, and possibly collagen, elastin, and proteoglycans (see Chan and Titze, 1999a, 1999b; Gray *et al.*, 1999). Such molecular differences and the larger number of interaction sites in the male vocal fold mucosa could be responsible for the gender-related difference in viscoelastic shear properties reported previously (Chan and Titze, 1999b).

Zhu *et al.* (1991, 1996) also found that the parameters η_0, η_∞, and λ_0 increase with increasing concentration of proteoglycan solutions, while η_0 and λ_0 increase with the relative content of collagen in collagen-proteoglycan mixtures. A comparison between the model parameters for the male and the female vocal fold mucosa showed that η_0, η_∞, and λ_0 were all larger for male than for female. This finding further supported the hypothesis that the male vocal fold mucosa can be modeled as a molecular network with a larger number of interaction sites than the female mucosa, as a result of higher concentrations of key molecular constituents like hyaluronic acid and proteoglycans. It also suggested that the higher elasticity and viscosity of the male vocal fold mucosa may be partly due to a higher relative content of *collagen* in the lamina propria extracellular matrix. Higher concentration of hyaluronic acid in the male vocal fold lamina propria has been reported (Hammond *et al.*, 1997), but further studies on the relative content of other molecular constituents are needed to elucidate their roles in the determination of viscoelastic shear properties in male versus female vocal fold mucosa.

TABLE IV. Correlation coefficients of curve-fitting with statistical network modeling of human female vocal fold mucosa (cf. Figs. 11 and 12).

Shear property	r
μ	0.8989
$\omega\eta$	0.9370
η	0.9515
ζ	0.8395

C. Theoretical extrapolations of tissue shear properties

Based on the two theories, extrapolations of the theoretical predictions of the viscoelastic shear properties to frequencies of phonation (>100 Hz) are possible, which allow for the predictions of shear properties at frequencies relevant to voice production. It has been shown analytically that the effective amount of damping in small-amplitude vocal fold oscillation depends critically on the viscous shear properties of the vocal fold mucosa (Chan, 1998; Titze, 1988). Specifically, it was shown that phonation threshold pressure is directly related to the viscous shear modulus $\omega\eta$ (or the dynamic viscosity η) of the vibrating mucosa (cover). On the other hand, the damping ratio ζ of the vocal fold mucosa is critical in determining whether or not self-sustained vocal fold oscillation is at all possible, i.e., whether oscillation would remain underdamped ($\zeta<1.0$) across different frequencies (Titze and Chan, 1998).

For both male and female vocal fold mucosa, extrapolation of the theoretical curves of $\omega\eta$ to a frequency above 100 Hz based on Fung's (1993) QLV showed that $\omega\eta$ remains

basically constant as frequency is increased to the range of phonation (Figs. 5 and 7). Extrapolation of the theoretical curves of ζ showed that ζ continues to decrease slowly with frequency, always remaining to be <1.0 up to frequencies of phonation, where it has a numerical value of approximately 0.1 (Figs. 6 and 8).

On the other hand, extrapolation of the theoretical curves of $\omega\eta$ and ζ to a frequency above 100 Hz based on Zhu's (1988, 1991) statistical network theory showed that both $\omega\eta$ and ζ begin to decrease with frequency quite dramatically, at a much faster rate than that predicted by the QLV (Figs. 9–12). It can be seen that for both male and female vocal fold mucosa ζ tends to decrease with frequency monotonically and approaches a numerical value on the order of 0.01 at frequencies of phonation (Figs. 10 and 12).

These findings suggested that vocal fold oscillation would remain underdamped and be able to sustain at a frequency above 100 Hz, since ζ remains <1.0. As frequency is increased, phonation threshold pressure, which is directly related to the viscous shear modulus $\omega\eta$, would remain basically constant according to the QLV, or it would decrease with frequency according to the statistical network theory, provided that other factors affecting phonation threshold pressure did *not* change with frequency. That is, vocal fold oscillation should remain as easy to initiate and sustain as frequency is increased. If such trends of extrapolations persist into even higher frequencies (200–1000 Hz), this may be the basis of why voice production is possible over a relatively wide range of fundamental frequencies in singing situations (i.e., 2–3 octaves) (Titze and Chan, 1998). As long as the viscous and damping properties of the vocal fold mucosa (as quantified by $\omega\eta$ and ζ) do not increase with frequency, the effective amount of damping on vocal fold oscillation would remain surmountable, resulting in realistic and achievable phonation threshold pressures even for phonation at high pitches. Moreover, individual differences in the ability to sing at high pitches may reflect differences in tissue shear properties of the vocal fold mucosa among different subjects, which may in turn reflect molecular and possibly genetic differences of the vocal fold lamina propria. This speculation is quite possible, as large intersubject differences in tissue shear properties of the vocal fold mucosa were indeed observed in our previous study (Chan and Titze, 1999b). Certainly, further empirical measurements at higher frequencies need to be done in order to validate these arguments as well as the extrapolation of the theoretical curves.

Solely based on the goodness of fit between theory and data in the frequency range where empirical measurements were made (0.01–15 Hz), it seemed that the statistical network theory was somewhat more accurate than the QLV in describing the shear properties of vocal fold mucosal tissues. However, the statistical network theory predicted that $\omega\eta$ and ζ continue to decrease with frequency quite dramatically, which suggested that the effective amount of damping and phonation threshold pressure may become unrealistically low at high frequencies (i.e., phonation being too easy with too high oscillation amplitudes). In contrast, the QLV predicted a relatively frequency-insensitive damping curve, which suggested a more appropriate amount of damping at high frequencies and more realistic phonation threshold pressures. The relatively flat damping curves were also more consistent with the findings for other biological soft tissues reported in the literature. It is not completely clear from these findings which of the two theories is more appropriate for the description of tissue shear properties of the vocal fold mucosa. Again, further empirical measurements should be made at higher frequencies so that the theoretical extrapolations can be validated and that this issue may be resolved.

V. SUMMARY AND CONCLUSION

Empirical data on the viscoelastic shear properties of human vocal fold mucosa were previously reported in a frequency range of 0.01–15 Hz (Chan and Titze, 1999b). The present investigation attempted to characterize these data theoretically based on two constitutive models: a quasilinear viscoelastic model (Fung, 1972, 1981, 1993) and a statistical network model (Zhu *et al.*, 1988, 1991). The quasilinear viscoelastic theory has been extensively applied to describe the viscoelastic properties of many biological tissues, including the shear properties of soft tissues. The statistical network theory, on the other hand, has been successfully applied to characterize the rheological properties of polymeric materials and extracellular matrices of connective tissues. Both theories provide a unique mathematical framework in which a continuous relaxation spectrum may be used to model the generally frequency-insensitive damping characteristics of soft tissues. Based on these theories, extrapolations of the dynamic shear data to frequencies of phonation (>100 Hz) are possible, which allow for the predictions of vocal fold shear properties at frequencies relevant to voice production.

Results of the constitutive modeling showed that there was generally reasonable agreement between the theoretical predictions and the empirical data within the frequency range of 0.01–15 Hz for both theories, although there were some discrepancies between theory and data at higher frequencies. These results suggested that the shear properties of the human vocal fold mucosa may be described parametrically by both theories under small-amplitude oscillation conditions. Theoretical extrapolations of the data to frequencies of phonation suggested that the damping properties of vocal fold mucosa may remain relatively constant and insensitive to frequency, or may even decrease with frequency. If similar patterns persist into higher frequencies (up to 1000 Hz), this may be the basis of why vocal fold oscillation may remain underdamped over a relatively wide range of fundamental frequencies, i.e., 2–3 octaves in singing situations. Further studies should involve the empirical measurements of viscoelastic shear properties at higher frequencies, so as to validate the theoretical extrapolations.

ACKNOWLEDGMENTS

This study was supported by Grant No. P60 DC00976 from the National Institute on Deafness and Other Communication Disorders, National Institutes of Health. R.W.C. thanks Reiner Wilhelms for his helpful comments.

APPENDIX: THE STATISTICAL NETWORK THEORY

The functions C (chain segment creation rate) and L (chain segment loss rate) are assumed to have the following specific forms (Zhu *et al.*, 1988, 1991):

$$C(\mathbf{\Pi}_1,\mathbf{\Pi}_2,s)=\frac{\eta(s)\exp[-(-2c+3)t_1(s)\sqrt{-\mathbf{\Pi}_1}]}{kT\lambda^2(s)\{1+[t_2(s)]^3\sqrt{\mathbf{\Pi}_1\mathbf{\Pi}_2}\}}, \quad \text{(A1)}$$

$$L(\mathbf{\Pi}_1,\mathbf{\Pi}_2,s)=\lambda(s)\exp[-(c-1)t_1(s)\sqrt{-\mathbf{\Pi}_1}]\times\{1+[t_2(s)]^3\sqrt{\mathbf{\Pi}_1\mathbf{\Pi}_2}\}, \quad \text{(A2)}$$

where c is a dimensionless constant, the function $t_1(s)$ modulates the effects of the rate of deformation ($\mathbf{\Pi}_1$) on the creation rate and loss rate of chain segments, and the function $t_2(s)$ modulates the effects of the acceleration of deformation ($\mathbf{\Pi}_2$) on chain segment creation and loss,

$$t_i(s)=\frac{t_i}{(1+s)^n} \quad \text{for } 0\leqslant s\leqslant s_0$$
$$=0 \quad s>s_0 \quad (i=1,2), \quad \text{(A3)}$$

where t_1 and t_2 are time constants associated with $\mathbf{\Pi}_1$ and $\mathbf{\Pi}_2$, respectively, and n is another dimensionless constant. The two parameters n and c control the dependence of chain segment creation rate (C) and loss rate (L) on $\mathbf{\Pi}_1$ and $\mathbf{\Pi}_2$.

For small-amplitude oscillations, the memory function $m(t,t')$ as defined in Eq. (26) can be greatly simplified, because $\mathbf{\Pi}_1$ and $\mathbf{\Pi}_2\approx 0$ when shear strain (γ_0) is small,

$$m(t-t')=\int_0^\infty \frac{\eta(s)}{\lambda^2(s)}\exp\left[-\frac{t-t'}{\lambda(s)}\right]ds. \quad \text{(A4)}$$

Substituting this memory function into the constitutive equation for the network [Eq. (24)], the final expressions for the complex shear modulus μ^* can be obtained [Eqs. (27) and (28)]. See Zhu *et al.* (1991) for further details of the derivation.

[1]Thixotropic materials show a gradual decrease of shear stress (and viscosity) with time under a constant strain rate, due to a breakdown of the molecular network during shearing (e.g., tomato ketchup).

[2]The second invariant ($\mathbf{\Pi}$) of a tensor $\mathbf{A}$ is defined as $\mathbf{\Pi}=[(\mathrm{tr}(\mathbf{A}))^2-\mathrm{tr}(\mathbf{A}^2)]/2$.

[3]The first Rivlin–Ericksen tensor $\mathbf{A}_1=\mathbf{L}+\mathbf{L}^T=2\mathbf{D}$, where $\mathbf{L}$ is the velocity gradient and $\mathbf{D}$ is the rate of strain or ''stretching'' tensor. The second Rivlin–Ericksen tensor $\mathbf{A}_2=\dot{\mathbf{L}}+\dot{\mathbf{L}}^T+2\mathbf{L}^T\mathbf{L}$.

Abramowitz, M., and Stegun, I. (**1964**). *Handbook of Mathematical Functions* (U.S. Department of Commerce, Washington, DC), p. 1027.

Alipour, F., and Titze, I. R. (**1983**). ''Simulation of particle trajectories of vocal fold tissue during phonation,'' in *Vocal fold Physiology: Biomechanics, Acoustics, and Phonatory Control*, edited by I. R. Titze and R. C. Scherer (Denver Center for the Performing Arts, Denver, CO), pp. 183–190.

Alipour, F., and Titze, I. R. (**1988**). ''A finite element simulation of vocal fold vibrations,'' Proceedings of Northeast Bioengineering Conference, IEEE Report 88 CH 2666-6, pp. 186–189.

Barnes, H. A., Hutton, J. F., and Walters, K. (**1989**). *An Introduction to Rheology* (Elsevier, Amsterdam), pp. 1–10; 37–54; 97–114.

Becker, R., and Doring, W. (**1939**). *Ferronmagnetismus* (Springer, Berlin).

Berry, D. A., and Titze, I. R. (**1996**). ''Normal modes in a continuum model of vocal fold tissues,'' J. Acoust. Soc. Am. **100**, 3345–3354.

Bilston, L. E., and Thibault, L. E. (**1996**). ''The mechanical properties of the human cervical spinal cord in vitro,'' Ann. Biomed. Eng. **24**, 67–74.

Bird, R. B., Armstrong, R. C., and Hassager, O. (**1977a**). *Dynamics of Polymeric Liquids. Fluid Mechanics* (Wiley, New York), Vol. 1, pp. 129–204; 275–303.

Bird, R. B., Hassager, O., Armstrong, R. C., and Curtiss, C. F. (**1977b**). *Dynamics of Polymeric Liquids. Kinetic Theory* (Wiley, New York), Vol. 2, pp. 471–580; 701–721.

Chan, R. W. (**1998**). ''Shear properties of vocal fold mucosal tissues and their effect on vocal fold oscillation,'' unpublished Ph.D. dissertation, The University of Iowa, Iowa City, IA.

Chan, R. W., and Titze, I. R. (**1998**). ''Viscosities of implantable biomaterials in vocal fold augmentation surgery,'' Laryngoscope **108**, 725–731.

Chan, R. W., and Titze, I. R. (**1999a**). ''Hyaluronic acid (with fibronectin) as a bioimplant for the vocal fold mucosa,'' Laryngoscope **109**, 1142–1149.

Chan, R. W., and Titze, I. R. (**1999b**). ''Viscoelastic shear properties of human vocal fold mucosa: Measurement methodology and empirical results,'' J. Acoust. Soc. Am. **106**, 2008–2021.

Chun, K. J., and Hubbard, R. P. (**1986**). ''Development of reduced relaxation function and stress relaxation with paired tendon,'' Adv. Bioeng. (ASME) **2**, 162–163.

De Kee, D., and Carreau, P. J. (**1979**). ''A constitutive equation derived from Lodge's network theory,'' J. Non-Newtonian Fluid Mech. **6**, 127–143.

Ferry, J. D. (**1980**). *Viscoelastic Properties of Polymers*, 3rd ed. (Wiley, New York).

Fung, Y. C. (**1972**). ''Stress-strain history relations of soft tissues in simple elongation,'' in *Biomechanics: Its Foundations and Objectives*, edited by Y. C. Fung, N. Perrone, and M. Anliker (Prentice-Hall, Englewood Cliffs, NJ), pp. 181–208.

Fung, Y. C. (**1981**). *Biomechanics. Mechanical Properties of Living Tissues* (Springer-Verlag, New York), pp. 22–61.

Fung, Y. C. (**1993**). *Biomechanics. Mechanical Properties of Living Tissues*, 2nd ed. (Springer-Verlag, New York), pp. 23–65; 242–320.

Gray, S. D., Titze, I. R., Chan, R., and Hammond, T. H. (**1999**). ''Vocal fold proteoglycans and their influence on biomechanics,'' Laryngoscope **109**, 845–854.

Hammond, T. H., Zhou, R., Hammond, E. H., Pawlak, A., and Gray, S. D. (**1997**). ''The intermediate layer: A morphologic study of the elastin and hyaluronic acid constituents of normal human vocal folds,'' J. Voice **11**, 59–66.

Lodge, A. S. (**1968**). ''Constitutive equations from molecular network theories for polymer solutions,'' Rheol. Acta **7**, 379–392.

Mak, A. F. (**1986**). ''Apparent viscoelastic behavior of articular cartilage-Contributions from intrinsic matrix viscoelasticity and interstitial fluid flow,'' J. Biomech. Eng. **108**, 123–130.

Neubert, H. K. P. (**1963**). ''A simple model representing internal damping in solid materials,'' Aeronaut. Q. **14**, 187–197.

Pinto, J. G., and Fung, Y. C. (**1973**). ''Mechanical properties of the heart muscle in the passive state,'' J. Biomech. **6**, 597–616.

Pinto, J. G., and Patitucci, P. J. (**1980**). ''Viscoelasticity of passive cardiac muscle,'' J. Biomech. Eng. **102**, 57–61.

Price, J. M., Patitucci, P. J., and Fung, Y. C. (**1979**). ''Mechanical properties of resting taenia coli smooth muscle,'' Am. J. Physiol. (Cell Physiol.) **236**, C211–C220.

Sauren, A. A. H. J., and Rousseau, E. P. M. (**1983**). ''A concise sensitivity analysis of the quasi-linear viscoelastic model proposed by Fung,'' J. Biomech. Eng. **105**, 92–95.

Simon, B. R., Coats, R. S., and Woo, S. L-Y. (**1984**). ''Relaxation and creep quasilinear viscoelastic models for normal articular cartilage,'' J. Biomech. Eng. **106**, 159–164.

Spirt, A. A., Mak, A. F., and Wassell, R. P. (**1989**). ''Nonlinear viscoelastic properties of articular cartilage in shear,'' J. Orthop. Res. **7**, 43–49.

Tanaka, T. T., and Fung, Y. C. (**1974**). ''Elastic and inelastic properties of the canine aorta and their variation along the aortic tree,'' J. Biomech. **7**, 357–370.

Theodorsen, T., and Garrick, E. (**1940**). ''Mechanism of flutter,'' U.S. National Advisory Committee on Aeronautics, Report #685.

Titze, I. R. (**1988**). ''The physics of small-amplitude oscillation of the vocal folds,'' J. Acoust. Soc. Am. **83**, 1536–1552.

Titze, I. R. (**1992**). ''Phonation threshold pressure: A missing link in glottal aerodynamics,'' J. Acoust. Soc. Am. **91**, 2926–2935.

Titze, I. R., and Chan, R. W. (**1998**). ''The effect of shear thinning in vocal fold tissues—or, why we can phonate over two octaves in pitch,'' *Proceedings of the 16th International Congress on Acoustics and the 135th*

Acoustical Society of America Meeting, Vol. IV, pp. 2669–2670.
Titze, I. R., and Story, B. H. (**1999**). ''Rules for controlling low-dimensional vocal fold models with muscle activities,'' J. Acoust. Soc. Am. (in review).
Wagner, K. W. (**1913**). ''Zur theorie der unvoll Kommener dielektrika,'' Ann. Phys. (Leipzig) **40**, 817–855.
Woo, S. L-Y., Gomez, M. A., and Akeson, W. H. (**1981**). ''The time and history-dependent viscoelastic properties of the canine medial collateral ligament,'' J. Biomech. Eng. **103**, 293–298.
Woo, S. L-Y., Gomez, M. A., Woo, Y-K., and Akeson, W. H. (**1982**). ''Mechanical properties of tendons and ligaments. I. Quasi-static and nonlinear viscoelastic properties,'' Biorheology **19**, 385–396.
Woo, S. L-Y., Johnson, G. A., and Smith, B. A. (**1993**). ''Mathematical modeling of ligaments and tendons,'' J. Biomech. Eng. **115**, 468–473.
Woo, S. L-Y., Simon, B. R., Kuei, S. C., and Akeson, W. H. (**1980**). ''Quasi-linear viscoelastic properties of normal articular cartilage,'' J. Biomech. Eng. **102**, 85–90.
Zhu, W., Iatridis, J. C., Hlibczuk, V., Ratcliffe, A., and Mow, V. C. (**1996**). ''Determination of collagen-proteoglycan interactions in vitro,'' J. Biomech. **29**, 773–783.
Zhu, W. B., Lai, W. M., and Mow, V. C. (**1986**). ''Intrinsic quasi-linear viscoelastic behavior of the extracellular matrix of cartilage,'' Trans. Orthopaedic Res. Soc. **11**, 407.
Zhu, W. B., Lai, W. M., and Mow, V. C. (**1988**). ''A second order rheological model to predict the time-dependent behavior of proteoglycan solutions,'' Adv. Bioeng. (ASME) **8**, 187–190.
Zhu, W. B., Lai, W. M., and Mow, V. C. (**1991**). ''The density and strength of proteoglycan-proteoglycan interaction sites in concentrated solutions,'' J. Biomech. **24**, 1007–1018.
Zhu, W. B., and Mow, V. C. (**1990**). ''Viscometric properties of proteoglycan solutions at physiological concentrations,'' in *Biomechanics of Diarthrodial Joints*, edited by V. C. Mow, A. Ratcliffe, and S. Woo (Springer-Verlag, New York), pp. 313–344.

Comparison between electroglottography and electromagnetic glottography

Ingo R. Titze and Brad H. Story
Department of Speech Pathology and Audiology and National Center for Voice and Speech, The University of Iowa and the Denver Center for the Performing Arts, Iowa City, Iowa 52242

Gregory C. Burnett
Department of Applied Science, University of California at Davis, and Lawrence Livermore National Laboratory, Livermore, California 94557

John F. Holzrichter and Lawrence C. Ng
Lawrence Livermore National Laboratory, Livermore, California 94551

Wayne A. Lea
Speech Sciences Institute, Apple Valley, Minnesota 55124

(Received 11 December 1998; revised 9 July 1999; accepted 14 July 1999)

Newly developed glottographic sensors, utilizing high-frequency propagating electromagnetic waves, were compared to a well-established electroglottographic device. The comparison was made on four male subjects under different phonation conditions, including three levels of vocal fold adduction (normal, breathy, and pressed), three different registers (falsetto, chest, and fry), and two different pitches. Agreement between the sensors was always found for the glottal closure event, but for the general wave shape the agreement was better for falsetto and breathy voice than for pressed voice and vocal fry. Differences are attributed to the field patterns of the devices. Whereas the electroglottographic device can operate only in a conduction mode, the electromagnetic device can operate in either the forward scattering (diffraction) mode or in the backward scattering (reflection) mode. Results of our tests favor the diffraction mode because a more favorable angle imposed on receiving the scattered (reflected) signal did not improve the signal strength. Several observations are made on the uses of the electromagnetic sensors for operation without skin contact and possibly in an array configuration for improved spatial resolution within the glottis. [S0001-4966(00)06201-9]

PACS numbers: 43.70.Jt [AL]

INTRODUCTION

Glottography is a measurement of the time variation of the glottis during phonation, where the glottis is defined as the airspace between the vocal folds. Glottography usually involves the transmission of a probe signal from one side of the larynx to the other, with the time variation of the glottis modulating the probe's properties. The modulation is then detected and interpreted in terms of the expected geometry of the glottis, which is formed by laryngeal tissues that are in partial stages of contact during the phonation cycle. The probes used in the past have been electrical current flow, ultrasonic waves, light transmission, and airflow as generated by the speaker. Recently, propagating high-frequency electromagnetic waves (EM waves) have been used to measure tissue motions in concert with glottal time variation (Holzrichter *et al.*, 1998). In this paper, the properties of such an EM wave device are compared to those of an electric current flow device, the EGG.

As in many imaging techniques, there are two traditional modes of probing an air–tissue interface: the transmission mode and the reflection mode. In the transmission mode the received signal passes through the interface (or a series of interfaces), whereas in the reflection mode, the received signal is scattered (i.e., reflected in the sense of ray optics) off the interface. As discussed below, when the wavelength of the probe becomes comparable or larger than the size of the object being detected, the concepts of transmission and reflection are better described by wave scattering than by ray optics. Examples are wave diffraction (usually defined as forward direction EM wave scattering), and backward EM wave scattering (due to a reflection from an interface). Generally speaking, the motion and geometry of a tissue interface can be detected in both forward and backward scattering modes. This is true provided there is adequate spatial and temporal resolution of the sending–receiving probe, and that there is a firm theoretical base on which to build an interpretation of the physical phenomena of tissue interface modulation.

Both transmission and reflection modes have been utilized in glottography. In almost all attempts in the past, the interface of interest has been the medial surface of the vocal folds. This interface (or pair of interfaces for two vocal folds) is on the order of 1 cm horizontally (front to back) and 0.5 cm vertically (top to bottom) and has significant curvature that varies over the glottal cycle. Thus any signal reflecting from this interface involves rapid changes in direction. For transmission, there are always at least two interfaces, first a tissue-to-air interface on one vocal fold and then an air-to-tissue interface on the other. When contact between the vocal folds occurs (over all or part of the medial sur-

faces), scattering from either of the interfaces begins to vanish and transmission approaches unity. The opening and closing of the glottis happens cyclically at frequencies of 100–1000 Hz; thus instrumentation resolution times are from several hundreds of microseconds to several milliseconds.

Under the highly variable reflection and transmission conditions of the vocal fold structure, the choice of a probe signal is important. As stated above, the classes of signals that have been tried have been electric, ultrasonic, and electromagnetic (in the form of visible light). In addition, flow glottography has been used, which uses the airflow signal that the larynx itself creates in the process of phonation.

With the use of electric current signals (electroglottography, or EGG), there is no scattering from the interfaces because the electric probe current does not propagate as a wave in the tissue; rather, electrons or ions are moving over very short mean free paths. The transmission mode reduces to a conduction mode. Wherever the tissues are in contact, there is conduction across the glottis; wherever there is an air gap, there is no direct conduction, but because the carrier signal is usually chosen to be an alternating current at a high frequency (in the MHz range), the capacitance of the vocal fold air gap does allow some displacement current to be transmitted across the gap. However, unless the gap is very small, the impedance of the gap is much larger than the impedance of the tissue, and the signal is determined by ionic conduction through the contacting tissues that surround the air gap (Titze, 1990).

With propagating transverse electromagnetic waves or longitudinal ultrasonic waves, there can be both transmission (forward scattering) and reflection (backward scattering) from the larynx tissues. Ultrasound waves used for tissue probing usually have wavelengths of 0.1 to 1 mm, and follow ray optic trajectories when used in probing glottal structures. Ideally, when used in the transmission probe, they have a relation to the contact area; when used in the reflection mode, they have a relation to the medial surface motion. Hamlet and Reid (1972) used ultrasonoglottography (UGG) in the transmission mode. The receiving transducer was placed on the distal side of the neck. Hamlet had better success with this arrangement than with reflection, but in general the contact area signal was not very stable. The amplitude was very sensitive to head and neck movement, especially vertical movement of the larynx within the neck. In the ultrasound reflection mode, Zagzebski *et al.* (1983) placed a signal transducer on one side of the neck, acting both as a sender and receiver. Owing to the nonparallel orientation of the transducer relative to the tissue–air interface in the glottis, the signal transducer received little of the reflected signal. Most of the wave was scattered away, making the detected interface signal very noisy.

Incoherent, visible light has been used as an electromagnetic probe, and is known as photoglottography (PGG). The measurement has been used for a number of decades (e.g., Löfqvist and Yoshioka, 1980). Although coherent light sources (i.e., lasers) can be used, light scattering in tissues is sufficiently intense that the measurement mode becomes essentially incoherent in nature. Because visible light is highly attenuated by tissue, a signal path has to be chosen that minimizes the loss. Usually, one transducer is placed above the glottis inside the throat (using a fiber-optic cable) while the other is placed outside the throat, usually below the thyroid prominence and, thereby, below the glottis. The signal propagation mode is transmission though the horizontal plane of the glottis and the surrounding vocal fold tissues, from top to bottom of the glottis. This direction of the probe signal is perpendicular to that used by UGG and EGG, which are directed along the horizontal plane of the glottis and perpendicular to the midsagittal plane. Thus PGG provides information that differs from UGG and EGG, a minimum projected *glottal area* rather than the *contact area* measured by EGG and UGG.

Finally, in flow glottography (FGG) the signal is associated with the stream of air forced through the glottis, from the lungs to the lips. As in all other forms of glottography, the movement of the vocal folds modulates the signal. What is profoundly different in FGG is that the probe is self-generated by the speaker. The signal is a natural part of the phonatory process. The FGG receiver is a flow mask placed over the mouth and nose, which measures the oral flow, as produced by the glottis and modulated by the vocal tract. From the measurement of oral airflow out of the nose and lips, the actual glottal flow versus time is estimated by inverse filtering, a process that attempts to remove the flow modulations imposed by the vocal tract. The estimated glottal airflow is then further inverse filtered to obtain the time-varying glottal area by using a nonlinear airflow model that has glottal area as an input (Rothenberg, 1973).

ELECTROMAGNETIC GLOTTOGRAPHY

Electromagnetic glottography (EMGG) is a new technique, whereby a transverse electromagnetic wave in the GHz range is propagated and then detected to obtain information on the condition of the larynx tissue interfaces (Holzrichter *et al.*, 1998). A transducer arrangement for combined EMGG and EGG measurements described herein is shown in Fig. 1. The EM antennae are placed on the front of the neck near the thyroid prominence (Adam's Apple). (In our experiment, EGG electrodes were placed additionally on both sides of the neck.) The transmitted EM signal is a wave packet (pulse) containing about ten wave cycles at 2.3 GHz, with a wavelength of 13 cm in air and 1.8 cm in tissue. The average power emitted is about 300 mW and the energy per pulse is $<10^{-9}$ J. The pulses form a train with a repetition rate of 2 MHz (see McEwan, 1994–1996), and reception is accomplished using a homodyne mode detector, signal integration, and bandpass filtering. The system can detect motion in the near, intermediate, or far field, with one antenna being used as a transmitting and the second as a receiving element. The transmit and receiver antennas are simple patch antennas, about 2 cm long, 1 cm wide, placed end to end, about 2 mm apart, along a common horizontal axis (Fig. 2, not drawn to scale).

The antenna radiation pattern is largely isotropic. In the horizontal plane of the sensor, cutting across the neck at the level of the vocal folds, the *E* field is horizontal, as shown by the arrows near the sending electrode. With the sensor centered on the mid-sagittal plane (0° azimuth), the transmit

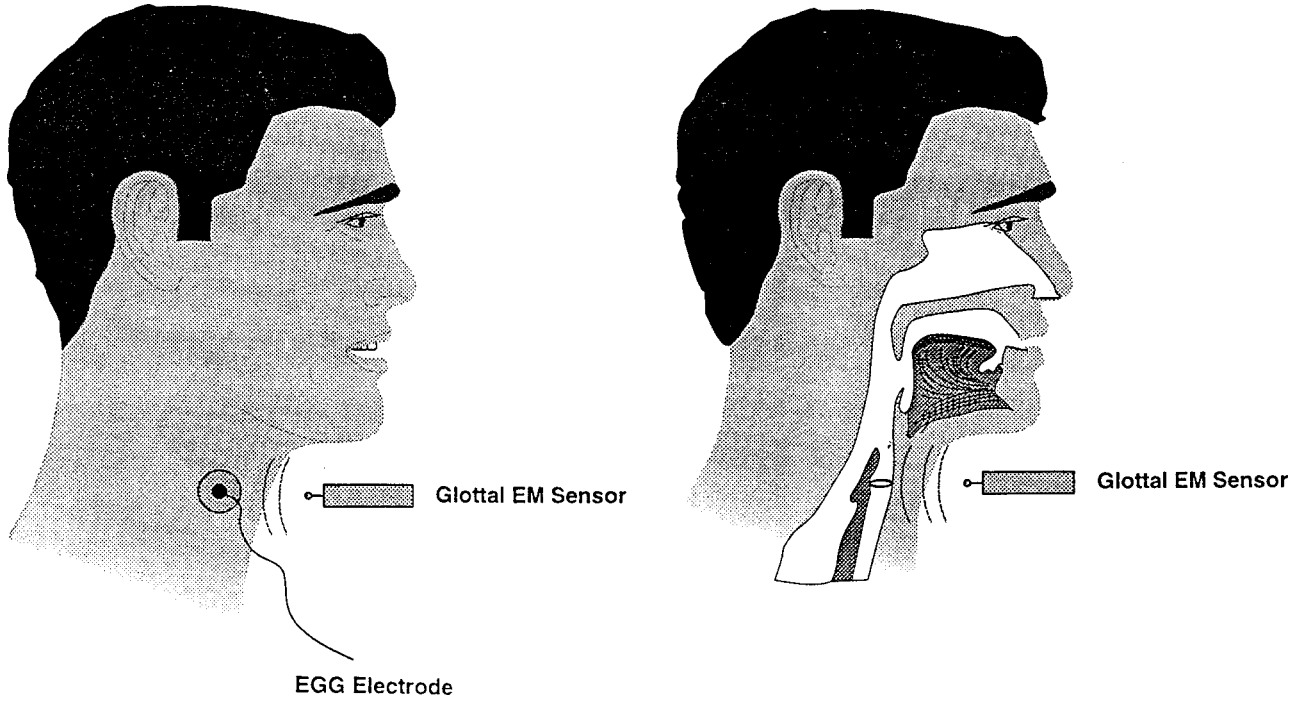

FIG. 1. Two right side-views of a subject, showing positions of EMGG and EGG sensors. The left image shows the locations of the EGG electrode and the EMGG sensor, and the right image illustrates the vocal tract, along the mid-sagittal plane of the neck and head, and the EMGG sensor location. The axis of the transmit and receive antennas of the EMGG is perpendicular to the figure plane. When the sensor is placed against the neck, below the thyroid prominence, the antenna axis is tangent to the neck at the mid-sagittal plane.

antenna is located about 1 cm to the right side of the mid-sagittal plane, and the receive antenna about 1 cm to the left. The angle of the sensor axis relative to the mid-sagittal plane, in the horizontal plane of the vocal folds, defines the azimuthal angle used in experiments described below.

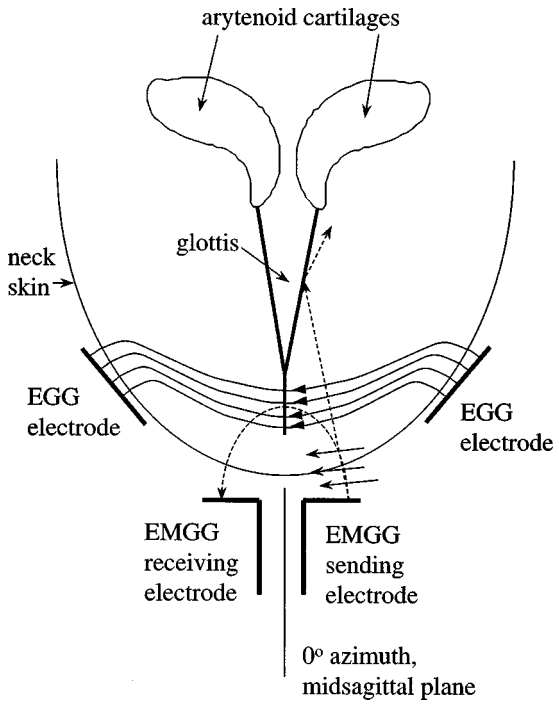

FIG. 2. EMGG and EGG electrode placement in a horizontal plane, with a cross section through the neck and larynx. Electric (*E*) field patterns are shown for the EGG electrodes from right to left across the glottis and the propagating *E* field is shown with arrows near the sending EMGG electrode.

Many other EM sensor modes of operation can be used. For example, for operation at a longer distance from the subject, a far-field mode sensor (i.e., radar mode with a directional antenna) can be employed (Skolnik, 1990). The EMGG device used for these experiments was operated in the near to intermediate field, where the antenna elements were about one wavelength from the internal glottal structure (the wavelength was about 13 cm in air or 1.8 cm in tissue, where the relative dielectric constant of the tissue is about 50). The 1.8-cm wavelength is similar in size to several of the glottal tissue structures and thus both wave scattering and diffraction methods are needed to describe the detailed EM wave trajectories. Simple analysis, as well as numerical modeling, have been used to validate this assumption (Burnett, 1999). The sensor transmits an EM wave pulse train toward the interior of the neck, receiving a return signal a nanosecond or so later. The return signal is either a backscattered (e.g., reflected) signal from tissue–air or tissue–tissue interfaces (the glottis or trachea) or a forward scattered (e.g., transmitted and diffracted) signal across or around the partially sealed glottal structure.

The signals received from each transmitted pulse are integrated and filtered (analog, single pole, high pass at 70 Hz, and low pass at 7 kHz) so that only those tissue interface motions in the voice harmonic frequency range are detected. A digital inverse filter is used later to restore the wave shape. Thus, reflections from stationary or slowly moving tissues, such as slow artery blood flow pulsation, are not detected. This high-pass filtered mode is called the ''field disturbance'' mode and is particularly useful for survey work, where absolute tissue interface locations relative to the antennae are uncertain, but movement is easily detected. The

field disturbance mode has the advantage that very small tissue interface motions, with position changes as small as 10 μm, are easily detected in the presence of other stationary anatomical structures. However, it has a disadvantage in that it is difficult to accurately identify the absolute locations of the moving, reflecting structures.

The initial experiments described in previous publications (Holzrichter *et al.*, 1998, 1996; Burnett *et al.*, 1997) showed that the EMGG sensors detect tissue motions that oscillate in phase with the closure and opening of the vocal folds. Because the antenna used with the EMGG was nonfocusing, and because several EM wave cycles were transmitted per pulse, it was not possible to measure which oscillating tissue interfaces were directly responsible for the signals. However, the position of the sensors, located directly under the thyroid prominence, together with the longitudinal range limit of the sensor (due to signal attenuation in the tissue) restricted the site of oscillation to either the vocal folds or the nearby tracheal walls. The association of the signal with specific tissue interfaces is ambiguous, as presently understood, because the sensors generate a signal that is a function of the product of tissue area and vibration amplitude (i.e., a volume displacement). As an example, for the vocal fold medial surface, the area is relatively small, 1–2 cm^2, but the amplitude of motion is relatively large, 0–0.5 cm; whereas for pressure induced tracheal wall motions, the area can be relatively large, 5–10 cm^2, with the amplitudes being relatively smaller, perhaps $<$0.1 cm. The waveforms for EMGG will be shown to be so consistent with EGG signals that it is ''natural'' to associate the EM scattering site with changes in the glottal tissue configurations. However, Burnett *et al.* (1997) stress that EM wave reflection from subglottal tracheal wall motion, induced by pressure buildup as the glottis closes, can lead to similar appearing EMGG signals, especially if placement of the sensor is lower on the neck. Focusing and time gated EM sensor systems are being developed to accurately measure the tissue interface motions of the differing tissues to determine the exact sources of EM wave reflections.

At this point both hypotheses, forward scatter (diffraction) and backscatter (reflection), must be considered. For forward scatter, the waves are diffracted (due to phase cancellations from boundary conditions at or near the electrodes) from the sending electrode around the glottal gap to the receiving electrode, as shown by the bent dashed lines in Fig. 2. The bending does not need to be a full 180°, as shown, but only a component of the scattered *E* field must be tangential to the receiving electrode. The anterior part of the glottal gap is the preferred path because the bending (diffracting) angle is less severe and the pathlength is smaller than for waves penetrating the posterior gap. For backscatter, the waves must first be reflected first from the vocal fold medial surfaces, toward the dorsal region of the neck, as shown by the straight dashed line and the scattering arrow. There would then have to be secondary reflections from cartilages and other interfaces back to the receiving electrode. It is not clear which part of the glottis would be favored for backscattering. In any case, a reflected signal from the air–tissue interface should assume more of the shape of the glottal area function (or PGG) than the contact area function (or EGG). If the backscatter is from the dorsal side of the tracheal wall, the signal would probably resemble neither EGG nor PGG.

For both types of scattering, the *E* field of the EMGG device can have the same orientation in the horizontal plane as the *E* field of the EGG device at the sending electrode (see arrows pointing to the left in Fig. 2). The electric field of the EGG device is less able to ''jump the glottal gap,'' but because the signal does have a high-frequency carrier, there is some capacitive conductance across the anterior portion of the gap. The EMGG signal can, in theory, propagate through both air and tissue interfaces, but this is unlikely due to the refraction indices.

At the receiving electrode, the direction of the *E* field of the EMGG device is not clear because of the uncertainty of the scattering mechanism. It is possible that an antenna angle less than the current 180° between sending and receiving electrodes would provide a more favorable reception for forwardscatter, but we had no freedom to change this design in our first experiment. Also, an angle $<$180° would complicate the comparison with the backward scatter, which is typically tested with 180° electrodes. Further studies are underway at Lawrence Livermore National Laboratories (Burnett, 1999) to determine the relative strengths and directions of EM wave scattering from laryngeal and tracheal tissues under varying conditions of electrode placement and design. The experiments presented in this report are intended to compare, under a limited set of conditions, well understood EGG signals associated with vocal fold contact to those obtained by a first version of an EMGG sensor.

METHODS

To test the scattering hypotheses, a side-by-side comparison of the EGG and EMGG devices was undertaken. Because of the difference in design and construction, the two devices did not interfere with each other, neither in terms of physical placement nor in terms of carrier frequency and spurious EM noise generation. Their simultaneous use enabled simple one-to-one comparisons of the two systems' measurements.

At the University of Iowa, four subjects were asked to perform phonatory tasks that produced a range of voice types and transducer placements. The subjects were all young to middle-aged males (ages 28, 31, 55, and 57). Males were recruited for this study because, in general, males have greater protrusion of the thyroid cartilage than females, making their EGG signals stronger. For this comparative study, we felt that the stronger signal-to-noise ratio was an advantage to tease out the signal differences. Also, none of the subjects had excessive fat in the neck, the presence of which would have limited the signal-to-noise ratio of the EGG signal (Titze, 1990). The subjects were identified by ascending age with the following symbols: S1, S2, S3, and S4.

The vocal conditions included three different levels of vocal fold adduction (normal, breathy, and pressed), three different registers (falsetto, modal and fry, and two pitches (low and high). It is known that variation in adduction and register cause major changes in the waveform of the EGG

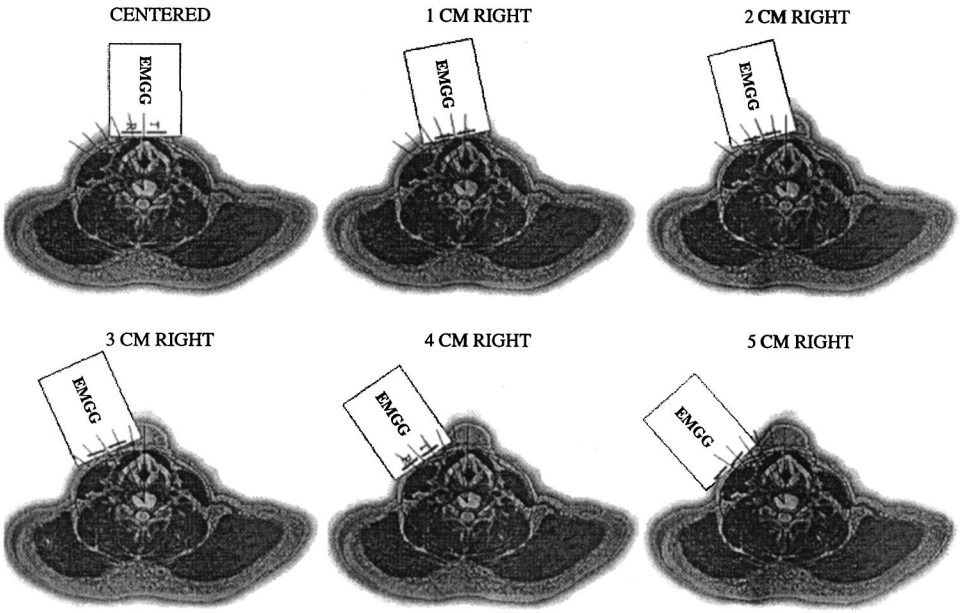

FIG. 3. Transverse sections through the neck at the level of the glottis, with the EMGG sensor placed at different locations around the neck.

signal (Childers *et al.*, 1986). In particular, breathy voice and pressed voice create differences in the vocal fold contact patterns in the anterior and posterior regions of the glottis. These differences should be noticeable in the glottographic signals. All in all, each subject phonated five tokens of a steady /ɑ/ vowel for each of three levels of adduction, three registers, and two pitches.

To test the scattering hypotheses, the EMGG electrodes were moved along the azimuth around the neck (Fig. 3), just touching the skin. (A few mm of distance between the electrode and the skin did not affect the signal, however. This is a major difference between EGG and EMGG.) The azimuthal rotation around the neck (away from 0°) should *increase* the EMGG signal strength if the transducer acts in a reflection mode because the scattering angle from the medial surface of the vocal folds would be reduced. However, the distance of the total signal path also increases with angle, making the advantage of off-axis placement somewhat less obvious. On the contrary, the azimuthal rotation should clearly *decrease* the EMGG signal strength if the transducer acts in the transmission mode because less contact surface would be in the field path. As seen in Fig. 3 for $\theta \approx 45°$ (5 cm right), any diffraction from one electrode to the other would include little of the glottis, whereas for $\theta = 0$ (centered) the anterior glottis is likely to be in the diffraction path.

The signals were recorded using a Sony PC-108M digital tape recorder at the University of Iowa, and processed at Lawrence Livermore with Matlab and other conventional signal processing software. As mentioned, instrumental induced filtering of the signals (i.e., internal high-pass and low-pass filtering) was removed from the data sets with inverse noncausal digital filtering (Burnett, 1999) before display in the following figures. This inverse filtering restored the proper wave shape for comparison to models.

RESULTS

Accurate glottal timing information was obtained from the EGG signal, which is unambiguously associated with the opening and closing of the glottis. The EMGG signal corresponded well to the EGG signal for the glottal closing event, but for some conditions of contact the waveforms differed considerably.

Figure 4 compares the EMGG signal with the acoustic (audio) signal and the EGG signal for modal (chest) voice, normal adduction, and low pitch (161 Hz) from subject 1. In this example, as in other figures to follow, the acoustic signal was shifted 1.4 ms in time to correct for the slower sound speed from the glottis to the microphone, in contrast to the near instantaneous (light) speed of the EGG and EMGG. The negative peak on the acoustic signal is associated with the closure of the glottis. Both sensor signals show agreement on glottal closure and glottal opening, as well as the general shape of the contact pattern. This is a case for best agreement between the two waveforms.

The timing between EMGG and photoglottography (PGG) have also been validated by employing high speed

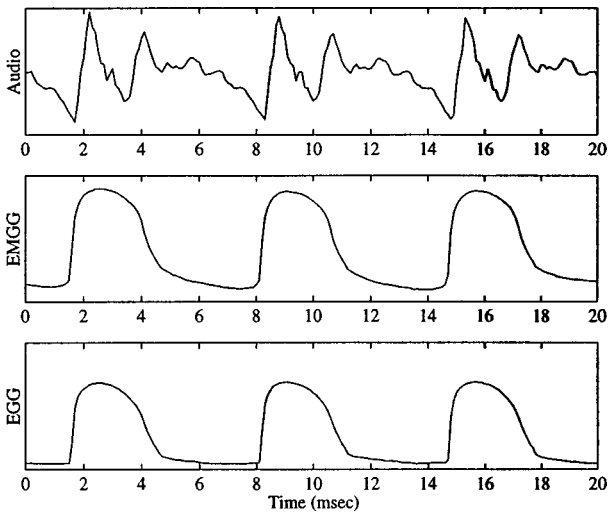

FIG. 4. An acoustic (microphone) signal, the EMGG signal, and the corresponding EGG signal recorded simultaneously from subject S1 for three pitch periods, modal phonation, and vowel /ɑ/.

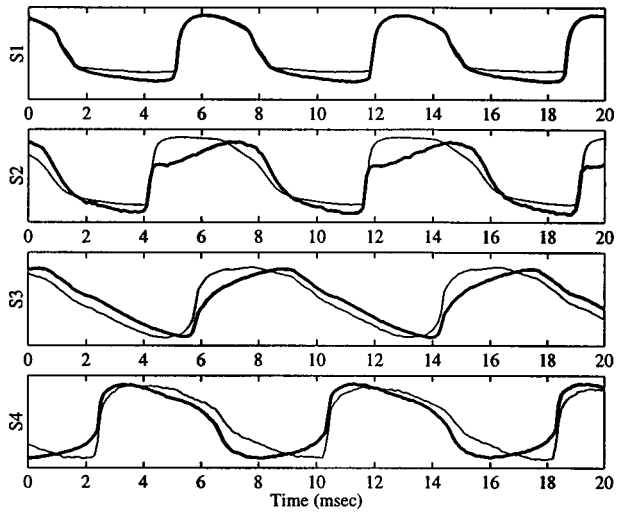

FIG. 5. Signals from EGG and EMGG for each of the four subjects for modal phonation and the vowel /ɑ/. Fundamental frequencies ranged between 100 and 120 Hz across subjects; EMGG is in bold lines and EGG in fine lines.

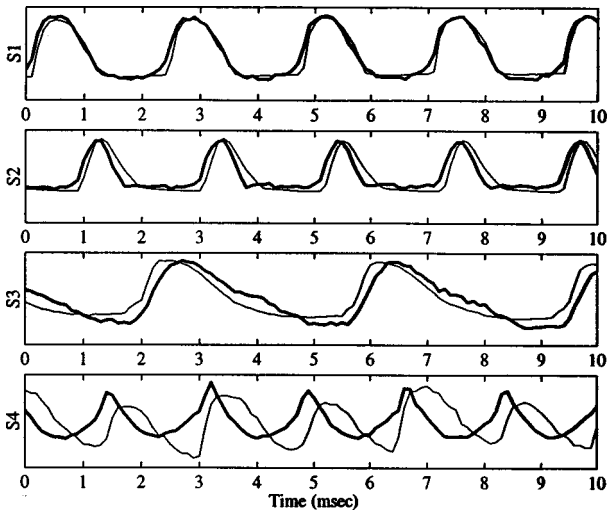

FIG. 6. Four examples of falsetto voice, with F_0 ranging form 266 to 578 Hz; EMGG is in bold lines and EGG in fine lines.

photography systems, coupled to a laryngoscope (Burnett *et al.*, 1997; Holzrichter *et al.*, 1996, 1998; Burnett and Leonard, 1999). Results showed that opening and closing events were consistently correlated.

The data in Fig. 5 show the EGG and EMGG signals from all four subjects, phonating in modal register. The fundamental frequency (F_0) was in the 100–120 Hz range for all subjects. Bold lines are for EMGG and fine lines for EGG. The waveforms have similarity, but there are considerable differences between them for all subjects except S1. Note, for example, the shape differences for subject S2 in the early contact phase. For a normalized amplitude, the EMGG does not rise to the same initial height as the EGG, but rises later. A similar effect is seen for S3. For subjects S1 and S4, the differences are greater in the low contact phase. These differences are likely to be the result of different field intensity distributions over different portions of the tissues in contact.

Figure 6 shows examples for falsetto voice, with F_0 ranging from 330 to 550 Hz. Waveforms for S1, S2, and S3 are similar, with the main differences being a slight phase offset for S2 and S3, but for subject S4 there is little similarity. The width of the contact pulse is smaller for EMGG than EGG for subject 54; since contact is incomplete in falsetto voice, the two systems may be measuring different spatial contact conditions.

Figure 7 shows examples of breathy voice for the four subjects. The fact that the overall agreement between the two sensor systems is best for this phonation type (except for subject S3) speaks in favor of the diffraction (forward scattering) hypothesis. This is because the primary contact region for breathy voice is expected to be in the anterior glottis (the nearest field region), where maximum diffraction would occur.

Figure 8 shows examples of pressed voice for the four subjects. There are substantial variations in the shapes of the EMGG signals compared to the EGG signals for all individuals. These larger differences again support the diffraction hypothesis because more contact area variation occurs in the posterior glottis during pressed voice than breathy voice, especially if the bottom of the vocal fold is not pressed as tightly as the top. But the reflection hypothesis would also claim less agreement for pressed voice because the tissue–air interfaces are only partially preserved with a high degree of contact over the entire vocal fold. In spite of these disclaimers, some of the important timing events, such as glottal closure, are preserved between the EGG and EMGG sensors. There is less agreement between the two signals with regard to the moment of glottal opening.

Figure 9 shows a modal-fry register transition for subject S2. Measured signals are again audio, EMGG, and EGG. In modal voice, represented by the first six or seven cycles, the waveforms have similar shapes, as previously discussed. After about 70 ms, the EMGG shows a strong negative spike that corresponds to glottal closure (the upward movement of the EGG). Here a reflected (backward scattered) signal from the rear wall of an expanding trachea may be starting to mix with the forward scattered signal through the glottis, which

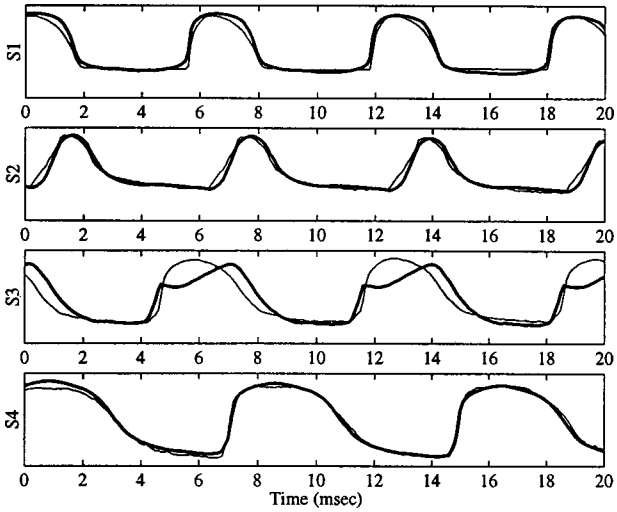

FIG. 7. Four examples of ''breathy'' voice; EMGG is in bold lines and EGG in fine lines.

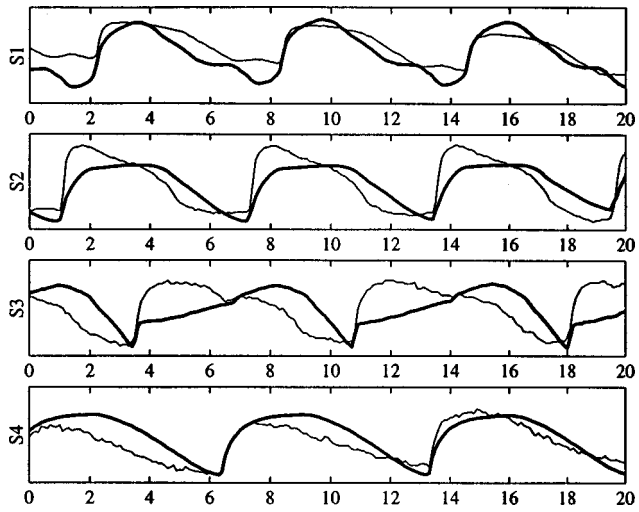

FIG. 8. Four examples of ''pressed'' voice; EMGG is in bold lines and EGG in fine lines.

gets smaller as the vibrational amplitude decreases in vocal fry. It is possible that the negative spike from the tracheal wall can cause a partial signal cancellation at glottal closure (Burnett *et al.*, 1997). Note that the basic waveform differences are similar to those seen in pressed voice from the same subject (S2) in Fig. 5, a lesser upward thrust with more symmetry in the wave shape.

Figure 10 shows the normalized root mean squared (rms) amplitude of the EMGG signal as a function of azimuth displacement (measured in cm around the neck in reference to the thyroid prominence). The sensor positions agree roughly with those shown in Fig. 3, although the transverse sections through the neck in Fig. 3 were not obtained from any of the four subjects. It is clear that the signal strength *decreases* in both directions with azimuth for all four subjects. There is a little ripple in the general maximization of the signal strength near zero, but this is attributed to system and measurement noise. These data are quite compelling in favor of the diffraction mode, for which the 0° azimuth is a clear advantage, as was argued earlier. However,

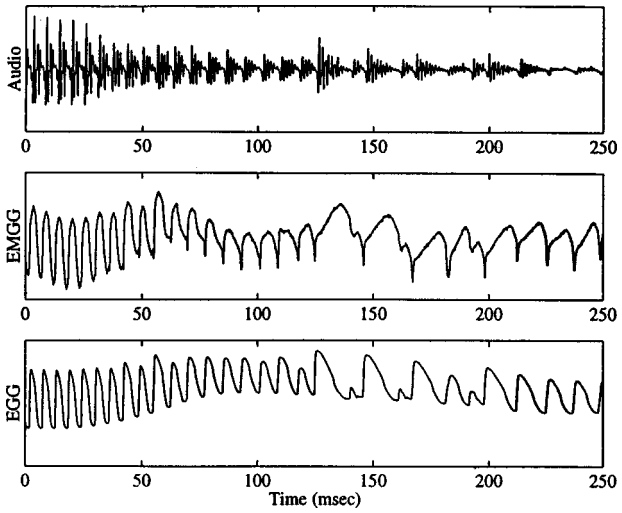

FIG. 9. Transition from ''modal'' register to vocal ''fry,'' spoken by subject S2. Recorded signals are audio, EMGG, and EGG.

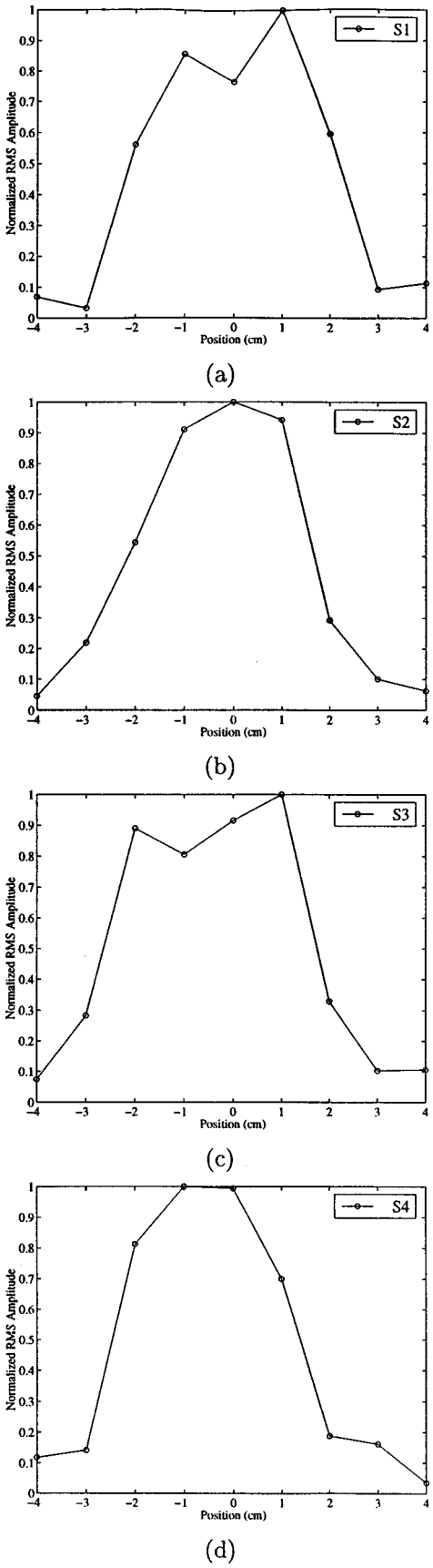

FIG. 10. Variation of the root mean square (rms) value of the EMGG signal as a function of azimuth position relative to the mid-sagittal plane.

because of the differences in path length, close range scattering, and multiple moving tissue surfaces (such as the trachea in combination with the medial surface of the vocal folds), the reflection mode hypothesis cannot be totally discarded.

CONCLUSIONS

It appears that electromagnetic glottography, EMGG, may be a viable alternative to electroglottography (EGG) for pitch extraction and vocal fold contact assessment. The EMGG signals are basically similar to those of EGG, but some differences exist as a function of phonation type, subject, and sensor placement. Closer agreement has been found with phonation types for which the anterior glottis is assumed to be the primary probing region, suggesting that the sensor operates more in a diffraction mode than in a reflection mode in this near- to mid-field region (about a wavelength from the source). However, another hypothesis by Burnett (1999), that the EMGG signals are significantly influenced by the tracheal wall motions, should be investigated in the future.

A clear advantage of the EMGG approach is that contact with the subject's skin is not needed. The capacity of the EMGG to provide sensing ''at a distance'' leaves space for other sensors to be used simultaneously in clinical applications. However, as shown in this study, there may be a confounding between reflected and diffracted waves. This confounding may be reduced by redesigning the angle between the electrodes. Because the EMGG signal has the potential of measuring all kinds of tissue movement (near the glottis and from the tracheal walls), under conditions of contact as well as noncontact, it is neither a pure contact area nor a pure glottal area detector. In the future, more spatial discrimination may be attainable with arrays of sensors or focusing antennas that could be designed to focus the EM wave onto a specific tissue subsurface to measure glottal positions as a function of both space and time.

ACKNOWLEDGMENTS

This work was supported by Grant No. DO02532 from the National Institute on Deafness and other Communication Disorders and under the auspices of the U.S. Department of Energy by Lawrence Livermore National Laboratory under Contract No. W-7405-Eng-48.

Burnett, G. C. (**1999**). ''The Physiological Basis of Glottal Electromagnetic Micropower Sensors (GEMS) and Their Use in Defining an Excitation Function for the Human Vocal Tract,'' Dissertation, University of California, Davis.

Burnett, G. C., and Leonard, R. (**1999**). ''Use of Kodak Ektapro high-speed digital cameras in laryngoscopy,'' Phonoscope **2**, 31–38.

Burnett, G. C., Gable, T. G., Holzrichter, J. F., and Ng, L. C. (**1997**). ''Voiced excitation functions calculated from micro-power impulse radar information,'' J. Acoust. Soc. Am. **102**, 3168(A). Available at the web site: http://speech.llnl.gov/

Childers, D., Hicks, D., Moor, G., and Alsaka, T. (**1986**). ''A model for vocal fold vibratory motion, contact area, and the electroglottogram,'' J. Acoust. Soc. Am. **80**, 1309–1320.

Hamlet, S., and Reid, J. (**1972**). ''Transmission of ultrasound through the larynx as a means of determining vocal-fold activity,'' IEEE Trans. Biomed. Eng. **19**, 34–37.

Holzrichter, J. F., Burnett, G. S., Ng, L. C., and Lea, W. A. (**1998**). ''Speech articulator measurements using low power EM-wave sensors,'' J. Acoust. Soc. Am. **103**, 622.

Holzrichter, J. F., Lea, W. A., McEwan, T. E., Ng, L. C., and Burnett, G. C. (**1996**). ''Speech Coding, Recognition, and Synthesis using Radar and Acoustic Sensors,'' University of California Report UCRL-ID-123687 (reprints available from the Office of Scientific and Technical Information, P.O. Box 62, Oak Ridge, TN 37831).

Löfqvist, A., and Yoshoika, H. (**1980**). ''Laryngeal activity in Swedish obstruent clusters,'' J. Acoust. Soc. Am. **68**, 792–801.

McEwan, T. E. U.S. Patents 5,345,471 (**1994**), 5,361,070 (**1994**), and 5,573,012 (**1996**). Generalized circuit descriptions are contained in these patents, however a wide range of EM sensor systems can be used for experiments similar to those described above.

Rothenberg, M. (**1973**). ''A new inverse filtering technique for deriving the glottal airflow waveform during voicing,'' J. Acoust. Soc. Am. **53**, 1632–1645.

Skolnik, M. I. (**1990**). *The Radar Handbook*, 2nd ed. (McGraw-Hill, New York).

Titze, I. (**1990**). ''Interpretation of the electroglottographic signal,'' J. Voice **4**, 1–9.

Zagzebski, J., Bless, D., and Ewanowski, S. (**1983**). ''Pulse echo imaging of the larynx using rapid ultrasonic scanners,'' in *Vocal Fold Physiology: Contemporary Research and Clinical Issues*, edited by D. M. Bless and J. H. Abbs (College-Hill, San Diego), pp. 210–220.

Effect of stimulation rate on phoneme recognition by Nucleus-22 cochlear implant listeners

Qian-Jie Fu[a] and Robert V. Shannon
Department of Auditory Implants and Perception, House Ear Institute, 2100 West Third Street, Los Angeles, California 90057

(Received 5 January 1999; revised 3 July 1999; accepted 13 October 1999)

This study investigated the effect of pulsatile stimulation rate on medial vowel and consonant recognition in cochlear implant listeners. Experiment 1 measured phoneme recognition as a function of stimulation rate in six Nucleus-22 cochlear implant listeners using an experimental four-channel continuous interleaved sampler (CIS) speech processing strategy. Results showed that all stimulation rates from 150 to 500 pulses/s/electrode produced equally good performance, while stimulation rates lower than 150 pulses/s/electrode produced significantly poorer performance. Experiment 2 measured phoneme recognition by implant listeners and normal-hearing listeners as a function of the low-pass cutoff frequency for envelope information. Results from both acoustic and electric hearing showed no significant difference in performance for all cutoff frequencies higher than 20 Hz. Both vowel and consonant scores dropped significantly when the cutoff frequency was reduced from 20 Hz to 2 Hz. The results of these two experiments suggest that temporal envelope information can be conveyed by relatively low stimulation rates. The pattern of results for both electrical and acoustic hearing is consistent with a simple model of temporal integration with an equivalent rectangular duration (ERD) of the temporal integrator of about 7 ms. [S0001-4966(00)06501-2]

PACS numbers: 43.71.Es, 43.71.Ky, 43.66.Ts [DOS]

INTRODUCTION

The continuous interleaved sampler (CIS) stimulation strategy is one of the most successful speech processing strategies for electrical stimulation of the auditory nerve. For speech processors with the CIS strategy, the spectral representation of speech sounds is encoded by the number of stimulated electrodes and temporal resolution is achieved by high-rate stimulation with short biphasic pulses interleaved in time across electrodes (Wilson *et al.*, 1991). A greater number of stimulated electrodes (channels) should provide better spectral resolution of speech sounds, while a higher rate of stimulation would improve the temporal sampling of the speech signal and possibly increase the stochastic response properties of the activated neurons (Rubinstein *et al.*, 1999; Wilson *et al.*, 1997a,b).

Many efforts have been made to understand the effect of the number of channels on speech performance of cochlear implant listeners (Fishman *et al.*, 1997; Lawson *et al.*, 1993; Brill *et al.*, 1997; Shannon *et al.*, 1995). The data from these studies have generally shown that performance improves with the number of channels up to about six to eight channels. Increase in the number of channels beyond eight has resulted in little improvement in performance.

Unlike the consistent results observed in studies of the number of channels, the pattern of results observed in studies of stimulation rates are much more variable. Lawson *et al.* (1996) measured consonant identification in five cochlear implant listeners using a six-channel CIS strategy at three stimulation rates: 250, 833, and 2525 pps/electrode. Although no statistical tests were performed, some individual listeners showed small, apparently significant improvements at one or both of the higher rates. However, across listeners the average consonant recognition was only 1.6% higher for the fast rate than the slow rate, and was 0.4% lower for the fast rate than for the medium rate.

Brill *et al.* (1998a,b) investigated the effect of stimulation rate with a fixed number of channel numbers in cochlear implant listeners using the Med-El COMBI 40+ device. In the first experiment, two pilot studies were conducted where the effect of stimulation rate in the CIS strategy was tested. Tests of consonant identification with one subject showed an increase in scores with increases in pulse rate from 625 pps/electrode to 1515 pps/electrode. In the second experiment, the stimulation rate was varied between 400 and 3030 pps/electrode in six-channel processors. The results showed a peak in performance of monosyllabic word recognition at the rate of 1515 pps/electrode for three subjects and at 3030 pps/electrode for the remaining two subjects. In the third experiment the stimulation rate was varied between 800 and 4545 pps/electrode in four-channel processors. The results showed peak in performance of monosyllabic word recognition at the rate of 1515 pps-per-electrode for one of the subjects, an asymptote in performance at 3030 pps-per-electrode for another subject, and increases in performance across rates for the remaining two subjects. Kiefer *et al.* (1999) also investigated the effect of variations in stimulus rate in cochlear implant users with the CIS speech coding strategy. They reported significant and sometimes large (e.g., 22%) improvements in monosyllable and vowel recognition when pulse rates were increased from 600 to 1500 pps, and reported for some patients improvements in performance with increases

[a]Electronic mail: qfu@hei.org

in rate to 2272 pps and to 4545 pps. A more recent investigation on the issue of the stimulation rate has been conducted by Loizou and Poroy (1999). They measured the monosyllable and phoneme recognition in six cochlear implant users with the CIS strategy at four different stimulation rates: 400 pps, 800 pps, 1400 pps, and 2100 pps. They reported a significant improvement in monosyllable and consonant recognition when pulse rates were increased from 400 to 800 pps as well as from 800 to 2100 pps. However, no significant improvement on the multi-talker vowel recognition was observed when the rates were increased from 400 to 2100 pps.

The effect of the stimulation rate on speech recognition is also investigated in cochlear implant users with the SPEAK strategy. Vandali *et al.* (1998) evaluated the effect of varying the stimulation rate on speech perception in five post-linguistically deaf adult users of the Nucleus 24 Cochlear Implant System with the SPEAK processing strategy. In their study, three different rates of electrical stimulation (250, 807, and 1615 pps/electrode) were employed on all 20 active electrodes. They found no statistically significant difference in performance between the low and medium stimulation rates. However, significantly poorer results were observed for the high-rate condition for some tests for some individuals. Lawson *et al.* (1996) also looked at SPEAK-like processors, which they termed ''n of m'' processors. In contrast to the Vandali *et al.* study, Lawson *et al.* found an improvement in performance at 833 pps/electrode compared to 250 pps/electrode in four out of five subjects. Arndt and Staller (1999) evaluated SPEAK (a slow rate strategy) and ACE (a strategy similar to SPEAK but with higher stimulation rate) on a within-subject basis in a sample of post-linguistically deafened adults implanted with the Nucleus 24 device. Results showed that the faster ACE strategy provided significantly better scores for sentence recognition in noise; however, the difference of the mean performance for sentences in quiet was not significant between the faster ACE strategy and the slower SPEAK strategy.

In general, findings with both CIS and SPEAK-like processors indicate a high variability in results across subjects, with some subjects showing little difference in performance as a function of stimulation rate, some showing a peak in performance at a particular stimulation rate, and other subjects showing significant increase in performance with increases in rate up to the maximum tested rate. One possible explanation is that some subjects cannot utilize the better temporal envelope cues provided by higher stimulation rates. A related question is how much temporal envelope information can be utilized by cochlear implant users. The importance of temporal envelope cues in speech recognition has been well documented in studies of normal-hearing listeners.

Rosen (1992) and Plomp (1983) have proposed a framework for understanding the role of temporal information in speech. Low-frequency temporal fluctuations (2–50 Hz) convey segmental information about prosody, duration, manner of articulation, and voicing. Temporal fluctuations in the 50–500 Hz range convey periodicity information that signals voicing and low first formant information. Temporal information above 500 Hz is primarily conveyed spectrally and provides information about fine structure. Since cochlear implant listeners have limited spectral resolution it has long been assumed that they could at least take advantage of the first two categories of temporal information. Psychophysical studies have shown that cochlear implants listeners can resolve temporal fluctuations at least as well as normal-hearing listeners (e.g., Shannon, 1983, 1992, 1993), and so should have access to all available temporal information in speech.

Steeneken and Houtgast (1980) measured temporal envelope information in speech by measuring the modulation spectrum of speech in octave bands. The shape of the modulation spectrum was similar in all spectral regions: a Gaussian-shaped curve on a logarithmic modulation frequency scale with a peak at 3–4 Hz (the word/syllable rate) and half-power points at 1 and 10 Hz. Thus most of the temporal modulations in running speech are between 1 and 10 Hz.

Perceptual studies have found a limit of 20–50 Hz for useful temporal cues in speech. Van Tasell *et al.* (1987) measured consonant recognition for noise modulated with the temporal envelope of speech. They observed an improvement in recognition when the low-pass filter on the envelope information was increased from 20 Hz to 200 Hz, but no significant difference between envelope filters of 200 and 2000 Hz. Shannon *et al.* (1995) extended this finding to the case of one, two, three, or four spectral bands of noise representing the spectral distribution of speech. Regardless of the number of spectral bands they found no difference in results between envelope filters of 50, 160, and 500 Hz. Drullman *et al.* (1994) found a limit of 16 Hz on the useful temporal information when speech was represented by 24, $\frac{1}{4}$-octave bands of noise each modulated by the low-pass filtered envelope signal from the respective spectral band. All of these studies show that envelope frequencies contribute to speech recognition only up to 16–50 Hz. For conditions in which no spectral cues are present, subjects may be forced to use temporal cues and may improve in performance up to envelope frequencies of 50 Hz. But when spectral cues are also available, the limit of temporal information appears to be 16–20 Hz. These results indicate that listener's psychophysical capability for detecting temporal fluctuations, which extends to 60–100 Hz as measured by temporal modulation transfer functions (Viemeister, 1979) is far better than is needed for detecting the useful envelope fluctuations in speech.

According to the sampling theorem, the stimulation rate needs to be only twice the highest frequency that we wish to represent. If temporal information is useful up to only 50 Hz, then sampling rate of 100 Hz should be sufficient to convey all temporal cues. The present study focuses on the effect of stimulation rate for representing temporal cues in speech. Vowel and consonant scores are measured as a function of stimulation rate over the range of 50–500 pulses/s/electrode in six Nucleus-22 cochlear implant listeners with four-channel CIS processors. The allocation of frequencies to electrodes and the electrode locations are held constant in these processors; only stimulation rate is varied.

TABLE I. Subject information for three Nucleus-22 cochlear implant listeners who participated in the present study. Frequency table refers to the frequency allocation used by the listener in their everyday processor. Frequency table 7 has a frequency range of 120–8658 Hz while frequency table 9 has a range of 150–10 823 Hz. Frequency table 9 is intended to be an approximate tonotopic map to the electrode locations for a full electrode insertion. Insertion depth is reported as the number of stiffening rings outside the round window from the surgical report. A full insertion would be 0 rings out. Sentence and vowel scores are from subjects' own Spectra 22 processor.

Subject	Age	Gender	Cause of deafness	Duration of use	Insertion depth	Freq. table	HINT score	Vowel score	Cons score
N3	57	M	Trauma	8 years	3 rings out	7	96.2%	69.5%	74.2%
N4	41	M	Trauma	6 years	4 rings out	9	100%	82.2%	82.0%
N7	56	M	Unknown	4 years	0 rings out	9	98.9%	67.7%	71.1%
N9	56	F	Hereditary	8 years	4 rings out	9	100%	68.3%	71.9%
N17	72	F	Unknown	3 years	10 rings out	7	81.0%	37.7%	51.2%
N19	68	M	Noise-induced	3 years	6 rings out	7	100%	77.2%	56.2%

I. EXPERIMENT 1: EFFECT OF STIMULATION RATE

This experiment measured vowel and consonant recognition as a function of stimulation rate in cochlear implant listeners fitted with a custom four-channel CIS speech processing strategy. Seven stimulation rate conditions were tested in the present study: 50, 100, 150, 200, 300, 400, and 500 pps-per-channel.

A. METHODS

1. Subjects

Six post-lingually deafened adults using the Nucleus-22 cochlear implant device participated in this study. All were native speakers of American English and had at least three years experience utilizing the SPEAK speech processing strategy. All implant subjects had 20 active electrodes available for use. Three subjects (N4, N7, and N9) used frequency allocation table 9 (150–10 823 Hz) in their clinical implant processor and three subjects (N3, N17, and N19) used frequency allocation table 7 (120–8658 Hz). Three subjects (N3, N4, and N7) had extensive experience in speech recognition experiments, while the other three (N9, N17, and N19) had relatively little experience in such experiments. Table I contains relevant information for the six subjects, including their most recent scores on the HINT sentence test and recent scores on the same multi-talker vowel and consonant tests used in this experiment, presented without lip-reading through their normal 20-electrode SPEAK processor.

2. Test materials and procedures

Speech performance was assessed using two measures: vowel and consonant identification. Vowel recognition was measured in a 12-alternative identification paradigm, including 10 monophthongs (/i ɪ ɛ æ u ʊ ɑ ʌ ɔ ɝ/) and 2 diphthongs (/o e/), presented in a /h/vowel/d/ context. The tokens for these closed-set tests were digitized natural productions from five men, five women, three boys, and two girls, drawn from the materials collected by Hillenbrand *et al.* (1995). Consonant recognition was measured in a 16-alternative identification paradigm, for the consonants /b d g p t k l m n f s ʃ v z θ dʒ/, presented in an /a/consonant/a/ context. Two exemplars of each of the 16 consonants were produced by 3 speakers (1 male, 2 female), and each was presented twice, for a total of 192 tokens (16 consonants* 3 talkers* 2 exemplars* 2 repeats).

Each test block included 180 tokens for vowel recognition (15 talkers* 12 vowels) and 192 tokens for consonant recognition. A stimulus token was randomly chosen from 180 tokens in vowel recognition and from 192 tokens in consonant recognition and presented to the subject. Following the presentation of each token, the subject responded by pressing one of 12 buttons in the vowel test or one of 16 buttons in the consonant test, each marked with one of the possible responses. The response buttons were labeled in a /h/-vowel-/d/ context (heed, hawed, head, who'd, hid, hood, hud, had, heard, hoed, hod, hayed) for the vowel recognition task and /a/-consonant-/a/ context following an example word for the consonant recognition task. Individual data points represent two runs in each condition (30 presentations of each vowel, and 24 presentations of each consonant).

All signals were presented at comfortable audible levels through a custom implant interface system (Shannon *et al.*, 1990). Subjects were instructed to maintain the same loudness scale across all test conditions. Subjects N3, N4, and N7 were highly familiar with the test materials and the test procedure from prior experiments, and were familiar with the experimental four-channel CIS processor from prior experiments. Subjects N9, N17, and N19 were less familiar with the test materials and procedures, and had no prior experience with CIS processors. The order of the seven rate conditions, and the order of the vowel and consonant tests, were counterbalanced across subjects. No feedback was provided.

3. Signal processing

The four-channel CIS processor was implemented through the custom interface (Shannon *et al.*, 1990), bypassing the subject's Spectra-22 speech processor. The signal was first pre-emphasized using a first-order Butterworth (6 dB/octave) high-pass filter with a cutoff frequency of 1200 Hz, and then bandpass filtered into four broad frequency bands using eighth-order Butterworth filters (96 dB/octave). The corner frequencies of the bands were at 300 Hz, 713 Hz, 1509 Hz, 3043 Hz, and 6000 Hz. The envelope of the signal in each band was extracted by half-wave rectification and

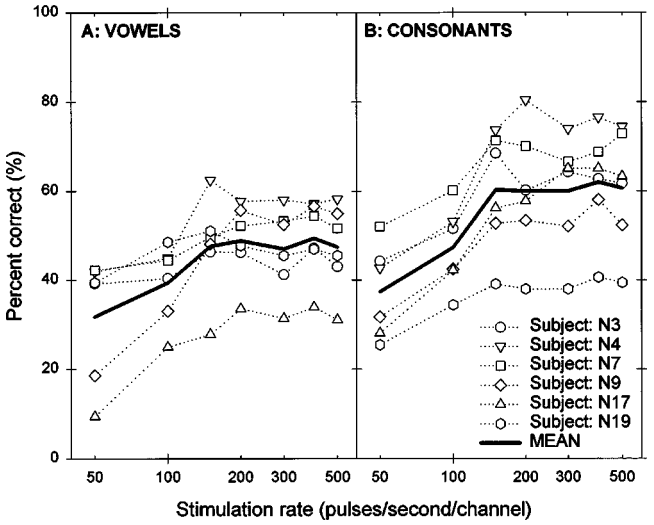

FIG. 1. Vowel and consonant recognition as a function of the stimulation rate for six Nucleus-22 cochlear implant users. (A) Vowel recognition; (B) consonant recognition. The cutoff frequency on the low-pass envelope filter was fixed at 40% of the stimulation rate. Error bars represent ± one standard deviation.

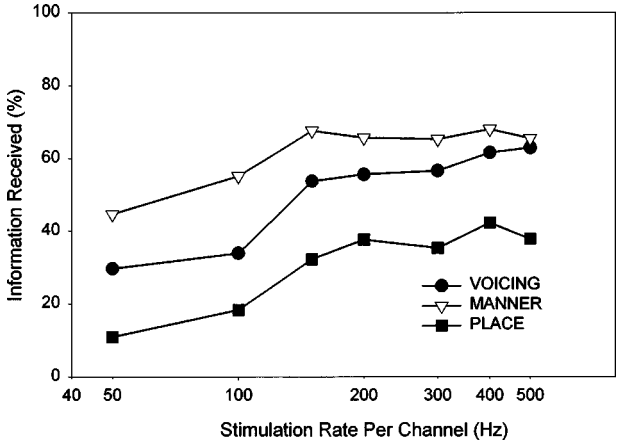

FIG. 2. Consonant information received on the production based features of voicing, manner, and place of articulation as a function of stimulation pulse rate.

low-pass filtering (eighth-order Butterworth: 48 dB/octave). To avoid any aliasing effects, the cutoff frequency of the low-pass envelope filters was set to 40% of the rate of stimulation. The acoustic amplitude (40-dB range) was transformed into electric amplitude by a power-law function with an exponent of 0.2 ($E=A^{0.2}$; Fu and Shannon, 1998) between each subject's threshold (*T*-level) and upper level of loudness (*C*-level). This transformed amplitude was then used to modulate the amplitude of a continuous biphasic pulse train with a 100 μs/phase pulse duration, and delivered to four electrode pairs interleaved in time: (18,22), (13,17), (8,12), and (3,7). Note that a relatively broad stimulation mode (BP+3) was used in the present study. The major reason was that several subjects could not reach upper level of loudness (*C*-level) on the apical electrode pairs with BP+1 stimulation mode. The rate of the biphasic pulse train was varied from 50 pps/channel to 500 pps/channel, for a total of 7 stimulation rate conditions. The highest stimulation rate tested was 500 pps/channel due to hardware limitations of the internal receiver in the Nucleus 22 cochlear implant—for 100 μs/phase stimulation reliable rates higher than 2000 pps (500 pps/channel) cannot be achieved. Also, the envelope waveform of all speech signals was preprocessed off-line and stored on PC computer disk. In each presentation, preprocessed buffers of stimulus information were transmitted to the subject through a custom implant interface system (Shannon *et al.*, 1990). This implementation precludes the possibility of acclimation with real-time connected speech.

B. Results and discussion

Figure 1 shows the vowel and consonant recognition scores as a function of stimulation rate. Panel (A) shows the individual and mean vowel recognition scores and panel (B) shows the individual and mean consonant recognition scores. When the stimulation rate was 50 pps/channel, 32% of vowels and 37% of consonants were correctly recognized. When the stimulation rate was increased from 50 pps to 150 pps/channel, mean vowel recognition increased significantly to 48% correct and mean consonant scores increased significantly to 61% correct. No significant improvement of vowel or consonant recognition was observed when the stimulation rate was further increased. For vowel recognition, there was a significant effect of stimulation rate [$F(6,42)=63.38$, $p<0.001$], of subjects [$F(5,42)=144.16$, $p<0.001$], and significant interaction between stimulation rate and subjects [$F(30,42)=6.95$, $p<0.001$]. For consonant recognition, there was a significant effect of stimulation rate [$F(6,42)=143.78$, $p<0.001$], of subjects [$F(5,42)=258.99$, $p<0.001$], and significant interaction between stimulation rate and subjects [$F(30,42)=5.19$, $p<0.001$]. *Post hoc* Tukey HSD tests indicate that both vowel and consonant scores were significantly lower for speech processors with stimulation rates lower than 100 pps.

In the present results there was no significant change in performance between stimulation rates of 500 and 150 pps/channel. Subjects did report a difference in speech quality when the stimulation rate was 200 pps or 150 pps, noting that speech sounded increasingly ''machinelike'' or ''weird.'' However, phoneme recognition performance deteriorated only when the stimulation rate was reduced to less than 150 pps.

Figure 2 presents the information received on the consonant features of voicing, manner, and place of articulation (Miller and Nicely, 1955). Reception of voicing, manner, and place cues all increased with stimulation rate up to 150 Hz, and then did not increase as the stimulation rate was increased above 150 Hz.

Phoneme recognition was significantly poorer when the stimulation rate was 100 pps-per-channel or lower. One possible explanation is that performance drop was due to the lower temporal resolution transmitted by the envelope filters. As described in the signal processing section, the cutoff frequency of envelope filters was reduced as the stimulation rate was decreased in order to remove any aliasing effects. For example, an envelope filter with a 60 Hz cutoff frequency was used when the stimulation rate was 150 pps, while 20 Hz was used for the stimulation rate of 50 pps. It is

possible that the loss of temporal envelope information within each channel was due to the envelope filter rather than the lower stimulation rate *per se*. It is important to distinguish if the limitation is due to the front-end speech processing or to the limitations of perception in electrical stimulation. To determine if the low-pass envelope filter cutoff frequency was the factor limiting speech recognition rather than the stimulation rate, an additional experiment was conducted.

II. EXPERIMENT 2: EFFECT OF ENVELOPE FILTER CUTOFF FREQUENCY

Experiment 2 measured phoneme recognition in conditions that held the stimulation rate per channel constant at 500 pps while reducing the envelope filter cutoff frequency. Vowel and consonant recognition was measured as a function of cutoff frequency of the envelope filters in both cochlear implant listeners using a custom four-channel CIS speech processor and in normal-hearing subjects listening to speech processed by a comparable four noise-band acoustic processor (Shannon *et al.*, 1995).

A. Method

1. Subjects

The six cochlear implant listeners from experiment 1 and five normal-hearing listeners aged 25 to 35 participated in this experiment. All normal-hearing subjects had thresholds better than 15 dB HL at audiometric test frequencies from 250 to 8000 Hz and all were native speakers of American English.

2. Test materials and procedures

The same test materials and procedures as experiment 1 were used in this experiment.

3. Signal processing

In electric hearing, the four-channel CIS processors were similar to those described in experiment 1 except that, when extracting the envelope in each band, the cutoff frequency of the envelope filters was varied from 2 Hz to 160 Hz. Seven cutoff frequencies were tested: 2, 5, 10, 20, 40, 80, and 160 Hz. The stimulation rate of pulse trains modulated with envelope information was fixed at 500 pps/channel.

In acoustic hearing, the speech signal was spectrally degraded using a four-band modulated noise processor (Shannon *et al.*, 1995). Envelope extraction in each band was the same as that in electric stimulation, except that the cutoff frequency of envelope filters was varied over a broader range: 2 Hz–640 Hz. Seven envelope filter cutoff frequencies were tested: 2, 5, 10, 20, 40, 160, and 640 Hz. Instead of modulating a continuous pulse train as in electric stimulation, the extracted envelope waveform in each band in the acoustic processor was used to modulate wideband noise that was subsequently spectrally limited by a bandpass filter with the same characteristics used for the analysis filter band. The outputs from all modulated noise bands were then summed and the processed speech tokens were equated in terms of rms energy. All processed speech stimuli were stored on computer disk and were presented via custom software to a 16-bit D/A converter (TDT DD1) at a 16 kHz sampling rate. A-weighted stimuli were presented to the listeners diotically through Sennheiser HDA200 headphones at 70 dB. Within each test, speech stimuli were presented in random order, and test conditions were pseudo-randomized for each subject.

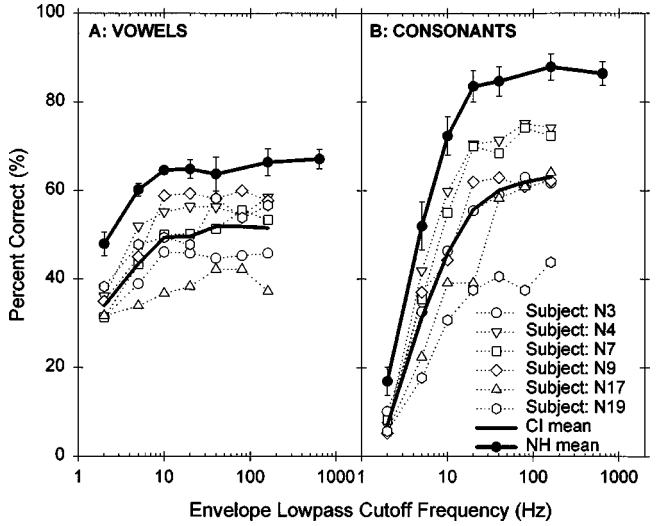

FIG. 3. Vowel and consonant recognition as a function of the cutoff frequency of the low-pass envelope filters for six Nucleus-22 cochlear implant users and five normal-hearing subjects. (A) Vowel recognition; (B) consonant recognition. Stimulation rate was fixed at 500 pps/electrode for the implant subjects. Noise bands were used as carriers for the NH listeners. Error bars represent ± one standard deviation.

B. Results and discussion

Figure 3 shows the vowel and consonant recognition scores as a function of the cutoff frequency of envelope filters. Figure 3(A) shows the individual and mean vowel scores from six cochlear implant users and the mean vowel scores from five normal-hearing listeners (results averaged because there was no significant effect of subjects [$F(4,30) = 0.361$, $p = 0.834$]). Vowel scores increased from 48% to 65% for normal-hearing listeners and from 34% to 49% for implant listeners when the cutoff frequency was increased from 2 Hz to 10 Hz. No significant improvement in either cochlear implant users or normal-hearing listeners was observed when the cutoff frequency was further increased above 10 Hz. There was a significant effect of the cutoff frequency on vowel recognition for both cochlear implant users [$F(6,35) = 5.52$, $p < 0.001$] and for normal-hearing listeners [$F(6,28) = 35.41$, $p < 0.001$]. *Post hoc* Tukey HSD tests indicated that the vowel score was significantly lower only when the cutoff frequency was 2 Hz. An ANOVA also showed a significant interaction between subjects and cutoff frequency for cochlear implant users [$F(30,42) = 4.15$, $p < 0.001$] but no significant interaction between electric hearing and acoustic hearing on vowel recognition [$F(6,63) = 0.215$, $p = 0.971$].

Figure 3(B) shows the individual and mean consonant scores from six cochlear implant users and the mean conso-

nant scores from five normal-hearing listeners (no significant effect of subjects [$F(4,30)=0.016$, $p=0.999$]). When the envelope cutoff frequency was 2 Hz, consonant recognition was nearly at a chance level for cochlear implant users. When the cutoff frequency was increased from 2 to 20 Hz, consonant scores increased dramatically to 56% correct. For normal-hearing listeners, consonant scores also increased dramatically from 17% to 84% when the cutoff frequency was increased from 2 Hz to 20 Hz. Similar to vowel recognition, no significant improvement was observed in either cochlear implant users or normal-hearing listeners when the cutoff frequency was further increased. An analysis of variance showed a significant effect of the cutoff frequency on consonant recognition for both cochlear implant users [$F(6,35)=21.60$, $p<0.001$] and for normal-hearing listeners [$F(6,28)=248.41$, $p<0.001$]. *Post hoc* Tukey HSD tests indicate that the consonant score was significantly lower when the cutoff frequency was 5 Hz or less. Further ANOVA tests showed a significant interaction between subjects and cutoff frequency for cochlear implant users [$F(30,42)=11.90$, $p<0.001$] but no significant interaction between electric hearing and acoustic hearing on consonant recognition [$F(6,63)=1.40$, $p=0.230$].

The fact that implant and normal hearing listeners showed a similar pattern of performance as a function of the envelope cutoff frequency suggests that the effect is not specific to electrical stimulation and likely represents a limitation in speech recognition that is common to electric and acoustic hearing. In previous psychophysical studies (e.g., Shannon, 1993) relatively little difference was observed between acoustic and electric hearing on measures of basic temporal processing. The present result extends this finding to the speech envelope domain.

Another interesting observation is that the effect of the envelope cutoff frequency on speech recognition was significantly different for vowels and consonants. Vowel recognition was only moderately reduced as the cutoff frequency was reduced to 2 Hz, where cochlear implant (CI) listeners still scored 34% percent correct and normal-hearing (NH) listeners scored 48% correct. However, consonant recognition scores dropped dramatically from 70% for implanted listeners and 90% for normal-hearing listeners to near-chance level as the cutoff frequency was reduced from 20 Hz to 2 Hz. This result indicates that both CI and NH listeners relied upon temporal envelope cues more for consonant recognition than for vowel recognition, consistent with the previous acoustic results (Drullman *et al.*, 1994).

One might think that high-frequency temporal envelope information would become less important as the number of spectral channels increases, i.e., temporal cues that are important when there are few spectral cues might be less important when more spectral cues are available. However, this does not seem to be the case. Temporal envelope information below 20 Hz can provide sufficient information for modest levels of consonant recognition, even in the complete absence of spectral information (Shannon *et al.*, 1995; Turner *et al.*, 1995; Van Tasell *et al.*, 1987, 1992), and temporal envelope information above 50–200 Hz does not increase phoneme recognition regardless of the spectral resolution

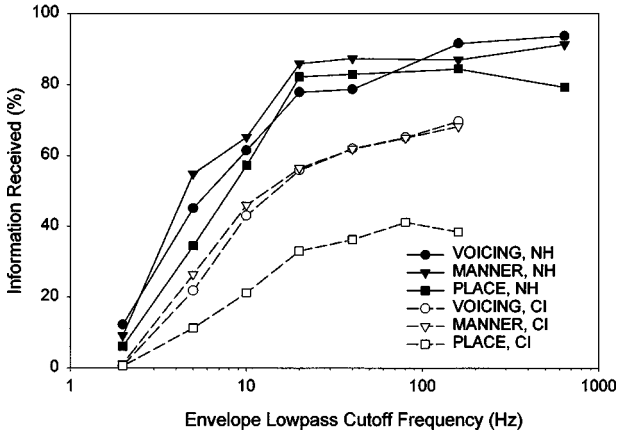

FIG. 4. The received information on consonant voicing (circles), manner (inverted triangles), and place (squares) as a function of the cutoff frequency of the low-pass envelope filters for six Nucleus-22 cochlear implant users (open symbols) and five normal-hearing subjects (filled symbols).

(Drullman *et al.*, 1994; Shannon *et al.*, 1995; Van Tasell *et al.*, 1987, 1992).

In summary, all of the abovementioned studies are consistent with a limit of useful temporal modulation information in speech between 16 and 50 Hz. It is possible that temporal information up to 50 Hz is important when all spectral cues are limited or missing, but when spectral information is available only temporal envelope modulations below 20 Hz are critical for speech recognition. One might think that periodicity information in the 50–300 Hz range would be important for correct identification of voicing. However, these studies show that voicing is well recognized when temporal envelope information is filtered below 20 Hz. It appears that there are sufficient cues to signal the presence of voicing even when the explicit F_0 pulses are not present, as is the case in whispered speech.

Figure 4 shows the analysis of consonant information received on the production-based features of voicing, manner, and place (Miller and Nicely, 1995) from the data of experiment 2. Information received for all three features increased as the envelope cutoff frequency increased up to 20 Hz. For normal-hearing listeners there was no change in information received on manner and place as the envelope cutoff frequency was increased above 20 Hz, but voicing information increased slightly up to 80 Hz. In implant listeners a similar pattern of results was observed on voicing, although the level of information received was about 20 percentage points lower than the normal-hearing results. However, for the implant listeners information received on both voicing and manner of articulation increased slightly for envelope frequencies higher than 20 Hz.

It is not too surprising that higher accuracy of information transmission for voicing was received in speech processors with higher cutoff frequency of envelope filters, presumably because the F_0 information could be at least partly transmitted by the temporal modulation when the cutoff frequency of envelope filters was increased above 80 Hz. However, it is quite puzzling that the information received for manner continued to increase in cochlear implant listeners and not in normal-hearing listeners. Whether this difference

is due to the high variability of the results across cochlear implant listeners or is an important perceptual difference between acoustic simulation and electric stimulation remains to be answered. One possibility is that rapid spectral transitions in consonants are important for correct identification of manner. In normal-hearing listeners, in whom the noise-band carriers are in the correct tonotopic location, the spectral transitions provide sufficient information that the temporal properties are not necessary for correct identification of manner. But the temporal information may be more important in implant listeners, in whom the spectral cues may not be properly represented by the electrode locations.

III. GENERAL DISCUSSION

The data from the present study show no significant differences in consonant or vowel recognition performance for experimental speech processors with stimulation rates ranging from 150 to 500 pps/channel. This suggests that increases in rate over this range may not provide a substantial benefit to speech recognition in electric hearing.

The results from the present study do show significantly lower scores in vowel and consonant recognition for speech processors with stimulation rates of 50 and 100 pps than for processors with higher stimulation rates. The drop in speech recognition could arise either from information reduction in the processor (processor domain) or from a perceptual limitation inherent to implants (perceptual domain). One way in which information is clearly reduced is when the cutoff frequency of envelope filters is decreased. In experiment 1, as the stimulation rate was reduced from 150 pps/channel to 50 pps/channel, the cutoff frequency of envelope filters decreased from 60 Hz to 20 Hz to avoid aliasing effects. The data from the experiment 2 showed no significant improvements in vowel or consonant recognition when the cutoff frequency of envelope filters was increased above 20 Hz. This implies that the observed performance drop at low stimulation rates in experiment 1 was not caused by the information reduction inherent in the envelope filtering in the speech processor.

Another possibility is that the performance drop in speech recognition at low stimulation rates was caused by a perceptual limitation of the implant listeners. One explanation is that pulse trains with lower rates produce their own distinctive pitch sensation that may interfere with the envelope information that is being transmitted. Rate pitch produced by an electrical pulse train is strongest in the 50–150 Hz range and becomes weaker as the pulse rate increases above 150 Hz. The pitch sensation generally saturates for pulse rates above 300 Hz (Shannon, 1983; Tong *et al.*, 1983; Townshend *et al.*, 1987; McKay *et al.*, 1996), however, a few ''star'' implant patients are able to detect pitch differences up to stimulation pulse rates as high as 1 kHz (Pijl and Schwarz, 1995; Wilson *et al.*, 1997c). A stimulation pulse train that produces its own strong pitch may interfere with the envelope information that is being transmitted. Even though there was no difference in phoneme recognition for stimulation rates of 150–300 Hz in the present study, patients did report that these processors produced strange and unpleasant sound quality, possibly due to the interfering pitch of the carrier signal.

Both the saturation of rate pitch with stimulation rate and the reduction in speech recognition at low stimulation rates might be explained by a relatively slow central temporal integration. Moore *et al.* (1996) found that the best equivalent rectangular duration for the central temporal integrator is about 7 ms. At a pulse rate of 150 pps the separation between two successive pulses is 6.67 ms, while at 100 pps the pulse separation is 10 ms. Poor central integration at 100 Hz may cause the envelope information to ''break up'' and not provide an adequate carrier for the speech envelope information, a phenomenon that might be comparable to exceeding the flicker fusion threshold in vision. The ability to compare successive time frames of speech patterns may influence speech perception. If consecutive frames occur quickly enough, close comparison between two frames provides enough information for speech temporal pattern recognition. If consecutive frames occur too far apart in time, the perceptual ''image'' breaks up in time, resulting in poorer speech recognition. However, the direct relationship between the central temporal integration and speech pattern recognition is still not clear. Implant patients who perceive rate pitch up to high stimulation rates may have shorter central temporal integration times and thus may be able to use temporal information in speech at stimulation rates higher than 150 Hz. To resolve this issue both pitch estimation and speech recognition would have to be measured as a function of stimulation rate in implant listeners with high-frequency pitch saturation.

One interesting aspect of the present data is the apparent conflict with recent studies of implant performance with high-rate stimulation (Brill *et al.*, 1998a,b; Pelizzone *et al.*, 1998; Wilson *et al.*, 1997a). These studies have shown improved performance at very high stimulation rates ($>$500 Hz), and have observed considerable individual variability in the stimulation rate that produced maximum speech recognition. In general, these studies all used much higher stimulation rates than the present study, which was limited to rates of 500 pps/electrode or lower.

It is not yet clear what additional information these implanted listeners were receiving that allowed improved speech recognition at higher stimulation rates. Based on the present data and previous studies on the limited range of temporal envelope information in speech, it is possible but unlikely that electrical stimulation of the auditory system via cochlear implants allows the use of temporal cues of speech sounds at higher rates than for normal-hearing listeners.

One possible explanation is that speech recognition is improved by additional neural mechanisms that modify the responses to electrical stimulation at high stimulation rates, as proposed by Wilson *et al.* (1997a) and Rubinstein *et al.* (1999). Wilson *et al.* (1997a,b) demonstrated from intracochlear compound action potential recordings that high stimulation rates can produce acousticlike stochastic neural discharge patterns, whereas lower stimulation rates produce abnormal nonstochastic neural phase-locking. These stochastic modes of neural activation, which might be beneficial for transmitting speech information, only occur for stimulation

rates exceeding 1000–2000 pps/electrode. Due to the hardware limitations of the speech processor, the maximum stimulation rate possible in the present study was 500 pps/channel. Thus the present data are not able to exclude the possibility of improvements in performance at higher stimulation rates.

IV. SUMMARY AND CONCLUSIONS

Results from the present experiments show an asymptote in phoneme recognition for stimulation rates in the range of 150 to 500 pps-per-electrode. The cutoff frequencies of envelope filters for different stimulation rates were not sufficient to explain the effect of the stimulation rate on speech recognition, suggesting that the limiting factor was perceptual rather than a limitation inherent to the signal processing. The results of the present experiments are consistent with previous psychophysical and speech results on normal-hearing listeners, which show 7 ms equivalent rectangular duration of the central temporal integrator. The data of the present experiments suggest that cochlear implant users cannot benefit from the improvement of temporal sampling of the speech signal as the stimulation rate in increased from 150 to 500 pps/electrode. However, the present data do not exclude the possibility that additional neuronal mechanism at electrical stimulation rates higher than 500 pps/electrode may be beneficial for electric stimulation of auditory nerve.

ACKNOWLEDGMENTS

We appreciate the efforts of all subjects, especially the six implant listeners for their tireless participation in our experiments. We thank Professor James Hillenbrand for allowing us to use the multi-talker vowel test materials. The assistance of Xiaosong Wang in data collection and John Galvin III in editorial comments are also greatly appreciated. Work funded by NIH Grants Nos. R03-DC-03861, R01-DC-01526, and Contract No. N01-DC-92100.

Arndt, P., and Staller, S. (**1999**). ''Within-subject comparison of advanced coding strategies in the Nucleus 24 cochlear implant,'' unpublished data from Cochlear Corporation.

Brill, S. M., Hochmair, I., and Hochmair, E. S. (**1998a**). ''The importance of stimulation rate in pulsatile stimulation strategies in cochlear implants,'' Presented at the XXIV International Congress of Audiology, Buenos Aires.

Brill, S. M., Schatzer, R., Nopp, P., Hochmair, I., and Hochmair, E. S. (**1998b**). ''JCIS:CIS with temporally jittering stimulation pulses: Effect of jittering amplitude and stimulation rate on speech understanding,'' Presented at the 4th European Symposium on Paediatric Cochlear Implantation, s-Hertogenbosch, The Netherlands.

Brill, S. M., Gstöttner, W., Helms, J., Ilberg, C. v., Baumgartner, W., Müller, J., and Kiefer, J. (**1997**). ''Optimization of channel number and stimulation rate for the fast continuous interleaved sampling strategy in the COMBI 40+,'' Am. J. Otolaryngol. **18**, S104–S106.

Drullman, R., Festen, J. M., and Plomp, R. (**1994**). ''Effect of temporal envelope smearing on speech reception,'' J. Acoust. Soc. Am. **95**, 1053–1064.

Fishman, K., Shannon, R. V., and Slattery, W. H. (**1997**). ''Speech recognition as a function of the number of electrodes used in the SPEAK cochlear implant speech processor,'' J. Speech Hear. Res. **40**, 1201–1215.

Fu, Q.-J., and Shannon, R. V. (**1998**). ''Effects of amplitude nonlinearity on speech recognition by cochlear implant users and normal-hearing listeners,'' J. Acoust. Soc. Am. **104**, 2570–2577.

Hillenbrand, J., Getty, L., Clark, M., and Wheeler, K. (**1995**). ''Acoustic characteristics of American english vowels,'' J. Acoust. Soc. Am. **97**, 3099–3111.

Kiefer, J., von Ilberg, C., Rupprecht, V., Huber-Egener, J., Baumgartner, W., Gstöttner, W., and Stephan, K. (**1999**). ''Optimized speech understanding with the CIS-speech coding strategy in cochlear implants: The effect of variations in stimulus rate and numbers of channels,'' in *Cochlear Implants*, edited by S. B. Waltzman and N. Cohen (Thieme Medical and Scientific, New York).

Lawson, D., Wilson, B., and Finley, C. (**1993**). ''New processing strategies for multichannel cochlear prostheses,'' in *Natural and Artificial Control of Hearing and Balance*, edited by J. A. Allum, D. J. Allum-Mecklenburg, F. P. Harris, and R. Probst, Progress in Brain Research, Vol. 97 (Elsevier, Amsterdam), pp. 313–321.

Lawson, D. T., Wilson, B.S., Zerbi, M., and Finley, C. C. (**1996**). ''Speech processors for auditory prostheses,'' Third Quarterly progress report, NIH project N01-DC-5-2103, Neural Prosthesis Program, National Institutes of Health, Bethesda, MD.

Loizou, P., and Poroy, O. (**1999**). ''A parametric study of the CIS strategy,'' Abstracts of 1999 Conference on implantable auditory prosthesis, p. 34.

McKay, C. M., McDermott, H. J., and Clark, G. M. (**1996**). ''The perceptual dimensions of single-electrode and nonsimultaneous dual-electrode stimuli in cochlear implantees,'' J. Acoust. Soc. Am. **99**, 1079–1090.

Miller, G., and Nicely, P. (**1955**). ''An analysis of perceptual confusions among some English consonants,'' J. Acoust. Soc. Am. **27**, 338–352.

Moore, B. C. J., Peters, R. W., and Glasberg, B. R. (**1996**). ''Detection of decrements and increments in sinusoids at high overall levels,'' J. Acoust. Soc. Am. **99**, 3669–3677.

Pelizzone, M., Tinembart, J., Francois, J., Steger, D., Boex, C., and Montandon, P. (**1998**). ''Very-high stimulation rates for cochlear implants,'' presented at the 4th European Symposium on Paediatric Cochlear Implantation, s-Hertogenbosch, The Netherlands.

Pijl, S., and Schwarz, D. W. F. (**1995**). ''Melody recognition and musical interval perception by deaf subjects stimulated with electrical pulse trains through single cochlear implant electrodes,'' J. Acoust. Soc. Am. **98**, 886–895.

Plomp, R. (**1983**). ''The role of modulation in hearing,'' in *Hearing—Physiological Bases and Psychophysics*, edited by R. Klinke and R. Hartmann (Springer-Verlag, Berlin), pp. 270–276.

Rosen, S. (**1992**). ''Temporal information in speech: acoustic, auditory and linguistics aspects,'' Philos. Trans. R. Soc. London, Ser. B **336**, 367–373.

Rubinstein, J. T., Wilson, B. S., Finley, C. C., and Abbas, P. J. (**1999**). ''Pseudospontaneous activity: Stochastic independence of auditory nerve fibers with electrical stimulation,'' Hear. Res. **127**, 108–118.

Shannon, R. V. (**1983**). ''Multichannel electrical stimulation of the auditory nerve in man: I. Basic psychophysics,'' Hear. Res. **11**, 157–189.

Shannon, R. V. (**1992**). ''Temporal modulation transfer functions in patients with cochlear implants,'' J. Acoust. Soc. Am. **91**, 1974–1982.

Shannon, R. V. (**1993**). ''Psychophysics of electrical stimulation,'' in *Cochlear Implants: Audiological Foundations*, edited by R. S. Tyler (Singular Pub. Grp., San Diego), pp. 357–388.

Shannon, R. V., Adams, D. D., Ferrel, R. L., Palumbo, R. L., and Grantgenett, M. (**1990**). ''A computer interface for psychophysical and speech research with the Nucleus cochlear implant,'' J. Acoust. Soc. Am. **87**, 905–907.

Shannon, R. V., Zeng, F.-G., Kamath, V., Wygonski, J., and Ekelid, M. (**1995**). ''Speech recognition with primarily temporal cues,'' Science **270**, 303–304.

Steeneken, H. J. M., and Houtgast, T. (**1980**). ''A physical method for measuring speech-transmission quality,'' J. Acoust. Soc. Am. **67**, 318–326.

Tong, Y. C., Blamey, P. J., Dowell, R. C., and Clark, G. M. (**1983**). ''Psychophysical studies evaluating the feasibility of a speech processing strategy for a multiple-channel cochlear implant,'' J. Acoust. Soc. Am. **74**, 73–80.

Townshend, B., Cotter, N., Van Compernolle, D., and White, R. L. (**1987**). ''Pitch perception by cochlear implant subjects,'' J. Acoust. Soc. Am. **82**, 106–115.

Turner, C. W., Souza, P. E., and Forget, L. N. (**1995**). ''Use of temporal envelope cues in speech recognition by normal and hearing-impaired listeners,'' J. Acoust. Soc. Am. **97**, 2568–2576.

Vandali, A. E., Grayden, D. B., Whitford, L. A., Plant, K. L., and Clark, G. M. (**1998**). ''An analysis of high rate speech processing strategies using the Nucleus 24 Cochlear Implant,'' presented at the meeting Cochlear Implants in Children, June 4–7, 1998, Iowa City, IA.

Van Tasell, D. J., Greenfield, D. G., Logemann, J. J., and Nelson, D. A. (**1992**). ''Temporal cues for consonant recognition: Training, talker generalization, and use in evaluation of cochlear implants,'' J. Acoust. Soc. Am. **92**, 1247–1257.

Van Tasell, D. J., Soli, S. D., Kirby, V. M., and Widin, G. P. (**1987**). ''Speech waveform envelope cues for consonant recognition,'' J. Acoust. Soc. Am. **82**, 1152–1161.

Viemaster N. F. (**1979**). ''Temporal modulation transfer functions based upon modulation threshold,'' J. Acoust. Soc. Am. **66**, 1364–1380.

Wilson, B. S., Finley, C. C., Lawson, D., and Zerbi, M. (**1997a**). ''Temporal representations with cochlear implants,'' Am. J. Otol. **18**, S30–S34.

Wilson, B. S., Finley, C. C., Lawson, D. T., Wolford, R. D., Eddington, D. K., and Rabinowitz, W. M. (**1991**). ''Better speech recognition with cochlear implants,'' Nature (London) **352**, 236–238.

Wilson, B., Finley, C., Zerbi, M., Lawson, D., and van den Honert, C. (**1997b**). ''Speech processors for auditory prostheses,'' NIH project N01-DC-5-2103, Seventh Quarterly progress report, Neural Prosthesis Program, National Institutes of Health, Bethesda, MD.

Wilson, B., Zerbi, M., Finley, C., Lawson, D., and van den Honert, C. (**1997c**). ''Speech processors for auditory prostheses,'' NIH project N01-DC-5-2103, Eighth Quarterly progress report, Neural Prosthesis Program, National Institutes of Health, Bethesda, MD.

The time-frequency characteristics of violin vibrato: Modal distribution analysis and synthesis[a)]

Maureen Mellody
Applied Physics Program, University of Michigan, Randall Laboratory, 500 East University Drive, Ann Arbor, Michigan 48109-1120

Gregory H. Wakefield
Department of Electrical Engineering and Computer Science, University of Michigan, Advanced Technology Laboratories Building, 1101 Beal Avenue, Ann Arbor, Michigan 48109-2110

(Received 16 February 1999; revised 26 August 1999; accepted 5 October 1999)

A high-resolution time-frequency distribution, the modal distribution, is applied to the study of violin vibrato. The analysis indicates that the frequency modulation induced by the motion of the stopped finger on the string is accompanied by a significant amplitude variation in each partial of that note. Amplitude and frequency estimates for each partial are extracted from the modal distribution of ten pitches that span the range of the violin instrument. The frequency modulation is well-represented by a single sinusoid with a mean rate of 5.9 Hz and a mean excursion of ± 15.2 cents. A spectral decomposition of the amplitude envelopes of the partials shows that the peaks lie primarily at integer multiples of the vibrato rate. These amplitude and frequency estimates are used in an additive synthesis model to generate synthetic replicates of violin vibrato. Simple approximations to these estimates are created, and synthesized sounds using these are evaluated perceptually by seven subjects using discrimination, nonmetric multidimensional scaling (MDS), and sound quality scoring tasks. It is found that the absence of frequency modulation has little effect on the perceptual response to violin vibrato, while the absence of amplitude modulation causes marked changes in both sound quality and MDS results. Low-order spectral decompositions of the amplitude and frequency estimates also occupy the same perceptual space as the original recording for a subset of the pitches studied.
[S0001-4966(00)05701-5]

PACS numbers: 43.75.De [WJS]

INTRODUCTION

Violin vibrato is created by the rhythmic motion of the performer's left forearm and wrist which enables the stopped finger to rock back and forth on the fingerboard, changing the effective string length. This change corresponds to a modulation of the pitch of the note played. While this basic mechanism for producing violin vibrato is well understood, violin vibrato has been the subject of several studies to determine more explicitly the effect of vibrato on the frequency and amplitude of a note's partials. These studies[1–5] utilized short-time Fourier analysis or analog filtering to reveal the presence of amplitude modulation of the violin partials, in addition to the expected frequency modulation. The source of amplitude modulation is the result of the interaction between the frequency-varying partials and the densely spaced resonances of the violin. Such body resonances have been theorized to be present roughly every 45 Hz above 1 kHz, which could account for the amplitude variation seen in the data.[6,7] Weinreich[7] recently confirmed these theoretical predictions through acoustical measurements of the violin body.

The present study employs the modal distribution, a bilinear time-frequency analysis method developed by Pielemeier and Wakefield,[8] to improve the accuracy of the measured frequencies and amplitudes of a note's partials. Using sinusoidal approximations of the frequency modulation present in vibrato signals, estimates based on the modal distribution have been shown to be accurate to within 4 cents, a factor of 5 improvement over estimates based on a spectrogram. Similarly, for sinusoidally amplitude modulated partials, the estimated modulated depth obtained from the modal distribution was 79% for 100% amplitude modulation, while it was only 28% as estimated by the spectrogram.[9] The present study addresses whether similar improvements in accuracy can be realized for violin signals.

We are also interested in the degree to which the fine-structure of the violin acoustic signal contributes to the auditory perception of violin vibrato. The viability of such a study is dependent upon the accuracy of the measurement method used to characterize a violin vibrato signal. In the test conditions described above, the measurement errors associated with estimates based on the spectrogram lie well above psychophysical detection thresholds, whereas those for the modal distribution are similar to the limits of auditory sensitivity.[10,11] The perceptual attributes of vibrato can influence the techniques used to produce sounds that are designed to emulate the violin. The complexity of any physical model of the violin grows with the number of resonances. This

[a)]Portions of this work were presented in ''A modal distribution study of violin vibrato,'' Proceedings of International Computer Music Conference, Thessaloniki, Greece, September 1997, and ''Modal distribution analysis of vibrato in musical signals,'' Proceedings of SPIE International Symposium on Optical Science and Technology, San Diego, CA, July 1998.

increase in complexity directly impacts the design costs and performance of digital synthesizers that emulate the acoustical behavior of a violin. However, if listeners are insensitive to such resonances, sources generated from a physical model with fewer resonances may be perceptually equivalent to those created by a more complex, but physically accurate, acoustical model. The contribution of the fine-structure of the violin is also important for research on alternative materials for violin construction. Solid-body instruments or open-body instruments built from synthetic polymers may be incapable of supporting the densely resonant structure of the violin, yet may be adequate in conveying the violin signal to a listener.

The rest of the paper is organized as follows. Section I describes the nature of the violin signals used in the study and the manner in which these signals are analyzed in time and frequency. Section II presents results for a set of violin signals using the modal distribution. In particular, we focus on the amplitude and frequency variations of the partials in a vibrato violin signal as a function of vibrato, pitch, and body type. Finally, in Sec. III results from several perceptual experiments are presented to evaluate the perceptual importance of the amplitude and frequency modulation reported in Sec. II.

I. METHODS

A. Acoustic violin signals

The acoustic violin signals were acquired from the McGill University Master Samples (MUMS) database of sounds and digitally transferred to computer for analysis. The MUMS recordings are mono, 16-bit linear digital sounds sampled at a rate of 44.1 kHz. Ten different pitches were studied, distributed across the typical range of the violin instrument: A3, B3, C4, F#4, G4, D5, A5, D6, E6, and G6. The violin used in the MUMS recordings is a Ferdinando Gagliano, dated from 1780. The violin was recorded using B&K condenser microphones model 4003 with matched B&K preamplifiers. Near-coincident stereo omnidirectional microphone arrangements along with spot cardioid microphones were used in the recording.[12]

B. Solid-body violin signals

Vibrato notes from an electric solid-body violin were also studied. A Mark O'Connor Signature Series Zeta violin, a solid-body instrument made from basswood, was used. This particular Zeta model uses a piezoelectric transducer for each string, located at the bridge, to sense the horizontal motion of the string. The first author played a two-octave G-Major scale using a student-quality standard bow. The signals were acquired by digitally sampling the line output from the Zeta instrument at a rate of 44.1 kHz.

C. Signal analysis: The modal time-frequency distribution

Like the spectrogram, the modal distribution, $M(t,\omega;\Phi)$, is a member of Cohen's class[13] of bilinear time-frequency distributions (TFD's), and can, therefore, be written as a two-dimensional linear transformation of the Wigner–Ville distribution, $W(t,\omega)$,

$$M(t,\omega)=\int_{-\infty}^{\infty}\int_{-\infty}^{\infty}W(\tau,\xi)\Phi(t-\tau,\omega-\xi)\,d\tau\,d\xi, \tag{1}$$

where, for some signal $s(t)$, its Wigner–Ville distribution is determined by taking the Fourier transform of the signal's local autocorrelation function $s^*(t-\tau/2)s(t+\tau/2)$, i.e.,

$$W(t,\omega)=\frac{1}{2\pi}\int_{-\infty}^{\infty}s^*\left(t-\frac{\tau}{2}\right)s\left(t+\frac{\tau}{2}\right)\exp(-j\omega\tau)\,d\tau. \tag{2}$$

As argued by Cohen,[13] the choice of the kernel function Φ is not only dependent on the specific signal class under study, but on the desired balance between simultaneous resolution in frequency and in time, and on the signal-dependent nonlinearities introduced by the local autocorrelation function. In the case of many musical signals, energy is concentrated about a set of partials, taking the form of the real part of

$$s(t)=\sum_{k=1}^{N}A_k(t)\exp(j\varphi_k(t)), \tag{3}$$

where $A_k(t)$ and $\varphi_k(t)$ are the slowly time-varying amplitude and phase of the k-th partial, respectively. The instantaneous frequency for each partial is given by the time derivative of the instantaneous phase, and is centered about an average frequency of ω_k for a given note. The Wigner–Ville distribution of such a signal consists of two sets of ridges, each of which parallels the time axis. The first set is located in the neighborhoods of the partial frequencies, $\{\omega_k\}$, and bears information about the instantaneous amplitudes and frequencies of the partials. The second set appears in the neighborhoods of the midpoint frequencies, $\{1/2(\omega_j+\omega_k)\}$, and oscillates at the difference frequency $\{\omega_j-\omega_k\}$. These additional ridges consist of the cross-products between partials in the original signal which appear as a result of the nonlinear form of the local autocorrelation function. This second set of ridges is known as the set of cross-terms of the distribution, and contains information about the relative phase of the partials. Since we are generally not interested in relative phase in musical acoustics, but would rather concentrate on the joint time-frequency properties of each partial in isolation, the modal distribution incorporates filtering to suppress the cross-terms. Specifically, the modal distribution uses a separable kernel in Eq. (1),

$$\Phi(t,\omega)=h(t)\,\delta(\omega), \tag{4}$$

where $h(t)$ is a low-pass filter used to suppress cross-terms. In theory, since we are not concerned with restricting the time support in Eq. (3), we use the Dirac delta function, $\delta(\omega)$, in the kernel, to obtain

$$M(t,\omega)=\int_{-\infty}^{\infty}W(\tau,\omega)h(t-\tau)\,d\tau. \tag{5}$$

Therefore, the modal distribution smooths the Wigner distribution of the signal along its time axis to average out the positive- and negative-going cross-terms. By choosing the

cutoff frequency of an ideal low-pass $h(t)$ to be half the minimum frequency difference between adjacent partials, such smoothing will attenuate the cross-terms without affecting the slowly varying instantaneous amplitude of each partial.

Time-frequency distributions are typically applied to sampled signals, for which discrete approximations become necessary. The pseudo-Wigner distribution was introduced by Claasen and Mecklenbraucker[14] as a discrete-time version of the Wigner distribution

$$W(n,k)=\sum_{l=-L}^{L} s^*(n-l)s(n+l)g(l)e^{-j2\pi kl/L}, \tag{6}$$

where the discrete local autocorrelation function is applied to the oversampled ($2\times$Nyquist rate) continuous-time signal $s(t)$, and $g(l)$ is introduced as a taper to control for the effects of truncating the time-support of the local autocorrelation function.[14] The discrete-time version of the modal distribution convolves the low-pass filter $h(n)$ with the pseudo-Wigner distribution for cross-term suppression, e.g.,

$$M(n,k)=\sum_{m=-P}^{P} W(m,k)h(n-m). \tag{7}$$

In this case, the low-pass filter is restricted to be finite impulse response (FIR), and, therefore, can no longer be an ideal low-pass operator. Denoting $W_{\text{rect}}(n,k)$ as the pseudo-Wigner distribution of the sampled signal for a rectangular taper, Eqs. (6) and (7) can be rewritten in a form more analogous with Eq. (1),

$$M(n,k)=\sum_{m=-P}^{P}\sum_{l=-L}^{L} W_{\text{rect}}(m,l)h(n-m)G(k-l), \tag{8}$$

where $G(k)$ is the discrete Fourier transform of the time-support taper $g(n)$. Pielemeier and Wakefield[8] proposed doubly convolved Hamming windows for $h(n)$ and $g(n)$ to yield cross-term suppression in excess of 40 dB while still preserving sufficient detail to allow for accurate local measures of amplitude and frequency.

To determine instantaneous amplitude and frequency of a signal's partials, we assume limited superposition; that is, we assume that regions in the neighborhood of each partial can be treated independently. The global operators for power, amplitude, and frequency as defined by Cohen[13] are then applied locally to each partial. The instantaneous power for a partial is determined from each time sample n by finding the location, $k_{\max}$, of the local maximum of the modal TFD for that partial and summing the modal distribution over a neighborhood of that maximum,

$$p(n,k_{\max})=\sum_{k=-\Delta K/2}^{\Delta K/2} M(n,k_{\max}-k), \tag{9}$$

where n is the discrete-time index, k is the discrete frequency index, and ΔK is the width of the averaging neighborhood. Typically, the width ΔK is chosen to be equal to the width (in bins) of the main lobe of the finite time-support filter $G(k)$. For real signals, the instantaneous amplitude of the partial in the neighborhood of $k_{\max}$ is computed by

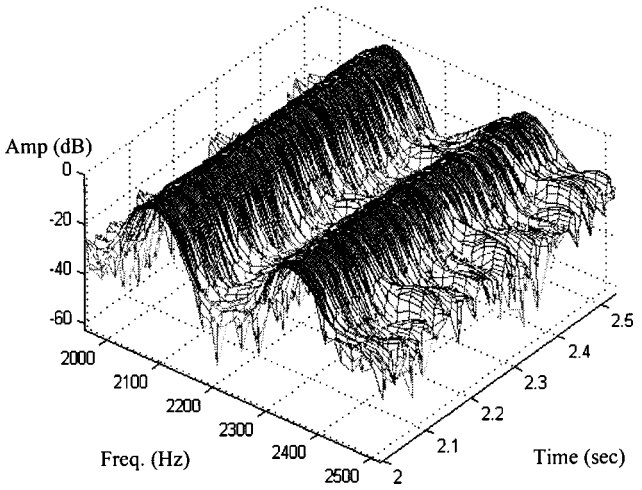

FIG. 1. Modal distribution of a nonvibrato C4 note, showing partials 8–9.

$$A(n,k_{\max})=\sqrt{2p(n,k_{\max})} \tag{10}$$

over positive frequencies. The instantaneous frequency for the partial in the neighborhood of $k_{\max}$ at time n is determined from the centroid of the time-frequency surface over the neighborhood of the peak

$$f(n,k_{\max})=\sum_{k=-\Delta K/2}^{\Delta K/2} \frac{(k_{\max}-k)M(n,(k_{\max}-k))}{P(n,k_{\max})}. \tag{11}$$

II. MODAL TFD ANALYSIS OF THE VIOLIN

The modal TFD was computed every 2 ms of the violin signal in order to obtain a dense sampling of the vibrato period, e.g., for a typical vibrato rate of 5 Hz, this update rate provides 100 samples/vibrato period. A 1024-point doubly convolved Hamming window was used to create the filter $G(k)$. Similarly, $h(n)$ was constructed from a doubly convolved Hamming window, where the length was chosen according to the fundamental frequency of each note. Measures of the instantaneous amplitude and frequency were obtained using Eqs. (10) and (11).

A. Time-frequency surfaces

A typical time-frequency surface for a note without vibrato is shown in Fig. 1, which displays a 500-ms section of the nonvibrato note C4, with a fundamental frequency of 262 Hz. The violin surface exhibits a 40-dB dynamic range. Time is shown in seconds, advancing from foreground to background, whereas frequency is shown in cycles per second (Hz), advancing from background to foreground. The figure focuses on the eighth and ninth partials of the note which form two ridges, one at 2089 Hz and the other at 2350 Hz, that parallel the time axis. Along the peaks of these ridges, the amplitudes appear relatively constant in these logarithmic units. In addition, the widths of the ridges show little variation over time; with respect to the location of the peaks, the surface rolls off monotonically reaching a minimum halfway between adjacent partials. The absence of any minor ridges in the valleys of this surface confirms the utility of the cross-term filter $h(n)$ in the modal distribution and is

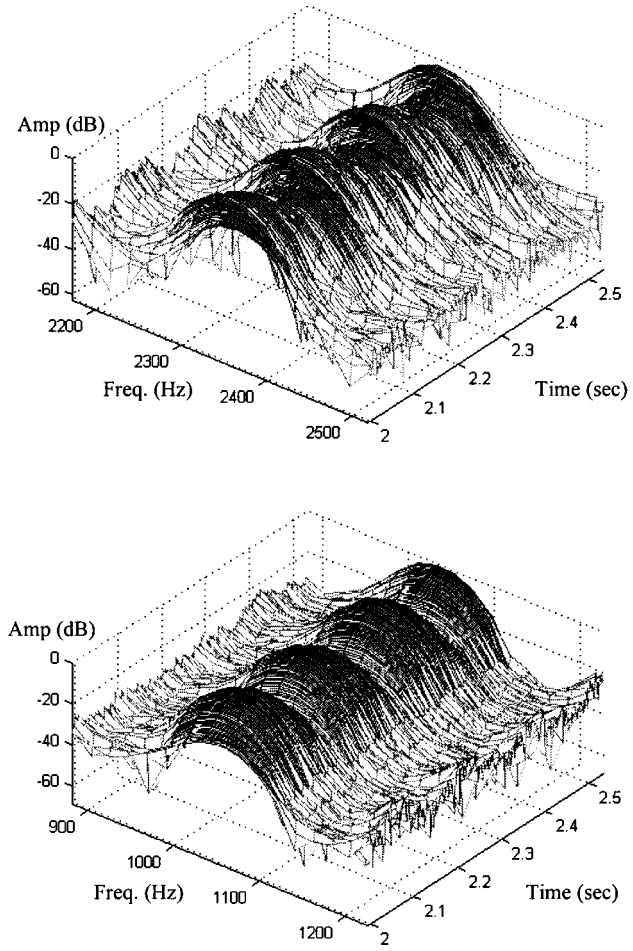

FIG. 2. Modal distribution of a vibrato C4 note; the top panel shows partial 9 and the bottom panel shows partial 4.

typical of the surfaces obtained for all partials: by properly choosing the cutoff frequency to match that of the fundamental, the cross-terms are at least 40 dB down from the signal's auto-terms. Furthermore, any cross-terms that occupy the same frequency region as an auto-term should be attenuated by at least the same magnitude as the cross-terms that lie between two adjacent auto-terms in the time-frequency plane.

Results similar to those shown in Fig. 1 are presented in the two panels of Fig. 2 for a violin note with vibrato. The top and bottom panels show the time-frequency surface for three periods of the ninth and fourth partials of C4, respectively. As was the case for nonvibrato signals, the surface exhibits a regular ''ridge/valley'' structure over a 40-dB range.

The differences between the nonvibrato and vibrato surfaces appear primarily in the behavior of the ridge. In both Figs. 1 and 2, the average trajectory of the ridge parallels the time axis. However, in the case of the vibrato note in Fig. 2, the location of the peak weaves periodically about this average frequency in accordance with the vibrato rate of the signal. In addition, the frequency excursion of the ridges increases with the harmonic index of the partial. In addition to the differences in ridge position over time, the height of the ridge differs between the partials shown in these two figures. The partial in the top panel of Fig. 2 exhibits greater variation in amplitude over time than those partials shown in the nonvibrato note of Fig. 1, but this is still far less than that shown for the partial in the bottom panel of Fig. 2. Even in these logarithmic units, the partial ridge in the bottom panel varies significantly in height as it modulates in frequency about its average value. When displayed in linear units, this variation is sufficiently large to practically eliminate the visibility of the ridge altogether at the amplitude minima of the partial.

The results shown in the two figures are typical of those found for the ten notes of our study. In general, when plotted in decibels, the surfaces exhibit well-defined ridges that correspond to the partials of the violin signal's harmonic series up to the maximum frequency of 11.025 kHz. The introduction of vibrato appears to generate variations in both the height and location of each partial's ridge. The temporal dependence of ridge location is consistent across partials and agrees with the basic model of vibrato as a periodic variation in the characteristic length of the string. In contrast, the amplitude variations tend to be specific to each partial. Although they co-vary with the vibrato cycle, the fine structure of the ridge heights appears to be frequency dependent, and supports the hypothesis that resonances in the violin body may significantly affect the amplitude of each partial as it undergoes frequency modulation.

B. Instantaneous amplitude and frequency

Measures of the instantaneous amplitude and frequency were obtained using Eqs. (10) and (11) within the neighborhood of each partial. Examples are shown in the panels of Fig. 3. The panels on the left show the instantaneous frequency extracted from the modal distribution surfaces, and those on the right show the corresponding instantaneous amplitude estimates. Estimates are shown for partials from a nonvibrato note (top row), a vibrato note with little amplitude modulation (second row), a vibrato note with a large degree of amplitude modulation (third row), and a solid-body instrument (bottom row). From these measures, we can determine that the vibrato rate is approximately 6 Hz and that the peak-to-trough ratio in the amplitude modulation is no larger than 15 dB in the data shown in Fig. 3. This is substantially greater than the variation observed in the absence of vibrato.

1. Accuracy of the measured variations in frequency and amplitude for each partial

Before proceeding with a more detailed analysis of the results, it is useful to understand the extent to which such details reflect properties of the violin signal, rather than interactions between the violin signal and the (nonlinear) modal distribution. The presence of cross-terms can severely contaminate estimates of instantaneous frequency and amplitude, which are based on local averages of the time-frequency surface. While the modal distribution has been designed to reduce the contributions of cross-terms to the time-frequency surface, it cannot entirely eliminate them. Furthermore, deviations in the observed signal from the model in Eq. (3) can introduce uncontrolled artifacts in the time-frequency surface.

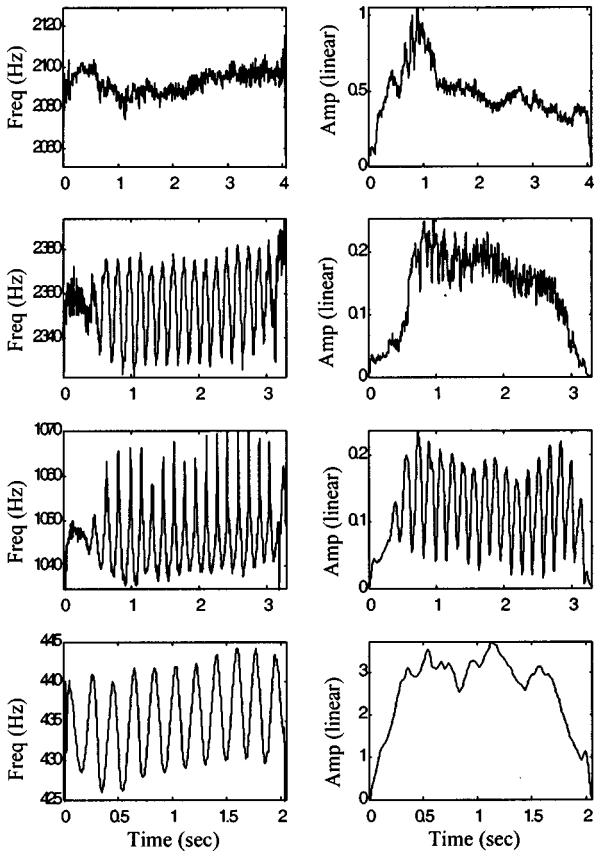

FIG. 3. Frequency estimates (left panels) and amplitude estimates (right panels) as a function of time for partial 8 of a nonvibrato C4 note (first row), partial 9 of a vibrato C4 note (second row), partial 4 of a vibrato C4 note (third row), and partial 1 of a solid-body A4 note (bottom row).

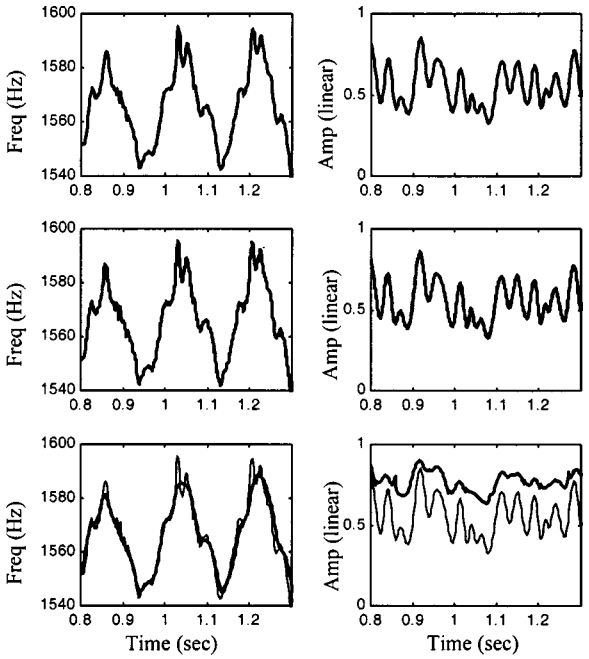

FIG. 4. Frequency estimates (left panels) and amplitude estimates (right panels) as a function of time for the fundamental of a synthesized G6 note. In each panel, the light line corresponds to the estimates used to create the synthesized note. The heavy lines correspond to the modal distribution estimates (top row), the phase vocoder estimates (middle row), and the spectrogram estimates (bottom row).

The accuracy of the modal distribution can be assessed by comparing the estimated amplitude and frequency variations of each partial against known values. A signal can be synthesized from known values of the instantaneous amplitude and phase functions in Eq. (3) and processed by the modal distribution. By comparing the estimated values of amplitude and phase based on local averages of the time-frequency surface with the known values, we can get a better sense for the validity of the results. Pielemeier and Wakefield[8] did such comparisons for sinusoidal forms of $A_k(t)$ and $\varphi_k(t)$. In our present case, the measured forms are generally more complicated, particularly for the instantaneous amplitude. Since the distribution is inherently nonlinear, it is difficult to generalize the results of Pielemeier and Wakefield to the vibrato signal at hand. In the absence of exact knowledge of the true signal, we can evaluate the consistency of the analysis method when applied to real data in the following way. Given a vibrato violin signal, estimates of $A_k(t)$ and $\varphi_k(t)$ can be extracted from the time-frequency surface and used in Eq. (3) to synthesize a new signal. This synthetic signal, in turn, can be analyzed using the modal distribution, or other analysis methods, to determine the values of $A_k(t)$ and $\varphi_k(t)$. Agreement between the estimated and actual values for the synthetic signal provides a measure of consistency: the accuracy of the original measurement is established if the original signal were identical to the synthetic signal.

An example of this consistency check is shown in the top row of Fig. 4. We first analyzed a G6 note with the modal distribution and synthesized a new signal according to Eq. (3). This signal was then analyzed again with the modal distribution, and the results are plotted together in the figure. The left panel shows a portion of the fundamental frequency estimate and the right shows a portion of the amplitude estimate for the first partial. A light line was used to indicate the original values, and a heavy line the reestimation of those values. In the case of the modal distribution, these lines are essentially exact, and any deviation is not visible on the figure. For this partial, the maximum frequency deviation observed was 3.7 cents (average $=0.7$ cents) and the maximum amplitude error was 34 dB down from the actual value.

Besides demonstrating the consistency of the method, we can compare the measured values of $A_k(t)$ and $\varphi_k(t)$ with those obtained using other signal analysis procedures. This is shown in the middle and bottom rows in Fig. 4 for a phase vocoder and spectrogram analysis, respectively.[29] We obtained virtually identical estimates as the original values using the phase vocoder, similar to the performance of the modal distribution. The spectrogram provided the poorest estimation of the original amplitude values, as the amplitude modulation was underestimated. The frequency modulation is also slightly smoothed relative to the original estimates in the case of the spectrogram. These characteristics of each method hold for all partials observed.

The preceding comparison assumes that the vibrato signals under analysis are well-represented by the test signal used (the synthesized note from the modal distribution estimates). If this is true, then the differences observed among the methods when applied to the synthesized signal should

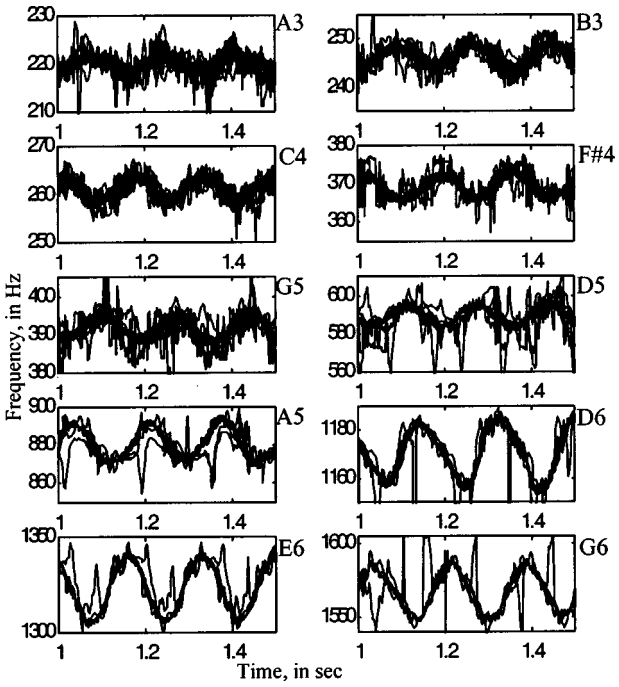

FIG. 5. Overlay of partial-predicted fundamental estimates for each pitch. A time interval corresponding to three vibrato periods is shown in each panel.

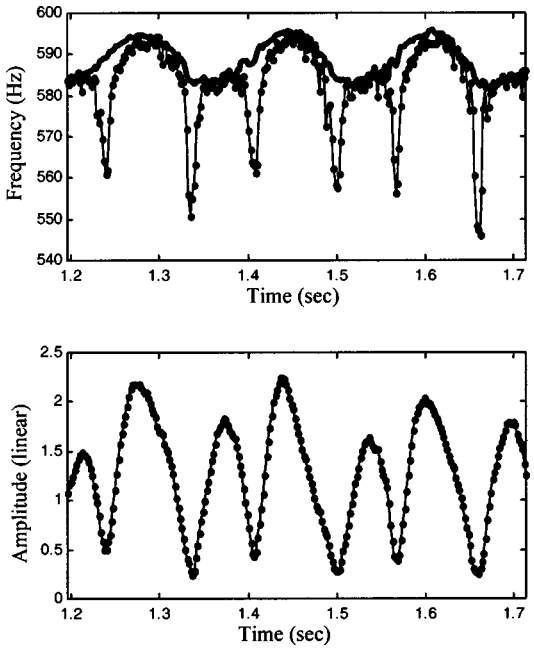

FIG. 6. The top panel shows frequency as a function of time for the fundamental of a D5 vibrato note (light solid line, with dots to indicate each data point) and the average partial-predicted fundamental frequency (heavy line). The lower panel shows the corresponding amplitude as a function of time for the D5 fundamental, with dots to indicate each data point. The deviations from sinusoidal FM appear at the low amplitude points in the vibrato cycle.

also be observed when applied to the original signal. In the case of the spectrogram, the same differences are observed: the estimates of both amplitude and frequency have less instantaneous variation, as is consistent with the known properties of the spectrogram. In the case of the phase vocoder, frequency estimates also exhibit jitter for the higher-frequency partials. For a partial in the neighborhood of 1500 Hz, for example, this jitter is on the order of 10–20 Hz, and, therefore, is relatively small in overall extent. This indicates that there is additional signal content in the recording which is not present in the synthesized version, possibly due to bow noise.

2. Analysis of frequency variations in partial estimates

Since the partials of a bowed violin note are expected to be harmonics of the fundamental, a simple test of the accuracy of the local average frequency estimates based on the modal distribution is to see how well each partial frequency is fit by an integer multiple of the fundamental at every time interval. To do this, the implied fundamental frequency for each partial was found by dividing each partial's frequency estimate by its partial number. Figure 5 shows an overlay of all partial-predicted fundamentals for the ten pitches studied.

In general, the partial-predicted fundamentals are within a few cents of one another at every time slice. However, when larger deviations from the mean occur, they tend to be associated with relatively small instantaneous amplitudes for a given partial. In many of the frequency estimates of these ten analyzed notes, the modulation did not follow a simple sinusoidal pattern, but rather had periodic deviations in the estimate as a function of time. The locations of these deviations varied in time from partial to partial. An example of this phenomenon is shown in the upper panel of Fig. 6, where the fundamental of a D5 note (light line) is compared with the average partial-predicted frequency estimate (heavy line). The lower panel of the figure shows the corresponding amplitude variation for this partial; the deviations in frequency appear at corresponding amplitude minima. In these instances, the partial frequencies do not follow the expected harmonic relationship, so it is unlikely these deviations are the result of an abrupt change in the driving function. It is also unlikely that these frequency discontinuities reflect artifacts in the estimate of instantaneous frequency in the neighborhoods of amplitude minima.[15] To test this, we created a synthesized note with integer multiples of the average fundamental and the amplitude estimates determined from the analysis of the original recording. The estimates of instantaneous frequency obtained from a modal distribution of this synthesized note showed no deviations and followed the expected sinusoidal pattern.

The deviations may be due to a rapid phase shift in the narrow-band partial that induces a change in frequency. Multiresonance systems undergo up to 180-deg phase shifts at the frequencies of resonance and antiresonance. It is therefore expected that as the driving frequency of the partial moves through either a resonance or an antiresonance of the body, the instantaneous frequency of the response will be distorted. This phase effect can be seen by examining the long-term phase spectrum of violin response functions, as reported by Cremer[6] and others. A similar phenomenon in acoustic instruments has also been seen by Dubnov and Rodet.[16] It should also be noted that these frequency deviations did not appear in the frequency estimates of notes played on a solid-body instrument. However, deviations

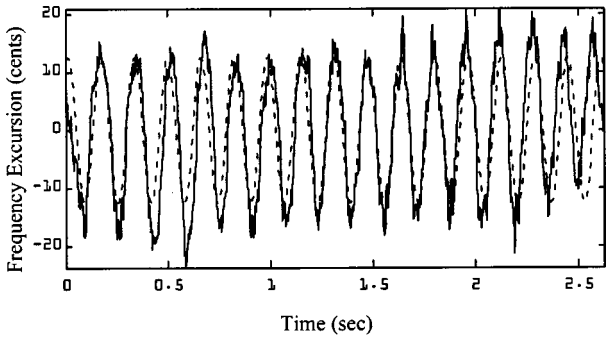

FIG. 7. The estimated fundamental frequency excursion, in cents (solid line), along with the best-fit sinusoid (dashed line) for a C4 vibrato violin note.

were not measurable at resonance conditions, only at antiresonance.

Except for these deviation conditions, the instantaneous frequencies appear to obey harmonic constraints. We can further represent the modulation function by refining the estimated vibrato rate in the frequency domain and then fitting the ''amplitude,'' i.e., maximum frequency excursion, and phase of this sinusoid to the time signal using a least-squares criterion. Figure 7 shows the frequency excursion of the actual vibrato (solid line) and best-fitting sinusoid (dashed line) for the fundamental of the C4 note. The excursion is reported in cents relative to the average fundamental. As can be seen, there appears to be a slight variation in the vibrato frequency over the duration of the signal. The greatest errors in fit are with respect to the maximum vibrato excursions, which do not appear to be purely constant.

Table I summarizes the least-squares fits to the fundamentals of the ten notes. Vibrato rate is presented in cycles per second, vibrato excursion is presented in cents, and the error in the fit is shown by the percent of variance accounted for by the best-fitting sinusoid. There does not appear to be a dependence of either vibrato rate or excursion on the frequency of the fundamental. In general, the average vibrato rate for this performer is 5.9 Hz, with a standard deviation of 0.2 Hz. The average excursion was 15.2 cents, with a standard deviation of 2.8 cents. This excursion represents just over a quarter of a semitone variation in pitch from minimum to maximum over each vibrato cycle.

TABLE I. Best-fit values of modulation rate and amplitude for FM, with the percent of the total variance accounted for shown by pitch.

Note name	Vibrato rate (Hz)	Excursion (cents)	Variance accounted
A3	6.2	10.6	67.5%
B3	5.8	16.1	83.3%
C4	6.1	12.7	67.4%
F#4	5.7	13.7	68.3%
G4	6.1	13.6	66.1%
D5	6.2	16.9	86.4%
A5	5.9	15.9	79.2%
D6	5.8	15.6	72.1%
E6	5.8	20.8	92.5%
G6	5.8	16.6	80.7%

3. Characterization of amplitude modulation for vibrato violin notes

The partial amplitudes exhibit rapid, periodic variations, as seen in the example in the third row of Fig. 3. In contrast, the partial amplitudes of the solid-body violin exhibit no such periodic variations, as seen in the bottom row of the same figure. The amplitude estimate of each solid-body partial resembles that of a nonvibrato partial, indicating that the amplitude variation observed in the acoustic signal is real and not the result of some cross-modulation effect occurring in the transformation.

The sinusoidal variations in fundamental frequency exhibited over the duration of each note simplify the parameterization of the frequency variation. In contrast, fitting a single sinusoid to each partial's amplitude estimate yields a very poor fit to the data. The two middle sequences shown in Fig. 3 are representative of the various degrees of amplitude variation observed for all ten notes. To analyze the amplitude modulation of each partial, we first separated the time variation into two components, one of short time scale and the other of long time scale. The short time-scale variations are presumably the ''vibrato'' part of the modulation, while the long time-scale portion is likely due to the natural evolution of a note as it progresses from onset to offset, and is a characteristic of bowing rather than of vibrato. These slowly varying, near-DC components were removed by smoothing each function over four vibrato periods and subtracting this near-DC component from the estimate to obtain the more rapidly varying residual.

In an attempt to characterize the complexity of the residual envelopes, we examined the peaks of the envelope spectrum. If residual envelopes are driven entirely by the periodic variation in frequency, then we would expect to see the location of the peaks in the envelope spectrum centering around integer multiples of the vibrato rate. As shown in Fig. 8, the actual results are more complicated. Each panel presents a scatter plot of the locations of the five largest peaks as a function of partial number. The horizontal lines indicate integer multiples of vibrato rate. As can be seen in the data, with few exceptions, those peaks found at, or above, the vibrato rate fall along these horizontal lines, as expected. Peaks are also found below the vibrato rate, suggesting the presence of a medium time-scale fluctuation in the original amplitude envelopes which is not eliminated by DC compensation. These conclusions do not depend on the number of peaks chosen; indeed, as more peaks are included, they tend to cluster around DC, well below the vibrato rate.

The resonance structure of the violin body introduces systematic variations in amplitude that depend primarily upon the center frequency of the frequency-modulated partial and upon the excursion of the modulation. Accordingly, we should expect that the phase of amplitude variation and the number of extrema in one vibrato cycle should vary from partial to partial, thereby resulting in a wide range of correlation coefficients between the amplitude estimates of any two partials. We find that correlation values range from -0.82 to 0.82 with an average of 0.065, essentially indicating that there is little or no systematic correlation in the amplitude variations across partials.

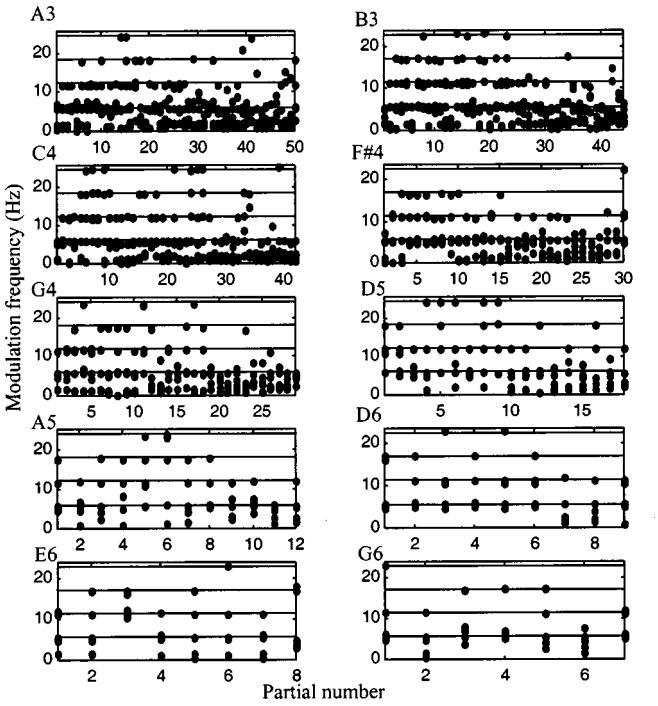

FIG. 8. Scatter plot of the principal spectral components of the amplitude modulation of the partials of each violin vibrato note. The *y*-axis is the frequency of each component, in Hz, and the *x*-axis is the partial number. The solid horizontal lines indicate integer multiples of the rate of the vibrato frequency modulation.

III. PERCEPTUAL RESPONSE TO SYNTHESIZED VIOLIN VIBRATO

The results of the preceding section raise several questions concerning the perceptual accuracy of our signal analysis. Are the rich amplitude and frequency structures of the partials necessary in the perception of violin vibrato, or has our analysis captured details that are relevant only to the physical characterization of the acoustical instrument? If such details are shown to be necessary, then is the representation sufficient, or do we require even more information to properly characterize the perceptual attributes of violin vibrato? By using the measured instantaneous frequency and amplitude functions in the signal model, we can compare the synthesized and original signals. If they differ perceptually, we can conclude that we have not captured the relevant information in the stimulus. If they do not differ, we can proceed to eliminate the fine structural features of the frequency and amplitude functions until a listener can hear the difference.[17]

In the following, we introduce the methods used to synthesize the signals, the ''coarser'' representations used to reduce the complexity of the signal, and the psychophysical methods used to measure the listener's perceptual response. The section concludes with a summary of the results from these experiments.

A. Signal processing methods

For each vibrato note, four synthesized versions of that note were created: one with the amplitude and frequency estimates directly extracted from the modal analysis (MODAL), one with a constant frequency approximation (FM-CONSTANT) and the original amplitude estimates, one with a constant amplitude approximation (AM-CONSTANT) and the original frequency estimates, and one with smoothed sinusoidal approximations (SINUSOID) to both amplitude modulation and frequency modulation. Each of these was then also synthesized with bow noise, for a total of eight synthesized sounds for each original recording. We discuss each of these synthesis methods below.

1. Additive synthesis (MODAL condition)

To synthesize violin vibrato notes, we used the real part of the signal model described in Eq. (3), where the instantaneous frequency is given by the time derivative of the instantaneous phase. The results of our modal analysis provide samples of the amplitude $[A_k(t)]$ and instantaneous phase $[\varphi_k(t)]$ functions for each of the k partials every 2 ms. These samples were then linearly interpolated over time to create amplitude and instantaneous phase functions at a sampling rate of 44.1 kHz. Synthetic violin vibrato notes were constructed using these interpolated functions.

2. Constant approximations to vibrato frequency and amplitude modulation (FM- and AM-CONSTANT conditions)

To assess the relative importance of frequency and amplitude modulation to the perception of vibrato, we replaced either of these two time-varying components with constant functions. For the FM-CONSTANT condition, the constant frequency was determined by finding the mean value of the note's fundamental frequency, and then using integer multiples of that value to represent the higher partials. For the AM-CONSTANT condition, the constant amplitude was determined by taking the running average of each partial's amplitude over four vibrato periods (cf. Sec. II B 3).

3. Sinusoidal approximations to vibrato frequency and amplitude modulation (SINUSOID condition)

To assess the extent to which the auditory system is sensitive to the detailed variations in amplitude and instantaneous frequency of each partial, sinusoidal approximations of each estimate were obtained. In the case of frequency modulation, we utilized the results from the analysis section to generate an harmonic series using the best-fitting sinusoid to the frequency modulation of the fundamental. In the case of amplitude modulation, the results from the analysis section suggested that five sinusoidal components were sufficient to represent vibrato-entrained amplitude modulation.

B. Synthesis of bow noise

Informal listening experiments suggested that the synthesized waveforms replicated the tonal content of the original waveform, but did not adequately replicate the sound of the bow across the strings, which was particularly pronounced for certain violin vibrato notes in the MUMS close-microphone recordings. While this bow noise had no bearing upon the characteristics of the violin vibrato, its absence provided a cue by which listeners could easily discriminate between the original and synthesized notes. To reduce the sa-

lience of this cue, bow noise was synthesized, according to the procedure outlined below, and added to the synthesized signals.

Since the modal distribution is not invertible, the simple technique of waveform subtraction, in which the difference between the original and synthesized signals is computed to obtain a residual, tends to capture both bow noise and tonal components whose phases and/or amplitudes differ between the original and synthesized signals. Therefore, a spectral subtraction technique was used.[18] Successive 2048-point sequences of the original and the synthesized waveforms were Fourier transformed and the difference in their magnitudes was computed. A random phase was paired with each magnitude component, and the inverse Fourier transform was taken to obtain a ''residual'' waveform.

C. Perceptual evaluation of synthesis methods

1. Same–different discrimination procedure

The discriminability between two signals was measured using a same–different psychophysical discrimination procedure. During each trial of this task, subjects listened to two observation intervals and determined whether the same signal was present on both intervals or each interval contained a different signal. ''Same'' and ''different'' trials were drawn randomly with equal probability over 42 trial blocks. Feedback was provided following each trial to help the subject learn the discrimination. The subject's performance is summarized by computing an index of discriminability (d') and converting this to a probability score. Final performance measures are reported by averaging discrimination scores from 3–5 blocks of trials.

2. Nonmetric multidimensional scaling

A nonmetric multidimensional scaling (MDS) procedure was used to better understand the perceptual space among acoustic signals that were highly discriminable by our subjects. Each trial in this procedure consisted of two observation intervals. The subject's task was to indicate the degree to which the signals heard in each interval were similar using an integer scale from 1 to 10, where 10 indicated the highest degree of similarity. Subjects were not instructed concerning the perceptual dimension along which they were to scale similarity. A complete unbalanced similarity matrix was determined for each set of N acoustic signals by presenting, in random order, all possible pairs under the assumption that the presentation order within a pair does not affect the subject's judgment. Thus one measure of the similarity matrix consists of $N(N-1)/2$ pairs of observations. For each similarity matrix, two measures were obtained.

Shepard[19] established the helical structure of pitch perception using nonmetric multidimensional scaling of similarity judgments. Such results suggest that human listeners perceive the pitch of a sound as a two-dimensional quantity where the chroma indicates the pitch class of the note (e.g., A, A#, B, C, etc.) and tone height indicates the octave placement of the fundamental. Since our analysis data span several octaves, we were concerned that perceptual differences due to synthesis method would be overwhelmed by the helical structure of the set of synthesized and original vibrato tones. Therefore, the stimulus set was broken up by pitch into ten separate conditions, i.e., A3, B3, C4, F#4, G4, D5, A5, D6, E6, G6, and the synthesized and original vibrato tones were scaled within each condition. This resulted in the scaling of nine stimuli (original vibrato note and four synthesis methods with or without bow noise) per condition.

3. Sound quality judgment

Finally, a third psychophysical procedure was used to determine the degree to which a sound was heard as a ''real,'' as opposed to ''synthesized'' violin. Subjects listened to each sound individually and judged their sound quality on a 10-point rating scale, where 10 indicates the highest and 1 indicates the lowest sound quality, respectively. Sounds from all pitches were presented in random order to form one block of measurements. Data from two blocks were averaged to estimate the judged sound quality of the violin vibrato signals.

4. Psychophysical testing apparatus and subjects

For each procedure, a subject was seated in a Tracoustics double-walled sound-proof booth. Stimuli were presented diotically (e.g., the same monaural signal was presented to both the left and the right channels) over Sennheiser HD 265 headphones. A microcomputer was used to control stimulus presentation, cue the subject, and record the response. Signals were synthesized digitally and a Digital Audio Lab digital-to-digital card was used to stream the digital data to an Otari DTR-8S DAC. All signals were synthesized at a rate of 44.1 kHz using 16 bits.

All subjects were determined to have normal audiometric thresholds for our laboratory. They were also highly trained listeners, several of whom were experienced in digital sound synthesis. Two subjects were used for the discrimination task. These subjects, along with another five, were used in the MDS scaling and sound quality tasks. Both authors participated as subjects in the MDS and sound quality scaling.

D. Results

1. Psychophysical discrimination

Unlike our success in applying the modal TFD analysis and additive-synthesis methods to piano,[20] our best attempts to synthesize a violin signal were always discriminable by two highly trained, expert listeners. Specifically, in the same–different task with feedback training, listeners discriminated ''same'' from ''different'' trials 100% of the time when asked to compare a violin vibrato note to a MODAL synthesis of that note. Performance did not degrade when synthetic bow noise was added to the MODAL signal. Subjects claimed that differences in the microstructure of the bow noise provided reliable cues to discriminate between the two signals. Given that signals generated by the most accurate synthesis method were discriminable from the original vibrato signal, we did not further study discrimination functions for less accurate synthesis methods. It should also be

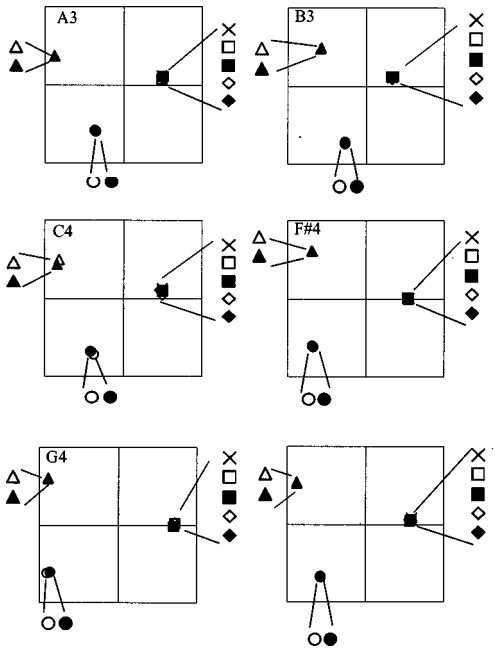

FIG. 9. Multidimensional scaling results for the five lowest pitches (A3, B3, C4, F#4, and G4); their composite response is plotted in the lower-right panel. The ''×'' indicates the original recording, squares are MODAL synthesis, diamonds are FM-CONSTANT synthesis, circles are AM-CONSTANT synthesis, and triangles are SINUSOID synthesis. The filled symbols indicate bow noise has been added and open circles indicate bow noise is absent. In all panels, the triangular symbols align in the upper-left corner, the circular symbols align in the lower-left corner, and all other symbols are clustered together to the right. In those instances in which the symbols are clustered together, the overlapping symbols are shown beside that region of the figure.

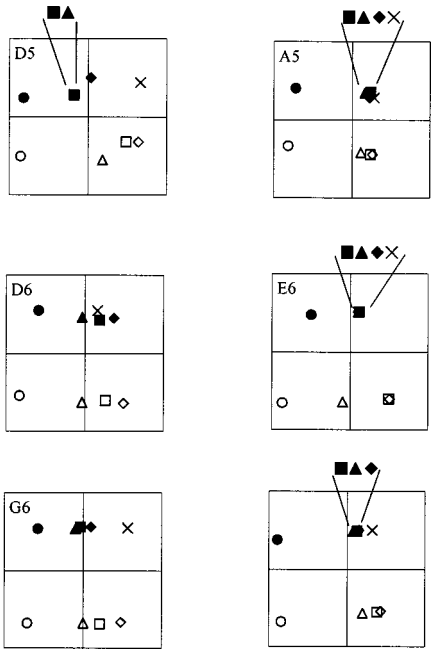

FIG. 10. Multidimensional scaling results for the five highest pitches (D5, A5, D6, E6, and G6); their composite response is plotted in the lower-right panel. The ''×'' indicates the original recording, squares are MODAL synthesis, diamonds are FM-CONSTANT synthesis, circles are AM-CONSTANT synthesis, and triangles are SINUSOID synthesis. The filled symbols indicate bow noise has been added and open circles indicate bow noise is absent. The circular symbols are isolated from the rest in all panels. In those instances in which the symbols are clustered together, the overlapping symbols are shown beside that region of the figure.

noted that discrimination of 100% was easily achieved when these notes were analyzed/synthesized using the phase vocoder and the spectrogram.

2. Nonmetric multidimensional scaling

Nonmetric multidimensional scaling was applied to similarity matrices that were averaged across seven subjects for ten pitch conditions.[21] We found that a two-dimensional solution for all conditions yielded stress values no greater than 0.1 (average of 0.06) and accounted for an average of 97% of the variance in the data. Reducing the dimension to one resulted in substantial increases in stress (average of 0.25) and reductions in percentage of variance accounted for (average of 84%). Increasing the dimension to three resulted in a small increase in performance, with an average stress value of 0.016 and a percentage of variance accounted for equaling 99.8%; in addition, three dimensions is typically considered to be too large for the relatively small number of stimuli presented in the experiment. Therefore, all subsequent analysis of the results is based on the two-dimensional solution.[22]

The two-dimensional MDS solutions for low- and mid-range pitches (A3, B3, C4, F#4, G4) is shown in the first five panels of Fig. 9. The symbols used are the following: the original signal is denoted by an ''×,'' the MODAL conditions by squares, the FM-CONSTANT conditions by diamonds, the AM-CONSTANT conditions by circles, and the SINUSOID conditions by triangles. Filled symbols indicate synthetic bow noise was added to the stimulus, and open symbols indicate no bow noise. In general, the data cluster in a triangular pattern according to synthesis method: one vertex is formed from stimuli synthesized by the SINUSOID algorithm, the second vertex is formed from the AM-CONSTANT stimuli, and the remaining vertex is a cluster of the FM-CONSTANT, MODAL, and original violin vibrato signals. Bow noise does not appear to be a perceptually salient feature, as stimuli that share the same synthesis method, with or without bow noise, lie in close proximity to each other in the solution space. Indeed, the data suggest a highly degenerate solution in which two of the synthesis methods stand out from all others.

In addition to bow noise, pitch does not appear to be a significant feature for the low- and mid-range pitches: the triangular solutions are similar across the five pitches. This observation is confirmed when we collapse the original similarity matrices across both subject and pitch before generating an MDS solution. As shown in the bottom right (sixth) panel of Fig. 9, the effect of this averaging is to further reduce the stress (from 0.1 to 0.0068) and increase the percentage of variance accounted (from 97% to 99.98%). In this collapsed case, the same pattern is readily apparent; the AM-CONSTANT and SINUSOID synthesis conditions are well-separated in the perceptual space from the remaining notes.

For the five highest pitches (D5, A5, D6, E6, G6), shown in the first five panels of Fig. 10, the results tend to separate by bow noise as well as by synthesis type. The symbols used are the same as in the previous figure. The data do not show the triangular pattern observed for the low- and

TABLE II. Sound quality scores for each synthesis type, separated by pitch region.

Synthesis type	Mean value: Lowest 5 pitches	Standard deviation: Lowest 5 pitches	Mean value: Highest 5 pitches	Standard deviation: Highest 5 pitches
Original	8.79	1.38	6.57	2.83
MODAL	8.36	1.73	7.87	1.66
MODAL bow	8.16	1.97	5.30	2.76
FM-CONSTANT	7.83	1.54	6.29	2.29
FM-CONSTANT bow	8.21	1.52	4.63	2.44
AM-CONSTANT	4.46	2.72	3.19	2.04
AM-CONSTANT bow	4.63	2.76	3.14	2.43
SINUSOID	2.23	1.38	5.66	2.07
SINUSOID bow	2.29	1.37	5.11	2.66

mid-range pitches; instead, one of the two orthogonal dimensions appears to be associated with bow noise, while the other is more weakly organized around the synthesis method. The original vibrato stimulus appears on the ''bow noise present'' end of the bow noise dimension. All five pitches suggest that, of the four synthesis methods, the AM-CONSTANT condition is perceived to be the most different from the original vibrato stimulus and that the absence of bow noise increases this difference. Otherwise, for the pitches that were evaluated, there is no clear ranking of the distance between stimuli generated by the other synthesis methods and the original vibrato. If we collapse the similarity matrices across the five highest pitches, the scaling solution shown in the sixth (bottom right) panel of Fig. 10 results. As above, the effect of this averaging is to significantly reduce the stress value to 0.006 and improve the variance accounted for to 99.98%. This average solution suggests that bowing followed by the AM-CONSTANT condition are dominant factors in determining the perceptual location of each of the stimuli.

3. Sound quality scaling

To assist in ''tiling'' the perceptual space found from the MDS solution into regions of acceptable and unacceptable violin vibrato, the same subjects who participated in the scaling experiment were asked to rate each note individually in terms of its quality. The mean scores, collapsed across subject and pitch group, are shown in Table II. For the lowest five pitches (A3, B3, C4, F#4, G4), the AM-CONSTANT and the SINUSOID conditions were given low quality scores, with an average value of 3.4 out of 10. The remaining synthesis conditions had higher quality scores, with an average value of 8.1. Bow noise did not significantly alter the quality scores for any of the synthesis methods in the lower pitch range. For the highest pitches (D5, A5, D6, E6, and G6), bow noise did alter the quality scores; those notes with bow noise tended to receive lower quality scores than their synthesized counterparts without bow noise. The scaling value of the original note also decreased from that of the lower five pitches. Two subjects, in particular, gave the original notes very low scores for the highest five pitches only (an average of 3.7), presumably from the increased amount of bow noise present in these signals. In addition, notes generated by the SINUSOID method improved in quality, but the AM-CONSTANT continued to receive very low quality scores, both with and without bow noise.

E. Discussion

The failure to properly synthesize a perceptually identical vibrato signal could stem from several factors. The estimates of instantaneous amplitude and frequency may contain errors which, when used in the additive synthesis model, generate a signal that listeners can discriminate. Even though the characterization studies discussed in Sec. II suggest virtually error-free measurements of the partials by the modal distribution, we cannot completely rule out measurement error as a source. Such characterizations of nonlinear operators are always conditional in nature: given that the true signal behaves exactly like the modeled signal, we expect estimator performance of the type described. Should the true signal deviate substantially from the modeled signal used to study performance, our characterizations may no longer be valid and the measurements may degrade. These comments are not isolated to our particular analysis/synthesis method: 100% discrimination was obtained in highly trained listeners under feedback conditions when analyzing these signals with the phase vocoder and with short-time Fourier-based methods.

The synthesis method may also be a source of perceptual error. Recall that the instantaneous envelope and frequency of each synthesized partially were computed by linearly interpolating in frequency and amplitude between samples taken every 2 ms. Therefore, errors between the original and interpolated values of amplitude and frequency could provide a cue for listeners in the discrimination task. A 2-ms update rate falls within most reported lower bounds of temporal resolution in the human auditory system,[23] so that it is unlikely that listeners are sensitive to interpolation error within each frame. Nevertheless, the cue could derive from the cumulative effects of many small errors across frames which become perceptible through a statistical combination of error over time.[24]

Finally, poorly measured out-of-band sources are a likely source of perceptual error based on the fact that bow noise can be identified throughout the original recordings. When only in-band information is used, we expect, and observe, high degrees of discrimination between the original and synthetic signals. However, when synthetic bow noise is added, the data indicate that listeners can still discriminate between the synthetic and original signals, but they verbally report that the differences between the original and synthetic bow noise provide a reliable cue. From these observations, we conclude that our synthesis method did not reproduce bow noise exactly. Indeed, the high-fidelity synthesis of such stochastic sources is a problem, in and of itself, for which spectral subtraction is one of the better methods that have been proposed.[18] Our data suggest that listeners can discriminate between different instantiations of the bow noise process and raise the possibility that better phase matching within each analysis frame of the spectral subtraction method could eliminate this discrimination cue.

From the discrimination data, it is difficult to determine conclusively the relative contributions of errors in measurement, interpolation, and bow noise synthesis to discrimination. The scaling data, however, address the question of synthesis quality from a different perspective. Nonmetric multidimensional scaling has been used to recover the perceptual dimensions of pitch,[19] timbre,[25] vowels,[26] and loudspeaker designs.[27] In the present case, the scaling data may shed some light on the relative perceptual fidelity of the various synthesis methods by determining whether some synthesis methods generate stimuli that lie closer to the original than others.

Two trends are apparent in the scaling data. Proper modulation in amplitude appears to be more important than proper modulation in frequency, if either one or the other is to be eliminated from synthesis. We find that the AM-CONSTANT condition lies farther from the original vibrato signal than the FM-CONSTANT/bow noise condition, which tends to cluster with the original vibrato signal, regardless of pitch. Our measurement shows little difference in the perceptual location when proper amplitude and frequency modulation (MODAL/bow noise) are present; these stimuli also cluster with the original vibrato signal. However, these observations run counter to the standard intuition concerning the importance of frequency modulation to the perception of vibrato.

A second trend concerns the effect of bow noise on the location of stimuli in the listener's perceptual space. For low- and mid-range pitches, the type of synthesis method appears to be the sole determining factor of spatial location, whereas both method type and bow noise synthesis are important for pitches in the upper range. The change from a triangular to rectangular spread in the scaling data as pitch increases suggests an interaction between bow noise, synthesis method, and pitch. Returning to the acoustic data, we find that bow noise is a low-pass random process that rolls off at a rate of 20–30 dB per decade starting at 100 Hz. For in-band synthesis, as fundamental frequency increases, the lowest frequency range that is synthesized must, by definition, increase as well, whereas the density of in-band ''sampling'' of the original signal's spectrum must decrease. Therefore, the low-pass spectrum of the bow noise is more likely to be captured as small perturbations of the in-band components for the lowest frequency fundamentals in our data. As the pitch of the violin note increases, proportionately more of the low-pass noise spectrum occupies frequencies below the lowest frequency range that is synthesized and proportionately less of the spectrum is sampled by the in-band analysis.

The scaling data provide some insight into the discrimination results. Although no synthesis method produced a stimulus that was perceptually identical to its original, several of the methods appear to do better than others. In particular, stimuli generated by MODAL/bow noise synthesis are perceived to be much more like their original vibrato counterparts than stimuli generated by some of the other synthesis conditions. Likewise, stimuli that share the same frequency modulation characteristics as the original vibrato note, but differ along the other synthesis dimensions, lie farthest from the original in these two-dimensional solutions.

The nonmetric MDS solutions allow us to make relative judgments among the different synthesis methods. Because they are based on ordinal measures of similarity, however, absolute distance cannot be inferred from the nonmetric MDS configurations. Thus the proximity of notes synthesized by the MODAL/bow noise method to the original may reflect the perception that the synthesized notes are effectively the same as the original, differing along qualitatively irrelevant dimensions, or that the synthesis, though poor, is still better than synthesis by the AM-CONSTANT method. It is for this reason that we included a quality scaling task among our psychophysical measures.

The results shown in Table II indicate that synthetic stimuli lying in close proximity to the original in the nonmetric MDS solutions receive virtually the same quality scores as the original. Conversely, synthetic stimuli lying far from the original receive significantly lower quality scores. Therefore, the clustering of synthetic stimuli in the neighborhood of the original, which is found in much of the data, particularly for the low- and mid-range pitches, is indicative of perceptually accurate synthesis.

The sound quality data also provide some insight into the importance of bow noise in synthesis. When bow noise is not a determinant of perceptual location (e.g., for the low- to mid-range pitches), the quality scores of all stimuli within the neighborhood of the original appear to be uniformly high. However, when bow noise is a determining factor, the average quality scores of all stimuli within the neighborhood of the original, including that of the original, go down. As noted in Sec. III D, the effect on the average quality score is more likely due to subject differences than to differences among stimulus conditions. In particular, two of the seven subjects consistently scored the bow noise conditions for the five highest pitches as poor in quality regardless of whether they were synthetic or original. The data from the five remaining subjects differ little as a function of pitch. Neither does it appear to be an independent factor for the first two subjects. When bow noise is not included in the synthesis, the quality score is purely a function of synthesis method. Indeed, the first two subjects gave their highest quality scores to stimuli synthesized by either the FM-CONSTANT or MODAL methods; they only judged stimuli containing bow noise to be of high quality for the low- and mid-range pitches.

F. Measurement of synthesis quality

The strongest indicator of synthesis quality is clearly when the synthetic stimulus cannot be discriminated from the original. If they are indiscriminable after sufficient training in an objective psychophysical discrimination task, then we expect that they will occupy the same location in the listener's perceptual space and will be judged to be identical in quality. Failure to meet this highest standard of quality, however, does not necessarily mean that the synthesis method is inadequate; rather, it means that the synthetic and original differ sufficiently along at least one perceptual dimension to support reliable discrimination. A trivial case is when the synthetic stimulus is the same as the original except that signal gain has been changed. No one would want

to argue that the synthesis method failed simply because of a difference in loudness. Nevertheless, no one would want to advance a psychophysical method of ''identity'' that coaches the subject into ignoring the experimenter-defined ''irrelevant'' stimulus dimensions because to do otherwise would introduce substantial bias into the measurement procedure.

In this present paper, we advocate the use of several measures of synthesis quality when the strongest test, perceptual equality, fails. Results based purely on measures of sound quality, as in judging the degree to which a stimulus sounds like a ''real violin,'' are always subject to bias when the stimuli are discriminable. Nonmetric MDS solutions, alone, cannot always determine whether any of the stimuli are sufficiently close to the original to be perceived as having the same perceptual quality as the original. By combining sound quality scaling with nonmetric MDS, we believe that much greater insight into the quality of the synthesis can be gained.

In theory, the combination of nonmetric MDS and measures of sound quality should help distinguish between those perceptual dimensions that are important to synthesis quality from those that are irrelevant. However, in practice, N, the number of stimuli required to identify perceptual dimensions using MDS techniques, grows linearly with the number of dimensions, while the number of pairs to be scaled is on the order of N^2. Experiments involving more than 20 stimuli are rare in the MDS literature, for no other reason than listener fatigue. Therefore, in all but the simplest cases when the number of dimensions is three or fewer, it is highly unlikely that the procedures would prove fruitful in the study of relevant perceptual dimensions.

How to best measure the quality of a synthesis method, when perceptual equality fails to hold, remains an open question. As noted above, we should not fault the synthesis method if the original and synthetic differ along irrelevant stimulus dimensions, such as loudness or duration. But should we necessarily fault the method if the two differ along relevant dimensions? We expect that repeated recordings of the same vibrato pitch will not only fail the test of perceptual equality, but fail to be identical along the relevant stimulus dimensions. Suppose that a synthesis method generates signals that lie within the bounds of covariation across each of the relevant dimensions. Would we reject this method because it failed to achieve a one-to-one match between a synthetic and original signal? Perhaps quality is more an issue of capturing and synthesizing the proper perceptual variations found over the ensemble of violin vibrato notes, rather than achieving one-to-one matching. The issue of one-to-one matching, or perceptual equality, may be more relevant to whether or not we can characterize the distribution of notes within the ensemble. Instead, it may be more appropriate to use procedures similar to those developed by Lutfi to study synthesis quality.[28]

IV. CONCLUSIONS

Our high-resolution time-frequency analysis has revealed rapidly varying amplitudes of the partials of vibrato notes, the result of an interaction between the frequency-modulated string motion and the densely spaced resonances of the violin body. We determined the spectral properties of both the frequency and amplitude modulation, and found that the frequency modulation was well-described by a single sinusoid, with a vibrato rate of roughly 6 Hz and a peak-to-trough variation of just over a quarter of a semitone. In contrast, the amplitude variations exhibited much richer spectra, with modulation depths up to 0.9 and many more peaks observed in a spectral decomposition of these envelopes. The majority of these spectral peaks fall at integer multiples of the vibrato rate, with little or no correlation in phasing and complexity in these envelopes across partials.

The perceptual importance of the measured temporal variations in frequency and amplitude was established through nonmetric multidimensional scaling and sound quality judgments by trained listeners. We discovered that the relative salience of amplitude and frequency modulation in violin vibrato runs counter to common intuition. Notes with proper frequency modulation (and no periodic amplitude modulation) were universally judged, both with MDS and quality scores, to lie well outside any ''perceptual distribution'' of violin vibrato sounds. On the contrary, notes with proper amplitude modulation (with proper frequency modulation or even without any frequency modulation) occupied a perceptual space that also encompassed the original recording. This suggests that a primary contribution of frequency modulation to the perception of violin vibrato is to create the perceptually important amplitude variations by interacting with narrowly spaced resonances in the violin body.

The sound quality scaling and MDS results support the fact that many of these synthetic sounds replicate vibrato produced by acoustic violins. The reasons that our techniques failed to produce perceptually identical synthetic violin vibrato signals from the original recordings are unknown, however. Inadequate bow noise synthesis is one likely source of discriminability. The modeling of a stochastic sound source, such as bow noise, is a well-studied, difficult problem and is not within the scope of this vibrato analysis. However, the absence of proper bow noise confounds the evaluation of vibrato synthesis, as the two cannot be decoupled in perceptual experimentation.

ACKNOWLEDGMENTS

This research was supported in part by a fellowship to the first author from the Regents of the University of Michigan, by a grant to the MusEn project from the Office of the Vice-President for Research at the University of Michigan, and by a University Research Foundation Grant from the Ford Motor Company. We would also like to thank the University of Michigan School of Music for the use of their Zeta violin.

[1] S. Ando and K. Yamaguchi, ''Statistical study of spectral parameters in musical instrument tones,'' J. Acoust. Soc. Am. **94**(1), 37–45 (1993).
[2] J. W. Beauchamp, ''Time-variant spectra of violin tones,'' J. Acoust. Soc. Am. **56**(3), 995–1004 (1974).
[3] H. Fletcher and L. C. Sanders, ''Quality of violin vibrato tones,'' J. Acoust. Soc. Am. **41**(6), 1534–1544 (1967).
[4] J. Meyer, ''New aspects of the violin vibrato,'' J. Acoust. Soc. Am. **89**, 1901–1902 (A) (1991).
[5] M. V. Mathews and J. Kohut, ''Electronic simulation of violin reso-

nances,'' J. Acoust. Soc. Am. **53**(6), 1620–1626 (1973).
[6] L. Cremer, *The Physics of the Violin* (MIT Press, Cambridge, Massachusetts, 1984), pp. 284–292.
[7] G. Weinreich, ''Directional tone color,'' J. Acoust. Soc. Am. **101**(4), 2338–2346 (1997).
[8] W. J. Pielemeier and G. H. Wakefield, ''A high-resolution time-frequency representation for musical instrument signals,'' J. Acoust. Soc. Am. **99**(4), 2382–2396 (1996).
[9] W. J. Pielemeier and G. H. Wakefield, ''Multi-component power and frequency estimation for a discrete TFD,'' Proceedings of IEEE Symposium on Time-Frequency and Time-Scale Analysis I., Philadelphia, PA, 1994, pp. 620–623.
[10] C. J. Plack and R. P. Carlyon, ''The detection of differences in the depth of frequency modulation,'' J. Acoust. Soc. Am. **96**(1), 115–125 (1994).
[11] G. H. Wakefield and N. F. Viemeister, ''Discrimination of modulation depth for SAM noise,'' J. Acoust. Soc. Am. **88**(3), 1367–1373 (1990).
[12] F. Opolko and J. Wapnick, *McGill University Master Samples User's Manual* (McGill University, Montreal, Canada, 1989).
[13] L. Cohen, *Time-Frequency Analysis* (Prentice-Hall, Englewood Cliffs, NJ, 1995), Chap. 8.
[14] T. A. C. M. Claasen and W. F. G. Mecklenbrauker, ''The Wigner distribution—a tool for time-frequency analysis, Part II: Discrete-time signals,'' Philips J. Res. **35**(4/5), 277–300 (1980).
[15] B. Picinbono, ''On instantaneous amplitude and phase of signals,'' IEEE Trans. Signal Process. **45**(3), 552–560 (1997).
[16] S. Dubnov and X. Rodet, ''Statistical modeling of sound aperiodicities,'' Proceedings of ICMC, Thessaloniki, Greece, 1997, pp. 43–50.
[17] S. McAdams, J. W. Beauchamp, and S. Meneguzzi, ''Discrimination of musical instrument sounds resynthesized with simplified spectrotemporal parameters,'' J. Acoust. Soc. Am. **105**(2), 882–897 (1999).
[18] X. Serra and J. O. Smith, ''Spectral modeling synthesis: A sound analysis/synthesis system based on a deterministic plus stochastic decomposition,'' Comput. Music J. **14**(4), 12–24 (1990).
[19] R. N. Shepard, ''Circularity in judgments of relative pitch,'' J. Acoust. Soc. Am. **36**, 2346–2353 (1964).
[20] R. C. L. Guevara and G. H. Wakefield, ''A modal distribution approach to piano analysis and synthesis,'' Proceedings of International Computer Music Conference, Hong Kong, 1996, pp. 350–351.
[21] Specifically, a commercial statistical software package, SYSTAT Version 5.05, was used to generate the solutions. Within this package, we used a Kruskal loss function and a monotonic regression to find the MDS solution.
[22] R. N. Shepard, ''Metric structures in ordinal data,'' J. Math. Psychol. **3**, 287–315 (1966).
[23] D. A. Eddins and D. M. Green, ''Temporal integration and temporal resolution,'' in *Hearing*, edited by B. C. J. Moore (Academic, San Diego, 1995), Chap. 6.
[24] N. F. Viemeister and G. H. Wakefield, ''Temporal integration and multiple looks,'' J. Acoust. Soc. Am. **90**(2), 858–865 (1991).
[25] R. Plomp, ''Timbre as a multidimensional attribute of complex tones,'' in *Frequency Analysis and Periodicity Detection in Hearing*, edited by R. Plomp and F. G. Smoorenburg (Sijthoff, Leiden, 1970), pp. 397–414.
[26] W. Klein, R. Plomp, and L. C. W. Pols, ''Vowel spectra, vowel spaces, and vowel identification,'' J. Acoust. Soc. Am. **48**(4), 999–1009 (1970).
[27] R. M. Aarts, ''A new method for the design of crossover filters,'' J. Audio. Eng. Soc. **37**(6), 445–454 (1989).
[28] R. A. Lutfi, K. A. Doherty, and E. Oh, ''Psychometric functions for the discrimination of spectral variance,'' J. Acoust. Soc. Am. **100**(4), 2258–2265 (1996).
[29] The phase vocoder result was obtained following the steps outlined by McAdams *et al.* [S. McAdams, J. W. Beauchamp, and S. Meneguzzi, ''Discrimination of musical instrument sounds resynthesized with simplified spectrotemporal parameters,'' J. Acoust. Soc. Am. **105**(2), 882–897 (1999)] for each pitch. The spectrogram was obtained using a 2048-point Hamming window, a 2048-point Fast Fourier transform (FFT), and an overlap such that the resulting time-frequency matrix was of equal size to the modal time-frequency matrix (for instance, in the G6 example, the overlap was set to 1962 points). The amplitude and frequency estimates were then obtained using a three-point parabolic fit to the log-magnitude spectra.

The extracellular matrix is an important source of ultrasound backscatter from myocardium

Christopher S. Hall,[a] Michael J. Scott, and Gregory M. Lanza
Washington University School of Medicine, St. Louis, Missouri 63110 and Barnes-Jewish Hospital, St. Louis, Missouri 63110

James G. Miller
Physics Department, Washington University, St. Louis, Missouri 63130

Samuel A. Wickline
Washington University School of Medicine, St. Louis, Missouri 63110 and Barnes-Jewish Hospital, St. Louis, Missouri 63110

(Received 23 March 1999; revised 25 August 1999; accepted 29 September 1999)

Ultrasound tissue characterization with measurement of backscatter has been employed in numerous experimental and clinical studies of cardiac pathology, yet the cellular components responsible for scattering from cardiac tissues have not been unequivocally identified. This laboratory has proposed a mathematical model for myocardial backscatter that postulates the fibrous extracellular matrix (ECM) as a significant determinant of backscatter. To demonstrate the importance of ECM, this group sought to determine whether measurements of backscatter from the isolated ECM could reproduce the known directional dependence, or anisotropy of backscatter, from intact cardiac tissues *in vitro*. Segments of left ventricular free wall from ten formalin fixed porcine hearts were insonified at 50 MHz, traversing the heart wall from endo- to epicardium to measure the anisotropy of myocardial backscatter, defined as the difference between peak (perpendicular to fibers) and trough (parallel to fibers) backscatter amplitude. The tissue segments were then treated with 10% NaOH to dissolve all of the cellular components, leaving only the intact ECM. Scanning electron micrographs (SEM) were obtained of tissue sections to reveal complete digestion of the cellular elements. The dimensions of the residual voids resulting from cell digestion were approximately the diameter of the intact myocytes (10–30 μm). These samples were reinsonified after seven days of treatment to compare the anisotropy of integrated backscatter. The magnitude of anisotropy of backscatter changed from 15.4 ± 0.8 to 12.6 ± 1.1 dB for intact as compared with digested specimens. Because digestion of the myocardium leaves only extracellular sources of ultrasonic scattering, and because the isolated ECM exhibits similar ultrasonic anisotropy as does the intact myocardium, it is concluded that there is a direct association between the ECM and the anisotropy of backscatter within intact tissue. Thus, it is suggested that ultrasonic tissue characterization represents a potentially clinically applicable method for delineating the structure and function of the ECM. © *2000 Acoustical Society of America.* [S0001-4966(00)05501-6]

PACS numbers: 43.80.Cs, 43.80.Ev, 43.80.Qf, 43.80.Vj [FD]

INTRODUCTION

The complex fibrous extracellular matrix of the heart plays an important role in the structural and mechanical properties of the heart muscle and is responsive to both external-loading conditions and to internal biochemical signaling pathways.[1] The extracellular collagenous matrix has been shown to possess a markedly greater tensile strength than the surrounding passive myocardium[2] and to provide the supporting frameworks for myocytes and fibroblasts.[3] The matrix consists of three parts: the epimysium that surrounds the myocytes, the perimysial fibers that course between the myocytes, and the endomysial collagen fibers that attach myocytes to one another.[4] The collagen fibrils form sheaths around individual cardiac myocytes to ensure the equal stretch of contiguous myocytes and to prevent slippage between cells. It has been suggested that the perimysial fibers may play a particularly important role in diastole.[4] These fibers have been described as coiled forms which stress gradually as they are forced to straighten by cardiac bending and untwisting, which suggests that their shape is of primary importance to their mechanical function.[5] Hence, the ability to nondestructively characterize the microscopic organization and composition of the cardiac extracellular matrix would be useful for evaluation of pathologies (e.g., hypertrophic cardiomyopathy, hypertensive heart disease, infarction, diabetes, and aging) that affect this component of the cardiovascular system.

The ultrasonic characterization of the high degree of organization of myocardial fibers in the myocardium has been reported extensively by our group and others. The specific alignment of the myofibers across the heart wall determines the acoustic properties of the heart such as the frequency dependence of the backscatter[6] and attenuation,[7] integrated or frequency-averaged magnitude of backscatter,[8–10] and

[a]Author to whom correspondence should be addressed.

speed of sound.[11,12] These properties can influence the appearance of clinical echocardiographic images as evidenced by the ''drop-out'' in the septal and lateral walls in the short axis echocardiographic view.[13]

In addition, normally contracting myocardium has been shown to exhibit a cardiac cycle-dependent variation of ultrasonic backscatter that is periodic with cardiac contraction and relaxation.[14–19] The presence of ischemic,[20,21] infarcted,[10,19] or cardiomyopathic tissue[22] affects this contractile dependence of ultrasonic backscatter. Although the principal cause of this cyclic variation and its relation to the microstructural components of the myocardium has been the source of many investigations, the exact physiologic mechanism responsible for cyclic variation and anisotropy of backscatter in heart muscle remains unknown. Other researchers have demonstrated a strong correlation between wall thickening and the magnitude of cyclic variation,[15,17] although after ischemic insult in patients with acute infarction, cyclic variation recovers before normal wall thickening in viable tissue that is salvaged by reperfusion therapy.[20,23] As the heart contracts and twists, the angular dependence of backscatter due to changes in scatterer geometry and orientation may play an important role in the observed cyclic variation. Evidence that suggests that this effect may occur has been demonstrated in observations of view-dependent cyclic variation parameters (magnitude and time-delay).[14,18]

We[24,25] and others[26–28] have proposed mechanisms to explain the experimentally measured anisotropy of acoustic parameters by developing a model for the fundamental scattering unit within the myocardium. Our laboratory has proposed that the fundamental cardiac scatterer manifests the typical geometric dimensions of a cardiac myocyte, and that the primary source of acoustic contrast is provided by the impedance mismatch between the stiff extracellular collagenous matrix and the waterlike myocyte itself. Linker *et al.* determined by acoustic microscopy that the autocorrelation length of normal myocardium was similar in size to the myofibers.[29] Initial results comparing the model's predictions of the anisotropy of backscatter with experimental results in fixed and fresh myocardium showed reasonable agreement. Other subsequent models have been proposed which employ many of the same assumptions about the extracellular matrix being the principal source of ultrasonic impedance mismatch while modeling the fundamental scatterer with slightly different shapes.

In order to test further our hypothesis that the extracellular matrix is a primary determinant for the observed anisotropy of backscatter, we sought to distinguish the scattering attributable solely to the extracellular matrix from that potentially arising from other components within the myocardium. Accordingly, we applied a method reported by Ohtani *et al.*[30] to dissolve the cellular components of the myocardial tissue by incubation of normal cardiac tissue in concentrated NaOH solution. After treatment, the remaining tissue contains only microfibrils associated with the extracellular matrix. In this paper, we report the results of measurements of ultrasonic backscatter from such treated tissues that have been excised from formalin-fixed porcine myocardium. By examining the acoustic properties of the myocardium before and after dissolution of the cellular material, we attempted to isolate the primary source of the anisotropy of ultrasonic scattering within myocardial tissues.

I. THEORY

We have previously presented a mathematical model to explain the dominant features of ultrasonic scattering from within the myocardium.[24] The model involves the assumption of a fundamental scatterer that is approximately the size of the cellular structure or myocyte within the myocardium. However, the primary impedance mismatch was postulated to exist between the extracellular collagen network and the myocyte.[31] In accordance with this view, we modeled the fundamental scatterer as an ellipsoidal shell where the shell possesses the physical characteristics of the extracellular matrix and the myocyte has the average properties of the surrounding waterlike medium. These shells (myofibers) comprise weak, independent scatterers (i.e., Born approximation) having a biologically reasonable distribution of physical parameters such as spatial orientation and elastic constants.

The backscatter from a single scatterer as a function of the material properties of the host medium and extracellular matrix can be expressed as

$$A_L(\omega) = -\frac{a_L^0 k_L^2}{4\pi}\left[\frac{\delta\rho}{\rho} + \frac{\delta\lambda + 2\delta\mu}{\lambda + 2\mu}\right] S_{LL}(\omega), \tag{1}$$

where ω is the angular frequency of insonification, $A_L(\omega)$ is the longitudinal to longitudinal scattering amplitude, a_L^0 is the amplitude of the insonifying wave, k_L is the wave number; ρ, λ, and μ are the density and Lame parameters of the host and intracellular media; and $\delta\rho$, $\delta\lambda$, and $\delta\mu$ are the changes of the densities and Lame parameters from the extracellular matrix to intracellular medium. The shape factor, $S_{LL}(\omega)$, represents the geometric properties of the scatterer and is the primary factor responsible for expressing the anisotropy of backscatter.

The predictions of this model have been presented in previous publications in comparison to experimentally measured results.[9,24] For the purpose of generating a comparison with the experimental results in this paper, it was necessary to convert the predicted backscatter coefficients to the ''apparent'' backscatter that has not been compensated for the effects of attenuation and beam diffraction arising from the finite beam width. To accomplish this goal, we applied a method of data reduction described by the group from the University of Wisconsin.[32] This method allows the calculation of the apparent backscatter from the equation,

$$\langle V_s(\omega) V_s^*(\omega)\rangle = \eta(\omega) \int_{\Omega}\int\int dr' \|J_\omega(r')\|^2, \tag{2}$$

where the apparent backscattered power is represented by $\langle V_s(\omega) V_s^*(\omega)\rangle$, ω represents the frequency of insonification, $\eta(\omega)$ is the backscatter coefficient, and $\int_{\Omega}\int\int dr' \|J_\omega(r')\|^2$ is the correction for beam diffraction and the attenuation occurring in the overlying tissue and within the gated volume Ω.

Figure 1 shows the predicted value of the backscattered power as a function of the angle of insonification for isolated

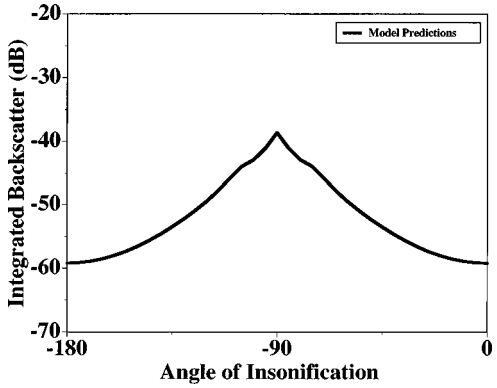

FIG. 1. The predicted value of the backscattered power as a function of the angle of insonification for isolated extracellular matrix.

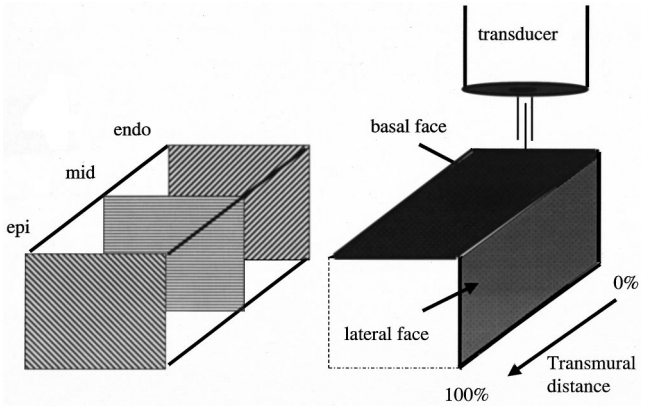

FIG. 2. The orientation between the transducer and the myocardial tissue sample. Insonification was performed as the transducer was translated transmurally across the heart wall.

extracellular matrix in water. The values for the parameters used in this calculation are given in Table I. The frequency range used for the modeling purposes in this paper is over a similar frequency range to that in the measurements, 30 to 50 MHz. The results in Fig. 1 are expressed in decibels, and measured relative to the amount of backscatter returned by a ''perfect'' planar reflector.

II. EXPERIMENTAL METHODS

A. Sample preparation

Ten samples were gathered from five excised, formalin-fixed pig hearts. The tissue had been fixed in 10% formalin for periods ranging from several months to years. The samples were cut from the left ventricular free wall in an orientation perpendicular to the axis from the apex to mitral valve. The samples were placed in a gelatin mold and then cut to have flat and parallel faces so that they could be scanned from the epicardial to endocardial surface (Fig. 2). After initial insonification, the hearts were then placed in a 10% NaOH solution for 7 to 10 days to allow for dissolution of the components not associated with the extracellular matrix.[30] The samples were then rinsed for a day in distilled water until the pieces became visually transparent.

B. Ultrasonic measurements

Measurements of backscatter were obtained from each tissue both before and after treatment with NaOH. The tissue was mounted so that interrogation was performed across the range of fibers spanning from epicardium to endocardium so that the effect of the fiber twist would be measured transmurally across the heart wall.[9] Figure 2 illustrates the manner in which the tissue was insonified. A transducer was translated across the basal face of the tissue so that the full range of transmural fiber angles would be examined. A 50-MHz transducer was translated in 100-μm steps from the epicardial surface extending to the endocardial border over roughly 120 independent intramural loci (each with different fiber orientations); at each fiber orientation seven site averages were obtained by translating the transducer laterally in 100-μm steps.

TABLE I. The physical parameters used for the theoretical calculation of integrated backscatter as a function of the angle of insonification.

Tissue	Myocyte semimajor axis (μm)	43.0 ± 10.0
	Myocyte semiminor axis (μm)	7.5 ± 2.0
Extracellular shell	Longitudinal velocity (cm/s)	2.9×10^5
	Shear velocity (cm/s)	0.4×10^5
	Density (g/cm^3)	1.3
Intracellular	Longitudinal velocity (cm/s)	1.58×10^5
	Shear velocity (cm/s)	0.1×10^5
	Density (g/cm^3)	1.05
Attenuation	Perpendicular to fibers (dB/cm)	1.2
	Parallel to fibers (dB/cm)	2.7

The acoustic microscope setup has been described previously. Briefly, a broadband pulse from a high-frequency pulser (Panametrics 5900) excited a 50-MHz piezoelectric, delay-line transducer (Panametrics). The received backscattered signal was amplified (Panametrics 5900) and digitized to 8 bits at 500 megaSamples/sec by a digitizing oscilloscope (Tektronix DSA 601). The signal was averaged 128 times in the time domain and then transferred to a computer (Macintosh IIfx) for off-line storage and analysis.

Analysis of the received signal was performed to determine the apparent backscatter transfer function (not compensated for attenuation) and the integrated backscatter for each intramural locus across the heart wall. A 600-ns gated region placed 150 ns below the front wall of the tissue was multiplied by a windowing function (Hamming) and Fourier transformed to calculate the power spectrum. For signal calibration, this tissue power spectrum was then referenced to a power spectrum returned by a polished steel plate to remove any dependence upon the electronic or transducer transfer functions. For the calculation of integrated backscatter, the resulting apparent backscatter transfer function is averaged over a usable bandwidth of 30–50 MHz.

In order to average the results of several measurements of the anisotropy of integrated backscatter from different specimens, it was necessary to account for the different transmural thickness of the myocardium exhibited by each heart. Therefore, we expressed the anisotropy of integrated backscatter as a percentage of the transmural distance across the left ventricular free wall. This expression takes into account the transmural twist of myofibers across the heart wall

so that the distance across the wall correlates with angle of insonification. In addition, we used a cross-correlation method to align the mid-myocardial regions between specimens. In the mid-myocardium, the backscattered power reaches a maximum due to the perpendicular insonification of the myofibers. This peak in the scattered power provided an appropriate feature to align the anisotropy curves of different specimens. After alignment according to the location of the maximum cross-correlation coefficient, the individual anisotropy of integrated backscatter curves was averaged together to obtain the reported result. The method described above has been used in several published papers.[6,11]

C. Histology measurements

Standard methods for preparation of the tissue for scanning electron microscopy were applied. Pig heart slices were fixed with glutaraldehyde, postfixed with OsO_4, and dehydrated in ascending concentrations (50%, 70%, 90%, and 100%) of ethyl alcohol (EtOH) for 20 min at each concentration. The slices were then cryofractured by inserting each slice into a tube of Parafilm, containing 100% EtOH, which was then sealed and dropped into a bath of liquid nitrogen. Each frozen tube was then fractured with a chilled razor blade, the frozen tissue halves placed into room temperature 100% EtOH and allowed to thaw. Cryofractured slices were transferred to a Polaron E3000 Critical Point Drying Apparatus (Polaron Equipment Limited). The 100% EtOH was replaced with liquid CO_2 and the tissues critical point dried after a one-hour soak in liquid CO_2. Dried samples were mounted onto aluminum specimen stubs (Electron Microscopy Sciences) with Carbon Conductive Tabs (Ted Pella, Inc); grounded with Colliodal Silver Liquid Paint (Ted Pella, Inc.), and sputter coated with about 300 Å (30 nm) of gold in a Polaron E5000 Sputter Coater (Polaron Equipment Limited). Samples were examined in a Hitachi S-450 Scanning Electron Microscope (Hitachi, Ltd.), operated at 20-KV accelerating voltage, and images were recorded on Polaroid 55 P/N film (Polaroid Corporation).

The collagen content was measured for both treated and intact tissues using a hydroxyproline assay. Two measurements of the collagen content were of interest: (i) the total amount of collagen, and (ii) the percentage collagen within the treated and intact tissues. To measure the total collagen, equal weights of wet tissue were obtained. One set of tissues was treated with NaOH to dissolve the cellular components while the other set was maintained intact in formalin. The absolute weight of the hydroxyproline (or indirectly the collagen) was obtained for both the dissolved and intact tissues. Any differences in these two weights would imply possible dissolution of the collagenous matrix with NaOH. Second, if the dissolved tissue were less than 100% collagen then the dissolution of the cellular components would be incomplete.

III. RESULTS

The structure of the intact and digested tissues was examined under scanning electron microscopy. Representative photomicrographs are shown in Fig. 3. The pictures were taken near the epicardial surface of the heart, and the myofiber orientation was arranged so that the major length of the myofiber was into the picture. The voids left after treatment of the tissue were roughly the size of myocytes. There were no cross struts or endomysial fibers, as the cellular components which would normally serve as anchors for these proteins had been removed. Examination under a dissecting microscope revealed that the shape and size of the digested piece of tissue were similar to those of the original, undigested tissue although the texture and coloration of the digested tissue were soft, gelatinous, and clear. This observation, coupled with the scanning electron micrographs, suggests that the cellular matrix geometry was left grossly intact by replacing the myocytes with fluid (NaOH or water during insonification).

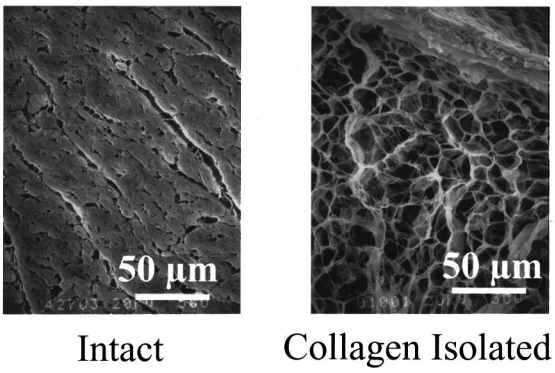

FIG. 3. Scanning electron micrographs of the intact and ECM-isolated tissue. The structure of the extracellular matrix is apparent in the right-hand picture.

Figure 4 shows the change in integrated backscatter measured transmurally across the myocardium for one sample (top panel) and the average for all ten specimens (middle panel) before digestion of the myocytes. The anisotropy measured within the single sample was maintained when averaged with the other nine samples showing a consistent anisotropy for porcine myocardium. The error bars are not shown on the graph for the sake of clarity, although the standard error of the mean is ± 0.8 dB for all ten animals at each angle of insonification.

The bottom panel of Fig. 4 shows the measurements of the anisotropy of backscatter across the heart wall before and after treatment of the tissue. The curves have been filtered with a three-point binomial filter to accent the overall trend. The anisotropy is preserved after treatment, although the overall scattering amplitude decreases with the removal of the cellular material. The magnitude of anisotropy of backscatter changed from 15.4 ± 0.8 to 12.6 ± 1.1 dB for intact as compared with digested specimens. Again, the error bars are reported by the standard deviation of the mean at ± 0.8 (intact) and ± 1.1 (ECM isolated) dB.

Figure 5 illustrates the amount of collagen in both intact and digested tissues as determined by the hydroxyproline assay. The control tissue was maintained in formalin and was measured to have a starting wet weight of 13.50 gm in comparison to the initial wet weight of 13.61 gm for the piece of tissue to be placed within NaOH. After one week of submersion in their respective fluids, the control tissue had a wet weight of 14.70 gm and the NaOH-treated tissue was 3.67

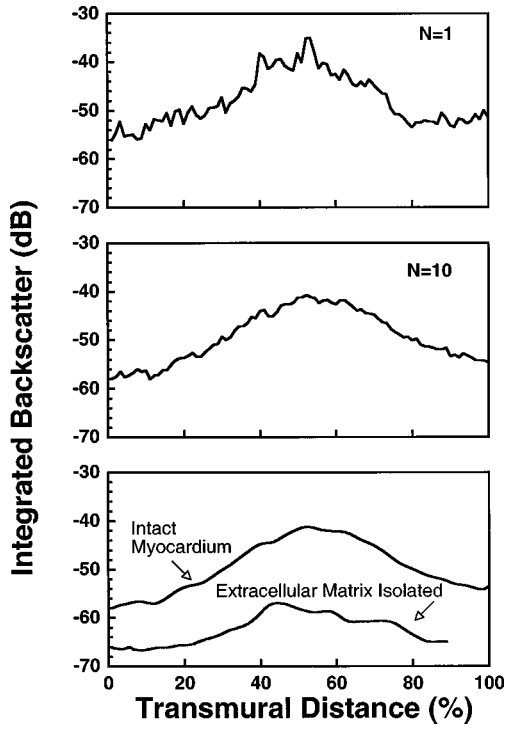

FIG. 4. The integrated backscatter averaged from 30 to 50 MHz as a function of the angle of insonification for a single sample (top) and the average of ten specimens (middle) of intact tissue. The comparison of the average of ten specimens of ECM-isolated and intact tissue is shown in the bottom panel.

gm. This difference in weights was due to dissolution of the cellular components. After lyopholization, the control tissue was 3.11 gm and the treated tissue was 0.12 gm. The hydroxyproline assay yielded results for the amount of collagen within the sample to be 139 ± 9 (control) and 58 ± 9 (treated) μg of collagen. These measurements imply that the treated tissue was 48% collagen while the untreated (control) tissue was 4.5% collagen.

IV. DISCUSSION

The myocardium represents a constantly changing microenvironment with the extracellular matrix continually being disassembled and reorganized by the action of proteolytic enzymes.[33] The extracellular matrix also undergoes reorganization in response to acute[34] and old myocardial injury[35] by the formation of scarred regions consisting of highly aligned collagen fibers. The collagenous extracellular matrix has been linked to the structural and functional properties of the myocardium. In particular, increased cross linking of the matrix has been implicated as the source of increased passive stiffness of the heart in both animal and human models. This decreased compliance of the heart muscle has been suggested as the principal cause of diastolic dysfunction associated with such diseases as diabetes and in the natural process of aging. Progressive nonenzymatic glycative mediated cross linking of the collagenous matrix has been proposed as a mechanism for diastolic dysfunction occurring in type-2 diabetes and in the natural process of aging.[36,37]

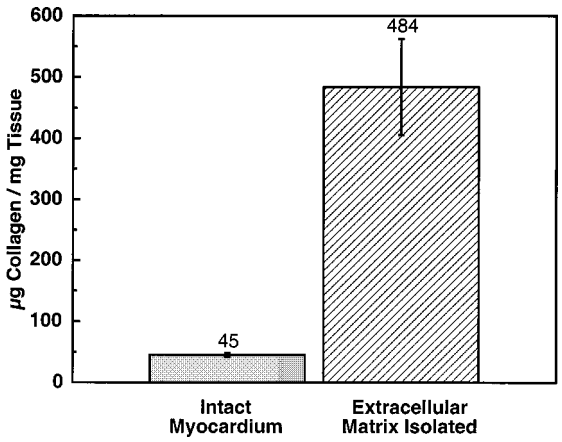

FIG. 5. The amount of collagen contained in equal original tissue wet weights after one set has been stored in formalin and the other treated with NaOH.

Clinical and experimental studies of cardiac diastolic dysfunction have not been well characterized because of the lack of a robust parameter that specifically delineates the extent of the ventricular compliance. The development of a tool to noninvasively monitor one possible microscopic source of ventricular compliance associated with diastolic dysfunction was a motivating factor of this study. We propose that quantitative backscatter may be useful as a noninvasive tool for the assessment of structural changes within the heart muscle that lead to diastolic dysfunction.

High-frequency ultrasound has been shown to be sensitive to changes in cardiac structure although the exact physical mechanisms responsible for the scattering of ultrasonic waves are poorly understood for biological tissues. The left ventricular free wall comprises a complex, three-dimensional fiber architecture that changes transmurally through the heart wall. This shift in fiber orientation allows the measurement of the angular dependence of specific ultrasonic parameters.[9] In the present study, we have measured the anisotropy of backscatter in a similar fashion both before and after treatment of the tissue to remove all cellular components, which presumably leaves only the extracellular matrix. We measured the magnitude of anisotropy to be 15.4 ± 0.8 dB in the case of the intact tissue, which compares favorably to the similar measurements by Recchia *et al.* of approximately 15 dB for canine myocardium over a similar ultrasonic frequency range.[9] Although these previous measurements were made on fixed tissue, a comparison of the anisotropy of fixed versus fresh tissues has yet to be reported in the literature. Fixation of tissue has been previously reported to increase the overall backscatter due to increases in the number of cross-linked collagenous proteins within the myocardium. These cross links may help the tissue maintain its structure after dissolution in this study, although they are not expected to significantly alter the measured anisotropy. The fact that the magnitude of backscatter and anisotropy of backscatter of the intact tissues is similar to previously published results suggests that this method of measuring anisotropy of backscatter across the heart wall yields robust and stable measurements.

We observed that the anisotropy of integrated backscatter was preserved in the ECM-isolated tissues despite the fact

that all of the cellular components had been removed. The magnitude of anisotropy, or difference between peak and trough in the anisotropy curves, shows that even after dissolution of the nonfibrous components, the backscatter still reaches a maximum for perpendicular insonification and a minimum at parallel incidence. The magnitude of anisotropy of the treated tissue (12.6 ± 1.1 dB) is comparable to that measured in the intact tissue (15.4 ± 0.8 dB). The slight diminution in the magnitude of anisotropy after cell dissolution may be due to the lack of a supporting structure (the cells and ground substance) in the dissolved tissue so that the precise angular orientation of the microfibers was not maintained. This change in the fiber orientation would affect the more sensitive measurements at perpendicular incidence, since the anisotropy function is very ''peaky'' or steep near perpendicular incidence. The fact that any anisotropy or directional dependence of scattering remains when the cellular components are removed suggests that the source of the observed anisotropy in cardiovascular tissue is largely due to the extracellular matrix and not the myocytes themselves. This observation has profound consequences for the monitoring of modifications to the extracellular matrix in response to tissue injury or drug treatment since even slight changes in the matrix may be reflected in changes in the degree to which anisotropy of ultrasonic backscatter is manifested.

A second noticeable feature of the comparison between the anisotropy curves in the bottom panel of Fig. 4 is that the dissolved tissue manifests considerably less overall backscatter than does the intact tissue. The reduction in backscatter is roughly 8 to 15 dB or a factor of 6 to 30 times. A few experimental conditions might contribute to the difference observed in the backscatter between the intact and treated tissues. The treatment of the intact tissue by placing it within concentrated NaOH could potentially disrupt portions of the extracellular matrix in addition to dissolving the intracellular components. The absence of some of the collagen network might result in a predicted decrease in overall magnitude of backscatter and perhaps a difference in the observed anisotropy of acoustic parameters. The results of the hydroxyproline assay suggest that this may be true since the amount of tissue left after treatment was 3.85% (0.12/3.11 gm) of the intact tissue. And of the remaining tissue after treatment, only 48% was determined to be collagen. The intact tissue was determined to be 4.5% collagen by weight, which implies that the remaining tissue after NaOH treatment represented only a portion of the total collagen present in the intact piece. Examination of the scanning electron micrograph reveals a complex three-dimensional weave of fibers. When the cellular components were removed, it is possible that some of the endomysial collagen fibers were also removed, since their primary function is to provide structural support between myocytes. The cell-free tissue may consist merely of the epimysial and perimysial fibers with the endomysial fibers absent once they have no place to anchor.

The SEM micrographs do not provide any information about the other 52% of the treated tissue that was determined to be components other than collagen. To account for the 52% of the remaining tissue that is not collagen, we have to examine the fundamental components of the extracellular matrix and myocardium. The myocardium contains the many noncirculating cells including myocytes and fibroblasts, in addition to the perfusion cells of erythrocytes and leukocytes. These components are dissolved by the treatment of the tissue with concentrated NaOH and are not evident in the SEM micrographs measured in our study. The extracellular matrix has been described as consisting of several different fibrous substances: elastin, microfibrils, collagen fibers, polyanionic lattice, and ground substance.[38] The elastin is primarily found in the epimysial layer near the endocardium,[38] and within blood vessels in the coronary vasculature. Microfibrils make up the dominant portion of the remaining extracellular matrix within our experiment.[39–41] The microfibrils have been measured to consist of the protein fibronectin existing as an independent structural entity, connecting or surrounding the collagen struts within the matrix. It has been observed by other investigators that fibronectin is a major component of the myocardial interstitium and may affect the compliance and control the motion of myocytes within the beating heart.[39] It is likely that the dominant, remaining, noncollagenous substance in the treated samples consists of fibronectin. The last component, ground substance, consists primarily of glycosaminoglycans and is dissolved by the treatment employed in this study.

Another experimental issue for treated tissues involved possibly enhanced relative absorbence of water (or edema) in the treated tissue in comparison with the intact tissue. The treated tissue grossly appeared to have the gelatinous consistency of a fragile, hydrated sponge. The increased capacity to absorb water would have the effect of spreading the collagenous fibers farther apart and therefore lowering the number density of scatterers. However, the amount of swelling of the tissue due to water was not enough to explain the decrease in backscatter in the treated tissue. All changes in volume were of order $<50\%$ where a 100% change or doubling in volume would only serve to reduce by half the scatterer number density, or, in other words, to decrease the magnitude of backscatter by 3 dB. However, if the collagen itself became more hydrated, its material properties could change in a way that would predict a decrease in backscatter amplitude.

The difference between the intact and treated tissues' anisotropy curves may also be due to a weakening of the fibrous matrix by partial dissolution of the collagen fibers. Although not detectable on the SEM picture in Fig. 3, the partial dissolution of the matrix could lead to changes in the acoustic properties of longitudinal or shear velocity of the extracellular medium. In a paper by Rose *et al.*, the anisotropy of integrated backscatter was highly dependent on the longitudinal velocity of the ECM. Varying the acoustic longitudinal velocity of the fibrous extracellular shell from 1800 to 2800 m/s yielded a predicted change in backscatter of 10 dB. Changes in the collagen matrix caused by hydration of the collagen protein could modify the acoustic velocity in a manner consistent with the observed decrease in backscatter.

The observed decrease in the overall magnitude of backscatter is significant because it suggests that some modifications to previously posed theoretical models may require

consideration. This experiment was performed essentially to assess the validity of some of the assumptions of the mathematical models developed to describe the backscatter returned by cardiac muscle. These models have mostly hypothesized that the principal source of the ultrasonic backscatter is the acoustic impedance mismatch between the intracellular medium and the extracellular matrix. In most of the treatments, the intracellular medium has been modeled as having the acoustic parameters of a waterlike medium. In this experiment, we have effectively removed the intracellular medium and replaced it with water. Ideally, this replacement should supply the exact conditions made by the approximations within the theoretical frameworks. However, the amount of backscatter decreases substantially in the case of the dissolved tissue. This observation may imply that the mechanism for ultrasonic scattering may not solely depend on the extracellular matrix. The exact mechanism for the unaccounted backscatter in the dissolved tissues is unknown at this time, although it could be accounted for by collagen dissolved by the NaOH.

In this study, we have attempted to delineate some of the primary sources of ultrasonic scattering within the myocardium. By removing all of the structures within the myocardium except for the fibrous extracellular matrix, we sought to isolate the scattering from the extracellular matrix and the cellular components. The isolated fibrous matrix possessed several interesting features of normal tissue, of which maintenance of the magnitude of the anisotropy of backscatter was the most remarkable characteristic. The sensitivity of the anisotropy of ultrasonic backscatter to the state of the underlying microstructure of the extracellular matrix suggests that ultrasonic tissue characterization may provide a useful diagnostic tool for defining derangements of cardiac microscopic architecture that influence heart function under pathologic conditions that specifically affect the matrix.

[1] K. T. Weber, ''Cardiac intersitium in health and disease: The fibrillar collagen network,'' J. Am. Coll. Cardiol. **13**, 1637–1652 (1989).

[2] S. L.-Y. Woo, P. O. Newton, D. A. MacKenna, and R. M. Lyon, ''A comparative evaluation of the mechanical properties of the rabbit medial collateral and anterior cruciate ligaments,'' J. Biomech. **25**, 377–386 (1992).

[3] J. B. Caulfield and T. K. Borg, ''The collagen network of the heart,'' Lab. Invest. **40**, 364–372 (1979).

[4] D. A. MacKenna, S. M. Vaplon, and A. D. McCulloch, ''Microstructural model of perimysial collagen fibers for resting myocardial mechanics during ventricular filling,'' Am. J. Physiol. **273**, H1576–1586 (1997).

[5] D. A. MacKenna, J. H. Omens, and J. W. Covell, ''Perimysial collagen fibers uncoil rather than stretch during diastolic filling,'' Basic Res. Cardiol. **91**, 112–122 (1996).

[6] C. S. Hall, E. D. Verdonk, S. A. Wickline, J. E. Perez, and J. G. Miller, ''Anisotropy of the apparent frequency dependence of backscatter in formalin fixed human myocardium,'' J. Acoust. Soc. Am. **101**, 563–568 (1997).

[7] E. D. Verdonk, B. K. Hoffmeister, S. A. Wickline, and J. G. Miller, ''Anisotropy of the slope of ultrasonic attenuation in formalin fixed human myocardium,'' J. Acoust. Soc. Am. **99**, 3837–3843 (1996).

[8] J. G. Mottley and J. G. Miller, ''Anisotropy of the ultrasonic backscatter of myocardial tissue: I. Theory and measurements *in vitro*,'' J. Acoust. Soc. Am. **83**, 755–761 (1988).

[9] D. Recchia, C. S. Hall, R. K. Shepherd, J. G. Miller, and S. A. Wickline, ''Mechanisms of the view-dependence of ultrasonic backscatter from normal myocardium,'' IEEE Trans. Ultrason. Ferroelectr. Freq. Control **42**, 91–98 (1995).

[10] J. Naito *et al.*, ''Myocardial integrated ultrasonic backscatter in patients with old myocardial infarction: Comparison with radionuclide evaluation,'' Am. Heart J. **132**, 54–60 (1996).

[11] E. D. Verdonk, S. A. Wickline, and J. G. Miller, ''Anisotropy of ultrasonic velocity and elastic properties in normal human myocardium,'' J. Acoust. Soc. Am. **92**, 3039–3050 (1992).

[12] B. K. Hoffmeister, S. M. Handley, S. A. Wickline, and J. G. Miller, ''Ultrasonic determination of the anisotropy of Young's modulus of fixed tendon and fixed myocardium,'' J. Acoust. Soc. Am. **100**, 3933–3940 (1996).

[13] D. Recchia, J. G. Miller, and S. A. Wickline, ''Quantification of ultrasonic anisotropy in normal myocardium with lateral gain compensation of two-dimensional integrated backscatter images,'' Ultrasound Med. Biol. **19**, 497–505 (1993).

[14] A. E. Finch-Johnston, H. M. Gussak, J. Mobley, M. R. Holland, O. Petrovic, J. E. Perez, and J. G. Miller, ''Effect of time delay on the apparent magnitude of cyclic variation of myocardial ultrasonic backscatter in standard echocardiographic views,'' Ultrason. Imaging **17**, 77 (1995).

[15] D. A. Lythall, R. B. Logan-Sinclair, C. J. Ilsley, S. S. Kushwaha, M. H. Yacoub, and D. G. Gibson, ''Relation between cyclic variation in echo amplitude and segmental contraction in normal and abnormal hearts,'' Br. Heart J. **66**, 268–276 (1991).

[16] M. R. Milunski, K. A. Wear, J. E. Perez, B. E. Sobel, J. G. Miller, and S. A. Wickline, ''The effect of frequency on the magnitude of cyclic variation of backscatter in dogs and its implications for prompt detection of the immediate consequences of myocardial ischemia,'' Circulation **80**, II-565 (1989).

[17] A. F. v. d. Steen, H. Rijsterborgh, C. T. Lancee, F. Mastik, R. Krams, P. D. Verdouw, J. R. Roelandt, and N. Bom, ''Influence of data processing on cyclic variation of integrated backscatter and wall thickness in stunned porcine myocardium,'' Ultrasound Med. Biol. **23**, 405–414 (1997).

[18] B. F. Vandenberg, L. Rath, T. A. Shoup, R. E. Kerber, S. M. Collins, and D. J. Skorton, ''Cyclic variation in normal myocardium is view dependent: Clinical studies with a real time backscatter imaging system,'' J. Am. Soc. Echocardiogr **2**, 308–314 (1989).

[19] K. A. Wear, M. R. Milunski, S. A. Wickline, J. E. Perez, B. E. Sobel, and J. G. Miller, ''The effect of frequency on the magnitude of cyclic variation of backscatter in dogs and implications for prompt detection of acute myocardial ischemia,'' IEEE Trans. Ultrason. Ferroelectr. Freq. Control **38**, 498–502 (1991).

[20] M. R. Milunski, G. A. Mohr, K. A. Wear, B. E. Sobel, J. G. Miller, and S. A. Wickline, ''Early identification with integrated backscatter of viable but stunned myocardium in dogs,'' J. Am. Coll. Cardiol. **14**, 462–471 (1989).

[21] S. A. Wickline, L. J. Thomas, J. G. Miller, B. E. Sobel, and J. E. Perez, ''Sensitive detection of the effects of reperfusion on myocardium by ultrasonic tissue characterization with integrated backscatter,'' Circulation **74**, 389–400 (1986).

[22] J. E. Perez, J. B. McGill, J. V. Santiago, K. B. Schechtman, A. D. Waggoner, J. G. Miller, and B. E. Sobel, ''Abnormal myocardial acoustic properties in diabetic patients and their correlation with the severity of disease,'' J. Am. Coll. Cardiol. **19**, 1154–1162 (1992).

[23] S. Takiuchi, H. Ito, K. Iwakura, Y. Taniyama, N. Nishikawa, T. Masuyama, M. Hori, Y. Higashino, K. Fujii, and T. Minamino, ''Ultrasonic tissue characterization predicts myocardial viability in early stage of reperfused acute myocardial infarction,'' Circulation **97**, 356–362 (1998).

[24] J. H. Rose, M. R. Kaufmann, S. A. Wickline, C. S. Hall, and J. G. Miller, ''A proposed microscopic elastic wave theory for ultrasonic backscatter from myocardial tissue,'' J. Acoust. Soc. Am. **97**, 656–668 (1994).

[25] S. A. Wickline, E. D. Verdonk, and J. G. Miller, ''Three-dimensional characterization of human ventricular myofiber architecture by ultrasonic backscatter,'' J. Clin. Invest. **88**, 438–446 (1991).

[26] K. N. Kumar and J. G. Mottley, ''Quantitative modeling of the anisotropy of ultrasonic backscatter from canine myocardium,'' IEEE Trans. Ultrason. Ferroelectr. Freq. Control **41**, 441 (1994).

[27] L. Landini and M. F. Santarelli, ''A regression model of ultrasound reflectivity from normal myocardium,'' Med. Eng. Phys. **17**, 141–144 (1995).

[28] M. F. Santarelli and L. Landini, ''A model of ultrasound backscatter for the assessment of myocardial tissue structure and architecture,'' IEEE Trans. Biomed. Eng. **43**, 901–911 (1996).

[29] D. T. Linker, B. A. J. Angelsen, and R. L. Popp, ''Autocorrelation length of normal and myopathic human myocardium measured by acoustic microscopy: Implications for clinical ultrasonic tissue characterization,'' Ultrasound Med. Biol. **16**, 793–799 (1990).

[30] O. Ohtani, T. Ushiki, T. Taguchi, and A. Kikuta, ''Collagen fibrillar networks as skeletal frameworks: A demonstration by cell-maceration/scanning electron microscope method,'' Arch. Histol. Cytol. **51**, 249–261 (1988).
[31] S. A. Wickline, L. J. Thomas III, J. G. Miller, B. E. Sobel, and J. E. Perez, ''A relationship between ultrasonic integrated backscatter and myocardial contractile function,'' J. Clin. Invest. **76**, 2151–2160 (1985).
[32] E. L. Madsen, M. F. Insana, and J. A. Zagzebski, ''Method of data reduction for accurate determination of acoustic backscatter coefficients,'' J. Acoust. Soc. Am. **76**, 913–923 (1984).
[33] F. G. Spinale, J. L. Zellner, W. S. Johnson, D. M. Eble, and P. D. Munyer, ''Cellular and extracellular remodeling with the development and recovery from tachycardia-induced cardiomyopathy—changes in fibrillar collagen, myocyte adhesion capacity and proteoglycans,'' J. Mol. Cell. Cardiol. **28**, 1591–1608 (1996).
[34] M. Zhao, H. Zhang, T. F. Robinson, S. M. Factor, E. H. Sonnenblick, and C. Eng, ''Profound structural alterations of the extracellular collagen matrix in postischemic dysfunctional (''stunned'') but viable myocardium,'' J. Am. Coll. Cardiol. **10**, 1322–1334 (1987).
[35] S. A. Wickline, E. D. Verdonk, A. K. Wong, R. K. Shepard, and J. G. Miller, ''Structural remodeling of human myocardial tissue after infarction,'' Circulation **85**, 259–268 (1992).
[36] E. D. Schleicher, E. Wagner, and A. G. Nerlich, ''Increased accumulation of the glycoxidation product *N*-epsilon (carboxymethyl) lysine in human tissues in diabetes and aging,'' J. Clin. Invest. **99**, 457–468 (1997).
[37] D. R. Sell, M. A. Lane, W. A. Johnson, E. J. Masoro, O. B. Mock, K. M. Reiser, J. F. Fogarty, R. G. Cutler, D. K. Ingram, G. S. Roth, and V. M. Monnier, ''Longevity and the genetic determination of collagen glycoxidation kinetics in mammalian senescence,'' Proc. Natl. Acad. Sci. USA **93**, 485–490 (1996).
[38] T. F. Robinson, L. Cohen-Gould, R. M. Remily, J. M. Capasso, and S. M. Factor, ''Extracellular structures in heart muscle,'' Adv. Myocardiol **5**, 243–255 (1985).
[39] G. G. Ahumada and J. E. Saffitz, ''Fibronectin in rat heart: A link between cardiac myocytes and collagen,'' J. Histochem. Cytochem. **32**, 383–388 (1984).
[40] E. Schwartz, S. Goldfischer, B. Coltoff-Schiller, and O. O. Blumenfeld, ''Extracellular matrix microfibrils are composed of core proteins coated with fibronectin,'' J. Histochem. Cytochem. **33**, 268–274 (1985).
[41] T. F. Robinson, S. M. Factor, J. M. Capasso, B. A. Wittenberg, O. O. Blumenfeld, and S. Seifter, ''Morphology, composition, and function of struts between cardiac myocytes of rate and hamster,'' Cell Tissue Res. **249**, 247–255 (1987).

Difference thresholds for intensity perception of whole-body vertical vibration: Effect of frequency and magnitude

Miyuki Morioka and Michael J. Griffin
Human Factors Research Unit, Institute of Sound and Vibration Research, University of Southampton, Southampton SO17 1BJ, United Kingdom

(Received 7 December 1998; revised 17 March 1999; accepted 25 August 1999)

Difference thresholds for seated subjects exposed to whole-body vertical sinusoidal vibration have been determined at two vibration magnitudes [0.1 and 0.5 ms^{-2} root mean square (r.m.s.)] and at two frequencies (5 and 20 Hz). For 12 subjects, difference thresholds were determined using the up-and-down transformed response method based on two-interval forced-choice tracking. At both frequencies, the difference thresholds increased by a factor of five when the magnitude of the vibration increased from 0.1 to 0.5 ms^{-2} r.m.s. The median relative difference thresholds, Weber fractions ($\Delta I/I$), expressed as percentages, were about 10% and did not differ significantly between the two vibration magnitudes or the two frequencies. It is concluded that for the conditions investigated the difference thresholds for whole-body vibration are approximately consistent with Weber's Law. A vibration magnitude will need to be reduced by more than about 10% for the change to be detectable by human subjects; vibration measurements will be required to detect reductions of less than 10%. [S0001-4966(99)03312-3]

PACS numbers: 43.80.Gx, 43.40.Ng, 43.66.Wv [FD]

INTRODUCTION

The human body is exposed to many sources of vibration: in all types of transport, in buildings, and from the operation of industrial equipment. People react to the vibration according to their perception, which depends, in part, on the vibration magnitude. The magnitude of the vibration to which the body is exposed can be expressed in terms of physical measurements (e.g., the displacement, velocity, or acceleration). However, the sensations experienced by people must be obtained using psychophysical measures (e.g., ratings of perceptibility, comfort, annoyance, or pain). While the physical magnitude of the motion may be quantified on well-known ratio scales (e.g., in meters, meters per second, or meters per second per second), psychophysical measures may have nominal, ordinal, interval, or ratio characteristics according to how they are obtained (Stevens, 1975). The interpretation of physical measurements, and the construction and interpretation of psychophysical scales, requires knowledge of how the perception of vibration varies with vibration magnitude.

Absolute thresholds for the perception of whole-body vibration have been determined in several experiments (e.g., Parsons and Griffin, 1988; see also review by Griffin, 1990). These show average absolute thresholds for the perception of vertical sinusoidal vibration at about 0.01 to 0.02 ms^{-2} r.m.s. over the range 5 to 20 Hz, but with appreciable differences between experimenters and between subjects.

Several studies have shown that for vibration magnitudes well above threshold (e.g., Miwa, 1968; Howarth and Griffin, 1988), increases in the magnitude, φ, of whole-body vibration results in increases in judgments of the sensation magnitude, ψ, which are approximately in accord with Steven's Power Law,

$$\psi = k \cdot \varphi^n,$$

where n is the ''growth function'' and k is a constant that depends on the system of units. Studies have found some values of n for vibration stimuli: 0.95, 0.81, and 0.62 at frequencies of 60, 120, and 240 Hz, respectively, for the fingertip (Stevens, 1959, 1968); 0.89 over the frequency range 25 to 350 Hz for the thenar eminence (Verrillo, 1970); 1.04 to 1.47 in the frequency range 4 to 60 Hz for whole-body vibration (Howarth and Griffin, 1988). This suggests that the sensation magnitude increases in approximately linear proportion to the acceleration magnitude.

For practical purposes, it is useful to know how much a vibration must be reduced for it to be perceived as being less uncomfortable. Attempts to reduce vibration discomfort for whole-body vibration have proceeded over recent years on the assumption that lower magnitudes of vibration will result in reduced discomfort. It has been assumed that, after applying a frequency weighting to allow for differences in sensitivity to different frequencies, reductions at any frequency that result in the same reduction in vibration magnitude will have the same beneficial effect. It has not been known when a reduction in vibration magnitude will not result in a noticeable improvement in discomfort.

For various stimuli, the ''difference threshold'' (sometimes called the ''difference limen,'' DL) has been measured: this quantifies human ability to differentiate between stimuli of different magnitudes. The difference threshold is defined as the change in a stimulus required for a human observer to recognize a ''just noticeable difference'' in the stimulus (Guilford, 1954).

The German psychologist, E. H. Weber, proposed that the size of the difference threshold is a constant ratio of the stimulus magnitude. Weber's law can be formulated as

$$\frac{\Delta I}{I} = \text{constant},$$

 1063-7834/2000/107(1)/5/$17.00

where ΔI represents the increment in stimulus intensity and I is the stimulus intensity; the ratio is called the Weber ratio, which varies according to the type of stimulus.

Two studies reported since the present study was conducted have investigated difference thresholds for whole-body vibration. Mansfield and Griffin (1999) determined difference thresholds for whole-body vertical vibration using a car seat, examining three vibration magnitudes (i.e., 0.2, 0.4, and 0.8 ms^{-2} r.m.s.) and two vibration waveforms recorded in a car driven on ''tarmac'' and ''pavé'' surfaces. On average, an increment of about 13% in stimulus intensity was just perceptible; this was independent of both the vibration magnitude and the vibration waveform when the stimulus was appropriately frequency-weighted. Pielemeier *et al.* (1997) determined difference thresholds on a car seat using a low level of stimulus: three types of narrow-band random vibration (i.e., center frequencies at 4, 8, and 15 Hz) at 8 mg r.m.s. (0.08 ms^{-2} r.m.s.). The difference thresholds were in the range 0.6 to 1.8 mg r.m.s. (7.5% to 22.5% of the stimulus magnitude).

There is a demand for a reduction of vibration not only in vehicles but also in other situations (e.g., in buildings, aircraft, ships) where the vibration contains a variety of characteristics. It is therefore desirable to identify perceptual sensitivity for a range of vibration stimuli so as to allow general predictions of the extent to which reductions in vibration magnitude will be perceived.

The present study involved the determination of difference thresholds for seated subjects exposed to *z*-axis (i.e., vertical) sinusoidal vibration. The effect of vibration frequency (at 5 and 20 Hz) on difference thresholds was examined with reference to two vibration magnitudes (0.1 and 0.5 ms^{-2} r.m.s.)

I. EXPERIMENTAL METHOD

A. Subjects

Twelve male volunteers, staff and students at the University of Southampton, participated in the experiment. All subjects were free of injury or history of relevant illness. They were aged between 21 and 30 (mean 23.5) years with an average stature of 181.2 cm and an average weight of 75.1 kg. The experiment was approved by the Human Experimentation Safety and Ethics Committee of the Institute of Sound and Vibration Research at the University of Southampton. Subjects were provided with written instructions (see Appendix) prior to participating in the experiment.

B. Apparatus

Whole-body sinusoidal vertical vibration was produced using a Derritron VP85 (6LA) electrodynamic vertical *z*-axis vibrator powered by a 1000-W amplifier. Subjects sat on a rigid flat wooden surface secured to an aluminum plate, 405 by 405 and 15 mm thick, attached to the vibrator. Subjects were positioned at the center of the seat surface; there was a stationary adjustable footrest but no backrest. Sinusoidal vertical vibration was generated and measured using *HVLab* software and a digital computer. The signals were generated at 300 samples per second and passed through 25-Hz low-pass filters. Vibration waveforms and the levels of the input and output signals were monitored on an oscilloscope. The vibration acceleration on the wooden seat surface was recorded during the presentation of every ''test'' motion using the *HVLab* system.

During the experiment, the ambient noise levels were in the range 55 to 60 dB(A); this noise was mainly caused by the vibrator cooling fan. So as to mask the ambient sounds of the vibrator, subjects wore ear defenders with integral speakers producing white noise at 70 dB(A), measured using a Knowles Electronics Manikin for Acoustic Research, KEMAR. They were exposed to this level for a maximum 60 min. Both the subject and experimenter were within easy reach of emergency buttons capable of stopping the motion of the vibrator.

C. Design and procedure

The difference thresholds were determined with vertical sinusoidal vibration in four conditions: two vibration frequencies (5 and 20 Hz) each presented at two different vibration magnitudes (0.1 and 0.5 ms^{-2} r.m.s.). The forced-choice tracking procedure, originally applied by Zwislocki *et al.* (1958) in auditory detection, was employed in the study in conjunction with the two-alternative forced-choice procedure. Subjects were exposed to a number of trials (about 35 to 60 trials per threshold determination); a trial consisted of a 4-sec ''reference'' stimulus, followed by a 1-sec pause, followed by a 4-sec ''test'' stimulus. The order of the ''reference'' and the ''test'' stimuli was randomized. The magnitude of the ''reference'' stimulus was constant at either 0.1 or 0.5 ms^{-2} r.m.s., depending on the condition being investigated. The ''test'' stimulus was presented at a greater magnitude than the ''reference'' stimulus with 0.25-dB (i.e., 2.9%) increment steps. The maximum magnitude of the ''test'' stimulus was 3 dB (i.e., 41%) greater than the ''reference'' stimulus. After each exposure to a pair of vibration stimuli the subject responded to the question:

> ''Did you judge the first or the second to be the greater?''

For the sequence of producing the ''test'' stimuli, the up-and-down transformed response method (UDTR method), proposed by Wetherill and Levitt (1965), was employed in the experiment. This method enables the estimation of observation probabilities other than the 50% level on a psychometric function; it has been used in some studies of absolute vibration perception thresholds at the finger (e.g., Maeda and Griffin, 1995; Maeda and Morioka, 1997) and on the hand (Morioka and Griffin, 1998), also to determine difference thresholds for whole-body vibration (Mansfield and Griffin, 1999) and hand-transmitted vibration (Morioka, 1998). The UDTR method has several alternative sequence patterns for obtaining thresholds at different probability levels (see Levitt, 1971). In the experiment, a three-down one-up rule (i.e., a decrease in the stimulus magnitude after three consecutive correct responses, an increase in the stimulus magnitude after one incorrect response) was selected because this gives thresholds at 79.4% correct response: close to half-way between a chance response (i.e., 50%) and certainty (100%).

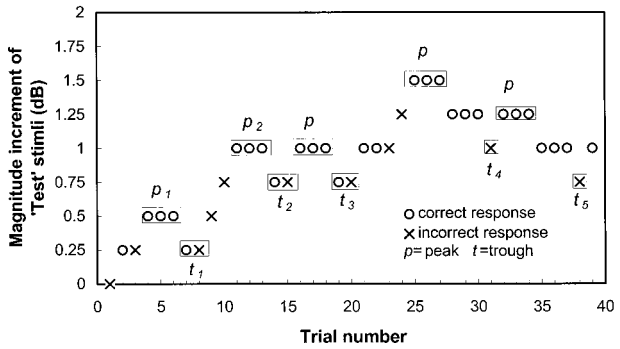

FIG. 1. Typical data for the difference threshold measurement using the UDTR procedure (three-down and one-up rule).

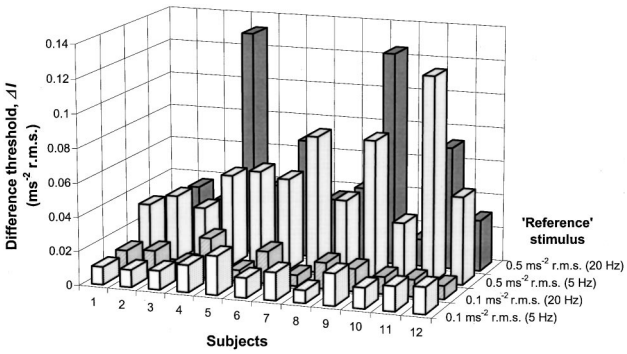

FIG. 2. Absolute difference thresholds for 12 subjects measured with four vibration stimulus conditions.

A typical set of data from the experiment is illustrated in Fig. 1. The ''test'' stimulus commenced with the same magnitude as the ''reference'' stimulus. In the example, an incorrect response was given after trial ''1,'' so the magnitude of the following ''test'' stimulus was increased to the next level. After trial ''2,'' a correct response was given, so the following stimulus was presented at the same level as in trial ''2.'' Subsequently, after trial ''3,'' three correct responses had been given consecutively, so the magnitude for trial ''7'' was decreased. A measurement was terminated after ten reversals (a point where the stimulus level reversed direction: either a peak or a trough). The four measurement runs were conducted with each subject on the same day, each requiring 10 to 15 min of experimentation.

D. Algorithm for determining difference thresholds

To determine difference thresholds, only the acceleration data at the reversal points (peaks and troughs) were used. Thresholds were calculated from the mean of the peaks and the troughs. Levitt and Rabiner (1967) suggested that the data from the first two reversals should be omitted from the calculation of the estimate in order to reduce starting errors, so difference thresholds were obtained by subtracting the ''reference'' value from the threshold value calculated from the average of the last four peaks and the last four troughs,

$$\text{Difference threshold} = \frac{[\Sigma_{i=2}^{i=5} p_i + \Sigma_{j=2}^{j=5} t_j]}{N} - R,$$

where p_i is the vibration magnitude of peak i, and t_j is the vibration magnitude of trough j; N is the number of reversals (i.e., 8); R is the reference magnitude.

II. RESULTS

A. Difference thresholds

Figure 2 shows the absolute difference thresholds obtained for all 12 subjects at the two magnitudes and the two frequencies. The difference thresholds ranged from 0.0064 to 0.0237 with the 0.1 ms^{-2} r.m.s. reference magnitude and ranged from 0.015 to 0.132 with the 0.5 ms^{-2} r.m.s. reference magnitude. It is clear that the difference thresholds were greater with the higher reference magnitude. Overall, the difference thresholds obtained with the four reference stimuli were significantly different (Friedman, $\chi^2 = 29.8$, $p < 0.0001$), whereas there was no significant difference between difference thresholds obtained with the 5- and 20-Hz reference stimuli at 0.1 ms^{-2} r.m.s., or between these two stimuli presented at 0.5 ms^{-2} r.m.s. (Wilcoxon, $p > 0.3$). From these results, it is concluded that there was no significant difference in the difference thresholds at the two vibration frequencies (i.e., at 5 and 20 Hz).

There were no significant correlations between difference thresholds and subject age or body size (i.e., height and weight) (Spearman, $p > 0.05$).

B. Weber fraction

In order to investigate the percentage change in magnitude required for a subject to notice that the vibration magnitude had changed, the ''absolute difference thresholds'' were expressed as ''relative difference thresholds'' using the Weber fraction, $\Delta I/I$ (i.e., the absolute difference threshold, ΔI, divided by the reference magnitude, I). Table I shows the relative difference thresholds, expressed as a percentage, for the four stimuli and the 12 subjects. The thresholds varied between subjects over the range 3.2% to 23.2%, with median thresholds of 11.6% at the low reference magnitude and 9.2% at the high reference magnitude. The analysis showed no significant difference in the Weber fractions be-

TABLE I. Relative difference thresholds (Weber fractions) expressed as percentages (%) with four reference stimuli for 12 subjects.

	Reference stimulus conditions			
	0.1 ms^{-2} r.m.s.		0.5 ms^{-2} r.m.s.	
Subjects	5 Hz	20 Hz	5 Hz	20 Hz
S1	8.51	11.16	6.40	4.86
S2	9.81	14.03	7.60	7.34
S3	10.49	7.41	6.42	5.82
S4	14.73	20.28	9.24	24.86
S5	20.40	6.96	11.40	9.14
S6	10.98	16.87	11.54	14.34
S7	16.01	6.84	14.70	6.89
S8	7.33	13.58	8.59	8.92
S9	14.69	13.57	15.49	23.18
S10	11.57	10.82	5.86	3.20
S11	13.40	10.55	24.52	14.63
S12	12.94	7.39	11.47	6.05
Median	12.25	10.99	10.32	8.13
Interquartile range	4.73	6.52	7.20	8.68

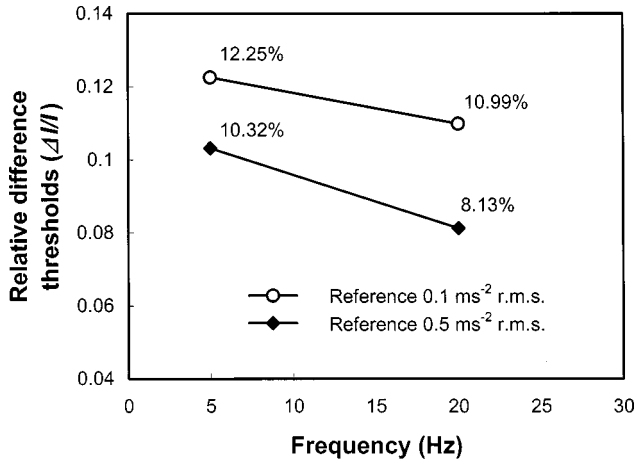

FIG. 3. Median relative difference thresholds for four vibration stimulus conditions.

tween the four stimuli (Friedman, $p>0.5$). The percentage of relative difference thresholds was slightly lower than those presented by Mansfield and Griffin (1999) (i.e., 11.8% to 14.1%) and much lower than those for hand-transmitted vibration presented by Morioka (1998) (i.e., about 15.6% to 18.6%).

III. DISCUSSION

The difference thresholds increased as the stimulus magnitude increased, with no frequency dependence: at both 5 and 20 Hz the difference threshold was almost five times greater at 0.5 than at 0.1 ms^{-2} r.m.s. When the difference threshold was expressed as a fraction of the vibration magnitude there was no significant difference between the two magnitudes. It seems that the difference thresholds for some types of whole-body vertical vibration are about 10% (between 8.1% and 12.3%) of the stimulus intensity. Although there was a trend for the Weber fractions to reduce with increasing vibration magnitude, the results are approximately consistent with Weber's law.

The results from the experiment may not be sufficient to predict detection sensitivity for other vibration stimuli. Figure 3 summarizes the median relative difference thresholds of the 12 subjects. Trends observed over the four stimuli may assist the extension of the results. At both frequencies, the relative difference threshold decreased (by about 2%) when the stimulus magnitude was increased from 0.1 to 0.5 ms^{-2} r.m.s. A similar phenomenon has been observed in some studies of difference thresholds at the thenar eminence where vibration intensity discrimination at 25 and 250 Hz is enhanced as intensity increases, but unaffected by frequency (Gescheider *et al.*, 1990). Discrimination sensitivity at 20 and 100 Hz has been found to be U-shaped or V-shaped, with a maximum enhancement at about 20-dB sensation level (Delemos and Hollins, 1996), which results in a ''near miss'' to Weber's Law.

Although the present results show no statistically significant change in the difference thresholds between 5 and 20 Hz, lower difference thresholds with the higher frequency were found at both magnitudes. This trend could indicate that detection sensitivity of vibration stimuli is greater at 20 than at 5 Hz. This implication does not support the use of frequency weightings that assume vertical vibration at 5 Hz produces significantly greater discomfort than vertical vibration at 20 Hz. Mansfield and Griffin (1999) concluded that the W_b frequency weighting from British Standard (BS) 6841 (1987) provided useful predictions of difference thresholds with different spectra of vertical vibration. The present results suggest that difference thresholds and Weber fractions of frequency-weighted stimuli may not be equal as the vibration frequency changes. However, the weighting W_b from BS 6841 (1987), which gives a high weighting to frequencies around 20 Hz relative to that in the old International Standard 2631 (1985) and the new International Standard 2631 (1997), may be sufficient if the vibration frequency is primarily within the range between 5 and 20 Hz.

During the experiment, some subjects reported they judged the difference between the stimuli by feeling the movement at a particular part of the body which varied according to the vibration conditions, such as movement of the head, knee, shoulder, or viscera at 5 Hz and movement of the upper leg or back at 20 Hz. The sensations generated by these two frequencies feel different and are generally perceived to be dominant in different parts of the body (see Whitham and Griffin, 1978). Although vibration may have been felt at different locations on the body, this does not appear to have resulted in a large difference in the difference thresholds at the two frequencies.

In accord with previous studies at the finger and the thenar eminence, it may be assumed that difference thresholds for whole-body vibration will depend on the method used for their determination (see Gescheider *et al.*, 1990). Higher or lower values could have been obtained by varying the psychophysical method. Further, difference thresholds probably depend on the interval between the presentation of the pairs of stimuli (see Gescheider *et al.*, 1996): a higher threshold may be expected if the interval is greater than that used here. Variations in the environment (e.g., noise or seating comfort) between two conditions may also be expected to increase difference thresholds. Hence, when comparing the ride in two vehicles, or the ride with two different seats, the present results suggest that changes in magnitude greater than 10% may be required for detection. However, this does not imply that vibration reductions below threshold are not worth achieving: the sum of several subthreshold changes can be expected to result in a noticeable improvement. The findings suggest that an improvement of less than 10% will not be easily detected by subjective testing. Consequently, it is desirable to use objective methods to optimize ride and seating dynamics, as these methods can measure improvements less than 10%.

IV. CONCLUSIONS

Difference thresholds for intensity perception of whole-body vertical vibration have been determined at two magnitudes (0.1 and 0.5 ms^{-2} r.m.s.) and at two frequencies (5 and 20 Hz) using a rigid flat seat. The difference thresholds increased in proportion to stimulus magnitude from 0.1 to 0.5 ms^{-2} r.m.s. The median relative difference thresholds, We-

ber fractions ($\Delta I/I$), expressed as a percentage, were about 10% (varying from 8.1% to 12.3%) and did not differ significantly between the two vibration magnitudes or the two frequencies.

It is concluded difference thresholds of whole-body vertical vibration may be approximately consistent with Weber's Law, but that further information is required in order to confidently predict detection sensitivity with the full range of complex motions in vehicles. It is suggested that reductions in vibration magnitude of more than 10% will often be required for a change to be detectable by human subjects. Improvements of less than 10% may be measured by suitable vibration instrumentation.

APPENDIX

Instructions for subjects

The aim of this experiment is to determine the difference threshold for vertical sinusoidal whole-body vibration.

(1) Before the experiment, the acceleration condition will be calibrated. During the calibration, you will sit in the seat.
(2) After the calibration, the experiment will be started. You will feel two vibration stimuli, then you will be asked;

''Did you judge the first or the second to be the greater?

Your task is to answer, either ''FIRST'' or ''SECOND.''
(3) Stimuli will be presented several times.

Note

- Please maintain the posture and concentrate on the stimuli during the measurement.
- FOUR measurements will be performed, it will take about 10 to 15 minutes for each.

Thank you very much for your co-operation.

British Standards Institution (**1987**). ''Guide to measurement and evaluation of human exposure to whole-body mechanical vibration and repeated shock,'' BS 6841.

Delemos, K. A., and Hollins, M. (**1996**). ''Adaptation induced enhancement of vibrotactile amplitude discrimination: The role of adapting frequency,'' J. Acoust. Soc. Am. **99**, 508–516.

Gescheider, G. A., Bolanowski, Jr., S. J., Verrillo, R. T., Arpajian, D. J., and Ryan, T. F. (**1990**). ''Vibrotactile intensity discrimination measured by three methods,'' J. Acoust. Soc. Am. **87**, 330–338.

Gescheider, G. A., Zwislocki, J. J., and Rasmussen, A. (**1996**). ''Effects of stimulus duration on the amplitude difference limen for vibrotaction,'' J. Acoust. Soc. Am. **100**, 2312–2319.

Griffin, M. J. (**1990**). *Handbook of Human Vibration* (Academic, London).

Guilford, J. P. (**1954**). *Psychometric Methods* (McGraw-Hill, New York).

Howarth, H. V. C., and Griffin, M. J. (**1988**). ''The frequency dependence of subjective reaction to vertical and horizontal whole-body vibration at low magnitudes,'' J. Acoust. Soc. Am. **83**, 1406–1413.

International Organization for Standardization (**1985**). ''Evaluation of human exposure to whole-body vibration-—Part 1: General requirements,'' ISO 2631/1, Geneva.

International Organization for Standardization (**1997**). ''Mechanical vibration and shock—Evaluation of human exposure to whole-body vibration—Part 1: General requirements,'' ISO 2631/1, Geneva.

Levitt, H., and Rabiner, L. R. (**1967**). ''Use of a sequential strategy in intelligibility testing,'' J. Acoust. Soc. Am. **42**, 609–612.

Levitt, H. (**1971**). ''Transformed up-down methods in psychoacoustics,'' J. Acoust. Soc. Am. **49**, 467–477.

Maeda, S., and Griffin, M. J. (**1995**). ''A comparison of vibrotactile thresholds on the finger obtained with different measuring algorithms,'' *Proceedings of Stockholm Workshop '94 Hand-Arm Vibration Syndrome: Diagnostics and Quantitative Relationships to Exposure*, pp. 85–95.

Maeda, S., and Morioka, M. (**1998**). ''A comparison of vibrotactile thresholds on the finger obtained with ISO type equipment and Japanese equipment,'' Industrial Health **35**, 343–352.

Mansfield, N. J., and Griffin, M. J. (**1999**). ''Difference thresholds for automobile seat vibration,'' Appl. Ergonomics (in press).

Miwa, T. (**1968**). ''Evaluation methods for vibration effect, Part 4. Measurements of vibration greatness for whole body and hand in vertical and horizontal vibrations,'' Industrial Health **6**, 1–10.

Morioka, M., and Griffin, M. J. (**1998**). ''Comparison of absolute thresholds for vibration at the fingertip and on the hand in two different postures,'' *Abstracts of the 8th International Conference on Hand-Arm Vibration*, Sweden.

Morioka, M. (**1998**). ''Difference thresholds for intensity perception of hand-transmitted vibration,'' *Proceedings of the 33rd Meeting of the UK Group on Human Response to Vibration*, The Health and Safety Executive, Buxton, Derbyshire, 16–18 September 1998.

Parsons, K. C., and Griffin, M. J. (**1988**). ''Whole-body vibration perception thresholds,'' J. Sound Vib. **121**, 237–258.

Pielemeier, W. J., Jeyabalan, V., Meier, R. C., and Otto, N. C. (**1997**). ''Just noticeable differences in vertical vibration for subjects on an automobile seat,'' *Proceedings of the 32nd United Kingdom Group Meeting on Human Response to Vibration*, ISVR, University of Southampton, 17–19 September 1997.

Stevens, S. S. (**1959**). ''Tactile vibration: Dynamics of sensory intensity,'' J. Exp. Psychol. **57**, 210–218.

Stevens, S. S. (**1968**). ''Tactile vibration: Change of exponent with frequency,'' Percept. Psychophys. **3**, 223–228.

Stevens, S. S. (**1975**). *Psychophysics, Introduction to its Perceptual, Neural and Social Prospects* (Wiley, New York).

Verrillo, R. T. (**1970**). ''Subjective magnitude functions for vibrotaction,'' IEEE Trans. Man-Machine Systems **1**, 19–24.

Wetherill, G. B., and Levitt, H. (**1965**). ''Sequential estimation of points on a psychometric function,'' Br. J. Mathematical Statistical Psychol. **18**, 1–10.

Whitham, E. M., and Griffin, M. J. (**1978**). ''The effects of vibration frequency and direction on the location of areas of discomfort caused by whole-body vibration,'' Appl. Ergon. **9**, 231–239.

Zwislocki, J., Maire, F., Feldman, A. S., and Rubin, H. (**1958**). ''On the effect of practice and motivation on the threshold of audibility,'' J. Acoust. Soc. Am. **30**, 254–262.

Range discrimination by big brown bats (*Eptesicus fuscus*) using altered model echoes: Implications for signal processing

W. Mitchell Masters and K. A. S. Raver
Ohio State University, Department of Evolution, Ecology, and Organismal Biology, 1735 Neil Avenue, Columbus, Ohio 43210

(Received 14 July 1999; revised 6 October 1999; accepted 12 October 1999)

The sonar emissions of two big brown bats (*Eptesicus fuscus*) were modeled to create a ''normal'' echolocation signal for each bat which was then used as an artificial echo to synthesize a phantom target. The bat's task was to indicate which of two phantom targets (presented singly) was the ''near'' target and which the ''far'' target. Threshold range discrimination at a nominal target distance of 80 cm was about 0.6 cm for both bats. The normal signal was then modified to change the relative energy in each harmonic, the signal duration, the curvature of the frequency sweep, the absolute frequency, the phase of the second and third harmonics relative to the first, or the Doppler shift of the signal. To determine which modifications affected ranging performance, the altered models were used in tests of range discrimination that were interleaved on a day-to-day basis with tests using the normal model. Of the 12 modifications tested, only those changing the curvature of the frequency sweep affected performance. This result appears not to be predicted by current models of echo processing in FM bats. *Eptesicus* may be able to compensate for certain types of distortions of a returning echo, an ability possibly related to Doppler tolerance or to the characteristics of the natural variation in a bat's emissions.
[S0001-4966(00)06301-3]

PACS numbers: 43.80.Ka, 43.80.Lb, 43.66.Gf [WA]

INTRODUCTION

The sonar signals bats use for echolocation vary considerably from species to species (Simmons and Stein, 1980; Fenton, 1995), from situation to situation (Simmons *et al.*, 1978; Zbinden, 1989; Rydell, 1993; Obrist, 1995), and from individual to individual (Vater *et al.*, 1985; Schnitzler *et al.*, 1987; Suga *et al.*, 1987; Thomas *et al.*, 1987; Brigham *et al.*, 1989; Masters *et al.*, 1991, 1995; Obrist, 1995). However, despite such variation, the signals of a particular bat in a particular situation are probably fairly similar to each other. Individual consistency of emissions is supported by the empirical finding that the signals recorded from a set of bats can be reliably assigned to the proper bat by discriminant function analysis (Masters *et al.*, 1995; Burnett *et al.*, 1998; Kazial *et al.*, 1998). A certain degree of consistency is also expected on theoretical grounds. If a bat is to extract the maximal amount of information from sonar echoes, it must process echoes optimally, implying some type of matched-filter reception (Woodward, 1953). To create a matched-filter receiver, the signal to be received must be previously specified (the more completely the better), otherwise the filter cannot be pre-adjusted to reject nonsignals. Matched-filter reception by itself does not demand exact emission-to-emission consistency from the bat because, in theory, the receiver could be modified on each emission to match the expected echo. However, as a practical matter one would not expect the bat's receiver to be infinitely adaptable; rather, it is more likely to be able to deal efficiently with signals only within a certain range of variation. Furthermore, the bat's receiver must be able to cope with variations in the echo imposed by the target, such as Doppler effects due to target motion and filtering due to target shape. Presumably these effects would be easier to interpret if emissions were reasonably similar.

A bat's emission can be described mathematically in terms of its duration, starting and ending frequencies, time-frequency structure, relative energy of harmonics, and envelope of each harmonic (Masters and Jacobs, 1989; Masters *et al.*, 1991). All of these descriptors vary from call to call, but it is possible to describe an average based on a number of calls. Previous research has shown that a bat can use the average signal obtained in this way to discriminate the range of an electronically synthesized ''phantom'' target created by playback of the signal as an artificial ''echo'' (Masters and Jacobs, 1989; Masters and Raver, 1996; Masters *et al.*, 1997). In this paper, we compared bats' ability to determine the relative range of two phantom targets using an echo with average characteristics for each bat (its ''normal model'') with their ability to determine range when one or a few parameters of the normal model were altered. The goal was to see which modifications caused difficulty for the bats, and what such difficulties might suggest about how bats process echoes. The only alteration that degraded a bat's ability to determine range was one producing a nonlinear change in the timing of pulse-echo frequency relationships, suggesting that big brown bats can process an echo so long as its time-frequency structure bears a quasi-linear relation to time-frequency structure of the emission. Examination of a bat's emissions suggests that their time-frequency structures may be related to each other in this same quasi-linear way.

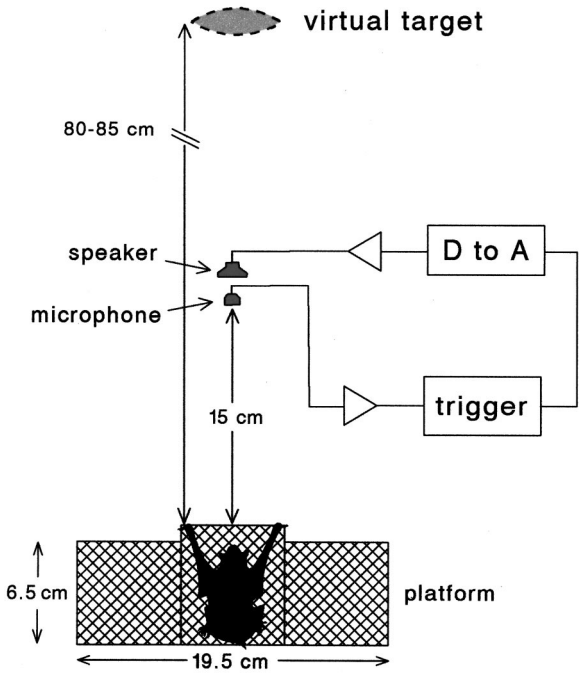

FIG. 1. Diagram of the target-presentation setup. The speaker and microphone were positioned one above the other but are separated here for clarity. The signal to be used as the artificial echo was loaded into the D/A converter before the trial began, and each sonar emission of the bat triggered playback of this signal so that the ''echo'' was time-locked to the bat's emissions.

I. METHODS

A. Subjects

We used two female big brown bats (*Eptesicus fuscus*) named Giggles and Guppy, born in the laboratory to wild-caught mothers who were pregnant when captured. Both were reared by their mothers for the first month and after that were housed individually in wooden cages patterned after those described by Barnard (1995). Water supplemented with vitamins and minerals was available *ad libitum*, and bats were fed mealworms (*Tenebrio molitor* larvae) reared in a vitamin and mineral-enriched flour-based medium (Barnard, 1995). They received sufficient mealworms to maintain their weight at 15–22 g during the experiments. At the start of testing, both bats were 11.5 months old.

B. Setup

Figure 1 shows the experimental setup used to generate phantom targets. The bat was placed on a horizontal platform 1.2 m above the floor and 1.5 m diagonally from one corner of a 2.9×3.4×2.9 m room whose walls were covered with echo-attenuating foam (Permafoam). A 6-mm Brüel and Kjær microphone (Model 4135) with an L-adapter and no protective grid was located 15 cm from the front of the platform. A 13-mm electrostatic speaker, designed following Kuhl *et al.* (1954), was mounted immediately above the microphone. The output of both microphone and speaker was ±3 dB over the range 25–110 kHz. The microphone picked up the bat's sonar emissions and relayed them to a trigger circuit consisting of a full-wave rectifier and level detector. The output of the level detector triggered playback of a computer-stored signal through a digital-to-analog converter at 500 kilosamples/s. The stored signal consisted of a model echo (see below) preceded by a variable number of zeros. Each additional zero added 2 μs to the delay of the model echo, thereby allowing the apparent distance to the virtual target to be set by the number of leading zeros. In all the tests described below, the distance to the near target was nominally 80 cm, corresponding to a 4.65-ms delay between emission and echo, of which 0.87 ms of the delay was provided by travel of the sound to and from the microphone/speaker, and the remaining 3.78 ms by zero-padding (1890 2-μs steps). To create a virtual target at a greater distance, the number of leading zeros was increased.

C. Model calls

Following the procedures given in Masters and Jacobs (1989) and Masters *et al.* (1991), the digital signal played to the bat to create the ''echo'' of the phantom target was designed to match the individual bat's typical emission. We first trained the bat to remain on the platform and emit sonar calls toward the microphone and speaker. Once the bat learned to do this, we recorded approximately 60 of its sonar emissions directly to computer memory while the bat was echolocating the phantom target. We analyzed these calls by a specially written computer program (Asyst programming language) to determine the value for each call of a number of different parameters, as well as the amplitude envelope of the call's first three harmonics. The analysis program also determined which of several functions fit most closely the downward frequency sweep of the first harmonic (Masters *et al.*, 1991). For both bats in this study the best fit was given by an exponentially falling frequency function:

$$f_1(t) = (F_s - F_a)e^{-1/T} + F_a, \tag{1}$$

where $f_1(t)$ is the frequency of the first harmonic at time t after the start of the call, F_s is the starting frequency at time $t=0$, F_a is the asymptotic frequency approached as t becomes large, e is the base of natural logarithms, and T is the decay constant. The ''normal model'' echo for a bat was based on the average parameters for the bat, thus creating a signal mimicking the typical sonar emission of that particular bat. Table I lists the values used to create normal models for Giggles and Guppy, and Fig. 2 shows the normal models graphically (Giggles upper, Guppy lower). Table I gives F_e, the ending frequency of the fundamental (i.e., the frequency when t equals the duration, D). F_a can be computed from F_e using

$$F_a = (F_e - F_s e^{-D/T})/(1 - e^{-D/T}). \tag{2}$$

We tested 12 signal alterations of the normal model falling into 7 classes designated *a* to *g* in the middle column of Table I. Those alterations involving a change in the signal's time-frequency structure are shown in Fig. 3 (for Giggles only), and the cross-correlations (XCs) of all altered models with the unaltered (normal) model are shown in Fig. 4 (Giggles on left, Guppy on right). The XCs are useful to consider under the assumptions that a bat behaves like a cross-correlation detector and that the normal emission is similar to its internal template. But regardless of whether

TABLE I. Characteristics of the normal and altered models for the bats Giggles and Guppy.

Model parameter	Giggles		Alteration type	Guppy	
	Normal model	Altered model		Altered model	Normal model
Ratio of 2nd to 1st harmonic, H_2/H_1	1.74	2.46	a_1	2.26	1.60
		1.23	a_2	1.13	
Ratio of 3rd to 1st harmonic, H_3/H_1	1.08	1.53	b_1	0.79	0.56
		0.77	b_2	0.39	
Duration, D (ms)	2.03	2.87	c_1	4.16	2.94
		1.44	c_2	2.08	
Decay constant, T (ms)	1.48	2.09	d_1	3.10	2.19
		1.05	d_2	1.55	
Sweep of first harmonic, F_s to F_e (kHz)	52.0–18.7	53.4–20.1	e_1	59.0–28.2	57.3–26.5
		50.6–17.3	e_2	55.6–24.8	
Phase of 2nd and 3rd harmonic *re*: 1st	0	180°	f	180°	0
Doppler factor	1.00	1.10	g	1.10	1.00

these assumptions are completely justified (see the Discussion), XCs are of interest because cross-correlation is the ideal signal processing method for range determination by sonar or radar (Woodward, 1953).

In alterations of type *a*, we changed the amplitude of the second harmonic relative to the first (Table I, H_2/H_1 ratio, where H_2 is the maximum amplitude of the second harmonic and H_1 the maximum amplitude of first harmonic, i.e., the fundamental). We increased this ratio by 3 dB in a_1 and decreased it by 3 dB in a_2 while simultaneously keeping the total power of the two harmonics (i.e., $H_1^2+H_2^2$) unchanged.

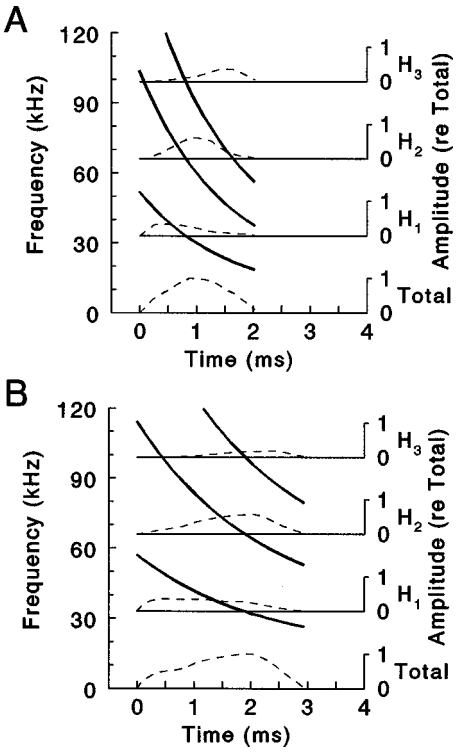

FIG. 2. Spectrograms of Giggles' (A) and Guppy's (B) average sonar emissions. Solid lines indicate the frequency of the three harmonics (scale on the left). Dashed lines show the envelopes of the three harmonics and of the total call (upper three curves and bottom curve, respectively, scales on the right).

In alterations of type *b*, we made similar changes to the ratio of third to first harmonic, H_3/H_1.

In alterations c_1 and c_2 [Fig. 3(A)] we increased or decreased, respectively, the duration, *D*, of the call by 1.41% and 0.71% (i.e., ± 3 dB). The call was extended or contracted at both the beginning and end of the frequency sweep. The envelopes of each harmonic (dashed lines in Fig. 2) were extended or contracted to fit the new duration. The main effect of these changes (Fig. 4) was to shift the position of the XC relative to that of the normal model (time zero in Fig. 4). For c_1 the peak occurs at a later point because adding material to the beginning of the signal delays the arrival of the portion of the waveform matching the normal model; for c_2 subtracting material at the beginning does the opposite. From the bat's point of view the shift should mean that target c_1 would seem farther away than the normal target because the critical portion of the echo is somewhat delayed, while c_2 should appear closer.

In alterations of type *d* [Fig. 3(B)], the decay constant, *T*, specifying the curvature of the first harmonic frequency sweep was increased (d_1) or decreased (d_2) by 3 dB. Increasing *T* makes the frequency sweep less curved and decreasing it makes the sweep more curved. In constructing these models, the beginning (F_a) and ending (F_e) frequencies of the first harmonic were kept the same as in the normal model and the asymptotic frequency F_a given by Eq. (2) was allowed to change. Like alteration *c*, these changes had the effect of delaying (d_1) or advancing (d_2) the XC relative to the normal model.

For alterations e_1 and e_2 [Fig. 3(C)] we shifted signal frequency up or down by 4%, respectively. The amount of the frequency shift was chosen to give approximately the same change in XC shift as produced by alterations d_1 and d_2. We adopted this criterion because the results of the behavioral tests showed that alterations of type *d* caused difficulties for the bats in ranging targets and we wished to produce a similar change in cross-correlation by a different method. A 4% shift in mid-frequency (the average of F_a and F_e) gave roughly the same XC shift as did alterations of type *d* (Fig. 4, traces e_1 and e_2 vs traces d_1 and d_2).

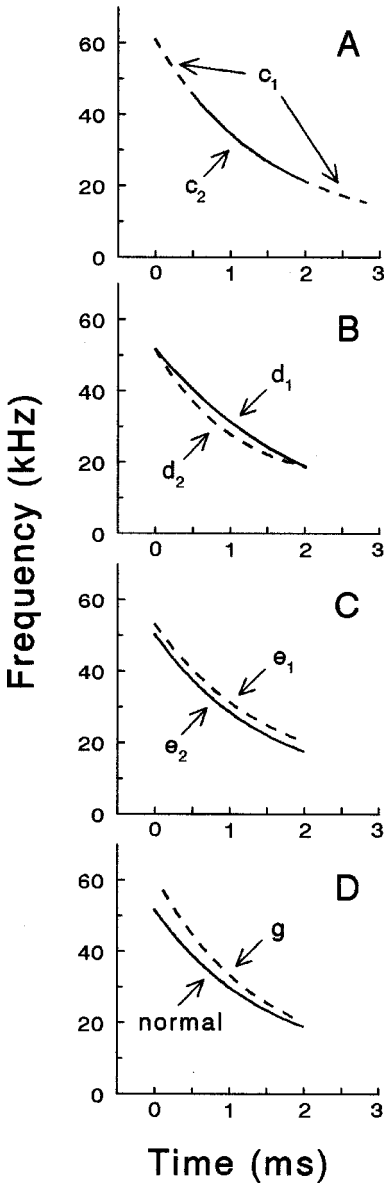

FIG. 3. Spectrograms (for Giggles only) of those altered models whose time-frequency structure differs from the normal model. For clarity, only the first harmonic of the signal is shown. The beginning of c_2 in (A) has been shifted rightward from time zero to show the correspondence between c_1 and c_2. The frequency sweep of the normal model also lies on the same curve as c_1 and c_2. Signal *g* in (D) has been shifted rightward slightly to separate it more clearly from the normal model. In (B) and (C), the normal model would lie midway between the two altered models shown.

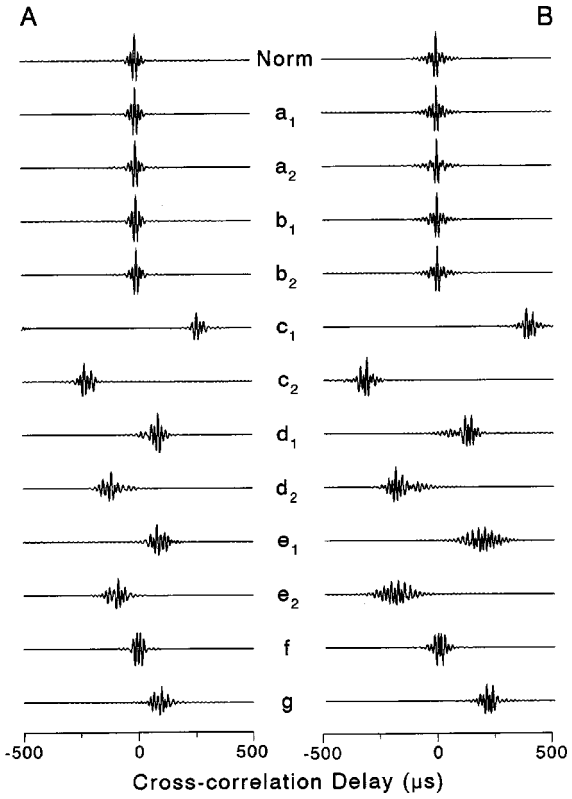

FIG. 4. Cross-correlations (XCs) of altered models versus the normal model. The top trace is the normal model versus itself (the autocorrelation). All signals were adjusted to unit energy before cross-correlation so that signal energy would not affect the XC. Letters *a* through *g* correspond to the signal alterations specified in the Methods section. The location of the peak of the normal XC was taken as time zero in all cases.

To determine whether the phase of the second and third harmonics relative to the first is important to the bat, we created signal *f* in which we inverted these two harmonics (i.e., phase shifted them by 180°) relative to the normal model. This did not change the location of the cross-correlation relative to the normal model (Fig. 4 trace *f*).

Alteration *g* [Fig. 3(D)] was an upward Doppler shift of the normal model, mimicking an echo from a target moving toward the bat (Masters *et al.*, 1991). We used a Doppler factor of 1.1, corresponding to a target approaching at 16.4 m/s, a closing speed that might be reached by two bats flying toward each other. This factor was chosen because it produced a displacement of XC (Fig. 4 trace *g*) similar to that of d_1. A Doppler shift of this magnitude causes each frequency in the signal to rise, and duration to decrease, by about 10%. This manipulation contrasts with *e* in that the frequency shift in *e* was constant across the whole call.

D. Testing

We trained bats to discriminate the range to phantom targets created using the model echoes described above. To start a trial, the bat crawled from the experimenter's hand onto the platform and emitted sonar sounds toward the phantom target. The bat then chose to move to the right or left side of the platform based on the distance to the phantom target. Bats were rewarded with a piece of mealworm for moving right when the target delay was set for 80 cm and for moving left when it was set for any greater distance. (As explained later in the Discussion, we believe that the bats followed the decision rule ''go right for the nearer target, left for farther target,'' rather than one based on absolute target distance.) For incorrect decisions the bat received no reward and a 10- to 15-s time-out. The distance to the target on a given trial was determined on the basis of a pseudorandom schedule (Gellermann, 1933) with equal numbers of presentations at near and far distances. We ran 20 trials per day, not including 3 to 5 preliminary trials. On any particular day, only one model (i.e., the normal model or one of the altered models) was used.

Before testing the altered models, we determined the range discrimination threshold for each bat using its normal model echo. Starting at a range difference of 5 cm (80 vs 85 cm), the difference was reduced to 4, 3, 2, 1.5, 1, 0.5, and 0.25 cm, with 40 trials at each level. After obtaining the threshold with the normal model, we began testing bats' range discrimination with the altered models at two range differences, 2 cm (80 vs 82 cm) and 1 cm (80 vs 81 cm). In order to avoid possible changes in baseline discriminatory ability, tests using altered models were alternated with tests using the normal model. For example, to test alteration a_1, targets were synthesized at 80 and 82 cm using a_1 on day 1, the normal model on day 2, a_1 on day 3, and the normal model on day 4. At 20 trials per day, this gave 40 trials with both the normal model and a_1 at a 2-cm range difference. We then repeated the procedure at a 1-cm range difference, thus completing the test of a_1. We then moved on to altered model a_2 following the same procedure, and so on through all 12 altered models in the order *a* to *g*. After completing this series of tests, we repeated the test of bats' range-discrimination threshold using the normal model in order to see whether their threshold had changed over the intervening ten months.

E. Statistics

The range-discrimination threshold for bats using their normal model echo was computed from the fraction of correct responses at different distances using a probit procedure (Finney, 1971, 1978; for further details see Masters and Raver, 1996). To determine the effect of altered models on range discrimination, we used three-way *G*-tests (Sokal and Rohlf, 1981) with the first factor being the type of model echo, the second the range difference (1 or 2 cm), and the third the outcome (number of correct and incorrect discriminations). All *G*-tests were two-tailed.

II. RESULTS

A. Range-discrimination threshold

The solid curves in Fig. 5 show range-discrimination performance of each bat using its normal model echo and before any testing with altered model echoes. The 75%-correct threshold determined by probit from these curves was 6.7±1.5 mm (mean±SE) for Giggles [Fig. 5(A)] and 5.4 ±1.9 mm for Guppy [Fig. 5(B)], meaning that the bats could distinguish a target at 80 cm from one at about 80.6 cm. The dashed curves show the bats' performance ten months later after having completed the series of tests using model echoes *a* through *g*. Thresholds were nearly unchanged (6.6±1.4 mm for Giggles and 6.0±1.1 mm for Guppy) and not significantly different for either bat from their earlier thresholds ($z=0.03$, $P\leqslant 0.98$, and $z=0.27$, $P\leqslant 0.79$, respectively).

B. Range-discrimination with altered models

Based on the psychometric curves in Fig. 5, we decided to use range differences of 1 and 2 cm to test bats' performance with modified echoes, considering these distances to be small enough to challenge the bats but not so small that the bats would become frustrated during extended testing. Table II gives the performance of the two bats using the altered model echoes compared with their performance determined concurrently using the normal model. Figure 6 shows their performance graphically in comparison to the average psychometric function (dashed line) from Fig. 5. The only modification that affected the bats' ability to discriminate range differences was *d*, in which the curvature of the frequency sweep was altered. The percentage of correct discriminations fell from around 90% with the normal model to around 75% with the altered model. For both bats, the effect of dropping the interaction between model (normal, d_1, or d_2) and performance (the number right and wrong) from the complete *G*-test was significant ($G_2=11.56$ and 8.37, $P\leqslant 0.003$ and 0.015 for Giggles and Guppy, respectively), indicating that the model used affects performance. We further partitioned these *G* values to reveal the effect due to alteration and the separate effect due to type of alteration. The comparisons of normal versus altered (d_1 and d_2) yielded large *G* values ($G_1=11.28$ and 8.23, $P\leqslant 0.001$ and 0.004, respectively), while the further comparison of d_1 vs d_2 was not significant ($G_1=0.28$ and 0.13, respectively), suggesting first that bats found modifications d_1 and d_2 more difficult to use than their normal model echo, and second that neither d_1 nor d_2 was significantly more difficult to use than the other.

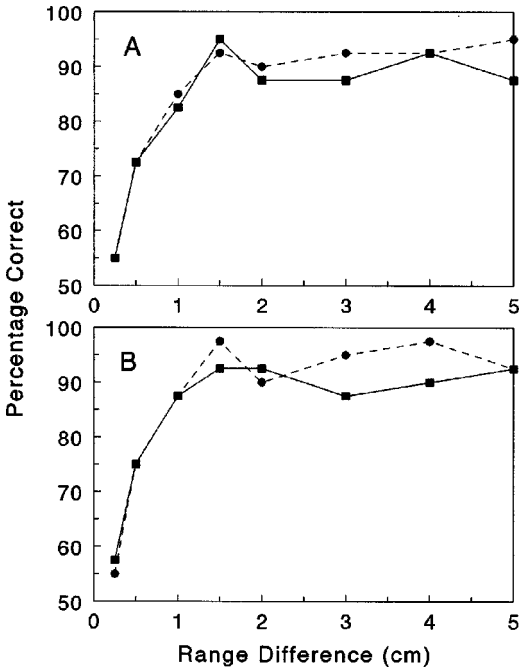

FIG. 5. The percentage of correct responses for Giggles (A) and Guppy (B) versus range difference using their normal model. The nominal distance to the nearer target was 80 cm; therefore, a range difference of 1 cm, for example, corresponds to discriminating a target at 80 cm from one at 81 cm. For both bats, performance drops below the 75% level at about 0.6 cm. The solid curve was obtained before beginning the series of tests with altered models and the dashed curve was obtained 11 months later after the series had been completed. Each point represents 40 trials. The average of each bat's two curves is shown as a dashed line in Fig. 6.

TABLE II. The number of correct discriminations out of 40 trials for each bat at the two range differences tested. The performance is given for the altered model echoes and for the concurrently tested normal model.

	Giggles			Guppy		
Test	80 vs 81 cm	80 vs 82 cm	Combined percentage	80 vs 81 cm	80 vs 82 cm	Combined percentage
Model a_1	36	34	87.50%	36	33	86.25%
Model a_2	36	35	88.75%	36	33	86.25%
Normal model	32	35	83.75%	35	35	87.50%
Model b_1	35	38	91.25%	36	35	88.75%
Model b_2	35	37	90.00%	33	35	85.00%
Normal model	35	36	88.75%	34	36	87.50%
Model c_1	34	34	85.00%	35	38	91.25%
Model c_2	34	37	88.75%	33	35	85.00%
Normal model	35	37	90.00%	35	37	90.00%
Model d_1	28	31	73.75%[a]	29	32	76.25%[a]
Model d_2	27	29	70.00%[a]	28	31	73.75%[a]
Normal model	36	36	90.00%	35	37	90.00%
Model e_1	35	37	90.00%	34	36	87.50%
Model e_2	34	38	90.00%	35	35	87.50%
Normal model	34	38	90.00%	35	35	87.50%
Model f	35	38	91.25%	34	35	86.25%
Normal model	34	37	88.75%	34	37	88.75%
Model g	36	36	90.00%	35	35	87.50%
Normal model	35	36	88.75%	35	37	90.00%

[a]Significantly different from the normal model at $P<0.01$.

III. DISCUSSION

A. Thresholds with the normal model

The bats' 75%-correct threshold for range discrimination using their normal models was about 0.6 cm (80.0 vs 80.6 cm), corresponding to an ability to discriminate echo arrival times differing by about 35 μs for near versus far target. The threshold remained unchanged over the course of the experiment. This threshold is essentially the same as obtained with other bats in the same situation (Masters and Raver, 1996; Masters *et al.*, 1997) and is toward the low end of the range of 0.6 cm to about 2 cm reported for different species using a number of different techniques (summarized in Moss and Schnitzler, 1995). The fact that the thresholds we obtained were as good as any found for any species using any technique (including real targets) suggests that the bats had no difficulty processing the normal model to determine target range.

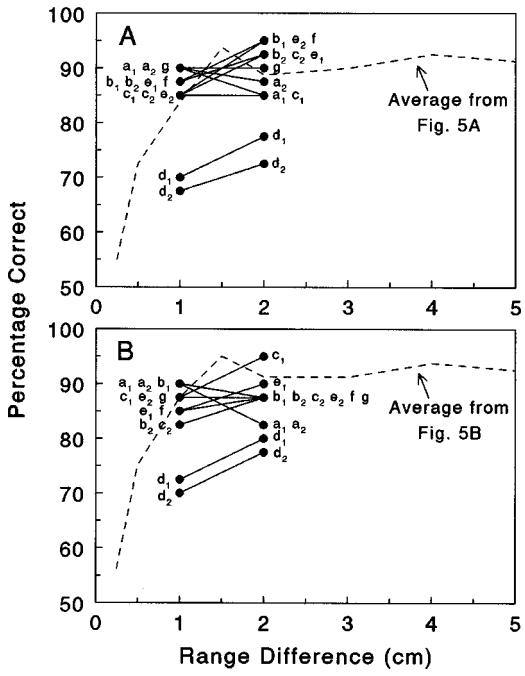

FIG. 6. Performance of Giggles (A) and Guppy (B) at a range difference of 1 and 2 cm using altered models *a* through *g*. The labels for each point correspond to the altered models listed in Table I. For each altered model, 40 trials were done at each range difference. The dashed line shows the bat's average psychometric curve obtained from Fig. 5.

Triggering playback of a simulated echo using a detector circuit that responds to the bat's emission, as in this paper, likely increases the uncertainty of the target's range due to trigger uncertainty or trigger ''jitter.'' The problem, in essence, is that no external device can synchronize precisely with the bat's unknown internal neural state (Masters *et al.*, 1997). As a consequence, the bat probably perceives some range variation in the phantom target from call to call even when the electronic delay remains fixed. Our estimates of the magnitude of triggering jitter suggest a standard deviation of the timing variation on the order of 70 μs (Masters *et al.*, 1997), which, because this is larger than the bats' observed threshold, implies that bats may average range estimates from two or more calls. Triggering jitter and the possibility of averaging make estimation of the bat's true neurophysiological uncertainty highly problematic. In the discussion that follows we are interested not so much in explaining the exact magnitude of the bat's threshold of 35 μs, but in com-

paring the bat's performance across the range of signals tested.

B. Cross-correlations and expected behavior

A useful concept from radar/sonar theory is that of an ideal observer or ideal receiver, i.e., a receiver that makes use of all the available information to reach some decision without adding additional ''noise'' of its own. Based on the characteristics of the expected signal (the echo, for bats) that are known *a priori*, an ideal receiver implements a filter matched to the expected signal. Assuming that the desired information is target range, the ideal matched-filter receiver is a cross-correlation detector, i.e., one that computes the cross-correlation (XC) between the emitted signal and the echo (Woodward, 1953). Cross-correlation can be carried out equivalently in either the time or frequency domain, and for mammalian auditory systems, cross-correlation may involve correlation of spectrogramlike representations of the emission and echo (Altes, 1980). Whether *Eptesicus* might be better characterized as a ''semi-coherent'' receiver able to use only the envelope of the XC, or as a ''coherent'' receiver able to use the fine structure within the envelope, is a question that has provoked a great deal of debate (Simmons, 1979, 1993; Simmons and Stein, 1980; Schnitzler and Henson, 1980; Schnitzier *et al.*, 1985; Menne and Hackbarth, 1986; Menne *et al.*, 1989; Moss and Schnitzler, 1989, 1995; Masters and Jacobs, 1989; Masters *et al.*, 1991; Schmidt, 1992; Moss and Simmons, 1993; Pollak, 1993). For the present discussion we assume the former, although the issue is not critical here.

If we view *Eptesicus* as an ideal receiver, we can use the XCs in Fig. 4 as a way of visualizing the possible effect of altered echoes on ranging performance. To do so we make the assumption that the normal model corresponds to the signal to which the bat's receiver is matched. The bat's actual ''template'' is unknown (and potentially varies from emission to emission), but this assumption is a reasonable starting point because the normal model was designed to correspond to the bat's typical sonar signal. For such a signal the expected echo would be very similar to the emitted pulse, at least for a point target such as synthesized by the target simulator.

The upper XC in Fig. 4 shows the correlation of the normal model with itself (i.e., the autocorrelation), which is the standard to which other XCs may be compared. This XC is quite compressed in the time dimension (much more so than the raw signal waveform) and sharply peaked. These characteristics make the XC useful for determining target range, which requires precise measurement of the time delay. A sharp peak in the XC means that the position of the peak (i.e., time of echo arrival) is easy to determine, and the width of the peak (or of the XC envelope if the bat behaves as a semi-coherent receiver) determines the uncertainty of the range estimate. Zero on the time axis in Fig. 4 is taken as the time delay for a target at a particular range. If the peak occurs at zero, then the perceived range of the target corresponds to its true range. Thus if the normal model corresponds to the bat's internal template and a target is generated using the normal model as an echo, then the target should appear to be at its true range. If the location of the XC is not at zero, the target should appear to be at a range other than its true range. Furthermore, because the peak of the normal XC is narrow, the target should appear compact or pointlike. When the XC becomes lower and broader, as it does for certain altered models, the target should appear more diffuse and its range less certain.

From Fig. 4 we see that alterations *a* and *b*, in which the relative amplitude of call harmonics was changed, had little effect on the XC. We would therefore not expect bats to have difficulty using these signals for range discrimination, and, in fact, they did not. On the other hand, alterations *c* through *g* had noticeable effects on the XC. One effect was a shift in location of the XC relative to zero. This shift should have made the target appear nearer (negative shift) or farther away (positive shift) than the nominal distance set by echo delay. The fact that bats had no difficulty doing range discrimination with targets generated by models *c*, *e*, and *g*, where XC shifts of about 100 to 400 μs (corresponding to about 2 to 7 cm) occur, suggests that bats based their decision on the relative rather than absolute distance to the target. In other words, the decision rule for the bats was probably ''go right if the nearer target is present, left if the farther target is present.'' Because we used only a single type of echo each day, and because we routinely gave several warm-up trials before data collection, the bat would have had a chance to determine the distances to near and far targets at the start of each session.

As seen in Fig. 4, the other major effect of altered models *c* through *g* is that the XCs of these models are all noticeably reduced in height and spread out more in time (Table III). For a cross-correlation receiver, the reduced ''peakiness'' of cross-correlations *c* through *g* should produce poorer time resolution and consequently increase the difficulty of determining echo delay and target range. In fact, only alteration *d* proved problematic for the bats, thereby raising the question of why this alteration affected discrimination while alterations *c*, *e*, *f*, and *g* did not.

C. Spectrogram correlation

A possible answer to this question is that the XCs in Fig. 4 do not truly represent the perceptual situation for the bat. Perhaps spectrogram correlation, in which the time-frequency structure of normal versus modified signals is compared, would produce a different picture. Table III gives the spectrogram correlation between normal and modified models computed by sliding the spectrogram of the normal model over that of the modified model until the highest correlation between the spectral energy distribution of the two signals was achieved (Masters and Raver, 1996).

We made two restrictions in computing spectrogram correlations as compared to cross-correlations. First, we restricted analysis to the first harmonic of the signals only. We did this because there is behavioral evidence that *Eptesicus* may use information in the first harmonic only, or at least rely more heavily on frequencies in the range of the first harmonic (Moss and Schnitzler, 1989; Mogdans and Schnitzler, 1990; Surlykke, 1992). Second, we restricted analysis to only those frequencies present in both the normal and modi-

TABLE III. Measures related to the temporal precision of different signal-processing approaches. For cross-correlation (XC) height, the two waveforms being cross-correlated were first normalized to unit energy, so the maximum achievable XC height is 1.0. The width of the XC was determined by computing the XC envelope using the analytic representation of the XC (Altes, 1980) and taking its width 6 dB below maximum. Spectrogram correlation was carried out using the method of Masters and Raver (1996); the maximum correlation is 1.0. The standard deviation (s.d.) of the cross-channel average (CCA) was computed from 100 frequency channels (see Fig. 7). The last columns give the (s.d.) after linear error correction (LEC) of the CCA values.

	Giggles					Guppy				
Normal vs	XC height	XC 6-dB width (μs)	Spectrogram corr.	CCA s.d. (μs)	CCA + LEC s.d. μs)	XC height	XC 6-dB width (μs)	Spectrogram corr.	CCA s.d. (μs)	CCA + LEC s.d. (μs)
Norm	1.00	25	1.00	0	0	1.00	21	1.00	0	0
a_1	0.99	27	0.99	0	0	0.99	22	1.00	0	0
a_2	0.99	23	0.99	0	0	0.99	20	1.00	0	0
b_1	0.99	26	1.00	0	0	1.00	21	1.00	0	0
b_2	0.99	24	1.00	0	0	1.00	21	1.00	0	0
c_1	0.61	27	0.91	0	0	0.67	50	0.97	0	0
c_2	0.74	54	0.97	0	0	0.87	45	0.93	0	0
d_1	0.85	26	0.98	30	30	0.67	49	0.98	43	43
d_2	0.64	54	0.95	41	41	0.75	47	0.98	60	58
e_1	0.68	54	0.98	37	3	0.54	119	0.98	64	9
e_2	0.68	25	0.97	37	3	0.53	126	0.96	64	9
f	0.69	50	1.00	0	0	0.68	53	1.00	0	0
g	0.60	71	0.92	31	5	0.65	47	0.96	20	8

fied models, because it is reasonable to suppose that a bat might ignore information about frequencies present only in the emission or only in the echo, but not in both. For example, a delay-tuned neuron (see below) requires two sound stimuli to respond optimally, so a neuron with best frequency in a region where only the emission or only the echo has energy would receive only one sound stimulus and so would not respond. In our analysis, therefore, we made the assumption that the same frequencies had to be present in both emission and echo to give rise to a delay-tuned response. Paschal and Wong (1994), who examined delay-tuned neurons in *Myotis*, found this assumption to be true only on average; in any particular case the essential frequency in the emission might be higher or lower than the essential frequency in the echo. However, there was no tendency for the essential emission frequency to be higher than the essential echo frequency or vice versa, so our assumption that they are the same seems heuristically reasonable.

With these changes in the way the correlation was computed, we found the values in Table III to be generally higher for spectrogram correlation than cross-correlation, but still there is no basis for expecting a bat's performance to be appreciably worse with alteration *d* than with *c*, *e*, or *g*. (The spectrogram correlations for alteration *c* are improved relative to their XCs but do not reach 1.0 because of differences in amount of energy at each frequency compared with the normal model, rather than because of differences in time-frequency structure.)

D. Neurally based model

Because neither cross-correlation nor spectrogram correlation accounts for the behavioral finding that alteration *d* was most deleterious, we considered a more neurophysiologically based model. The most complete model of sonar processing for *Eptesicus* is the spectrogram correlation and transformation (SCAT) model proposed by Saillant *et al.* (1993) and Simmons *et al.* (1996). In the SCAT model, as in others (Sullivan, 1982; Suga, 1990; Park and Pollak, 1993), distance to a target is assumed to be computed from the responses of delay-tuned neurons. Delay tuning is one of the most prominent features of many neurons in bats' higher auditory centers. Delay-tuned neurons respond preferentially to pairs of sounds. Such neurons usually respond best when a loud initial sound representing the emitted pulse (*P*) is followed by a softer sound representing a returning echo (*E*). For delay-tuned neurons, the time delay between *P* and *E* is important, with maximal neuronal response occurring at a particular pulse-echo (PE) delay. Such neurons are obvious candidates for measuring echo arrival time and for perception of target distance, and, at least in the bat *Pteronotus parnellii* [a bat that uses a constant frequency (CF) signal], there is evidence that delay-tuned neurons are involved in range perception. In *Pteronotus*, the FM–FM area of the auditory cortex maps delay-tuning (corresponding to target distance) in an orderly array, and inactivation of the FM–FM area selectively disrupts the bat's ability to determine target range (Riquimaroux *et al.*, 1991). Delay-tuned neurons are also found in *Eptesicus fuscus* and *Myotis lucifugus* [bats that use frequency modulated (FM) signals], but in these bats delay-tuned neurons seem not to be confined to particular areas of the auditory cortex, nor does delay tuning appear to be mapped in such an orderly fashion as in *Pteronotus* (Dear *et al.*, 1993; Paschal and Wong, 1994).

Although we assume that delay-tuned neurons provide range information, one difficulty with ascribing a bat's perception of range directly or solely to these neurons is that

their tuning is ordinarily rather broad, on the order of several milliseconds. For instance, a delay-tuned neuron that responds maximally at a PE delay of 5 ms may have a 50%-response region between 3 and 7 ms. Since each millisecond of delay corresponds to 17 cm of target range, this neuron would respond to targets located anywhere between 50 and 120 cm, implying rather poor range specificity. Behaviorally, in contrast, bats show very good ability to estimate range, with range-discrimination thresholds as low as 30–40 μs (Miller, 1991; Masters and Jacobs, 1989; Masters and Raver, 1996; this study). For detecting target jitter (that is, back and forth motion of the target), time resolution is even better, certainly under 1 μs (Simmons, 1979; Menne *et al.*, 1989; Moss and Schnitzler, 1989; Moss and Simmons, 1993; Masters *et al.*, 1997). *Eptesicus* may possibly detect jitter as small as 10–15 ns (Simmons *et al.*, 1990).

The discrepancy between neural and behavioral range resolution suggests that the range-tuning curves of delay-tuned neurons may not suffice to explain bats' ranging ability, at least without extensive population averaging. Ultimately the accuracy with which the time of echo arrival can be specified will be limited by neuronal variability in response at the level of the auditory system where range information is extracted and by the extent of population averaging. If the latency between an auditory event (such as a pulse-echo pair with a particular time separation) and the neuronal response is quite variable, it then becomes more difficult for the nervous system to know the exact time of occurrence of the event. On the other hand, if the variability is low, it might be possible for a bat to determine the time of occurrence of the event with great accuracy even with little averaging. Variability in the latency of neuronal responses has been measured at different levels of the auditory system for *Eptesicus* (Covey and Casseday, 1991; Haplea *et al.*, 1994) and can be as low as 30 μs. For delay-tuned neurons, variability in firing latency can be as low as 300 μs (Dear and Suga, 1995). These values are much closer to the bat's behavioral capabilities than are the response profiles of delay-tuned neurons, suggesting that the timing of neural events, and not just their occurrence or nonoccurrence (which indicates range only crudely), may be important in measuring target distance (Simmons *et al.*, 1996).

In the following, we assume that neuronal entities with properties like those of delay-tuned neurons are used to make measurements of time intervals between acoustic events, but that precise information about timing of neuronal response is incorporated into the range estimate in some as-yet-undetermined way, thus enabling the bat to determine target distance more accurately than the width of the tuning functions of delay-tuned neurons would suggest. Specifically, following the approach used in the SCAT model, we assumed that the bat's auditory system is composed of a number of different frequency channels arrayed across the bandwidth of the sonar signal and that the bat measures the time between the occurrence of energy in a particular frequency channel in the pulse and the occurrence of energy in the same channel in the echo. The estimate of target range is based on the average time delay measured in the different frequency channels, so we will refer to this as the cross-channel average

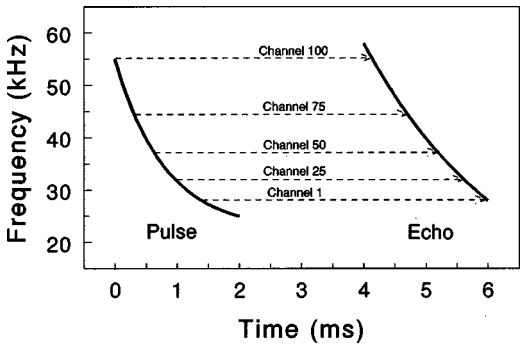

FIG. 7. Schematic of the cross-channel average (CCA) model of signal processing. The frequency range over which the emitted pulse and returning echo both contain energy was divided into 100 channels equally spaced by period, and in each channel an estimate is obtained of the time delay between occurrence of that frequency in the pulse and in the echo. The average of these estimates across channels is assumed to correspond to the bat's estimate of target range. When the shape of the pulse differs from that of the echo, as shown here, the time estimates of different frequency channels will differ. The degree to which the different channels disagree was quantified by the standard deviation of the CCA in Tables III, V, and VI.

(CCA) model. In *Eptesicus* and *Myotis*, delay-tuned neurons with the same best delay may have very different latencies so that their responses relative to the emission are dispersed over tens of milliseconds (Dear *et al.*, 1993). Nevertheless, from the point of view of recovering PE delay for target ranging, the important point is that the time of occurrence of different delay-tuned neurons is predictable, and so, in principle, timing information can be integrated across frequency channels and across different delay-tuned neurons within a channel.

To predict the effect of different alterations of the model echo on the bat's performance, we assumed the normal model represents the bat's pulse (or internal standard) and the modified model represents the returning echo (Fig. 7). For the reasons given earlier, we used only the first harmonic of each signal, and only those frequencies common to both pulse and echo. Furthermore, we assumed the frequency channels to be equally distributed along a period (i.e., inverse frequency) scale, thus weighting lower frequencies more heavily in computing the CCA. There is some neurophysiological evidence for this assumption (Simmons *et al.*, 1996). For each frequency channel, we subtracted the time of occurrence of energy in the pulse from the time of occurrence of energy in the echo, and then averaged across all channels to obtain the CCA. When the time-frequency structure of the echo does not exactly match that of the pulse, discrepancies will exist across channels in the time delay between pulse and echo, thus engendering uncertainty as to the true time delay. The higher the variability among channels, the more difficult it should be for the bat to determine target range. Therefore, the variability of cross-channel delay estimates can be used to estimate the bat's likely difficulty in judging target range in behavioral tests.

The standard deviations across frequency channels for CCA estimates are shown in Table III. The deviations are low for alterations *a*, *b*, *c*, and *f*, suggesting that these modifications of the model echo should cause the bat little difficulty, a result in agreement with the observed behavioral

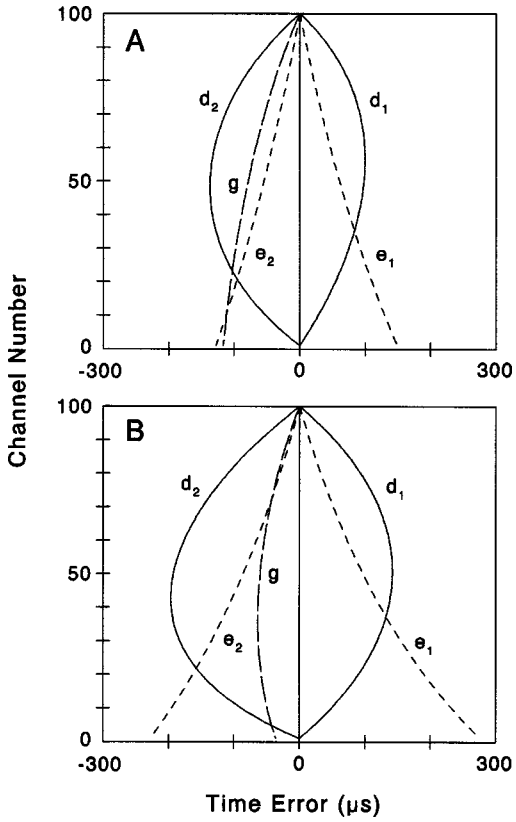

FIG. 8. Time estimates of echo delay across 100 frequency channels (see Fig. 7) for altered models d_1, d_2, e_1, e_2, and g (the echo) versus the normal model (the pulse). These time estimates are compared to those that would be obtained when pulse and echo match precisely (line at time zero).

thresholds. However, alterations *d*, *e*, and *g* all resulted in high variability across channels, suggesting that each of these alterations should have worsened the bat's range discrimination, when in fact only alteration *d* did so.

When the CCA estimates for alterations *d*, *e*, and *g* are plotted with respect to the normal model (Fig. 8), a difference appears between alteration *d* and the other two that may provide a clue to why bats find alteration *d* more disruptive than *e* or *g*. For alterations of type *d*, the PE delay estimates from high- and low-frequency channels are very close to those for the normal model (the zero line on the graph), but for intermediate frequencies the delay estimates diverge substantially from the those of the normal model, thus resulting in a nonmonotonic change in delay estimate across channels. For the other two types of alterations, the divergence in PE delay estimate from that of the normal model tends to increase more or less monotonically. This raises the possibility that a bat might be able to compensate for those altered signals in which PE delay diverges in a manner that is roughly linear with frequency (assuming a period-weighted frequency representation). If we make the simplest assumption, namely that the bat applies a linear correction based on frequency, the reduction in CCA variance the bat would achieve (and hence the decrease in range uncertainty) can be estimated from the residual variation around the best fitting straight line. We will refer to this procedure as linear error correction (LEC) of cross-channel delay estimates. LEC leads to a marked reduction in cross-channel PE delay variability, as shown in Table III. If an approach similar to LEC were in fact used by the bats, the detrimental effect of alteration *d*, and the lack of effect of alterations *e* and *g*, would be understandable.

TABLE IV. Mean values and variability for model parameters as measured from the set of ~400 calls analyzed for each bat.

Model parameter	Giggles			Guppy		
	Mean	s.d.	CV	Mean	s.d.	CV
H_2/H_1	2.02	0.54	27%	1.73	0.40	23%
H_3/H_1	1.63	0.69	42%	0.69	0.42	60%
Duration D (ms)	2.11	0.25	12%	3.35	0.72	21%
Decay Const. T (ms)	1.52	0.31	20%	2.49	0.57	23%
Start Freq. F_s (kHz)	49.0	4.5	9%	54.8	3.4	6%
End Freq. F_e (kHz)	17.3	1.1	6%	25.0	1.4	6%
Asymp. Freq. F_a (kHz)	7.0	3.7	53%	13.7	6.0	44%

LEC of cross-channel delay estimates is a hypothetical strategy to account for our behavioral results, and at present there is no neurophysiological evidence for such processing. However, analysis of the natural variability of bats' emissions suggests that LEC is an idea worth considering. There is variation among calls (including successive calls) even when a bat is performing a standard task in a static situation (e.g., range discrimination in our laboratory tests). This variation includes changes in T [Eq. (1)], the rate constant controlling the curvature of the frequency sweep. Since T is the very constant we changed to produce alteration *d*, it might seem that a bat could not afford to change T, or at least that variation in T should be kept small. Over the course of our experiments with the two bats, we recorded 411 calls from Giggles and 448 from Guppy. When we analyzed these calls, we found, as shown in Table IV, that the coefficient of variation for T was not particularly low (20%–23%). However, unlike the artificially constructed signal *d*, in which only T but not D or F_e was changed, when a bat changes T, it also tends to change other call parameters simultaneously. We used regression to develop functions relating T to other call parameters and used these functions to predict the value of these parameters for any given value of T. Then, for a specified T, we could create a model similar to the emission a bat would produce for that value of T. As Table V shows, changes in T of $\pm 35\%$ (i.e., about 1.5 standard deviations, encompassing about 90% of all recorded emissions) gave uncorrected CCA deviations from 57 to 242 μs (equivalent to 1–4 cm of range) with reference to a model based on the average of T for all recorded calls. Correction by LEC reduced the standard deviations to between 17 and 30 μs with improvement factors of 2.3–14. Thus despite large changes in T by the bat, LEC echo delay estimates remain reasonably small and of a magnitude commensurate with bats' range discrimination threshold of about 35 μs. (The values in Table V ignore within-channel noise, which will also contribute to CCA variability.)

TABLE V. Standard deviations of the cross-channel average (CCA) and after linear error correction (LEC) for a change of ±35% in the decay constant, *T*. The other parameters in the model were changed to accord with the new value of *T* (see text), and this model was then compared to the normal model. The improvement factor gives the improvement using LEC.

Change in decay constant *T*	Giggles			Guppy		
	CCA s.d. (μs)	CCA+LEC s.d. (μs)	Improvement factor	CCA s.d. (μs)	CCA+LEC s.d. (μs)	Improvement factor
35%	57	25	2.3	235	17	14.0
−35%	124	30	4.1	242	28	8.6

E. Echo processing by *Eptesicus*

In the foregoing discussion we have tried to justify the plausibility of CCA plus LEC as a strategy for echo processing, yet some important theoretical considerations remain unaddressed. First, it should be pointed out that most models of bat range determination, including the SCAT (Simmons *et al.*, 1996) and CCA approaches, do not require the emission to follow any particular form (except that it be brief and broadband). Because the bat is assumed to compare the echo with the previous emission, a change in the emission should have no effect on the PE delay estimate in any particular frequency channel, and consequently the PE delay estimates seen across channels will be consistent *ipso facto*. Essentially, the bat is conceived to construct anew the template for its matched filter on each emission. Given that a model echo will not likely match each emission closely, the question arises as to how a bat can, with any success, use a model echo—as opposed to a real echo or an echo that is a delayed rebroadcast of its emission—to accomplish target ranging. We know, of course, that bats can use model echoes successfully, as demonstrated by their low range-discrimination thresholds. In addition, *Eptesicus* can, under some circumstances, discriminate a model echo that is jittering in delay by 1 μs from one which is not jittering (Masters *et al.*, 1997). This temporal acuity is remarkable for a biological system, although not as good as the jitter thresholds achieved with targets generated by delayed rebroadcast of the bat's emissions (Simmons, 1979; Menne *et al.*, 1989; Moss and Schnitzler, 1989; Simmons *et al.*, 1990; Moss and Simmons, 1993). Whether bats can process a model echo as well as they do an actual echo or a delayed replica of their emission is still unknown, but they do surprisingly well, and this requires some explanation.

The explanation could lie in the incorporation of an operation similar to LEC into the bat's echo processing. In Table III we assumed that the bat's template was the normal model and compared altered models to this reference, but biologically the process is likely to be the reverse, i.e., the altered model (the echo) is compared to the emission. We can simulate this process by comparing the model echoes we used in our experiments with the 400+ emissions recorded for each bat. Table VI shows the standard deviation of CCA and LEC delay estimates for the recorded calls with the normal model and altered models *c*, *d*, *e*, and *g*. (The time-frequency structure of models *a*, *b*, and *f*, are the same as the normal model and so provide no additional information.) We see that the mean cross-channel variation in delay estimates for Giggles ranges from 45 to 75 μs, while for Guppy it ranges from 152 to 252 μs. These values are all well above the bats' threshold of about 35 μs. With LEC, however, the mean variation for the normal model and models *c*, *e*, and *g* is reduced to 6–13 μs for Giggles and 10–35 μs for Guppy. On the other hand, for alterations d_1 and d_2, although variation is reduced by LEC, it remains relatively high (28 and 36 μs for Giggles and 42 and 56 μs for Guppy). If we compare the models that the bats had no difficulty using (normal, *c*, *e*, and *g*) with the ones they had difficulty using (d_1 and d_2), we find that on average the cross-channel standard deviation using CCA alone is a factor of only about 1.2 times lower for the first group. However, the residual variation after correc-

TABLE VI. Comparison of the cross-channel average (CCA) and CCA+linear error correction (LEC) for the ~400 calls ultimately recorded from each bat versus a model based on the average of the ~400 calls (top row) or versus the normal model (next row), or versus altered models (following rows).

All calls vs	Giggles			Guppy		
	CCA avg. s.d. (μs)	CCA+LEC avg. s.d. (μs)	Improvement factor	CCA avg. s.d. (μs)	CCA+LEC avg. s.d. (μs)	Improvement factor
Mean of calls	65	12	5.4	235	31	7.5
Norm	63	11	5.8	214	25	8.6
c_1	70	13	5.2	251	35	12.6
c_2	45	6	7.8	152	12	7.3
d_1	70	28	2.5	222	42	5.3
d_2	75	36	2.1	223	56	4.0
e_1	68	9	7.6	176	20	8.7
e_2	68	13	5.3	252	30	8.4
g	55	10	6.4	171	10	10.0

tion by LEC is 2–3 times lower—perhaps enough to account for the bat's greater difficulty using model echoes of type *d*.

Another question that arises concerns how a LEC-type system could have evolved. If, in nature, the echo a bat receives is always a near-copy of its emission, what would supply the selective pressure to evolve such an error correction system? One possible answer may be that the bat's receiver must be able to cope with moving targets producing Doppler-shifted echoes. It has been shown that for a particular type of frequency modulation (linear period modulation or hyperbolic frequency modulation), the relative time-frequency structure (i.e., time of occurrence of one frequency relative to another) of the Doppler-shifted echo does not differ from that of the original signal (Kroszczynski, 1969; Altes and Titlebaum, 1970). For such signals, LEC would be unnecessary. Yet *Eptesicus* appears not to use exact linear period modulation (Masters *et al.*, 1991) and consequently a Doppler shift changes the time-frequency structure of the echo slightly [Fig. 3(D)]. LEC compensates for the changed temporal relationship among frequencies very nicely (Tables III and VI, bottom rows). Furthermore, the system works despite variability in a bat's emissions because the variation is apparently not random. Instead, a bat's emissions are all members of a family of signals having the property that they produce approximately linear cross-channel error when compared with the bat's average signal model (Table V). Consequently, emissions also produce approximately linear cross-channel error when they are compared with altered models that are themselves related to the average emission by linear cross-channel error (e.g., alterations *e* and *g*). However, when emissions must be compared with an altered model such as *d*, where the cross-channel error is not linear along the neural frequency axis (and therefore not like a Doppler shift), LEC cannot reconcile the cross-channel time estimates and, the result, we speculate, is greater difficulty using *d* to judge target range.

ACKNOWLEDGMENTS

We would like to thank Dr. Karl Kornacker, Dr. Douglas Nelson, Stephen Burnett, Karry Kazial, Anne Moffat, and two anonymous reviewers for their comments on the manuscript. This work was supported by NIH Grant No. RO1-DC001251 to WMM.

Altes, R. A. (**1980**). ''Detection, estimation, and classification with spectrograms,'' J. Acoust. Soc. Am. **67**, 1232–1246.

Altes, R. A., and Titlebaum, E. L. (**1970**). ''Bat signals as optimally Doppler-tolerant waveforms,'' J. Acoust. Soc. Am. **48**, 1014–1020.

Barnard, S. M. (**1995**). *Bats in Captivity* (Wild Ones Animal Books, Springville, CA).

Brigham, R. M., Cebek, J. E., and Hickey, B. C. (**1989**). ''Intraspecific variation in the echolocation calls of two species of insectivorous bats,'' J. Mammal. **70**, 426–428.

Burnett, S. C., Kazial, K. A., and Masters, W. M. (**1998**). ''Echolocation call descriptors that differentiate calls of handheld and flying big brown bats (*Eptesicus fuscus*),'' Abstr. 78th Annual Meeting Amer. Soc. Mammal.

Covey, E., and Casseday, J. H. (**1991**). ''The monaural nuclei of the lateral lemniscus in an echolocating bat: Parallel pathways for analyzing temporal features of sound,'' J. Neurosci. **11**, 3456–3470.

Dear, S. P., and Suga, N. (**1995**). ''Delay-tuned neurons in the midbrain of the big brown bat,'' J. Neurophysiol. **73**, 1084–1100.

Dear, S. P., Fritz, J., Haresign, T., Ferragamo, M., and Simmons, J. A. (**1993**). ''Tonotopic and functional organization in the auditory cortex of the big brown bat, *Eptesicus fuscus*,'' J. Neurophysiol. **70**, 1988–2009.

Fenton, M. B. (**1995**). ''Natural history and biosonar signals,'' in *Hearing by Bats*, edited by A. N. Popper and R. R. Fay (Springer-Verlag, New York), pp. 37–86.

Finney, D. J. (**1971**). *Probit Analysis* (Cambridge University Press, London).

Finney, D. J. (**1978**). *Statistical Methods in Biological Assay* (Griffin, London).

Gellermann, L. W. (**1933**). ''Chance orders of alternating stimuli in visual discrimination experiments,'' J. Gen. Psychol. **42**, 206–208.

Haplea, S., Covey, E., and Casseday, J. H. (**1994**). ''Frequency tuning and response latencies at three levels in the brainstem of the echolocating bat, *Eptesicus fuscus*,'' J. Comp. Physiol. A **174**, 671–683.

Kazial, K. A., Burnett, S. A., and Masters, W. M. (**1998**). ''Discriminability of big brown bat (*Eptesicus fuscus*) echolocation calls by age, sex, and individual,'' Abstr. 78th Annual Meeting Amer. Soc. Mammal.

Kroszczynski, J. J. (**1969**). ''Pulse compression by means of linear period modulation,'' Proc. IEEE **57**, 1260–1266.

Kuhl, W., Schodder, G. R., and Schröder, F. K. (**1954**). ''Condenser transmitters and microphones with solid dielectric for airborne ultrasonics,'' Acoustica **4**, 519–532.

Masters, W. M., and Jacobs, S. C. (**1989**). ''Target detection and range resolution by the big brown bat (*Eptesicus fuscus*) using normal and time-reversed model echoes,'' J. Comp. Physiol. A **166**, 65–73.

Masters, W. M., and Raver, K. A. S. (**1996**). ''The degradation of distance discrimination in big brown bats (*Eptesicus fuscus*) caused by different interference signals,'' J. Comp. Physiol. A **179**, 703–713.

Masters, W. M., Jacobs, S. C., and Simmons, J. A. (**1991**). ''The structure of echolocation sounds used by the big brown bat *Eptesicus fuscus*: Some consequences for echo processing,'' J. Acoust. Soc. Am. **89**, 1402–1413.

Masters, W. M., Raver, K. A. S., and Kazial, K. A. (**1995**). ''Sonar signals of big brown bats, *Eptesicus fuscus*, contain information about individual identity, age and family affiliation,'' Anim. Behav. **50**, 1243–1260.

Masters, W. M., Raver, K. A. S., Kornacker, K., and Burnett, S. C. (**1997**). ''Detection of jitter in intertarget spacing by the big brown bat *Eptesicus fuscus*,'' J. Comp. Physiol. A **181**, 279–290.

Menne, D., and Hackbarth, H. (**1986**). ''Accuracy of distance measurement in the bat *Eptesicus fuscus*: Theoretical aspects and computer simulations,'' J. Acoust. Soc. Am. **79**, 386–397.

Menne, D., Kaipf, I., Wagner, I., Ostwald, J., and Schnitzler, H. U. (**1989**). ''Range estimation by echolocation in the bat *Eptesicus fuscus*: Trading of phase versus time cues,'' J. Acoust. Soc. Am. **85**, 2642–2650.

Miller, L. A. (**1991**). ''Arctiid moth clicks can degrade the accuracy of range difference discrimination in echolocating big brown bats, *Eptesicus fuscus*,'' J. Comp. Physiol. A **168**, 571–579.

Mogdans, J., and Schnitzler, H. U. (**1990**). ''Range resolution and the possible use of spectral information in the echolocating bat, *Eptesicus fuscus*,'' J. Acoust. Soc. Am. **88**, 754–757.

Moss, C. F., and Schnitzler, H. U. (**1989**). ''Accuracy of target ranging in echolocating bats: Acoustic information processing,'' J. Comp. Physiol. A **165**, 383–393.

Moss, C. F., and Schnitzler, H. U. (**1995**). ''Behavioral studies of auditory information processing,'' in *Hearing by Bats*, edited by A. N. Popper and R. R. Fay (Springer-Verlag, New York), pp. 87–145.

Moss, C. F., and Simmons, J. A. (**1993**). ''Acoustic image representation of a point target in the bat *Eptesicus fuscus*: Evidence for sensitivity to echo phase in bat sonar,'' J. Acoust. Soc. Am. **93**, 1553–1562.

Obrist, M. (**1995**). ''Flexible bat echolocation: the influence of individual, habitat, and conspecifics on sonar signal design,'' Behav. Ecol. Sociobiol. **36**, 207–219.

Park, T. J., and Pollak, G. D. (**1993**). ''GABA shapes a topographic organization of response latency in the mustache bat's inferior colliculus,'' J. Neurosci. **13**, 5172–5187.

Paschal, W. G., and Wong, D. (**1994**). ''Frequency organization of delay-sensitive neurons in the auditory cortex of the FM bat, *Myotis lucifugus*,'' J. Neurophysiol. **72**, 366–379.

Pollak, G. D. (**1993**). ''Some comments on the proposed perception of phase and nanosecond time disparities by echolocating bats,'' J. Comp. Physiol. A **172**, 523–531.

Riquimaroux, H., Gaioni, S. J., and Suga, N. (**1991**). ''Cortical computational maps control auditory perception,'' Science **251**, 565–568.

Rydell, J. (**1993**). ''Variation in the sonar of an aerial-hawking bat (*Eptesicus nilssonii*),'' Ethology **93**, 275–284.
Saillant, P. A., Simmons, J. A., Dear, S. P., and McMullen, T. A. (**1993**). ''A computational model of echo processing and acoustic imaging in frequency-modulated echolocating bats: The spectrogram correlation and transformation receiver,'' J. Acoust. Soc. Am. **94**, 2691–2712.
Schmidt, S. (**1992**). ''Perception of structured phantom targets in the echolocating bat, *Megaderma lyra*,'' J. Acoust. Soc. Am. **91**, 2203–2223.
Schnitzler, H. U., and Henson, O. W. (**1980**). ''Performance of animal airborne sonar systems: I. Microchiroptera,'' in *Animal Sonar Systems*, edited by R. G. Busnel and J. F. Fish (Plenum, New York), pp. 109–181.
Schnitzler, H. U., Menne, D., and Hackbarth, H. (**1985**). ''Range determination by measuring time delays in echolocating bats,'' in *Time Resolution in Auditory Systems*, edited by A. Michelsen (Springer-Verlag, New York), pp. 180–204.
Schnitzler, H. U., Kalko, E., Miller, L., and Surlykke, A. (**1987**). ''The echolocation and hunting behavior of the bat, *Pipistrellus kuhli*,'' J. Comp. Physiol. A **161**, 267–274.
Simmons, J. A. (**1979**). ''Perception of echo phase information in bat sonar,'' Science **204**, 1336–1338.
Simmons, J. A. (**1993**). ''Evidence for perception of fine echo delay and phase by the FM bat, *Eptesicus fuscus*,'' J. Comp. Physiol. A **172**, 533–547.
Simmons, J. A., and Stein, R. A. (**1980**). ''Acoustic imaging in bat sonar: Echolocation signals and the evolution of echolocation,'' J. Comp. Physiol. **135**, 61–84.
Simmons, J. A., Fenton, M. B., and O'Farrell, M. J. (**1978**). ''Echolocation and pursuit of prey by bats,'' Science **203**, 16–21.
Simmons, J. A., Ferragamo, M., Moss, C. F., Stevenson, S. B., and Altes, R. A. (**1990**). ''Discrimination of jittered sonar echoes by the echolocating bat, *Eptesicus fuscus*: The shape of target images in echolocation,'' J. Comp. Physiol. A **167**, 589–616.
Simmons, J. A., Saillant, P. A., Ferragamo, M. J., Haresign, T., Dear, S. P., Fritz, J., and McMullen, T. A. (**1996**). ''Auditory computations for biosonar target imaging in bats,'' in *Auditory Computation*, edited by H. L. Hawkins, T. A. McMullen, A. N. Popper, and R. R. Fay (Springer-Verlag, New York), pp. 401–468.
Sokal, R. R., and Rohlf, F. J. (**1981**). *Biometry* (Freeman, New York).
Suga, N. (**1990**). ''Cortical computational maps for auditory imaging,'' Neural Networks **3**, 3–21.
Suga, N., Niwa, H., Taniguchi, I., and Margoliash, D. (**1987**). ''The personalized auditory cortex of the mustached bat: Adaptation for echolocation,'' J. Neurophysiol. **58**, 643–654.
Sullivan, W. E. (**1982**). ''Neural representation of target distance in auditory cortex of the echolocating bat *Myotis lucifugus*,'' J. Neurophysiol. **48**, 1011–1032.
Surlykke, A. (**1992**). ''Target ranging and the role of time-frequency structure of synthetic echoes in big brown bats, *Eptesicus fuscus*,'' J. Comp. Physiol. A **170**, 83–92.
Thomas, D. W., Fenton, M. B., and Barclay, M. R. (**1979**). ''Social behavior of the little brown bat, *Myotis lucifugus*,'' Behav. Ecol. Sociobiol. **6**, 129–136.
Vater, M., Feng, A. S., and Betz, M. (**1985**). ''An HRP-study of the frequency-place map of the horseshoe bat cochlea: morphological correlates of the sharp tuning to a narrow frequency band,'' J. Comp. Physiol. A **157**, 671–686.
Woodward, P. M. (**1953**). *Probability and Information Theory, with Applications to Radar* (Pergamon, London) (reprinted by Artech House Books, Dedham, MA, 1980).
Zbinden, K. (**1989**). ''Field observations on the flexibility of the acoustic behaviour of the European bat *Nyctalus noctula* (Schreber, 1774),'' Rev. Suisse Zool. **96**, 335–343.

Sperm whale clicks: Directionality and source level revisited

B. Møhl, M. Wahlberg, and P. T. Madsen
Department of Zoophysiology, Århus University, Building 131, C. F. Møllers Alle, DK-8000 Århus C, Denmark

L. A. Miller and A. Surlykke
Center for Sound Communication, Institute of Biology, Odense University, Campusvej 55, DK-5230 Odense M, Denmark

(Received 24 August 1999; accepted for publication 8 October 1999)

In sperm whales (*Physeter catodon L.* 1758) the nose is vastly hypertrophied, accounting for about one-third of the length or weight of an adult male. Norris and Harvey [in Animal Orientation and Navigation, NASA SP-262 (1972), pp. 397–417] ascribed a sound-generating function to this organ complex. A sound generator weighing upward of 10 tons and with a cross-section of 1 m is expected to generate high-intensity, directional sounds. This prediction from the Norris and Harvey theory is not supported by published data for sperm whale clicks (source levels of 180 dB *re* 1 μPa and little, if any, directionality). Either the theory is not borne out or the data is not representative for the capabilities of the sound-generating mechanism. To increase the amount of relevant data, a five-hydrophone array, suspended from three platforms separated by 1 km and linked by radio, was deployed at the slope of the continental shelf off Andenes, Norway, in the summers of 1997 and 1998. With this system, source levels up to 223 dB *re* 1 μPa peRMS were recorded. Also, source level differences of 35 dB for the same click at different directions were seen, which are interpreted as evidence for high directionality. This implicates sonar as a possible function of the clicks. Thus, previously published properties of sperm whale clicks underestimate the capabilities of the sound generator and therefore cannot falsify the Norris and Harvey theory. © *2000 Acoustical Society of America.* [S0001-4966(00)03301-4]

PACS numbers: 43.80.Ka, 43.80.Gx [WA]

INTRODUCTION

In 1972, Norris and Harvey presented a seminal paper on the possible function of the nasal structures of the sperm whale as a gigantic generator of sound. To appreciate the boldness of this proposal, one should keep in mind the unique size and proportions of this Odontocete. Old males can weigh upwards of 50 tons (Berzin, 1971), 1000 times more than the smallest member of the suborder, *Phocoena*. About $\frac{1}{3}$ of total body weight—and body length—is allocated for the soft structures of the nose, which is aptly coined the ''biggest nose on record'' (Raven and Gregory, 1933). Apart from its scale, the ''design'' of this nose is quite unlike that of other Odontocetes. The spermaceti case is an elongated, horn-shaped structure of connective tissue containing up to 2 tons of liquid wax and extending throughout the length of the nose. It is bound in the front and rear by air sacs. The case rests on a similarly sized structure (the ''junk'' in whaling parlance), a longitudinally, stacked series of lens-shaped bodies of spermaceti, each surrounded by connective tissue.

At the time of publication of the Norris and Harvey theory (1972), the basic properties of sperm whale clicks were known from several papers, notably the one by Backus and Schevill (1966). The trademark of clicks from this species is a multi-pulsed structure, in which pulses are spaced at fixed intervals and with decaying amplitude (Fig. 1). The Norris and Harvey theory (1972) explains this pattern by proposing a single pulse being generated at one end of the spermaceti sac, traveling down the sac, and being reflected at the air sac at the other end. On return, part of the energy is intercepted by the opposing sac, giving rise to the next pulse. Thus each trailing pulse is derived from the preceeding pulse as a diverted fraction of the energy of the former. The authors' prime suspected location of click generation is the ''monkey muzzle,'' a structure of tough, connective tissue surrounding the distal end of the right nasal passage at the anterior termination of the spermaceti organ.

Norris and Harvey (1972) also performed experiments with a multiple reflection model that generated trains of decaying pulses from single clicks. They published the first measurement of velocity of sound in spermaceti and combined this knowledge with their theory and with the measured value of the pulse interval from recordings of a subadult sperm whale of known length. A ''remarkable correspondence'' between the observed length of the animal and the prediction from their theory was obtained.[1]

Overall, they made a pretty good case for the proposal that the nose of the sperm whale is a generator of sound. However, a rather basic question was not dealt with at the time: What is the survival value of investing so much of the whale's developmental resources just to make sound? This question was subsequently addressed in a paper by Norris and Møhl (1983), in which a number of observations were presented to illuminate the hypothesis that Odontocetes—and sperm whales in particular—could use intense sound to debilitate prey.

This hypothesis has problems of its own. While peak pressures in clicks of Bottlenose dolphins (*Tursiops truncatus M.*) were known to be just high enough (Au *et al.*, 1974)

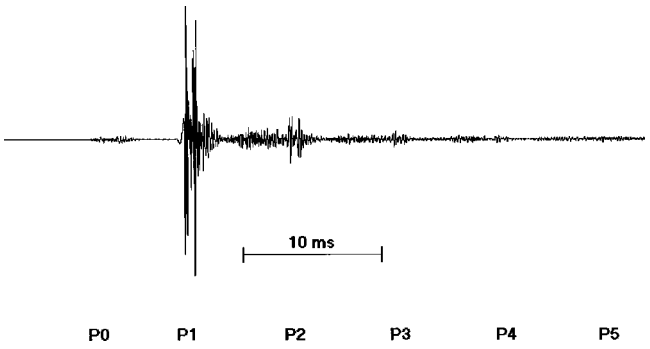

FIG. 1. Waveform of sperm whale click, selected to illustrate the multipulse pattern. Pulses are labeled P0–P5. Note the constant interpulse interval between pulses $P_n - P_{n+1}$ for $n>0$, which is the essence of the Norris and Harvey theory (1972). The low-amplitude P0 pulse precedes the P1 pulse with a slightly shorter interpulse interval than found for the remaining intervals. The doublet pattern is caused by surface reflection.

to have debilitating effects on fish (see Zagaesky, 1987), the most commonly cited source level (SL) for sperm whale clicks of 180 dB *re* 1 μPa (Watkins, 1980) is about 40 dB below debilitating levels.

Another observation of Watkins (1980) is that sperm whale clicks lack directionality. This counter-indicates biosonar as a function of the clicks. Additionally, it is not supportive of the hypothesis of the sperm whale nose as being the largest biological generator of sound, since directionality generally follows the ratio of transmitter cross section to wavelength (Urick, 1983). With an aperture on the order of 1 m and wavelengths on the order of 0.1 m, directionality in sperm whales should be as good as, or better than, that of dolphins, which have a pronounced directionality (Au *et al.*, 1986, 1987). Instead, Watkins' observation implicates a smallish generator. And smallish is definitely not a property of the nose of sperm whales.

Thus, either the Norris and Harvey theory (1972) of sperm whale click generation is not realized, or the reported properties of clicks are not fully representative.

This paper deals with the latter alternative. To obtain measures of the properties of sperm whale clicks beyond waveform and repetition rates is not a trivial matter. The species is found at the slope of the continental shelves, where they habitually dive to depths of 1000 m or more. To get recordings near the whales requires deep water hydrophones, which are costly and difficult to handle. Once recordings have been made, source level determination involves a series of processes: deriving the received sound pressure, measuring the sound velocity profile (SVP) of the medium, and positioning the whale. The positioning process dictates the use of an array of hydrophones. The spacing of the latter is a compromise. They have to be sufficiently widely spaced to yield a proper position and to present a set of significantly different angles to the whale. Yet, the hydrophones must also be sufficiently close to each other so that they can all pick up signals from the same source. A special problem is to know the relative locations of the hydrophones. Above all, the whale should comply and direct its clicks towards one of the hydrophones (if directionality is indeed present). This can never be ascertained, but the probability that it occurs can be increased with the number of hydrophones deployed, and by increasing the time spent recording.

Here, we report our attempts to meet the above requirements. The data obtained shows several properties expected from high directionality, as well as extremely high peak pressures in certain sperm whale clicks, which presumably were recorded close to the acoustic axis of the source.

I. METHODS

Recordings were made between 14 and 28 July 1997, and between 8 and 24 July 1998, in an area about 10 NM (nautical miles) northwest of Andenes, Northern Norway. Geographical coordinates of the center of the area of operations are 69°25′N, 15°45′E. Here, an undersea canyon brings the slope of the continental shelf to within 8 NM of the coast. The depth drops rapidly from about 130 to 1000 m. In this area solitary, presumably foraging male sperm whales are found and usually spaced some kilometers apart when surfaced. The water is part of the Gulf Stream and the Norwegian Coastal Current, running NE at an average speed of 1 knot (Johannesen, 1986). Recordings were made at sea state 2 or below.

The array was deployed from three platforms and utilized four hydrophones in 1997, five in 1998. The main platform was a 41-ft auxiliary ketch (''R/V NARHVALEN'') in which a Racal Store 7D instrumentation tape recorder was installed (wow and flutter specification: 0.2%–0.35%, time base error: ± 4 μs). This was normally operated at $7^{1/2}$ ips (inches per second), occasionally also at 30 ips. The frequency response is within ± 3 dB between 0.1 and 37.5 kHz at $7^{1/2}$ ips, 0.2 and 150 kHz at 30 ips. The tape used was Ampex 456, recorder bias being adjusted accordingly.

The dynamic range of instrumentation recorders (about 35 dB) is not sufficient to cover the range of amplitude variations in sperm whale clicks, and the most intense clicks will cause saturation. For the instrumentation recorder, an input–output function for low saturation levels was established and used to correct SL values. This extended the dynamic range by 4 dB (Weber, 1963). Filters as described in Table I largely set the limitations in frequency response.

From the main platform two B&K 8101 hydrophones were lowered, one with 30 m and one with 100 m of cable.

TABLE I. Frequency response of the hydrophone chains.

Chain	N30+N100	N460	B30+R30+M30
Recorder	Racal 7D	Racal 7D	Sony DAT
± 3 dB bandpass (kHz)	0.3−37.5	0.3−6[a]	0.08−11.5[a]
Filter slope (dB/oct)	HP=24, LP=30[b]	6	6

[a]Equalized to 20 kHz in analyses.
[b]Tape recorder gap effect.

TABLE II. Key data showing maximum level clicks from sequences selected for source positioning. From each sequence the click of max ASL was selected and its P1-component properties derived for all elements of the array. TL: transmission loss, ASL: apparent source level, ERRrms: root-mean-square error from error propagation analysis, BWrms: root-mean-square bandwidth, see Sec. I, n.a.: not available for directions towards the array with the whale in endfire position. Heading: the general heading of the whale relative to the array (A) or platform M.

Sequence	Click no.	Hydrophone	TL (dB)	ASL (dB *re* 1μ Pa)	ERR rms, dB+	ERR rms, dB−	BW rms (kHz)	Heading
4*t* 1640	5	M30	47	175	11	n.a.	3.6	towards M
⋯	⋯	G30	61	192	5	⋯	2.9	⋯
⋯	⋯	N30	64	197	2	⋯	3.3	⋯
⋯	⋯	N100	64	197	2	⋯	3.2	⋯
4*t* 1659	7	M30	47	191	22	n.a	3.1	towards M
⋯	⋯	G30	61	202	10	⋯	3.3	⋯
⋯	⋯	N30	64	190	8	⋯	2.7	⋯
⋯	⋯	N100	64	188	13	⋯	2.6	⋯
4*t* 1808b	2	M30	66	191	13	n.a.	8.2	n.a.
⋯	⋯	G30	62	189	16	⋯	7.5	⋯
⋯	⋯	N30	54	189	23	⋯	8.7	⋯
⋯	⋯	N100	54	188	23	⋯	8.5	⋯
4*t* 1817	4	M30	60	184	2	4	4.4	par. w. A.
⋯	⋯	G30	61	187	2	4	3.5	⋯
⋯	⋯	N30	55	195	3	2	7.4	⋯
⋯	⋯	N100	55	193	3	2	8.9	⋯
7*t* 898	19	N30	56	218	14	n.a.	12.4	towards A
⋯	⋯	N100	56	218	14	⋯	12.5	⋯
⋯	⋯	N460	56	192	14	⋯	8.3	⋯
⋯	⋯	B30	66	207	7	⋯	8.4	⋯
⋯	⋯	R30	66	194	7	⋯	6.4	⋯
7*t* 954	8	N30	65	221	5	10	7.5	towards A
⋯	⋯	N100	65	220	5	10	7.4	⋯
⋯	⋯	N460	65	209	5	11	7.0	⋯
⋯	⋯	B30	69	205	4	5	6.3	⋯
⋯	⋯	R30	68	193	4	7	7.0	⋯
7*t* 990	41	N30	64	223	2	3	9.7	towards A
⋯	⋯	N100	64	217	2	3	10.4	⋯
⋯	⋯	N460	63	192	2	3	7.8	⋯
⋯	⋯	B30	68	200	1	2	6.2	⋯
⋯	⋯	R30	66	185	1	1	6.2	⋯
7*t* 1036	17	N30	58	208	12	n.a.	11.6	towards A?
⋯	⋯	N100	58	220	12	⋯	8.4	⋯
⋯	⋯	N460	58	195	12	⋯	7.8	⋯
⋯	⋯	B30	67	204	6	⋯	7.3	⋯
⋯	⋯	R30	67	193	6	⋯	7.3	⋯

All 8101 hydrophone cables were B&K AO 113 or AO 114. In 1998, an additional (spherical) hydrophone, (HS/150, Sonar Products, Ltd.) having a maximum operating depth of 1500 m was lowered to depths of between 400 and 600 m, using a 3 mm o.d., multi-stranded, nylon-insulated, single-wire cable to return the signal from a pressure-resistant canister. This housed batteries, an Etec hydrophone preamplifier, a sweep generator for calibration, and a line driver. The sea was used as the return path. The upper −3 dB cutoff was 20 kHz in most of the recordings, except for the session generating data for Table II. On this occasion, a leak in the cable reduced the upper −3 dB frequency to 6 kHz. Equalization of the response to 20 kHz was carried out during analysis. The three hydrophones and their associated electronics (chains) are referred to as N30, N100, and N460.

The two satellite platforms (in 1997 a 38-ft ketch, ''Mette-Marie,'' and a 12-ft Zodiac, and in 1998 two Zodiacs) were spaced 0.5 to 1 NM from each other and from the main platform. After deployment of the hydrophones, changes in geometry occurred only passively by differential drifting. Each satellite platform had a B&K 8101 hydrophone (referred to as G30 and M30 in 1997 and B30 and R30 in 1998), powered from a B&K 2804 power supply. It was lowered with 30 m of cable. A Sony DAT recorder (TCD-D7 or D8) preceded by an antialiasing filter (1998 only) completed the chains. The recording chains were adjusted so that the tape recorders were the amplitude-limiting instruments rather than the preceding electronics in front of the recorders.

Radio links (using VHF in 1997 and UHF in 1998) relayed the signals from the hydrophones of the satellite platforms to the instrumentation recorder at the main platform. The links had limited bandwidth (0.5 to 2 kHz) and low dynamic range, but preserved the timing of the sperm whale signals.

On each of the platforms, the continuous output from a

Garmin 45 GPS (global positioning system) receiver was converted to a FSK (frequency shift keying) signal that was recorded along with the acoustic signals on the DATs and the instrumentation recorder. The latter, on the main platform, thus received simultaneous inputs from the three local hydrophones, from the two telemetry links, and from a GPS signal. The seventh channel was used to record the electrical current applied to the blasting caps, used for fine-scale positioning of the hydrophones, as described below.

All B&K hydrophones were calibrated before each session with B&K 4223 hydrophone calibrators, the calibration signal being recorded on tape. Fixed gain was used in the DAT chains. On the instrumentation recorder, step attenuators were sparsely used to adapt the limited dynamic range to the received levels, changes being annotated on the commentary channel.

The frequency responses of the various recording chains are given in Table I. Filters were present or introduced for various reasons. The high-pass filters were used to reduce hydrodynamic and electric noise. The low-pass (LP) filter of the N460 chain is an inherent property of the cable/sea water transmission path. In the DAT chains, antialiasing filters were necessary to avoid folding of high-frequency components. The effect of the LP filters on frequency response was compensated for at analyzing time by properly weighted amplification. Finally, the low-pass filter of the Racal reflects the gap effect (Weber, 1963).

Sound velocity profiles (SVP) for the top 150 m were determined only in 1998, using a custom built ''sing-around-device.'' The SVP slope we measured was identical to those measured to a depth of 1000 m in 1997 and 1998 by the Institute of Marine Research, Bergen, Norway. The SVP profile shows a decrease from 1495 m/s at the surface to 1480 m/s at a depth of 50 m. Below 50 m, the SVP varies little from 1480 m/s. This information was used for ray tracings, which showed only minor reductions in received sound level for shallow, distant sources. There was no indication of transmission losses (TLs) less than predicted from spherical spreading. Accordingly, TL was computed as $20\log(r)$, where r is the distance in meters from the source to the receiver.

Positions of the platforms were derived from the GPS signals. The specified rms error of this system is 100 m (set by US Department of Defense, DOD), which suffices for approximate fixes of favorably located sound sources and array legs of the large size used here. Some reduction of GPS error was achieved by making running averages of positions of the slowly drifting platforms. However, for whales in array end-fire directions (i.e., sources close to the line through a pair of hydrophones, outside the array), standard GPS determination of array geometry is inadequate, as, e.g., in sequence 898 (Fig. 5). Also, the sway of the cables for the deeper hydrophones, due to differential drift of the platform and the deeper layers of water, introduces an uncertainty in the position of the hydrophones. To reduce this uncertainty, a series of transients generated by blasting caps were set off in 1998 from the three platforms, and from a third, GPS-positioned dinghy. From such data the actual acoustic travel times between the various platforms and all the hydrophones

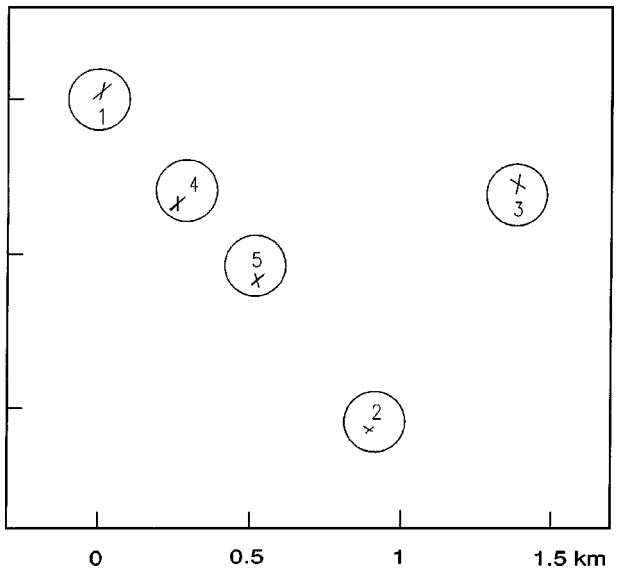

FIG. 2. Recording geometry in the 1998 recordings. Numbers refer to calibrating shots, 1 to 3 being fired from the three platforms, 4 and 5 from a GPS positioned dinghy. Circles signify GPS positions of platforms, with the centers obtained through linear regression of 5 min of continuous recordings. Diameter represents the DOD imposed RMS uncertainty. The crosses at 1 to 3 represent measured distances of travel for the transient signals to the two other platforms, assuming a sound velocity of 1490 m/s. The crosses at 4 and 5 are derived from acoustical localization of the transient and subsequent derivation of the distances to the three platforms.

were determined and used to define the residual uncertainties. The latter was then used in error propagation analysis of the acoustic localization of whales (Wahlberg, 1999a, b). However, this kind of calibration was only done in two sessions. The acoustic data from 1998 reported below was selected for being close in time (within less than 6 min) to the transient events.

In 1997, the GPS signal of the N-platform fell out in the session from which data for Table II was derived. The relative positions of platforms were instead reconstructed from the Radar log.

The recordings were subsequently digitized in stereo (using the 30-m hydrophone signals from the main platform as a reference in one channel) by standard PC sound-card-compatible hardware (digitizing rate: 44.1 kHz). This resulted in four files, describing one sequence of clicks. In addition, the DAT recordings from the satellite platforms were digitized, using the GPS timing for rough synchronization and the telemetry linked series for absolute synchronization under operator control. The precision of this process is in the order of fractions of a millisecond.

The digitized series were analyzed by commercially available sound-editing software (COOLEDIT96, SYNTRILLIUM), as well as by custom-built software (A. Heerfordt) for rms bandwidth determination. The effect of the antialiasing filters was compensated for by postrecording frequency weighting.

All levels are given in peak equivalent root-mean-square (peRMS) which is the rms sound pressure level of a continuous pure tone having the same amplitude as the transient. Traditionally, levels are given as peak-to-peak levels with the rms sensitivity of the hydrophone as the reference. This

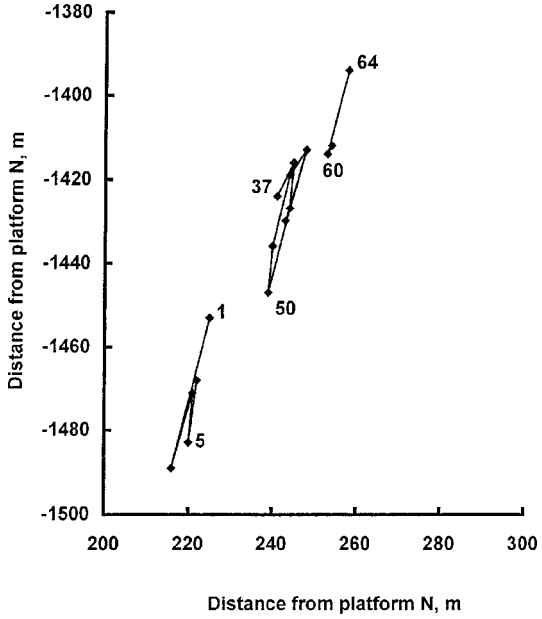

FIG. 3. Partial track of a whale. Positions from sequence 990/98, (plotted in Fig. 4). The origin refers to the location of the N-platform in Fig. 4. The first and last click in the three consecutive segments where clicks are detectable at all three platforms are identified with click numbers from Fig. 4.

method leads to 9 dB higher values than with the notation used here. For a discussion of this topic, see Møhl (1988).

Bandwidths of isolated P1 pulses (see Fig. 1) were measured as rms bandwidth, which is a weighted distance of the frequencies in the spectrum from the frequency 0 Hz (Menne and Hackbarth, 1986):

$$\text{Brms} = \left(\left(\int_{-\infty}^{\infty} f^2 |S(f)|^2 df \right) \Big/ \left(\int_{-\infty}^{\infty} |S(f)|^2 df \right) \right)^{1/2}.$$

Source positioning of 1998 data was calculated analytically with a 3-D algorithm adapted to Matlab 4.2 after Watkins and Schevill (1971). A modified version of this algorithm was used for 2-D positioning of the 1997 data. In a few situations a vertical array configuration was used, utilizing surface-reflected signals as if recorded by virtual hydrophones (Møhl *et al.*, 1990). Error propagation analysis (Taylor, 1997) was implemented in Matlab to estimate the rms error in the calculated source positions due to uncertainties in sound velocity, receiver positions, and time-of-arrival differences (TOAD) measurements (Wahlberg, 1999a, b).

Absorption at the centroid frequency of the clicks at 10

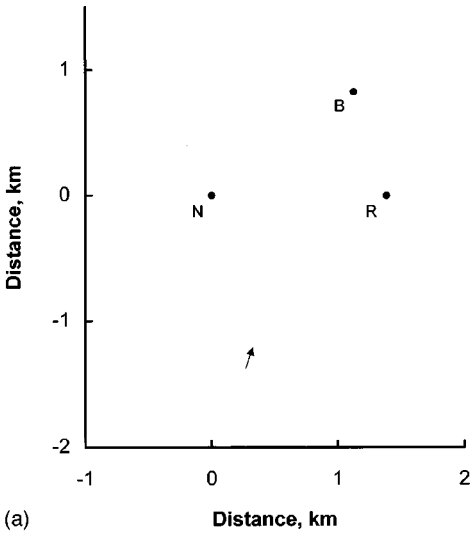

(a)

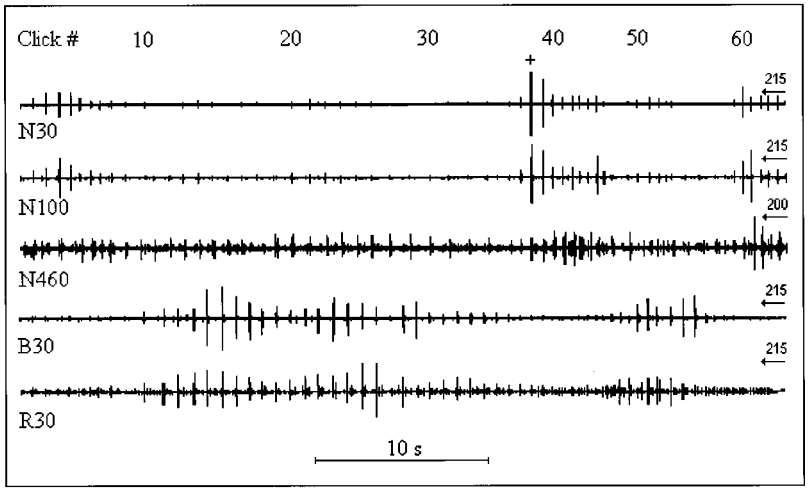

(b)

FIG. 4. Sequence 990/98 showing geometry (a) and time series (b). (a) The arrow shows the position and general heading of the whale. N, R, and B are the three platforms, with N in origin. (b) Synchronized time series (oscillogram format), recorded at the five hydrophones. The series are normalized *re* max amplitude of each channel. Arrows at the right signify the specified ASLs in dB *re* 1 μPa peRMS, valid only for the positioned whale. Clicks, overloading the recording, are marked with a +. Low-level clicks from other whales set the noise background and dominate the N-traces between clicks 9 and 37.

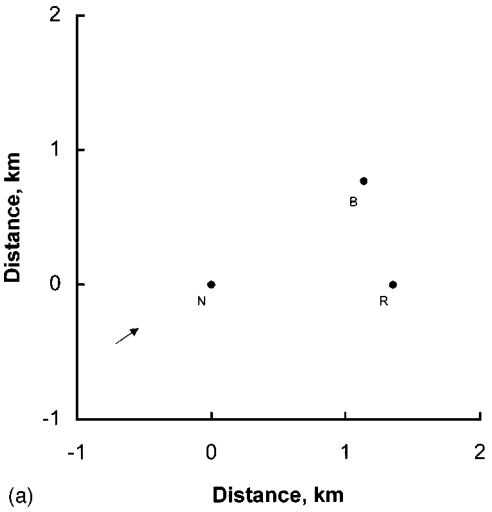

(a)

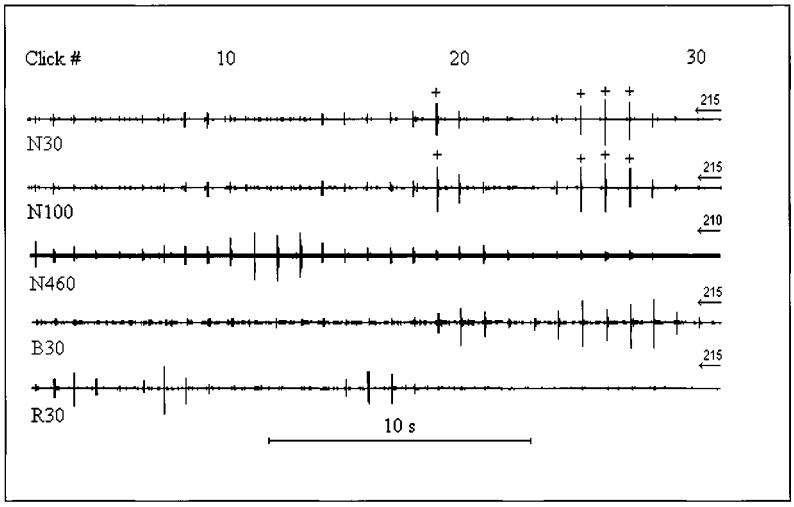

(b)

FIG. 5. Sequence 898/98 showing geometry (a) and time series (b). Symbols as in Fig. 4.

kHz (see Madsen and Møhl, 2000) is a minor factor, reducing the recorded levels by about 1 dB/km (Urick, 1983). This correction has been applied to the apparent source level (ASL) numbers in Table II.

II. RESULTS

The criteria applied for the selection of the data presented in this paper were that clicks belonging to the same sequence should be identifiable at all hydrophones of all three platforms. For 1998, an additional condition was for the sequences to occur within 6 min of the period in which array geometry was established by the firing of the blasting caps. In this period 20 sequences were identified, 4 of which were simultaneously detectable on all platforms. From 1997, 15 sequences were examined, 4 of which yielded position data. The start and end of a sequence are determined by the operator, not necessarily by the whale. The shortest sequence analyzed consisted of 5 consecutive clicks, the longest of 64. Within a sequence, the time-of-arrival differences (TOADs) did not vary by more than a couple of milliseconds from one click to the next.

Figure 2 shows the GPS positions of blasting-cap-generated transients (shots), used in 1998 to establish the geometry of the array. Shots 1 to 3 were set off from the recording platforms. Shots 4 and 5 were fired from an independent, GPS-positioned platform. Also given are the acoustically derived locations generated from observed travel times to the recording platforms (the crosses).

In Fig. 3, the track of the whale generating sequence 990/98 is plotted (geometry and click pattern of this sequence are presented in Fig. 4). The track is interrupted during two periods, where it was not possible to detect the same click at all three platforms.

Figures 4–6 show the recording geometry, plotted in 2-D format with the associated time series of three sequences. The time scale is chosen so as to illustrate a conspicuous feature: the smoothly varying, yet profound change in amplitude over the course of the sequences. With the scales used it is not possible to identify clicks as belonging to the same sequence; contributions from other whales contaminate the picture somewhat, as described in the legends.

The influence of recording geometry shows up in the rms error of positioning, given in Table II. In Fig. 4, uncertainty of the position only moderately affects the SL determination. Figure 5 illustrates a situation with a whale in line with two of the platforms (end-fire position). Here the linear error propagation model is not applicable for the positioning

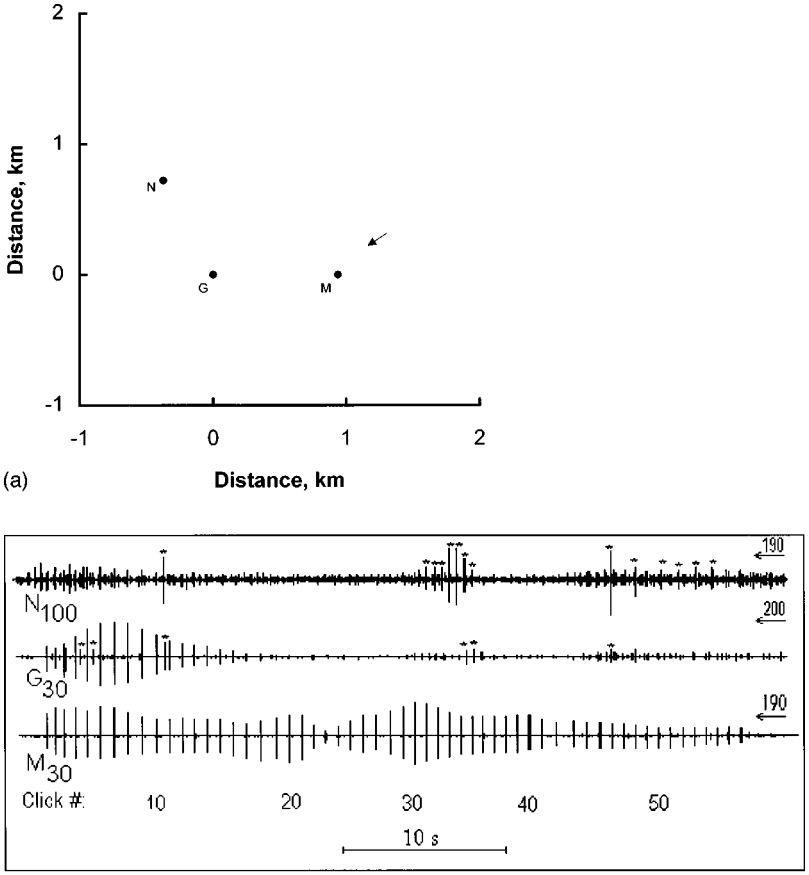

FIG. 6. Sequence 1659/97 showing geometry (a) and time series (b). Symbols are as in Fig. 4. (a) Platform G is at the origin. Only three hydrophones used. Platform N is positioned by a transposed radar fix, while G and M are positioned by GPS. (b) Oscillograms. At the far hydrophone (N100) a second whale is dominating (marked *).

error in the direction towards the array. From the 2-D array in 1997 there is data from three such sequences presented in Table II. From the 3-D array in 1998 there is data from two whales in end-fire positions (Table II). In the 3-D cases the vertical array configuration from platform N was used to check the position given by the 3-D algorithm. The estimated range from the whale to the array obtained with the linear array was within 200 m from the 3-D solution for both sequences.

The amplitude span of the clicks at each hydrophone exceeds 20 dB. However, the patterns of the amplitude changes are not correlated between the three platforms. In time series from the three hydrophones suspended from the main platform, changes in click amplitudes from the one at a depth of 460 m are only weakly correlated with those from the upper hydrophones. This is most evident for sequence 898/98 (Fig. 5), for which the source is fairly close to platform N, resulting in increased angular separation for the string of N hydrophones.

From Figs. 4–6, it is evident that the derived SLs of each click as seen at the different hydrophones cover a wide range. As we interpret such differences to be caused by directionality, we propose to refer to them as source level anomalies, and we call the derived source levels ASLs (apparent source levels). This is done to signify the interpretive aspect.

Table II lists key data on maximum level clicks from sequences selected for source positioning. From each sequence the click of maximum ASL was selected and the properties of the P1 component were derived for all elements of the array (the P1 component is defined in Fig. 1). The amplitude spectra of the P1 component from the same click are highly variable between platforms, sometimes multipeaked, sometimes flat. As an attempt to quantify the spectral properties in a way that is not sensitive to the shape of the spectra or to arbitrary definitions, we have computed the rms bandwidth. This measure defines the range resolution properties of a pulse in a sonar system that use all information available (Menne and Hackbarth, 1986). With a rather uniform low-frequency cutoff at 2 kHz, the rms bandwidth describes the extent of spectral energy. A correlation can be established between ASL and bandwidth (Fig. 7). The trend is statistically significant at $\alpha = 0.01$ level, but explains only some 15% of the variation [linear regression ANOVA test (Zar, 1996)]. Note that the clicks analyzed come from different sequences, different geometries, different equipment, an unknown number of individuals, and from recordings obtained in two different years.

Waveforms of the blasting cap signals could not be reliably recovered due to overload of the recorders.

III. DISCUSSION

A. Array properties

Figure 2 demonstrates a fair correspondence between acoustically derived positions and GPS-determined positions. It should be understood, however, that this represents the easy case of a source close to the plane of the hydro-

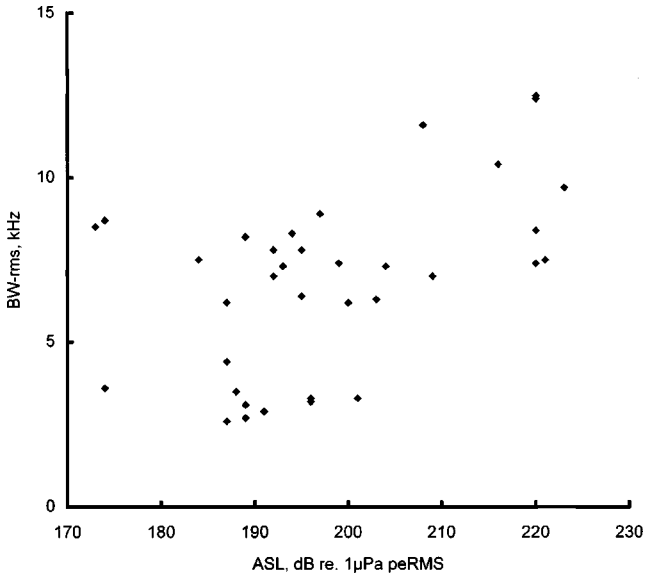

FIG. 7. Plot of RMS bandwidth versus ASL for clicks listed in Table II.

phones, and at the very borders of the array. For distant and deep sources, and for sources in end-fire positions, a number of factors combine to increase uncertainty about the position of the source. This is illustrated by the rms error values in Table II. The whale generating the data in Fig. 5 was in the end-fire direction of the array where the rms error of position becomes particularly high. In this case, the vertical array configuration of the N hydrophones was used for distance assessment. For sequence 1659/97 (plotted in Fig. 6), the large rms error in source positioning is caused by positioning uncertainty of the N platform.

The data in Fig. 2 does show that the combined system of a GPS fixed array, telemetry of signals, sound velocity measurements, and time stability of recording and analyzing processes is acceptable for the task of positioning. The main source of uncertainty lies in the geometry of the recording situation, rather than in the equipment.

The omnidirectionality of the transient blasting cap sources expected from theoretical reasoning was indirectly demonstrated by the invariable, intense reverberation following the first echo from the bottom (Madsen and Møhl, 2000). The time constant of this reverberation was on the order of 600 ms.

The track of a whale in Fig. 3 illustrates how positioning on a macro-scale is quite consistent, with the whale progressing along a rather stable course towards the array. On a micro-scale, the track is erratic and with many reversals. This pattern is characteristic for a geometry with the source well outside the array. The micro-perturbations are not believed to reflect movements of the whale, but are considered to be consequences of noise *sensu latu* in the system.

B. Source anomaly and directionality

The variation in SL seen in Figs. 4–6 is found in all series examined. The variation in click amplitude is gradual. This is most simply explained by directional effects, combined with scanning movements of the source, rather than by some kind of source modulation. The lack of correlation of SL changes between platforms—or at times a negative correlation—is consistent with this view. The sequences last less than 1 min, during which period the geometry of the recording situation is essentially unchanged. This counter-indicates transmission path effects as being the cause of the change in patterns observed.

In smaller Odontocetes it is established that scanning is obtained by moving the head with its fixed acoustical axis relative to the body (Norris *et al.*, 1961). It is not obvious that this solution will be feasible in sperm whales, where about 10 tons of tissue with its surrounding water would have to be moved. Another possibility is that the scanning mechanism is within the sound generating organs. Our data only suggests that scanning takes place, not by which mechanism.

The course of amplitude changes (see, e.g., the alternation of ensonification between platforms in Figs. 4 and 5, and the onset of sequence 1659/97 in Fig. 6) further suggests that click amplitude for any given series is largely constant. This conjecture, however, is not testable, and is not important for the discussion of the data.

It is interesting to compare the reverberation pattern of the omni-directional blasting cap transients (Madsen and Møhl, 2000) with that of the sperm whale clicks. While the ASLs of the more intense clicks were approaching the magnitude of the SLs of the transient (231 dB *re* 1 μPa peRMS, measured at 40 m and referred to 1 m, data from Thiele and Oedegaard, 1983), the reverberation patterns for the clicks were either absent or quite different from the smoothly decaying pattern of the transients. Notably, in cases where reverberation caused by clicks can be seen, the echo pattern changes from click to click. This difference between transients and clicks can again be explained by ascribing high directionality to the clicks, combined with scanning so that not all clicks are directed towards the bottom and, if they are, only a limited patch of the bottom is ensonified by each click. A similar variability is seen with reflections from the surface: at times they are prominent, at other times not detectable at all.

When ASLs of individual clicks are compared between platforms, as well as between real and virtual hydrophones, we find differences as large as 35 dB (the entire dynamic range of the instrumentation recorder). Without knowledge of the acoustical axis of the animal it is not possible to establish SL or directional indices (DIs). However, some guidance can be obtained by means of the theory of a vibrating plane piston in an infinite baffle. Although it may be a little hard to imagine that the anatomy of the sperm whale's nose fits this description, it helps to recall that this model has been useful in describing directionality in a number of other biological cases, including small Odontocetes (Au, 1993). The piston model predicts a behavior of the transmitter somewhat akin to that of a low-pass filter with the cutoff frequency being inversely proportional to the off-axis angle. Figure 7 is a scatter plot of bandwidth versus ASL for all clicks in Table II. The trend is qualitatively in agreement with piston theory, but hardly a good starting point for quantitative arguments.

It is instructive to consider the consequences if indeed sperm whale clicks were omnidirectional, as previously re-

ported (Watkins, 1980). The power emitted by an omnidirectional point source is

$$\mathrm{Po} = 4\pi r^2 I,$$

where r is distance and I is the acoustic intensity, given by $I = p^2/\rho c$ (ρc is density and sound velocity of the medium, respectively). Using the measured maximum value of 223 dB *re* 1 μPa peRMS from Table II for p, the emitted acoustic power will be 22 dB *re* 1 kW or about 167 kW. This would indeed be surprisingly high. A directivity index in the order of 30 dB, similar to that found in dolphins (Au, 1993), would reduce this number to a more reasonable 167 W. This would still be a very powerful sound, about three times as powerful as the most intense signals recorded from dolphins (Au, 1993, table 7.2).

In Figs. 4(a)–6(a) the general heading of the sources is given (course from source position at sequence onset to position at sequence end). The value of this information is problematic for several reasons, one of which is that it is a 2D statement about a 3D world, another that it does not account for scanning or other movements. Still, a tendency is seen in Table II that in sequences with high ASLs, the whales are approaching the array, while in lower level sequences they are moving away from, or parallel to it. The concept of directionality is consistent with this tendency, which is of a different nature than that of SL anomalies seen within a sequence from an individual whale. The observation also underlines the importance of the completely uncontrollable condition of having the whales pointing towards the array during measurements of maximum levels. Our lack of knowledge of direction of the acoustic axis of the whales precludes any statement about the maximum capability of the sound generator. We can only report on the maximum levels that our hydrophones happened to register.

The data in Table II do not indicate that deep hydrophones are essential for the recording of maximum ASL. This observation may be biased because the N460 chain was deliberately operated at high gain, leading to a high rate of occurrence of saturation. The prime purpose of this hydrophone was to provide time information.

C. ASL

The most difficult condition to meet for the derivation of ASL is the requirement to localize the source. This is the basis for the estimate of the transmission loss (TL), numerically the largest element in ASL calculations. The problem of localization is dealt with in Wahlberg (1999a, b). It should be recalled that the data in Fig. 2 shows positioning accuracies of the system that will produce only fractional dB errors in transmission loss estimates. Larger errors are to be expected for sources far from the array, and in end-fire positions, as evidenced by the occasionally large standard deviations of ASL, given in Table II. In sequences such as 898/98 the rms error is so large so as to make determinations of ASL rather meaningless. However, the vertical array of platform N was advantageously used here to get a better confidence interval in determining source positions.

With the source localized, TL can be calculated from the law of spherical spreading, which describes the propagation of the click as the distribution of sound pressure on an ever-expanding sphere. For straight, vertical SVPs this relation is a good description, but with increasing velocity in the top layers the sphere becomes distorted, resulting in lowered ASLs for distant, shallow sources. This might introduce an offset or bias of SL anomaly for certain recording geometries. Since geometry during sequences of about 1-min duration is largely constant, this effect cannot explain the fast, relative changes in ASL between platforms (Figs. 4–6).

Determining the sound pressure impinging on the hydrophones is, in principle, straightforward with knowledge of the transfer functions for the various recording chains available. The use of fixed gain results in the occasional, strong signals overloading the electronics, which might lead to underestimated ASLs. While overloading leaves its footprint on the analog tapes and thus can be taken into account, the situation is more complicated with the DAT recordings. The limited bandwidth of the various recording chains will also reduce the derived ASLs. Thus, most of the known sources of errors combine to bias the derived ASLs in a negative direction, with positioning errors being neutral.

Because of the large anomalies observed and from the direction of the various errors discussed, it is clear that any kind of mean, standard deviation, or similar measurement is not a meaningful description of SL, as long as the orientation of the acoustic axis remains unknown and constantly varying. Instead, ASLs are given for the most intense click from each sequence as such clicks are likely to have been recorded closer to the acoustic axis. The levels found for the eight sequences of Table II are large, some of them extremely large, some 40 or 50 dB above generally cited values for sperm whales (Watkins, 1980). In fact, all levels above 219 dB *re* 1 μPa peRMS^2 are larger than any level previously reported from any Odontocete species (Au, 1993, Table 7.2).

The fact that sound levels reported here are within the range given by Zagaesky (1987) for debilitating effects in fish solves one of the problems with the debilitation hypothesis of Norris and Møhl (1983). It is emphasized, however, that the general properties of the sequences recorded, particularly their rather constant and slow repetition rates, are suggestive of sonar as the function of the clicks (Goold and Jones, 1995), rather than the capture of prey. Other proposed functions of sperm whale clicks such as communication (Watkins, 1980) cannot readily be deduced from our recordings.

D. Comparison with previous data

Why have such extreme source levels and high directionality in sperm whale clicks remained undetected for so long? There is no single answer to this question. A part of the explanation may be that our recordings are from the northernmost population, a population exclusively made up of adult, foraging males (Berzin, 1971), whereas all other recordings are from lower latitudes, where females and calves are also found. Sexual dimorphism leads to nonallometric growth of the nasal (i.e., sound producing) organs in male sperm whales (Nishiwaki *et al.*, 1963). Thus, clicks

from old males may simply be more intense than those from females and calves, as suggested by Weilgart and Whitehead (1988).

Another part of the explanation is that a number of analyses on sperm whale clicks have not been designed to include SL, measurements (e.g., Gordon, 1991; Weilgart and Whitehead, 1988; Goold and Jones, 1995). However, as we show, on-axis signals are so intense that they can hardly go unnoticed. Weilgart and Whitehead (1988) do in fact report about ''loud, distinctive clicks,'' but the recording procedure used in their studies involved spotting the whales at the surface, approaching them and identifying them, and making recordings as they dive. This procedure was likely to increase the probability of getting signals from the rear of the animal, opposite the putative acoustic axis.

Further, we have specifically looked for, and have set up our instruments to record, high ASLs. Despite this, only some of our sequences contain a few clicks with very large ASLs, while in several of the sequences the levels were more comparable to previously published maximum levels (Watkins, 1980; Dunn, 1969; Levenson, 1974).

The other conspicuous difference between our data and those found in the literature on sperm whale clicks is the pronounced directionality we infer from our observations. The simplest explanation of this difference is that a cumbersome array of considerable size is required to detect the anomalies. To the best of our knowledge the array we used here is unique. The sonobuoy technique presently used by Orion aircraft for submarine surveillance would be ideal for such measurements, but dedicated missions for civilian use of data by this system appear unlikely at present. The fact that the early use of this technique by Dunn (1969) and Levenson (1974) did not result in findings as reported here can be explained by short exposure times and by the limited number of hydrophones deployed (one and three, respectively).

Finally, our findings may not be that unique as they are not very different from early work by Whitney (1968). His report, however, has largely been overlooked. He describes properties of sperm whale clicks recorded with a large-aperture, two-hydrophone array. Directionality is inferred from alternating illumination of the hydrophones, as well as from a relationship between spectral composition and SL akin to that shown in Fig. 7 of the present paper. Maximum source levels are stated to be in the range of 175 to 200 dB re1 μ Pa. From this it is tempting to conclude that the use of small as opposed to large-aperture arrays can explain some of the differences between currently accepted properties of sperm whale clicks (e.g., Watkins, 1980) and those described by Whitney (1968) and us (this paper).

IV. CONCLUSION

Results from recordings of sperm whales at high latitudes with a large-aperture array are interpreted to show high directionality, with maximum recorded SLs exceeding 220 dB re 1 μPa peRMS. Such levels are 40 to 50 dB above previously published levels. The findings support the Norris and Harvey (1972) theory of sound generation in the sperm whale by demonstrating high outputs from the putative largest known biological generator of sound. Acoustically, the sperm whale may thus no longer be thought of as an aberrant, degenerated odontocete species without biosonar [as may be implicated from previous data, apart from those of Whitney (1968)], but rather as a specialized one with noteworthy properties. That it may also use its sound generator for other purposes such as communication (Watkins, 1980) is only to be expected, since biosonar generally has such a collateral function. From this, more specialized communication, such as coda exchanges, may have evolved.

ACKNOWLEDGMENTS

This paper is dedicated to the late Kenneth Steven Norris, who pioneered the field of echolocation in Odontocetes. His unique insights, visions and personal inspiration are fundamental to the work in this field.

We thank the crews of Mette Marie and R/V NARHVALEN for hard, difficult and excellent teamwork, and The Andenes Cetacean Research Unit and Andenes Whale Safari for providing shore-based facilities and zodiacs. We thank A. Thode for bringing the report of W. Whitney (1968) to our attention, L. Rendell and K. Fristrup for fruitful discussions, and G. Timmins and H. Strager for help with the manuscript. This work was funded by the Danish Research Foundation through the Center for Sound Communication, Odense University.

[1]The measurements were carried out by K. J. Diercks of the Defense Research Laboratory, University of Texas. The value obtained, about 2.7 m/ms, has not been found by other researchers and is now considered to be off by a factor of 2 (Goold *et al.*, 1996). In a correspondence between Diercks and Møhl (in 1976), Diercks proposed that the value might apply for a transversal or shear mode of propagation. Such modes are conceivable since spermaceti crystallizes in a range of temperatures just below normal body temperature.

[2]Note that 9 dB should be added to the levels given here to make them comparable with previous figures for, e.g., *Tursiops* (Au *et al.*, 1974), as explained above.

Au, W. W. L. (**1993**). *The Sonar of Dolphins* (Springer-Verlag, New York).

Au, W. W. L., Moore, P. W. B., and Pawloski, D. (**1986**). ''Echolocation transmitting beam of the Atlantic bottlenose dolphin,'' J. Acoust. Soc. Am. **83**, 688–691.

Au, W. W. L., Penner, R. H., and Turl, C. W. (**1987**). ''Propagation of beluga echolocation signals,'' J. Acoust. Soc. Am. **83**, 807–813.

Au, W. W. L., Floyd, R. W., Penner, R. H., and Murchison, A. E. (**1974**). ''Measurements of echolocation signals of the Atlantic bottlenose dolphin, *Tursiops truncatus Montagu*, in open waters,'' J. Acoust. Soc. Am. **56**, 1289–1290.

Backus, R., and Schevill, W. E. (**1966**). ''Physeter clicks,'' in *Whales, Porpoises and Dolphins*, edited by K. S. Norris (Univ. Calif.), pp. 510–528.

Berzin, A. A. (**1971**). *The Sperm Whale*, Pacific Sci. Res. Inst. Fisheries Oceanogr., Trans. 1972 (Israel Program for Scientific Trans., no. 600707, Jerusalem).

Dunn, J. L. (**1969**). ''Airborne measurements of the acoustic characteristics of a sperm whale,'' J. Acoust. Soc. Am. **46**, 1052–1054.

Goold, J. C., and Jones, S. E. (**1995**). ''Time and frequency domain characteristics of sperm whale clicks,'' J. Acoust. Soc. Am. **98**, 1279–1291.

Goold, J. C., Bennell, J. D., and Jones, S. E. (**1996**). ''Sound velocity measurements in spermaceti oil under the combined influences of temperature and pressure,'' Deep-Sea Res. **43**, 961–969.

Gordon, J. C. D. (**1991**). ''Evaluation of a method for determining the length of sperm whales, *Physeter catodon*, from their vocalisations,'' J. Zool. London **224**, 301–314.

Johannesen, O. M. (**1986**). ''Brief overview of the physical oceanography,'' in *The Nordic Seas*, edited by B. G. Hurdle (Springer-Verlag, New York), Chap. 4, pp. 105–126.
Levenson, C. (**1974**). ''Source level and bistatic target strength of the sperm whale (*Physeter catodon*) measured from an oceanic aircraft,'' J. Acoust. Soc. Am. **55**, 1100–1103.
Madsen, P. T., and Møhl, B. (**2000**). ''Sperm whales (*Physeter catodon L.* 1758) do not react to sounds from detonators,'' J. Acoust. Soc. Am. **107**, 668–671.
Menne, D., and Hackbarth, H. (**1986**). ''Accuracy of distance measurement in the bat *Eptesicus fuscus*: Theoretical aspects and computer simulations,'' J. Acoust. Soc. Am. **79**, 386–397.
Møhl, B. (**1988**). ''Target detection by echolocating bats,'' in *Animal Sonar*, edited by P. E. Nachtigall and P. W. B. Moore (Plenum, New York), pp. 435–450.
Møhl, B., Surlykke, A., and Miller L. A. (**1990**). ''High intensity Narhwal clicks,'' in *Sensory Abilities of Cetaceans*, edited by J. A. Thomas and R. A. Kastelein (Plenum, New York), pp. 295–304.
Nishiwaki, N., Oshumi, S., and Maeda Y. (**1963**). ''Changes of form in the sperm whale accompanied with growth,'' Sci. Rept. Whales Res. Inst., Tokyo, Vol. 17, 1–13.
Norris, K. S., and Harvey, G. W. (**1972**). ''A theory for the function of the spermaceti organ of the sperm whale (*Physeter catodon L.*),'' in *Animal Orientation and Navigation*, edited by S. R. Galler (NASA SP-262), pp. 397–417.
Norris, K. S., and Møhl, B. (**1983**). ''Can Odontocetes debilitate prey with sound?,'' Am. Nat. **122**, 85–104.
Norris, K. S., Prescott, J. H., Asa-Dorian, P. V., and Perkins, P. (**1961**). ''An experimental demonstration of echolocation behaviour in the porpoise, *Tursiops truncatus* (Montagu),'' Biol. Bull. **120**, 163–176.
Raven, H. C., and Gregory, W. K. (**1933**). ''The spermaceti organ and nasal passages of the sperm whale (*Physeter catodon*) and other Odontocetes,'' Am. Mus. Novitates **677**, 1–17.
Taylor, J. R. (**1997**). *An Introduction to Error Analysis. The Study of Uncertainties in Physical Measurements*, 2nd. ed. (University Science Books, Sausalito, CA), pp. 73–76.
Thiele, L., and Oedegaard, J. (**1983**). ''Underwater noise from the propellers of a triple screw container ship,'' Report no. 82.54, Oedan, Greenland Fisheries Investigations, Copenhagen, Denmark.
Urick, R. J. (**1983**). *Principles of Underwater Sound*, 3rd ed. (McGraw–Hill, New York).
Wahlberg, M. (**1999a**). ''Positioning accuracy of a large-aperture array for sperm whale research,'' J. Acoust. Soc. Am. **105**, 1318 abstract.
Wahlberg, M. (**1999b**). ''Estimating source position accuracy in acoustic localization of marine mammals,'' Masters thesis, Dept. of Physics, Gothenburg University, Sweden, 63 pp.
Watkins, W. A. (**1980**). ''Sperm whale clicks,'' in *Animal Sonar Systems*, edited by R.-G. Busnel and J. F. Fish (Plenum, New York), pp. 283–290.
Watkins, W. A., and Schevill W. E. (**1971**). ''Four hydrophone array for acoustic three-dimensional location,'' Woods Hole Oceanographic Institution Tech. Rep. No. 71-60, Woods Hole, MA.
Weber, P. J. (**1963**). ''The tape recorder as an instrumentation device,'' Ampex Corporation.
Weilgart, L. S., and Whitehead, H. (**1988**). ''Distinctive vocalizations from mature male sperm whales (*Physeter macrocephalus*),'' Can. J. Zool. **66**, 1931–1937.
Whitney, W. (**1968**). ''Observations of Sperm Whale Sounds from great depths,'' MPL-U-11/68, Marine Physical Laboratory, Scripps Institution of Oceanography, 8 pp.
Zagaesky, M. (**1987**). ''Some observations on the debilitation hypothesis,'' Marine Mammal Science **3**, 275–278.
Zar, J. H. (**1996**). *Biostatistical Analysis* (Prentice–Hall, Englewood Cliffs, NJ), 3rd ed., pp. 327–330.

Source levels and estimated yellowfin tuna (*Thunnus albacares*) detection ranges for dolphin jaw pops, breaches, and tail slaps

James J. Finneran
Biosciences Division, Space and Naval Warfare Systems Center, San Diego (PL-BS), D3503, 49620 Beluga Road, San Diego, California 92152

Charles W. Oliver
NOAA, National Marine Fisheries Service, Southwest Fisheries Science Center, P.O. Box 271, La Jolla, California 92038

Kurt M. Schaefer
Inter-American Tropical Tuna Commission, Scripps Institution of Oceanography, 8604 La Jolla Shores Drive, La Jolla, California 92037-1508

Sam H. Ridgway
Biosciences Division, Space and Naval Warfare Systems Center, San Diego (PL-BS), D3503, 49620 Beluga Road, San Diego, California 92152

(Received 18 December 1998; revised 14 September 1999; accepted 27 September 1999)

Tuna fishers in the eastern Pacific Ocean often exploit an association between a few genus of dolphin (*Stenella* and *Delphinus*) and yellowfin tuna (*Thunnus albacares*) to locate and capture the tuna. Identification of a mechanism which facilitates the tuna/dolphin bond may provide a means of exploiting the bond and capturing tuna without catching dolphin. To investigate if tuna may be attracted to low-frequency sounds produced by dolphins, source levels of bottlenose dolphin (*Tursiops truncatus*) jaw pops, breaches, and tail slaps were experimentally measured and used to estimate the maximum range at which yellowfin could detect similar sounds produced by pelagic species. The effective acoustic stimulus to the tuna was defined as the maximum one-third-octave level between 200 and 800 Hz, the frequency range where *T. albacares* is most sensitive. Spherical spreading was assumed to predict transmission loss with range. Breaches and jaw pops produced maximum one-third-octave source levels between 200 and 800 Hz of 153 ($\pm$4) and 163 ($\pm$2) dB *re:* 1 μPa-m, respectively, which resulted in estimated detection ranges of 340–840 and 660–1040 m, respectively. Tail slaps had lower source levels [max. 141 ($\pm$3) dB *re:* 1 μPa-m] and a maximum detection range of approximately 90–180 m.
[S0001-4966(00)03001-0]

PACS numbers: 43.80.Lb, 43.80.Ka [WA]

INTRODUCTION

For over 50 years, tuna fishers in the eastern Pacific Ocean (EPO) have exploited an association between a few species of dolphins (pantropical spotted dolphin, *Stenella attenuata*, spinner dolphin, *Stenella longirostris*, and short-beak common dolphin, *Delphinus delphis*), and yellowfin tuna, *Thunnus albacares*, to locate and capture the tuna (Perrin, 1968; Perrin, 1969; National Research Council, 1992). Similar associations have been noted and exploited in other oceans, but the association is especially strong in the EPO. Improvements in purse seine fishing nets and refrigeration equipment in the 1950's allowed fishers to set their nets around schools of dolphins and capture the associated tuna, producing nearly one-fourth of the world's tuna catch. However, the practice also produced large numbers of dolphin mortalities and focused research on the fishing practice and dolphin populations. Although dolphin mortalities in this fishery have been significantly reduced through education, gear innovations, and quotas, the reason for the strong tuna/dolphin association in the EPO is still unclear (Edwards, 1992; Scott and Cattanach, 1998). Identification of a mechanism which facilitates the tuna/dolphin bond may provide a means of breaking the bond prior to encircling dolphins, thus enabling the capture of tuna without catching dolphins.

Fishers believe larger yellowfin tuna are attracted to the dolphins (National Research Council, 1992), which raises the question of how tuna might detect dolphins. Although fish possess light, sound, and chemical sense organs, only sound allows long-range transmission of information underwater (Rogers and Cox, 1988). It thus seems likely that the tuna/dolphin attraction is somehow facilitated by acoustic cues.

Schaefer and Oliver (1999) suggested that yellowfin tuna may be attracted to sounds produced by dolphins. Dolphins actively generate a wide variety of whistles, clicks, jaw pops (or jaw claps), and pulse bursts (Lilly, 1962; Marten *et al.*, 1988; Smolker and Richards, 1988; Au, 1993; Connor and Smolker, 1996). In addition to these sounds, dolphins may also generate sound through their interaction with the water: by swimming, jumping high in the air and landing on their sides or back (breaching), or striking the water's surface

with their flukes (tail slaps) or head (head slaps) (Würsig and Würsig, 1980).

The vast majority of fish studied have been shown to have a relatively narrow audible frequency range that does not extend to the frequencies dominant in high-frequency dolphin sounds such as vocalizations and echolocation clicks (Fay, 1988; Au, 1993). Although some species of fish have been shown to be sensitive to ultrasound, including clicks similar to those produced by echolocating dolphins or whales (Astrup and Møhl, 1993; Mann *et al.*, 1998a), it is unlikely that ultrasonic detection is widespread in fish (Mann *et al.*, 1998b). Ultrasonic detection has been demonstrated only in clupeids and cod. Clupeids possess a unique ear structure in which two air-filled tubes project anteriorly from the swimbladder and terminate in small air chambers near the inner ears (Blaxter *et al.*, 1981). Yellowfin do not possess any similar morphological adaptations, thus it seems unlikely that yellowfin could detect higher-frequency dolphin sounds such as whistles and echolocation clicks. Although cod also lack any specialized adaptations to their peripheral auditory system, their ultrasonic thresholds are rather high, approximately 194 dB *re:* 1 μPa (Astrup and Møhl, 1993). Astrup and Møhl (1993) estimated that cod could detect echolocating odontocetes at ranges of 10–30 m, which is well below the detection ranges deemed necessary for tuna to locate dolphins within the EPO. The combination of poor hearing and high sound attenuation at high frequencies makes the lower-frequency dolphin sounds more likely to be detected at a distance by fish. The source levels of the lower-frequency dolphin sounds are therefore of particular interest with regards to the identification of a mechanism responsible for the tuna/dolphin bond.

Yellowfin have been shown to respond to pure tones at frequencies from 50–1100 Hz (Iversen, 1967). Sounds produced by dolphins with significant frequency content within this range include breaches, tail slaps, and jaw pops (Marten *et al.*, 1988; Smolker and Richards, 1988). Many of these sounds have been described as being ''loud'' (Marten *et al.*, 1988; Smolker and Richards, 1988); however, few data exist regarding the actual source levels and frequency content of these sounds.

This report presents the first measured source levels and frequency spectra for some low-frequency sounds (jaw pops, breaches, and tail slaps) produced by the bottlenose dolphin, *Tursiops truncatus*, and estimated distances at which yellowfin could detect these sounds (sound propagation was assumed to obey spherical spreading). Although *Tursiops* is not one of the pelagic dolphin species associated with yellowfin in the EPO, the use of *Tursiops* to model low-frequency sound production in pelagic species was attractive because of the availability of trained bottlenose dolphins. Expected source level differences between *Tursiops* and pelagic species are discussed.

The source levels and estimated detection ranges are presented here in an attempt to determine the potential of yellowfin to locate dolphin within the EPO by cueing on low-frequency sounds produced by dolphins. Dolphins have a highly developed auditory system and yellowfin do generate sound (Iversen, 1967), thus it is possible that it is the dolphins that locate the tuna, rather than vice versa; however, investigation of this hypothesis was considered beyond the scope of the current study.

TABLE I. Experimental animals used in this study.

Name	Species	Age	Weight (kg)	Sex	Task
IAY	*Tursiops truncatus gilli*	19[a]	255[a]	M	Jaw pops
APR	*Tursiops truncatus*	14	169	F	Beach/tail slaps
MAK	*Tursiops truncatus*	28	207	M	Breach

[a]December 1983.

I. METHODS

A. Experimental animals

Table I lists the individual dolphins used in this study. Breaches were performed by both APR and MAK. Jaw pops and tail slaps were recorded from IAY and APR, respectively. The dolphins were housed, and the experimental measurements conducted, in floating net enclosures (9×9 or 9×18 m) located in San Diego Bay, California.

B. Jaw pop recordings

Jaw pops (or jaw claps) are loud pops or snaps produced by dolphins, presumably as a social display of dominance or agitation during an aggressive situation. The name ''jaw pop'' originated from the pronounced lower jaw motions that accompany the sound. In fact, the sound appears to be produced within the nasal cavities, not by the closing of the jaws, which produce only a low-frequency ''thud'' (Lilly, 1962). The jaw motions may be part of a social display or threat (Lilly, 1962), or may be related to pressurization events necessary to produce the loud pop sounds (Marten *et al.*, 1988).

Jaw pops were recorded on two separate dates: 1 November 1983 and 1 June 1988. These recordings were not the result of trained behaviors, but rather fortuitous circumstances. On these dates, the dolphin IAY voluntarily assumed a fixed position, underwater facing the net (looking out of the pen), and began to spontaneously (i.e., not under the direction of a trainer) produce jawpops. In one case, the pops were directed toward dolphins housed in an adjacent pen; in the other, the pops appeared to be directed at a wild California sea lion (*Zalophus californianus*) which had approached the outside netting of the pen. These behaviors were consistent with previous observations that jaw pops were typically produced by this animal when he became agitated.

Jaw pop production continued for several minutes, with the animal returning to the same general position after each trip to the surface for air. After IAY had taken up station and begun to emit pops, a small hydrophone (B&K 8103) was positioned underwater in front of the animal, at the same depth (approximately 2 m), and along the animal's longitudinal axis. For the 1983 data, the nominal distance between the animal and the hydrophone was 1 m. The hydrophone was periodically moved to adjust for any differences in the animal's position (e.g., after surfacing). The distance from

the sound source to the receiving hydrophone was estimated to be within the range 0.5–1.5 m. For the 1988 data, the hydrophone was approximately 25 m from the animal and the dolphin's position did not vary by more than ±2 m, thus the range was estimated to be between 23 and 27 m. The angle between the animal and the receiving hydrophone could not be determined from the 1988 data.

On each date, the hydrophone signal was bandpass filtered (2 Hz–200 kHz) and amplified (B&K 2635 charge amp) and recorded on magnetic tape (RACAL Store 7DS). A separate voice track was also recorded to allow future identification of the signals. The tape speed was 60 in/s(ips) for the 1983 data and either 15 or 60 ips for the 1988 data. The tape recorder frequency bandwidth was 0.1–75 kHz at 15 ips tape speed and 0.3–300 kHz at 60 ips. The recorded tapes were stored in a controlled environment, where they remained for several years. The recorded signals were later digitized at 705.6 and 88.2 kHz (Iotech WaveBook/512) for the tapes recorded at 60 and 15 ips, respectively.

The peak-to-peak (p-p) source level, $SL_{\text{p-p}}$, and root-mean-square (rms) source level, SL_{rms}, were calculated for each jaw pop identified within the digitized data series. The rms source level was calculated using

$$SL_{\text{rms}} = 10 \log_{10}\left(\frac{1}{T}\int_0^T p^2(t)\,dt\right), \tag{1}$$

where $p(t)$ is the recorded pressure and T is the signal duration. The pressure density spectrum, octave, and one-third-octave band levels were also computed using a fast Fourier transform (FFT) algorithm.

Source levels are normally expressed as the sound pressure level (SPL) at a reference distance of 1 m. Equation (2) was therefore used to convert the SPL measured at a distance r from the source, SL_r, to the source level at 1 m, SL_1,

$$SL_1 = SL_r + TL, \tag{2}$$

where TL is the transmission loss. For the frequencies of interest, assuming spherical spreading, the transmission loss TL may be written as

$$TL = 20 \log_{10}(r) + ar, \tag{3}$$

where r is the distance from source to target (m) and a is the absorption coefficient (dB/m) (Kinsler *et al.*, 1982). At 1 kHz the absorption coefficient $a \approx 0.000\,06$ dB/m, so the second term in Eq. (3) may be neglected at the frequencies considered here; at low frequencies and relatively short ranges the primary loss is due to the geometric (in this case spherical) spreading of the sound beam. The transmission loss is thus approximately equal to

$$TL \approx 20 \log_{10}(r). \tag{4}$$

The absolute error in the jaw pop source levels was estimated to be ±5 dB for the 1983 recordings and ±2 dB for the 1988 data. The primary source of error was the uncertainty in the distance between the animal and the receiving hydrophone.

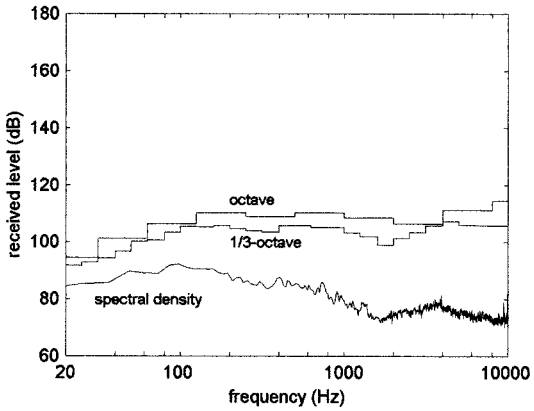

FIG. 1. Ambient noise level measured at the test site in San Diego Bay. The dB reference is 1 μPa^2 Hz for the spectral density and 1μPa for the octave and one-third-octave levels. The analysis frequency bandwidth is 12.2 Hz.

C. Breach and tail slap recordings

The breach and tail slap recordings were carried out in a 9×18-m floating net enclosure in San Diego Bay. Breaches and tail slaps were elicited from animals specifically trained to perform these tasks. Upon receiving a cue from the trainer, animals were free to breach anywhere within the enclosure (normally near the center). Tail slaps were performed by an animal trained to station on the trainer's outstretched hand, remain horizontal, and slap the water with its tail flukes.

Underwater sounds were recorded using a hydrophone (B&K 8103) mounted to a pvc frame and submerged to a depth of 1.2 m. The hydrophone was located at the midpoint of one of the long sides of the pen and extended 0.75 m toward the pen interior. The output from the hydrophone was bandpass filtered (2 Hz–200 kHz) and amplified (B&K 2635 charge amp), then digitized at 100 kHz (National Instruments PCI-MIO-16E-1). Video tape recordings were made of each trial and used to estimate the timing of the events and the position of the animal relative to the receiving hydrophone. The distance from the receiving hydrophone to the animal was estimated individually (from the video) for each breach and tail slap. These distances ranged from 4–7 m for the breaches and were approximately 2 m for the tail slaps. The maximum position error was estimated to be ±1.5 m for the breaches and ±0.5 m for the tail slaps.

The hydrophone recordings were digitally high-pass filtered (20 Hz cutoff frequency) and analyzed using a moving-window FFT algorithm to determine the envelope pressure density spectrum for each recorded event. The octave and one-third-octave band levels were also calculated from the pressure density spectrum. The p-p source levels were calculated for the breaches and tail slaps; however, rms levels were not computed because the signal duration could not be accurately determined in each case. Absolute errors in the source levels were estimated to be ±4 dB for the breaches and ±3 dB for the tail slaps.

II. RESULTS

A. Ambient noise levels

Ambient noise at the test site in San Diego Bay was dominated by ship and boat traffic and biological sources

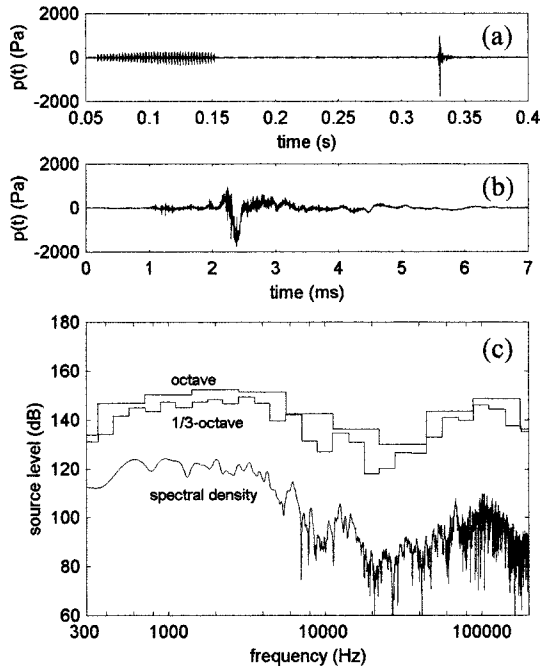

FIG. 2. (a) Jaw pop recording showing the pop and its precursor. (b) Pressure recording for the actual pop of (a). (c) Pressure density, octave, and one-third-octave spectrum levels of the jaw pop from (b). The analysis frequency bandwidth was 21.5 Hz. The dB reference is 1 (μPa-m)^2/Hz for the pressure density spectrum and 1 μPa-m for the octave and one-third-octave levels.

such as snapping shrimp and other animals housed at the facility. Figure 1 shows ambient noise levels measured during this study (with the same equipment used for the breach and tail slap recordings). Ordinate units are dB *re:* 1 μPa^2/Hz for the spectral density and dB *re:* 1 μPa for the octave and one-third-octave levels. Spectral density levels represent the sound power in a 1-Hz band and are therefore lower than one-third-octave levels, which represent the power in a frequency band whose width is 23% of the center frequency. Similarly, octave bands, which contain three one-third-octave bands, have higher levels than one-third-octave bands (Richardson *et al.*, 1995). Noise spectral density levels ranged from approximately 80 to 90 dB *re:* 1 μPa^2/Hz at frequencies below 1000 Hz. Octave and one-third-octave levels were between 100 and 110 dB *re:* 1 μPa. These noise levels were high enough to mask some of the low-level tail slaps but were well below the amplitudes measured for the breaches and jawpops.

B. Source levels

1. Jaw pops

Figure 2(a) shows a typical jaw pop recording. Each actual pop was usually preceded by a precursor consisting of a number of intense pulses or clicks having p-p source levels as high as 180–190 dB *re:* 1 μPa-m (1μPa at a distance of 1 m). The precursor clicks have a rather high frequency content, with the bulk of the power between 50 and 150 kHz. The actual jaw pop has a broad spectrum with both low-frequency (below 10 kHz) and high-frequency (50–200 kHz) components.

Figure 2(b) shows the acoustic pressure measured for the actual jaw pop of Fig. 2(a). Figure 2(c) shows the pressure density, octave, and one-third-octave spectrum levels for the signal in Fig. 2(b). The units for the ordinate in Fig. 2(c) are in dB *re:* 1 (μPa-m)^2/Hz (1 μPa at 1 m in a 1-Hz band) for the pressure density spectrum and dB *re:* 1 μPa-m for the octave and one-third-octave levels. The pop has a relatively short duration, on the order of 5 ms. The p-p and rms source levels are 188 ($\pm$5) and 163 ($\pm$5) dB *re:* 1 μPa-m, respectively. The main signal power exists between 0.4 and 3 kHz.

Since much of the signal power exists at frequencies above the tuna's audible range, the rms level is not an appropriate measure of the actual stimulus to the tuna. The pressure density spectrum also does not seem appropriate because the use of a 1-Hz frequency bandwidth, while convenient, does not have any special significance to the auditory system of fish. To estimate the effective stimulus to the tuna, we therefore rely upon the concept of the critical bandwidth, which is ''the frequency range within which the intensity of the stimulus summates over frequency in its effect on the auditory system'' (Fay, 1988). The critical bandwidth concept approximates the ear as a bank of parallel bandpass filters, each with some finite bandwidth (the critical bandwidth). Critical bandwidths between 8% and 40% have been measured in goldfish and cod at center frequencies between 160 and 500 Hz (Hawkins and Chapman, 1975; Tavolga, 1974). These bandwidths are roughly in line with those of a one-third-octave filter, which has a 23% bandwidth at all frequencies. For this reason, we define the effective source level SL_e as the maximum one-third-octave level within the 200–800 Hz frequency range, which is the frequency range over which the yellowfin is most sensitive (Iversen, 1967). The data recorded at 60 ips have a low-frequency limit of 300 Hz, therefore the effective source levels for these data were calculated using the frequency range 300–800 Hz.

A total of 26 jaw pops were examined. The p-p levels for all jaw pops varied from 175 ($\pm$5) to 201 ($\pm$2) dB *re:* 1 μPa-m. The rms levels for the jaw pops varied from 156 ($\pm$5) to 184 ($\pm$2) dB *re:* 1 μPa-m. Effective source levels for the jaw pops varied from 130 ($\pm$2) to 163 ($\pm$2) dB *re:* 1 μPa-m. The mean value for SL_e was 152 ($\pm$2) dB *re:* 1 μPa-m.

2. Breaches

Figure 3(a) shows the pressure recorded during one of the breaching trials. As the animal approached the water surface, it continuously echolocated, presumably to judge the distance to the surface. These echolocation clicks may be seen in Fig. 3(a), beginning near the 1.5-s mark and continuing until the animal became airborne near 4.5 s. The interclick interval decreased dramatically as the surface was approached. The animal remained airborne for approximately 1.5 s and reached a height of approximately 2 m. The animal reentered the water near the 6.1-s mark, producing a large transient followed by lower-frequency disturbances. The short impulse visible near the 5.1-s mark was produced by the experimenter striking an underwater pipe and was used as a timing reference to synchronize the video and hydro-

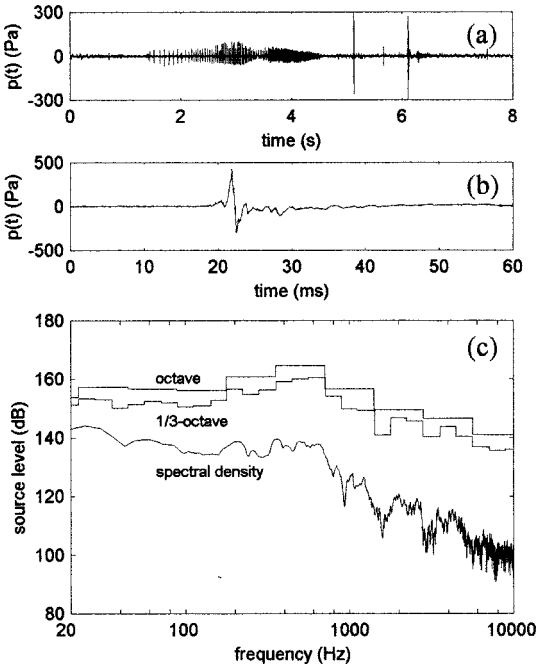

FIG. 3. (a) Pressure recorded during a breach showing echolocation clicks and reentry sounds. The transient near 5.1 s was caused by the experimenter striking an underwater pipe and was used as a timing reference. (b) Pressure recording for a breach reentry sound only. (c) Pressure density, octave, and one-third-octave spectrum levels of the reentry sound from (b). The analysis frequency bandwidth was 6.1 Hz. The dB reference is 1 (μPa-m)^2/Hz for the pressure density spectrum and 1 μPa-m for the octave and one-third-octave levels.

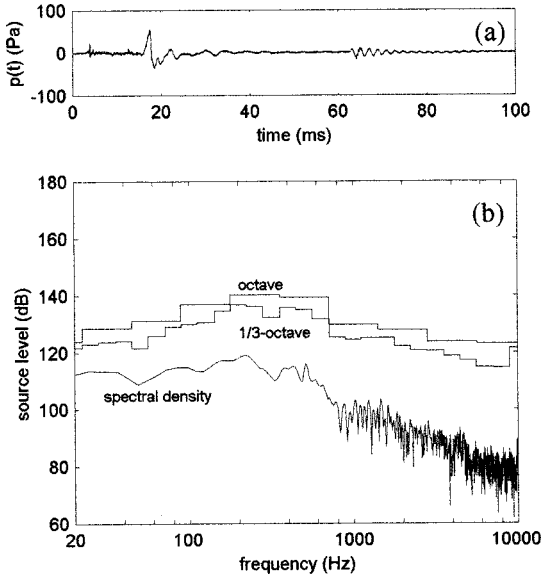

FIG. 4. (a) Time trace and (b) pressure density spectrum, octave, and one-third-octave band levels for a tail slap recording. The dB reference is 1 (μPa-m)^2/Hz for the pressure density spectrum and 1 μPa-m for the octave and one-third-octave levels. The pressure density spectrum bandwidth is 12.2 Hz.

phone recordings. Figure 3(b) shows the reentry sounds from one of the breaches. Figure 3(c) shows the pressure density spectrum, octave band, and one-third-octave band levels for the signal of Fig. 3(b). The spectra are broad and show significant components at frequencies up to approximately 1000 Hz. For this recording, SL_e is 160 ($\pm$4) dB *re:* 1 μPa-m.

A total of 11 breach recordings were examined. The p-p levels for all breach recordings varied from 155 ($\pm$4) to 189 ($\pm$4) dB *re:* 1 μPa-m. Effective source levels for all breaches varied from 119 ($\pm$4) to 153 ($\pm$4) dB *re:* 1 μPa-m. The mean value for SL_e was 144 ($\pm$4) dB *re:* 1 μPa-m.

3. Tail slaps

A total of six tail slap recordings were analyzed. Figure 4(a) and (b) show the time trace and frequency spectra, respectively, for a representative tail slap. The main spectral amplitude from the tail slaps was often within the 100–600-Hz range. The p-p levels for all tail slap recordings varied from 154 ($\pm$3) to 168 ($\pm$3) dB *re:* 1μPa-m. Effective source levels for tail slaps varied from 127 ($\pm$3) to 141 ($\pm$3) dB *re:* 1 μPa-m. The mean value for SL_e was 135 ($\pm$3) dB *re:* 1 μPa-m.

The source levels for the three different signal types are summarized in Table II.

C. Yellowfin hearing thresholds and estimated detection range

Figure 5 illustrates the behavioral audiogram for yellowfin tuna measured by Iversen (1967). The symbols indicate the individual thresholds measured for both yellowfin tuna tested. The solid line is the mean yellowfin threshold at each frequency and is considered (for this study) to be the hearing threshold for yellowfin. The best sensitivity occurs between 200–800 Hz, where mean thresholds range from 89–100 dB *re:* 1 μPa.

The tuna hearing thresholds presented in Fig. 5 are based on continuous wave (cw), pure tone stimuli. For finite duration sounds, thresholds decrease as the sound duration increases and eventually approach the cw value (Hawkins, 1981; Fay and Coombs, 1983). Temporal summation or integration such as this is a feature common to the auditory systems of all vertebrates (Fay, 1988). The sounds considered here are of relatively short duration, approximately 5–50 ms, therefore it seems reasonable to adjust (increase) the hearing thresholds from Fig. 5 to include the effects of temporal summation.

No data exist for the effects of signal duration on the hearing thresholds in tuna. Fay and Coombs (1983) measured hearing thresholds in goldfish as a function of stimulus duration for 200, 400, and 800 Hz pure tones and broadband noise. For the goldfish, the threshold decreases as the signal duration increases up to approximately 800 ms, where the threshold approaches the cw value. A least-squares fit to these data was performed using the equation

$$\Delta T = m \log(\tau) + b, \tag{5}$$

where ΔT is the increase in dB over the cw threshold, τ is the stimulus duration in ms, and m and b are constants. The least-squares fit yielded $m = -8.3$ and $b = 23.5$. Equation (5) was then used to estimate the expected increase to the tuna threshold for the jaw pop, breach, and tail slap sounds. For representative signal durations of 10, 50, and 50 ms for the jaw pops, breaches, and tail slaps, respectively, the resulting threshold increases (ΔT) are 15, 9, and 9 dB, respectively.

TABLE II. Measured source levels and estimated yellowfin detection range for the jaw pops, breaches, and tail slaps.

		SL_e (dB *re:* 1 μPa-m)		$SL_{p\text{-}p}$ (dB *re:* 1 μPa-m)		SL_{rms} (dB *re:* 1 μPa-m)		Estimated detection
	n	mean	range	mean	range	mean	range	range (m)
Jaw pop	26	152(±2)	130(±2)–163(±2)	194(±2)	175(±5)–201(±2)	174(±2)	156(±5)–184(±2)	660–1040
Breach	11	144(±4)	119(±4)–153(±4)	177(±4)	155(±4)–189(±4)			340–840
Tail slap	6	135(±3)	127(±3)–141(±3)	163(±3)	154(±3)–168(±3)			90–180

To estimate the maximum range at which the tuna could hear each of the different sounds, we assume that the effective source level minus the transmission loss equals the tuna average hearing threshold (within the 200–800-Hz band) plus the threshold correction for the finite stimulus duration,

$$SL_e - TL = T_{cw} + \Delta T, \tag{6}$$

where T_{cw} is the cw threshold within the 200–800-Hz range. The transmission loss *TL* is given in Eq. (4), which assumes spherical spreading with zero absorption. Spherical spreading loss is a reasonable approximation given the water depth in the EPO (up to 5 km) (Rees, 1998) and the relatively short maximum audible ranges anticipated (less than 2 km). At the low frequencies considered here, absorption would not be a significant factor at ranges less than 2 km. Substituting Eq. (4) into Eq. (6) and solving for *r* yields

$$r = 10^{(SL_e - T_{cw} - \Delta T)/20}, \tag{7}$$

Equation (7) was solved using the maximum SL_e for each *Tursiops* sound and the minimum yellowfin hearing threshold (89 dB *re:* 1 μPa). This yields the estimated detection range for each signal type. The results are included in Table II. The jaw pops have the largest estimated detection range (660–1040 m), followed by the breaches (340–840 m). The maximum estimated detection range for the tail slaps is 90–180 m.

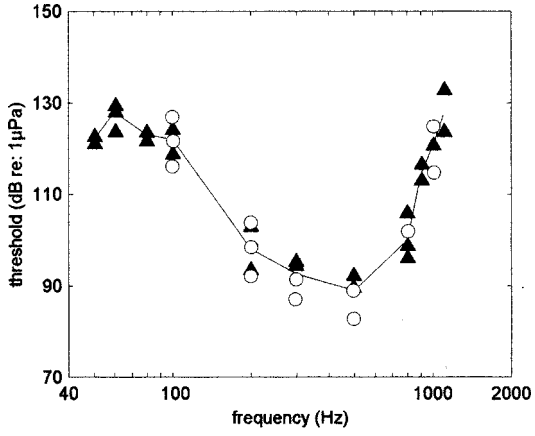

FIG. 5. Behavioral audiogram for yellowfin tuna (*Thunnus albacares*) (Iversen, 1967). The symbols are the thresholds measured from two individual yellowfin; the solid line indicates the mean yellowfin threshold.

III. DISCUSSION

The capacity to detect sounds in the 200–800-Hz range provides *T. albacares* the opportunity to detect some prey. Moulton (1960) contains spectrograms at these frequencies for anchovy schools, *Anchoviella choerostoma*, and Iversen *et al.* (1963) suggests squid may also produce sounds at these frequencies. *Stenella spp*. and *T. albacares* all feed on epipelagic fish, squid, and crustaceans in the EPO (Perrin *et al.*, 1973). The combination of species-specific sounds produced by many individuals in a dolphin herd, and favorable oceanographic conditions for horizontal sound propagation (Rees, 1998), may provide the mechanism for the tuna/dolphin association in the EPO. In the absence of nearby prey, tuna may home on dolphin-produced sounds as part of their foraging strategy.

The source levels and estimated detection ranges are based on a relatively small sample of sounds obtained from three animals. Source level measurements were hampered by the difficulty of accurately measuring the distance between the animal and the receiving hydrophone in each trial. This variability, together with the scatter present in the yellowfin threshold data (as much as 11 dB at any one frequency), makes estimating the detection range somewhat difficult—a cumulative error of 6 dB results in a doubling (or halving) of the estimated range. There was no way to ascertain if the animals were producing the ''loudest'' signals possible. Because the jaw pops were spontaneous and measured in San Diego Bay (as opposed to a tank), these levels are probably a fair representation of levels produced by *Tursiops* in the wild. Tail slaps were elicited from a trained animal who quickly lost interest, thus higher levels may possibly be measured from a highly motivated animal tail-slapping as part of a social display.

Because the angle between the receiving hydrophone and the animal could not be precisely determined for each jaw pop, these data must be used with some caution. Several jaw pops recorded at 25 m had complex time signatures, presumably because the hydrophone was located off axis. It seems reasonable to expect the jaw pops to have some directivity pattern with a main lobe projecting forward from the animal's head, similar to that of other sounds produced within the nasal cavities, with perhaps a broader main lobe because the frequency content is lower. Higher source levels may have been recorded for some of the jaw pops if the hydrophone had been located on axis. The data shown in Fig. 2 were recorded at 1-m range with the hydrophone on axis.

The directivity patterns of the tail slaps and breaches are also unknown. Because the hydrophone was not located beneath the animal, there is the possibility that source levels for these sounds are underestimated. Neither the breaches or tail slaps are represented well by simple source models; however, for the tail slaps, a dipole source may be a reasonable approximation, suitable for the discussion here. For a dipole, the maximum levels exist along the source axis (vertical in this case). Off-axis amplitudes vary as $\cos\theta$, where $\theta = \tan^{-1}(h/v)$ and h and v are the horizontal and vertical distances from the source. For the tail slaps, $\cos\theta$ is approximately 0.5, which leads to a source level error of 6 dB and a doubling of the maximum detection range. We hesitate to apply the same analysis to the breaches because of the size of the (whole) dolphin compared to the wavelengths and the complexity of the sound generation mechanics; we simply acknowledge that higher levels (and thus larger detection distances) may have been obtained if the hydrophone were located beneath the animal, although this was not considered practical or safe.

The detection range estimates rely on hearing thresholds for yellowfin based on the mean values from the two individuals tested by Iversen (1967). These data are for 50 and 60 cm fish, which are considerably smaller than those typically associated with dolphin in the EPO. The effect of yellowfin size on hearing threshold is currently unknown. Popper (1971) found no relationship between size and hearing ability in goldfish; however, swimbladder resonance frequencies in goldfish are above the range of best hearing (Popper, 1974; Derenburger *et al.*, 1997). Larger yellowfin may have swimbladder resonance frequencies within their audible range and improved hearing sensitivity as a result (Schaefer and Oliver, 1999). The lowest threshold observed by Iversen for either fish was 83 dB *re:* 1 μPa at 500 Hz. If this value (rather than the lowest mean threshold of 89 dB *re:* 1 μPa) is used to estimate the maximum audible range for the breaches and jaw pops, the maximum ranges are approximately 1600 and 2000 m, respectively.

Ambient noise in the wild will affect the ability of the tuna to discern these sounds from the background noise and lower the estimated detection ranges presented here. Because of the scarce data on hearing thresholds in tuna and complete lack of information regarding hearing of broadband signals and the required signal-to-noise ratio, it is difficult to predict the effects of ambient noise. We simply note that the presence of ambient noise levels will decrease the maximum audible range of these sounds.

The sounds investigated in this study were produced by bottlenose dolphins, *Tursiops truncatus*, which, while found in association with yellowfin tuna in the EPO, are exploited by tuna fishers to a much lesser extent than other dolphin species. Tuna fishers set upon larger herds of dolphins more often than smaller herds (Scott and Cattanach, 1998), which may result from the fishers's past experience that larger herds carry more tuna and the likelihood that larger herds are easier to see. In their study on aggregations of pelagic dolphins and tuna from data obtained by observers on tuna seiners in the EPO, Scott and Cattanach (1998) present median herd-size ranges for *Tursiops truncatus* (10–15), *Stenella attenuata* (150–305), *Stenella longirostris* (138–300), mixed *Stenella spp.* (600–800), and *Delphinus delphis* (200–350). We used *Tursiops* to model the more pelagic species (i.e., *Stenella spp.* and *Delphinus delphis*) because trained *Tursiops* were available. *Tursiops* are in the same family, delphinidae, and there is apparently much overlap in the types of sounds produced (Evans, 1995; Herzing, 1996). Most delphinids also exhibit a variety of aerial and other behaviors (e.g., breach, tail slap, head slap), which can result in percussive sound (Ridgway and Harrison, 1994; Ridgway and Harrison, 1999). Although *Tursiops* are generally larger than *Stenella spp.* and *Delphinus delphis*, and may be expected to produce higher source levels in a breach, the height of the breaches studied here (1.5–2.5 m) was less than the 3–4 m-jumps observed by *Stenella spp.* and *Delphinus delphis* in the wild. It may be possible that source levels produced by the smaller animals jumping higher could be as large as the values reported here.

Future measurements of source levels within the frequency band audible to *T. albacares*, for various sounds produced by *Stenella spp.* and *Delphinus delphis* in the EPO, would provide more appropriate source levels and maximum detection range estimates. Additional threshold data for yellowfin are also needed, preferably for larger individuals exposed to both cw and impulsive sounds.

Identification of an acoustic mechanism enabling the tuna/dolphin bond may provide a means of exploiting the bond without encircling dolphins, but still allow the capture of tuna (Schaefer and Oliver, 1999). If yellowfin are attracted to all, or part, of the sound repertaire emanating from dolphin schools, it may be possible to aggregate tuna using playback sounds beneath floating platforms, or mask the sounds in order to separate tuna from dolphins just prior to capture.

ACKNOWLEDGMENTS

Don Carder and Mark Todd provided technical assistance. Tricia Kamolnick, Jennifer Carr, Monica Chaplin, and Lauryn Crosthwaite trained the dolphins to breach or tail slap on cue. The Office of Naval Research supported recording equipment. James Finneran was supported by a National Research Council Research Associateship. We thank Whitlow Au, Art Popper, Bill Evans, and two anonymous reviewers for their helpful comments, which significantly improved this manuscript.

Astrup, J., and Møhl, B. (**1993**). ''Detection of intense ultrasound by the cod *Gadus morhua*,'' J. Exp. Biol. **182**, 71–80.

Au, W. W. L. (**1993**). *The Sonar of Dolphins* (Springer-Verlag, New York).

Blaxter, J. H. S., Denton, E. J., and Gray, J. A. B. (**1981**). ''Acousticolateralis system in clupeid fishes,'' in *Hearing and Sound Communication in Fishes*, edited by W. N. Tavolga, A. N. Popper, and R. R. Fay (Springer-Verlag, New York).

Connor, R. C., and Smolker, R. A. (**1996**). '''Pop' goes the dolphin: A vocalization male bottlenose dolphins produce during consortships,'' Behaviour **133**, 643–662.

Derenburger, C., Hastings, M. C., and Finneran, J. J. (**1997**). ''A comparison of experimentally determined swimbladder resonances in two species of fish,'' Proceedings of the ASME Noise Control and Acoustics Division, NCA, **24**, 299–306.

Edwards, E. F. (**1992**). ''Energetics of associated tunas and dolphins in the eastern tropical Pacific Ocean: A basis for the bond,'' Fish. Bull. **90**, 678–690.
Evans, W. E. (**1995**). ''White-bellied porpoise *Delphinus delphis* Linnaeus, 1758,'' in *Handbook of Marine Mammals*, edited by S. H. Ridgway and R. Harrison (Academic, San Diego), Vol. 5, pp. 191–224.
Fay, R. R. (**1988**). *Hearing in Vertebrates: A Psychophysics Databook* (Hill-Fay, Winnetka, IL).
Fay, R. R., and Coombs, S. (**1983**). ''Neural mechanisms in sound detection and temporal summation,'' Hear. Res. **10**, 69–92.
Hawkins, A. D. (**1981**). ''The hearing abilities of fish,'' in *Hearing and Sound Communication in Fishes*, edited by W. N. Tavolga, A. N. Popper, and R. R. Fay (Springer-Verlag, New York).
Hawkins, A. D., and Chapman, C. J. (**1975**). ''Masked auditory thresholds in the cod, *Gadus morhua* L.,'' J. Comp. Physiol. **103**, 209–226.
Herzing, D. L. (**1996**). ''Vocalizations and associated underwater behavior of free-ranging Atlantic spotted dolphins, *Tursiops truncatus*,'' Aquatic Mammals **22**, 61–79.
Iversen, R. T. B. (**1967**). ''Response of the yellowfin tuna (*Thunnus albacares*) to underwater sound,'' in *Marine Bioacoustics*, edited by W. N. Tavolga (Pergamon, Oxford), Vol. 2.
Iversen, R. T. B., Perkins, P. J., and Dionne, R. D. (**1963**). ''An indication of underwater sound production by squid,'' Nature (London) **199**, 250–251.
Kinsler, L. E., Frey, A. R., Coppens, A. B., and Sanders, J. V. (**1982**). *Fundamentals of Acoustics*, 3rd ed. (Wiley, New York).
Lilly, J. C. (**1962**). ''Vocal behavior of the bottlenose dolphin,'' Proc. Am. Philos. Soc. **106**(6), 520–529.
Mann, D. A., Lu, Z., Hastings, M. C., and Popper, A. N. (**1998a**). ''Detection of ultrasonic tones and simulated dolphin echolocation clicks by a teleost fish, the American shad (*Alosa sapidissima*),'' J. Acoust. Soc. Am. **104**, 562–568.
Mann, D. A., Lu, Z., and Popper, A. N. (**1998b**). ''Detection of ultrasound and marine mammal echolocation clicks by the American shad (*Clupeidae*),'' Proc. 16th Int. Con. Acoust. **II**, 1025–1026.
Marten, K., Norris, K. S., Moore, P. W. B., and Englund, K. A. (**1988**). ''Loud impulse sounds in odontocete predation and social behavior,'' in *Animal Sonar Processes and Performance*, edited by P. E. Nachtigall and P. W. B. Moore (Plenum, New York).
Moulton, J. M. (**1960**). ''Swimming sounds and the schooling of fishes,'' Biol. Bull. **119**, 210–223.
National Research Council, Committee on Reducing Porpoise Mortality from Tuna Fishing (**1992**). *Dolphins and the Tuna Industry* (National Academy, Washington, DC).
Perrin, W. F. (**1968**). ''The porpoise and the tuna,'' Sea Frontiers **14**(3), 166–174.
Perrin, W. F. (**1969**). ''Using porpoise to catch tuna,'' World Fishing **18**, 42–45.
Perrin, W. F., Warner, R. W., Fiscus, C. L., and Holts, D. B. (**1973**). ''Stomach contents of porpoise, *Stenella spp.*, and yellowfin tuna, *Thunnus albacares*, in mixed species aggregation,'' Fish. Bull. **71**, 1077–1092.
Popper, A. N. (**1971**). ''The effects of size on the auditory capacities of the goldfish,'' J. Aud Res. **11**, 239–247.
Popper, A. N. (**1974**). ''The response of the swimbladder of the goldfish (*Carassius auratus*) to acoustic stimuli,'' J. Exp. Biol. **60**, 295–304.
Richardson, W. J., Greene, C. R., Jr., Malme, C. I., and Thomson, D. H. (**1995**). *Marine Mammals and Noise* (Academic, San Diego).
Rees, C. D. (**1998**). ''Active towed-array acoustic system design study for yellowfin tuna in the eastern tropical Pacific fishery area,'' NOAA-TM-NMFS-SWFSC-251.
Ridgway, S. H., and Harrison, R. (**1994**). *Handbook of Marine Mammals* (Academic, San Diego), Vol. 5.
Ridgway, S. H., and Harrison, R. (**1999**). *Handbook of Marine Mammals* (Academic, San Diego), Vol. 6.
Rogers, P. H., and Cox, M. (**1988**). ''Underwater sound as a biological stimulus,'' in *Sensory Biology of Aquatic Animals*, edited by J. Atema, R. R. Fay, A. N. Popper, and W. N. Tavolga (Springer-Verlag, New York).
Schaefer, K. M., and Oliver, C. W. (**1999**). ''Shape, volume, and resonance frequency of the swimbladder of yellowfin tuna (*Thunnus albacares*),'' submitted to Fish. Bull.
Scott, M. D., and Cattanach, K. L. (**1998**). ''Diel patterns in aggregations of pelagic dolphins and tunas in the eastern Pacific,'' Marine Mammal Sci. **14**, 401–428.
Smolker, R., and Richards, A. (**1988**). ''Loud sounds during feeding in Indian Ocean bottlenose dolphins,'' in *Animal Sonar: Processes and Performance*, edited by P. E. Nachtigall and P. W. B. Moore (Plenum, New York).
Tavolga, W. N. (**1974**). ''Signal/noise ratio and the critical band in fishes,'' J. Acoust. Soc. Am. **55**, 1323–1333.
Würsig, B., and Würsig, M. (**1980**). ''Behavior and ecology of the dusky dolphin, *Lagenorhyncus obscurus*, in the South Atlantic,'' Fish. Bull. **77**, 871–889.

LETTERS TO THE EDITOR

Localized vibration modes in free anisotropic wedges

A. L. Shuvalov[a] and V. V. Krylov
Department of Civil and Structural Engineering, The Nottingham Trent University, Burton Street, Nottingham NG1 4BU, United Kingdom

(Received 5 April 1999; revised 26 July 1999; accepted 1 October 1999)

Propagation of flexural localized vibration modes along edges of anisotropic wedges is considered in the framework of the geometrical-acoustics approach. Its application allows for straightforward evaluation of the wedge-mode velocities in the general case of arbitrary elastic anisotropy. The velocities depend on the wedge apex angle and on the mode number in the same way as in the isotropic case, but there appears to be additional dependence on elastic coefficients. The velocities in tetragonal wedges (with the midplane orthogonal to the four-fold axis) and in ''weakly'' monoclinic wedges are explicitly calculated and analyzed. Bounds of the wedge-wave velocity variation in tetragonal materials are established. © *2000 Acoustical Society of America.* [S0001-4966(00)02901-5]

PACS numbers: 43.20.Jr [ANN]

INTRODUCTION

The existence of antisymmetric localized waves propagating along edges of elastic solid wedges in contact with vacuum was predicted in 1972 by Lagasse[1] and Maradudin *et al.*[2] By using numerical calculations, it was shown in Refs. 1 and 2 that such waves, now often called wedge acoustic waves, have low propagation velocities (generally much lower than that of Rayleigh waves), and that their elastic energy is concentrated in the area of about one wavelength near the wedge tips. Since 1972, wedge acoustic waves have been investigated in a number of papers with regard to their possible applications to signal processing, nondestructive testing of special engineering constructions, structural dynamics, etc. (see, e.g., Refs. 3–12).

Because of the complexity of the problem even for wedges made of elastically isotropic materials, no exact analytical theory of the localized wedge modes is available which could describe their propagation for an arbitrary wedge apex angle. However, for slender wedges, the approximate analytical theory[5,6] has been developed on the basis of the geometrical acoustics approach, which interprets the problem in terms of the quasiplane flexural waves propagating in a plate of variable thickness. In Ref. 5 the case of elastic isotropy in the wedge midplane has been envisaged (for brevity, we will be referring to such transversal isotropy as simply the isotropy). Reference 6 has been concerned with a slender wedge of weakly anisotropic material, whose departure from the isotropic state can be described by a single (and) small parameter. In this framework it was demonstrated that weak anisotropy does not affect the dependence of wedge-wave velocities on the wedge apex angle θ and the mode number n.

In the present paper, we consider antisymmetric localized waves in a generally anisotropic slender wedge. The relation for wedge-wave velocities is obtained which reveals the same dependence on θ and n as in the isotropic case, but acquires additional dependence on elastic coefficients. As an example, the velocities are explicitly calculated and analyzed for tetragonal wedges, with the midplane orthogonal to the four-fold axis, and also for ''weakly'' monoclinic wedges.

I. CONSIDERATIONS FOR AN ARBITRARY ANISOTROPY

According to Refs. 5 and 6, the velocities of antisymmetric localized modes $c=\omega/\beta$ in an elastic wedge with a small apex angle θ are defined by the equation

$$\int_C [k_a^2(x,\varphi)-\beta^2]^{1/2}dx = 2\pi n \quad (n=1,2,\ldots), \tag{1}$$

where n is the mode order,

$$\beta = k_a(x,\varphi)\cos\varphi, \tag{2}$$

φ is the polar angle varying in the midplane of the wedge, k_a is the wave number of flexural mode in a plate of the small

[a]Author to whom correspondence should be addressed. Permanent address: Institute of Crystallography, Leninskii pr. 59, Moscow 117333, Russia; electronic mail: ashuv@mechan.incr.msk.su

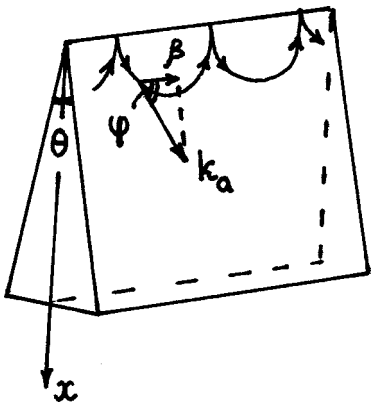

FIG. 1. Geometry of the problem.

variable thickness $h=\theta x$ (Fig. 1). The integration path C follows the ray trajectory, which starts from the edge $x=0$ where $\varphi=\pi/2$, passes the turning point x_t corresponding to $\varphi=0$, and ends up at the edge $x=0$ having $\varphi=-\pi/2$. In the case of isotropic material,

$$k_a^2(x)=\frac{2\sqrt{3}\omega}{\theta x c_{0p}}, \tag{3}$$

where c_{0p} is the speed of the longitudinal dilatational mode in an isotropic thin plate. This leads to the result of Ref. 5 for the antisymmetric-mode velocity in the isotropic wedge,

$$c^{(\mathrm{iso})}=c_{0p}\frac{\theta n}{\sqrt{3}}. \tag{4}$$

It can be shown[13] that in the case of generally anisotropic material with the density ρ and the tensor of elastic moduli c_{ijkl}, the squared value $k_a^2(x,\varphi)$ becomes

$$k_a^2(x,\varphi)=\frac{2\sqrt{3}\omega}{\theta x\sqrt{f(\varphi)}}, \tag{5}$$

where

$$f(\varphi)=\frac{1}{\rho}\mathbf{m}\cdot[(mm)-(mn)(nn)^{-1}(nm)]\mathbf{m}, \tag{6}$$

$\mathbf{m}=\mathbf{m}(\varphi)$ is the unit vector turning about the angle φ in the midplane, $\mathbf{n}$ is the unit normal to the midplane, and $(\ldots)$ are the matrices written by means of notation

$$(ab)\equiv a_j c_{ijkl} b_k \quad \text{for any vectors } \mathbf{a},\ \mathbf{b}. \tag{7}$$

In the generic case, $f(\varphi)$ (6) is a homogeneous polynomial of the 4th degree in $\sin\varphi$,$\cos\varphi$ with the coefficients depending on elastic moduli. Because the matrix, enclosed in brackets in (6), is positive-definite for an arbitrary tensor c_{ijkl} and any vectors $\mathbf{m}$, $\mathbf{n}$,[14] the quadratic form $f(\varphi)$ is positive and so the flexural-mode wave number (5) is well-defined for an arbitrary anisotropy.

In the presence of anisotropy, conjunction of (2) and (5) cannot provide explicit $\varphi(x)$, but it readily yields $x(\varphi)$,

$$x(\varphi)=\frac{2\sqrt{3}\omega}{\theta\beta^2}\frac{\cos^2\varphi}{\sqrt{f(\varphi)}}. \tag{8}$$

It is therefore convenient to pass to the integration over φ, writing Eq. (1) with the aid of (2) as

$$\beta\int_{\pi/2}^{-\pi/2} x'(\varphi)\tan\varphi\, d\varphi=2\pi n. \tag{9}$$

Inserting (8) into (9) results in the following relation for the wedge-wave velocities c:

$$c=\frac{\theta n\pi}{\sqrt{3}J}, \tag{10}$$

where

$$J=\int_{\pi/2}^{-\pi/2}[f^{-1/2}(\varphi)\cos^2\varphi]'\tan\varphi\, d\varphi, \tag{11}$$

and $f(\varphi)$ is defined by (6). The obtained relation describes the velocities c in an arbitrary anisotropic wedge. It may also be cast into the form

$$c=c^{(\mathrm{iso})}\frac{\pi}{c_{0p}J}, \tag{12}$$

where $c^{(\mathrm{iso})}$ is given by (4). The dimensionless coefficient $(\pi/c_{0p}J)$ shows the anisotropy-induced change of the wedge-wave velocities with respect to the reference (transversely) isotropic medium, characterized by the dilatational plate-mode speed $\sqrt{f(\varphi_{\mathrm{ref}})}=c_{0p}$, where a polar angle φ_{ref} may be chosen optionally. Once picked, φ_{ref} sets c_{0p} and, thereby, specifies a particular reference isotropic medium.

Comparing (4) and (10), (12) confirms that the impact of unrestricted elastic anisotropy does not affect the dependence of velocities c on the apex angle θ and mode number n. It is also noteworthy that c does not depend on the orientation of the wedge edge in the given midplane due to the period π of $f(\varphi)$ (6), which merely reflects the inversion symmetry of elastic-wave properties in an arbitrary anisotropic medium.

II. TETRAGONAL WEDGE

As a simple example, consider a tetragonal wedge, whose midplane is orthogonal to the four-fold axis. It is convenient to choose the edge orientation so that $\varphi=0$ corresponds to the direction of the two-fold axis in the midplane. In this case, (6) simplifies to

$$f(\varphi)=f_0\left(1-\frac{C}{2f_0}\sin^2 2\varphi\right), \tag{13}$$

where

$$f_0=\frac{1}{\rho}\left(c_{11}-\frac{c_{13}^2}{c_{33}}\right),\quad C=\frac{1}{\rho}(c_{11}-c_{12}-2c_{66}), \tag{14}$$

C being the parameter of anisotropy which measures the deviation of a given tetragonal material from the transversely isotropic state.

Positive-definiteness of elastic strain energy leads to the condition[14]

$$(c_{11}+c_{12})c_{33}>2c_{13}^2, \tag{15}$$

which in turn demands that $f_0>0$ and $C<2f_0$. Thus the dimensionless parameter $C/2f_0$ is always less then one, and

may take either positive or negative values in different anisotropic materials. Strictly speaking, $C/2f_0$ is not bounded from below. However, invoking (15) reveals that the inequality $c_{66}>c_{11}$ is the necessary condition for $C/2f_0<-1$. Shear moduli exceeding extensional ones is quite a rare occasion, so the low bound $C/2f_0>-1$ is well applicable for almost all tetragonal materials.

Substituting (13) into (11) gives

$$J=\frac{1}{\sqrt{f_0}}\int_{-\pi/2}^{\pi/2}\left\{-\frac{(C/4f_0)\sin 4\varphi\sin 2\varphi}{[1-(C/2f_0)\sin^2 2\varphi]^{3/2}}+\frac{1-\cos 2\varphi}{[1-(C/2f_0)\sin^2 2\varphi]^{1/2}}\right\}d\varphi$$

$$=\frac{1}{2\sqrt{f_0}}\int_{-\pi}^{\pi}\frac{dx}{[1-(C/2f_0)\sin^2 x]^{1/2}}, \tag{16}$$

which is obviously positive by virtue of $C/2f_0<1$. Provided that the parameter of anisotropy C in a given material is positive,

$$J=\frac{2}{\sqrt{f_0}}F\left(k,\frac{\pi}{2}\right),\quad k=\sqrt{\frac{C}{2f_0}}, \tag{17}$$

where $F(k,\pi/2)$ is the full elliptical integral of the first order,

$$F(k,\pi/2)\equiv\int_0^{\pi/2}\frac{dx}{(1-k^2\sin^2 x)^{1/2}}, \tag{18}$$

which is defined at $0\leqslant k^2<1$. It equals $\pi/2$ at $k=0$ and monotonically increases toward a logarithmic pole at $k^2\to 1$. If C is negative, J may be written in the form

$$J=\frac{1}{\sqrt{f_0[1-(C/2f_0)]}}\int_{-\pi/2}^{\pi/2}\frac{d\varphi}{\left[1-\left(\frac{C}{C-2f_0}\right)\sin^2 2\varphi\right]^{1/2}}$$

$$=\frac{2}{\sqrt{f_0[1-(C/2f_0)]}}F\left(k,\frac{\pi}{2}\right),\quad k=\sqrt{\frac{C}{C-2f_0}}. \tag{19}$$

Inserting (17) or (19) into (10), we may present the wedge-wave velocities c in terms of the elliptical integral $F(k,\pi/2)$ in two alternative forms, depending on whether the parameter of anisotropy C is positive or negative, namely,

$$c=\frac{\pi\theta n}{2\sqrt{3}}\frac{\sqrt{f_0}}{F\left(\sqrt{\frac{C}{2f_0}},\frac{\pi}{2}\right)}\quad\text{if}\quad C\geqslant 0, \tag{20}$$

$$c=\frac{\pi\theta n}{2\sqrt{3}}\frac{\sqrt{f_0-(C/2)}}{F\left(\sqrt{\frac{C}{C-2f_0}},\frac{\pi}{2}\right)}\quad\text{if}\quad C\leqslant 0. \tag{21}$$

Let us analyze the obtained result. At $C=0$, i.e., when the material is transversely isotropic, f_0 in (14) is equal to the dilatational plate-mode speed c_{0p}, and Eqs. (20), (21) merge into the relation (4) obtained in Ref. 5. This limit may be naturally regarded as the reference state for evaluating the effect of tetragonal anisotropy.

Provided that anisotropy is weak, i.e., $|C|/2f_0\ll 1$, either of the equations (20), (21) yields the following approximation for c:

$$c\approx\theta n\sqrt{\frac{f_0}{3}}\left[1-\frac{1}{4}\left(\frac{C}{2f_0}\right)-\frac{5}{64}\left(\frac{C}{2f_0}\right)^2\right], \tag{22}$$

which corrects the corresponding result of Ref. 6. Equation (22) shows that the increase of positive parameter C stipulates the decrease of the wedge-wave velocities c, while the increase of the absolute value of C entails increase of c (provided that f_0 is kept constant). Note that, by (22), the effect of (weak) anisotropy on the velocities c is stronger in case of $C>0$.

In view of $\pi/2\leqslant F(k,\pi/2)<\infty$ at $0\leqslant k^2<1$, the same conclusions follow from Eqs. (20), (21) which evaluate the impact of an arbitrary measure of tetragonal anisotropy. In the limit $C/2f_0\to 1$, the flexural plate-mode velocity,

$$c_a(\varphi)=\sqrt{\frac{f(\varphi)}{12}}k_a\theta x, \tag{23}$$

tends to zero for the direction $\varphi=\pi/4+\pi l/2$ ($l=0,1,\ldots$), and so do the wedge-wave velocities due to the presence of the logarithmic pole in the denominator of (20). If C is negative and $-1<C/2f_0<0$, the argument of F in (21) varies from 0 to 1/2, which confirms that the effect of anisotropy with a given $|C|$ is relatively stronger in case of positive C.

Consider the bounds for the wedge-wave velocities. According to (13), at $\varphi=\pi l/2$ and $\varphi=\pi/4+\pi l/2$, the function $f(\varphi)$ reaches its extremal values,

$$f_{\text{ext}}(\varphi)=f_0;\quad f_0-(C/2), \tag{24}$$

being, respectively, maximum and minimum at $C>0$, and vice versa at $C<0$. Suppose that $C\geqslant 0$. Combining (20) with (24), and recalling that the elliptical integral F which appears in (20) is bounded from behind by $\pi/2$, we obtain the inequality

$$\theta n\sqrt{\frac{f_{\min}}{3}}\leqslant c\leqslant\theta n\sqrt{\frac{f_{\max}}{3}}, \tag{25}$$

where $f_{\max}=f_0$ and $f_{\min}=f_0-(C/2)$ at $C\geqslant 0$. If $C\leqslant 0$, then manipulating (21) leads to the same inequalities (25), in which now $f_{\max}=f_0-(C/2)$ and $f_{\min}=f_0$. It can also be shown[13] that the extremal values of the velocity $c_p(\varphi)$ of the dilatational mode in a thin tetragonal plate are

$$[c_p(\varphi)]_{\text{ext}}=\sqrt{f_0},\quad\sqrt{f_0-(C/2)}. \tag{26}$$

Thus the bounds (25) for wedge-wave velocities are proportional to the extrema of the velocities of the dilatational plate-mode, so that

$$\frac{\theta n}{\sqrt{3}}[c_p(\varphi)]_{\min}\leqslant c\leqslant\frac{\theta n}{\sqrt{3}}[c_p(\varphi)]_{\max}. \tag{27}$$

Both equalities in (27) are obviously associated with the case of transverse isotropy $C=0$. In the formal limit $f_0\to 0$ (hence $C\to 0$ due to $C/2f_0<1$), which implies that the flexural plate-mode velocity $c_a(\varphi)$ tends to zero in any direction φ, both bounds in (27), naturally, tend to zero as well. Also,

as mentioned above, $c \to 0$ at $C/2f_0 \to 1$. Note that the wedge-wave velocity bounds may be also presented via extrema of the flexural plate-mode velocity, see (23), (24).

III. MONOCLINIC WEDGE

Consider a monoclinic wedge with the midplane orthogonal to the symmetry plane. Bearing in mind that the wedge-wave velocities are independent of the edge orientation, we choose to measure the polar angle φ from the direction orthogonal to the symmetry plane. Then the function $f(\varphi)$ (6) may be written in the form

$$f(\varphi) = a_1 \cos^4\varphi + a_2 \cos^2\varphi \sin^2\varphi + a_3 \sin^4\varphi$$
$$= \tilde{f}_0 \left(1 - \frac{\tilde{C}}{2\tilde{f}_0} \sin^2 2\varphi + b \cos 2\varphi \right), \tag{28}$$

where, at taking crystallographic axes X_1, X_2 as, say, orthogonal ($\varphi = 0$) and parallel ($\varphi = \pi/2$) to the edge, respectively,

$$a_1 = \frac{1}{\rho}\left[c_{11} - \frac{c_{14}^2 c_{33} - 2c_{13}c_{14}c_{34} + c_{13}^2 c_{44}}{c_{33}c_{44} - c_{34}^2} \right],$$
$$a_2 = \frac{1}{\rho}\left[c_{22} - \frac{c_{24}^2 c_{33} - 2c_{23}c_{24}c_{34} + c_{23}^2 c_{44}}{c_{33}c_{44} - c_{34}^2} \right], \tag{29}$$
$$a_3 = \frac{2}{\rho}\left[c_{12} + 2c_{66} - 2\frac{c_{45}^2}{c_{55}} - \frac{c_{14}(c_{33}c_{24} - c_{23}c_{34}) + c_{13}(c_{23}c_{44} - c_{24}c_{34})}{c_{33}c_{44} - c_{34}^2} \right],$$

and

$$\tilde{f}_0 = \frac{1}{2}(a_1 + a_2), \quad \frac{\tilde{C}}{2\tilde{f}_0} = \frac{a_1 + a_2 - a_3}{2(a_1 + a_2)}, \quad b = \frac{a_1 - a_2}{a_1 + a_2}. \tag{30}$$

It is seen that the effect of monoclinic anisotropy is characterized by two dimensionless parameters $(\tilde{C}/2\tilde{f}_0)$ and b. The first one is similar to the parameter $(C/2\tilde{f}_0)$ introduced above for the case of tetragonal symmetry, whereas the second one describes specifically the departure of the given monoclinic medium from the tetragonal state. Imposing no restrictions on the parameter $(\tilde{C}/2\tilde{f}_0)$, let us suppose that the parameter b is small which is often valid for monoclinic and orthorhombic materials. Inserting (28) into (11) and evaluating the integrals to the first order in $b \ll 1$, we obtain the relation for the wedge-wave velocities in exactly the same form (20), (21), but with the parameters f_0 and $(C/2f_0)$ replaced, respectively, by $\tilde{f}_0$ and $(\tilde{C}/2\tilde{f}_0)$. This shows that the impact of departure of monoclinic anisotropy from the tetragonal one reveals itself only in the second order in small parameter b.

IV. CONCLUSIONS

Conjunction of the geometrical acoustics approach with the plate theory yields the positive-definite relation for the velocities of localized vibration modes in a slender wedge of an arbitrary elastic anisotropy. The velocities retain the same dependence on the wedge apex edge and the mode number as in the isotropic case, but acquire an additional factor depending on elastic coefficients. Explicit analysis is carried out for tetragonal wedges with the midplane orthogonal to the four-fold axis, and for ''weakly'' monoclinic wedges. In particular it is shown that the bounds of the wedge-wave velocity value appear to be proportional to extrema of the plate-mode velocities.

ACKNOWLEDGMENTS

This work was supported by the Nottingham Trent University Research Grant No. REF-EX5-97 and the European Commission Grant No. INTAS-96-441.

[1] P. E. Lagasse, ''Analysis of a dispersion free guide for elastic waves,'' Electron. Lett. **8**, 372–373 (1972).
[2] A. A. Maradudin, R. F. Wallis, D. L. Mills, and R. L. Ballard, ''Vibrational edge modes in finite crystals,'' Phys. Rev. B **6**, 1106–1111 (1972).
[3] P. E. Lagasse, I. M. Mason, and E. A. Ash, ''Acoustic surface waveguides—analysis and assessment,'' IEEE Trans. Sonics Ultrason. **20**(2), 143–154 (1973).
[4] S. L. Moss, A. A. Maradudin, and S. L. Cunningham, ''Vibrational edge modes for wedges of arbitrary interior angles,'' Phys. Rev. B **8**, 2999–3008 (1973).
[5] V. V. Krylov ''Geometrical-acoustics approach to the description of localized vibrational modes of an elastic solid wedge,'' Sov. Phys. Tech. Phys. **35**(1), 137–140 (1990).
[6] V. V. Krylov and A. V. Shanin, ''Influence of elastic anisotropy on the velocities of acoustic wedge modes,'' Sov. Phys. Acoust. **37**, 65–67 (1991).
[7] V. V. Krylov and D. F. Parker, ''Harmonic generation and parametric mixing in wedge acoustic waves,'' Wave Motion **15**, 185–200 (1992).
[8] S. V. Biryukov, Yu. V. Gulyaev, V. V. Krylov, and V. P. Plessky, *Surface Acoustic Waves in Inhomogeneous Media* (Springer-Verlag, Berlin, 1995).
[9] J. R. Chamuel, ''Flexural edge waves along free and immersed elastic waveguides,'' *Review of Progress in Quantitative Nondestructive Evaluation*, Proceedings of the 16th Symp. Quant. Nondestruct. Eval., July 28–August 2, 1996, Brunswick, Maine, edited by D. O. Thompson and D. E. Chimenti (Plenum, New York, 1996), pp. 129–136.
[10] M. de Billy, ''On the influence of loading on the velocity of guided acoustic waves in linear elastic wedges,'' J. Acoust. Soc. Am. **100**(1), 659–662 (1996).
[11] A.-C. Hladky-Hennion, P. Langlet, and M. de Billy, ''Finite element analysis of the propagation of acoustic waves along waveguides immersed in water,'' J. Sound Vib. **200**(4), 519–530 (1997).
[12] V. V. Krylov, On the velocities of localized vibration modes in immersed solid wedges,'' J. Acoust. Soc. Am. **103**(2), 767–770 (1998).
[13] A. L. Shuvalov, ''On the theory of wave propagation in anisotropic plates,'' Proc. R. Soc. London, Ser. A (submitted).
[14] T. C. T. Ting, *Anisotropic Elasticity* (Oxford U.P., New York, 1996).

Displacement of droplets and deformation of thin liquid layers using flexural vibrations of structures. Influence of acoustic radiation pressure

S. Biwersi, J. F. Manceau, and F. Bastien
Laboratoire de Physique et de Métrologie des Oscillateurs–UPR 3203, Institut des Microtechniques de Franche-Comté–FR 0067, CNRS (Associated with Université de Franche-Comté) 32, Avenue de l'Observatoire–25044 Besançon Cedex, France

(Received 21 July 1998; revised 3 August 1999; accepted 11 October 1999)

In this paper observations concerning some effects of vibrating structures on fluids are presented, followed by a tentative theoretical analysis. First, a brief description of a caterpillar-like structure is made. This structure is almost equivalent to an infinite beam which allows the choice of positions of the nodal lines of a vibrating mode. Displacement of liquid droplets using switching between two modes of this structure is then presented. This phenomenon is supposed to be induced by acoustic radiation pressure. Possible extensions of this principle are then discussed. After this, results are reported concerning deformations of thin liquid layers. © *2000 Acoustical Society of America.* [S0001-4966(00)06001-X]

PACS numbers: 43.35.Bf [HEB]

INTRODUCTION

The basic principles of acoustic radiation pressure theory have been established by Lord Rayleigh and completed by several studies.[1,2] Moreover, the study of the effects of acoustic waves on liquid interfaces has led to many phenomena with interesting applications: acoustic streaming,[3,4] acoustic levitation of droplets[5–8] or large objects,[9] atomization of liquids,[10,11] etc. Our work on piezoelectric traveling wave ultrasonic motors using the combination of standing vibration modes in several types of plates[12,13] has led us to study the effect of vibrations on droplets or thin liquid layers placed upon them. First, we will explain how we managed to obtain the displacement of liquid droplets on a caterpillar-like structure which allows the production of standing waves at a given frequency with arbitrary positions of nodal lines. After this, observations concerning the deformations of thin liquid layers placed on this structure will be presented.

I. PRINCIPLE OF THE CATERPILLAR-LIKE STRUCTURE

In a classical beam with arbitrary boundary conditions, it is impossible to excite one flexural mode with different nodal lines positions. This can theoretically be achieved only in infinite beams. Nevertheless, let us now consider the structure represented in Fig 1. It has been shown that in a first approximation, it can be assimilated to an infinite beam. This means that we can excite the *n*th flexural vibration mode at the frequency f_n with geometrically shifted nodal lines, which means that we can get *n* degenerated modes.

We applied this principle in order to manufacture a linear ultrasonic actuator producing a traveling wave by combining the 11th flexural mode of such a structure excited by two sets of bulk Pz26 piezoelectric ceramics geometrically shifted by a quarter of a wavelength and electrically shifted by $\pi/2$.

II. APPLICATION TO THE DISPLACEMENT OF DROPLETS

Let us consider a droplet of diameter $d<\lambda_n/2$ (corresponding in our case to an average diameter of a few millimeters). If we excite one of the sets of ceramics, we observe that the droplet will move toward the antinode of the corresponding mode. Now, if we excite the other mode, even if the frequency is not exactly the same as the previous one, the droplet moves towards the antinode of this mode. Then, if we successively excite each mode, the droplet moves between the two antinodes. If the droplet has a diameter $d>\lambda_m/2$, when one mode is excited the droplet splits in two droplets, and each part moves toward an antinode. We also managed to assemble again the original droplet by recombining the droplets. Using the caterpillar-like structure, we can consider exciting not only two but *m* degenerate modes with several geometrical phase shifts. This would have the advantage to allow the choice of the direction of displacement only by switching between the frequency corresponding to each nodal lines configuration.[14]

Let us give the example of four different positions for the nodal lines. It can then easily be shown that we expect to move a droplet with an adapted diameter with successive and variable steps in any direction. We also expect that this principle could be adapted to other types of plates. The main cause of this phenomenon seems to be the radiation pressure. In order to verify this hypothesis, we have performed an experiment on thin liquid layers where the interpretation is easier.

III. DEFORMATION OF THIN LIQUID LAYERS

A. Experimental observations

When a thin liquid layer (thickness of some millimeters) is placed on the caterpillar-like actuator and one vibration

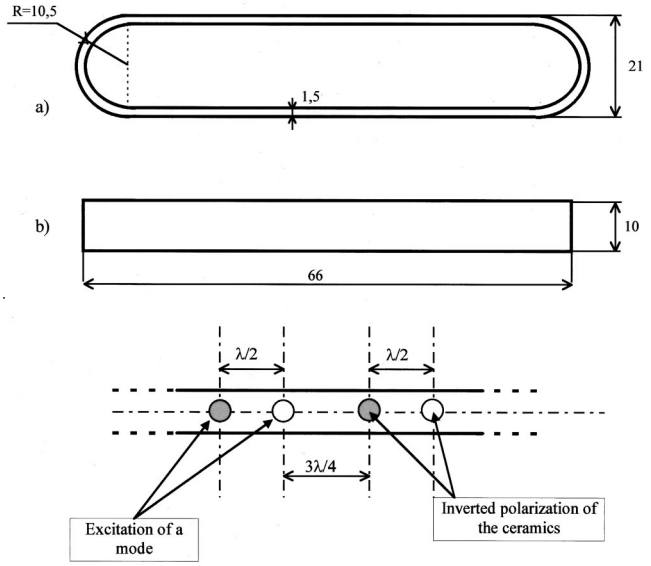

FIG. 1. Sketch of a caterpillar-like structure: (a) front view; (b) top view.

mode is excited, the layer presents a time-independent deformation. This has been observed with several liquids, especially water (Fig. 2) and isopropanol.

Using experimental pictures of the modes, we verified that maximum deformations of the layer correspond to the antinodes of the vibration. As we switch the excitation to the mode geometrically phase-shifted by $\lambda_n/4$, the maximum of the deformation shifts to the antinodes of this mode.

B. Interpretation of the results

We have found no similar observations in the literature, but there is an extensive body in the literature describing the interaction of deformable free-liquid surfaces of finite surface with ultrasound. Nevertheless, some results obtained with high-frequency ultrasonic transducers[15–17] suggest that acoustic radiation pressure is the cause of the deformations.

Let us consider a thin air slice submitted to an unidirectional standing acoustic field. The classical equation of propagation is only an approximation; a more accurate one is given by[18]

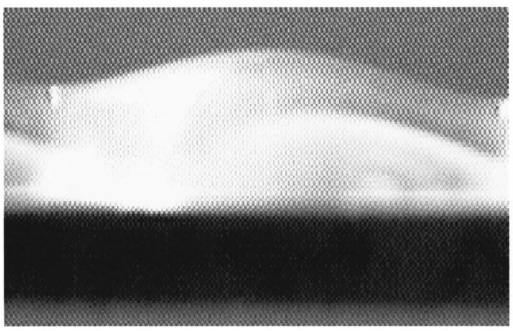

FIG. 2. Maximum deformation of a water layer ($h \approx 2.5$ mm) under 150 V.

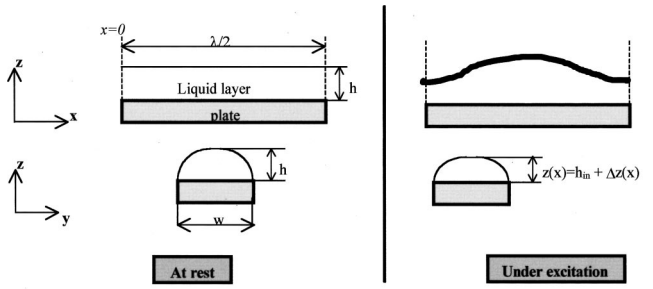

FIG. 3. Parameters of the considered slice of liquid.

$$\frac{\partial^2 u}{\partial t^2} = c^2 \frac{\dfrac{\partial^2 u}{\partial x^2}}{\left(1+\dfrac{\partial u}{\partial x}\right)^{1+\gamma}}, \tag{1}$$

where γ is the parameter of nonlinearity in a fluid.

On the assumption that $\partial u/\partial x \ll 1$, the first-order development of (1) leads to

$$\frac{\partial^2 u}{\partial t^2} = c^2 \frac{\partial^2 u}{\partial x^2}\left(1-(1+\gamma)\frac{\partial u}{\partial x}\right), \tag{2}$$

which yields

$$\Delta P = \rho c^2 \left\{ -\frac{\partial u}{\partial x} + \frac{(1+\gamma)}{2}\left(\frac{\partial u}{\partial x}\right)^2 \right\}, \tag{3}$$

where ΔP is the excess of pressure that would be exerted on a plane.

The time average of the first right-hand term is zero, but the second term of (3) is quadratic so that its time-average value will be different from zero and defines a general equation for acoustic radiation pressure

$$P_r = \rho c^2 \frac{(1+\gamma)}{2}\left\langle \left(\frac{\partial u}{\partial x}\right)^2 \right\rangle. \tag{4}$$

In order to study the effect of the amplitude of the vibration, we took pictures of water and isopropanol layers under different excitation voltages. The maximum deformations $d_{\max}$ have been measured. The results clearly indicate a quadratic variation which, added to the time independency of the phenomena, tends to confirm the influence of acoustic radiation pressure. It also can be noticed that we have deformations up to 900 μm where typical vibration amplitudes are about 1 μm.

Let us consider a liquid with an initial thickness h_{in} placed on horizontal structure. Nevertheless, in order to simplify the calculation, we will only consider a slice placed at $y = w/2$ (see Fig. 3), taken between $x = 0$ and $x = \lambda/2$ and far from the borders, so that its liquid–air interface is initially horizontal. The equilibrium of the pressures at any point of the liquid–air interface is given in these conditions by the Laplace equation[19]

$$P_2 - P_1 = \sigma\left(\frac{1}{R_x}+\frac{1}{R_y}\right), \tag{5}$$

where P_2 and P_1 are the pressures inside and outside the layer, respectively, and σ the surface tension of the liquid. If

we consider a radiation pressure $P_r(x)$ acting on the liquid–air interface, we have

$$P_2 = P_{\text{in}} - \rho g z(x) + P_r(x), \tag{6}$$

where P_{in} is the reference pressure in the liquid layer. This yields, if we take $P_1 = P_o$ near the interface (where P_o is the room pressure)

$$P_{\text{in}} - P_o = \rho g z(x) + \sigma\left(\frac{1}{R_x} + \frac{1}{R_y}\right) - P_r(x). \tag{7}$$

The equilibrium point is the result of the action of three different pressures: radiation pressure, induced by the vibration of the actuator, hydrostatic pressure due to gravity, and capillary pressure, induced by surface tension σ.

In the general case, the curvature radius at any point along the x direction is given by

$$R_x = -\frac{(1+z'^2)^{3/2}}{z''} \quad \text{or} \quad R_x \approx -\frac{1}{z''(x)}. \tag{8}$$

As a first approximation, we can consider that at any moment the profile of any (yz) section of the layer is elliptic. In that case, the curvature radius at $y = w/2$ is given, in the y direction, by

$$R_y = \frac{w^2}{4z(x)}. \tag{9}$$

Under this approximation, we can write, following (8) and (9):

$$\rho g z(x) + \sigma\left(\frac{4z(x)}{w^2} - z''(x)\right) = P_r(x) + P_{\text{in}} - P_o. \tag{10}$$

If we consider that the origin $x = 0$ corresponds to a node of the vibration and the surface displacement of the actuator is given by

$$\xi = \xi_o \sin(kx)\cos(\omega t), \tag{11}$$

with $k = 2\pi/\lambda$.

Following (4), we have

$$P_r(x) = \tfrac{1}{4}\rho\omega^2\xi_o^2(1+\gamma)\sin^2(kx). \tag{12}$$

In the case of fluids, we replace γ by[20]

$$\gamma = 1 + \frac{B}{A} = 1 + \frac{\rho_o^2\left(\dfrac{\partial^2 p}{\partial \rho^2}\right)_{S,\rho=\rho_0}}{\rho_0\left(\dfrac{\partial p}{\partial \rho}\right)_{s,\rho=\rho 0}}. \tag{13}$$

We look for solutions expressed as $z(x) = a_1 + a_2 \sin^2 kx$, which inserted into (10) gives the system

$$a_2 = \frac{A_o}{4k^2\sigma + \beta}$$
$$P_{\text{in}} - P_o = -2k^2\sigma a_2 + \beta a_1$$

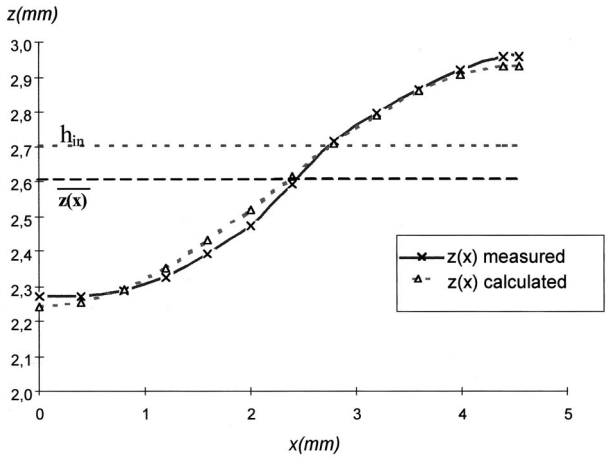

FIG. 4. Experimental and corrected calculated values of $z(x)$ for a water layer with $\xi_o = 0.75\ \mu$m.

$$\text{with} \quad \begin{cases} A_o = \dfrac{1}{4}\left(2 + \dfrac{B}{A}\right)\rho\omega^2\xi_o^2 \\ \beta = \rho g + \dfrac{4\sigma}{1^2}. \end{cases} \tag{14}$$

It can be seen that knowledge of ξ_o gives the value of a_2. In order to calculate a_1, we can use the conservation of the liquid quantity on the considered slice

$$\frac{\lambda}{2}h = \int_0^{\lambda/2} z(x)dx = \int_0^{\lambda/2} (a_1 + a_2 \sin^2(kx))dx, \tag{15}$$

which yields to

$$a_1 = h - \frac{a_2}{2}. \tag{16}$$

C. Analysis of experimental results

We computed several values of $z(x)$ measured on the pictures of deformed layers, for $x \in [0...\lambda/2]$. Then, we sought the value of ξ_o which minimizes the difference between measured and calculated values of $z(x)$.

First, we studied a water layer with the following parameters: $h_{\text{in}} = 2.7$ mm, $B/A \approx 5.2$, $\rho = 1000$ kg/m^3, and $\sigma = 72$ mJ m^{-2}.

We then found $a_1 = 2.36$ mm and $a_2 = 0.69$ for $\xi_o = 0.75\ \mu$m.

Nevertheless, it appears that there is a constant difference between the curves. This is explained by the fact that the average value $\overline{z(x)}$ of the measured deformation is different from h_{in}. This can be due to the fact that a certain quantity of water ''leaves'' the slice, for example because of change of the contact angles in the transversal direction (y axis in Fig. 3).

Taking this into account, we recalculated a_1 using $\overline{z(x)}$ instead of h_{in}. We then obtain a good correlation between the two curves (Fig. 4). An isopropanol layer was also studied with similar results.

Finally, it can be noticed that in both cases, coincidence is obtained for vibration amplitudes in the range of what we can expect on such structures (about 1 μm).

The previous results confirm that acoustic radiation pressure is an important factor and that it plays a major role in the phenomena we have described here.

IV. CONCLUSION

We have related some interesting phenomena concerning the effect of a vibrating plate on small quantity of fluids (either layers or droplets). The displacement of droplets on plates offers potential applications which could be applied to more complex structures.

Concerning deformation of liquid layers, the theoretical analysis of the final state of the liquid layer gives quite good accuracy with experimental data and tends to prove the influence of two main parameters: acoustic radiation pressure and surface tension. Yet further studies should be performed in order to understand the dynamic aspect of the deformation.

[1] R. T. Beyer, ''Radiation pressure–History of a mislabeled tenor,'' J. Acoust. Soc. Am. **63**, 1025–1030 (1978).
[2] C. P. Lee and T. G. Wang, ''Acoustic radiation pressure,'' J. Acoust. Soc. Am. **94**, 1099–1109 (1994).
[3] J. Lighthill, ''Acoustic streaming,'' J. Sound Vib. **61**, 391–418 (1978).
[4] R. M. Moroney, R. M. White, and R. T. Howe, ''Microtransport induced by ultrasonic Lamb waves,'' Appl. Phys. Lett. **59**(7), 774–776 (1991).
[5] T. G. Wang, ''Acoustic levitation and manipulation for space applications,'' Proc. IEEE Ultr. Symp. 79CH1482-9, 471–475 (1979).
[6] N. Jacobi and M. Barmatz, ''Equilibrium shapes of acoustically levitated drops,'' Proc. IEEE Ultr. Symp. 79CH1482-9, 476–481 (1979).
[7] E. Trinh, J. Robey, N. Jacobi, and T. Wang, ''Dual temperature acoustic levitation and sample transport apparatus,'' J. Acoust. Soc. Am. **79**, 604 (1986).
[8] S. Min, R. Holt, and R. Apfel, ''Simulation of drop dynamics in an acoustic positioning chamber,'' J. Acoust. Soc. Am. **91**, 3157 (1992).
[9] Y. Hashimoto, Y. Koike, and S. Ueha, ''Near-field acoustic levitation of planar specimens using flexural vibration,'' J. Acoust. Soc. Am. **100**, 2057–2061 (1996).
[10] A. Lang, ''Ultrasonic atomization of liquids,'' J. Acoust. Soc. Am. **34**, 6–8 (1962).
[11] A. Giovannini, D. Guyomar, M. Gschwind, and G. Fonze, ''Evaluation and design of new piezoelectrical droplets generator,'' Proc. IEEE Ultr. Symp. 94CH3468-6, 611–614 (1994).
[12] J. F. Manceau and F. Bastien, ''Linear ultrasonic motor using a quasi-traveling wave in a rectangular plate,'' Ultrasonics **34**, 257–260 (1996).
[13] S. Biwersi, J. F. Manceau, and F. Bastien, ''Linear and circular ultrasonic actuators: miniaturization and new concepts,'' Proc. Eurosensors XI, Warsaw, 21–23 September 1997, pp. 775–778.
[14] F. Bastien, S. Biwersi, and J. F. Manceau, French Patent, request no. 98/02351, deposited 26 February 1998.
[15] C. Cinbis, N. N. Mansour, and B. T. Khuri-Yakub, ''Effect of surface tension on the acoustic radiation pressure-induced motion of the water–air interface,'' J. Acoust. Soc. Am. **94**, 2365–2372 (1994).
[16] P. Marston, S. LoPorto-Arione, and G. Pullen, ''Quadrupole projection of the radiation pressure on a compressible sphere,'' J. Acoust. Soc. Am. **69**, 1499 (1981).
[17] Y. Tian, R. Holt, and R. Apfel, ''Deformation and location of an acoustically levitated liquid drop,'' J. Acoust. Soc. Am. **93**, 3096 (1993).
[18] R. T. Beyer, *Nonlinear Acoustics* (Naval Sea Systems Command, Washington D.C., 1974).
[19] J. Lyklema, *Fundamentals of Interface and Colloid Science—Vol. 1: Fundamentals* (Academic, New York, 1993), 2.94.
[20] R. T. Beyer, ''Parameter of nonlinearity in fluids,'' J. Acoust. Soc. Am. **32**, 719–721 (1960).

A principle of least complexity for musical scales

Alpar Sevgen
Department of Physics, Boğaziçi University, Bebek 80815, Istanbul, Turkey

(Received 28 September 1998; revised 15 September 1999; accepted 16 September 1999)

The following properties of equally tempered scales are demonstrated in this Letter: For N semitones and M notes, each distinct scale (interval) structure can be represented by an associated multiplet of N scales. These scales allow themselves to be labeled by a set of integers $\{c\}$. Each label c is the difference between the number of sharps and flats in a given scale. The equivalence classes $[c]$ modulo N form a commutative ring with unity. When the ratio N/M cannot be simplified further, then each member of a given multiplet will have a unique label (modulo N), different from the other members of the same multiplet. Because this labeling depends *not* on the interval structure of the multiplet but only on N and M, different multiplets with the same N and M values will have members carrying the same respective labels. Each equally tempered scale (interval) structure possesses a property which will be referred to as *complexity*. This Letter proposes a quantitative measure for complexity which distinguishes between different scale (interval) structures. For the particular case where $N=12$ and $M=7$, out of 462 possible different equally tempered scale structures, those with minimum complexity are the major scale and the modes, which suggests a minimum principle in music based on equally tempered scales. This simplicity of structure allows the practical use of key signatures in music.
[S0001-4966(00)02501-7]

PACS numbers: 43.75.Bc [WJS]

In order to study the properties of the equally tempered scales mathematically, we first define note objects and shift operators that act on these objects. Since such an approach may not be familiar, examples from the well-known major scale are provided.

As defined in this Letter, a *note object*, denoted henceforth by **t**, is an entity with an inflection property having to do with sharps and flats as explained below. We divide an octave $(\ln 2)$ into N equal intervals called semitones. These N intervals provide $N+1$ frequency values or frequency points. Any one of the discrete frequency points within an octave can be expressed in terms of **t**, with an appropriate value of the inflection property. The inflection property of a note object can take all positive and negative integer values including zero. The collection of all these values and the frequencies they imply define the note object. *Note* is defined, on the other hand, as a note object with a certain inflection value. Each note has a definite frequency since it corresponds to a fixed value of the inflection property. Two note objects are different if they have different frequencies for the same value of the inflection property. We associate the inflection value n $(n>0)$ with n sharps $\sharp$ and $-n$ with n flats $\flat$. For example, a **C** note object is a collection of notes $\{\ldots,C^{\flat\flat},C^{\flat},C,C^{\sharp},C^{\sharp\sharp},\ldots\}$ and **C** and **D** are two different note objects. With more than one note object, any frequency point can be expressed by any note object inflected appropriately. Such notes are different but enharmonically equivalent, meaning they have the same frequency. If n_1 denotes the number of semitones between $\mathbf{t}_1(0)$ and $\mathbf{t}_2(0)$, then

$$t_1^{k\sharp}\sim t_2^{(n_1-k)\flat} \tag{1}$$

(for example, for the major scale, there are two semitones between C and D, and for $k=2$ we have $C^{\sharp\sharp}\sim D$). We now define the shift operators $\mathbf{s}_{a+}$ and $\mathbf{s}_{a-}$ that increase and decrease, respectively, the inflection property of the note object $\mathbf{t}_a$ by unit value,

$$\mathbf{s}_{a\pm}\mathbf{t}_a(q)=\mathbf{t}_a(q\pm 1). \tag{2}$$

Note that the shift operators $\mathbf{s}_{a\pm}$ act only on $\mathbf{t}_a$ and not on other note objects with $b\neq a$. We now construct a scale with M distinct notes. Let $t_1,\ldots,t_M$ denote a collection of M distinct notes with increasing values of frequency, where $t_a \equiv \mathbf{t}_a(0)$. The first note t_1, the tonic, is at the first frequency point. The other notes $t_2,\ldots,t_M$ are distributed over the remaining $N-1$ points, keeping their numerical order but with a varying number of semitones between each. This numerical ordering is very important; it imposes the correct musical syntax on our scale where every note object occurs once and only once in the scale irrespective of its inflection value and follows a predetermined order, e.g., {C,D,E,F,G,A,B}. The number of scales generated this way is given by the binomial coefficient $\binom{N-1}{M-1}$. For $N=12$ and $M=7$ there are 462 different scale (interval) structures, each one is a 12-member multiplet. Hence, the major scale is one out of 462 possible scales. A particular scale (i) is uniquely determined by its interval structure

$$\mathbf{n}(i)=\{n_1^{(i)},\ldots,n_M^{(i)}\}. \tag{3}$$

As an example, the interval structure of the major scale is $\mathbf{n}(\text{major})=(2212221)$. We can now define the shift operators $\mathbf{S}_{\pm}$ for the entire scale as follows:

$$\mathbf{S}_{\pm}\equiv\prod_{a=1}^{M}\mathbf{s}_{a\pm}. \tag{4}$$

The shift operators $\mathbf{S}_{\pm}$ for a scale are applied to step through the different members of the multiplet. One particular mem-

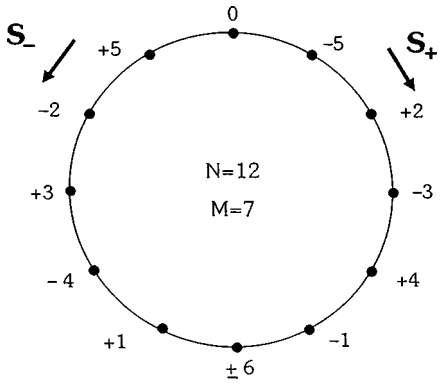

FIG. 1. The circle of nearest neighbors for 462 distinct scales of 12 semitones and 7 notes. The clockwise generator of the scale labels is $c_1=-5$.

ber of a multiplet where all note objects have zero inflection values will be denoted as the reference scale $|0\rangle$

$$|0\rangle \equiv \{t_1,\ldots,t_M\}. \tag{5}$$

In Eq. (5) above, we used the following definition for the scale label L:

$$L \equiv (\text{number of sharps } \sharp) - (\text{number of flats } \flat). \tag{6}$$

Clearly, the value of L is zero for the reference scale. We now consider the scales and their labels obtained by applying the scale shift operator $\mathbf{S}_+$ on the reference scale k times

$$(\mathbf{S}_+)^k|0\rangle = \{t_1^{k\sharp},\ldots,t_{M-1}^{k\sharp},t_M^{k\sharp}\} = |kM\rangle, \tag{7}$$

$$\sim\{t_2^{(n_1-k)\flat},\ldots,t_M^{(n_{M-1}-k)\flat},t_1^{(n_M-k)\flat}\} = |kM-N\rangle, \tag{8}$$

$$\sim\{t_M^{(n_M+k)\sharp},t_1^{(n_1+k)\sharp},\ldots,t_{M-1}^{(n_{M-1}+k)\sharp}\} = |kM+N\rangle. \tag{9}$$

In the two relations that follow Eq. (7) above, we used as enharmonic equivalents the neighboring note objects inflected properly and followed the musical syntax. Clearly the scale labels ''L'' are equivalent modulo N. And, we are entitled to pick a ''principal value,'' say c_k, for the labels. The integer c_k is chosen as that integer smallest in absolute value in the corresponding equivalence set of modulo N. Since the equivalence sets of modulo N are $[0],[1],\ldots,[N-1]$, the value of c_k is obtained from $[kM]$ as

$$c_k = \begin{cases} j & \text{if } j \leqslant \dfrac{N}{2} \\ j-N & \text{if } j \geqslant \dfrac{N}{2}. \end{cases} \tag{10}$$

For $N=12$ semitones and $M=7$ notes the scale labels c_k are computed using Eq. (10) and because of the periodicity in N we may represent these labels around a circle, which is denoted as the ''circle of nearest neighbors,'' as shown in Fig. 1 below. This circle is the same for all 462 scale (interval) structures having 12 semitones and 7 notes; each scale structure is a 12-member multiplet. The circle of nearest neighbors has certain symmetries as explained below.

The equivalence classes $[kM]$ modulo N form a commutative ring with unity[1] and the circle of nearest neighbors embodies the symmetries involved. For $N=12$ semitones and $M=7$ notes, the scale labels c_k satisfy the following symmetry relations as dictated by the ring structure:

$$c_k + c_q = c_{k+q} = (k+q)c_1, \tag{11}$$

$$c_k \times c_q = c_{7kq} = kq. \tag{12}$$

For example, the fact that the circle of nearest neighbors is asymmetric about the vertical diameter is due to the first of the relations above with $q=N-k$ and $c_N=c_0=0$. We also see that $c_1=-5$ is the generator of the labels in the clockwise direction. The scale labels shown in the figure reminds one immediately of the key signatures used in music: for example, the $|\text{D major}\rangle$ has 2 sharps and $|\text{E}^\flat\text{ major}\rangle$ has 3 flats and the scale labels here are $+2$ and -3, respectively. However, the scale labels do not give information about how the sharps and flats are distributed over the individual notes. We present two examples with the scale label $c_2=+2$:

(a) major scale $\mathbf{n}=(2212221)$

$$\{\text{DEF}^\sharp\text{GABC}^\sharp\} = |+2\rangle, \tag{13}$$

(b) another scale $\mathbf{n}=(1111116)$

$$\{t_2^\sharp t_3^\sharp t_4^\sharp t_5^\sharp t_6^\sharp t_1^{4\flat}\} = |+2\rangle. \tag{14}$$

Obviously, Eq. (14) represents a scale structure more complex compared to the $|\text{D major}\rangle$. Complementary scales, i.e., those where notes are replaced by no notes and vice versa, exhibit the same properties: the scale complementary to the major scale is the pentatonic scale $\mathbf{n}=(23223)$, whose reference scale is {CDFGA}. The interval structure complementary to the one given in part (b) above is: $\mathbf{n}=(11118)$. The clockwise generator of the circle of nearest neighbors is $c_1=+5$. The scales complementary to those given in Eqs. (13) and (14), respectively, have the scale label $c_2=-2$ and are

$$\{\text{DF}^\flat\text{GAC}^\flat\}, \tag{15}$$

and

$$\{t_2^\sharp t_3^\sharp t_4^\sharp t_5^\sharp t_1^{6\flat}\}. \tag{16}$$

Note that $N=12$ and $M=7$ are relative primes; that is, N/M cannot be simplified further, so that all members of the ring $I/(12)$ are represented as scale labels on the circle of nearest neighbors. If, on the other hand, N and M can be written as $N=qn$ and $M=qm$ where n/m cannot be simplified further, then the action of $\mathbf{S}_+$ on the reference scale $|0\rangle$ generates scale labels which are elements not of the full ring but that of the subring $I/(N/q)$. In that case the string of labels $\{c_0,c_1,\ldots,c_{N/q}\}$ is repeated q times. (For example, for $N=12$ and $M=8$ the greatest common divisor is $q=4$ and the string of labels $\{0,-4,4\}$ is repeated four times clockwise around the circle of nearest neighbors.) It is clear that the scale labels imply key signatures if the number of inflections do not exceed the number indicated by the key signature; that is, the $|\text{D major}\rangle$ scale allows the practical use of key signatures, but for the scale given in Eq. (14) key signature would not be useful (the same conclusion also holds for their complementary scales).

As the examples given by relations (13) and (14) show, cancellation among the sharps and flats in the computation of

scale labels hides the complexity of the scales. In order to avoid the cancellations among the sharps and flats and thereby bring out the complexity of the scales to the fore, we define *complexity* as the total number of inflections in the whole multiplet. For $N=12$ and $M=7$,

$$C(i)=\sum_{q=-5}^{6}(n_{\sharp}^{i}(q)+n_{\flat}^{i}(q)), \quad i=1,...,462. \tag{17}$$

Complexity reflects the details of the interval structure **n**, whereas scale labels are independent of them. It is important to note that all 462 scales are treated on equal terms; that is, their reference scales do not involve inflected notes. A cyclic permutation of notes $\{t_1,\ldots,t_M\}$, though it changes the interval structure, does not change the exponents of the individual notes in Eq. (7). Hence, an interval structure $(n_1,\ldots,n_7)$ and its cyclical permutations have the same complexity. We have found the greatest complexity in the interval structure (1111116) and its cyclical permutations; the complexity number of this most complex structure is $C=140$. [A member of this multiplet was shown in Eq. (14).] The least complex structure, on the other hand, is the major scale (2212221) and its cyclic permutations; the complexity number of this least complex structure is $C=36$. One should also note that the cyclic permutations of this scale are called *modes*, which have been used in music and which go under the names[2] of Dorian, Phyrigian, Lydian, Mixolydian, and Locrian. (Complementary scales have the same complexity as their partners, hence the complexity of the pentatonic scale is also $C=36$.) The complexity $C=36$ is the sum of the absolute values of integers appearing in the circle of nearest neighbors; hence, for major scales (and for the modes) either sharps or flats occur in a given scale, never both. This allows us to use the key signatures without the need to introduce a scale operator, say **R**. (**R** provides further inflections in addition to those declared by the key signature.) An example of **R** is seen in the harmonic minor scale, where the seventh note is sharped for all members of the multiplet. This inflection is in addition to those declared by the key signature. The usefulness of key signatures is reduced as complexity increases; sharp and flat signs occur simultaneously in the same scale. It is still practical, however, to use key signatures with the help of scale operators for scales which differ only slightly from the major scale.

In conclusion, it is interesting that the simplest scale structure (major scale together with modes and its complementary partner pentatonic scale) is also the one which has been favored over the centuries by composers, musicians, and instrument makers alike.

The importance of minimum principles in physics is quite well-known.[3] That we should encounter a minimum (complexity) principle in music too attests to the pervasiveness of minimum principles in general.

ACKNOWLEDGMENT

I would like to thank my student Alper Akgün for carrying out the numerical work to compute the complexity numbers.

[1] N. H. McCoy, *Introduction to Modern Algebra* (Allyn and Bacon, Boston, 1964).

[2] J. W. Duarte, *Melody and Harmony for Guitarists* [Universal Edition (Australia) Pty. Ltd., London, 1980].

[3] R. P. Feynman, R. B. Leighton, and M. Sands, *The Feynman Lectures on Physics*, Vol. II (Addison-Wesley, Reading, MA, 1963).

Sperm whales (*Physeter catodon L.* 1758) do not react to sounds from detonators

P. T. Madsen[a] and B. Møhl
Department of Zoophysiology, Aarhus University, Building 131, C. F. Møllers Alle, 8000 Aarhus C, Denmark

(Received 17 June 1999; accepted for publication 8 October 1999)

A number of observations show that sperm whales (*Physeter catodon L.* 1758) react to various man-made pulses with moderate source levels. The behavioral responses are described to vary from silence to fear. Click rates of five submerged male sperm whales were measured during the discharge of eight detonators off Andenes, northern Norway. In addition, the behavioral response of a surfaced specimen was observed. Click rates of the submerged whales and the behavior of the surfaced specimen did not change during the discharges with received sound levels of some 180 dB *re* 1 μPa peRMS. The apparent lack of response to the discharges could be due to similarity between sperm whale clicks and detonations. Accordingly, it can be speculated that the discharges may have been perceived as isolated clicks from conspecifics. © *2000 Acoustical Society of America.* [S0001-4966(00)03401-9]

PACS numbers: 43.80.Gx, 43.80.Nd [WA]

INTRODUCTION

The interest on marine mammals and anthropogenic noise has been extensive in the last decade, with discussions on the possible effects on the physiology and behavior of the animals exposed (e.g., Richardson, *et al.*, 1995). Several investigators have reported on sperm whale reactions to man-made noise.

Watkins and Schevill (1975) showed that sperm whales in the Caribbean react to pinger pulses [6–13 kHz, source levels (SL, dB *re* 1 μPa referred to 1 m) between 110 and 130 dB *re* 1 μPa] by interrupting their click production for 2 min or more. André *et al.* (1997) have investigated sperm whale reactions to a number of artificial sounds with SL of 180 dB *re* 1 μPa: Artificial codas caused the same reactions, as reported by Watkins and Schevill (1975), and 10-kHz pulses induced startle reactions among surfaced specimens, whereas observations on the acoustical responses to other artificial sounds with similar SLs were lacking or inconclusive. Two coda-exchanging sperm whales apparently reacted to high-level submarine sonar pulses by click interruption and immediate submersion (Watkins *et al.*, 1993). Mate *et al.* (1992) report that the number of sperm whales decreased when airguns was used in seismic surveys in the Gulf of Mexico, and investigations by Bowles *et al.* (1994) indicated that low-frequency sounds (209–220 dB *re* 1 μPa at 57 Hz) from the Heard Island Feasibility Test may have caused sperm whales to fall silent or to leave the test area. Watkins and Tyack (1991) and Whitehead *et al.* (1990) have reported that splashes when missing darts, used for tagging and biopsy, hit the water caused a startle reaction and defecation from sperm whales. To summarize, it seems fair to conclude that sperm whales in general are sensitive to man-made sound pulses.

In this paper we describe and discuss click rates from five submerged male sperm whales and behavior of one surfaced specimen during discharges of eight detonators off the continental shelf at Andenes, northern Norway (N69.23, E15.45)

I. METHODS

The detonators in the present study were used for calibration of hydrophone positions in a large aperture array [see Møhl *et al.* (2000) for details]. The detonators, containing 1.0 g TNT (Thiele and Oedegaard, 1983), were set off at depths between 3 and 15 m within 5 min on the 23 July (detonations 1–3) and the 24 July (detonations 4–8) 1998. The detonation produces an omnidirectional pressure wave consisting of a steep front with exponential pressure decay (Urick, 1983). After approximately 600 ms, bottom reverberation follows with exponentially decaying amplitude (Fig. 1). As the recording chains were adapted to sperm whale clicks, the detonations caused minor saturation of the recorders for which reason the derived SL of the detonators would be underestimated. Thiele and Oedegaard (1983) have measured a SL of similar detonators to be 231 dB *re* 1 μPa peRMS (peak equivalent root mean square), which have been applied in the present study. Only one of the whales monitored (*t*71036, Møhl *et al.*, 2000) could be positioned by time of arrival differences (TOADs) of the clicks at all five hydrophones of the array. The distance between this whale and the detonation was 840 m, which, based on a SL of 231 dB *re* 1 μPa peRMS and spherical spreading, yields an estimated received sound level (RL) at the whale of about 173 dB *re* 1 μPa peRMS. Clicks from the four other whales monitored could not be detected at all hydrophones of the array. However, the TOADs at the hydrophones of the vertical part of the array indicated that the distances between these whales and the detonations were similar or greater than in the case of the positioned specimen. In addition, the distance to a surfaced whale was determined by a *F*-band radar to be 450 m from the detonation. Estimation of the RL of a

[a]Electronic mail: ptm@bio.aau.dk

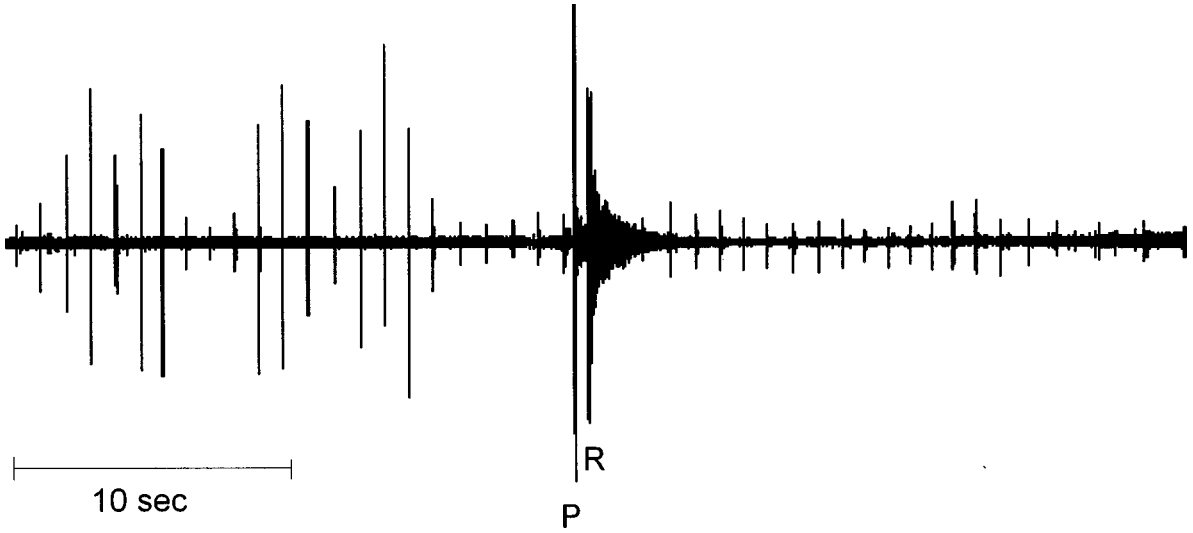

FIG. 1. Click train and discharge of the first detonator, *P*, pressure wave and *R*, reverberation. Note that the click train is masked by the reverberation within the first seconds after the discharge.

surfaced whale has some uncertainty, because of Lloyd mirror and other surface-related effects. An estimate neglecting such effects results in a RL at the whale of 179 dB *re* 1 μPa peRMS.

Click intervals in a period of 40 s, bracketing the discharge, were used as a measure of the behavioral response of the clicking whales to the detonations (Fig. 2). The pressure wave of the detonation and the following reverberation temporarily masked the click train (Fig. 1). Due to spectral similarity between clicks and detonations [Fig. 3(a) and (b)], it has not been possible to isolate the clicks from the reverberation by filtering within 2–3 s, after the onset. Consequently, the masking precludes any statements about putative clicks and their intervals in this period.

To insure that it was the same whale clicking before and after the onset, the TOAD of the clicks at three hydrophones (at 30, 100, and 460 m) in the vertical part of the array were measured throughout the sequences. No changes larger than half a millisecond before and after onset were found. Similarly, the interpulse intervals (Norris and Harvey, 1972) of the clicks before and after discharge were unchanged. These methods allowed us to distinguish between five different specimens exposed to eight detonations (Fig. 2).

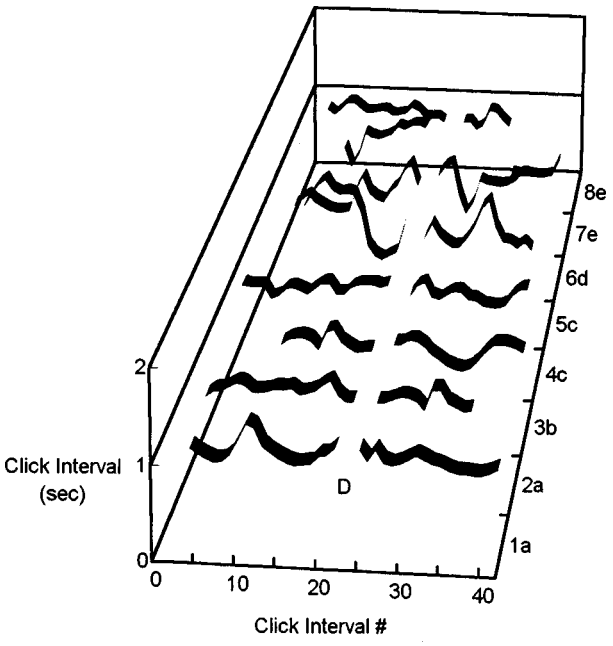

FIG. 2. Click intervals 20 sec before and after discharge of eight detonators (1-8). Letters a–e denote whales investigated. D marks the detonations.

II. RESULTS

In seven out of eight events, the whales did not interrupt their click production outside the aforementioned 2 s, of masking (Fig. 2). There is, however, no evidence to suggest that the whales interrupted their click production during the masking, as the click intervals following the discharges were largely unchanged compared to those prior to the discharges (Fig. 2). None of the changes in click intervals following the discharges were larger than what can be ascribed to the normal jitter (Fig. 2, Goold and Jones, 1995). In the case of the seventh discharge, the amplitudes of the clicks were decaying towards noise level prior to the discharge, and the clicks were not detectable within the next 13 s [Fig. 2; Fig. 7(e)]. Whether that was due to a poor signal-to-noise ratio or an actual interruption of the click production is not possible to say. The former interpretation is supported by the observation that the next discharge 35 s later does not cause any interruption or change in the click intervals from the same whale [Fig. 2; Fig. 8(e)]. One could imagine that the whales, if indeed aroused by the high-level detonations, would direct their putative sonar towards the source for examination. However, the click trains show no profound increase in click amplitudes after discharge (e.g., Fig. 1) at the hydrophone closest to the transient source.

We also made one visual observation of a surfaced sperm whale exposed to one discharge with a RL of 179 dB *re* 1 μPa peRMS. During the discharge, it remained at the surface without any visible movements and kept ventilating.

III. DISCUSSION

The observations reported here are coincidental in the sense that they do not come from an experiment designed to provide data on sperm whale reactions to the discharge of detonators.

The overall picture is, with the uncertainties and the risk of anomalous behavior inherent to limited sampling, that male sperm whales do not interrupt nor change their click production or alter their behavior in any detectable way in response to a broadband pressure wave from a detonating blasting cap with a received sound level of some 180 dB *re* 1 μPa peRMS.

Watkins (1986) has shown that cetaceans normally respond to sudden increases in sound level when these are in excess of 12 dB relative to the ambient sound level, for which the discharges in the present study qualify within a range of tens of kilometers. In the case of sperm whales, a number of observations show that they react to anthropogenic pulses from, e.g., splashes, pingers, airguns, and sonars (see the Introduction). Why do sperm whales not seem to react to high-intensity transients from detonating blasting caps?

One answer could be that most of the sounds, which have been reported to cause a reaction, are repetitive or quasi-continuous in contrast to the single event transients generated by the detonators. This explanation, however, is not supported by the sperm whale reactions to splashes from missing tagging darts.

Since the RLs of the detonations are likely to be higher than the SL of the above-mentioned sounds, it could be speculated that the nonreacting sperm whales in the present study are familiar with high-intensity, broadband pulses. A number of sources can potentially cause habituation, but the most likely source of such pulses is the whales themselves. The sperm whales off the continental slope at Andenes produce long-lasting trains of broadband [Fig. 3(a)], high-intensity clicks, with apparent SLs (ASLs) 40 dB higher than the RL of the detonations (Møhl *et al.*, 2000). Furthermore, the durations of sperm whale clicks (see Møhl *et al.*, 2000) and that of a detonation are both in the order of 1 ms. It is likely that sperm whales can tell the difference between detonations and clicks, but the transient nature and the spectral similarity [Fig. 3(a) and (b)] may be close enough to make the sperm whales perceive the detonations as isolated clicks from conspecifics.

Watkins and Schevill (1975) have suggested that interruption of click production as a reaction to the onset of pingers is due to resemblance between the pinger pulses and communicative codas of the sperm whales, who may fall silent because they listen. If indeed the detonations are perceived as single clicks from conspecifics, they are apparently not interpreted as communication attempts in the sense of codas, since the whales keep clicking. This can be due to the fact that the detonations are single events, while codas consist of a set of clicks (Watkins and Schevill, 1977). Moreover, communicative codas are very seldom heard among sperm whales in northern Norway, perhaps because high latitude stocks consist exclusively of solitary, feeding males (Berzin, 1971).

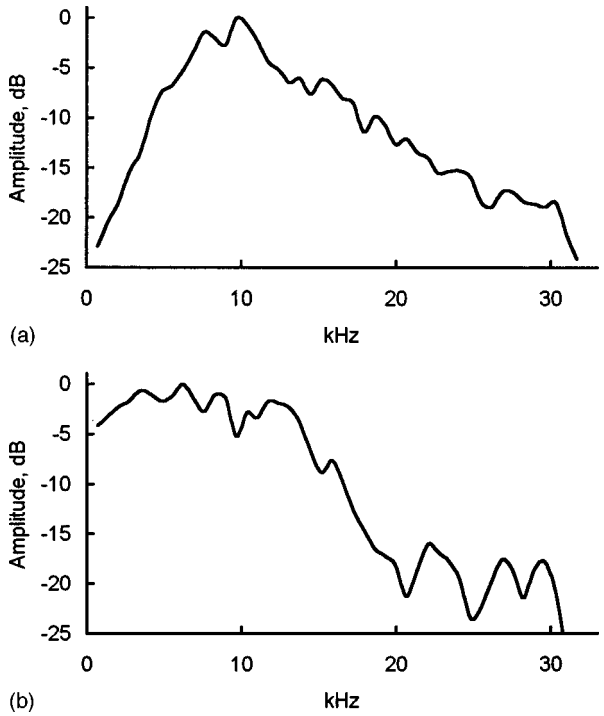

FIG. 3. (a) Amplitude spectrum of the P1 pulse in a sperm whale click. HP-filter at 300 Hz. Sample rate 88.2 kHz. Binwidth 345 Hz. (b) Amplitude spectrum of the pressure wave from a detonator. HP-filtering at 300 Hz. Sample rate 88.2 kHz. Binwidth 345 Hz.

ACKNOWLEDGMENTS

We thank the crew of R/V NARHVALEN: Mads F. Cristoffersen, Niels U. Kristiansen, Lee A. Miller, Lotte Møhl, Bjarke K. Nielsen, Annemarie Surlykke, Peter T. Sørensen, Ulf Toke, and Magnus Wahlberg for excellent teamwork. We also thank Andenes Cetacean Research Unit (ANCRU) and Andenes Whale Safari for provision of shorebase facilities and zodiacs. This work was funded by the Danish Research Foundation through Center for Sound Communication, OU.

André, M., Terada, M., and Watanabe, Y. (**1997**). ''Sperm whales (*Physeter macrocephalus*) behavioral response after playback of artificial sounds,'' Report of The International Whaling Commission Vol. 47, pp. 499–504.

Berzin, A. A. (**1971**). ''The Sperm Whale,'' Jerusalem, Israel Program for Scientific Translations, IPST Cat. No. 600707.

Bowles, A. E., Smultea, M., Würsig, B., DeMaster, D. P., and Palka, D. (**1994**). ''Relative abundance and behavior of marine mammals exposed to transmissions from the Heard Island Feasibility Test,'' J. Acoust. Soc. Am. **96**, 2469–2484.

Goold, J. C., and Jones, S. E. (**1995**). ''Time and frequency domain characteristics of sperm whale clicks,'' J. Acoust. Soc. Am. **98**, 1279–1291.

Mate, B. R., Stafford, K. M., and Ljungblad, D. K. (**1992**). ''A change in sperm whale (*Physeter macrocephalus*) distribution correlated to seismic surveys in the Gulf of Mexico,'' J. Acoust. Soc. Am. **96**, 3268–3269.

Møhl, B., Wahlberg, M., Madsen, P. T., Miller, L. A., and Surlykke, A. (**2000**). ''Sperm whale clicks: Directionality and source revisited,'' J. Acoust. Soc. Am. **107**, 638–648.

Norris, K. S., and Harvey, G. W. (**1972**). ''A theory for the function of the spermaceti organ of the sperm whale (*Physeter catodon L.*),'' in *Animal Orientation and Navigation*, edited by S. R. Galler, NASA sp-262, pp. 397–417.

Richardson, W. J., Greene, C. R., Malme, C. I., and Thompson, D. H. (**1995**). *Marine Mammals and Noise* (Academic, San Diego, CA).

Thiele, L., and Oedegaard, J. (**1983**). ''Underwater noise from the propellers

of a triple screw container ship,'' Report No. 82.54, Greenland Fisheries Investigations, Copenhagen.
Urick, R. J. (**1983**). *Principles of Underwater Sound* (McGraw–Hill, New York).
Watkins, W. A. (**1986**). ''Whale reactions to human activities in Cape Cod waters,'' Marine Mammal Science **2**, 251–262.
Watkins, W. A., and Schevill, W. E. (**1975**). ''Sperm whales react to pingers,'' Deep-Sea Res. **22**, 123–129.
Watkins, W. A., and Schevill, W. E. (**1977**). ''Sperm whale codas,'' J. Acoust. Soc. Am. **62**, 1485–1490.
Watkins, W. A., and Tyack, P. (**1991**). ''Reaction of sperm whales (*Physeter catodon*) to tagging with implanted sonar transponder and radio tags,'' Marine Mammal Science, **7**(4), 409–413.
Watkins, W. A., Daher, M. A., Fristrup, K. M., and Howald, T. J. (**1993**). ''Sperm whales tagged with transponders and tracked underwater by sonar,'' Marine Mammal Science **9**(1), 55–67.
Whitehead, H., Gordon, J., Matthews, E. A., and Richard, K. R. (**1990**). ''Obtaining skin samples from living sperm whales,'' Marine Mammal Science **6**(4), 316–326.